UCRL-ID-146350

International Workshop on the Physics of Compressible Turbulent Mixing

Edited By: O. Schilling

November 28, 2001

U.S. Department of Energy

Lawrence
Livermore
National
Laboratory

Approved for public release; further dissemination unlimited

8th International Workshop on the Physics of Compressible Turbulent Mixing, Pasadena, CA (2001)

Disclaimer and Auspices

This document was prepared as an account of work sponsored by an agency of the United States Government. Neither the United States Government nor the University of California nor any of their employees, makes any warranty, express or implied, or assumes any legal liability or responsibility for the accuracy, completeness, or usefulness of any information, apparatus, product, or process disclosed, or represents that its use would not infringe privately owned rights. Reference herein to any specific commercial product, process, or service by trade name, trademark, manufacturer, or otherwise, does not necessarily constitute or imply its endorsement, recommendation, or favoring by the United States Government or the University of California. The views and opinions of authors expressed herein do not necessarily state or reflect those of the United States Government or the University of California, and shall not be used for advertising or product endorsement purposes.

This work was performed under the auspices of the U.S. Department of Energy by University of California, Lawrence Livermore National Laboratory under Contract W-7405-Eng-48.

Instructions for use of the CD-ROM

To View Presentations

To view the contributed, unedited presentations from the 8th International Workshop on the Physics of Compressible Turbulent Mixing, open the PDF document **CONTENTS.PDF** and click with the cursor on the presentation number, animation, or title (for the Summary and Review Talks): this will open the corresponding presentation in Adobe® Portable Document Format (PDF), graphic (`gif` format), or animation (`avi` format). See below to obtain freely-downloadable software to view these files.

The summary presentation "Summary of the 8th International Workshop on the Physics of Compressible Turbulent Mixing (9-14 December 2001, Pasadena, CA)" (Schilling) can be viewed, and has links to all of the contributed presentations on the CD-ROM.

To View the Abstract Book

To view the Abstract Book in PDF, navigate to the bottom of **CONTENTS.PDF** and click on **ABSTRACT BOOK**.

To View the Program Summary

To view the Program Summary in PDF, navigate to the bottom of **CONTENTS.PDF** and click on **PROGRAM SUMMARY**.

To View the Author Contact Information

To view the Author Contact Information in PDF, navigate to the bottom of **CONTENTS.PDF** and click on **AUTHOR CONTACT INFORMATION**.

To View the Photographs from the Banquet and Workshop

To view the Photographs from the Banquet and Workshop in PDF, navigate to the bottom of **CONTENTS.PDF** and click on **PHOTOGRAPHS FROM THE BANQUET AND WORKSHOP**.

To Obtain Adobe® Acrobat® Reader®

To obtain the freely available Adobe® Acrobat® Reader®, click on http://www.adobe.com/products/acrobat/readstep.html

To Obtain RealOne™ Player

To obtain the freely available RealOne™ Player for avi files, click on http://www.real.com/realoneplayer.html

8th International Workshop on the Physics of Compressible Turbulent Mixing, Pasadena, CA (2001)

CD-ROM Table of Contents

OVERVIEW

O. Schilling
Summary of the 8th International Workshop on the Physics of Compressible Turbulent Mixing

CONTRIBUTED REVIEW PRESENTATIONS

J.-F. Haas and S. G. Zaytsev
Review on RTI, RMI and TM Experiments

D. L. Youngs
Review of Numerical Simulation of Mixing due to Rayleigh-Taylor and Richtmyer-Meshkov Instabilities

D. Kartoon, D. Oron, L. Arazi, A. Rikanati, O. Sadot, A. Yosef-Hai, U. Alon, G. Ben-Dor, and D. Shvarts
Three Dimensional Multi-Mode Rayleigh-Taylor and Richtmyer-Meshkov Instabilities at All Density Ratios (T14)

CONTRIBUTED EXPERIMENTAL PRESENTATIONS

Yu. A. Kucherenko, S. I. Balabin, R. I. Ardashova, O. E. Kozelkov, A. V. Dulov, and I. A. Romanov
Experimental Study of the Influence of the Stabilizing Properties of Transitional Layers on the Turbulent Mixing Evolution (E3)

C. W. Barnes, S. H. Batha, A. M. Dunne, N. E. Lanier, G. R. Magelssen, T. J. Murphy, K. W. Parker, S. Rothman, J. M. Scott, and D. Youngs
Improvements to Convergent Cylindrical Plasma Mix Experiments Using Laser Direct Drive (E4)

S. H. Batha, K. W. Parker, C. W. Barnes, A. M. Dunne, N. E. Lanier, G. R. Magelssen, T. J. Murphy, S. Rothman, J. M. Scott, and D. L. Youngs
Mixing Between Two Compressing Cylinders (E5)

M. Bliznetsov, V. Dudin, S. Gerasimov, L. Houas, G. Jourdan, A. Logvinov, E. Meshkov, and Yu. Vlasov
Development of the Method for Interaction Between Shock Wave and Flame (E6)

M. V. Bliznetsov, E. E. Meshkov, N. V. Nevmerzhitzky, A. A. Nikulin, E. D. Sen'kovsky, and E. A. Sotskov
Influence of Scales of Initial Perturbations on Rayleigh-Taylor Instability Growth on Gas-Liquid Interface (E7)

M. Brouillette and C. H. Hebért
Formation and Propagation of Shock-Generated Vortex Rings (E8)

R. P. Drake
Design of Flyer-Plate-Driven Compressible-Turbulent-Mix Experiments (E9)

R. P. Drake, P. Keiter, K. E. Korreck, K. Dannenberg, H. A. Robey, T. S. Perry, J. O. Kane, O. A. Hurricane, B. A. Remington, D. D. Ryutov, R. J. Wallace, J. Knauer, R. Teyssier, A. Calder, B. Fryxell, R. Rosner, Y. Zhang, J. Glimm, J. Grove, D. Arnett, R. McCray, N. Turner, and J. Stone,
Compressible Hydrodynamics on the Omega Laser: Motivated by Astrophysics (E10)

S. G. Glendinning, D. G. Braun, M. J. Edwards, W. W. Hsing, B. F. Lasinski, H. Louis, A. Miles, J. Moreno, T. A. Peyser, B. A. Remington, H. F. Robey, E. J. Turano, C. P. Verdon, and Y. Zhou
An Experimental Study of the Effect of Shock Proximity on the Richtmyer-Meshkov Instability at High Mach Number (E12)

D. A. Holder, C. J. Barton, A. V. Smith, and D. L. Youngs
Mix Experiments Using a Two-Dimensional Convergent Shock Tube (E13)

J. M. Holford, S. B. Dalziel, and D. Youngs
Rayleigh-Taylor Instability at a Tilted Interface in Incompressible Laboratory Experiments and Compressible Numerical Simulations (E14)

S. H. R. Hosseini and K. Takayama
Production of Diverging and Converging Spherical Shock Waves and Eccentric Interaction of Converging Shock Waves with Cylindrical Interfaces (E15)

L. Houas, G. Jourdan, L. Schwaederle, and E. E. Meshkov
Linear and Non-Linear Stages of the Richtmyer-Meshkov Instability Development in a Large Cross Section Shock-Tube (E17)

J. W. Jacobs and V. V. Krivets
Experimental Investigation of Richtmyer-Meshkov Instability After a Second Interaction with a Reflected Shock Wave (E18)

D. H. Kalantar, J. Belak, J. D. Colvin, M. Kumar, K. T. Lorenz, K. O. Mikaelian, S. Pollaine, B. A. Remington, S. V. Weber, L. G. Wiley, J. S. Wark, A. Loveridge, A. M. Allen, M. A. Meyers, and M. Schneider
Laser-Based High Pressure, High-Strain-Rate Materials Experiments (E19)

Yu. A. Kucherenko, O. E. Shestachenko, S. I. Balabin, and A. P. Pylaev
RFNC-VNIITF Multifunctional Shock Tube for Investigating the Evolution of Instabilities in Unstationary Gasdynamic Flows (E20)

G. Layes, G. Jourdan, P. Roualdes, and L. Houas
Hydrodynamic Instabilities at a Shock Accelerated Bubble Gas-Gas Interface (E22)

K. Levy, Sadot, A. Rikanati, D. Kartoon, Y. Srebro, A. Yosef-Hai, G. Ben-Dor, and D. Shvarts
Scaling in the Shock-Bubble Interaction (E23)

C. E. Niederhaus and J. W. Jacobs
Single-Mode Incompressible Richtmyer-Meshkov Instability Experiments (E26)

M. H. Anderson, J. G. Oakley, B. Puranik, and R. Bonazza
Experimental Study of a Strongly Shocked Gas Interface with Visualized Initial Conditions (E27 and animation)

Yu. A. Kucherenko, O. E. Shestachenko, Yu. A. Piskunov, E. V. Sviridov, V. M. Medvedev, and A. I. Baishev
Experimental Investigation into the Self-Similar Mode of Mixing of Different Density Gases in the Earth's Gravitational Field (E28)

S. Pollaine, D. Petersen, D. Kalantar, B. Remington, J. Belak, J. Colvin, M. Kumar, T. Lorenz, S. Weber, J. Wark, A. Loveridge, A. Allen, and M. Meyers
Modeling Laser Material Strength Experiments (E29)

K. Prestridge, C. Tomkins, C. Zoldi, M. Marr-Lyon, P. Vorobieff , P. Rightley, and R. Benjamin
Experiments and Simulations of Instabilities in Shock-Accelerated Gas Cylinders (E30)

Yu. A. Kucherenko, A. P. Pylaev, V. D. Murzakov, A. V. Belomestnih, V. N. Popov, and A. A. Tyaktev
Experimental Study into Rayleigh-Taylor Turbulent Mixing Zone Heterogeneous Structure (E31)

M. J. Andrews and P. Ramaprabhu
Measurements of Turbulence Correlations in Low Atwood Number Rayleigh-Taylor Mixing (E32, animation1, animation2, and animation3)

H. F. Robey, T. S. Perry, R. I. Klein, J. A. Greenough, H. Louis, P. Davis, J. O. Kane, and T. R. Boehly
Experimental Study of the Interaction of a Strong Shock with a Spherical Density Inhomogeneity (E34)

H. F. Robey, Y. K. Zhou, A. C. Buckingham, P. Keiter, B. A. Remington, and R. P. Drake
Turbulent Transition in a High Reynolds Number, Rayleigh-Taylor Unstable Plasma Flow (E35)

O. Sadot, A. Rikanati, D. Oron, A. Yosef-Hai, G. Ben-Dor, and D. Shvarts
High Mach Number and High Initial Amplitude Effects on the Evolution of the Single-Mode Richtmyer-Meshkov Instability─An Experimental Study (E36)

L. Schwaederlé, G. Jourdan, L. Houas, and J.-F. Haas
Measurements Within a Richtmyer-Meshkov Mixing Zone Using a Triple Hot Wire Probe Technique (E37)

Yu. A. Kucherenko, O. E. Shestachenko, Yu. A. Piskunov, E. V. Sviridov, V. M. Medvedev, and A. I. Baishev
Experimental Investigation into the Evolution of Turbulent Mixing of Gases by Using the Multifunctional Shock Tube (E38)

A. V. Smith, D. A. Holder, C. J. Barton, A. P. Morris, and D. L. Youngs
Shock Tube Experiments on Richtmyer-Meshkov Instability Across a Chevron Profiled Interface (E39, animation1, and animation2)

C. Tomkins, K. Prestridge, P. Rightley, M. Marr-Lyon, R. Benjamin, J. Doyle, M. Schneider, P. Vorobieff, and C. Zoldi
The Evolution and Interaction of Two Shock-Accelerated, Unstable Gas Cylinders (E40)

R. I. Klein, H. Robey, T. Perry, J. Kane, J. Greenough, and M. Marinak
The Interaction of Supernova Blast Waves with Interstellar Clouds: Experiments on the Omega Laser (E42)

H. Azechi et al.
Ablative Rayleigh-Taylor Instability at Short Wavelengths (E45)

H. F. Robey, S. G. Glendinning, J. A. Greenough, and S. V. Weber
A Vortex Model for Studying the Effect of Shock Proximity on Richtmyer-Meshkov Instability at High Mach Number (E46)

CONTRIBUTED COMPUTATIONAL PRESENTATIONS

M. G. Anuchin, V. E. Neuvazhayev, and I. E. Parshukov
Application of Kε-Model for the Description of an Atmospheric Surface Layer (C2)

W. Ashurst and A. Kerstein
Computational Modeling of Low-Mach-Number High-Atwood-Number Turbulent Mixing (C4)

A. W. Cook, W. Cabot, J. A. Greenough, and S. V. Weber
Spectral and High-Order Methods for Shock-Induced Mixing (C8)

R. M. Darlington and K. S. Budil
Numerical Simulation of Mode Coupling in Laser-Driven Rayleigh-Taylor Instability Experiments (C9)

S. Dutta, E. George, J. Grove, J. Glimm, X. Li, A. Marchese, D. Sharp, Z. Xu, and Y. Zhang
Numerical Methods for Determination of RT and RM Mixing (C11 and animation)

R. Epstein, J. A. Delettrez, V. Yu. Glebov, V. N. Goncharov, P. W. Mckenty, P. B. Radha, S. Skupsky, V. A. Smalyuk, C. Stoeckl, J. Frenje, C. K. Li, R. D. Petrasso, and F. H. Séguin
One-Dimensional Simulation of the Effects of Unstable Mix on Neutron and Charged-Particle Yield from Laser-Driven Implosions (C13)

E. S. Gavrilova, E. V. Gubkov, V. A. Zhmailo, and Yu. V. Yanilkin
3D Computation for Surface Perturbations Evolution in Plasma Cloud During its Expansion in Magnetic Field (C14)

J. A. Greenough, W. J. Rider, C. Zoldi, and J. R. Kamm
Code-to-Code Comparisons for the Problem of Shock Acceleration of a Diffuse Dense Gaseous Cylinder (C16)

B. Grieves
Implementation of a Turbulent Mix Model in a 2D ALE Code (C17)

E. V. Gubkov, V. A. Zhmailo, and Yu. V. Yanilkin
Semiempirical Model of Turbulent Magnetic Field Diffusion to Driven Plasma (C19)

N. J. Zabusky, S. Gupta, Y. Gulak, G. Peng, and R. Samtaney
Localization and Spreading of Interfaces (Contact Discontinuities) in PPM and WENO Simulations of the Compressible Euler Equations (C20)

S. W. Haan, T. Dittrich, G. Strobel, M. Marinak, D. Munro, G. Glendinning, P. Amendt, and R. Turner
Instability Modeling for NIF Ignition Targets and Omega Experiments (C22)

I. G. Lebo and V. D. Zvorykin
Laser Shock Tube for the Study of Supersonic Gas Flows and the Development of Hydrodynamic Instabilities in Layered Media (C25)

K. Nishihara, V. Zhakhovskii, and M. Abe
Molecular Dynamics Simulation of Shocks and Richtmyer-Meshkov Instability in Cylindrical Geometry (C26, animation 1, and animation 2)

G. Peng, S. Gupta, S. Zhang, and N. J. Zabusky
Dispersal of Mass and Circulation Following Shock-Sphere and Shock-Cylinder Interactions: Effects Arising from Shock-Cavity Collapse, Vortex Bilayers, Density-Gradient Intensification and Vortex Projectiles (C29)

W. J. Rider, J. R. Kamm, and C. Zoldi
A Numerical Study of Shocked Gas Cylinders (C31)

R. Samtaney, D. I. Pullin, T. Voelkl, and D. J. Hill
Large Eddy Simulation of Strong-Shock Richtmyer-Meshkov Instability (C33)

P. Seytor and M. Legrand
Numerical Investigation of a Laser Induced Turbulent Mixing Zone (C35)

D. Souffland and F. Renaud
A Mix-Model For One-Dimensional Simulations of Laser-Driven Implosion Experiments (C36)

Y. Srebro, D. Kushnir, Y. Elbaz, and D. Shvarts
Modeling Turbulent Mixing in Inertial Confinement Fusion Implosions (C37)

H. Takabe, S. Yamada, K. Kobayashi, A. Mizuta, and K. Nomoto
Turbulent Mixing Nuclear Burning in Type Ia Supernova Explosion Based on Bubble Statistical Mechanics (C38)

N. Toqué
Turbulent Diffusion in Solar Type Star (C39)

E. Vold
Recent Computational Simulations of Rayleigh-Taylor Mix Layer Growth With a Multi-Fluid Model (C40)

S. P. Wang, M. H. Anderson, J. G. Oakley, and R. Bonazza
An Efficient and High Resolution Solver for the Two-Dimensional Numerical Simulation of the Richtmyer-Meshkov Instability (C41)

S. V. Weber, G. Dimonte, and M. M. Marinak
ALE Simulations of Turbulent Rayleigh-Taylor Instability in 2-D and 3-D (C42)

Yu. V. Yanilkin, V. P. Statsenko, S. V. Rebrov, O. G. Sin'kova, and A. L. Stadnik
Study of Gravitational Turbulent Mixing at Large Density Differences Using Direct 3D Numerical Simulation (C44)

D. L. Youngs
Development and Validation of a 2D Turbulent Mix Model (C46)

D. L. Youngs and A. Llor
Preliminary Results of LES Simulations of Self-Similar Variable Acceleration RT Mixing Flows (C47)

S. Zhang and N. J. Zabusky
Shock-Planar Curtain Interactions: Strong Secondary Baroclinic Deposition and Emergence of Coherent and Random Vortex Projectiles (VPs), and Decaying Stratified Turbulence (C48)

S. Zhang, N. J. Zabusky, K. Nishihara, and Y.-G. Kang
Rapid Turbulization Arising from Vortex Double Layers in Interactions of "Complex" Blast Waves and Cylindrical/Spherical Bubbles (C49)

C. A. Zoldi
Simulations of a Shock-Accelerated Gas Cylinder and Comparison with Experimental Images and Velocity Fields (C50)

A. N. Razin, V. I. Kozlov, and I. V. Sapozhnikov
Simulations of Turbulent Mixing of Two Fluids With Variable Acceleration Laws (C51)

V. I. Kozlov and A. N. Razin
The Behaviour of Axial Variance Resulting from Turbulent Mixing Zone Interaction with Shocks (C52)

D. E. Eliason, W. H. Cabot, and Y. Zhou
A New Two-Scale Mix Model: Towards a Multi-Component Model of Turbulent Mixing (C53)

W. S. Don, D. Gottlieb, C.-W. Shu, and L. Jameson
High Order Methods for 2D Richtmyer-Meshkov Instability (C54)

A. M. Dimits
Examination of Rayleigh-Taylor α in Three Cases: PPM Simulations, Vasilenko et al. Shock Tube Experiment, and Meshkov-Nevmerzhitsky Accelerated Tank Experiment (C55)

A. Cook, P. Dimotakis, and T. Mattner
Transition Stages of Rayleigh-Taylor Instability Between Miscible Fluids (C56)

A. Miles, J. Edwards, and G. Glendinning
CALE Simulation of Richtmyer-Meshkov Instability Experiments at High Mach Number (C57)

S. M. Bakrakh, N. A. Volodina, P. N. Nizotsev, V. F. Spiridonov, and E. V. Shuvalova
Numerical Simulation of Initial Perturbation Growth in Oblique Impact of Metal Plates

CONTRIBUTED THEORETICAL PRESENTATIONS

S. I. Abarzhi
Nonlinear Evolution of Unstable Fluid Interface (T1)

S. I. Abarzhi, J. Glimm, and A. der Lin
Nonlinear Asymptotic Solutions to Rayleigh-Taylor and Richtmyer-Meshkov Problems for Fluids With a Finite Density Contrast (T2)

S. I. Abarzhi
Turbulent Mixing in RTI as Order-Disorder Process (T3)

P. Bailly and A. Llor
A New Turbulent Two-Fluid RANS Model for KH, RT and RM Mixing Layers (T4)

R. E. Breidenthal
How to Inhibit Rayleigh-Taylor Mixing (T5)

B. Cheng, J. Glimm, and D. Sharp
Theoretical Methods for the Determination of Mix (T7)

T. Clark and F. Harlow
Modeling Radiation Effects in Mixing Layers (T8)

S. B. Dalziel
Toy Models for Rayleigh-Taylor Instability (T10)

Y. Elbaz, Y. Srebro, O. Sadot, and D. Shvarts
A General Buoyancy-Drag Model for the Evolution of the Rayleigh-Taylor and Richtmyer-Meshkov Instabilities (T11)

N. Inogamov, M. Tricottet, A. Oparin, and S. Bouquet
Nonlinear RT and RM Single Modes (Analytic) (T13)

V. M. Ktitorov
Stability of Diverging Shock Waves (T15)

V. M. Ktitorov
Stability of Reflected from the Center Self-Similar Converging Shock Wave (T16)

A. Llor
Response of Turbulent RANS Models to Self-Similar Variable Acceleration RT-Mixing: An Analytical "0D" Analysis (T18)

K. Nishihara, C. Matsuoka, and Y. Fukuda
Nonlinear Evolution of an Interface in the Richtmyer-Meshkov Instability (T19)

A. Rikanati, U. Alon, and D. Shvarts
Vortex-Merger Statistical Model for the Late Time Self-Similar Evolution of the Kelvin Helmholtz Instability (T22)

A. Rikanati, D. Oron, O. Sadot, and D. Shvarts
High Mach Number and High Initial Amplitude Effects on the Evolution of the Single-Mode Richtmyer-Meshkov Instability─Theoretical Study (T23)

D. D. Ryutov
Compressible MHD Turbulence in Strongly Radiating Molecular Clouds in Astrophysics (T25)

O. Schilling
Single-Velocity, Multi-Component Turbulent Transport Models for Interfacial Instability-Driven Flows (T26)

O. Schilling and A. W. Cook
Large- and Small-Scale Dynamics of Variable-Density Rayleigh-Taylor Instability-Induced Turbulent Mixing (T28)

M. Tricottet and S. Bouquet
Analytical Study of the RTI in Compressible Fluids (T30)

M. Vandenboomgaerde
Analytical Growth Rate of a Non-Linear Single-Mode R-M Instability (T31)

M. Vandenboomgaerde, S. Gauthier, D. Galmiche, C. Cherfils, and P. A. Raviart
Efficient Perturbation Methods for Richtmyer-Meshkov and Rayleigh-Taylor Instabilities: Weakly Nonlinear Stage and Beyond (T32)

P. Wilson, M. Andrews, and F. Harlow
Combined Shear and Buoyancy Instabilities (T33)

J. G. Wouchuk
Rate of Growth of the Linear Richtmyer-Meshkov Instability (T34)

A. Yosef-Hai, O. Sadot, D. Kartoon, D. Oron, L. A. Levin, E. Sarid, Y. Elbaz, G. Ben-Dor, and D. Shvarts
The Dependence of the Shock Induced Richtmyer-Meshkov Instability on Dimensionality and Density Ratio (T35)

Y. Zhou, H. F. Robey, and A. C. Buckingham, B. A. Remington, A. Dimits, W. Cabot, J. Greenough, S. Weber, O. Schilling, T. A. Peyser, D. Eliason, P. Keiter, and R. P. Drake
Mixing Transition in Time-Dependent Flows (T36)

A. L. Kuhl and R. E. Ferguson
Spherical Combustion Layer in a TNT Explosion (T37)

B. Afeyan, P. Ramaprabhu, and M. J. Andrews
Discrete Wavelet Transform Techniques for Denoising, Pattern Detection and Compression of Turbulent Rayleigh-Taylor Mix Data (T39)

ABSTRACT BOOK

PROGRAM SUMMARY

AUTHOR CONTACT INFORMATION

PHOTOGRAPHS FROM THE BANQUET AND WORKSHOP

UCRL-ID-146350

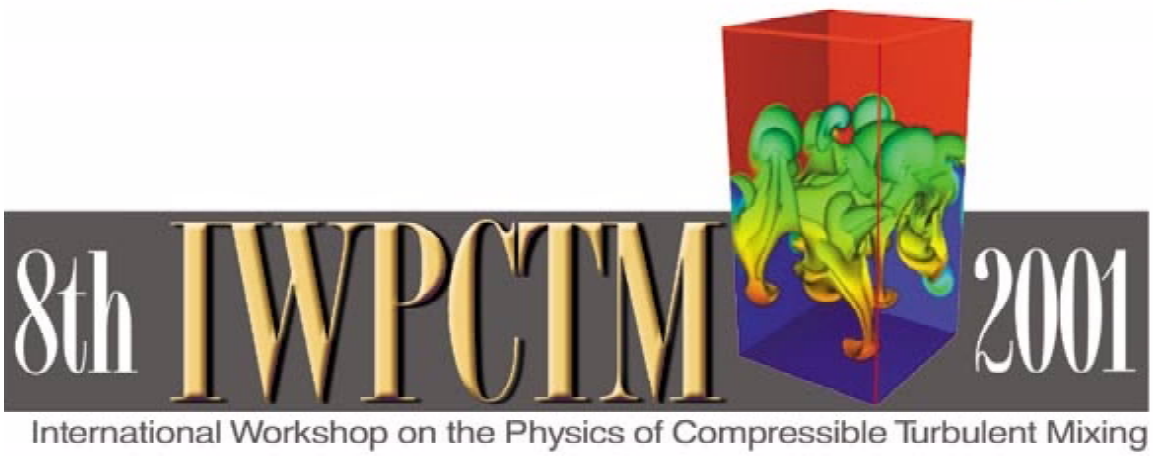

December 9-14, 2001
Pasadena, California, USA

ABSTRACTS

Oleg Schilling, Chairman

DISCLAIMER

This document was prepared as an account of work sponsored by an agency of the United States Government. Neither the United States Government nor the University of California nor any of their employees, makes any warranty, express or implied, or assumes any legal liability or responsibility for the accuracy, completeness, or usefulness of any information, apparatus, product, or process disclosed, or represents that its use would not infringe privately owned rights. Reference herein to any specific commercial product, process, or service by trade name, trademark, manufacturer, or otherwise, does not necessarily constitute or imply its endorsement, recommendation, or favoring by the United States Government or the University of California. The views and opinions of authors expressed herein do not necessarily state or reflect those of the United States Government or the University of California, and shall not be used for advertising or product endorsement purposes.

This work was performed under the auspices of the U. S. Department of Energy by the University of California, Lawrence Livermore National Laboratory under Contract No. W-7405-Eng-48.

This report has been reproduced
directly from the best available copy.

Available to DOE and DOE contractors from the
Office of Scientific and Technical Information
P.O. Box 62, Oak Ridge, TN 37831
Prices available from (423) 576-8401
http://apollo.osti.gov/bridge/

Available to the public from the
National Technical Information Service
U.S. Department of Commerce
5285 Port Royal Rd.,
Springfield, VA 22161
http://www.ntis.gov/

OR

Lawrence Livermore National Laboratory
Technical Information Department's Digital Library
http://www.llnl.gov/tid/Library.html

Local Organizing Committee

G. Dimonte, Lawrence Livermore National Laboratory, Livermore, CA, USA
B. Goodwin, Lawrence Livermore National Laboratory, Livermore, CA, USA
D. Meiron, California Institute of Technology, Pasadena, CA, USA
T. McAbee, Lawrence Livermore National Laboratory, Livermore, CA, USA
T. Peyser, Lawrence Livermore National Laboratory, Livermore, CA, USA
B. Remington, Lawrence Livermore National Laboratory, Livermore, CA, USA
O. Schilling (Chairman), Lawrence Livermore National Laboratory, Livermore, CA, USA
C. Verdon, Lawrence Livermore National Laboratory, Livermore, CA, USA

International Scientific Committee

G. Ben-Dor, Ben-Gurion University of the Negev, Beer-Sheeva, IL
D. Besnard, Commissariat à l'Energie Atomique, FR
A. Buckingham, Lawrence Livermore National Laboratory, Livermore, CA, USA
T. Clark, Los Alamos National Laboratory, Los Alamos, NM, USA
S. Dalziel, University of Cambridge, Cambridge, UK
D. Galmiche, Commissariat à l'Energie Atomique, FR
S. Gauthier, Commissariat à l'Energie Atomique, FR
J. Glimm, State University of New York at Stony Brook, NY, USA
B. Goodwin, Lawrence Livermore National Laboratory, Livermore, CA, USA
N. Hoffman, Los Alamos National Laboratory, Los Alamos, NM, USA
L. Houas, IUSTI Universite de Provence, Marseille, FR
J. Jacobs, University of Arizona, Tuscon, AZ, USA
Yu. Kucherenko, Russian Federal Nuclear Center-VNIITF, Snezhinsk, RU
P. Linden, University of California at San Diego, San Diego, CA, USA
D. Meiron, California Institute of Technology, Pasadena, CA, USA
E. Meshkov, Russian Federal Nuclear Center-VNIIEF, Sarov, RU
V. Neuvazhaev, Russian Federal Nuclear Center-VNIITF, Snezhinsk, RU
T. Peyser, Lawrence Livermore National Laboratory, Livermore, CA, USA
J. Redondo, Universitat Politecnica de Catalunya, Barcelona, SP
B. Remington, Lawrence Livermore National Laboratory, Livermore, CA, USA
V. Rozanov, P. N. Lebedev Physical Institute, Moscow, RU
O. Schilling, Lawrence Livermore National Laboratory, Livermore, CA, USA
D. Sharp, Los Alamos National Laboratory, Los Alamos, NM, USA
D. Shvarts, Nuclear Research Center, Beer-Sheeva, IL
E. Son, Moscow Physical and Technical Institute, Moscow, RU
H. Takabe, ILE, Osaka University, Osaka, JP
K. Takayama, Tohoku University, Sendai, JP
D. Youngs, Atomic Weapons Establishment, Aldermaston, UK
S. Zaytsev, ENIN, Moscow, RU

General Information

The workshop is hosted by the Lawrence Livermore National Laboratory and is held at the California Institute of Technology.

Schedule (Oral and poster presentations will be at the California Institute of Technology):

Day	Date	Time	Activity
Sunday	December 9, 2001	5:00 PM – 9:00 PM	Registration – Pasadena Hilton
Sunday	December 9, 2001	6:00 PM – 9:00 PM	Reception – Pasadena Hilton
Monday	December 10, 2001	8:15 AM – 4:15 PM	Opening Remarks/Oral Presentations
Monday	December 10, 2001	4:15 PM – 6:00 PM	Poster Presentations
Tuesday	December 11, 2001	8:15 AM – 4:15 PM	Announcements/Oral Presentations
Tuesday	December 11, 2001	4:15 PM – 6:00 PM	Experimental Discussion/ Computational and Theoretical Poster Presentations
Wednesday	December 12, 2001	8:15 AM – 4:15 PM	Announcements /Oral Presentations
Wednesday	December 12, 2001	4:15 PM – 6:00 PM	Computational Discussion/Experimental and Theoretical Poster Presentations
Wednesday	December 12, 2001	6:00 PM – 9:00 PM	Banquet – Pasadena Hilton
Thursday	December 13, 2001	8:15 AM – 4:15 PM	Announcements /Oral Presentations
Thursday	December 13, 2001	4:15 PM – 6:00 PM	Theoretical Discussion/Computational and Experimental Poster Presentations
Friday	December 14, 2001	8:15 AM – 12:00 PM	Announcements/Oral Presentations/Summary Remarks/Closing Remarks

Invited Guest Speakers:

Dr. Edward I. Moses, National Ignition Facility (NIF) Project Manager at the Lawrence Livermore National Laboratory, will be the guest speaker at the Reception on Sunday evening, December 9. Z. Nagin Cox, Mission Operations Engineer for the Mars Sample Return Mission at the NASA Jet Propulsion Laboratory, will be the guest speaker at the Banquet on Wednesday evening, December 12.

Message Line:

A phone will be located in the lobby of the Beckman Institute Auditorium for messages: the telephone number is (626) 395-5035.

Shuttles:

The Pasadena Hilton will provide shuttles to and from the hotel and Caltech in the morning and afternoon (parking on or near campus is extremely limited).

Pasadena Convention Center:

The Pasadena Convention Center will have representatives available for scheduling tourist activities. Representatives will be available on Sunday during the Registration and Tuesday through Thursday from 4:00 PM – 8:00 PM in the Pasadena Hilton Hotel lobby.

Administrative Staff:

C. Cantlin, Lawrence Livermore National Laboratory, Livermore, CA, USA
S. Davis, Lawrence Livermore National Laboratory, Livermore, CA, USA
K. Evans, Lawrence Livermore National Laboratory, Livermore, CA, USA

8th International Workshop on the Physics of Compressible Turbulent Mixing, Pasadena, CA (2001)

Table of Contents

REVIEW TALKS 1

J.-F. Haas and S. G. Zaytsev
A Review on RT and RM Instability and TM Experiments 2

S. G. Zaytsev
The Experimental Study of Excitation and Development of the Hydrodynamic Instability in the Mixing Zone Separating Gases of Different Densities at their Accelerated Motion 3

D. L. Youngs
Review of Numerical Simulation of Mixing due to Rayleigh-Taylor and Richtmyer-Meshkov Instabilities 4

D. Shvarts
Modeling Late-Time Nonlinear Evolution of Hydrodynamic Instabilities and their Role in Inertial Confinement Fusion 5

EXPERIMENTAL ABSTRACTS 6

Yu. A. Kucherenko, S. I. Balabin, R. I. Ardashova, A. P. Pylaev, O. E. Kozelkov, and V. D. Murzakov
Experimental Investigations of the Heavy and Light Media Separation in the Rayleigh-Taylor Turbulence Zone at Different Atwood Numbers (E2) 7

Yu. A. Kucherenko, S. I. Balabin, R. I. Ardashova, O. E. Kozelkov, A. V. Dulov, and I. A. Romanov
Experimental Investigations into Influence of Stablizing Properties of Transitional Layers Upon the Turbulent Mixing Evolution (E3) 8

C. W. Barnes, S. H. Batha, A. M. Dunne, N. E. Lanier, G. R. Magelssen, T. J. Murphy, K. W. Parker, S. Rothman, J. M. Scott, and D. Youngs
Improvements to Convergent Cylindrical Plasma Mix Experiments Using Laser Direct Drive (E4) 9

S. H. Batha, K. W. Parker, C. W. Barnes, A. M. Dunne, N. E. Lanier, G. R. Magelssen, T. J. Murphy, S. Rothman, J. M. Scott, and D. Youngs
Mixing Between Two Compressing Cylinders (E5) 10

M. Bliznetsov, V. Dudin, S. Gerasimov, L. Houas, G. Jourdan, A. Logvinov, E. Meshkov, and Yu. Vlasov
Development of a Method for Studying the Interaction Between Shock Wave and a Flame Front (E6) 11

M. Bliznetsov, E. Meshkov, N. Nevmerzhitzky, A. Nikulin, E. Sen'kovsky, and E. Sotskov
The Influence of Scaling for Periodical Perturbations on Development of Turbulent Mixing on a Gas-Liquid Interface (E7) 12

M. Brouillette and C. H. Hebért
Compressible Vortex Rings (E8) 13

R. P. Drake
Design of Flyer-Plate-Driven Compressible Turbulent Mix Experiments (E9) 14

R. P. Drake, P. Keiter, K. E. Korreck, K. Dannenberg, H. A. Robey, T. Perry, J. O. Kane, B. A. Remington, R. J. Wallace, O. A. Hurricane, D. D. Ryutov, J. Knauer, R. Teyssier, A. Calder, R. Rosner, B. Fryxell, D. Arnett, Y. Zhang, J. Glimm, N. Turner, J. Stone, R. McCray, and J. Grove
Compressible Hydrodynamics on the Omega Laser, Motivated by Astrophysics (E10) 15

O. B. Drennov, A. L. Mikhaylov, P. N. Nizovtsev, and V. A. Raevskii
Growth of Perturbation on Metals Interface at Oblique Collission with Supersonic Velocity of Contact Point Motion (E11) 16

S. G. Glendinning, D. G. Braun , M. J. Edwards, W. W. Hsing, B. F. Lasinski, H. Louis, J. Moreno, T. A. Peyser, B. A. Remington, H. F. Robey, E. J. Turano, C. P. Verdon, and Y. Zhou
An Experimental Study of the Effect of Shock Proximity on the Richtmyer-Meshkov Instability at High Mach Number (E12) 17

D. A. Holder, C. Barton, and A. V. Smith
Mix Experiments using a Two Dimensional Convergent Shock Tube (E13) 18

J. M. Holford, S. B. Dalziel, and D. Youngs
Rayleigh-Taylor Instability at a Tilted Interface in Incompressible Laboratory Experiments and Compressible Numerical Simulations (E14) 19

S. H. R. Hosseini and K. Takayama
Study of Diverging and Converging Spherical Shock Waves Induced by Micro Explosives and their Interaction with Product Gases (E15) 20

S. H. R. Hosseini and K. Takayama
Interaction of Converging Shock Waves with Cylindrical Heavy Gas Interfaces in an Eccentric Arrangement (E16) 21

L. Houas, G. Jourdan, L. Schwaederle, and E. E. Meshkov
From Linear to Turbulent Stages of the Richtmyer-Meshkov Instability Development in a Large Cross Section Shock Tube (E17) 22

J. W. Jacobs and V. V. Krivets
PLIF Flow Visualization of a Shock-Accelerated Air/SF_6 Interface (E18) 24

D. H. Kalantar, J. Belak, J. D. Colvin, M. Kumar, K. T. Lorenz, K. O. Mikaelian, S. Pollaine, B. A. Remington, S. V. Weber, L. G. Wiley, A. M. Allen, A. Loveridge-Smith, J. S. Wark, and M. A. Meyers
Laser-Based High Pressure, High Strain-Rate Solid-State Experiments (E19) 25

Yu. A. Kucherenko, O. E. Shestachenko, S. I. Balabin, and A. P. Pylaev
RFNC-VNIITF Multifunctional Shock Tube to Investigate the Evolution of Instabilities in Nonstationary Gas Dynamic Flows (E20) 26

A. Lassis, P. Montlaurent, C. Rayer and J.-F. Haas
Planar Laser Sheet Visualization and Laser Doppler Velocity Measurements in Shock-Induced Turbulent Mixing Zones (E21) 27

G. Layes, G. Jourdan, P. Roualdes, and L. Houas
Hydrodynamic Instabilities at a Shock Accelerated Bubble Gas-Gas Interface (E22) 29

K. Levy, O. Sadot, D. Oron, Y. Srebro, Y. Elbaz, A. Josef-Hai, G. Ben-Dor, and D. Shvarts
Experimental and Numerical Study of Shock Wave–Bubble Interaction (E23) 30

K. T. Lorenz, D. Kalantar, J. Edwards, J. D. Colvin, and B. Remington
Laser-Driven Near Isentropic Compression of an Aluminum Flyer Plate (E24) 31

C. E. Niederhaus and J. W. Jacobs
Single-Mode Incompressible Richtmyer-Meshkov Instability Experiments (E26) 32

J. G. Oakley, M. H. Anderson, and R. Bonazza
Experimental Study of a Strongly-Shocked Gas Interface with Visualized Initial Conditions (E27) 33

Yu. A. Kucherenko, O. E. Shestachenko, Yu. A. Piskunov, E. V. Sviridov, V. M. Medvedev, and A. I. Baishev
Experimental Investigations of the Self-Similar Mixing Mode of Different Density Gases in the Earth's Gravitational Field (E28) 34

S. Pollaine, D. Kalantar, B. Remington, J. Belak, J. D. Colvin, J. Edwards, R. Minich, K. O. Mikaelian, K. T. Lorenz, S. V. Weber, L. G. Wiley, D. Paisley, A. Hauer, J. S. Wark, A. Loveridge, A. M. Allen, T. R. Boehly, and M. A. Meyers
Modeling Laser Material Strength Experiments (E29) 35

K. Prestridge, C. A. Zoldi, P. Vorobieff , P. M. Rightley, and R. F. Benjamin
Experiments and Simulations of Instabilities in a Shock-Accelerated Gas Cylinder (E30) 36

Yu. A. Kucherenko, A. P. Pylaev, V. D. Murzakov, A. V. Belomestnih, V. N. Popov, and A. A. Tyaktev
Experimental Study into Rayleigh-Taylor Turbulent Mixing Zone Heterogeneous Structure (E31) 37

P. Ramaprabhu and M. J. Andrews
Measurements of Turbulence Correlations in Low Atwood Number Rayleigh-Taylor Mixing (E32) 38

H. F. Robey, T. S. Perry, R. I. Klein, J. A. Greenough, J. O. Kane, and T. R. Boehly
Experimental Study of the Interaction of a Strong Shock with a Spherical Density Inhomogeneity (E34) 39

H. F. Robey, Y. K. Zhou, A. C. Buckingham, P. Keiter, B. A. Remington, and R. P. Drake
Turbulent Transition in a High Reynolds Number, Rayleigh-Taylor Unstable Plasma Flow (E35) 40

O. Sadot, A. Yosef-Hai, A. Rikanati, D. Oron, G. Ben-Dor, and D. Shvarts
Effects of High Initial Amplitudes and High Mach Numbers on the Evolution of the RM Instability II. Experimental Study (E36) 41

L. Schwaederlé, G. Jourdan, L. Houas, and J.-F. Haas
Measurements within a Richtmyer-Meshkov Mixing Zone using a Triple Hot Wire Probe Technique (E37) 42

Yu. A. Kucherenko, O. E. Shestachenko, Yu. A. Piskunov, E. V. Sviridov, V. M. Medvedev, and A. I. Baishev
Experimental Study into Evolution of Gravitational Turbulent Mixing of Gases at the Multifunctional Shock Tube (E38) 44

A. V. Smith, D. A. Holder, C. J. Barton, A. P. Morris, and D. L. Youngs
Shock Tube Experiments on Richtmyer-Meshkov Instability Across a Chevron Profiled Interface (E39) 45

C. Tomkins, K. Prestridge, P. Rightley, C. Zoldi, and R. Benjamin
The Evolution and Interaction of Two Shock-Accelerated Unstable Gas Cylinders (E40) 46

D. J. Ward, K. S. Budil, T. A. Peyser, B. A. Remington, P. L. Miller, R. J. Wallace, H. Louis, and A. Demiris
Doubly-Shocked Richtmyer-Meshkov Instability Experiments at Nova (E41) 47

R. I. Klein, H. Robey, T. Perry, and J. Greenough
The Interaction of Supernova Blast Waves with Interstellar Clouds: Experiments on the OMEGA Laser (E42) 48

S. G. Zaytsev, V. V. Krivets, I. M. Mazilin, S. N. Titov, E. I. Chebotareva, V. V. Nikishin, V. F. Tishkin, S. Bouquet, and J.-F. Haas
Evolution of the Mixing Zone of Different Densities Gases Being Interaction to Compression Waves (E43) 49

A. Lebedev, P. Nizovtcev, and V. Raevsky
Studies of Rayleigh-Taylor Instability in Aluminum Under Shock-Wave and Shock Less Loading (E44) 50

H. Azechi, T. Sakaiya, M. Nakai, H. Shiraga, K. Shigemori, N. Miyanaga, M. Nishikino, S. Fujioka, Y. Tamari, H. Nagatomo, H. Takabe, and A. Sunahara
Ablative Rayleigh-Taylor Instability at Short Wavelengths (E45) 51

H. F. Robey and S. G. Glendinning
A Vortex Model for Studying the Effect of Shock Proximity on Richtmyer-Meshkov Instability at High Mach Number (E46) 52

COMPUTATIONAL ABSTRACTS 53

V. I. Anisimov and A. V. Polionov
Modes' Interaction on Nonlinear Stage of Richtmyer-Meshkov Instability Evolution (C1) 54

M. G. Anuchin, V. E. Neuvazhayev, and I. E. Parshukov
Application of Kε-Model for the Description of an Atmospheric Surface Layer (C2) 55

Wm. T. Ashurst and A. R. Kerstein
Computational Modeling of Low-Mach-Number High-Atwood-Number Turbulent Mixing (C4) 56

A. W. Cook, W. H. Cabot, and J. A. Greenough
Spectral and High-Order Compact Methods for Shock-Induced Mixing (C8) 57

R. M. Darlington and K. S. Budil
Numerical Simulation of Mode Coupling in Laser-Driven Rayleigh-Taylor Instability Experiments (C9) 58

G. Dimonte, A. Dimits, S. Weber, D. L. Youngs, A. C. Calder, B. Fryxell, J. Biello, L. Dursi, P. MacNeice, K. Olson, P. Ricker, R. Rosner, F. Timmes, H. Tufo, Y.-N. Young, M. Zingale, M. J. Andrews, P. Ramaprabhu, S. Wunsch, C. Garasi, and A. Robinson
A Comparison of High-Resolution 3D Numerical Simulations Of Turbulent Rayleigh-Taylor (RT) Instability: Alpha-Group Collaboration (C10) 59

S. Dutta, E. George, J. Glimm, J. Grove, X. Li, A. Marchese, D. H. Sharp, Z. Xu, and Y. Zhang
Numerical Methods for Determination of Mix (C11) 60

Y. Elbaz, A. Rikanati, D. Oron, and D. Shvarts
Rayleigh-Taylor Instability in Compressible Fluids (C12) 61

R. Epstein, J. A. Delettrez, V. Yu. Glebov, V. N. Goncharov, P. W. Mckenty, P. B. Radha, S. Skupsky, V. A. Smalyuk, and C. Stoeckl
One-Dimensional Simulation of the Effects of Unstable Mix on Neutron and Charged-Particle Yield from Laser-Driven Implosion Experiments (C13) 62

E. S. Gavrilova, E. V. Gubkov, V. A. Zhmailo, and Yu. V. Yanilkin
3D Computation for Surface Perturbation Evolution of Plasma Cloud During its Expansion in Magnetic Field (C14) 63

M. J. Graham, K. S. Budil, J. Grove, and B. A. Remington
The Richtmyer-Meshkov Instability in Cylindrical Geometry: Experiments and Simulation (C15) 64

J. A. Greenough, W. J. Rider, C. A. Zoldi, and J. R. Kamm
Code to Code Comparisons for the Problem of Shock Acceleration of a Diffuse Dense Gaseous Cylinder (C16) 65

B. Grieves
Implementation of a Turbulent Mix Model in a 2D ALE Code (C17) 66

J. W. Grove
Error Estimation for Strong Shock Hydrodynamics (C18) 67

E. V. Gubkov, V. A. Zhmailo, and Yu. V. Yanilkin
A Semi-Empirical Model for Turbulent Diffusion of Magnetic Field to Accelerated Plasma (C19) 68

S. Gupta, N. J. Zabusky, R. Samtaney, and Y. Gulak
Localization and Spreading of Interfaces (Contact Discontinuities) in Direct Numerical Simulations of the Compressible Euler Equations (C20) 69

S. W. Haan, T. Dittrich, S. Hatchett, D. Hinkel, M. Marinak, D. Munro, O. Jones, S. Pollaine, and L. Suter
Update on Instability Modeling for the NIF Ignition Targets (C22) 70

J. O. Kane, D. D. Ryutov, B. A. Remington, S. G. Glendinning, J. Nash, M. Pound, and D. Arnett
Pillars of Creation (C23) 71

I. G. Lebo and V. D. Zvorykin
Application of a Laser Shock Tube for the Study of Supersonic Gas Flows and the Development of Hydrodynamic Instabilities in Layered Media (C25) 72

K. Nishihara, V. Zhakhovskii, and M. Abe
Molecular Dynamic Simulation of Shock and Richtmyer-Meshkov Instability in Cylindrical Geometry (C26) 73

C. Pantano and S. Sarkar
Compressibility Effects in a High-Speed, Reacting Shear Layer: An Investigation Using DNS (C27) 74

K. W. Parker, A. M. Dunne, S. Rothman, D. Youngs, C. W. Barnes, S. H. Batha, N. E. Lanier, G. R. Magelssen, T. J. Murphy, and J. M. Scott
Computational Modeling of Two-Shell Cylindrical Implosions with Mix (C28) 76

G. Peng and N. J. Zabusky
Dispersal of Mass and Circulation Following M = 2.5 – M = 10 Shock-Bubble Interactions: Effects Arising from Shock-Cavity Collapse-& Re-Expansion, Vortex Double Layers (Vdls) and Vortex Projectiles (Vps) (C29) 77

V. A. Raevski, S. N. Sinitsina, and Yu. V. Yanilkin
Influence of Turbulent Mixing Zone on Growth of Local Perturbation in Environments of Rayleigh-Taylor Instability (Numerical Simulation) (C30) 78

W. J. Rider, J. R. Kamm, and C. A. Zoldi
A Statistical Comparison of Gas Cylinder Experiments with their Simulation (C31) 79

R. Samtaney, T. Voelkl, and D. I. Pullin
Large Eddy Simulation of Strong Shock Richtmyer-Meshkov Instability (C33) 80

P. Seytor and M. Legrand
Numerical Investigation of a Laser Induced Turbulent Mixing Zone (C35) 81

D. Souffland and F. Renaud
A Mix-Model For One-Dimensional Simulations of Laser-Driven Implosion Experiments (C36) 82

Y. Srebro, D. Kushnir, Y. Elbaz, and D. Shvarts
Modeling Turbulent Mixing in Inertial Confinement Fusion Implosions (C37) 83

H. Takabe, S. Yamada, K. Kobayashi, A. Mizuta, and K. Nomoto
Turbulent Mixing Nuclear Burning in Type Ia Supernova Explosion Based on Bubble Statistical Mechanics (C38) 84

N. Toqué
Turbulent Diffusion in Solar Type Star (C39) 85

E. Vold
Recent Computational Simulations of Rayleigh-Taylor Mix Layer Growth With a Multi-Fluid Model (C40) 86

S. P. Wang, M. H. Anderson, J. G. Oakley, and R. Bonazza
An Efficient and High Resolution Solver for the Two-Dimensional Numerical Simulation of the Richtmyer-Meshkov Instability (C41) 87

S. V. Weber, G. Dimonte, and M. M. Marinak
ALE Simulations of Turbulent Rayleigh-Taylor Instability in 2-D and 3-D (C42) 88

Yu. V. Yanilkin, V. P. Statsenko, S. V. Rebrov, N. I. Selchenkova, O. G. Sin'kova, A. L. Stadnik, and A. Ya. Uchayev
Study of Turbulent Gravitational Mixing at Large Density Differences Using Direct 3D Numerical Simulation (C44) 89

D. L. Youngs
Development and Validation of a 2D Turbulent Mix Model (C46) 90

D. L. Youngs, X. Silvani, J. Magnaudet, and A. Llor
Preliminary Results of DNS and LES Simulations of Self-Similar Variable Acceleration RT-Mixing Flows (C47) 91

S. Zhang and N. J. Zabusky
Shock–Planar Curtain Interactions: Strong Secondary Baroclinic Deposition and the Emergence of Coherent and Random Vortex Projectiles (*VPs*) and Decaying Stratified Turbulence (C48) 92

S. Zhang, Y.-G. Kang , K. Nishihara, N. J. Zabusky, and H. Kim
Rapid Turbulization Arising from Vortex Double Layers in Interactions of "Complex" Blast Waves and Cylindrical and Spherical Bubbles (C49) 93

C. A. Zoldi, K. Prestridge, P. M. Rightley, and R. F. Benjamin
Simulations of a Shock-Accelerated Gas Cylinder and Comparison with Experimental Images and Velocity Fields (C50) 94

V. I. Kozlov, A. N. Razin, and I. V. Sapozhnikov
Turbulent Flow Simulations of Two Fluids Moving with Different Laws of Acceleration (C51) 95

V. I. Kozlov and A. N. Razin
The Behaviour of Velocity Variance Resulting from Turbulent Mixing Zone-Shock Interaction (C52) 96

D. E. Eliason, W. H. Cabot, and Y. Zhou
An Assessment of Multi-Velocity Versus Single Velocity in a Multi-Component Model of Turbulent Mixing (C53) 97

W.-S. Don, D. Gottlieb, L. Jameson, and C.-W. Shu
High Order Numerical Methods for the 2D Richtmyer-Meshkov Instability (C54) 98

A. M. Dimits
Mixing Due to the Rayleigh-Taylor Instability (C55) 99

A. W. Cook and P. E. Dimotakis
Transition Stages of Rayleigh-Taylor Instability Between Miscible Fluids (C56) 100

A. Miles, J. Edwards, and G. Glendinning
CALE Simulation of Richtmyer-Meshkov Experiments at High Mach Number (C57) 101

THEORETICAL ABSTRACTS 102

S. I. Abarzhi
Nonlinear Evolution of Unstable Fluid Interface (T1) 103

S. I. Abarzhi
Nonlinear Asymptotic Solutions to RT and RM Problems for Fluids With Close Densities (T2) 104

S. I. Abarzhi
Turbulent Mixing in RTI as Order-Disorder Process (T3) 105

P. Bailly and A. Llor
A New Turbulent Two-Fluid RANS Model for KH, RT and RM Mixing Layers (T4) 106

R. E. Breidenthal
Super-Exponential Rayleigh-Taylor Flow (T5) 107

B. Cheng, J. Glimm, and D. H. Sharp
Theoretical Methods for Determination of Mix (T7) 108

T. Clark and F. Harlow
Modeling Radiation Effects in Mixing Layers (T8) 109

J. D. Colvin, M. Legrand, B. A. Remington, G. Schurtz, and S. V. Weber
A Model for Instability Growth in Accelerated Solid Metals (T9) 110

S. B. Dalziel
Toy Models for the Growth Rate of Rayleigh-Taylor Instability (T10) 111

Y. Elbaz, Y. Srebro, O. Sadot, and D. Shvarts
A General Buoyancy-Drag Model for the Evolution of the Rayleigh-Taylor and Richtmyer-Meshkov Instabilities (T11) 112

N. A. Inogamov, A. M. Oparin, M. Tricottet, and S. Bouquet
3D Rayleigh-Taylor and Richtmyer-Meshkov Single-Modes (T12) 113

N. A. Inogamov, M. Tricottet, A. M. Oparin, and S. Bouquet
Rayleigh-Taylor Instability for Compressible and Incompressible Media (T13) 114

D. Kartoon, D. Oron, L. Arazi, A. Rikanati, U. Alon, and D. Shvarts
Three Dimensional Multi-Mode Rayleigh-Taylor and Richtmyer-Meshkov Instabilities at All Density Ratios (T14) 115

V. M. Ktitorov
Stability of Diverging Shock Waves (T15) 116

V. M. Ktitorov
Stability of Reflected from the Center Self-Similar Converging Shock Wave (T16) 117

R. R. Linn and F. H. Harlow
Using a Turbulence Transport Approach to Study Shocks Through Polycrystalline Metal (T17) 118

A. Llor
Response of Turbulent RANS Models to Self-Similar Variable Acceleration RT-Mixing: An Analytical 0D Analysis (T18) 119

C. Matsuoka, K. Nishihara, and Y. Fukuda
Nonlinear Evolution of an Interface in the Richtmyer-Meshkov Instability (T19) 120

K. O. Mikaelian
Evolution of Arbitrary Perturbations in the Richtmyer-Meshkov Instability (T20) 121

A. M. Oparin, N. A. Inogamov, and A. Yu. Dem'yanov
RT Turbulence: Dramatic Dynamics of Interpenetration (Fast Jets, Sharp Decelerations and Accelerations) (T21) 122

A. Rikanati, U. Alon, and D. Shvarts
Statistical Mechanics Large Scale Model for the Evolution of the Multi-Mode Kelvin Helmholtz Instability (T22) 123

A. Rikanati, D. Oron, O. Sadot, and D. Shvarts
Effects of High Initial Amplitudes and High Mach Numbers on the Evolution of the RM Instability: I. Theoretical Study (T23) 124

D. D. Ryutov and B. A. Remington
Compressible MHD Turbulence in Strongly Radiating Molecular Clouds in Astrophysics (T25) 125

O. Schilling
Single-Velocity, Multi-Component Turbulent Transport Models for Interfacial Instability-Driven Flows (T26) 126

O. Schilling and A. W. Cook
Large- and Small-Scale Dynamics of Variable-Density Rayleigh-Taylor Instability-Induced Turbulent Mixing (T28) 127

M. Tricottet and S. Bouquet
Analytical Study of the Rayleigh-Taylor Instability in Compressible Fluids (T30) 128

M. Vandenboomgaerde
Analytic Nonlinear Growth of A Single-Mode Richtmyer-Meshkov Instability (T31) 129

M. Vandenboomgaerde, C. Cherfils, D. Galmiche, S. Gauthier, and P. A. Raviard
Efficient Perturbation Methods for Richtmyer-Meshkov and Rayleigh-Taylor Instabilities: Weakly Nonlinear Stage and Beyond (T32) 130

P. N. Wilson, M. J. Andrews, and F. H. Harlow
Combined Shear and Buoyancy Instabilities (T33) 131

J. G. Wouchuk
Rate of Growth of the Linear Richtmyer-Meshkov Instability (T34) 132

A. Yosef-Hai, O. Sadot, D. Kartoon, D. Oron, E. Sarid, G. Ben-Dor, and D. Shvarts
The Dependence of the Shock Induced Richtmyer-Meshkov Instability on Dimensionality and Density Ratio (T35) 133

Y. Zhou, H. F. Robey, and A. C. Buckingham
A New Framework for Transitional and Turbulent Mixing (T36) 135

A. L. Kuhl and R. E. Ferguson
Spherical Combustion Layer in a TNT Explosion (T37) 136

V. F. Tishkin and N. V. Zmitrenko
Spectral Analysis of Turbulent Flows Induced by RT and RM Instabilities (T38) 137

B. B. Afeyan, P. Ramaprabhu, and M. J. Andrews
Pattern Detection, Compression and Denoising of Rayleigh-Taylor Mix Data Using Discrete Wavelet Transform Techniques (T39) 138

Author Contact Information 139

Author Index 181

REVIEW TALKS

A Review on RT and RM Instability and TM Experiments

J.-F. Haas[1] and S. G. Zaytsev[2]
[1]*Commissariat à l'Energie Atomique, Bruyères-le-Châtel, France*
[2]*Krzhizhanovsky Power Engineering Institute, Moscow, Russia*

We analyse the state of the art for experiments on Rayleigh-Taylor, Richtmyer-Meshkov instabilities (RTI, RMI) and the resulting (possibly compressible) turbulent mixing (TM). There is a very wide spectrum of state of matter (in addition to acceleration history and magnitude) ranging from « ordinary » gas or liquid dynamics experiments, through intermediate complexity detonation-driven setups often involving materials with strength, all the way to large laser driven experiments for the study of high energy density plasmas. Experiments are needed for a better understanding of fundamental mechanisms (e.g. nonlinear regime of the RTI and RMI, complex natural phenomena (supernovae explosions) and future applications (inertial confinement fusion). We consider first the field of « simple » gas dynamics RMI and TM experiments performed in ordinary shock tubes. It was suggested at the experimental roundtable of the 7th IWPCTM that the experiment type could be presented on a map with an horizontal axis for a compressibility parameter (such as the incident shock Mach number) and a vertical axis for the instability strength (e.g., according to the linear RMI formula, the product of Atwood number, perturbation wave number and initial amplitude). A second map was proposed, with a horizontal axis tentatively called « usefulness to theory » and a vertical one labelled « complexity of diagnostics ». The classical visualization by refractive effects (shadowgraph, schlieren, Mach-Zehnder or differential interferometry) is useful for geometrical observations of the mixing zones and instability patterns, but of limited quantitative value in TM. The modern laser sheet method provides a 2D map of the density or concentration field (via Mie or Rayleigh scattering or fluorescence). Flash X-rays absorption by Xe, infrared emission or infrared CO_2 laser absorption by shock heated CO_2 allow density measurements within binary mixing zones containing these gases. Laser Doppler Velocimetry (giving the velocity history at a given position) and Particle Image Velocimetry (giving a velocity map at a given time) have recently been introduced. The Hot Wire Anemometer provides the time evolution at a fixed position of the Nusselt number, which depends on velocity, concentration and temperature. The initial gas separation is best membrane-less for RMI and with microfilm for fine scale TM. Often, a good experiment for theory benefits from an imaginative conception while advanced diagnostics are useful for a quantitative comparison with numerical simulation and TM modelling. Among the cold hydrodynamics RTI experiments, some based on gravitational mixing of liquids (molecularly miscible or not, with or without surface tension) increasingly benefit from modern diagnostics. The experiments on gases in modified shock- or combustion tubes allow the investigation of compressibility and acceleration nonsteadiness, but with usually less precise diagnostics. There is a variety of gas detonation or combustion experiments in which the effect of cylindrical geometries are tested. Effects of initial interfacial perturbations and material strength can be investigated with jellies. Solid explosive drivers are needed for the measurement of such RT/RM processes in metals. Among recent high energy laser driven plasma experiments, the high quality visualizations in some very high Mach number experiments are fascinating. Our challenge is to insure that simpler and cheaper gas or liquid dynamics experiments will remain useful with the advent of the next generation of ICF lasers.

PACS Nos.: 42.79, 47.20, 47.27, 47.40, 52.57

The Experimental Study of Excitation and Development of the Hydrodynamic Instability in the Mixing Zone Separating Gases of Different Densities at their Accelerated Motion

S. G. Zaytsev
Krzhizhanovsky Power Engineering Institute, Moscow, Russia

The properties of the mixing zone between gases of different densities during accelerated and decelerated motion caused by compression waves have been analyzed. The design of the experimental set-up for study of the mentioned processes has been described.

The wave diagrams of possible regimes of flows and basic parameters such as velocity u, acceleration g, density ρ, pressure p, and temperature T have been under consideration.

The properties of excitation and development of the Rayleigh-Taylor instability (RTI) at the stages of accelerated and decelerated motion of the mixing zone have been described.
The characteristics of the mixing zone at the stage of "stratification" caused by interaction with a reflected compression wave - non-shocked deceleration - have been defined. The mixing zone volume decreases in this case.

The generation of shocks during evolution of compression waves and their interaction with the mixing zone results in growth of the mixing volume caused by excitation of the Richtmyer-Meshkov instability (RMI).

The amount of the substance involved into mixing during accelerated motion of the mixing zone separating gases of different densities has been defined. The problem of influence of the working media compressibility on process of the mixing has been discussed.

Review of Numerical Simulation of Mixing due to Rayleigh-Taylor and Richtmyer-Meshkov Instabilities

D. L. Youngs
Atomic Weapons Establishment, Aldermaston, United Kingdom

Since the late 1960s numerical simulation has been very successfully used to gain insight into the non-linear growth of Rayleigh-Taylor (RT) and Richtmyer-Meshkov (RM) instabilities. The first calculations were for single-mode growth in 2D. Then in the 1980s, 2D multimode simulations became feasible. 3D simulations of fully-developed turbulent mixing in simple situations have been performed during the past few years. There are many examples where numerical simulation has been used to study the affect of additional physical processes, such as ablation stabilisation or material strength, on instability growth. The progress made is reviewed and instances where numerical simulation has enhanced our understanding are highlighted. The main emphasis of this review will be on RT and RM instability. However, some reference will be made to simulations of turbulent shear flow and homogeneous turbulence, especially where ideas from these areas are relevant to RT/RM studies.

The numerical methods used will be discussed. RT and RM problems involve discontinuities, contact surfaces or shocks. TVD schemes have proved popular and number of researchers have used interface tracking techniques. For 3D LES (Large Eddy Simulation) dissipation at high-wavenumbers is needed. Many researchers, especially those who work on turbulent shear flow, favour the use of an explicit sub-grid model to represent this effect. The TVD methods have high-wavenumber dissipation inherent in the numerical scheme and when applied to turbulence simulations are referred to as MILES schemes (Monotone Implicit LES). There have been a number of examples of the application of MILES to RT and RM turbulent mixing and also some examples of 3D DNS (Direct Numerical Simulation) in which the effects of viscosity and diffusivity are resolved.

The future role of numerical simulation will be discussed. 2D simulation will continue to be useful for understanding complex experiments or the effect of additional physics, where 3D simulation is impractical. However, with the advent of very powerful supercomputers, 3D simulation (LES or DNS) will become increasingly useful and will give a detailed understanding of turbulent mixing in simplified situations. It is likely that RANS (Reynolds-AveragedNavier-Stokes) models will contine to be essential for modelling the most complex real applications. However, 3D simulation can make an important contribution here as well. In addition to experimental data, the results of 3D simulations should be used to validate the RANS models in simplified situations.

Modeling Late-Time Nonlinear Evolution of Hydrodynamic Instabilities and their Role in Inertial Confinement Fusion

D. Shvarts
Ben-Gurion University, Beer Sheeva, Israel and Nuclear Research Center, Negev, Israel

Abstract not available at time of printing.

EXPERIMENTAL ABSTRACTS

Abstract No. E2

Experimental Investigations of the Heavy and Light Media Separation in the Rayleigh-Taylor Turbulence Zone at Different Atwood Numbers

Yu. A. Kucherenko, S. I. Balabin, R. I. Ardashova, A. P. Pylaev, O. E. Kozelkov, and V. D. Murzakov
Russian Federal Nuclear Center – VNIITF, Snezhinsk, Russia

In the paper the experimental results with respect to the nondimensional rate of separation in the Rayleigh-Taylor turbulence zone are presented. In the experiments two different density liquids separated by a plane contact boundary were accelerated so that in the first phase of acceleration the Rayleigh-Taylor instability evolved and the definite zone of the turbulent mixing formed. At the second phase the sign of acceleration was jumpwise changed into the opposite one. As a result, the system of two different density liquids became stable. At these instants of time, in the turbulent mixing zone the separation processes of the heavy and light liquids evolved.

For three values of Atwood numbers the experiments were performed. for each of Atwood numbers the nondimensional rate of separation was determined.

Abstract No. E3

Experimental Investigation into Influence of Stabilizing Properties of Transitional Layers Upon the Turbulent Mixing Evolution

Yu. A. Kucherenko, S. I. Balabin, R. I. Ardashova, O. E. Kozelkov, A. V. Dulov, and I. A. Romanov
Russian Federal Nuclear Center – VNIITF, Snezhinsk, Russia

It is presented the results of the experimental investigation of the transitional layers width influence upon the evolution of turbulent mixing caused by the Rayleigh-Taylor instability. In experiments, mutual soluble liquids with density relation been equal to two were used. A transitional layer having continuous distribution of density arises in the region of liquids contact because of molecular diffusion. In experiments, it has been determined the dependence of the turbulent mixing evolution delay on both the initial perturbation region size and the characteristic width of the transitional layer.

Abstract No. E4

Improvements to Convergent Cylindrical Plasma Mix Experiments Using Laser Direct Drive

C. W. Barnes[1], S. H. Batha[1], A. M. Dunne[2], N. E. Lanier[1], G. R. Magelssen[1], T. J. Murphy[1], K. W. Parker[2], S. Rothman[2], J. M. Scott[1], and D. Youngs[2]
[1]*Los Alamos National Laboratory, Los Alamos, NM*
[2]*Atomic Weapons Establishment, Aldermaston, United Kingdom*

Experiments studying mix in a compressible, convergent, miscible, plasma system are being conducted on the OMEGA Laser at the Laboratory for Laser Energetics at the University of Rochester.[1,2] Thin-walled polystyrene cylinders 2.25-mm long and 0.86 mm inner diameter with foam inside are directly illuminated with 351-nm wavelength light from 50 laser beams in a 1-ns square laser pulse. The turbulence driven by the Richtmyer-Meshkov instability by shock passage across a density discontinuity mixes marker material that is radiographically opaque. Initial work using a high-density, high-opacity marker layer of gold between the plastic ablator and foam clearly demonstrated significant measurable mix width[2]. However, the high opacity of the gold prevented determination of a density profile in the mix region, and it was also overly sensitive to hydrodynamic effects at the end of the marker layer. Use of lower opacity marker material will be described and its impact on end effects and the measurements of mix density profile described.

1 C. W. Barnes *et al., Rev . Sci. Instrum.* **70** (1999) 471.
2 C. W. Barnes *et al.,* submitted to *Physical Review Letters* (2001).

Abstract No. E5

Mixing Between Two Compressing Cylinders

S. H. Batha[1], K. W. Parker[2], C. W. Barnes[1], A. M. Dunne[2],
N. E. Lanier[1], G. R. Magelssen[1], T. J. Murphy[1], S. Rothman[2],
J. M. Scott[1], and D. Youngs[2]
[1]*Los Alamos National Laboratory, Los Alamos, NM*
[2]*Atomic Weapons Establishment, Aldermaston, United Kingdom*

Foam-filled cylinders have been imploded by the OMEGA laser at the University of Rochester. A marker layer of heavier material is placed between the foam and the outside ablator. The marker layer is hydrodynamically unstable when a strong shock passes through both these interfaces and the marker layer material mixes into the foam and the ablator. These experiments thus measure mix in the compressible, convergent, miscible, strong-shock regime.

These experiments are being extended by placing a solid cylinder at the center of the foam, forming a set of concentric cylinders separated by foam. The initial shock converges on the central cylinder and then rebounds and expands. The shock is predicted to create even more mixing of the marker layer as it traverses the previously mixed region. We present experimental measurements of this configuration.

Abstract No. E6

Development of a Method for Studying the Interaction Between Shock Wave and a Flame Front

M. Bliznetsov[1], V. Dudin[1], S. Gerasimov[1], L. Houas[3], G. Jourdan[3], A. Logvinov[1,2], E. Meshkov[1,2], and Yu. Vlasov[1,2]

[1]*Russian Federal Nuclear Center - VNIIEF, Sarov, Russia*

[2]*SarPTI, Sarov, Russia*

[3]*IUSTI/CNRS, Université de Provence, Marseille, France*

Tomsk University has carried out research into explosive method for extinguishing the wild fires (A.M.Grishin, Kovalev Yu.M., 1994, Grishin, 1994, Grishin et al., 2000). This method has been experimentally checked but it is not currently used in practice. According to Grishin's hypothesis (A.M.Grishin, Kovalev Yu.M., 1994, Grishin, 1994), the explosive method for extinguishing the wild fires is based on "blowing out" the flame by a shock. There exists another idea (Meshkov, 1999) according to which this extinguishing is due to development of hydrodynamic instabilities. Experimental study of this method in natural conditions is rather complex, dangerous, and expensive. Hence, modeling this method in laboratory conditions is of interest. We report on results of an experimental study of developing such a method for interaction between shock and flame.

References

Grishin A.M., Babaev V.M., Gruzin A.D., Zverev V.G., Abaltusov V.E., Mamontov G.Ya. (1985). Meaning of extinguishing wild fires A.D. 1136811 USSR. Published 30.01.85. Bul.4

Grishin A.M., Kovalev Yu.M. (1989). Experimental and theoretical study of the interaction between explosion and crown fire. FGV, 6, pp. 72-79

Grishin A.M., Zima V.P., Mashovich A.Ya., Samoilov V.I. (2000). Experimental study of the interaction between a shock induced by point charges, and crowns. Proceedings of international conference "Common problems on mechanics and ecology", Tomsk University, pp.83-85

Meshkov E.E. (2000). Turbulent mixing associated with hydrodynamic instabilities in modern practical problems. Proceedings of international conference "Common problems on mechanics and ecology", Tomsk University, pp.156-158.

Abstract No. E7

The Influence of Scaling for Periodical Perturbations on Development of Turbulent Mixing on a Gas-Liquid Interface

M. Bliznetsov, E. Meshkov, N. Nevmerzhitsky, A. Nikulin, E. Sen'kovsky, and E. Sotskov
Russian Federal Nuclear Center – VNIIEF, Sarov, Russia

We report on results of experimental study of the influence of scaling for 3D periodical perturbations on dynamics of turbulent mixing on a gas-liquid interface, associated with R-T instability. The liquid was modeled with layers of a low-strength (= 0.01 MPa) water-solved gelatin jellies driven in a squared (40x40-mm) channel with helium compressed to 13 atm. The perturbations imposed on unstable surface had quadrilateral pyramidal structures with a height equal to the perturbation wavelength (=(0=0.25; 1; 2, 2.86 mm. The experimental results obtained in tests without imposed perturbations of a given shape are also presented. The acceleration of layers was of $3x10^4 m/s^2$. The obtained results show:

- When the perturbations are not originally given or when they have (=(0=0.25 on unstable surface, the turbulent mixing develops with an initial delay, and then it grows linearly as (l=dhl/d(2S)=0.12(0.025, where (l- intensity for penetration of light substance into heavy, hl- depth of the gas- into- jelly penetration, S - layer displacement,

- For (=(0=0.25; 1; 2, 2.86, the R-T instability grows simultaneously with the layer movement, and turbulent mixing has linear regime for light-into-heavy penetration (l=0.1(0.14. (l increases from 0.13 to 0.42 with growing the perturbation amplitude; hence, for the given range of initial periodical perturbations their amplitudes influence weakly on the rate of the light-into-heavy penetration, but sufficiently on the heavy-into-light.

Abstract No. E8

Compressible Vortex Rings

M. Brouillette and C. Hébert
Université de Sherbrooke, Quebec, Canada

We present the results of an experimental study aimed at characterising compressible and viscous effects on the generation and propagation of vortex rings. The overall aim of this study is to characterise basic vortical structures in the context of compressible turbulence, but these findings also have applications in the study of shock-vortex interaction, for example. In the context of the Richtmyer-Meshkov instability, these rings can be viewed as rapidly mushrooming spikes at moderate Atwood numbers.

The vortices are produced by the diffraction of a shock wave from the open end of the driven section of a specially-built shock tube. By varying the pressure ratio across the driver and driven sections we could control the strength of the incident shock wave. Also, by altering the length of the driver, we could modify the ejection velocity history, also known as the ejection velocity program, at the orifice end of the tube. Finally, by changing the diameter of the end orifice, we could change the size, i.e., Reynolds number, of the vortex ring. Our instrumentation comprised fast-response piezoelectric pressure transducers and flow visualisation was achieved with shadow and schlieren photography along with holographic interferometry.

A major difference between incompressible and compressible vortex ring formation is in the maximum circulation attained in the ring. Previous studies have found that the vorticity saturation threshold of incompressible vortex rings was not a strong function of the ejection velocity program; we found that this was not the case for compressible vortex rings. In the present study, we found that a higher normalised circulation was possible, for a given incident shock wave, with a continuous jet at the exit of the tube than with a rapidly attenuated jet.

The appearance of a shock wave within the recirculating region of the vortex ring is also strongly dependant on the amount of vorticity deposited within the ring. In fact, the onset of appearance of this shock wave and other shock and vortical features around the main vortex ring can now be related to vorticity deposition through the ejection velocity program.

Although the vortex formation mechanism of the present study is inherently compressible and non-linear, the propagation of these vortex rings is similar to that of incompressible rings reported in numerous previous studies. The principal compressibility effect is in the structure of the vortex core, which appears to exhibit a Reynolds number dependence.

Because of the wide range of viscous and convective scales present in this problem, experiments such as these can also pose an interesting challenge to direct numerical simulation in the context of compressible turbulence.

Abstract No. E9

Design of Flyer-Plate-Driven Compressible Turbulent Mix Experiments

R. P. Drake
University of Michigan, Ann Arbor, MI

In this work we consider the optimization of experiments that use flyer plates to study compressible turbulent mixing. There are now at least two types of flyer plates that can be used for such purposes. The recent advent of high-velocity (>20 km/s), solid state flyers on the Z machine at Sandia National Laboratories, along with the pending activation of x-ray backlighting, will make possible very clean experiments. In addition, any large laser can shock and accelerate a slab of material, producing a "plasma flyer" that can deliver energy and momentum to a desired target. If the laser is large enough (~ 1 kJ), then the plasma flyer can have sufficient lateral size to permit studies of mixing. Here we consider the problem of designing of an optimized experiment.

This poster will discuss the optimization of a flyer-driven experiment for either Rayleigh Taylor (RT) or Richtmyer Meshkov (RM) experiments. In RT experiments, one wants to decelerate an interface immediately after it is shocked (with minimum coasting time), and to move the interface as far as possible. In RM experiments, one wants to cause the interface to coast steadily after it is shocked, for the longest possible time. This poster will present an analysis and analytic relations that can guide the achievement of these goals, and hydrodynamic simulations showing what one can do using flyer plates on Z.

Abstract No. E10

Compressible Hydrodynamics on the Omega Laser, Motivated by Astrophysics

R. P. Drake[1], P. Keiter[1], K. E. Korreck[1], K. Dannenberg[1], H. A. Robey[2], T. Perry[2], J. O. Kane[2], B. A. Remington[2], R. J. Wallace[2], O. A. Hurricane[2], D. D. Ryutov[2], J. Knauer[3], R. Teyssier[4], A. Calder[5], R. Rosner[5], B. Fryxell[5], D. Arnett[6], Y. Zhang[7], J. Glimm[7], N. Turner[8], J. Stone[8], R. McCray[9], J. Grove[10]

[1]*University of Michigan, Ann Arbor, MI*
[2]*Lawrence Livermore National Laboratory, Livermore, CA*
[3]*Laboratory for Laser Energetics, University of Rochester, Rochester, NY*
[4]*Commissariat à l'Energie Atomique, Saclay, France*
[5]*University of Chicago, Chicago, IL*
[6]*University of Arizona, Tuscon, AZ*
[7]*State University New York Stony Brook, Stony Brook, NY*
[8]*University of Maryland, College Park, MD*
[9]*University of Colorado, Boulder, CO*
[10]*Los Alamos National Laboratory, Los Alamos, NM*

Compressible turbulent mixing is an inherent feature in supernovae, supernova remnants, and related systems. Our scientific team collaborates to produce, in the laboratory, hydrodynamic mechanisms that are important for the evolution of such systems. These experiments are designed to be well scaled from astrophysical systems to the laboratory. This talk will provide an overview of this work and will highlight our most recent results. Our work is motivated by the specific fact that high-resolution 2D and 3D numerical simulations have proven unable to reproduce certain aspects of observations of supernova SN 1987A, and by the general need to provide experimental tests of modeling of hydrodynamic systems. The experiments take place on the Omega Laser at the Laboratory for Laser Energetics, University of Rochester. We have explored the coupling between unstable interfaces, instability growth in a diverging system, the comparison of 2D and 3D systems, the comparison of single mode and multimode systems, and the production and diagnosis of a radiative-precursor shock. In each of these cases, the experiment begins by using the laser to drive a strong shock into a target material. This produces a hydrodynamic initial state that can be modeled by any astrophysical or laboratory hydrodynamics code. The shock subsequently interacts with other structures in the target, which we design in order to explore a specific physical issue. In each case, we then compare the results of the experiments with those of computer simulations. The US DOE and NASA supported this work.

This work was performed under the auspices of the U.S. Department of Energy by the University of California Lawrence Livermore National Laboratory under contract No. W-7405-Eng-48.

Abstract No. E11

Growth of Perturbations on Metals Interface at Oblique Collission with Supersonic Velocity of Contact Point Motion

O. B. Drennov, A. L. Mikhaylov, P. N. Nizovtsev, and V. A. Raevskii
Russian Federal Nuclear Center – VNIIEF, Sarov, Russia

By now the subsonic mode of collision is studied in detail. In the supersonic mode, when shock waves arrive to the contact point, jet formation is impossible. It is assumed that perturbations growth at metals interface is also impossible. It is obtained in our experiments that perturbations are formed in the mode of supersonic jetless oblique collision at the metals interface. Analytical consideration of the problem determined existence of the critical value of Mach number characterizing transition from the stability area to the instable area. Numerical calculations with use of the two-dimensional Lagrange technique showed presence of an area with large gradient of velocity and high intensity of strains near the contact point. It results in fulfillment of the conditions for growth of Kelvin-Helmholtz instability. Comparison of calculated and experimental values of amplitude of occurred perturbations showed a rather good agreement between them.

Abstract No. E12

An Experimental Study of the Effect of Shock Proximity on the Richtmyer-Meshkov Instability at High Mach Number

S. G. Glendinning, D. G. Braun , M. J. Edwards, W. W. Hsing, B. F. Lasinski, H. Louis, J. Moreno, T. A. Peyser, B. A. Remington, H. F. Robey, E. J. Turano, C. P. Verdon, and Y. Zhou
Lawrence Livermore National Laboratory, Livermore, CA

The effect of shock proximity on the non-linear evolution of Richtmyer-Meshkov instability of a sinusoidal perturbation at high Mach number was examined on experiments at the Omega laser at the Laboratory for Laser Energetics, University of Rochester. We will present results from experiments using a laser drive of about $3X10^{13}$ W/cm^2 and targets made with polycarbonate as a pusher and carbon foam (ρ=0.1 g/cc) as a payload. This provided an incident shock of Mach number ~10, a nearly constant interface velocity for 10 ns, and a transmitted shock to interface velocity ratio of about 1.22. Wavelengths studied varied between 50 μm and 150 μm. Different amplitudes were chosen to allow linear growth, nonlinear growth, or proximate-shock growth to dominate.

This work was performed under the auspices of the U.S. Department of Energy by the University of California Lawrence Livermore National Laboratory under contract No. W-7405-Eng-48.

Abstract No. E13

Mix Experiments using a Two Dimensional Convergent Shock Tube

D. A. Holder, C. Barton, and A. V. Smith
Atomic Weapons Establishment, Aldermaston, United Kingdom

This paper reports on the first Richtmyer Meshkov instability mix experiments using the improved version of the AWE detonation driven Convergent Shock Tube (CST). Results from an early prototype presented at the 7th IWPCTM demonstrated concept feasibility, but also the need for refinement of the multi-point ignition process that critically controlled cylindricity of the generated shock. This paper includes a brief description of the modifications undertaken to achieve the required performance; also images recording the origin of the detonation wave formation and combination process. The CST facility has been created to allow an extension of earlier RMI studies using a conventional linear shock tube at low Mach number to two-dimensional studies at Mach number 2 – 3.

The current configuration is as shown, with height (internal) 1.02m: depth 50mm: apex angle 30^0. Detonation of an oxy-acetylene gas mixture by 30 sparkplugs drives a cylindrically converging shock of order 10 bar into a dense gas region, bounded by cylindrically curved microfilm membranes, supported by fine wire meshes. Maximum compression of the dense gas during its motion into the apex region is ~40 for sulphur hexafluoride, or optionally, ~20 for xenon.

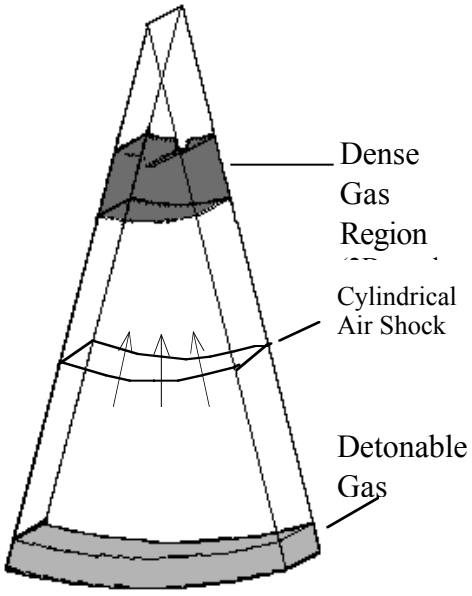

Visualisation is currently by shadowgraphy using a pulsed copper vapour laser and drum camera. This provides a timed sequence of images of the mixing development over the dense gas region. Results from basic experiments with two unperturbed interfaces will be presented, with comparisons to TURMOIL3D code calculations.

Additionally results will be shown from the first experiments to feature a perturbation superimposed on one interface. These will serve as a forerunner to the proposed investigations in 2D geometry of a series of perturbation profiles previously investigated using the AWE linear shock tube [1]. The results will be used to validate 2D turbulent mix models.

Proposals will also be included for incorporating improved diagnostic techniques including the laser sheet technique with ICCD camera recording to facilitate image analysis and derivation of quantitative data.

PACS No.: 47.20.Ma

Abstract No. E14

Rayleigh-Taylor Instability at a Tilted Interface in Incompressible Laboratory Experiments and Compressible Numerical Simulations

J. M. Holford[1], S. B. Dalziel[1], and D. Youngs[2]
[1]*Cambridge University, Cambridge, United Kingdom*
[2]*Atomic Weapons Establishment, Aldermaston, United Kingdom*

An important feature of Rayleigh-Taylor (RT) instability is the significant amount of molecular mixing that occurs, due to the small scales that are created. Molecular mixing is important both as a control on the rate of reaction between chemically active species, and because it creates a sink for available energy by allowing the background potential energy of the flow to increase. RT instability is the most efficient known mixing process, and laboratory measurements show that, over the whole flow evolution, up to 40% of the initial available energy increases the potential energy of the background stratification, while the balance is lost to viscous dissipation.

Regions of locally unstable stratification are frequently created in perturbed stratified flows, for example in breaking gravity waves and shear-driven billows. However, in these naturally occurring statically unstable regions, the initial conditions are far from the idealised classical RT instability. In this study, we investigate the mixing that occurs in RT instability at an interface that is initially tilted at an angle to the horizontal, introducing a competition between the local overturning of RT instability and a large-scale overturning within the whole domain.

RT instability is initialised in a water tank in the laboratory by withdrawing a barrier separating dense salt water above from fresh water below. Measurements of both the density distribution and in-plane velocity field are made in a vertical slice through the centre of the tank. For the first time, measurements of the instantaneous efficiency of mixing are made. The instantaneous efficiency at early times can be higher than the cumulative efficiency, with the rate of increase of potential energy of the background stratification reaching 50% of the rate of decrease of available energy. The reduction in the cumulative mixing efficiency as the angle of the initial interface increases is quantified.

The experiments have been modelled numerically using the compressible code TURMOIL3D. The initial conditions are carefully chosen to model the incompressible experiments as closely as possible. Analyses of energy and concentration fluctuation spectra are used to understand the mixing and dissipation processes. The combination of experimental and computational modelling is shown to be useful both as a validation of the numerical methods and as a tool for understanding the basic dynamics of the flow.

Abstract No. E15

Study of Diverging and Converging Spherical Shock Waves Induced by Micro Explosives and their Interaction with Product Gases

S. H. R. Hosseini and K. Takayama
Tohoku University, Sendai, Japan

The paper reports an experimental study of production and propagation of spherical shock waves. In order to quantitatively observe spherical shock waves and the flow field behind them, an aspheric spherical transparent test section was designed and constructed. This 150 mm inner-diameter aspheric lens shaped test section permits the collimated visualization laser beam to traverse the test section parallel and emerge parallel. Spherical diverging shock waves were produced at the center of the spherical test section. In order to generate shock waves, irradiation of a pulsed Nd:YAG laser beam on micro silver azide pellets were used. The weight of silver azide pellets ranged from 5 to 20 mg, with their corresponding energy of 9 to 36 J. Pressure histories at different points over the test section were measured to validate production of uniform shock waves. After reflection of spherical shock wave from the test section, a converging spherical shock wave was produced and its interaction with the interface of explosive product gas was studied. Double exposure holographic interferometry and time resolved high speed photography were used for flow visualization. The whole sequence of diverging and converging spherical shock waves propagation and their interaction with product gases were observed.

PACS No.: 47.40.Nm

Abstract No. E16

Interaction of Converging Shock Waves With Cylindrical Heavy Gas Interfaces in an Eccentric Arrangement

S. H. R. Hosseini and K. Takayama
Tohoku University, Sendai, Japan

Paper reports a study on interaction of converging and diverging cylindrical shock waves in air with non-uniform gaseous media and resulting Richtmyer-Meshkov instability. An annular vertical co-axial diaphragmless shock tube was used to produce converging cylindrical shock waves. Cylindrical soap bubbles filled with SF_6 heavy gas were placed out of the geometrical center of shock tube's test section. As a result of asymmetry between converging cylindrical shock waves and cylindrical interfaces, a complex wave motion and interaction was produced. Pressure histories at different radii were measured during the converging and diverging shock wave propagation in the test section after interaction. A strong secondary shock wave focusing in the SF_6 test gas with a high peak overpressure was observed. Double exposure holographic interferometry was used for flow visualization. The time evolution of turbulent mixing zone between the air/ SF_6 light/heavy gases and interfacial deformations were quantitatively studied. After the secondary shock wave focusing in the SF_6 a relatively strong jet, which was penetrating to the air in the direction of geometrical center, was produced.

PACS No.: 47.40.Nm

Abstract No. E17

From Linear to Turbulent Stages of the Richtmyer-Meshkov Instability Development in a Large Cross Section Shock Tube

L. Houas[1], G. Jourdan[1], L. Schwaederlé[1], and E. E. Meshkov[2]
[1]*IUSTI, CNRS, Université de Provence, Technopôle de Château-Gombert, Marseille, France*
[2]*Russian Federal Nuclear Center – VNIIEF, Sarov, Russia*

The aim of the present investigation is to contribute to the understanding of the turbulence transition phases by the help of the development of the Richtmyer-Meshkov instability (RMI). In this way, we have built a new shock tube which allows to follow a Richtmyer-Meshkov instability induced mixing from its beginning to the fully turbulent developed stage with both control and knowledge of the initial conditions. Up today, all experiments developed to study the RMI have been focussed on the observation of the growth of the initial perturbations in the linear and the non-linear regimes and not far, or the investigation of the turbulent phase without knowing the real initial conditions, i.e. when the shock wave interacts with the thin membrane which initially separates the two fluids of different densities. Thus, the new shock tube has first a large square cross section (20 cm by 20 cm) in order to prevent from wall effects. Furthermore a suitable experimental chamber permits to observe and control the initial perturbations we impose to the thin material interface which initially separates the two gases expected to mix together after the incident shock wave accelerates their common interface. The total length of the shock tube is of 7 m, the experimental chamber is 50 cm total length and its field of view starts from 4 cm before the initial position of the interface to 46 cm after. To follow the development of the initial perturbations and the mixing of the two gases, we have carried out a Mie scattering laser sheet technique. A 50 Khz Oxford copper vapor laser beam is transformed as a laser sheet before crossing the experimental chamber in its length direction. This ultra rapid laser is coupled with a 321 Cordin model high speed camera, which together allow to record, during the same run, about 100 plane frames of the experiment spaced by 100 to 20 µs depending on the laser frequency (from 10 to 50 Khz). The maximum recorded image rates is of about 50,000 pictures per second. Moreover, a suitable rotating mirror device accurately coupled and synchronized with the laser-camera system, permits to translate, during the same run, the laser sheet from the center axis of the experimental chamber to its walls in order to obtain a 3D visualization of the phenomenon. The gas initially present in the experimental chamber is seeded with water vapor particles. The test gases are air/He, air/Ar and air/Kr in order to investigate the cases where the shock wave passes from a heavy to a light gas and vice-versa. The initial pressure is 1 atm. and the shock wave Mach number in air is of 1.3. The principle of the experiment and a view of the experimental set up are shown on Figure 1. We are now running the first experiments and we hope to present in the full paper the first results illustrating, during the same run, the development of the different

stages of the instability, the transient phases as well as some information on the fully turbulent regime.

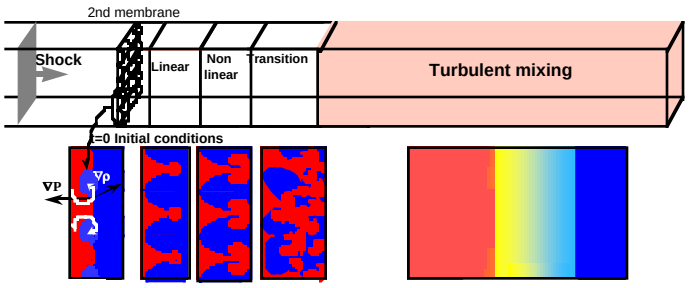

(a)

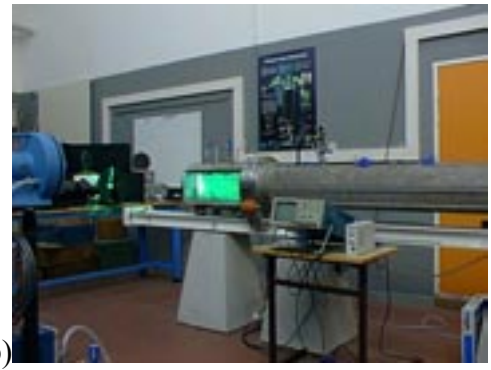

(b)

Fig. 1: Principle of the experiment (a) and view of the new large cross section shock tube of IUSTI coupled with a Copper vapor Mie scattering laser sheet technique (b).

Abstract No. E18

PLIF Flow Visualization of a Shock-Accelerated Air/SF_6 Interface

J. W. Jacobs and V. V. Krivets
University of Arizona, Tucson, AZ

A vertical shock tube is used to study the Richtmyer-Meshkov instability of a membraneless Air/SF_6 interface. The two gases enter the shock tube at opposite ends of the driven section and are allowed to exit through slots in the shock tube wall to produce a flat, slightly diffuse interface in the test section. A sinusoidal perturbation is then given to the interface by oscillating the shock tube in the lateral direction to produce standing waves. Planar laser induced fluorescence (PLIF) is used to visualize the flow by seeding the air with acetone vapor and illuminating it with a sheet of light produced by a pulsed Nd:YAG laser. The resulting fluorescent signal is then recorded using a cooled CCD camera. Images obtained from these experiments show very clearly the development of the instability far into the nonlinear regime in which the interface is contorted into pronounced mushroom structures. New results using M = 1.3 shock waves will be presented which clearly show the transition to turbulence in this flow at late times. The transition process begins with the development of Kelvin-Helmholtz instability on the vortex spirals. After formation, the initially coherent Kelvin-Helmholtz pattern very quickly decays into turbulence. Eventually the turbulence, which is initially confined to the vortex cores, begins to erode the remainder of the mushroom structures. Experiments will also be presented that study the effects of reshock on different stages of the instability. In these experiments a false wall is used to vary the distance between the initial interface location and the end wall in order to control the arrival time of the reflected shock wave.

Abstract No. E19

Laser-Based High Pressure, High Strain-Rate Solid-State Experiments

D. H. Kalantar[1], J. Belak[1], J. D. Colvin[1], M. Kumar[1], K. T. Lorenz[1], K. O. Mikaelian[1], S. Pollaine[1], B. A. Remington[1], S. V. Weber[1], L. G. Wiley[1], A. M. Allen[2], A. Loveridge-Smith[2], J. S. Wark[2], and M. A. Meyers[3]

[1]*Lawrence Livermore National Laboratory, Livermore, CA*

[2]*Oxford University, Oxford, United Kingdom*

[3]*University of California at San Diego, San Diego, CA*

We have performed a high pressure solid state instability growth experiment using an x-ray ablative drive on the Nova laser [1]. In this experiment, an Al foil is shock compressed to a peak pressure of 1.8 Mbar with a sequence of shocks. A preimposed sinusoidal modulation grows by the Rayleigh-Taylor instability. At early time, the growth is nearly fluid-like, but it is suppressed at late time. The growth of the instability provides information about the strength of the metal at high pressure [2, 3]. In order to model this experiment, we invoke softening by shear bands and recovery of strength following dissipation of the heat associated with the localized shear bands.

In order to develop a lattice level understanding of response of these samples at high pressure, we perform dynamic x-ray diffraction of shocked materials to verify the state of the material under compression. In these experiments, we record x-rays diffracted from orthogonal lattice planes of shock compressed single crystal Cu. The shift of the Bragg diffraction from these orthogonal planes confirms that the lattice undergoes a 3D compression. By comparison, Si is observed to respond with uniaxial compression. [4]

We are also developing shocked sample recovery techniques to characterize the residual deformation microstructure. This residual structure is studied by optical and electron microscopy techniques.

Results of the RT, diffraction, and recovery experiments will be discussed.

---

[1] D. H. Kalantar, B. A. Remington, J. D. Colvin, *et al*, Phys. Plasmas **7**, 1999 (2000).
[2] J. F. Barnes, P. J. Blewett, R. G> McQueen, *et al*, J. Appl. Phys. **45**, 727 (1974).
[3] A. I. Lebedev, P. N. Nizovtsev, V. A. Raevskii, V. P. Solov'ev, Phys. Dokl. **41**, 328 (1996).
[4] A. Loveridge-Smith, A. Allen, J. Belak, *et al*, Phys. Rev. Letters **86**, 2349 (2001).

This work was performed under the auspices of the U.S. Department of Energy by the University of California Lawrence Livermore National Laboratory under contract No. W-7405-Eng-48.

Abstract No. E20

RFNC-VNIITF Multifunctional Shock Tube to Investigate the Evolution of Instabilities in Nonstationary Gas Dynamic Flows

Yu. A. Kucherenko, O. E. Shestachenko, S. I. Balabin, and A. P. Pylaev
Russian Federal Nuclear Center – VNIITF, Snezhinsk, Russia

In the paper, at the shock tube operation in three modes, the parameters of the flows in the RFNC-VNIITF were given.

In the first mode, in the shock tube the stationary shock waves are formed. This makes it possible to investigate the evolution of the Richtmyer-Meshkov instability and turbulence.

In the second mode, in the shock tube a nonstationary shock wave is formed that makes it possible to carry out the investigation of the behaviour of the contact boundaries between different density gases when there are conditions for the evolution of the Rayleigh-Taylor and Richtmyer-Meshkov instabilities.

In the third mode, in the shock tube a compression wave is formed. This makes it possible to investigate the evolution of the Rayleigh-Taylor instability and turbulence.

Abstract No. E21

Planar Laser Sheet Visualization and Laser Doppler Velocity Measurements in Shock-Induced Turbulent Mixing Zones

A. Lassis, P. Montlaurent, C. Rayer, and J.-F. Haas
Commissariat à l'Energie Atomique, Bruyères-le-Châtel, France

We plan to present measurements on gaseous turbulent mixing arising from the Richtmyer-Meshkov instability (RMI) in a vertical shock tube of driver (below) and driven (above) sections lengths 1 m and 4-5 m respectively and of square internal cross section throughout (13 cm by 13 cm). In its present configuration, the maximum driver pressure is 8 bar and the driven section is initially at local atmospheric pressure (1 bar), thus the shock tube is limited to Mach numbers of about 1.5 maximum. The main diaphragm is made of two plastic layers (kapton) with conducting wires between them. In a typical low Mach number experiment, the initial pressure of air in the driver is set at 3 bar, and a Mach 1.2 shock is driven in the test section air at a controlled time by Joule heating the wires and locally melting (and weakening) the kapton.

We will characterize the mixing arising when the shock wave (propagating upwards in the z direction) accelerates a planar horizontal contact surface made of a thin (0.5 μm) nitrocellulose membrane laid against a thin stainless steel wire mesh (wire diameter and spacing 1010 and 80 μm). The purpose of the film-mesh combination is to force the small scales (1 by 1 mm in the x and y directions) of the RMI, thus insuring an early transition to turbulence of a thin planar mixing zone after shock passage. The gas pairs of initial interest are SF6-air and air-SF6. As it was several years ago, our primary goal is to provide an experimental data base (density structure and turbulent kinetic energy) for verification and validation of turbulent mixing models (1) imbedded in one- or two-dimensional hydrodynamic codes. The same laser-doppler velocimeter will be used (Dantec two component system) for the measurement of the kinematic parameters of the mixing zone. Compared to the earlier effort performed in a shorter (3.8m) and narrower shock tube (cross section 8 by 8 cm), we expect to improve the quality of the flow because the wall

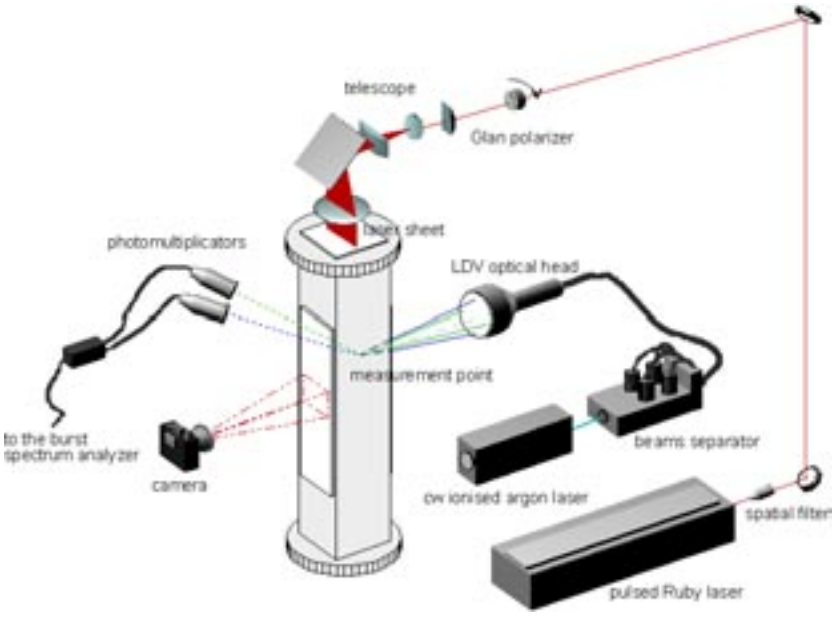

effects will be much less disruptive. We are also preparing a planar visualization system using a short pulse ruby laser to produce a light sheet (thickness 0.5 to 1 mm) entering the shock tube from the top end-plate. Thus we hope to measure the local structure of the mixing zone without the optical signature from wall-located mixing which perturbed our earlier visualizations in the smaller tube (2).

References :

1. D. Souffland et al., Measurements and Simulations of the Turbulent Energy Levels in Mixing Zones Generated in Shock Tubes. pp. 486-491 in the proceedings of the 6th IWPCTM, Marseilles, June 1997, Jourdan and Houas eds.
2. I. Galametz at al., Visualization of shocked mixing zones using differential interferometry and X-rays. pp. 178-184 in the proceedings of the 5th IWPCTM, Stony Brook, July 1995, Young, Glimm and Boston eds., World Scientific.

Abstract No. E22

Hydrodynamic Instabilities at a Shock Accelerated Bubble Gas-Gas Interface

G. Layes[1], G. Jourdan[1], P. Roualdes[2], and L. Houas[1]
[1]*IUSTI, CNRS, Université de Provence, Technopôle de Château-Gombert, Marseille, France*
[2]*Centre d'Etudes de Gramat, Gramat, France*

The aim of the present work is to investigate the interaction of a plane shock wave with one gas bubble within another gas of different density in order to better understand the Richtmyer-Meshkov instability process in spherical geometry. These experiments are performed in the new 500 mm circular cross section shock tube installation of IUSTI (donation of DGA Gramat). It is a 12 m total length shock-tube with a 2 m high pressure chamber long and an experimental chamber total field of view of 475 mm long by 320 mm high. The shock tube is coupled with a Schlieren high speed camera system and PCB piezoelectric transducers are flush mounted on the shock tube side walls for both recording the pressure evolutions and triggering the acquisition device.

Spherical volumes of gas (He, Ar or Kr) with density, and sound speed, differing from that of the surrounding atmosphere (air) are accelerated by a relatively weak shock wave. The incident shock wave Mach number in air is around about 1.2. From successive Schlieren pictures (up to 30 000 frames per second), we hope to investigate the hydrodynamic interface instability and the bubble distortion. Finally, we plan to generate several neighboring bubbles in the experimental chamber in order to study the bubble coupling during their acceleration.

Abstract No. E23

Experimental and Numerical Study of Shock Wave–Bubble Interaction

K. Levy[1,2], O. Sadot[1,2], D. Oron[1,2], Y. Srebro[2], Y. Elbaz[2], A. Yosef-Hai[1,2],
G. Ben-Dor[3], and D. Shvarts[1,2]
[1]*Ben-Gurion University, Beer-Sheva, Israel*
[2]*Nuclear Research Center - Negev, Israel*

This work presents a study of the interaction of a shock wave with a spherical bubble, which results in the formation of vortex rings and a jet. Similar studies which presents various stages of the interaction evolution were published in [1-5].

In the present work two configurations were studied in which a spherical bubble of SF6 (Heavy bubble) or He (light bubble) was imbedded in the shock tube at ambient conditions. The evolution of the flow due to the interaction of the shock wave with the bubble was followed experimentally and numerical. The results reveal that in the first case a jet is formed due to a converge shock wave towards the bubble center, which formed high-pressure region on the bubble axis that forced the heavy fluid forward. In the second case a vortex ring is formed around the bubble creating a region of high pressure in the heavy gas forcing the heavy fluid forward and forming a jet. A good agreement was found comparing the results of the experiments to those of the simulations.

References

1. Quirk et al., J. Fluid Mechanics, 318, pp. 129 (1996).
2. Picone et al., J. Fluid Mechanics, 189, pp. 23 (1988).
3. Yang, et al., J. Fluid Mechanics, 258, pp.217 (1994).
4. Haas et al., J. Fluid Mechanics, 181, pp. 41 (1987).
5. Smith et al. in the proceeding of the MIX 91 workshop.

Abstract No. E24

Laser-Driven Near Isentropic Compression of an Aluminum Flyer Plate

K. T. Lorenz, D. Kalantar, J. Edwards, J. D. Colvin, and B. Remington
Lawrence Livermore National Laboratory, Livermore, CA

A new design for producing a ramped pressure wave for the study of material response in solid media under nearly isentropic compression conditions will be discussed. A plasma source, initiated from laser heating of a low-density carbon foam, unloads across a vacuum gap onto an Al target to provide a ramped, shockless, pressure load. Experiments using HE to create shockless drives have previously been demonstrated by Barnes, *et al*. [1] and Levedev, *et al.* [2,3]. This type pressure drive is coupled to targets having modulated surfaces for the study of material response and strength. The current design configuration of our near isentropic drive will provide peak pressures and strain rates on order of 0.4Mbar and $10^6 - 10^7 sec^{-1}$, respectively. Initial experiments using VISAR, x-ray radiography and thin Al foils will examine both the planarity and the time-dependent nature of the pressure loading in the target. Recent experimental results and as well as experimental simulations scaled to the laser drive conditions will be presented.

[1] J.F. Barnes, P.J. Blewett, R.G. McQueen, K.A. Meyer and D. Venable, *J. Appl. Phys.* **45**, 727 (1974).

[2] A.I. Lebedev, P.N. Nizovtsev, V.A. Rayevsky, in the *Proceedings of the 4th International Workshop on the Physics of Compressible Turbulent Mixing*, 29 March – 1 April, Cambridge, England (Cambridge University Press, Cambridge, 1993), p. 81.

[3] A.I. Lebedev, P.N. Nizovtsev, V.A. Raevskii and V.P. Solov'ev, *Dokl. Akad. Nauk.* **349** (MAIK Nauka / Interperiodica Publishing, Moscow July 1996), pp. 332-4. Translation: *Phys. Dokl.* **41**, 328 (1996).

This work was performed under the auspices of the U.S. Department of Energy by the University of California Lawrence Livermore National Laboratory under contract No. W-7405-Eng-48.

Abstract No. E26

Single-Mode Incompressible Richtmyer-Meshkov Instability Experiments

C. E. Niederhaus[1] and J. W. Jacobs[2]
[1]*NASA Glenn, Cleveland, OH*
[2]*University of Arizona, Tucson, AZ*

The Richtmyer-Meshkov instability of a moderate Atwood number, miscible, two-liquid system is experimentally investigated. The instability is generated by dropping a fluid container onto a coil spring, producing a nearly impulsive acceleration followed by a period of freefall. The initial density interface has a well-defined, 2-D, single-mode sinusoidal perturbation generated by laterally oscillating the fluid container. The perturbation quickly inverts and then grows in amplitude after undergoing the impulsive acceleration. Planar laser-induced fluorescence is used for flow visualization, providing clear views of the fluids far into the nonlinear regime. Disturbance amplitudes are measured and compared to theoretical predictions in the linear, weakly nonlinear, and nonlinear regimes. The effects of Reynolds number (based on circulation) on the vortex core evolution and overall growth rate of the interface are also investigated. In addition, an instability in the vortex cores is observed and criteria established for its occurrence.

Abstract No. E27

Experimental Study of a Strongly-Shocked Gas Interface with Visualized Initial Conditions

J. G. Oakley, M. H. Anderson, and R. Bonazza
University of Wisconsin at Madison, Madison, WI

The Richtmyer-Meshkov (RM) instability is studied for a strongly shocked gas-gas interface in the nonlinear regime. The impulsive acceleration of the interface by a shock wave imparts a velocity to the interface and baroclinic vorticity ($\nabla\rho \times \nabla p$) causes the amplitude of a single mode perturbation to grow. Experiments for studying the compressible, turbulent mixing of a gas-gas interface are conducted in a shock tube. The shock tube is oriented vertically (9.3 m high), has a large square cross-section (25.4 cm), is modular (for studying interfaces of different ages) and has a structural capacity of 20 MPa [1]. The driven and test section gases are initially separated with a thin copper plate that has been formed with a sinusoidal perturbation along its length. The sine wave plate has three wavelengths of λ=38.1 mm and an amplitude, a_0=3.2 mm which forms an initial condition in the linear to nonlinear transition with a wavelength amplitude product of ka_0=0.52. The sine wave plate is retracted from the shock tube forming a membraneless, single-mode perturbation between the driven and test gases. Using a heavy-above-light gas configuration, the Rayleigh-Taylor (RT) instability develops and the perturbation amplitudes grow in time forming the initial condition for the RM experiment. A continuous wave laser is used in the interface section to illuminate the interface, and the RT instability is imaged using a 256x256 pixel array, 8-bit CCD camera framing at 100 fps. The test gas is seeded with smoke particles (~0.5 μm) and Mie scattering is used to visualize the interface the two interface gases. After acceleration by the planar shock wave, the interface travels down the shock tube and is imaged in the test section using a pulsed YAG laser and 1024x1024 pixel array, 16-bit CCD camera. One post-shock image is obtained per experiment. The experimental images are processed to determine the initial and post-shocked perturbation amplitudes. The experimental results are compared with linear and nonlinear RM theories. The gas pair combination CO_2-air is studied in the strongly shocked regime, M=2.90.

[1] Anderson, M.H., B.P. Puranik, J.G. Oakley, P.W. Brooks and R. Bonazza, "Shock tube Investigation of Hydrodynamic Issues Related to Inertial Confinement Fusion," *Shock Waves*, **10**(5), pp. 377-387, 2000.

Abstract No. E28

Experimental Investigations of the Self-Similar Mixing Mode of Different Density Gases in the Earth's Gravitational Field

Yu. A. Kucherenko, O. E. Shestachenko, Yu. A. Piskunov,
E. V. Sviridov, V. M. Medvedev, and A. I. Baishev
Russian Federal Nuclear Center – VNIITF, Snezhinsk, Russia

At the installation OSA the experiments on the investigation of the self-similar mixing mode of different density gases in the Earth's gravitational field were performed. When so doing the heavy gas was placed over the light one. By means of the specter-diaphragm the gases were separated. At some instant of time the specter-diaphragm was quickly ruptured into small-scale fragments under the action of the external force. At the formed contact boundary of two different density gases the Rayleigh-Taylor instability and the unstationary zone of turbulent mixing were evolved.

For three values of Atwood numbers the experiments were carried out. In the experiments the trajectories of the mixing fronts in the light and heavy gases were registered. The mixing asymmetry coefficient and the constant alpha specifying the nondimensional mixing rate were determined.

Abstract No. E29

Modeling Laser Material Strength Experiments

S. Pollaine[1], D. Kalantar[1], B. Remington[1], J. Belak[1], J. D. Colvin[1], J. Edwards[1], R. Minich[1], K. O. Mikaelian[1], K. T. Lorenz[1], S. V. Weber[1], L. G. Wiley[1], D. Paisley[2], A. Hauer[2], J. S. Wark[3], A. Loveridge[3], A. M. Allen[3], T. R. Boehly[4], and M. A. Meyers[5]

[1]*Lawrence Livermore National Laboratory, Livermore, CA*
[2]*Los Alamos National Laboratory, Los Alamos, NM*
[3]*Oxford University, Oxford, United Kingdom*
[4]*Laboratory for Laser Energetics, University of Rochester, Rochester, NY*
[5]*University of California at San Diego, San Diego, CA*

We have done many experiments on the Omega and Janus lasers to measure material strength and other properties of Al, Si and Cu at high pressures (100 kb – 1 Mb) and strain rates (1.e5 – 1.e8). These experiments are diagnosed by VISAR (velocity measurement), x-ray diffraction and material recovery. We simulate these experiments with the Steinberg-Guinan constitutive model that includes shear strength, yield and melting temperature as a function of pressure and temperature.

This work was performed under the auspices of the U.S. Department of Energy by the University of California Lawrence Livermore National Laboratory under contract No. W-7405-Eng-48.

Abstract No. E30

Experiments and Simulations of Instabilities in a Shock-Accelerated Gas Cylinder

K. Prestridge[1], C. A. Zoldi[1,2], P. Vorobieff [3], P. M. Rightley, and R. F. Benjamin[1]
[1]*Los Alamos National Laboratory, Los Alamos, NM*
[2]*State University New York, Stony Brook, Stony Brook, NY*
[3]*University of New Mexico, Albuquerque, NM*

The interaction of a planar (M=1.2) shock with a heavy-gas SF6, round cylinder surrounded by air produces strong vorticity, driven by the shock wave's pressure gradient interacting with density gradients at the air/SF6 interface. The growth of the cylinder is measured using six images of the density profiles of each experimental event, unlike earlier studies, which captured only one image per event. The velocity field is measured at one time using Particle Image Velocimetry (PIV). We also present two-dimensional computational simulations, using the RAGE code, which utilize the actual initial conditions measured in the experiment. The simulation has the same spatial resolution as the experimental diagnostics, and for the first time, the width of the computational domain has been matched to that of the experiment, allowing us to consider sidewall effects. Experimental images show an instability growth rate somewhat higher than the results of the RAGE simulation. Velocity fields measured experimentally qualitatively agree with simulations, but the quantitative difference in velocity magnitudes is substantial.

Abstract No. E31

Experimental Study into Rayleigh-Taylor Turbulent Mixing Zone Heterogeneous Structure

Yu. A. Kucherenko, A. P. Pylaev, V. D. Murzakov, A. V. Belomestnih, V. N. Popov, and A. A. Tyaktev
Russian Federal Nuclear Center – VNIITF, Snezhinsk, Russia

The heterogeneous structure study has been performed by means of a "light-sheet" technique at the SOM gas-dynamic accelerator. The investigated system consisted of three layers of different density liquids. For leading out the information from the mixing zone inner region illuminated by the "light-sheet", visualizing particles were seeded into one of the liquids. The visualizing particles, which got into the "light-sheet", diffused light, and at the same time photo images of the liquid fragments, contained the visualizing particles, were formed by a light-sensitive receiver. For the error reduction refractive indexes of all the three liquids were equalized. A special test has been conducted for determining of measurements inaccuracy. Experiments have been performed for two values of acceleration of artificial field of gravity. Distributions of liquid fragments sizes are showed in the form of bar charts for different moments of time.

Abstract No. E32

Measurements of Turbulence Correlations in Low Atwood Number Rayleigh-Taylor Mixing

P. Ramaprabhu and M. J. Andrews
Texas A & M University, College Station, TX

Simultaneous measurement of velocity and density fields in a statistically-steady, low Atwood number (~ 10^{-3}), Rayleigh-Taylor experiment have been made. The experiment allows long data collection times and thus extensive spectral characterization. The method used is referred to as Particle Image Velocimetry-Scalar (PIV-S), and is a variant of the PIV technique. The PIV-S method uses different concentrations of particles to mark fluids of different densities. Tracking the motion of individual particles yields velocity measurements, while local particle concentrations gives density measurements. Two-dimensional fields of $\langle \rho'^2 \rangle$, $\langle u'^2 \rangle$, $\langle v'^2 \rangle$, $\langle u'v' \rangle$, $\langle \rho'u' \rangle$, and $\langle \rho'v' \rangle$ correlations, with associated power spectra will be presented. The density measurements compare well with corresponding temperature data from thermocouple experiments.

Abstract No. E34

Experimental Study of the Interaction of a Strong Shock with a Spherical Density Inhomogeneity

H. F. Robey[1], T. S. Perry[1], R. I. Klein[1, 2], J. A. Greenough[1], J. O. Kane[1], and T. R. Boehly[3]

[1]*Lawrence Livermore National Laboratory, Livermore, CA*

[2]*University California at Berkeley, Department of Astronomy, Berkeley, CA*

[3]*Laboratory for Laser Energetics, University of Rochester, Rochester, NY*

Laser-driven experiments conducted on the Omega Laser are described which probe the interaction of a very strong shock with a spherical density inhomogeneity. The interaction is viewed simultaneously from two orthogonal directions. This enables visualization of both the initial distortion of the sphere into a double vortex ring structure as well as the onset of an azimuthal instability that ultimately results in the three-dimensional breakup of the ring. The experimental results are compared with three-dimensional numerical simulations using an adaptive mesh refinement technique. The agreement between experiment and simulation is shown to be quite good. The experimental results completely define the three-dimensional topology of the flow, and the three-dimensional breakup is shown to be in remarkable agreement with the incompressible theory of Widnall et al.

This work was performed under the auspices of the U.S. Department of Energy by the University of California Lawrence Livermore National Laboratory under contract No. W-7405-Eng-48.

Abstract No. E35

Turbulent Transition in a High Reynolds Number, Rayleigh-Taylor Unstable Plasma Flow

H. F. Robey[1], Y. K. Zhou[1], A. C. Buckingham[1],
P. Keiter[2], B. A. Remington[1], and R. P. Drake[2]
[1]*Lawrence Livermore National Laboratory, Livermore, CA*
[2]*University of Michigan, Ann Arbor, MI*

A high Reynolds number, Rayleigh-Taylor unstable plasma flow driven by laser radiation is described. Given enough time at these experimental conditions, the interfacial mixing layer will eventually transition to turbulence. The experiments are limited, however, in the very short time duration of the available flow. The Reynolds number characterizing the mixing layer is determined from the experimentally measured length and velocity scales together with the plasma kinematic viscosity determined from a corresponding 1D numerical simulation. From these, the Reynolds number is determined to be sufficiently large ($Re > 10^5$) to support a turbulent flow. An estimate of the developing Taylor and Kolmogorov dissipation scales, however, shows that the temporal duration of the flow is insufficient to allow for the appearance of a turbulent inertial subrange. A methodology is described for estimating the time required for the development of a fully turbulent flow at these conditions.

This work was performed under the auspices of the U.S. Department of Energy by the University of California Lawrence Livermore National Laboratory under contract No. W-7405-Eng-48.

Abstract No. E36

Effects of High Initial Amplitudes and High Mach numbers on the Evolution of the RM instability: II. Experimental Study

O. Sadot[1,2], A. Yosef-Hai[2], A. Rikanati[1,2], D. Oron[1], G. Ben-Dor[2], and D. Shvarts[1,2]
[1]*Nuclear Research Center Negev, Israel*
[2]*Ben-Gurion University, Beer-Sheva, Israel*

Recent theoretical work [Rikanati et. al. this conference] suggested that the reduction in the RM instability initial growth rate observed in recent experiments [1, 2] is mainly a result of high initial amplitudes used in those experiments, rather then high Mach number effects.

In the present work, effects of high initial amplitudes and high Mach number are studied experimentally. Results from a shock tube apparatus at low Mach number (M=1.2) with high initial amplitudes shows velocity reduction similar to the theoretical predictions. Preliminary experiments studying the RM instability at high Mach numbers were done, using a newly constructed shuck tube, to confirm the velocity reduction due to effects of high Mach numbers.

References

1) Aleshin *et. al.*, in Proceedings of the Sixth International Workshop on the Physics of Compressible Turbulent Mixing edited by G. Jourdan & L. Houas, Marsielle France 1997. Page 1.

2) Dimonte G., Frerking C.E., Schnider M. and Remington B., Phys. of Plasmas **12**, 304 (1996).

Abstract No. E37

Measurements within a Richtmyer-Meshkov Mixing Zone using a Triple Hot Wire Probe Technique

L. Schwaederlé[1], G. Jourdan[1], L. Houas[1], and J.-F. Haas[2]
[1]*IUSTI, CNRS, Université de Provence, Technopôle de Château-Gombert, Marseille, France*
[2]*Commissariat à l'Energie Atomique, Bruyères-le-Châtel, France*

A triple probe constant temperature hot wire anemometer (CTHWA) investigation is undertaken in a shock tube to characterize the turbulent mixing zone induced by the Richtmyer-Meshkov instability (RMI) when the shock wave propagates through the interface between two gases of different densities. The first gas is air and the second is He (lighter), Ar (moderately heavier) and Kr (much heavier). The experiments are conducted in a 8.5cm square cross section shock tube of which test section is represented on Fig. 1. The two gases are separated by a thin (0.4μm) nitrocellulose film resting on an orthogonal grid made of 9_9 wires (180μm diameter, 8.5mm spacing) which is accelerated by a Mach number 1.25 shock wave in air at atmospheric pressure. Fig 2. summarizes the principle and the aim of the present investigation.

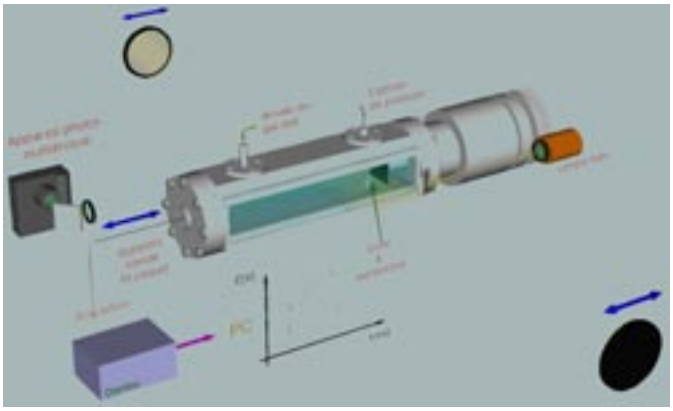

Fig 1. Experimental set-up

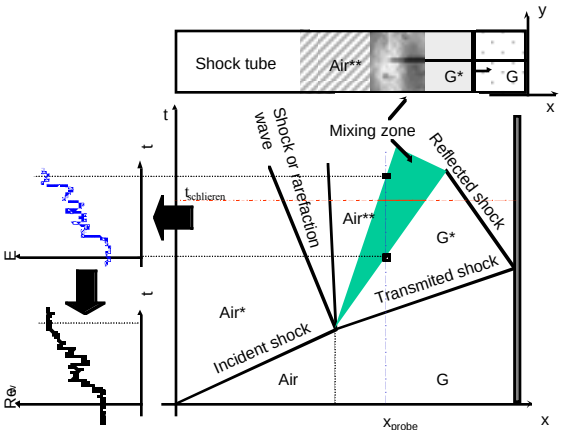

Fig 2. Principle of the investigation

The CTHWA output voltage is a function of local Reynolds number, heat conductivity and temperature with empirical constants. With the simplifying assumption of linear profiles for both temperature (with a jump less than 30K in all cases) and heat conductivity across the mixing zone, and using the Rankine-Hugoniot calculations in pure and premixed gases, the determination of the constants, given by a suitable calibration procedure with varying concentrations (by steps of 10%), provides the evolution of the Reynolds number within the mixing zone. An example of both (a) raw hot-wire signal and (b) deduced Reynolds number evolution in air/Ar mixing zone are represented in Fig 3.

(a) (b

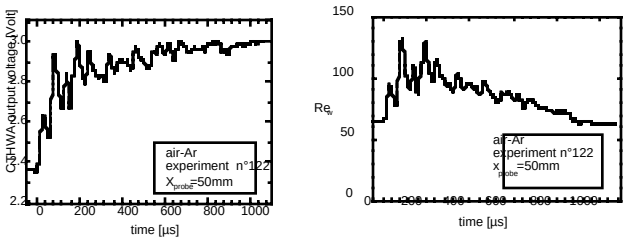

Fig. 3. Typical hot-wire signal and local Reynolds number evolution

In order to obtain separately the mixing density, temperature and velocity we positioned three HWA probes (5 µm in diameter and 1.25 mm in length), inserted from the end plate along the shock tube axis and working at different temperatures. We intend to present the local Reynolds number evolution across the mixing zone, the estimates of density, velocity and temperatures with statistical results based on identical shock tube experiments, and carry this study at different positions both axially and laterally.

Abstract No. E38

Experimental Study into Evolution of Gravitational Turbulent Mixing of Gases at the Multifunctional Shock Tube

Yu. A. Kucherenko, O. E. Shestachenko, Yu. A. Piskunov, E. V. Sviridov,
V. M. Medvedev, and A. I. Baishev
Russian Federal Nuclear Center – VNIITF, Snezhinsk, Russia

At initial moment of time investigated different density gases are placed inside the multifunctional shock tube and separated with the "Spectre-diaphragm". Next the "Spectre-diaphragm" is destroyed into small-scale fragments by an external force. The gaseous interface is accelerated by a compression wave formed in the shock tube. At that, the Rayleigh-Taylor instability arises at the contact boundary of different density gases, and a non-stationary zone of gravitational turbulent mixing forms. According to the experimental results, the dependence of the turbulent mixing zone width on the interface displacement has been built, and the non-dimensional rate of mixing alpha has been obtained.

Abstract No. E39

Shock Tube Experiments on Richtmyer-Meshkov Instability Across a Chevron Profiled Interface

A. V. Smith, D. A. Holder, C. J. Barton, A. P. Morris, and D. L. Youngs
Atomic Weapons Establishment, Aldermaston, United Kingdom

This paper reports on the latest experiment in the series of Richtmyer-Meshkov instability (RMI) shock tube experiments. They feature a dense gas / air interface in the form of a chevron of central obtuse angle 157º and full test cell height. The interest in an inclined interface of this angle was initiated at the 5th IWPCTM [1].

The experiments were conducted at shock Mach number 1.26 (70kPa overpressure), using the 200 x 100 mm shock tube with a three zone test cell arrangement of air / dense gas / air. The dense gas is optionally sulphur hexafluoride (SF_6) or xenon (Xe) which provide Atwood numbers of 0.67 and 0.64 respectively. Gas separation was by means of microfilm membranes, supported by fine wire meshes. Visualisation of the gas mixing was by laser sheet illumination of the seeded dense gas using a copper vapour laser pulsing at 12.5kHz. Mie scattered light was recorded using a 35mm rotating drum camera to capture a sequence of 50 images per experiment; or alternatively a single image from an ICCD camera.

Sample laser sheet images are compared to those from corresponding 3-D hydrocode calculations. Quantitative analysis will be of the form of derived relative intensity data from line-outs through experimental images and their code equivalents. Comparisons will reveal substantial agreement on major features.

A video will also be available showing a full sequence of images from one experiment with corresponding computed code images.

1. Bashurov et al. Experimental and Numerical Evolution Studies for 2-D Perturbations of the Interface Accelerated by Shock Waves. 5th IWPCTM

PACS No.: 47.20.Ma

Abstract No. E40

The Evolution and Interaction of Two Shock-Accelerated Unstable Gas Cylinders

C. Tomkins, K. Prestridge, P. Rightley, C. Zoldi, and R. Benjamin
Los Alamos National Laboratory, Los Alamos, NM

The interaction of two Richtmyer–Meshkov-unstable gas cylinders is investigated experimentally. The dense-gas cylinders are initially configured with separation S in the spanwise direction (S = 1.1 to 2.0 times the diameter, center-to-center), and subject to acceleration by a planar shockwave. The evolution of the resulting flow structures is captured downstream by flow visualization and PIV.

In the single-cylinder case (Prestridge *et al*.), the flow structure is dominated by two spanwise-separated vortices. In the double-cylinder configuration, the innermost vortices interact (e.g., Figure 1). The nature and degree of the interaction—and hence the morphology of the resulting flow structures—is observed to be highly sensitive to the initial cylinder spacing. The effects of the interaction on both the initial baroclinic vorticity production, and the subsequent evolution of this deposited vorticity, are investigated.

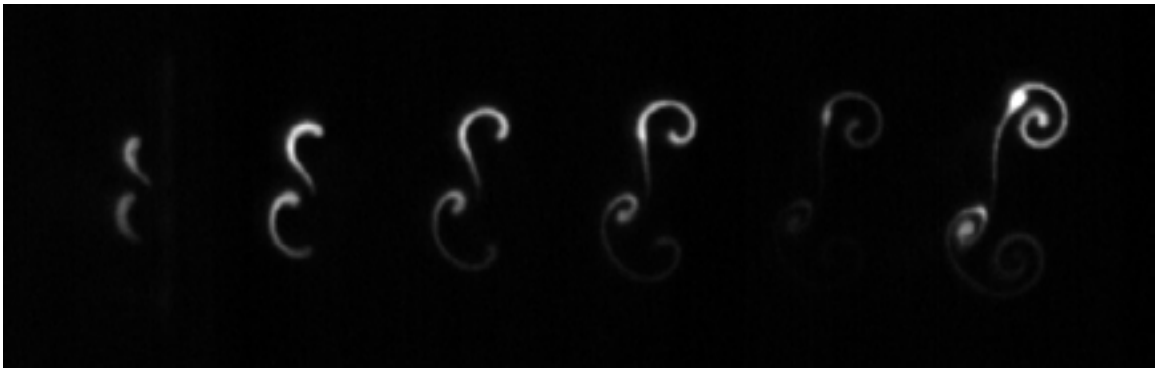

Figure 1. Flow visualization example of interaction between adjacent shock-accelerated gas cylinders.

References

K. Prestridge, *et al*., "Experiments and Simulations of Instabilities in a Shock-Accelerated Gas Cylinder", submitted to *Phys. Fluids*.

PACS No.: 47.20Ma

Abstract No. E41

Doubly-Shocked Richtmyer-Meshkov Instability Experiments at Nova

D. J. Ward, K. S. Budil, T. A. Peyser, B. A. Remington,
P. L. Miller, R. J. Wallace, H. Louis, and A. Demiris
Lawrence Livermore National Laboratory, Livermore, CA

Hydrodynamic instabilities are present in many physical systems, ranging from very small inertial confinement fusion capsules to supernovae. A great deal of effort, computational, theoretical and experimental, has been focused on the evolution of buoyancy-driven (Rayleigh-Taylor), shear-driven (Kelvin-Helmholz) and shock-driven (Richtmyer-Meshkov) instabilities. For astrophysics the interaction of shock waves with molecular clouds in the interstellar medium is a common occurrence and a problem that has been studied extensively. A slightly more complex problem is the interaction of multiple shock waves with such a cloud, in either a co- or counter-propagating geometry. This is the system that we chose to address with these experiments.

We will present the results of a series of experiments that investigated hydrodynamic instabilities in doubly shocked systems. A half-hohlraum driver was used to launch a shock into a miniature shock tube that then crossed a rippled interface, causing the ripples at the interface to grow via the Richtmyer-Meshkov instability. A second, counterpropagating shock was launched from the opposite end of the shock tube by a second half-hohlraum driver that impacted the developing mix region at some later time. This unique geometry allowed independent control of the relative timing of the two shocks and their relative strength. However, for ease of experimental implementation we have chosen to begin with the case of two roughly equal strength, counter-propagating shock waves. The evolution of the mixing region was observed via radiography.

The quality of the data obtained in this experiment was greatly improved over prior experiments by the use of a layered ablator, constructed by using two density matched plastic materials, only one of which was radiographically opaque to the backlighter X rays. The opaque material was confined to the central 100 microns along the line-of-sight, thus virtually eliminating the complications due to shock curvature in that direction. The initial perturbation was a 100 μm wavelength ripple with an initial amplitude of 1 μm.

The experimental results show good agreement with two-dimensional radiation-hydrodynamics code simulations. We will also discuss comparisons to existing analytic models for the evolution of the RM instability.

This work was performed under the auspices of the U.S. Department of Energy by the University of California Lawrence Livermore National Laboratory under contract No. W-7405-Eng-48.

Abstract No. E42

The Interaction of Supernova Blast Waves with Interstellar Clouds: Experiments on the OMEGA Laser

R. I. Klein[1,2], H. Robey[1], T. Perry[1], and J. Greenough[1]
[1]*Lawrence Livermore National Laboratory, Livermore, CA*
[2]*University of California at Berkeley, Berkeley, CA*

The interaction of strong shock waves, such as those generated by the explosion of supernovae with interstellar clouds, is a problem of fundamental importance in understanding the evolution and the dynamics of the interstellar medium (ISM) as it is disrupted by shockwaves.. The physics of this essential interaction is critical to understanding the evolution f the ISM, the mixing of interstellar clouds with the ISM and the viability of this mechanism for triggered star formation. We present the results of a series of new OMEGA laser experiments investigating the evolution of a high density sphere embedded in a low density medium after the interaction of a strong shock wave, emulating the supernova shock-cloud interaction. The interaction is viewed from two orthogonal directions using face-on and side-on x-ray radiography enabling visualization of the both the initial distortion of the sphere into a vortex ring as well as the onset of a powerful azimuthal 3D instability that ultimately results in the three-dimensional breakup of the ring. These studies augment the previous studies of Klein et al. (2000, 2001) on the NOVA laser by enabling the full three-dimensional topology of the interaction to be understood. We compare the experimental results for the vortex ring with the incompressible theory of Widnall et al. 1974 and we discuss high resolution 3D numerical simulations that recover all of the essential features of the interaction including Richtmyer-Meshkov, Rayleigh-Taylor and Kelvin-Helmholtz instabilities. We discuss implications for mixing in the ISM.

This work was performed under the auspices of the U.S. Department of Energy by the University of California Lawrence Livermore National Laboratory under contract No. W-7405-Eng-48.

Abstract No. E43

Evolution of the Mixing Zone of Different Densities Gases Being Interaction to Compression Waves

S. G. Zaytsev[1], V. V. Krivets[1], I. M. Mazilin[1], S. N. Titov[1], E. I. Chebotareva[1], V. V. Nikishin[2], V. F. Tishkin[2], S. Bouquet[3], and J.-F. Haas[3]
[1]*Krzhizhanovsky Power Engineering Institute, Moscow, Russia*
[2]*Institute of Mathematical Modeling, Moscow, Russia*
[3]*Commissariat à l'Energie Atomique, Bruyères-le-Châtel, France*

The experimental and numerical study of the mixing zone evolution between a combustible mixture (hydrogen-oxygen, molecular weight is 18.5) and argon was carried out during accelerated, and then decelerated motion. The accelerated motion was formed by compression waves generated by a flame front in a combustible mixture. The magnitude of acceleration was about 10^4 acceleration of gravity. In experiments the density distribution and shape of the mixing zone in the test-section were observed.
One-dimensional (1D) and two-dimensional (2D) models of process were used in numerical calculations.

The analysis of numerical and experimental results has shown:

1. The one-dimensional model satisfactorily describes a trajectory of the mixing zone motion and density distribution outside the mixing zone during accelerated, and then decelerated motion.
2. The shape of perturbations in the mixing zone generated as a result of the Rayleigh-Taylor instability evolution at the stage of accelerated motion is satisfactorily described by two-dimensional model.
3. At the stage of deceleration two qualitatively different ways of the mixing zone evolution are observed:
4. At deceleration caused by the reflected shock, the decrease of the perturbation amplitude is observed – **non-shocked deceleration.**
5. In the given design of experiments, there are waves, which observed sometimes inside the incident compression wave. They form reflected shock waves with the Mach number just slightly exceeding M=1. The interaction of these extremely weak shocks with the mixing zone resulted in the perturbation amplitude growth inside the mixing zone – **shock-induced deceleration**.

Abstract No. E44

Studies of Rayleigh-Taylor Instability in Aluminum Under Shock-Wave and Shock Less Loading

A. Lebedev, P. Nizovtcev, and V. Raevsky
Russian Federal Nuclear Center – VNIIEF, Sarov, Russia

The paper present results of experimental studies of Rayleigh-Taylor instability growth in aluminum alloys AMg-6 and 6061-T6 subjected to shock-wave and shock less loading up pressures of 45Gpa. Fast growth of perturbations was recorded at the initial stage of acceleration in experiments with shock-wave loading. This testifies to short-time reduction of strength of tested material. To explain this phenomenon, the authors suggest a relaxation model of aluminum strength, taking into account heterogeneous character of deformation at shock wave front. Results of micro structural analysis of samples subjected to shock less and shock-wave loading are presented.

The study was performed at financial support under Agreement 512964 between Lawrence Livermore National Laboratory University of California and All-Russia Research Institute of Experimental Physics

Abstract No. E45

Ablative Rayleigh-Taylor Instability at Short Wavelengths

H. Azechi[1], T. Sakaiya[1], M. Nakai[1], H. Shiraga[1], K. Shigemori[1], N. Miyanaga[1], M. Nishikino[1], S. Fujioka[1], Y. Tamari[1], H. Nagatomo[1], H. Takabe[1], and A. Sunahara[2]
[1]*Osaka University, Osaka, Japan*
[2]*University of Rochester, Rochester, NY*

The Rayleigh-Taylor (RT) instability in inertial confinement fusion (ICF) targets and in some astrophysical objects has an essential difference from the classical RT instability: material ablation. Since the ablation removes the RT perturbation away from the unstable surface, the RT growth is expected to be substantially reduced from its classical growth. Accordingly the RT instability at short wavelengths provides a critical test of various theories. To date, few experiment has addressed the short wavelength RT instability because of the wavelength of interest is around or even below the diagnostic spatial resolution. We will report in this Workshop the short wavelength RT instability growth rates which are measured for the first time by utilizing the newly innovated moiré interferometry. The measured growth rates are reasonably well reproduced by the simulation that solves the Fokker-Plank equation for non-local heat transport.

Abstract No. E46

A Vortex Model for Studying the Effect of Shock Proximity on Richtmyer-Meshkov Instability at High Mach Number

H. F. Robey and S. G. Glendinning
Lawrence Livermore National Laboratory, Livermore, CA

The effect of shock proximity on the non-linear evolution of Richtmyer-Meshkov instability of a sinusoidal perturbation at high Mach number is investigated analytically using a vortex model. The presence of the time-dependent shock boundary condition is incorporated using a system of image vortices of opposite sign located at the shock-to-interface distance ahead of the shock. For certain conditions, the perturbation growth rate is predicted by the linear theory to exceed the velocity of the transmitted shock relative to the mean interface. The effect of the image vortices is to initially suppress the growth of the perturbation while the shock remains close to the unstable interface. Later in time as the shock separates from the interface, the growth rate rebounds to a value slightly greater than would have occurred in the absence of the proximity effect. The model is compared with data from recent high Mach number RM experiments conducted on the Omega Laser and is shown to provide very reasonable agreement.

This work was performed under the auspices of the U.S. Department of Energy by the University of California Lawrence Livermore National Laboratory under contract No. W-7405-Eng-48.

COMPUTATIONAL ABSTRACTS

Abstract No. C1

Modes' Interaction on Nonlinear Stage of Richtmyer-Meshkov Instability Evolution

V. I. Anisimov and A. V. Polionov
Russian Federal Nuclear Center – VNIITF, Snezhinsk, Russia

Universal dependence, permitting to describe linear and non-linear stages of Richtmyer-Meshkov instability evolution for single mode for the wide range of Mach and Atwood numbers was obtained earlier. In the present paper we are making an attempt to describe modes' interaction. For each single mode its own turbulent viscosity is determined. During modes interaction it is supposed that evolution of each mode damps because of total viscosity all modes being in the presence. The obtained results are compared with direct numerical simulation by MACH code.

Abstract No. C2

Application of Kε-Model for the Description of an Atmospheric Surface Layer

M. G. Anuchin, V. E. Neuvazhayev, and I. E. Parshukov
Russian Federal Nuclear Center – VNIITF, Snezhinsk, Russia

The problem on determination of non-dimensional characteristics of turbulent flow in atmospheric surface layer is considered within kε-model. Kε-equations and their singular points are investigated. The mathematical program for calculations of characteristics of turbulent flow in surface atmospheric layer is developed. From the set of integral curves those curves are chosen which correspond to the solution of formulated task and ensure the satisfactory experiments description. Here the basic model constants are chosen according to the conventional criteria. At the same it is shown that the parameter responding to convection source term of an ε-equation should be chosen depending on stability conditions. The best agreement with experimental results is reached if for steady stratification and for unstable stratification. By a numerical choice of value and factor of turbulent diffusion the quite satisfactory description of experimental observations known as analytical interpolar dependencies is received.

Abstract No. C4

Computational Modeling of Low-Mach-Number High-Atwood-Number Turbulent Mixing

Wm. T. Ashurst and A. R. Kerstein
Sandia National Laboratories, Livermore, CA

A prerequisite for physical understanding of compressible turbulent mixing is clarification of low-Ma high-At turbulent mixing mechanisms. Remarkably, uncertainty persists concerning the interpretation of the fundamental experiments in this regime, such as the seminal mixing-layer study by Brown and Roshko [1] and subsequent GALCIT experiments. It is difficult to perform numerical simulations directly comparable to the pertinent experiments, and theoretical progress has been limited. The present study provides an integrated picture of low-Ma high-At turbulent mixing using a new computational model for stochastic simulation of variable-density turbulent mixing. Comparison of model results to various published and unpublished experimental and numerical results clarifies the physical mechanisms underlying the diverse results and demonstrates novel predictive capabilities. A planned extension of the model to compressible flow is outlined.

G. L. Brown and A. Roshko, *J. Fluid Mech.* 64, 775 (1974).

PACS Nos.: 47.27.Eq, 47.27.Nz, 47.27.Jv

Abstract No. C8

Spectral and High-Order Compact Methods for Shock-Induced Mixing

A. W. Cook, W. H. Cabot, and J. A. Greenough
Lawrence Livermore National Laboratory, Livermore, CA

A methodology, based on high-order compact and spectral schemes, is described for computing multicomponent turbulent flows at any Mach number. Filters are employed to stabilize the numerical integration and high-order artificial transport coefficients are introduced to control Gibbs oscillations. The equations and numerical scheme are formulated such that, under grid refinement, the method approaches a DNS. The method is evaluated for flows in 1, 2, and 3 dimensions, including comparisons with lower-order schemes. The dissipative character of the filter and artificial terms appears to be of little consequence for strongly forced flows which evolve over short periods of time; however, the dissipation is more noticeable for unforced flows which evolve over long periods of time.

PACS Nos.: 02.70.Hm, 47.20.Ma

This work was performed under the auspices of the U.S. Department of Energy by the University of California Lawrence Livermore National Laboratory under contract No. W-7405-Eng-48.

Abstract No. C9

Numerical Simulation of Mode Coupling in Laser-Driven Rayleigh-Taylor Instability Experiments

R. M. Darlington and K. S. Budil
Lawrence Livermore National Laboratory, Livermore, CA

This study addresses the simulation of multimode laser-driven Rayleigh-Taylor instability experiments. The linear and transition stages of the instability will be examined, with particular study of the mode coupling between short and long wavelengths. The experiments, conducted at the Nova laser facility at LLNL, consisted of ablatively-accelerated planar composite foils mounted onto the side of a gold hohlraum. A modulation was machined at the interface between a brominated plastic ablator layer (40 um thick) and a titanium payload (15 um thick) and its growth was diagnosed by measuring the changing optical depth modulation via face-on radiography. In this work we will focus on the evolution of a superposition of a 20 and a 4 um mode and contrast this to the evolution of a 20 um single mode perturbation. The shape and growth rate of
the resulting instability will be examined, as well as the effect of numerical methods on the simulation. Similar simulations will also be used to examine the evolution of this perturbation in a more idealized situation where the target layers will be much thicker in order to mitigate thin foil effects, and the laser drive can be sustained for much longer durations. This will allow us to investigate the experimental conditions required to follow the instability further toward the turbulent regime.

This work was performed under the auspices of the U.S. Department of Energy by the University of California Lawrence Livermore National Laboratory under contract No. W-7405-Eng-48.

Abstract No. C10

A Comparison of High-Resolution 3D Numerical Simulations Of Turbulent Rayleigh-Taylor (RT) Instability: Alpha-Group Collaboration

G. Dimonte[1], A. Dimits[1], S. Weber[1], D. L. Youngs[2], A. C. Calder[3], B. Fryxell[3], J. Biello[3], L. Dursi[3], P. MacNeice[4], K. Olson[4], P. Ricker[3], R. Rosner[3], F. Timmes[3], H. Tufo[3], Y.-N. Young[3], M. Zingale[3], M. J. Andrews[5], P. Ramaprabhu[5], S. Wunsch[6], C. Garasi[6], and A. Robinson[6]

[1]*Lawrence Livermore National Laboratory, Livermore, CA*

[2]*Atomic Weapons Establishment, Aldermaston, United Kingdom*

[3]*University of Chicago, Chicago, IL*

[4]*NASA Goddard Space Flight Center, Greenbelt, MD*

[5]*Texas A & M University, College Station, TX*

[6]*Sandia National Laboratories, Livermore, CA*

The RT instability is investigated by comparing high resolution (256 x 256 x 512 zones) simulations using various (5-7) numerical techniques with identical initial conditions. The fluids have a density ratio $\rho_2/\rho_1 = 3$ and an ideal gas specific heat ratio of $\gamma = 5/3$. The hydrostatic equilibrium is adiabatic with a pressure $\sim 2\pi\ (\rho_1+\rho_2)gL$ (g = acceleration, L = box width) at the interface to keep the velocities sub-sonic (Mach < 0.2). The initial perturbations have an RMS amplitude $h_o/L \sim 3 \times 10^{-4}$ with mode numbers randomly distributed in a cylindrical shell $32 \leq n \leq 64$. This paper compares the self-similar growth $\sim gt^2$ of the mixing zone and internal scales, the atomic mixing, and the energy budget from the different codes and with available experiments.

This work was performed under the auspices of the U.S. Department of Energy by the University of California Lawrence Livermore National Laboratory under contract No. W-7405-Eng-48.

Abstract No. C11

Numerical Methods for Determination of Mix

S. Dutta[1], E. George[1], J. Glimm[1,3], J. Grove[2], X. Li[1],
A. Marchese[1], D. H. Sharp[2], Z. Xu[1], and Y. Zhang[1]
[1]*State University of New York at Stony Brook, Stony Brook, NY*
[2]*Los Alamos National Laboratory, Los Alamos, NM*
[3]*Brookhaven National Laboratory, Brookhaven, NY*

We present numerical studies of the growth of a 3D mixing layer due to Rayleigh-Taylor (RT) or Richtmyer-Meshkov(RM) instabilities. Simulations based on the Front Tracking code FronTier give a mixing rate alpha for the bubble growth in planar RT mixing within the range determined by experiments of Youngs-Reed, Smeeton-Youngs and Dimonte et. al. Identical simulation problems, solved with a TVD capturing code, give an alpha below this range of experiment. We present an analysis (based on theory and on diagnostics from the two simulations) to indicate that the difference between simulations is primarily due to diffusion of mass across the fluid interface in the TVD (capturing) simulation.

Axisymmetric 3D spherical RM mixing studies show dependence of the mixing rate on the azimuthal angle, especially after reshock. Statistical mix quantities (volume fraction, etc.) are recorded and compared with mix model equations of the authors and co-workers.

PACS Nos.: 47.20Bp, 47.52+j

Abstract No. C12

Rayleigh-Taylor Instability in Compressible Fluids

Y. Elbaz[1,2], A. Rikanati[1,2], D. Oron[3], and D. Shvarts[1,2]
[1]*Nuclear Research Center Negev, Israel*
[2]*Ben Gurion University, Beer-Sheva, Israel*
[3]*Weizmann Institue of Science, Rehovot, Israel*

The behavior of the single mode and multimode Rayleigh-Taylor (RT) instability in compressible fluids is studied using full two-dimensional numerical simulations and analytical theoretical models. Due to the finite mass of the heavier fluid above the bubble, resulting from the initial density distribution, the perturbation growth causes a state of pressure non-equilibrium on the heavier fluid, leading to a bulk acceleration of the heavier fluid as in the case of RT instability in a finite layer of an incompressible fluid. Also, the finite sound speed of the heavier fluid causes an effective mass accumulation in time, therefore changing the pressure gradient on the interface with time.

Analyzing the instability dynamics in a frame of reference moving with the accelerated physical system shows a small effect of compressibility on the instability dynamics. In this frame of reference the simulation results coincide with the known incompressible results - a constant velocity in the single mode case and α~0.04-0.06 in the multimode case. However, due to the bulk acceleration of the heavier fluid, in the laboratory frame of reference the bubble velocity continuously increases in the single mode case, and in the multimode case an αgt^2 growth rate is obtained, with α continuously increasing as well.

Abstract No. C13

One-Dimensional Simulation of the Effects of Unstable Mix on Neutron and Charged-Particle Yield from Laser-Driven Implosion Experiments

R. Epstein, J. A. Delettrez, V. Yu. Glebov, V. N. Goncharov, P. W. McKenty,
P. B. Radha, S. Skupsky, V. A. Smalyuk, and C. Stoeckl
Laboratory for Laser Energetics, University of Rochester, Rochester, NY

The effects of Rayleigh–Taylor flow in laser-driven implosion experiments are simulated in one dimension by the hydrodynamics code *LILAC*. Mix is modeled as a diffusive transport process affecting material constituents, thermal energy, and turbulent mix-motion energy within a mix region whose boundaries are derived from a saturable, linear, multimode model of the Rayleigh–Taylor instability. The growth rates and the coupling between perturbations of different unstable interfaces are obtained analytically in terms of the one-dimensional fluid profiles. The initial perturbations are due to beam-energy imbalance, hydrodynamic imprint of short-scale laser nonuniformity, and target surface roughness. The effects of fuel–pusher mix on neutron production and secondary particle yields are characterized and compared with data from implosion experiments. The limitations of one-dimensional mix as an approximation to the multidimensional distortion of the fuel–pusher interface will be considered.

Abstract No. C14

3D Computation for Surface Perturbation Evolution of Plasma Cloud During its Expansion in Magnetic Field

E. S. Gavrilova, E. V. Gubkov, V. A. Zhmailo, and Yu. V. Yanilkin
Russian Federal Nuclear Center – VNIIEF, Sarov, Russia

Previously, ref. [1] considered the 2D problem of initially spherical plasma cloud expansion in the axial magnetic field. In particular, it was noted that the plasma surface was unstable to evolution of perturbations (of "chute" type).

This paper solves the above problem with taking into account the growth of the perturbations. The computation is performed with 3D code TREK [2]. Two methods to solve the problem are discussed:

- it is assumed that outside the cloud there is plasma of quite low density as well which magnetic field is "frozen into", in this case appropriate MHD equations are used to compute magnetic field variations;
- it is assumed that outside the cloud there is vacuum, in this case quasi-stationary approximation [1] is used to compute the magnetic field.

Two initial perturbation types are given: one mode and random. The computed data for the linear stage of the one mode perturbation growth is compared to the analytical data.

The results of the problem computation with random perturbations are averaged (over azimuth). Thus obtained plasma density and magnetic field profiles, in particular, dependence of the transition zone width in the profiles on the problem parameters are considered. Applicability of this plasma model is discussed.

1. Bakhrakh S.M., Gubkov E.V., Zhmailo V.A., Terekhin V.A. "Plasma cloud expansion in homogeneous magnetic field". PMTF, 1974, No. 4, pp. 146-150.

2. Yanilkin Yu.V., Tarasov V.I., Stadnik A.L., Bazhenov S.V., Bashurov V.V., Belyaev S.P., Bondarenko Yu.A., Bykova E.A., Gavrilova E.S., Gorev V.V., Dibirov O.A., Ivanova G.G., Kovalev N.P., Korol'kova T.V., Pevnaya P.I., Sofronov V.N., Toropova T.A., Shanin A.A. Program System TREK for Numerical Simulation of 3D Multi-component Medium Flows. Proceedings of workshop "New Models and Numerical Codes for Shock Wave Processes in Condensed Media", Oxford, 1997, pp 413-422, 1997.

Abstract No. C15

The Richtmyer-Meshkov Instability in Cylindrical Geometry: Experiments and Simulation

M. J. Graham[1], K. S. Budil[1], J. Grove[2], and B. A. Remington[1]
[1]*Lawrence Livermore National Laboratory, Livermore, CA*
[2]*Los Alamos National Laboratory, Los Alamos, NM*

Hydrodynamic instabilities are fundamentally important to a wide range of fields, including astrophysics, inertial confinement fusion (ICF), and inertial fusion energy (IFE). The most common of these instabilities is the Rayleigh-Taylor (RT), or buoyancy-driven instability, is caused when a material of higher density is accelerated by a material of lower density. The Richtmyer-Meshkov (RM), or shock-driven instability is produced when an incident shock wave impulsively accelerates a material interface causing small disturbances to grow.

The RT interface is unstable only when the external force acts from the heavy material to the lighter material, whereas the RM instability is present whether the incident shock travels from light to heavy or vice versa. The majority of the theoretical, computational and experimental work has been successfully performed for the RM instability in planar geometry. In most physical applications the RM instability occurs in a curved geometry, either cylindrical or spherical. This curved geometry complicates the system considerably. For example, the unperturbed system does not have an analytical solution, while the unperturbed system in plane geometry does. The occurrence of re-acceleration or re-shock of the material interface caused by the waves reflecting back from the origin is unavoidable in curved geometry.

The Nova Laser was used to test critical ingredients of our understanding of the fundamental properties of the RM instability in the strong-shock, high-compression regime. A shock was launched into a copper hemicylinder with a thin plastic ablator layer by focusing 6 KPP-smoothed, 1 ns square laser beams at 3ω onto the interior of the target. A single-mode sinusoidal perturbation was machined onto the outer surface of the copper, which was embedded in a thick layer of plastic. The expanding interface was diagnosed by side-on radiography and radiographs were recorded at several times.

We will show numerical simulations of this experiment using two difference codes: FronTier and CALE. In the FronTier method a lower dimensional grid is fitted to and moves dynamically with discontinuities in the flow. CALE is a continuous adaptive Lagrangian Eulerian method.

PACS Nos.: 52.35.Tc, 47.11+j

Abstract No. C16

Code to Code Comparisons for the Problem of Shock Acceleration of a Diffuse Dense Gaseous Cylinder

J. A. Greenough[1], W. J. Rider[2], C. A. Zoldi[2], and J. R. Kamm [2]
[1]*Lawrence Livermore National Laboratory, Livermore, CA*
[2]*Los Alamos National Laboratory, Los Alamos, NM*

The current computational study is motivated by large-scale (and small-scale) discrepancies between ongoing calculations and experiments of a shock wave accelerating a diffuse cylinder of SF_6 ("Experiments and simulations of instabilities in a shock accelerated cylinder," K. Prestridge, C. A. Zoldi, P. Vorobieff, P.M. Rightley, and R. F. Benjamin, Los Alamos Report LAUR –00-3973). Three different Eulerian based codes, Rage (LANL), Cuervo (LANL) and Raptor (LLNL), are applied to an idealized two-dimensional version of the experiment. The model problem consists of a Gaussian shaped SF_6 inhomogeneity in air that is accelerated by a M=1.2 shock wave. The initial diffuse cylinder evolves into a quasi-vortex dipole at intermediate times until finally becoming unstable at late times. The integral (large) scale features, which include the length and width of the evolving structure, will be measured from the calculations and compared. The sub-integral scale, small-scale vortical features in the central roll-up, will also be examined quantitatively and compared at intermediate times. An assessment of the degree of convergence of the simulations as well as factors accounting for computed differences will be discussed.

This work was performed under the auspices of the U.S. Department of Energy by the University of California Lawrence Livermore National Laboratory under contract No. W-7405-Eng-48.

Abstract No. C17

Implementation of a Turbulent Mix Model in a 2D ALE Code

B. Grieves
Atomic Weapons Establishment, Aldermaston, United Kingdom

The addition of a turbulent mix model to a two dimensional finite element ALE hydrocode, CORVUS, is discussed. Use is made of the existing mixed-cell data structure to facilitate the inclusion of the model.

This first stage of the model is based on the multiphase flow equations, and is a simplified form of the model implemented by Youngs (See paper at this workshop) in a 2D Eulerian Code. This is applicable to simple Rayleigh-Taylor and Richtmyer-Meshkov instabilities, and some results are presented.

A simple buoyancy-drag model is used to calculate the early stages of the instability growth at interface nodes, and this is used to initialise the turbulent mix model calculation.

Abstract No. C18

Error Estimation for Strong Shock Hydrodynamics

J. W. Grove
Los Alamos National Laboratory, Los Alamos, NM

The quantification of uncertainty is a fundamental problem in mathematical modeling. Sources of uncertainty include incomplete physical models, poorly defined initial conditions, and the effect of numerical methods. Traditional numerical analysis is extremely limited in accessing the accuracy of a computation, especially in highly nonlinear regimes. Predictive calculations require a more detailed assessment of solution error, including a quantitative model for the probability distribution of the error in a simulation.

This talk will describe a prototype methodology, developed in collaboration with researchers at the University at Stony Brook, for studying uncertainty in a computational model. We apply this methodology to a simple strong shock refraction test problem. Assuming known probability distributions for a set of initialization and flow parameters, we perform a statistical study of the generation and propagation of solution error. Error is computed by comparing fine and coarse grid computations for different mesh sizes, and numerical methods. We obtain a space-time field of probability distributions for a variety of state variables, and seek stochastic models for the generation and propagation of solution error as a function of flow state and numerical method.

PACS Nos.: 07.05.Tp, 47.11.+j, 47.40.-x

Abstract No. C19

A Semi-Empirical Model for Turbulent Diffusion of Magnetic Field to Accelerated Plasma

E. V. Gubkov, V. A. Zhmailo, and Yu. V. Yanilkin
Russian Federal Nuclear Center – VNIIEF, Sarov, Russia

A nonlinear phase of instability development at the accelerated plasma/magnetic field interface is studied. The paper considers the case with short wavelength and incidental initial perturbations. A semi-empirical model which structure is similar to that of the hydrodynamic model from /1/ is proposed to describe perturbations of such a kind.

Two problems are solved using the proposed model: a one-dimensional problem of a converging cylindrical liner with axial magnetic field in cavity (ultra-high magnetic field generator "MK-1" /2/); a two-dimensional problem of a plasma cloud expansion in external magnetic field /3-5/.

By comparing computation results with the corresponding experimental data, some constants introduced to the model are determined, as well as frames of its applicability are specified.

1. Yanilkin Yu.V., Nikiforov V.V., Zharova G.V. A Two-Equation Model and a Method for Turbulent Mixing Computations in 2D Compressible Flows. – VANT, Ser.:MMPhP, 1994, Iss.4.
2. Sakharov A.D., LudaevR.Z., Smirnov E.N., Plyushcheyev Yu.I., Pavlovskii A.I., et al. DAN SSSR, 1965, V.196, No.1, pp.65-68.
3. Bakhrakh S.M., Gubkov E.V., Zhmailo V.A., Terekhin V.A. Expansion of a Plasma Cloud in Uniform Magnetic Field. – PMTPh, 1974, No.4, pp.146-150.
4. Zakharov Yu.P., Orishich A.T., Ponomarenko A.G. "Plasma Physics" Journal, 1986, V.12, p.674.
5. Pisarczuk T., Kasprczuk A., Karpinski L., et al. Application of Interferometric Methods to Investigation of Laser-Produced Plasma in Strong External Magnetic Field. –In "Advances in laser interaction with matter and inertial fusion", Madrid, 1996.

Abstract No. C20

Localization and Spreading of Interfaces (Contact Discontinuities) in PPM and WENO Simulations of the Inviscid Compressible Euler Equations

S. Gupta, N. J. Zabusky, R. Samtaney, and Y. Gulak
Rutgers, StateUniversity of New Jersey, Piscataway, NJ

The physical or numerically- "motion" of interfaces or contact discontinuities (CD) between two fluids of different density or temperature governs the mixing of species, particularly during the late time ("asymptotic ") epochs.

Using the methods of Vorozhtzov and Yanenko, [1] we show that for the equation $\frac{f\rho}{ft} + u_0 \frac{f\rho}{fx} = 0$, the continuum limit yields $\frac{f\rho}{ft} + u_0 \frac{f\rho}{fx} = (-1)^{r+1} \mu(h, \tau, u_0, p_0) \frac{f^{r+1}\rho}{fx^{r+1}}$ (A) where r is the order of the scheme (r = 1 for 1st order schemes, such as Lax, etc.), h is the grid size and τ is the time-step of the integration. For r = 1 and 2, the exact solution of (A) with a discontinuous initial density function, $(\rho = \rho_1, x < x_0; \rho = \rho_2, x > x_0)$, is $\rho(x,t) = (\rho_1 + r\rho_2)/(r+1) + (\rho_2 - \rho_1)\, F(\xi(x,t))$, (B), where $\xi(x,t) = (x - x_0 - u_0 t)/(c_r \mu t)^{1/(r+1)}$ and **F** is the solution of an ODE arising in a self-similar study. In our numerical PPM [3] solutions, we find accurate agreement with the constant term in (B), i.e. the center of a spreading interface depends on r. This explains the lack of convergence in attempting to localize the CD previously [2]. However, the numerical spreading, $\xi_{PPM}(x,t)$, produced by PPM artificially steepens the density over two grid intervals if $\rho_2 > \rho_1$ and spreads it according to a power law if $\rho_2 < \rho_1$. This asymmetry will prove troublesome for reshock and reacceleration problems at late time epochs. We also comment on higher-order algorithms [4] and the effects of vorticity on the interface in 2D.

[1] E. V. Vorozhtzov and N. N. Yanenko, 1990. Methods for the Localization of Singularities in Numerical Solutions of Gas Dynamics Problems, Springer.
[2] R. Samtaney and N. J. Zabusky, 2001. High gradient compressible flows: Visualization, feature extraction and quantification, In *Flow Visualization: Techniques and Examples*, Editors T. T. Lim and A. Smits, Imperial College Press.
[3] J.M Blondin *et al* at NCSU.VH-1. A Lagrangian remap code based on PPM.
[4] Ravi Samtaney, Caltech . Higher order WENO code

Abstract No. C22

Update on Instability Modeling for the NIF Ignition Targets

S. W. Haan, T. Dittrich, S. Hatchett, D. Hinkel, M. Marinak, D. Munro, O. Jones, S. Pollaine, and L. Suter
Lawrence Livermore National Laboratory, Livermore, CA

This talk is a general update on the hydrodynamic instability modeling that we do for ignition targets for the National Ignition Facility. Recent results include design of a polystyrene-ablator target, analysis of Rayleigh-Taylor growth on beryllium targets driven at 250eV at various scales, simulations of the effect of fill tubes on the implosion,, and simulations of 3D asymmetry and its impact. Hydrodynamic instability modeling is done with direct numerical simulations, since the targets are designed to avoid short wavelength instability growth.

PACS Nos.: 52.57.Bc, 52.57.Fg

Abstract No. C23

Pillars of Creation

J. O. Kane[1], D. D. Ryutov[1], B. A. Remington[1], S. G. Glendinning[1], J. Nash[1], M. Pound[2], and D. Arnett[3]
[1]*Lawrence Livermore National Laboratory, Livermore, CA*
[2]*University of Maryland, College Park, MD*
[3]*University of Arizona, Tuscon, AZ*

The towering 'Pillars of Creation' of the Eagle Nebula are a long-standing astrophysical mystery. A new initiative is underway to develop a model for the formation of the Pillars, employing three-dimensional numerical modeling and scaled verification experiments using intense lasers. In the Rayleigh-Taylor instability (RT) model of the Pillars advanced almost fifty years ago by Spitzer and Frieman (Spitzer, L. 1954, ApJ 120, 1, Frieman, E. A. 1954, ApJ 120, 18), radiation from nearby stars photo-evaporates and accelerates the cloud surface, and the Pillars are falling 'spikes' of dense gas. Recently, fluid velocities and column densities in the Pillars have been measured (Pound, M. W. 1998, ApJ 493, L113). Preliminary two-dimensional numerical simulations of the RT model have been performed which produce results consistent these observations, assuming compressible fluids and a thin initial cloud. Since the radiation may impact the surface at an angle, a 'Tilted Radiation' instability (LLNL report UCRL-JC-138744, May 2000; .D. Ryutov, B.A. Remington, H.F. Robey, R.P. Drake. Phys. Plasmas, 8, 1804 (2001)) can cause the spikes to translate as waves whose tips may 'break', producing the small gas 'bullets' visible near the Pillars in images taken by the Hubble Space Telescope. In an alternate model for the Pillars, the cometary model, the Pillars consist of gas swept behind dense preexisting nuclei, but it appears difficult to reproduce the observed velocities and densities in numerical models with dense preexisting nuclei as the initial condition. . However, the effect of radiative cooling and magnetic fields remains to be explored. The maturing field of laser astrophysics presents an opportunity for testing models for the Pillars in the laboratory. Theoretical and numerical evaluations of various models, implications for observations, and plans for verification experiments are presented.

This work was performed under the auspices of the U.S. Department of Energy by the University of California Lawrence Livermore National Laboratory under contract No. W-7405-Eng-48.

Abstract No. C25

Application of a Laser Shock Tube for the Study of Supersonic Gas Flows and the Development of Hydrodynamic Instabilities in Layered Media

I. G. Lebo[1] and V. D. Zvorykin[2]
[1]*Tekhnikal University-MIREA, Moscow, Russia*
[2]*P. N. Lebedev Physical Institute of the Russian Academy of Sciences, Moscow, Russia*

The study of the evolution of hydrodynamic instabilities of the interface between two media found in the field of acceleration is a problem of great importance in inertial confinement fusion (ICF), physics of high energy densities, cosmology, and astrophysics. The passage of strong shock waves (with Mach number M>>1) through contact surfaces of two gases or plasma with different densities causes the formation and development of complex vortex structures, which are of interest for present-day nonlinear hydrodynamics and for studying the problem of a change from an ordered state to chaos. Another problem, which is important for the development of modern aerospace engineering and protecting the Earth from collisions with space objects, is the study of supersonic flow past bodies of complex shape at large Mach numbers. Usually, such experiments in gases are carried out at relatively small Mach numbers M=1-4 with help of shock tubes. The pressure amplitudes in shock wave are about 2-10 bar. The design of a miniature laser shock tube for the study of a wide range of hydrodynamic phenomena in liquids at pressures greater than 10 kbar and supersonic flows in gases with large Mach numbers (greater than 10) is discussed in this paper. In the system considered here, the confinement of a laser-produced plasma and the excitation of plane shock waves take place inside a miniature tube, which restricts lateral unloading. The design of such a laser shock tube (LST) is based on the use of the following basic components: a shock tube chamber; a powerful KrF laser [1]; an original laser focusing system; and 2D numerical codes. The technique proposed here for exciting shock waves in gases and compression waves in liquids by KrF laser radiation has some advantages in comparison with the conventional technique used in experiments with shock tubes: 1) large Mach numbers in gas flows (M>20) and pressure pulses greater than 10 kbar in liquids [2]; 2) economy of noble gases and other supplies (laser driven shock tube volume is less in ~ 10^3-10^4 times). This study is supported by RFBR, grant N0101-00023

References.

1. Zvorykin V.D., Lebo I.G. Laser and Particle Beams, 17, 69, 1999
2. Zvorykin V.D., Lebo I.G. Quantum Electronics, 30, 540, 2000

Abstract No. C26

Molecular Dynamic Simulation of Shock and Richtmyer-Meshkov Instability in Cylindrical Geometry

K. Nishihara, V. Zhakhovskii, and M. Abe
Osaka University, Osaka, Japan

Molecular dynamic (MD) approach has been applied to study the converging cylindrical shock waves and the Richtmyer-Meshkov instability in a dense Lennard-Jones fluid. MD method is based on tracking of the atom motion and hence it has fundamental advantages over hydrodynamic methods that assume a shock as a structureless discontinuity and require an equation of state. In addition, hydrodynamic simulation has a limitation in grid resolution, especially, in the cylindrical geometry. It is found that the one million particles is enough to simulate propagation of a cylindrical shock in close detail due to small thickness of shock fronts (a few Angstroms for Argon) in liquid.

We investigate the stability of converging shocks with different perturbation modes and its mixture for different Mach numbers. The converging shock is unstable for low mode number perturbation in large Mach number. It was shown that the amplitude of a shock front ripple increases and the Mach stems are formed. Supersonic jets generated by interaction of reflected shocks in downstream flow are observed. We also study the Richtmyer-Meshkov instability of an interface between two L-J liquids of different densities in the cylindrical geometry. The turbulent mixing is observed when the reflected shock near the center passes again through the unstable interface.

Abstract No. C27

Compressibility Effects in a High-Speed, Reacting Shear Layer: An Investigation Using DNS

C. Pantano and S. Sarkar
University of California at San Diego, La Jolla, CA

In technological applications such as combustion, high-speed propulsion and energetic devices, the variation in thermodynamic variables associated with large heat release interacts with and modifies the underlying turbulent flow. Direct numerical simulations of the reacting shear layer using up to 20 million grid points are performed over a wide range of heat release rates and convective Mach numbers to quantify and understand some of these modifications to the turbulence evolution and structure. Large heat release rates typical of hydrocarbon combustion are considered, and not only the overall growth characteristics but also the turbulence structure is investigated. The single-step irreversible combustion of a diluted methane stream mixing with an air stream is considered. An infinitely fast reaction rate is assumed, that is, the heat release is confined to an infinitely thin region in mixture fraction space located at the stoichiometric value.

A longitudinal snapshot of the density field is shown in Fig. 1. The upper air stream moves to the left while the lower fuel stream moves to the right. The mean location of the flame sheet is displaced to the upper air side. However, the convective stirring of the flame sheet by the turbulent motion spans the entire width of the shear layer so that an instantaneous snapshot such as Fig.1 shows a *wide* central core of hot, low-density fluid separated from the cold, high-density fluid on either side by thin regions with large values of the density gradient. The thickness growth rate of the shear layer is the overall quantity of primary interest. With increasing values of convective Mach number, the growth rate of the nonreacting cases shows the well-known large reduction. What is perhaps less expected is the effect of Mach number on the growth rate of the reacting cases. The growth rate is already quite low at the low-Mach number reacting case and a further increase in the Mach number causes only a relatively small additional reduction. The Reynolds shear stress profiles show that, in the low-speed case, there is a significant reduction of its peak value in the case with the highest heat release. However, at the largest convective Mach number, any additional change in the Reynolds shear stress is relatively small. The width of the profiles of Reynolds shear stress (not shown) as well as other Reynolds stresses scale well with the vorticity thickness but not the momentum thickness. The full paper will present results regarding all Reynolds stress components as well as thermodynamic correlations and cross-correlations

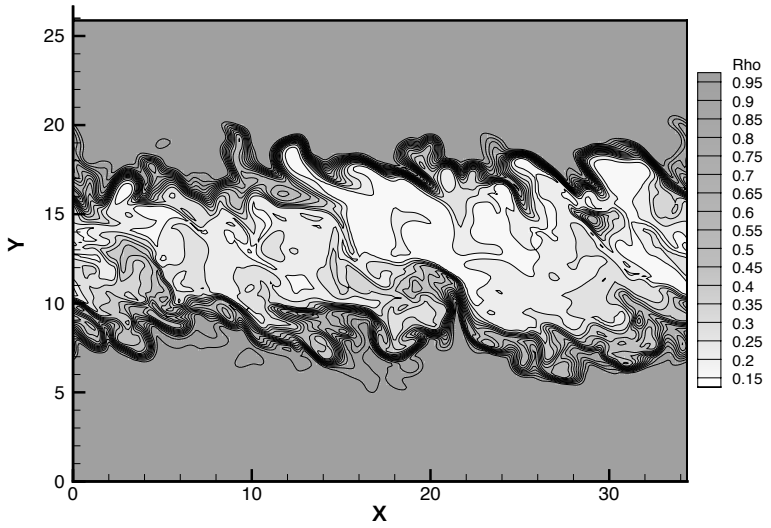
Rho
0.95
0.9
0.85
0.8
0.75
0.7
0.65
0.6
0.55
0.5
0.45
0.4
0.35
0.3
0.25
0.2
0.15
Y
X
0
5
10
15
20
25
0
10
20
30

Abstract No. C28

Computational Modelling of Two-Shell Cylindrical Implosions with Mix

K. W. Parker[1], A. M. Dunne[1], S. Rothman[1], D. Youngs[1], C. W. Barnes[2], S. H. Batha[2], N. E. Lanier[2], G. R. Magelssen[2], T. J. Murphy[2], and J. M. Scott[2]
[1]*Atomic Weapons Establishment, Aldermaston, United Kingdom*
[2]*Los Alamos National Laboratory, Los Alamos, NM*

Experiments to look at mix in a compressible, convergent geometry have been carried out on the Omega Laser Facility. These employ a radio-graphically opaque marker layer, which is sandwiched between the polystyrene ablator and low-density foam. As the implosion proceeds, a strong shock is launched which causes the marker to become mixed into both the foam and the ablator. More recently, these experiments have introduced a high-density core to the targets, such that a shock is reflected from the core back through the mix layer at late time. Presented here are calculations for these '2-shell' targets. Where possible, comparisons are made to the experimental results.

Abstract No. C29

Dispersal of Mass and Circulation Following Shock-Sphere (axisymmetric) and Shock Cylinder Interactions: Effects Arsing From Shock Cavity Collapse, Vortex Double Layers; Density-Gradient Intensification and Vortex Projectiles

G. Peng, S. Gupta, S. Zhang, and N. J. Zabusky
Rutgers, StateUniversity of New Jersey, Piscataway, NJ

We quantify and scale the dispersal and mixing (transport) of mass and vorticity following a spherical (axisymmetric) shock-bubble interaction. We use planar shocks of Mach =2.5, 5.0 and 10 and a density ratio - bubble/ambient- of 10.0, a parameter domain beyond that explored earlier [1], where new effects arise. We correlate and scale the transports with: the primary circulation layer deposited by the passing incident shock in epoch 1; the collapsing *transmitted shock cavity circulation layer* (TSCCL); and a vortex "double layer" (VDL) on the downstream boundary. The TSCSL is generated at the sharp kink of the collapsing transmitted shock (where numerous shocklets arise, e.g. a "penta-point" shock for M= 2.5) and is responsible for an epoch 1 appearing and upstream-moving Vortex Projectile (VP) (with an associated density enhancement). The VDL arises from two shock wave sources incident on the downstream side of the bubble: from inside, the re-expanding cavity and from outside the incident shock as it passes the rear side of the bubble. These phenomena evolve into a chaotic downstream array of vortex projectiles (VPs) which in axisymmetry are complex-shaped stratified rings of *opposite* polarity. We observe strong circulation generating baroclinic effects during this epoch [2]. In 3D, these VPs will be rapidly unstable and lead to domains of reconnecting vortices and stratified turbulence. The collapse of the shock cavity produces: large short-time enhancements of pressure, density and temperature, which we scale; and subsequent *reverberation effects* in the bubble interior and exterior, which we quantify. We simulated the 2d axisymmetric Euler equations with the Colella & Woodward (1984) PPM in a Galilean frame translating uniformly with the velocity equal to 20 percent of the post-shock velocity. Our study was made at three resolutions, (z, r): (1){803,123}; (2){1606,246} and {3212,492}. At our high Mach numbers and resolutions fast instabilities arise which yield coherent structures (e.g.[3]) and we comment on their relevance to the new observed phenomena.

[1] N.J. Zabusky and S-M. Zeng, J. Fluid Mechanics 362, pp. 327-346, 1998. Shock cavity implosion morphologies and vortical projectile generation in axisymmetric shock-spherical F/S bubble interactions. Also,: N.J. Zabusky, Annual Review Fluid Mechanics 31, pp. 495-536, 1999

[2] S. Zhang and N. J. Zabusky Shock –planar curtain interactions: Strong secondary baroclinic deposition and the emergence of coherent and random vortex projectiles (VPs) and decaying stratified turbulence. 8th IWPCTM: International Workshop on the Physics of Compressible Turbulent Mixing (this volume)

[3] R. Samtaney and D.I. Pullin, Physics of Fluids 8, pp. 2650-2655, 1996

*This work was supported mainly by DOE (Grant No. DE-FG0293ER25179.A000) and monitored by Dr. Daniel Hitchcock. Additional support was provided by Rutgers University SROA program
This paper is dedicated to Brad Sturtevant whose experiments inspired important configurations for accelerated flows.

PACS Nos.: 47.40.-x, 47.40.Nm, 52.57.Fg, 47.20 Ma, 47.27.-I, 47.27.Eq, 47.11.+j

Abstract No. C30

Influence of Turbulent Mixing Zone on Growth of Local Perturbation in Environments of Rayleigh-Taylor Instability (Numerical Simulation)

V. A. Raevski, S. N. Sinitsina, and Yu. V. Yanilkin
Russian Federal Nuclear Center – VNIIEF, Sarov, Russia

It is common knowledge that self-similar growth of local perturbation occurs following the law in the case of absence of turbulent mixing zone. The growth constant is about 3 times higher than the constant of growth of self-similar turbulent mixing zone. Basing on two-dimensional numerical computations by Euler technique EGAK, it is revealed that continuous continuum of self-similar solutions occurs, where is function of the relation and, if at the initial time there are local perturbation and the perturbations forming further the turbulent mixing zone.

Abstract No. C31

A Statistical Comparison of Gas Cylinder Experiments with Their Simulation

W. J. Rider, J. R. Kamm, and C. A. Zoldi
Los Alamos National Laboratory, Los Alamos, NM

We present the statistical analysis of the evolution of a diffuse cylinder of SF_6 shocked by a Mach 1.2 shock. The cylinder baroclinically develops a vortical structure and subsequently mixes with the surrounding air. The experimental diagnostics are images of tracer particles in the SF_6 and particle image velocimetry. We examine the nature of the mixing using a variety of tools including image analysis using correlations, wavelets, and fractal dimension. Our efforts follow the path of earlier investigations of a gas curtain geometry. There we found significant departures in behavior between the details of the experimentally measured mixing and that computed with the hydrodynamic codes. These statistics from the experiment are then compared with complementary simulations using several computer codes. In each case, we examine the sensitivity of the results to variations in mesh resolution and numerical algorithms. Figure 1 contains plots showing that both the integral size of the evolving cylinder and the magnitude of the velocity field computed in hydrodynamic codes do not match the experimentally measured results.

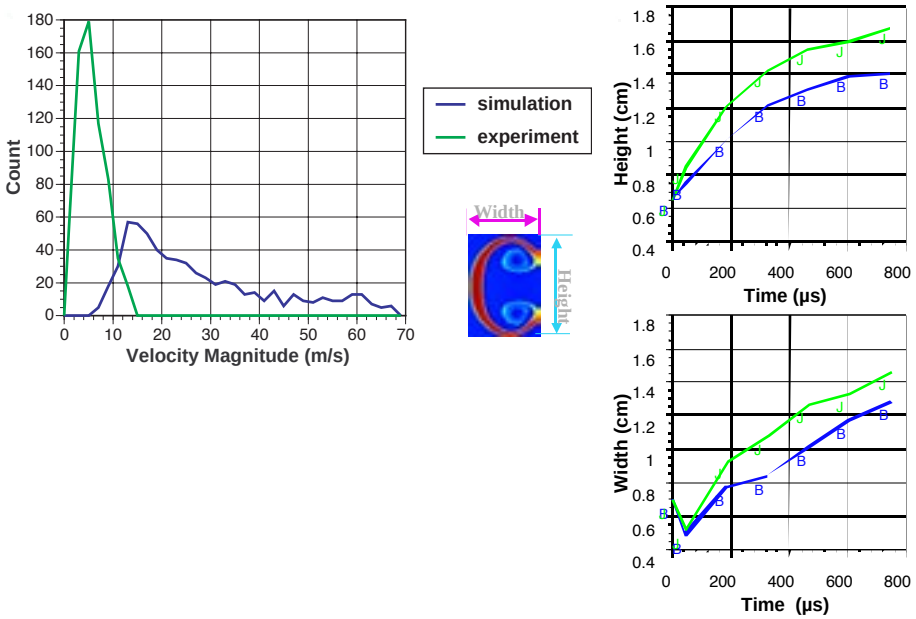

Fig. 1. The plot on the left shows a distribution of the velocity magnitude for the experiment (green) and simulation (blue). The plots on the right show the time evolution of the height and width of the evolving shocked cylinder structure.

Abstract No. C33

Large Eddy Simulation of Strong Shock Richtmyer-Meshkov Instability

R. Samtaney, T. Voelkl, and D. I. Pullin
Graduate Aeronautical Laboratories, California Institute of Technology, Pasadena, CA

In previous studies of isotropic compressible turbulence [1], it was demonstrated that low-order difference schemes are unsuitable for large eddy simulations (LES) of compressible turbulence. In this paper, we present results from formally high-order accurate LES of the Richtmyer-Meshkov (RM) instability. We chose fifth and seventh-order accurate Weighted Essentially Non-Oscillatory (WENO) schemes as the numerical method. These were suitably modified to suppress the so-called carbuncle numerical instability of the shock front. The physical details of the simulations are as follows. The physical domain is a shock-tube of square cross-section. A smooth flat interface with a hyperbolic tangent profile between two gases is initially deformed with a prescribed spectrum giving it multiple harmonic perturbations. This interface is accelerated with a strong (Mach number = 10) shock. The boundary conditions are periodic in the transverse directions, and inflow and reflecting along the length of the shock-tube.

The sub-grid-scale (SGS) model employed in the LES is the stretched vortex (SV) SGS model [2]. This model assumes sub-grid motion to be generated by nearly axisymmetric vortices. The sub-grid heat flux is modeled by advection of a passive scalar taken as the temperature. This model was successfully demonstrated in *a posteriori* comparisons between LES and direct numerical simulations of moderate turbulent Mach number decaying isotropic compressible turbulent simulations in the presence of shocklets [1]. It requires the velocity gradient tensor and the temperature gradient, both of which are calculated with an explicit fourth-order finite difference method.

We will present the evolution of the mixing width as a function of time computed using a level-set approach and a variety of diagnostic procedures, the transverse spectra and evolution of the turbulent kinetic energy (both sub-grid and resolved). In particular, we focus on the effects on these variables due to reshock. Finally, we will endeavor to shed light on the modified wavenumber characteristics of the WENO method and it's suitability for the LES of RM flows.

Acknowledgement: We gratefully acknowledge support of this work by the Academic Strategic Alliances Program of the Accelerated Strategic Computing Initiative (ASCI/ASAP) under subcontract no. B341492 of DOE contract W-7405-ENG-48. Useful discussions with Paul Dimotakis, Tony Leonard, Dan Meiron, and Branko Kosovic are gratefully acknowledged.

References:

[1] Branko Kosovic, Dale I. Pullin, and Ravi Samtaney. *Subgrid-scale modeling for large-eddy simulation of compressible turbulence.* Physics of fluids, sub-judice.

[2] Tobias Voelkl and D.I Pullin. A physical-space version of the stretched-vortex subgrid-stress model for large-eddy simulation. Physics of Fluids, Vol. 12, pp1810-1825

Abstract No. C35

Numerical Investigation of a Laser Induced Turbulent Mixing Zone

P. Seytor and M. Legrand
Commissariat à l'Energie Atomique, Bruyères-le-Châtel, France

We have used high Mach number (M~30) mix instability experiments[1] which have been conducted using Nova laser system to investigate the growth of the Richtmyer-Meshkov instability resulting from a strong shock wave. The initial nonlinear single-mode two dimensionnal pertubation was machined into a brominated plastic ablator (1.22 g/cm^3) adjacent to a low density carbon foam (0.10 g/cm^3). We compared the experimental measurements with LLNL simulations (CALE 1D/2D) and our own numerical simulations (FCI1/FCI2). We found both experiment and simulation to be in good agreement with a k-_ model and also with recent theories for the non linear evolution of instability relevant to an other work presented at this meeting[2].

[1]D.R. Farley, L. M. Logory, S.D. Murray and E. W. Burke PHYS; Plasmas **6**, 4304, (1999).

[2]M. Vandenboomgaerde this meeting 8th IWPCTM 2001.

Abstract No. C36

A Mix-Model For One-Dimensional Simulations of Laser-Driven Implosion Experiments

D. Souffland and F. Renaud
Commissariat à l'Energie Atomique, Bruyères-le-Châtel, France

In laser-driven implosion experiments, hydrodynamic instabilities can growth at interfaces between components as well as at ablation fronts. These processes have various origins and evolve through different ways, but they have in common to favor interpenetration of different fluid components or of fluid regions differing only by their thermodynamic states. The complete study of these intrinsically three-dimensional phenomena, involving a large range of length scales, is still unworkable. We thus need simplified models to assess the impact of variations in the definition of the target, the hohlraum or the laser drive.

The main hypothesis for the present mix-model is that, at the scale of the mesh size, an intimate mixing can simulate the interpenetration region. The description of the model, called hereafter MeDiC, specifies the treatment for the two main cases: density interface instabilities and non-material front instabilities. Diffusive terms are added to model heat and momentum transfers. In the first case, an additional equation for the mass concentration of one component of the mixing is calculate, when, for the second one, the boundaries of the mixing region are imposed. The thickening of the interpenetration zone is, indeed, supposed to be known from experimental data or from post-processing of two-dimensional computations results. This information is used to set the boundary locations, in the non-material front instabilities case, and, in both cases, to calculate the evolution of the diffusion coefficients.

We will discuss examples of mixings due to the Richtmyer-Meshkov instability occurring at the interface between the plastic shell and the fuel, on one hand, and to the ablation front instability occurring at the edge of the hot spot during its formation, on the other hand.

PACS Nos.: 52.57.Fg, 51.20, 42.27.Qb

Abstract No. C37

Modeling Turbulent Mixing in Inertial Confinement Fusion Implosions

Y. Srebro[1,2], D. Kushnir[2,3], Y. Elbaz[1,2], and D. Shvarts[1,2]
[1]*Ben-Gurion University, Beer-Sheva, Israel*
[2]*Nuclear Research Center, Negev, Israel*
[3]*Hebrew University, Jerusalem, Israel*

A series of high uniformity spherical implosion experiments has recently been conducted on the OMEGA laser system in the University of Rochester. In these experiments 3-15atm gas-filled plastic shells of diameter ~1mm were irradiated with 1ns square laser pulses of total energy ~20kJ. Fusion yields were measured experimentally to be 10-40% of one-dimensional numerical simulations' prediction, probably because of core-shell mixing.
Perturbations to these implosions include inner and outer surface roughness, beam-to-beam power imbalance and single-beam laser nonuniformity, which has been reduced to a minimal level using 1THz 2D-SSD.
Two-dimensional numerical simulations, describing the Rayleigh-Taylor growth of multimode perturbations during the deceleration-stage, were performed to determine mix region width. Reductions in the temporal neutron production rate, attained from the simulations assuming various levels of atomic mixing in the mixed region, were compared to experimental results for implosions with different convergence ratios.

Abstract No. C38

Turbulent Mixing Nuclear Burning in Type Ia Supernova Explosion Based on Bubble Statistical Mechanics

H. Takabe[1], S. Yamada[1], K. Kobayashi[1], A. Mizuta[1], and K. Nomoto[2]
[1]*Osaka University, Osaka, Japan*
[2]*University of Tokyo, Tokyo, Japan*

It is well known that Type Ia supernovae explode when the masses of white dwarfs become close to the Chandrasekhar limiting mass. This is the reason why the Type Ia explosion is used as a standard candle in the universe to determine, for example, the Hubble constant and dark energy. The scale of explosion has been well studied with one-dimensional code with some mixing model; however, the physical mechanism has not determined from the first principle, yet. There are many works to understand the physics with large scale computing based on hydrodynamics in two-dimension or mostly three-dimension in these days [1]. It seems, however, that the smaller scale fluctuation appears, the smaller the grid size, and it is still open question how the instability grows and evolves into nonlinear stage and enhance the energy release by nuclear reactions.

In the present report, we would like to model the growth of the Rayleigh-Taylor instability coupled with the Landau-Darrieus instability. In the nonlinear stage, we consider the statistical mechanics of the bubbles following the way developed by Don Shvarts[2] and estimate the increase in the nuclear burning rate due to the increase in the surface area of the burning wave in the form of fractal structure. This model is coupled with the multi-dimensional explosion code to predict the scale of explosion. Such work is expected to be used to identify the physical mechanism of the time evolution of the burning wave, which may change from deflagration wave to detonation wave.

Reference:
[1]W. Hillebrandt and J. Niemeyer, Ann. Rev. Astron. Astrophys. 38, 191-230 (2000)
[2]D. Shvarts et al, Physics of Plasmas 2. 2465 (1995).

Abstract No. C39

Turbulent Diffusion in Solar Type Star

N. Toqué
University of Montreal, Quebec, Canada

The shear layers with the instability of Kelvin-Helmoltz are common topics of the fluids mechanics. They are less common when they are assumed to be in a solar type star to partly explain the anomalies of abundances at the photosphere. Thanks to the rolling-up of the convective zone, the ionized species, which are produced in the radiative core of the star, such as the Lithium, have to migrate to the top of it. However, they are not enough detected at the photophere to validate the standard stellar model. So, it is assumed that at the vicinity of the tachoclyne, the goin-up of the light abundances is blocked by horizontal turbulence in shear layers.

This poster introduces the content of the numerical 2D code and the assumptions made to simplify the modelisation of the physical problem. It shows results which enforce the influence of the turbulence and quantify its effect on the going-up of the ionized species to the photophere of the star.

Abstract No. C40

Recent Computational Simulations of Rayleigh-Taylor Mix Layer Growth With a Multi-Fluid Model

E. Vold
Los Alamos National Laboratory, Los Alamos, NM

Recent results of computational simulations of the Rayleigh-Taylor mix layer are presented and discussed. Our previous work is summarized briefly comparing mix layer growth characteristics observed in different simulation modes including single fluid with initial density discontinuity, two-fluids with interface reconstruction and in a full multi-fluid dynamic approach. Recent comparisons under varying compressibility are presented showing negligible influence of compressibility on the mix layer growth rate. Using spectral analyses, perturbations intentionally introduced in the initial conditions are compared to long wave length perturbations introduced inadvertently in these initial conditions. The influence of these initial conditions on late time growth and growth rate are explored. The compressible multi-fluid model allows each fluid to have its own 'drift velocity' relative to the mass averaged fluid velocity. This can be applied in several ways within the mix layer to represent a real molecular mixing, a turbulent enhanced diffusive mixing, or an individual species 'sub-grid' convective drift flux. Examples of these in the Rayleigh-Taylor mix layer are discussed. Finally, we consider the combination of these factors which best matches the experimental results for mixing layer growth rates in incompressible experiments, and how these results may apply to compressible fluids.

Abstract No. C41

An Efficient and High Resolution Solver for the Two-Dimensional Numerical Simulation of the Richtmyer-Meshkov Instability

S. P. Wang, M. H. Anderson, J. G. Oakley, and R. Bonazza
University of Wisconsin at Madison, Madison, WI

The development of a consistent and fully conservative model and a corresponding efficient and high resolution solver for the numerical simulation of multicomponent or multifluid flows is presented. This theoretical and numerical work was developed to support the Wisconsin shock tube investigation of hydrodynamic issues related to the Richtmyer-Meshkov and Rayleigh-Taylor instabilities.

A consistent and fully conservative treatment of contact discontinuities is proposed for the simulation of compressible multifluid flows. The model is capable of capturing contact discontinuities with significantly reduced numerical uncertainties compared to conventional conservative models. Starting from the concept of total enthalpy conservation for the mixture, a new formulation is defined for the determination of the ratio of the specific heats of the mixture, and a governing equation in conservative form for pressure is obtained subsequently. With continuity equations for the individual components, a governing equation in conservative form for the ratio of specific heats of the mixture is easily derived. These two derived equations, combined with mass balance and momentum balance equations form the full system for the description of multifluid flows.

The conservative governing equations are then solved with an efficient and high resolution Godunov-type solver which is based upon the exact Pike(1993) Riemann solver. To improve the accuracy of the scheme, by preserving monotonicity of the variables at shock waves and contact surfaces, a Monotonic Upstream-Centred Scheme for Conservation Laws (MUSCL) technique for the data reconstruction of fluxes is used. Second order accuracy is achieved by using a piece-wise linear method and a piece-wise spline method is introduced to achieve higher-order accuracy especially useful for capturing contact discontinuities such as the Richtmyer-Meshkov instability (fourth order accuracy has been achieved even for non-uniform mesh sizes).

Several 1-D multifluid flows with both strong and weak shocks are simulated using the model. Comparisons of numerical results obtained by the proposed model, conventional models and exact solutions are made. They show that the proposed model and the methods are accurate, robust and generate oscillation-free solutions near material interfaces. Finally, the proposed model and method are extended to 2-D multifluid flow problems and compared to experimental Richtmyer-Meshkov instability growth measurements conducted in the University of Wisconsin shock tube.

Abstract No. C42

ALE Simulations of Turbulent Rayleigh-Taylor Instability in 2-D and 3-D

S. V. Weber, G. Dimonte, and M. M. Marinak
Lawrence Livermore National Laboratory, Livermore, CA

We have performed simulations of the evolution of the turbulent Rayleigh-Taylor instability with the ALE code HYDRA3, including interface reconstruction. The test problem is that of the "alpha group", discussed in the presentation of Dimonte *et al*. at this conference. Perfect γ=5/3 gases of densities 1 and 3 are accelerated by constant gravity. The initial interface perturbation is a random spectrum of modes in the range $32 \leq n \leq 64$. We employed meshs of 256 x 512, 512 x 1028, and 1028 x 2048 in two dimensions (2-D) and 128^2 x 512 and 256^2 x 512 in 3-D. The shortest seed modes have only 4 zones/wavelength at the nominal (coarsest) resolution. Consequently, linear growth is suppressed by under-resolution, and is not fully converged even at the highest resolution. However, as the growth transitions toward turbulence, turn-over of the growth rate in the 2-D simulations occurs earlier and at smaller amplitude with higher resolution. Results for mixing layer growth in the self-similar $\sim gt^2$ regime and sub-structure of the mixing layer will be discussed.

1 M. Marinak *et al*., *Phys. Plasmas* **3**, 2070 (1996).

This work was performed under the auspices of the U.S. Department of Energy by the University of California Lawrence Livermore National Laboratory under contract No. W-7405-Eng-48.

Abstract No. C44

Study of Turbulent Gravitational Mixing at Large Density Differences Using Direct 3D Numerical Simulation

Yu. V. Yanilkin, V. P. Statsenko, S. V. Rebrov, N. I. Selchenkova, O. G. Sin'kova, A. L. Stadnik and A. Ya. Uchayev
Russian Federal Nuclear Center – VNIIEF, Sarov, Russia

3D hydrocode TREK is used for numerical study of turbulence evolution in the field of gravity at a plane interface between two incompressible fluids (gases) with a large density difference, $3 \le \rho_2/\rho_1 \le 40$.

The computations were conducted on a fine computational grid with parallelization on several tens of processors.

The computed data was processed (averaged) in order to obtain moments of hydrodynamic values: diagonal components of Reynolds tensor (turbulent energy), turbulent flows, density profiles and mean-square pulsation. The resultant values are compared to predictions with phenomenological turbulence models and known experimental data.

The dissipation problems in these computations are disscussed.

A one-point function of concentration probability density is constructed using processed results of the direct numerical simulation. The results are compared to computed data obtained elsewhere.

A fractal analysis of turbulent vortex scales is also conducted, which demonstrates that in the turbulent mixing zone the fractal size does not essentially change and is close to the measured value and the value from 3D computations by other investigators.

Abstract No. C46

Development and Validation of a 2D Turbulent Mix Model

D. L. Youngs
Atomic Weapons Establishment, Aldermaston, United Kingdom

A 2D turbulence model based on the equations of multiphase flow with turbulent diffusion effects added, is used to model mixing by Rayleigh-Taylor and Richtmyer-Meshkov instabilities in situations where the mean flow is two dimensional. For simple 1D flows it is relatively easy to check that the turbulence model gives satisfactory mix distributions. However, this is much more difficult to do for the case when the mean flow is two dimensional. In order to validate the 2D turbulence model, results are compared to the tilted-interface Rayleigh-Taylor mixing experiments presented by J.M.Holford at this meeting and the 'chevron' shock tube experiments presented by A.V.Smith at this meeting. Experimental measurements of mix distributions are difficult to make in 2D. Hence 3D Large Eddy Simulation is able to make a very useful contribution. The TURMOIL3D code is used to perform 3D simulations which give a satisfactory match to the experimental results. The mix distributions obtained by averaging the calculational results in the third dimension may then be compared directly with the 2D turbulence model results.

At present 3D LES is often not practical for complex real applications. However, 3D LES for simplified problems does have a very useful role in helping to validate the turbulence models which can be applied to complex problems.

Abstract No. C47

Preliminary Results of DNS and LES Simulations of Self-Similar Variable Acceleration RT-Mixing Flows

D. L. Youngs[1], X. Silvani[2], J. Magnaudet[2], and A. Llor[3]
[1]*Atomic Weapons Establishment, Aldermaston, United Kingdom*
[2]*Institut de Mécanique des Fluides de Toulouse, Toulouse, France*
[3]*Commissariat à l'Energie Atomique, Bruyères-le-Châtel, France*

The importance of self-similar variable acceleration RT flows (SSVARTs) for the design an calibration of turbulent mixing models has been shown in an other presentation to the present workshop.

Because experimental results on SSVARTs are not, and will probably not be available in any close future, we are currently investigating such flows by means of DNS and LES.

This first presentation of our preliminary results will be devoted to discussing the technical issues (compressibility effects, subgrid models, initial conditions, mesh size, Atwood number...) whose influence must be carefully controled due to the lack of experimental data. The behaviour of the observed growth rates and large scale turbulent structures will also be analysed.

Abstract No. C48

Shock–Planar Curtain Interactions: Strong Secondary Baroclinic Deposition and the Emergence of Coherent and Random Vortex Projectiles (*VPs*) and Decaying Stratified Turbulence

S. Zhang and N. J. Zabusky
Rutgers, State University of New Jersey, Piscataway, NJ

We continue our previous investigation [1] of the interaction of a shock with a planar, inclined curtain (s/f/s) to higher Mach numbers, (M=1.5, 2.5 & 5.0), longer times (epochs) and alternate configurations in 2D and 3D (e.g. a fast/slow/fast or (f/s/f)). In all cases, the qualitative features may be explained in terms of opposite-signed vortex layers (deposited by shock waves in epoch 1) that move in opposite directions and collide at one boundary to form a complex ***v**ortex **d**ouble **l**ayer* (***VDL***) that traverses the shock tube. (This causes early-time ``breakthrough'' [1]). We focus on longer evolution times where, eventually, the transversely moving VDLs collide with the opposite horizontal boundary and evolve into upstream & downstream moving stratified ***v**ortex **p**rojectile**s*** (***VPs***) [2]. In 2D, we compare these near-stationary, inhomogeneous coherent structures to the Lamb-Chaplygin vortex of 2D homogeneous flow. We also display and quantify: (1) *strong* non-acoustic circulation generation via baroclinic processes during traversal of the VDL across the shock tube (epoch 2); and (2) evolution and decay (epochs > 2). of a stratified turbulent domain that arises between the two dominant VPs. We compare with images from Sturtevant' s 1985 experiments and comment on the unusual advantages of this configuration as well as the convergence of results under mesh refinement.

[1] Yang, X. , N.J. Zabusky, and I-L. Chern. Phys. Fluids A 2(6),892-895, **1990.**
"Breakthrough" via Dipolar-Vortex/Jet Formation in Shock-Accelerated Stratified Layers.
[2] N.J. Zabusky and S-M. Zeng, J. Fluid Mechanics 362, pp. 327-346, **1998**.
Shock cavity implosion morphologies and vortical projectile generation in axisymmetric shock-spherical F/S bubble interactions.

*This work was supported mainly by DOE (Grant No. DE-FG0293ER25179.A000) and monitored by Dr. Daniel Hitchcock. Additional support was provided by SROA program and the Jacobs Chair of Applied Physics at Rutgers University

Abstract No. C49

Rapid Turbulization Arising from Vortex Double Layers in Interactions of "Complex" Blast Waves and Cylindrical and Spherical Bubbles

S. Zhang[1], Y.-G. Kang [2], K. Nishihara, N. J. Zabusky[1], and H. Kim[2]
[1]*Institute of Laser Engineering, Osaka, Japan*
[2]*Rutgers, State University of New Jersey, Piscataway, NJ*

[1]We examine the interaction of both cylindrical and spherical bubbles and a *complex* blast wave which consists of an approaching shock/contact discontinuity/shock . Such configurations arise following a supernova explosion, e.g. SN 1987A where a complex blast wave is presently approaching a high density ring ("inner circumstellar"), and may lead to rapid onset of turbulence on the *upstream* part of the bubble[2], not an occurrence at low Mach numbers and density ratios[3]. The mixing in this turbulent domain will affect the electromagnetic radiation processes. Using PPM[4], we examine a parameter domain containing SN 1987A parameters to validate the occurrence of this process which is related to shock reverberations and vortex double layers and their rapid instabilities.

*At Rutgers, this work was supported mainly by DOE (Grant No. DE-FG0293ER25179.A000) and monitored by Dr. Daniel Hitchcock. Additional support was provided by the SROA program and the Jacobs Chair of Applied Physics at Rutgers University.[2]Laser Plasma Laboratory, Dept. of Materials Sci. & Eng., Kwangju Institute of Science and Technology, 1 Oryong-dong, Puk-gu, Kwangju, Korea

---

[1]Y-G Kang, et al , "A novel experiment on the blast wave-sphere interaction using a laser produced plasma" Phys. Rev E , submitted May 2001.
[2]K.J.Borkowski, J.M. Blondin and R. McCray. Astrophys J. **477**, 281-293, 1997
[3]N.J. Zabusky and S-M. Zeng, J. Fluid Mechanics **362**, 327-346, 1998.
[4]M. Blondin et al, Code VH-1 , NCSU. A lagrangian remap code based on PPM.

Abstract No. C50

Simulations of a Shock-Accelerated Gas Cylinder and Comparison with Experimental Images and Velocity Fields

C. A. Zoldi[1,2], K. Prestridge[1], P. M. Rightley[1], and R. F. Benjamin[1]
[1]*Los Alamos National Laboratory, Los Alamos, NM*
[2]*State University New York at Stony Brook, Stony Brook, NY*

The evolution of a cylinder of SF_6 gas accelerated by a Mach 1.2 shock wave is studied both experimentally and computationally. Images of the initial conditions and the time evolution of the cylinder are obtained from the experiment. Velocity measurements are determined at one time using Particle Image Velocimetry. Using an image of the experimental initial conditions, 2D simulations are performed with the adaptive mesh Eulerian code, RAGE. Although qualitative agreement is achieved, significant differences exist in quantitative measurements. The linear dimensions of the cylinder measured over time are approximately 15% smaller in the simulation than in the experiment. In addition, although the directions of the velocity vectors are similar, the peak magnitude of the velocity is a factor of three larger in the simulation. The effect of turbulent mixing, which has not been considered in previous analyses, is examined using the BHR K-S-a-b mix model recently added to the RAGE code.

PACS No.: 47.20.Ma

Abstract No. C51

Turbulent Flow Simulations of Two Fluids Moving with Different Laws of Acceleration

V. I. Kozlov, A. N. Razin, and I. V. Sapozhnikov
Russian Federal Nuclear Center – VNIIEF, Sarov, Russia

With Dimonte tests as an example, turbulent mixing (TM) evolution is discussed that results from Rayleigh-Taylor instability at the interface between two fluids. In these tests, an ampoule with two molecularly immiscible fluids (freon and water) was accelerated while the acceleration law being varied in these tests.

The VIKHR code was used for the numerical simulations of the Dimonte's tests. This VIKHR technique includes V.V. Nikiforov's semiempirical model of turbulent mixing. This model treats various characteristics of a turbulent field, like the kinetic energy of turbulence, the turbulence energy dissipation rate, the average square density fluctuations and the turbulent mass transfer velocity.

The calculations were performed with a sequence of refined grids with different initial TM zone widths for increasing, decreasing, pulse and constant accelerations of the ampoule (the acceleration laws were the same as those given in the paper by Dimonte). TM zone growth laws versus the ampoule's path and the initial TM zone width have been obtained. The numerical results have been shown to be in good agreement with the measured data provided additional constrains have been included in the V.V. Nikiforov's model. These constraints can be interpreted as effective treatment of turbulent motion energy being transferred to the interface energy of the boundary between the fluids that are molecularly immiscible.

References

Dimonte Guy, Schneider Marilyn. Turbulent Rayleigh-Taylor instability experiments with variable acceleration // Physical Review E, 1996, v. 54, p.3740-3743.

Abstract No. C52

The Behaviour of Velocity Variance Resulting from Turbulent Mixing Zone-Shock Interaction

V. I. Kozlov and A. N. Razin
Russian Federal Nuclear Center – VNIIEF, Sarov, Russia

Turbulent mixing (TM) caused by Richtmyer-Meshkov instability at an interface between two gases with different densities is discussed. VIKHR code simulations of shock tube tests by Poggi et al have been performed. The feature of these tests is that the fluid's instantaneous mass velocities were measured by Doppler's laser anemometer.

The VIKHR code includes the 1D version of the semiempirical TM model suggested by V.V. Nikiforov that treats eddies' anisotropy. The VIKHR technique permits to precisely calculate various quantities of a turbulent field, like for instance, the average square variance of different velocity components and the average square density fluctuations, along with the flow's gas-dynamical parameter distributions.

The calculations gave TM zone width and location versus time. The temporal evolution of the average square axial velocity variance was also obtained for several Eulerian points. No special calculation algorithm for turbulence quantities was used at the shock front in these calculations.

On the whole, there is satisfactory agreement with the test data by Poggi et al. Meanwhile, behind the front of the first wave (whose intensity is the highest) reflected from the tube's dead end is approximately two time higher than that measured in the tests. (Note that the same quantity calculated by Souffland et. al. exceeds the observed value by an order of magnitude). These results have shown that the correlations used in the Nikiforov's model to treat shock wave-turbulent field interactions, need to be improved.

References

1. *F. Poggi, M.-H. Thorembey, G. Rodriguez.* Physics of Fluids, v. 10, _ 11, 1998, pp. 2698-2700.
2. *D Souffland, O. Gregoire, S. Gauthier, F. Poggi, J.M. Koenig.* 6th International Workshop on the physics of compressible turbulent mixing (Marseille, France), 1997, pp. 486-491.

Abstract No. C53

An Assessment of Multi-Velocity Versus Single Velocity in a Multi-Component Model of Turbulent Mixing

D. E. Eliason, W. H. Cabot, and Y. Zhou
Lawrence Livermore National Laboratory, Livermore, CA

Turbulent mixing of the fluids in a multi-componentsystem is of interest in situations such as inertial confinement fusion (ICF) and core-collapse supernovae [1]. We report results of a project to include a model of turbulent mixing in a multi-component hydrodynamics and physics model called KULL, which is used for ICF. Because KULL is a complex, multi-dimensional model, we have developed a simplified, one-dimensional version called sKULL to speed-up the development of the turbulent mixing model.

Of primary interest in the development of a turbulent mixing model for a multi-component fluid is the question of whether it is necessary to allow each component of the fluid to retain its own velocity. A recently developed model of turbulent mixing, consisting of an extended buoyancy-drag model and two-equation turbulent transport model [2], treats all components of the fluid as if they had the same velocity. In contrast, multi-velocity turbulent mixing models allow separate velocities for each component of the fluid [3]. However, the necessity to carry separate velocities for each component of the fluid greatly increases the memory requirements and complexity of the computer implementation. We will report results of a comparison between single velocity and multi-velocity turbulent mixing models in sKULL with the intention of answering the question of whether the full multi-velocity treatment is really necessary.

This work was performed under the auspices of the U.S. Department of Energy by the University of California Lawrence Livermore National Laboratory under contract No. W-7405-Eng-48.

[1] Remington, B.A., D. Arnett, R.P. Drake, and H. Takabe, Modeling Astrophysical Phenomena in the Laboratory with Intense Lasers, *Science*, **284**, 1488 (1999).

[2] Zhou, Y., G. Zimmerman, and E.B. Burke, submitted to *Phys. Rev. E.*, (2001).

[3] Youngs, D.L., *Laser & Particle Beams* **12**, 725 (1994).

Abstract No. C54

High Order Numerical Methods for the 2D Richtmyer-Meshkov Instability

W.-S. Don[1], D. Gottlieb[1], L. Jameson[2], and C.-W. Shu[1]
[1]*Brown University, Providence, RI*
[2]*Lawrence Livermore National Laboratory, Livermore, CA*

The primary goal of this presentation is to examine several numerical methodologies with high order accuracy for the investigation of the two dimensional (and eventually three dimensional) Richtmyer-Meshkov instability. The high order schemes employed are the Spectral methods and the high order Weighted Essentially Non-Oscillatory (WENO) finite difference scheme. We will briefly discuss several important aspects of the numerical schemes when applied to the Euler equations. Multi-species full Navier-Stokes equations will be implemented in the near future.

A series of numerical simulations are carried out to investigate the convergence properties of the schemes and long time behavior of the interface evolution. Numerical results from the simulation of shock interaction with a single mode perturbation of interface separating the heavy (Xenon) to light (Argon) gases will be presented with various interface thickness and different Mach numbers. It can be observed that the large and median scale structures such as the spike and bubble, transmitted shock, shocked-interface velocity and shock triple point obtained by the different schemes are basically in excellent agreement with each other and with available experimental data. Also convergence studies had been made. Some minor discrepancies of the finest scale structures along the gaseous interface, as can be expected for numerical simulations of the Euler equations with this sensitive nature, are observed.

This work was performed under the auspices of the U.S. Department of Energy by the University of California Lawrence Livermore National Laboratory under contract No. W-7405-Eng-48.

Abstract No. C55

Mixing Due to the Rayleigh-Taylor Instability

A. M. Dimits
Lawrence Livermore National Laboratory, Livermore, CA

Several aspects of mixing due to the Rayleigh-Taylor (RT) instability are investigated.

Analysis of 3D multimode simulations using the PPM code [D.H. Porter and P.R. Woodward, Astrophys. J. Suppl. 93, 309 (1994), and references therein.] show that there are regions of the parameter space of the initial conditions in which the growth rate is independent of variations in the initial conditions. The simulated growth rates are found to increase as the Navier-Stokes viscosity is increased. It is investigated whether this couterintuitive result is due to the suppression of material mixing at the molecular level for larger viscosities.

Analyses of two RT experiments, one in which water is accelerated by a compressed gas (E.E. Meshkov and N.V. Nevmerzhitsky, Proc. 3rd Int. Workshop. on the Physics of Compressible Turbulent Mixing, 1991) and one in which an interface between gases of different density is decellerated in the post-shock region of a shock in an electromagnetic shock tube (A.M. Vasilenko et al., ibid.), are presented. Direct compressibility effects on the RT growth are shown to be negligible in the former. Various effects of the expansion of the gases in the region of the interface on the RT growth rates are investigated for the latter experiment, both analytically and with 1D simulations. These effects are found to be insufficient to reconcile the growth rates observed in the Vasilenko et al. experiments with some other experimental and simulation results.

This work was performed under the auspices of the U.S. Department of Energy by the University of California Lawrence Livermore National Laboratory under contract No. W-7405-Eng-48.

Abstract No. C56

Transition Stages of Rayleigh-Taylor Instability Between Miscible Fluids

A. W. Cook and P. E. Dimotakis
Lawrence Livermore National Laboratory, Livermore, CA
California Institute of Technology, Pasadena, CA

Direct Numerical Simulations are presented of three-dimensional, Rayleigh-Taylor instability between two incompressible, miscible fluids, with a 3:1 density ratio. Periodic boundary conditions are imposed in the horizontal directions of a rectangular domain, with no-slip top and bottom walls. Solutions are obtained for the Navier-Stokes equations, augmented by a species transport-diffusion equation, with various initial perturbations. Three of the simulations (Cases A, B and C) were performed at a resolution of 256 x 256 x 1024 grid points, and the fourth simulation (Case D) was performed at a resolution of 512 x 512 x 2040 grid points. The A, B and C cases achieved outer-scale Reynolds numbers, based on height and rate of growth of mixing-zone, in excess of 3000; Case D achieved an outer-scale Reynolds number of 5500. Initial diffusive growth is captured in the simulations. The onset of nonlinear growth is as predicted by linear stability theory. Following the diffusive stage, growth rates are found to depend on the initial perturbations through the end of the simulations. Mixing is found to be even more sensitive to initial conditions than growth rates. Taylor microscales and Reynolds numbers are anisotropic throughout the simulations. Improved collapse of many statistics is achieved if the height of the mixing zone, rather than time, is used as the progress variable. Mixing has dynamical consequences for this flow, since it is driven by the action of the imposed acceleration field on local density differences.

This work was performed under the auspices of the U.S. Department of Energy by the University of California Lawrence Livermore National Laboratory under contract No. W-7405-Eng-48.

Abstract No. C57

CALE Simulation of Richtmyer-Meshkov Experiments at High Mach Number

A. Miles[1,2], J. Edwards[2], G. Glendinning[2]
[1]*Lawrence Livermore National Laboratory, Livermore, CA*
[2]*University of Maryland, College Park, MD*

Richtmyer-Meshkov instability experiments, recently conducted on the Omega laser, are simulated via the C-based Arbitrary Lagrangian-Eulerian (CALE) hydrodynamics code in 2D. In the experiments, a high Mach number shock ($M \approx 10$) is incident on a corrugated plastic-foam interface ($ka = 0.92$). The ratio of plastic to foam density is 12:1. After passage of the incident shock, the perturbation amplitude grows in time. Computational grids initially rectangular and conforming to the initial amplitude perturbation are both considered, as are zoning effects. Discrepancies between the experiment and simulation are considered, including the growth rate at early times, the post-shock amplitude, and the shock-interface proximity as the transmitted shock propagates through the foam. A modified input velocity source is presented which results in a time-dependent growth rate that agrees with the experimental observations much better than does the original source, which is produced by a 1D Lasnex simulation. Various EOS models are used, and their predictions compared.

THEORETICAL ABSTRACTS

Abstract No. T1

Nonlinear Evolution of Unstable Fluid Interface

S. I. Abarzhi
State University of New York at Stony Brook, Stony Brook, NY

We study the nonlinear evolution of the fluid interface generated by the Richtmyer-Meshkov instability. For the first time we find the theoretical solutions, which capture the interplay of harmonics in the nonlinear dynamics of 3D and 2D flows. A new type of the evolution of the bubble front in RMI is discovered [1]. It is shown that the nonlinear RM bubbles flatten in time and the shapes of Rayleigh-Taylor and Richtmyer-Meshkov bubbles differ significantly.

To perform the multi-mode analysis for the RM flow, we generalized the method developed in [2] for RTI, and based our approach on symmetry theory. From the conservation aws we derived a dynamical system governing the local dynamics of the nonlinear bubble. To capture the interplay of harmonics in the local dynamics, we extended the functional space, involved all bubbles allowed by symmetry of the flow, and found a family of regular asymptotic solutions. The physically dominant solution in this family, i.e. the fastest stable one, corresponds to a flattened bubble, not to a bubble with finite curvature as in [3].

The theory reveals deficiency of previous theoretical approaches in [3], explains existing experiments, and establishes control parameters to be monitored in experiments.

1.S.I.Abarzhi, Nonlinear evolution of unstable fluid interface, Phys.Rev.Lett. submitted
2.S.I.Abarzhi, PRL89, 1332 (1998)
3.J.Hecht, U.Alon, D.Shvarts, Phys.Fluids 6, 4019 (1994); N.A.Inogamov, Sov.Phys.JETP 80, 890 (1995); K.O.Mikaelian, Phys.Rev.Lett.80, 508 (1998); Q.Zhang, Phys.Rev.Lett. 81,3391 (1998); S.Abarzhi, Phys.Fluids 12, N12 (2000).

Abstract No. T2

Nonlinear Asymptotic Solutions to RT and RM Problems for Fluids With Close Densities

S. I. Abarzhi
State University of New York at Stony Brook, Stony Brook, NY

We consider the interface dynamics in the Rayleigh-Taylor and Richtmyer-Meshkov instabilities for fluids with close densities, the Atwood number A<1. We find the analytical solutions to the equations governing the interface dynamics in 3D and 2D (conservation laws, potential approximation), and analyze their regular and singular asymptotic behavior. First we derive a nonlinear solution of the Layzer-type, i.e. single-mode solution [1]. For this solution the normal component of velocity is discontinuous, and the flux of mass through the interface is significant. We resolve this paradox and find a multi-mode nonlinear solution with NO FLUX of MASS through the interface. This solution is the fastest one in the family of asymptotic solutions to the conservation laws [1].

The theory [1] determines parameters to distinguish between the Layzer-type solution and the nonlinear solution with NO FLUX. In RTI the bubble with NO FLUX is in few times narrower than the Layzer-type bubble, while in RMI the bubble with NO FLUX is flattened. The singular asymptotes (spikes) are also analyzed, and the influence of vorticity on the spike motion is evaluated. We conclude that there is a non-trivial dependence on the Atwood number for the parameters of the nonlinear motion (such as velocity of the bubble or spike) in either RTI or RMI cases. The RT/RM mixing process is discussed.

1. S.I.Abarzhi, The dependence of the nonlinear RT/RM motion on the Atwood number, in preparation, 2001.

Abstract No. T3

Turbulent Mixing in RTI as Order-Disorder Process

S. I. Abarzhi
State University of New York at Stony Brook, Stony Brook, NY

The cascades of energy and the dynamics of large-scale coherent structure are fundamental issues in the problem of Rayleigh-Taylor turbulent mixing. The large-scale structure is a periodic array of bubbles and spikes in the plane normal to the direction of gravity. We study dynamics of this structure based on group theory, and analyze transitions associated with the growth of length scale of the flow. In the limiting case of 2D flow, the scale growth occurs as a doubling of the spatial period, in agreement with Sharp and Wheeler model, and a stable observable coherent structure appears under this transition. In contrast, for a 3D flow the growth of length scale leads eventually to anisotropy of the flow in the plane normal to the direction of gravity and no isotropic structure occurs. We see that in RT turbulent mixing a balance between the inverse and direct cascades is required to keep isotropy of the flow. These two processes may lead in a generation of an internal structure with hexagonal symmetry and with close packing in the plane normal to the direction of gravity. The concept of self-similarity in the RT mixing is discussed.

Abstract No. T4

A New Turbulent Two-Fluid RANS Model for KH, RT and RM Mixing Layers

P. Bailly and A. Llor
Commissariat à l'Energie Atomique, Bruyères-le-Châtel, France

Our aim is to develop an accurate turbulent mixing model for combined RT, RM and KH type of instabilities, with arbitrarily variable accelerations.
Following the recent analysis of the RT and RM cases by G. Dimonte, and of the self-similar variable acceleration RT flows (SSVARTs) in an other presentation to the present workshop, we have considered as crucial to capture the following physical aspects by the corresponding model features:

- the directed transport by a two-fluid approach,
- the correct buoyancy force by including mass transfer between the fluids,
- the turbulence diffusion by including most of the standard k-ε features,
- the geometrical aspects by consistent closures of the length scales.

This yielded a two-fluid two-turbulence model whose specific and original features will be discussed. 1D numerical results of this model applied to self-similar flows will be presented.

Abstract No. T5

Super-Exponential Rayleigh-Taylor Flow

R. E. Breidenthal
University of Washington, Seattle, WA

A new class of forced, self-similar turbulence is proposed. In it, the rotation period of the large-scale vortices is forced to decrease by a constant factor at each rotation. This is achieved by imposing an e-folding time scale on the flow that decreases linearly with time. Based on experimental results in analogous flows, super-exponential turbulence may exhibit extraordinarily low entrainment and mixing rates. One application is in inertial-confinement fusion, where super-exponential acceleration may play a useful role in achieving ignition. It is shown that super-exponential flows are the mirror image of unforced turbulence, and both are members of a closely related family of self-similar turbulence.

Abstract No. T7

Theoretical Methods for Determination of Mix

B. Cheng[1], J. Glimm[2,3], and D. H. Sharp[1]
[1]*Los Alamos National Laboratory, Los Alamos, NM*
[2]*State University of New York at Stony Brook, Stony Brook, NY*
[3]*Brookhaven National Laboratory, Brookhaven, NY*

We present a theoretical description of the growth of a planar 3D mixing layer due to Rayleigh-Taylor (RT) or Richtmyer-Meshkov (RM) instabilities. The methods yield agreement with all known experiments. They also possess advantageous theoretical features, such as real characteristic speeds and improved mixed cell EOS.

The first method is a bubble merger model, validated by comparison to experiments of Smeeton and Youngs and of Dimonte et al. The model is based on a renormalization group fixed point calculation, incorporating the self similar behavior of RT instability. The second method is based on the dynamic motion of the RT center of mass; it couples the bubble and spike mixing zone edges, and predicts the RT spike growth as a function of the RT bubble growth. The third method is a drag buoyancy model, with a phenomenological drag coefficient, set to agree with the RT edge motion models above. This model predicts RM edge motion. The final method is a mix model, i.e. a set of averaged equations, with prediction of the behavior of mixed average flow quantities such as volume fraction, as a function of the mixing zone edges.

PACS Nos.: 47.20Bp, 47.52+j

Abstract No. T8

Modeling Radiation Effects in Mixing Layers

T. Clark and F. Harlow
Los Alamos National Laboratory, Los Alamos, NM

Radiative heat transport and resulting material phase changes can have a pronounced effect on the evolution of Rayleigh-Taylor and Richtmyer-Meshkov mixing layers. For sufficiently high temperature differences across the materials in these layers, the radiation effects may significantly alter the rate of growth of these mixing layers. Direct numerical simulation of these processes is generally not possible for practical circumstances due to the rapid growth of fine-scale structures as well as the inherent stochasticity of the mixing process. Consequently, we are developing a turbulent mix model that incorporates the effects of radiative heat transfer and ablation in a computationally tractable fashion. The model under development describes the ablation of the cold material as a surface phenomenon in which a thin skin of the cold material is ablated by the radiation through a thin skin of the hot material. As a first approximation we have assumed that only two materials are present. Thus after the cold material is ablated it is indistinguishable from the hot material. The goal of the model is to derive a model with sufficient predictive power to determine the mixing layer growth rates, and to distinguish the circumstances under which the ablation process (i.e., "fire-polishing") will overwhelm the tendency towards hydrodynamic mixing intrinsic to these mixing layers. We will discuss both model development and computed results.

PACS Nos.: 47.27.Eq, 47.27.Te, 47.55.Kf, 47.70.Mc

Abstract No. T9

A Model for Instability Growth in Accelerated Solid Metals

J. D. Colvin[1], M. Legrand[2], B. A. Remington[1], G. Schurtz[2], and S. V. Weber[1]
[1]*Lawrence Livermore National Laboratory, Livermore, CA*
[2]*Commissariat à l'Energie Atomique, Bruyères-le-Châtel, France*

We present the derivation of an approximate analytical dispersion relationship for elastic-plastic acceleration-driven instability growth. We have applied this model, where applicable, to perturbation growth measurements made in three separate types of experiments: HE-driven planar Al plates, HE-driven implosions of steel cylinders, and planar Al foils driven indirectly by LLNL's Nova laser. We have also compared the analytical modeling with 2-D simulations. We find that for the moderate strain rates of the HE experiments the simulations and analytical modeling agree with each other and with the data, with an equivalent plastic viscosity consistent with the von Mises criterion. For the high strain rates of the Nova experiments, on the other hand, the viscosity needed in the analytical model to match the data is about one-tenth of what the simulations predict. This initial material weakening, followed by a relaxation to a strengthened state, is consistent with a "relaxation model" in which plastic flow at high strain rate is confined to discrete shear bands. We also derive a characteristic scale for the plastic viscosity and find under what conditions the growth is independent of initial amplitude.

This work was performed under the auspices of the U.S. Department of Energy by the University of California Lawrence Livermore National Laboratory under contract No. W-7405-Eng-48.

Abstract No. T10

Toy Models for the Growth Rate of Rayleigh-Taylor Instability

S. B. Dalziel
Cambridge University, Cambridge, United Kingdom

There remains an on-going debate about one of the most basic characteristics of the instability: the growth-rate coefficient α. In many respects this is surprising, but at the same time it is perhaps inevitable. After undergoing a period of convergence between experiments and numerics for values of this important quantity, some recent studies show a continued decline in the growth rate for some numerical models, at the same time as the models offer overall improvement in the resolution and quality of results. This paper makes use of a range of toy models for Boussinesq Rayleigh-Taylor instability in an effort to understand and reconcile the issues.

The paper begins by returning to the classical Layzer model and reconciles it with the behaviour of other buoyancy-driven flows, before exploring the possible growth rates it predicts for the developing instability. Attention is then turned to a shell model for the instability. Shell models are normally used to help explain the behaviour of turbulence in homogeneous fluids subject to forcing at low wavenumbers. In this study, a very simple model is adapted to take account of buoyancy-driven forcing over the entire range of available scales. The results offer an interesting comparison with Rayleigh-Taylor instability, and offer insight into the behaviour that determines the growth rate α.

Abstract No. T11

A General Buoyancy-Drag Model for the Evolution of the Rayleigh-Taylor and Richtmyer-Meshkov Instabilities

Y. Elbaz[1,2], Y. Srebro[1,2], O. Sadot[2], and D. Shvarts[1,2]
[1]*Ben-Gurion University, Beer-Sheva, Israel*
[2]*Nuclear Research Center - Negev, Israel*

The growth of a single-mode perturbation is described by a buoyancy-drag equation, which describes all instability stages (linear, non-linear and asymptotic) at time-dependant Atwood number and acceleration profile. The evolution of a multi-mode spectrum of perturbations from a short wavelength random noise is described using a single characteristic wavelength. The temporal evolution of this wavelength allows the description of both the linear stage and the late time self-similar behavior.

The model includes additional effects, such as shock compression and spherical convergence. In addition to the mixing zone fronts, the internal density profile of the mixing region has been investigated using a simple diffusion-like model.

Model results are compared to full 2D and 3D numerical simulations and shock-tube experiments of random perturbations, studying the various stages of the evolution.

Abstract No. T12

3D Rayleigh-Taylor and Richtmyer-Meshkov Single-Modes

N. A. Inogamov[1], A. M. Oparin[2], M. Tricottet, and S. Bouquet[3]
[1]*Landau Institute for Theoretical Physics, Moscow, Russia*
[2]*Institute for Computer Aided Design, Moscow, Russia,*
[3]*Commissariat à l'Energie Atomique, Bruyères-le-Châtel, France*

We study 3D topology of Rayleigh-Taylor (RT) and Richtmyer-Meshkov (RM) single-modes. 3D case is much richer than 2D case. For example, in addition to the well-known bubbles and jets, 3D saddles appear. Saddles are points of stagnation - as are the tips of bubbles and jets - and, therefore, they play the same important role. We present a 3D analytic description of the interface as a whole,from bubbles to jets. Hexagonal, square and triangular lattices of bubbles are investigated both analytically and numerically.

Abstract No. T13

Rayleigh-Taylor Instability for Compressible and Incompressible Media

N. A. Inogamov[1,2], M. Tricottet[2], A. M. Oparin[3], and S. Bouquet[2]
[1]*Landau Institute for Theoretical Physics, Moscow, Russia*
[2]*Commissariat à l'Energie Atomique, Bruyères-le-Châtel, France*
[3]*Institute of Computer-Aided Design, Moscow, Russia*

After a brief Reminding of the role played by Rayleigh-Taylor Instabilities in astrophysics (Type II supernovae, supernovae remnants, insterstellar clouds driven by ablation), some developments concerning instability criteria, linear growth for compressible media will be presented.
Then, the 3D structure of non-linear single-mode instability interfaces is investigated, and proves to be much richer than in 2D. Accumulation points are analytically studied, up to high-order development, for arbitrary long times - including asymptotic behaviour.
Finally, some comparisons will be effected to numerical simulations with the predictions concerning this points and some shape factor.

PACS Nos.: 47.20.Ma, 47.40.Nm

Abstract No. T14

Three Dimensional Multi-Mode Rayleigh-Taylor and Richtmyer-Meshkov Instabilities at All Density Ratios

D. Kartoon[1,2], D. Oron[1], L. Arazi[3], A. Rikanati[1,2], U. Alon[4], and D. Shvarts[1,2]
[1]*Nuclear Research Center Negev, Israel*
[2]*Ben-Gurion University, Beer-Sheva, Israel*
[3]*Tel-Aviv University, Tel-Aviv, Israel*
[4]*Weizmann Institute, Rehovot, Israel*

The three dimensional turbulent mixing zone (TMZ) evolution was studied using two approaches. First, an extensive numerical study was made, investigating the growth of a random three dimensional (3D) perturbation under Rayleigh-Taylor and Richtmyer-Meshkov unstable conditions in a wide range of density ratios. Following that, a new 3D statistical model was developed based on the same logic as the 2D statistical model – binary interactions between bubbles growing at a 3D asymptotic rate.

The results for the growth rate of the 3D bubble front attained from the theoretical model show good agreement with both the experimental [1] and the 3D simulation results. The simulation results also agree well with the experimental spike front growth rate. Further approval for the theoretical model was gained by detailed comparison of the bubble size distribution to the numerical simulations, and by comparison to a 3D multi-mode drag-buoyancy model [2].

The good agreement between the theoretical models, the 3D numerical simulations and the experimental results, together with the clear differences between the 2D and the 3D results, suggest that the discrepancies between the experiments and the previously developed models are due to geometrical effects.

[1] G. Dimonte, Phys. Plasmas 6, 2009 (1999).
[2] D. Oron, L. Arazi, D. Kartoon, A. Rikanati, U. Alon, D. Shvarts, Phys. Plasmas 8 (June 2001)

Abstract No. T15

Stability of Diverging Shock Waves

V. M. Ktitorov
Russian Federal Nuclear Center – VNIIEF, Sarov, Russia

For the first time the self-similar approach was successfully applied to the stability problem of diverging shock waves when calculating evolution of small perturbations of self-similar point blast wave. The new sort of Rayleigh-Taylorinstability was found in this case when $\gamma<1.2$ (See instability region on Fig.1 /1/). The results of calculations were later proved in laboratory experiment /2/ as well as in computer simulation /3/.

In this paper we summarize the solutions of stability problems of various types of diverging shock waves (both spherical and cylindrical) which were obtained with the help of the self-similar approach. The following cases are considered:
Point blast wave in non-ideal gas and in the gas which density depends on radius,
Reflected from the center converging shock wave.

We calculate the values of complex exponents of power time dependence of front perturbations in a wide region of values of harmonic number and of gas adiabatic exponent. We also determine the region of instability.

V.M.Ktitorov, Khim.Fizika(Chem.Phys.Issues),V.14,No2-3,p.169,1995
J.Grun et al, Phys.Rev.Let.,V.66,No21,p.2738,1991
V.Ktitorov,V.Meltsas, Proceedings of the 6thIWPCTM,Marseille,1997

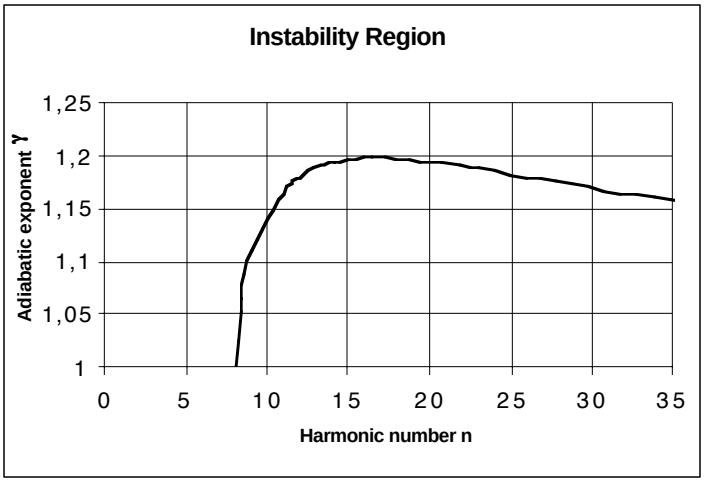

Abstract No. T16

Stability of Reflected from the Center Self-Similar Converging Shock Wave

V. M. Ktitorov
Russian Federal Nuclear Center – VNIIEF, Sarov, Russia

The technique first used in /1-3/ for solving the point blast wave stability problem is applied for the one of the self-similar converging shock wave after focusing.

Small (linear) perturbations of the shock wave are expanded into spherical harmonics the components of expansion being presented in the self-similar form. The stability problem is reduced to the solving of the system of the ordinary differential equations, which are to be solved simultaneously with the main spherically symmetric equations of the shock wave.

The eigenvalue problem is formulated. This problem is solved, complex values of power exponent (they describe a time dependence of front perturbations) are calculated as eigenvalues. The eigenvalues are calculated numerically in the general case of arbitrary values of harmonic number n and gas adiabatic exponent γ. The region of instability is defined on the plane n-γ.

V.M.Ktitorov (Russian Atomic Science and Technique Issues, Ser. Theoretical and Applied Physics), No2, p.28, (1984);
D.Ryu and E.T.Vishniac, Astrophys.J. 313, 820 (1987);
V.M.Ktitorov, Khimicheskaya Fizika (Chemical Physics Issues) V.14, No 2-3, p.169, (1995);

Abstract No. T17

Using a Turbulence Transport Approach to Study Shocks Through Polycrystalline Metal

R. R. Linn and F. H. Harlow
Los Alamos National Laboratory, Los Alamos, NM

A polycrystalline metal is composed of close packed crystals in each of which the elastic modulus is non-isotropic to a degree that ranges from slight to extreme (as in delta-phase plutonium where there is a seven to one variation). We have made considerable progress in the development of a stochastic model by which to describe the collective behavior as a strong shock or rarefaction passes through the material. The basic idea is to start with the laws of mass, momentum, and energy conservation, decompose each variable into mean and fluctuating parts, ensemble average the equations, and then derive transport equations and closures for the higher-order moments. The first version has been obtained and tested numerically for a self-similar traveling wave, and results show deficiencies, together with strong clues for their remediation. We have made much progress in developing a second, improved version for which results will be presented during the talk.

Abstract No. T18

Response of Turbulent RANS Models to Self-Similar Variable Acceleration RT-Mixing: An Analytical 0D Analysis

A. Llor
Commissariat à l'Energie Atomique, Bruyères-le-Châtel, France

So far, the validation of RANS models applicable to variable acceleration RT mixing flows (as found in ICF) has mostly been carried out by fitting experimental or numerical data obtained for constant (RT) and impulsive (RM) accelerations. Further checks are also possible on the few available data for variable acceleration, such as in mixing-demixing flows induced by reverting the gravity field. Although this approach is widely applied and accepted, it is unsatisfactory because of the complex relationship between the model features and coefficients and the experimental measurements.

It is shown here that self-similar variable acceleration RT (SSVART) provides an appealing alternative since it extends the usual calibration techniques of turbulent RANS models based on simple self-similar flows. The general model equations in 1D (PDEs) are still too complex for full analytical calculations of SSVART flows, but using reasonable assumptions, simple 0D (ODEs) approximations can be derived and solved analytically.

This approach is applied to an extended k-ε model derived from Andronov's and to Young's two-fluid model. The behaviour of the mixing layer growth rate and integral turbulent scales provides important informations on the accuracy of these models.

Finally, general qualitative arguments will be discussed showing the importance and the difficulty of capturing accurately a broad range of SSVARTs with a single simple model.

Abstract No. T19

Nonlinear Evolution of an Interface in the Richtmyer-Meshkov Instability

C. Matsuoka[1], K. Nishihara[2], and Y. Fukuda[2]
[1]*Ehime University, Ehime, Japan*
[2]*Institute of Laser Engineering, Osaka University, Osaka, Japan*

We have developed an analytical model that describes a fully nonlinear evolution of an interface in the Richtmyer-Meshkov instability. Proper boundary conditions at the interface are derived and the temporal evolution of the interface is investigated as a vortex sheet using them. It is shown that the created vorticity on the interface has a strong inhomogeneity, which causes the stretching and compression of the sheet. We discuss the inhomogeneity in detail, from which we show the interface has a double spiral structure. We also show a good agreement in the analytical solutions of the interface shape with two-dimensional hydrodynamic simulations.

We present the proper kinematic boundary condition, the modified Birkhoff-Rott equation, in order to describe the nonlinear evolution of the interface with the temporal evolution of the circulation, corresponding to the Bernoulli equation, on the interface for an arbitrary Atwood number. The analytical solutions show that the interface is stretched to the tangential direction proportional to time. In the nonlinear stage, the modes in the normal and tangential directions mutually interact to yield to the large deformation of the spike. By introducing the self-similar form of the velocity potential first found by Rott, we can construct a fully nonlinear evolution of the double spiral structure in the spike.

Abstract No. T20

Evolution of Arbitrary Perturbations in the Richtmyer-Meshkov Instability

K. O. Mikaelian
Lawrence Livermore National Laboratory, Livermore, CA

We present analytical and numerical calculations on the evolution of arbitrarily shaped initial perturbations undergoing the Richtmyer-Meshkov instability. In many cases a simple, explicit, analytic formula can be written down for the linear regime. These formulas serve as nontrivial tests of hydrocodes, and we present simulations with the Arbitrary Lagrangian-Eulerian hydrocode CALE that cover the linear as well as the deeply nonlinear regime of the instability. A brief outline and code calculations for possible experiments will also be presented.

PACS No.: 52.35.Py

This work was performed under the auspices of the U.S. Department of Energy by the University of California Lawrence Livermore National Laboratory under contract No. W-7405-Eng-48.

Abstract No. T21

RT Turbulence: Dramatic Dynamics of Interpenetration (Fast Jets, Sharp Decelerations and Accelerations)

A. M. Oparin[1], N. A. Inogamov[2], and A. Yu. Dem'yanov[3]
[1]*Institute for Computer Aided Design, Moscow, Russia*
[2]*Landau Institute for Theoretical Physics, Moscow, Russia*
[3]*Moscow Institute for Physics and Technology, Moscow, Russia*

Dynamics of turbulent mixing due to the Rayleigh-Taylor instability is considered. The mixing layer consists of a single horizontal array of large scale structures. The characteristics of these structures are studied by the spectral and statistical methods. Stimulation of mixing by long-wavelength noise is studied. It is demonstrated that, for a typical homogeneous unscaled noise,time-squared self-similarity is retained. The threshold amplitude of random broadband noise is determined, below which these noise can be ignored. The mixing deceleration by the side boundaries is studied. The stimulation and deceleration effects sizably influence the mixing coefficient, increasing and decreasing it respectively.

Abstract No. T22

Statistical Mechanics Large Scale Model for the Evolution of the Multi-Mode Kelvin Helmholtz Instability

A. Rikanati[1,2], U. Alon[3], and D. Shvarts[1,2]
[1]*Nuclear Research Center Negev, Israel*
[2]*Ben-Gurion University, Negev, Israel*
[3]*Weizmann Institute of Science, Israel*

The nonlinear growth of the multi-mode incompressible Kelvin-Helmholtz (KH) shear flow instability at all density ratios is treated by a large scale statistical-mechanics eddy-pairing model, based on a vortex model for the single eddy behavior and the process of two eddy-pairing. Using an adaptation of the statistical merger model by Alon et. al [1994], a linear time growth of the mixing zone is obtained, resulting in the linear time growth coefficient for several density ratios as well as an asymptotic lognormal eddy size distribution and the average eddy life time probability. Very good agreement with full numerical simulations and experiments is achieved.

References:

U. Alon, J. Hecht, D. Mukamel and D. Shvarts, Phys. Rev. Lett. 72, 2867 (1994).

Abstract No. T23

Effects of High Initial Amplitudes and High Mach Numbers on the Evolution of the RM Instability: I. Theoretical Study

A. Rikanati[1,2], D. Oron[1], O. Sadot[1,2], and D. Shvarts[1,2]
[1]*Nuclear Research Center Negev, Israel*
[2]*Ben-Gurion University, Beer-Sheva, Israel*

Recent shock tube experiments [Aleshin et al. 1997] and laser driven experiments [Dimonte et al.1998] resulted in an initial bubble growth velocity smaller then that predicted by the matching impulsive models [Richtmyer et. al. 196? and Meyer-Blewett 1972]. It was suggested that the reduction can be attributed to effects of both High Mach number and high initial amplitudes [Holems 2000].

In the present work two models are formulated describing the velocity reduction caused by the two effects. A vorticity deposition model is formulated for effects of high initial amplitudes and a "wall" model is formulated for describing effects of high Mach number caused by the proximity of the shock wave with the two fluid interface. Both in good agreement with the matching experimental results.

Implementing the above models for a range of initial conditions (low to high initial amplitudes and Mach numbers) and with the aid of full numerical simulations, previous experiments and new low and high Mach number shock tube experiments [Sadot et. al., present conference], the range of initial conditions is divided into regions of high Mach dominance, regions of high initial amplitudes dominance and "classical " regions were the two effects are negligible. Using the above mapping, it was found that effects of high initial amplitudes dominates most of the previous experiments.

References:

Aleshin et. al., in Proceedings of the Sixth International Workshop on the Physics of Compressible Turbulent Mixing edited by G. Jourdan & L. Houas, Marsielle France 1997. Page 1.

Dimonte G., Frerking C.E., Schnider M. and Remington B., Phys. of Plasmas 12, 304 (1996).

Holmes et. al., J. Fluid Mech 187, 329 (1999).

Meyer K.M. and Blewett P.J., Phys. of. Fluids 15, 753 (1972).

Richtmyer R.D., Commun. Pure Appl. Math. 13, 297 (1960).

Abstract No. T25

Compressible MHD Turbulence in Strongly Radiating Molecular Clouds in Astrophysics

D. D. Ryutov and B. A. Remington
Lawrence Livermore National Laboratory, Livermore, CA

Molecular clouds in astrophysics are often subjected to intense irradiation by nearby young stars. The ablation process ensues and a strong shock is driven into the cloud. In a number of cases, the radiative cooling time of the shocked matter is much shorter than the dynamical time of the cloud evolution. In such situations, possible pre-existing turbulent motions and turbulent magnetic fields can potentially contribute to the "stiffness" of the shocked material. We suggest simple models allowing quick evaluation of these effects. We conclude that the presence of a turbulent magnetic field can play a significant role, provided its amplitude is beyond some critical level, whereas the turbulent ram pressure of the unmagnetized medium can play only a relatively minor role. Implications for the dynamics of astrophysical molecular clouds are discussed.

PACS Nos.: 47.27.Jv, 47.65.+a, 95.30.Qd. 98.58.Db

This work was performed under the auspices of the U.S. Department of Energy by the University of California Lawrence Livermore National Laboratory under contract No. W-7405-Eng-48.

Abstract No. T26

Single-Velocity, Multi-Component Turbulent Transport Models for Interfacial Instability-Driven Flows

O. Schilling
Lawrence Livermore National Laboratory, Livermore, CA

A family of two-equation turbulent transport models is proposed for three-dimensional, single-velocity, multi-component turbulent flows driven by Rayleigh-Taylor, Richtmyer-Meshkov, and Kelvin-Helmholtz instabilities. The models are compressible versions of *K*-*Z* models, where *K* is the turbulent kinetic energy and *Z* is an auxiliary variable such as the turbulent kinetic energy dissipation rate, turbulent frequency, or turbulent lengthscale. Terms are proposed in these equations that account for buoyancy and compressibility effects. The relative merits of different *K*-*Z* models will be discussed, and preliminary *a priori* and *a posteriori* tests of the models using direct numerical simulation data for Rayleigh-Taylor instability-induced turbulent mixing will be presented. Future plans for model tests and applications to Richtmyer-Meshkov instability-induced turbulent mixing will also be discussed.

PACS Nos.: 47.20.Ma, 47.27.Eq, 47.40.Nm

This work was performed under the auspices of the U.S. Department of Energy by the University of California Lawrence Livermore National Laboratory under contract No. W-7405-Eng-48.

Abstract No. T28

Large- and Small-Scale Dynamics of Variable-Density Rayleigh-Taylor Instability-Induced Turbulent Mixing

O. Schilling and A. W. Cook
Lawrence Livermore National Laboratory, Livermore, CA

The statistical dynamics of the large- and small-scales in a three-dimensional turbulent mixing layer induced by Rayleigh-Taylor instability is studied using 512^2 x 2040 direct numerical simulation data. The terms in the evolution equations for the density-weighted kinetic energy, density-weighted enstrophy, and squared density are evaluated to study their relative contributions during the time-evolution. Particular consideration is given to the role of the baroclinic production and turbulent diffusion terms, as well as to the coupling between the density and velocity fields. The traditional method used to study the flow of energy between resolved (supergrid) and unresolved (subgrid) scales by introducing a cutoff wavenumber in Fourier space is generalized using a multi-resolution wavelet analysis, and used to quantify the forward cascade of kinetic energy, enstrophy, and the squared density from large to smaller scales, as well as the backward cascade from small to larger scales. The implications of this study for developing and assessing subgrid-scale and backscatter models for large-eddy simulation of Rayleigh-Taylor mixing are discussed. Wavelet analysis is ideally suited to studying evolving, anisotropic turbulent mixing, as wavelet-transformed spectra yield information regarding both the *scale* of structures and their *location* within the flow. The use of wavelet methods provides additional insight into the coupling between the large-scale, coherent flow (the bubbles and spikes formed during the merger process) and the small-scale, incoherent background flow (the smaller scale turbulence induced by Kelvin-Helmholtz instability and the turbulent energy transfer process).

PACS Nos.: 47.20.Ma, 47.27.Eq

This work was performed under the auspices of the U.S. Department of Energy by the University of California Lawrence Livermore National Laboratory under contract No. W-7405-Eng-48.

Abstract No. T30

Analytical Study of the Rayleigh-Taylor Instability in Compressible Fluids

M. Tricottet and S. Bouquet
Commissariat à l'Energie Atomique, Bruyères-le-Châtel, France

Since the observation of the explosion of the type II supernova, SN87a, Rayleigh-Taylorinstabilities (RTI) are suspected to play a key-role during the process of expansion of the envelope (due to the passage of the shock) [1,2,3,4].
In this paper we perform an analytical study of the RTI. In contrast to most of all previous studies [5,6,7], we examine the case of compressible fluids. In addition, both the static (time-independent acceleration) and the dynamical (time-dependent acceleration) cases are presented.
For these two cases we are able to derive a non-trivial analytical dispersion relationship. Comparisons are made, first, with the models developped for incompressible fluids and, as expected, for wave number, k, going to infinity (wavelengths going to zero) we recover the well-known result valid for incompressibility.
On the other hand, the influence of the time-dependence in the acceleration is shown and the differences with the static case are emphasized.

[1] Clayton, Principles of Stellar Evolution and Nucleosynthesis, Univ. of Chicago Press (1983)
[2] Fryxell et al., ApJ. 367, 619 (1991)
[3] Glanz, Science 276, 351 (1997)
[4] Kane et al., ApJ. Lett. 478, 75 (1997)
[5] Abarzhi, Phys. Rev. Lett. 81(2), 337 (1998)
[6] Velasquez et al., Astron. Astrophys. 334, 1060 (1998)
[7] Mikaelian, Phys. Rev. Lett. 80(3), 508 (1998)

Abstract No. T31

Analytic Nonlinear Growth of A Single-Mode Richtmyer-Meshkov Instability

M. Vandenboomgaerde
Commissariat à l'Energie Atomique, Bruyères-le-Châtel, France

Perturbation method where only the most secular terms are retained gives a simple result for the weakly nonlinear growth of a single-mode shock-accelerated interface [M.Vandenboomgaerde, C.Mugler, and S.Gauthier, Proceedings, 7th IWPCTM, St. Petersbourg, 1999]. This result writes as a series in integer powers of time. It can be considered as the Taylor expansion of an analytic function. We believe that such a function has been identified; it describes the evolution of the instability from the linear to intermediate nonlinear regime. Whereas the series has a finite radius of convergence, the function has no singularity. The accuracy of this analytic formula is checked against various 2D simulations. Comparisons with previous theoretical models are also presented.

Abstract No. T32

Efficient Perturbation Methods for Richtmyer-Meshkov and Rayleigh-Taylor Instabilities: Weakly Nonlinear Stage and Beyond

M. Vandenboomgaerde, C. Cherfils, D. Galmiche, S. Gauthier, and P. A. Raviard
Commissariat à l'Energie Atomique, Bruyères-le-Châtel, France

A perturbation method has been derived by Q.Zhang and S-I.Sohn [Phys.Fluids 9, 1106 (1997)] in order to predict the weakly nonlinear stage of the Richtmyer-Meshkov instability. Retaining the most secular terms has allowed us to drastically simplify this theory [M.Vandenboomgaerde, C.Mugler, and S.Gauthier, Proceedings, 7th IWPCTM, St Petersbourg, 1999].
We use this simplified but accurate approach to show the importance of the sign of the amplitude of the modes in the selection mode process. Such process is also studied beyond the weakly nonlinear stage. A class of homothetic interfaces is deduced fromthe theory. Its validity is checked against 2D simulations, even in the intermediate nonlinear regime.
Finally, this approach is used in order to solve the equations of the nonlinear stage of the Rayleigh-Taylor instability. We present comparisons between theory and various published test cases.

Abstract No. T33

Combined Shear and Buoyancy Instabilities

P. N. Wilson[1], M. J. Andrews[1], and F. H. Harlow[2]
[1]*Texas A & M University, College Station, TX*
[2]*Los Alamos National Laboratory, Los Alamos, NM*

Mixing layer experiments were performed at Texas A&M University with flows in shear, with an unstable buoyancy configuration and combined shear and (stabilizing, de-stabilizing) buoyancy. Two-time density correlations were measured, as well as single-point, second-order velocity correlations for the various flow configurations. A turbulence spectral transport model and a single-point turbulence transport model were investigated with their local formulation and later with non-local formulation in both physical and wave number space. Numerical simulations of the mixing layer were compared with experimental data and gave good agreement with the addition of terms to model non-local processes, such as, pressure fluctuations propagating into the surrounding fluid from the mix region, advection of small-scale eddies by large-scale structures, and vortex pairing resulting from Kelvin-Helmholtz instabilities. Results of the comparisons between theoretical models and numerical simulations and experimental data are presented.

Abstract No. T34

Rate of Growth of the Linear Richtmyer-Meshkov Instability

J. G. Wouchuk
E. T. S. I. Industriales, University of Castilla, Salamanca, Spain

A theoretical model is presented that calculates the exact asymptotic rate of growth of the perturbations present at a shocked corrugated contact surface. The model covers both situations: whether a shock or a rarefaction are reflected back in the first fluid. The asymptotic growth rate can be calculated with the desired accuracy for any value of the incident shock Mach number, fluids compressibilities or initial density contrast. The growth rate is obtained as the solution, either of a system of two coupled functional equations in the shock reflected situation, or of only one functional equation in the rarefaction reflected case. The model includes the compressible history of the sound wave reverberations between the corrugated fronts and the material interface. It is seen a quite high speed of convergence for the intermediate calculations. Good agreement with previous numerical and experimental works is shown.

PACS Nos.: 47.20.-k, 52.35.Py-, 52.35-T

Abstract No. T35

The Dependence of the Shock Induced Richtmyer-Meshkov Instability on Dimensionality and Density Ratio

A. Yosef-Hai[1], O. Sadot[1,2], D. Kartoon[1,2], D. Oron[2], E. Sarid[2], G. Ben-Dor[1], and D. Shvarts[1,2]
[1]*Ben-Gurion University, Beer-Sheva, Israel*
[2]*Nuclear Research Center, Negev, Israel*

The RM instability occurs when a shock wave passes through a perturbed interface between two fluids. As a result of the instability, small perturbations on the initial interface develop into an array of bubbles and spikes. The bubble front was found to be dominated by bubbles rising and competing[1]. It was previously shown that this evolution of a multi-mode random initial perturbations is strongly related to the evolution of the single-mode case.

For a single-mode perturbation the instability can be described by a linear stage, during which the growth is characterized by a constant velocity, followed by a nonlinear stage, during which the growth velocity reaches an asymptotic 1/t behavior[2]. Simple drag-buoyancy considerations can be used to derive the acceleration of a single bubble. Assuming two fluids with different densities ρ_H and ρ_L and bubble of wave length λ the equation of motion is:

$$(1)\quad (\rho_L + C_a\rho_H)\frac{dU}{dt} = (\rho_H - \rho_L)g - \frac{C_d}{\lambda}\rho_H U^2$$

The two constants C_a and C_d, which are the added mass coefficient and the drag coefficient respectively, are determined by equating Eq. 1 to the prediction of a potential flow model[2]. For the 2D case C_a=2 and C_d=6π, for the 3D case C_a=1 and C_d=2π. The asymptotic solution of Eq. 1 for RM is achieved by neglecting the effect of the shock (g=0). By doing so the bubble asymptotic acceleration is derived:

$$(2)\quad \frac{dU}{dt} = -\frac{a' H}{\rho_L + C_a\rho_H}\cdot\frac{U}{\lambda}$$

The growth rate is the solution of Eq.2. By introducing the coefficients as described above, the dependence of the late time growth rate on the dimensionality and density ratio is found. The results are summarized in the following Table:

	$\rho_H/\rho_L \to 1$	$\rho_H/\rho_L \to \infty$
2D	$\frac{1}{\lambda}$	$\frac{3\pi}{\lambda}$
3D	$\frac{1}{\lambda}$	$\frac{1}{\lambda}$

In the present work a set of shock tube experiments were made to verify the model's prediction. A thin membrane, on which the 2D and 3D initial perturbations were imposed, separated the two gases. Different pairs of gases were used to achieve different density ratios. The evolution of the shock-wave induced mixing zone was measured by high speed laser schlieren photography. The linear and asymptotic stages were observed. The results were found to be in good agreement with both model and simulations. See the following Figure for the case of $\rho_H / \rho_L = 5$.

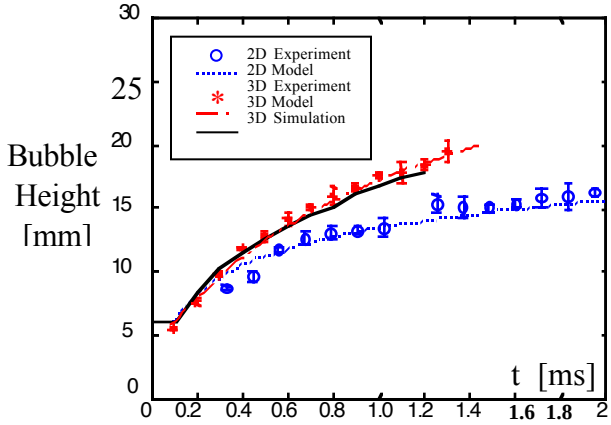

References:

[1] Alon U., Hecht J., Ofer D. and Shvarts D. 1995 Phys. Rev. Lett. 74, 534.

[2] Hecht J., Alon U. and Shvarts D., 1994 Phys. Fluids 6, 4019.

Abstract No. T36

A New Framework for Transitional and Turbulent Mixing

Y. Zhou, H. F. Robey, and A. C. Buckingham
Lawrence Livermore National Laboratory, Livermore, CA

We develop a framework, based on the current knowledge of turbulence theory and using phenomenological treatment, for the characterization of turbulent mixing evolving from shock and gravity driven instabilities. The procedure is designed to supplement and connect the history of the flow development from the early stages of the Rayleigh-Taylorand Richtmyer-Meshkovinstabilities into the fully developed turbulent flow regime under the conditions of high pressure, high temperature, elevated Reynolds number flow and material mixing. We first demonstrate an analogy between the buoyancy drag model and the one equation turbulence transport closure model. We show that in simplifying the latter transport model to form the buoyancy drag model, the multiple length scales of physical turbulence are drastically reduced to essentially a single, dominant length scale. Furthermore, we show that in the buoyancy drag model several other terms representing specific additional contributions of physical turbulence in the one equation transport model are omitted in the simplification. Next, we compile the key parameters that are needed to characterize both initial transitional flow and its subsequent evolution into fully developed turbulent flow. Although all important length scales are well known and well described in turbulent fluid dynamics literature, we pay special attention here to their time dependent features because of our special focus on description of the transient states and their evolution in transitional and turbulent material mixing. As a result, we have formed a generalization of the transition criteria proposed by Dimotakis (*J. Fluid Mechanics, **409,*** 69 (2000)). We illustrate the utility of our framework for transitional and turbulent mixing by applying it to a classical fluid dynamics RTI experiment conducted at Cambridge University and, a laser experiment carried out in the Omega laser facility at the University of Rochester.

This work was performed under the auspices of the U.S. Department of Energy by the University of California Lawrence Livermore National Laboratory under contract No. W-7405-Eng-48.

Abstract No. T37

Spherical Combustion Layer in a TNT Explosion

A. L. Kuhl[1] and R. E. Ferguson[2]
[1]*Lawrence Livermore National Laboratory, Livermore, CA*
[2]*Krispin Technologies Inc, Rockville, MD*

A theoretical model of combustion in explosions at large Reynolds, Peclet and Damkohler numbers is described. A key feature of the model is that combustion is treated as material transformations in the Le Chatelier plane, rather than "heat release". In the limit considered here, combustion becomes concentrated in thin exothermic sheets (boundaries between fuel and oxidizer). The products expand along the sheet, thereby inducing vorticity on either side of the sheet that continues to feed the process. The results illustrate the linking between turbulence (vorticity) and exothermicity (dilatation) in the limit of fast chemistry, thereby demonstrating the controlling role that fluid dynamics plays in such flows.

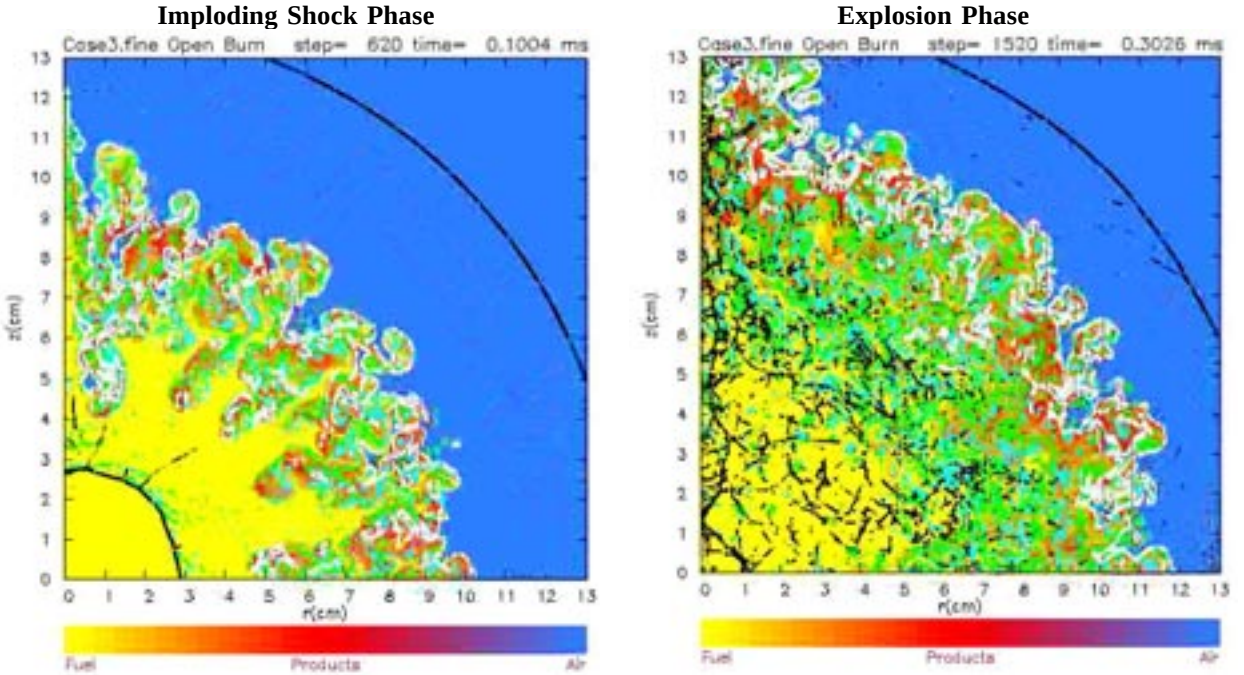

Figure 1. Cross-sectional view of the combustion field generated by the detonation of a 1-g spherical TNT charge. TNT explosion products (shown as *yellow*) mix with air (depicted in *blue*) to form combustion products (represented as *red*). Exothermic cells are marked with *white* dots. Vorticity contours are *turquoise* (positive) and *chartreuse* (negative), while compressional dilatation contours are *black*.

This work was performed under the auspices of the U.S. Department of Energy by the University of California Lawrence Livermore National Laboratory under contract No. W-7405-Eng-48.

Abstract No. T38

Spectral Analysis of Turbulent Flows Induced by RT and RM Instabilities

V. F. Tishkin and N. V. Zmitrenko
Institute for Mathematical Modeling of the Russian Academy of Sciences, Moscow, Russia

The results of analysis of spectral characteristics of a velocity field for two unstable hydrodynamic problems are examined in this report. One of this problem involves direct simulation of turbulent mixing experiment, which has done for the case of Richtmyer-Meshkov instability. Results of simulation describe main characteristics of developing mixing zone, i.e. shape and sizes of turbulent layer. The spectral analysis has revealed a presence of an interval connected with an enstrophy transfer to small-scale oscillations.
Another problem relates to classic case or Rayleigh-Taylor instability. The analysis of this case has shown that an inertial interval is observed.
Both problems were treated with the help of 3D hydrodynamic code NUT. The spectral analysis was fulfilled by means of specially alaborated for this problems code SPAN.

Supported by ISTC project # 1495.

Abstract No. T39

Pattern Detection, Compression and Denoising of Rayleigh-Taylor Mix Data Using Discrete Wavelet Transform Techniques

B. B. Afeyan[1], P. Ramaprabhu[2], and M. J. Andrews[2]

[1]*Polymath Research Incorporated, Pleasanton, CA*
[2]*Texas A & M University, College Station, TX*

Sequential single point density measurements have been collected from a statistically steady Rayleigh-Taylor mix. The experiment allows long collection times, and thus highly detailed statistical analyses are possible. We have studied this data using a number of discrete wavelet transform techniques in order to denoise, compress and detect patterns and correlations in these ideal representations of intermittent data. By comparing the statistical properties of the evolution of RT at various points downstream, we can establish the minimum number of wavelet coefficients whose evolution can capture the most significant aspects of the turbulent flow. To this end, scale based as well as largest coefficient thresholding are compared and contrasted and the choice of optimum wavelets for the tasks as hand identified. instability-induced turbulent mixing will also be discussed.

8TH INTERNATIONAL WORKSHOP ON THE PHYSICS OF COMPRESSIBLE TURBULENT MIXING

December 9 – 14, 2001

CALIFORNIA INSTITUTE OF TECHNOLOGY
PASADENA, CALIFORNIA, USA

PROGRAM SUMMARY

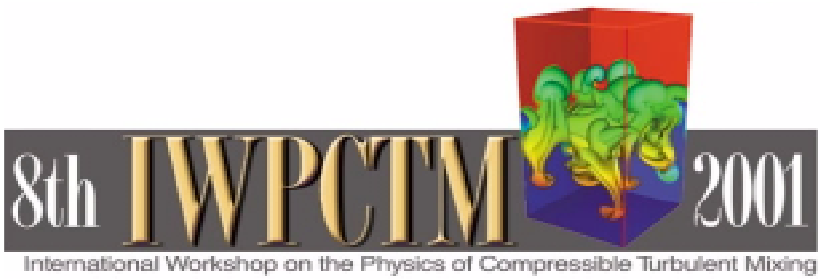

The 8th IWPCTM
is hosted by the
Lawrence Livermore National Laboratory
and is co-hosted by the
California Institute of Technology†

All oral sessions and discussions will be held in the Beckman Institute Auditorium

Poster sessions will be held in the Winnett Lounge and Club Room

†Partial financial support was generously provided by the California Institute of Technology

Transportation

Buses depart from the Pasadena Hilton to campus
at 7:45 Monday – Friday, December 10 – 14.

Buses depart from campus to the Pasadena Hilton
at 17:50 Monday – Thursday, December 10 – 13,
and at 12:15 on Friday, December 14.

Refreshments

Refreshments will be available at 8:00 and at breaks
Monday – Friday, December 10 – 14.

SUNDAY, DECEMBER 9, 2001

17:00 – 21:00	Registration Pasadena Hilton
18:00 – 21:00	Reception Pasadena Hilton
Guest Speaker:	**E. I. Moses** **NIF Project Manager** **(Lawrence Livermore National Laboratory)**

MONDAY, DECEMBER 10, 2001

8:15 – 8:30 Welcome and Opening Remarks:
S. Koonin / O. Schilling

Experimental Session I
Chair: H. F. Robey
(Lawrence Livermore National Laboratory)

8:30 – 9:30 Review Talk:
A Review on RT and RM Instability and TM Experiments
J.-F. Haas and S. G. Zaytsev (Comissariat à l'Energie Atomique and Krzhizhanovsky Power Engineering Institute)

9:30 – 9:50 The Influence of Scaling for Periodical Perturbations on Development of Turbulent Mixing on a Gas-Liquid Interface (E7)
M. Bliznetsov, E. Meshkov, N. Nevmerzhitsky, A. Nikulin, E. Sen'kovsky, and E. Sotskov (Russian Federal Nuclear Center-VNIIEF)

9:50 – 10:10 Experimental Study Into Rayleigh-Taylor Turbulent Mixing Zone Heterogeneous Structure (E31)
Yu. A. Kucherenko, A. P. Pylaev, V. D. Murzakov, A. V. Belomestnih, V. N. Popov, and A. A. Tyaktev (Russian Federal Nuclear Center-VNIITF)

10:10 – 10:30 Rayleigh-Taylor Instability at a Tilted Interface in Incompressible Laboratory Experiments and Compressible Numerical Simulations (E14)
J. M. Holford, S. B. Dalziel, and D. L. Youngs (Cambridge University and Atomic Weapons Establishment)

10:30 – 10:50 Break: Beckman Institute (courtyard)

Experimental Session II
Chair: J.-F. Haas
(Commissariat à l'Energie Atomique)

10:50 – 11:10 Measurements of Turbulence Correlations in Low Atwood Number Rayleigh-Taylor Mixing (E32)
P. Ramaprabhu and M. J. Andrews (Texas A & M University)

11:10 – 11:30 Experimental Investigations of the Self-Similar Mixing Mode of Different Density Gases in the Earth's Gravitational Field (E28)
Yu. A. Kucherenko, O. E. Shestachenko, Yu. A. Puskunov, E. V. Sviridov, V. M. Medvedev, and A. I. Baishev (Russian Federal Nuclear Center – VNIITF)

11:30 – 11:50 Mix Experiments Using a Two Dimensional Convergent Shock Tube (E13)
D. A. Holder, C. Barton, and A. V. Smith (Atomic Weapons Establishment)

12:00 – 13:15 Lunch: Winnett Lounge

Experimental Session III
Chair: J. W. Jacobs
(University of Arizona)

13:15 – 13:35 The Evolution and Interaction of Two Shock-Accelerated Unstable Gas Cylinders (E40)
C. Tomkins, K. Prestridge, P. Rightley, C. A. Zoldi, and R. Benjamin, (Los Alamos National Laboratory)

13:35 – 13:55 PLIF Flow Visualization of a Shock-Accelerated Air/SF6 Interface (E18)
J. W. Jacobs and V. V. Krivets (University of Arizona, Tuscon)

13:55 – 14:15 Shock Tube Experiments on Richtmyer-Meshkov Instability Across a Chevron Profiled Interface (E39)
A. V. Smith, D. A. Holder, C. J. Barton, A. P. Morris, and D. L. Youngs (Atomic Weapons Laboratory)

14:15 – 14:35 Study of Diverging and Converging Spherical Shock Waves Induced by Micro Explosives and Their Interaction with Product Gases (E15)
S .H. R. Hosseini and K. Takayama (Tohoku University)

14:35 – 14:55 Break: Beckman Institute (courtyard)

Experimental Session IV
Chair: K. Budil
(Lawrence Livermore National Laboratory)

14:55 – 15:15 The Dependence of the Shock Induced Richtmyer-Meshkov Instability on Dimensionality and Density Ratio (T35)
A. Yosef-Hai, O. Sadot, D. Kartoon, D. Oron, E. Sarid, G. Ben-Dor, and D. Shvarts (Ben-Gurion University, Nuclear Research Center, Negev)

15:15 – 15:35 Effects of High Initial Amplitudes and High Mach Numbers on the Evolution of the RM Instability: II. Experimental Study (E36)
O. Sadot, A. Yosef-Hai, A. Rikanati, D. Oron, G. Ben-Dor, and D. Shvarts (Nuclear Research Center, Negev and Ben-Gurion University)

15:35 – 15:55 Experimental Study of a Strongly-Shocked Gas Interface With Visualized Initial Conditions (E27)
J. G. Oakley, M. H. Anderson, and R. Bonazza (University of Wisconsin, Madison)

15:55 – 16:15 Compressible Vortex Rings (E8)
M. Brouillette and C. Hébert (Université de Sherbrooke)

16:15 – 17:45 General Poster Session: Winnett Lounge and Club Room

TUESDAY, DECEMBER 11, 2001

8:15 – 8:30 Announcements: O. Schilling

Experimental Session V
Chair: T. A. Peyser
(Lawrence Livermore National Laboratory)

8:30 – 9:30 Review Talk: The Experimental Study of Excitation and Development of the Hydrodynamic Instability in the Mixing Zone Separating Gases of Different Densities at their Accelerated Motion
S. G. Zaytsev (Krzhizhanovsky Power Engineering Institute)

9:30 – 9:50 Compressible Hydrodynamics on the Omega Laser, Motivated by Astrophysics (E10)
R. P. Drake, P. Keiter, K. E. Korreck, K. Dannenberg, H. F. Robey, T. Perry, J. O. Kane, B. A. Remington, R. J. Wallace, O. A. Hurricane, D. D. Ryutov, J. Knauer, R. Teyssier, A. Calder, R. Rosner, B. Fryxell, D. Arnett, Y. Zhang, J. Glimm, N. Turner, J. Stone, R. McCray, and J. Grove (University of Michigan, Lawrence Livermore National Laboratory, University of Rochester, Laboratory for Laser Energetics, Comissariat à l'Energie Atomique, University of Chicago, University of Arizona, State University of New York, Stony Brook, University of Maryland, University of Colorado, and Los Alamos National Laboratory)

9:50 – 10:10 Improvements to Convergent Cylindrical Plasma Mix Experiments Using Laser Direct Drive (E4)
C. W. Barnes, S. H. Batha, A. M. Dunne, N. E. Lanier, G. R. Magelssen, T. J. Murphy, K W. Parker, S. Rothman, J. M. Scott, and D. Youngs (Los Alamos National Laboratory and Atomic Weapons Establishment)

10:10 – 10:30 The Interaction of Supernova Blast Waves with Interstellar Clouds: Experiments on the OMEGA Laser (E42)
R. I. Klein, H. Robey, T. Perry, and J. Greenough (Lawrence Livermore National Laboratory and University of California, Berkeley)

10:30 – 10:50 Break: Beckman Institute (courtyard)

Experimental Session VI
Chair: G. Dimonte
(Lawrence Livermore National Laboratory)

10:50 – 11:10 An Experimental Study of the Effect of Shock Proximity on the Richtmyer-Meshkov Instability at High Mach Number (E12)
S. G. Glendinning, D. G. Braun, M. J. Edwards, W. W. Hsing, B. F. Lasinski, H. Louis, J. Moreno, T. A. Peyser, B. A. Remington, H. F. Robey, E. J. Turano, C. P. Verdon, and Y. Zhou (Lawrence Livermore National Laboratory)

11:10 – 11:30 A Vortex Model for Studying the Effect of Shock Proximity on Richtmyer-Meshkov Instability at High Mach Number (E46)
H. F. Robey and S. G. Glendinning (Lawrence Livermore National Laboratory)

11:30 – 11:50 Laser-Based High Pressure, High Strain-Rate Solid-State Experiments (E19)
D. H. Kalantar, J. Belak, J. D. Colvin, M. Kumar, K. T. Lorenz, K. O. Mikaelian, S. Pollaine, B. A. Remington, S. V. Weber, L. G. Wiley, A. M. Wiley, A. Loveridge-Smith, J. S. Wark, and M. A. Myers (Lawrence Livermore National Laboratory, Oxford University, and University of California, San Diego)

12:00 – 13:15 Lunch: Winnett Lounge

Computational Session I
Chair: T. L. McAbee
(Lawrence Livermore National Laboratory)

13:15 – 13:35 A Comparison of High-Resolution 3D Numerical Simulations of Turbulent Rayleigh-Taylor (RT) Instability: Alpha-Group Collaboration (C10)
G. Dimonte, A. Dimits, S. Weber, D. L. Youngs, A. C. Calder, B. Fryxell, J. Biello, L. Dursi, P. MacNiece, K. Olson, P. Ricker, R. Rosner, F. Timmes, H. Tufo, Y.-N. Young, M. Zingale, M. J. Andrews, P. Ramaprabhu, S. Wunsch, C. Garasi, and A. Robinson (Lawrence Livermore National Laboratory, Atomic Weapons Establishment, University of Chicago, NASA Goddard Space Flight Center, Texas A & M University, and Sandia National Laboratories)

13:35 – 13:55 Study of Turbulent Gravitational Mixing at Large DensityDifferences Using Direct 3D Numerical Simulation (C44)
Yu. V. Yanilkin, V. P. Statsenko, S. V. Rebrov, N. I. Selchenkova, O. G. Sin'kova, A. L. Stadnik, and A. Ya. Uchayev (Russian Federal Nuclear Center – VNIIEF)

13:55 – 14:15 Numerical Methods for Determination of Mix (C11)
S. Dutta, E. George, J. Glimm, J. Grove, X. Li, A. Marchese, D. H. Sharp, Z. Xu, and Y. Zhang (State University of New York, Stony Brook, Los Alamos National Laboratory, and Brookhaven National Laboratory)

14:15 – 14:35 Effects of High Initial Amplitudes and High Mach Numbers on the Evolution of the RM Instability: II. Experimental Study (E36)
O. Sadot, A. Yosef-Hai, A. Rikanati, D. Oron, G. Ben-Dor, and D. Shvarts (Nuclear Research Center, Negev and Ben-Gurion University)

14:35 – 14:55 Break: Beckman Institute (courtyard)

Computational Session II
Chair: H. Takabe
(Osaka University)

14:55 – 15:15 Numerical Investigation of a Laser Induced Turbulent Mixing Zone (C35)
P. Seytor and M. Legrand (Commissariat à l'Energie Atomique)

15:15 – 15:35 Development and Validation of a 2D Turbulent Mix Model (C46)
D. L. Youngs (Atomic Weapons Establishment)

15:35 – 15:55 Computational Modeling of Low-Mach-Number High-Atwood-Number Turbulent Mixing (C4)
Wm. T. Ashurst and A. R. Kerstein (Sandia National Laboratories)

15:55 – 16:15 Simulation of a Shock-Accelerated Gas Cylinder and Comparison with Experimental Images and Velocity Fields (C50)
C. A. Zoldi, K. Prestridge, P. M. Rightley, and R. F. Benjamin (Los Alamos National Laboratory and State University of New York, Stony Brook)

16:15 – 17:45 Experimental Discussion: Beckman Institute Auditorium

---

Computational and Theoretical Poster Session: Winnett Lounge

WEDNESDAY, DECEMBER 12, 2001

8:15 – 8:30 Announcements: O. Schilling

Computational Session III
Chair: J. Glimm
(State University of New York, Stony Brook)

8:30 – 9:30 Review Talk:
Review of Numerical Simulation of Mixing due to Rayleigh-Taylor and Richtmyer-Meshkov Instabilities
D. L. Youngs (Atomic Weapons Establishment)

9:30 – 9:50 Transition Stages of Rayleigh-Taylor Instability Between Miscible Fluids (C56)
A. W. Cook and P. E. Dimotakis (Lawrence Livermore National Laboratory and California Institute of Technology)

9:50 – 10:10 Application of a Laser Shock Tube for the Study of Supersonic Gas Flows and the Development of Hydrodynamic Instabilities in Layered Media (C25)
I. G. Lebo and V. D. Zvorykin (Technical University MIREA and P. N. Lebedev Physical Institute)

10:10 – 10:30 Shock-Planar Curtain Interactions: Strong Secondary Baroclinic Deposition and the Emergence of Coherent and Random Vortex Projectiles (VPs) and Decaying Stratified Turbulence (C48)
S. Zhang and N. J. Zabusky (Rutgers University)

10:30 – 10:50 Break: Beckman Institute (courtyard)

Computational Session IV
Chair: J. Grove
(Los Alamos National Laboratory)

10:50 – 11:10 One-Dimensional Simulation of the Effects of Unstable Mix on Neutron and Charged-Particle Yield from Laser-Driven Implosion Experiments (C13)
R. Epstein, J. A. Delettrez, V. Yu. Glebov, V. N. Goncharov, P. W. McKenty, P. B. Radha, S. Skupsky, V. A. Smalyuk, and C. Stoeckl (University of Rochester, Laboratory for Laser Engineering)

11:10 – 11:30 Modeling Turbulent Mixing in Inertial Confinement Fusion Implosions (C37)
Y. Srebro, D. Kushnir, Y. Elbaz, and D. Shvarts (Ben-Gurion University, Nuclear Research Center, Negev, and Hebrew University)

11:30 – 12:00 Dispersal of Mass and Circulation Following Shock-Sphere (Axisymmetric) and Shock Cylinder Interactions: Effects Arising from Shock Cavity Collapse, Vortex Double Layers; Density-Gradient Intensification and Vortex Projectiles (C29)
G. Peng, S. Gupta, S. Zhang, and N. J. Zabusky (Rutgers University)

12:00 – 13:15 Lunch: Winnett Lounge

Computational Session V
Chair: N. J. Zabusky
(Rutgers University)

13:15 – 13:35 Code to Code Comparisons for the Problem of Shock Acceleration of Diffuse Dense Gaseous Cylinder (C16)
J. A. Greenough, W. J. Rider, C. A. Zoldi, and J. R. Kamm (Lawrence Livermore National Laboratory and Los Alamos National Laboratory)

13:35 – 13:55 Molecular Dynamic Simulation of Shock and Richtmyer-Meshkov Instability in Cylindrical Geometry (C26)
K. Nishihara, V. Zhakhovskii, and M. Abe (Osaka University, Institute of Laser Engineering)

13:55 – 14:15 Large Eddy Simulation of Strong Shock Richtmyer-Meshkov Instability (C33)
R. Samtaney, T. Voelkl, and D. I. Pullin (California Institute of Technology)

14:15 – 14:35 Spectral and High-Order Compact Methods for Shock-Induced Mixing (C8)
A. W. Cook, W. Cabot, and J. A. Greenough (Lawrence Livermore National Laboratory)

14:35 – 14:55 Break: Beckman Institute (courtyard)

Computational Session VI
Chair: B. T. Goodwin
(Lawrence Livermore National Laboratory)

14:55 – 15:15 Turbulent Mixing Nuclear Burning in Type Ia Supernova Explosion Based on Bubble Statistical Mechanics (C38)
H. Takabe, S. Yamada, K. Kobayashi, A. Mizuta, and K. Nomoto (Osaka University, Institute of Laser Engineering and University of Tokyo)

15:15 – 15:35 High Order Numerical Methods for the 2D Richtmyer-Meshkov Instability (C54)
W.-S. Don, D. Gottlieb, L. Jameson, and C.-W. Shu (Brown University and Lawrence Livermore National Laboratory)

15:35 – 15:55 Compressibility Effects in a High-Speed, Reacting Shear Layer: An Investigation Using DNS (C27)
C. Pantano and S. Sarkar (University of California, San Diego)

15:55 – 16:15 A Semi-Empirical Model for Turbulent Diffusion of Magnetic Field to Accelerated Plasma (C19)
E. V. Gubkov, V. A. Zhmailo, and Yu. V. Yanilkin (Russian Federal Nuclear Center-VNIIEF)

16:15 – 17:45 Computational Discussion: Beckman Institute Auditorium

---

Experimental and Theoretical Poster Session:
Winnett Lounge

18:00 – 21:00 Banquet: Pasadena Hilton
Guest Speaker: Z. Nagin Cox
(NASA, Jet Propulsion Laboratory)

THURSDAY, DECEMBER 13, 2001

8:15 – 8:30 Announcements: O. Schilling

Theoretical Session I
Chair: D. I. Meiron
(California Institute of Technology)

8:30 – 9:30 Review Talk:
Three Dimensional Multi-Mode Rayleigh-Taylor and Richtmyer-Meshkov Instabilities at All Density Ratios (T14)
D. Kartoon, D. Oron, L. Arazi, A. Rikanati, U. Alon, and D. Shvarts (Nuclear Research Center, Negev, Ben-Gurion University, Tel-Aviv University, and Weizmann Institute)

9:30 – 9:50 Theoretical Methods for Determination of Mix (T7)
B. Cheng, J. Glimm, and D. H. Sharp (Los Alamos National Laboratory, State University of New York, Stony Brook, and Brookhaven National Laboratory)

9:50 – 10:10 Effects of High Initial Amplitudes and High Mach Numbers on the Evolution of the RM Instability: I. Theoretical Study (T23)
A. Rikanati, D. Oron, O. Sadot, and D. Shvarts (Nuclear Research Center, Negev and Ben-Gurion University)

10:10 – 10:30 Evolution of Arbitrary Perturbations in the Richtmyer-Meshkov Instability (T20)
K. O. Mikaelian (Lawrence Livermore National Laboratory)

10:30 – 10:50 Break: Beckman Institute (courtyard)

Theoretical Session II
Chair: S. B. Dalziel
(Cambridge University)

10:50 – 11:10 Spectral Analysis of Turbulent Flows Induced by RT and RM Instabilities (T38)
V. F. Tishkin and N. V. Zmitrenko (Institute for Mathematical Modeling, Russian Academy of Sciences)

11:10 – 11:30 A New Framework for Transitional and Turbulent Mixing (T36)
Y. Zhou, H. F. Robey, and A. C. Buckingham (Lawrence Livermore National Laboratory)

11:30 – 11:50 Raleigh-Taylor and Richtmyer-Meshkov Instabilities for Fluids with a Finite Density Contrast (T2)
S. I. Abarzhi, J. Glimm, and A der Lin (State University of New York, Stony Brook)

12:00 – 13:15 Lunch: Winnett Lounge

Theoretical Session III
Chair: T. T. Clark
(Los Alamos National Laboratory)

13:15 – 13:35 Nonlinear Evolution of an Interface in the Richtmyer-Meshkov Instability (T19)
K. Nishihara, C. Matsuoka, and Y. Fukuda (Ehime University and Osaka University Institute of Laser Engineering)

13:35 – 13:55 Nonlinear Evolution of Unstable Fluid Interface (T1)
S. I. Abarzhi (State University of New York, Stony Brook)

13:55 – 14:15 Analytical Study of the Rayleigh-Taylor Instability in Compressible Fluids (T30)
M. Tricottet and S. Bouquet (Commissariat à l'Energie Atomique)

14:15 – 14:35 Non-Linear Stages for the RT and RM Instabilities (T13))
N. A. Inogamov, M. Tricottet, A. M. Oparin, and S. Bouquet (Landau Institute for Theoretical Physics, Institute of Computer-Aided Design, and Commissariat à l'Energie Atomique)

14:35 – 14:55 Break: Beckman Institute (courtyard)

Theoretical Session IV
Chair: D. L. Youngs
(Atomic Weapons Establishment)

14:55 – 15:15 Rate of Growth of the Linear Richtmyer-Meshkov Instability (T34)
J. G. Wouchuk (University of Castilla)

15:15 – 15:35 Efficient Perturbation Methods for Richtmyer-Meshkov and Rayleigh-Taylor Instabilities: Weakly Nonlinear Stage and Beyond (T32)
M. Vandenboomegaerde, C. Cherfils, D. Galmiche, S. Gauthier, and P. A. Raviard (Commissariat à l'Energie Atomique)

15:35 – 15:55 Response of Turbulent RANS Models to Self-Similar Variable Acceleration RT-Mixing: An Analytical 0D Analysis (T18)
A. Llor (Commissariat à l'Energie Atomique)

15:55 – 16:15 Combined Shear and Buoyancy Instabilities (T33)
P. N. Wilson, M. J. Andrews, and F. H. Harlow (Texas A & M University and Los Alamos National Laboratory)

16:15 – 17:45 Theoretical Discussion: Beckman Institute Auditorium

---

Experimental and Computational Poster Session: Winnett Lounge

FRIDAY, DECEMBER 14, 2001

8:15 – 8:30 Announcements: O. Schilling

Theoretical Session V
Chair: O. Schilling
(Lawrence Livermore National Laboratory)

8:30 – 8:50 Rayleigh-Taylor Instability in Compressible Fluids (C12)
Y. Elbaz, A. Rikanati, D. Oron, and D. Shvarts (Nuclear Research Center Negev, Ben Gurion University, and Weizmann Institute of Science)

8:50 – 9:10 A Model for Instability Growth in Accelerated Solid Metals (T9)
J. D. Colvin, M. Legrand, B. A. Remington, G. Schurtz, and S. V. Weber (Lawrence Livermore National Laboratory and Comissariat à l'Energie Atomique)

9:10 – 9:30 Toy Models for the Growth Rate of Rayleigh-Taylor Instability (T10)
S. B. Dalziel (Cambridge University)

9:30 – 9:50 Spherical Combustion Layer in a TNT Explosion (T37)
A. L. Kuhl and R. E. Ferguson (Lawrence Livermore National Laboratory and Krispin Technologies)

9:50 – 10:10 3D Rayleigh-Taylor and Richtmyer-Meshkov Single -Modes (T12)
N. A. Inogamov, A. M. Oparin, M. Tricottet, and S. Bouquet (Landau Institute for Theoretical Physics, Institute for Computer Aided Design, and Commissariat à l'Energie Atomique)

10:10 – 10:30 Modeling Radiation Effects in Mixing Layers (T8)
T. Clark and F. H. Harlow (Los Alamos National Laboratory)

10:30 – 10:50 Break: Beckman Institute (courtyard)

10:50 – 11:10 Large- and Small-Scale Dynamics of Variable-Density Rayleigh-Taylor Instability-Induced Turbulent Mixing (T28)
O. Schilling and A. W. Cook (Lawrence Livermore National Laboratory)

11:10 – 11:55 Summary Remarks

11:55 – 12:00 Closing Remarks: O. Schilling / D. Meiron

EXPERIMENTAL POSTERS

Experimental Investigation of the Heavy and Light Media Separation in the Rayleigh-Taylor Turbulence Zone at Different Atwood Numbers (E2*)*
Yu. A. Kucherenko, S. I. Balabin, R. I. Ardashova, A. P. Pylaev, O. E. Kozelkov, and V. D. Murzakov (Russian Federal Nuclear Center – VNIITF)

Experimental Investigation into Influence of Stabilizing Properties of Transitional Layers Upon the Turbulent Mixing Evolution (E3)
Yu. A. Kucherenko, S. I. Balabin, R. I. Ardashova, O. E. Kozelkov, A. V. Dulov, and I. A. Romanov (Russian Federal Nuclear Center – VNIITF)

Mixing Between Two Compressing Cylinders (E5)
S. H. Batha, K. W. Parker, C. W. Barnes, A. M. Dunne, N. E. Lanier, G. R. Magelssen, T. J. Murphy, S. Rothman J. M. Scott, and D. Youngs (Los Alamos National Laboratory and Atomic Weapons Establishment)

Development of a Method for Studying the Interaction between Shock Wave and a Flame Front (E6)
M. Bliznetsov, V. Dudin, S. Gerasimov, L. Houas, G. Jourdan, and A. Logvinov (Russian Federal Nuclear Center – VNIIEF, SarPTI, IUSTI/CNRS)

Design of Flyer-Plate-Driven Compressible Turbulent Mix Experiments (E9)
R. P. Drake (University of Michigan)

Growth of Perturbations on Metals Interface at Oblique Collision with Supersonic Velocity of Contact Point Motion (E11)
O. B. Drennov, A. L. Mikhaylov, P. N. Nizovtsev, and V. A. Raevskii (Russian Federal Nuclear Center – VNIIEF)

From Linear to Turbulent Stages of the Richtmyer-Meshkov Instability Development in a Large Cross Section Shock Tube (E17)
L. Houas, G. Jourdan, E. E. Meshkov, and L. Schwaederlé (Université de Provence and Russian Federal Nuclear Center – VNIIEF)

RFNC-VNIITF Multifunctional Shock Tube to Investigate the Evolution of Instabilities in Nonstationary Gas Dynamic Flows (E20)
Yu. A. Kucherenko, O. E. Shestachenko, S. I. Balabin, and A. P. Pylaev (Russian Federal Nuclear Center – VNIITF)

Hydrodynamic Instabilities at a Shock Accelerated Bubble Gas-Gas Interface (E22)
G. Layes, G. Jourdan, P. Roualdes, and L. Houas (IUSTI and Centre d'Etudes de Gramat)

Experimental and Numerical Study of Shock Wave-Bubble Interaction (E23)
K. Levy, O. Sadot, D. Oron, Y. Srebro, Y. Elbaz, A. Josef-Hai, G. Ben-Dor, and D. Shvarts (Ben-Gurion University and Nuclear Research Center, Negev)

Laser-Driven Near Isentropic Compression of an Aluminum Flyer Plate (E24)
K. T. Lorenz, D. Kalantar, J. Edwards, J. D. Colvin, and B. Remington (Lawrence Livermore National Laboratory)

Single-Mode Incompressible Richtmyer-Meshkov Instability Experiments (E26)
C. E. Niederhaus and J. W. Jacobs (NASA Glenn and University of Arizona)

Modeling Laser Material Strength Experiments (E29)
S. Pollaine, D. Kalantar, B. Remington, J. Belak, J. D. Colvin, J. Edwards, R. Minich, K. O. Mikaelian, K. T. Lorenz, S. V. Weber, L. G. Wiley, D. Paisley, A. Hauer, J. S. Wark, A. Loveridge, A. M. Allen, T. R. Boehly, and M. A. Meyers (Lawrence Livermore National Laboratory, Los Alamos National Laboratory, Oxford University, University of Rochester, and University of California, San Diego)

Experiments and Simulations of Instabilities in a Shock-Accelerated Gas Cylinder (E30)
K. Prestridge, C. A. Zoldi, P. Vorobieff, P. M. Rightley, and R. F. Benjamin (Los Alamos National Laboratory, State University New York, Stony Brook, and University of New Mexico)

Experimental Study of the Interaction of a Strong Shock with a Spherical Density Inhomogeneity (E34)
H. F. Robey, T. S. Perry, R. I. Klein, J. A. Greenough, J. O. Kane, and T. R. Boehly (Lawrence Livermore National Laboratory, University of California, Berkeley, University of Rochester)

Turbulent Transition in a High Reynolds Number, Rayleigh-Taylor Unstable Plasma Flow (E35)
H. F. Robey, Y. K. Zhou, A. C. Buckingham, P. Keiter, B. A. Remington, and R. P. Drake (Lawrence Livermore National Laboratory and University of Michigan)

Measurements Within a Richtmyer-Meshkov Mixing Zone Using a Triple Hot Wire Probe Technique (E37)
L. Schwaederlé, G. Jourdan, L. Houas, and J.-F. Haas (IUSTI and Commissariat à l'Energie Atomique)

Experimental Study into Evolution of Gravitational Turbulent Mixing of Gases at the Multifunctional Shock Tube (E38)
Yu. A. Kucherenko, O. E. Shestachenko, Yu. A. Piskunov, E. V. Sviridov, V. M. Medvedev, and A. I. Baishev (Russian Federal Nuclear Center – VNITF)

Doubly-Shocked Richtmyer-Meshkov Instability Experiments at Nova (E41)
D. J. Ward, K. S. Budil, T. A. Peyser, B. A. Remington, P. L. Miller, R. J. Wallace, H. Louis, and A. Demiris (Lawrence Livermore National Laboratory)

Evolution of the Mixing Zone of Different Densities Gases Being Interaction to Compression Waves (E43)
S. G. Zaytsev, V. V. Krivets, I. M. Mazlin, S. N. Titov, E. I. Chebotareva, V. V. Nikishin, V. F. Tishkin, S. Bouquet, and J.-F. Haas (Krzhizhanovsky Power Engineering Institute, Institute of Mathematical Modeling, and Commissariat à l'Energie Atomique)

Studies of Rayleigh-Taylor Instability in Aluminum Under Shock-Wave and Shock Less Loading (E44)
A. Lebedev, P. Nizovtcev, and V. Raevsky (Russian Federal Nuclear Center – VNIIEF)

Ablative Rayleigh-Taylor Instability at Short Wavelengths (E45)
H. Azechi, T. Sakaiya, M. Nakai, H. Shiraga, K. Shigemori, N. Miyanaga, M. Nishikino, S. Fujioka, Y. Tamari, H. Nagatomo, A. Sunahara, and H. Takabe (Osaka University and Rutgers University)

Computational Posters

Modes' Interaction on Nonlinear Stage of Richtmyer-Meshkov Instability Evolution (C1)
V. I. Anisimov and A. V. Polionov (Russian Federal Nuclear Center-VNIITF)

Application of kε-Model for the Description of an Atmospheric Surface Layer (C2)
M. G. Anuchin, V. E. Neuvazhayev, and I. E. Parshukov (Russian Federal Nuclear Center-VNIITF)

Numerical Simulation of Mode Coupling in Laser-Driven Rayleigh-Taylor Instability Experiments (C9)
R. Darlington and K. Budil (Lawrence Livermore National Laboratory)

3D Computation for Surface Perturbation Evolution of Plasma Cloud During its Expansion in Magnetic Field (C14)
E. S. Gavrilova, E. V. Gubkov, V. A. Zhmailo, and Yu. V. Yanilkin (Russian Federal Nuclear Center – VNIIEF)

The Richtmyer-Meshkov Instability in Cylindrical Geometry: Experiments and Simulation (C15)
M. J. Graham, K. S. Budil, J. Grove, and B. A. Remington (Lawrence Livermore National Laboratory and Los Alamos National Laboratory)

Implementation of a Turbulent Mix Model in a 2D ALE Code (C17)
B. Grieves (Atomic Weapons Establishment)

Error Estimation for Strong Shock Hydrodynamics (C18)
J. W. Grove (Los Alamos National Laboratory)

Localization and Spreading of Interfaces (Contact Discontinuities) in PPM and WENO Simulations of the Inviscid Compressible Euler Equations (C20)
Y. Gupta, N. J. Zabusky, R. Samtaney, and Y. Gulak (Rutgers University)

Update on Instability Modeling for the NIF Ignition Targets (C22)
S. W. Haan, T. Dittrich, S. Hatchett, D. Hinkel, M. Marinak, D. Munro, O. Jones, S. Pollaine, and L. Suter (Lawrence Livermore National Laboratory)

Pillars of Creation (C23)
J. O. Kane, D. D. Ryutov, B. A. Remington, S. G. Glendinning, J. Nash, M. Pound, and D. Arnett (Lawrence Livermore National Laboratory, University of Maryland, and University of Arizona)

Computational Modeling of Two-Shell Cylindrical Implosions with Mix (C28)
K. W. Parker, A. M. Dunne, S. Rothman, D. Youngs, C. Barnes, S. H. Batha, N. E. Lanier, G. R. Magelssen, T. J. Murphy, and J. M. Scott (Atomic Weapons Establishment and Los Alamos National Laboratory)

Influence of Turbulent Mixing Zone on Growth of Local Perturbation in Environments of Rayleigh-Taylor Instability (Numerical Simulation) (C30)
V. A. Raevski, A. N. Sinitsina, and Yu. V. Yanilkin (Russian Federal Nuclear Center – VNIIEF)

A Statistical Comparison of Gas Cylinder Experiments with Their Simulation (C31)
W. J. Rider, J. R. Kamm, and C. A. Zoldi (Los Alamos National Laboratory)

A Mix-Model for One-Dimensional Simulations of Laser-Driven Implosion Experiments (C36)
D. Souffland and F. Renaud (Commissariat à l'Energie Atomique)

Turbulent Diffusion in Solar Type Star (C39)
N. Toqué (University of Montreal)

Recent Computational Simulations of Rayleigh-Taylor Mix Layer Growth with a Multi-Fluid Model (C40)
E. Vold (Los Alamos National Laboratory)

An Efficient and High Resolution Solver for the Two-Dimensional Numerical Simulation of the Richtmyer-Meshkov Instability (C41)
S. P. Wang, M. H. Anderson, J. G. Oakley, and R. Bonazza (University of Wisconsin, Madison)

ALE Simulations of Turbulent Rayleigh-Taylor Instability in 2-D and 3-D (C42)
S. V. Weber, G. Dimonte, and M. M. Marinak (Lawrence Livermore National Laboratory)

Preliminary Results of DNS and LES Simulations of Self-Similar Variable Acceleration RT-Mixing Flows (C47)
D. L. Youngs, X. Silvani, J. Magnaudet, and A. Llor (Atomic Weapons Establishment, Institute de Mécanique des Fluides de Toulouse, and Commissariat à l'Energie Atomique)

Rapid Turbulization Arising from Vortex Double Layers in Interactions of "Complex" Blast Waves and Cylindrical and Spherical Bubbles (C49)
S. Zhang, Y.-G. Kang, K. Nishihara, N. J. Zabusky, and H. Kim (Rutgers University and Kwangju Institute of Science and Technology)

Turbulent Flow Simulations of Two Fluids Moving with Different Laws of Acceleration (C51)
V. I. Kozlov, A. N. Razin, and I. V. Saphzhnikov (Russian Federal Nuclear Center – VNIIEF)

The Behavior of Velocity Variance Resulting From Turbulent Mixing Zone-Shock Interaction (C52)
V. I. Kozlov and A. N. Razin (Russian Federal Nuclear Center-VNIIEF)

An Assessment of Multi-Velocity Versus Single Velocity in a Multi-Component Model of Turbulent Mixing (C53)
D. Eliason, W. Cabot, and Y. Zhou (Lawrence Livermore National Laboratory)

Mixing Due to the Rayleigh-Taylor Instability (C55)
A. M. Dimits (Lawrence Livermore National Laboratory)

CALE Simulation of Richtmyer-Meshkov Experiments at High Mach Number (C57)
A. Miles, J. Edwards, and S. G. Glendinning (Lawrence Livermore National Laboratory and University of Michigan)

THEORETICAL POSTERS

Nonlinear Asymptotic Solutions to RT and RM Problems for Fluids with Close Densities (T2)
S. I. Abarzhi (State University of New York at Stony Brook)

Turbulent Mixing in RTI as Order-Disorder Process (T3)
S. I. Abarzhi (State University of New York at Stony Brook)

A New Turbulent Two-Fluid RANS Model for KH, RT, and RM Mixing Layers (T4)
P. Bailly and A. Llor (Commissariat à l'Energie Atomique)

Super-Exponential Rayleigh-Taylor Flow (T5)
R. E. Breidenthal (University of Washington)

A General Buoyancy-Drag Model for the Evolution of the Rayleigh-Taylor and Richtmyer-Meshkov Instabilities (T11)
Y. Elbaz, Y. Srebro, O. Sadot, and D. Shvarts (Ben Gurion University and Nuclear Research Center)

Stability of Diverging Shock Waves (T15)
V. M. Ktitorov (Russian Federal Nuclear Center – VNIIEF)

Stability of Reflected From the Center Self-Similar Converging Shock Wave (T16)
V. M. Ktitorov (Russian Federal Nuclear Center – VNIIEF)

Using a Turbulence Transport Approach to Study Shocks Through Polycrystalline Metal (T17)
R. R. Linn and F. H. Harlow (Los Alamos National Laboratory)

Statistical Mechanics Large Scale Model for the Evolution of the Multi-Mode Kelvin Helmholtz Instability (T22)
A. Rikanati, U. Alon, and D. Shvarts (Nuclear Research Center, Ben-Gurion University, and Weizmann Institute of Science)

Compressible MHD Turbulence in Strongly Radiating Molecular Clouds in Astrophysics (T25)
D. D. Ryutov and B. A. Remington (Lawrence Livermore National Laboratory)

Single-Velocity, Multi-Component Turbulent Transport Models for Interfacial Instability-Driven Flows (T26)
O. Schilling (Lawrence Livermore National Laboratory)

Analytic Nonlinear Growth of a Single-Mode Richtmyer-Meshkov Instability (T31)
M. Vandenboomgaerde (Commissariat à l'Energie Atomique)

Pattern Detection, Compression and Denoising of RT Mix Data Using Discrete Wavelet Transform (T39)
B. B. Afeyan, P. Ramaprabhu, and M. J. Andrews (PolyMath Research Incorporated and Texas A & M University)

Numerical simulation of initial perturbation growth in oblique impact of metal plates

Bakhrakh S.M., Volodina N.A., Nizovtsev P.N., Spiridonov V.F., Shuvalova E.V.
VNIIEF-RUSSIA

Introduction

An oblique impact of metal layers results in development of intensive shear strains at their interface, the near-boundary metal layers become severely heated and produce shaped jets. These effects lead to the interface profile distortion. Both regular and asymmetric distorted waves appear. In this case a hydrodynamic instability, the Kelvin-Helmholtz instability, appears [1].

The subsonic regime of the oblique impact has been comprehensively studied recently, where $U_c<C_s$ (U_c – contact point velocity, C_s – sound speed in the material). Under these loading conditions, a shaped jet forms at the contact point, if the pressure about the impact point is higher than the metal strength.

The initial perturbation growth is known to occur in the subsonic impact conditions in the gas dynamics approximation. The situation is more complex in the supersonic impact of strong plates.

When the impact angle is constant, there is critical velocity U_{cr}. If $C_s<U_c<U_{cr}$, detached oblique shock waves form in the flow. During the transition across the wave front the flow transforms from supersonic to subsonic. In the impact zone the shaped jet forms and the perturbations grow like in the case of the subsonic impact.

When $U_c> U_{cr}$, attached oblique shock waves are established at the contact point and no jet formation is observed. The perturbation evolution is considered as impossible in this case, as there is no principal perturbation generator, i.e. the shaped jet.

The material interface state in such supersonic loading conditions has been inadequately studied. It was anticipated that essentially prompt cessation of the perturbation evolution process would be obtained in the transition to the jet-free conditions of the plate impact. That is, as soon as $U_c= U_{cr}$, no peturbations should appear. However, the perturbation growth was observed in the experiments. Ref. [2] analyzes the experimental data and explains this phenomenon theoretically.

The direct numerical simulation of the experiments is of interest.

1. Numerical codes. Setting up problems

The numerical simulations were performed with the program complex that implements code LEGAK [3].

The strength properties are included using code [4].

The material state was described in the elastic-plastic approximation. Pressure was estimated by Mie-Grueneisen equation of state [5] with the following parameters:

$$\rho_0 = 2.64\frac{g}{cm^3},\ c_0 = 5.55\frac{km}{s},\ \boldsymbol{n = 3.2},\ \boldsymbol{\Gamma = 2.14}.$$

Yield strength was taken as a function of pressure and temperature:

$$\boldsymbol{Y = Y_0 (1 + \alpha \cdot P)\left(1 - \beta \cdot \frac{E_T}{E_m}\right)},$$

where $\boldsymbol{Y_0 = 0.3}$, $\alpha = \frac{1}{3}$, $\beta = 1$, E_T is heat energy, $E_m = 1.1\frac{kJ}{g}$ is melting energy, $\vartheta = \mathbf{0.33}$ is Poisson ratio.

The problem geometry is presented in Fig.1. Impact of two aluminum plates at an angle of 14 degrees was simulated. The perturbation of $\lambda_0 = 0.5mm$ wavelength and $a_0 = 0.01mm$ amplitude was given on the surface of the lower rod (Fig.2).

The computational grid is depicted in Fig.3.

Domain 1: impacting plate of 4 mm thickness.

Domain 2: immovable plate of 15 mm thickness, on the external boundary of which initial perturbation $\boldsymbol{a = a_0 \cdot \sin \frac{2\pi}{\lambda_0} x}$ is given.

Domain 3: vacuum.

During the computation the grid remains immovable, fixed. The material moves relative to the immovable computational grid. This allows computations with severe interface strains.

To follow the evolution of the interface between the upper and lower aluminum rods, they were marked with different marks, to be more exact, as “different materials” with identical physical properties. Hence, if material from the upper and lower plates gets into the same computational cell, it is possible to determine the plate interface position by the material concentrations and follow the perturbation evolution.

The computational grid was taken such, that there were on the order of 20 computational cells per wavelength. The total number of the points is 1120x740=828800. The computations in the scalar (one-processor) regime are problematic. So the computations were performed on the shared memory multi-processor computer with complex LEGAK-MP [6].

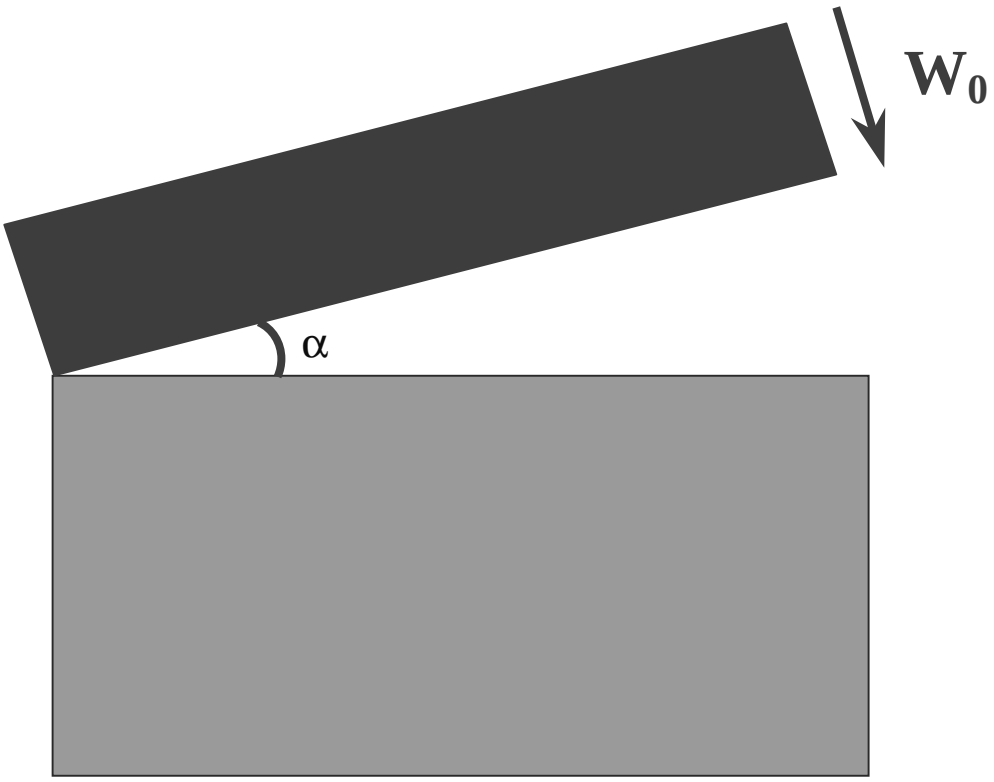

Fig.1 *Problem geometry*

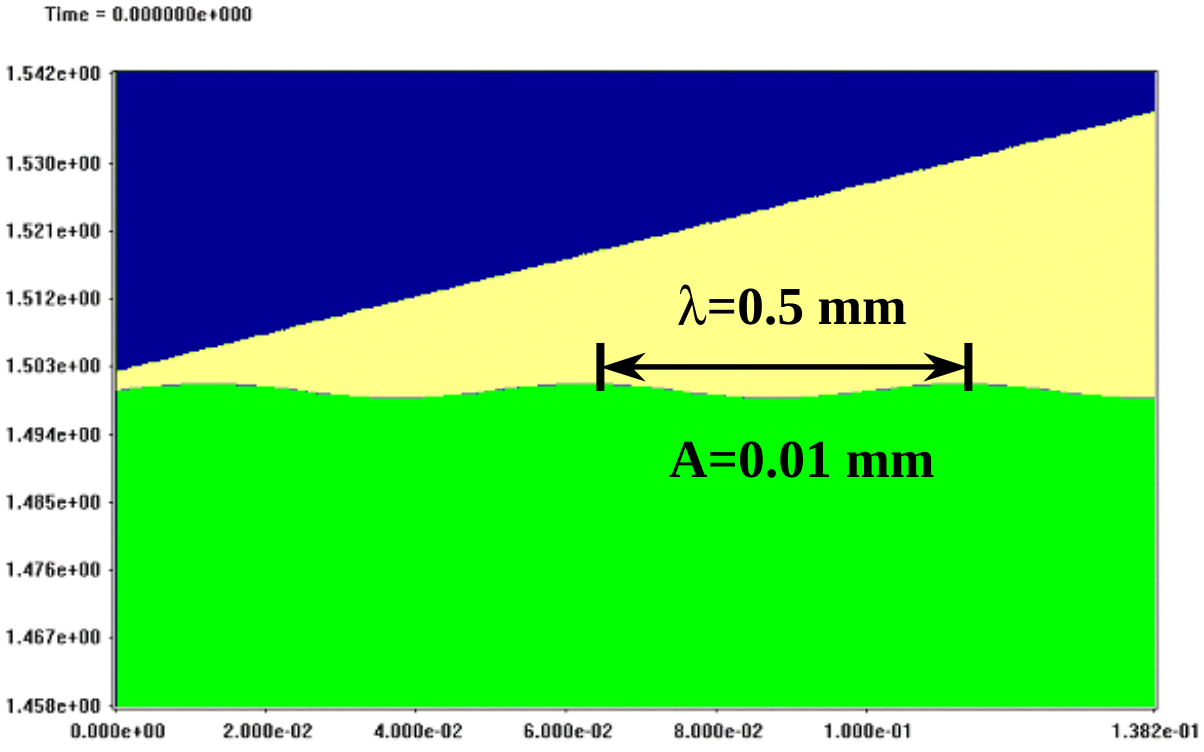

Fig.2 *Initial perturbation*

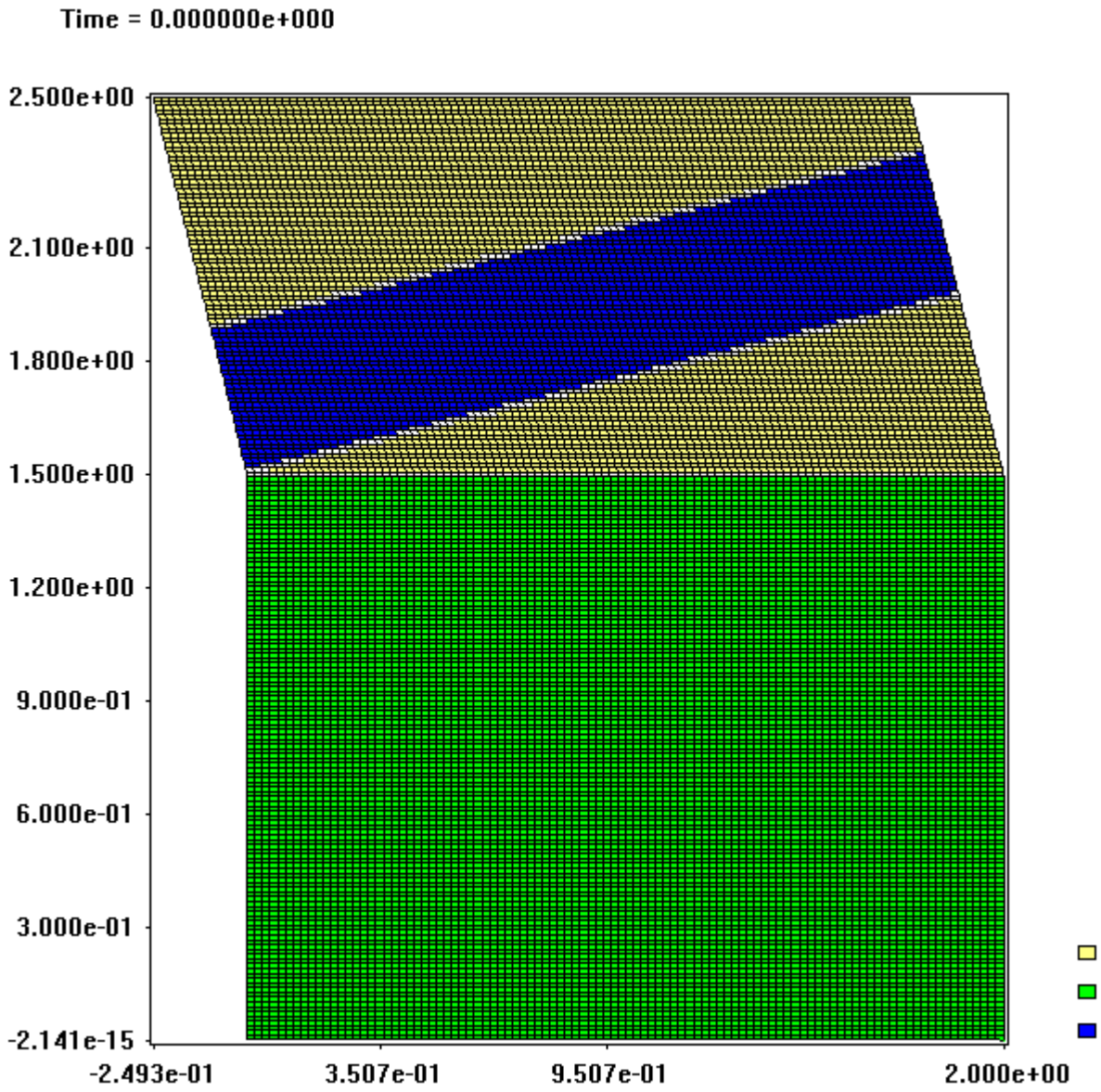

Fig.3 *Computational grid (Eulerian computation)*

At the initial study phase, the computations were performed in the quasi-Lagrangian formulation. In these computations, both the upper (launched) and lower plates were considered as separate regions, whose boundaries were Lagrangian lines, between which there was no interaction. In the areas of the plates, the distances between which became less than ***0.1h*** (where ***h*** is the computational grid size) during the motion, their boundary segments were integrated, thereby the inter-plate interaction was given. A number of computations were conducted in this formulation. The computed data for early times are in a good agreement with the computations on the Eulerian grid. However, because of the grid distortion (due to the complex flow) and other computational "phenomena" it was impossible to perform the computations up to the times of our concern. For this reason our choice was in favor of the computations on the immovable Eulerian computational grid.

2 Results of the computations

Several computational series were conducted. The following was varied in the computations:

- plate impact velocity W_0;
- perturbation wavelength λ_0;
- material properties:
  - gas-dynamic approximation;
  - elastic-plastic approximation with different medium parameters:
    - — variations of strengthening α,
    - — variations of yield strength Y_0,
    - — variations of melting heat E_m,
    - — determination of E_m according to the Lindemann model.

It is of interest to perform the computations including the elastic stress relaxation. This model is being introduced to the program complex LEGAK, and we are planning the studies at the next phase of the work. We are inspired by the fact that the relaxation models most adequately describe material shear strain that is responsible for the perturbation growth in the oblique impact of plates.

2.1 Impact velocity effect

The impact velocity was varied in the computations.
The results for all the computations are presented for the time, when the contact point has traveled a distance of ***L= 20mm***.

The computations were conducted with strengthening factor $\alpha = \frac{1}{3}$, melting heat $E_m = 1.1\frac{kJ}{g}$, and perturbation wavelength $\lambda_0 = 0.5mm$.

The computed amplitude increase factors are summarized in Table 1.

Table 1

Initial velocity W_0, km/s	Amplitude increase factor a/a_0
1.5	6
1.75	2.5
2	1

The perturbation evolution pattern for W_0=1.5 and 1.75 km/s is presented in Figs. 8 and 4.

Thus, the direct numerical simulation reproduces the experimentally detected effect of the perturbation increase.

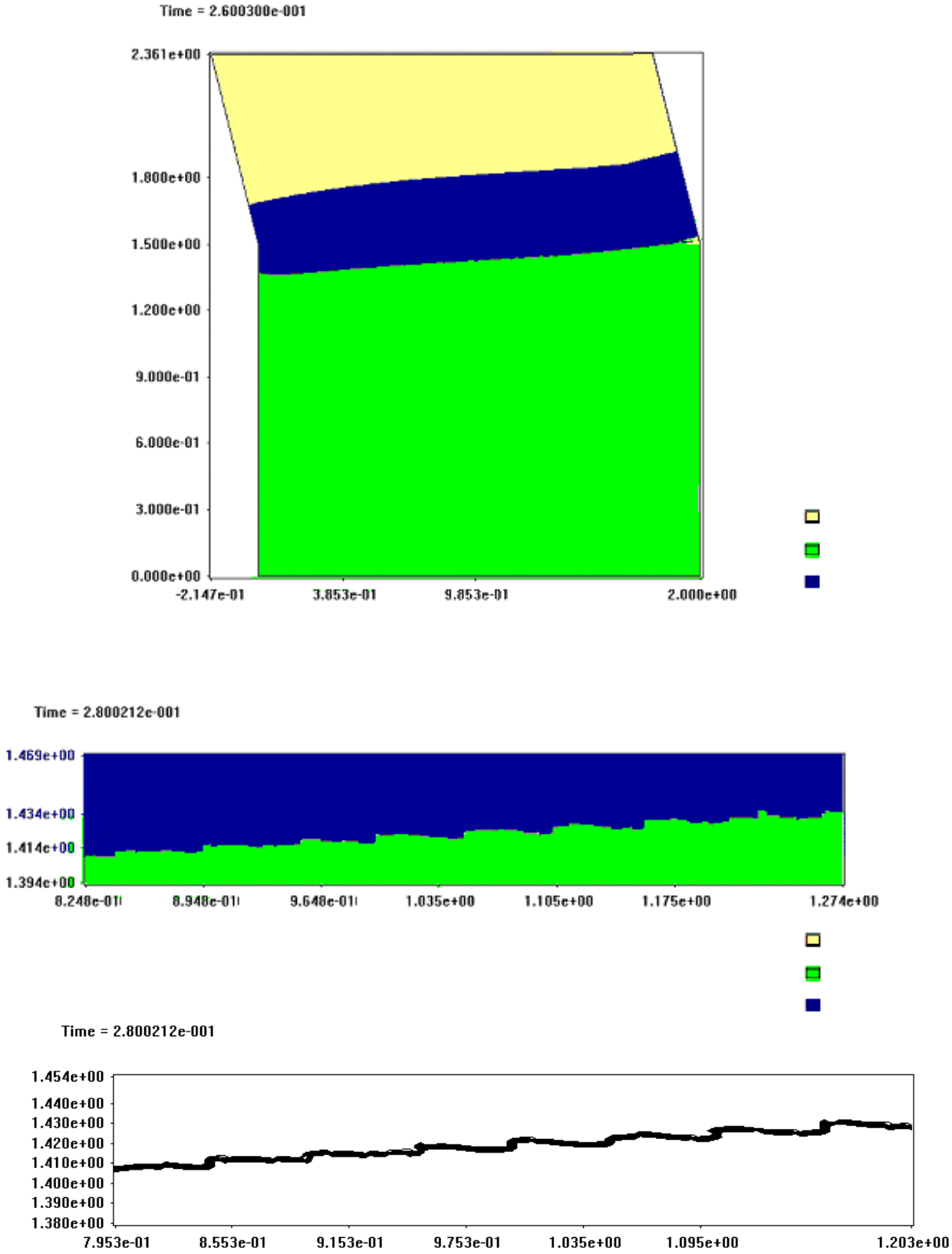

Fig.4 Geometry and isolines (UP $\alpha=1/3$, $U_0=1.75$, $\lambda_0=0.5mm$)

2.2 Simulation of metal interface instability with change in strength properties

The material strength properties were varied in the computations.

The computations were conducted with initial velocity W_0=1.5km/s, melting heat $E_m = 1.1\frac{kJ}{g}$, and perturbation wavelength $\lambda_0 = 0.5mm$.

The perturbation growth pattern is depicted in Figs. 5-8. The material strength effect on the perturbation growth is summarized in Table 2.

Table 2

Material model	Amplitude increase factor a/a_0
Gas dynamics	93
Elasticity-plasticity $\alpha = 0$	65
Elasticity-plasticity $\alpha = 0.1$	53
Elasticity-plasticity $\alpha = 1/3$	6
Elasticity-plasticity $\alpha = 2/3$	2
Elasticity-plasticity $\alpha = 1$	1

2.3 Simulation of metal interface instability with different values of melting heat

The value of melting heat was varied in the computations.

The computations were conducted with initial velocity W_0=1.5km/s, strengthening factor $\alpha = \frac{1}{3}$, and perturbation wavelength $\lambda_0 = 0.5mm$.

The effect of different melting heat values on the perturbaton growth is summarized in Table 3.

Table 3

Melting heat $E_m\left(\frac{кДж}{г}\right)$	Amplitude increase factor a/a_0
0.4	29
1.1	6
1.5	2
2.0	1

2.4 Simulation of metal interface instability with different initial perturbation wavelengths

The computations were conducted in the elastic-plastic approximation ($Y_0 = 0.3$, $\alpha = \frac{1}{3}$, $\beta = 1$) for initial velocity W_0=1.5km/s with different initial perturbation wavelengths.

The results are summarized in Table 4.

Table 4

Initial wavelength (*mm*)	Amplitude increase factor a/a_0
0.25	1
0.5	6
1.0	1

Thus, the ~ 0.5-mm-wavelength perturbations grow most intensively under the discussed conditions. This can explain the fact that among the whole spectrum of the perturbations that take place on “smooth” plates by virtue of their machining it is ~ $0.5 \div 0.6$-mm-wavelength perturbations that grow and are observed in the experiments.

2.5 Change in perturbation wavelength

The computations revealed an interesting fact of increase in the initial perturbation wavelength. The computed data for initial velocity W_0=1.5km/s and wavelength $\lambda_0 = 0.05cm$ are presented in Table 5.

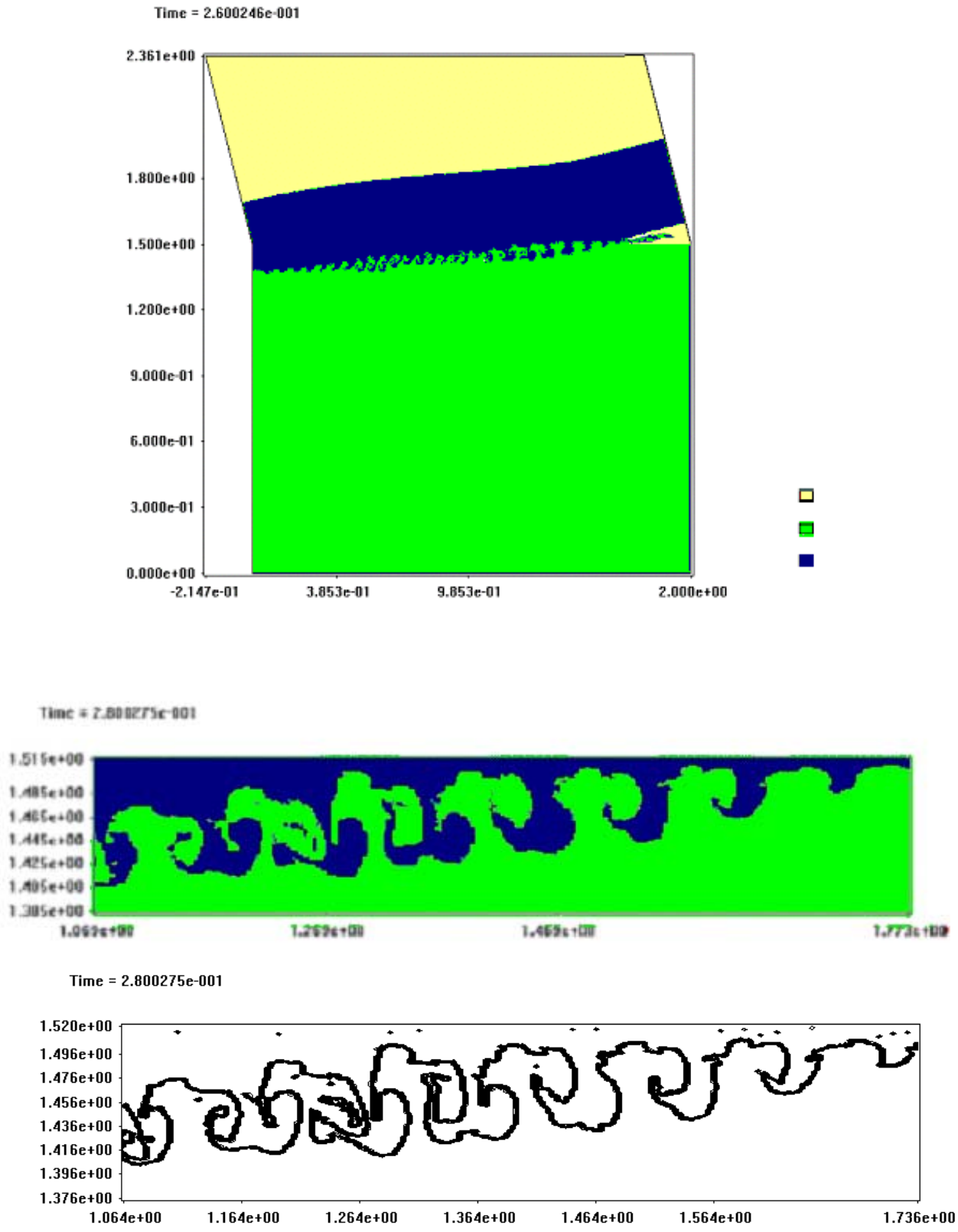

Fig.5 Geometry and isolines (*GD*, U_0*=1.5*, λ_0*=0.5mm)*

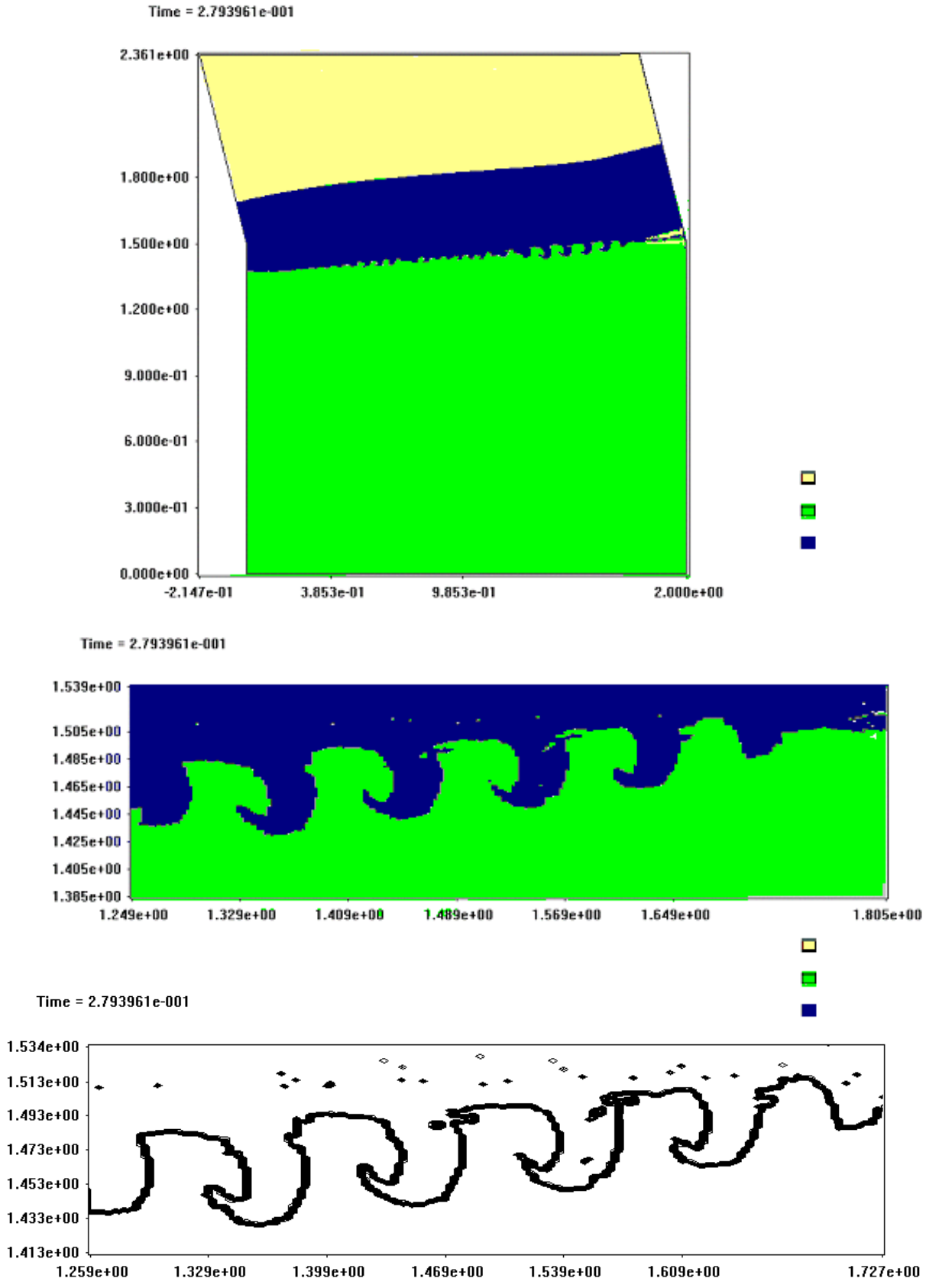

Fig.6 Geometry and isolines (*UP* $\alpha=0$, $U_0=1.5$, $\lambda_0=0.5mm$)

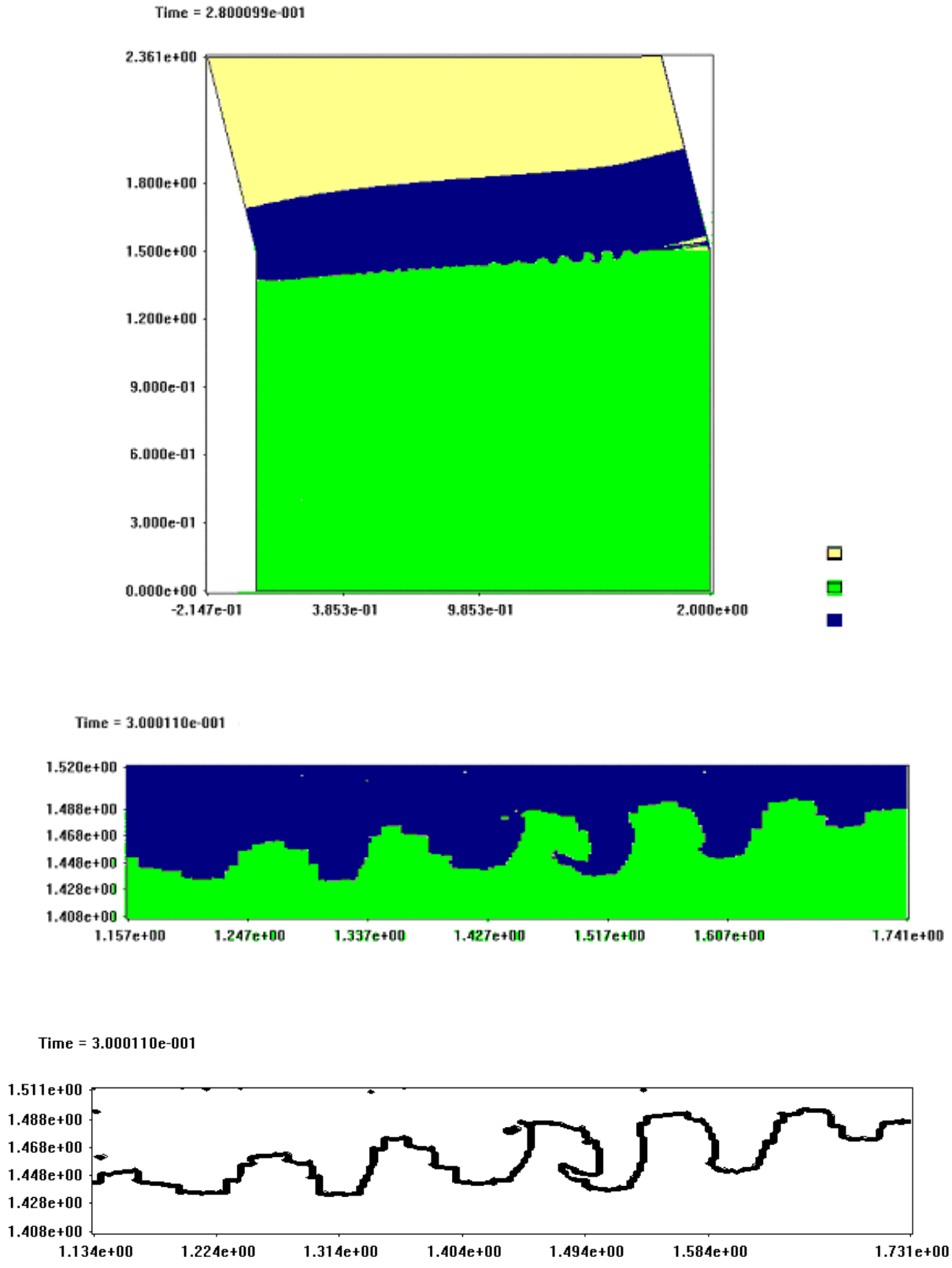

Fig.7 Geometry and isolines (*UP* α*=0.1,* U_0*=1.5,* λ_0*=0.5mm)*

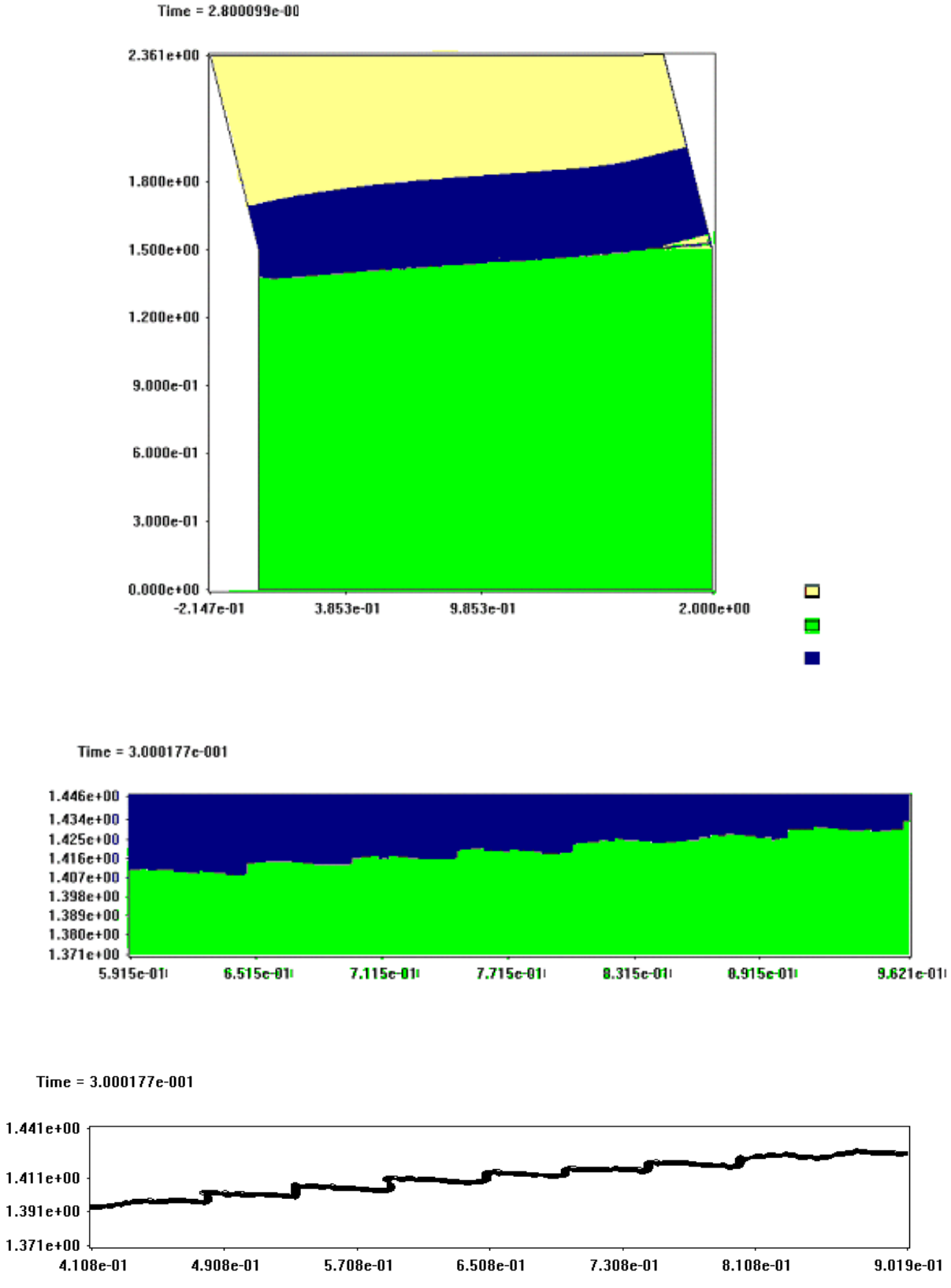

Fig.8 Geometry and isolines (*UP* α*=1/3,* U_0*=1.5,* λ_0*=0.5mm)*

Table 5

Material model	Final wavelength λ *(mm)*
Gas dynamics	1
Elasticity-plasticity $\alpha = \mathbf{0}$	0.9
Elasticity-plasticity $\alpha = \mathbf{0.1}$	0.8
Elasticity-plasticity $\alpha = \mathbf{1/3}$	0.5

Whereas the wavelength increases by a factor of about 2 in the gas-dynamic approximation, it remains essentially unchanged in strong medium. This phenomenon requires more comprehensive study, both numerical and experimental.

Conclusion

The computed data for the oblique plate impact agrees with the experimental data. In particular, it is numerically corroborated that the perturbations of wavelength λ=0.5mm grow most intensively. The numerical simulation revealed the effect of the wavelength growth in low-strength material, which needs more comprehensive study, both experimental and computational.

The work was carried out under the support by Russia Fundamental Research Foundation, Grant 99-01-00812 and 02-01-00796, and LNLN/VNIIEF Agreement B512135.

References

1. Deribas A.A. Strengthening and explosive welding physics. Novosibirsk, Nauka Publishers. 1980.

2. Drennov O.B., Mikhailov A.L., Nizovtsev P.N., Rayevsky V.A. Perturbation evolution at metal interface in oblique impact with contact point moving at supersonic velocity. VANT. Ser. Teoreticheskaya i Prikladnaya Fizika (to be published).

3. Bakhrakh S.M., Spiridonov V.F., Shanin A.A. A method for heterogeneous medium gas-dynamic flow computations in Lagrangian-Eulerian coordinates// DAN SSSR, 1984, V. 278, No. 4, pp. 829-833.

4. Bakhrakh S.M., Kovalev N.P., Pavlusha I.N. A method for elastic-plastic flow computations// Proceedings of All-Union Conference on Numerical Methods of Elasticity and Plasticity Theory. Part I. Novosibirsk, Nauka Publishers. 1974, pp.22-36.

5. Zeldovich Ya.B., Raizer Yu.P. Physics of shock waves and high-temperature hydrodynamic phenomena. Moscow, Fizmatgiz Publishers, 1963, 632p.

6. Avdeyev P.A., Artamonov M.V., Bakhrakh S.M., Velichko S.V., Volodina N.A., Vorobyeva N.M., Yegorshin S.P., Yesayeva E.N., Kovaleva A.D., Luchinin M.V., Pronevich S.N., Spiridonov V.F., Taradai I.Yu., Tarasova A.N., Shuvalova E.V. Program complex LEGAK and principles of its parallelization on multiprocessor computers// VANT. Ser. Matematicheskoye Modelirovaniye Fizicheskikh Protsessov (to be published).

APPLICATION OF Kε-MODEL FOR THE DESCRIPTION OF AN ATMOSPHERIC SURFACE LAYER

Anuchin M.G., Neuvazhayev V.E., Parshukov I.E.

(RFNC-VNIITF, Snezhinsk, Chelyabinsk region)

The problem on determination of non-dimensional characteristics of turbulent flow in atmospheric surface layer is considered within kε-model. Kε-equations and their singular points are investigated. The mathematical program for calculations of characteristics of turbulent flow in surface atmospheric layer is developed. From the set of integral curves those curves are chosen which correspond to the solution of formulated task and ensure the satisfactory experiments description. Here the basic model constants are chosen according to the conventional criteria. At the same it is shown that the parameter C_θ responding to convection source term of an ε-equation should be chosen depending on stability conditions. The best agreement with experimental results is reached if $C_\theta = 0$ for steady stratification and $C_\theta \neq 0$ for unstable stratification. By a numerical choice of value C_θ and factor of turbulent diffusion $\hat{\alpha}$ the quite satisfactory description of experimental observations known as analytical interpolar dependencies is received.

Introduction

Semiempirical $K\varepsilon$ models of turbulence are widely used for the description of different classes of turbulent flows [1-3] (jet streams and channels streams, gravitational turbulent mixing of fluid layers with different densities and others).

$K\varepsilon$ model was used for solving of the micrometeorology problems as well. In [4,5] the calculations of universal profile functions of atmosphere surface layer were conducted. On the basis of $K\varepsilon$ model the technique of calculation reconstruction of vertical profiles of meteorological values in the atmosphere boundary layer was developed according to the data of standard surface meteorological measurements [6,7].

In the current paper we are also analyzing the problem about atmosphere surface layer (ASL) within the frameworks of $K\varepsilon$ model. ASL is an example of the stratified flow, which is interested by the fact that it includes simultaneously both shear and convective (gravitational) mechanisms of turbulence generation. Moreover, the profile characteristics of stationary ASL have been studied experimentally quite well up to present. These conditions make the ASL problem by a good test for any semiempirical turbulence model.

The conducted theoretical and numerical investigations of the problem under consideration allowed to perform the procedure of selection of the empirical model constants more accurately and to obtain more accurate description of the experimental profiles as compared with the previous papers [4,5]. As the analysis showed, the best agreement with the observation data is obtained in case we assume the empirical parameter C_θ (which regulates the convective source of turbulence in ε equation) depends on the ASL stability status: $C_\theta = 0$ in the stable stratification area and $C_\theta \neq 0$ in the unstable stratification area.

1. Atmosphere surface layer. Theory of similarity, dimensionless form of equations of *K*ε model.

To describe turbulent flow in stationary and horizontally homogeneous ASL the following system of equations is applicable

$$k\frac{\partial U}{\partial z}=u_*^2; \tag{1.1}$$

$$-\alpha_\theta k\frac{\partial \theta}{\partial z}=q; \tag{1.2}$$

$$k\left(\frac{\partial U}{\partial z}\right)^2-\frac{g}{T}\alpha_\theta k\frac{\partial \theta}{\partial z}-\varepsilon+\alpha_b\frac{\partial}{\partial z}k\frac{\partial b}{\partial z}=0; \tag{1.3}$$

$$C_{\varepsilon 1}k\left(\frac{\partial U}{\partial z}\right)^2-C_\theta\alpha_\theta\frac{g}{T}k\frac{\partial \theta}{\partial z}-C_{\varepsilon 2}\varepsilon+C_\varepsilon\frac{b}{\varepsilon}\frac{\partial}{\partial z}\frac{b^2}{\varepsilon}\frac{\partial \varepsilon}{\partial z}=0; \tag{1.4}$$

$$k=C\frac{b^2}{\varepsilon}.$$

Here the axis *oz* is up-directed, *T* is temperature of ground surface, θ is potential temperature, *U* is velocity, *g* is gravitational acceleration, u_* is dynamic friction velocity, which determines turbulent frictional force between horizontal layers, *q* is turbulent temperature flow on the surface, *b* is turbulent energy pulsation (turbulent kinetic energy), ε is turbulent energy dissipation, *k* is turbulent viscosity (diffusion) coefficient. $\alpha_b, \alpha_\theta, C_\varepsilon, C_{\varepsilon 1}, C_{\varepsilon 2}, C_\theta, C$ are empirical constants.

At the height much above the significant dimensions of surface roughness the dimensional parameters of the problem are: u_*, q, $\frac{g}{T}$. With them it is possible to construct the single length parameter $L=-\frac{u_*^3}{\kappa\frac{g}{T}q}=\frac{u_*^2}{\kappa\frac{g}{T}\theta_*}$ presenting the characteristic of stratification (relational influence of dynamic and heat factors). Here κ is Karman constant, $\theta_*=-\frac{q}{u_*}$ is temperature scale.

If $L>0$, turbulent heat flow is down-directed (air substratum is cooled with a colder ground surface), stratification is stable. If $L<0$, turbulent heat flow is up-directed (air is heated with a hotter surface), stratification is unstable. The limit $L\to\infty$ corresponds to neutral stratification (heat flow equals to zero, thermal convection is absent).

All ASL characteristics are the functions of dimensionless height $\xi=\frac{z}{L}$ and may be presented in the form

$$U(z)=\frac{u_*}{\kappa}u_n(\xi),\quad k(z)=\kappa u_* L k_n(\xi),\quad b(z)=\frac{u_*^2}{\sqrt{C}}b_n(\xi),\quad \varepsilon(z)=\frac{u_*^3}{\kappa L}\varepsilon_n(\xi),\quad \theta(z)=\theta_0+\frac{\theta_*}{\kappa\alpha_\theta}\theta_n(\xi).$$

Here the dimensionless functions are indicated with the index "*n*", the empirical constants are traditionally introduced for convenience.

In the dimensionless variables instead of (1.1)-(1.4) after some transformations we finally have the following system of equations:

$$\frac{1}{k_n} - 1 - \varepsilon_n + \hat{\alpha}\frac{d}{d\xi}k_n\frac{db_n}{d\xi} = 0, \qquad (1.5)$$

$$\frac{C_{\varepsilon 1}}{k_n} - C_\theta - C_{\varepsilon 2}\varepsilon_n + \hat{\sigma}\frac{b_n}{\varepsilon_n}\frac{d}{d\xi}k_n\frac{d\varepsilon_n}{d\xi} = 0, \qquad (1.6)$$

$$k_n = \frac{b_n^2}{\varepsilon_n}.$$

Here $\hat{\alpha} = \alpha_b\frac{\kappa^2}{\sqrt{C}}$; $\hat{\sigma} = C_\varepsilon\frac{\kappa^2}{\sqrt{C}}$.

To interpret the experimental observations we use the dimensionless function $\varphi_u(\xi) = \frac{k\,z}{u_*}\frac{dU}{dz} = \xi\frac{\partial u_n}{\partial\xi} = \frac{\xi}{k_n}$ and Richardson flow number $Rf(\xi) = -\frac{\frac{g}{T}q}{u_*^2\frac{\partial U}{\partial z}} = \frac{\xi}{\varphi_u} = k_n$, which is monotonous and single-valued function of ξ.

For limiting cases of neutral stratification ($z/L \to 0$), strong instability ($z/L \to -\infty$) and strong stability ($z/L \to +\infty$) the similarity considerations allow to make a number of specific conclusions without solving the system (1.5)-(1.6).

If $\xi = z/L \to 0$ ($L \to \infty$ or $q \to 0$ or $z \to 0$), the parameter q ceases to be the parameter of the problem, and dependence of the functions $\frac{\partial U}{\partial z}$, $\frac{\partial\theta}{\partial z}$, ε upon it should fall out. The length scale also disappears, i.e. that regime is self-similar. It is possible only if at $\xi \to 0$ $\frac{\partial u_n}{\partial\xi}, \frac{\partial\theta_n}{\partial\xi}, \varepsilon_n \to \frac{1}{\xi}$, hence it follows that the values of universal functions approach the constants: $\varphi_u(0) = 1$, $\varphi_\varepsilon(0) = 1$. Such constant values are provided by Karman constant κ previously introduced into the definition of universal functions.

Thus, near to zero the following decompositions are true:

$$\left.\begin{aligned} u_n &= \ln\xi + \beta_1\xi + const \\ \theta_n &= \ln\xi + \beta_1\xi + const \\ b_n &= 1 + \gamma_1\xi + \cdots \\ \varepsilon_n &= \frac{1}{\xi} + \delta_1 + \cdots \\ k_n &= \xi(1 - \beta_1\xi) + \cdots \\ \varphi_u &= 1 + \beta_1\xi + \cdots \end{aligned}\right\}, \qquad (1.7)$$

It is verified by multiple atmosphere observations and laboratory experiments by studying surface layers in unstratified fluid.

According to the necessity of asymptotic (1.7) existence if $\xi \to 0$, the additional limitation for the values of $K\varepsilon$ model empirical constants follows: $\hat{\sigma} = C_{\varepsilon 2} - C_{\varepsilon 1}$. At this for the decomposition coefficients it is possible to obtain:

$$\gamma_1 = \frac{1}{\hat{\alpha} - 2}; \qquad \delta_1 = \frac{3C_{\varepsilon 1} - C_{\varepsilon 2} - C_\theta(2 - \hat{\alpha})}{2(2 - \hat{\alpha})\hat{\sigma}}; \qquad \beta_1 = \delta_1 - 2\gamma_1 = \frac{3C_{\varepsilon 2} - C_{\varepsilon 1} - C_\theta(2 - \hat{\alpha})}{2(2 - \hat{\alpha})\hat{\sigma}} \qquad (1.8)$$

The limiting case $z/L \to -\infty$ is the regime of purely convective turbulence, which may be obtained at $u_* \to 0$, i.e. u_* falls out from the determining parameters of the problem, hence it

follows: $\varphi_u \approx C_u(-\xi)^{-1/3}$, $\varphi_\theta \approx C_\theta(-\xi)^{-1/3}$, $\varphi_\varepsilon \approx -C_\varepsilon\xi$. Then $Rf = k_n \approx -\frac{1}{C_u}(-\xi)^{4/3}$, $b_n \approx C_b(-\xi)^{2/3}$ (C_u, C_θ, C_ε, C_b are constants.)

The obtained asymptotic presents just qualitative information about behavior of universal functions and does not allow uniquely formulating the boundary conditions for b and ε for numerical solution of the system of equations (1.5), (1.6) at finite integrating interval.

The universal functions are considered rather well known, though different authors propose different formulas for experimental data interpolating. However, for the stratification, which is not very far from indifferent ($|\xi|<1$), different sources give close results especially for convective conditions. In [10] by processing of multiple experiments the formula adjusted for convective and stable conditions was obtained:

$$\varphi_u = \frac{\xi}{k_n} = \begin{cases} 1+\xi\left\{1+0.667\exp(-0.35\xi)\left[1+0.35(14.3-\xi)\right]\right\}, & \xi>0; \\ (1-19\xi)^{-1/4}, & \xi<0. \end{cases} \qquad (1.9)$$

Below we present the results of calculations of ASL characteristics within the frameworks of $K\varepsilon$ model.

2. Statement of boundary problem. Selection of values of kε model empirical constants.

As the basic sought functions we will use b_n and k_n. b_n corresponds to turbulent kinetic energy and is a positive and monotone decreasing function. Function k_n is also monotone and, according to the experimental observations, increase from $-\infty$ up to some finite value $k_n(\infty)\le 1$. Thus, the system of equations (1.5)-(1.6) is to be solved, which, if $\hat\alpha \ne 0$, with the variables b_n and k_n assumes the following form:

$$k_n b_n'' + k_n' b_n' = \frac{1}{\hat\alpha k_n}\left(b_n^2 + k_n - 1\right) \qquad (2.1)$$

$$b_n k_n'' + 4k_n' b_n' - 2\frac{k_n}{b_n}b_n'^2 - \frac{b_n k_n'^2}{k_n} == \frac{1}{\hat\alpha\hat\sigma k_n}\left[\left(2\hat\sigma - \hat\alpha C_{\varepsilon 2}\right)b_n^2 + \left(2\hat\sigma - \hat\alpha C_\theta\right)k_n + \hat\alpha C_{\varepsilon 1} - 2\hat\sigma\right] \qquad (2.2)$$

Here the stroke sign denotes ξ differentiation.

If we head for the dependencies (1.7) and (1.9) and attempt to approach them along the whole interval $-\infty<\xi<+\infty$, the boundary conditions for the system (2.1)-(2.2) will be as follows, taking into account the form of the functions k_n, b_n:

$$b_n = +\infty,\ k_n = -\infty \text{ at } \xi = -\infty \qquad (2.3)$$

$$b_n = 0,\ k_n = 1 \text{ at } \xi = +\infty. \qquad (2.4)$$

$$b_n = 1,\ k_n = 0 \text{ at } \xi = 0 \qquad (2.5)$$

Formally the model constants $C_{\varepsilon 2}, C_{\varepsilon 1}, C_\theta, \hat\alpha$ remain undefined. The constants $C_{\varepsilon 2}, C_{\varepsilon 1}, \hat\sigma = C_{\varepsilon 2} - C_{\varepsilon 1}, \hat\alpha$ are supposed to be uniform for the whole area $-\infty<\xi<+\infty$, where the solution is sought. If we consider the decomposition of the function (1.9), obtained from the experimental data, in series in the neighborhood $\xi = 0$, we will obtain different decompositions to the right and to the left. Taking into account (1.7) the coefficient β_1 should be discontinuous that is C_θ should be taken as piecewise with discontinuity at $\xi = 0$.

In meteorology the following constant values are considered to be conventional $C_{\varepsilon 2}=2; C_{\varepsilon 1}=1.45; \hat{\sigma}=C_{\varepsilon 2}-C_{\varepsilon 1}=0.55$; $\hat{\alpha}=0.54$; $C_\theta=1$.

However such selection of the constants is not unique [2,14]. For example, in [2] the description of self-similar profiles in experiments [13] is the basis for constant selection, and it is obtained that $C_{\varepsilon 2}=1.92; C_{\varepsilon 1}=1.43$; $\hat{\alpha}=1.7\cdot\hat{\sigma}=0.83$.

Values $C_{\varepsilon 2}, C_{\varepsilon 1}$ in these sets differ insignificantly. One can notice the difference in $\hat{\alpha}$ and the value C_θ remains virtually indefinite.

Below we describe the algorithms for selecting the values $\hat{\alpha}$, C_θ for best description of the experimental observations at the finite interval $\xi\in[-a;+a]$ for the both nominal sets of constants $C_{\varepsilon 2}$ and $C_{\varepsilon 1}$ (which are assumed already known).

3. Behavior of solutions of the systems of equations of surface layer.

Let us investigate the behavior of the integral curves of the system (2.1), (2.2). We equate the right-hand sides to zero and obtain:

$$b_{n1}^2=\frac{C_{\varepsilon 1}-C_\theta}{C_{\varepsilon 2}-C_\theta}; \qquad k_{n1}=\frac{C_{\varepsilon 2}-C_{\varepsilon 1}}{C_{\varepsilon 2}-C_\theta}. \tag{3.1}$$

The obtained flock of points is the solution of the system. Decomposition of the sought solution in the neighborhood $\xi=0$ is presented with the formulas (1.7), and the behavior of the integral curves near this point will be considered below.

It is known that $C_{\varepsilon 2}>C_{\varepsilon 1}$. We consider the behavior of the solution of the equations (2.1)-(2.2) at $\xi\in(0;+\infty)$. It would be natural to suppose that the solution should pass through the critical points $b_n\big|_{\xi=0}=1$, $k_n\big|_{\xi=0}=0$ и $b_n\big|_{\xi=+\infty}=b_{n1}$, $k_n\big|_{\xi=+\infty}=k_{n1}$. Since $0<k_{n1}\le 1$ and $b_{n1}^2\ge 0$ should be satisfied, then one should assume $0\le C_\theta\le C_{\varepsilon 1}$ at $\xi>0$.

When $\xi=-\infty$, the empirical formula (1.9) gives $k_n\big|_{\xi=-\infty}\approx c_k(-\xi)^{5/4}$. Let us find the decomposition of the solution of the equations (2.1)-(2.2) in the neighborhood $\xi=-\infty$ in the form $k_n\big|_{\xi=-\infty}\approx c_k(-\xi)^\alpha$, $b_n\big|_{\xi=-\infty}\approx c_b(-\xi)^\beta$. We obtain that the exponents α and β depend on the used values of the parameters $C_{\varepsilon 1}, C_{\varepsilon 2}, C_\theta, \hat{\alpha}$. From the allowed decompositions at $\xi=-\infty$ we select those, which correspond to the physical meaning of the problem, i.e. along the whole interval $\xi\in(-\infty;0)$ the conditions of monotone increase of the function k_n from $-\infty$ to 0 and monotone decrease of b_n from $+\infty$ to 1 should be satisfied. We obtain $3/2\le\alpha<2$ and $\beta=2-\alpha$ (that is $0<\beta\le 1/2$). Thus, at no values of the used parameters it is possible to obtain the solution of the equations (2.1)-(2.2), which would satisfy asymptotic of the empirical formula (1.9) at $\xi=-\infty$.

We consider the behavior of the solution at $\xi\approx 0$. Taking into account (1.7), at the fixed values $C_{\varepsilon 1}, C_{\varepsilon 2}$ it is always possible to select values C_θ, $\hat{\alpha}$, which allow to obtain coincidences for solution of the problem (2.1)-(2.2) with the values of the experimental curve slope at the right and at the left of $\xi=0$.

Thus, while solving the equations (2.1)-(2.2) for the selected fixed values $C_{\varepsilon 1}, C_{\varepsilon 2}$, at the expense of selecting $\hat{\alpha}$ and value C_θ discontinuous at $\xi=0$, one may accurately describe individually or the behavior of the experimental curve in the neighborhood $\xi=0$ or $\xi=+\infty$.

Though decompositions by $\xi=\pm\infty$, following from $K\varepsilon$ model, do not agree with the experimental formulas, which have different asymptotic at infinity with different authors, there

may be no sense to try to satisfy them accurately. The experimental observations relate to the limited interval of change of dimensionless height, therefore the numerical integration of the equations (2.1)-(2.2) should be performed at the limited interval of height change. If we do not try to satisfy the empirical asymptotic at $\xi = \pm\infty$, but consider just the mean square deviation of the obtained solution from the experimental data at the limited interval, for example $-2 \le \xi \le 2$, then one may obtain good agreement with the experiment at the expense of parameter selection $C_\theta, \hat{\alpha}$.

4. Numerical integration of surface layer system of equations

We solve the system of equation (2.1)-(2.2) for the functions k_n, b_n. Since the coefficients included into the equations may be discontinuous at $\xi = 0$, integrating is performed by the two intervals: $[0.01; 2]$ and $[-2; -0.01]$. In the points $\xi_0 = \pm 0.01$ the values b_n and k_n are determined from the decomposition (1.7).

Let us determine the right boundary condition at the interval $[0.01; 2]$. The performed studying of the problem shows that at the right the values b_n and k_n quickly approach some constant positive values, which are formally dependent on the constants $C_{\varepsilon 1}, C_{\varepsilon 2}, C_\theta, \hat{\alpha}$. Therefore it is natural to take $\left.\frac{db_n}{d\xi}\right|_{\xi_R} = \left.\frac{dk_n}{d\xi}\right|_{\xi_R} = 0$ as a boundary condition.

We consider the interval $[-2; -0.01]$. $k_n \to -\infty$, $b_n \to +\infty$ is to be satisfied within the limit $\xi \to -\infty$. If we take into account the kind of the solution decomposition at $\xi = -\infty$, $\left.\frac{db_n}{d\xi}\right|_{\xi=-\infty} = 0$ is to be satisfied as well. This condition is satisfied with adequate accuracy already for values ξ at small module, therefore one may take the derivative value close to zero: $\left.\frac{db_n}{d\xi}\right|_{\xi_L} = -0.001$ as the left boundary condition for b_n. The value of k_n in the point $\xi_L = -2$ we determine from the condition $k_n(\xi_L = -2) = \frac{\xi_L}{\varphi_u(\xi_L)} \approx -\frac{2}{0.4}$, where $\varphi_u(\xi_L = -2) = 0.4$ is the experimental value determined from (1.9).

The system of equations (2.1)-(2.2) with specified boundary conditions was solved numerically by chaser method at the intervals $[0.01; 2]$ and $[-2; -0.01]$. The program of numerical solution of the given system was created. Calculations were made with various number of points *N*. Convergence of the results was obtained at *N*>50 in positive and negative areas.

It was assumed that the values $C_{\varepsilon 1}, C_{\varepsilon 2}$ have been determined earlier and are constant for both intervals. Value $\hat{\alpha}$ is assumed to be constant and value C_θ is assumed to be discontinuous: $C_\theta = \begin{cases} C_{\theta+}: & \xi > 0 \\ C_{\theta-}: & \xi < 0 \end{cases}$. A great number of calculations with different values of $\hat{\alpha}, C_\theta$ was performed with the purpose to determine such their values, which allow to obtain numerical solution describing in the best way (that is mean–square deviation) the empirical functional dependence (1.9) at the interval $\xi \in [-2; 2]$.

5. Comparison of numerical solution with experimental observations

As we have noted above, the following set of constant values is typically used in meteorology: $C_{\varepsilon 2}=2; C_{\varepsilon 1}=1.45; \hat{\sigma}=C_{\varepsilon 2}-C_{\varepsilon 1}=0.55$; $\hat{\alpha}=0.54$; $C_\theta=1$.

It was obtained that the resulting solution at $\xi>0$ very weekly depends on $\hat{\alpha}$ and strongly depends on C_θ. At this the calculated values k_n, b_n approach very quickly (just at $\xi\approx 1$) the constant values, which coincide with the values in the critical points (3.1) (that verifies the correctness of the numerical solution of the problem).

Actually, having numerical solution at the finite right interval of height change and knowing the solution behavior beyond the interval at large values of ξ, we can construct the solution along the whole interval $\xi\in(0;+\infty)$. For k_n the best agreement with the empirical dependence is obtained at $C_\theta=0$.

Thus, it is necessary to assume $C_\theta=0$ at $\xi\in(0;+\infty)$ and it is required to match $\hat{\alpha}$ and C_θ at the left integrating interval.

Let us take the value $C_\theta=1$ at $\xi<0$. According to calculation results the optimal value of the left parameter $\hat{\alpha}=1$ was selected, which provides the best agreement between calculation and experimental data. The results of calculation of the case $\hat{\alpha}=1$, $C_\theta=\begin{cases}0: & \xi>0\\ 1: & \xi<0\end{cases}$ are presented in Figure 1 as compared with the empirical data.

Let $\hat{\alpha}=0.54$. According to the calculation results the optimal value $C_\theta=1.6$ at $\xi<0$. The results of calculation of the case $\hat{\alpha}=0.54$, $C_\theta=\begin{cases}0: & \xi>0\\ 1.6: & \xi<0\end{cases}$ are presented in Figure 1 as well and almost coincide with the previous case.

Above we presented another used set of constants of *ke* model $C_{\varepsilon 2}=1.92; C_{\varepsilon 1}=1.43$; $\hat{\alpha}=1.7\cdot\hat{\sigma}=0.83$. The results of calculation of this case provide the following optimal values of parameters $C_\theta=\begin{cases}0: & \xi>0\\ 1.2: & \xi<0\end{cases}$. The calculating results are presented in Figure 1 as well.

As is seen, the solutions for all the obtained sets of constants almost coincide between each other and are close to the experimental data. The calculations at various values of parameters $\hat{\alpha}$ and C_θ were conducted, however, the available results would not be improved.

If we know the values of the used parameters, we may determine the character of the solution behavior at $\xi\approx 0$ and $\xi=\pm\infty$.

For example, the set of parameters $C_{\varepsilon 2}=2; C_{\varepsilon 1}=1.45; \hat{\sigma}=0.55$; $\hat{\alpha}=1$, $C_\theta=\begin{cases}0: & \xi>0\\ 1: & \xi<0\end{cases}$ provides the following behavior of the functions: $k_n\big|_{\xi=-\infty}\sim(-\xi)^{1.62}$, $b_n\big|_{\xi=-\infty}\sim(-\xi)^{0.38}$, and the decomposition coefficient for k_n in the neighborhood $\xi\approx -0$ (see (1.7)) $\beta_1=3.23$. At $\xi>0$ the values k_n, b_n quickly approach the constant values coincident with the values in the critical points (3.1), at this in the neighborhood $\xi\approx +0$ the value $\beta_1=4.17$.

The parameter set $C_{\varepsilon 2}=2; C_{\varepsilon 1}=1.45; \hat{\sigma}=0.55$; $\hat{\alpha}=0.54$, $C_\theta=\begin{cases}0: & \xi>0\\ 1.6: & \xi<0\end{cases}$ provides the following results: $k_n\big|_{\xi=-\infty}\sim(-\xi)^{1.54}$, $b_n\big|_{\xi=-\infty}\sim(-\xi)^{0.46}$, $\beta_1=1.38$ at $\xi\approx -0$ and $\beta_1=2.83$ at $\xi\approx +0$.

If $C_{\varepsilon 2}=1.92; C_{\varepsilon 1}=1.43;$; $\hat{\alpha}=0.83$, $C_\theta=\begin{cases}0: & \xi>0\\ 1.2: & \xi<0\end{cases}$, then $k_n\big|_{\xi=-\infty}\sim(-\xi)^{1.59}$, $b_n\big|_{\xi=-\infty}\sim(-\xi)^{0.41}$, $\beta_1=2.55$ at $\xi\approx -0$ and $\beta_1=3.78$ at $\xi\approx +0$.

Thus, the values of the model parameters are obtained, at which the numerical solutions of the system (2.1)-(2.2) describe well the experimental dependence (1.9) along the interval $\xi\in[-2;2]$.

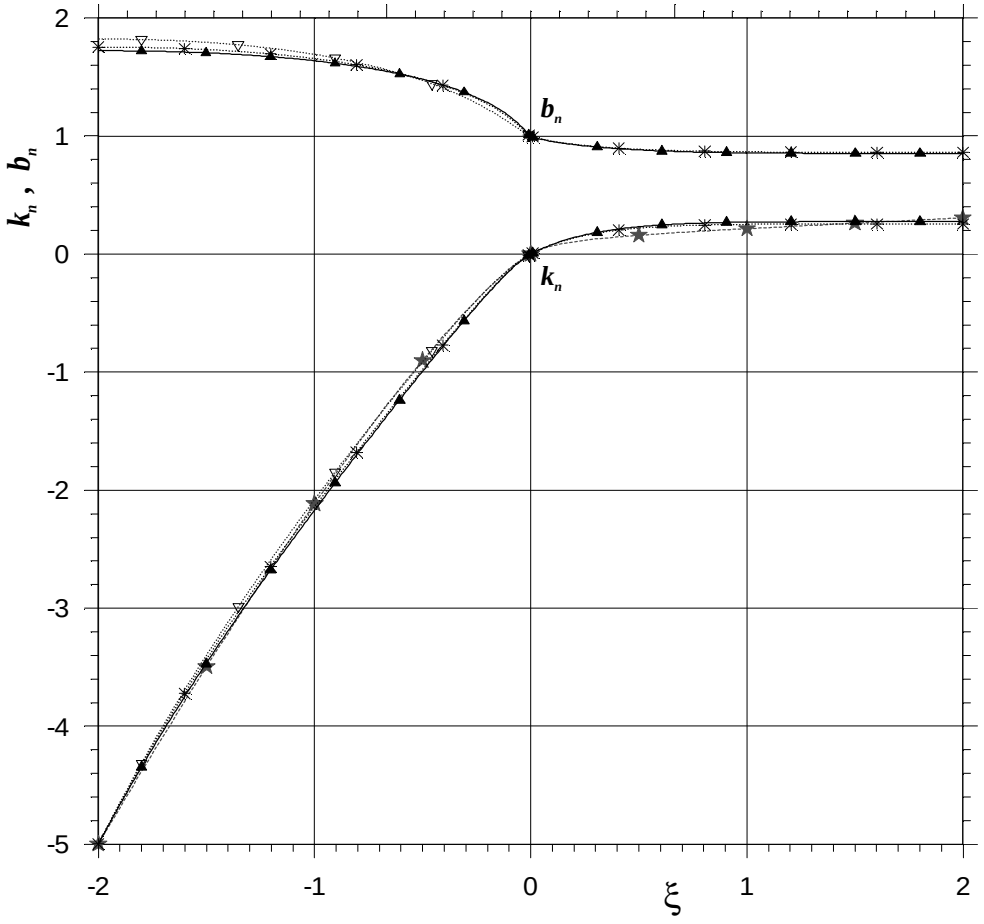

Figure 1. Dependence of functions k_n, b_n on dimensionless height ξ:

--▲-- calculation with $C_{\varepsilon 2}=2; C_{\varepsilon 1}=1.45;\ \hat{\sigma}=0.55$; $\hat{\alpha}=1$, $C_\theta=\begin{cases}0: & \xi>0\\ 1: & \xi<0\end{cases}$;

- - - - calculation with $C_{\varepsilon 2}=2; C_{\varepsilon 1}=1.45;\ \hat{\sigma}=0.55$; $\hat{\alpha}=0.54$, $C_\theta=\begin{cases}0: & \xi>0\\ 1.6: & \xi<0\end{cases}$;

- - ※ - - calculation with $C_{\varepsilon 2}=1.92; C_{\varepsilon 1}=1.43;$; $\hat{\alpha}=0.83$, $C_\theta=\begin{cases}0: & \xi>0\\ 1.2: & \xi<0\end{cases}$;

- - ⋆ - - the empirical curve [10],

Conclusions

Within the frameworks of *K*ε-model the problem about determination of dimensionless characteristics of turbulent flow in atmosphere surface layer is considered.

The complete investigation of *K*ε-equations and their critical points are conducted. From the variety of the integral curves the ones are selected, which correspond to the solution of the stated problem and describe quite satisfactorily all experiments. At this the basic empirical constants of the model $(C_{\varepsilon 1}, C_{\varepsilon 2})$ are selected according to the conventional criteria. At the same time it is shown that parameter C_θ responsible for the convective source term in the equation for ε should be selected different depending on stability status of the surface layer. At this the best agreement with experimental observations is obtained, if $C_\theta = 0$ in the area of stable stratification and $C_\theta \neq 0$ in the area of unstable stratification.

The program, which allows solving the obtained model equations, is created. The calculations for various values C_θ and $\hat{\alpha}$ are conducted.

By the numerical matching of values C_θ and turbulent diffusion coefficient $\hat{\alpha}$ the quite satisfactory description of the experimental observations is obtained at the finite interval of dimensionless height change for any state of atmosphere stability.

Taking into account the obtained asymptotic of the model equation solutions for the values of dimensionless height $\xi = \pm\infty$, the solution is virtually constructed along the whole interval $\xi \in (-\infty; +\infty)$.

References

1. Kharsha P. Turbulent kinetic energy transfer models. // Turbulence. Application principles. M., Mir, 1980, pp. 207-261.
2. Neuvazhayev V.E., Yakovlev V.G. Description of gravitational turbulent mixing by ke-model // VANT, Theoretical and Applied Physics, 1986, V1, p. 28.
3. Neuvazhayev V.E. Characteristics of models of gravitational turbulent mixing in non-self-similar problems // VANT, Mathematical Modeling of Physical Processes, 1994, V3, pp.3-10.
4. Nadezhina E.D. On using differential equations for second moments in models of atmosphere boundary layer // GTO Proceedings, 1975, V362, pp. 3-14.
5. Vager B.G., Nadezhina E.D. Using differential equation of dissipation transfer at modeling of atmospheric surface layer // News of AS USSR. Physics of atmosphere and ocean, 1976, V12, № 4, pp. 345–355.
6. Shneidman V.A., Bondarenko V.N. Quantitative description of vertical structure of surface sublayer in model of planet boundary atmosphere layer // IEM Proceedings, 1981, V 27 (100), pp. 22-28.
7. Stepanenko S.N., Shneidman V.A. Comparison of results of generalization of experimental data with calculations by three-parameter model of atmosphere boundary layer // GTO Proceedings, 1983, V 481, pp. 144-151.
8. Matveev L.T. Course of general meteorology. Aerophysics. – Leningrad: Gidrometeoizdat, 1976.
9. Atmosphere. Reference Book. – Leningrad: Gidrometeoizdat, 1991.
10. Boughton B.A. and DeLaurentis A.M. Description and validation of ERAD: an atmospheric dispersion model for high explosive detonations, Sandia National Laboratories Report №SAND92-2069, 1992.
11. Leichtman D.L. Physics of atmosphere boundary layer.– Leningrad: Gidrometeoizdat, 1970.
12. Simonov V.V. On using of equation for dissipation velocity while modeling turbulent flow above wavy surface // GTO Proceedings, 1986, V504, pp. 119-132.
13. Anuchina N.N., Kucherenko Yu.A., Neuvazhayev V.E. et al. Turbulent mixing at accelerating interface of fluids of different densities // MZhG, 1978, №6, pp. 157-160.
14. Sonin A.A. Calibration of the ke turbulence model for the diffusion of turbulence // Phys. Fluids, 1983, 26, 2769.

Computational Modeling of Low-Mach-Number High-Atwood-Number Turbulent Mixing (C4)

William Ashurst and Alan Kerstein
ashurs@ca.sandia.gov and kerstein@ca.sandia.gov
Sandia National Laboratories, Livermore

Introduction

One Dimensional Turbulence (ODT) is a stochastic model which tries to capture the essence of turbulent combustion: fully resolved molecular fluxes within a turbulent flow. To do this task a three dimensional velocity vector is described along a line (assumed to be the inhomogeneous direction in a temporal or spatially developing flow). Molecular processes are solved numerically and the turbulent flow effects of compressive strain rate and entrainment are accomplished with rearrangement events which are called the eddies. Upon random selection of an eddy length and location, guided by an assumed probability distribution, the proposed eddy energy is used to determine the eddy time scale, or frequency. This time scale is compared with an event rate distribution using a Bernoulli trial process; the eddy acceptance probability is kept low by the choice of the eddy time step so that the probability of more than one eddy occuring at one time vanishes. The action of the eddy is to rearrange all quantities within the eddy length – this is done by compressing the spatial scale to one-third of the eddy length, making two copies of the compressed result and placing them to fill out the eddy domain, the middle copy is then reversed. This triplet map will make a sawtooth curve out of a region with a linear gradient. Repeated application of the triplet map, at random locations, will generate a lognormal distribution of gradients.

In addition to the triplet mapping the eddy exchanges energy (energy flux) in the temporal (spatial) flow to mimic the pressure-strain-rate effects in turbulence. Using available direct numerical simulations (DNS) of Navier-Stokes turbulence in two shear flows, planar shear layer and planar wake, we have calibrated the ODT model by setting one rate term in order to match the temporal growth rate found in the DNS simulations. Comparison of first, second and third order turbulence quantities reveals nice agreement considering the simplicity of the ODT assumptions (Kerstein *et al.*, 2001).

New ODT work considers the temporal and spatial planar mixing layers in which the density of one stream may be a thousand times larger than the density of the other stream. This density contrast is achieved within incompressible flow by using two species with different molecular weights.

In this presentation we compare the variable density temporal shear with recent DNS compressible simulations by Pantano and Sarkar (2002). The spatially evolving ODT results are compared with the experiments performed by Brown and Roshko (1974). These experiments approximate incompressible flow while the DNS temporal simulations with density ratios up to eight were done with a convective Mach number of 0.7.

ODT Flow Equations

We achieve variable-density, incompressible flow by using two species which have different molecular weights. The number density is constant and pressure gradients are also neglected (boundary layer approximation). We apply ODT to a shear layer which evolves in time (temporal) or in space (spatial) and conservation of streamwise momentum yields different governing equations between these two cases. The streamwise momentum in two dimensions is

$$\frac{\partial \rho u}{\partial t} + \frac{\partial \rho u^2}{\partial x} + \frac{\partial \rho uv}{\partial y} = vis$$

where vis is the viscous term. In the temporal case this reduces to $\partial \rho u / \partial t = vis$ and there is no convective velocity, that feature is accomplished by the eddies. In steady spatial flow the momentum relation reduces to

$$\frac{\partial \rho uU}{\partial x} + \frac{\partial \rho uV}{\partial y} = vis$$

where U, V are the convection velocities with $U = u$, but $V \neq v$ because convection is accomplished by the eddies. Thus, in the spatial case it is the flux of momentum which is conserved while in the temporal it is the momentum itself which is conserved. To mimic pressure scrambling of turbulence we exchange kinetic energy among the vector components in the temporal flow, but we exchange kinetic energy flux in the spatial flow, that is, exchange $\rho u^2 U$ with $\rho v^2 U$ and $\rho w^2 U$.

Time Developing Flow Equations

The ODT velocity components on the 1D domain are denoted $v_i(y,t)$, $i = 1,\ 2,\ 3$, where y (corresponding to $i = 2$) is the domain coordinate. These velocities do no convection, convection is done by the eddies. The number density is constant (incompressible flow), but in a binary mixture with unequal molecular weights, the mass and momentum fluxes are not zero when the species gradient is not zero.

Density diffusion:

$$\frac{\partial \rho}{\partial t} = \kappa \frac{\partial^2 \rho}{\partial y^2}.$$

Momentum:

$$\frac{\partial \rho v_i}{\partial t} = \mu \frac{\partial^2 v_i}{\partial y^2} + \kappa \frac{\partial}{\partial y} v_i \frac{\partial \rho}{\partial y}$$

Spatially Developing Flow Equations

Each ODT realization is a steady, planar flow. The streamwise advecting velocity U is the same as v_1, while the lateral advecting velocity V is different from v_2. This distinction is made because the v_i velocities are regarded as being storage of kinetic energy, and this energy is displaced by the eddy mappings. Therefore, the v_i velocities are not convective but evolve formally as passive scalars advected by U and V and diffused by viscosity.

Continuity:

$$\frac{\partial \rho U}{\partial x} + \frac{\partial \rho V}{\partial y} = 0$$

Density diffusion:

$$\frac{\partial U}{\partial x} + \frac{\partial V}{\partial y} = -\frac{\partial}{\partial y} \frac{\kappa}{\rho} \frac{\partial \rho}{\partial y}$$

note: incompressible flow has zero volume flux, and the mass average velocity is the sum of volume flux V' plus the diffusion flux, $V = V' - (\kappa/\rho)(\partial \rho / \partial y)$.

Momentum:

$$\frac{\partial \rho v_i U}{\partial x} + \frac{\partial \rho v_i V}{\partial y} = \mu \frac{\partial^2 v_i}{\partial y^2}$$

Temporal Shear Layer

In our ODT temporal shear layer the one-dimensional line is in the lateral direction and we impose streamwise boundary velocities of $U_1 = 0.5$ for $y > 0$ and $U_2 = -0.5$ for $y < 0$. We normalize velocities with $\Delta U = U_1 - U_2$ and set $\rho_2 = s\rho_1$ with $\rho_1 = 1$. With incompressible flow there is no equation of state.

Pantano and Sarkar (2002) have performed compressible DNS of the temporal shear layer using an ideal gas with constant specific heats, dynamic viscosity, thermal conductivity and diffusion. The energy equation is expressed as a dynamical equation for the pressure. Reference values are: L_o, ρ_o, p_o, U_o with the condition that $\gamma M a_o^2 = 1$ leading to $p_o = \rho_o U_o^2$. The convective Mach number is $M_c = \Delta U/(c_1 + c_2)$. The average density is fixed to unity $\rho_o = (\rho_1 + \rho_2)/2 = 1$ with $s = \rho_2/\rho_1$ and $s \geq 1$ (by symmetry the flow with $s = 1/s$ is the same flow). Their flow is periodic in the spanwise (z) and streamwise (x) directions while a free boundary is used in the lateral direction (y). The initial conditions include broadband fluctuations, isotropic turbulence spectrum, in the shear region with an initial turbulence intensity of ten percent. They computed with convective Mach numbers of 0.3, 0.7 and 1.1 with a density ratio different from unity only in the 0.7 case.

The ODT parameters are those developed in the constant density work (Kerstein *et al.*, 2001), no new parameters were needed to include variable density, only the specification of a diffusivity was required. With constant dynamic viscosity μ, the diffusivity is $D_{12} = 0.6\mu((\rho_1 + \rho_2)/(\rho_1\rho_2))$. The ODT mean streamwise velocity and density profiles agree with the DNS results ($s = 1, 2, 4, 8$) and the ODT results indicate a reduced growth rate with increasing density ratio, similar to the behavior of the compressible layer. The ODT turbulent kinetic energy production, dissipation and transport have a peak amplitude which is about twice that of the compressible results. Future ODT work which includes a compressible velocity component may show that this amplitude difference is a compressibility effect.

Temporal Shear Layer

Comparison with Compressible DNS, $M_c = 0.7$

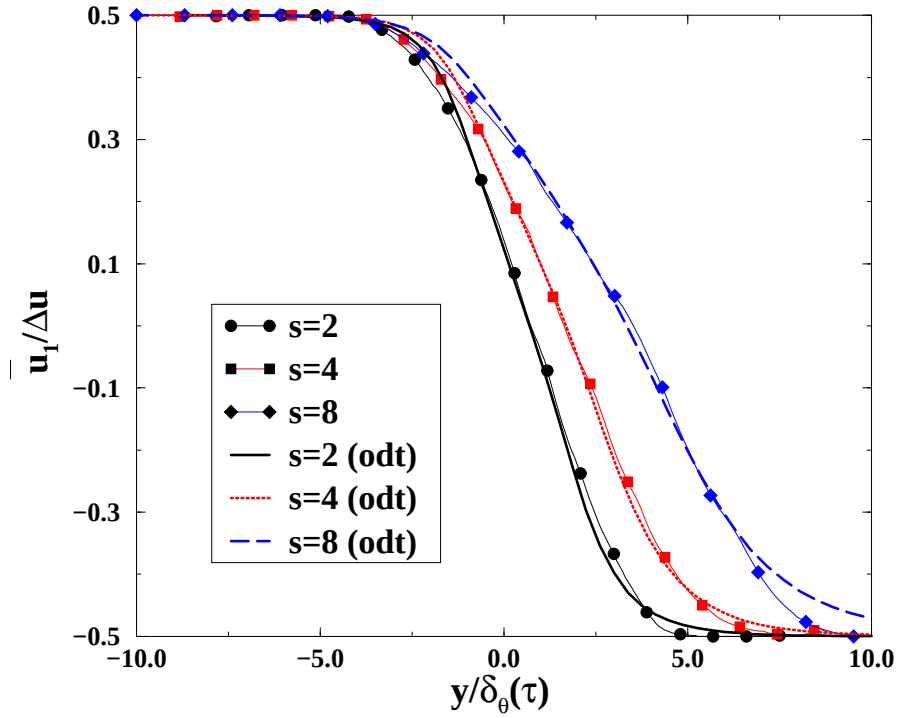

Mean streamwise velocity u from Pantano & Sarkar (JFM).

Momentum Thickness (Favre velocity: $\tilde{u} = \overline{\rho u}/\bar{\rho}$)

$$\delta_\theta = \frac{1}{\rho_o \Delta U^2} \int \bar{\rho}(u_1 - \tilde{u})(\tilde{u} - u_2) dy$$

Temporal Shear Layer

Comparison with Compressible DNS, $M_c = 0.7$

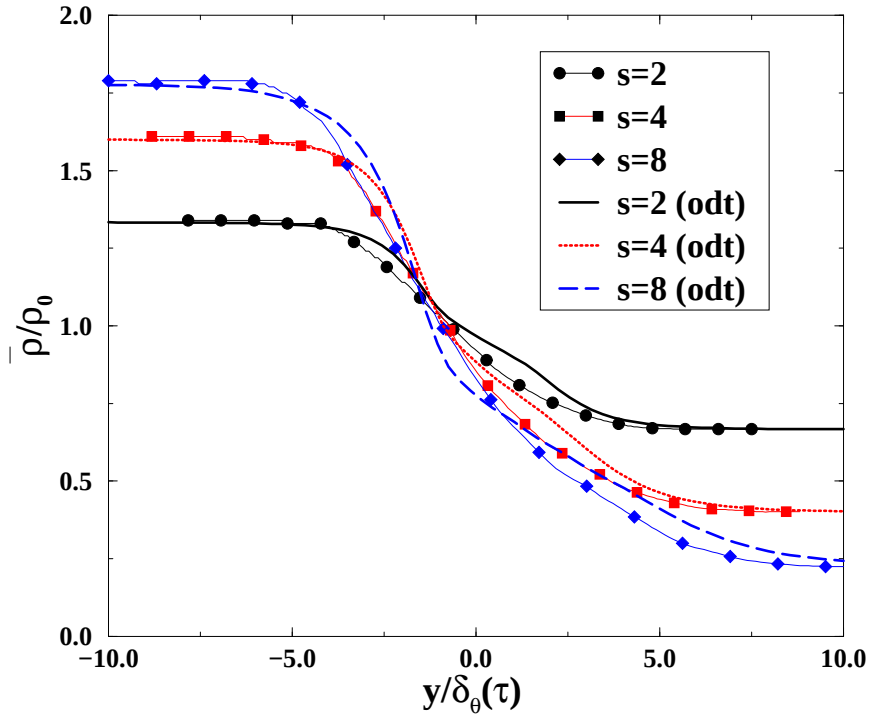

Mean density ρ from Pantano & Sarkar (JFM).

Temporal Shear Layer

Comparison with Compressible DNS, $M_c = 0.7$

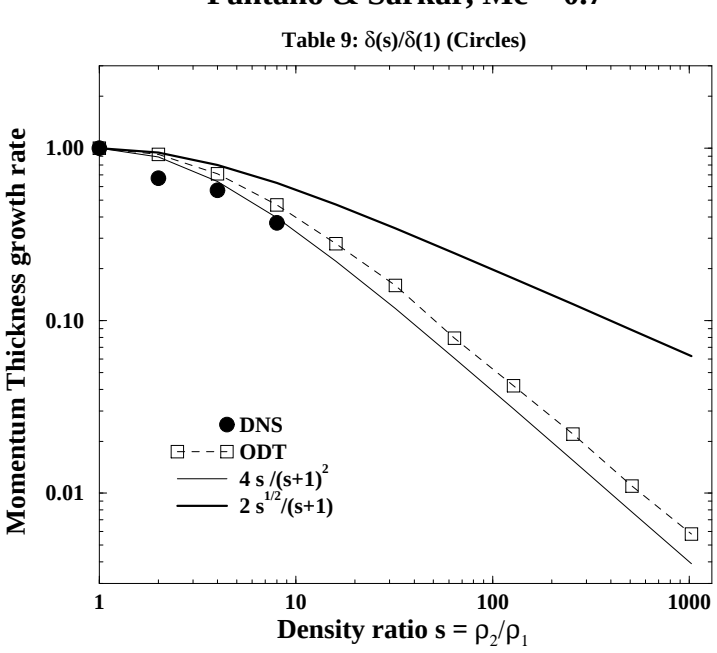

Momentum Thickness δ_θ growth rate from Pantano & Sarkar (JFM).

$$\delta_\theta = \frac{2}{(\rho_1 + \rho_2)(\Delta U)^2} \int \bar{\rho}(u_1 - \tilde{u})(\tilde{u} - u_2) dy$$

Favre velocity: $\tilde{u} = \overline{\rho u}/\bar{\rho}$

Ramshaw (2000) has presented a model of shear layer growth, which when only the Kelvin-Helmholtz instability is active becomes

$$h \approx \Delta U \quad t \quad \frac{\sqrt{\rho_1 \rho_2}}{(\rho_1 + \rho_2)}$$

however, the ODT results indicate that the square of the density term is a better approximation

$$h \approx \Delta U \quad t \quad \frac{\rho_1 \rho_2}{(\rho_1 + \rho_2)^2}$$

which, with density ratio $s = \rho_2/\rho_1$ gives the $s/(s+1)^2$ effect shown in the figure above. Of course, being unit-less, there is no way to determine the exponent of this term by scaling laws.

Temporal Shear Layer

Comparison with Compressible DNS, $M_c = 0.7$

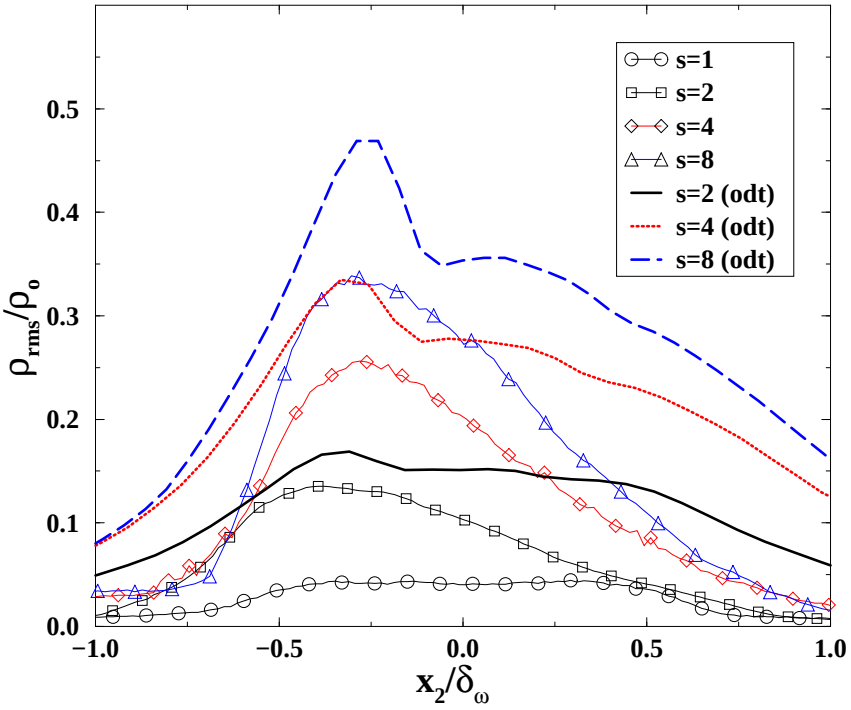

Density rms versus vorticity thickness δ_ω
(from Pantano & Sarkar, JFM)

Vorticity Thickness $\delta_\omega = \Delta U/(\partial u/\partial y)_{max}$

Temporal Shear Layer

Comparison with Compressible DNS, $M_c = 0.7$

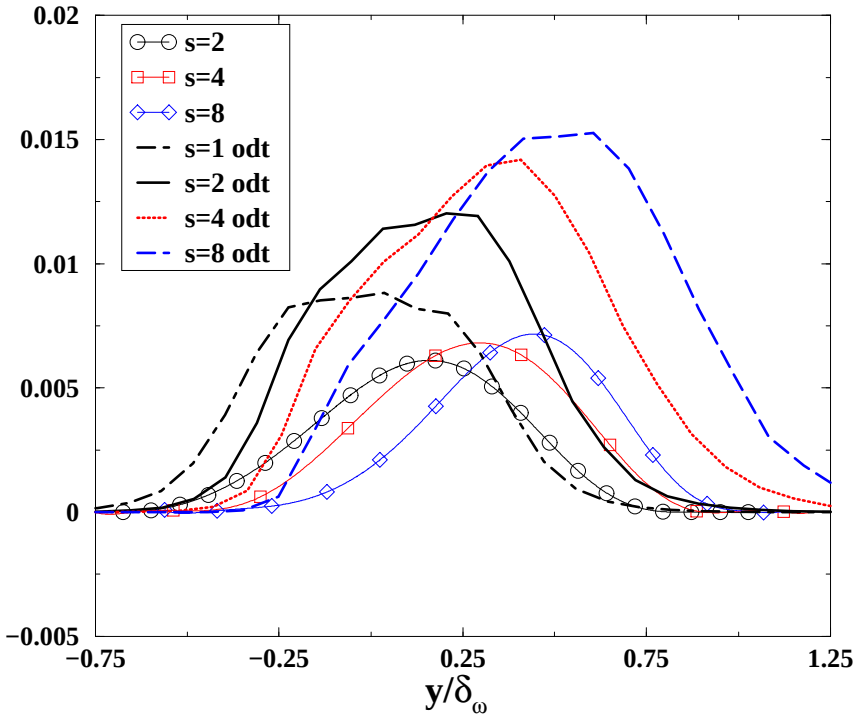

Turbulent kinetic energy production versus vorticity thickness δ_ω

(from Pantano & Sarkar, JFM)

Vorticity Thickness $\delta_\omega = \Delta U/(\partial u/\partial y)_{max}$

Temporal Shear Layer

Comparison with Compressible DNS, $M_c = 0.7$

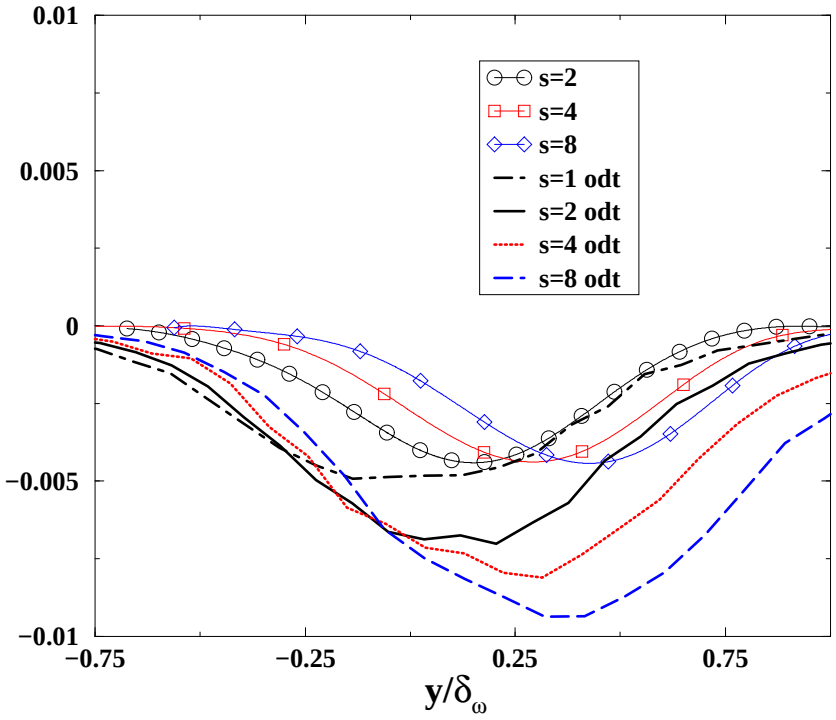

Turbulent kinetic energy dissipation versus vorticity thickness δ_ω
(from Pantano & Sarkar, JFM)

Temporal Shear Layer

Comparison with Compressible DNS, $M_c = 0.7$

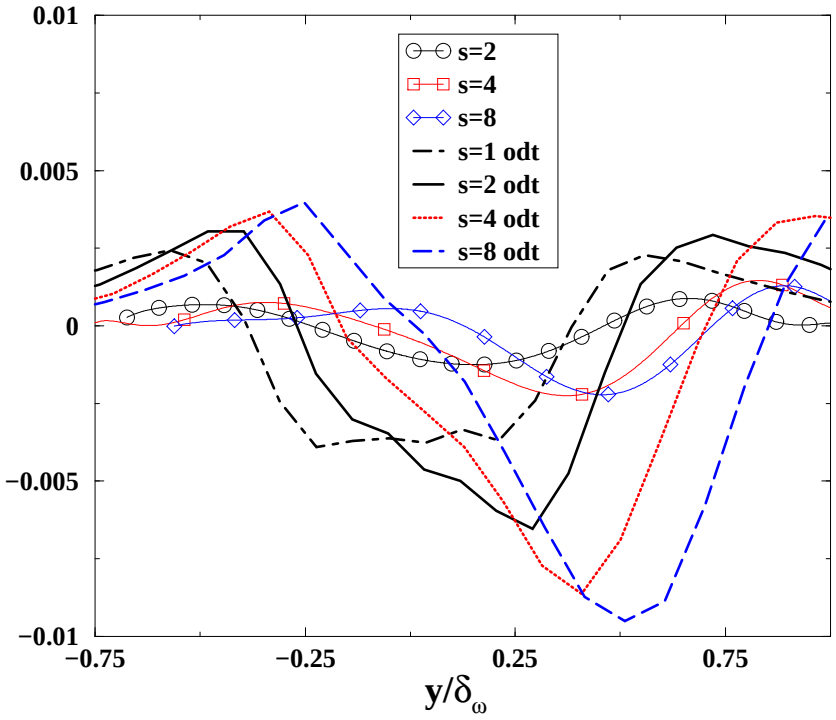

Turbulent kinetic energy transport versus vorticity thickness δ_ω
(from Pantano & Sarkar, JFM)

SPATIALLY DEVELOPING SHEAR LAYER

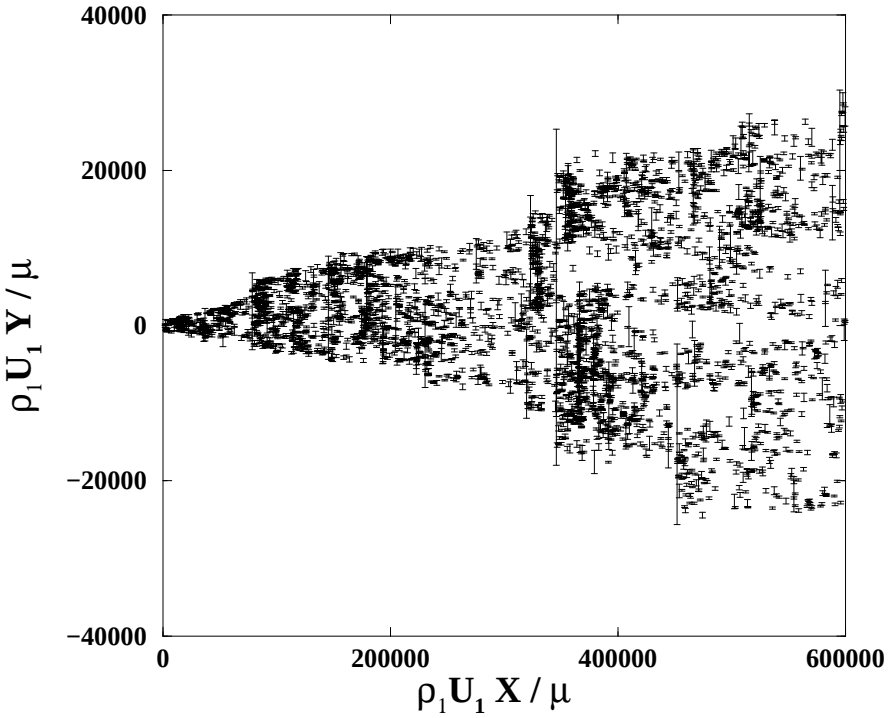

The density ratio is unity $s = 1$, the upper flow has $U_2 = 0.38$ and the lower flow has $U_1 = 1$, the Reynolds number is comparable to the experimental value.

One ODT realization is shown by drawing vertical lines corresponding to the eddy length and location. To be accepted the eddy energy, given by velocity component in the direction of the ODT line, combined with the eddy length must give a time scale which is smaller than the viscous time scale for that eddy length. An additional barrier to accepting an eddy is examination of eddy segments, each segment is one-third of the eddy, if any segment fails to be acceptable then the eddy is rejected. In this manner an eddy may protrude into the quiet freestream and thus cause an abrupt growth in the layer thickness. Notice the increased eddy activity downstream of the larger eddies, the larger eddy has enhanced the local shear which favors smaller eddies – thus forming a cascade of shear to small length scales.

SPATIALLY DEVELOPING SHEAR LAYER

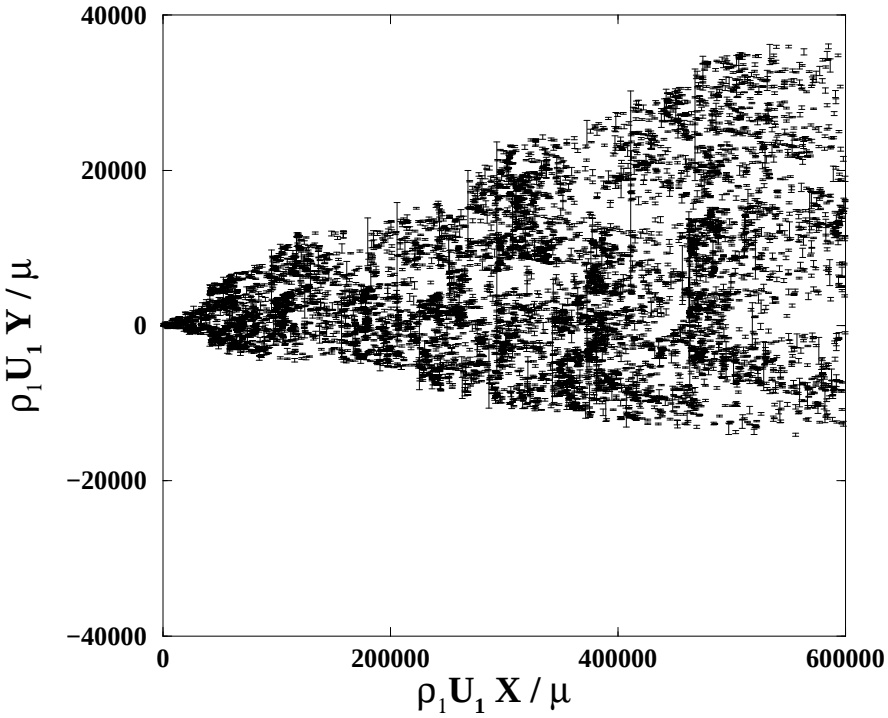

The density ratio is $s = 7 = \rho_2/\rho_1$, the upper flow has $U_1 = 1$ and the lower flow has $U_2 = 0.38$.

Notice that the spreading of the eddies into the lower flow, which has the larger inertia, is reduced by comparison with the upper flow.

SPATIALLY DEVELOPING SHEAR LAYER

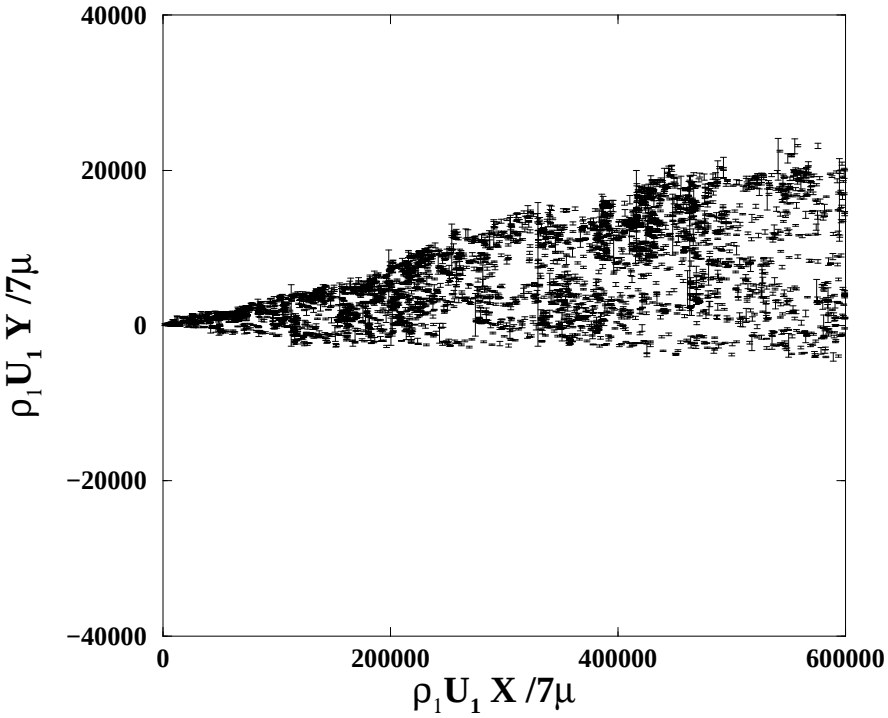

The density ratio is $s = 1/7 = \rho_2/\rho_1$, the upper flow has $U_2 = 0.38$ and the lower flow has $U_1 = 1$.

Notice that the faster flow which now has the larger inertia has very few eddies, and the overall growth rate is much less than when the denser flow is the slower stream (previous case with $s = 7$).

SPATIALLY DEVELOPING SHEAR LAYER

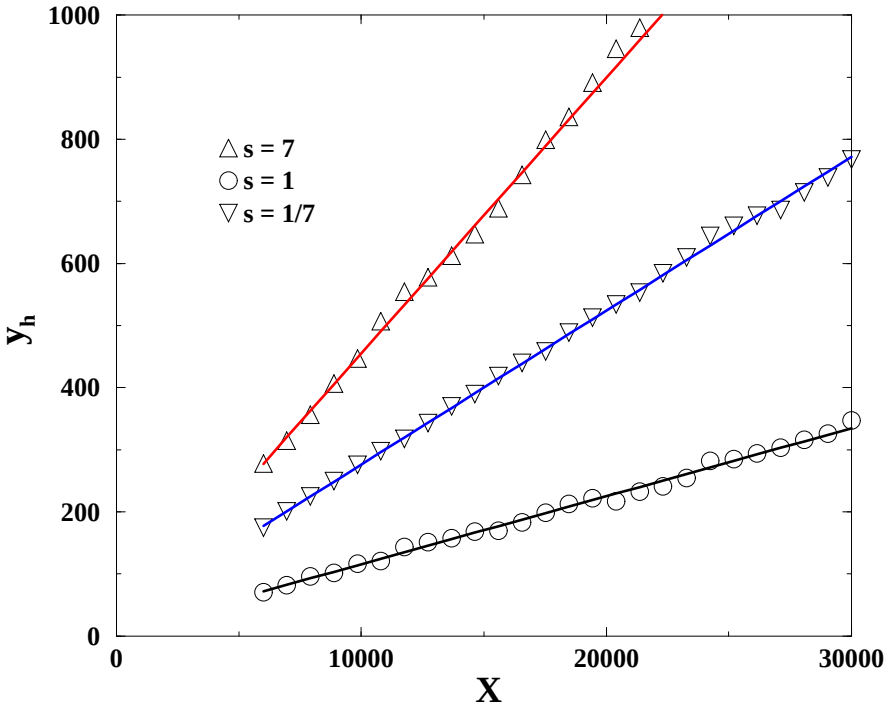

With each density ratio $s = 7, 1, 1/7$, one thousand realizations are used to determine mean profiles. An origin in the lateral direction is determined by the location where the Favre velocity equals the mean of the freestream velocities, $\tilde{u} = (U_1 + U_2)/2$, this defines y_h. The symbols denote y_h locations and the lines are least square fits which determine the virtual origin x_o and the growth rate. The lateral profiles will be shown as a function of the similarity coordinate $(y - y_h)/(x - x_o)$. In the spatial units shown here the dynamic viscosity has the value of $1/20$.

SPATIALLY DEVELOPING SHEAR LAYER

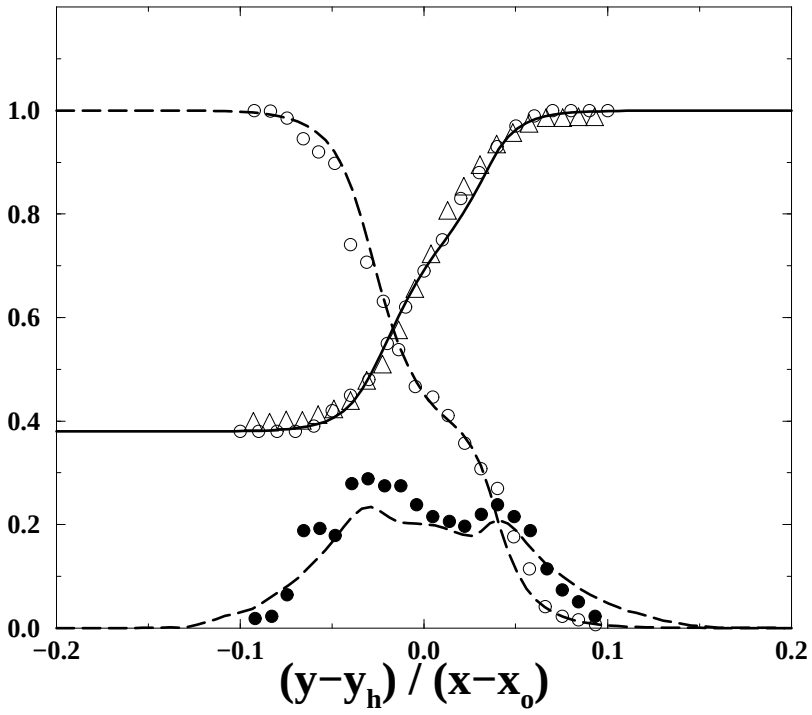

Lateral profiles of velocity (ODT, solid line) and concentration and concentration rms values (ODT, dashed lines) with constant density $s = 1$; the open triangles are from Brown & Roshko (velocity only) and the circles are from Konrad (velocity and concentration, open circle and concentration rms, filled circle). The ODT and Konrad's results have been scaled to match the velocity integral thickness of Brown & Roshko; this sets the eddy rate constant in the ODT simulations (which is used in the other density cases) and requires a factor of 0.7 times Konrad's lateral coordinate values. The velocity is reduced by the maximum velocity.

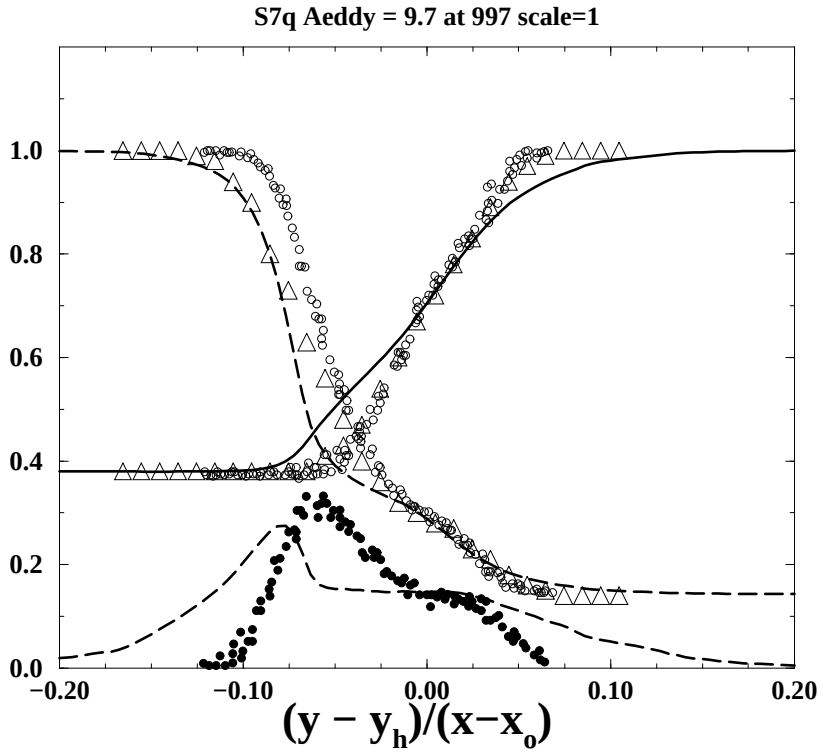

Lateral profiles of velocity (ODT, solid line) and density and rms density values (ODT, dashed lines) with density ratio $s = 7$; the open triangles are from Brown & Roshko (velocity and density only) and the circles are from Konrad (velocity and density, open circle and rms density, filled circle). The lateral scale factors are the same as given in $s = 1$ results; the density, and its rms, are normalized by the maximum density.

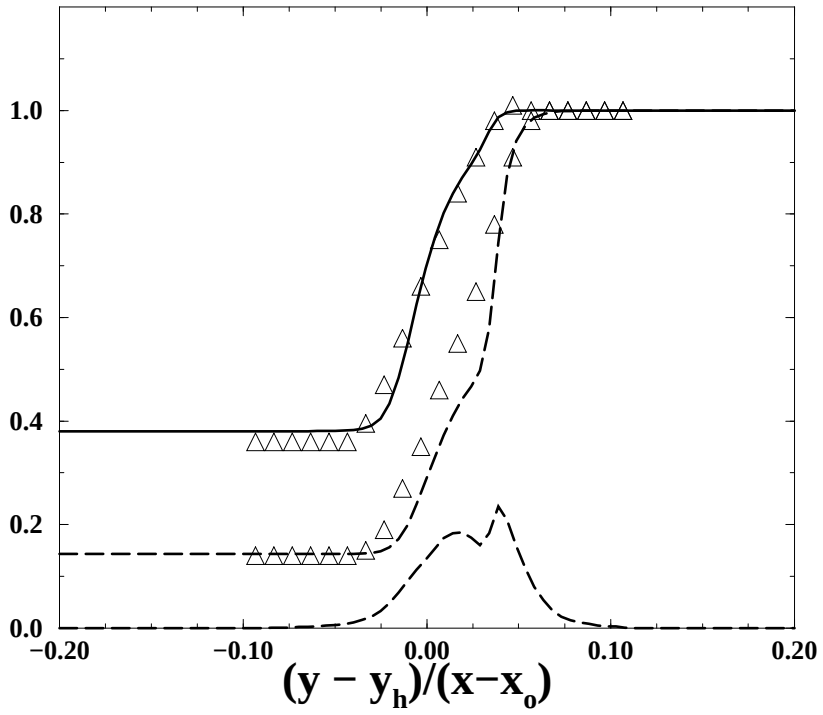

Lateral profiles of velocity (ODT, solid line) and density and rms density values (ODT, dashed lines) with density ratio $s = 1/7$; the open triangles are from Brown & Roshko (velocity and density only). The lateral scale factors and normalizations are the same as given in $s = 7$ results.

SPATIALLY DEVELOPING SHEAR LAYER

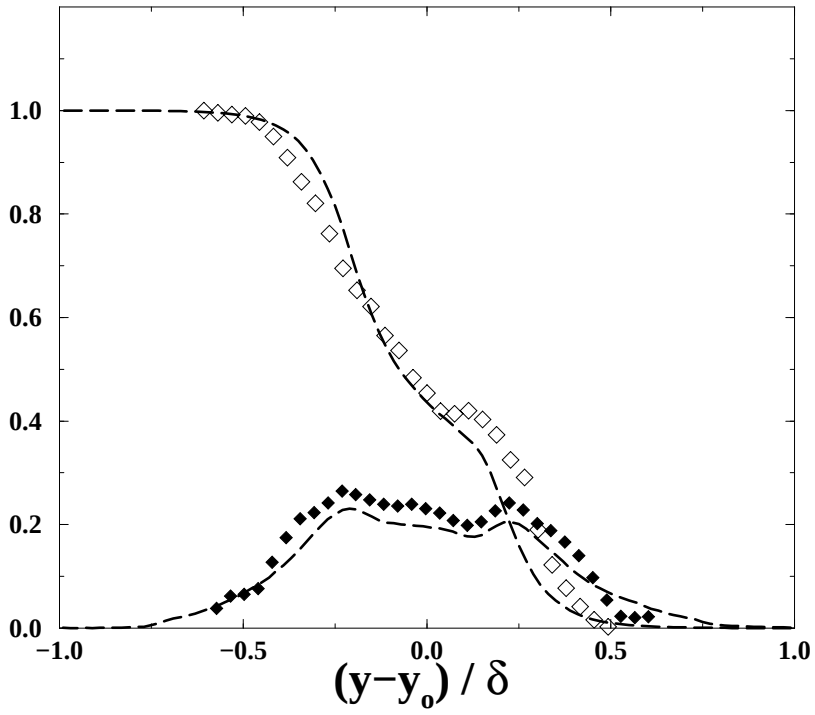

Concentration, and its rms, in constant density flow, velocity ratio of 0.4 (Pickett and Ghandhi, Phys. Fluids, 2002, symbols) and ODT (dashed lines). Lateral scaling is from the concentration one-percent distance δ, the lateral origin is the mean of those locations. The high speed stream is at positive y values.

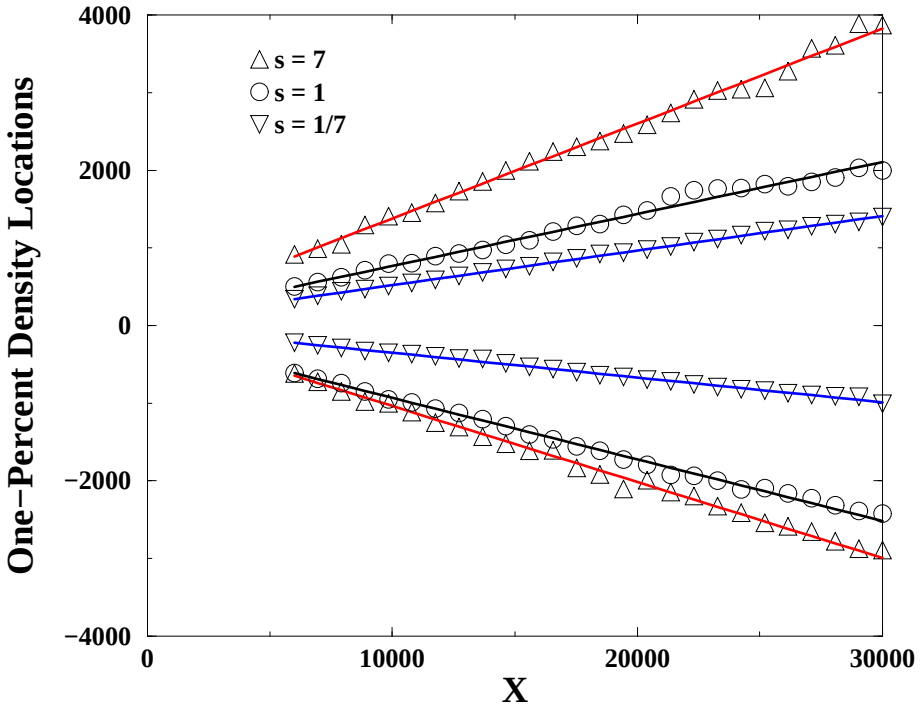

With each density ratio $s = 7, 1, 1/7$, one thousand realizations are used to determine mean profiles. The symbols denote the locations where the concentration is at a one-percent difference from its freestream value. The lines are least-square fits and the slope differences give the density growth rate.

SPATIALLY DEVELOPING SHEAR LAYER

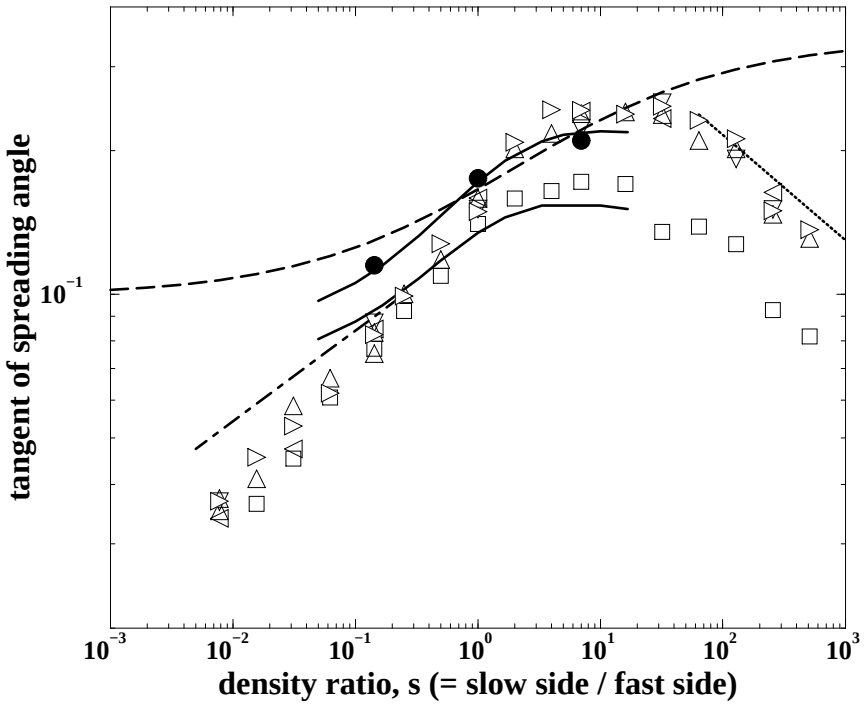

Density growth rate as a function of density ratio s and velocity ratio $r = U_2/U_1$. The ODT simulations have been matched to the experimental velocity integral thickness at $s = 1$, $r = 0.38$, no other adjustments have been made for other density ratios or the other velocity ratio. The visual growth rate from Brown & Roshko (their figure 7) are given by the filled circles. The model of Dimotakis is the dashed line, while the two solid lines are given by the laminar stability of a compressible boundary layer, recently computed by Sandham at velocity ratios of 0.38 (upper) and 0.48 (lower). The ODT results ($r = 0.38$, triangles and $r = 0.48$, squares) indicate a power-law behavior when s is very small and when s is large. Similar behavior has been found in round jets: Siebers has found an exponent of 0.19 over the range of $0.005 < s < 0.24$ in spray jets and Witze has found an exponent of -0.22 over the range of $1 < s < 7$ in gaseous jets. These exponents of 0.19 (dot-dash) and -0.22 (dotted) are shown above with amplitudes to allow comparison with the ODT behavior.

Acknowledgments

We thank Professor Sarkar and Dr. Pantano for sharing their DNS results and thank Professor Sandham for providing the stability results. Discussions with Professor Roshko have been helpful. This work supported by the Division of Chemical Sciences, Office of Basic Energy Sciences, U. S. Department of Energy.

References

Brown, G. L. and Roshko, A., "On density effects and large structure in turbulent mixing layers", J. Fluid Mech. **64**, 775 (1974).

Dimotakis, P. E., "Two-Dimensional Shear-Layer Entrainment", AIAA Jour. **24**, 1791 (1986).

Kerstein, A. R., Ashurst, W. T., Wunsch, S. and Nilsen, V., "One-dimensional turbulence: vector formulation and application to free shear flows", J. Fluid Mech. **447**, 85 (2001).

Konrad, J. H., "An Experimental Investigation of Mixing in Two-Dimensional Turbulent Shear Flows with Application to Diffusion-Limited Chemical Reactions", Project SQUID Tech. Rept. CIT-8-PU, Dec. 1976.

Pantano, C. and Sarkar, S., "A study of compressibility effects in the high-speed turbulent shear layer using direct simulation", J. Fluid Mech. **451**, 329 (2002).

Ramshaw, J. D., "Simple model for mixing at accelerated fluid interfaces with shear and compression", Phys. Rev. E **61**, 5339 (2000).

Sandham, N. D. and Reynolds, W. C., "Compressible mixing layer: Linear theory and direct simulation", AIAA J. **28**, 618 (1990) and private communication (2001).

Siebers, D. L., "Scaling Liquid-Phase Fuel Penetration in Diesel Sprays Based on Mixing-Limited Vaporization", SAE Paper 1999-01-0528.

Witze, P. O., "Centerline Velocity Decay of Compressible Free Jets", AIAA Jour. **12**, 417 (1974).

Numerical Methods for Determination of RT and RM Mixing

S. Dutta, E. George, J. Grove, J. Glimm, ***X. L. Li,***
A. Marchese, D. Sharp, Z. Xu and Y. Zhang
Department of Applied Math and Statistics
SUNY at Stony Brook
Stony Brook, NY 11794

Outline of the Talk

- Tracking the contact interface
- Simulations of Random RT Mixing
- Comparison with untracked code
- Analysis of buoyancy acceleration
- Simulation of axisymmetric RM mixing
- Conclusion

The Front Tracking Method

- Interface divides space into subdomains
- Riemann solution to propagate interface
- Finite difference with ghost cells
- Coupling interface-interior solutions
- Dynamic resolution of interface topology
- Clear separation of discontinuous states
- Clear separation of material (EOS)

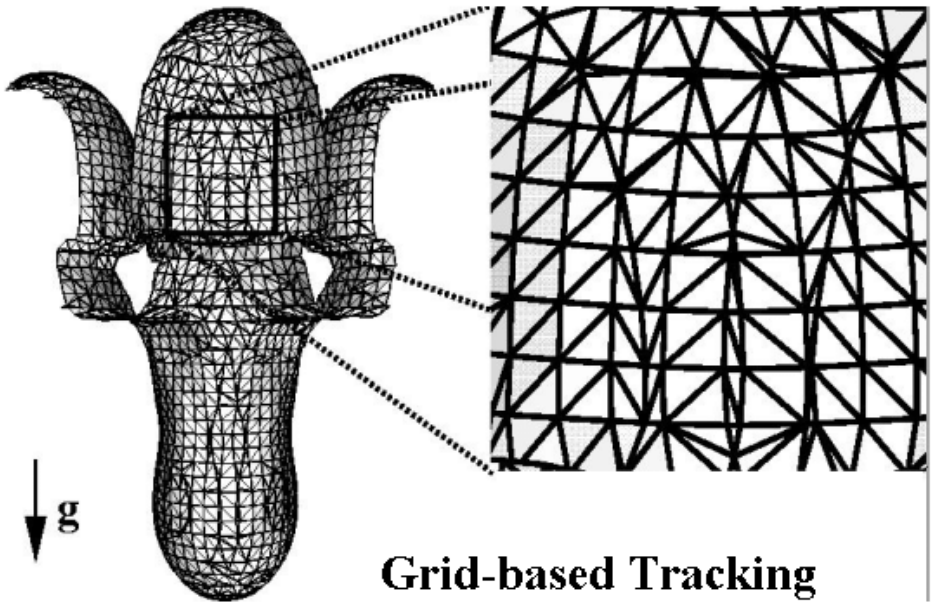
g
Grid-based Tracking

Basic FronTier Test Simulations

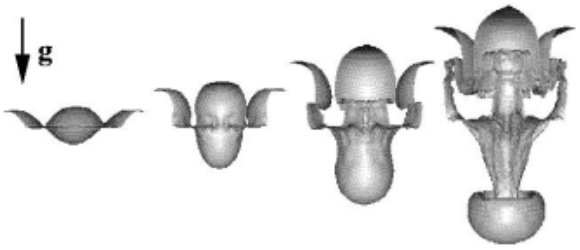

Case Single-2

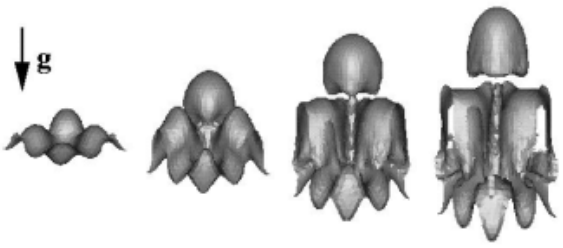

Case Bifure-1

Separating fluids via ghost-cell

1. Ghost-cell method
   Front Tracking (Glimm, McBryan, etc 1980)

2. Ghost cell has been the key design component of front tracking

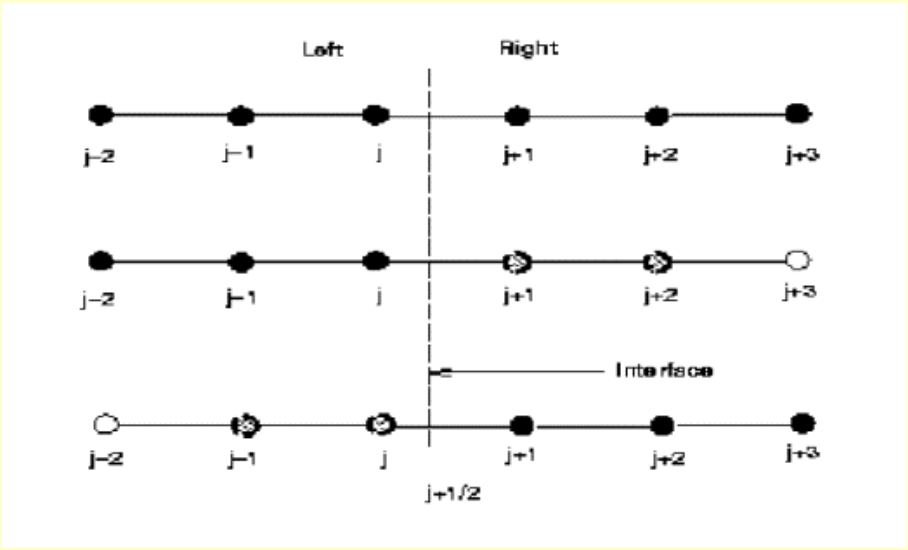

The ghost-cell method

Numerical diffusion in 1st order upwinding

$$Du = u_t - au_x = 0$$

$$D_h u = \frac{u_j^{n+1} - u_j^n}{\Delta t} - a\frac{u_j^n - u_{j-1}^n}{\Delta x} = 0$$

$$D_h u - Du = -\frac{a\Delta x}{2}\left(1 - a\frac{\Delta t}{\Delta x}\right)u_{xx}$$

$$a\frac{\Delta t_{CFL}}{\Delta x} = 1$$

Numerical diffusion is large if $\Delta t << \Delta t_{CFL}$

Numerical dissipation at contact discontinuity

1. Most higher order schemes switch to 1st order at discontinuity to avoid oscillation, using either artificial viscosity or limiter.

2. For three characteristic wave speed $u \pm c$, u, the motion of contact is the inertial motion with speed u.

3. For first order scheme, the smaller is Δt away from the CFL condition, the more dissipative it becomes.

4. It is particularly dissipative at contact for low compressibility

$$c >> u \qquad \Delta t = CFL \times \frac{\Delta x}{|u| + c} << CFL \times \frac{\Delta x}{|u|}$$

The α Paradox

$$h_b = \alpha A g t^2$$

David Youngs and K.Read
(1984)

Read's Experiment (1984)

3D alcohol/air	Exp # 29	Alpha = 0.073
	39	0.076
	58	0.077
3D NaI soln./Pentane	Exp # 33	Alpha = 0.066
	35	0.071
3D NaI soln./Hexane	Exp # 62	Alpha = 0.063
	60	0.073

Summary of Experiments

Experiments			
Read/Youngs	'84	$\alpha_b \sim 0.58 - 0.65$	2D
		$\alpha_b \sim 0.063 - 0.077$	3D
Kucherenko	'91	$\alpha_b \sim 0.07$	3D
Snider/Andrews	'94	$\alpha_b \sim 0.07 \pm 0.007$	3D
Schneider/Dimonte/Remington	'99	$\alpha_b \geq 0.054$	3D
Dimonte/Schneider	'99	$\alpha_b \sim 0.05 \pm 0.01$	3D

Bliznetsov	0.1
Shestachchenko	0.04

FronTier Simulation of Random RT Mixing

Simulation Random-3

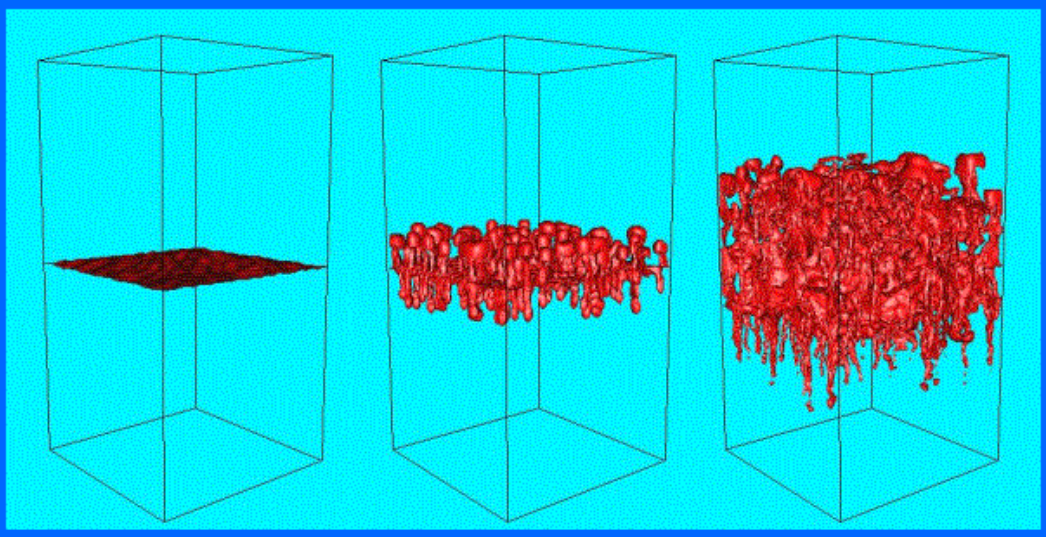

Compressibility = 0.06 **Alpha ~ 0.08**

Movie Random-4

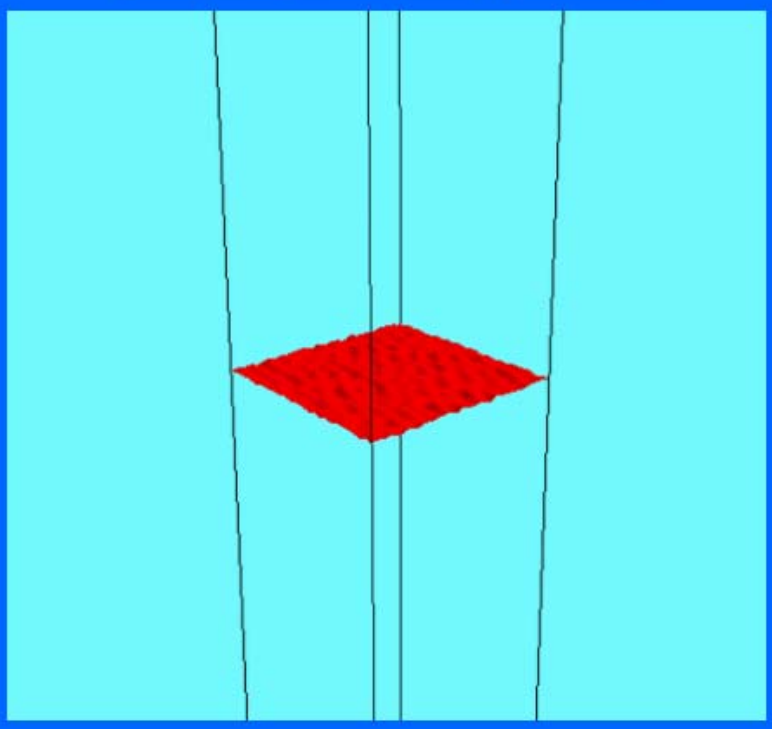

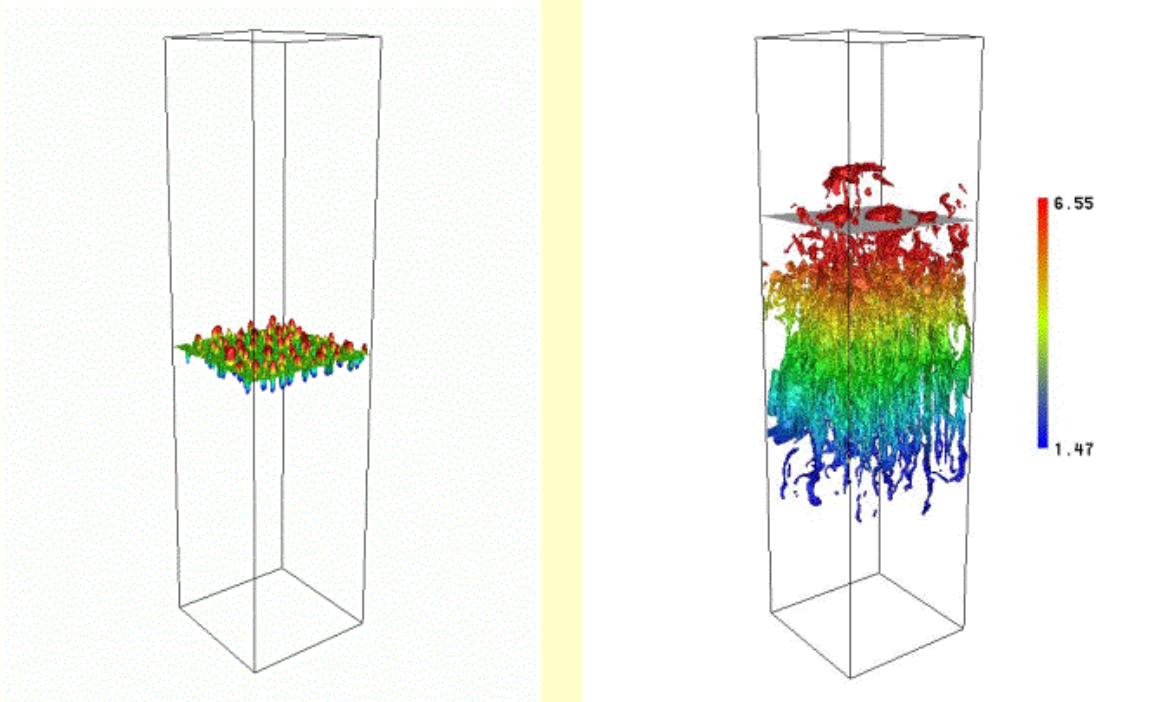

FronTier simulation of RT mixing, with A = 0.5.

Left: early time. Right: late time. On 128*128*512 grid

The Alpha of Bubbles

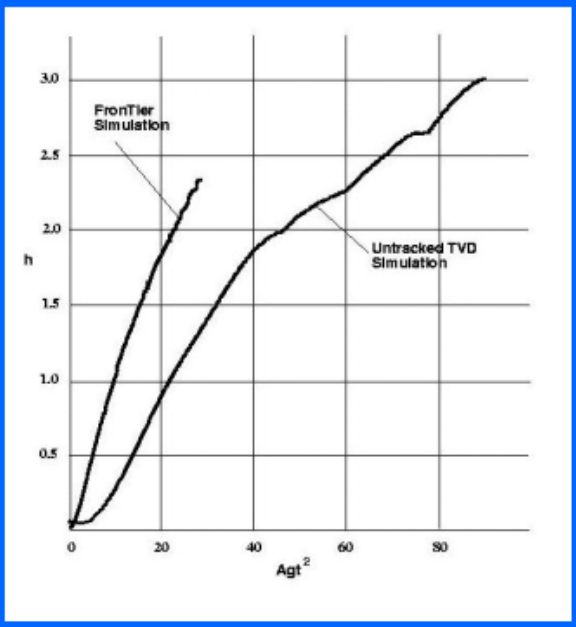

FronTier:
Alpha = 0.08

TVD:
Alpha = 0.025-0.045

FronTier **TVD**

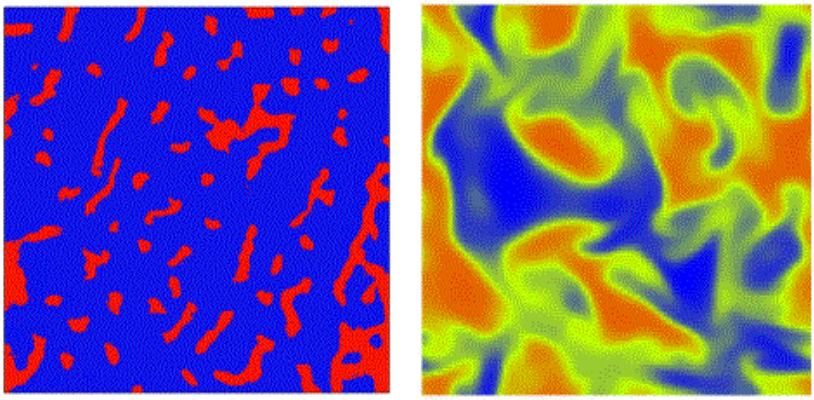

Agt $= \frac{2}{2}$ 25.3 h = 4.16 Density plot

The Archimedes Principle

- The buoyancy force on an immersed body equals to the weight of the fluid the immersed body has repelled.

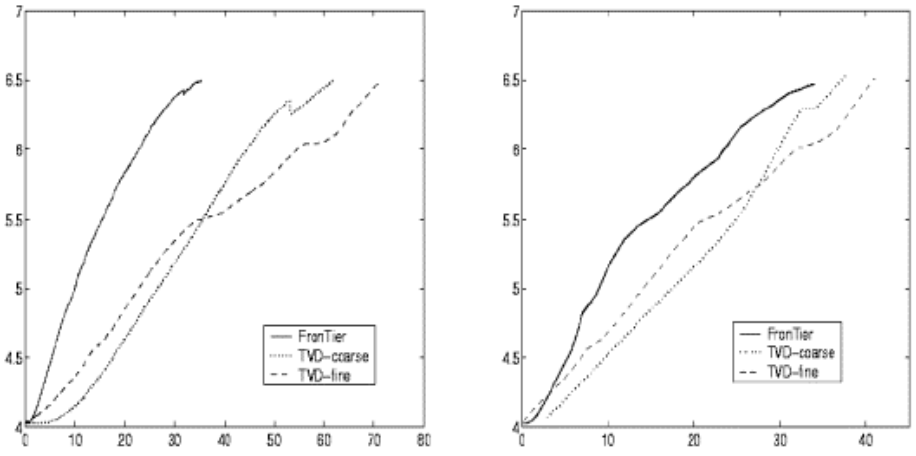

Normalization of alpha with effective Atwood number

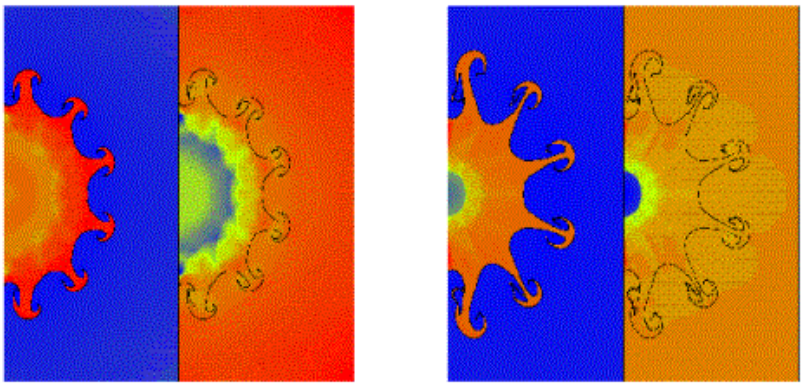

A 2D simulation of spherical RM instability with axisymmetry
The Mach number of the imploding shock is 1.2 and the Atwood number is 2/3. The inner gas is SF_6 and the outer gas is air.

FronTier Simulation of NLUF 2 Experiment

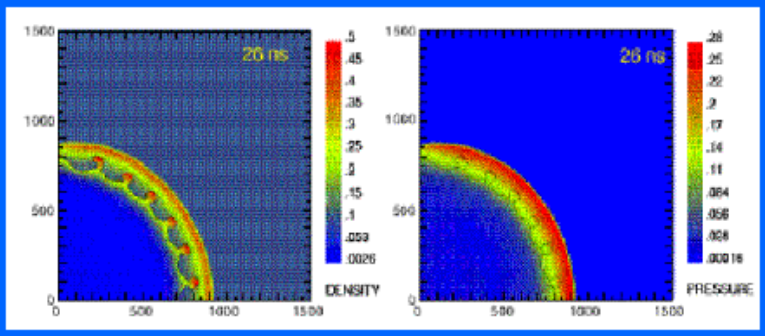

CHGe capsule surrounded by CRF foam. The RM instability is driven by strong shock of Mach number 300 by the Omega laser

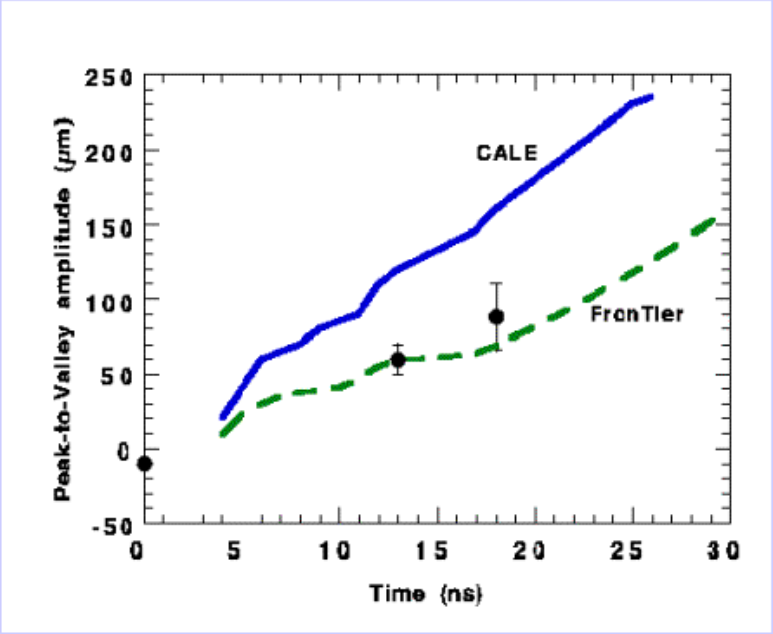

Comparison of *FronTier* amplitude and the CALE Simulation with the experiment

Conservative Interface-Interior Coupling

The conservation law:

$$u_t + f(u)_x = 0$$

The Rankine-Hugoniot condition:

$$f(u_L) - su_L = f(u_R) - su_R$$

Neglect higher order term and note that

$$\int_{\Delta V} u dV = \int_{S_M} u v_n dS \Delta t$$

We have the integral form of conservation

$$\frac{\partial}{\partial t}\int_V u dV - \int_{S_M} u v_n dS + \oint_S F_n(u) dS = 0$$

This can also be written as

$$\frac{\partial}{\partial t}\int_V u dV + \int_{S_F} F_n(u) + \int_{S_M} (F_n(u) - v_n u) dS = 0$$

Or simply

$$\frac{\partial}{\partial t}\int_V u dV + \oint_S (F_n(u) - v_n u) dS = 0$$

Conclusion

1. Numerical diffusion is a serious problem in simulation of contact surface in gas dynamics, especially when c >> u.

2. Front tracking prevents such diffusion through ghost-cell method, retains correct buoyancy force in RT simulation.

3. The introduction of local effective Atwood number bridges the gap between tracked and untracked simulations.

4. Front tracking shows agreement in axisymmetric spherical RM instability.

5. Front tracking is will replace ghost-cell by conservative tracking using dynamic flux at a cell with moving boundary.

One-Dimensional Simulation of the Effects of Unstable Mix on Neutron and Charged-Particle Yield from Laser-Driven Implosions

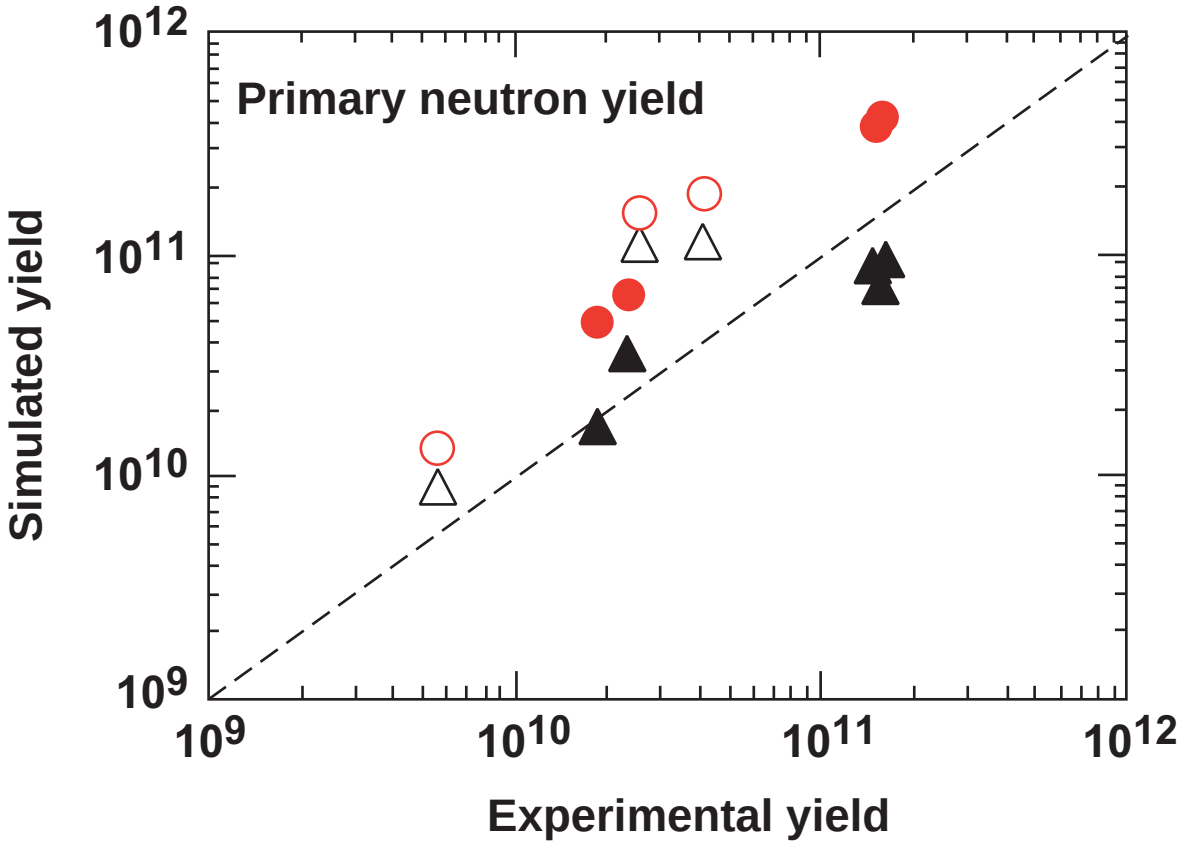

R. Epstein
University of Rochester
Laboratory for Laser Energetics

8th International Workshop on the Physics of Compressible Turbulent Mixing
Pasadena, CA
10–14 December 2001

Collaborators

J. A. Delettrez, V. Yu. Glebov, V. N. Goncharov, P. W. McKenty, P. B. Radha, S. Skupsky, V. A. Smalyuk, and C. Stoeckl

Laboratory for Laser Energetics
University of Rochester

J. Frenje, C. K. Li, R. D. Petrasso, and F. H. Séguin

Massachusetts Institute of Technology

Summary

Mix effects on particle yields can be described effectively by mix modeling in the 1-D hydrocode *LILAC*

UR LLE

MIT

- **The mix model includes the transport of target constituents, thermal energy, and turbulent energy due to both the acceleration and deceleration instabilities.**

- **Including mix in 1-D simulations of experiments provides improved predictions of primary and secondary particle yields over a broad range of target performance.**

Outline

- Modeling of mix in 1-D
- Comparison of simulated and experimental yields
- Secondary neutron and proton production
- Conclusions

“Bubble and spike” mixing thickness is obtained from a multimode Rayleigh–Taylor perturbation model*

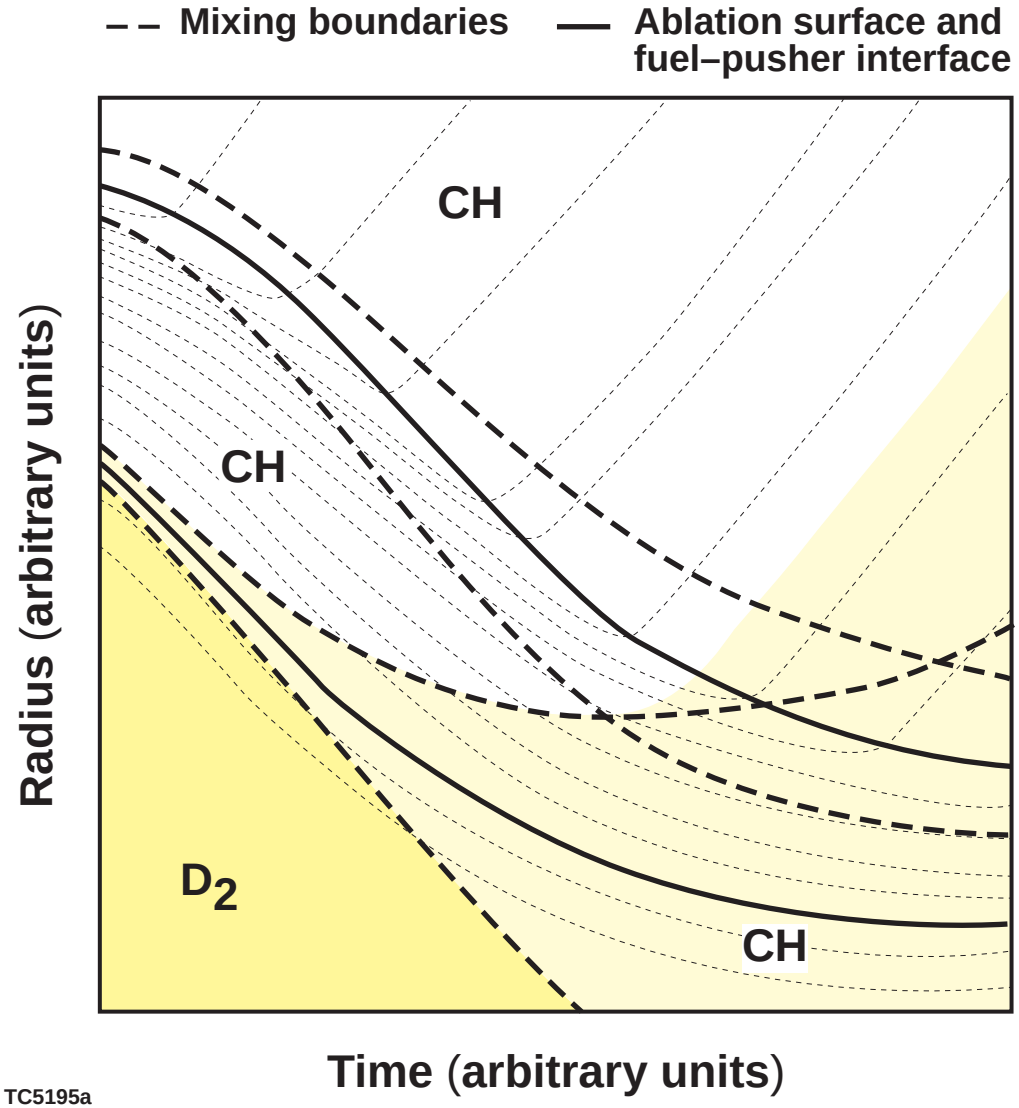

- $\frac{d^2}{dt^2} A_\ell = \gamma^2(t)\, A_\ell$ including Bell-Plesset effects
- Takabe/Betti form for $\gamma^2(t)$
- Haan saturation procedure for

$$A_\ell(t) > \frac{2R(t)^*}{\ell^2}$$

- Initial perturbation spectrum $A_\ell(t = t_0)$ specified at ablation surface and fed through to fuel–pusher interface over time.
- Mix is modeled as a diffusive transport process.

*S. W. Haan, Phys. Rev. A 39, 5812 (1989).

TC5195a

The mix model is based on carefully formulated phenomenology

UR LLE

- **Perturbations due to single-beam imprint were obtained from *ORCHID* calculations based on measured single-beam nonuniformity.**
- **Beam-imbalance effects are based on power-imbalance measurements from each shot and the geometrical superposition of the acceleration distributions of 60 beams.**
- **The formulation of the perturbation growth using fully time-dependent perturbation equations allows secular nonuniform irradiation effects and "feedthrough" from the outer to the inner instabilities to be treated as driving terms, rather than as instantaneous effects.**
- **Plausible flux limitation of the diffusive mix transport is obtained by allowing that the mixed constituent profiles can remain self-similar under expansion.**

Perturbation equations are best written in terms of a mass amplitude

UR LLE

Incompressible planar approximation

$$\frac{d^2}{dt^2} A_\ell = \gamma_0^2 \, A_\ell \qquad \gamma_\pm = \pm\gamma_0$$

$$A_{\ell\pm} = A_{\ell 0} \, e^{\gamma_\pm t} \qquad \gamma_0^2 = \frac{\ell}{R}\left(\frac{\rho_2 - \rho_1}{\rho_2 + \rho_1}\right)\ddot{R}$$

Compressible spherical solution (i.e., Bell–Plesset*)

$$\left(-\gamma_\rho - \gamma_R + \frac{d}{dt}\right)\frac{d}{dt}\left(A_\ell \rho R^2\right) = \gamma_0^2 \left(A_\ell \rho R^2\right) \qquad \gamma_R = \dot{R}/R,\ \gamma_\rho = \dot{\rho}/\rho$$

$$\gamma_0^2 = \frac{\ell(\ell+1)}{R}\frac{(\rho_2 - \rho_1)\,\ddot{R}}{[\ell\rho_2 + (\ell+1)\rho_1]} \qquad \gamma_\pm = \frac{1}{2}\left(\gamma_\rho + \gamma_R\right) \pm \sqrt{\gamma_0^2 + \frac{1}{4}\left(\gamma_\rho + \gamma_R\right)^2}$$

*G. I. Bell, Los Alamos National Laboratory, Report No. LA-1321 (1951).
M. S. Plesset, J. Appl. Phys. 25 (1), 96-98 (1954).

Mix is modeled in 1-D as a diffusive transport process

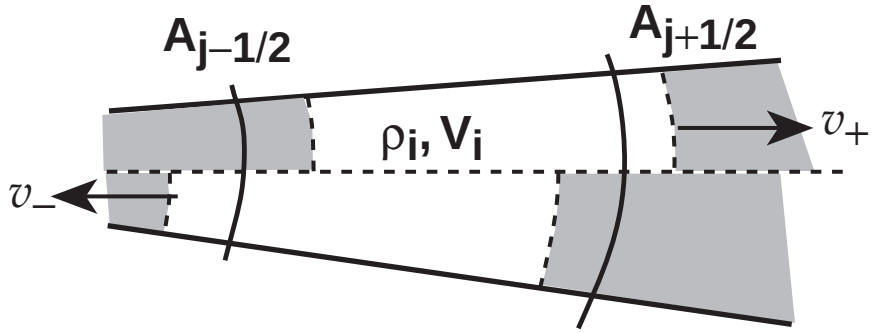

Advection to and from nearest-neighbor zones is expressed as diffusion in 1-D.

$$\frac{\partial}{\partial t}\begin{bmatrix}\rho\\ n_e\\ n_H\\ C_v T_e\\ \vdots\end{bmatrix} = \frac{1}{r^2}\frac{\partial}{\partial r}\left(r^2 \frac{\sigma}{\beta_m}\frac{\partial}{\partial r}\begin{bmatrix}\rho\\ n_e\\ n_H\\ C_v T_e\\ \vdots\end{bmatrix}\right), \quad \text{where } \sigma = v_{mix}\lambda * \frac{4(r_b - r)(r - r_s)}{(r_b - r_s)^2}$$

v_{mix}: obtained from trajectories of mix-region boundaries

λ: scale length of turbulence structure from rms perturbation wavelength

f: "flux limit" parameter $\frac{\sigma}{\beta_m}\left|\frac{\partial \rho}{\partial r}\right| \Rightarrow \text{Min}\left[\frac{\sigma}{\beta_m}\left|\frac{\partial \rho}{\partial r}\right|, f\rho v_{mix}\right]$

The mix computation is done as a separate step within the 1-D hydrocode

- **Diffusive transport of constituent densities $\{\phi\}$ keeps zone masses constant:**

$$\frac{d}{dt}(V\phi)_j = \left[A\left(u + \frac{\sigma}{\beta_m}\frac{\partial}{\partial r}\right)\phi\right]_{j+1/2} - \left[A\left(u + \frac{\sigma}{\beta_m}\frac{\partial}{\partial r}\right)\phi\right]_{j-1/2}$$

$$(\rho u)_{j+1/2} = -\left[\frac{\sigma}{\beta_m}\frac{\partial \rho}{\partial r}\right]_{j+1/2}$$

$$\frac{d}{dt}M_j = \frac{d}{dt}(V\rho)_j = 0$$

- **Hydrodynamics in terms of total mass velocity*** $v_{j+1/2} = \langle v_{j+1/2} \rangle + u_{j+1/2}$

$$\frac{d\rho}{dt} = \frac{-\rho}{r^2}\frac{\partial}{\partial r}\left(r^2 v\right), \qquad \rho\frac{dv}{dt} = -\frac{\partial}{\partial r}(P + Q + P_T + Q_T)$$

*Leith, UCRL-96036 (1986).

Mix-motion energy is computed as turbulent energy in a "k–λ" model

UR LLE

- **Turbulent energy density k:**

$$P_T = \frac{2}{3}k, \quad Q_T = -\frac{4}{3}\frac{\sigma}{\beta_q}\frac{\partial v}{\partial r}, \quad \sigma = v_{mix}\,\lambda \qquad (\beta_q = 1.0)$$

- **Buoyant force as source of k:**

$$S = \max\left(\rho u \frac{dv}{dt}, 0\right), \quad \rho u = -\frac{\sigma}{\beta_m}\frac{\partial \rho}{\partial r} \qquad (\beta_m = 0.7)$$

- **Dissipation rate:**

$$\varepsilon = C_\varepsilon \frac{k^{3/2}}{\rho^{1/2}\lambda} \qquad (c_\varepsilon = 0.09)$$

- **Evolution:**

$$\frac{dk}{dt} = \frac{1}{r^2}\frac{\partial}{\partial r}\left(r^2 \frac{\sigma}{\beta_k}\frac{\partial k}{\partial r}\right) - (P_T + Q_T)\frac{1}{r^2}\frac{\partial}{\partial r}\left(r^2 v\right) + S - \varepsilon \qquad (\beta_k = 0.715)$$

$$\frac{dE_i}{dt} = \frac{1}{r^2}\frac{\partial}{\partial r}\left(r^2 \frac{\sigma}{\beta_m}\frac{\partial E_i}{\partial r}\right) + \varepsilon - S + \ldots \text{etc.}$$

TC3962

Growth rates of perturbations of arbitrary density profiles are estimated using Sturm–Liouville theory

- The Rayleigh perturbation equation for an arbitrary density profile is a Sturm–Liouville eigenvalue equation:

$$\frac{1}{r^2}\frac{d}{dr}\left[r^2\rho\frac{dw_\ell}{dr}\right]-\rho\frac{\ell(\ell+1)}{r^2}w_\ell+\frac{1}{\gamma_\ell^2}\frac{\ell(\ell+1)}{r^2}g\frac{d\rho}{dr}w_\ell=0$$

- The perturbation growth rate is given by a variational expression:

$$\frac{\gamma_\ell^2}{g}=\text{Max}\left\{\int_0^\infty\frac{\ell(\ell+1)}{r^2}\frac{d\rho}{dr}w_\ell^2r^2dr\Big/\int_0^\infty\rho\left[\left(\frac{dw_\ell}{dr}\right)^2+\frac{\ell(\ell+1)}{r^2}w_\ell^2\right]r^2dr\right\}$$

- Estimates obtained using only moderately accurate eigenfunctions are accurate to second order in variations of the postulated eigenfunction:

$$w_\ell\approx\left[(r/L)^\ell,\ r<L/2;\ a+b\left(r-r_0\right)+c\left(r-r_0\right)^2,-L/2<r<L/2;\ (r/L)^{-(\ell+1)},\ r>L/2\right]$$

A constrained set of static model core properties reproduces most experimental observables

- 1-ns square, 23 kJ, 20-μm-CH shells, 15 atm fill, CR ~ 15

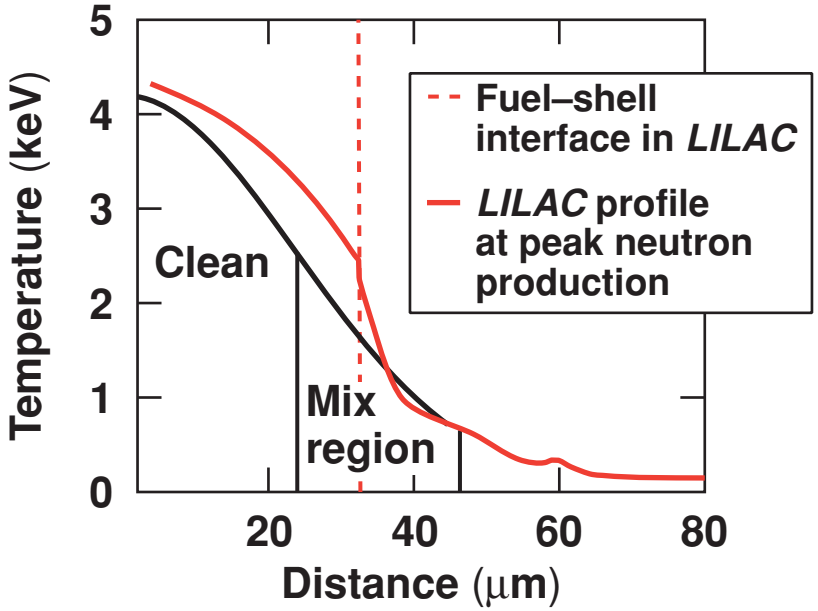

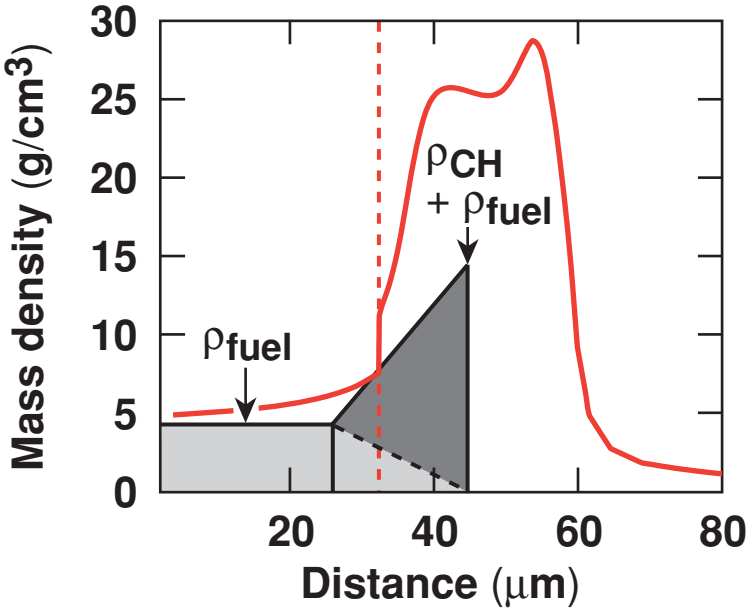

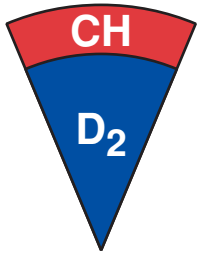

	Measured	% of model
Max: neutron rate	$(9\pm2)\times10^{20}$	120
Burn width (ps)	170±20	94
T_{ion} (D_2) (keV)	3.7±0.5	90
Secondary neutron ratio	$(2.1\pm0.4)\times10^{-3}$	90
Secondary proton ratio	$(1.8\pm0.3)\times10^{-3}$	100

TC5855

Mix modeling improves the agreement of simulated primary neutron yield with implosion data

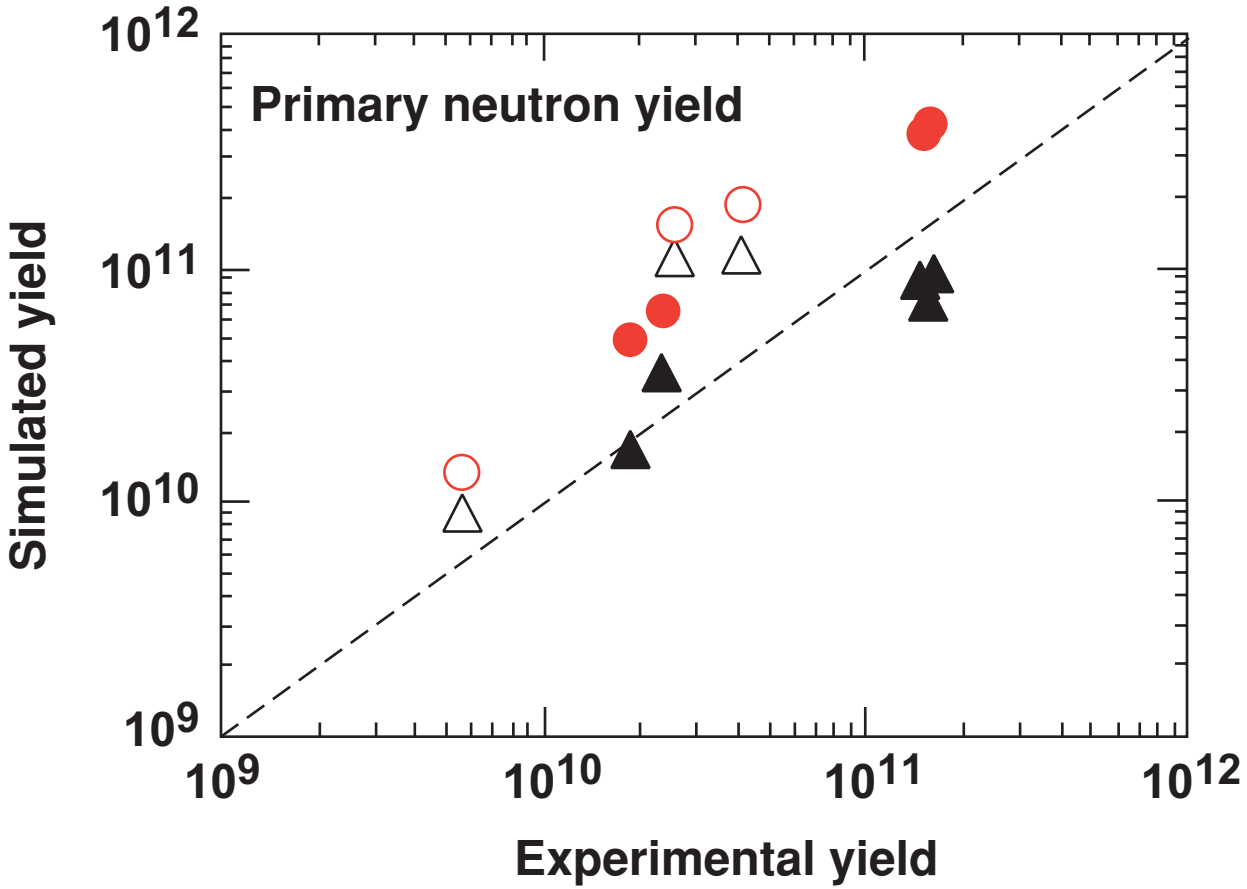

- Data from eight shots (August 2000)
- Pure-CH shells, 20–27 μm, 900-μm diameter, D_2 fill, 3–25 atm

TC5667

Primary yield ratios indicate that implosion degradation is comparable to the predictions of mix modeling

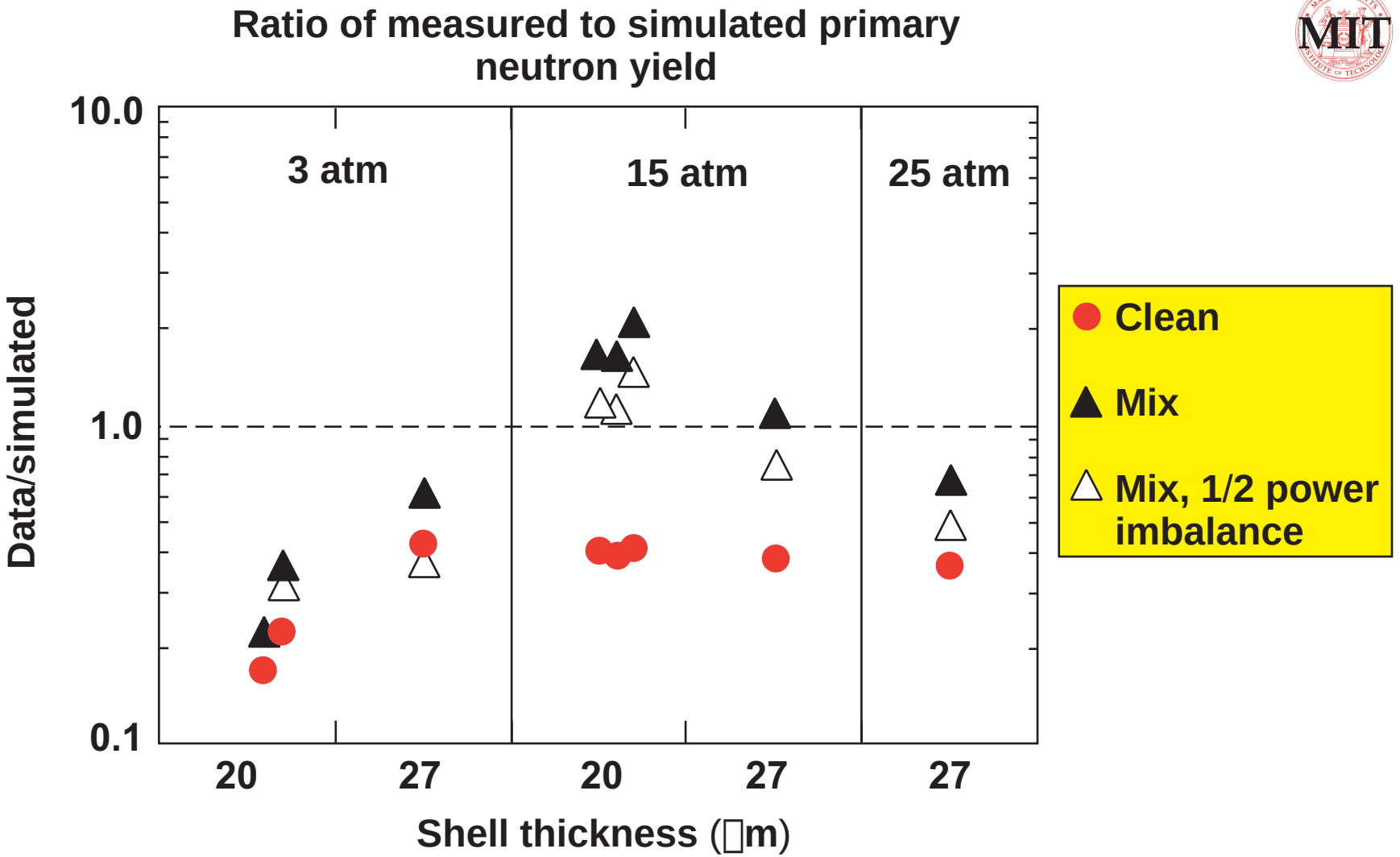

TC5668

Simulated and measured neutron-averaged temperatures show some improved agreement with mix modeling

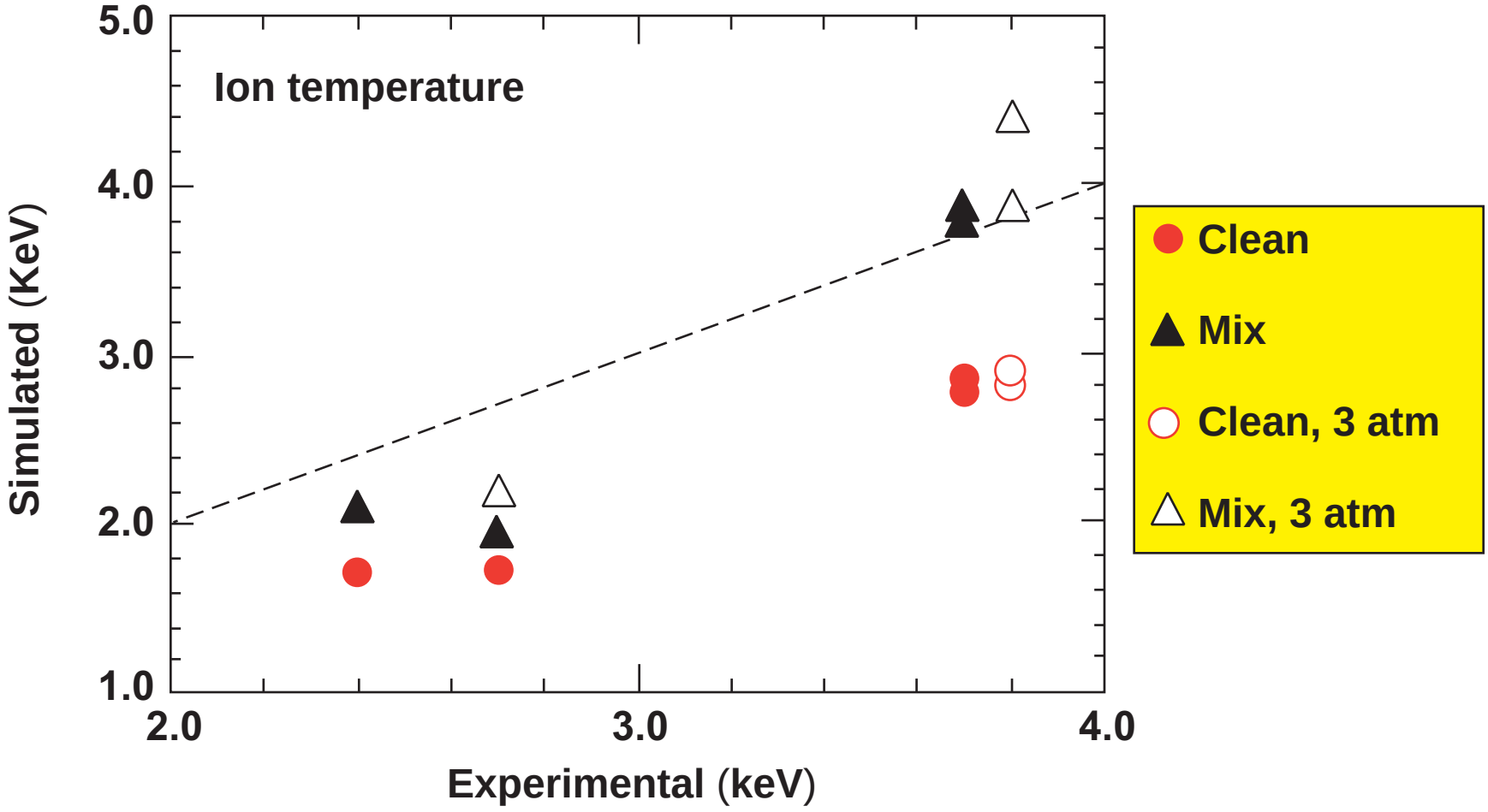

TC5669

Secondary particle yields reflect different slowing rates and cross sections with contrasting energy dependence

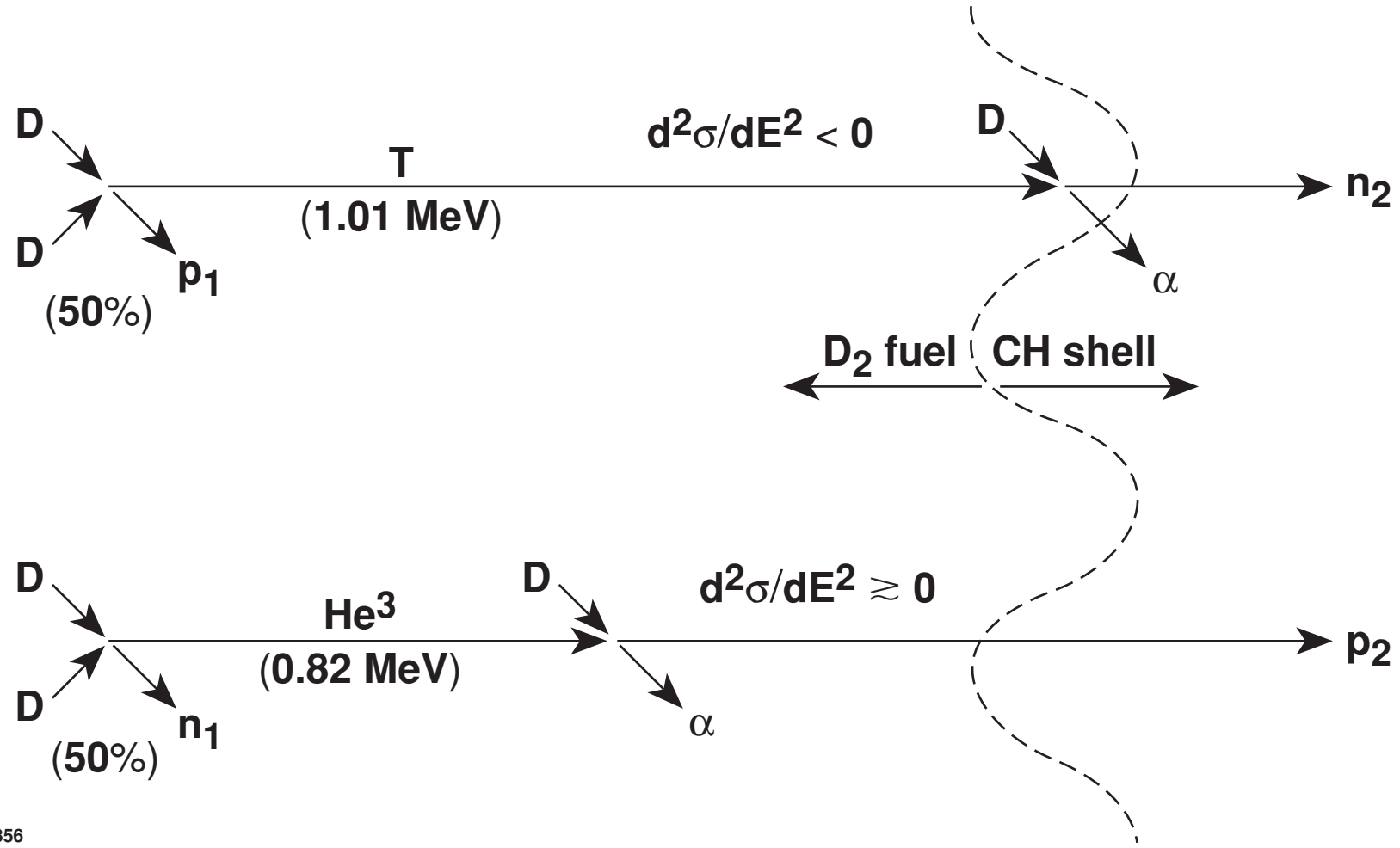

TC5856

Comparison of simulated with measured secondary particle yield ratios suggests sensitivity to dynamics

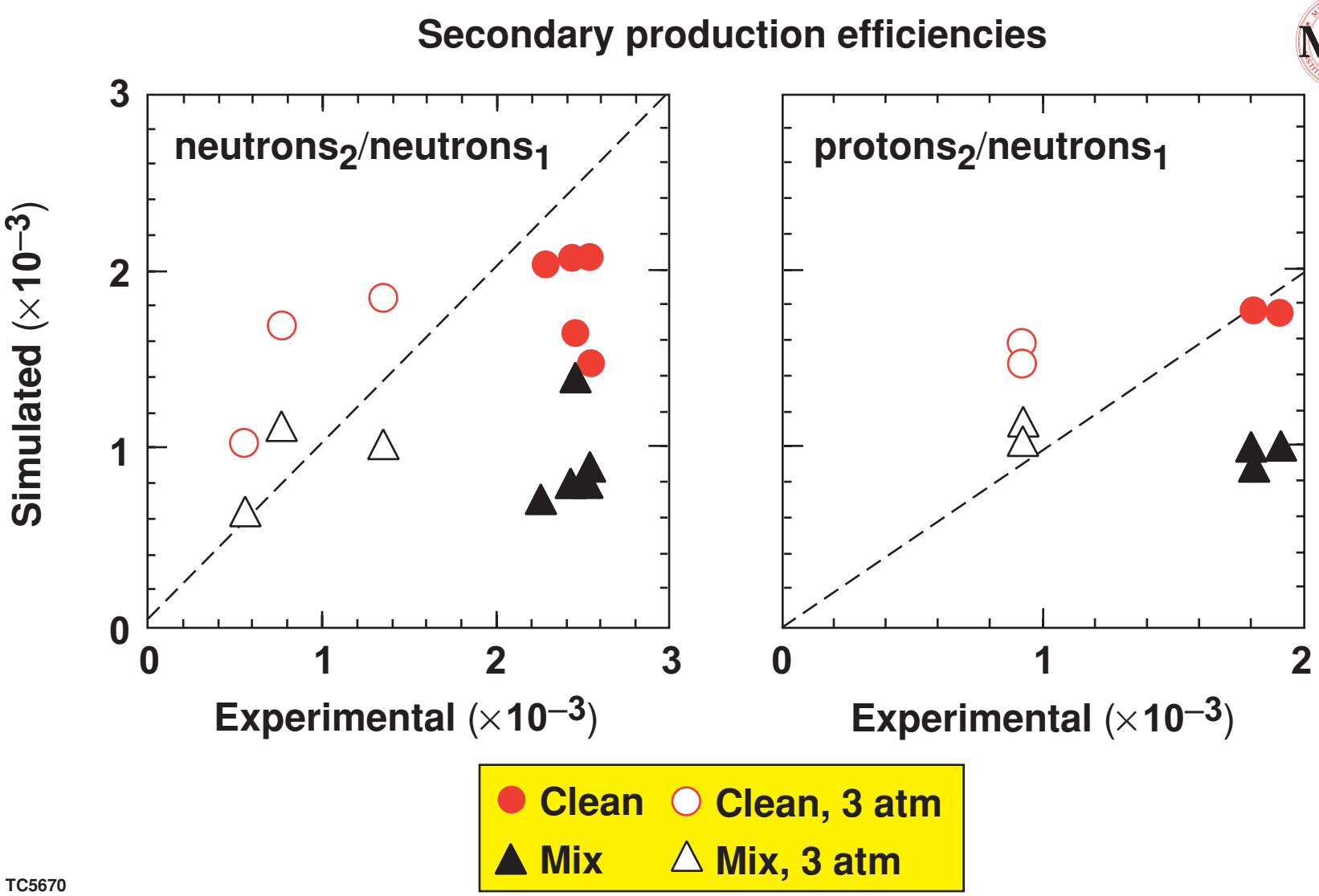

TC5670

The spatial distribution of secondary particle production depends on the extent of mix

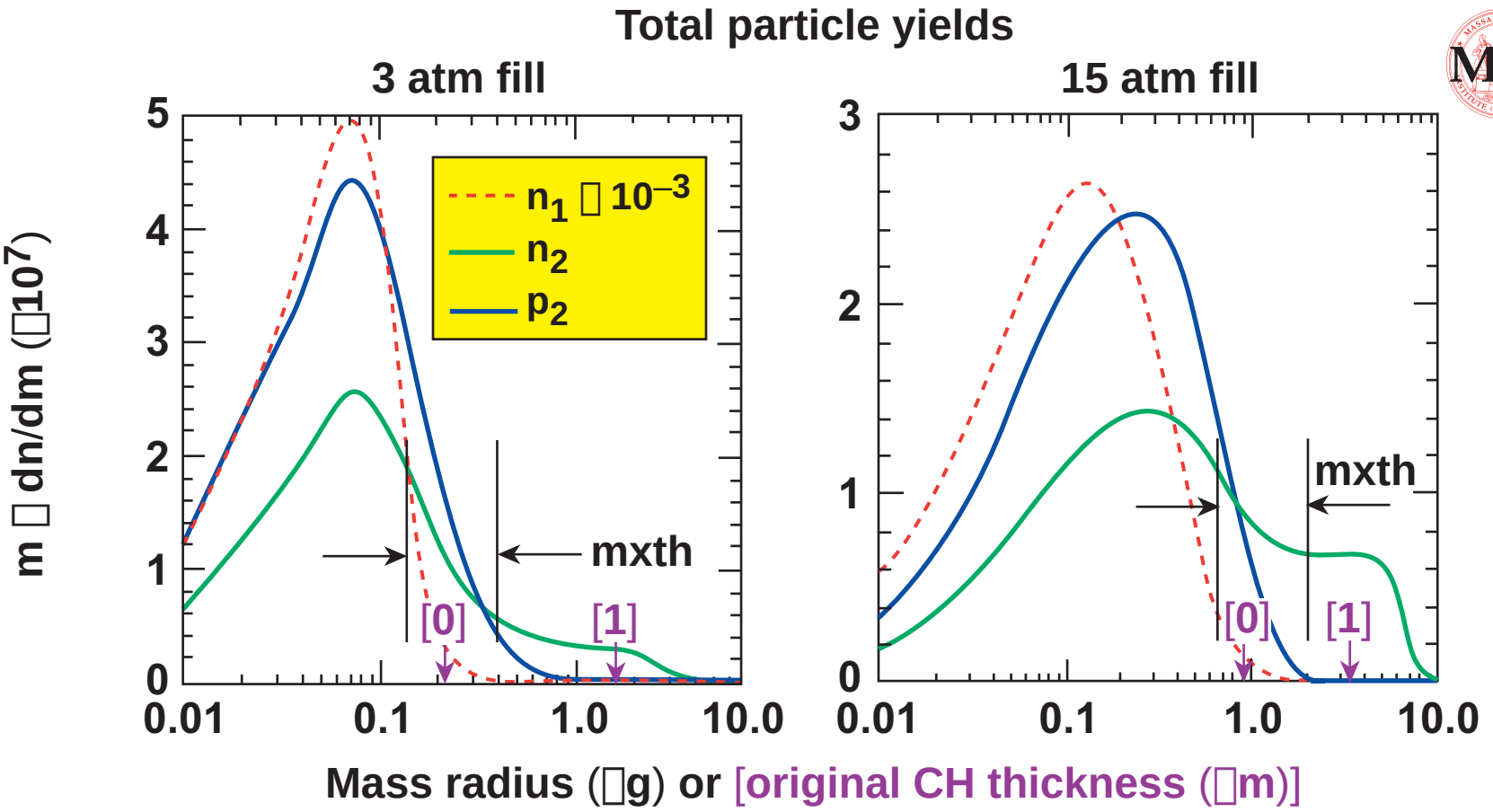

- Mix thickness (mxth) is from the 1:3 to 3:1 mix points at the time of peak n_1 production rate.
- With the mass-spatial distribution as plotted here, the area under the curve is preserved.

TC5671

The relative timing of peak neutron production and peak compression does not affect the coincidence of primary and secondary production times

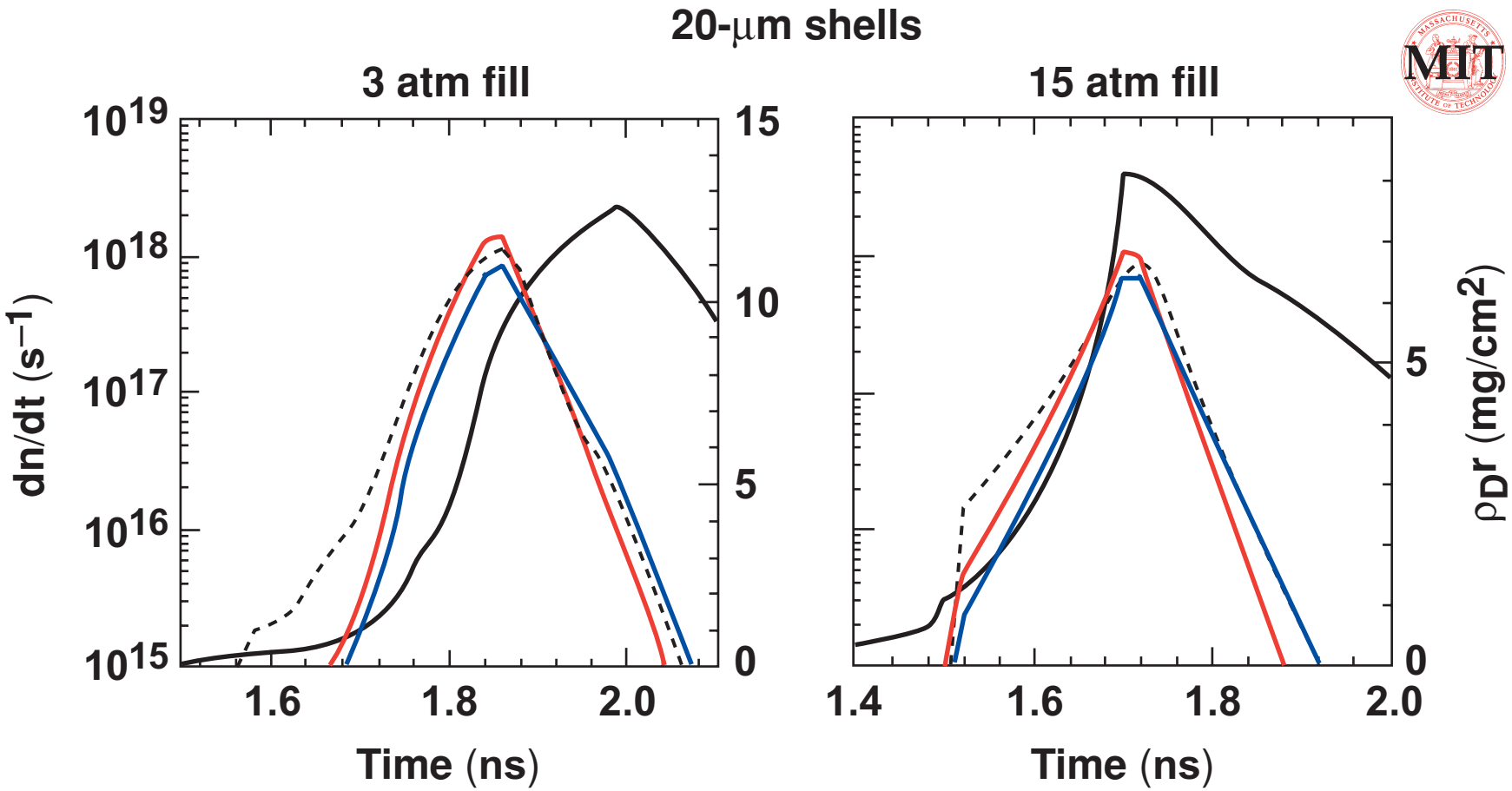

TC5672

Summary/Conclusion

Mix effects on particle yields can be described effectively by mix modeling in the 1-D hydrocode *LILAC*

UR LLE

MIT

- The mix model includes the transport of target constituents, thermal energy, and turbulent energy due to both the acceleration and deceleration instabilities.
- Including mix in 1-D simulations of experiments provides improved predictions of primary and secondary particle yields over a broad range of target performance.
- The validity of approximating multidimensional hydrodynamics with a spherically symmetric model remains an issue.

3D computation of surface perturbations evolution in plasma cloud during its expansion in magnetic field.

E.S. Gavrilova, E.V. Gubkov, V.A. Zhmailo, Yu.V. Yanilkin
RFNC-VNIIEF, 607190, Sarov, Nizhni Novgorod region
E-mail: vaz@vniief.ru

Paper presented at the 8th International Workshop on the Physics of Compressible Turbulent Mixing (8th IWPCTM, Pasadena, 2001)

Previously, refs. [1-3] considered a 2D problem of initially spherical plasma cloud expansion in axial magnetic field. The papers indicated, in particular, that the cloud surface was nonresistant to "chute" type instability evolution and estimated the instability growth increments.

The objective of the paper is tracking the evolution of the above instabilities with account for their actual, i.e. three-dimensional, nature.

Two approaches are used for this purpose:

- the initial stage of the perturbation growth is considered analytically under the assumption of the perturbation smallness,
- the nonlinear stage is computed with 3D numerical code TREK [4].

1. Unperturbed plasma cloud dynamics in magnetic field.

Recall the features of solving the problem of dynamics of a plasma cloud expanding in the external magnetic field.

Consider a cloud of energy E, mass M and assume the magnetic field to be axial, homogeneous, of strength $\vec{H} = (0,0,H_0)$ with r→∞. Also, assume that the initial shape cloud is spherical of radius r_0.

A detailed pattern of the cloud expansion and deformation is obtained by numerical computations and discussed in ref. [3]. To find out the qualitative pattern, an approximate model can be used, which implies that the motion of each "sector" of the cloud depends on magnetic pressure on its surface. If the pressure is given (by relations presented in ref. [1]), then we can obtain the equation for the cloud surface radius:

$$R(\Theta,t) = \left[r_0^3 + R_0^3 \cdot \frac{\sin^2 \omega t}{\sin^2 \Theta} \right]^{\frac{1}{3}} \qquad (1.1)$$

where $u_0 = \left(\frac{E}{M}\right)^{\frac{1}{2}}$ is initial expansion rate, $\omega(\Theta) = \frac{\omega_0}{\sin\Theta}$, $\omega_0 \cong \frac{u_0}{R_0}$, $R_0 = \left(\frac{E}{\frac{4}{3}\pi \cdot p_m^0}\right)^{\frac{1}{3}}$,

$p_m^0 = \frac{H_0^2}{8\pi}$, Θ is an angle with respect to the axis of symmetry.

Thus, from the solution it follows that the expanding cloud is decelerated by the magnetic field, its radius periodically changes depending on time t, with the deceleration being most noticeable at the "equator" ($\Theta = \frac{\pi}{2}$) and missing at the poles ($\Theta = 0$).

As the comparison to the data of ref. [3] suggests, this simple cloud dynamics model is valid at $\omega_0 t \le \pi$.

The plasma cloud deceleration by the magnetic field leads to the perturbation evolution on the cloud surface (by analogy with the R-T instability in hydrodynamics: the role of the "heavy" fluid is played by the cloud plasma, that of the "light" by the magnetic field).

2. Linear stage of instability growth

When considering this stage of the perturbation growth on the plasma cloud surface, of interest to us will be most hazardous of them, that is such, for which increment $\gamma >> \omega_0$. In this case the unperturbed surface can be considered as spherically symmetric and the unperturbed magnetic field near the surface as having only one, tangential, component $H_\Theta = \frac{3}{2} H_0 \sin\Theta$ [1].

If the surface perturbation form is given as

$$R(\Theta,\varphi,t) = R_0(t) + \sum_{lm} \xi_{lm}(t) \cdot Y_{lm}(\Theta,\varphi) \qquad (2.1)$$

where $Y_{lm}(\Theta,\varphi)$ are spherical harmonics, then, by extending the well-known conclusion [5] for plane plasma-magnetic field interface to the spherical case under consideration, the following equation system can be obtained for harmonics $\xi_{lm}(t)$:

$$\frac{\partial}{\partial t}\left(R^2 \frac{\partial \sigma_{lm}}{\partial t} \right) = \sum_{k=l,l\pm2} a_{km}^{lm} \cdot \sigma_{km} \qquad (2.2)$$

where $a_{km}^{lm} = -\left[\ddot{R}_0 \cdot R_0 \cdot \lambda_{km}^{lm} + c_A^2 \cdot \mu_{km}^{lm} \right] \cdot l$ (2.3)

where $c_A^2 = \frac{\left(\frac{3}{2} H_0\right)^2}{4 \cdot \pi \cdot \rho_0(t)}$, λ_{km}^{lm} and μ_{km}^{lm} are algebraic functions l and m. The expressions for the functions prove quite cumbersome, here it is sufficient to note that for $l >> 1$, $\lambda_{km}^{lm} \sim \delta_{kl} + \delta\lambda_{km}^{lm}$, where $\delta\lambda_{km}^{lm} \sim \frac{1}{m+1}$, $\mu_{km}^{lm} \sim (l-m)$.

Note that the "engagement" of harmonics l and l±2 in equation system (2.2) is a consequence of the fact that the pressure of the unperturbed magnetic field on the surface depends on Θ ($p_m \sim \sin^2\Theta$). This "engagement" disappears, when the initial perturbation is localized at $\Theta = \Theta_0 \pm \Delta\Theta$, where $\Delta\Theta << 1$. Assuming m=0 and l such that $l\Delta\Theta >> 1$, equation (2.2) can be reduced to a simpler form:

$$\frac{\partial}{\partial t}\left(R^2 \frac{\partial \sigma_{lm}}{\partial t} \right) = -\sigma_{lm}\left[l \cdot \ddot{R}_0(\Theta_0) \cdot R_0 + c_A^2(\Theta_0) \cdot l^2 \right] \qquad (2.4)$$

where $\ddot{R}_0(\Theta_0) \sim c_A^2(\Theta_0) \sim \sin^2\Theta_0$ are surface acceleration and Alfven velocity characteristic of a given angle.

In the quasi-static case ($\gamma >> \omega_0$) from (2.4) it follows that

$$\gamma_l^2 = -\left[k \cdot \ddot{R}(\Theta_0) + c_A^2(\Theta_0) \cdot k^2 \right] \qquad (2.5)$$

where $k = \frac{l}{R_0}$. This expression coincides with that obtained previously [5] for the plane interface with parameters corresponding to angle Θ_0.

If we continue to consider l>>1, but m=l-Δ, where Δ~1, then from (2.2) it readily follows that

$$\frac{\partial}{\partial t}\left(R^2 \frac{\partial \sigma_{lm}}{\partial t} \right) = -\sigma_{lm}\left[l \cdot \ddot{R}_0 \cdot R_0 + c_A^2 \cdot l \cdot \Delta \right] \qquad (2.6)$$

As seen from the comparison between (2.3) and (2.5), for such perturbations the stabilizing role of the magnetic field (addend ~c^2_A in 2.5) is noticeably less than that for m=0. In

particular, for $c_A^2 << (\ddot{R}_0 \cdot R_0)$ (2.5) yields an expression for increment γ_{lm} similar to that known [6] for a cylindrical problem with longitudinal magnetic field ($\gamma \sim \sqrt{-m\frac{\ddot{R}_0}{R_0}}$).

3. Numerical calculations

The computations were with code TREK [3]. The scaling was as follows: $p_1 = \frac{H_0^2}{8\pi}$ for pressure, $r_1 = \left(\frac{E}{\frac{4}{3}\pi \cdot p_1}\right)^{\frac{1}{3}}$ for length, $u_1 = \left(\frac{E}{M}\right)^{\frac{1}{2}}$ for velocity, $\frac{r_1}{u_1}$ for time, $\rho_1 = \frac{M}{\frac{4}{3}\pi \cdot r_1^3} = \frac{p_1}{u_1^2}$ for density.

The magnetic pressure on the cloud surface was calculated using two apporoaches:

- Vacuum was assumed outside the cloud; the magnetic field in it was calculated using quasi-stationary approximation [2]. In this case the problem is characterized with an only dimensionless parameter, $r_0' = \frac{r_0}{r_1}$, with the dependence on the parameter disappearing at $r_0' << 1$, $r' \sim 1$.
- "Background" plasma of quite a small density with a magnetic field frozen in it was assumed outside the cloud. In this case the magnetic field changes are calculated using MHD approximation; besides the parameter r_0, the problem is also characterized with parameter $M_A^2 = \frac{u_1^2}{c_A^2}$, where $c_A^2 = \frac{H_0^2}{4\pi \cdot \rho_1}$; options with $M_A^2 << 1$ were considered, in which the dependence on M_A^2 disappears.

At t=0, sphere surface radial velocity perturbations were given, i.e.

$$u(0, \mu, \varphi) = u_0 + u_{lm} \cdot Y_{lm}(\mu, \varphi) \qquad (3.1)$$

was assumed. Here $u_0 = \sqrt{\frac{10}{3}}u_1$ is free expansion velocity of "cold" spherical cloud having a linear velocity profile and constant density. $u_{lm} = \alpha \cdot u_0$ was assumed.

Four problems were calculated.

In the first of them, α=0 (unperturbed surface) was assumed. The results of the calculation are plotted in Figs. 1 through 3 ($M_A^2 = 0.05$, $r_0' = 1$, t=0.25;2.0 and 3, respectively). The expansion pattern qualitatively agrees with relation (1.1): the plasma spreading in the longitudinal direction and oscillating motion (with period ~π) in the transversal direction occur.

In the second problem, "meridional" velocity perturbations were given at the initial time: α=0.1, l=12, m=0, the other parameters are the same as in problem 1. The calculation results are illustrated in Figs. 4 and 5.

In this case the ratio of the first addend to the second in (2.3) is $\sim \frac{u_0^2}{c_A^2 \cdot l} << 1$ (here c_A^2 is estimated by plasma cloud density $\rho_0 \sim 1$ at t≤1), hence, a significant perturbation growth stabilization can be expected thanks to the magnetic field.

This assumption is confirmed by comparison between the results of the calculation and similar calculation 3, which differs from the former in the fact that instead of "magnetic" pressure, "thermal" pressure of the same magnitude is given in the "external" plasma. In this case the cloud dynamics will remain about the same as in problem 2, however, the perturbation growth depends only on the first addend in (2.3), i.e. is significantly faster than in problem 2.

Problem 4 differs from problem 2 in given m=l=12, i.e. the initial perturbation was localized near "equator" and its amplitude depended on azimuthal angle φ. Its solution results appear in Figs. 8 and 9. In this case, according to (2.6), we can expect that increment $\gamma^2>0$ (unsteady conditions) and that the cloud surface will be perturbed, in the main, across azimuth. These assumptions agree with the calculated data presented in Figs. 8 and 9.

Conclusion

More extensive computational series with varying parameters r_0, M_A^2, l, m, as well as setting "random" surface perturbations are being planned.

The authors are thankful to T. Yu. Odintsova for the performed numerical computations and assistance in the paper execution.

References

1. Raizer Yu.P. "On plasma cloud expansion into a vacuum magnetic field". RMTF, 1967, No.5
2. J.W.Poukey "Expansion of a Plasma Shell into a Vacuum Magnetic Field", Phys FI, 1969, vol12, No.7, pp 1452
3. Bakhrakh S.M., Gubkov E.V., Zhmailo V.A., Terekhin V.A. "Plasma cloud expansion in homogeneous magnetic field". RMTF, 1974, No.4, pp 146-150
4. Yanilkin Yu.V., Tarasov V.I., Stadnik A.L. "Program System "TREK" for Numerical Simulation of 3D Multicomponent Medium Flows". Proceedings of Workshop "New models and Numerical Codes for Shock Processes in Condensed Media", Oxford, 1997, pp 413-422
5. Kruskal M., Schwarzschild M., "Some instabilities of completely ionized plasma", Proc. of the Roy. Soc., vol223, p 348-361, 1954
6. Harris E.G. "Rayleigh-Taylor Instabilities of a Collapsing Cylindrical Shell in a Magnetic Field", Phys FI, 1962, vol5, No.9, pp 1057-1062

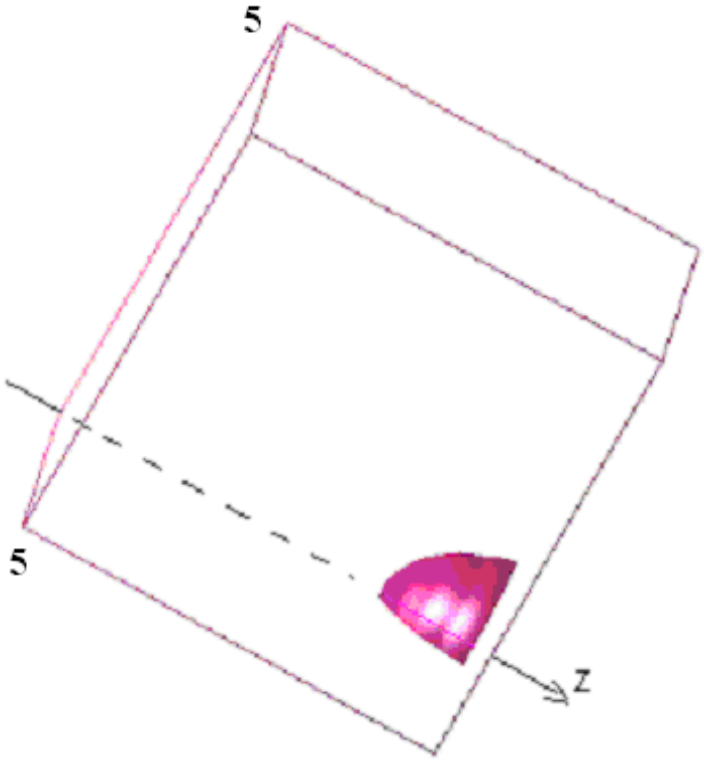

fig1. Plasma cloud expansion in the magnetic field (unperturbed surface), t=0.25, $M_A^2 = 0.05$

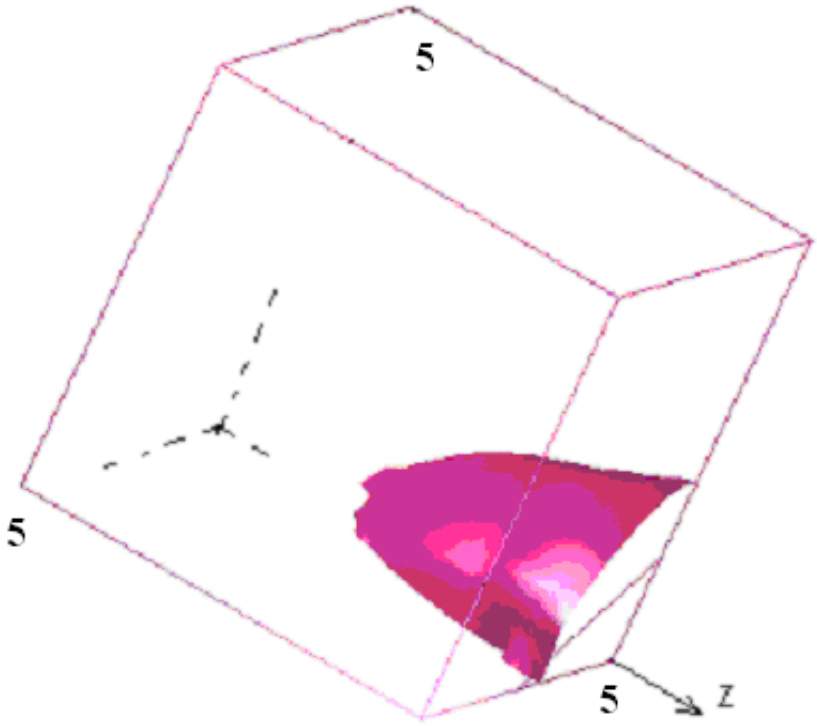

fig2. Plasma cloud expansion in the magnetic field (unperturbed surface), t=2.0, $M_A^2 = 0.05$

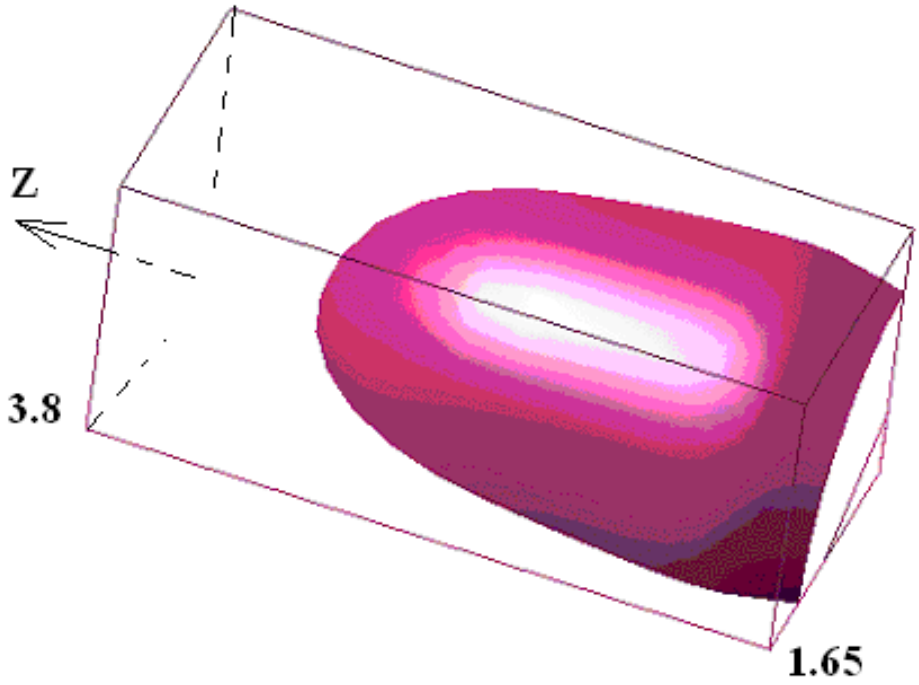

fig3. Plasma cloud expansion in the magnetic field (unperturbed surface), t=3.0, $M_A^2 = 0.05$

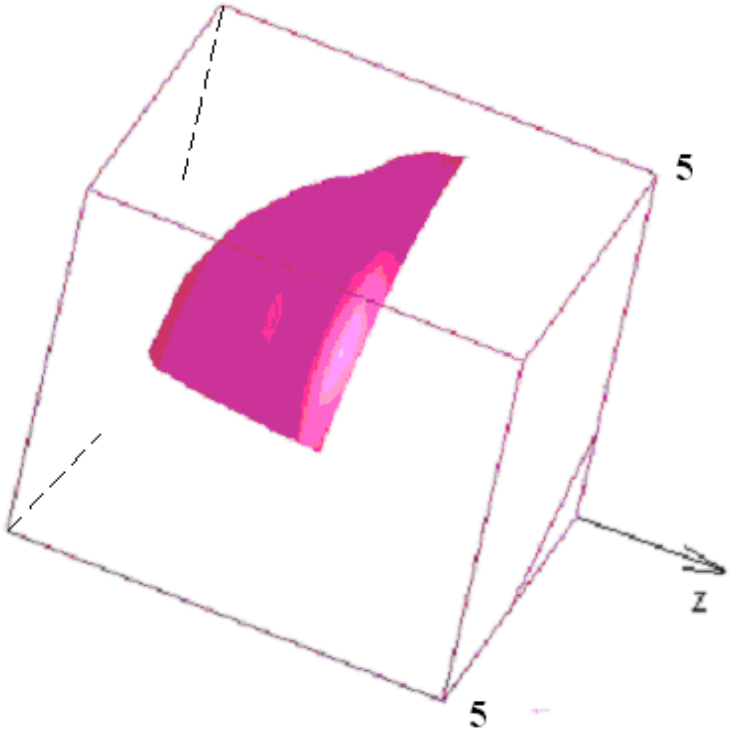

fig4. Plasma cloud expansion in the magnetic field (meridianal perturbations, l=12, m=0, $M_A^2 = 0.05$), t=0.25

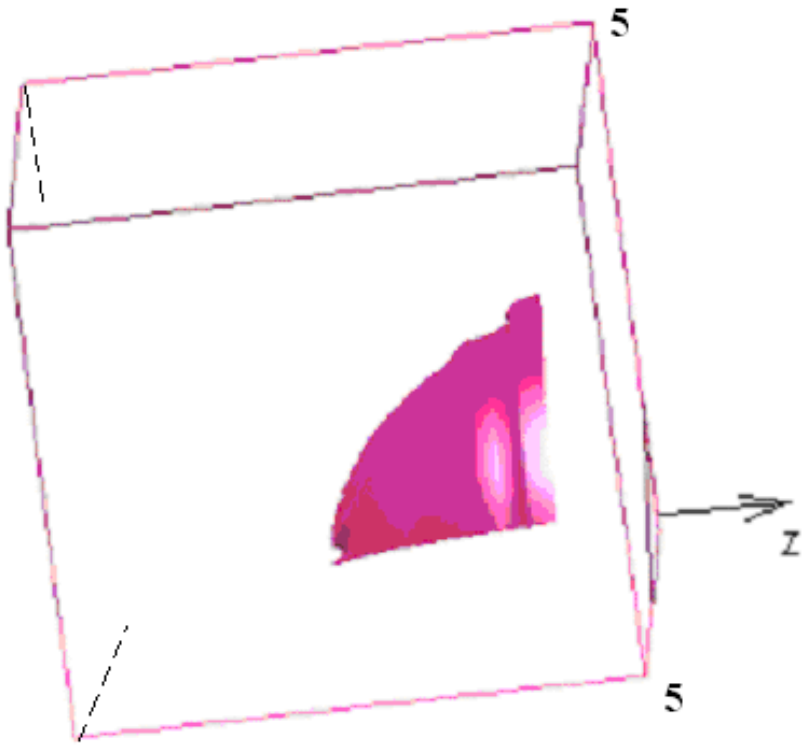

fig5. Plasma cloud expansion in the magnetic field (meridianal perturbations, l=12, m=0, $M_A^2 = 0.05$), t=0.5

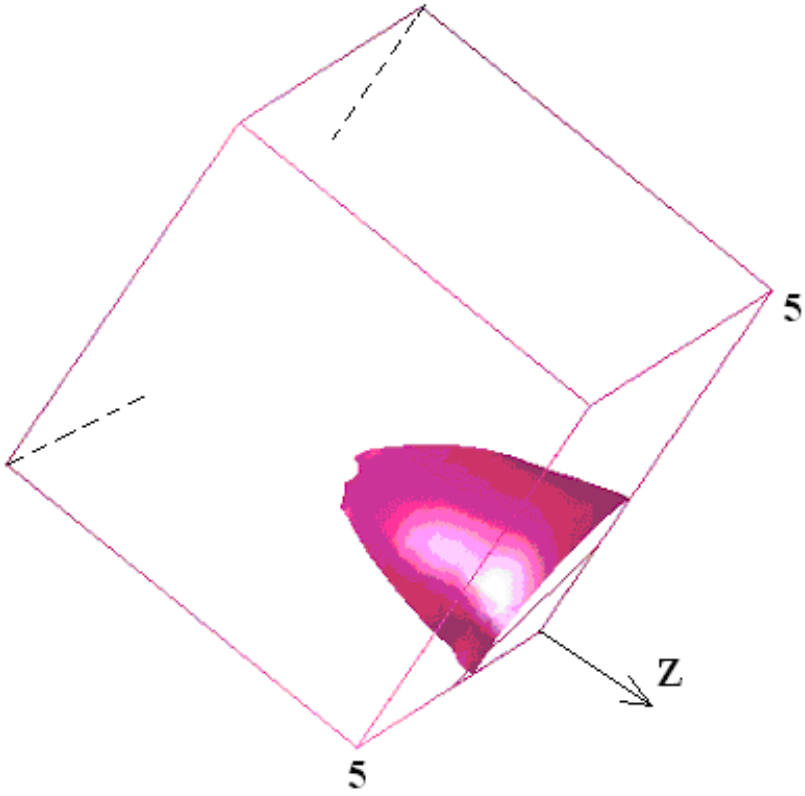

fig6. Plasma cloud expansion against termal pressure (meridianal perturbations), $M_{th}^2 = 0.05$, P_m=0, l=12, m=0, t=0.5

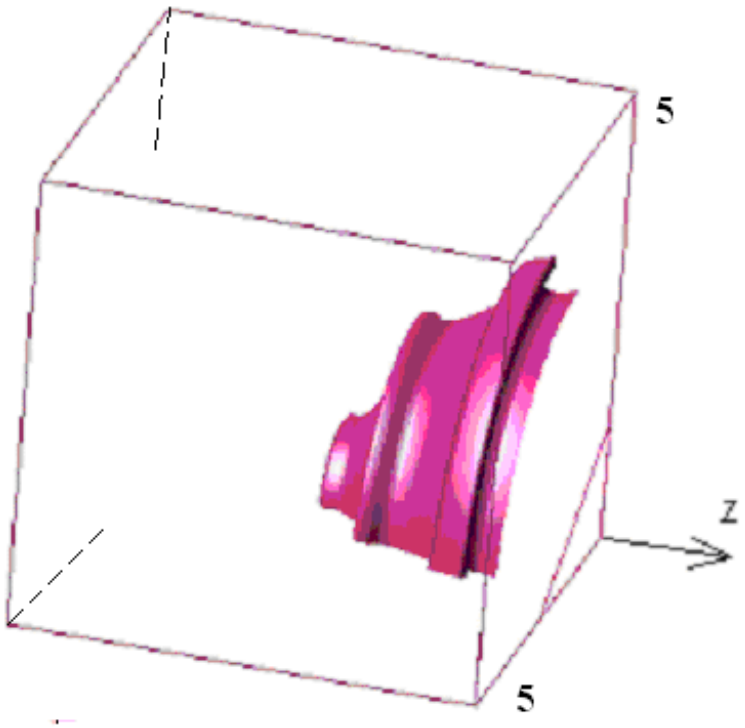

fig7. Plasma cloud expansion against termal pressure (meridianal perturbations), $M_{th}^2 = 0.05$, P_m=0, l=12, m=0, t=3.0

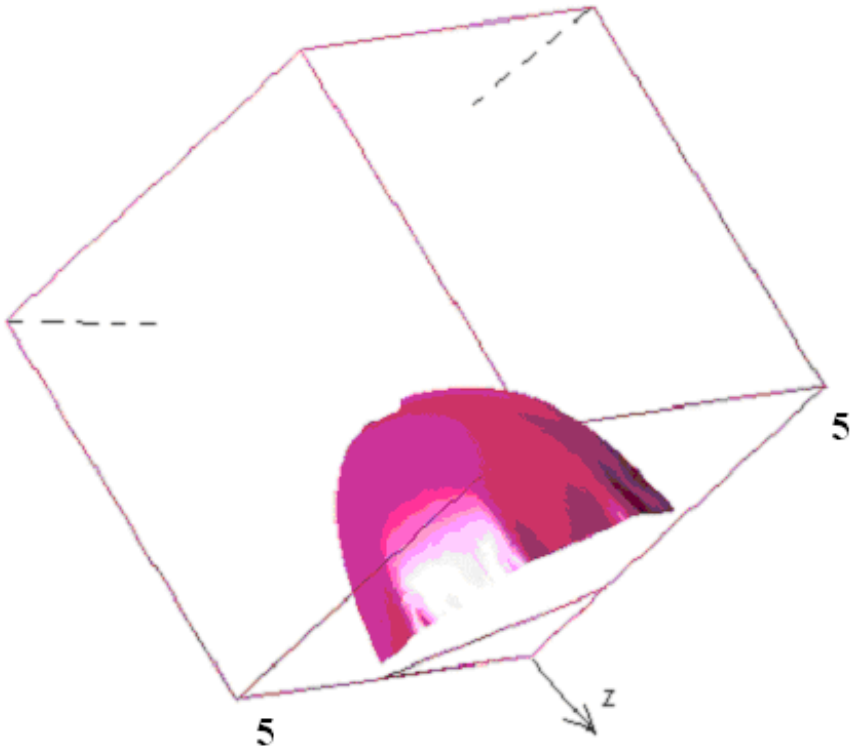

fig8. Plasma cloud expansion in the magnetic field (perturbation l=12, m=12, $M_A^2 = 0.05$), t=0.4

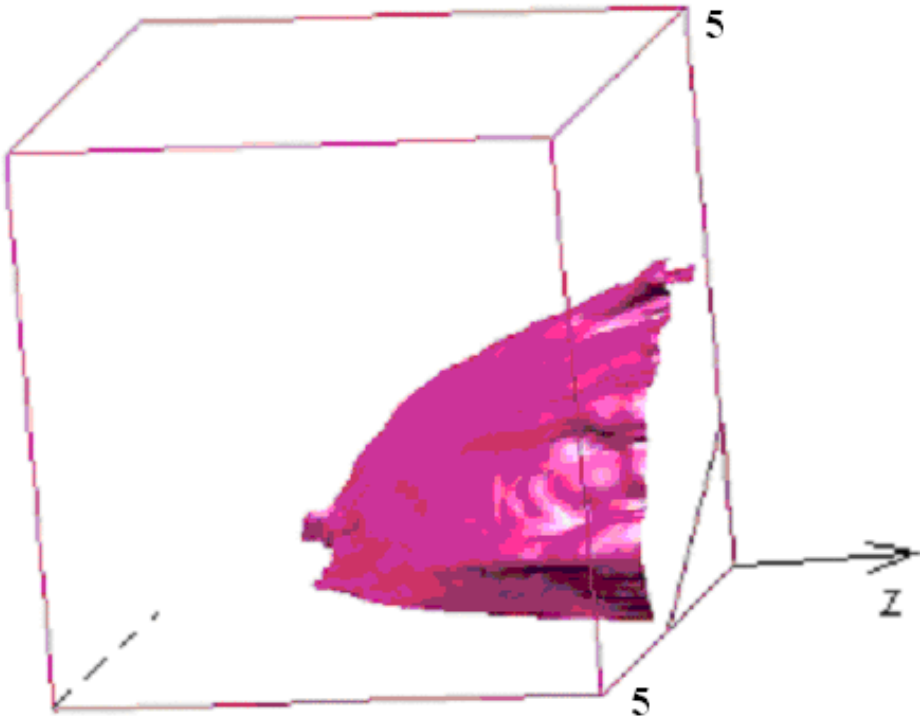

fig9. Plasma cloud expansion in the magnetic field (perturbation l=12, m=12, $M_A^2 = 0.05$), t=1.

Code-to-Code Comparisons for the Problem of Shock Acceleration of a Diffuse Dense Gaseous Cylinder

J.A. Greenough[1], W.J. Rider[2], C. Zoldi[2], J.R. Kamm[2]

8th IWPCTM
December 9-14, 2001
Pasadena, CA

[1]Lawrence Livermore National Laboratory, [2]Los Alamos National Laboratory

Motivation

- Focus on computational issues as cause for disagreement between Rage and ongoing LANL shock/cylinder experiments:
    - Large scale (dipole aspect ratio) differences
    - Quantitative velocity measurements (PIV)
- Remove experimental uncertainities/unknowns:
    - Use well-defined initial conditions
    - Analysis and comparisons based on computational data
    - Use different codes for comparison

Motivation

- Use this research to also examine:
    - What does convergence mean for evolving flows & instabilities?
    - What are the resolution requirements for “fully-resolved” calculations of this class of flow?
    - What quality of results can we obtain from low-order codes (second-order) in this regime?
- Our guide will be existing & on-going experiments

Experimental Configuration

- "Pour" SF_6 in the shocktube as a laminar stream

- LANL experiments seed gas with glycol/water droplets (original CalTech experiments used biacetyl)

- Laser sheet illumination with multiple frames per experiment

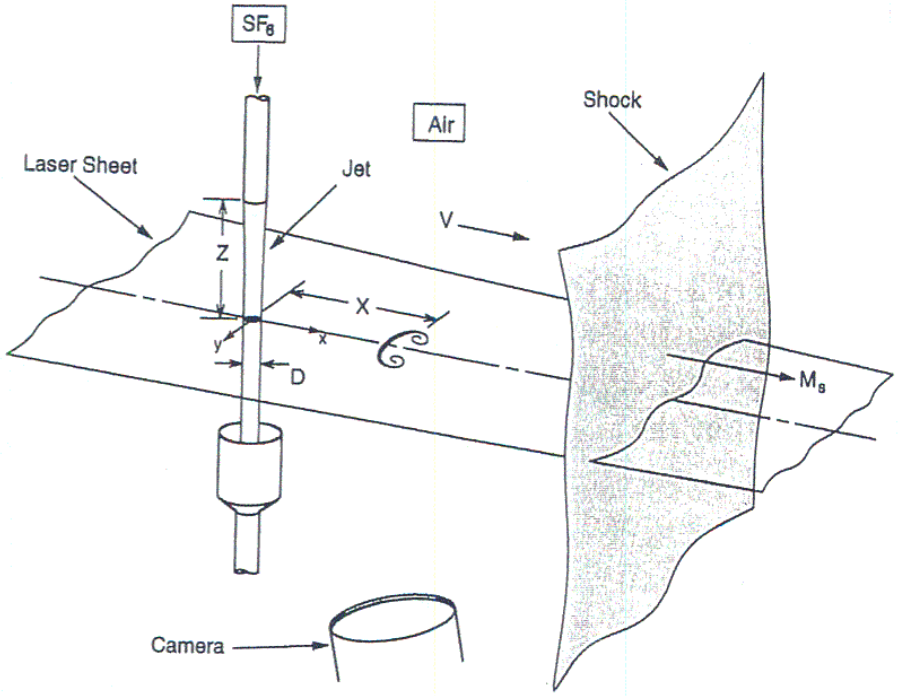

FIG. 1. Drawing of the jet/PLIF configuration.

Comparison Between Experiment and Simulation

50 μs 190 μs 330 μs 470 μs 610 μs 750 μs

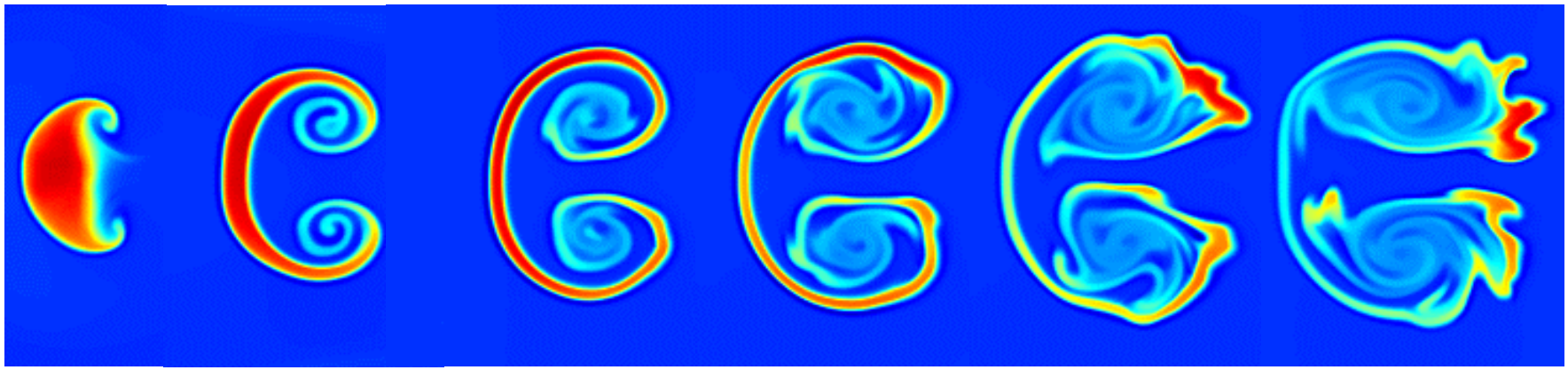

Quantitative Measurements

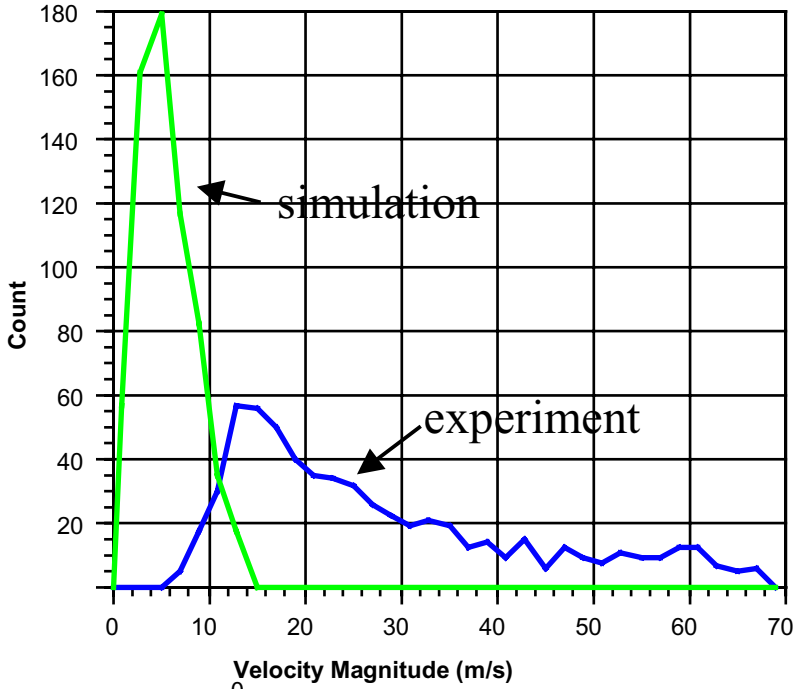

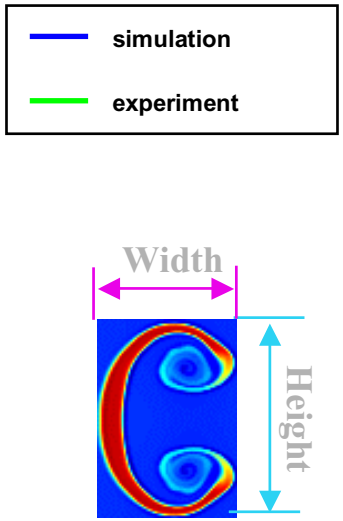

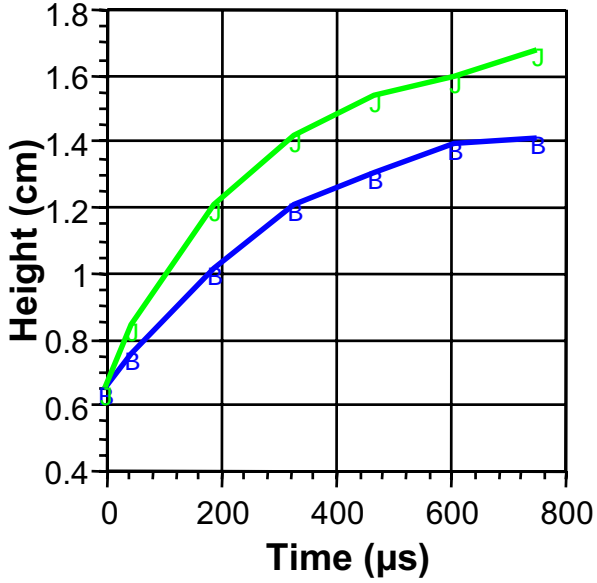

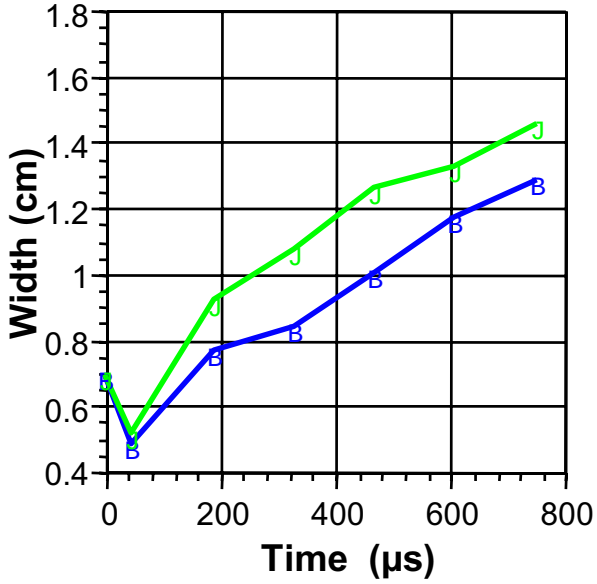

Simulation has larger velocities and smaller lengths compared to the experimental data.

Codes

- Rage (LANL; Gittings et al.)
  - Eulerian (Lagrange + Remap); directionally split
  - Unstructured AMR (point-wise adaptivity)
  - Multi-component formulation (mass fraction); one energy equation
  - Euler equations (inviscid)

- Cuervo (LANL; Rider & Kamm)
  - Eulerian (direct); directionally and temporally unsplit
  - Rectangular uniform grids
  - single-component formulation (gamma blending); one energy equation
  - Navier-Stokes equations (constant properties)

- Raptor (LLNL; Greenough et al.)
  - Eulerian (direct); directionally split
  - Block-structured AMR (patch-based adaptivity)
  - VOF formulation (volume fraction); N energy equations
  - Navier-Stokes equations (Chapman-Enskog, Sutherland's formula)

Model Problem

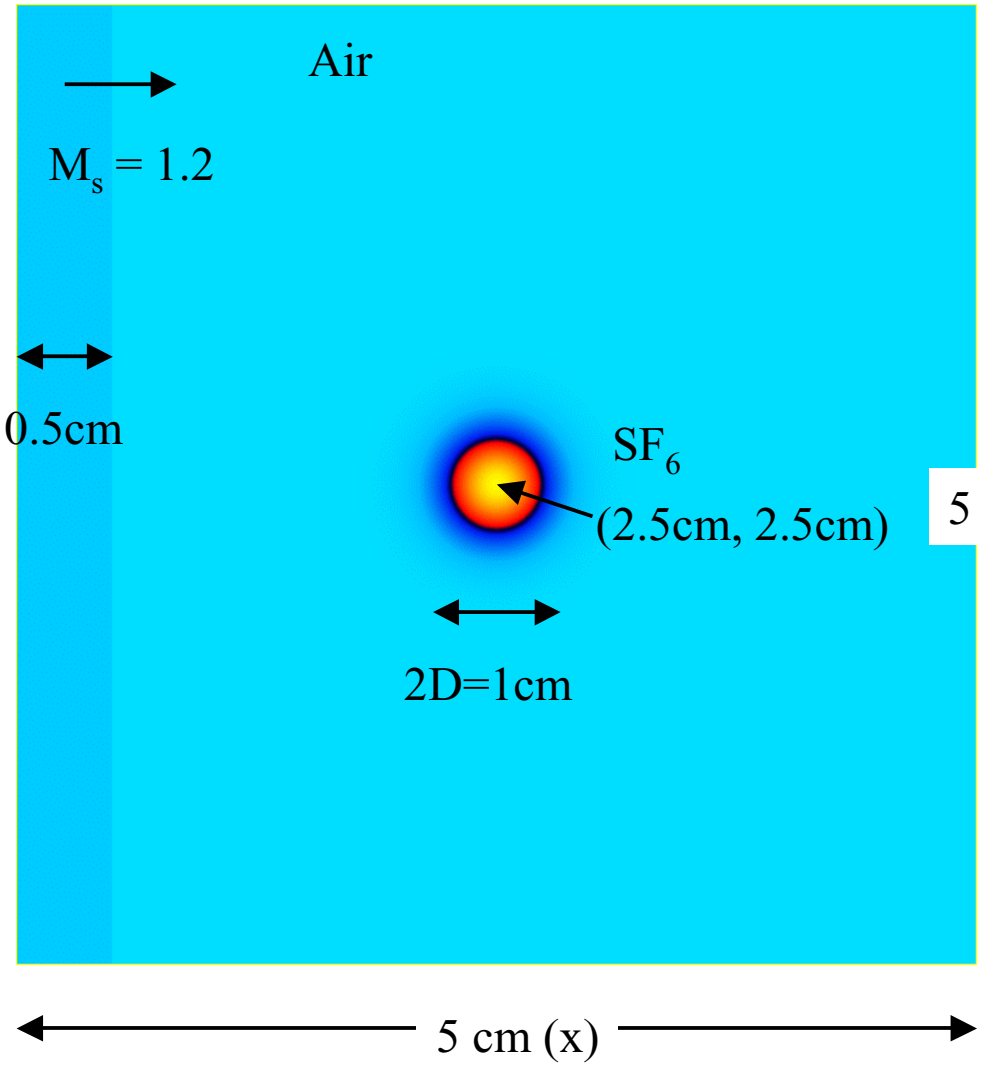

- Inflow/outflow B.C.'s
- Moving frame with post-interaction velocity near zero
- $\rho_{SF_6} = \rho_0 \exp(-r^2/\delta)$, $r=\sqrt{(x-x_0)^2+(y-y_0)^2}$, $\delta=0.0902$; D=0.5cm
- LANL pre-shock conditions
- t_{final} = 0.8 msec
- Δx = 125µm, 62.5µm, 31.25µm, 15.625µm, 7.8125µm

Integral Lengths/Flow

125 micron zoning, t = 0.8 msec

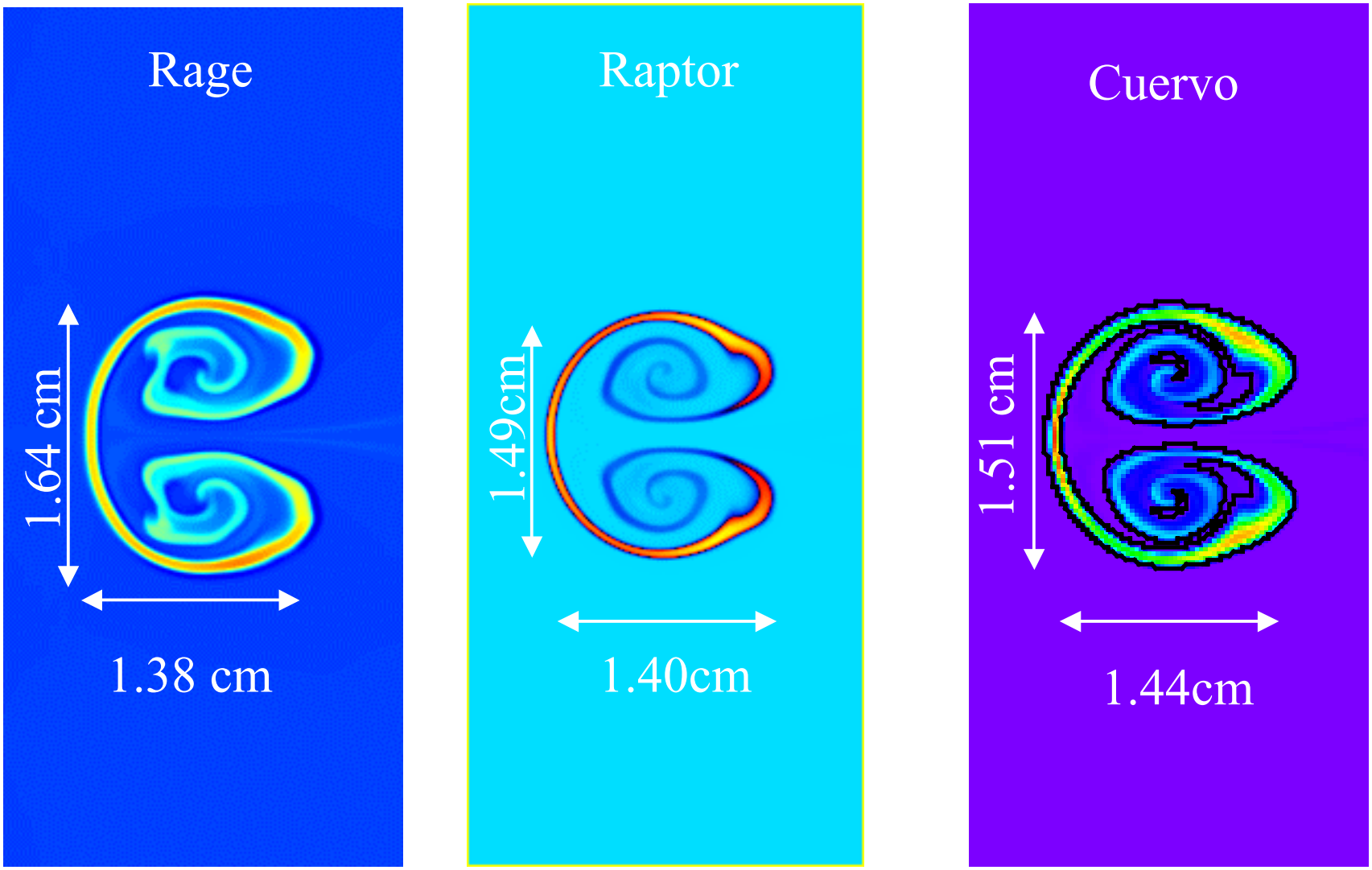

Integral Lengths/Flow

62.5 micron zoning, t = 0.8 msec

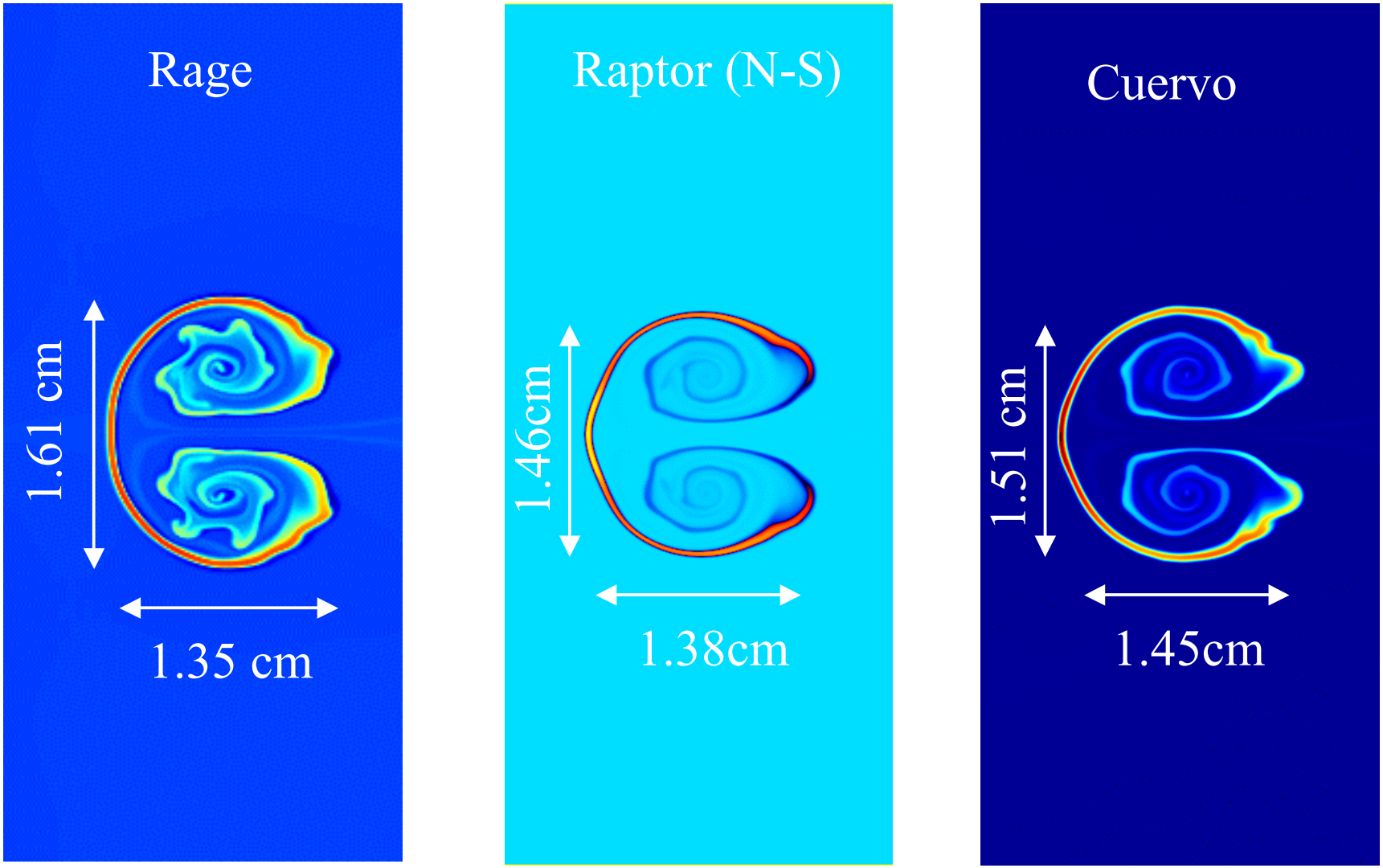

Integral Lengths/Flow

31.25 micron zoning, t = 0.8 msec

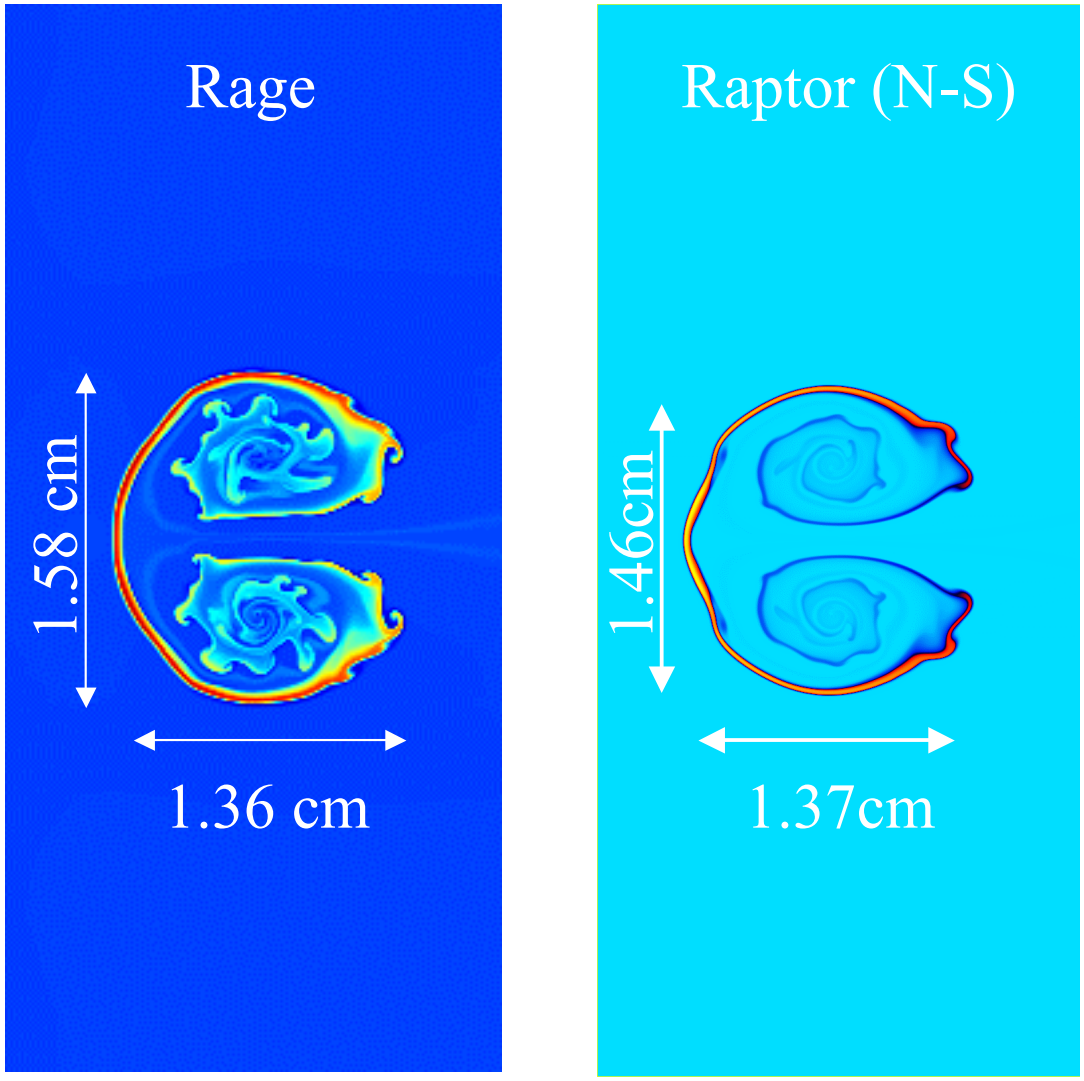

Integral Lengths/Flow

15.125 micron zoning

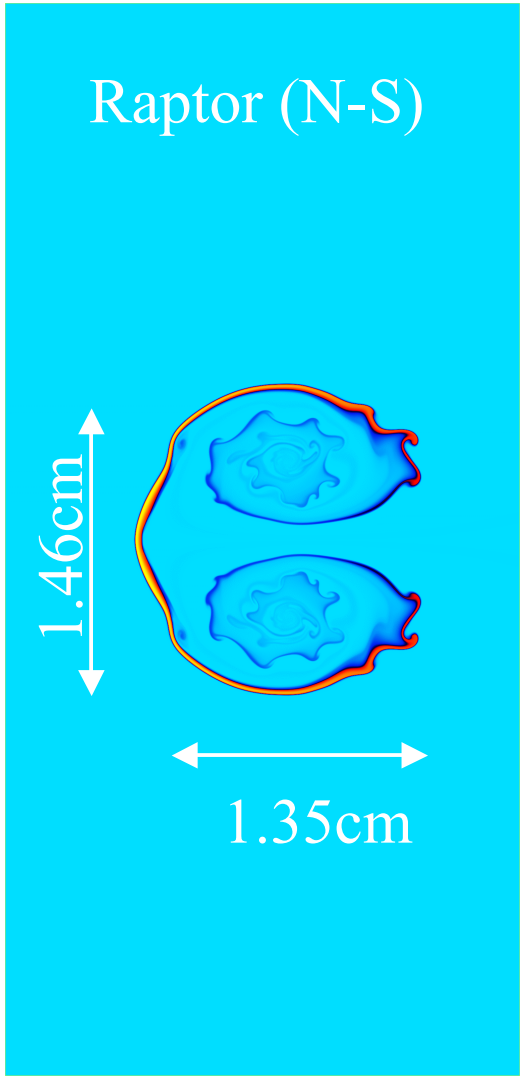

7.8125 micron zoning

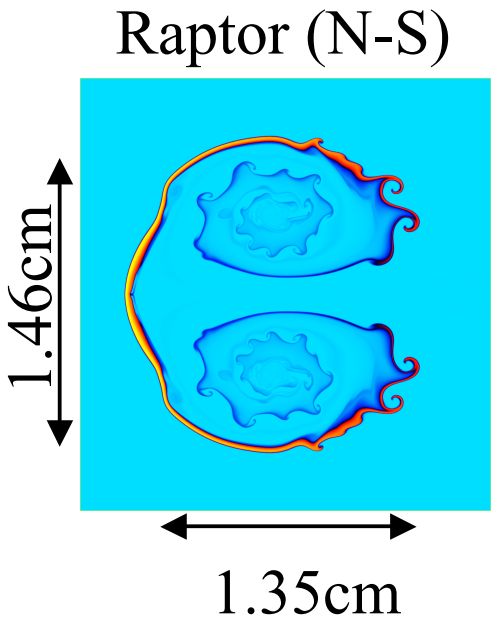

3.90625 micron zoning

Integral Lengths - Summary

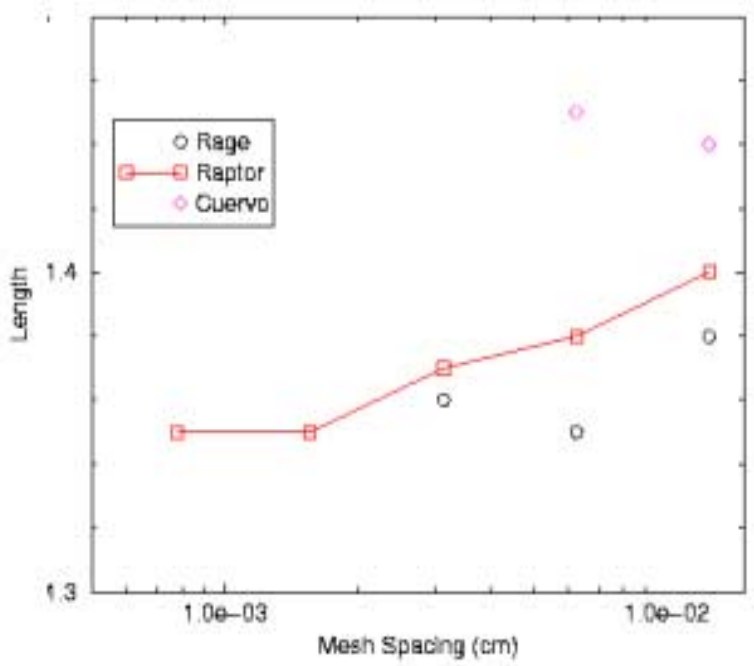

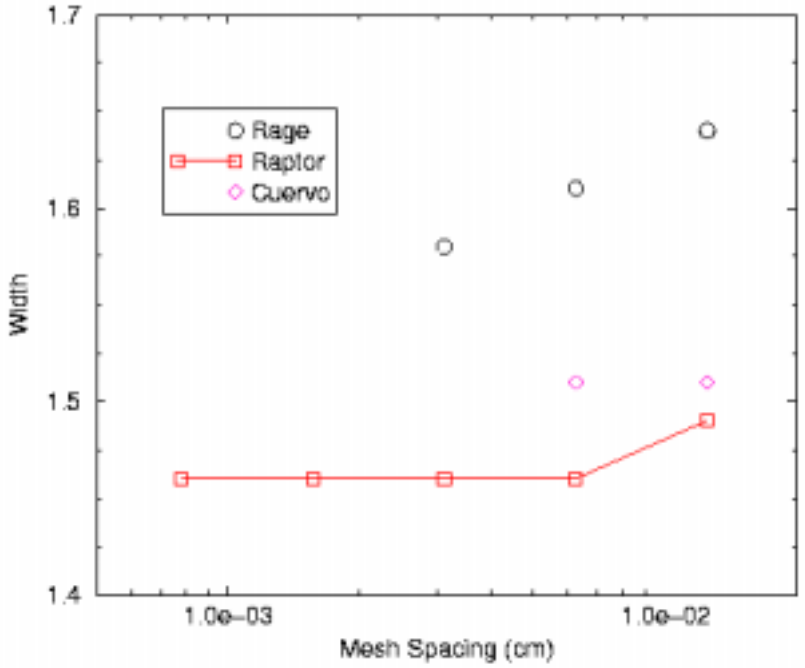

Convergence Rates

Cuervo ~ $\Delta x^{1.28}$

Raptor ~ $\Delta x^{1.58}$

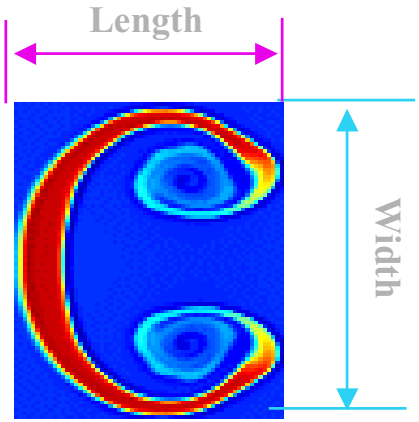

Convergence Rates

Cuervo ~ $\Delta x^{0.74}$

Raptor ~ $\Delta x^{0.28}$

Mixing Fraction

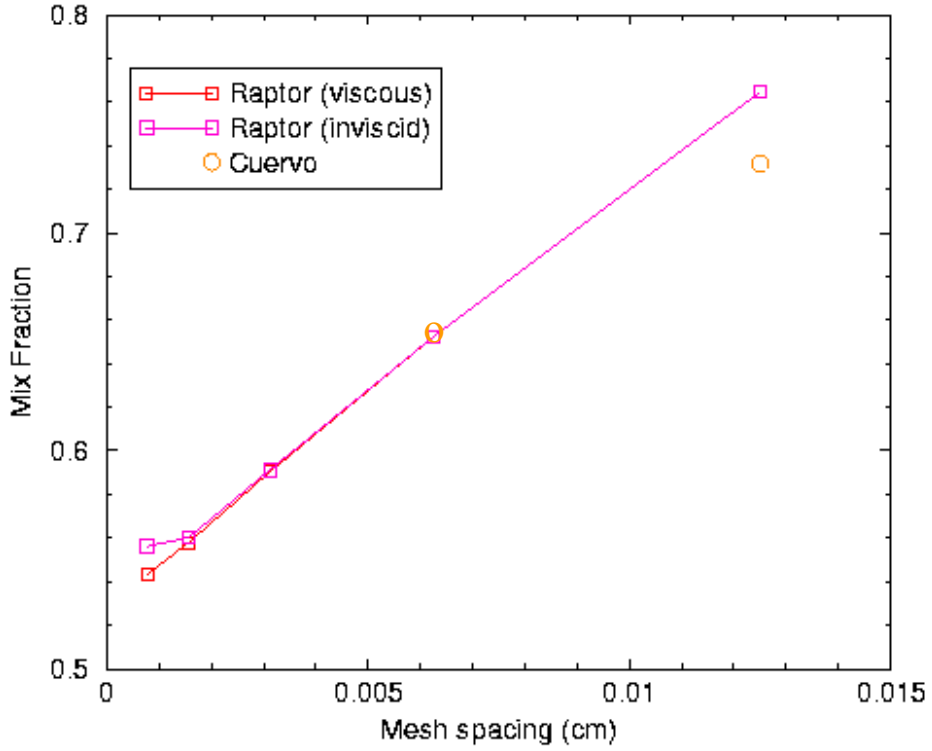

$$\theta = \frac{\Sigma\, f_{SF_6}\,(1-f_{SF_6})\,\Delta x\,\Delta y}{(\Sigma\, f_{SF_6}\,\Delta x\,\Delta y)\,(\Sigma\,(1-f_{SF_6})\,\Delta x\,\Delta y)}$$

Convergence Rates

Cuervo ~ $\Delta x^{0.28}$

Raptor ~ $\Delta x^{1.02}$

Vortex Spacing

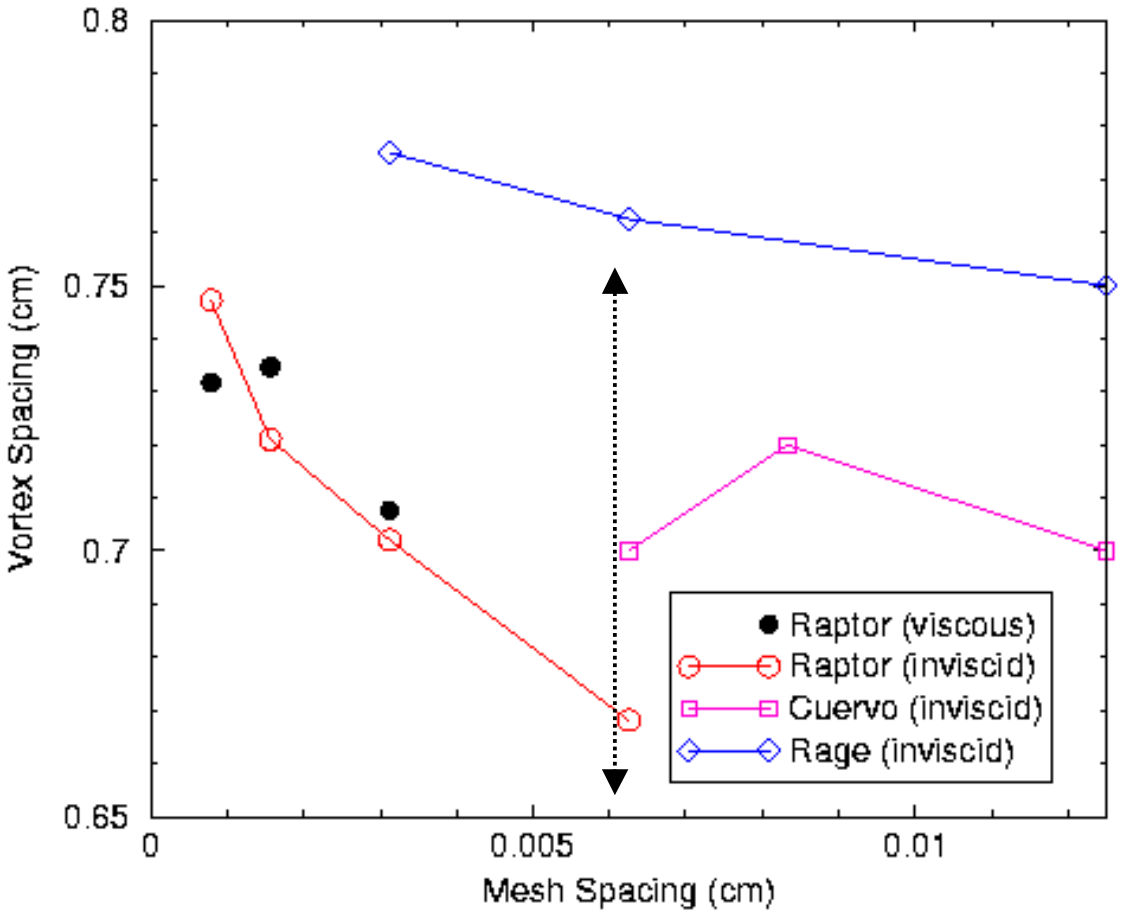

• Experimental data range shown for comparison

• cf. J.W. Jacobs, Phys. Fluids 1993; M=1.095, D=0.43

Convergence Rates

Raptor ~ $\Delta x^{0.87}$

Circulation Budget

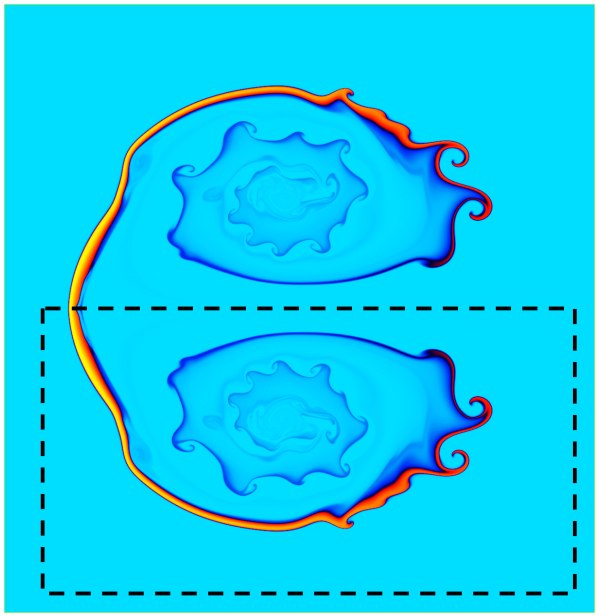

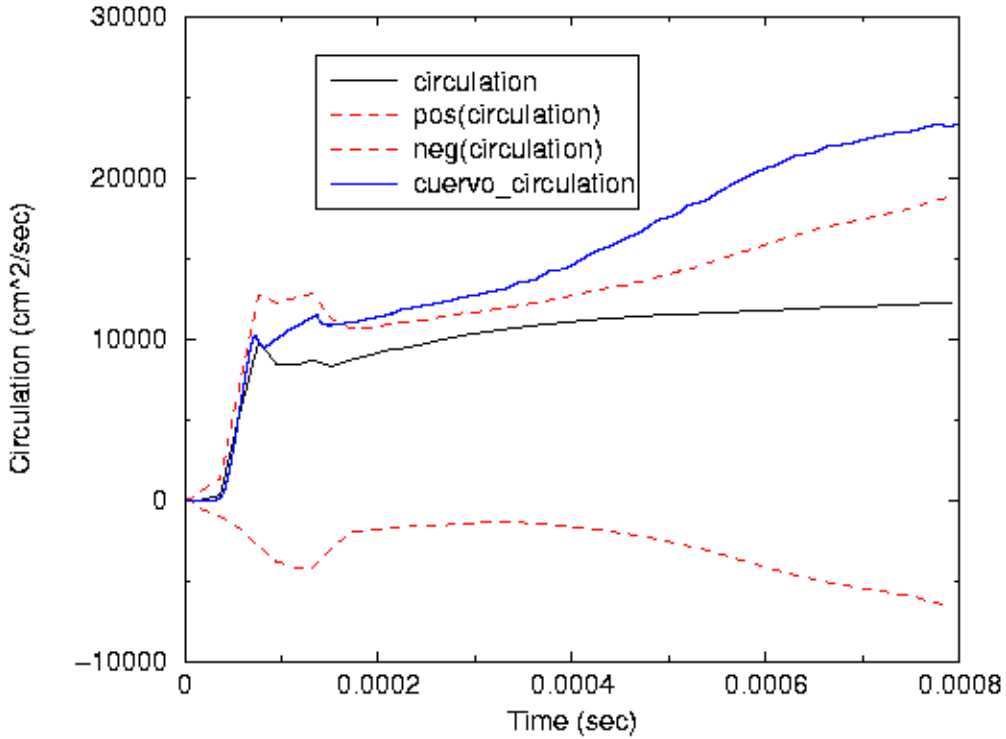

- Deposition by shock (positive)
- Counter-sign production (baroclinic)
- Late-time equilibration

Flow Dynamics

- Early time
  - Vortex blob deposition (shock-passage time ~ 30 μsec)
- Intermediate time
  - Blob dipole transformation
  - Counter-sign production
- Later time
  - Dipole configuration established
  - Balanced net vorticity (i.e. $\Gamma \sim$ constant)

Flow Dynamics - Density

t = .08msec

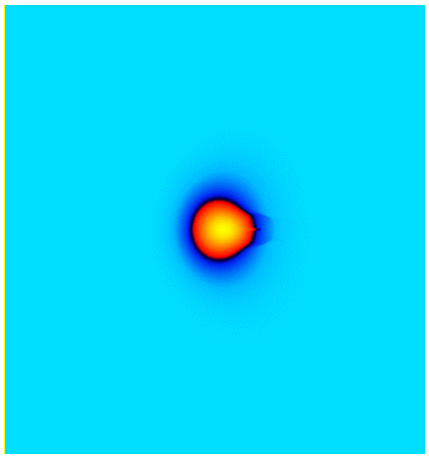

t = .12msec

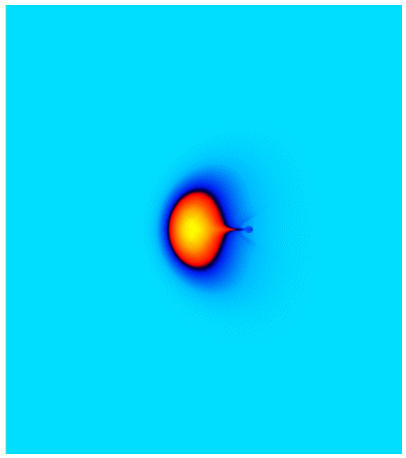

t = .22msec

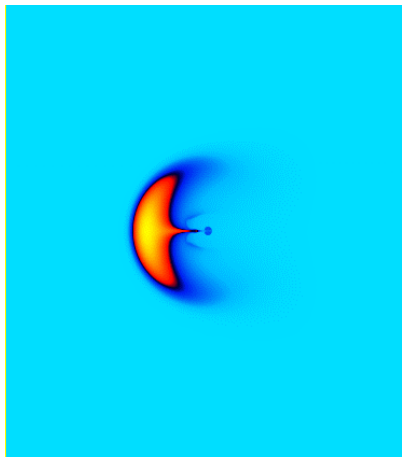

t = .35msec

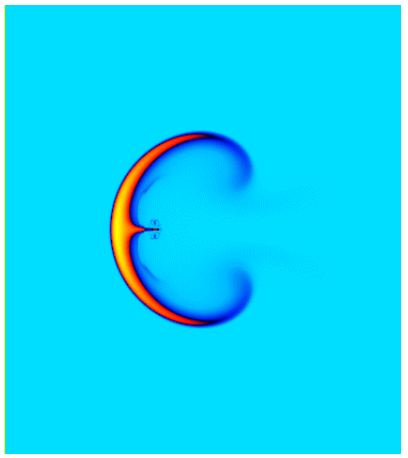

t = .47msec

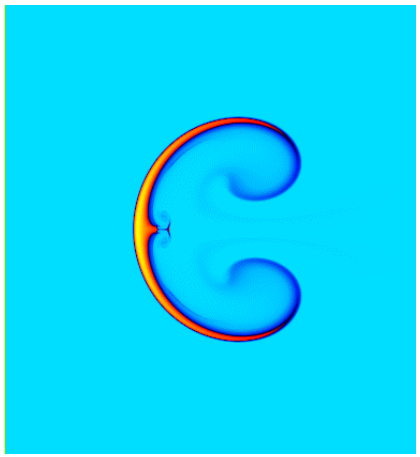

t = .58msec

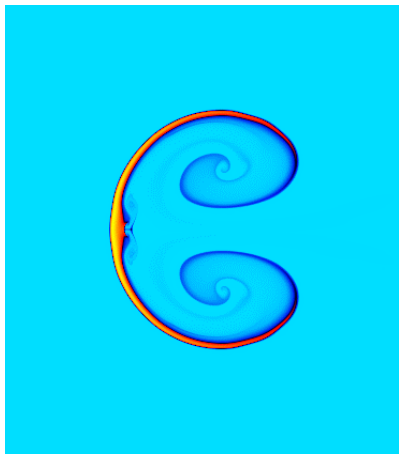

t = .70msec

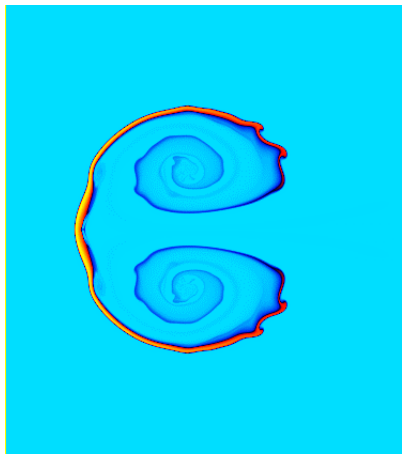

t = . 82msec

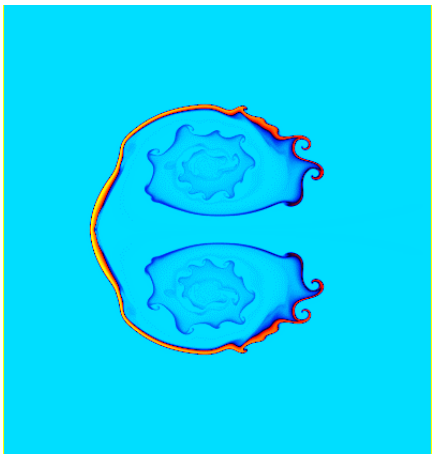

Flow Dynamics - Vorticity

t = .08msec

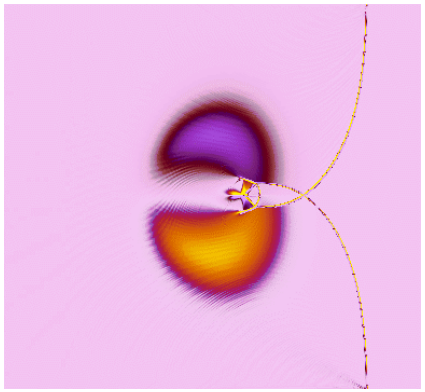

t = .12msec

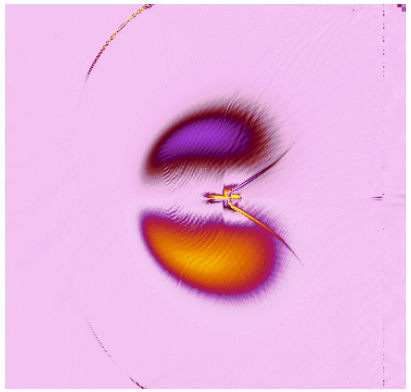

t = .22msec

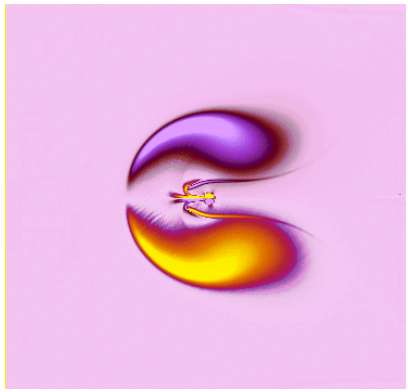

t = .35msec

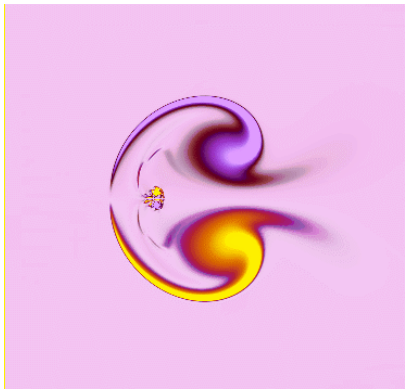

t = .47msec

t = .58msec

t = .70msec

t = . 82msec

Flow Dynamics – Baroclinic Generation

t = .08msec

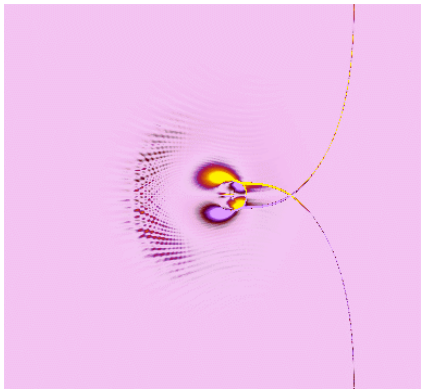

t = .12msec

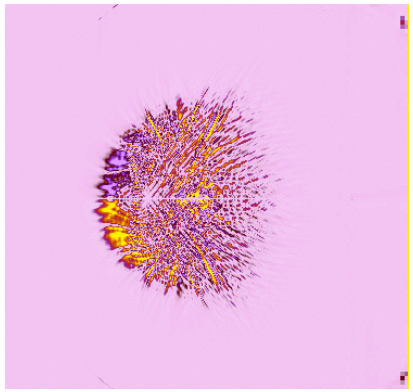

t = .22msec

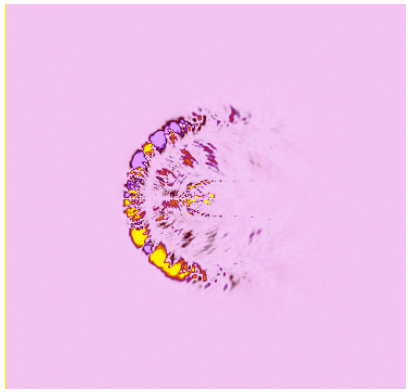

t = .35msec

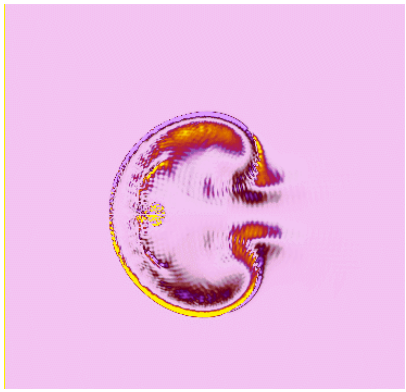

t = .47msec

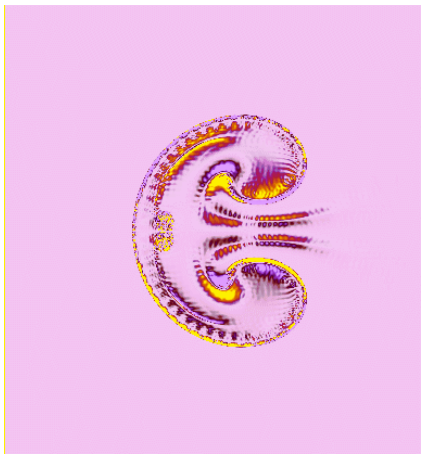

t = .58msec

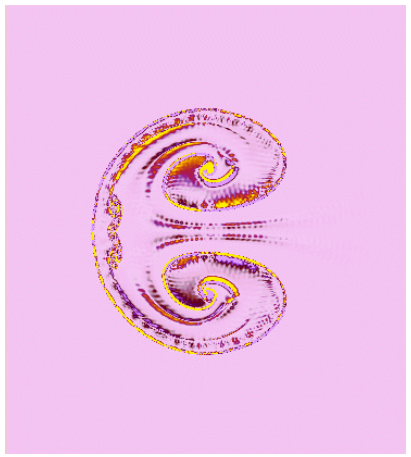

t = .70msec

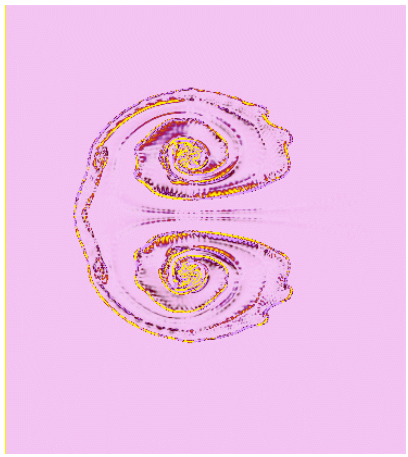

t = . 82msec

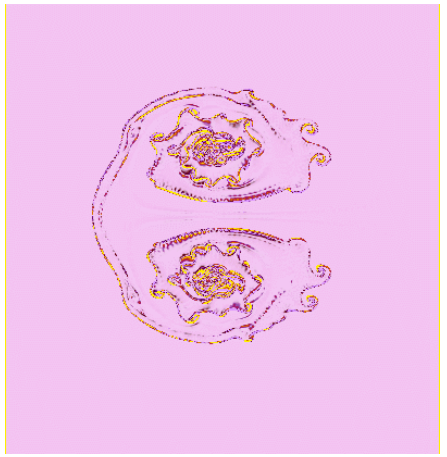

Raptor Summary

31.25µm, 15.625µm, 7.8125µm

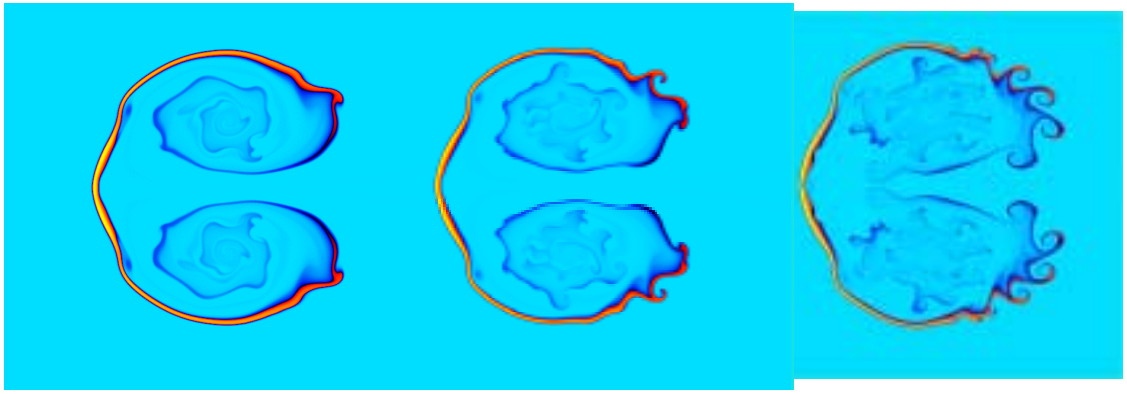

Increasing Resolution

Inviscid

Increasing Resolution

Viscous

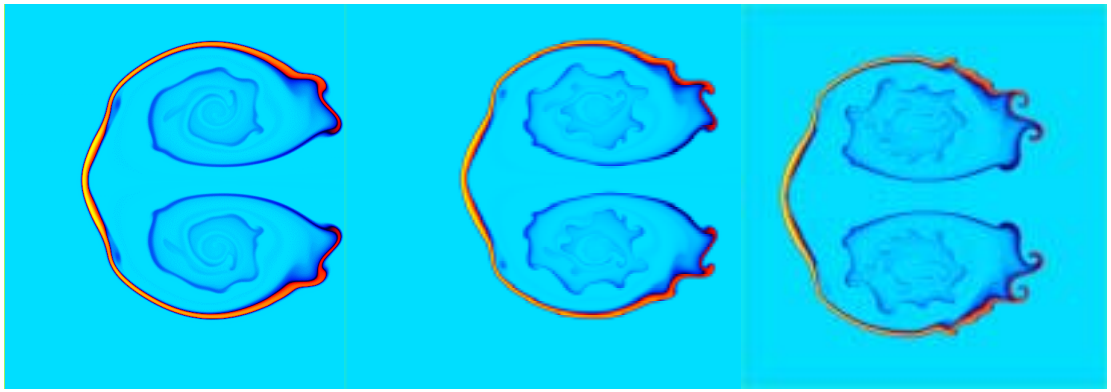

NEW Raptor Summary
No prelax, viscosity fix

31.25µm, 15.625µm, 7.8125µm

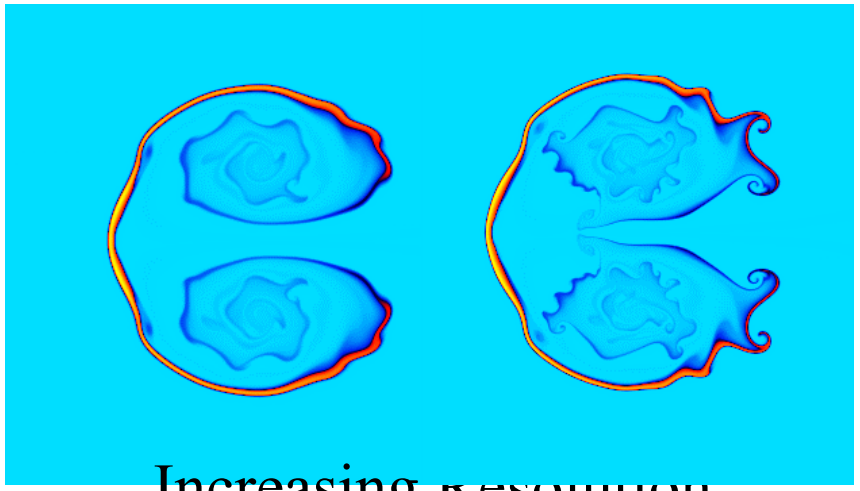

Increasing Resolution

Inviscid

Increasing Resolution

Viscous

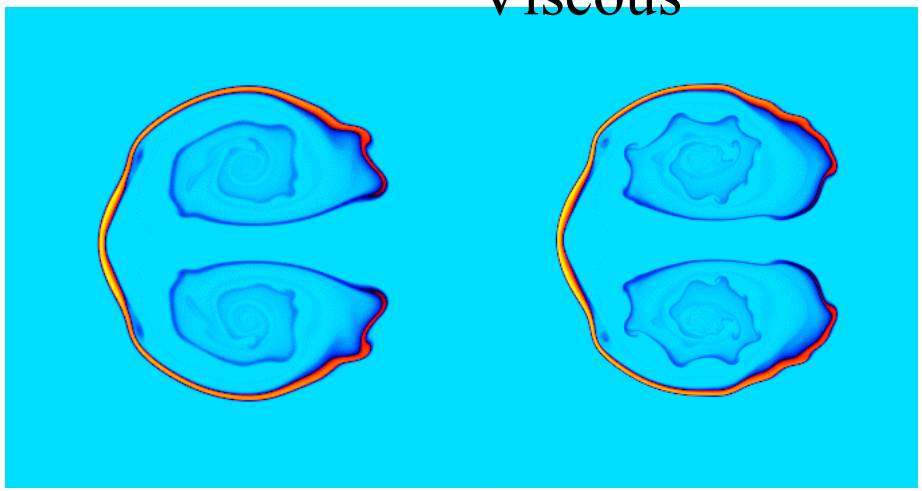

Lengthscale estimates

- Using order of magnitude considerations (Tennekes and Lumley)
  - $U \approx 2{,}000$ cm/sec, $\nu \approx 0.1$ cm^2/sec, $L = 0.1$ cm Re = 2,000
  - $\eta/L \sim Re^{-0.75}$ $\eta \sim 3$ μm (Kolmgorov scale)
  - $\lambda/L \sim Re^{-0.5}$ $\lambda \sim 90$ μm (Taylor scale)

- At 7.8125 μm resolution, we have about 12 points/λ resolvable

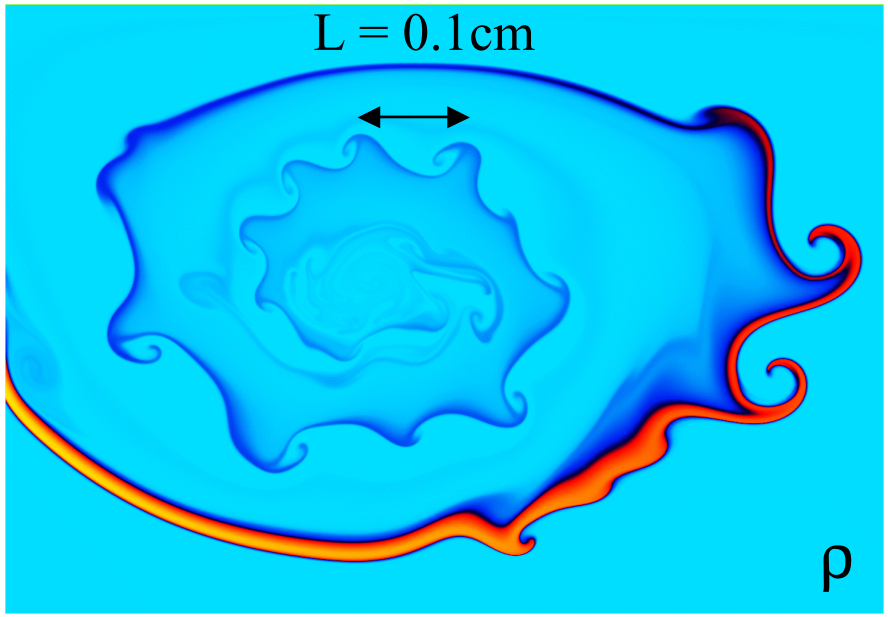

Conclusions

- Have we demonstrated convergence?
  - Maybe. Some diagnostics show convergence while others do not.
  - Include addition diagnostics (statistical, wavelet analysis).

- Have demonstrated what resolutions and physics are required for resolved calculations.

- Directly compute mm wavelength vortices. This is a robust feature present in analogous flow (Jacobs' Diffuse Interface R-M).

- Rage calculations appear to be the outlier; much more structure and different integral measurements. Vorticity?

M=1.2 Diffuse Interface R-M

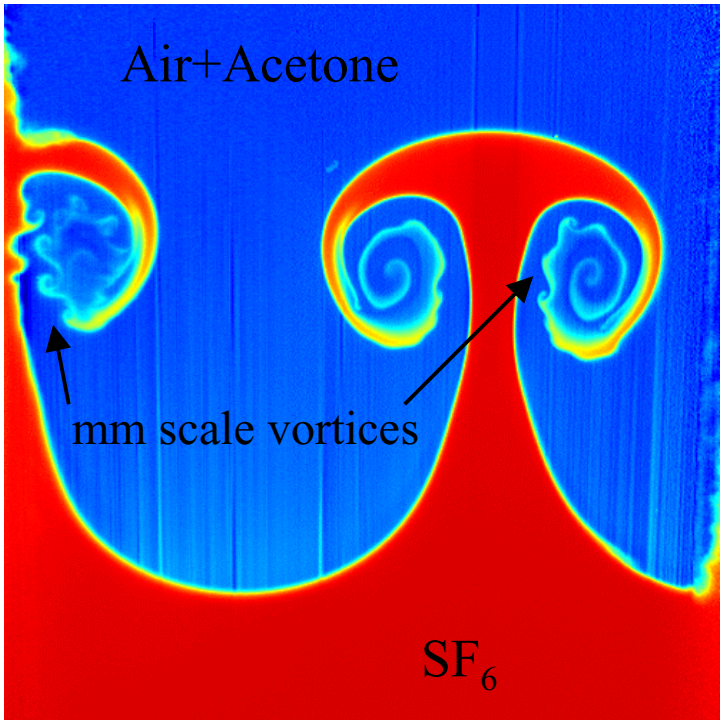

Courtesy of Prof. J.W. Jacobs

NEEDS

- High(er) resolution experimental imaging
    - PLIF visualization. LANL facility appears to generate a "more stable" evolving flow better pictures. Isolate mm-scale vortices
- More direct measurements
    - Mixing measurements (Rayleigh scattering). Complementary to Helium jet work by J. Budzinski.
- More computing resources (never have enough) would allow definitive simulations.
    - e.g. highest resolution run took ~ 70 hrs wall clock on 128 CPU's of an SP-3; AMR required 4.7 Mzones compared to 43 Mzones single grid.

LANL Experimental Activity

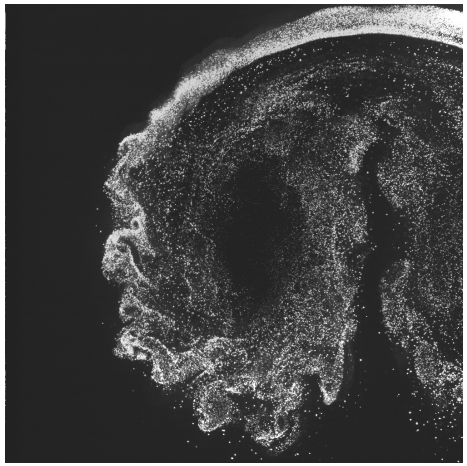

- No outer flow seeding

Varying the seeding densities & light intensity

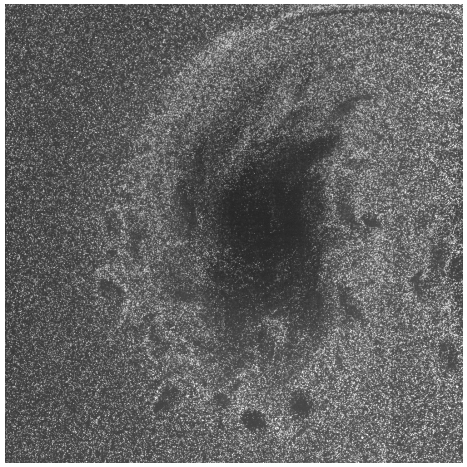

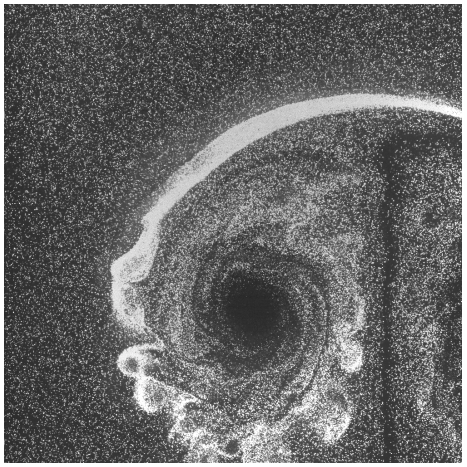

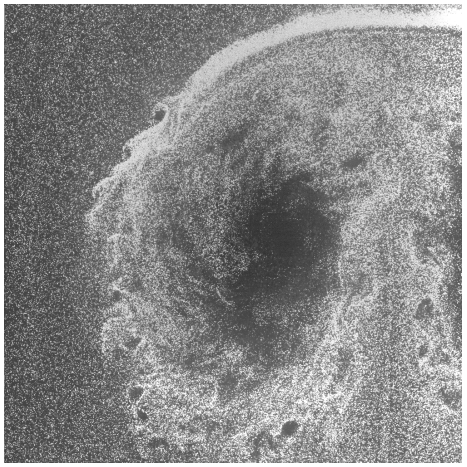

Images courtesy C. Tomkins, LANL, DX-3

Implementation of a Turbulent Mix Model in a 2D ALE Code

B Grieves

AWE

Abstract

The addition of a turbulent mix model to a two dimensional finite element ALE hydrocode, CORVUS, is discussed. Use is made of the existing mixed-cell data structure package to facilitate the inclusion of the model.

This first stage of the model is based on the multiphase flow equations, and is a simplified form of the model implemented by Youngs (see paper at this workshop) in a 2D eulerian code. This is applicable to simple Rayleigh-Taylor and Richtmyer-Meshkov instabilities and some results are presented.

A simple buoyancy-drag model is used to calculate the early stages of the instability growth at internal nodes, and this is used to initialise the turbulent mix model calculation.

2D ALE Code, CORVUS

Corvus is a 2D finite element arbitrary lagrangian eulerian (ALE) hydrocode. It uses a staggered quadrilateral grid which is explicitly integrated using bilinear finite elements; pressure and internal energy are cell centred and the velocity is node centred. Each region is logically quadrilateral and ALE works across adjacent regions. The time step is split into a lagrangian and rezone phase.

Corvus uses a predictor corrector scheme for time discretisation and the rezone is accomplished using a second order van leer scheme. This gives a nominal second order accuracy both spatially and temporally. Corvus also incorporates strength, slide, friction, void opening and void closure.

The purpose of this work is to add a mixing phase to the time step.

A. J. Barlow, "ALE in Corvus", proceedings of new models and numerical codes for shock wave processes in condensed media, oxford, 1997, 581-596

The Model

Equations for the transport of mass, momentum and internal energy.

$$\frac{\partial}{\partial t}(f_r \rho_r) + \frac{\partial}{\partial x_j}(f_r \rho_r u_{rj}) = 0$$

$$\frac{\partial}{\partial t}(f_r \rho_r u_{ri}) + \frac{\partial}{\partial x_j}(f_r \rho_r u_{ri} u_{rj}) = -f_r \frac{\partial p}{\partial x_i} + \sum_s A_{rsi} + \sum_s D_{rsi} + f_r \rho_r g_i$$

$$\frac{\partial}{\partial t}(f_r \rho_r e_r) + \frac{\partial}{\partial x_j}(f_r \rho_r e_r u_{rj}) = -h_r f_r \rho_r \frac{\partial \bar{u}_j}{\partial x_j} + f_r \varepsilon$$

f_r = volume fraction of material r
ρ_r = density of material r
e_r = internal energy of material r
g_i = gravity
h_r = compressibility factor of material r
u_{rj} = velocity of material r in direction j
A_{rsi} = Added mass of fluid r due to s
D_{rsi} = Drag on fluid r due to s

The Model - Mixing phase

Volume fluxes calculated

$$f^1_{rj}\, V^1_j = f^0_{rj}\, V^0_j + \delta V_{rj} - \delta V_{rj+1}$$

$$\delta V_{rj} = A_j f^x_{rj}\, (u^0_{rj} - \bar{u}^0_j + \delta u)\, \Delta t$$

A_j = area

f^x_{rj} = van leer limited advection value

u^0_{rj} = fluid r velocity

δu = correction used to ensure $\Sigma \delta V = 0$

Density Fluxes

$$\rho^1_{rj} f^1_{rj}\, V^1_j = \rho^0_{rj} f^0_{rj}\, V^0_j + \delta M_{rj} - \delta M_{rj+1}$$

Internal Energy

$$e^1_r \rho^1_{rj} f^1_{rj}\, V^1_j = e^1_r \rho^0_{rj} f^0_{rj}\, V^0_j + \delta E_{rj} - \delta E_{rj+1}$$

The model - Van Leer

Van Leer limited advection flux calculated as follows
if $(u^0_{rj} - \bar{u}^0_j + \delta u) > 0$ then a=j-2, b=j-1, c=j
otherwise a=j+1, b=j, c=j-1

define $\varepsilon_{rj} = (|u^0_{rj} - \bar{u}^0_j + \delta u| A_j \Delta t)/V_b$ then

$f^x_{rj} = f^x_{rb} + (1- \varepsilon_{rj}) D_{rj}/2$

D_{rj} which represents the change in f across the upwind cell is obtained by Van Leer limiting. This is the minimum of:

$\Delta_1 = f^0_{rb} - f^0_{ra}$

$\Delta_2 = f^0_{rc} - f^0_{rb}$

$$D^{\Diamond}_{rj} = V_b \left(p \frac{\Delta_1}{\frac{1}{2}(V_a + V_b)} + (1-p) \frac{\Delta_2}{\frac{1}{2}(V_b + V_v)} \right)$$

$$where \quad p = \frac{V_a + \varepsilon_{rj} V_b}{V_a + V_b + V_c}$$

Similarly $\delta M_{rj} = \rho^x_{rj} \delta V_{rj}$ and $\delta E_{rj} = e^x_{rj} \delta M_{rj}$ where ρ^x_{rj} and e^x_{rj} are also Van Leer limited values

Implementation in Corvus

The mix model is initialised by specifying the interfaces across which the mixing is calculated. A list of cells is generated on each side of this interface.

The mixing routines are then called after the lagrangian and rezone phases of each time step. The equations are solved along “rows” and “columns” of cells. The cell numbers of the edges are stored and the line of cells between these edges is generated and passed to the mixing routines one at time. The volume fractions are stored using the ALE package which calculates the effect of mesh movement. Other variables are stored on a “mixed cell” basis, in the same way as the ALE package. This minimises storage and utilises the pre-existing code.

Results - buoyancy-drag model

A simple problem is used to illustrate the model. This is two regions of density 1 and 3. The Equation of State of both fluids is $-\frac{1}{\rho}\frac{\partial p}{\partial x} = 0.5$ with boundary conditions p=400 and p=200. This gives mixing limits of 54.0 and 70.0 at t=60.

The table below gives the results.

Time	Mix penetration	Mix penetration
0.000E+00	1.000E-05	1.000E-05
2.500E+00	1.243E-01	9.594E-02
5.000E+00	4.918E-01	3.794E-01
1.000E+01	1.955E+00	1.508E+00
1.500E+01	4.391E+00	3.387E+00
2.000E+01	7.798E+00	6.015E+00
2.500E+01	1.217E+01	9.394E+00
3.000E+01	1.753E+01	1.352E+01
3.500E+01	2.385E+01	1.840E+01
4.000E+01	3.115E+01	2.403E+01
4.250E+01	3.516E+01	2.712E+01
4.500E+01	3.942E+01	3.041E+01
4.750E+01	4.392E+01	3.388E+01
5.000E+01	4.866E+01	3.753E+01
5.250E+01	5.364E+01	4.138E+01
5.500E+01	5.887E+01	4.541E+01
5.750E+01	6.434E+01	4.963E+01
6.000E+01	7.006E+01	5.404E+01

Results - buoyancy-drag model

This is a mesh plot, the stars show the mixed cells.

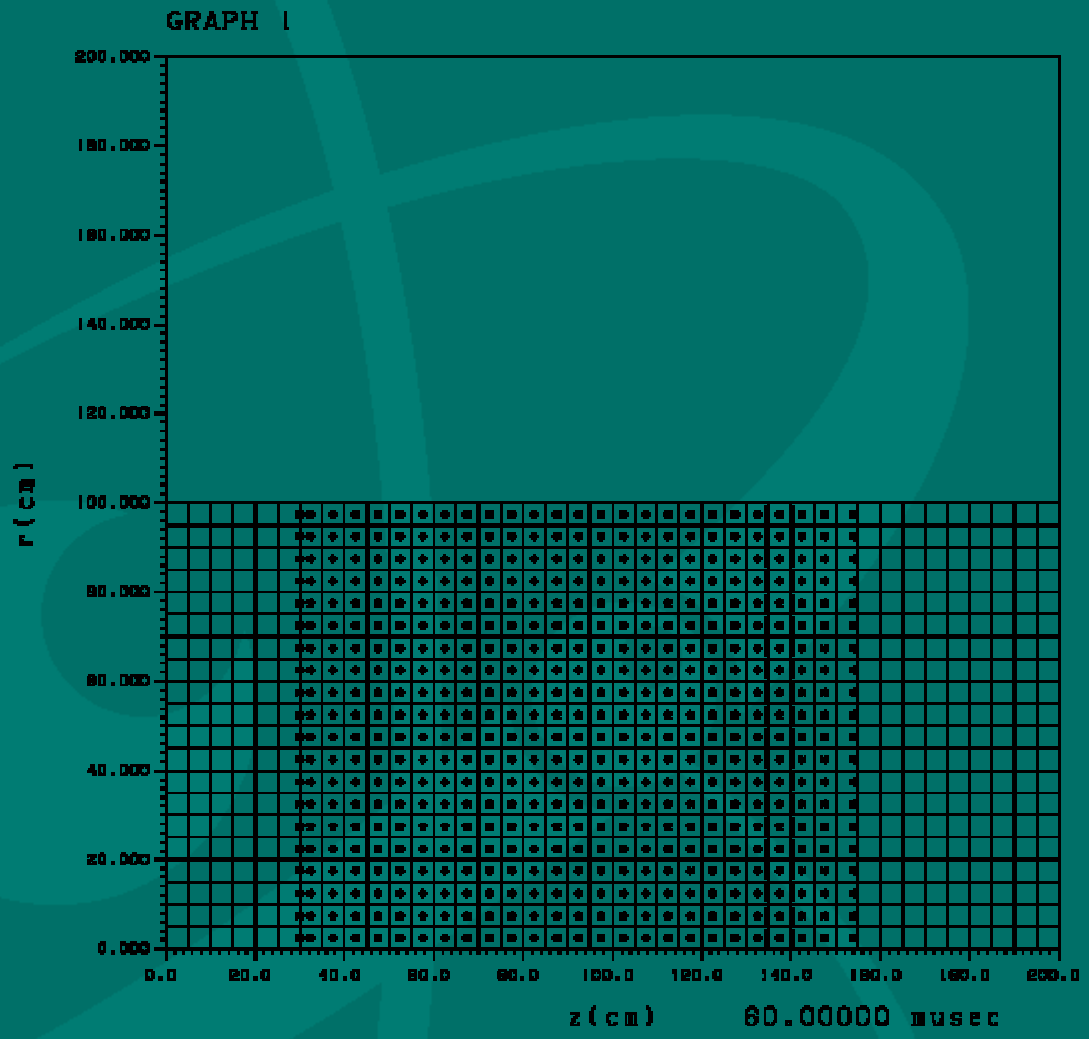

Results

These are the volume fractions along a line.

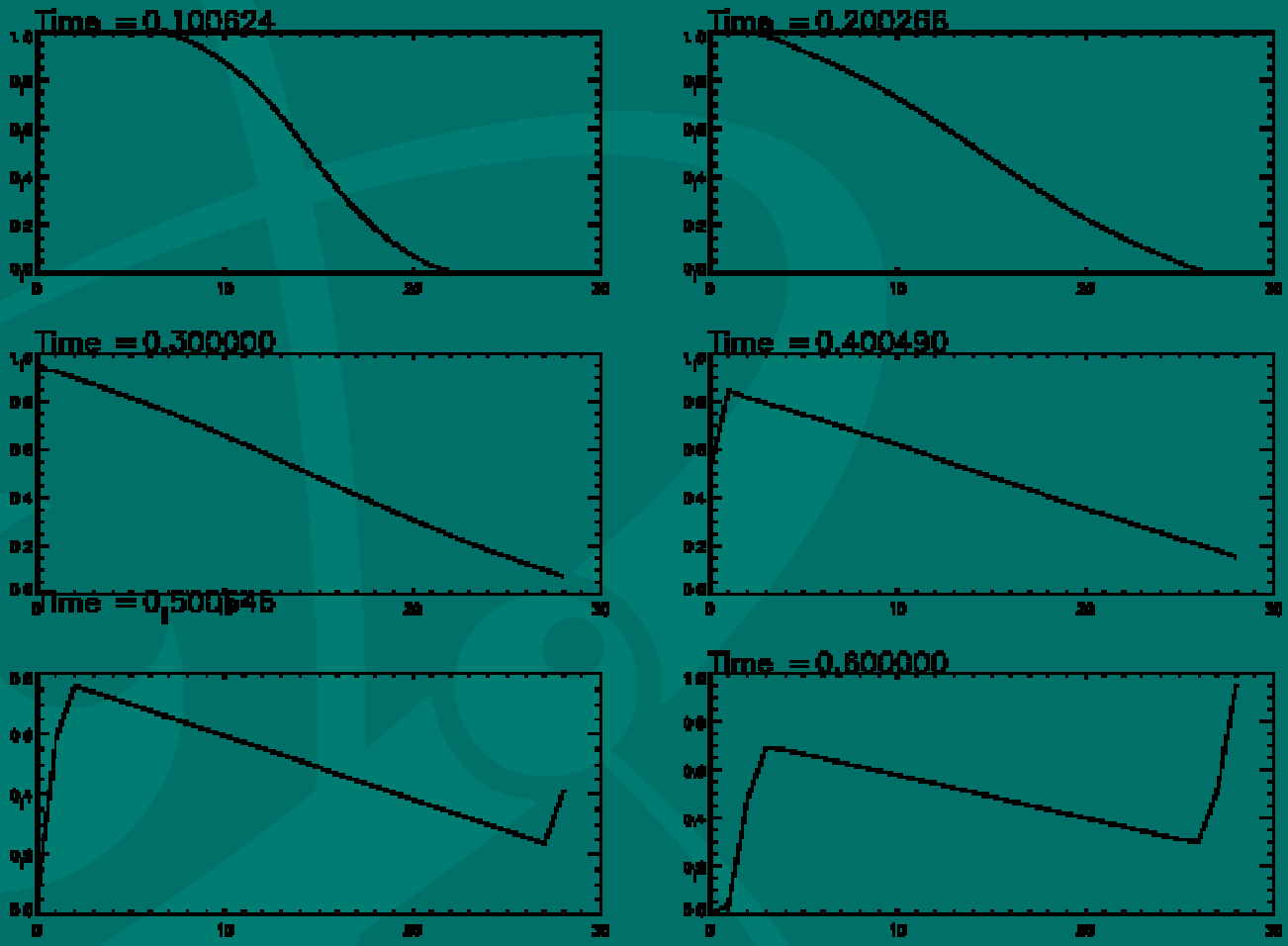

Results

This is a meshplot showing volume fractions.

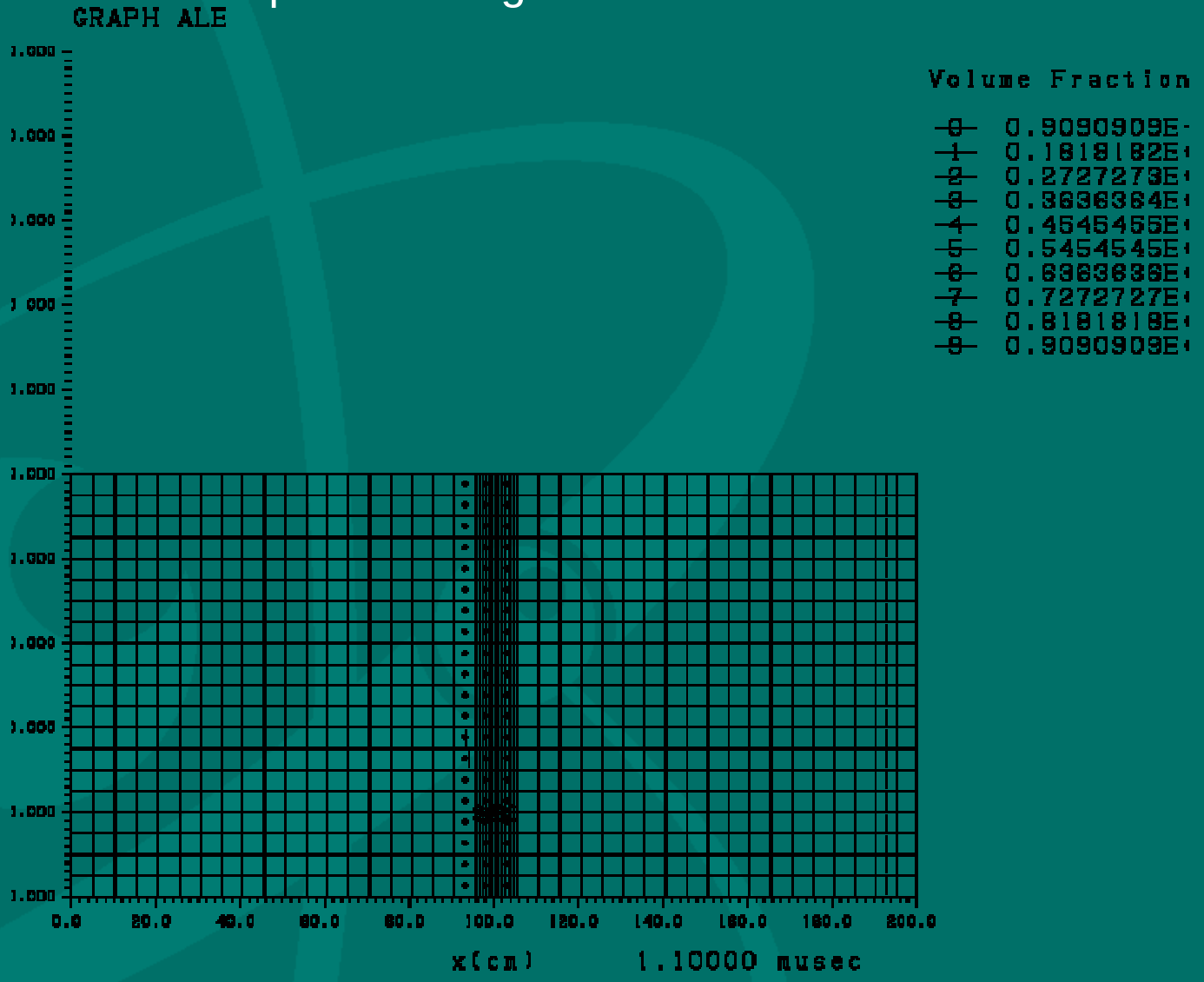

Further work

Initialisation using a simple buoyancy-drag model to start the turbulent model, this should increase the accuracy of the early time behaviour on a course mesh.

Mass exchange in the cells. Currently each mix cell consists of separate fluids.

Conclusions

A turbulent mix model has been implemented in a 2D ALE code, Corvus. It has been used on a simple problem and the results shown.

Semiempirical model of turbulent magnetic field diffusion to driven plasma

E.V.Gubkov, V.A.Zhmailo, Yu.V.Yanilkin

RFNC-VNIIEF, 607190, Sarov, Nizhni Novgorod region

E-mail: vaz@vniief.ru

Paper to be presented at the 8th IWPCTM, Pasadena, 2001.

There are quite many astrophysical and geophysical problems [1,2] as well as CTF related problems [3], in which a significant role is played by plasma-magnetic field interface instability. Among the numerous types of the instability, the magnetohydrodynamic instabilities were studied first. A most well-known example of this instability type is a so-called “chute” instability arising at the plasma-magnetic field interface during the interface acceleration.

This instability type is studied in a large number of papers, (see ref. [3]). The papers, as a rule, consider the linear stage of its evolution. The studies of the later, nonlinear stage became possible only recently thanks to availability of numerical methods. The approaches can be exemplified by refs. [4,5,8]. The first of them treats collisionless plasma and uses a “hybrid” model, the others consider plasma as “collisional” and perform the computation in the MHD approximation.

It was possible to obtain many useful results for the RT instability evolution at the plasma-magnetic field interface using this kind of approaches, however, all examples known to us of using these approaches are limited to problems, where unperturbed flow is one-dimensional. (A typical example is plasma cylinder expansion.) This limitation relates to the fact that such approaches prove quite complex, cumbersome, and do not allow us to follow the computed flow behavior in quite small scales.

A similar difficulty is encountered in unstable flow computations in hydrodynamics. A method to avoid this is using “semiempirical” turbulent mixing (TM) models. The model for “gravitational” TM problems was formulated for the first time in ref. [6], later the “semiempirical” models were developed quite extensively, became more complex, and found wide use for computation of a different kinds of turbulent flows. The models can be exemplified with those of refs. [7,12,13].

The studies of the RT instabilities in hydrodynamics and MHD flows revealed quite a close analogy between them at the linear stage [3]. This fact allows us to expect that this analogy may be also valid for a later, "turbulent" stage of the problem.

This paper discusses a semiempirical model for computing characteristics of a transitional layer at the accelerated plasma cloud – magnetic field interface. The model was developed on the basis of the hydrodynamic models [6,7] with using the above-mentioned analogy. Results of some 1D and 2D computations by the model are presented.

1. Derivation of governing equations

Assume that the flow can be described by MHD equations [9].

Thus, we have:

$$\frac{\partial \rho}{\partial t} + \mathrm{div}\rho\vec{u} = 0 \qquad (1.1)$$

$$\frac{\partial(\rho\vec{u})}{\partial t} + \mathrm{Div}(\vec{S}) = \vec{f} \qquad (1.2)$$

$$\frac{\partial Q}{\partial t} + \mathrm{div}\left[\rho\vec{u}\left(\frac{u^2}{2} + \omega\right) - (\vec{u}\cdot\ddot{\sigma}) + \frac{1}{4\pi}\left[\vec{H}\vec{E}\right]\right] = 0 \qquad (1.3)$$

$$\vec{f} = \frac{1}{4\pi}\left[\mathrm{rot}\vec{H}\cdot\vec{H}\right] \qquad (1.4)$$

where $S_{ik} = P\delta_{ik} + \rho u_i u_k - \sigma_{ik}$ (1.5)

$$Q = \frac{\rho u^2}{2} + \rho E + \frac{H^2}{8\pi} \qquad (1.6)$$

$$\vec{E} = \frac{1}{c}\left[\vec{u}\vec{H}\right] - \frac{c}{4\pi\Sigma}\mathrm{rot}\vec{H} \qquad (1.7)$$

$$\omega = E + \frac{P}{\rho} \qquad (1.8)$$

$\ddot{\sigma}$ is viscous stress tensor, Σ - conductivity, other notations are conventional.

This system is complemented with equations for magnetic field:

$$\frac{\partial\vec{H}}{\partial t} + (\vec{u}\nabla)\vec{H} = (\vec{H}\nabla)\vec{u} + \nu_m\Delta H \qquad (1.9)$$

$$\mathrm{div}\vec{H} = 0 \qquad (1.10)$$

where $\nu_m = \frac{C^2}{4\pi\sigma}$ is "magnetic" viscosity factor, as well as with the equation for different concentrations α_i:

$$\frac{\partial \rho_i}{\partial t} + \mathrm{div}\rho_i\vec{u} = \mathrm{div}(\rho i\ \nabla\alpha_i) \qquad (1.11)$$

where $\rho_i = \rho\alpha_i$, D – coefficient of molecular diffusion, and equation of state:

$$P = P(\rho, E, \alpha_i) \qquad (1.12)$$

As usual, divide the quantities to be calculated into low- and high-frequency addends, then make appropriate averaging [10,11], and use the commonly accepted expressions for the addends containing the third or higher order moments to obtain the following from set 1.1 through 1.12 for averaged values:

For density: Eq. 1.1

For velocity: Eq. 1.2

For concentrations : Eq. 1.11

For "magnetic" force: Eq. 1.4.

The equations for velocity and density therewith involve the "turbulent" tensor of viscous pressures, σ_t, and diffusion coefficient, D_t, instead of relevant "molecular" values.

For internal energy:

$$\frac{\partial}{\partial t}(\rho \cdot E) + div(\rho E\vec{u}) = c_\alpha div(\rho D\nabla(\alpha E)) - Pdiv\vec{u} + \rho\varepsilon + \frac{(\vec{j})^2}{\Sigma_T} \qquad 1.13$$

$$\vec{j} = \frac{c}{4\pi} rot\vec{H} \qquad 1.14$$

Here ε is dissipation rate of turbulent energy k, Σ_T is effective conductivity.

The following relations are used for functions σ_t and D_t [7]:

$$D_t = C_D \frac{k^2}{\varepsilon} \qquad 1.15$$

$$\sigma_t^{ij} = \rho D_t \left[\frac{\partial u_i}{\partial x_j} + \frac{\partial u_j}{\partial x_i} - \frac{2}{3}\delta_{ij}\frac{\partial u_r}{\partial x_r} \right] - \frac{2}{3}\rho k\delta_{ij} \qquad 1.16$$

Also, note that relations 1.11 to 1.16 were derived assuming Reynolds numbers Re and $\mathrm{Re}_{mag} \to \infty$ and addends, such as "turbulent pressure" $\mathrm{P_T}$ and "magnetic turbulent pressure, were neglected.

A number of additional assumptions were used in this paper to calculate averaged magnetic field:

- cylindrical symmetry of the problem was assumed,
- the geometry of the initial magnetic field was assumed "poloidal",
- "magnetic viscosity" can be neglected.

Under these assumptions, the magnetic field components $\mathrm{H_\rho}$ and $\mathrm{H_z}$ (where z is axis of symmetry) are related with $\mathrm{A_\phi}$, azimuthal potential vector component, as

$$\mathrm{H_\rho} = -\frac{\partial \mathrm{A_\varphi}}{\partial \mathrm{z}} \qquad 1.17$$

$$\mathrm{H_z} = \frac{1}{\rho}\frac{\partial}{\partial \rho}\left(\mathrm{A_\varphi}\rho\right) \qquad 1.18$$

$$\mathrm{A_\varphi}\rho = \mathrm{m} \qquad 1.19$$

where

$$\frac{\partial \mathrm{m}}{\partial \mathrm{t}} + \vec{\mathrm{u}}\nabla \mathrm{m} = \mathrm{div}\vec{\mathrm{R}}_\mathrm{m} \qquad 1.20$$

$$\vec{\mathrm{R}}_\mathrm{m} = -\left\langle \vec{\mathrm{u}}'\mathrm{m}' \right\rangle = \tilde{\mathrm{D}}\nabla \mathrm{m} \qquad 1.21$$

Assume that $\tilde{\mathrm{D}} = \mathrm{C_m D}$, where $\mathrm{C_m}$ is an empirical constant.

When considering the equations for turbulent values k and ε, turbulence anisotropization by magnetic field must be included. To do this, a simplest method is using the equation system for $k_{ij} = \left\langle u_i' u_j' \right\rangle$ instead of a single equation for k [7]. By analogy with this equation [7], the following can be written for diagonal components $\mathrm{k_j}$:

$$\frac{\partial}{\partial t}(\rho k_j) = \rho(G_j - \varepsilon_j) + C_k div \rho D_j \nabla k_j + \Phi_j - \mathrm{Re}l(\rho k_j) - div \rho k_j \vec{u} - \frac{2}{3}\rho k_j div \vec{u} \qquad 1.22$$

$$G_j = G_j^{(1)} + G_j^{(2)} \qquad 1.23$$

$$G_j^{(1)} = \sigma_{jl}\frac{\partial u_j}{\partial x_l} \text{ - shear generation} \qquad 1.24$$

$$G_j^{(2)} = \frac{w_j \gamma_j}{\rho} \text{ - gravitational generation} \qquad 1.25$$

$$\vec{\gamma} = \nabla(P + P_m) - \frac{1}{4\pi}(\vec{H}\nabla\vec{H}) \qquad 1.26$$

$$\vec{w} = \frac{\nabla P}{\gamma P} - \frac{\nabla \rho}{\rho}, \quad \vec{w} \text{ - turbulent flow} \qquad 1.27$$

$$\mathrm{Re}\, l(\rho k_j) = \frac{\varepsilon}{k}\rho\left(k_j - \frac{k}{3}\right) \qquad 1.28$$

Φ_j - exchange term (between velocity and magnetic field fluctuation)

$$\Phi_j = \frac{1}{4\pi}\cdot 2\cdot\left[H_l < u_j \frac{\partial h_j}{\partial x_l} > + \frac{\partial H_j}{\partial x_l} r_{jl} - \left\langle u_j \frac{\partial}{\partial x_j} P_m' \right\rangle\right] \qquad 1.29$$

here $r_{jl} = \langle u_j h_l \rangle$, $P_m{}' = \left(H_k + \frac{h_k}{2}\right)h_k$, h_k - fluctuating part of magnetic field, ε_j - dissipation of the k_j.

To "close" system 1.21-1.29, Φ_j and ε_j should be expressed in terms of the previously introduced functions.

The last addend in 1.29 can be written (by analogy with Rotta's hypothesis [10]) as a sum of the diffusion and relaxation terms for tensor components $\pi_{ik} = \langle h_i h_k \rangle$. If then the first addend in 1.29 is neglected, it is possible to express function Φ_j in terms of r_{jl} and π_{ik}.

The equation system for these functions can be derived from 1.2 and 1.9. By solving this system, they can be expressed in terms of k_{ij} and average velocities and fields.

The equation for ε_j can be written, following [11], as

$$\varepsilon_j = \frac{k_j^{\frac{3}{2}}}{l_j} \qquad 1.31$$

where l_j is the mixing path length that depends on the orientation of unit vector $\vec{e}_j$ relative to the magnetic field. When $\vec{e}_j \parallel \vec{H}$ the $l_j \to \infty$ if $\vec{H} \to \infty$ [11].It is suggested that the methods for determination of Φ_j and ε_j should be discussed separately.

2. Setting up the computations and discussion

The computations discussed below assumed that the magnetic field was not very strong and its effect on the anisotropy and turbulence dissipation could be neglected. This allowed us to neglect addend Φ_j in 1.22, i.e. to use one equation for k and one equation for ε presented in [7].

In so doing the magnetic field action on plasma is expressed in terms of force $\vec{f}$ in equation 1.2 and by relevant addends $\vec{\gamma}$ (1.26) in "generation" term G_2 for turbulent energy.

The plasma action on magnetic field leads to its displacement, however turbulence causes field diffusion into the plasma, with the diffusion coefficient itself depending on the field.

Two problems of plasma cloud expansion to surrounding, "background", low-density plasma ("vacuum") with magnetic field were calculated.

Problem 1. One-dimensional problem of cylindrical plasma cloud expansion in magnetic field.

It is agreed that at t=0 there is a cylindrical symmetric plasma cloud of radius r_0, energy E, and mass M (per unit length) surrounded by cold "background" plasma of density ρ_0 and by magnetic field oriented along axis of symmetry z, i.e. $\vec{H} = (0,0,H_1)$.

It is convenient to consider this problem in dimensionless variables. Introduce scaling: $u_1 = \left(\frac{E}{M}\right)^{1/2}$ for velocity, $r_1 = \left(\frac{E}{P_1}\right)^{1/2}$ for distance, $\frac{r_1}{u_1}$ for time, $\frac{M}{r_1^2}$ for density, H_1 for magnetic field (here P_1 is unperturbed magnetic field pressure).

In this scaling the problem is characterized with two dimensionless parameters, r_0' and $\rho_0' = \frac{\rho_0}{\rho_1} = \left(\frac{u_1}{C_A}\right)^2$, where $C_A^2 = \frac{H_1^2}{4\pi\rho_0}$.

Next, restrict our consideration to $\rho_0' \to 0$, i.e. "sub-Alfven" plasma expansion.

The dimensionless initial data are summarized in Table 2.1

Table 2.1

	ρ	ε	u	H
$r < r_0$	$\frac{1}{\pi r_0'^2}$	1	0	0
$r > r_0$	ρ_0'	0	0	1

To calculate the turbulent mixing with the code of ref. [7], the data of initial turbulent energy profiles k and turbulent energy dissipation ε should be added to these initial data. It was assumed that at t=0 these functions are nonzero only in the layer of thickness $\delta r_0 << r_0$ near boundary r_0. In the computation, $C_m = 1$.

The computed data for $\rho_0' = \frac{10^{-2}}{\pi}$ and $r_0 = 0.1$ is plotted in Figs. 1.1-1.3.

The figures depict turbulent mixing zone (TMZ) boundaries with tine (here $R_1(t)$ is radius determined by level $H(R_1) = 0.05$, $R_2(t)$ is that by level $H(R_2) = 0.95$) (Fig. 1); magnetic field profiles at times $t = 0.5\tau$, and τ, where τ is period of one cylinder radius oscillation (Fig. 2), plasma density profiles at the same times (Fig. 3).

As seen in these figures, a noticeable magnetic field and plasma interpenetration ("turbulent diffusion") is observed. At $\rho_0' << 1$ and $r_0' << 1$ the result weakly depends on specific magnitudes of the parameters and on initial profiles k and ε.

Problem 2. Two-dimensional problem of spherical cloud expansion.

Assume that at t=0 there is a spherical plasma cloud of energy E, mass M, radius r_0 surrounded with "background" plasma of density ρ_0, thermal pressure P_0 and by magnetic field, whose strength tends to $\vec{H} = (0,0,H_0)$ with $r \to \infty$.

Like previously, introduce scaling $u_1^2 = \frac{E}{M}$ for velocity, $r_1 = \left(\frac{E}{P_1}\right)^{1/3}$ for distance, $P_1 = \frac{\left(\frac{3}{2} H_0\right)^2}{8\pi} + P_0$ for pressure, $H_1 = H_0$ for magnetic field.

It was solved two spherical tasks №2.1 and 2.2. We assumed H_0=0, $P_0 \neq 0$ in the task 2.1 (so, this task become one-dimensional) and $H_0 \neq 0, P_0 = 0$ in the task 2.2.

The dimensionless initial data for the problem are summarized in Table 2.2.

Table 2.2

	ρ	ε	u	H
$r < r_0$	$\frac{3}{4\pi r_0^3}$	1	0	0
$r > r_0$	0,1	ε_0	0	H_0

Here ε_0=10, H_0=0 in the task 2.1 and ε_0=0, H_0=1 in task 2.2, r_0=0,5, $\gamma = 2$,

In contrast to Problem 1, here magnetic field in region $r > r_0$ is not constant and corresponds to the dipole magnetic field of radius r_0 in the external field of strength (0,0,1).

The initial data for the "turbulent" functions k and ε were given like in Problem 1: in a thin layer near interface r_0.

It was assumed that $C_m = 1$.

The results of the computation are plotted in the figures 4-9.

The first of them depicts the TMZ time dependence for 1D task 2.1. We can see TMZ width L_t is comparable with the cloud radious.

The fig. 5 depict the TMZ time dependence for 2D task 2.2 ($\theta = \frac{\pi}{2}$).

Comparing fig. 4 and 5 we can note although the plasma clouds dynamics are similar, but the magnetic field diminish value of L_t.

Figs. 6,7 plot the plasma density isolines at times t=0,4, 0,6, Figs. 8,9 depict the magnetic pressure isolines at the same times .

As seen, a noticeable field and plasma inter-diffusion is observed in this problem as well at the selected value of C_m, with this being significantly stronger at the $\theta = \frac{\pi}{4}$.

Conclusion

This paper discusses first our attempt to develop a semi-empirical model of turbulent mixing in inhomogeneous plasma with magnetic field.

To describe the MHD effects, the simplest form of the model is shown to require setting two additional constants determining the turbulent magnetic field diffusion factor and dissipative addends in the equation of energy.

To determine the constants, it is reasonable to involve experimental data on pinches and plasma liners.

It is being planned to make more accurate 2D computation and include turbulent energy anisotropy in it.

The authors would like to thank A.S.Pavlunin for his assistance in the computations and L.A. Rogacheva for help in execution of this paper.

References

1. Shklovsky I.S. Supernovae. Moscow, Nauka Publishers, 1976.
2. Dahlburg J.P., Fyfe D.E., Gardner J.H. et al., Phys. Plasmas 2. 2453(1995).
3. Kadomtsev B.B. Collective phenomena in plasma. Moscow, Nauka Publishers, 1988.
4. Winske Dan, "Regimes of magnetized RT instability" LA-UR-96-818, 1996
5. Hassam A.B., Huba J.D., Phys Fluids 31, 318(1988).
6. Belen'ky S.Z., Fradkin E.S. Theory of turbulent mixing. Trudy FIAN. V. XXIX, 1965.
7. Yanilkin Yu.V., Nikiforov V.V., Zharova G.V. A two-equation model and a code for turbulent mixing in 2D flows. VANT, Ser. MMFP, No.4, 1994.
8. Zhmailo V.A., Yanilkin Yu.V. "Direct numerical simulation of magnetic field turbulent diffusion into accelerated plasma", 7th IWPCTM, St. Petersburg, 1999
9. Landau L.D., Lifshits E.M. Continuum electrodynamics. Moscow. 1962.
10. Monin A.S., Yaglom A.M. Statistical hydromechanics. V.1. Moscow, Nauka Publishers, 1965.
11. Ievlev V.M. Turbulent high-temperature media flow. Moscow, Nauka Publishers, 1975.
12. Levellen V. A method for invariant modeling. In: Turbulence: Principles and Applications. Moscow, Mir Publishers, 1980.
13. Bakhrakh S.M., Darova N.S., Statsenko V.P., Zhmailo V.A. "The effects of turbulence and viscosity on structure of thin vortex rings" 4th JWPCTM, Cambridge, 1993.

Cylindrical cloud.

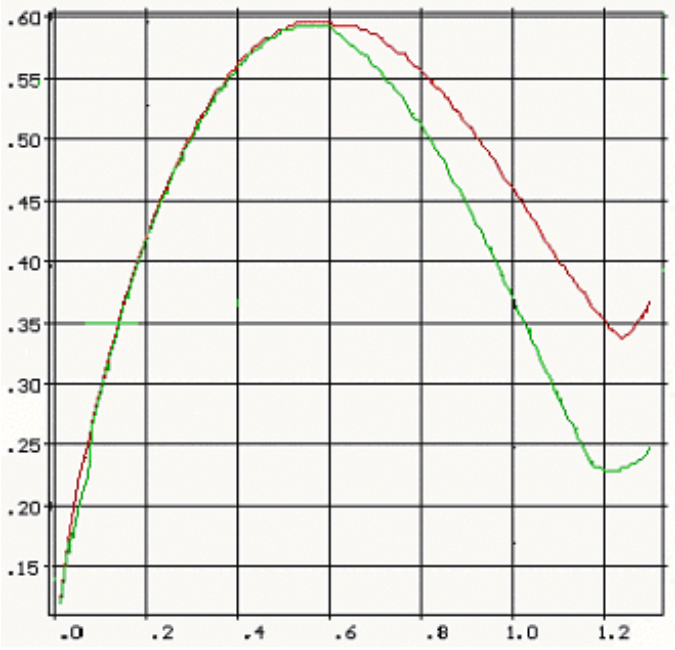

fig1. TMZ time dependence
(concentration levels 0.05 and 0.95), cylindr. task, P_m=1.0

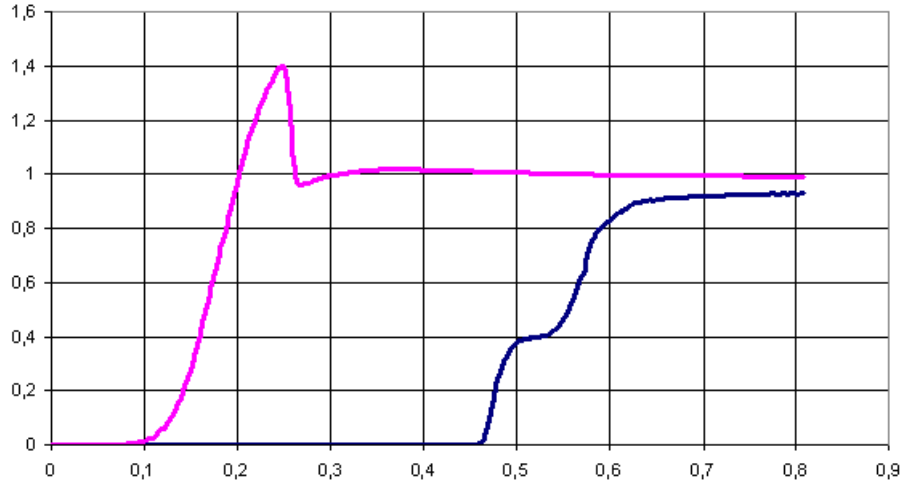

fig2. Magnetic field profiles, cylindr. task, P_m=1.0, t=0.6, t=1.2

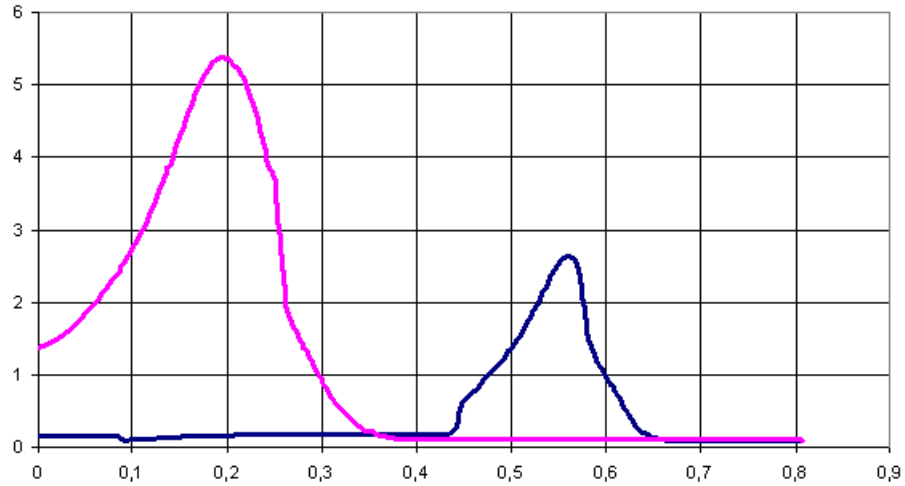

fig3. Plasma density profiles, cylindr. task, P_m=1.0, t=0.6, t=1.2

Spherical cloud.

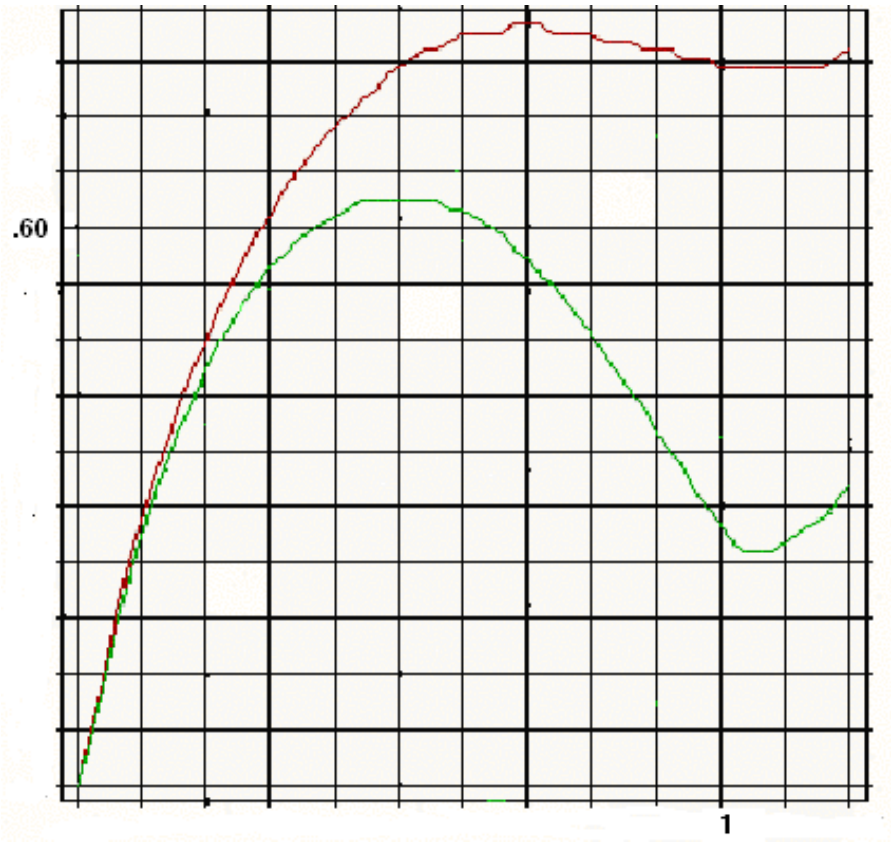

fig4. TMZ time dependence, spher. task, P_{th}=0.1, P_m=0

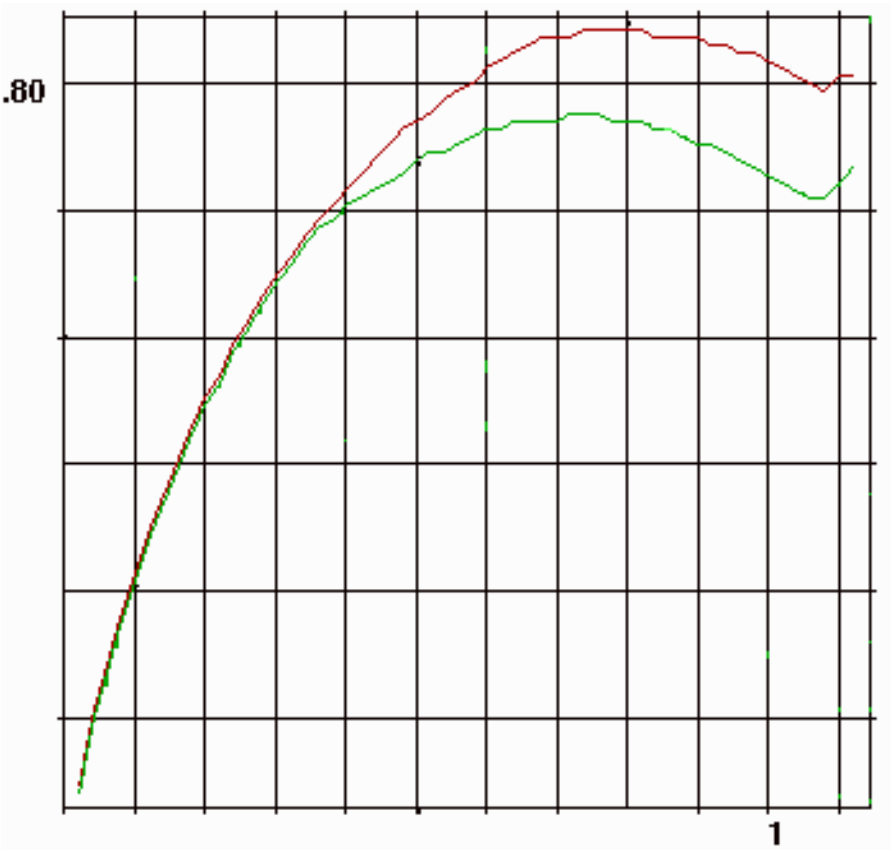

fig5. TMZ time dependence, 2D task, P_m=0.44, $\Theta=\pi/2$ (equator)

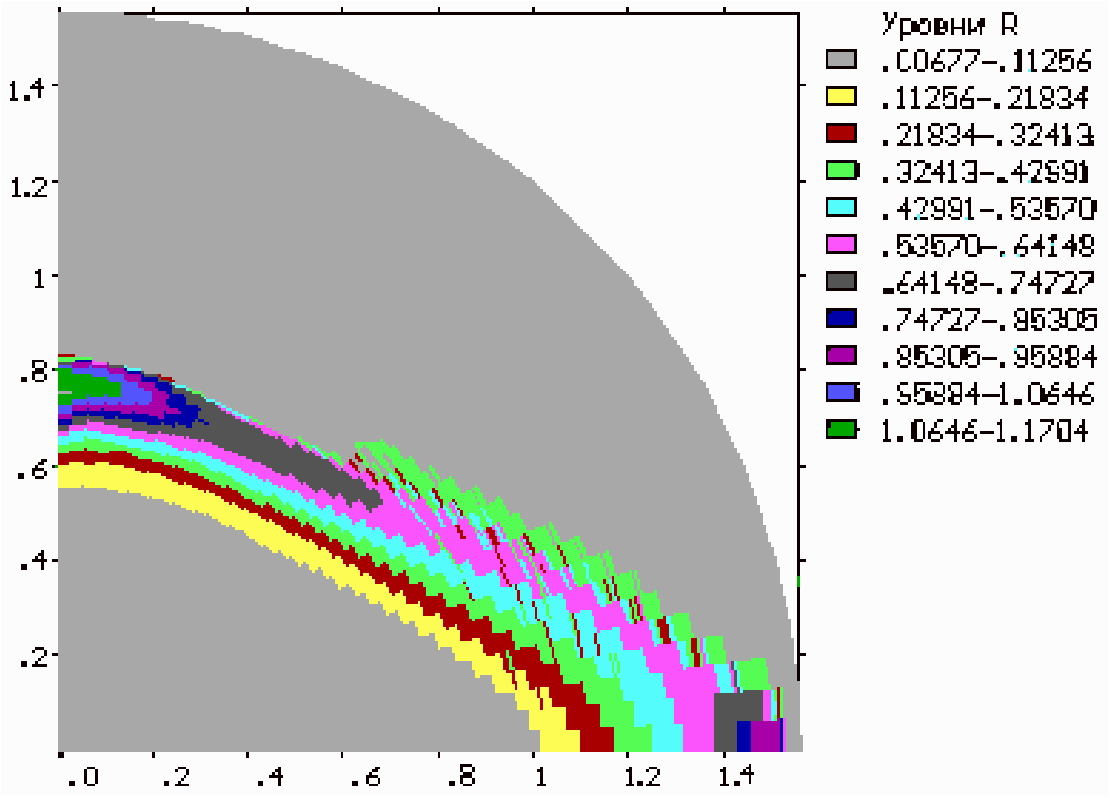

fig6. Plot of the plasma density, 2D task, P_m=0.44, t = 0.8

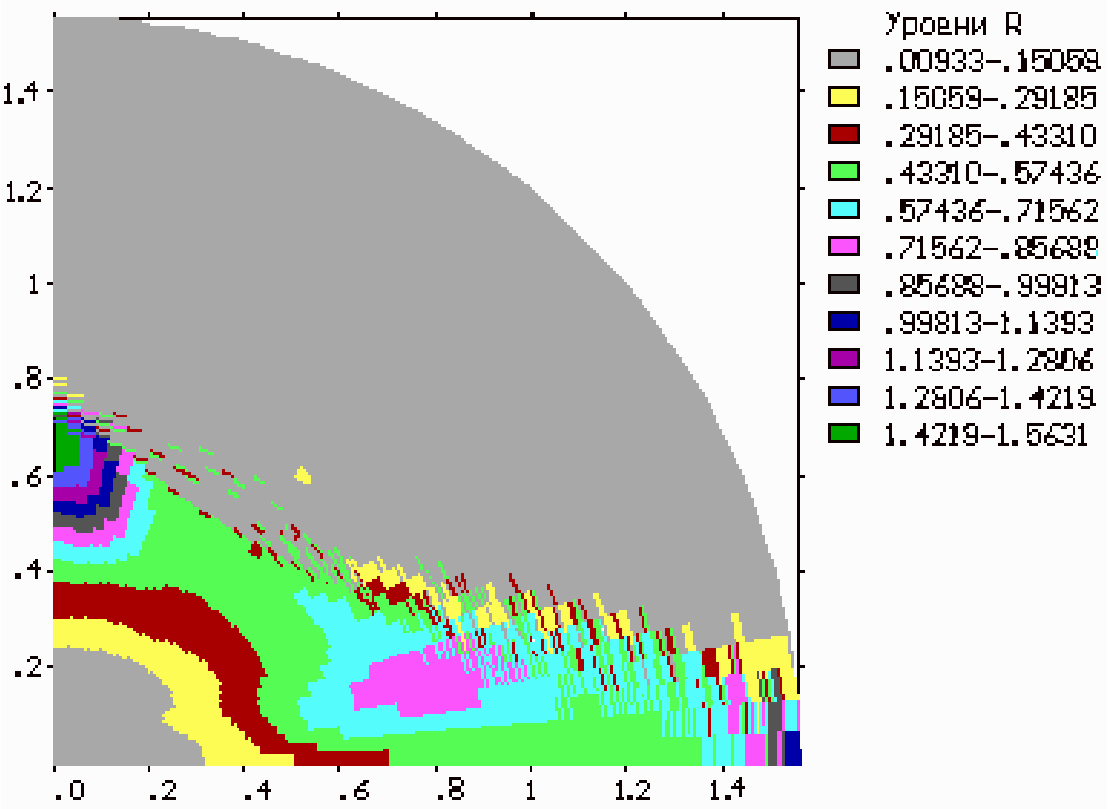

fig7. Plot of the plasma density, 2D task, P_m=0.44, t = 1.2

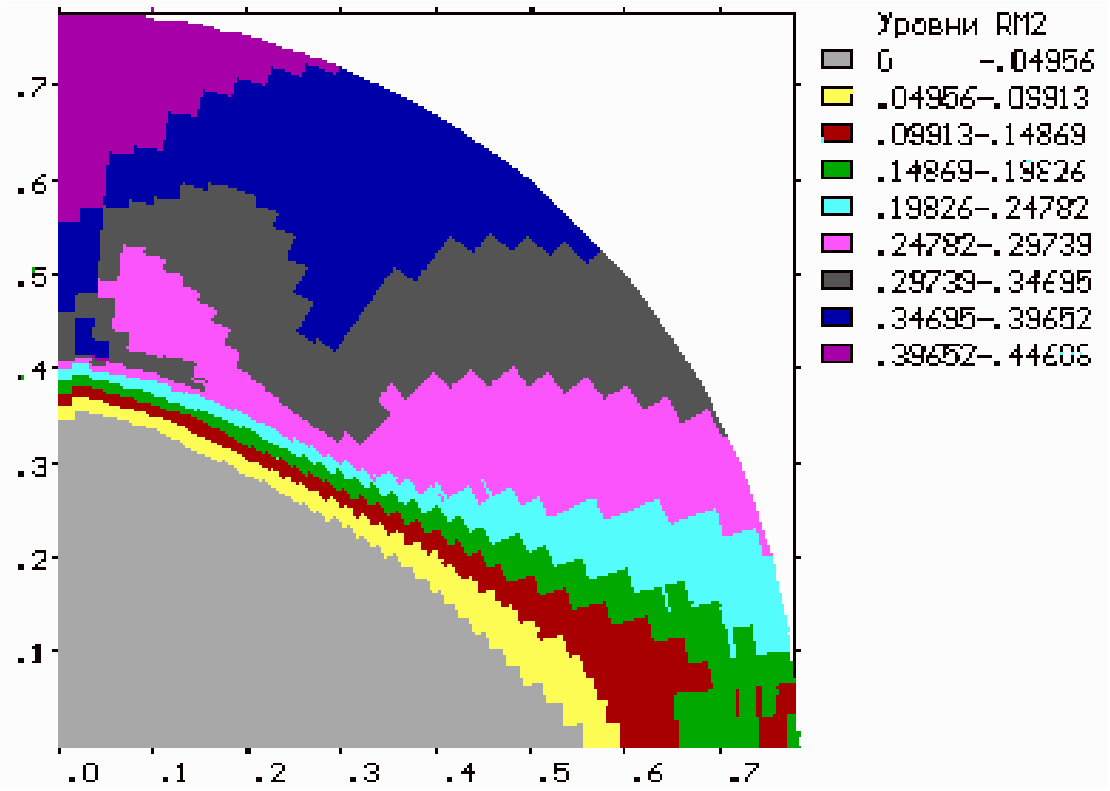

fig8. Plot of the “magnetic” pressure, 2D task, P_m=0.44, t = 0.4

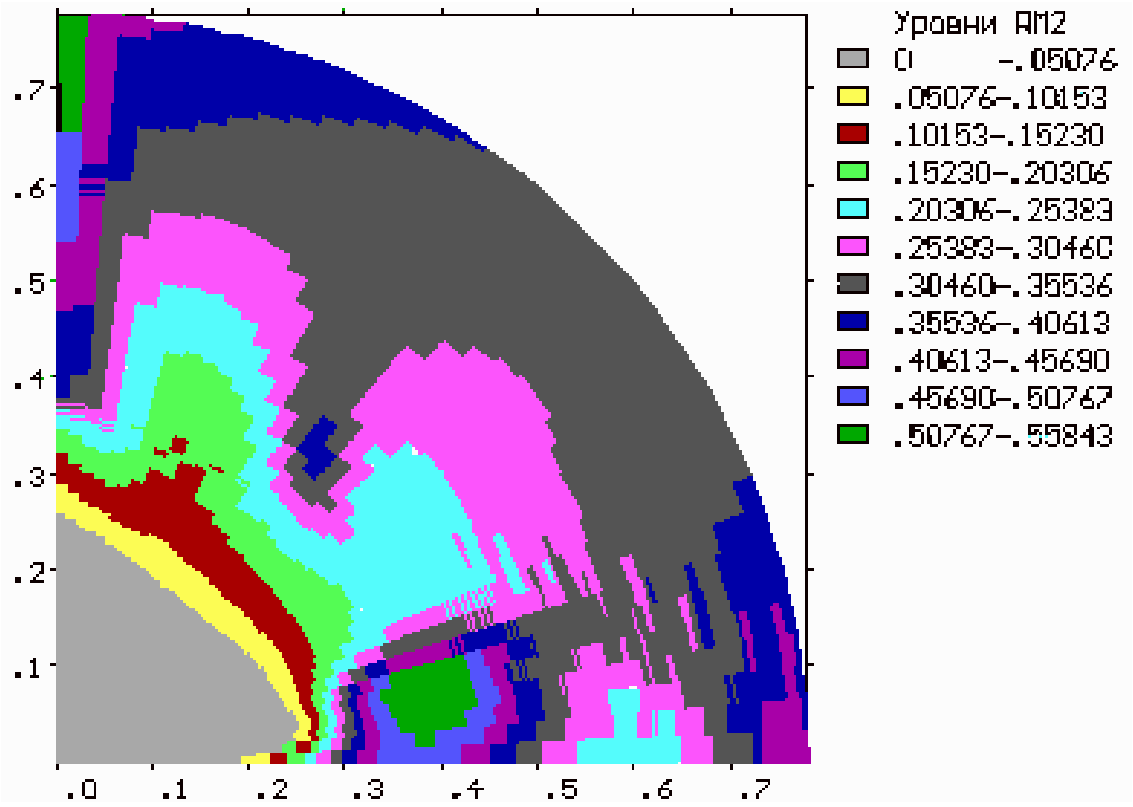

fig9. Plot of the “magnetic” pressure, 2D task, P_m=0.44, t = 0.6

LOCALIZATION AND SPREADING OF INTERFACES (CONTACT DISCONTINUITIES) IN PPM AND WENO SIMULATIONS OF THE INVISCID COMPRESSIBLE EULER EQUATIONS

N.J Zabusky[1], S. Gupta[1], Y. Gulak[1], G. Peng[1] , R. Samtaney[2] ,

[1]Rutgers University,NJ [2]Princeton Plasma Physics Lab.,NJ

OBJECTIVE

- Systematic approach to examine localization and temporal spreading of contact discontinuities(CDs) in 1D and 2D.
- Validity of near contact simulations of accelerated flows of high-gradient compressible media (RT and RM).
- Evolution of sinusoidal RM interface at late time and interfacial growth rate.

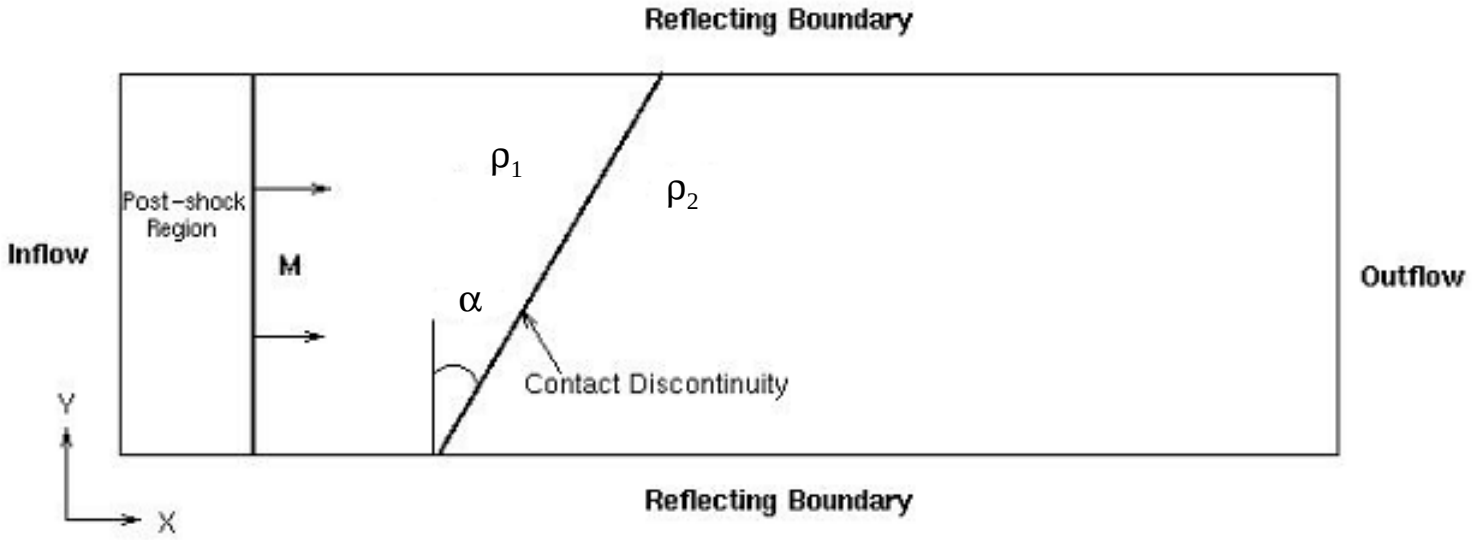

Schematic of Shock Interaction with an Inclined Discontinuity. M is the Mach number, α is the angle between shock and contact discontinuity, ρ_1 and ρ_2 are the densities of two gases.

MOTIVATION

- Study by Samtaney & Zabusky: Visualization and quantification of compressible flows in *Flow Visualization(1999)*.
- Non-convergence of position of contact discontinuity(x_{num}-x_{anal})/h to exact analytical solution for 1D.

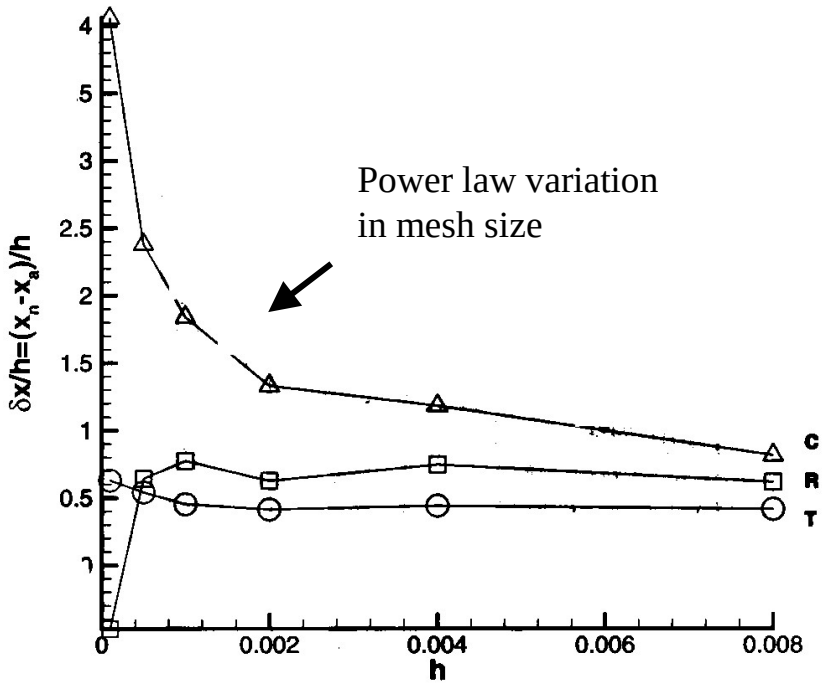

Convergence study using difference in the numerical and analytical locations of high gradient regions (shocks and CDs) vs **mesh size** h. M = 3.0 shock interacts with a density discontinuity (CD, ρ_2/ρ_1= 3.0) and yields a moving CD (C), upstream reflected shock (R), and downstream transmitted shock (T).

CONTINUUM LIMITS & DIFFERENTIAL APPROXIMATION

Consider a 1D Riemann problem for Euler System

$$\frac{\partial \mathrm{U}}{\partial \mathrm{t}} + \frac{\partial F(\mathrm{U})}{\partial \mathrm{x}} = 0.$$

with initial conditions,

$$\mathrm{u}(\mathrm{x},0)=\mathrm{u}_0,\ \ \mathrm{p}(\mathrm{x},0)=\mathrm{p}_0,\ \rho(\mathrm{x},0) = \begin{cases} \rho_1, \mathrm{x} < \mathrm{x}_0 \\ \rho_2, \mathrm{x} > \mathrm{x}_0 \end{cases}$$

Using **Differential Approximation** (Vorozhtsov and Yanenko, Springer1990) for a numerical method of **r-th** order spatial accuracy, system reduces to,

$$\frac{\partial \rho}{\partial \mathrm{t}} + \mathrm{u}_0 \frac{\partial \rho}{\partial \mathrm{x}} = (-1)^{\mathrm{r}+1} \mu_{\mathrm{r}+1} \frac{\partial^{\mathrm{r}+1} \rho}{\partial \mathrm{x}^{\mathrm{r}+1}}$$

For r = 1,

$$\rho(\mathrm{x},\mathrm{t}) = 0.5(\rho_1 + \rho_2)[1 + \mathrm{erf}(\chi)] \qquad (1)$$

For r = 2,

$$\rho(\mathrm{x},\mathrm{t}) = (2\rho_2 + \rho_1)/3 + (\rho_2 - \rho_1) \int_0^{\chi} \mathrm{Ai}(\chi') \, \mathrm{d}\chi' \qquad (2)$$

where

$$\chi(\mathrm{x},\mathrm{t}) = (\mathrm{x} - \mathrm{x}_0 - \mathrm{u}_0 \mathrm{t})/((\mathrm{r}+1)\mu_{\mathrm{r}+1}\mathrm{t})^{1/\mathrm{r}+1} \qquad (3)$$

EXTRACTION OF CONTACT DISCONTINUITY

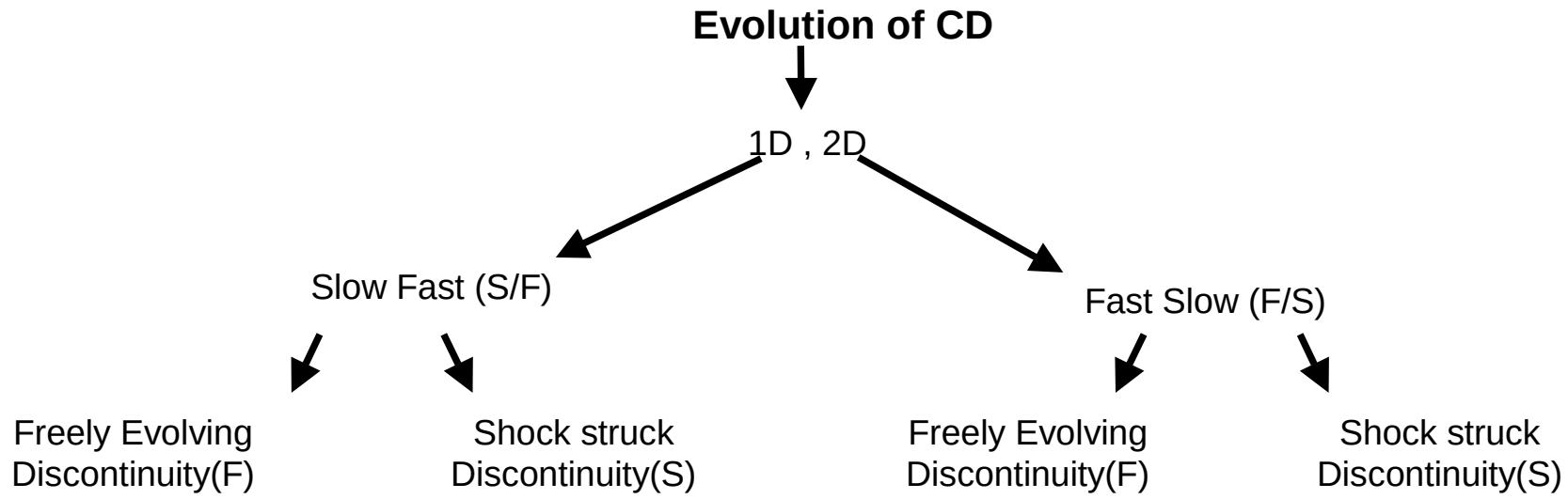

For 2D case, we examine a slice at y=YMAX/2

NUMERICAL METHODS

- Piecewise Parabolic Method (**PPM**)
- Weighted Essentially Non- Oscillatory (**WENO**,r=5)

EXTRACTION PROCEDURE FOR CD

- Point-wise Algorithm (A variation of edge detection technique)
- Width of CD = $X(d^2\rho_{max}) - X(d^2\rho_{min})$ where $d^2\rho$ is the second central difference
- Shock – Elimination using cost functions
  - Divergence of velocity $|\nabla.U| < |\nabla.U|_{thresh}$
  - Normalized pressure jump $dP < dP_{thresh}$

LOCALIZATION OF CD UNDER MESH REFINEMENT

PPM

Intersection point $\approx (2*\rho_1 + \rho_2)/3$

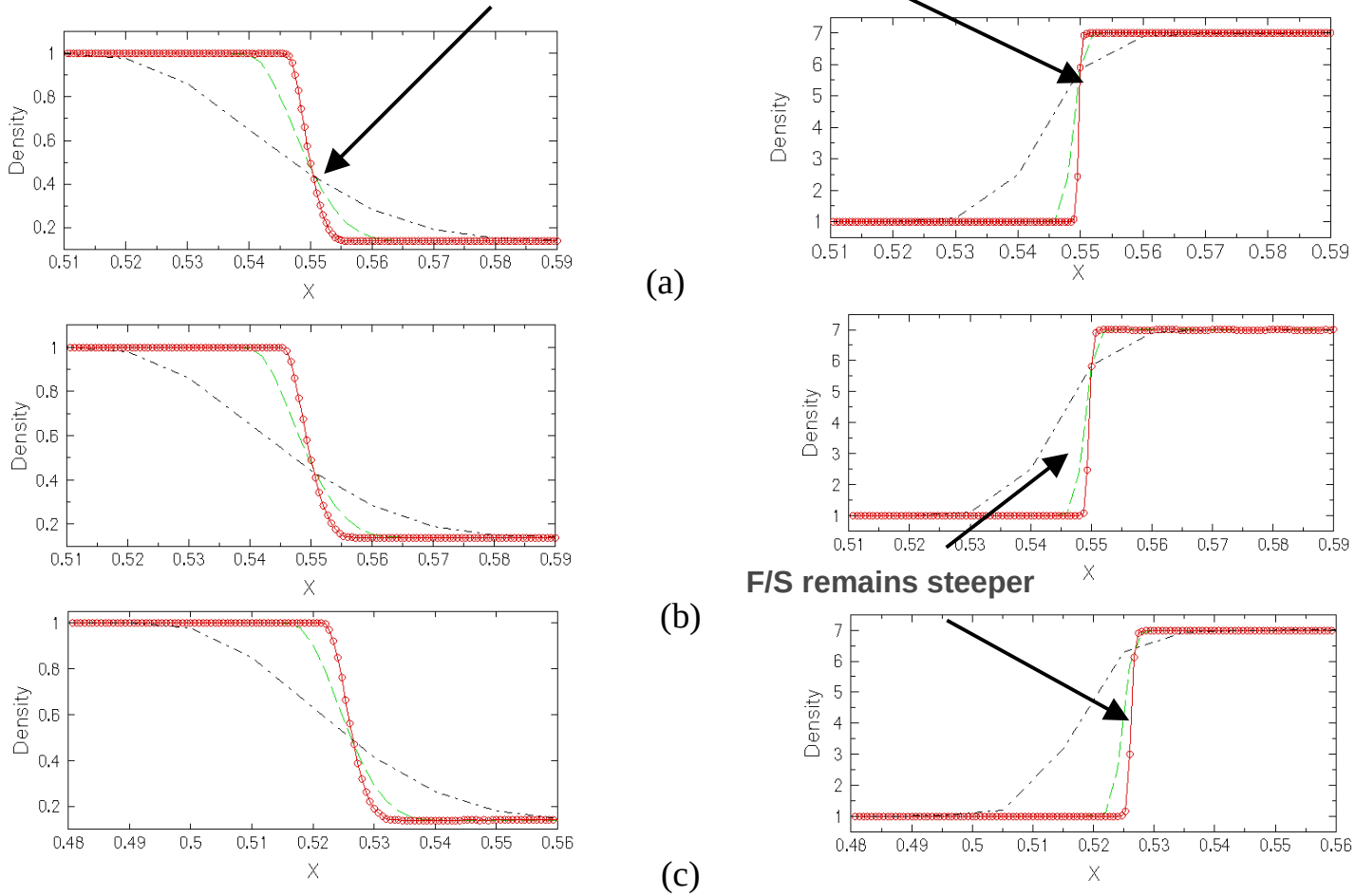

S/F(density ratio=0.14)

F/S (density ratio=7.0)

Density profiles for **Diffusing Contact Discontinuity** (u0 =1.5) at t=0.3. Top to Down (a) 1D (b) 2D, α =0 (c) 2D, α =30. The solid line with open circles is the highest resolution 0.0005 and - - - and - · - · - are 0.002 and 0.01 respectively.

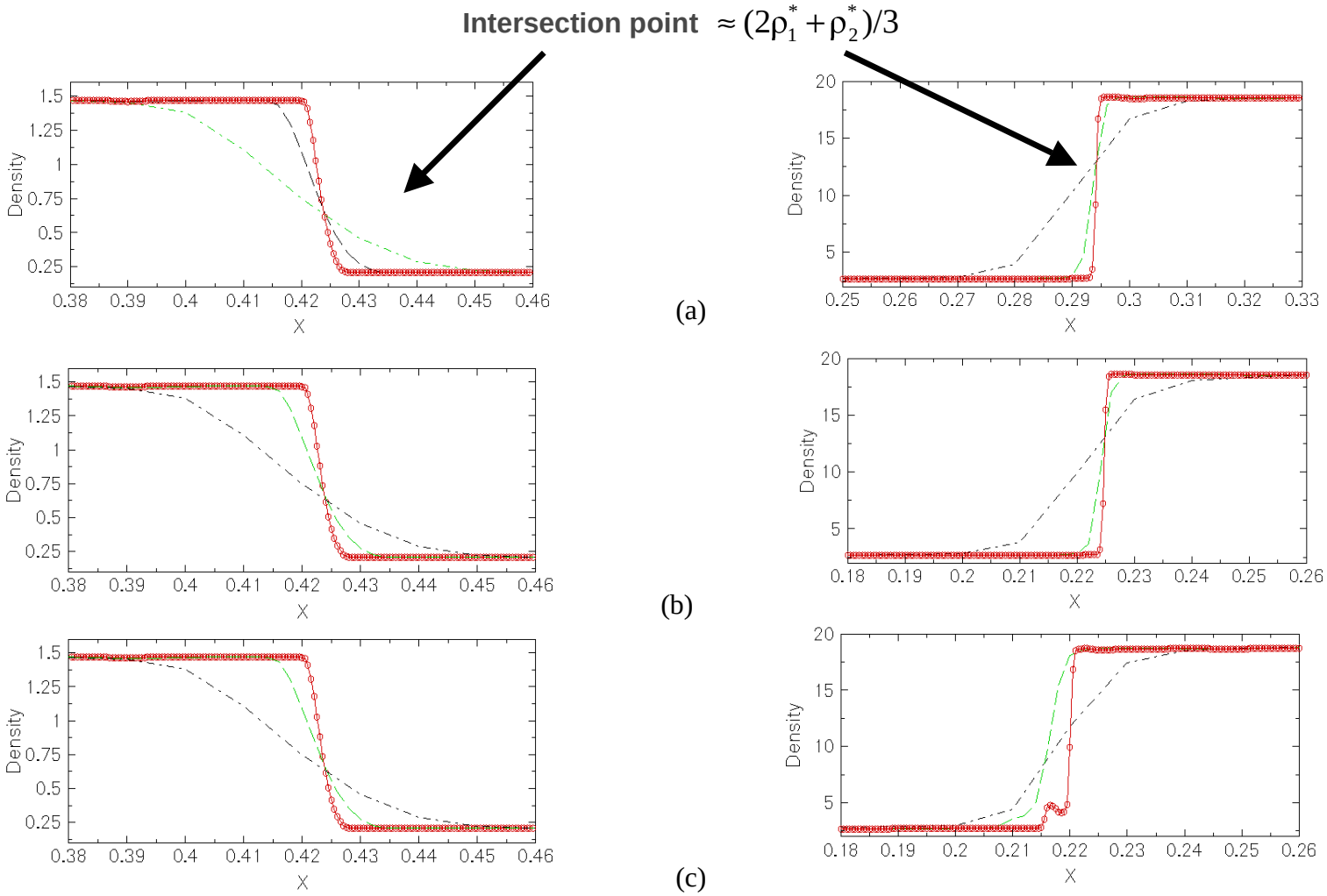

Density profiles for **Shock Contact Discontinuity Interaction** (M=1.5) at t=0.3. Top to Down (a) 1D (b) 2D, α =0 (c) 2D, α =10. The solid line with open circles is the highest resolution 0.0005 and - - - and - · - · - are 0.002 and 0.01 respectively. ρ_1^*, ρ_2^* are the post shock densities.

LOCALIZATION OF CD UNDER MESH REFINEMENT(CONT.)

WENO

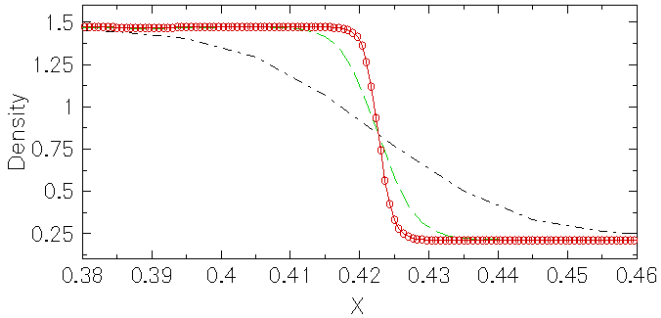

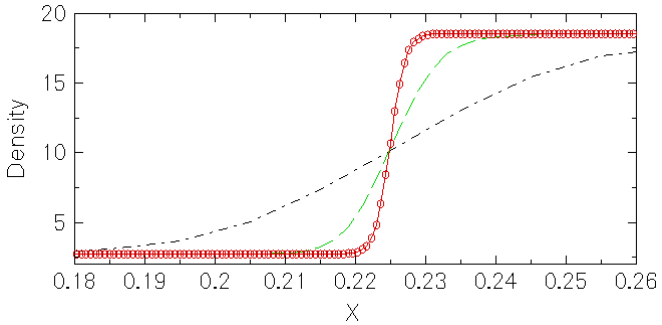

Density profiles for 1D **Shock Contact Discontinuity Interaction** (M=1.5) at t=0.3.The solid line with open circles is the highest resolution 0.000667 and - - - and - · - · - are 0.002 and 0.01 respectively.

SPREADING OF CD UNDER MESH REFINEMENT

PPM (width $\propto t^{1/3}$)

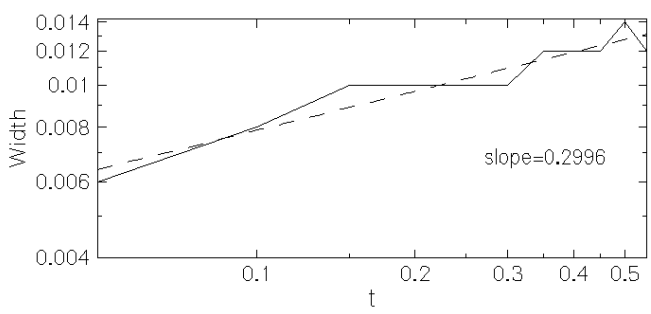

(a)

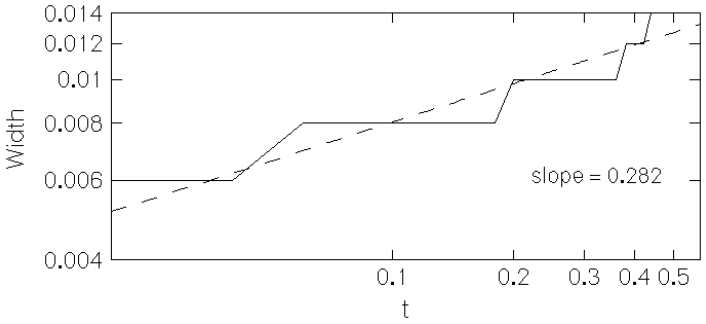

(b)

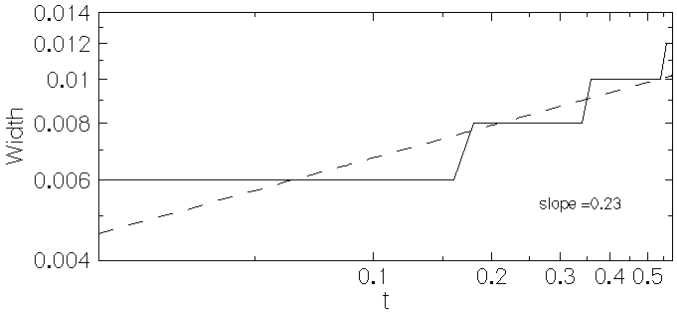

(c)

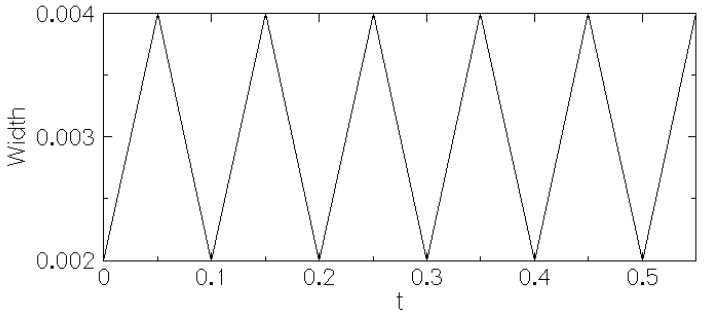

(d)

Growth of width of CD with time in **Diffusing Contact** for a resolution of 0.002 (a) S/F (1D) (b) S/F(2D, α=0) (c) S/F (2D, α =30). For (d)F/S, 1D **Width oscillates** between two values. Dashed line is the power law fit.

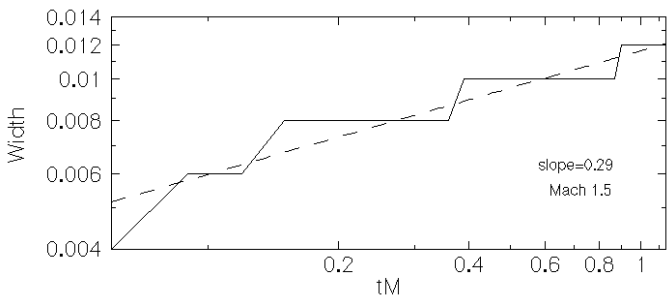

(a)

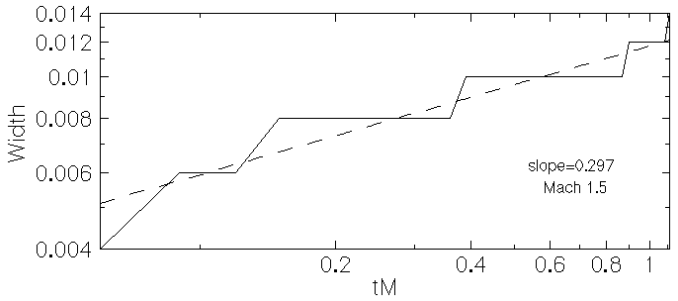

(b)

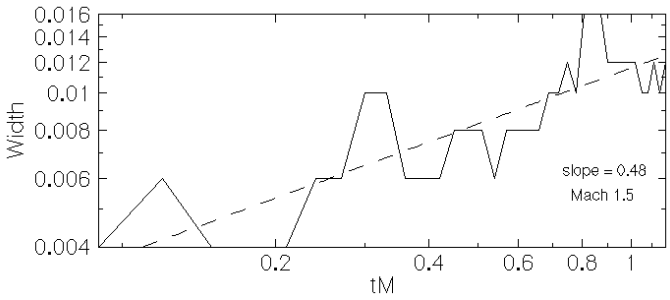

(c)

Growth of width of CD with time in **Shock Contact** interaction (Mach 1.5) for a resolution of 0.002 (a) S/F (1D) (b) S/F(2D, α =0) (c) S/F (2D, α =10). Dashed line is the power law fit.

WENO (width $\propto t^{1/4}$)

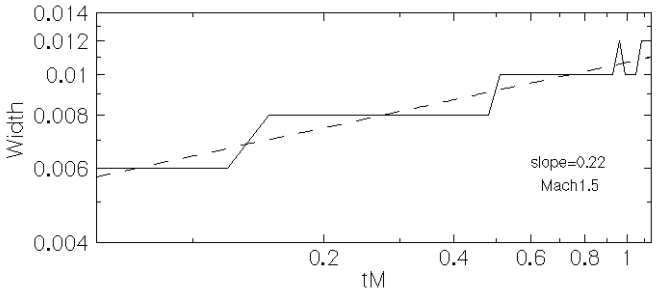

(a)

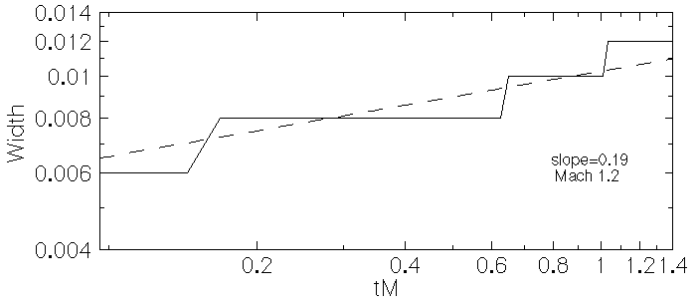

(b)

Growth of width of CD with time in **Shock Contact** interaction for a resolution of 0.002 (a)S/F (b) F/S Dashed line is the power law fit.

SPREADING RATES

Evolution	η or η*	Vel(U_0or M)	nD	α	C/r	Exponent(p)
F	0.14	1.5	1	N/A	PPM/2	0.2996
F	0.14	1.5	2	0	PPM/2	0.282
F	7.0	1.5	1	N/A	PPM/2	Oscillating
S	0.142	1.2	1	N/A	PPM/2	0.245
S	0.142	1.5	1	N/A	PPM/2	0.31
S	0.142	2.0	1	N/A	PPM/2	0.337
S	0.142	2.5	1	N/A	PPM/2	0.327
S	0.142	1.5	2	0	PPM/2	0.297
S	0.142	1.2	2	10	PPM/2	0.26
S	0.142	1.5	2	30	PPM/2	0.16
S	0.142	1.2	1	N/A	WENO/3	0.18
S	0.142	1.5	1	N/A	WENO/3	0.22
S	0.142	2.0	1	N/A	WENO/3	0.25
S	6.83	1.2	1	N/A	WENO/3	0.19
S	6.83	2.0	1	N/A	WENO/3	0.25

F or S – Freely evolving or Shock struck η or η* - Density ratio before and after shock passage

U_0 or M – Constant initial velocity or Mach number

nD – Number of dimensions C/r - Code/Order of code

VORTEX LOCALIZATION & NONLINEAR EVOLUTION SINGLE-MODE RM INTERFACE

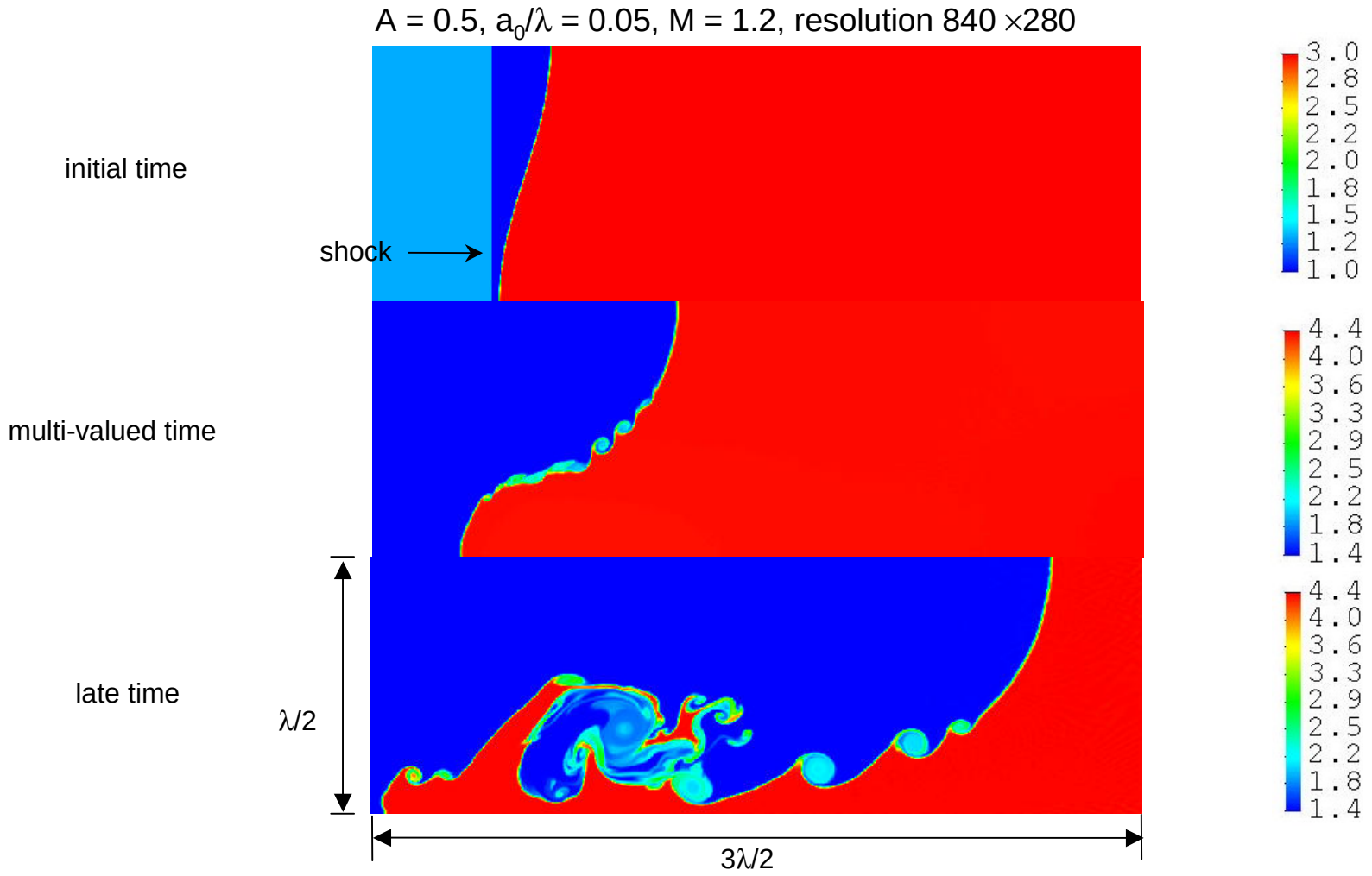

Three stages(*density*) of RM instability in shock-sinusoidal interaction : “initial time”, “multi-valued” and “late time.” The actual times are 0, 6.0 and 36; Atwood number is 0.5; initial density ratio is 3.0; Incident shock is M = 1.2; the perturbation is a_0/λ = 0.05; resolution 840 ×280 (PPM)

INTERFACIAL GROWTH RATE AND GLOBAL CIRCULATION

A = 0.5, a_0/λ = 0.05, M = 1.2

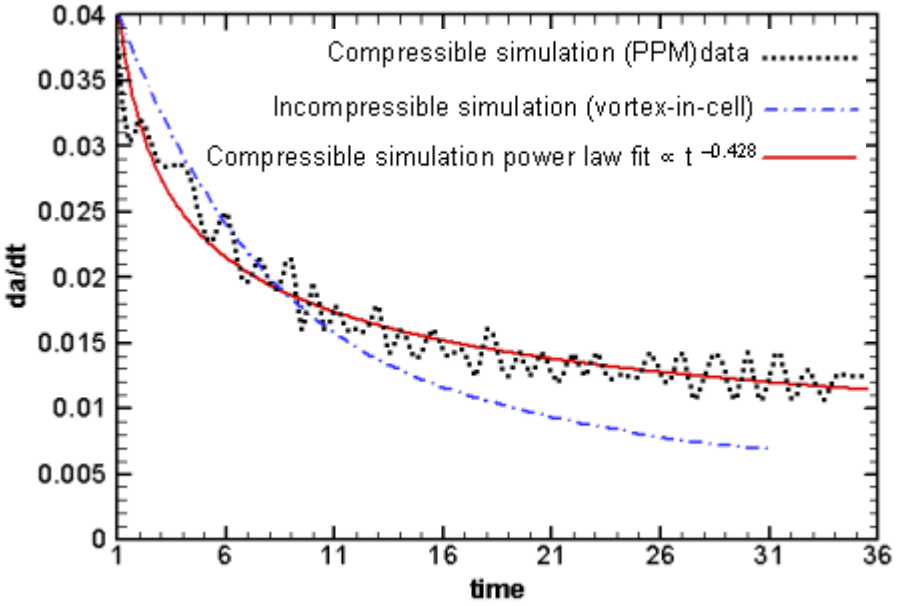

Interfacial growth rate obtained from compressible simulation(PPM), incompressible simulation (vortex-in-cell) and power law fitting for compressible simulation (PPM) data. For the power fitting: total RMS error ~ 8.7%, but for 16 < t < 36, da/dt = 0.013-0.15/ t and RMS error ~ 7%.

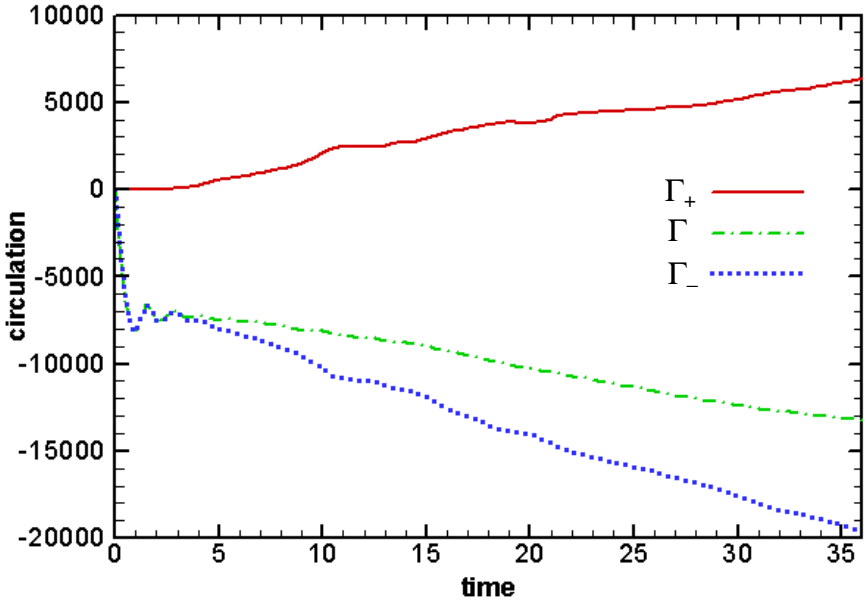

Positive (Γ_{+}), negative (Γ_{-}) and net (Γ) circulations obtained from compressible simulation (PPM). Secondary vorticity generation and associated instability contribute to interfacial growth rate.

CONCLUSIONS

- We present a systematic approach to quantify interfacial localization and temporal spreading in one dimension.
- We observe asymmetry in interfacial spreading rates for the one and two dimensional PPM simulations for F/S and S/F configurations. These are not present in a WENO simulations.
- Evolution of sinusoidal RM interface at late time exhibits large growth of positive and negative “secondary” baroclinic circulation. Interfacial growth rate is not (1/t) and depends on Atwood number.

Instability modeling for NIF ignition targets and Omega experiments

**S W Haan, T Dittrich,
G Strobel, M Marinak,
D Munro, G. Glendinning,
P. Amendt, and R. Turner**

X-division

University of California
**Lawrence Livermore
National Laboratory**

**Presented to:
IWCTM 2001
Pasadena
Dec 2001**

*This work was performed under the auspices of the U.S. Department of Energy by the University of California, Lawrence Livermore National Laboratory under contract No. W-7405-Eng-48.

Summary: We are continuing to explore hydro instability issues on NIF targets, and verifying modeling with Omega experiments

Specifications are being completed for a variety of indirect drive targets:

- **Beryllium, polyimide, CH(Ge) ablators**
- **Drive temperatures 250 - 350 eV, spectra for gold or cocktail hohlraum**
- **Scales from 100 kJ to 600 kJ into capsule (NIF energy ~1.8 MJ)**

Details such as ^{3}He buildup in the core are being analyzed

Modeling of Omega planar polyimide Rayleigh-Taylor foils is close to experiments

A new design for convergent Rayleigh-Taylor experiments on Omega will test other aspects of the modeling

Generically the ignition targets all look the same as for the last 10 years or so

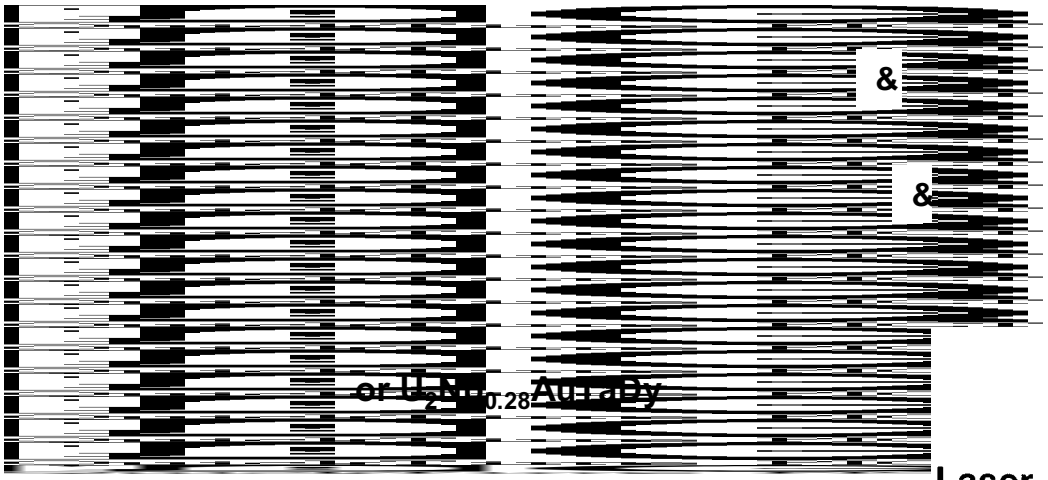

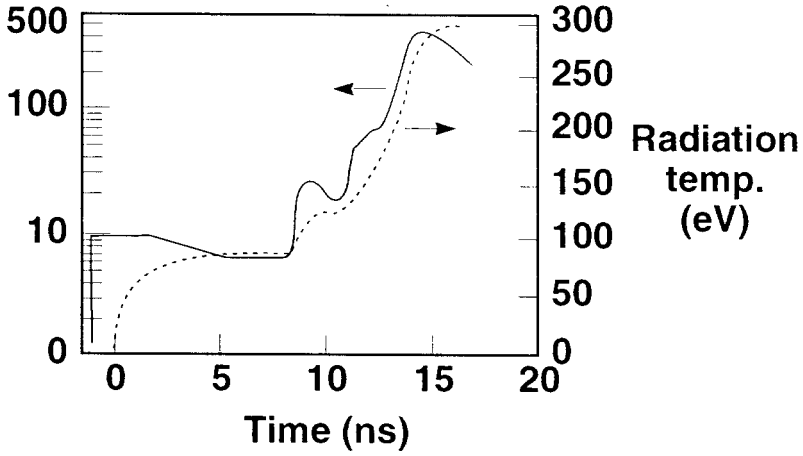

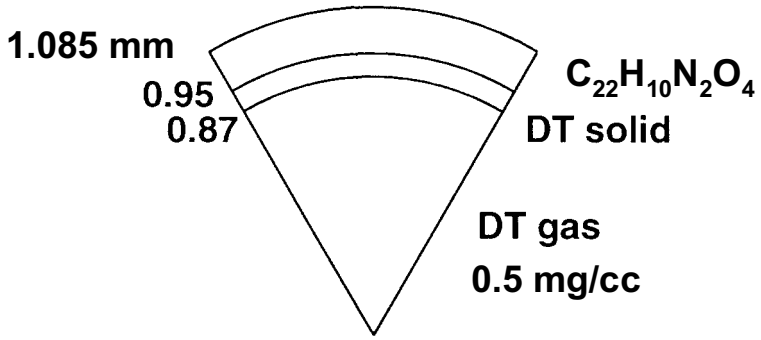

Our current instability modeling is based entirely on explicit full simulations of perturbation growth and its impact on ignition and burn

- Single shell cryogenic capsules are ablatively stabilized on outside during acceleration, and on inside during deceleration
- Simulations indicate that modes beyond about 120 do have any appreciable amplitudes at any times of interest
- Experiments have generally been compatible with simulations giving us confidence in them
- Modeling is done in 2D (LASNEX and Hydra) and 3D (HYDRA) for single modes, and for multiple modes over various solid angles
- Biggest uncertainties are considered to be in the input: spectrum of drive radiation, opacities, characterization of initial perturbations

There are three failure modes we see in our simulations

- **Acceleration: Modes l ~100 grow and disrupt the shell**
  Especially a problem if shell is too thin
- **Deceleration: Modes l ~15 create spikes that cool the hotspot**
  Especially a problem if shell is too thick
- **Low modes: If there is much solid angle with $\rho r < 1$ g/cm^2, bubbles blow out and yield is reduced**

A successful target is optimized to trade off the first two issues, and has enough 1D ρr to minimize the third. Requires power and energy to have room to trade them off!

This plot summarizes ablator-seeded Rayleigh-Taylor results for the different capsules

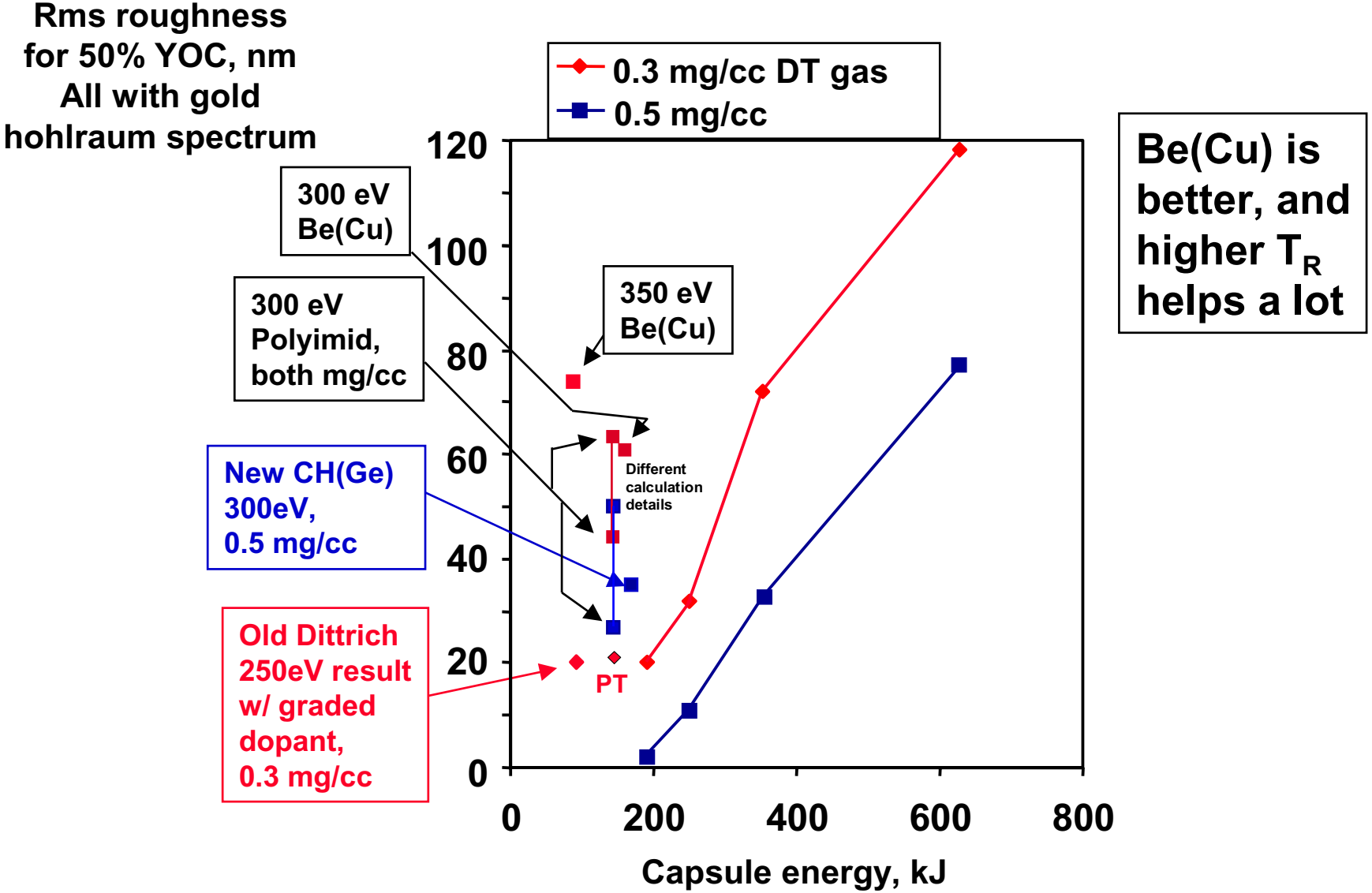

600 kJ capsules might be constrained in foot length, at a significant energy price

Largest scale might have foot increased in order to keep total pulse length close to 20 ns

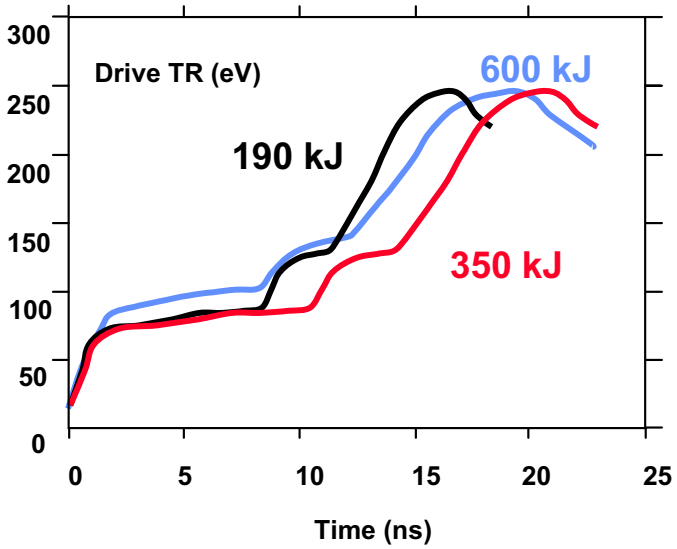

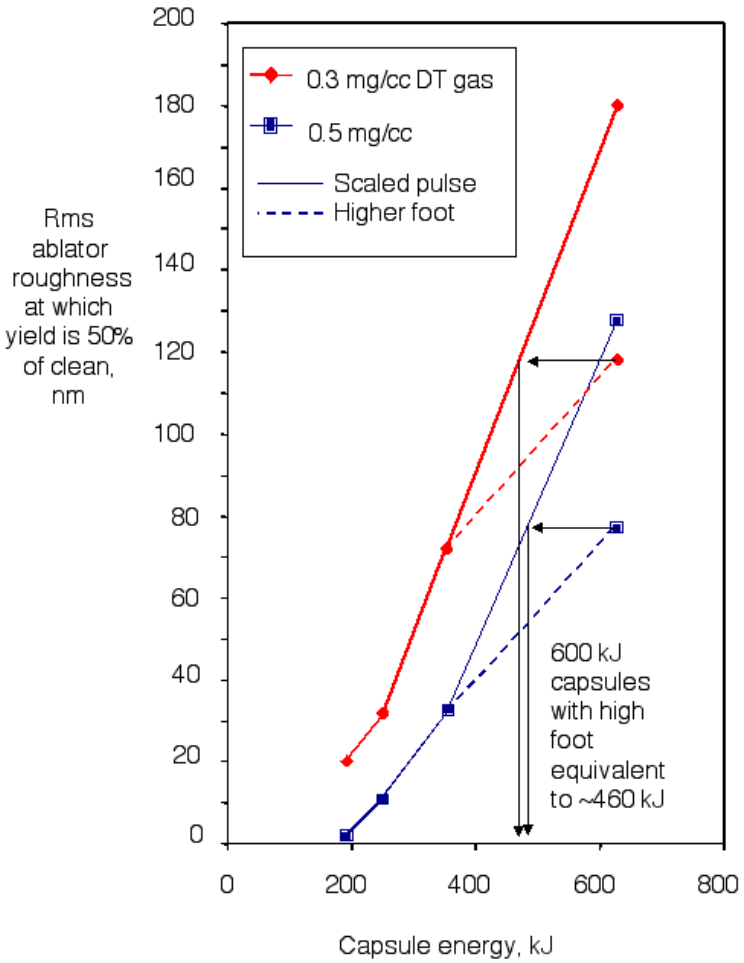

If shock-crossing time is fixed,
velocity ~ S^1
foot level flux F ~ S^2
Adiabat β ~ $S^{1.2}$
Margin ~ $S^3\beta^{-1.5}$ ~ $S^{1.2}$ ~ $E^{0.4}$ instead of E^1

Surface roughness specifications are tighter if there is ^{1}H or ^{3}He in the central gas

- Both are "dead weight" w/ respect to hydro, ignition & burn
- Atom-for-atom, ^{3}He is worse—more electrons and ion charge, increases radiative and conductive losses
- But gram-for-gram, ^{1}H is slightly worse—3x more atoms/g

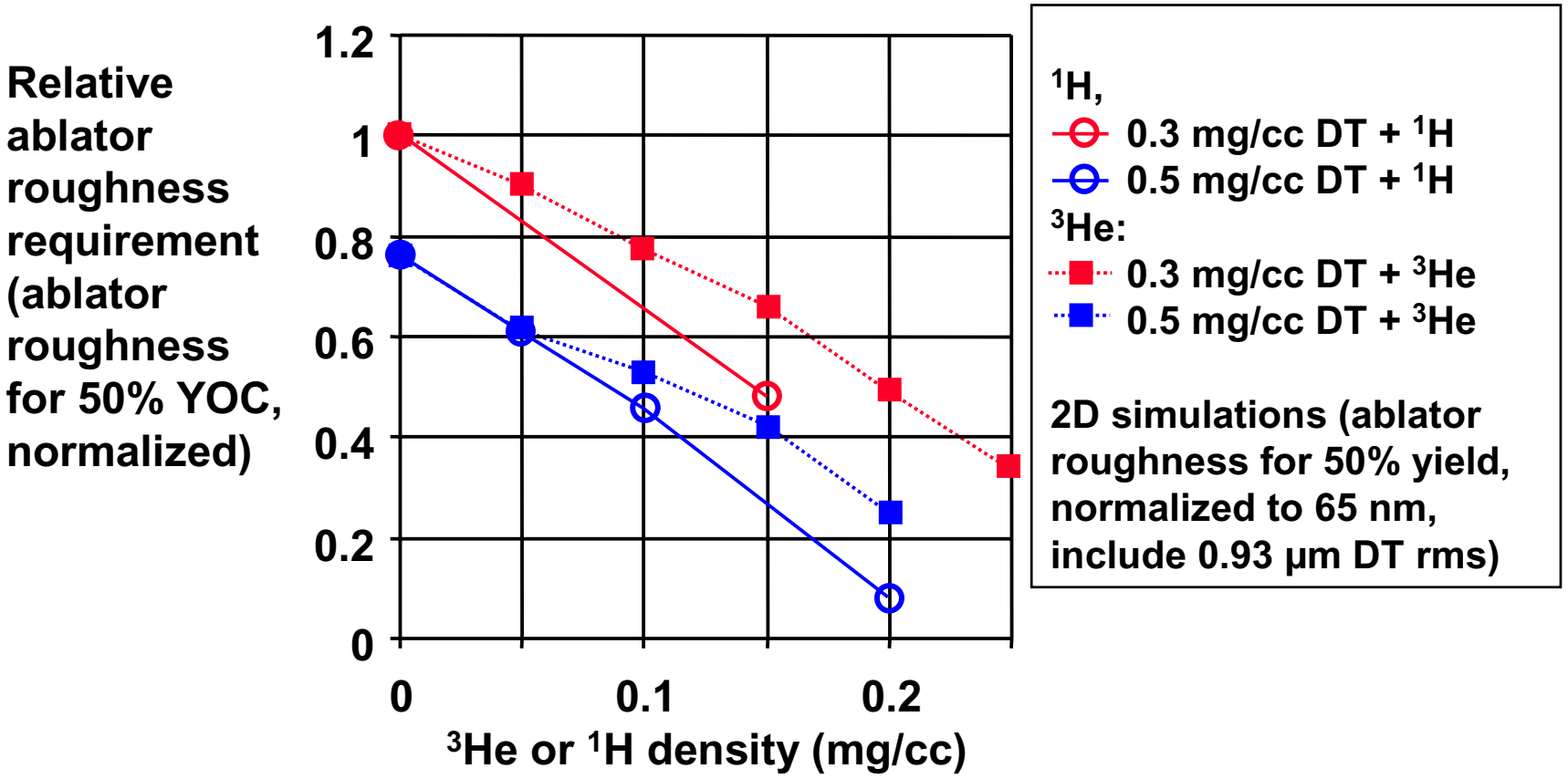

The calculated NIF cocktail spectrum is intermediate between Planckian and gold

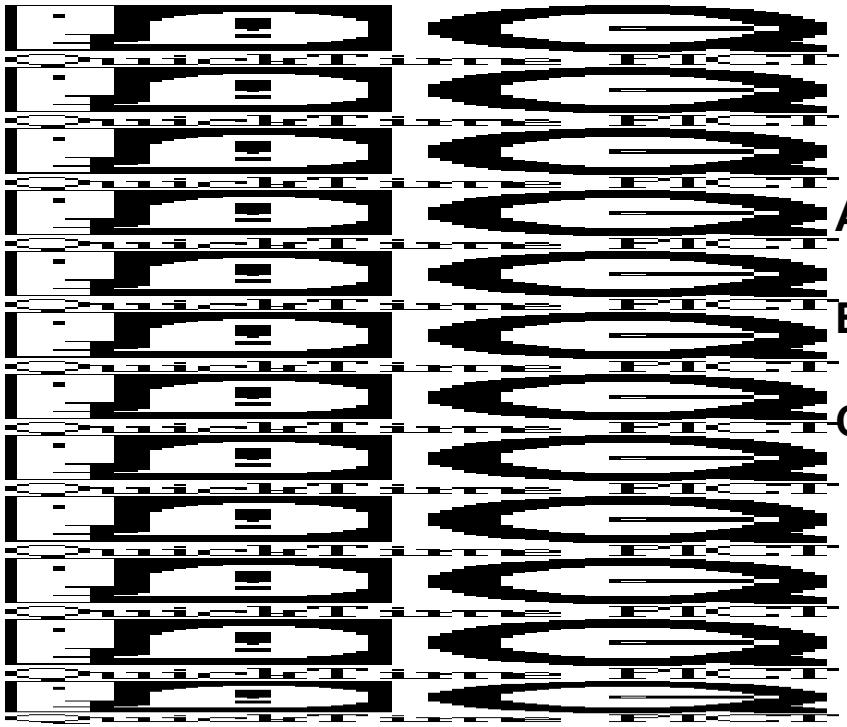

A (black) typical gold spectrum

B (red) cocktail calculation (Pollaine)

C (blue) Planckian w/ same flux

Need to do simulations of effect on Rayleigh-Taylor of actual cocktail spectrum

With a Planckian drive, baseline polyimide NIF capsule shows 85% more Rayleigh-Taylor growth

Growth in 2D simulations, very small multi-mode pert on ablator initially

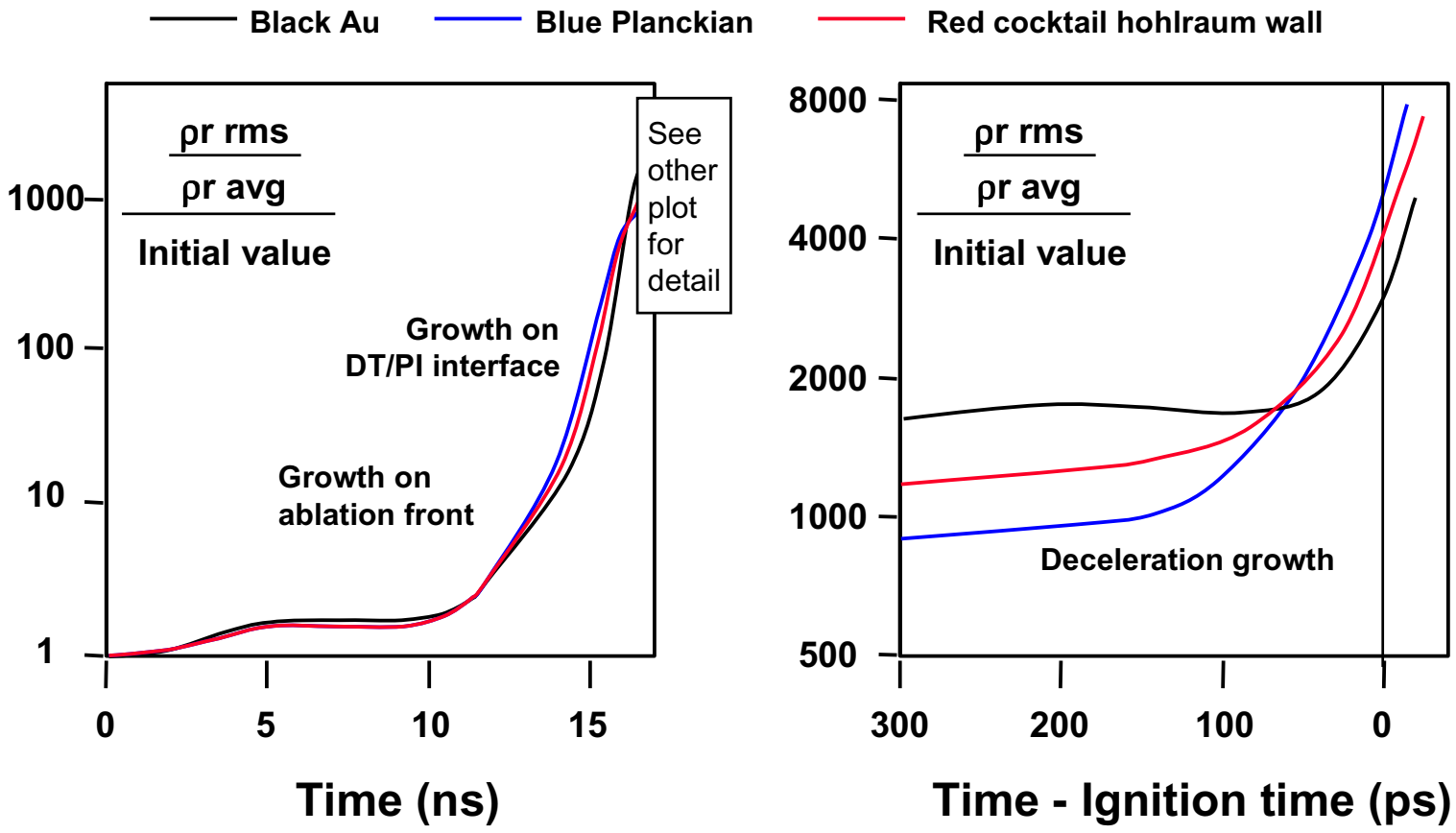

Complicated interplay of growth on the various interfaces
With doped ablators, may be able to reoptimize w/ cocktail wall

We are doing Rayleigh-Taylor experiments on Omega to verify modeling of polyimide

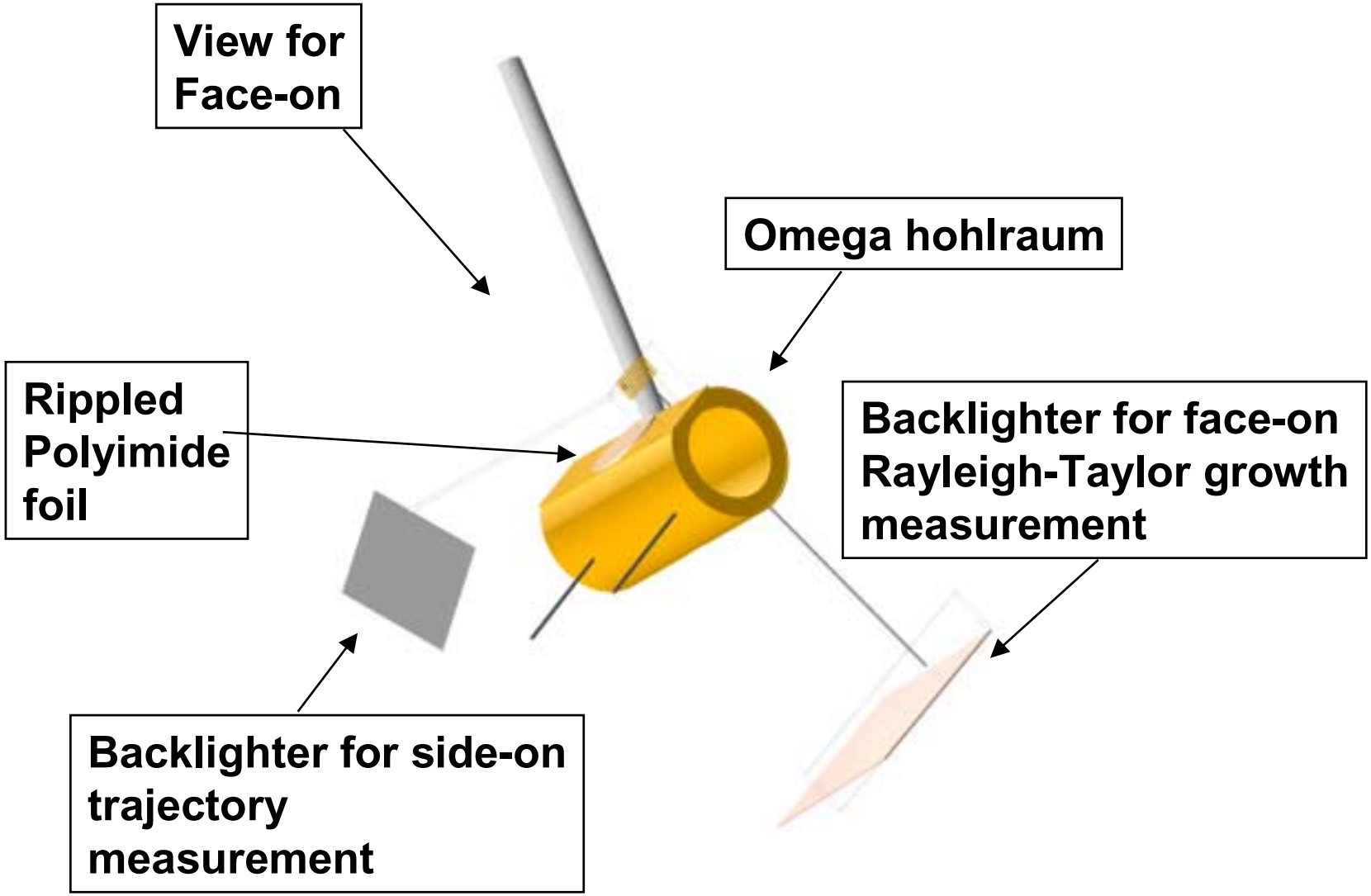

Peter Amendt has done hohlraum simulations that fit the Dante flux measurement

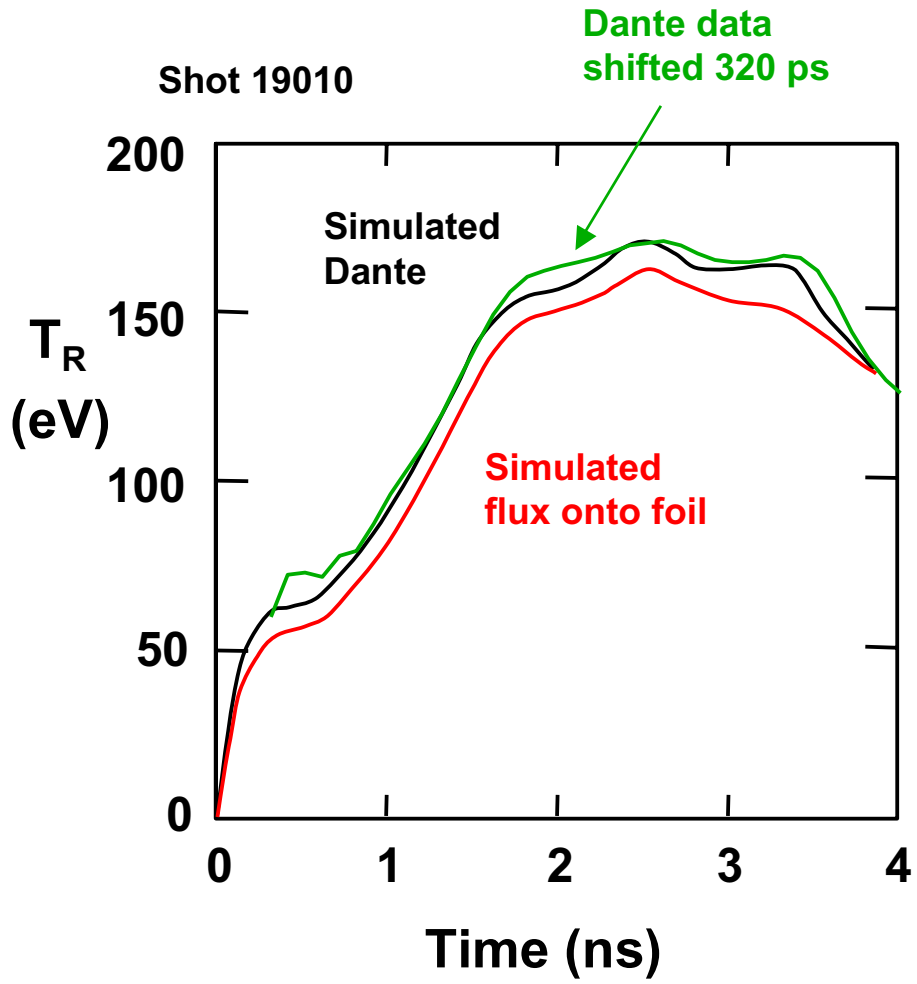

Post-process to simulate Dante: almost high enough to fit data (black curve compared to green).

Simulated drive for package is red curve, about 10 eV lower

There's a significant geometrical correction (like the old albedo correction, but now in the other direction) that we need to incorporate

Simulated drive extracted from Peter's hohlraum calculations makes sideons very close to data

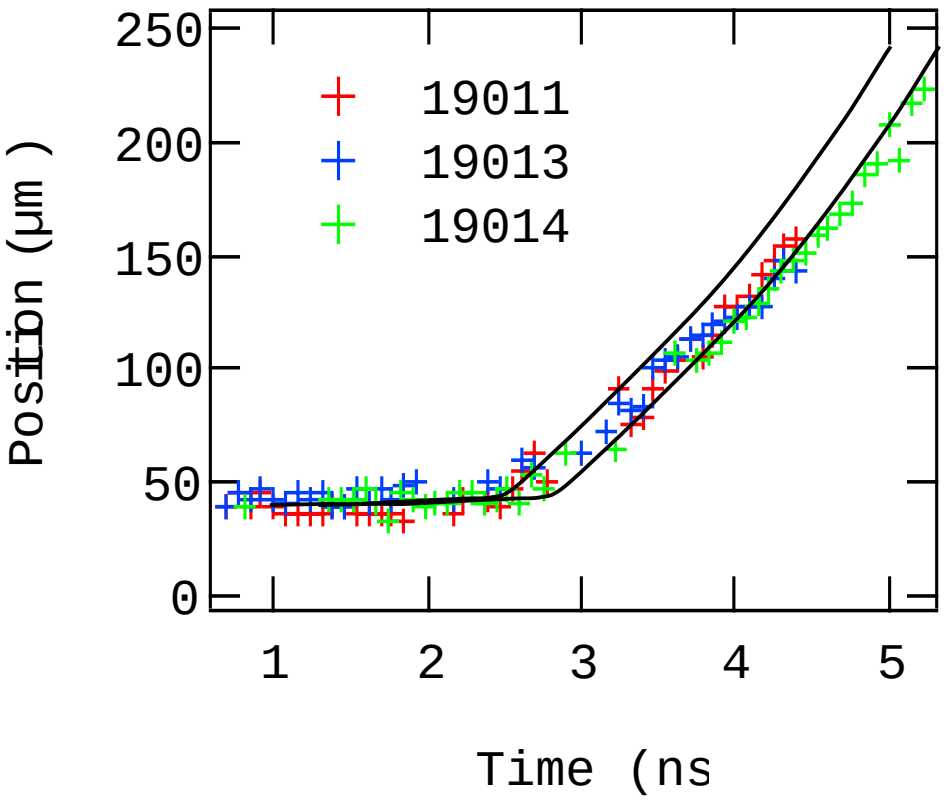

Simulation using Peter's simulated drive

Also shown shifted in time, improves fit

Peter's hohlraum simulations include a foil, its side-on motion agrees with my foil-only simulation

I have finished one case faceon and sideon from June 00 shots with the new source info

Source was Dante-25eV, with M-band adjusted (by factor of several) to match Dante M-band fraction

Gail says this is the one reliable side-on from this series

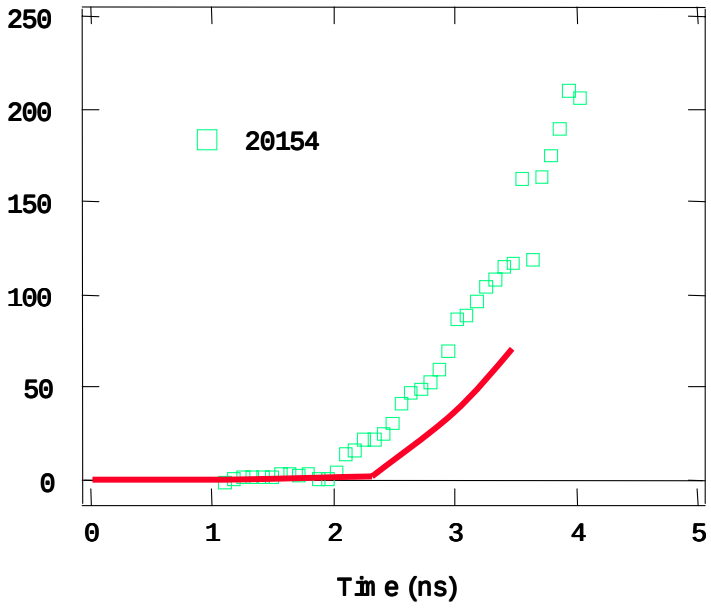

Face-on

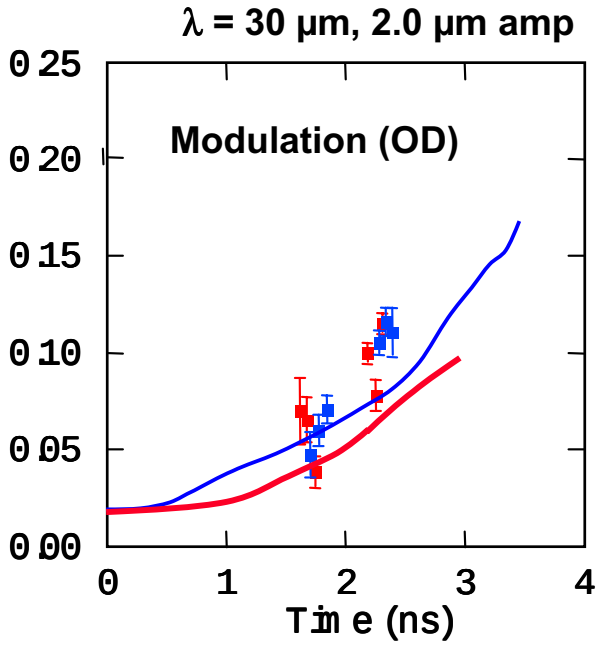

Old drive
New drive

This is late and slow, meaning we've overcorrected the drive, which is very good news

The simulations I've shown previously for the June 00 faceons used this drive profile

Profile I used for old face-on work

19010 simulated source from Peter (aruguably fits sideons)

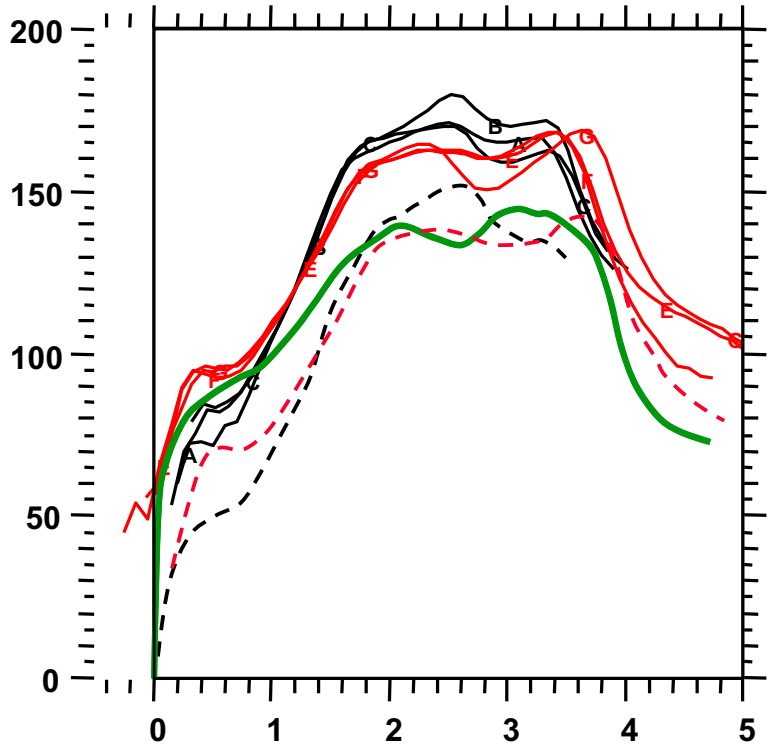

Dante:

Black 19010, 1, 3 (Feb 00)
(sideons we've been trying to fit)

Red 20154 5 6 (June 00)
(faceon shots)

All Dante retimed to go through (1.2 ns ,120 eV)

All plots are with CEA calibration

Black solid to black dashed is geometry correction + ~10 eV that Dante is still high compared to simulations. (Arguably fits sideons) Same correction to red curves would be "right" profile, compare to green curve.

Red dash is face-on Dante -25eV, shifted 0.1ns to get good time 0 -- best guess at drive for faceons 20154-6. On old green profile, foot was too high, peak not bad

With that profile I had a decent fit, need to revisit now that sideons are more or less sorted out

- Better simulations use opacity tables generated from OPAL code
- Increases growth slightly, improves agreement at 30 microns

Simulations using XSN opacities, Dante drive, calculated spectrum (same as above)
OPAL opacities, drive shown above and calculated spectrum
OPAL opacities, Planckian spectrum

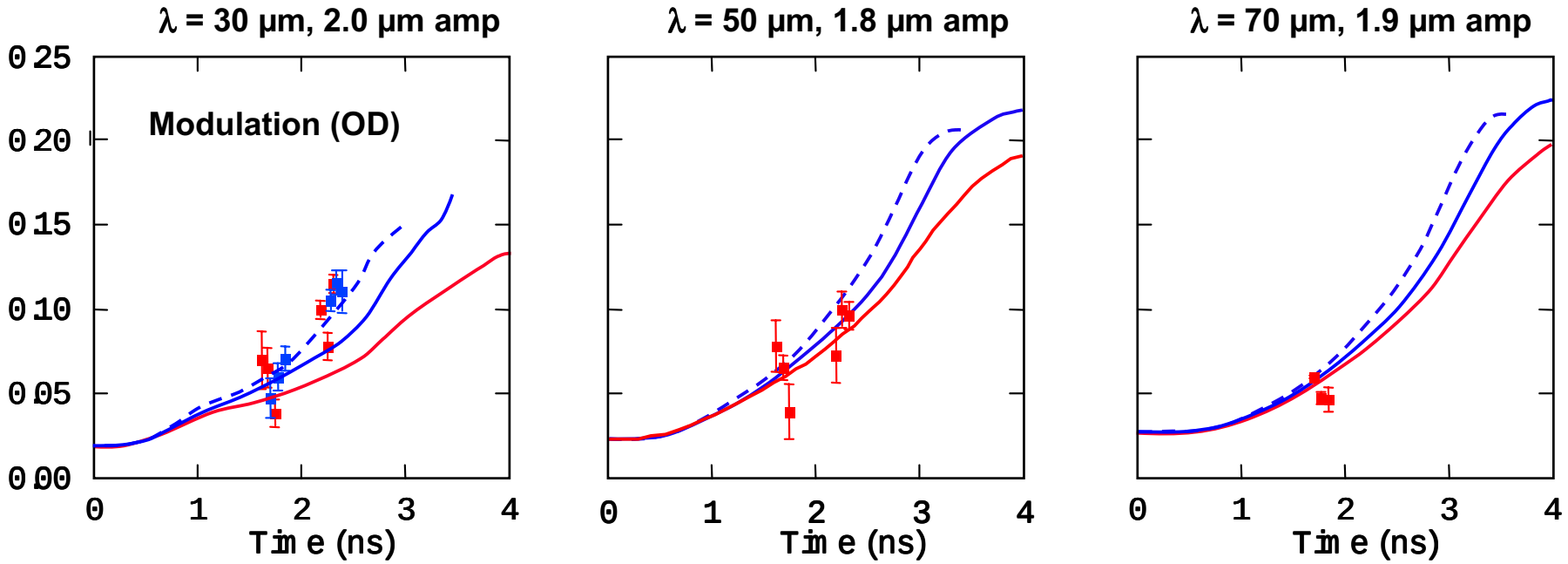

Recent shots in cocktail hohlraum had this drive

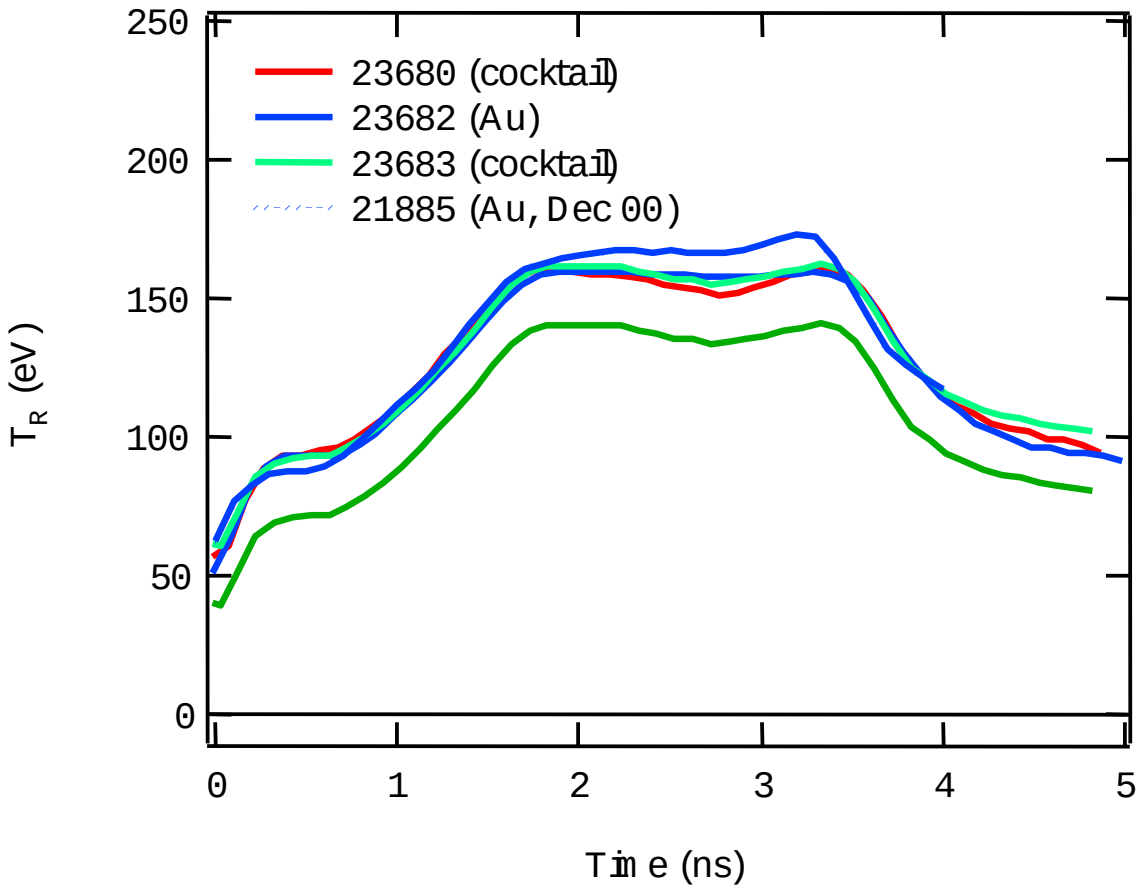

Dante curve 23683, minus 25 eV from "typical" temperature for this series, shifted +200ps for Dante timing -- used as source for foil simulations

At 70 micron wavelength, we see good agreement between simulated and observed perturbation growth

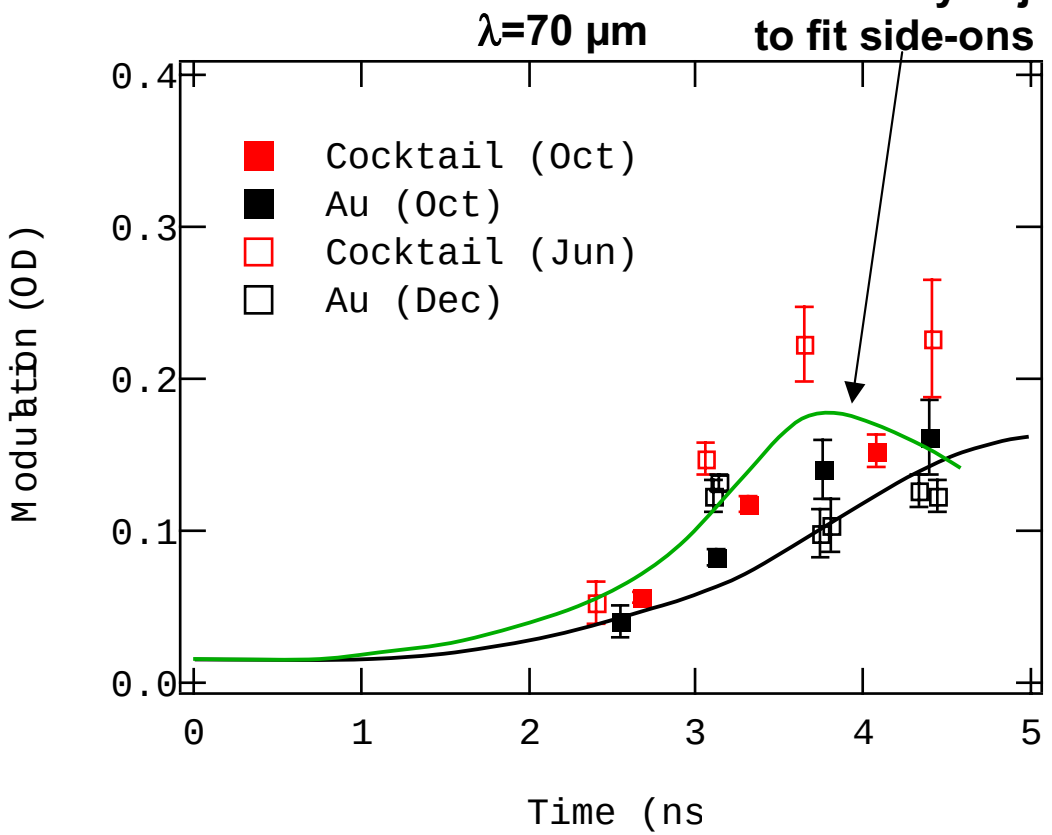

17eV lower, too low to fit side-ons

70 μm happens to be the wavelength at which experiments have worked to date. Need to get data comparing Au and cocktails at smaller wavelengths!

At 70 μm wavelength there is no difference between Au and cocktail drives in modulation growth. Early shots seemed to show experimental difference, but not more recent data

We are also planning convergent Rayleigh-Taylor experiments with a mock fuel layer

- On NIF capsules, perturbation ends up growing on interface between ablator and fuel, which becomes increasingly unstable as shells implode

- Converging geometry is a big part of the physics determining densities, plus something we haven't done enough with yet

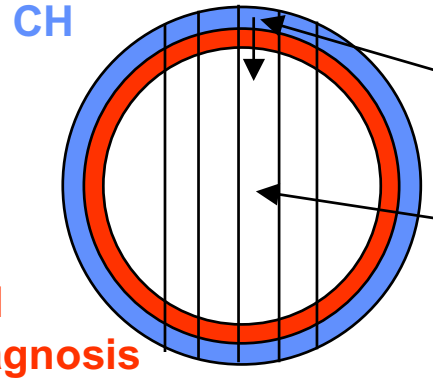

Impose perturbations, view face-on

Image here may give "side-on" growth measurement

Image here will give "face-on" ρr growth measurement

Be stays at density > CH
Doped with silver for diagnosis

Similar to experiment calculated by Dittrich for 0.6-scale NIF noncryo

With a beryllium mock fuel layer we do a decent job of mocking up the interface instability

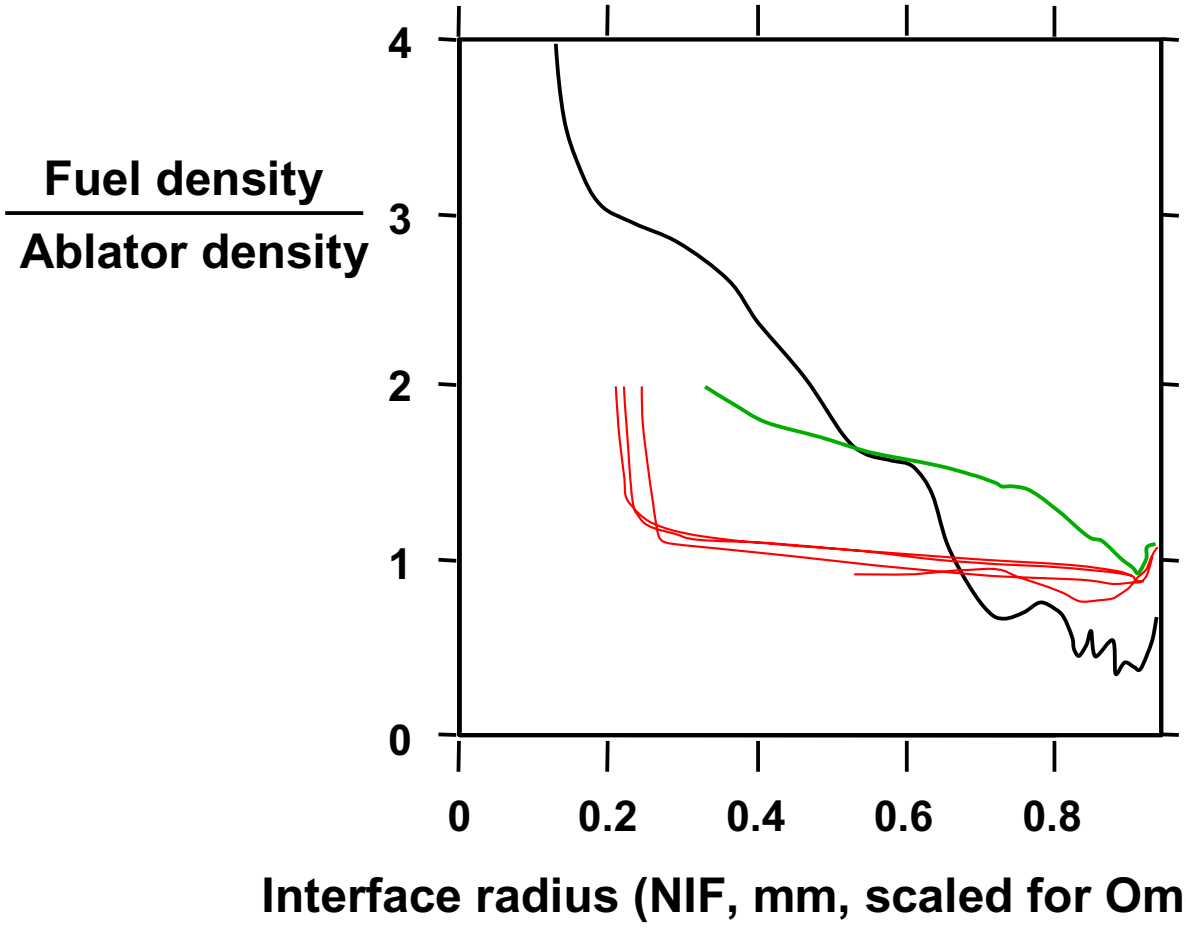

Black NIF

Green CH over Be(Cu)

Also tried
CH(Ge) over CH(Ti)
Ge= 0,1,2.5, and 4%
(red curves)

We are working on optimizing this experiment

Current thinking: ramp pulse that pushered single shell program developed, they are verifying symmetry

Capsule 210 μm outer radius,
23 μm CH / 4μm Be+0.5% Ag / 3 μm mandrel

Gives good density profiles, and good images

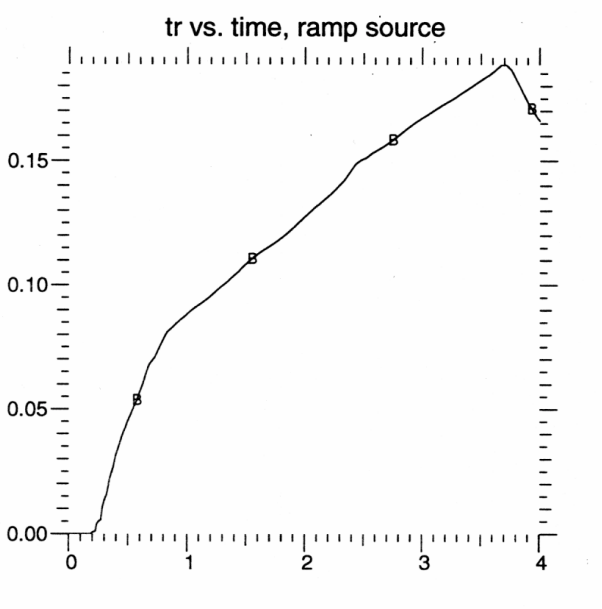

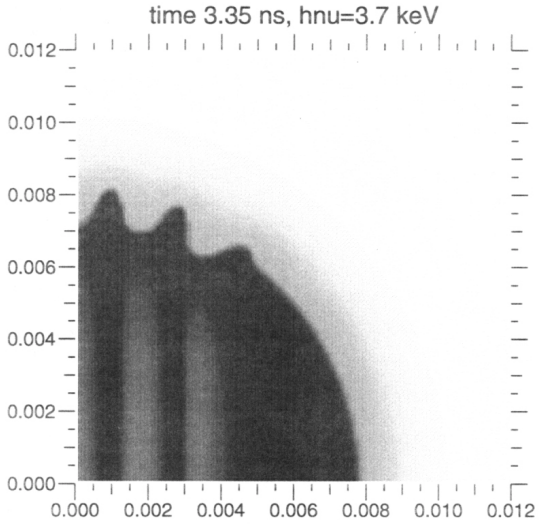

Simulated image from 1 μm initial amp, 50 μm initial wavelength, 2 1/2 waves at waist cut into ablator

Molecular Dynamics Simulation of Shocks and Richtmyer-Meshkov Instability in Cylindrical Geometry

angular velocity at t = 30

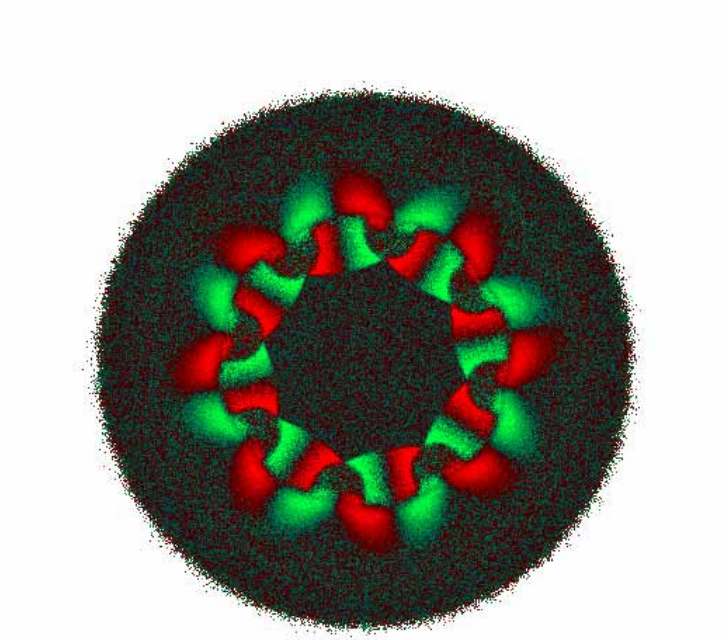

density at t = 100

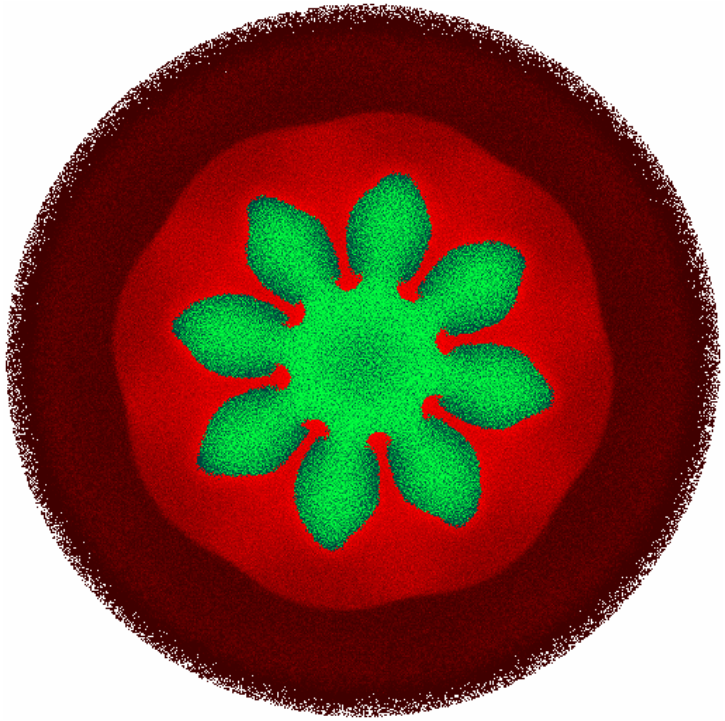

K. Nishihara, V. Zhakhovskii and M. Abe
Institute of Laser Engineering, Osaka University
www.ile.osaka-u.ac.jp/research/TSI/Vasilii

18 IWPCTM,
December 10-14, 2001
Pasadena, USA

Introduction

Difficulty in hydrodynamic simulation in converging geometry

ILE OSAKA

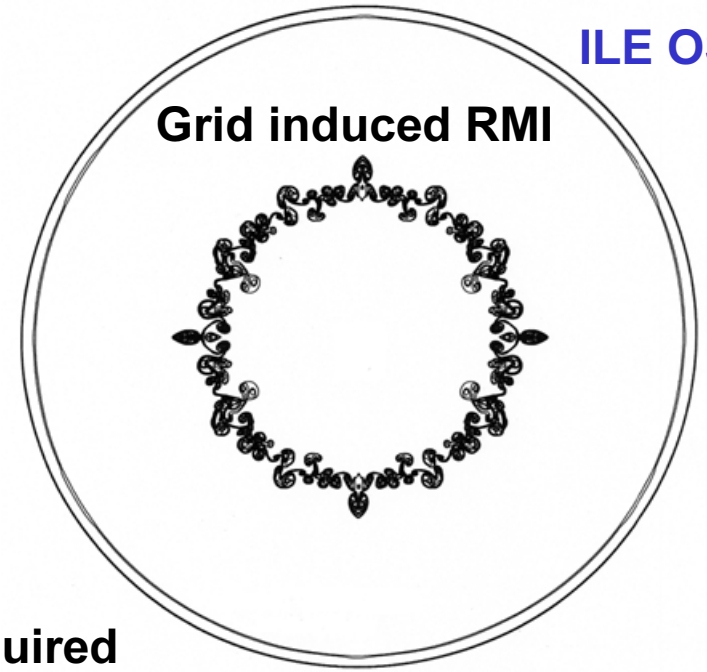

- Singularity at the center
- Numerical instability and viscosity depend on the grid structure

↓

Molecular Dynamic Simulation

Advantage

spatial mesh and EOS are not required
non LTE system can be treated
viscosity, heat conduction are automatically taken into account
conservation laws are automatically satisfied

Disadvantage

system size limited by computer power
limited temperature

Today's hydrodynamic codes looks well but they are still inaccurate

RM gas curtain experiments and simulations

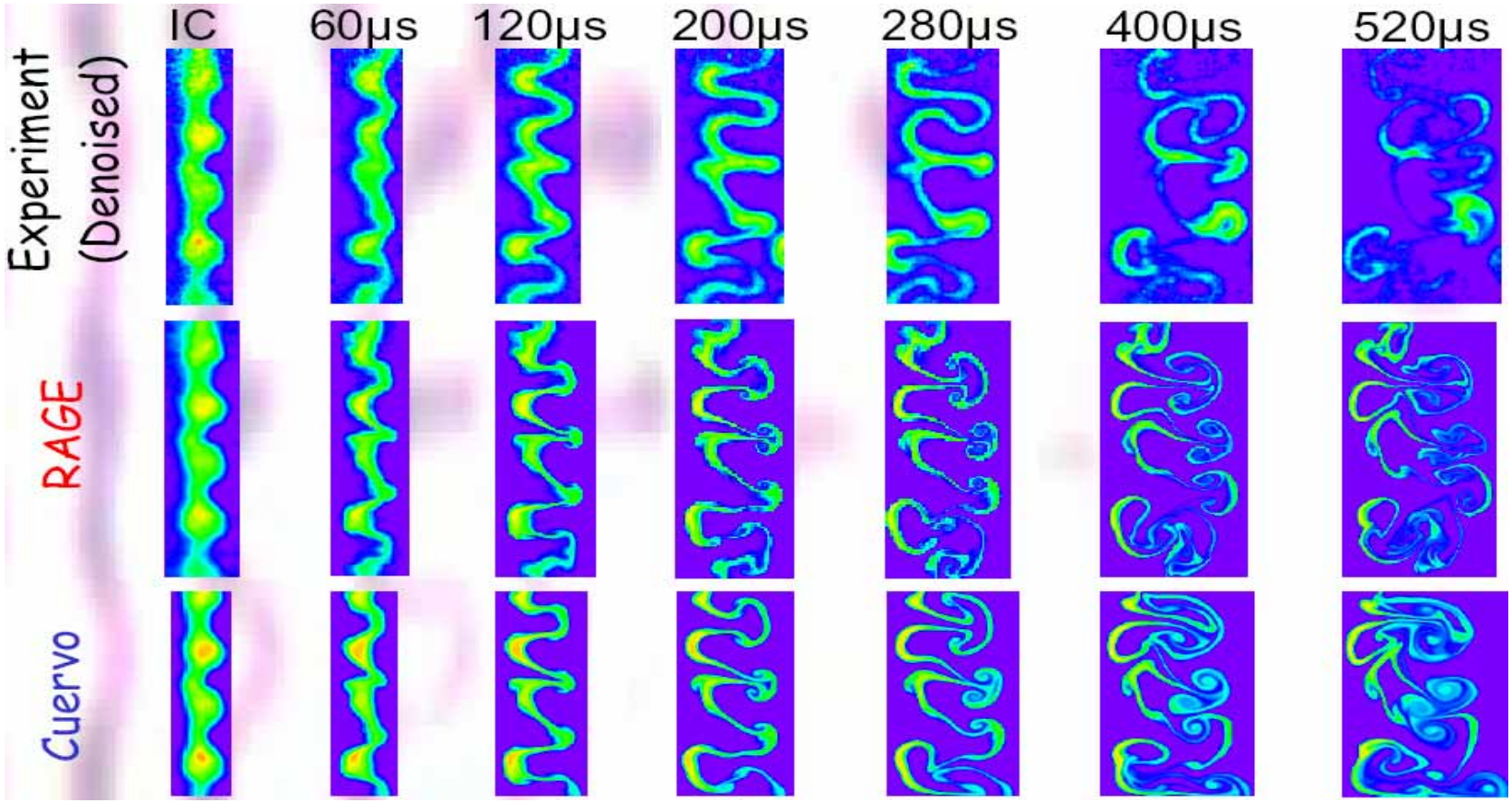

Pictures from W.Rider and J.Kamm, LANL

executive summary

- MD simulation provides a new tool for a study of hydrodynamic instabilities, when CFD fails.
- Mode dependence of nonlinear growth is investigated for cylindrical RMI. Higher mode decays slower.
- Growth of mixing zone in cylindrical RMI is much larger than that in planar RMT (shocks hit interface repeatedly).
- In a shell case (two interfaces), many higher modes appear on its inner surface, and thickness of mixing zone is thinner than that on single interface.

Outline of Talk

- Introduction of Molecular Dynamic simulation
- Shock wave in cylindrical geometry

  structure and stability of rippled front
- Richtmyer-Meshkov instability in cylindrical geometry

  nonlinear dynamics of RMI

  dependence of nonlinear growth on mode number

  comparison with planar geometry

  shell structure

  (animation)

Molecular dynamics simulation technique

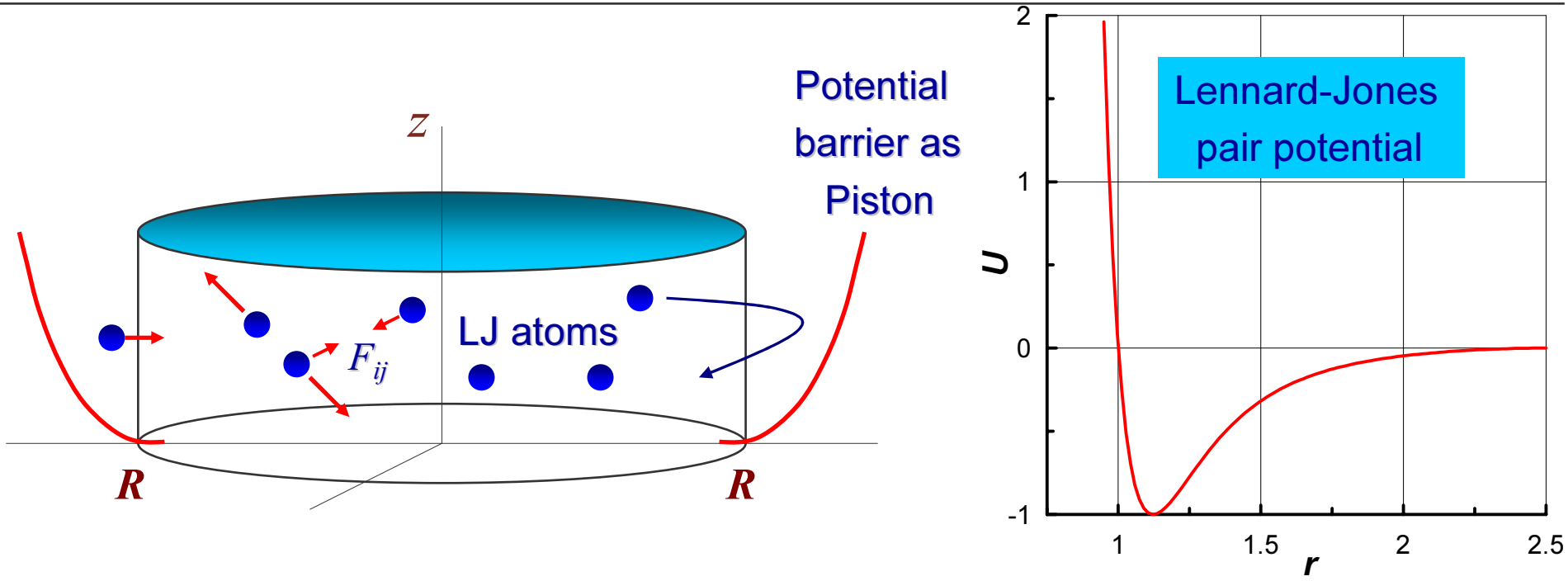

- **Periodical boundary conditions are imposed on the system along z-axis**
- **The atoms interact via Lennard-Jones (LJ) pair potential with cutoff at r_c**

$$\phi_{LJ}(r) = 4\varepsilon[(\sigma/r)^{12} - (\sigma/r)^{6}] \quad \text{if} \quad 0 < r < r_c = 2.5\sigma$$

- **The piston is simulated by an external potential ~$[\, r_i - R(\phi_i, t)]^2$ and its position may depend on angles in case of perturbed boundary as well as on time to generate shock waves.**

Shock R-H relations are satisfied within accuracy of 10^{-5}

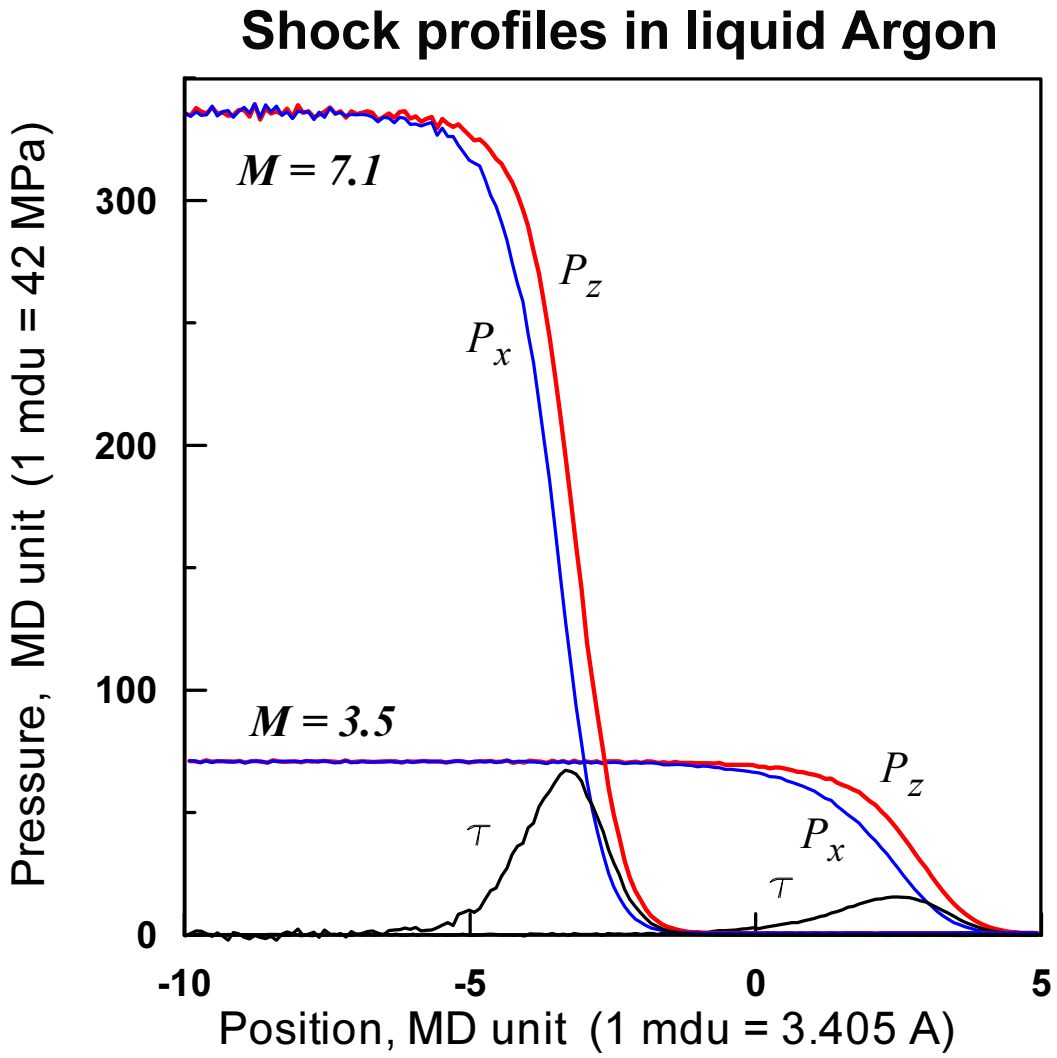

V. Zhakhovskii, K. Nishihara,
S.I. Anisimov, and S. Zybin
JETP Lett., v.65, 755 (1997)
JETP Lett., v.66, 99 (1997)
PRL, v.83, 1175 (1999)

Shock front thickness is enough thin compared with perturbation amplitude

Molecular dynamics simulation technique

Typical snapshots of MD systems at the beginning of compression

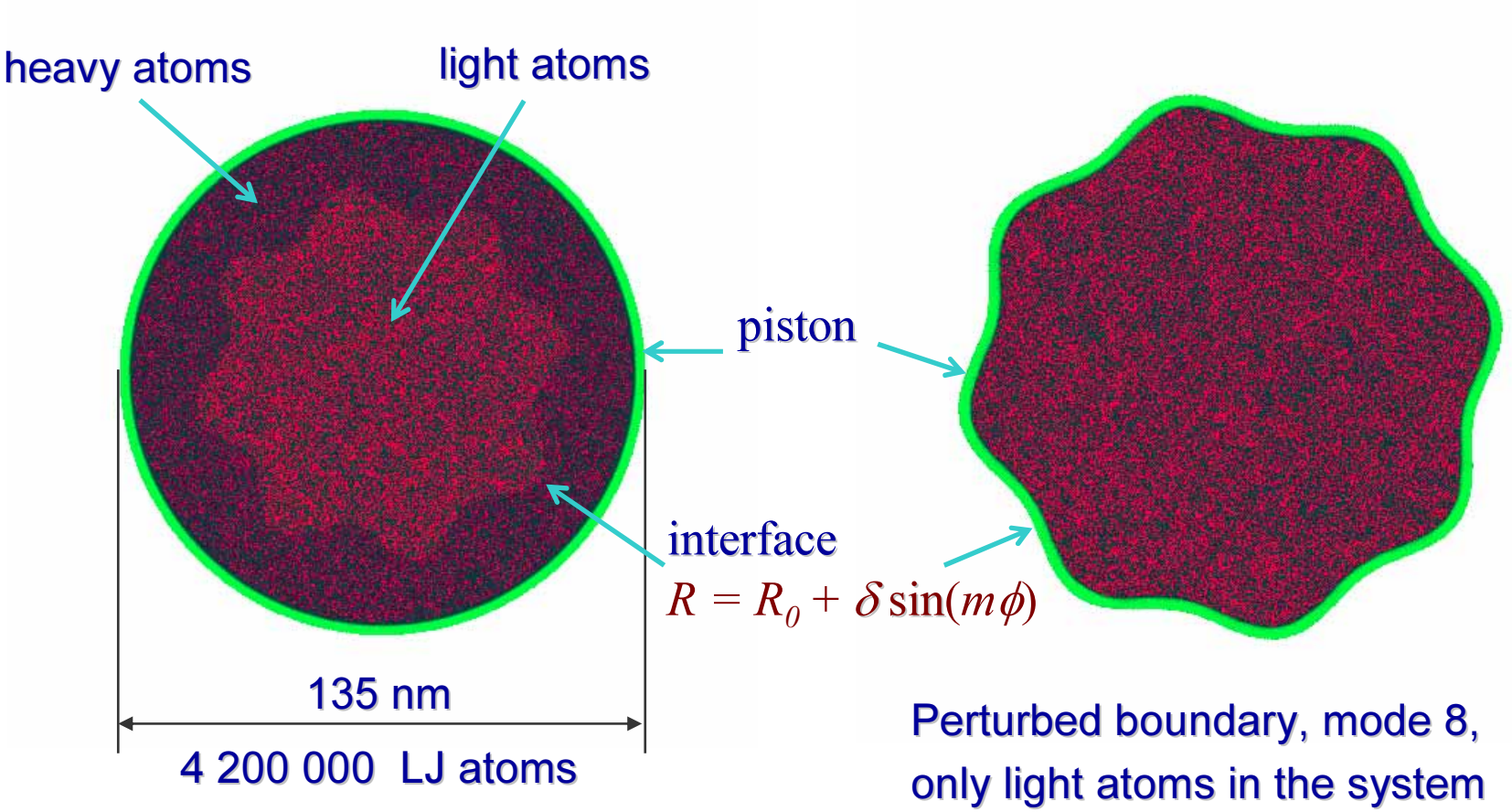

- Each pixel represents a small domain, which is occupied approximately 30 atoms
- Green colors correspond negative radial velocity of a domain, red colors mean positive velocity. *Brightness* is proportional to absolute values and balances according maximal amplitude.

MD simulation of perturbed shock front, of which ripples oscillate in time.

First generation of Mach stems appears at very early stage of SW converging

Brightness is proportional to density.

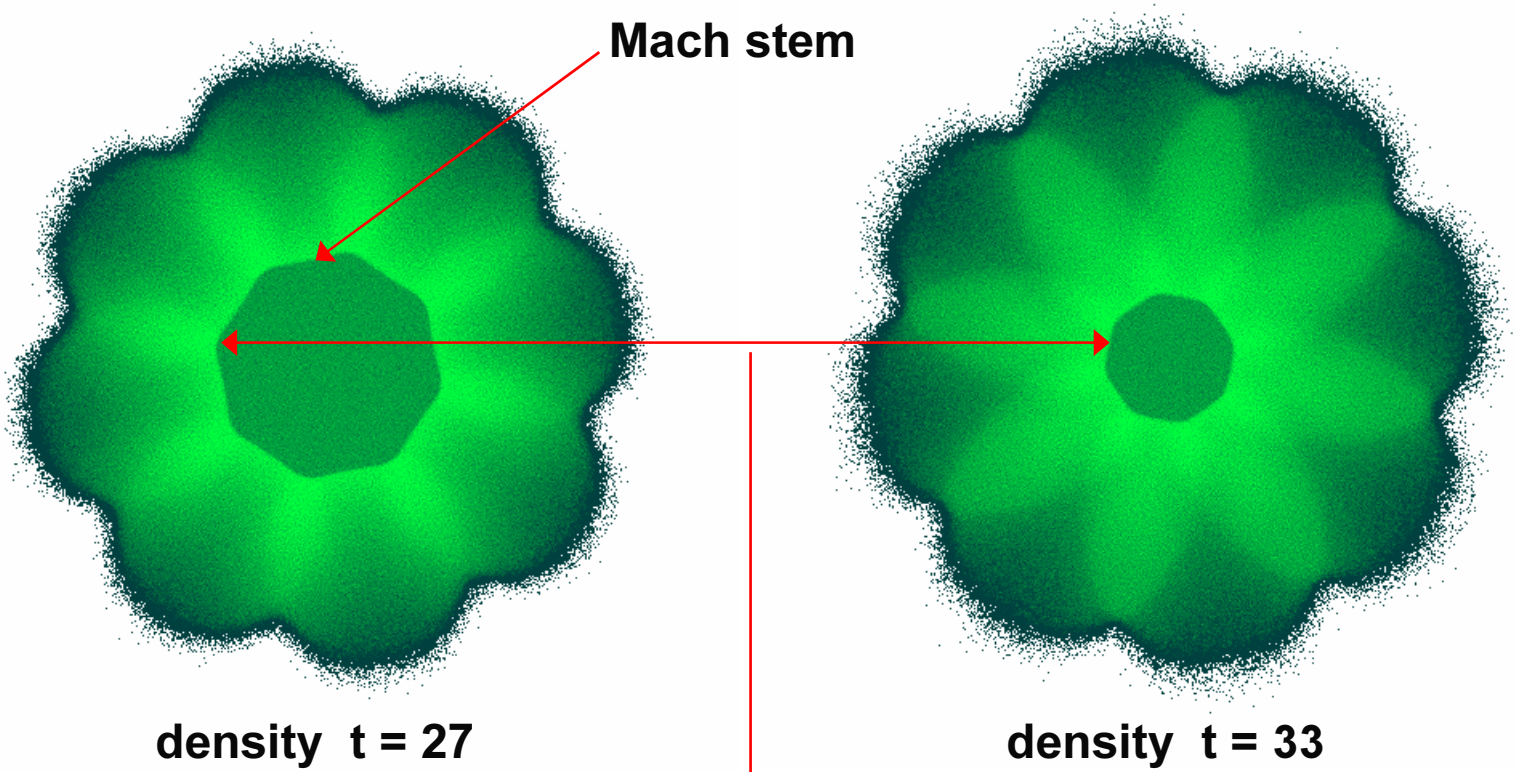

instead of circle the polygons (8 or 16 sides for mode 8) converge to center

Converging shock wave is unstable for low mode number

initial Mach number M = 3.1

$$\frac{\delta R(t)}{R(t)} = a\left(\frac{R(t)}{R_0}\right)^{\gamma}$$

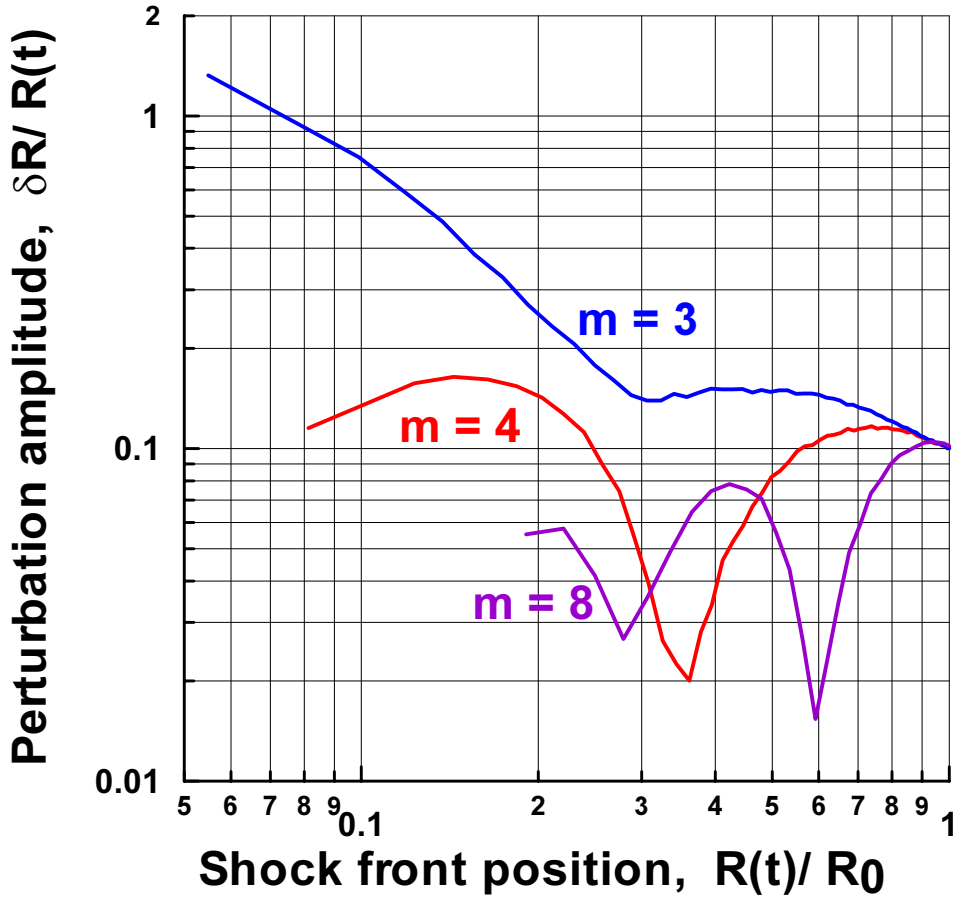

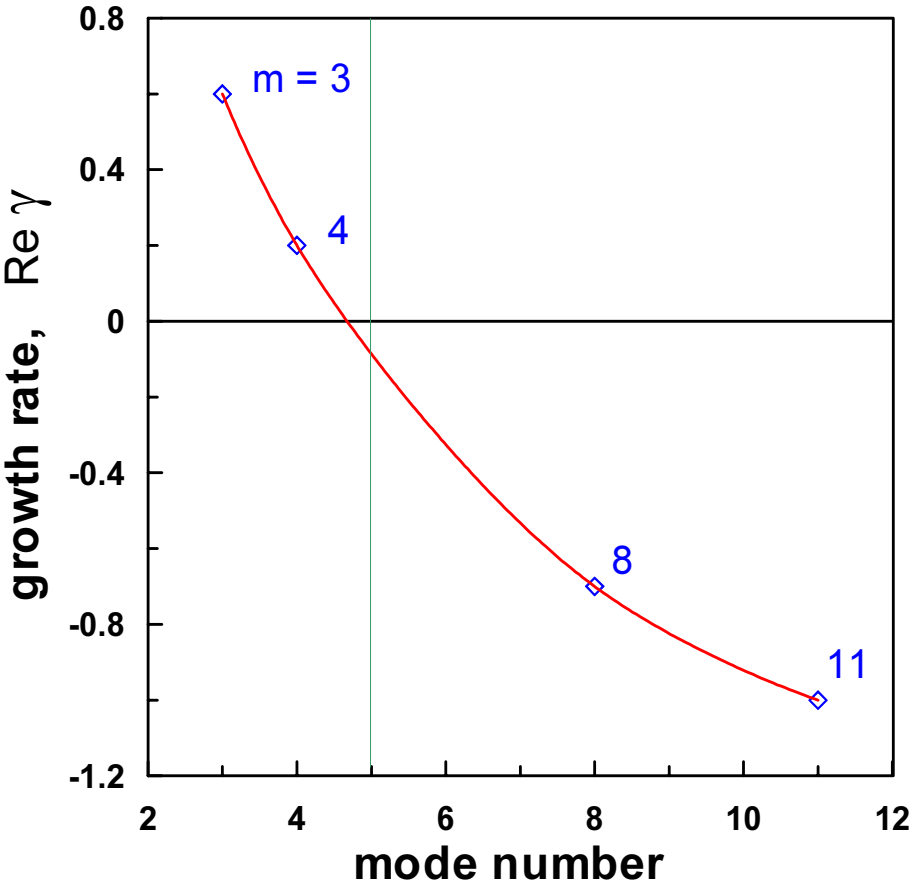

Perturbations grows if the mode number m < 5

MD simulation of RM instability

Vorticity at the interface causes RM instability

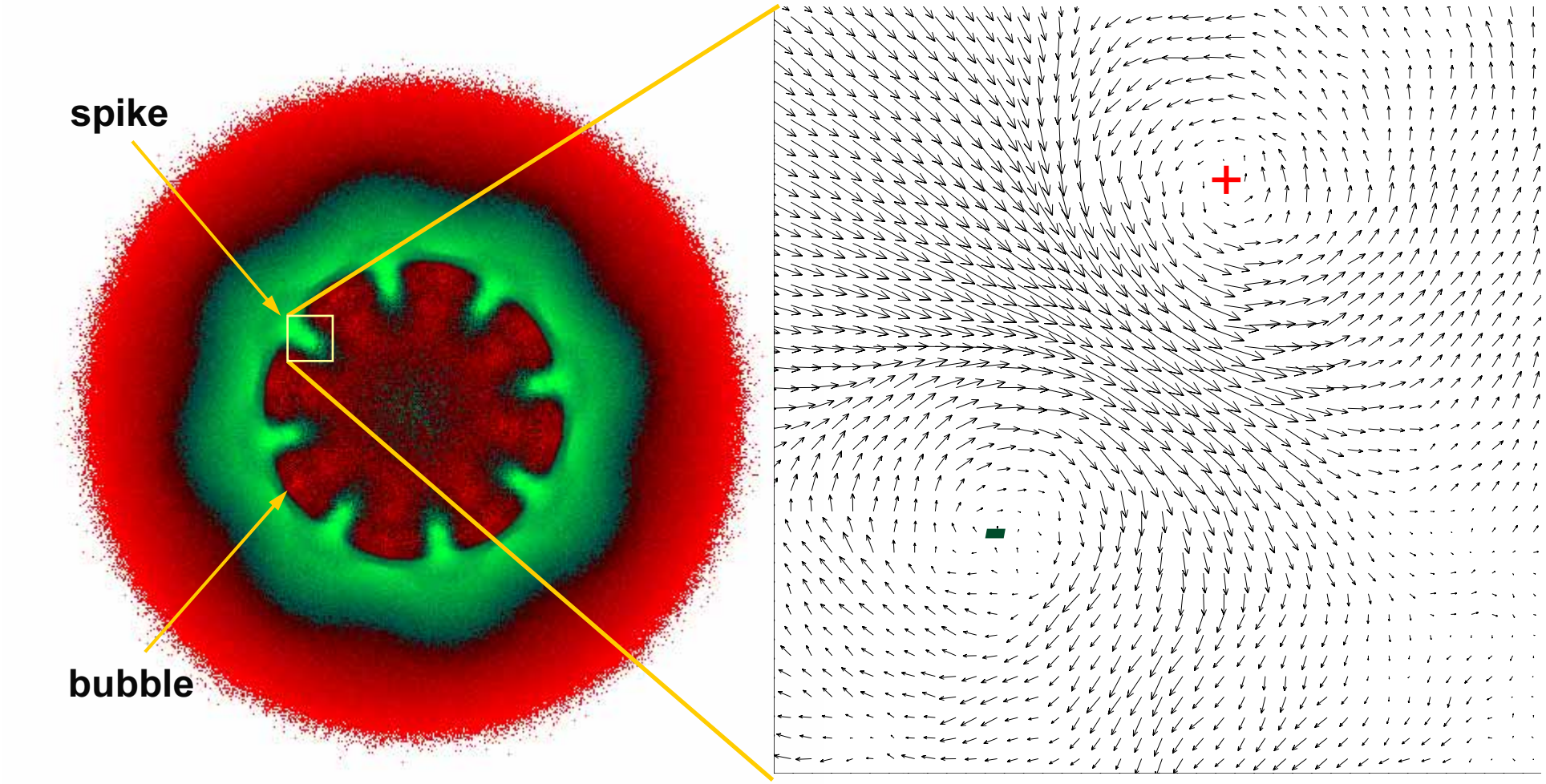

Radial velocity map,
green means negative value (to origin)

Velocity field, each arrow indicates
average velocity of about 100 atoms

Richtmyer-Meshkov instability in cylindrical geometry

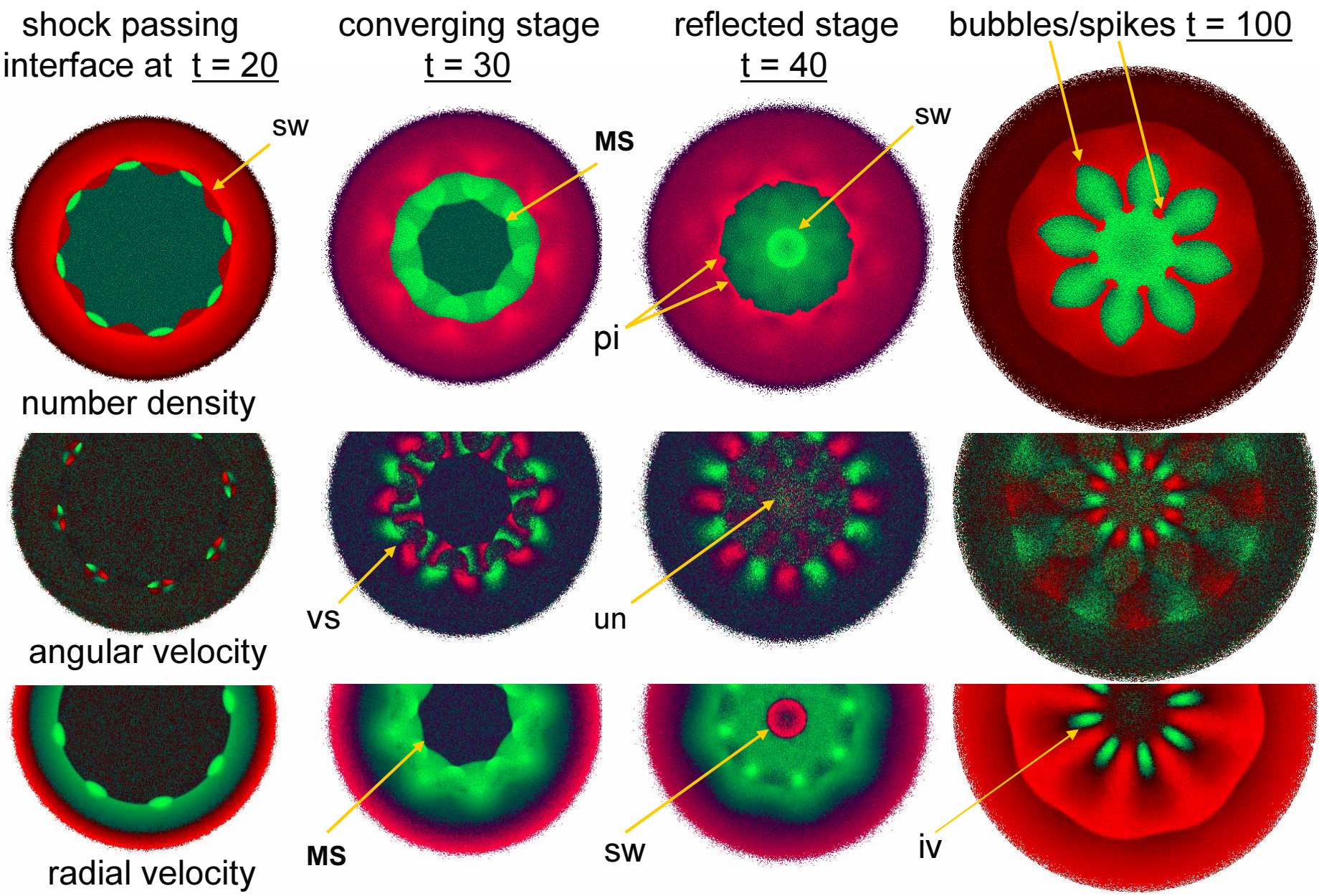

Molecular dynamics simulations show RM growth driven by multiple shocks for different mode numbers.

Decay of nonlinear growth is mode dependent and higher mode decays slower

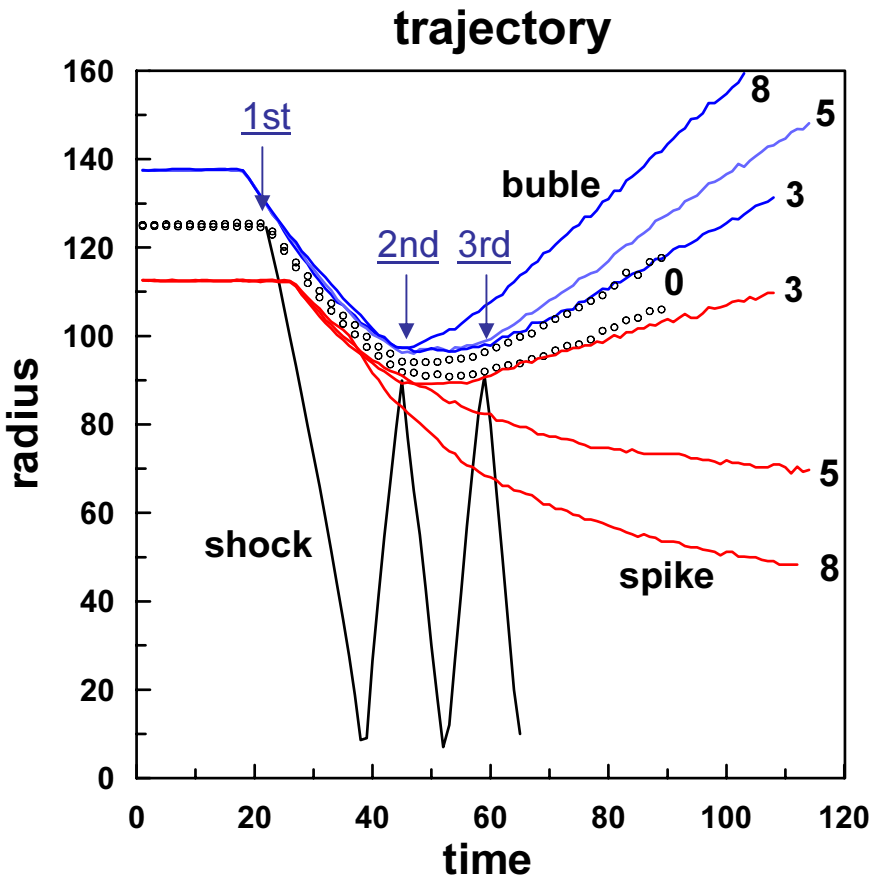

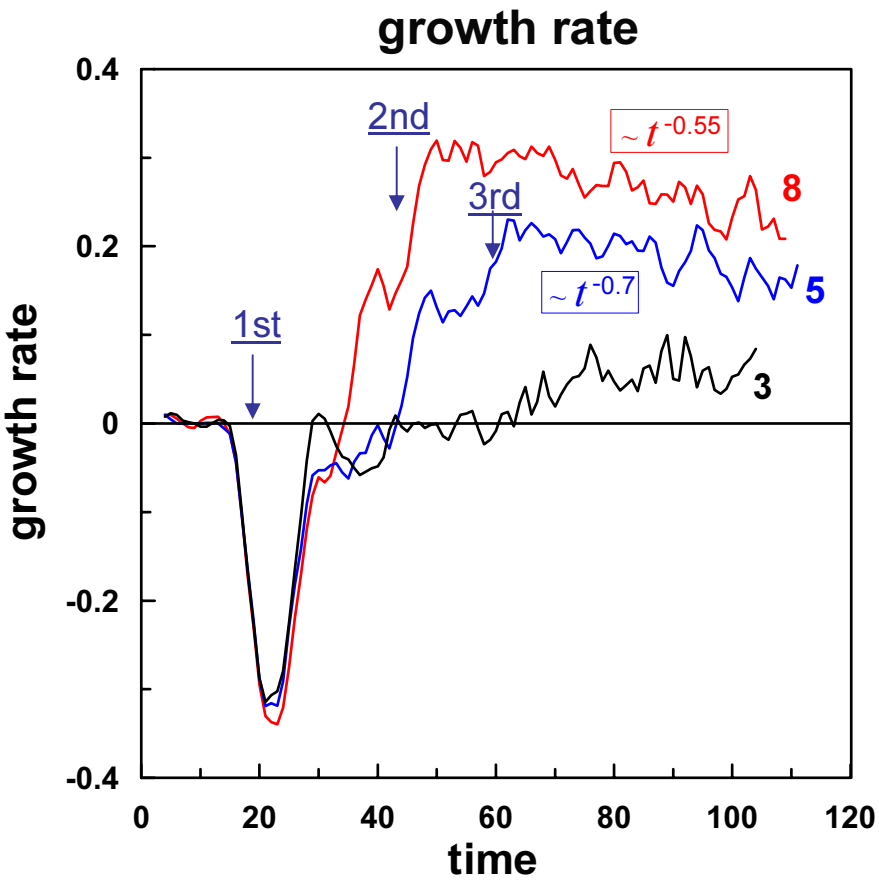

Richtmyer-Meshkov instability in planar geometry

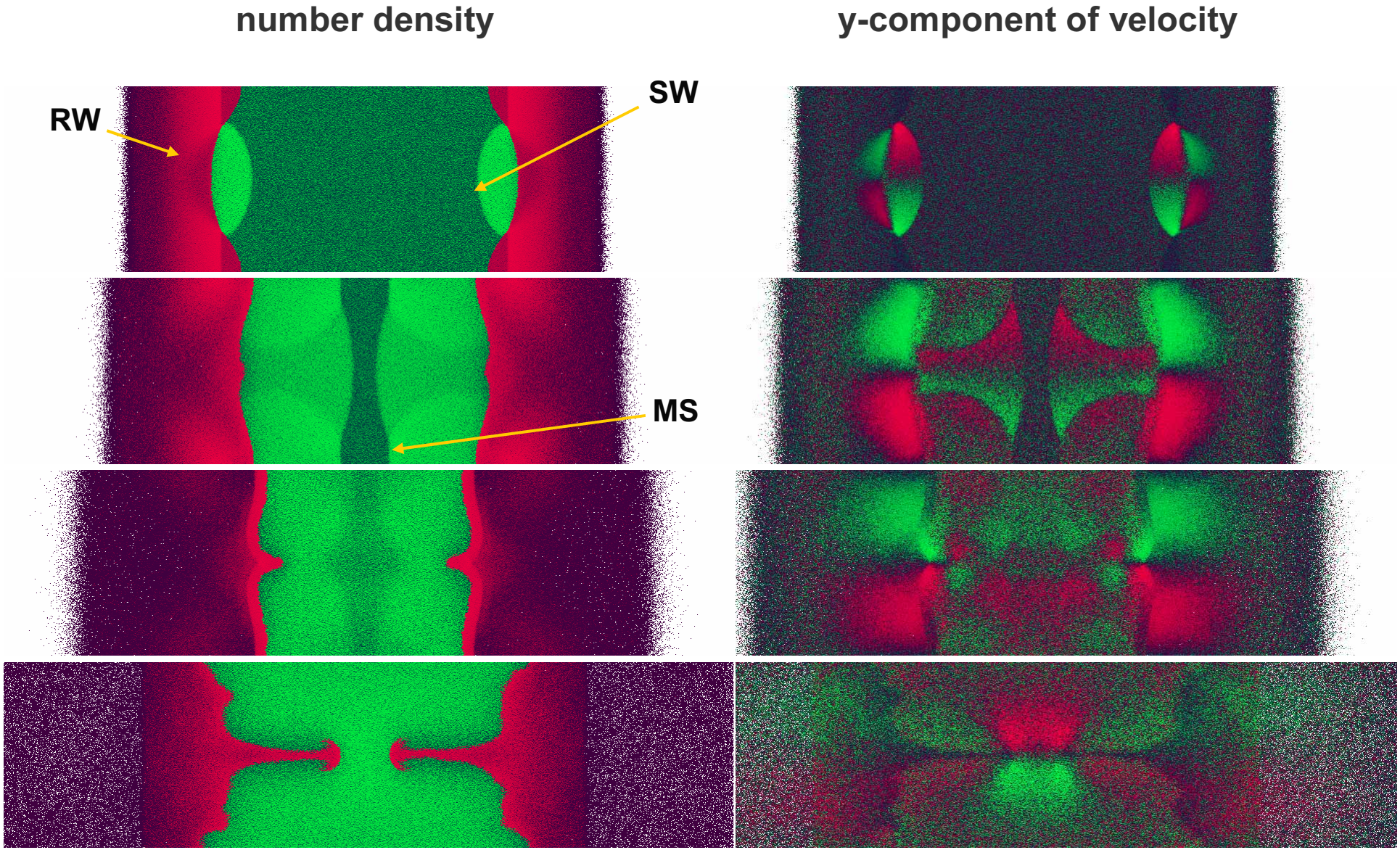

Growth of mixing zone in cylindrical RMI is much larger than in planar RMI

In both cases shocks hit interface repeatedly and growth rate increases

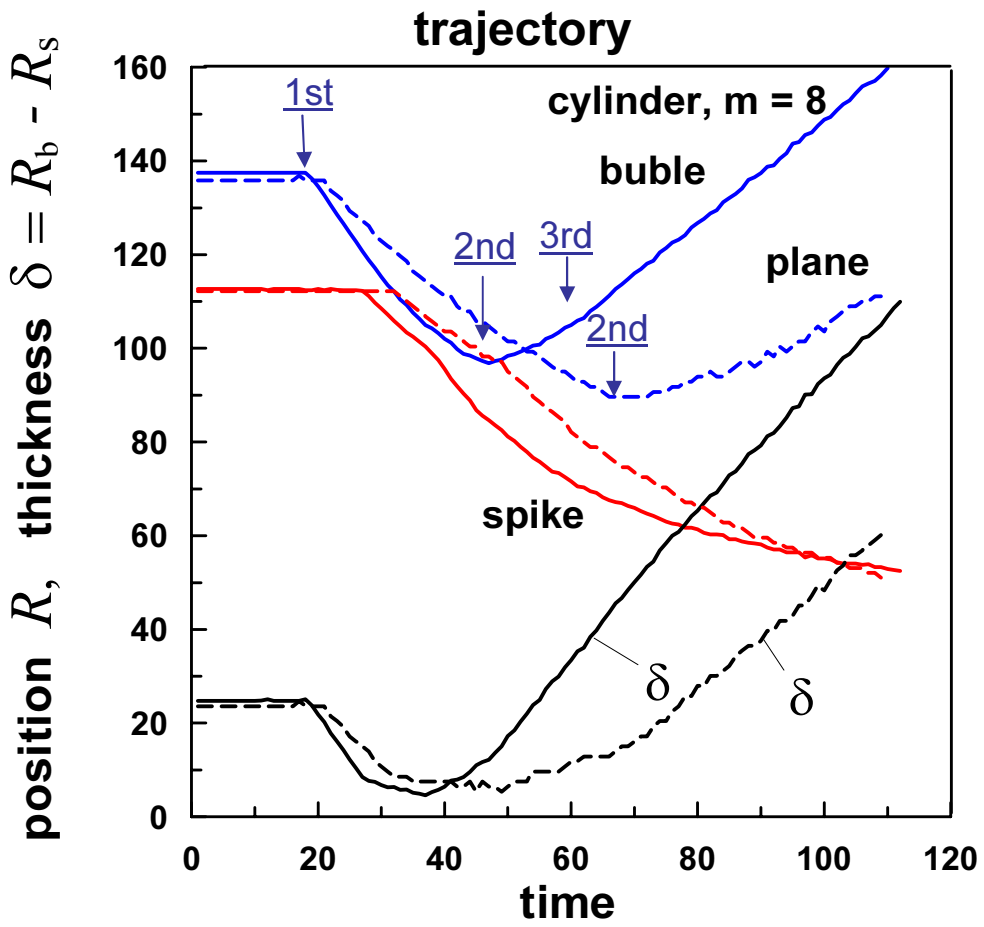

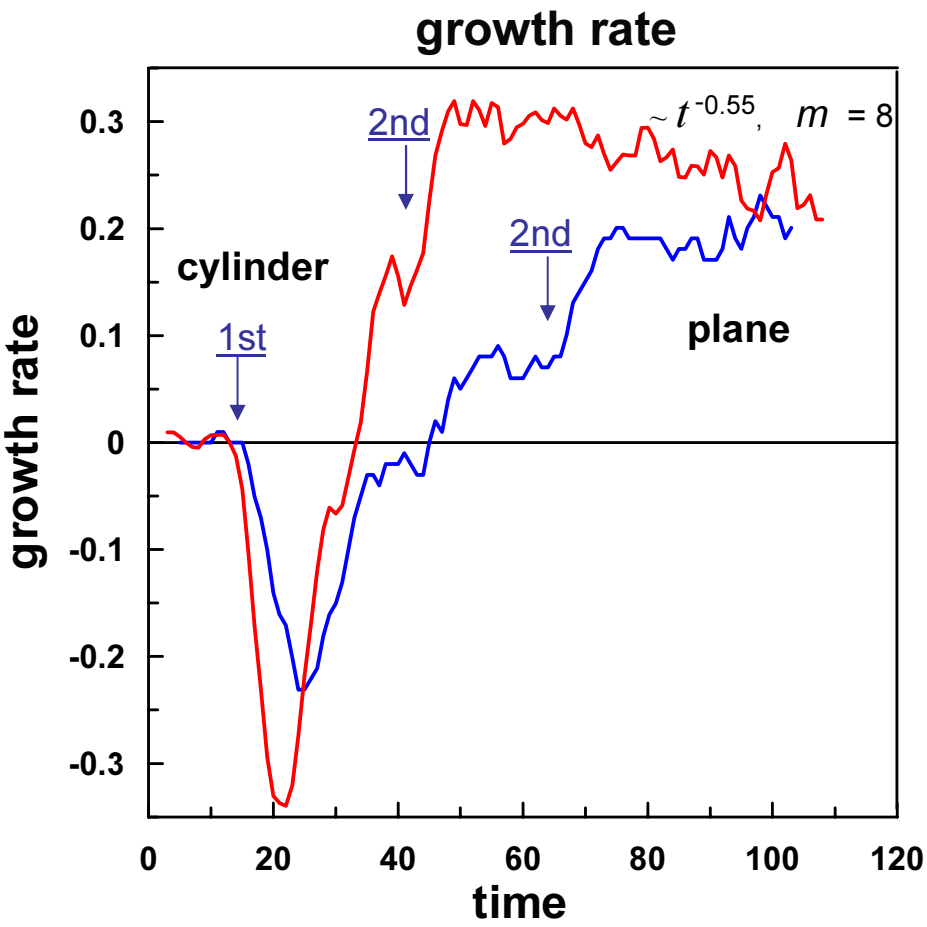

Richtmyer-Meshkov instability at shell surfaces

Many higher mode appear on inner surface.

Thickness of mixing zone is thinner than that on single interface.

number density

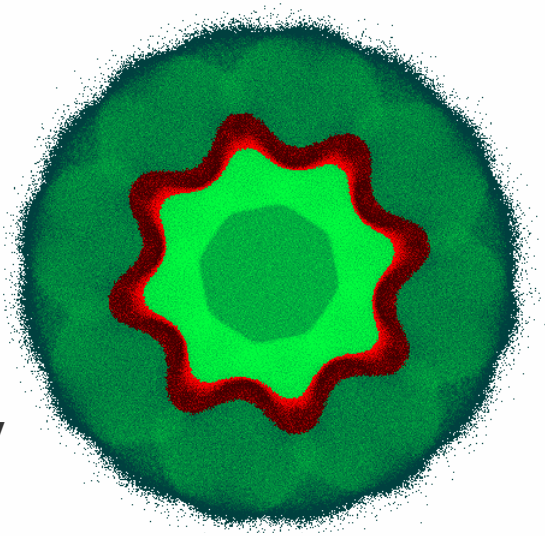

number density of heavy fluid

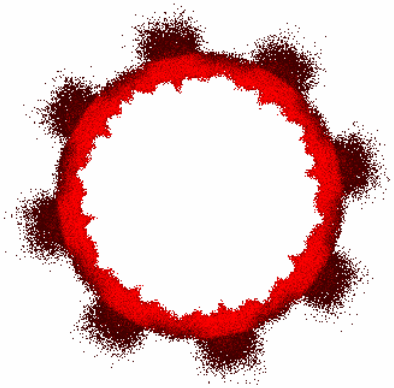

shell

angular velocity

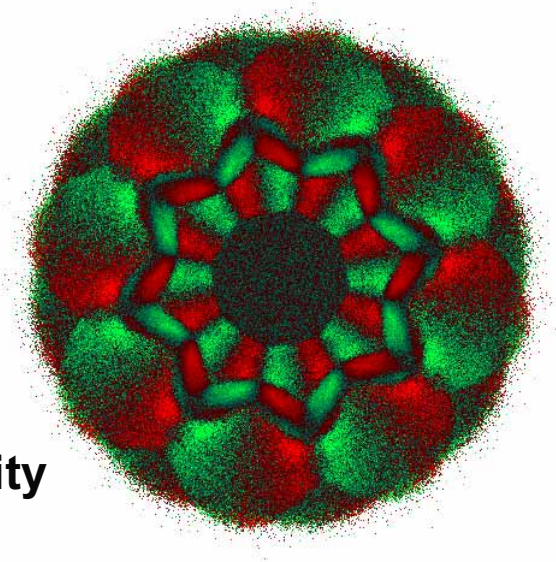

single interface

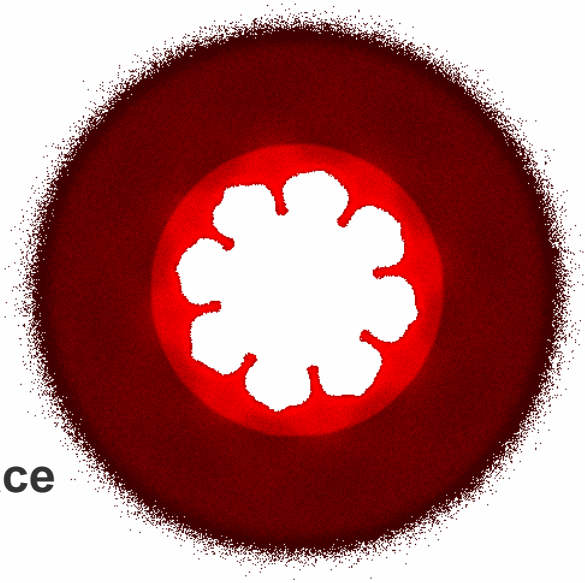

Conclusion

- **MD simulation provides a new tool for a study of hydrodynamic instabilities, when CFD fails.**
- **Mode dependence of nonlinear growth is investigated for cylindrical RMI. Higher mode decays slower.**
- **Growth of mixing zone in cylindrical RMI is much larger than that in planar RMT (shocks hit interface repeatedly).**
- **In a shell case (two interfaces), many higher modes appear on its inner surface, and thickness of mixing zone is thinner than that on single interface.**
- *www.ile.osaka-u.ac.jp/research/TSI/Vasilii*

A Numerical Study of Shocked a Gas Cylinders

William J. Rider, James R. Kamm and Cindy Zoldi
Los Alamos National Laboratory

- The gas curtain setup (1997)

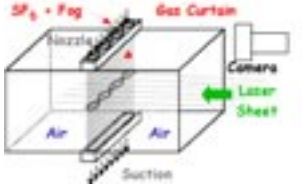

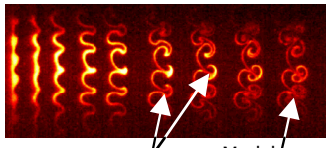

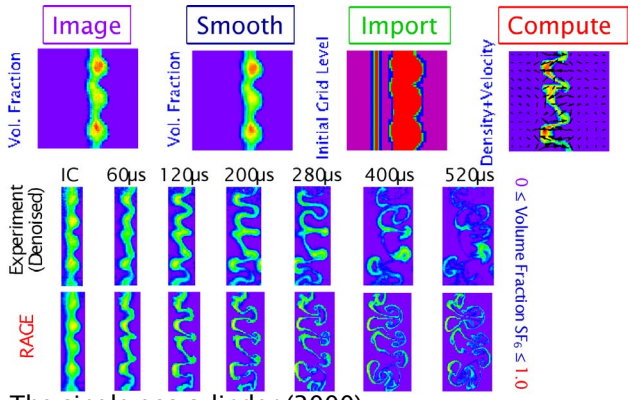

- The single gas cylinder (2000)

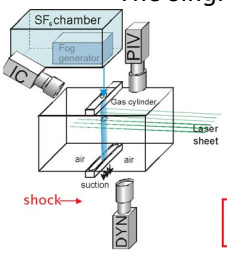

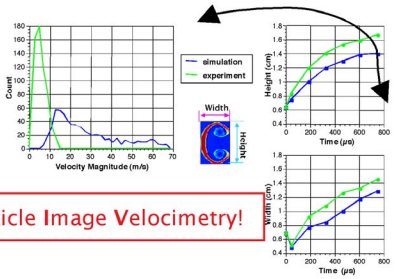

Particle Image Velocimetry!

Initial PIV shows 5:1 difference in velocities between the experiment and calculation.

The integral scales also do not match!

- The double gas cylinder (2001)

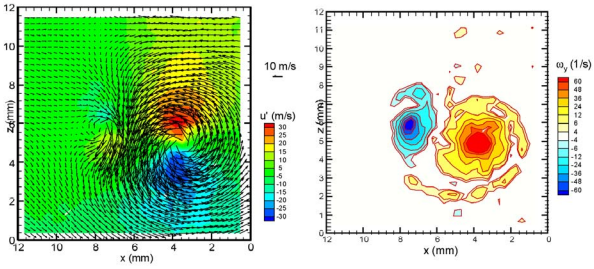

New PIV shows 5:3difference in velocities between the experiment and calculation. The air and SF6 have both been seeded giving the complete velocity field.

Double Cylinder Experiment ICs

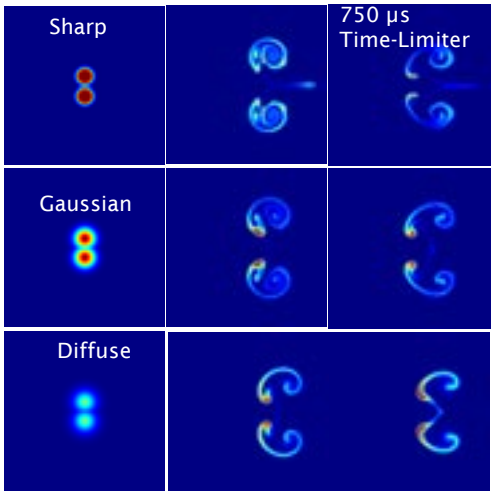

The initial conditions have not been imaged for the double cylinder. Here, we test various initial conditions with two schemes, the standard method and a modified method. With a sharper IC and the modified scheme, the most consistent results are found.

Double Cylinder Experiments

The behavior of the cylinders shows considerable variation with spacing with a spacing of 1.5 D being a critical value in the behavior.

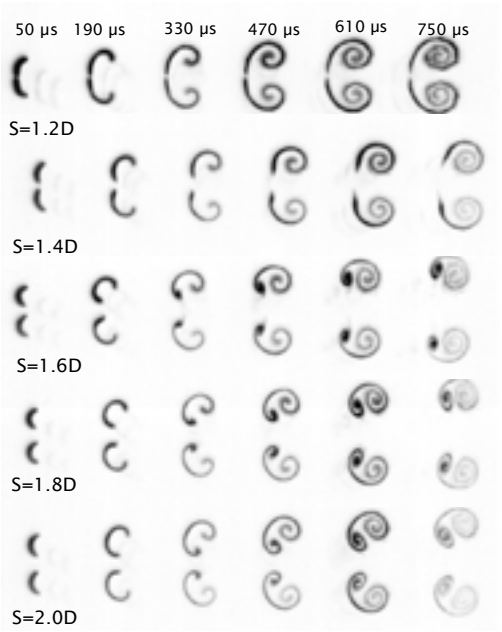

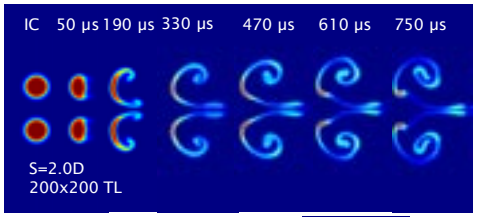

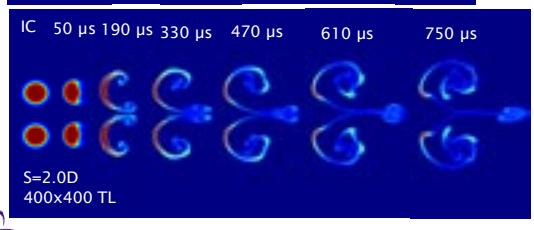

In general the results are not as variable with S as the experiments. This related to the strength of the inner vortices. The TL method does show less jetting and greater qualitative similarity than the standard MUSCL type scheme.

Double Cylinder Simulations

The simulations do not show the experimental variability

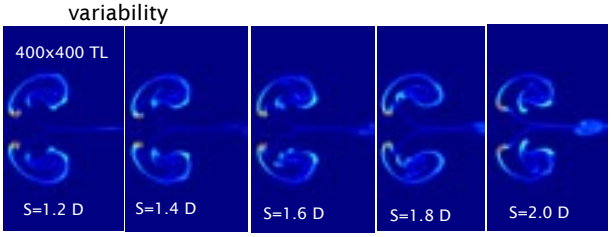

Gas Curtain - Effect of Mesh Refinement

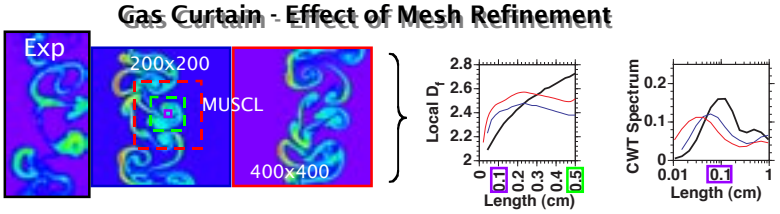

TVD Scheme (Lax&Liu) Results

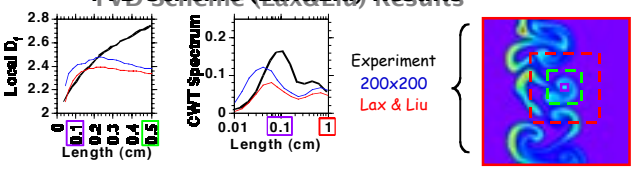

All standard modern schemes tested (MUSCL, WENO, PPM, TVD,…showed similar results. All results with these schemes were not consistent with the scaling exhibited by the experimental data. Mesh refinement does not provide improved results, but first-order methods show more consistent scaling (below). We also show a modified method (time-limiter) that has second-order accuracy while providing scaling consistent with the experimental data.

Ideal Gas Cylinder - 750 µs

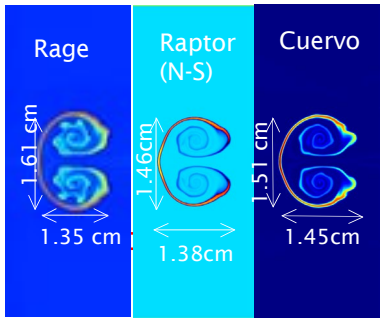

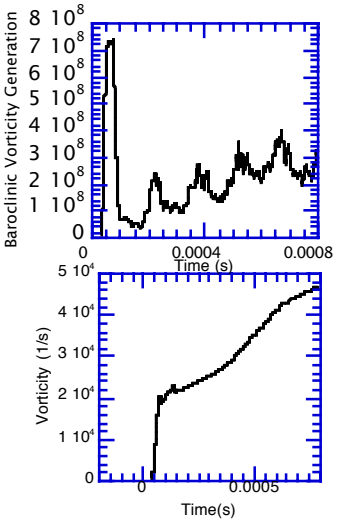

Experimental & Ideal Cylinder Analysis ?

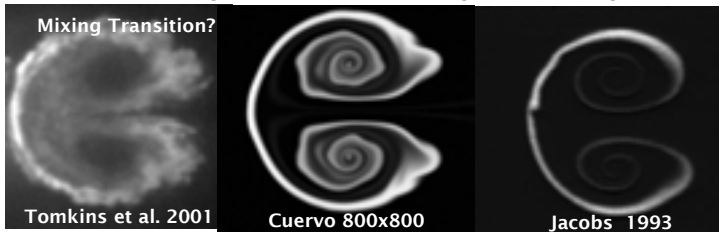

Tomkins et al. 2001	Cuervo 800x800	Jacobs 1993
$\tau = 9.4$, $\mathrm{Re} \approx 24{,}000$	$\tau = 15$	$\tau = 6.3$, $\mathrm{Re} \approx 12{,}000$
$U = 10^{-2}$ cm/µs	$U = 10^{-2}$ cm/µs	$U = 5 \times 10^{-3}$ cm/µs
D = 0.794 cm	D = 0.5 cm	D = 0.794 cm
t = 750 µs	t = 750 µs	t = 998 µs

$$\tau = \frac{tU}{D}$$

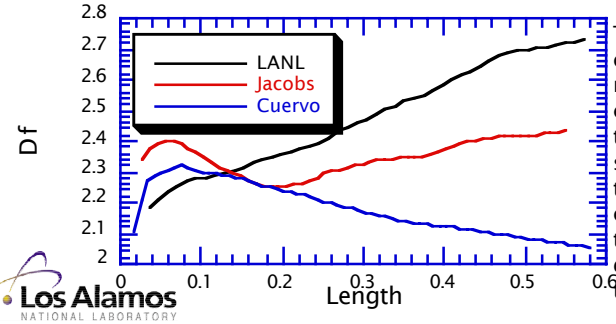

The results of the computations are most like Jacobs experiment, while the LANL exps. show scaling like that seen in the curtain and unlike that computed despite its long time scale.

Discontinuous Galerkin Results

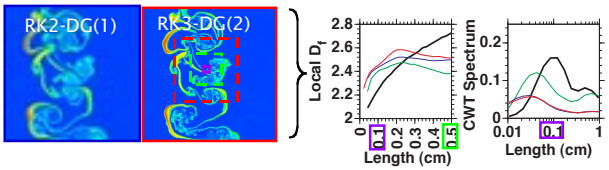

New Time Limiter Results

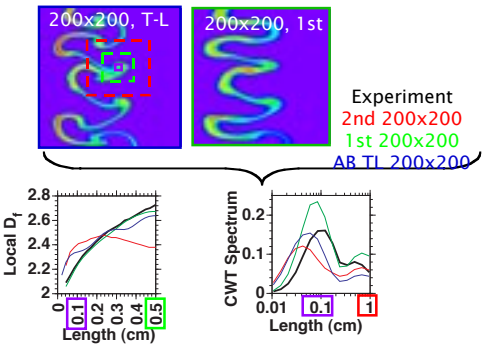

Numerical Method

- Solves conservation equations

$$U_t + F(U)_x + G(U)_y = 0$$

for the variables $U = [\rho, \rho u, \rho v, \rho E]^T$
and flux $F(U) = [\rho u, \rho u^2, \rho uv, u(\rho E + p)]^T$
with $p = p(\rho, e)$, $E = e + (u^2 + v^2)/2$

- Eq'ns are cast in "primitive" form for parts of the numerics and analysis:

$$V_t + A\,V_x + B\,V_y = 0$$
$$A \equiv \partial F/\partial V \quad B \equiv \partial G/\partial V \quad V \equiv [\rho, u, v, p, \rho e]^T$$

1 Compute "limited" spatial gradients
$$V^n(x) = \bar{V}^n + \nabla V^n(\bar{x} - x)$$
2 Advance data in time $V^{n+1/2}(x) = V^n(x) + \Delta t V_t / 2$
3 Solve the Riemann problem
$$F(U) = R(U_-, U_+)$$
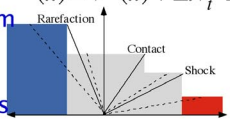

4 Advance conservation laws
$$\bar{U}_j^{n+1} = \bar{U}_j^n + \Delta t\left(F_{j+1/2}^{n+1/2} - F_{j-1/2}^{n+1/2}\right)/\Delta x$$
5 Update constitutive laws $p^{n+1} = p(\rho^{n+1}, e^{n+1})$

New Time Limiter

- 2nd Order Adams-Bashforth

$$\frac{\partial V}{\partial t} = \frac{V^n - V^{n-1}}{\Delta t} \rightarrow V^{n+1/2} = V^n + \frac{\Delta t}{2}\frac{\partial V}{\partial t}$$

- Stiff ODE integrators control order dynamically $V + \Delta t V_t + C\Delta t^2 V_{tt}; C < 1$
- Use standard scheme to limit

$$\frac{\partial V}{\partial t} := \varphi \frac{\partial V}{\partial t} \text{ and } \nabla V := \varphi \nabla V, \text{ with}$$
$$\varphi = \max\left[0, \min\left(1, \frac{2\partial V/\partial t}{-A\nabla V}, \frac{-2A\nabla V}{\partial V/\partial t}\right)\right]$$

Large Eddy Simulation of Strong-shock Richtmyer-Meshkov Instability

R. Samtaney

D. I. Pulin

T. Voelkl

D. J. Hill

Graduate Aeronautical Laboratories

Caltech

IWPCTM

December 9-14. 2001. Caltech

Acknowledgement

- ASCI Compressible Turbulence Group
  - *P. E. Dimotakis*
  - *A. Leonard*
  - *D. Meiron*
  - *B. Kosovic*
- ASCI/ASAP subcontract no. B341492 of DOE contract W-7405-ENG-48.
- Computational resources: LLNL Blue Pacific, LANL nirvana.

Outline

- Objectives and physical problem setup
- Equations and numerical method
- Subgrid scale model description
  - *Stretched vortex SGS model for LES*
- Decaying isotropic turbulence test
  - *comparison between Pade and WENO*
    - *modified wave number behavior*
- RM Simulation results
  - *Plane averages and rms quantities*
  - *mixing width (with and w/o SGS models)*
- Conclusion

Strong-shock Richtmyer-Meshkov Instability (RMI)

- Objectives:
  - *Pseudo-DNS of Richtmyer-Meshkov flow with strong shocks*
    - *shocks not resolved (requires shock-capturing method)*
    - *numerical method reverts to high-order in regions away from shocks*
  - *LES with the stretched-vortex model of same flow*
- Requirements:
  - *Shock-capturing method with good resolution characteristics in the high-wavenumber range (not only formally high-order)*
    - *WENO (Shu et al.)*
    - *Hybrid (Pade + WENO) (Adams and Shariff)*
    - *Spectral methods for compressible flows (Gottlieb et al.)*
  - *Numerical method compatible with AMR*
  - *SGS-Model applicable to flows with strong shocks*
    - *Stretched Vortex SGS (Pullin and co-workers)*

RM instability: Setup

- Strong shocks (M=10)
- Density ratios
  - *light to heavy (fast/slow) (5/1)*
  - *heavy to light (slow/fast)*
- Periodic boundary conditions in transverse directions
  - *homogeneous turbulence in cross-plane*

Shock reflects off end

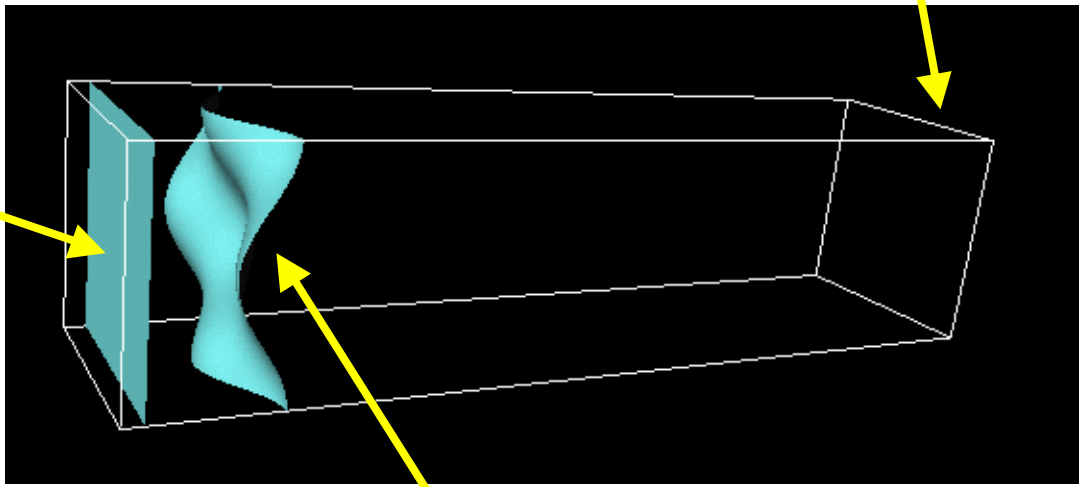

Incident shock

Interface (multiple harmonic perturbation)

Favre filtered NS equations

- Favre average: $\widetilde{q} = \bar{\rho} q / \bar{q}$
- Continuity

$$\frac{\partial \bar{\rho}}{\partial t} + \frac{\partial \bar{\rho} \widetilde{u}_i}{\partial x_i} = 0$$

- Momemtum

$$\frac{\partial \bar{\rho} \widetilde{u}_i}{\partial t} + \frac{\partial (\bar{\rho} \widetilde{u}_i \widetilde{u}_j + \bar{p}/\gamma M^2 \delta_{ij})}{\partial x_j} = Re^{-1} \left(\frac{\partial \widetilde{\sigma}_{ij}}{\partial x_j} \right) - \frac{\partial T_{ij}}{\partial x_j}$$

where

$$T_{ij} = \bar{\rho}(\widetilde{u_i u_j} - \widetilde{u}_i \widetilde{u}_j) \equiv \bar{\rho}\, \tau_{ij}$$

Subgrid stress

Favre filtered NS equations

Energy

$$\frac{\partial \bar{E}}{\partial t} + \frac{\partial (\bar{E} + \bar{p}/\gamma M^2)\widetilde{u}_i}{\partial x_i} = \frac{1}{PrRe(\gamma-1)M^2}\frac{\partial}{\partial x_i}\left(k\frac{\partial \widetilde{T}}{\partial x_i}\right)$$

$$+ Re^{-1}\frac{\partial(\widetilde{\sigma}_{ij}\widetilde{u}_j)}{\partial x_i}$$

$$- \frac{1}{(\gamma-1)M^2}\frac{\partial(\bar{\rho}q_i)}{\partial x_i}$$

$$- \frac{1}{2}\frac{\partial[\bar{\rho}(\widetilde{u_j u_j}u_i - \widetilde{u_j u_j}\widetilde{u}_i)]}{\partial x_i}$$

$$+ Re^{-1}\frac{\partial(\widetilde{\sigma_{ij}u_j} - \widetilde{\sigma}_{ij}\widetilde{u}_j)}{\partial x_i}$$

$$\bar{E} = \frac{\bar{p}}{(\gamma-1)\gamma M^2} + \frac{1}{2}\bar{\rho}(\widetilde{u}_j\widetilde{u}_j) + \frac{1}{2}\bar{\rho}(\widetilde{u_j u_j} - \widetilde{u}_j\widetilde{u}_j)$$

$$q_i = \widetilde{Tu_i} - \widetilde{T}\widetilde{u}_i$$

$$\bar{p} = \bar{\rho}\widetilde{T}$$

Heat flux

Triple correlation

Viscous work

Subgrid KE

Numerical method: WENO

- Finite difference formulation WENO (Jiang & Shu) for inviscid fluxes in the governing equations
- Conservative approximation of flux derivatives

$$\frac{1}{\Delta x_i}\left[\hat{f}_n(x_{i+1/2}) - \hat{f}_n(x_{i-1/2})\right] = \partial f_n(x_i)/\partial x + O(\Delta x^k)$$

  - *Fluxes calculated in characteristic coordinates*
  - *Characteristics -eigenvalues and eigenvectors evaluated using Roe state*
- Runge-Kutta (TVD) time discretization

Prevention of Instabilities

- "H-correction" by Sanders, Morano & Druguet adapted for FD-WENO

$$\hat{\lambda}^{*}_{p;i+1/2;j} = \max\left(\hat{\lambda}_{p;i+1/2;j}, \eta^{H}_{i+1/2;j}\right)$$

where

$$\eta^{H}_{i+1/2,;j} = \max\left(\eta_{i+1/2;j}, \eta_{i;j+1/2}, \eta_{i;j\ \ 1/2}, \eta_{i+1;j+1/2}, \eta_{i+1;j\ \ 1/2}\right)$$

$$\eta_{i+1/2;j} = \frac{1}{2}\max_{p}\left(\left|\lambda_{p}(\boldsymbol{U}_{i+1;j}, \boldsymbol{e}_{x}) - \lambda_{p}(\boldsymbol{U}_{i;j}, \boldsymbol{e}_{x})\right|\right)$$

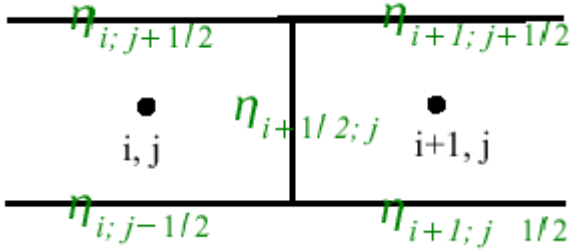

LES Model - Pullin SGS vortex model

- Extension of stretched vortex sub-grid stress model (Misra & Pullin 1997) to compressible turbulence
- Structure-based approach
  - *Subgrid motion represented by nearly axisymmetric vortex within each cell.*
- Subgrid stresses are:

$$T_{ij} = K\,(\delta_{ij} - e_i\,e_j)\,,$$

$$K = \int_{k_c}^{\infty} E(k)\,dk.$$

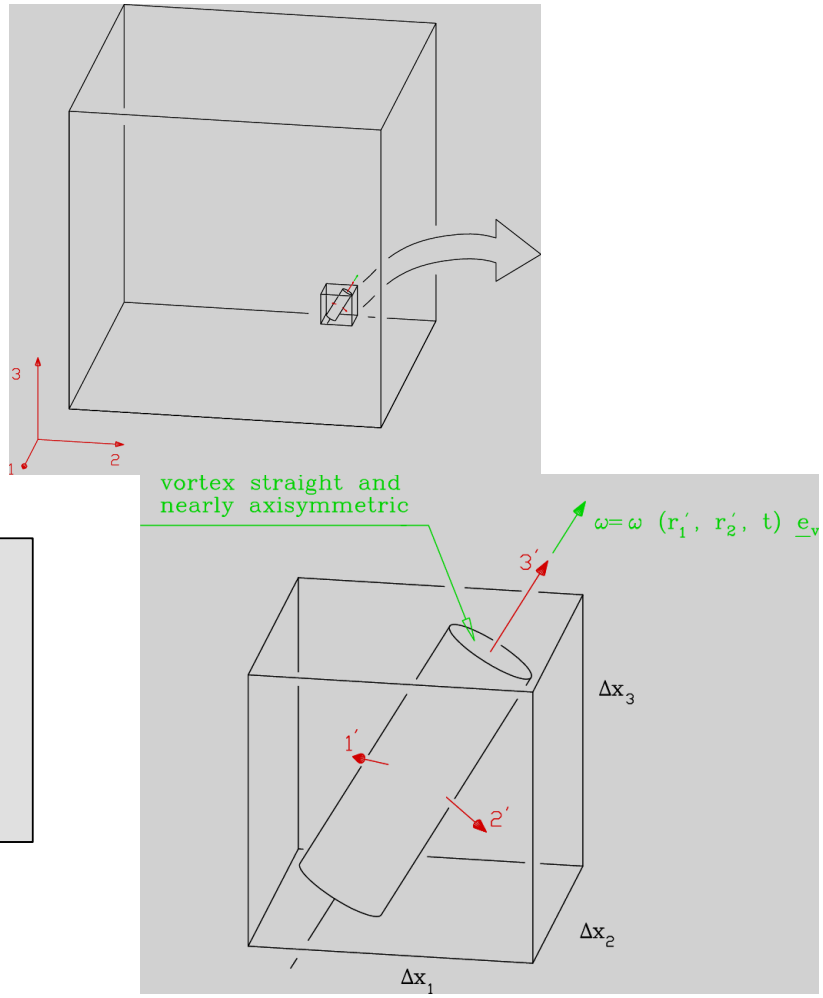

Pullin SGS vortex model

- Lundgren form assumed for subgrid energy spectrum:

$$K_0\,\epsilon^{2/3}\,k^{-5/3}\,\exp(-2\,k^2\,\nu/(3\,|a|))$$

$$a = \tilde{S}_{ij}\,e_i^v\,e_j^v$$

- PDF for vortex orientation in each cell

$$P(\mathbf{e}) = \mu\,\wp\,(\mathbf{e}^{\mathbf{v}} \mid \tilde{\mathbf{e}}_{\mathbf{3}}) + (1-\mu)\,\wp\,(\mathbf{e}^{\mathbf{v}} \mid \tilde{\mathbf{e}}_{\omega})$$

$$\mu = \frac{\lambda_3}{\lambda_3 + \parallel \tilde{\boldsymbol{\omega}} \parallel}$$

- Subgrid temperature flux (analytical solution for the winding of the local resolved temperature by the elemental vortex)

$$[q_i]_{mod} = \frac{1}{2}\,\Delta\,K^{1/2}\,\left(\delta_{ij} - \mathrm{e}_i^v\,\mathrm{e}_j^v\right)\,\frac{\partial \tilde{T}}{\partial x_j}$$

Pullin SGS vortex model

- $\mathcal{K}_0\ \epsilon^{2/3}$ estimated locally by matching local resolved flow 2'nd-order velocity structure function to local subgrid estimate
- Stretched-vortex model is *not* an eddy-viscosity model
  - *allows "back scatter"*
- Elements of subgrid stress tensor and subgrid energy calculated directly
  - *Important for scalar and other subgrid quantities*
- No explicit filtering
- No explicit treatment for shock
  - *verified using aposteriori tests with DNS of decaying isotropic turbulence in the presence of shocklets at modest turbulent Mach numbers (0.3-0.5)*
- Plug-in model: ease of implementation

Comparison of DNS with LES + SGS

Decay of turbulent kinetic energy using Pullin stretched-vortex SGS model

("SGS modeling for LES of compressible turbulence" Kosovic, Pullin and Samtaney. To appear in Phys. Fluids)

$$M_t = 0.488 \quad Re_l = 175 \quad O(h^{10}) \quad 256^3 \quad \text{IC4}$$

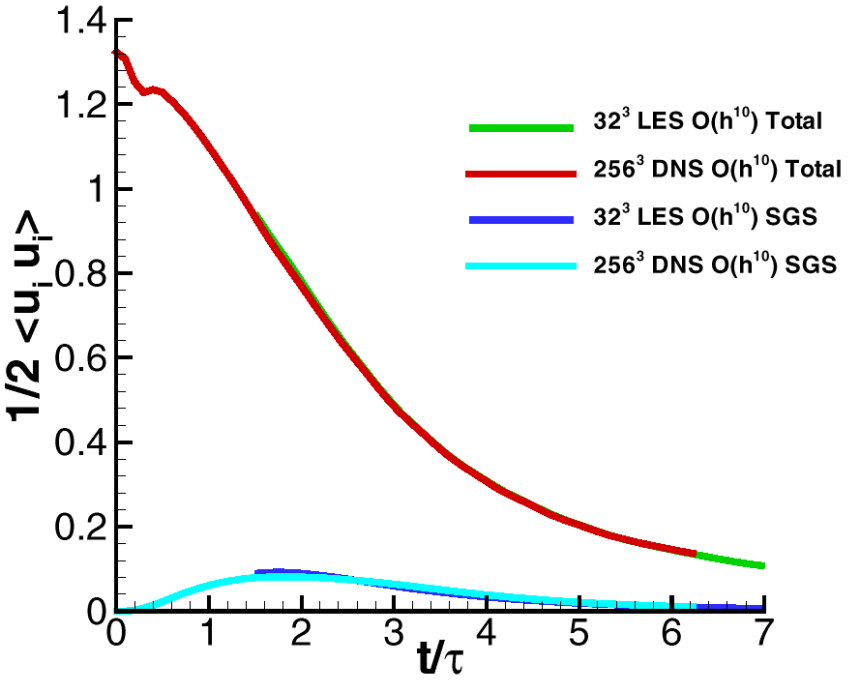

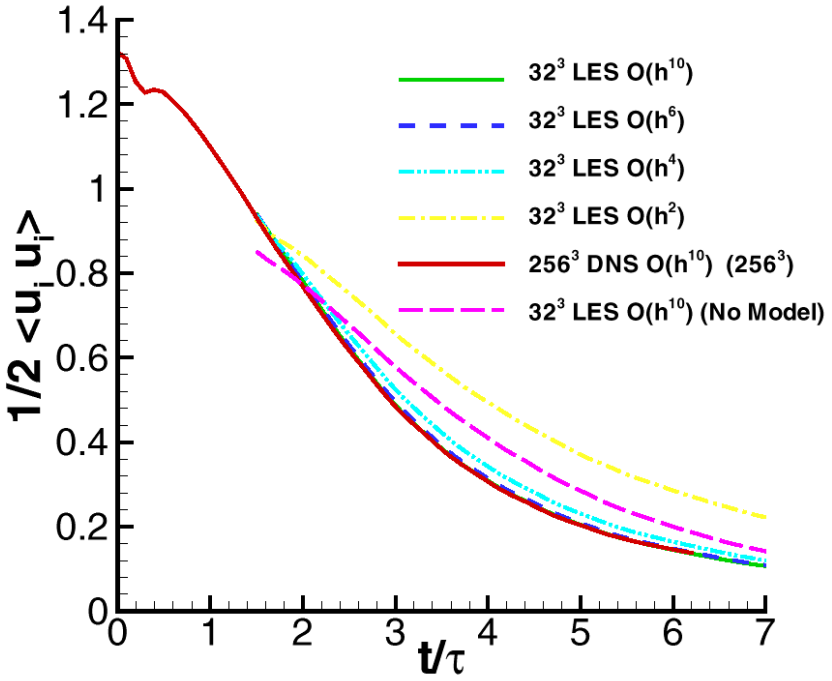

"DNS of decaying isotropic turbulence" - Samtaney, Pullin, Kosovic in Phys. Fluids, May 2001

Comparison of spectra (LES vs. DNS)

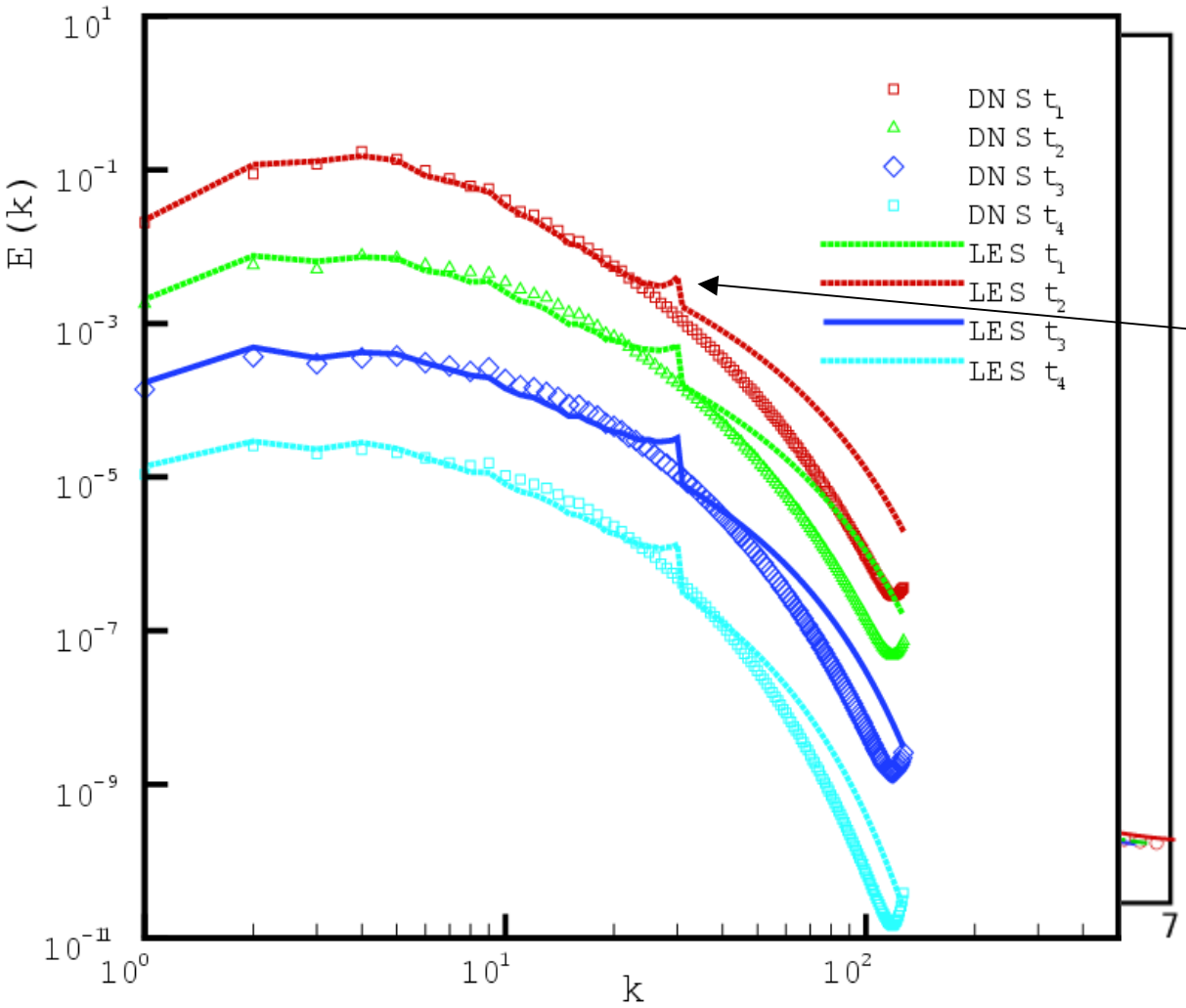

Pile-up is due to aliasing

Pade vs. WENO

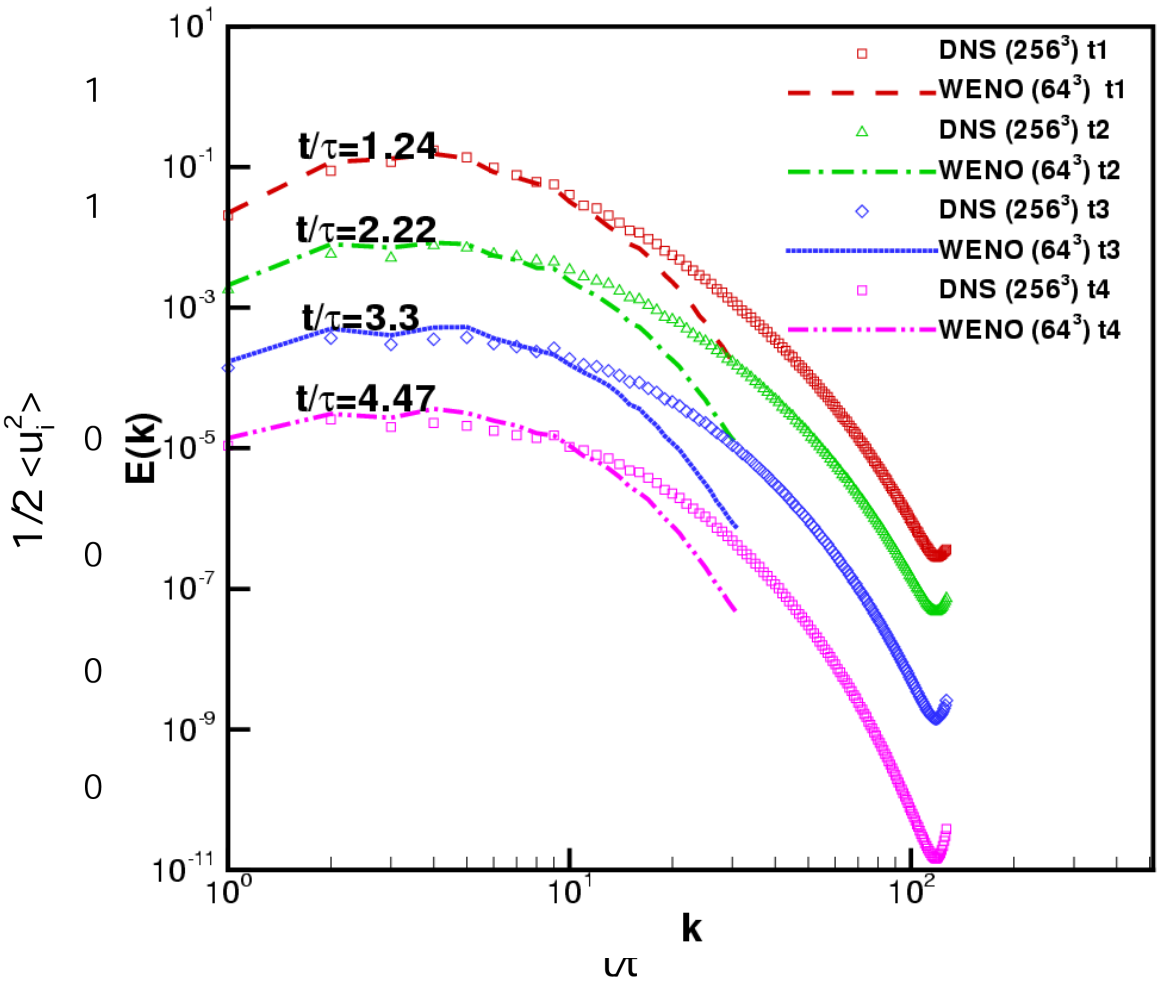
DNS (256³) t1
WENO (64³) t1
DNS (256³) t2
WENO (64³) t2
DNS (256³) t3
WENO (64³) t3
DNS (256³) t4
WENO (64³) t4
t/τ=1.24
t/τ=2.22
t/τ=3.3
t/τ=4.47
E(k)
1/2 <u_i^2>
k
kη

Pade vs. WENO (Modified Wave number)

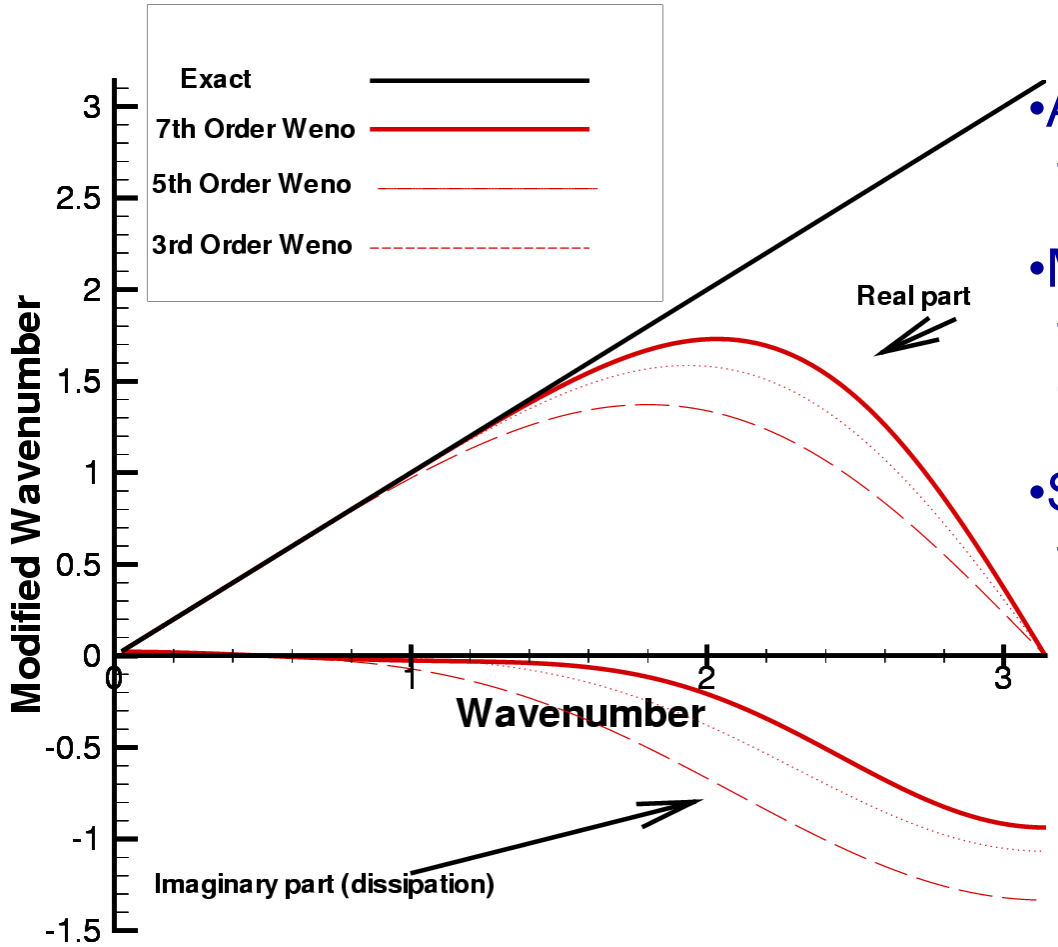

- Analysis assume periodic functions
- Modified wavenumber for WENO done for the optimal stencil
- See Lele (JCP 1992) for a discussion of modified wave number

WENO-RMI: Run Parameters

- Shock Mach number M=10
- Density ratio 1:5
- Interface Initial condition: Multi-mode perturbation with random phases and prescribed spectrum
- BC: Inflow (left), Reflecting (right), Periodic (transverse)
- Physical Domain $16\pi \times 2\pi \times 2\pi$
- 7th-order (formally) WENO with H-correction
- Three runs
  - *(A) 1024x128x128 (No SGS model)*
  - *(B) 512x64x64 (No SGS model)*
  - *(C) 512x64x64 (SV SGS model)*
- Simulations on ASCI Blue Mountain (nirvana)
  - *1024x128x128 on 128 procs., 18400 timesteps (40s/timestep)*
  - *512x64x64 on 64 procs., 10000 timesteps (20s/timestep)*

WENO- RMI simulation: Initial Condition

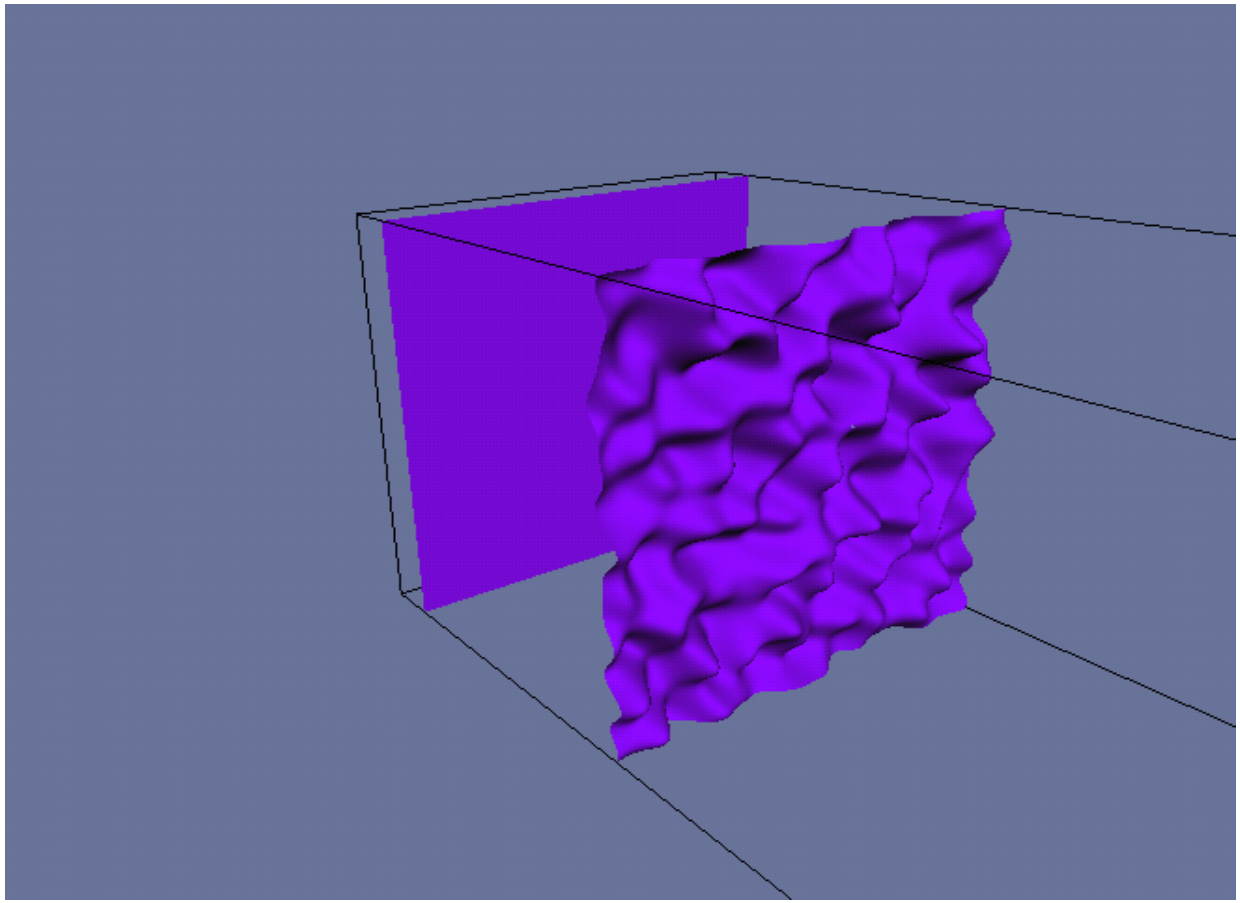

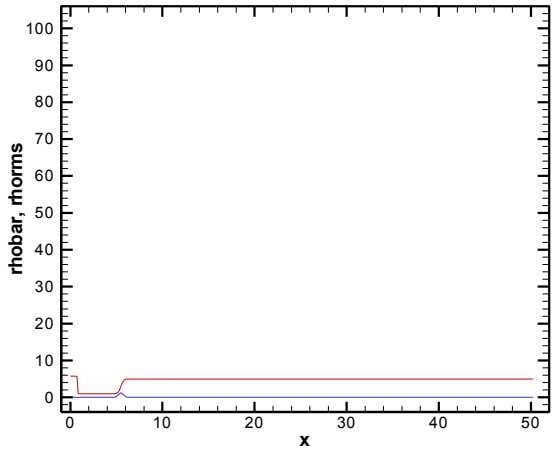

$$\rho = 3$$

RMI: Before reshock (Run A)

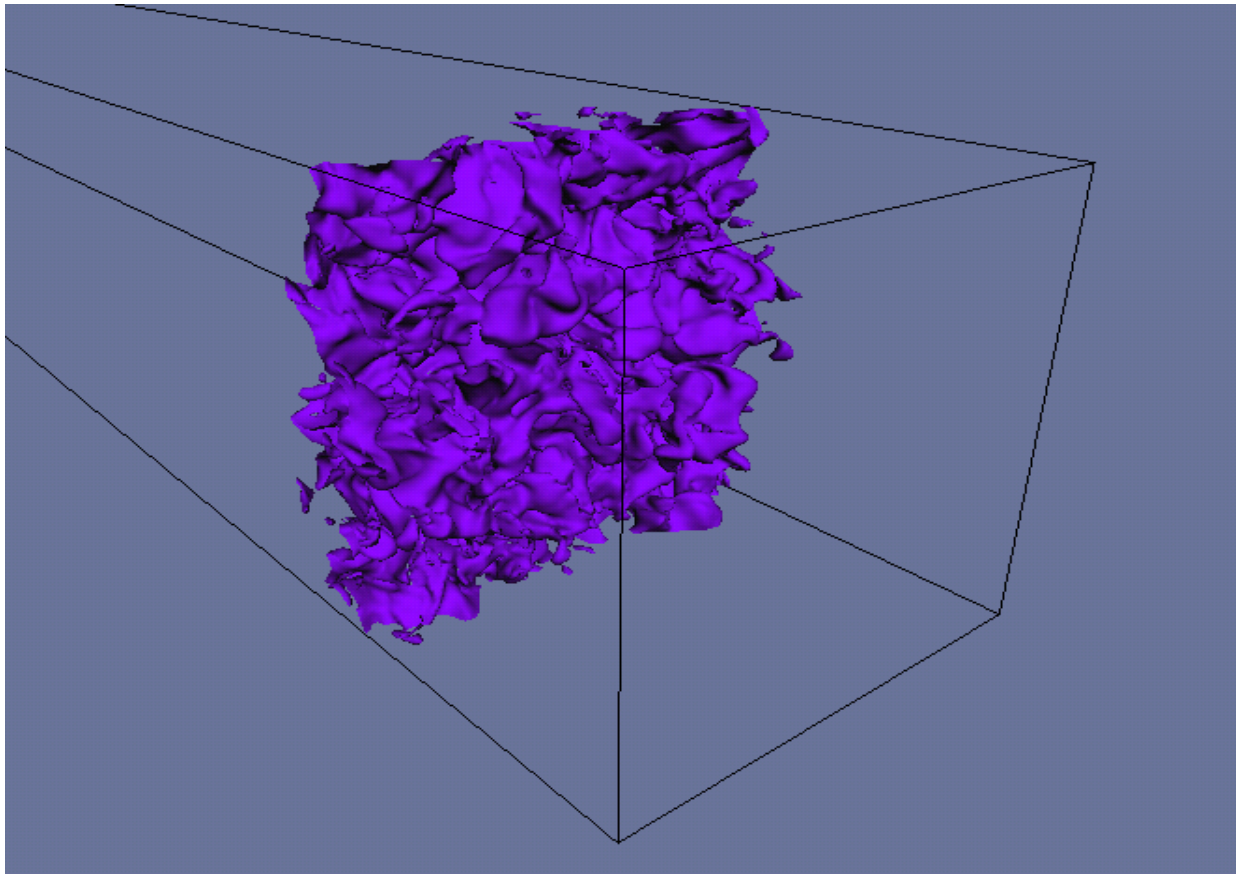

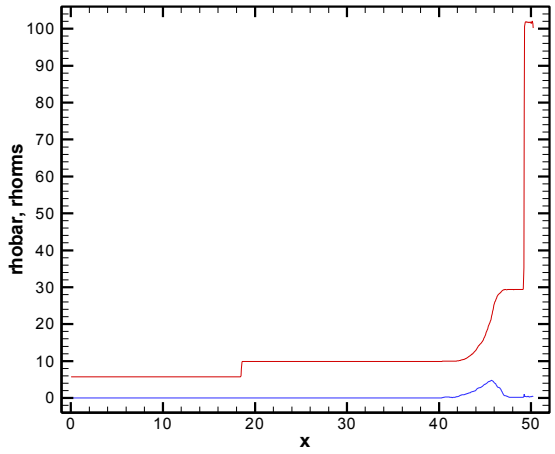

$$\rho = 20$$

RMI: After reshock (Run A)

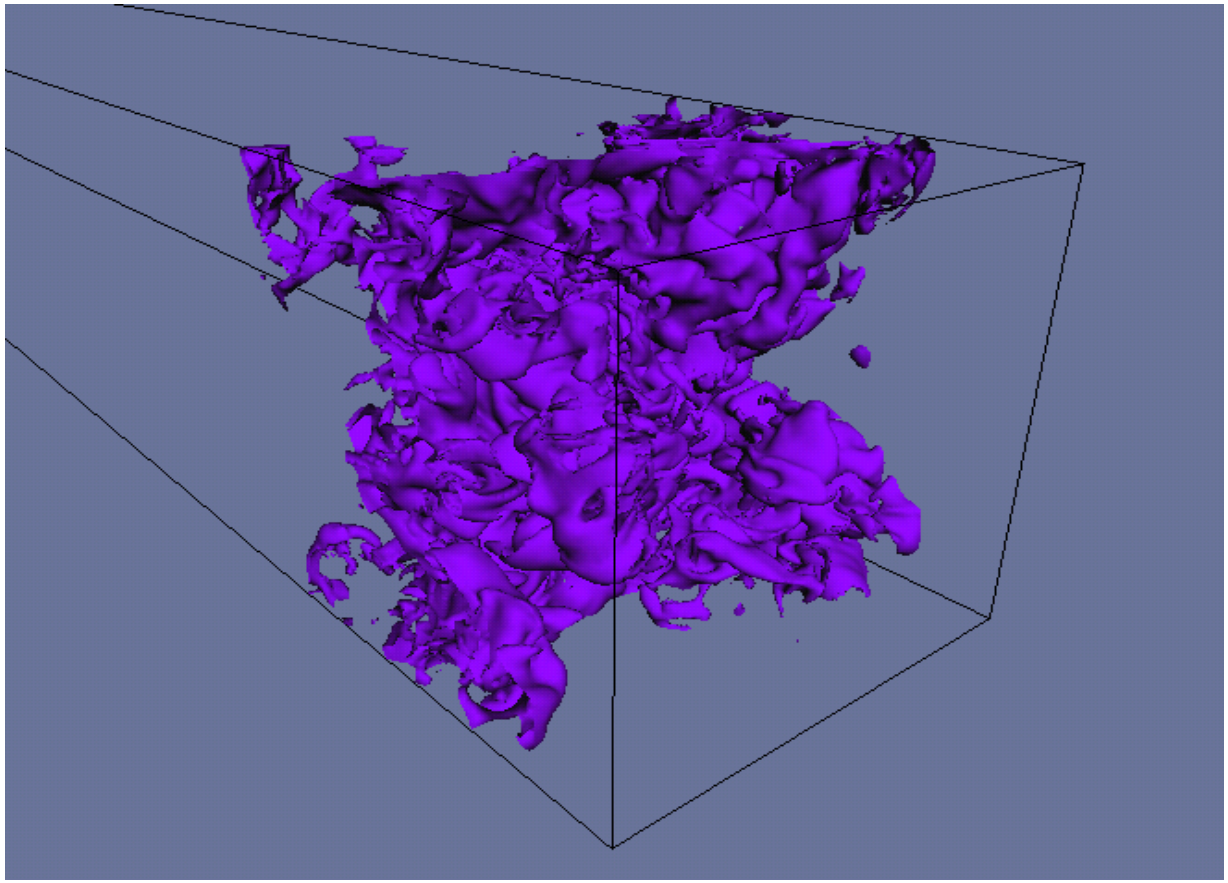

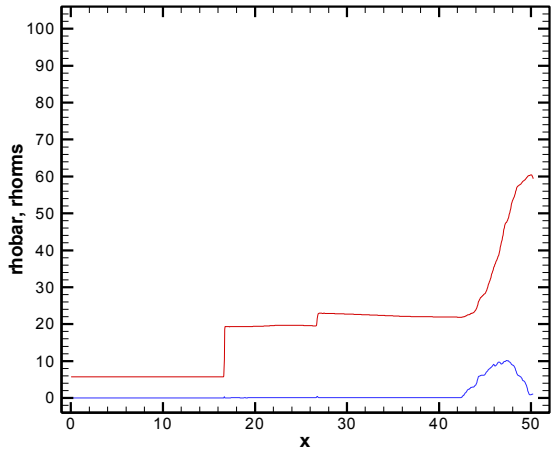

$$\rho = 42$$

RMI: Spectra (Run A)

- 2D spectra in planes normal to shock–propagation direction
- Location of plane determined by zero crossing of $\bar{\phi}$

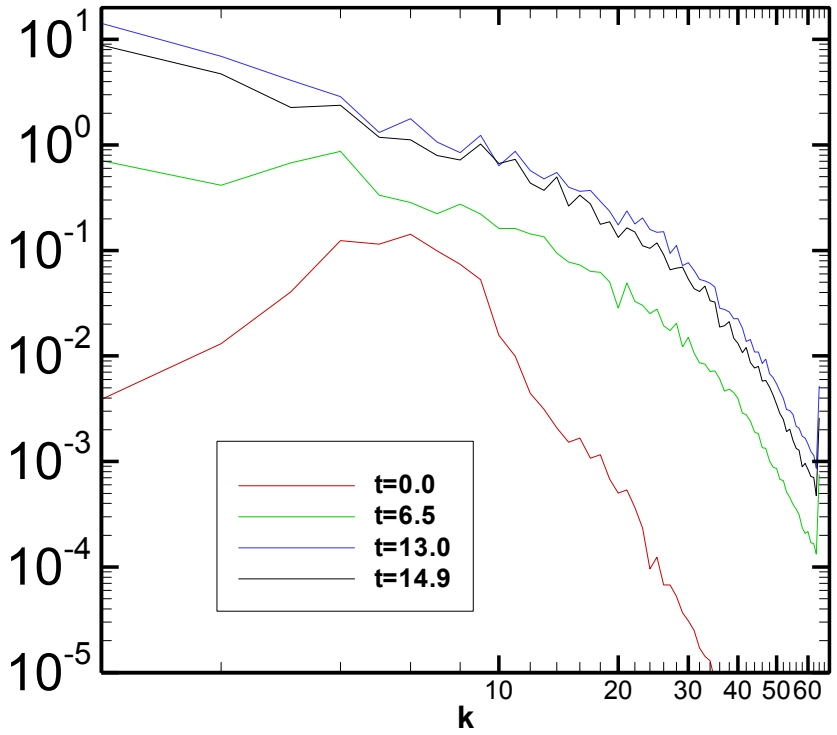

density spectra

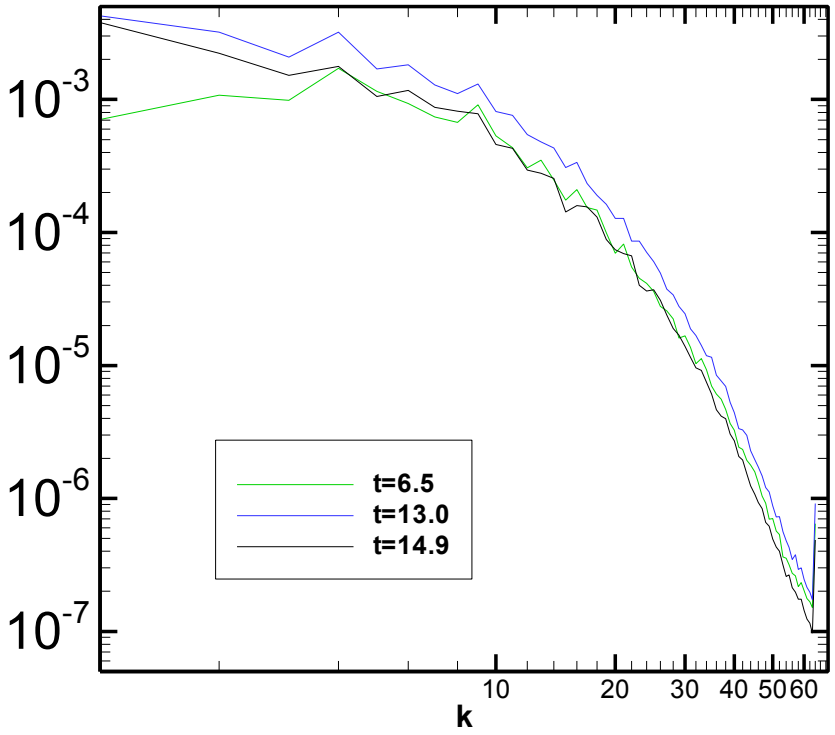

velocity spectra

RMI: Density plane averages and rms

Run A

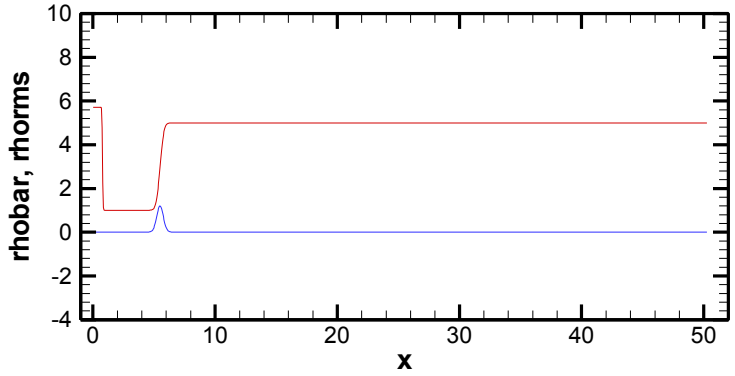

t=0.0

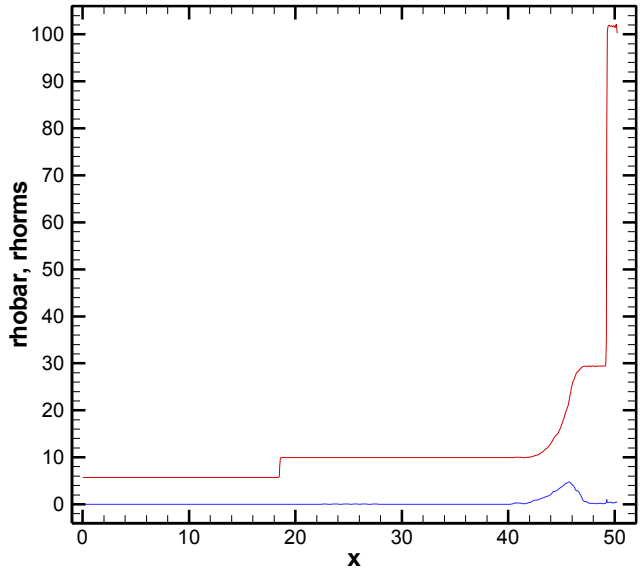

t=6.5

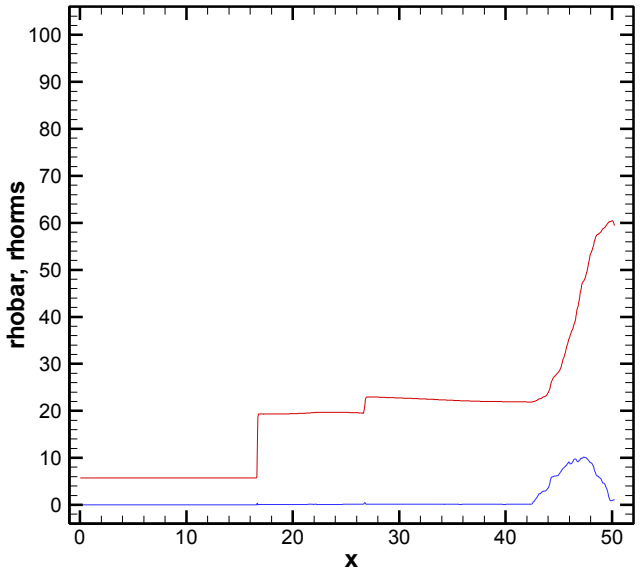

t=13.0

RMI: Plane averages and rms (Run C)

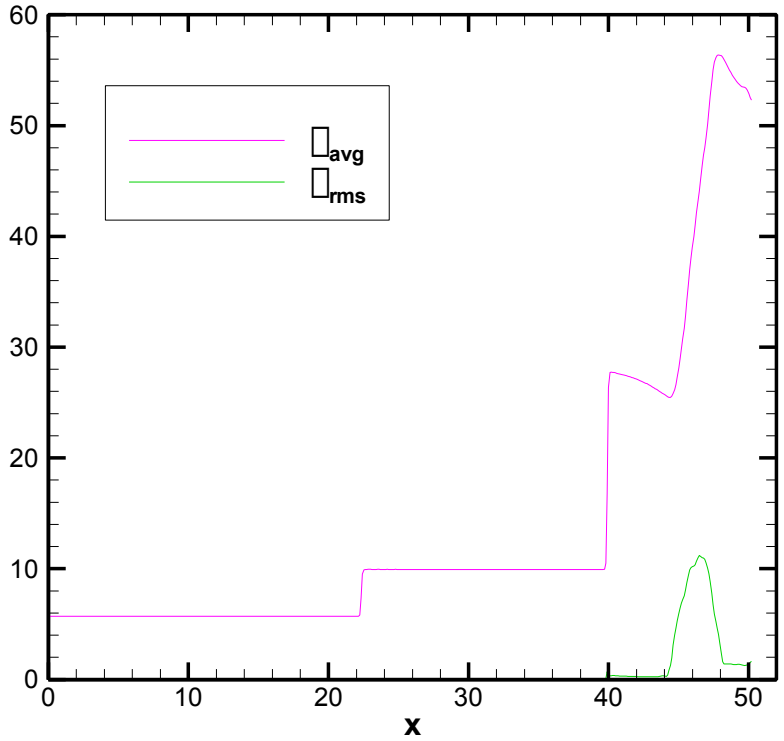

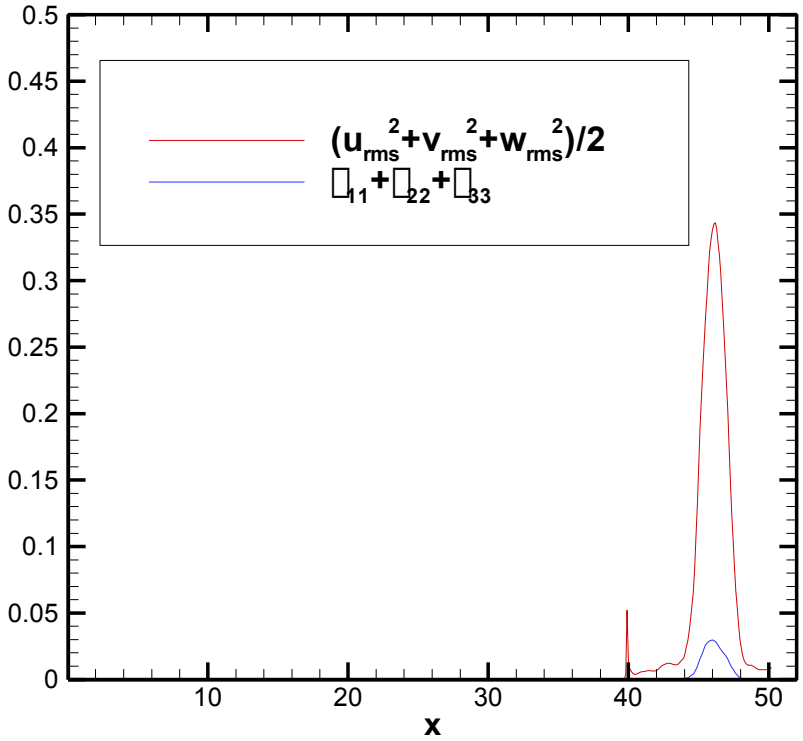

t=8.3 (after reshock)

Turbulent Mach number is approx. 0.13 (0.1-0.35 after reshock)

RMI: Mixing width (Integral Measure)

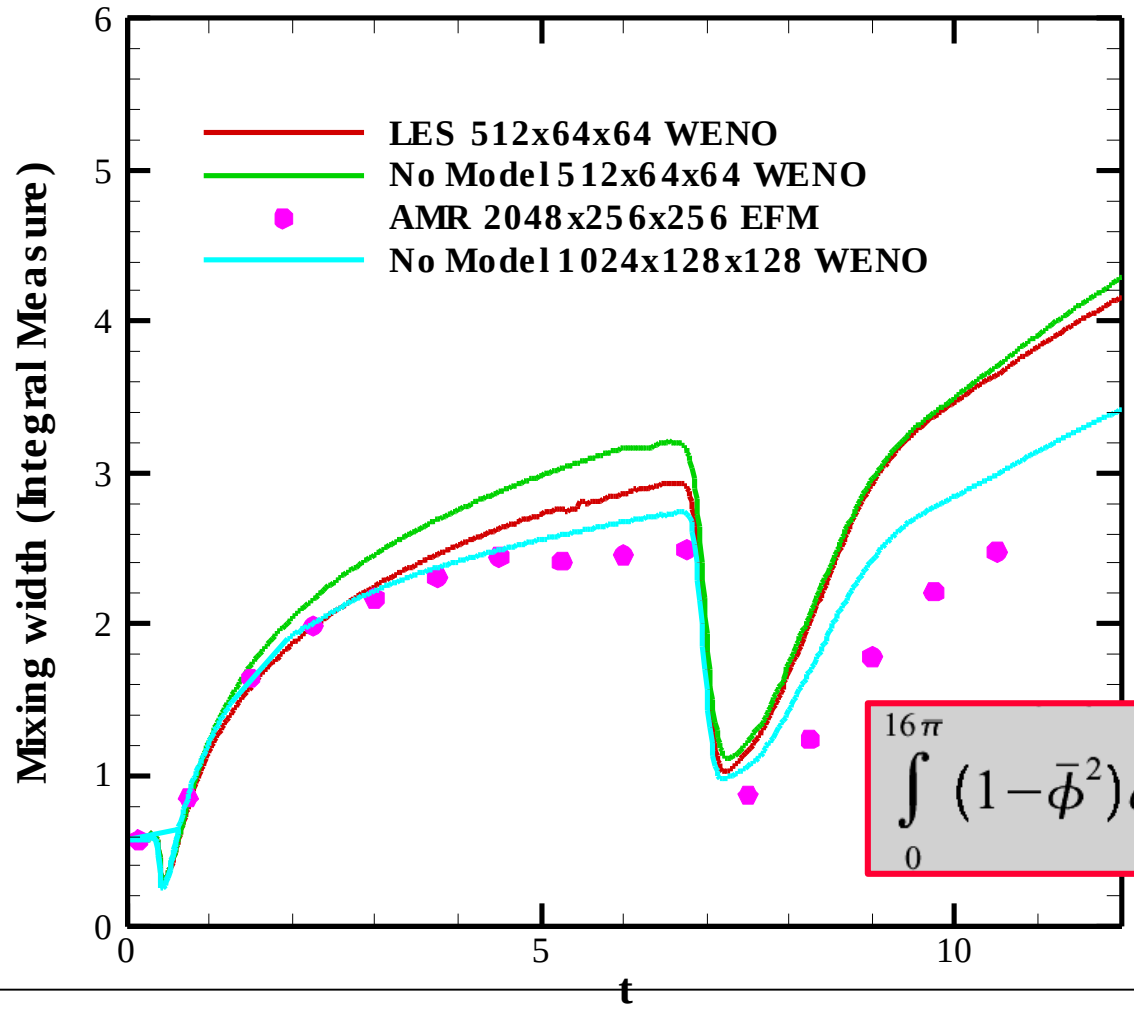

$$\int_0^{16\pi} (1-\bar{\phi}^2)\,dx \quad \text{with} \quad \phi \in [-1;1]$$

AMR done with EFM, no SGS model and with reflecting BC

RMI: Width of density interface

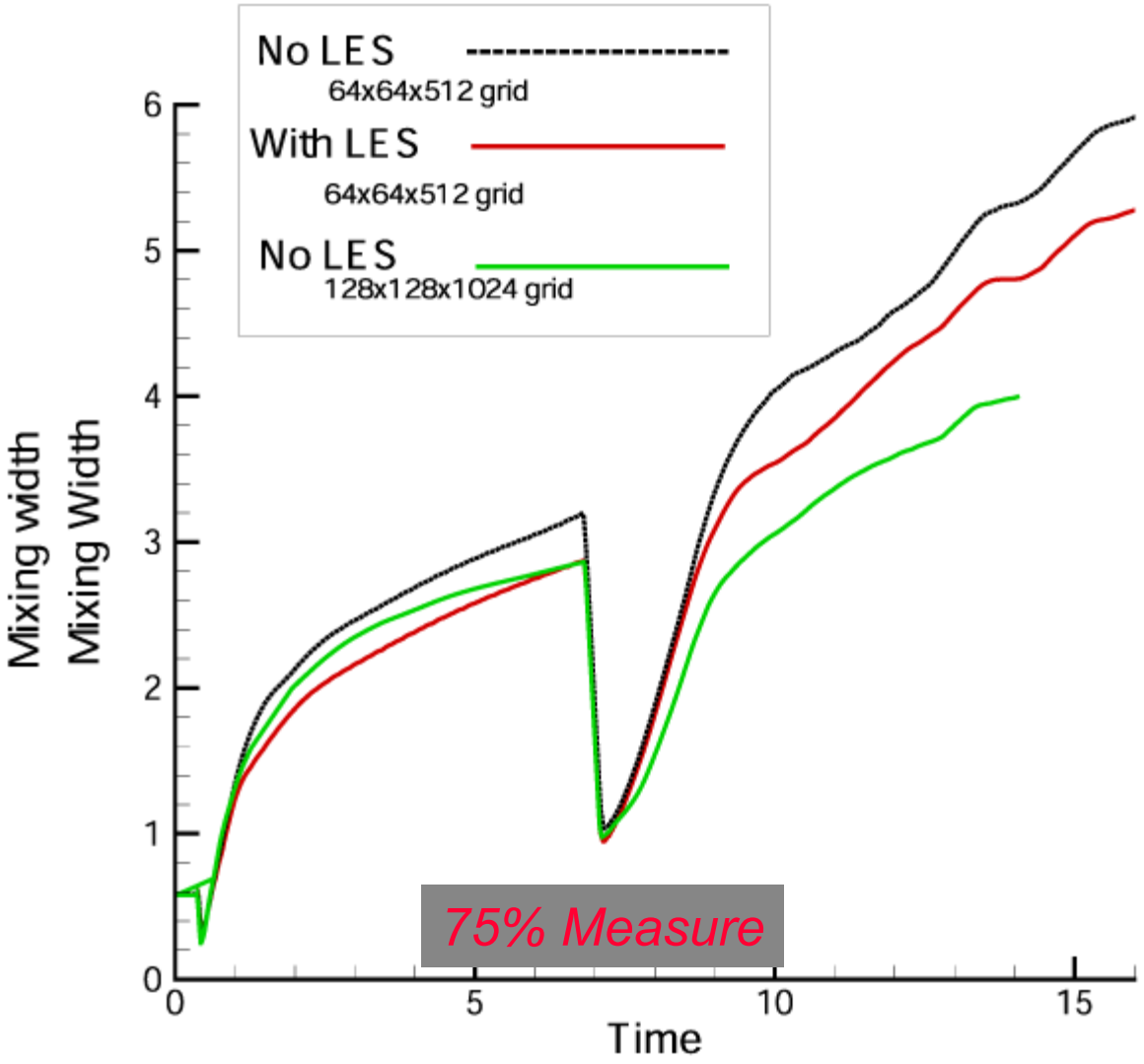

Conclusion

- Requirement of shock-capturing and higher-order is difficult to achieve in practice
  - *WENO schemes investigated*
    - *Compared with Pade schemes for decaying isotropic turbulence*
    - *High modified wavenumber behaviour not favourable*
    - *Require "Carbuncle fix" to stabilise the shock*
- LES of strong-shock RM performed using the stretched vortex SGS model
  - *SV - SGS model implemented in the WENO code*
    - *works as a plug-in*
    - *no explicit filtering*
    - *SGS model is robust (I.e., no. numerical stability issues)*
- Compared LES with SV model and LES with no model
  - *SGS model active but subgrid TKE is a small fraction of the totalTKE (~10%)*
  - *Small differences in the "mixing width" with and w/o SGS model*

Numerical Investigation of a Laser Induced Turbulent Mixing Zone

P. Seytor and M. Legrand
CEA/DAM Ile de France, BP12, 91680, Bruyères le Châtel, France

We have used high Mach number (M ≈ 20) mix instability experiments which have been conducted using the NOVA laser system to investigate the growth of the Richtmyer-Meshkov instability resulting from a strong shock wave. The initial nonlinear single-mode two dimensional perturbation was machined into a brominated plastic ablator (density : 1.22 g/cc) adjacent to a low density carbon foam (0.10 g/cc). We compared the experimental results with LLNL simulations (CALE code) and with our own numerical simulations (FCI2 code). A non linear model (Ramshaw [1]) has been previously used to analyze the growth of a mixing zone in this experiment (Farley *et al.* [2]). We propose here to consider the possibility of a long turbulent phase in this type of experiment. We found mix width results to be in good agreement with the k-ε statistical model included in a 1D code when the transition time to turbulence is correctly estimated (high Mach number effects).

The first section of this talk describes the experimental setup. The instability phases of the flow are discussed in section II. The Ramshaw non linear model is described in section III and the necessary conditions for turbulence in section IV. High Mach number effects on the transition time to turbulence are discussed in section V (HESIONE 2D eulerian code) and k-ε computations are described in section VI. This is followed by a summary in section VII.

[1] J. D. Ramshaw
Simple model for linear and non linear mixing at unstable fluid interfaces with variable acceleration
Phys. Rev. E, **58**, N5, 1998

[2] D. R. Farley et al.
High Mach number mix instability experiments of an unstable density interface using a single mode, nonlinear initial perturbation
Physics of plasmas, **6**, N11, 1999

Experimental Setup

Farley et *al.*

Front View

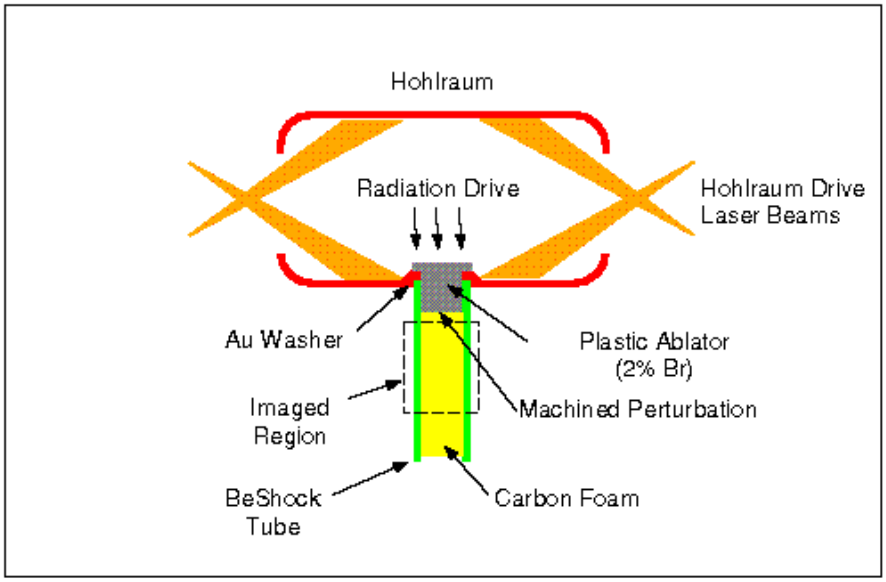

Hohlraum : 3080 µm long and 1600 µm diameter hollow cylinder

Shock tube : 2200 µm long **beryllium cylinder**
outer diameter : 700 µm
inner diameter : 500 µm
ablator : 300 µm long (ρ = 1.22 g/cm3)
carbon foam : 1900 µm long (ρ = 0.1 g/cm3)

Hohlraum drive : 1ns square pulse (≈ 20kJ)
Radiation drive : peak flux temperature = 230 eV (±10 eV)

Instability phases

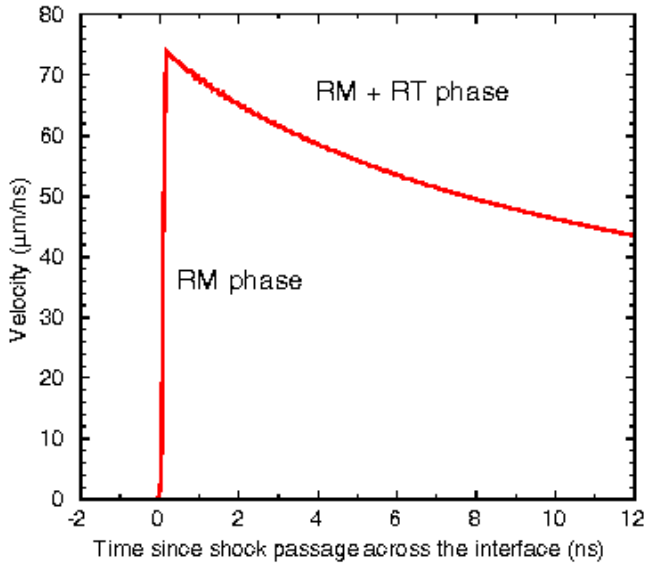

❒ A Richtmyer-Meshkov Instability (RMI) is induced by the shock passage across the interface

❒ This RM phase is followed by a slow decay of velocity which generates a Rayleigh-Taylor Instability (RTI)

❒ These results obtained with our 1D Radiation Hydrodynamics code are very close to Farley's (CALE 1D, [1])

[1] D. R. Farley et al.
High Mach number mix instability experiments of an unstable density interface using a single mode, nonlinear initial perturbation
Physics of Plasmas, **6**, N11, 1999

Nonlinear Model

• Ramshaw [1] uses a Lagrangian formulation to derive an ODE for the growth of a perturbed density interface subjected to an arbitrary acceleration g(t) in uncompressible fluids :

$$b|a|\dot{a} + \frac{ba}{2|a|}\dot{a}^2 + 2\pi c|\dot{a}|\dot{a} - 2\pi A a g(t) = 0$$

a is the amplitude of the perturbation, A is the Atwood number, b is a nondimensional constant related to the RT α parameter and to the RM power law exponent θ {$b = \pi\theta/\alpha(2-\theta)$} and c is a dissipation factor of order unity.

• Farley *et al.* [2] use this model to fit the experimental results of the laser experiment.

[1] J. D. Ramshaw
Simple model for linear and non linear mixing at unstable fluid interfaces with variable acceleration.
Phys. Rev. E, **58**, N5, 1998

[2] D. R. Farley *et al.*
High Mach number mix instability experiments of an unstable density interface using a single mode, nonlinear initial perturbation.
Physics of Plasmas, **6**, N11, 1999

Nonlinear model

Farley *et al.*

❒ The amplitude (experiment) is equal to mix half-width

❒ The Ramshaw model is uncompressible and the experimental results have to be decompression-corrected in order to be compared to modelization.

❒ The initial values of a and da/dt are given by a 2D eulerian computation (CALE code)

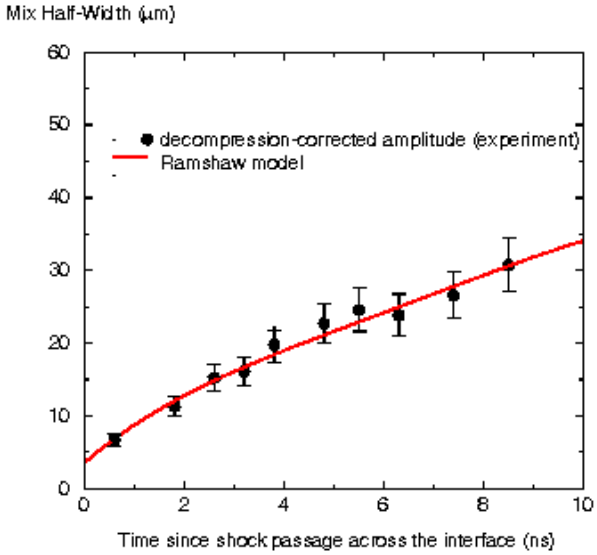

The authors obtain a very reasonable fit of experimental data

Necessary conditions for turbulence

- The Reynolds number of the flow must be enough
  - Reynolds number estimation

- The experiment duration must be greater than the transition time to turbulence
  - Transition time model

Necessary conditions for turbulence

Reynolds number estimation

$$\mathrm{Re} = \frac{ul}{\nu}$$

ν = 0.001 μm^2/ns [1]

We propose [2] the following definitions for u and l :

$$u = \dot{a}(t_s) = 10 \mu m / ns$$

$$l = \lambda = 23 \mu m$$

$\mathrm{Re} \approx 10^5$ (≈ Farley's result [1])

Grégoire [2] founds the following result for three classical shock tubes :

$5.\ 10^3 < \mathrm{Re} < 8.\ 10^4$

The laser induced instability can lead to turbulence

[1] D. R. Farley et al.
High Mach number mix instability experiments of an unstable density interface using a single mode, nonlinear initial perturbation
Physics of Plasmas, **6**, N11, 1999

[2] O. Grégoire
CEA/DIF internal report, 2000

Necessary conditions for turbulence
Transition time model [1]

$$\tau_{tr} = t_{nl} + t_{turb}$$

$\tau_{tr} = t_{nl} + t_{turb}$ ← "filling" of the spectrum

↑ end of the non linear phase

❑ t_{nl} $\quad a(t) = a_0^+ + \dot{a}_{IM}(t - t_0)$

linear phase, Impulsive model (IM)

$$t_{as}(a) = t - t_0 = \frac{a - a_0^+}{\dot{a}_{IM}} \qquad (d = ka < 1)$$

End of the linear phase :

Heuristic geometrical argument : $a(t_{nl}) = \lambda/2$ $\quad (d = \pi)$

$$t_{nl} = \frac{\pi - d_0^+}{k\dot{a}_{IM}}$$

Grégoire [1] uses Vandenboomgaerde's impulsive model [2] valid for low Mach numbers to evaluate $\dot{a}_{IM}$

$$t_{nl} = \frac{2}{k}\left\{\frac{\pi - d_0^-\left(1 - \frac{\Delta U}{W}\right)}{\Delta U d_0^-\left[A^+\left(1 - \frac{\Delta U}{W}\right) + A^-\right]}\right\}$$

[1] O. Grégoire
CEA/DIF internal report, 2000

[2] M. Vandenboomgaerde et al.
Phys. Rev. E, 58 (2), 1874 – 1882, 1998

Necessary conditions for turbulence
Transition time model [1]

❑ t_{turb} : the initial spectrum is a $\delta(k-k_0)$ distribution. t_{turb} is the time necessary to establish the Kolmogorov cascade :

$$t_{turb} = \frac{\theta_T}{k\sqrt{K}}$$ (K is the fluctuating kinetic energy)

$$\theta_T = 2.1$$ (Clark *et al.* [2])

$$K \approx \frac{1}{2}\dot{a}^2_{t=t_{nl}}$$ (Grégoire [1])

$$t_{turb} = \frac{2}{k}\left\{\frac{\theta_T\sqrt{2}}{\Delta U d_0^-\left[A^+\left(1-\frac{\Delta U}{W}\right)+A^-\right]}\right\}$$

❑ We will use an alternate expression for $\dot{a}_{IM}$ (Meyer *et al.* [3]):

$$\dot{a}_{IM} = kA^+a_0^*\Delta U \qquad \text{with} \qquad a_0^* = \frac{1}{2}\left(a_0^- + a_0^+\right)$$

τ_{tr} =0.44 ns after shock passage across the interface in the laser experiment (valid for low Mach number)

[1] O. Grégoire. CEA/DIF internal report, 2000
[2] T. T. Clark *et al.* Symmetries and the approach to statistical equilibrium in isotropic turbulence. Physics of Fluids, **10** (11),, 2846-2858,1998
[3] Meyer et al. Numerical investigation of the stability of a shock-accelerated interface between two fluids. Phys. Fluids 15, 753-75

2D eulerian computations (HESIONE code)

Initial setup

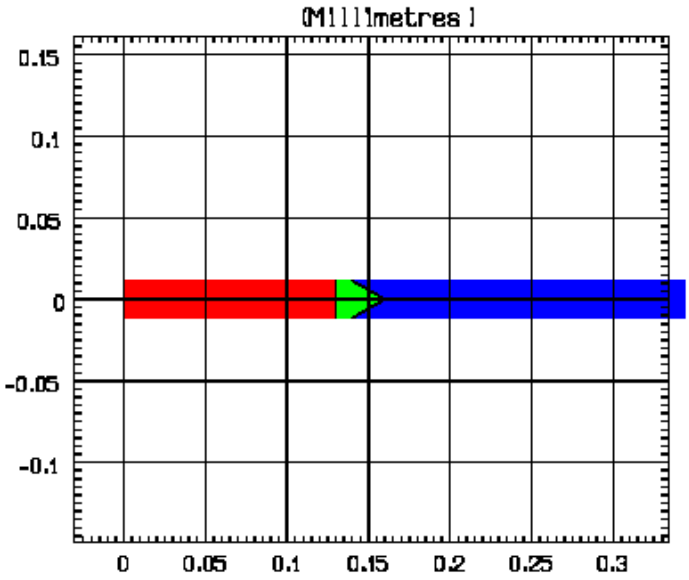

shocked CHBr (red) length : 130 µm

unshocked CHBr (green) length : 20 µm

carbon foam (blue) length : 250 µm

- Pure RMI computation (35 Mbar incident shock)
- Planar geometry
- Rigid walls computation box
- No radiation effects
- Standard EOS
- 100 zones/wavelength
- Computations valid till ≈ 2ns (non physical rarefaction waves effects)

2D eulerian computations (HESIONE code)

Interface history

❒ Vx map + interface

❒ Time is referenced to when the shock completes the interface traversal for a0 = 10 μm

a0 = 1 μm

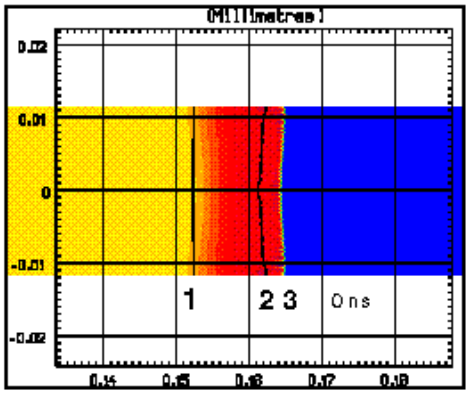

a0 = 10 μm

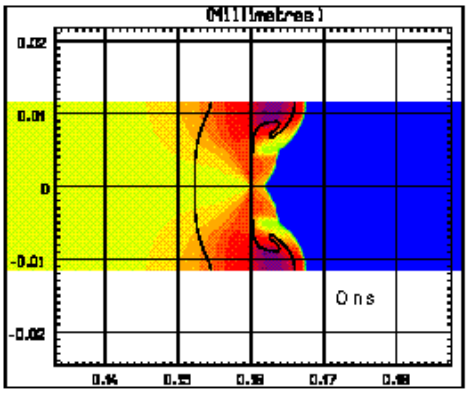

1 : artifact; **2** : interface; **3** : shock

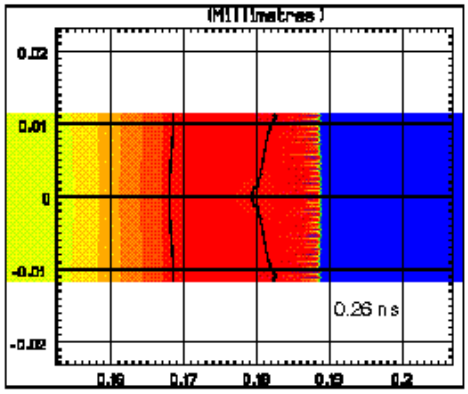

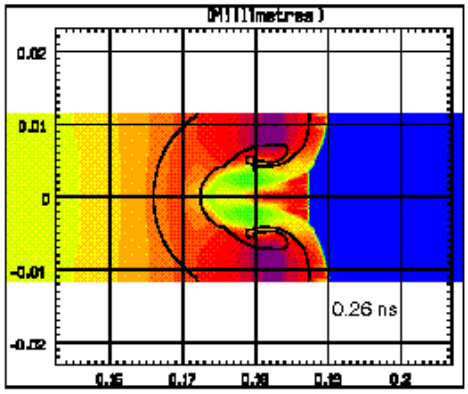

❒ The spike tip cannot overtake the transmitted shock (this penetration is energetically prohibitive)

⇒ **da/dt** ≤ **st - uc** (st : transmitted shock speed; uc : interface speed)

2D eulerian computations (HESIONE code)

Amplitude and growth rate history of the perturbation

The following analysis was proposed by Holmes et al. [1]

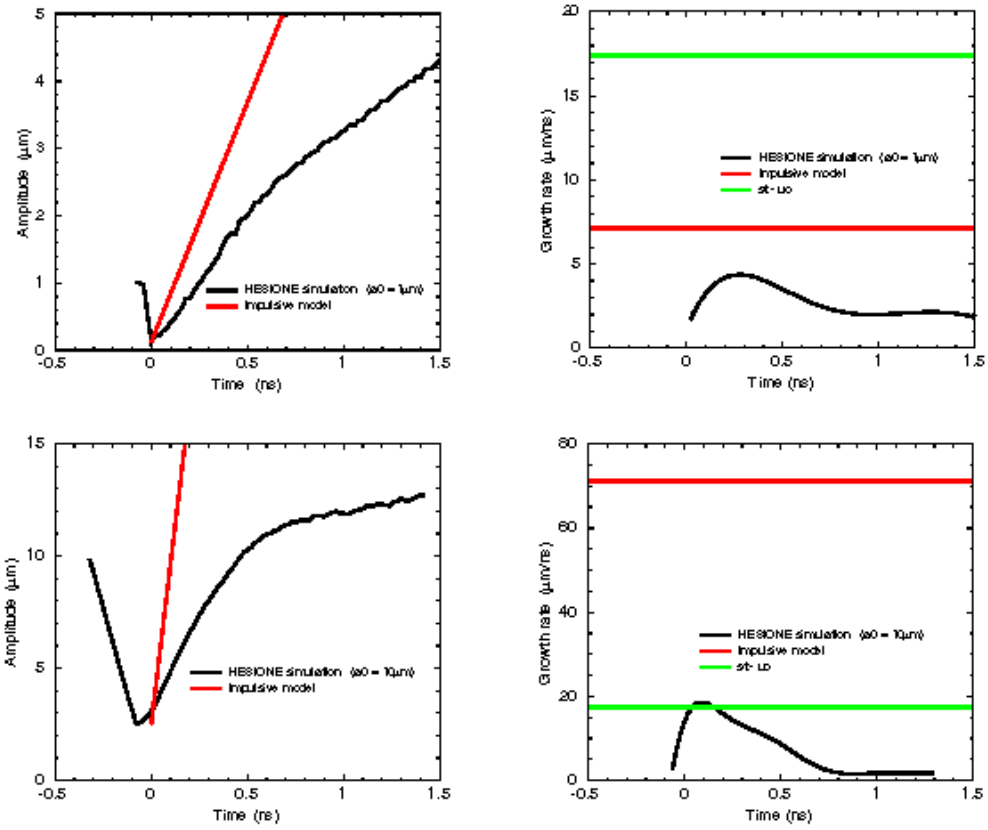

❒ Time is referenced to when the shock completes the interface traversal for each of the computations.

❒ For a0 = 1µm the impulsive model leads to a growth rate lower than st-uc.
⇒ The maximum growth rate given by HESIONE is of the order of 60% of the growth rate given by the impulsive model.

❒ For a0 = 10µm the growth rate given by the impulsive model is four times higher than st-uc which is the limiting factor (the maximum growth rate given by HESIONE is of the order of st-uc).

[1] R. L. Holmes *et al.*
Richtmyer-Meshkov Instability growth : experiment, simulation and theory
J. Fluid Mech., vol. 389, pp. 55-79 (1999)

2D eulerian computations (HESIONE code)

Saturation of the growth rate

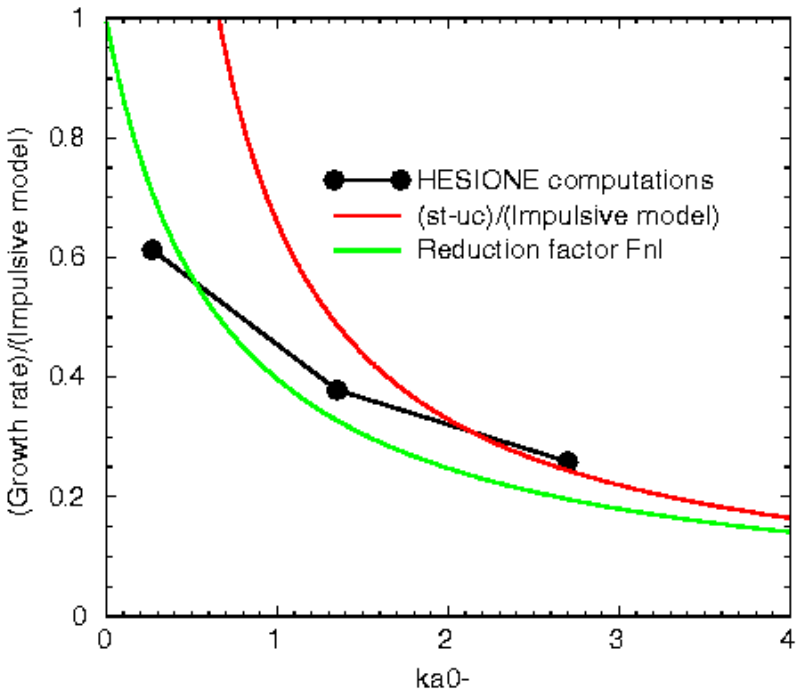

❒ The ratio of the actual growth rate to the IM growth rate (IMgr) is lower than 1 and lower than (st-uc)/IMgr

❒ Holmes *et al.* [1] propose a heuristic reducing factor Fnl which gives the IM growth rate in the linear limit :

$$Fnl = 1/\{1 + IMgr/(st - uc)\}$$

❒ Our results ($M \approx 20$) are similar to Holmes ($M = 15.3$)

[1] R. Holmes *et al.*
Richtmyer-Meshkov instability growth : experiment, simulation and theory
J. Fluid Mech., vol. 389, pp. 55-79 (1999)

2D eulerian computations (HESIONE code)

Estimation of the transition time

Modifications of the Gregoire's model :

❒ The IM growth rate is replaced by the maximum growth rate given by the simulation to calculate tnl and tturb (low value of τtr)

❒ The growth rate at tnl can be used instead of the maximum growth rate to calculate tturb (high value of τtr)

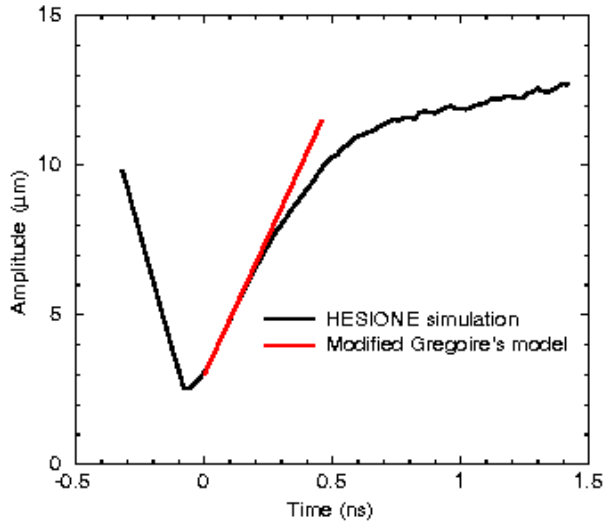

$1.2\ ns < \tau tr < 1.9\ ns$

(after shock passage across the interface)

k-ε computations [1]
Initial conditions

- The k-ε model is a two equations statistical model (one equation for k, the turbulent kinetic energy and one equation for ε, its dissipation rate)

- k and ε have to be defined at τ_{tr}

- k and ε have the same extension L at τ_{tr} (the mixing zone width at τ_{tr}) and have a symmetric triangular shape

$$L = 2\alpha(1+\beta)A^{+}\Delta U\tau_{tr} \text{ (Mikaelian [2])}$$

$$k_{max} = \frac{4}{3}\alpha\left(A^{+}\Delta U\right)^{2}$$

$$\varepsilon_{max} = C\frac{k_{max}^{3/2}}{L}$$

This simple model has been widely used in classical shock tubes computations.

[1] S. Gauthier et al.
A k-ε model for turbulent mixing in shock tube flows induced by Rayleigh-Taylor instability
Phys. Fluids. A **2** (9) 1685-1694, 1990

[2] K. O. Mikaelian
Turbulent mixing generated by Rayleigh-Taylor and Richtmyer-Meshkov instabilities
Physica D, **36**, 343, 1989

k-ε computations

Transition time estimation

k-ε computations were carried out for three arbitrary values of τtr (0.5, 1.0 and 1.5 ns)

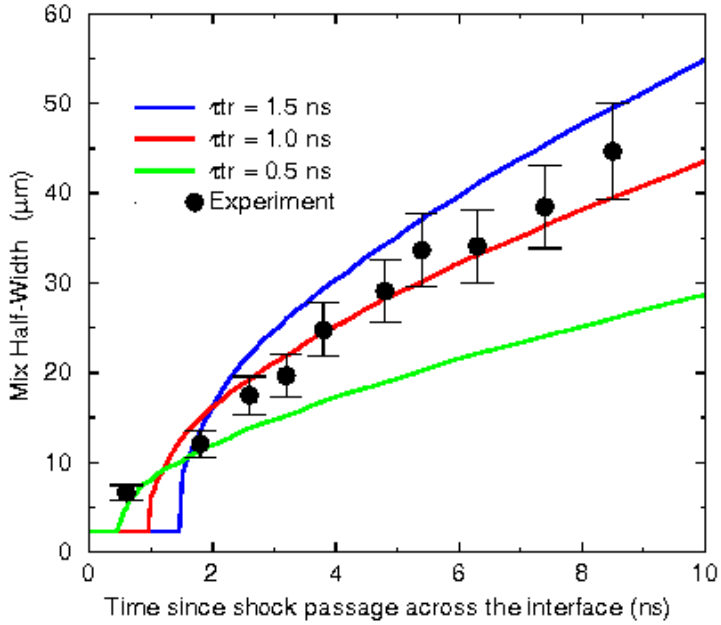

❒ The amplitude (Mix half-Width) history for τtr ≈ τtrIM (τtr = 0.5 ns) doesn't fit the experimental data

❒ A reasonable fit for the long term amplitude is obtained for 1.0 ns < τtr < 1.5 ns

❒ This τtr range reasonably agrees with the Gregoire's model applied to HESIONE computations :

1.2 ns < τtr < 1.9 ns

k-ε computations

Ramshaw model [1] and k-ε model

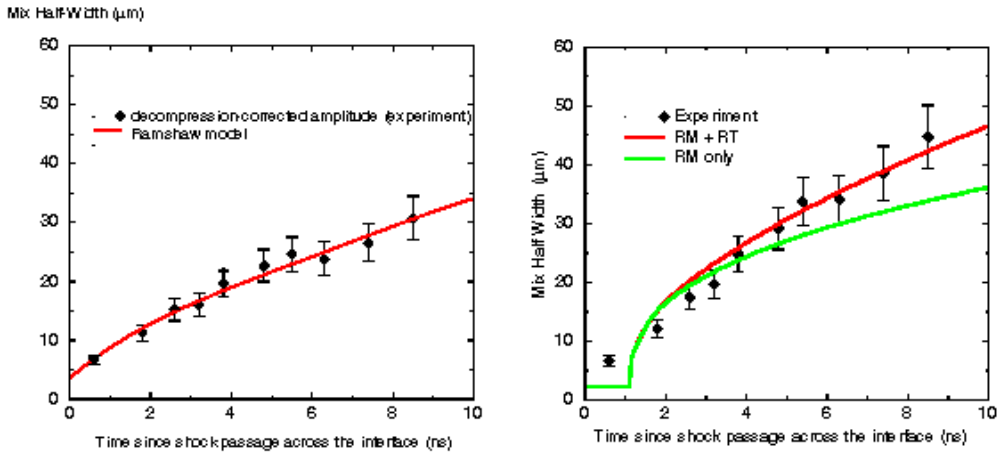

❒ **A reasonable fit for the long term amplitude is obtained either with the Ramshaw model or with the k-ε model (τtr = 1.125 ns)**

❒ The k-ε transient phase doesn't permit a satisfactory description of the beginning of the perturbation growth

❒ The pure RM case has also been considered in [1] (aRM/aRM+RT = 0.81 at 10 ns) and the k-ε model leads to a similar result (aRM/aRM+RT = 0.78 at 10 ns)

[1] D. R. Farley et al.
High Mach number mix instability experiments of an unstable density interface using a single mode, nonlinear initial perturbation.
Physics of Plasmas, **6**, N11, 1999

Summary

❑ The Reynolds number of the flow induced by laser in the experiment analyzed here is of the order of magnitude of the Reynolds number obtained in classical shock tube experiments

❑ The transition time related to the Impulsive Model growth rate is very small as compared to the duration of the experiment

❑ The transition time related to the growth rate evaluated through 2D computations stays very shorter than the duration of the experiment

❑ The k-ε computations fit the experimental data in a range of τ_{tr} compatible with the former result

A Mix-Model for One-Dimensional Simulations of Laser-Driven Implosion Experiments

D. Souffland and F. Renaud

(Commissariat à l'Énergie Atomique, DAM Île-de-France)

BP 12, 91680 Bruyères-le-Châtel, France

DAM - Île de France

Acknowledgments: D. Galmiche, C. Cherfils-Clérouin, A. Grisollet (CEA/DIF)

MéDiC: A tool to mimic hydrodynamic instability effects on laser targets

- Context:
  Design of laser targets for LMJ facility
  Studies upon the reduction of implosion efficiency due to the development of interface and front perturbations
  Usefulness of 1D quick parametric studies

- By previous theoretical, experimental or multidimensional simulation studies, temporal evolution of the "mixing zone" is known
  (thickness = peak-to-valley distance, exchange area, mass, ...)

- Basic hypothesis:
  Influence of the interpenetration of matter is modelized through diffusion processes although transition to full turbulent mixing do not occur
  (short wavenumber perturbations, in weakly non-linear stage, are still dominant)

Application to the hydrodynamic instabilities at the ablator-fuel interface

- Cumulative effects of various processes: Richtmyer-Meshkov instability, feed-in, Bell-Plesset instability ...
  Preliminary stages of the mixing of two separate fluids
  Main process: mass transport

- Goal: interpretation of the HEP4 experiments at Omega

- Derivation of the mix model from a classical two-fluid formulation

DAM - Île de France

Averaging the Two-Fluid Model $\Longrightarrow$

a mono-fluid model

Hyp. : The 2 fluids have the same presssure

$$\frac{\partial \rho}{\partial t} + \frac{\partial}{\partial x}(\rho u) = 0,$$

$$\frac{\partial}{\partial t}(\rho c) + \frac{\partial}{\partial x}(\rho c u + \rho c\,(1-c)\,u_r) = 0,$$

$$\frac{\partial}{\partial t}(\rho u) + \frac{\partial}{\partial x}\left(\rho u^2 + P + \rho c\,(1-c)\,u_r^2\right) = 0,$$

$$\frac{\partial}{\partial t}(\rho E) + \frac{\partial}{\partial x}\left(\rho E u + P u + \rho c\,(1-c)\,(h_1 - h_2)\,u_r \quad + \rho c\,(1-c)\left(u u_r^2 + \left(\frac{1}{2} - c\right) u_r^3\right)\right) = S$$

where ρ, u, P and E are the density, the velocity, the pressure and the total energy of the mixture. c the mass fraction of fluid 1, $h_{1,2}$ are the partial enthalpies of each fluid and u_r the relative velocity between each fluid.

Basic hypothesis: Diffusion type closure $\rho c\,(1-c)\,u_r \equiv -\rho \mathcal{D} \dfrac{\partial c}{\partial x} \Longrightarrow$

Equations for the mixing in a monofluid 1D lagrangian code

Extra hypothesis: isothermal mixing ($h_i = \mathcal{F}(\rho_i, T)$)
relative velocity is small ($u_r << u$) $\Longrightarrow$ "green terms" neglected
Source terms for internal energies equations: thermal conduction, thermalization and radiative contributions

$$\frac{\partial \rho}{\partial t} + \frac{\partial}{\partial x}(\rho u) = 0,$$

$$\rho \frac{Dc}{Dt} = \frac{\partial}{\partial x}\left(\rho \mathcal{D} \frac{\partial c}{\partial x}\right),$$

$$\rho \frac{Du}{Dt} = -\frac{\partial P}{\partial x},$$

$$\rho \frac{De_i}{Dt} = -P\frac{\partial u}{\partial x} + \frac{\partial}{\partial x}\left(\rho\,(h_1 - h_2)\,\mathcal{D}\frac{\partial c}{\partial x}\right) + \frac{\partial}{\partial x}\left(\mathcal{K}_i \frac{\partial T_i}{\partial x}\right) + \text{Therm.}$$

$$\rho \frac{De_e}{Dt} = -P\frac{\partial u}{\partial x} + \frac{\partial}{\partial x}\left(\mathcal{K}_e \frac{\partial T_e}{\partial x}\right) - \text{Therm.} + \text{Rad.}$$

with $\frac{D}{Dt}$ the Lagrangian derivative, e_i, e_e, T_i and T_e are the internal energies and temperatures

+ Multigroupe radiative method

$\equiv$ Modelling of the mass transport by "molecular mixing" with diffusion coefficient $\mathcal{D}$

Determination of the diffusion coefficient

The diffusion coefficient in the mass concentration equation, $\mathcal{D}(t)$, must be adjusted to give the requested mixing zone widening, $L_{mix}(t)$

- For an interface at constant velocity the exact solution is known:
  $\mathcal{D}(t) = \frac{1}{8\,\xi^2} L_{mix} \frac{dL_{mix}}{dt}(t)$, with $\xi = 1.163$ for a 5 - 95 % concentration profile
- For an homogeneous compression in spherical geometry,
  the flow is defined by the evolution of the interface location $\Lambda(t)$
  A good approximation is given by $\mathcal{D}(t) = \frac{1}{8\,\xi^2} L_{mix} \left[\frac{dL_{mix}}{dt} - \frac{L_{mix}}{\Lambda}\frac{d\Lambda}{dt}\right]$

Moreover, the mass of the mixing zone can be approximate by $M_{mix} \approx (\rho_h + \rho_l)\, 4\pi\Lambda^2\, L_{mix}/2$
As, in these ideal flows, we have $\rho(t) \propto \Lambda^{-3}$, we get $M_{mix}(t) \propto \frac{L_{mix}}{\Lambda}(t)$
If we know $M_{mix}(t)$ and $L(t)$, we thus can use the alternative expression
$\mathcal{D}(t) = \frac{1}{8\,\xi^2} L_{mix}^2 \left[\frac{1}{M_{mix}}\frac{dM_{mix}}{dt}\right]$

DAM - Île de France

First results

The mix-model is implemented and validated for simple configurations
(two fluids with the same initial temperature mix without global motion)

Example of He / DT mixing at T=30000 K. Evolution of temperature, density and pressure profiles

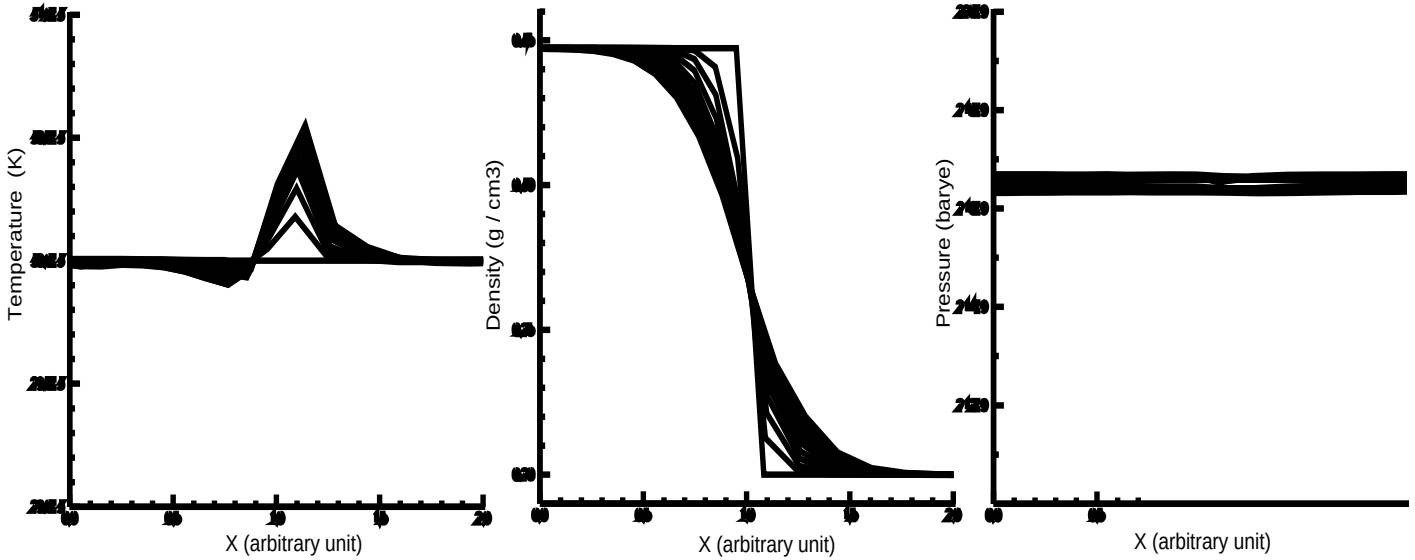

Future work: application to HEP4 experiments

Application to the hydrodynamic instabilities at the hot spot

Characteristics:

- Development of an "ablation front like" instability inside the fuel volume between the heavy and cold corona and the light and hot central spot
- Here, the front is not linked to a material interface:
  its location has to be determined by appropriate criterium
- Partial enthalpy difference transport term is ineffective
  (same fluid, isothermal mixing)
- Perturbation of the isotherms increase exchange area for thermal conduction

DAM - Île de France

Perturbation at the edge of the "in progress" hot spot

In cryogenic capsules, the DT of the hot spot at ignition is made up of the internal part of cryogenic DT corona

During the implosion, an ablation front propagate into the initially cryogenic DT

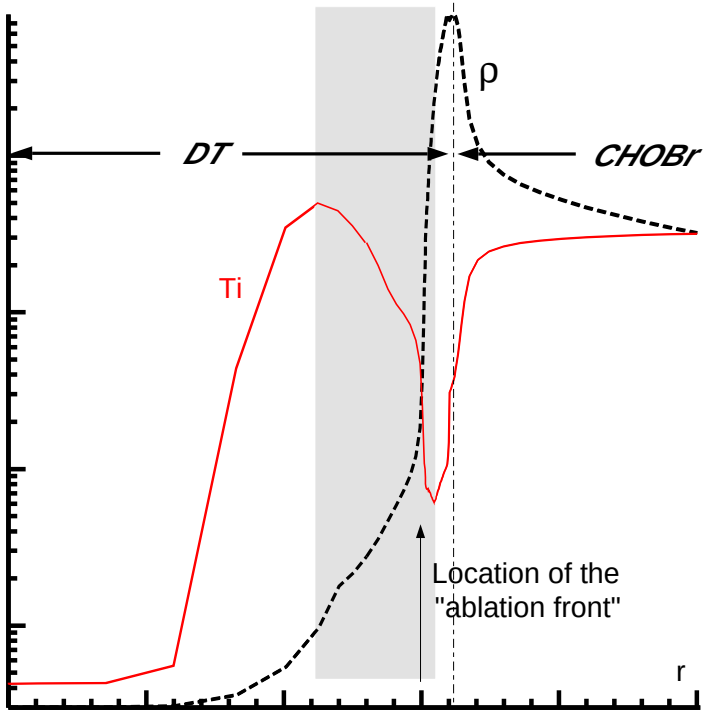

Temperature and density profiles during the implosion (1D unperturbed simulation)

We assume identity of hot spot edge, R_{hs}, and ablation front location

Ablation front location determination:

$$Max\left[2\frac{\rho^{I+1}-\rho^{I}}{\rho^{I+1}+\rho^{I}}\times(T_{ion}^{I}-T_{ion}^{I-1})\right]$$

(based upon R-T instability criterium, first part $\longrightarrow$ local Atwood number)

Good agreement with other definitions of the hot spot, within the last ns before the ignition time (see below)

DAM - Île de France

Modelling the instable front perturbation in a 1D code

Previous modelling through a "mass transfer" is inappropriate

(perturbations within the DT, where $\Delta h_i = 0$: added term do not affect energy balance)

The main process is assumed to be the increase of exchange surface for thermal conduction:

within the perturbated zone ($R_{hs} - L_{mix}/2 < x < R_{hs} + L_{mix}/2$)

thermal conduction fluxes will be multiplied by the ratio of areas $Ra(t) = S_{perturb}/S_{sph}$

Modified set of equations (plane geometry):

$$\frac{\partial \rho}{\partial t} + \frac{\partial}{\partial x}(\rho u) = 0,$$

$$\rho \frac{Du}{Dt} t = -\frac{\partial P}{\partial x},$$

$$\rho \frac{De_i}{Dt} = -P\frac{\partial u}{\partial x} + \frac{\partial}{\partial x}\left(Ra\, \mathcal{K}_i \frac{\partial T_i}{\partial x} \right) + \text{Therm.}$$

$$\rho \frac{De_e}{Dt} = -P\frac{\partial u}{\partial x} + \frac{\partial}{\partial x}\left(Ra\, \mathcal{K}_e \frac{\partial T_e}{\partial x} \right) - \text{Therm.} + \text{Rad.}$$

R_{hs} is calculated through above method; $L_{mix}, Ra(t)$ are deduced from 2D simulation

Alternative modelling through a "diffusive model"

Hypothesis: we add "mix" viscous and conductive terms

within the perturbated zone $(R_{hs} - L_{mix}/2 < x < R_{hs} + L_{mix}/2)$

"mix viscosity", $\mathcal{D}_u$, and "mix conductivity", $\mathcal{D}_e$, (homogeneous to l^2/t)

are deduced from $\mathcal{D}(t) = \dfrac{1}{8\,\xi^2}\, L_{mix}^2 \left[\dfrac{1}{M_{mix}} \dfrac{dM_{mix}}{dt}\right]$ (see above)

Modified set of equations (plane geometry):

$$\frac{\partial \rho}{\partial t} + \frac{\partial}{\partial x}(\rho u) = 0,$$

$$\rho \frac{Du}{Dt} t = -\frac{\partial P}{\partial x} + \frac{\partial}{\partial x}\left(\frac{4}{3}\rho \mathcal{D}_u \frac{\partial u}{\partial x}\right),$$

$$\rho \frac{De_i}{Dt} = -P\frac{\partial u}{\partial x} + \frac{\partial}{\partial x}\left(\rho \mathcal{D}_e \frac{\partial e_i}{\partial x}\right) + \frac{\partial}{\partial x}\left(\mathcal{K}_i \frac{\partial T_i}{\partial x}\right) + \text{Therm.} + \left(\frac{4}{3}\rho \mathcal{D}_u \frac{\partial u}{\partial x}\right)\frac{\partial u}{\partial x},$$

$$\rho \frac{De_e}{Dt} = -P\frac{\partial u}{\partial x} + \frac{\partial}{\partial x}\left(\rho \mathcal{D}_e \frac{\partial e_e}{\partial x}\right) + \frac{\partial}{\partial x}\left(\mathcal{K}_e \frac{\partial T_e}{\partial x}\right) - \text{Therm.} + \text{Rad.}$$

DAM - Île de France

Example: simulations of the L1215 capsule

to recover nonlinear multimode 2D simulations

Description of the configuration and simulations (Cherfils *et al.*, APS 43rd Annual Meeting, Long Beach CA, 2001):

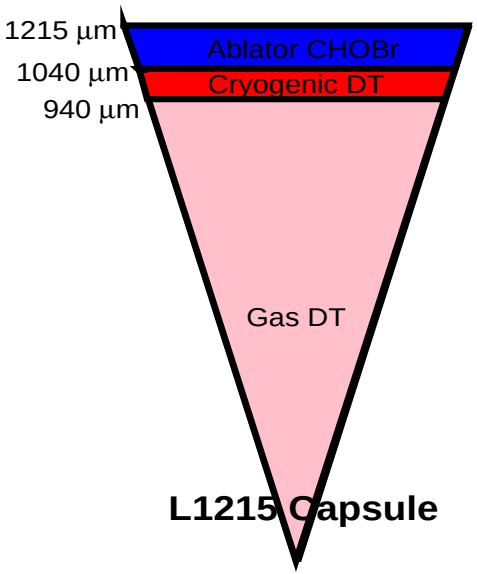

Half-spheres simulations

FCI2 code ("driven" ALE method)

$t_i = 17.45ns$,

$V_{DT}{}^{max} = 3.9\,10^7 cm/s$

Multimode initial perturbations:

Ablation surface $rms(l \geq 10) = 10\,nm$,

Cryogenic DT surface $rms(l \geq 10) = 1\,\mu m$

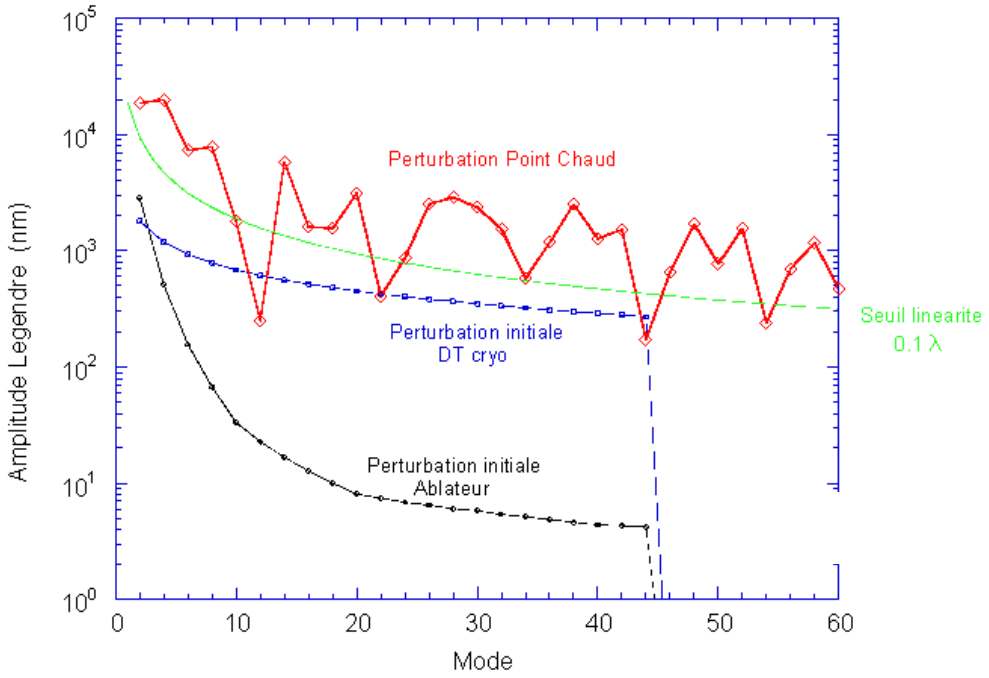

DAM - Île de France

Hot Spot front tracking

3 ways to track the Hot Spot front :

1) Search the isotherm T_{ion}=50 MK (—).

2) Search the isotherm T_{ion}= Max(T_{ion})/10 (—).

3) Search the location of the instable front:

$\left[2\frac{\rho^{I+1}-\rho^{I}}{\rho^{I+1}-\rho^{I}} \times (T^{I}_{ion} - T^{I-1}_{ion}) \right]$ maximum, for each angle θ (—)

this last method can be applied even before the converging time of the shock waves

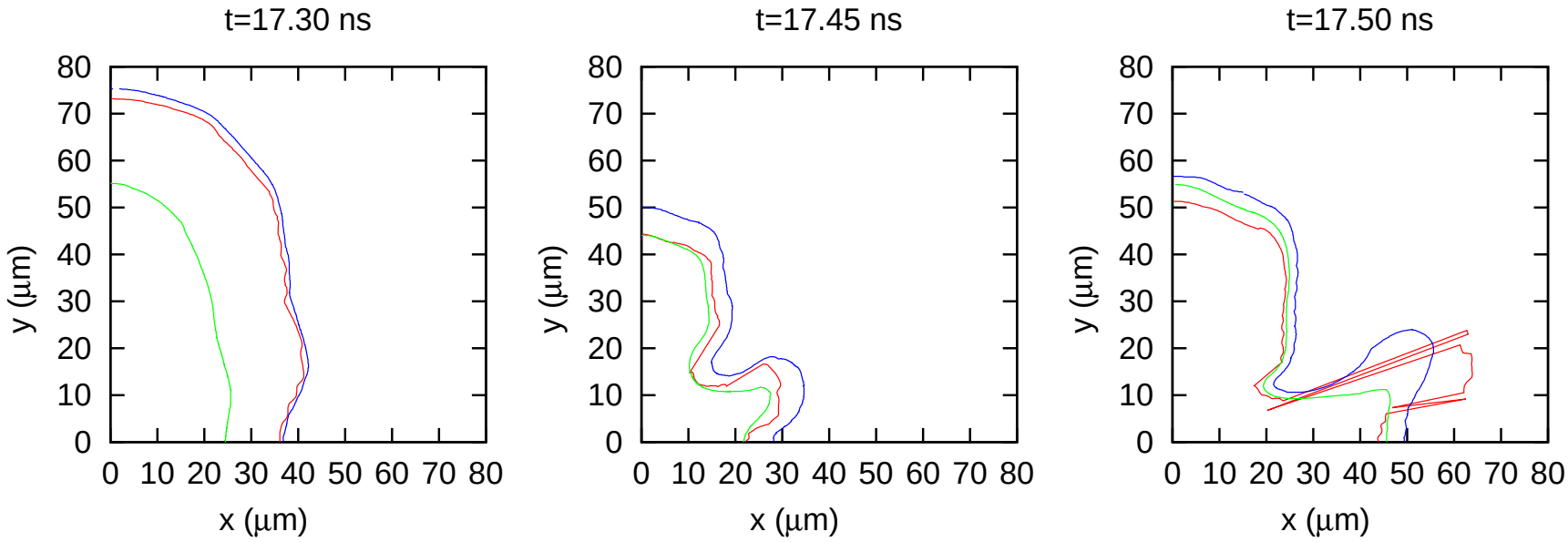

Comparison of Hot Spot fronts for 2D simulation around the ignition time

DAM - Île de France

Post-processing 2D simulation results

From the instable front contour

Minimal radius and maximal radius of the Hot Spot front

$$\Longrightarrow \text{1D mixing length } L_{\text{mix}} \text{ and mean radius } R_{\text{hs}}$$

Integration of the Hot Spot front

$$\Longrightarrow \text{1D thermal exchange surface in the mixing zone } S_{\text{perturb}}$$

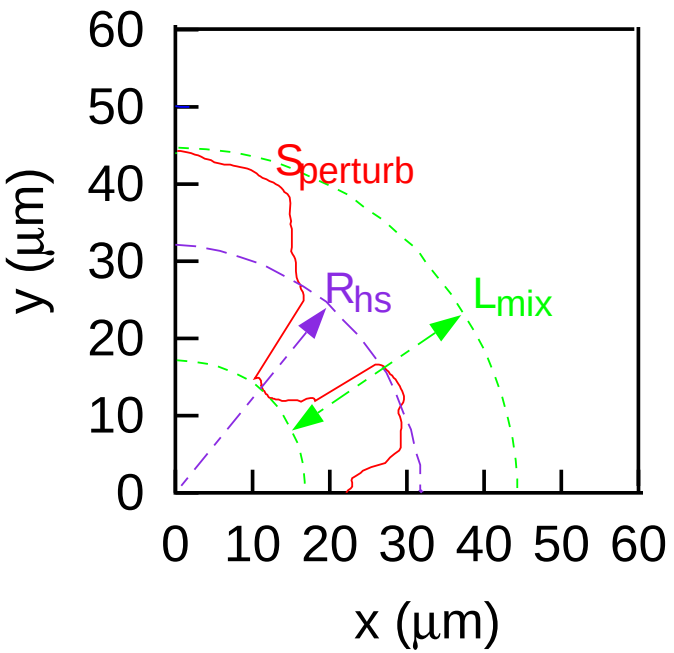

DAM - Île de France

1D Mixing length and thermal exchange surface

2D mixing length and thermal exchange area are fitted to be used in 1D code

Scaling of L_{mix} by the Hot Spot mean radius R_{hs}
Scaling of S_{perturb} by the Hot Spot mean surface $4\pi R_{\text{hs}}^2$

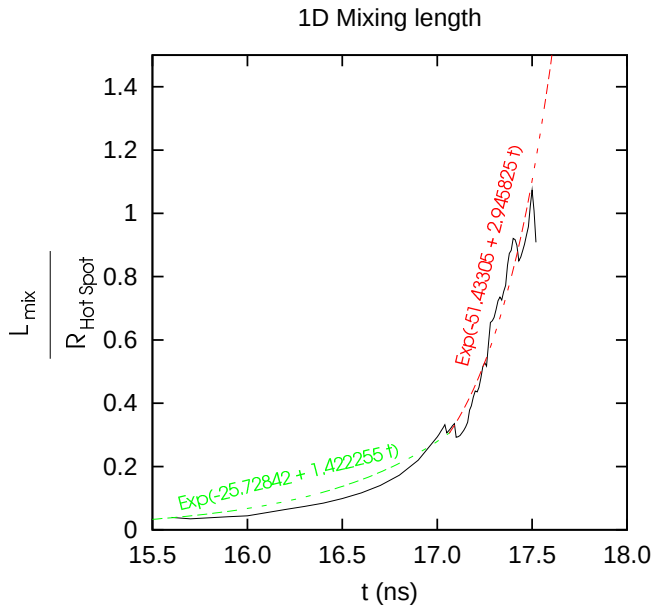

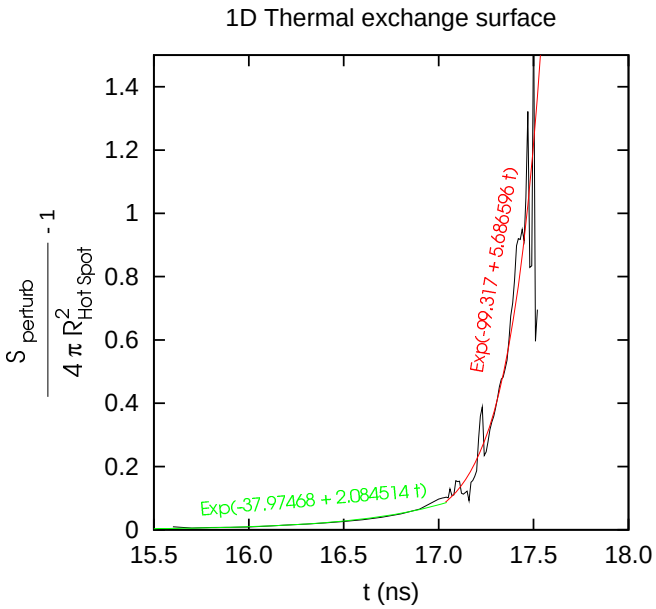

Satisfactory description of the mean hot spot characteristics

The evolution of the mass of DT within the hot spot

and its mean ionic temperature are simulated in 1D calculations

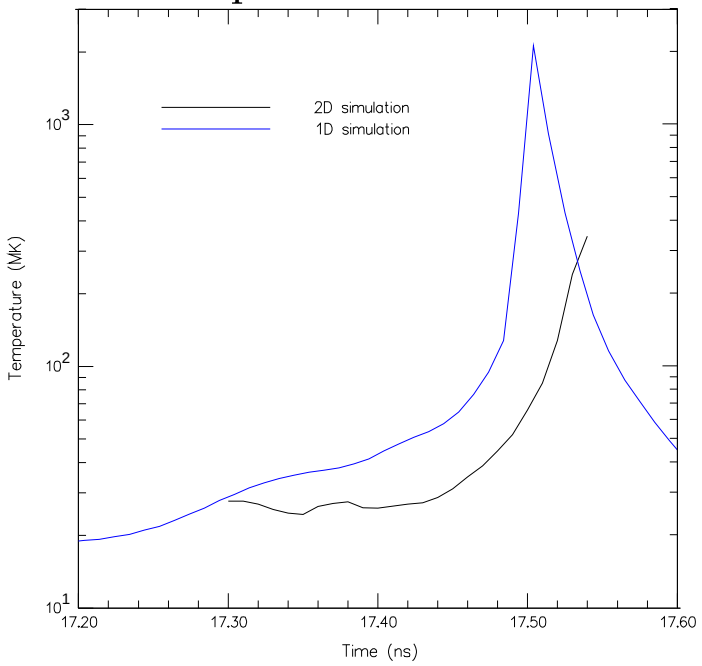

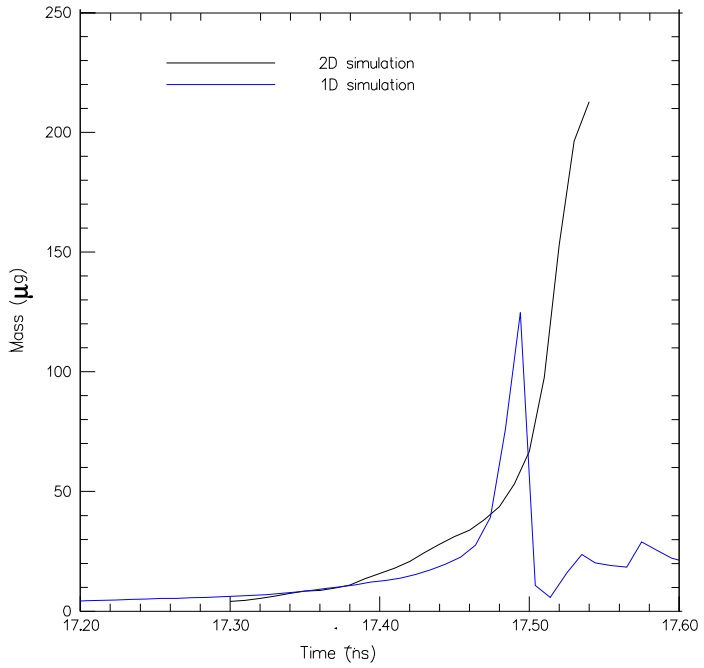

DAM - Île de France

1D models fail to represent all 2D flow complexity

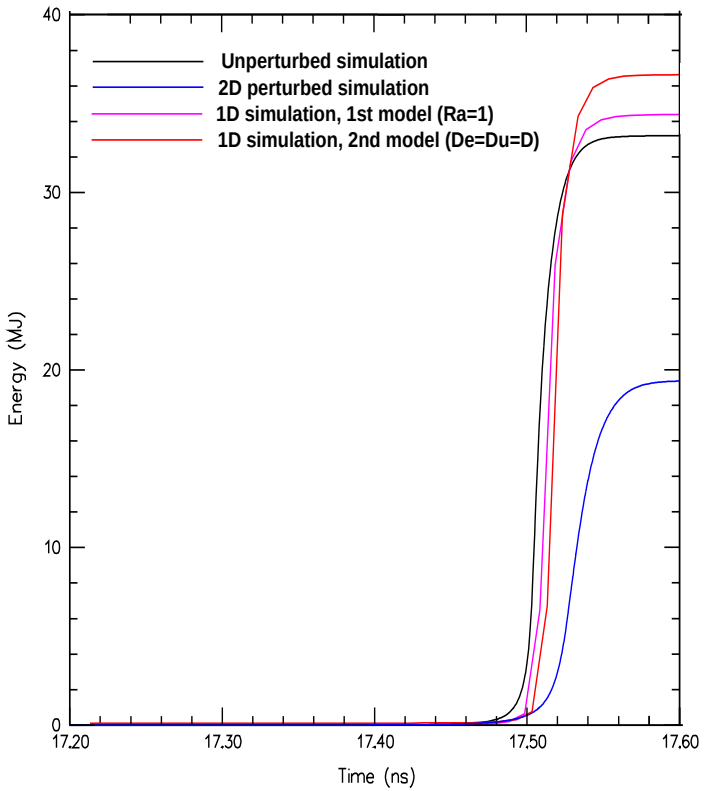

Comparison of energy evolution

With the two mix models,

the relative delay to ignition is underestimated

The implosion is more efficient but closer to the threshold

The non-sphericity of perturbed 2D implosion explain the spread of the energy production

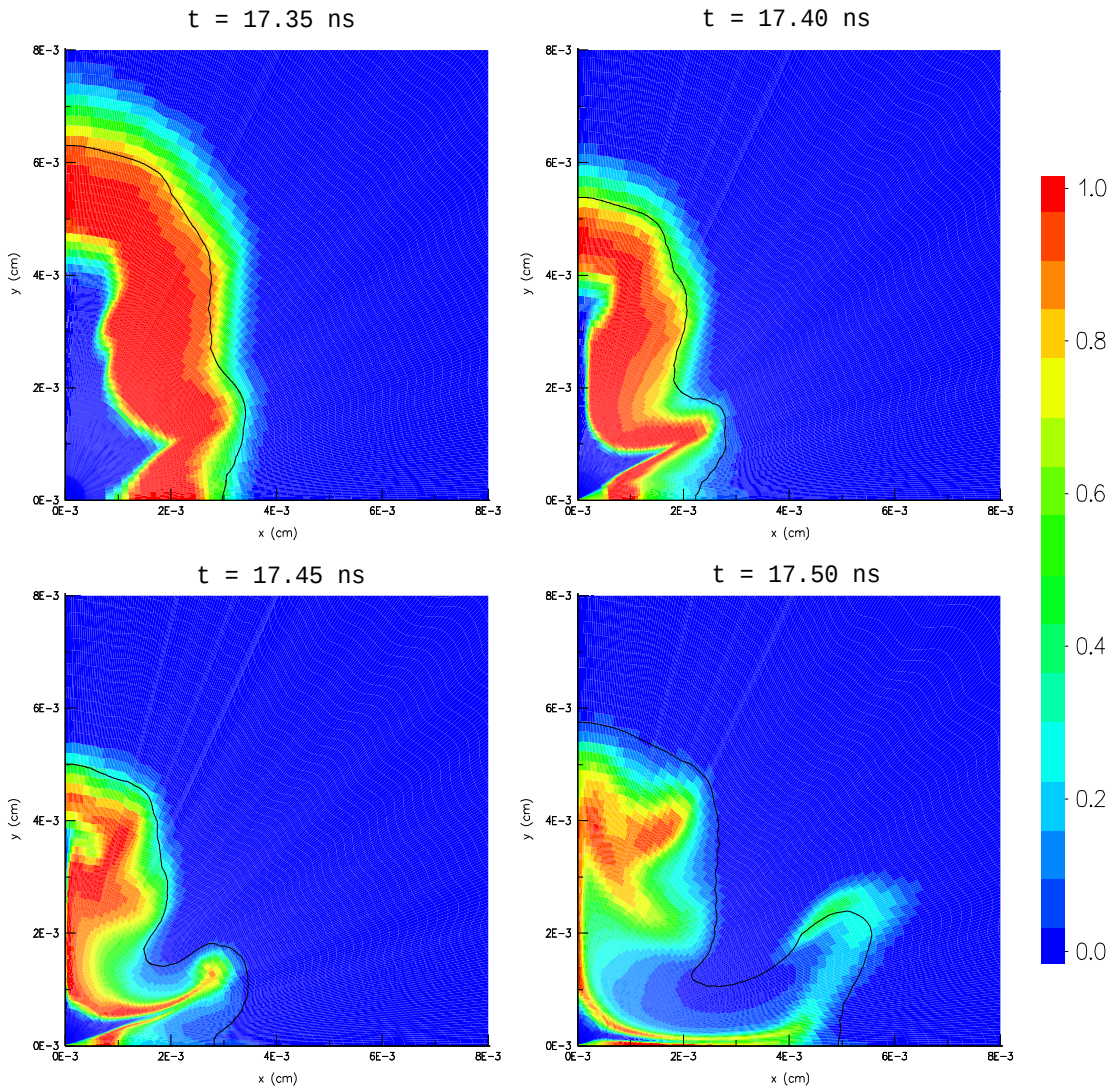

Comparison of the Hot Spot contours ($T = (MaxT_{ion})/10$) with the mass concentrations of the cryogenic DT entering in the Hot Spot at the ignition time.
Iso-concentration contours are more perturbed than Iso-temperature contours

Simulation of the ignition threshold

2D specific behavior (low mode deformation of the Hot Spot contours, possible mean viscous effects,) is not recovered by nominal values of 1D models

We realize parametric studies on Ra and $\mathcal{D}_e/\mathcal{D}$ to obtain ignition threshold

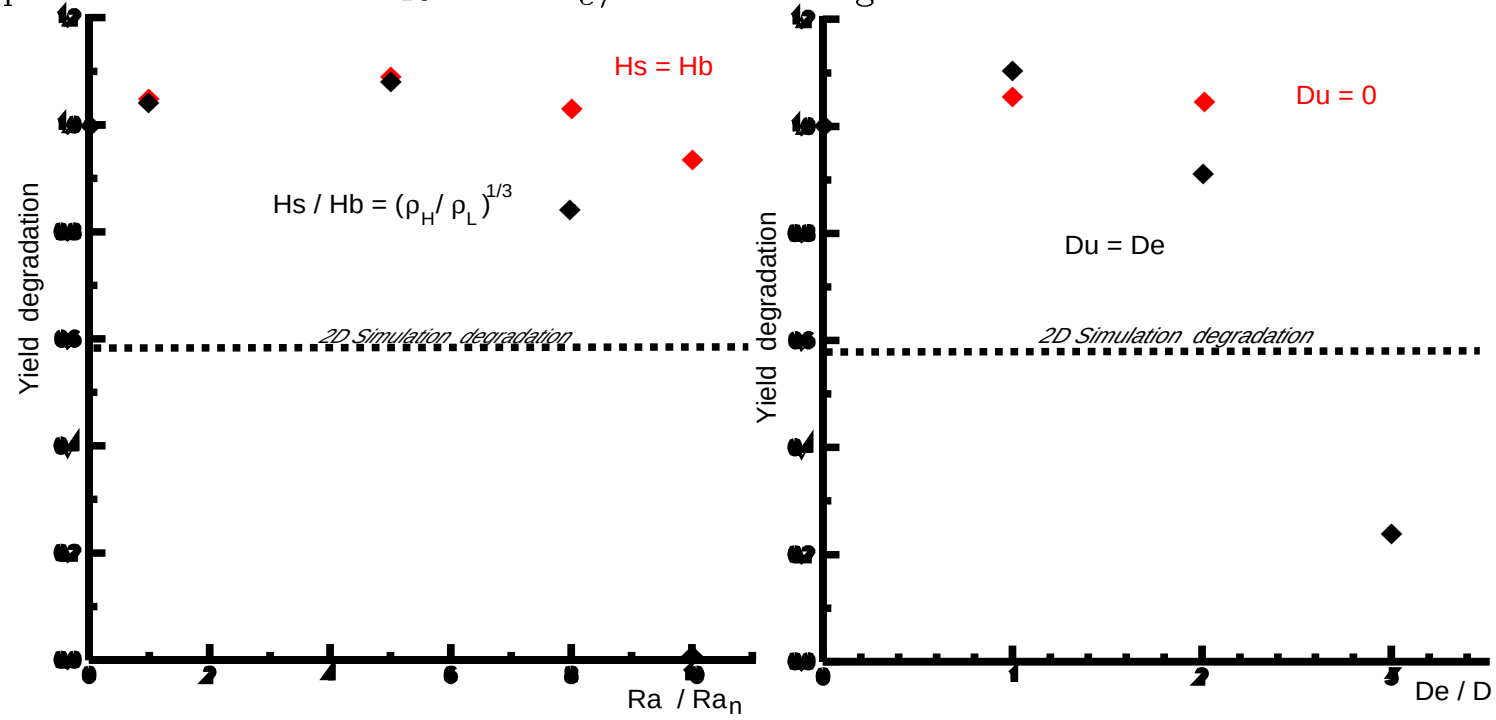

To recover the 2D simulation degradation we need to multiply by 8 the nominal ratio area

$Ra_n \equiv S_{perturb}/S_{sph}$ (with an asymetric development of "spikes" and "bubbles")

The simulation with the "diffusive model" show the importance of the added term in velocity equation

DAM - Île de France

Prospects

- These preliminary results open several ways
- For Hot Spot perturbations we envisage to model separately low modes and high modes
- The modelling of an "average viscous effect" on the velocity profiles seems essential
- The modelling of hydrodynamic instabilities at interfaces could take advantage of the above ideas

DAM - Île de France

Modeling Turbulent Mixing in Inertial Confinement Fusion Implosions

Y. Srebro, D. Kushnir, Y. Elbaz and D. Shvarts

Nuclear Research Center - Negev, Israel.

Ben-Gurion University, Beer-Sheva, Israel.

Hebrew University, Jerusalem, Israel.

Experiments

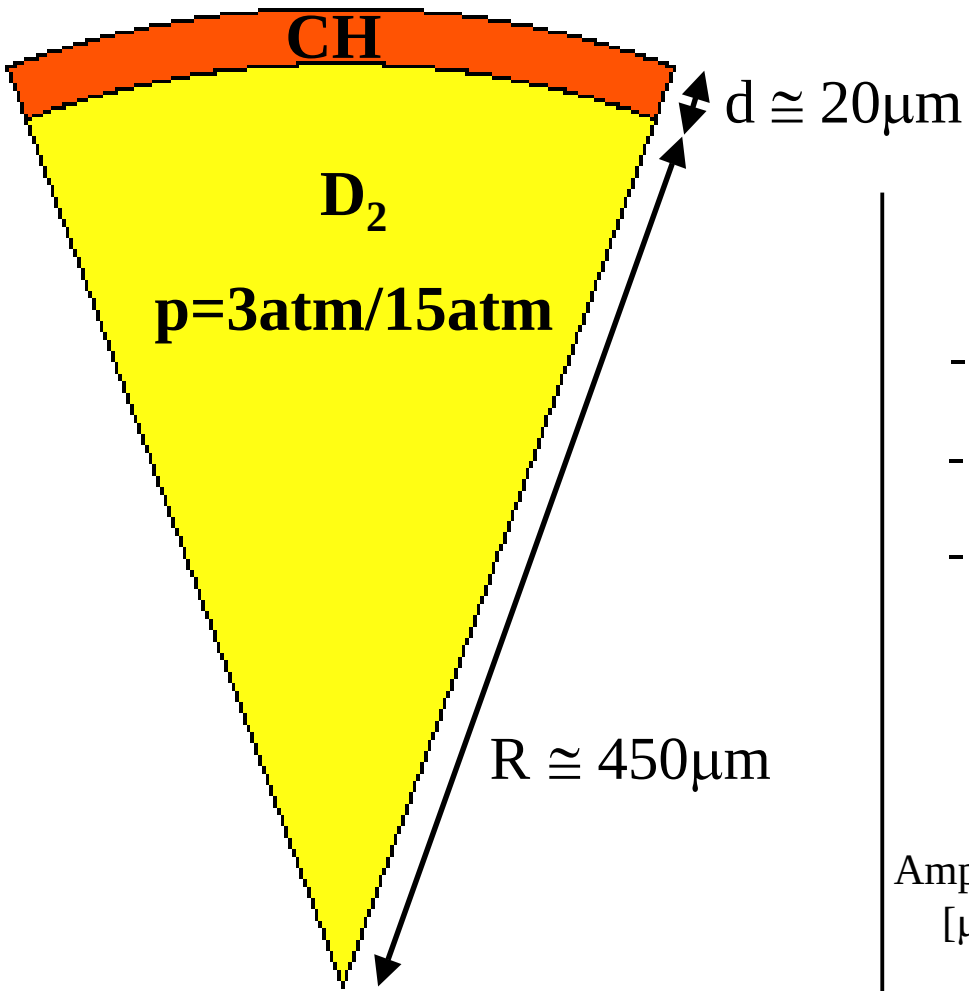

Laser :

E ≅ 20kJ t ≅ 1ns

Perturbations :

- Surface roughness (outer and inner)
- Power imbalance between beams
- Beam nonuniformity (1THz 2D-SSD)

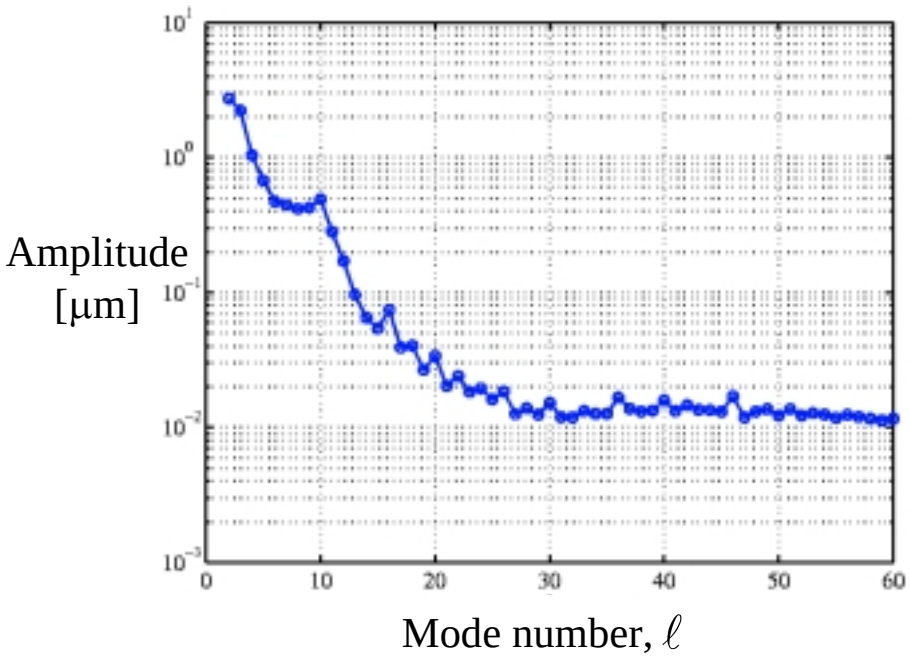

Experiments held at Laboratory for Laser Energetics, U. of Rochester

Experimental results

$$Y.O.C. = \frac{Y_{exp}}{Y_{1D}}$$

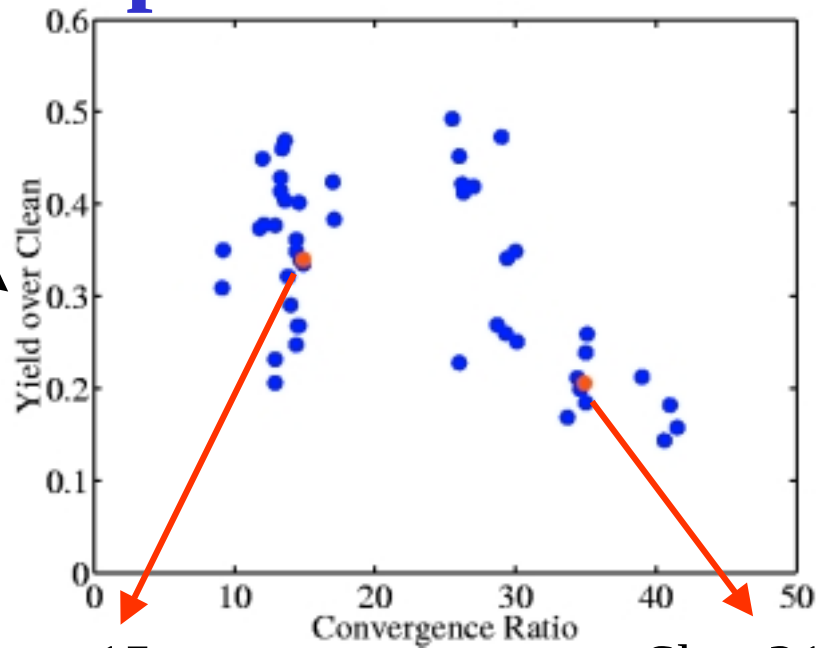

Shot 20690 - p=15atm

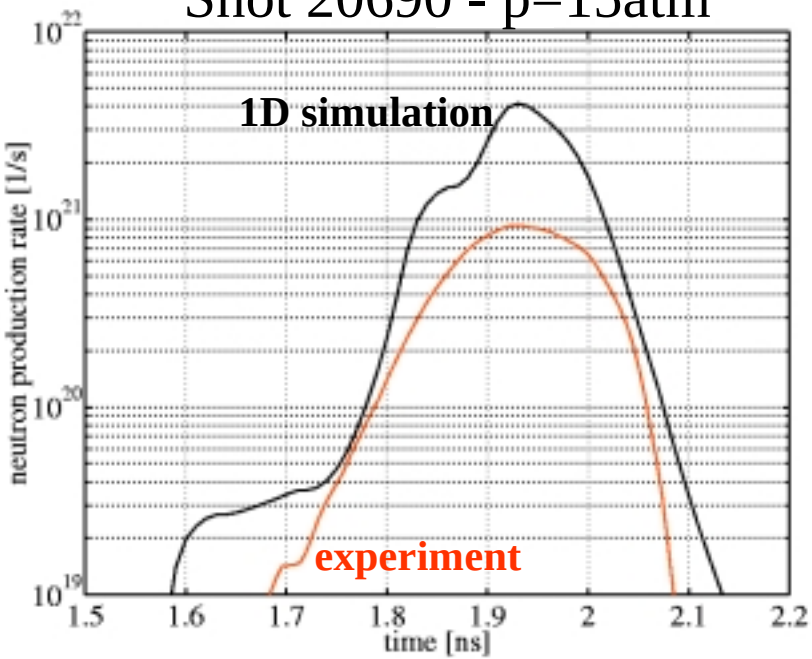

Shot 21216 - p=3atm

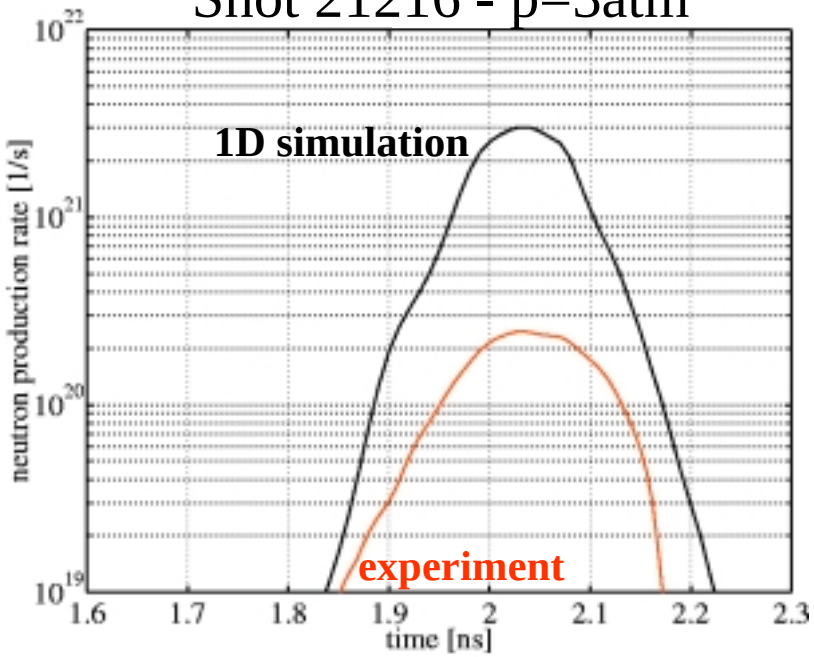

1D Simulation

(Shot 20690 - p=15atm)

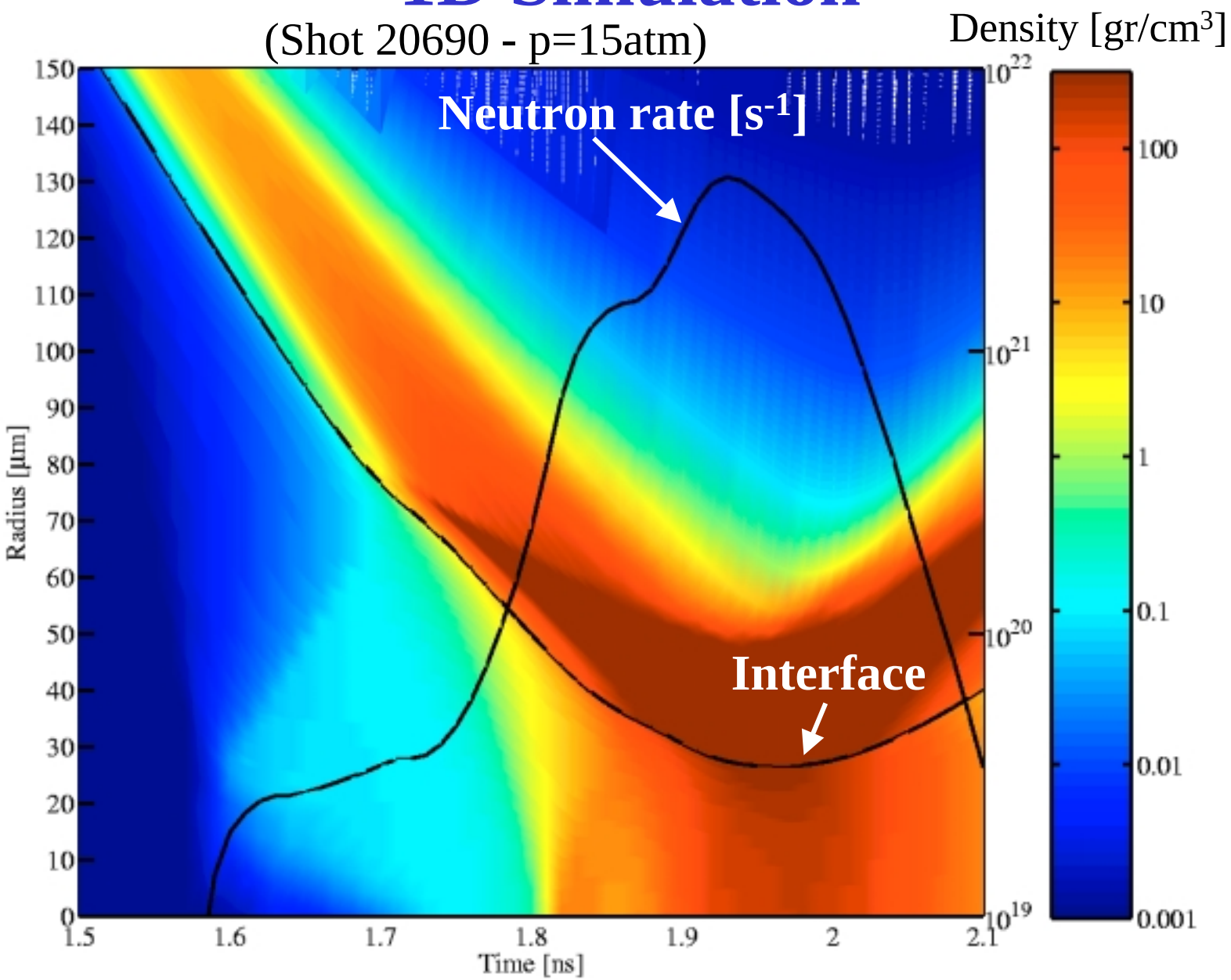

Fusion rate is dominated by shock dynamics

2D multi-mode simulation

(Shot 20690 - p=15atm)

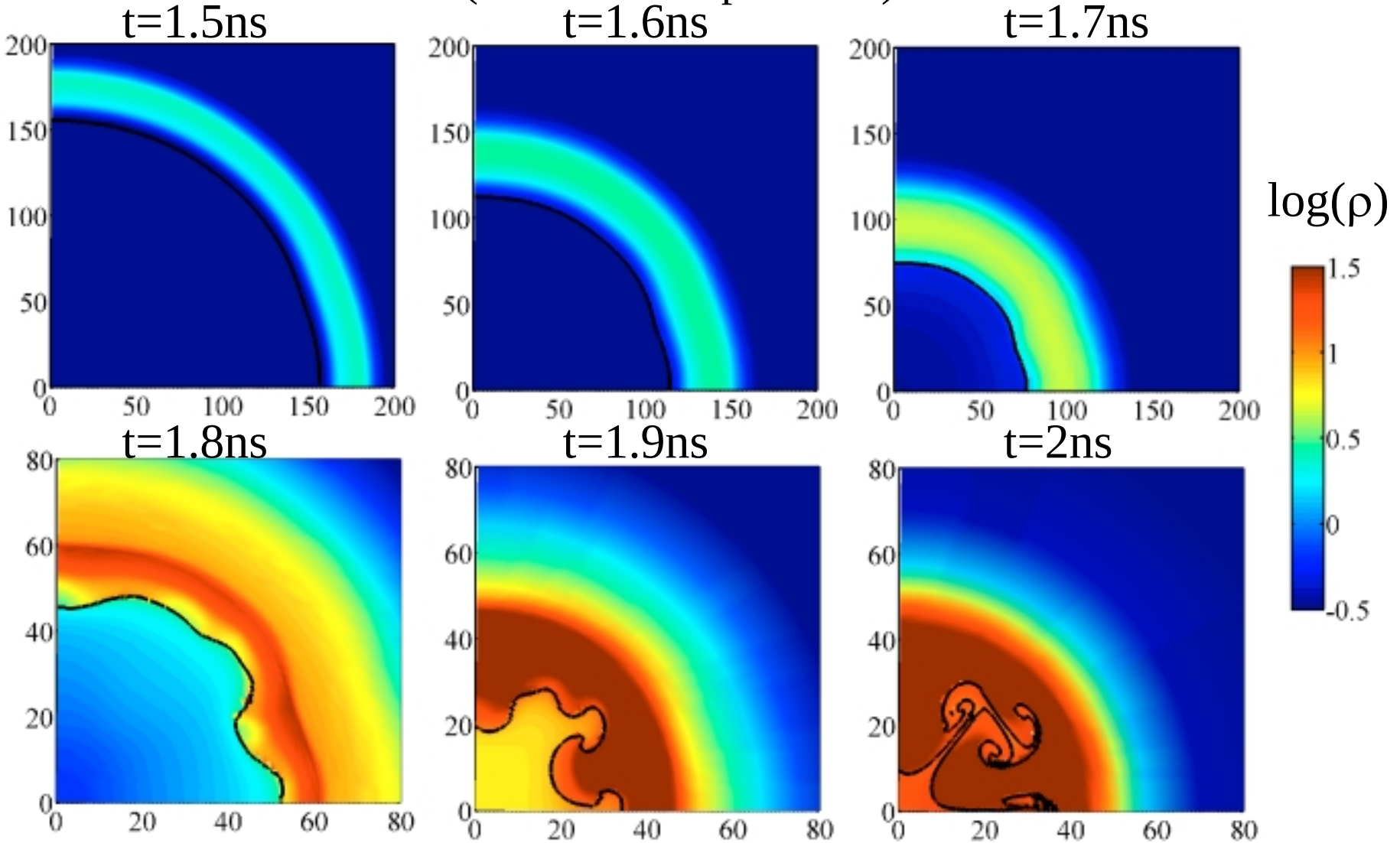

Perturbation dominated by power imbalance ($\ell \approx 6$)

Bubble and spike growth

Shot 20690 - p=15atm

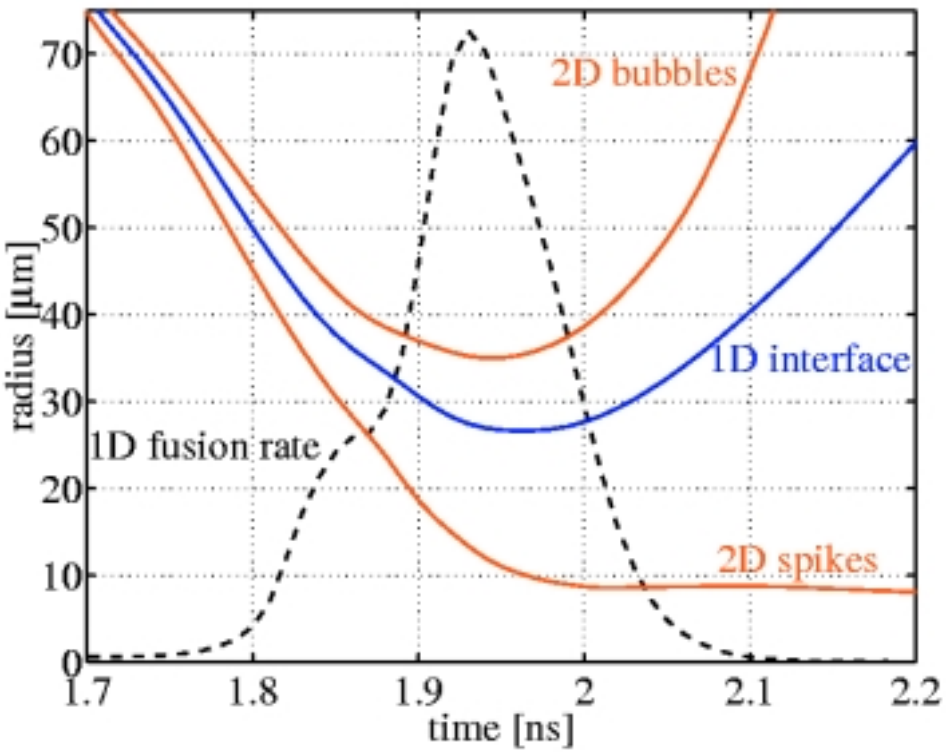

Shot 21216 - p=3atm

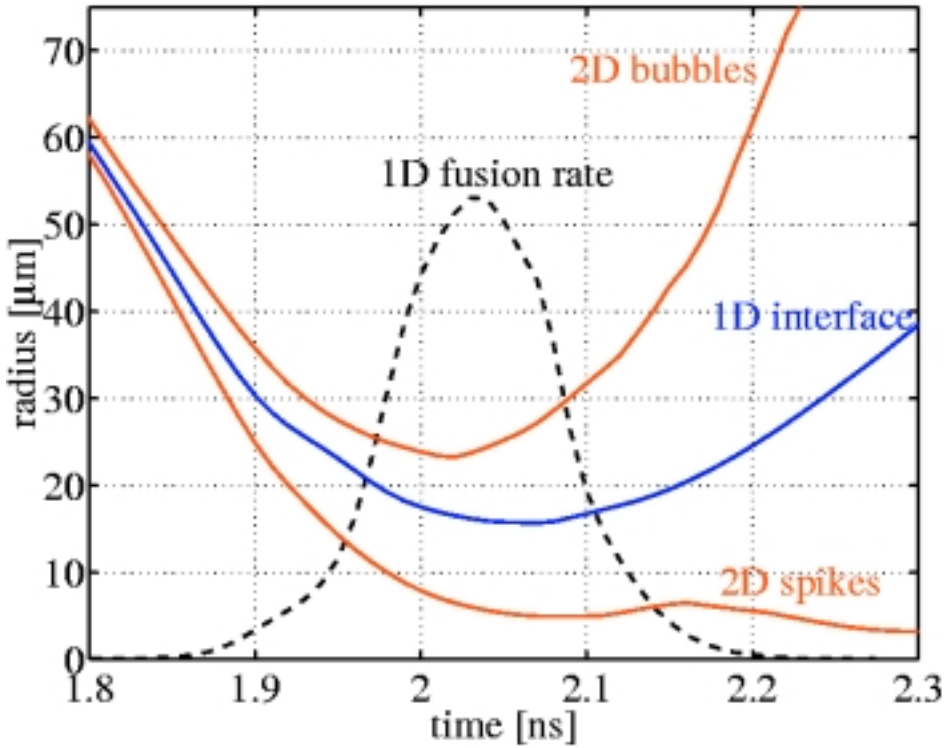

Neutron yield

Shot 20690 - p=15atm

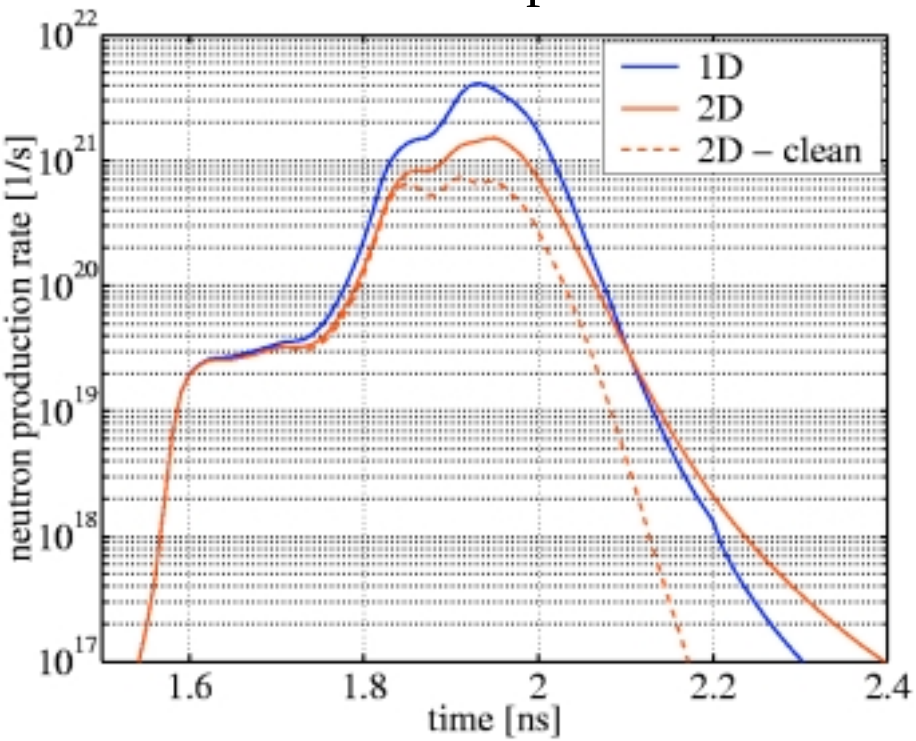

Shot 21216 - p=3atm

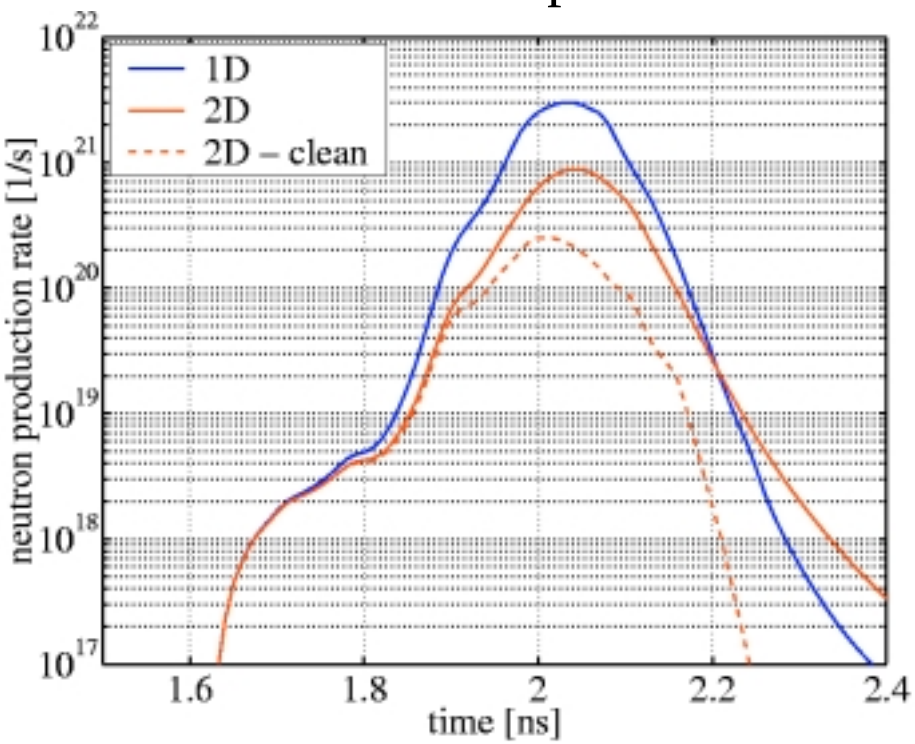

- 2D yield lower by factor 2-3 from 1D.
- Fully developed turbulent mixing:

Worst case - fusion only in clean zone defined by most penetrating spike.

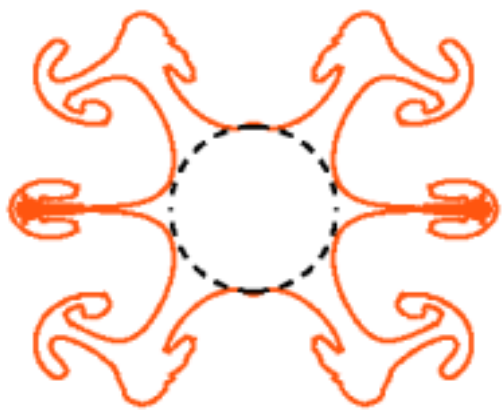

Neutron yield degradation

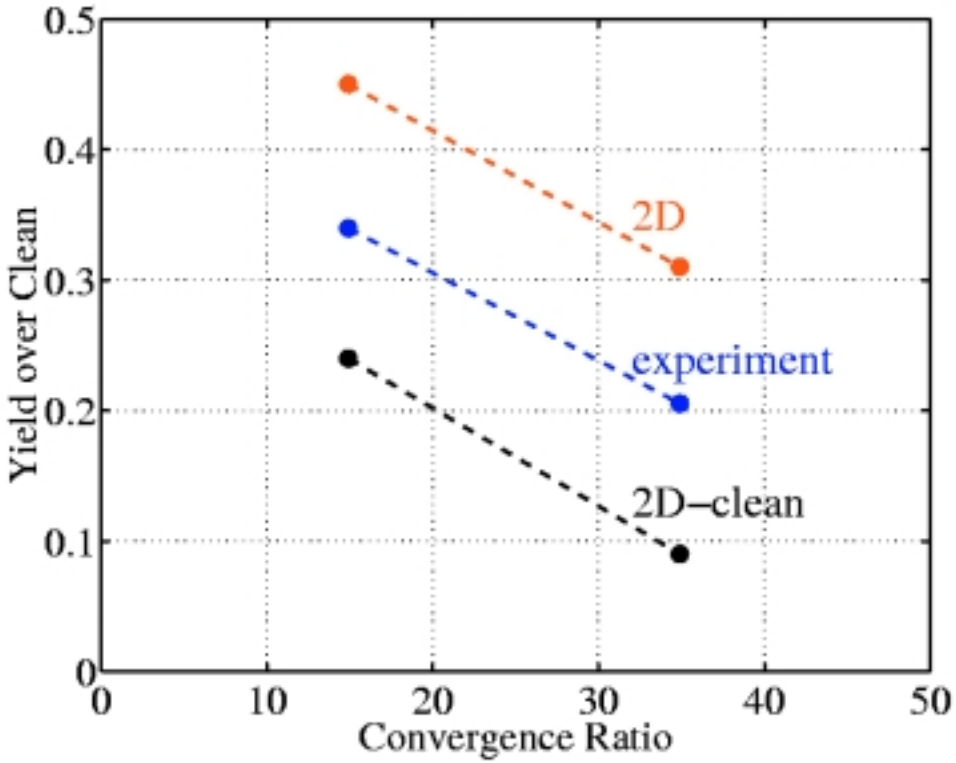

- 2D simulations underestimate degradation.
- Assuming fusion only in clean area overestimates degradation.

Cumulative fusion rate

$$\left(N(R) = \int_0^R n(r) d^3 r\right)$$

(shot 20690 - p=15atm)

t=1.7ns

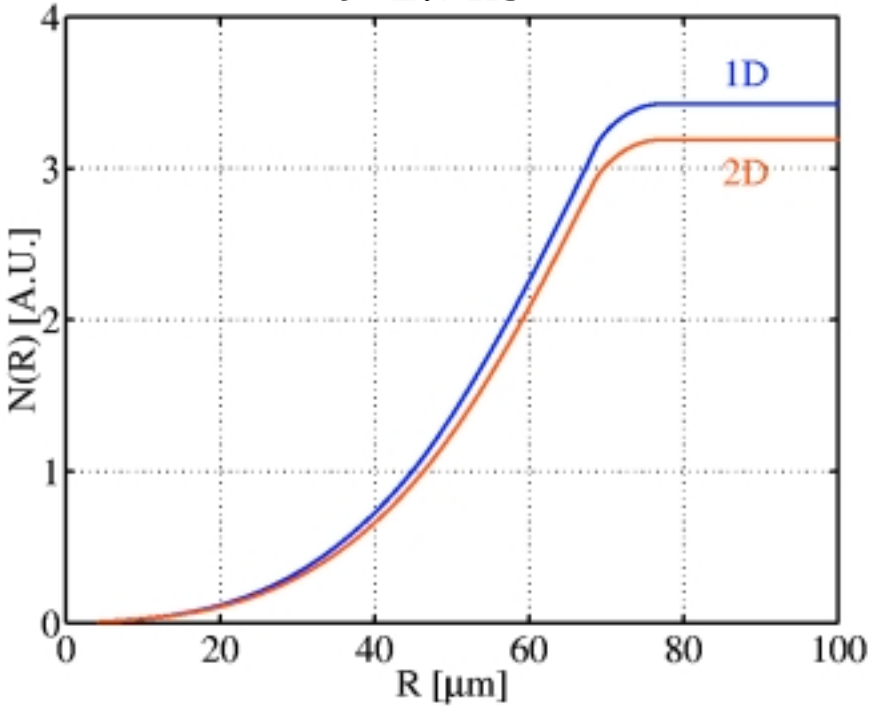

t=2ns

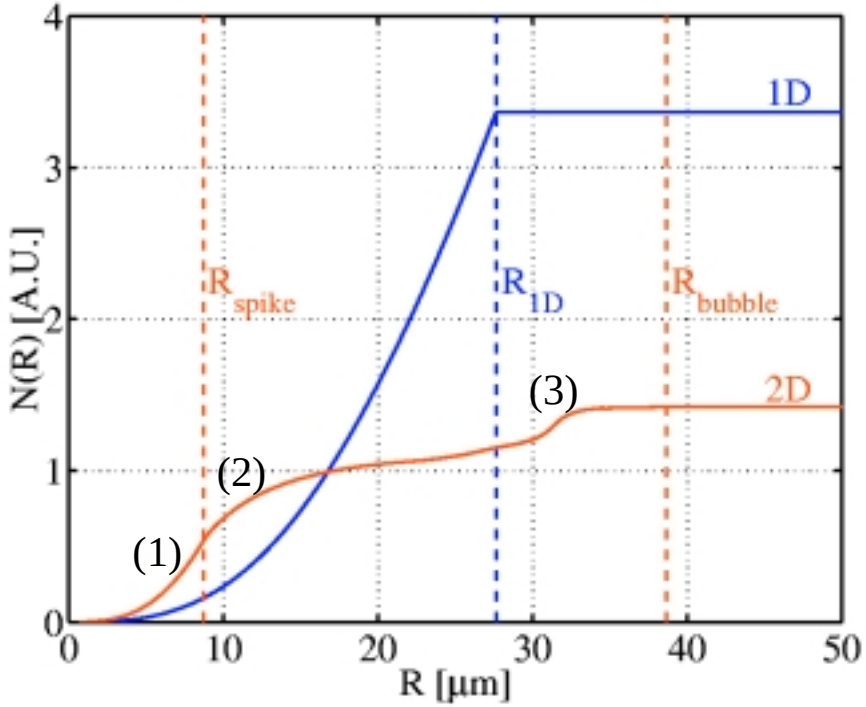

1) Higher 2D yield from central region.

2) Slight redefinition of R_{clean} will significantly change yield.

3) Contribution of bubbles to fusion yield.

Difference in yield from central region

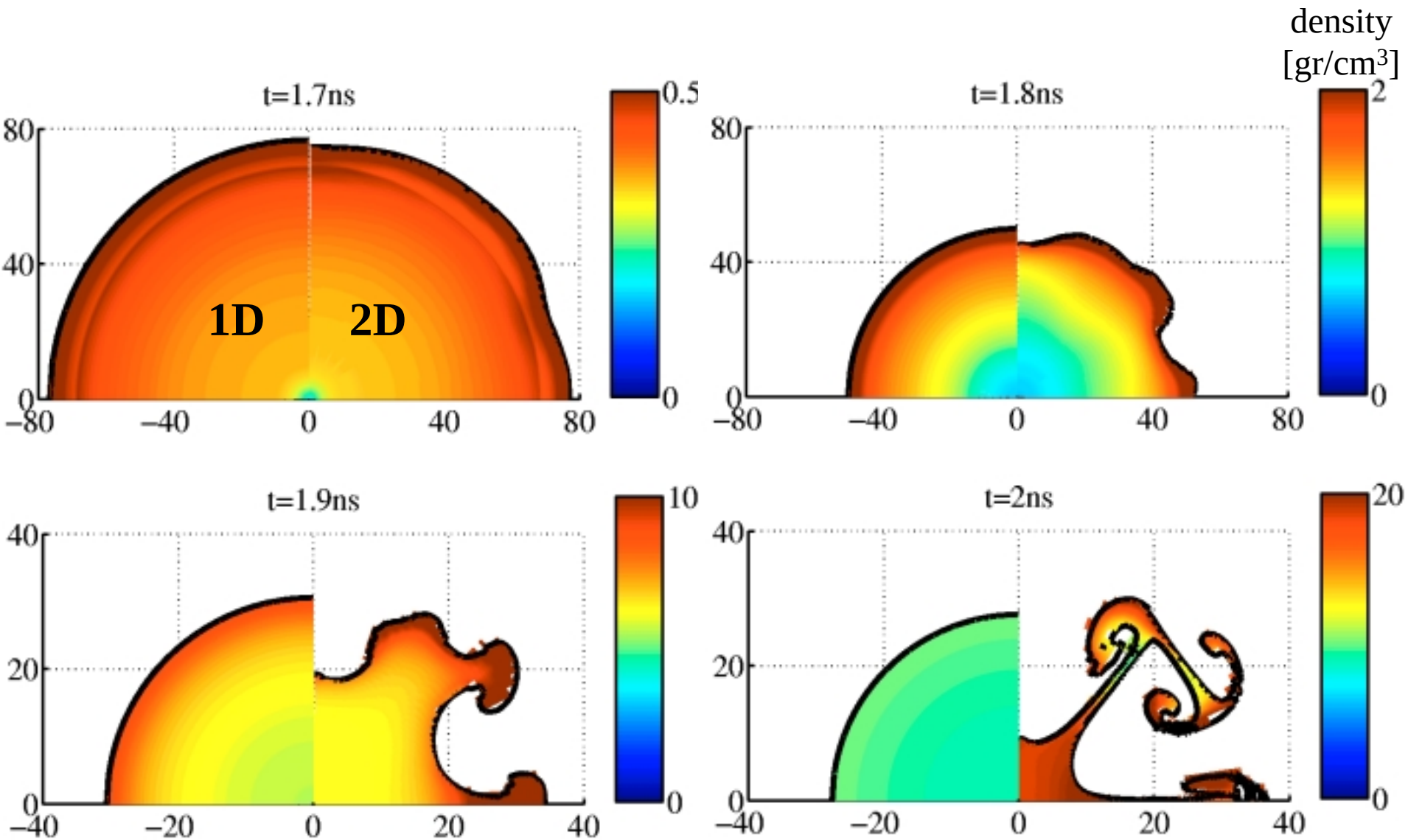

2D central density is higher due to differences in shock dynamics.

Redefinition of clean region

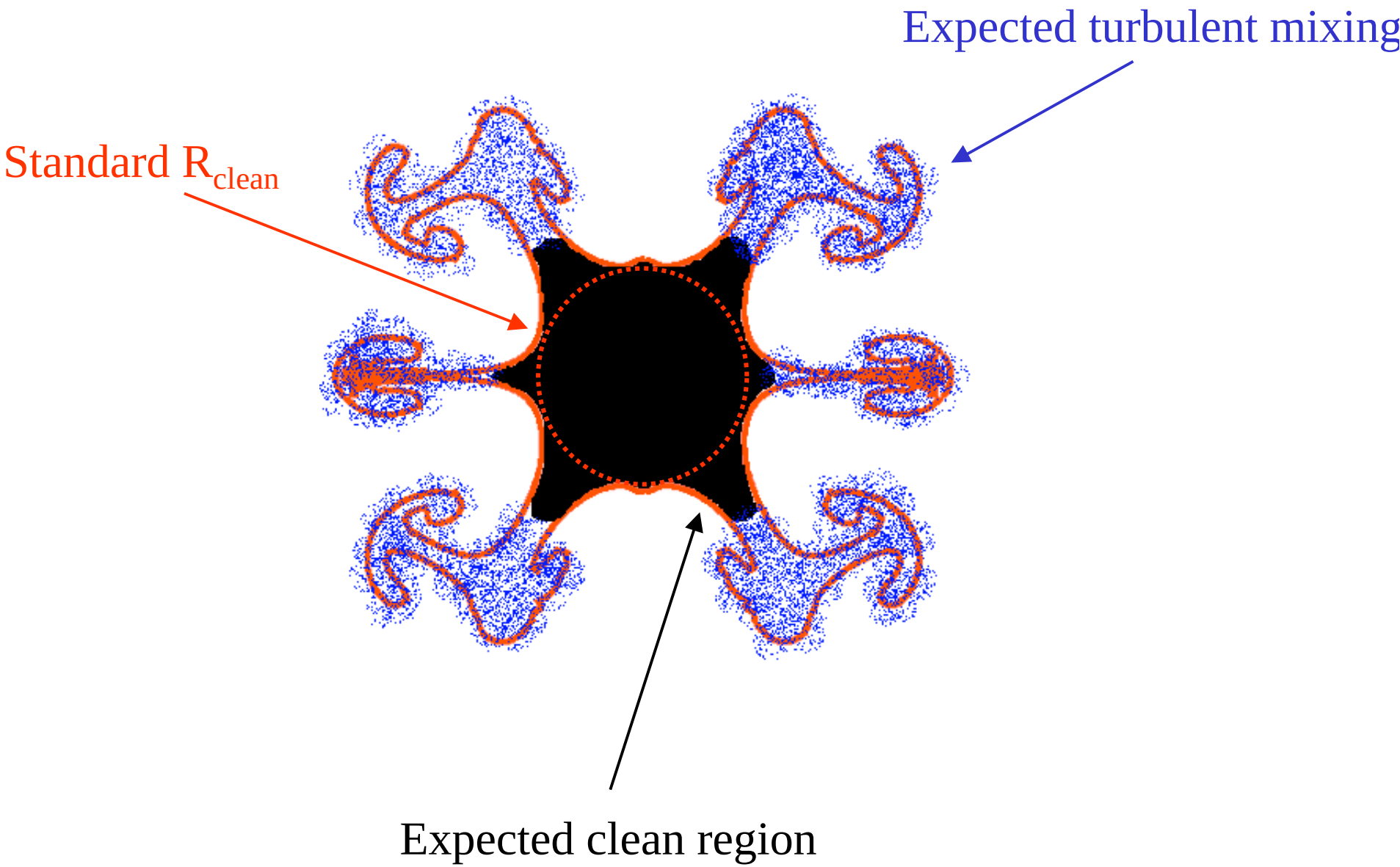

Redefinition of R_{clean}

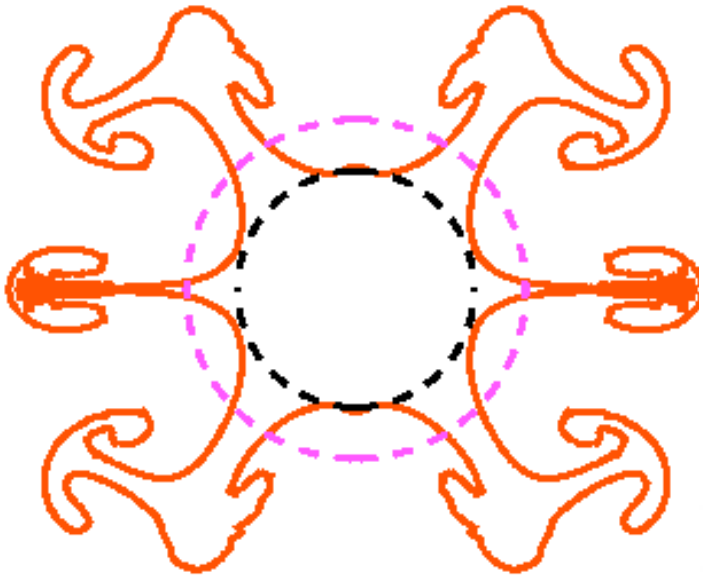

$$R_{clean}=R_{spike}+f(R_{bubble}-R_{spike})$$

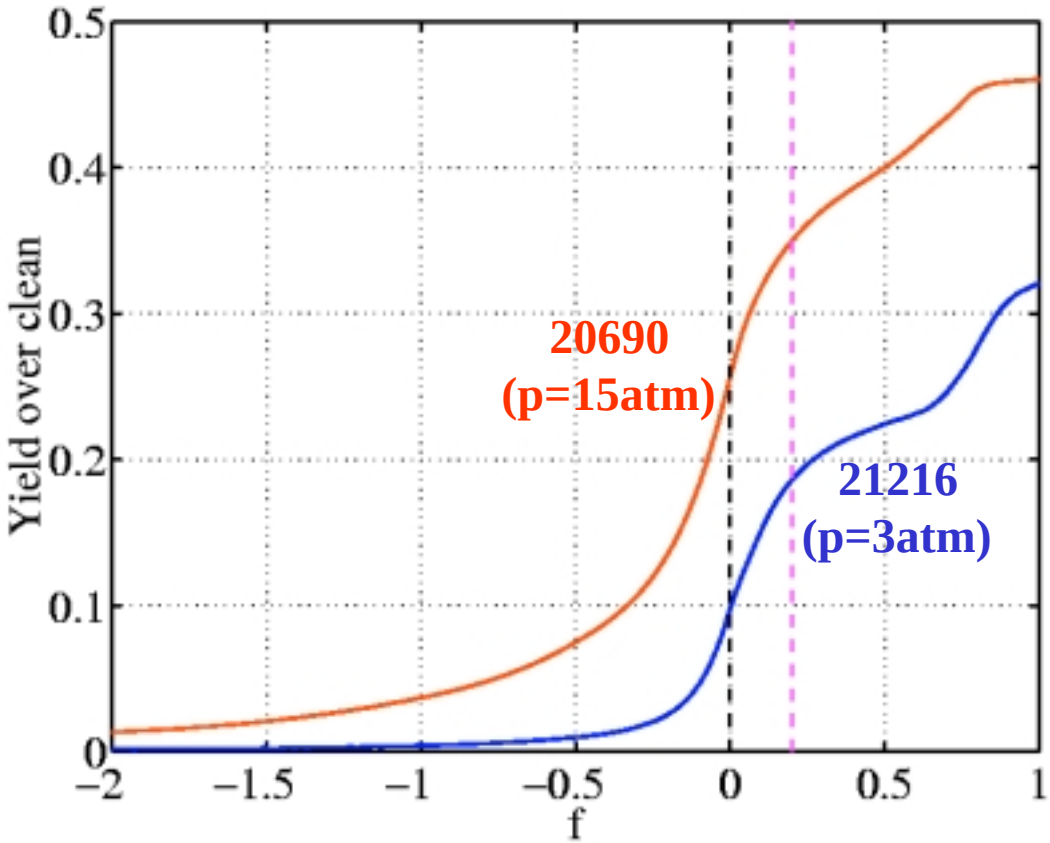

Sharp rise ends at f=0.2, coinciding with clean region boundaries.

Re-definition of clean region improves agreement with experimental results

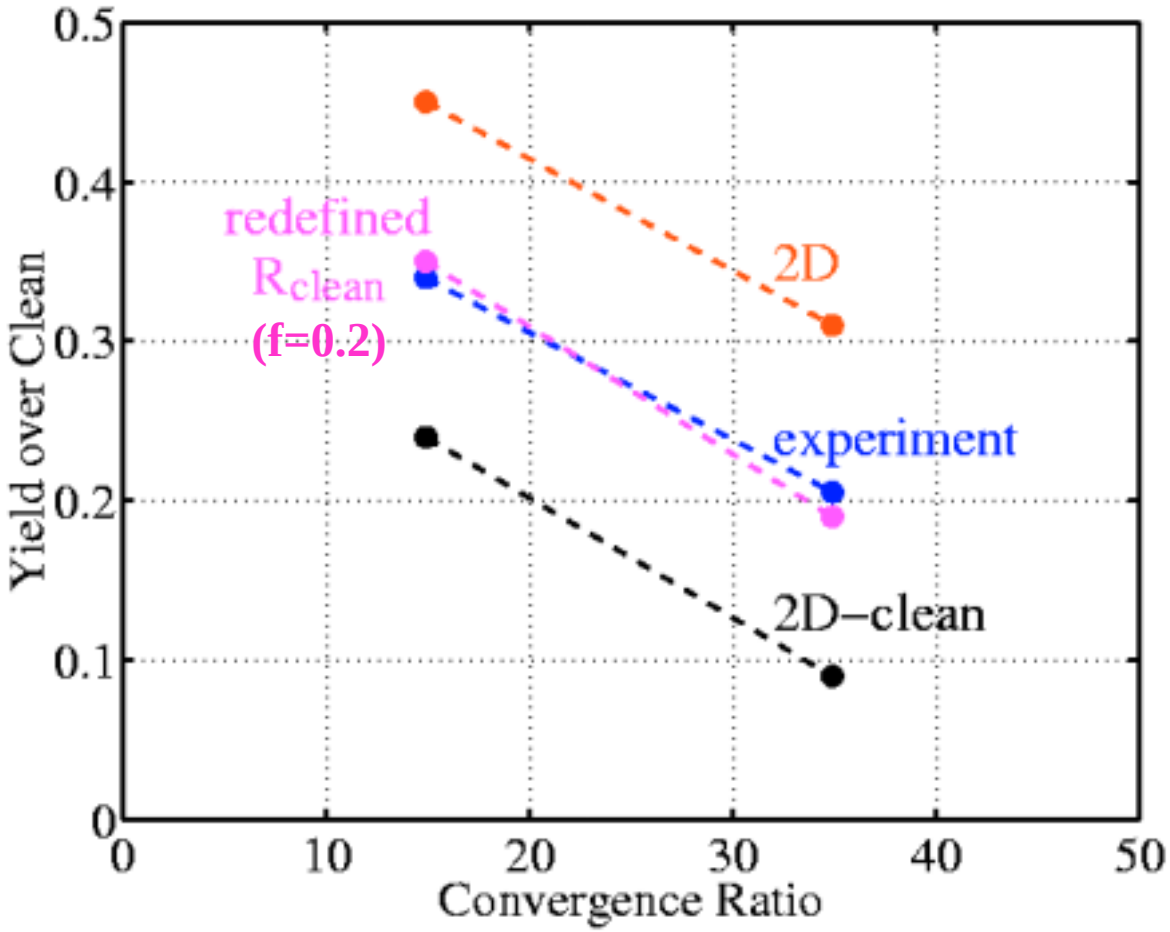

Conclusions

- Recent ICF experiments have been analyzed by comparing full 2D and 1D numerical simulations.
- Assuming no mixing, bubbles raise fusion yield above experimental results.
- Differences in central pressure, density and fusion rate at high perturbation amplitudes imply that mix effects are not limited to the mix region, hence full 2D simulations are needed.
- Regions slightly beyond R_{clean} contribute significantly to fusion yield. New definition for R_{clean} improves agreement with experimental results.

Turbulent Mixing Nuclear Burning in Type Ia Supernova Explosion based on Bubble Statistical Mechanics

H. Takabe, S. Yamada, K. Kobayashi, A. Mizuta, and K. Nomoto*

Institute of Laser Energetics and Graduate School of Science, Osaka University

****Department of Astronomy, Graduate School of Science, University of Tokyo***

E-mail: takabe@ile.osaka-u.ac.jp

(This viewgraph was prepared for "the 8th International Workshop on the Physics of Compressible Turbulent Mixing (8th IWPCTM) " held at the California Institute of Technology (Caltech) in Pasadena, California, USA, from December 9-14, 2001. The Workshop will be held on campus in the Beckman Institute Auditorium, and is hosted by Lawrence Livermore National Laboratory (LLNL).)

It is well known that Type Ia supernovae explode when the masses of white dwarfs become close to the Chandrasechar's limiting mass. This is the reason why the Type Ia explosion is used as a standard candle in the universe to determine, for example, the Hubble constant and dark energy. The scale of explosion has been well studied with one-dimensional code with some mixing model; however, the physical mechanism has not determined from the first principle, yet. There are many works to understand the physics with large scale computing based on hydrodynamics in two-dimension or mostly three-dimension in these days[1]. It seems, however, that the smaller scale fluctuation appears, the smaller the grid size, and it is still open question how the instability grows and evolves into nonlinear stage and enhance the energy release by nuclear reactions.

In the present report, we would like to model the growth of the Rayleigh-Taylor instability coupled with the Landau-Darrieus instability. In the nonlinear stage, we consider the statistical mechanics of the bubbles following the way developed by Don Shvart's group[2] and estimate the increase in the nuclear burning rate due to the increase in the surface area of the burning wave in the form of fractal structure. This model is coupled with the multi-dimensional explosion code to predict the scale of explosion. Such work is expected to be used to identify the physical mechanism of the time evolution of the burning wave, which may change from deflagration wave to detonation wave.

Reference:

[1] W. Hillebrandt and J. Niemeyer, Ann. Rev. Astron. Astrophys. **38**, 191-230 (2000)

[2] D. Shvarts et al, Physics of Plasmas **2**. 2465 (1995).

1. Introduction

- We are promoting a new scientific field of "Laser Astrophysics".

- Many issues regarding hydrodynamics instabilities and turbulent mixings.

- Recent review of LA.
  H. Takabe, "*Astrophysics with intense and ultra-intense lasers –Laser Astrophysics- "*, Progress of Theoretical Physics Suppl. No. **143**, 202-265 (2001).

- Many works on hydrodynamic instabilities and mixings have been done in the case of Type-II supernova explosion, especially SN1987A, in the framework of LA. (B. Remington, P. Drake et al.)

- More sophisticated physics scenario should be studied in the case of Type-Ia SN explosion.

2. What is Type-Ia Supernova ?

- Type II
  - Massive star (~ 20 M_{Sun} for SN1987A), Single
- H_α line emission.

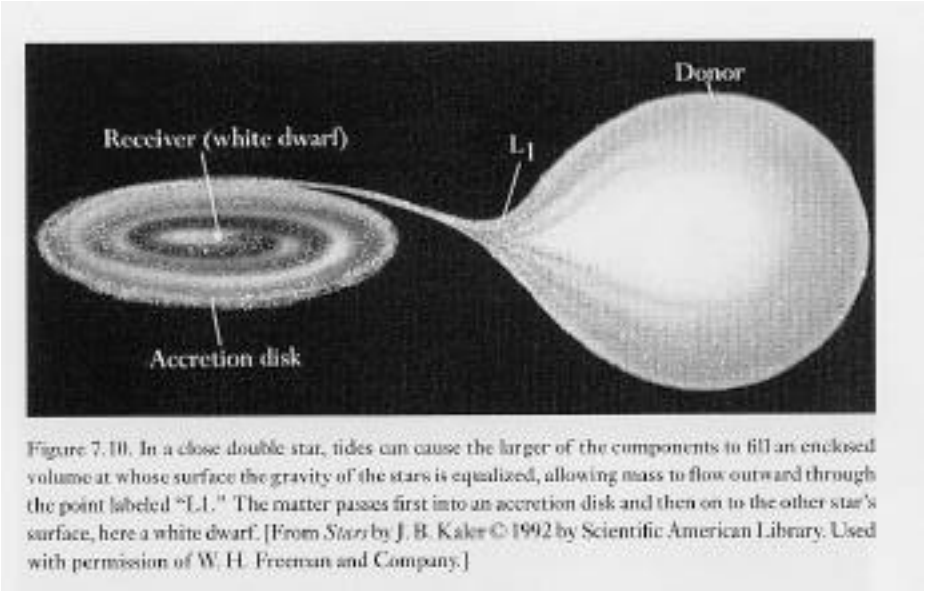

Figure 7.10. In a close double star, tides can cause the larger of the components to fill an enclosed volume at whose surface the gravity of the stars is equalized, allowing mass to flow outward through the point labeled "L1." The matter passes first into an accretion disk and then on to the other star's surface, here a white dwarf. [From *Stars* by J. B. Kaler © 1992 by Scientific American Library. Used with permission of W. H. Freeman and Company.]

Fig. 1 (J. Kaler, "Extreme Stars" (Cambridge, 2001) p.158)

-

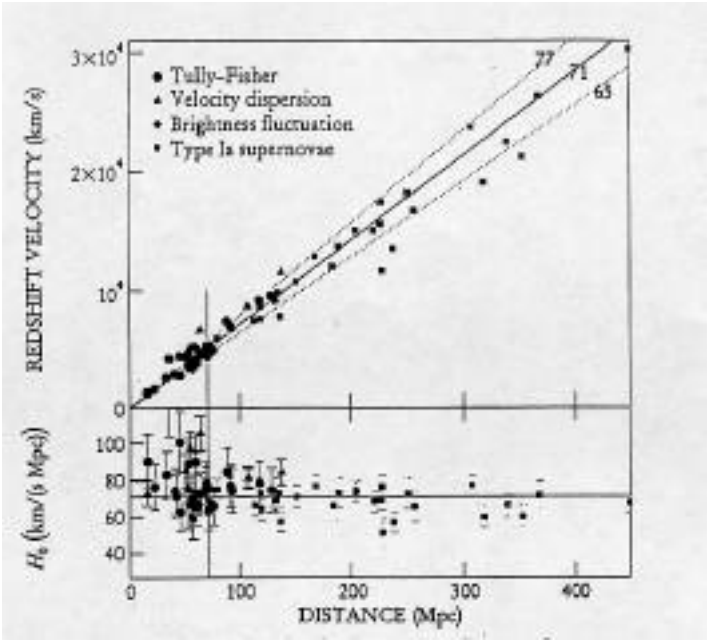

Fig. 2 (Physics Today, August (1999) p.20)

- Type Ia
  - White Dwarf, Binary system, Chandrasekhar-mass (~ 1.4 M_{Sun}) See Fig. 1.
  - No H_α line emission.

- Light curve of Type Ia SNe.

- Why important?

- Precise determination of Hubble constant
  H_0 = (velocity)/(distance) for Z <0.1
  See Fig. 2

- Einstein constant is finite? Dark energy. For Z<1.0

  (cf: $Z = (\lambda-\lambda_0)/\lambda_0$, L = 1 B-ly for Z = 0.1)

3. Hydrodynamic Instability in Laser Implosion

- Mixing reduces neutron yields --- Degrades thermonuclear reaction and burn. [cf: H. Takabe et al, Phys. Fluids **31**, 2884 (1988)]

- Multi-dimensional simulation with surface-tracking is necessary. See Fig. 3

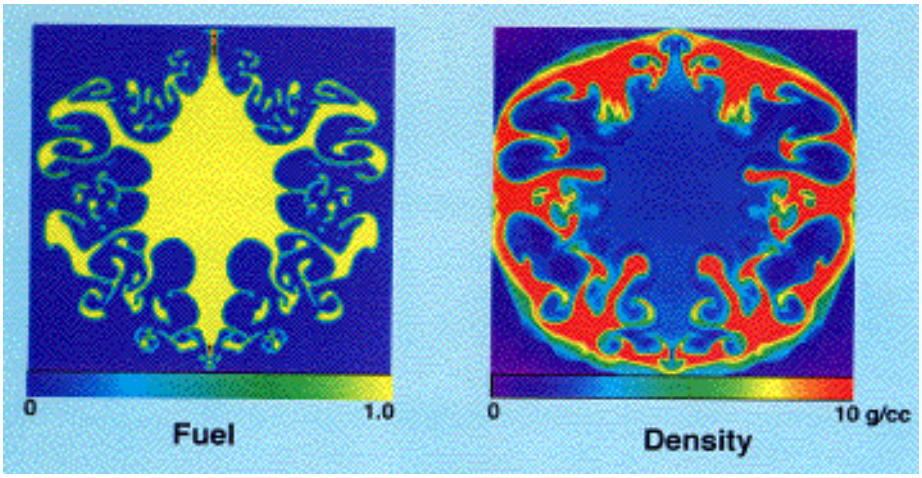

Fig. 3 (2D simulation of laser implosion. by H. Takeuchi and H. Takabe)

4. Spherical Symmetry Scenario of Nuclear Burning Wave Propagation in Chandrasekhar-mass WD.

- Very sharp wave front [(thickness) < mm] compared to the size of WD (~ 10000 km). See Fig. 4

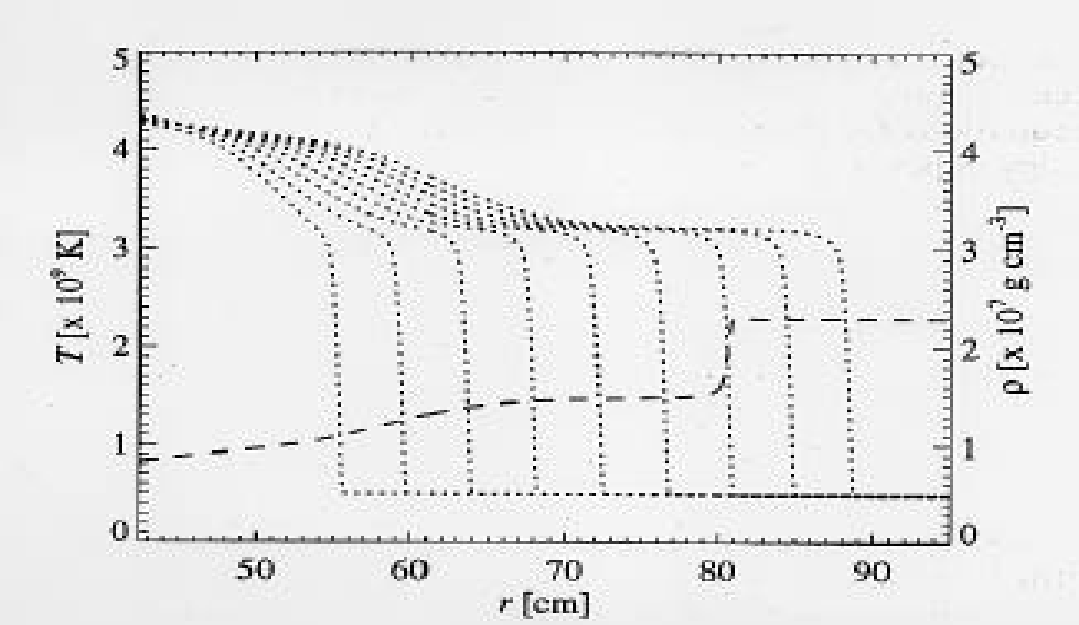

FIG. 2.—Propagation of an $X(^{12}C) = X(^{16}O) = 0.5$ conductive flame. The sequential temperature profiles (*dotted lines*) are shown at times $t = 1.3 \times 10^{-4}$, 3.0×10^{-4}, 6.5×10^{-4}, 8.3×10^{-4}, 1.01×10^{-3}, 1.19×10^{-3}, 1.36×10^{-3}, and 1.51×10^{-3} s. The dashed line is the density profile at $t = 1.19 \times 10^{-3}$ s. The carbon flame already moves in a steady state, while the temperature rise at the left-hand side comes from oxygen burning as a result of the energy stored at the initial state of the simulation.

Fig. 4 [A. M. Lisewski et al., ApJ **537**, 405 (2000)]

- Very week deflagration wave or combustion wave (M ~0.01).

- No explosion:
  (Released fusion energy) < -(Gravitational binding energy).

- Multi-dimensional physics scenario is necessary.

- Unstable to R-T instability.
- Unstable to Landau-Darius instability
- K-H instability is also important.

5. Fractal Dimension of the Nuclear Burning Wave Front.

- Effective area and velocity of the burning front (F. X. Timmes, ApJ, 1994)

$$A_{eff} = (l_{max}/l_{min})^{D-2} A_0$$

$$V_{eff} = (l_{max}/l_{min})^{D-2} V_{conduction}$$

D: Fractal dimension (D>2)

- Fractal dimension (S. I. Blinnikov, PRE, 1996).

$(l_{max}/l_{min})^{D-2} \sim 7$ Compare: we need ~ 100 !

See Fig. 5

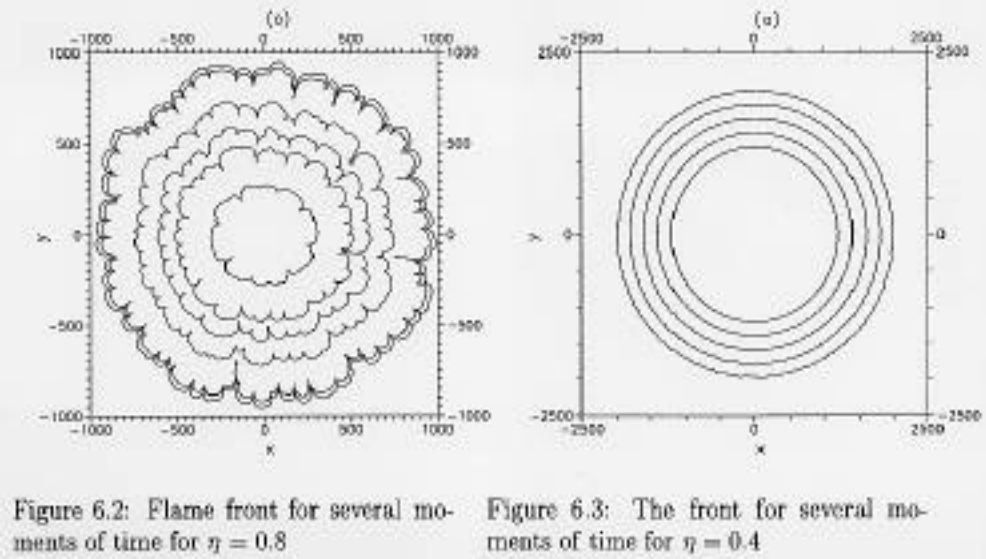

Figure 6.2: Flame front for several moments of time for $\eta = 0.8$

Figure 6.3: The front for several moments of time for $\eta = 0.4$

Fig. 5 (S. I. Blinnikov, Phy. Rev. E, 1996)

6. Multi-Dimensional Simulation (LES-like)

- Intensive works by W. Hillebrandt group (MPA).
  References:
  1. W. Hillebrandt and J. C. Niemeyer, Annu. Rev. Astron. Astrophys. **38**, 191 (2000).
  2. A. M. Lisewski et al., ApJ **537**, 405 (2000).
  3. M. Reinecke et al., A&A **347**, 739 (1999).
  4. M. Reinecke et al., astro-ph/0111473, 26 Nov (2001).
  5. M. Reinecke et al., astro-ph/0111475, 26 Nov (2001).

- Central ignition
- Off-center ignition
- Mesh-size dependence in 2-D simulation
- 3-D simulation See Fig. 6

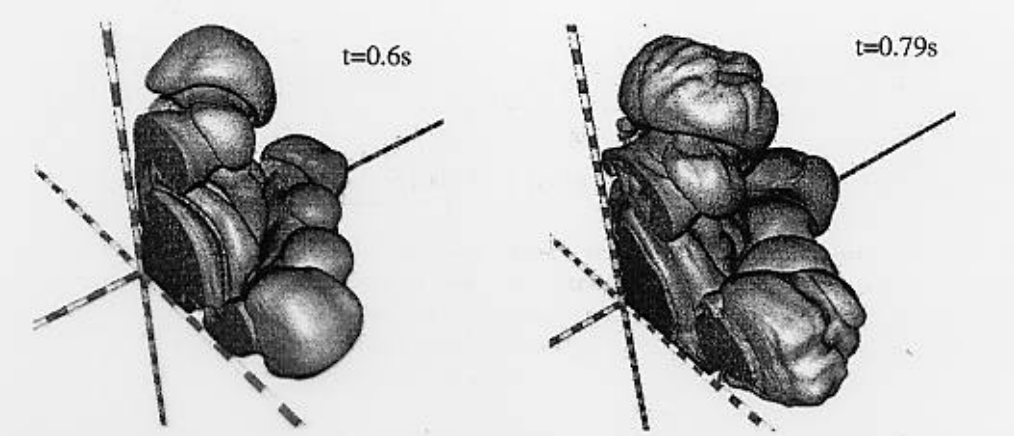

Fig. 3. Burning front geometry evolution of model c3_3d_256. One ring on the axes corresponds to 10^7cm.

Fig. 6 [M. Reinecke et al., astro-ph/0111473, 26 Nov (2001)]

7. Statistical Bubble Model is applicable to this case?

- Large-Eddy-type simulation based on the spectra by U. Alon et al. (PRL, 74, 534 (1995)). Possible ?

- Review by Don Shvarts in this morning session.

8. Summary

We have started numerical study to see more detail and complete explosion scenario of Type Ia supernovae. They are unstable to Rayleigh-Taylor instability and Landau-Darrius instability. The increase of the surface of the nuclear burning front determines and enhances the rate of thermonuclear energy release. It determines the fraction of the production of ^{56}Nn, which finally nuclear decays to ^{56}Fe. This is the origin of iron in the universe.

Type Ia is so bright, the peak luminosity is 10^{11} time the solar luminosity, and the luminosity is thought to be almost constant, so that it can be used to discuss not only to determine the Hubble constant precisely but also to know the existence of cosmological term in Einstein equation..

The project is not so simple. As summarized in Fig. 7, we have to start from one-dimensional code with realistic equation of state (EOS) in which Fermi pressure in relativistic regime should be modeled. The calculation of thermonuclear burn requires to calculate the equations of concentrations for original element (C/O) and burn product (Fe). Two dimensional simulations have been carried out by many authors, while the numerical resolution was a big issue. Prof. I. Hachisu, our collaborator at University of Tokyo, thinks that 2D is enough and no sub-grid model is necessary. He is think of usage of Earth simulator, the world-highest-speed vector-parallel computer at Yokohama.

The authors think of developing our original sub-grid model based on the accomplishment in relation to laser implosion physics. The simulation will be done in 2D and finally 3D. To check the sub-grid model we need to do a variety of local 3D simulations. We hope to relate such explosion simulation to the observable light curve.

Final point of this project is to find a new mixing model to be installed in 1D code so that many-parameter study is able to be done by supernova observation groups. Very tough job but very attractive, isn't it.

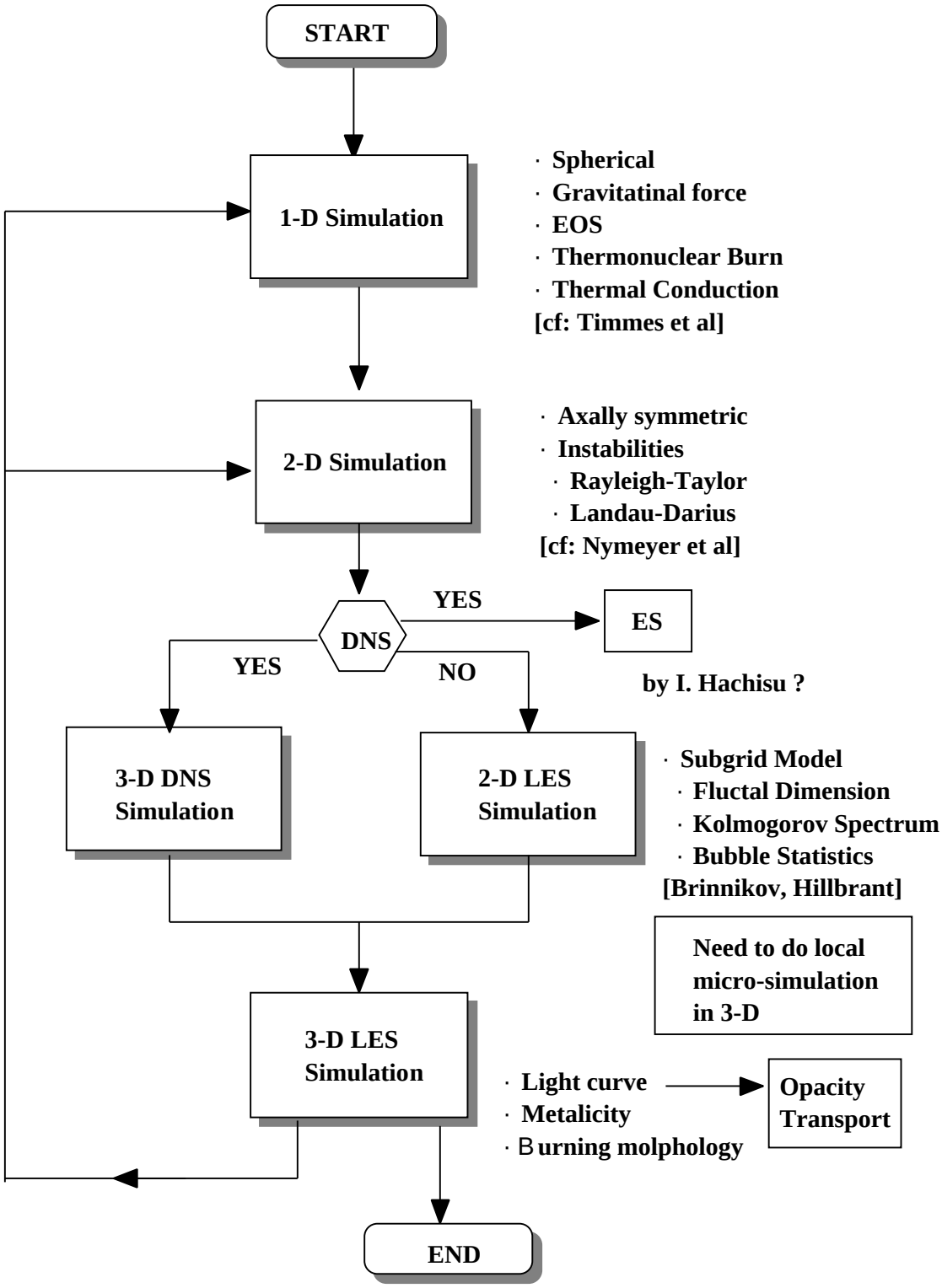

Fig. 7 Flow Diagram of the Present Project (H. Takabe)

Turbulent diffusion in solar type star

How may be trapped light elements as lithium in differential rotation zones of solar type star

Nathalie Toqué

Departement of Physics of the University of Montreal, Canada

PhD Supervisor : Prof. Alain Vincent

Setup of the study

Tachocline: Differential rotation zone of about 35000 km thickness between the convective and radiative parts

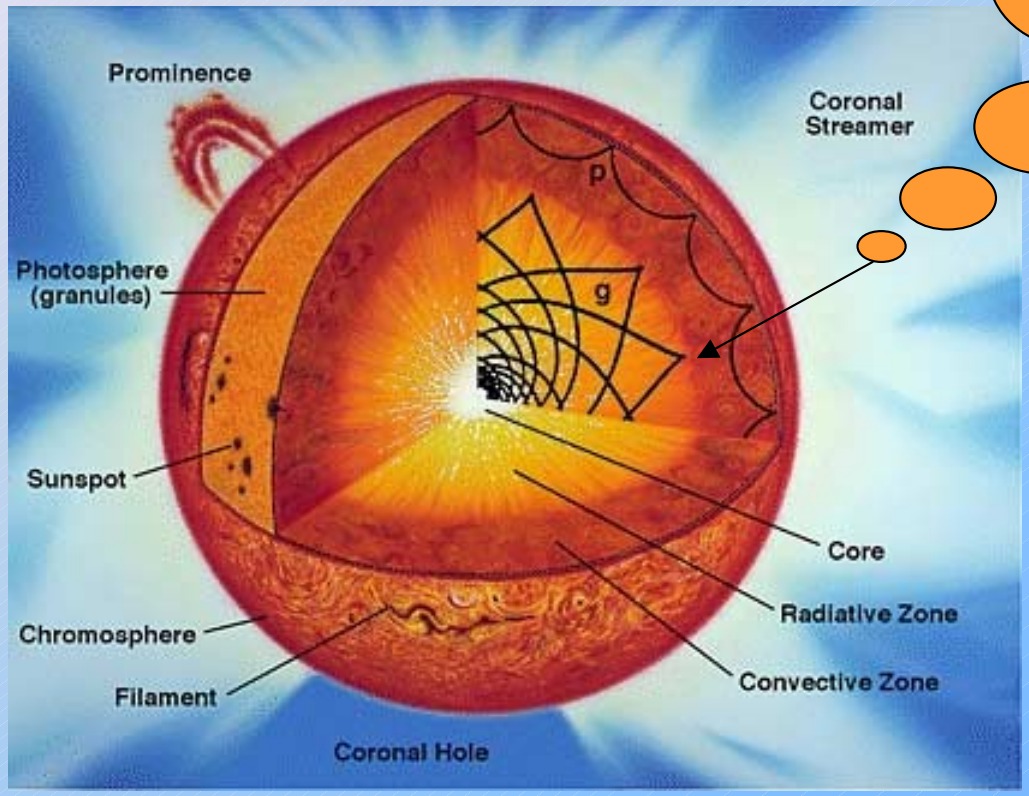

The tachocline is approximated by a 2D shear layer as follows

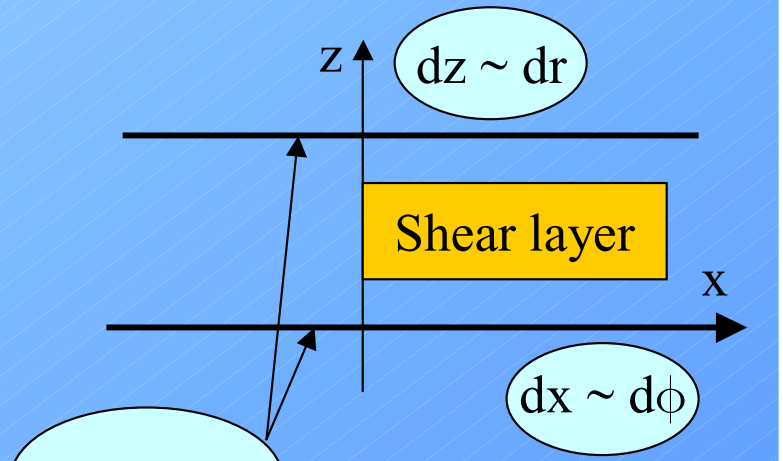

Hypothesis of the model

Contribution from convective and radiative zones reduced to a **forcing in velocity** along the x direction and depending on the solar latitude coordinate

Perfect gas approximation for the fluid

Uncompressible and **isentropic** flow

No Boussinesq approximation, no thermic dissipation, kinetic and hydrostatic pressure gradients

Free-slip conditions on the surfaces, otherwise periodic

A concentration with an initial gaussian profile versus the z coordinate is convected by the flow. Its diffusion is studied for different values of the Reynolds number depending on the intensity of the forcing

Theory

$$\begin{cases} \partial_x V_x + \partial_z V_z = 0 \\ \partial_t V_x = -\partial_x P - R_x + \frac{1}{Re}\left\{\partial_x{}^2 V_x + \partial_z{}^2 V_x\right\} + \Phi \\ \partial_t V_z = -\partial_z P - R_z + \frac{1}{Re}\left\{\partial_x{}^2 V_z + \partial_z{}^2 V_z\right\} \\ \partial_t C = -\partial_x (V_x\, C) - \partial_z (V_z\, C) + \frac{1}{Pe}\left\{\partial_x{}^2 C + \partial_z{}^2 C\right\} \end{cases}$$

with

$$\begin{cases} R_x = V_z\ (\partial_z V_x - \partial_x V_z) \\ R_z = V_x\ (\partial_x V_z - \partial_z V_x) \end{cases}$$

Re is the Reynolds number

Pe is the Peclet number

$\boldsymbol{\Phi}$ is the forcing along the horizontal direction

$(\partial_z V_x - \partial_x V_z)$: Vorticity component perpendicular to the domain of study

The theoretical equations are solved in spectral space

Written in spectral space with the following decompositions,

$$\begin{cases} C(t,x,z) = \sum_{\mathbf{k}} \hat{C}(t,\mathbf{k}) e^{ik_x x} \sin(k_z z) \\ V_z(t,x,z) = \sum_{\mathbf{k}} \hat{V}z(t,\mathbf{k}) e^{ik_x x} \sin(k_z z) \\ V_x(t,x,z) = \sum_{\mathbf{k}} \hat{V}x(t,\mathbf{k}) e^{ik_x x} \cos(k_z z) \end{cases}$$

The equations under study become

$$\begin{cases} \mathbf{i}k_x \hat{V}_x + \mathbf{i}k_z \hat{V}_z = 0 \\ \partial_t \hat{V}_x = -\mathbf{i}k_x \hat{P} - \hat{R}_x - \frac{({k_x}^2 + {k_z}^2)}{Re} \hat{V}_x + \hat{\Phi} \\ \partial_t \hat{V}_z = -\mathbf{i}k_z \hat{P} - \hat{R}_z - \frac{({k_x}^2 + {k_z}^2)}{Re} \hat{V}_z \\ \partial_t \hat{C} = -\mathbf{i}k_x \widehat{(V_x\, C)} - \mathbf{i}k_z \widehat{(V_z\, C)} - \frac{({k_x}^2 + {k_z}^2)}{Pe} \hat{C} \end{cases}$$

The time iteration is made with

- ★ the **implicit** Cranck-Nicholson method for the **diffusion terms**
- ★ the **explicit** Leapfrog scheme for the **advection terms**

The time iteration is divided in two steps for the velocity components. After the first step, the pressure is calculated with the condition :

$$\widehat{\nabla.\mathbf{V}} = 0$$

The contribution of the small scales of turbulence is carried out by a subgrid model

Subgrid Model

(M.Lesieur&R.Rogallo, 1989)

$$\nu_t(k/k_c) = (A + Be^{C(k_c/k)})[E(k_c)/k_c]^{1/2}$$

A = 0.267, **B** = 9.21 and **C** = -3.03

An extra-diffusion term is added to the equations governing the velocity components and the concentration as follows :

$$\begin{cases} \hat{V}_x^{n+1} = \hat{V}_x^{n+1} - 2dt\ \nu_t\ k^2 \hat{V}_x^{n+1} \\ \hat{V}_z^{n+1} = \hat{V}_z^{n+1} - 2dt\ \nu_t\ k^2 \hat{V}_z^{n+1} \\ \hat{C}^{n+1} = \hat{C}^{n+1} - 2dt\ \nu_t\ k^2 \hat{C}^{n+1} \end{cases}$$

Simulation philosophy

Given a Reynolds number, a simulation is made in **two steps** with a forcing on several layers

First step : Stationarity of the anisotropy

The purpose of the forcing is to create a strong sheared flow with a constant mean value of the anisotropy defined as follows

$$A(t) = \sqrt{\frac{<V^2{}_x(x,z,t)> - <V_x(x,z,t)>^2}{<V^2{}_z(x,z,t)> - <V_z(x,z,t)>^2}}$$

Second step : Vertical diffusion of the concentration

The aim of the forcing is to produce the vertical diffusion of the concentration in the flow with a constant anisotropy.
The concentration is named after **C**

Quantities measuring the turbulent diffusion

Anisotropy

Turbulent diffusion coefficient

Flux

x averaged variancy

z averaged variancy

$$
\begin{cases}
A(t) = \sqrt{\dfrac{<V^2{}_x(x,z,t)> - <V_x(x,z,t)>^2}{<V^2{}_z(x,z,t)> - <V_z(x,z,t)>^2}} \\
D_T(z,t) = \dfrac{<V_z(x,z,t) \times C(x,z,t)>_x}{<\frac{dC(x,z,t)}{dz}>_x} \\
F(z,t) = < V_z(x,z,t) \times C(x,z,t)>_x \\
\sigma^2{}_x(z,t) = < (C(x,z,t) - < C(x,z,t)>_x)^2>_x \\
\sigma^2{}_z(x,t) = < (C(x,z,t) - < C(x,z,t)>_z)^2>_z
\end{cases}
$$

After averages on time and space coordinates,
it involves one value for **A**, $\mathbf{D_T}$, $\mathbf{F_{max}}$, $\sigma^2{}_\mathbf{x}$ and $\sigma^2{}_\mathbf{z}$

D_T, F_{max} versus the anisotropy

$dx = dz = 1.2 \times 10^{-2}$
$dt = 10^{-5}$ and $Pe = 1$

Re = 140000

Re = 1400000

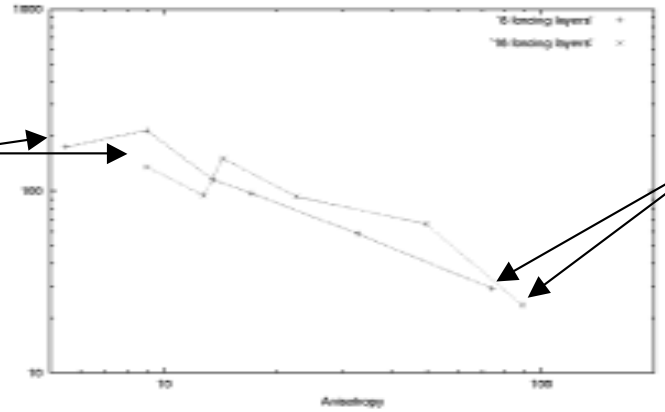

FIG. 1 – Dimensionless turbulent diffusion coefficient $D_T/(l_{0z}v_{0z})$ versus anisotropy

Re = 700000

Number of forcing layers

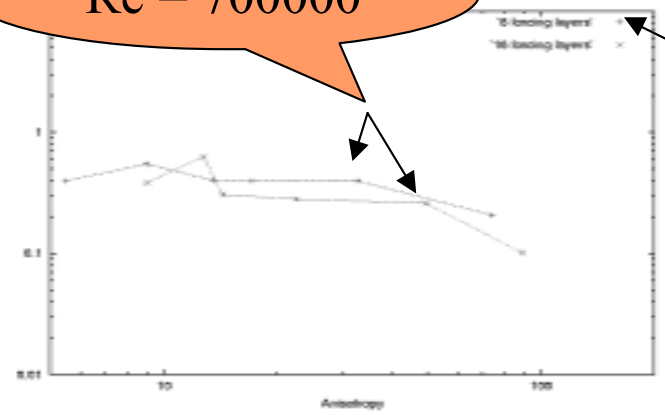

FIG. 2 – Maximum flux versus anisotropy

σ^2_x and σ^2_z versus the anisotropy

$dx = dz = 1.2 \times 10^{-2}$
$dt = 10^{-5}$ and $Pe = 1$

Re = 140000

Re = 1400000

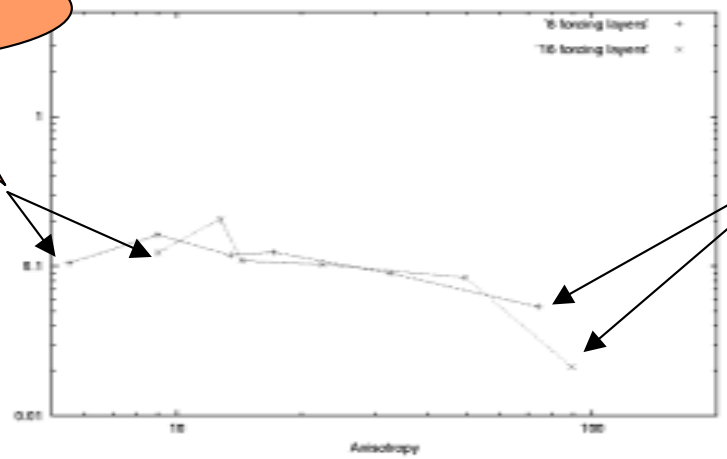

FIG. 3 – Variancy σ^2_x versus anisotropy

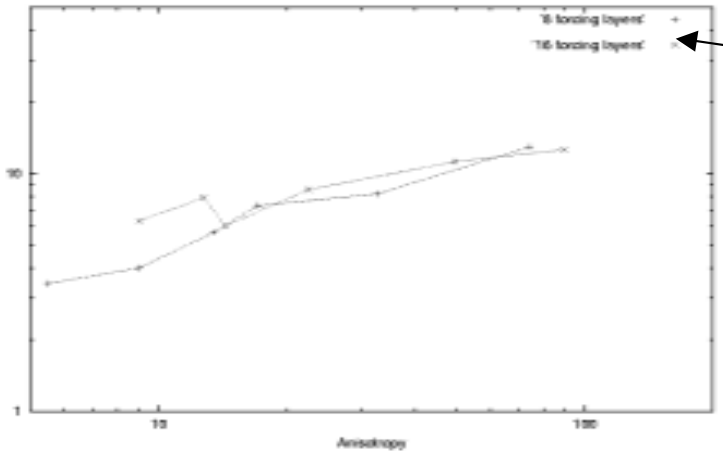

Number of forcing layers

FIG. 4 – Variancy σ^2_z versus anisotropy

Total kinetic energy, Re = 700000

16 forcing layers

$$dx = dz = 1.2 \times 10^{-2}$$
$$dt = 10^{-5} \text{ and } Pe = 1$$

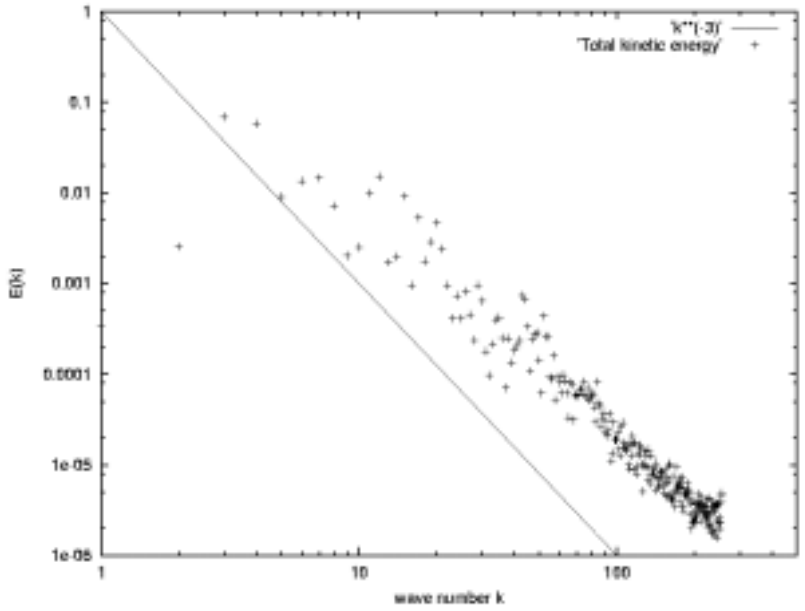

FIG. 5 – Total kinetic energy at the time of maximum vertical flux of the concentration in the flow

The curves 1 to 4 show that for increasing Reynolds numbers, the turbulent diffusion coefficient, the maximum flux and the variancy σ^2_x are growing down for anisotropy values upper than 40, and the variancy σ^2_z is growing up

More forcing layers move down the maximum flux of the concentration in the flow because the integral scale and the quadratic fluctuation of vertical velocity are lower

The variances seem not influenced by the number of layers. They measure the turbulent homogenization in the two directions. For a conservative flow, less kinetic energy in the vertical direction involves more in the horizontal direction. So, the turbulent homogenization is better in the x direction than in the z direction. For increasing Reynolds numbers, the variancy σ^2_x decays and the variancy σ^2_z grows up.

The total kinetic energy evolves as k^{-3} as shown on the diagram 5

Vorticity component perpendicular to the domain of study, Re = 700000

16 forcing layers

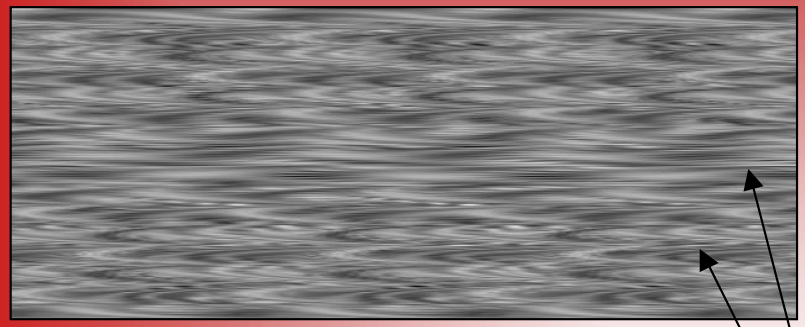

z

x

t = 0.001

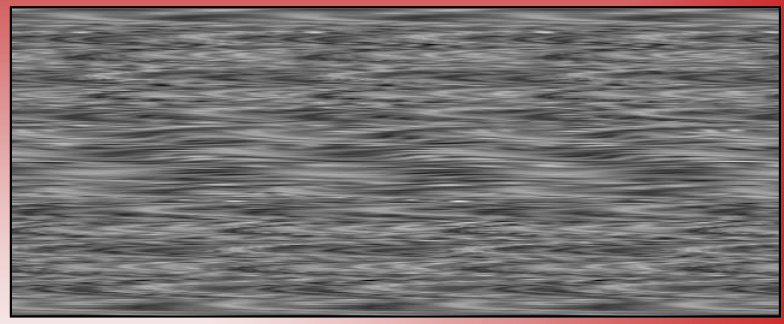

t = 0.002

Time of maximum vertical flux of the concentration

Small whirls

An unhomogeneous flow at the beginning of the simulation

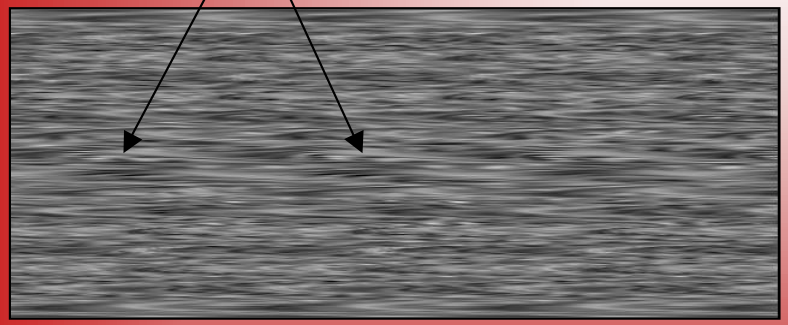

t = 0.003

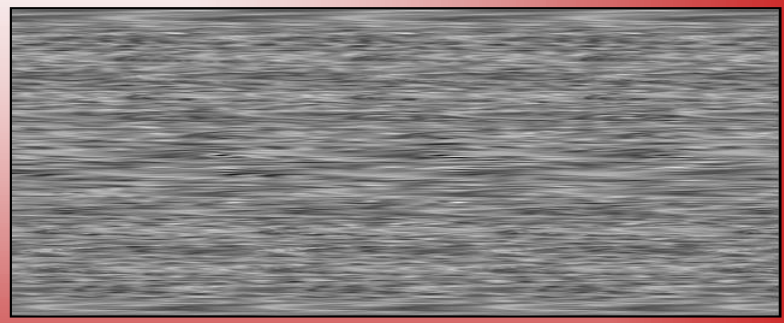

t = 0.004

Vorticity component perpendicular to the domain of study, Re = 700000

16 forcing layers

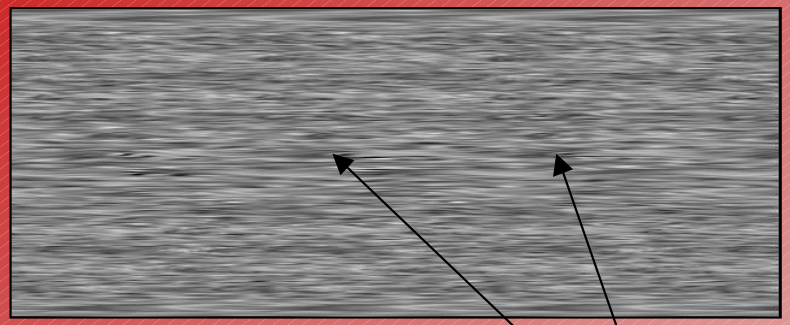

t = 0.005

t = 0.006

Whirls are getting thinner and thinner and flattened

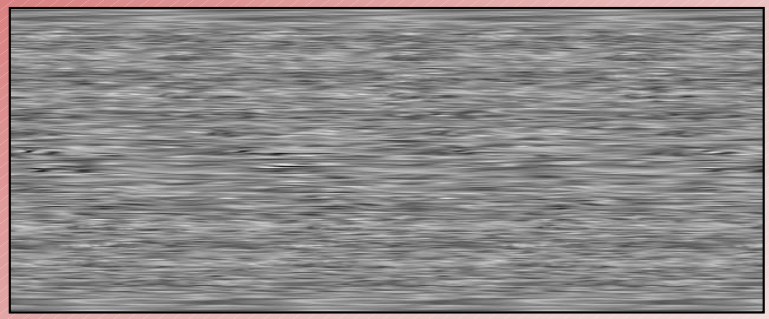

t = 0.007

No more evidence of inhomogeneity between the center, the top and the bottom of the flow

Continuation of the study

- Simulations with different values of the Peclet number
- Boussinesq approximation to take into account a temperature stratification
- Forcing with internal waves to quantify their part on the turbulent diffusion in differential rotation zones
- 3D compressible simulations

Los Alamos NATIONAL LABORATORY

Recent Computational Simulations of Rayleigh-Taylor Mix Layer Growth with a Multi-fluid Model

Erik Vold
Los Alamos National Laboratory

w/ acknowledgements to A.J.Scannapieco,
Tim Clark, John Grove, Chuck Cranfill, et.al.

Presented at the 8th International Workshop on
The Physics of Compressible Turbulent Mixing
Pasadena, CA, Dec.10-14, 2001

Los Alamos NATIONAL LABORATORY

disclaimer

This is a partial sub-set of the viewgraphs presented at the 8th IWCTM.

The work on ‘resolved scale’ simulations is currently being prepared for publication, to be submitted to Physics of Fluids.

The work on ‘sub-grid drift flux’ simulations will be prepared for publication soon, to be submitted to a journal TBD.

Los Alamos NATIONAL LABORATORY

Recent computational simulations of Rayleigh-Taylor mix layer growth with a multi-fluid model.

Erik Vold
Los Alamos National Laboratory

Abstract - LA-UR-01-2562

Recent results of computational simulations of the Rayleigh-Taylor mix layer are presented and discussed. Our previous work is summarized briefly comparing mix layer growth characteristics observed in different simulation modes including single fluid with initial density discontinuity, two-fluids with interface reconstruction and in a full multi-fluid dynamic approach. Recent comparisons under varying compressibility are presented showing negligible influence of compressibility on the mix layer growth rate. Using spectral analyses, perturbations intentionally introduced in the initial conditions are compared to long wave length perturbations introduced inadvertently in these initial conditions. The influence of these initial conditions on late time growth and growth rate are explored. The compressible multi-fluid model allows each fluid to have its own 'drift velocity' relative to the mass averaged fluid velocity. This can be applied in several ways within the mix layer to represent a real molecular mixing, a turbulent enhanced diffusive mixing, or an individual species 'sub-grid' convective drift flux. Examples of these in the Rayleigh-Taylor mix layer are discussed. Finally, we consider the combination of these factors which best matches the experimental results for mixing layer growth rates in incompressible experiments, and how these results may apply to compressible fluids.

Los Alamos NATIONAL LABORATORY

Introduction

- Goals:
  - simulate Rayleigh-Taylor mix layers accurately to predict atomic / molecular mixing (e.g., a reactive R-T mixing front) in macroscopic geometries.
  - use 'resolved simulations' to model mix layer growth and use drift flux (subgrid) simulations to model the mix layers atomically mixing components.
  - match experimental 'alpha' (α), $h = \alpha A_t g t^2$
  - match refined experimental findings related to mixing front details.

focus today

- Central Issues
  - numerical mixing must be small enough to have a negligible effect on mix layer growth rates so that 'sub-grid' mixing can be represented realistically.
  - Hypothesis: the growth rate seen in computations, which have no subgrid mixing and small numerical diffusion, should equal or exceed the experimental value IF the experiment contains small scale dissipation which reduces the growth rate in the experiment.

Los Alamos NATIONAL LABORATORY

Summary of Relevant Work

- Experimental
  - wide range of experiments (mostly incompressible) show a mix layer growth rate which closely approximates the scaling, $h = \alpha A_t g t^2$
  - alpha bubble, $\alpha_b \sim 0.06$-0.07 (earlier work, e.g., Youngs and Read et.al.,) - and ~ 0.05 (recent work, e.g., Dimonte, Schneider, et.al.)
- Computational
  - alpha bubble results range from ~ 0.03 - ~0.1
  - many 3-D methods (compressible or incompressible) trending towards low end, $\alpha_b \sim 0.03$ ~ half experimental mean
  - front tracking w/ 2 distinct fluids ('Frontier code', Glimm, et.al.) at higher end, ~0.07-0.08
  - large variance in alpha just due to random seed in initial perturbation
    - (~ 0.05 +/- 20-50%, in 2-D compressible isothermal fluids, T. Clark, 2001)
  - 2-D results ~ 15% greater than 3-D results (Youngs, 1994)

Summary of Our Methods

- Methods
  - 2-D multi-fluid Eulerian AMR formulation
  - compressible Euler equations in appropriate limit to recover incompressible approximation, supplemented with fluid volume fractions
  - ideal gas equation of state for each fluid
  - advection of fluid volume fractions in mixed cells at the interface
    - mixed cell treatment (Bowers and Wilson,1991)
    - interface reconstruction (D.Youngs, 1984, 1989)
  - high-order, monotonic Van Leer advection of fluid quantities
  - each fluid has its own density, internal energy and pressure in its fluid volume fraction within the 'mixed cells' (containing the interface)
  - in 'drift flux' representation of sub-grid mixing, each fluid has its own 'drift momenta' relative to the mass average which can be adjusted to represent realistic molecular diffusion or a range of assumed turbulent flux forms

Los Alamos NATIONAL LABORATORY

Summary of Our Previous Results

- Previous Results
  - alpha bubble was found on a 128 x 128 grid with no sub-grid mix model, to be ~ 0.08 - 0.1, somewhat larger than experiments.
  - interface algorithm does not alter the growth rates significantly.
  - molecular mixing (by the drift flux) does not influence the mix layer growth rate but does create a unique distribution of molecularly mixed materials controlled primarily by the volume fraction of the lighter material.
  - drift flux mixing significantly above the molecular diffusion level reduces the mix layer growth rate (for the set-up in these results, a drift flux ~ 50 times greater matches experimental range (α_{bub}~ 0.055)

Los Alamos NATIONAL LABORATORY

Issues in Matching 'alpha' [and what our set-up uses]

- **Numerical**
  - grid resolution [128^2 or 256^2 or 512^2]
  - Interface treatment [mix cell volume fraction advection w/ Young's interface reconstruction]
  - Differencing schemes [high order monotonic Van Leer like scheme]
  - 2-D vs. 3-D [2-D only]
- **Initial Conditions**
  - initial perturbation magnitudes, [volume fractions, Vf, set to match interface perturbation]
    - perturbation on density [$\rho = \rho_1 Vf_1 + \rho_2(1.-Vf_1)$]
    - perturbation on internal energy [$\varepsilon = \varepsilon_1 Vf_1 + \varepsilon_2(1.-Vf_1)$]
  - wavelength spectrum, [30 modes, mode numbers 30 - 60, random phase, unit amplitude]
  - hydrostatic equilibrium by e(z), or $\rho(z)$ [e(z), w/ $\rho = \rho_o$]
- **Physics**
  - compressible or incompressible formulation (w/ or w/o internal energy) [compressible]
    - degree of compressibility [varied Ma^2 by 2 orders of magnitude]
  - fluid equations: Euler, viscid, internal or total energy [Euler using internal energy w/ optional multi-fluid drift flux for 'species momenta' relative to mass averaged single fluid velocity.]
  - Interface physics: surface tension, slip or traction, molecular diffusion, sub-grid mixing

Los Alamos
NATIONAL LABORATORY

rt256bc4 den at t=20,40,60,80

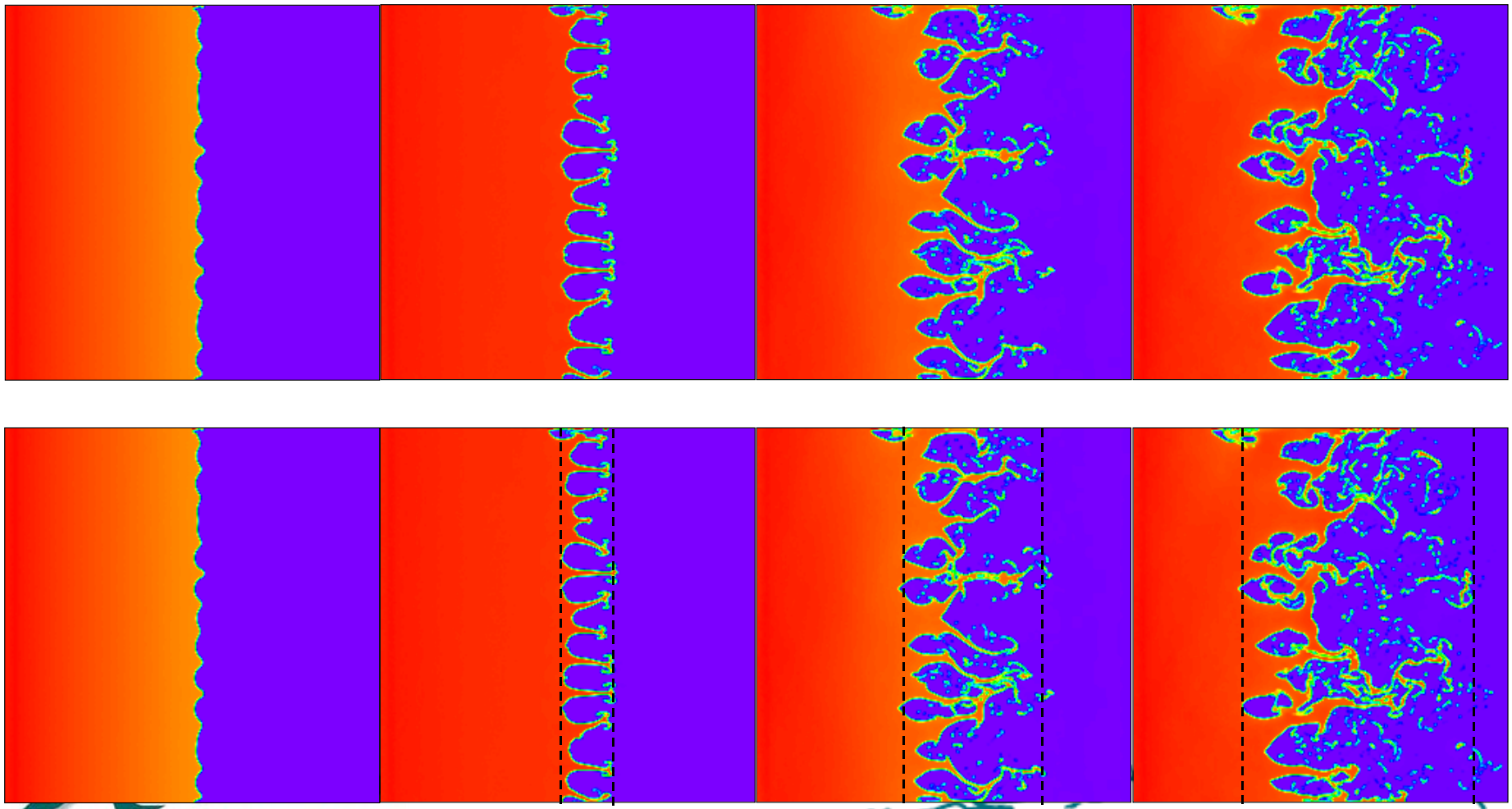

Los Alamos NATIONAL LABORATORY

RT mix width for 256 case

mix layer width, h

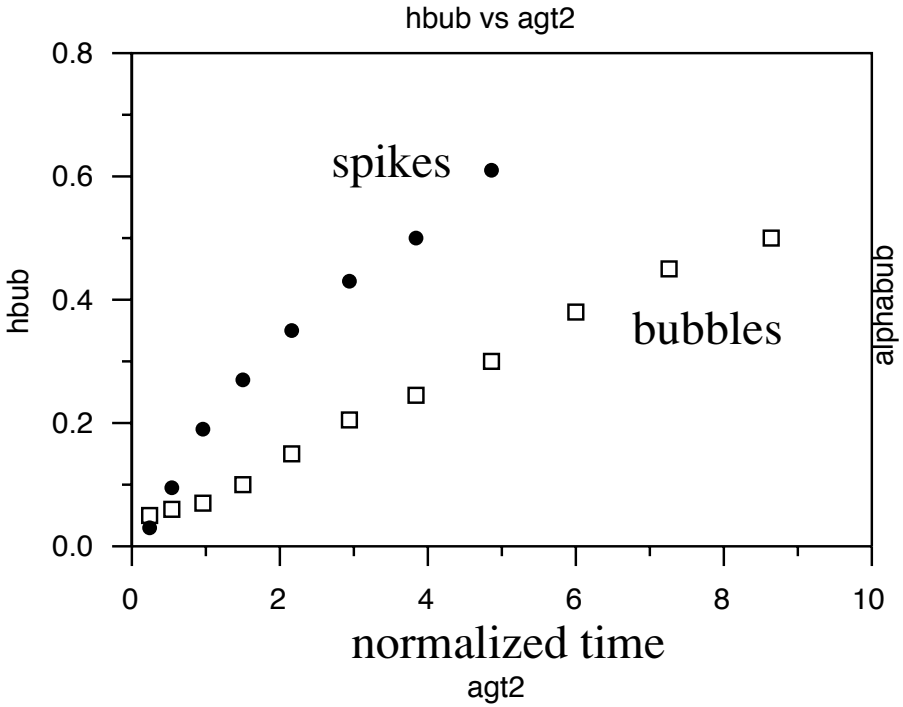

mix width growth coef, α

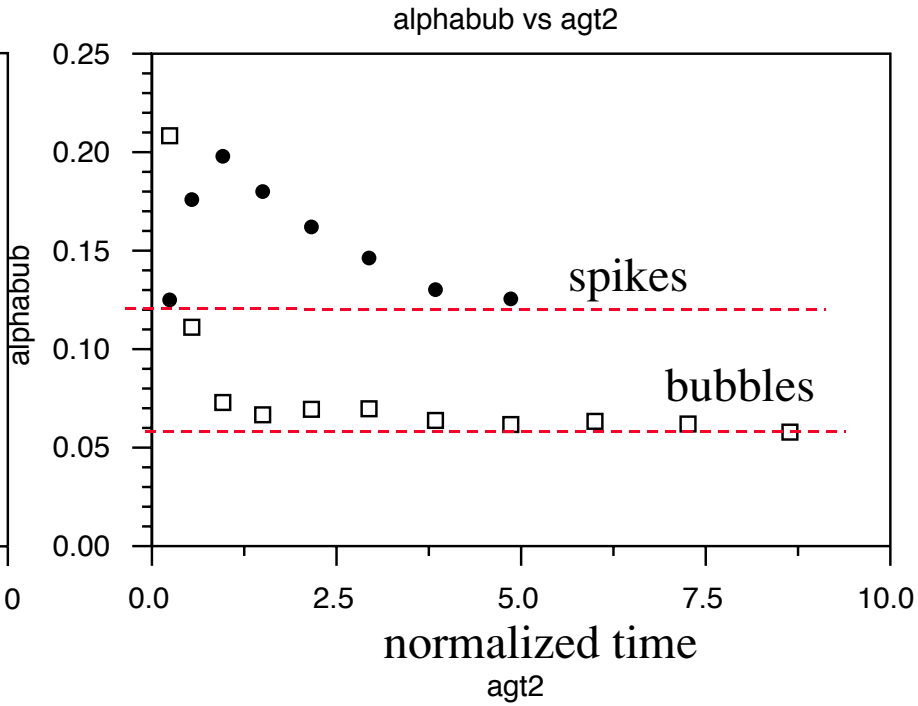

Los Alamos NATIONAL LABORATORY

RT mix width for varying compressibility

total mix layer width, h

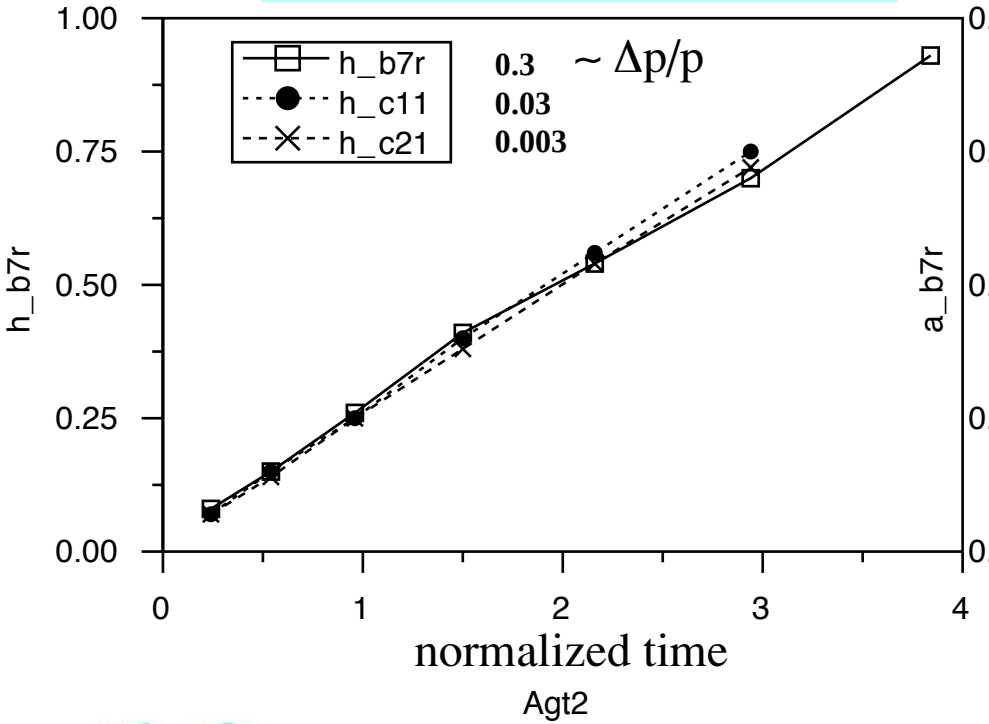

mix width growth coef, α

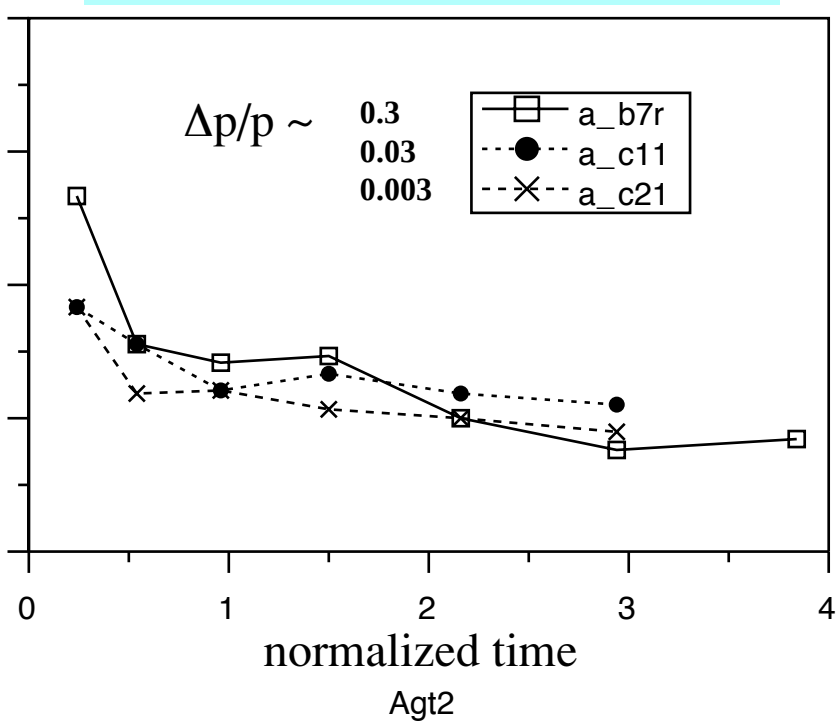

Los Alamos NATIONAL LABORATORY

BC4- Zint(IC) fixed

grids 128^2, 256^2 & 512^2 - each grid result on 512^2

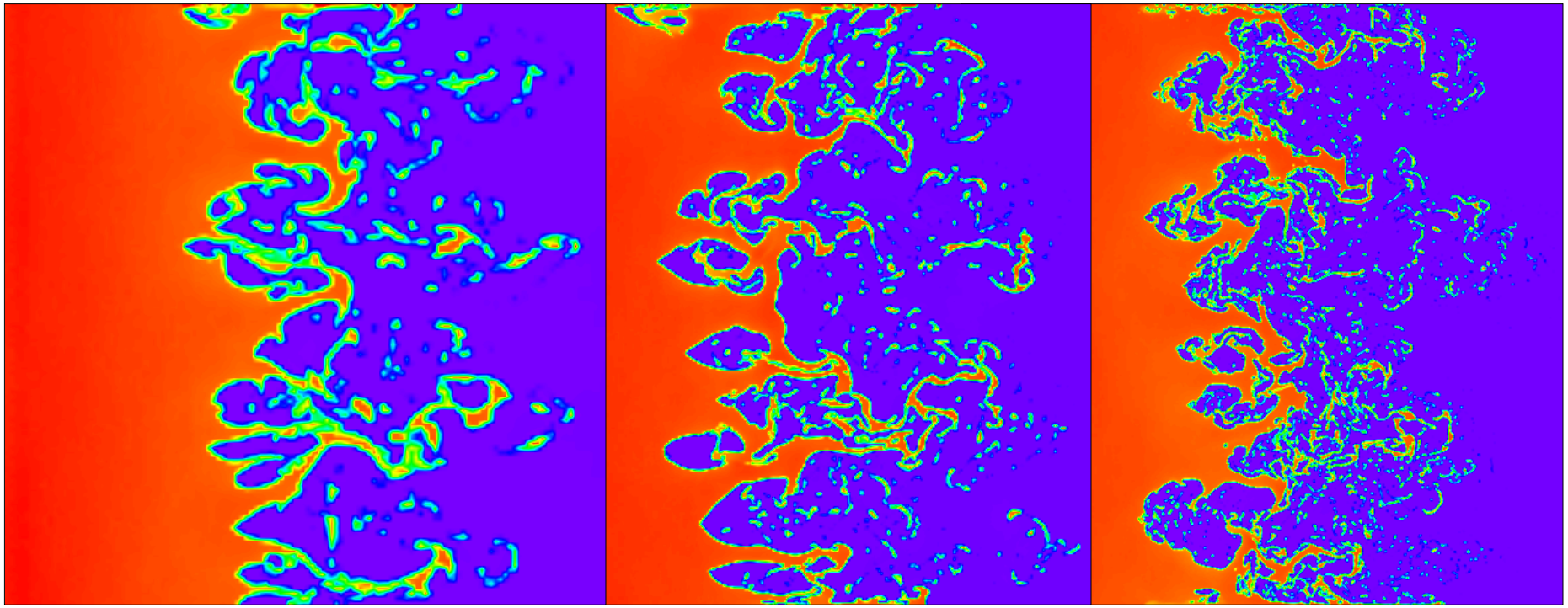

Los Alamos NATIONAL LABORATORY

BC4- Zint(IC) fixed

grids 128^2, 256^2 & 512^2 - actual grid results

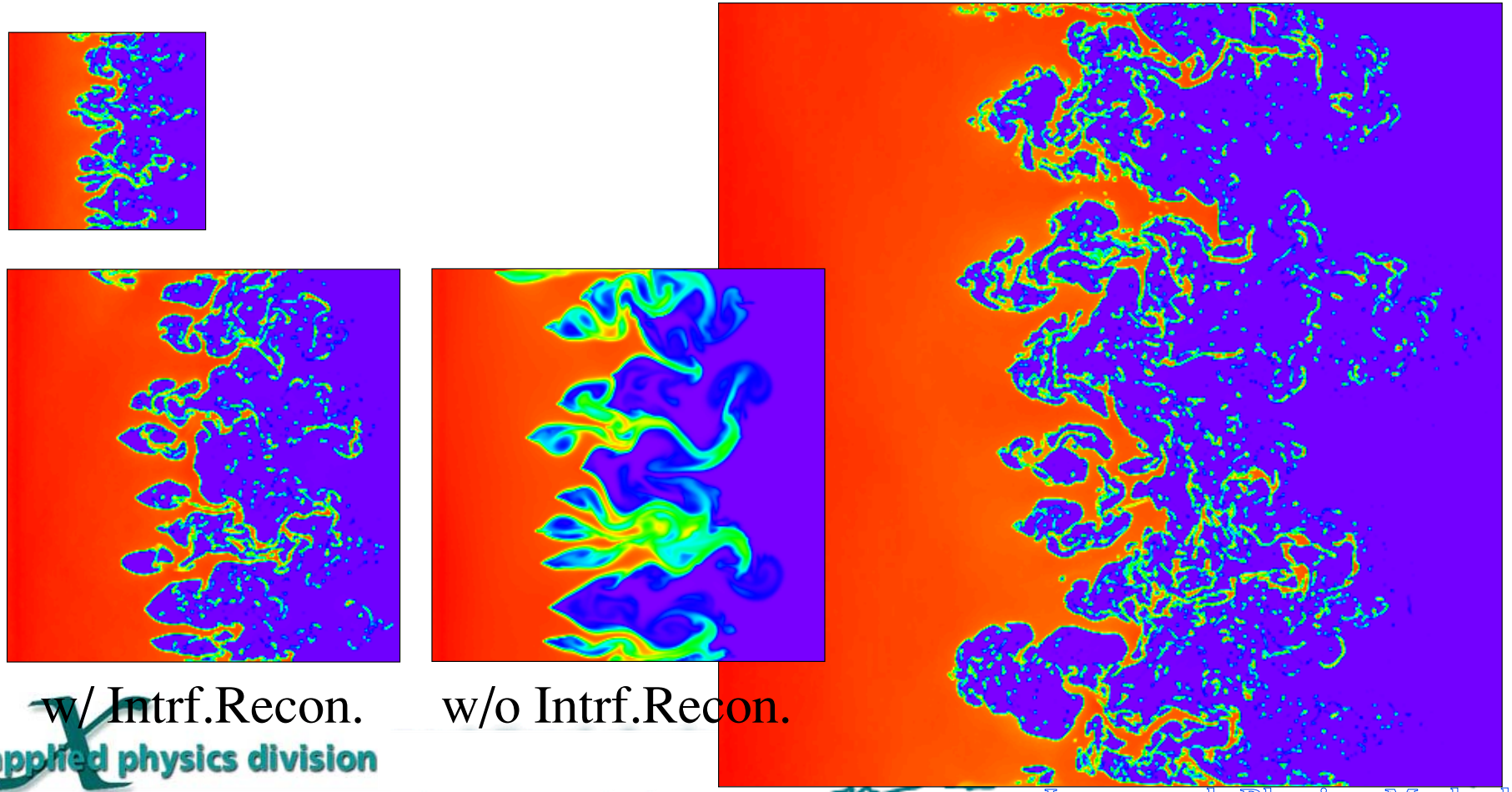

w/ Intrf.Recon. w/o Intrf.Recon.

Alpha (RT mix growth rate)

E.L.Vold

BC4 -fixed Zint(IC) - varying grid res. and w/ & w/o Intrf.Recon.

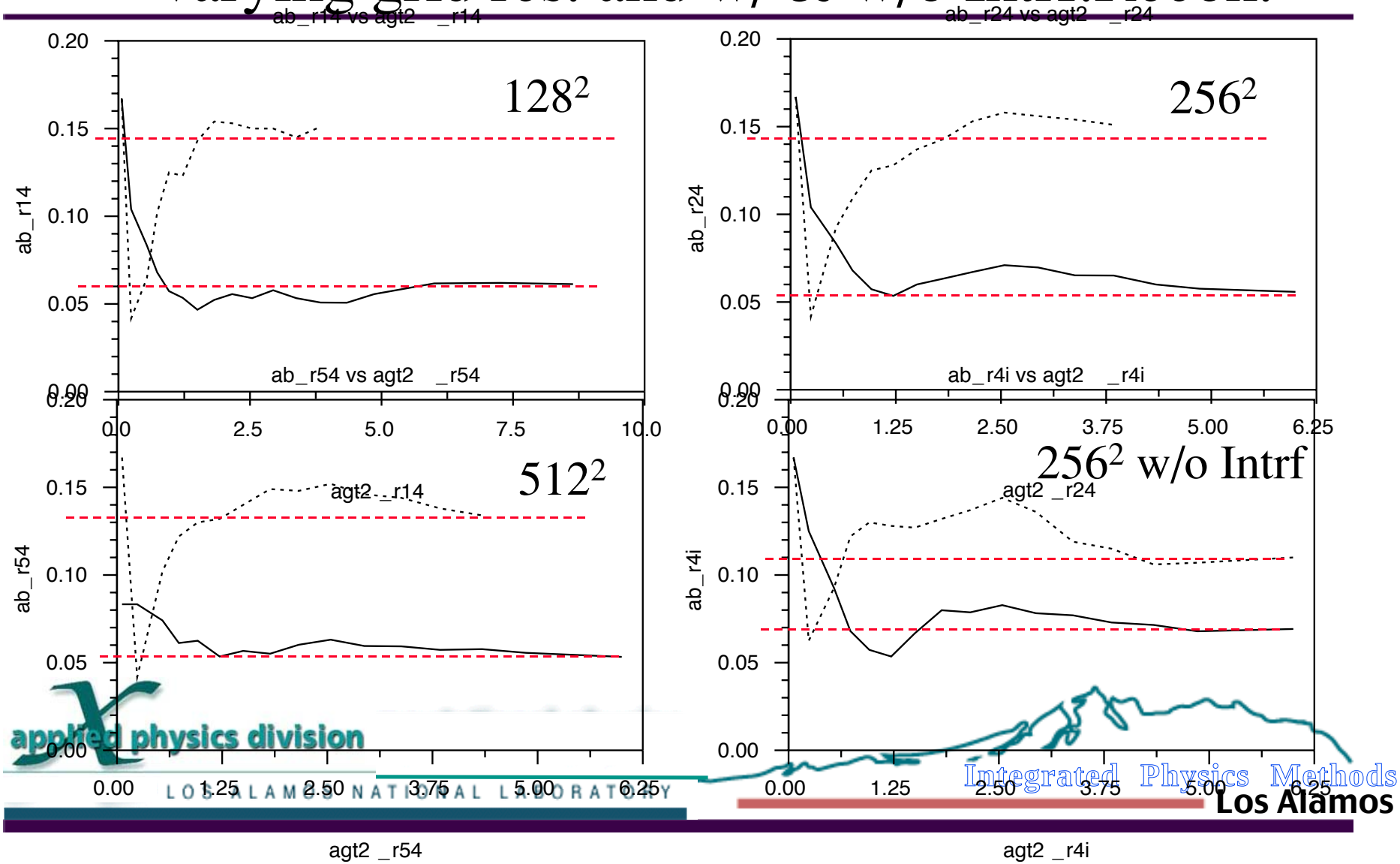

applied physics division

LOS ALAMOS NATIONAL LABORATORY

Integrated Physics Methods

Los Alamos

BC2- Vf(IC) fixed

E.L.Vold

grids 128^2, 256^2, 512^2 actual grid dimensions

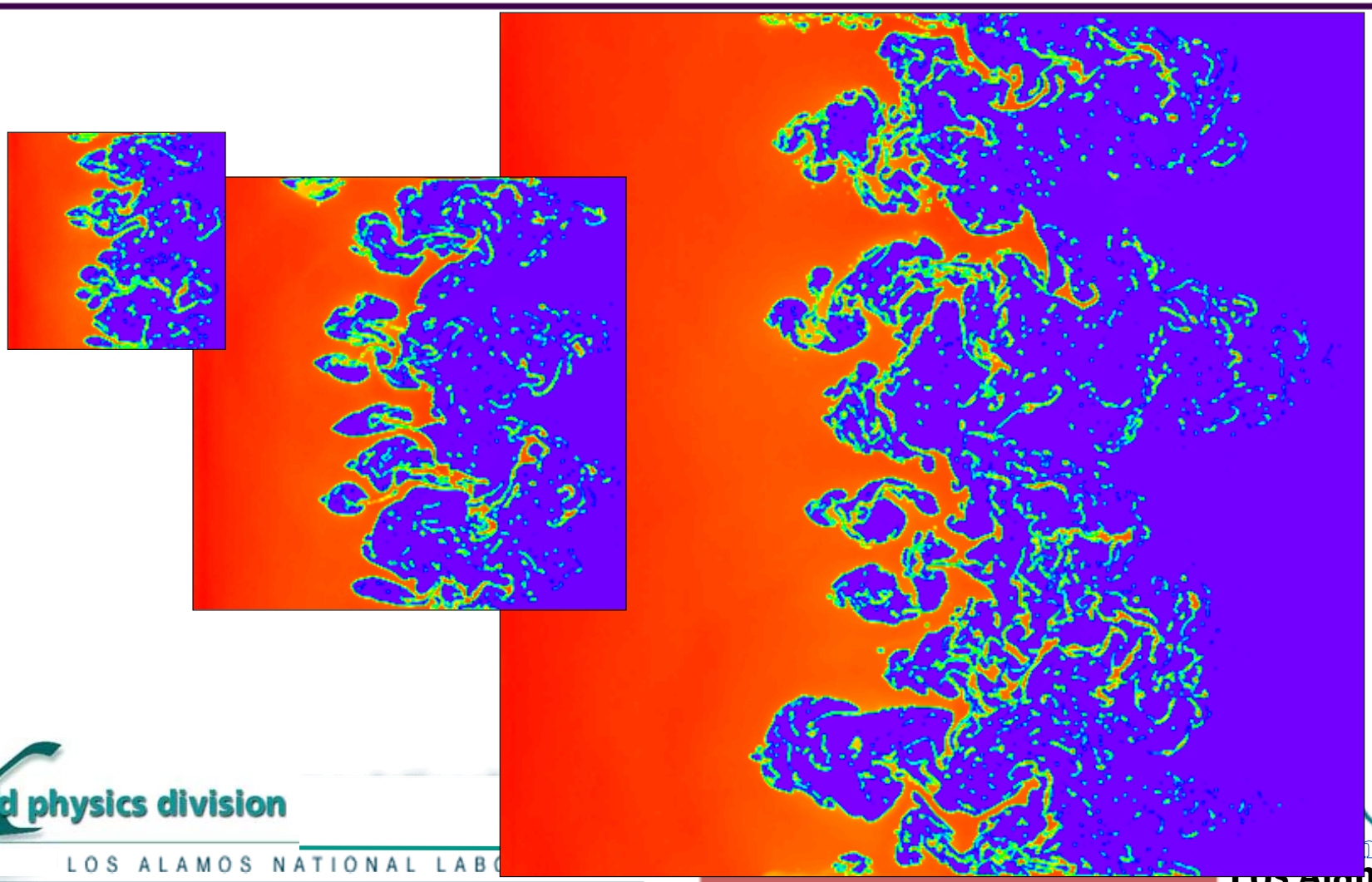

Alpha (RT mix growth rate)

E.L.Vold

BC2 -fixed V_f(IC) - varying grid res. and w/ & w/o Intrf.Recon.

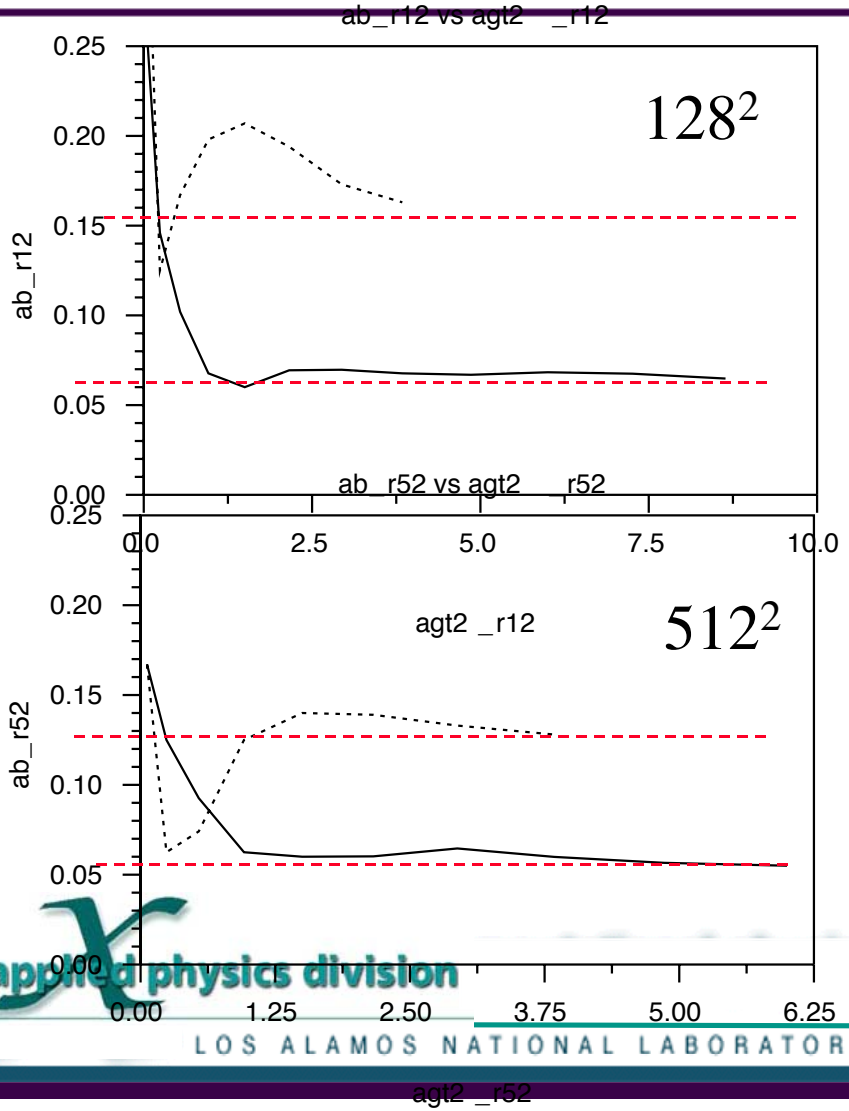

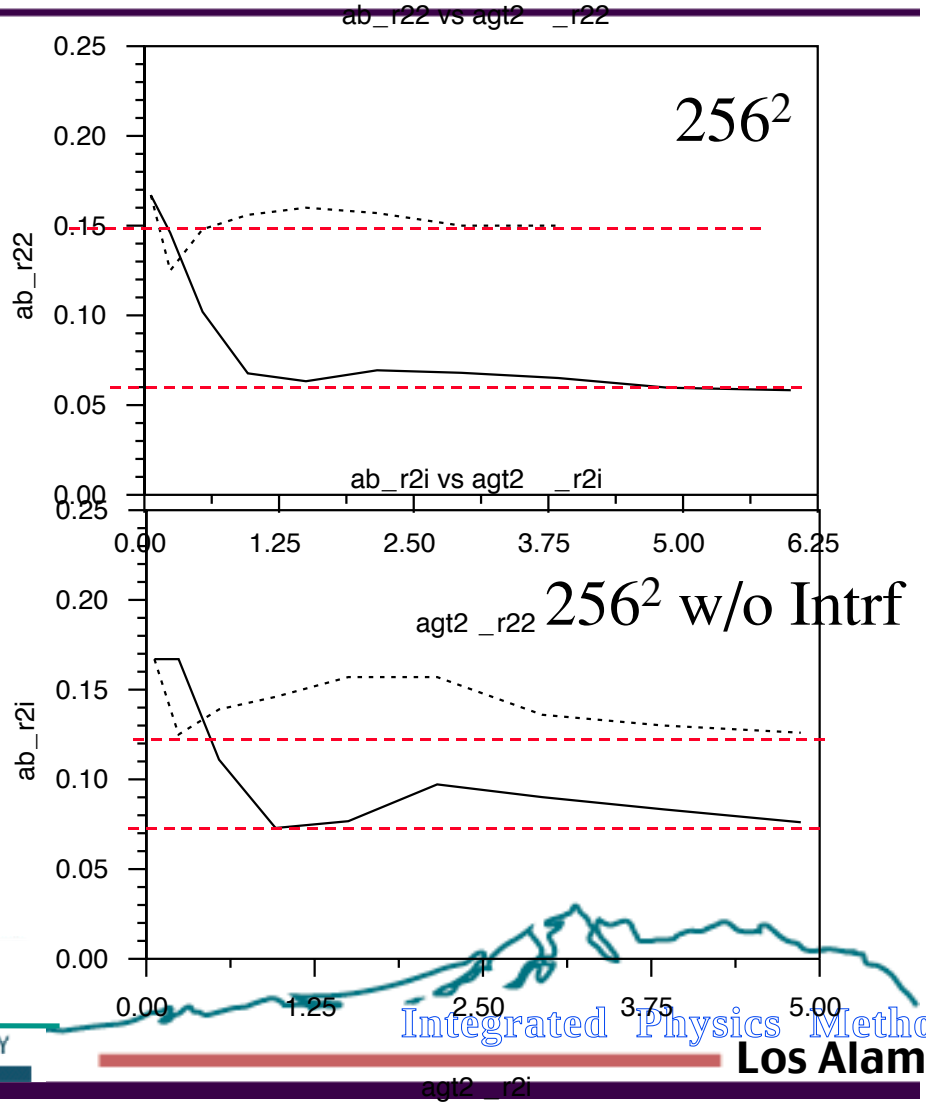

BC2 (fixed VF(IC)) vs. BC4 (fixed Zint(IC))

E.L.Vold

are the same structures seen across grid res. in either case?

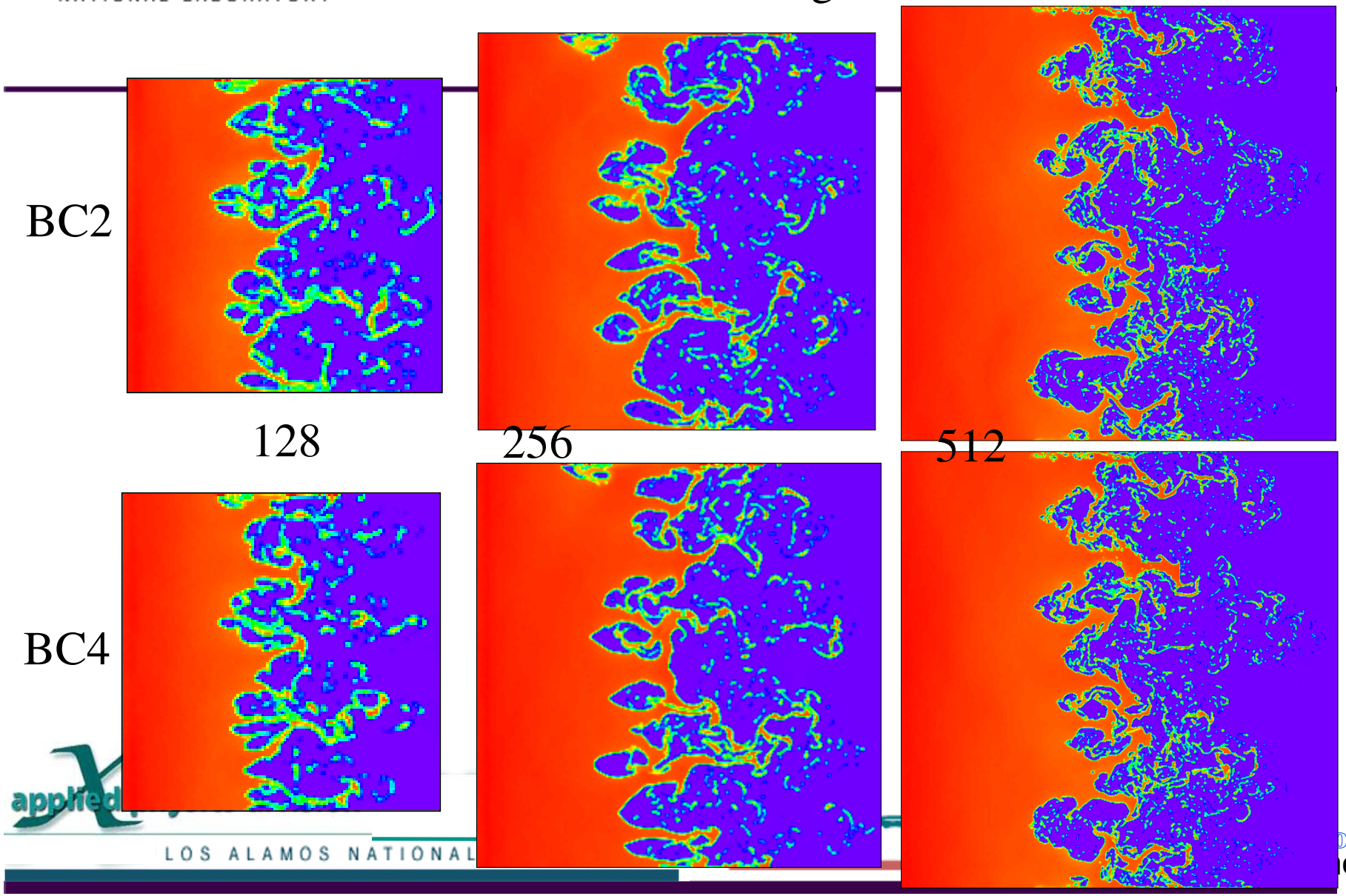

RT resolved simulation cases alpha summary for At=0.8

- Base cases - spikes
- Base cases - bubbles
- delta(IC)= delta(base case)/2 - bubble or spike
- IC: $e = e_0$, $\rho = \rho(z)$.
- x-ave contours eval.
- w/af- atomic mixing by drift flux momenta

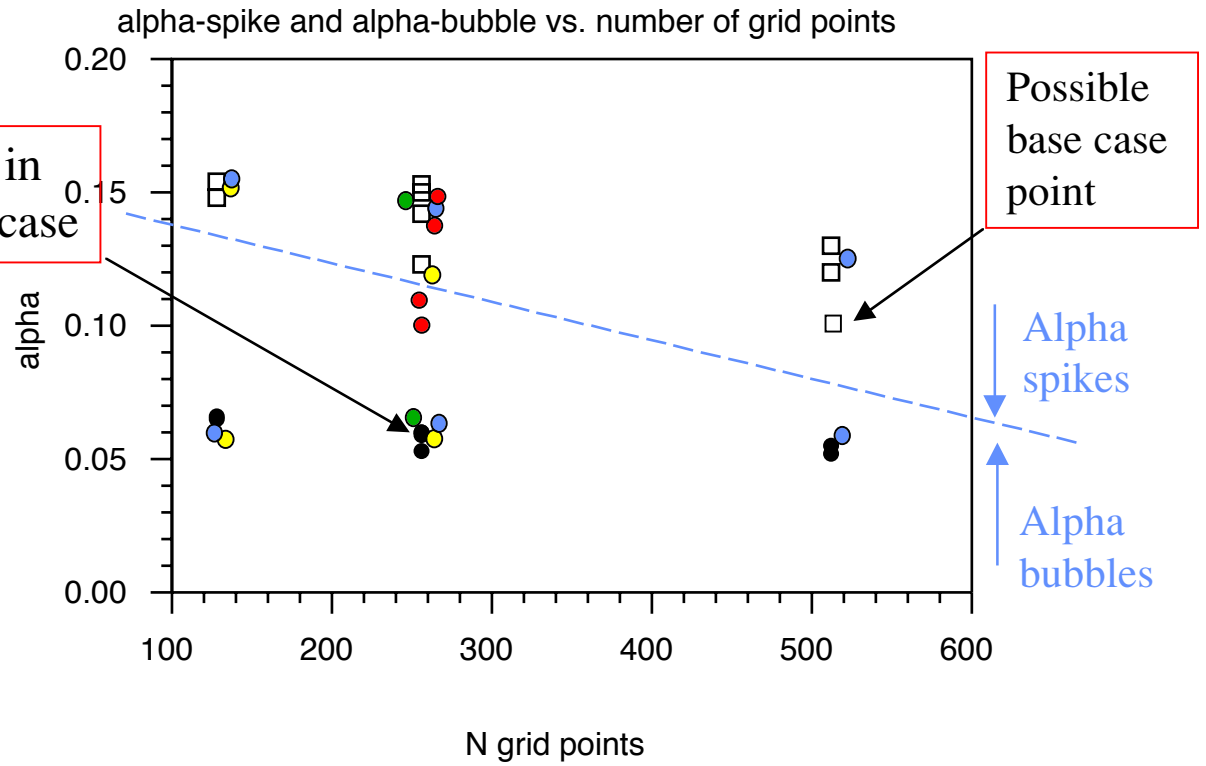

Analytic model compared to fluid equations

Analytic model:

$$\frac{\partial h}{\partial t} = u$$

$$\frac{\partial u_i}{\partial t} + C_{Di}\frac{u_i^2}{(\delta_o + \alpha_o h_i)} = \beta_i Ag$$

Fluid model:

$$\frac{\partial h_m}{\partial t} \sim u_g$$

$$\frac{\partial u}{\partial t} + u\cdot\nabla u = a \sim Ag - \frac{\nabla p}{\rho}$$

OR: $$\frac{\partial u}{\partial t} + \frac{\nabla u_s^2}{2} - u\times\omega = a$$

OR: $$\frac{\partial u}{\partial t} + \frac{u_x^2}{2L_x} + \frac{u_y^2}{2L_x} - u\times\omega \sim a$$

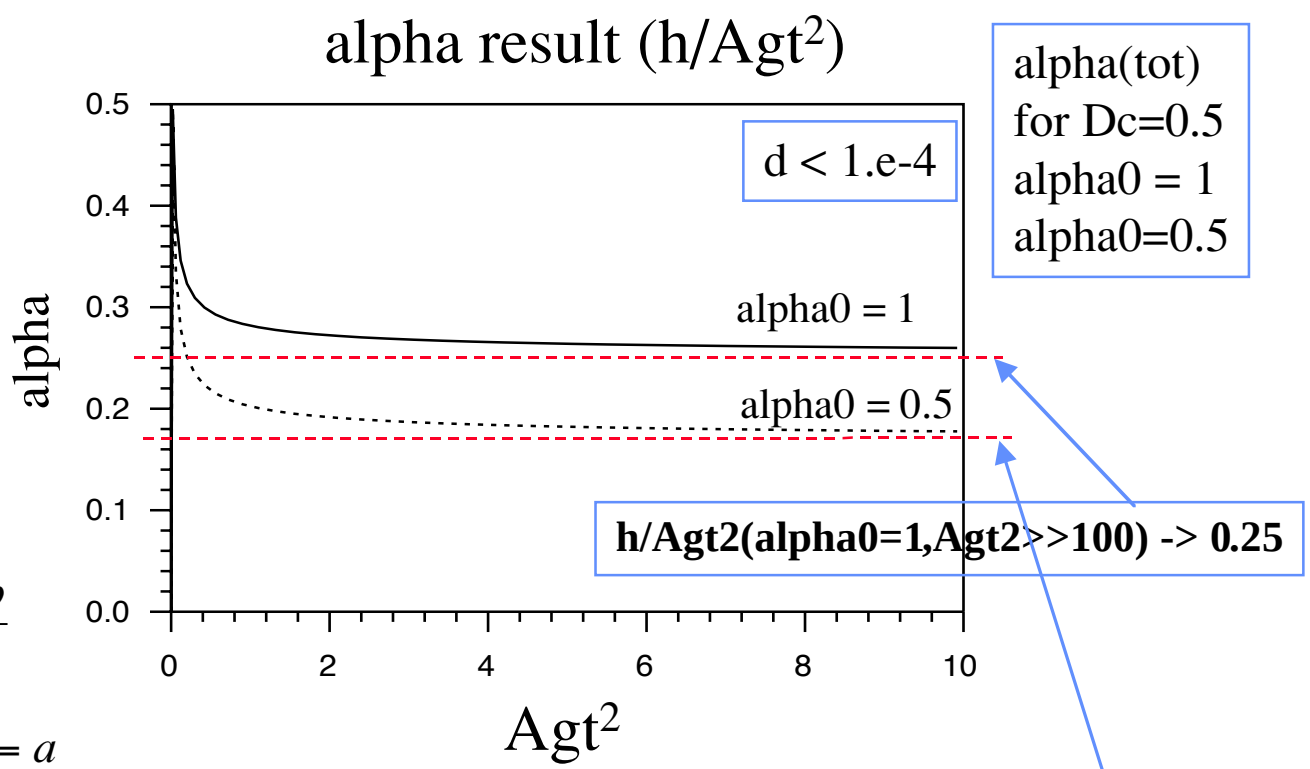

h/Agt2 as f[delta0]

v determined as:

$$\frac{\partial v}{\partial t} + \frac{v^2}{(\delta_o + \alpha_c \int v\, dt)} = a$$

hoh0_hintvt:

$\alpha_c = 0.12$

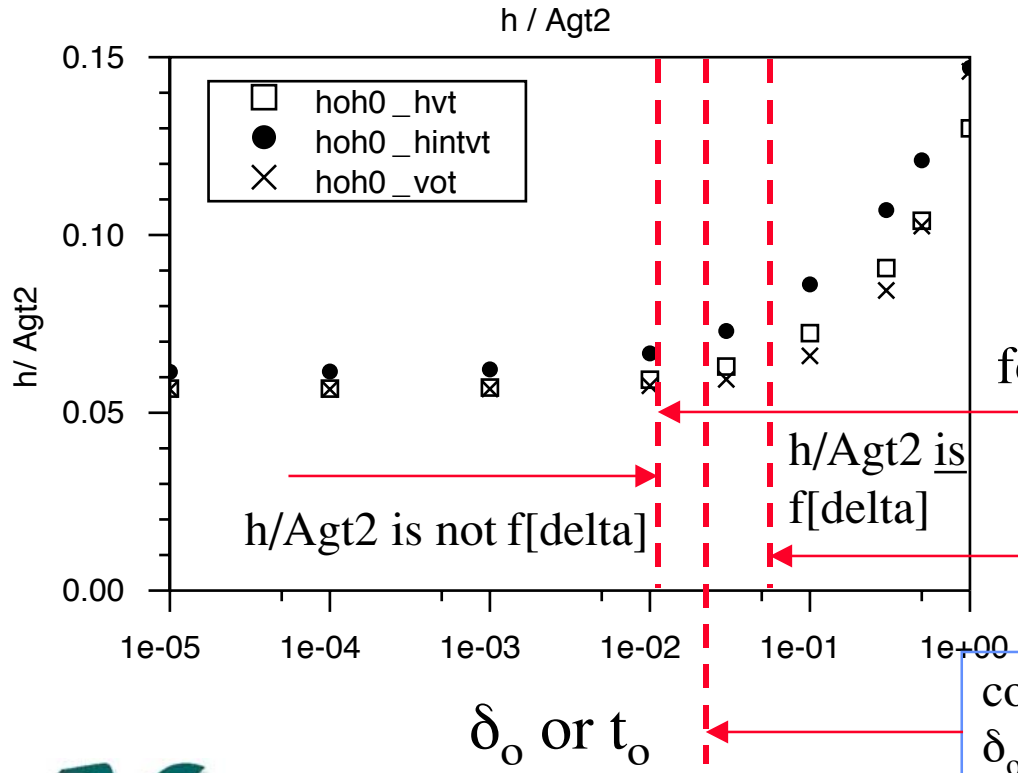

Normalize δ_o to $L = Agt^2$

δ_o ~ variance of Vf(IC)

for comparison to comput. setup

$\delta_o/L=1.e-2/5=0.002$

comput on 128 grid:
δ_o/L~var(Vf-IC)/L~0.7dx/70dx
or $\delta_o/L(128)$~1.e-2

comput on 256 grid:
δ_o/L~var(Vf-IC)/L~0.7dx/140dx
or $\delta_o/L(256)$~0.5e-2

RT spectral density for IC perturbation w/ modes k=30-60: $z_{int}(t=0) \sim Vf$

E.L.Vold

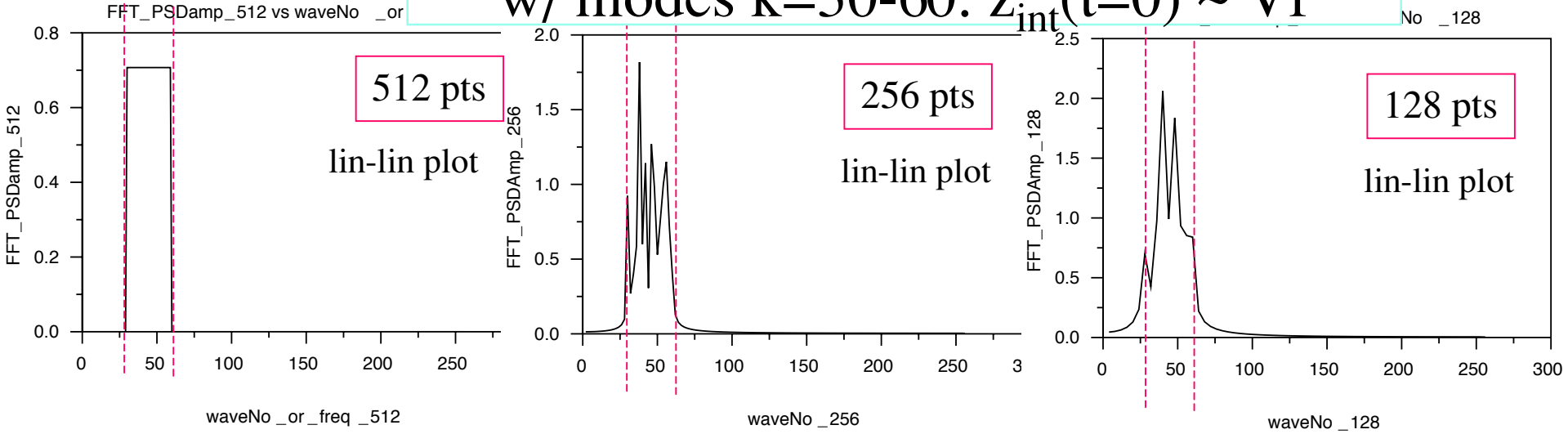

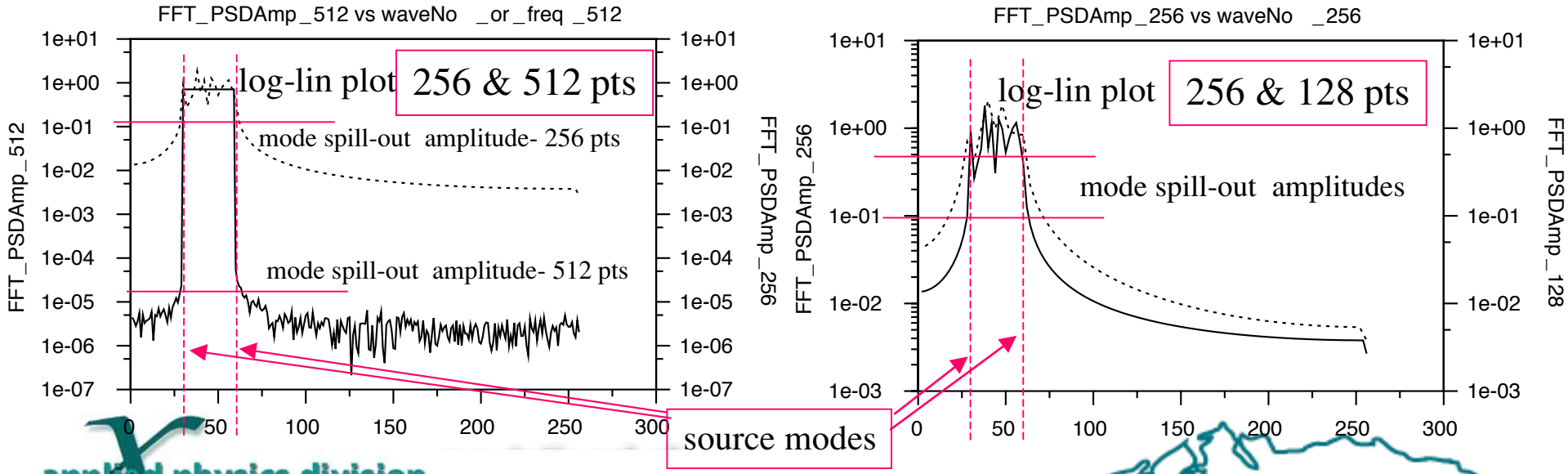

locations for FFTs at t80

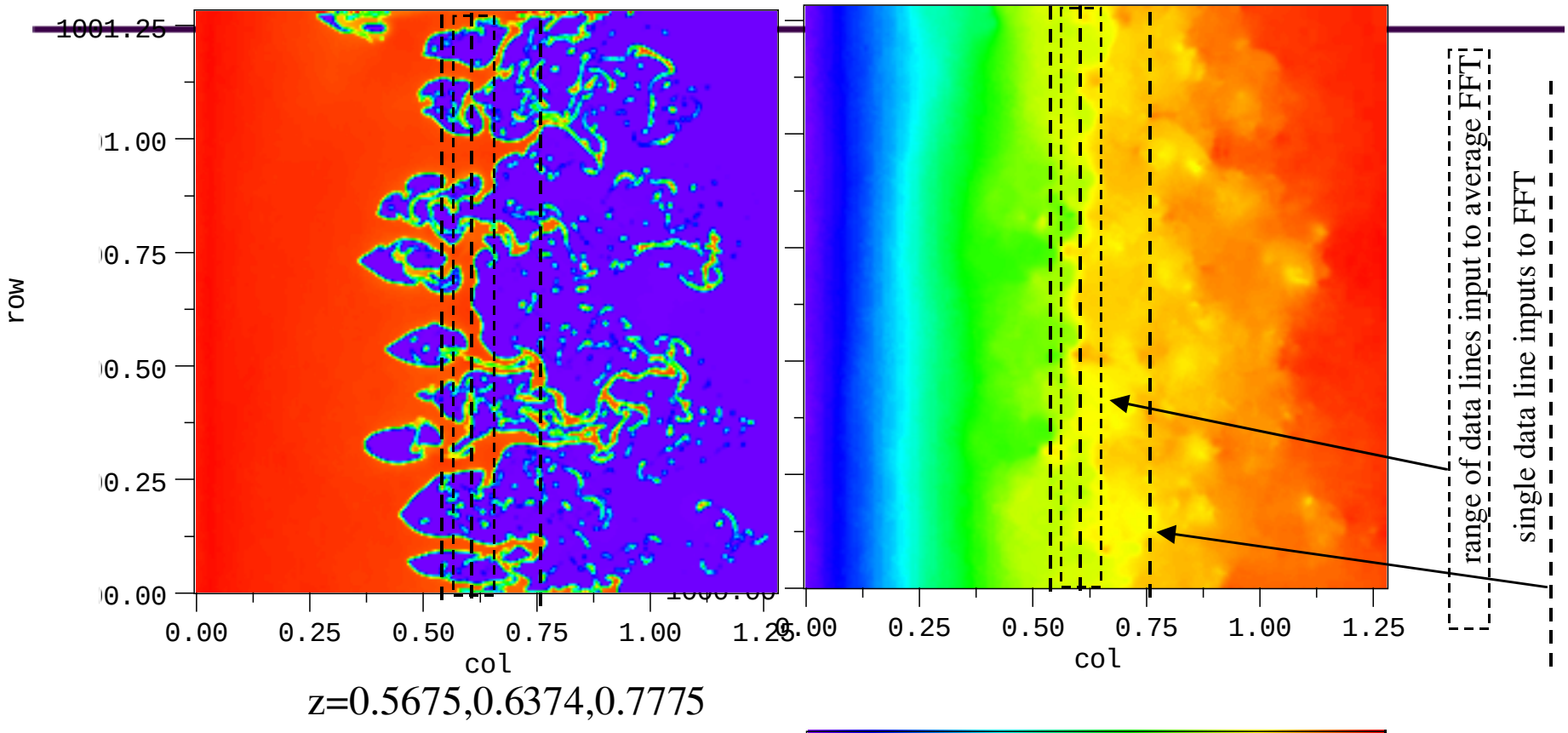

FFTs p-t80 128 & 512

p spectra (left) w/ 10x shift on 512 grid (right) to compare

p-t80 128 & 512

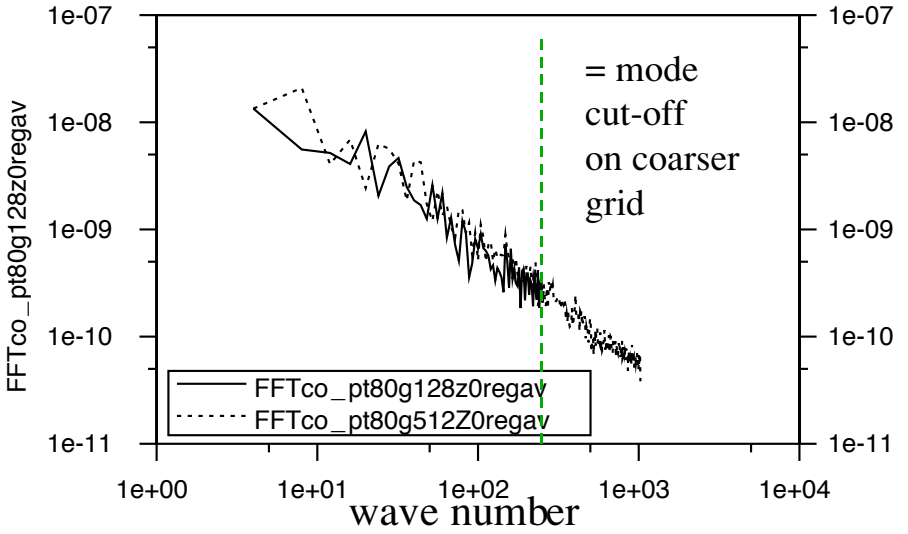

p-t80 128 & 10x p-t80 512

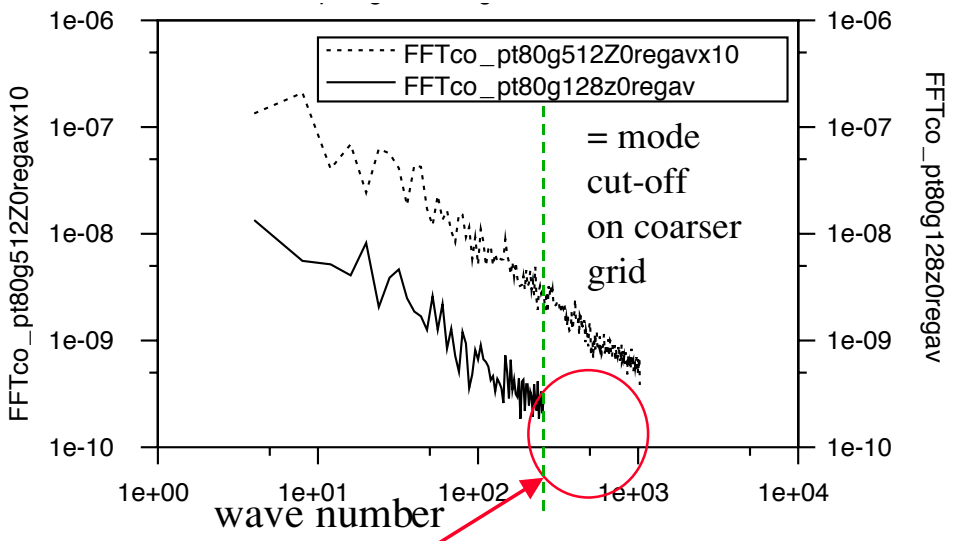

Therefore, unresolved components on 128 grid appear to be irrelevant to small k, long wavelength mode growth**.

** alternative explanation: numerical errors on 128 grid and resolved high mode numbers on 512 grid both have the same effect on the small k, long wavelength mode growth***.

*** alternative alternate: the alternate is true and the effect in either case is ~ 0.

FFTs p-t80, grids compared

128 & 512, 256 & 512, 128 & 256

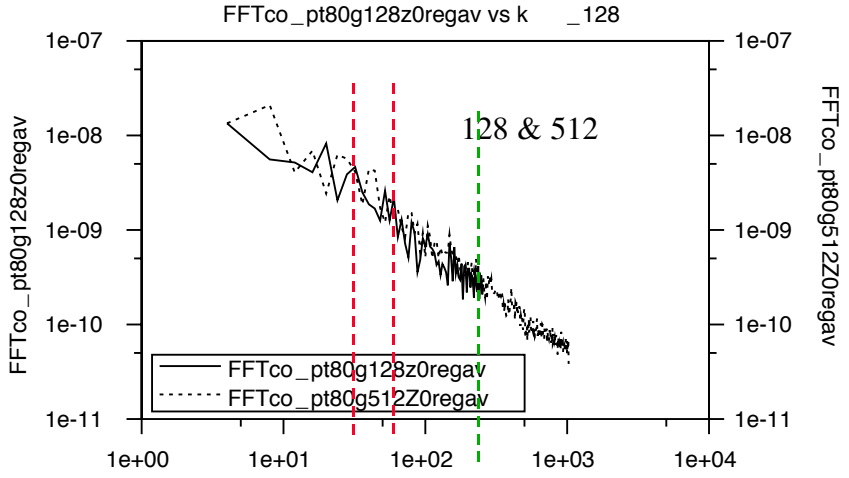

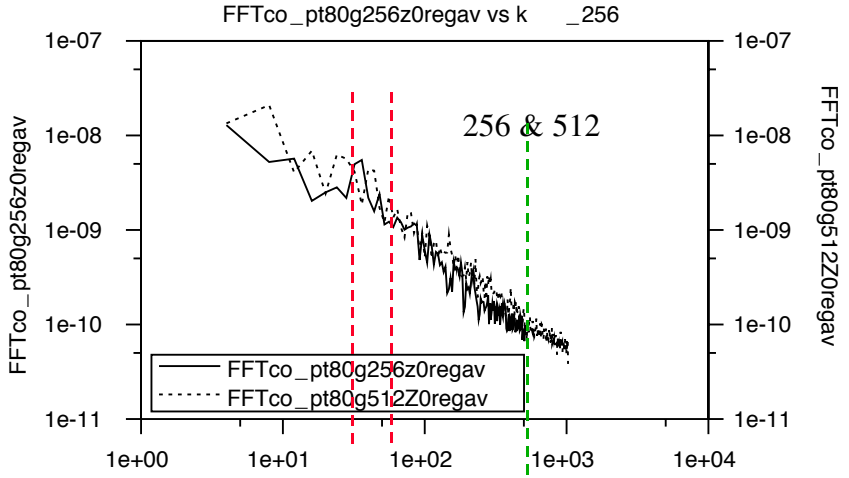

k_128

= mode cut-off on coarser grid

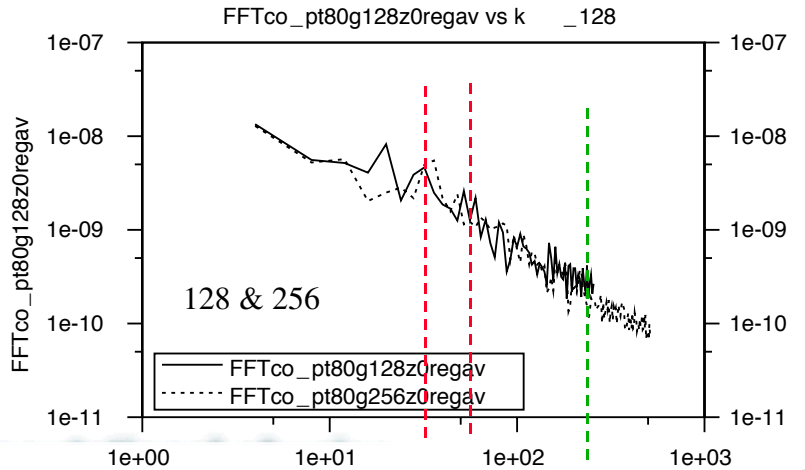

k_256

= range of IC modes

k_128

E.L.Vold

RT mix at late time -varying Atw

At = 0.96
ρ1/ρ2 = 50
t = 60 (z = 2.6)

At = 0.8
ρ1/ρ2 = 9
t = 80 (z = 3.84)

At = 0.33
ρ1/ρ2 = 2
t = 120 (z = 3.6)

At = 0.048
ρ1/ρ2 = 1.1
t = 320 (z = 3.66)

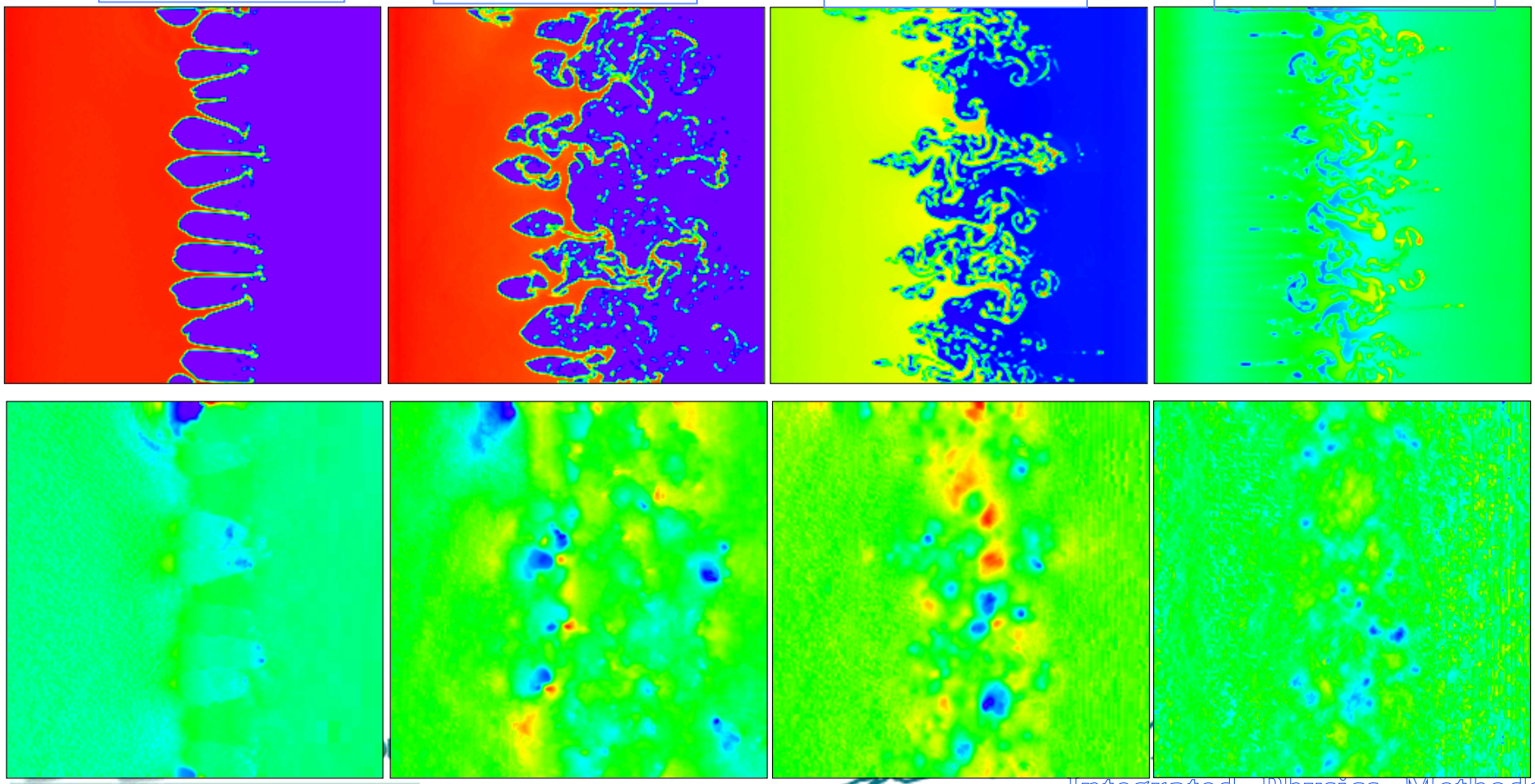

Alpha (RT growth rate)

for varying Atwood number and w/ & w/o Interface Recon.

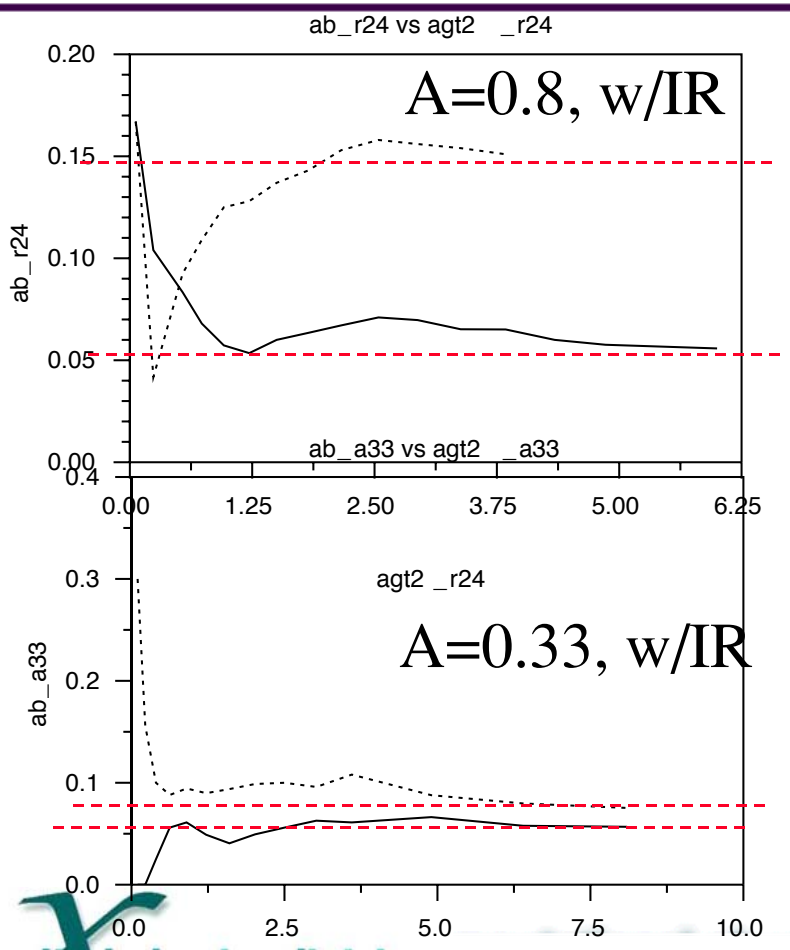

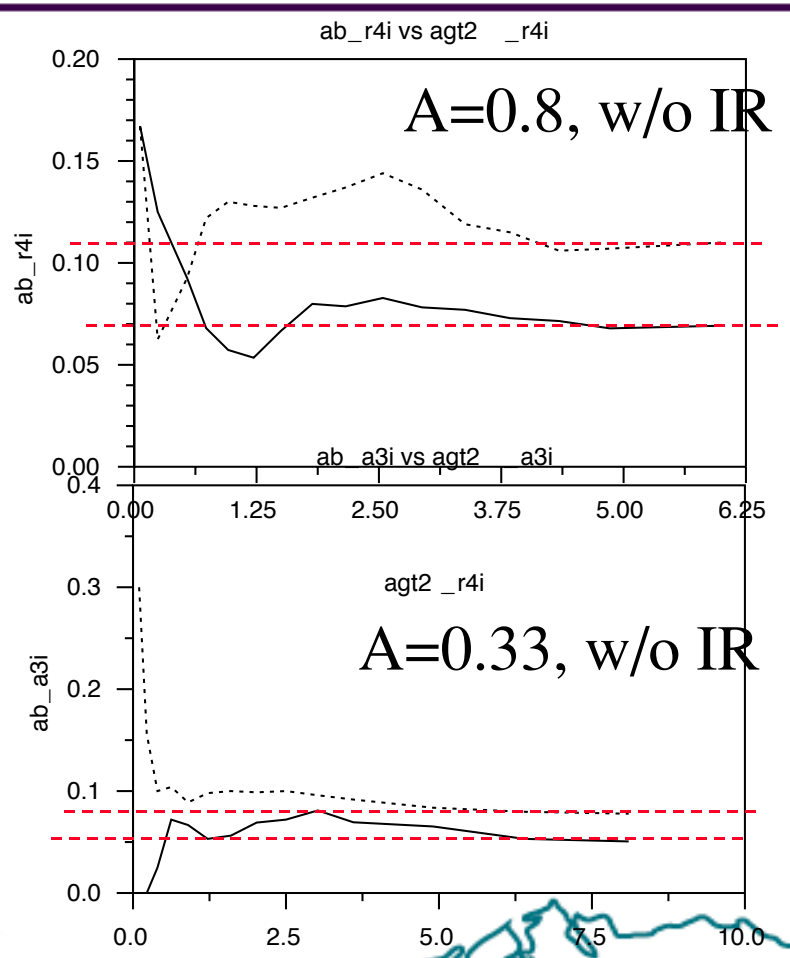

Alpha (RT growth rate)

for varying Atwood number and w/ & w/o Interface Recon.

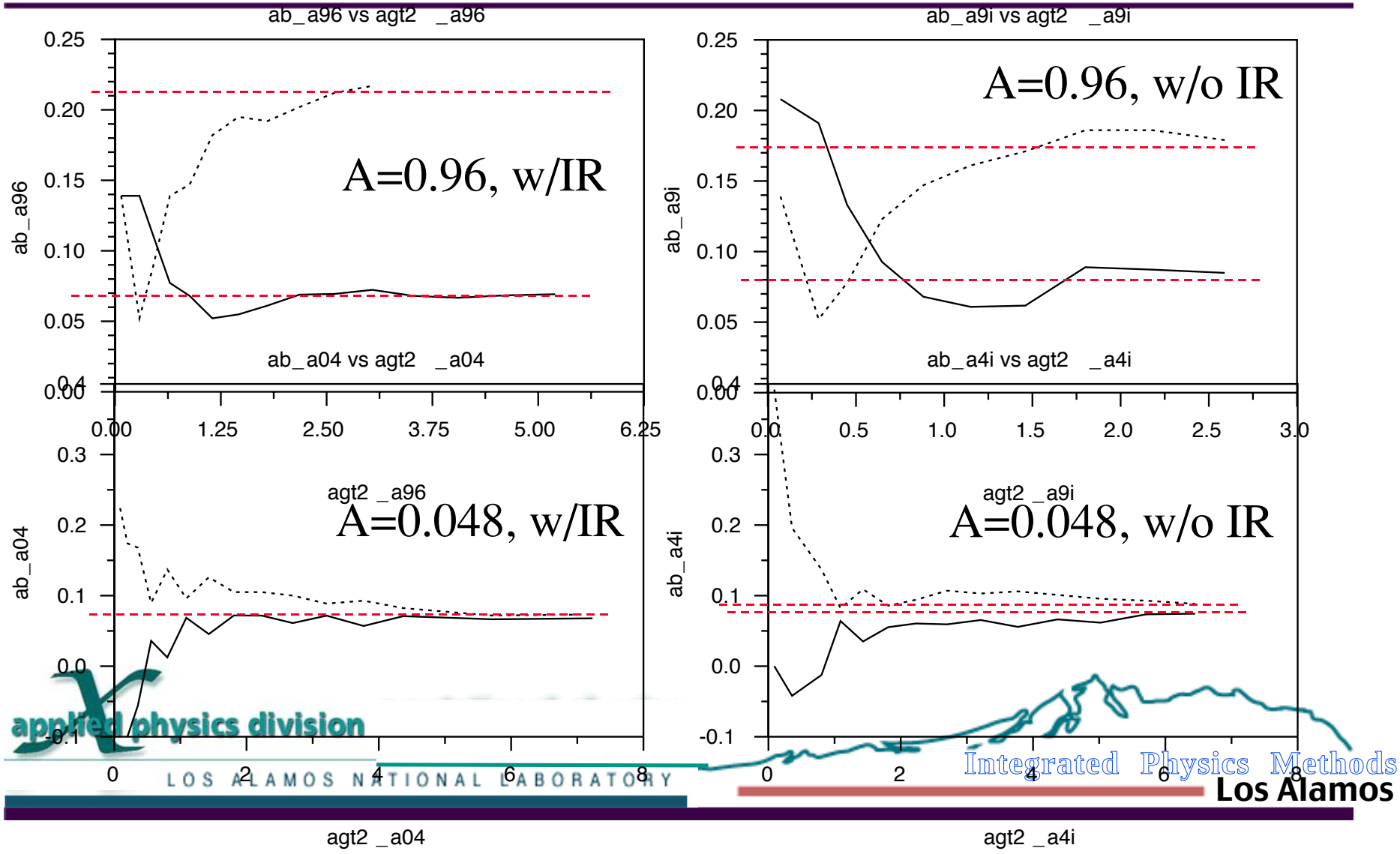

Los Alamos NATIONAL LABORATORY

Conclusions: R-T Mix Layer Growth

- **Results apply to 2-D multi-mode-IC simulations for At=0.8**
- **Grid convergence is good for alpha bubbles - less certain for alpha spikes.**
- **Alpha bubble computed here, ~ 0.05-0.065, agrees with experimental data.**
- **Discrepancy with other computations predicting lower alpha (~0.03)**
  - may be mostly due to treatment of internal energy discontinuity at interface and/or the internal energy in the long wavelength IC which contributes to growth rate through energy fluctuations.
  - a smaller difference (~15%) is expected between 2-D and 3-D.
  - It is shown to be unlikely that discrepancy is related to compressibility, hydrostatic equilibrium form, IC mode amplitudes or IC mode spectra details, or front evaluation methods..
- **Internal energy fluctuations dominate over density fluctuations where (e_o/ρ_o) is sufficiently small in the mix layer -**
  - this occurs in the heavier fluid even in limit as compressibility becomes 'negligible'.
  - e_o is irrelevant in 'ideal' incompressible fluid, so only density fluctuations matter.
- **Transition from early time IC dominated regime to later time self-similar solutions is evident and agrees with analytic results.**
- **The resolved simulations appear to be adequately represented in the multi-fluid model so that we can now proceed to use the multi-fluid drift-flux model to represent the molecular mixing and/or sub-grid scale turbulent mixing within the Rayleigh-Taylor unstable mix layer.**

An Efficient and High Resolution Solver for the Two-Dimensional Numerical Simulation of the Richtmyer-Meshkov Instability

University of Wisconsin - Madison, Fusion Technology Institute

S.P. Wang, M.H. Anderson, J.G. Oakley and R. Bonazza

Key features of the Solver

The solver based on the model developed byWang *et al.* (2001), which uses a thermodynamically consistent fully conservative approach for the treatment of contact discontinuities based upon the concept of Total Enthalpy Conservation of the Mixture (ThCM), is implemented to study the Richtmyer-Meshkov instability. This method utilizes a high resolution Godunov-type scheme based upon a fast exact Riemann solver and the Piece-wise Spline Method (PSM) for data reconstruction of primitive variables at cell interfaces with fourth order accuracy.

ThCM Model

In the two-dimensional simulation of the Richtmyer-Meshkov instability, the hyperbolic conservation laws with the ThCM model are given by:

$$\mathbf{U}_t + \mathbf{F}(\mathbf{U})_x + \mathbf{G}(\mathbf{U})_y = 0$$

where **U** are the conservative variables and **F** and **G** are the conservative fluxes in the *x* and *y* directions respectively.

$$\mathbf{U}=\begin{pmatrix}\rho\\ \rho\phi\\ \rho u\\ \rho v\\ H-p\end{pmatrix};\quad \mathbf{F}=\begin{pmatrix}\rho u\\ \rho u\phi\\ \rho u^2+p\\ \rho uv\\ uH\end{pmatrix};\quad \mathbf{G}=\begin{pmatrix}\rho v\\ \rho v\phi\\ \rho uv\\ \rho v^2+p\\ vH\end{pmatrix}$$

where *H*, the total enthalpy per unit volume, is given by:

$$H = \Gamma p + \frac{1}{2}\rho\left(u^2+v^2\right)$$

In the model, the pressure is calculated following the current value of the conservative variable term (*H-p)* as follows:

$$p = \frac{(H-p) - \frac{1}{2}\rho\left(u^2+v^2\right)}{\Gamma - 1}$$

Where Γ is introduced in the ThCM model to simplify the expression of the governing equations and is defined as:

$$\Gamma = \frac{\gamma}{\gamma - 1} = \phi_1\Gamma_1 + \phi_2\Gamma_2$$

A splitting scheme is employed for the system in two spatial dimensions defined as follows:

$$(A)\quad for\quad x-sweep:\qquad \begin{pmatrix}\rho\\ \rho u\\ \rho\phi\\ H-p\\ \rho v\end{pmatrix}_t + \begin{pmatrix}\rho u\\ \rho u^2+p\\ \rho u\phi\\ uH\\ \rho uv\end{pmatrix}_x = 0;$$

$$(B)\quad for\quad y-sweep:\qquad \begin{pmatrix}\rho\\ \rho v\\ \rho\phi\\ H-p\\ \rho u\end{pmatrix}_t + \begin{pmatrix}\rho v\\ \rho v^2+p\\ \rho v\phi\\ vH\\ \rho uv\end{pmatrix}_y = 0.$$

The tangential velocity component, *v(u)* in the *x*-sweep(*y*-sweep), is passively advected with the normal velocity component, *u(v)*. A two-step process shown is used to accomplish the integration from time *n* to *n*+1 using a Godunov scheme:

$$\mathbf{U}_{i,j}^{n+1/2} = \mathbf{U}_{i,j}^{n} + \frac{\Delta t}{\Delta x}\left(\mathbf{F}_{i-1/2,j}^{n} - \mathbf{F}_{i+1/2,j}^{n}\right); \quad \forall j \quad (a)$$

$$\mathbf{U}_{i,j}^{n+1} = \mathbf{U}_{i,j}^{n+1/2} + \frac{\Delta t}{\Delta y}\left(\mathbf{G}_{i,j-1/2}^{n+1/2} - \mathbf{G}_{i,j+1/2}^{n+1/2}\right); \quad \forall i. \quad (b)$$

The PSM and following slope limiters, similar to those developed by Ren *et al. (1996),* are used for the data reconstruction of the conservative variables for the local Riemann problem solutions at cell interfaces.

$$\mathbf{U}_i^L = \mathbf{U}_i^n - \frac{\Delta x_i}{2}\mathbf{m}_i + \frac{(\Delta x_i)^2}{8}\mathbf{M}_i - \frac{(\Delta x_i)^3}{48}\mathbf{M}_i^{(3)} \quad (a)$$

$$\mathbf{U}_i^R = \mathbf{U}_i^n + \frac{\Delta x_i}{2}\mathbf{m}_i + \frac{(\Delta x_i)^2}{8}\mathbf{M}_i + \frac{(\Delta x_i)^3}{48}\mathbf{M}_i^{(3)} \quad (b)$$

$$\mathbf{U}_i^L = \mathbf{U}_i^n - \frac{1}{2}\mathrm{minmod}(\mathbf{m}_{i-1},\mathbf{m}_i,\mathbf{m}_{i+1})\Delta x_i + \frac{1}{8}\mathrm{minmod}(\mathbf{M}_{i-1},\mathbf{M}_i,\mathbf{M}_{i+1})(\Delta x_i)^2 - \frac{1}{48}\mathrm{minmod}(\mathbf{M}_{i-1}^{(3)},\mathbf{M}_i^{(3)},\mathbf{M}_{i+1}^{(3)})(\Delta x_i)^3$$

$$\mathbf{U}_i^R = \mathbf{U}_i^n + \frac{1}{2}\mathrm{minmod}(\mathbf{m}_{i-1},\mathbf{m}_i,\mathbf{m}_{i+1})\Delta x_i + \frac{1}{8}\mathrm{minmod}(\mathbf{M}_{i-1},\mathbf{M}_i,\mathbf{M}_{i+1})(\Delta x_i)^2 + \frac{1}{48}\mathrm{minmod}(\mathbf{M}_{i-1}^{(3)},\mathbf{M}_i^{(3)},\mathbf{M}_{i+1}^{(3)})(\Delta x_i)^3$$

and

$$\mathrm{minmod}(g_{i-1},g_i,g_{i+1}) = \begin{cases}\min\left(|g_{i-1}|,|g_i|,|g_{i+1}|\right)sign(g_i) & if\ \min(g_{i-1},g_i,g_{i+1})\cdot\max(g_{i-1},g_i,g_{i+1})>0\\ 0 & else\end{cases}$$

Simulations of the Wisconsin RM Shock Tube Experiments

Total Length	9.2 m
Driven Length	6.8 m
Inner square cross section	0.25 m
Maximum Driver Pressure	100 atm

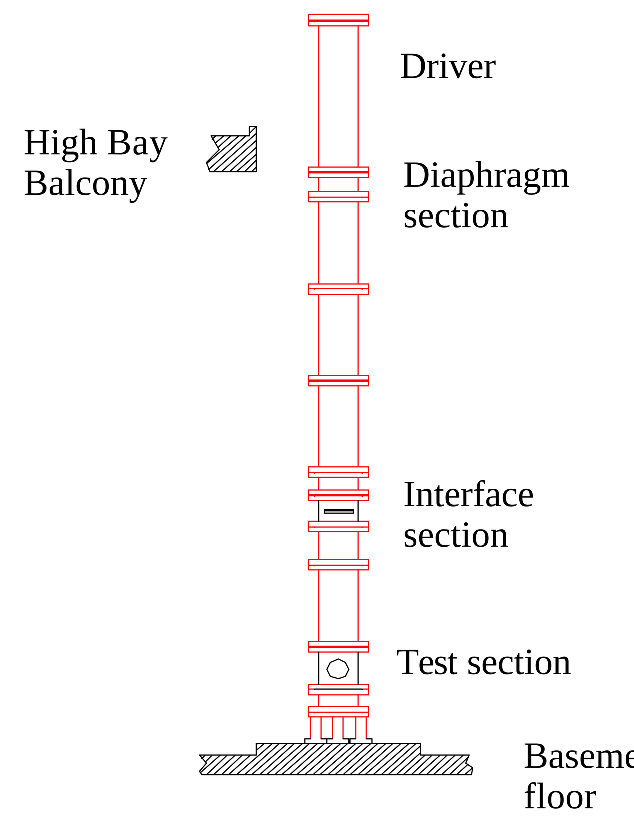

A series of two Richtmyer-Meshkov instability experiments were conducted in the University of Wisconsin's shock tube and have been simulated with the numerical model. In these experiments, the distance from the interface to the center of the test section was 0.457 m and an initial condition was created by the retraction of a sinusoidal copper plate which resulted in a Rayleigh-Taylor instability. The RT formed initial condition just prior (< 10 ms) before the shock interaction was recorded, and a sine series representation of the initial condition was used as the input initial condition for the simulation. The parameters of each of the experiments and the details of the calculations are presented below.

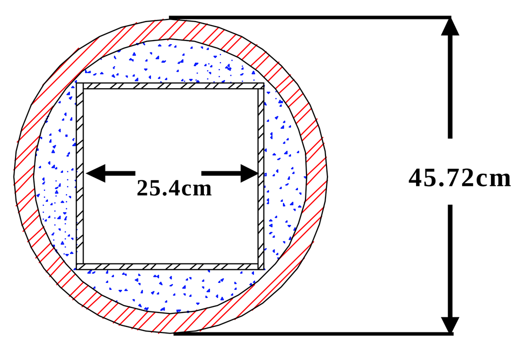

Driven cross section of shock tube

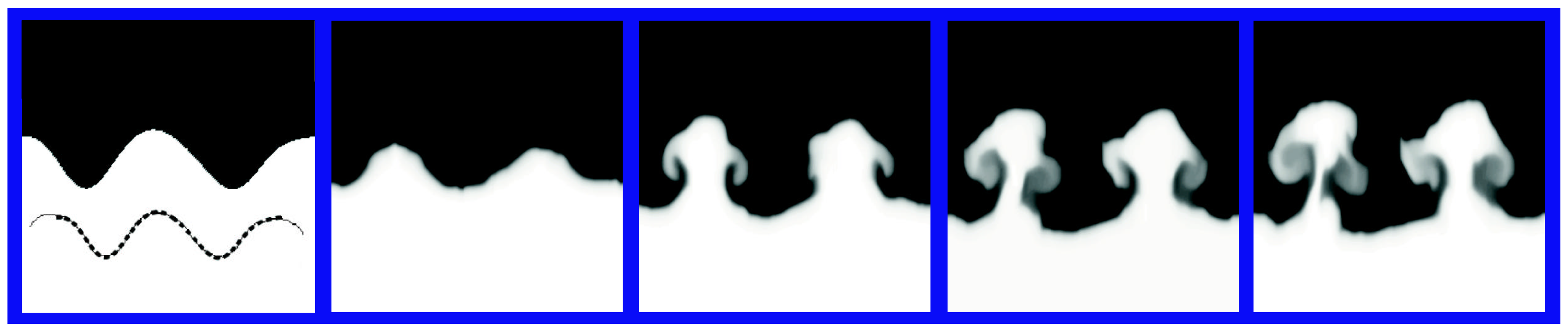

t=0 ms *t*=0.17 ms *t*=0.47 ms *t*=0.72 ms *t*=0.87 ms

Test 319	Shocked Ar	Unshocked Ar	Unshocked Air
Density (x 10^{-4} g/cm^3)	46.83	16.22	11.38
Pressure (bar)	9.68302	1	1
Mass velocity (km/sec)	0.5908	0	0
γ	1.667	1.667	1.4

Numerical Domain 2480x200 cells with a spatial resolution of 0.381mm CPU time ~24 h on a 1.13 GHz Pentium 4

The growth rate from the simulation at the time of the experiment is 9.4 m/s.

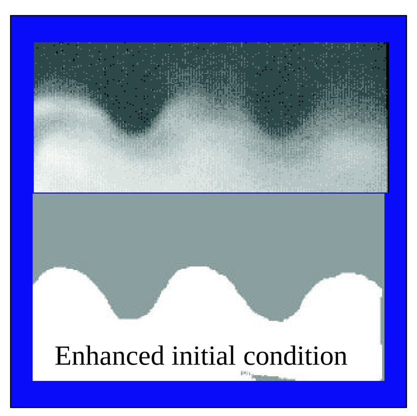

Enhanced initial condition

Initial condition

$$\eta_{IC}(x) = \sum_{i=1}^{5} a_i \sin\left(\frac{i\pi}{W}x + \phi_i\right)$$

Coefficients of sine series	Expt.319 Ar/N_2 M=2.80
a_1 (mm)	0.811
a_2 (mm)	7.13
a_3 (mm)	0.736
a_4 (mm)	0.996
a_5 (mm)	0.198
ϕ_1	6.04
ϕ_2	1.98
ϕ_3	0.0359
ϕ_4	5.45
ϕ_5	5.64

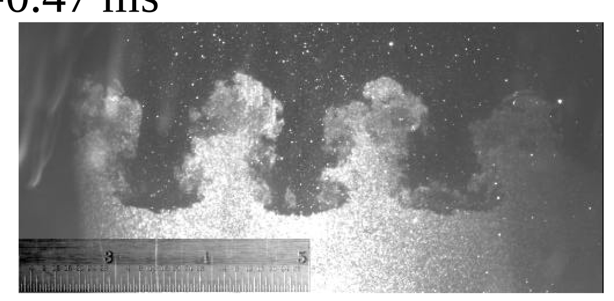

Experimental image at t=0.70 ms after shock interaction. Measured amplitude η=17.52 mm

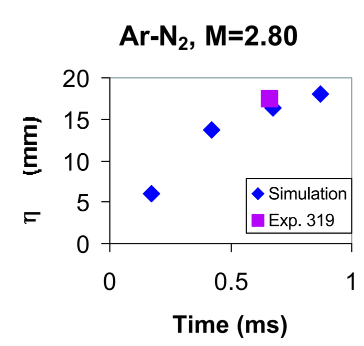

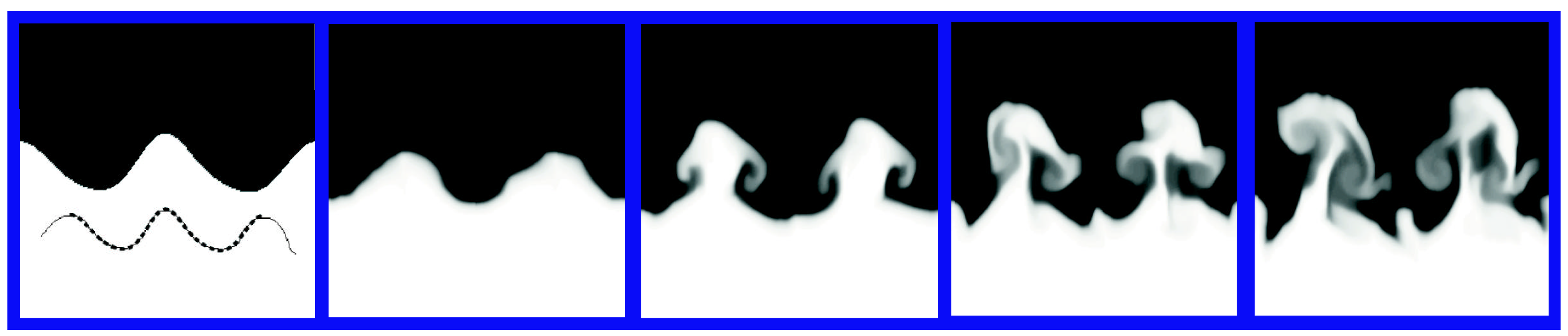

t=0 ms *t*=0.17 ms *t*=0.42 ms *t*=0.67 ms *t*=0.87 ms

Test 333	Shocked CO_2	Unshocked CO_2	Unshocked Air
Density (x 10^{-4} g/cm^3)	80.87	17.88	11.77
Pressure (bar)	10.72	1	1
Mass velocity (km/sec)	0.6504	0	0
γ	1.297	1.297	1.402

Numerical Domain 2480x200 cells with a spatial resolution of 0.381mm CPU time ~24 h on a 1.13 GHz Pentium 4

The growth rate from the simulation at the time of the experiment is 16.6 m/s.

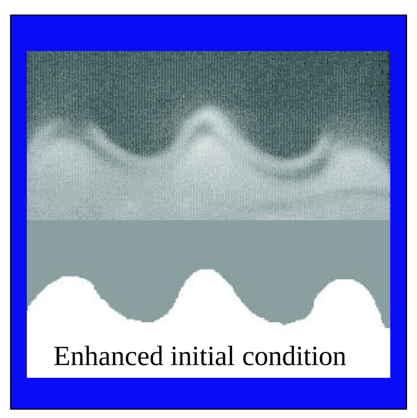

Enhanced initial condition

Initial condition

$$\eta_{IC}(x) = \sum_{i=1}^{5} a_i \sin\left(\frac{i\pi}{W}x + \phi_i\right)$$

Coefficients of sine series	Expt.333 CO_2/Air M=3.08
a_1 (mm)	0.747
a_2 (mm)	6.80
a_3 (mm)	0.365
a_4 (mm)	0.916
a_5 (mm)	0.118
ϕ_1	5.28
ϕ_2	1.50
ϕ_3	5.41
ϕ_4	2.03
ϕ_5	5.30

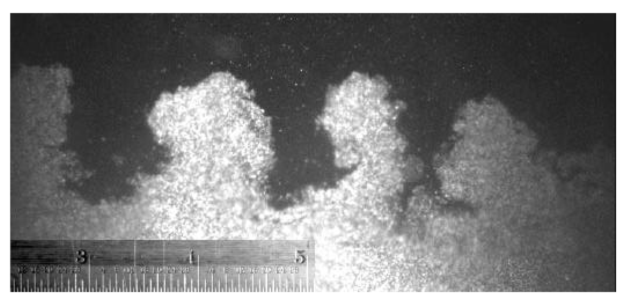

Experimental image at t=0.66 ms after shock interaction. Measured amplitude η=15.29 mm

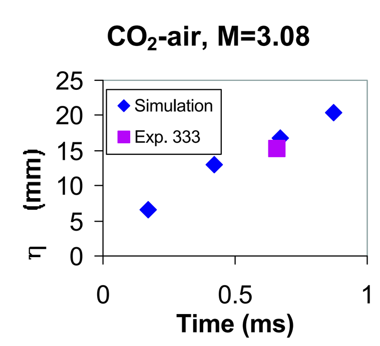

Simulation of Test Problem #1

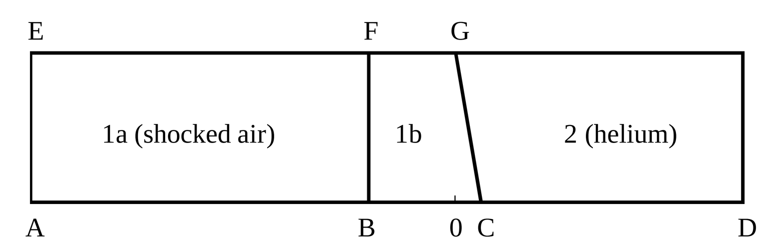

Boundary condition

Inflow condition of air with parameters behind shock is set on the left boundary and other boundaries are rigid walls.

Mesh

The mesh is square for x>-2cm. Zone size of 0.2 cm and 60 zones per region width.

AB=38cm, BC=3.2cm, 0D=20cm, AE=12cm, FG=0.8cm. Initially the average position of the interface is x=0 (point 0). Regions 1a,b contain Air (1a - shocked air, 1b - unshocked air), region 2 contain He. The incident shock moves from left to right, i.e. From Air to He. The full width of the tube is 12 cm and the full perturbation amplitude is 2.4 cm.

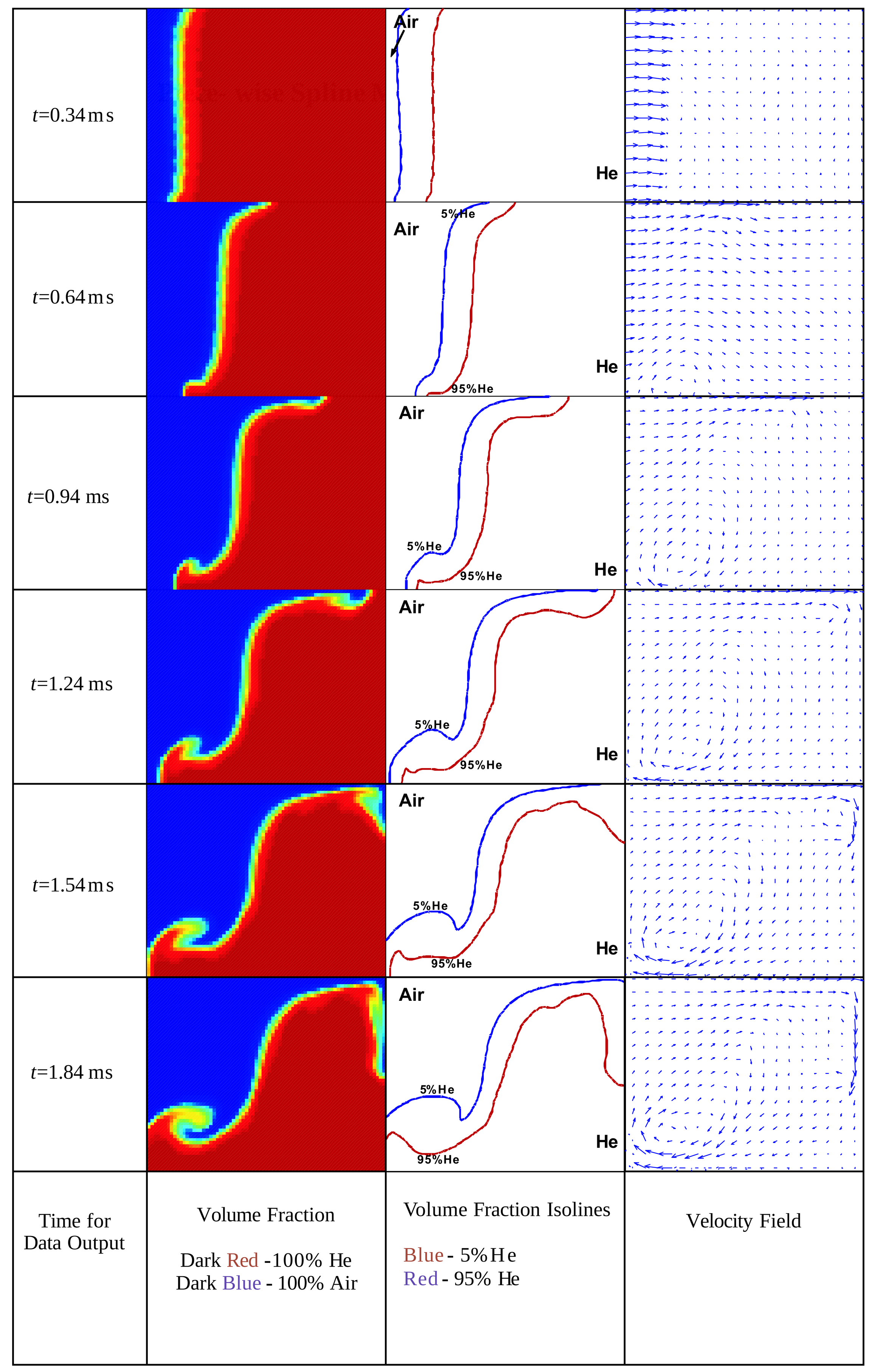

Initial conditions

	Shocked Air	Unshocked Air	Unshocked He
Density (x 10^{-4} g/cm^3)	18.2641	12.05	1.67
Pressure (bar)	1.804997	1	1
Mass velocity (km/sec)	0.15076	0	0
γ	1.4	1.4	1.63

Results

The left most series of images shows the volume fractions of the two gas species as a function of time. The center set of images are 5% and 95% volume fraction isolines. The third column shows the local velocity vectors

.

The graph below shows the total mass of each material in the mixing zone (from 5% to 95% of the volume fraction). The points on the graph correspond to the times in the images on the left.

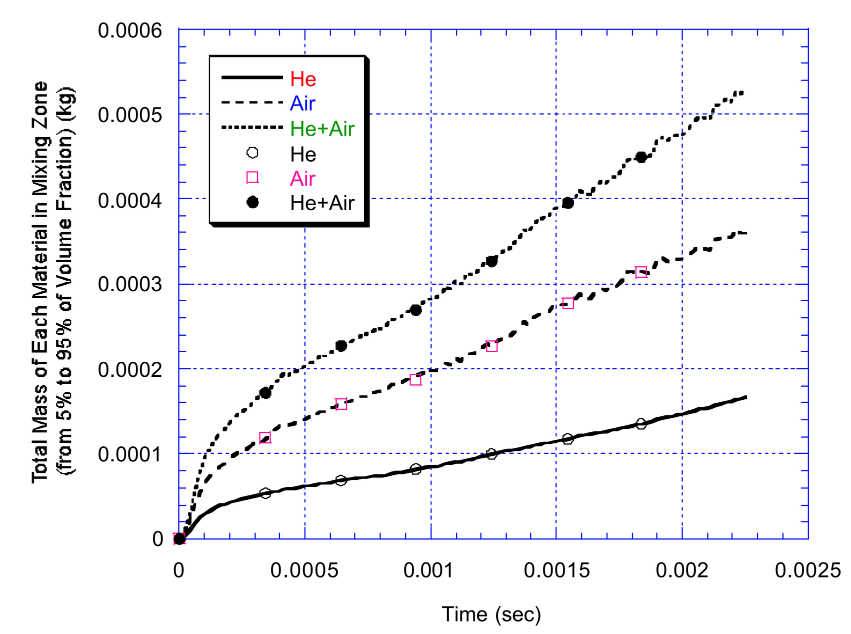

Wang, S.P., Anderson, M.H., Oakley, J.G., Corradini, M.L., Bonazza, R., A thermodynamically consistent and fully conservative treatment of contact discontinuities for compressible multicomponent flows submitted to *J. Comput. Phys.* (2001)

Ren, Y.X., Liu, Q.S.,Wang, S. P., Shen, M. Y., A high order accurate, non-oscillating finite volume scheme using spline interpolation for hyperbolic conservation laws, *ActaAerodynamica Sinica* **14**, 281 (1996)

UCRL-PRES-143896

ALE Simulations of Turbulent Rayleigh-Taylor Instability in 2-D and 3-D

S. V. Weber, G. Dimonte, and M. M. Marinak
Lawrence Livermore National Laboratory

2001 International Workshop on the Physics
of Compressible Turbulent Mixing
Pasadena, CA
December 10-14, 2001

We have simulated the "α - group" turbulent Rayleigh-Taylor problem in 2-D and 3-D with the ALE code, Hydra

- Weakly compressible RT with a random initial surface spectrum restricted to short wavelength modes (4-8 zones/λ)
- Hydra is a 3-D parallel ALE code with interface reconstruction
- Zoning convergence is suspect
  - Simulated linear growth rates for the seed modes are as low as 15% of the correct classical value
  - In 3-D, modes with *k* aligned with the mesh grow faster than others
- We use a initial surface comprised of cosine modes to avoid aliasing due to reflection span-wise boundary conditions
- 2-D simulations show weak dependence on zoning up to 1024$\times$2048
- 3-D simulations with interface reconstruction predict α_b ~ 0.03-0.055, α_s ~ 0.06
- Simulations without interface reconstruction show only slightly lower penetration but much more small-scale mixing

Initial configuration & adiabatic equilibrium

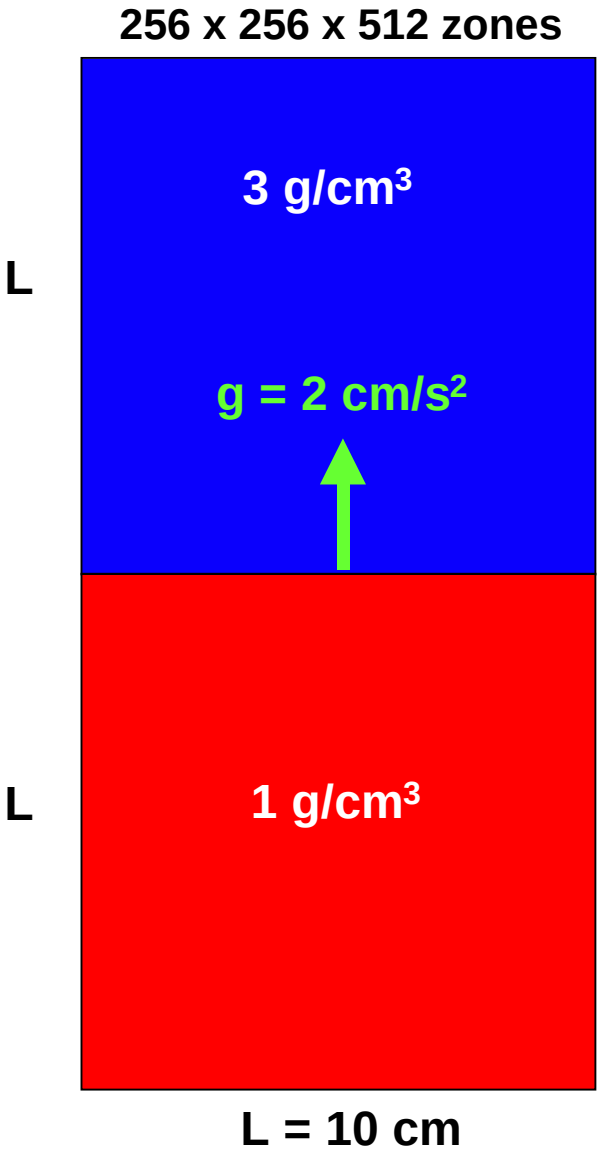

$$\frac{dP}{dz} = -\rho g$$

$$P = P_o\left(\frac{\rho}{\rho_o}\right)^{\gamma}$$

$$\rho = \rho_o\left(1 - \frac{\gamma - 1}{\gamma}\frac{\rho_o g z}{P_o}\right)^{\frac{1}{\gamma - 1}}$$

$\gamma = 5/3$, $P_o = 500$ dyne/cm²

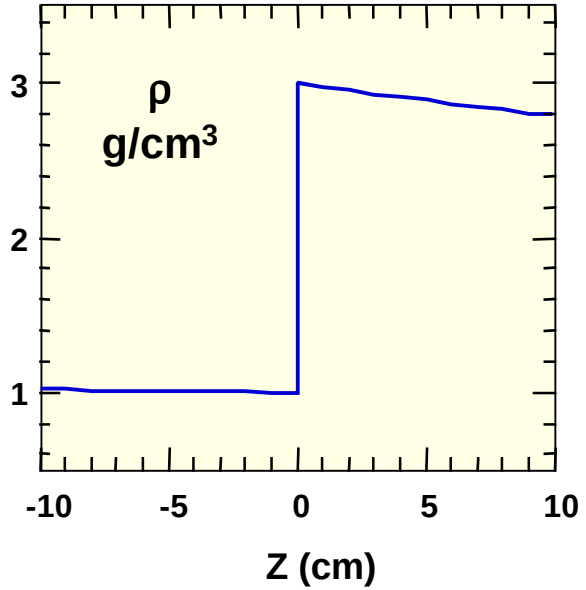

Initial conditions (David Youngs) are random & distributed in wavenumber shell (modes 32-64) close to Nyquist limit

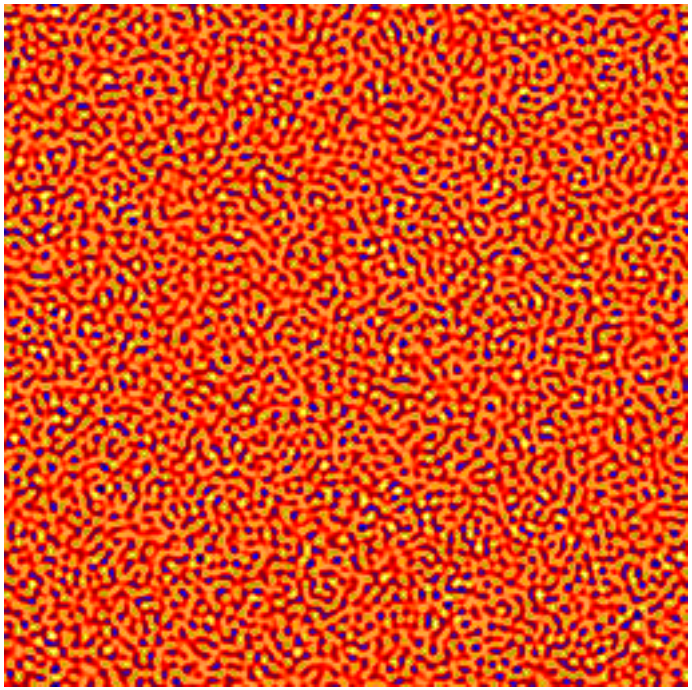

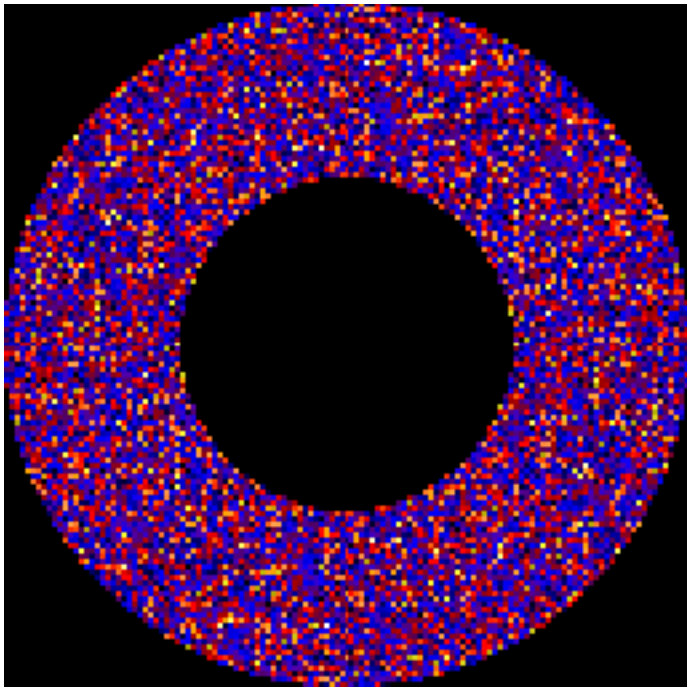

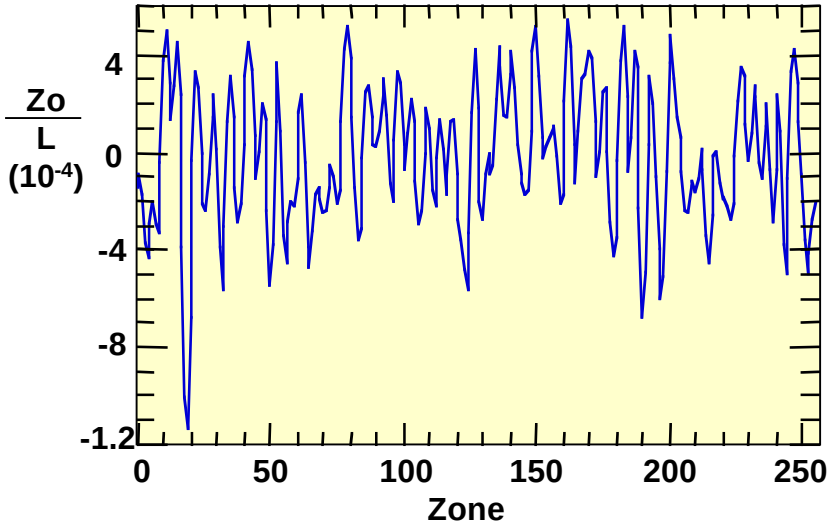

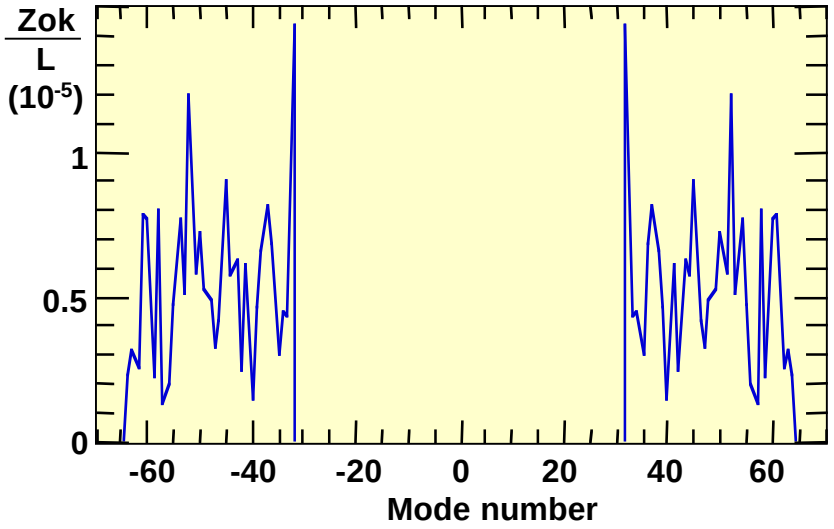

Simulated linear growth rates of seed modes are far below classical due to under-resolution

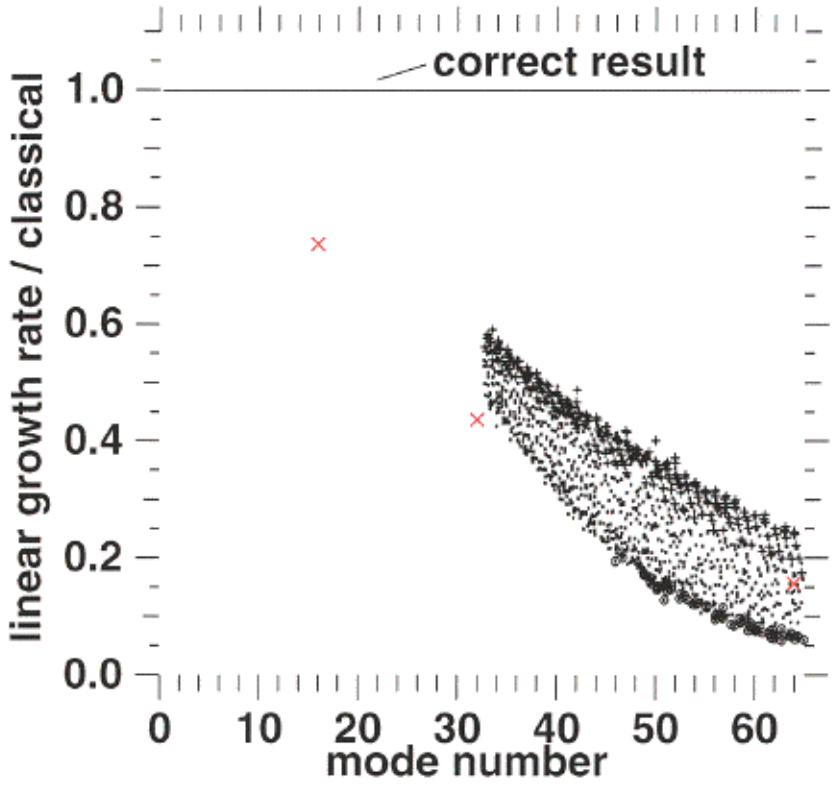

× 2-D, single mode simulation
+ 3-D, *k* along mesh direction
◦ 3-D, *k* diagonal to mesh
· 3-D, all *k*

- If the simulation were converged, all modes would grow at the classical rate
- Also note that the simulated growth rate depends upon the orientation of the wave vector, *k*, to the mesh

In 2-D, the mix *extent* at late times does not change much with zoning refinement

2-D 256×512 (1x)

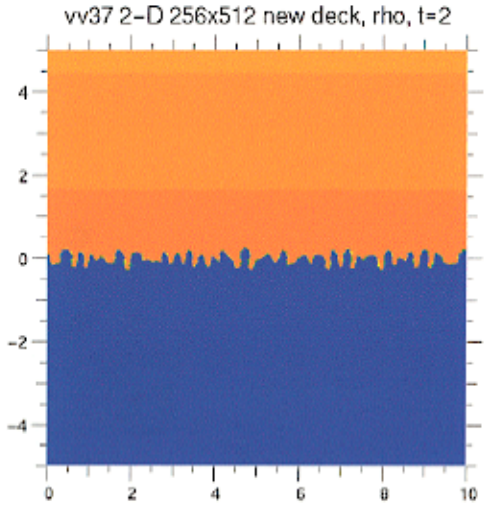

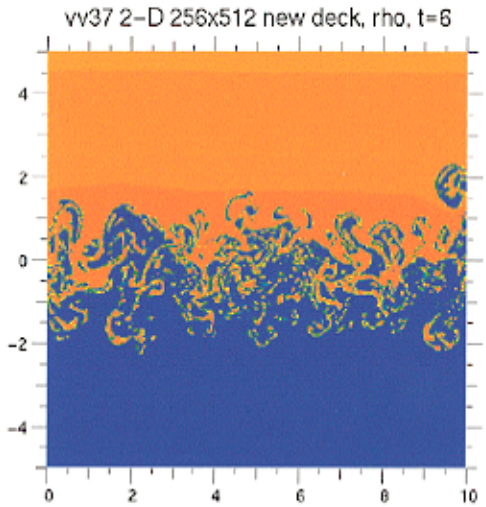

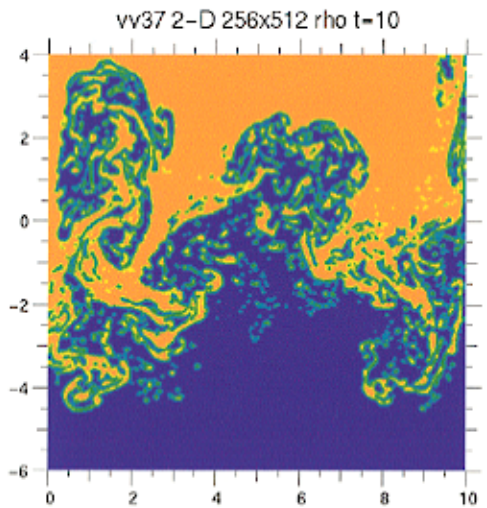

2-D 1024×2048 (4x)

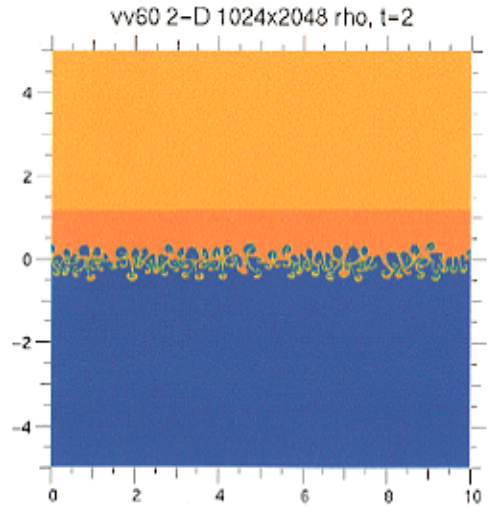

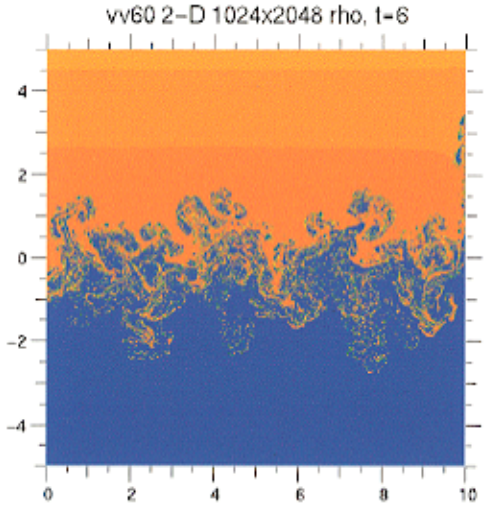

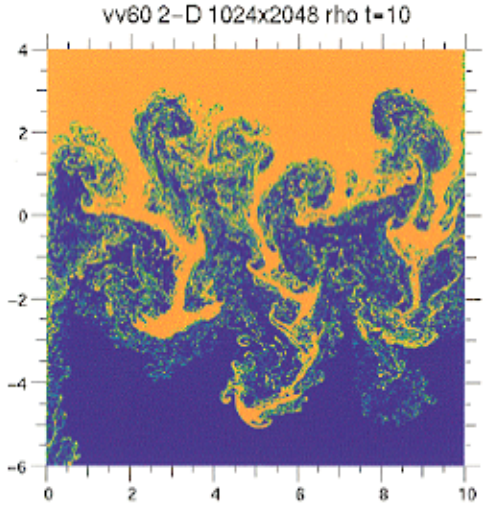

- **The seed modes are clearly under-resolved with nominal zoning**

Zoning refinement beyond the nominal resolution does not significantly affect the mix extent in 2-D runs

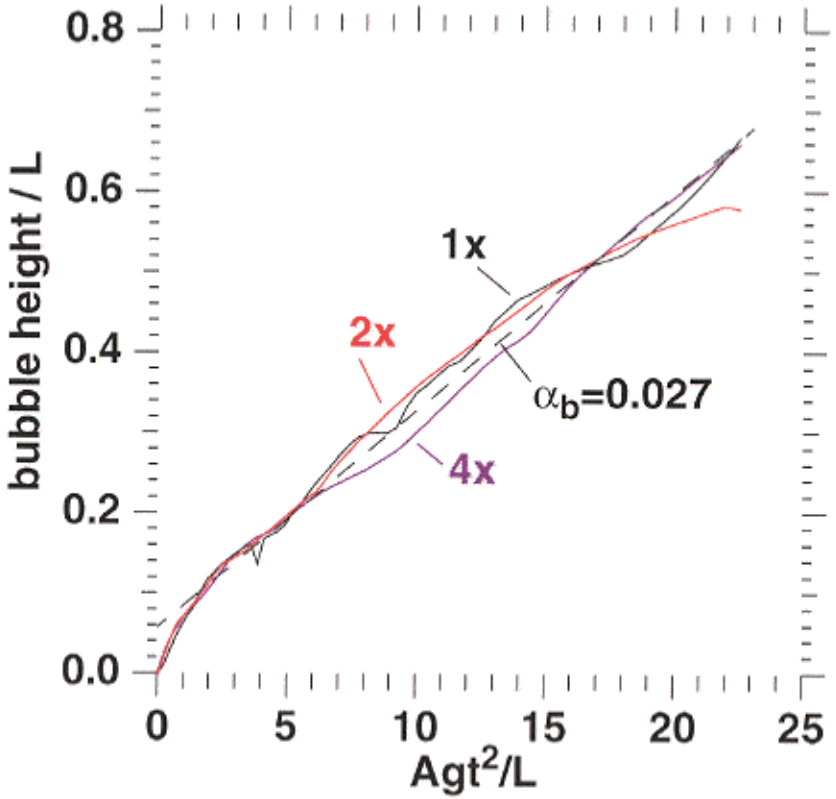

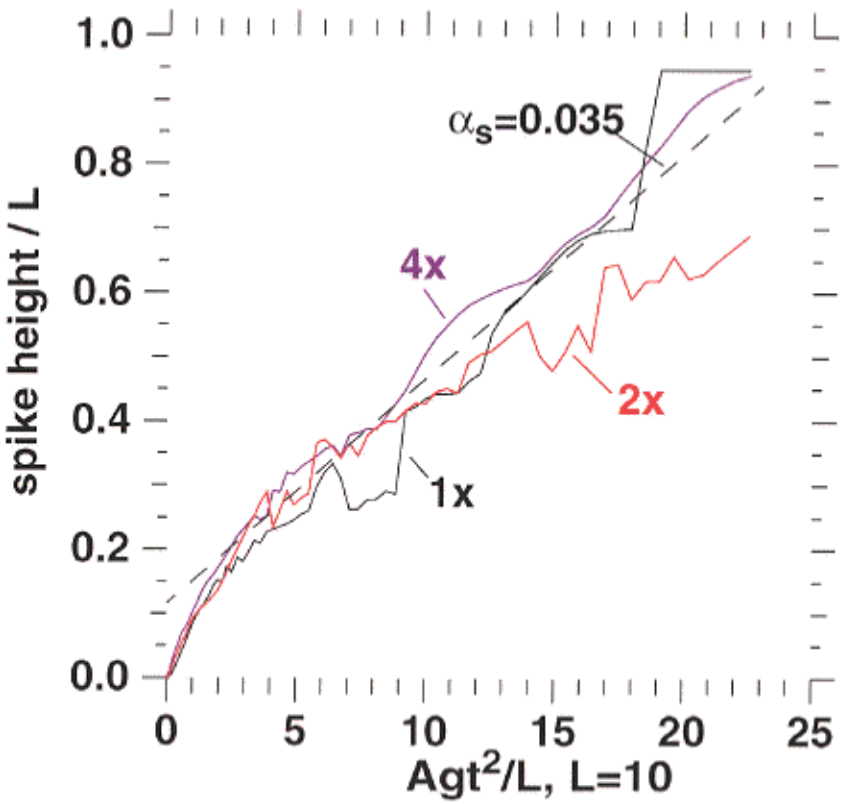

- 1x - nominal 256×512, 2x - 512×1024, 4x - 1024×2048
- Bubble and spike limits are taken at 1% volume fraction within $2 < x < 8$
- The small number of large bubbles or spikes at later times introduces uncertainty due to selection statistics

We have performed $128^2 \times 512$ 3-D simulations in one quadrant of the nominal α problem

- We use 1/4 of the specified initial interface, a 5x5 cm square
- The zone size, initial amplitude, initial wavelengths, and g are preserved from the nominal problem (not scaled by L)
- This preserves three of the four dimensionless length ratios of the problem
  - λ_0/l
  - a_0/l
  - $P/(\rho g \lambda_0)$
  - L/l not preserved
  - l - zone size, a_0 - initial amplitude, L - box size
- Results are expected to be nearly the same as for the full problem until the mix extent becomes comparable to the box width
  - This will occur earlier in time by a factor ~$2^{1/2}$ than for the full problem
- We have recently completed the full size $256^2 \times 512$ problem without interface reconstruction

Under-resolution of the initial perturbations results in mesh imprinting - a numerical artifact

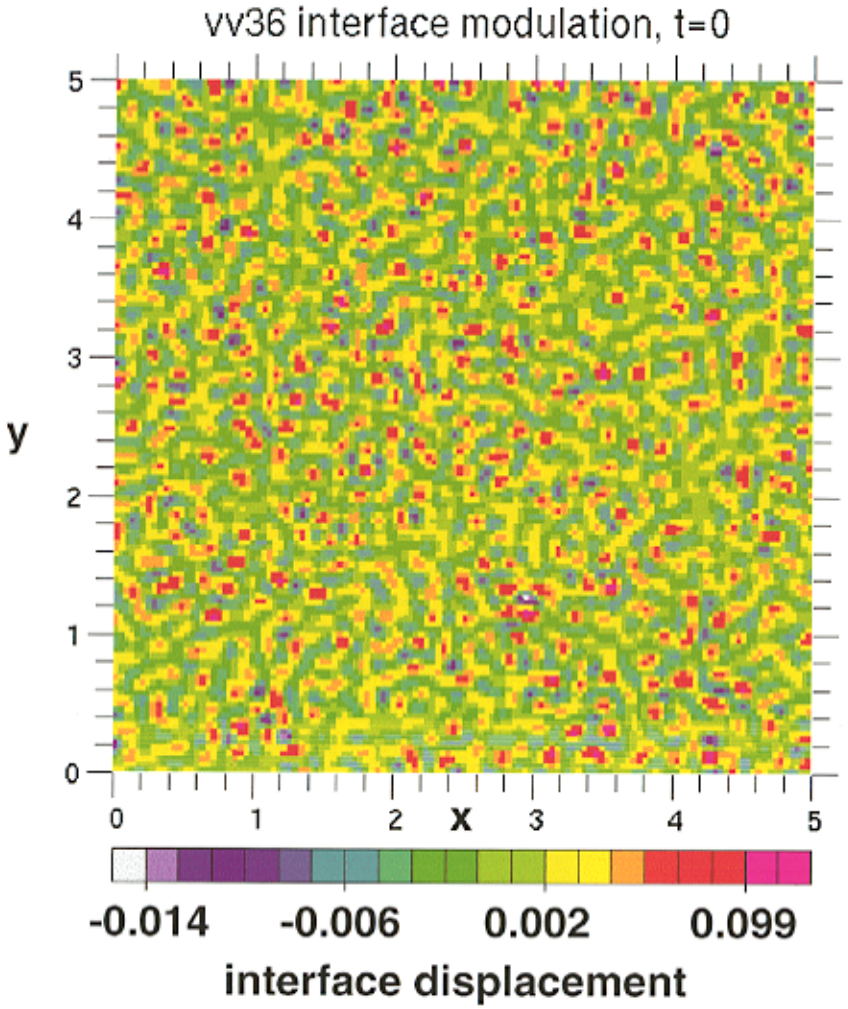

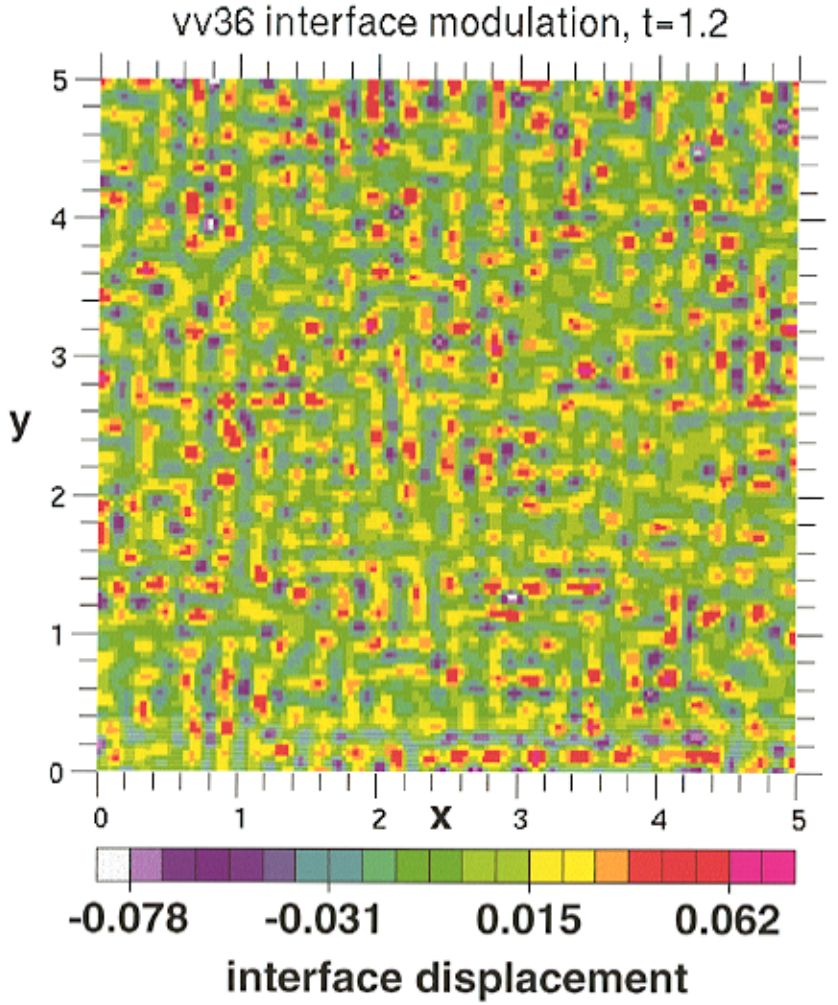

- The random isotropic initial surface evolves into a "checker board" pattern because of more rapid linear growth of modes aligned with the mesh

The surface finish definition including sine and cosine modes should not be used with reflection boundary conditions

- Reflection boundary conditions support a spectrum consisting of integer and half-integer cosine modes
- Sine modes in the original surface definition are aliased into half-integer cosine modes. A "sine" mode with reflection bc has a cusp ot the boundary resulting in excessive growth near the boundary even in the linear phase
- Therefore, we used a surface finish obtained from Youngs containing only cosine modes, but which looks very similar to the original surface

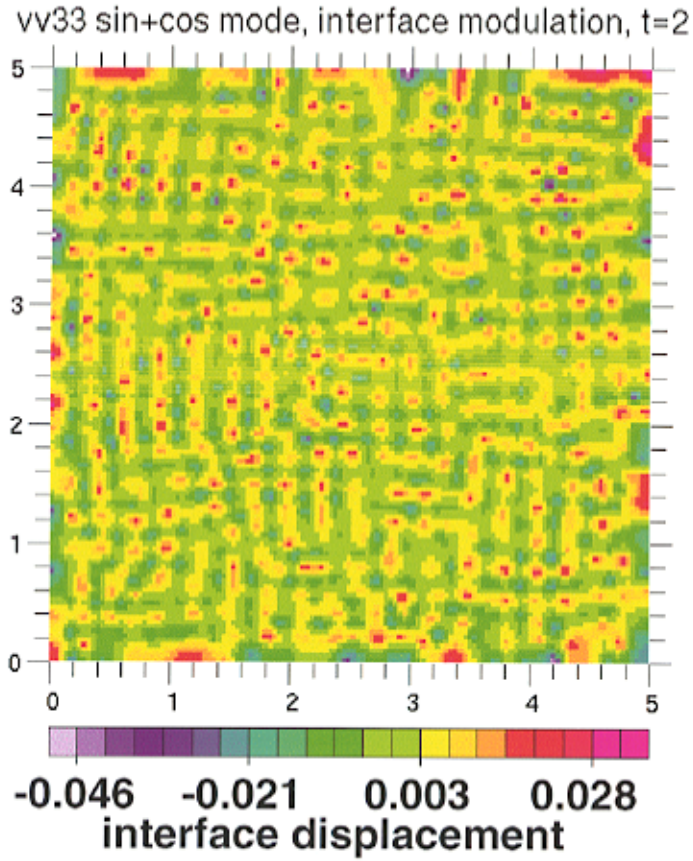

Spurious enhanced penetration at faces and corners is probable a consequence of reflection boundary conditions

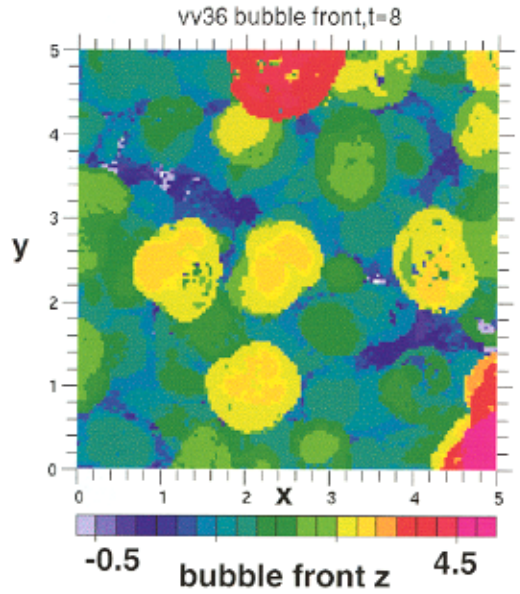

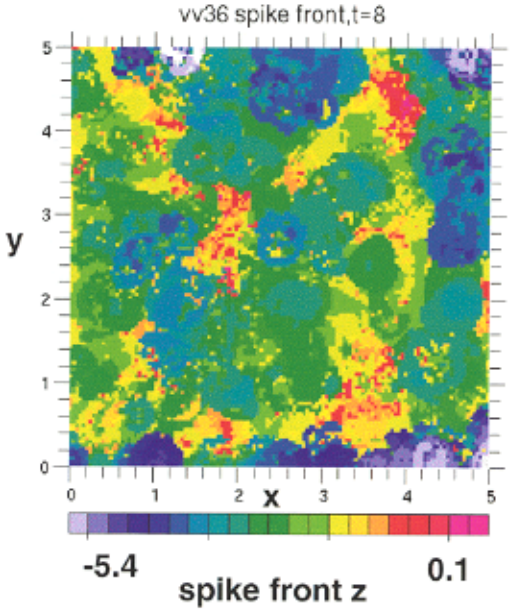

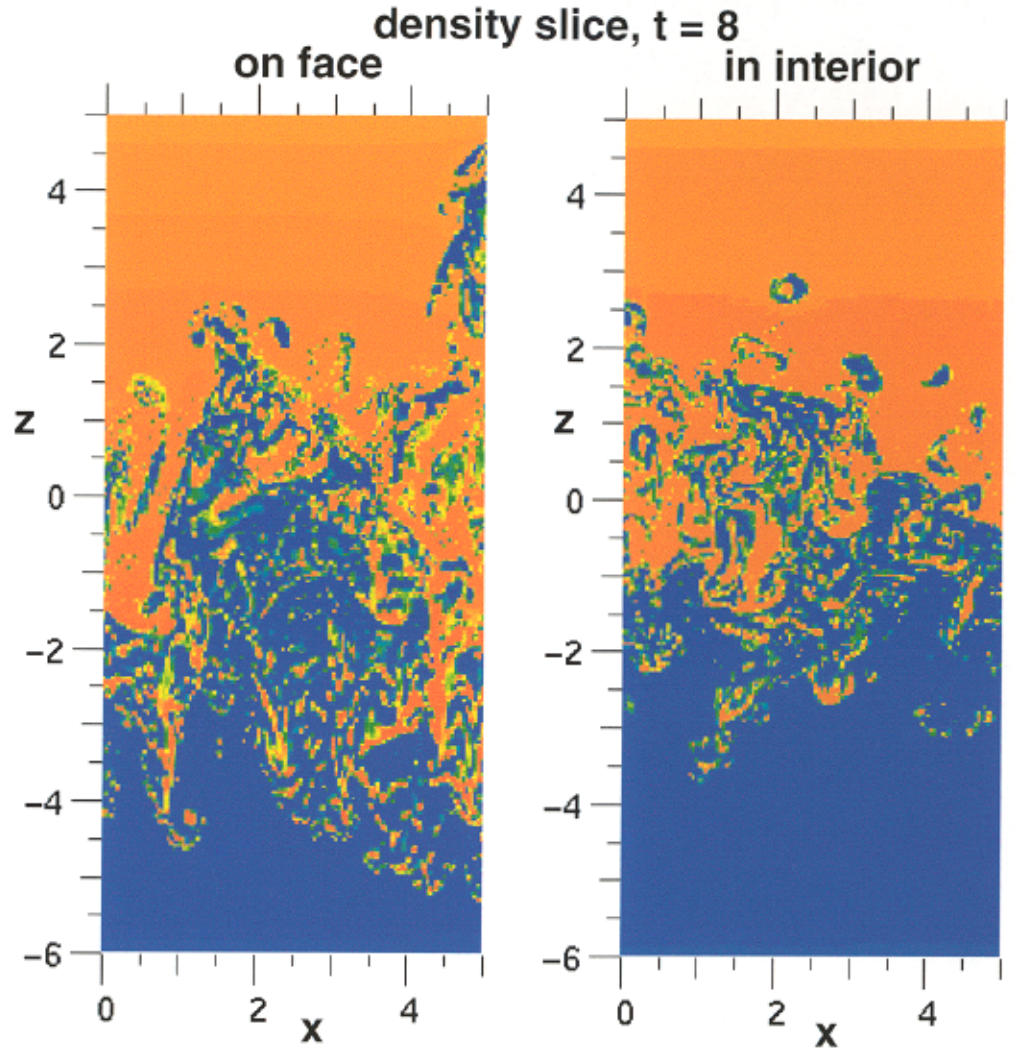

- This may result from higher symmetry of the flow at edges and corners

- Data analysis excludes volume near boundaries to minimize the influence of this effect

The simulation with interface reconstruction shows breakup into many small drops at late times

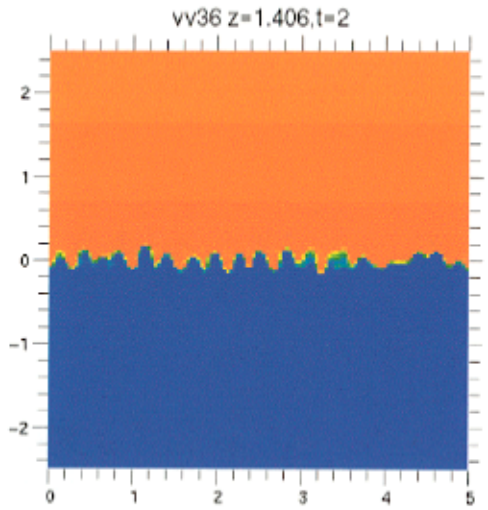

t = 2

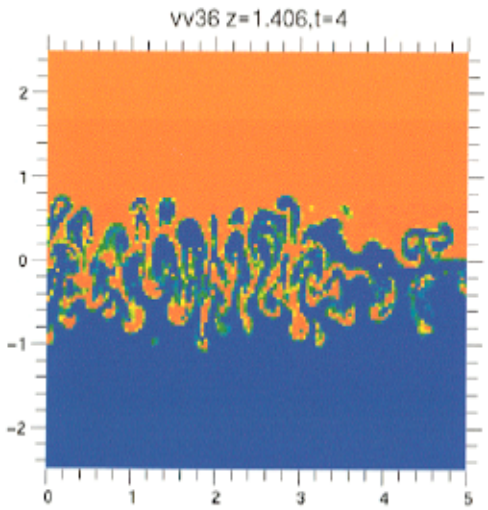

t = 4

- Sequence of density cuts of 3-D 1282x512 simulation in the interior (away from a face)

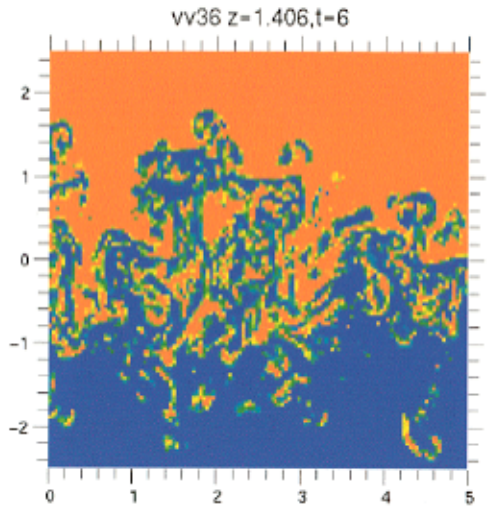

t = 6

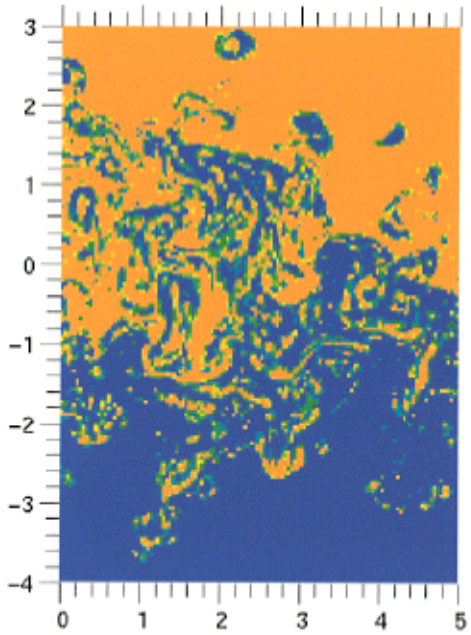

t = 8

Simulations without interface reconstruction predict a mix extent only slightly lower, but show much more small scale mixing

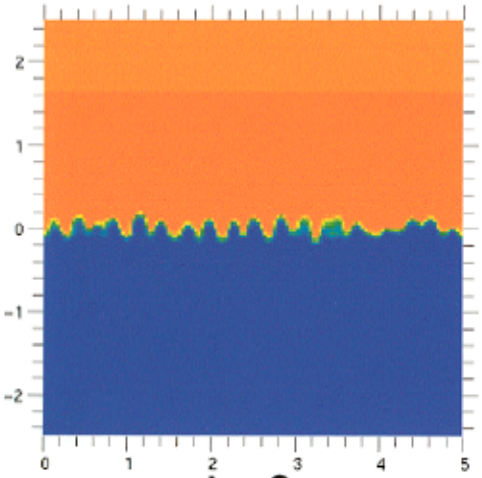

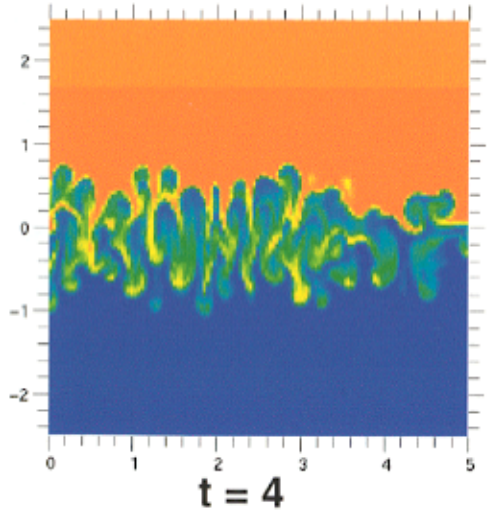

density cuts in 3-D $128^2 \times 512$ simulation without interface reconstruction

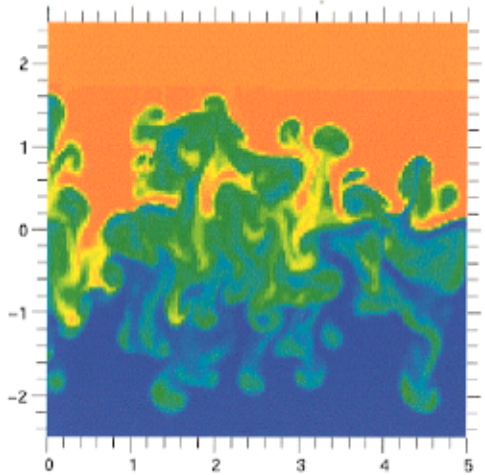

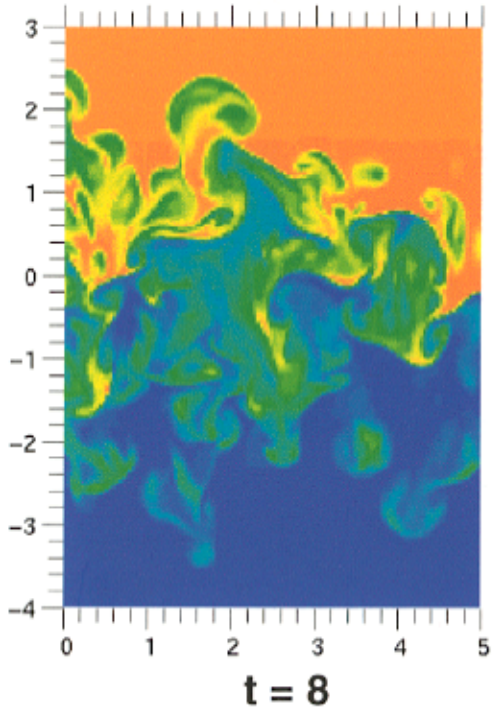

The 3-D simulation shows the expected transition to turbulence, followed by bubble merger

visualization of interface, identified as $\rho = 2$ contour

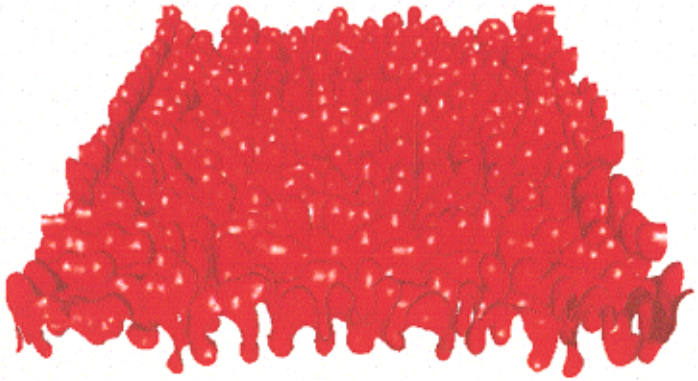

t = 2

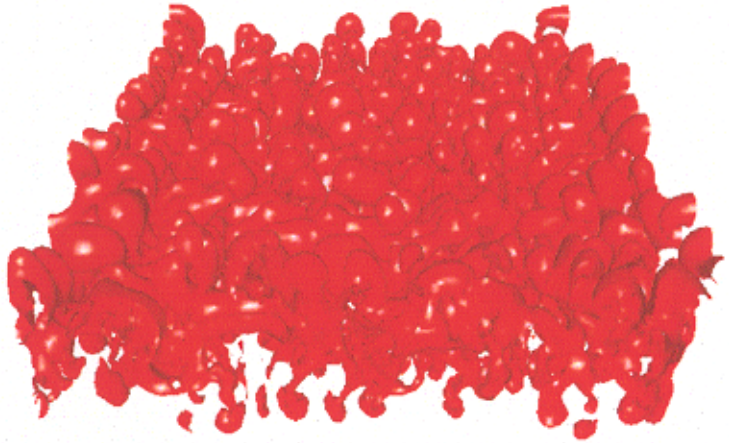

t = 4

t = 6

It is not apparent that the mix extent ever reaches an asymptotic t^2 growth

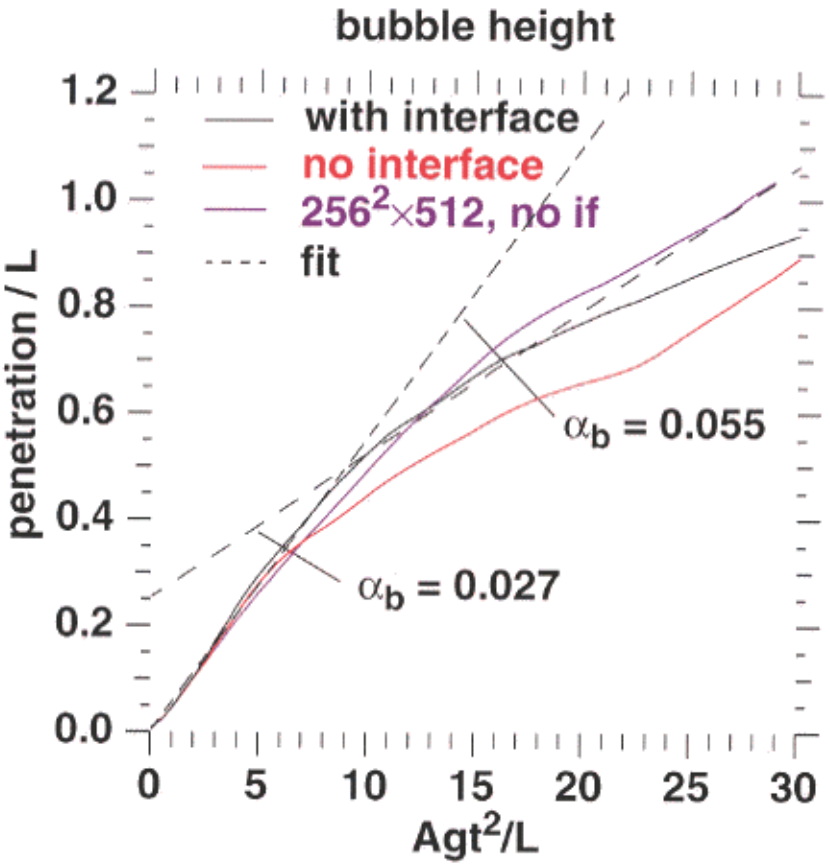

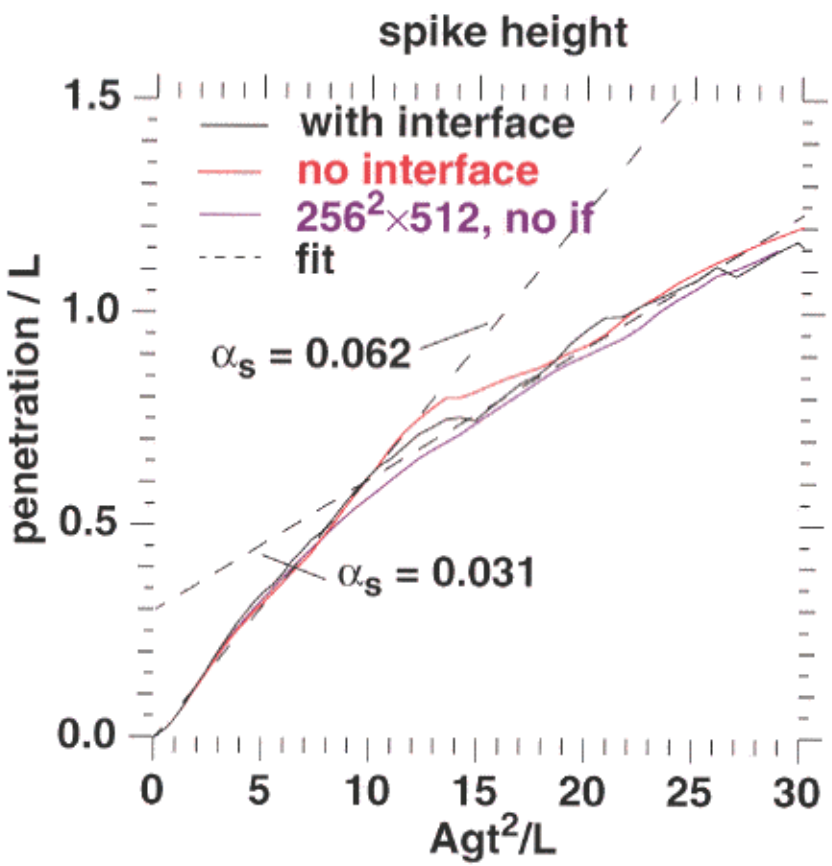

- "fit" lines are drawn by eye
- Interface reconstruction gives only modestly higher growth, only on the bubble side
- All cases show the slope, α, decreasing with time
- On the bubble side, the full scale problem retains a higher growth rate later in time as it can grow bigger bubbles (all curves are scaled as L=5)
- The growth of the spikes does not change with problem size

The total mix width and integral width measure also exhibit decreasing slope with time

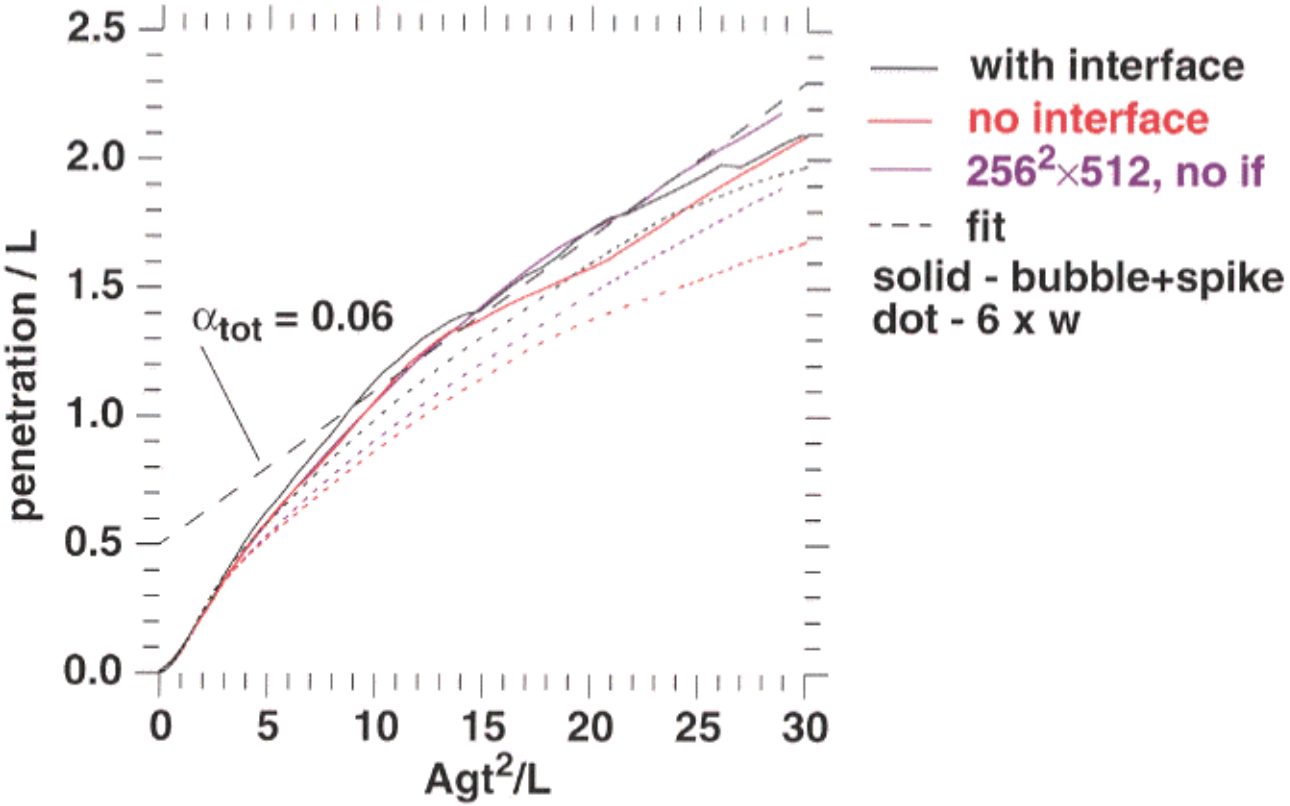

- w - Andrews and Spalding integral width
- The full scale and one quadrant simulations nearly overlay when scaled with the *same L* (5 here) as the initial amplitude and wavelength were not scaled with L
- We believe that the box size affects the growth only by limiting the size of the largest bubbles late in time, which is a *breakdown* of self-similarity rather than a feature of the scaling

Simulations lie below the LEM data when scaled by the box size; however, the slope is about right

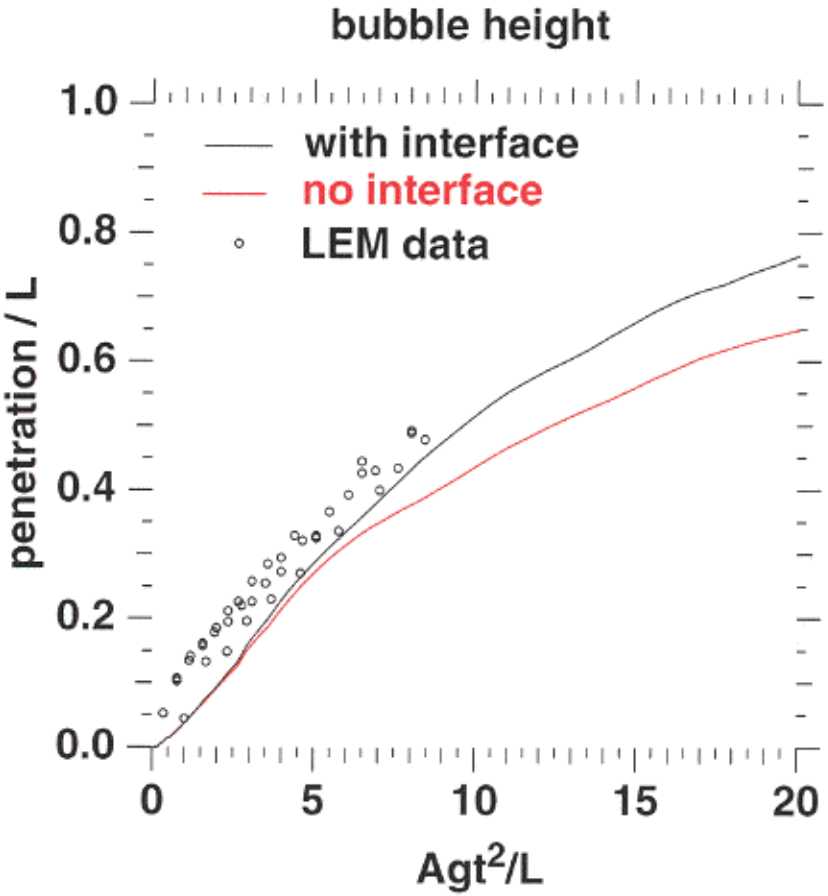

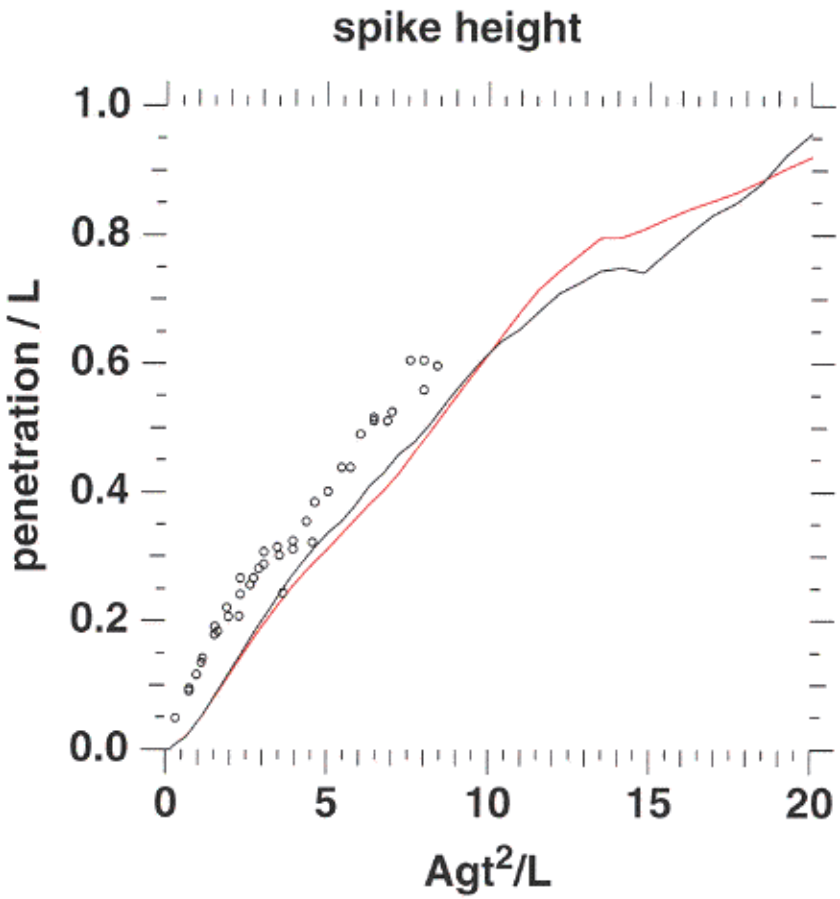

The simulation without interface reconstruction gives atomic mixing ~0.7, but similar dissipation to the run with tracking

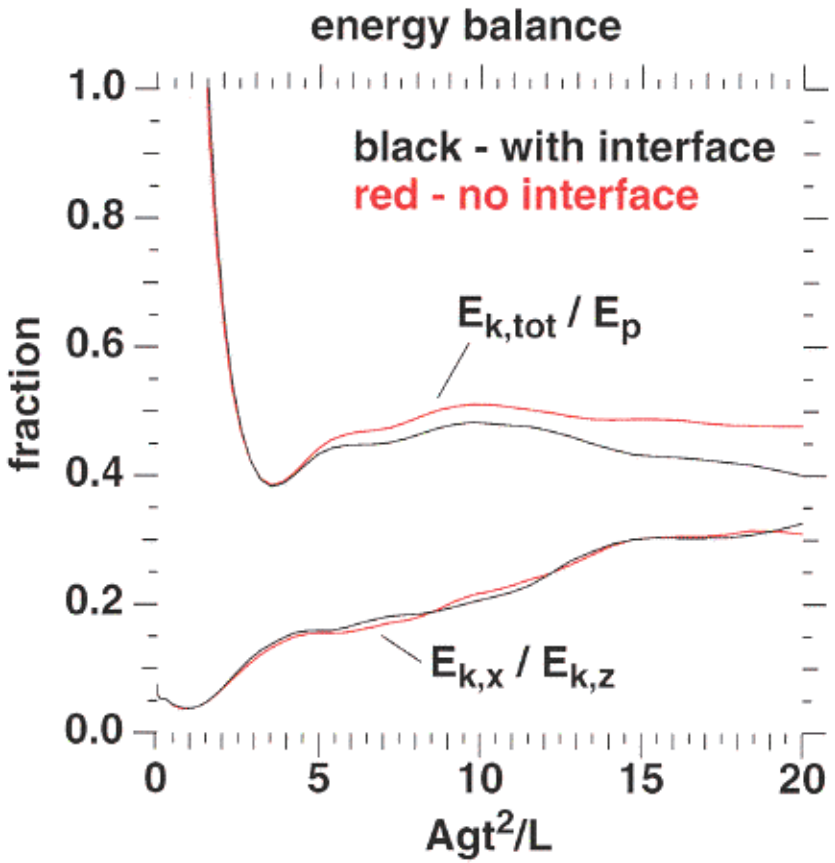

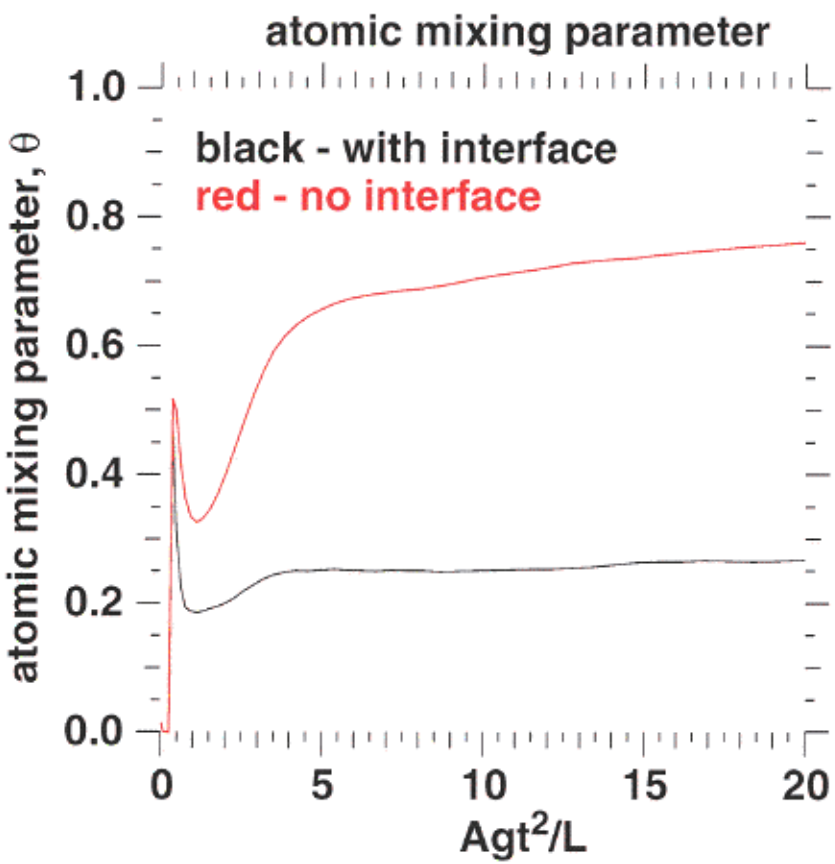

- E_p - potential energy drop, dissipated energy, $E_{k,z}$ kinetic energy in streamwise direction, $E_{k,x}$ kinetic energy in one spanwise direction, $E_{k,tot}$ - total kinetic energy
- The atomic mixing parameter for the interface reconstruction run is an upper limit because post-processing does not account for the interface reconstruction and treats zones through which the interface passes as mixed

Volume fraction histograms are also very similar with or without interface reconstruction

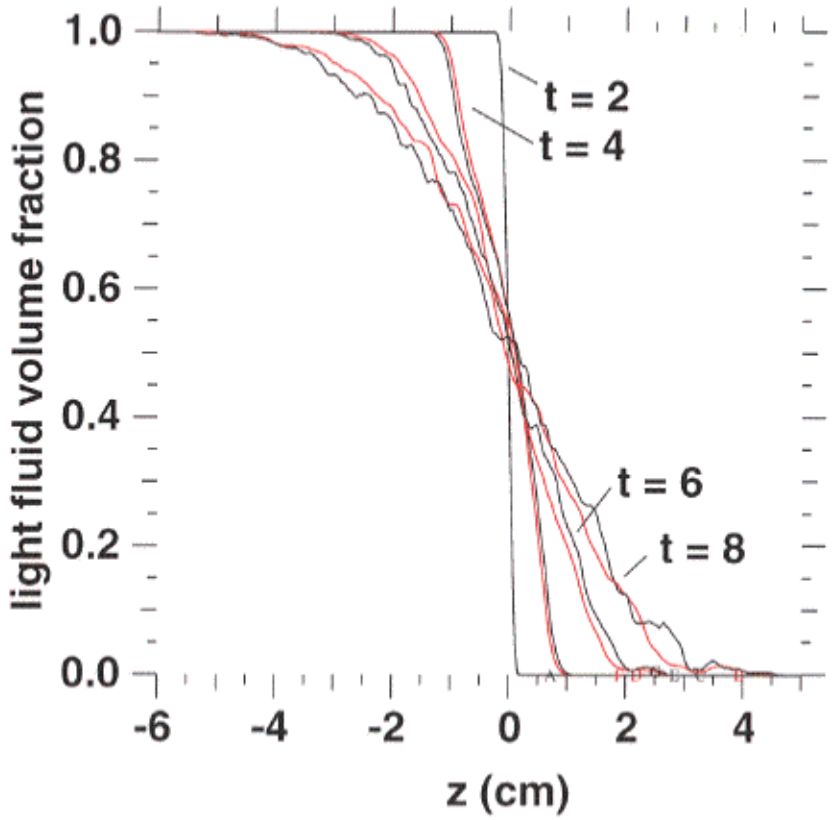

black - with interface reconstruction

red - no interface

Conclusions

- Under-resolution of the initial perturbations introduces numerical artifacts, but it is uncertain if the simulated mix extent is compromised
  - 2-D runs show no significant change in mix extent with zoning refinement
- Interface reconstruction has only a modest effect on mixing extent
  - However, internal structure of the mixing zone is affected
- These runs do not appear to specify a definite value of α
  - 3-D simulations of one quadrant of the nominal α problem show monotonically decreasing α with increasing time
  - α_b drops from ~0.055 at early times to ~0.03 later in time
  - α_b remains high longer for the full scale problem
  - α_s ~ 0.06 at early times; also appears to drop later in time
- Simulations lie below the LEM bubble, spike penetration data
  - slope of spike penetration and early time slope of bubble penetration are close to measured slopes of penetration vs. t^2

STUDY OF GRAVITATIONAL TURBULENT MIXING AT LARGE DENSITY DIFFERENCES USING DIRECT 3D NUMERICAL SIMULATION

Yu.V.Yanilkin, V.P.Statsenko, S.V.Rebrov, O.G.Sin'kova, A.L.Stadnik

Paper to be presented at the 8th International Seminar on Turbulent Mixing of Compressible Matter (8th IWPCTM, Pasadena, USA)

The problem of turbulent mixing under action of a constant gravity force (constant acceleration) on a plane interface of two gases was numerically studied by a number of papers [1, 2], however the studies are essentially missing for large density differences in mixing materials.

This paper makes an attempt of direct 3D numerical simulation of the above problem with code TREK [3] for gases of different densities, such that $n=\rho_2/\rho_1=3\text{-}40$. With these density differences, the numerical simulations involve severe difficulties in achievement of the self-similar regime of a turbulent flow, so the difference scheme and the number of the computational cells were varied in the computations. A large number of the computations were conducted, it is impossible to demonstrate results of all the computations, however, note that the results agree well with each other. Below are results of computations by the same difference scheme and on the same computational grid.

Numerical arrays of hydrodynamic quantities from 3D computations are used to find moments of the quantities (Reynolds tensor, turbulent flows, profiles of density and its mean square pulsation). Besides, they are also used for construction of one-point concentration probability density function (PDF). Spectral analysis of velocity and density pulsations in TMZ was conducted: the effect on the approximation to the Kholmogorov spectrum for the quantities was studied.

The computed data is compared to known experimental data [4-9]. The analysis of the computed and experimental data suggests that the flow is not self-

similar at the initial quite long stage, and the stage should be excluded to when determining the well-known self-similar constant α. In view of this it seems to us that most experimental data need to be corrected.

1. Setting up TREK computations

The problem is formulated similar to ref. [1]: at the initial time two half-spaces separated with plane $z=z_c=0$ are filled with ideal gases in rest having densities $\rho_1=1$ и $\rho_2=n$ (n=3, 10, 20, 40). The initial geometry is presented in Fig.1. The gravitational acceleration, $g_z = -1 \equiv - g$, is directed from the heavy material to the light. At the initial time, at the interface (in a layer one cell thick), a random-number generator gives random density perturbations $\delta\rho= \pm \rho_1\delta$, where $\delta= 0.1$.

Gas dynamics equations for ideal two-component medium (with zero molecular viscosity and heat conduction) are solved. The computational domain is a parallelepiped with height $\Lambda=2$. Its horizontal face is a square with side $L_x=L_y=1$.

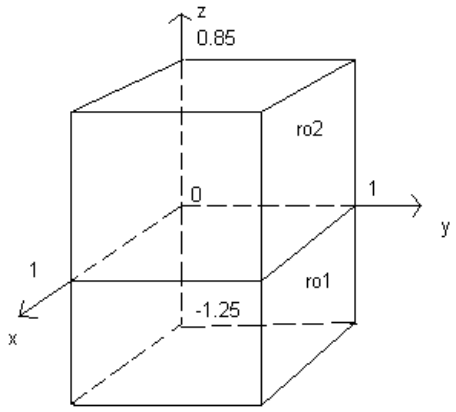

Fig.1. Initial geometry

The initial pressure profile was given using the hydrostatic equilibrium condition $p(z) = p_0 - \int_{z_2}^{z} \rho(z) \cdot g \cdot dz$. Here the coordinate of the upper face is $z_2=0.85$, that of the lower face $z_1= -1.15$, $p_0=100$. Note that the pressure ($p \approx p_0$)

is such, that the following non-compressibility condition was met well for the turbulent flow $k=\xi L_t g << \gamma p/\rho$, where $\xi=const<<1$, $L_t<\Lambda$, L_t is turbulent mixing zone (TMZ) width, k is turbulent energy.

The equation of state is ideal gas with adiabatic constant $\gamma=1.4$. The computational grid is uniform, having $N_x=200$, $N_y=200$, $N_z=400$ cells. The "rigid wall" type condition was posed on all the computational domain boundaries.

2. Results of 3D computations, integral characteristics

The flow evolution observed in all the computations is similar on the whole to the previous computations [2] for small density differences: whirl enlargement with time and change over to the self-similar regime are observed.

The latter shows up for this problem, in particular, as transition to the linear dependence of TMZ width function $L_t(t)$:

$$F \equiv \frac{1}{t_L}\sqrt{\frac{L_t}{Ag}}\,. \qquad (1)$$

Here the unit of measurement for time is $t_L \equiv \sqrt{\frac{L_x}{g}}$ and $L_t(t)$,

$$L_t \equiv z_2 - z_1, \qquad (2)$$

is TMZ width along z determined by points z_1, z_2, at which quite small value of ε of a hydrodynamic quantity, for example, concentration, is achieved. Next, assume that $c_2(z_1)=\varepsilon$, $c_2(z_2)=1-\varepsilon$, where c_2 is mass fraction of the material whose initial density was $\rho_2 = n$.

The angle of inclination, dF/dt, therewith determines the value of coefficient $\alpha_a=(dF/dt)^2$ in the relation for the TMZ width at the self-similar stage:

$$L_{ta} = \alpha_a A g t^2\,. \qquad (3)$$

Fig. 2 plots F(t) from the computations using relations (1) and (2).

For n=8.5-29, the α_a obtained in the experiments [7] range from 0.15 to 0.2 and slightly increase with increasing n. The relevant straight lines also appear in Fig.2.

As seen from Fig.2, there are two flow segments differing in the angle of inclination dF/dt, at the initial segment this is larger than in the experiment, at the second segment this is, on the contrary, less. Prior to us, similar results were obtained by Youngs [1]. A comprehensive analysis of the flow suggests that at the first segment there is no flow self-similarity, although the inclination dF/dt is close to constant. The self-similarity takes place only at the second stage, therefore it is this segment that the self-similar constant α should be measured at, where it proves less than the known experimental data. We assume, that it is caused by that at processing the specified data was not excluded initial nonself-similar a stage.

What this can result in can be seen from the experimental data of Kucherenko et al., which we analyzed.

Fig.3 plots function $F_2(t) \equiv \frac{1}{t_L}\sqrt{\frac{z_2 - z_c}{Ag}}$ versus time for coordinate z_2 of the penetration of the heavy liquid into the light. At the final stage, where the self-similar regime is achieved, our computation for n=40 results in the angle of inclination dF_2/dt close to the observed: Fig.3 presents minimum and maximum quantities measured in [9] for n=36.5. Note that by α_2=0.078 ($\alpha_2=(dF_2/dt)^2$) taken in [9] the angle of inclination is larger than the observed. Apparently, this value was obtained without exclusion of the initial segment, at which the self-similarity also does not take place.

A similar dependence for smaller density differences is shown in Fig.4. Apparently, the self-similar regime is not achieved in the experiment (for n=3.65): the angle of inclination decreases about in the same manner as in our computation (for n=3) at the initial stage, where the self-similar regime is not also achieved. In [9] α_2=0.078, this is significantly higher than the observed and corresponds just to the initial (non-self-similar) stage.

Fig.5 plots the scaled TMZ width:

$$\alpha(t) = \frac{L_t}{Ag(t - t_0)^2}, \qquad (4)$$

that follows from our computations. Here t_o corresponds to the intersection of the extrapolated self-similar segment of curve F(t) estimated by the data of Fig. 2 with the abscissa axis.

In the computations with n=10, 20, 40, α approaches approximately constant values (which corresponds to the self-similar stage): $\alpha_a \approx 0.11, 0.15, 0.16$, respectively, which is somewhat less than the experimental quantities [8]. Note that the self-similar stage is achieved earlier with increasing **n**, but its duration becomes shorter.

Processing similar to (4) was performed for coordinates z_1, z_2 of the penetration of the heavy liquid into the light and the light into the heavy, respectively. Their scaled values are

$$\alpha_1 \equiv \frac{z_c - z_1}{Ag(t-t_0)^2}, \qquad \alpha_2 \equiv \frac{z_2 - z_c}{Ag(t-t_0)^2} \tag{5}$$

The results are plotted in Fig.6. On the whole, $\alpha_1(t), \alpha_2(t)$ behave like $\alpha(t)$. In so doing, as might be expected, TMZ grows faster toward the light material. Asymmetry increases with increasing **n** and reaches ≈2 for n=40.

For this problem the self-similar regime also shows up by the fact that the following quantity becomes time-independent:

$$E(t) \equiv \frac{k_m}{L_t g}, \tag{6}$$

where $k_m(t) \equiv \max(\langle k \rangle(z,t))$ is maximum averaged turbulent energy over the TMZ width:

$$k(z) = \frac{\langle (u_j)^2 \rangle - \langle u_j \rangle^2}{2}, \tag{7}$$

the averaging (denoted with <>) is over the entire horizontal section z=const.

As seen from Fig.7, at the initial stage E(t) is large enough [at this stage, there is a small number of computational cells per TMZ, which leads to insufficiently correct values of E(t)] and increases with increasing **n** in all the computations. At a later stage this quantity approaches approximately constant $E=E_a$ in the computations with n=3, n=10, and n=20. The E_a also increases with increasing **n**.

To draw a more justified conclusion about whether or not the self-similar regime is achieved, other turbulent quantities have to be considered.

The TMZ maximum value, R_m, of density pulsation function R versus time is plotted in Fig.7,

$$R_m \equiv \max(R), \qquad R \equiv \frac{<\rho'^2>}{\rho^2}. \tag{8}$$

From the figure it is clear that at the self-similar stage the R_m quite confidently approaches approximately constant $R_m \approx R_a$ in all the computations. The R_a increases with increasing **n**.

Fig.9 plots the TMZ maximum turbulent mass flow versus time:

$$R_{zm} \equiv \max(\widetilde{R}_z), \widetilde{R}_z \equiv \frac{R_z}{\sqrt{L_t g}}, R_z \equiv <\rho' u_z'> \tag{9}$$

Like for the R_m, from Fig.9 it follows that at the self-similar stage the R_{zm} approaches approximately constant $R_{zm} \approx R_{zma}$ increasing with increasing **n**.

Thus, the analysis shows that at the initial flow stage the self-similar regime is not established and this segment should be excluded when considering self-similar flow characteristics. This is also true for the experiments, in which initial perturbations able to affect the flows under study for long are always present.

3. Velocity and density pulsation spectra

The computed data was used as a basis to study the velocity pulsation spectrum according to relation

$$\begin{aligned} &E_{iil}^{(s)}(x,y) = \langle u_i^2 \rangle_{|_{l,x,y,z}} - \langle u_i \rangle^2_{|_{l,x,y,z}} \qquad ; \qquad s = 1,2....N_z \\ &E_{iil}(z) = E_{iil}^{(s)} = \langle E_{iil}^{(s)}(x,y) \rangle \qquad ; l = rh, \qquad r = 2,3....N_x. \end{aligned} \tag{10}$$

Here averaging $\langle\rangle_{|_{1,x,y}}$ is performed in the s-layer (over z) in a square with side l (l=rh, h is computational cell size), whose center coordinates are x,y, and then averaging ($\langle\rangle$) is made over all possible values x, y of the squares with the l in the entire s-th layer. In (10) there is no summation over **i**.

Next: $$E_l = \sum_{i=1}^{i=3} E_{iil} \qquad (11)$$

Fig. 10 plots the results of the computation for t=2, n=40 (where K=2π/l) along with Kolmogorov spectrum

$$\lg E_l = -2K/3 + \text{const.} \qquad (12)$$

Inside the TMZ ($|\zeta| \le 0.3 \div 0.4; \quad \zeta \equiv \frac{z - z_c}{L_t}$, here L_t was computed by model [2]), the computed spectrum of total energy E_l approaches the 3D Kolmogorov spectrum, with this being less confidently for highest n. Fig. 10 also shows that at small space scales (large K) the velocity pulsations become isotropic: all components E_{iil} approach each other.

A similar quantity is calculated for the squared density pulsations:

$$\begin{aligned} &\rho_l^s(x,y) = \langle \rho^2 \rangle_{|_{l,x,y,z}} - \langle \rho \rangle^2_{|_{l,x,y,z}} \quad ; \quad s = 1,2....N_z \\ &\rho_l(z) \equiv \langle \rho_l^s(x,y) \rangle \quad ; l = rh, \quad r = 2,3....N_x; \end{aligned} \qquad (13)$$

this is depicted in Fig. 11. As seen, at the TMZ center the spectrum of net ρ_l at small scales approaches the Kolmogorov spectrum. In contrast to the velocity pulsation spectrum, the density pulsation spectrum is closer to the Kolmogorov spectrum with increasing **n**.

4. Concentration probability density function

The one-point heavy material mass concentration probability density function was determined by the computed data:

$$F(c_2, z, t) = \frac{N(c_1^{(ik)}(z) \ge c_2) - N(c_2^{(ik)}(z) \ge (c_2 + \Delta c))}{N_0 \Delta c}, \qquad (14)$$

here $N(c_2^{(ik)}(z) \ge c_2)$ is the quantity of points in a given horizontal plane z, at which current concentration $c_2^{(ik)}$ is higher than c_2, $N_o(z)$ is the total number of the points in the plane. The c_2 runs through a sequence of M numbers:

$$c_2 = (0, \quad 1, \quad 2, \quad ...., \quad M-1)\Delta c,$$

where $M\Delta c = 1$; in our computations, M=100.

When the initial concentration array is used, because of circuit features of calculation of concentration in separately taken cell the maximal values $F(c_2)$ are achieved basically (inside TMZ) near to borders of an interval of values of concentration, that is, at $c_2 \approx 0$ or ≈ 1. Thus inside an interval $0 < c < 1$ values $F(c_2)$ are small, that is, the integral is gathered basically at edges of an interval. Near to border TMZ, adjoining to heavy substance, $F(c_2)$ looks like δ-function concentrated at $c_2 \approx 1$.

However, with use of averaging of an initial concentration array on squares with the side n_o, in calculation for variant N=1.6107, n=10 with increase n_o from 2 up to 4 it is observed (as shows rice 12) fast approach to certain established kind $F(c_2)$, not dependent from n_o. Its characteristic feature is almost uniform distribution on c_2 inside TMZ, that is, $F(c_2) \approx 1$ - and the integral is gathered almost uniformly on all interval.

The form of the function is similar for other **n**.

References

1. Youngs D.L., Numerical simulation of mixing by Rayleigh-Taylor and Richtmyer-Meshkov instabilites, Laser and Particle Beams, vol 12, no. 4, pp. 725-750 (1994).
2. Sinkova O.G., Stadnik A.L., Statsenko V.P., Yanilkin Yu.V., Zhmailo V.A., Three-Dimensional Direct Numerical Simulation of Gravitational Turbulent Mixing, 6rd Inter. Workshop on the Physics of Compressible Turbulent Mixing, Marseille France, pp.470-479 (1997).
3. Stadnik A.L., Shanin A.A., Yanilkin Yu.V. Eulerian code TREK for computing 3D gas-dynamic multicomponent medium flows// VANT. Ser. Mat. Modelir. Fiz. Protsessov, No.4 (1994).
4. Read, K.I. Experimental investigation for turbulent mixing by Rayleigh-Taylor instability //Physica D12, 45 (1984).
5. Youngs, D.L. Modeling turbulent mixing by Rayleigh-Taylor instability //Physica D37, 270 (1989).

6. Yu.A.Kucherenko, L.I.Shibarshov, V.I Chitajkin at al. Experimental study of the gravitational turbulent mixing self-similar mode //3-rd International Workshop on the physics of compressible turbulent mixing, pp.345-356 (1991).
7. Linden P.F., Redondo J.M., Youngs D.L., Molecular mixing in Rayleigh-Taylor instability, J. Fluid Mech, vol.265, pp.97-124, (1994).
8. Youngs, D.L., Three-dimensional numerical simulation of turbulent mixing by Rayleigh-Taylor instability, Phys. Fluids, A3, 1312 (1991).

Kucherenko Yu.A., Shestachenko O.E., Piskunov Yu.A., Sviridov E.V., Medvedev V.M., Baishev A.I. Experimental study for self-similar mode of different-density gas mixing in the Earth's field gravity. Paper presented at the 6th Zababakhin Scientic Talks, 24-28September 2001, Snezhinsk, Russia.

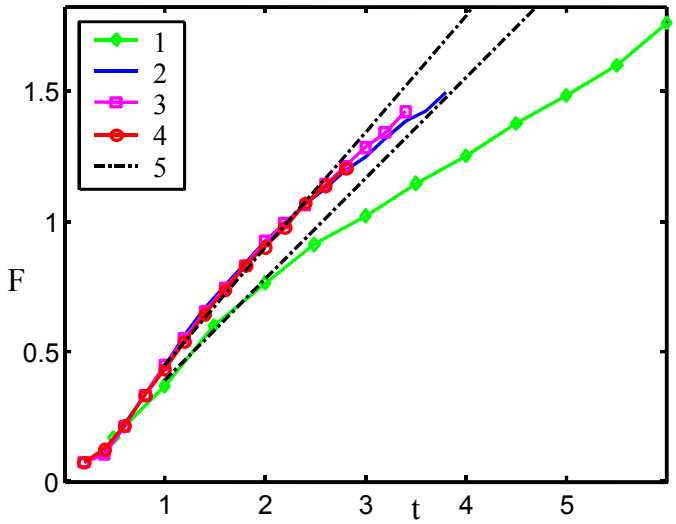

Fig. 2. Function F of TMZ width *L* versus *t*;
our computations: 1 – n=3, 2 – n=10, 3 – n=20, 4 – n=40, 3 – by α taken in [7]

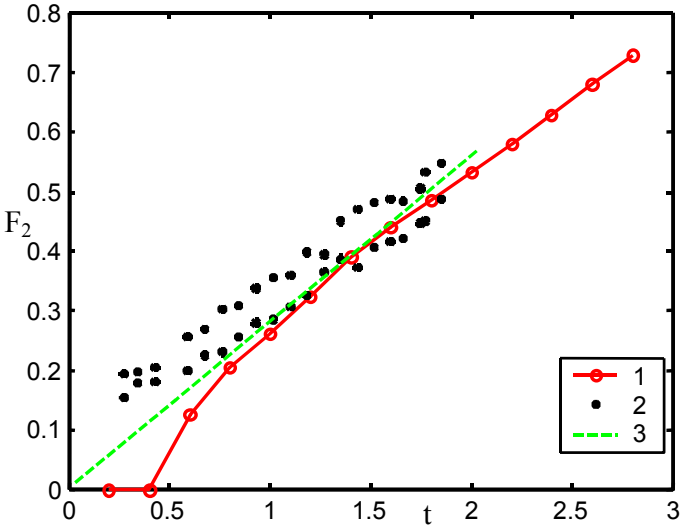

Fig. 3. Function F_2 of coordinate z_2 of heavy liquid penetration into light liquid versus time t: 1 – our computation for n=40, 2 –minimum and maximum values measured in ref. [9] for n=36.5, 3 – by α_2=0.078 taken in [9]

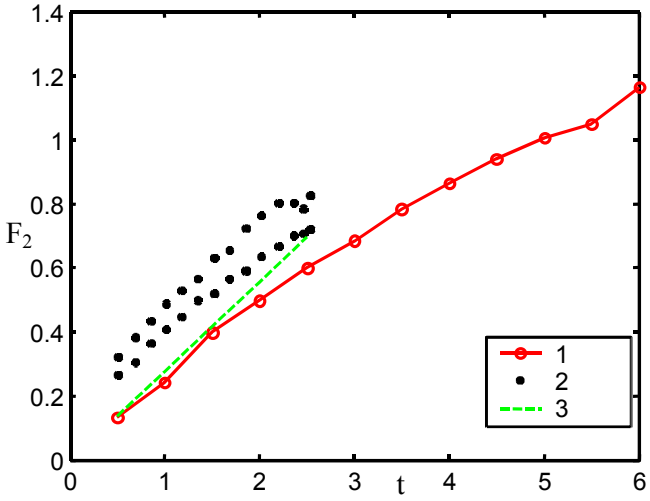

Fig. 4. Function F_2 of coordinate z_2 of heavy liquid penetration into light liquid versus time t: 1 – our computation for n=3, 2 – minimum and maximum values measured in ref. [9] for n=3.65, 3 – by α_2=0.078 taken in [9]

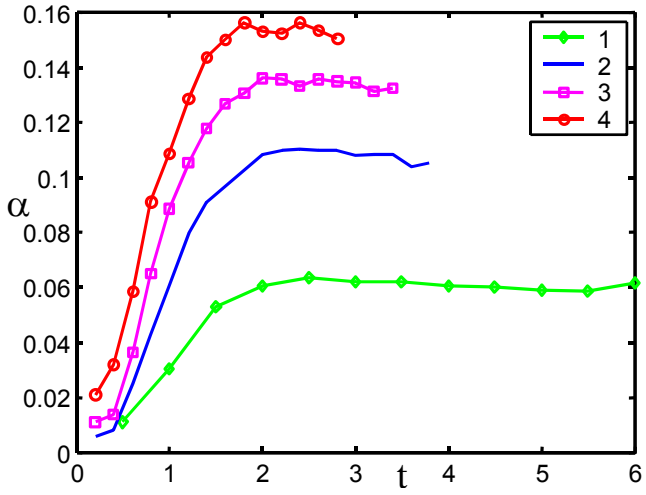

Fig. 5. Scaled TMZ width versus time. The notations are like those in Fig.2

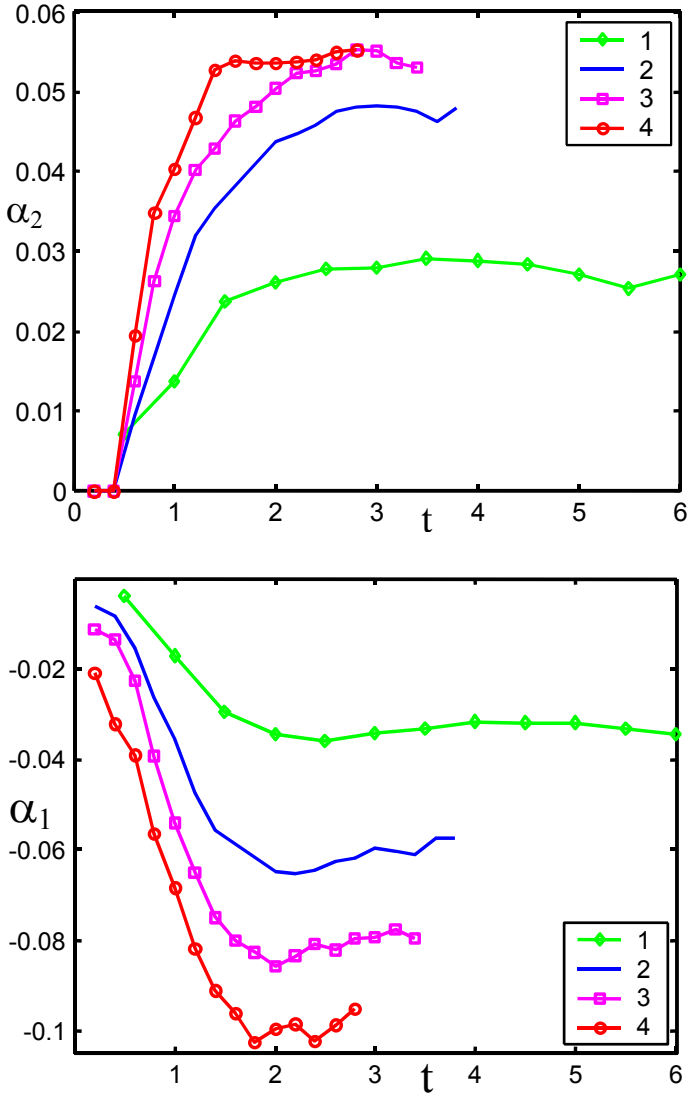

Fig. 6. Scaled TMZ boundary coordinate in light material (α_1) and heavy material ($\alpha 2$) versus time. The notations are like those in Fig.2

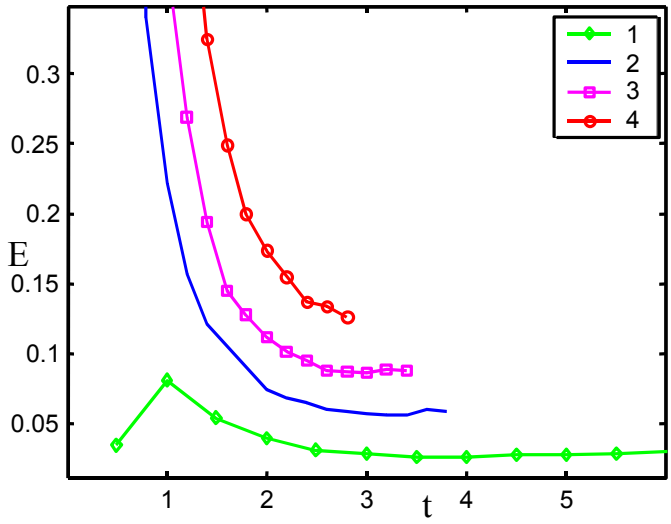

Fig. 7. TMZ maximum scaled turbulent energy versus time.
The notations are like those in Fig.2

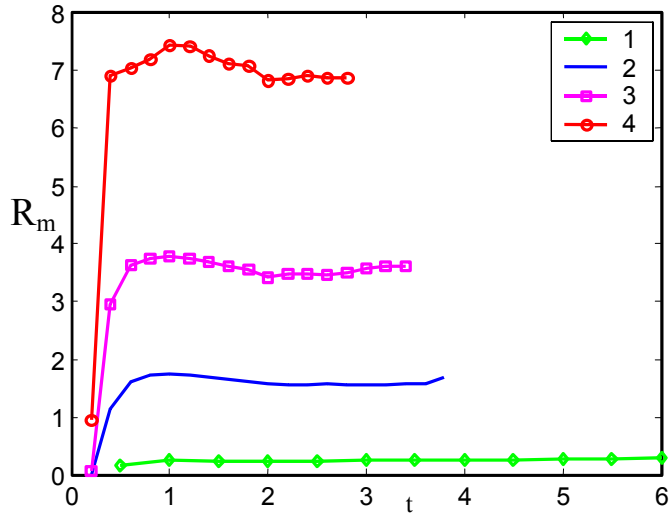

Fig. 8. TMZ maximum density pulsation function versus time.
The notations are like those in Fig.2

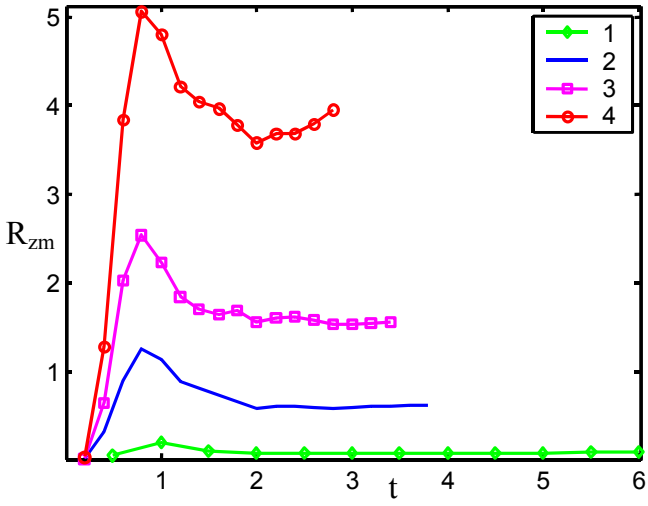

Fig. 9. TMZ maximum turbulent mass flow versus time. The notations are like those in Fig.2

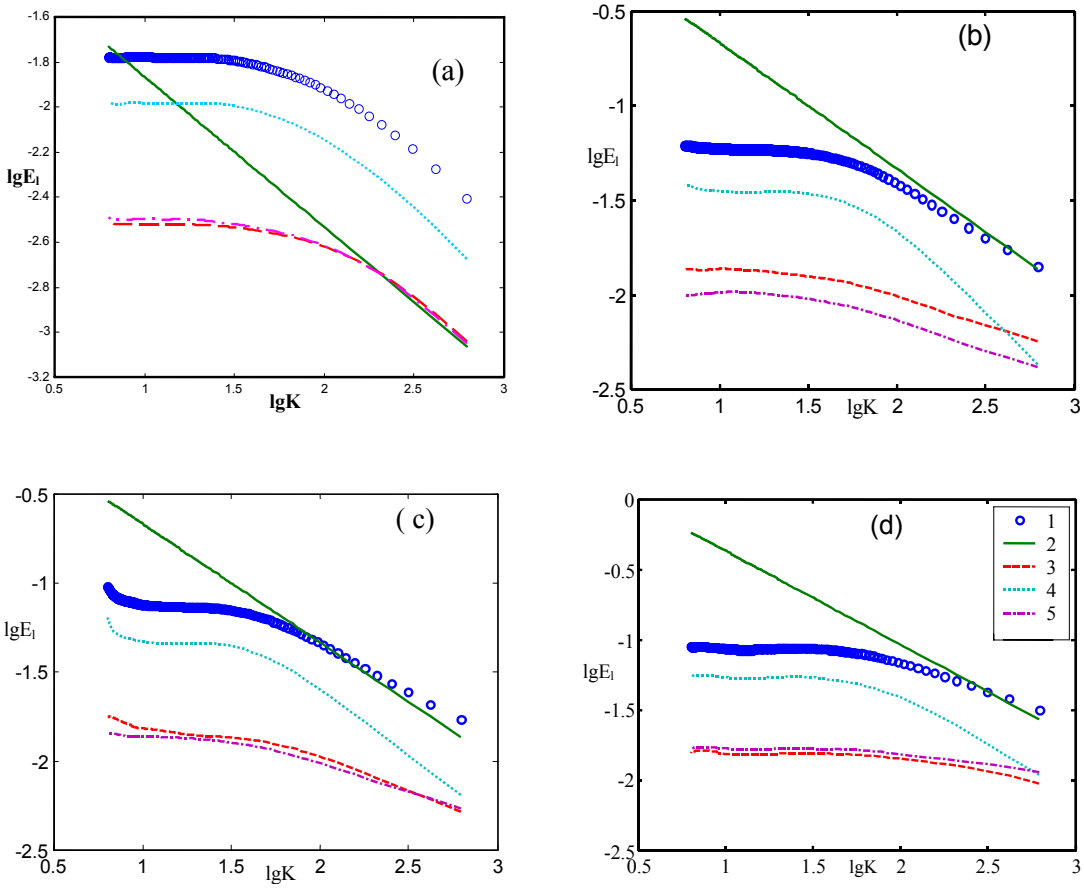

Fig. 10. Velocity pulsation spectrum,
(a) n=3, t =3.5, ζ=-0.076, (b) n=10, t =2.5, ζ=-0.076, (c) n=20, t =2.5, ζ =0.055, (d) n=40, t =2, ζ= - 0.36; 1 – E_l, 3 - E_{xxl}, 4 - E_{zzl}, 5 - E_{yyl}; 2 – Kolmogorov spectrum.

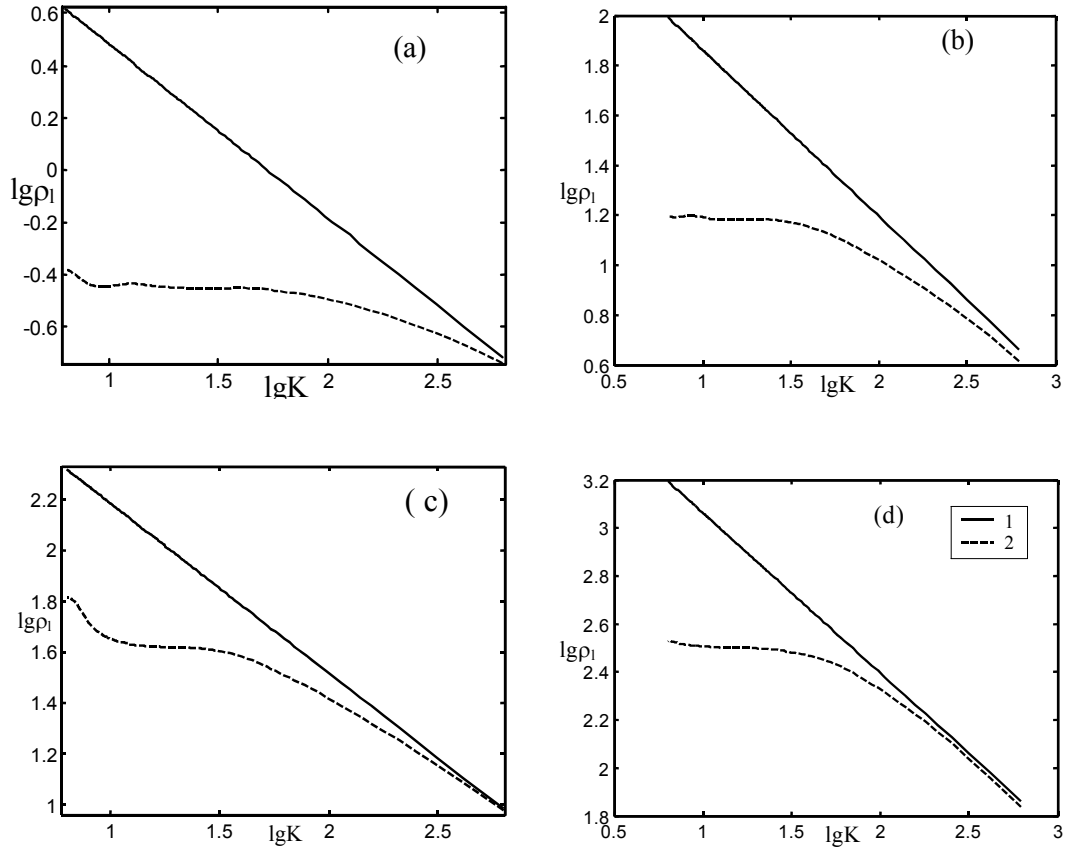

Fig. 11. Density pulsation spectrum,
(a) n=3, t =4.5, ζ= 0.137, (b) n=10, t =2.5, ζ=0.236, (c) n=20, t =2.5, ζ=0.22,
(d) n=40, t =1.8, ζ=0.19; 1 – ρ_l, 2 - Kolmogorov spectrum.

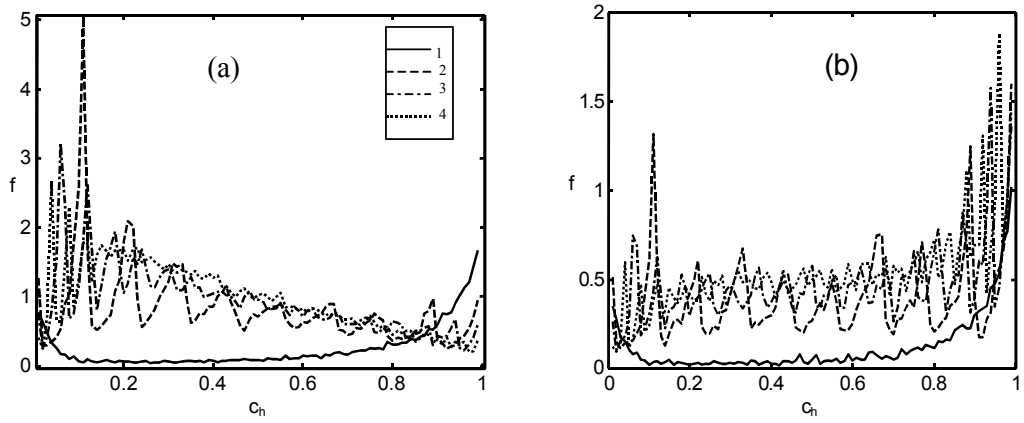

Fig. 12. Heavy material mass concentration probability density function, n=10, t=2;
M=100. 1 – n_o=1, 2 – n_o=2, 3 – n_o=3, 4 – n_o=4; a) ζ= -0.187, b) ζ=0.41089.

DEVELOPMENT AND VALIDATION OF A 2D TURBULENT MIX MODEL

David L Youngs

AWE, Aldermaston

UK

8th IWPCT M

Pasadena, December 2001

Problems of interest

- **Compressible flow with interfaces between fluids of widely differing densities.**
- **High Reynolds No.**
- **Turbulent mixing at interfaces. Due to RT instability, RM instability. KH instability also important.**

Need to model turbulent mixing in flows which are on average 1D or 2D.

Strategy for Numerical Simulation

- **3D Large Eddy Simulation (LES) impractical for real complex applications but can be successfully applied to simplified problems.**

- **High-resolution 3D LES is applied to simplified problems for which experimental results are available.**

- **A combination of 3D simulation results and experimental data is then used to set model coefficients used in a turbulence model (RANS model).**

- **The turbulence model is used to calculate the average mixing behaviour in 1D and 2D numercial simulations of complex real applications.**

TURMOIL 3D

- **Simple 3D compressible Eulerian hydrocode used for turbulent mixing studies (LES).**

- **Same numerical method as the AWE 2D and 3D Eulerian production codes, but without interface tracking.**

- **Moving mesh option:-**

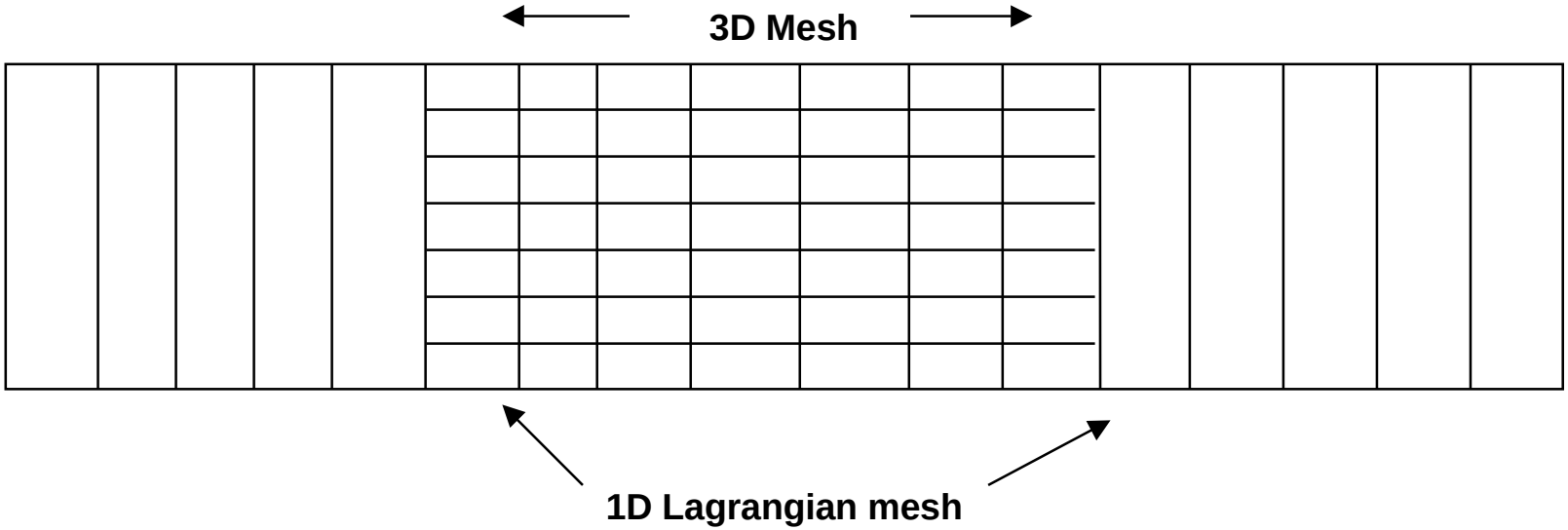

Used for shock tube applications

- **Explicit numerical method ideally suited to parallelisation. Low Mach no. calculations used to approximate incompressible flow.**

- **Lagrangian phase - non-dissipative except in the presence of shocks. Quadratic artifical viscous pressure used.**

- **Rezone or Advection phase.**
  Monotonic advection method of Van Leer used for all fluid variables.

- **Monotonic advection considered essential for problems considered here with shocks and initial density continuities.**
  $\Rightarrow$ non-linear dissipation at high wave numbers.

- **Example of MILES (Monotone Integrated Large Eddy Simulation).**

- **No need for an additional sub-grid dissipation model.**

THE 2D TURBULENCE MODEL (RANS MODEL)

Implemented in a 2D Eulerian hydrocode (which also has the moving mesh option)

Novel form of turbulence model - based on modelling the dynamics of the large scale structures (bubbles of light-fluid, drops of heavy fluid) rather than 1st or 2nd order closure assumptions for the fluctuating quantities)

Combines three basic ideas

1. **Mixing induced by a pressure gradient or shock on fluids of different density.**
2. **Turbulent diffusion in the presence of concentration gradients.**
3 **Exchange of mass between the initial fluids is used to model the decay of concentration fluctuations [2].**

Uses multiphase flow equations with turbulent diffusion terms added [1].

Bouyancy - drag model used to calculate initial behaviour - approximate representation of the initial conditions[3].

References: 1. D.L.Youngs, Laser and Particle Beams, vol 12, p725 (1994)
2. D.L. Youngs, Proceedings of 5th IWPCTM, Stony Brook(1995)
3. J.C.V. Hansom et al., Laser and Particle Beams, vol 8, p51(1990)

The simple incompressible RT problem $(\rho_1, \rho_2,$ g constant$)$ is the key problem for fixing the turbulence model coefficients.

Loss of memory of initial conditions tends to occur $\rightarrow$ self-similar mixing with length scale gt^2:

Bubble penetration $h_1 = \alpha \dfrac{\rho_1 - \rho_2}{\rho_1 + \rho_2} gt^2$

α **~ 0.05 to 0.06**

(AWRE Foulness, LLNL (LEM), Chelyabinsk 70)

TURMOIL3D calculations with short-wavelength initial perturbations (growth purely by mode coupling) give α ~ 0.03, less than observed.

Need to add long wavelength initial perturbations:-

$$\sigma^2 = \int_0^\infty P(k)\, dk$$

where $$\left\{ \int_{2\pi/\lambda}^{\infty} P(k)\, dk \right\}^{\frac{1}{2}} = \varepsilon \lambda$$

ε **= 0.0005 gives self-similar growth with α ~ 0.05. It is assumed that this corresponds to a typical experimental situation.**

Model coefficients are chosen to fit the key quantities for RT mixing

α : **growth rate coefficient**

$\frac{D}{P}$: $\frac{\text{turbulence KE dissipated}}{\text{Loss of potential energy}}$

θ : **molecular mixing fraction**

$$\frac{\int \overline{f_1 f_2}\, dz}{\int \bar{f}_1 . \bar{f}_2\, dz}$$

Values used are based on TURMOIL3D calculations (800 x 400 x 400 zones, ε = 0.0005): -

α	=	0.05
D/P	=	0.4 (no experimental data)
θ	=	0.7 (some experimental confirmation)

Still leaves one key degree of freedom

$$\Delta = \frac{\Delta u_D}{\Delta u_D + \Delta u_P}$$

Δu_D = **mixing velocity due to turbulent diffusion**

Δu_P = **mixing velocity induced by pressure gradient**

Results shown here for $\Delta = 0.4$

TYPICAL 2D TURBULENCE MODEL APPLICATION

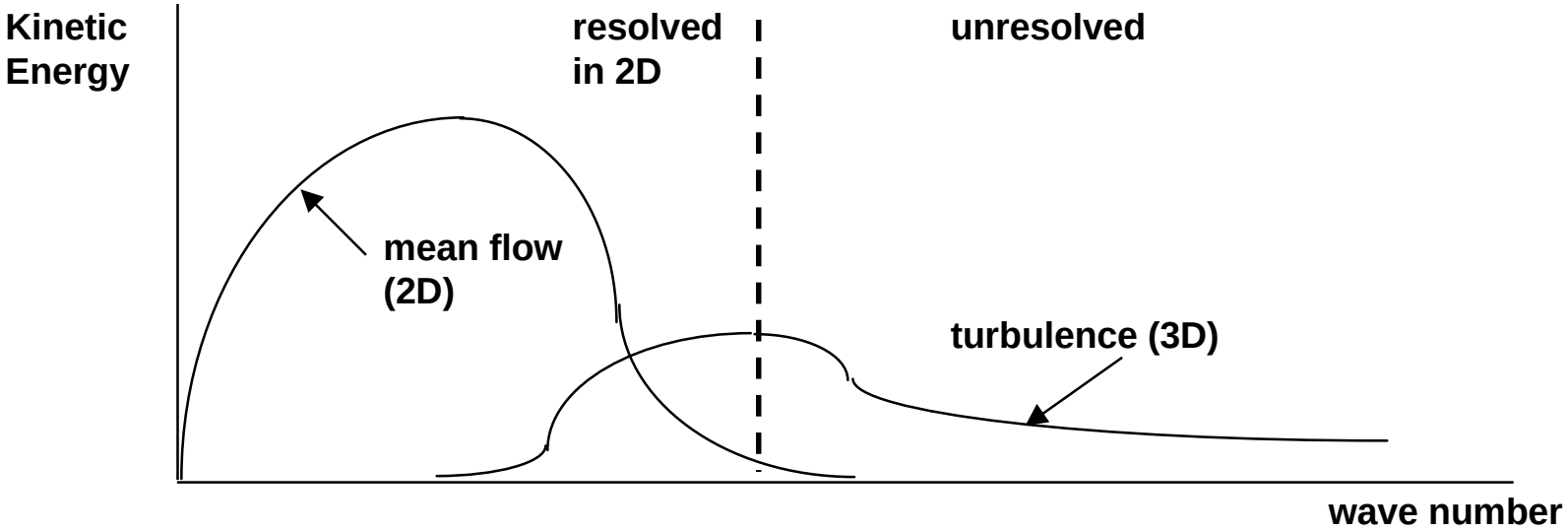

Mean flow (2D) : calculated
Turbulence (3D) : modelled

Points of concern

(a) Likely to be some overlap between the mean flow scales and the turbulence scales - is double counting an issue?

(b) Some of the turbulence scales are resolved (but only in 2D). Does this matter?

(c) Does the turbulence model give the correct spatial distribution in a complex 2D situation.

RAYLEIGH-TAYLOR EXPERIMENT
(CAMBRIDGE UNIVERSITY)
Dalziel, Linden, Youngs, JFM 1999

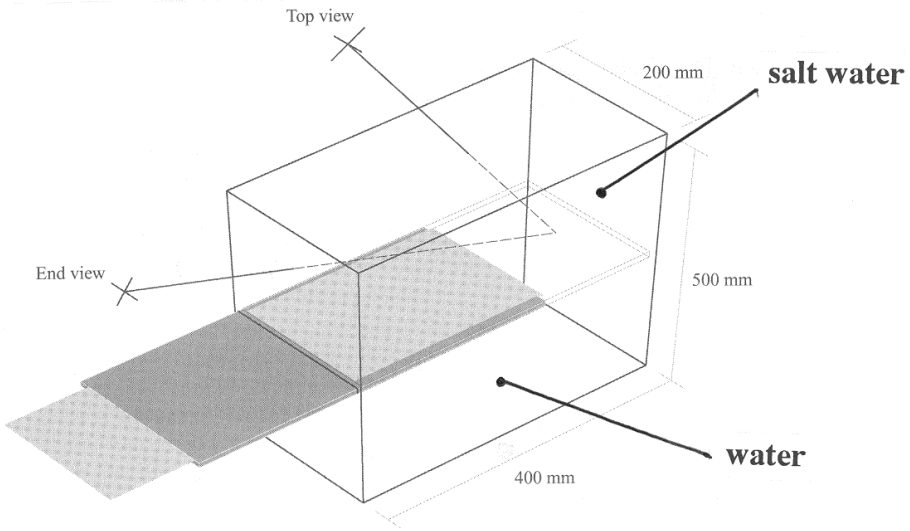

3D calculation : 400 x 320 x 160 zones
Random perturbation ($\varepsilon = 0.0005$)
2D initial velocity field used to represent effect of barrier removal $\Rightarrow$ 2D on average

2D turbulence model calculation
100 x 80 zones
barrier perturbation included

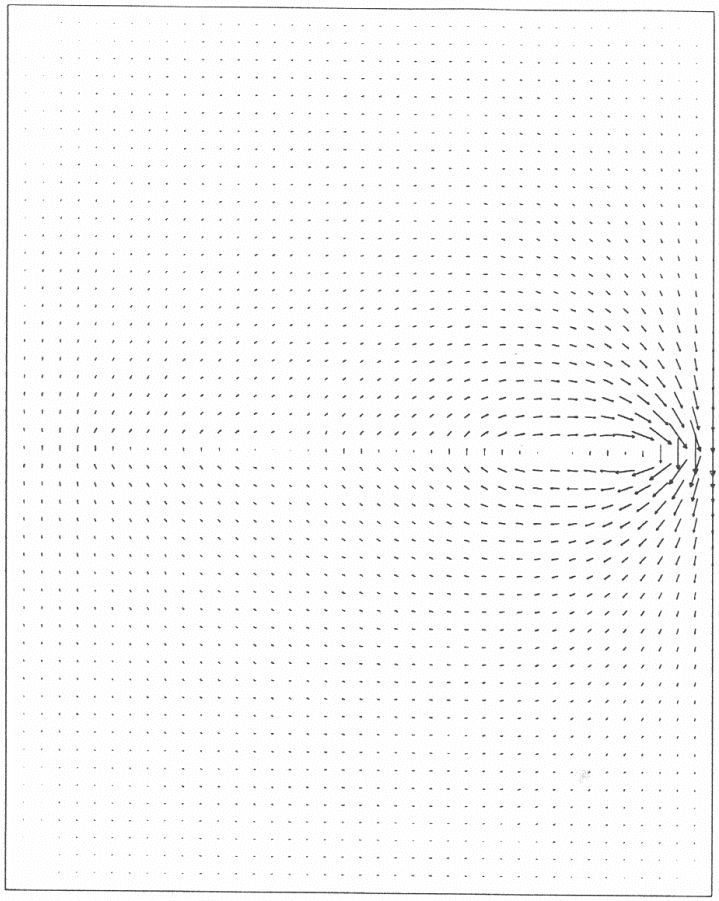

Model for barrier perturbation

Initial velocity field (2D)

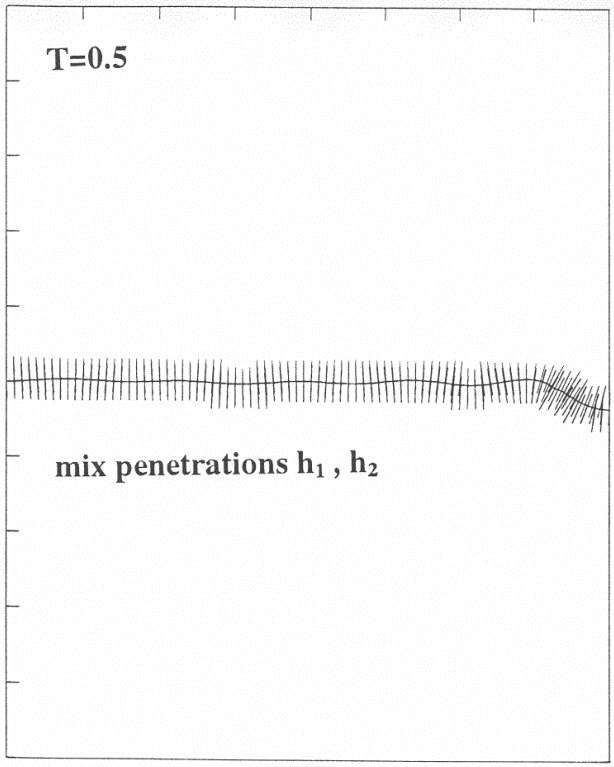

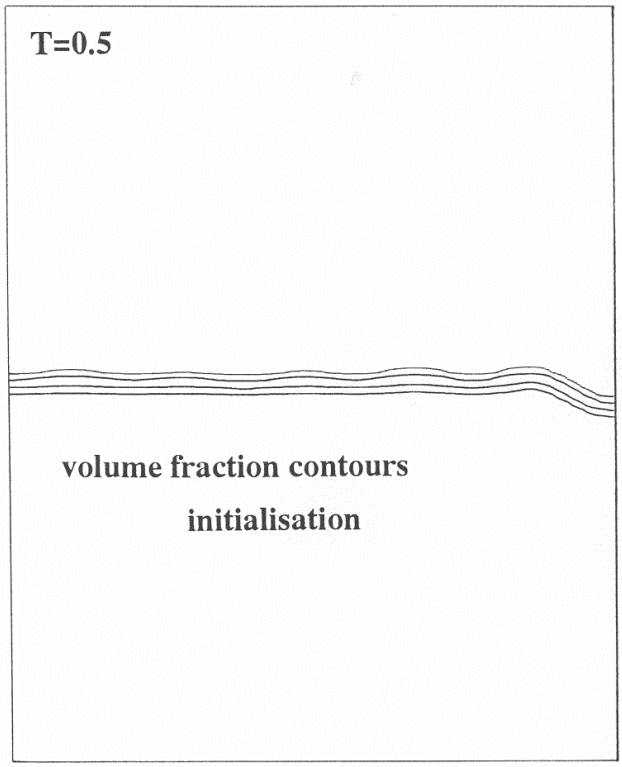

2D turbulence model calculation – run to t=0.5 with interface tracking and initial conditions model.

(a) (b) (c)

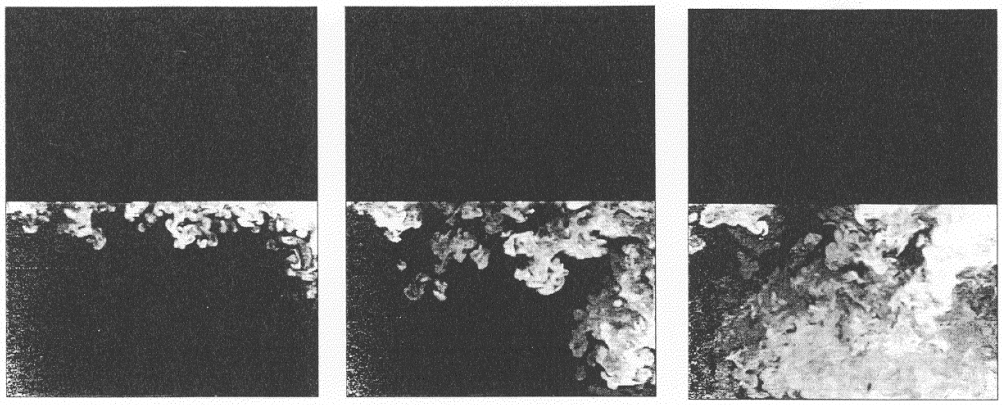

Experiment (lower half of tank)

3D Numerical Simulation (200x160x80 zones)

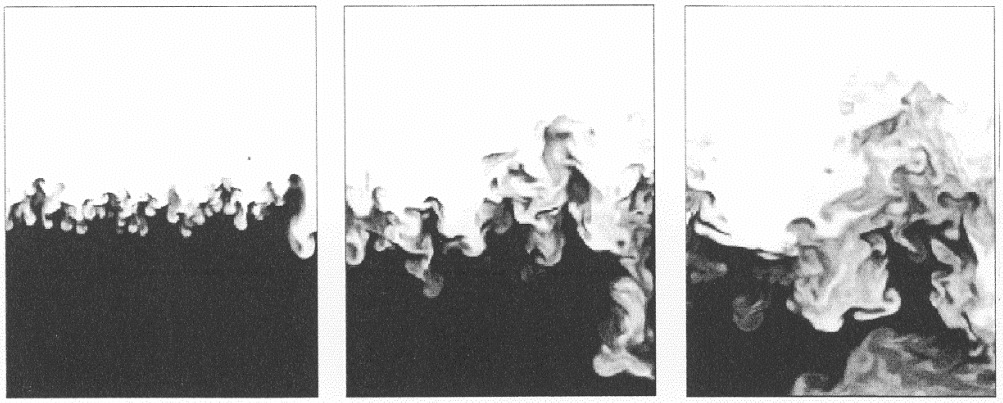

T=1.0 T=2.0 T=3.0

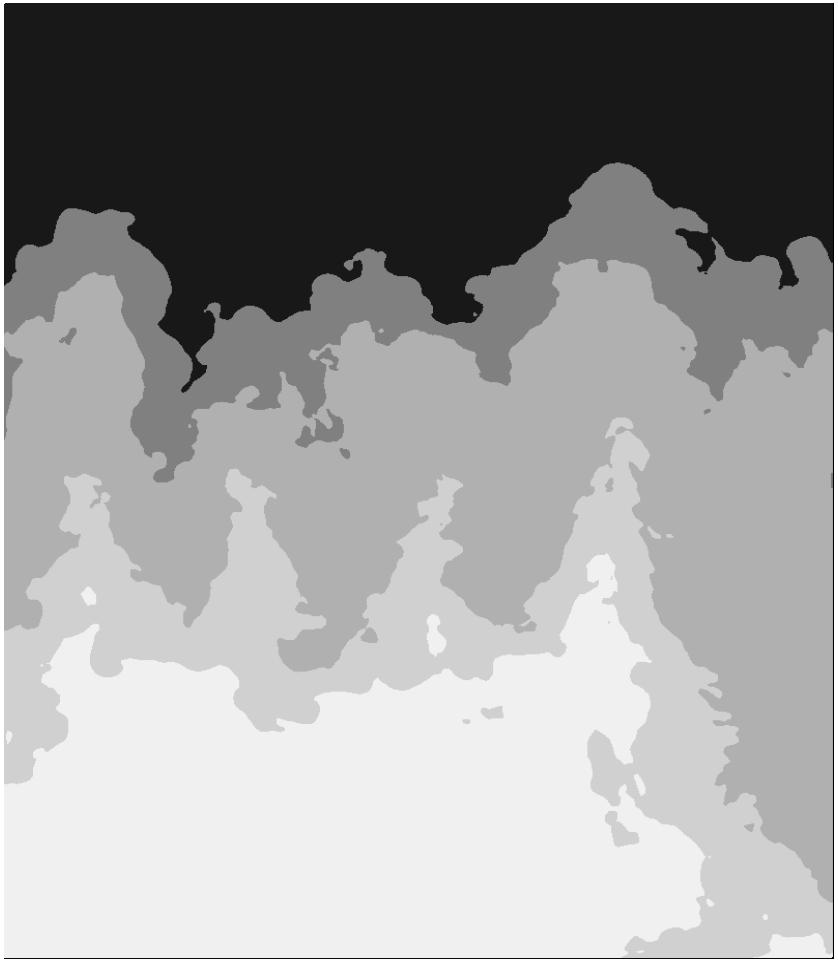

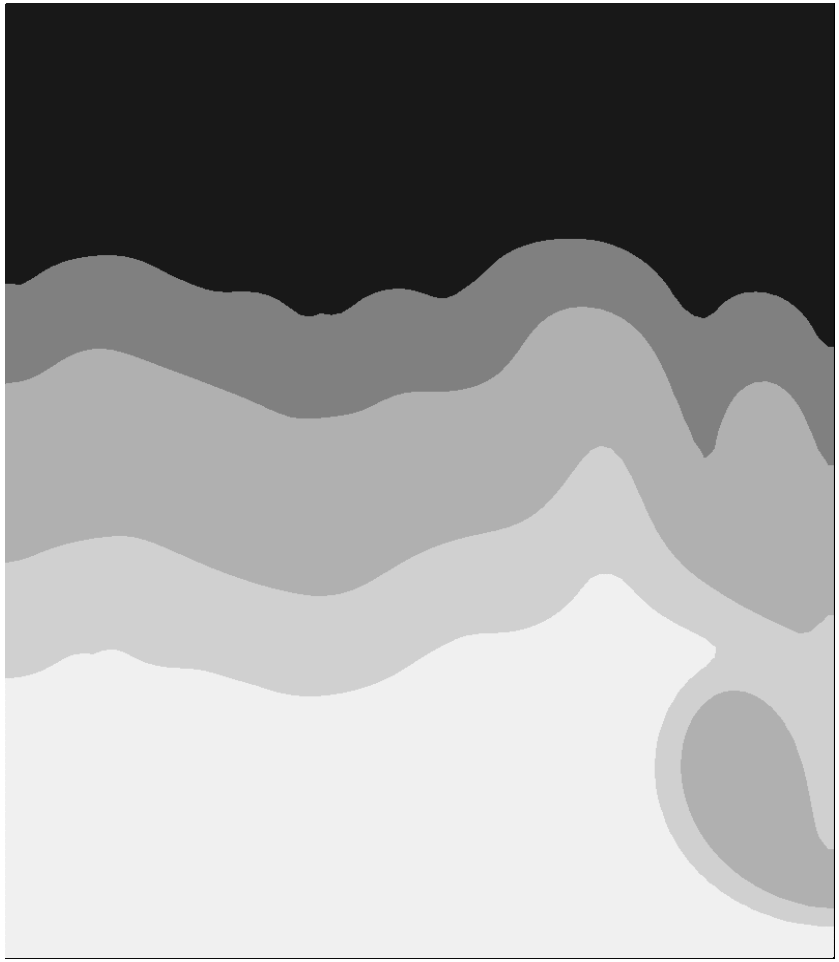

3D simulation at t = 2.0

2D turbulence model at t = 2.0

Mean volume fraction contours: 0.05, 0.25, 0.75, 0.95

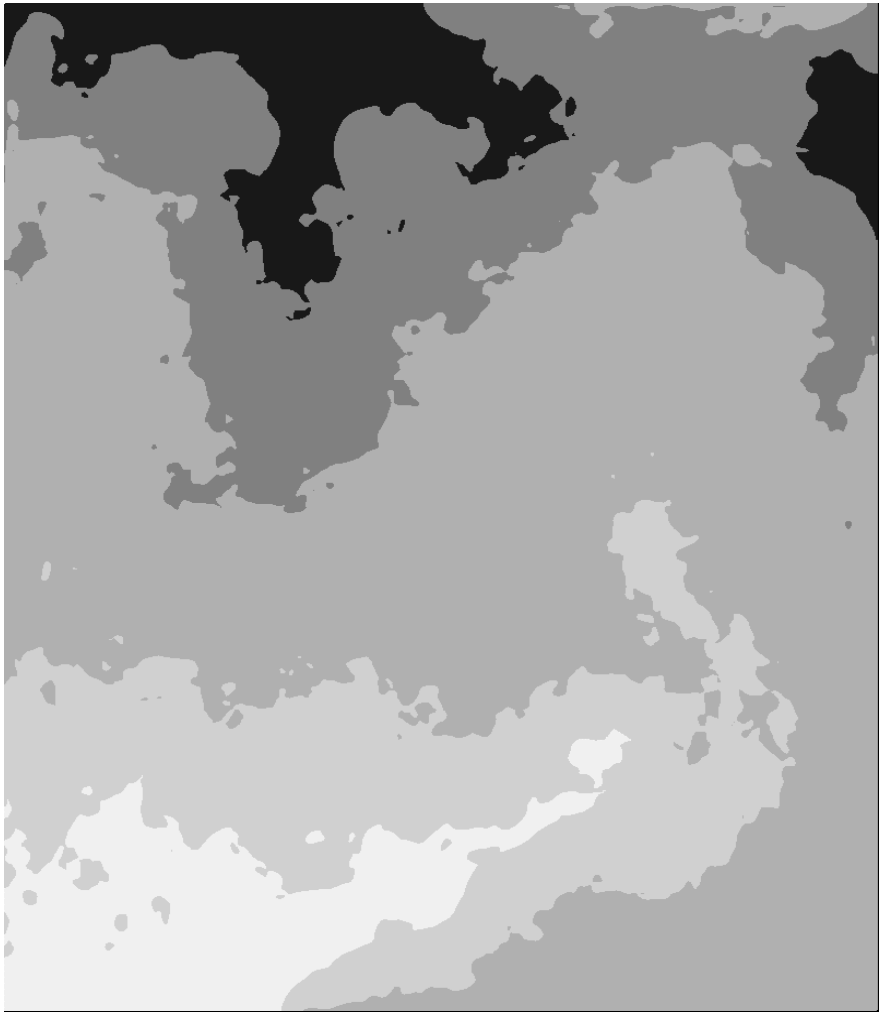

3D simulation at t = 3.0

2D simulation at t = 3.0

SHOCK TUBE EXPERIMENT (AWE)

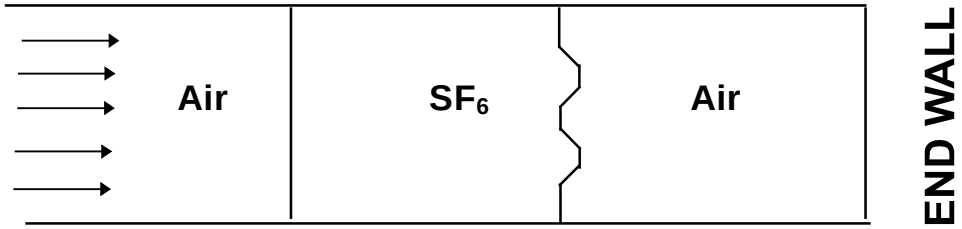

Cross-section 20 x 10 cm

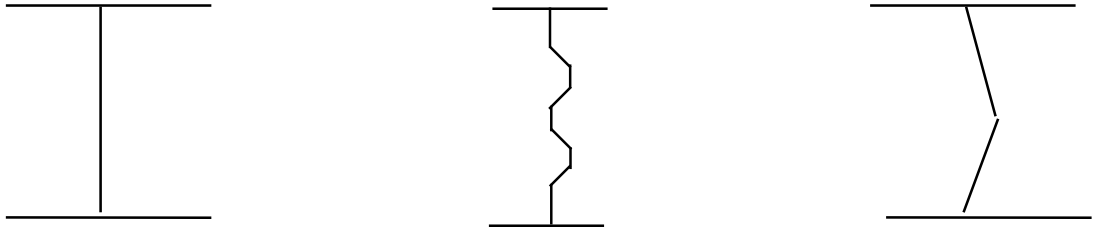

(a) flat **(b) double bump** **(c) chevron**

Moving mesh option used (semi-Lagrangian calculations)

3D LES: **400 x 320 x 160 zones**
random interface perturbations (models effect of membrane rupture)
wavelengths **0.5 to 5 cm**
s.d **0.01 cm**

2D turbulence model calculation
200 x 160 zones
initial conditions model
a_o = 0.02 cm, λ_0 = 0.5 cm

Shock tube experiment : flat interface

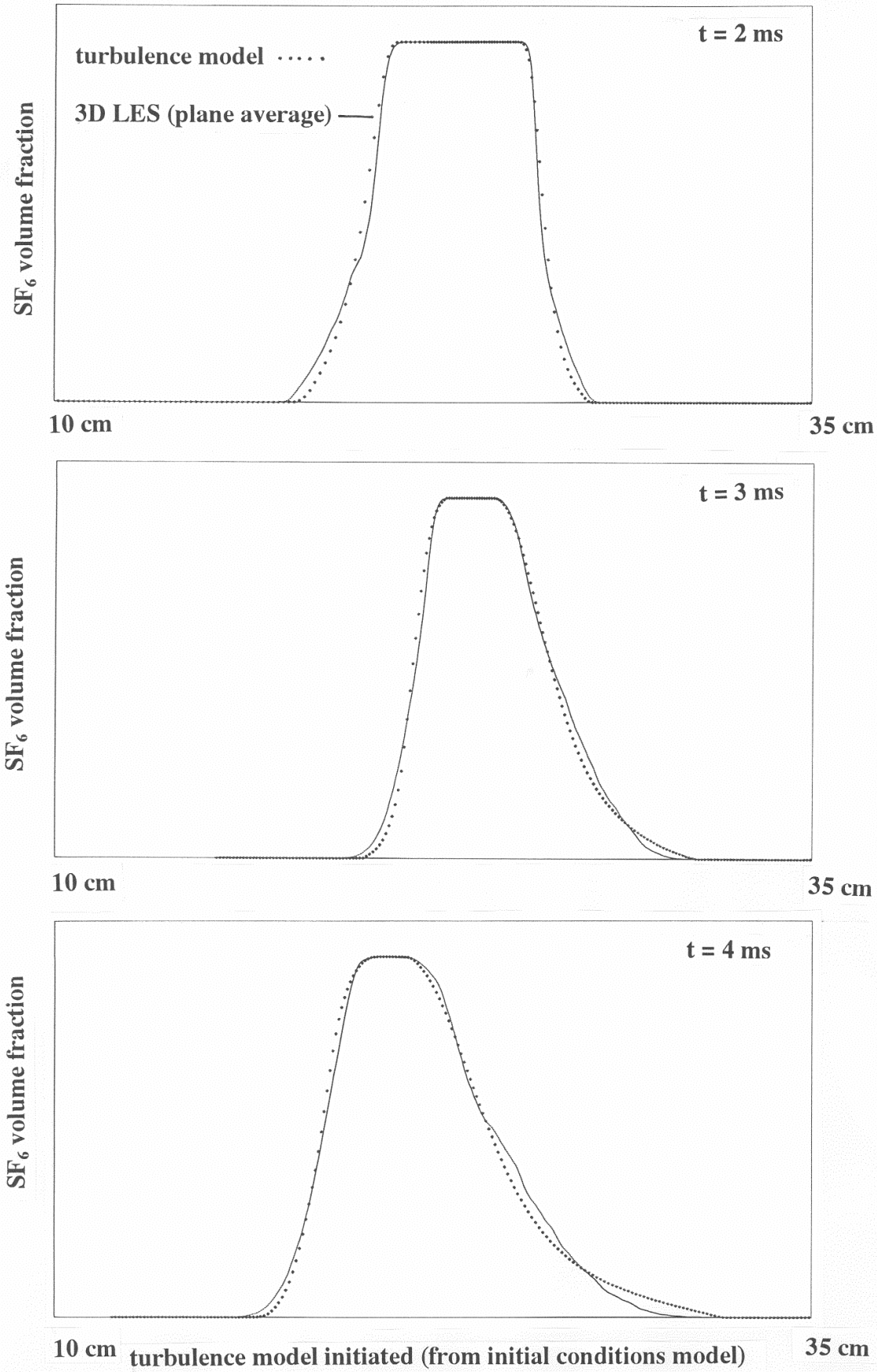

turbulence model initiated (from initial conditions model)
at t = 0.2 ms (first interface), t=1.1 ms (second interface)
initial molecular mixing fraction = 0.5

AWE Shock Tube Experiment

Double Bump results (0.0 - 1.9 ms)

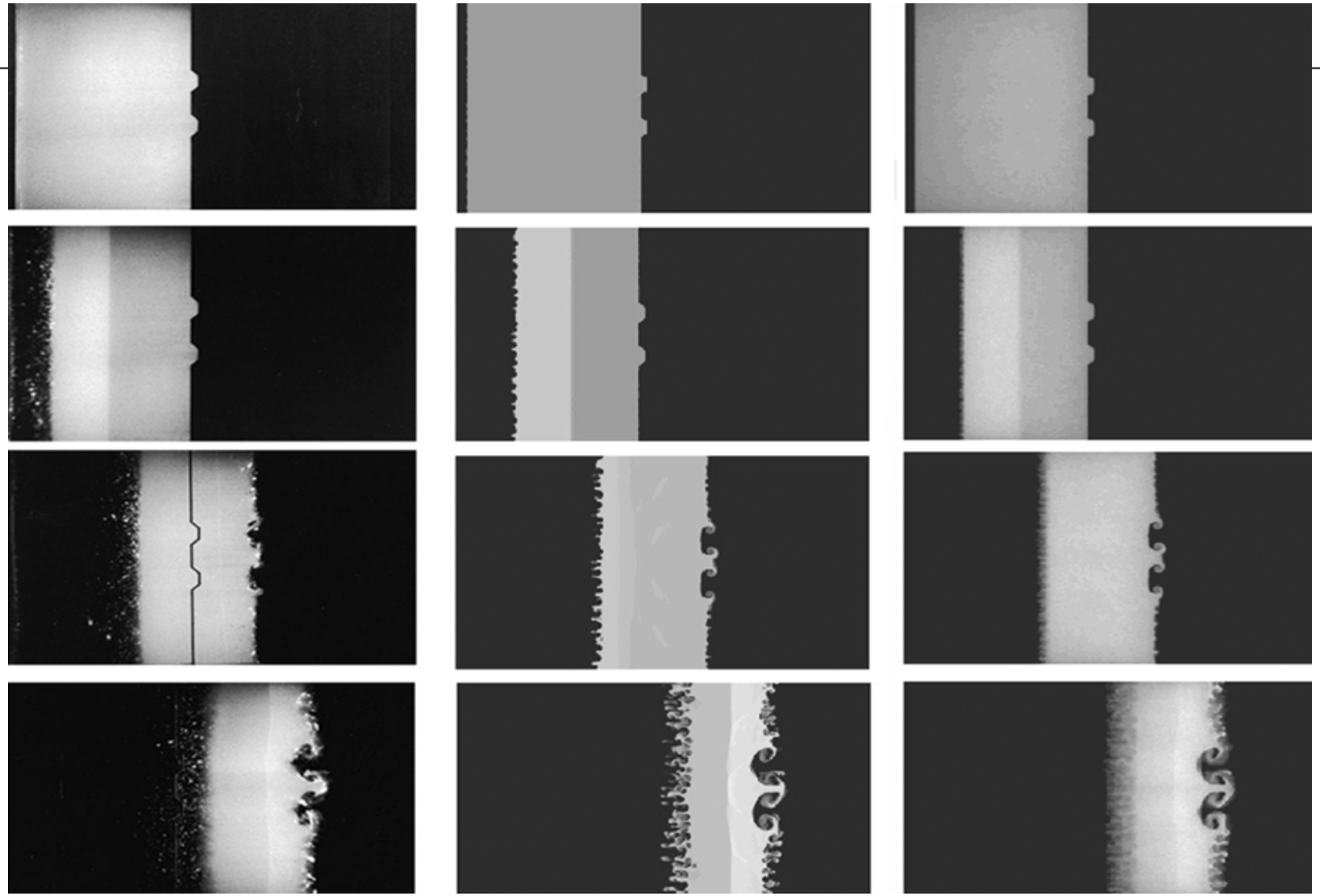

Experiment

3D simulation

3D simulation (scattered image)

AWE Shock Tube Experiment

Double Bump results (2.2 - 3.9 ms)

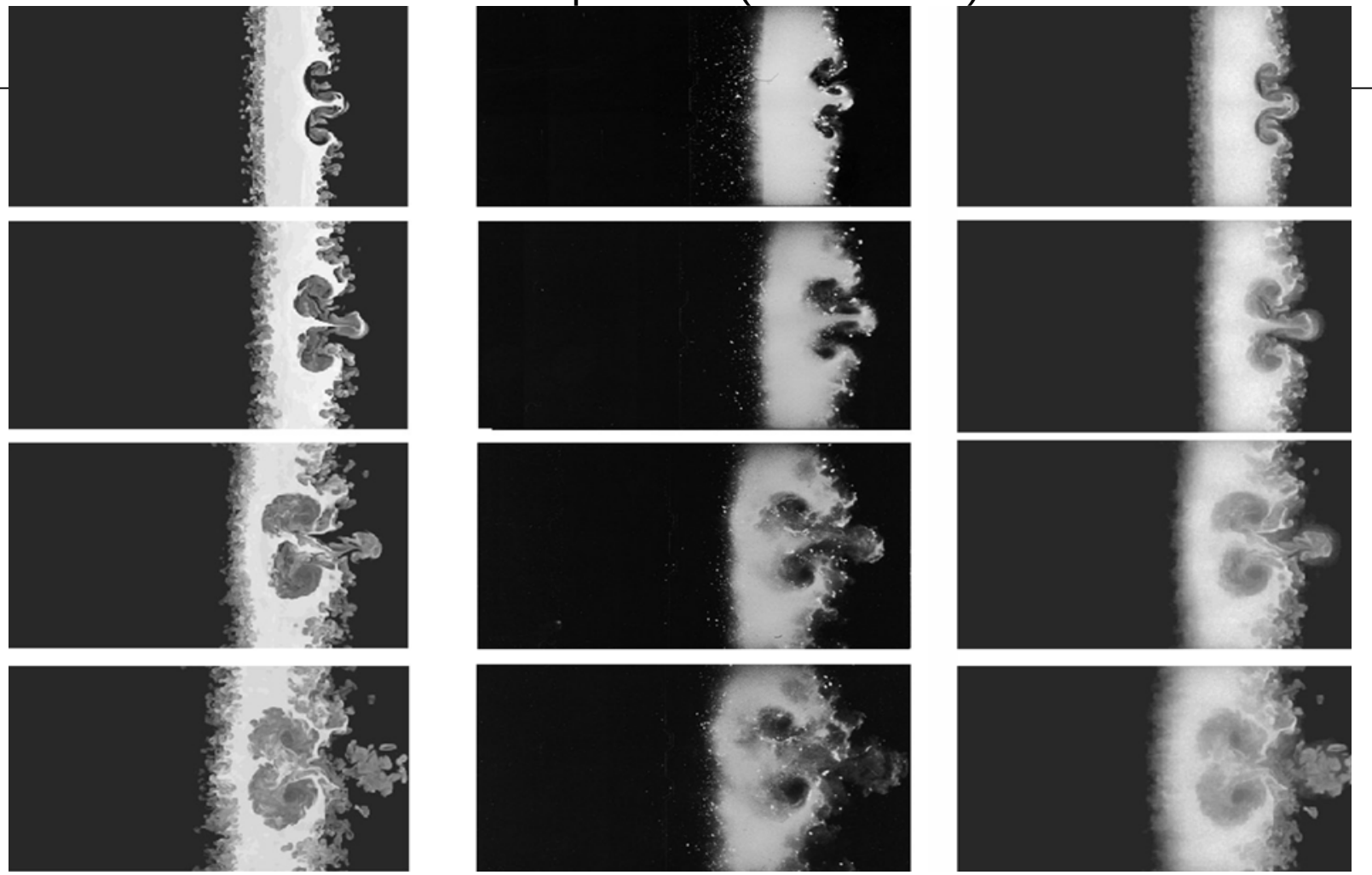

3D simulation | Experiment | 3D simulation(scattered image)

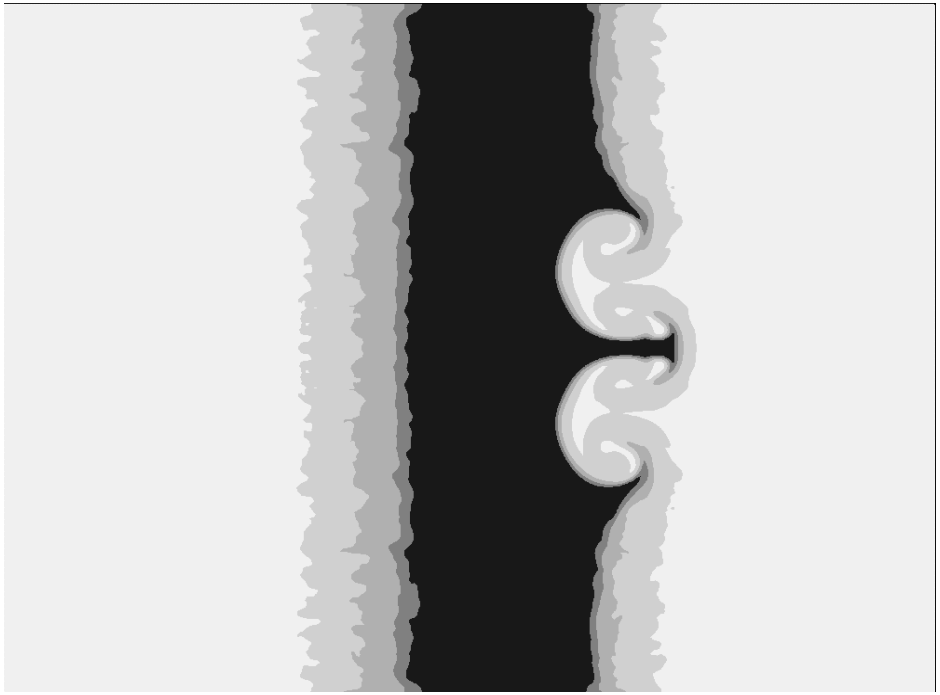

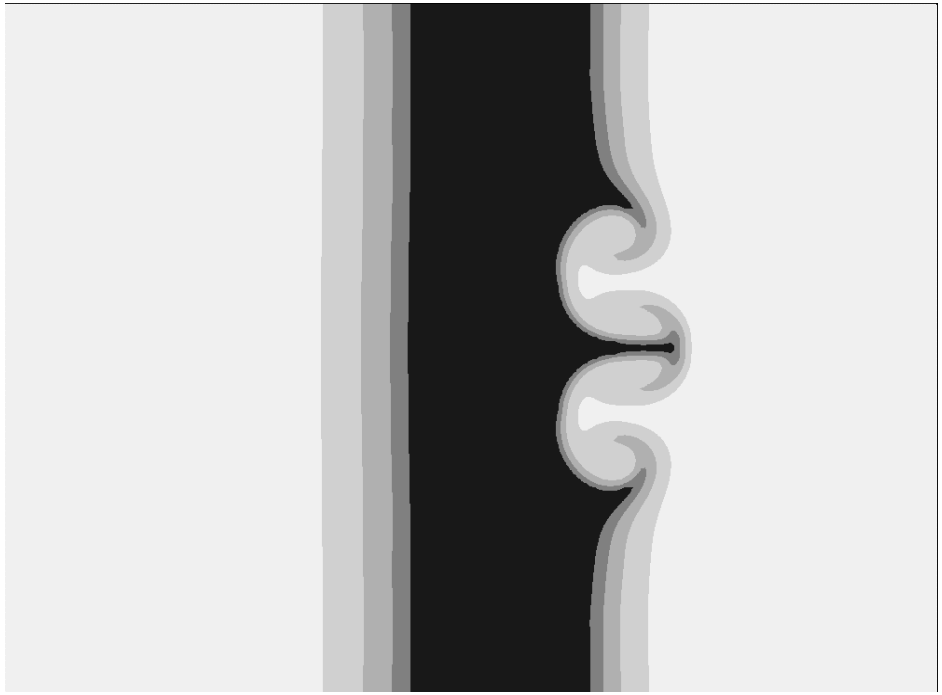

3D simulation at t = 2.0ms

2D turbulence model at t = 2.0ms

Double bump experiment

mean volume fraction contours: 0.05, 0.3, 0.7, 0.95

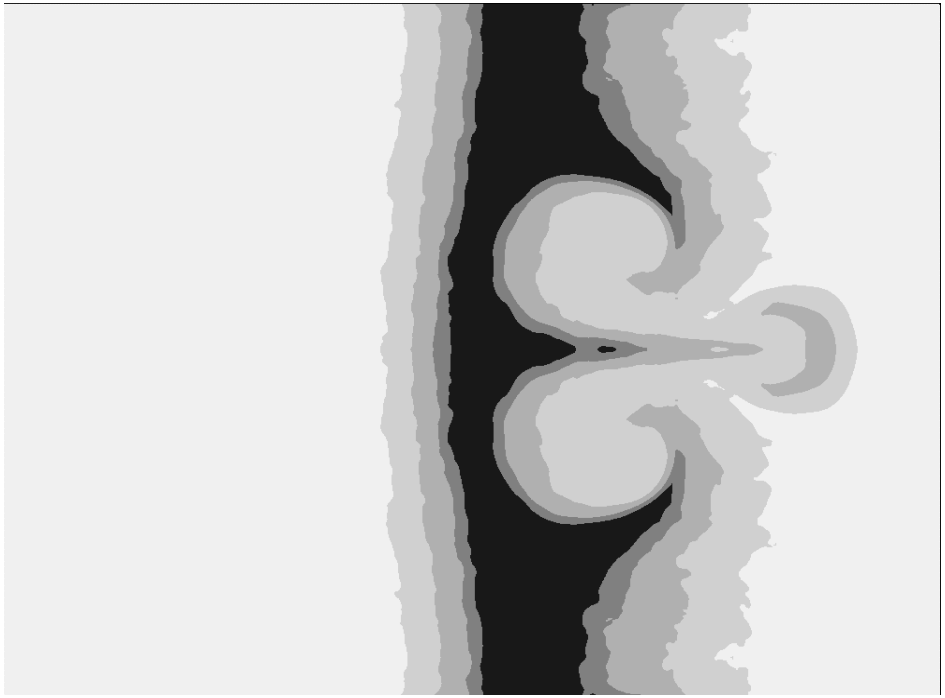

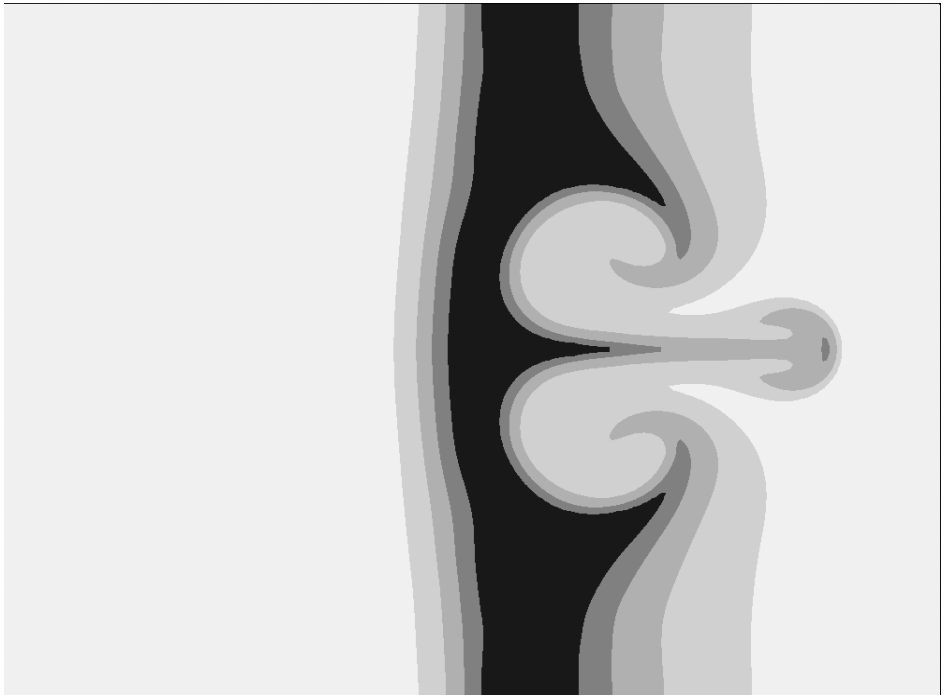

3D simulation at t = 3.0ms

2D turbulence model at t = 3.0ms

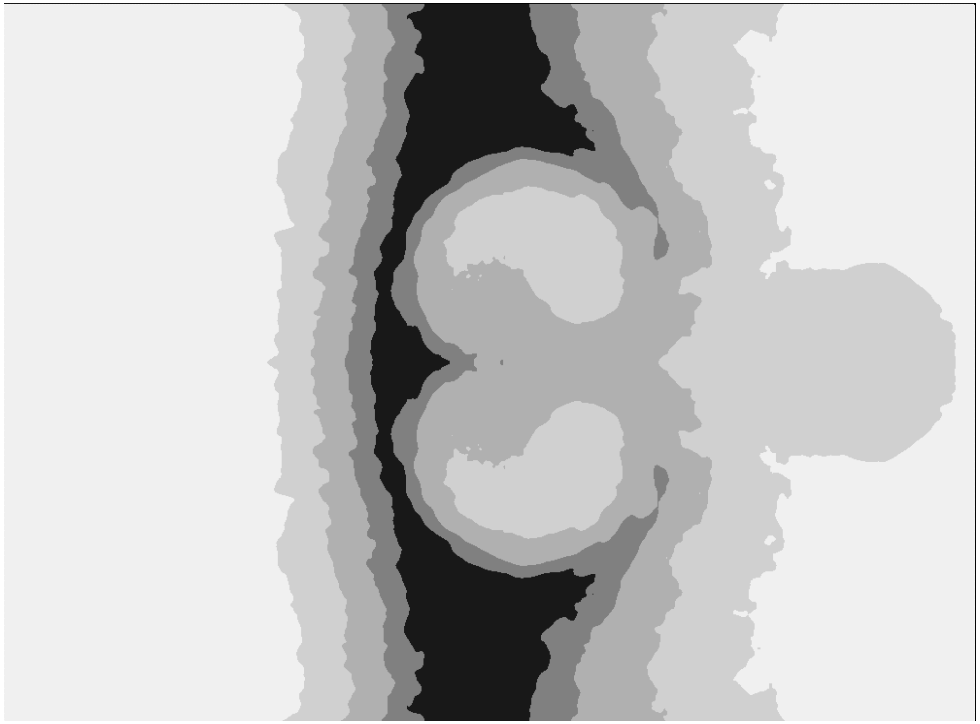

3D simulation at t = 4.0ms

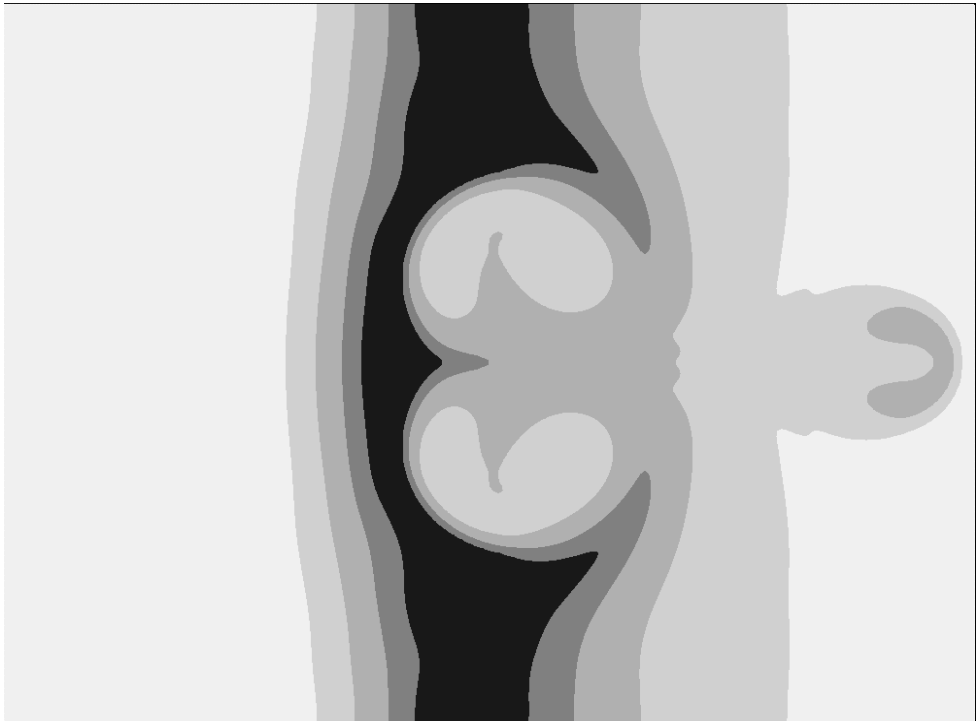

2D turbulence model at t = 4.0ms

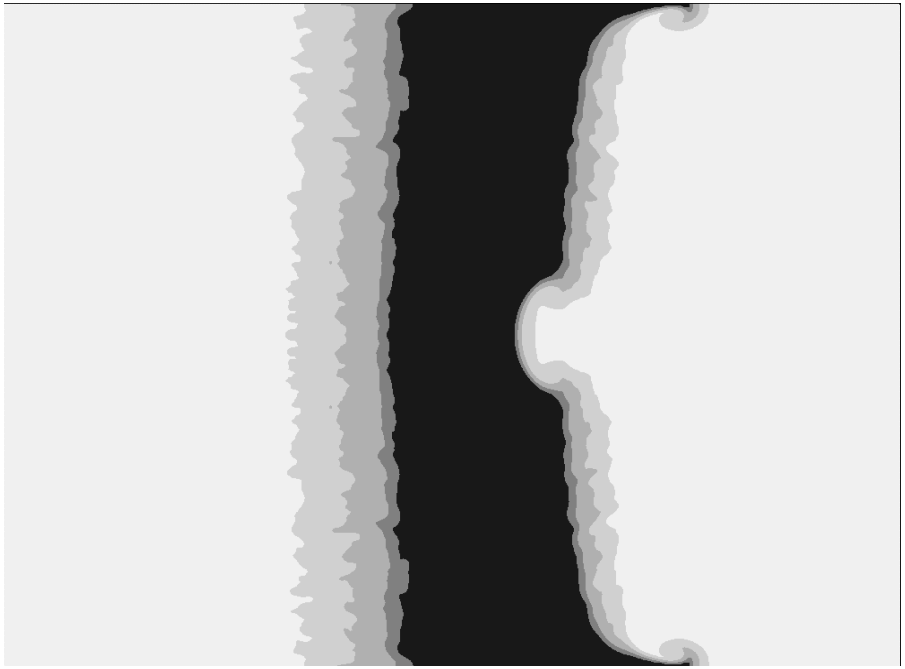

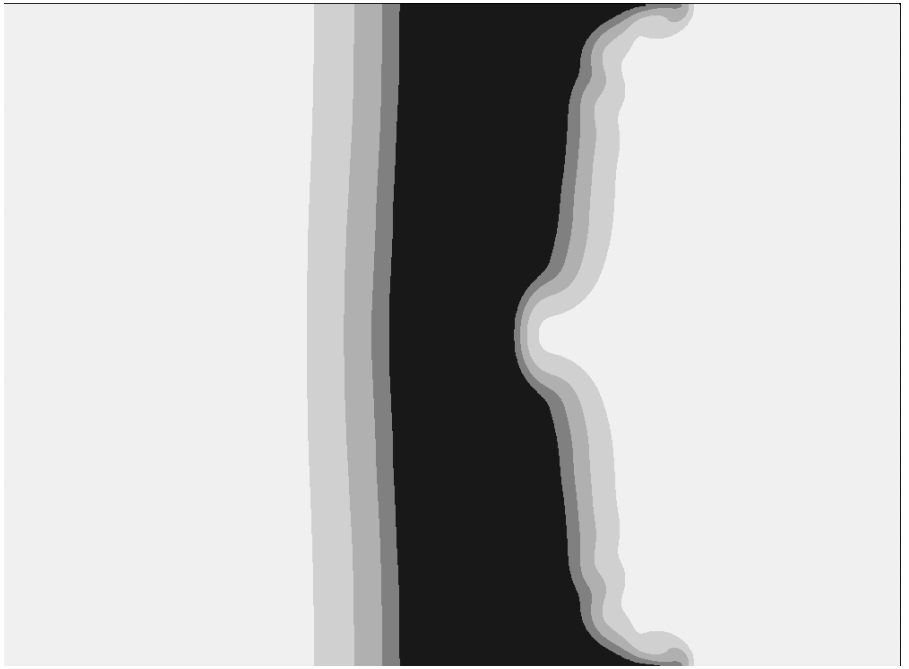

3D simulation at t = 2.0ms

2D turbulence model at t = 2.0ms

mean volume fraction contours: 0.05, 0.3, 0.7, 0.95

Chevron experiment

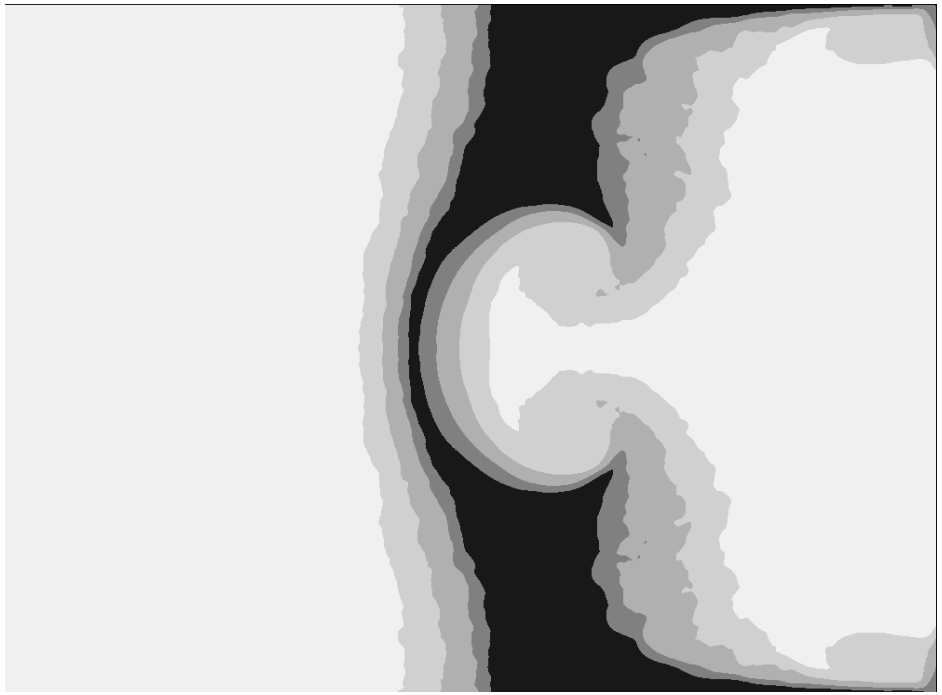

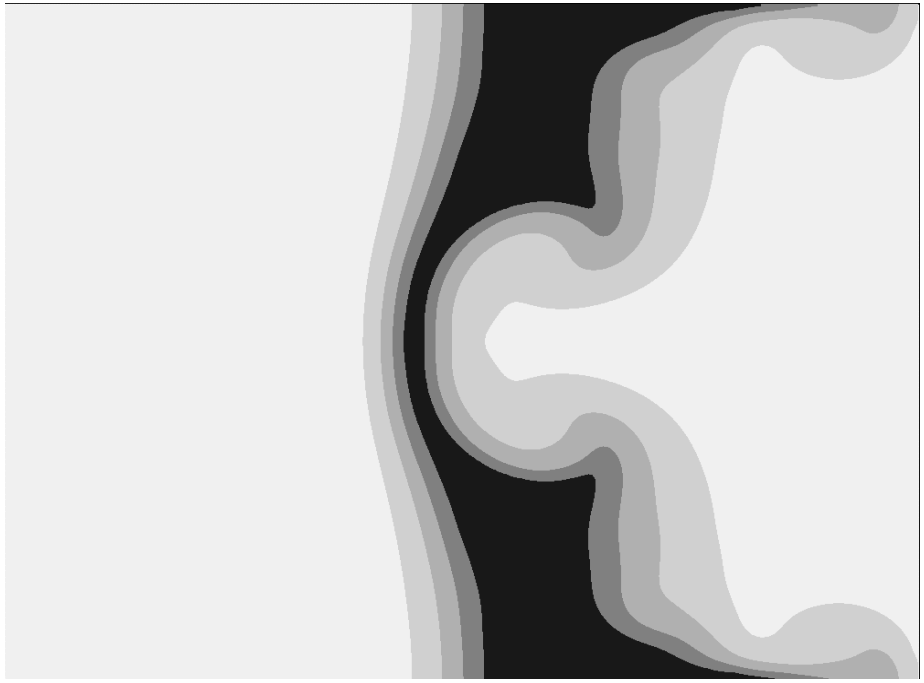

3D simulation at t = 3.0ms

2D turbulence model at t = 3.0ms

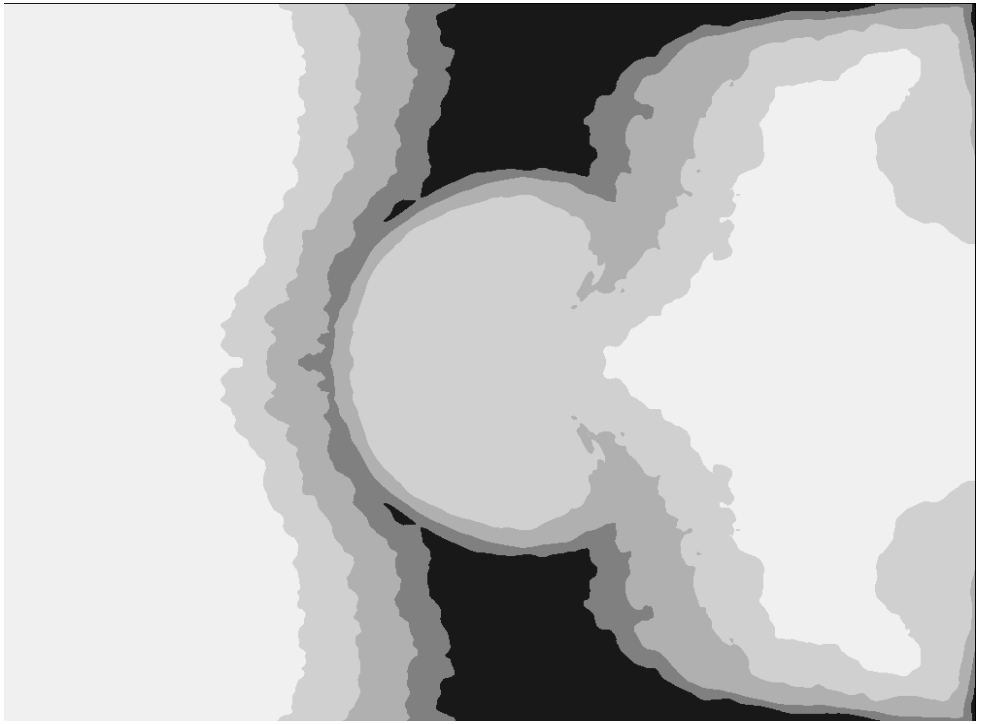

3D simulation at t=4.0ms

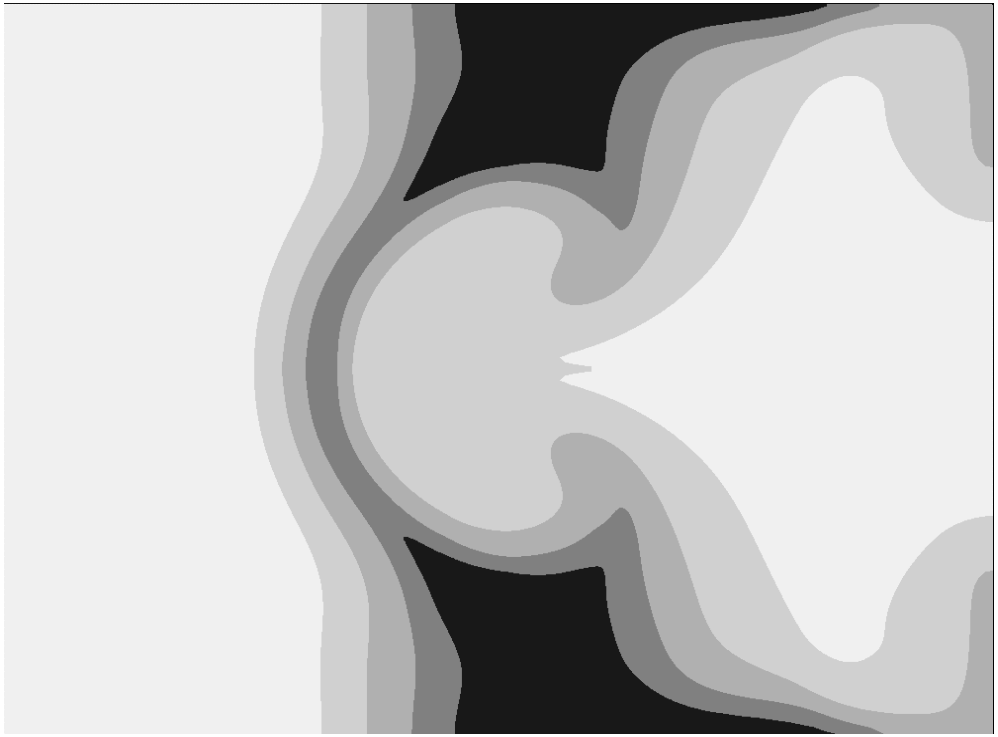

2D turbulence model at t=4.0ms

FINAL REMARKS

- **The 2D turbulence model based on the equations of multiphase flow, using a single set of model coefficients has given satisfactory results for**

  RT self-similar mixing
  A 2D RT experiment
  The double-bump shock tube experiment
  The chevron shock tube experiment

- **3D LES for simplified problems, in conjunction with experimental data, is making a very valuable contribution to the validation of the turbulence model.**

- **In the near future (after AWE's next supercomputer procurement) a more detailed comparison, (including 2D distributions of k and θ) will be made between the 2D turbulence model results and higher resolution LES.**

PRELIMINARY RESULTS OF LES SIMULATIONS OF SELF-SIMILAR VARIABLE ACCELERATION RT MIXING FLOWS

D L YOUNGS
AWE
ALDERMASTON, UK

A LLOR
CEA
BRUYÈRES-LE-CHÂTEL, FRANCE

The importance of self-similar variable acceleration RT flows (SSVARTs) for the design and calibration of turbulent mixing models is shown in the presentation by Antoine Llor at this workshop.

Because experimental results on SSVARTs are not, and will probably not be available in the near future, we are currently investigating such flows by means of LES.

In these incompressible flows the acceleration has the form

$$g = kt^n$$

and for self-similar mixing the mixing zone width grows in proportion to t^{n+2}.

Preliminary results, using low-resolution LES are given for n = 0, 1 and -1, using the TURMOIL3D code.

Results are compared with simple theoretical models.

THE TEST PROBLEM

This is based on the test problem proposed by Guy Dimonte (see presentation at this workshop).

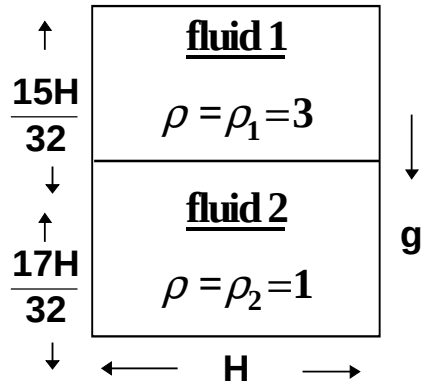

Computational domain	**:**	**H x H x 2H**
Zoning	**:**	**128 x 128 x 256**
Dimension	**:**	**H =1**
Acceleration	**:**	**(a) g = 2** **(b) g = t** **(c) g = 9/(4t)**

Run to t = 4.5, when for each case

$\left(\int \sqrt{g}\, dt\right)^2 = 40.5$

Compressible calculation with Mach number < 0.2

The major calculational problem is the treatment of variable g within a compressible calculation.

For incompressible flow, the pressure distribution adjusts at each instant of time to maintain $\mathrm{div}\,\underline{u} = 0$. **If no mixing occurs this implies hydrostatic equilibrium.**

$$\frac{\partial p}{\partial z} = \rho g$$

In the compressible simulations an appropriate pressure gradient is maintained by adding an internal energy source.

Initially adiabatic hydrostatic equilibrium (uniform entropy/neutral stability within each fluid) is assumed:-

$$\frac{\partial p_0}{\partial z} = \rho_0 g_0$$

$p_0 = k\rho_0^{\gamma}$, **in each region**

$$\rho_0 = \begin{cases} 3 & \text{just above the interface} \\ 1 & \text{just below the interface} \end{cases}$$

$\gamma = \frac{5}{3}$ **for both fluids**

If $g_{n+\frac{1}{2}}$ is the value of g for the n-th time step, at the start of the time step

the internal energy is scaled:-

$$\varepsilon' = \varepsilon . \frac{g_{n+\frac{1}{2}}}{g_{n-\frac{1}{2}}}$$

This maintains hydrostatic equilibrium outside the mixing zone and uniform entropy within each fluid.

The acceleration history needs to be modified slightly to give finite non-zero g at t = 0:-

case (b) $g = \max \{0.01, t\}$

case (c) $g = \min \{50, 9/(4t)\}$

The initial interface pressure is chosen high enough to ensure that the Mach no. of the flow remains small (M<0.2) at all times and also high enough to give small (<4%) variation in the initial density of each region.

THE INITIAL PERTURBATION

RT experiments with constant g give bubble penetration

$$h_1 = \alpha \frac{\rho_1 - \rho_2}{\rho_1 + \rho_2} gt^2 \quad \text{, with } \alpha \sim 0.05 \text{ to } 0.06$$

TURMOIL3D calculations with short wavelength initial perturbations (growth purely by mode coupling) give $\alpha \sim 0.03$.

Need to assume long wavelength initial perturbations with amplitude $\propto$ wavelength (as proposed by Inogamov [1]) to give self-similar growth with $\alpha \sim 0.05$.

Perturbation used $\xi(x,y) = \xi_S + \xi_L$

ξ_S : **wavelengths** **$4\Delta x$ to $8\Delta x$**
s.d **=** **$0.02\ \Delta x$**

ξ_L : **power spectrum** **P(k)**

$$\sigma_\lambda = \left\{ \int_{2\pi/\lambda}^{\infty} P(k)dk \right\}^{\frac{1}{2}} = \varepsilon\lambda$$

$$\Rightarrow P(k) \propto 1/k^3$$

$\varepsilon = 0.0005$

wavelengths in the range $4\Delta x$ **to** $\frac{H}{2}$

RESULTS SHOWN

f_1 , f_2 : volume fractions of fluids 1 and 2

$\overline{f_1}$, $\overline{f_2}$: plane averaged values

$W = \int \overline{f_1}\ \overline{f_2}\ dz$ integral mix width

h_1 : bubble penetration - measured to point where $\overline{f_1} = 0.99$.
Approximation used here : $h_1 = 3.3W$

θ = $\dfrac{\int \overline{f_1 f_2}\ dz}{\int \overline{f_1}.\overline{f_2}\ dz}$, molecular mixing fraction

$\dfrac{D}{P}$ = $\dfrac{\text{KE dissipated}}{\text{KE production}}$

$S = \dfrac{\rho_1 - \rho_2}{\rho_1 + \rho_2}\left(\int \sqrt{g}\ dt\right)^2$

Fig 1 : initial long wavelength perturbation
Fig 2 : isosurfaces for the case g = k
Fig 3 : profiles of $\overline{f_1}$
Fig 4 : plots of h_1
Fig 5 : plots of θ
Fig 6 : plots of D/P

Figure 1

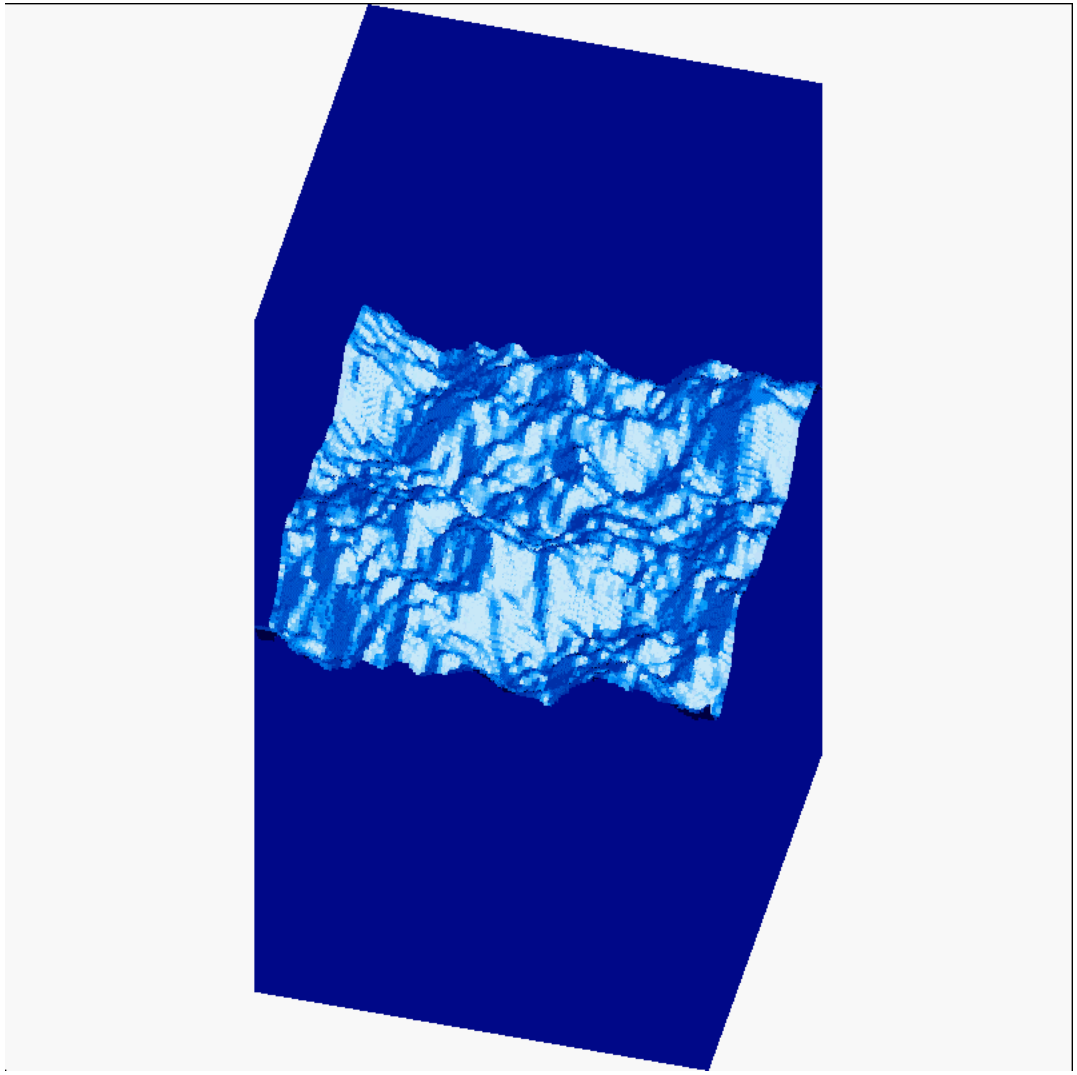

ε = 0.005, initial perturbation x 200

Figure2: Isosurfaces (f_1 = 0.99) for g =k

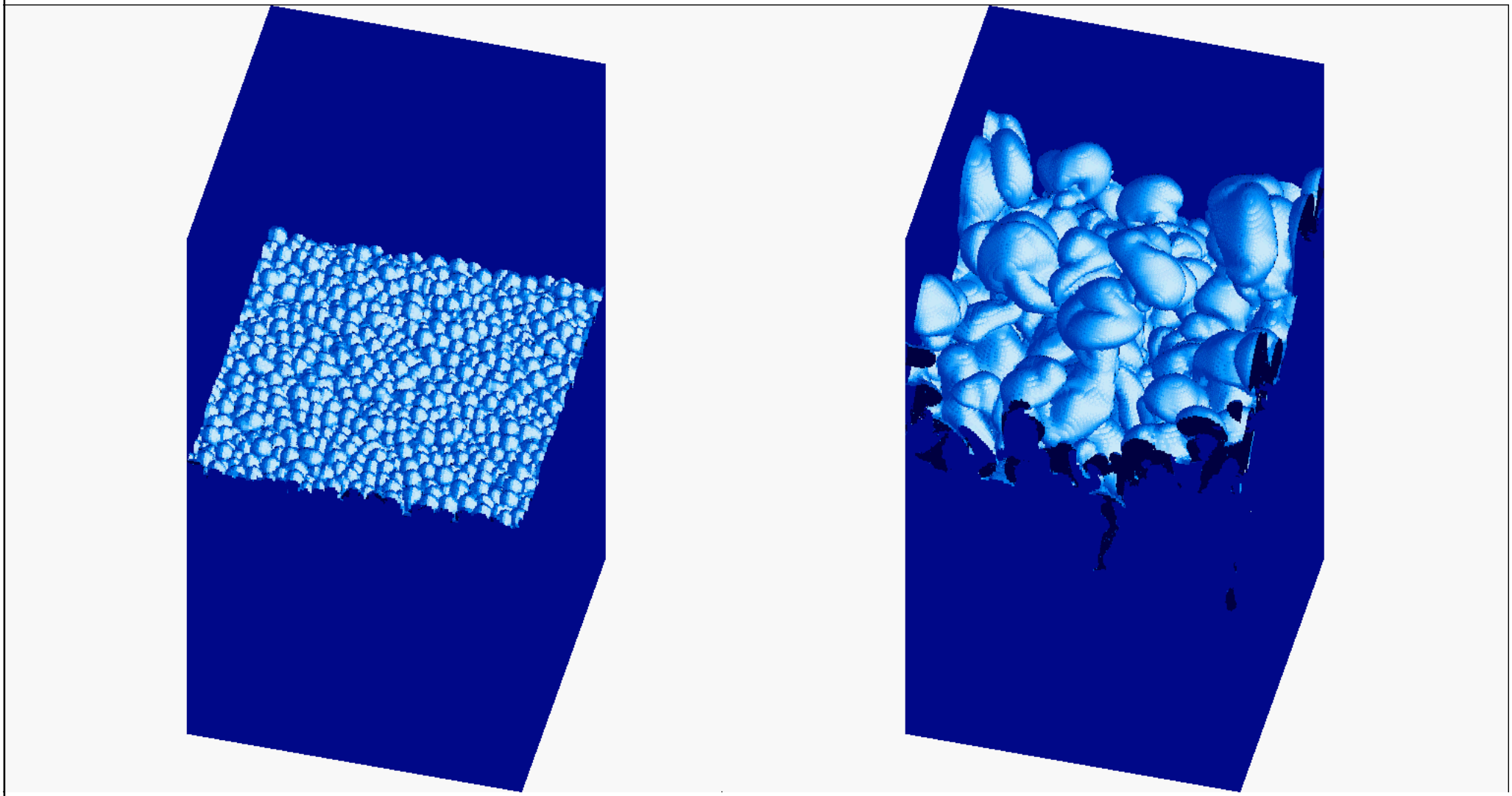

t = 0.9 **t = 3.5**

Figure3

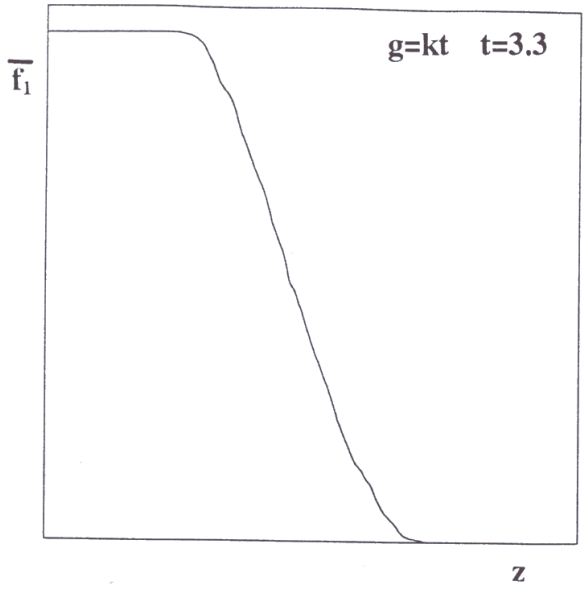
g=kt t=3.3
$\overline{f_1}$
z

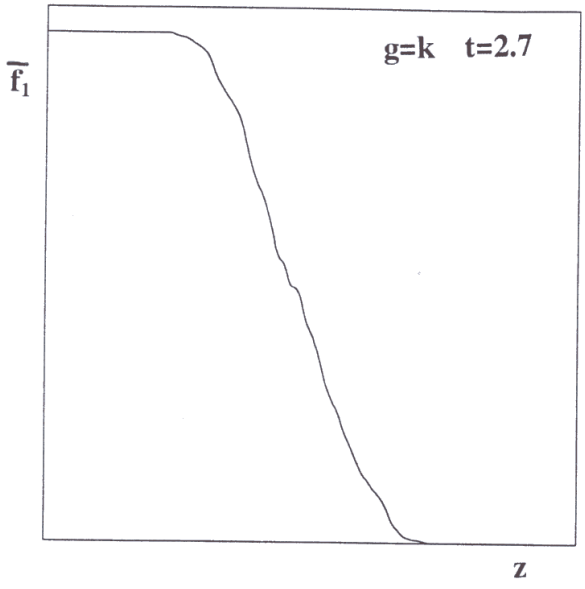
g=k t=2.7
$\overline{f_1}$
z

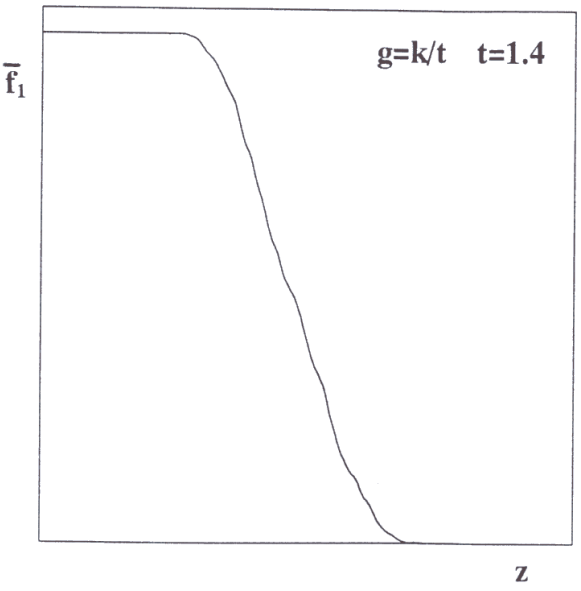
g=k/t t=1.4
$\overline{f_1}$
z

Figure4

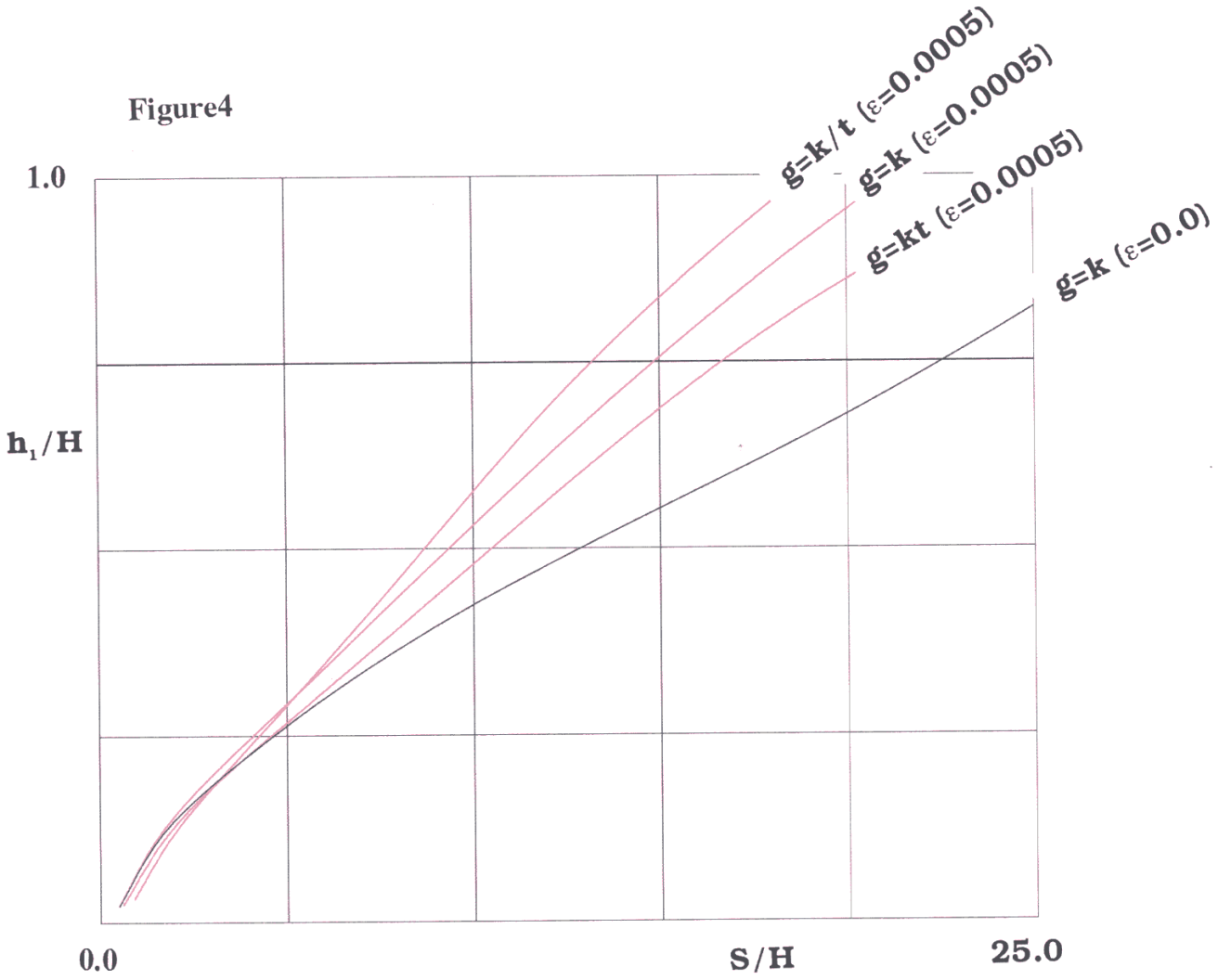

Figure5

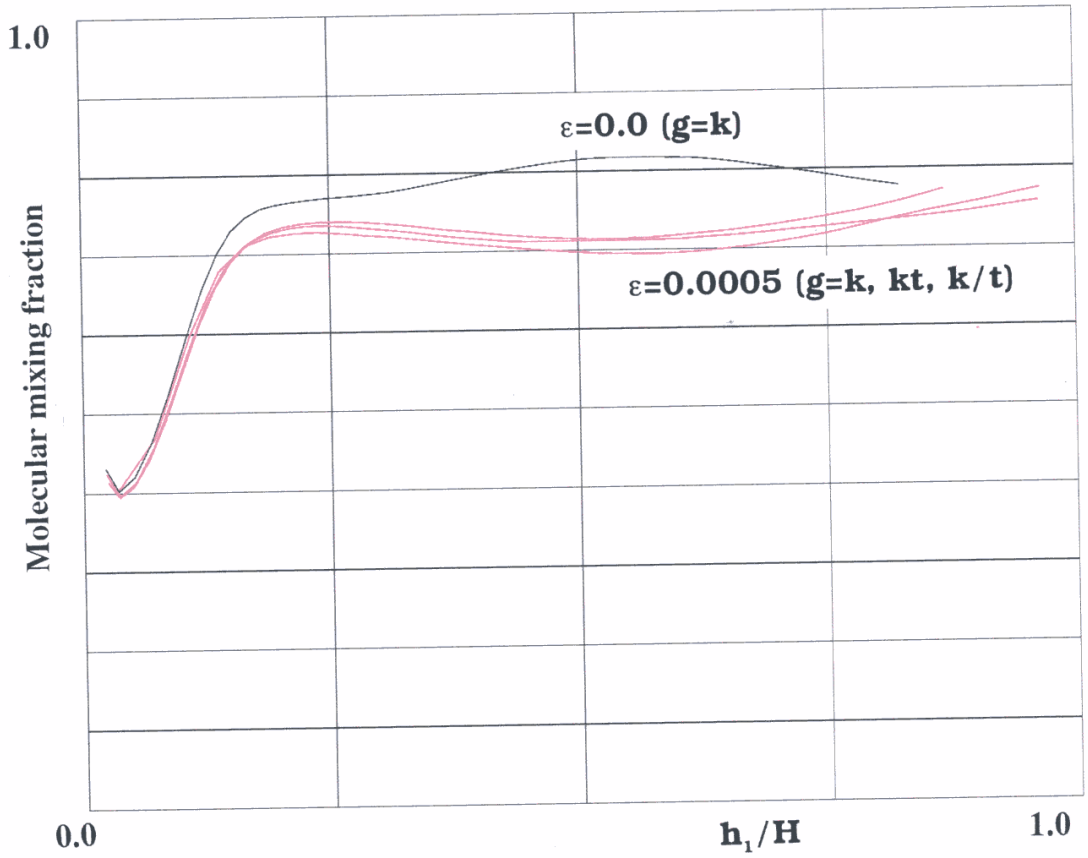

Figure6

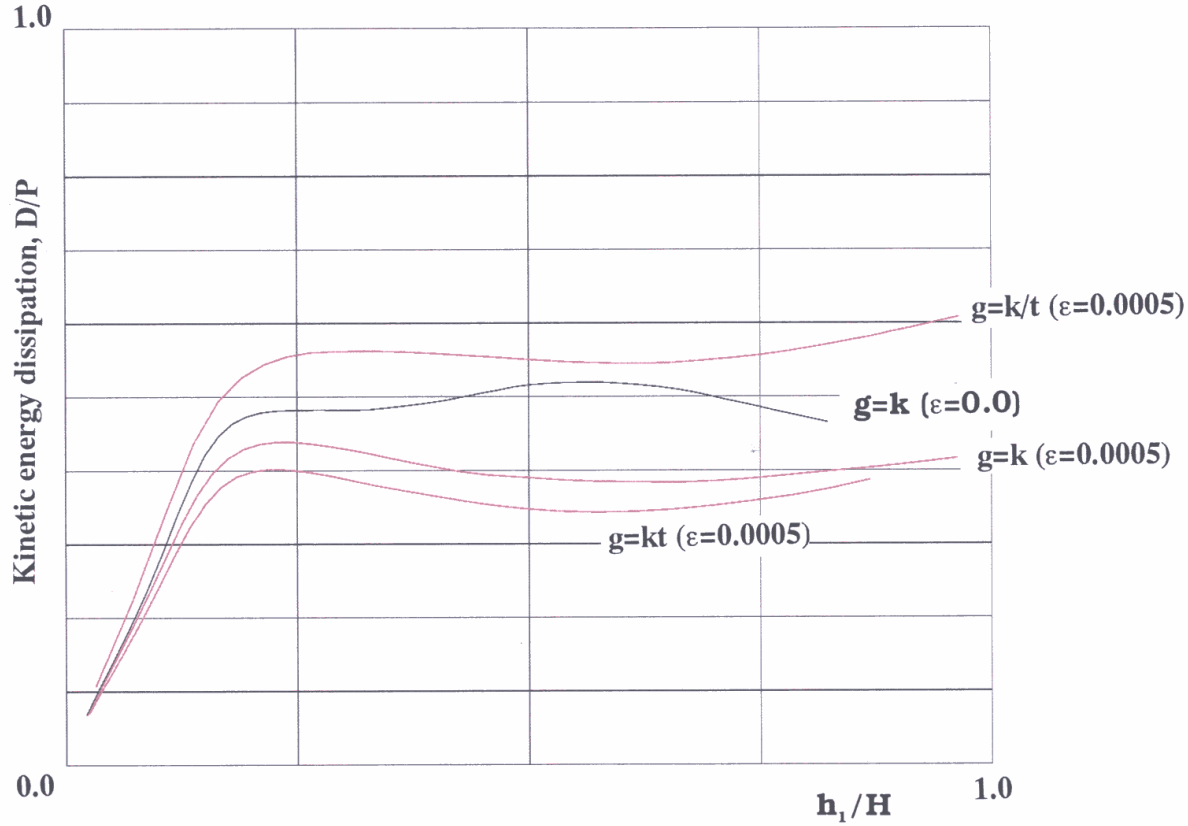
1.0
Kinetic energy dissipation, D/P
0.0
1.0
h1/H
g=k/t (ε=0.0005)
g=k (ε=0.0)
g=k (ε=0.0005)
g=kt (ε=0.0005)

Figure7 : Probability distributions for f_1 within a plane z=constant

Wilson and Andrews At =0.001

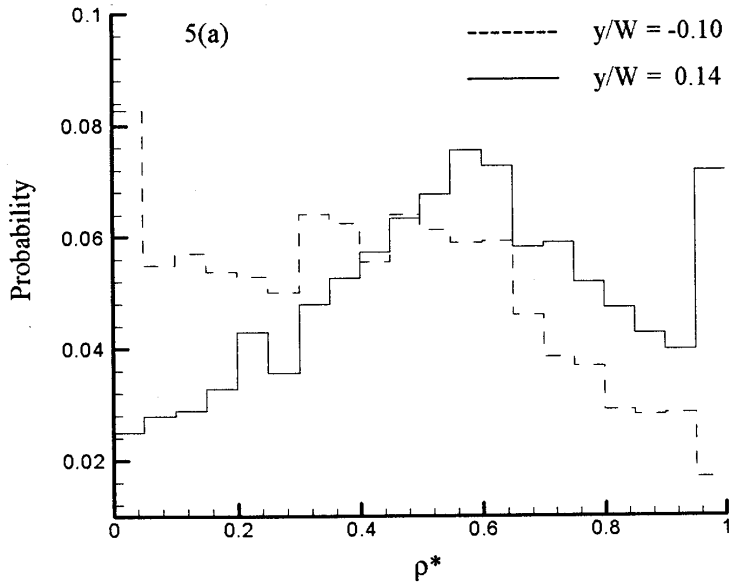

TURMOIL3D calculation
At=0.5
128x128x256 zones

g=constant

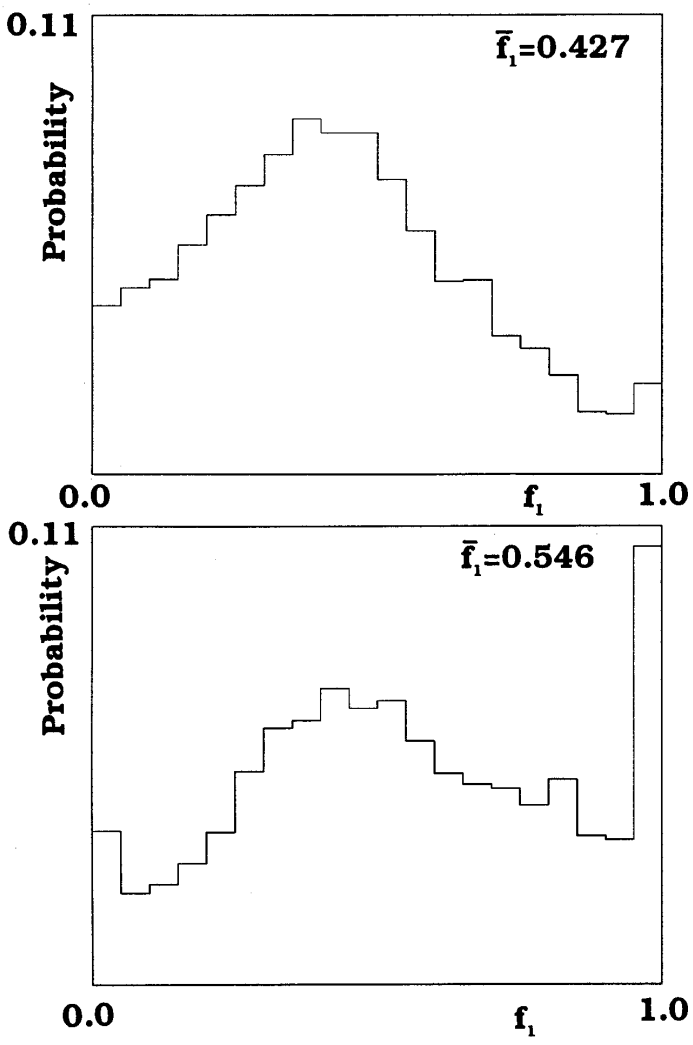

COMPARISON OF RESULTS WITH SIMPLE MODELS

(A) The Simplest Model

Bubbles of radius R have a limiting velocity ~ $\sqrt{AgR}$. If it is assumed that $R \sim h_1$, then

$$\dot{h}_1 = c\sqrt{Agh_1}$$

ie $$h_1 = \alpha A\left\{\int_0^t \sqrt{g(t')}\, dt'\right\}^2 = \alpha S \qquad \ldots(1)$$

Figure 5 shows plots of h_1 vs S. The slopes of the curves (for the range h_1/H = 0.25 to 0.75) give; for $\varepsilon = 0.0005$

n = 0	,	α	=	0.0464
n = 1	,	α	=	0.0415
n = -1	,	α	=	0.0559

The model works surprisingly well, but there is some variation of α with n:-

$$\frac{\alpha_1}{\alpha_0} = 0.89$$

$$\frac{\alpha_{-1}}{\alpha_0} = 1.20$$

(B) A Buoyancy - Drag Model

A model of this type, based on a modified form of Layzer's equation for a bubble rising in a cylindrical tube, was used by Hansom et al [2].

$$\ddot{h}_1 = Ag - \frac{C_D\left(\dot{h}_1\right)^2}{h_1} \qquad \text{. . . (2)}$$

acceleration = buoyancy - drag

For constant g, $C_D = 4.5$ gives $\alpha = 0.05$. Then if α is defined as in equation (1):-

$$\frac{\alpha_1}{\alpha_0} = 0.97$$

$$\frac{\alpha_{-1}}{\alpha_0} = 1.11$$

This is closer to the TURMOIL3D results than taking α independent of n but the change is not large enough.

Dimonte and Schneider [3] include a factor $\beta < 1$ in front of the Ag term in equation (2). This improves agreement with the 3D simulations.

(C) An Energy Balance Model

This is version of the model proposed by Ramshaw [4], but with different settings for the model coefficients.

Let $K = \frac{1}{2}\left(\rho_1 + \rho_2\right) h_1 V^2$ = kinetic energy within the mixing layer.

$\dot{P}$ = KE production rate (loss of potential energy)

$\dot{D}$ = dissipation rate

Then the model equations used are

$$\dot{K} = \dot{P} - \dot{D}$$

$$\dot{P} = c_1\left(\rho_1 - \rho_2\right) g\, h_1 \dot{h}_1$$

$$\dot{D} = c_2 \frac{1}{2}\left(\rho_1 + \rho_2\right) V^3$$

$$\dot{h}_1 = c_3 V$$

The coefficient c_1 depends on the shape of the volume fraction profile. For a linear distribution $c_1 = 1/3$. For the TURMOIL3D profiles (figure 4) $c_1 = 0.30$, and this is the value used here.

If for constant g we assume, α = 0.05 and D/P = 0.4 (figure 7) then

$c_2 = 1.4055$

$c_3 = 1.0541$

The equation $\dot{K} = \dot{P} - \dot{D}$ gives

$$\ddot{h}_1 = c_1 c_3^2 Ag - \frac{c_2 + c_3}{2c_3} \frac{\left(\dot{h}_1\right)^2}{h_1}$$

$$= \frac{1}{3} Ag - \frac{7}{6} \frac{\left(\dot{h}_1\right)^2}{h_1} \qquad \ldots (3)$$

This has the same form as the buoyancy - drag model (2). The coefficient in front of the Ag term is less than unity as in Dimonte and Schneider [3].

This choice of the coefficients gives

$\frac{\alpha_1}{\alpha_0} = 0.91$

$\frac{\alpha_{-1}}{\alpha_0} = 1.43$

also	D/P	=	0.40 assumed for n = 0
	D/P	=	0.36 for n = 1
	D/P	=	0.57 for n = -1

α_1/α_0 agrees with the 3D simulations

α_{-1}/α_0 appears to be somewhat too high. However, the variation of D/P with n (see fig. 6) is represented very well.

FUTURE PLANS

- Values of n outside the range [-1, 1]
- Higher resolution TURMOIL3D calculations
- Use of the SSVARTs results to differentiate between various types of RANS models.

REFERENCES

1. N A Inogamov et al, Proceedings of the 3rd IWPCTM, Royaumont (1991)
2. J C V Hansom et al, Laser and Particle Beams, Vol 8, p 51 (1990)
3. G Dimonte and M Schneider, Phys Rev E54, p 3740 (1996)
4. J D Ramshaw, Phys Rev E58, p 5834 (1998)

Shock – planar curtain interactions

Strong Secondary baroclinic deposition and emergence of coherent and random vortex projectiles (VPs), and decaying stratified turbulence

Shuang Zhang and Norman J. Zabusky

Laboratory of Visiometrics and Modeling
Department of Mechanical and Aerospace Engineering
Rutgers, The State University of New Jersey

Brief Review

Common geometries for studying accelerated inhomogeneous flows (**aifs**)

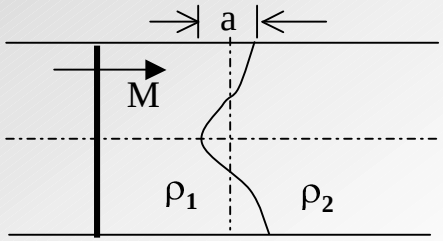

Linear, Nonlinear & Vortex: growth rate

… å …

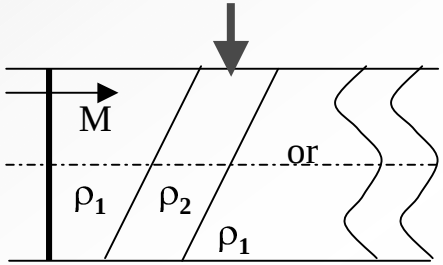

Curtain: inclined or perturbed (Sturtevant, 87; Benjamin et al, 84)

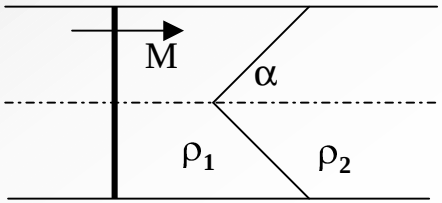

Self-similar Solution; Quantification on: Circulation, baroclinic effects & convergence

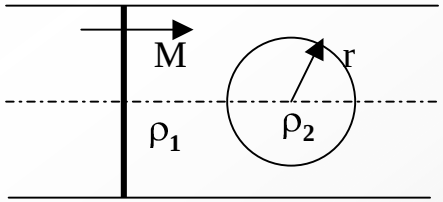

Circular Cylinder or Sphere (axisymmetric or 3D): Vortex separation & vortex projectiles (VPs)

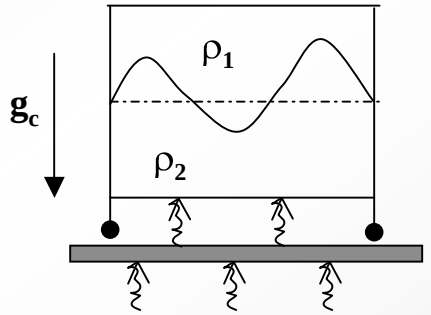

Reaccelerated tank (Jacobs & Niederhaus, 97)

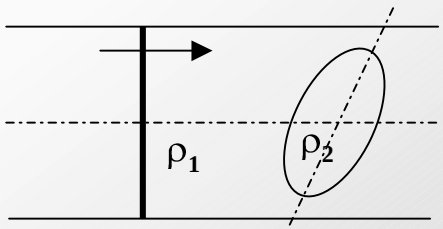

Elliptical cylinder or ellipsoid: Cavity implosion, vortex separation & vortex projectiles (VPs)

Motivations

Visualize, ***Quantify*** and ***Model*** the vortex dominated physical process, including:

1. Baroclinic vorticity
   - Main baroclinic vorticity deposition by the shock wave: *vortex double layers (VDL*)
   - Secondary baroclinic vorticity deposition by vortex interaction
   - Scaling with regard to Mach number
2. Emergence, evolution and modeling of "*Vortex Projectiles*" (**VP**) or coherent dipolar vortex structures
3. Turbulent mixing and rapid turbulization at high Mach number
4. Study of 3D effects

Computational Domain

1. Schematic (following [Yang, Zabusky & Chern, 1990]):

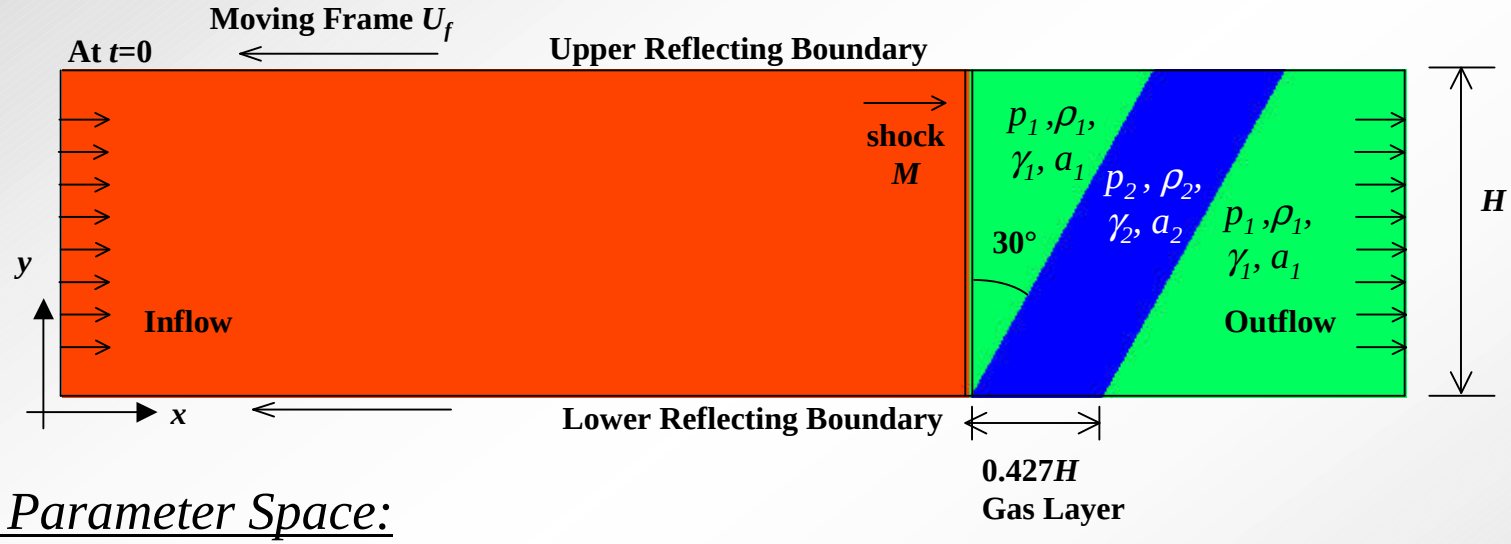

2. Parameter Space:

- **Density ratio:** $\eta = \rho_2 / \rho_1$ **(Slow/Fast/Slow (0.14)**
- **Mach #: 1.5, 2.0, 5.0**
- **Resolution(2D & 3D):**

  800×160(H)

  200×80×80

3. Numerical Method:

- Compressible Euler Equation
- Piecewise Parabolic Method [Woodward & Colella, 1984]

Global Quantification I: Evolution of normalized circulation

Normalization factors:

• M=1.5 circulation: $\max\Gamma_{+|M=2.0}/\max\Gamma_{+|M=1.5}\approx 1.4$

• M=5.0 circulation: $\max\Gamma_{+|M=2.0}/\max\Gamma_{+|M=1.5}\approx 0.39$,

• t_n: a plain shock traveling through length of the curtain thickness horizontally without inhomogeneity.

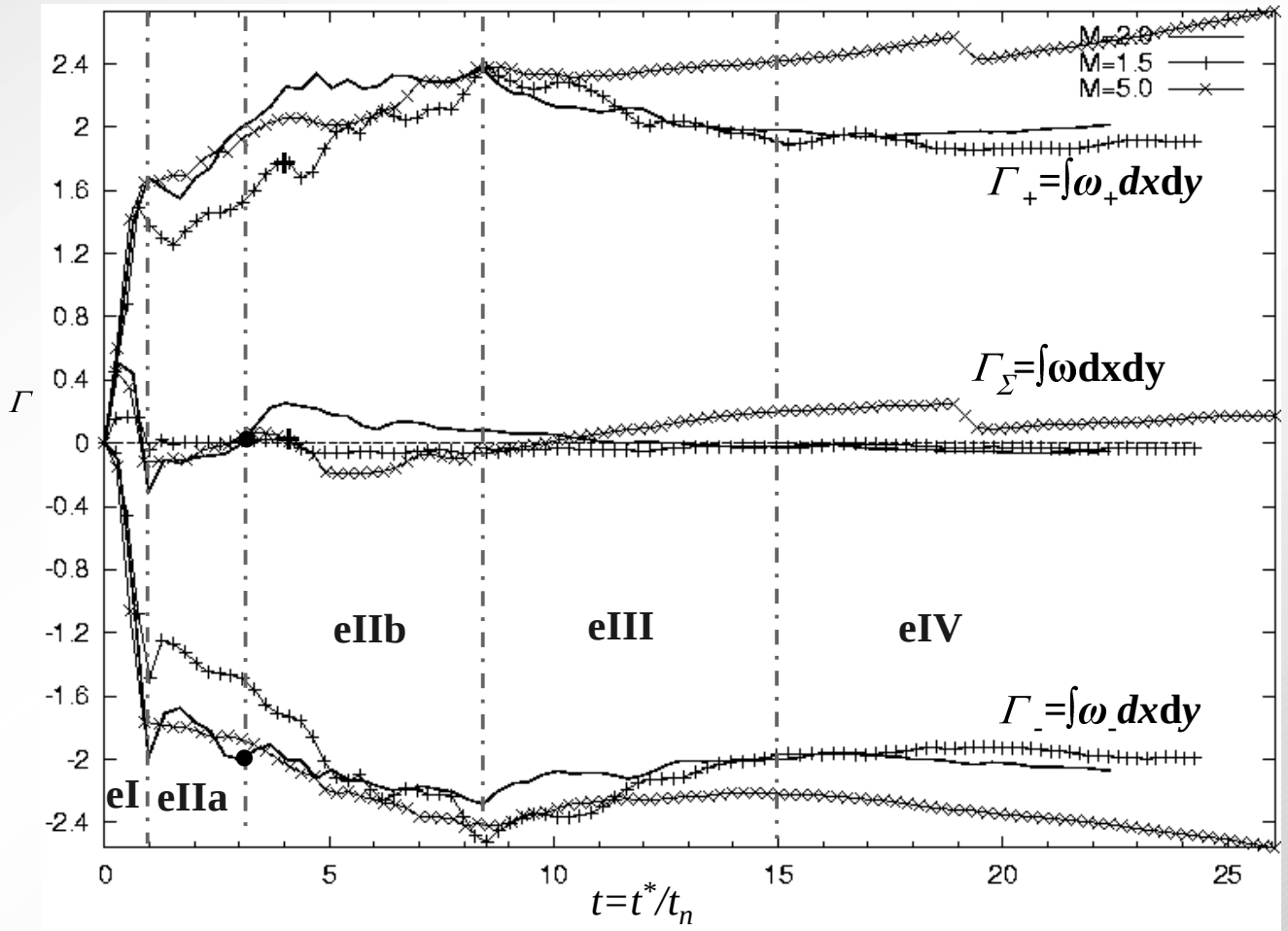

Note

• The time epoch: according to M=2.0 run, good for most of M=1.5 run

• Separation point of eIIa and eIIb, characterized by the time *VP1* hit the upper boundary, • *for* M=2.0 and + *for* M=1.5, are identified via negative circulation for M=2.0 and positively circulation for M=1.5 respectively.

Time Epoch, Feature Phenomena and Physical Processes

Time Epochs	Feature Phenomena		Physical Processes
	Density	Vorticity	
e①	Shock wave passes the curtain: reflection (upstream expansion wave), refraction and transmission.	Opposite sign vortex sheet deposition and approach; Circulation increases with significant rate.	Primary baroclinic effects
e②	Curtain "breakthrough"; Mushroom structure hits the upper boundary; Secondary reflected shock wave hits the deformed curtain	Collision of vortex layers; "Vortex binding" of oppositely signed; Formation of complex VP1; VP1 hits the boundary Circulation increases with lower rate but longer term (total amount almost the 50% as e①)	Secondary baroclinic effect due to mutual acceleration of inhomogeneity and vortex interaction
e③	Complete formation of upstream and downstream bubbles (VP's); Translating dipolar structures; Transition to turbulence	Separation of VPs; Vortex binding with image; Circulation decreasing	Vortex merging; and turbulent mixing
e④	Emergence of dipolar VP's which are well isolated; and intermediate turbulent interval	Approach to nearly stationary configuration of VPs and intermediate turbulent domain; nearly constant circulation	Dissipation and baroclinic re-acceleration

S. Zhang & N. Zabusky, 12/12/2001

Simulations

Early time snapshots for *M*=1.5:

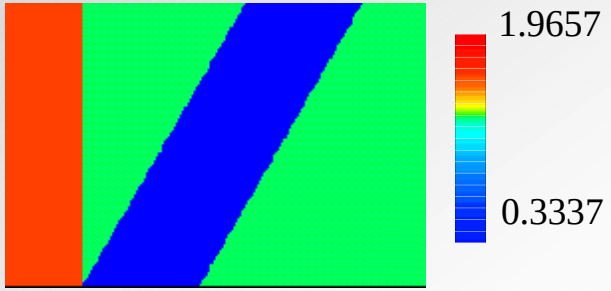

t=0

- Juxtaposition of density, vorticity, baroclinic term $\nabla\rho\times\nabla p/\rho^2$, and dilatation $\nabla\bullet\mathbf{u}$
- *VDL*, shock wave patterns, breaking through process and dominant *VP1*
- Following our previous work [Yang, Zabusky & Chern, 1990]

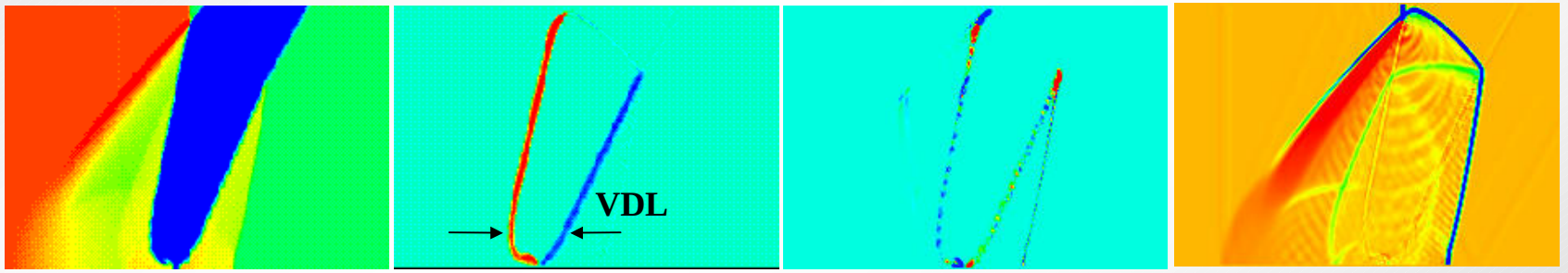

density **vorticity** $\nabla\rho\times\nabla p/\rho^2$ $\nabla\bullet\mathbf{u}$ *t*=0.9, eI

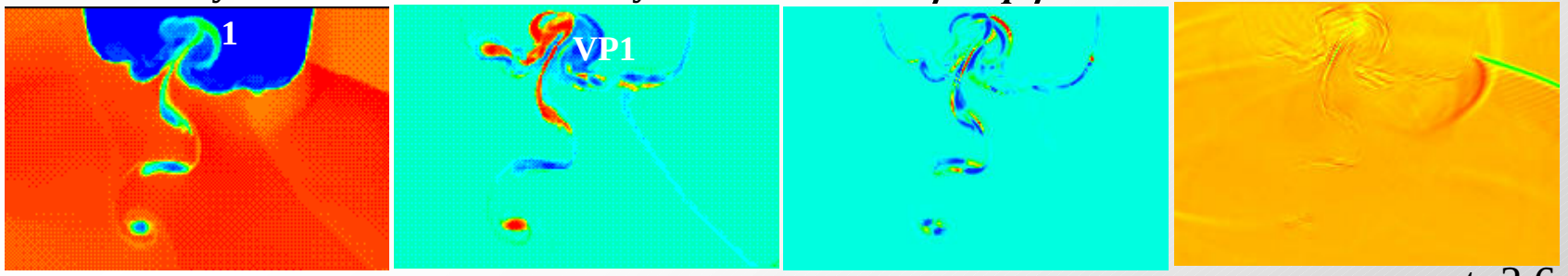

t=3.6, eIIa

Early time snapshots for *M*=2.0

- Similar to M=1.5: VDL, breaking through process, and dominant VP1
- More generic VP configuration

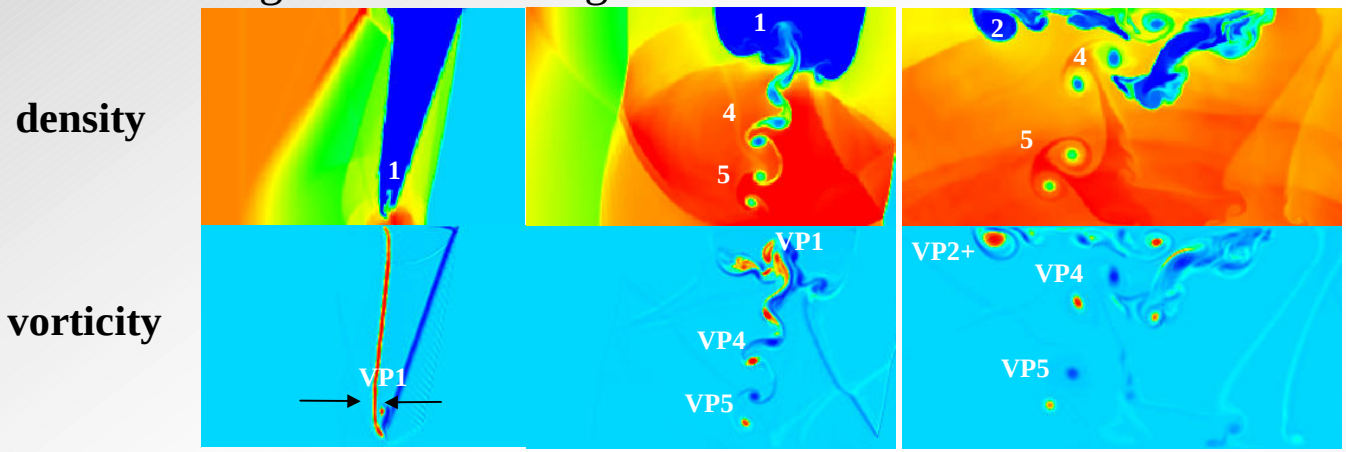

(a) t=0.95, eIIa begins (b) t=2.62, during eIIa (c) t=7.25, during eIIb

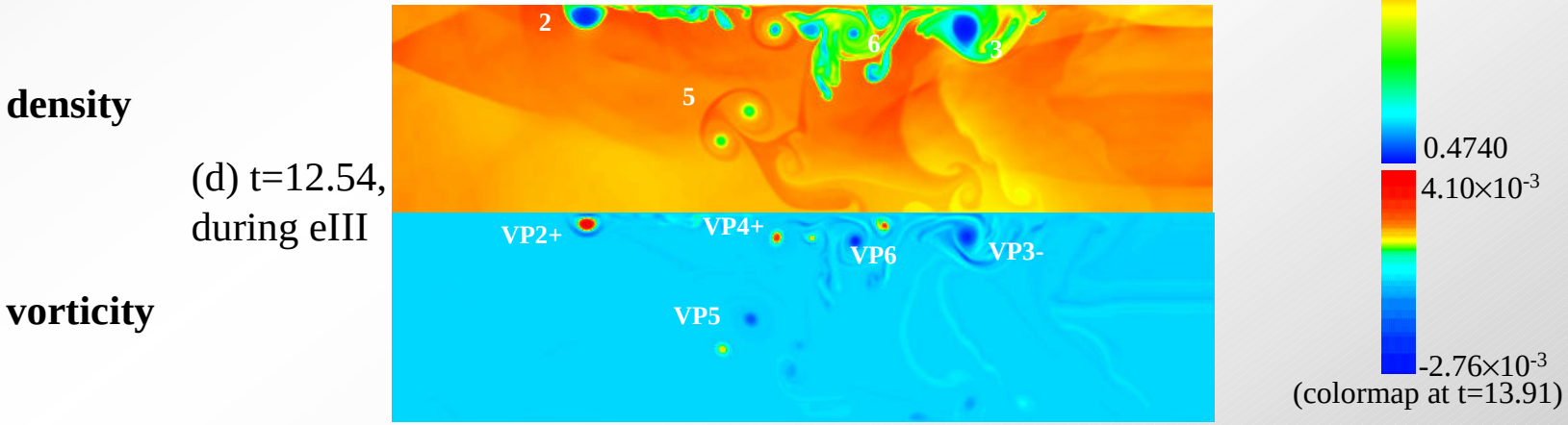

(d) t=12.54, during eIII

S. Zhang & N. Zabusky, 12/12/2001

Late time snapshots: M=1.5 and M=2.0

Simulation Cont.

M = 1.5
t =23.76
eIV

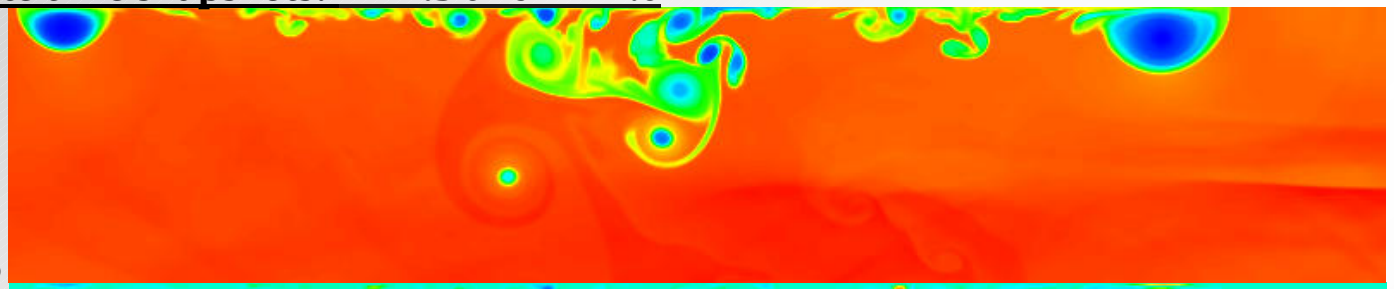

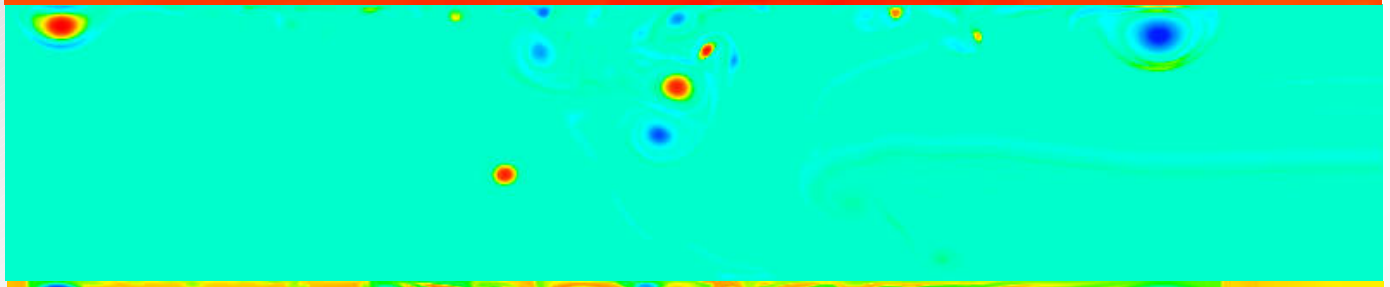

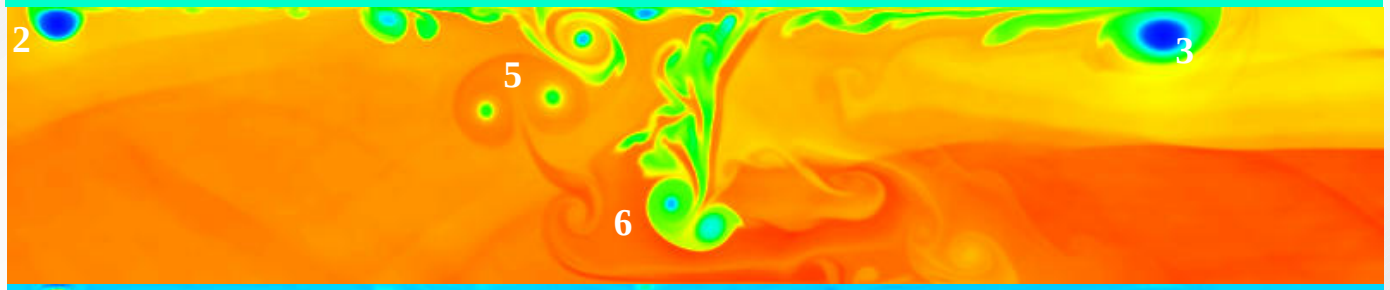

M = 2.0
t =21.88
eIV

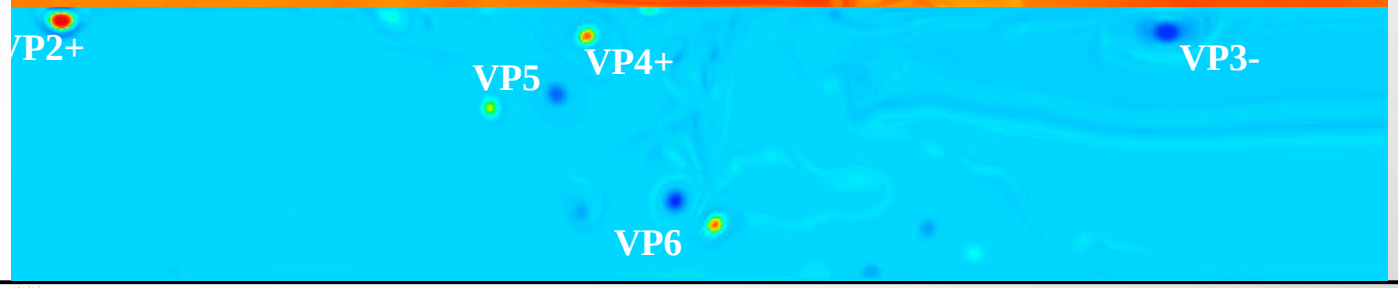

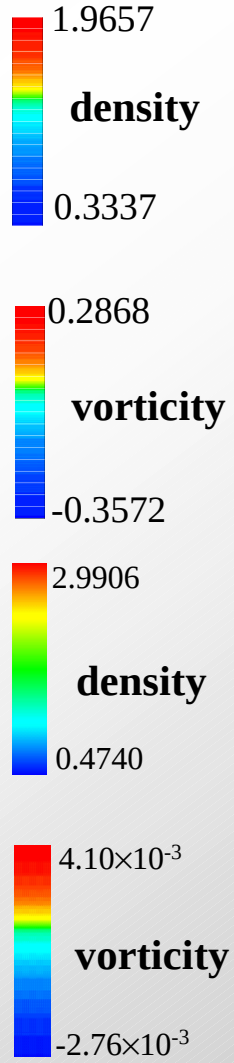

Rutgers
Welcome to
The State University of New Jersey

VIZLAB

Simulation Cont.

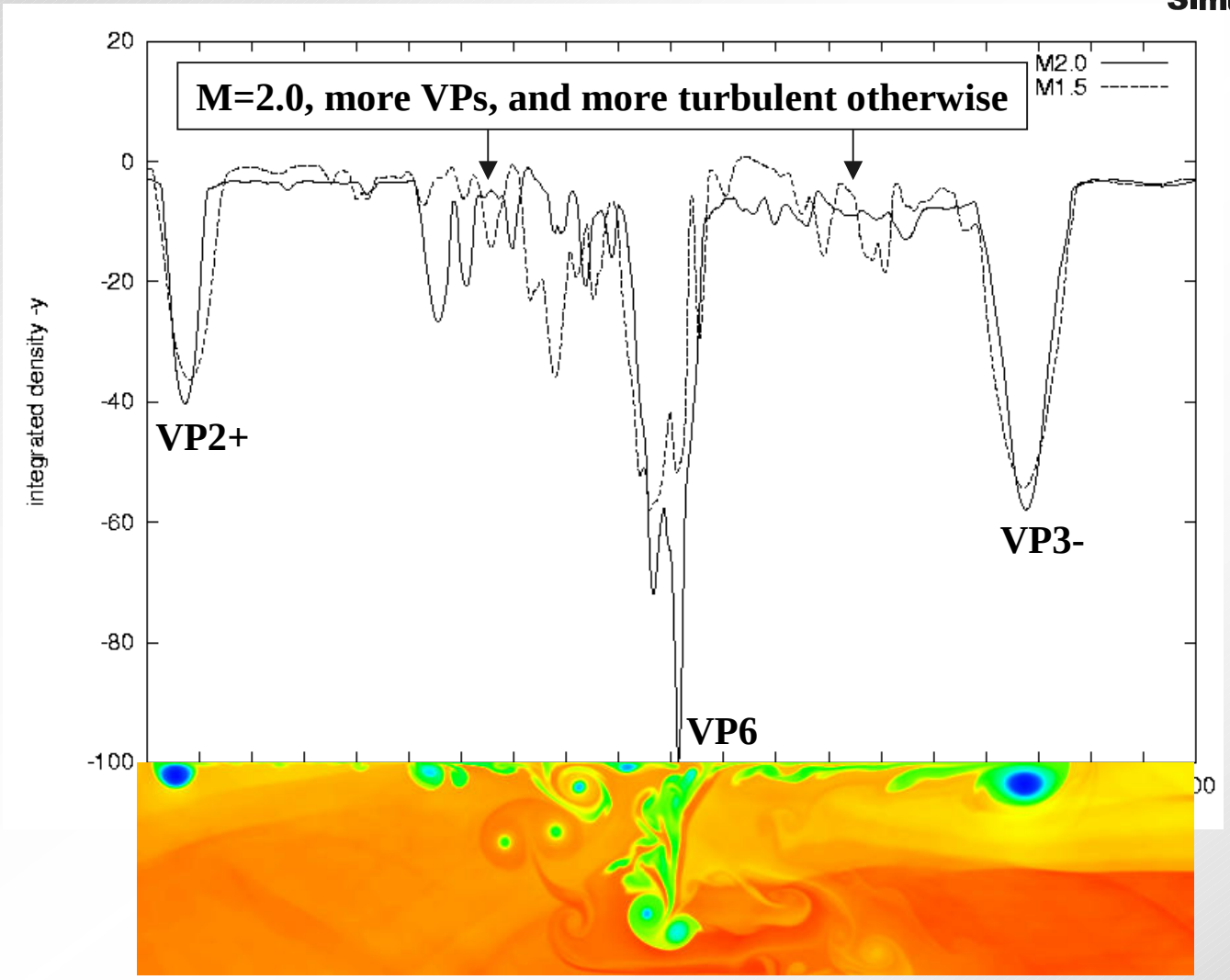

Y-integrated density (filtered the ambient density)

S. Zhang & N. Zabusky, 12/12/2001

Simulation Cont.

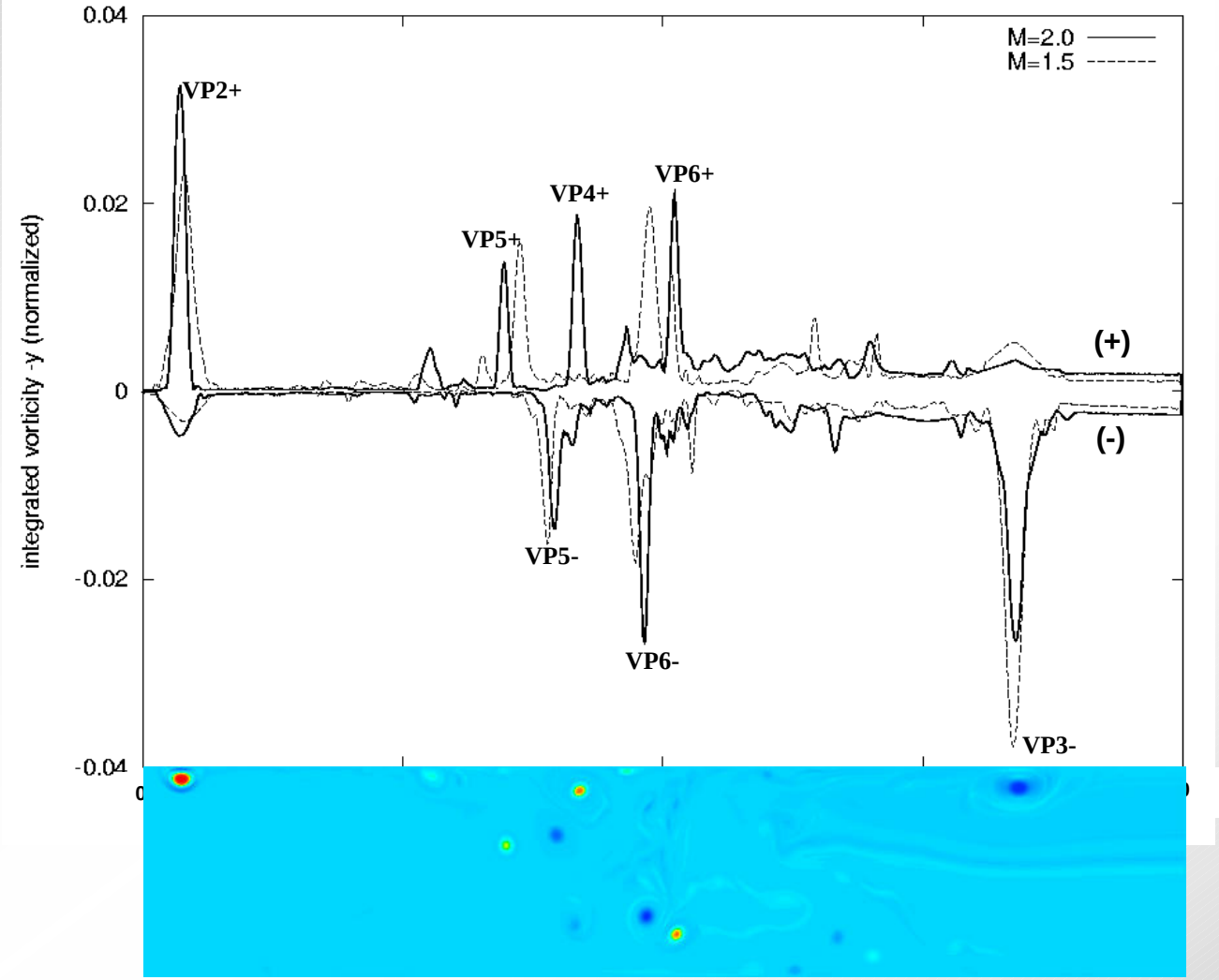

Y-integrated vorticity

Global Quantification II: Integrated enstrophy evolution equation

- Emphasizes larger magnitude vortex domains;
- Normalization factor E_n: enstrophy at the end of eI.

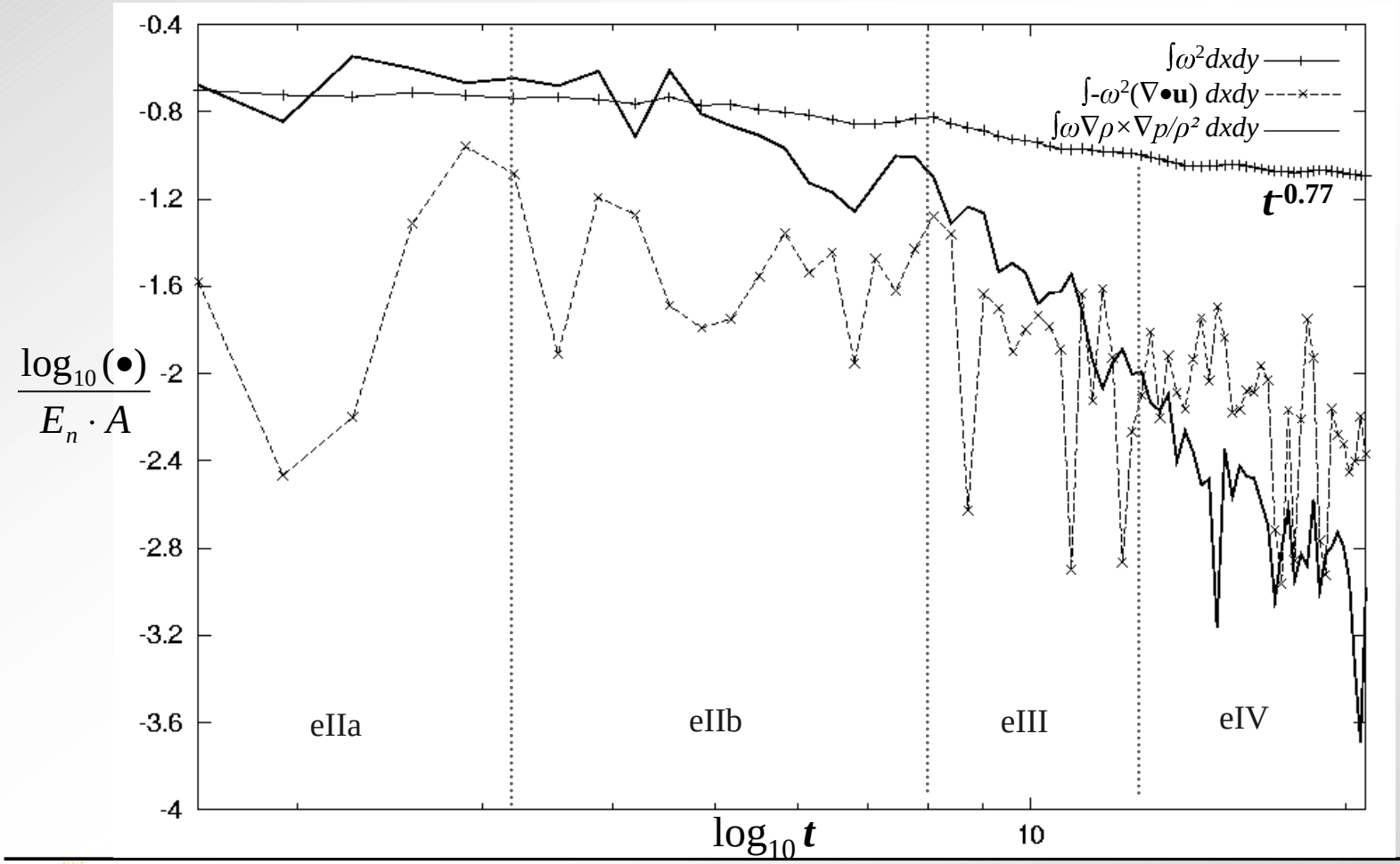

Local Structures' Quantification

Quantification of vortex projectiles

- VP2+ for upstream and VP3- for downstream, respectively
- M=1.5 and M=2.0 ($|\Gamma_{VP2+}|+|\Gamma_{+VP3-}|+\Gamma_{affi}|=30\%(|\Gamma_{-}|+|\Gamma_{+}|)$
- Extraction threshold: 4% of the extremum of vorticity

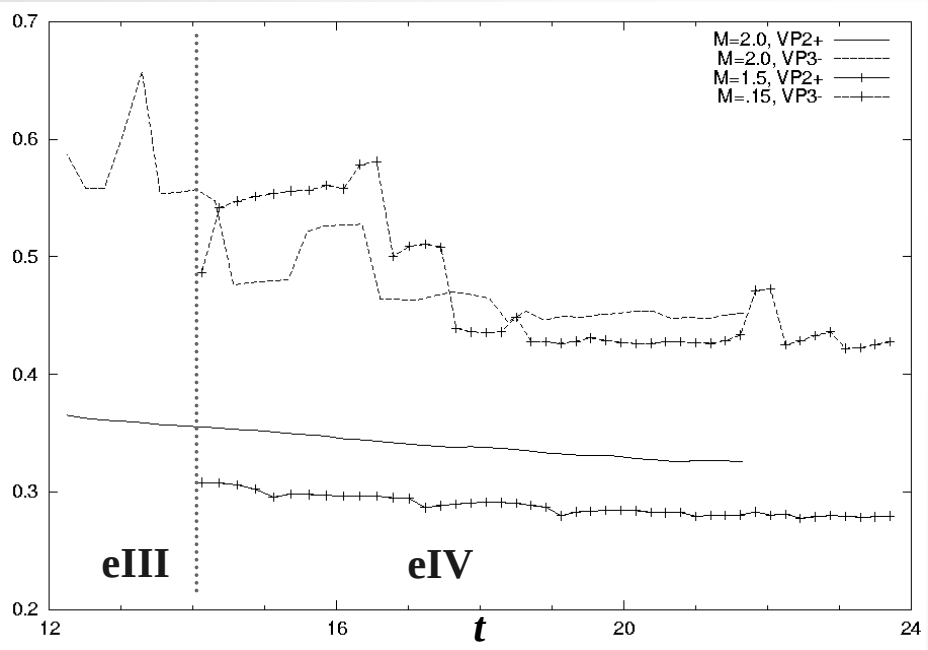

(a) Evolution of local circulation

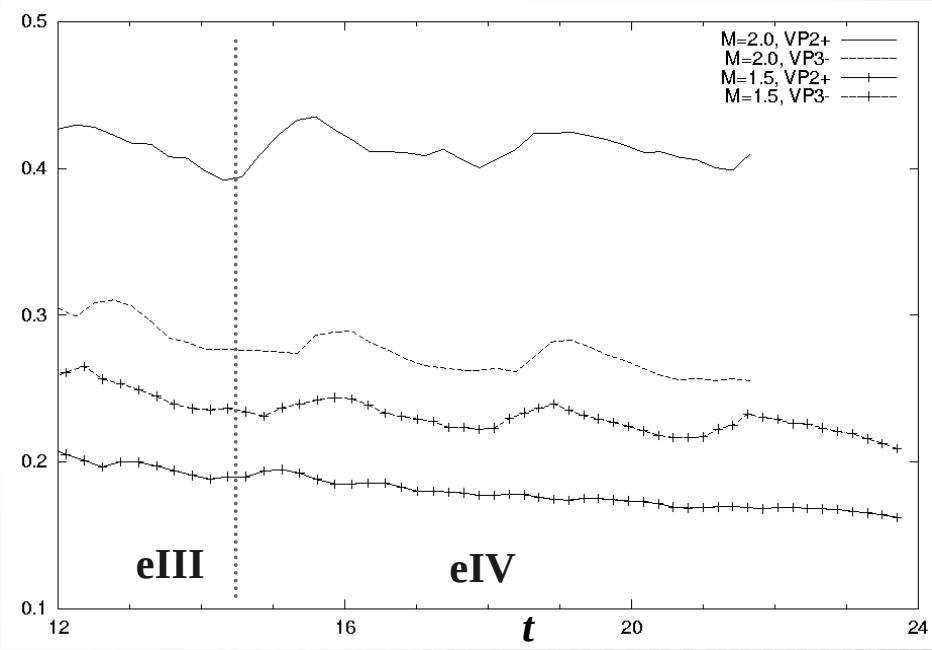

(b) Evolution of local vorticity maxima

Point vortex modeling (*M*=2.0)

Modeled translational velocity: $u_x = \frac{\Gamma}{2\pi d}$

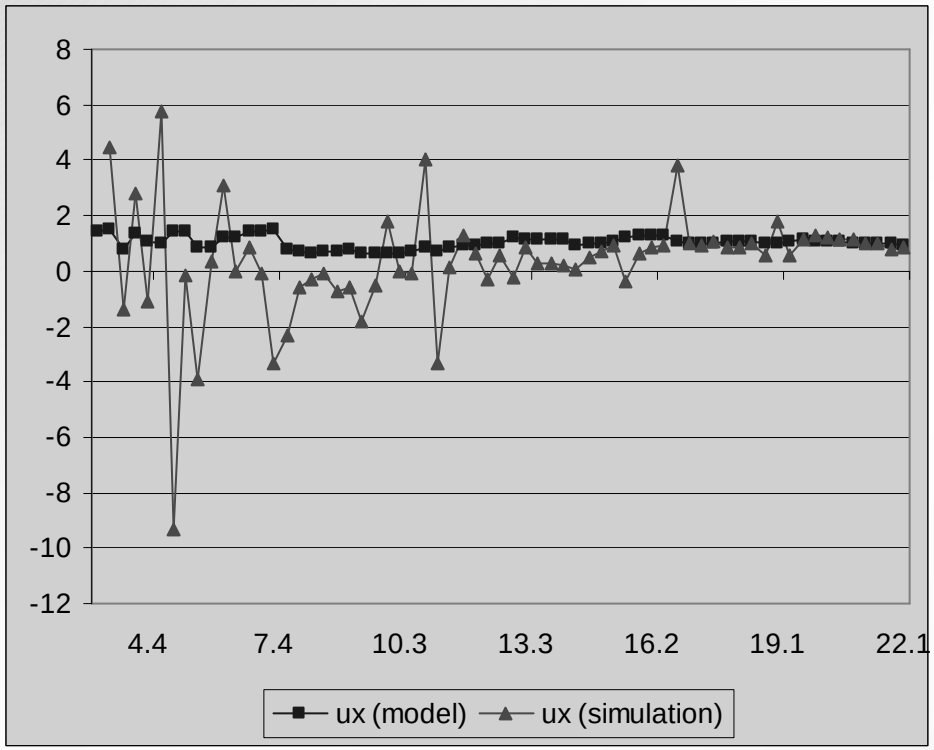

Downstream VP3-

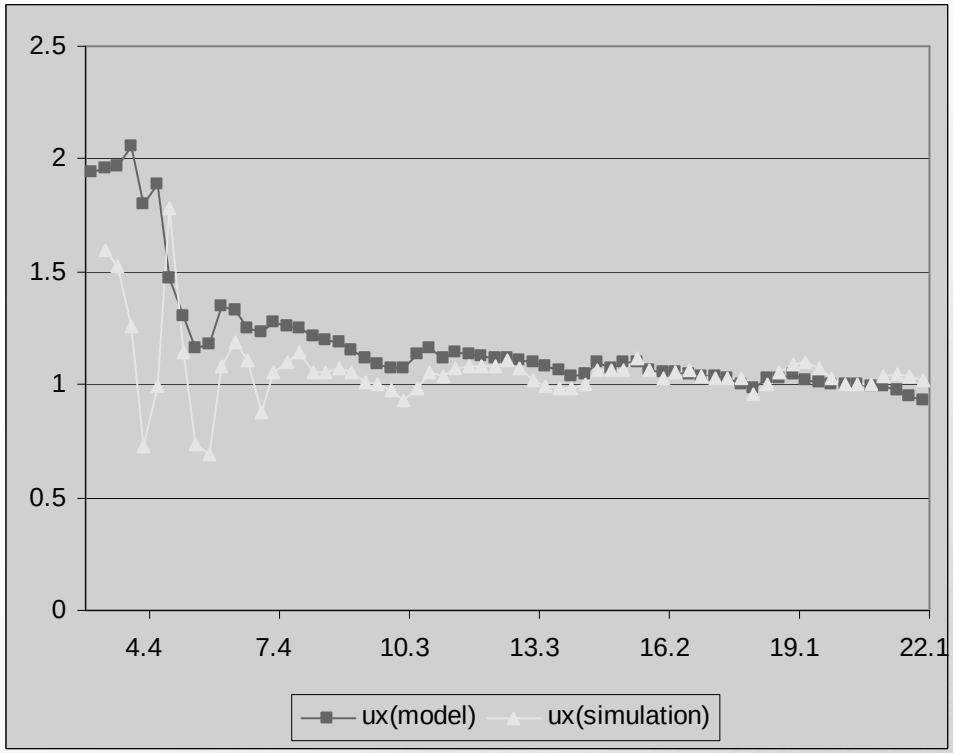

Upstream VP2+

Density distribution

Turbulent mixing

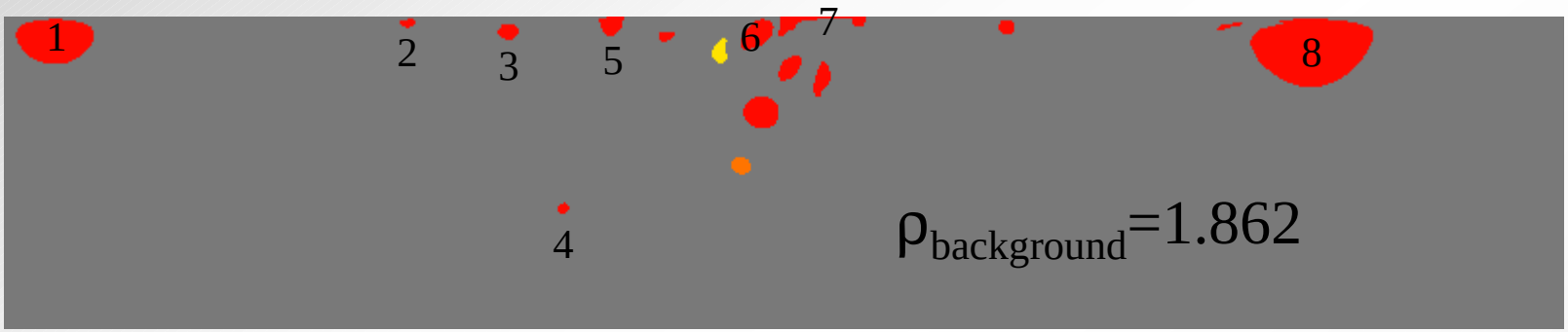

- Initial Density Ratio: 0.14

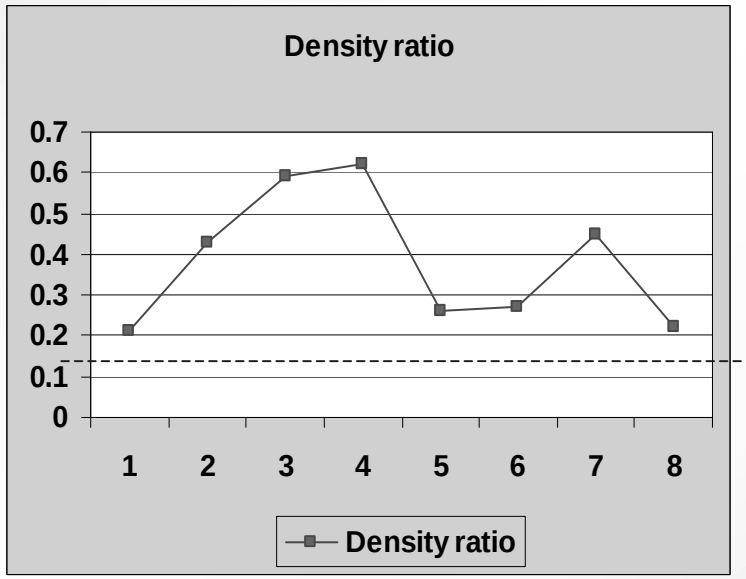

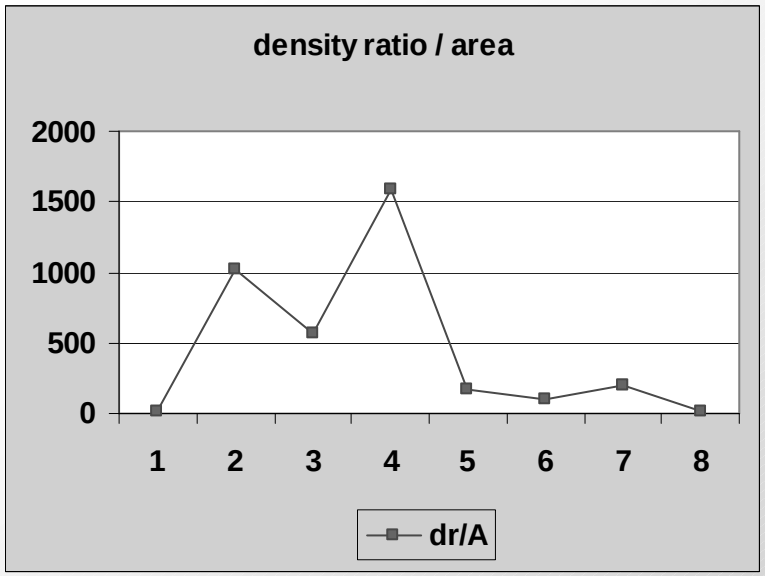

Rapid Turbulization at High Mach number (*M*=5.0)

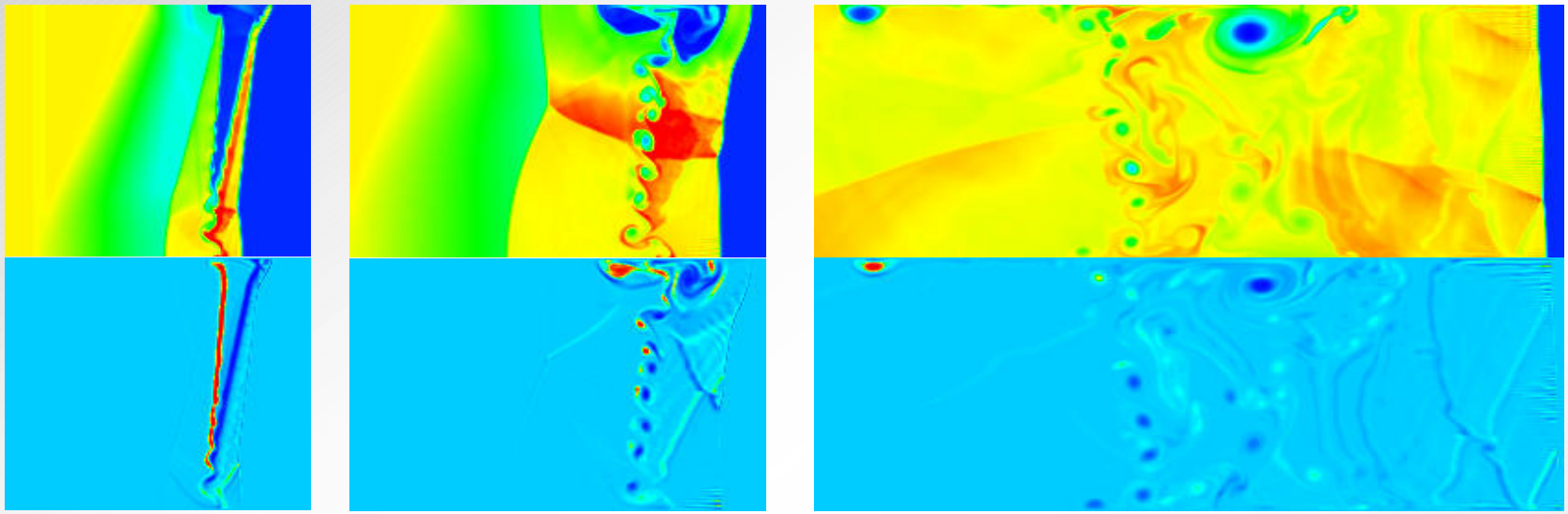

t=1.0 t=2.0 t=6.0

t=15.0

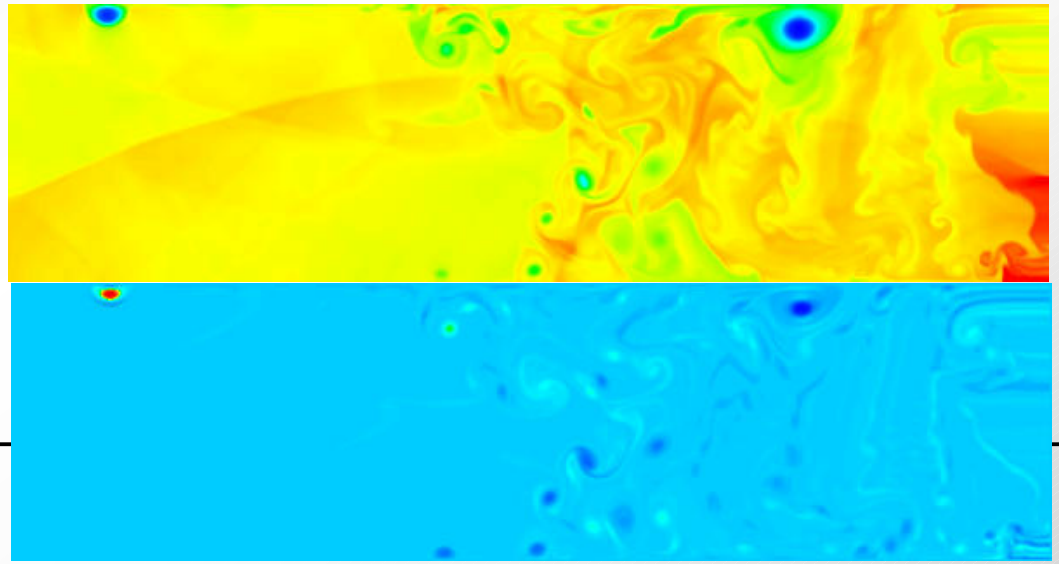

density

vorticity

3D Curtain study

Main approaches: Simulation with adaptive mesh; quantification via data projection;

2 vertical slices

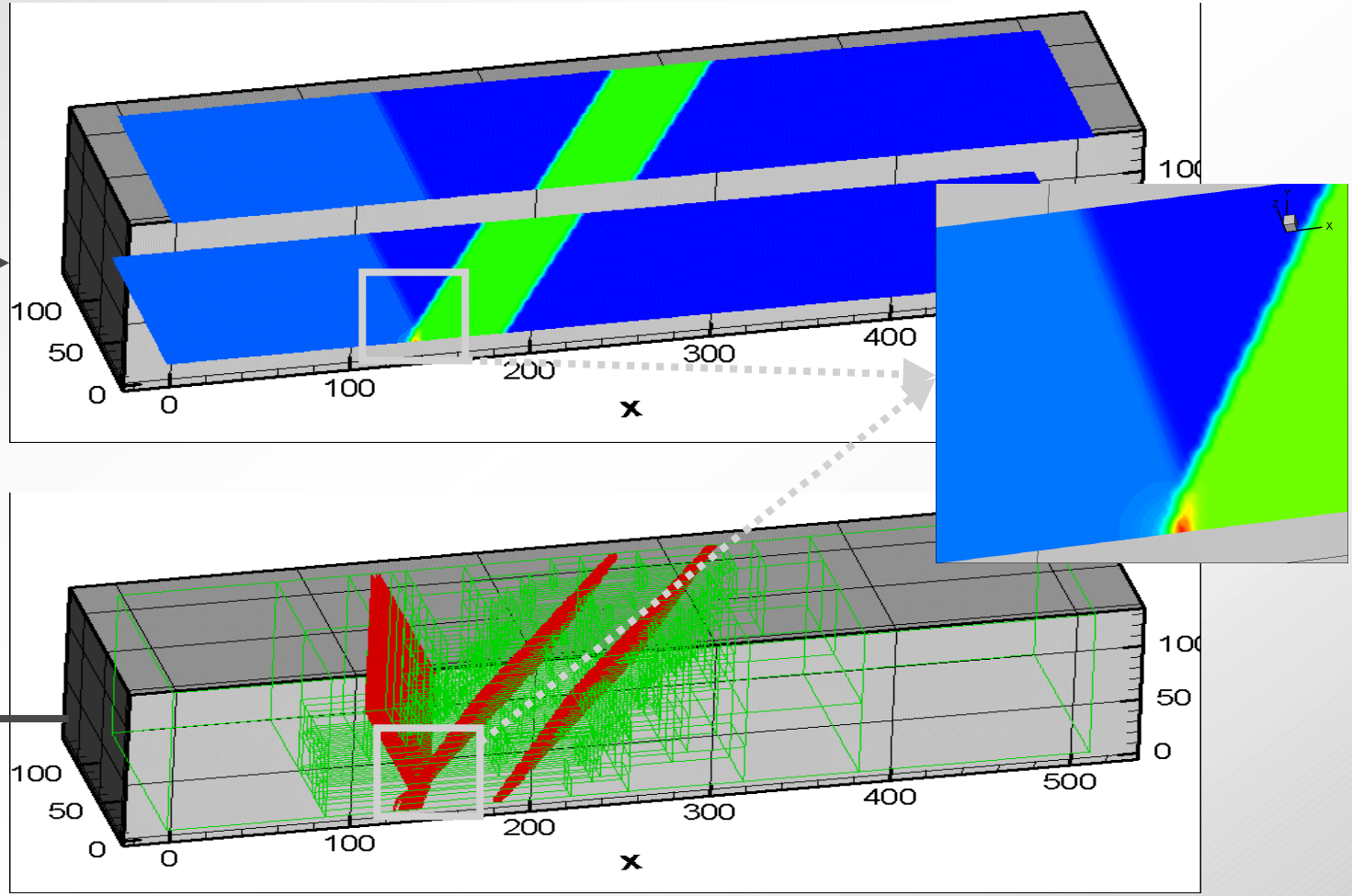

Data Projection: quasi-2D (Resolution: 200*80*80)

3D curtain cont.

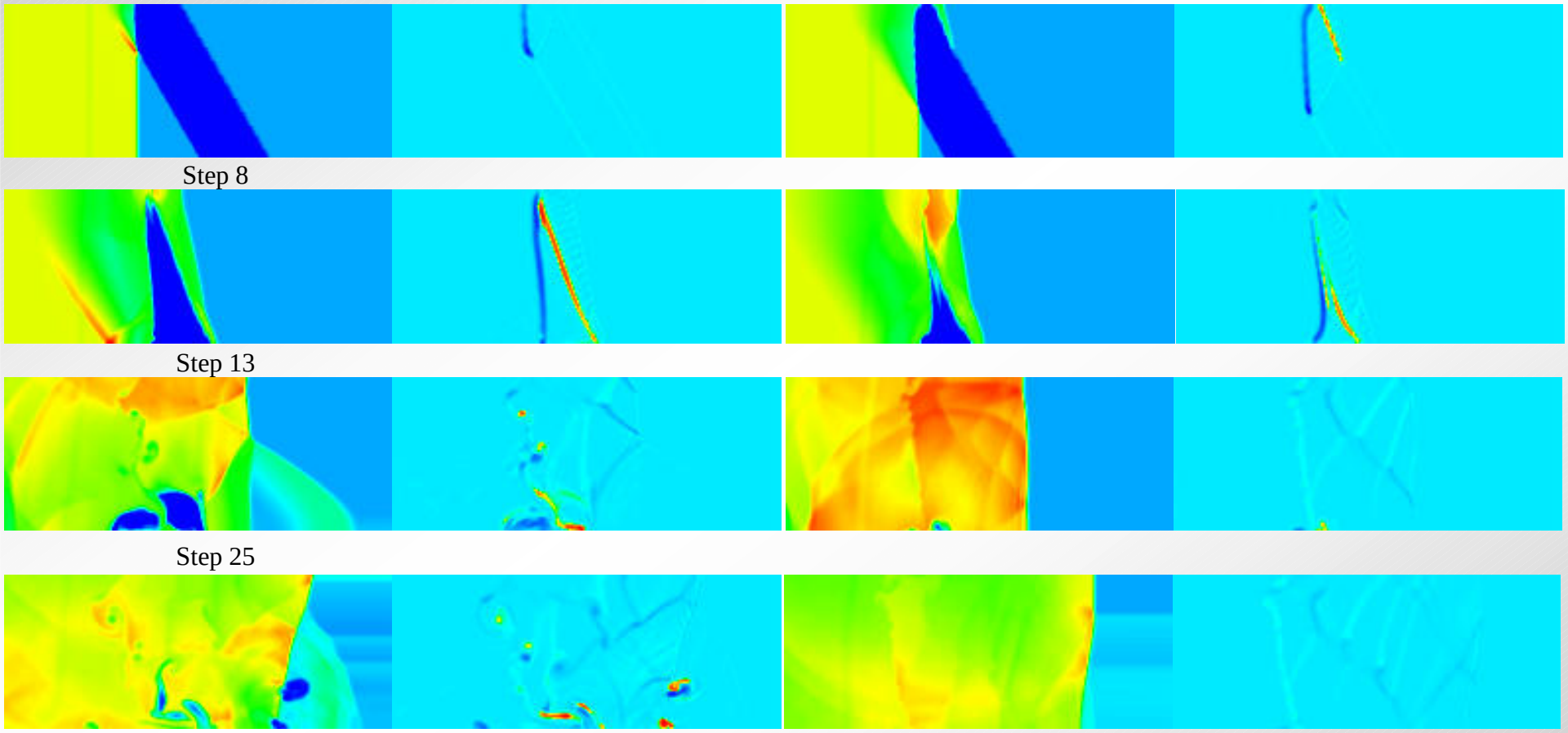

3D curtain cont.

3D effects: juxtaposition of quasi-2D and 2D global circulation

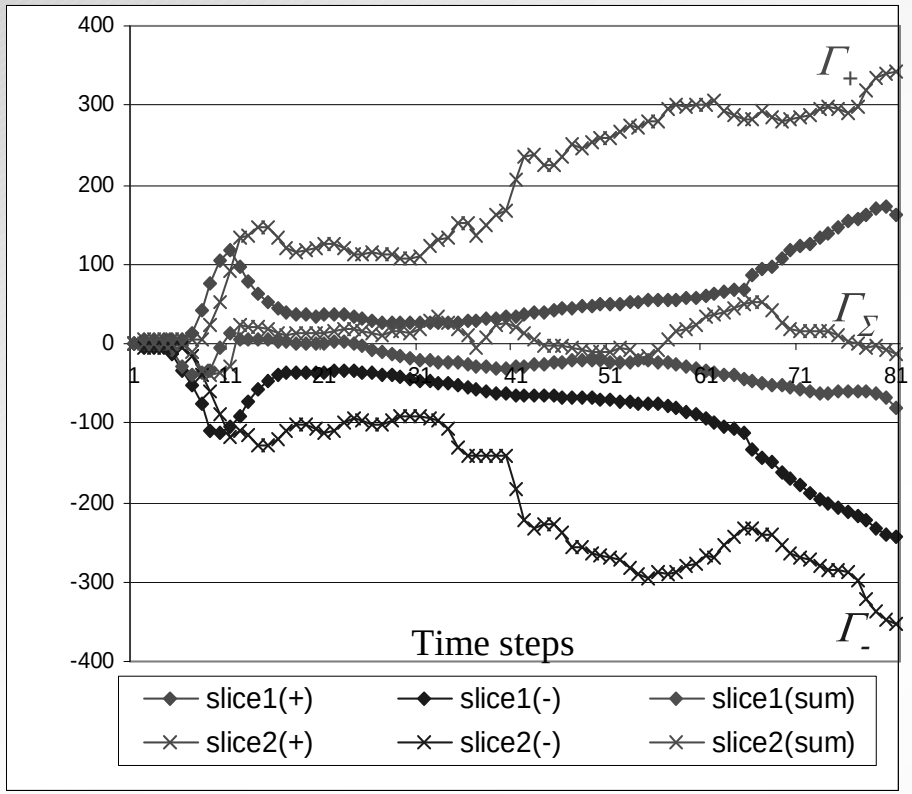

2 of the 3D slices slice1 (y=8), slice2 (y=40)

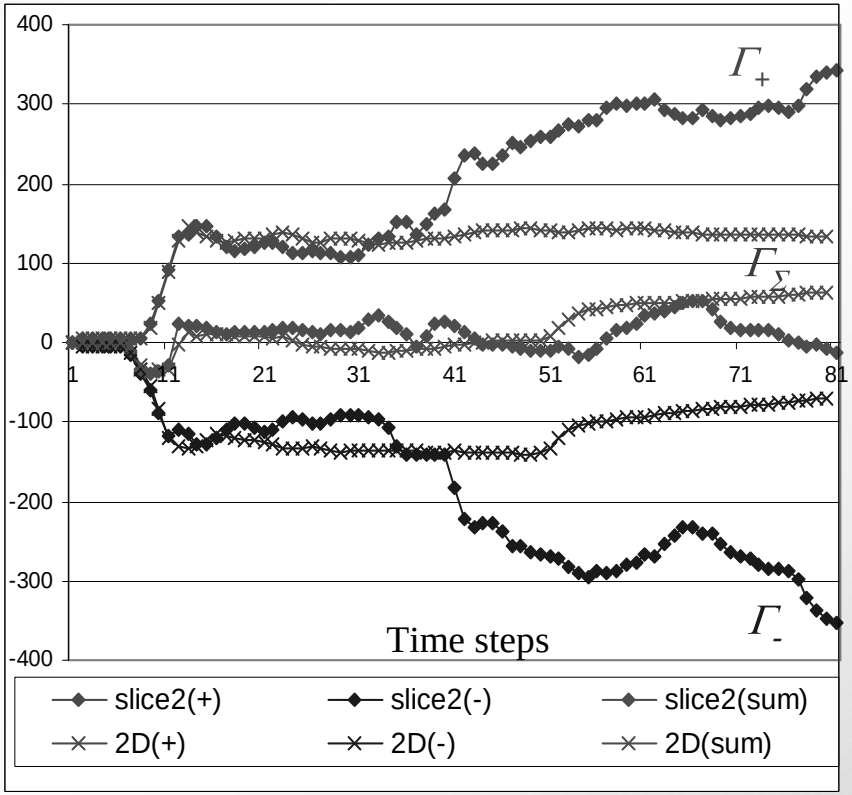

3D center slice (y=40) and 2D

Note:

1). Resolution: 200*80*80; 2). Early time, the curtain behaves similar to 2D – No obvious 3D effects; 3). The slice near the boundary influenced by 3D early; 4). 3D effects become important and dominant when vortex structures localized

Summary & Future Directions

- Simulations of s/f/s curtain with M=1.5 to 5.0;
- Vortex double layers and large baroclinic circulation evolution;
- Visiometrics of vortex “layer” collisions and binding; Strong secondary baroclinic deposition,;
- Vortex projectiles emergence: quantitative study and modeling;
- Preliminary study of stratified turbulence domain;
- Preliminary adaptive mesh simulation of 3D planar curtain evolution; quantification via juxtaposition of slices.

Rapid Turbulization Arising from Vortex Double Layers in Interactions of "Complex" Blast Waves and Cylindrical/Spherical Bubbles

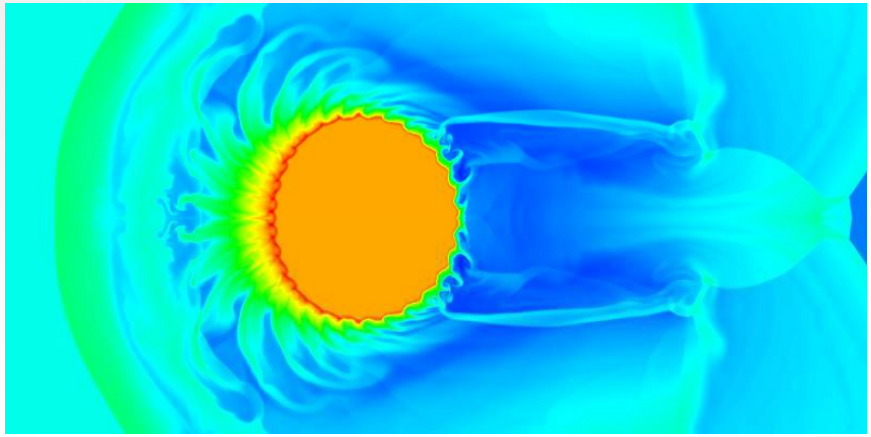

S. Zhang[1], N. J. Zabusky[1], K. Nishihara[2], and Y-G. Kang[2]

VIZLAB

[1] Lab of Visiometrics and Modeling, Dept. of Mechanical & Aerospace Engineering, Rutgers University, USA

[2]Institute of Laser Engineering, Osaka University, Japan

Motivations

1. Supernova 1987A: Hydrodynamics of complex blast wave (*shock-contact-shock*) and ring interaction;
2. Upstream-ring erosion [Borkowski, Blondin & McCray, 1997];
3. Emergence and significance of vortex double layer, vortex projectiles due to the primary and secondary deposition of baroclinic vorticity;
4. Numerical simulations (PPM) at extremely high density ratio (up to 5500) and Mach numbers (up to 70);
5. Compare simulation with laser experiment[Kang et al, 2001];
6. Prediction of the late time behavior

Motivations Cont.

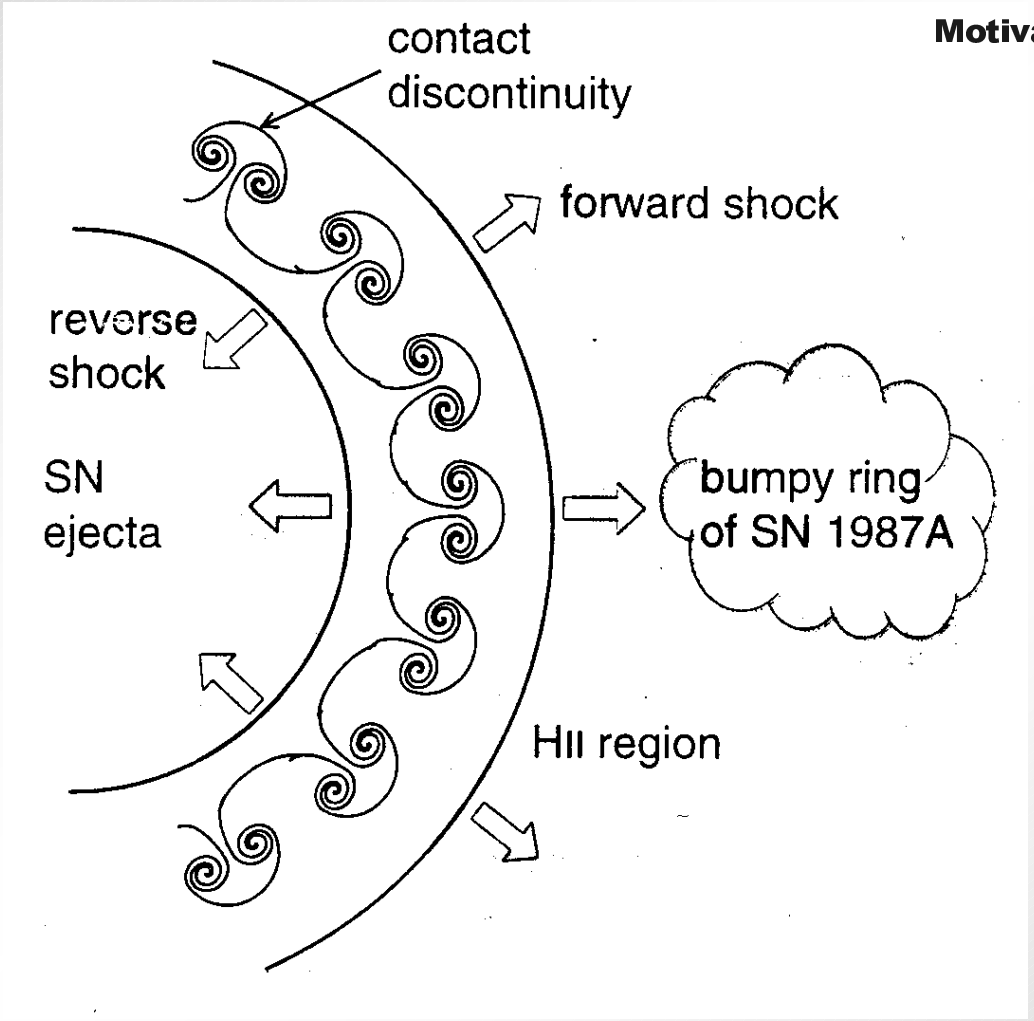

Fig.1. Turbulent contact discontinuity of the circumstellar region and the bumpy ring of SN 1987A: a more realistic situation

Motivations Cont.

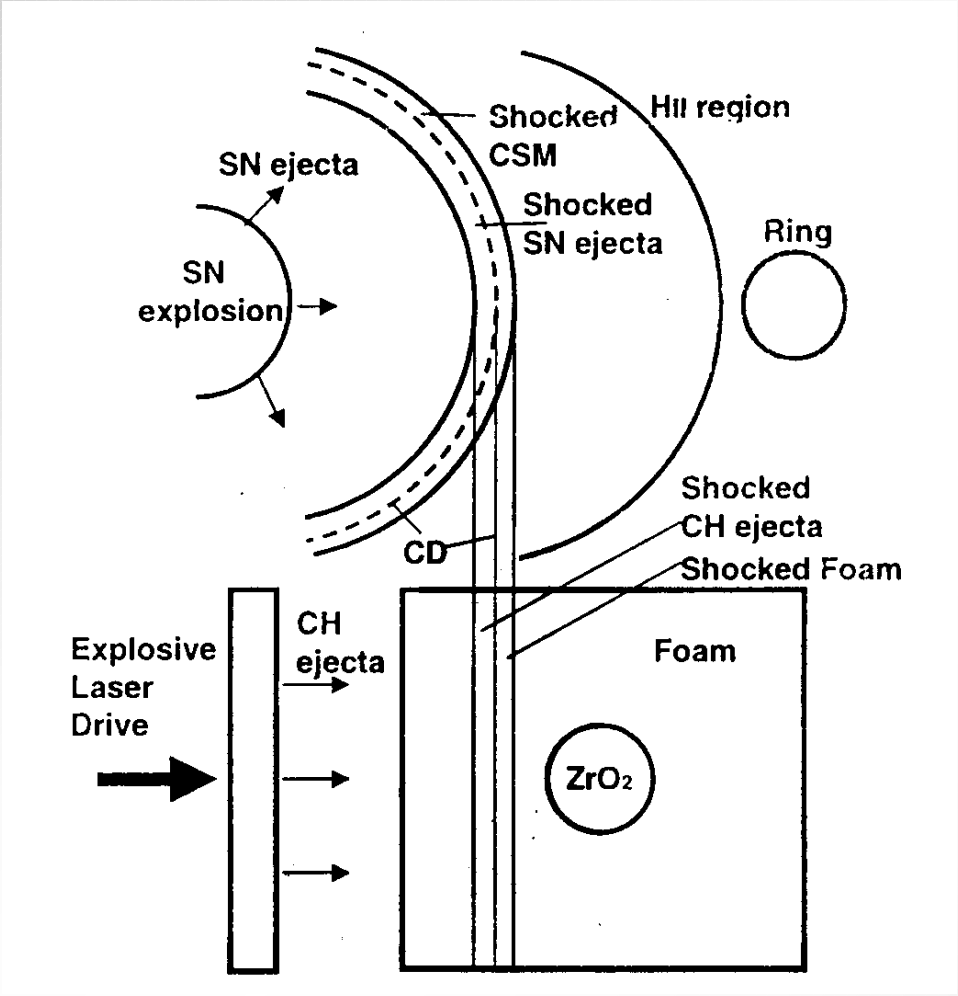

Fig. 2. Schematic structure of the shocked region, the circumstellar region and the ring of SN1987A with an laboratory experiment. The ejected material (SN ejecta and the CH ejecta) and the low density medium (CSM and the foam) are separated by a contact discontinuity (CD).

Part I: Simulations ---- Cylindrical bubble

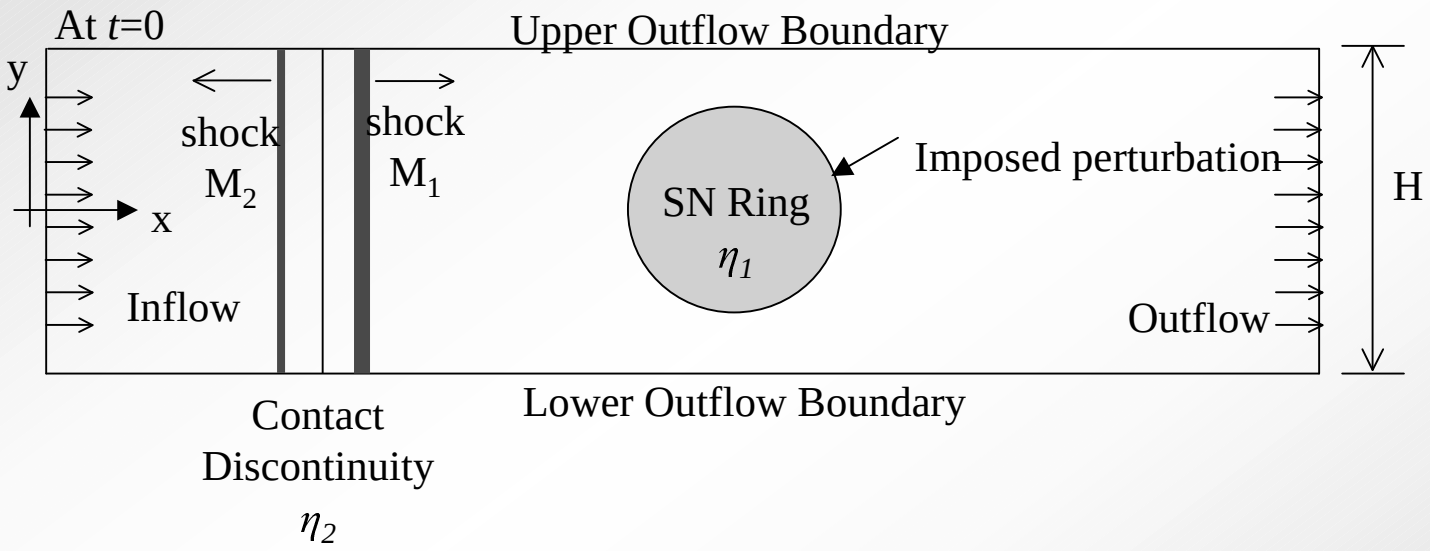

Fig. 3 Schematic of the computational domain and initial condition: Blast wave/SN Ring

Part I: Simulations Cont.

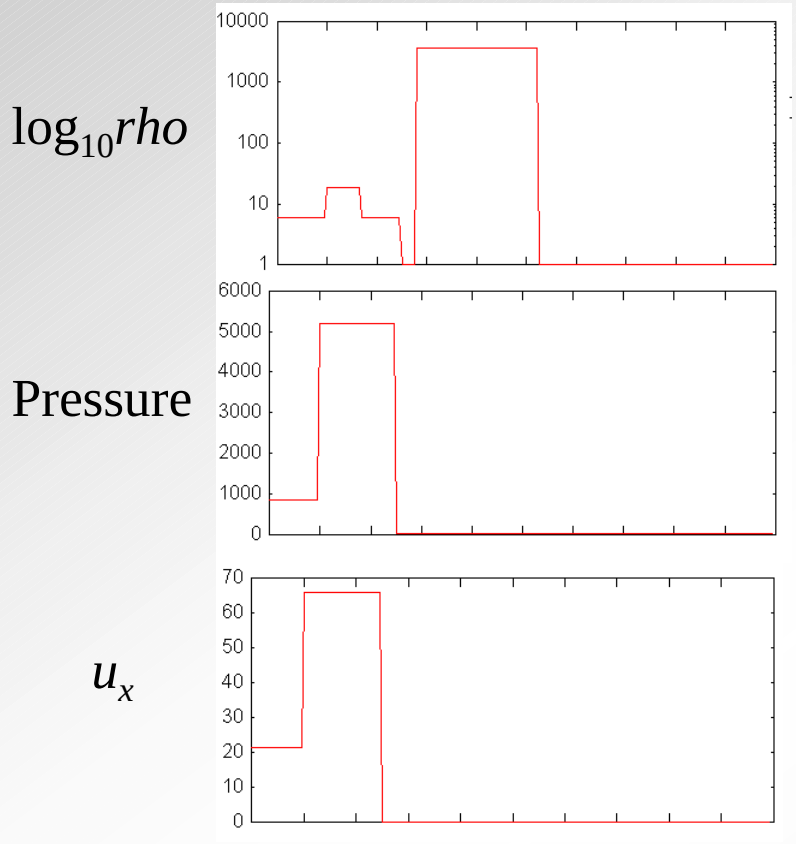

Fig. 4 Initial profiles of density (log scale), pressure, and x-velocity

Parameter Space:

- M_1 = 66.77
- η_1=5000
- η_2=4.0

Numerical Method:

- Compressible Euler Equation
- Piecewise Parabolic Method [Woodward & Colella, 1984]

Global quantification:

Part I: Simulations Cont.

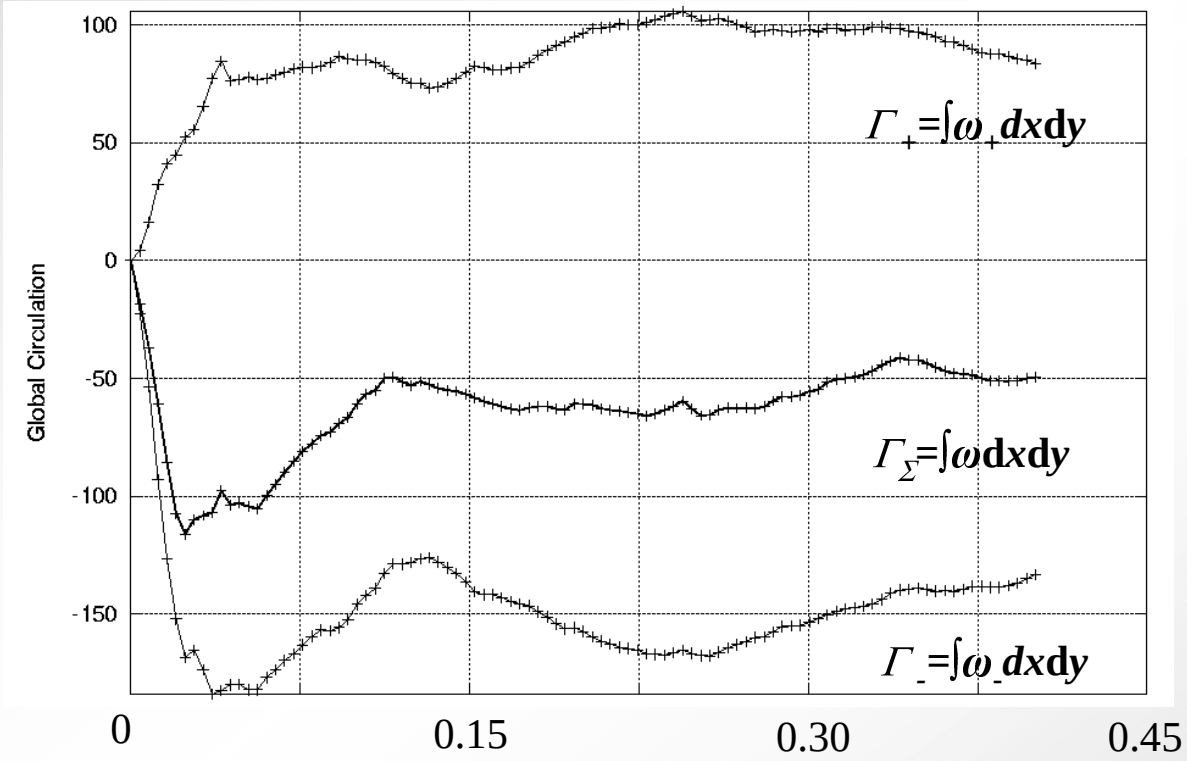

Fig. 5 Evolution of global circulation (positive, negative and sum integrated over the whole domain), t=0.01 corresponds approximately 4 years

S. Zhang et al, 12/12/2001

Simulation Snapshots I: Early time, juxtaposition of density (log scale), vorticity and div(u), vortex double layers, vortex projectiles, and upstream erosion

Part I: Simulations Cont.

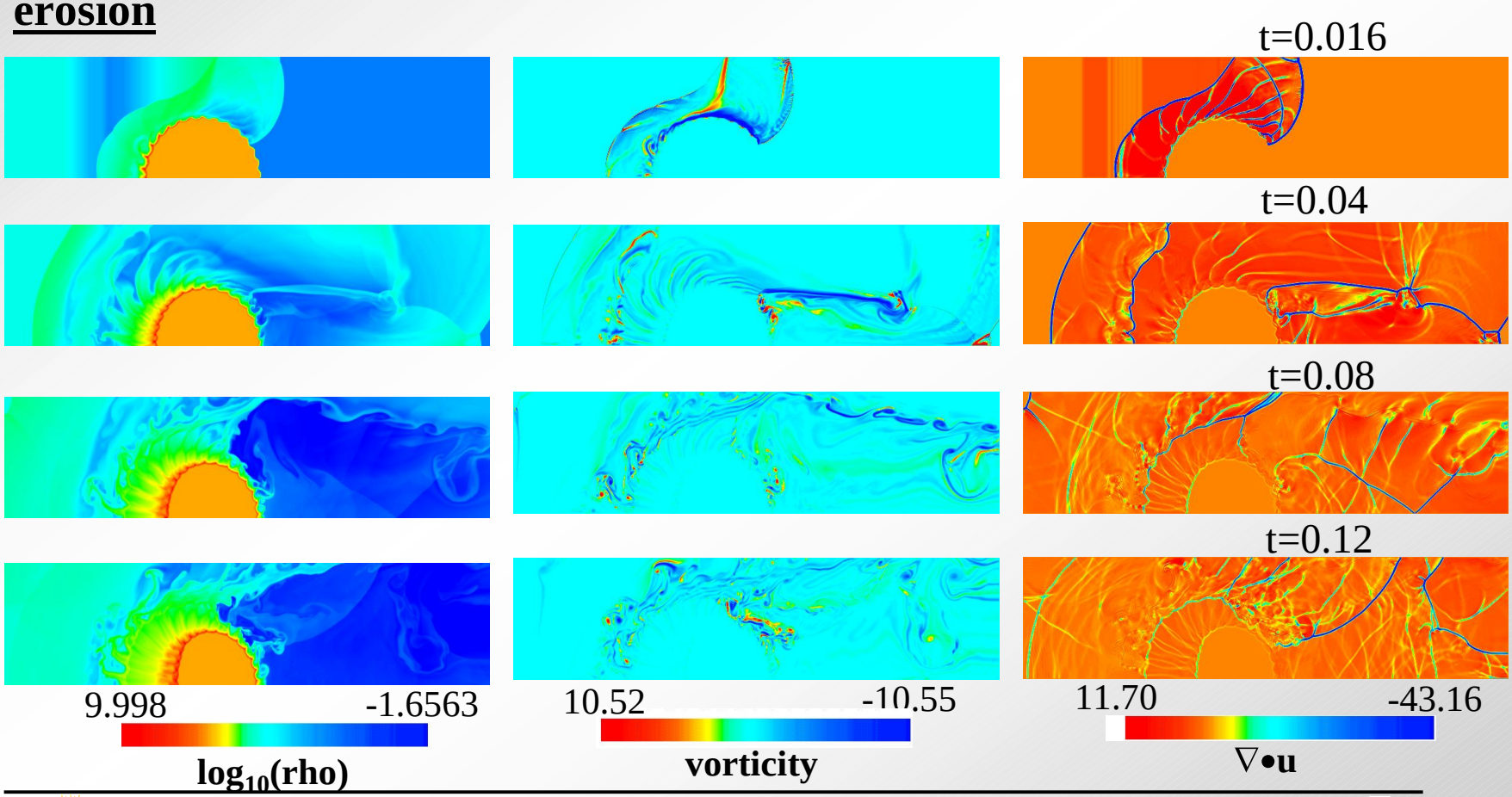

Upstream Erosion:

Part I: Simulations Cont.

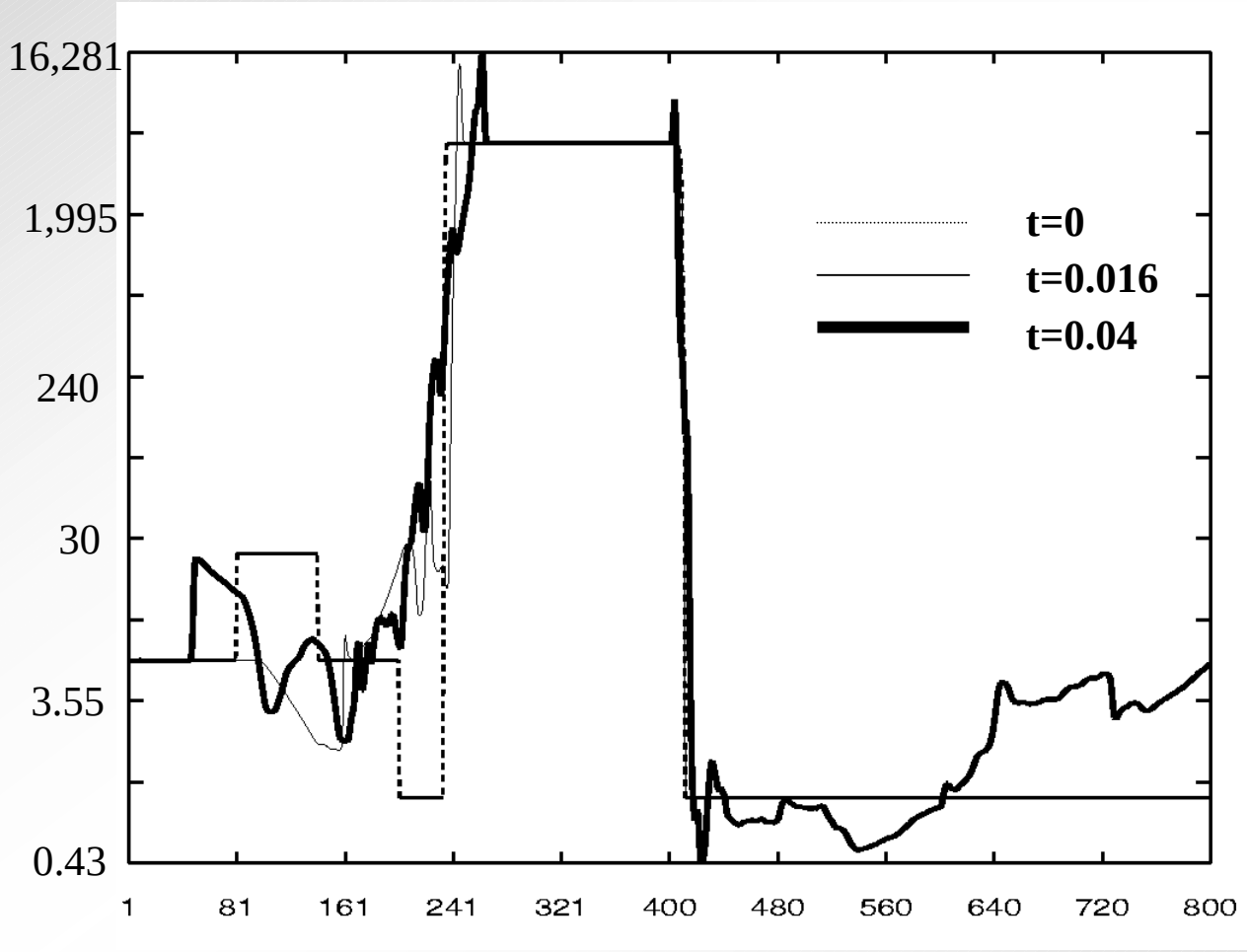

Fig. 6. Evolution of density (log scale) Slice at j=10

S. Zhang et al, 12/12/2001

Late time predictions

Part I: Simulations Cont.

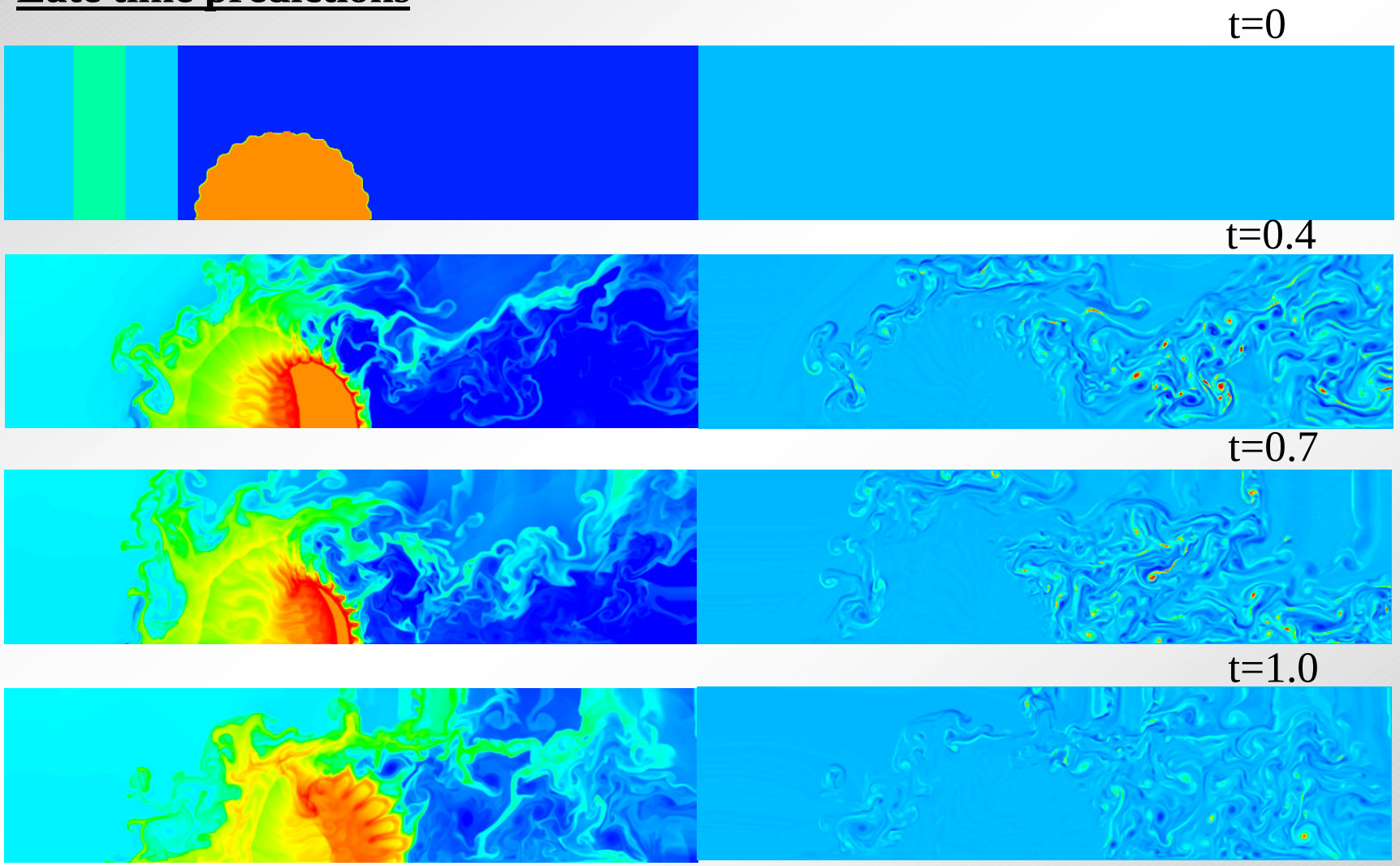

S. Zhang et al, 12/12/2001

Part I: Simulations Cont.

t=1.4

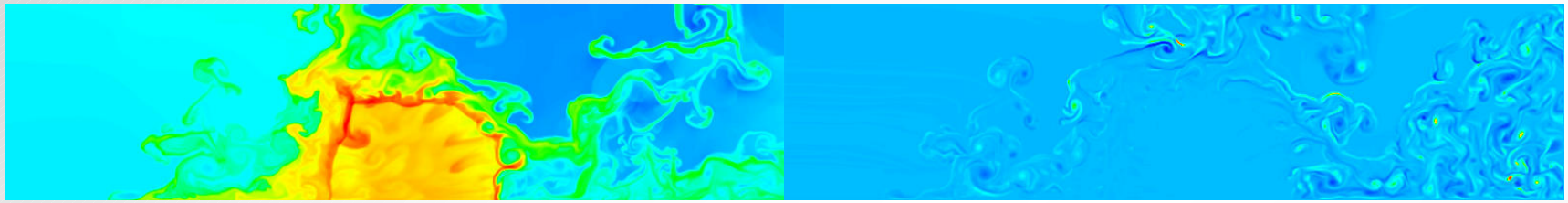

t=2.1

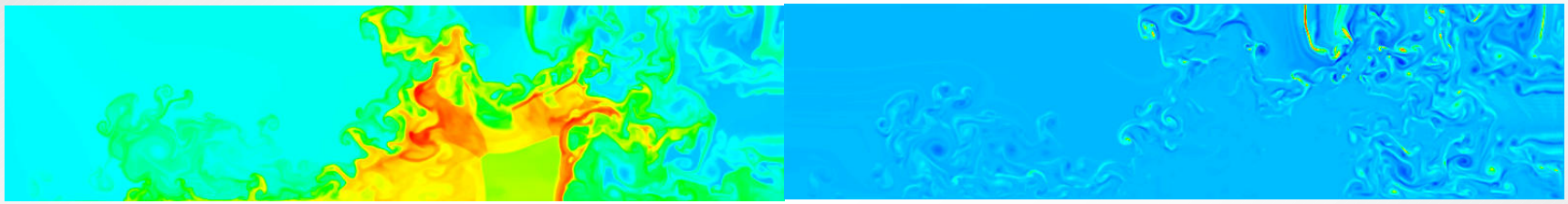

t=2.9

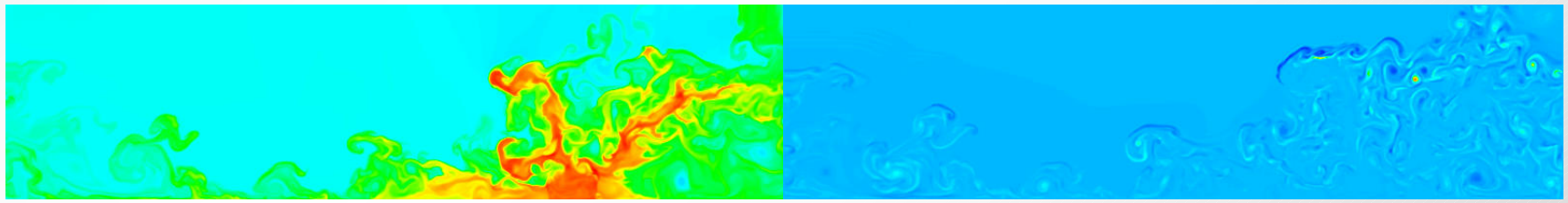

4.33 -0.17

$\log_{10}$(rho)

6.26 -4.85

vorticity

Conclusions

1. We simulate a complex blast wave – cylindrical bubble interaction at M=66.77 and η=5000 with PPM;
2. We observe strong early time positive and negative circulation and vortex double layers due to complex blast wave structure;
3. We study the upstream erosion, which is consistent with [Borkowski et al 1997];
4. At intermediate time, we observe the primary vorticity deposition separates from the interface in an *elongated* vortex layer
5. We observe late time cavity collapse and re-expansion and corresponding fragmentation of the SN ring.

Laser shock tube for the study of supersonic gas flows and the development of hydrodynamic instabilities in layered media.

Lebo I.G.[1),2),] Zvorykin V.D.[2)]

[1)] Technical University-MIREA, Russia, Moscow, Vernadsky prospect, 78,
[2)] Lebedev Physical Institute, Russia, Moscow, Leninsky prospect, 53,
Fax: (095)- 132-11-96, e-mail: lebo@sci.lebedev.ru

Abstract.

The design of miniature laser shock tube for the study of a wide range of hydrodynamic phenomena in liquids at pressures greater than 10 kbar and supersonic flows in gases with large Mach numbers(greater than 10) is discussed. A substance filling a chamber of quadratic cross section, with a characteristic size of several centimeters, is compressed and accelerated due to local absorption of 100-ns, 100-J KrF laser pulses ("GARPUN" installation, Lebedev Phys. Institute, Moscow) near the entrance window. It is proposed to focus a laser beam by a prism raster, which provides a uniform intensity distribution over the tube cross section. The system used to study the hypersonic flow past objects of complex shape and the development of hydrodynamic instabilities in the case of a passage of a shock wave or a compression wave through the interfaces between different media. The numerical simulations are used to model the laser shock tube experiments.

1. Introduction.

The stability of an interface between two media found in the field of constant or pulsed acceleration is a fundamental problem of fluid and gas mechanics.

In the first case, the contact surface is unstable if the gradients of pressure and density have opposite directions (Rayleigh-Taylor instability) /1/.

In the case of pulsed acceleration caused by the passage of a shock wave through a contact surface between two liquids or gases or a sharp deceleration of a substance, which previously moved, the interface is unstable for any arrangement of layers (Richtmyer-Meshkov instability-RMI) /2,3/.

The study of the evolution of hydrodynamic instabilities is a problem of great importance in inertial fusion, physics of high energy densities, cosmology and astrophysics. The passage of strong shock waves through contact surfaces of two gases with different densities causes the formation and development of complex vortex structures, which are of interest for present-day nonlinear hydrodynamics and for studying the problem of a change from an order state to chaos. Another problem, which is important for the development of modern aerospace engineering and protecting the Earth from collisions with space objects, is the study of supersonic flow past bodies of complex shape at large Mach numbers. The problems mentioned above are studied by numerical methods using 2D and 3D codes, in laboratory experiments with shock tubes /3-5/, special rocket and gun facilities /6,7/ using high -power lasers /8,9/ and explosions /10,11/.

Lasers are used to study hydrodynamic flows and instabilities in plane, cylindrical, and spherical geometries, both in the case of direct target heating and in the case of converting laser radiation to x-rays. However, the multichannel and multielement laser facilities used for this

purpose, such as ISKRA-5 (Russia), VULCAN (Great Britain), GEKKO-XII (Japan), NIKE, NOVA and OMEGA (USA) with radiation energy of order of 10 kJ are extremely expensive. In typical laser experiments, the radiation intensity q in focal spot of size *(0.1-1) mm* is 10^{13}-10^{15} *W/cm*^{2} and the pulse duration is of order of *1-10 ns*. In this time, a shock wave travels in a solid path *1-10* μ*m* long, which determines the characteristic scale of a phenomenon being studied, because the unloading wave rapidly weakens the shock wave after the termination of a laser pulse. The development of instability in condensed media, as a rule, is studied with complex and expensive x-ray techniques, which often give only time- and space integrated information.

We propose a new technique for exciting shock waves in gases and compression waves in liquids by a pulsed KrF-laser with considerably lower radiation energy *(~100 J)* for modelling a wide range of hydrodynamic phenomena mentioned above at a spatial scale of *1-10 mm* in a range of microsecond duration. The idea is based on two known facts:

(1) lasers with pulse duration of *10-100 ns*, when irradiating the surface of a solid coated with a thin transparent layer, which hampers a rapid unload of the evaporated substance, produce pressure jumps with amplitudes more then 10 kbar at moderate radiation intensities 10^8-10^9 *W/cm*^{2};

(2) unloading target excites strong shock waves with Mach number more then 10 in the atmospheric air surrounding it.

2. Design of laser shock tube.

The design of such a laser shock tube is based on the use of following basic components: a miniature shock tube chamber, a powerful KrF laser, a laser focusing system and 2D numerical codes. The shock tube chamber is shown in **Fig.1a,b.**

Figure 1. Schematic of laser shock tube for investigation of RMI (a) and hypersonic flow past objects of complex shape (b).

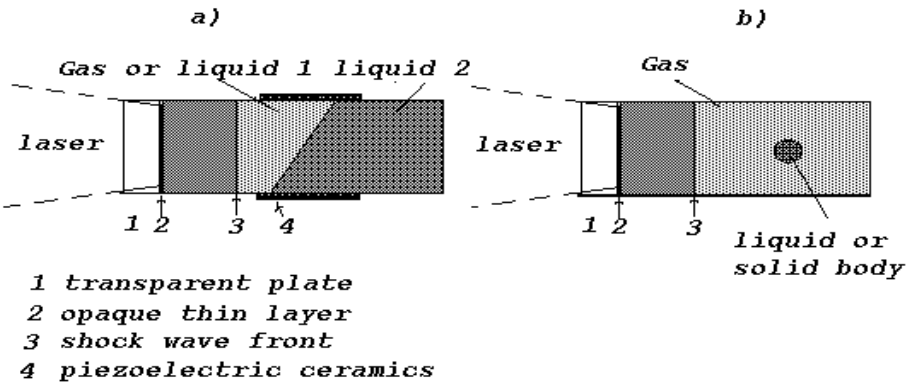

Laser radiation enters through a transparent window (1) inside a chamber, which is filled with a liquid or gas. Radiation is absorbed in a thin layer (2) adjacent to the window, resulting in a compression wave travelling in both directions from the energy release region.

Initial perturbations on the contact surface between two liquids or a liquid and gas can be produced by a piezoceramic transducer (4) attached to the chamber wall or with help of a thin shaped film. One can place liquid drops or solid particles of different shape inside the chamber which is filled with a gas (see **Fig.1b**). Because the liquids and gases under study are transparent to probing visible radiation, one can use conventional high-speed shadow and schlieren photography. In detail it is possible to find the description of laser shock tube in /12/.

3. Numerical simulation of the propagation of pressure waves in laser shock tube.

The numerical calculations modeling the formation and propagation of a pressure wave were made using 2D Lagragian code “ATLANT” /13/ and 2D Euler code “NUTCY” /14/ in cylindrical geometry. A laser beam traveled along z-axis. Laser shock tube has length of 12 cm and contains three (or four) subregions: transparent layer of silica glass with density *2.5 g/cm*^{3}, aluminium foil with thickness of 2 μm and *Xe*-gas filled chamber with initial density *5.4 mg/cm*^{3}. Laser radiation was incident from the right, passed through a transparent layer, and was totally absorbed in aluminium layer. A KrF laser pulse had a trapezoidal form, with leading and trailing edges 20 ns long and a region of constant intensity *3.1x10*^{8} *W/cm*^{2} 60 ns long. Because of heating and evaporation of a thin Al-foil, a pressure jump with the amplitude about 10 kbar occurred and compression wave in glass and shock wave in gas was produced. **Fig.2** shows the results of calculation modeling the propagation of a shock wave in Xe-gas filled chamber. The sound speed in xenon and glass was *174 m/s* and *3.7 km/s*, respectively. One can see that strong shock wave

with Mach numbers M~40 is formed in gas, and this wave gradually damps during its position. By a moment of *700* ns, it travels a *4 mm* path, but its velocity remains rather high and corresponds to *M≥20*.

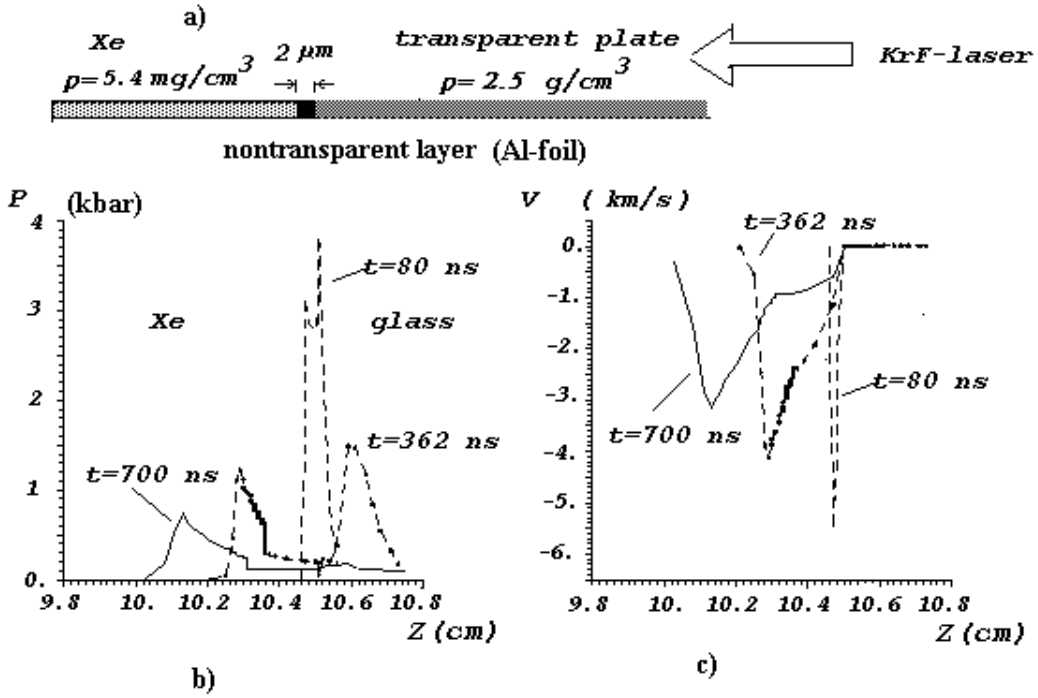

Figure 2. Results of calculation. Schematic of the experiment (a); the distributions of pressure (b), and velocity (c) along the z-axis at the moments of time t=80 (1), 362(2), and 700 (3) ns.

4. Preliminary experiments.

The experiments have been performed at GARPUN electron-beam pumped KrF laser installation in Lebedev Physical Institute (Moscow) /15/. Laser beam was focused on the targets by an optical system consisting of the prism raster and the lens. Overlapping of 25 individual beamlets provided non-uniformity less then few percents across the square spot. By moving the lens we could vary a spot size from *20x20* to several mm. For a fixed 7x7 mm focal spot laser intensities were changed in the range of *0.1-1 GW/cm*^{2} by attenuating incident laser energy. The targets were set inside an evacuated chamber filled with an air, which pressure being varied in the range of p_0*=0.0001-1 bar*. Gasdynamic processes that developed under laser-target interaction were studied with the help of high-speed optomecanical camera in combination with schlieren or shadow technique /16/. Slit scanning images of the self-luminescence laser-produced plasma were combined with images of flying foil targets and shock wave (SW) propagating in surrounding air.

It was observed that during laser pulse action plasma front propagated towards an incident radiation together with the SW front. The velocities in dependence on laser intensity (**Fig.3**) and air pressure (**Fig.4**) are shown. Solid lines in Fig.3 correspond to calculated velocities of laser-

supported detonation wave (LSDW) /17/, dashed lines are the results of numerical simulations using “ATLANT_C”-code /18/.

The most part of laser radiation (up to 90%) penetrated to the target. At lower air pressures $p_0 < 0.1$ *bar* (Fig.4) the absorption in air reduced and did not influence on SW velocity (≅ *30 km/s*).

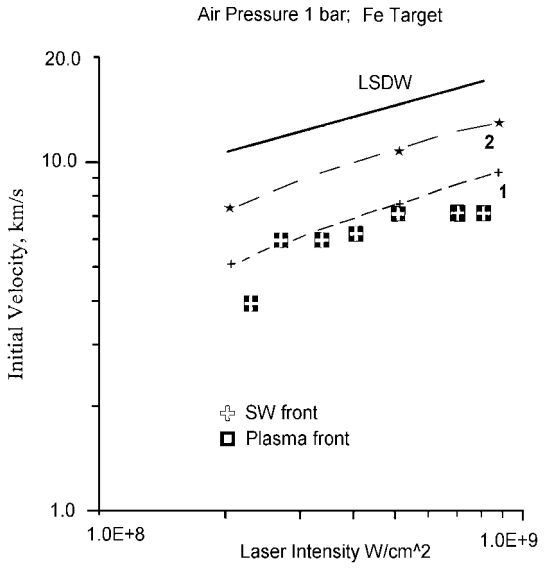

Fig.3. The dependence of plasma front velocity from laser intensity. Dashed lines – the results of numerical simulations with allowance for ionization processes (1) and when Z=const (2).

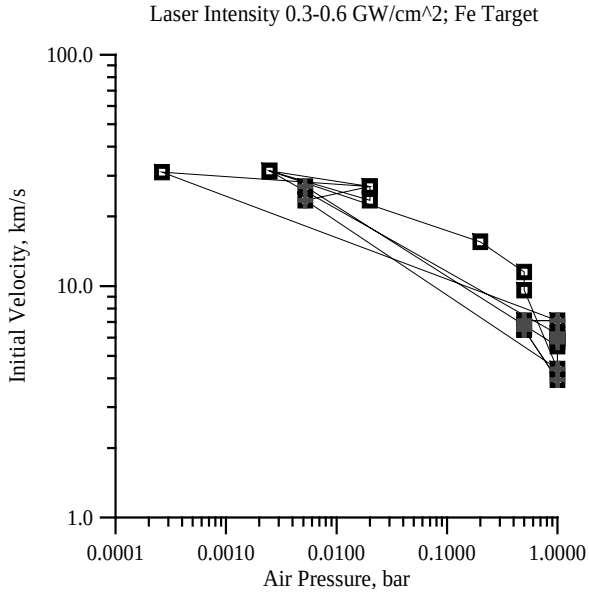

Fig.4. The dependence of plasma front velocity from gas pressure. Laser intensity is 0.3-0.6 GW/cm^2.

5. Conclusions.

The technique proposed here for exiting shock waves in gases and compression waves in liquids by KrF laser radiation has some advantages in comparison with the conventional technique used in experiments with nanosecond laser pulses. The typical scale of gas-dynamic flow is of the order of 1 mm, and the duration of processes reaches several microseconds. This enables one to use conventional optical techniques to observe the spatial and time evolution of instabilities at the interfaces between different media and to study the supersonic gas flow past objects of complex shape. One can also study the effect of a repeated initiation of acceleration by several shock waves, which are produced by a tandem of laser pulses.

The advantages of laser shock tube in comparison of ordinary shock tube are

1) the generation of large pressure pulse (as a result high Mach number ≥ 20 shock wave) and

2) the economy of noble gases and other supplies.

The preliminary experiments show that in contrast of CO_2 laser-plasma experiments the radiation of UV KrF laser comes through atmosphere and reach condense target. It allows to carry out experiments with solid targets and background gases with the initial pressure is about 1 bar.

Acknowledgments.

We are grateful to Prof.V.F.Tishkin and Dr.A.B.Iskakov for help of numerical modeling of laser plasma jet formation and shock wave expansion in Air (see Fig.3).

This work was supported by the Russian Foundation for Basic Research, project N 01-01-00023.

References.

[1] G.Taylor Proc. Roy. Soc., A201, 192, (1950)

[2] R.D.Richtmyer, Commun. Pure Appl. Math.,13, 297, (1960)

[3] E.E.Meshkov, Izv. Akad. Nauk SSSR, Mekh. Zhidk. Gasa, 5, 151, (1969)

[4] J.Haas, B.J.Sturtevant. Fluid Mech., 1281, 41, (1987)

[5] A.N. Aleshin, E.V.Lazareva, S.G.Zaytsev et al. Dokladi Akademii Nauk SSSR, 310, 1105, (1990)

[6] K.I.Read, Physica D, 12, 45, (1984)

[7] Yu.A. Kucherenko et al., In: Proc. of 3rd International Workshop on Physics of Compressible Turbulent Mixing at Royaumont, France, 1991, p.427

[8] C.J.Pawlew et al. Phys. Plasmas, 4, 1969, (1997)

[9] D.H.Kalantar et al., Phys. Plasmas, {4}, 1985, (1997)

[10] R.F.Benjamin. In: Proc. of 3rd International Workshop on Physics of Compressible Turbulent Mixing at Royaumont, France, (1991)

[11] A.Lebedev et al., In: Proc. of 5th International Workshop on Physics of Compressible Turbulent Mixing at Stony Brook, USA, 1995, p.213

[12] V.D.Zvorykin, I.G.Lebo Quantum Electronics, 30, 540, (2000)

[13] I.G.Lebo et al. J. Russ. Laser Research, 15, 136, (1993)

[14] I.G. Lebo et al., In: Proc. of 6th International Workshop on Physics of Compressible Turbulent Mixing at Marcellie, France, 1997, Institute Universitaire des Systemes Thermiques Industriels 1997, p.312

[15] V.D.Zvorykin, I.G.Lebo, Laser and Particle Beams, 17, 69, (1999)

[16]. V.A.Danilychev, V.D.Zvorykin. In: Trudi Fiz. Insit. P.N.Lebedeva Akad. Nauk SSSR, {142}, 117, (1983)

[17] Yu.P.Raizer Sov. Phys.-JETP, 21,1009, (1965)

[18] A.B.Iskakov, I.G.Lebo, V.F.Tishkin. J. Russ. Laser Research, 21,247, (2000)

Simulations of a Shock-Accelerated Gas Cylinder and Comparison with Experimental Images and Velocity Fields

Cindy A. Zoldi

(Los Alamos National Laboratory and SUNY at Stony Brook)

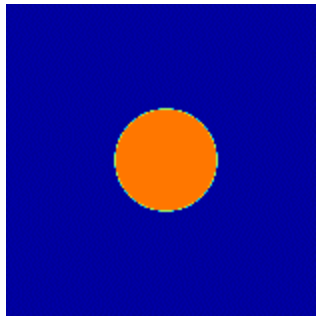

8th IWPCTM

California Institute of Technology
Pasadena, California

December 9-14, 2001

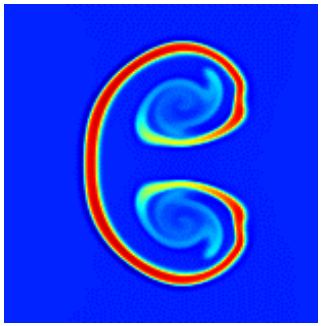

Collaborators

Experimenters:

Kathy Prestridge (LANL, DX-3)
Bob Benjamin (LANL, DX-3)
Paul Rightley (LANL, DX-3)
Peter Vorobieff (UNM)
Chris Tomkins (LANL, P-22/DX-3)
Mark Marr-Lyon (LANL, DX-3)

Computational Scientists:

RAGE: Mike Gittings (LANL/SAIC, X-2)
Mike Steinkamp (LANL, X-3)

Cuervo: Bill Rider (LANL, CCS-2)
Jim Kamm (LANL, CCS-2)

CHAD: Barbara Devolder (LANL, X-5)
Manjit Sahota (LANL, T-3)

Thesis Advisors:

James Glimm (Stony Brook)
David Sharp (LANL, T-3)

Outline

- Purpose of research
- Experimental apparatus
- Simulation setup
- Qualitative and quantitative comparisons
- Future work

Our View of Scientific Modeling

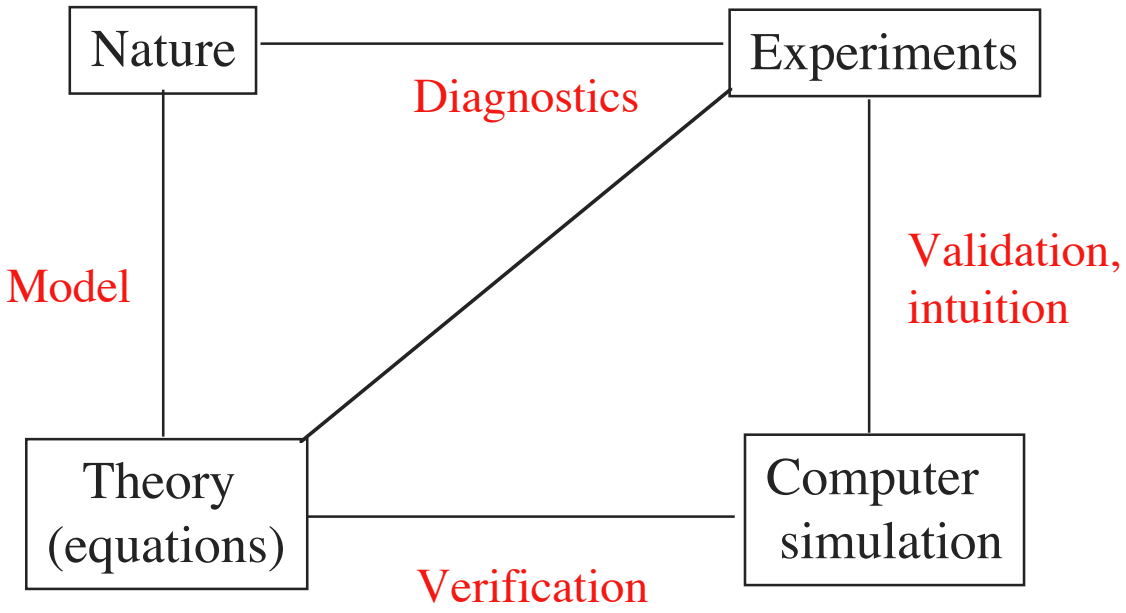

How well do computer simulations approximate nature?

Richtmyer-Meshkov Instability

What is the Richtmyer-Meshkov instability?

It occurs when a shock wave collides with an interface between two different materials causing perturbations on the interface to grow.

Example: Shock moving from air into SF_6 gas (Note: $\rho_{air} < \rho_{SF6}$)

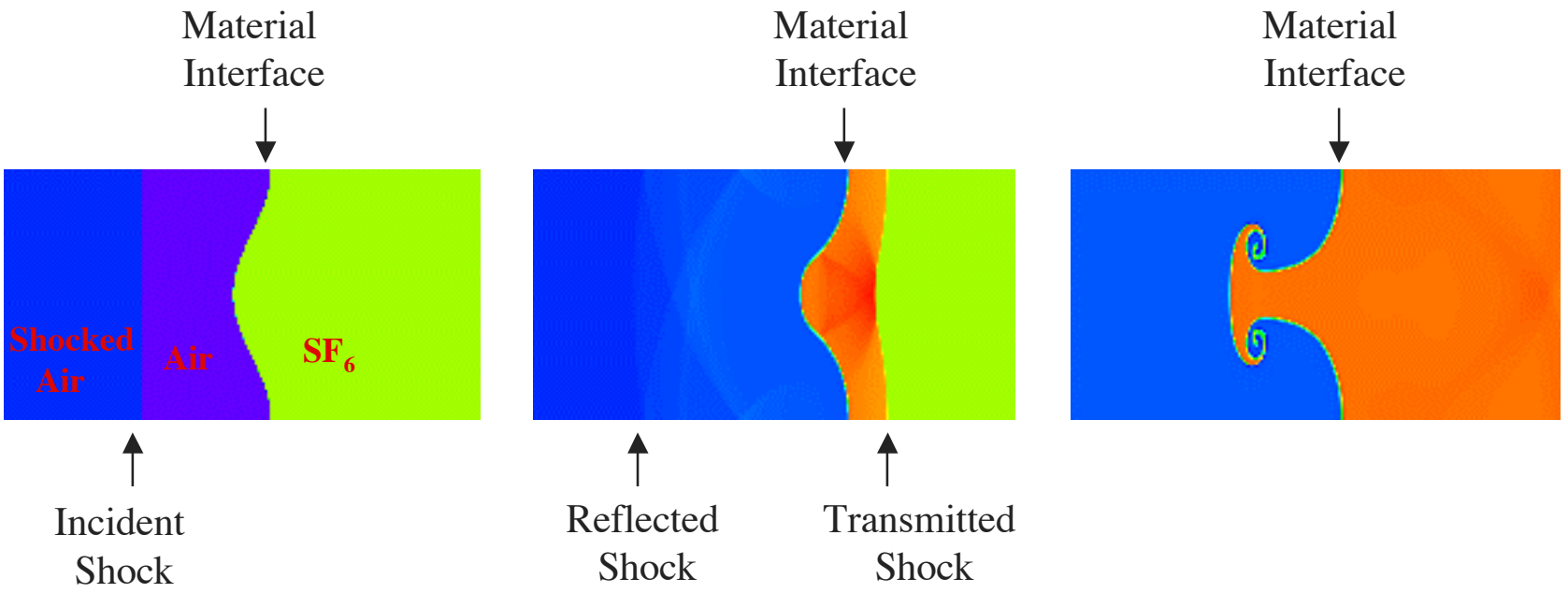

DX-3 Gas Shock Tube

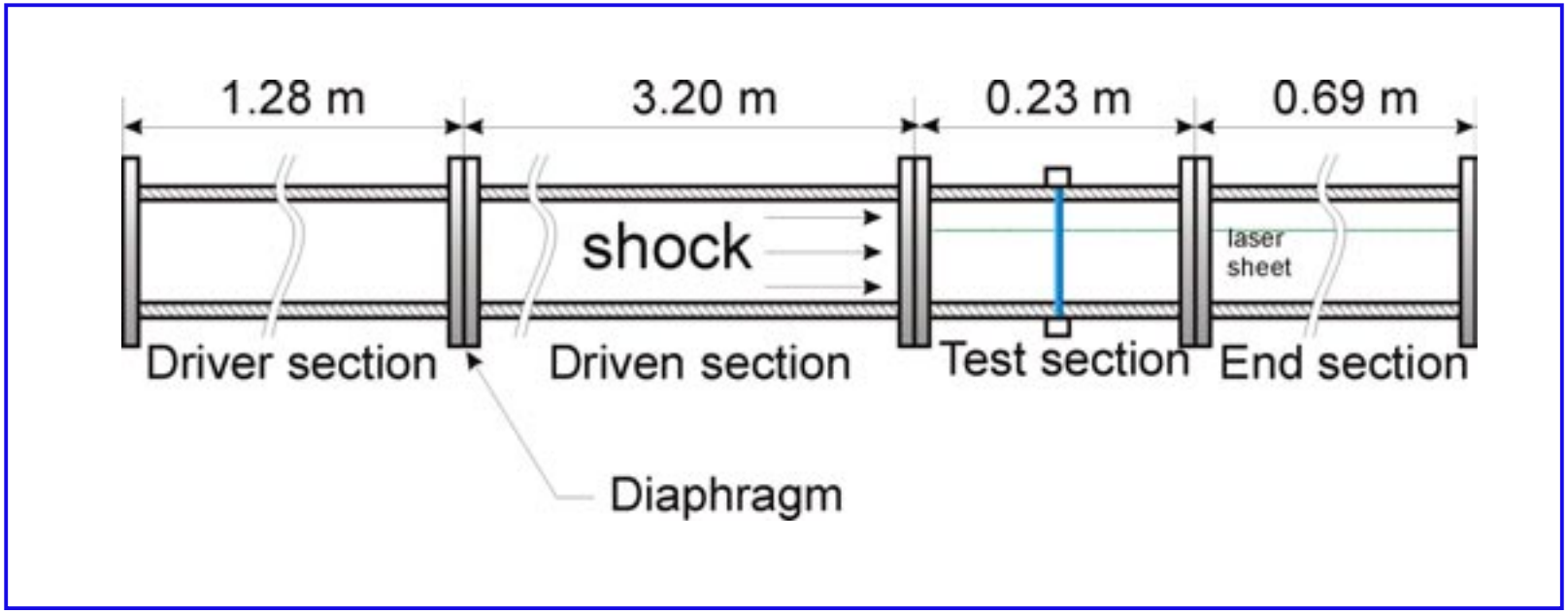

- Gas cylinder composed of SF_6 and surrounded by ambient air
- SF_6 seeded with glycol droplets to aid in visualizing the flow and to enable the PIV capability

Consult the following paper for more information on the experimental setup: P. M. Rightley, P. Vorobieff, and R. F. Benjamin. Evolution of a shock-accelerated thin fluid layer. *Phys. Fluids*, 9(6):1770-1782, 1997.

Test Section of the Shock Tube

- 2 lasers:
  - Customized, frequency doubled Nd:YAG
  - 10 Hz 'New Wave' at 532 nm
- 3 cameras:
  - Intensified CCDs, 1134x468
  - Initial Conditions (IC), Dynamic (DYN), and PIV
- 8 pulses:
  - 7 pulses for ICs and dynamic images with $\Delta t=140\mu s$
  - 8th pulse for PIV

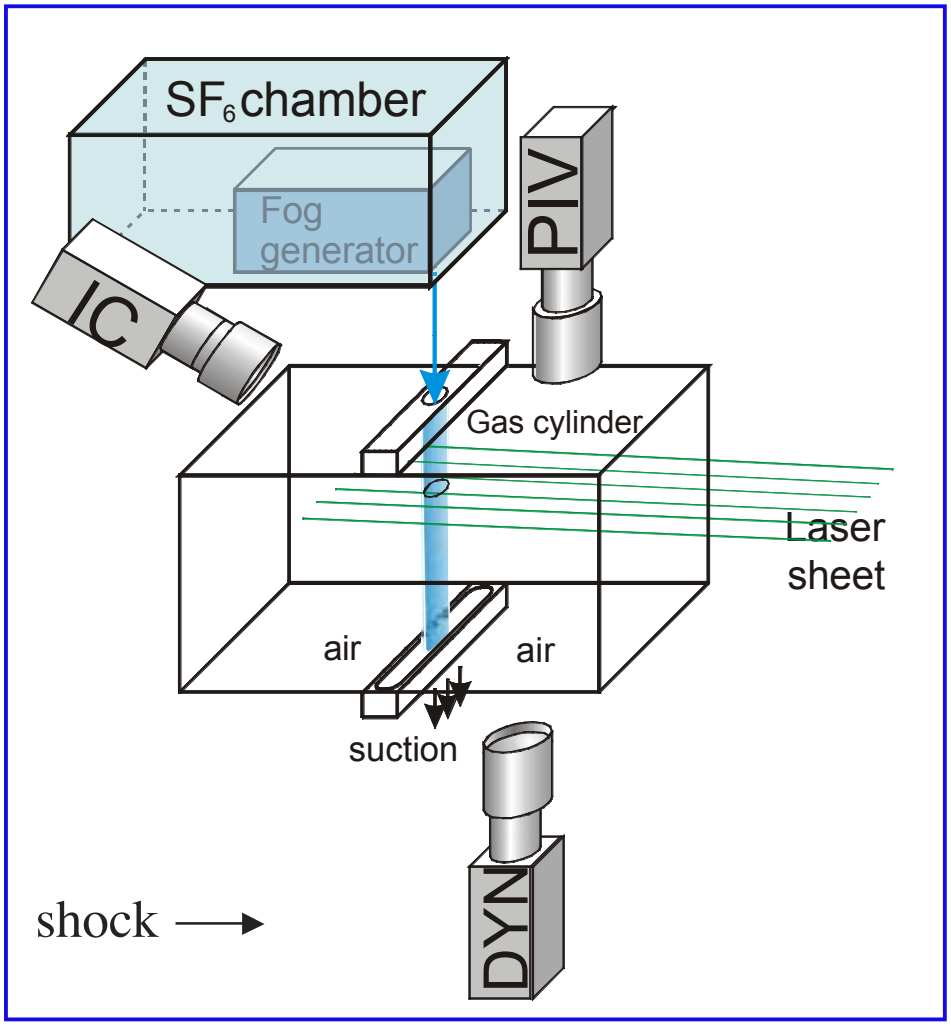

RAGE: Radiation Adaptive Grid Eulerian Code

- Multi-dimensional Eulerian hydrodynamic code
- Directionally-split second order Godunov scheme

- Continuous adaptive mesh refinement (CAMR)
  - Each cell can be coarsened or refined by a factor of two in each timestep
  - Only one level of refinement change possible between adjacent cells
  - Refinement decisions can be modified for each material or defined for regions of computation

- Running in parallel on ASCI machines (Blue Mountain)
- Substantial validation has been performed on shocked interface problems
  - Shocked curtain, single mode RMI, NOVA experiments

RAGE was originally developed by Michael L. Gittings

Initial grid -- level 1

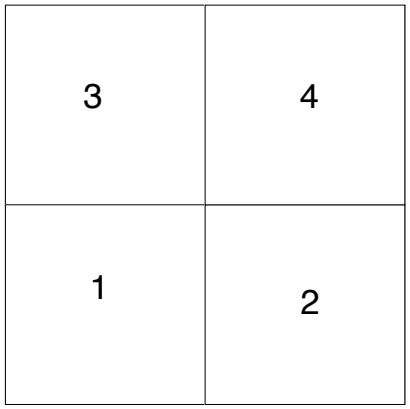

Subdivided cells 2 and 6

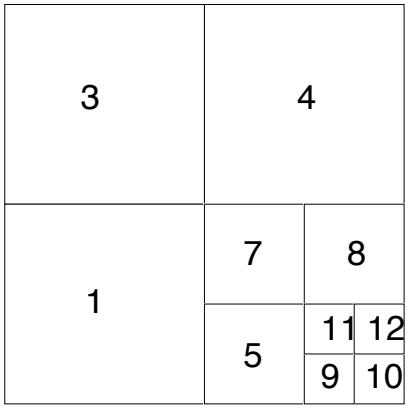

Cylinder Simulation Setup

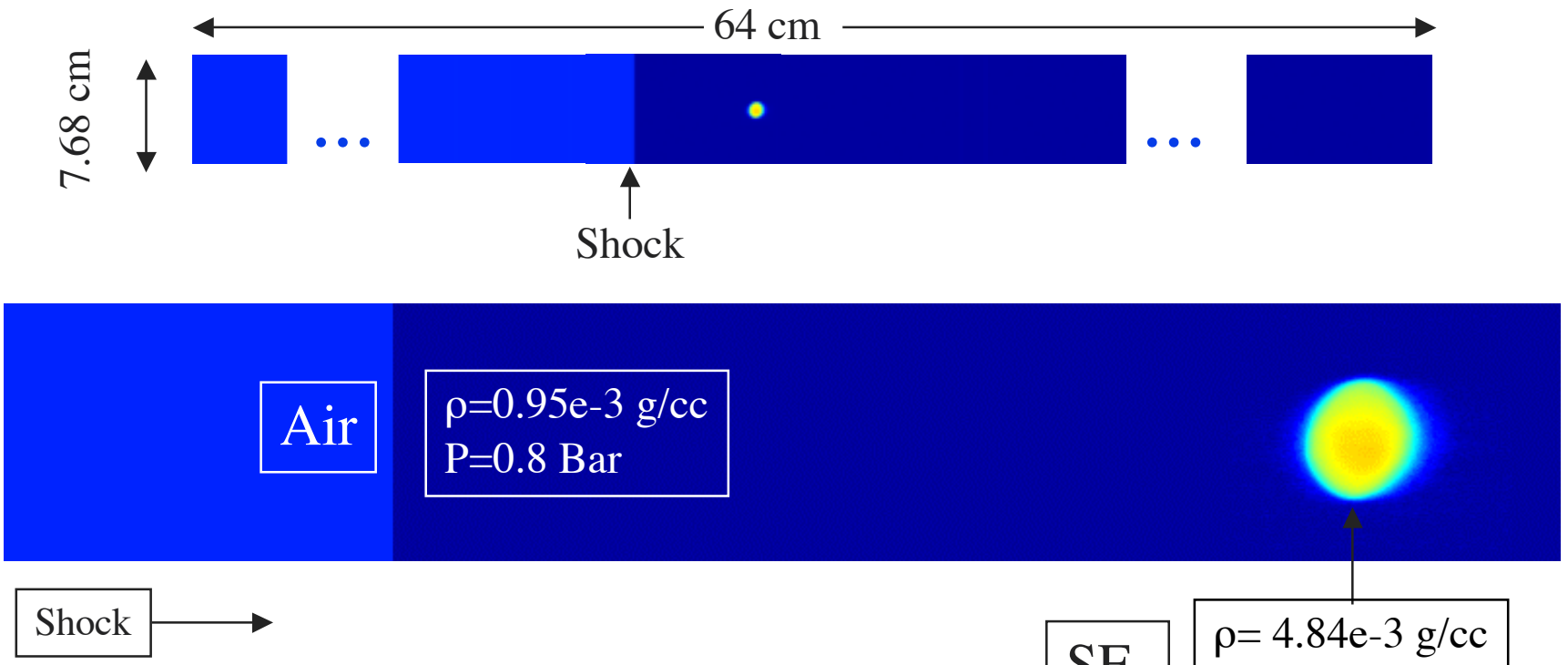

- Mach 1.2 shock in air hitting a cylinder of SF_6
- Ideal gases: $\gamma_{SF6} = 1.09$ $\gamma_{air}=1.4$
- RAGE grid: level 1 = 0.64 cm (approx 80 zones across the diameter of the initial cylinder)
  level 7 = 0.01 cm

Comparison Between Experimental and Computational Images

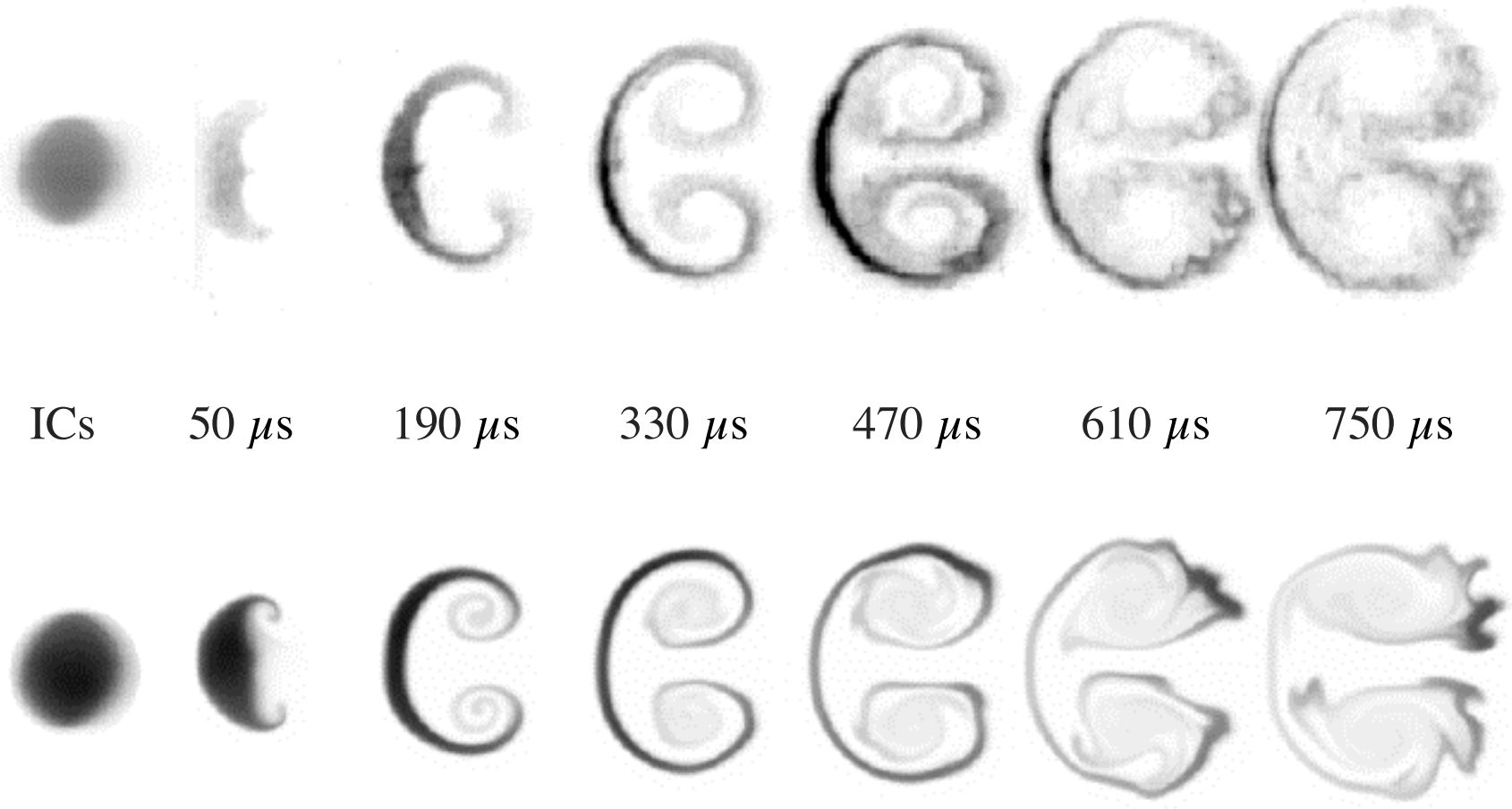

Quantitative Measurements

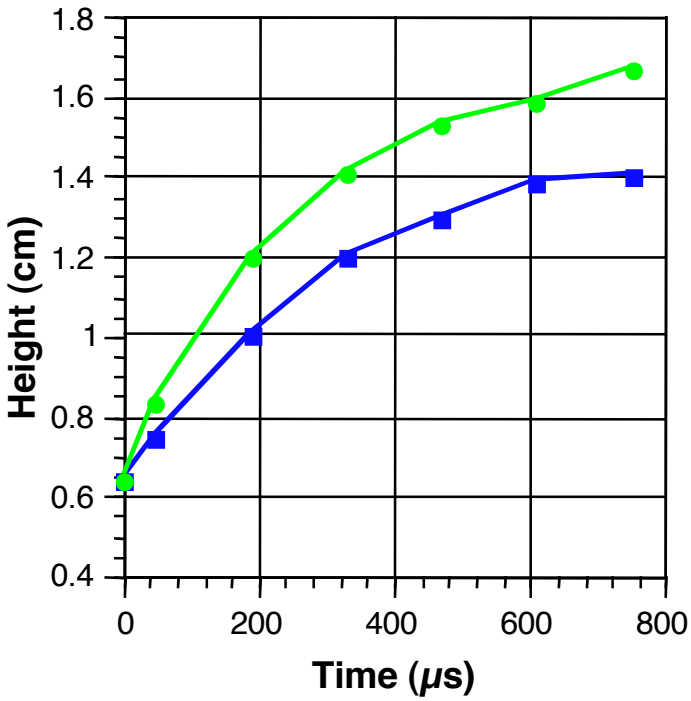

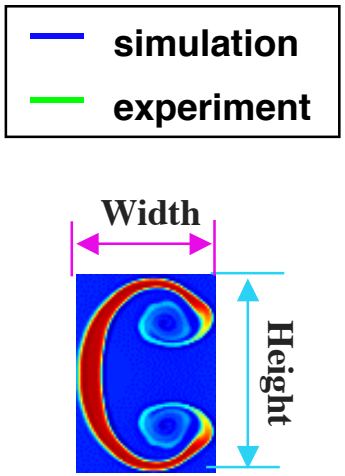

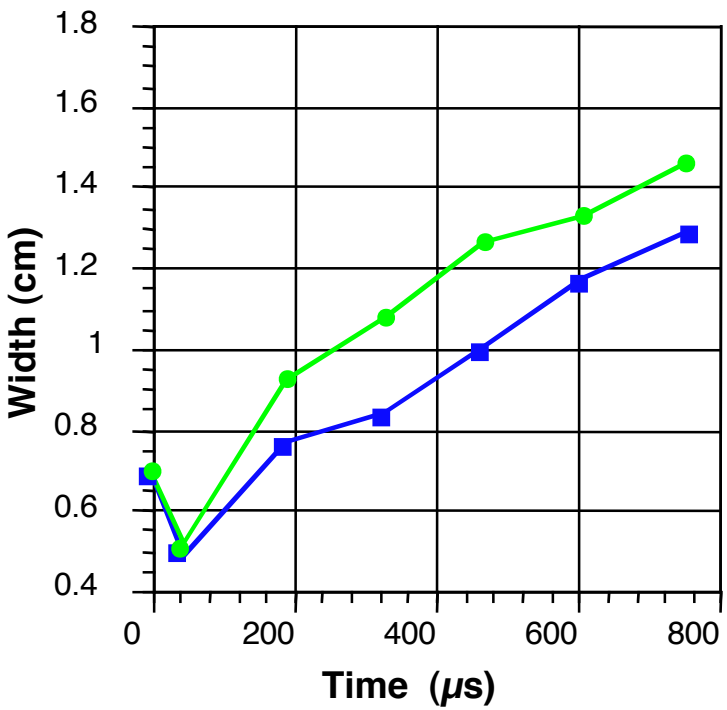

The height and width of the evolving cylinder are 15% larger in the experiment than in the simulation

Velocity Fields

Experiment

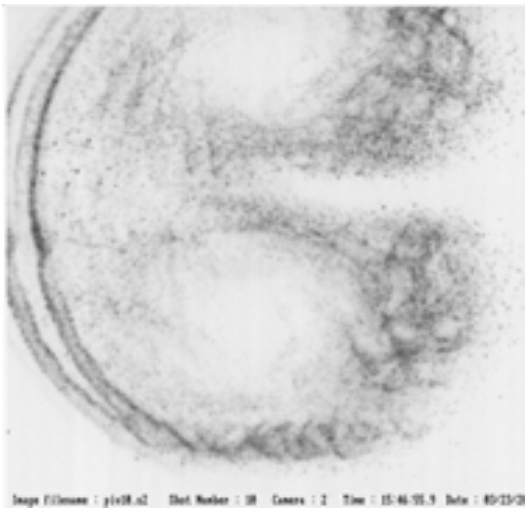

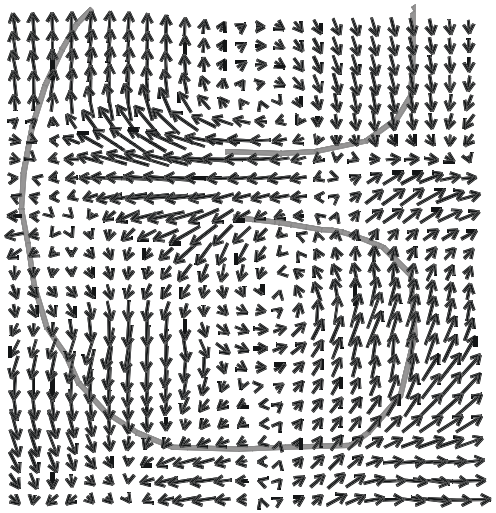

→ 10 m/s

Simulation

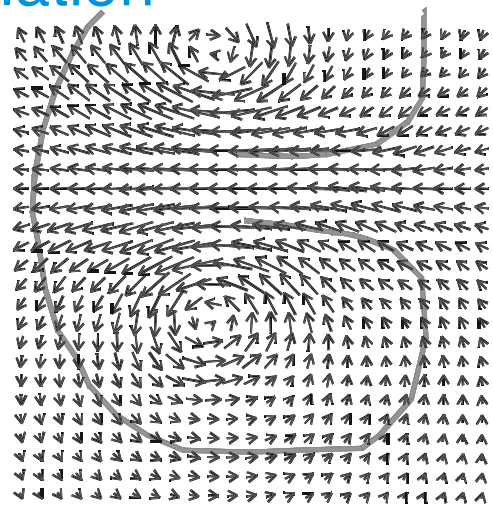

→ 50 m/s

Varying Peak SF_6 Concentration

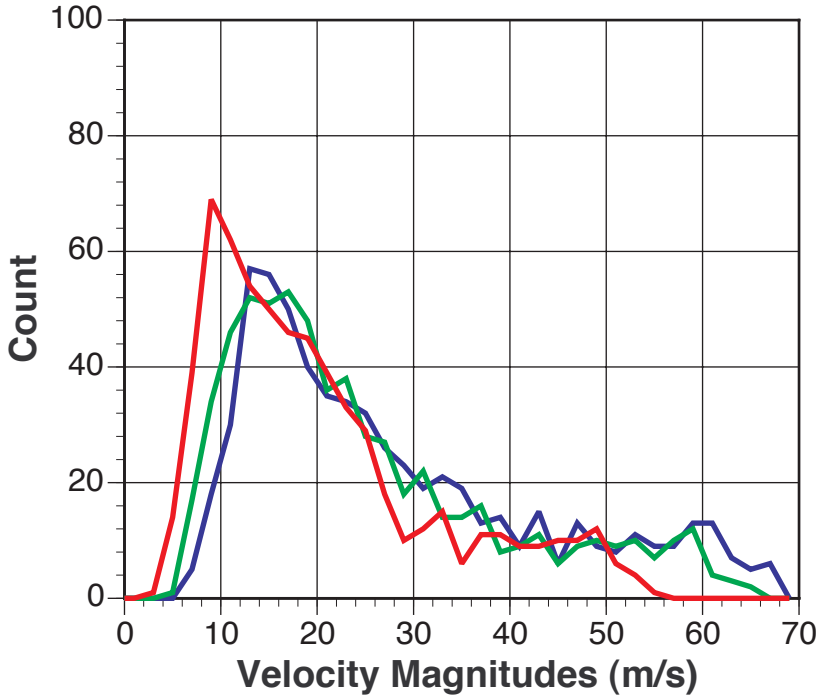

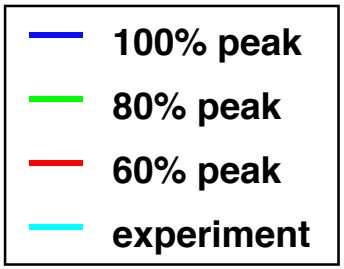

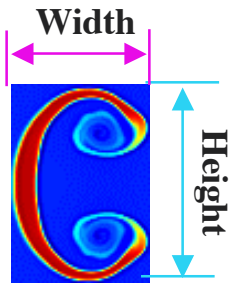

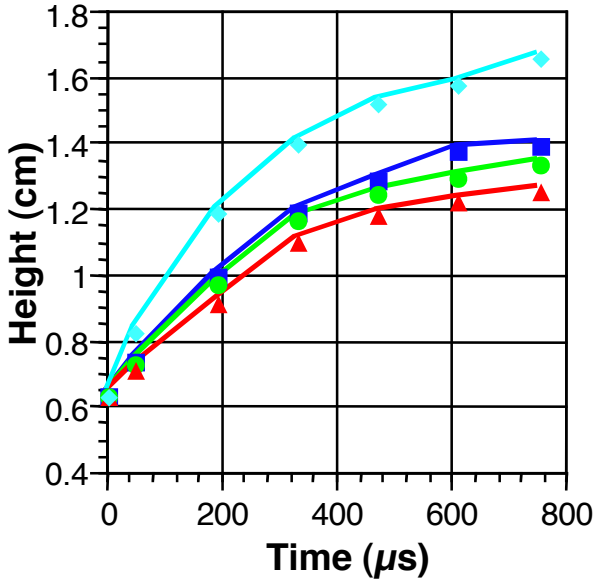

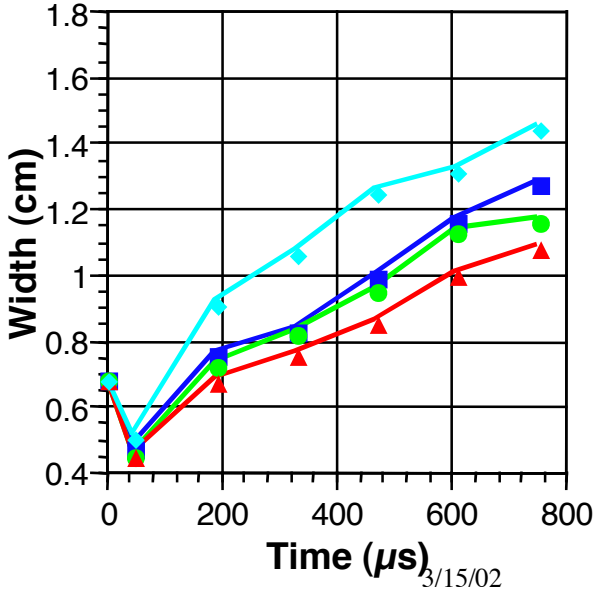

Smaller peak SF_6 concentrations result in smaller velocities and smaller lengths

Varying Density Gradient at the Air/ SF_6 Interface

Experiment

Experimental Initial Conditions

Sharp Interface

Diffuse Interface

- Differences are visible in the density images with the initially diffuse interface producing the best visual agreement with the experiment
- No significant differences exist in the heights/widths and velocities

How well characterized are the experimental initial conditions?

Mesh Refinement

Experiment

Diffuse Interface - fine $\Delta x = 0.01$

Diffuse Interface - coarse $\Delta x = 0.02$

A coarser simulation shows "better" visual agreement with the experiment

Jet velocity:
- coarse simulation: 62 m/s
- fine simulation: 69 m/s

Coarser resolution:
- less rollup in vortex
- less evidence of secondary instability
- smaller jet velocity

New Velocity Measurements

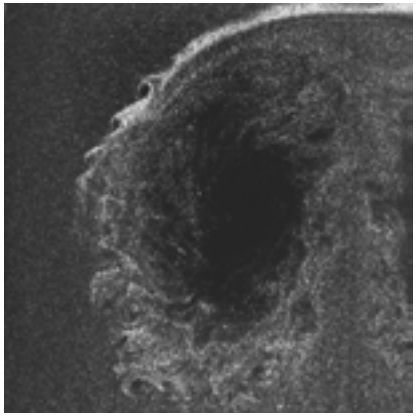

PIV image

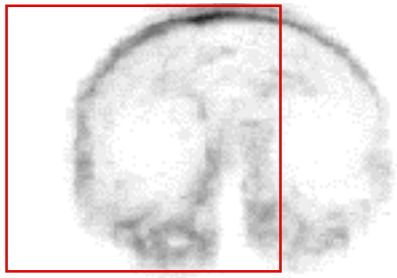

Last dynamic image

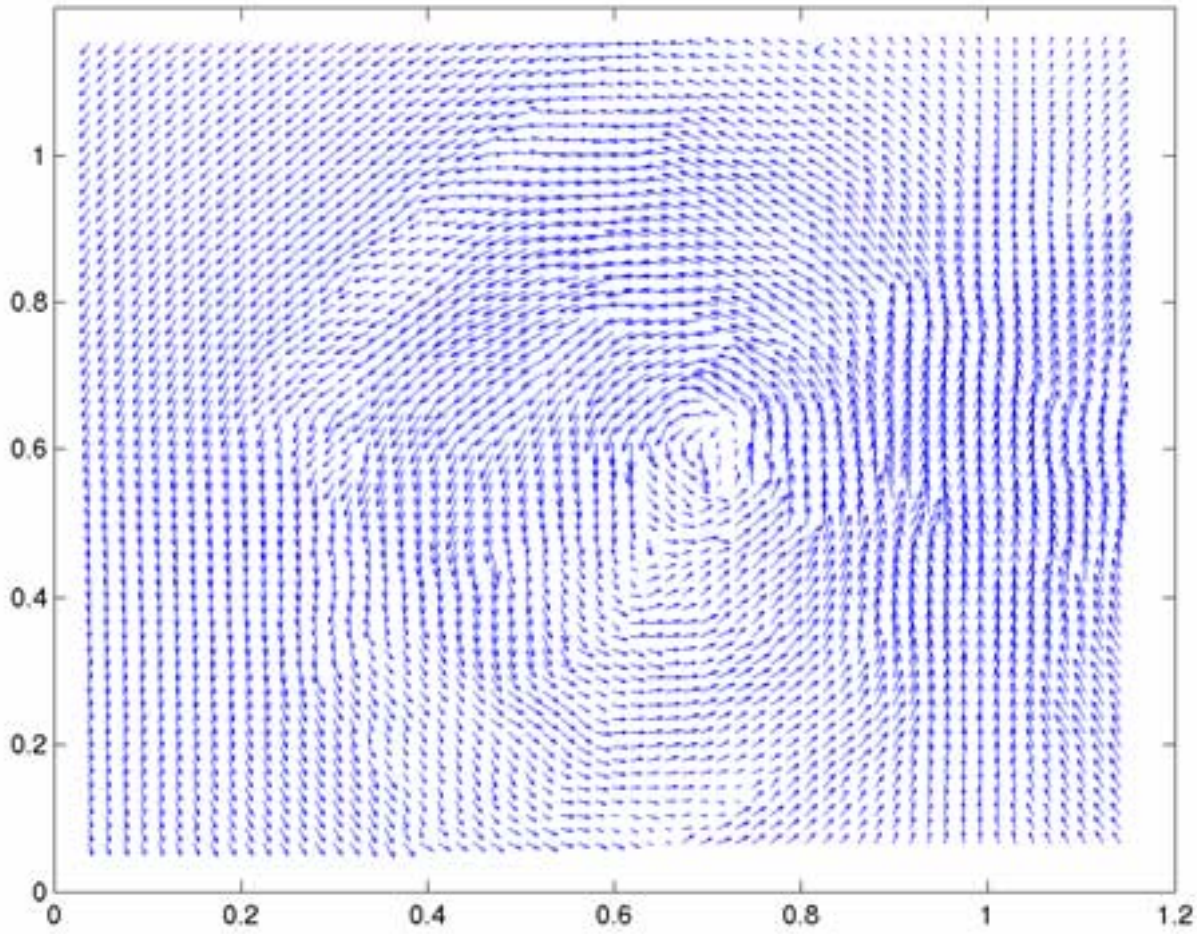

The new velocity field has vectors every 187 μm compared to every 537 μm obtained previously.

Location of Velocity Magnitudes

Experiment

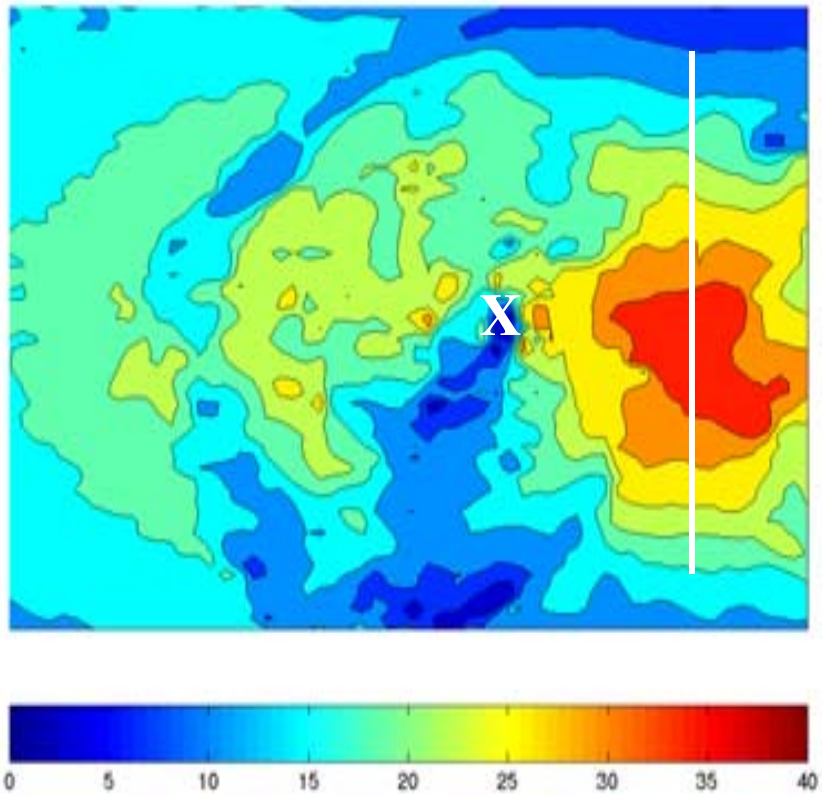

Simulation

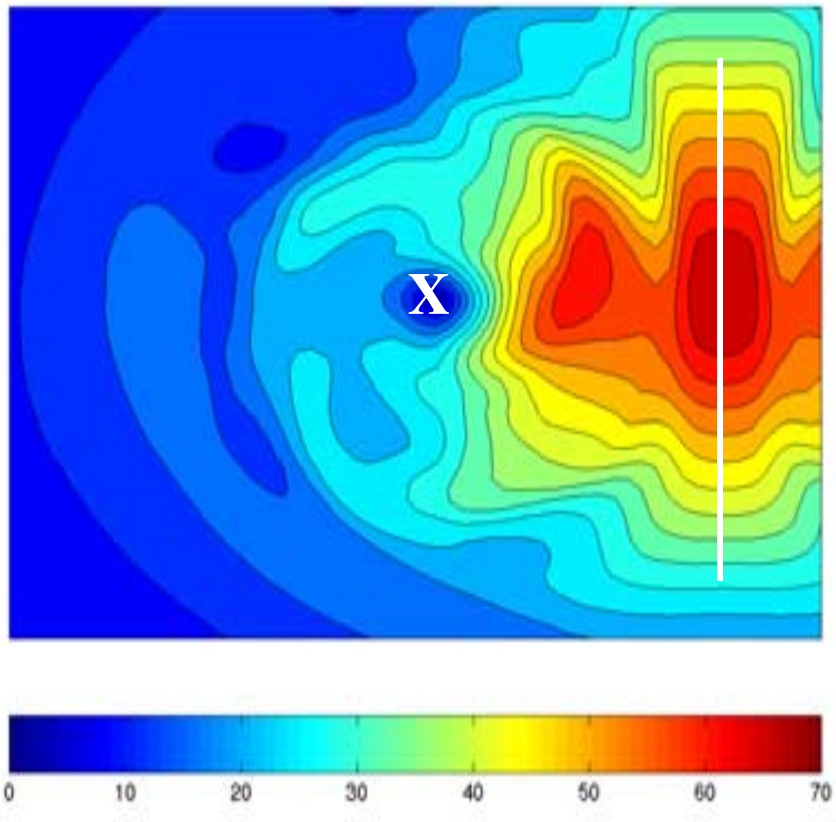

Largest velocities occur in the back-flow area and the smallest velocities occur in the vortex core

Comparison of Experimental and Computational Velocity Magnitudes

Experiment

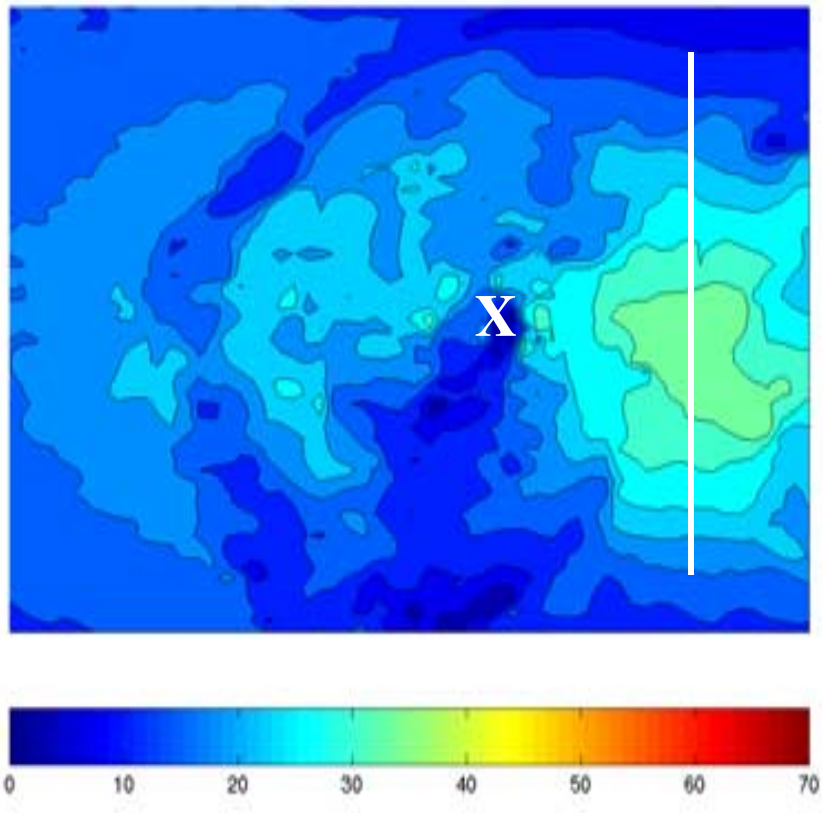

Simulation

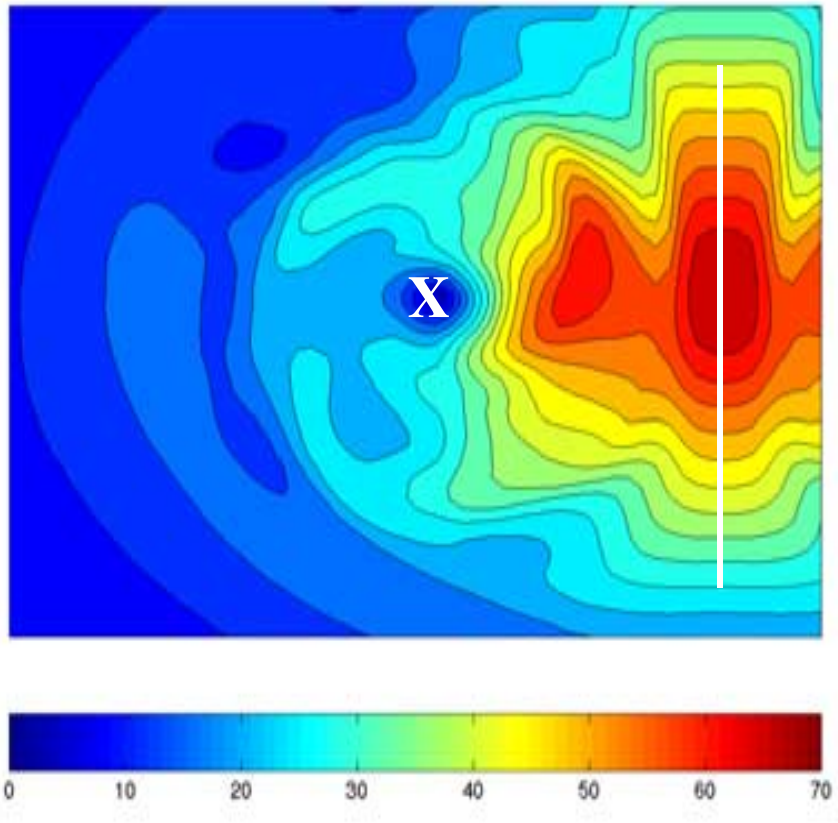

The experiment and the computation have similar velocities in the vortex core

Histogram of Velocity Magnitudes

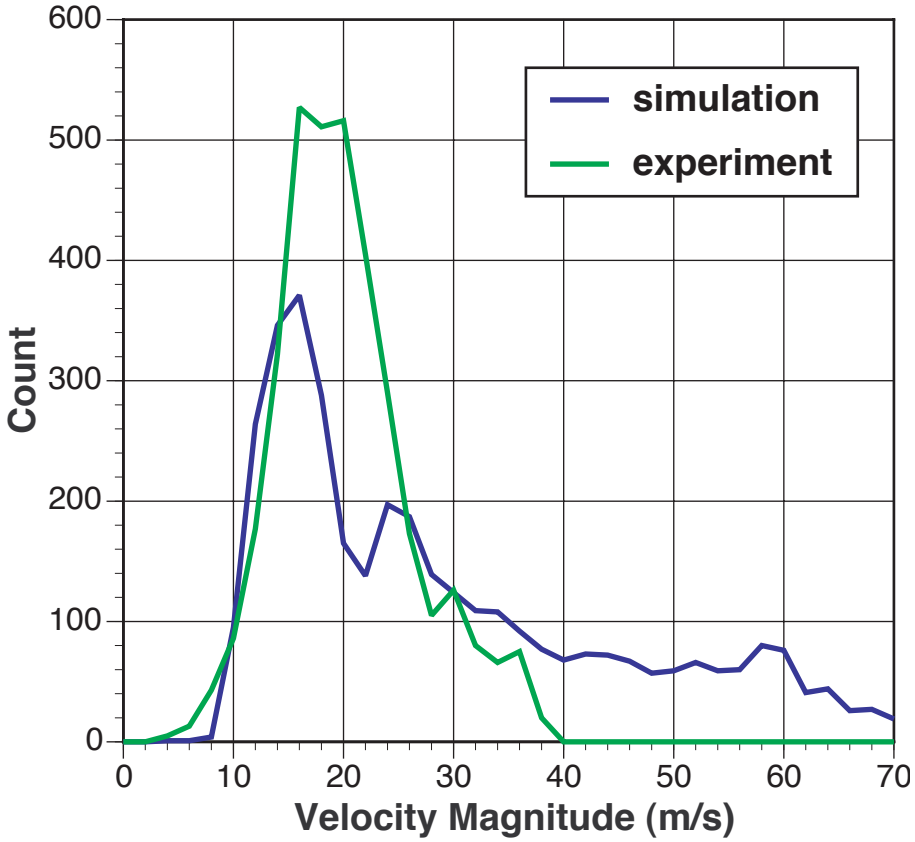

Both the experiment and the computation have a peak velocity of 15 m/s.

The magnitudes of the back-flow velocities form the tail of the histogram.

Large disagreement still exists between the experimental and computational back-flow velocities.

Jet Velocity of a Vortex Pair

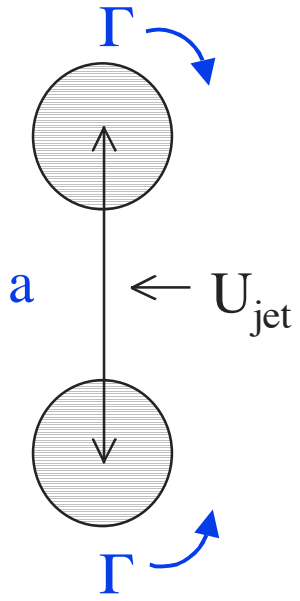

Model the evolving cylinder as a vortex pair composed of two idealized incompressible rectilinear vortices with equal and opposite circulations

For steady state flow (i.e., vortices stationary), the jet velocity U_{jet} between the two vortices is equal to*:

$$U_{jet} = 3\Gamma / 2\pi a$$

Simulation: U_{jet} = 59 m/s (predicted)
U_{jet} = 69 m/s (observed)

Experiment: U_{jet} = 37 m/s (predicted)
U_{jet} = 36 m/s (observed)

Are the predicted velocities qualitatively consistent with the circulation and vortex spacings measured in the experiment and the simulation?

*L. Prandtl and O.G. Tietjens. Fundamentals of Hydro- and Aeromechanics, McGraw-Hill Book, 1934.

Vortex Spacing

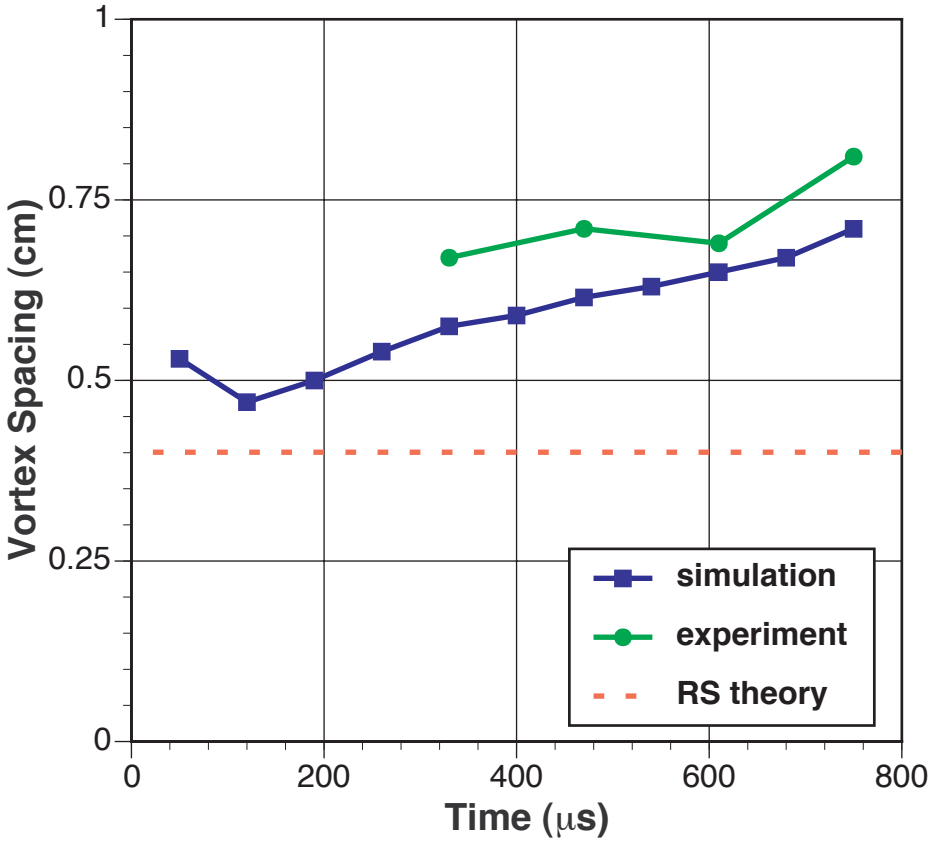

The experiment has larger vortex spacings compared to the simulation

The experimental and computational vortex spacings are in the range of Jacobs' measurements*

Note: The vortex spacing is determined using flow visualization

*J. W. Jacobs. The dynamics of shock accelerated light and heavy gas cylinders. *Phys. Fluids A*, 5(9):2239, 1993.

Circulation Values

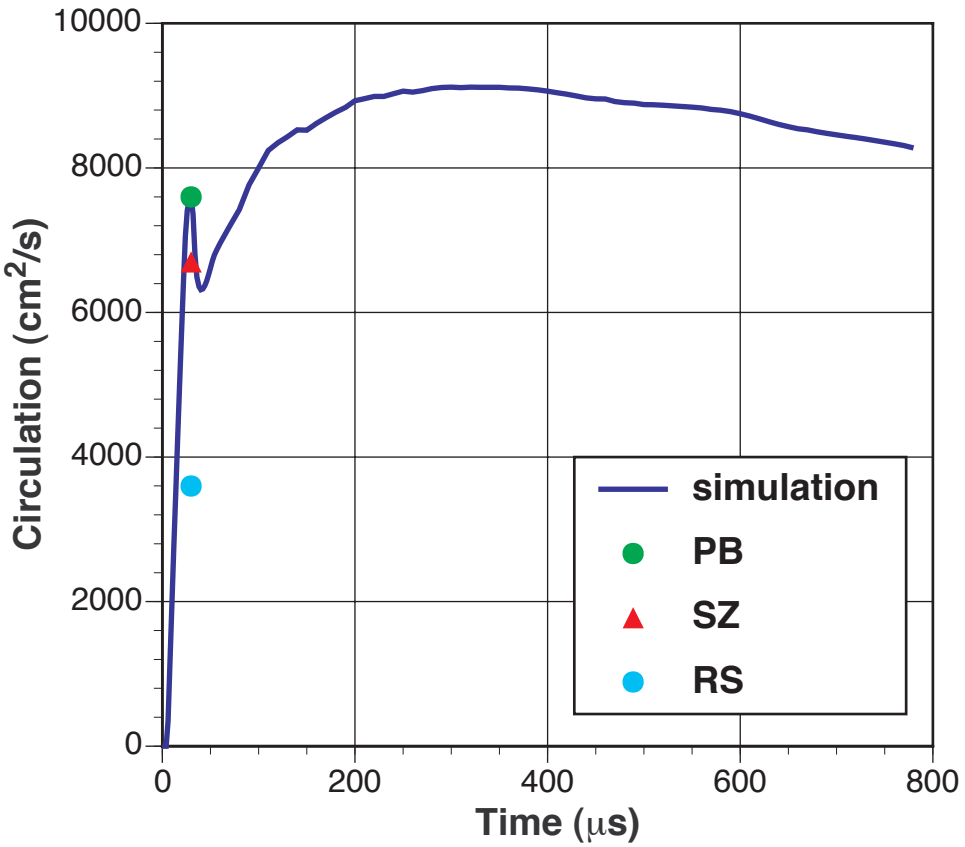

Predictions of circulation:
RS: Rudinger & Somers (1960)
PB: Picone and Boris (1988)
SZ: Samtaney & Zabusky (1994)

The computational circulation value right after shock passage agrees well with the theoretical predictions of PB and SZ.

We need early-time PIV to determine the corresponding experimental circulation value.

Using the PIV results at 750 μs we find that: $\Gamma_{experiment} < \Gamma_{simulation}$

Summary

- Higher experimental velocities are observed with the improved PIV diagnostic, resulting in better agreement with the computational velocities
- The experiment and the simulation have similar velocities in the vortex core
- The computational jet velocity is approximately twice the value of the experimental jet velocity
- The differences in the jet velocities may be resolved by:
  - Examining the early-time shock-cylinder interaction in the experiment
  - Comparing the RAGE simulations with other hydrodynamics codes

Future Work

- Continue to investigate the length and velocity differences between the experiment and the simulation
- Redesign the experimental hardware to allow for high-resolution PIV at early time
- Obtain a better characterization of the experimental initial conditions
- Examine the effects of mix on the cylinder development using the new mix model added to the RAGE code
- Perform simulations using different computer codes
  - Cuervo (Bill Rider, Jim Kamm)
  - CHAD (Barbara Devolder, Manjit Sahota)
- Perform statistical analysis of the experimental and computational images (Bill Rider, Jim Kamm)

SIMULATIONS OF TURBULENT MIXING OF TWO FLUIDS WITH VARIABLE ACCELERATION LAWS

A.N. Razin, V.I. Kozlov, I.V. Sapozhnikov
(RFNC – VNIIEF)

Dimonte's experiments have been simulated with the VIKHR technique. The progress of the turbulent mixing zone has been considered resulting from Raleigh-Taylor instability at the interface between two immiscible fluids. The calculations were performed with variable initial turbulent zone width and a sequence of refined grids for increasing, decreasing, pulse and constant accelerations. The turbulent mixing zone growth rate was obtained as a function of the path and initial zone width. It has been shown that the numerical results are in good agreement with the test data.

INTRODUCTION.

At present, the VIKHR technique [1] with V.V. Nikiforov's turbulent mixing (TM) model is widely used in VNIIEF for numerical simulations of flows with turbulent mixing. The Nikiforov's model has been tested many times against TM tests with gases [2-5], including shock tube tests.

Shock tube tests on TM at an interface of two gases with different densities have a number of specific features. First, in these tests, the gases are initially separated by a thin film, which prevents their diffusion before the mixing starts. After the film is ruptured by a shock wave, an initial turbulent mixing zone forms. In this case, the film's mechanical properties have a considerable effect throughout the TM zone evolution. In particular, TM zone width after the test may vary considerably with the film's thickness and strength. Therefore, a physical model that would treat film rupture and the initial phase of TM zone evolution is required for testing turbulent mixing calculation techniques. As such model does not exist, in VIKHR calculations we set initial fluctuations of density. Their values are specified so that to describe the measurements adequately.

Second, TM zone in shock tube tests is formed by means of intense interaction of shock waves and turbulent eddies. In numerical simulations of turbulent flows with

shocks, gas-dynamic gradients at a shock front are inversely proportional to numerical point size. As a result, solutions of TM difference equations are highly dependent on a numerical grid, since gas-dynamic gradients are included in turbulence generation terms of the TM equations.

This is the reason why tests where these uncertainties are absent or insignificant are especially interesting for testing TM numerical techniques. Dimonte's experiments [6] belong to these tests.

In Dimonte's experiments two immiscible fluids were placed in a sealed ampoule: freon ($\rho = 1.57$ g/cm^3) at the bottom and water ($\rho = 1$ g/cm^3) at the top. The interface here is planar, except for the menisci at the ampoule walls due to surface tension that are small compared to the ampoule size. Initial perturbations of the interface are low and result from thermal fluctuations. Interface acceleration resulting into a Raleigh-Taylor instability is caused by the ampoule acceleration by a so-called electric motor (a conductor moving along guide electrodes under the influence of a magnetic field). Four acceleration laws have been obtained by varying the current and magnetic induction in [6]: constant, decreasing, increasing and pulse accelerations. The acceleration was directed from the heavy fluid into the light one.

This paper presents numerical results obtained for the tests [6] with four ampoule acceleration laws. The calculations were performed with the VIKHR technique with the incompressible fluid assumption (as the maximum ampoule velocity is within ~31 м/с, the resulting flow inside the ampoule is definitely subsonic). Surface tension effects were not taken into account.

PROBLEM DEFINITION.

The numerical geometry of the tests [6] is given in the fig. 1. The domain 1 ($0 \le r \le 10$ cm) is filled with water with the density $\rho_1^0 = 1$ g/cm^3, the domain 2 ($10 \le r \le 20$ cm) has liquid freon with the density $\rho_2^0 = 1.57$ g/cm^3. The boundary conditions at the left and right are: rigid wall. In our calculations we used the following equation of state for weakly compressible fluids:

$$P = 1000 + 25[(\rho/\rho_c)^3 - 1]/3,$$

where $\rho_c = \rho_1^0\rho_1^0/(c_1\rho_2^0 + c_2\rho_1^0)$, c_1 and c_2 are the mass fractions of water and freon respectively. In all calculations, the TM zone width was found from the mass fraction levels: c_1=0.02 for the right boundary, c_2=0.02 for the left boundary.

Numerical and experimental results are given as a function $h(Z)$, where h is the depth to which the light fluid penetrates into the heavy one, $Z = \int_0^t dt' \int_0^{t'} dt'' g(t'')$ is the ampoule path ($g(t)$ is the ampoule's variable acceleration). In our calculations we assumed that at small density difference the mixing occurs nearly symmetrically (in [7], for instance, the mixing asymmetry of $\approx 3\%$ was obtained for $\rho_2/\rho_1 \approx 1.5$), so the light-into-heavy fluid penetration depth was found as $h = 0.5(r_1 - r_2)$, where r_1 and r_2 are the coordinates of the right and the left boundaries of the TM zone. For the constant acceleration we also used $S = Z = 0.5gt^2$ for the ampoule's path.

NUMERICAL RESULTS

All calculations were performed with a uniform distribution of numerical points across the domains. The following notation is used in the figures: the first value in brackets is the number of points in the first domain, the second value gives that in the second domain; the notation 1+1 corresponds to initial density fluctuations set in one point at the left and one point at the right from the interface, the notation 2+2 corresponds to initial density fluctuations set in two points to the left and two points to the right from the interface, an so on. The initial density fluctuation in all calculations was set to $R_0 = 0.05$, the initial width of the TM zone was L_0 (the length of the interval where the density fluctuations were set to the non-zero value).

Constant acceleration.

The fig. 2.a and 2.b depict the simulation results for the constant acceleration of the ampoule, the data from [6] are also presented. The fig. 2.a shows that when the grid is refined (which makes the initial TM zone width smaller) the calculations give smaller light-to-heavy fluid penetration depth. So, a twofold increase of the number of points in the differencing grid reduces h at the end of a calculation by about 8%. If we increase the number of points 3-fold, h at the end of a calculation becomes about 12% smaller, and a

4-fold increase makes h at the same time about 14% smaller. The influence of L_0 and the cell linear size is pronounced throughout the calculation, though the ratio $\Delta h/h$ decreases with time.

At the initial phase of TM zone evolution (to $Z \leq 10$) there is a discrepancy between the numerical data and the experiments. In our opinion, this discrepancy can be accounted for by the fluid's interface surface tension, which was not taken into consideration in the calculations (this is also true for the other acceleration laws).

The fig. 2.b present h as a function of L_0. One can see that the dependence of the TM zone growth rate dh/dS on L_0 is most pronounced at the initial phase of the perturbation evolution. With the developed turbulence at $20 < Z < 80$ (in the interval where the ampoule's acceleration is constant) dh/dS shows almost no dependence on L_0:

$$dh/dS \approx 0.0235 \approx 0.11A \tag{1}$$

where $A = (\rho_2 - \rho_1)/(\rho_2 + \rho_1)$ is the Atwood number.

In the references [7÷9] the zone growth rate is to a certain extent dependent on the density level at the left and right boundaries of the TM zone that are used to measure the experimental zone width. For example, the following dependencies are presented in [7] where the TM zone width was found from the dimensionless density profile $\delta = (\rho(x) - \rho_1)/(\rho_2 - \rho_1)$:

$$dh/dS = (0.14 \pm 0.005)A \text{ at } \delta = 1, \tag{2}$$

$$dh/dS = (0.11 \pm 0.01)A \text{ at } \delta = 0.98. \tag{3}$$

(2) and (3) yield at $A = 0.222$ (for the system of water and freon): $dh/dS \approx 0.0244 \div 0.031$, which is higher than the value (1), produced by the VIKHR calculation.

The numerical result (1) and the test data [7÷9] show considerable discrepancies with the dependence derived by Nikiforov [10]:

$$dh/dS = 0.325A, \tag{4}$$

which in our case at $A = 0.222$ yields a noticeably higher TM growth rate $dh/dS \approx 0.072$. The correlation (4) was obtained in TOGA technique calculations and was first given in [10]. The VIKHR calculations performed in the standard manner produced a similar result. According to Nikiforov [11], the reason for these discrepancies between the law (4) and the test data is that the turbulence energy dissipation mechanism, which takes

place when two molecularly immiscible fluids are mixed, is different from that specific for gases.

VIKHR calculations have shown that satisfactory agreement with the test data can be achieved if we introduce a restriction on the function $f_1 = \overline{\rho'^2}/\rho/\rho R$ at the initial phase of a calculation, while preserving the model parameters (all the results, given in this paper were obtained with the restriction on this function). The function f_1 in the Nikiforov's model is a measure of deviation of liquid particles' acceleration from the gas-dynamic acceleration $\nabla P/\rho$, and it is represented as $f_1 = (1 + R - D_t \nabla R/W)^{-1}$. For a heterogeneous mixture of two immiscible fluids there is an analytical expression for this function: $f_1 = \delta[\delta - (\delta - 1)c]^{-2}$, where $\delta = \rho_h/\rho_l$, ρ_h and ρ_l are the densities of the heavy and the light fluid, c is the mass fraction of the light fluid. The value of the function f_1 for an arbitrary turbulent mixture cannot be higher than its heterogeneous value. Meanwhile, the representation of f_1, used in the model at the beginning of TM calculations can result into overestimated f_1. For this reason, a restriction on f_1 is used in calculations, which is equivalent to a restriction on the archimedian forces' work to move the liquid particles. As a result, the turbulence kinetic energy and the turbulent diffusivity decrease, which, in turn, leads to smaller growth of TM zone width. The restriction on the structural function can thus be interpreted as effective consideration of the turbulence energy conversion to the interface surface energy.

Increasing acceleration.

The fig. 3.a, 3.b and 3.c present the numerical results for the increasing acceleration of the ampoule. The fig. 3.a shows that when the grid is refined (which results into a decrease of the initial TM zone width) the light-to-heavy fluid penetration depth slightly decreases. And throughout the calculation h depends on L_0, though the relative change of h decreases with time.

The influence of L_0 on the dependence $h(Z)$ on a fixed grid is shown in the fig. 3.b and 3.c (the data in the fig. 3.c were obtained on a grid with a doubled number of points compared to the fig. 3.b). One can see that when L_0 is changed, it changes $h(Z)$ by a constant value Δh, that is almost independent on the ampoule's path Z. Indeed, the fig. 3.b

shows that at $20 < Z < 70$ the rate of penetration of the light fluid into the heavy one dh/dZ decreases from 0.0314 for $L_0 = 0.02778$ cm to 0.0308 for $L_0 = 0.1111$ cm. If the grid has 2 times more cells (see the fig. 3.c) at $20 < Z < 70$ the value of dh/dZ does not depend on L_0 and equals to 0.0298. This result can be approximated by the dependence

$$dh/dZ \approx 0.135A.$$

Decreasing acceleration.

The numerical results for the decreasing acceleration of the ampoule are given in the fig. 4.a and 4.b. The fig. 4.a shows that an increase of numerical point size results into an increase of TM zone width. At the end of the calculations the light-to-heavy fluid penetration depth is: $h \approx 2.143$ cm on the grid with $L_0 = 0.0833$ cm, $h \approx 1.922$ cm on the grid with $L_0 = 0.0417$ cm, $h \approx 1.831$ cm on the grid with $L_0 = 0.02778$ cm и $h \approx 1.775$ cm on the grid with $L_0 = 0.02083$ cm.

The influence of L_0 on the dependence $h(Z)$ on a fixed grid is shown in the fig. 4.b. One can see that when L_0 increases it results into an increase of the the light-to-heavy fluid penetration depth by a constant value Δh, which weakly depends on the ampoule's path Z.

Pulse acceleration.

The numerical results with the ampoule's pulse acceleration are shown in the fig. 5.a and 5.b. The fig. 5.a shows that if the number of points in the differencing grid is increased by a factor of 1.5 (respectively, L_0 decreases by a factor of 1.5) h at the end of calculations decreases by about 5.6%, and a twofold increase results into h at the end decreasing by about 16%. In this case there is a slight dependence of the growth rate dh/dZ on L_0 through out the calculation.

The fig. 5.b shows the influence of L_0 on the dependence $h(Z)$ on a fixed grid. One can see that the most pronounced dependence of dh/dZ on L_0 is observed at the beginning of TM calculations. At the phase of the developed TM the influence of L_0 becomes weaker. Comparing the results obtained for the constant, decreasing, increasing and pulse accelerations, one can note that the influence of L_0 on the dependence $h(Z)$ is the most pronounced for the pulse acceleration.

CONCLUSION.

Numerical simulations of Dimonte's experiments[6] on Raleigh-Taylor mixing of two molecularly immiscible fluids have been performed with the VIKHR technique. The calculations have been performed for four ampoule acceleration laws. There is satisfactory agreement with the data [6]. Thus, we can state that V.V.Nikiforov's TM model provides adequate treatment of turbulent flow evolution in absence of shock waves.

REFERENCES.

1. *V.A. Andronov, V.I. Kozlov, V.V. Nikiforov, A.N. Razin, Yu.A. Yudin* Turbulent mixing calculation technique for 1D flows (the VIKHR technique) // Voprosy Atomnoy Nauki i Techniki. Series: Mathematical modeling of physical processes. 1994, issue 2, p. 59-64.
2. *V.A. Andronov, V.V. Nikiforov* Turbulence evolution calculations with an axially symmetric strain // Voprosy Atomnoy Nauki i Techniki. Series: Theoretical and applied physics. 1990, issue 1, p. 34-36.
3. *V.A.Andronov, S.M.Bakhrakh, E.E.Meshkov, V.V.Nikiforov, A.V.Pevnitsky, A.I.Tolshmyakov* An experimental study and numerical simulations of turbulent mixing in 1D flows // Doklady AN SSSR. 1982, vol. 264, № 1, p. 76-82.
4. *V.V.Nikiforov, V.A.Andronov, A.N.Razin* Turbulent mixing zone evolution under shock impact // Doklady AN SSSR. 1995, vol. 343, # 3, p. 323-325.
5. *V.A.Andronov, S.A.Bel'kov, A.V.Bessarab et.al.* Investigation of turbulent mixing in thin layers with different densities during laser acceleration of plane multilayer targets at the ISKRA-4 facility// JETF, 1997, vol. 111, issue 3, p. 882-888.
6. *Dimonte Guy, Schneider Marilyn.* Turbulent Rayleigh-Taylor instability experiments with variable acceleration // Physical Review E, 1996, v. 54, № 4, p.3740-3743.
7. *Kuchtrenko Yu.A., Shibarshov L.I., Chitaikin V.I., Balabin S.I., Pylaev A.P.* Experimental study of the gravitational turbulent mixing self-similar mode. 3rd International Workshop on the physics of compressible turbulent mixing (Abbey of Royaumont, France), 1991, p. 427.

8. *D.L. Youngs*, Physica 12 D, 32, 1984.

9. *K.I. Read* Experimental investigation of turbulent mixing by Rayleigh-Taylor instability, Part 1. // Atomic Weapons Research Establishment, Foulness, England, 1984.

10. *V.V.Nikiforov* Turbulent mixing at an interface of different-density fluids. // Voprosy Atomnoy Nauki i Techniki. Series: Theoretical and applied physics. 1985, issue 1, p. 3÷8.

11. *V.V.Nikiforov* Calculations of gravitational turbulent mixing in non-self-similar flows // Voprosy Atomnoy Nauki i Techniki. Series: Theoretical and applied physics. 1993, issue 1, c. 3-13.

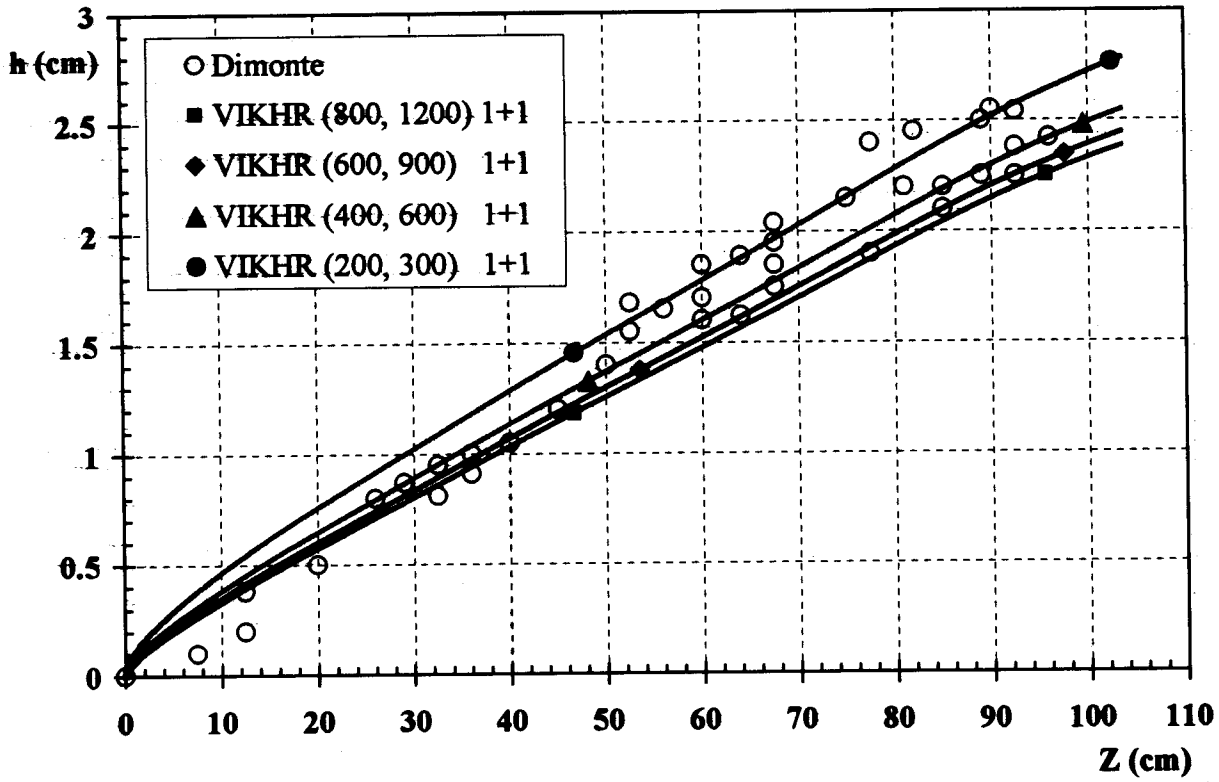

Fig. 2,a. Constant acceleration: calculations with a sequence of refined grids. (Initial density fluctuations are set in one point to the left and one point to the right of the interface.)

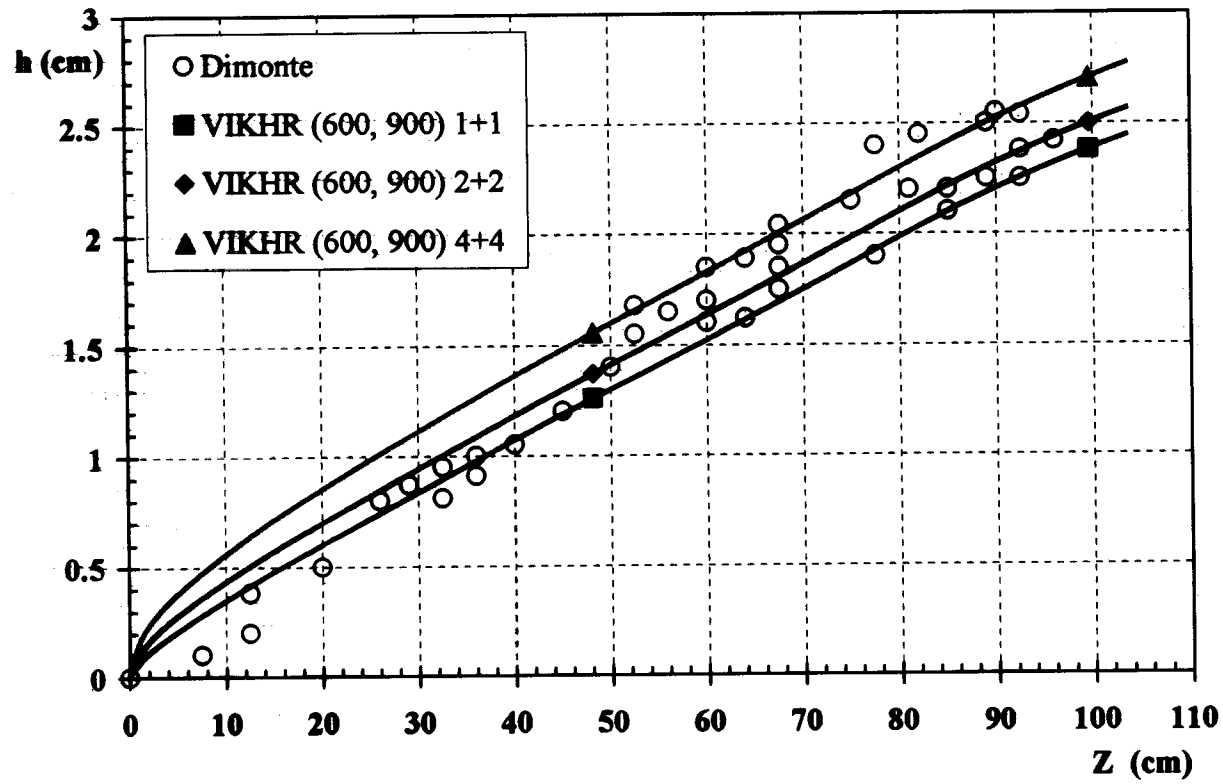

Fig. 2,b Constant acceleration: calculations with variable initial zone width L_0 on a fixed grid. (L_0 is given by the number of numerical points to the left and to the right of the interface where the initial density fluctuations are set.)

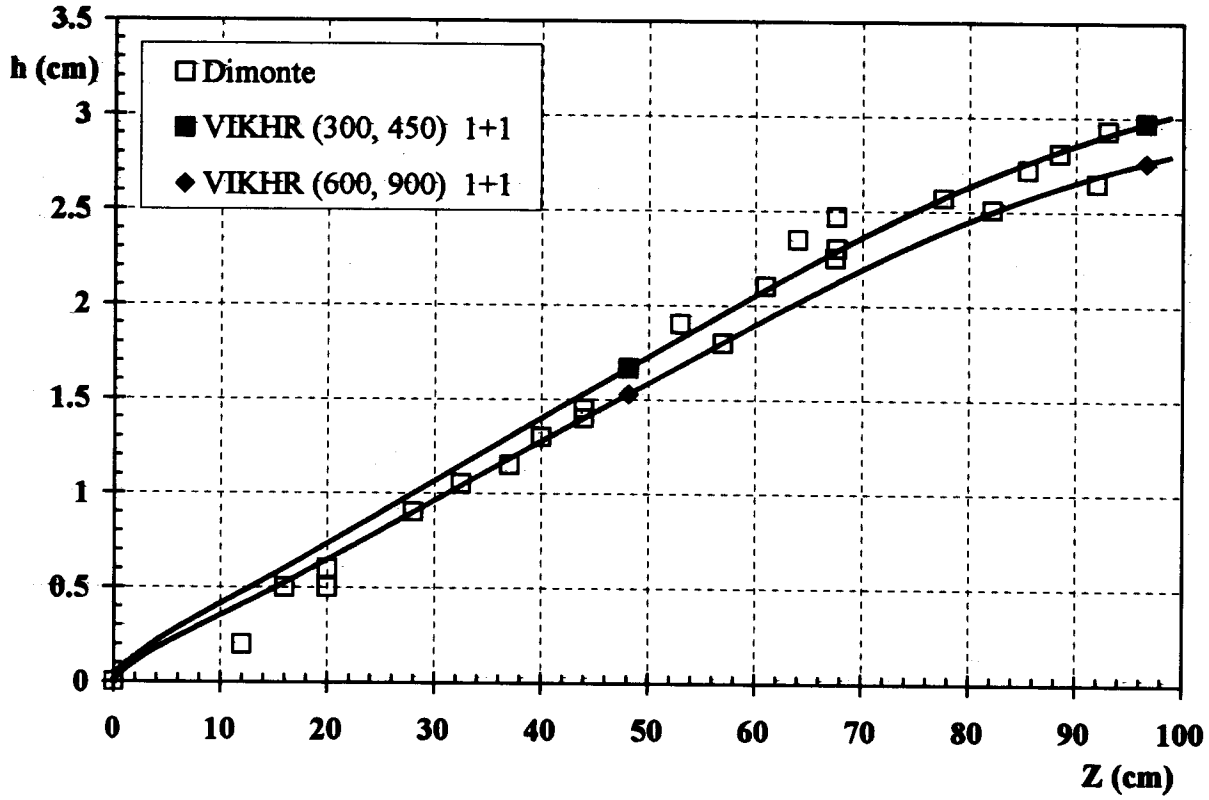

Fig. 3,a. Increasing acceleration: calculations with a sequence of refined grids. (Initial density fluctuations are set in one point to the left and one point to the right of the interface.)

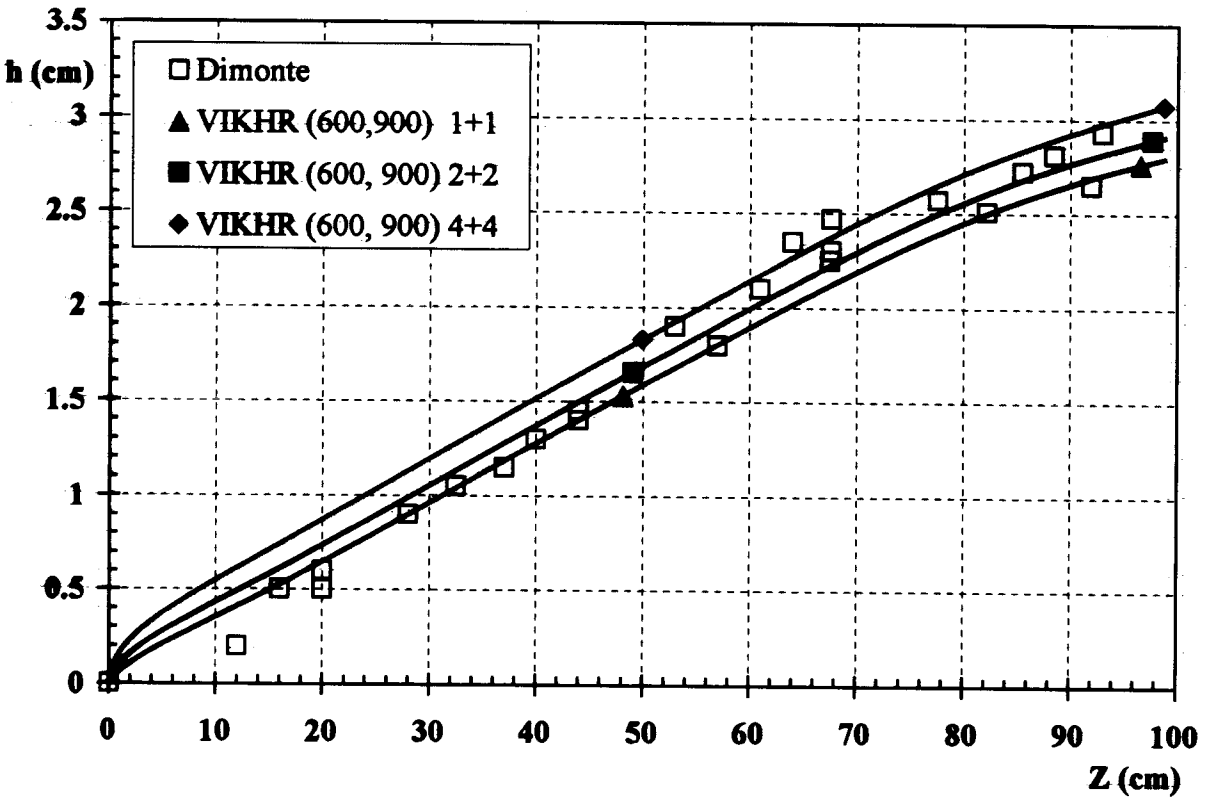

Fig. 3,b. Increasing acceleration: calculations with variable initial zone width L0 on a fixed grid. (L_0 is given by the number of numerical points to the left and to the right of the interface where the initial density fluctuations are set.)

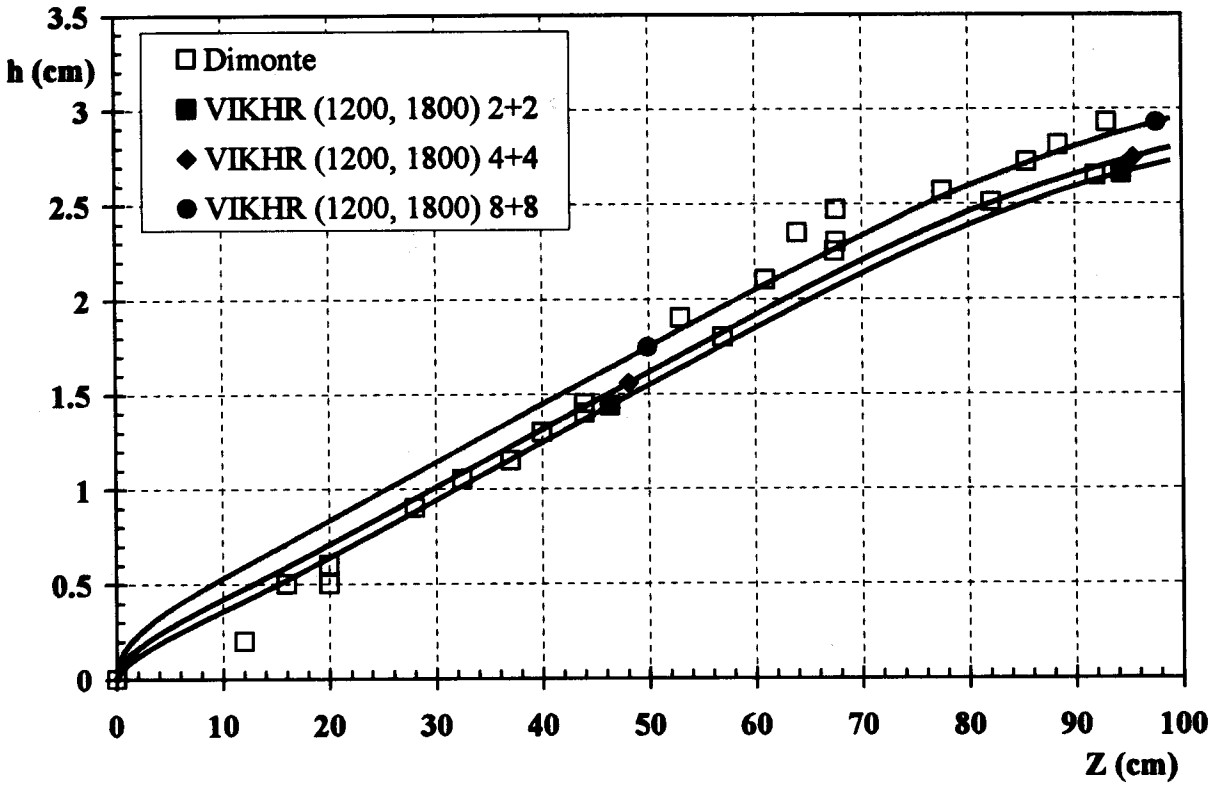

Fig. 3,c. Increasing acceleration: calculations similar to those shown in the fig. 3.b, but the number of numerical points increased twofold.

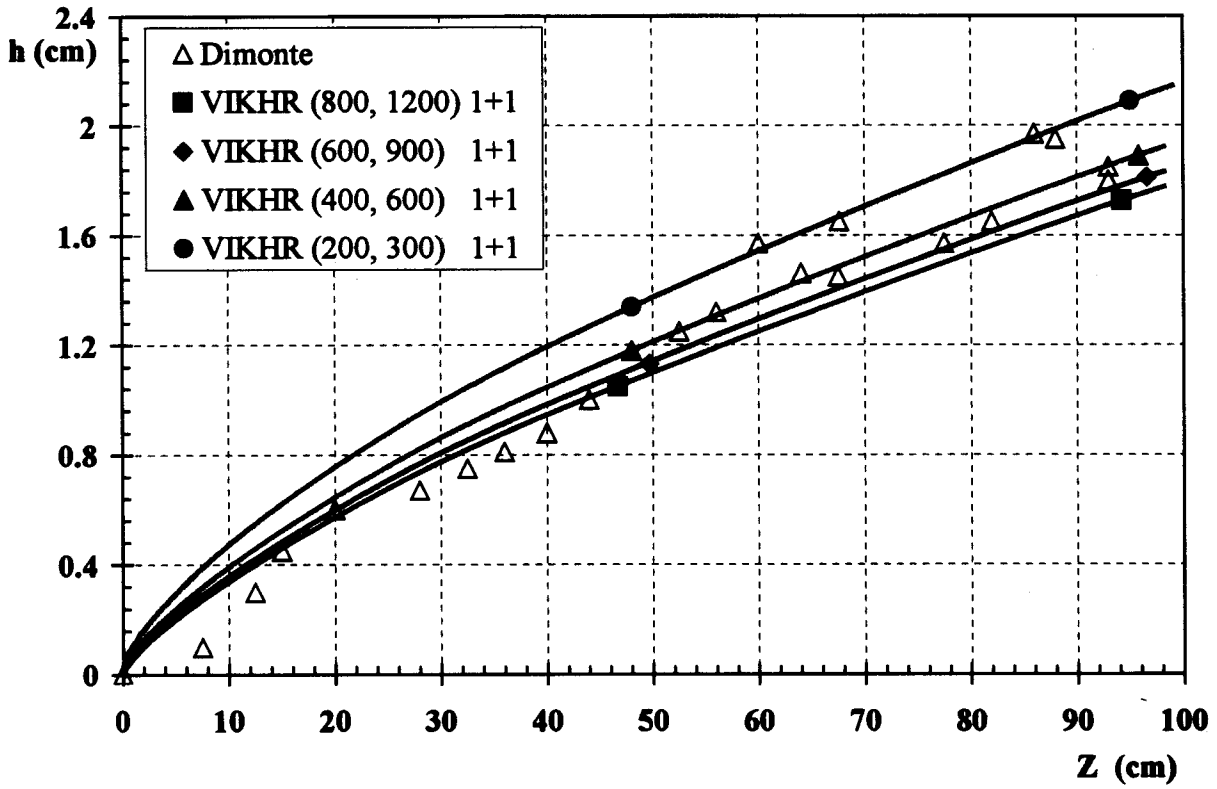

Fig. 4,a. Decreasing acceleration: calculations with a sequence of refined grids. (Initial density fluctuations are set in one point to the left and one point to the right of the interface.)

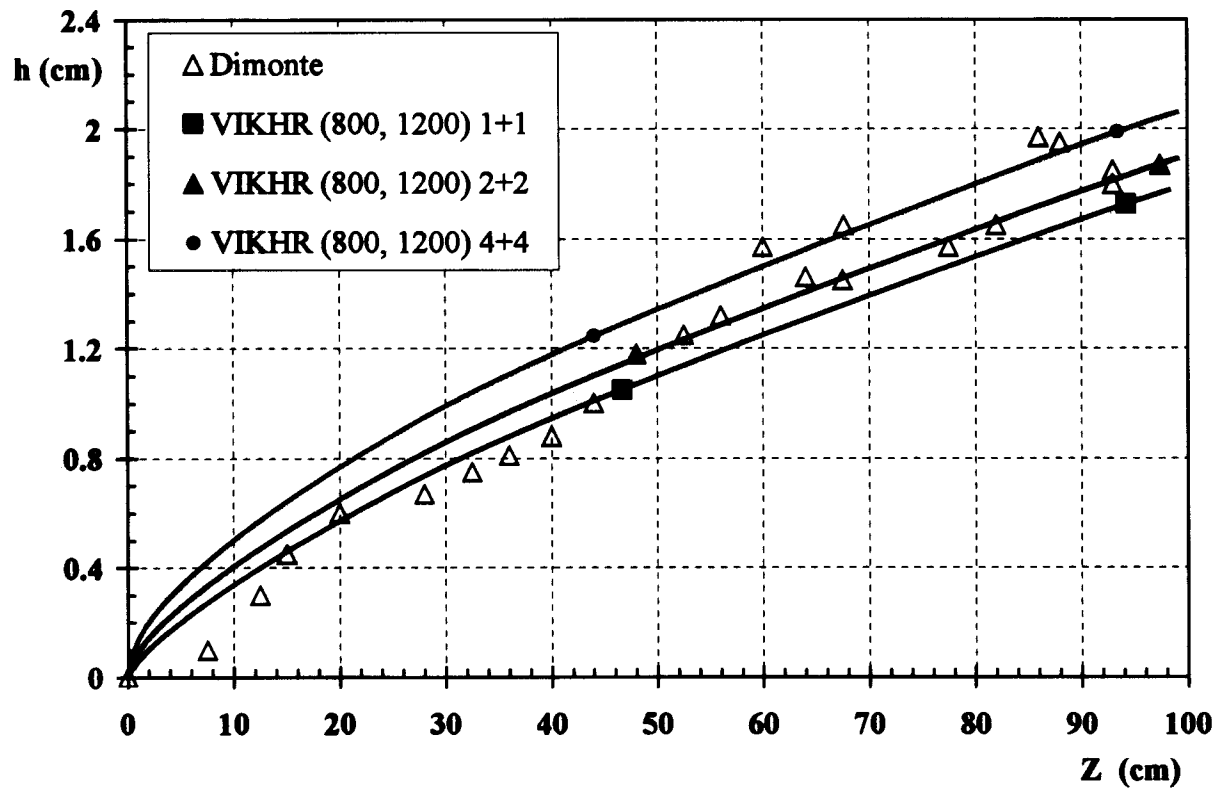

Fig. 4,b. Decreasing acceleration: calculations with variable initial zone width L_0 on a fixed grid. (L_0 is given by the number of numerical points to the left and to the right of the interface where the initial density fluctuations are set.)

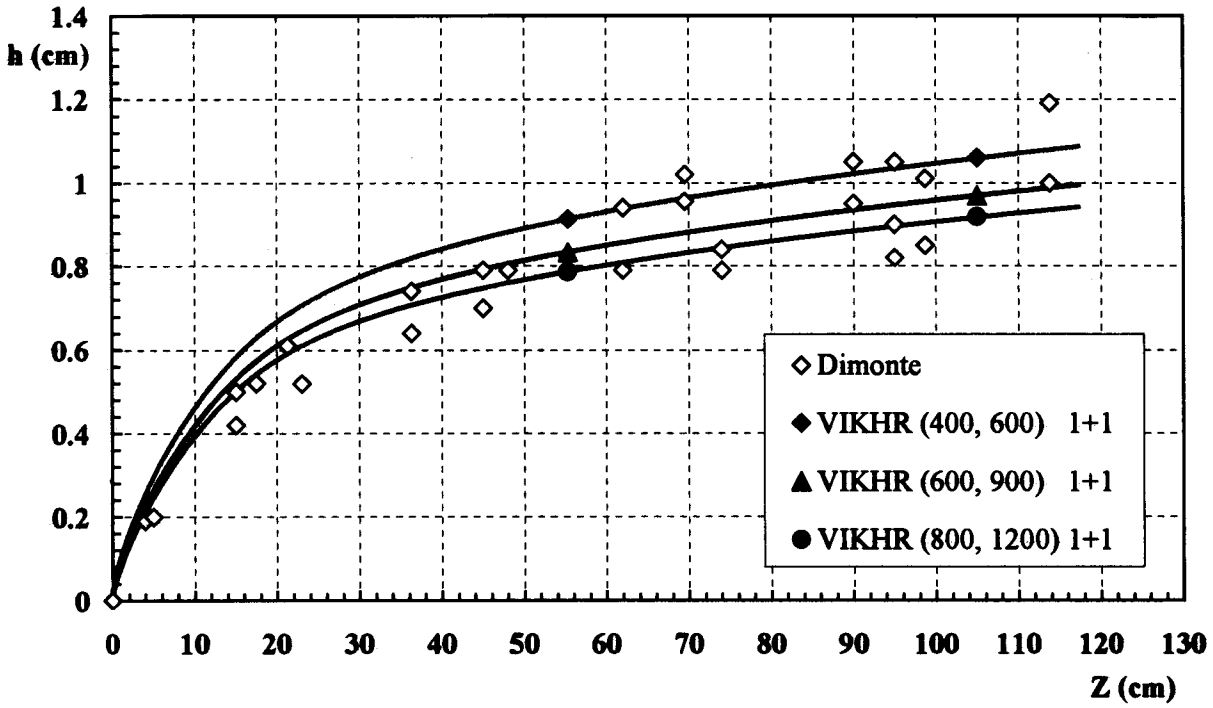

Fig. 5,a. Pulse acceleration: calculations with a sequence of refined grids. (Initial density fluctuations are set in one point to the left and one point to the right of the interface.).

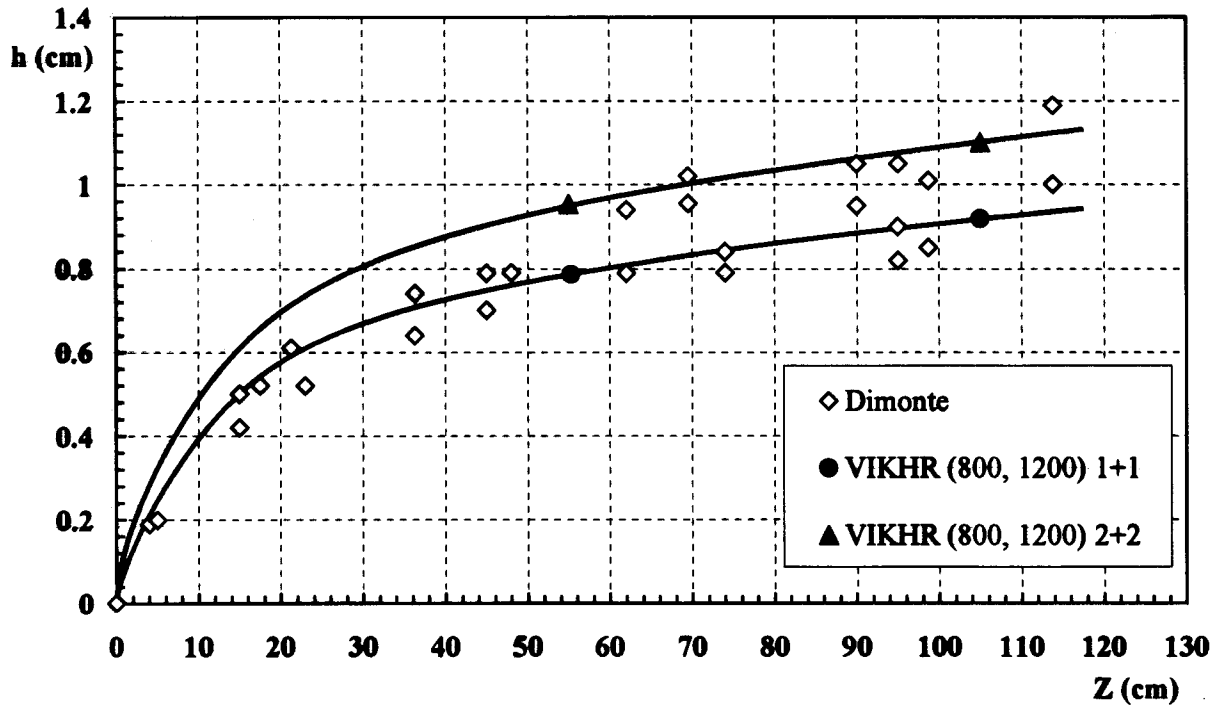

Fig. 5,b. Pulse acceleration: calculations with variable initial zone width L_0 on a fixed grid. (L_0 is given by the number of numerical points to the left and to the right of the interface where the initial density fluctuations are set.)

AXIAL

THE BEHAVIOR OF VARIANCE RESULTING FROM TURBULENT MIXING ZONE INTERACTION WITH SHOCKS

V.I. Kozlov, A.N. Razin
(RFNC – VNIIEF)

We have compared numerical and experimental data on turbulent mixing of two gases in a shock tube induced by Richtmeyer-Meshkov's instability. The calculations were performed with the 1D technique VIKHR. This technique implements Nikiforov's semi-empirical model. We compared both the mixing zones and the average variances of the velocity component parallel to the tube axis. There was no special algorithm for calculations of turbulent quantities at the shock front.

INTRODUCTION.

Nikiforov suggested the turbulent mixing model [1] to treat transient turbulent flows stipulated by Raleigh-Taylor and Richtmeyer-Meshkov instabilities. This model has been implemented in the difference form with the VIKHR technique [2]. Numerical simulations of various tests has shown that the model [1] provides satisfactory treatment of turbulent flows of multicomponent fluids without changing the model's constants [3÷5].

Basing on [3÷5] we can conclude that the information given by shock tube tests that only measure TM zone width as a function of time and the distribution of average density across this zone is incomplete. In fact, the width is an integral characteristic of the TM zone, and just this quantity taken alone is not sufficient to study in detail the interaction of the TM zone with shocks. On the other hand, TM models based on quite different principles can yield similar average density distributions without noticeable changes of TM zone width as a function of time. Still these model treat the TM zone "fine" structure (the distributions of turbulence intensity, turbulent energy dissipation rate, density fluctuations intensity, etc.) differently. If there is only one shock passing through the TM zone, the fine structure may have no considerable effects on the zone evolution (apparently, this accounts for the fact that different models yield similar results

for simple flows). Complex flows often have several TM zones that evolve simultaneously under the influence of multiple shocks, and different zones can join. More detailed information about TM zone structure and the mechanism of interaction with shocks is required for such flows.

New results in this direction have been obtained by French researchers in their tests [6]. These tests, which were arranged similarly to Meshkov's shock tube tests, were the first to systematically measure instantaneous flow velocities in the TM zone. The evolution of fluctuations of the axial mass flow velocity (the velocity component parallel to the tube axis) in the TM zone before and after it interacted with shocks reflected from the tube dead-end has been studied by means of Doppler's laser anemometry. Mean square fluctuations of the axial velocity have been calculated in five Eulerian points by statistical averaging of the multiple measurements.

This paper gives VIKHR numerical results on the experiments [6]. On the whole, there is good agreement with the experiments of both the TM zone width as a function of time and the axial variance $\overline{u_1'^2}$ as a function of time. Meanwhile, we must note that the calculation considerably overestimates (nearly twofold) the maximum $\overline{u_1'^2}$ when the TM zone interacts with the first shock reflected from the tube dead-end (this is the most intensive shock). In addition, the calculations have shown faster attenuation of $\overline{u_1'^2}$ with time compared to the experiments.

At present we are working on further development of the TM physical model implemented in the VIKHR technique. In particular, we are improving the correlations for turbulent transport and dissipative processes, and study the mechanism of TM zone interaction with shocks in more detail. The results calculated with the modified VIKHR will be presented upon completion of this work.

NUMERICAL RESULTS

The numerical domain of the problem is shown in the fig. 1. The initial gas pressure is equal to the atmospheric pressure of 1 bar. The initial air density is 0.0012 g/cm^3, that of SF_6 – 0.006 g/cm^3. Air and SF_6 were treated as perfect gases, the adiabatic index of air was $\gamma = 1.4$, that of SF_6 was $\gamma = 1.094$. The shock tube dead-end has

the co-ordinate 0 cm, the dead end being regarded as a rigid wall. The interface co-ordinate is 30 cm. At the right boundary (120 cm from the shock tube dead end) a constant pressure of 2.15 bar is set, which causes a shock in SF_6 with the front velocity of 197 m/s.

The comparison of the experimental data and the numerical data calculated with the VIKHR code is given in the fig. 2÷4. Note that $2e_1$ from VIKHR corresponds to the axial variance $\overline{u_1'^2}$.

The fig. 2 shows the R-t diagram of the TM zone boundaries. The start of the calculation is the reference time (the time when the shock reaches the interface is $t \approx 4.55$ ms), and the coordinate center is at the shock tube dead end (rigid wall). One can see that the experimental and numerical data are, on the whole, in satisfactory agreement. The R-t diagram of the finite-difference shock center calculated ~~with the algorithm [7]~~ is also given here. The fig. 2 shows that three shocks reflected from the dead end pass through the TM zone. In the calculation, however, only two waves can be regarded as shocks. As a matter of fact, an analysis of calculations with a sequence of refined grids has shown that the gas-dynamic gradients at the fronts of the first two waves are inversely proportional to the numerical point size, with much less pronounced dependence for the third wave. Thus, the third finite-difference wave can be regarded as a compression wave.

The fig. 3 shows the numerical (solid line) and experimental (step line) axial variance. The coordinates of the Eulerian points (transducers) where the velocity was measured, are given in mm from the initial interface location, and the time (ms) is counted from the moment when the shock reaches the interface.

The fig. 3 shows that before the first reflected shock enters the TM zone, the numerical and the experimental variance are in satisfactory agreement (according to the two transducers nearest to the interface: 51 mm and 125.5 mm). Note that when the TM zone passes through these ~~transducers~~, there are no shocks in the TM zone.

As for the third ~~transducer~~ (161 mm), the numerical variance is considerably higher than the experimental data. The fig. 2 shows that when the TM zone passes through this ~~transducer~~, the most intensive (the first) reflected shock is within the TM zone.

On the fourth transducer (169 mm) the numerical variance satisfactorily agrees with the experimental data. The fig. 2 shows that when the TM zone passes through this transducer, there are no shocks in the TM zone.

For the fifth transducer (178.5 mm) the numerical variance is lower than the experimental data, though the numerical data are close to the experimental data statistical scatter range. When the TM zone passes through this transducer two last reflected shocks are crossing the TM zone.

For the detailed analysis of the variance on the fifth transducer, numerical variance has been calculated as a function of time in three extra Eulerian points in the vicinity of the fifth transducer. The results are shown in the fig. 4 (the co-ordinates of the Eulerian points are counted from the dead-end).

According to the fig. 2, the left TM zone boundary (the one closer to the tube's dead-end) passes through the transducer with R = 12 cm earlier than it crosses the transducers with R = 11.5 cm and R = 11 cm. The second shock reflected from the rigid wall passes through the transducer with R = 12 cm later than it passes through those with R = 11.5 cm and R = 11 cm. It is shown in the fig. 4 as gradual increase of the signal recording time from R = 12 cm to R = 11 cm and decreasing maximum variance until the second reflected shock enters the TM zone. As the second shock, when it crosses the transducers, is in different Lagrangian points of the TM zone with different turbulence intensity, the peaks due to shock-TM zone interaction have different amplitudes at different transducers.

It is shown in the fig. 2 that the third reflected shock passes through the TM zone at 6.95 ms < t < 7.2 ms. In the fig. 4, one can see an increase of variance at the transducer with R = 11 cm during this time interval, while the other two transducers do not show any increase of the variance. The main reason for this is, apparently, that the third reflected shock (which is the weakest) interacts with the TM zone in Lagrangian points with different turbulence intensities, the turbulent intensity being the lowest at the transducers with R = 11.5 cm and R = 12 cm (the corresponding Lagrangian points are near the right boundary of the zone).

On the whole, we can state satisfactory agreement between the numerical results and experimental data, except for the transducer located at 161 mm from the shock tube

dead end. The numerical peak value for this ~~transducer~~ $2e_1$ is about 2 times higher than the experimental measurement $\overline{u_1'^2}$ (for the other ~~transducers~~ the numerical results are within the measurement uncertainty). Since when the TM zone passes through this ~~transducer,~~ the most intensive first reflected shock is in the TM zone, we can conclude that one of the reasons for this discrepancy can be that the model [1] unsatisfactorily describes the mechanism of shock-TM zone interaction. (As a matter of fact, the closure correlations of the model [1] have been developed for finite, rather small gas-dynamic gradients. Meanwhile, shocks in turbulent flows are discontinuity surfaces, like those in perfect fluids. This results from the fact that the minimum turbulent eddy size from the dissipative (Kolmogorov's) interval of spectrum is at least an order of magnitude higher than the interatomic distance).

REFERENCES.

1. *V.V.Nikiforov* Turbulent mixing at an interface of different-density fluids. // Voprosy Atomnoy Nauki i Techniki. Series: Theoretical and applied physics. 1985, issue 1, p. 3-8.

2. *V.A.Andronov, V.I.Kozlov, V.V.Nikiforov, A.N.Razin, Yu.A.Yudin* Turbulent mixing calcualtion technique for 1D flows (the VIKHR technique). // Voprosy Atomnoy Nauki i Techniki. Series: Mathematical modeling of physical processes. 1994, issue 2, s. 59-64.

3. *V.A.Andronov, S.M.Bakhrakh, E.E.Meshkov et.al.* An experimental study and numerical simulations of turbulent mixing in 1D flows // Doklady AN SSSR, 1982. vol. 264, № 1, p. 76-82.

4. *V.V.Nikiforov* Calculations of gravitational turbulent mixing in non-self-similar flows. // Voprosy Atomnoy Nauki i Techniki. Series: Theoretical and applied physics. 1993, issue 1, p. 3-12.

5. *V.V.Nikiforov, V.A.Andronov, A.N.Razin* Evolution of a turbulent mixing zone under shock impact // Doklady AN SSSR, 1995. vol. 343, № 3. p. 323-325.

6. ***Francoise Poggi, Marie-Helene Thorembey, Gerard Rodriguez.*** Velocity measurements in turbulent gaseous mixtures induced by Richtmyer-Meshkov instability. Physics of Fluids, v. 10, n. 11, 1998, pp. 2698-2700.

7. ***A.N.Razin*** An algorithm for finite-difference shock center location. // Voprosy Atomnoy Nauki i Techniki. Series: Theoretical and applied physics. 2001, issue 1, p. 43-50 .

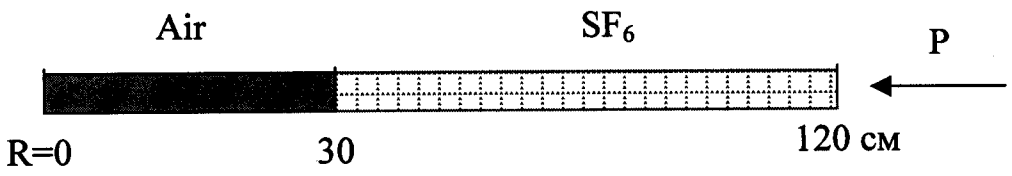

Fig. 1 Numerical geometry.

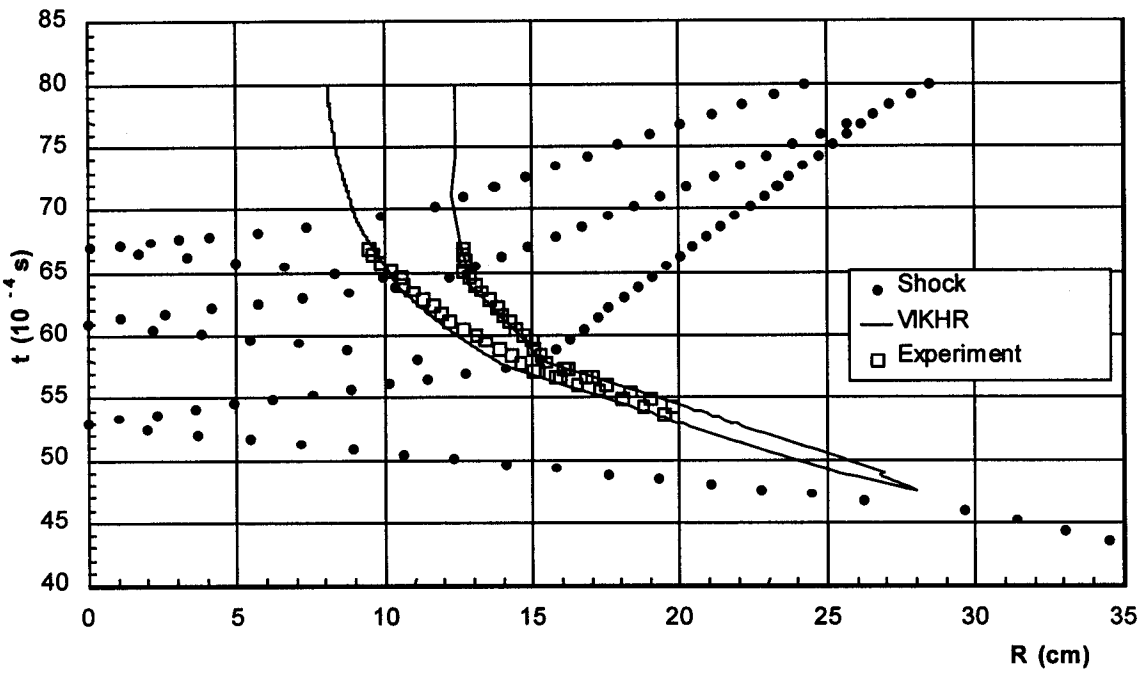

Fig. 2 R-t diagrams of the TM zone boundary and the shock

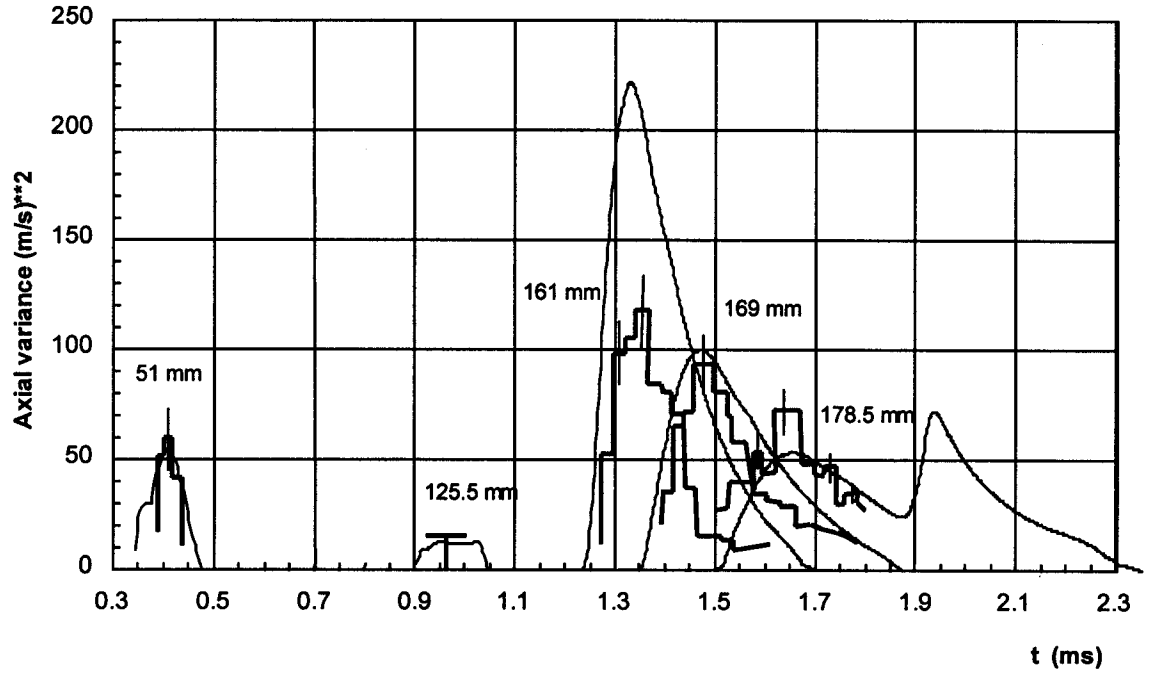

Fig. 3 Variance as a function of time given by different transducers

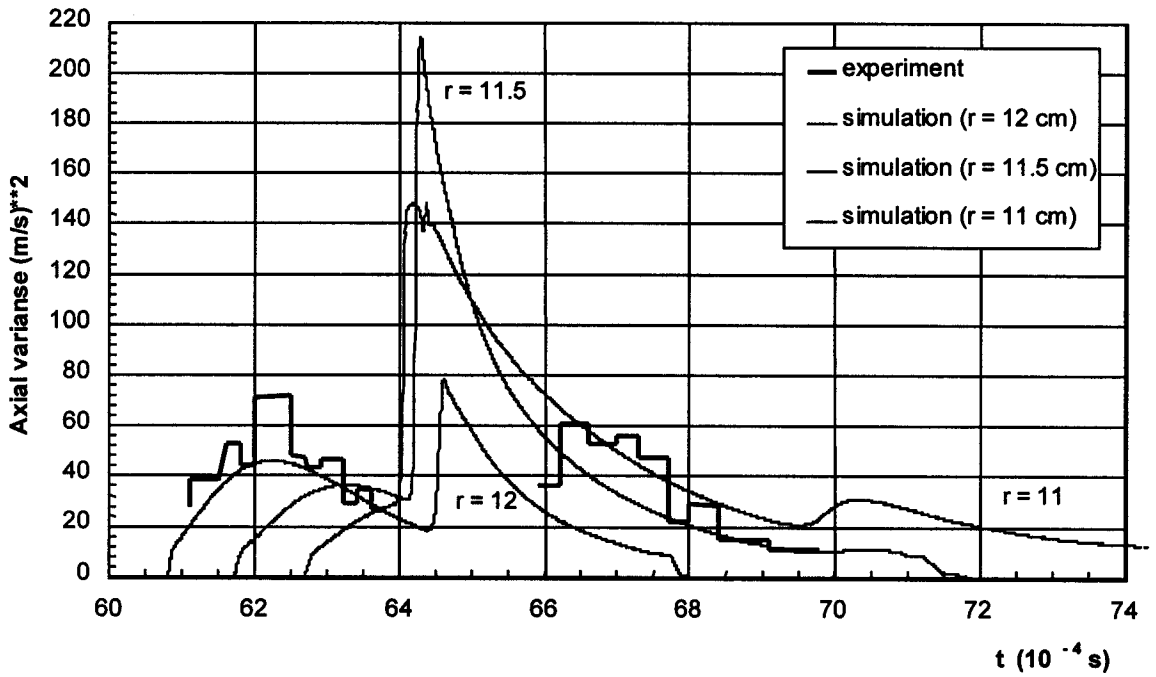

Fig. 4 Variance as a function of time in the vicinity of hte 5th transducer

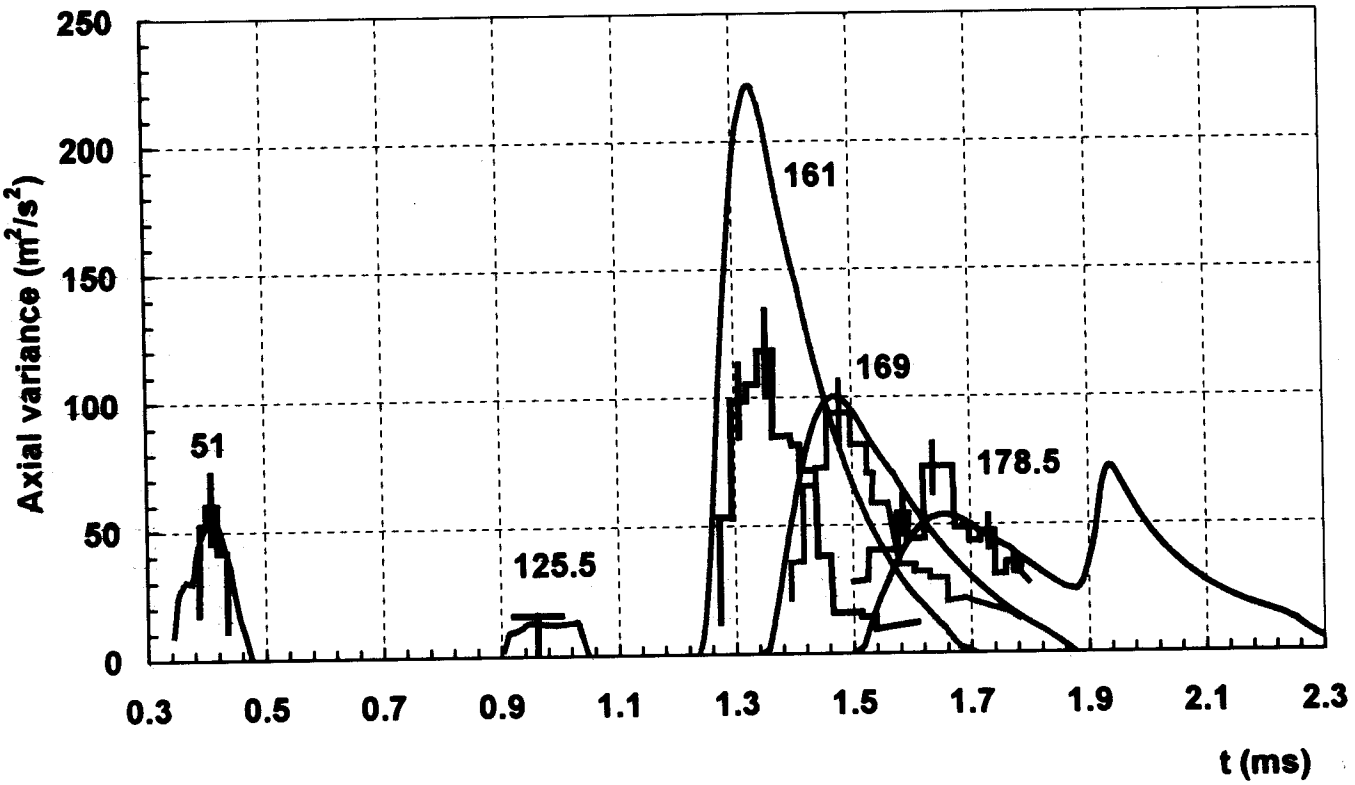

Fig. 3 Variance as a function of time given by different LDA probes.

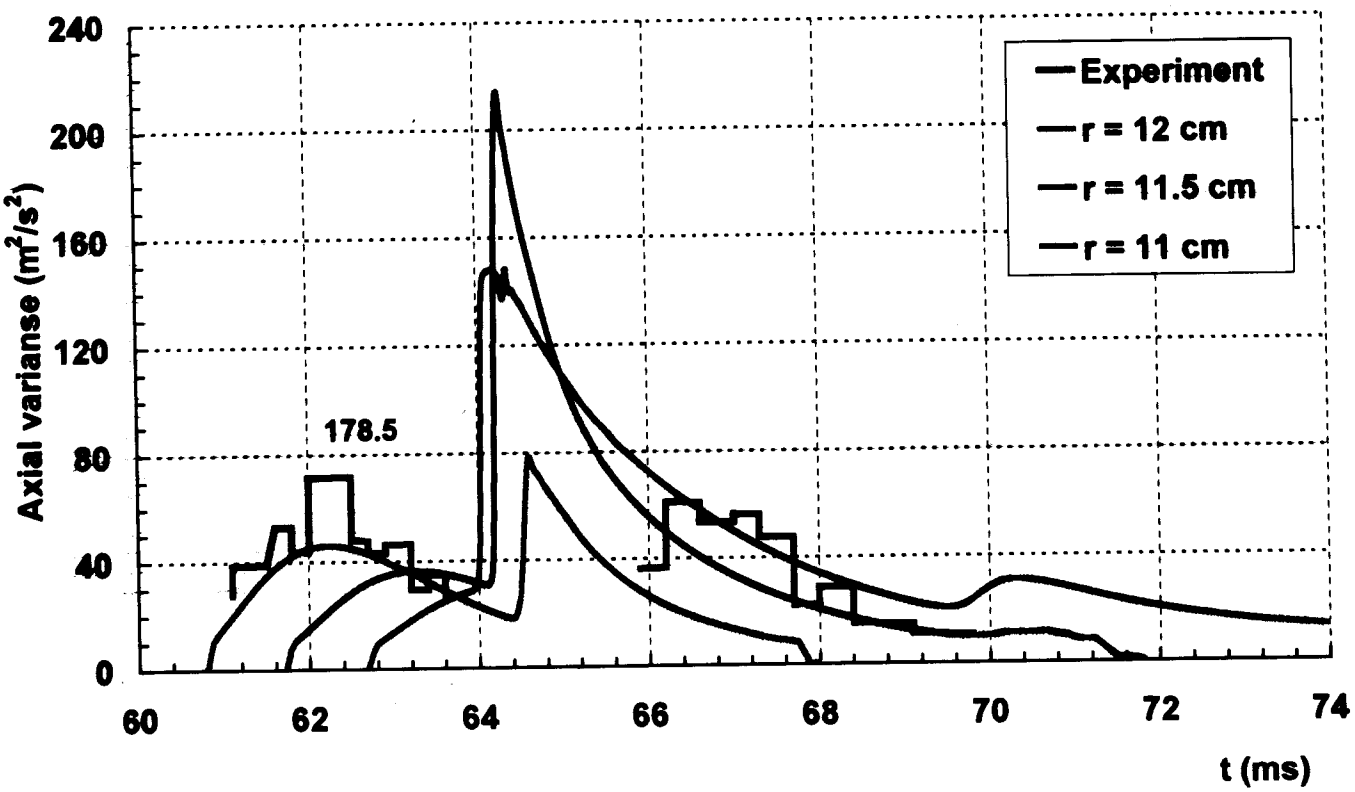

Fig. 4 Variance as a function of time in the vicinity of the 5th LDA probe.

NIKIFOROV'S MODEL OF TURBULENT MIXING (slab geometry)

$$\frac{d\rho}{dt}=-\rho\,\mathrm{div}U;\qquad \frac{dU}{dt}=-\frac{1}{\rho}\nabla\left(P+P_t\right);\qquad P_t=2\rho\frac{e_1}{e}\Phi;$$

$$\frac{dE}{dt}=-\frac{P}{\rho}\mathrm{div}\left(U-W\right)+\frac{1}{\rho}\mathrm{div}\left(\rho D\nabla E\right)+\frac{Q}{e}\Phi;\qquad \frac{dc_i}{dt}=\frac{1}{\rho}\mathrm{div}\left(\rho D\nabla c_i\right)$$

$$\frac{de_1}{dt}=\mathrm{div}\left(3D_t\nabla e_1-We_1\right)-e_1\mathrm{div}W-2V_{11}e_1+\left(1-\frac{\alpha k}{5}\right)f_1GW-\gamma\frac{Q}{e}\left(e_1-\frac{1}{3}e\right)-\frac{Q}{3};$$

$$\frac{de_2}{dt}=\mathrm{div}\left(D_t\nabla e_2-We_2\right)-e_2\mathrm{div}W+\frac{\alpha k}{10}f_1GW-\gamma\frac{Q}{e}\left(e_2-\frac{1}{3}e\right)-\frac{Q}{3};$$

$$\frac{d\Phi}{dt}=\frac{1}{\rho}\mathrm{div}\left[\rho\left(3D_t\nabla\Phi-W\Phi\right)\right]-2\frac{V_{11}e_1}{e}\Phi-W\frac{dU}{dt}-\frac{Q}{e}\Phi;$$

$$\frac{dQ}{dt}=\mathrm{div}\left(\frac{5}{3}D_t\nabla Q-WQ\right)-Q\mathrm{div}W-\frac{4}{3}\left(1+\frac{\gamma}{2}\frac{e_1-e_2}{e}\right)V_{11}Q+\frac{f_1GW}{3e_1}Q+$$

$$\beta\left(\frac{\alpha k}{5}f_1GW+\frac{2\gamma}{3}\frac{e_1-e_2}{e}Q\right)\frac{AW}{R}\left(1+R\right)-2\frac{Q^2}{ke};$$

$$\frac{dW}{dt}=\frac{1}{\rho}\mathrm{div}\left[\rho\left(2D_t\nabla W-W^2\right)\right]-V_{11}W+2Ae_1+f_1GR-k_1\frac{Q}{e}W;$$

$$\frac{dR}{dt}=\frac{1}{\rho^2}\mathrm{div}\left[\rho^2\left(D_t\nabla R-WR\right)\right]+R\mathrm{div}W+2AW-\frac{3}{2}\frac{Q}{e}R.$$

Here: $\nabla\equiv\frac{\partial}{\partial r};\quad \mathrm{div}\equiv\frac{\partial}{\partial r};\quad V_{11}=\frac{\partial}{\partial r}\left(U-W\right);\quad A=\frac{\nabla P}{\gamma_{ad}P}-\frac{\nabla\rho}{\rho};G=\frac{1}{\rho}\nabla P;$

$$e=e_1+2e_2;\qquad k=\frac{3e_2}{e}\sqrt{\frac{3e_1}{e}};\quad e_1=\overline{u_1'^2}/2;\qquad e_2=\overline{u_2'^2}/2;\qquad R=\overline{\rho'^2}/\rho^2;$$

$$W=\overline{\rho'u_1'}/\rho;\qquad \Phi=e+\overline{\rho'u_k'^2}/2\rho;\qquad f_1=\left(1+R-\frac{D_t}{W}\nabla R\right)^{-1}.$$

$$D=\begin{cases}W/A & if\ AW>0\\ 0 & f\ AW\le 0\end{cases};\qquad D_t=\frac{16\alpha_1e_1}{k_3+b};\qquad k_3=2\frac{Q}{e}\left(\gamma+\frac{e}{3e_1}+3\right);$$

$$b=\alpha_1\left(\xi+|\xi|\right);\quad \xi=\frac{2AW}{R}-k_2\frac{Q}{e}.$$

LDA probe positions from interface:

5.1 cm, 12.55 cm, 16.1 cm, 16.9 cm, 17.85 cm

Fig. 1 Numerical geometry.

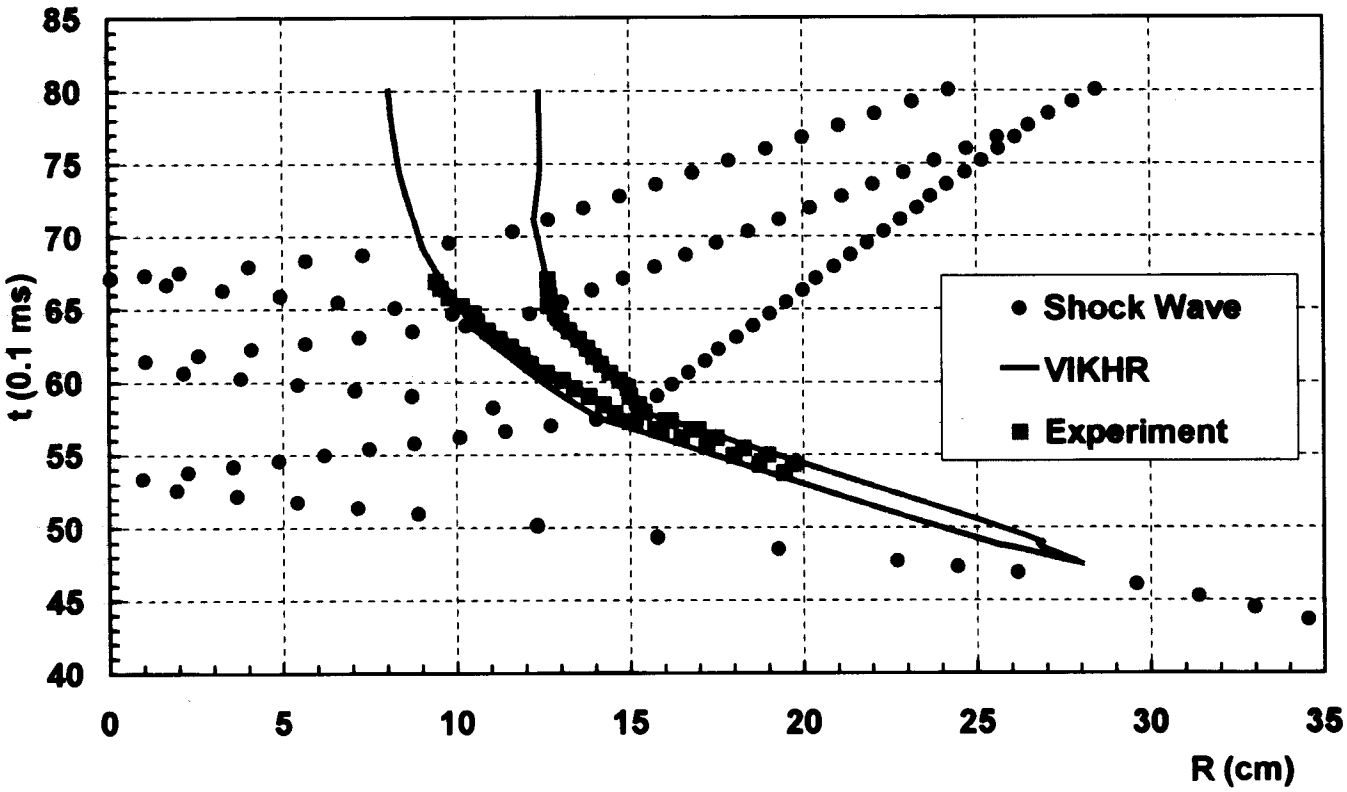

Fig. 2 R-t diagrams of the TM zone boundary and the shock

A New Two-Scale Mix Model: Towards a Multi-Component Model of Turbulent Mixing*

Presented to the 8th International Workshop on the Physics of Compressible Turbulent Mixing

Donald E. Eliason, William H. Cabot, and Ye Zhou

AX-Division, Lawrence Livermore National Laboratory

11 December 2001

*This work was performed under the auspices of the U.S. Department of Energy by the University of California Lawrence Livermore National Laboratory under contract No. W-7405-Eng-48.

Abstract

Turbulent mixing of the fluids in a multi-component system is of interest in situations such as inertial confinement fusion (ICF) and core-collapse supernovae[1]. We report results of a project to include a model of turbulent mixing in a multi-component hydrodynamics and physics model called KULL, which is used for ICF. Because KULL is a complex, multi-dimensional model, we have developed a simplified, one-dimensional version called sKULL to speed-up the development of the turbulent mixing model.

Of primary interest in the development of a turbulent mixing model for a multi-component fluid is the question of whether it is necessary to allow each component of the fluid to retain its own velocity. Generally a multi-component, multi-velocity turbulent mixing model should allow separate velocities for each component of the fluid[2]. However, the necessity to carry separate velocities for each component of the fluid greatly increases the memory requirements and complexity of the computer implementation. In contrast, we present a new two-scale formulation of the K-ε turbulent mixing model, with production terms based on a recent scaling analysis[3], which treats all components of the fluid as if they had the same velocity. We also show that our new method for the initial conditions of the uncoupled two-scale K-ε model yields asymptotic growth. Future work will compare the results of using this single velocity model with those from a more complete multi-velocity formulation of turbulent mixing, to decide whether the multi-velocity formulation needs to be used in KULL.

The goal of this work is to develop a turbulent mixing model for the ICF code called KULL

- **Turbulent mixing of the fluids in a multi-component system is of interest in situations such as inertial confinement fusion (ICF) and core-collapse supernovae[1]**
- **We report results of a project to include a model of turbulent mixing in a multi-component hydrodynamics and physics model called KULL, which is used for ICF**
- **Because KULL is a complex, multi-dimensional code, we have developed a simplified, one-dimensional version called sKULL to speed-up the development of the turbulent mixing model**

[1]Remington, B.A., D. Arnett, R.P. Drake, and H. Takabe, Modeling Astrophysical Phenomena in the Laboratory with Intense Lasers, *Science* **284**, 1488 (1999).

Three areas of this research are highlighted

- **sKULL reproduces KULL's multi-component hydrodynamics and numerics**

- **A single velocity, multi-component, two-scale K-ε turbulent mixing model has been developed within sKULL**

- **A new method for the uncoupled two-scale K-ε initial conditions yields asymptotic growth**

We have an appropriate path to develop a turbulent mixing model for KULL

Classic KULL:

ALE Hydrodynamics

Single sKULL:

Duplicates KULL's

ALE Hydrodynamics

Multi-sKULL:

Multi-

Component

and

Multi-Velocity

The most general model of turbulent mixing is multi-component and multi-velocity

sKULL is the right platform in which to develop a turbulent mixing model for KULL

- sKULL duplicates KULL's hydrodynamics
  - Side-by-side runs of KULL and sKULL on the Sod shock produce the same results
  - We tested the Lagrangian, Eulerian,and ALE capabilities of sKULL to ensure they matched KULL's

- The simplified nature of sKULL, due both to 1-D and no additional physics, allows it to run more quickly
  - Faster run times lead to shorter turn-around times for testing turbulent mixing models

Side-by-side runs of KULL and sKULL on the Sod shock problem produce the same results

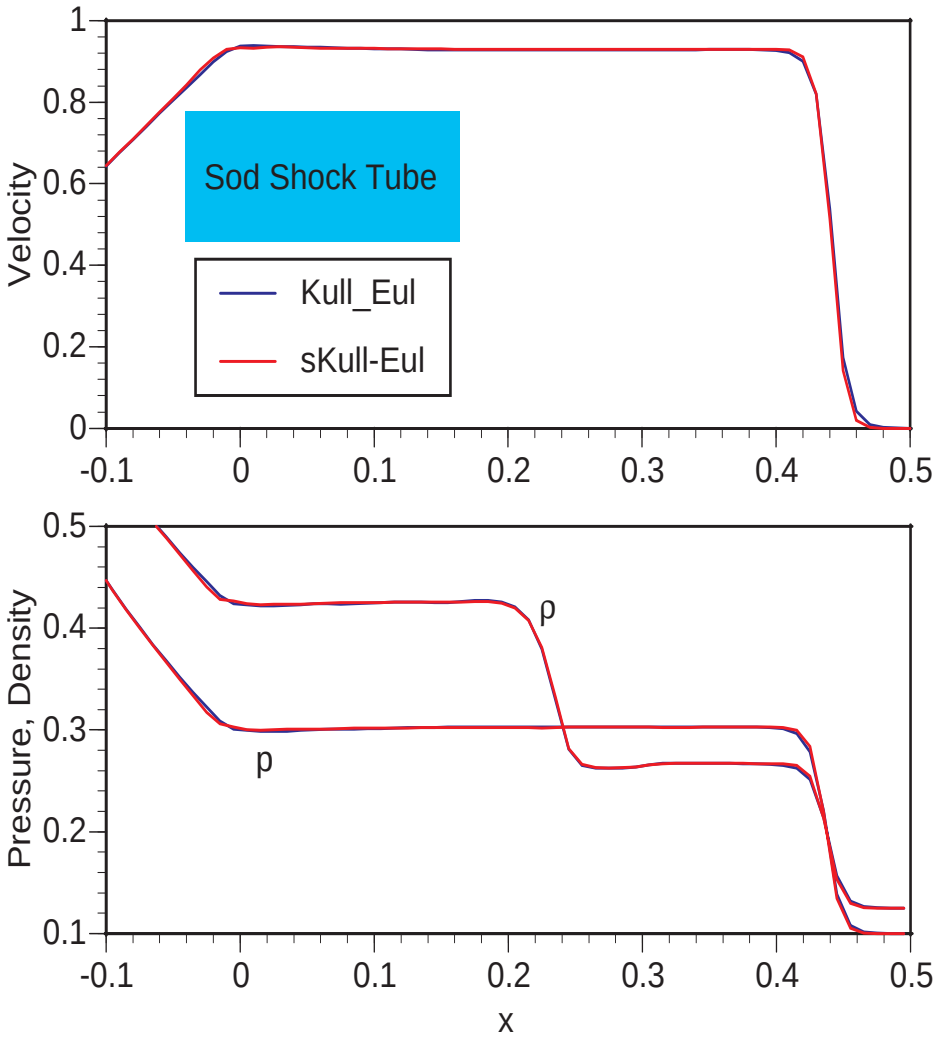

- Duplication of KULL results on selected problems w/ sKULL verifies that we've duplicated KULL's numerics
- Sod (1978) shock tube problem:

ρ = 1	ρ = 0.125
p = 1	p = 0.1
u = 0	u = 0

- Standard test problem
- Compared Lagrangian, Eulerian, and ALE results to ensure that the results from the two codes agreed

sKULL MC-1V's simulation of the Benjamin air-SF_6 shock tube agrees well with the exact solution

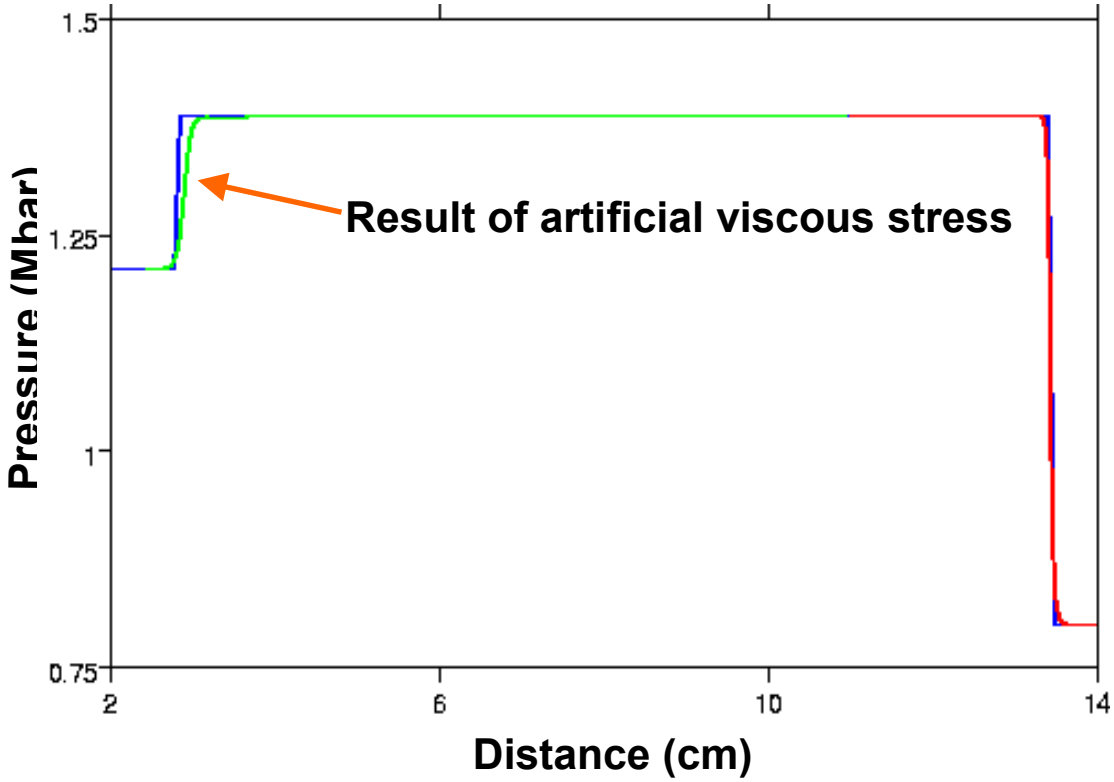

- Benjamin *et al.* (1993) air-SF_6 shock tube:

Air*	SF_6
$\rho = 1.27\times10^{-3}$	$\rho = 4.85\times10^{-3}$
$u = 1.05\times10^{4}$	$u = 0$
$p = 1.21\times10^{6}$	$p = 8.00\times10^{5}$

Shock (Ma=1.2)

- Pressure results from the MC-1V Lagrangian simulation versus exact solution at time 232 μs show good agreement

A multi-component, multi-velocity (MC-MV) approach needs to be considered for the turbulent mixing model

- In RTI/RMI, zones may contain more than one component, each with its own velocity
  - Component interactions (e.g., drag) can lead to mixing
  - From the rocket rig experiments, this led David Youngs (AWE) to create his MC-MV mixing model[2]

- The MC-MV equations add a great deal of complexity
  - Carrying separate velocities increases the memory requirement
  - The drag term may require an implicit treatment

[2]Youngs, D.L., *Laser & Particle Beams* **12**, 725 (1994).

sKULL will be used to test multi-velocity versus single velocity-based turbulent mixing models

Because of sKULL's simplified nature it is faster and cheaper than KULL

- **The extra memory requirement of MC-MV will be manageable**
- **Additional computation for interactions will be do-able**
- **Different numerical treatments of the drag term can be tested (explicit vs. implicit vs. iterated)**

Faster and cheaper makes sKULL the ideal platform to test whether MC-MV might be needed in KULL

The MC-MV equations (Youngs[2]) add a great deal of complexity

ALE: "Grid Velocity" u = $\begin{cases} u_r, \text{ Lagrangian} \\ 0, \text{ Eulerian} \end{cases}$

"ALE"-like,

g = 0 if shock tube,

Interactions,

Turbulence Transport

$$\frac{\partial x}{\partial t} = u$$

$$\frac{\partial (f_r \rho_r)}{\partial t} = -\frac{\partial}{\partial x}\left[f_r \rho_r (u_r - u)\right] - f_r \rho_r \frac{\partial u}{\partial x}$$

$$\frac{\partial (f_r \rho_r u_r)}{\partial t} = -\frac{\partial}{\partial x}\left[f_r \rho_r u_r (u_r - u)\right] - f_r \rho_r u_r \frac{\partial u}{\partial x} - f_r \frac{\partial P}{\partial x} + f_r \rho_r g + \sum_s (D_{rs} + M_{rs}) - m_r \frac{\partial \tau}{\partial x}$$

$$\frac{\partial (f_r \rho_r e_r)}{\partial t} = -\frac{\partial}{\partial x}\left[f_r \rho_r e_r (u_r - u)\right] - f_r \rho_r e_r \frac{\partial u}{\partial x} - h_r P_r \frac{\partial \bar{u}}{\partial x} + \frac{\partial}{\partial x}\left(f_r \rho_r \nu_r \frac{\partial e_r}{\partial x}\right) + f_r \varepsilon$$

Because of the MC-MV equations' complexity, we've first developed a single velocity version, MC-1V

sKULL MC-1V Lagrangian equations with a new two-scale K-ε mixing model

$$\frac{dx}{dt} = u$$

$$\frac{dV_r}{dt} \approx h_r \frac{dV}{dt}, V = \sum_r V_r$$

$$\rho \frac{Du}{Dt} = -\frac{\partial P}{\partial x} - \frac{\partial \tau}{\partial x}$$

Reynolds stress

Turbulent dissipation

$$f_r \rho_r \frac{De_r}{Dt} = -h_r P_r \frac{\partial u}{\partial x} + f_r \rho_r \varepsilon_t + \frac{\partial}{\partial x}\left(f_r \rho_r \frac{\nu_r}{\sigma_e} \frac{\partial e_r}{\partial x} \right)$$

Kinematic viscosity/Schmidt number

The use of the compressibility in the effective pressure allows the simplification to single velocity

$$P = \frac{\sum_r P_r f_r K_r}{\sum_r f_r K_r}, P_r = p_r + q_r$$

Effective pressure (includes artificial viscosity)

$$K_r^{-1} = \rho_r \left.\frac{\partial P_r}{\partial \rho_r}\right|_{e_r} + \frac{P_r}{\rho_r}\left.\frac{\partial P_r}{\partial e_r}\right|_{\rho_r}, h_r = \frac{f_r K_r}{\sum_s f_s K_s}$$

Inverse effective compression;

Relative compression

For an ideal gas and $q_r = 0$, $K_r^{-1} = \gamma_r p_r$ (adiabatic compres-sibility), and $h_r = [f_r/(\rho_r c_r^2)]/[\sum_s f_s/(\rho_s c_s^2)]$ (Youngs[2])

The viscosity for energy diffusion and Reynolds stress comes from the two-scale K-ε model

$$\tau = \frac{2}{3}\rho K_p - \frac{4}{3}\rho \nu_p \frac{\partial u}{\partial x}$$

Reynolds stress

$$\nu_\alpha = \nu_0 + \nu_{T\alpha}$$

Kinematic visc.

Molecular **Turbulent**

$$\nu_{T\alpha} = C_\mu \frac{K_\alpha^2}{\varepsilon_\alpha}$$

Equations for K_α and ε_α are needed for closure

The two-scale K-ε equations describe evolution of the production and turbulence scales

$$\frac{DK_p}{Dt} = P_{R*} - \varepsilon_p + \frac{\partial}{\partial x}\frac{\nu_p}{\sigma_K}\frac{\partial K_p}{\partial x} - \frac{\tau}{\rho}\frac{\partial u}{\partial x}$$

Production scale

Production

$$\frac{DK_t}{Dt} = \varepsilon_p - \varepsilon_t + \frac{\partial}{\partial x}\frac{\nu_t}{\sigma_K}\frac{\partial K_t}{\partial x}$$

Turbulence scale

$$\frac{D\varepsilon_p}{Dt} = C_{p1}\frac{\varepsilon_p}{K_p}P_{R*} - C_{p2}\frac{\varepsilon_p^2}{K_p} + \frac{\partial}{\partial x}\frac{\nu_p}{\sigma_\varepsilon}\frac{\partial \varepsilon_p}{\partial x}$$

$$\frac{D\varepsilon_t}{Dt} = C_{t1}\frac{\varepsilon_p\varepsilon_t}{K_t} - C_{t2}\frac{\varepsilon_t^2}{K_t} + \frac{\partial}{\partial x}\frac{\nu_t}{\sigma_\varepsilon}\frac{\partial \varepsilon_t}{\partial x}$$

The production terms P_{R*} for the two-scale K-ε equations parameterize mixing caused by RTI or RMI

Based on a recent scaling analysis[3] of RT and RM instabilities, the production term may be written as

Rayleigh-Taylor

$$P_{RT} = 4C_{RT}\varepsilon_p^{1/2}(gA)^{3/4}(k_0^{-1/4} - k_1^{-1/4})$$

Richtmyer-Meshkov

$$P_{RM} = 2C_{RM}\varepsilon_p^{1/2}(A\Delta u)^{3/2}(k_1^{1/2} - k_0^{1/2})$$

[3]Zhou, Y., A scaling analysis of turbulent flows driven by Rayleigh-Taylor and Richtmyer-Meshkov instabilities, *Phys. Fluids* **13**, 538–543 (2001).

Wave numbers k_0 and k_1 for the production terms evolve with the flow

Initially k_0 and k_1 are set by the initial perturbation scales, but thereafter evolve according to the computed production and turbulence scales

Production scale

Rayleigh-Taylor

$$k_0 = \left[\frac{\frac{4}{7} C_{RT} \varepsilon_p^{1/2} (gA)^{1/4}}{\frac{4}{7} C_{RT} \varepsilon_p^{1/2} (gA)^{1/4} k_1^{-3/4} + K_p} \right]^{4/3}$$

Richtmyer-Meshkov

$$k_0 = \frac{4 C_{RM}^2 \varepsilon_p A \Delta u}{\left[2 C_{RM} \left(\varepsilon_p A \Delta u \right)^{1/2} k_1^{-1/2} + K_p \right]^2}$$

Turbulence scale

$$k_1 = \varepsilon_t \left(\tfrac{3}{2} C_K / K_t \right)^{3/2}$$ **RT or RM**

The change in total energy is due to production minus dissipation and surface fluxes

$$\underbrace{\frac{D}{Dt}\int \rho\left(u^2/2+e+K\right)dV}_{\text{Total Energy Change}} = \underbrace{\int \rho\left(P_{R^*}-\varepsilon_t\right)dV}_{\text{Production - Dissipation}} \underbrace{-\left[u\left(P+\tau\right)+F_e+F_K\right]_S}_{\text{Surface Fluxes}}$$

$$F_e = -\frac{\nu}{\sigma_K}\frac{\partial e}{\partial x}, F_{K_\alpha} = -\frac{\nu_\alpha}{\sigma_K}\frac{\partial K_\alpha}{\partial x}$$

$$F_K = F_{K_p} + F_{K_t}$$

Diffusive fluxes of internal and turbulent kinetic energies

Results from Orszag and Speziale will be used to provide ICs for the two-scale turbulent mixing model

- **Steve Orszag's work for the ASCI Turbulence Group:**

$$K_p < \tilde{P}_{R0}\sqrt{\nu_0 / C_\mu}, \tilde{P}_{R0} = P_{R0} / \varepsilon_{p0}^{1/2}$$

Initial RT or RM Production

$$\frac{C_\mu K_{p0}^2}{\nu_0} < \varepsilon_{p0} < \tilde{P}_{R0}^2$$

If violated: too much turbulence initially, interface dies out

If violated: no turbulent viscosity develops, Orszag's high Re run blew up

- **Is this result consistent w/ Speziale's fixed point analysis?**

The result using Orszag's approach is consistent with Speziale's fixed point analysis

- **The "fixed points" from Speziale's analysis[4] act as attractors**
- **Initialize with fixed points that are consistent with desired long-term behavior**
  - **Leads more quickly to the desired long-term state**
- **Speziale's analysis yields the following fixed points:**

$$\varepsilon_{pf} = f_p P_{R0}, \varepsilon_{tf} = f_t \varepsilon_{pf}$$

$$f_p = (C_{p1} - 1)/(C_{p2} - 1), f_t = (C_{t1} - 1)/(C_{t2} - 1)$$

suggesting

$$\varepsilon_{p0} = f_p^2 \tilde{P}_{R0}^2$$

consistent with Orszag's approach if $f_p < 1$

[4]Speziale, C.G., and N. Mac Giolla Mhuiris, On the prediction of equilibrium states in homogeneous turbulence, *J. Fluid Mech.,* **209**, 591-615 (1989).

The Orszag-Speziale ICs yield asymptotically growing solutions for the two-scale turbulent mixing model

- **Current recommended values $C_{p1} = 1.5$, $C_{p2} = 2$ give $f_p = 1/2$**
  - **➔ The result using Orszag's approach is consistent with Speziale's fixed point analysis**
  - **➔ Also consistent with constraints $C_{*2} > 1$ and $C_{*2} > C_{*1} > 1/2$ needed to get asymptotically growing solutions**
- **Solution of the two-scale turbulent mixing model equations as ODEs using the Orszag-Speziale ICs produced the expected asymptotically growing results**
  - **➔ The Orszag-Speziale ICs will be used in the two-scale turbulent mixing model for sKULL MC-1V**

A test of the Orszag-Speziale ICs w/ the uncoupled two-scale K-ε model yields asymptotic growth

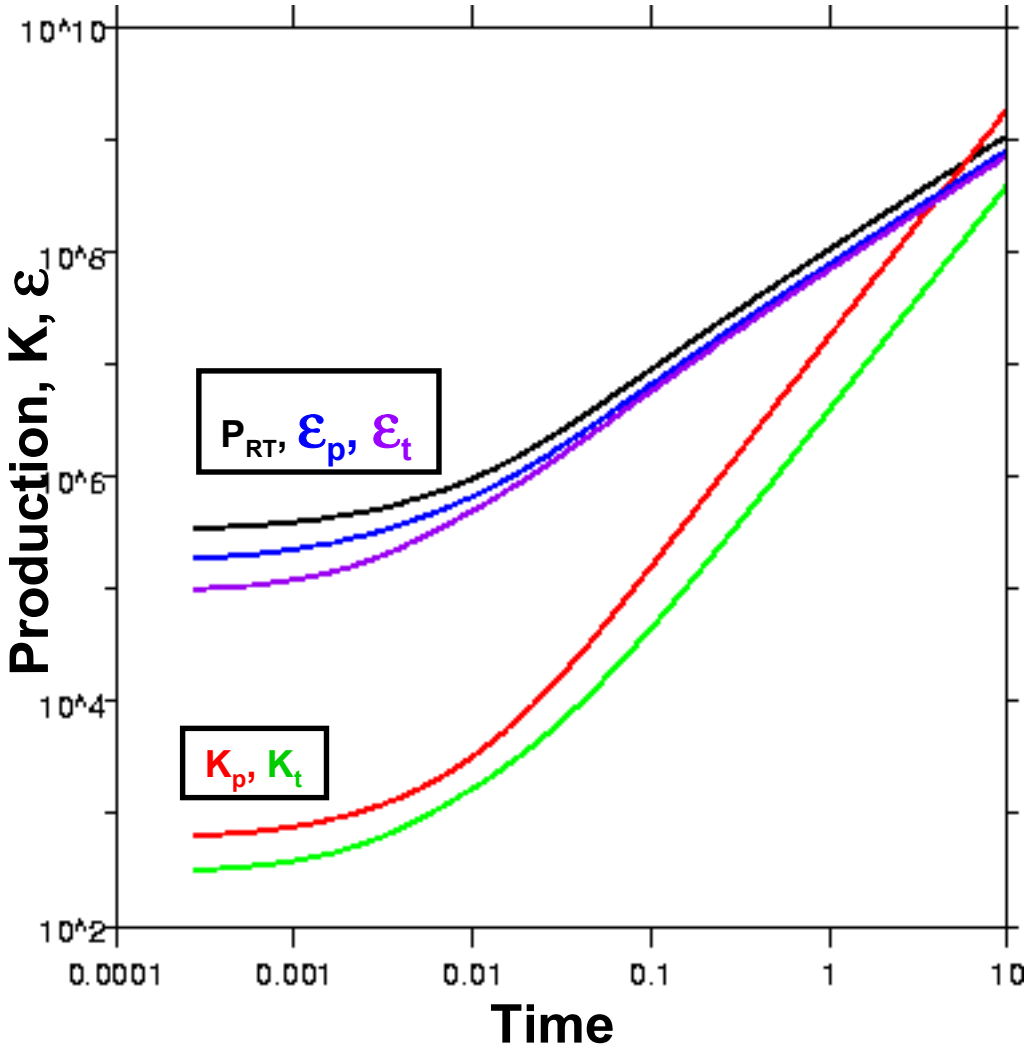

Rayleigh-Taylor Test

- gA = 4000
- $k_1(0) = 10k_0(0) = 20\pi$
- $C_K = C_{RT} = 1.5$
- $C_{p1} = 1.5$, $C_{p2} = 2.0$
- $C_{t1} = 1.08$, $C_{t2} = 1.15$

- Constraints for asymptotic growth are satisfied, and asymptotic growth achieved

Consistency with a stand-alone ODE solution demonstrates that the uncoupled two-scale K-ε equations have been correctly implemented in sKULL

Summary and Future Work

- A simplified version of the ICF code KULL has been developed which reproduces KULL's multi-component hydrodynamics
  - The purpose of simplified KULL, sKULL, is to serve as a test-bed for implementation of multi-component turbulent mixing models
  - Tests show that sKULL faithfully duplicates KULL's numerics
- A single velocity, multi-component, two-scale K-ε turbulent mixing model has been developed within sKULL
  - A new method for the uncoupled two-scale K-ε initial conditions yields asymptotic growth
- Future work will compare these single velocity results with those from a more complete multi-velocity formulation of turbulent mixing, to decide whether the multi-velocity formulation needs to be used in KULL

Table of Symbols #1

Quantity	Description
D_{rs}	Drag force on fluid r due to fluid s
e_r	Specific internal energy of fluid r
ε_p	Dissipation at production scale
ε_t	Dissipation at turbulence scale
f_r	Volume fraction of fluid r
g	Acceleration (e.g., gravitational)
h_r	Relative compressibility of fluid r
K_p	Turbulence kinetic energy at production scale
K_t	Turbulence kinetic energy at turbulence scale
m_r	Mass fraction of fluid r

Table of Symbols #2

Quantity	Description
M_{rs}	Added mass effect for fluid r due to fluid s
ν_{0r}	Molecular viscosity of fluid r
$\nu_T = \nu_p + \nu_t$	Total turbulent viscosity
ν_p	Turbulent viscosity, production scale
ν_t	Turbulent viscosity, turbulence scale
$\nu_r = \nu_{0r} + \nu_T$	Total viscosity of fluid r
$P_r = p_r + q_r$	Effective pressure of fluid r
$P = p + q$	Effective mean pressure
$p = \sum_r h_r p_r$	Mean pressure
$p_r = p_r(\rho_r, e_r)$	Pressure of fluid r from EOS

Table of Symbols #3

Quantity	Description
$q = \sum_r f_r q_r$	Mean artificial viscous stress
q_r	Artificial viscous stress of fluid r
$\rho = \sum_r f_r \rho_r$	Mean density
ρ_r	Density of fluid r
t	Time
u	Mean velocity
$\bar{u} = \sum_r f_r \bar{u}_r$	Volume-weighted mean velocity
$\bar{u}_r = u_r + \frac{\nu_r}{\rho_r}\frac{\partial \rho_r}{\partial x}$	Volume-weighted velocity of fluid r
u_r	Velocity of fluid r
x	Position at time t

High order methods for 2D Richtmyer-Meshkov Instability

Wai Sun Don, David Gottlieb, Chi-Wang Shu
Division of Applied Mathematics
Brown University

Leeland Jameson
Lawerance Livermore National Laboratory
University of California

This research is supported under the auspices of the US Department of Energy by the University of California Lawerance Livermore National Laboratory.

Richtmyer-Meshkov Instability

- Shock induced instability of the interface between fluids of different density (Theoretized by Richtmyer and experimented by Meshkov.)
- Growth of the interface amplitude and secondary shear instability promote the onset of turbulence mixing.
- Applications included but not limited to mixing enhancement and inertial confinement fusion (ICF).

Richtmyer-Meshkov Instability (Cont.)

The two-dimensional Euler equations,

$$\mathbf{Q}_t + \mathbf{F}_x + \mathbf{G}_y = 0.$$

The state vector $\mathbf{Q}$ is

$$\mathbf{Q} = (\rho, \rho u, \rho v, E)^{\mathrm{T}} .$$

The inviscid fluxes $\mathbf{F}$ and $\mathbf{G}$ are given by

$$\begin{aligned} \mathbf{F} &= (\rho u, \rho u u + P, \rho u v, (E + P)u)^{\mathrm{T}} , \\ \mathbf{G} &= (\rho v, \rho u v, \rho v v + P, (E + P)v)^{\mathrm{T}} . \end{aligned}$$

where

$$P = (\gamma - 1)(E - \frac{1}{2}\rho \mathbf{U} \cdot \mathbf{U}) .$$

Richtmyer-Meshkov Instability (Cont.)

Initial Condition :

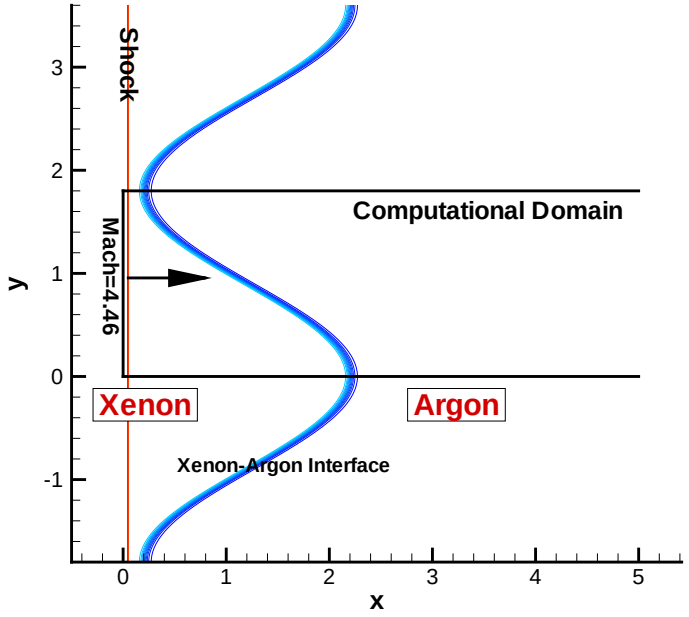

- Hugoniot-Rankine condition for the shock
- Pre-Shock Temperature $T = 296\ K$
- Pre-Shock Pressure $P = 0.5\ atm$
- Xenon and Argon density are $\rho_{Xe} = 2.90 \times 10^{-3}\ \frac{g}{cm^3}$ and $\rho_{Ar} = 0.89 \times 10^{-3}\ \frac{g}{cm^3}$ respectively, at half of the normal atmospheric pressure
- Specific heat ratio $\gamma = \frac{5}{3}$
- Atwood number $At = 0.54$
- Mach number $M = 2, 4.46, 8, 10$
- Wave Length $\lambda = 36\ mm$
- Amplitude $a = 1, 2.5, 5, 10, 15\ mm$

Richtmyer-Meshkov Instability (Cont.)

Xenon-Argon interface definition :

$$S(x,y) = \exp(-\alpha|d|^{\beta}) \qquad 0 < d < 1$$

where

- $$d = \frac{(x_i + a\cos(2\pi y/\lambda) + \delta) - x}{2\delta}$$

- $\delta = a/5$ is the interface thickness,
- $\beta = 8$ is the interface order,
- $\alpha = -\ln\epsilon$ with ϵ being the machine zero.

Richtmyer-Meshkov Instability (Cont.)

Regions of Interest :

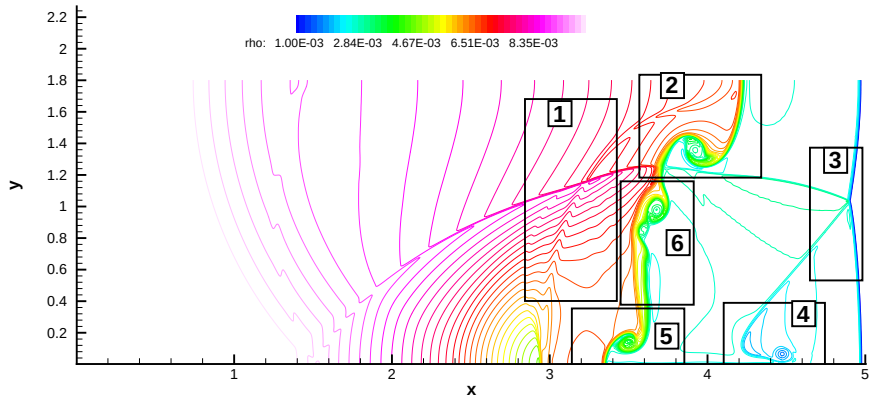

1. Reflected shock generated by the shock refraction;
2. The penetration of the heavy (Xe) to light (Ar) fluid forms the Spike;
3. Triple point on the transmitted shock;
4. A small jet and its vortical structure. The Kelvin-Helmholtz instability caused the instability along the contact discontinuity in long time simulation;
5. The penetration of the light (Ar) to heavy (Xe) fluid forms the Bubble;
6. Vortical rollups of the gaseous interface.

Richtmyer-Meshkov Instability : Algorithms

- Spatial Algorithm : (Spectral)
  1. Combined Chebyshev (x) and Fourier collocation method (y)
     - Differentiation and Smoothing operations are done via an optimized library PseudoPack (Costa & Don);
     - a 10'th and 9'th order exponential filter used for the differentiation and solution smoothing respectively.
     - Incremental domain size in x as shock moved downstream.
     - Parallelized with OpenMP.
  2. WENO fifth order finite difference scheme (WENO) with Lax-Frederick flux.
  3. Symmetry property in y is utilized to reduce the cost of computation.
- Temporal Algorithm :
  Third order TVD Runge Kutta method (Shu and Osher).

Spectral Methods - Introduction

The solution of an equation is assumed to be in a space $\mathcal{B}_\mathcal{N}$ spanned by smooth basis functions $\{\phi_k\}$.

- For periodic problems

$$\phi_k = e^{ikx}$$

- for non-periodic problems in finite intervals
  - Either

$$\phi_k = T_k(x)$$

    where T_k are the Chebyshev polynomials.
  - Or

$$\phi_k = L_k(x)$$

    where L_k are the Legendre polynomials.

Spectral Methods - Introduction (Cont.)

The approximation is obtained in one of two ways:

- Galerkin projection:

$$\mathcal{P}_{\mathcal{N}} F(x) = \sum_{k=0}^{N} (F, \phi_k)\phi_k(x)$$

  where

$$(F, \phi_k) = \int \omega(x) F(x) \phi_k(x)\ dx$$

Spectral Methods - Introduction (Cont.)

- The Pseudo-spectral approximation

$$\mathcal{I}_{\mathcal{N}} F(x) = \sum_{k=0}^{N} (F, \phi_k)_N \phi_k(x)$$

where

$$(F, \phi_k)_N = \sum_{i=0}^{N} \omega_i F(x_i) \phi_k(x_i)$$

  - x_i and ω_i are the Gauss-Lobatto Quadrature nodes and weights respectively.
  - Thus

$$\int f(x)\omega(x)dx = \sum_{i=0}^{N} \omega_i f(x_i) \phi_k(x_i)$$

when $f(x)$ is a polynomial or trigonometrical polynomial of degree $2N - 1$.

Spectral Methods - Introduction (Cont.)

- Alternatively

$$\mathcal{I}_{\mathcal{N}} F(x) = \sum_{i=0}^{N} F(x_i) g_i(x)$$

  where

  – $g_i(x)$ is a polynomial of degree N such that $g_i(x_k) = \delta_{i,k}$.

This leads naturally to the formula:

$$\frac{d}{dx}\mathcal{I}_{\mathcal{N}} F(x_k) = \sum_{i=0}^{N} F(x_i) g_i'(x_k)$$

and defines the *Differentiation Matrix*

$$\mathcal{D} = g_i'(x_k)$$

Approximation Results

$$||F - \mathcal{P}_N F|| \leq K \frac{||F||_s}{N^s}$$
$$||F - \mathcal{I}_N F|| \leq K \frac{||F||_s}{N^s}$$

Filtering

- To solve most *nonlinear* PDE, for example Burgers' Equation, some form of dissipation (natural or numerical) is generally required for stability by damping the growth of the high modes.
- Spectral methods is a conservative method.
- Stabilization of the spectral methods requires *Low Pass Filter*.

Filters in the Transform Space

Force the Fourier/Chebyshev coefficient a_k decays faster.

Replace

$$f_N(x) = \sum_{k=0}^{N} a_k e^{ikx}$$

by

$$\hat{f}_N(x) = \sum_{k=0}^{N} \sigma(\frac{k}{N}) a_k e^{ikx} \quad .$$

Filtering (Cont.)

Definition of Filters

A filter of p order $\sigma(x)$ is defined as

$$\begin{aligned} \sigma(0) &= 1 \\ \sigma^l(0) &= 0 \quad 1 \leq l \leq p-1 \\ \sigma^l(1) &= 0 \quad 1 \leq l \leq p-1 \end{aligned}$$

Theorem (Vandeven 1989)

$$|f(x) - \hat{f}_N(x)| \leq C_p N^{1-p} d(x)^{1-p} ||f||$$

where $d(x)$ is the distance from the discontinuity.

If p is proportional to N, accuracy can be recovered *away from the discontinuity.*

Filtering (Cont.)

Exponential Filter

$$\sigma(\frac{k}{N}) = \exp\left(-\alpha\left(\frac{k}{N}\right)^{\gamma}\right)$$

where $\alpha = -\ln\epsilon$, ϵ is the machine zero.

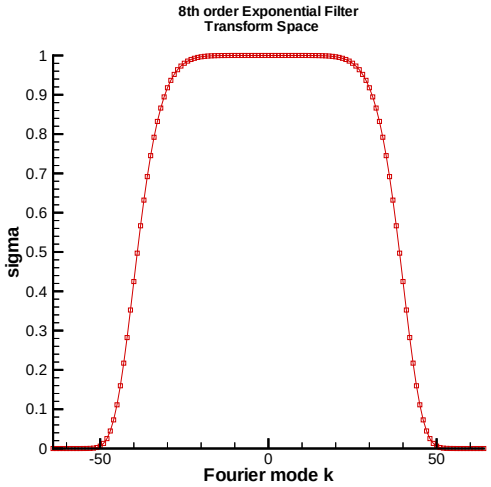

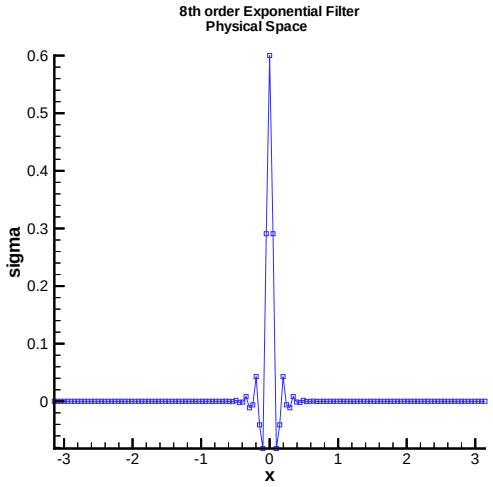

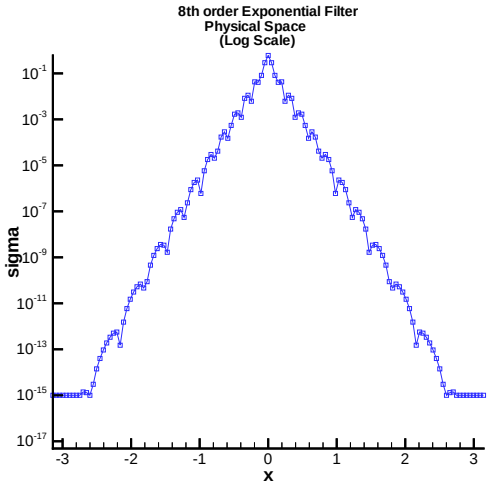

Time Stepping Scheme

The algorithm employs the third order TVD Runge-Kutta scheme (Shu & Osher) to solve the system of ODE's produced by the spatial differencing.

It has the form of

$$\begin{aligned}
\vec{U}^1 &= \vec{U}^n + \Delta t L(\vec{U}^n) \\
\vec{U}^2 &= \frac{1}{4}(3\vec{U}^n + \vec{U}^1 + \Delta t L(\vec{U}^1)) \\
\vec{U}^{n+1} &= \frac{1}{3}(\vec{U}^n + 2\vec{U}^2 + 2\Delta t L(\vec{U}^2))\,.
\end{aligned}$$

L is the spatial operator.

$\vec{U}^n$and $\vec{U}^{n+1}$ are the data arrays at the n-th and $(n+1)$-th time step, respectively. $\vec{U}^1$and $\vec{U}^2$ are two temporary arrays at the intermediate Runge-Kutta stages.

The scheme is stable for CFL < 1.

Mapping for Chebyshev Method

Consider the scalar hyperbolic equation

$$\begin{aligned} U_t &= U_x \quad -1 \le x \le 1 \\ U(1,t) &= 0\,. \end{aligned}$$

In the semi-discreet form

$$\frac{\partial}{\partial t} U_N(t) = D U_N(t)$$

where D is the Chebyshev differentiation matrix with the first row and column removed.

Disadvantages :

1. Roundoff Error grows as $O(N^{2k})$.
2. Restrictive CFL conditions for explicit time stepping scheme with $\Delta t \approx O(N^{-2k})$.

with k being the number of derivatives taken.

Mapping for Chebyshev Method (Cont.)

Kosloff-Tal-Ezer Mapping

$$x = g(\xi, \alpha) = \frac{\sin^{-1}(\alpha\xi)}{\sin^{-1}\alpha}$$

where ξ_j and x_j are the original and mapped Chebyshev collocation points respectively.

If $\alpha \in [0, 1]$ is chosen as

$$\alpha = \alpha(N, \epsilon) = \operatorname{sech}\left(\frac{|\ln \epsilon|}{N}\right),$$

then the approximation error is roughly ϵ. Note that α is not a constant but a function of N.

By choosing ϵ to be machine zero, the error of the coordinate transformation is essentially guaranteed to be harmless.

Under the mapping, the differentiation matrix D becomes

$$\mathcal{D} = \mathcal{M}D$$

where $\mathcal{M}$ is a diagonal matrix with element $\mathcal{M}_{ii} = g'(\xi_i, \alpha)^{-1}$.

Mapping for Chebyshev Method (Cont.)

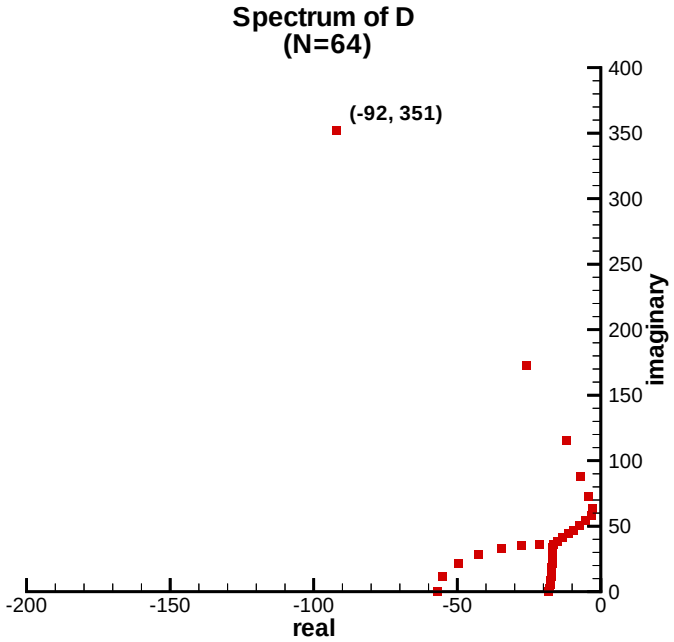

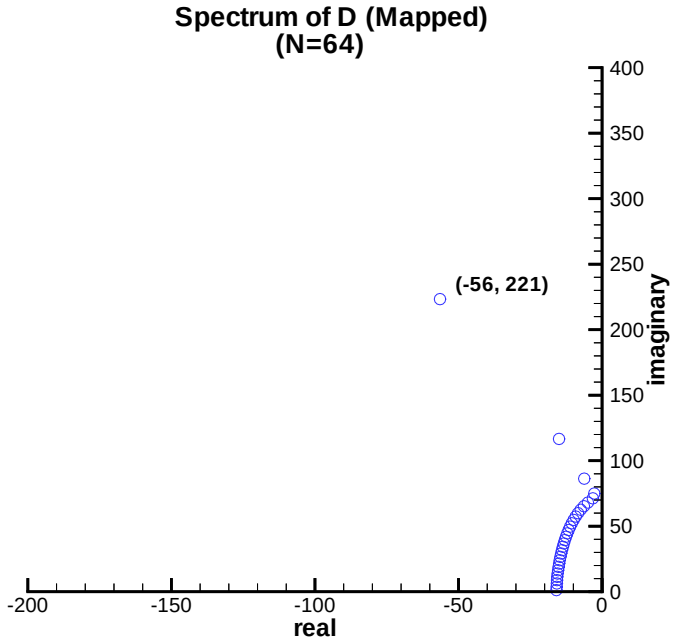

Mapping for Chebyshev Method (Cont.)

Advantages

- Reduction of roundoff error from $O(N^{2k}\epsilon)$ to $O(N^k\epsilon)$.

N	No Mapping	with Mapping
32	0.47E-09	0.20E-09
64	0.62E-08	0.20E-08
128	0.71E-07	0.13E-07
256	0.35E-05	0.21E-06
512	0.98E-05	0.33E-06
1024	0.13E-02	0.21E-05

Table I: Absolute maximum error for the second derivative of $\sin(2x)$.

Mapping for Chebyshev Method (Cont.)

- Reduction of the spectral radius of the differentiation matrix from $O(N^{2k})$ to $O(N^k)$ asymptotically for D and $\mathcal{D}$ respectively.

N	$\lambda(D)$	Growth Rate	$\lambda(\mathcal{D})$	Growth Rate
32	91.6		80.8	
64	263.8	2	230.4	1.50
128	1452.7	2	555.4	1.27
256	5808.4	2	1219.1	1.13
512	23231.3	2	2553.5	1.07
1024	92922.8	2	5225.8	1.03

Table II: The spectral radius λ of D and $\mathcal{D}$.

k is the order of differentiation.

Results

Richtmyer-Meshkov Instability (Cont.)

$(M = 4.46, a = 10\ mm, \delta = 6\ mm, t = 50\ \mu s)$: **Density**

Spectral

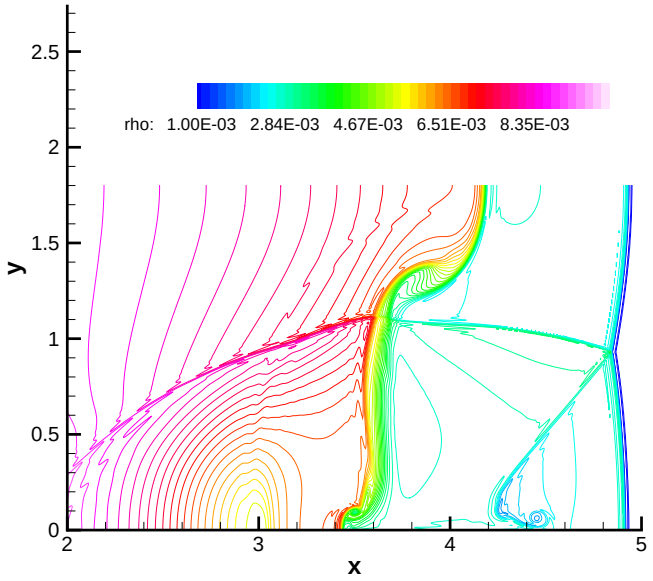

WENO

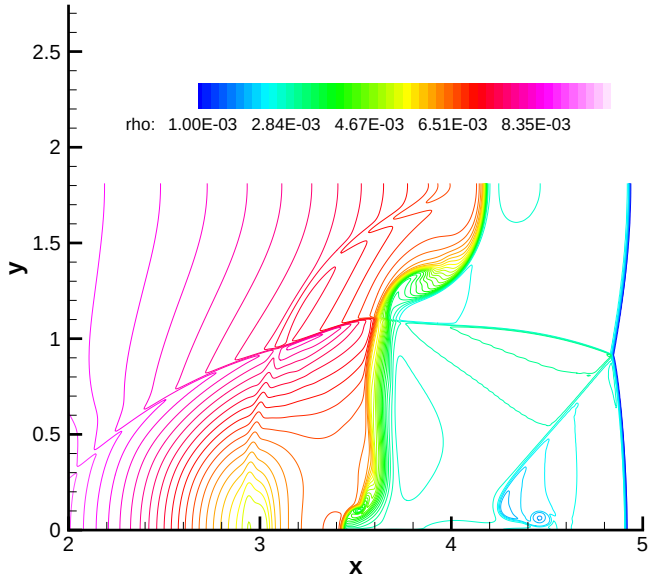

- Grid size for the Spectral and WENO schemes are 1024x512.

Richtmyer-Meshkov Instability (Cont.)

$(M = 4.46, a = 10\ mm, \delta = 6\ mm, t = 50\ \mu s)$: **V-Velocity**

Spectral

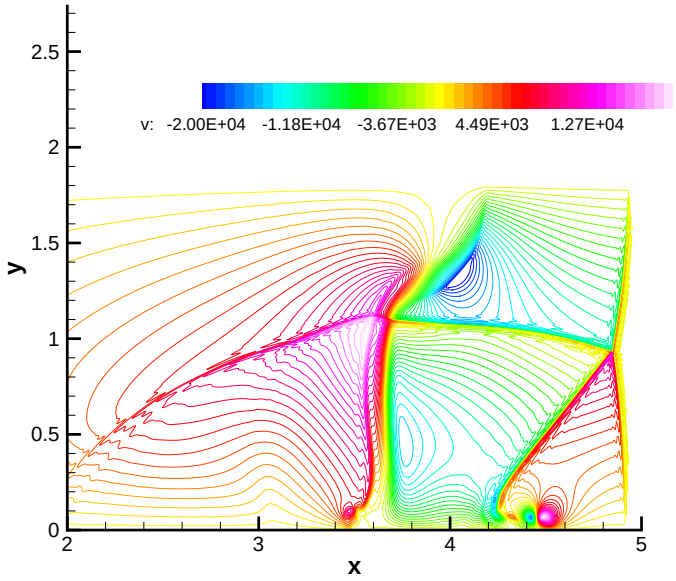

WENO

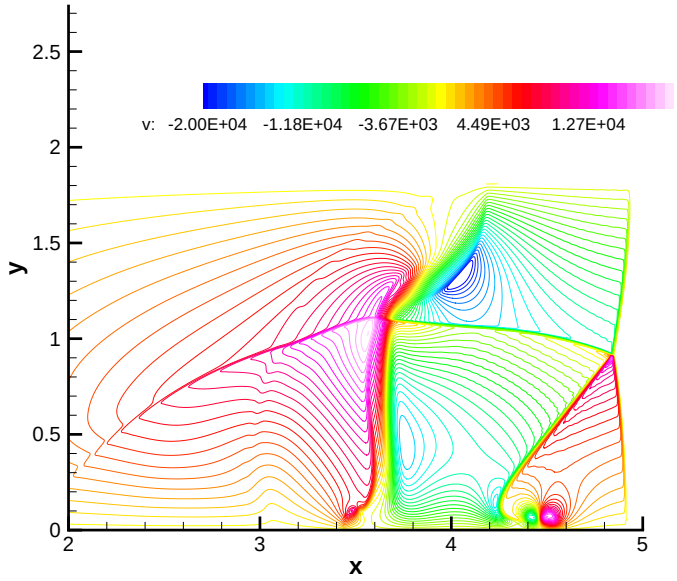

- Grid size for the Spectral and WENO schemes are 1024x512.

Richtmyer-Meshkov Instability (Cont.)

$(M = 4.46, a = 10\ mm, \delta = 2\ mm, t = 50\ \mu s)$: **Density**

Spectral

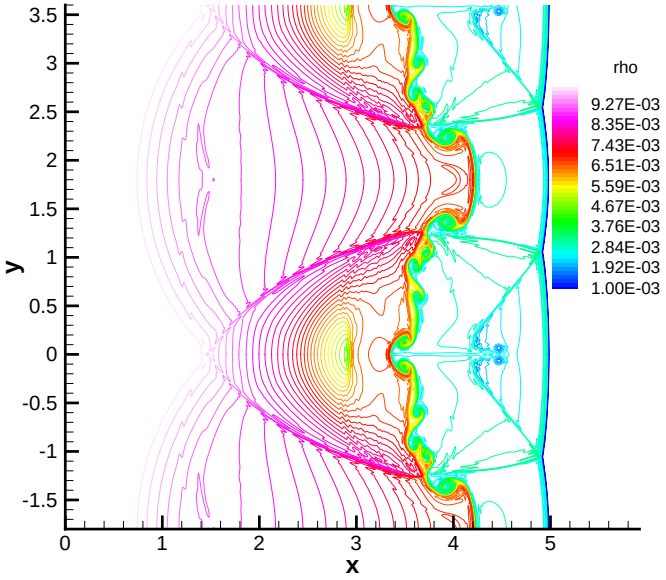

WENO

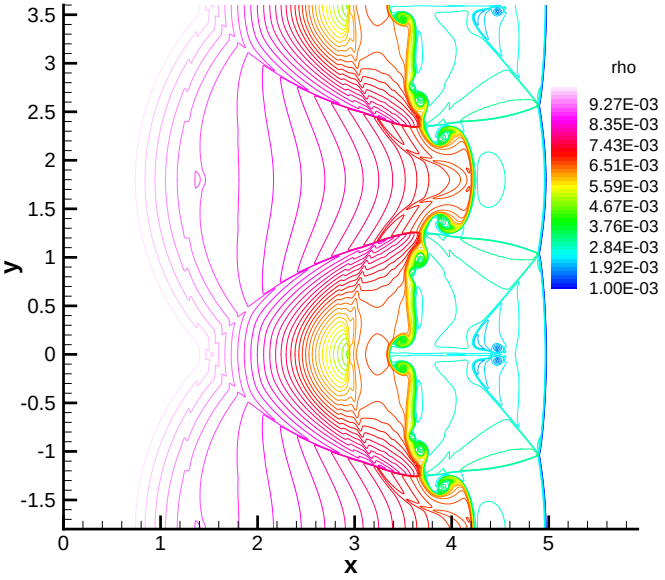

- Grid size for the Spectral and WENO schemes are 1024x256 and 1024x512 respectively.

Richtmyer-Meshkov Instability (Cont.)

$(M = 4.46, a = 10\ mm, \delta = 2\ mm, t = 50\ \mu s)$: **V-Velocity**

Spectral

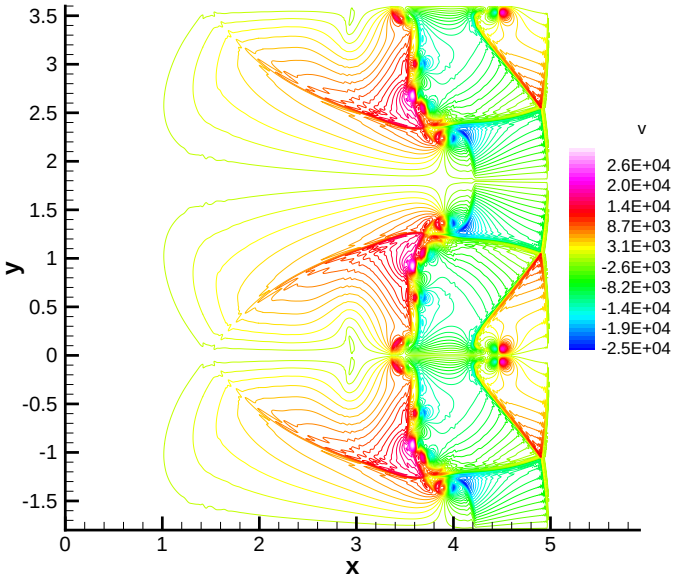

WENO

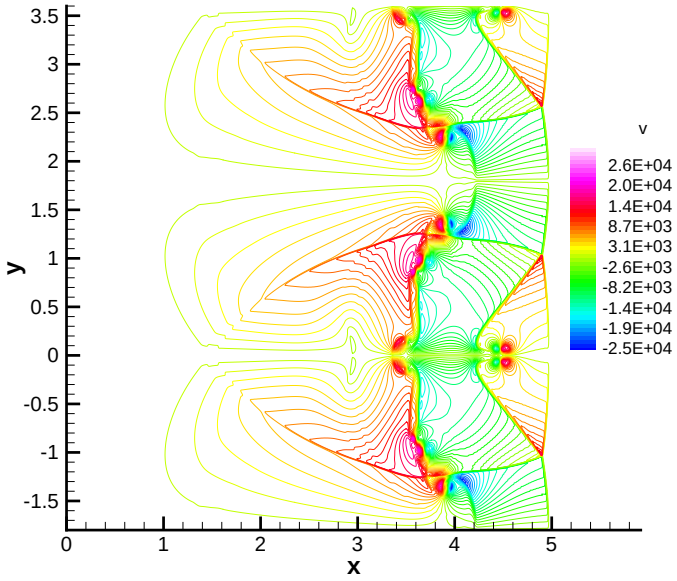

- Grid size for the Spectral and WENO schemes are 1024x256 and 1024x512 respectively.

Richtmyer-Meshkov Instability (Cont.)

Long time Case ($M = 4.46, a = 10\ mm, \delta = 2\ mm, t = 124\ \mu s$) **: Density**

Spectral

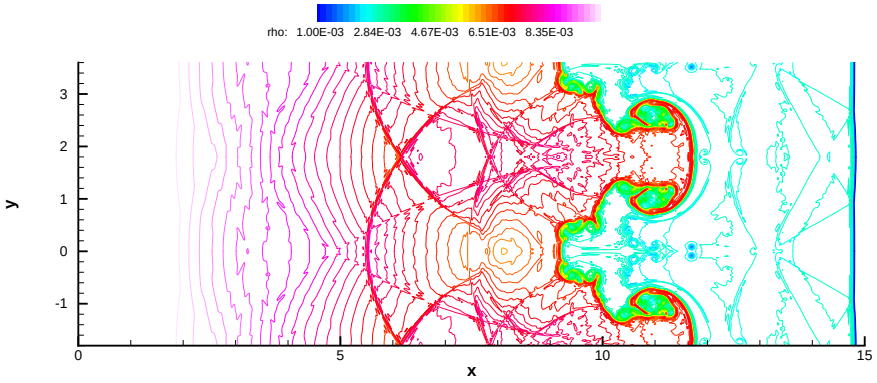

WENO

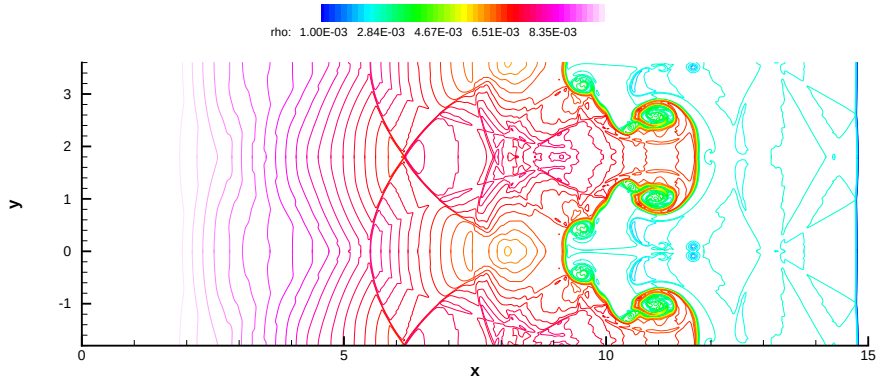

Richtmyer-Meshkov Instability (Cont.)

Long time Case ($M = 4.46, a = 10\ mm, \delta = 2\ mm, t = 124\ \mu s$) **: V-Velocity**

Spectral

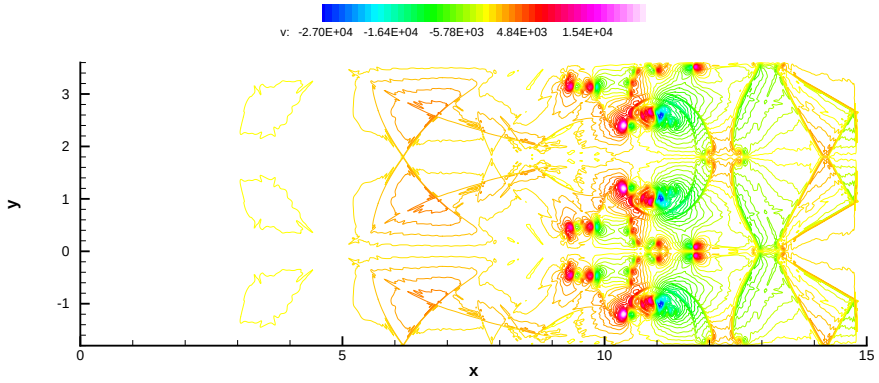

WENO

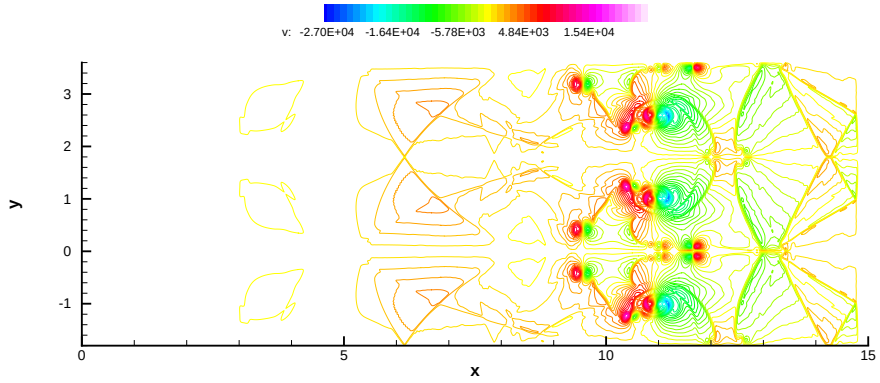

Richtmyer-Meshkov Instability (Cont.)

Large Domain Case ($M = 4.46, a = 10\ mm, \delta = 2\ mm, t = 237\ \mu s$) **: Spectral scheme**

Density

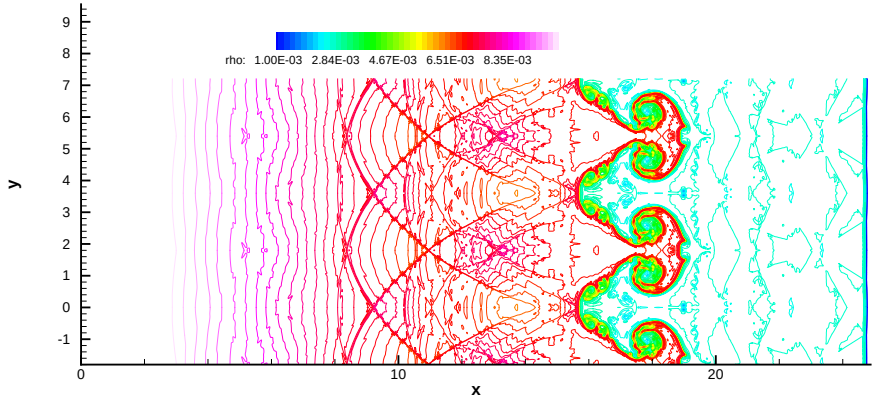

V-Velocity

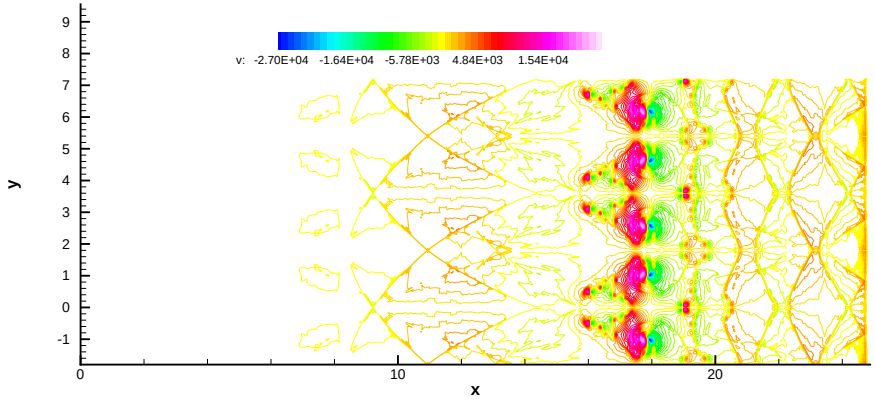

Richtmyer-Meshkov Instability (Cont.)

High Mach Number ($M = 8, a = 10\ mm, \delta = 2\ mm, t = 200\ \mu s$) **: Spectral scheme**

Density

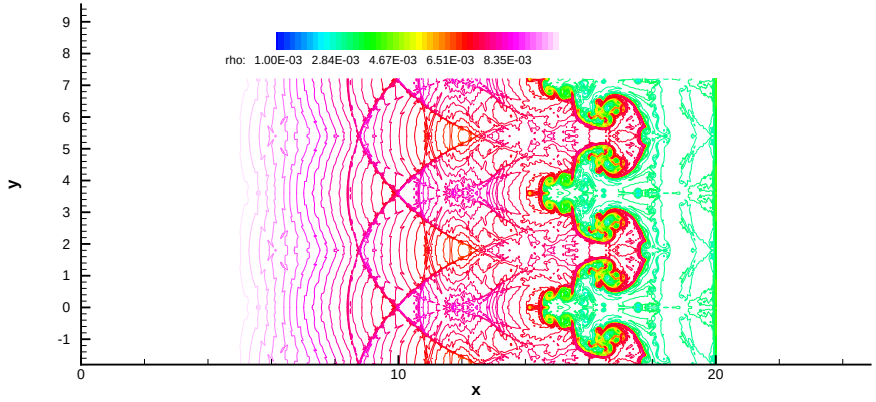

V-Velocity

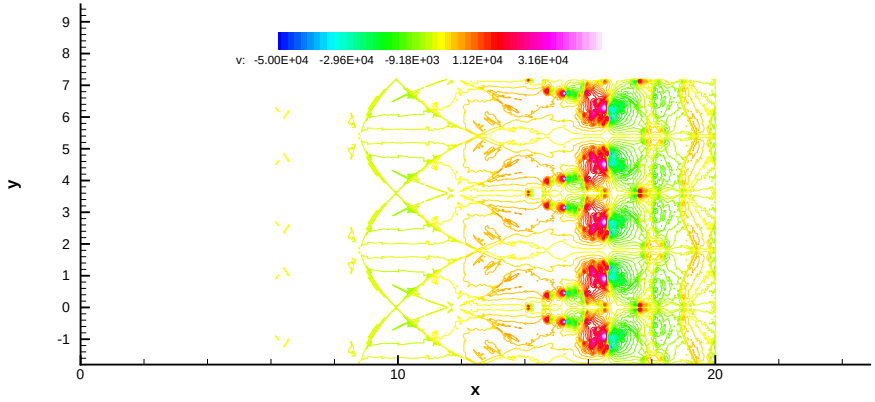

Richtmyer-Meshkov Instability (Cont.)

Amplitudes vs. Displacement

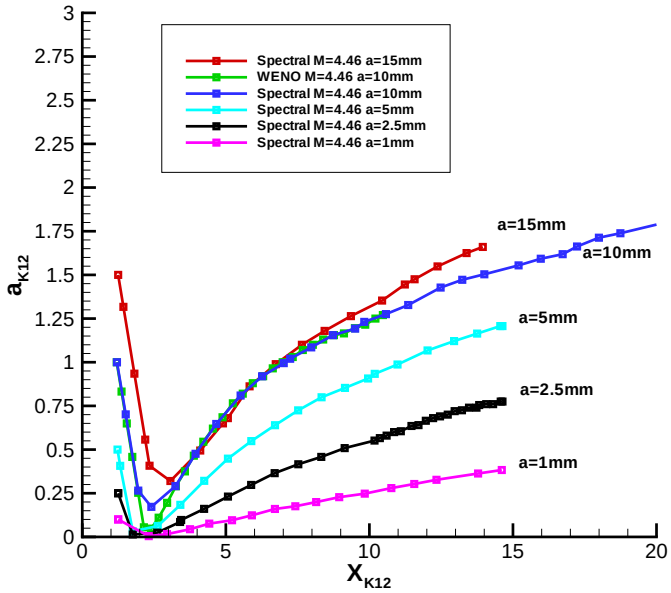

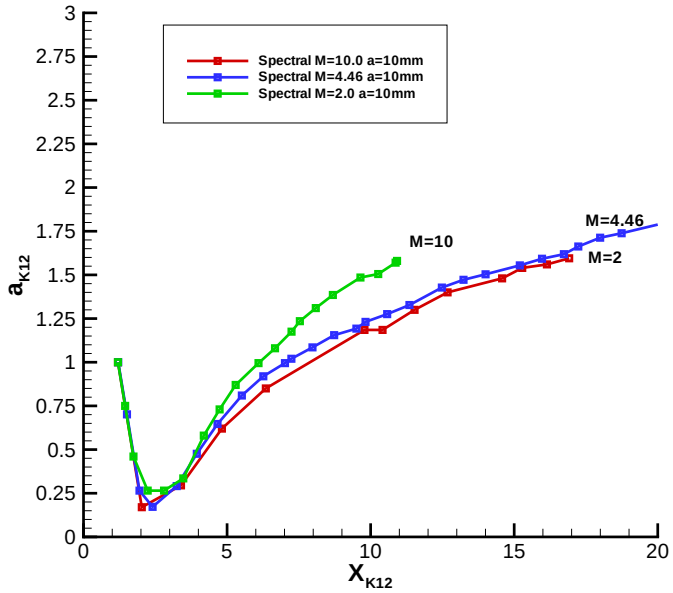

- Consistent with the experimental observations by Aleshin et al.
  1. Linear growth of a within "soft regular" regime;
  2. Decrease growth of a within the irregular regime.

Richtmyer-Meshkov Instability : Conclusion

Summary :

- Good agreement of the global large and medium features between the Spectral scheme and the WENO scheme.
- Some discrepancy of the fine scale vortical structures along the gaseous interface as expected for simulations of this sensitive nature to small perturbation (physically and/or numerically).
- Good agreement with the experimental data (Aleshin et al.)

Examination of Rayleigh-Taylor α in Three Cases: PPM Simulations, Vasilenko et al. Shock Tube Experiment, and Meshkov-Nevmerzhitsky Accelerated Tank Experiment

UCRL-PRES-146443

A.M. Dimits

Lawrence Livermore National Laboratory

Acknowledgments: E.W. Burke, A.W. Cook, G. Dimonte, J.A. Greenough, D. Klem T.A. Peyser, D.H. Porter, D. Youngs, Y. Zhou.

Presented at the 8th IWPCTM, Caltech, Pasadena, CA, 12/9-12/14/01.

This work was performed under the auspices of the U.S. Department of Energy by the University of California, Lawrence Livermore National Laboratory under Contract No. W-7405-Eng-48

Abstract

Several aspects of mixing due to the Rayleigh-Taylor (RT) instabilityare investigated.

Analysis of 3D multimode simulations using the PPM code [D.H. Porter and P.R. Woodward, Astrophys. J. Suppl. 93, 309 (1994), and references therein.] show that there are regions of the parameter space of the initial conditions in which the growth rate is independent of variations in the initial conditions. The simulated growth rates are found to increase as the Navier-Stokes viscosity is increased. It is investigated whether this couterintuitive result is due to the suppression of material mixing at the molecular level for larger viscosities.

Analyses of two RT experiments, one in which water is accelerated by a compressed gas (E.E. Meshkov and N.V. Nevmerzhitsky, Proc. 3rd Int. Wkshp. on the Physics of Compressible Turbulent Mixing, 1991) and one in which an interface between gases of different density is decellerated in the post-shock region of a shock in an electromagnetic shock tube (A.M. Vasilenko et al., ibid.), are presented. Direct compressibility effects on the RT growth are shown to be negligible in the former. Various effects of the expansion of the gases in the region of the interface on the RT growth rates are investigated for the latter experiment, both analytically and with 1D simulations. These effects are found to be insufficient to reconcile the growth rates observed in the Vasilenko et al. experiments with some other experimental and simulation results.

RAYLEIGH-TAYLOR EVOLUTION IS OF WIDE INTEREST

- Nonlinear Rayleigh-Taylor evolution arises in
  - astrophysics - collapsed stars, supernovae
  - performance degradation of inertial fusion capsules
- Rayleigh-Taylor evolution is of general basic interest as a paradigm for phenomena in
  - atmospheric and space sciences
  - magnetic fusion
  - combustion

High-Resolution 3D PPM simulations of Rayleigh-Taylor instability give the following results.

- Lower growth rates (α) than experiments and many other simulations.
- α increases with Navier-Stokes viscosity ν.
- α is insensitive to changes in system size and spatial scale of initial perturbations.
- There appears to be a single large scale of the evolution; i.e.,
  - amplitudes from concentration thresholds and profile overlap, and perpendicular integral correlation length scales agree for most cases.
- Cases with very different a have very similar atomic mix fraction profiles.

THE PPM CODE IS AN ESTABLISHED HYDRO CODE USED EXTENSIVELY IN ASTROPHYSICS

- PPM = Piecewise Parabolic Method
  - Godunov-type code
  - Uses piecewise parabolic interpolation
  - Woodward-Porter version
    - Lagrange + remap to Euler mesh
    - 3D; Directionally split
    - Has Navier-Stokes dissipation
- Robust for high-Mach-number flows
- Runs well on large parallel computers

Baker, Meiron, and Orszag RT cases were used as validation tests of PPM.

- G.H. Baker, D.I. Meiron, and S.A. Orszag, Phys. Fluids 23, 1485 (1980).
- A=0.33 case.
- PPM and Baker et al. agree well for bubble and spike amplitudes.
- Qualitative appearance of interface is similar, apart from discrete polygon nature of Baker et al. results, and slightly more roll up and some evidence of residual secondary Kelvin-Helmholtz notches in the PPM case.

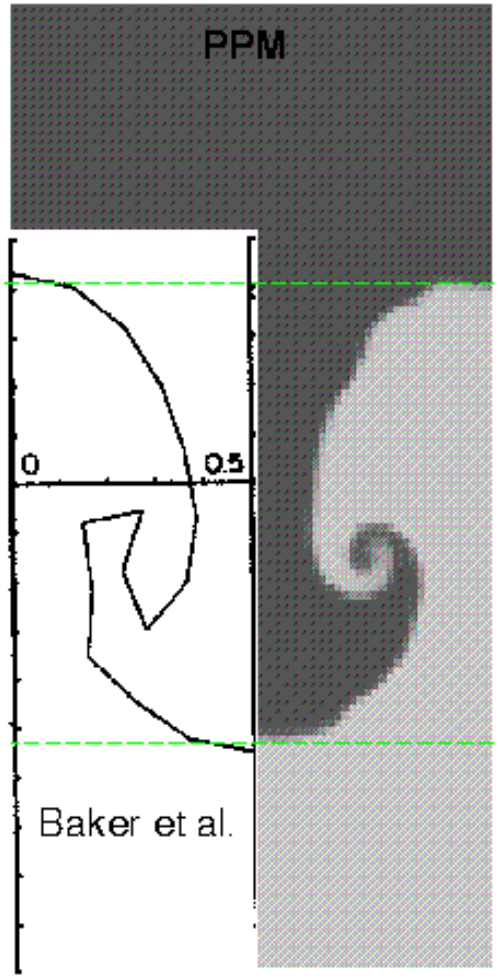

For A=0.048, PPM gives amplitudes slightly lower than Baker et al.

- Qualitative appearance of interface is similar, apart from discrete polygon nature of Baker et al. results and slightly more roll up in the PPM case.

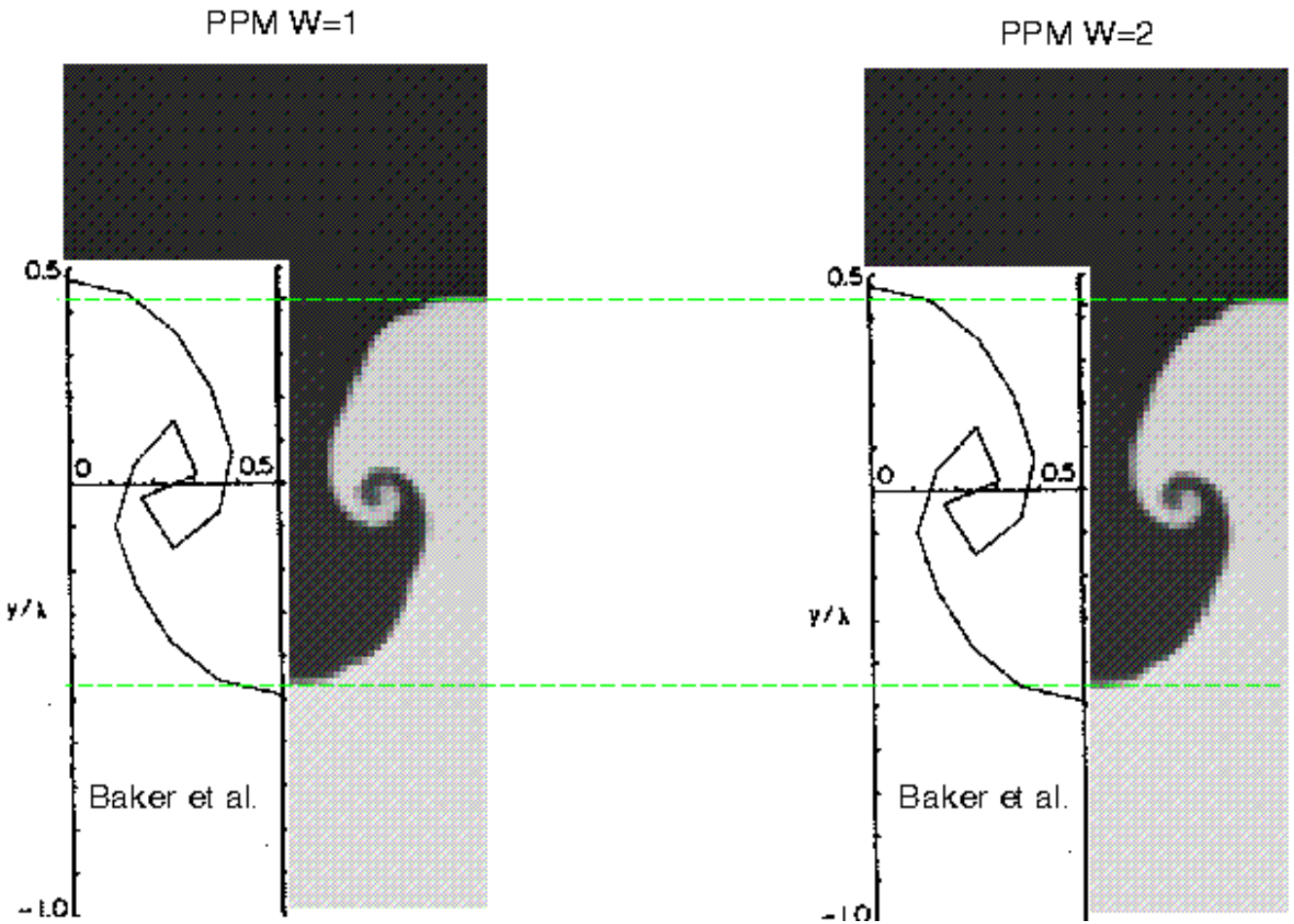

THE SETUP MOST USED HERE HAS UNIFORM TEMPERATURES ABOVE AND BELOW THE INTERFACE

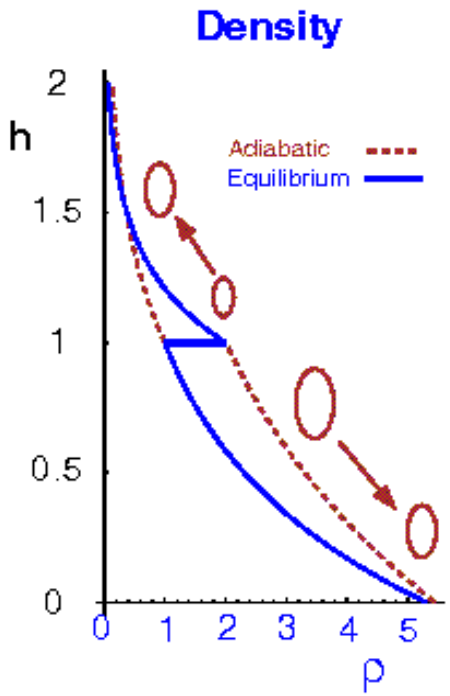

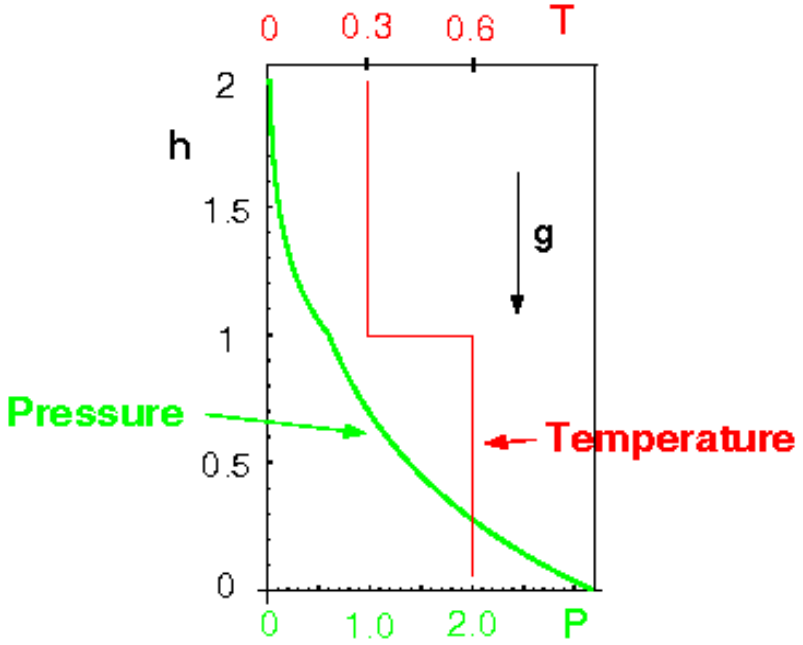

- ideal, single-γ (=5/3) gas
- density discontinuity supported by a discontinuity in the temperature or the molecular mass
- exponential density and pressure profiles above and below interface
- near-incompressible low-level initial velocity perturbations
  - multi-mode – quasi-Gaussian with a specified peak k

A RANGE OF RESOLUTIONS, NAVIER-STOKES DISSIPATION VALUES, AND SYSTEM SIZES IN THE NEAR-INCOMPRESSIBLE REGIME WERE USED

- ρ_h/ρ_l = 2-3 (A=1/3-1/2)
- $\nu=\kappa$=0, 1/6.5, 1/2.3 $g\Delta^{3/2}$
- L=0.02, 0.04, 0.08 c^2/g
- 256^3, $256^2\times512$, 512^3
- Low-level initial velocity perturbations
- Peak wavenumber varied

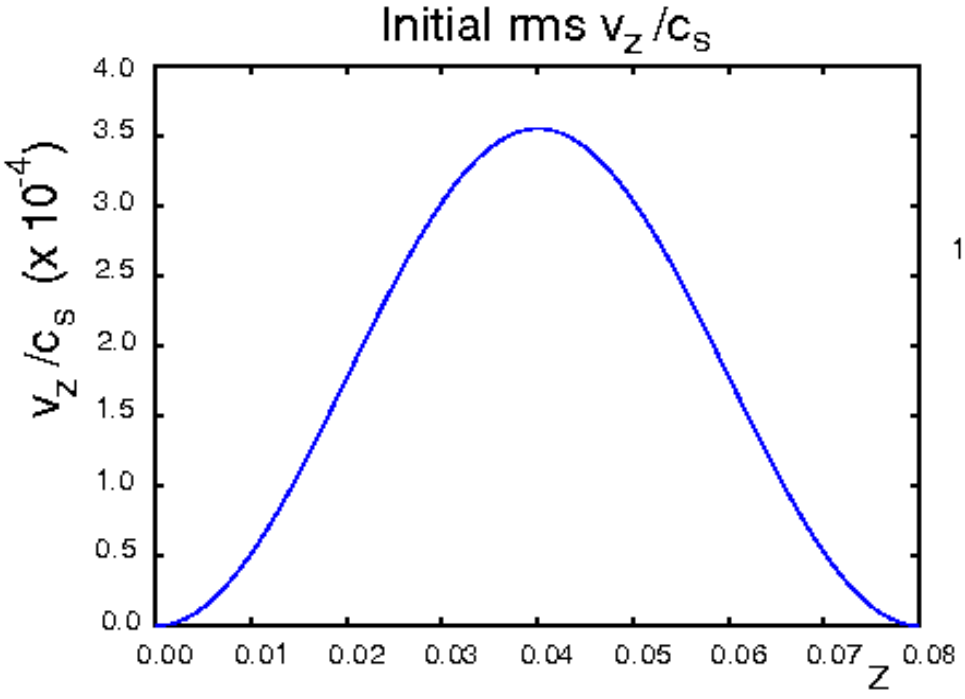

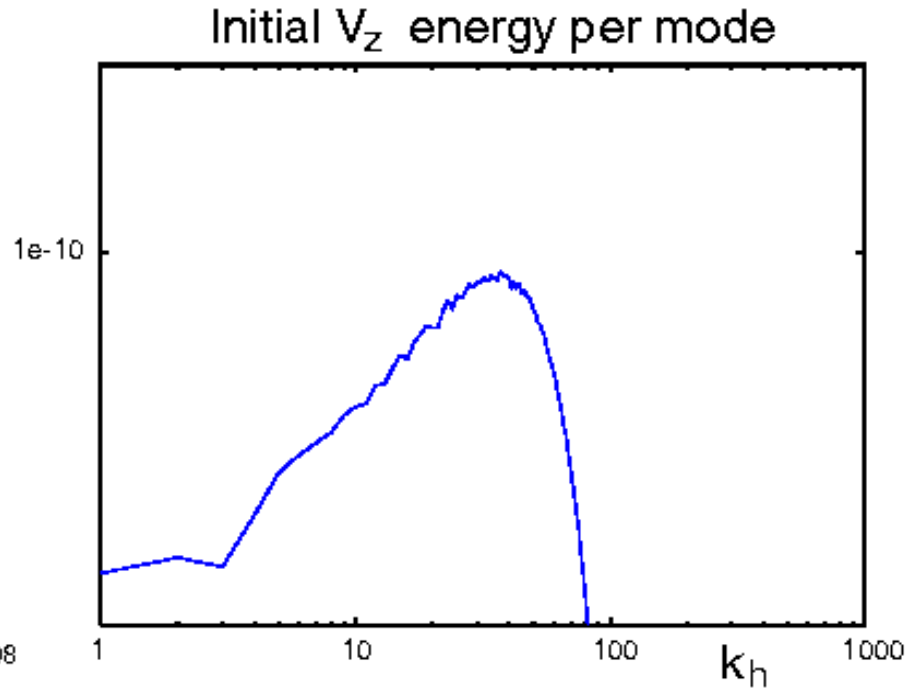

PPM AND PPM+NS SIMULATIONS OF RAYLEIGH-TAYLOR EVOLUTION SHOW BUBBLES, SPIKES, AND ROBUST "BUBBLE MERGER"

t=0.1 c/g

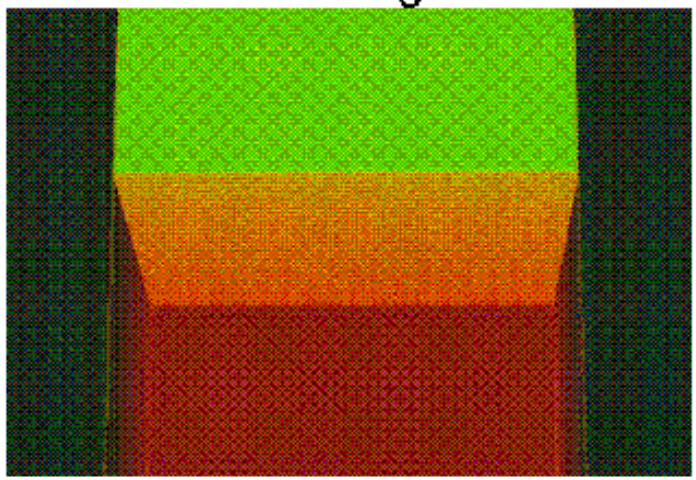

t=0.35 c/g

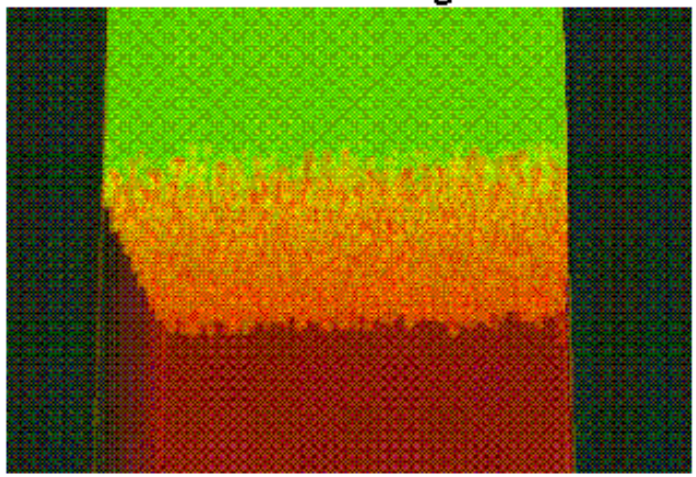

t=1.125 c/g

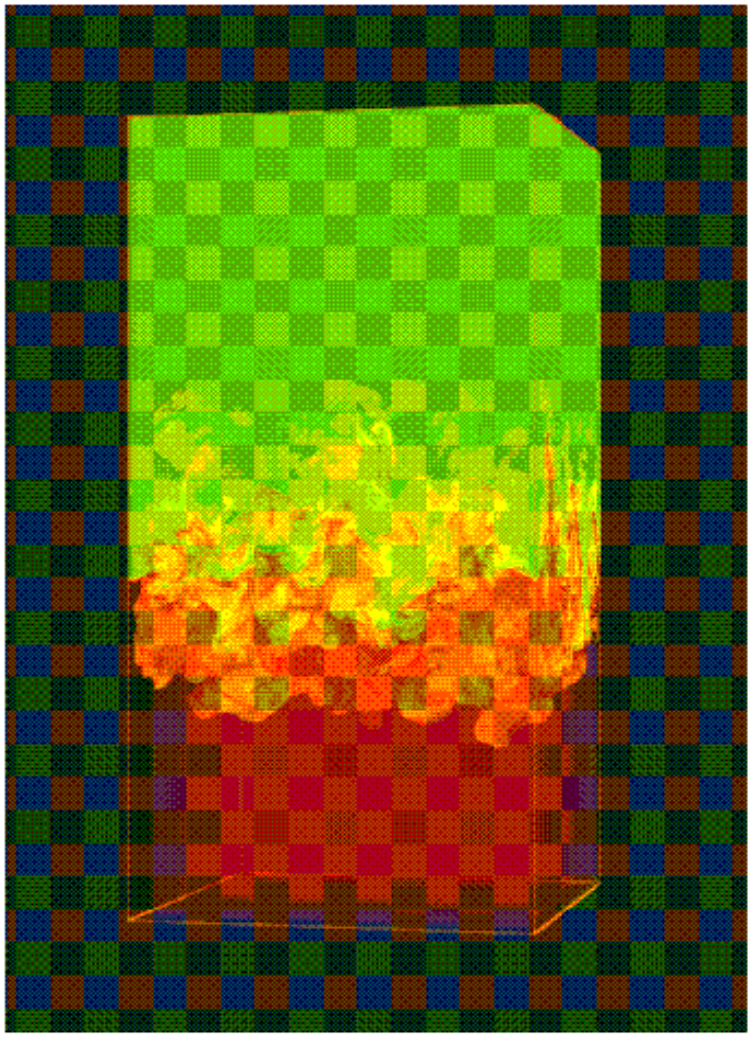

THE LATE-TIME EVOLUTION OF INCOMPRESSIBLE MULTIMODE RAYLEIGH-TAYLOR LAYERS IS THOUGHT TO BE SELF-SIMILAR

- All spatial scales l grow as $l(t) = F(f)\cdot g\cdot(t-t_0)^2$, where f is the density ratio, and t is a "movable" time origin.

- Common characterization:
  - bubble heights have $F(f) = \alpha\cdot A$
  - $A = (f-1)/(f+1)$ is the "Atwood number"
  - α_{bubble} is a key parameter for comparisons.

- l_{bubble} is obtained as the height at which the volume fraction of fluid originating below the interface is 1%.

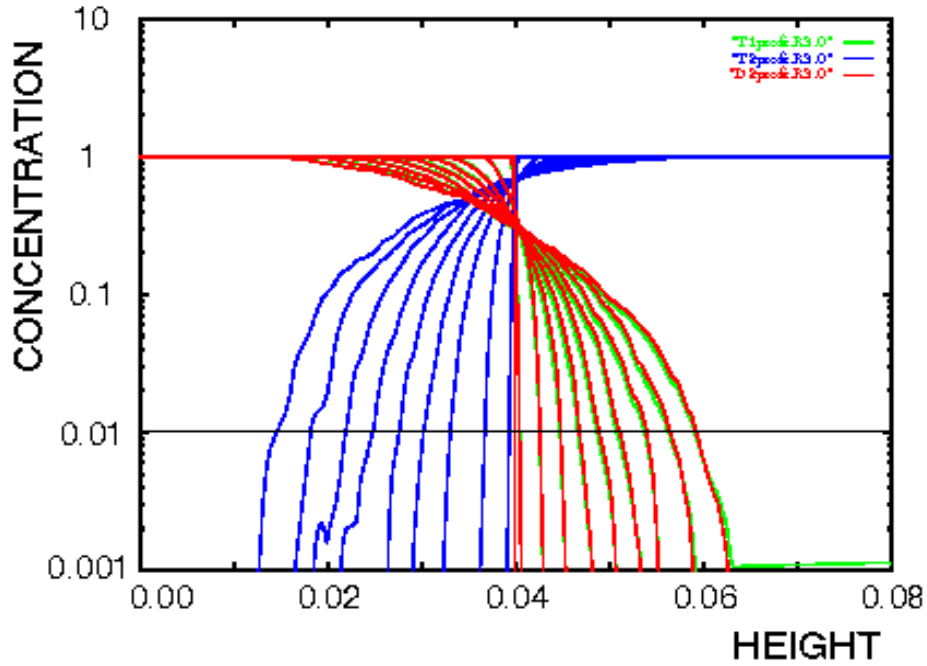

AT LATE TIME (>0.4), PPM-NS CALCULATIONS ARE IN THE t^2 ASYMPTOTIC REGIME

- α is sensitive to the criterion for determining the envelope of the mixing layer.

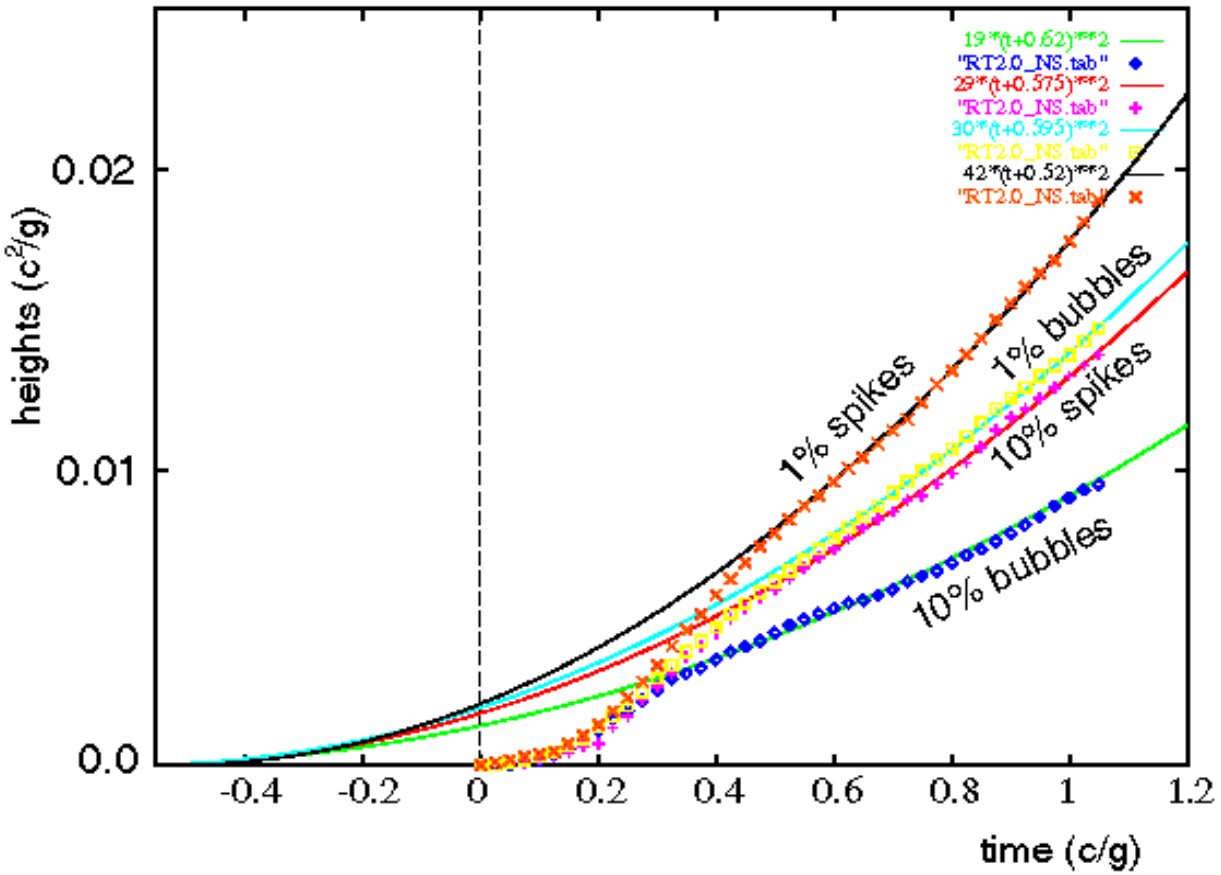

3D PPM SIMULATIONS GIVE LOWER VALUES OF α_b THAN EXPERIMENTS AND OTHER CODES

Code/Exp.	Author	A	Resolution	$y^{\frac{1}{2}}\Delta^{\frac{3}{2}}/\nu$	α_b
Turmoil	Youngs	0.50	$\leq 1025 \times 512^2$	∞ Van Leer	0.025–0.028
Turmoil	Youngs	0.20	240×160^2	∞	0.027
Turmoil	Youngs	0.90	240×160^2	∞	0.029
PPM-NS		0.33–0.5	256^3–512^3	2.3–18.4	0.012–0.026
PPM		0.33	256^3	∞ - PPM	0.011–0.013
rocket	Read	0.23	na		0.06
LEM	Dimonte	0.22	na		0.06

- References:
  - Simulations by D.L. Youngs [Laser and Particle Beams 12, 725 (1994)].
  - Experiments by K.I. Read [Physica D 12, 45 (1984).], G. Dimonte et al., [Phys. Rev. E54 3740 (1996).]

α_b in PPM+NS simulations increases with ν

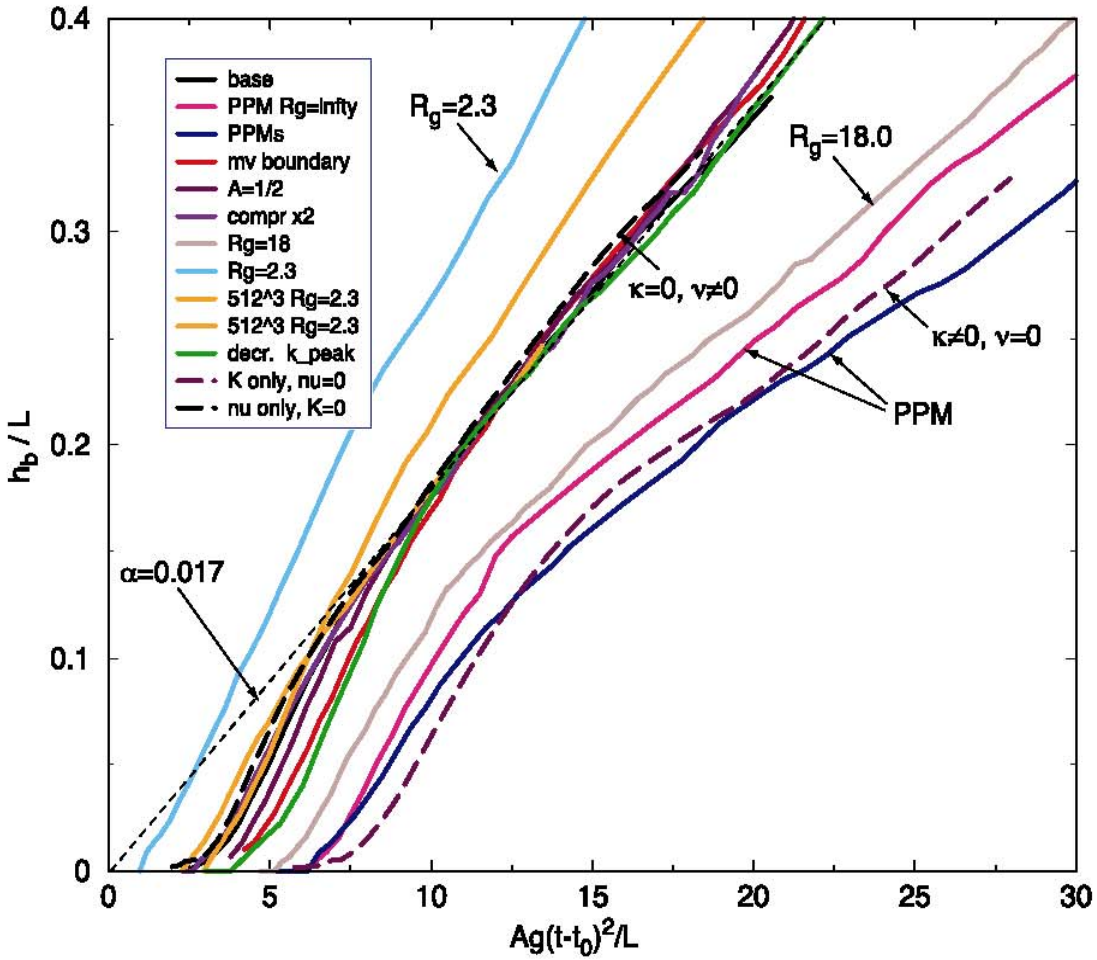

α_b is insensitive to
- boundary position
- A
- compressibility
- k_h of IC spectrum

CHANGING THE BOX SIZE AND A DOES NOT CHANGE α_b in 3D PPM SIMULATIONS

Model	Comment	A	Resolution	$g^{\frac{1}{2}}\Delta^{\frac{3}{2}}/\nu$	α_b
PPM-NS		0.33	256^3, $k_p - 32$	6.5	0.018
PPM-NS	incr. L_z	0.33	$256^2 \times 512$	6.5	0.018
PPM-NS	change A	0.5	$256^3 \times 512$	6.5	0.018
PPM-NS	lower k_p	0.33	256^3, $k_p - 16$	6.5	0.018
PPM-NS	$L_z - 0.08$	0.33	256^3	6.5	0.018
PPM-NS	incr. ν, κ	0.33	256^3	2.3	0.028
PPM-NS	decr. ν, κ	0.33	256^3	18.4	0.012
PPM-NS	incr. res.	0.33	512^3	2.3	0.022 *
PPM	no NS	0.33	256^3, $k_p - 32$	∞ - PPM	0.0125
PPM		0.33	256^3, $k_p - 64$	∞ - PPM	0.011

- Increasing (decreasing) Navier-Stokes dissipation raises (lowers) α_b.
- Increasing compressibility has no effect on α_b.
- Run with lower initial $k_p(=16)$ - α unaffected.

PPM simulations of RT show a single large scale.

- In RT studies, the large scales commonly diagnosed are measures of the vertical scale, e.g.,
  - amplitudes from threshold concentration levels,
  - integral measures of overlap of concentration profiles.
- In much of fluid dynamics “integral” correlation length scales are used.
  - Integral scales measured at the position the interface would have in the absence of RT instability provide measures of the transverse scale.
- In high resolution 3D multimode PPM simulations of RT, these scales usually maintain a proportionality with ratios independent of time.

Bubble and spike amplitudes and integral scales track if NS dissipation is used.

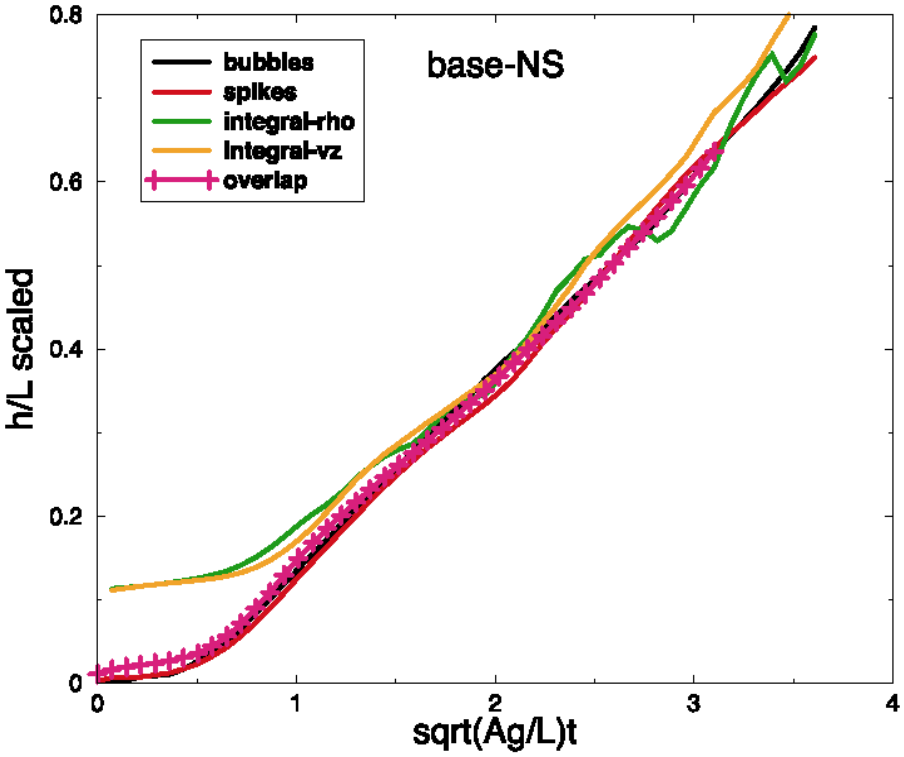

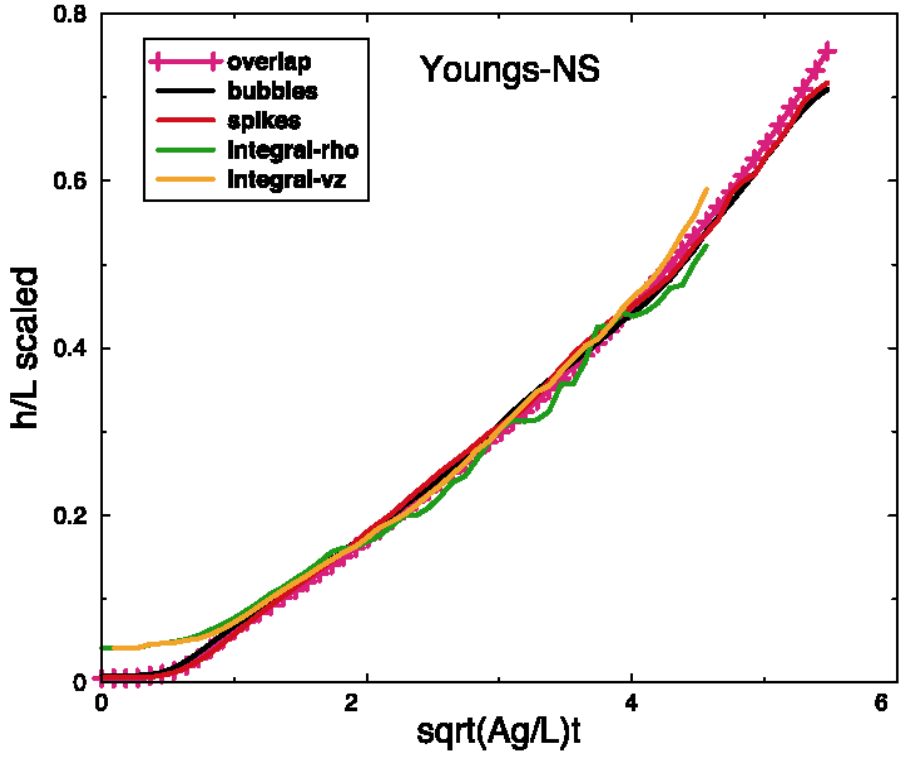

Perpendicular integral scales track vertical scales less well for pure PPM.

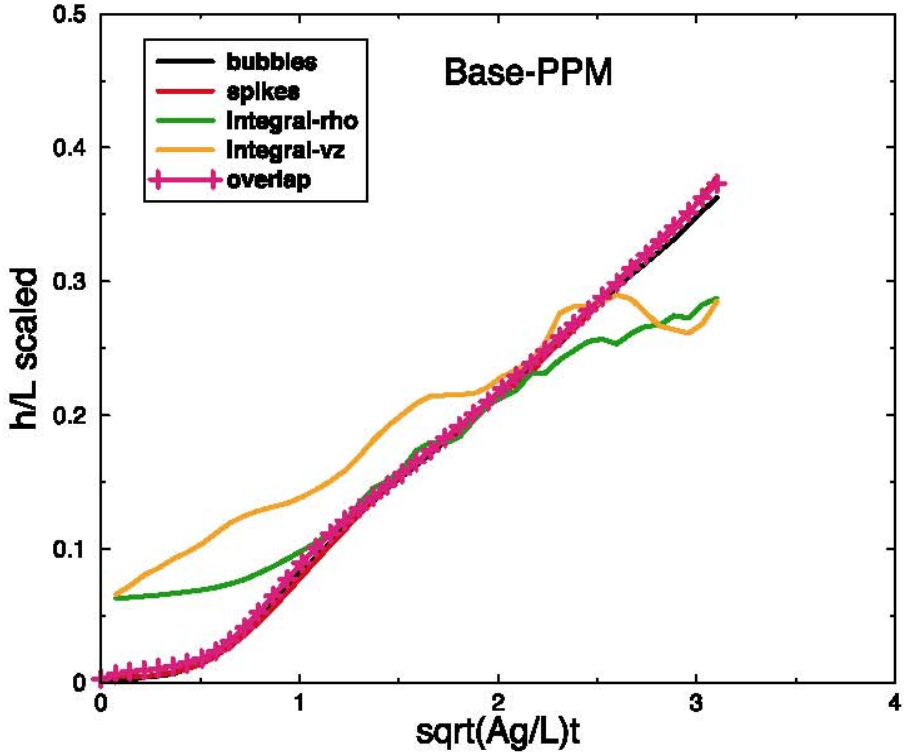

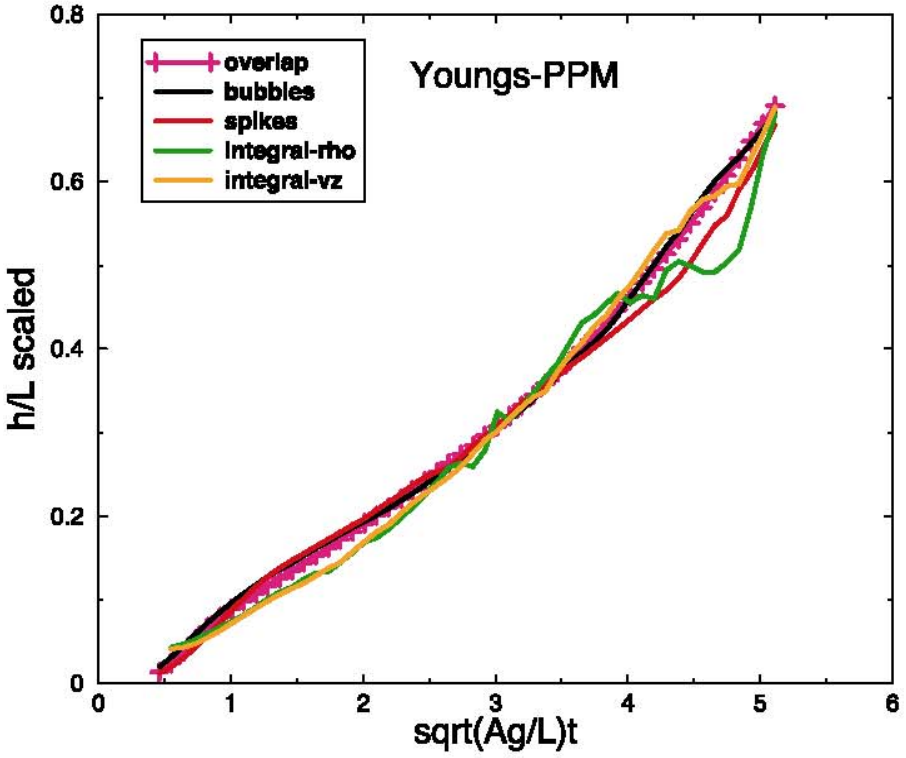

A hypothesis that low α's are associated with hight atomic mix fraction was tested.

- If the mixing fraction is large, bubbles and spikes are impure and experience small buoyancy relative to the surrounding fluid.
  - This might be expected to result in low growth rates.

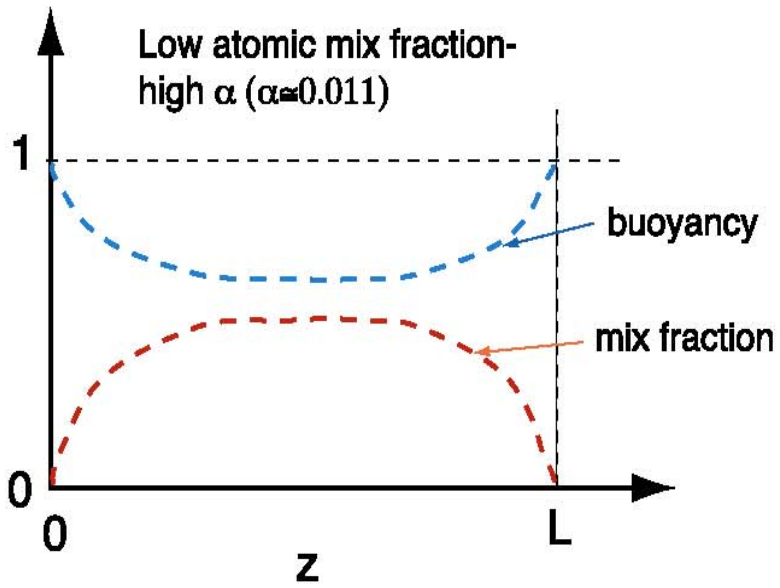

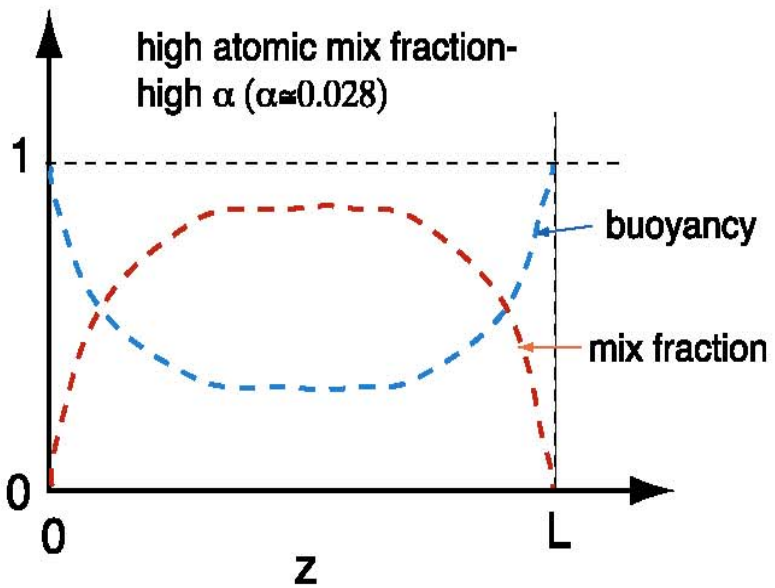

Cases with very different α show very similar atomic mix fraction profiles.

- PPM and R_g=6.5 have similar mix fraction profiles, different α (α_b=0.013, 0.018).
- R_g=2.3 has slightly lower mix fraction, highest α (α_b=0. 028).

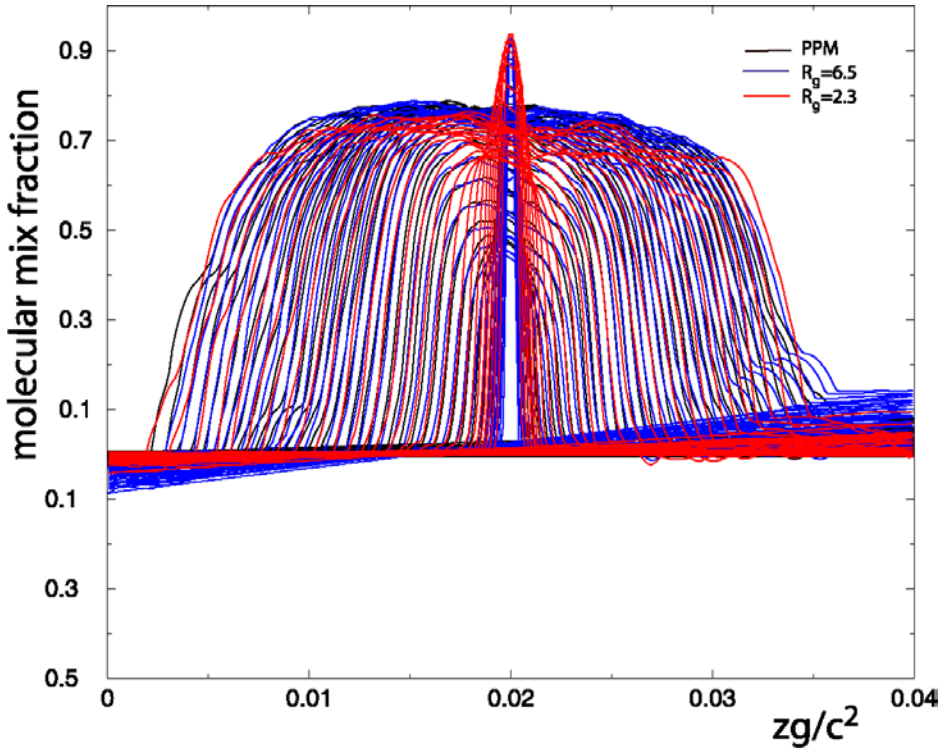

Summary of Results From High Resolution 3D PPM Simulations of Rayleigh-Taylor Instability Evolution

- Lower growth rates (α) than experiments and many other simulations.
- α increases with Navier-Stokes viscosity ν.
- α is insensitive to changes in system size and spatial scale of initial perturbations.
- There appears to be a single large scale of the evolution; i.e.,
  - amplitudes from concentration thresholds and profile overlap, and perpendicular integral correlation length scales agree for most cases.
- Cases with very different α have very similar atomic mix fraction profiles.
- Demonstrated that simulations are in a regime where compressibility is negligible.

The experiments by E.E. Meshkov and N.V. Nevmerzhitsky were reexamined because they appeared to give large values of α and an apparent increase of α with acceleration.

- Rayleigh-Taylor experiment (3rd. IWPCTM, France, 7/91.)

- Water accelerated by compressed air or Helium

- Atwood number A≅1

- Membrane breaks; plywood plate detaches; water and plate accelerated downwards by compressed air

- Authors conclude that α_{bubble} increases with p_c

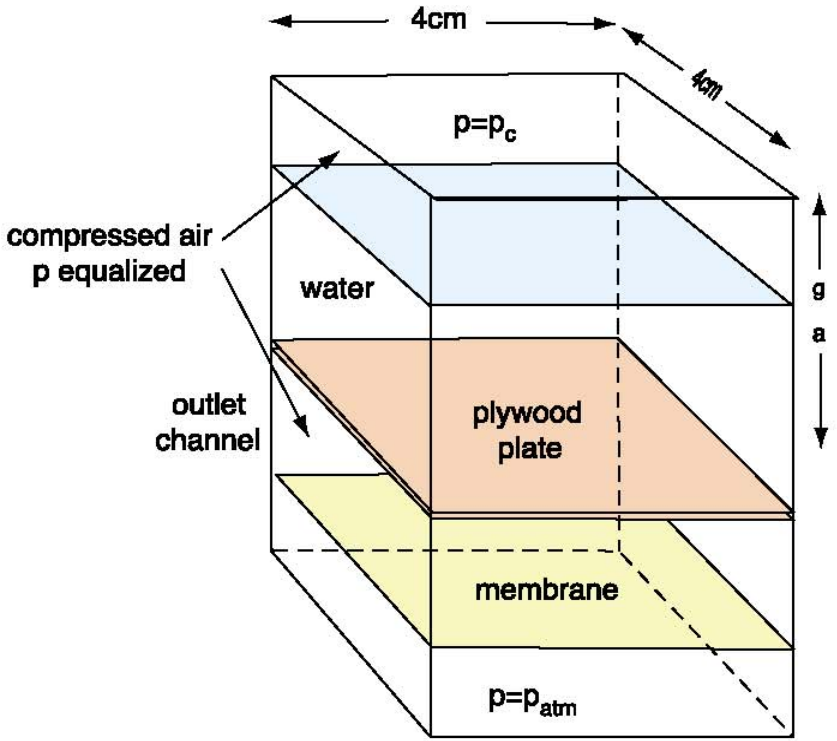

The results shown in the Meshkov-Nevmerzhitsky `91 IWPCTM paper do not demonstrate a systematic increase in α due to compressibility.

- Data shown for expts #422 and #446.
- Different curve fitting to #422 data can revise α_b down slightly from 0.128 to ≈0.1.
- α_b for #446 has large uncertainty.
- Compressibility effects are highest, but negligible, in #422.

Meshkov et al., Expt. 422

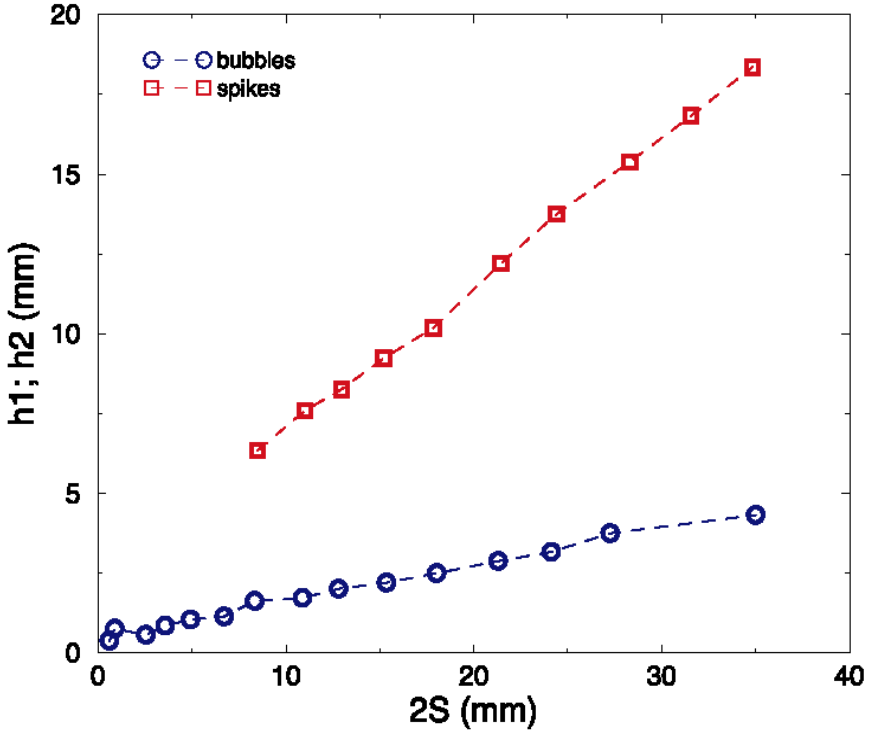

Meshkov et al., Expt. 446

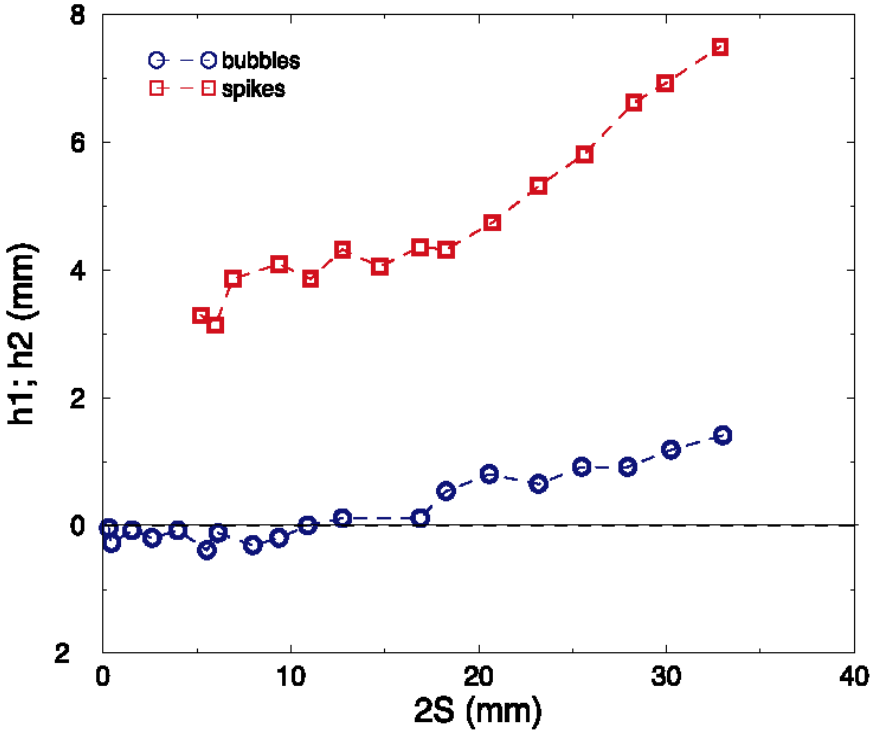

Compressibility is negligible in Meshkov - Nevmerzhitsky experiment #422.

- Subsonic
  - $M_{bubbles} \leq 0.04$, $M_{spikes} \leq 0.13$.
- Bubble expansion due to change in relative pressure small
  - $\delta l_{exp}/l \leq 0.03$ for isolated bubble
  - $\delta l_{exp}/l$ negligible for open-cell bubble structure
- Change in drag due to bubble expansion results in < 2% change in bubble height.

Conclusions on Meshkov - Nevmerzhitsky Experiments

- Expt. #422 has higher α_b than experiments by Read and by Dimonte and Schneider (but has higher density ratio).
- Difference not explained by compressibility
  - more likely connected with initial conditions.
- For the other experiments, α_b is highly uncertain (e.g., #446) or data is insufficient to demonstrate a trend.

The experiments of Vasilenko et al. were reexamined because α's were found that were much larger than in other experiments and simulations.

- Miscible (gas) Rayleigh-Taylor experiment
- S_c ($\equiv \nu/D$) = $O(1)$ (>>1 for liquids)
- $W = \alpha A g t^2$; $(\alpha = \alpha_{bubble} + \alpha_{spike})$
- α = 0.29 - 0.34, (for ρ_2/ρ_1 = 1.4 - 20)
- Conflict with other data:
  - experiment: $\alpha_{bubble} \approx 0.06$, $\alpha_{spike}/\alpha_{bubble} \approx 1+A$
  - simulation: $\alpha_{bubble} \approx 0.02$ - 0.06

Experiment by A.M. Vasilenko, V.I. Olhovskaya, O.V. Buryakov and V.G. Yakovlev

- Rayleigh-Taylor experiment
  (3rd. IWPCTM, France, 7/91.)

- Electromagnetic shock tube

- Impulsive shock with rarefaction passing through
  3 noble gases (e.g., He-Ar-He, He-Kr-He, He-Xe-Kr)

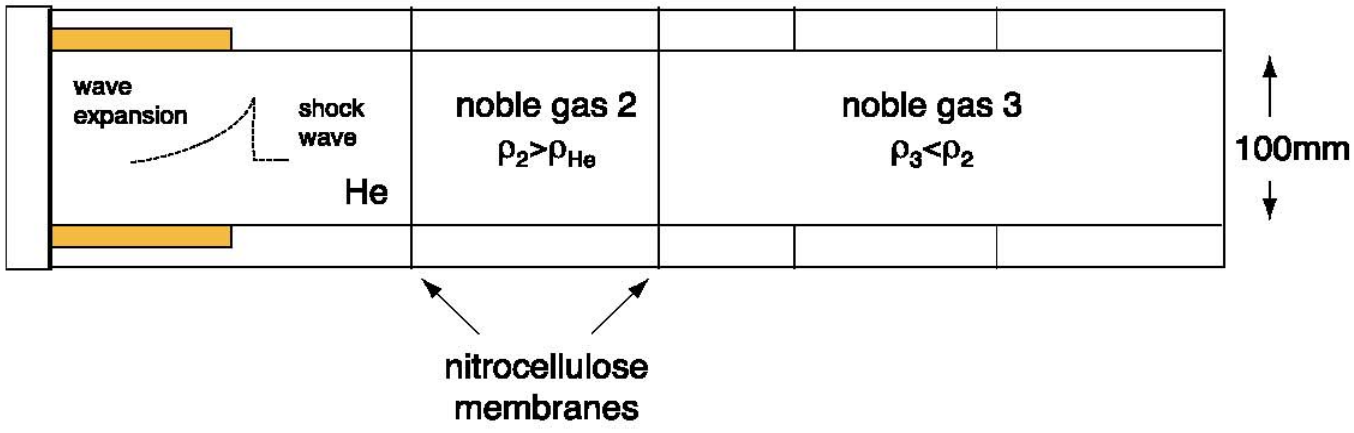

Expansion behind the shock front does not directly account for differences in α.

- $A<<1$ - analytical estimate of expansion effect using 1D Sedov wave based model

- General A : 1D HAMR computations show that propagation of a Sedov wave through light-heavy-light gases can be modeled as a shift in origin of Sedov wave.
  - Same analysis applies for bounds on expansion effect.

- Analysis by Zhou and Dimits (Zhou et. al, this meeting) finds that experiments do not reach turbulence transition.
  - Expect significant influence of initial conditions.

Effect of expansion on layer width for A<<1

- Approximate shock/rarefaction as 1D Sedov wave.
- $u \approx u_0 \xi/\xi_0$; $\xi \equiv r[\rho_0/(E\,t^2)]^{1/(2+d)}$ (supported by 1D simulations); $r_0(t) \equiv$ shock position; $u_0 \cong CV_s$; $C \cong (\gamma-1)/(\gamma+1)$; $V_s \equiv$ shock speed.
- Then $u \approx 2C/(2+d)(r/t)$ for $0 \le r \le r_0$
- Define $r_1(t) \equiv$ Lagrangian trajectory of fluid element that coincides with shock at $t = t_1$ [i.e.,$r_1(t_1) = r_0(t_1)$].
- Then $r_1(t)/r_0(t_1) = (t/t_1)^{2C/(2+d)}$

Effect of expansion for A<<1

- Define decceleration path:
  - $R_a(t) \equiv u_0 .(t- t_1)-[r_1(t) - r_1(t_1)]$.
- Suppose layer width $h \approx \alpha R_a(t)$.
- Contribution of expansion to h' is $h'_{exp} = h \, \partial u / \partial r$.
- Then h'_{exp} / h' obtainable analytically.

RT growth enhancement by expansion is less than ≈1.3

- $h'_{exp}/h' \leq 0.2 \Rightarrow$ less than factor 1.3 direct enhancement of layer width by expansion.

- Indirect effects? - need 2D or 3D simulation.

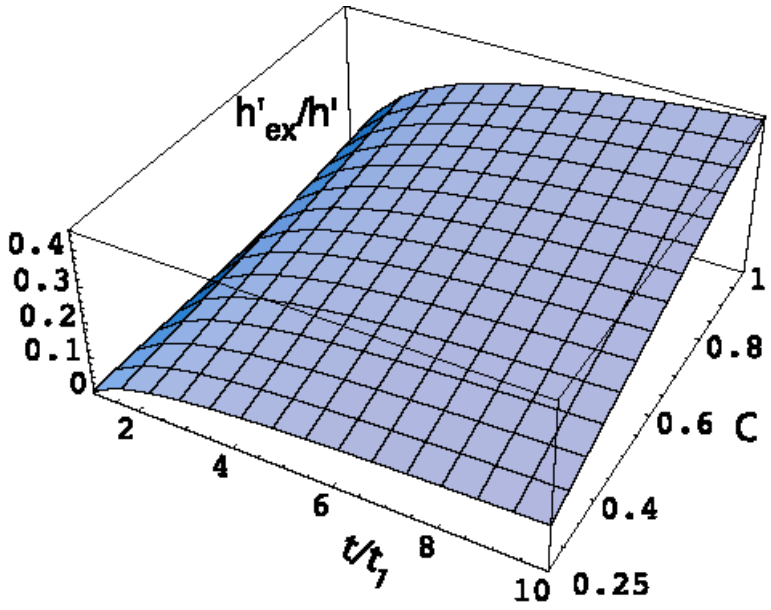

1D HAMR simulations support the application of the A<<1 analytical model to cases where A<<1 does not hold.

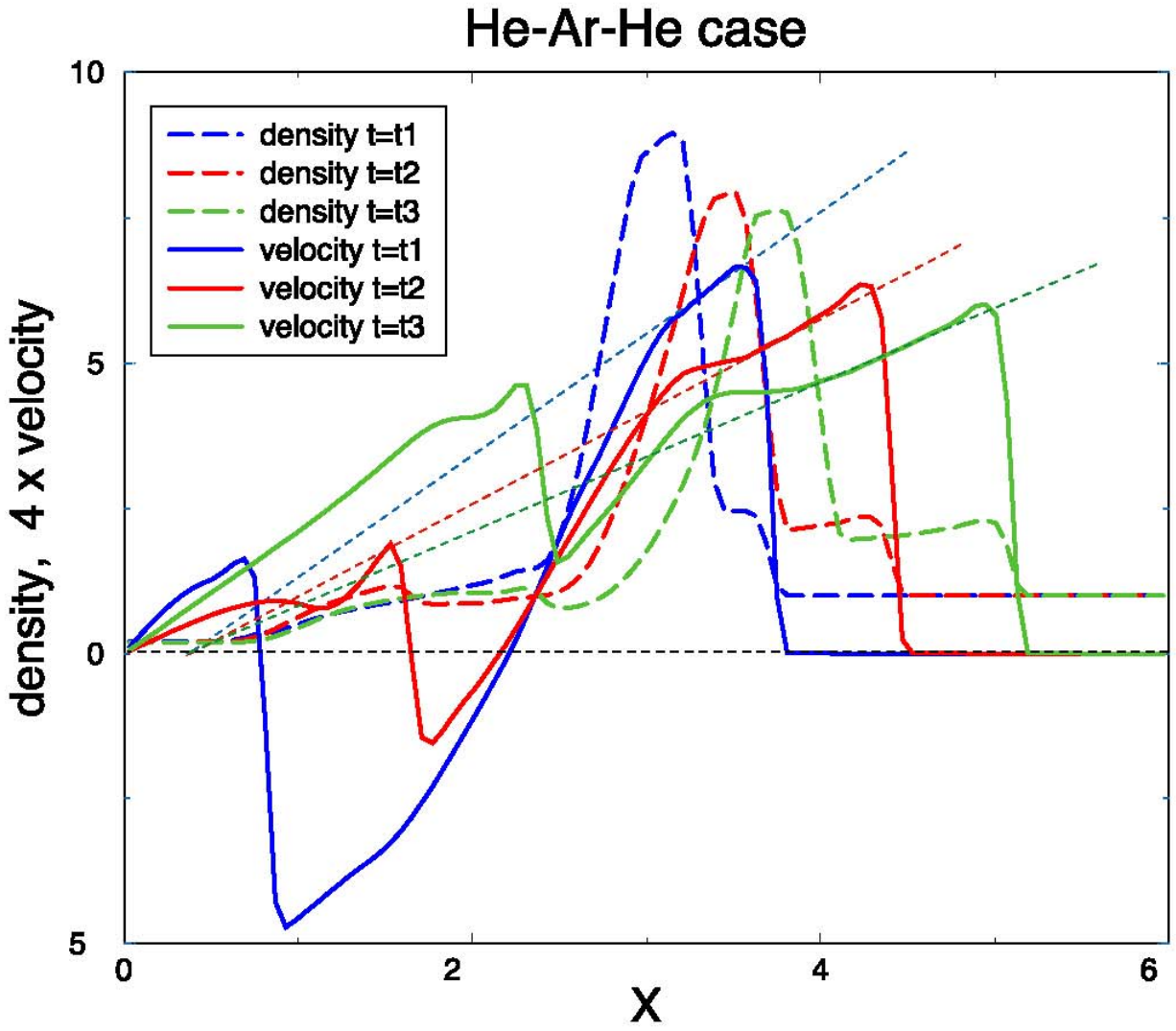

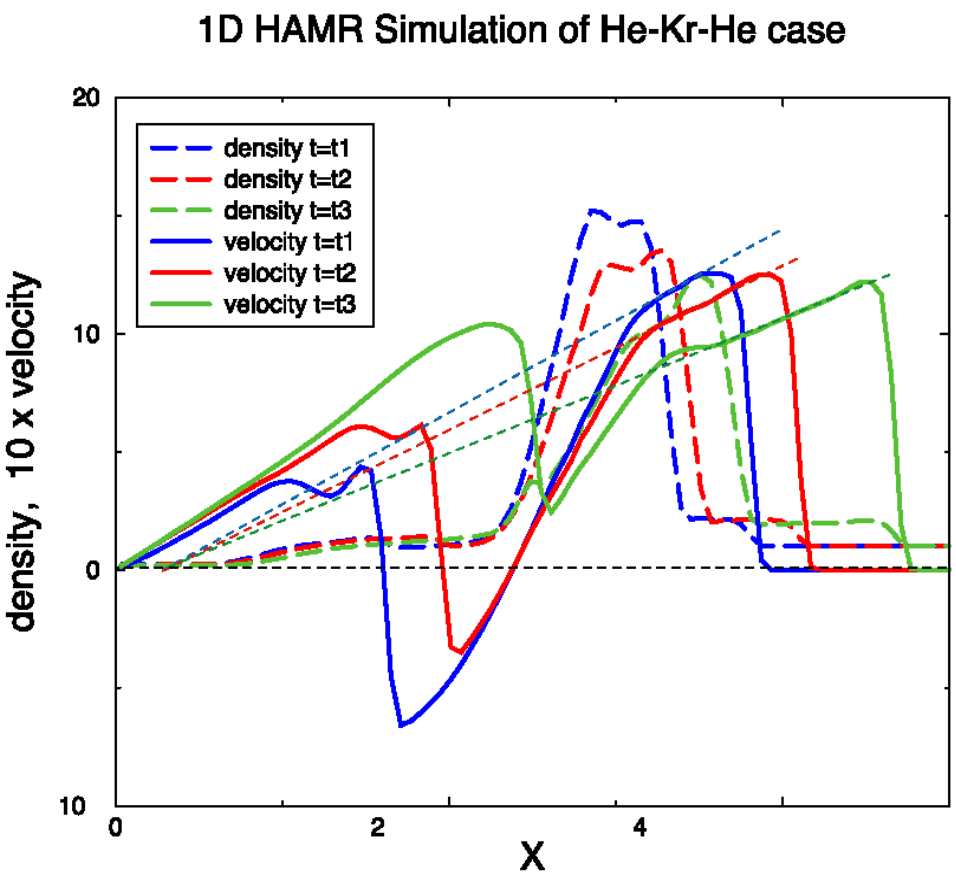
1D HAMR Simulation of He-Kr-He case
density t=t1
density t=t2
density t=t3
velocity t=t1
velocity t=t2
velocity t=t3
density, 10 x velocity
X
20
10
0
10
0
2
4

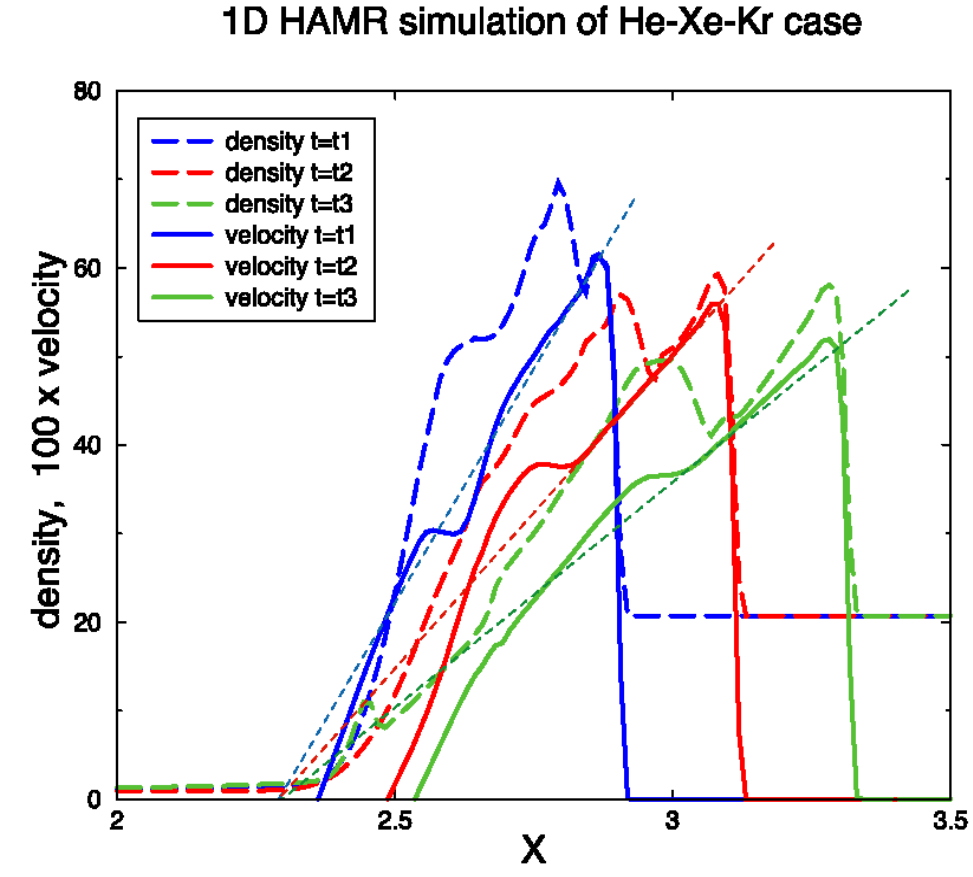
1D HAMR simulation of He-Xe-Kr case
density t=t1
density t=t2
density t=t3
velocity t=t1
velocity t=t2
velocity t=t3
density, 100 x velocity
X
80
60
40
20
0
2
2.5
3
3.5

Summary an Conclusions Concerning Experiments by Vasilenko *et al.*

- Expansion behind the shock front does not account for differences in α between Vasilenko *et al.* experiments and other results.
- Estimated effect of expansion on α using a 1D Sedov-wave based model, valid for A<<1.
- 1D HAMR computations support the extension and application of this model to cases where A<<1 does not hold.
- Turbulence-transition analysis by Zhou and Dimits (Zhou *et al.*, this meeting) suggests a significant influence of initial conditions on α as a possible explanation of the discrepancy.

Transition Stages of Rayleigh-Taylor Instability between Miscible Fluids

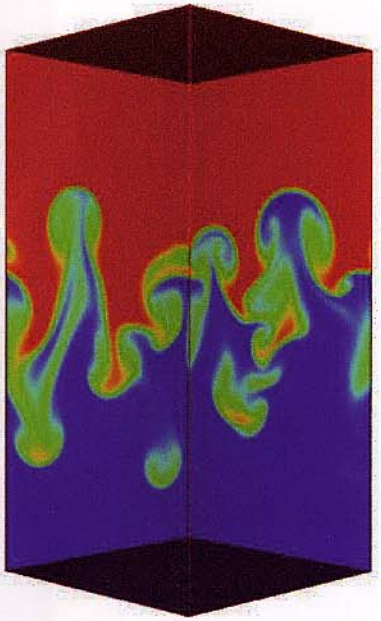

Andrew Cook

Paul Dimotakis

Trent Mattner

This work was performed under the auspices of the U.S. Department of Energy by the University of California Lawrence Livermore National Laboratory, under contract No. W-7405-Eng-48, the DOE/Caltech ASCI/ASAP subcontract B341492, and by the Air Force Office of Scientific Research Grant Nos. F49620-94-1-0353 and F49620-98-1-0052.

Overview

- Three 256x256x1024-point and one 512x512x2040-point Direct Numerical Simulations (DNS) were performed of Rayleigh-Taylor instability with different initial conditions.
- The smaller jobs executed on 128 CPU's of ASCI Blue-Pacific (IBM SP2) at LLNL. Simulation times varied from 200 to 300 machine hours.
- The larger job executed on 1024 CPU's and took roughly 50 machine days.
- Small and large simulations attained outer-scale Reynolds numbers of 3000 and 5500, respectively.
- **Mixing-zone growth exhibits an initial diffusion stage, followed by a nonlinear stage.**
- **Growth and mixing are sensitive to initial conditions for duration of simulations.**
- **For many statistics, height of mixing zone (h) is a better progress variable than time (t).**

Governing equations

$$\frac{\partial \rho}{\partial t} + u_j \frac{\partial \rho}{\partial x_j} = -\rho \frac{\partial u_j}{\partial x_j} = \frac{\rho}{\mathrm{Re}\, Sc} \frac{\partial}{\partial x_j}\left(\frac{1}{\rho}\frac{\partial \rho}{\partial x_j}\right)$$

$$\frac{\partial \rho u_i}{\partial t} + \frac{\partial \rho u_i u_j}{\partial x_j} = -\frac{\partial p}{\partial x_i} + \frac{1}{\mathrm{Re}} \frac{\partial \tau_{ij}}{\partial x_j} - \frac{\rho \delta_{i3}}{Fr^2}$$

$$\tau_{ij} = \frac{\partial u_i}{\partial x_j} + \frac{\partial u_j}{\partial x_i} - \frac{2}{3}\delta_{ij}\frac{\partial u_k}{\partial x_k}$$

$$\frac{\partial \rho Y}{\partial t} + \frac{\partial}{\partial x_j}\left(\rho u_j Y\right) = \frac{1}{\mathrm{Re}\, Sc} + \frac{\partial}{\partial x_j}\left(\rho \frac{\partial Y}{\partial x_j}\right)$$

$$X = \frac{\rho - \rho_1}{\rho_2 - \rho_1}$$

$$\rho Y = \rho_2 X$$

ρ = density

u_j = velocity vector

p = pressure

τ_{ij} = viscous stress tensor

Y = heavy fluid mass-fraction

X = heavy fluid mole-fraction

ρ_1 = density of light fluid

ρ_2 = density of heavy fluid

$\mathrm{Re} = \rho_1 l U / \mu = (2\pi l/N)^{-4/3}$

$Sc = \mu / \rho_1 D = 1$

$Fr = U/(gl)^{1/2} = 1$

N = number of x grid points

l = scaling length

U = scaling velocity

g = acceleration

Numerical method

- Spatial derivatives:
  - Spectral in x and y
  - Eighth-order compact in z
- Time integration of density equation:
  - 3rd-order, Adams-Bashforth-Moulton method
- Time integration of momentum equation:
  - (1) account for advection and diffusion
  - (2) solve Poisson equation for pressure
  - (3) add pressure and acceleration effects
- Boundary conditions:
  - periodic in x and y
  - walls in z (Neumann pressure, no through flow)

Initial conditions

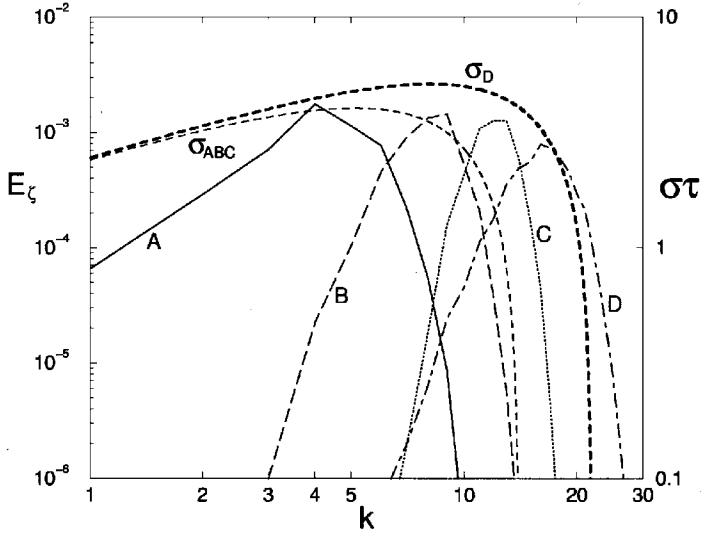

- $E_\zeta(k)$ = spectrum of initial interfacial perturbations
- k = 2-D (x-y) wavenumber
- $\sigma\tau$ = nondimensional growth rate from Linear Stability Theory (LST)
- High wavenumber perturbations are initially damped by diffusion

Time-evolution of R-T instability for DNS Case C

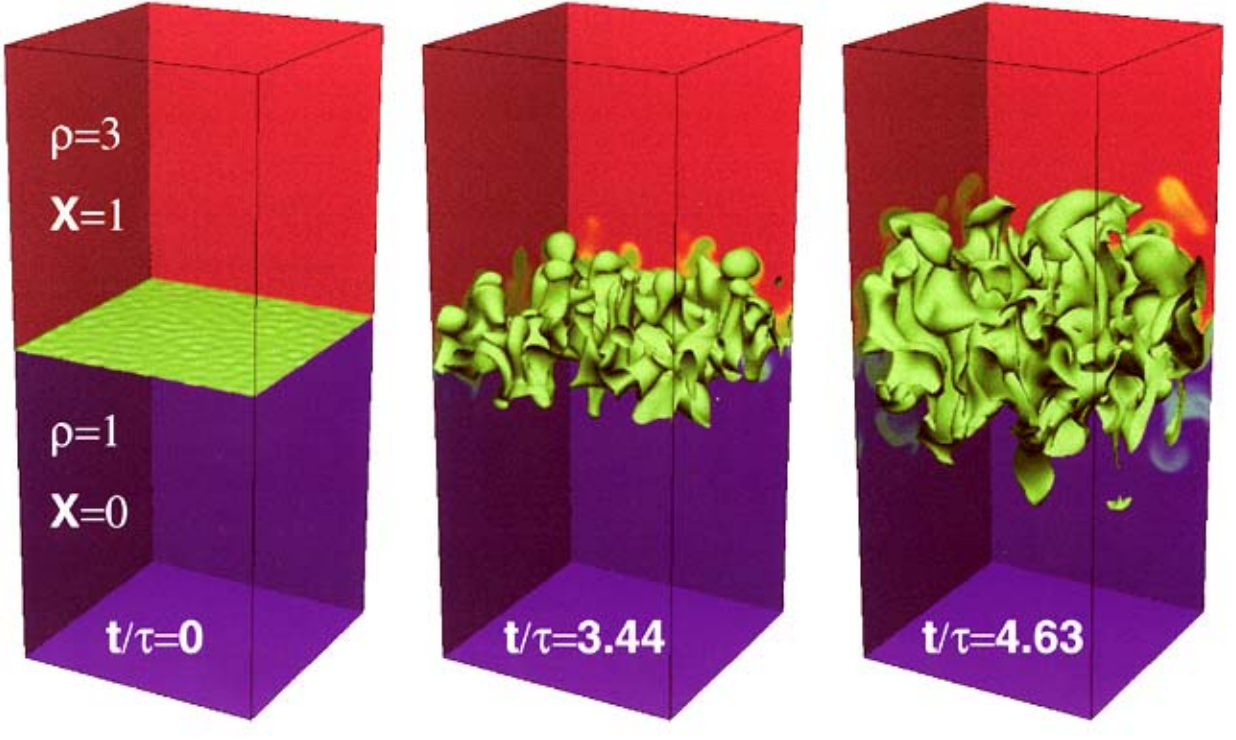

Time-evolution of horizontally-averaged mole-fraction profiles for Case C

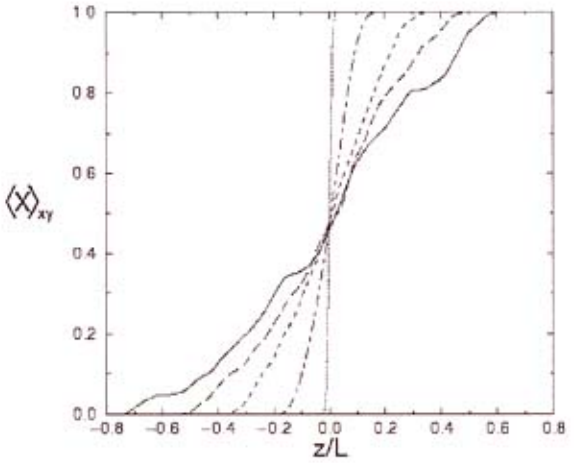

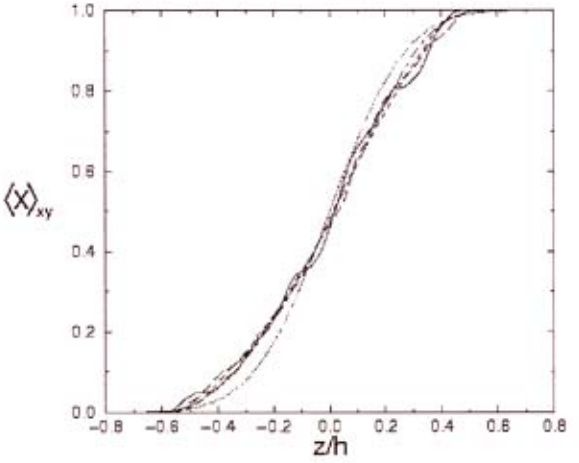

Dotted line: $t/\tau=0.0$, Short-long dashed line: $t/\tau=2.26$, Short dashed line: $t/\tau=3.40$, Long dashed line: $t/\tau=3.95$, Solid line: $t/\tau=4.52$

- Mix height h defined as range of z for which: $0.01 < X < 0.99$
- **Profiles collapse when plotted vs. z/h**

Growth rates of bubbles and spikes

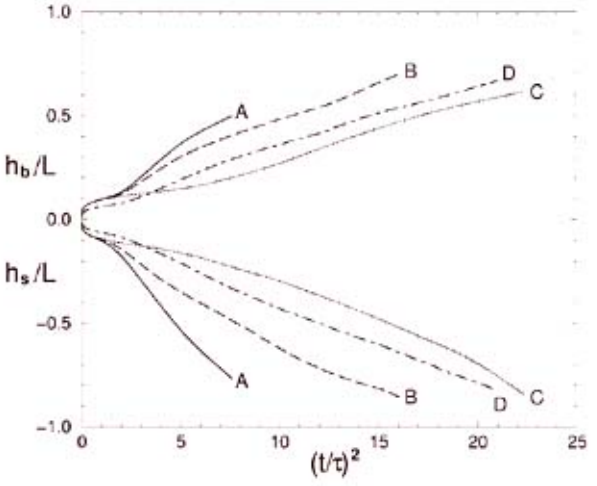

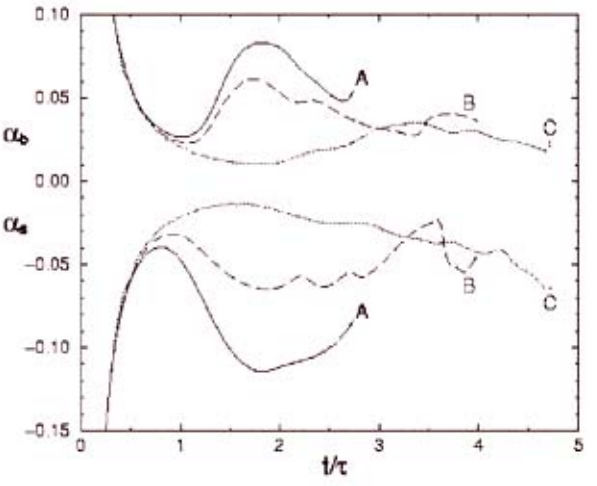

h_b = height of bubbles, h_s = height of spikes, i.e., $h = h_b - h_s$

α_b = growth coefficient of bubbles, α_s = growth coefficient of spikes, i.e., $h_i = \alpha_i A g t^2$

- **Growth rates can vary by factor of 2 depending on initial conditions**
- **α_b and α_s do not approach constant values**

Growth of mixing layer

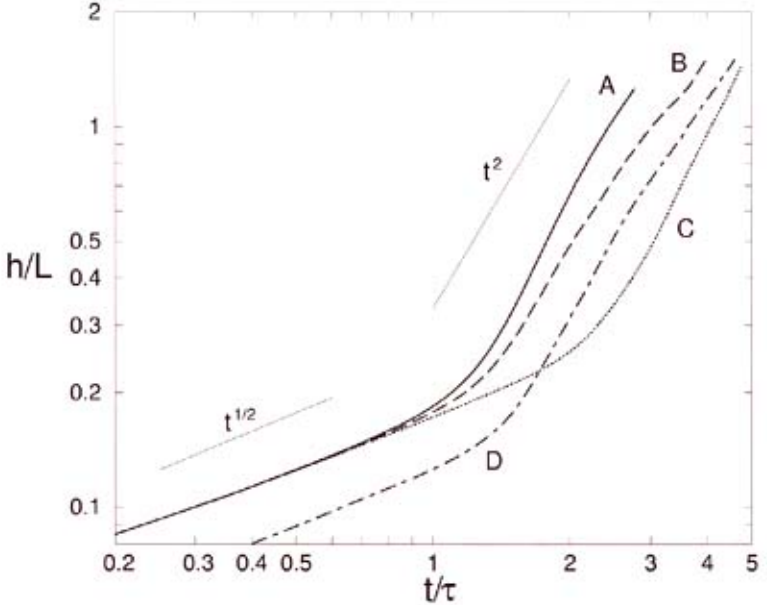

h = height of mixing layer

L = $2\pi l$ = width of flow domain

t = time

$\tau = (L/Ag)^{1/2}$

A = Atwood number

g = gravity

Early growth is diffusive, i.e., $t^{1/2}$; later, growth $\propto t^2$

Bubble merger from initial perturbations

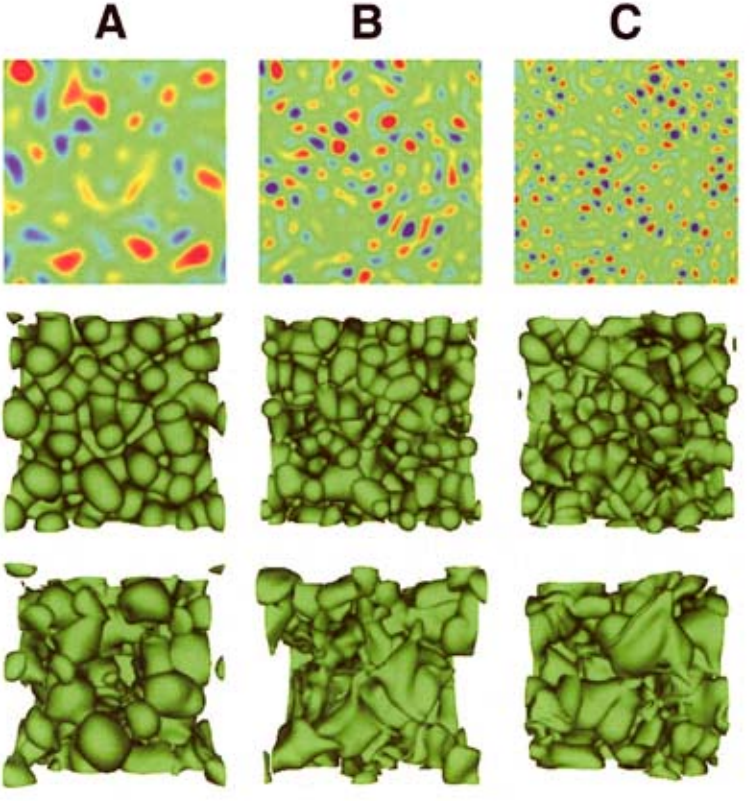

- Top Row: Initial perturbations at z = 0, blue: X = 0.35, green: X = 0.5 and red: X = 0.65
- Middle Row: X = 0.5 isosurface when h/L = 0.6
- Bottom Row: X = 0.5 isosurface when h/L = 1.25

- **Case A: bubbles rise more or less independently**
- **Case B: bubbles begin to merge when 0.6 < h/L < 1.25**
- **Case C: significant bubble merger for both h/L = 0.6 and h/L = 1.25**

Outer-scale Reynolds numbers

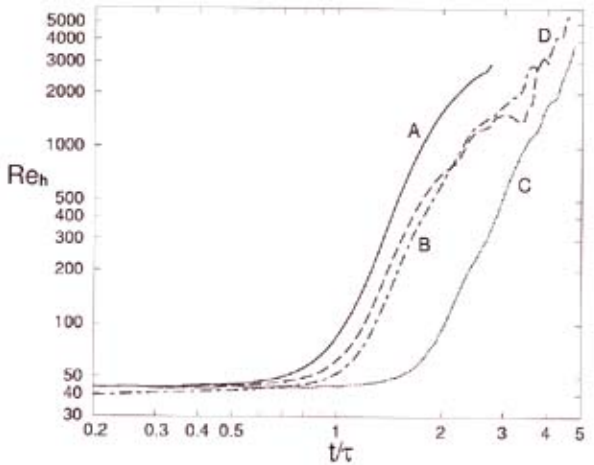

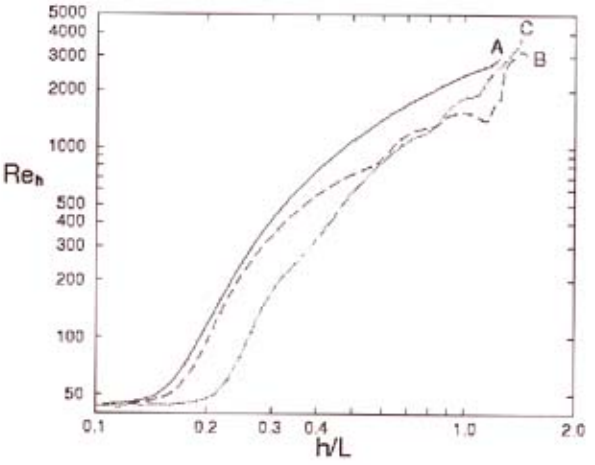

$$Re_h = \bar{\rho} h \dot{h} / \mu, \text{ where } \bar{\rho} = (\rho_1 + \rho_2)/2$$

- Cases reach outer-scale Reynolds numbers of 3000-5500.
- Improved collapse achieved by replacing t with h as progress variable.

Mixing

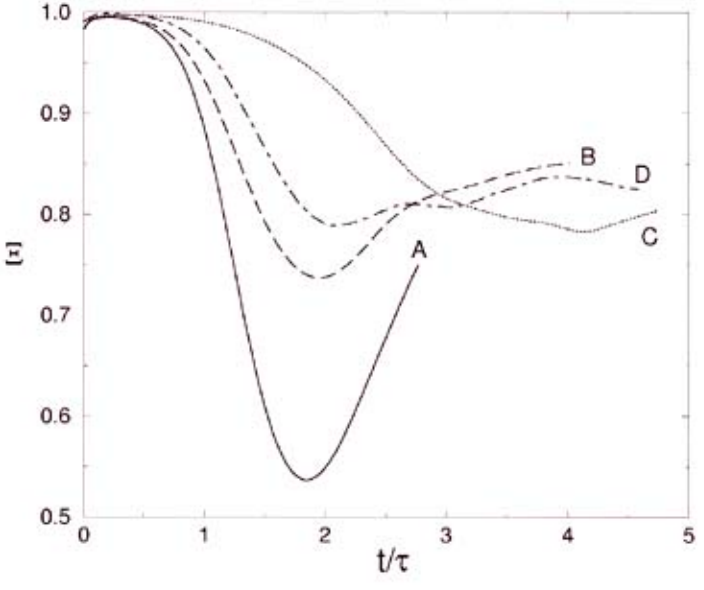

- Considering an equilibrium chemical reaction between fluids (stoichiometric mole ratio: $X_s = 1/2$), Ξ is the ratio of maximum possible product to actual product.
- $\Xi = 1$ corresponds to complete mixing within layer, whereas $\Xi = 0$ indicates no mixing (immiscible case).
- **Rates of mixing and entrainment do not come into balance within timespan of simulations.**

Spectra

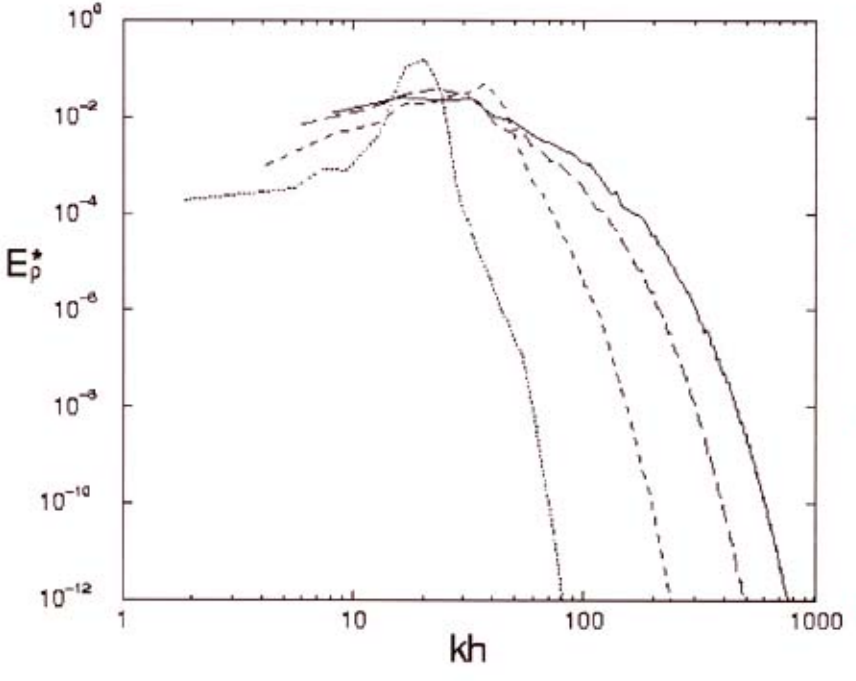

- Normalized 2-D density spectra in z = 0 plane for Case C. Lines of increasing solidity denote increasing time.
- Beginning of a collapse at low wavenumber is evident towards end of simulation.
- Low-(kh) collapse indicates large-scale structures scale with mixing zone height.
- Full spectrum is still evolving, however, due to low Reynolds number.

Taylor microscales

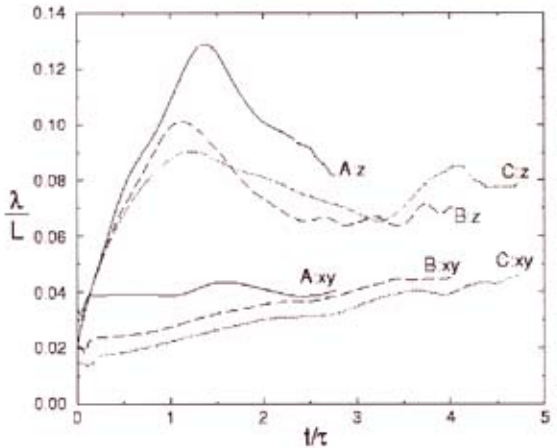

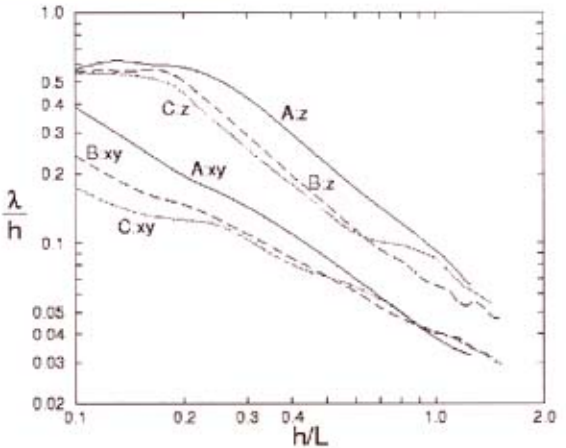

- Initial values for horizontal microscales are ranked in order of peaks of initial perturbation spectra.
- Vertical microscales grow much faster than horizontal scales due to directed body force.
- Flows exhibit strong anisotropy between horizontal and vertical microscales for duration of simulations.

Taylor Reynolds numbers

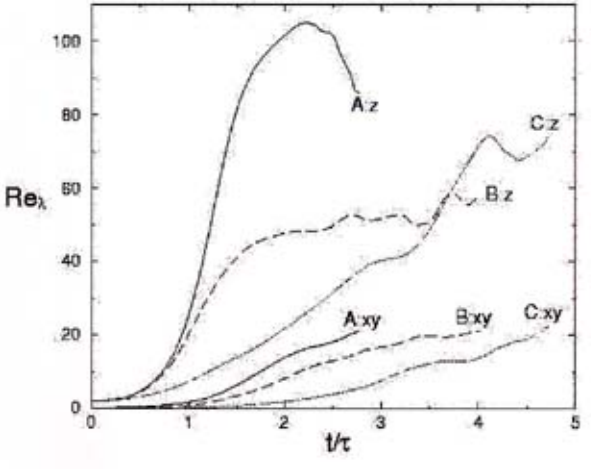

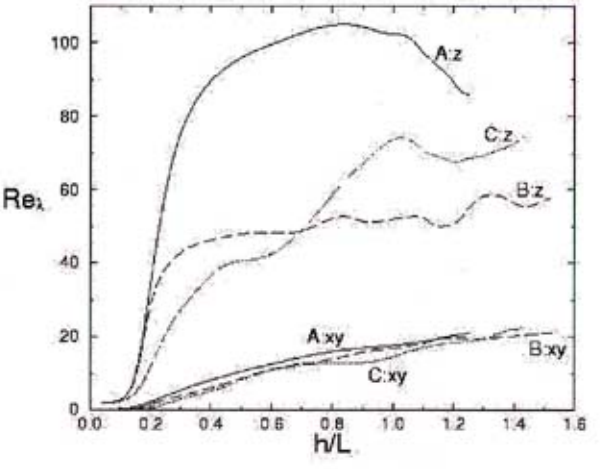

- Anisotropy in microscales also manifest in Taylor Reynolds numbers
- Vertical Taylor Reynolds numbers extremely sensitive to initial conditions with no collapse for either independent variable
- Near perfect collapse of horizontal Reynolds numbers when plotted vs. h/L

Conclusions

- Growth of R-T mixing layer depends sensitively on initial conditions.
- Ranking of growth rates is in same order as suggested by Linear Stability Theory.
- Mixing exhibits greater sensitivity to initial conditions than growth rates.
- Density-fluctuation spectra in interior of mixing zone indicate that imprint of the initial perturbation spectra is eventually lost; furthermore, the spectra exhibit good collapse at low wavenumbers by late simulation time.
- Taylor microscales and Reynolds numbers are also sensitive to initial conditions, nonmonotonic in their temporal evolution and reflect considerable and persistant anisotropy in the flow.
- Mixing zone height is a better progress variable than time, i.e., improved collapse occurs if statistics are compared at the same value of h and if spatial scales are nondimensionalized in terms of h.

UCRL-PRES-146184-REV-1

CALE simulation of Richtmyer-Meshkov instability experiments at high Mach number

A. Miles[1,2], J. Edwards[1], G. Glendinning[1]

[1]Lawrence Livermore National Laboratory

[2]University of Maryland at College Park

8th International Workshop on the
Physics of Compressible Turbulent Mixing
Pasadena, CA
Dec 9-14, 2001

This work was performed under the auspices of the U.S. Department of Energy by the University of California, Lawrence Livermore National Laboratory under contract No. W-7405-Eng-48.

Experiment:

- Omega laser used to generate a strong shock (M≈10) in a plastic pusher
- Shock drives a corrugated plastic - foam interface (ka=0.92) at near constant velocity
- Richtmyer-Meshkov instability produces growth of the initial perturbation

Simulation:

- C-based Arbitrary Lagrangian-Eulerian (CALE) used to simulate the experiments
- Discrepancies between experiment and simulation are investigated

This experiment uses an 11 ns laser drive to create a steady shock incident on a modulated interface

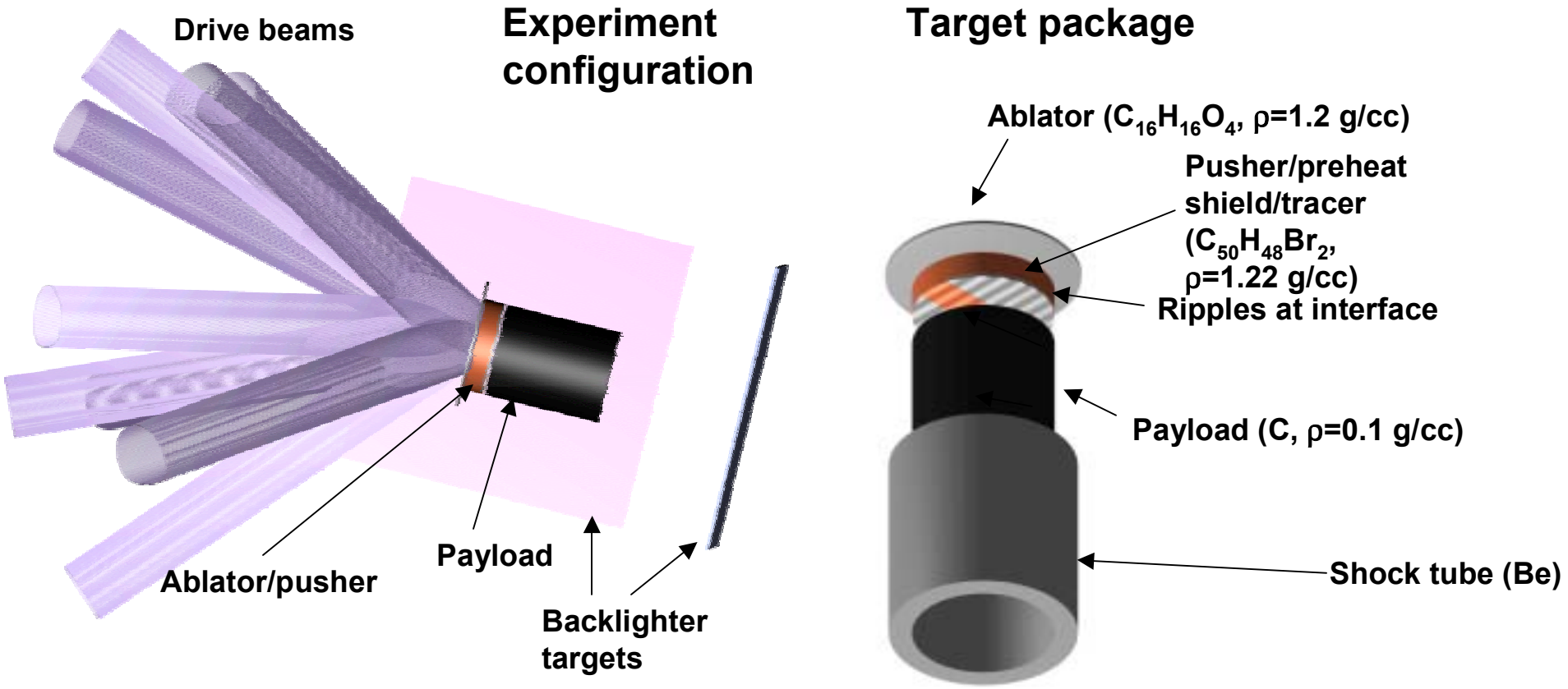

- Backlighting is done on two axes, along target axis and perpendicular to modulations
- Target package is encased in a beryllium shock tube
- The incident shock and interface velocities are constant within ±5% RMS
- The shock is incident on a 12:1 density contrast
- The interface position is measured by side-on radiography

Computational Parameters (CALE)

- $\rho_{plastic} = 1.1$ g/cc
- $\rho_{foam} = 0.1$ g/cc
- $\rho_{void} = 0.001$ g/cc
- $a = 22$ μm
- $\lambda = 150$ μm
- Computational grid dimensions: $\lambda /2$ x 700 μm
- With EOP EOS:
  - $c_{plastic} = 1.84$ μm/ns
  - $c_{foam} = 0.11$ μm/ns
  - $P_{plastic} = 728$ barr
  - $P_{foam} < 1$barr

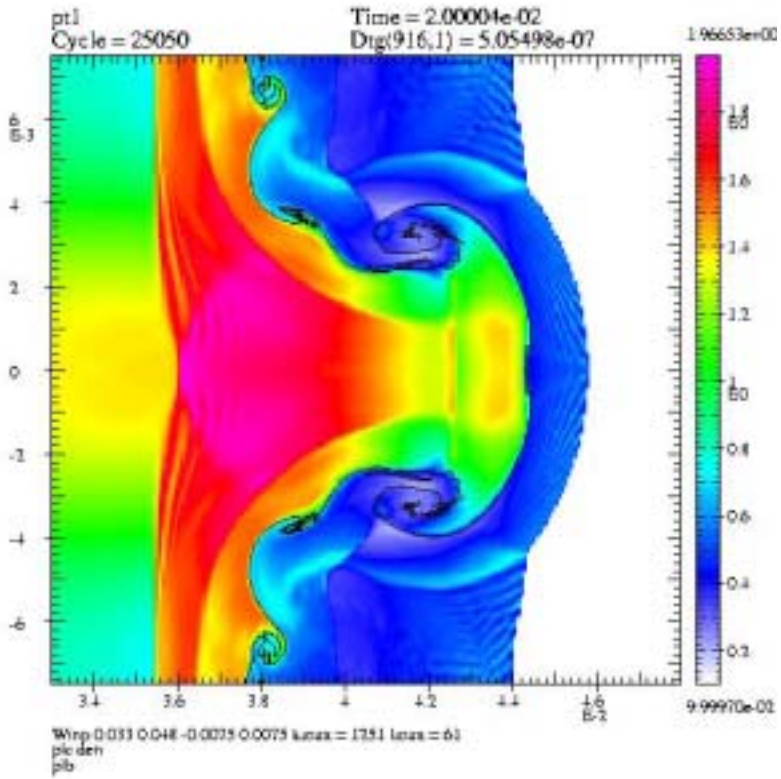

T = 20 ns

Typical side-on data at 20 ns

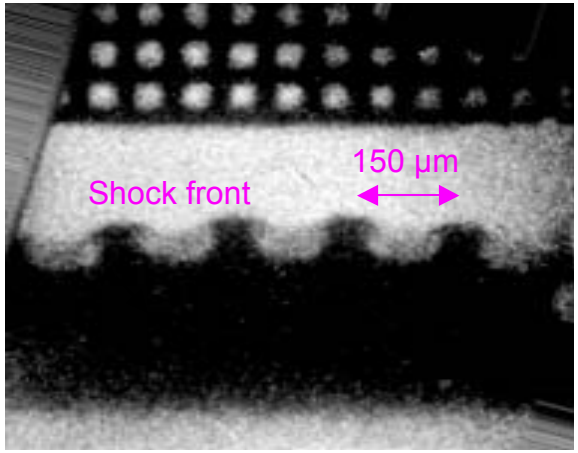

Discrepancies between experiment and simulation:

1. Post-shock amplitude a* is much too large in simulation - 9 µm instead of 5 µm.
2. Growth rate from 14 - 18 ns is higher in simulation than experiment.
3. The standoff distance of the shock from the interface is larger in the simulation than in the experiment.

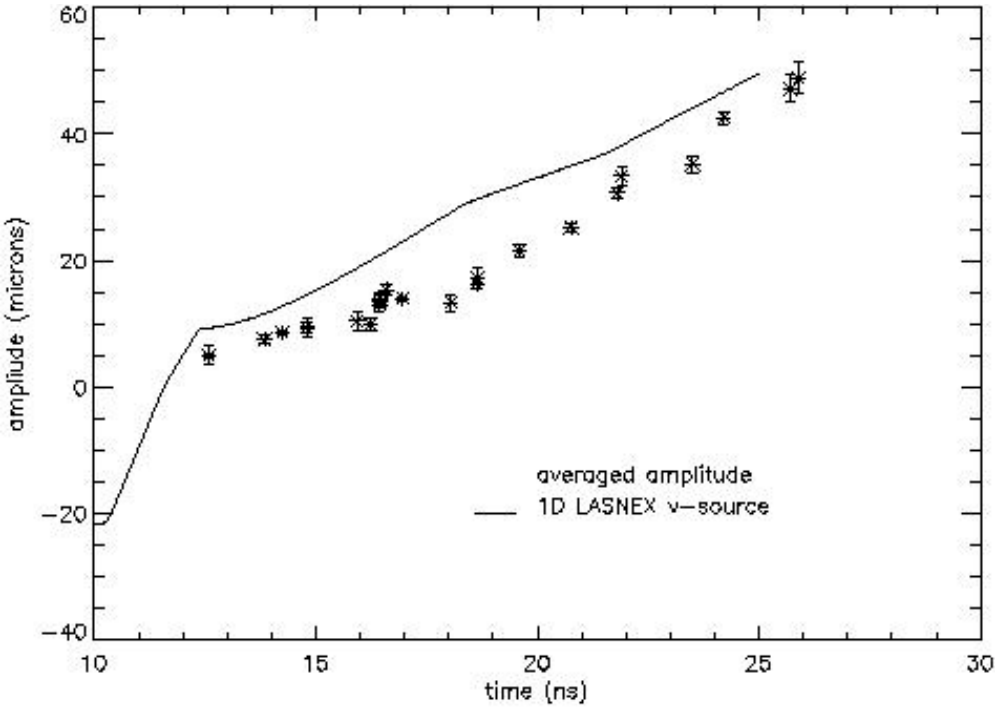

Zoning

Two grid configurations used:

- Rectangular grid

  Typical parameters:
  - 120 cells/wavelength
    1.25 μm/cell
  - Cell dimensions:
    1.25 μm x 0.5 μm

- Conforming mesh

  Typical parameters:
  - 120 cells/wavelength
  - Plastic and foam "interface"
    68% mass-matched
    - 0.1 μm/cell at plastic-void interface
    - 0.75 μm/cell at void-foam interface

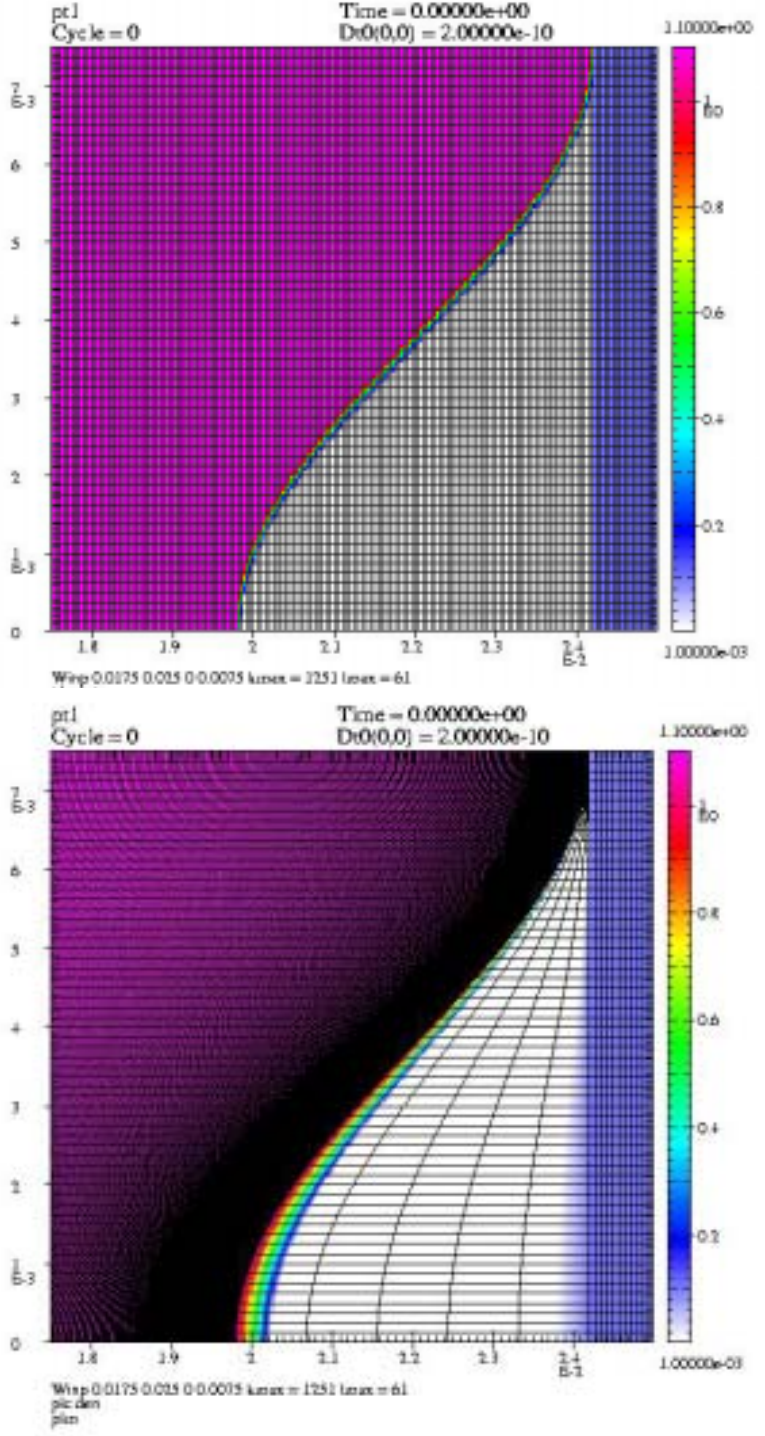

Zoning Effects* I: Conforming Mesh

Cells/wavelength	Cell width across interface (μm)	a* (μm)	a (25ns) (μm)
120	0.1 - Δ_{void}/5 - 0.75	10	41
120	0.01 - Δ_{void}/5 - 0.1 (plastic and foam mass-matched at interface)	11	45
240	0.01 - Δ_{void}/5 - 0.1	12	47

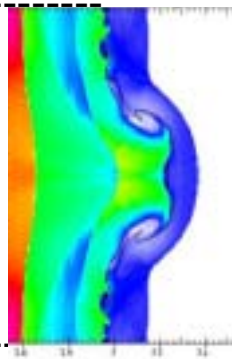

When the number of cells/wavelength ≤ 240, a “dimple” forms in the center of the spike.This yields a smaller amplitude, which is defined as half the distance from bubble tip to spike tip. A further increase of cells/wavelength to 480 looks identical to the 240 case, suggesting convergence by 240.

Zoning Effects II: Rectangular Grid

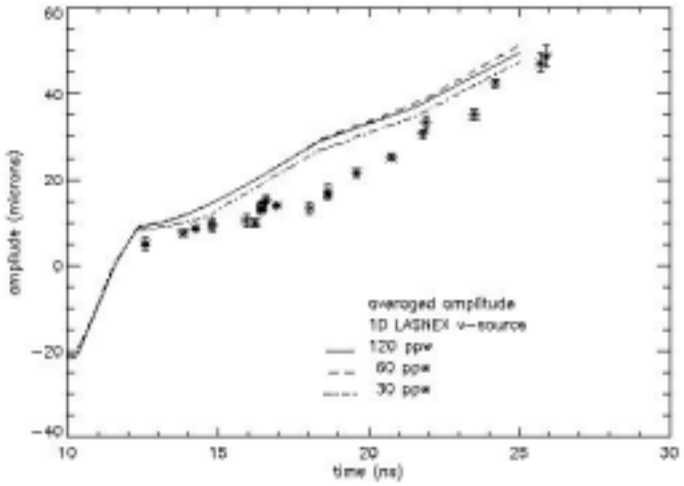

Cells/wavelength	Cell dimensions (μm)
120	1.25 x 0.5
60	2.50 x 1.0
30	5.00 x 2.0

Further increase of cells/wavelength to 240 looks identical to the 120 case, suggesting convergence by 120.

Beyond 15 ns, the converged conforming and rectangular zoning schemes show virtually identical growth rates. The post shock amplitude a* is about 1.5 μm lower here than in the converged conforming mesh case, and the growth rate at early times is slightly smaller. In what follows, the above grid is used unless otherwise specified.

A one-dimensional study of the effects of cell size for zones mass-matched across the plastic-foam interface shows virtually no change in interface position $z_i(t)$ when the cell size in the plastic at the plastic-void interface is varied from 0.1 - 0.001 μm. Over this range, $z_i(t)$ is also shown to be insensitive to whether CALE is run in pure lagrangian mode or lagrangian-eulerian hybrid mode.

Comparison of simulations of Aleshin experiment

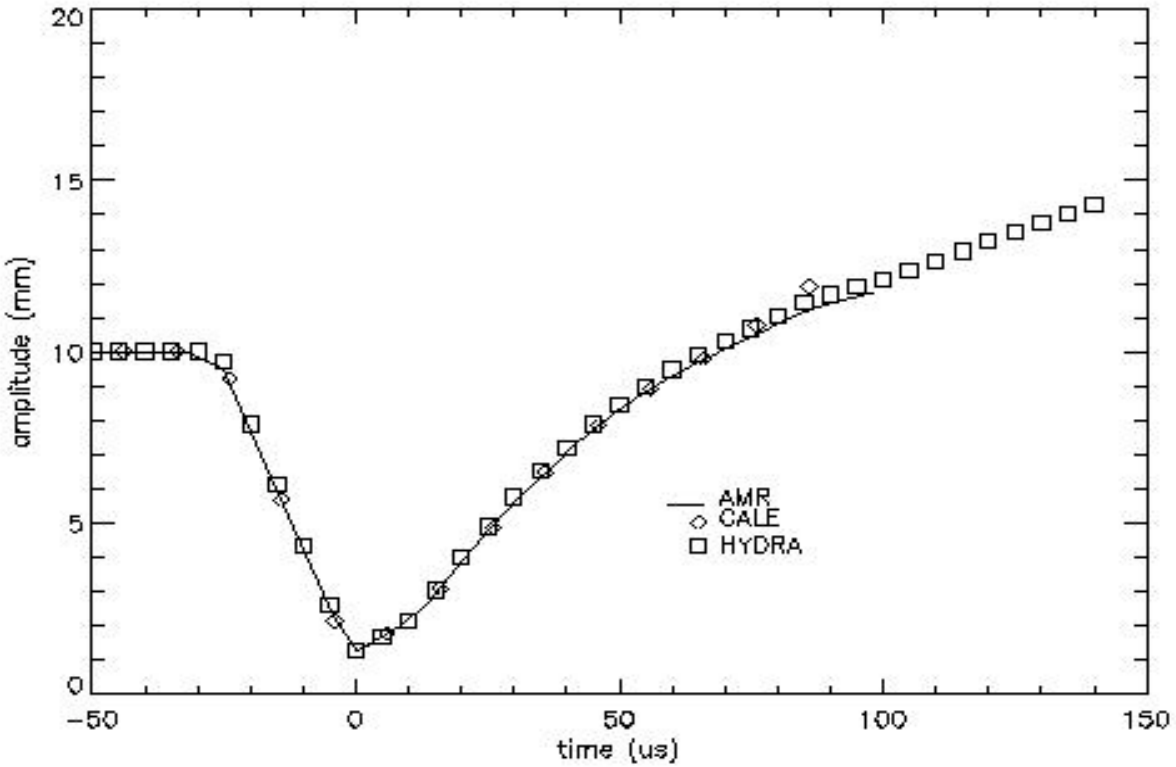

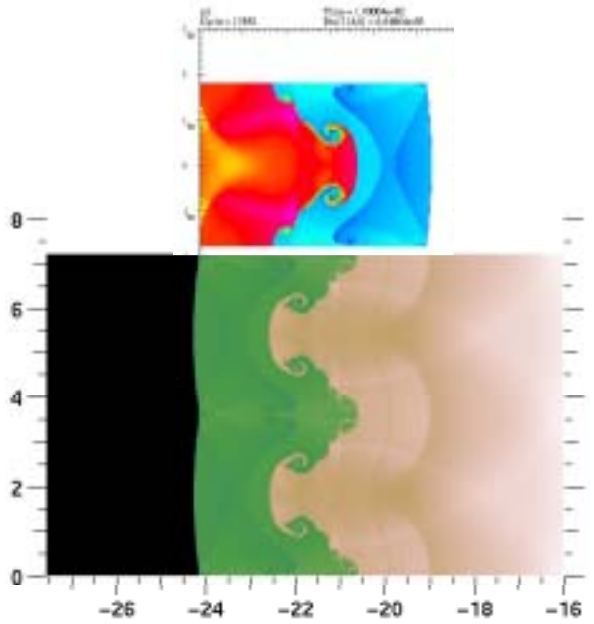

HYDRA (below) and CALE (above) at approx. 80 μs

Gas-tube experiment with M = 4.5 shock across Xe-Ar interface with ρ_{Xe} = 2.95 g/l, ρ_{Ar} = 2.95 g/l (ρ_{Xe} / ρ_{Ar} = 0.30), ak = 1.75

- AMR (Greenough, 2001) and ALE (CALE and HYDRA (Weber, 2001)) simulations of the Aleshin experiment (Aleshin et al., 1996).
- The RAPTOR and HYDRA simulations include 2560 and 512 cells/wavelength, respectively. The CALE simulation was run with only 120 cells/wavelength.
- Despite differences in coarseness, the three simulations show very good agreement in their predictions of amplitude history, and all three are in good agreement with the experimental data (not shown).
- The number of cells/wavelength and the initial ratio of cell dimensions (cell width along / perpendicular to the unperturbed interface) in the above CALE simulation is 2.5 - the same as in simulations of the Omega experiments.

Velocity Source I

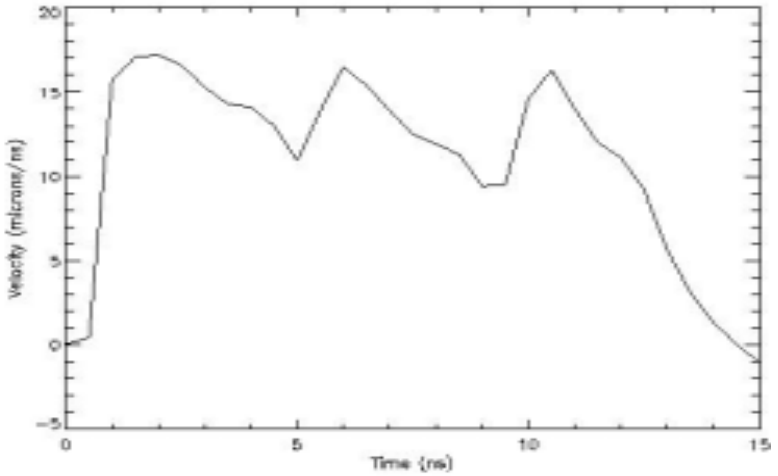

A 1D Lasnex simulation translates the 11 ns laser pulse into a velocity source. The result is used as a source input for CALE.

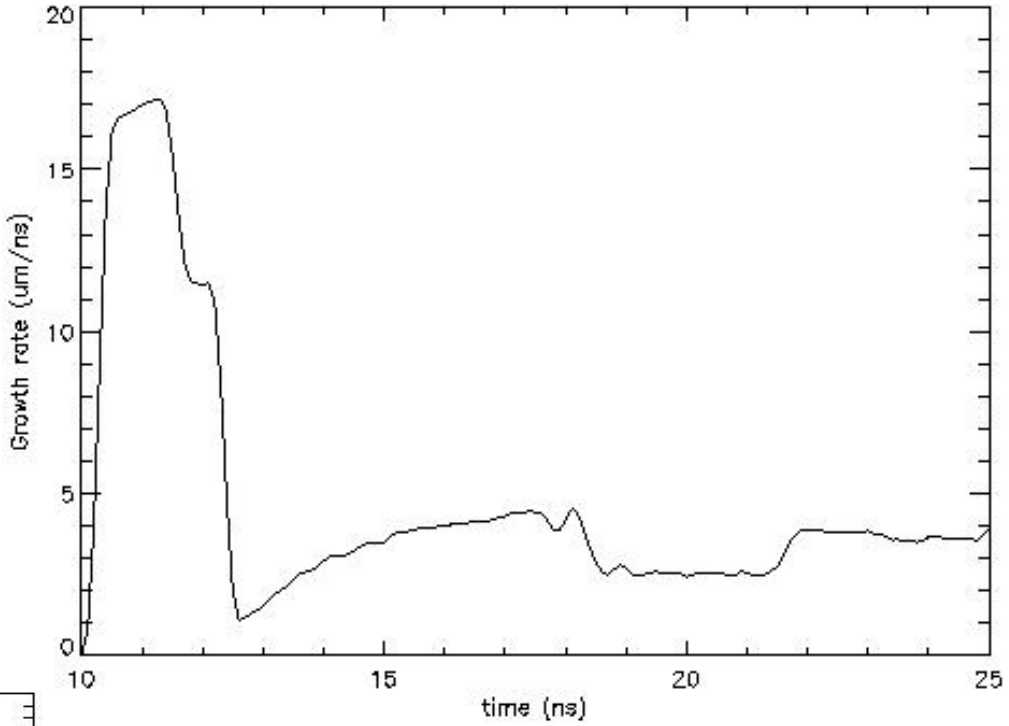

The RM instability growth rate is obtained by numerically differentiating the averaged amplitude history.

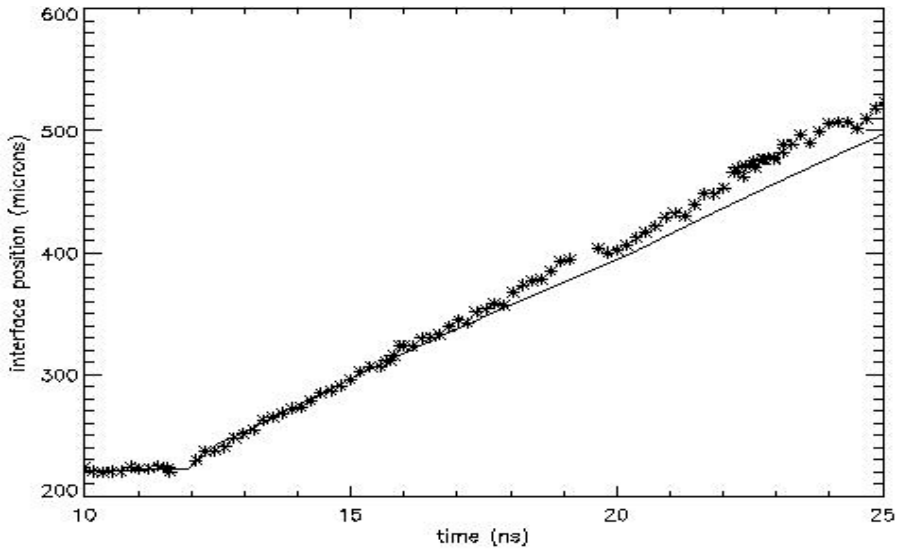

The interface position is obtained from a 1D CALE simulation. The CALE-predicted interface velocity is apparently smaller than in the experiment.

Velocity Source II

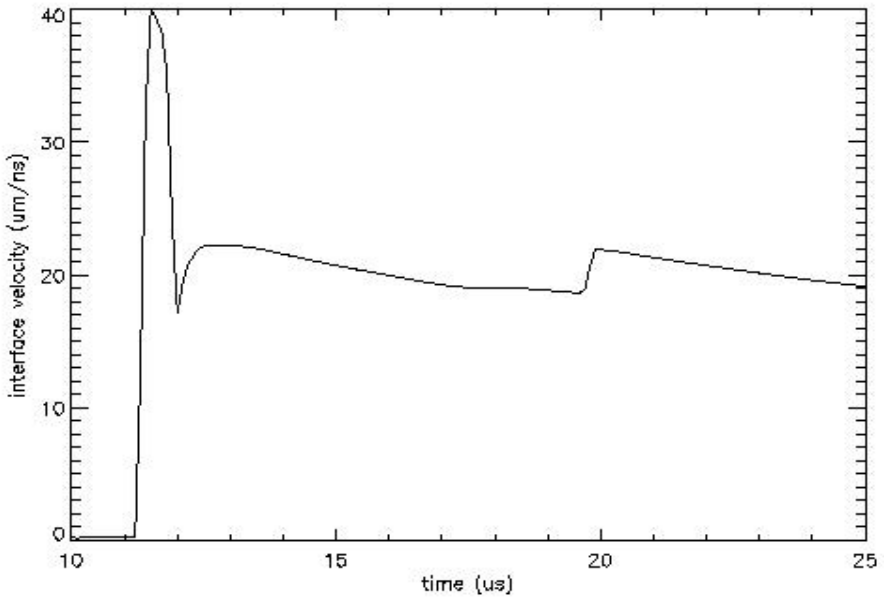

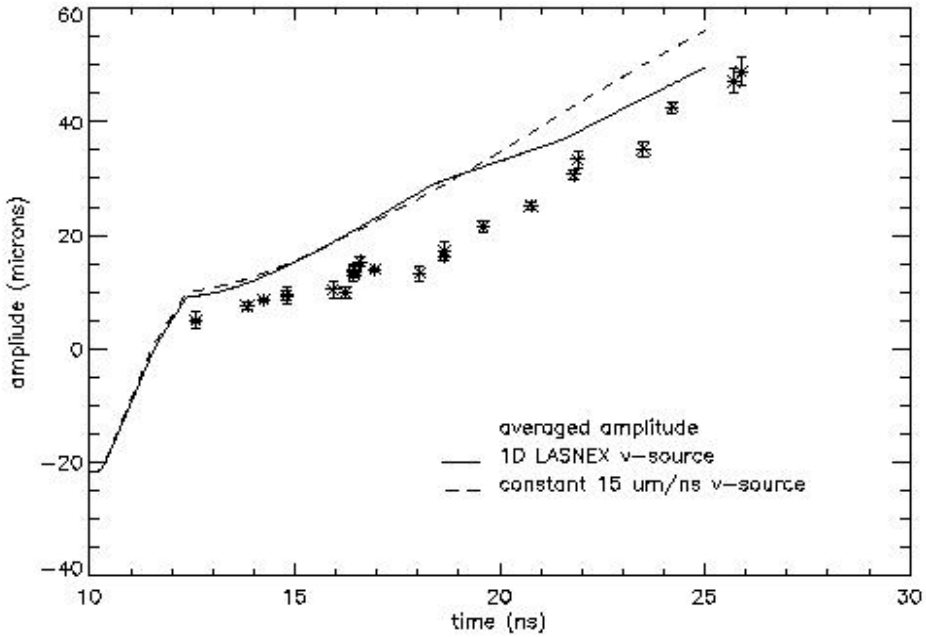

The interface velocity $u_i(t)$ is obtained by differentiating the interface position. It shows that the reduction in growth rate from 18-22 ns corresponds to the arrival at the interface of a second shock. Investigation of modified velocity sources has demonstrated that this second shock corresponds in turn to the third peak in the velocity source.

Effect of velocity source details on amplitude history. The instability develops initially as if driven by a constant velocity (15 μm/ns) piston. The two histories diverge significantly only upon the arrival of the second shock at the bubble. The shock associated with the second peak in the velocity source has overtaken the incident shock just before the beginning of the interaction.

Modified Velocity Source I

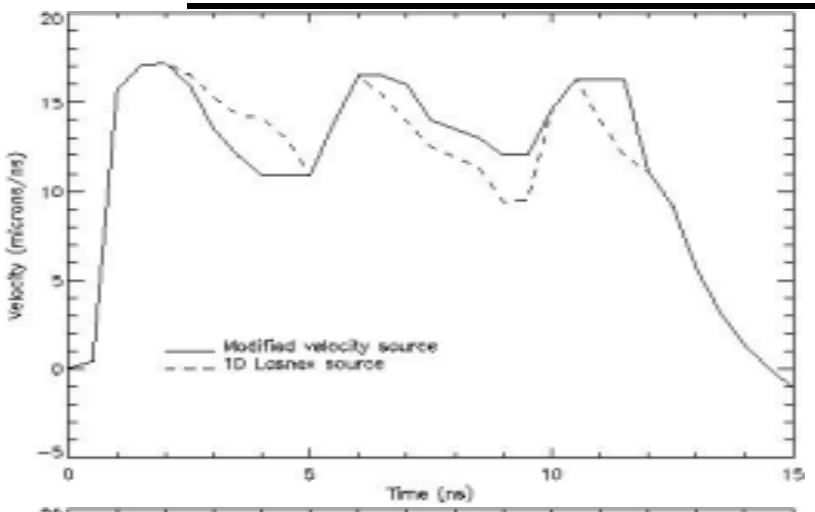

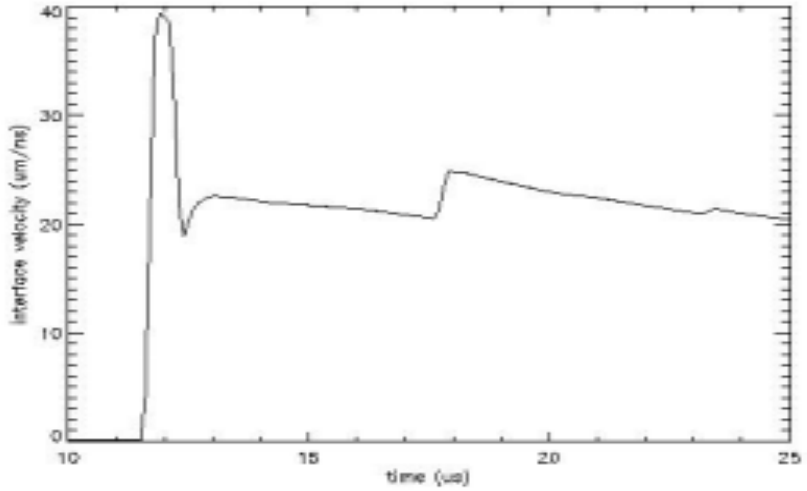

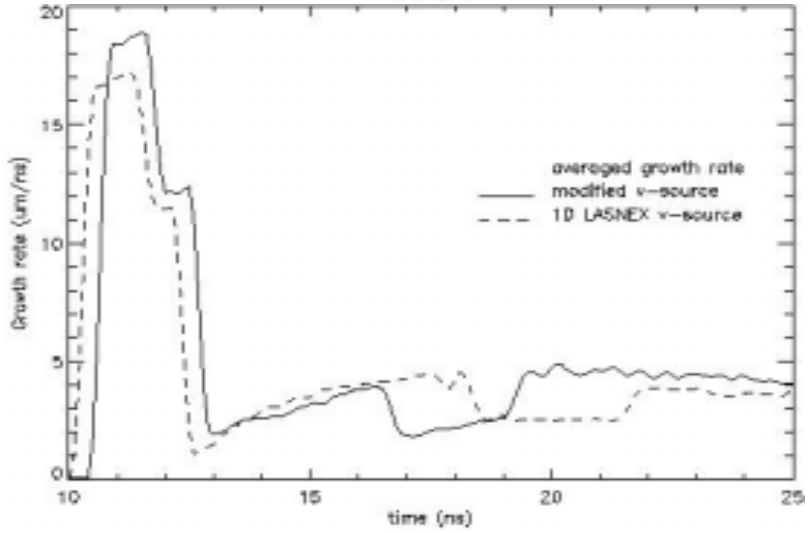

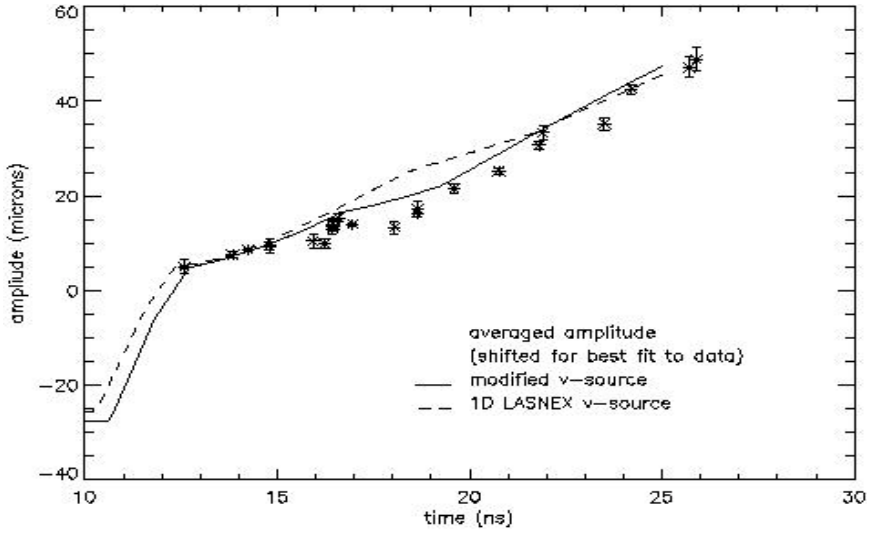

Small changes in the velocity source strengthen the second shock and decrease its arrival time. The resulting amplitude history more closely matches the experimental data.

However, the post-shock amplitude is further increased to 11 μm (from 9 μm).

Modified Velocity Source II

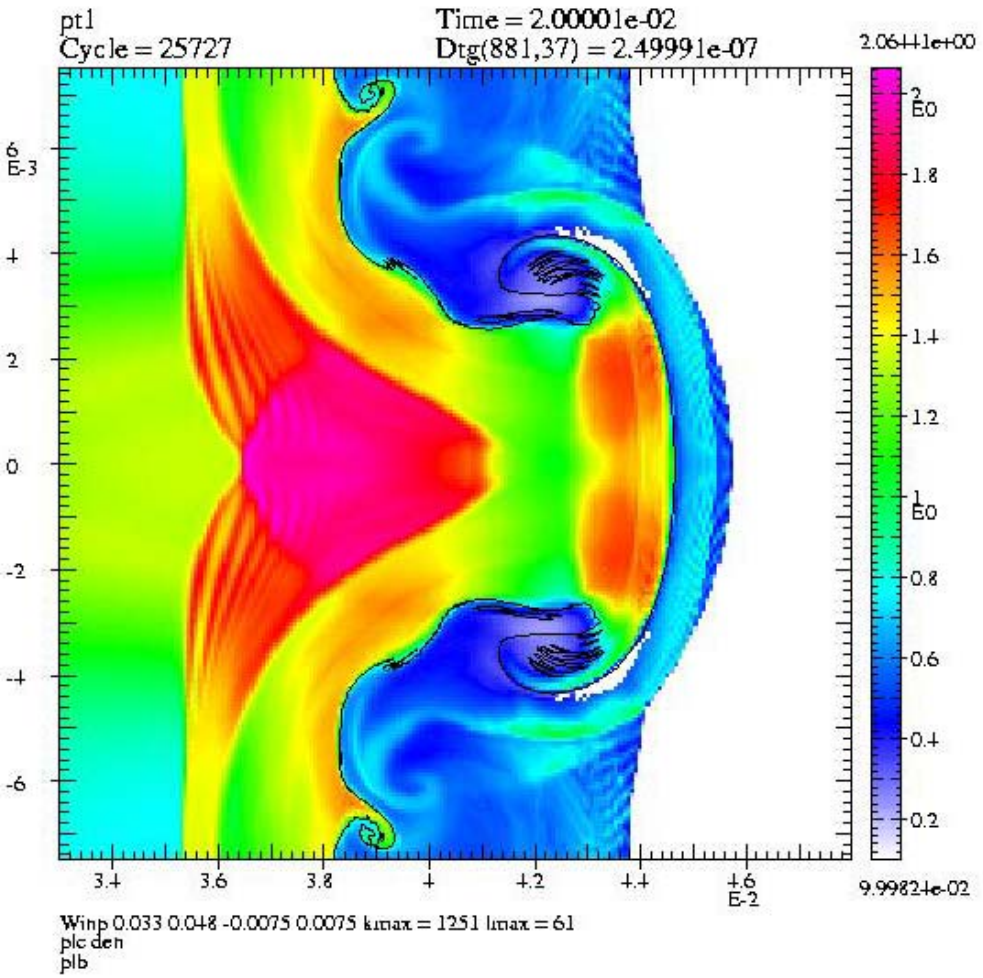

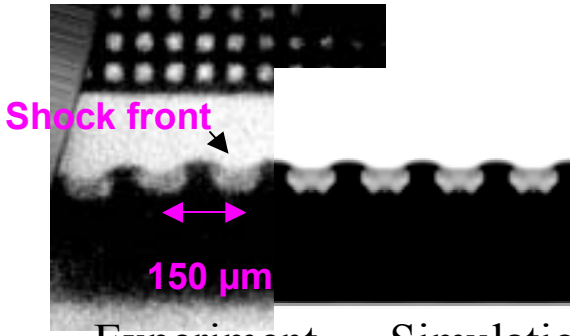

Experiment Simulation

Comparison of simulated x-ray radiograph with experimental x-ray snapshot at 20 ns shows very good agreement.

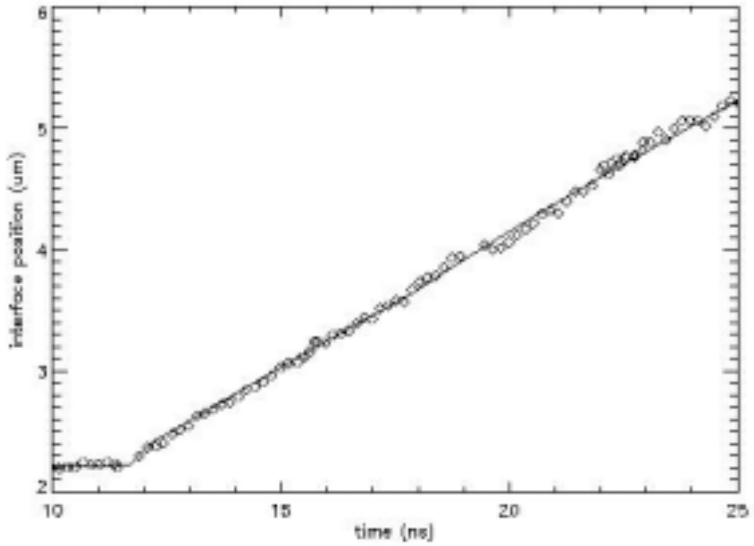

The time-dependent interface position (from 1D CALE simulation) agrees well with experimental measurements.

2D LASNEX Velocity Source I

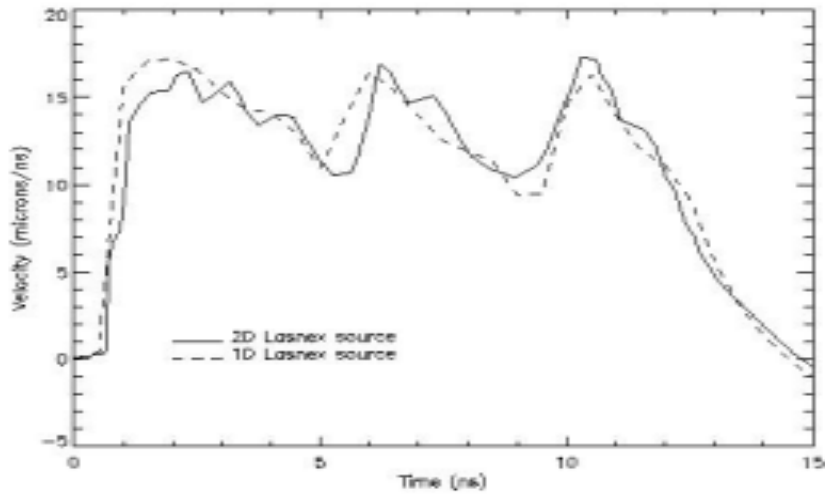

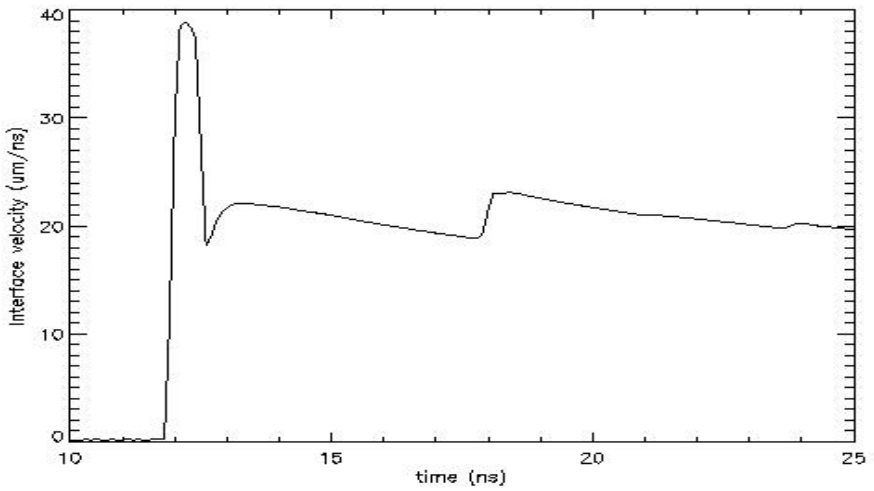

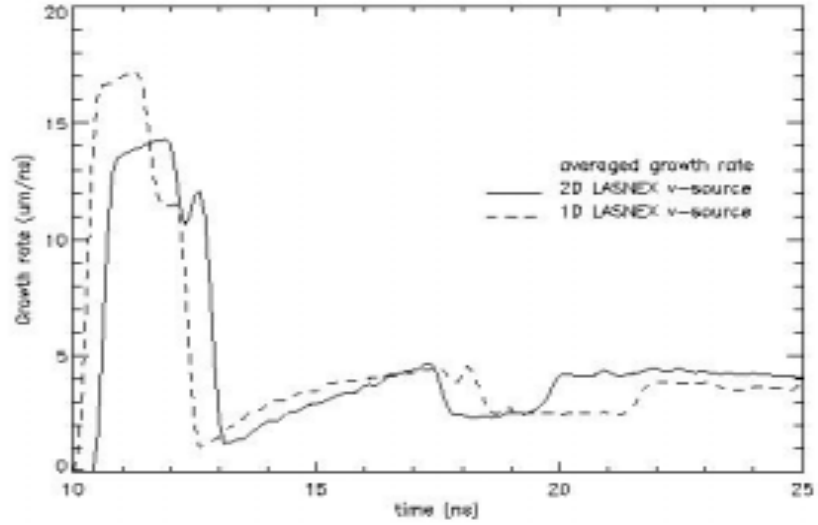

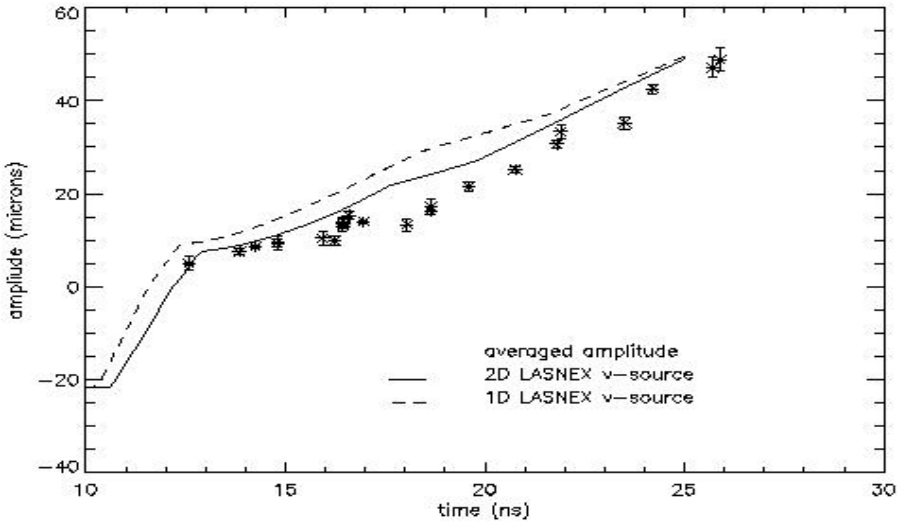

A 2D LASNEX simulation produces a velocity source that differs slightly from the 1D LASNEX prediction. The average interface velocity is increased from 20.4 μm/ns to 21.0 μm/ns. The resulting amplitude history more closely matches the experimental data. Notably, the post-shock amplitude is decreased to 7.7 μm (from 9 μm).

2D LASNEX Velocity Source II

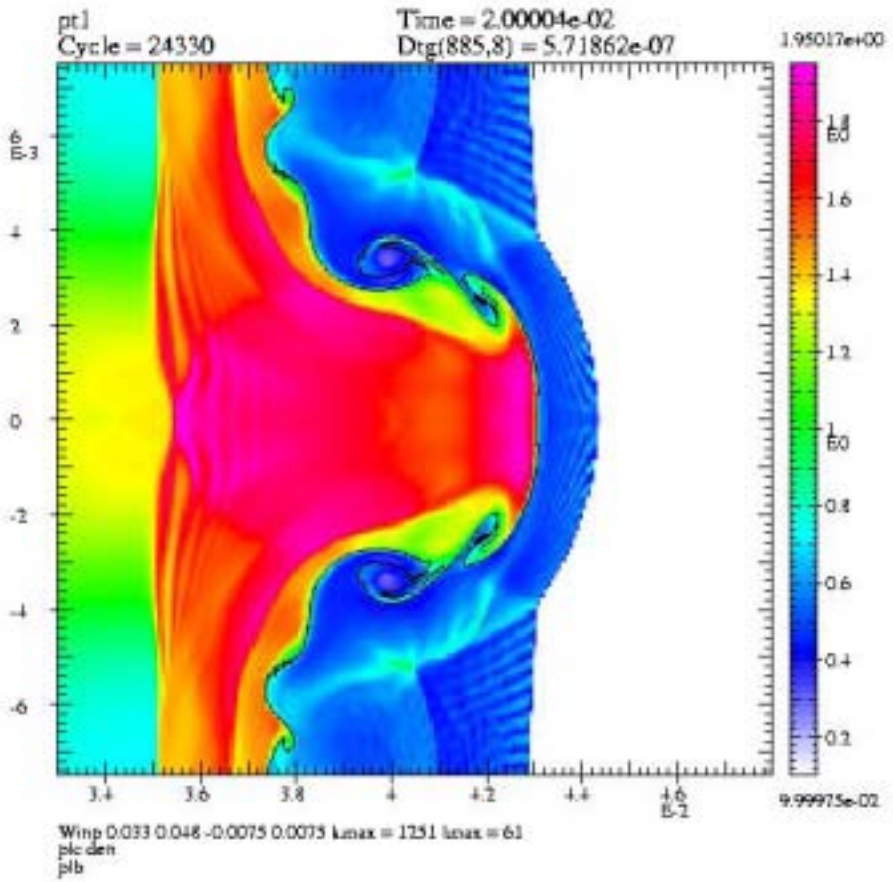

Density plot at 20 ns.

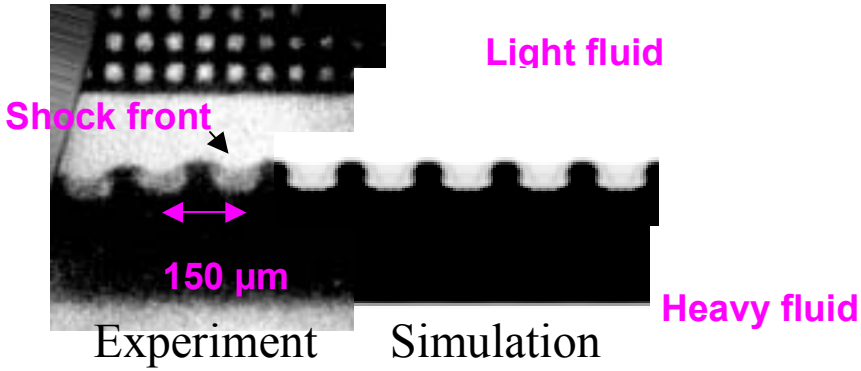

Comparison of simulated x-ray radiograph with experimental x-ray snapshot at 20 ns shows good agreement. However, the CALE-predicted shock is flatter than in the experiment.

2D LANSEX Velocity Source III

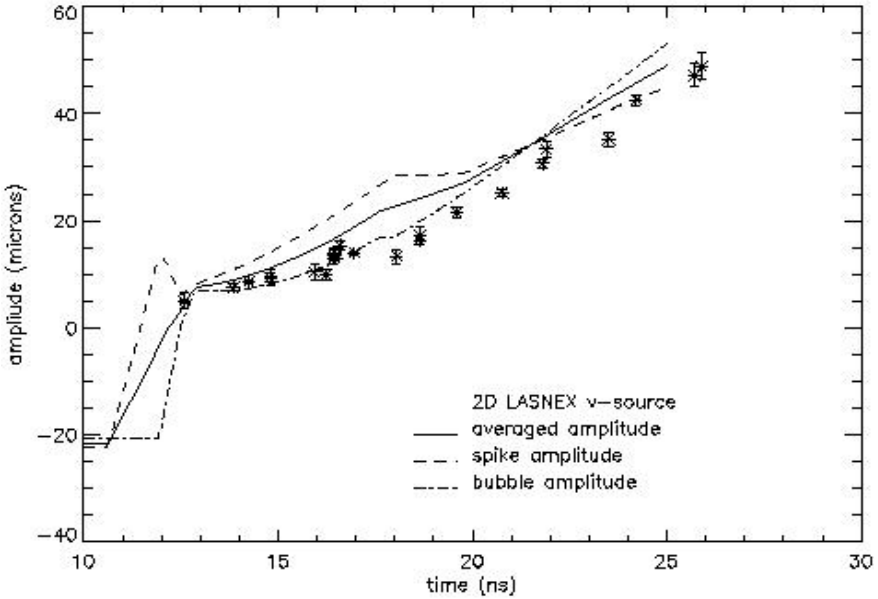

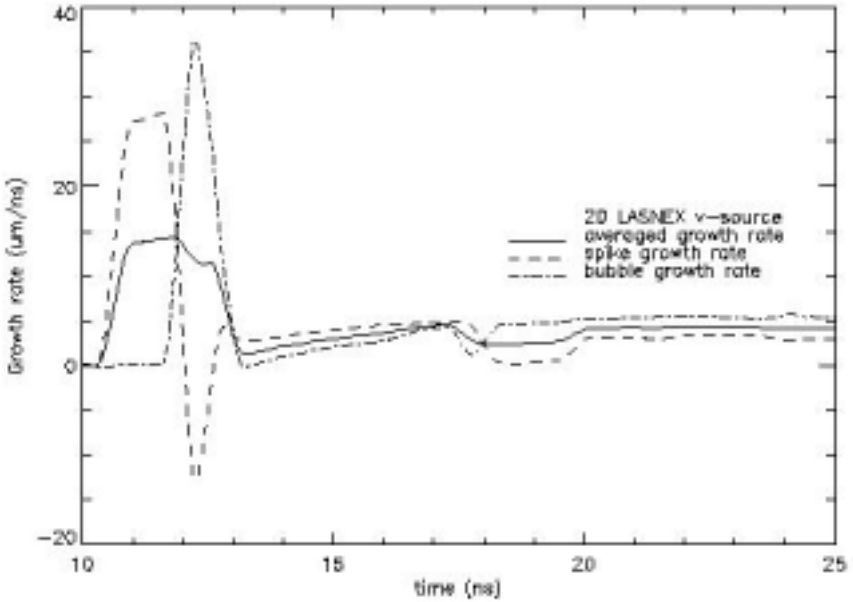

Separate spike and bubble amplitudes and growth rates. The reference time-dependent interface position is obtained from a 1D simulation including a 22 μm gap separating the plastic and foam regions.

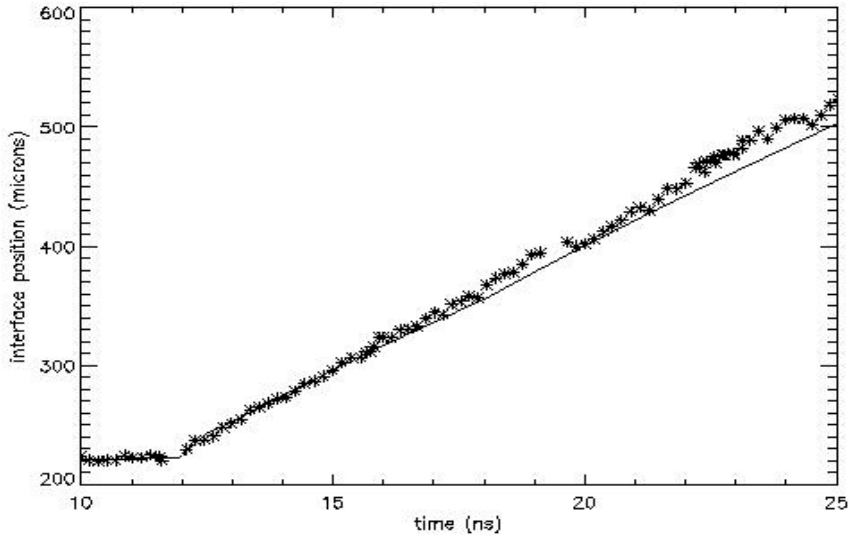

The time-dependent interface position (from 1D CALE simulation) is shown to agree well with experimental measurements at early times. After 15 ns, however, the interface velocity is too low.

2D LASNEX Velocity Source IV

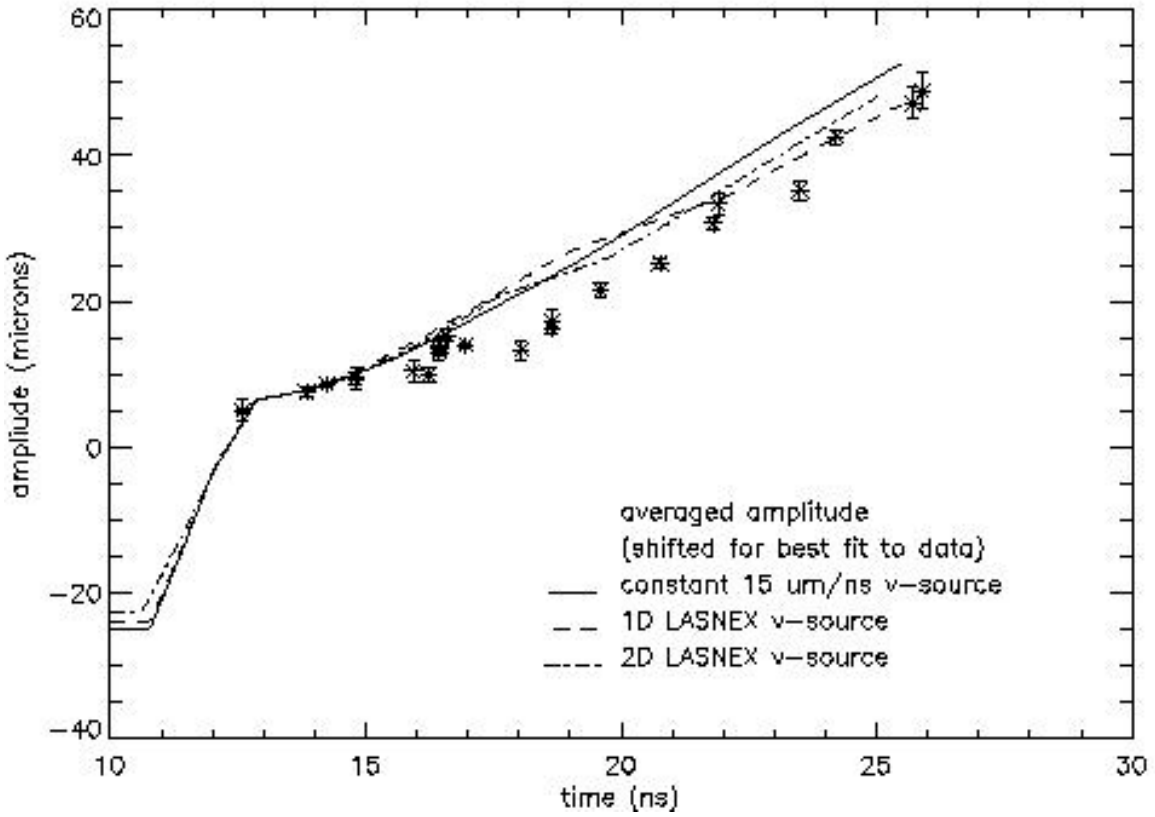

2D LASNEX: t, a - 1.0 μm; 1D LASNEX: t + 0.5 ns, a - 2.5 μm; Flat source: t + 0.5 ns, a - 3.5 μm

Aside from a shifts in time and amplitude, the constant velocity 15 μm/ns velocity source provides early time instability growth that agrees well with the 2D as well as 1D LASNEX v-source.

Effect of Pusher Velocity

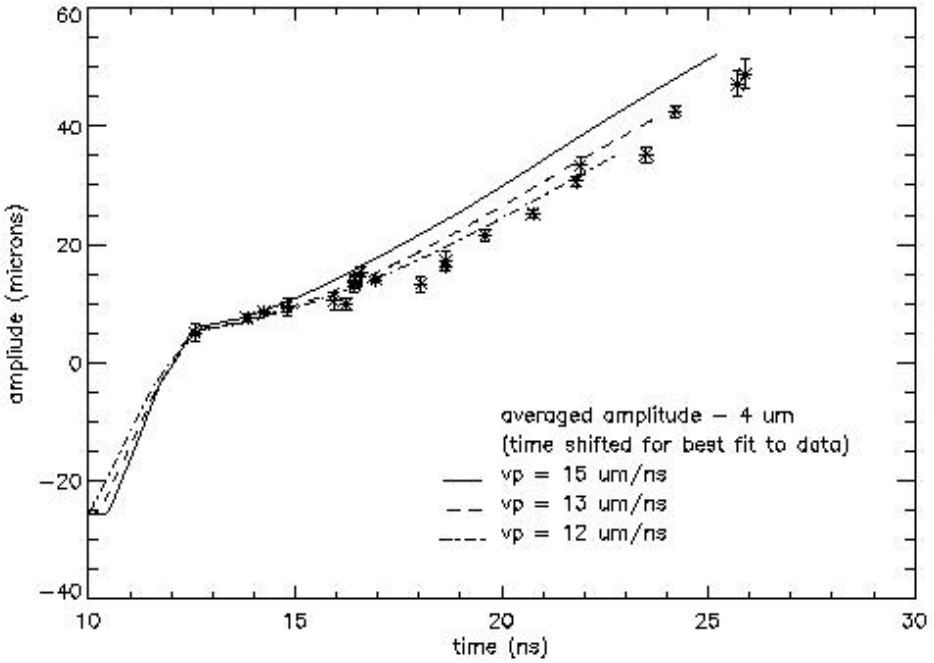

22 μm initial amplitude

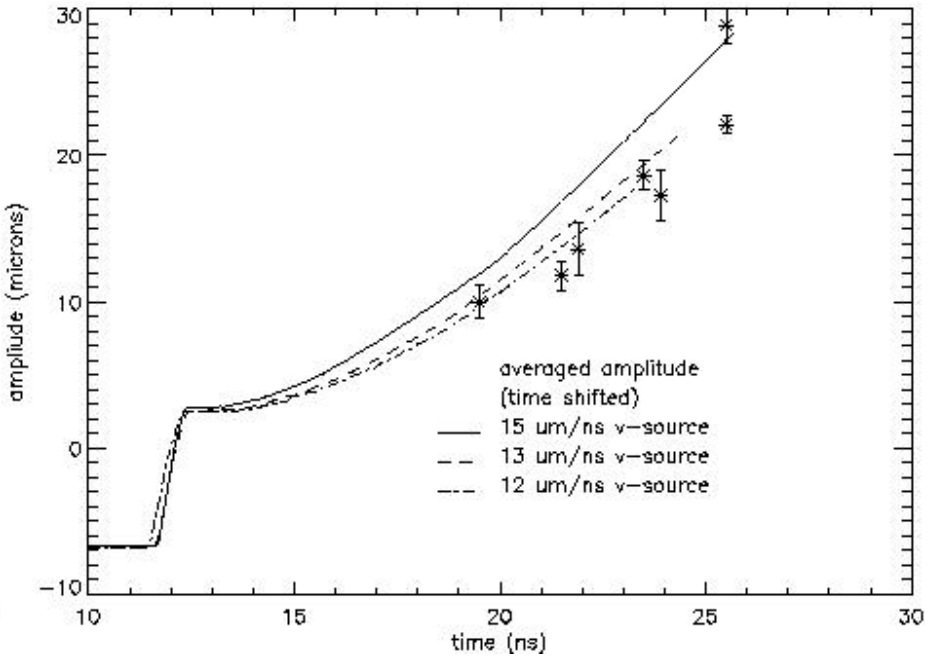

7 μm initial amplitude

The post-shock amplitude is insensitive to the piston velocity over a range of several μm/ns. For comparison, the average velocities of the 1 and 2D Lasnex v-sources from 1 - 11 ns are 14.0 and 13.9 μm/ns, respectively. The analogous averages taken from the first to the second peak in the velocity profiles are 15.0 and 14.1 μm/ns.

2D LASNEX Velocity Source V

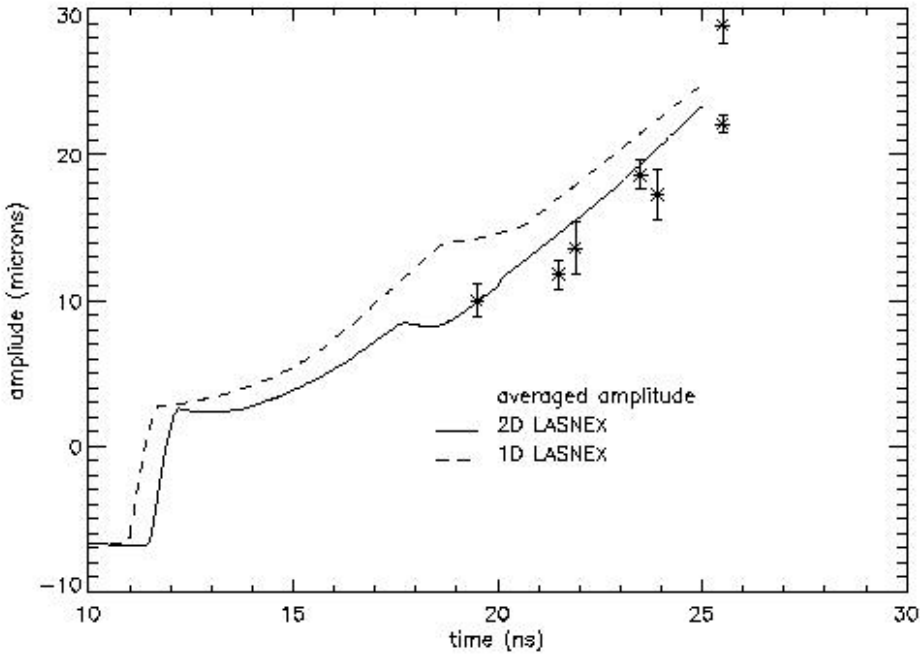

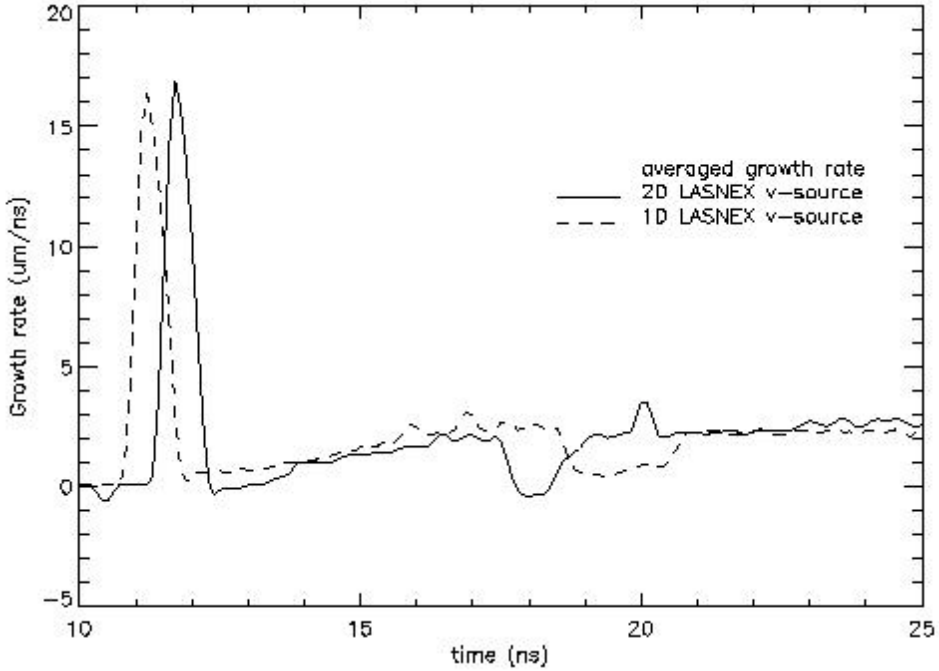

The simulation with the 2D LASNEX velocity source is also in closer agreement with experimental data obtained from experiments with small initial perturbation amplitude ($a = 7\ \mu m$, $ka = 0.29$).

Equation of State I:

Effect on basic parameters, post-shock amplitude, and early-time growth rate

All lengths are in μm, times in ns.

	v_1 (ave 2-8 ns)	γ_1^{eff}	u_i	v_2 (v_2^{rel})	γ_2^{eff}	a*	da/dt ave(t* - 18ns)	da/dt††
Exp	22.0 ± 0.2	1.93 ± 0.03	21.9 ± 1	26.1 ± 0.5 (4.2)	1.38	5.0	≈ 1.9±0.1	
EOP-1D†	20.9	1.80	20.4	25.1 (4.7)	1.46	9.0	3.4	4.3
EOP-2D†	20.8		21.0	26.1 (5.1)		7.7	3.0	4.5
EOP	19.6		22.2	27.0 (4.8)		10.5	2.8	4.0
LEOS	18.9	1.67	22.9	29.4 (6.5)	1.66	13.0	3.1	4.5
γ/EOP		1.5				13.5		2.1
γ/EOP		1.9				11.0		4.9
γ/EOP		2.0				7.0		5.0
γ/EOP		2.2				7.0		5.5
EOP/γ					1.1	11.0		3.2
EOP/γ					1.2			3.5
EOP/γ					1.3			3.8
EOP/γ					1.4			3.9
EOP/γ					1.5	10.5		4.0

†Simulation run with drive from LASNEX calculation - all others run with modified v-source.

†† Peak growth rate over interval from t*, defined by a(t*)=a*, to instant where second shock reaches the bubble front.

v_2^{rel} is shock speed in interface frame

Equation of State II: Shock Proximity

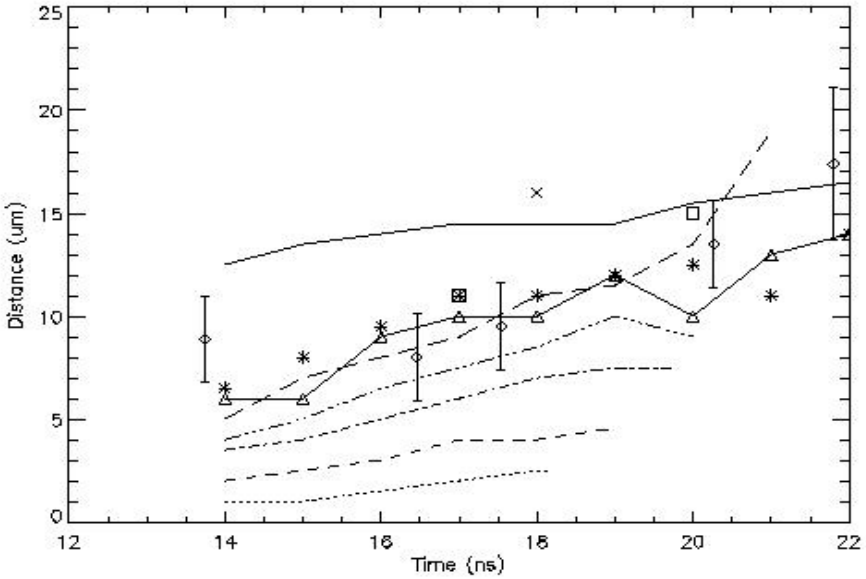

Distance from spike to shock

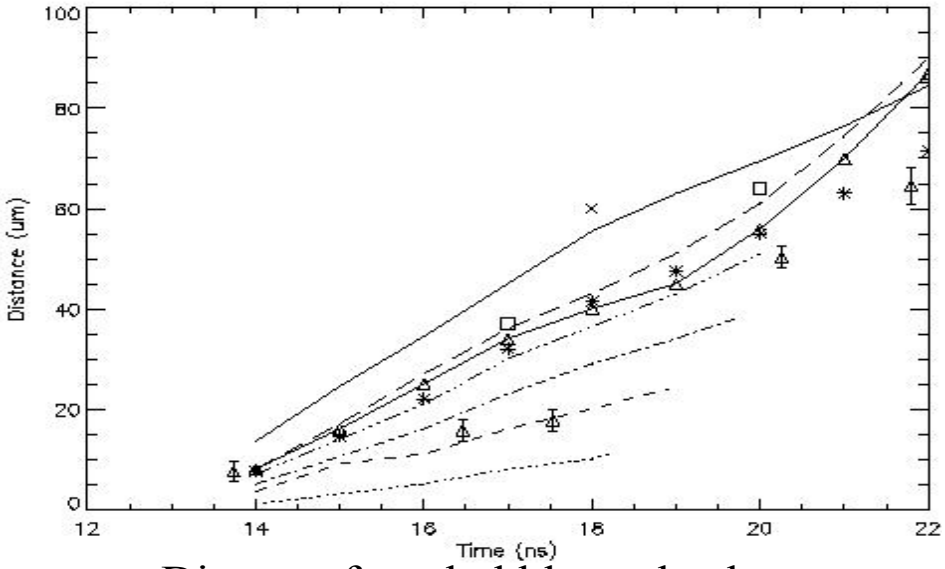

Distance from bubble to shock

Modified v-source and EOP EOS unless otherwise specified

—Δ— EOP
x LEOS
□ 1D LASNEX v-source
* 2D LASNEX v-source
____ 1D LASNEX v-source, foam-filled gap

···· ····· ·· $\gamma_{fom} = 1.1$
---------- $\gamma_{fom} = 1.2$
— · — · — $\gamma_{fom} = 1.3$
— · · · — $\gamma_{fom} = 1.4$
———— $\gamma_{fom} = 1.5$

Shock proximity and distortion compared for various EOS models and velocity source profiles. No one combination of EOS model and v-source matches all of the data. The discrepancy between data and experiment on the bubble proximity is generally consistent with the discrepancy in perturbation amplitude.

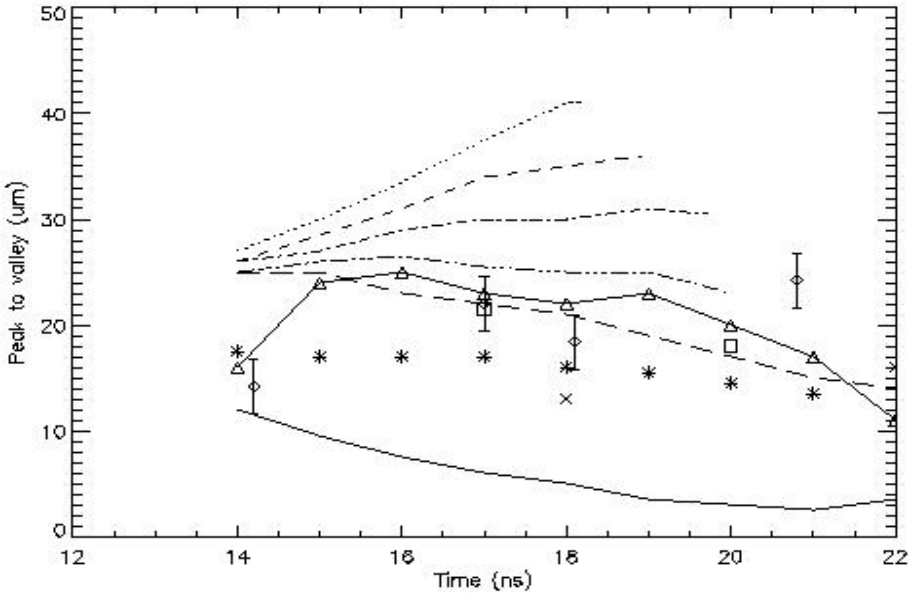

Shock distortion

Shock-Proximity vs Amplitude

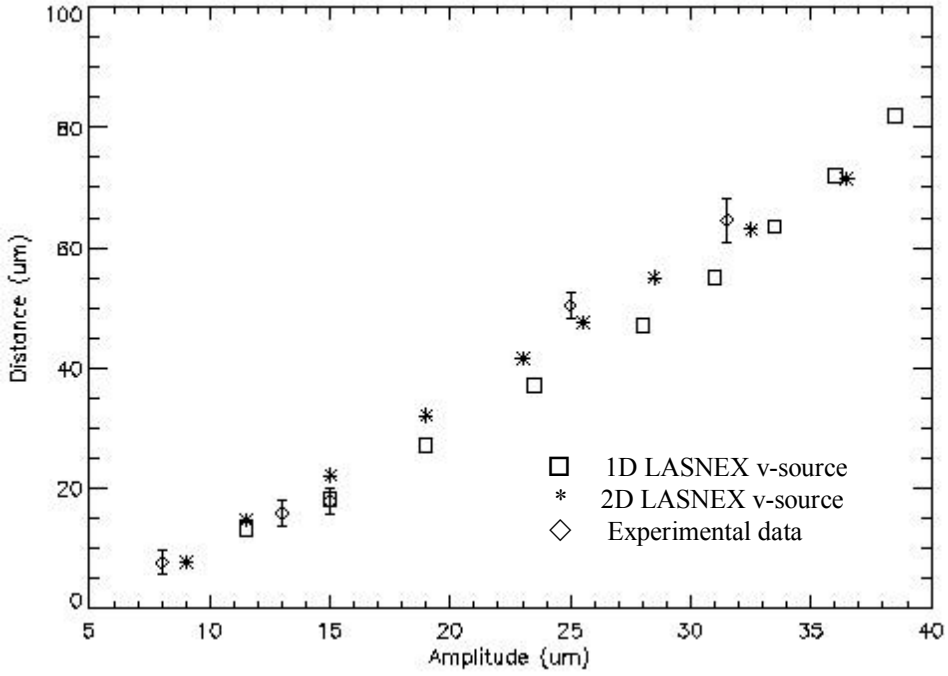

Distance from bubble to shock

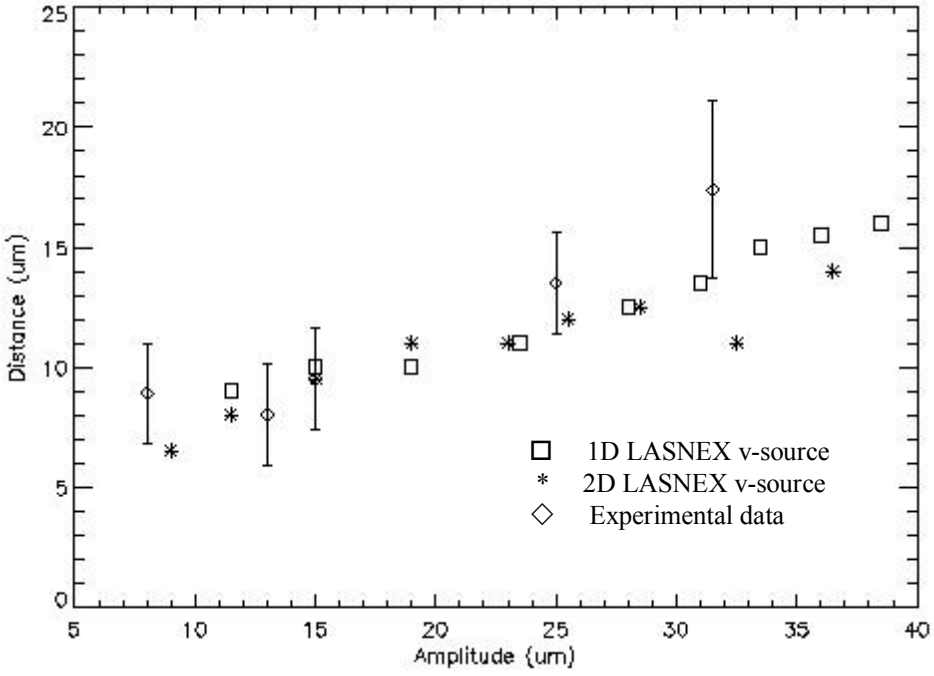

Distance from spike to shock

Post-shock amplitude

- a* has been shown to exhibit only weak dependence on EOS and zoning issues.
- a* is defined by half the bubble to spike distance at the instant the shock completely crosses the interface, and is determined by the compression factor:

$$\frac{a^*}{a} = u_i \left(\frac{1}{v_1} - \frac{1}{u_g} \right)$$

Where u_i is the interface velocity, v_1 is the shock speed in the plastic, and u_g is the interface velocity in the gap. This reduces to the usual expression in the absence of a gap, when $u_g = u_i$.

- For the reported experimental amplitude and velocity values, this requires $u_g = 28.5 \pm 1.3$ μm/ns. If the incident shock and interface velocities at the time of interaction are used (rather than their average values), we find $u_g = 26.5$ μm/ns. A rough measurement from the data suggests $u_g = 20 \pm 10$ μm/ns. The analogous calculation for the simulations with an EOP EOS gives $u_g = 33.9$ μm/ns (modified v-source), $u_g = 36.0$ μm/ns (1D LASNEX v-source), and $u_g = 31.8$ μm/ns (2D LASNEX v-source), while, for LEOS, $u_g = 36.9$ μm/ns (modified v-source). The actual values from the three simulations are 37±1, 34±1, 28±1 and 40±1 μm/ns, respectively.

Post-shock Amplitude II: Modified gap

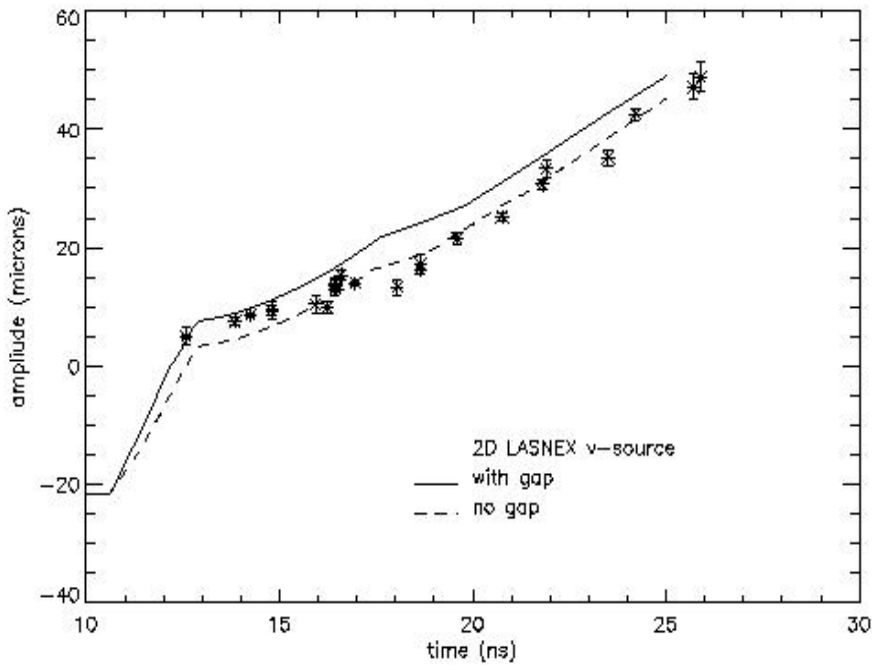

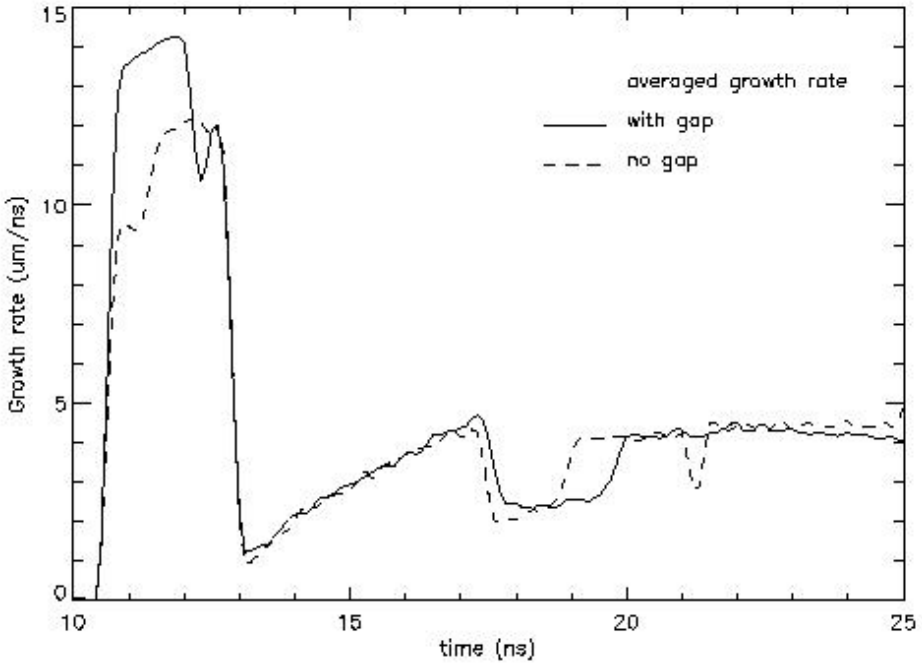

When the gap is "filled in" with foam, the breakout speed of the interface into the gap region is reduced. The speed of the interface in the gap is one-half the instability growth rate until the moment that the incident shock reaches the position of the unperturbed interface. The reduction in breakout speed produces a corresponding reduction in post-shock amplitude.

Conclusions I

- CALE simulations of high Mach number RM experiments have been performed.
- Results obtained using computational grids initially rectangular or conforming agree with one another provided the number of zones/wavelength is sufficiently large. Convergence is obtained more rapidly for rectangular grid.
- Although the general features of the experiments are correctly predicted by he simulations, there are discrepancies.
- The discrepancy between the experimental and simulation a* does not appear to appear to be caused by EOS issues. It has been shown most sensitively dependent on the details of: the composition of the gap region, the shock-gap dynamics, and the velocity source.

Conclusions II

- Relatively small details of the velocity source can significantly affect the post-shock amplitude and the instability growth rate. CALE simulations in which the input velocity source was obtained from a 2D rather than 1D Lasnex simulation show improved agreement of a* and da(t)/dt with the experimental data. This is true for both both the large and small amplitude cases.
- The discrepancy between experimental and simulation da(t)/dt from 17 - 20 ns does not appear to be caused by zoning or EOS issues. Simulations with a modified v-source suggest that, in the experiment, the second shock (observed with both Lasnex velocity sources) reaches the perturbation about 1 ns earlier than in the CALE simulation with 2D Lasnex v-source. This in turn suggests that further refinement of the velocity source will be required for more accurate simulations of the experiment.
- The long-term shock proximity observed in the experiments suggests that the foam may more compressible than predicted by the EOP tables, and is certainly more compressible than predicted by the LEOS tables. The degree of shock proximity remains the most significant discrepancy between the experiments and simulations.

LA-UR-01-6602 (Rev)

Improvements to Convergent Cylindrical Plasma Mix Experiments using Laser Direct Drive

Cris W. Barnes*, Steven H. Batha*, A. M. Dunne#, N. E. Lanier*, Glenn R. Magelssen*, Thomas J. Murphy*, Kenneth W. Parker#, Stephen Rothman#, John M. Scott*, David Youngs#

*Los Alamos National Laboratory, Los Alamos, NM USA

#AWE, Aldermaston, UK

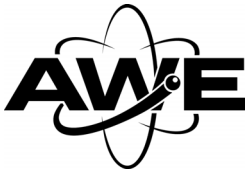

Abstract- LA-UR-01-2545

- Experiments studying mix in a compressible, convergent, miscible, plasma system are being conducted on the OMEGA Laser at the Laboratory for Laser Energetics at the University of Rochester. Thin-walled polystyrene cylinders 2.25-mm long and 0.86 mm inner diameter with foam inside are directly illuminated with 351-nm wavelength light from 50 laser beams in a 1-ns square laser pulse. The turbulence driven by the Richtmyer-Meshkov instability by shock passage across a density discontinuity mixes marker material that is radiographically opaque. Initial work using a high-density, high-opacity marker layer of gold between the plastic ablator and foam clearly demonstrated significant measurable mix width. However, the high opacity of the gold prevented determination of a density profile in the mix region, and it was also overly sensitive to hydrodynamic effects at the end of the marker layer. Use of lower opacity marker material will be described and its impact on end effects and the measurements of mix density profile described.
  - **C. W. Barnes et al., Rev . Sci. Instrum. 70 (1999) 471.**
  - **C. W. Barnes et al., submitted to Physical Review Letters (2001).**

Why use direct-drive cylindrical implosions to study mix?

- **Purpose**
  - Study Richtmyer-Meshkov (RM) instability in *compressible, convergent, miscible, plasma* system
- **Method**
  - Implode cylinder with an unstable interface and measure resulting mix
  - Diagnostic advantages, fewer ends to affect experiment, convergent
- **Strategy**
  - Compare results from wide variations in initial conditions
    - » Smooth Cl vs. Rough Au interfaces (no mix vs. lots of mix)
    - » Smooth Au vs. Rough Au interfaces
    - » Vary surface roughness
  - Improve design (to make less sensitive to small amounts of marker material) using Al marker and epoxy ablator

We have established a useful, laser-based test bed for mix experiments

- Implode cylinder with thick ablator with 1-ns square pulse direct laser irradiation
- Hydrodynamically unstable at plastic/Au and Au/foam interfaces
- Backlight with x rays through cylinder
- Measure radial extent of "mix layer" of Au into adjacent materials
- 1D convergent experiment with Mach number ≈ 20 (pre-shock; Mach ≈ 5 post-shock), convergence ≈ 4, Pressure > 45 Mbars, Reynold's number ≈10^6*

*Galmiche and Gauthier, *Jpn. J. Appl. Phys.* 35 (1996) 4516

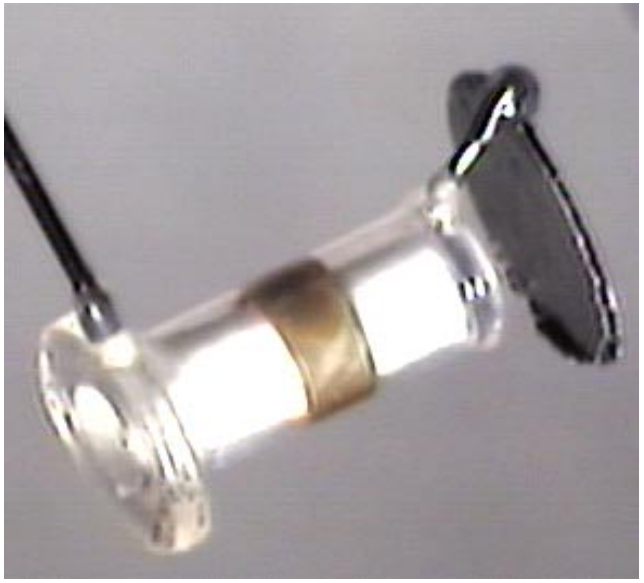

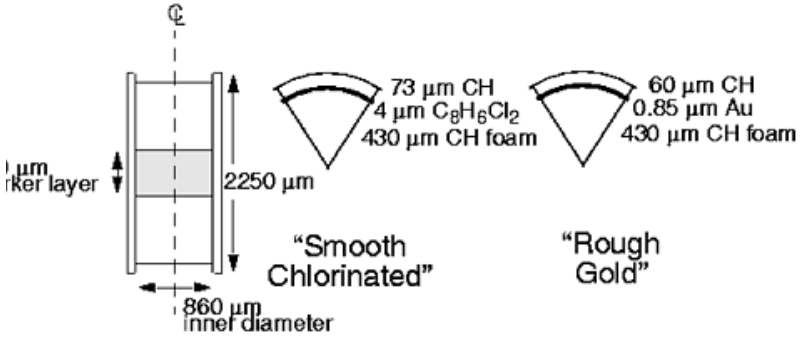

Compressibility and convergence matter to mix

- What mix width do we expect?
- Planar Meyer-Blewett:
  - dH/dt ~ A* U <k>< a_0> ≈ 140 μm in 4ns
    (estimated using measured surface roughness)
- Incompressible Bell-Plesset:
  - Convergence ratio ≈ 4
  - Thickness ≈ 1/δR ≈ 4x more than planar
  - Would be big effect

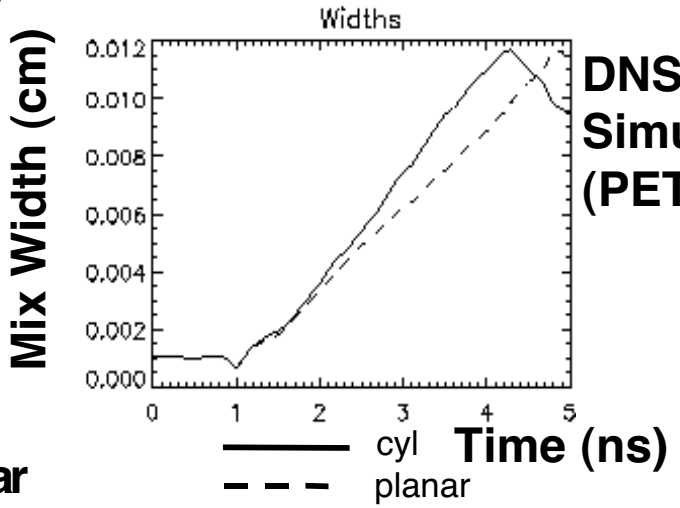

DNS Simulation (PETRA)

- Compressible Bell-Plesset:
  - Shock increases density
  - Convergence also increases density eventually
  - Thickness ≈ 1/δ(ρR) ≈ 1.25x planar, consistent with simulations

Complete Diagnostic Coverage Available

Diagnostics for Shot 13315

(example from thin ablator Rayleigh-Taylor experiments)

Imaging X-Ray Streak Camera

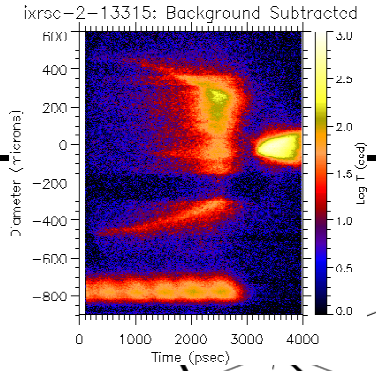

SSC1 Streak of Backlighter

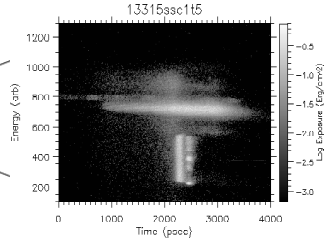

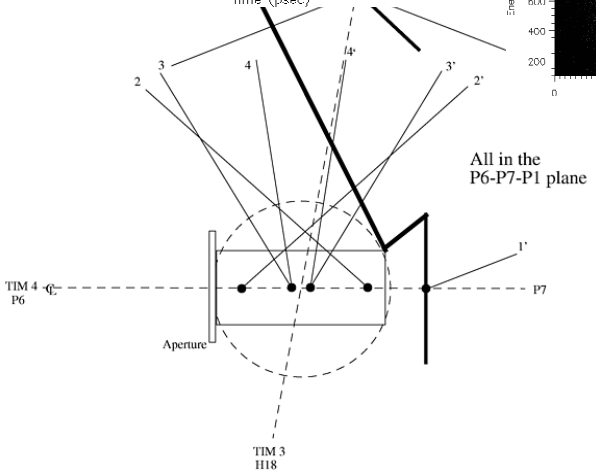

XRFC4 Axial Radiography

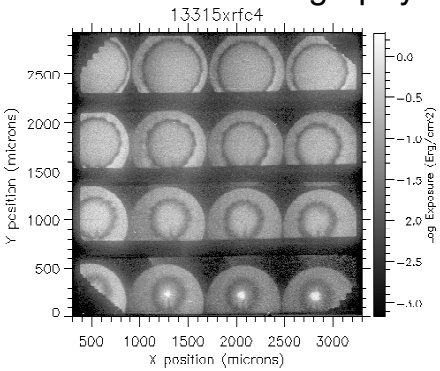

XRFC1 View of Backlighter

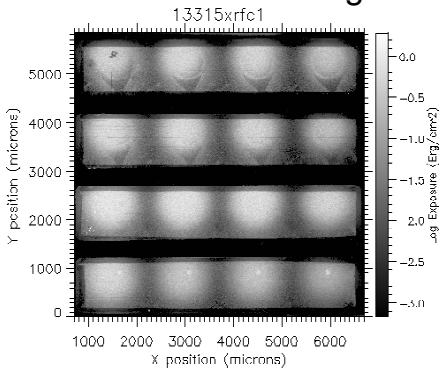

XRFC3 Transverse View of Self-Emission

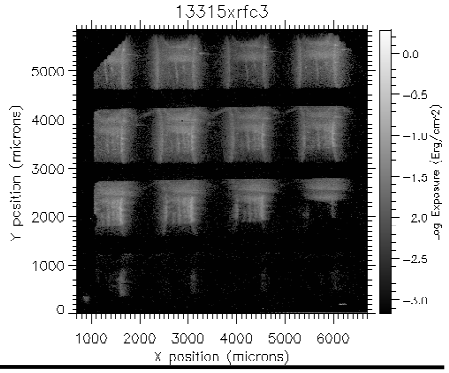

LLE X-Ray Spectrometer Streak of Chlorine Emission

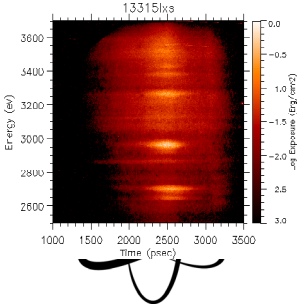

Extremes of mix/no-mix measured, demonstrating principle of experiment

- Different surface roughness
- Different marker layer density
  - Did not change the Atwood number significantly
  - Changed the behavior at the end of the marker layers

Smooth-Cl

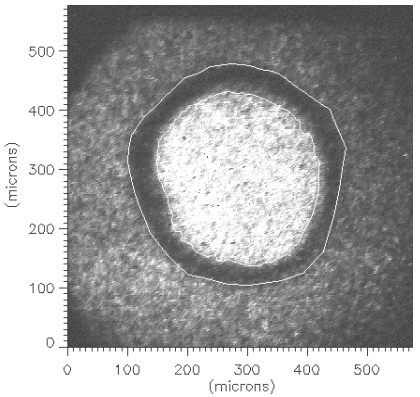

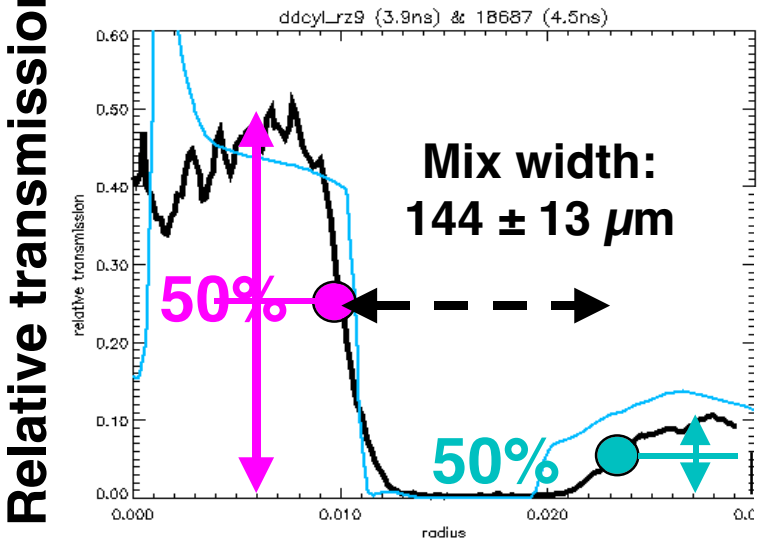

Rough-Au

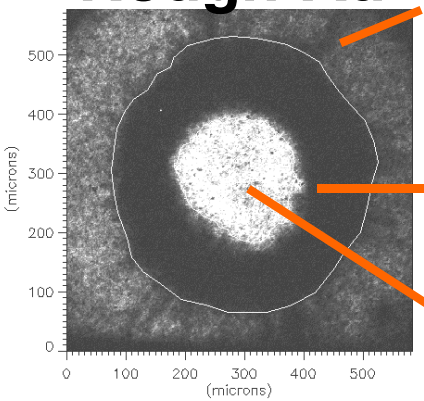

Creation of vorticity at ends of marker layer can increase apparent marker layer width

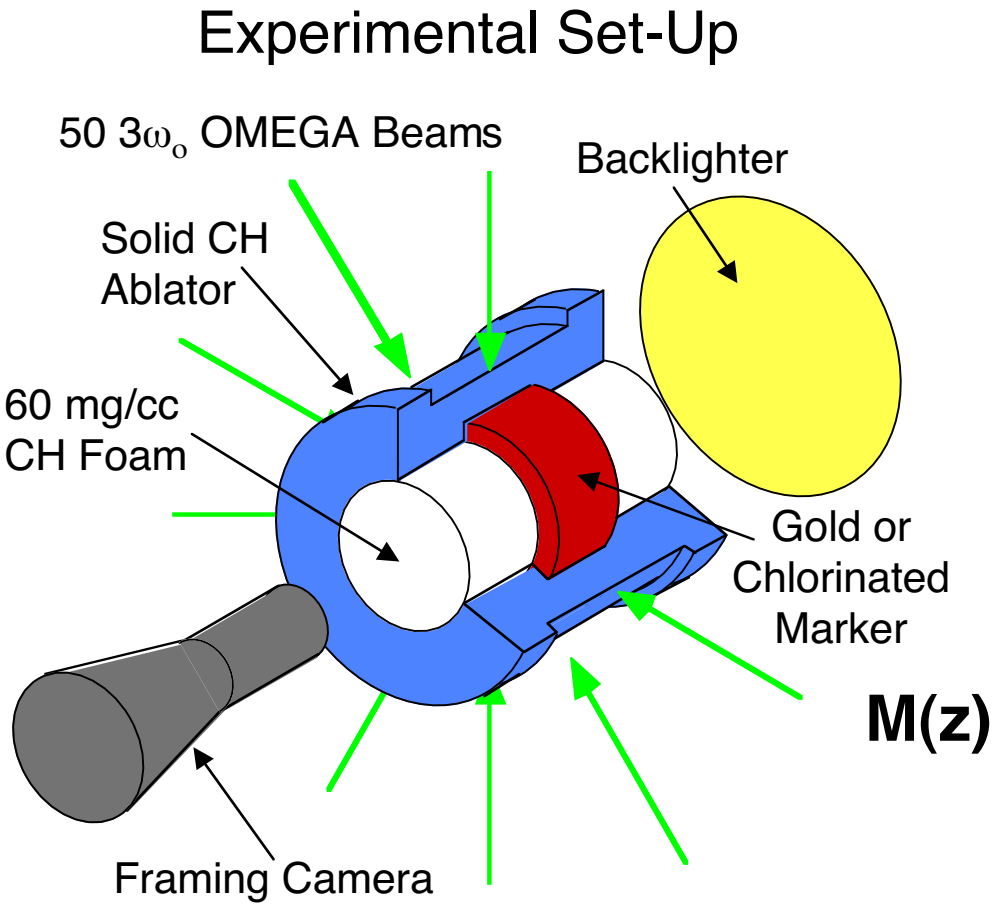

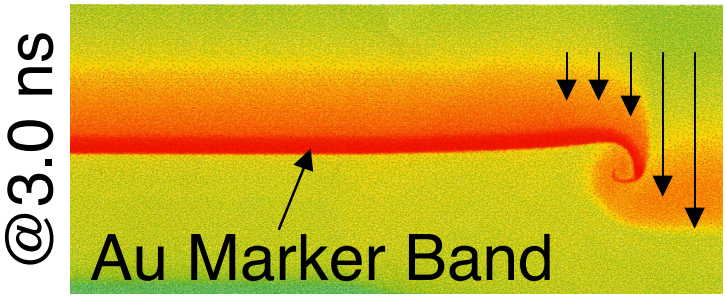

$$M(z) = \int_0^\infty \rho(r,z)\, dr$$

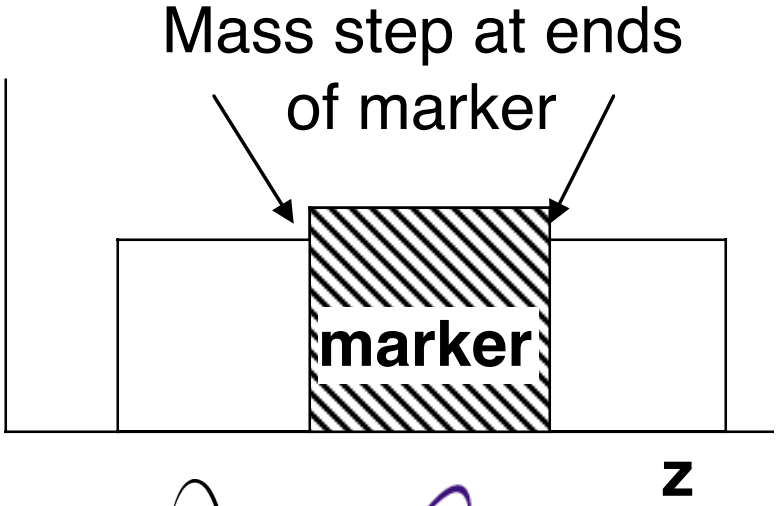

Smoother surfaces don't show as much mix

- Same material
  - Same Atwood number and end effects
- Smooth mix width: ≈ 95 μm
- Rough mix width: 144 μm
- Mixing from larger surface roughness overwhelms end effect, which dominates smooth case

RAGE DNS calculation

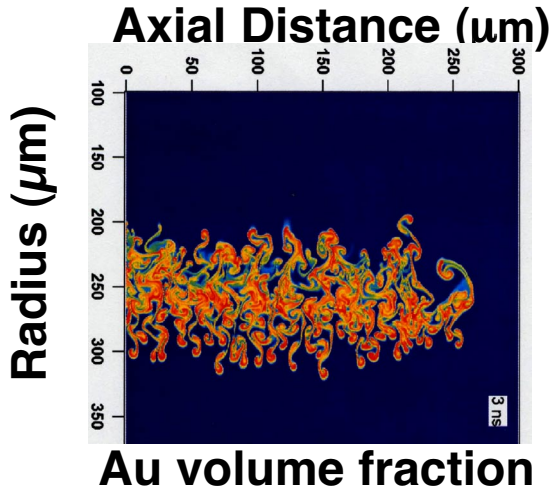

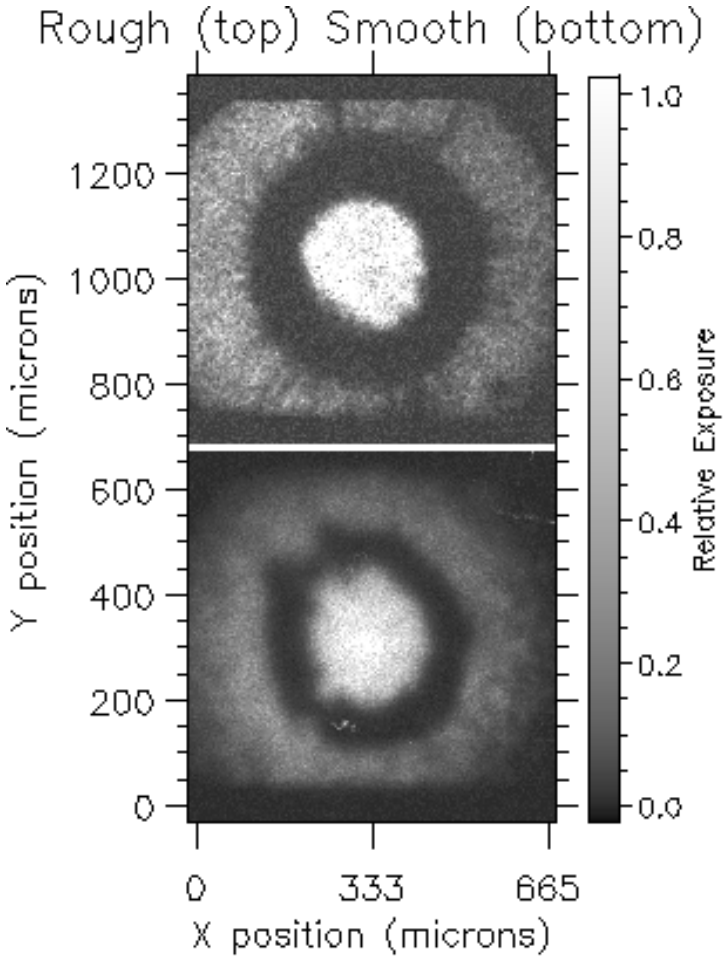

Numerical simulations help uncover the important physics in mix

A wide range of simulations are underway at LANL and AWE

- SOXO : 1D Lagrangian + dynamic mix model
- PETRA : 2-D R-Θ and R-Z semi Eulerian
- TURMOIL : 2D & 3D perfect fluid code
- LASNEX : 2D R-Z
- RAGE : 2D R-Z and R-Θ

Can use measured surface roughness

RAGE does highly resolved simulations*

- **RAGE is an Eulerian, radiation-hydrodynamics code with continuous adaptive mesh refinement**
- **Unlike LASNEX, RAGE can calculate *Rough* surfaces**
- **All calculations included:**
  - **One group (grey) radiation diffusion used in *smooth* cases**
  - **Radiation transport was turned 'off' for *rough* simulations**
    - » **Similar radiographs are produced with radiation transport 'On'**
  - **Sesame equation-of-state and opacities**
  - **LTE**
- **Caveat :**
  - **Rage lacks 3-D Laser raytrace package**
    - » **Laser energy is deposited directly into cylinder surface with an energy source**

***See poster by John Scott**

Calculated axial transmission profiles from more detailed simulations agree with experiments

- **PETRA and RAGE (short dashed lines) predictions in general agreement with observations (solid curve) from initially rough gold markers.**

- **Simulations with smooth initial conditions (as with LASNEX, long dashed lines) predict much smaller mix widths**

- **Some modeling uncertainties remain:**
  - **Absorbed energy affects zero-order hydro**
  - **R-Z and r-Θ calculations differ at 7% level**

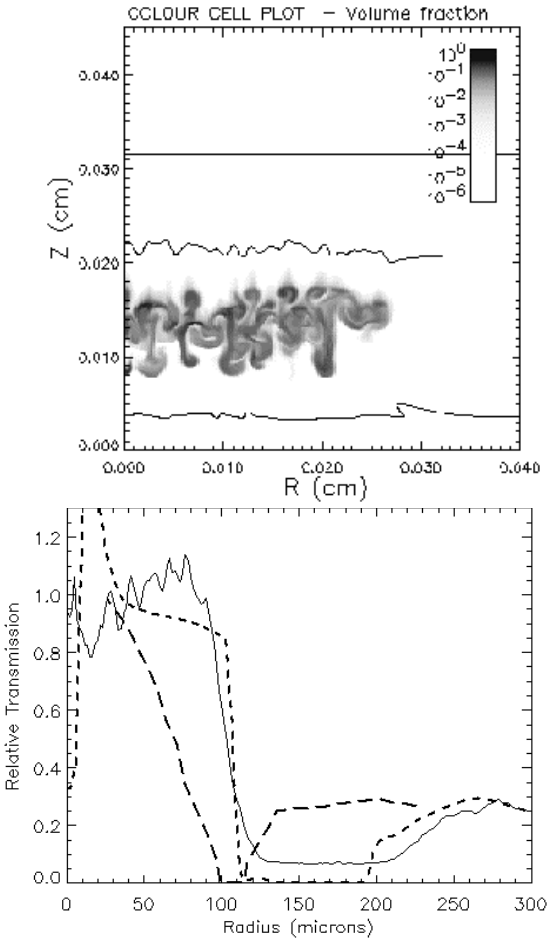

RAGE can simulate as shot *Rough* interfaces, in both R-Z and R-Θ geometries

- **Initial R-Z and R-Q setups with as-shot *rough* surface finish**

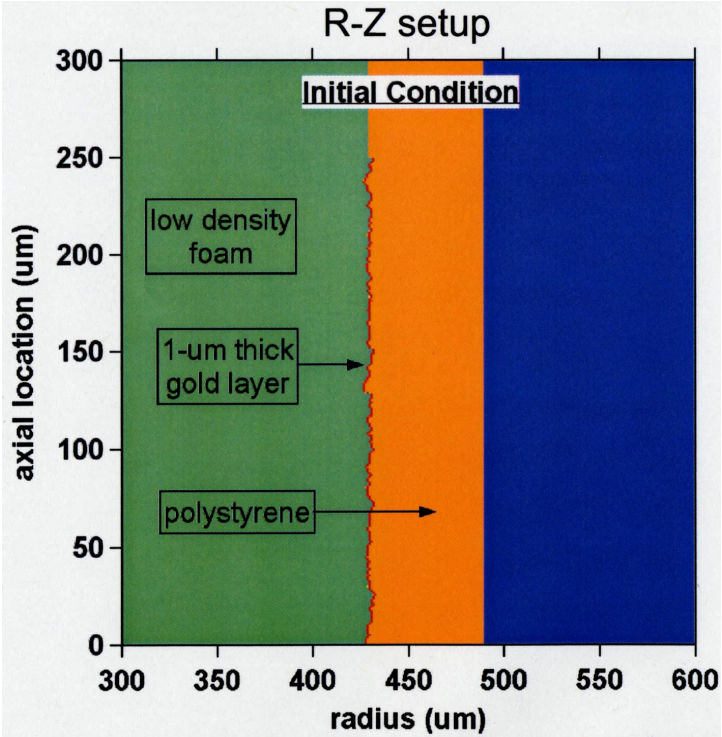

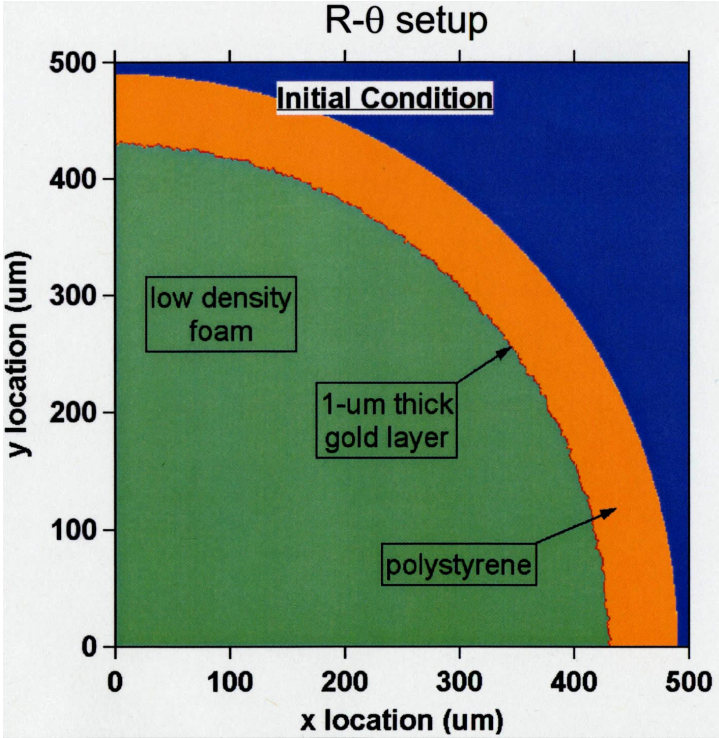

RAGE predicts mix from *Rough* surfaces overwhelms the filigree

R-Z Mix at 3.0 ns

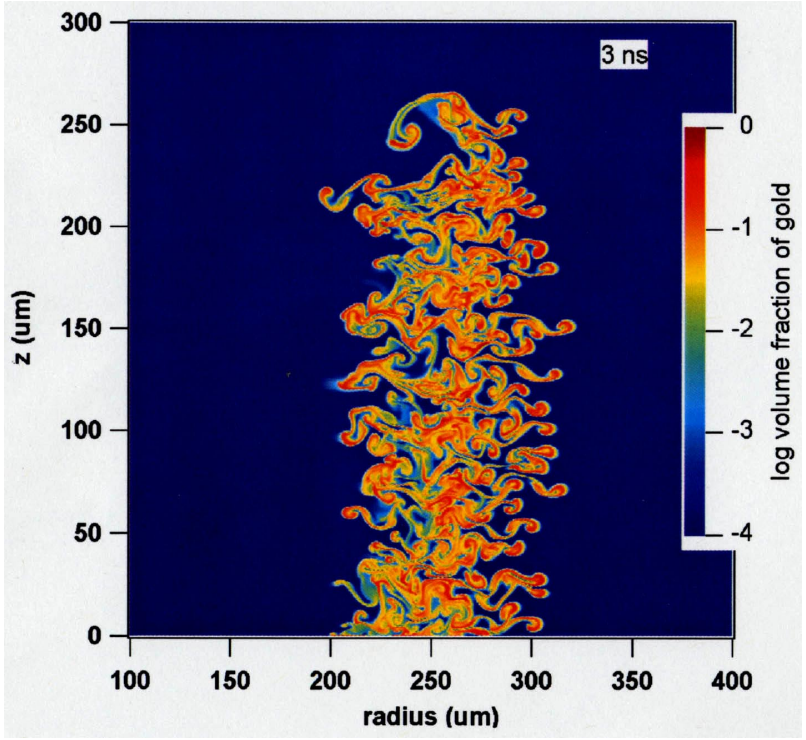

R-Θ Mix at 3.0 ns

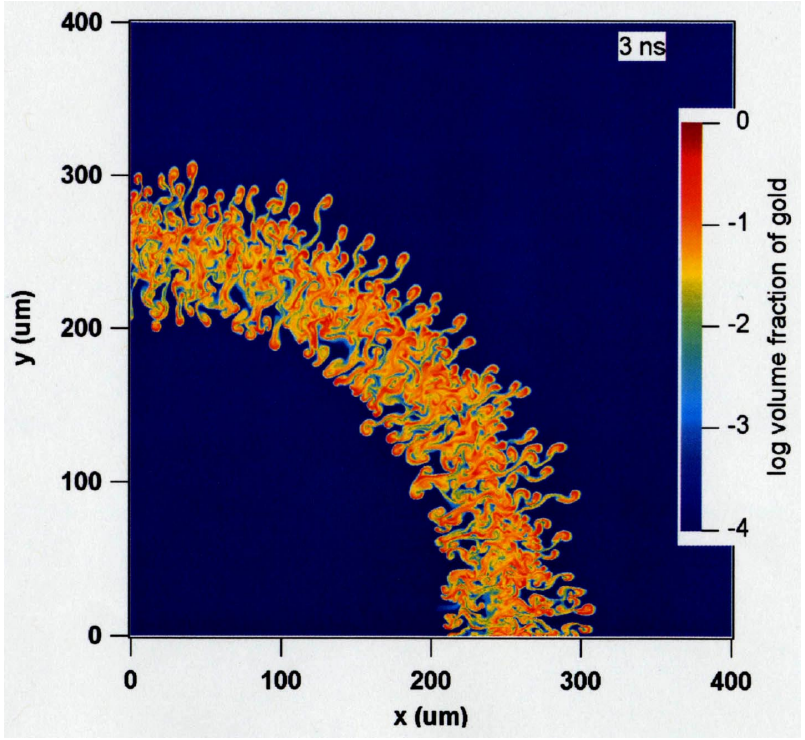

- **Even at 3.0 ns, predicted mix is significant**
- **Of order ~100 *μ*m**

R-θ and R-Z calculations in RAGE agree in implosion hydro and volume fraction

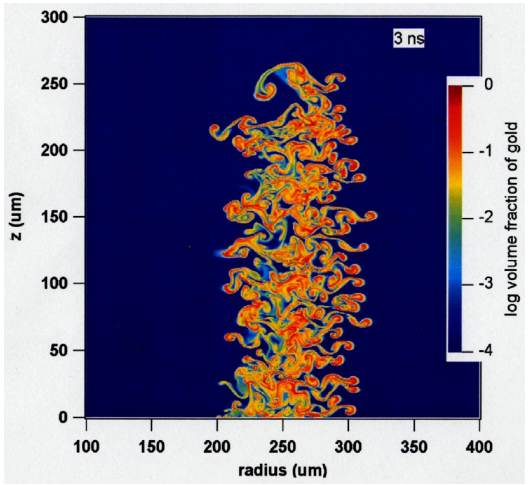

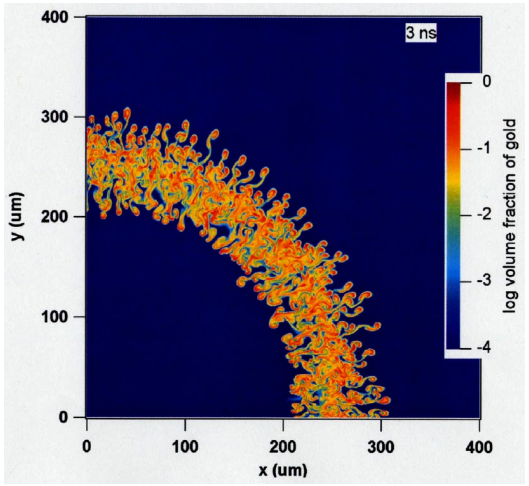

- The zeroth-order hydro is the *same* in RAGE for R-Z and R-θ calculations (same implosion for same energy boundary condition)
- The volume fraction profiles are the same
- The mix width of simulated radiography transmission profiles in R-θ calculations is greater than in R-Z calculations.

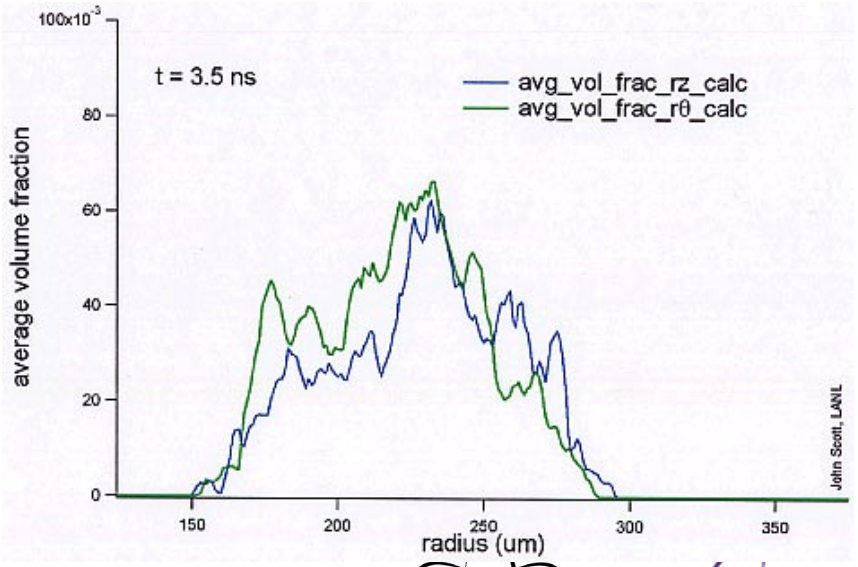

What kind of temporal evolution is expected?

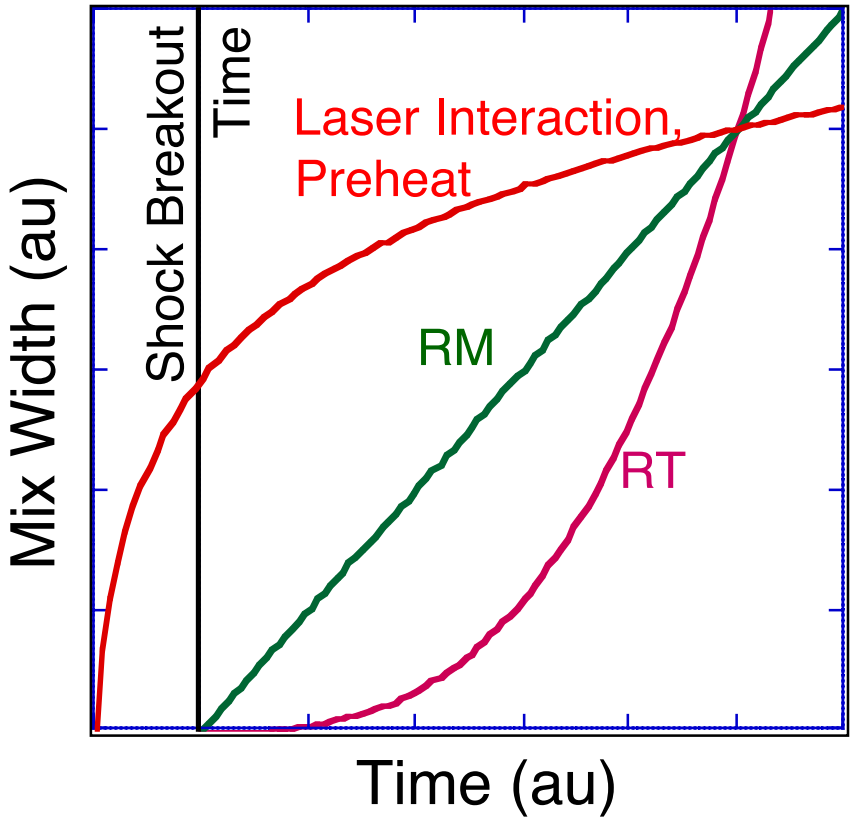

- Preheat effects or strong laser interaction with marker, could make marker initially very wide with little or no subsequent evolution.
- Late-time Rayleigh-Taylor from deceleration could make marker grow quadratic or faster late in time.
- Linear evolution would be consistent with Richtmyer-Meshkov growth.

Multiple measurements in time required to discern cause of mixing.

Time dependent measurements of compressible mix in a convergent geometry have been made

Comparison of cylindrical mix experimental data with simulation

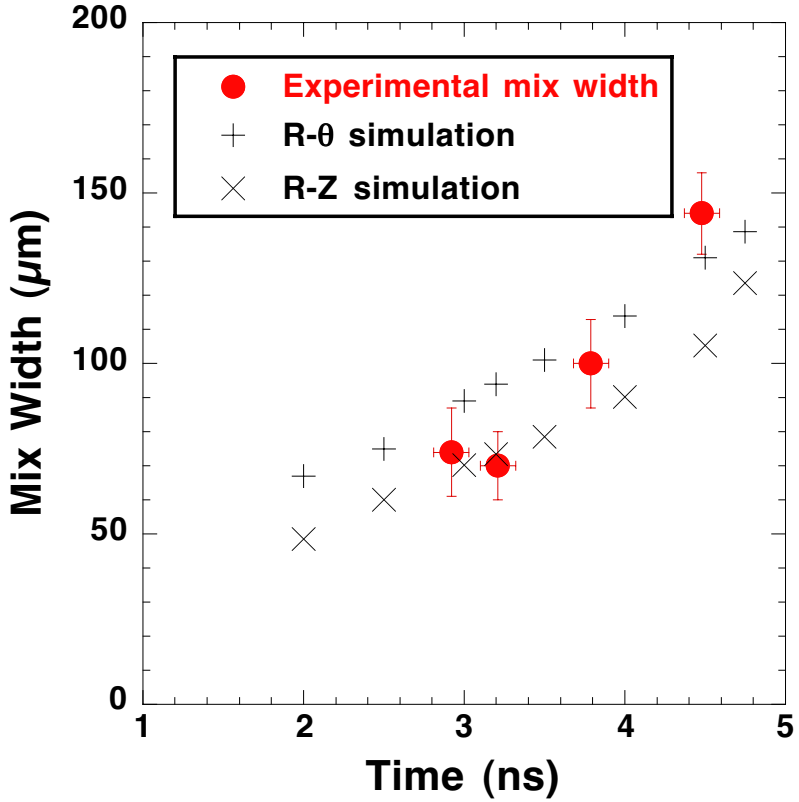

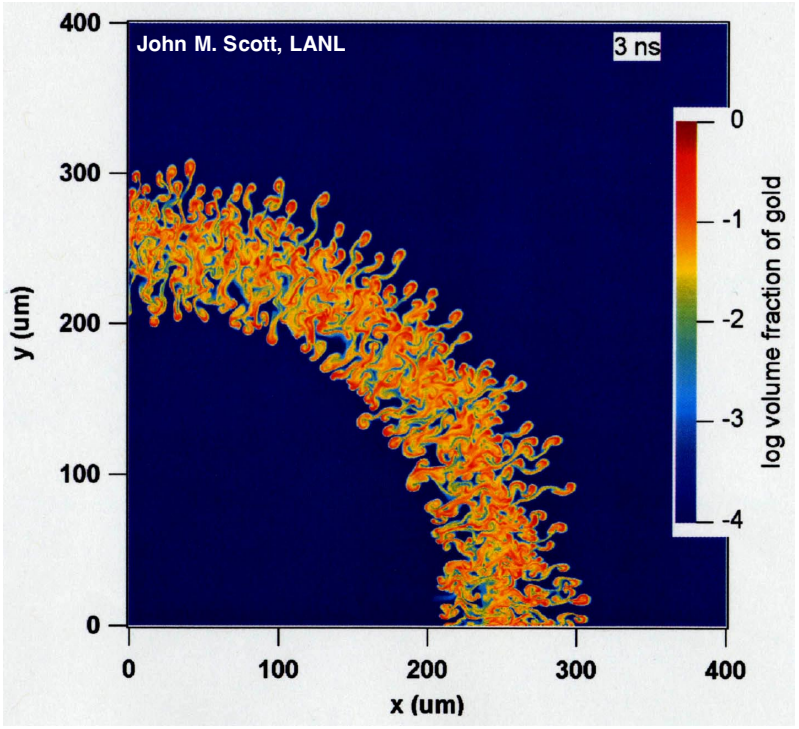

RAGE simulation of experiment

2D and fully 3D TURMOIL calculations predict similar mixing profiles

2D results

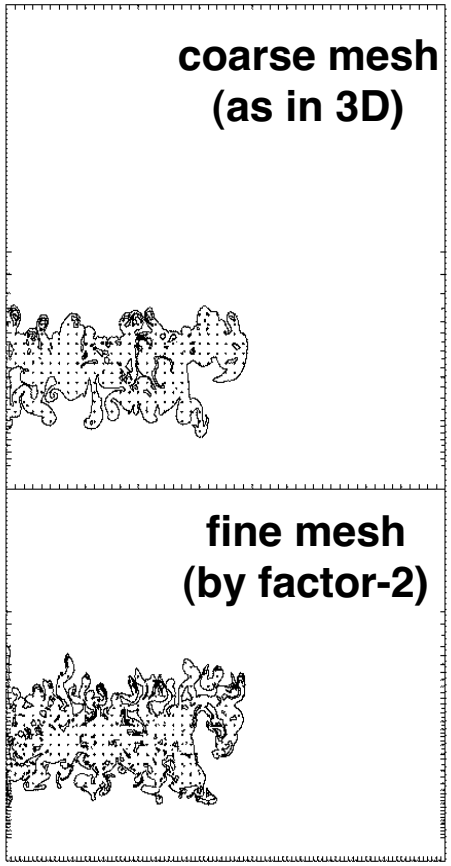

3D results

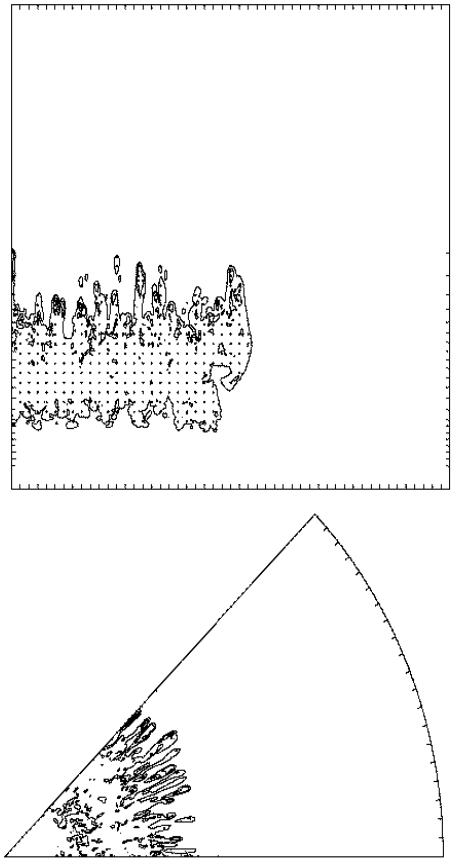

3D code calculates short-wavelength streamers penetrating to high radius (as seen in experiment?)

Overall mix profile similar

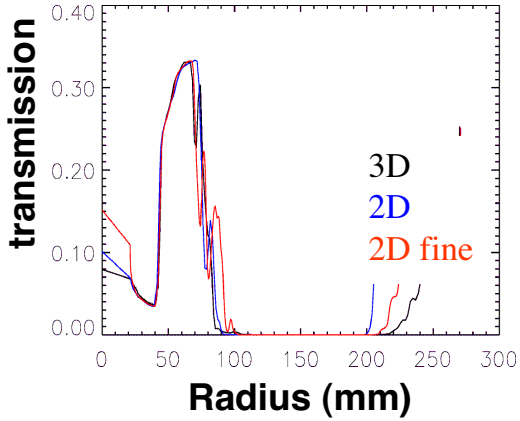

Conclusions

- We have established a useful, laser-based test bed for convergent, compressible, plasma mix experiments
- With sufficiently rough initial surfaces, we see measurable mix which increase close to linearly in time
- Results are in agreement with 2-D (in r-Z and r-θ) and 3-D fully resolved direct numerical simulations
- Future improvements: A lower opacity marker layer will eliminate the end-effect vortical structures

LA-UR-01-6658

Mixing Between Two Compressing Cylinders

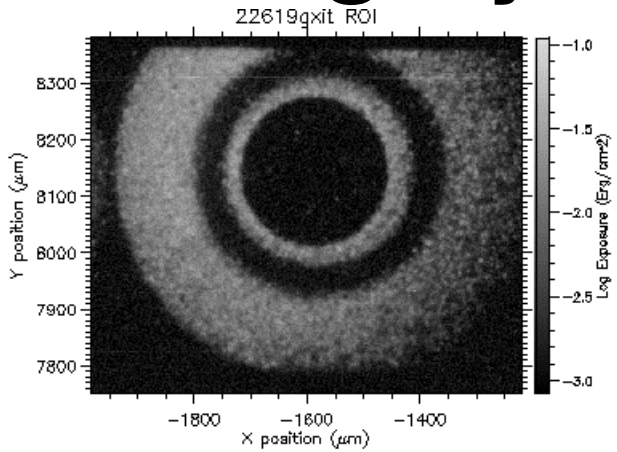

Steven H. Batha

Los Alamos National Laboratory

K. W. Parker,# C. W. Barnes,* A. M. Dunne, # N. E. Lanier,*

G. R. Magelssen,* T. J. Murphy,* S. D. Rothman,#

J. M. Scott,* and D. L. Youngs#

***LANL, #AWE**

8th International Workshop on Compressible Turbulence and Mix

Poster E5; Pasadena, CA December 11, 2001

AWE

Los Alamos

Abstract

- **Foam-filled cylinders have been imploded by the OMEGA laser at the University of Rochester. A marker layer of heavier material is placed between the foam and the outside ablator. The marker layer is hydrodynamically unstable when a strong shock passes through both these interfaces and the marker layer material mixes into the foam and the ablator.**
- **These experiments thus measure mix in the compressible, convergent, miscible, strong-shock regime. These experiments are being extended by placing a solid cylinder at the center of the foam, forming a set of concentric cylinders separated by foam. The initial shock converges on the central cylinder and then rebounds and expands. The shock is predicted to create even more mixing of the marker layer as it traverses the previously mixed region. We present experimental measurements of this configuration.**

- **LA-UR-01-2575:** ***This document was produced by the Los Alamos National Laboratory under the auspices of the United States Department of Energy under contract no. W-7405-ENG-36.***

Why direct-drive cylindrical implosions?

- **Purpose**
  - **Study Richtmyer-Meshkov (RM) instability in *compressible, convergent, miscible* systems undergoing *strong shocks***
  - ***Examine mixing due to reflectance of a shock from the center (reshock)***
- **Method**
  - **Implode cylinder with an unstable interface and measure resulting mix**
  - **Diagnostic advantages, fewer ends to affect experiment, convergent**

- **This poster presents initial experimental results**
- **See Kenny Parker's poster for design information**
  - **"Computational Modeling of 2 – Shell Cylindrical Implosions with Mix" for design information**

We have established a useful, laser-based test bed for mix experiments

- Implode cylinder with thick ablator with 1-ns square pulse direct laser irradiation
- Hydrodynamically unstable at plastic/Au and Au/foam interfaces
- Backlight with x rays through cylinder
- Measure radial extent of "mix layer" of Au into adjacent materials
- 1D convergent experiment with Mach number ≈ 20 (pre-shock; Mach ≈ 5 post-shock), convergence ≈ 4, Pressure > 45 Mbars, Reynold's number ≈10^6*

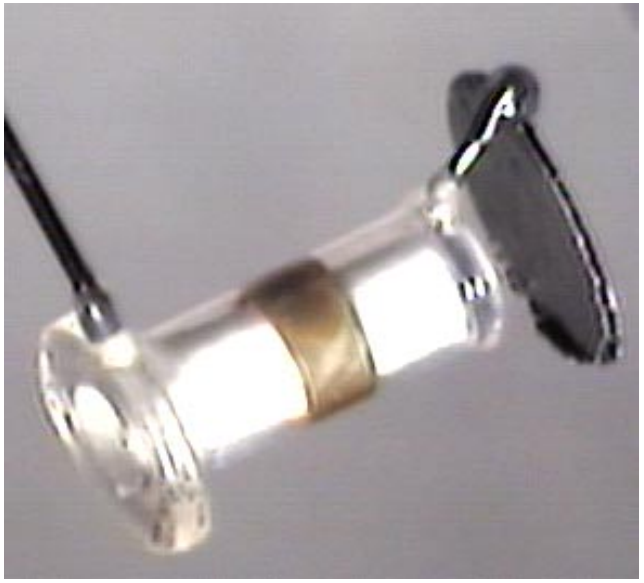

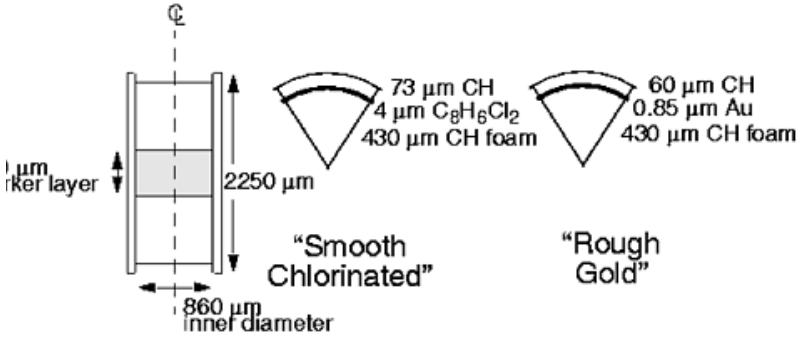

*Galmiche and Gauthier, *Jpn. J. Appl. Phys.* 35 (1996) 4516

We use the Omega laser at the University of Rochester

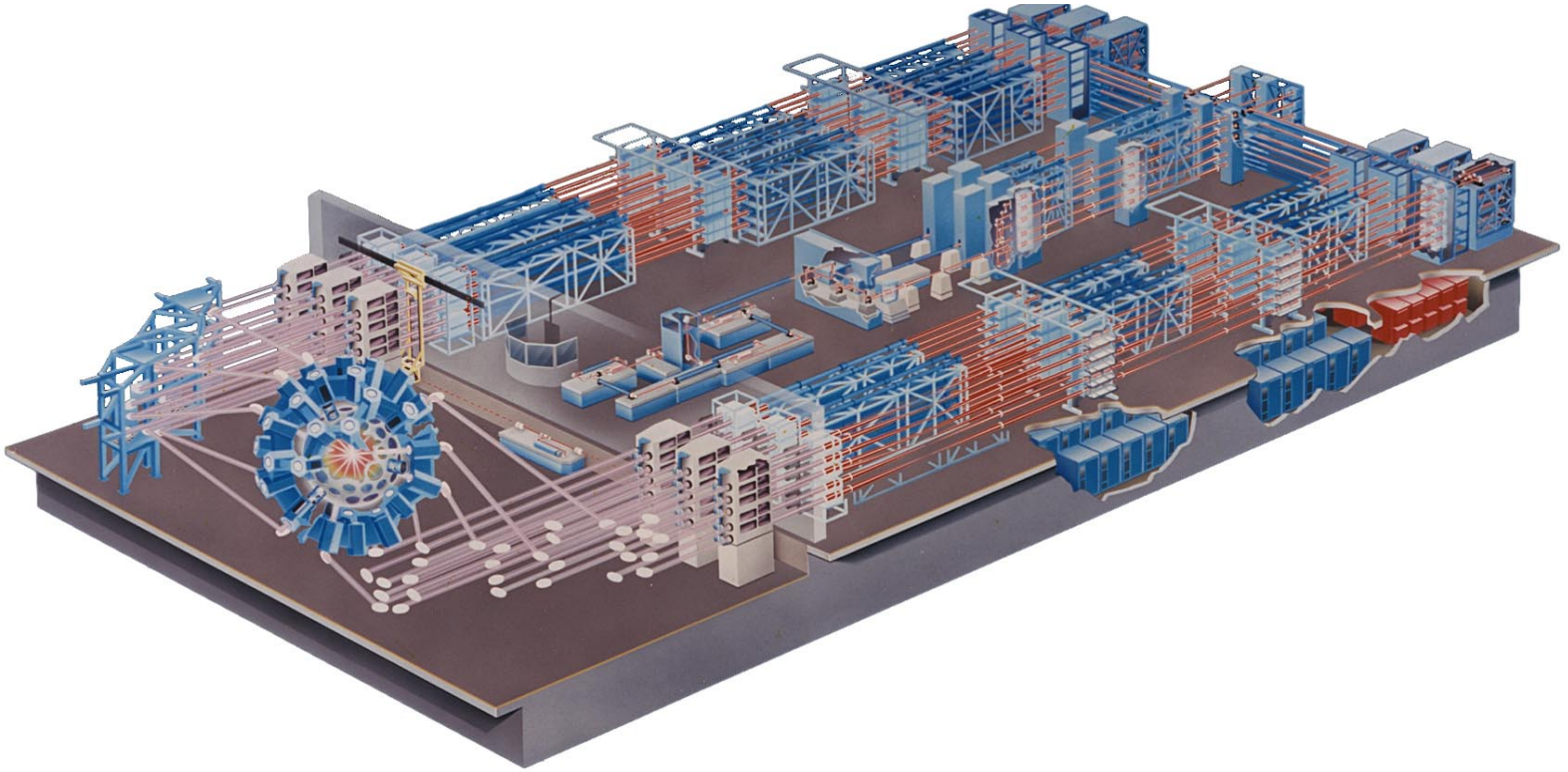

- 60 beams
- >30 kJ UV on target
- 1%–2% irradiation nonuniformity
- Flexible pulse shaping
- Short shot cycle (1 h)

Complete Diagnostic Coverage Available

- **Diagnostics for shot 13315**

Imaging X-Ray Streak Camera

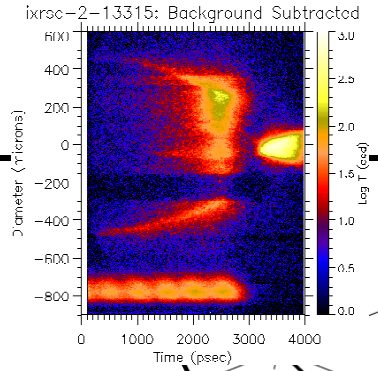

SSC1 Streak of Backlighter

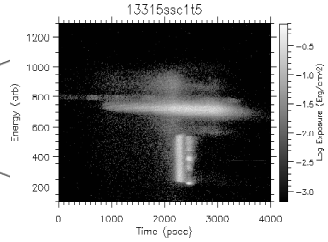

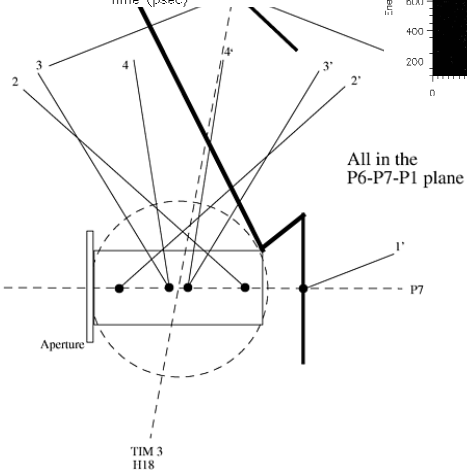

XRFC4 Axial Radiography

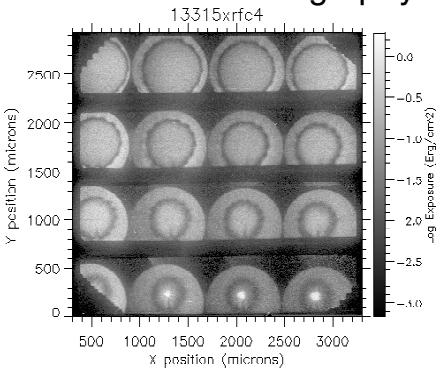

XRFC1 View of Backlighter

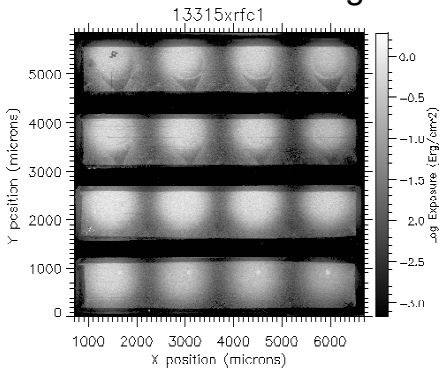

XRFC3 Transverse View of Self-Emission

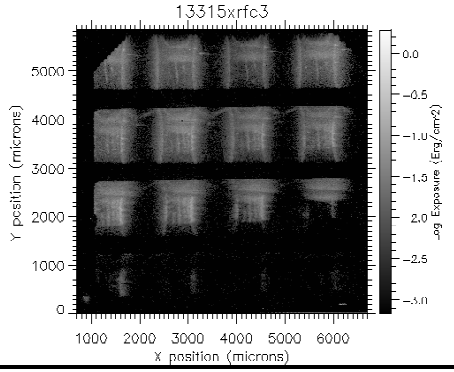

LLE X-Ray Spectrometer Streak of Chlorine Emission

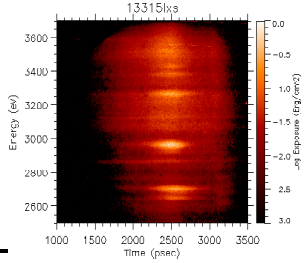

Double cylinder adds an inner shell

- Al or Cu wire in center provides a hard reflector for the main shock
- Wire: 700 μm long
- Marker layer: 500 μm long

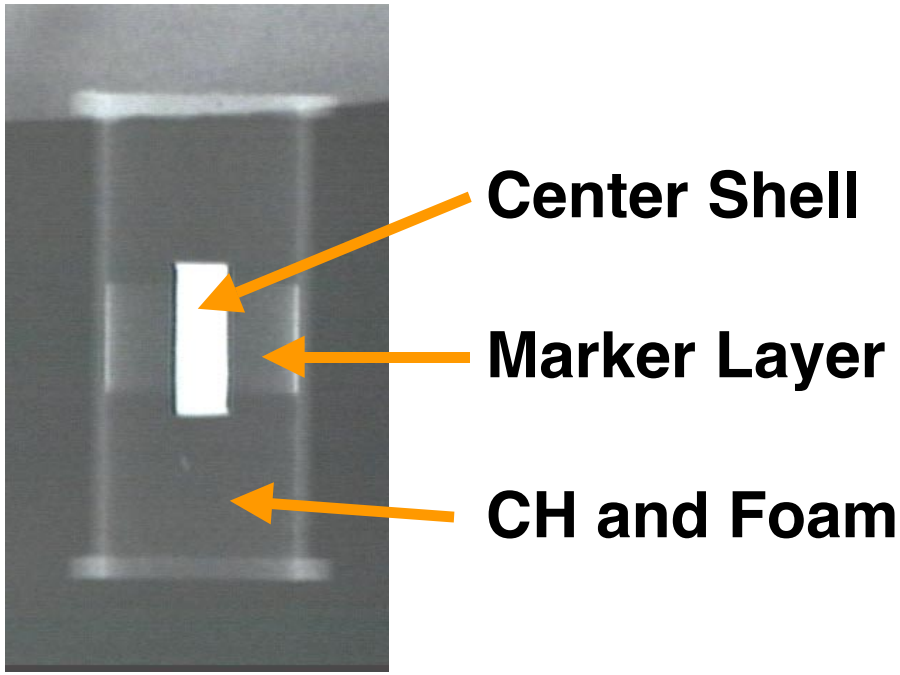

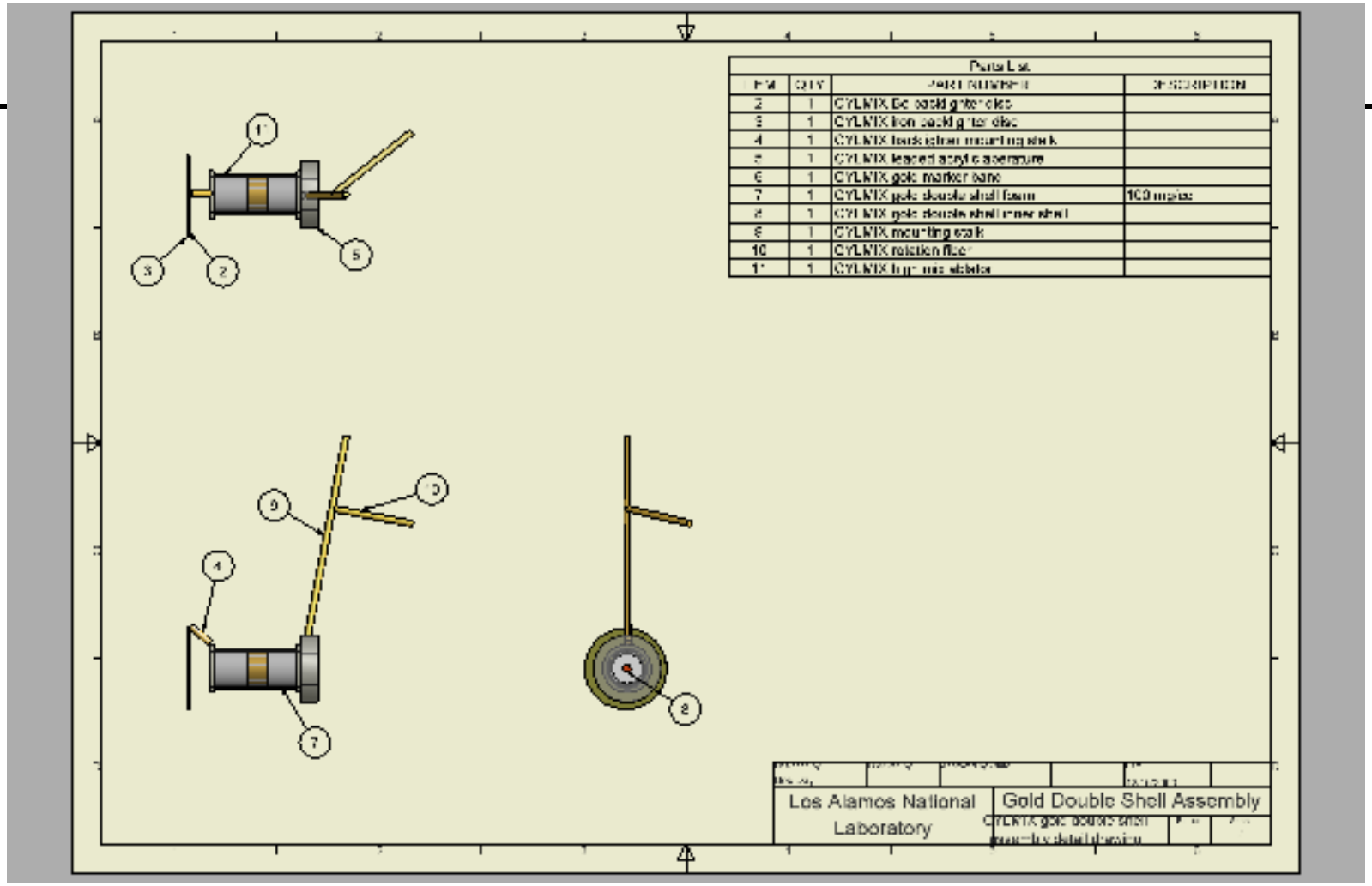
Parts List
ITEM
QTY
PART NUMBER
DESCRIPTION
2 1 CYLNDX Be solid glow plug
3 1 CYLNDX Iron solid glow plug
4 1 CYLNDX back-iron mounting stalk
5 1 CYLNDX leaded acrylic aperture
6 1 CYLNDX gold marker cone
7 1 CYLNDX gold double shell foam 100 mg/cc
8 1 CYLNDX gold double shell inner shell
9 1 CYLNDX mounting stalk
10 1 CYLNDX rotation fiber
11 1 CYLNDX high-mass stalktop
Los Alamos National Laboratory
Gold Double Shell Assembly

Intershell region undergoes strong shocks and mix

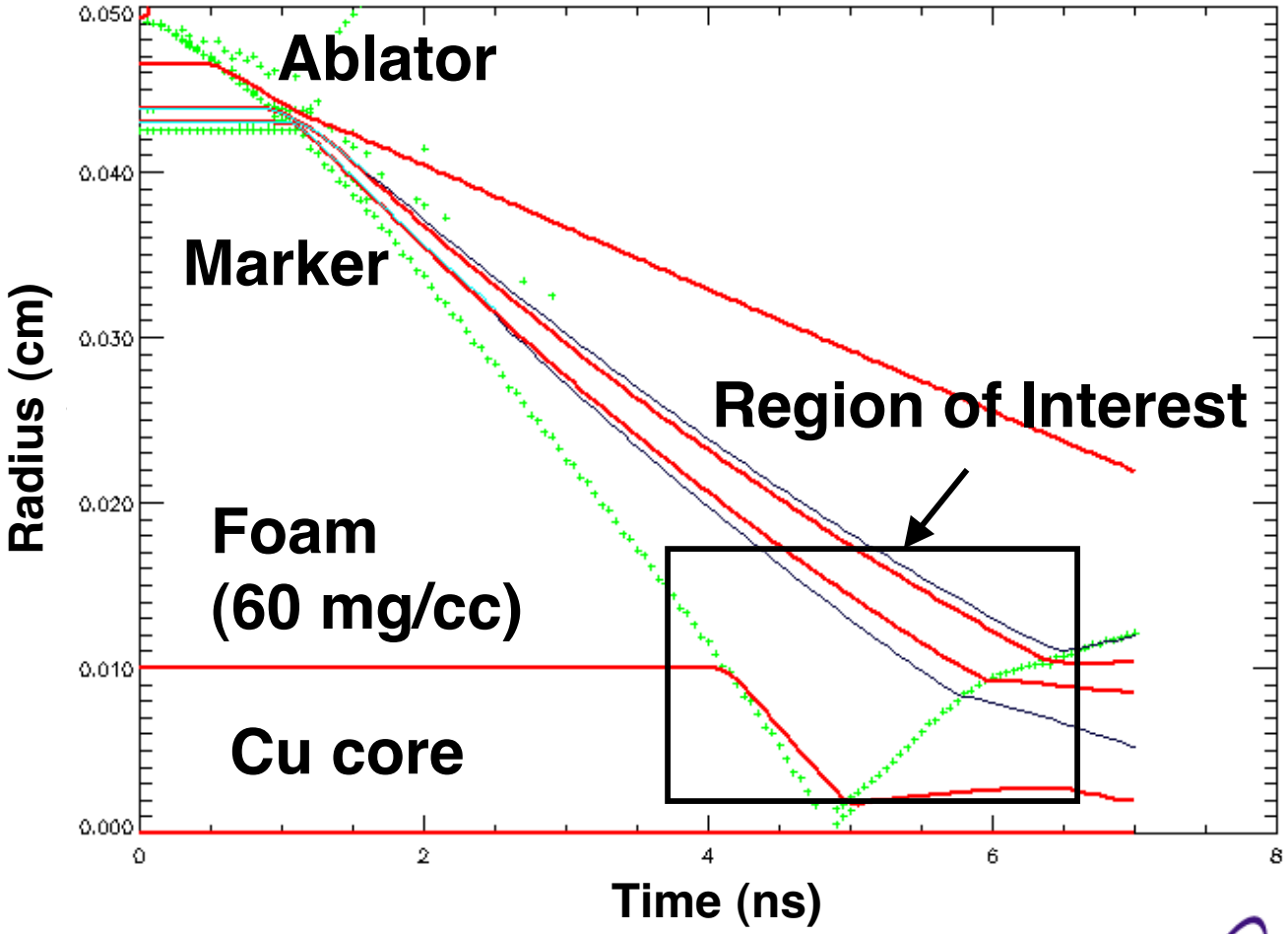

Time/space regions of interest

- Proof-of-principle experiment based on low-mix design
- Solid, centered Al “shell”
- Want to diagnose mix between shells

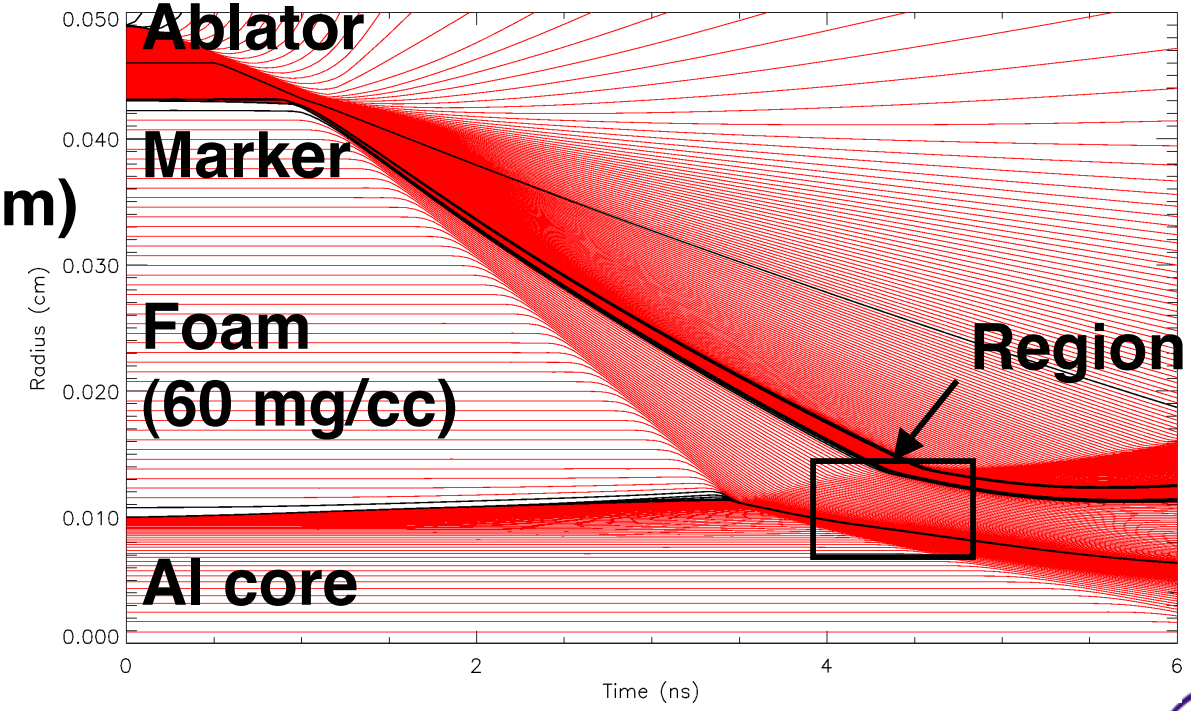

Radius (cm)

Time (ns)

Intershell region clearly visible

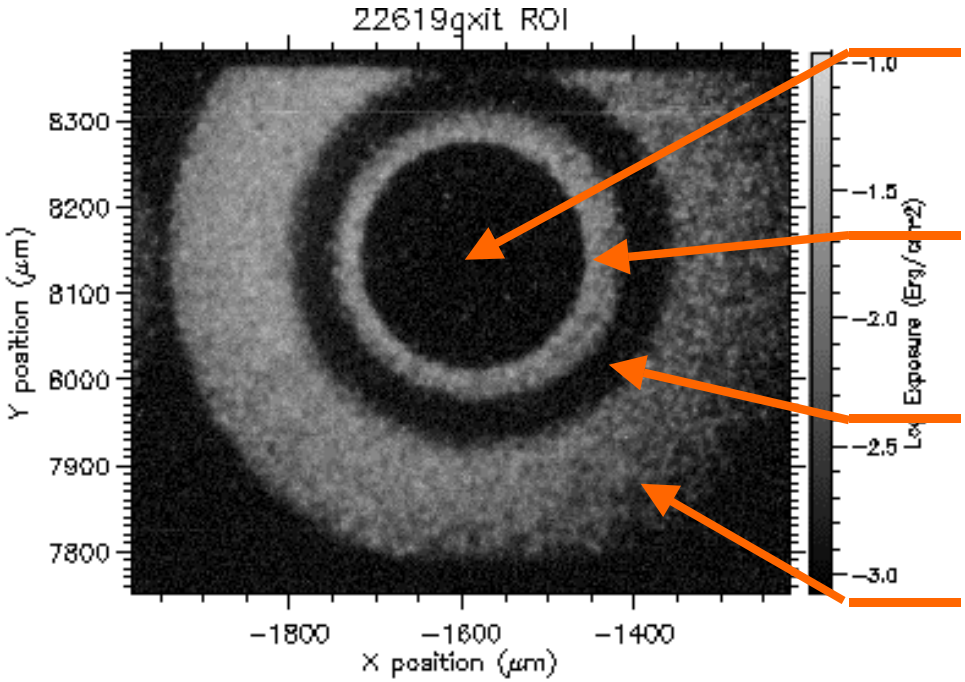

Cu center shell (opaque)

Foam between shells (transparent)

Ni marker layer (opaque)

Plastic ablator (transparent)

- **Marker mixes into foam and ablator**
- **Radiograph at 6.9 keV (Fe K-shell)**
- **Backlighter intensity varies smoothly across image**

Radial lineout shows different regions

- **Average radial transmission profile**

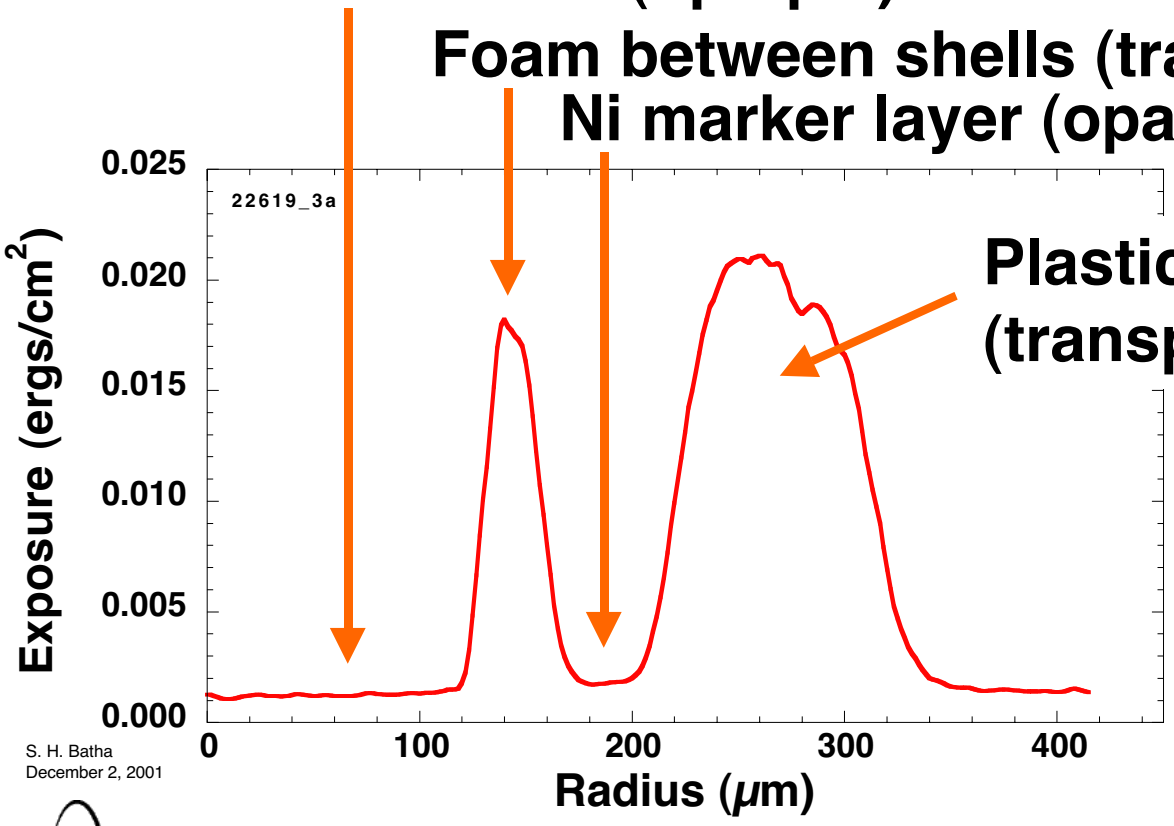

Compare double to single cylinders

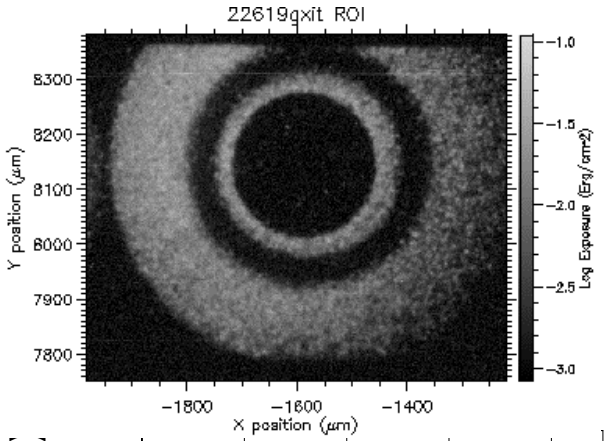

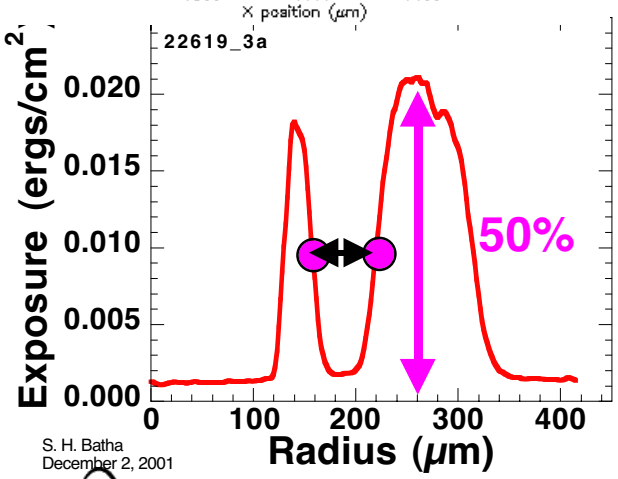

50%

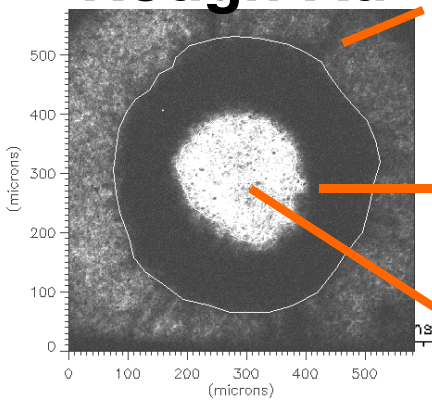

Rough-Au

Outer Ablator

Mix Region

Foam Core

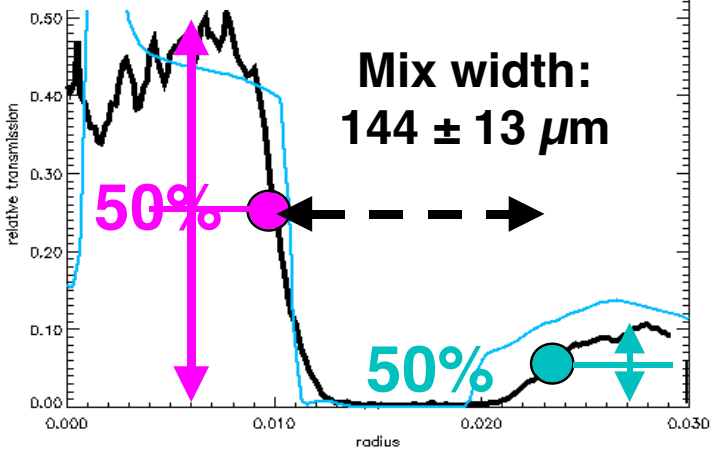

S. H. Batha
December 2, 2001

Marker layer has expanded near peak compression

- Marker/inner shell separation initially 290 μm
- 4-μm-thick Ni marker
- Mix width ≈ 65 μm

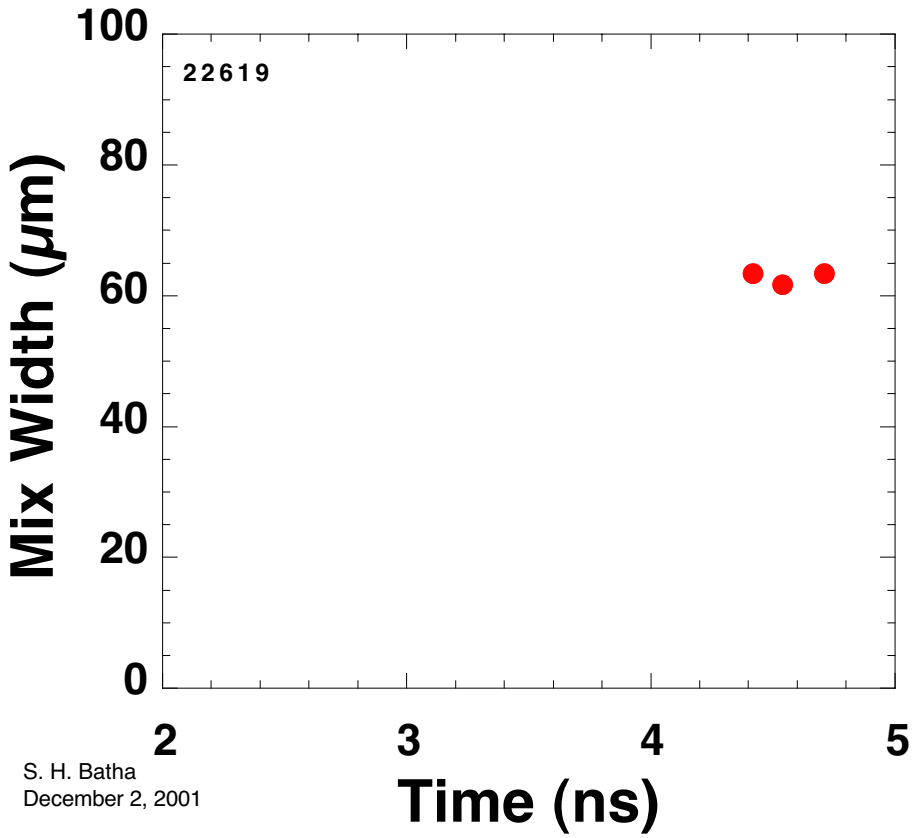

S. H. Batha
December 2, 2001

Dynamics of implosion as expected

- Little change in outer-shell radius seen over 400 ps
- Central shell has not expanded (initial radius ≈ 140 μm)

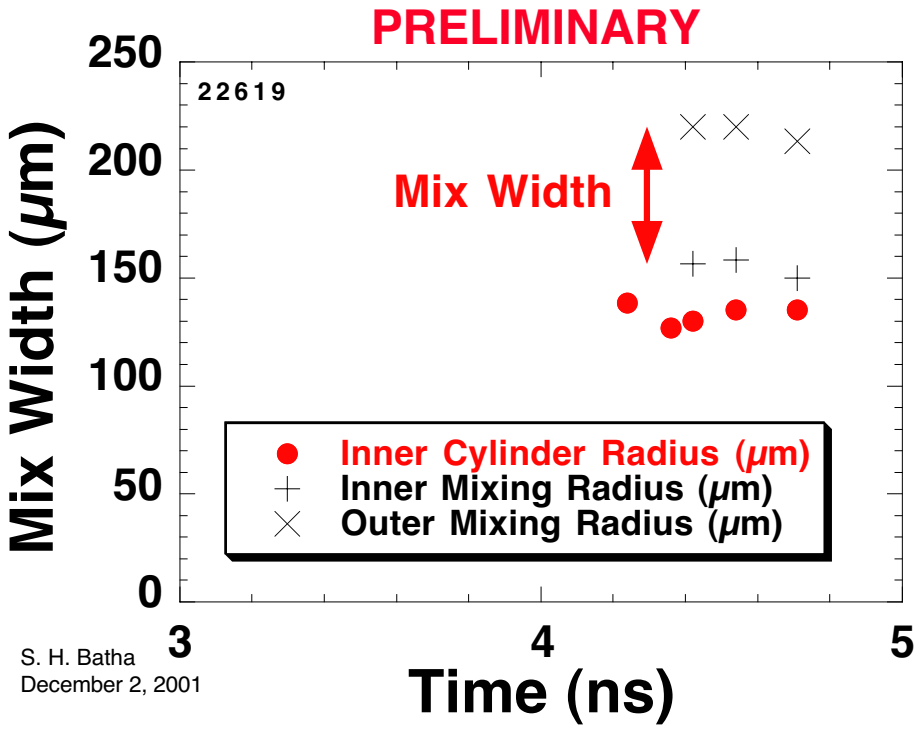

Conclusions

- Double-cylinder targets can be built and fielded
- Excellent radiographic data of intershell region obtained
- Central shell does not expand during experiment
- Mixing observed
- See Kenny Parker's poster (C28)

DEVELOPMENT OF THE METHOD FOR INTERACTION BETWEEN SHOCK WAVE AND FLAME

M.Bliznetsov[1], *V.Dudin*[1], *S.Gerasimov*[1], *L.Houas*[3], *G.Jourdan*[3], *A.Logvinov*[1,2], *E.Meshkov*[1,2], *Yu.Vlasov*[1]

[1]Russian Federal Nuclear Center – Institute of Experimental Physics (VNIIEF), 607190, Sarov,Russia
[2]Sarov Physics Technical Institute, 607190, Sarov, Russia
[3]IUSTI/CNRS UMR 6595, Universite de Provence, Technopole de Chateau-Gombert, 13013, Marseille, France

1. Introduction.

Wild fires are disastrous events damaging the environment. Numerous examples show that extinguishing the wild fires is a hard line, which does not ever finish successfully. Let us remember, for example, the fire in the Los Alamos region in spring, 2000.

There is a method of extinguishing the wild fires by means of exploding of longitudinal charge located before the flame front [1,2]. Here, there is observed the amplifying of the shock wave after it passing through the flame zone. The effectiveness of the method was experimentally demonstrated [3]. However, it is not put into practice.

According to the authors' hypothesis [3] this extinguishing is due to blowing a flame off by a shock. Amplifying the shock is considered in terms of additional explosion of a mixture consisting of air and pyrolysis products (PP) from crown fragments (pine needles, small branches, and leaves). This additional explosion is supposed to follow a shock from initial explosion.

There is another hypothesis [4], which considers the process is due to growing the hydrodynamic instabilities.

On explosion of a cylindrical longitudinal charge, an expanding non-steady shock is generated. The substance accelerates on the shock wave front, and, then decelerates. When the shock wave passes through the flame front, this corresponds to its propagation from a substance with a more high density (PP-air mixture) into another of lower one (flame). As a result, we have conditions for occurrence of instability induced by the shock wave [5,6], and then, the conditions of Rayleigh-Taylor instability arise for the flow behind the front of shock wave because the acceleration directs from light to heavy substance [7,8].

Thus, the instability of flame front grows, and an intense mixing between flame and PP-air mixture should arise, so it should effect the sharp combustion of this mixture. A rapid (or possibly, explosive) combustion of the mixture should result in generation of a compression wave (or series of compression waves) overrunning and amplifying the shock wave generated by the charge explosion.

Experimental research with a real wild fire is rather complex, dangerous, and expensive. That is why the new methods for study the interaction between non-steady shock with a flame front in cases close to a crown forest fires are of actual interest.

The results obtained at developing such method are presented below.

The most complex problem here is to create a model even qualitatively related to peculiarities of crown fire propagation:

- generation of gaseous explosive mixtures before flame front due to its high temperature
- high rate for the flame front propagation

For study the interaction between non-steady shock with a flame front we suggest a spatial model consisting of parallel (or diverging from a point) threads or rods along which an inflammable substance able to be fume before a flame front is distributed.

A non-steady shock could be generated towards the flame front propagating through the model; so, one can observe the process of the shock-flame interaction. The means for generating the non-steady shock could be different for different scales:

- electrical explosion of a wire tightened before the lame front;
- shock tube with compressed gas or gaseous explosive mixture as a driver [9];
- explosion of a longitudinal HE (for example, detonation flex).

2. Experimental research for the spatial thread model.

First stage dealt with laboratory experiments using a small spatial model consisting of threads diverging from a point.

At first we performed experiments with one and two threads. The threads were saturated with combustible liquid. Such liquids were alcohol, acetone, solvent 646, and kerosene. As it turned out kerosene was the most suitable. Kerosene as well as PP is a limiting hydrocarbon.

The flame propagation was visualized by video.

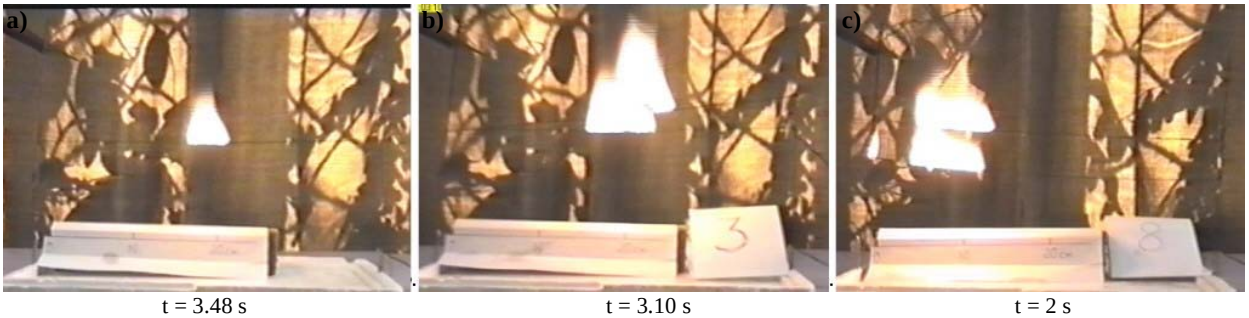

t = 3.48 s t = 3.10 s t = 2 s

Figure 1. Flame propagation along a) a thread saturated with kerosene, b) two threads diverging from a point, c) two parallel threads

Figure 1 presents the frames of the flame propagation a) along a thread, b) along two threads diverging from a point, and c) along two parallel threads. The frames show that in b) case the upper flame overruns the low – it was due to the dependence of flame rate on slope tangent. We performed a series of tests varying the slope tangent. The results obtained were handled (Figure 2). Ought to note the linear character for the dependence.

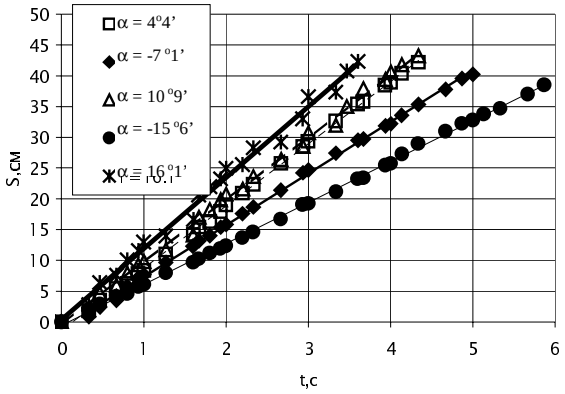

Figure 2. Dependence in time *t* of the flame front propagation *S* along a thread on its slope tangent α. The angle is counted from skyline, positive direction at propagation from below.

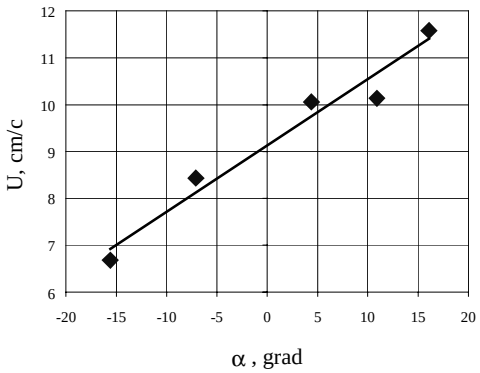

Figure 3. Dependence of rate of flame propagation *U* along a thread against its slope tangent α.

The measured rate of flame propagation for the tests is presented in Figure 3.

Figure 4 shows the frames for flame propagation in a model consisting of 25 threads diverging from a point. The ends of threads were fixed in knots of a grid (5×5) with a cell of 2 cm. The threads were saturated with kerosene.

Figure 5 shows the results of measurements for this model.

It should be noted that at recording the process from side one could find a) a weak acceleration of the flame front and b) overrunning for the second thread from the top (Figure 4,a a frame at 3.15 s.) but not for the upper. Simultaneously, at recording from above one could observe the overrunning in the middle region (Figure 4,b).

These effects could be related to the heating of the threads before the flame front and evaporating of the combustible liquid from the threads. A more intensive heating of the threads should be realized in the middle region of the front. Due to the more intensive heating a more intensive evaporation of the combustible liquid is realized that corresponds to a more rapid propagation of the flame front.

These effects are weakly found here owing to the small sizes of the model; apparently, increasing the scale of these effects should follow increasing the model sizes.

3. Shock wave and flame interaction. Preliminary tests.

We have performed a few preliminary tests for the shock wave and flame interaction. There were two types of the tests:

1. The shock wave was induced by electrical explosion of a thin metal wire (nickel-chrome, 0.05mm) through which there was realized a discharge from a capacity of 0.1mcF at 60kV. It was followed by a cylindrical shock wave.

The shadow pattern of the interaction between the shock wave and the flame propagating along a thread saturated with kerosene was visualized with a high-speed camera.

The thread and wire were located in the same plane; the axis of the thread was normal to the wire's.

The frames for the interaction process are presented in Figure 6. One can find the following stages of the process:

- some displacement of the flame under shock wave
- generation of a part of the shock wave passed through the flame and overrunning the main part of the front (ShW_1)
- growth of perturbations on the initially smooth, laminar flame front with its further turbulence. In this test the flame was more probably extinguished due to blowing it off. But it is a fact that the flame being initially laminar with a rather smooth front got unstable and turbulent.

2. In test (Figure 8) the shock wave was generated through detonation of a layer (8×8×2 cm) of gaseous explosive mixture of acetylene and oxygen. Initially, the mixture filled the volume of a shock tube [9] with rigid lateral and back walls; the output window was closed with a thin mylar film of 0.9mm - thickness.

In this case the flame was generated on a spatial model with 25 parallel threads saturated with kerosene. Figure 8 shows the frames of shadow pattern for the interaction process. The shock wave was stronger (2-3 Mach) in this case. The flame was extinguished with the wave. There were observed both the perturbation growth and sufficient displacement of the flame under the wave.

a)

t = 0 s.

t = 1.14 s

t = 3.15 s

t = 5 s

b)

t=0 s

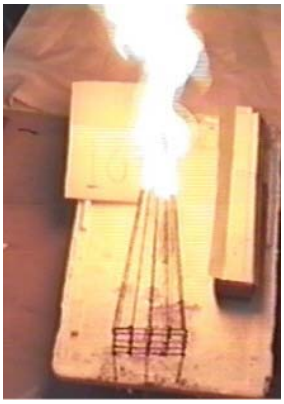

t = 2.15 s

t = 4 s

Figure 4. Flame propagation along spatial model consisting of 5×5 threads diverging from a point a) side view, b) from above view (test N16 and 18)

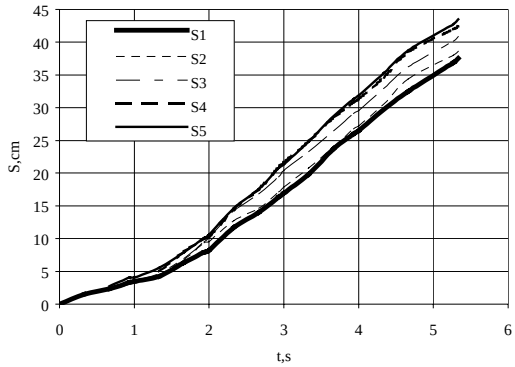

Figure 5. Dependence of flame propagation *S* along diverging threads saturated with kerosene on time *t*

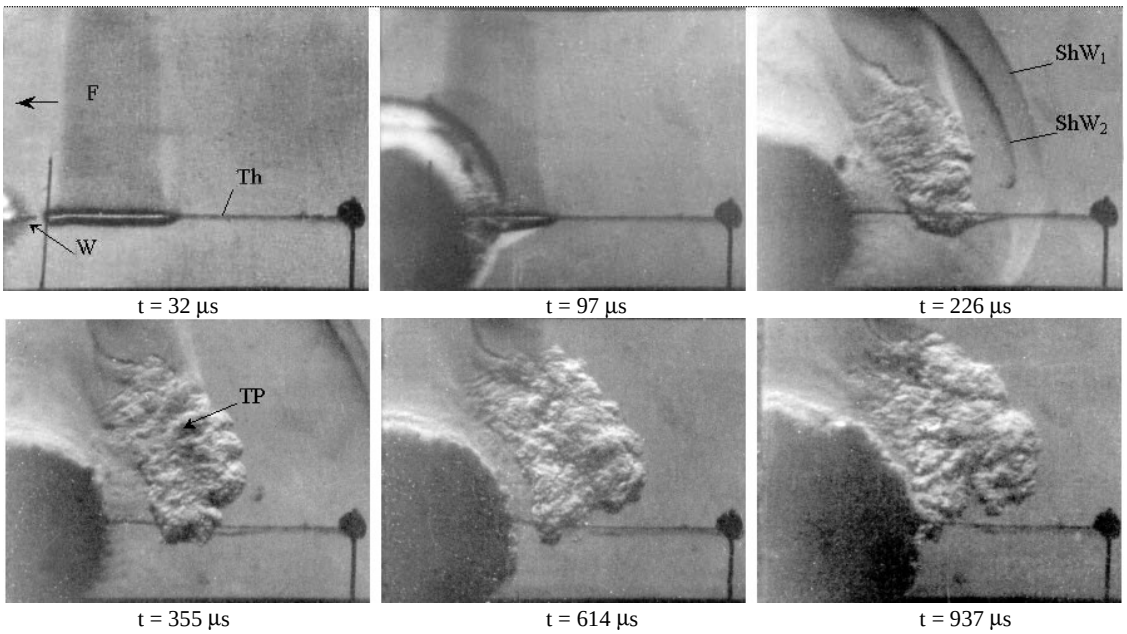

Figure 6. Frames for interaction between a shock wave generated by electrical explosion of a thin wire and flame propagating along a thread saturated with kerosene. Notations: F – flame; W – electrically exploded wire (its axes is normal to plane of picture); ShW_1 – shock wave, that passed region of flame; ShW_2 – that spread in air (outside flame); Th – thread; TP – turbulized products of burning. Time is counted from the moment of wire explosion.

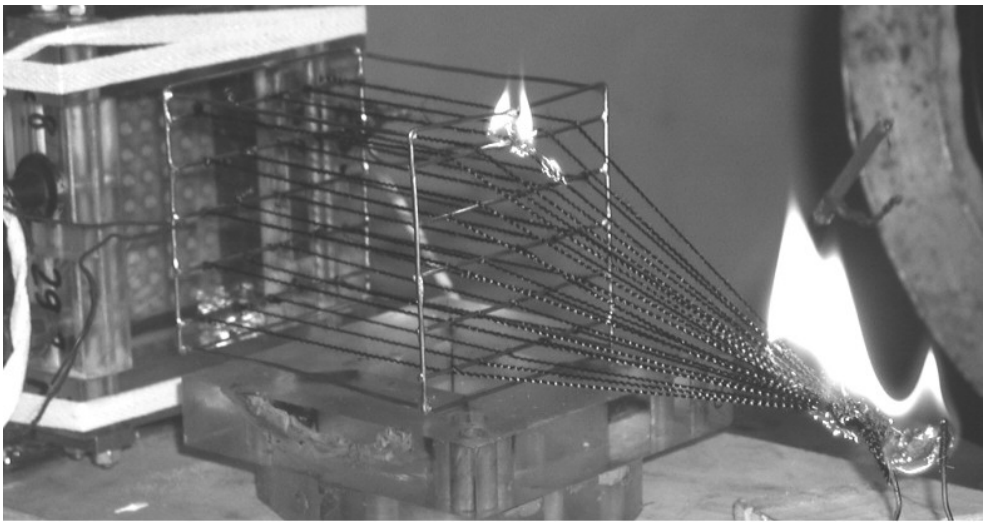

Figure 7 Experimental assembly

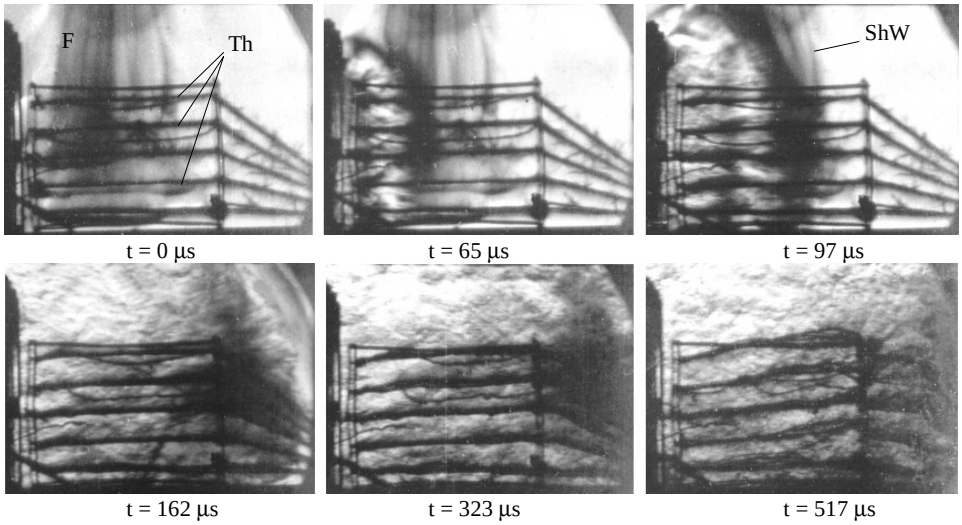

Figure 8. Frames for interaction between shock wave and flame propagating through spatial model of 25 parallel threads saturated with kerosene. Notations: F – flame; ShW – shock wave; Th – thread. Time is counted from the moment of gas explosive mixture detonation.

4.Summary and conclusion

A method for study the interaction between non-steady shock wave and the flame front at conditions close to crown fire is on progress.

An experimental, laboratory model for generating a quasi-flat flame front propagating along a spatial structure of threads saturated with combustible liquid (kerosene), was supposed.

A series of experiments for study the flame propagation both along 1-2 threads and along a spatial structure of 5x5 = 25 threads diverging from a point, was performed.

A series of experiments for the interaction between flame front and the non-steady shock generated by a) electrical explosion of a wire and b) explosion of a thin layer of a gaseous explosive mixture was performed.

The obtained results for the shock-flame interaction show:

- the flame displacement under shock wave
- a part of shock, that has passed through the flame, overruns the main front
- a flame front being initially smooth gets turbulent

Further steps in developing this method should be done by increasing the model scale and applying the improved methods of recording. The development of a model with a grid of 1-2 m size is supposed to be the next step; in this case the most suitable generation of a shock could be done with a longitudinal HE. In the case of favorable results with using the model it could be done a device with characteristic sizes close to real – of several tens of meters.

The development of the method for study the interaction between shock and flame could develop new methods for fighting the forest fires or could improve the existing ones.

Besides, the study in terms of the described above models could be used for checking the corresponding numerical methods.

This work is partially supported by Conseil Generale de Bouche du Rhone (France) and Joint Intersectorial Science – Technical Program of Minatom and Ministry of Education of Russia (grant 749/01).

References.

1. A.M.Grishin Physics of wild fires. Tomsk. Iss. by Tomsk Univer., 1994, p.218
2. A.M.Grishin, V.P.Zima, A.Ya.Mashovich, V.I.Samoilov Experimental study between shock generated with point charges and crowns. Proceedings of international conference “Common problems of mechanics and ecology”. Tomsk, Iss. by Tomsk University, 2000, pp 83-85
3. A.M.Grishin, Yu.Kovalev, Experimental and theoretical study of action of explosion on a crown wild fire. FGV, 1989, №6, pp 72-79
4. E.E.Meshkov Turbulent mixing associated with hydrodynamic instabilities in modern problems. Proceedings of international conference “Common problems of mechanics and ecology”. Tomsk, Iss. by Tomsk University, 2000, pp 156-158
5. Richtmyer Taylor instability in shock acceleration of compressible fluids. Commun.Pure Appl.Math., 1960, v.13,p.297.
6. E.E.Meshkov Instability of interface between two gases accelerated by a shock. MZhG, 1969, N5, 151-158
7. Lord Rayleigh Proc.London Math Soc, 1983, v.14, p.170
8. G.I.Taylor The instability of liquid surfaces when accelerated in a direction perpendicular to their planes. I. Proc.Roy.Soc., 1950, v.A201,p.192
9. Yu.A.Vlasov, S.I.Gerasimov, E.B.Gubkov, V.A.Dudin, V.P.Kopyshev, E.E.Meshkov, A.A.Nikulin, V.P.Ryabov, V.A.Til’kunov Shock tube with GEM as a driver. Sarov, preprint VNIIEF, 1996, 47-96

Influence of Scales of Initial Perturbations on Rayleigh-Taylor Instability Growth on Gas-Liquid Interface

M.V.Bliznetsov, E.E.Meshkov, N.V.Nevmerzhitsky, A.A.Nikulin, E.D.Sen'kovsky, E.A.Sotskov

RFNC-VNIIEF, Sarov, Russia

8th IWPCTM, Pasadena, USA

Abstract: Results on the influence of scales of periodical 3D perturbations on the turbulent mix growth associated with the Rayleigh-Taylor (RT) instability evolution at the gas-liquid interface, are reported. A layer of low-strength, dissolved-in-water- gelatin was employed for modeling the liquid driven with compressed helium. The perturbations given on an obviously unstable surface were 4-hedral pyramids with a height Δ equal to the perturbation wavelength $\Delta = \lambda_0$ =0.25,1,2,2.86 mm. The results obtained in RT experiments with no initial perturbations are also presented. The width of the turbulent mix zone was found growing with increasing the perturbation scales.

Introduction

The dynamics of turbulent mix (TM) growth caused by RT instability [1] is known to be in relation with a series of parameters such as surface tension, viscosity, initial perturbations on the interface [2,3,4].

According to current recognition, viscosity and surface tension of liquid at considerable acceleration g of the layer does not practically affect the TM growth. More complex case is the relation between initial perturbations and TM growth.

Self-similar turbulence occurs, in particular, at "forgetting" the initial perturbations.

As it has been shown in theoretical-numerical work [4], the rate and how the rate goes to self-similar form depend on perturbation density within the initial transition zone. Moreover, this work has shown, that TM (TMZ) does not occur when initial perturbations are lacking.

Currently, in experimental as well as in theoretical plane there are some questions of interest: what are initial given perturbations on the interface to be further "forgotten", when it occurs, and whether they are "forgotten" in terms of the experimental data we have or for all practically significant cases.

Jelly technique [5] intended for studying non-stationary hydrodynamic flows allows us to answer partly the questions. The core of the technique is modeling a liquid layer by a low-strength gelatin dissolved in water. For example, the jellies, using gelatin dissolved in water at

the concentration of C ≈ 4.4%, posses some strength (σ ≈ 0.005 MPa), and they are capable of conserving their shapes initially imposed on. When these jellies are driven by compressed gas at about 10 atm pressure, they would show behavior similar to that of incompressible liquids [5]. Any perturbation can be imposed on the surface of the jelly; further, its evolution could be recorded during dynamic experiment [6-8].

The subject matter of the paper is experimental results for the influence of the scales of 3D periodical perturbations given on unstable surface of a plane jelly driven by a compressed gas on TM evolution.

1. Experimental

Schematically, the experiment setup is shown in Fig.1. By this technique, a section of the acceleration channel of 40×40 mm sectional area, was placed on a matrix which surface had the following 3D perturbations a) of height (amplitude) $\Delta = 0.25$ mm and wavelength $\lambda_0 = 0.1$ mm, b) $\Delta = 1$ mm, $\lambda_0 = 1$ mm, c) $\Delta = 2$ mm, $\lambda_0 = 2$ mm, d) $\Delta = 2.86$ mm, $\lambda_0 = 2.86$ mm. (The perturbations had a regular shape of 4-hedral pyramid. Apex angle was directed to the jelly. Accuracy of manufacturing the perturbations using matrix was of about 0.07mm.) The section of the acceleration channel (which wall surfaces were greased thinly with vaseline) was filled with gelatin solution (C=4.4%) above which was placed a 4mm thick plywood to prevent the jelly from sagging. On soliciting, the matrix was removed, so the free surface of the jelly had perturbations being mirror images of ones imposed on the matrix. We also performed experiments with jellies without artificially given perturbations on their unstable surfaces. In this case, the jellies were manufactured in a thin transparent container (Fig.1, variant1). Unstable surfaces of such jellies had roughness with convexity ≈0.05 mm high due to vaseline. The mass of a jelly was about 47-52g.

The section with jelly was put in the acceleration channel. An end of the channel was tightly sealed with a cap, another one was closed with a 0.1mm thick millar diaphragm. The acceleration channel (on either side of the jelly) was filled with compressed helium of P = 13 atm. The diaphragm was broken with the electrical explosion of a nichrome wire glued on to it, so that the gas under the jelly would rapidly flow out to the atmosphere, and the jelly accelerated. The motion of jellies was visualized using high-speed frame filming in transmitted light.

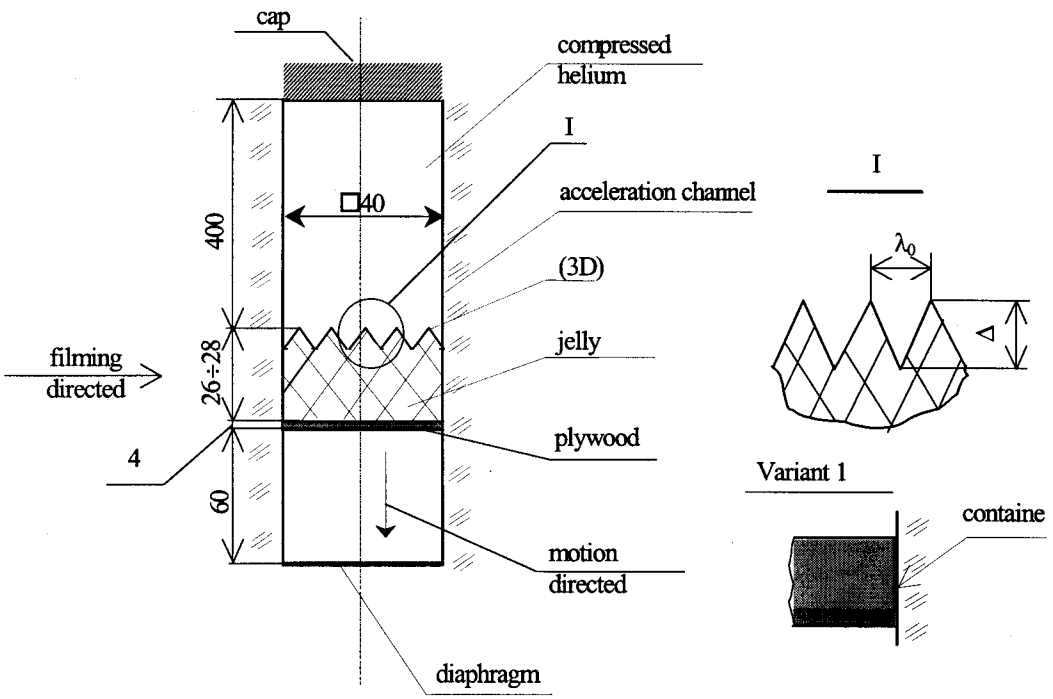

Fig.1 Schematic of the experiment setup

2.Experimental results. Analysis.

Fig.2 shows separate frames for the experiments performed with jellies without artificially given initial perturbations on their unstable surfaces and for jelly experiments with the perturbations: $\lambda_0 = \Delta = 0.25$ mm, : $\lambda_0 = \Delta = 1$ mm , $\lambda_0 = \Delta = 2$ mm, $\lambda_0 = \Delta = 2.86$ mm.

Accelerations for all the experiments were almost equal and constant ($g \approx 3 \cdot 10^4$ m/s^2).

Fig.3 presents the handling results for these experiments:

- the dependence of the averaged penetration depth (bubbles into jelly) h_{lh} on double jelly displacement S;
- the dependence of the averaged penetration depth (jelly(jets) into gas) h_{hl} on double jelly displacement S;
- the dependence of the total width of mixing zone H on double jelly displacement S ($H = h_{lh} + h_{hl}$).

At S > 20mm, the dependencies are close to be linear. The error in measuring the front h_{lh} was about ± 0.5mm. The error in measuring the front h_{hl} was estimated as ± 0.5mm for the initial stage of the TM growth and as ± 2mm for the final stage of recording. Such range is due to jet character for penetration of heavy material into a lighter – jet front is hardly processed from photos.

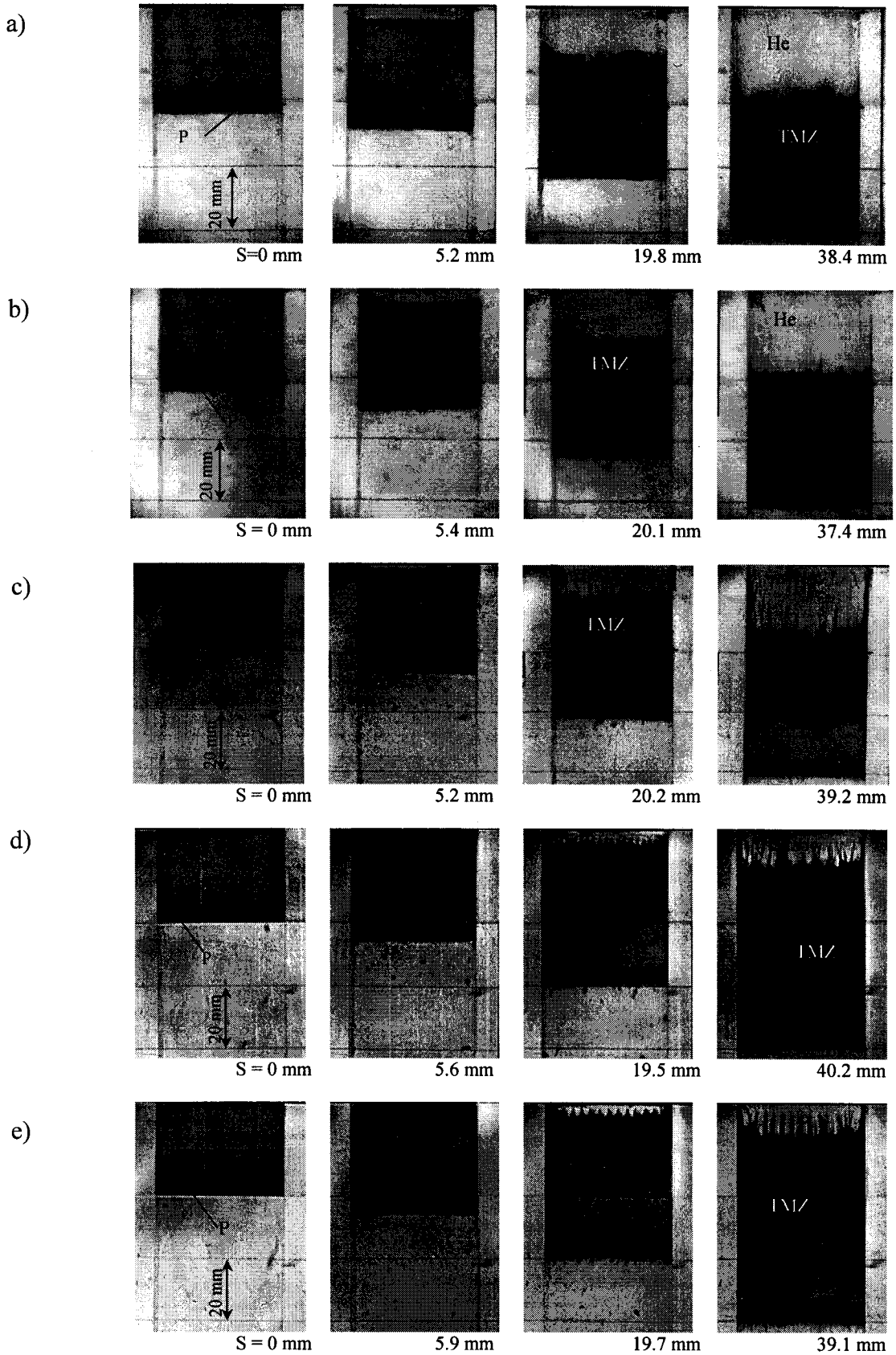

Fig.2. Frames for evolution of the TM zone on unstable surface of jellies with different initial perturbations a) without perturbations, b) $\lambda_0 = \Delta = 0.25$mm, c) $\lambda_0 = \Delta = 1$mm,d) $\lambda_0 = \Delta = 2$mm,e) $\lambda_0 = \Delta = 2.86$mm. Notations: J-jelly; He-compressed helium, TMZ-turbulent mix zone, P – plywood, S - displacement

a)

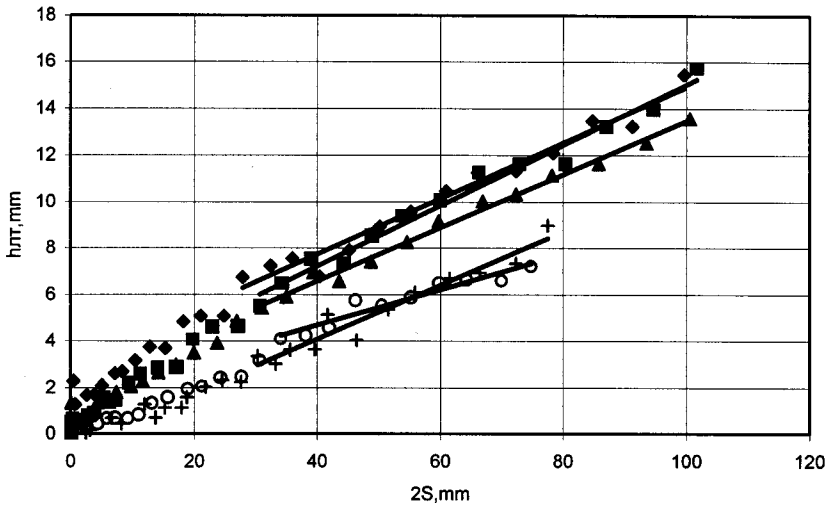

b)

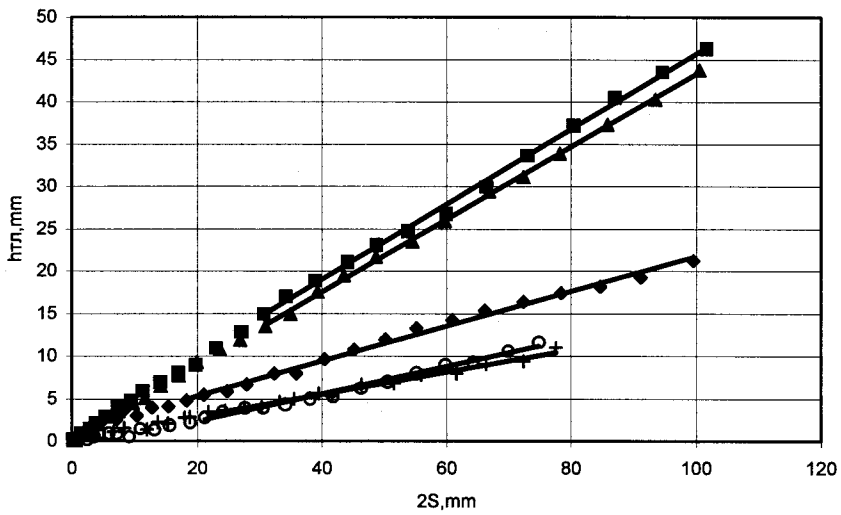

c)

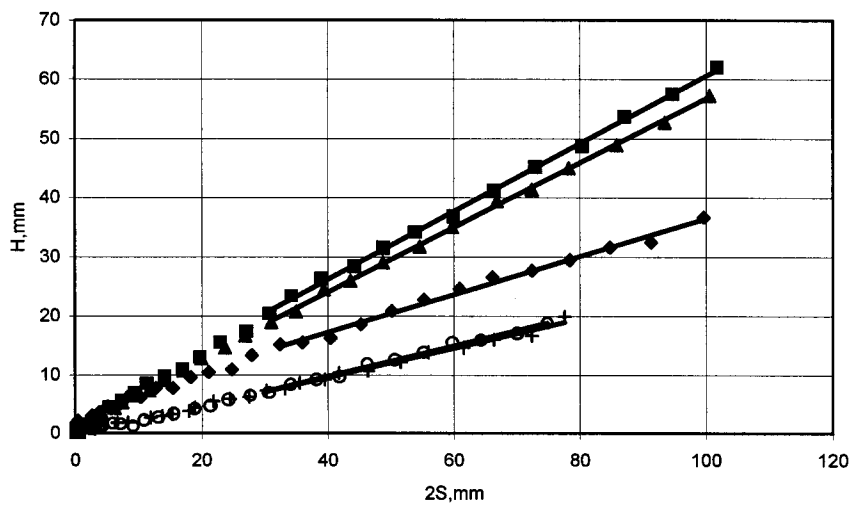

Fig.3. Processed results: a) dependence of penetration depth of gas into jelly h_{lh} versus double displacement 2S; b) dependence of penetration depth of jelly into gas h_{hl} versus double displacement 2S; dependence of total width of turbulent mix zone H versus double displacement 2S. Notations: ◆ - $\lambda_0 = \Delta$ =1mm, ▲ - $\lambda_0 = \Delta$ =2mm, ■ - $\lambda_0 = \Delta$ = 2.86mm, +-without perturbations, o- $\lambda_0 = \Delta = 0.25$мм.

Particular attention is given for the following:

- somewhat unusual long stage of the non-linear jet growth; the perturbation amplitude increases fifteen times while the laminar flow takes place
- There is a delay in mixing at unstable interface for the jelly experiments without given initial perturbations with respect to ones with given initial perturbations.
- At $0<S\leq 20$mm, the front of bubbles is more smooth for jellies with $\lambda_0 = \Delta = 1,2,2.86$ mm with respect to jellies without perturbations and with $\lambda_0 = \Delta = 0.25$mm. It may be assumed that, for this range of S and for jellies with $\lambda_0 = \Delta = 1,2,2.86$ mm, the TM growth is determined, in general, by given perturbations; i.e. random perturbations are, in some extent, suppressed.
- Intensity of the light-into-heavy penetration) β_{lh}, determined for a linear stage, is higher than the presented above dependencies; $\beta_{lh}=dh_{lh}/d(2S)$, $\beta_{lh}\approx 0.12$ for jellies with $\Delta\approx 0.05$mm and $\Delta\approx 0.25$mm; with Δ increases from 1 to 2.86mm, β_{lh} grows from 0.1 to 0.14. However, this growth lies within measurement error which is $\delta\beta_{lh}=0.025$. So, due to low accuracy ($\approx 20\%$), we can't unambiguously say about "forgetting" these perturbations for the recorded jelly displacement.
- Intensity of the heavy-into-light penetration β_{hl}, determined for a linear stage in the same manner as β_{lh}, increases from ≈ 0.13 to ≈ 0.42 (i.e. threefold) with increasing the Δ from 0.05 to 2.86. Such growth is much more than the value of errors in measuring, thus, the initial perturbations are not "forgotten" during the penetration of heavy material into a lighter (at least, for the $S \leq 50$mm).
- The total width of the TM zone H grows with the scale of initial perturbations; this growth is, in general, due to high intensity of the heavy-into-light penetration.

Conclusion

The experimental results show that the width of turbulent mix zone grows with the scale of initial, periodical 3D perturbations.

The data obtained could be used for testing numerical techniques.

References

1. G.I.Taylor. The instability of liquid surfaces when accelerated in a direction perpebdicular to their planes.Proc.Roy.Soc.,VA2016P.192,1950.
2. D.H.Sharp. An Overview of Rayleigh-Taylor Instability.Physica 12D,3-8, 1984
3. Yu.A.Kucherenko, G.G.Tomashev, L.I.Shibarshov. Experimental study of gravitational turbulent mix for self-similar regime. VANT, is. Th.and Ap. Ph., 1,p.13,1988

4. V.V.Nikiforov. Turbulent mixing on an interface between media different in density VANT, is. Th.and Ap. Ph., 1,p.3,1983
5. O.I.Volchenko, I.G.Zhidov, B.A.Klopov, E.E.Meshkov et al. A mean for modeling non-stationary flows of incompressible liquid A.S.1026154,MKI 09 B23/12
6. M.V.Bliznetsov, E.E.Meshkov,N.V.Nevmerzitsky, P.I.Nizovtsev, E.D.Sen'kovsky, E.A.Sotskov, L.V.Tochilina. On possibility of modeling some cases of RT instability in strength media VANT, is. Th.and Ap. Ph., 3,p.54-57,2000
7. S.T.Weir, E.A.Chandler and B.T.Goodwin. Rayleigh-taylor instability growth experiments in a cylindrically convergent geometry. The Proc. of 6th IWPCTM, Marseilles, 1997,(France)
8. E.E.Meshkov, N.V.Nevmerzhitsky,V.G.Rogachev,I.G.Zhidov. The use of jelly technique to study hydrodynamic perturbation evalution at unstable plane and cylindrical surfaces. The Proc. of 5th IWPCTM, Stony Brook, 1995, (USA). P.243-250

Formation and propagation of shock-generated vortex rings

Martin Brouillette and Christian Hébert

Laboratoire d'ondes de choc
Université de Sherbrooke
Sherbrooke (Québec) CANADA

Outline

1. Introduction
2. Experimental considerations
3. Vortex propagation
4. Vortex formation — Circulation standpoint
5. Other features — Shock formation by vortex
6. Summary

Introduction

Explore compressible turbulence via the standpoint of compressible vorticity and its building blocks.

Compressible vorticity is also important from both fundamental and practical standpoints, in:

- Blade-vortex interaction, including sound generation, for rotary wing aircraft applications.
- Shock-vortex interaction, including sound generation, for jet noise applications.

Objectives

Experimental study of isolated vortices as building blocks of compressible turbulence.

For example, in the Richtmyer-Meshkov instability:

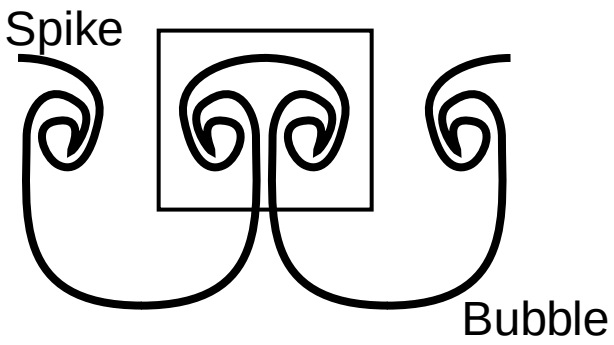

In particular,
— What exactly are compressible vortices?
— How are they different from incompressible vortical structures?

Specific experimental objectives

- Characterize the effects of the generator on the production and propagation of compressible vortices.
- Examine the effects of compressibility and scale on these properties.
- Compare with incompressible results.

Experimental considerations

Experiments are performed with a modified shock tube:

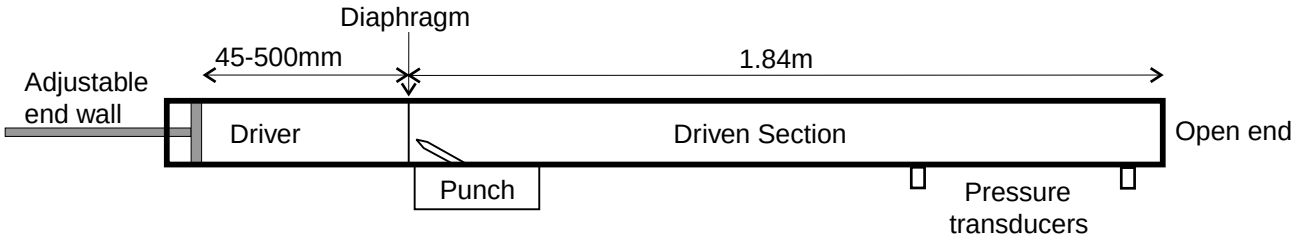

Open driven end, with 3 different exit nozzle diameters: 6.4, 12.7 and 25.4 mm

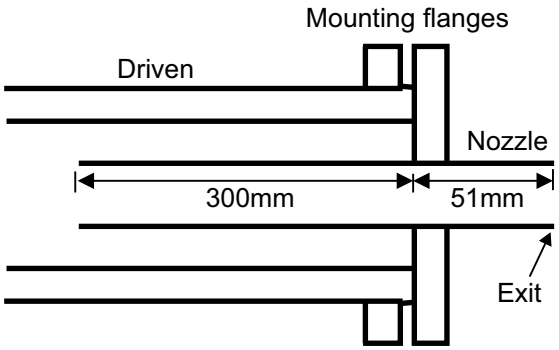

Features of this setup:

- Produce shear-driven vortices (Kelvin-Helmoltz instability) as opposed to baroclinically-driven vortices (Rayleigh-Taylor or Richtmyer-Meshkov instabilities)
- High vorticity production rates.
- Fluid piston analogous to high speed spike in RMI.

Effect of driver length on fluid ejection history

Standard (= long) driver

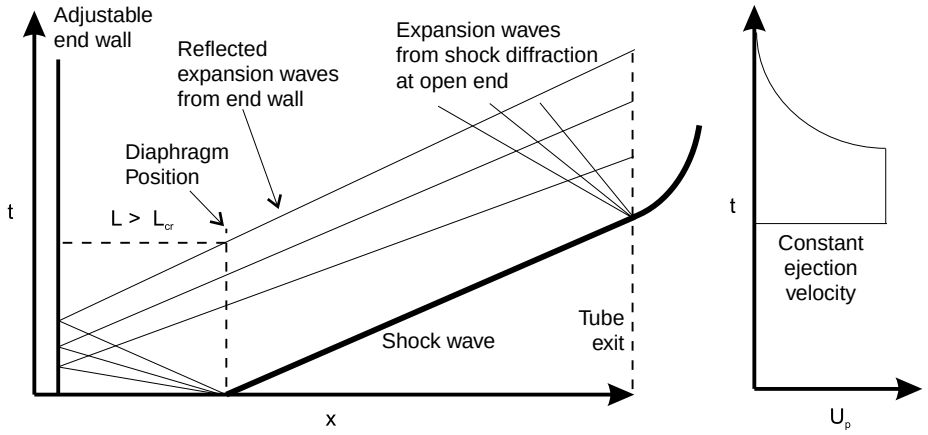

Analogous to RMI followed by RTI.

Tuned driver

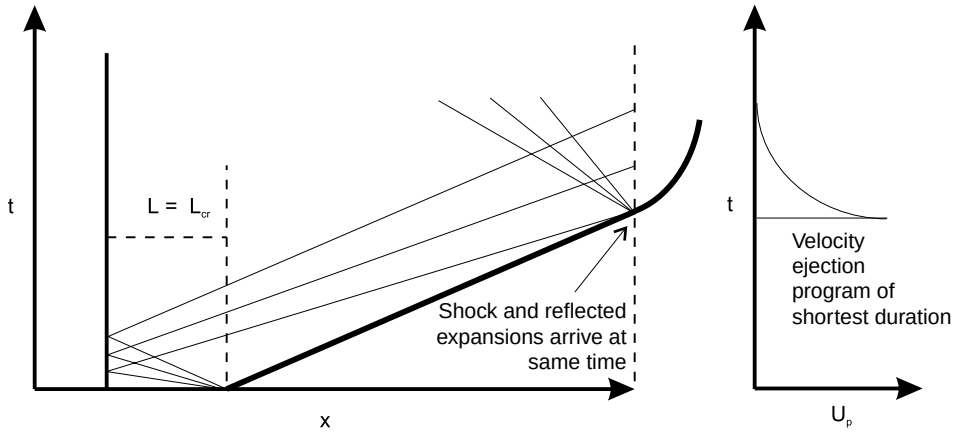

Analogous to “almost only” RMI.

Flow diagnostics

- Piezoelectric pressure transducers.
- Flow visualization (shadowgraph, schlieren, holographic interferometry).

Vortex propagation

Three regimes of propagation

Low shock Mach number → regime 1

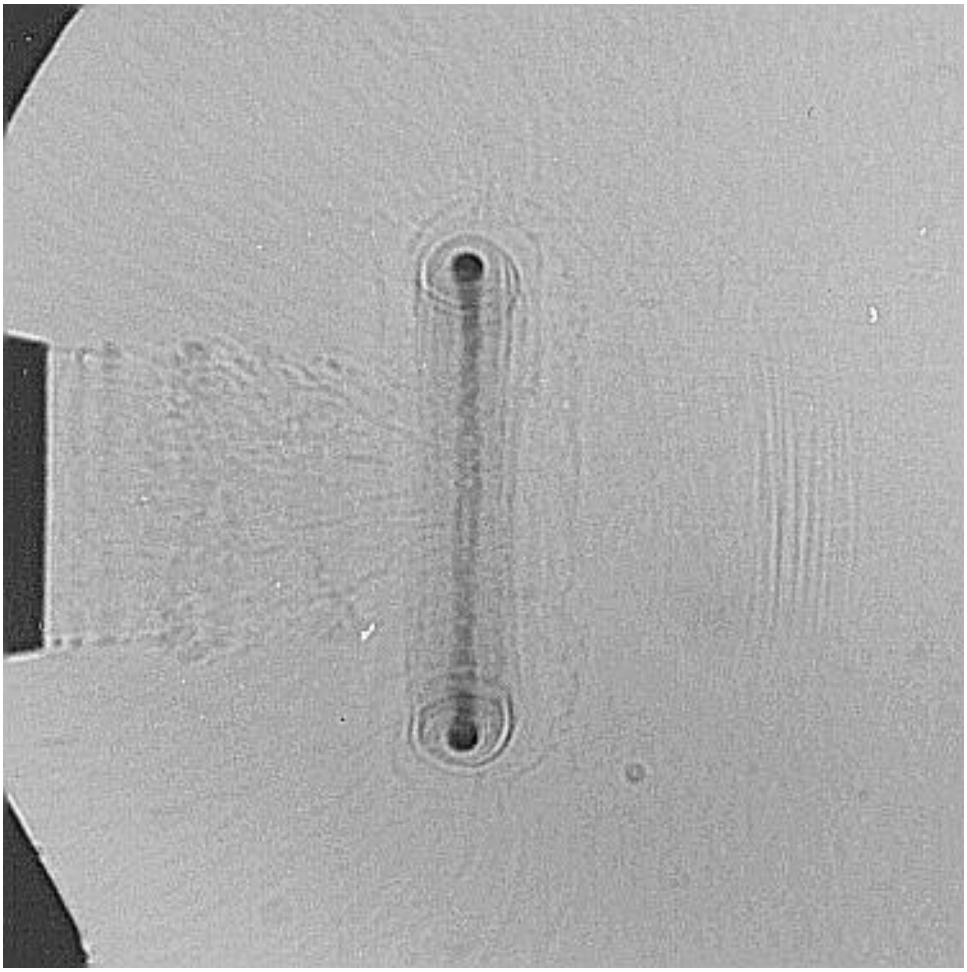

Regime 1 — Development of circonferential instabilities (oblique view)

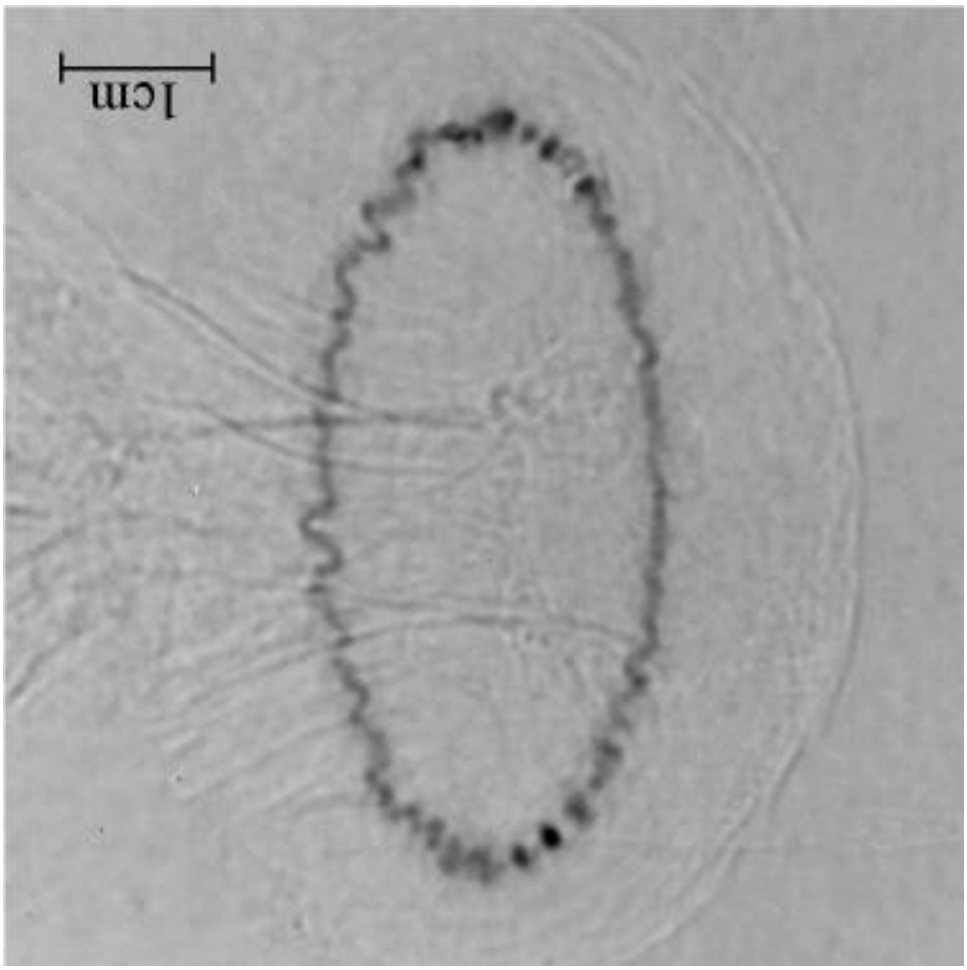

Oblique spark shadowgraph, $M_s = 1.32$, $D_p = 38$ mm: $t = 1.42$ ms, $x/D_p = 3.30$

As M_s is increased:

Regime 2 — Appearance of shocks

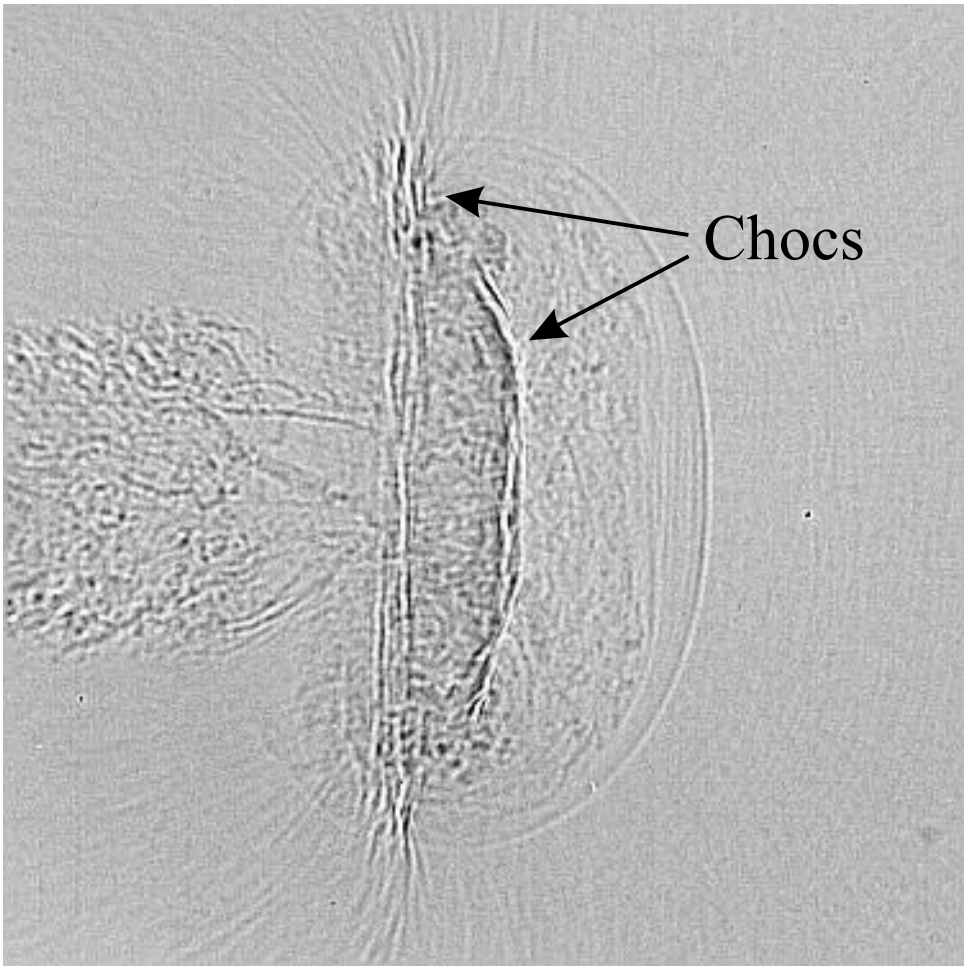

As M_s is further increased:

Regime 3 — Secondary vorticity generation

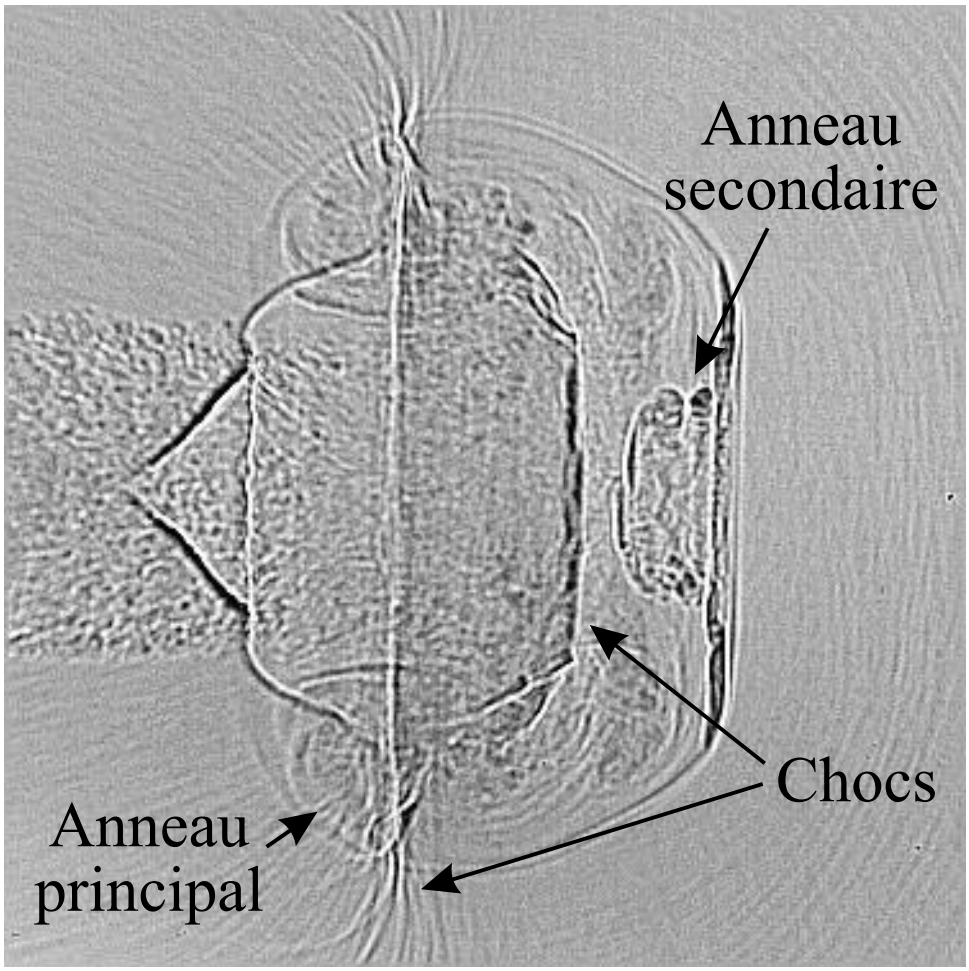

Vortex propagation (37 mm orifice)

	Standard driver	Tuned driver
Regime 1	$1 < M_s < 1.34$	$1 < M_s < 1.44$
Regime 2	$1.34 < M_s < 1.45$	$1.44 < M_s < 1.60$
Regime 3	$M_s > 1.45$	$M_s > 1.60$

We know that for the same shock Mach number, impulse is larger for standard driver.

Regimes appear at lower Mach numbers for the standard case.

Vortex propagation — Position vs time

Results normalized with orifice diameter D_p and maximum fluid velocity U_p as:

$$x^* = \frac{x}{D_p} \qquad t^* = \frac{tU_p}{D_p}$$

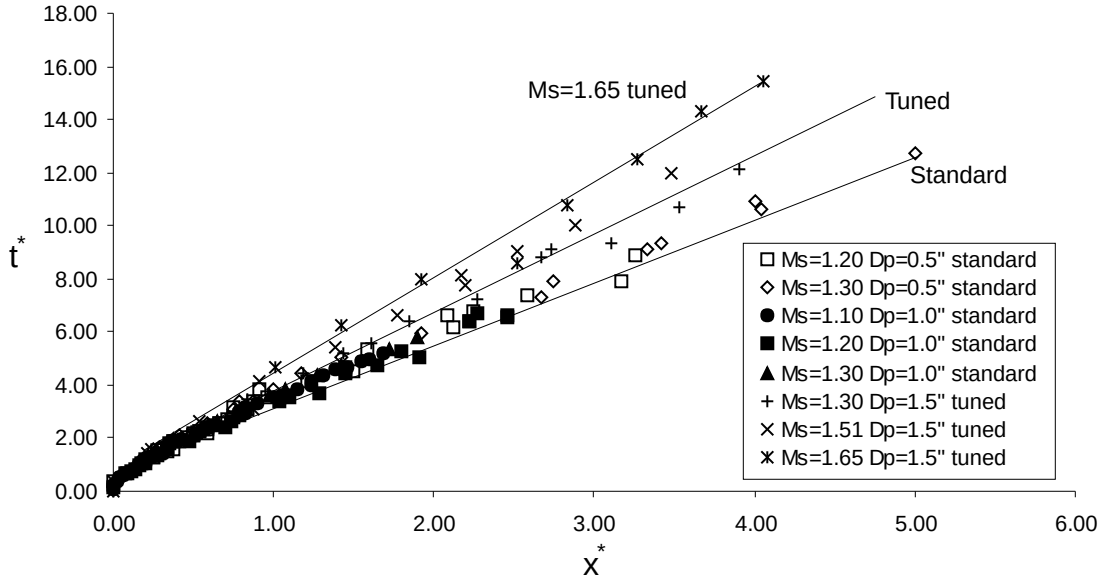

Observations:

- Speed of vortex rings increases with shock strength.
- Rings produced with the tuned driver propagate slower $U^* \approx 0.34$ than with the standard driver $U^* \approx 0.42$.
- Within experimental error, not possible to detect compressibility effects.

Vortex formation

In incompressible experiments, typically use a piston to eject a slug of fluid (liquid).

- Ejection Mach number near zero.
- Normalized ejected slug length relatively much smaller than in the present study.
- Vortex propagation mostly free from the effects of the generating jet.

Examine vortex formation in terms of circulation deposition history:

Use a normalized circulation

$$\Gamma^* = U^* d^*$$

Normalized circulation vs normalized time

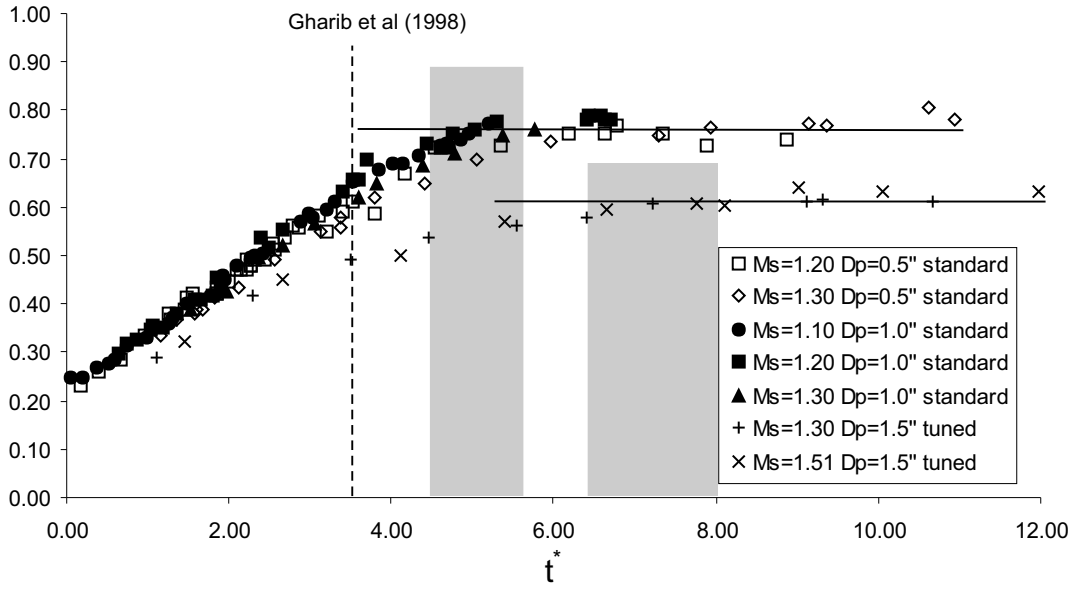

Observations:

- Vortex ring is formed when a vorticity saturation threshold is reached.
- Concept of vortex formation number (Gharib et al. 1998).
- Formation number higher for compressible rings.
- Maximum circulation similar between incompressible results and standard driver results.
- Lower circulation with tuned driver.
- Non-zero "initial" circulation (purely impulsive ejection history).

Other features — Shock formation by vortex

Onset of appearance of shock wave within recirculating region:

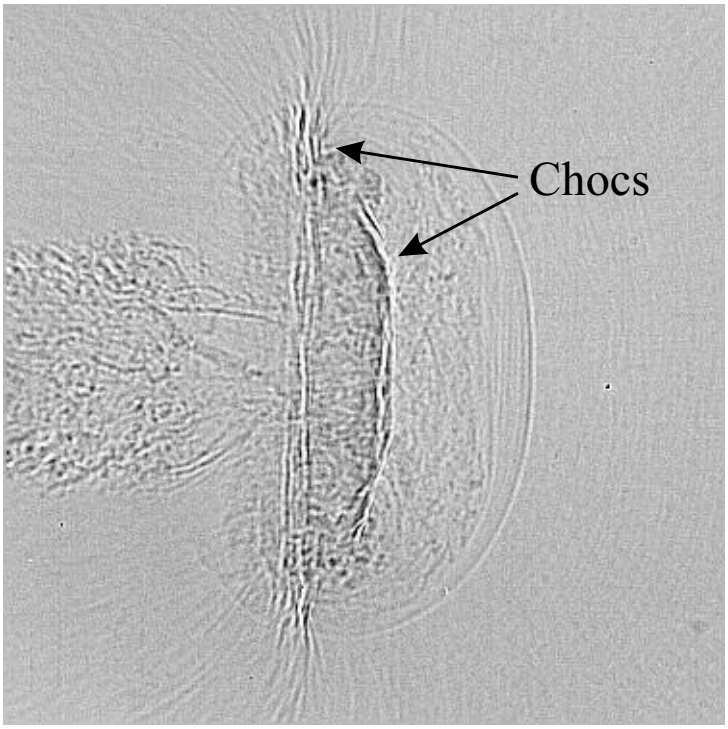

For the standard driver, this shock appears at $M_s = 1.34$ ($U_p = 339$ m/s).

For the tuned driver, this shock appears at $M_s = 1.44$ ($U_p = 425$ m/s).

This threshold is reached when flow velocities within ring recirculating region become sonic $u/c = 1$.

But since $u \sim \Gamma/d$ this threshold occurs when:

$$\frac{\Gamma}{d\ c} = 1$$

With $\Gamma \sim Ud$, then $\Gamma = \Gamma^*\ U_p\ D_p$. and this threshold can then be expressed as:

$$\frac{\Gamma^* U_p D_p}{d\ c} = 1$$

If this criterion is satisfied for both tuned and standard cases, then:

$$\frac{\Gamma^*_{tuned}\ U_{p_{tuned}}\ D_{p_{tuned}}}{d_{tuned}\ c_{tuned}} = \frac{\Gamma^*_{std}\ U_{p_{std}}\ D_{p_{std}}}{d_{std}\ c_{std}}$$

For identical test gases $c_{tuned} = c_{std}$, for identical orifices $D_{p_{tuned}} = D_{p_{std}}$ and we observe that $d_{tuned} = d_{std}$. Therefore

$$\frac{\Gamma^*_{tuned}}{\Gamma^*_{std}} = \frac{U_{p_{std}}}{U_{p_{tuned}}}$$

is satisfied if postulate is correct!

Experimental data:

Standard driver: $\Gamma^*_{std} = 0.76$

Tuned driver : $\Gamma^*_{tuned} = 0.61$

$$\frac{\Gamma^*_{tuned}}{\Gamma^*_{std}} = 0.80$$

Standard driver: transition at $M_s = 1.34$ $U_{p_{std}} = 339$ m/s

Tuned driver: transition at $M_s = 1.44$ $U_{p_{tuned}} = 425$ m/s.

$$\frac{U_{p_{std}}}{U_{p_{tuned}}} = 0.80$$

at the onset of appearance of the shock within the recirculating region.

Postulate appears satisfied!

- For a given size, shock appears at a given ring circulation.
- The estimation of ring circulation rests on solid ground.

Consequences:

In a compressible turbulent flow, shocklets would appear if sufficient vorticity is locally present.

For a purely impulsive (delta function) fluid ejection history, since the maximum vorticity deposition Γ^* is small, a shock would appear at a very large ejection velocity. Our limited experiments at $M_s = 2$ support this.

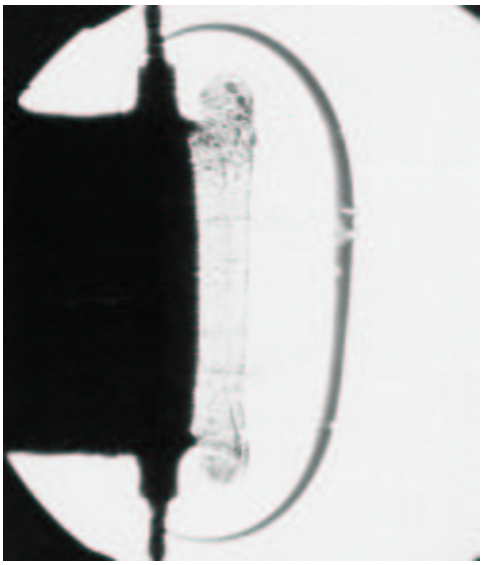

Conclusions

- The behavior of compressible vortices is somewhat similar to that of incompressible vortices, but they attain circulation saturation slower.
- Vortex rings can only absorb a maximum amount of circulation.
- The most sustained and higher vorticity production rate lead to faster normalized formation and higher circulation.
- Can use this point of view to explain he appearance of shocks within vortical structures.

Design of Flyer-Plate-Driven, Compressible-Turbulent-Mix Experiments

R. P. Drake
University of Michigan

IWPCTM, Pasadena, December 2001

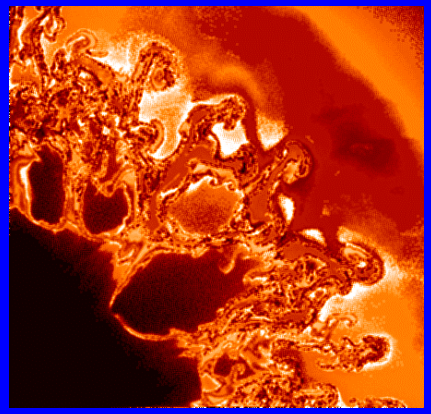

Supernova Simulation

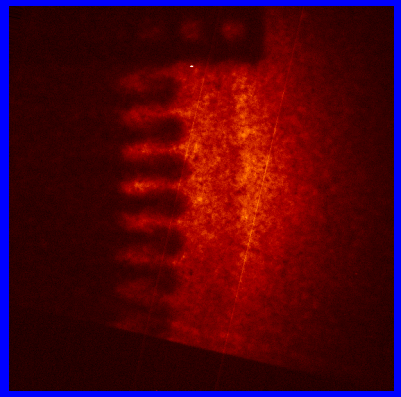

Omega Laser Experiment

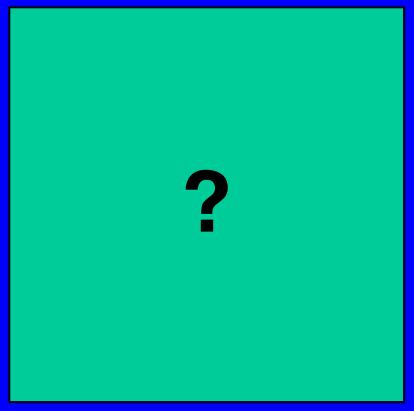

Z Flyer Experiment

Work supported by the U.S. Department of Energy under grants DE-FG03-99DP00284, DE-FG03-00SF22021 and other grants and contracts

Z has opened up new experimental possibilities

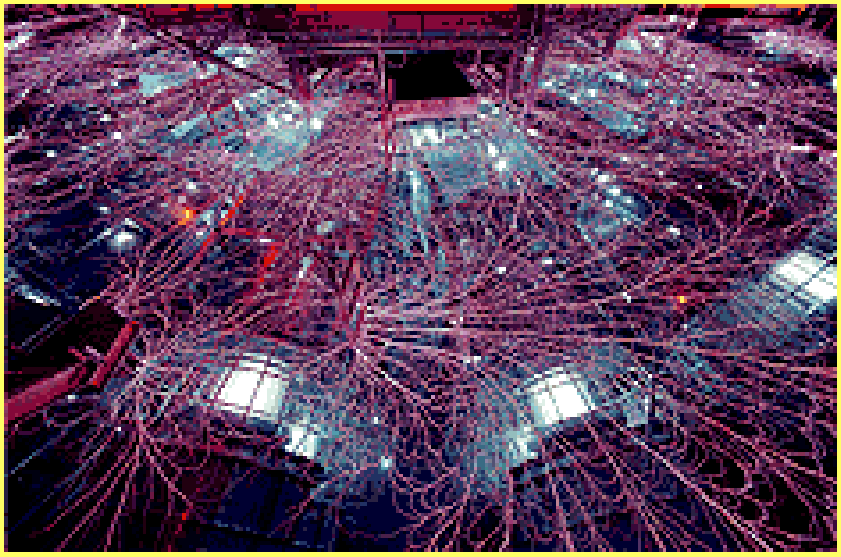

Shown above are pictures of the Z-pinch:
(left) prior to firing (right) during firing

By imploding hundreds of wires, Z can make MJ of x-rays

When the wires collide they produce up to 2 Mega-Joules of x-rays

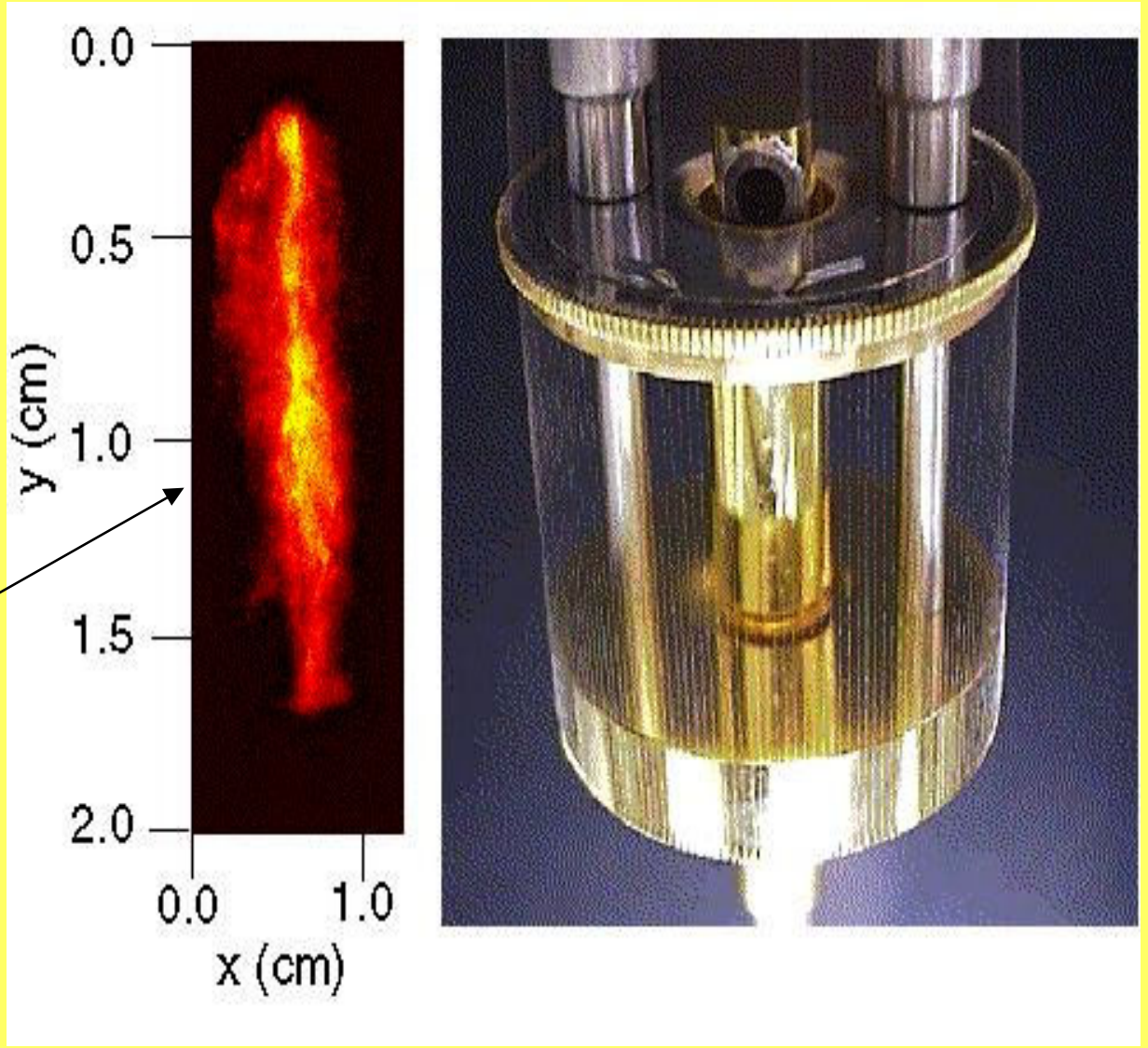

December, 2001

What matters here: Z can use J X B forces to launch Al flyer plates at > 20 km/s

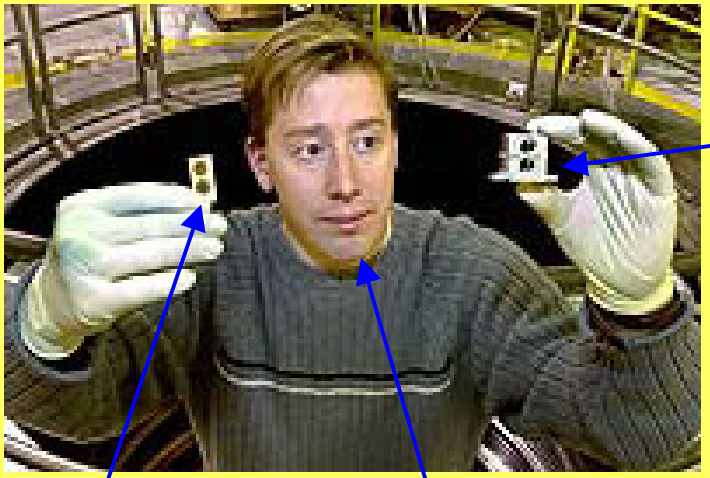

The "gun" J X B launching structure

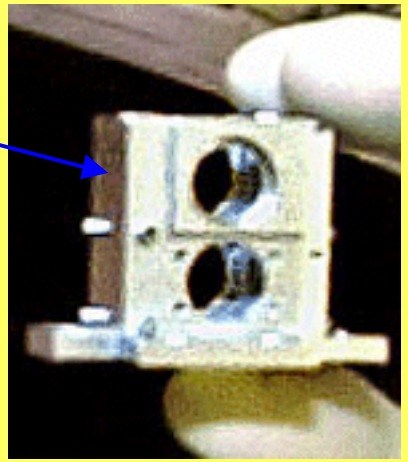

Flyer Plates

???
(your caption here)

Photo: www.spacedaily.com/news/milspace-tech-01a.html

Acknowledgements: useful discussions with

M. D. Knudson, J. R. Asay, C. Deeney

Sandia National Laboratory

S.G. Glendinning, H.A. Robey, J.O. Kane,

Lawrence Livermore National Laboratory

Flyer-plate mix experiments differ from flyer-plate EOS experiments

- **EOS experiments**
  - Need rock-steady shock
  - Experiment ends when shock exits material

- **Mix experiments**
  - Experiment begins when interface of interest is shocked
  - May not want steady shock
  - Even steady shock need not meet EOS constraints

Basic geometry for flyer plate experiments

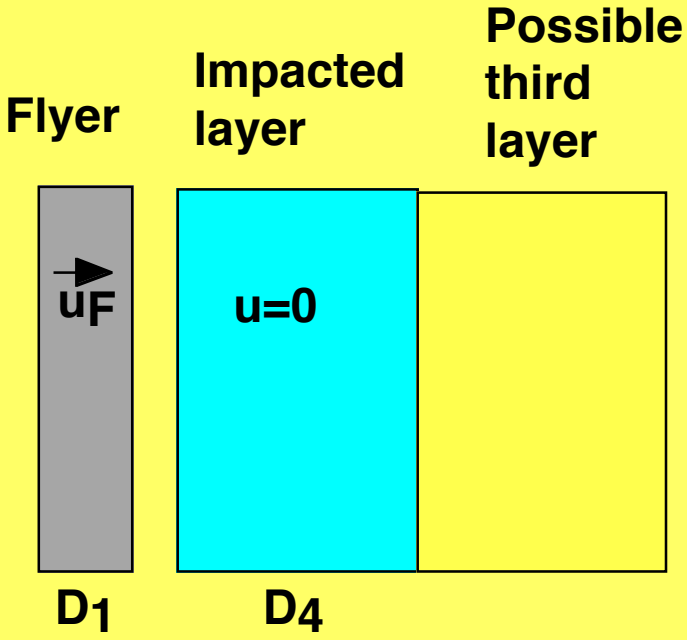

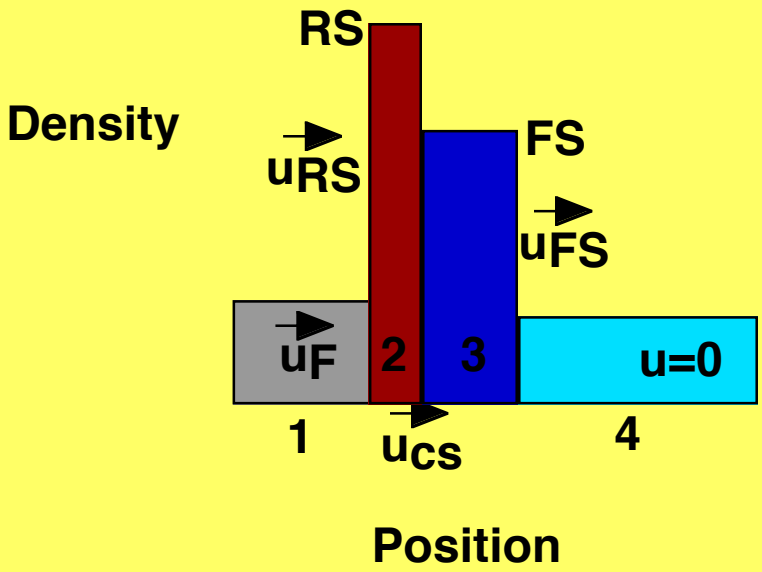

In the following:

Analytic results use γ-law gas, strong shock equations

Simulations used the HYADES Lagrangian hydrocode with SESAME EOS

Basic relationships for strong shocks in this system

In lab frame:

$$u_{cs} = \frac{1}{1+\sqrt{\rho_4/\rho_1}}u_F$$

$$u_{RS} = \left(1-\frac{\gamma-1}{2}\sqrt{\frac{\rho_4}{\rho_1}}\right)\frac{u_F}{1+\sqrt{\rho_4/\rho_1}}$$

$$u_{FS} = \frac{\gamma+1}{2}\frac{u_F}{1+\sqrt{\rho_4/\rho_1}}$$

In flyer frame:

$$u''_{RS} = \frac{-\sqrt{\rho_4/\rho_1}}{1+\sqrt{\rho_4/\rho_1}}\frac{\gamma+1}{2}u_F$$

Sound speeds:

$$c_3 = \sqrt{\frac{\gamma(\gamma-1)}{2}}u_{CS} = \sqrt{\frac{\gamma(\gamma-1)}{2}}\frac{u_F}{1+\sqrt{\rho_4/\rho_1}}$$

$$c_2 = \sqrt{\frac{\gamma(\gamma-1)}{2}}(u_F-u_{CS}) = \sqrt{\frac{\gamma(\gamma-1)}{2}}\frac{\sqrt{\rho_4/\rho_1}}{1+\sqrt{\rho_4/\rho_1}}u_F$$

In mix experiments one will often not use an Aluminum impact layer

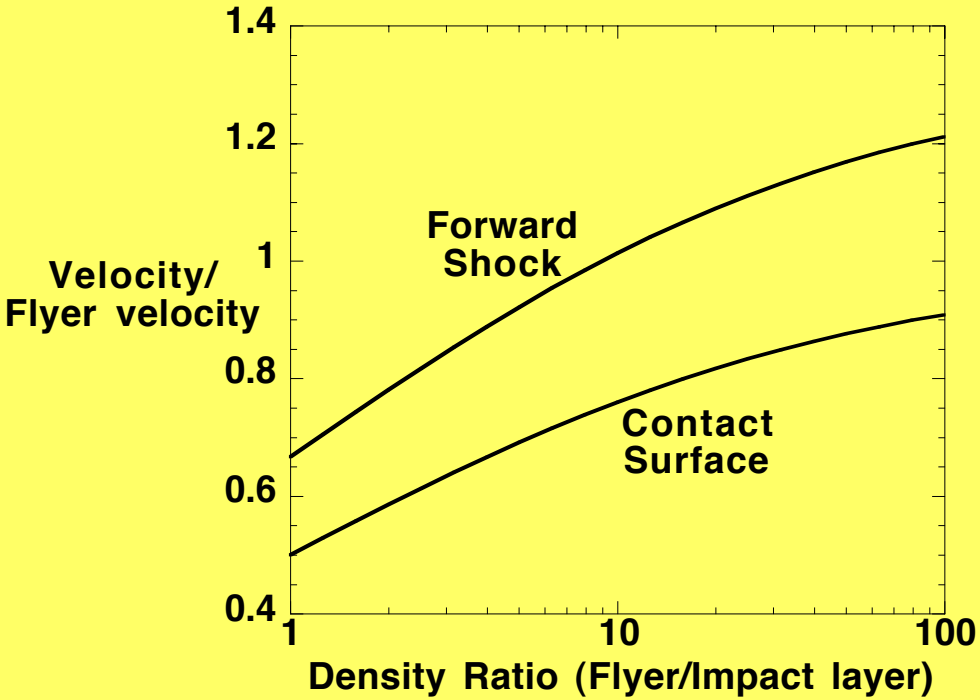

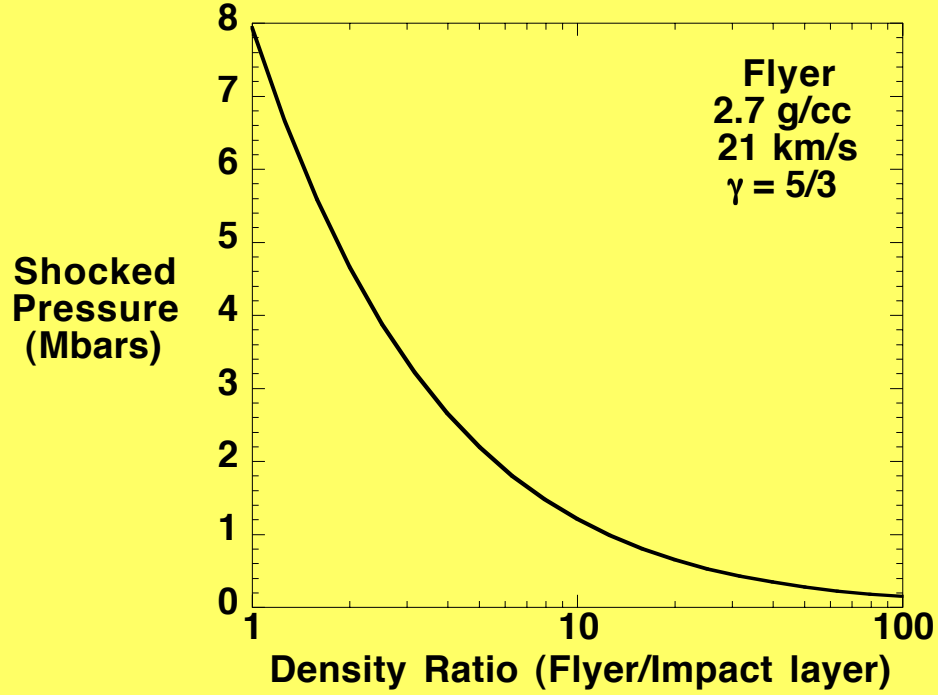

At lower impact layer density, one can drive steady shocks over larger distances

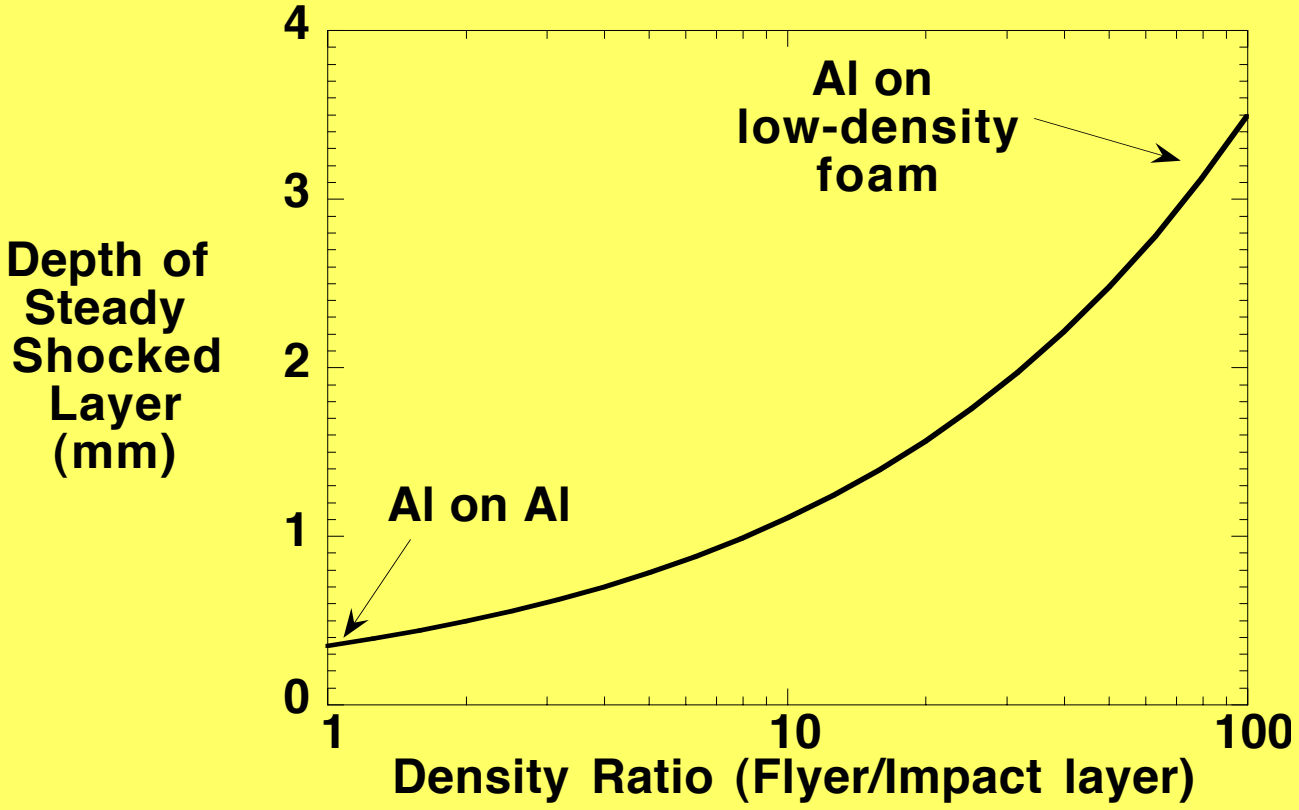

350 μm, Al (2.7 g/cc) flyer

Time until the shock reaches the rear of the flyer plate

$$t = \frac{D_1}{\left|u''_{RS}\right|}$$

How far the shock goes into the impact layer

$$D_4 = u_{FS}t = \frac{u_{FS}}{\left|u''_{RS}\right|}D_1 = \sqrt{\frac{\rho_1}{\rho_4}}D_1$$

For RT experiments, one creates a blast wave

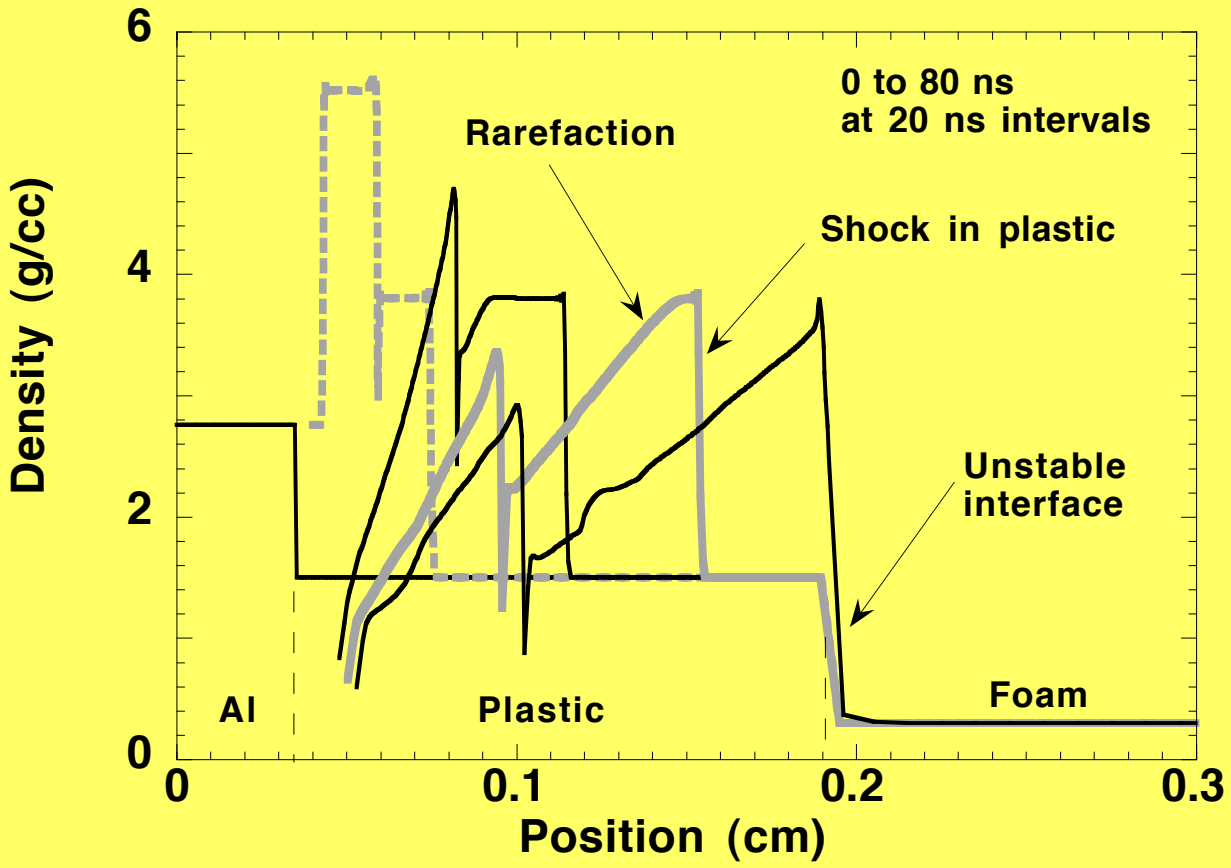

Goal: waste none of the deceleration

$$t_4 = \frac{D_4}{u_{FS}} = \frac{D_4}{u_F}\frac{2(1+\sqrt{\rho_4/\rho_1})}{\gamma+1}$$

$$t_1 = \frac{D_1}{\left|u''_{RS}\right|} + \frac{\gamma-1}{\gamma+1}\frac{D_1}{c_2} + \frac{\gamma-1}{\gamma+1}\frac{D_4}{c_3}$$

$t_4 = t_1$ so

$$\frac{D_4}{D_1} = \sqrt{\frac{\rho_1}{\rho_4}}\frac{(1+\sqrt{(\gamma-1)/2\gamma})}{(1-\sqrt{(\gamma-1)/2\gamma})}$$

The unstable interface moves several mm

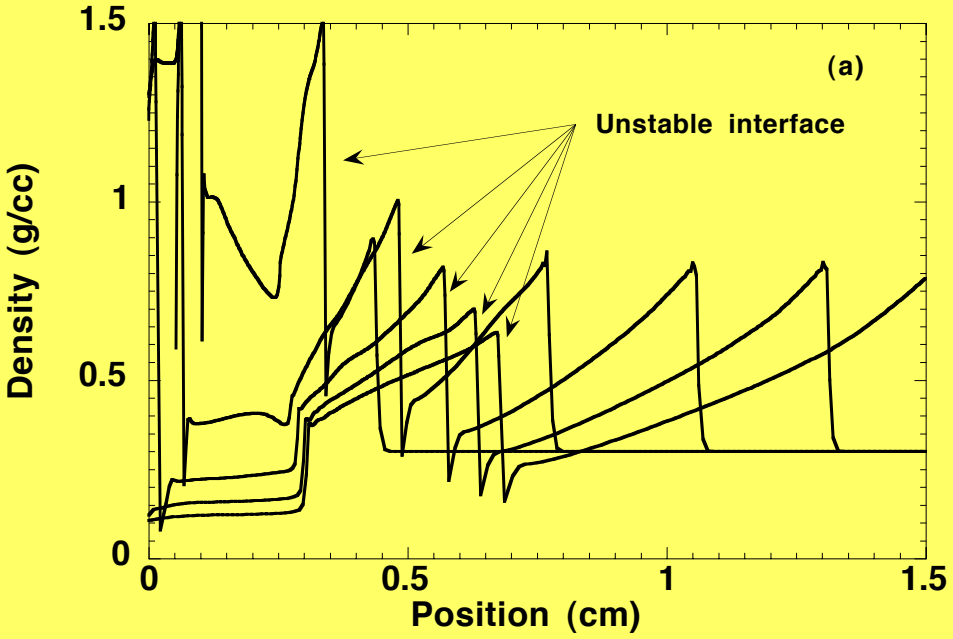

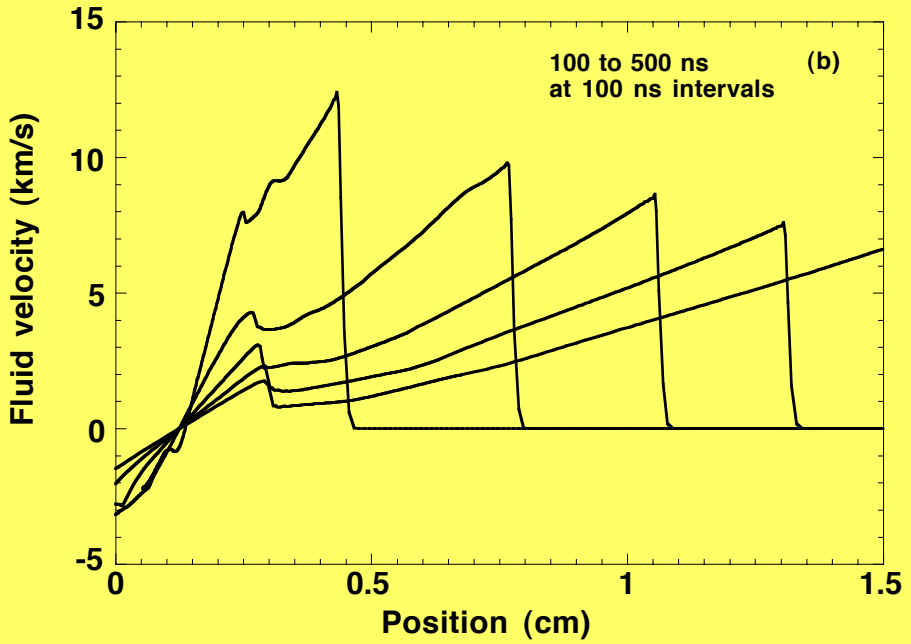

This graph shows the interface behavior

- The linear growth exponent is ~ 30 by 1.5 μsec

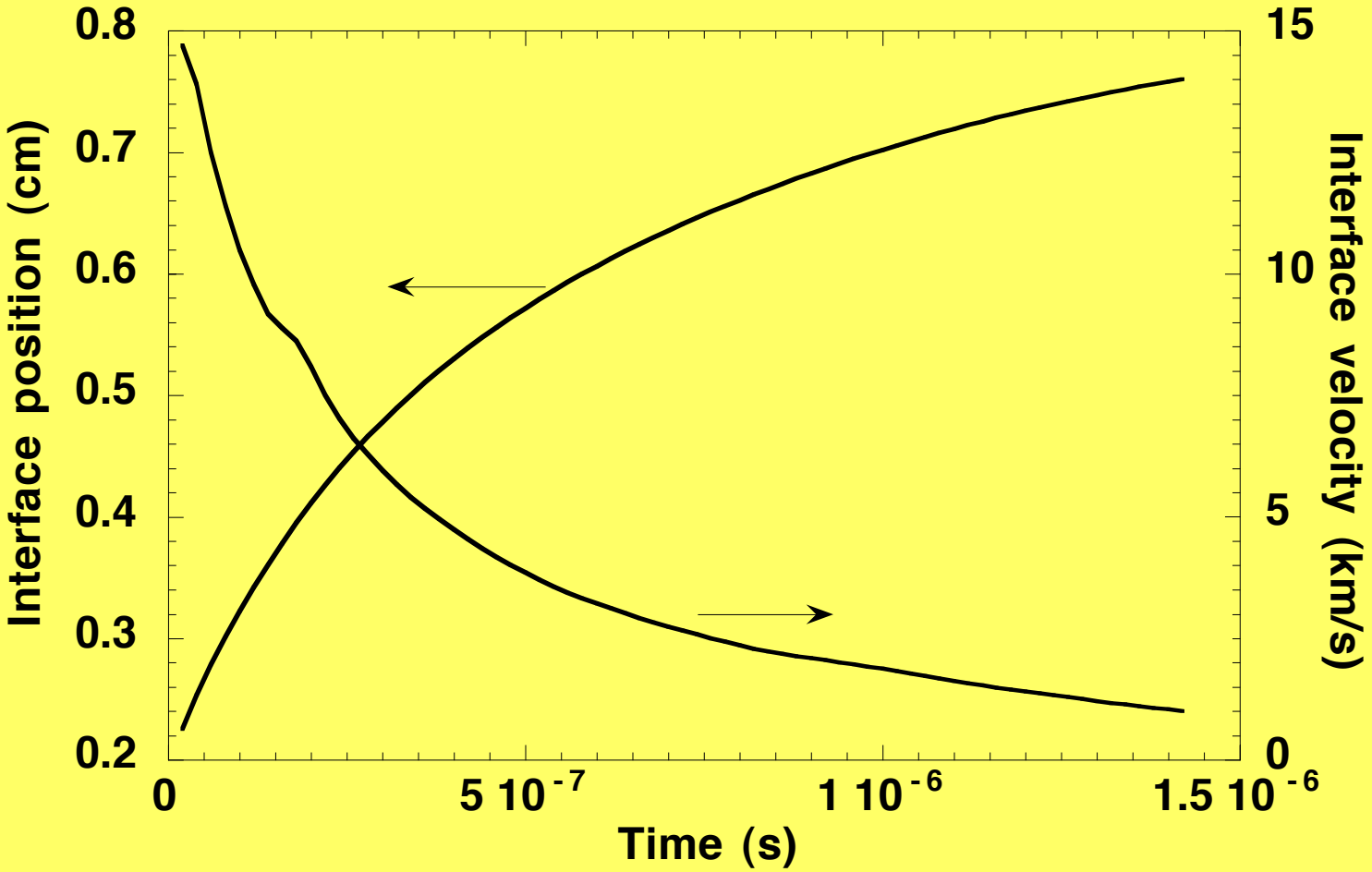

Richtmyer-Meshkov experiments are harder

Goal: maximum steady post-shock motion of interface

Means: make rarefactions in flyer and impact layer meet at contact surface

$$t_1 = \frac{D_1}{\left|u''_{RS}\right|} + \frac{\gamma - 1}{\gamma + 1}\frac{D_1}{c_2} = \frac{D_1}{u_F}\frac{(1+\sqrt{\rho_4/\rho_1})}{\sqrt{\rho_4/\rho_1}}\left(\frac{2}{\gamma+1} + \sqrt{\frac{2}{\gamma(\gamma-1)}}\right)$$

$$t_4 = \frac{D_4}{u_{FS}} + \frac{\gamma - 1}{\gamma + 1}\frac{D_4}{c_3} = \frac{D_4}{u_F}(1+\sqrt{\rho_4/\rho_1})\left\{\frac{2}{\gamma+1} + \sqrt{\frac{2}{\gamma(\gamma-1)}}\right\}$$

$t_4 = t_1$ so

$$D_4/D_1 = \sqrt{\rho_1/\rho_4}$$

An example where the rarefactions meet

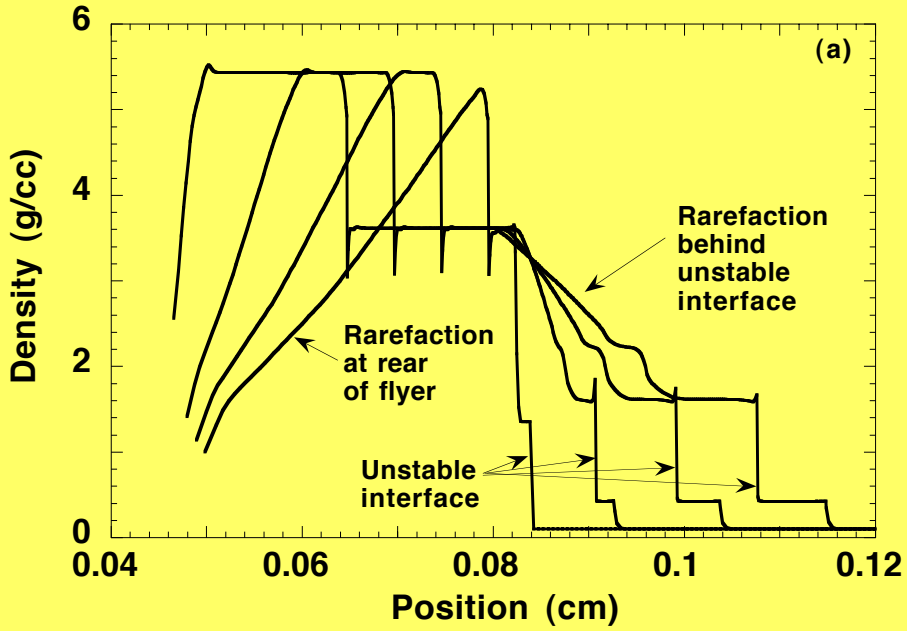

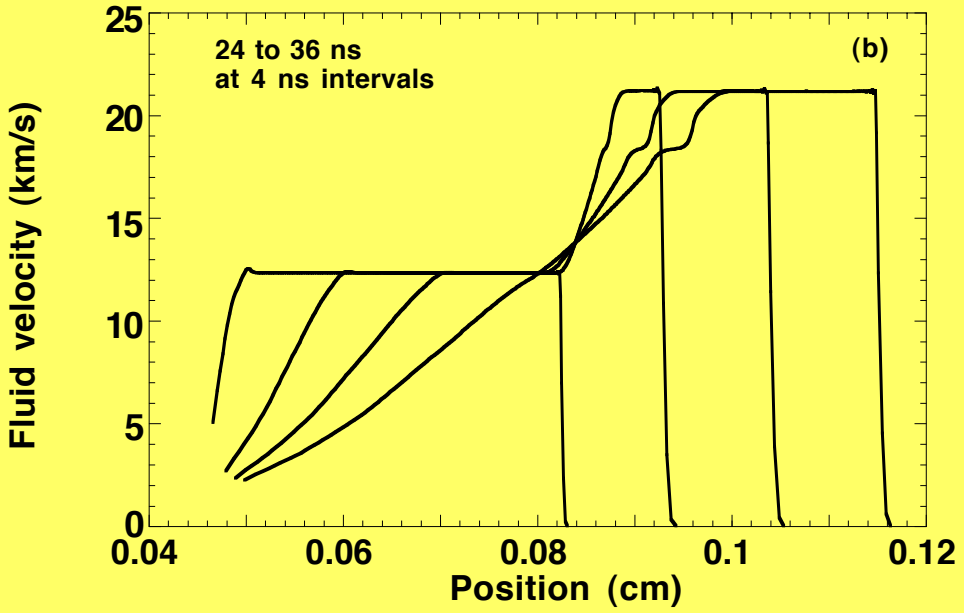

350 μm thick, 21 km/s flyer

The unstable interface moves steadily for ~ 1mm

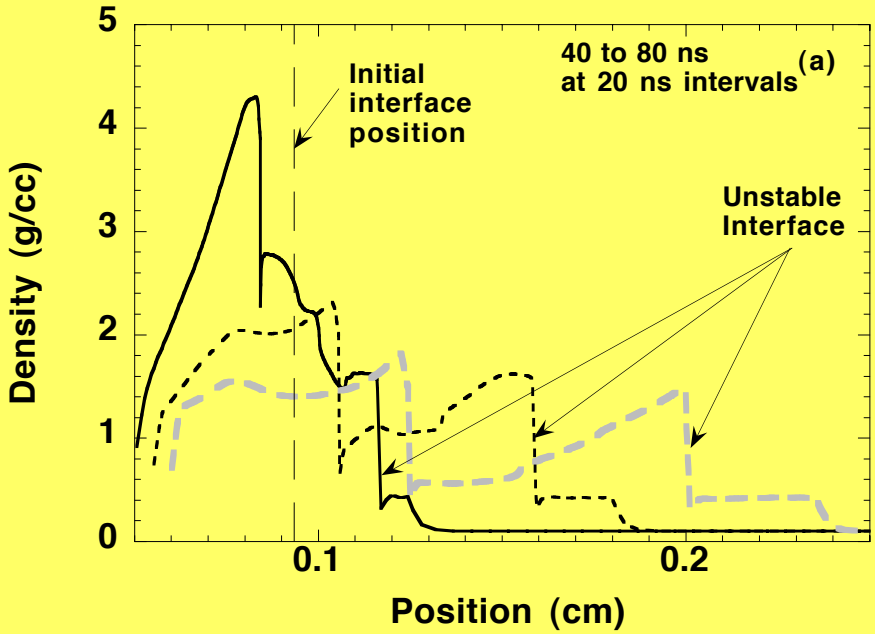

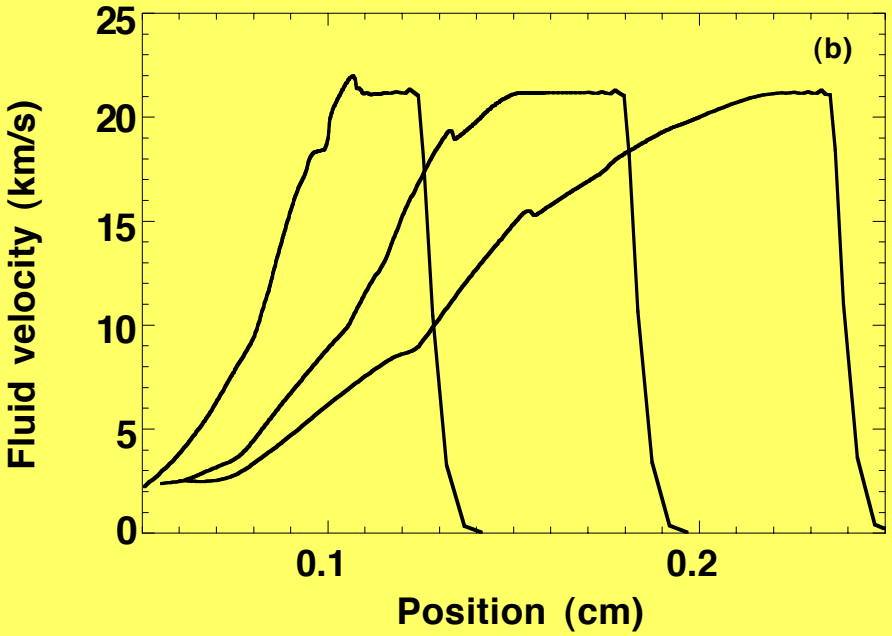

Conclusions

- This poster has described design approaches for flyer-driven RT and RM experiments on Z
- The advent of the Z backlighter makes these timely
- Z should be able to accomplish *very interesting* compressible turbulent mix experiments

- Join us the February 23-25, 2002 for the
- *4th International Conference on High Energy Density Laboratory Astrophysics*
- At the University of Michigan in Ann Arbor

Compressible Hydrodynamics on the Omega Laser: Motivated by Astrophysics

R. P. Drake, P. Keiter, K.E. Korreck, K. Dannenberg
University of Michigan

H.A. Robey, T.S. Perry, J.O. Kane, O.A. Hurricane, B.A. Remington, D.D. Ryutov, R.J. Wallace
Lawrence Livermore National Laboratory

J. Knauer, *University of Rochester*
R. Teyssier, *CEA Saclay, France*
A. Calder, B. Fryxell, R. Rosner, *U. Chicago*
Y. Zhang, J. Glimm, *SUNY Stony Brook*
J. Grove, *Los Alamos National Laboratory*
D. Arnett, *University of Arizona*
R. McCray, *Univ. of Colorado*
N. Turner, J. Stone, *Univ. of Maryland*

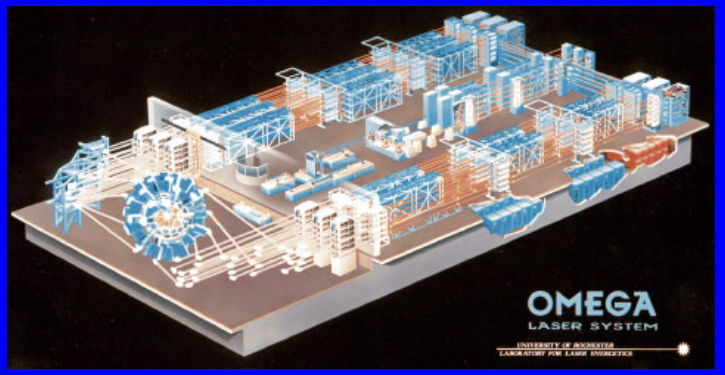

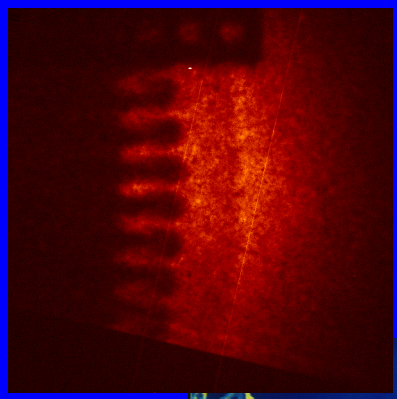

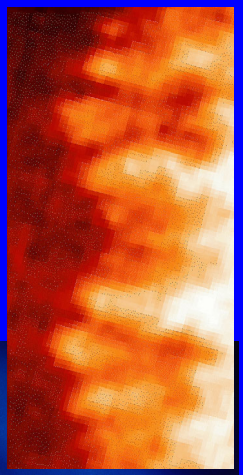

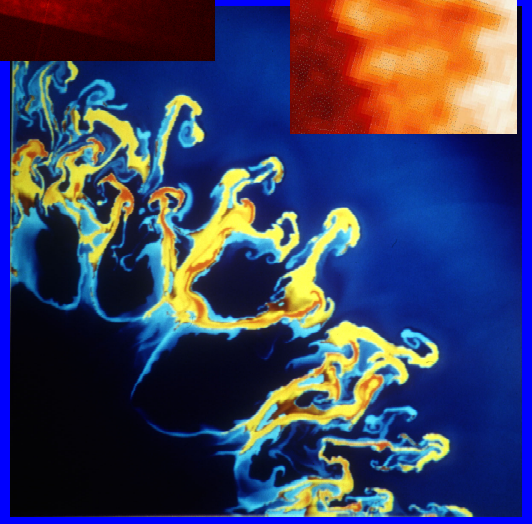

IWPCTM, Pasadena, CA, December 2001

Work supported by the U.S. Department of Energy under grants DE-FG03-99DP00284, DE-FG03-00SF22021 and other grants and contracts

We use the Omega laser to explore phenomena that matter for astrophysics

- **Our goal is to experimentally ground the understanding of important mechanisms**
  - **Theory or simulation suggests explanations for astrophysical data**
  - **The important mechanisms have often never been observed anywhere**
  - **We produce and observe these mechanisms in scaled experiments**
  - **This tests the theory and simulations**

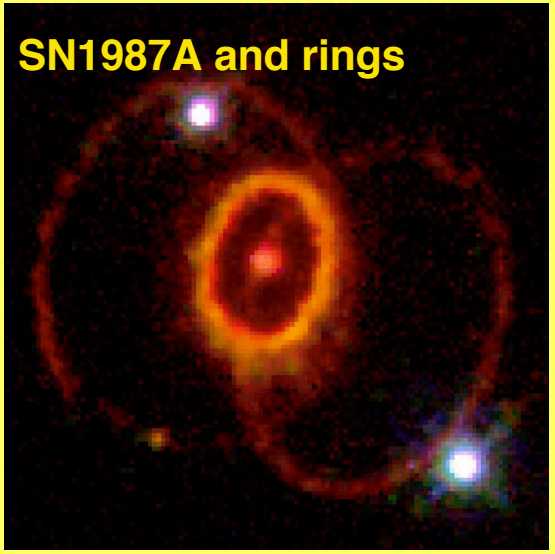

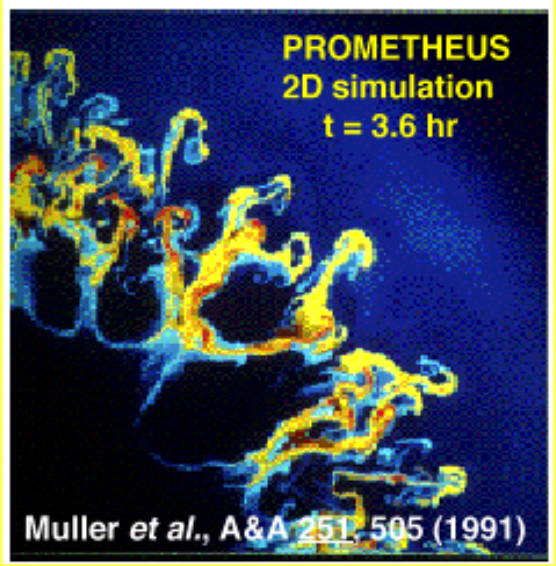

Astrophysical systems provide strong motivations for hydrodynamic studies

2D Simulation of SN 1987A

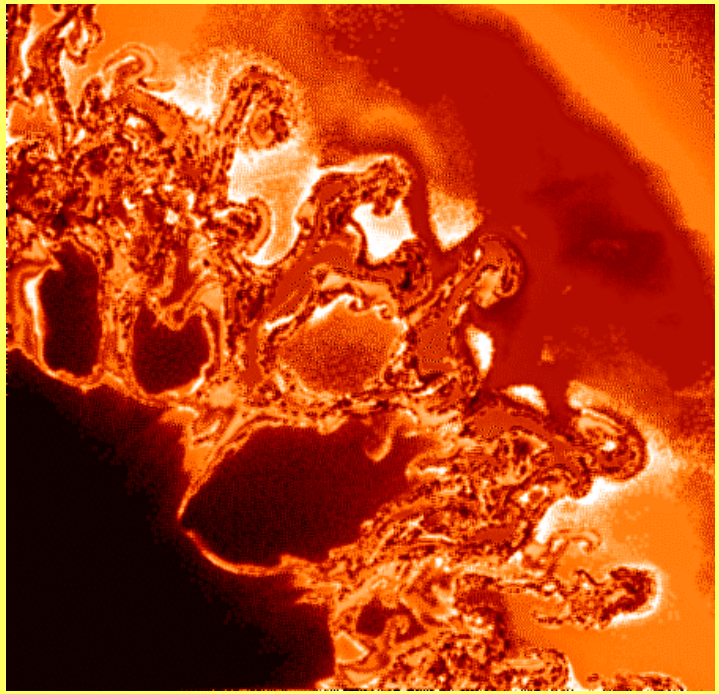

Muller, Fryxell, and Arnett (1991)

The velocities of the heavy element remain larger than predicted.

SN 1987A provided compelling evidence that hydrodynamic instabilities are essential to supernovae

- **Light curve**
- **Spectra**

Compressible turbulent mixing is also present in other astrophysical systems

- **Supernova Remnants**
- **Jets**
- **Shocks into clouds**

Well-scaled experiments are feasible: ***D.D. Ryutov, et al. ApJ 518, 821 (1999) ApJ Suppl. 127, 465 (2000) Phys. Plasmas 8, 1804 (2001)***

We often must explain to astrophysicists that we don't understand hydrodynamics

- We understand the *EQUATIONS* of hydrodynamics
- But NOT numerical simulations
  - They are like series solutions to differential equations without the ability to quantify errors
  - Vanishing metrics add complications
  - No stochastic backscatter in current simulations (Leith '90, Piomelli '91)
  - Also no full turbulence

Codes disagree about asymptotic growth rates [*Glimm et al. 2001*]

Simulation	RT growth factor, α
'91 Youngs	0.04-0.05
'91 Youngs	0.03
'99 S.Y. Chen	0.043
'99 Dimits et al.	0.016
'99 Cheng et al.	0.08
'99 Glimm et al.	0.07
'99 Oparin	0.075

Codes disagree about structure

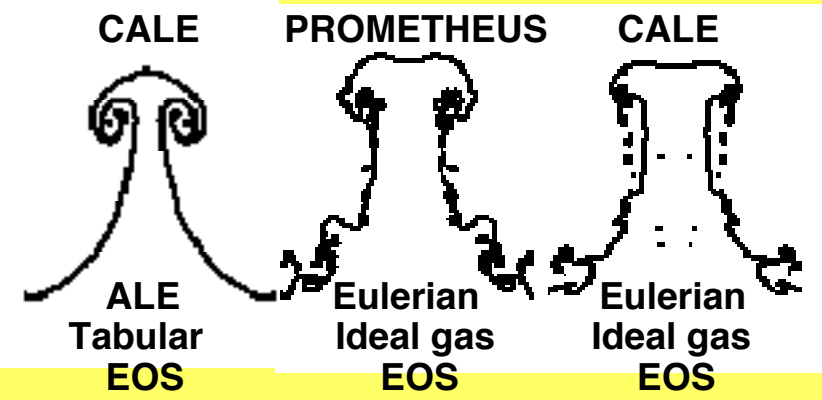

- This can matter for astrophysics
- Examples:
  - Size of mix layers is uncertain
  - Small details affect production of "hydrodynamic bullets" or other important structures

Our hydrodynamic experiments all use similar target packages

Photograph of target

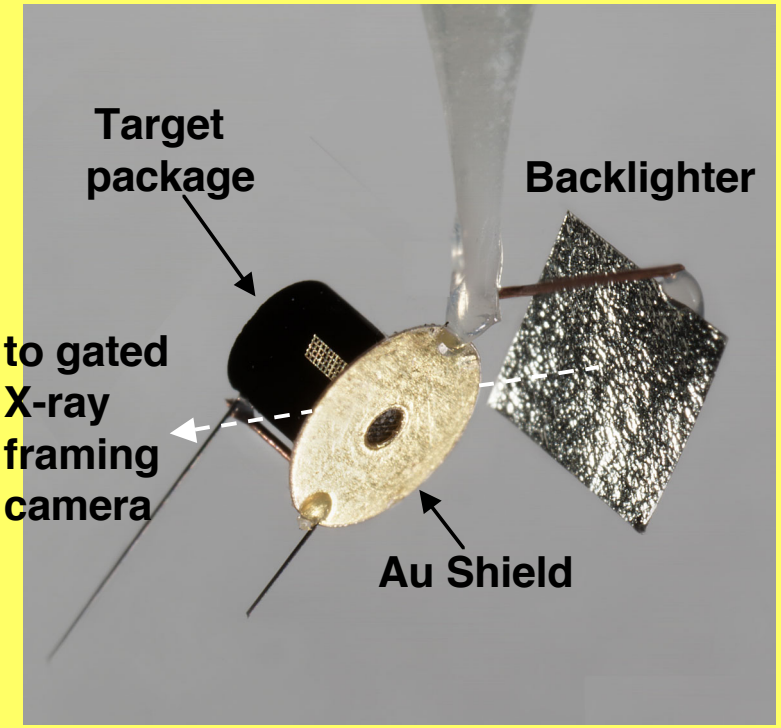

CAD drawing of target & beams

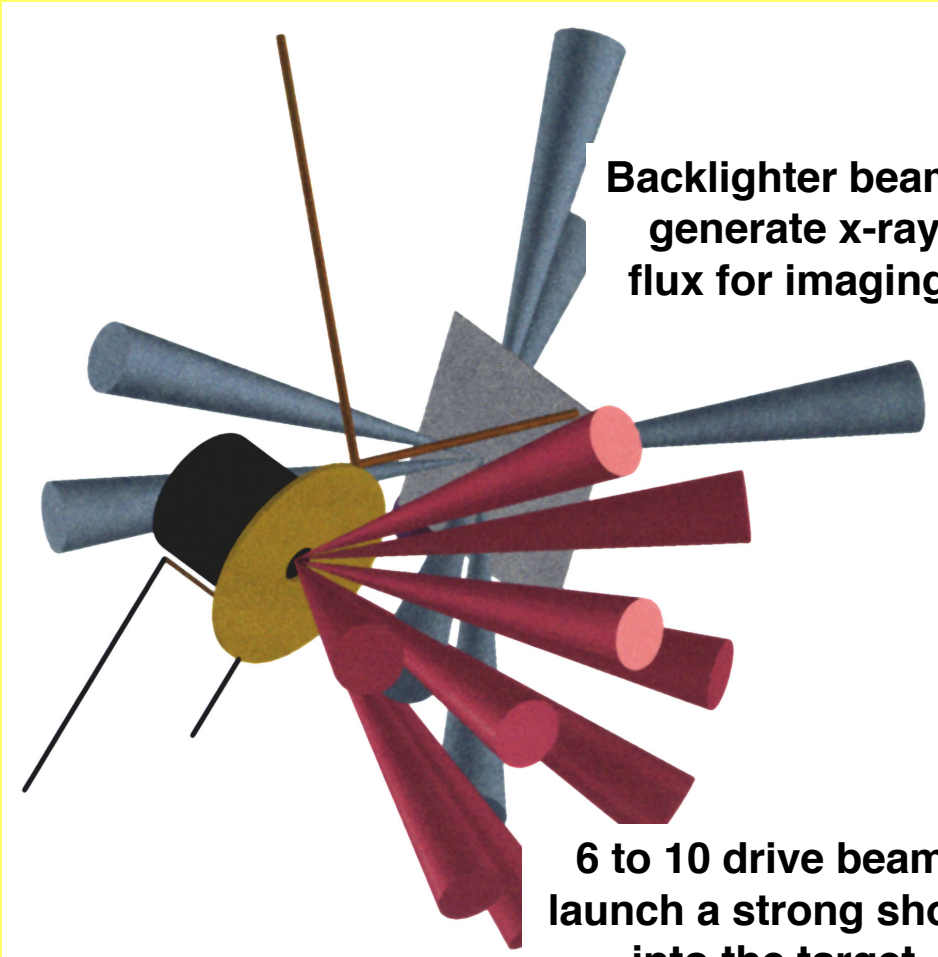

Backlighter beams generate x-ray flux for imaging

6 to 10 drive beams launch a strong shock into the target materials

Our experiments have been aimed at addressing the obvious first question:

- **THE FIRST QUESTION: Can the codes follow the evolution of such hydrodynamics deep into the nonlinear regime?**

Our experiments at Omega have addressed this question while probing several mechanisms present in supernova explosions

Spherical divergence

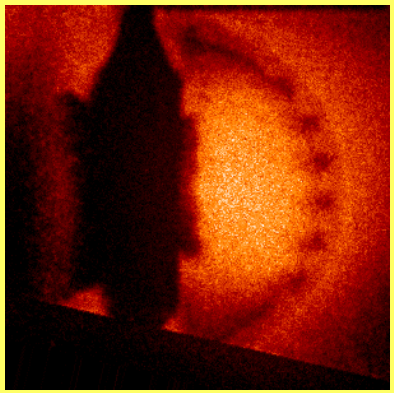

Drake et al., ApJ Jan. '02

2D simulation of SN1987A
Muller, Fryxell, and Arnett (1991)

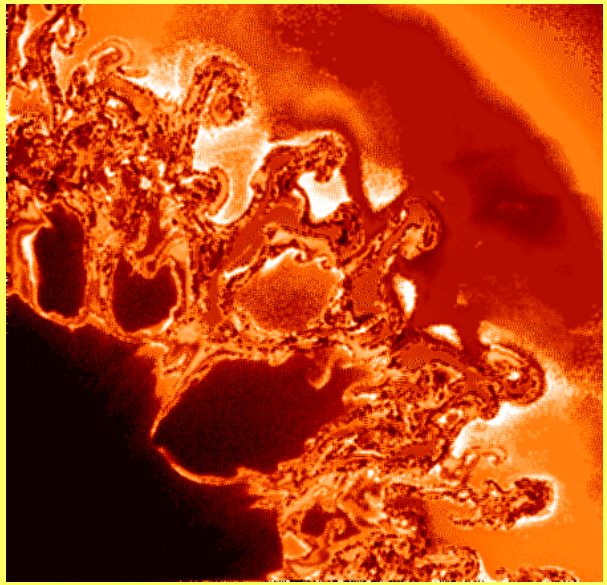

2D vs. 3D instability

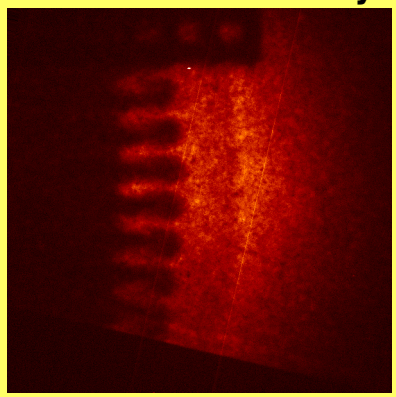

Finished in September

Multi-interface coupling

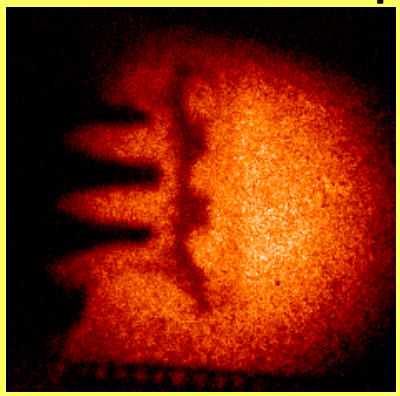

Kane et al., PRE 63, 55401 (2001)

Multi-mode instability

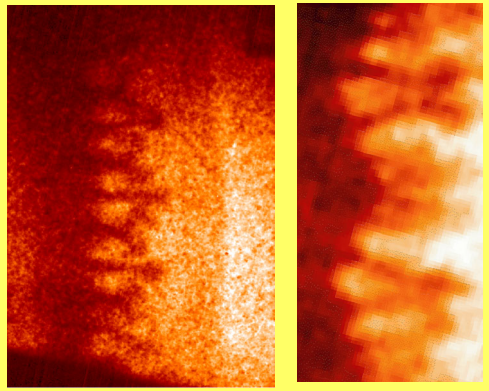

Ongoing experiments

Coupling between spatially separated interfaces in a SN is studied with a multi-layer target

Exploded view of multi-layer target

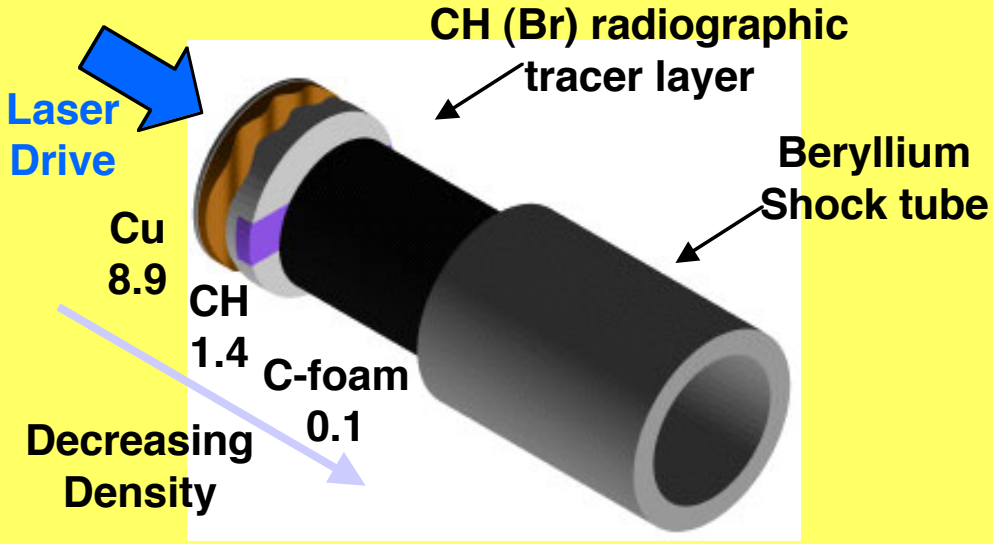

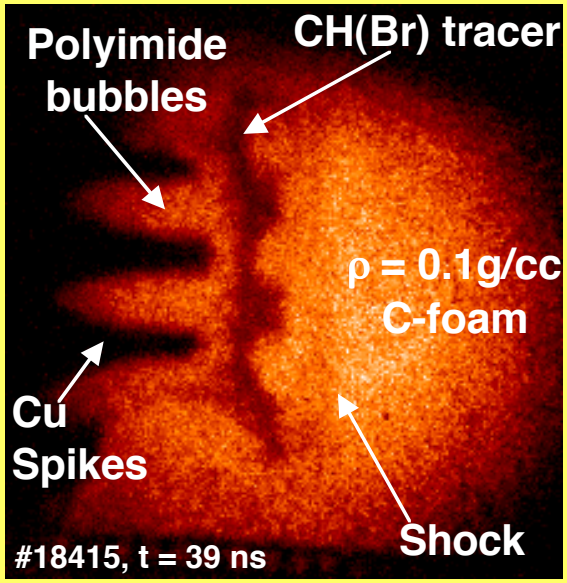

Simulation of this experiment by the ASCI code FLASH at Chicago

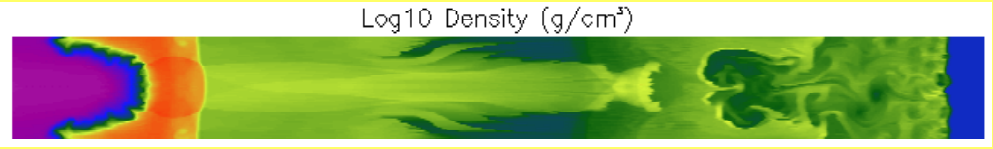

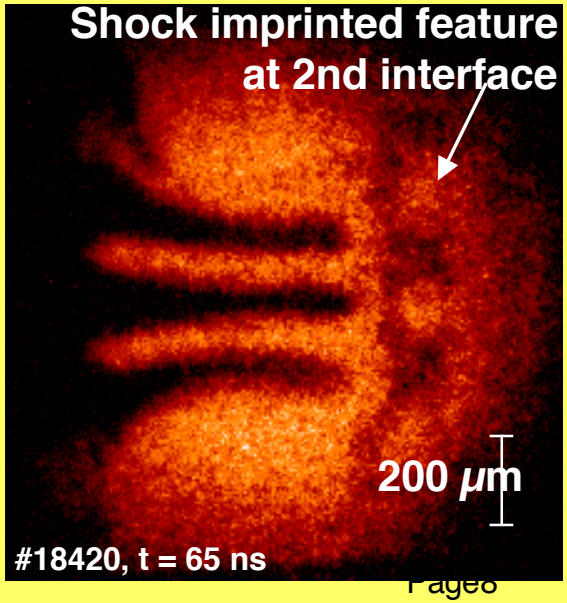

The interface coupling experiments are typical of what we have found

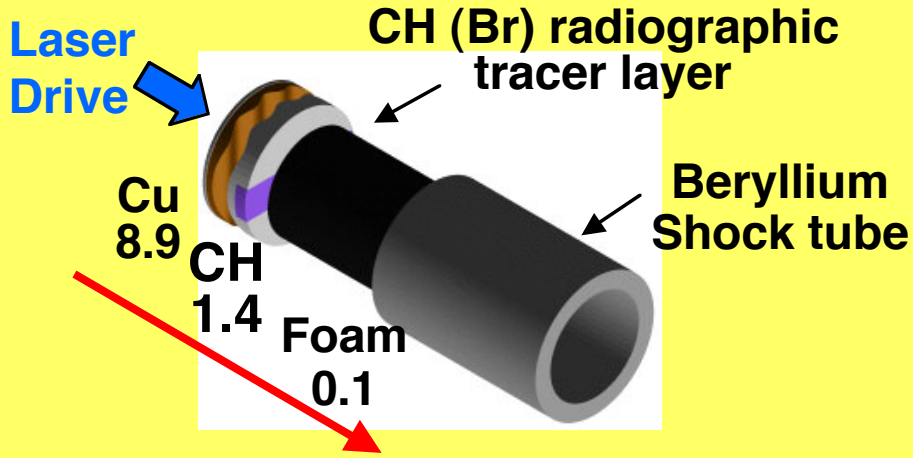

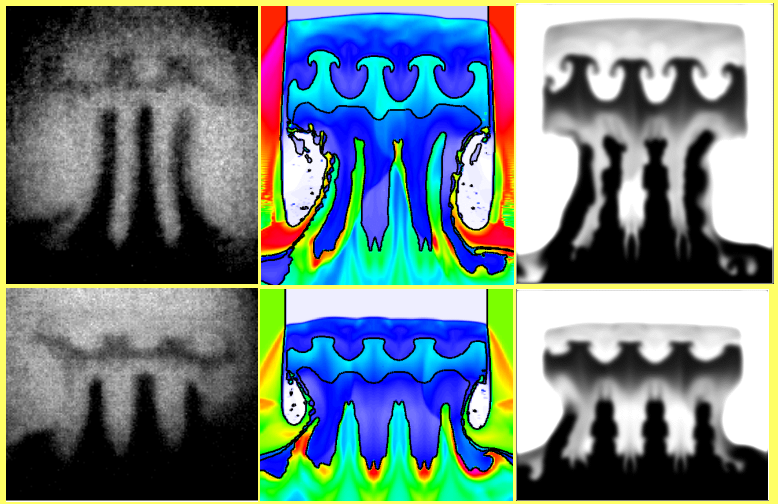

THE FIRST QUESTION: Can the codes follow the evolution of such hydrodynamics deep into the nonlinear regime?

ANSWER: Yes, eventually, based on work to date.

But not in the first run in every version.

Another example: effect of spherical divergence is studied by laser illumination of a perturbed hemispherical shell

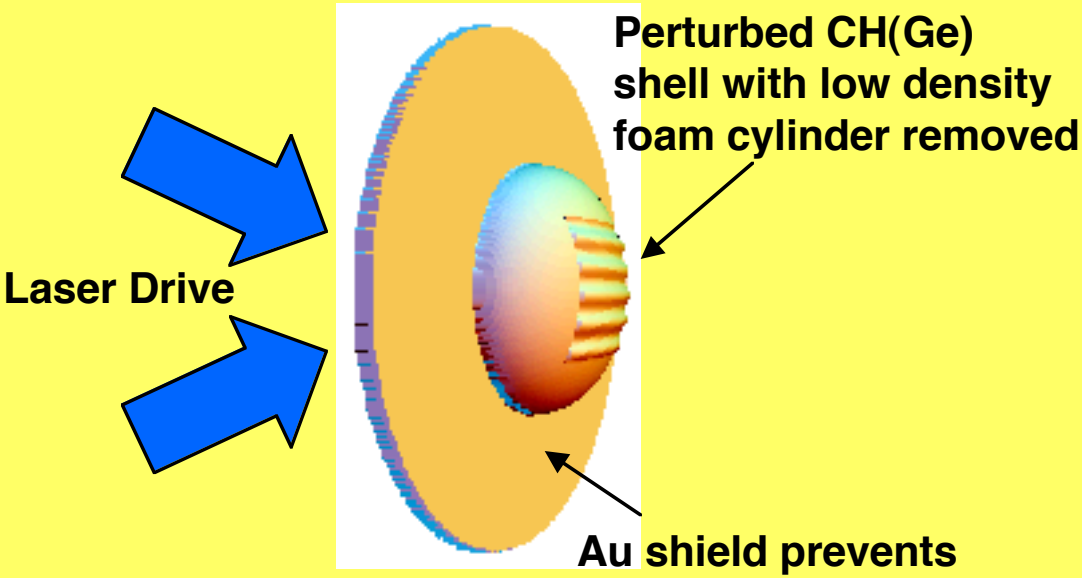

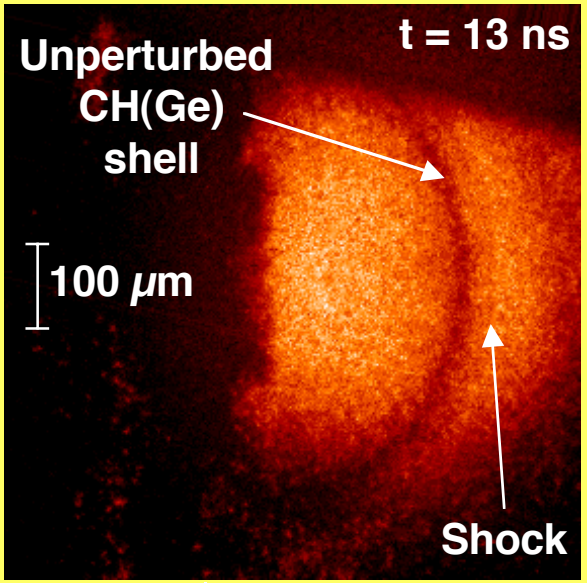

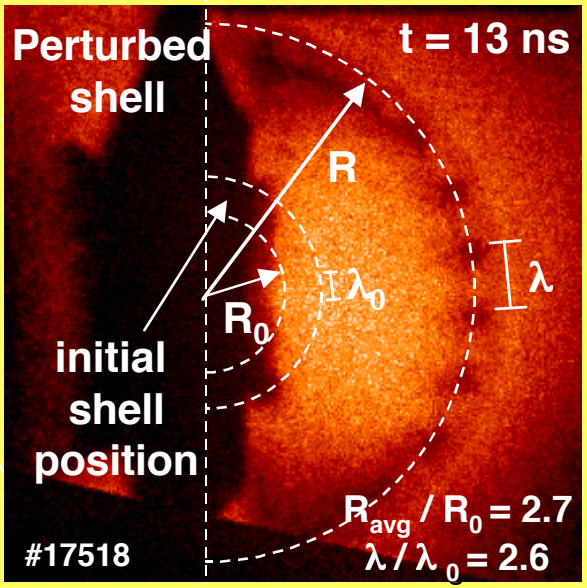

- The unperturbed hemispherical shell remains intact indicating no significant perturbation from the laser drive
- The perturbed shell (λ=70μm, a_{P-V}=10μm) breaks up due to R-T and R-M instability

Perturbation growth in spherical geometry is observed to be significantly smaller than in planar geometry

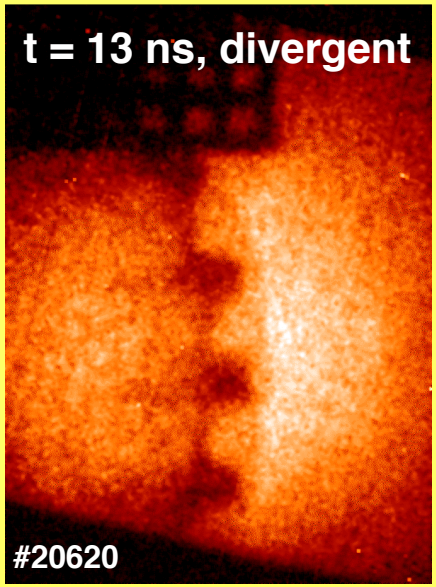

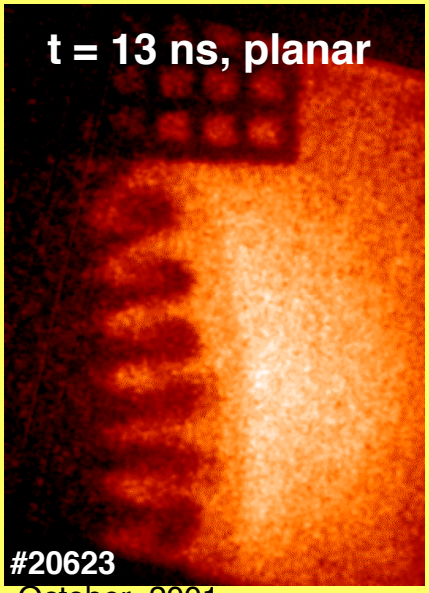

CALE vs. data

Comparison of spherical vs. planar

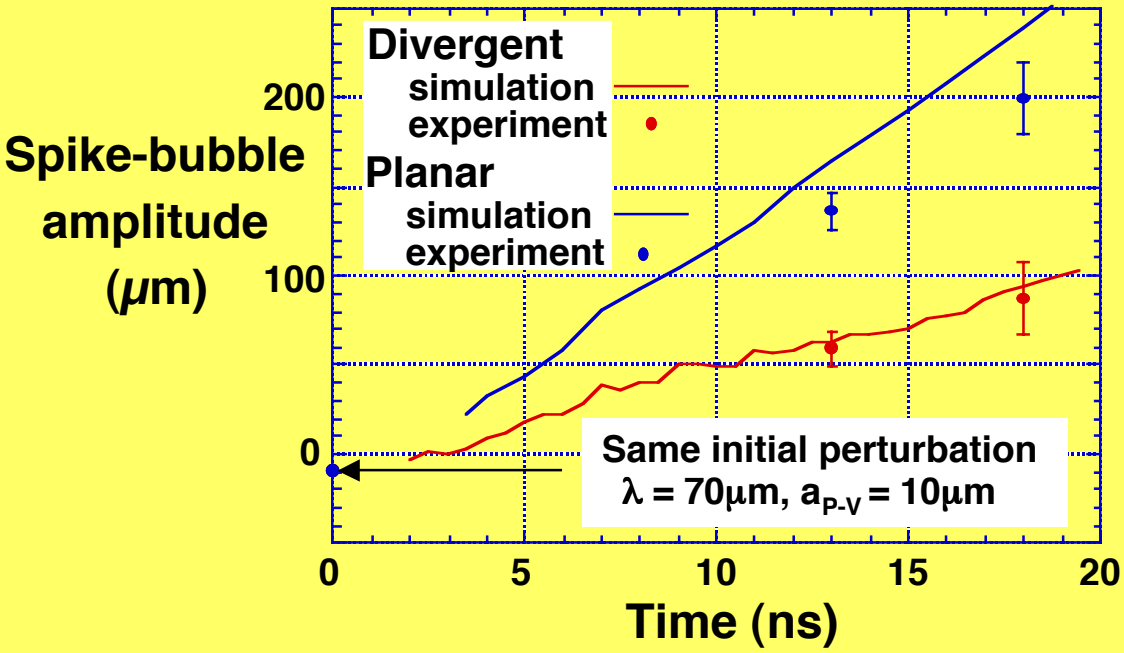

Growth in spherical geometry is reduced due to :

- **Wavelength increase due to divergence**
- **Possible effect of shock proximity**

CALE results show spike development

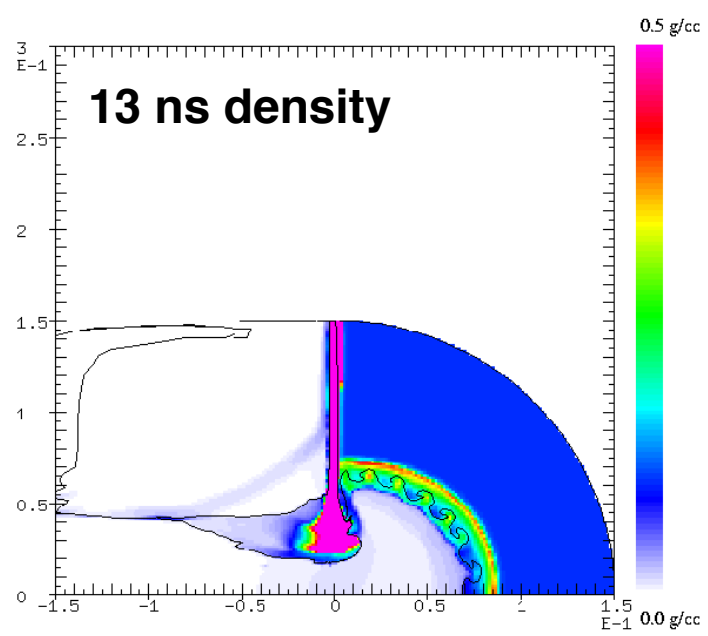

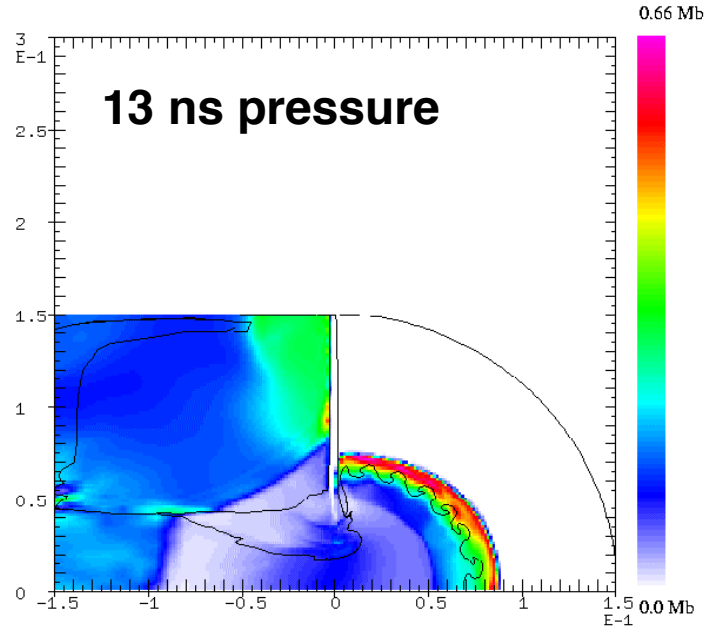

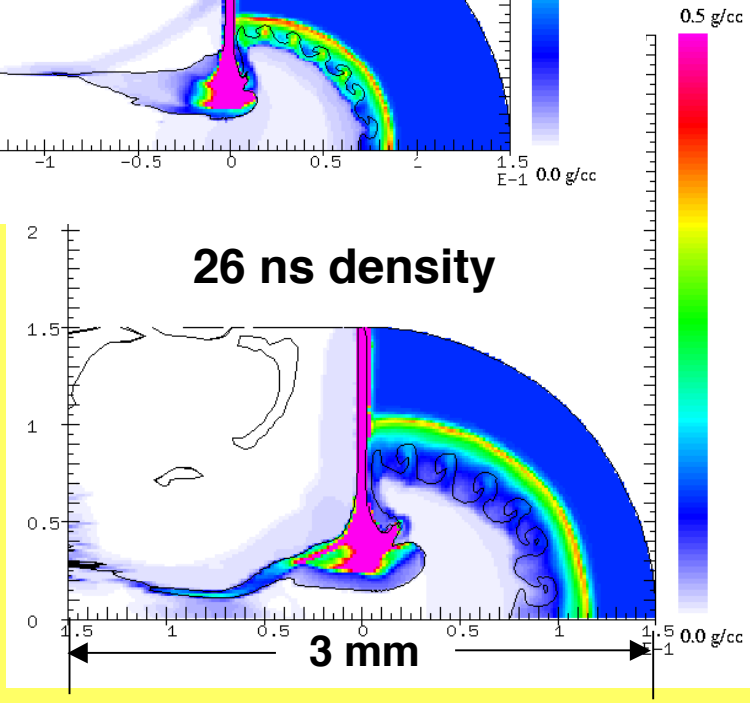

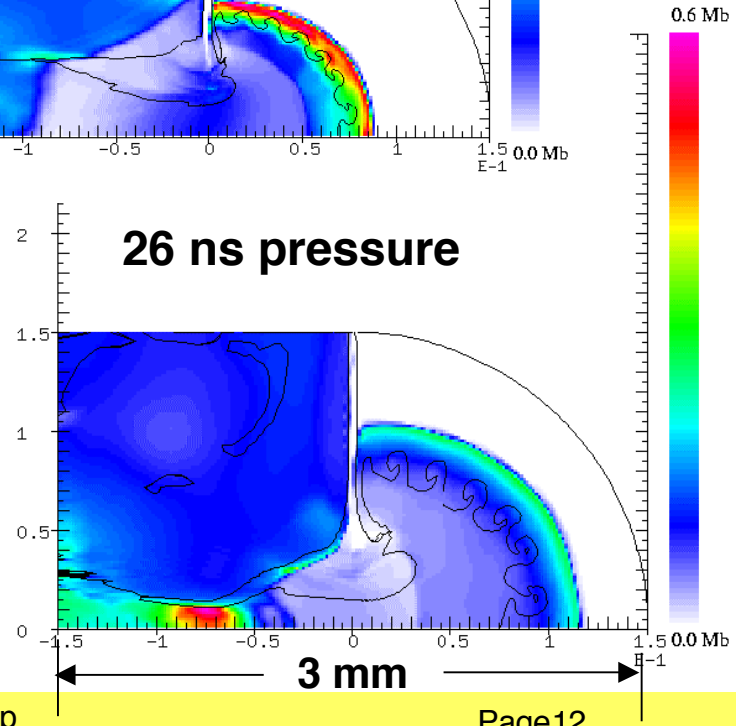

We used FronTier to demonstrate mapping to a purely hydrodynamic code

- FronTier
  - Front tracking by independent updating on the two sides of the discontinuity: there is never finite differencing across the front
  - The common MUSCL (Monotonic Upstream-centered Scheme for Conservation Laws) approach is used to advance the hydro normal to the front and elsewhere
  - For this problem, outgoing boundary conditions are used within the capsule and at the outer boundaries; the remainder of the axis of symmetry is a reflecting boundary
  - Results shown on 1.5 mm x 1.5 mm scale

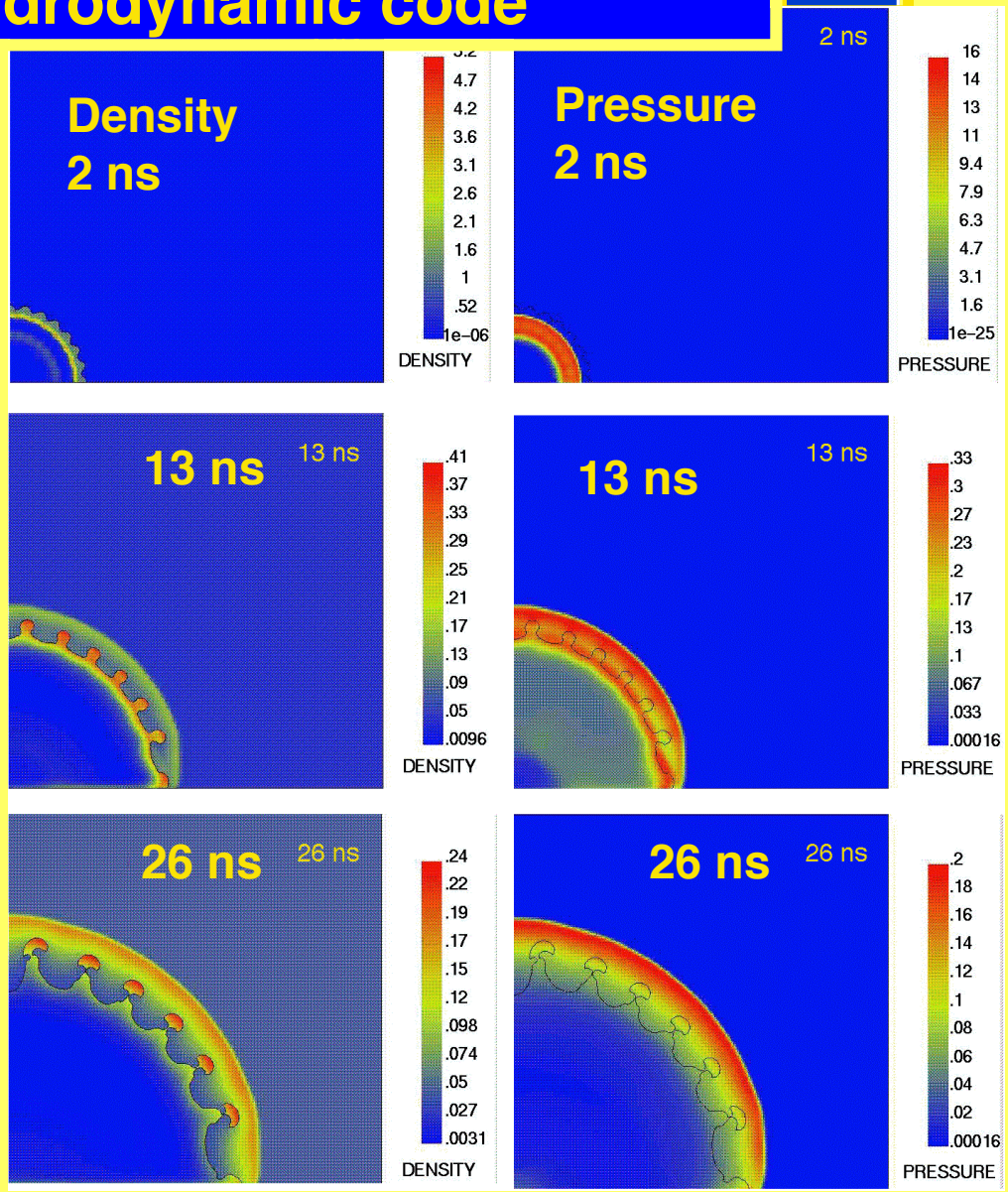

Our hydrodynamic experiments are ready to ask the second question

- **THE SECOND QUESTION: Does this medium (plasma) exhibit a transition to turbulence like that seen in fluids?**
- **A: In ongoing experiments, we are working to find out.**
  - **If so, this will be a much bigger challenge for simulations.**
  - **It will probably also mean that much published astrophysical hydrodynamics is wrong.**

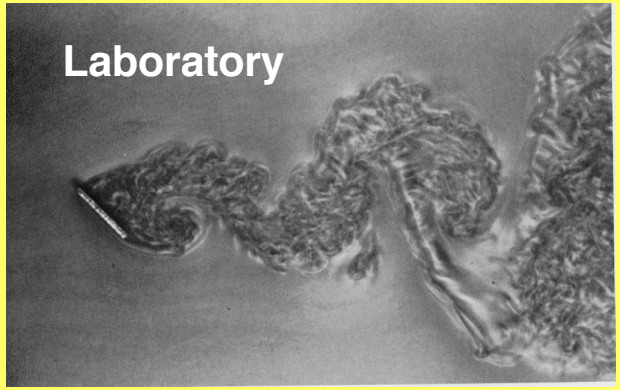

Re = 4300 Cantwell, *Ann. Rev. Fluid Mech.*, 13, 457 (1981)

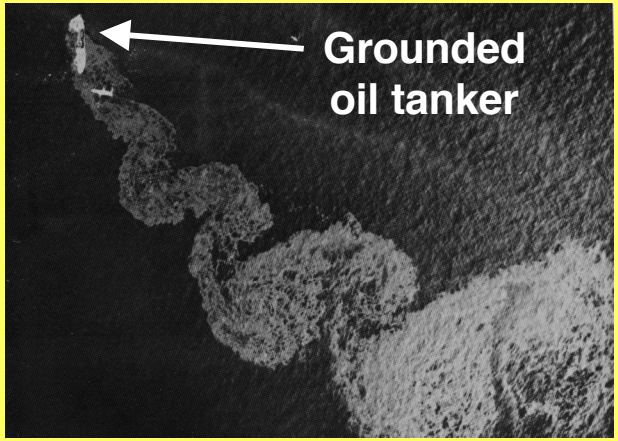

Re = 10^7 Van Dyke, "An Album of Fluid Motion", Parabolic Press, p.100 (1982)

We are excited about our progress and look forward to forthcoming experiments

- We've made demanding tests of deep nonlinear hydrodynamics at high energy density
- Next: Push high energy density systems into the "fully turbulent" regime

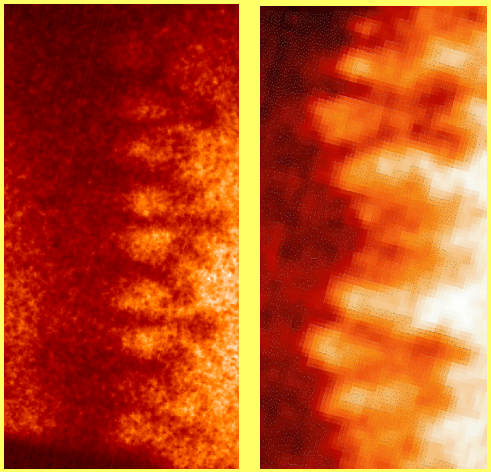

- Join us the February 23-25, 2002 for the
- *4th International Conference on High Energy Density Laboratory Astrophysics*
- At the University of Michigan in Ann Arbor

An experimental study of the effect of shock proximity on the Richtmyer-Meshkov instability at high Mach number

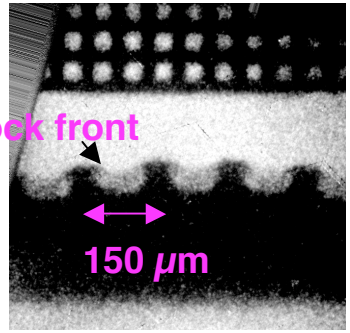

S. G. Glendinning, D.G.Braun , M.J.Edwards, W.W.Hsing, B.F.Lasinski, H.Louis, A. Miles, J.Moreno, T.A.Peyser, B.A.Remington, H.F.Robey, E.J.Turano, C.P.Verdon, Y.Zhou

LLNL

Presented to: 8th International Workshop on the Physics of Compressible Turbulent Mixing
Pasadena, CA
11 December, 2001

This work was performed under the auspices of the U. S. Department of Energy by the University of California, Lawrence Livermore National Laboratory under Contract No. W-7405-Eng-48.

Summary

- We have used the Omega laser to generate a nearly steady interface velocity for Richtmyer-Meshkov experiments
  - The interface is a heavy-to-light (12:1) density step
  - The incident shock Mach number is ~10
  - The shock velocity is only about 20% higher than the interface velocity
- An initially sinusoidal perturbation with λ=150 μm, λ_0=7 μm ($k\lambda_0$=0.3) grows according to incompressible models
- The growth of with λ=150 μm, λ_0=22 μm ($k\lambda_0$=0.9) is about half that predicted from incompressible models
  - The shock remains very close to the spike tips as the perturbation grows
  - An analytical model which accounts for the effect of the shock proximity predicts the reduced growth

The Richtmyer-Meshkov instability occurs at an interface impulsively accelerated by a shock

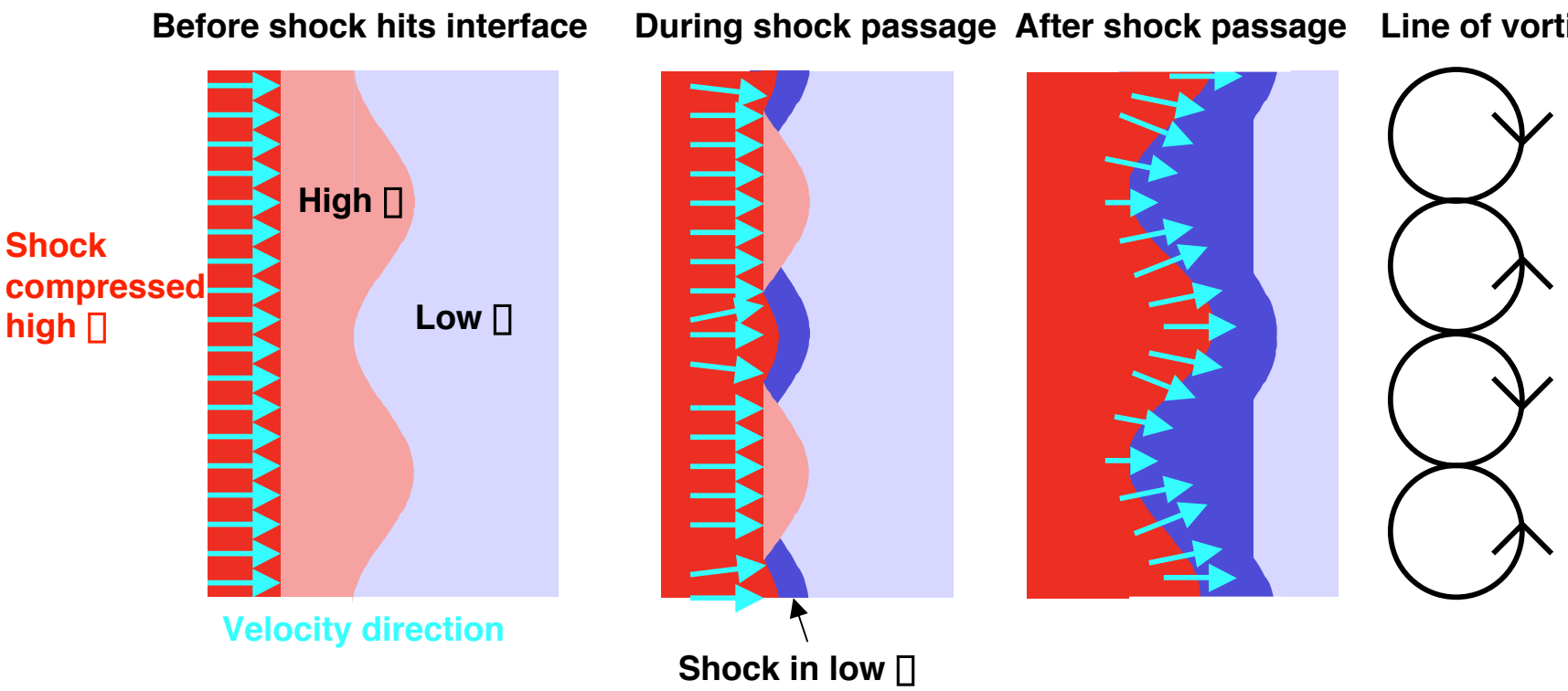

- The interface may be at a density decrease or increase in the propagation direction
  - These experiments are at a density decrease
- A perturbation at the interface creates a velocity perturbation (vorticity field)
- The perturbation grows linearly as $\eta(t) = kA^{*}\left(\frac{\rho^{*}+\rho_0}{2}\right)u_c t$ (Meyer and Blewett, 1972)

Laser experiments are important to understand effects of compressibility (high Mach number)

- Compressibility results in a shock front which remains close to the interface
  - $u_c \sim s_f$, where u_c is the interface speed and s_f is the receding shock speed
- Incompressible models (Meyer-Blewett, 1972; Sadot, 1998) predict that spike tip moves faster than shock
- Various models predict reduction in growth rate due to shock proximity:
  - Holmes et al., (1999) $\dot{\eta} = \dot{\eta}_{IM} / \left[1 + \dot{\eta}_{IM} / (s_f - u_c)\right]$, where $\dot{\eta}_{IM}$ is $ku_cA^*(\eta^*+\eta_0)/2$.
  - Hurricane et al., (2000) $\dot{\eta} = u_c(1-u_c/s_f)\tanh\left[\dot{\eta}_{IM}/u_c(1-u_c/s_f)\right]$
- Laser experiments at Mach ~15 (Dimonte, 1996; Holmes, 1999; Farley 1999) may show large amplitude effects rather than compressibility effects (Ben-Dor et al., 2001)
  - $k\eta_0 = 2$ (Dimonte/Holmes), $k\eta_0 \sim 2.7$ (Farley)
  - Rikanati et al. (2000) predicts $\dot{\eta}/\dot{\eta}_{IM}$ at Mach 15 of ~0.9 for $k\eta_0 = 0.9$, 0.65 for $k\eta_0 = 2$
- On Omega we have investigated this with $k\eta_0 = 0.9$, $u_c = 21.9$ μm/ns, $s_f = 26.1$ μm/ns

A model of vortex evolution (Rikanati, 1998) was proposed for low Atwood number RMI

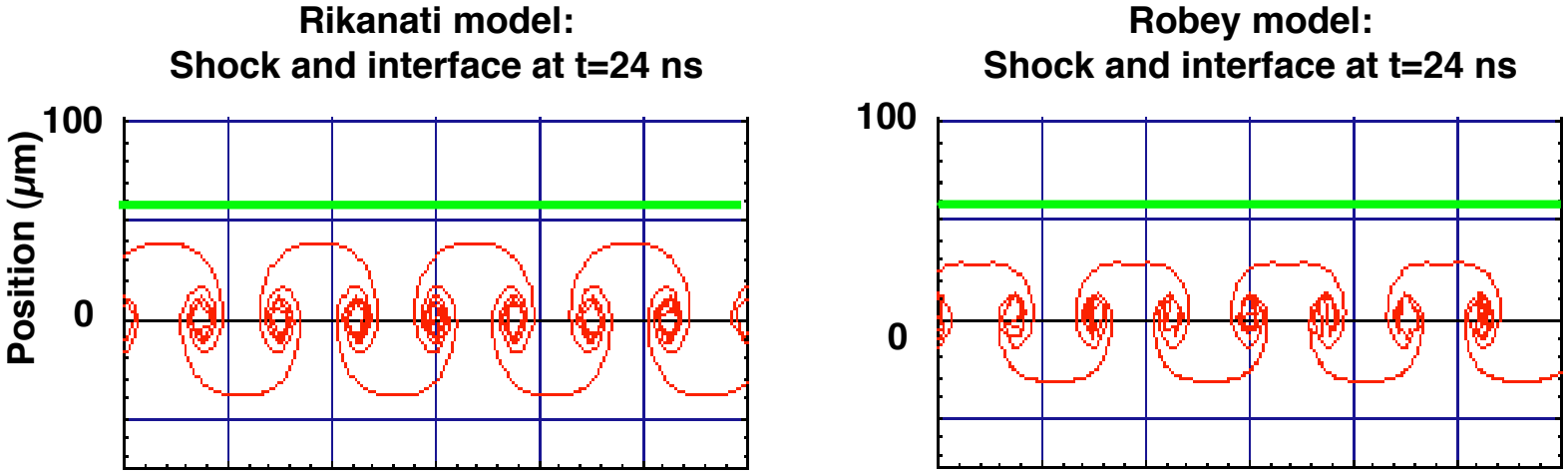

- This model calculates growth rates from analytical solutions to vortex flow problem
- An extension of this model (Robey, 2001) constrains the shock front to be flat by introducing mirror image vortices
  - However, the shock front is not in reality flat
- Robey's is the only model which predicts an increase in growth rate after initially slow growth

This experiment uses an 11 ns laser drive to create a steady shock incident on a modulated interface

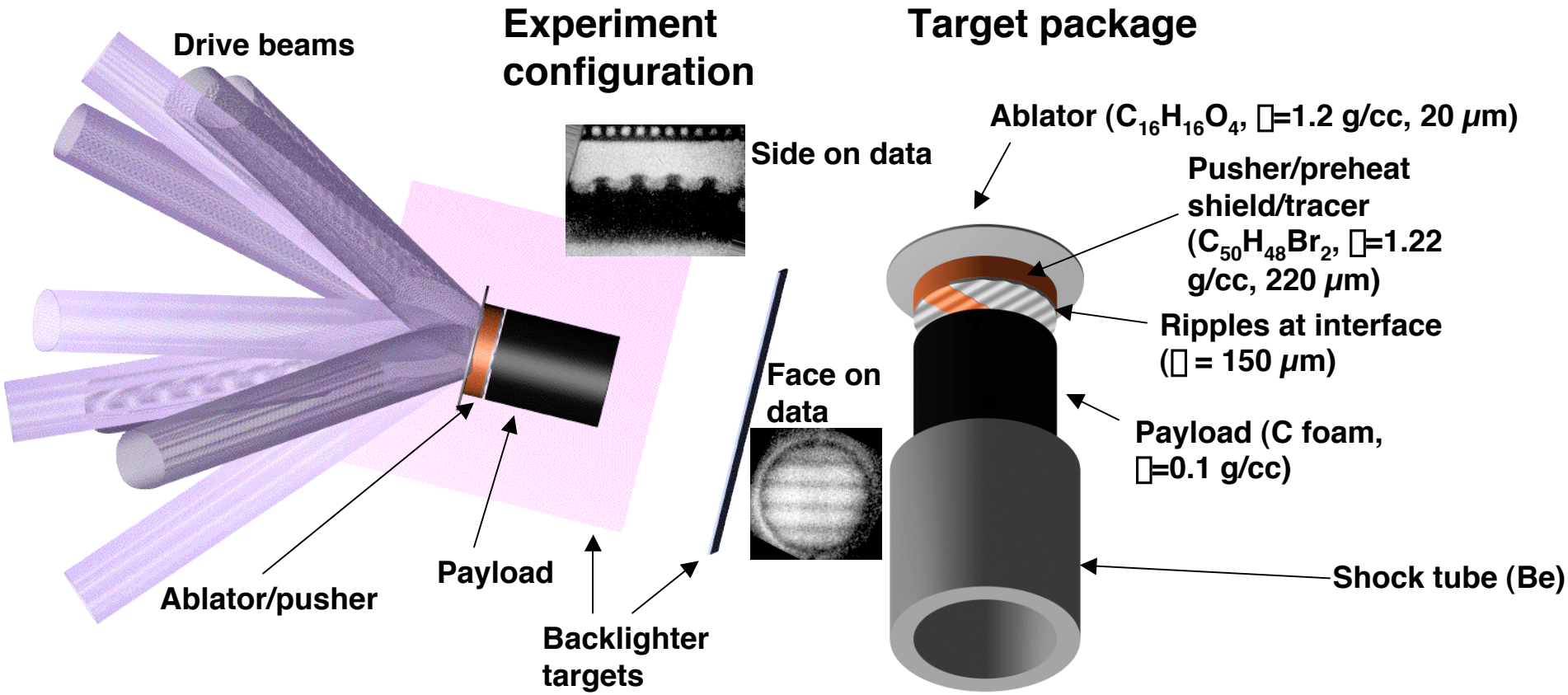

- Radiography is done on two axes, along target axis and perpendicular to modulations
- Target package is encased in a beryllium shock tube

The incident shock and interface velocities are constant within ±5% RMS

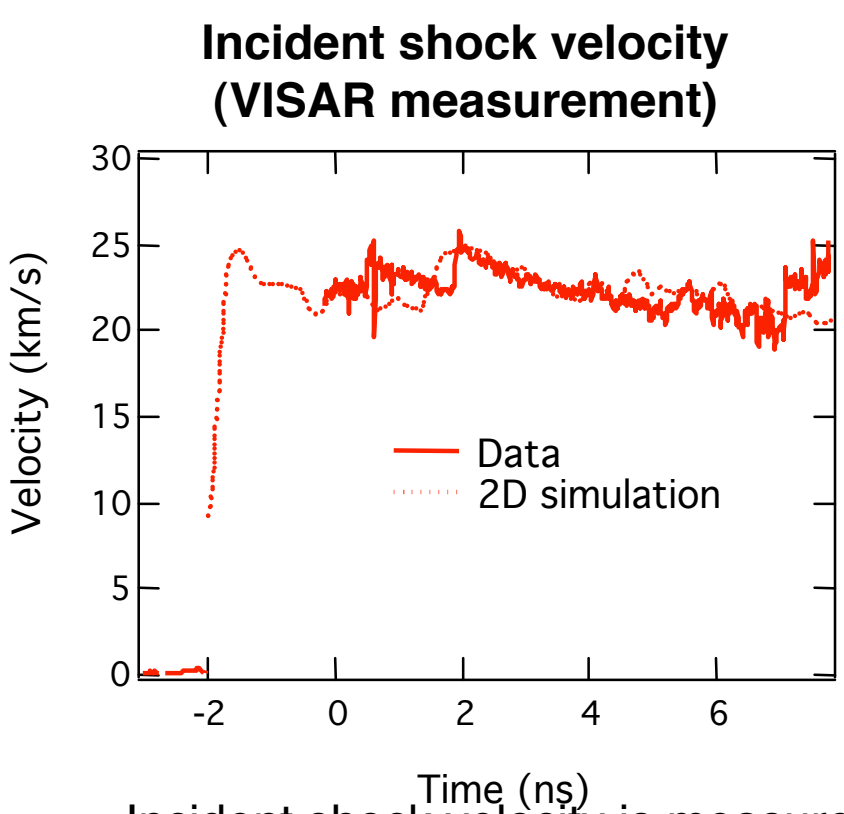

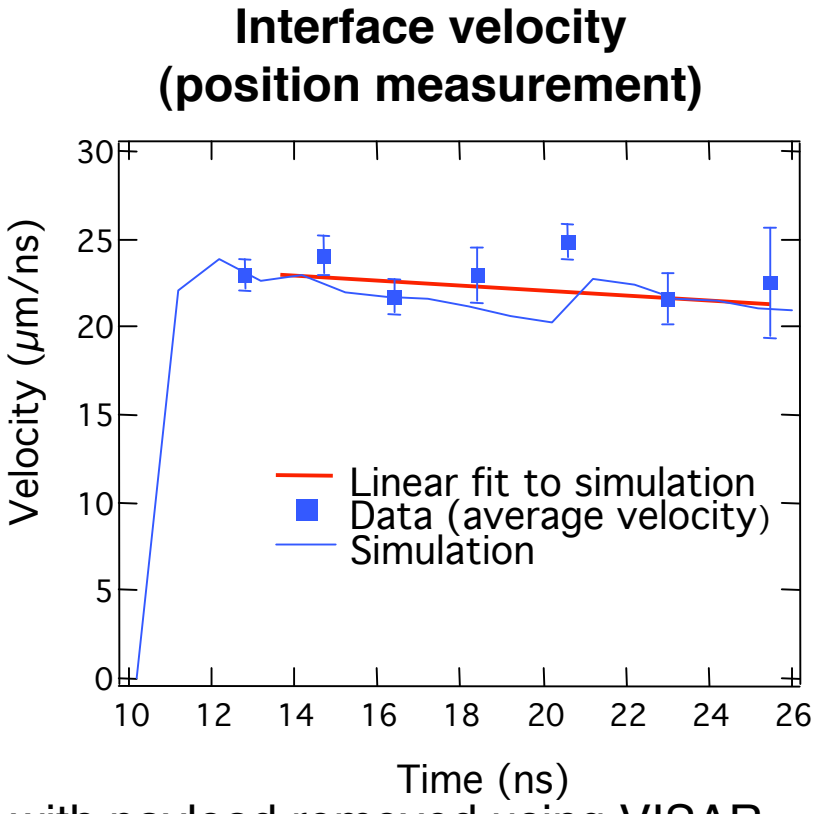

- Incident shock velocity is measured with payload removed using VISAR
  - Result 22.0±0.2 μm/ns, ±5% (RMS) variations
- The shock is incident on a 12:1 density contrast
- The interface position is measured by side-on radiography
  - Average interface velocity 21.9±1.0 μm/ns
  - Transmitted shock velocity 26.1±0.5 μm/ns

At low initial amplitude results show no effect of shock proximity and little nonlinearity

Side-on radiographs, η_0=7 μm

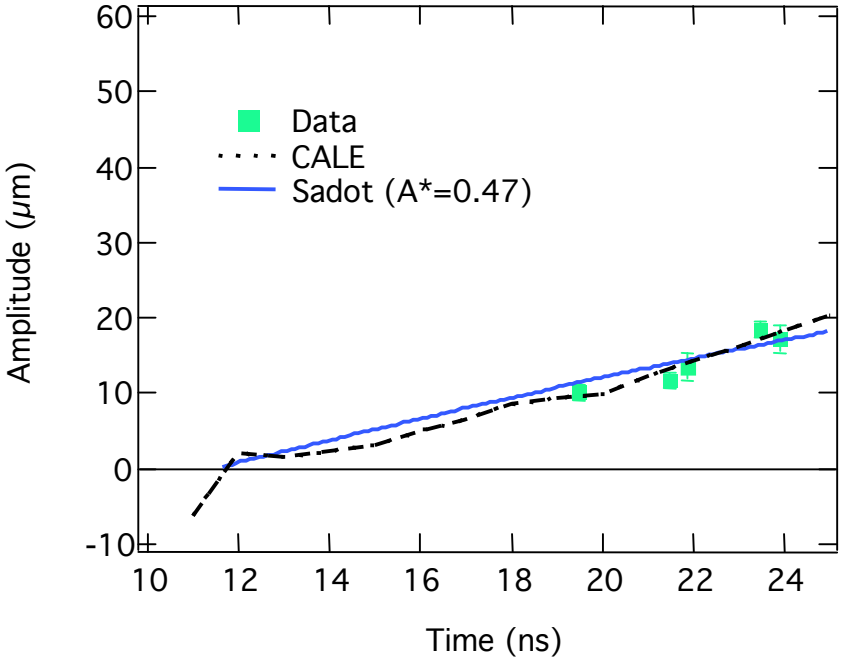

Face-on radiographs, η_0=7 μm

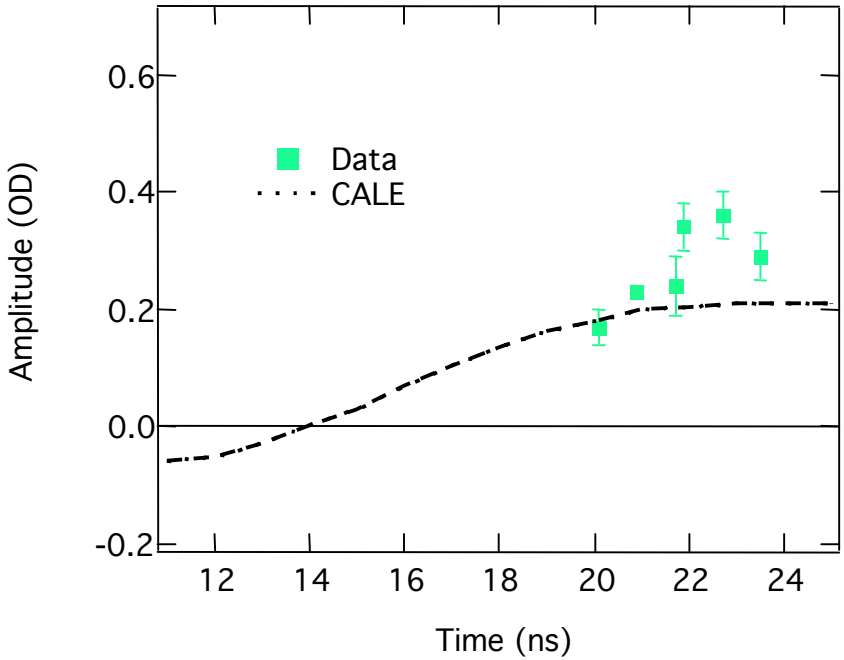

- The nonlinear, incompressible model of Sadot (1998) was used to describe the side-on data with an inferred post-shock Atwood number of 0.47
  - Atwood number of 0.47 agrees with one-dimensional simulations
- Linear growth rate $\dot{\eta}$ is 1.5 μm/ns
- CALE simulations agree with the data

Larger initial amplitude results show reduced growth due to shock proximity

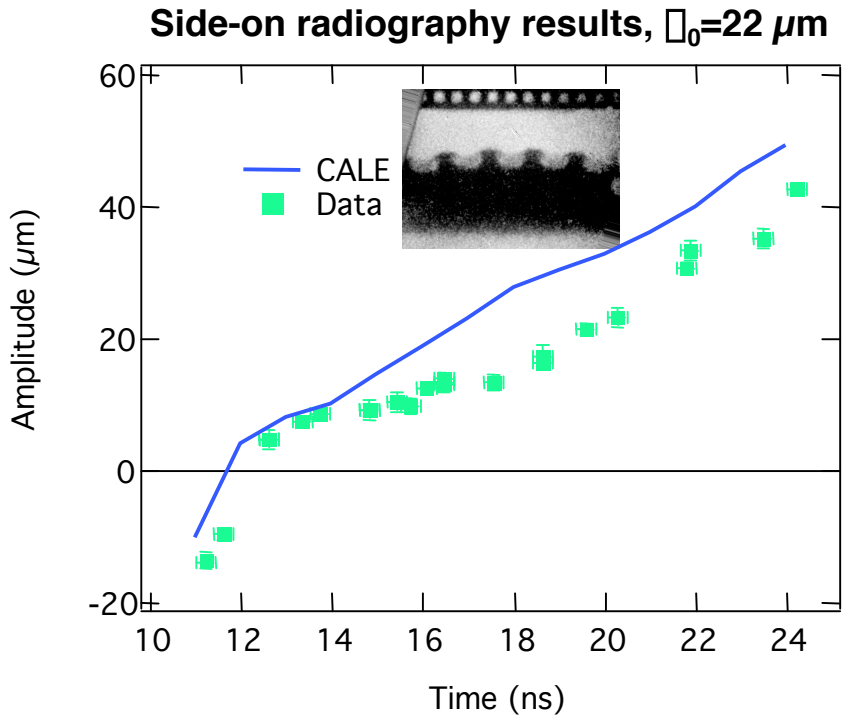

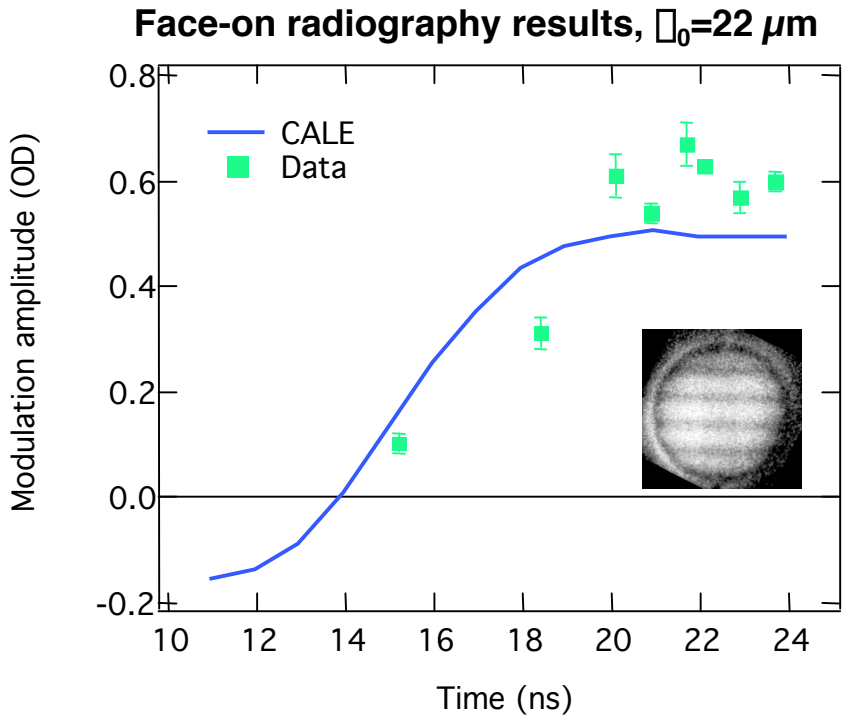

- Linear growth rate would be 4.8 μm/ns
- The average $\dot{\eta}$ is 2.4±0.1 μm/ns
  - Before 18 ns $\dot{\eta}$ is about 1.9±0.1 μm/ns
- The CALE simulation gives a growth rate of 3.9 μm/ns before 18 ns, 3.7 μm/ns average 12-24 ns

We may constrain the CALE simulations to come closer to the modulation growth at □=150, □$_0$=22 by changing the drive

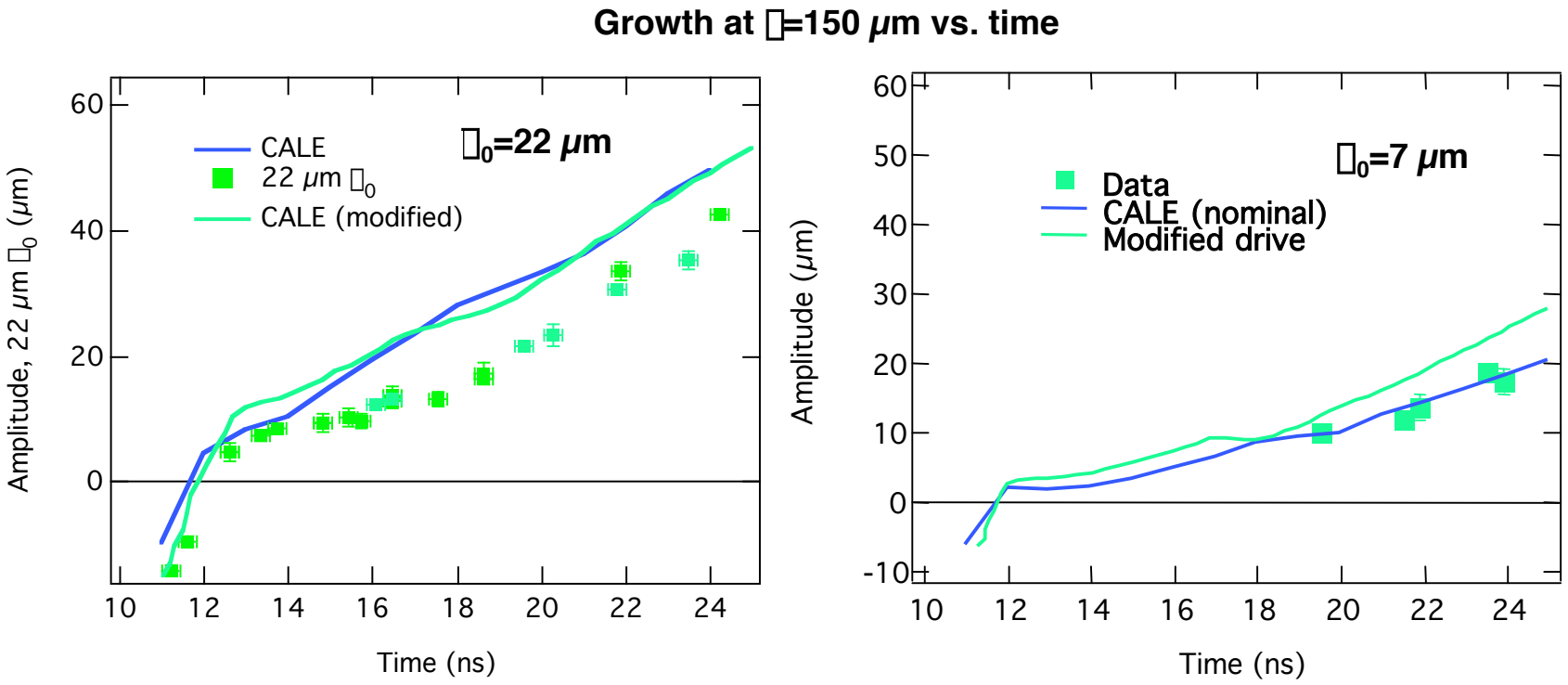

- The modified drive gives a growth rate at early time of 3.0 μm/ns
- The modified drive does not predict the □=150 μm, □$_0$=7 μm data
- We are currently investigating EOS issues
- The discrepancy between CALE and the data is currently not understood

The vortex model of Robey does predict growth very much like that seen

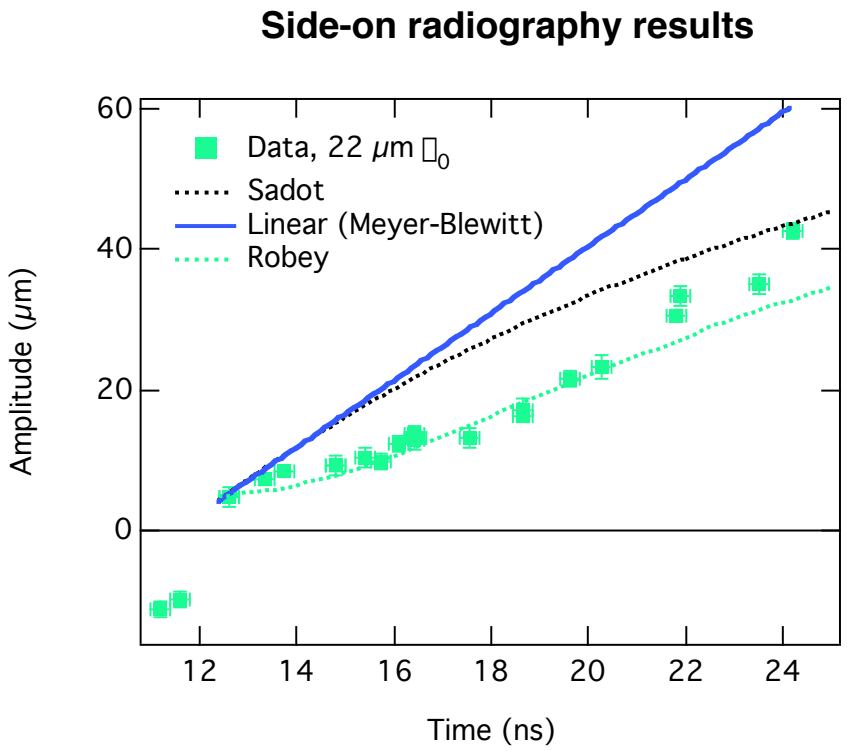

- The model predictions are offset to the first observed data point

The data may be compared with the shock tube data of Aleshin et al.

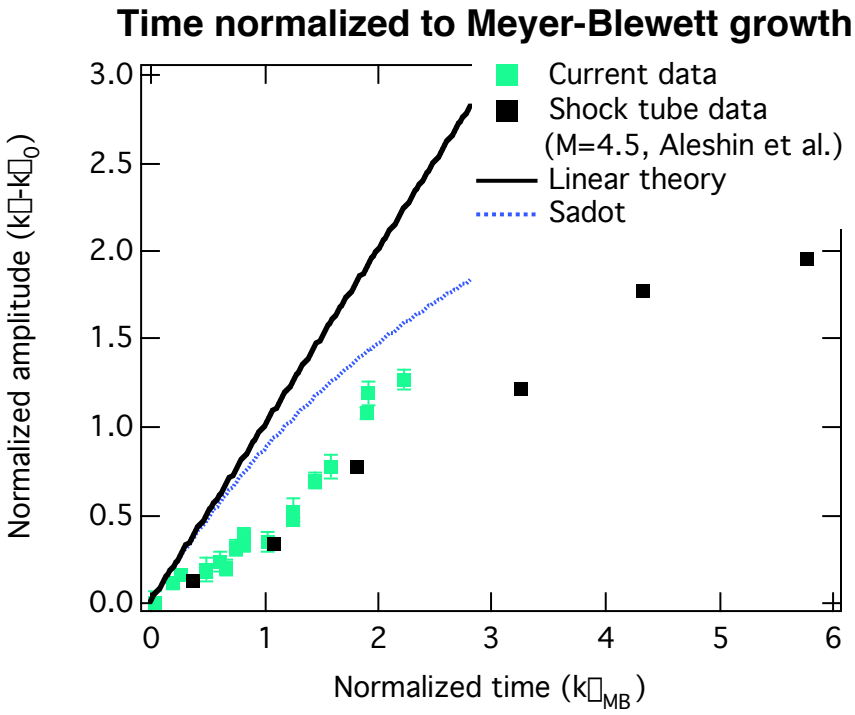

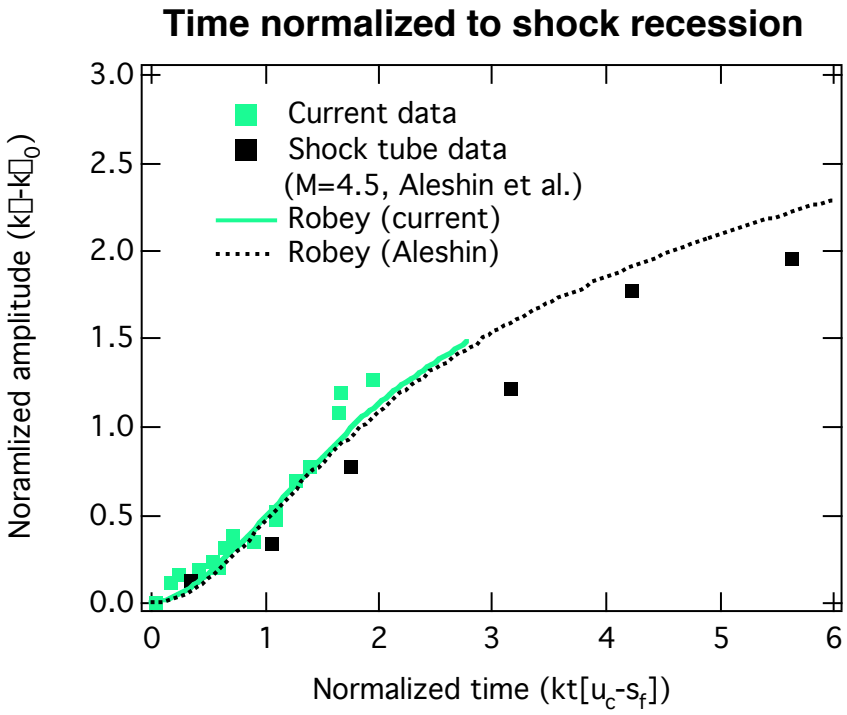

- One normalization is k□ vs. k□$_{IM}$ (Meyer-Blewett, shows nonlinearity)
- Another normalization is k□ vs k*(u_c-s_f)*t (shows shock proximity)

The initial growth rate is much lower than linear or large-initial-amplitude models predict

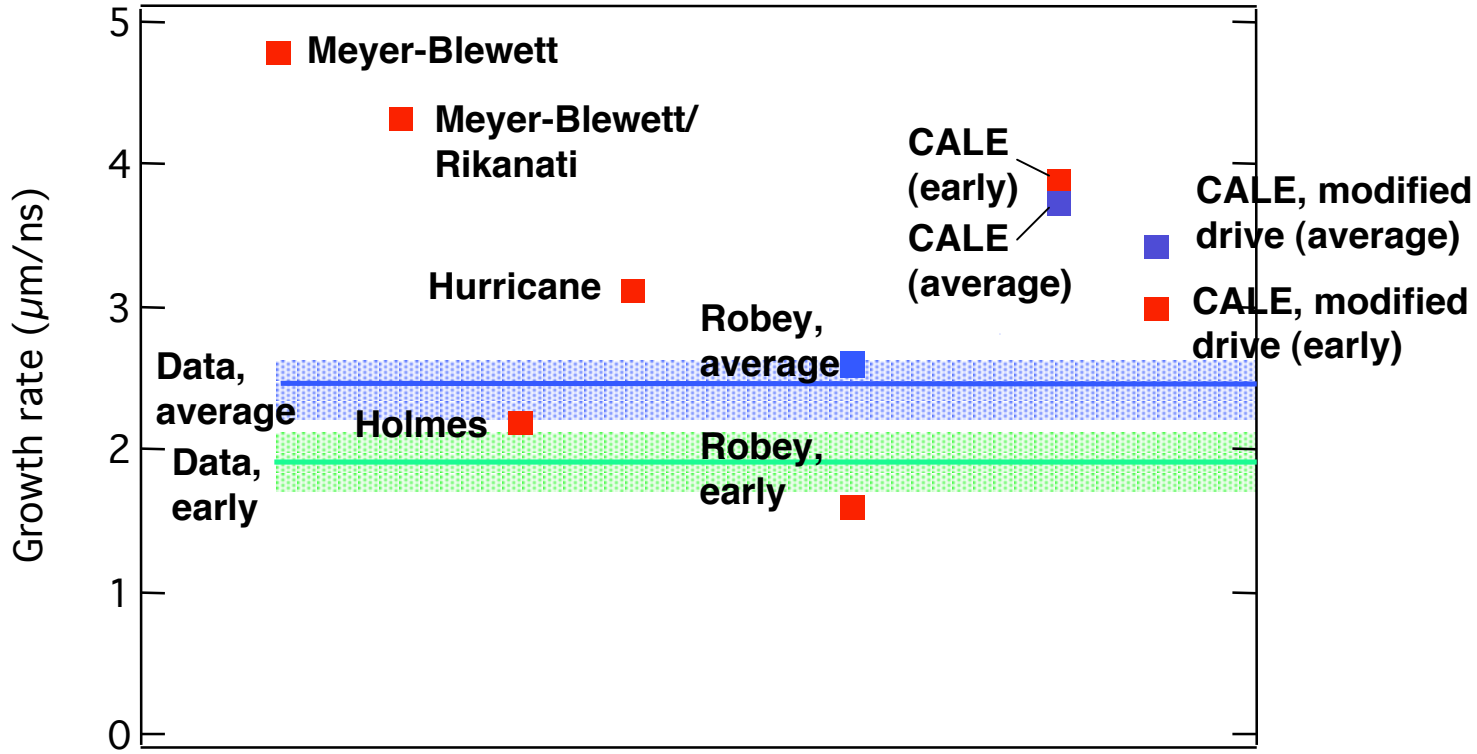

- Only the Robey model predicts an increase in velocity later in time (as the shock recedes)

Summary

- We have used the Omega laser to generate a nearly steady interface velocity for Richtmyer-Meshkov experiments
  - The interface is a heavy-to-light (12:1) density step
  - The incident shock Mach number is ~10
  - The shock velocity is only about 20% higher than the interface velocity
- An initially sinusoidal perturbation with λ=150 μm, λ_0=7 μm ($k\lambda_0$=0.3) grows according to incompressible models
- The growth of with λ=150 μm, λ_0=22 μm ($k\lambda_0$=0.9) is about half that predicted from incompressible models
  - The shock remains very close to the spike tips as the perturbation grows
  - An analytical model which accounts for the effect of the shock proximity predicts the reduced growth

Mix Experiments using a Two-Dimensional Convergent Shock Tube

D A Holder, C J Barton, A V Smith, D L Youngs

AWE Aldermaston UK

Principle of Design

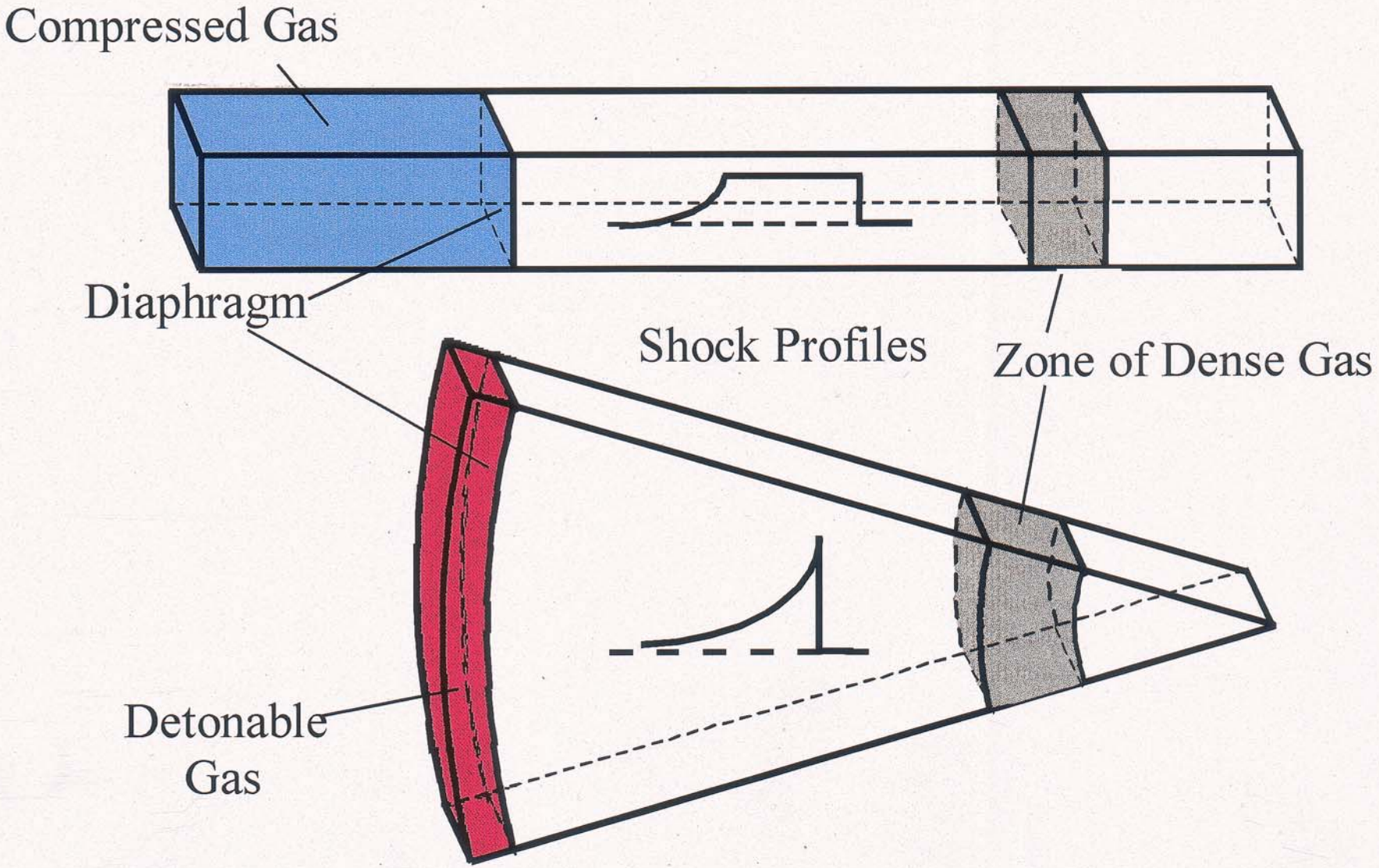

Experiments performed

Basic cylindrical

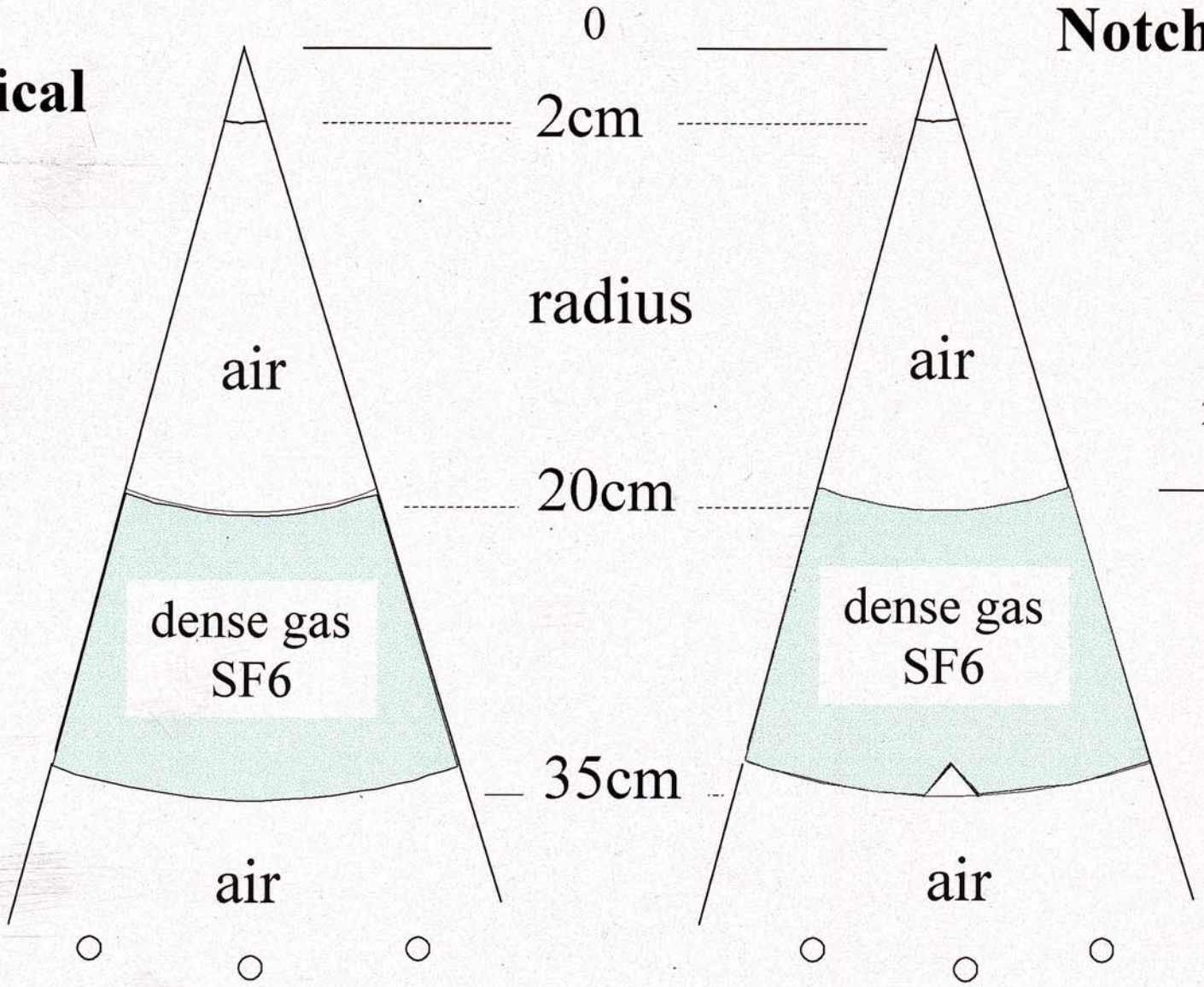

Notch

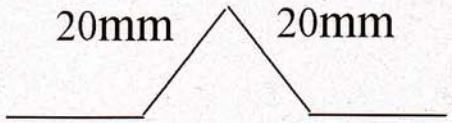

Shock Pressure Waveform

Radius 50cm

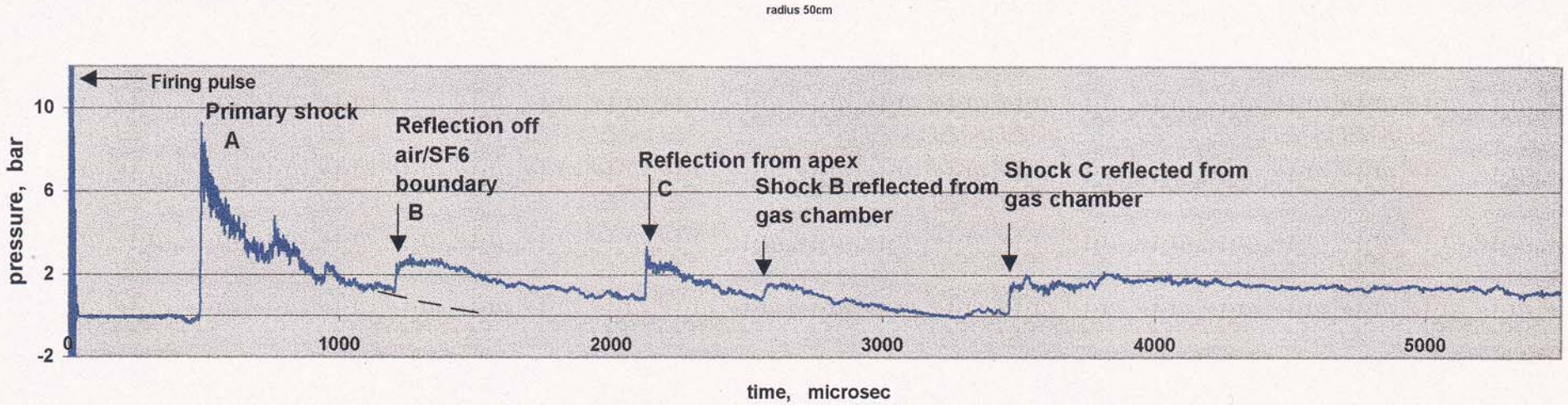

Details of the Dense Gas Containment

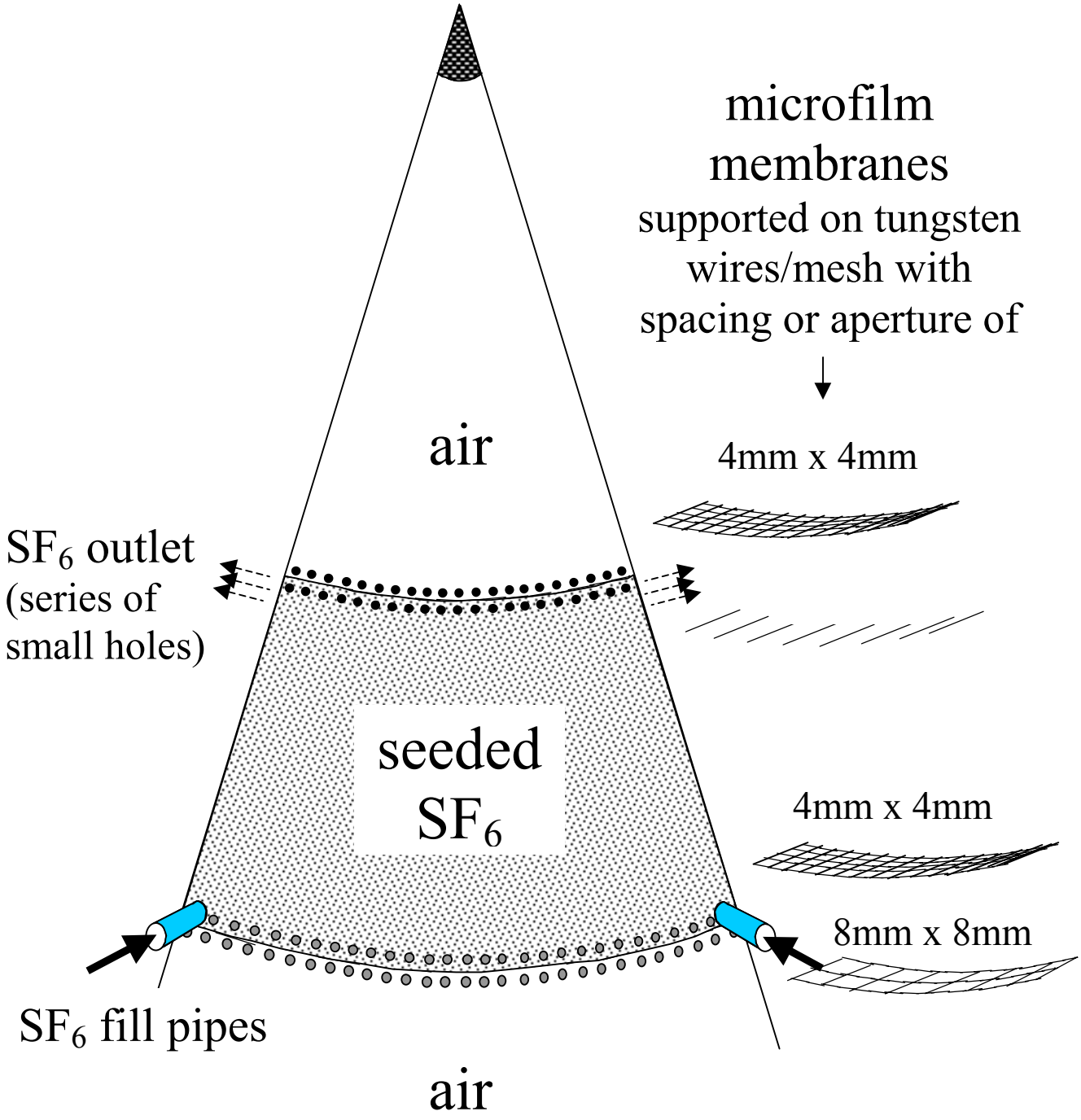

Detonable Gas Chamber

Oxy-acetylene gas chamber

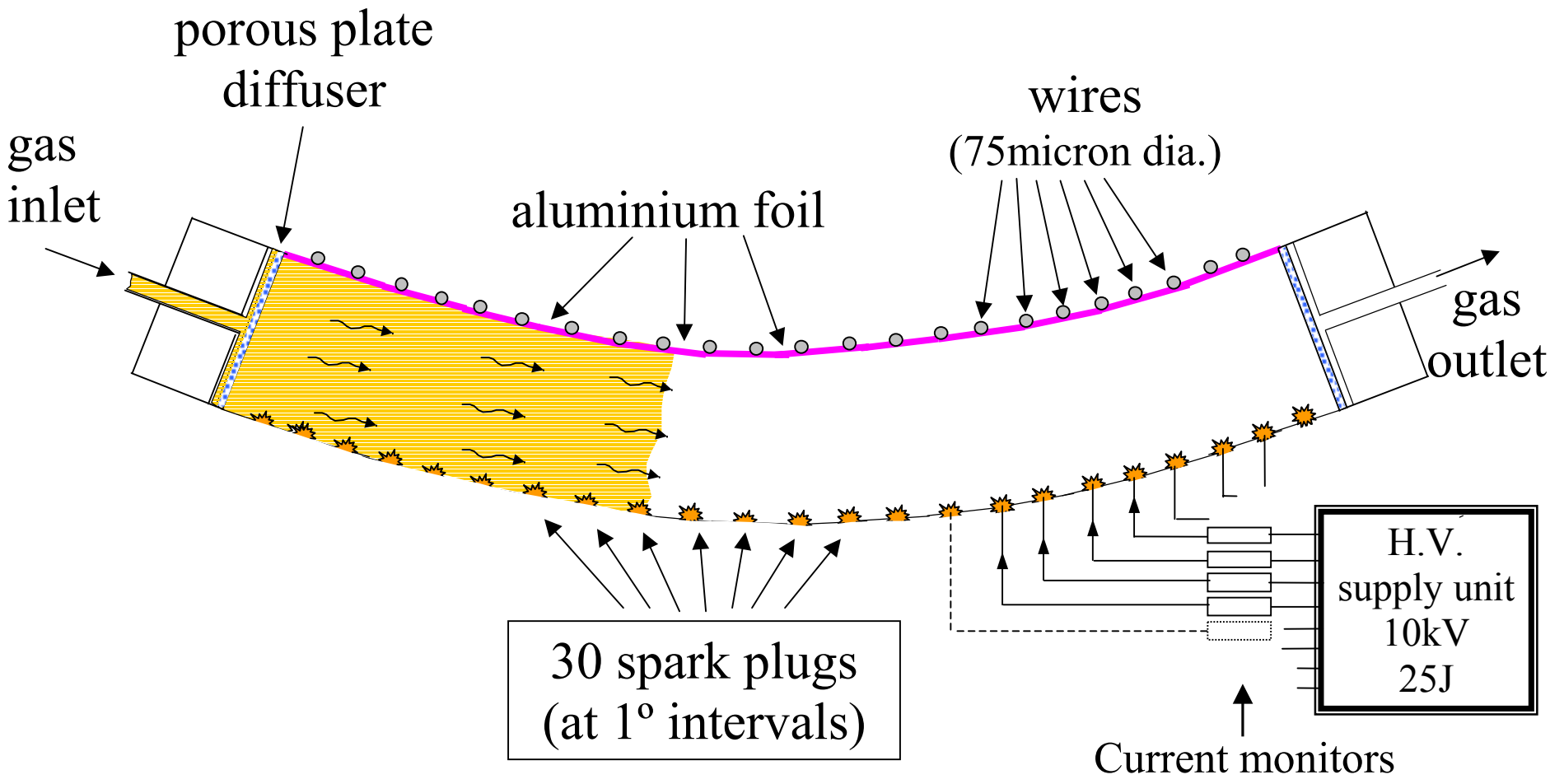

Small Detonation Test-cell

to check for simultaneity of multi-point detonation

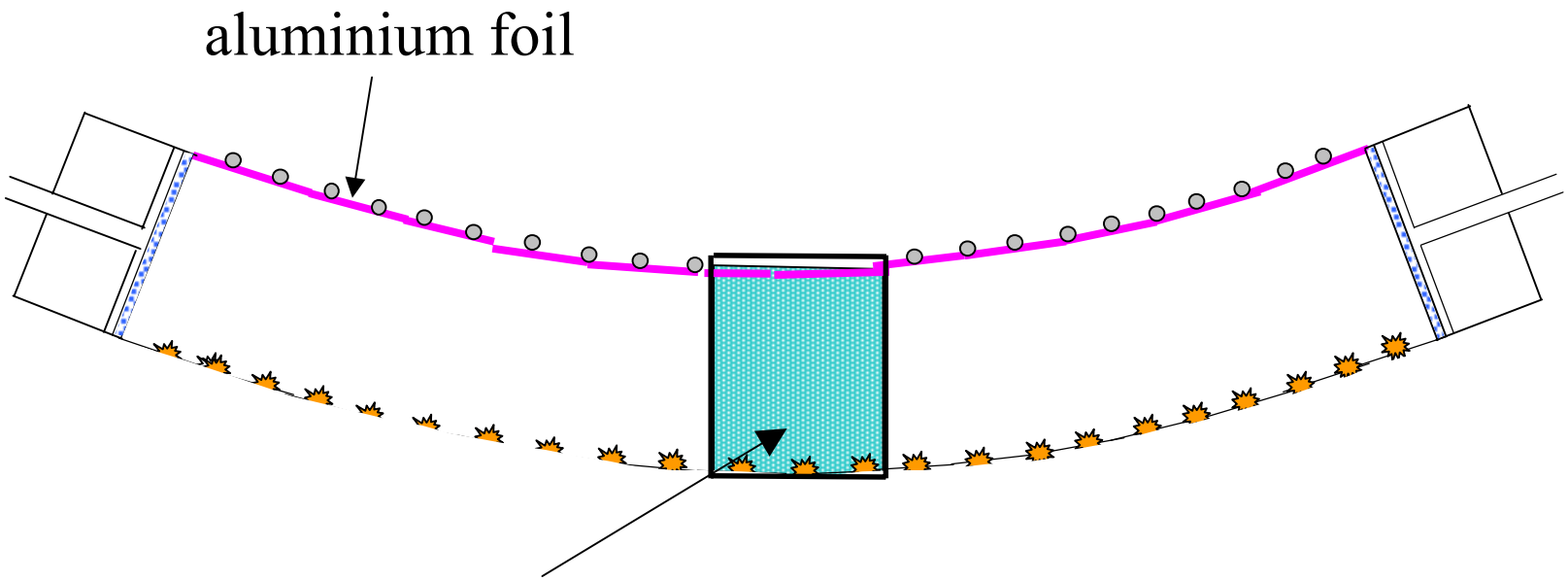

Optical test cell representing a 1/10 volume of the gas chamber - features 3 spark plugs. It allows photographic study of the detonation process

Small Detonation Test Cell - Sample Images

Detonation test cell

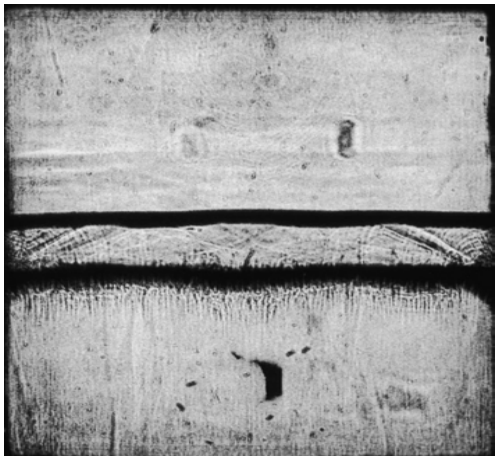

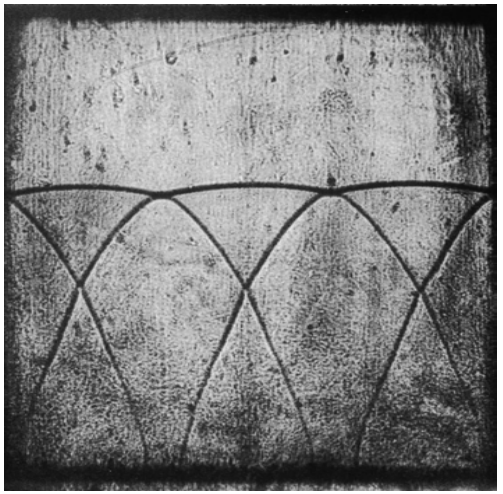

Example of non-simultaneous spark ignition

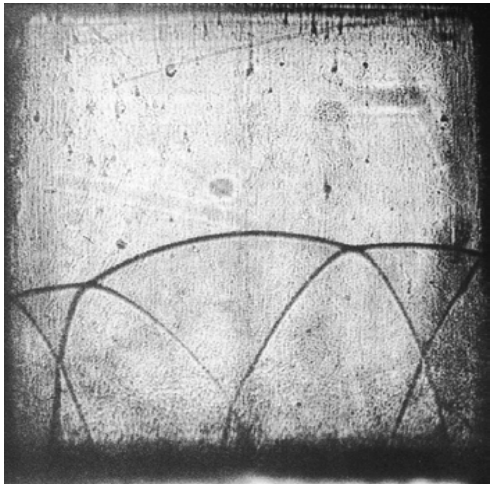

Shadowgraph Images

(air / SF_6 / air cylindrical experiment)

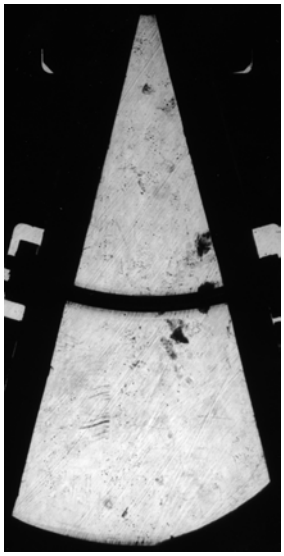

0ms

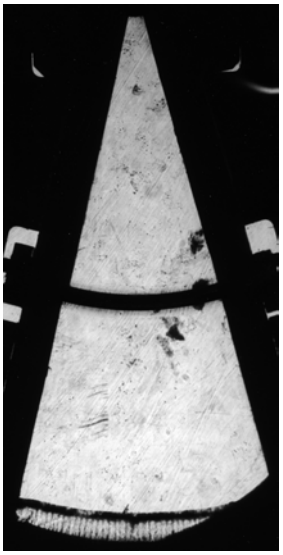

0.73ms

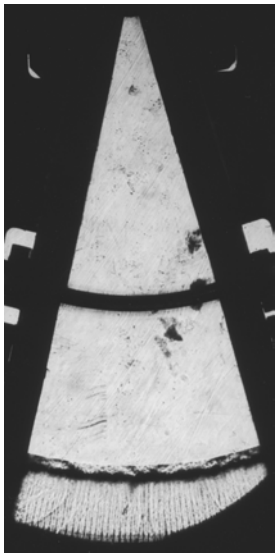

0.80ms

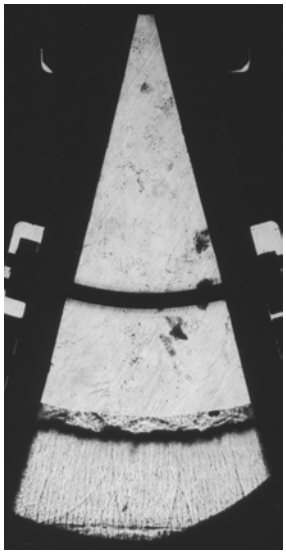

0.87ms

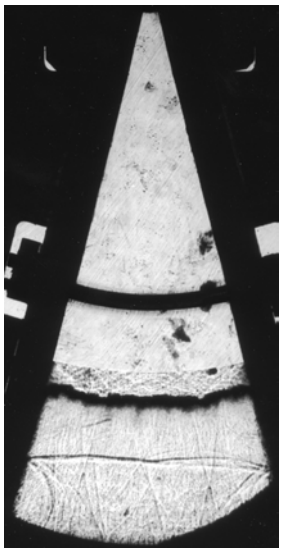

0.93ms

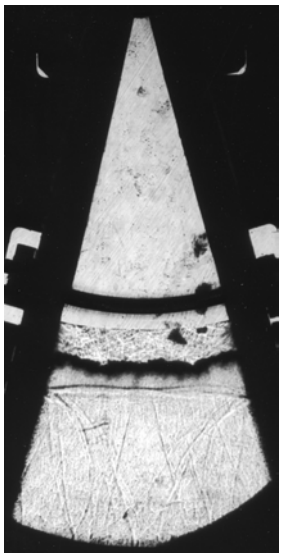

1.00ms

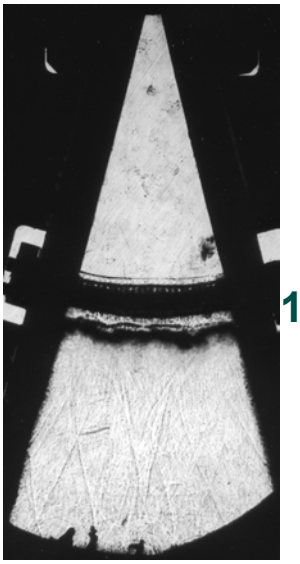

1.07ms

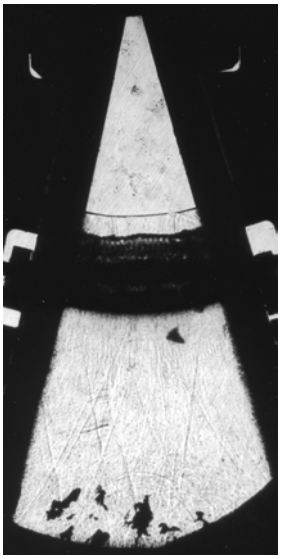

1.13ms

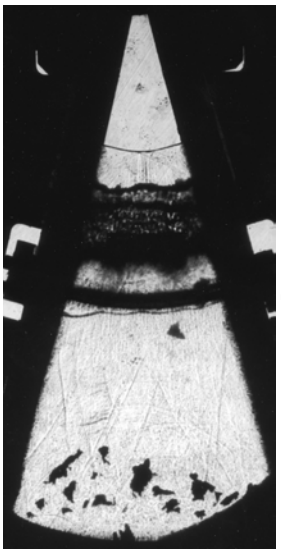

1.20ms

Shadowgraph Images

(air / SF_6 / air cylindrical experiment)

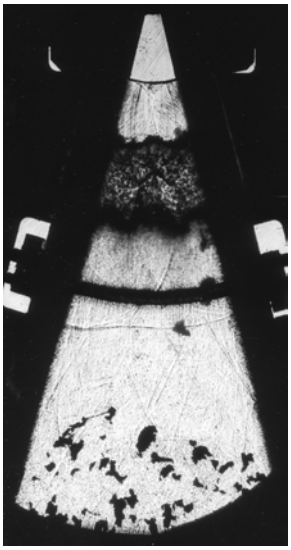

1.27ms

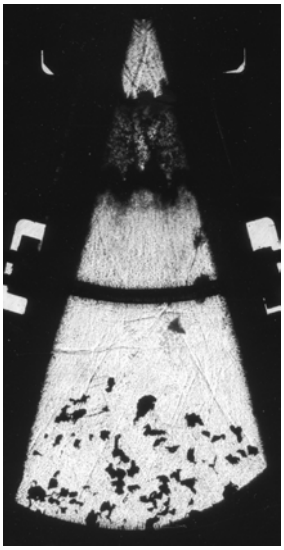

1.33ms

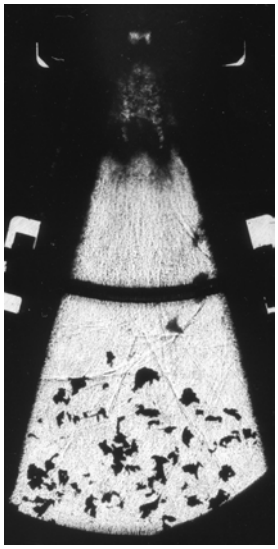

1.40ms

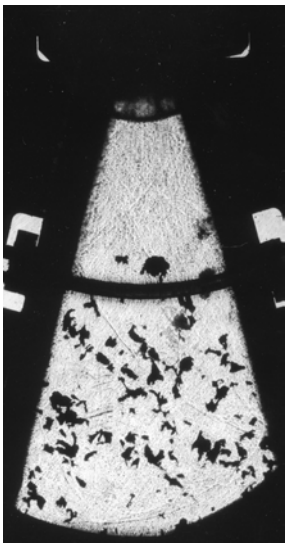

1.67ms

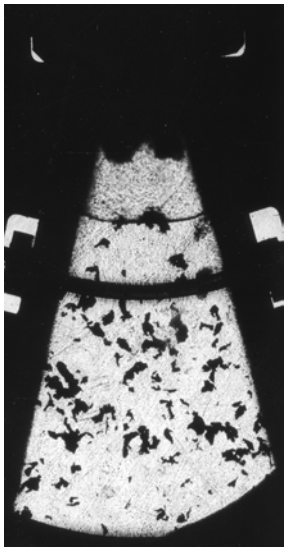

1.80ms

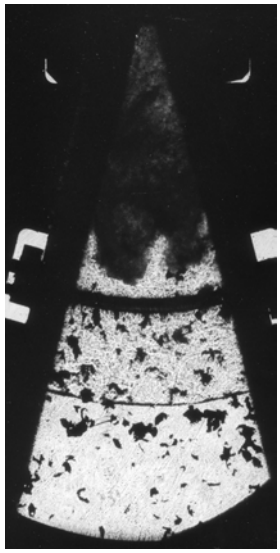

2.00ms

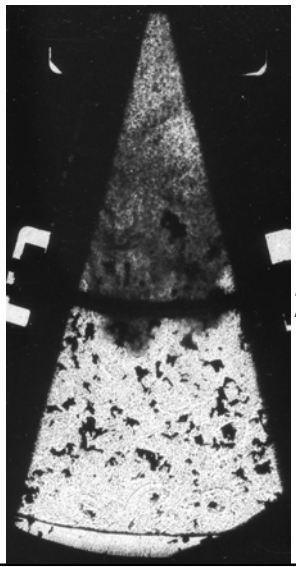

2.13ms

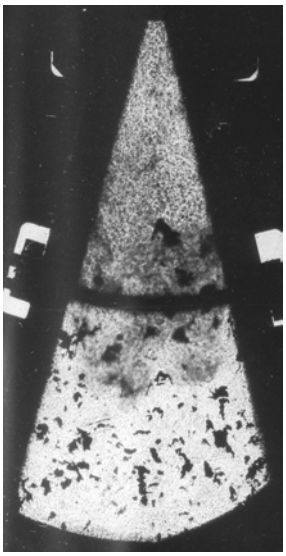

2.27ms

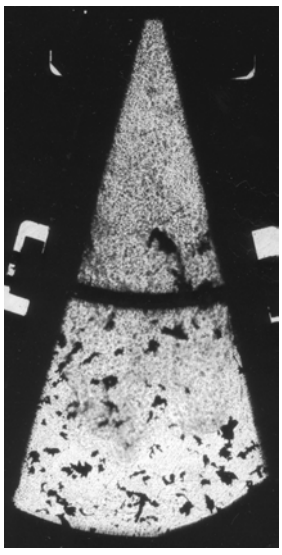

2.40ms

Shadowgraph Images

(air / SF_6 / air cylindrical experiment)

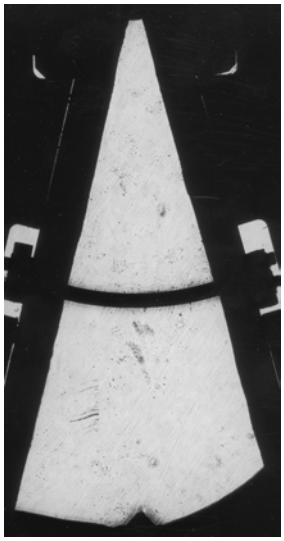

0ms

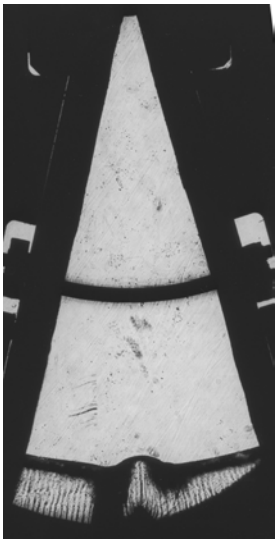

0.73ms

0.80ms

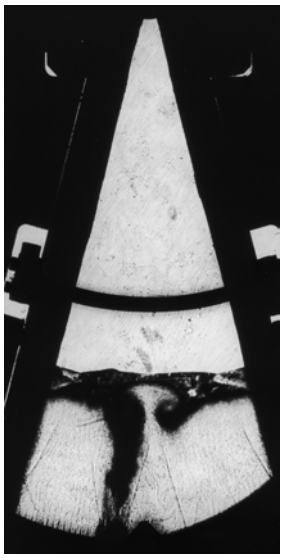

0.87ms

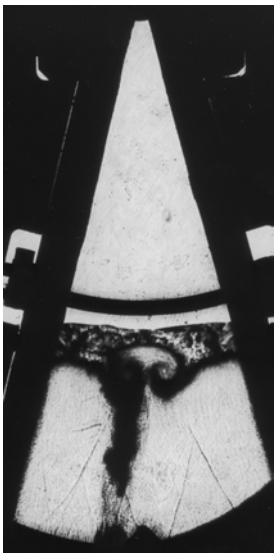

0.93ms

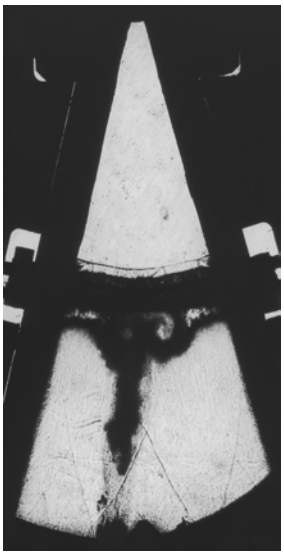

1.00ms

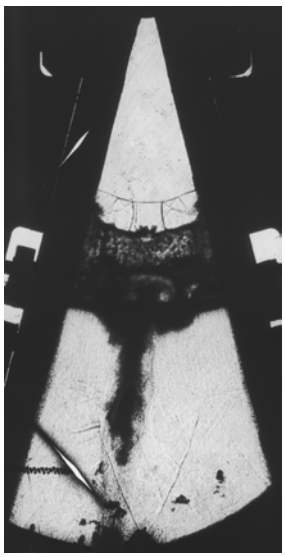

1.07ms

1.13ms

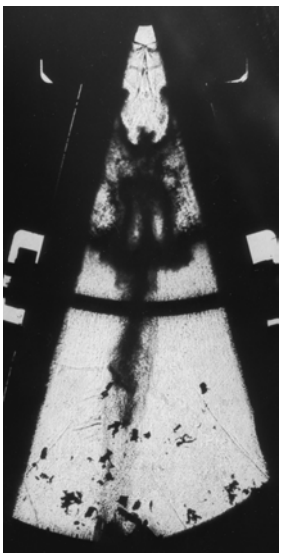

1.20ms

Shadowgraph Images

(air / SF_6 / air cylindrical experiment)

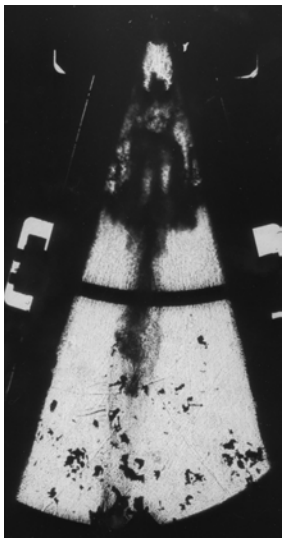

1.27ms

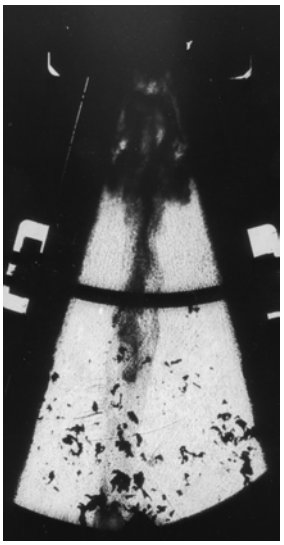

1.33ms

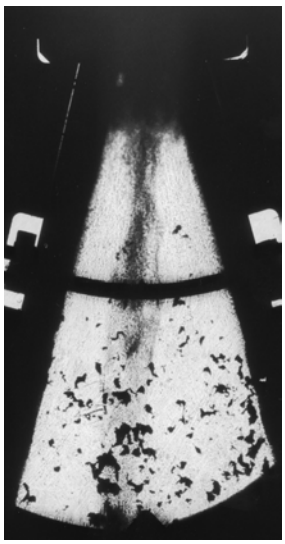

1.47ms

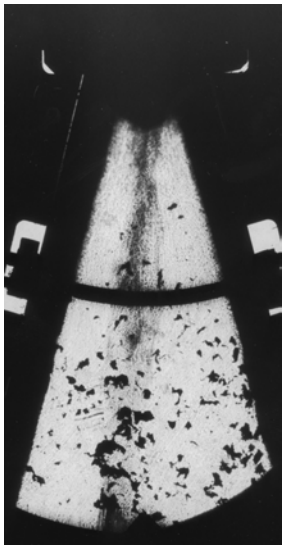

1.53ms

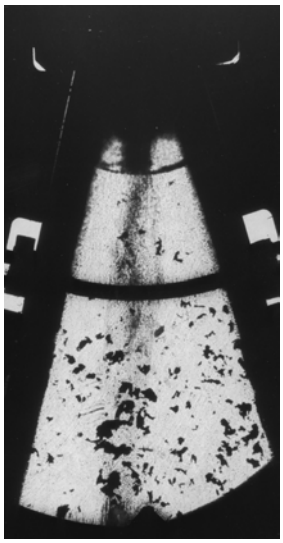

1.60ms

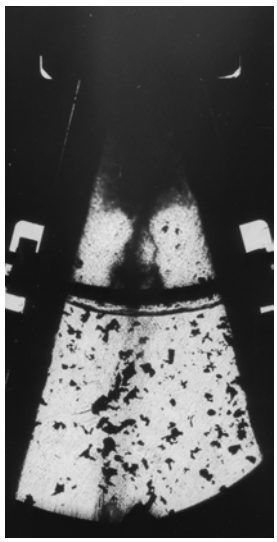

1.73ms

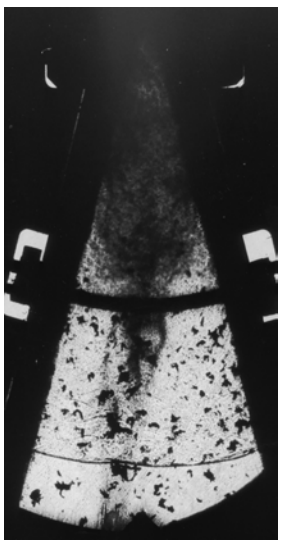

1.87ms

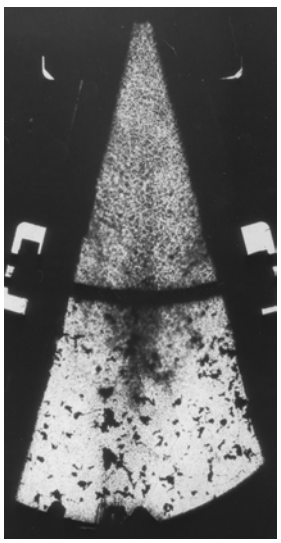

2.07ms

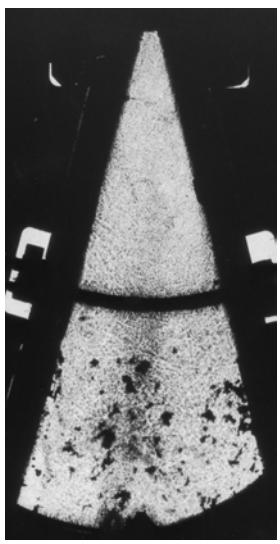

2.33ms

TURMOIL 3D Simulation

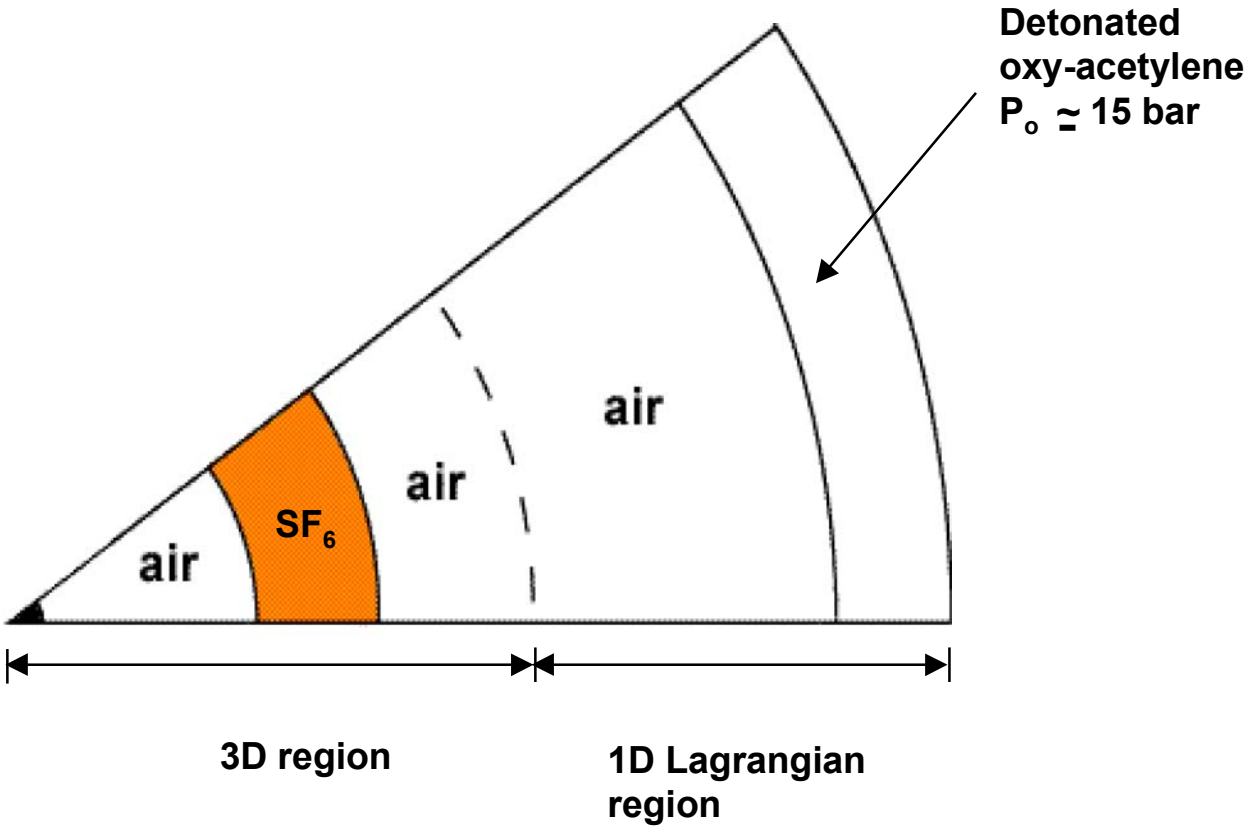

Cylindrical polar mesh.

Semi-Lagrangian calculation - r - direction mesh moves with the mean fluid velocity.

Mesh used in the 3D region (r, θ, z): 344 x 200 x 140.

Random pertubations imposed at each interface:

Wavelengths: 0.5 to 5.0cm
s.d: 0.01cm

Notch Experiment

Experiment

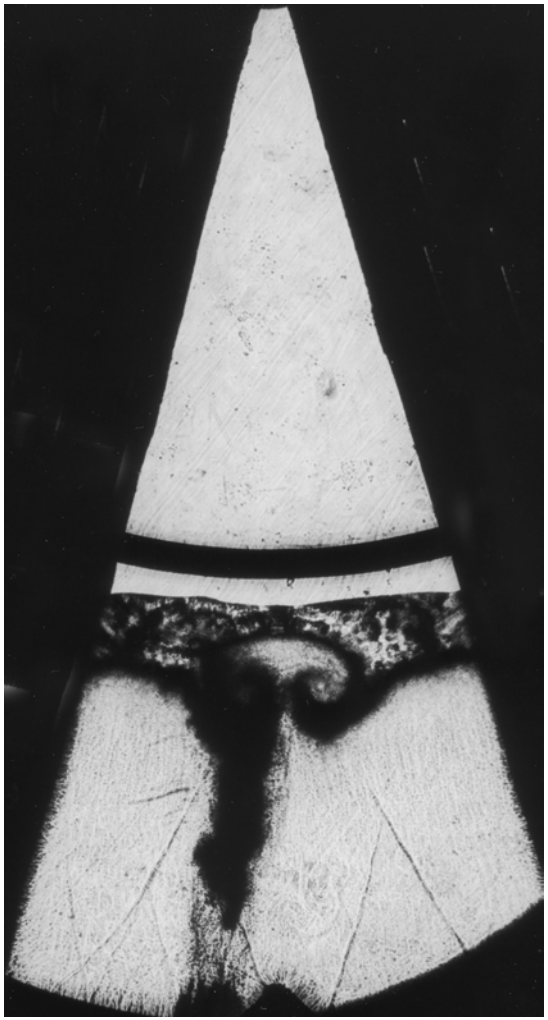

0.93ms

Turmoil 3D code

0.9ms

Notch Experiment

Experiment

1.13ms

Turmoil 3D code

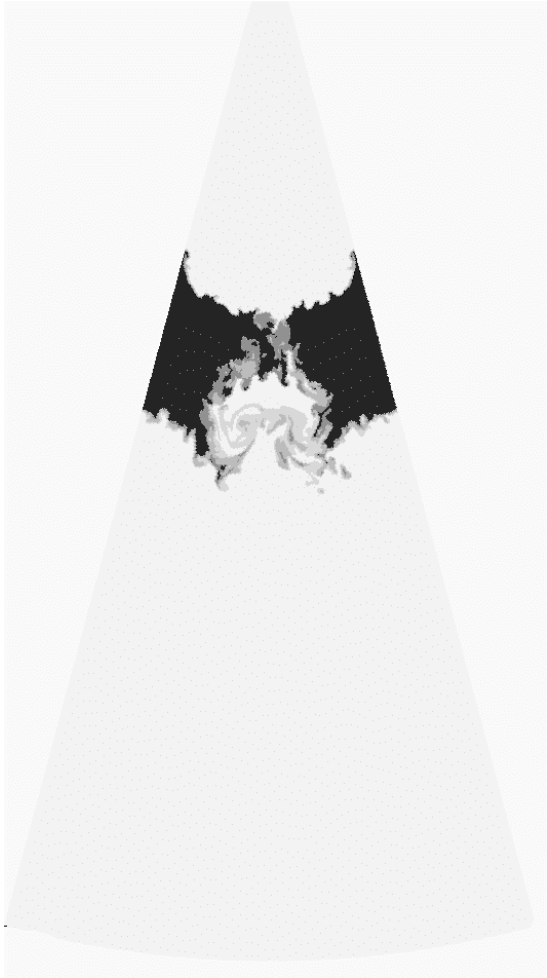

1.05ms

Notch Experiment

Experiment

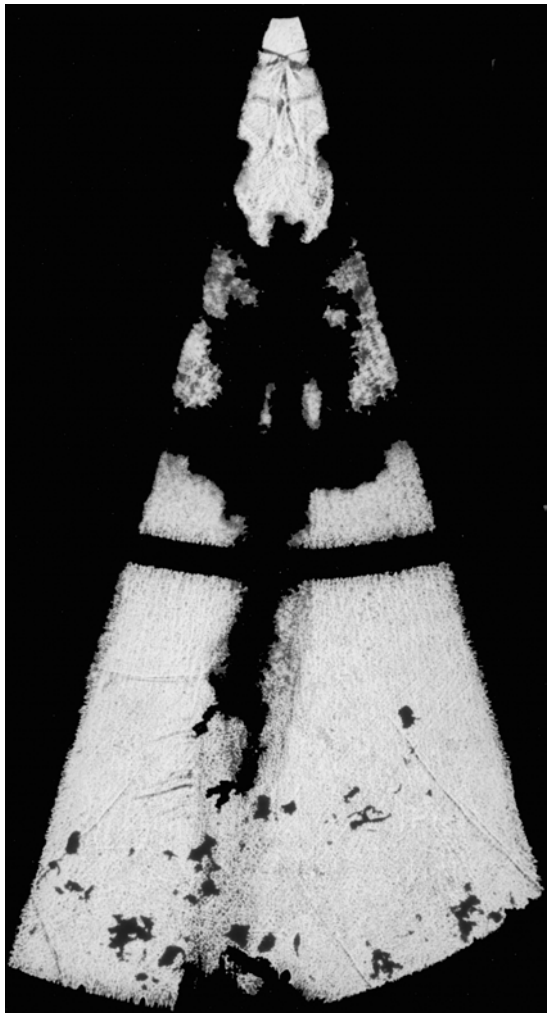

1.20ms

Turmoil 3D code

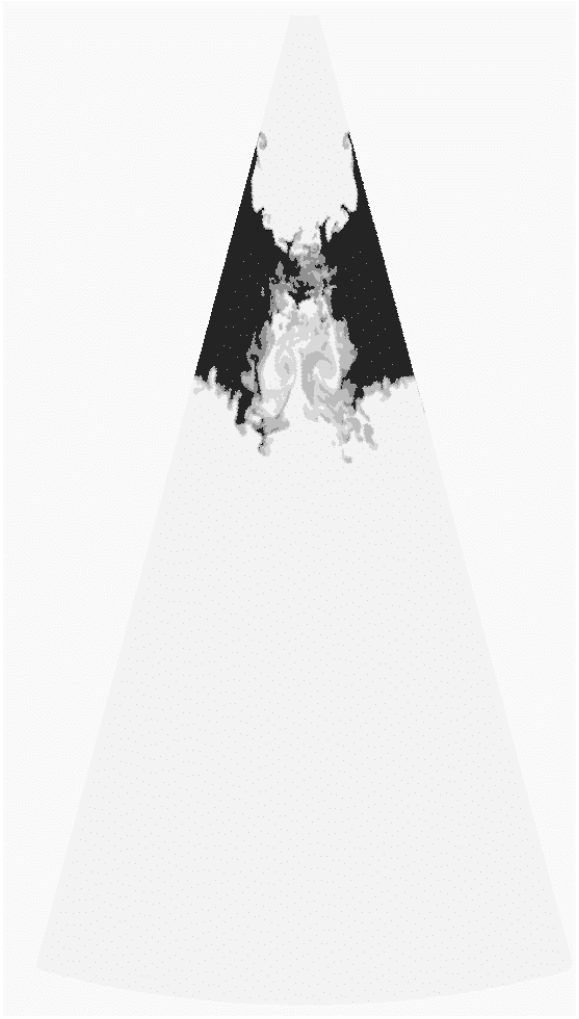

1.15ms

Notch Experiment

Experiment

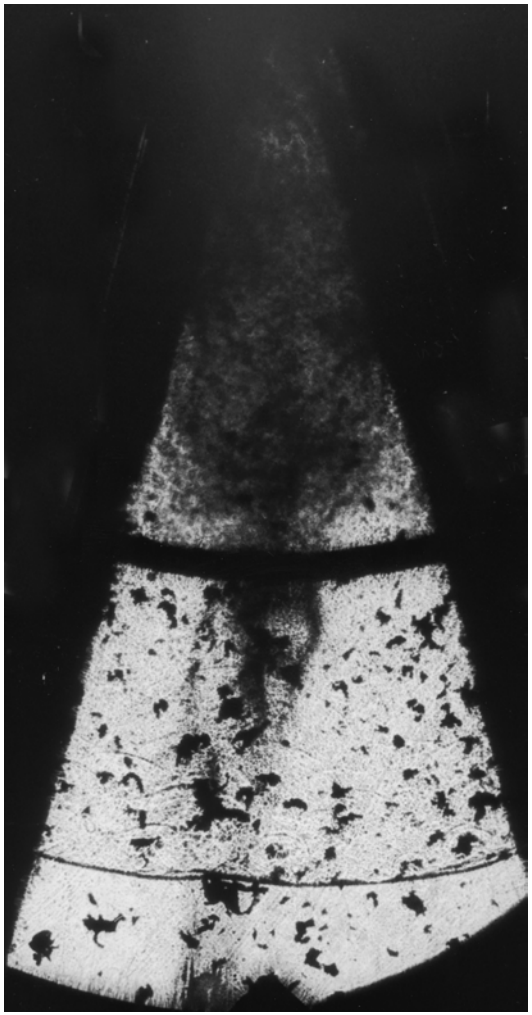

1.87ms

Turmoil 3D code

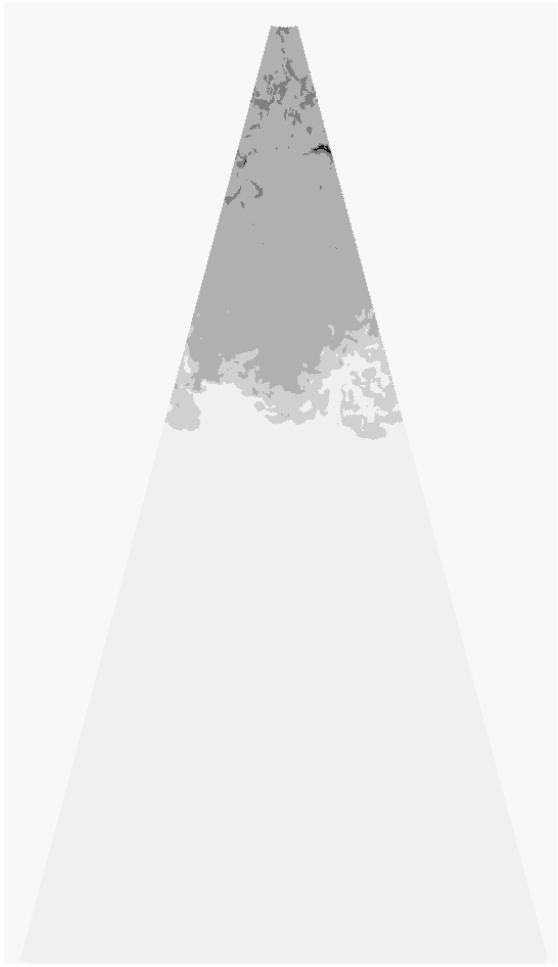

1.75ms

Turmoil 3D Calculations

Cylindrical Experiment

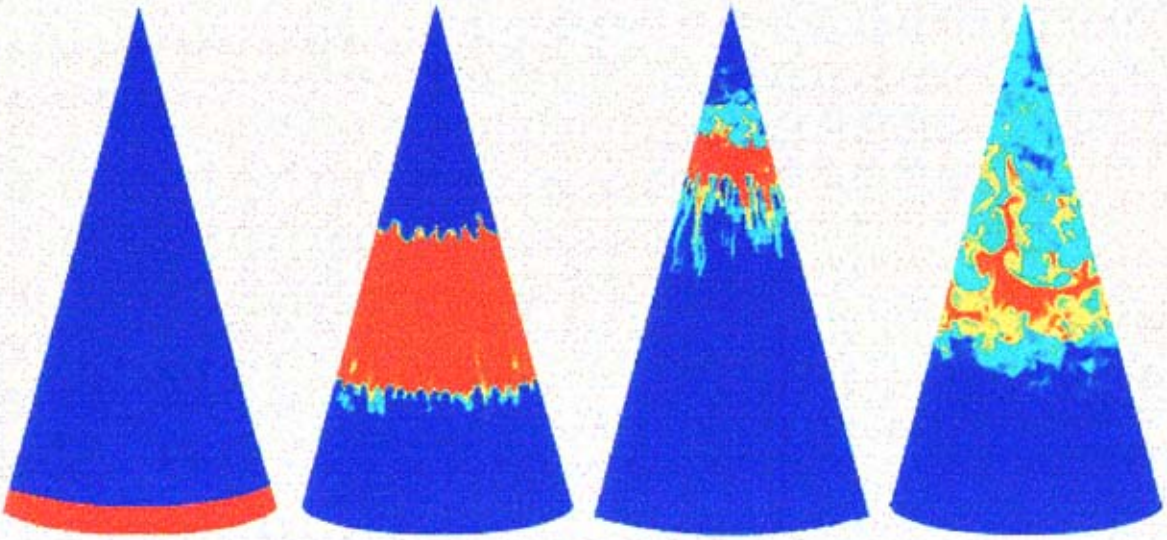

0 1.2 ms 1.5 ms 1.8 ms

Conclusions

1. Successfully demonstrated suitability of a Convergent Shock Tube for performing R-M experiments with gases in 2D geometry

2. Achieved compressions of dense gas of typically 25 : 1 using shock Mach No. ~ 3

3. Achieved good understanding of design requirements for constructing a new improved Convergent Shock Tube

Future Work

- Construct new Convergent Shock Tube which operates with the laser sheet diagnostic (and variants)
- Establish seeding with fluorescent gas suitable for:-
  - use of notch filter to 'remove' laser light scattered from membrane fragments
  - seeding at high gas compression
- Continue experiments with different perturbation profiles
- Substitute Xe gas for SF_6
- Establish calibration technique for gas data analysis of laser sheet images
- [Consider 'inverse' experiment to check the influence of the side walls]

Rayleigh-Taylor instability at a tilted interface

in incompressible laboratory experiments and compressible numerical simulations

Joanne M. Holford[†]

Stuart B. Dalziel[†]

David Youngs[‡]

[†]DAMTP, University of Cambridge, Silver Street, Cambridge CB3 9EW, UK

[‡]AWE Aldermaston, Reading, Berkshire, RG7 4PR, UK

Outline

- Introduction

  RT instability at a tilted interface

  Mixing, available energy and mixing efficiency

- Laboratory experiments

  At DAMTP, in the Fluid Dynamics Laboratory

  Incompressible water, NaCl to create density contrast

- Numerical simulations

  At AWE, using Turmoil3D (with David Youngs)

  Compressible code, for a mixture of two ideal gases

- Conclusions and further work

Introduction

- RT instability

Instability of dense fluid accelerated into less dense fluid

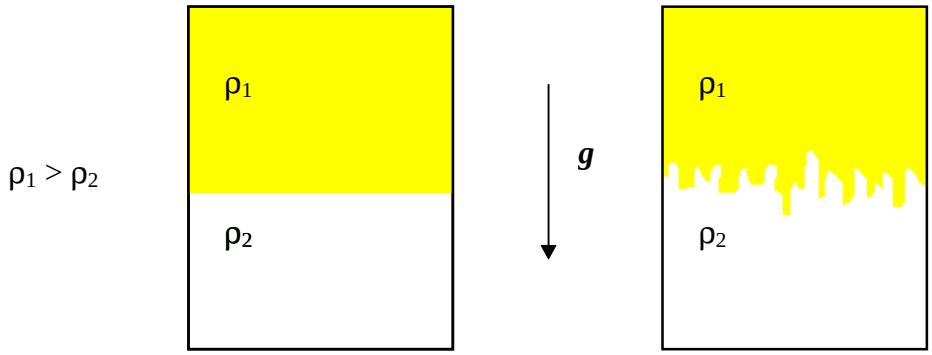

Non-dimensional parameter Atwood number $A = \left(\frac{\rho_1 - \rho_2}{\rho_1 + \rho_2} \right) = \frac{g'}{2g}$

For an external lengthscale H, timescale $\tau = \sqrt{\frac{H}{Ag}}$

Much more efficient mixing than other mechanisms (shear instability, mechanical stirring)

An important mixing process within larger-scale flows (3D instability of 2D shear billows)

In environment, R-T instability has non-ideal initial conditions

At a tilted interface, there is competition between local instability and large-scale overturning

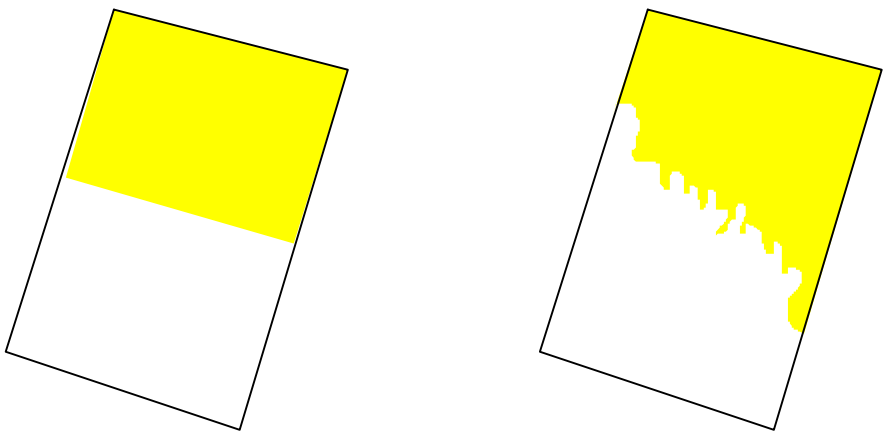

• Definitions of mixing

Distinguish between reversible and irreversible mixing:

Reversible mixing - interleaving of fluid with different properties - “reversible mixing = stirring”

Irreversible mixing - homogenisation of fluid properties at the molecular scale - “irreversible mixing = stirring + diffusion”

Irreversible mixing is important for

- chemical reactions
- removal of available energy when mixing density gradients across a gravitational field

• How do we measure mixing?

Mixing can be measured by a molecular mixing fraction

For two fluids, volume fractions f and $(1-f)$:

$$\vartheta(\boldsymbol{x},t) = f(\boldsymbol{x},t)(1-f(\boldsymbol{x},t))$$

Alternatively, for fluids of varying density in a gravitational field, can measure the mixing efficiency η

For a fluid at rest, stirred by an energy input and returning to rest,

$$\eta = \frac{\text{increase in potential energy}}{\text{amount of energy added}}$$

fraction of energy lost to fluid motion doing work against gravity

• Mixing in R-T instability

Measurements of η in laboratory experiments - high values with some dependence on A

Linden & Redondo (1991)

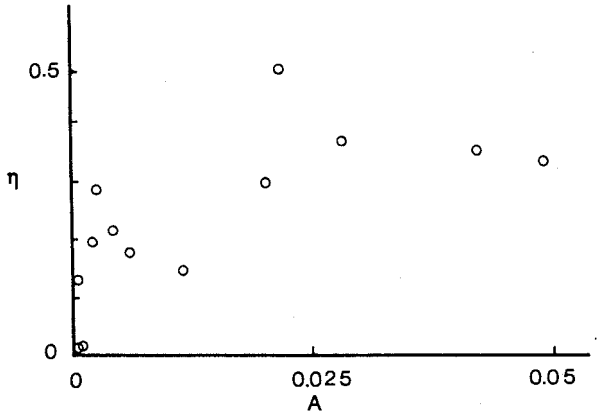

Numerical simulations show sensitivity to initial conditions

Linden, Redondo & Youngs (1991), Cook & Dimotakis (2001)

• Diffusion and viscosity in incompressible fluids

Mechanical energy density per unit volume $E_v = \frac{1}{2}\rho|u|^2 + \rho g z$

$$\frac{\partial}{\partial t} E_v(\boldsymbol{x},t) + \nabla . \boldsymbol{f}_v(\boldsymbol{x},t) = -\varepsilon_v(\boldsymbol{x},t),$$

$\boldsymbol{f}_v$ energy flux

ε_v energy dissipation

Water/salt system - $\nu = 1.0\times10^{-2}\text{cm}^2\text{s}^{-1}$ kinematic viscosity

$\kappa = 1.4\times10^{-5}\text{cm}^2\text{s}^{-1}$ diffusivity

concentration fluctuations persist at smaller scales than velocity fluctuations - $Pr = \frac{\nu}{\kappa} = 700$

Turbulent flows - eddy viscosity = eddy diffusivity

effectively $Pr = 1$

- Available energy in incompressible flow

Mechanical energy in whole fluid $E = \int_V E_v \, dV$ decomposes:

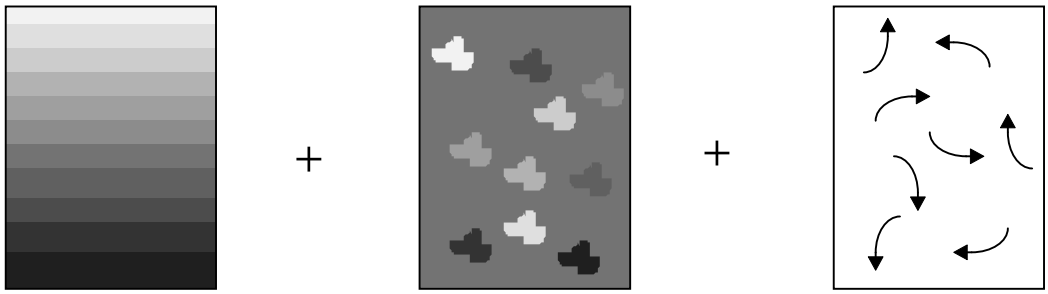

PE_{back} PE_{avail} KE

E_{back} E_{avail}

Lorenz (1955), Thorpe (1977), Winters et al. (1995)

In unforced, decaying flow

$$\frac{d}{dt}\left(E_{back} + E_{avail}\right) = -\varepsilon$$

loss of E due to turbulent dissipation

$$\frac{d}{dt}\left(E_{back}\right) = q$$

gain in E_{back} due to molecular mixing

Define cumulative mixing efficiency

$$\eta_{cumulative} = \frac{\int_{t_0}^{t} q \, dt}{\int_{t_0}^{t} q + \varepsilon \, dt} = \frac{\Delta PE_{back}}{-\Delta E_{avail}}$$

and instantaneous mixing efficiency

$$\eta_{instantaneous} = \frac{q}{q + \varepsilon} = \frac{\delta PE_{back}}{-\delta E_{avail}}$$

• Available energy in compressible flow

Now concerned with total energy (mechanical + internal) so $E_V = \frac{1}{2}\rho|u|^2 + \rho g z + \rho e$, e internal energy. In whole fluid:

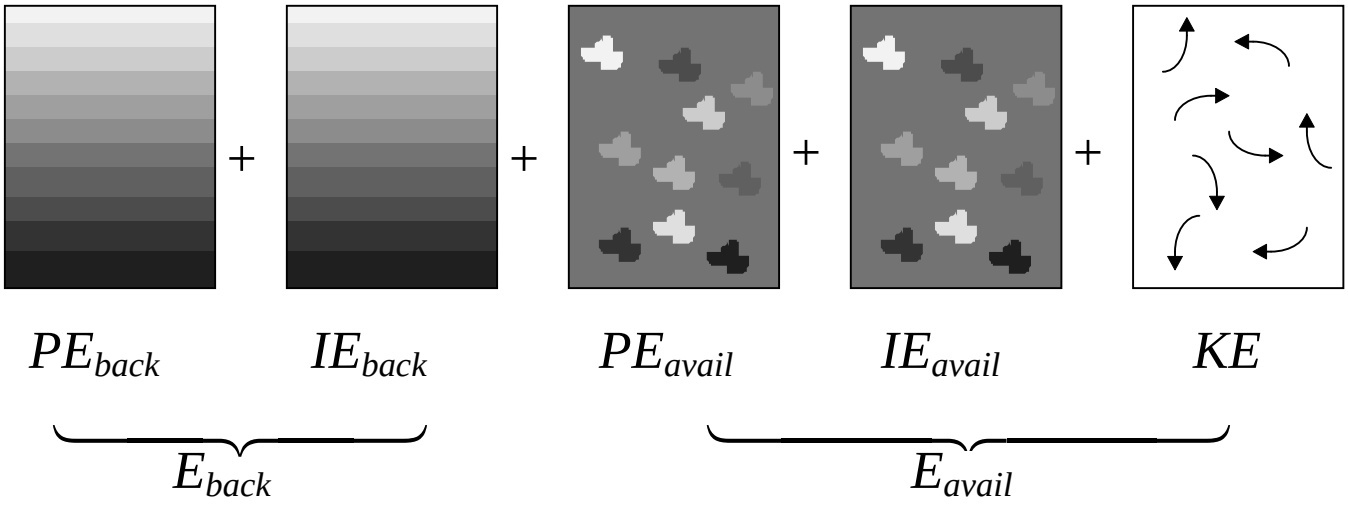

Lorenz (1955), Andrews (1981), Shepherd (1993)

In unforced, decaying flow

$\frac{d}{dt}\left(E_{back} + E_{avail}\right) = 0$ E is conserved

$\frac{d}{dt}\left(IE_{back}\right) = \varepsilon$ gain in IE_{back} due to turbulent dissipation and molecular mixing

$\frac{d}{dt}\left(PE_{back}\right) = q$ gain in PE_{back} due to molecular mixing

Same definitions of mixing efficiency apply, so η is still

fraction of energy lost to fluid motion (reduction in E_{avail}) doing work against gravity (gain in E_{back})

Laboratory Experiments

- Configuration

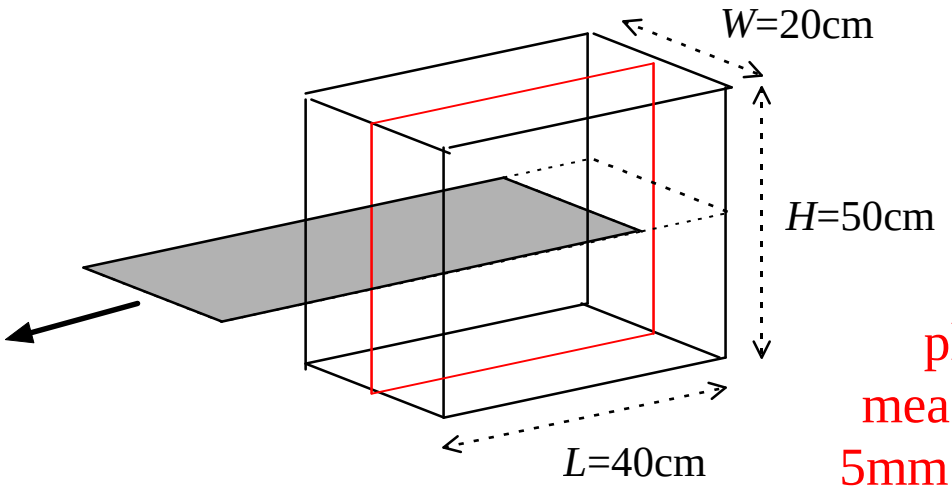

plane of measurement: 5mm light sheet

- Initial conditions

A solid barrier introduces significant shear

Reduced shear barrier: *Dalziel, Linden & Youngs (1999)*

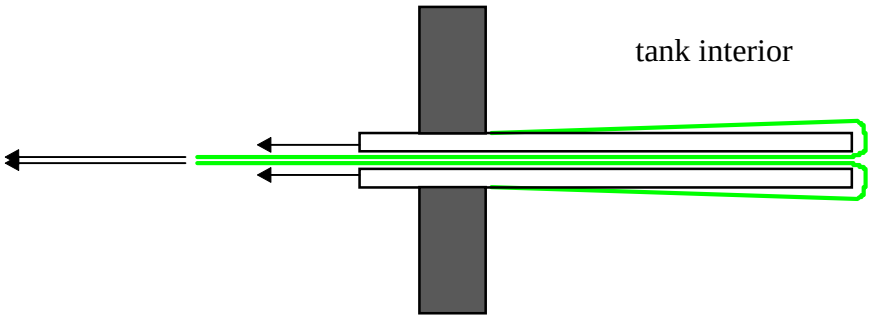

SIDE VIEW

fabric

Removal of finite thickness barrier causes initial velocity field

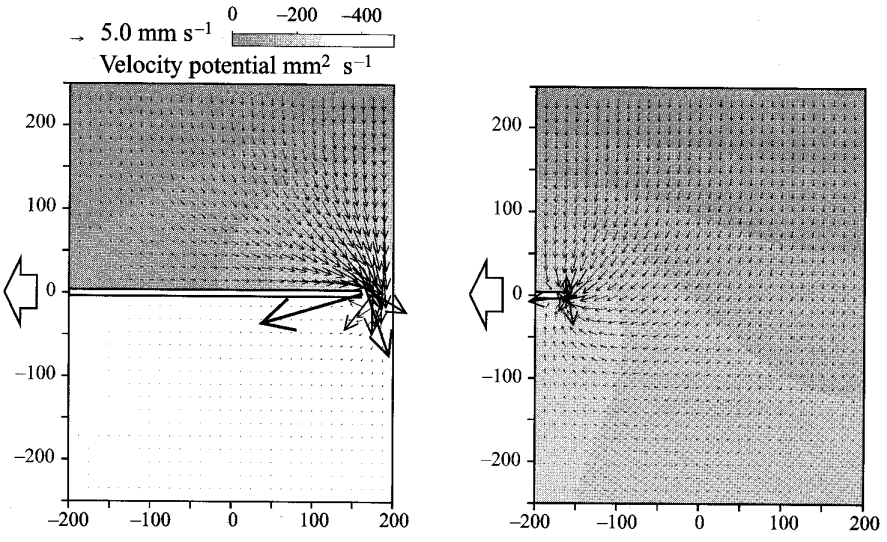

• Diagnostic measurements

Image analysis: spatial resolution 1 pixel ≅ 0.1cm
temporal resolution 25Hz

Assume statistical homogeneity across tank

Add propanol to fresh water to match refractive index

Density measurement

Dense fluid dyed with fluorescent dye

Images corrected for divergence of light sheet and attenuation

Velocity measurement

Fluid seeded with 400μm neutrally-buoyant particles

Lagrangian tracks for particles from tracking a frame sequence
Interpolating onto a grid gives Eulerian velocities

Gridded at two scales: 1cm - resolved velocity
3cm - mean velocity
(overcomes lack of similarity between experiments)

Assume isotropy at small scales ⇒ estimate of total KE

• Parameters

Atwood number $0.5\times10^{-3} < A < 2.5\times10^{-3}$ ⇒ Boussinesq

Timescale $10s > \tau > 4.5s$

RMS velocity $0.8cms^{-1} < |\boldsymbol{u}| < 2cms^{-1}$

Integral lengthscale $1.8cm < l < 2.5cm$

Reynolds number $150 < Re < 500$

divergence

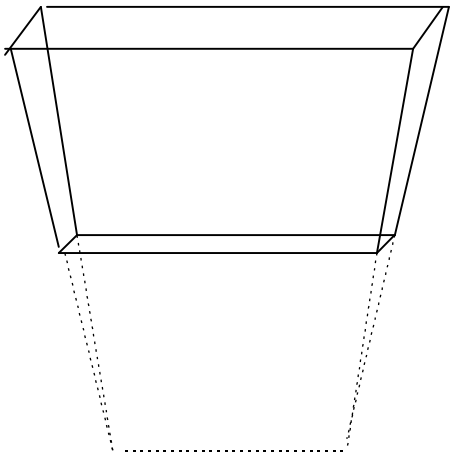

light source

corrected for
by comparing
fluorescence
pattern of image
with uniform dye
concentration

attenuation

(of incident,
not fluoresced
light)

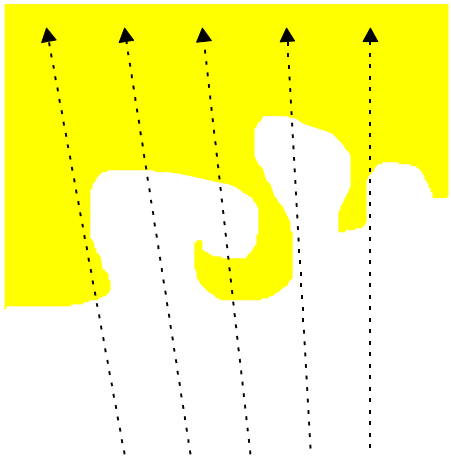

light rays

corrected for
by integrating
along rays to
determine the
actual illumination
and fluorescence
at each point

Density field $\theta = 5°$ $A = 2.6 \times 10^{-3}$

$\frac{t}{\tau} = 0.4$

$\frac{t}{\tau} = 0.9$

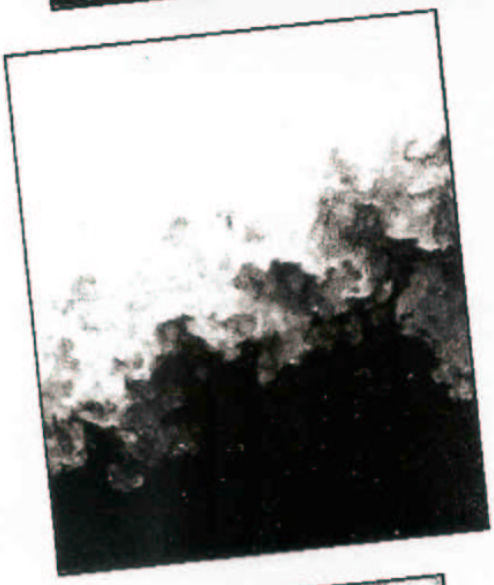

$\frac{t}{\tau} = 1.8$

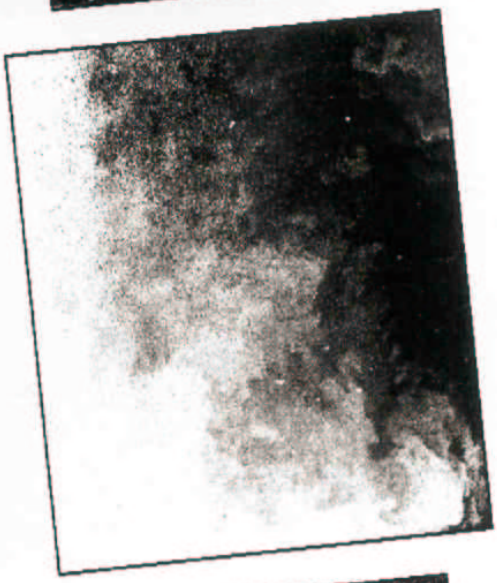

$\frac{t}{\tau} = 3.5$

maximum KE

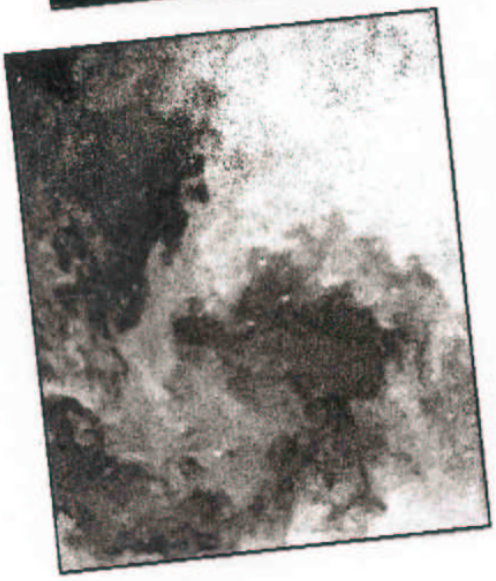

$\frac{t}{\tau} = 6.0$

minimum KE

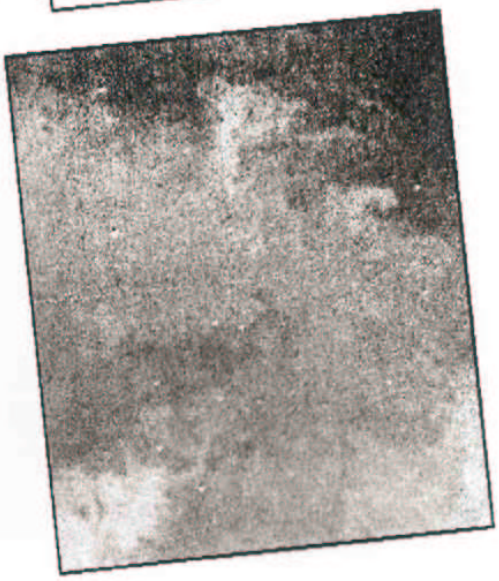

$\frac{t}{\tau} = 8.5$

maximum KE

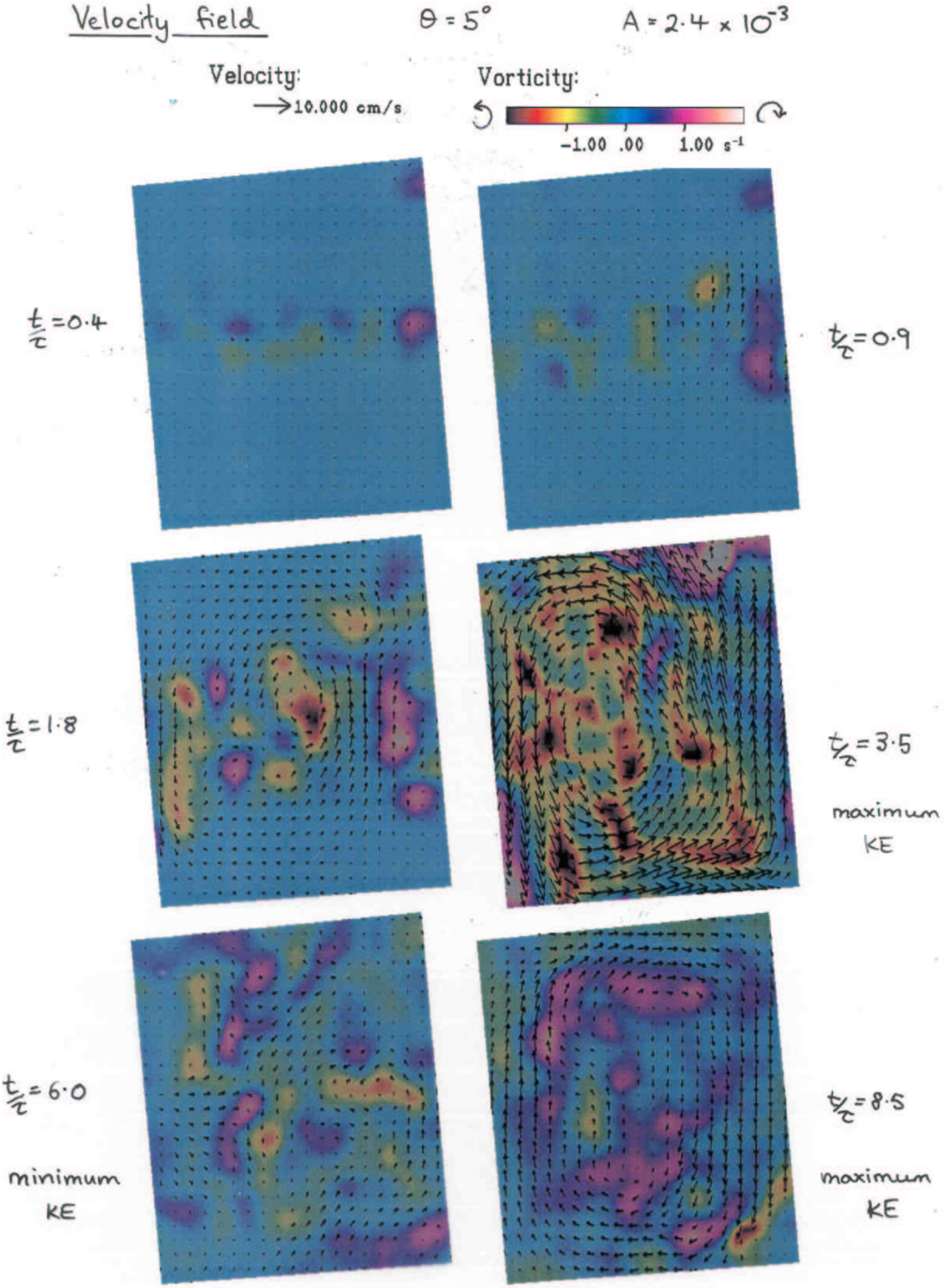
Velocity field
θ = 5°
A = 2·4 × 10⁻³
Velocity:
10.000 cm/s
Vorticity:
-1.00 .00 1.00 s⁻¹
t/τ = 0·4
t/τ = 0·9
t/τ = 1·8
t/τ = 3·5
maximum KE
t/τ = 6·0
minimum KE
t/τ = 8·5
maximum KE

Energy evolution $\Theta = 5^\circ$

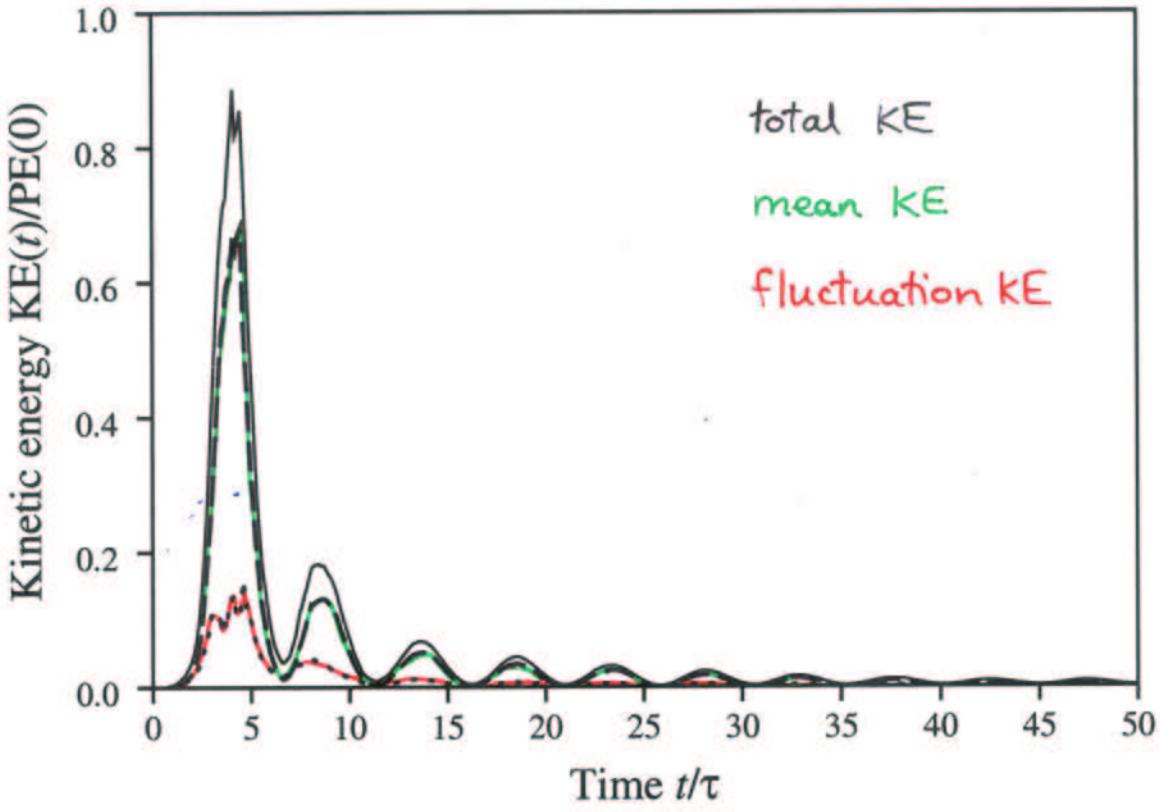

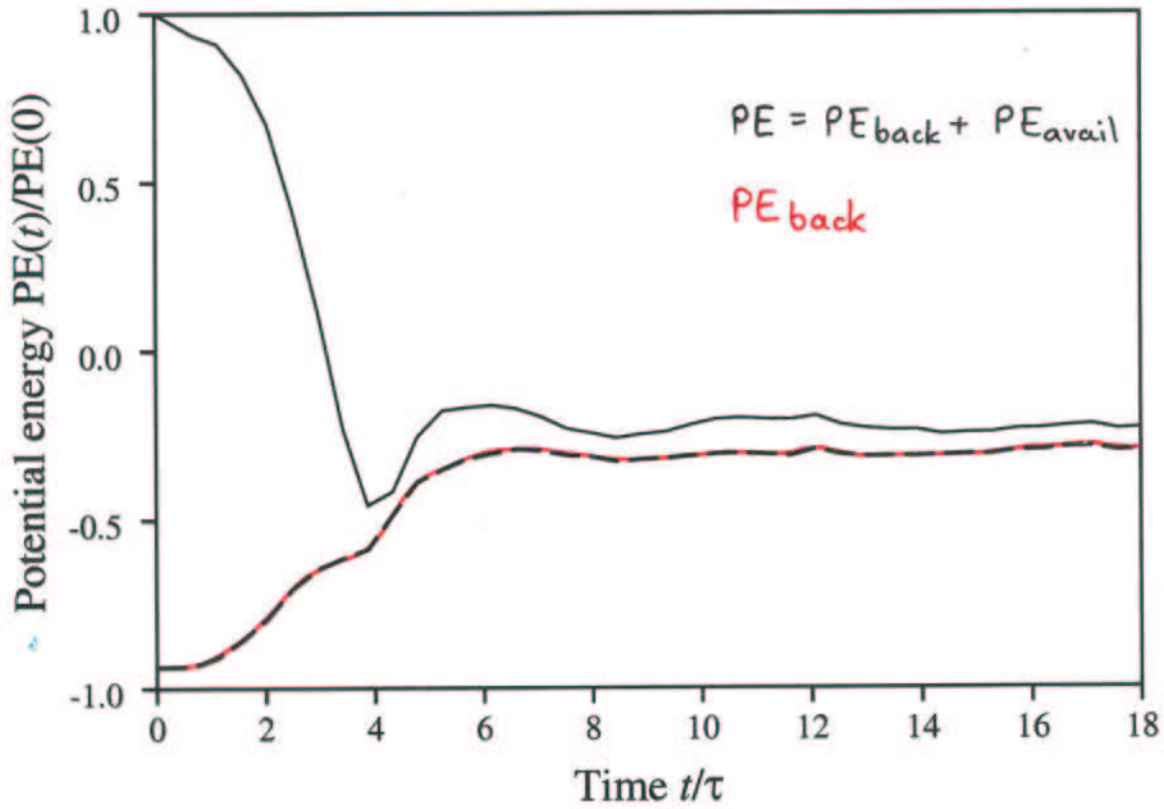

Energy evolution $\theta = 0°$

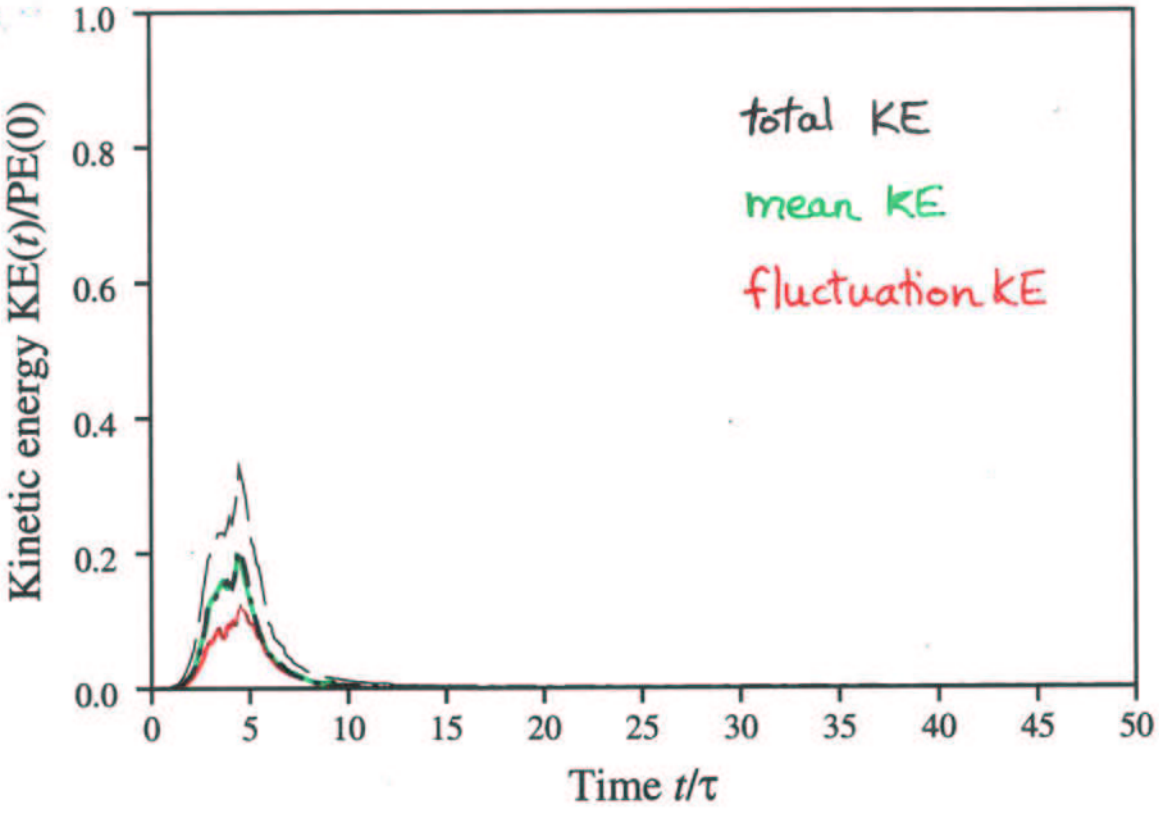

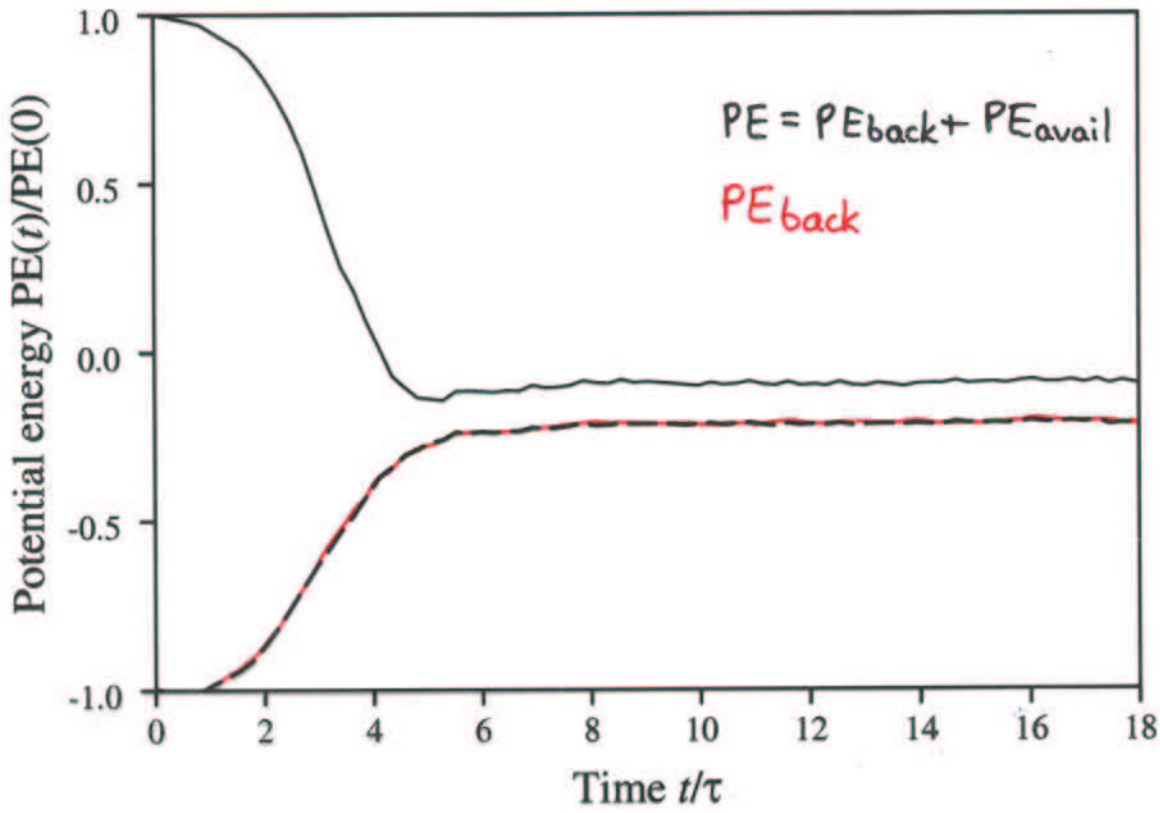

Numerical Simulations

- Code type

  Semi-Lagrangian finite volume code

  (conservation of fluid masses and momentum)

  Two ideal gases ($\gamma = 5/3$)

  Typical simulation: 3D at resolution 200×160×80

- Viscosity and diffusion

  Loss of resolution at grid scale ⇒ diffusion-like behaviour

  for mass fractions, analogous to molecular mixing

  for KE, analogous to dissipation, and added to IE

  In some runs, an explicit viscosity was added

- Approximating an incompressible fluid

  Normalisation: choose $H = 1$, $Ag = 1$, $\rho_1 = 1$

  Non-dimensional parameters (ideally small):

Density ratio	$B = \frac{\Delta\rho}{\rho_0} = \frac{2}{g}$	≈ 0.18
Mach number	$M = \sqrt{\frac{AgH\rho}{p\gamma}} \approx \sqrt{\frac{3}{5p_0}}$	≈ 0.08
Incompressibility ratio	$I = \frac{gH\rho^2}{5p\Delta\rho} \approx \frac{g^2}{10p_0}$	≈ 0.12

  Compromise $g = 11$, $p_0 = 100$

• Initial conditions - basic distribution

Away from interface:

Since $\boldsymbol{u} \approx 0$, require $\frac{\partial p}{\partial z} = -\rho g$.

Require neutral stability, buoyancy frequency

$N^2 = \frac{g}{T}\left(\frac{\partial T}{\partial z} + \frac{g}{c_p}\right) = 0 \Leftrightarrow$ isentropic fluid $p = k(s)\rho^{\gamma}$.

At interface:

Choose specific heats at constant volume, c_{v1} and c_{v2}.

Require temperature continuous $\Leftrightarrow c_{v1}\rho_1 = c_{v2}\rho_2$.

Everywhere:

Pressure field cannot be entirely hydrostatic.

Require $\boxed{\frac{\partial}{\partial t}(\nabla.\boldsymbol{u}) = 0}$.

Ignoring terms of $O(u^2)$, require

$$\nabla.\left(\frac{1}{\rho}\nabla p\right) \propto \nabla.\left(k^{1/\gamma}\nabla p^{(\gamma-1)/\gamma}\right) = 0,$$

with $\frac{\partial p}{\partial n} = -\rho g \hat{\boldsymbol{n}}.\hat{\boldsymbol{z}}$ on boundaries with outward normal $\hat{\boldsymbol{n}}$.

• Initial conditions - perturbations

2D velocity field with vorticity at interface models experimental barrier withdrawal.

3D random perturbation to interface position, wavelengths $\frac{L}{40} < \lambda < \frac{L}{20}$, rms amplitude $\sigma = \frac{H}{2500}$.

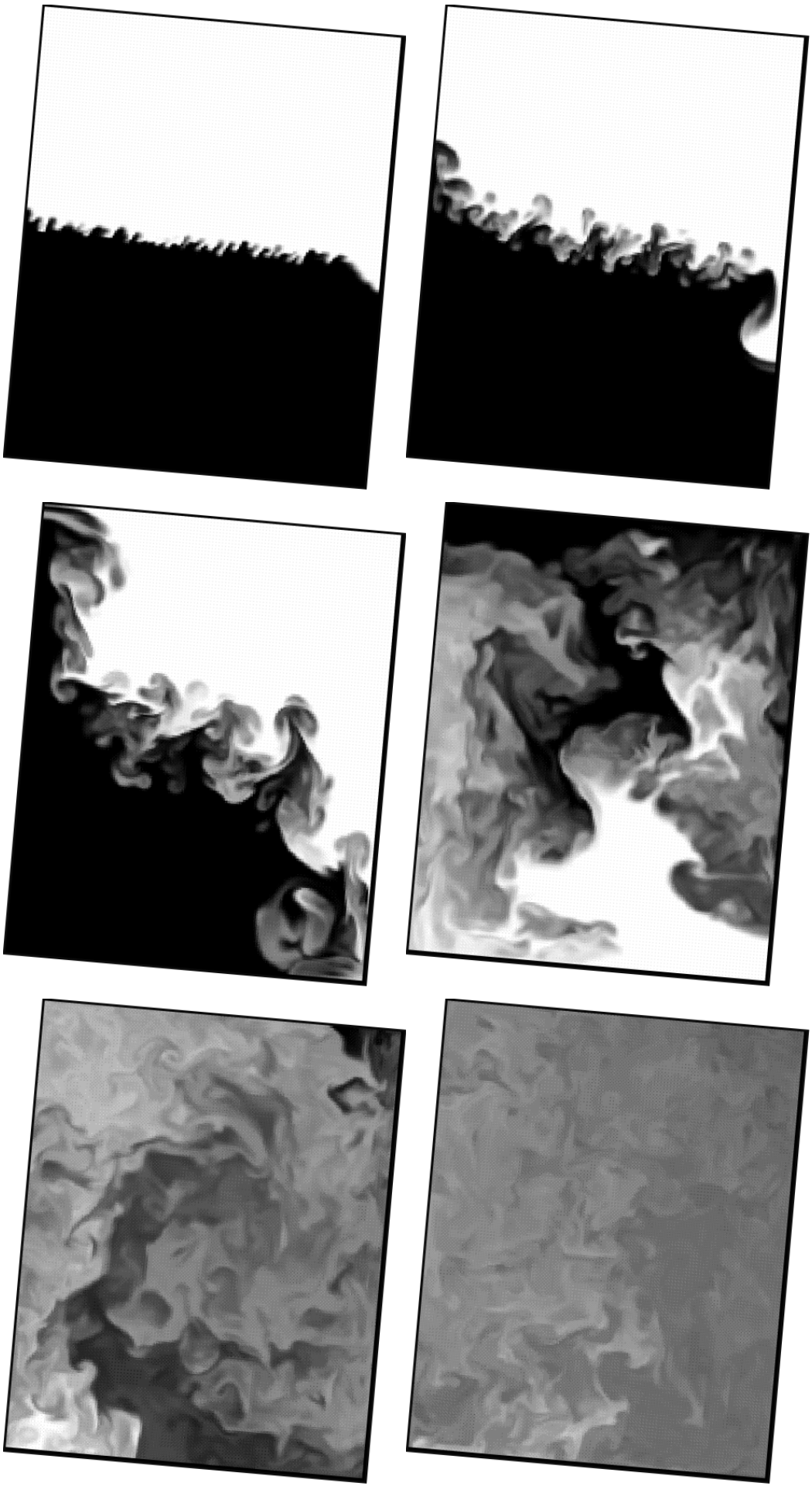

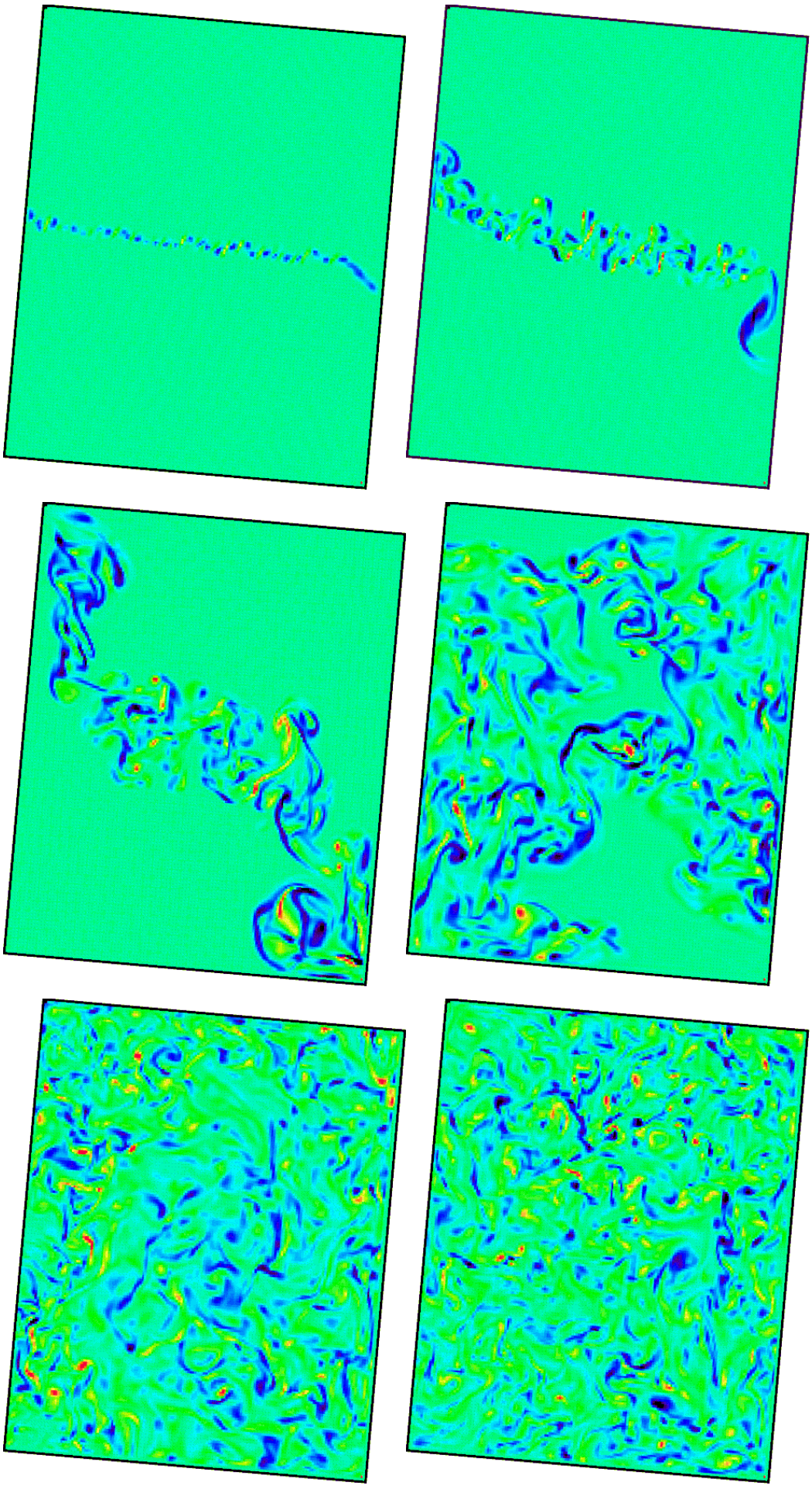

Energy budget

Numerical results $\eta \approx 0.48$

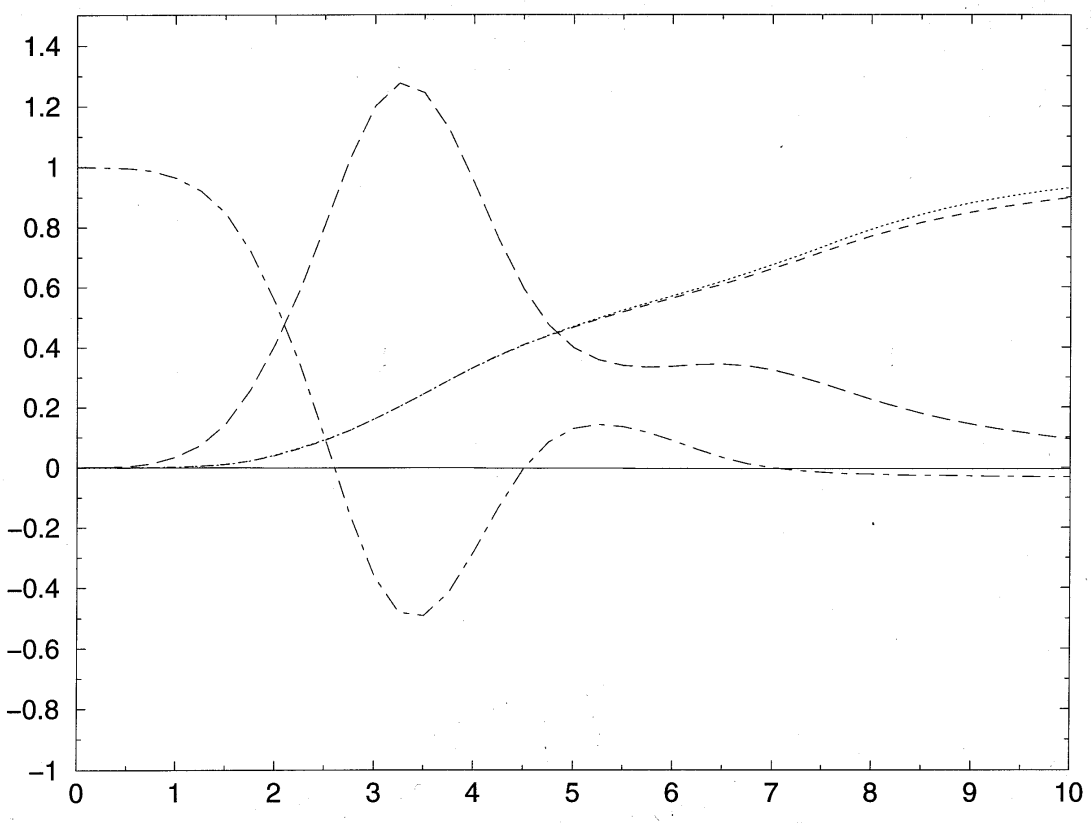

Typical experimental results $\eta \approx 0.38$

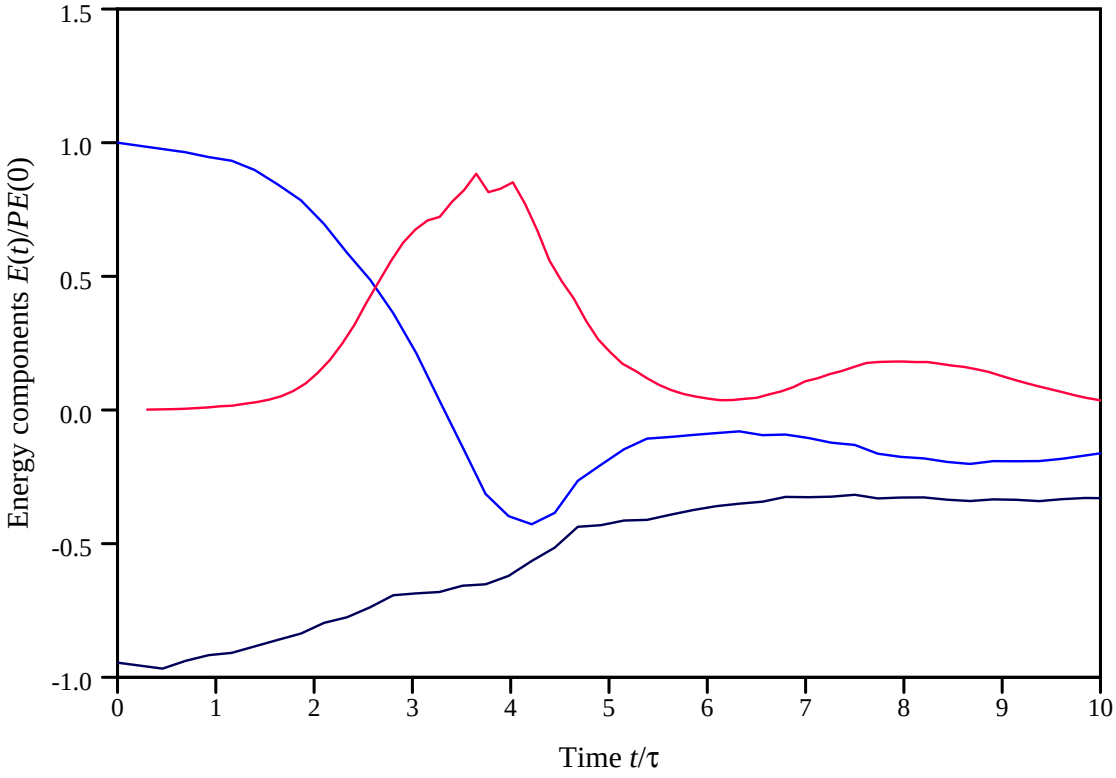

• Why the difference in energy budgets?

Numerical diffusion not ∇^2

2D advection test pattern

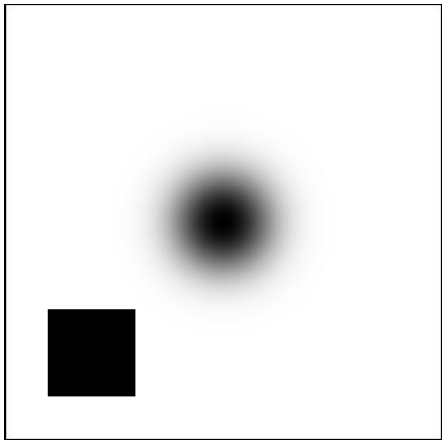

Numerical viscosity acts preferentially at small scales and is resolution and velocity-dependent

Total dissipation is unaffected by ratio of explicit/numerical viscosity until explicit viscosity dominates

Re of experiments is low

But experiments do not show *Re* dependence

Energy conservation

Small departures from energy conservation in stable waves

Sensitivity to initial conditions

But there is no change when λ_{random} increased by 4

Different molecular Pr

Does small-scale dynamics adjust to forcing from larger scales?

Instantaneous mixing efficiency

$\theta = 0°$

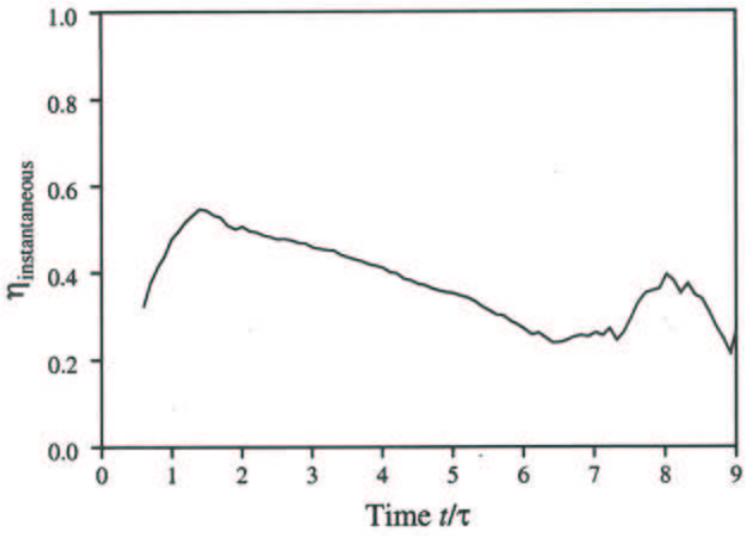

peak values

$\eta_{instantaneous} \approx 0.5$

around

$t/\tau = 1$

for $\theta = 0°, 5°$

$\theta = 5°$

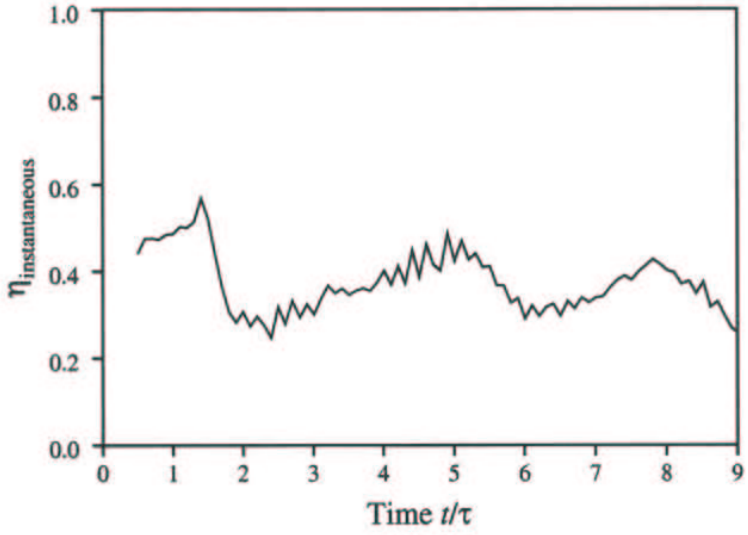

typical values

0·2–0·4

$\theta = 10°$

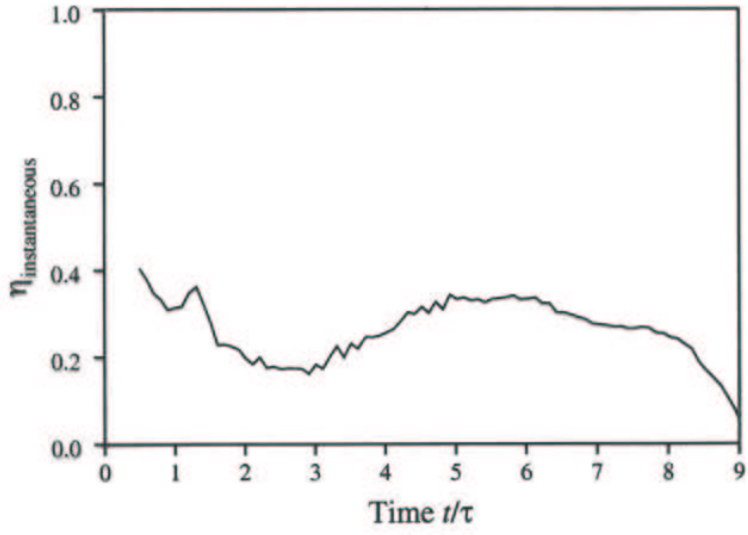

Dominant contribution to $\eta_{cumulative}$ when E_{avail} decreases most rapidly - during overturning

Cumulative mixing efficiency

theoretical maximum

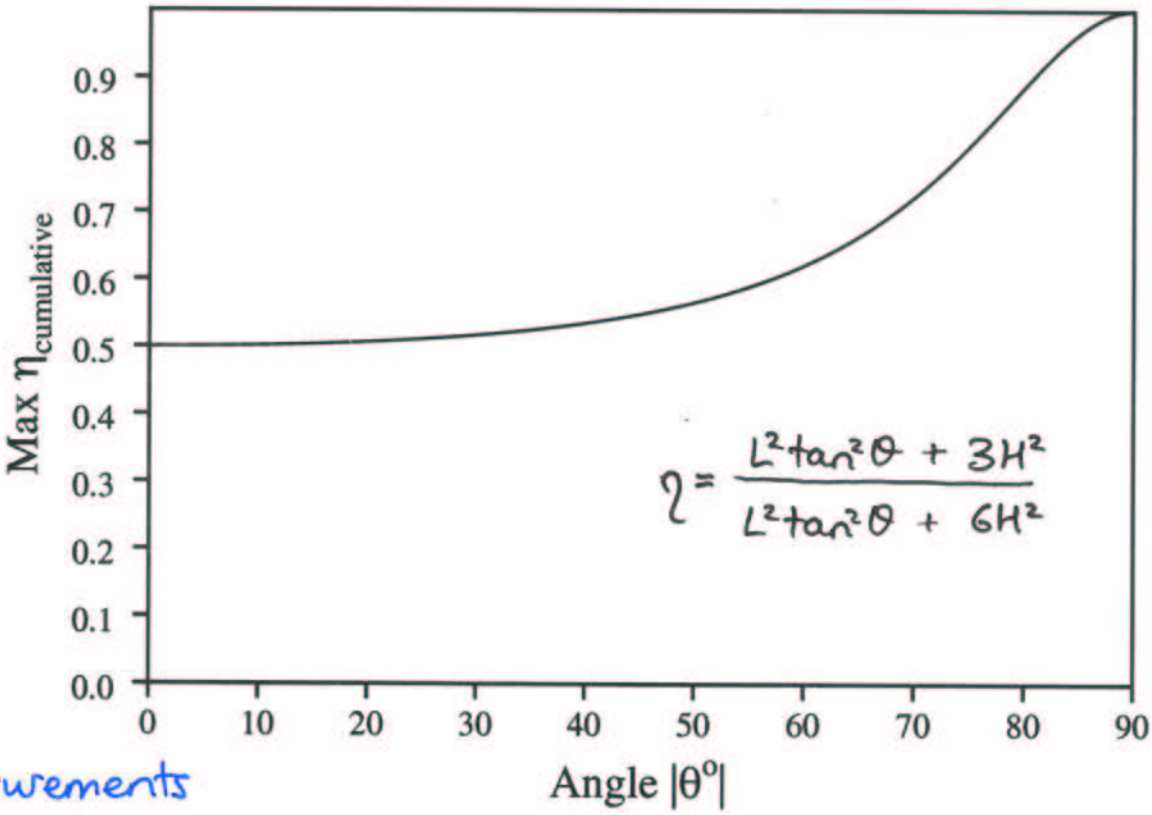

measurements

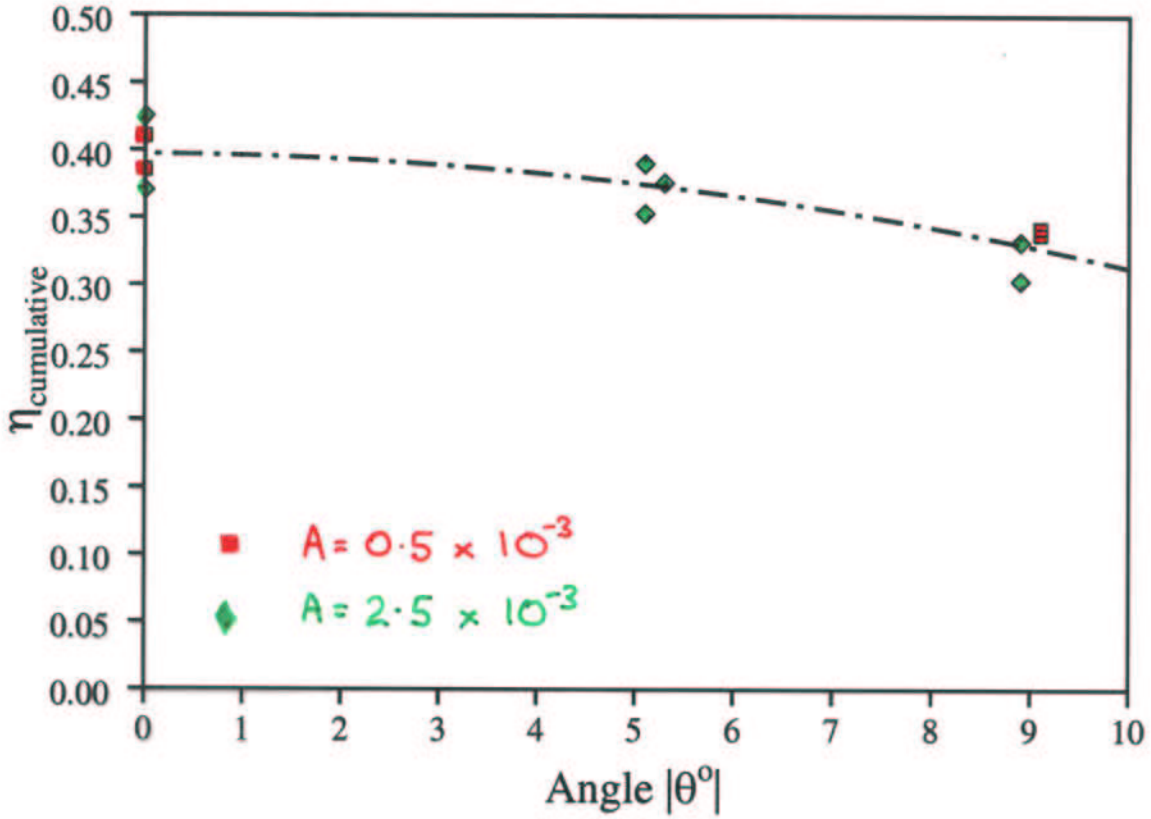

Conclusions and further work

- Laboratory experiments
  - $\theta = 0^\circ$ - $\eta_{cumulative} \approx 0.4$
  - As $\theta \uparrow$, $\eta_{cumulative} \downarrow$
  - For $\theta \leq 5^\circ$, $\eta_{instantaneous} \approx 0.5$
- Numerical simulations
  - Models experiments at suitable parameters
  - Good agreement in large-scale overturning
- Further work
  - Investigate sensitivity of mixing to various factors
  - Investigate instability at higher angles - up to limiting case:

  - Extend study of mixing efficiency to more complex stratifications

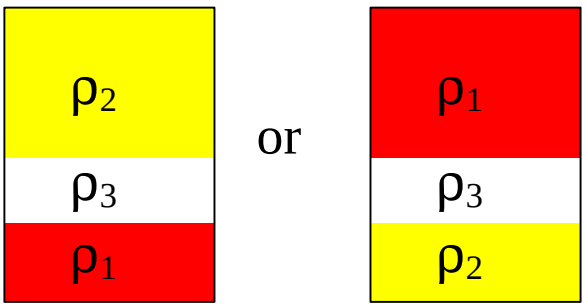

$\rho_1 > \rho_2 > \rho_3$

Dalziel & Jacobs (2000)

The 8th International Workshop on the Physics of Compressible Turbulent Mixing
Dec. 9-14, 2001, Pasadena, CA

Production of diverging and converging spherical shock waves and eccentric interaction of converging shock waves with cylindrical interfaces

S.H.R. Hosseini and K. Takayama

Shock Wave Research Center, I.F.S., Tohoku University, Sendai, Japan

Introduction

- **Upon focusing of spherical or cylindrical shock waves, high pressures and temperatures created at the center of convergence and have been used for various scientific and industrial applications.**
- **It is not necessarily easy in laboratories to produce uniformly converging shock waves.**
- **Applications of R-M instability appearing in converging spherical and cylindrical geometries, such as inertial confinement fusion, supersonic combustion, and astrophysics, made it of considerable interest.**
- **In the present research, results of recent experiment of R-M instability will be reported.**

Shock Wave Research Center, I. F. S., Tohoku University

Aspheric spherical test section

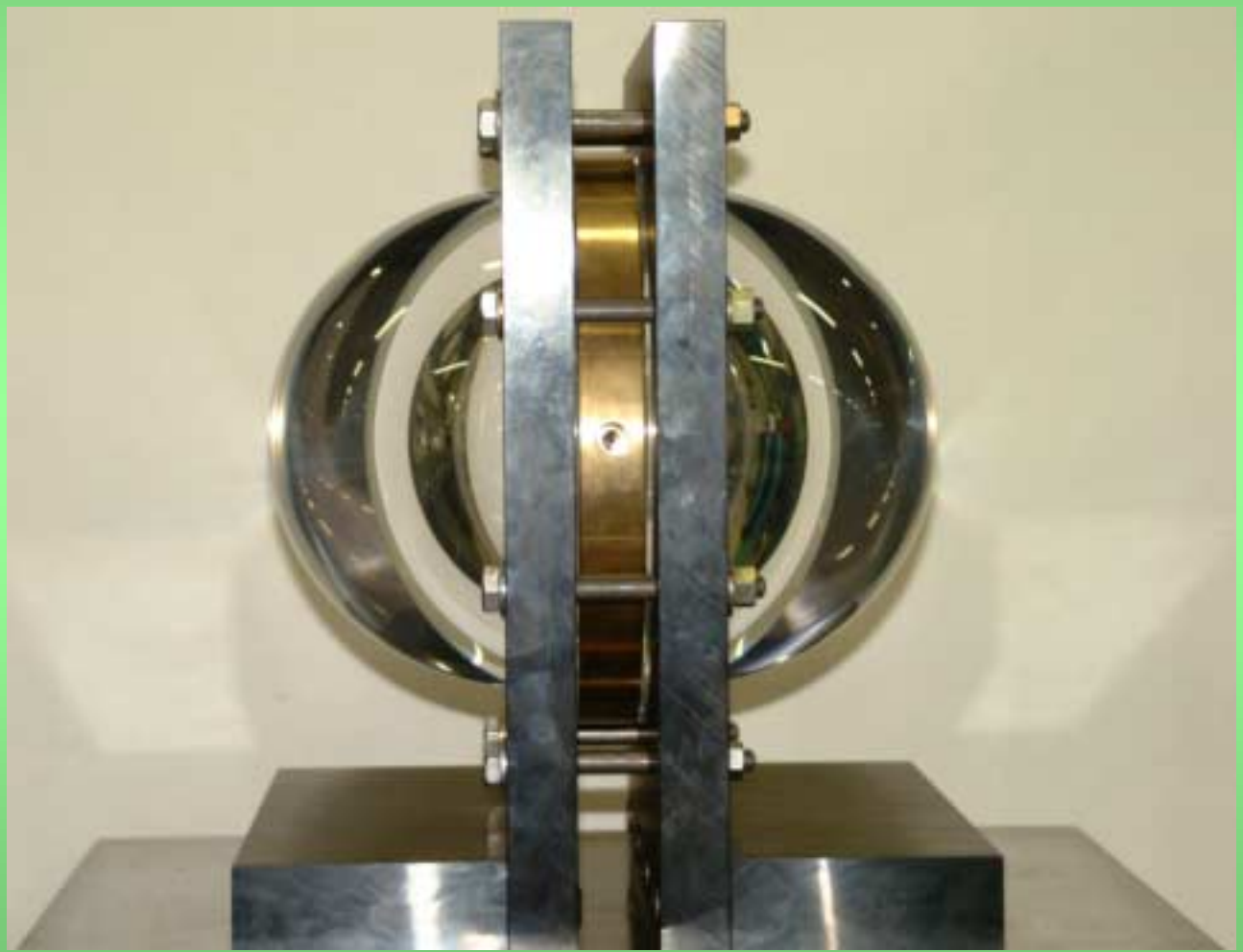

Shock Wave Research Center, I. F. S., Tohoku University

Front view of the aspheric spherical test section

Laser light rays in the aspheric test section

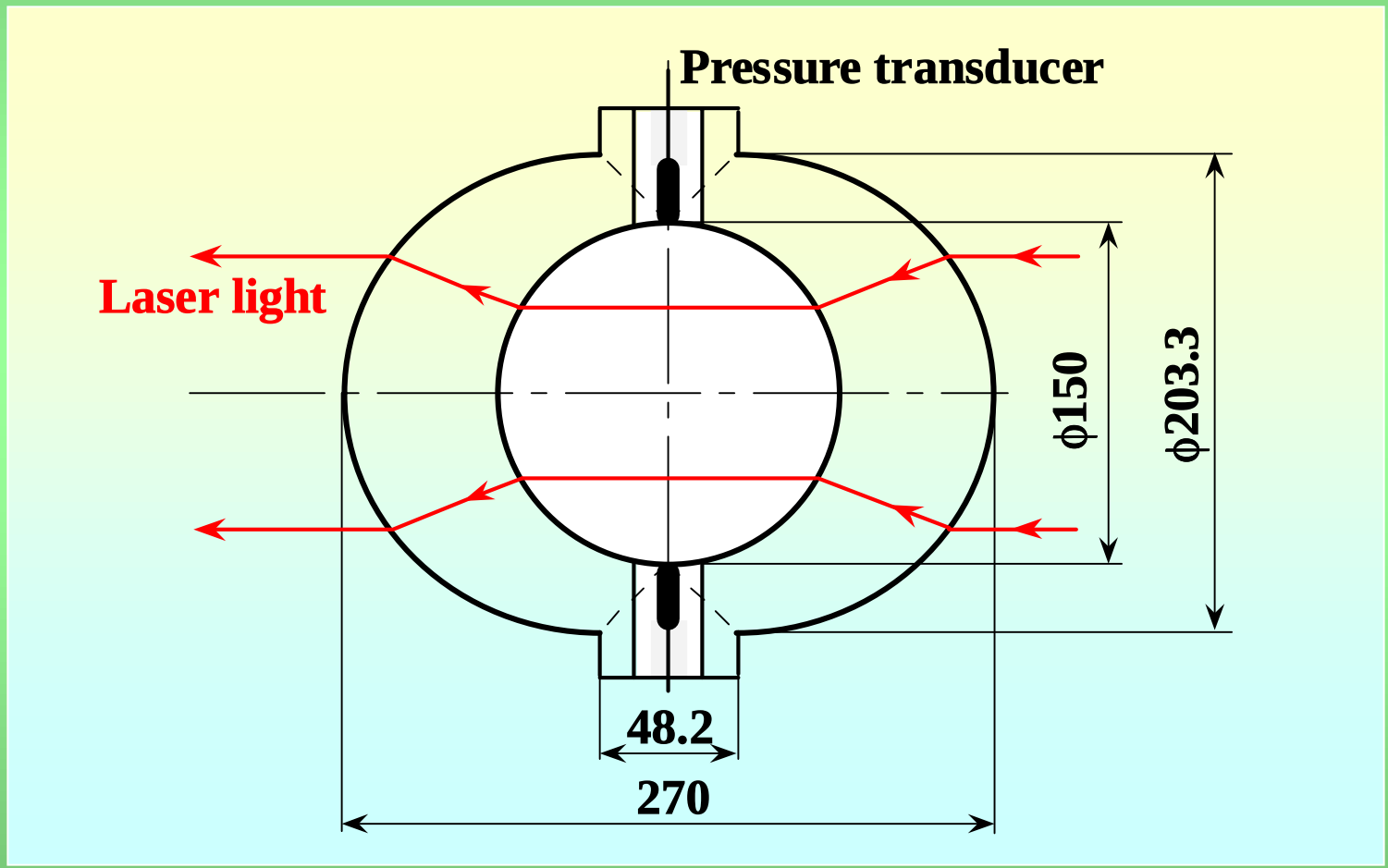

Double exposure holographic interferometric optical set-up

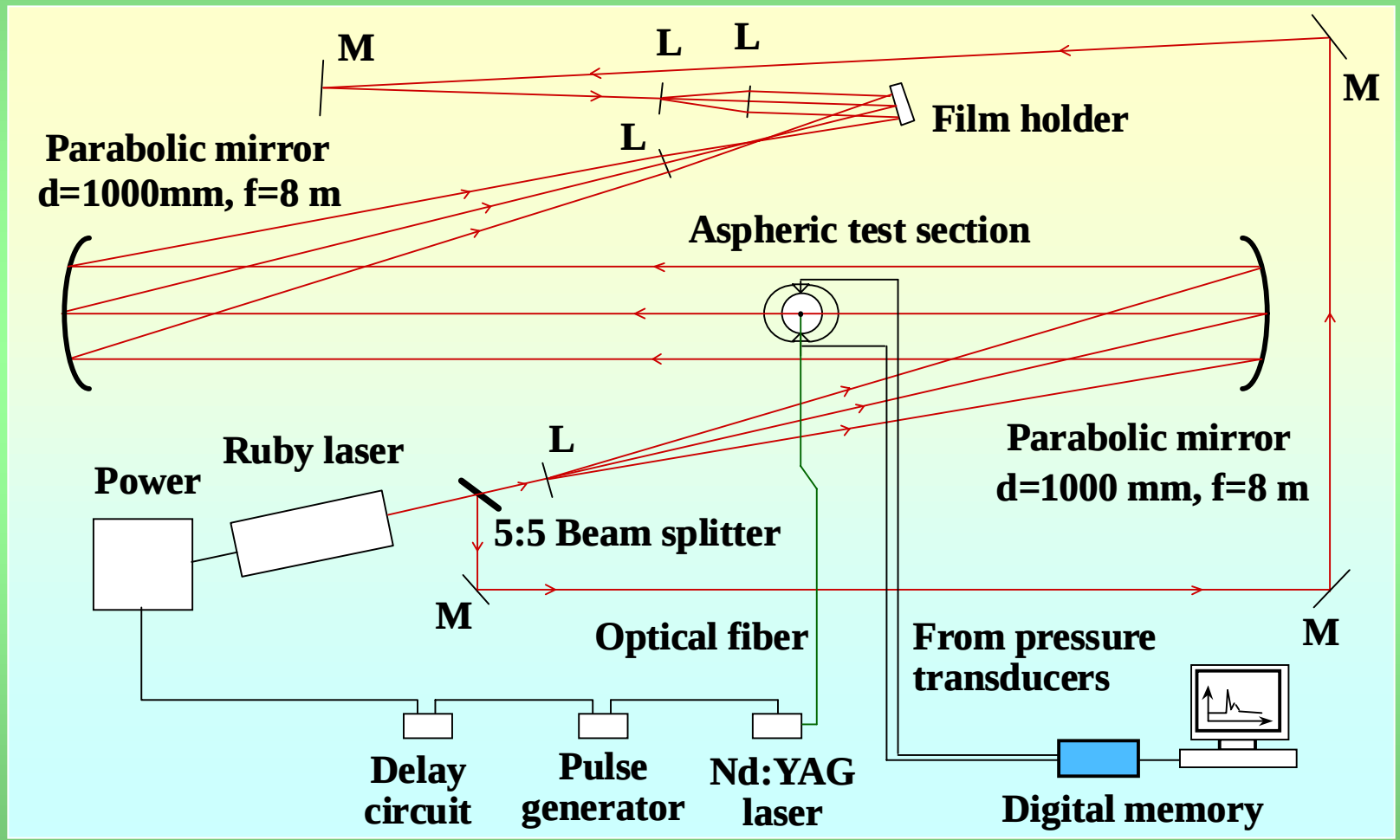

Shock Wave Research Center, I. F. S., Tohoku University

Structure of vertical diaphragmless shock tube

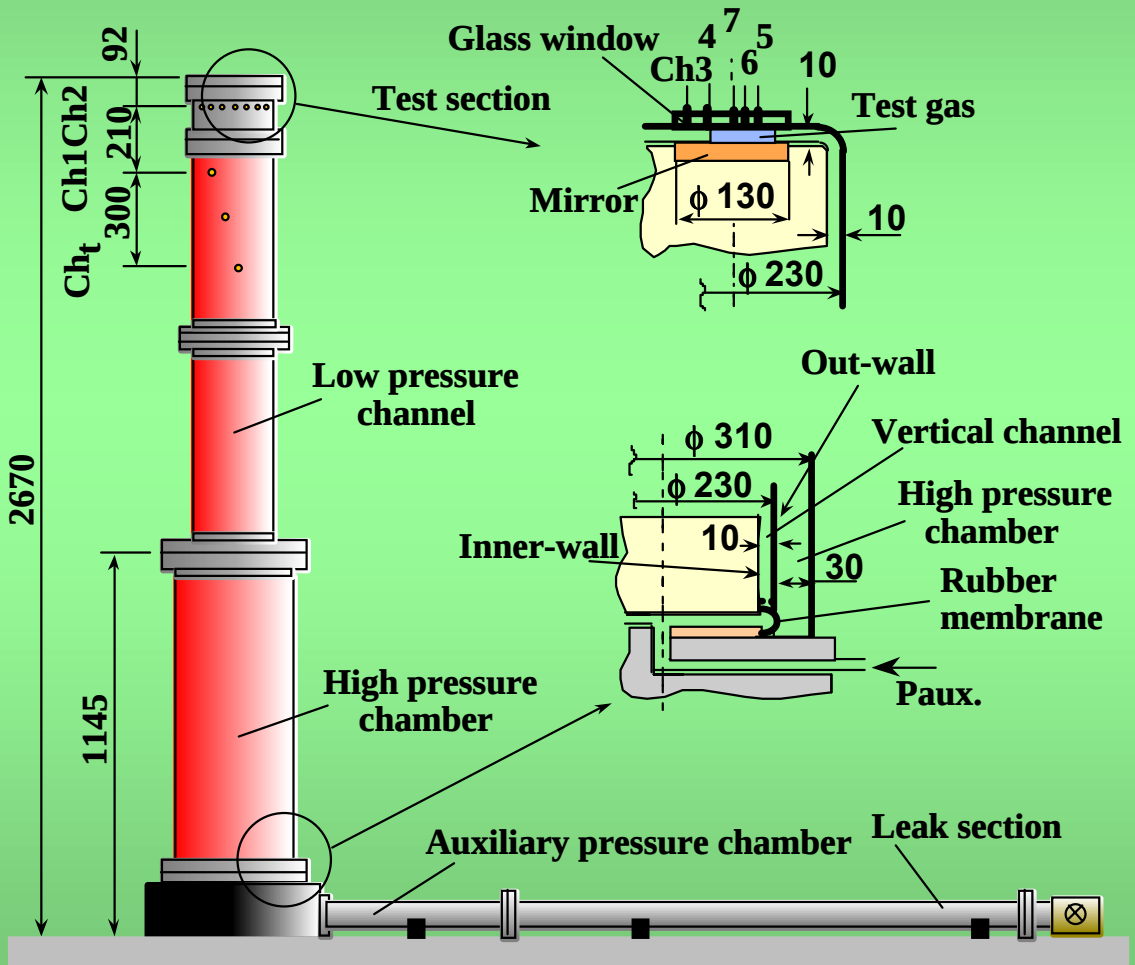

Shock Wave Research Center, I. F. S., Tohoku University

Double exposure holographic interferometry

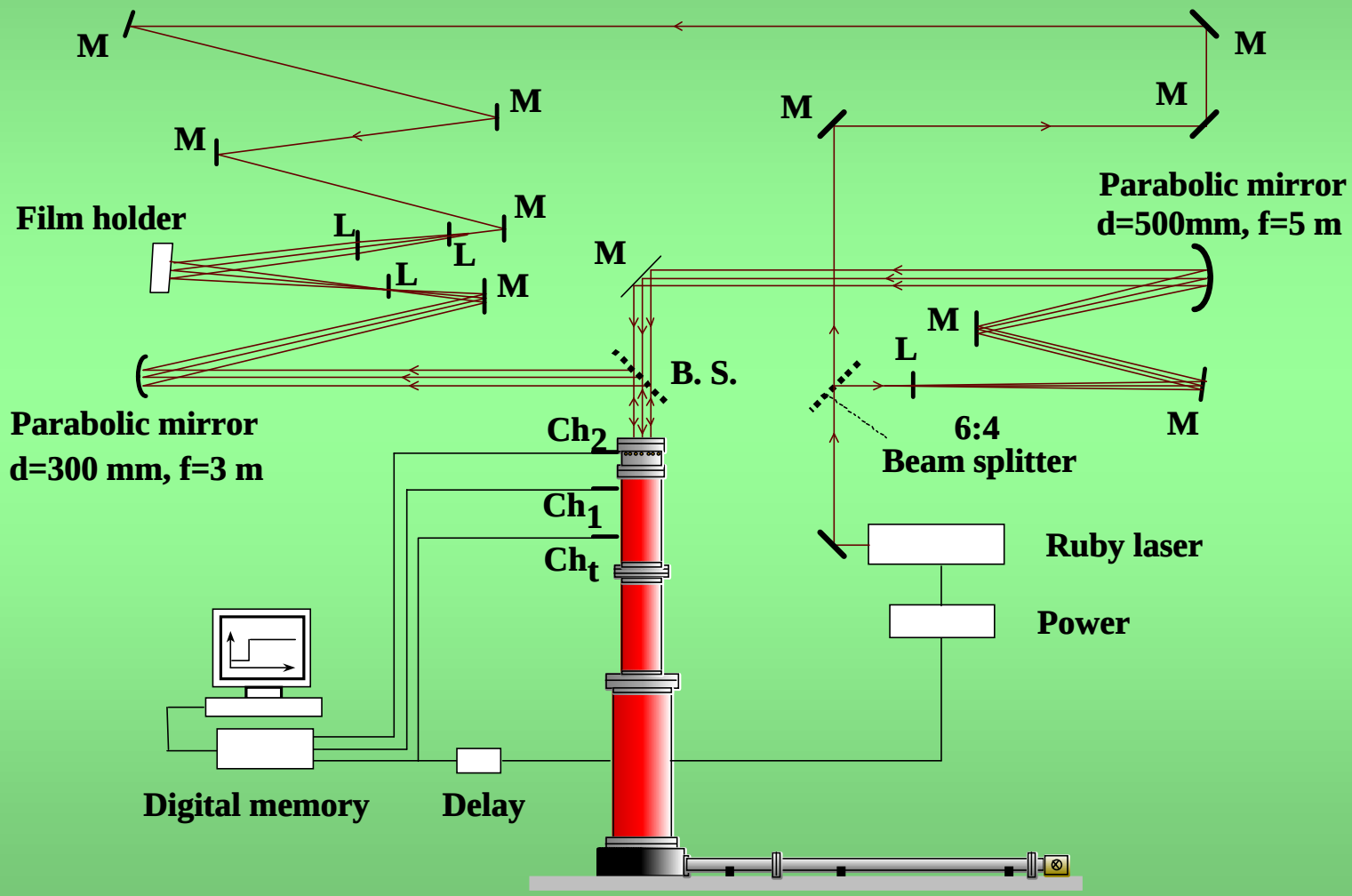

Shock Wave Research Center, I. F. S., Tohoku University

Test section with cylindrical bubble

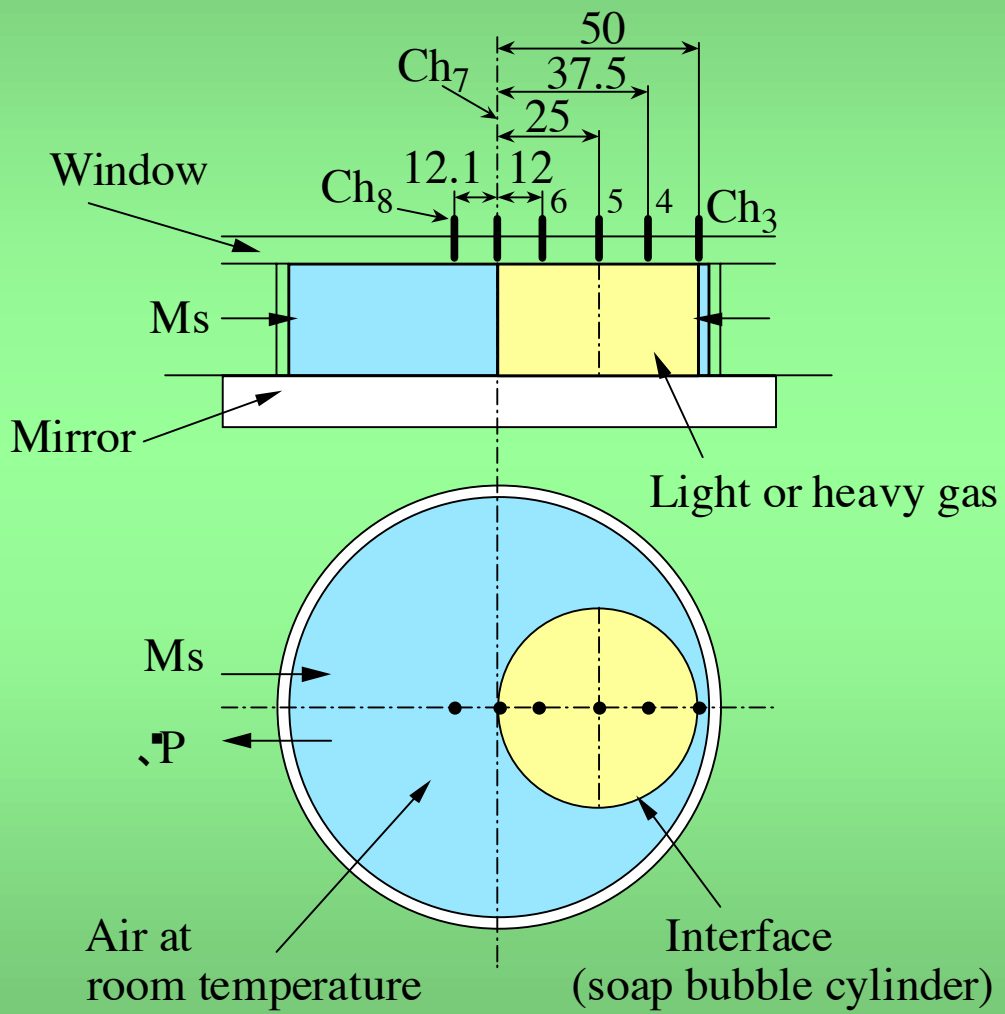

Pressure histories at the test section for eccentric interaction of cylindrical shock wave with cylindrical SF_6 bubble, Ms_i=1.18, P_0=101.13 kPa

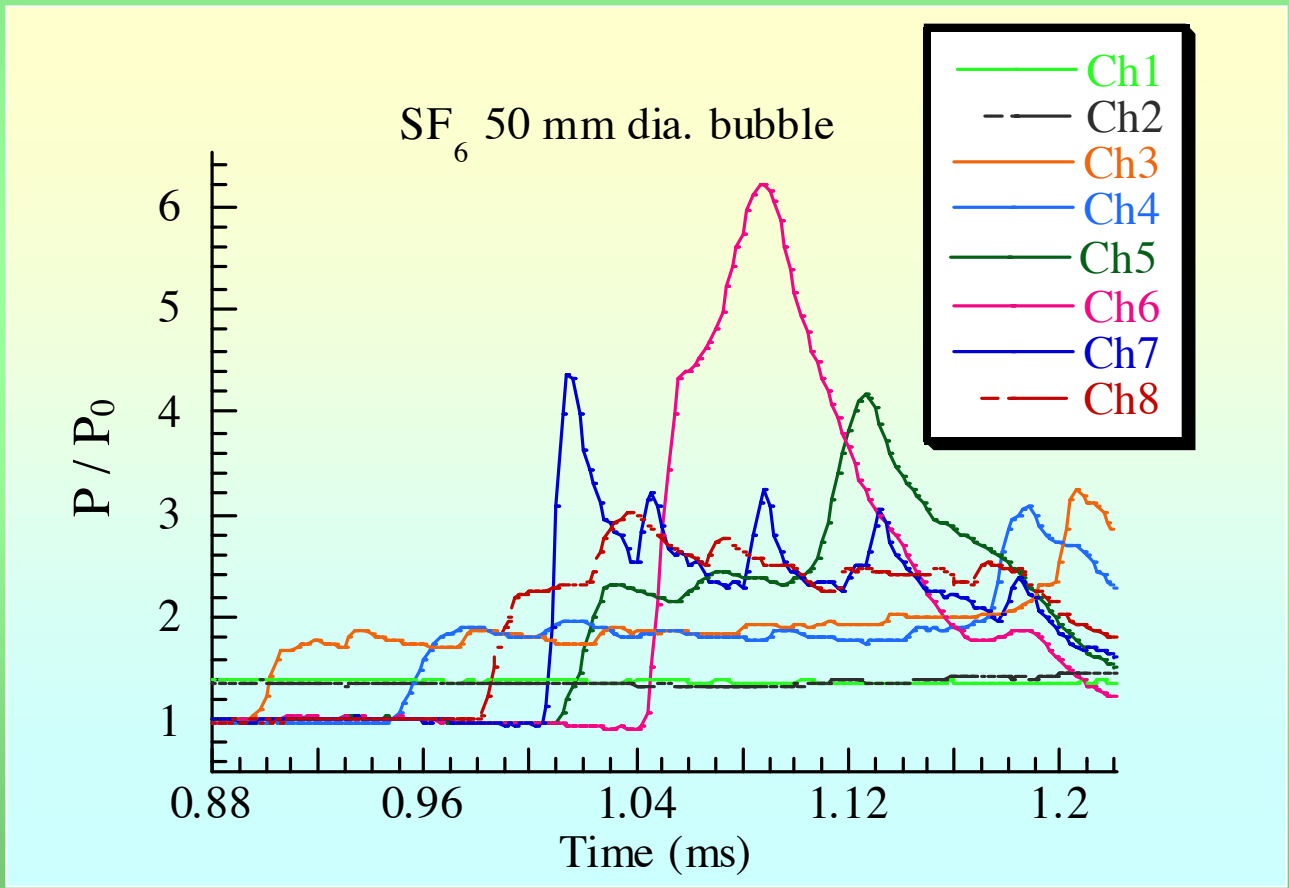

Ms_i=1.18 in air, P_0=100.3 kPa, D_{SF_6}=50mm

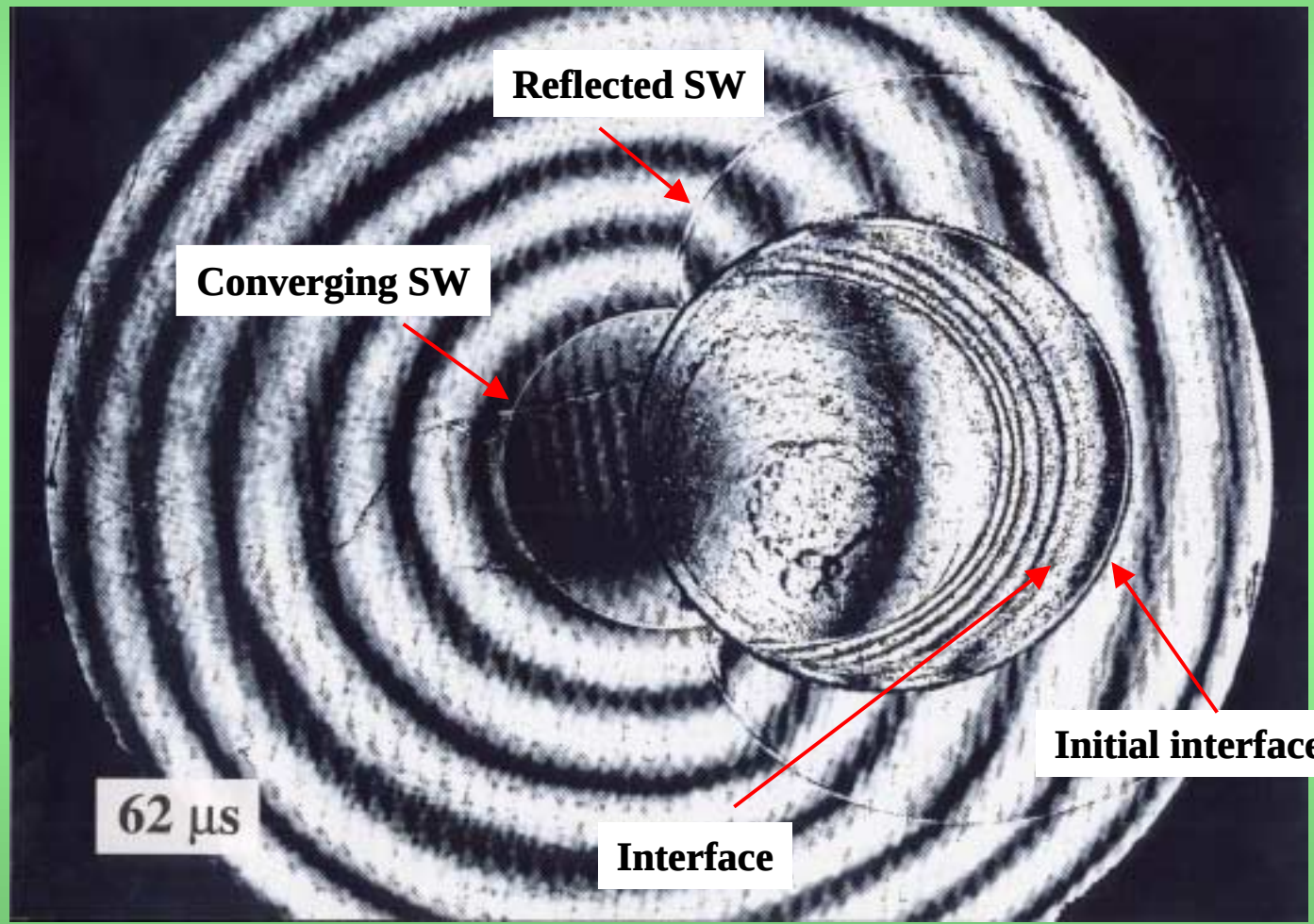

Shock Wave Research Center, I. F. S., Tohoku University

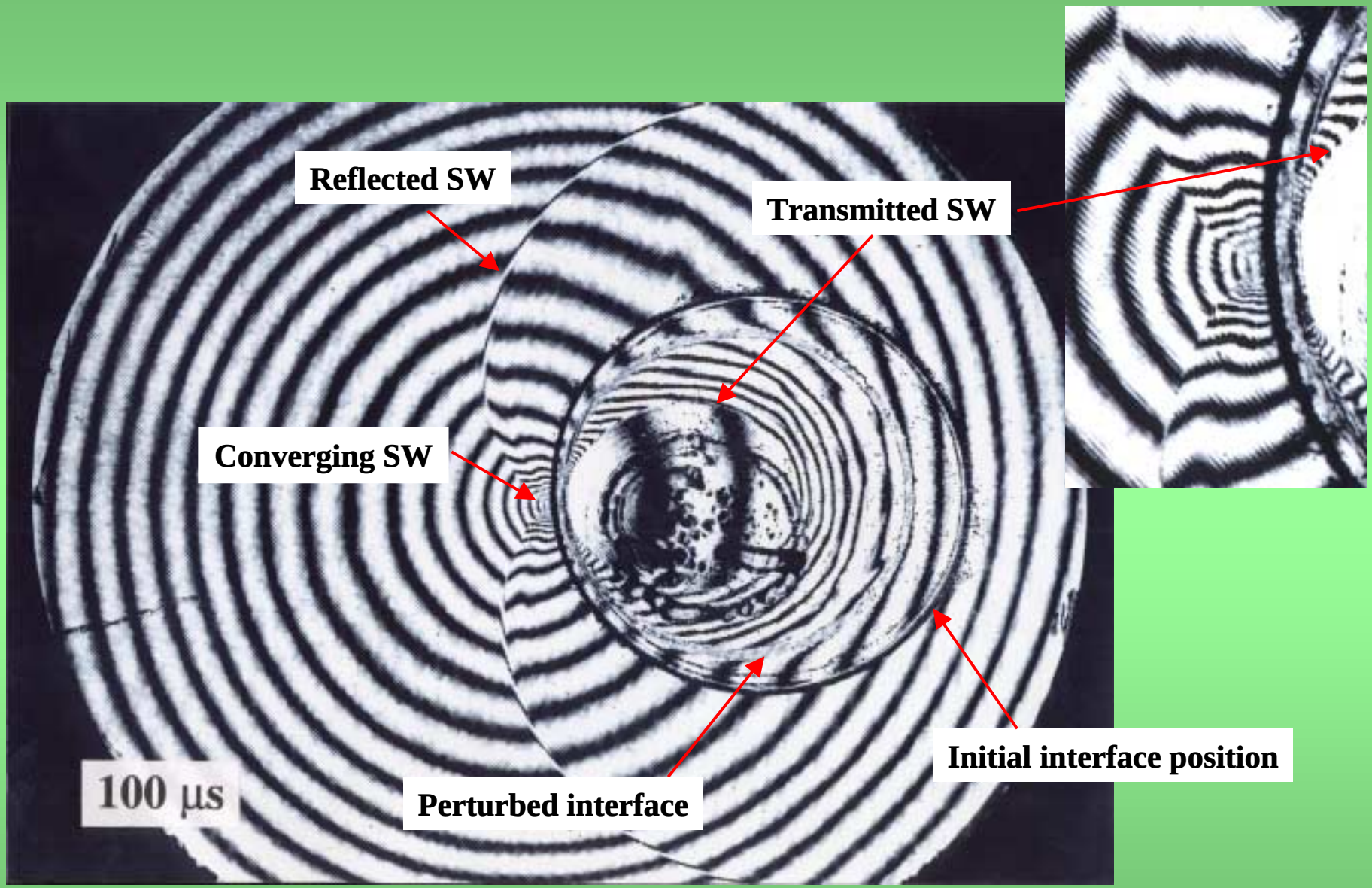

Shock Wave Research Center, I. F. S., Tohoku University

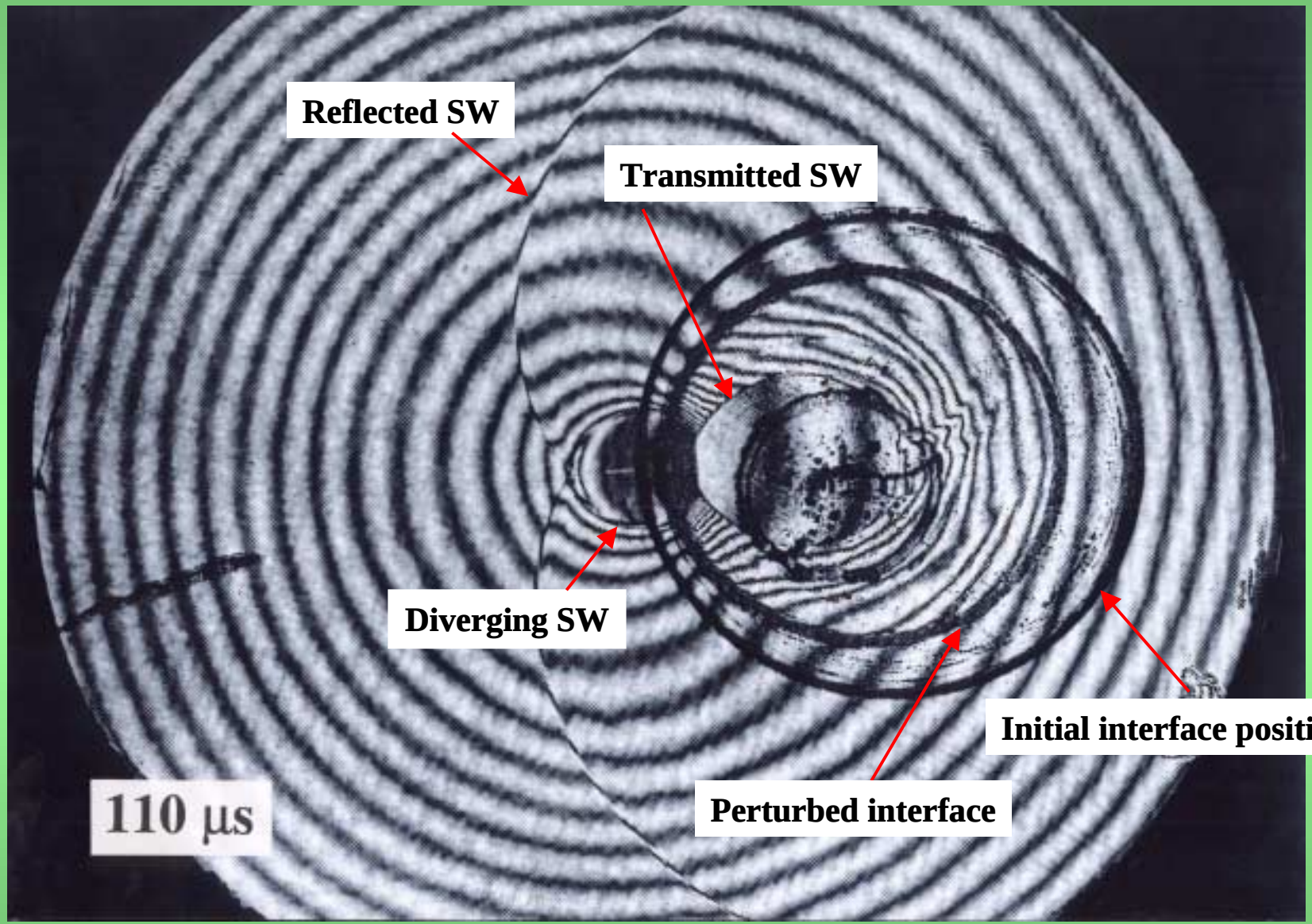

Shock Wave Research Center, I. F. S., Tohoku University

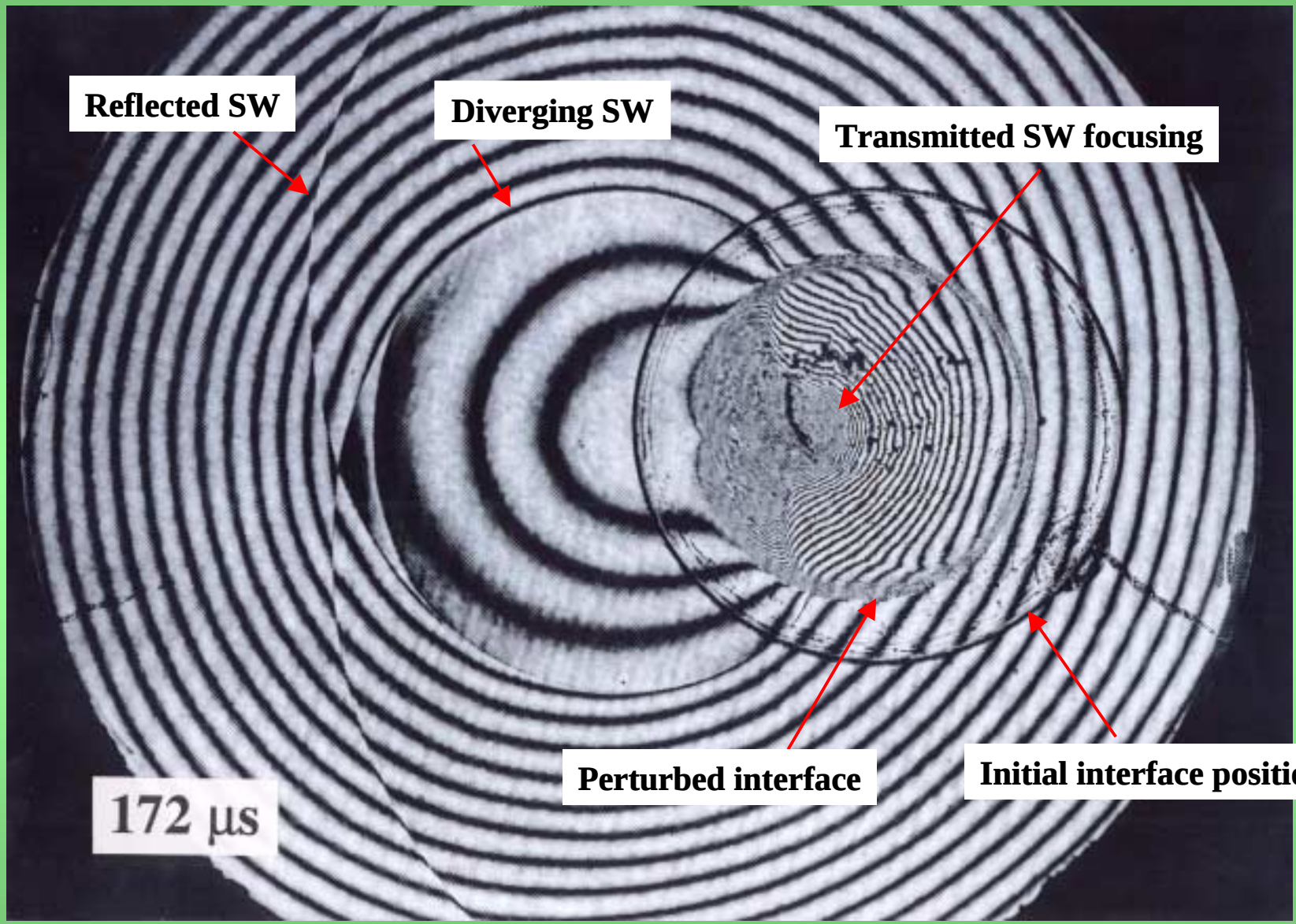

Shock Wave Research Center, I. F. S., Tohoku University

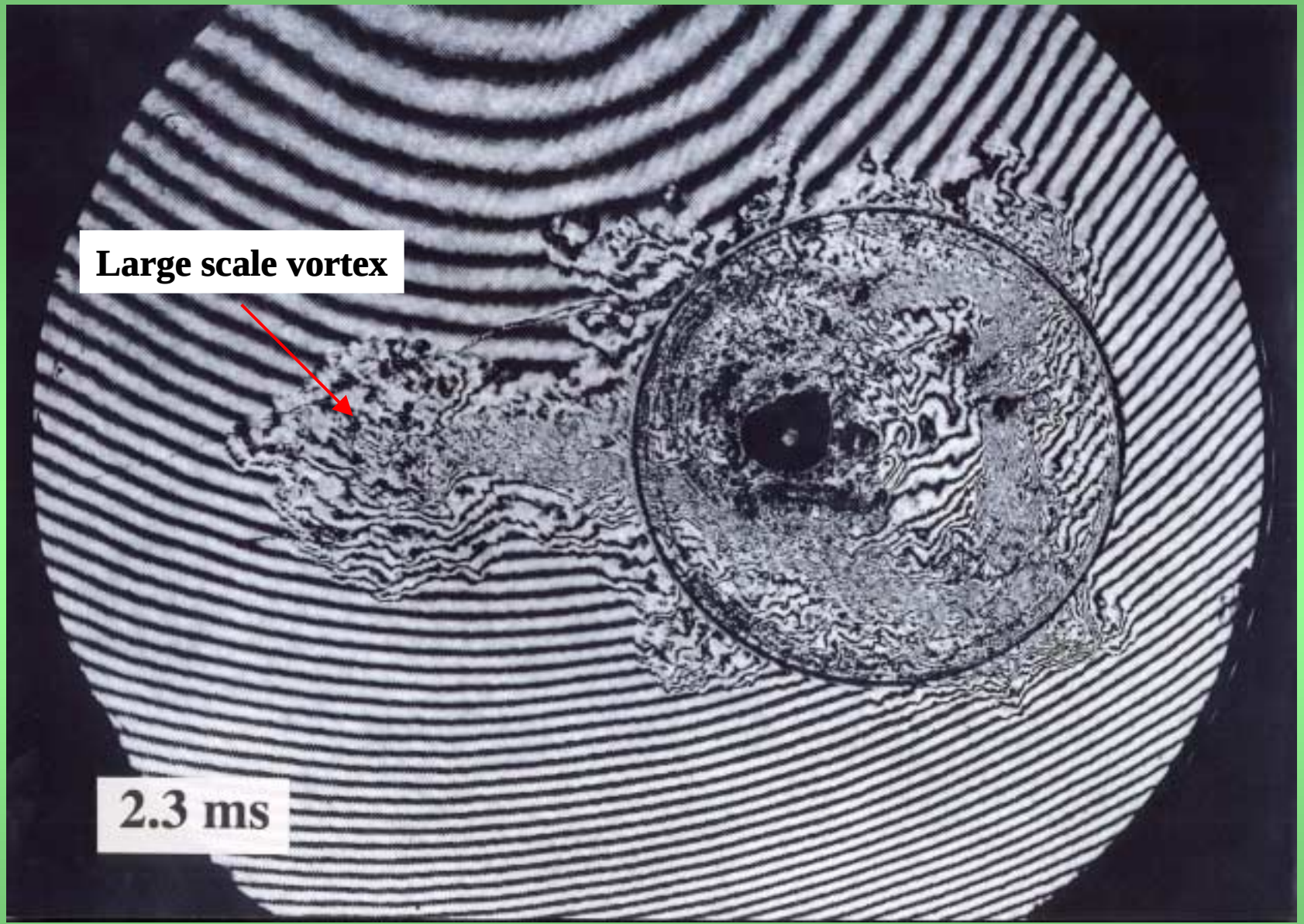

Shock Wave Research Center, I. F. S., Tohoku University

Time variation of average SF_6 jet velocity in air

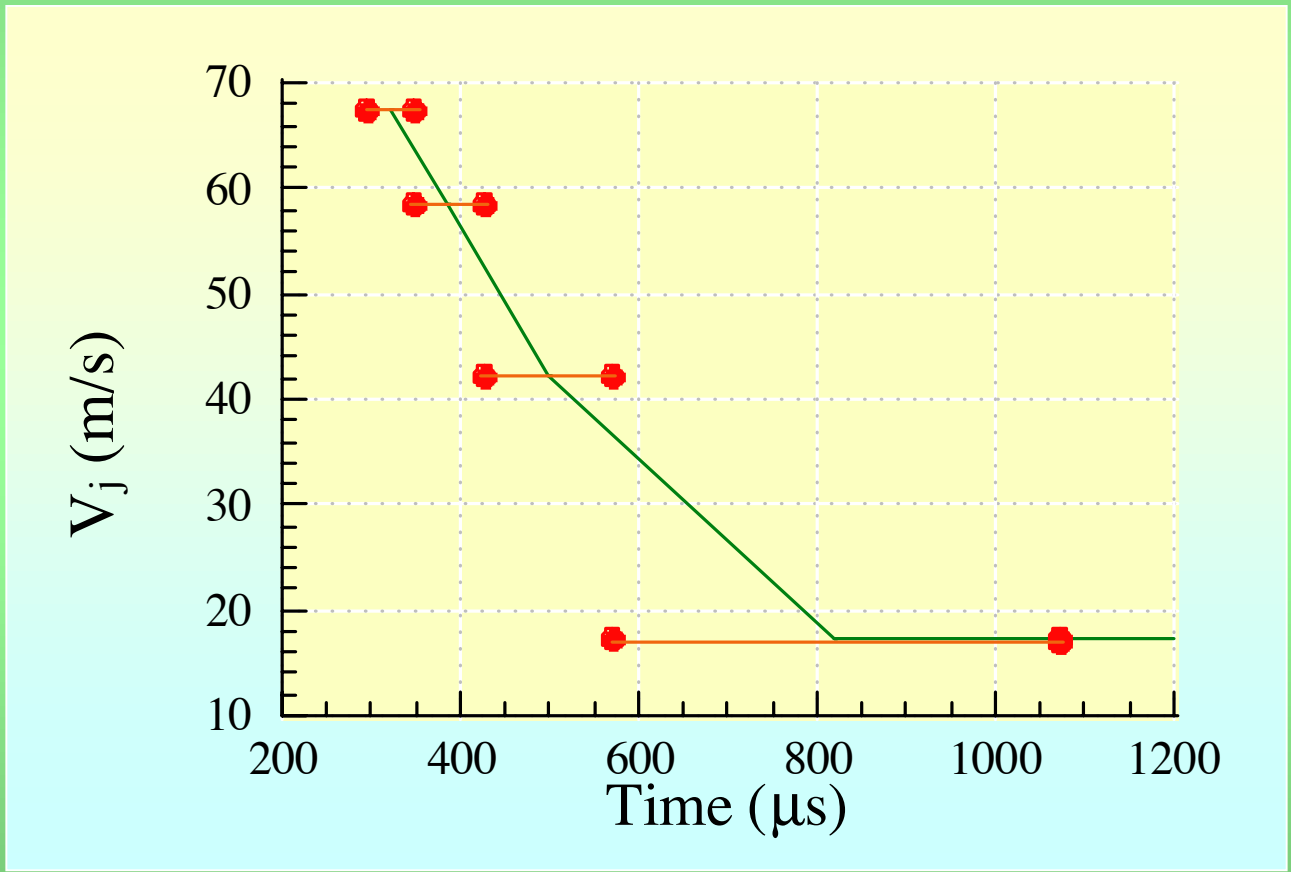

Summary

1) **Converging spherical shock waves and their interaction with micro-explosive product gases were investigated by using a spherical transparent test section.**

2) **Using double exposure holographic interferometry, the interactions of converging shock waves with light/heavy cylindrical gaseous interface were quantitatively visualized. A relatively strong secondary shock wave focusing in SF_6 heavy gas bubble resulted a strong SF_6 jet in air, which made the final distortion of the bubbles to be different from planar shock wave loading.**

Shock Wave Research Center, I. F. S., Tohoku University

LINEAR AND NON-LINEAR STAGES OF THE RICHTMYER-MESHKOV INSTABILITY DEVELOPMENT IN A LARGE CROSS SECTION SHOCK-TUBE

L.HOUAS*, G. JOURDAN*, L. SCHWAEDERLE* and E.E. MESHKOV♣

*IUSTI, UMR CNRS 6595, Université de Provence, Technopôle de Château-Gombert, 5 rue Enrico Fermi, 13453 Marseille Cedex 13, FRANCE

♣Russian Federal Nuclear Center, Institute of Experimental Physics, 607190 Sarov, RUSSIA

CENTRE NATIONAL DE LA RECHERCHE SCIENTIFIQUE

I- INTRODUCTION

Present research topic: Fundamental research

- - Characterization of the transition phases to turbulence from the development of hydrodynamic instabilities within a shock accelerated interface

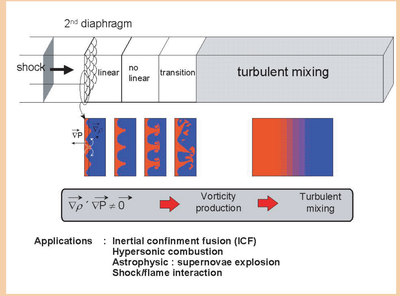

The Richtmyer Meshkov instability

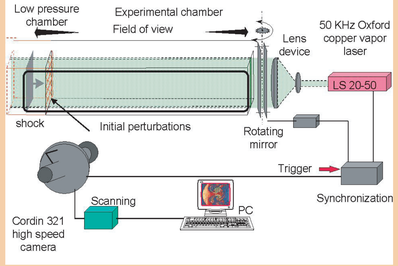

Principle of the measurements

II- THE NEW LARGE CROSS SECTION SHOCK TUBE OF IUSTI

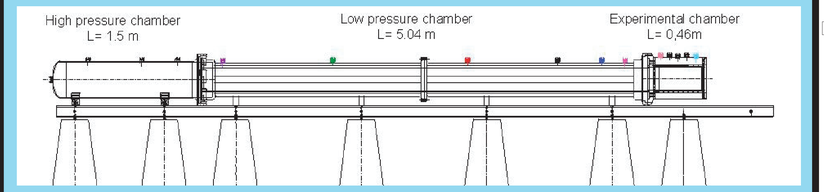

Characteristics and usual performances

- - Square cross section: 20x20 cm2
- - Length: 7.04 meters
- - Mach number: from 1.1 to 3
- - Initial pressure: from 0.5 atm to 1 atm

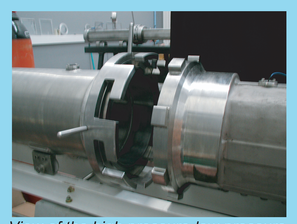

View of the high pressure-low pressure chamber connection

First diaphragm before and after run (Aluminium, thickness=1 mm, ϕ=360 mm)

Control of the initial conditions

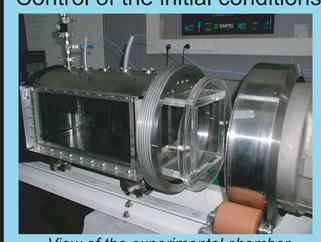

View of the experimental chamber

Initial interface materialized by a 0.8 µm thick nitrocellulose membrane resting over metallic horizontal lines

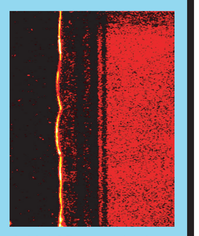

Initial 2D perturbations

III- DIAGNOSTIC SYSTEM - Laser sheet high speed visualization

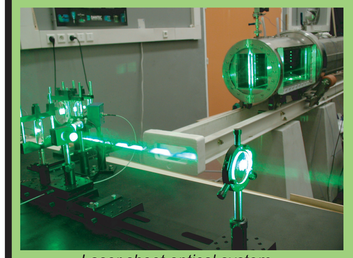

Laser sheet optical system

View of the general experimental device

- - Source: from 2 to 50 kHz pulsed copper vapour Oxford laser
- - Camera: 321 Cordin streak camera
- - External shutter: Electro-optical shutter
  - *Response time: ~ 1 µs*
- - Acquisition device: 720 Tektronix scope
  - *4 channels*
- - Trigger: signal from PCB pressure gauge

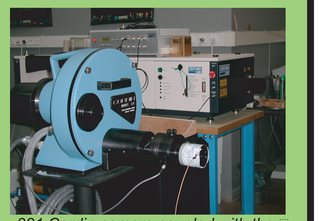

321 Cordin camera coupled with the LS 20-50 copper vapour Oxford laser

IV- INITIAL CONDITIONS

P_{Exp} ~ 1 atm | P_{LP} ~ 1 atm | P_{HP} ~ 3 bars

Gas test He or Kr | Driven= air + smoke | Driver= air

M_{is} ~ 1.32 in air | W_{is} ~ 460 m/s

Heavy/light case (air/He)

$A_{air/He} = \frac{\rho_{He} - \rho_{air}}{\rho_{He} + \rho_{air}} = -0.7$

W_{ts}=1111 m/s
$U_{mz/is}$ = 226 m/s
$U_{mz/rs}$ = 99 m/s

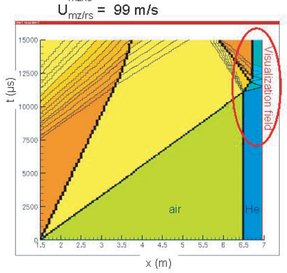

Light/heavy case (air/Kr)

$A_{air/Kr} = \frac{\rho_{Kr} - \rho_{air}}{\rho_{Kr} + \rho_{air}} = +0.5$

W_{ts}=322 m/s
$U_{mz/is}$ = 115 m/s
$U_{mz/rs}$ = 9 m/s

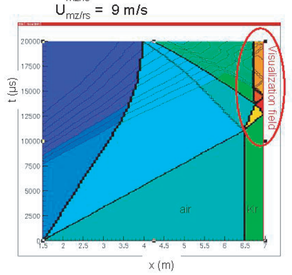

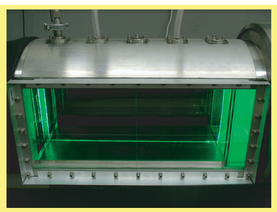

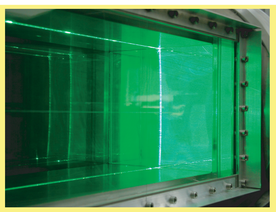

Pictures taken just before the run. Air at right is seeded by smoke cigarette and mosquito incense. Pure helium or krypton are used in the left part in order to study both the heavy/light and light/heavy configurations for the same initial shock wave. The initial interface is materialized by two layers of a thin membrane of nitrocellulose (0.4 µm thick) resting over fine metallic horizontal lines which create 2D perturbations of different wavelengths (2 cm and 4 cm).

V- FIRST RESULTS

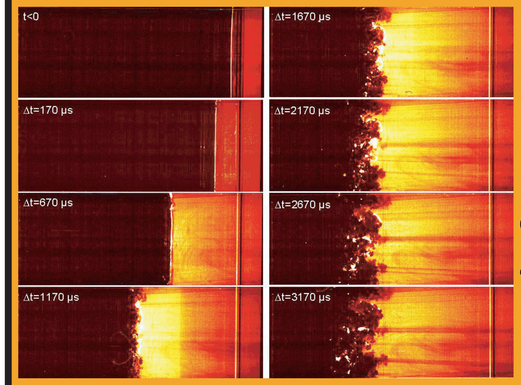

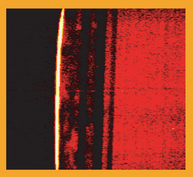

Sequences of a heavy/light (air/He) experiment with an initially non perturbated interface. (burst frequency: 2 kHz camera, velocity: 40 m/s) Air at right is initially seeded and helium is pure. The thin membrane of nitrocellulose is not completely destroyed by the incident shock wave but by the reflected one.

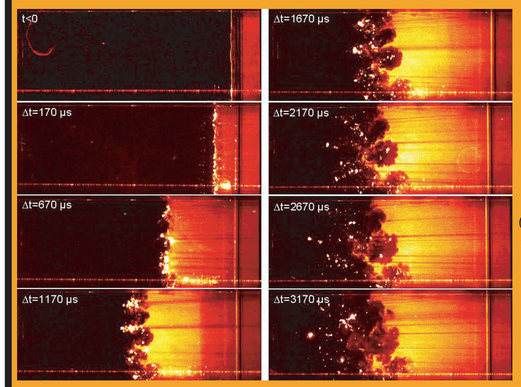

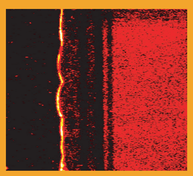

Sequences of a heavy/light (air/He) experiment with an initially perturbated interface. (burst frequency: 2 kHz camera, velocity: 40 m/s) Air at right is initially seeded and helium is pure.

Both heavy/light (air/He) and light/heavy (air/Kr) experiments with an initially perturbated interface. The incident shock wave Mach number in seeded air is 1.3 and the initial pressure of the test gases is 1 atm.

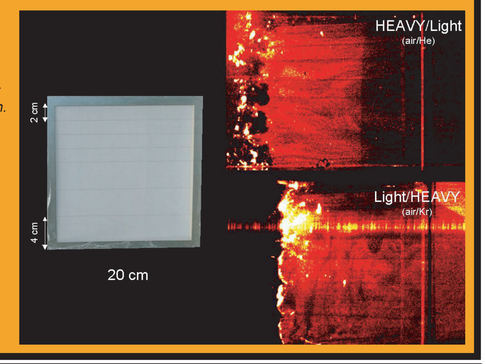

VI- CONCLUSIONS AND PERSPECTIVES

- *First results in a new shock tube coupled with a high frequency laser sheet technique have been obtained for the study of the transition phases to turbulence initiated by the RIchtmyer-Meshkov instability.*
- *The 20 cm large square cross shock tube prevents from wall boundary layer effects and the special device realized for the control of the initial conditions is succesfully available.*
- *The growing up of the initial perturbations at the interface and the RIchtmyer-Meshkov mixing process are cleary visible.*
- *Runs with a higher observation frequency have to be realized (up to 50 kHz).*
- *The quality of the picture and in particular the homogeneity of the seeding have to be improved.*

Experimental Investigation of Richtmyer-Meshkov Instability after a Second Interaction with a Reflected Shock Wave

J.W. Jacobs and V.V. Krivets

Department of Aerospace and Mechanical Engineering
University of Arizona

Supported by:

Lawrence Livermore National Laboratory

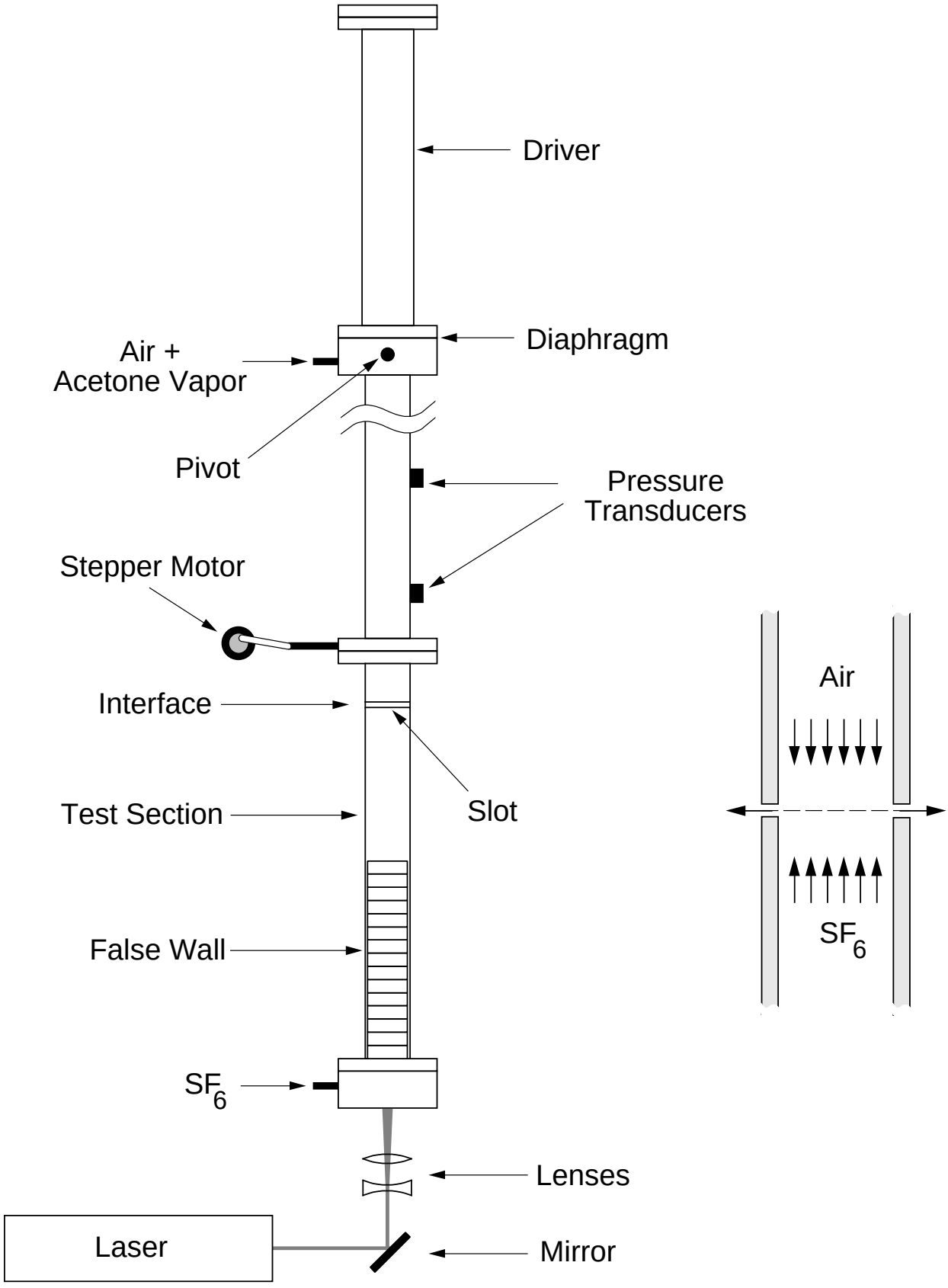
Driver
Diaphragm
Air +
Acetone Vapor
Pivot
Pressure
Transducers
Stepper Motor
Interface
Slot
Test Section
False Wall
SF6
Lenses
Laser
Mirror
Air
SF6

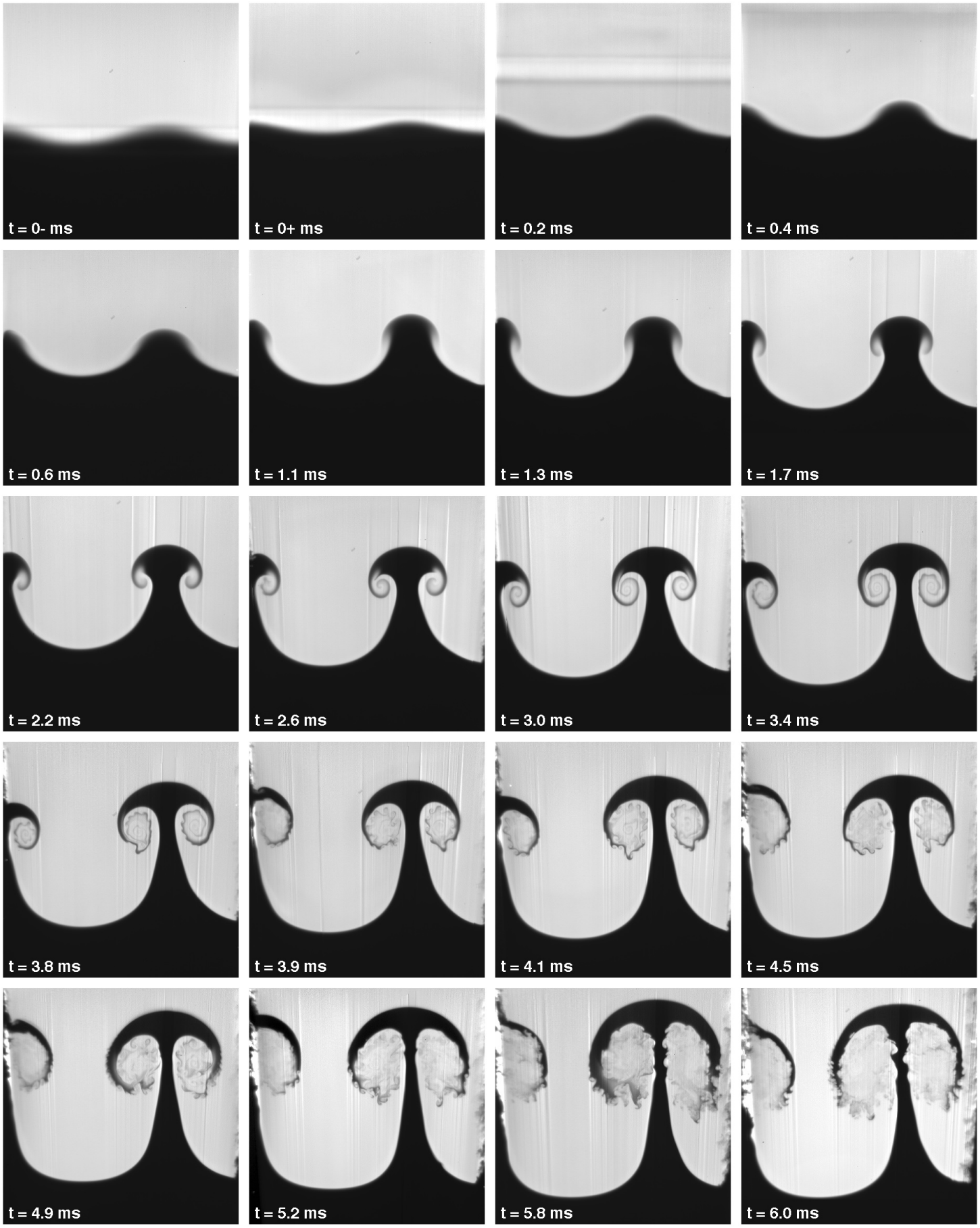
t = 0- ms
t = 0+ ms
t = 0.2 ms
t = 0.4 ms
t = 0.6 ms
t = 1.1 ms
t = 1.3 ms
t = 1.7 ms
t = 2.2 ms
t = 2.6 ms
t = 3.0 ms
t = 3.4 ms
t = 3.8 ms
t = 3.9 ms
t = 4.1 ms
t = 4.5 ms
t = 4.9 ms
t = 5.2 ms
t = 5.8 ms
t = 6.0 ms

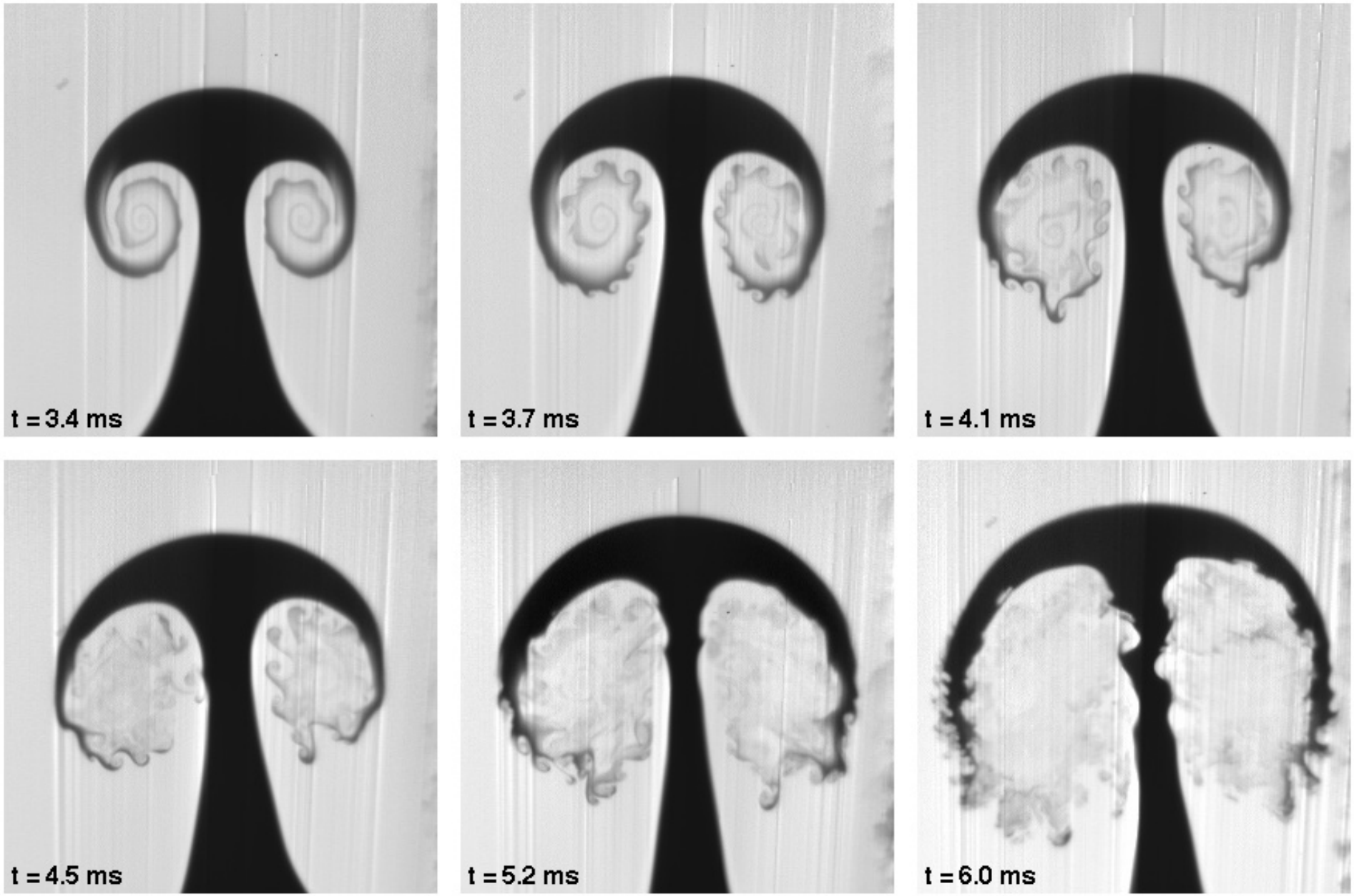
t = 3.4 ms
t = 3.7 ms
t = 4.1 ms
t = 4.5 ms
t = 5.2 ms
t = 6.0 ms

Reynolds Number

$$\mathrm{Re} = \frac{U\ell}{\nu}$$

Let, $\ell \sim h = 2a$, $U \sim \frac{dh}{dt}$, $\nu =$ average viscosity

At time of transition,

$$\mathrm{Re} \sim \frac{h\dot{h}}{\nu} \approx 50{,}000$$

Alternatively let, $\mathrm{Re} = \frac{\Gamma}{\nu}$

Linear stability theory gives, $\Gamma = \frac{2}{\pi}\lambda \dot{a}_0$

Then,

$$\mathrm{Re} = \frac{2}{\pi}\frac{\lambda \dot{a}_0}{\nu} \approx 42{,}000$$

Nonlinear Models

Zhang & Sohn (1997)

$$v_{b/s} = \frac{v_0}{1 + v_0 a_0 k^2 t + \max\left[0,\ a_0^2 k^2 - A^2 + \frac{1}{2}\right] v_0^2 k^2 t^2} \mp \frac{A v_0^2 k t}{1 + 2k^2 a_0 v_0 t + 4k^2 v_0^2 \left[a_0^2 k^2 + \frac{1}{3}(1 - A^2)\right] t^2}$$

when $A^2 \le \frac{1}{2} + a_0^2 k^2$

$$v = \tfrac{1}{2}(v_b + v_s) \to \frac{v_0}{\left[a_0^2 k^2 - A^2 + \frac{1}{2}\right] v_0^2 k^2 t^2} \quad \frac{1}{t^2} \quad \text{as} \quad t \to \infty$$

Sadot el al. (1998)

$$v_{b/s} = \frac{v_0 (1 + v_0 k t)}{1 + (1 \pm A) v_0 k t + \left[\frac{1 \pm A}{1 + A}\right] \frac{1}{2\pi C} v_0^2 k^2 t^2}$$

where

$$C = \begin{cases} 1/3\pi & A \ge 0.5 \\ 1/2\pi & A \to 0 \end{cases}$$

$$v \to \left(\frac{1}{1 - A}\right) \frac{C\lambda}{t} \quad \frac{1}{t} \quad \text{as} \quad t \to \infty$$

Late Time Growth

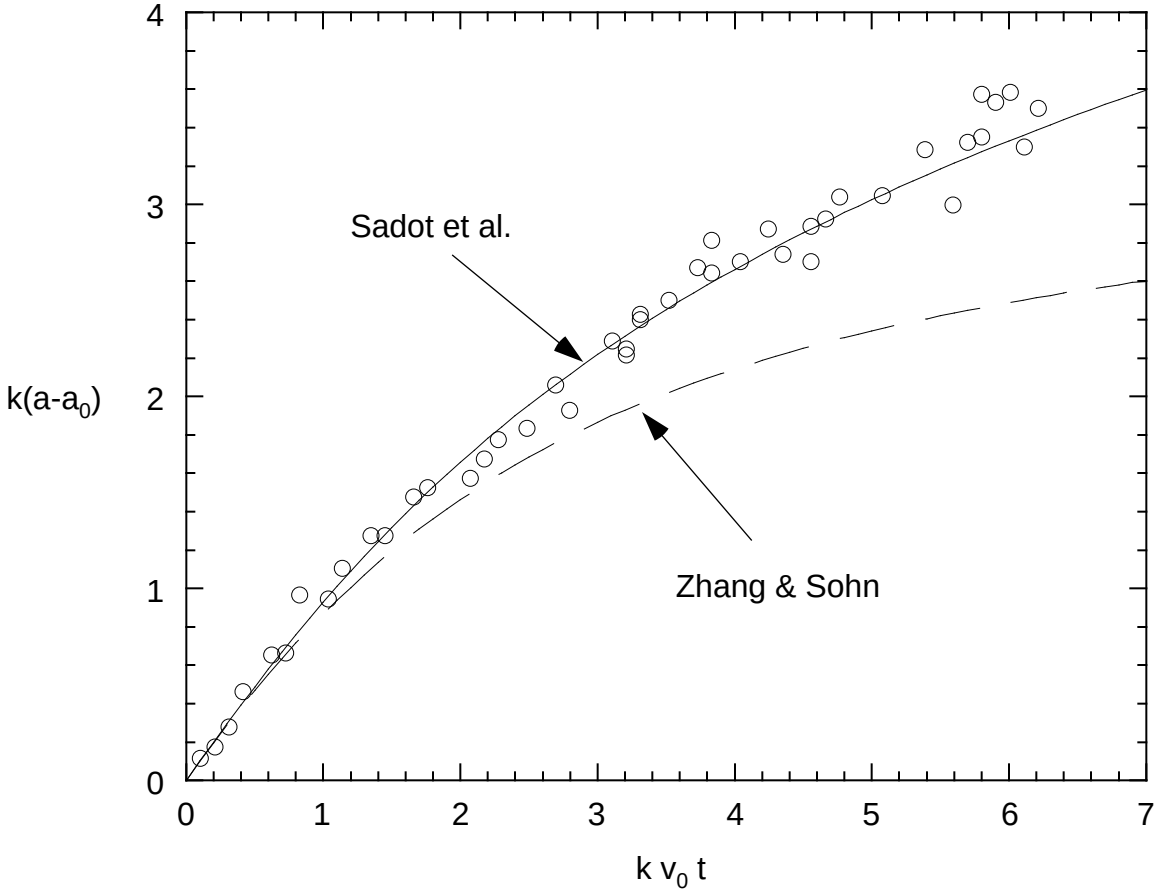

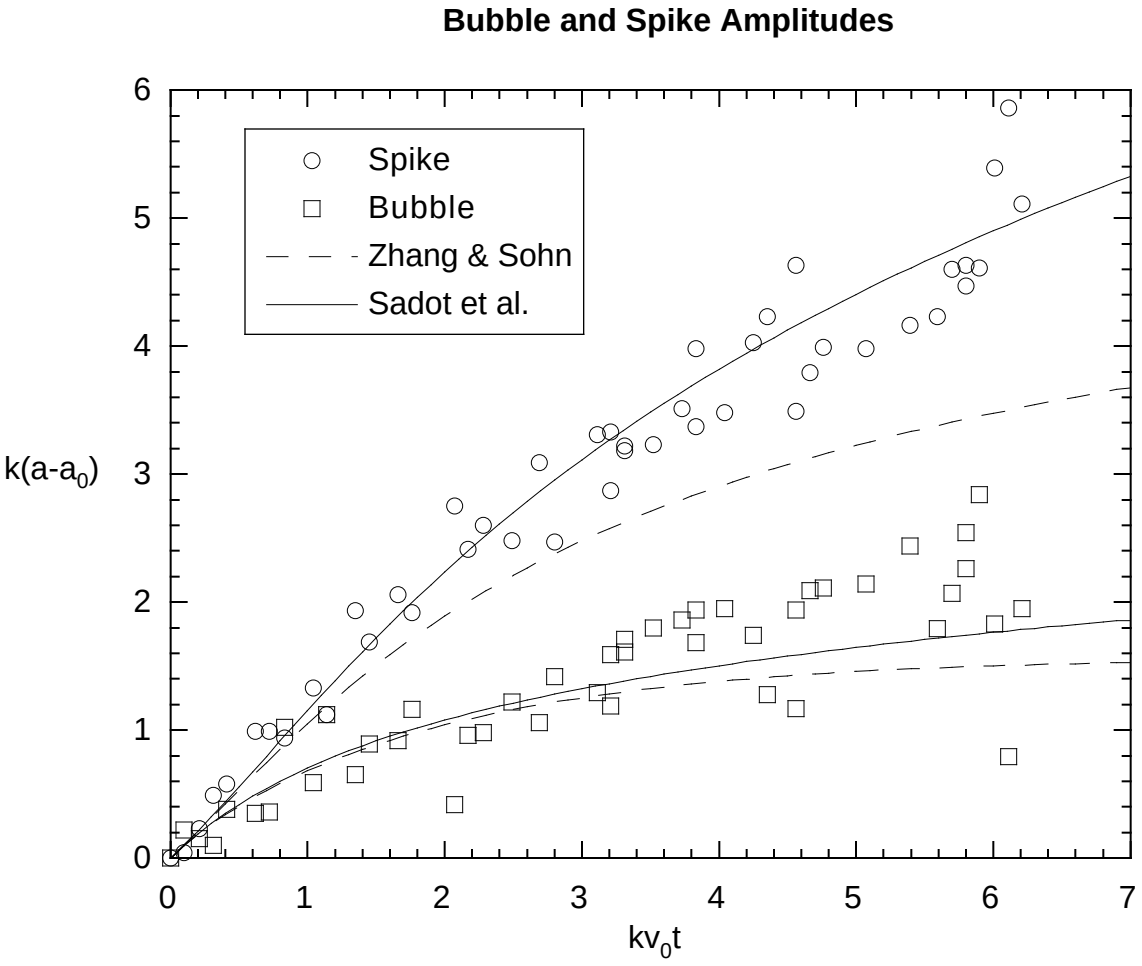
Bubble and Spike Amplitudes
Spike
Bubble
Zhang & Sohn
Sadot et al.
k(a-a0)
kv0t
0
1
2
3
4
5
6
7

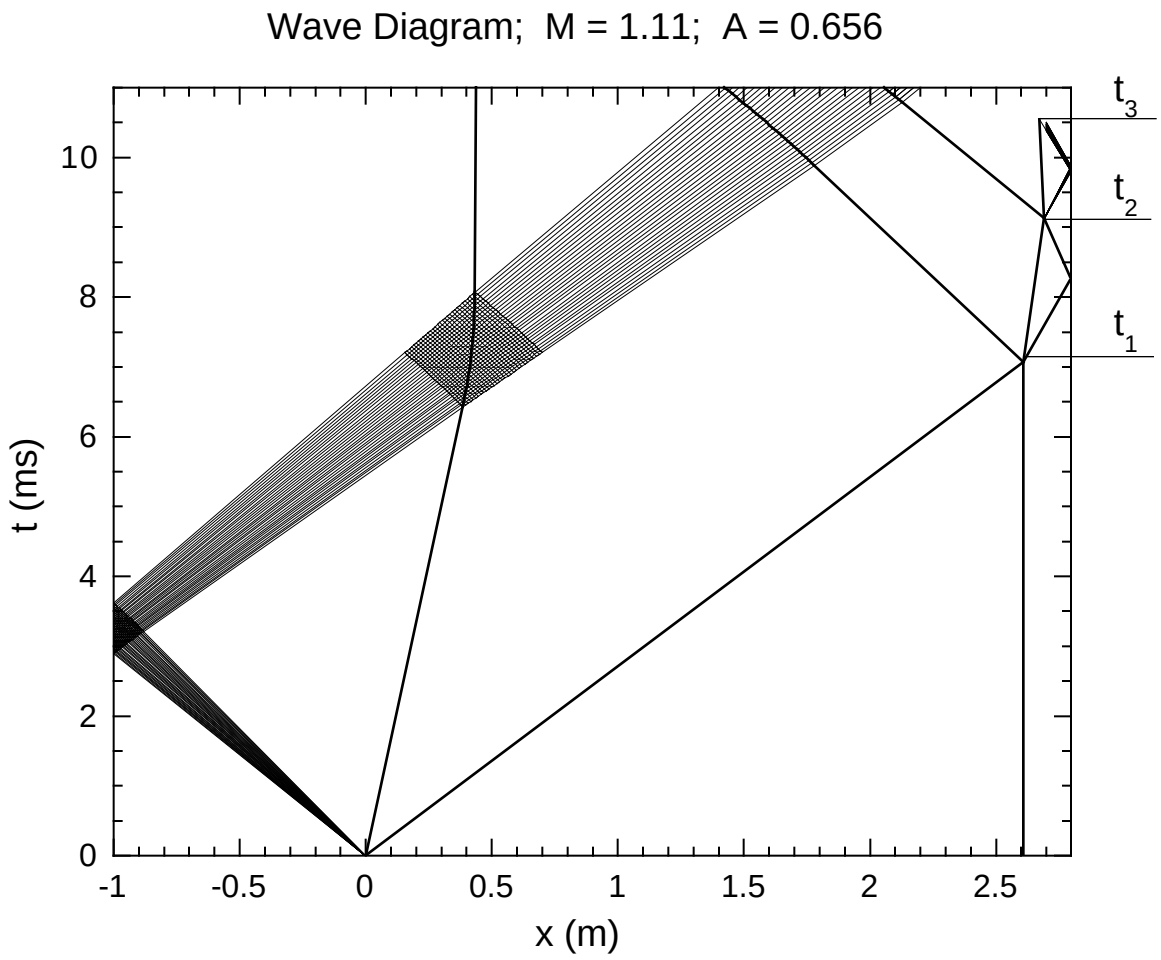
Wave Diagram; M = 1.11; A = 0.656
t (ms)
x (m)
0
2
4
6
8
10
-1
-0.5
0
0.5
1
1.5
2
2.5
t3
t2
t1

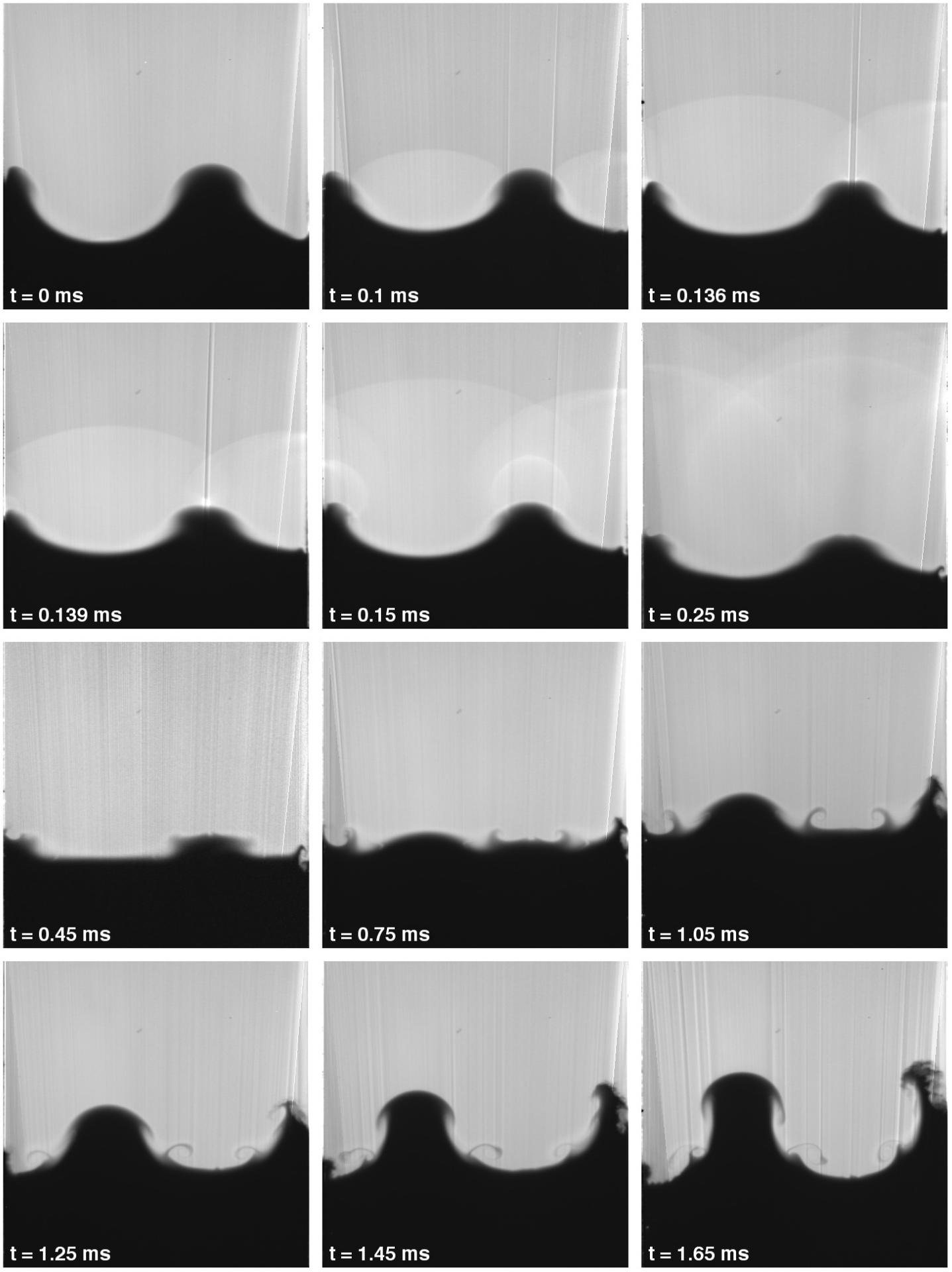
t = 0 ms
t = 0.1 ms
t = 0.136 ms
t = 0.139 ms
t = 0.15 ms
t = 0.25 ms
t = 0.45 ms
t = 0.75 ms
t = 1.05 ms
t = 1.25 ms
t = 1.45 ms
t = 1.65 ms

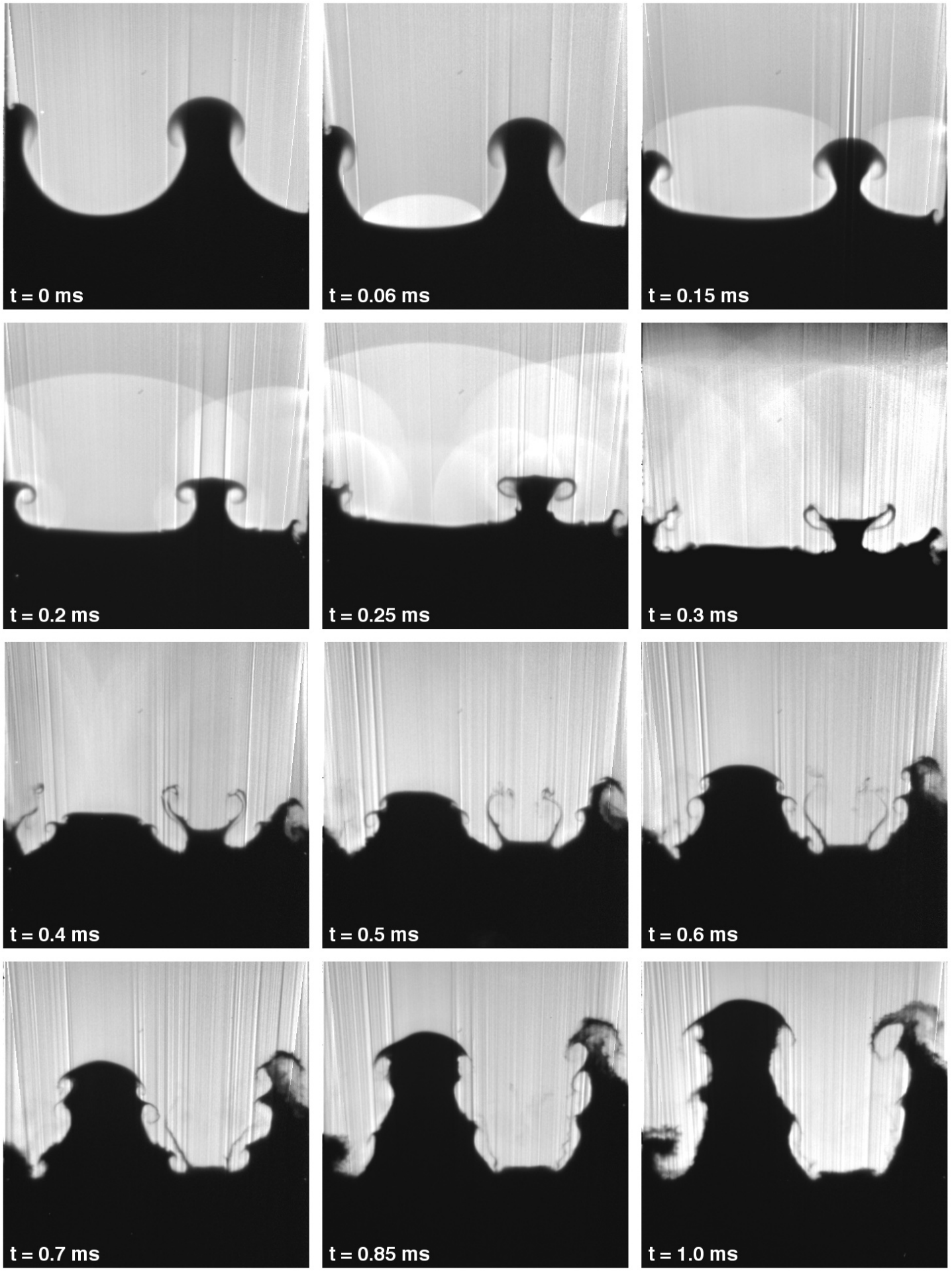
t = 0 ms
t = 0.06 ms
t = 0.15 ms
t = 0.2 ms
t = 0.25 ms
t = 0.3 ms
t = 0.4 ms
t = 0.5 ms
t = 0.6 ms
t = 0.7 ms
t = 0.85 ms
t = 1.0 ms

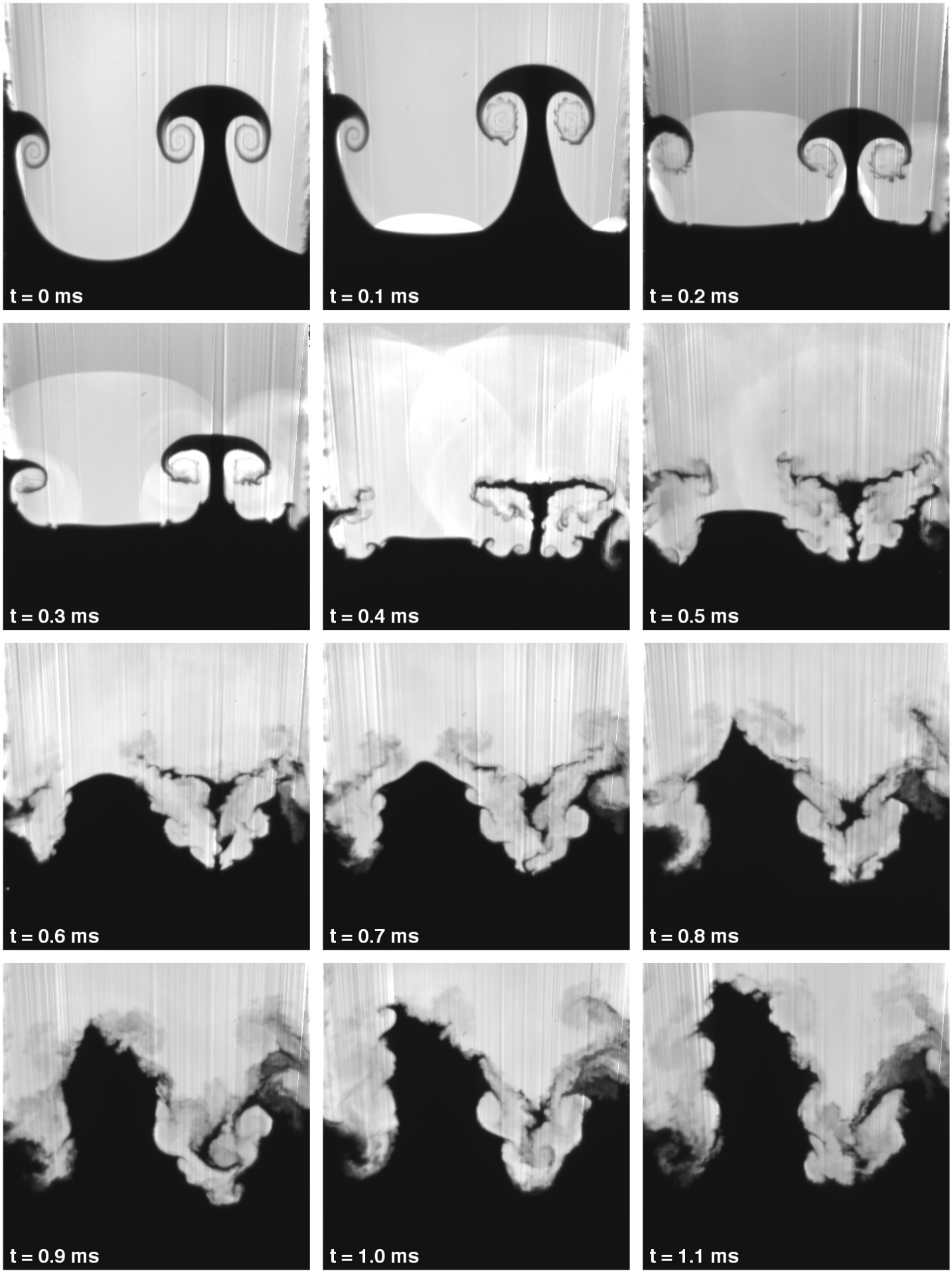
t = 0 ms
t = 0.1 ms
t = 0.2 ms
t = 0.3 ms
t = 0.4 ms
t = 0.5 ms
t = 0.6 ms
t = 0.7 ms
t = 0.8 ms
t = 0.9 ms
t = 1.0 ms
t = 1.1 ms

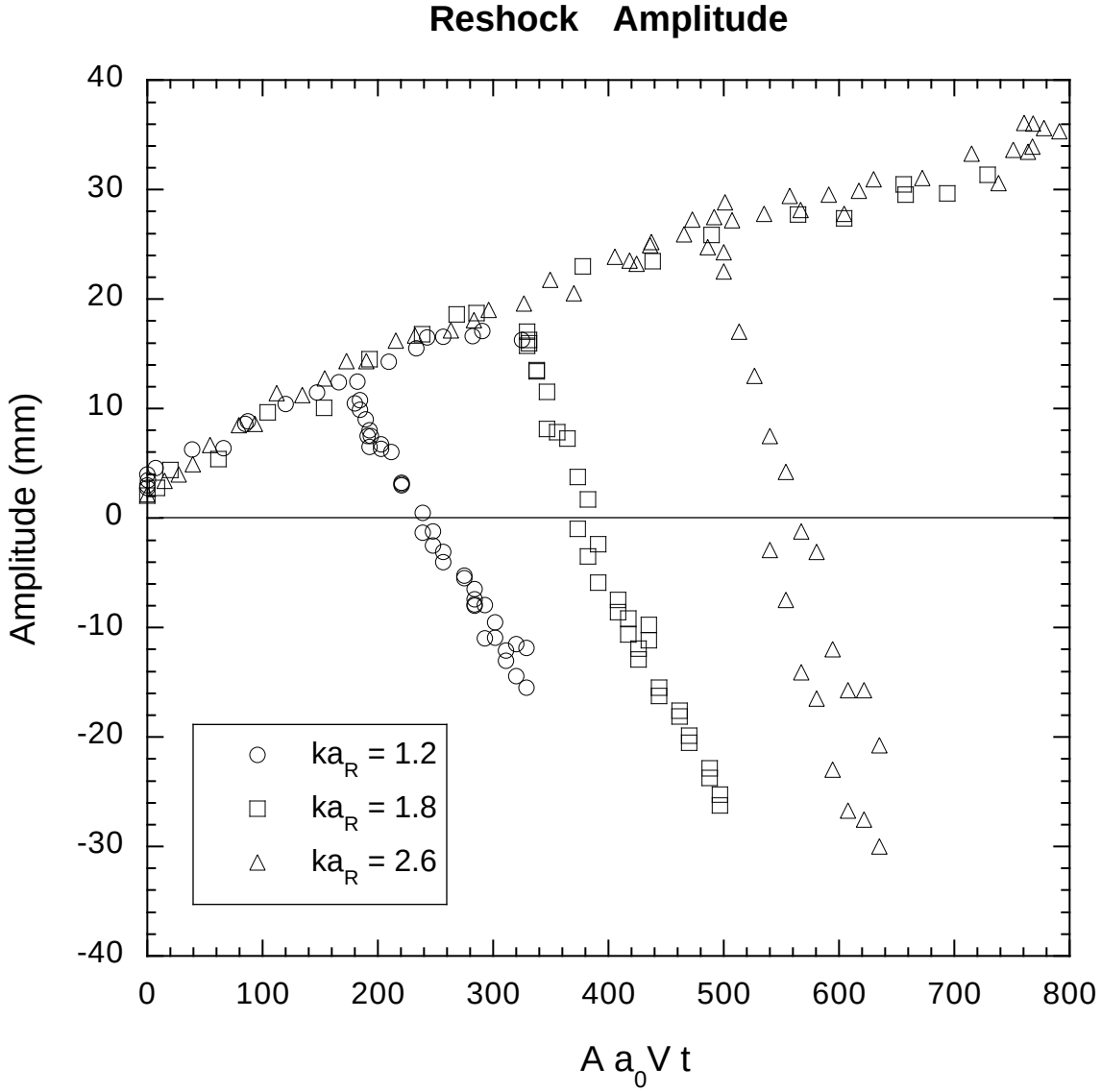
Reshock Amplitude
Amplitude (mm)
40
30
20
10
0
-10
-20
-30
-40
0
100
200
300
400
500
600
700
800
A a0 V t
kaR = 1.2
kaR = 1.8
kaR = 2.6

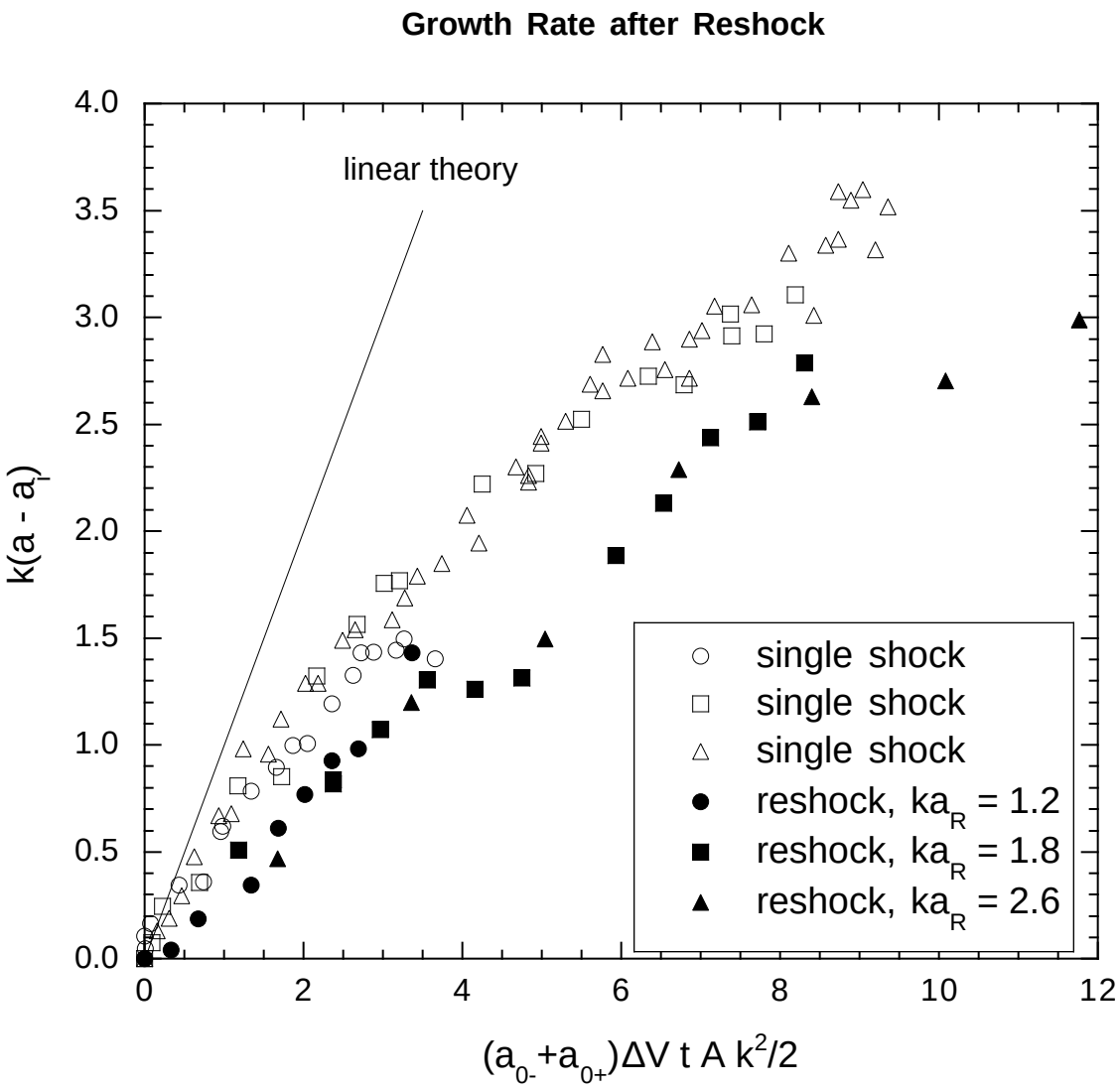
Growth Rate after Reshock
linear theory
single shock
single shock
single shock
reshock, ka$_R$ = 1.2
reshock, ka$_R$ = 1.8
reshock, ka$_R$ = 2.6
k(a - a$_i$)
(a$_{0-}$+a$_{0+}$)ΔV t A k^2/2
0.0
0.5
1.0
1.5
2.0
2.5
3.0
3.5
4.0
0
2
4
6
8
10
12

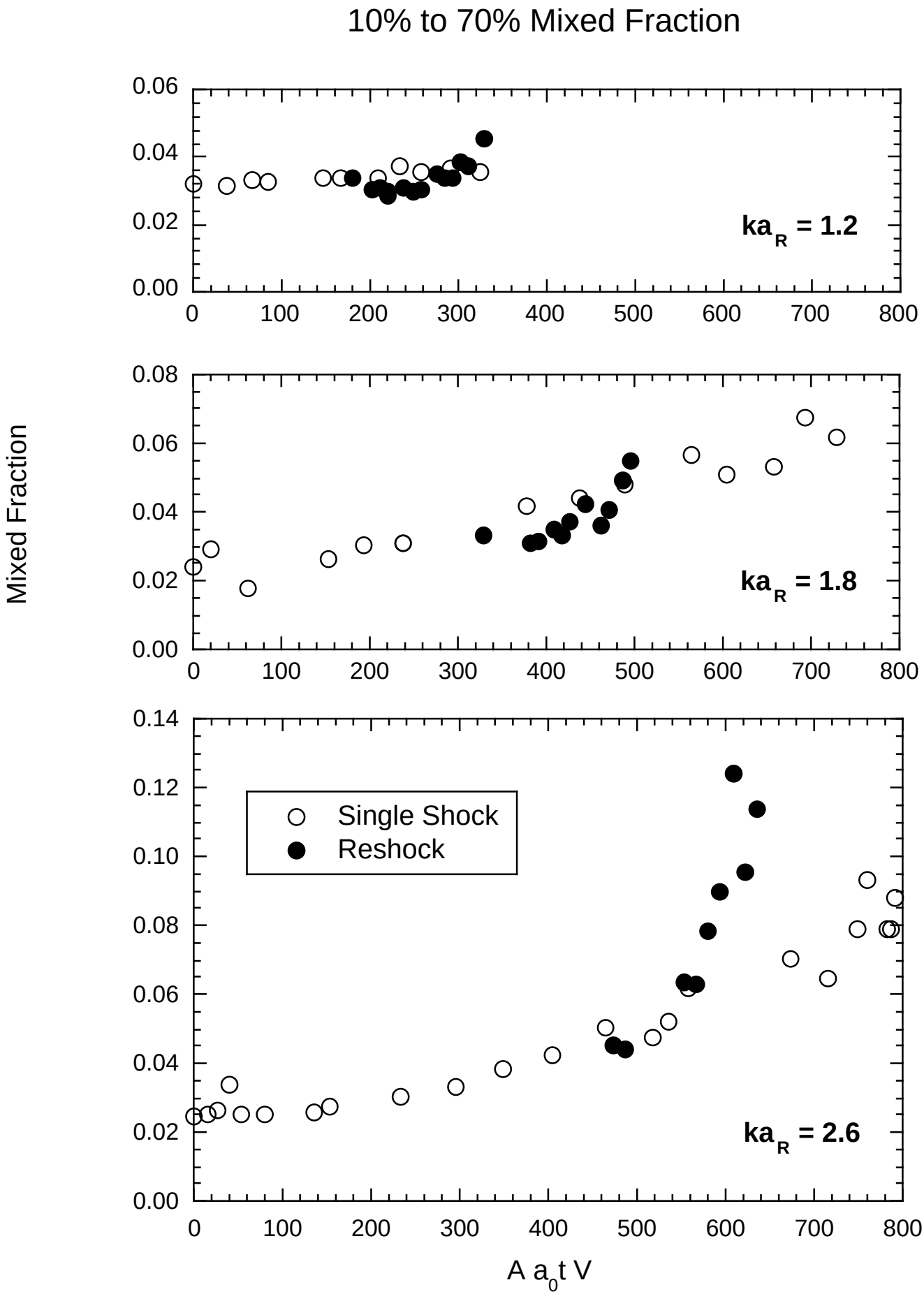
10% to 70% Mixed Fraction
Mixed Fraction
0.06
0.04
0.02
0.00
0
100
200
300
400
500
600
700
800
ka$_R$ = 1.2
0.08
0.06
0.04
0.02
0.00
ka$_R$ = 1.8
0.14
0.12
0.10
0.08
0.06
0.04
0.02
0.00
Single Shock
Reshock
ka$_R$ = 2.6
A a$_0$ t V

Conclusions

- Single-mode RM experiments show a transition to turbulence in the vortex cores at Re ≈ 50,000.
- Late-time amplitude measurements show excellent agreement with the model of Sadot et al. (1998).
- Penetration depth measurements for the three reshock conditions collapse when plotted in dimensionless form and have a growth rate approximately 1/3 that given by linear stability theory.
- Reshock at early stages of the instability show similar evolution to that of single interaction with little increase in the mixing rate.
- Reshock at late stages of the instability produces a complex interface pattern and a significant increase in the mixing rate.

Laser-based high-pressure, high-strain-rate materials experiments

Daniel H. Kalantar - Lawrence Livermore National Laboratory

Presented by Thomas Lorenz

8th International Workshop on the Physics of Compressible Turbulent Mixing
Pasedena, CA - December 9-14, 2001

J. Belak, J. D. Colvin, M. Kumar, K. T. Lorenz, K. O. Mikaelian, S. Pollaine, B. A. Remington,
S. V. Weber, L. G. Wiley (LLNL),
J. S. Wark, A. Loveridge, A. M. Allen (University of Oxford), M. A. Meyers, M. Schneider (UCSD)

This work was performed under the auspices of the US DOE by UC LLNL under contract No. W-7405-48-Eng.
Supported in part through the Science Use of Nova Program, DOE Grants program, and NLUF program (OMEGA).

Outline

- Introduction
  - Solid-state experiments at high pressure on a laser
- High pressure strength
  - RT instability in solid Al at high pressure to infer Y(P)
- Dynamic material response
  - Dynamic x-ray diffraction of the lattice level response in Si and Cu
- Wave profile and residual deformation
  - VISAR measurement, sample recovery and characterization

The high pressure response of materials is of interest for many reasons; lasers provide a way to access high pressures and strain rates

- The core of the earth is Fe at 3 Mbar, both solid and liquid
  - Long time scale, diamond anvil experiments
- Survivability of passengers in a car crash depend on the material response of the car
  - ms-μs time scale, Hopkinson bar and gun experiments
- Space station wall integrity from space debris, dust, micro-asteroids
  - μs time scale, gun and high explosives experiments

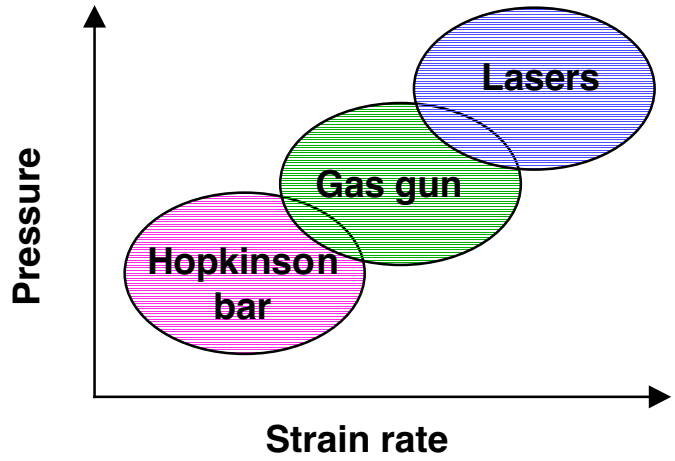

Lasers access unique high pressure, high strain rate regime of material response to test the limits of theories and scaling laws

Example - strength measurements at high pressure using a high explosive drive and modulated Al plate

- Shockless HE drive used to compress and accelerate a plate with pre-imposed modulations
- Pre-imposed modulations grow by the Rayleigh-Taylor instability
- The growth is reduced from classical (fluid) due to material strength

Al plate experiment

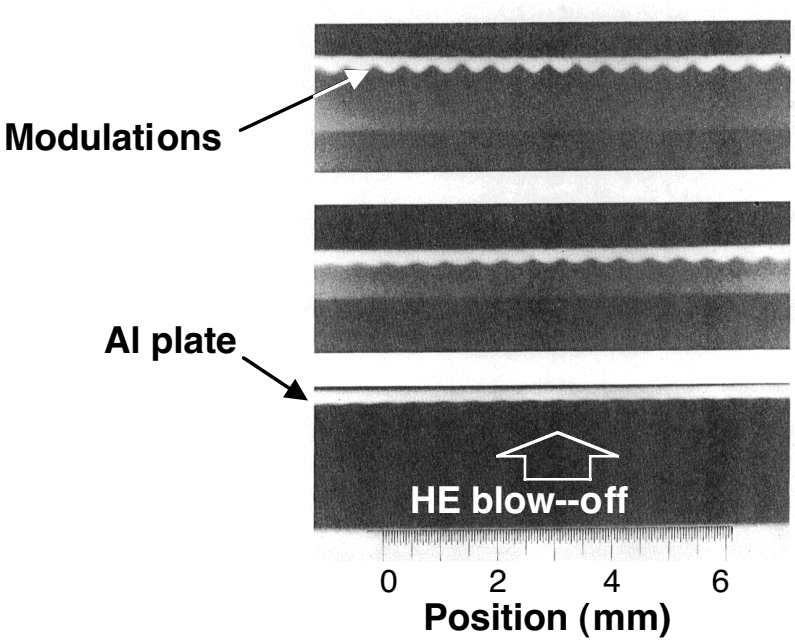

Growth is reduced from fluid

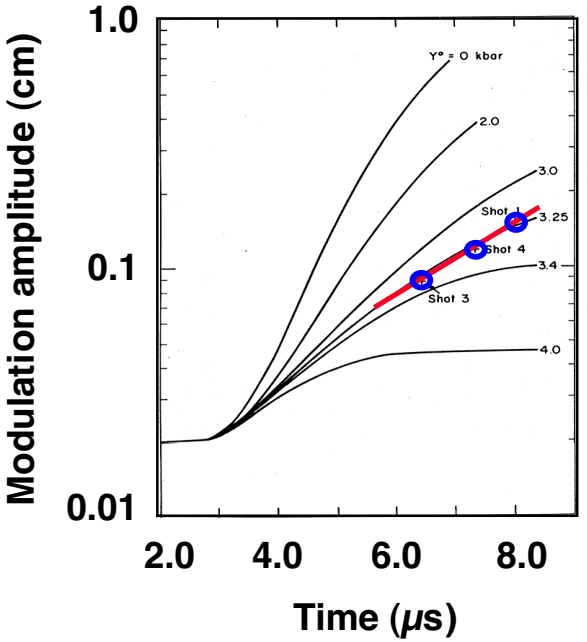

Barnes *et al*, J. Appl. Phys. 45, 727 (1974).

Also Rayevsky and Lebedev

1. Solid state RT instability experiment

- An internally shielded hohlraum is used to shock compress an Al-6061 metal foil at high pressure
- Internal shields block hard x-rays from preheating package
- A shaped laser pulse generates a series of gentle shocks for nearly isentropic compression

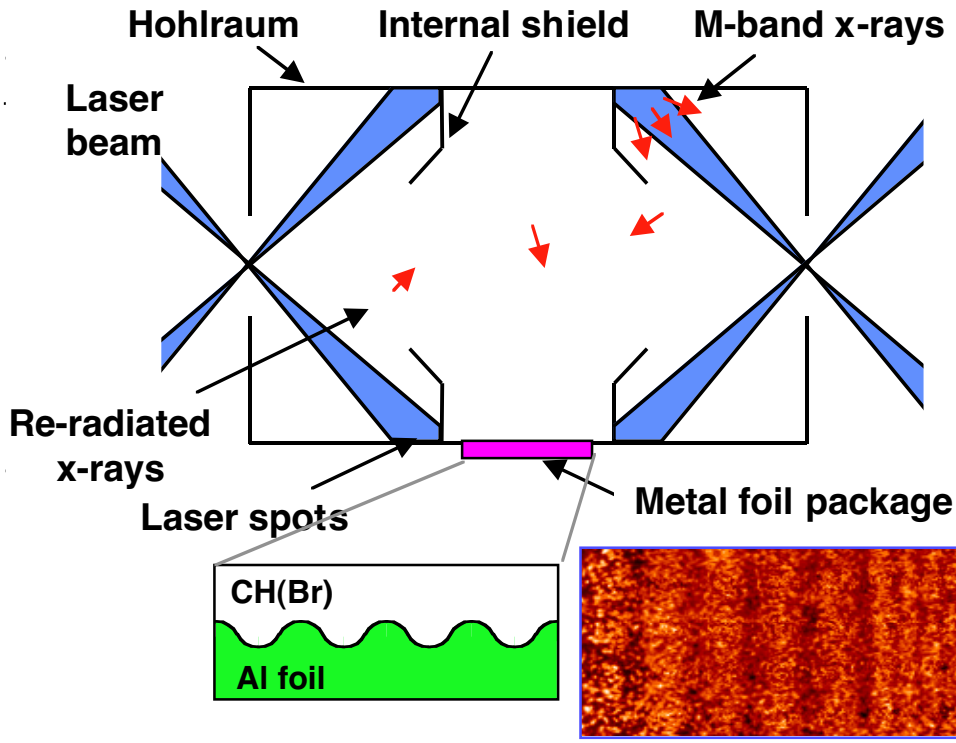

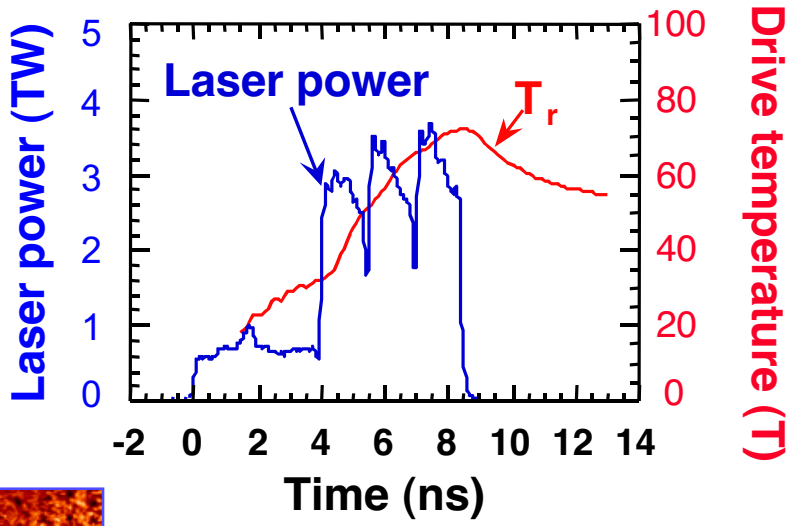

Detailed simulations predict that the Al foil remains solid throughout the experiment

- The Al remains below the melt curve
- The foil trajectory is nearly isentropic to 1.8 Mbar

Lindemann melt model $T_m = T_{m_o} e^{2a(1-\eta)} \eta^{2(\gamma_o - a - 1/3)}$

Pressure and temperature at the embedded interface

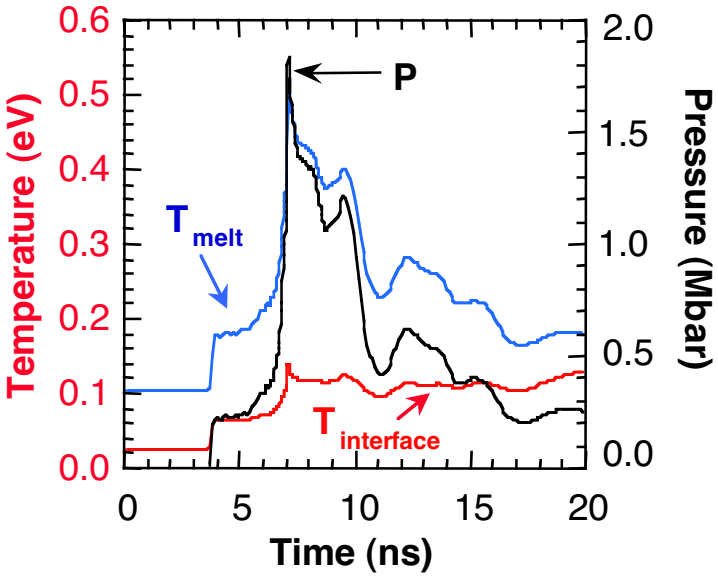

Calculated internal energy trajectory

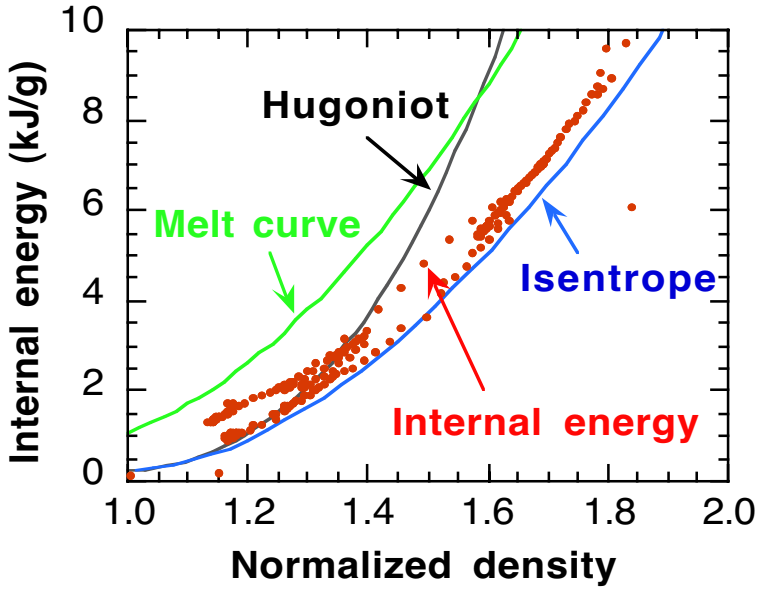

Simulations of the instability growth demonstrate sensitivity to the strength of the Al

- Growth rates with strength are expected to be reduced from classical (fluid)

Steinberg-Guinan constitutive model

$$Y = Y_o\left(1+\beta\left(\varepsilon+\varepsilon_i\right)\right)^n \frac{G(P,T)}{G_o}$$

$$G = G_o\left(1+\left(\frac{G'_P}{G_o}\right)\frac{P}{\eta^{1/3}}-\left(\frac{G'_T}{G_o}\right)(T-300)\right)$$

Rayevsky Stability boundary formula

$$\eta_c = \eta_D\left[1-0.86e^{-\frac{2\pi H}{\sqrt{3}\lambda}}\right]\left\{\left[1-e^{-\frac{2\pi H}{\sqrt{3}\lambda}}\right]^2-\left[\frac{\lambda}{\lambda_M}\right]^2\right\}$$

$$\eta_D = \frac{2Y}{\rho g} \qquad \lambda_M = \frac{4\pi G}{\rho g}$$

Predicted growth factors λ=20 μm

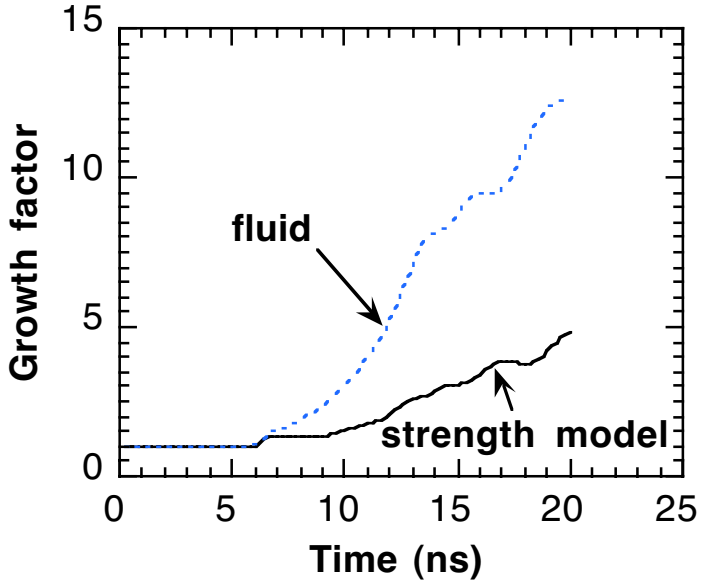

Stability curve (Nizovtsev and Rayevsky, 1991)

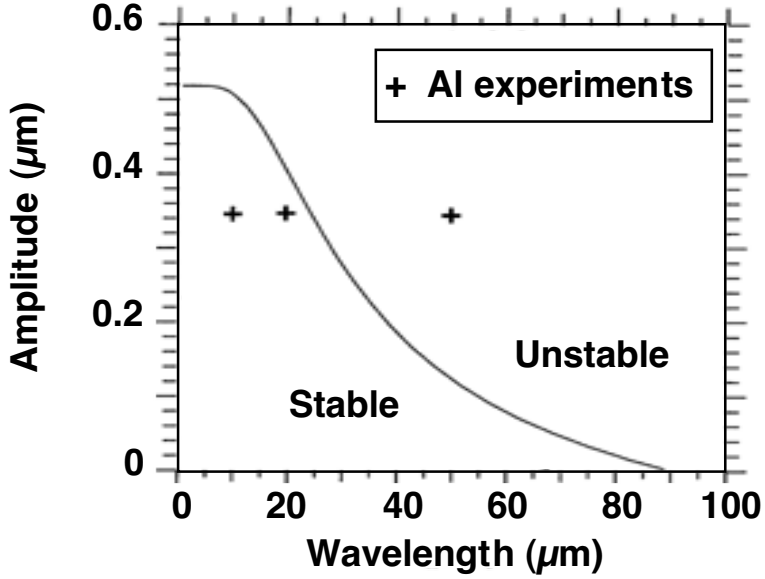

The RT growth is nearly fluid at early times, but it is suppressed at later times

- Experiments were conducted with 10, 20 and 50 μm wavelengths
- Modeling was done assuming the following:
  - Fluid
  - Nominal Steinberg-Guinan
  - Fluid until 13 ns, then S-G with theoretical maximum Y=G/10

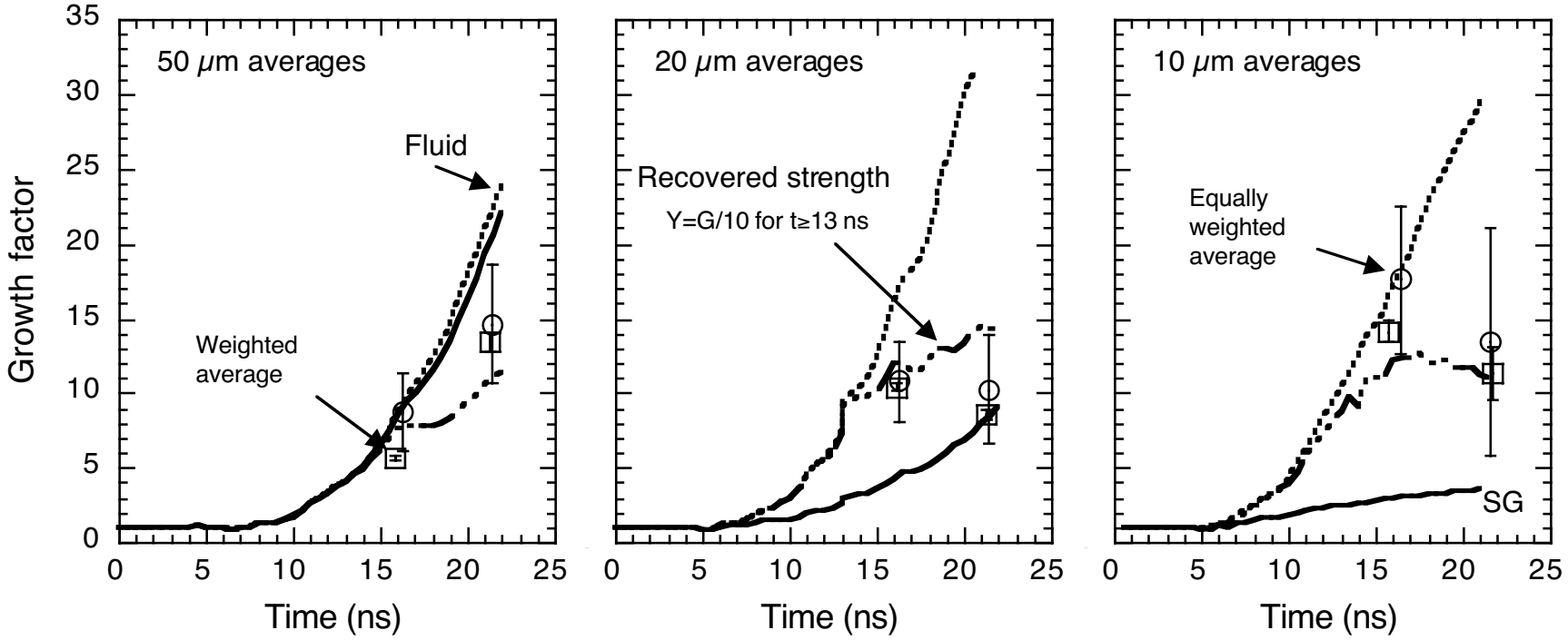

The RT growth is nearly fluid at early times, but it is suppressed at later times; suggestive of model from Grady/Asay and data by Rayevsky and Lebedev

- High pressure strain causes localized heating and softening in shear bands; bulk Al flows as fluid due to localized deformation
- As heat conducts into the bulk material, the metal regains bulk solid strength and continued growth is inhibited

Optical emission from shocked quartz

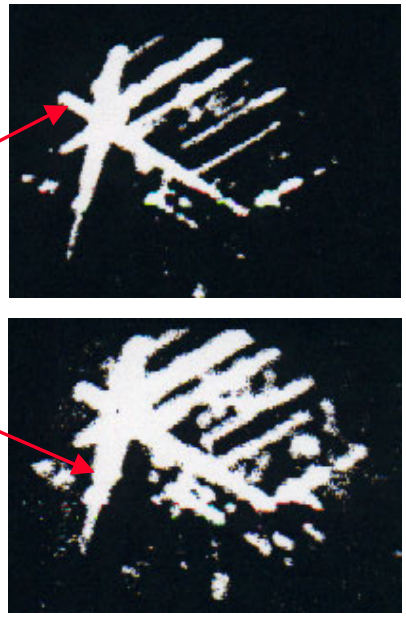

Brannon *et al*, SCCM 1983.

Shocked HE experiments show fluid-like response with saturation

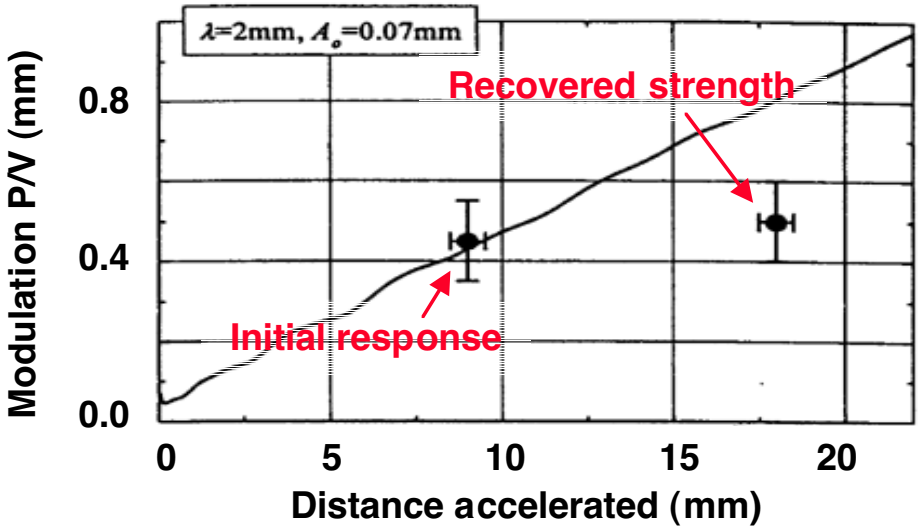

Rayevsky *et al*, IWPCTM, 1999.

The late time images show features that may be due to hydrodynamic imprinting of the grain structure

- The spatial scale of the late-time modulation is similar to initial grain structure
- 2D simulations incorporating the grain boundaries start to show effects at t=18 ns, 3D simulation has been started

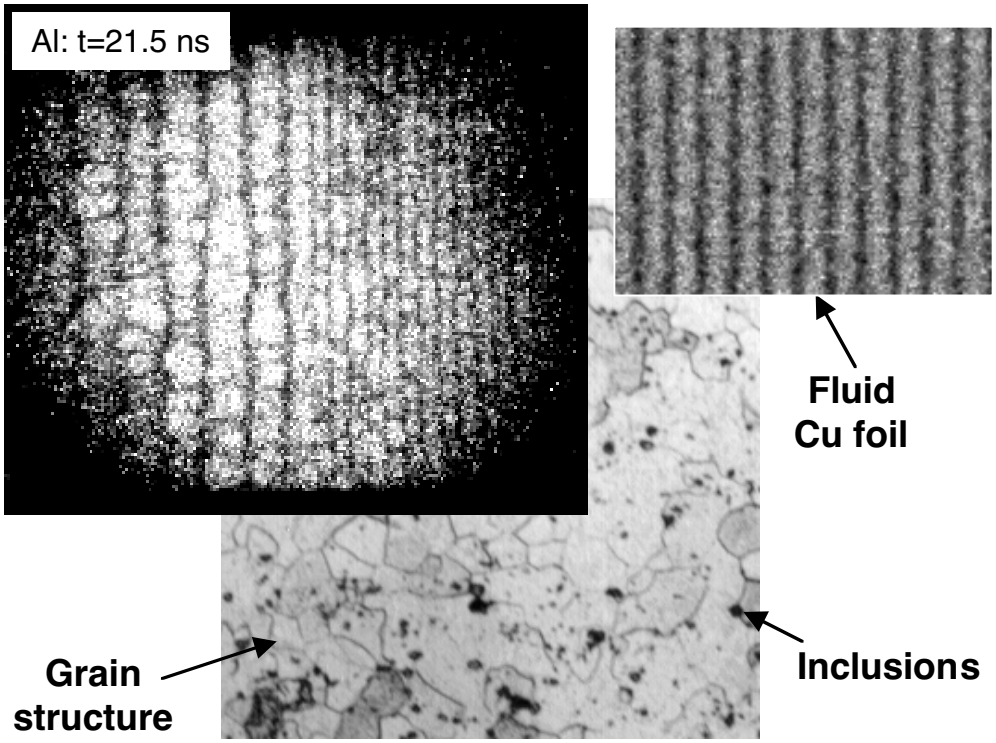

2D simulation including grain structure

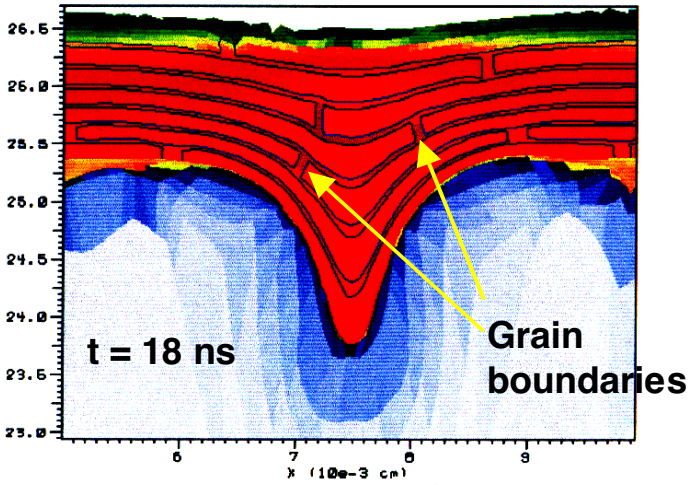

$Y_{grain} = Y_{SG}$ $Y_{boundary} = 0$

Simulations by G. Bazan, 2001

2. Dynamic x-ray diffraction

- *In situ* x-ray diffraction probes the long range lattice order under shock compression
- Shock pressure generated using a hohlraum x-ray drive or by direct laser irradiation
- Time-resolution with x-ray streak cameras provides information on dynamic lattice response

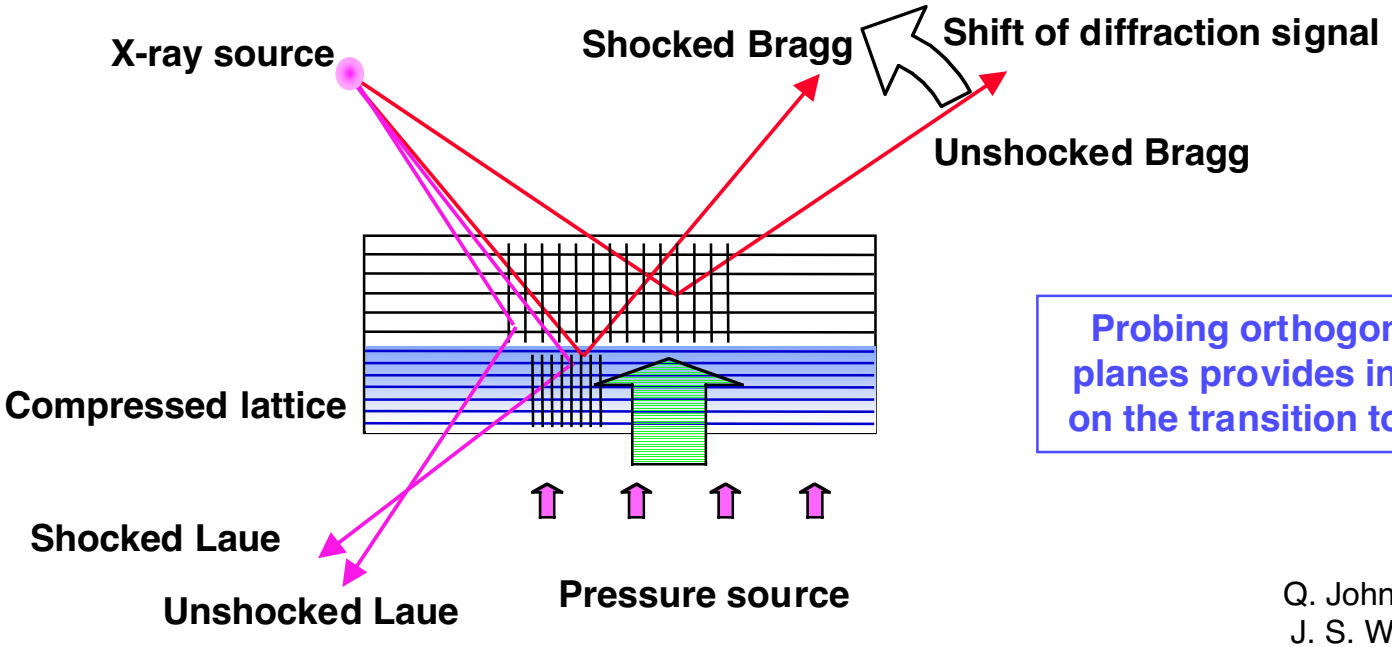

Probing orthogonal lattice planes provides information on the transition to plasticity

Q. Johnson *et al*, 1970;
J. S. Wark *et al*, 1989.

Simultaneous measurements of orthogonal planes indicates Si responds uniaxially on a ns time scale

- 40 μm thick Si shocked along (100) axis
- P=115-135 kbar; HEL=84 kbar

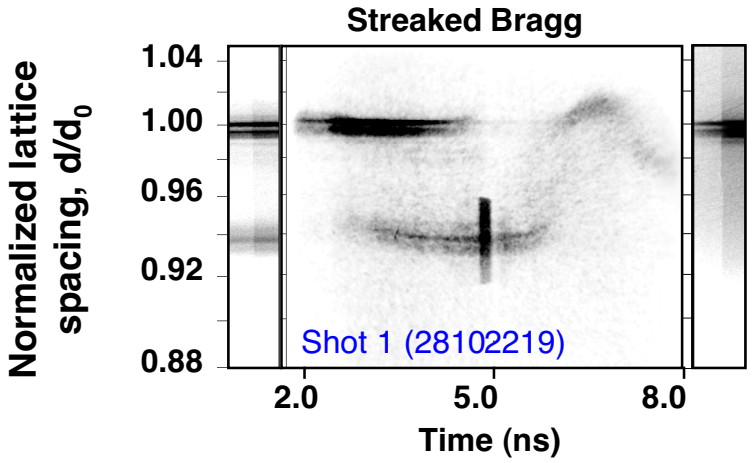

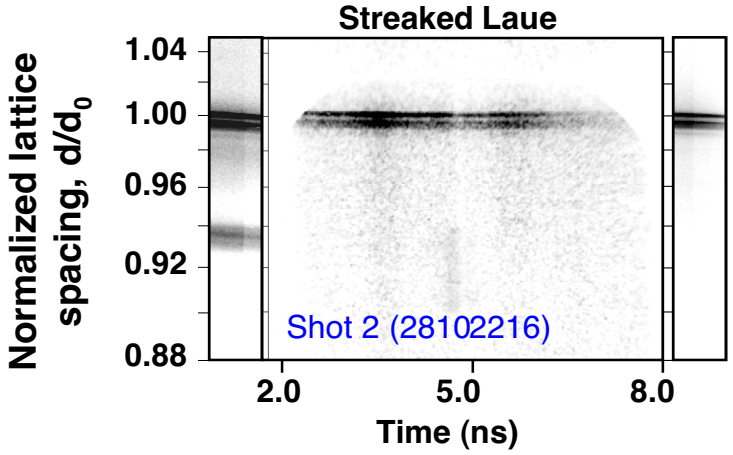

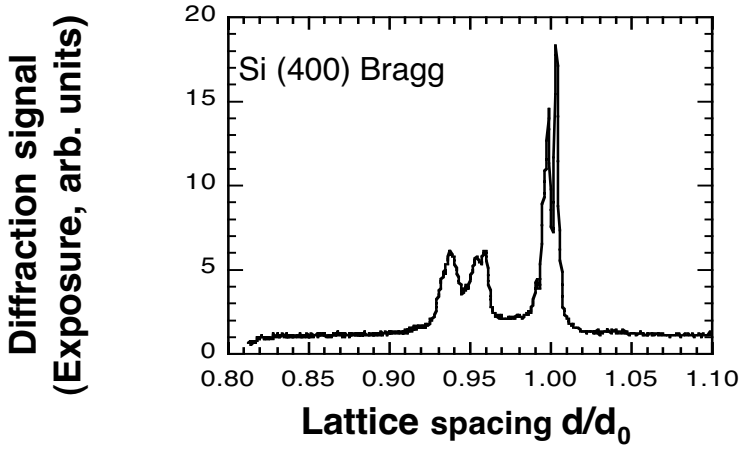

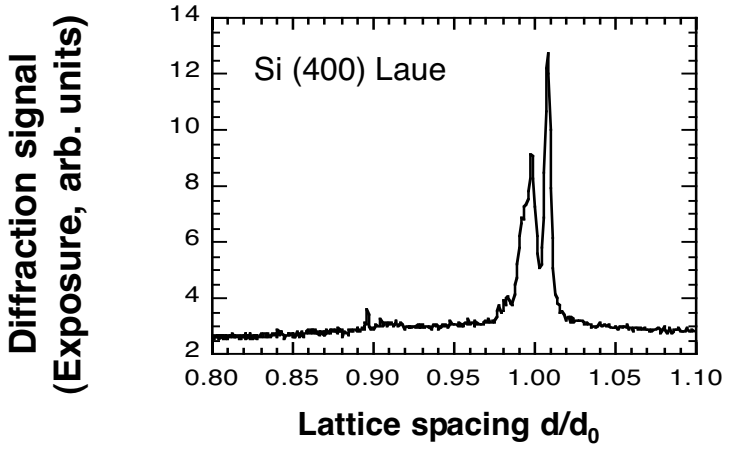

Cu undergoes a transition to 3D lattice compression at high pressure

- 8 μm single crystal Cu shocked along (100) axis
- P = 180 kbar; HEL ~ 2 kbar

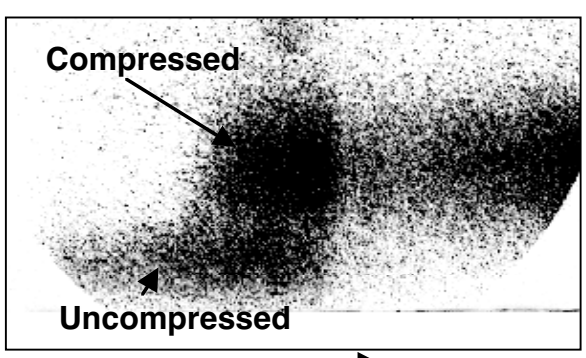

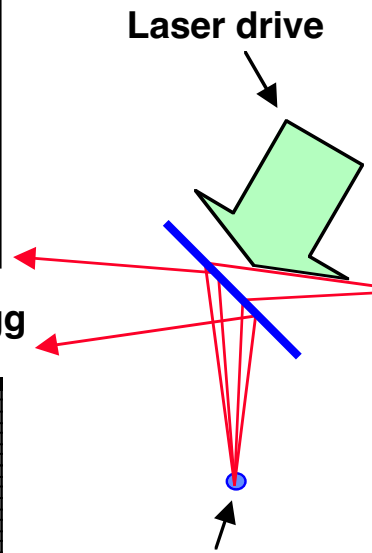

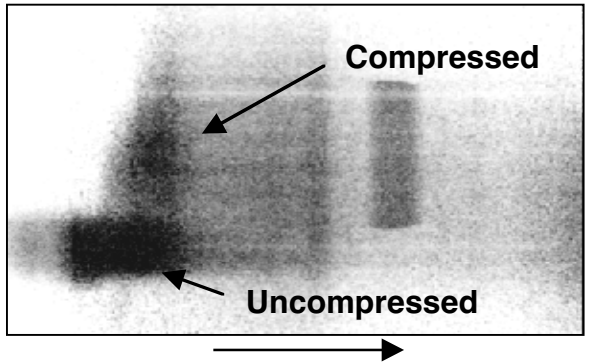

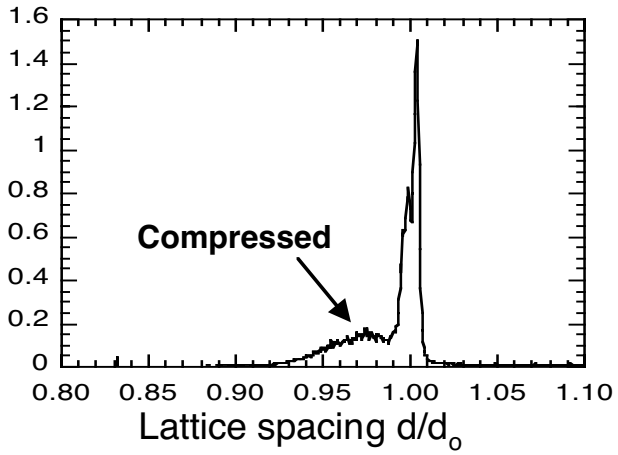

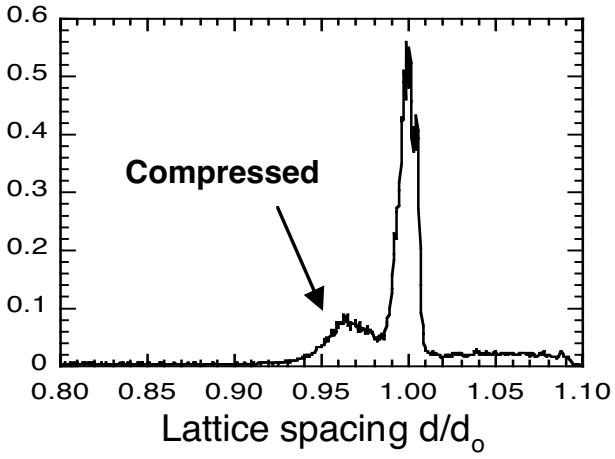

The timescale for plastic deformation in Si is much longer than for Cu based on Orowan's equation

Orowan equation: $\frac{\Delta\varepsilon}{\Delta t} = N\,|\mathbf{b}|\,\mathbf{v}$

Silicon

- **$\Delta t > 1\ \mu s$: dislocations do not move**
  - —5% strain, dislocations separated by at least the Burger's vector (3.8 Å) (diffraction linewidth indicates $N < 10^{14}\ m^{-2}$)
  - —Linear extrapolation of dislocation velocity in Si (0.1 mm/s)

Copper

- **$\Delta t < 10$ ps : dislocations do move**
  - —5% strain, dislocations separated by at least the Berger's vector (2.5 Å)
  - —Velocity of dislocations calculated to be 400 m/s in MD simulations

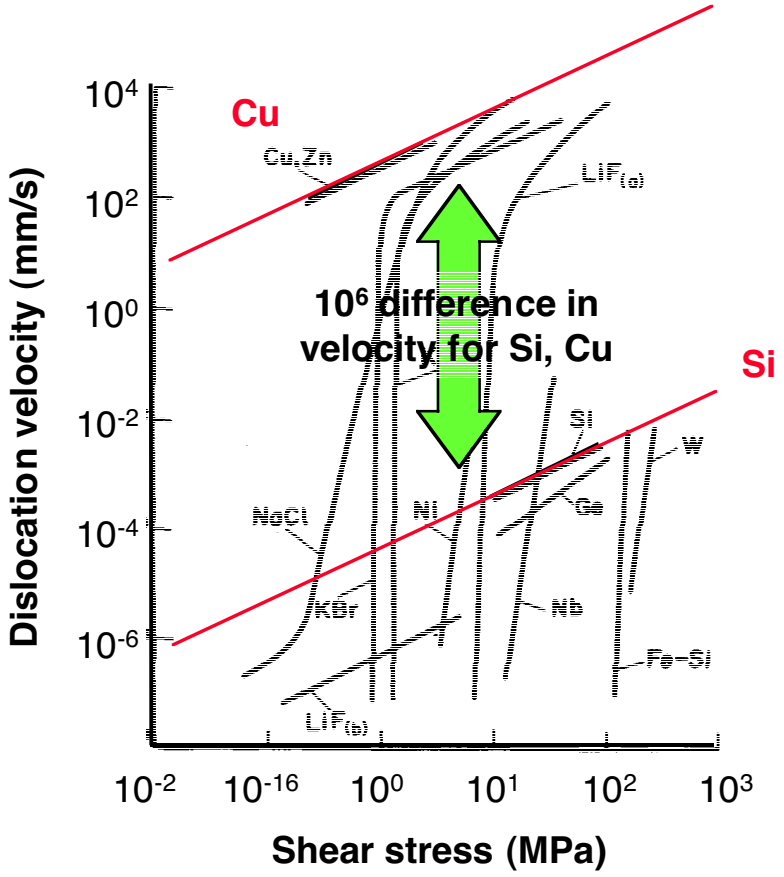

Introduction to Dislocations, Hull and Bacon (Fig. 3.12)

The time scale for plastic deformation in Si is much longer than for Cu, due to its high Peierls barrier and activation energy

- For $\sigma < Y_P$: thermal activation regime, and

$$t = t_{wait} = \frac{1}{\nu_{attempt} \exp\left[\frac{-\Delta F}{kT}\left(1 - \frac{\sigma}{Y_P}\right)^2\right]}$$

- For $\sigma > Y_P$: phonon drag regime, $t = t_{run} = \frac{aB}{\sigma b}$

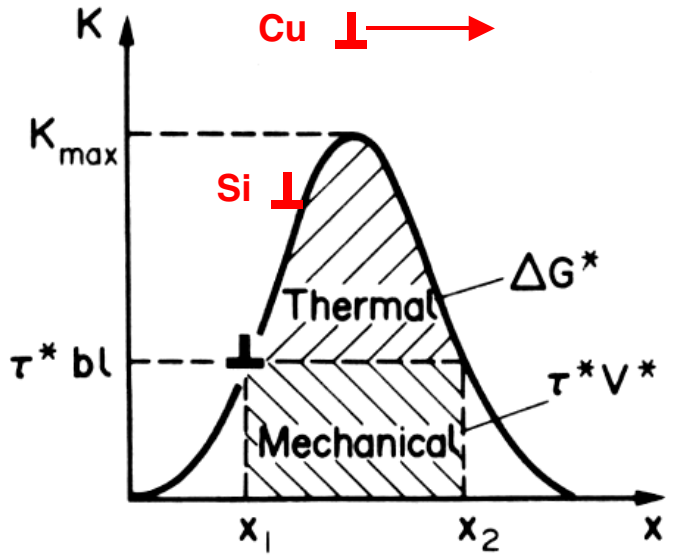

Assume that σ = 3 GPa, and kT = 0.05 eV:

For Si:

$Y_P = 0.07G_0(1+AP/\eta^{1/3}) > 0.07G_0$
giving $Y_P > 0.07$ (63.7 GPa) = 4.5 GPa,
$\Delta F = 0.2Gb^3 = 0.2$ (63.7GPa) (3.83 A)^3 = 4.5 eV

So $\sigma < Y_P$, and kT << ΔF: thermal activ. regime

Assume $\nu_{attempt} = \nu_{Debye}/100 = 10^{11}$ s^{-1} ,
So $1/t_{wait} = (10^{11}$ s$^{-1}) \exp[-(4.5/.05)(1- 3/4.5)^2]$

Giving t_{wait} > ~150 ns, meaning slow

For Cu:

$Y_P = (6.3 \times 10^{-3})G_0(1+AP/\eta^{1/3}) = 0.42$ GPa
So $\sigma > Y_P$, meaning phonon drag regime

Assume B = 10^{-10} MPa·s, and a/b < 10^3,

So $t_{run} < (10^3)(10^{-10}$ MPa·s)/(3 GPa) = 30 ps: fast

A new wide-angle film detector is used to record many more lattice planes

- X-rays diffracted from orthogonal lattice planes are recorded with 2 x-ray streak cameras
- A segmented film assembly records x-rays diffracted over a π-solid angle from many more lattice planes

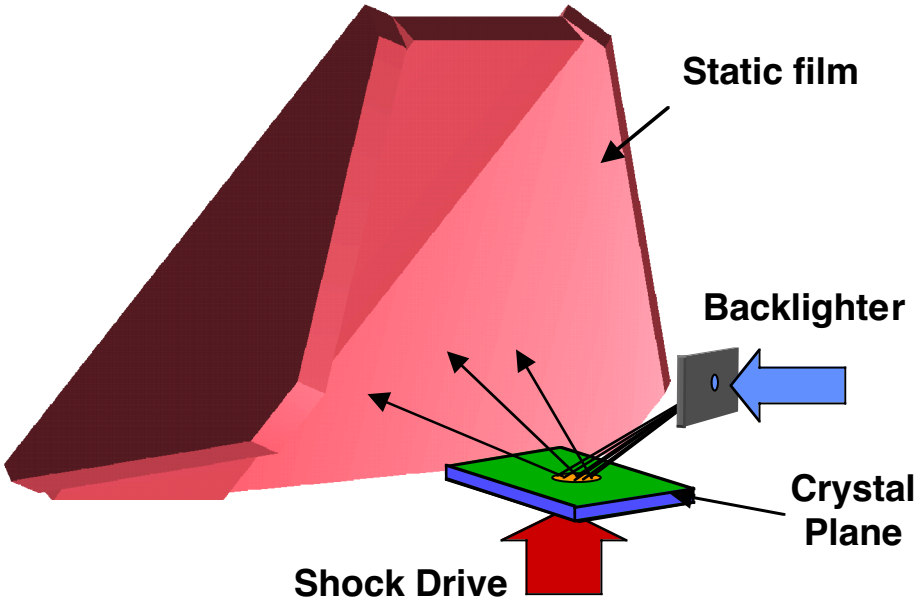

Calculated diffraction pattern from static Cu

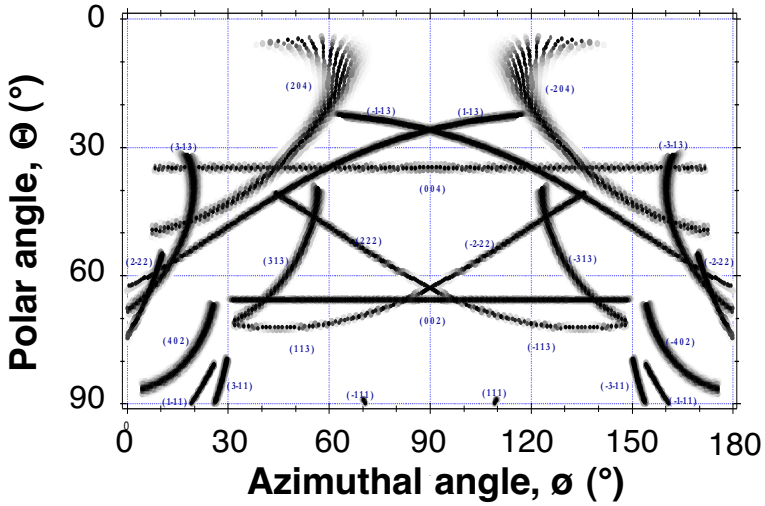

Detailed response of the lattice is better understood by recording diffraction from other lattice planes

- Large angle detector has been fielded on Si shock experiments
- Shift of many different lines is observed; details are being studied

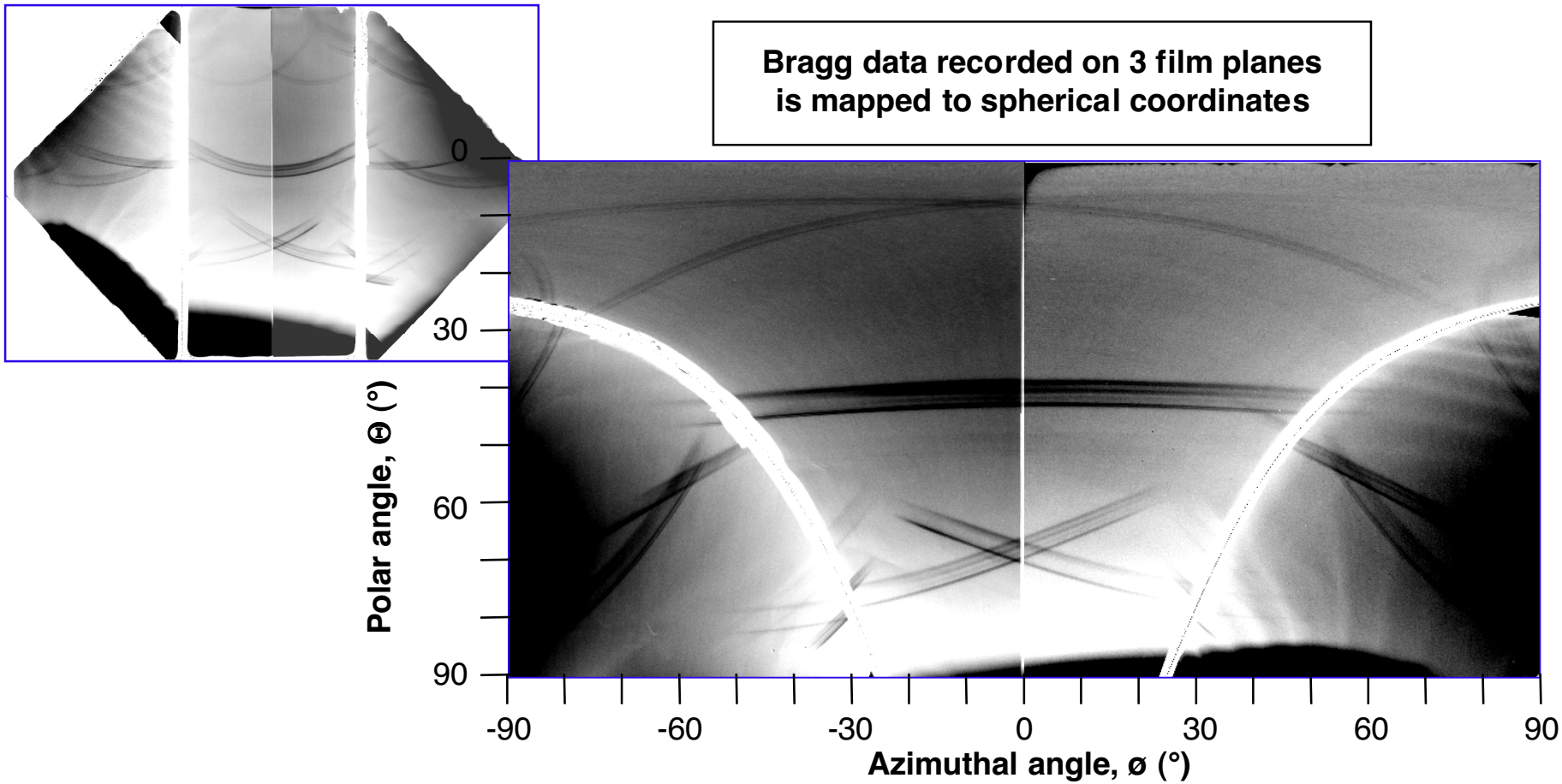

3. VISAR wave profiles and sample recovery

- **Al-6061 wave profile measurements show elastic-plastic response with spall on release**
- **Fitting the shock breakout wave profile provides best-fit strength parameters**

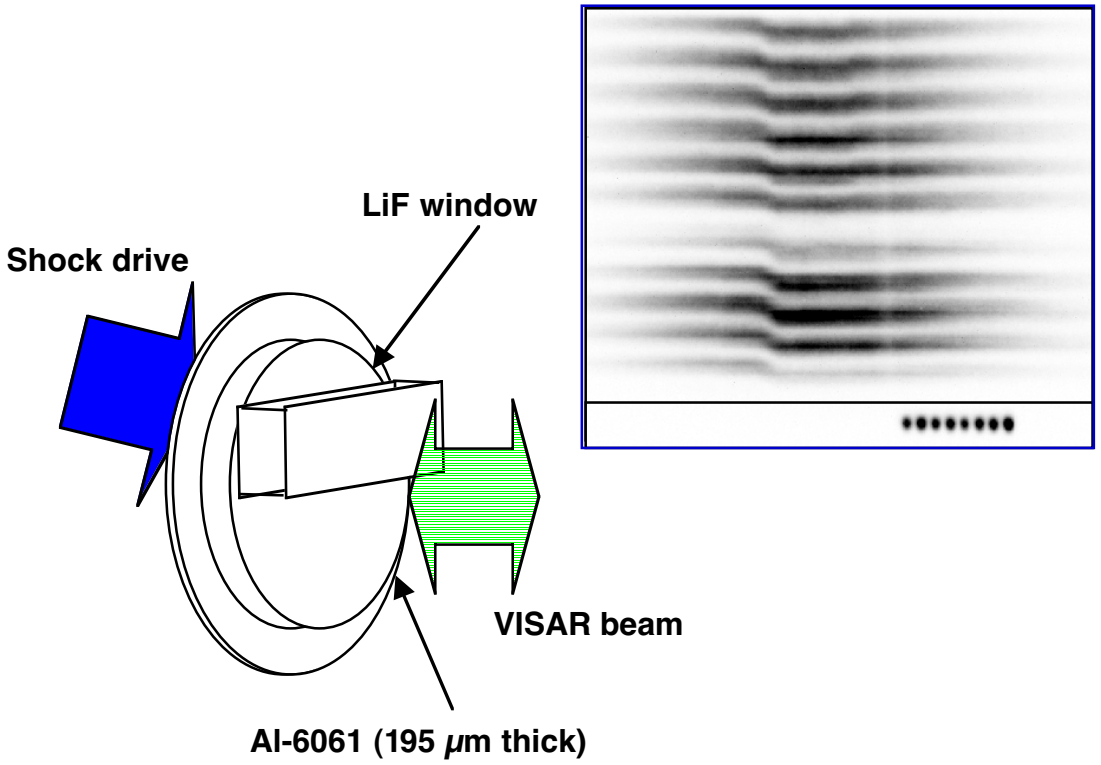

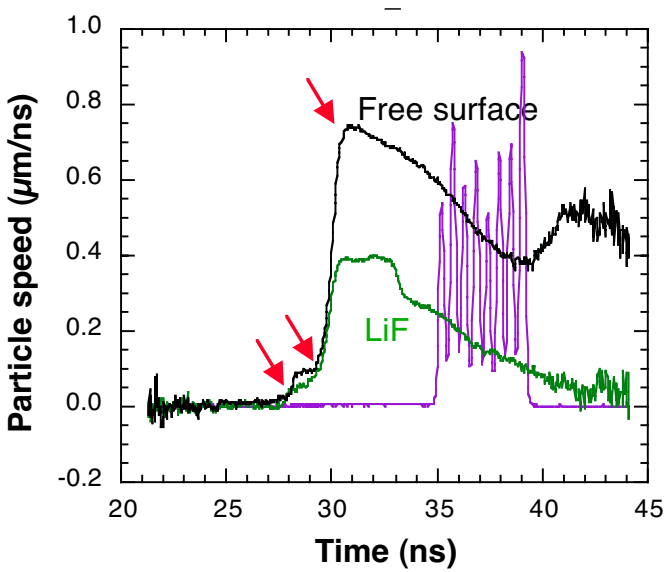

VISAR wave profiles provide information on the strength parameters for the shocked metal

- **The wave profile is sensitive to the constitutive model parameters for the metal foil**
- **Best-fit wave profile provides model parameters:**
  - **Shear modulus G=320 kbar (276)**
  - **Bulk modulus K=794 kbar (742)**
  - **Yield strength Y=4.27 kbar (2.9)**

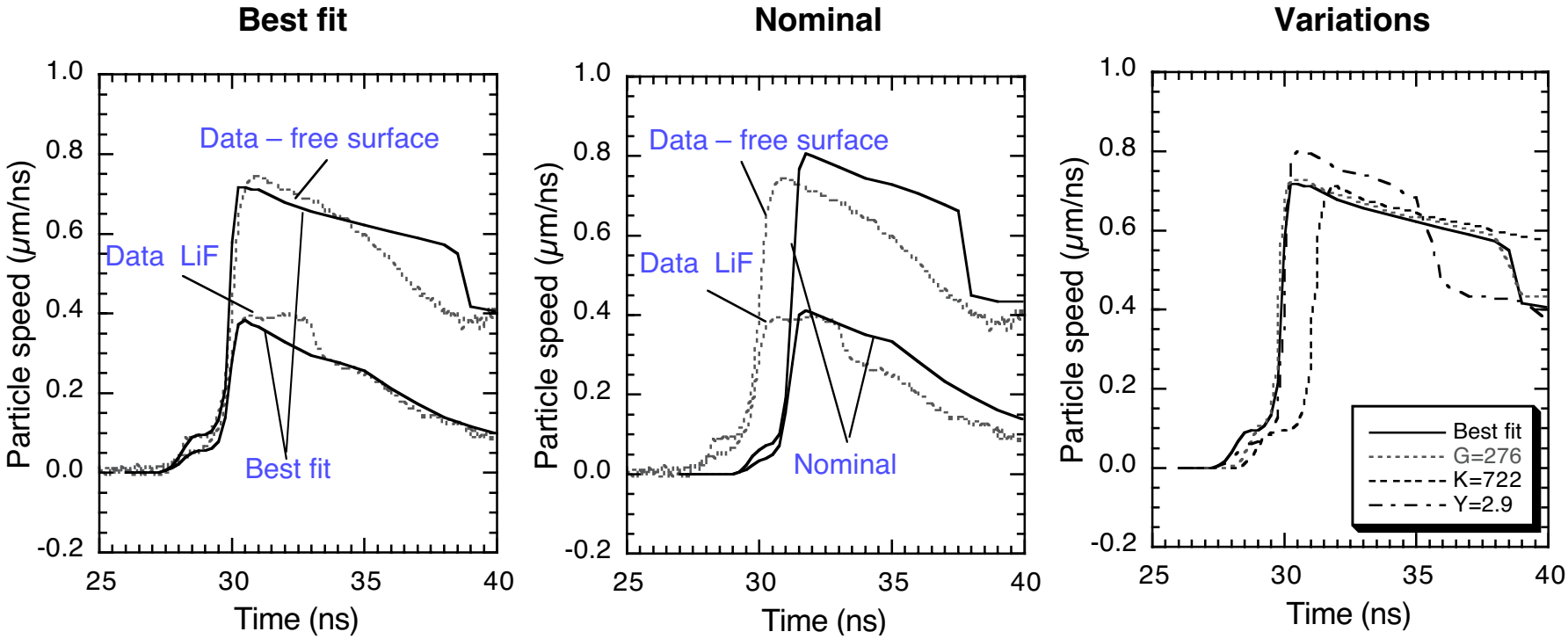

Transmission electron and optical microscope analysis shows residual structure that depends on the drive conditions

- Shocked samples are recovered in a low density foam-filled tube
- Preliminary tests done at OMEGA; shock pressure is ~400 kbar, decays to ~25 kbar at the rear surface

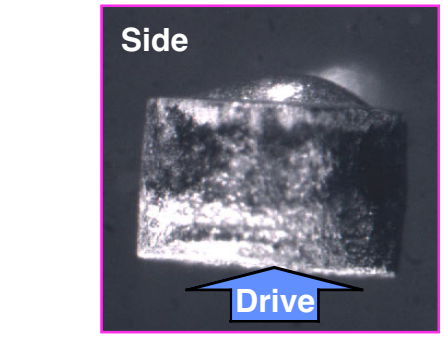

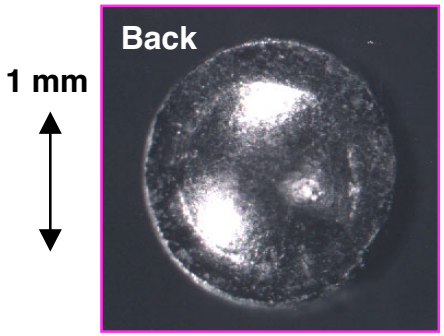

1 mm

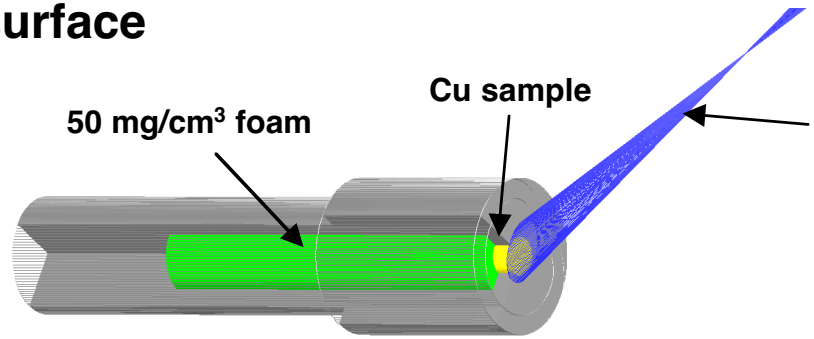

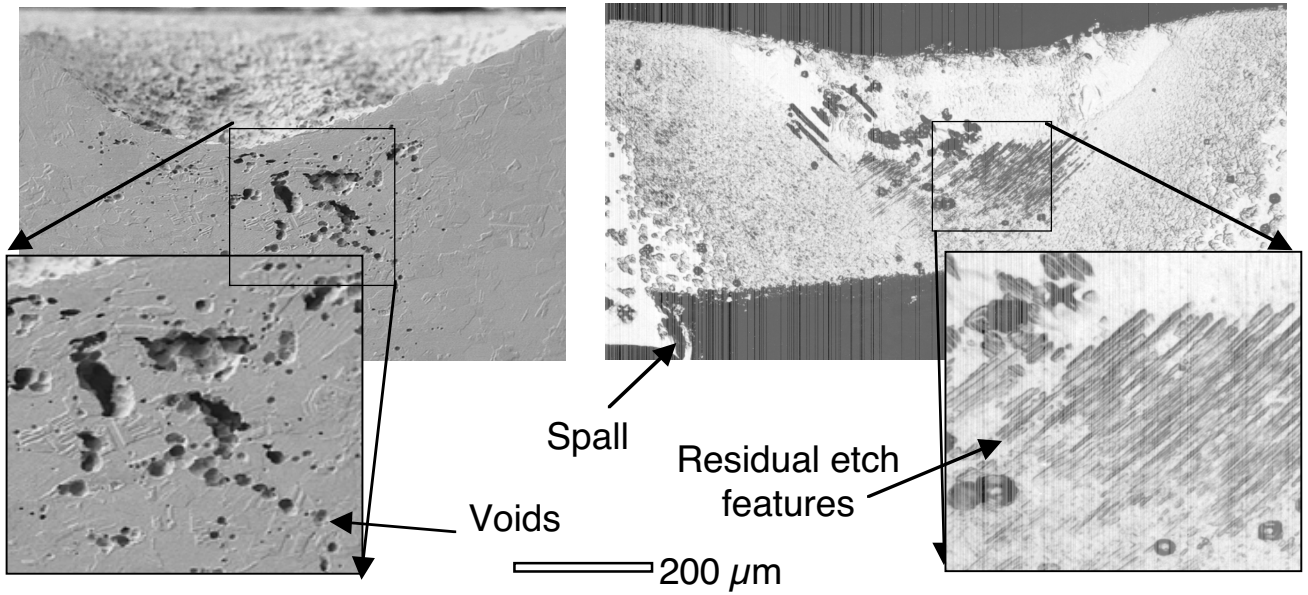

TEM analysis of recovered Cu shows the residual microstructure

- Residual microstructure of recovered single crystal Cu samples
- Higher pressures show twinning

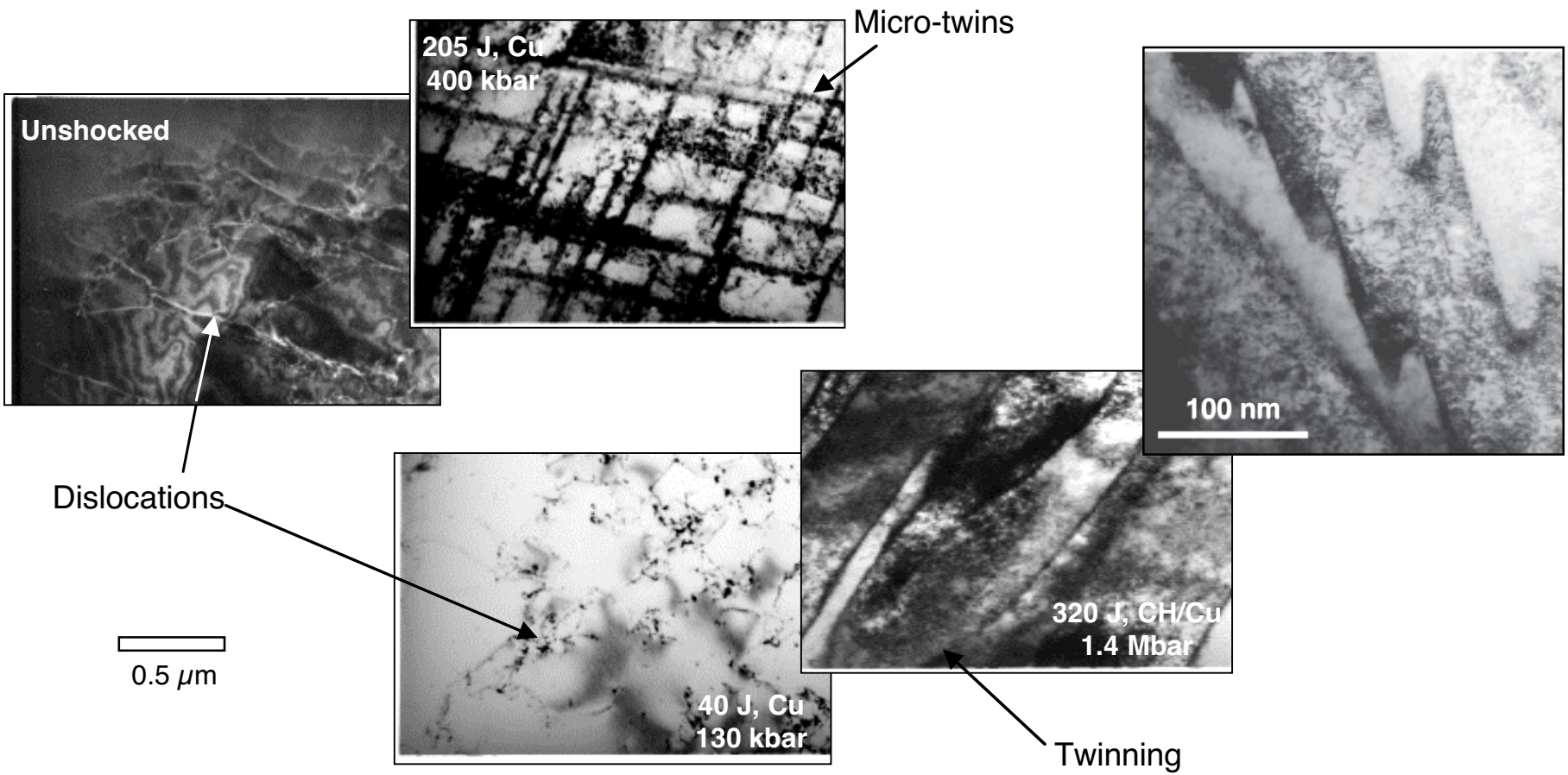

Summary

- Solid state hydrodynamic instability
  - RT instability in Al to infer Y(P)
  - There is possible imprinting due to the initial grain structure
- In situ dynamic x-ray diffraction
  - Time-resolved diffraction relates the lattice behavior to the macroscopic response of Si and Cu under shock loading
  - Si responds uniaxially, Cu deforms plastically
- Shock/recovery experiments
  - Residual deformation structure in Cu depends on the shock pressure

8th International Workshop on Physics of Compressible Turbulent Mixing
Pasadena, USA, December 9 – 14, 2001

RFNC-VNIITF MULTIFUNCTIONAL SHOCK TUBE FOR INVESTIGATING THE EVOLUTION OF INSTABILITIES IN UNSTATIONARY GASDYNAMIC FLOWS

Yu. A. Kucherenko, O. E. Shestachenko, S. I. Balabin, and A. P. Pylaev

Russian Federal Nuclear Center – Academician E. I. Zababakhin
All-Russian Research Institute of Technical Physics (RFNC-VNIITF)
456770 Snezhinsk, Chelyabinsk region, P.O.245, Russia
E-mail: kucherenko@five.ch70.chel.su

Abstract

Parameters of flows in the RFNC-VNIITF shock tube at its operation under three modes are given. In the first, ode a stationary shock wave is formed. This makes it possible to investigate the evolution of the Richtmyer-Meshkov instability and the turbulence induced by it. In the second mode, in the shock tube a nonstationary shock wave is formed that makes it possible to investigate the behaviour of the contact boundaries of different density gases when the conditions for the evolution of the Richtmyer-Meshkov and Rayleigh-Taylor instability are realized. In the third mode a compression wave is formed that makes it possible to investigate the evolution of the Rayleigh-Taylor instability and the turbulence induced by it.

1 Introduction

In spite of a great number of investigations performed with a view to study the evolution of hydrodynamic instabilities and turbulent mixing associated with them in gases, there are many questions hat have not been studied as a result of the experimental technique imperfection.

When studying the turbulence induced by the action of the Richtmyer-Meshkov instability, a great uncertainty takes place, which is associated with the parameters of diaphragms separating the different density gases at the initial instant of time. At the same time, the influence of the diaphragms is such that the obtained turbulent flow "does not forget" the initial conditions. This leads to the turbulent flow structure distortion and, as a consequence, to great errors when measuring the turbulence parameters.

When studying the turbulence induced by the action of the Rayleigh-Taylor instability, the role of the separating diaphragms is also rather important. This problem is especially significant when studying the self-similar mode of mixing at which it is important to have the self-similar spectrum of perturbations at the contact boundary of different density gases. A great uncertainty is, possibly, associated with this circumstance in the determination of the non-dimensional rate of different density gases in the self-similar mode. This mode is characterized by the constant rate of the mixing zone width growth, at the same time, the mixing zone width $\mathbf{L}$ depends only on the density ratio of miscible media $\mathbf{n}$ or Atwood number $A = (\mathbf{n}—1) / (\mathbf{n} + 1)$, the contact boundary acceleration $\mathbf{g}_1$ and time $\mathbf{t}$:

$$L \sim A g_1 t^2. \qquad (1)$$

The self-similar mode of the gravitational turbulent mixing is everywhere used both for the calibration of the semiempirical models of mixing and for the mathematical modeling of mixing processes due to the minimum number of parameters determining this mode. The proportionality coefficient in the relation (1), which represents the non-dimensional rate of mixing, is determined in experiments and is estimated at the numerical modeling.

It is known [1] that the gravitational turbulent mixing process of different density media is processed of the definite asymmetry which consists in the fact the fronts of the penetration of the light medium into the heavy one and the heavy medium into the light one are spreading with different

velocity. Historically the non-dimensional rate α_b of spreading the light medium front into the heavy one is assumed to be the characteristic of the gravitational turbulent mixing [2]. Denoting the light medium penetration front coordinate counted off from the contact boundary as L_{12}, it is possible to write down

$$L_{12} = 2\alpha AS, \qquad (2)$$

where $\mathbf{S} = \mathbf{gt}^2/2$.

Results obtained in experiments with different density liquids [1- 4] give the value of **a** being found in the range of

$$\alpha = 0.06 - 0.07$$

At the same time, the results obtained in the work [5] with different density gases give the magnitude of this value, which exceeds the above one shown more than by a factor of two. The reasons of such a difference have not been elucidated up to now. It may be proposed that in the work [5] either the conditions of self-similarity were not satisfied in the set-up of experiments or the measurements were made a the nonlinear stage of the Rayleigh-Taylor instability evolution, when the initial experimental conditions "were not yet forgotten". The last argument is supported by the absence of the direct control of the initial conditions when performing experiments in this work. Moreover, the factor of compressibility can exert an influence on the result in the work [5]. However, the investigations performed in the work [6] with compressible media have shown that the values of α_b for different combinations of gases are found in the range of

$$\alpha = 0.052 - 0.098.$$

In the works [7,8] the numerical three-dimensional modeling of the gravitational turbulent mixing evolution has been carried out by means of different mathematical codes. In the work [7] the value of

$$\alpha \approx 0.052$$

was obtained, but in work [8] this value is in the range of

$$\alpha = 0.04 - 0.06.$$

Thus, it is seen that the results obtained in the work [5] for gases are contradictory. This contradiction is, most likely, associated with the experimental technique imperfection. The study of the turbulence induced by the successive action of the Richtmyer-Meshkov and Rayleigh-Taylor instabilities has not yet been performed up to now. However, this situation is rather often realized when studying the operation of laser targets in the problem of the inertial thermonuclear fusion. The absence of such work being set up under laboratory conditions is, apparently, associated with the absence of the appropriate experimental technique.

The multifunctional shock tube (MST) being developed at present in RFNC-VNIITF will make it possible to solve a number of fundamental problems of nonstationary turbulence which were described above. In the present work three modes of the MST operation associated with the shown problems are described. This development has been the result of the RFNC-VNIITF and LLNL collaboration and initially it has been known as the Project "BIZON".

2 Multifunctional shock tube with driver I

The physical scheme of MST with driver I is presented in Fig 1.

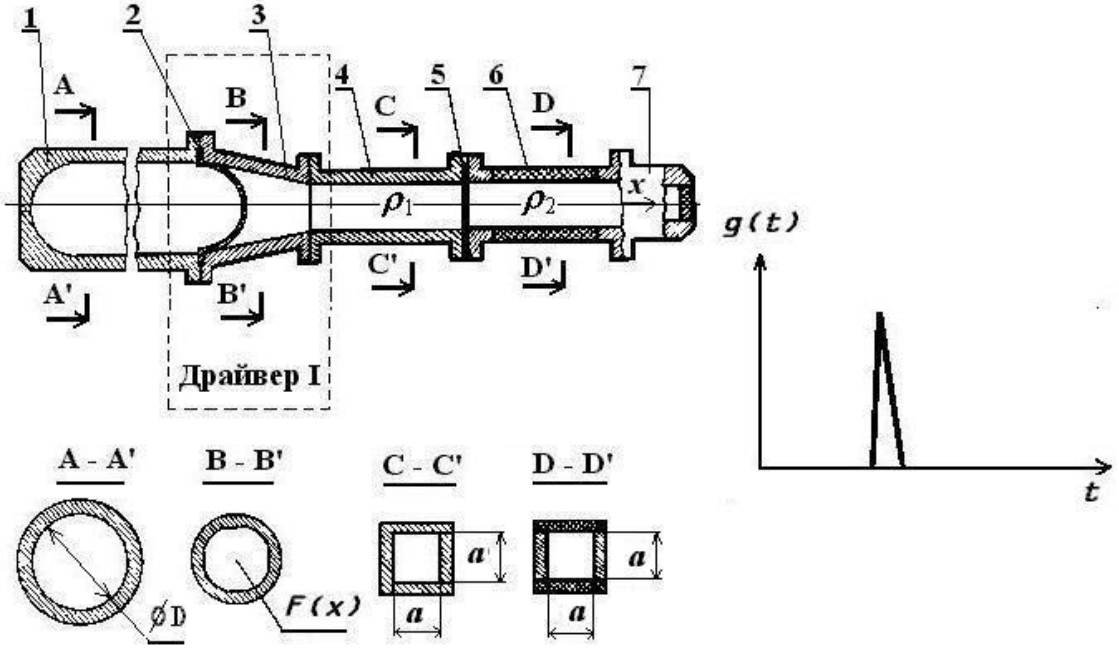

Fig. 1. The physical scheme of MST with driver I

This driver intends to be used for studying the Richtmyer-Meshkov instability and the turbulent mixing induced by it. One of the investigated gases with density ρ_1 is located in the measuring section I (4), second gas with density ρ_2 - in the measuring section II (6). At the initial instant of time a separating membrane (5) is found between gases. The composition of driver I includes a high pressure chamber (1), a high pressure membrane (2), a transitional section (3) and a part of the measuring section I. Driver I operates as follows. Gas is forced into the high-pressure chamber up to such pressure $\mathbf{P}_o$, at which the high-pressure membrane is opened. The gas flow rushes into the transitional section and then into the measuring section I creating a shock wave (SW). The function of the transitional section consists in coordinating the round cross-section **A-A** of the high-pressure chamber with the square cross-section **C-C** of the measuring section I. The cross-section **A-A** of the high-pressure chamber is chosen to be round proceeding from the considerations of its strength and technology to mount the high-pressure membrane on it. **C-C** and **D-D** cross-section of the measuring sections were chosen to be right-angled (square), proceeding from the convenience to register the turbulent mixing parameters by the light techniques. The cross-section of the other form would induce difficulties associated either with taking into account the additional refraction of light beams or with mounting the plane transparent windows on the non-planar walls of the measuring sections. The transitional section along the axis x is of a variable cross-section **F(x)** which changes from the round cross-section to the square one. At the same time, the gas flow form is smoothly changed. The intensity of the shock wave (SW) being created is determined by the value of pressure $\mathbf{P}_o$. The part of the measuring section I is used to generate a stationary SW propagating through a low-pressure gas. The required length of the stationary SW determines the length of this part of the measuring section. As a result of the SW passage through the contact boundary of gases, the contact boundary undergoes he impulsive acceleration whose character is shown in the right part of Fig.1. Mach number of the stationary SW generated by the driver I amounts to $\mathbf{M} \leq 5$.

The separating membrane (5) performs two functions. Firstly, it stabilizes the contact boundary (CB) of different density gases while preventing the mixing of gases prior to the SW arrival at CB. Secondly, by means of this membrane, at the initial instant of time, the zone of initial perturbations with specified parameters is created at the contact boundary. Such a membrane has, actually, been developed and has been named the "specter-diaphragm". Its distinctive features are its initiation from the external force and its disappearance just after the creation of the initial perturbations zone.

The length of the measuring section II is chosen depending on the problem being solved. If a single passage of SW through the zone of mixture is required, then the outlet section (7) is used for this purpose, which prevents from the creation of the reflected shock waves.

3 Multifunctional shock tube with driver II

The physical scheme of MST with driver II is presented in Fig.2.

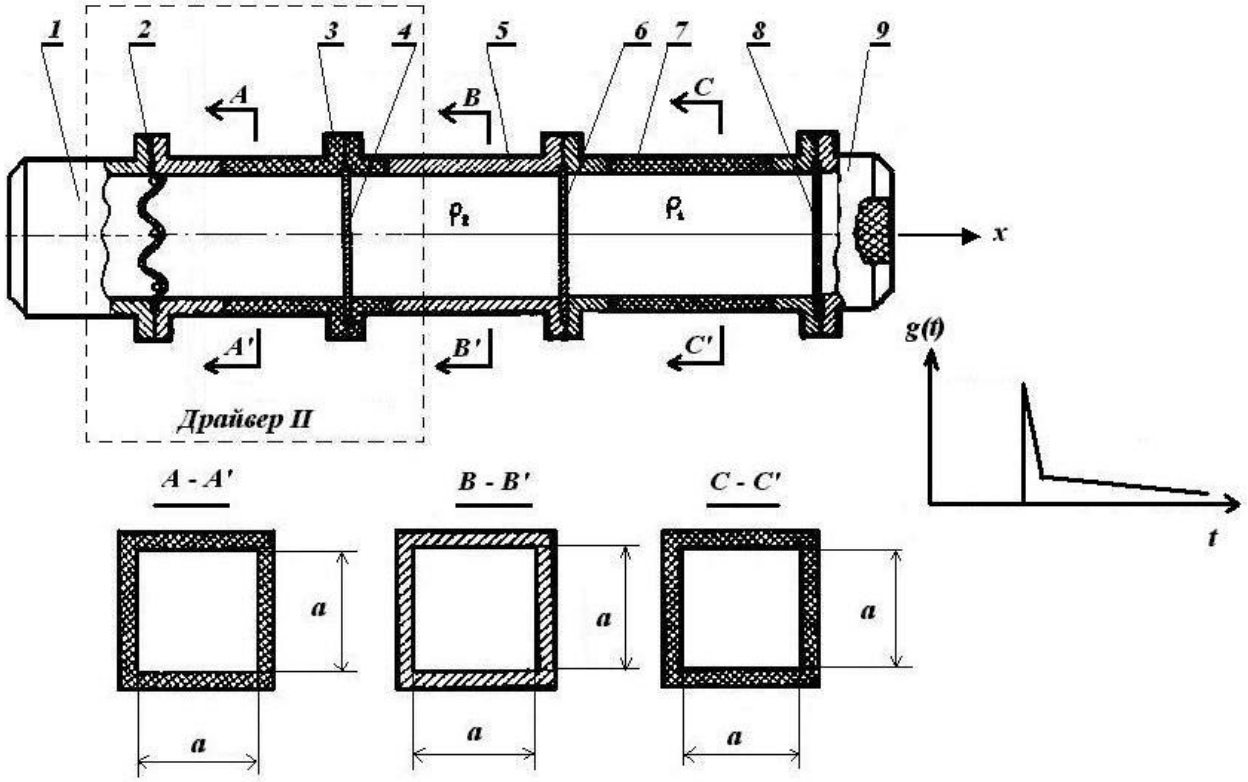

Fig.2. The physical scheme of MST with driver II

This driver intends to be used for investigating the successive action of the Richtmyer-Meshkov and Rayleigh-Taylor instabilities and the turbulent mixing induced by them. One of the gases (heavier one) being investigated and having density ρ_2 is placed into the measuring section I (5), but the lighter gas of density ρ_1 is placed into the measuring section II (7). At the initial instant of time the separating membrane (5) separates gases. This membrane performs the same function as in the case with driver I. Driver II includes a vacuum section (1), a restraining membrane (2), a section of the electrically exploded foil (EEF) (3) and the electrically exploded metal foil (4). The metal foil separates the measuring sections I from the section of EEF. The restraining membrane separates the section of EEF from the vacuum section. At the moment of the metal foil blasting a shock wave (SW) is formed which propagates into both sides. When reaching the restraining membrane (2), AW ruptures

it, and gas moving behind SW begins to flow into vacuum. As a result, a rarefaction wave is formed which propagates toward the side of the measuring section I. This rarefaction wave overtakes SW, which propagate along the measuring section I. As a result, a nonstationary SW with pressure sharply dropping at the back front falls on the contact boundary. Pressure at the leading front of SW can reach $5*10^5$ Pa at the distance of 500 mm from the point of the electrically exploded foil location. Thus, the leading front of the shock wave creates the Richtmyer-Meshkov instability after passing through the contact boundary of gases and then the different density gases underwent the action of the Rayleigh-Taylor instability in the region of the contact boundary, because the gradients of pressure and density are directed in the opposite sides. For MST with the driver II the contact boundary acceleration dependence on time is shown in the right part of Fig.2. At first the contact boundary is accelerated in the pulsed mode, then it moves with almost constant acceleration. In case of MST with driver II all the section have the same square cross-section.

4 Multifunctional shock tube with driver III

The physical scheme of MST with driver III is presented in Fig.3.

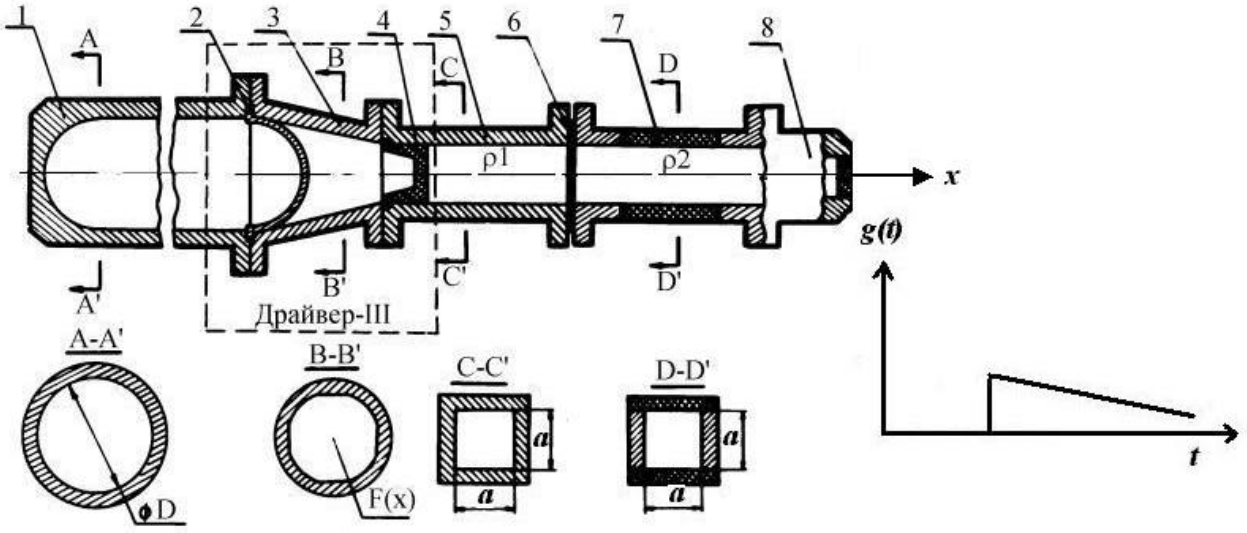

Fig.3. The physical scheme of MST with driver III

This driver intends to be used for studying the Rayleigh-Taylor instability and the turbulent mixing induced by this instability. The Lighter gas of density p_1 is placed into the measuring section I (5), the other heavier gas of density p_2 is located in the measuring section II (7). The separating membrane (6) separates gases. This membrane performs the same functions as in two preceding cases with drivers II and I. Driver III includes a high-pressure chamber (1), a high-pressure membrane (2), a transitional section (3) and a piston (4). The high-pressure chamber, the high-pressure membrane (2) and the transitional section of the driver III perform the same functions as in the driver I. However, here the gas flow does not form the stationary shock wave after passing through the transitional section, but accelerates the light piston. Then piston moving with acceleration creates a compression wave before itself, which is transformed into a shock wave in time. In the case of driver III the separating membrane and, consequently, the contact boundary of gases should be arranged at some distance from the initial position of the piston in order that by the moment of the arrival at the contact boundary the compression wave could not be transformed into SW. The pressure profile in the

compression wave is such that pressure drops in the positive direction of the axis **x**. Therefore, the gradients of pressure and density in the region of the contact boundary of different density gases will be directed to the opposite sides, therefore, the contact boundary of gases will be found under condition of the Rayleigh-Taylor instability. This boundary will move along the axis **x** with almost constant acceleration whose dependence on time is shown in the right part of Fig.3. The maximum value of the contact boundary acceleration may reach the value of $g_1 = 10^5\mathbf{g}$, where **g** is the acceleration of the Earth's gravitational field. The registration of the evolution process of the instability and the turbulent mixing of gases in the region of the contact boundary during its motion with acceleration is completed in the measuring section II before the piston will reach this region. Subsequently, the piston will get into the outlet section (8) where its deceleration takes place. For the same reasons which are shown when describing MST with driver I, the high pressure chamber cross-section is chosen to be round, but the cross-section of the measuring sections – to be square one. The transitional section is of the variable cross-section **F(x)** that ensures the smooth change of the form of the gas flow at its transition from the high pressure chamber to the measuring section I.

5.**Conclusion**

The multifunctional shock tube, which has been developed in RFNC-VNIITF in collaboration with colleagues from Lawrence Livermore National Laboratory and has made it possible to realize three different modes of nonstationary gas dynamic flows, will give possibility to accomplish applied tasks in the interests of solving the inertial thermonuclear fusion problems and for the development of different cumulative devices.

The multifunctional shock tube provides the following parameters of gas dynamic flows:

- in the mode with driver I a stationary shock wave with Mach number $\mathbf{M} \leq 5$ is generated;
- in the mode with driver II a nonstationary shock wave is generated whose initial pressure at the front is $5*10^6$ Pa with the acceleration of the contact boundary of different density gases behind the wave front $\mathbf{g}_1 \leq 10^6\ \mathbf{g}$, where **g** is the acceleration of the Earth's gravitational field;
- in the mode with driver III a compression wave is generated which ensures the acceleration of the contact boundaries of different density gases $\mathbf{g}_1 \leq 10^5\ \mathbf{g}$.

In all three modes the gases with density ration $p_2/p_1 \leq 34$ may be used.

References

1. Yu. Kucherenko et al. "Experimental Study of the Gravitational Turbulent Mixing in Self-Similar mode". The 3rd Int. Workshop on Physics of Compressible Turbulent Mixing. Abbey of Royamont, France, 1991.
2. K. Read. "Experimental Investigation of Turbulent Mixing by Rayleigh-Taylor Instability". Physica 12D, 1984.
3. D. Youngs. "Experimental Investigation of Turbulent Mixing by Rayleigh-Taylor Instability". Advances in Compressible Turbulent Mixing.
   W. P. Dannevik, A. C. Buckingham, C. E. Leith Editors, 1992.
4. Yu. Kucherenko, G. G. Tomashev, L. I. Shibarshov . "Experimental Investigation of the Gravitational Turbulent Mixing in Self-Similar mode". Rus. J. VANT, Series Theoretical and Applied Physics, Issue 1,1988.

5. A. Vasilenko, V. Olhovskaya, O. Buryakov, V.Yakovlev . “Experimental Investigations for Turbulent Mixing of Gases at the Interface under the Influence of the Decelerating shock wave”. The 3rd Int. Workshop on Physics of Compressible Turbulent Mixing. Abbey of Royaumont, France, 1991.
6. S. G. Zaitsev et al. “Evolution of the Rayleigh-Taylor Instability in Compressible Media”. Report under ISTC Project ¹ 96-029.
7. N. Anuchina, V. Gordeichuk, N. Es`kov, O. Ilyutina, O. Kozyrev, V. Volkov. “Three-dimensional Numerical Simulation of Rayleigh-Taylor Instability by MAH-3 Code”. The 6th Int. Workshop on Physics of Compressible Turbulent Mixing. Marseilles, France, 1997.
8. D. Youngs. “Three-dimensional Numerical Simulation of Turbulent Mixing by Rayleigh-Taylor Instability”. Phys. Fluids A3 (5), 1991.,

HYDRODYNAMIC INSTABILITIES AT A SHOCK ACCELERATED BUBBLE GAS-GAS INTERFACE

G. LAYES*, G. JOURDAN*, P. ROUALDES♣ and L.HOUAS*

*IUSTI, UMR CNRS 6595, Université de Provence, Technopôle de Château-Gombert, 5 rue Enrico Fermi, 13453 Marseille Cedex 13, FRANCE

♣Centre d'Etudes de Gramat, 46500 Gramat, FRANCE

I- Schematic representations of the interaction between a shock wave and a gas bubble

slow/fast or heavy/light case: helium bubble in air

t — **Shock wave is coming from right to left** — 0

Bubble is growing from right to left

fast/slow or light/heavy case: freon 22 in air

II- Shadowgraphs of the interaction between a shock wave in air (Mach 1.5) and a helium bubble (run #156)

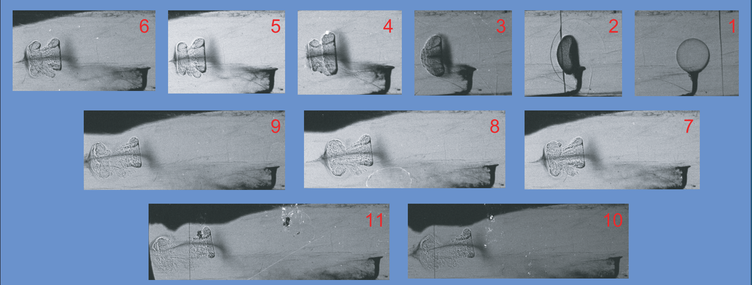

Experimental conditions:
- Incident shock wave Mach number in air: 1.5
- Bubble diameter: 28 mm
- Initial pressure of air and helium: 1 bar
- 70 µs between 2 consecutive pictures

Picture's default are coming from too slow opening of the shutter

III- Shadowgraphs of the interaction between a shock wave in air (Mach 1.5) and a krypton bubble (run #153)

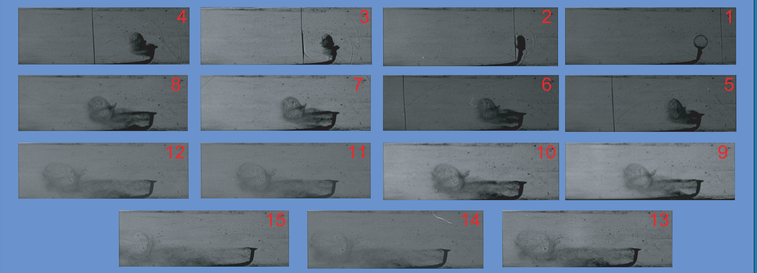

Experimental conditions:
- Incident shock wave Mach number in air: 1.5
- Bubble diameter: 18 mm
- Initial pressure of air and krypton: 1 bar
- 70 µs between 2 consecutive pictures

IV- Experimental device

Characteristics of the shock tube:
- Square cross section: 8 x 8 cm2
- Shock wave Mach number: up to 5
- Total lenght: 3.75 m (25 cm of visualization field)

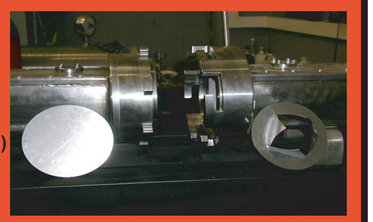

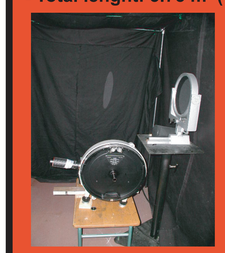

Diagnostic system: **shadowgraph photography**
- Nanolite 20 kHz maximum frequency
- Strobodrum camera
- Acquisition device: tecktronix 720 scope
- Trigger: signal from PCB pressure gauge

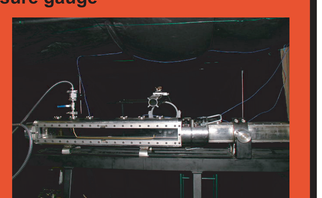

Bubble system:
- 50% solution in water of shampoo
- 1 cm diameter bubble support
- Pressure reducer : 1.2 bar (He) - 1.05 bar (Kr)

V- Experimental preliminary results

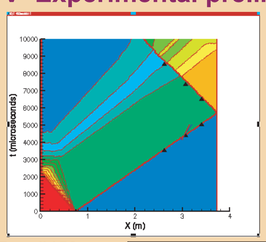

Wave diagrams

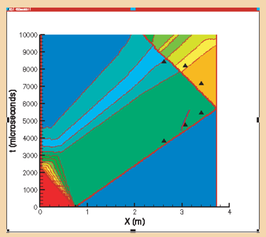

Run #152
Helium bubble

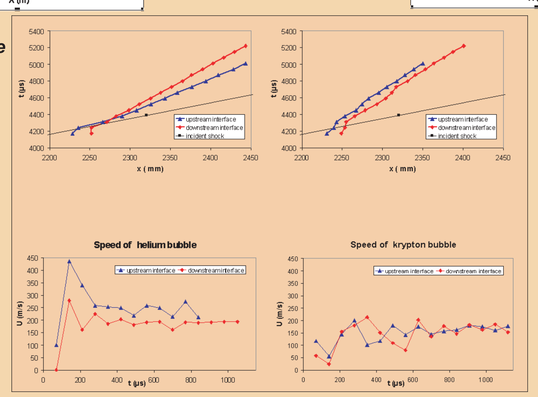

Run #153
Krypton bubble

VI- Next steps

Improvements: - Bubble injection system design
- Shampoo solution

Experimental Program: - Heavy/light case
- Close densities case
- Light/heavy case

Installation of the system on the new large diameter shock tube
- 500 mm diameter circular section
- Length: 12 meters
- Visualization field: Lenght: 475 mm, Height: 322mm, Width: 282 mm

Scaling in the Shock-Bubble Interaction

K. Levy[1,2], O. Sadot[1,2], A. Rikanati[1,2], D. Kartoon[1,2], Y. Srebro[1,2], A. Yosef-Hai[1,2], G. Ben-Dor[1], D. Shvarts[1,2]

1) Ben-Gurion Univeristy, Beer Sheva, Israel

2) Nuclear Research Center Negev, Israel

Introduction

The phenomenon of shock-bubble interaction is of importance in several differently scaled situations, from fragmentation of gallstones or kidney stones by shock waves (*Gracewski et al. 1993*) to the interaction of supernovae shock waves with interstellar clouds (*Klein et al. 2000*). Therefore the scalability of the interaction is important. The passage of a shock wave through a spherical bubble results in the formation of a vortex ring. In the present study, simple dimensional analysis shows that the circulation is linearly dependent on the surrounding speed of sound c_s and the initial bubble radius R. In addition, it is found that the velocities characterizing the flow field are linearly dependent on the speed of sound, and are independent of the initial bubble radius. The dependence of the circulation on the shock wave Mach number M is derived by *Samtaney & Zabusky (1994)* as $(1+1/M+2/M^2)(M-1)$. Using the dimensional analysis the velocities are shown to have a similar dependence. Full numerical simulations and experiments were conducted for slow/fast (air-helium) and fast/slow (air-SF_6) interactions. Good agreement was achieved. From the results it is seen that in both cases, according to the proposed scaling, the vortex ring velocity is bubble radius independent. The numerical results for the slow/fast interaction show that the proposed Mach scaling is valid for $M<2$. Above $M\cong2$ the topology of the bubble changes due to a competition between the upstream surface of the bubble and the incident shockwave.

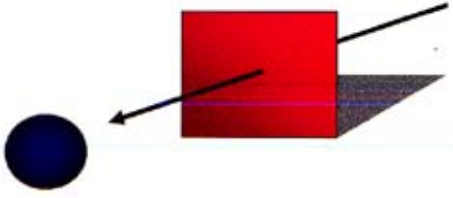

Computational method

- Leeor-2D*: ALE, interface-tracking, finite differences

Initial condition

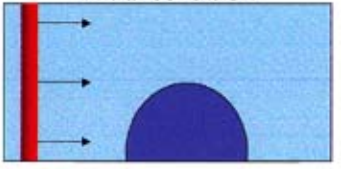

Computational grid (450x100)

- Ambient gas - air, $E = (\gamma - 1) \cdot P / \rho$
- Heavy bubble (f/s) - Sf_6, η=5.034, r_0=1.3cm
- Light bubble (s/f) - Helium, η=0.138, r_0=1.63cm
- Mach range - 1.05 to 4
- Boundary conditions - free slip
- Shock tube width - 4 cm

$$\eta = \rho_{bubble} / \rho_{ambient\_gas}$$

*D. Shvarts et al., Phys. Plasma 2, 2465 (1995)

Experimental Apparatus

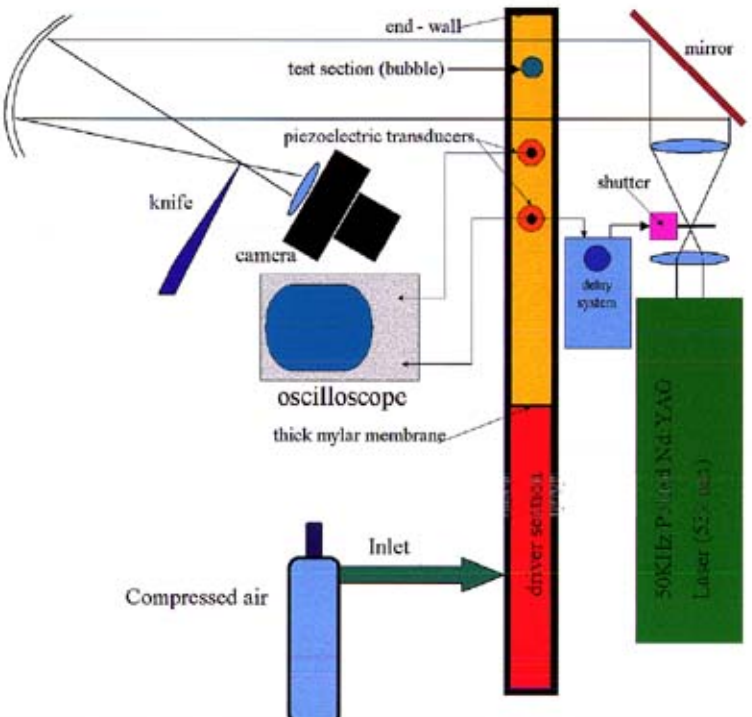

Experiment/simulation comparison

slow/fast (air-helium), M=1.22

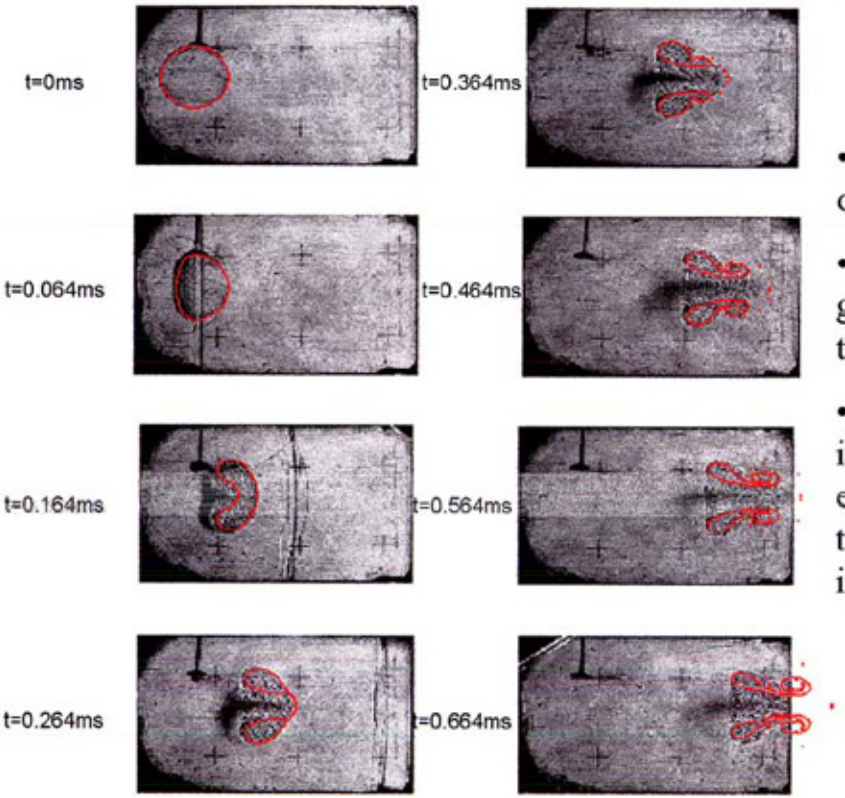

- Schliren images of the experiment
- Red contour: gas interface from the simulation
- Good agreement is found during the early and late times of the interaction.

Experiment/simulation comparison

fast/slow (air-SF_6), M=1.17

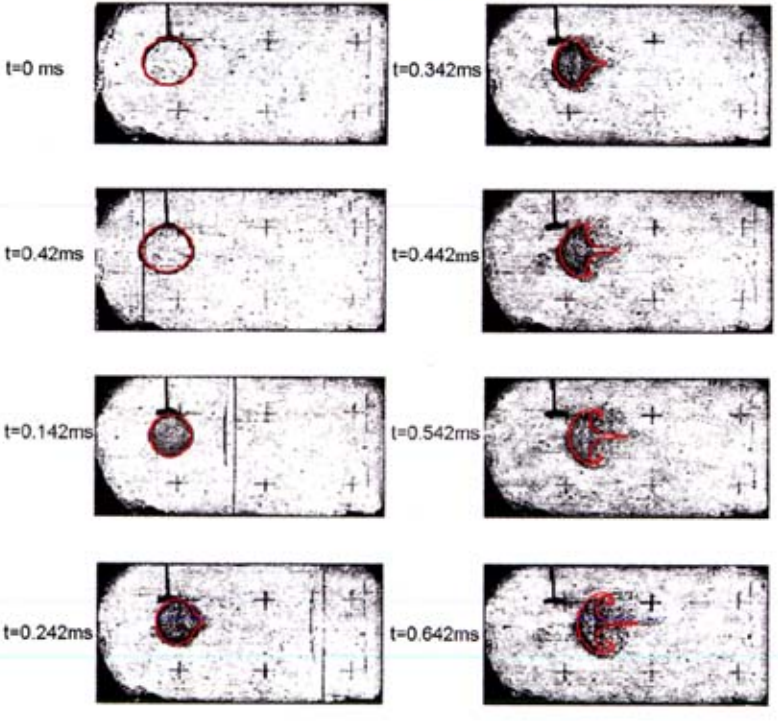

- Schliren images of the experiment
- Red contour: gas interface from the simulation
- Good agreement is found during the early and late times of the interaction.
- Emerging jet is highly sensitive to resolution changes.

Circulation Dimensional Analysis

- Circulation: $[\Gamma]=[\text{length}]^2/[\text{time}]$
- Flow parameters: c_s - *speed of sound*, R - *bubble radius*, dimensionless parameters: M - *Mach number*, η - *density ratio*, γ - *ratio of specific heats of both gases*

$$\Gamma = f(M,\gamma,\eta)\cdot R\cdot c_s$$

- Using a vorticity deposition model*:

$$\Gamma = (1+\frac{\pi}{2})\cdot\frac{2\gamma^{1/2}}{1+\gamma}(1-\eta^{-1/2})(1+\frac{1}{M}+\frac{2}{M^2})(M-1)\cdot R\cdot c_s$$

*Samtaney & Zabusky, JFM. 269 (1994)
Zabusky & Zeng, JFM. 362 (1998)

Velocity Dimensional Analysis

- Velocity: [U]=[length]/[time]
- Since the flow velocities are determined by the vorticity distribution in the flow:

$$U_i = g_i \cdot \frac{\Gamma}{R} = g_i \cdot f(M,\eta,\gamma) \cdot c_s$$

i - ring, jet, etc...

g_i - is a constant representing the influence of the topology of the problem, the boundary conditions and the specific velocity U_i.

For example: the velocity of an ideal vortex ring*:

$$U_{ring} = \frac{1}{4\pi}\left\{\log\left(\frac{8R}{\delta}\right) - 1/4\right\}\frac{\Gamma}{R}$$

R - vortex ring radius,

δ - radius of core section (or average of ellipse axes)

*Lim & Nickels in "Fluid Vortices" edited by S.I. Green (1995)

Typical simulation

slow/fast, M=1.22

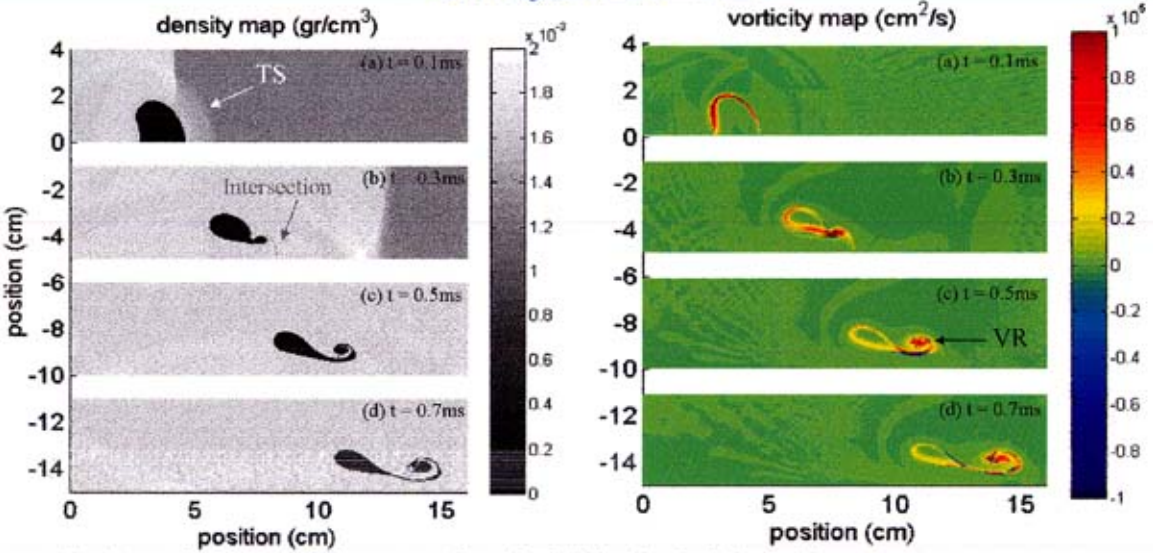

(a) - Transmitted wave (TS) emerges from the bubble ahead of the incident wave.

(b) - Upstream side of bubble reaches the downstream side. There is vorticity on the inner side of the bubble because of the shear velocity.

(c) - The vortex ring (VR) has formed at the downstream side.

(d) - The vortex ring is moving at a steady speed. The vortex ring separates from the upstream remains of the bubble.

Vortex ring formation - velocity field

low/fast, M=1.22

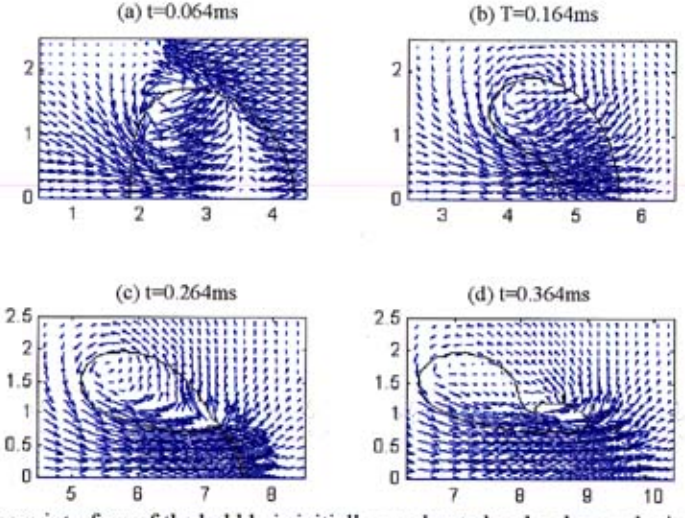

The velocity field is drawn in a coordinate moving with the shocked air

(a) The upstream interface of the bubble is initially accelerated and a shear velocity is formed leading to rotational flow.

(b) The ambient gas moves in to fill the space left by the bubble.

(c) The bubble is penetrated through the center creating a torus-like shape

(d) The vortex ring is formed

Vortex ring velocity definition

slow/fast, M=1.22

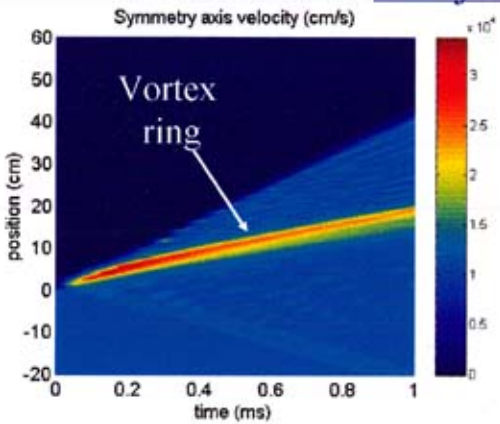

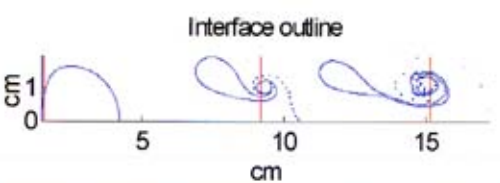

Vertical lines represent position of maximum velocity

- The motion of the vortex ring is characterized by the region of high velocity.
- The maximum velocity on the symmetry axis is located at the center of the vortex ring.
- The vortex ring velocity is derived from the movement of this point.

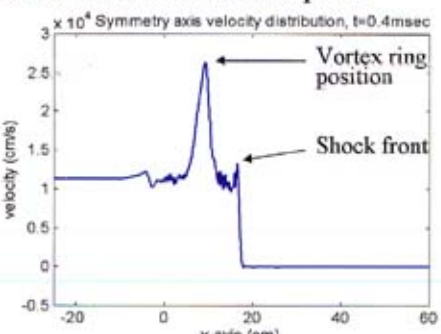

Vortex ring velocity development

slow/fast, M=1.22

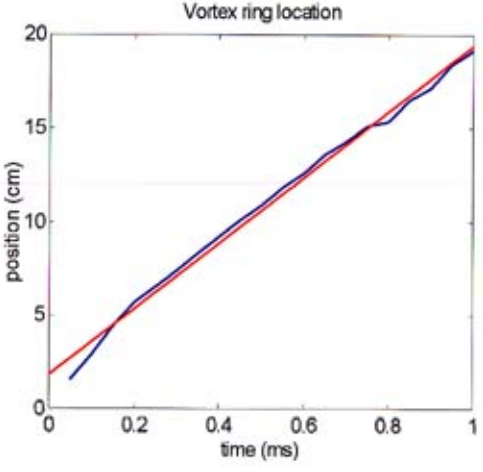

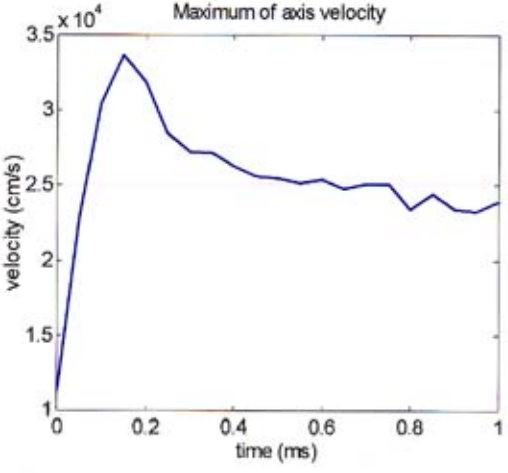

- From $t = 0.2\ ms$ the maximum axis velocity and the vortex ring velocity stabilize.
- Resulting vortex ring velocity is approximately 176 m/s.

Circulation

slow/fast, M=1.22

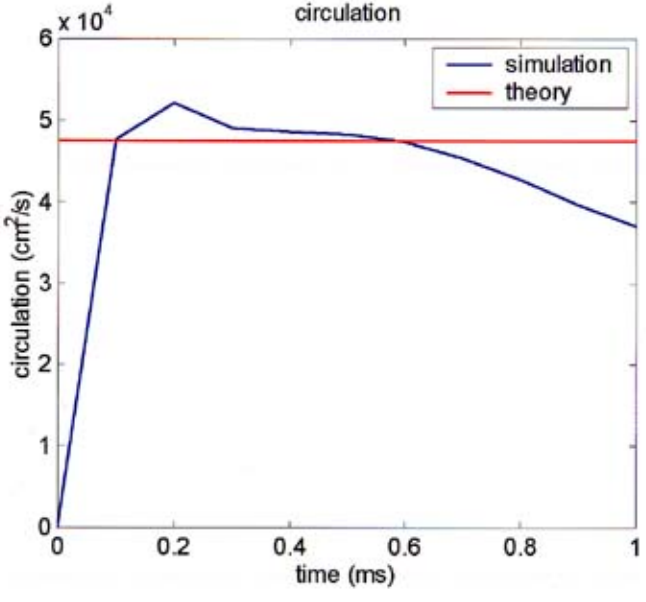

Circulation from simulation:

$$\Gamma = \int_A \omega \cdot dA$$

where ω is the vorticity:

$$\omega = \frac{\partial v}{\partial x} - \frac{\partial u}{\partial y}$$

- The circulation is in good agreement with Zabusky's model in early times.
- The decrease after t = 0.6ms is a result of numerical viscosity

Radius scaling

slow/fast, M=1.22

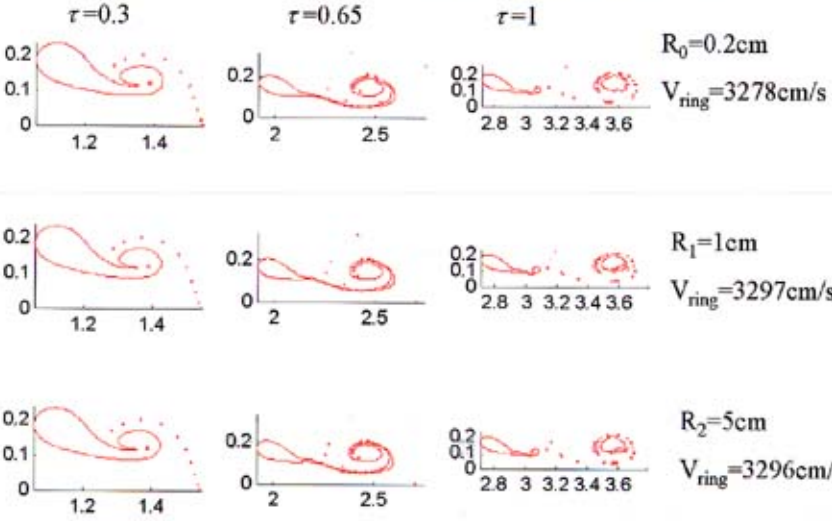

Scaling:

$$\tau = t \cdot R_0 / R_i$$

$$\zeta = x \cdot R_0 / R_i$$

$$\xi = y \cdot R_0 / R_i$$

The ring velocity in the three cases differs by less than 1%. Furthermore, the full evolution of the ring is also velocity independent.

$$v \neq f(R)$$

Mach scaling, slow/fast

scaling factor: $(1+1/M+2/M^2)(M-1)$

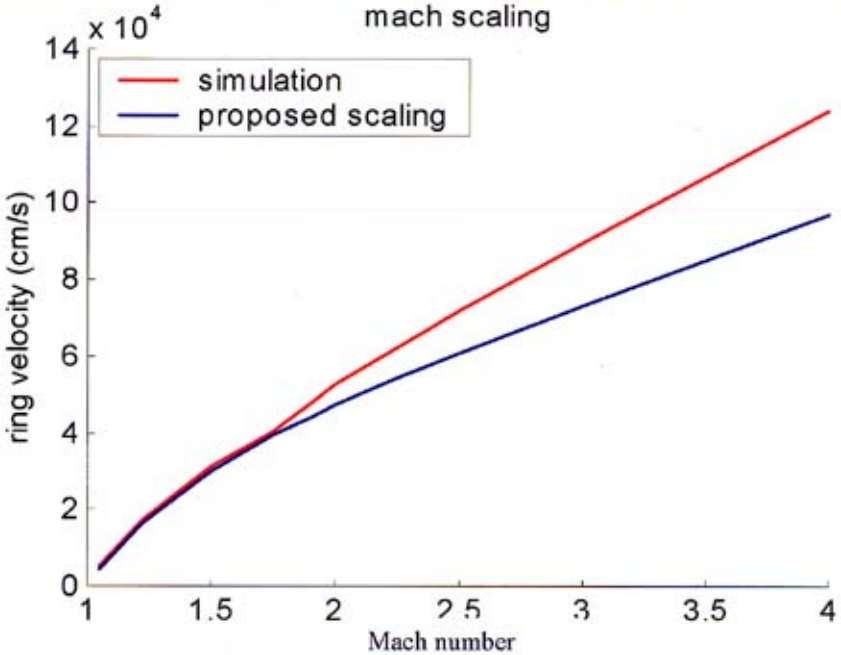

- Good agreement is found for M<2.

Early shock/upstream interface competition

pressure contours

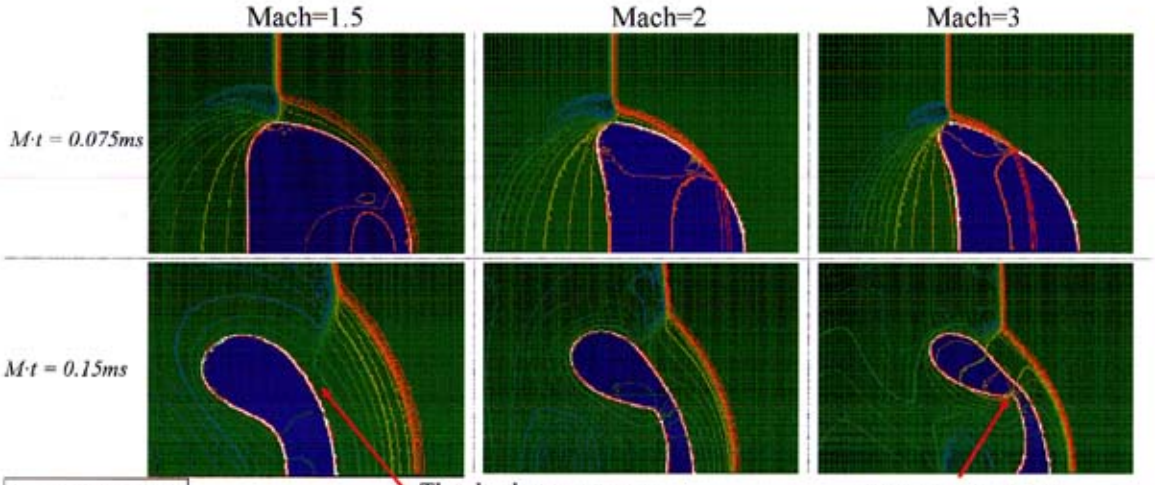

The results show that for M>2 the upstream surface reaches the downstream side of the bubble before the incident shock wave. In this case the incident wave deposits the vorticity on an interface different from the M<2 case. This phenomenon is not considered in the scaling rendering it invalid for M>2.

Late shock/upstream interface competition

vorticity maps (1/s)

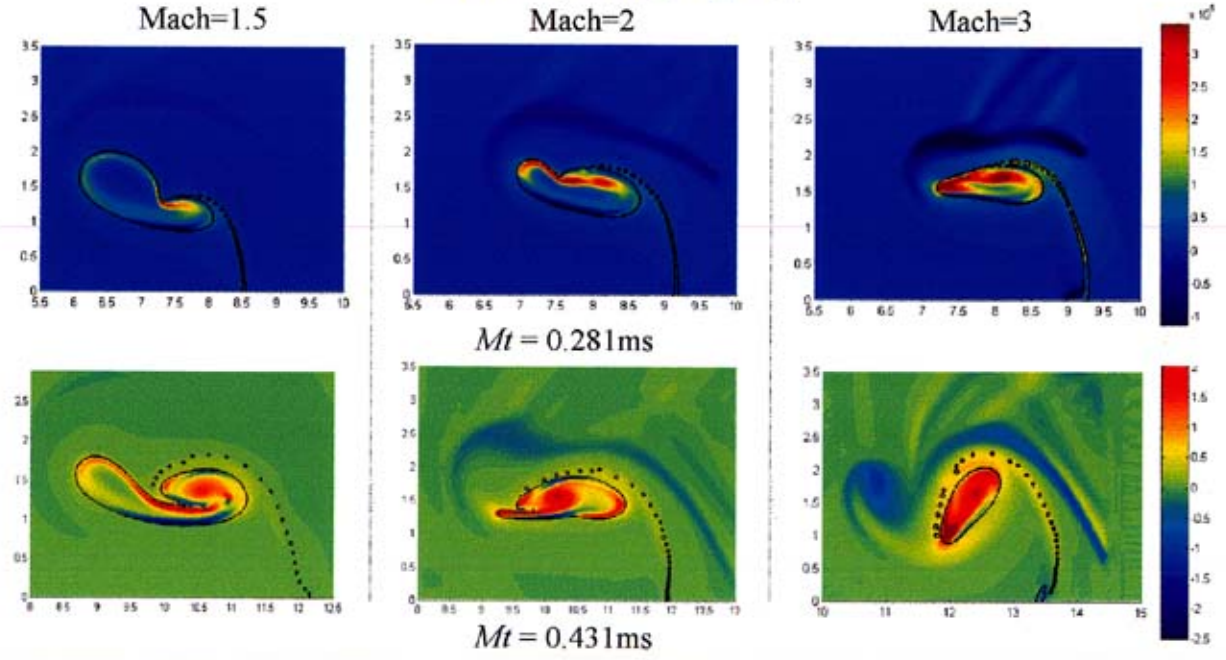

The main difference between the results is that for higher mach numbers the vorticity is more concentrated at the vortex ring, whereas for mach=1.5 there is a distribution of the vorticity on the remains of the upstream side of the bubble. In addition, for M=3 the vortex ring is spinning around its axis. These differences are a possible cause for the increase in velocit.

Summary

- The phenomenon of a shock wave bubble interaction was investigated using shock tube experiments and simulations. A comparison of the bubble interface shows very good agreement.
- Using dimensional analysis and a previously suggested Mach scaling, a new velocities scaling of the shock bubble interaction is proposed.
- The velocities in the interaction were found to be independent of the initial bubble radius.
- For slow/fast interactions (air/helium) the mach scaling factor was found to be valid for $M<2$.
- It is shown that the scaling is invalid for $M>2$ due to a change in the topology of the ring evolution.

Single-Mode Incompressible Richtmyer-Meshkov Instability Experiments

C. E. Niederhaus[1] and J. W. Jacobs
University of Arizona
[1]Currently at NASA Glenn Research Center

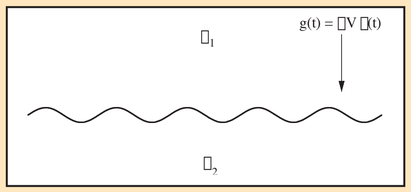

Richtmyer-Meshkov (R–M) instability occurs when two different density fluids are impulsively accelerated in the direction normal to their nearly planar interface. The instability causes small perturbations on the interface to grow and possibly become turbulent given the proper initial conditions. R–M instability is similar to the Rayleigh-Taylor (R–T) instability, which is generated when the two fluids undergo a constant acceleration. R–M instability is a fundamental fluid instability that is important to fields ranging from astrophysics to high-speed combustion. For example, R–M instability is currently the limiting factor in achieving a net positive yield with inertial confinement fusion.

The experiments described here utilize a novel technique that circumvents many of the experimental difficulties previously limiting the study of the R–M instability. A Plexiglas tank contains two unequal density liquids and is gently oscillated horizontally to produce a controlled initial fluid interface shape. The tank is mounted to a sled on a high-speed, low-friction linear rail system, constraining the main motion to the vertical direction. The sled is released from an initial height and falls vertically until bouncing off of a movable spring, imparting an impulsive acceleration in the upward direction. As the sled travels up and down the rails, the spring retracts out of the way, allowing the instability to evolve in freefall until the sled impacts a shock absorber at the end of the rails. The impulsive acceleration provided to the system is measured by a piezoelectric accelerometer mounted on the tank, and a capacitive accelerometer measures the low-level drag of the bearings. Planar Laser-Induced Fluorescence is used for flow visualization, with an Argon ion laser illuminating the flow and a CCD camera mounted to the sled capturing images of the interface.

This experimental study investigates the instability of an interface between incompressible, miscible liquids with an initial sinusoidal perturbation. The lighter fluid is an isopropyl alcohol and water solution, and the heavier fluid is a calcium nitrate salt solution. The resulting Atwood number A (density difference over density sum) is 0.155. The amplitude of the disturbance during the experiment is measured and compared to theories. The results are nondimensionalized using the wave number k and initial growth rate $\dot{a}_0$. The initial growth rate and time for zero amplitude are obtained from an integration routine utilizing linear theory along with measured initial conditions and accelerations. The amplitude measurements are compared to several theories in the linear, weakly nonlinear, and late-time nonlinear regimes. The effect of Reynolds number on the vortices' evolution is also investigated. At higher Reynolds Number (based on circulation), an instability of the vortex cores has been observed. While time limitations of the apparatus prevent determination of a critical Reynolds Number, the lowest Reynolds Number this vortex instability has been observed at is 2000.

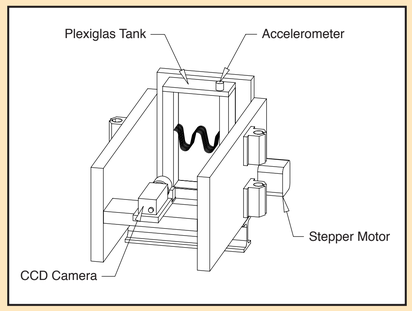

Experimental fluid container mounted on the sled.

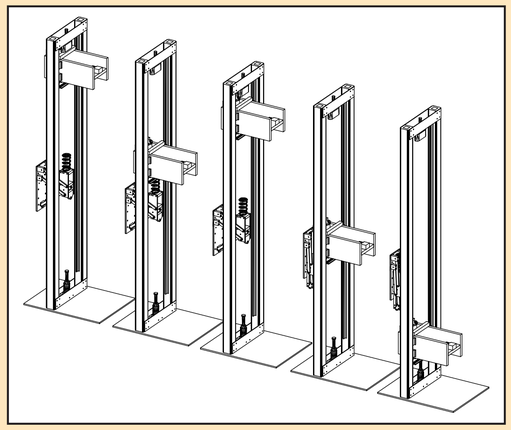

Animation of sled traveling along drop tower rails.

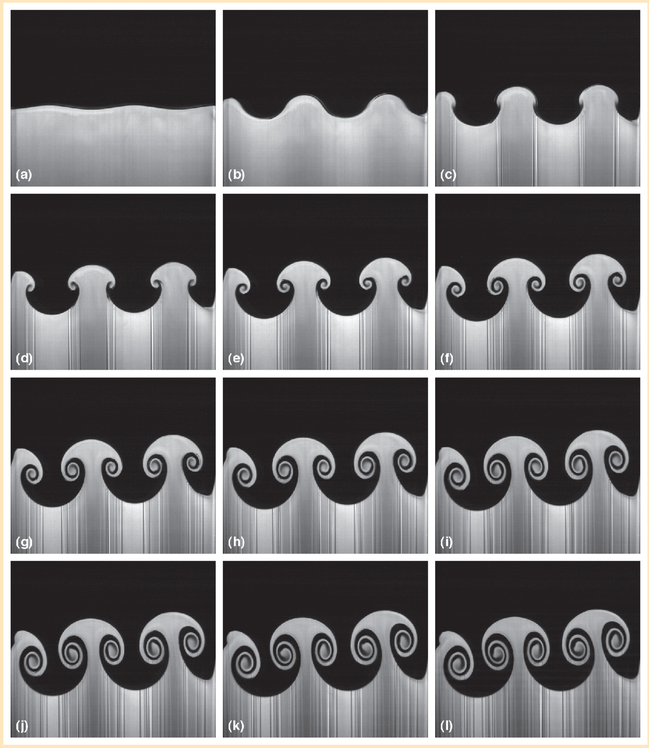

The above sequence of PLIF images shows the evolution of the Richtmyer-Meshkov instability generated from a sinusoidal initial perturbation with ka_i = 0.16 and 2 1/2 waves inside the experiment tank. Image (a) was taken just before the sled impacted the spring and thus shows the initial interface shape. The impulsive acceleration in these experiments is directed from the heavier fluid into the lighter fluid, causing the initial perturbation to invert before growing. Immediately after inversion, the interface retains a sinusoidal shape, but with time the vorticity begins to concentrate at points midway between the crests and troughs. These vortices roll the interface around their centers, forming a spiral pattern. Note that, characteristic of the instability with small density differences, the interface retains its top-to-bottom symmetry well into the nonlinear regime.

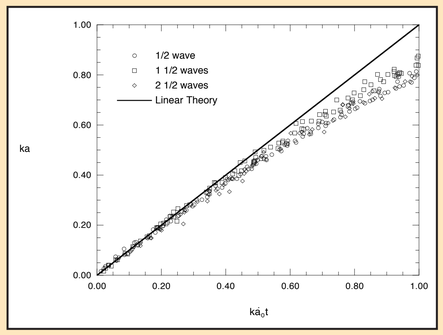

The nondimensional amplitude versus time is shown for the early stages of the instability. Linear theory (Richtmyer, *Commun. Pure Appl. Math* **13**, 1960) is shown by the solid line. The experiments show excellent agreement with linear theory up to $k\dot{a}_0 t$ = 0.3 and are within 10% of linear theory at $k\dot{a}_0 t$ = 0.7, where nonlinear effects start to become important. It should be noted that linear theory is derived assuming $|ka| << 1$ and is surprisingly accurate at moderate values of ka. Also, the ka_i (dimensionless amplitude before impact) for these experiments ranged from 0.07 to 0.66 and does not seem to effect the agreement with linear theory.

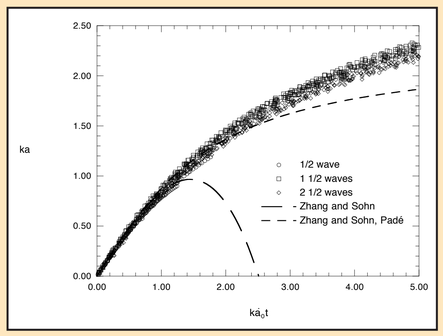

Intermediate-time amplitude measurements are shown along with two theories developed by Zhang and Sohn (*Phys. Fluids* **9**, 247, 1997) that are a function of Atwood number. The first is a weakly nonlinear fourth order perturbation theory, shown for a representative A of 0.155. This solution agrees with experimental data to within 10% up to $k\dot{a}_0 t$ = 1.3, but then rapidly becomes invalid due to its cubic form. Recognizing the limited range of validity, Zhang and Sohn used this solution to develop a Padé approximate for velocity which was then integrated to determine amplitude. This extended the range of agreement (to within 10%) up to $k\dot{a}_0 t$ = 3.

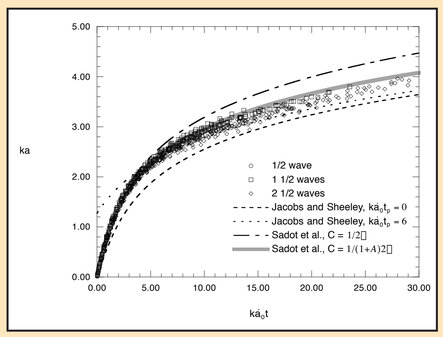

Late-time amplitude measurements are shown along with nonlinear theories. Jacobs and Sheeley (*Phys. Fluids* **8**, 405, 1996) modeled the late-time flow as a row of point vortices in fluids with A = 0, where $k\dot{a}_0 t_p$ is the time when the vorticity has coalesced into a point. Sadot et al. (*Phys. Rev. Lett.* **80**, 1998) used several models' results to develop a rational equation for growth that captures the early stages to second order (with A dependence) and converges to the correct asymptotic velocity. The parameter C is a function of the asymptotic velocity, with the functional form of A dependence developed in Niederhaus (Ph.D. dissertation, University of Arizona, 2000).

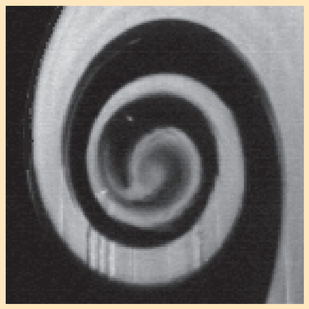

One parameter that has not received previous study is the influence of Reynolds number on the flow. The Reynolds number for this vortex dominated flow is defined using the circulation of the vortices and the average kinematic viscosity of the fluids, i.e. /. While the overall amplitude was not found to be a function of the Reynolds number, the dynamics of the vortex core was influenced by the flow Reynolds number. Measurements were made of when the interface first became multi-valued, and when the vortex had completed a given number of turns. The image to the left shows a vortex that has just made 2 complete turns.

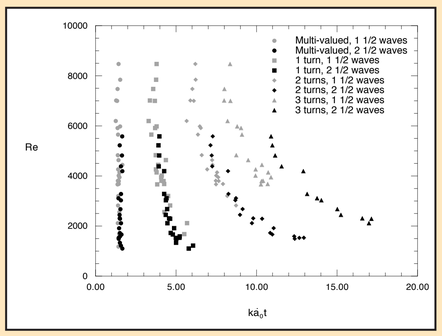

This graph shows the evolution of the vortex core as a function of the experimental Reynolds number. At early-times when the vorticity is still distributed along the interface, the flow is not a function of Reynolds number and the interface first becomes multi-valued at $k\dot{a}_0 t$ 1.5 for all Reynolds numbers investigated. After the vorticity has concentrated, the lower Reynolds number experiments have a slower turning rate due to viscous diffusion of vorticity from the cores. However, because perturbation amplitudes were not found to be a function of Reynolds number, the size of the vortex core is still small compared to the perturbation amplitude.

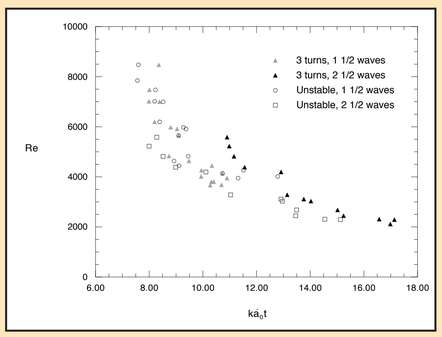

Shown on the graph to the left is the nondimensional time when the disturbance amplitude equals the spiral thickness (see images to right) for those experiments exhibiting the secondary instability. Higher Reynolds number experiments become unstable sooner, with the lower Reynolds number experiment taking more than twice as long to exhibit the instability. The instability appears to be correlated to the number of turns in the vortex core, occurring roughly after three turns over the Reynolds number range investigated. Due to experimental time limitations, a critical Reynolds number for the secondary instability cannot be determined.

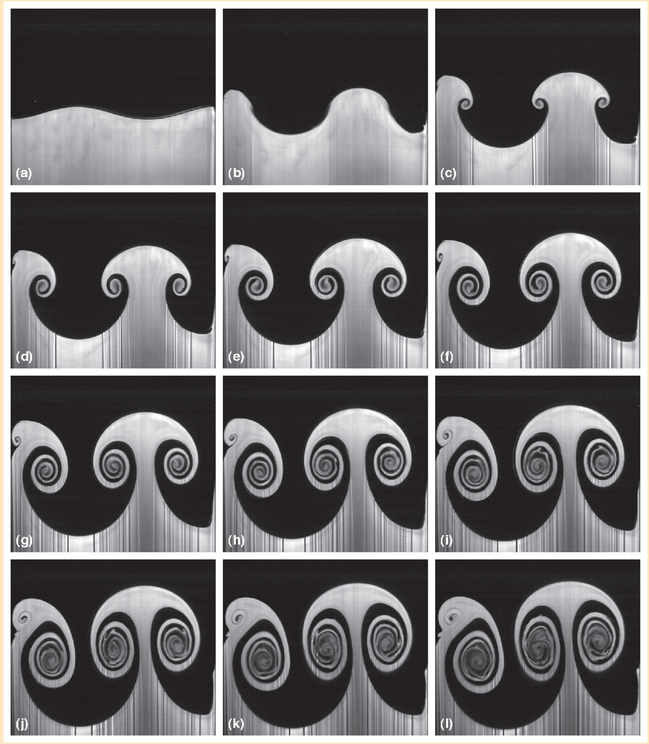

Shown above is a sequence of images from an experiment with ka_i = 0.29 and 1 1/2 waves inside the tank. The Reynolds number (based on circulation) of the experiment is 4830. Initially the instability develops very similarly to the lower Reynolds number cases. Starting at frame (h), however, one can see the start of a secondary instability in the core of the vortex. The secondary instability takes the form of oscillations superimposed on the vortex spiral. The waves start near the center of the core and grow in size and extent until all layers of the core spiral are effected. By frame (k) the instability has spread throughout the vortex core and it appears that the interface is no longer sharp and the fluids are starting to mix on a smaller scale.

Experimental Study of a Strongly Shocked Gas Interface with Visualized Initial Conditions

8th International Workshop on the Physics of Compressible Turbulent Mixing

California Institute of Technology,

Pasadena, California, USA, Dec. 9-14, 2001

Mark Anderson,
Jason Oakley,
Bhalchandra Puranik,
Riccardo Bonazza

Department of Engineering Physics
University of Wisconsin –Madison

Outline

- University of Wisconsin Shock-Tube Laboratory (WiSTL)
- Interface preparation
- Shocked interfaces
- Comparisons with non-linear theories
- Conclusions

WiSTL (Wisconsin Shock Tube Laboratory)

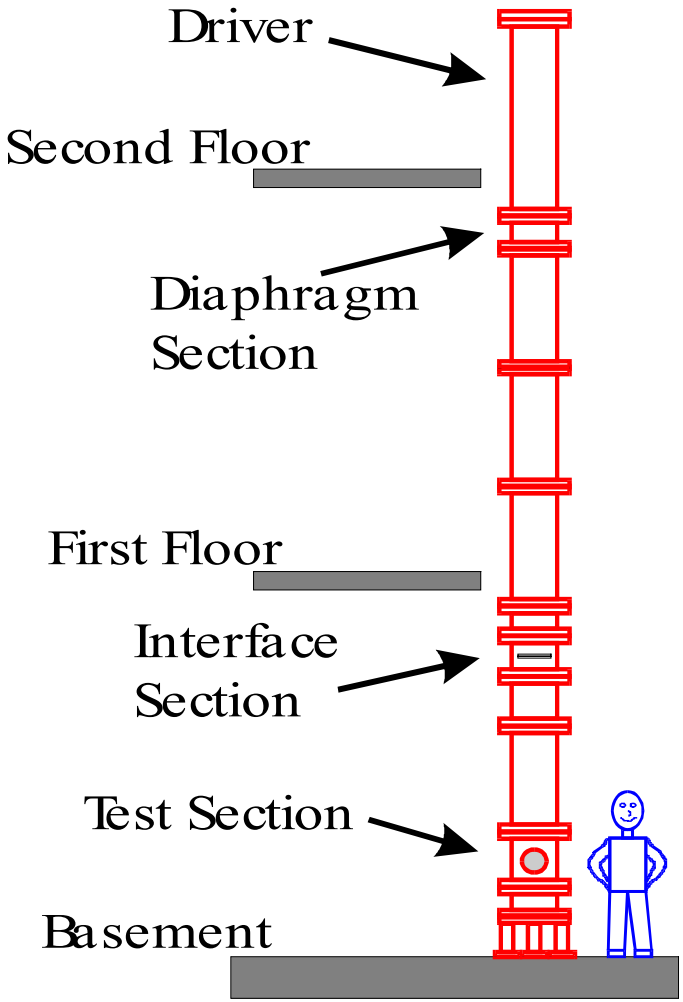

- Vertical Orientation
- Large Internal Square Cross-Section (25 cm square)
- Total Length=9.2 m
  Driven Length=6.8 m
- Structural Capacity 20 Mpa
- Modular Construction

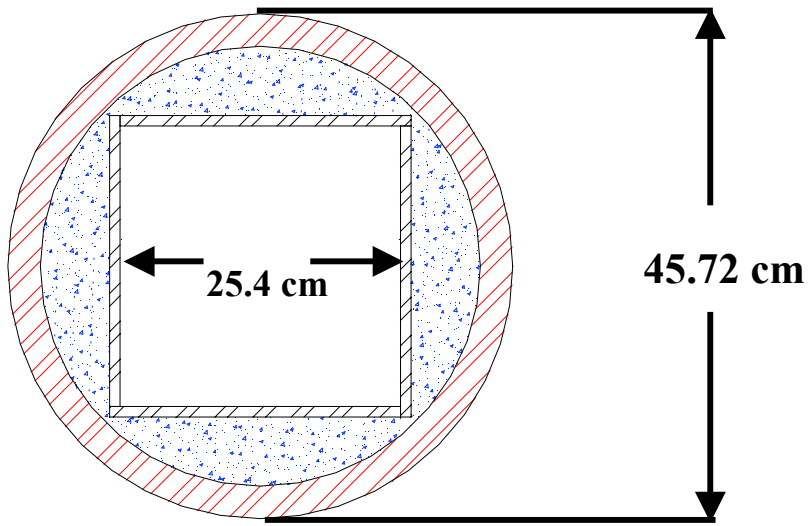

Interface Preparation

- Use of a retractable metal plate formed into a sinusoidal shape
- Copper plate, 0.6 mm thick
- Plastic deformation by rolling operation
- Sine wave parameters:
  - Amplitude = 3.18 mm
  - Wavelength = 38.1 mm
  - η_0/λ = 0.083

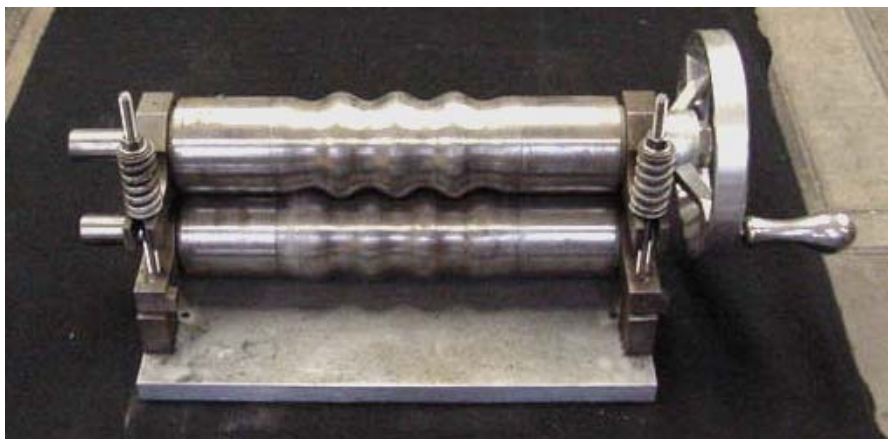

Rollers

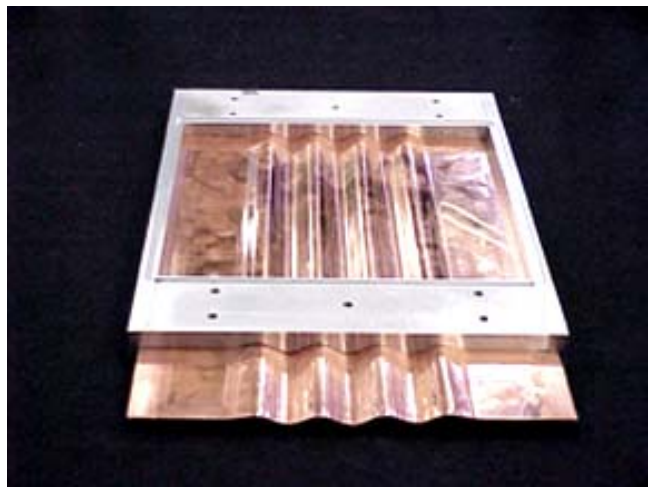

Formed plate

Study of initial conditions

- $P_{initial}$ = 1 atm, $T_{initial}$ = 298 K
- Ar-ion laser @ λ=514 and 488 nm, CW
- Planar Mie scattering visualization
- CCD camera: 256 x 256 pixel array, 8 bit/pixel
- Two-stage retraction (τ_1 ~ 250 ms, τ_2 ~ 80 ms)

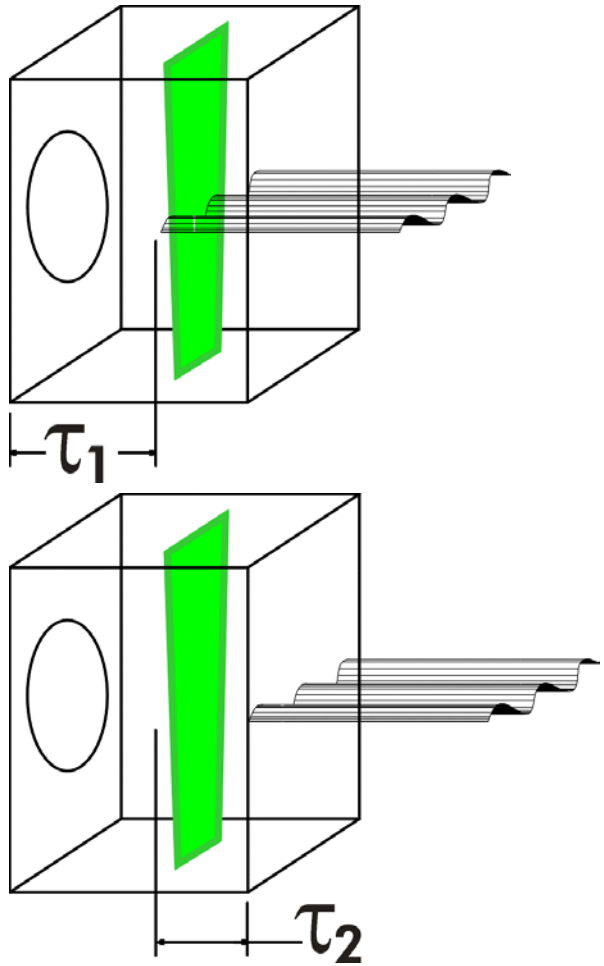

RT Unstable Interface (CO_2/Air)

CO_2

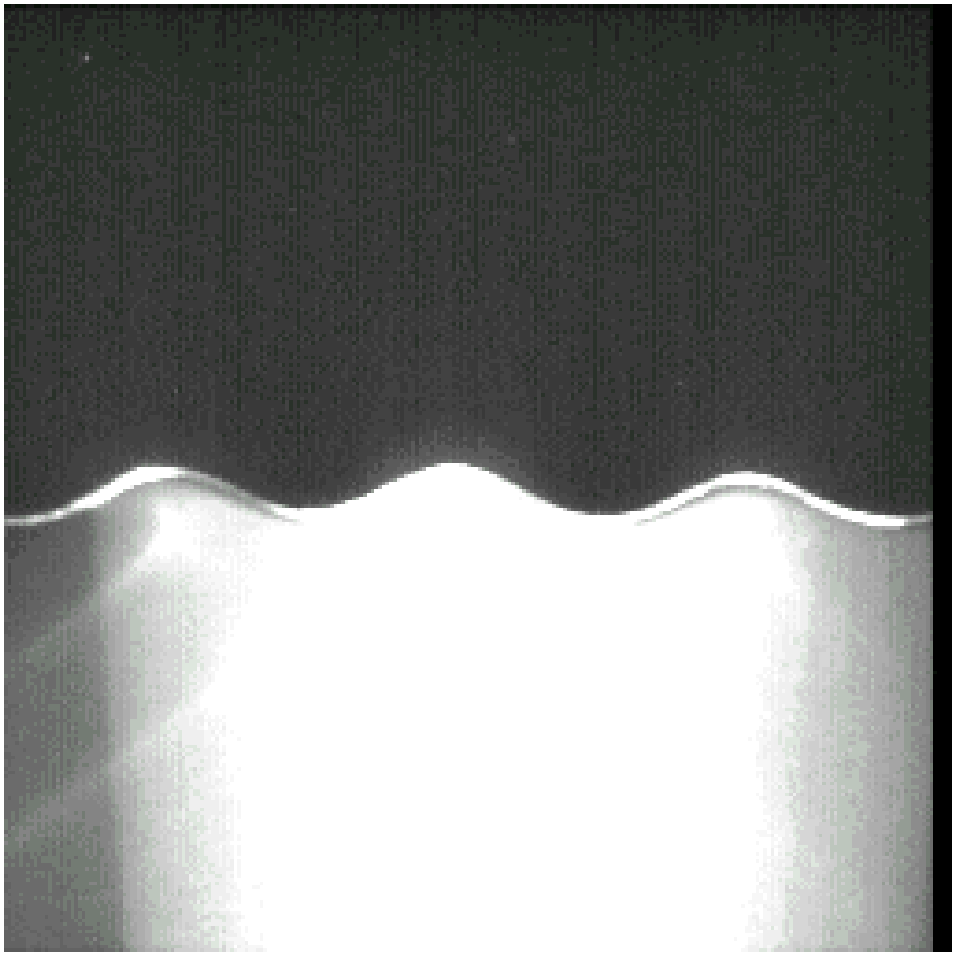

Air seeded with smoke

Desired τ_{RT}<120 ms for RM Initial Condition

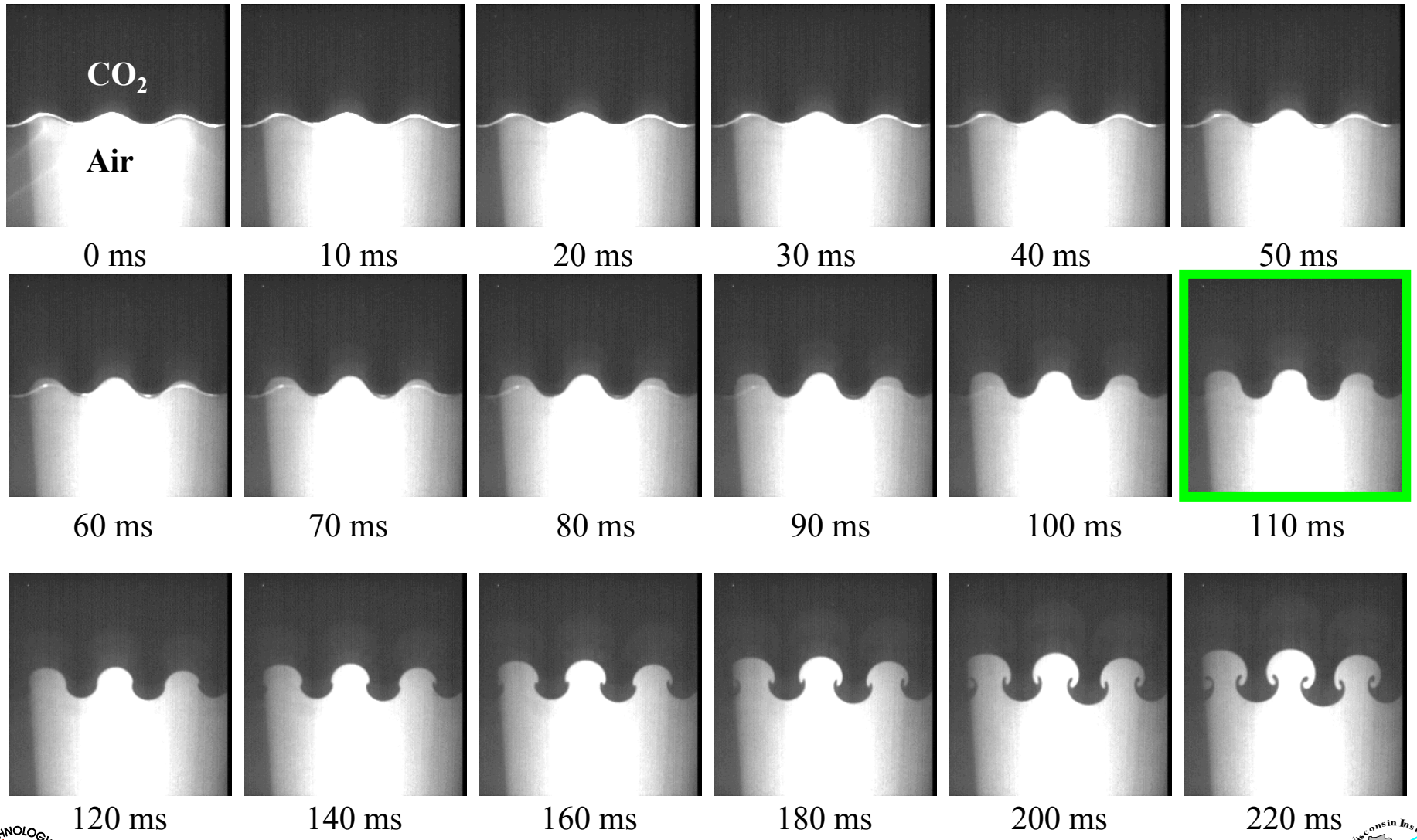

R-M instability visualization results

- CO_2/Air, A_{post} = 0.246, A_{pre}= 0.206
- Very early interaction of the M=3.06 shock wave with the sinusoidal interface
- Development of phase reversal (heavy/light configuration)

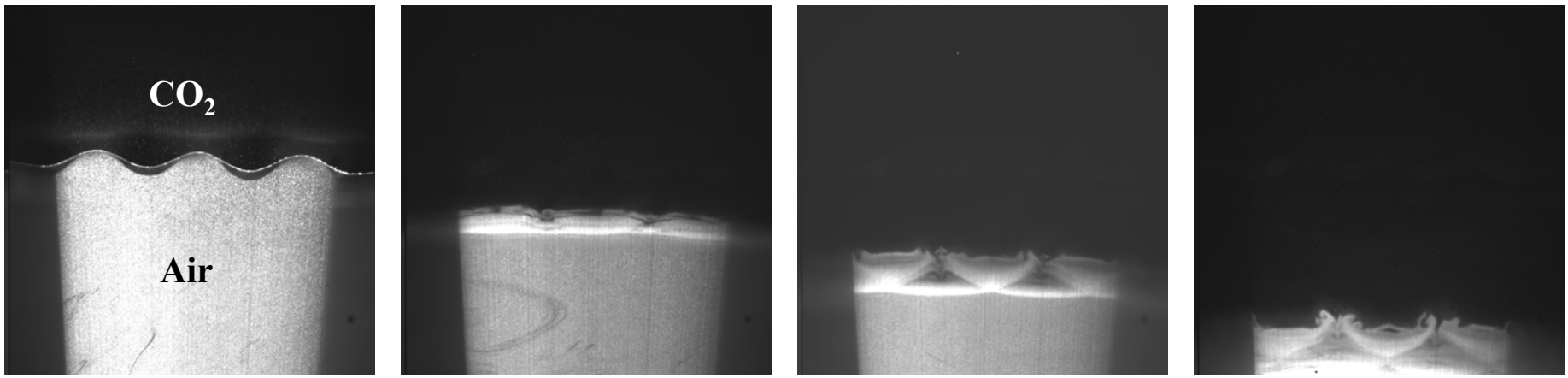

(a) (b) (c) (d)

- (a): Pre-shocked interface (Note the location of peaks and troughs)
- (b): Shocked interface ~ 5 μs after initial shock acceleration
- (c): Shocked interface ~ 36 μs after initial shock acceleration
- (d): Shocked interface ~ 39 μs after initial shock acceleration

R-M instability visualization results (Cont'd)

I.C. 0s

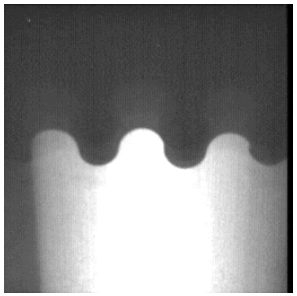

0.64 ms

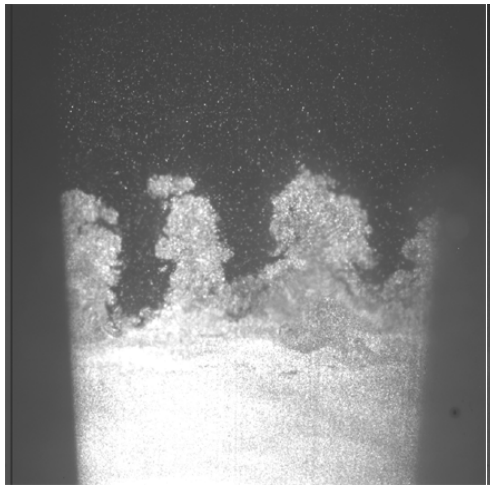

1.08 ms

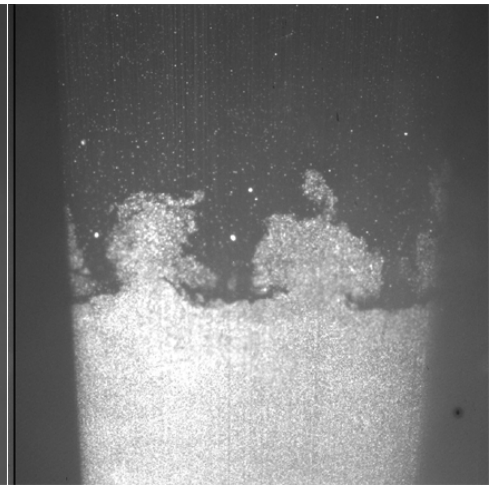

1.37 ms

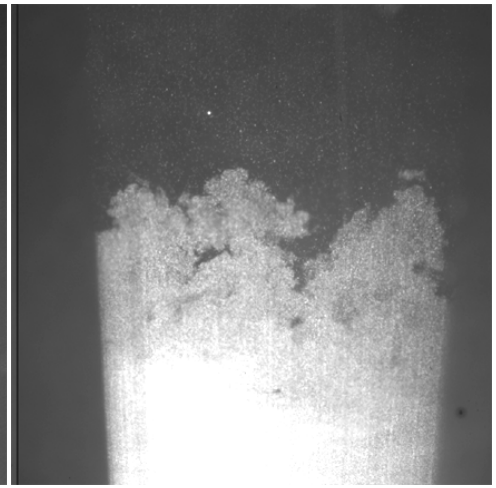

1.80 ms

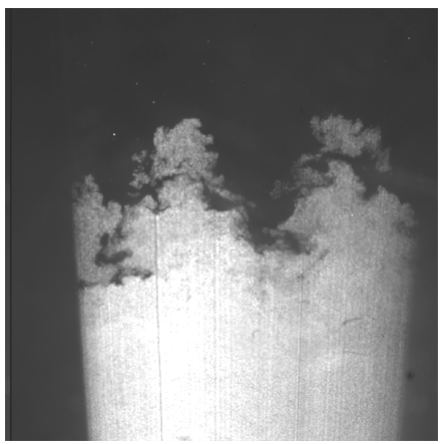

2.1 ms

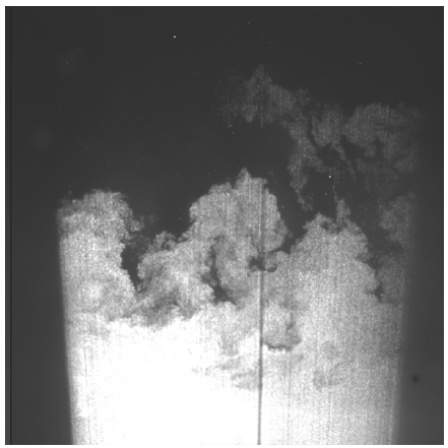

- Evolution of interface growth for the same nominal initial condition.
- Each image was taken in a separate experiment with a M~3.06 shock.
- Initial condition inferred from time of shock interaction and RT experiments.

Experiments: Image Analysis

- Images
  - Initial condition: 3 peaks, 2 troughs
  - Shocked image: 1-4 peaks, 1-3 troughs
  - Median filter
  - Excess noise removed in driven and test gases manually
  - Convert to black and white, then apply Sobel operator to detect edge
- Perturbation amplitude:

$$\eta = \frac{1}{2}\left(\overline{P}_{PIX} - \overline{V}_{PIX} - 1\right)P_{DIM}$$

$\overline{P}_{PIX}$ = average pixel row number of perturbation peaks
$\overline{V}_{PIX}$ = average pixel row number of perturbation valleys
P_{DIM} = pixel dimension (mm/pixel)

- Error less than 2 pixels: 0.8 mm for initial condition, 0.4 mm for shocked interface

Analytic theories

Richtmyer (1960) impulsive model: $\eta(t) = k[u_p]A\eta_0 t$

Sadot *et al.* (1998) nonlinear theory: $\left(\frac{d\eta}{dt}\right) = \left(\frac{d\eta}{dt}\right)_{LIN}\left(\frac{1+Bt}{1+Dt+Et^2}\right)$

$$D_{b/s} = (1 \pm A')\left(\frac{d\eta}{dt}\right)_{imp} k \qquad E_{b/s} = [(1 \pm A')/(1+A')] \times (1/2\pi C)\left(\frac{d\eta}{dt}\right)_{imp}^2 k^2$$

$C = 1/2\pi$ for low A'

Zhang and Sohn (1997) nonlinear theory:

$$\left(\frac{d\eta}{dt}\right)_{total} = \frac{\left(\frac{d\eta}{dt}\right)_{lin}}{1+\left(\frac{d\eta}{dt}\right)_{lin}\eta_0' k^2 t + \max\{0, \eta_0'^2 k^2 - A'^2 + 1/2\}\left(\frac{d\eta}{dt}\right)_{lin}^2 k^2 t^2}$$

Comparison with Theories

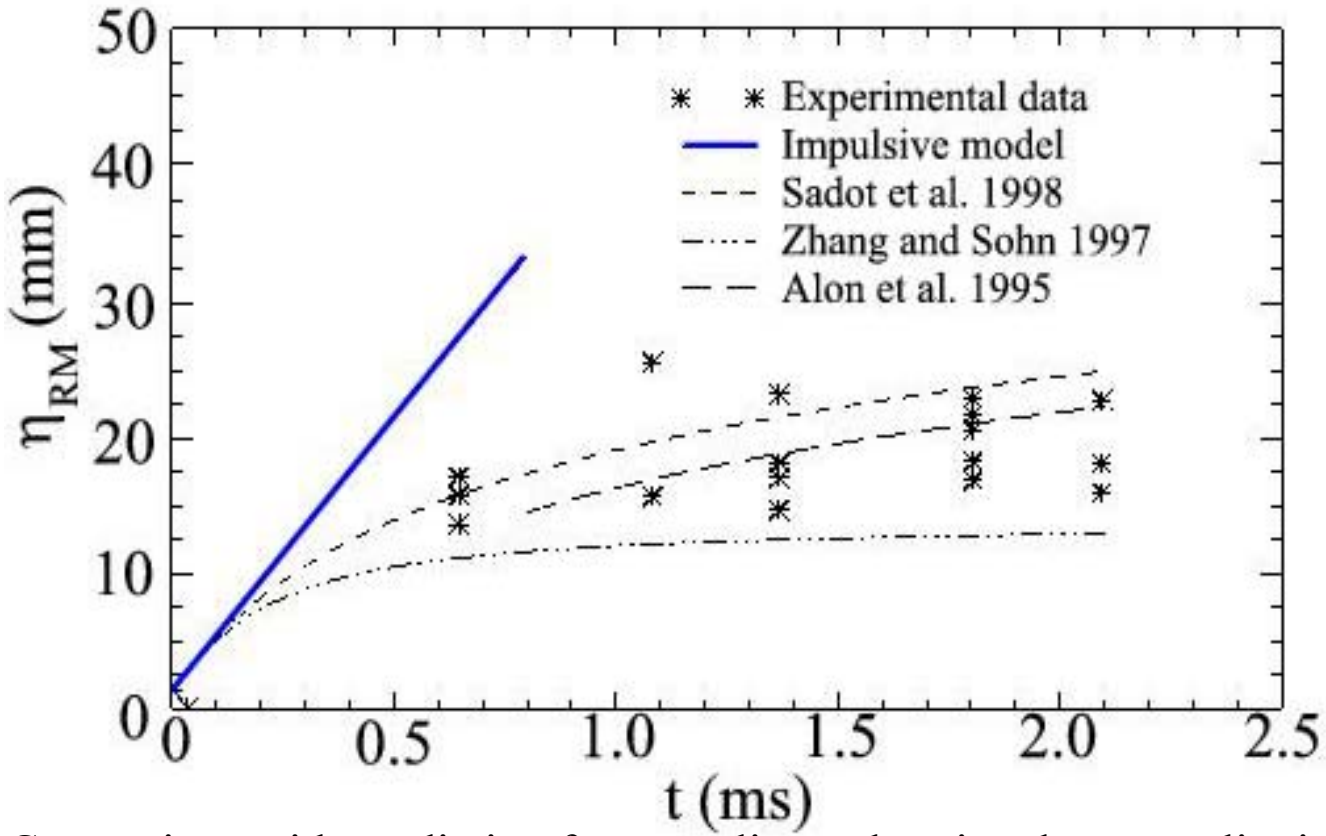

- Comparison with prediction from nonlinear theories shows qualitative agreement
  - - - Sadot *et al*. theory overpredicts at late times
  — · · · Zhang and Sohn theory underpredicts at all times

Experiment: Combined Imaging Setup

Previously, the RM initial condition was inferred from a reference set of RT experiments.

Dynamic imaging of the interface, prior to being shocked, provides interfacial initial condition data for each RM experiment.

Provides the interface geometry of the initial condition which may be used in a numerical simulation.

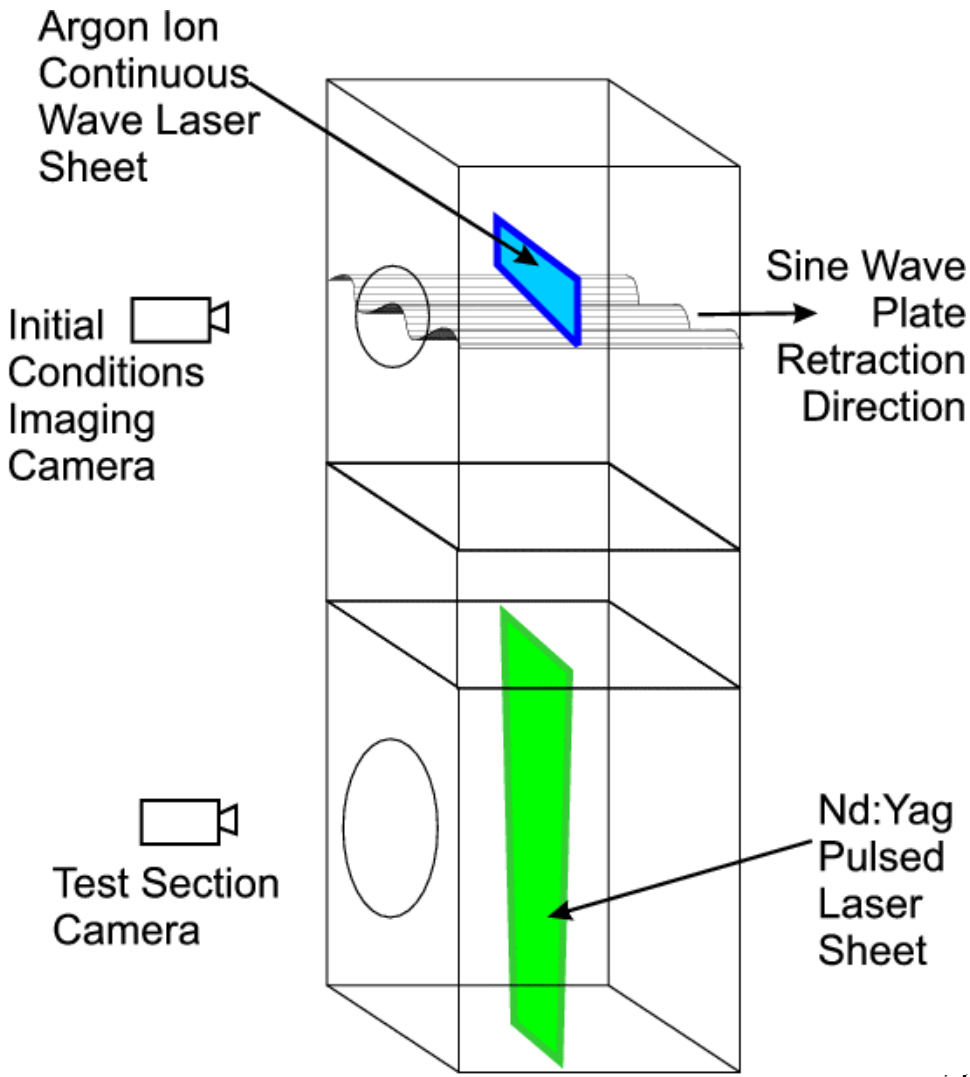

Experimental conditions

- Incident shock wave: M=2.90, in CO_2
- $P_{initial}$ = 1 atm, $T_{initial}$ = 300 K
- Post-shock A'=0.245 (A=0.206, $A=(\rho_1-\rho_2)/(\rho_1+\rho_2)$)
- Planar Mie scattering visualization, smoke particles
- Two-stage retraction ($\tau_1 \sim 250$ ms, $\tau_2 \sim 80$ ms)
- Interface section
  - Ar+ laser @ λ=488 nm, continuous wave
  - CCD camera, 256 x 256 pixel array, 8 bit/pixel, framing @ 100 fps
- Test section
  - Nd:YAG laser @ λ=532 nm, 10 ns pulse
  - CCD camera: 1024 x 1024 pixel array, 16 bit/pixel, one shocked image per experiment

Experiment: CO_2-air M=2.90

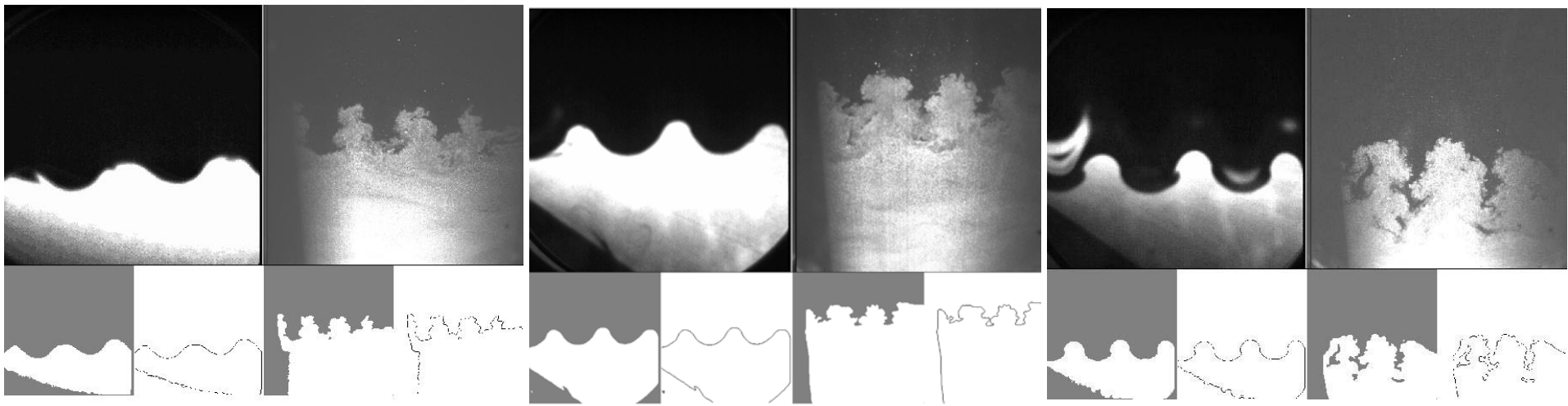

Experiment 322
x = 0.457 m
η_{IC} = 4.64 mm
η_{RM} = 13.83 mm
τ_{RM} = 0.70 ms

Experiment 351
x = 0.756 m
η_{IC} = 5.90 mm
η_{RM} = 12.3 mm
τ_{RM} = 1.13 ms

Experiment 363
x = 0.987 m
η_{IC} = 7.81 mm
η_{RM} = 28.0 mm
τ_{RM} = 1.57 ms

- Initial condition well into nonlinear regime ($\eta_0/\lambda > 0.2$)
- Phase inversion of shocked interface

Comparison with Theories

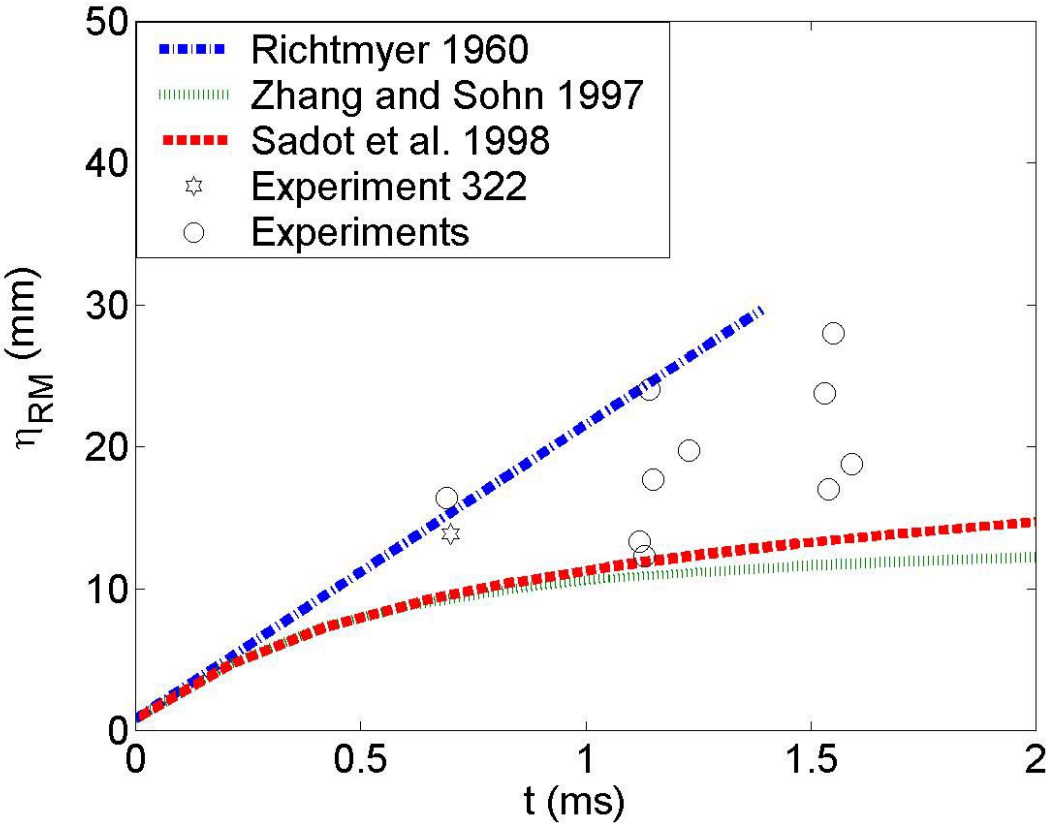

Comparison with prediction from theories shows qualitative agreement and experimental data bounded by the linear (upper) and nonlinear theories (lower)

Conclusions

- Two dimensional gas-gas interface without a membrane
- Strongly shocked interface (CO_2-air, M up to 3.06)
- Initial condition geometry imaged for each experiment
- Scatter in data attributed to extreme sensitivity to initial conditions
- Results are similar to existing linear theories
- Needed improvements
  - Better retraction mechanism for more repeatable initial condition
  - Diagnostic upgrade to obtain more than one shocked image per experiment

Lower Mach # Experiment: CO_2-air M=1.41

A=0.2061, A'=0.2242, Al3003 0.508 mm diaphragm

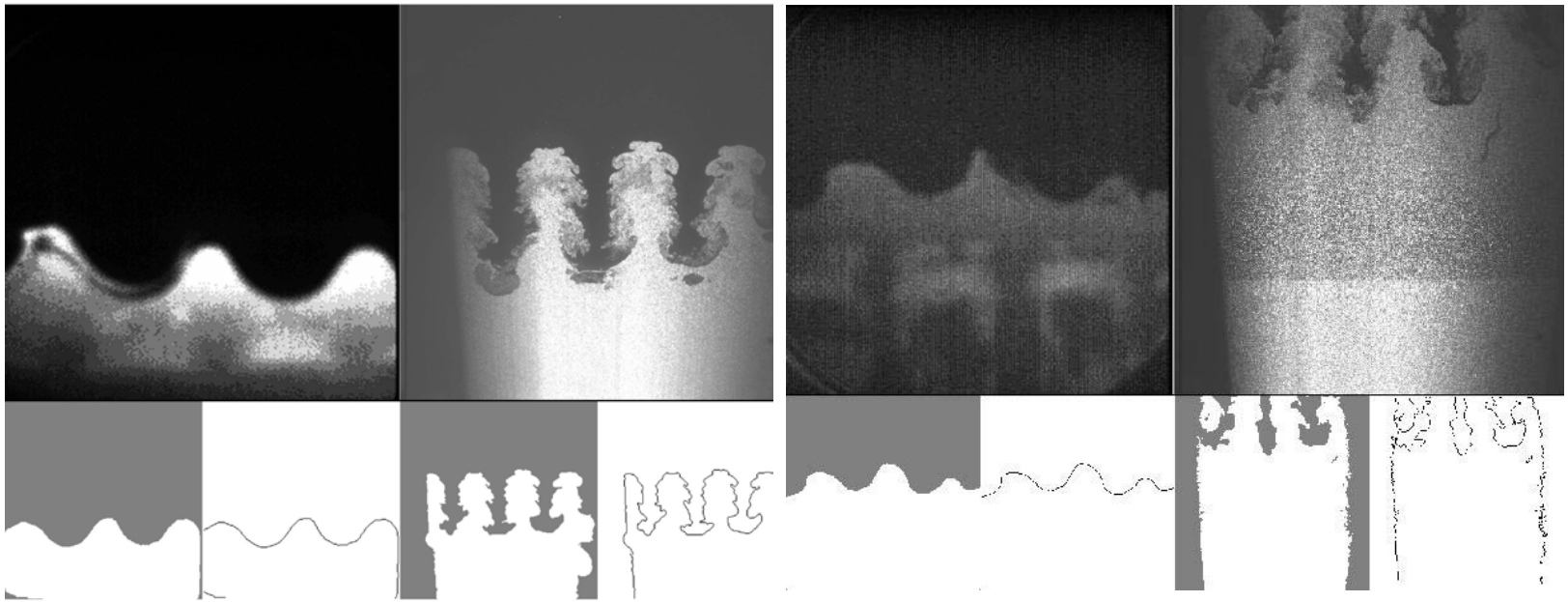

Experiment 327
x = 0.457 m
η_{IC} = 6.12 mm
η_{RM} = 25.3 mm
τ_{RM} = 2.60 ms

Experiment 343
x = 0.756 m
η_{IC} = 5.45 mm
η_{RM} = 23.0 mm
τ_{RM} = 3.97 ms

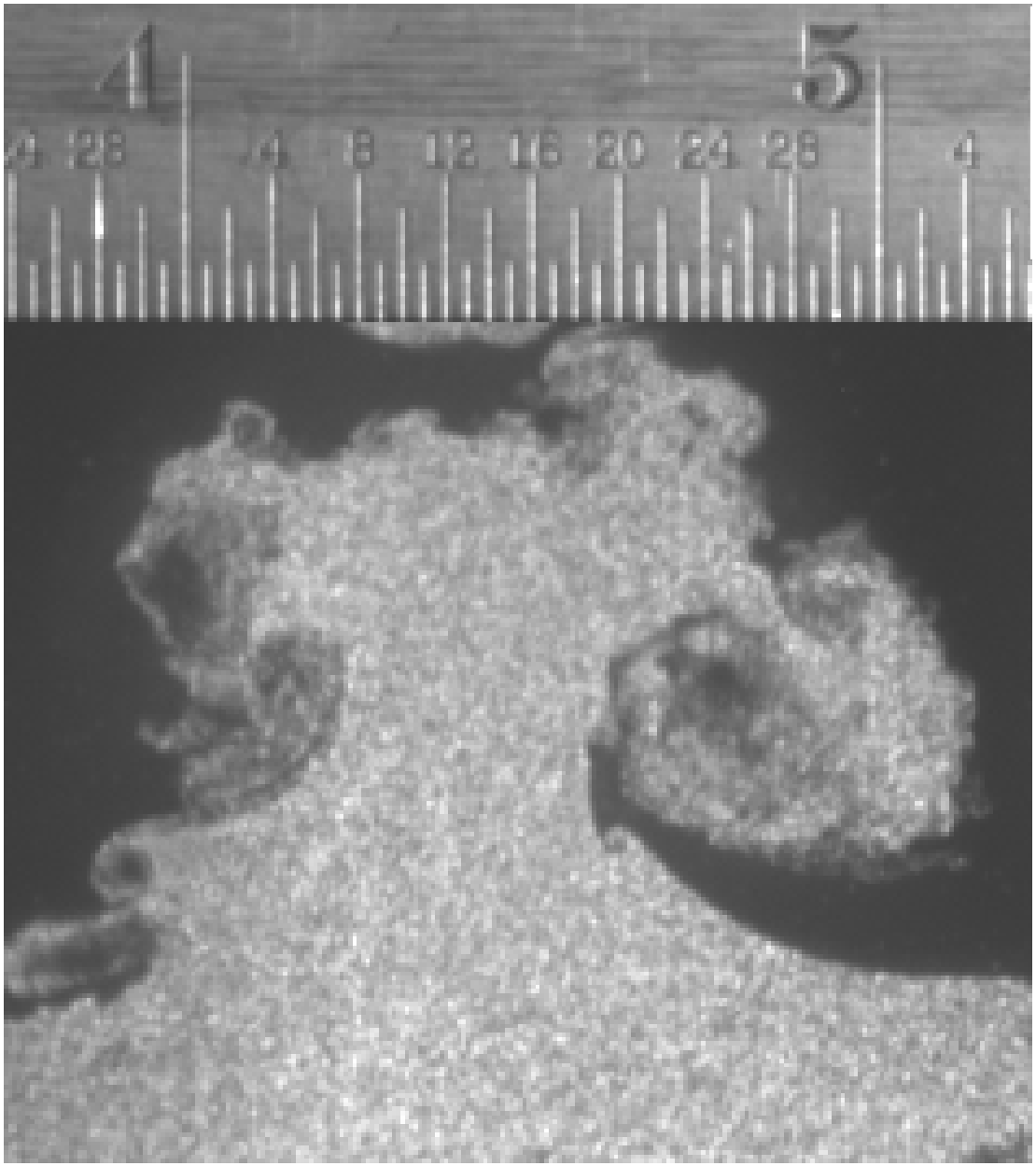

Magnified image of one peak from test 327, the scale above the instability is in inches.

Paper at VIII International Workshop on the Physics
of Compressible Turbulent Mixing

California Technological Institute, Pasadena, California, USA

Experimental Investigation into the Evolution of Turbulent Mixing of Gases by Using the Multifunctional Shock Tube

Yu.A.Kucherenko, O.E.Shestachenko, Yu. A. Piskunov, E.V. Sviridov,
V.M.Medvedev, A.I.Baishev

Russian Federal Nuclear Center – Academician E. I. Zababakhin
All-Russian Research Institute of Technical Physics
456770 Snezhinsk, Russia

At the initial instant of time, different density gases being investigated are found in the multifunctional shock tube and are separated by a "specter-membrane". Then the specter-membrane is destroyed into small-scale fragments by the external force. The contact boundary of gases is accelerated by means of a compression wave, which is formed in the shock tube. At the same time, at the contact boundary of different density gases, the Rayleigh-Taylor instability arises and the unstationary zone of the gravitational turbulent mixing forms. On the basis of the experimental results the dependence of the turbulent mixing zone width on the contact boundary displacement has been constructed, and the gravitational turbulent mixing constant alpha has been determined.

1. INTRODUCTION

In most of problems associated with the fast compression processes of a matter the situation arises when a matter of less density (a light matter) and a more dense matter (a heavy matter) have a surface of their contact (a contact surface) and are moving with acceleration. In case of constant acceleration the contact surface is said to be subjected to the action of the Rayleigh-Taylor instability (RTI). If the pulsed acceleration (for example, at the passage of shock waves) takes place, then any contact surface is unstable, because the Richtmyer-Meshkov instability (RMI) arises.

The instability means that any small perturbation has a tendency to an unlimited growth, the mutual penetration of media and the destruction of structures under the action of shear turbulence take place, the turbulent mixing zone (TMZ) arises. The evolution of instabilities on the contact surface of different density media exerts an influence on the dynamics of the compression, restricts the limiting value of compression and the dynamics of subsequent processes.

The determining parameter to take into account the gravitational turbulent mixing influence is the turbulent mixing zone width which depends on the density ratio of different density media, the time of the unstable situation existence, etc. In a number of problems, taking into account the compressibility media being found along the different sides of the contact surface becomes important.

Under laboratory conditions the investigation of RTI and arising gravitational turbulent mixing (GTM) is performed with using different density liquid and gaseous media at the installations EKAP and SOM. The installation OSA makes it possible to investigate different kinds of instability (RTI, RMI) by using three replaceable drivers for these purposes. The distinctive feature of the experiments is the usage of the controlled separating membrane making it possible to form the evolution process of GTM of different gases with preset initial conditions.

The aim of the present work is to perform experiments by using the shock tube OSA creating RTI and to apply the controlled separating membrane for these investigations.

2. SET- UP OF EXPERIMENTS

For performing experiments regarding the gravitational turbulent mixing investigation the scheme presented in Fig.1 was used. The $0 < x < x_1$ region is filled up with the compressed gas and represents a high pressure chamber. From the rest of the shock tube part the chamber is separated by a light piston which is found at the point $\tilde{o} = \tilde{o}_1$. The $\tilde{o}_1 < \tilde{o} < \tilde{o}_2$ region is filled up with a light working gas **1** of density ρ_1 and represents the low pressure chamber. The $\tilde{o} > \tilde{o}_2$ region is filled up with a heavy working gas **2** of density ρ_2 and represents a measuring chamber by which the mixing process registration is carried out. In the point $\tilde{o} = \tilde{o}_2$ the separating membrane is found which prevents from the mixing of working gases during the experiment preparation. At the specified instant of time the separating membrane is destroyed into pieces of definite size by the external force. The installation operates as follows. At the instant of time $t=t_0$ the piston begins to move with constant acceleration in the positive direction of the axis X under the action of the compressed gas in the high pressure chamber. From the piston a compression wave begins to propagate in the

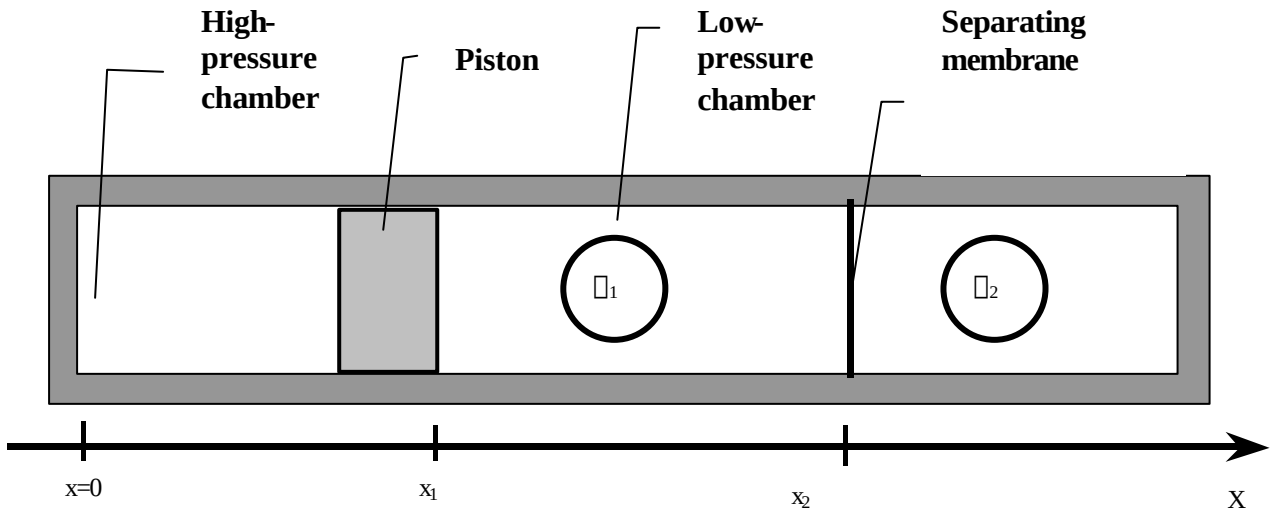

Fig. 1 Physical scheme of the experiment

positive direction of the axis X with velocity $\tilde{N}_1$, where $\tilde{N}_1$- sound velocity in the working gas **1**. At the instant of time $t = (x_2 - x_1)/C_1$ the compression wave arrives at the interface of gases $\tilde{o} = \tilde{o}_2$. At the same time, the external destructive force is applied to the separating membrane, and the contact boundary between gases begins to be accelerated. As the contact boundary acceleration profile is slightly falling and the pressure gradient in the compression wave is directed oppositely to the density gradient at the contact boundary, then the conditions are created for the RTI occurrence.

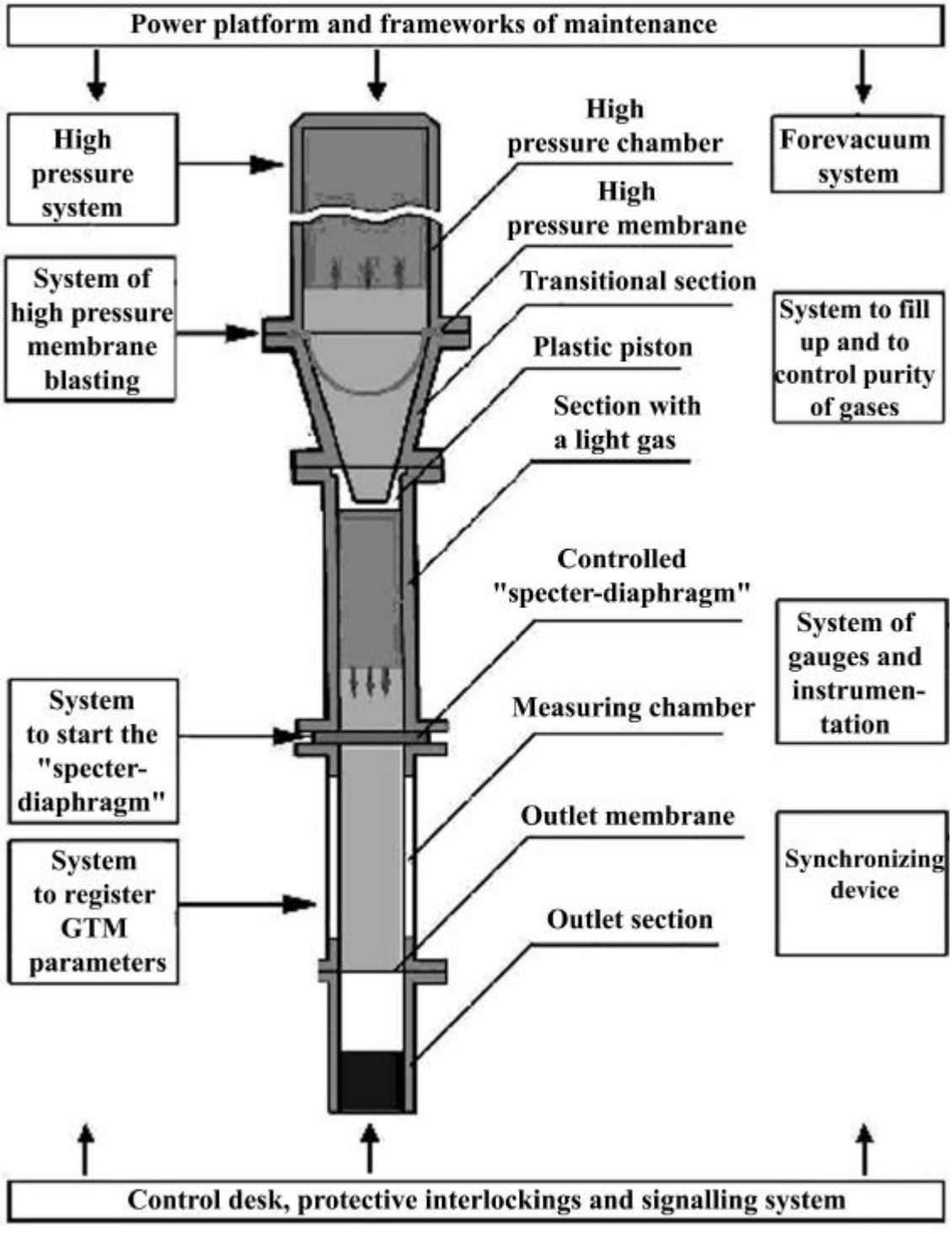

Fig.2. Functional scheme of the installation OSA

Fig.2 shows the functional scheme of the installation OSA. The total height of the installation amounts to ≈ 5 m. In the upper part of the installation the high pressure chamber is located. It represents a thick-walled vessel consisting of three parts connected among themselves by flanges. The operating pressure in the chamber is up to 2 MPa. At the upper flange of the high pressure chamber there is the emergency valve of pressure drop, pipelines for gas inlet and outlet. From the rest of the shock tube part the high pressure chamber is separated by the aluminum membrane. The membrane thickness amounts to 1 mm or 0.5 mm and determines the limiting pressure of gas in the reservoir. For the membrane destruction at the specified instant of time, a strong electric explosion is used. A sliding contact in the form of a metal needle touches the membrane in the center. The needle is connected to the positive pole of the capacitor bank by means of cables, but the membrane – to the negative pole. At the instant of time $t = t_0$ the pulse of current burns through the aluminum membrane in the center. Gas begins to flow out of the reservoir and opens the membrane completely. The gas flow passes through the conical part of the transitional section and begins to push a plastic piston. In the compression wave the pressure profile and amplitude depend on the piston mass. Under the action of the compressed gas the piston is moving with acceleration along the section with a light gas. The section with a light gas is filled up with gas of density ρ_1. The internal cross-section of the light gas section is equal to 138 × 138 mm^2, but the length amounts to 500 mm. The contact boundary acceleration profile depends on the light gas section. The further the contact boundary of gases from the piston is, the more the acceleration differs from the constant one and approaches to the delta-shaped one.

Prior to the experiment performing the section with a light gas is filled up with the working gas of density ρ_1 through the gas inlet system. Simultaneously, the measuring chamber is filled up with the working gas of density ρ_2 through the gas inlet system. The gas inlet system controls the extent of purity of working gases. Between the light gas section and the measuring chamber the controlled separating membrane is located. It is designed to prevent from the mixing of working gases during the experiment preparation.

The controlled measuring membrane represents the interweaved grid of microconductors, 20 μm in diameter and 4 mm in step. To this grid the liquid film of the soapy solution is applied. The film thickness amounts to ≈ 1 μm. At the specified instant of time the electric current is passed through the grid. Microconductors are heated, and the liquid film begins to be destroyed into the pieces with the typical scale ≈ 4 mm in the places of contact with microconductors. Then the surface tension forces tighten the pieces of liquid film into small balls which act as initial perturbations at the contact boundary of working gases. When the compression wave reaches the boundary between gases, the contact boundary begins to be accelerated. As acceleration is directed from the light gas to the heavy one, the conditions are created for the gravitational turbulent mixing zone evolution.

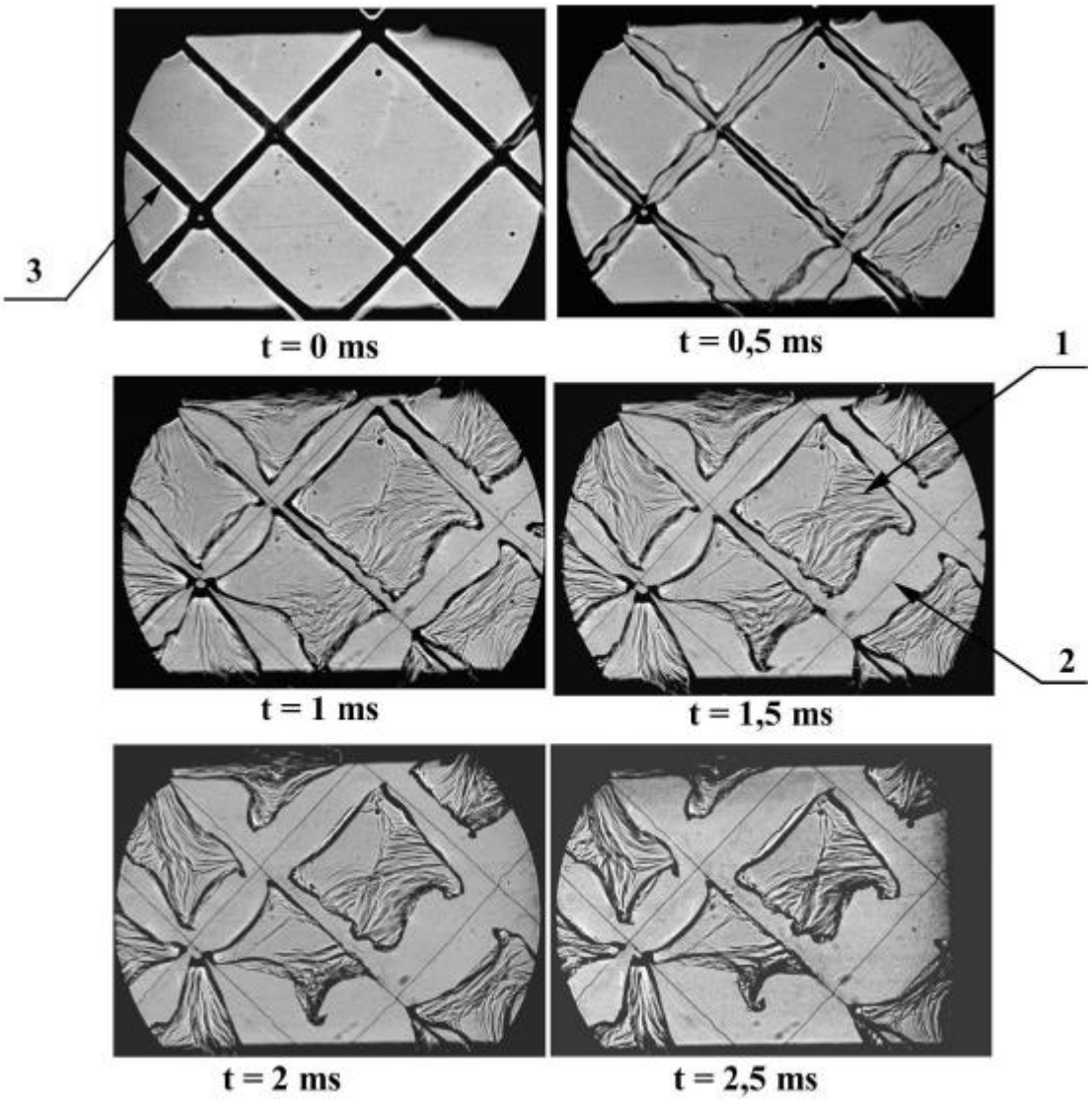

Fig. 3 Characteristic photographic images of the liquid film destruction process.

Fig.3 shows the characteristic photographic images of the separating membrane destruction process at different instants of time. In this figure microconductors are denoted by number **1**, liquid film pieces – by number **2,** the microconductor with the liquid film around it – by number **3**. From this figure it is seen that after applying the current pulse to the grid the liquid film begins to separate from microconductors and then, under the action of the surface tension forces, it is tightened into a drop.

After the block with the controlled separating membrane, the measuring section is located. It is filled with the working gas of density ρ_2. The measuring chamber has two transparent walls of high-quality optical glass. This makes possible to perform the photographic record of the turbulent mixing zone by means of a schlieren (photograph) technique. If it is necessary to investigate the late stages of the turbulent mixing process, then the additional chamber of low pressure is mounted between the block of the controlled separating membrane and the measuring section.

After the measuring chamber the low pressure chamber, 260 mm in length, is found. It is also filled up with the working gas of density ρ_2.

This chamber is necessary so that the reflected compression wave does not exert an influence on the photographic record of the turbulent mixing zone. After terminating the photographic record and passing of the piston into the low pressure chamber, it is necessary to slow down the piston. For this purpose the special outlet section is designed. When the piston passes into the low pressure chamber its velocity is $\sim 100 \div 150$ m/sec. Gas being pushed by the piston ruptures the outlet membrane which is located between the measuring chamber and the outlet section. Gas pressure before the piston becomes gradually higher than the pressure behind the piston, and the latter begins to be decelerated. When moving the piston along the outlet section the pressure of the decelerating gas increases. In order to decrease the acceleration of retardation and to prevent the reverse motion of the piston, it is necessary to release gas from the inlet section into atmosphere. For this purpose in the outlet section there are exhaust windows in which the membranes of lavsan are found. When reaching the ultimate strength the membranes are ruptured and gas gets into atmosphere. The rubber shock – absorber located at the bottom of the outlet section is designed to cancel the residual speed of the piston.

The registration of flow arising at the contact surface (CS) of two different density gases after its acceleration was carried out through the peepholes in the measuring section by the schlieren device IAB-451. The device is consistent with the high-speed camera VFU, operating in the mode of a time magnifier. Illuminating was carried out by a flash lamp. The light pulse duration was equal to 4 msec. The flash lamp, the camera VFU-1 and the phenomenon itself were synchronized is such a way that the phenomenon registration was performed at the required stage of evolution. The optical method to register transparent inhomogeneities is based on the dependence of the refractive index of gases on density.

3. Discussion of results

In the given work argon Ar (density ρ = 1.78 kg/m^3) and Kr gas (density ρ = 3.7 kg/m^3) were used as working gases. The density ratio for the given pair of gases n = 2.1, but the Atwood number $A = \dfrac{\rho_2 - \rho_1}{\rho_2 + \rho_1}$ for the given pair of gases was equal to À = 0.35. For these experiments the acceleration of the contact boundary of gases amounted to $g \sim 40000$ m/sec^2. The photographic record of the turbulent mixing process was carried out when changing the parameter $S = gt^2/2$ from 0.1 m to 0.5 m.

Fig. 4 shows the characteristic photographic records of the gravitational turbulent mixing process. The turbulent mixing zone is seen in photos in the form of a wide dark band. It is seen that the zone width is increased with time, but the zone itself is mixing downwards. For the correct determination of the image scale, reference bench marks are set before the measuring chamber glasses.

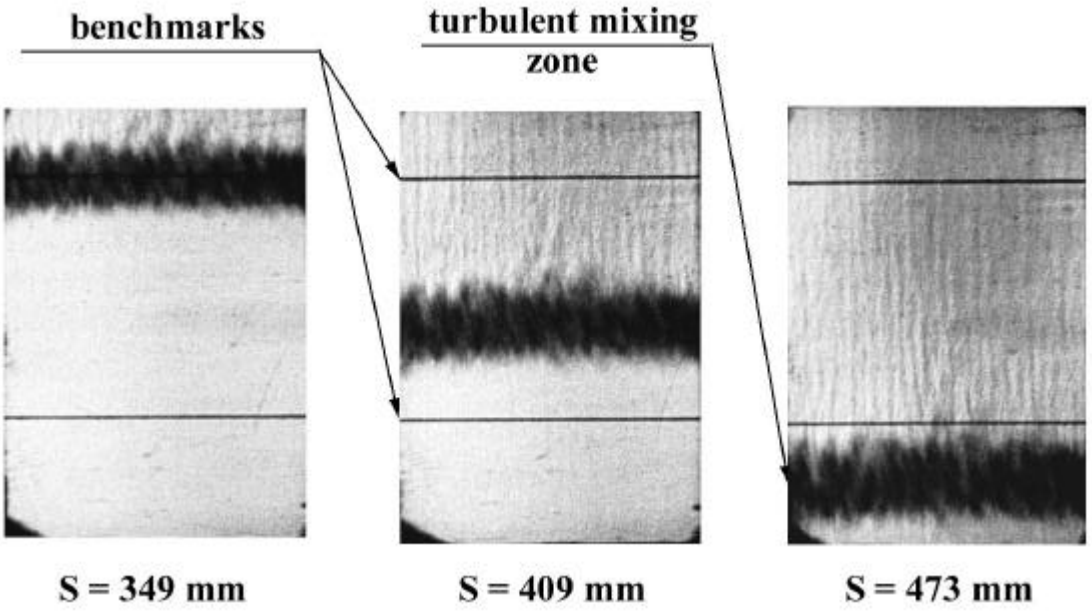

Fig. 4 Characteristic photographic images of the gravitational turbulent mixing process

Fig.5 shows the dependence of the turbulent mixing zone width on the parameter S for the pair of gases Ar – Kr. The conditions of self-similarity for the given experiment

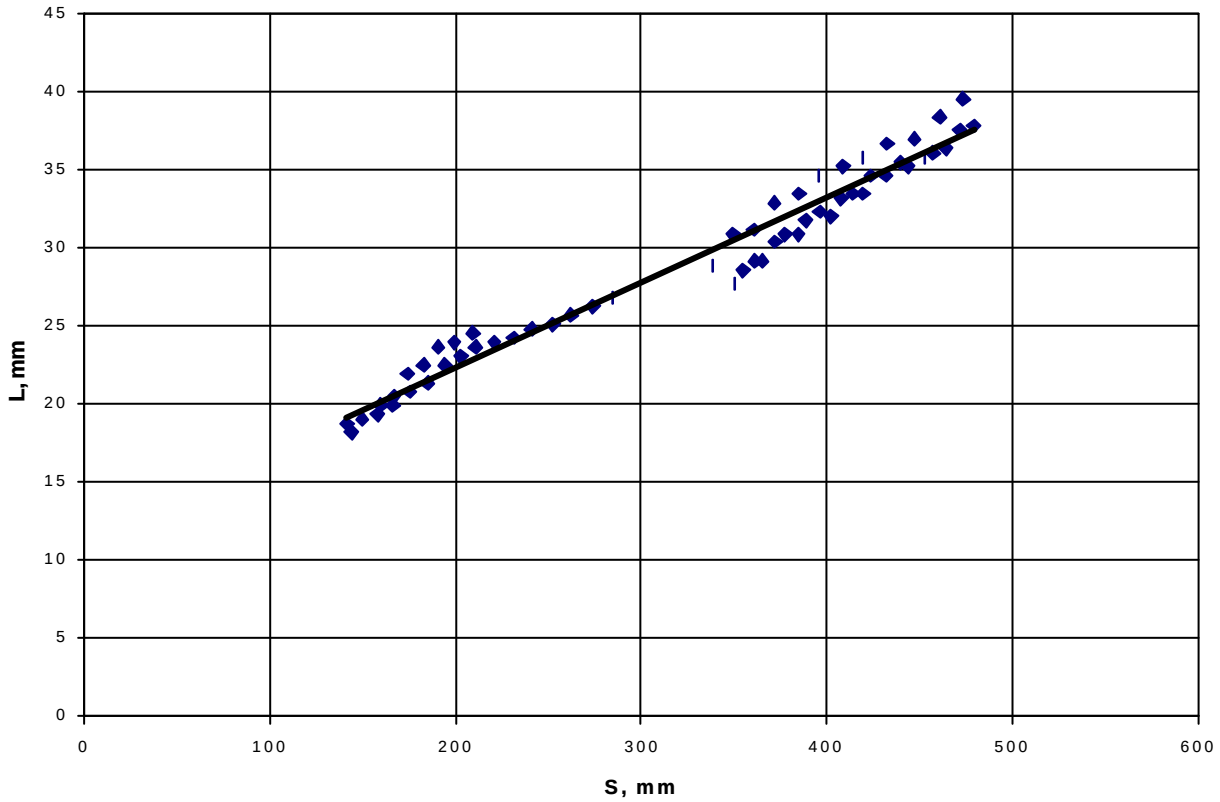

Fig.5. Dependence of the turbulent mixing zone width on the parameter S for the pair of gases Ar – Kr.

are carried out at S ≥ 100 mm. It means that the turbulent mixing zone growth does not depend on the initial conditions on the contact boundary of gases. All the totality of experimental points at S ≥ 100 mm can be described by the formula L = 2αAS, where the parameter S = gt^2/2 is the contact boundary displacement, $A = \frac{r_2 - r_1}{r_2 + r_1}$ is Atwood number and α is the dimensionless velocity of turbulent mixing. On the basis of experimental results the constant α = 0.04 has been determined.

4. Conclusion

In the given work the Rayleigh-Taylor instability for gaseous media was studied. Ar and Kr were used as working gases. Density ratio r_2/r_1 was taken to be equal to 2.1, but Atwood number $A=(r_1-r_2)/(r_1+r_2)$ was equal to 0.35.

At the initial instant of time, different density gases being investigated were located in the multifunctional shock tube and were separated by the controlled separating membrane. Then the separating membrane was destroyed by the external force into small – scale fragments with the typical size ≈ 4 mm.

The contact boundary of gases was accelerated by means of a compression wave, which was generated by the piston being accelerated. The initial acceleration of the contact boundary of gases amounted to ≈ 40000 m/sec^2.

According to the results of experiments, the dependencies of the turbulent mixing zone width on the contact boundary displacement S have been constructed. The parameter S was changed from 100 mm to 500 mm. At the self-similar stage of the turbulent mixing evolution the dimensionless velocity of turbulent mixing α was determined to be equal to 0.04.

Modeling Laser Material Strength Experiments

Steve Pollaine
David Petersen
Lawrence Livermore National Laboratory

8th IWPCTM
December 10-14, 2001

D. Kalantar, B. Remington, J. Belak, J. Colvin,
M. Kumar, T. Lorenz, S. Weber
Lawrence Livermore National Laboratory

J. Wark, A. Loveridge, A. Allen
University of Oxford

M. Meyers
University of California, San Diego

This presentation was reviewed and released as UCRL-PRES-143513-REV-2.
This work was performed under the auspices of the U.S. Department of Energy by University of California, Lawrence Livermore National Laboratory under Contract W-7405-Eng-48.

Outline of poster

- Material strength model
  - Elastic-plastic flow
  - Steinberg-Guinan and Steinberg-Lund models
- VISAR velocity measurement
  - Experiment
  - Model
- Diffraction
  - Experiment
  - Model
- Sample recovery
  - Experiment
  - Decay of shock strength
- Summary and future developments

The constituitive properties of metals is of general scientific interest

Laser experiments give us access to new regimes
- High pressures
- High strain rates

How materials deform at strain rates > 10^8/s is unknown

Relevant for impact of micrometeorites on space hardware

Diagnostics
- VISAR
- X-ray diffraction
- Recovery

Infer properties such as EOS, K, G, Y

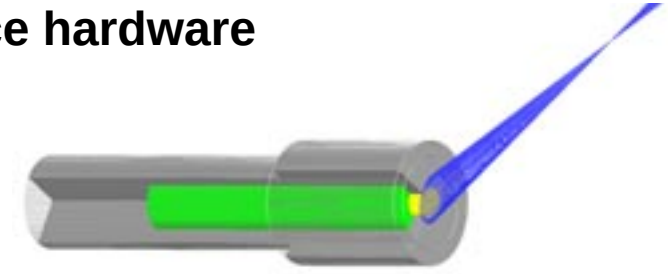

Recovery

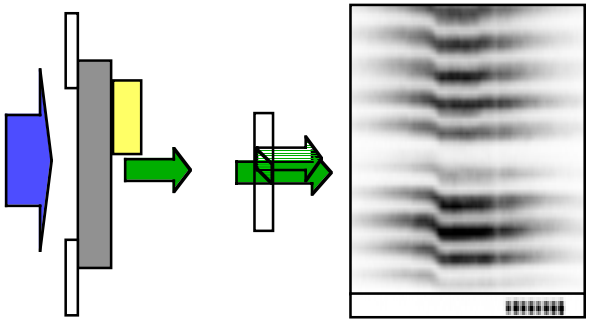

VISAR

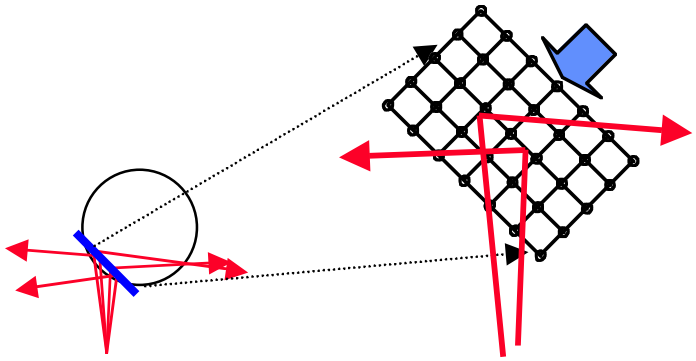

X-ray diffraction

Moderate shocks show both elastic and plastic waves

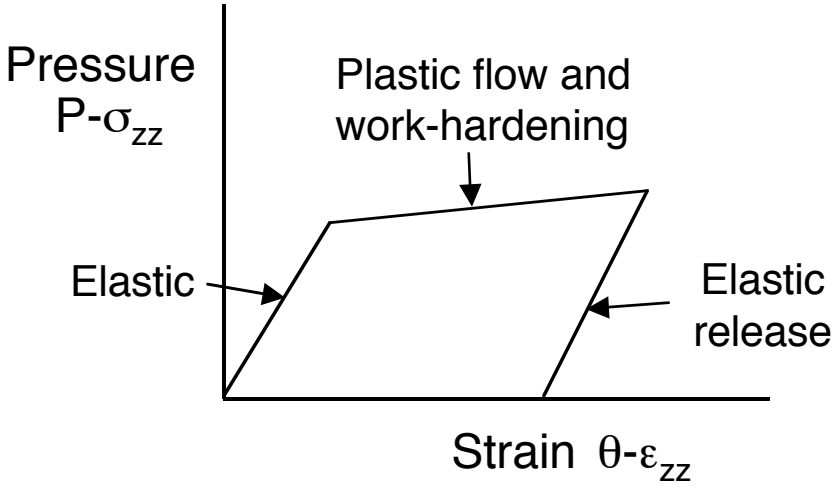

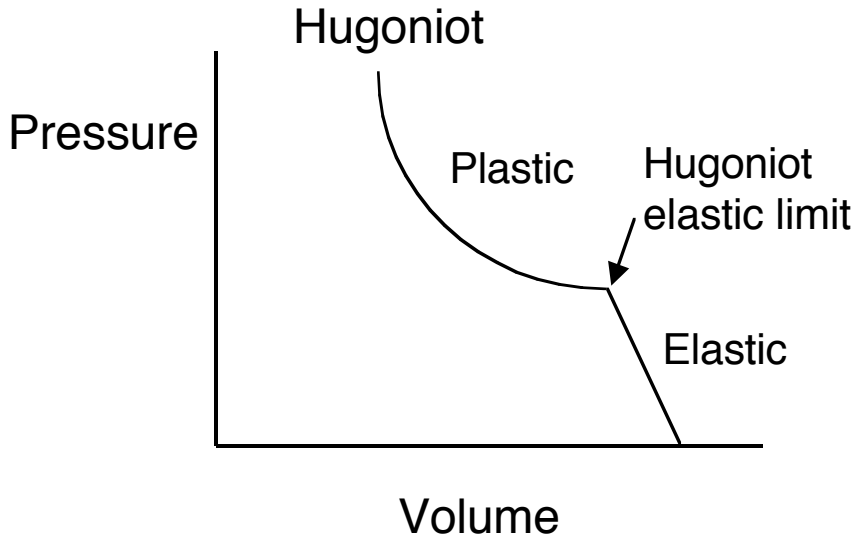

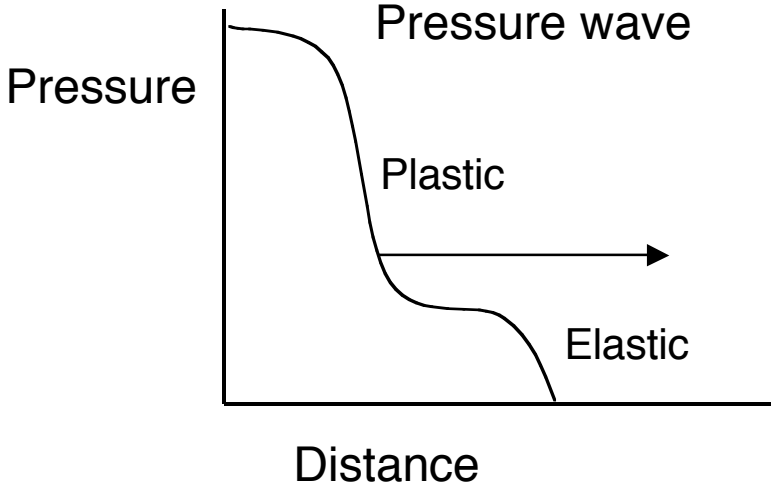

We use a material strength package in our code

Newton's law

$$\rho \ddot{v}_r = -\frac{\partial}{\partial r}\left(P - \sigma_{rr}\right) + \frac{\partial}{\partial z}\sigma_{rz} + \frac{1}{r}\left(2\sigma_{rr} + \sigma_{zz}\right)$$

$$\rho \ddot{v}_z = -\frac{\partial}{\partial z}\left(P - \sigma_{zz}\right) + \frac{\partial}{\partial r}\sigma_{rz} + \frac{1}{r}\sigma_{rz}$$

ρ= density
v= velocity
P= hydrodynamic pressure
σ= deviatoric stress
θ= hydrodynamic strain
ε= deviatoric strain
K= bulk modulus
G=shear modulus

Definition of strain

$$\dot{\theta} = \frac{\partial v_r}{\partial r} + \frac{\partial v_z}{\partial z} + \frac{v_r}{r}$$

$$\dot{\varepsilon}_{rr} = \frac{1}{3}\left(2\frac{\partial v_r}{\partial r} - \frac{\partial v_z}{\partial z} - \frac{v_r}{r}\right)$$

$$\dot{\varepsilon}_{zz} = \frac{1}{3}\left(2\frac{\partial v_z}{\partial z} - \frac{\partial v_r}{\partial r} - \frac{v_r}{r}\right)$$

$$\dot{\varepsilon}_{rz} = \frac{1}{2}\left(\frac{\partial v_r}{\partial z} + \frac{\partial v_z}{\partial r}\right)$$

EOS with strain

$$\dot{P} = -K\dot{\theta} - \dot{P}^{inelastic}$$

$$\dot{\sigma}_{rr} = 2G\dot{\varepsilon}_{rr} - \dot{\sigma}_{rr}^{inelastic} + 2\sigma_{rz}\omega + (\sigma_{zz} - \sigma_{rr})\omega^2$$

$$\dot{\sigma}_{zz} = 2G\dot{\varepsilon}_{zz} - \dot{\sigma}_{zz}^{inelastic} - 2\sigma_{rz}\omega - (\sigma_{zz} - \sigma_{rr})\omega^2$$

$$\dot{\sigma}_{rz} = 2G\dot{\varepsilon}_{rz} - \dot{\sigma}_{rz}^{inelastic} + 2(\sigma_{rz} - \sigma_{rr})\omega - 2\sigma_{rz}\omega^2$$

$$\omega = \frac{1}{2}\left(\frac{\partial v_r}{\partial z} - \frac{\partial v_z}{\partial r}\right)$$

We use a von Mises yield criterion for the onset of plastic flow

Deviatoric strain invariant $J = \sqrt{\frac{4}{3}\left(\sigma_{rr}^2 + \sigma_{zz}^2 + \sigma_{rz}^2 + \sigma_{rr}\sigma_{zz}\right)}$

Effective pressure $P_e = P - \sqrt[3]{\left(\sigma_{rr} + \sigma_{zz}\right)\left(\sigma_{rz}^2 - \sigma_{rr}\sigma_{zz}\right)/16}$

When J > Y(P_e), the elastic limit is exceeded and plastic flow begins

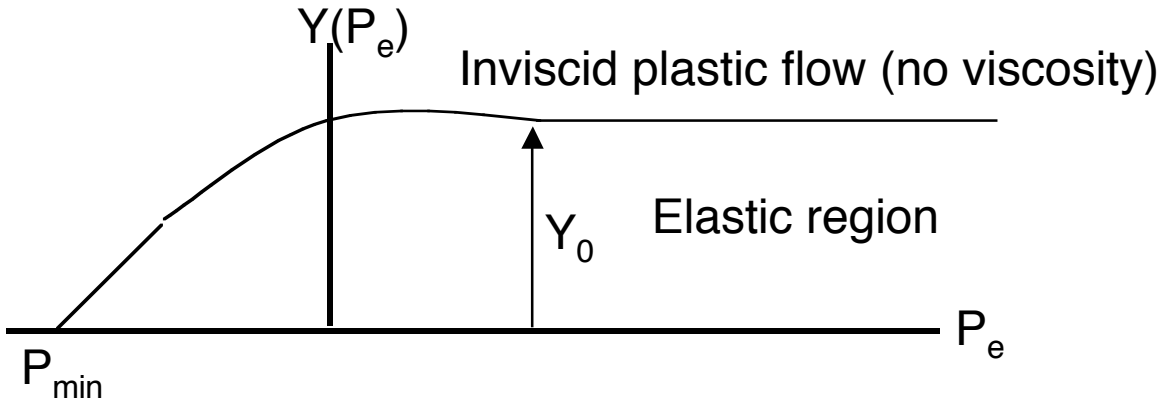

von Mises, Z. Angew. Math. U. Mech. **8** (1928),
translated in UCRL Trans. 872

Uniaxial strain equations

$$\rho \dot{v}_z = \frac{\partial}{\partial z}\left(-P + \sigma_{zz}\right)$$

$$\dot{\theta} = \frac{\partial v_z}{\partial z}$$

$$\dot{\varepsilon}_{zz} = \frac{2}{3}\frac{\partial v_z}{\partial z}$$

$$\dot{P} = -K\dot{\theta} - \dot{P}^{inelastic}$$

$$\dot{\sigma}_{zz} = 2G\dot{\varepsilon}_{zz} - \dot{\sigma}_{zz}^{inelastic}$$

$$P_e = P - \tfrac{1}{4}\sigma_{zz}$$

$$J = \left|\sigma_{zz}\right|$$

$$\text{Sound speed } c_{11} = \sqrt{\left(K + \tfrac{4}{3}G\right)/\rho}$$

Steinberg-Guinan Model

$$G(P,T) = G_0\left(1 + \frac{1}{G_0}\frac{\partial G}{\partial P}\frac{P}{\eta^{1/3}} - \frac{1}{G_0}\frac{\partial G}{\partial T}(T-300)\right)$$

$$Y = Y_0 f(\varepsilon_p)\, G(P,T)/G_0$$

$$Y_0 f(\varepsilon_p) = Y_0\left(1 + \beta(\varepsilon_p + \varepsilon_i)\right)^n \le Y_{\max}$$

$$T_{melt} = T_0 \exp\left(2a(1-\tfrac{1}{\eta})\eta^{2(\gamma_0 - a - 1/3)}\right), \quad \eta = \frac{\rho}{\rho_0}$$

D.J. Stenberg, S.G. Cochran and M. W. Guinan, J. Appl. Phys. **51**, 1498 (1980)
D.J. Steinberg, UCRL-MA-106439 (1991)

Steinberg-Lund Model

$$Y = \{Y_T(\varepsilon_p, T) + Y_A f(\varepsilon_p)\} G(P,T)/G_0$$

$$\varepsilon_p = \{\frac{1}{C_1}\exp[\frac{2U_K}{kT}(1-\frac{Y_T}{Y_P})^2] + \frac{C_2}{Y_T}\}^{-1}$$

$$Y_A f(\varepsilon_p) = Y_A\left(1+\beta(\varepsilon_p+\varepsilon_i)\right)^n \le Y_{\max}$$

$$Y_T \le Y_P$$

D.J. Stenberg and C.M. Lund, J. Appl. Phys. **65**, 1528 (1989)

VISAR measures the surface velocity history

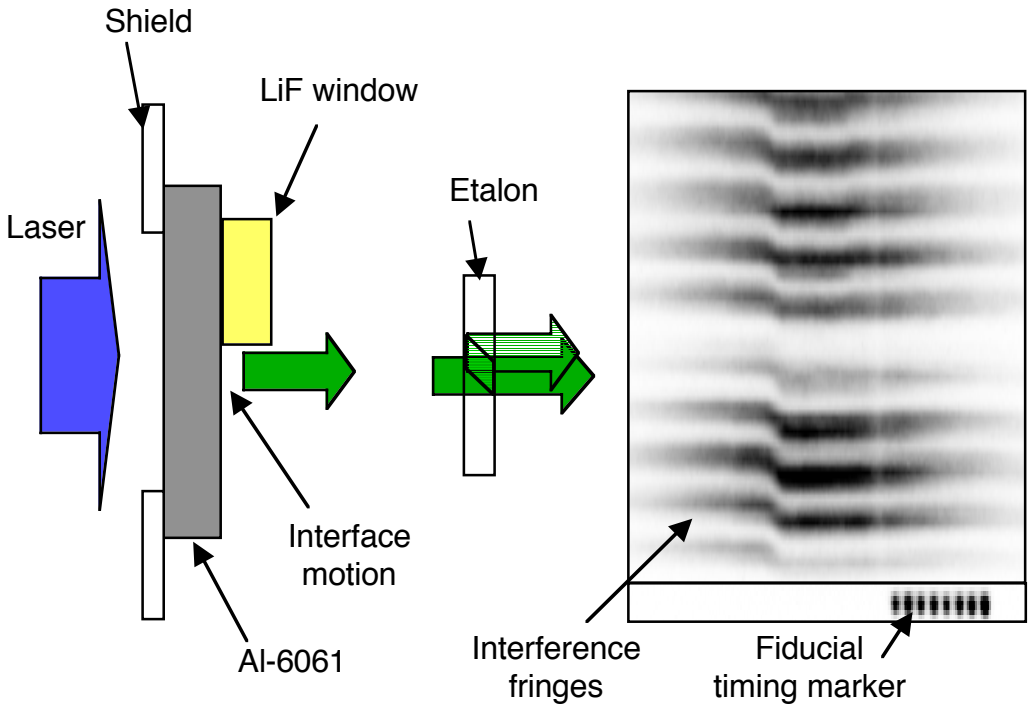

•An optical laser pulse is reflected from the free surface of the foil and injected into an interferometer
•The phase of the fringe is proportional to the velocity of the free surface
•Spatial resolution of the VISAR system provides data on the rear-surface motion with and without the LiF window

VISAR measurement of elastic-plastic wave breakout in Al-6061

- 195 μm Al-6061, LiF over half of the rear surface
- Omega shot #21382 - 19 J on target

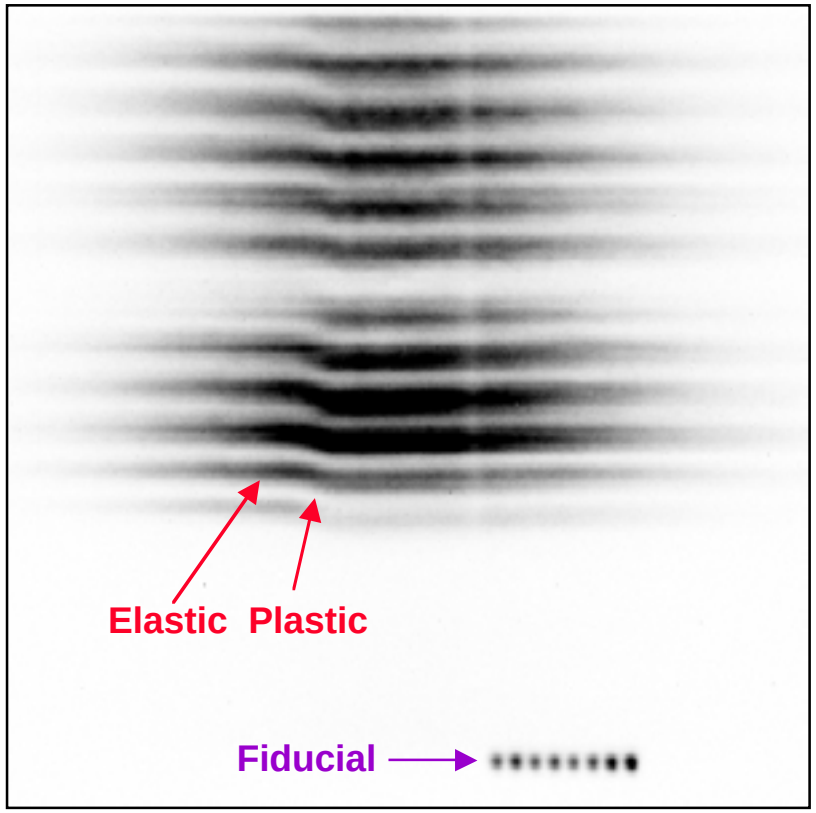

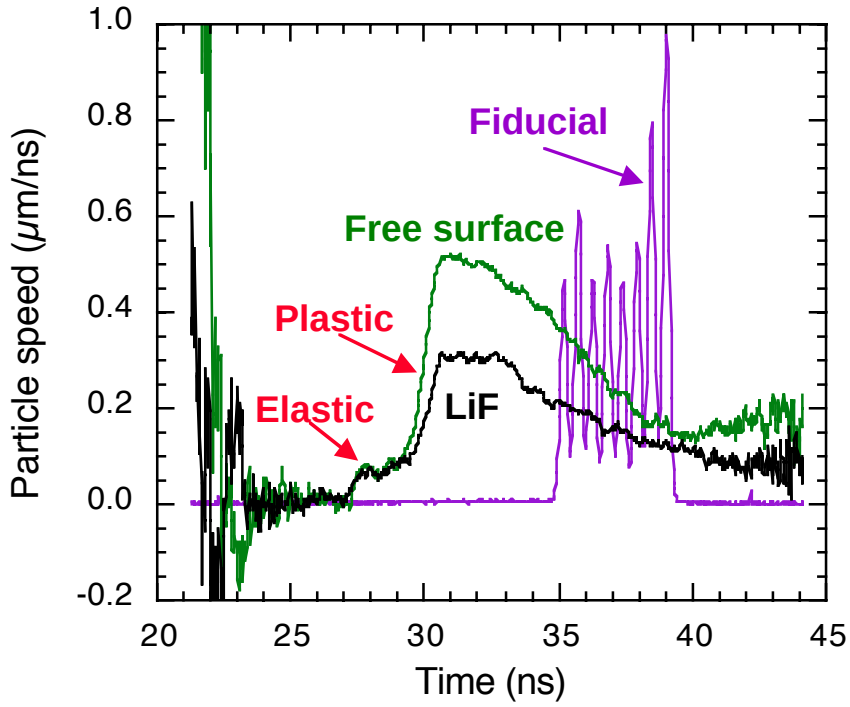

The wave profile shows a pull-back at higher drive pressure

- 195 μm Al-6061, LiF over half of the rear surface
- Omega shot #21384 - 33 J on target

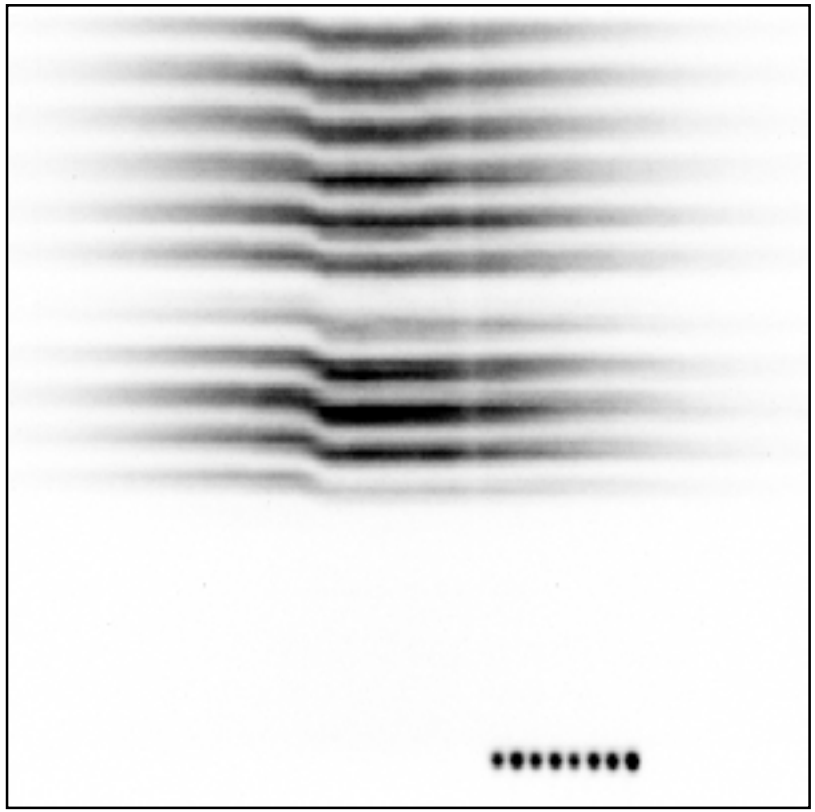

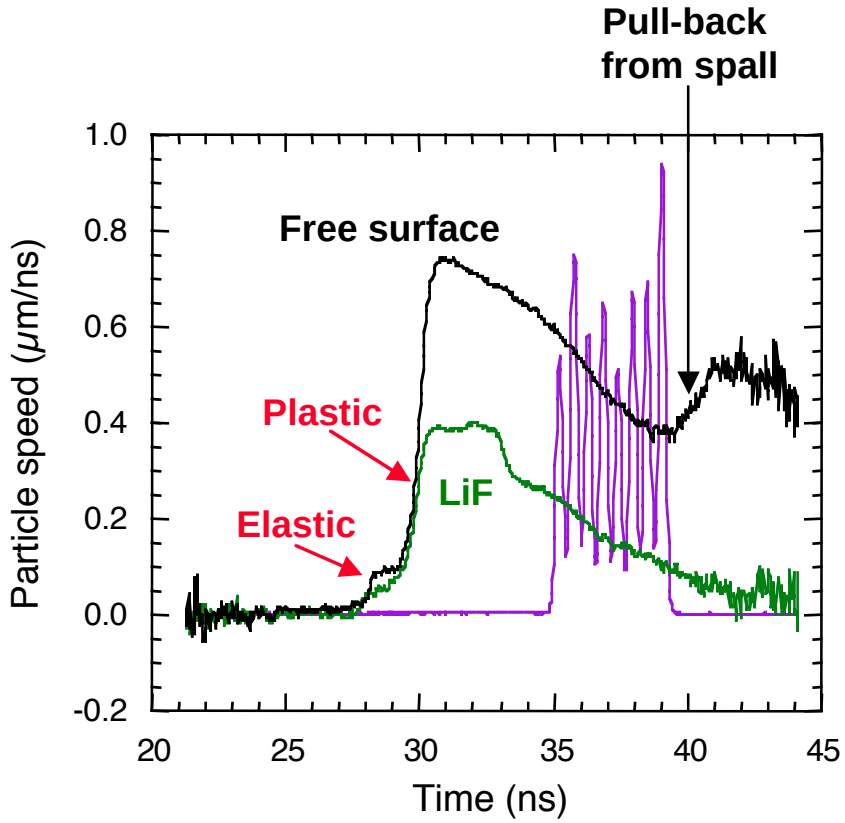

We use VISAR data to determine the shear modulus, bulk modulus and yield strength

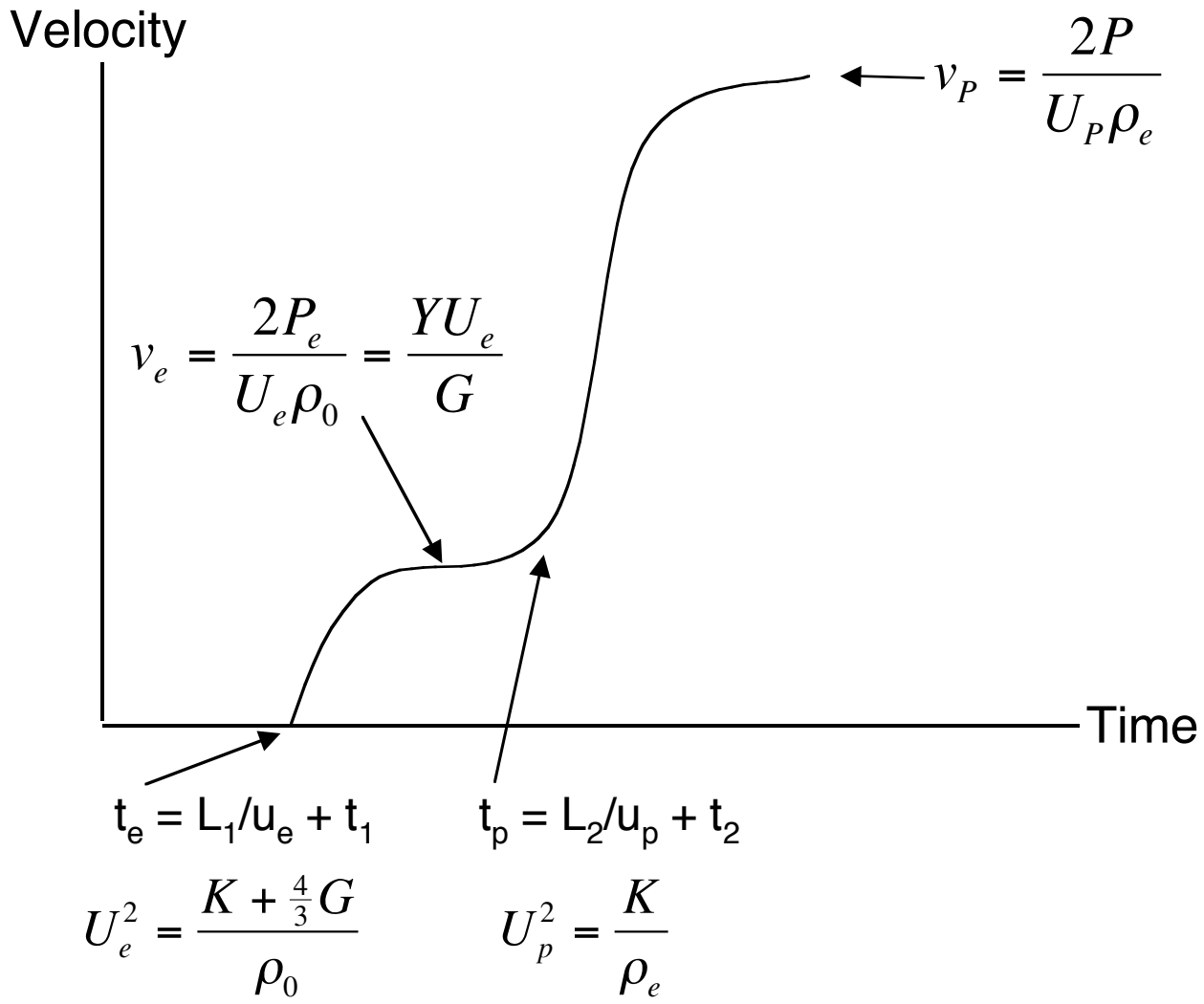

Shocks lose strength as they propagate

$$\left.\frac{dP}{dx}\right)_{shock} = -\left.\frac{dP}{dx}\right)_{rarefaction}\left(\frac{u_{material} + c_s}{U_{shock}} - 1\right)$$

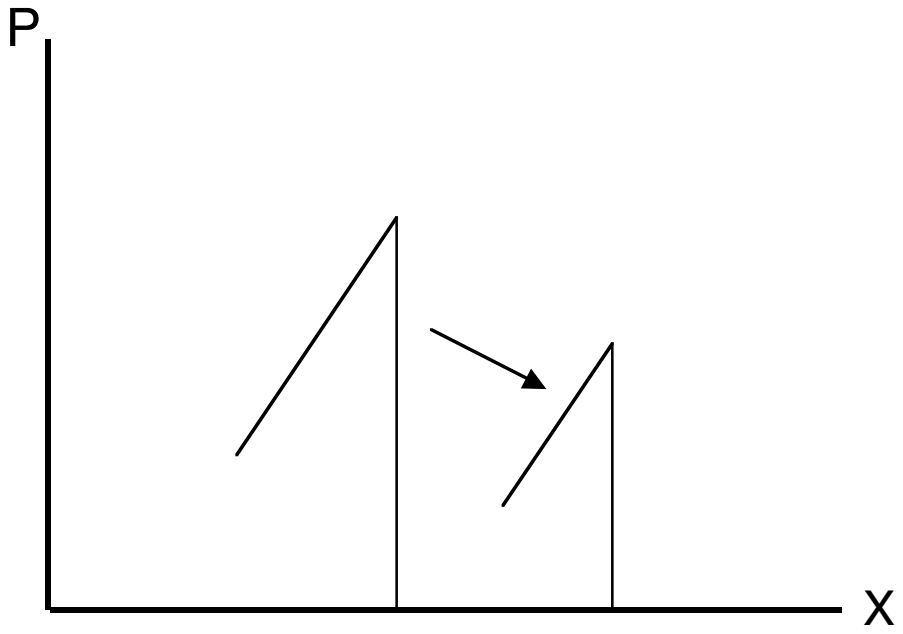

The shear modulus, bulk modulus and yield strength affect the rise time and velocity of the VISAR data

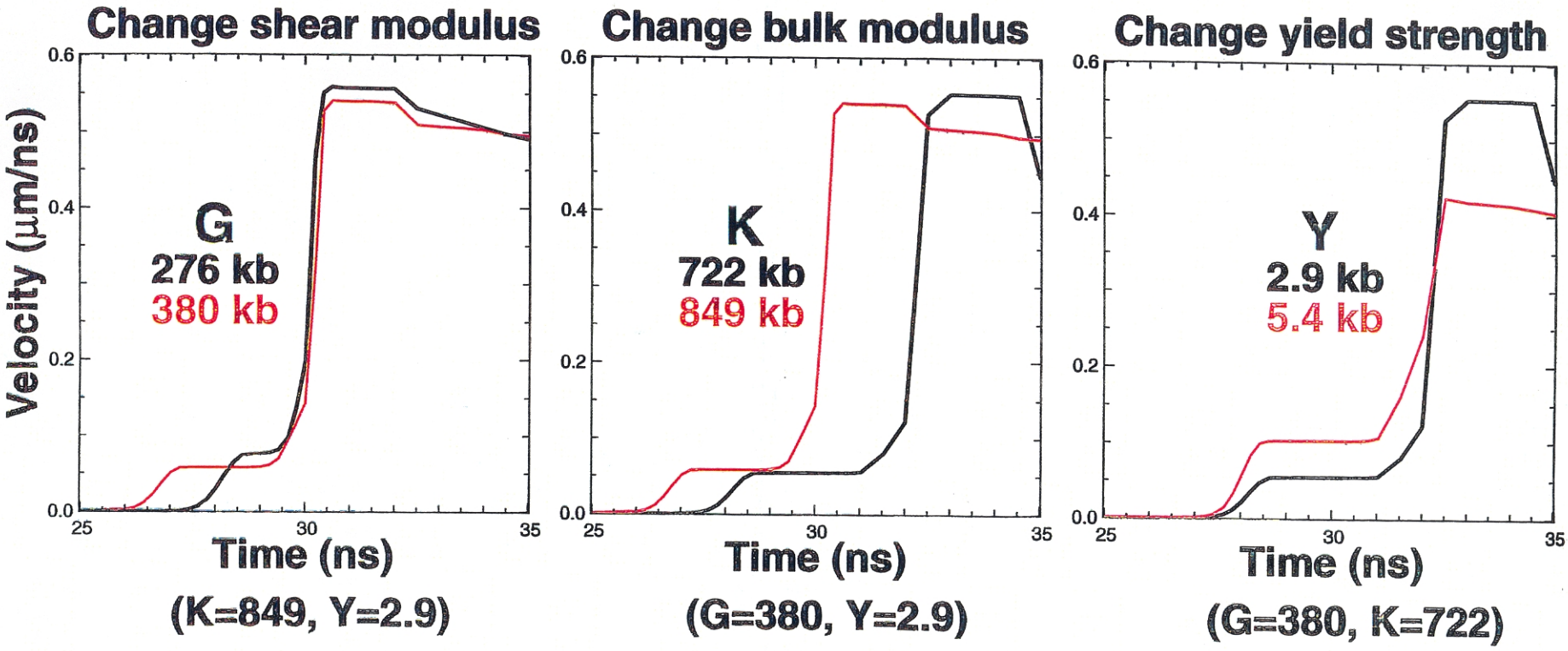

The shock strength decreases more rapidly with increasing yield strength

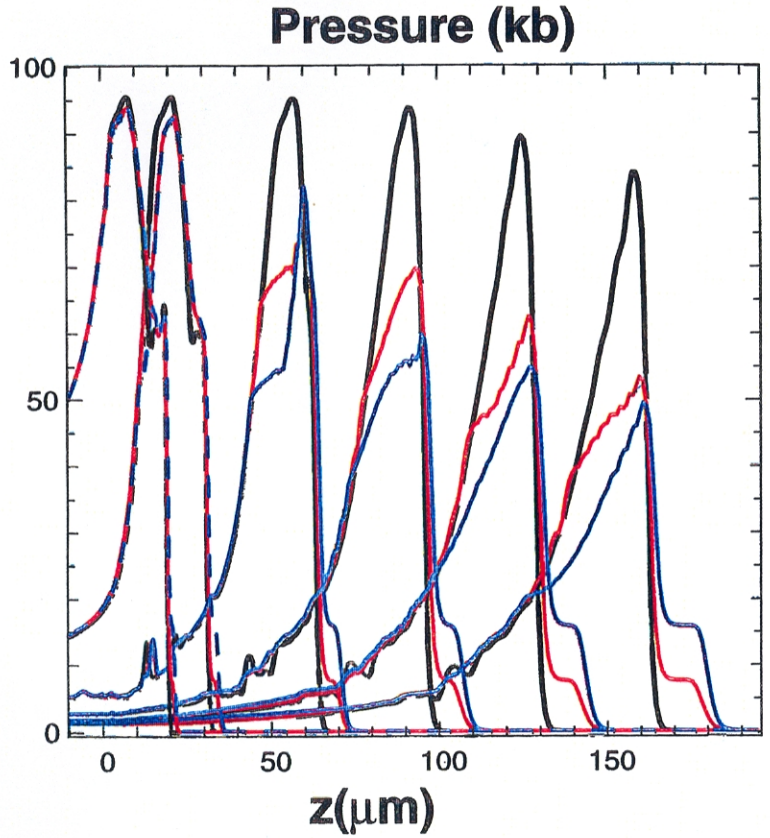

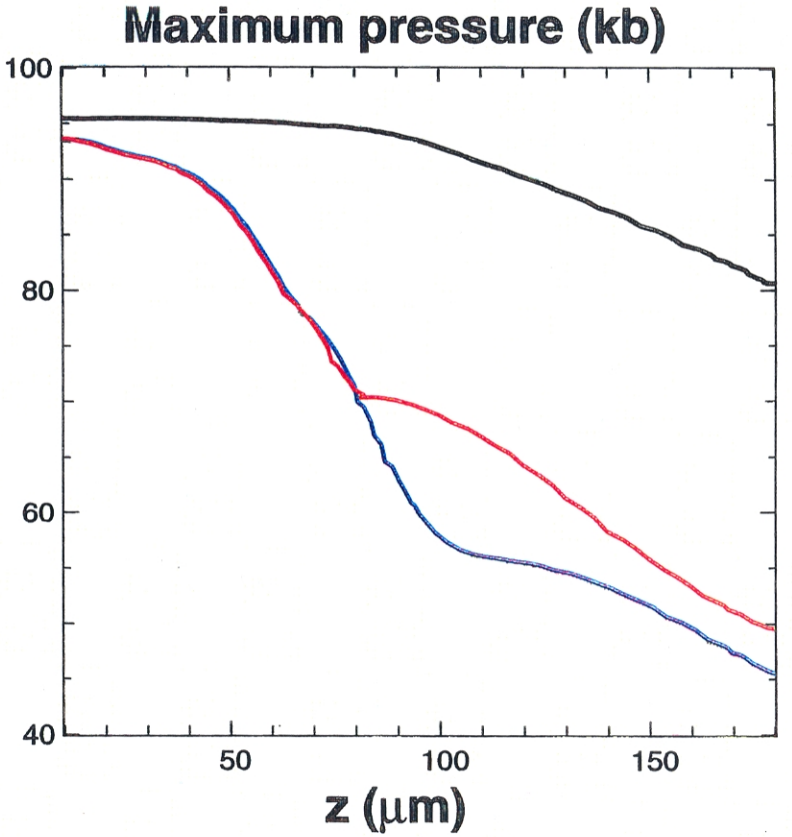

Yield strength = 0

Yield strength = 3.34 kb

Yield strength = 6.8 kb

We can match rise times and velocities by varying bulk modulus, shear modulus and yield strength

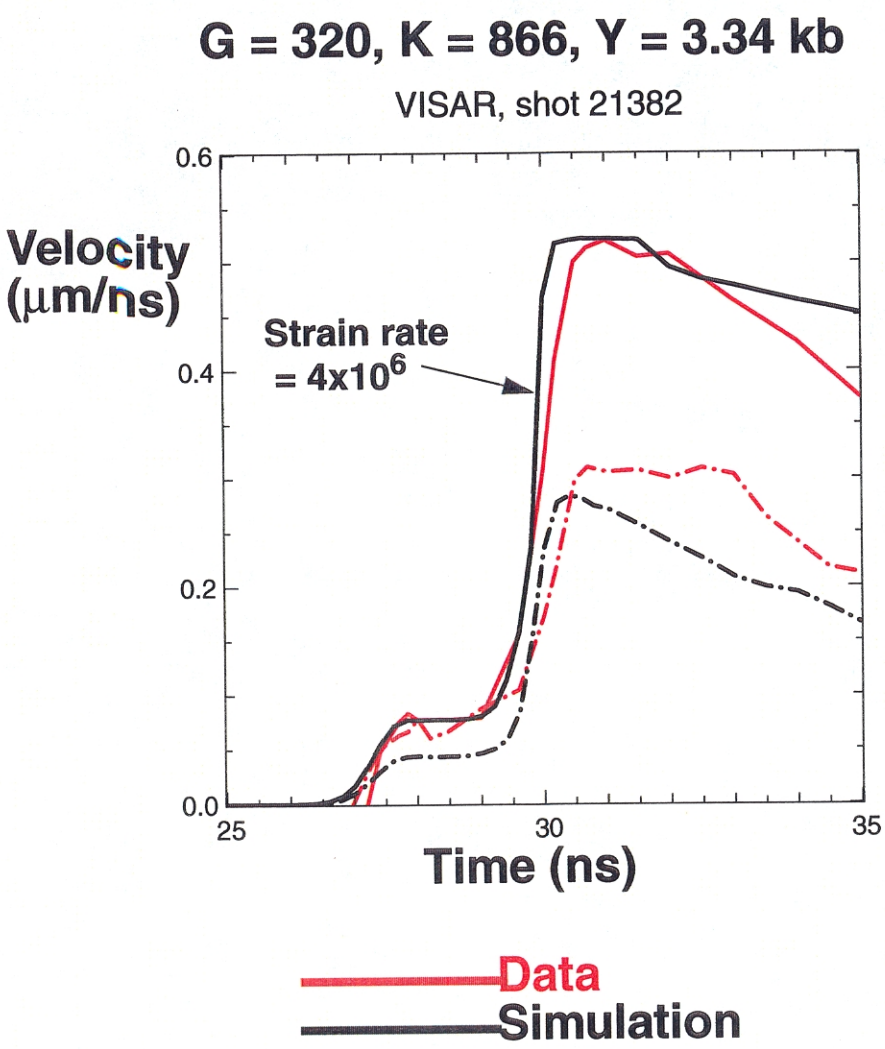

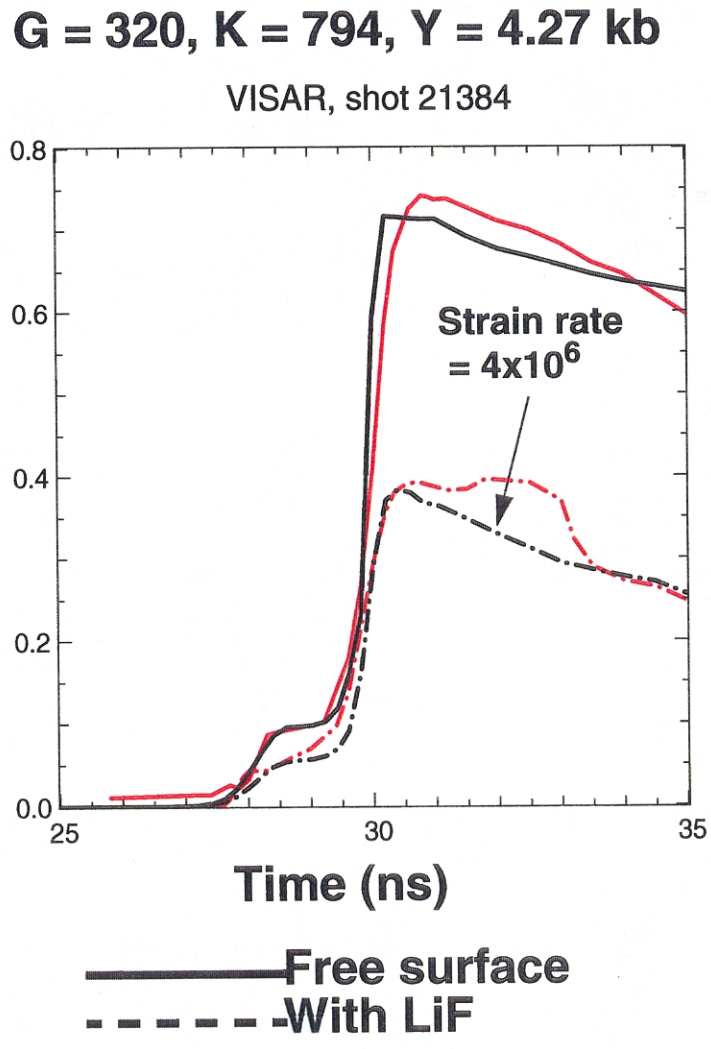

The Steinberg-Guinan model by itself gives a spall time that is too late compared to the data

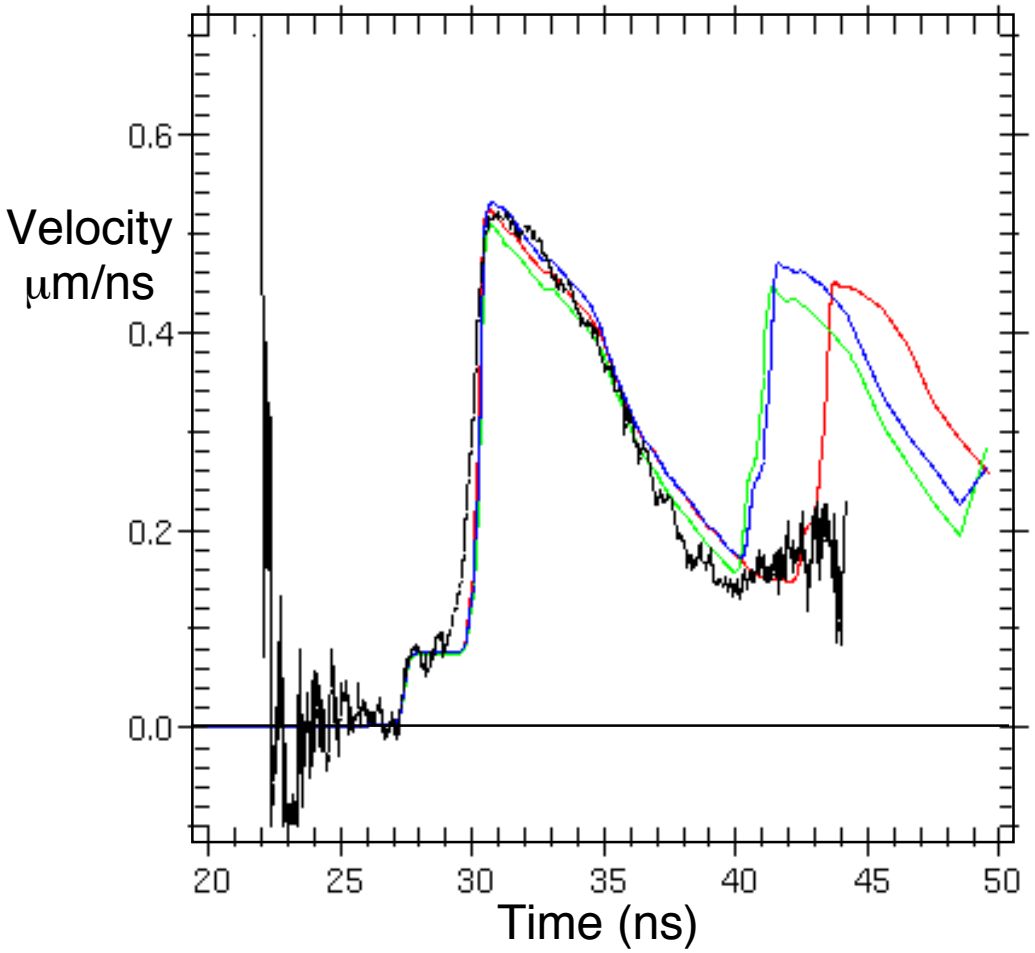

Data

Steinberg-Guinan

Steinberg-Lund

SG+Steinberg-Tipton failure model

eps_{max} = 0.25, $(\rho/\rho_0)_{min}$= 0.9665

Steinberg-Tipton Failure Model

Damage ranges from 0 to 1

Broken material: $Y_b < P$, $G_b/G_0 = Y_b/Y_0$

$\{P,G,Y\} = \text{damage}*\{P_0,G_0,Y_0\} + (1\text{-damage})*\{P_b,G_b,Y_b\}$

$$\frac{d}{dt}\text{Damage} = \begin{cases} \dfrac{RC_s}{\Delta X_{zone}} & \sum_i \max(0, \dfrac{f_i}{fmax_i})^2 > 1 \\ 0 & \sum_i \max(0, \dfrac{f_i}{fmax_i})^2 < 1 \end{cases}$$

$$C_s = \sqrt{\frac{4G_0}{3\rho}}$$

$f_i = \{\text{eps}, \rho/\rho_0 - 1, P, \sigma, \Delta\sigma\}$

Parameters

- **Steinberg-Guinan**
  - **p_{min} = -30 kb**
  - **ρ/ρ_0 = 0.9665**
  - **K= 940 kb**
  - **G_0 = 325 kb**
  - **Y = 3.335 kb**
  - **eps_{max} = 2.0**
- **Steinberg-Tipton**
  - **$\rho/\rho_0 - 1$ = -.0335**
  - **eps = .25**
  - **$R = 10^{20}$**
- **Steinberg-Lund**
  - **Y = 1.5 kb**
  - **c_1 = .71**
  - **c_2 = .12**
  - **u_k = .31**
  - **y_{prl} = 1.9 kb**

Dynamic x-ray diffraction measures density and crystal structure

- In situ x-ray diffraction allows us to probe the material state by providing information on the lattice under compression
- Technique applied on laser experiments at Nova and elsewhere (Janus, Vulcan, Trident, OMEGA) and powder and gas gun facilities

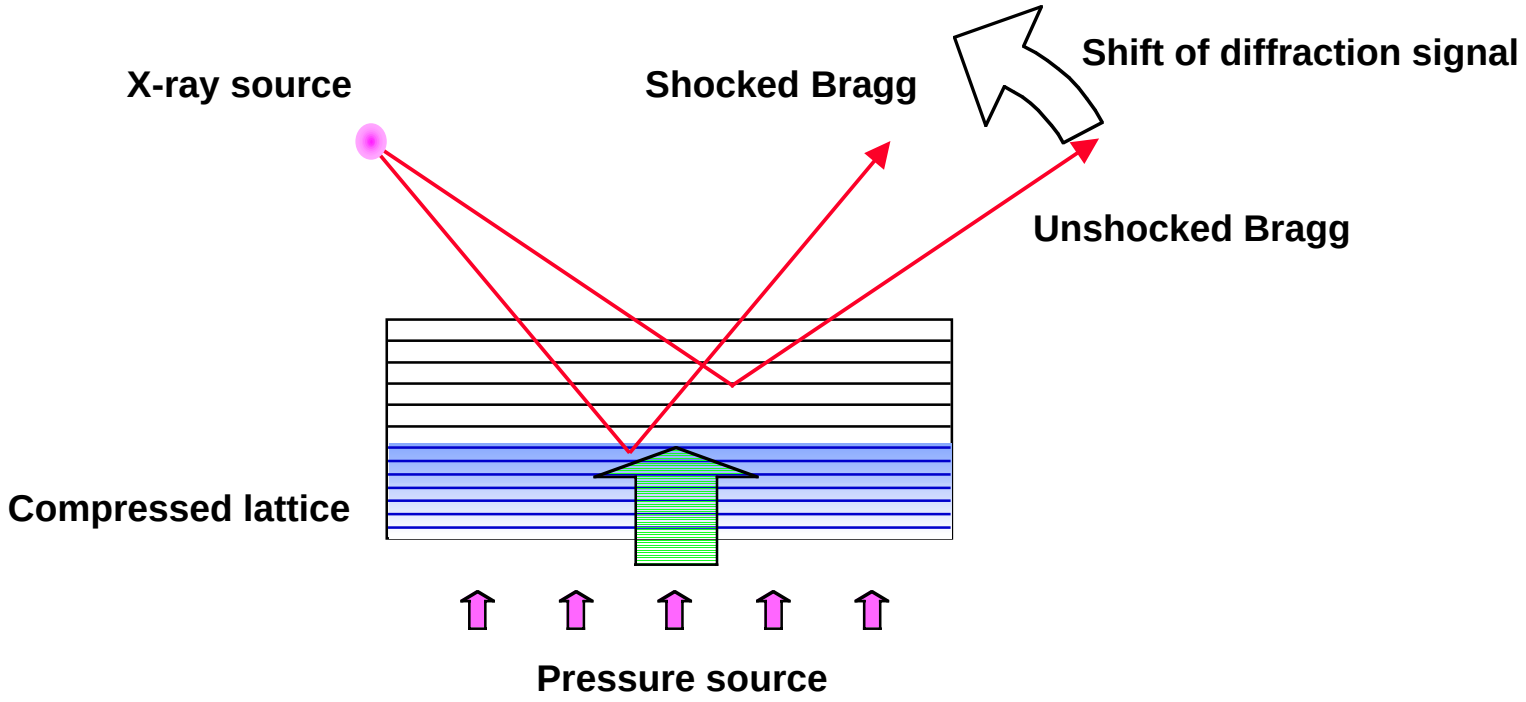

Q. Johnson, A. Mitchell, R.N. Keeler, L. Evans, *Phys Rev Lett* **25**, 1099 (1970)
J..S Wark, R.R. Whitlock, A.A. Hauer, J.E. Swain, P.J. Solone, *Phys Rev B* **40**, 5705 (1989)

Diffraction from shock compressed Si has been demonstrated on Nova

- Low intensity square laser pulse generates a single shock drive
- Displacement of the diffraction signal indicates a compression of the lattice spacing

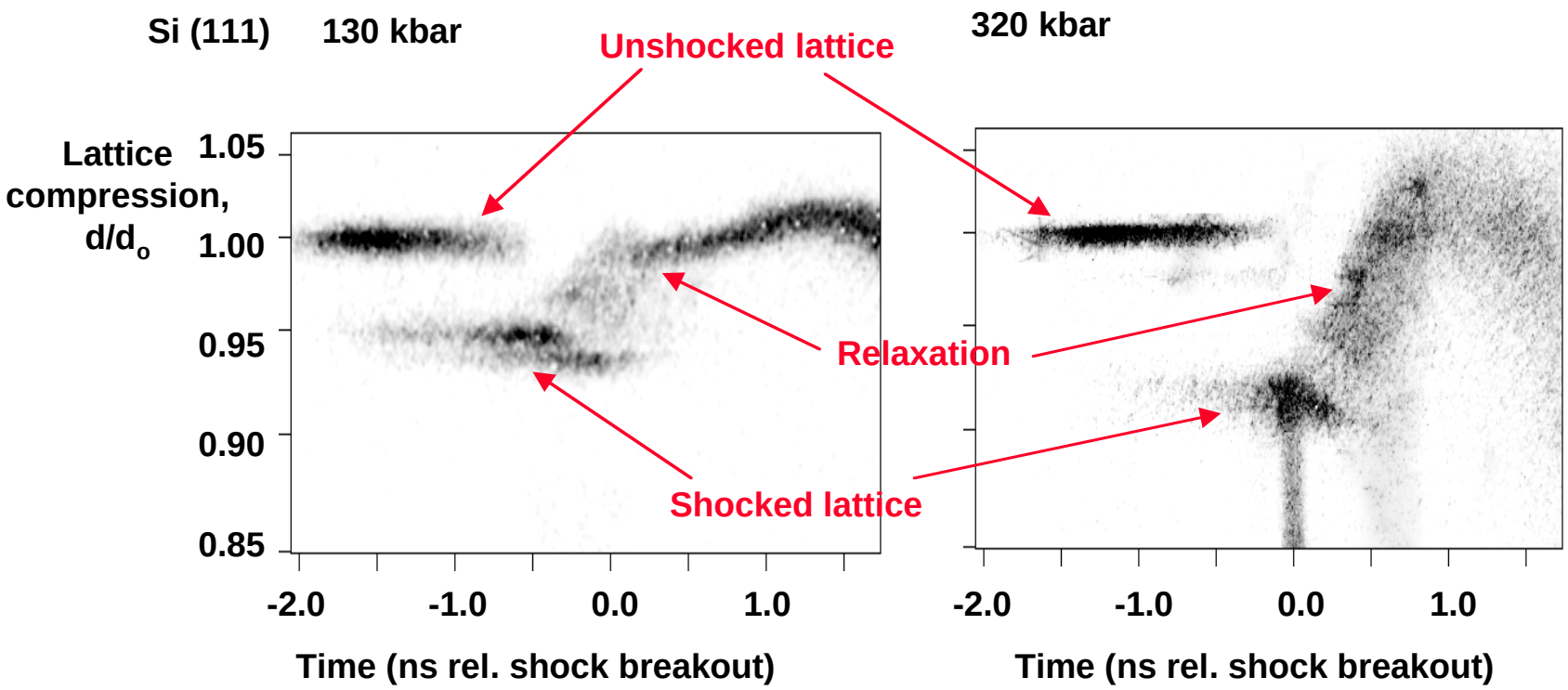

Diffraction from orthogonal lattice planes provides information on the transition to plasticity

- Simultaneous measurements are made of compression of orthogonal lattice planes
- Shock compression above the HEL for Si and Cu show very different behavior on the ns time scale[1]
  - Si responds uniaxially
  - Cu shows plastic deformation

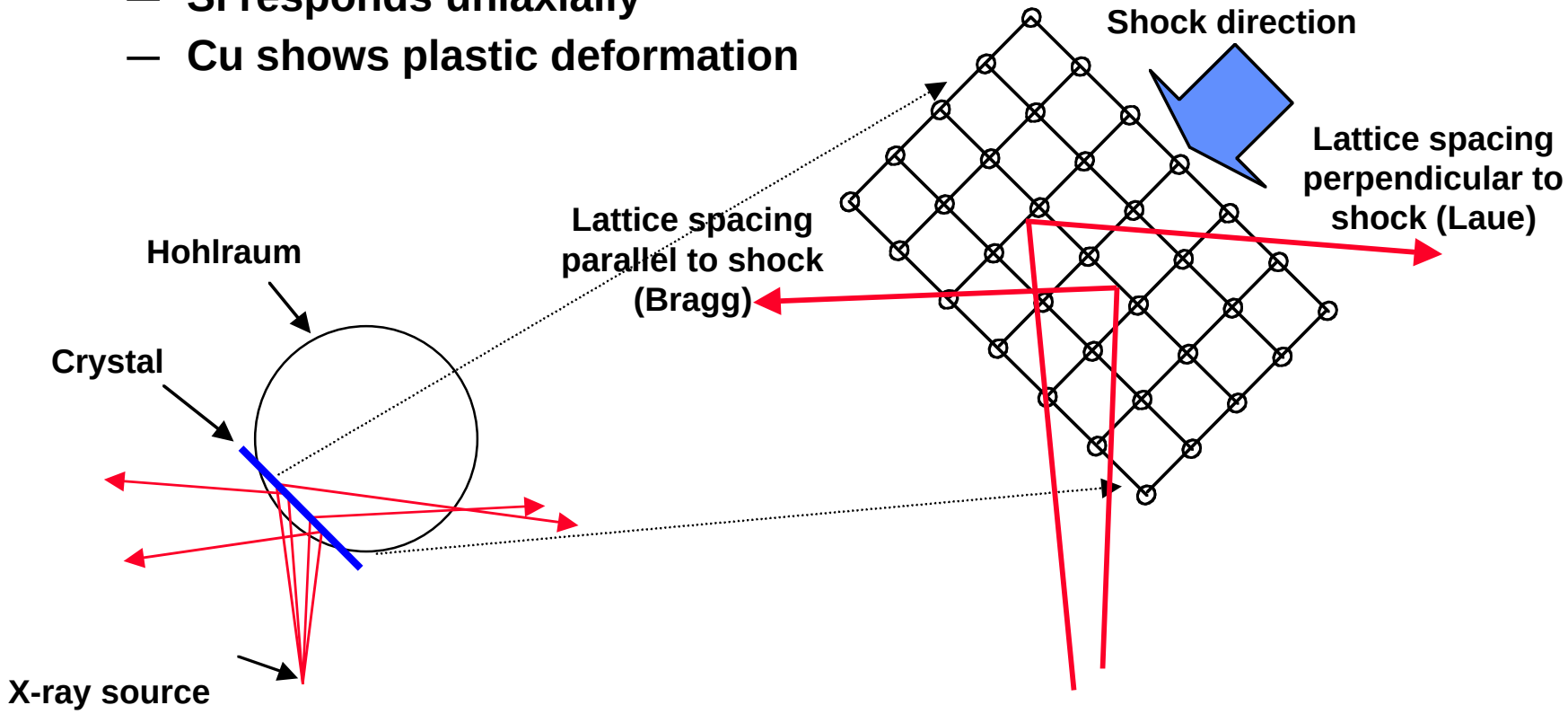

[1] A. Loveridge et al, *"Anomalous elastic response of silicon to uniaxial shock compression on nanosecond timescales"*, Phys. Rev. Letters **86**, 2349 (2001)

Simultaneous measurements of orthogonal planes indicate Si responds uniaxially on a ns time scale

- Si shock compressed along (400); probed along (400), (040)
- P = 115-135 kbar; HEL = 84 kbar, 40 μm thick Si
- Simultaneous measurements of Bragg and Laue diffraction

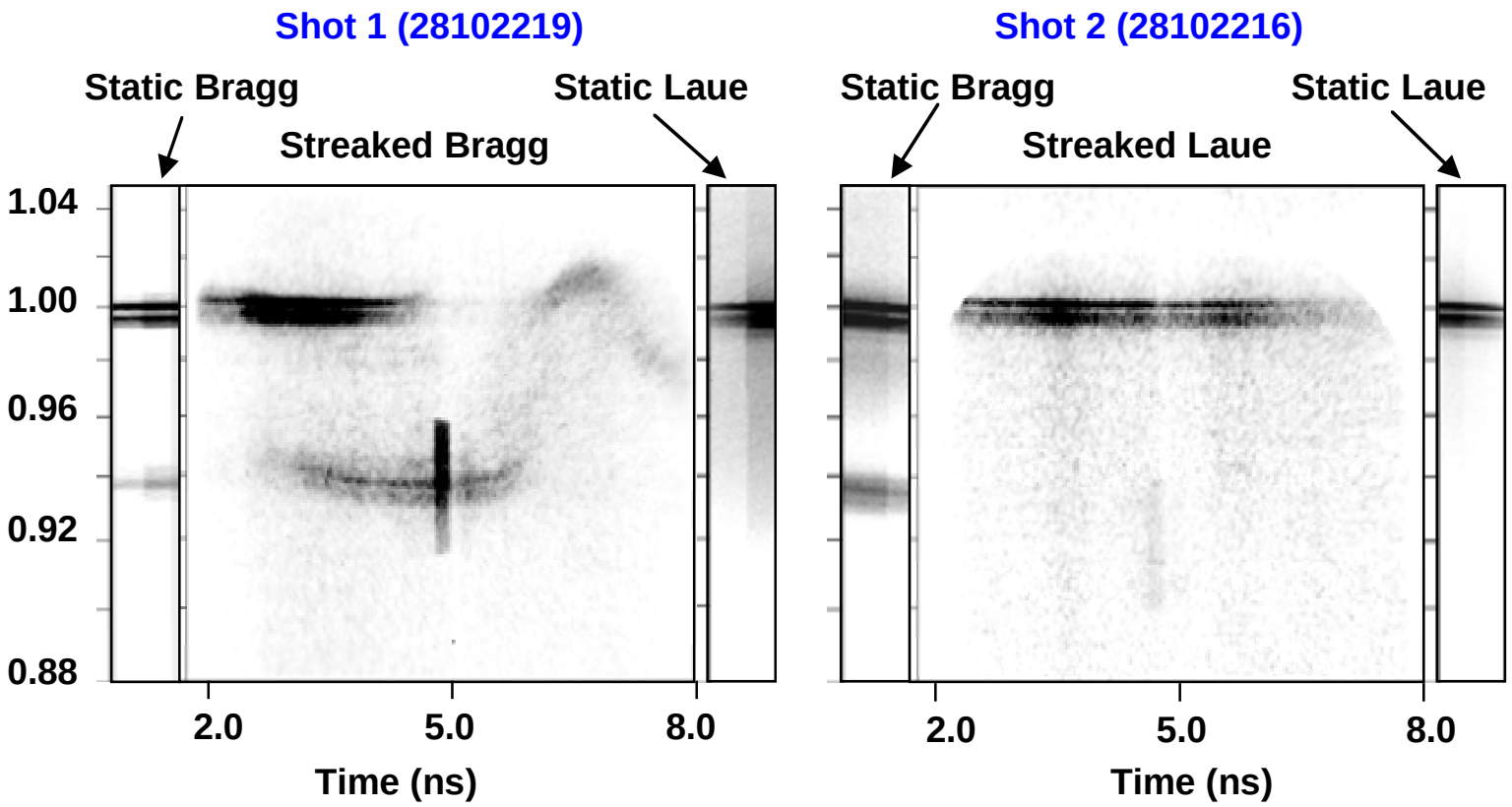

1-D compression in Si is due to high Peierls barrier

X-ray diffraction of 40 μm Si shows density features that vary with drive temperature

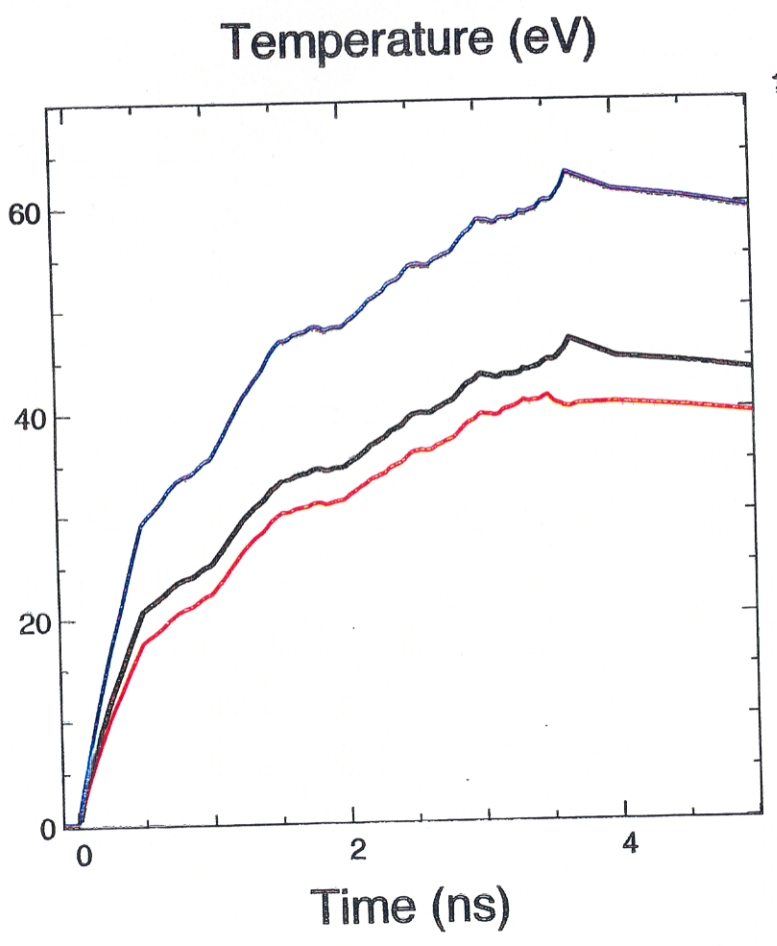

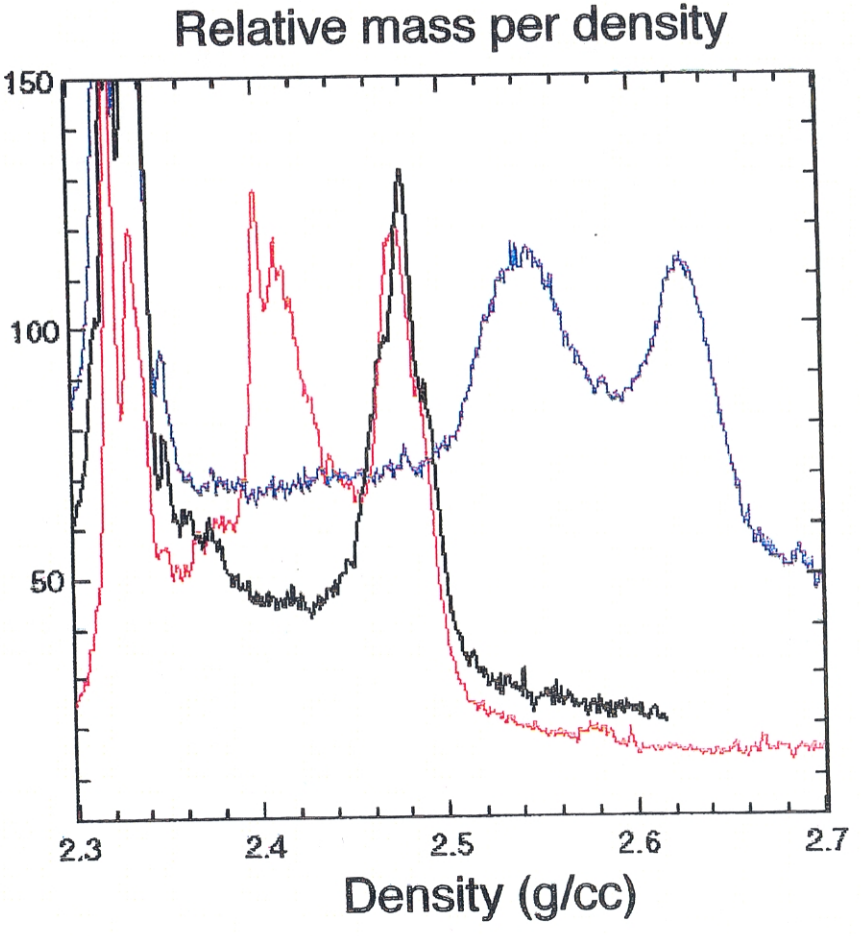

Molecular dynamic simulations show that the Si longitudinal stiffness increases with pressure

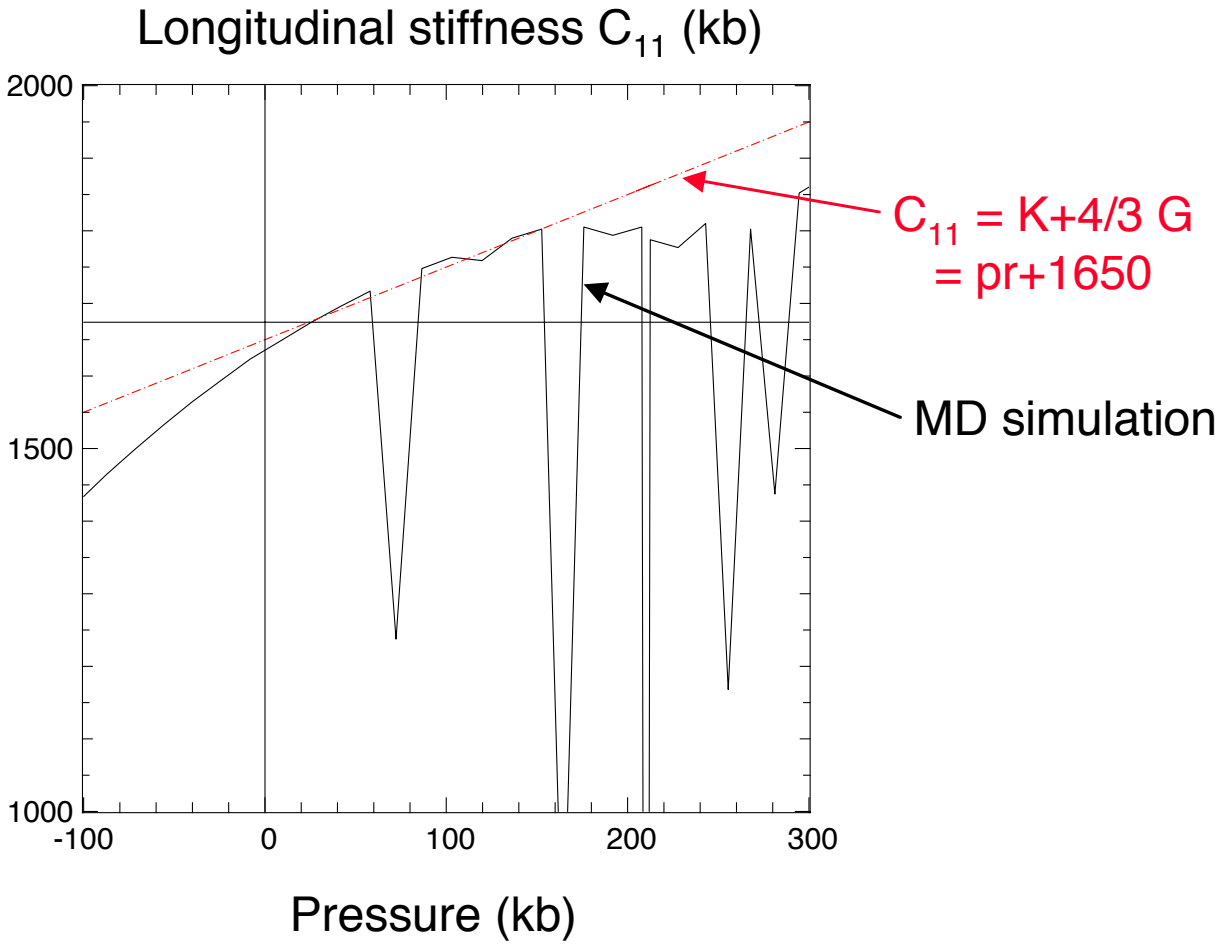

Simulation done by D. J. Roundy

The density structure depends in a complicated way on the drive temperature

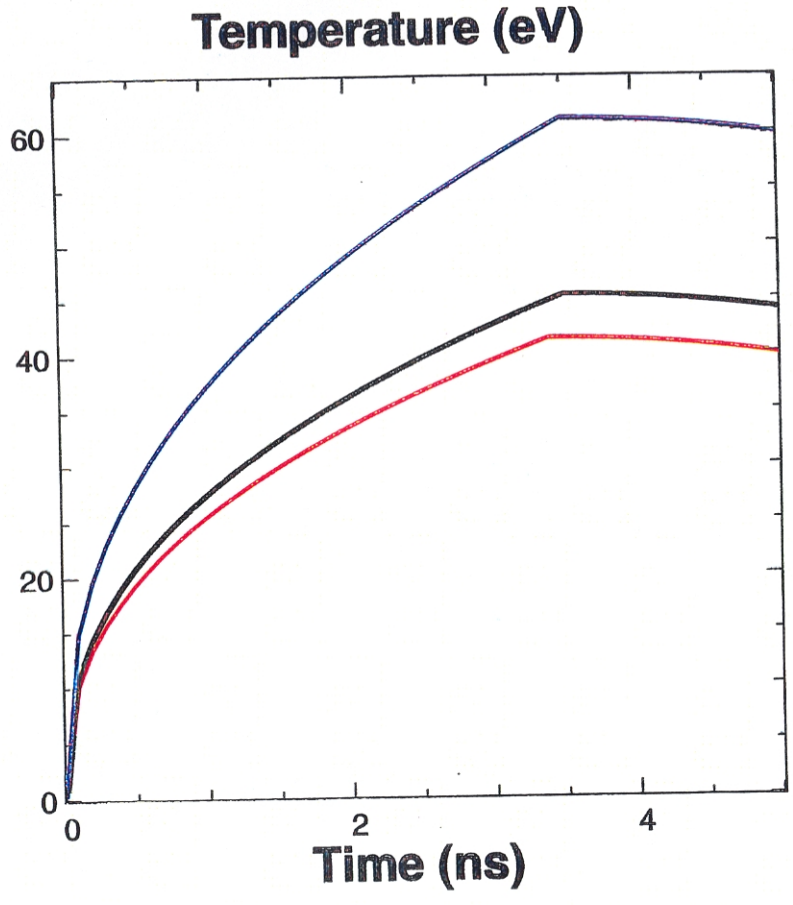

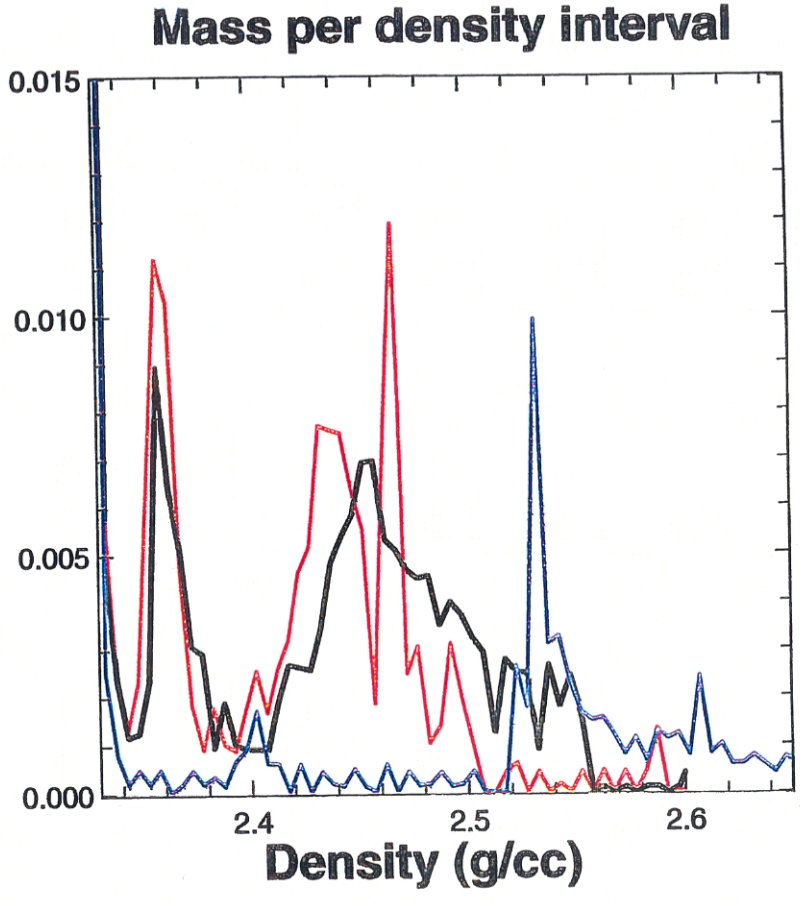

By increasing the drive, we can match part of the data

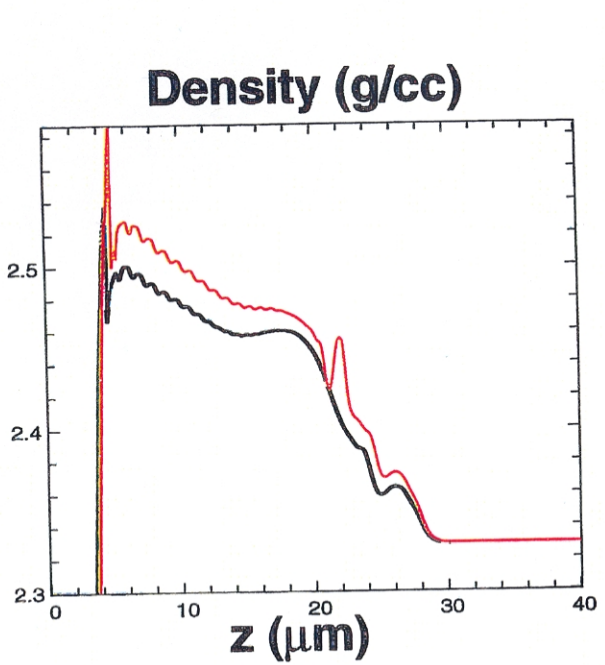

Relative fraction of material

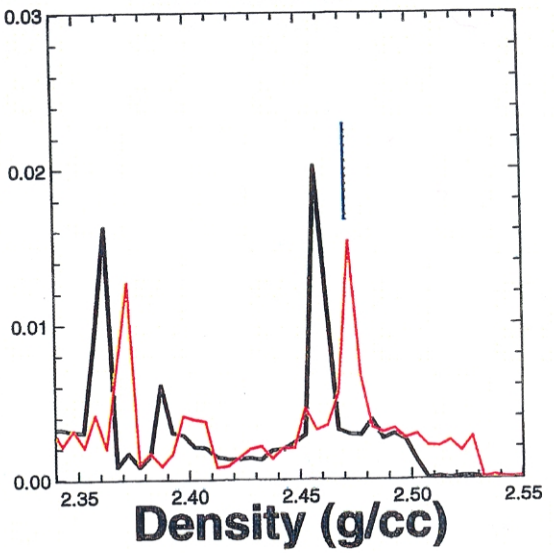

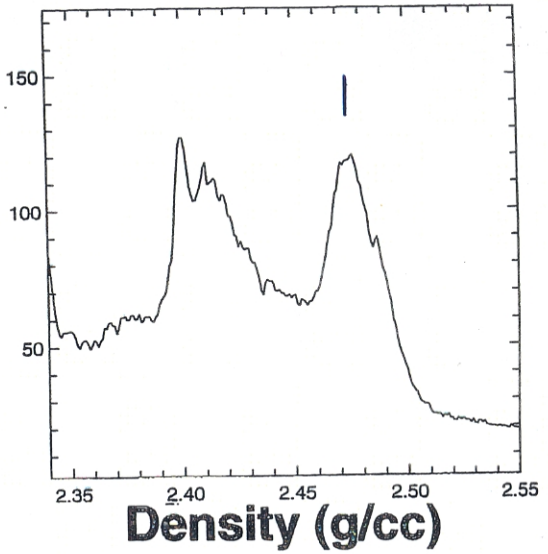

Nominal drive

Tr x 1.06

We have recovered samples to study the residual effects due to these high strain rate laser experiments

- Single crystal Cu samples were shocked by direct laser irradiation and captured in a foam-filled cavity
- Preliminary tests done at OMEGA; shock pressure is >1 Mbar, decays to ~50 kbar at the rear surface

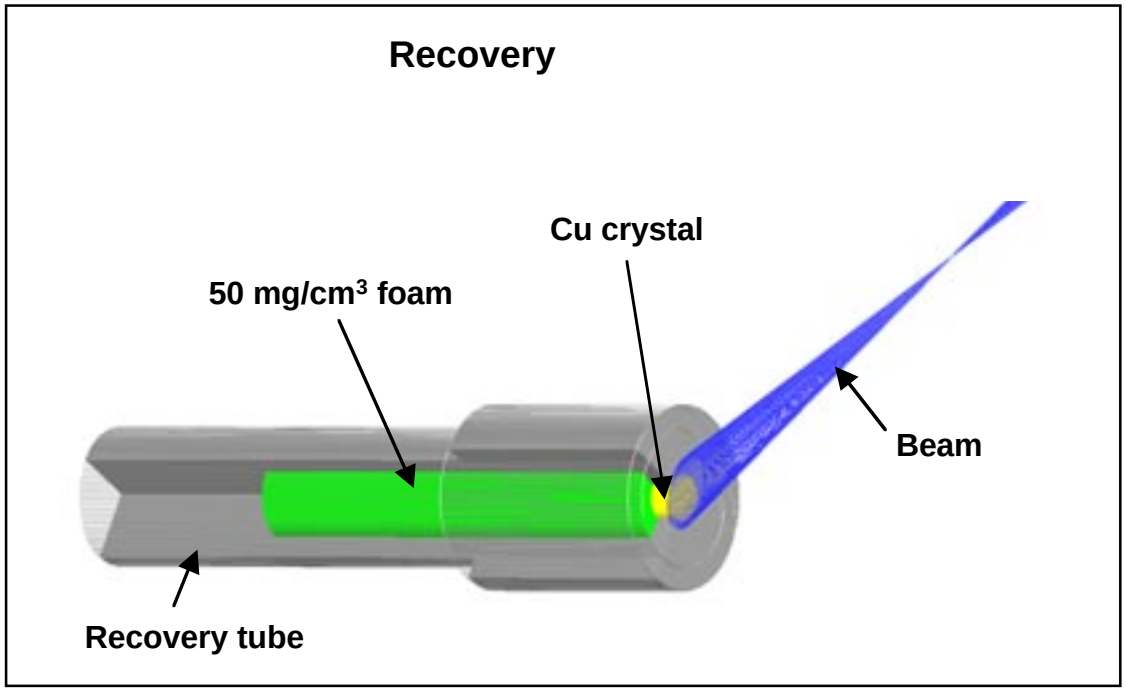

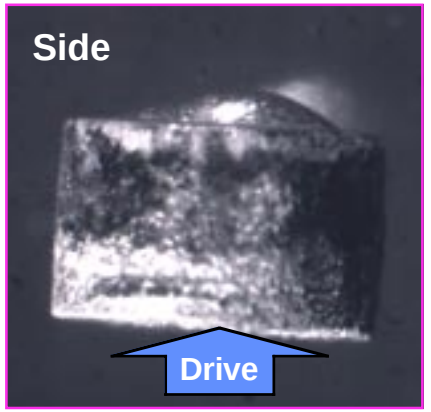

1 mm

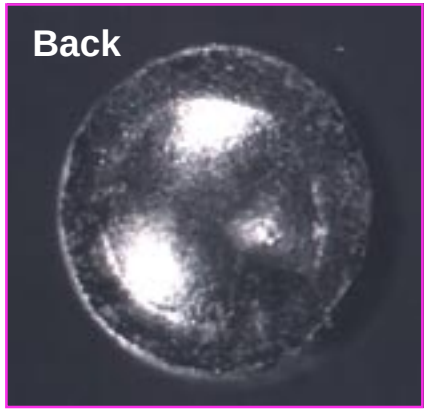

We see spall on a Cu sample driven by Janus

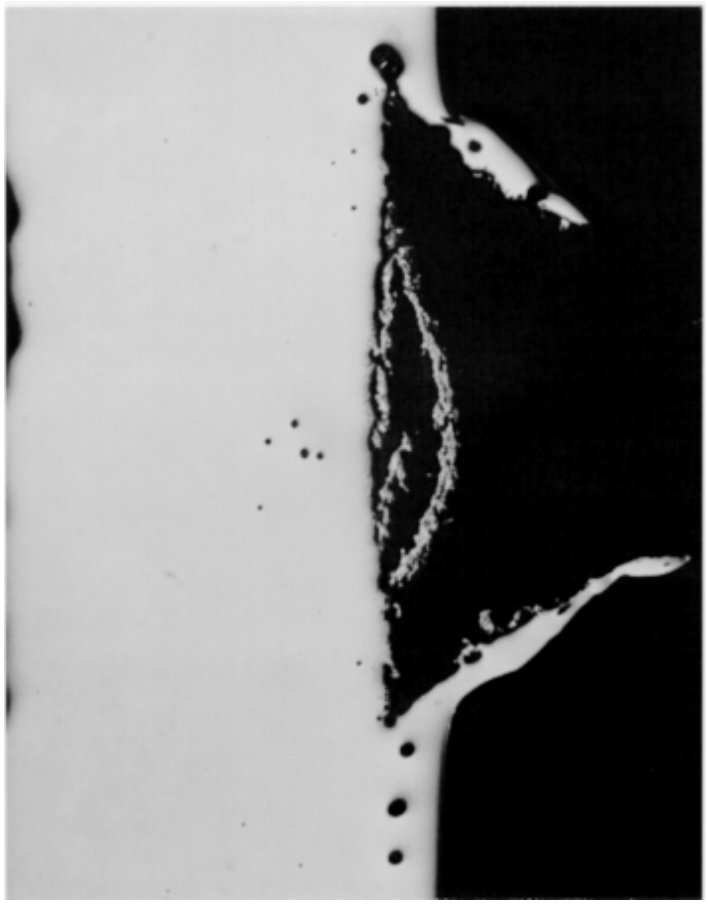

Shock strength falls roughly as distance$^{-3/4}$ in Cu

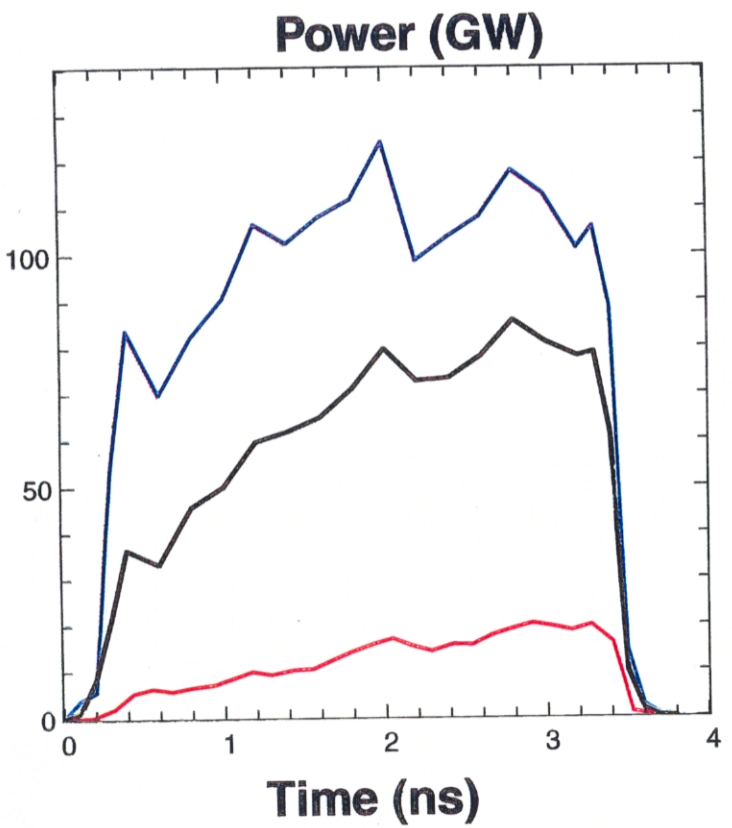

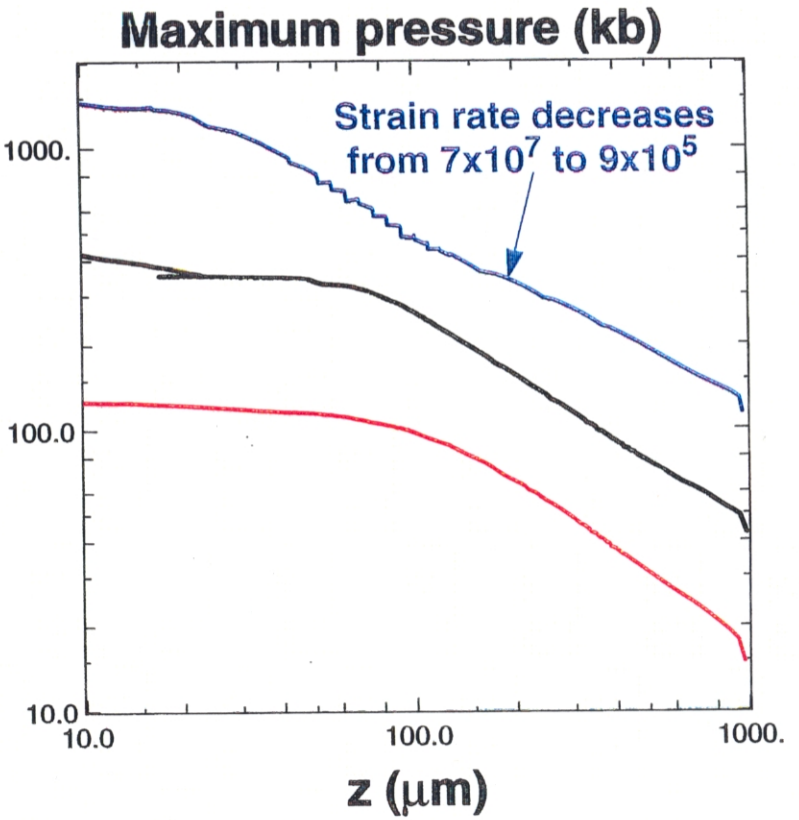

Summary and future work

- VISAR provides free surface velocity history
  - Gives shear modulus, bulk modulus and yield strength
  - Gives information on fracture model and spall
- X-ray diffraction provides information about lattice deformation

- Future work
  - Correlate VISAR with x-ray diffraction
  - Relate VISAR with post-shock recovery and residual deformation of structure

Experiments and simulations of instabilities in shock-accelerated gas cylinders

K. Prestridge[1], C. Tomkins[1], C. Zoldi[1,2], M. Marr-Lyon[1], P. Vorobieff[3], P. Rightley[1], R. Benjamin[1]

1 Los Alamos National Laboratory

2 SUNY Stony Brook

3 University of New Mexico

Shock-accelerated gas cylinder

Shock Tube Facility

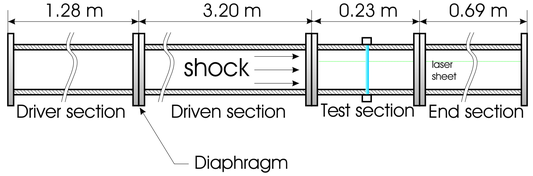

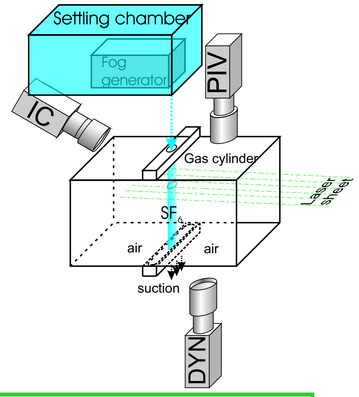

- Comparison between experimental density-field images and density-field images from a 2-D adaptive-mesh Eulerian code simulation reveal that the simulation has smaller lengths in the spanwise and streamwise directions.
- When velocity fields are compared at one instant in time, the higher magnitudes appear in the backflow region and the lower magnitudes appear in the vortex cores for both experiment and simulation. The overall magnitudes of the velocities in the simulation are higher than those of the experiment.

Particle Image Velocimetry

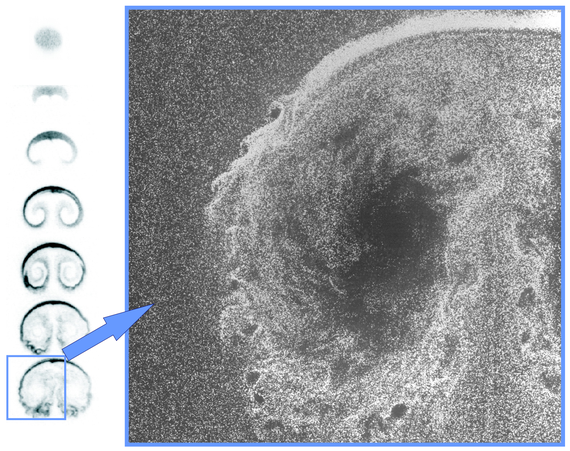

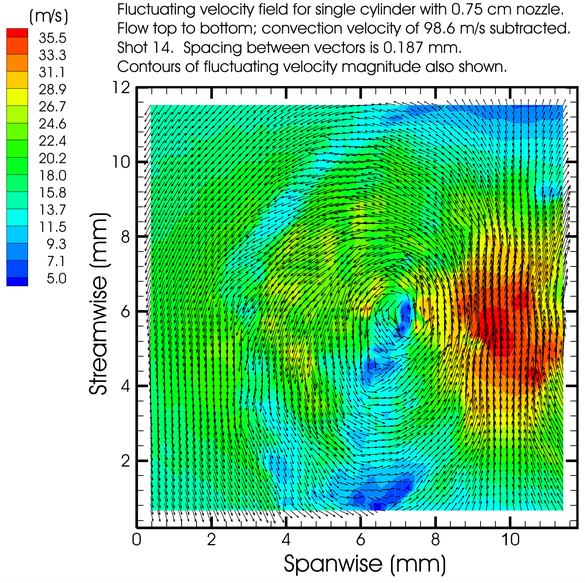

Fluctuating velocity field for single cylinder with 0.75 cm nozzle.
Flow top to bottom; convection velocity of 98.6 m/s subtracted.
Shot 14. Spacing between vectors is 0.187 mm.
Contours of fluctuating velocity magnitude also shown.

Density Fields

Experiment

Resolution of ICs = 55 μm/pixel
Dynamic Images = 100 μm/pixel

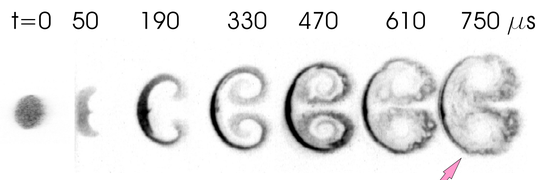

Simulation (using experimental ICs)

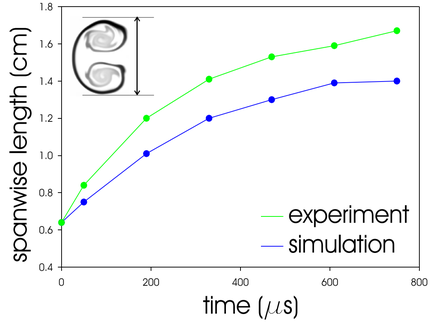

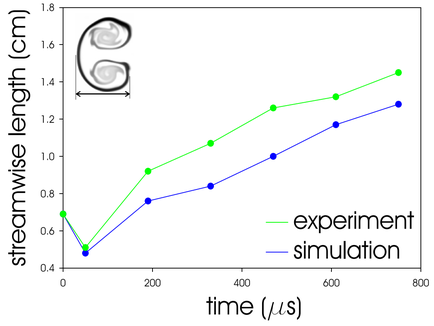

Velocity Magnitudes

Experiment

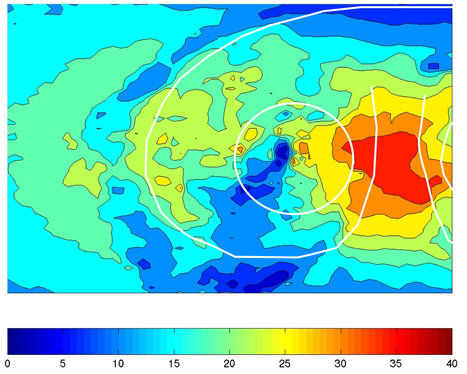

Simulation

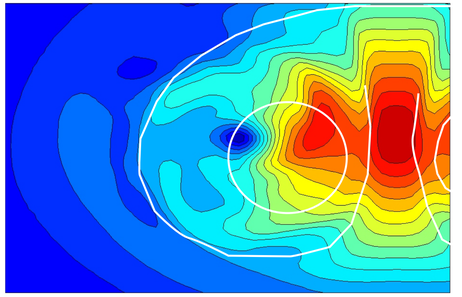

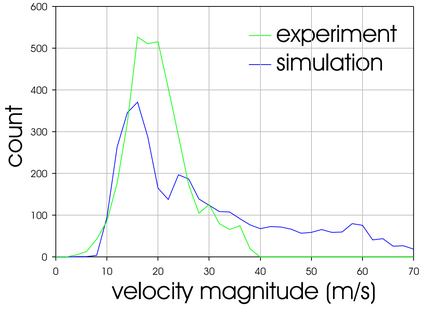

Pairs of cylinders

Experimental Density Fields

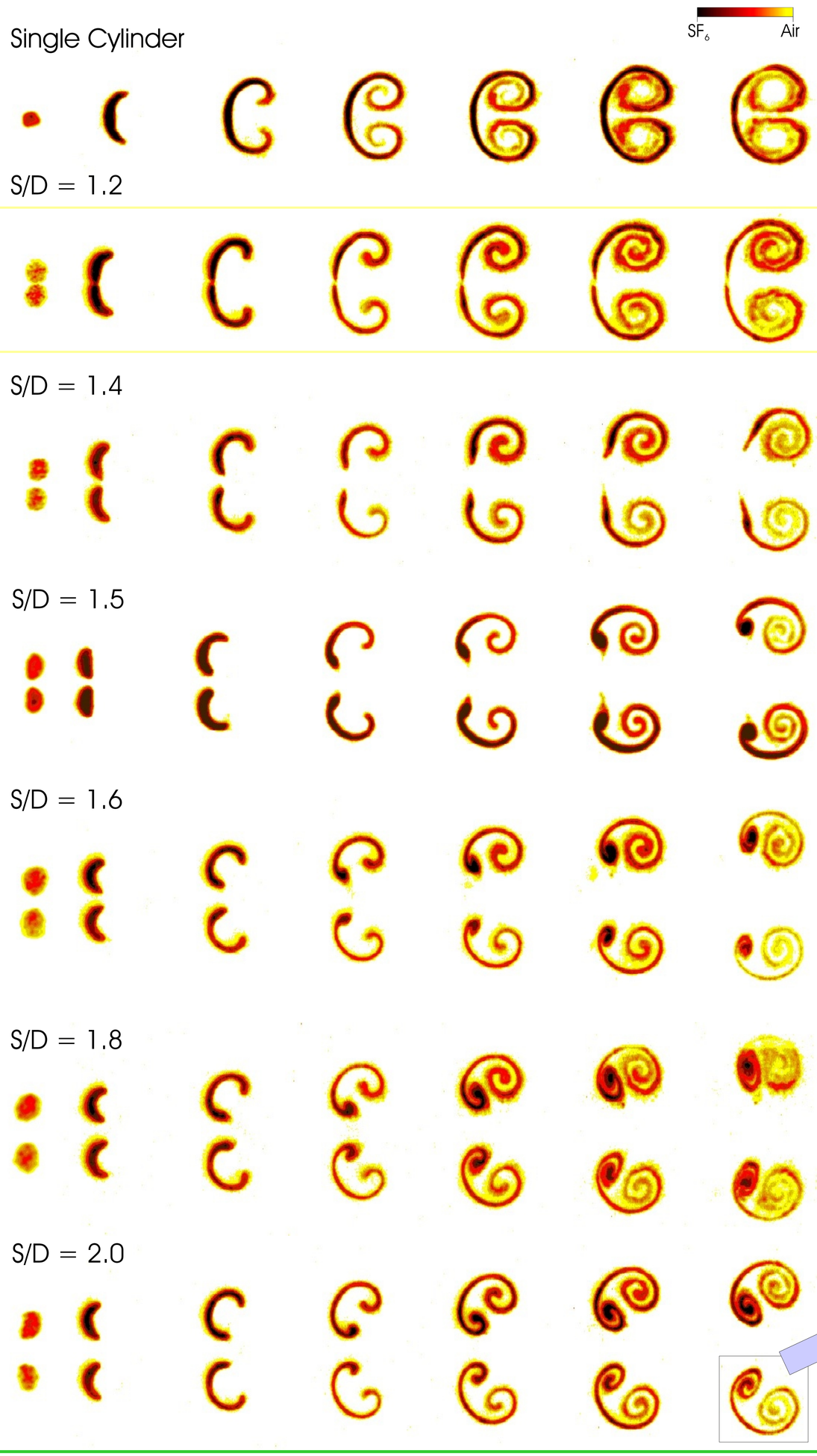

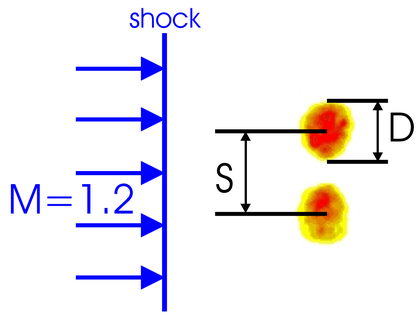

Anticipated results from a simple vortex blob model: Assumes 2 pairs of equal-strength counter-rotating vortices deposited by shock passage.

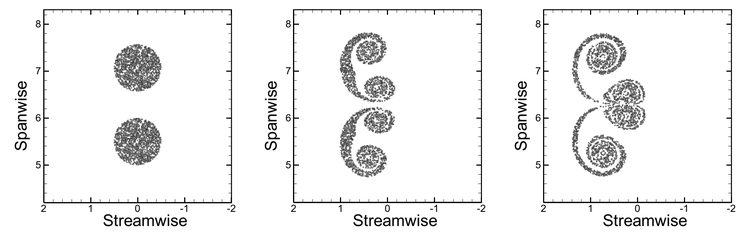

REPRODUCIBILITY

Ensemble-averaged over many shots– large-scale features preserved

Variation in Mixing and ICs with S/D

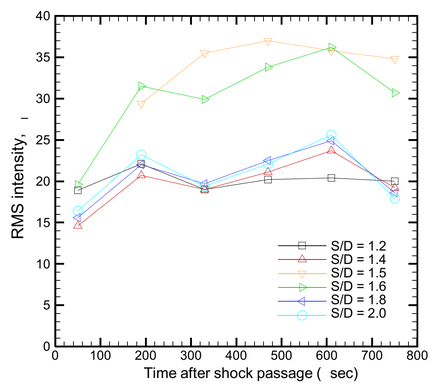

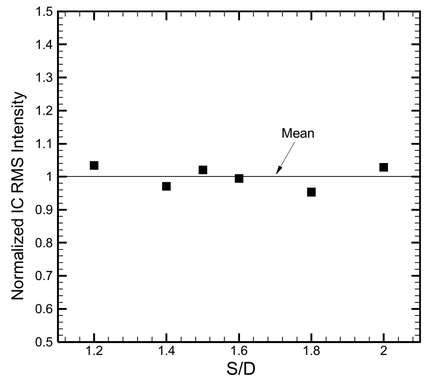

- Effects of shock impact on variably-spaced cylinders were not what we expected based on a simple model of vorticity deposition.
- There are various levels of interaction among the vortices depending upon the initial spacing of the cylinders.
- These results are highly reproducible from experiment to experiment, based on correlation-based ensemble averaging. Large-scale features are preserved.
- Particle Image Velocimetry was performed using cross-correlation and seeding of the background air.
- PIV reveals high velocity magnitudes in the region between the counter-rotating vortices and lower magnitudes in the cores.
- The vorticity field from PIV reveals a larger outer vortex with about four times the circulation of the inner vortex. Also visible is the vorticity along the outer edge of the vortex pair caused by shear.

Particle Image Velocimetry

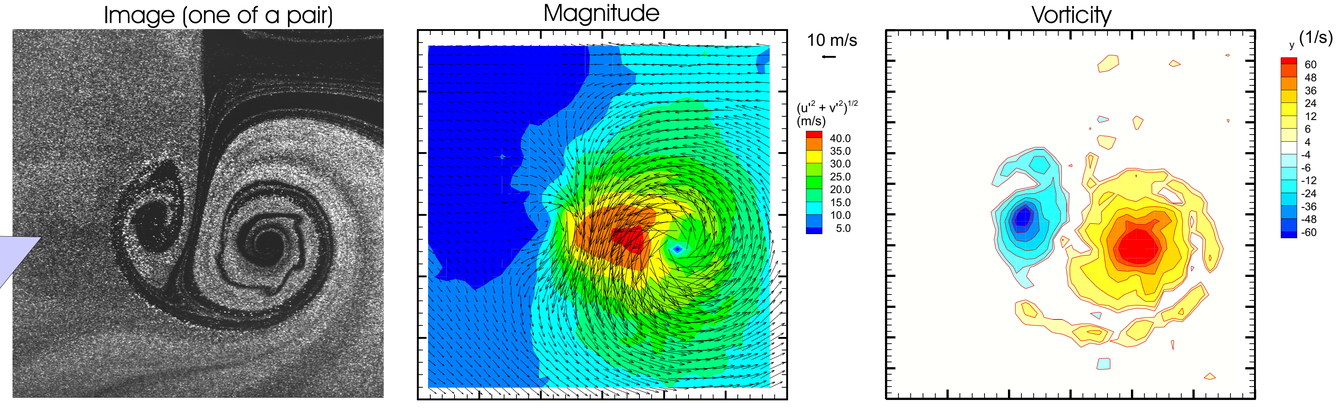

The 8th International Workshop on the Physics of Compressible Turbulent Mixing

Experimental study into Rayleigh-Taylor turbulent mixing zone heterogeneous structure

Yu. A. Kucherenko, A. P. Pylaev, V. D. Murzakov, A. V. Belomestnih, V. N. Popov, A. A. Tyaktev

Academician E. I. Zababakhin Russian Federal Nuclear Center – All-Russian Research Institute of Technical Physics
P. O. 245, Snezhinsk, Chelyabinsk region, 456770, Russia
E-mail: kucherenko@five.ch70.chel.su

Abstract: The heterogeneous structure study has been performed by means of a "light-sheet" technique at the SOM gas-dynamic accelerator. The investigated system consisted of three layers of different density liquids. For leading out the information from the mixing zone inner region illuminated by the "light-sheet", visualizing particles were seeded into one of the liquids. The visualizing particles, which got into the "light-sheet", diffused light, and at the same time photo images of the liquid fragments, contained the visualizing particles, were formed by a light-sensitive receiver. For the error reduction, refractive indexes of all the three liquids were equalized. A special test has been conducted for determining of measurements inaccuracy. Experiments have been performed for two values of acceleration of artificial field of gravity. Distributions of liquid fragments sizes are showed in the form of bar charts for different moments of time.

1 Introduction

Up to the present, the gravitational turbulent mixing heterogeneous structure is insufficiently known though it has been made considerable efforts for solution of this problem. There had been made an attempt to value fragments scales of different density miscible liquids at their gravitational mixing by an electro contact technique in experimental work [1]. In this work, a qualitative result had been obtained. According to this result, mixing at the unstable stage occurred by large fragments but at the turbulent mixing stage fragment sizes amounted 1 mm. In work [2] structure of the Richtmyer-Meshkov turbulent mixing of different density gases had been studied by a "laser knife" technique. In this work, there had been obtained photo images of non-uniformities in inner sections -of the mixing zone that gave an idea of the gases mixing character. In experimental & numerical works [3,4] the structure of gravitational turbulent mixing of miscible liquids with educing of molecular component had been studied for low Atwood numbers. Molecular part evaluations of mixing and density fluctuations were obtained in these works. In experimental & numerical work [5] fractal dimension evaluations of constant concentration contours had been obtained for the Rayleigh-Taylor turbulent mixing of liquids for low Atwood numbers. In work [6] density profiles of mixing liquids had been obtained from photo images of mixing zone sections by a "laser sheet" technique.

In the present work, an attempt of direct determination of immiscible liquids fragments sizes at their Rayleigh-Taylor turbulent mixing has been made. A "light sheet" technique has been employed for this study. It is known that for immiscible liquids the smallest size of fluid elements, which are in result of fragmentation, depends on relation between inertial forces determining by acceleration of a system and resistant forces determining by surface tension of given couple of liquids (Kolmogorov's criterion). A. V. Polionov offered the following relation for evaluation of the minimum size of fluid elements:

$$d \approx 4{,}3\left(\frac{\sigma / \rho}{A g_1}\right)^{4/7} \frac{1}{L^{1/7}}. \qquad (1)$$

© RFNC-VNIITF, 2001

Here **s** is surface tension value, ρ is density, $A = \frac{\rho_2 - \rho_1}{\rho_2 + \rho_1}$ is Atwood number, g_1 is acceleration of artificial field of gravity, ***L***- is turbulent mixing zone size. So the minimum size of fluid elements for chosen experimental system containing immiscible liquids depends on acceleration value g_1. Therefore experiments have been performed for two essentially different accelerations.

2 Experimental technique

Experiments were performed at the SOM installation described in work [7]. The measuring module of the installation represents a vertical channel, in upper part of which an ampoule containing studied liquids is placed at initial moment of time. The ampoule is accelerated by a gas flow, and a liquid system placed inside of the ampoule becomes unstable because of the acceleration is directed from a heavy liquid to a light one in the coordinate system connected with the ampoule. Owing to unstable a turbulent mixing arises at the contact boundary of the liquids. In the present work the measuring module was equipped with 14 horizontal light channels located with a step of 56 mm. Each channel contained the "light sheet»-forming block. The sketch of a horizontal section of the light channel is shown in Fig. 1.

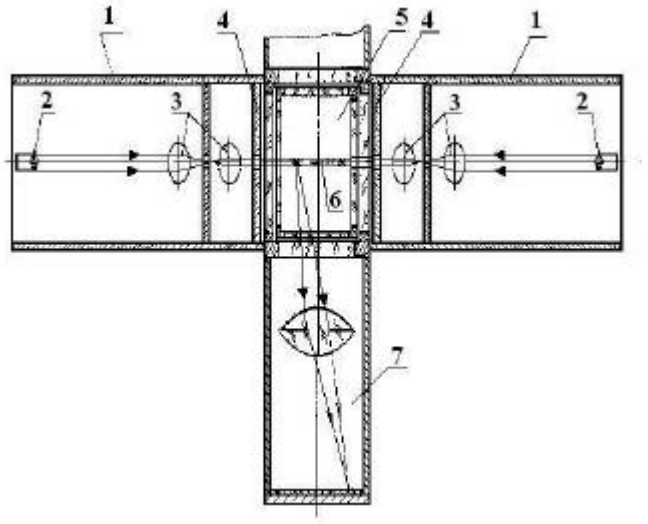

Fig. 1. Sketch of a horizontal section of the light channel

Light radiated by a pair of impulse sources (2), which is located in case (1), transforms by means of cylindrical optics (3) and diaphragms (4) to a luminous flux having a form of "light sheet" of thickness $\approx$ 1.5 mm. The "light sheet" comes into the ampoule (5) from two sides and illuminates chosen section of the mixing zone. Scheme with two-side coming of the "light sheet" is chosen from consideration of uniform illumination of chosen section along the ampoule length.

Visualizing particles inserts into one of the liquids. Light scattered by the visualizing particles, which are in the "light sheet" section, finds itself in the photo recorder (7) where a photo image of the mixing zone section forms. This photo image is some set of fragments of that liquid which contains visualizing particles.

3 Sensitivity of the technique

The light channel sensitivity, i. e. the least registered size of non-uniformities, depends on a set of factors, so that it was determined by the most direct method – with using some models. There

used jets specified size and form as models of non-uniformities. The jets formed by special formers two of which is shown in Fig. 2.

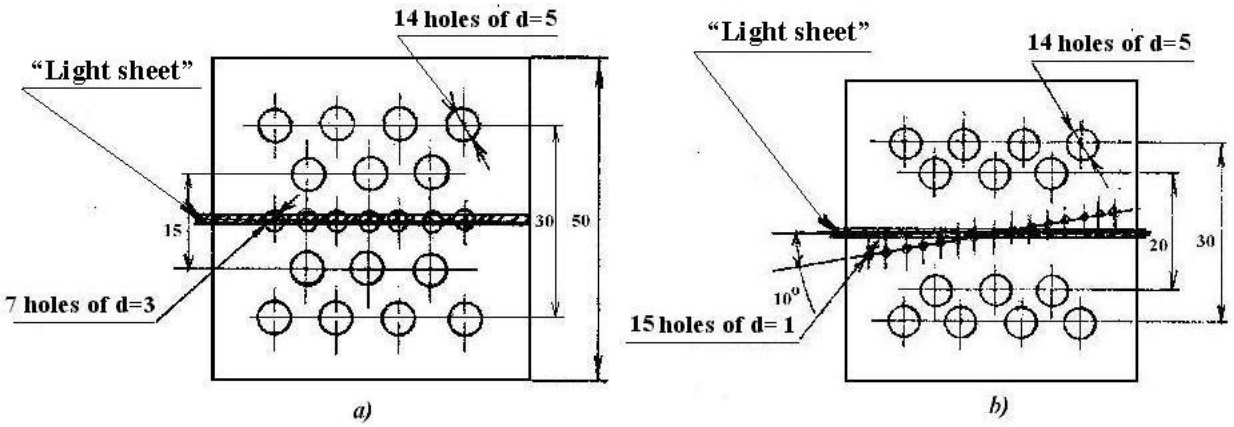

Fig.2. Formers for jets forming

The formers were located inside the ampoule at the contact boundary of the liquids which were aqueous solution of glycerin and benzine with the density ratio $\boldsymbol{n}$ = 1.6. Visualizing particles were in the aqueous solution of glycerin. At moving a former down, the heavy liquid containing visualizing particles passes through the holes producing jets, form and diameter of which corresponds to the form and diameter of the holes in the former. The photo recorder only takes those images for which jets find themselves in the "light sheet" section. Photo images of the jets are shown in Fig. 3. In Fig. 3*a*, there are distinctly seen four jets of diameter 5 mm found themselves in the "light sheet" section and not seen other jets not found themselves there. In Fig.3*b*, there are distinctly seen seven jets of diameter 3 mm formed with applying the former shown in Fig. 2*a*. In Fig. 3*c* and Fig. 3*d*, there are seen by four jets of diameter correspondingly 2 mm and 1 mm. These jets were formed with the former shown in Fig. 2*b*. Holes of that former were placed on an angle to the "light sheet". It is seen that the images only correspond to those jets which found themselves in the "light sheet" section. Jets of diameter less than 1 mm do not practically have images. Obtained results give a possibility to assert that:

1. Concentration of visualizing substance is enough for sharp image acquisition of non-uniformities of sizes not less than 1 mm;
2. Those non-uniformities, which do not find themselves in the "light sheet" section, do not have photo images.

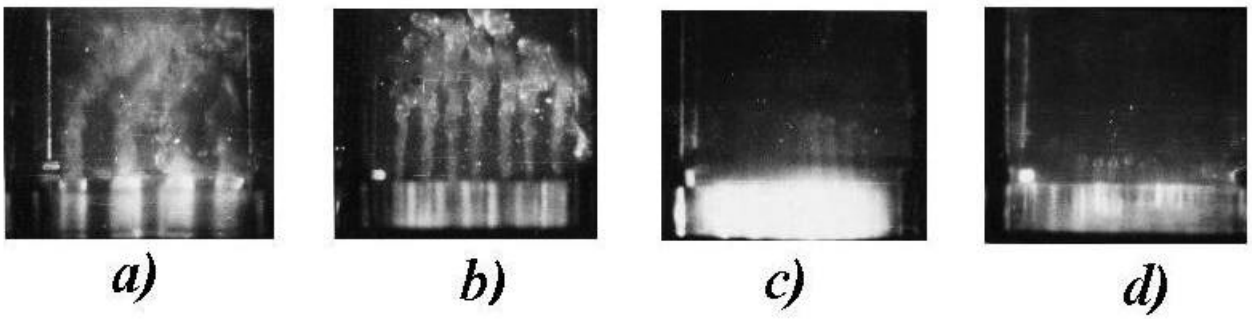

Fig. 3. Photo images of jets taken with special formers

4 Set up of experiments

Scheme of set up of experiments is shown in Fig. 4.

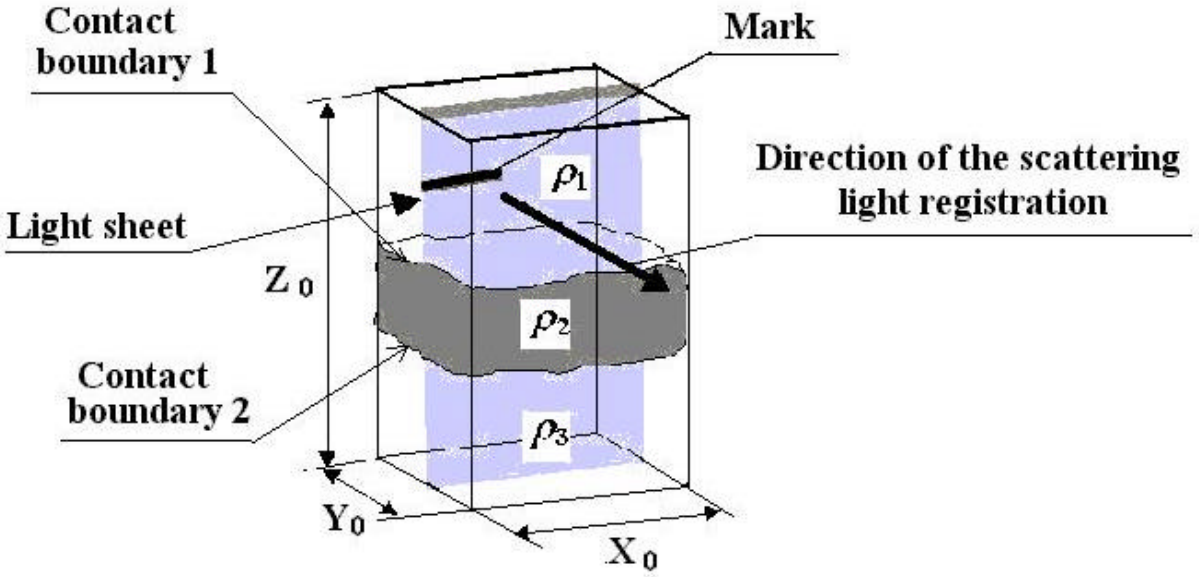

Fig.4. Scheme of set up of experiments

Experiments were performed with the system consisted of three layers of different density liquids placed inside of a hermetically ampoule. The lower layer was an aqueous solution of sodium hyposulfite (Na_2SO_3) with adding of glycerin of density ρ_3 = 1.24 g/cm^3 and viscosity ν_3 = 1.95 CSt. The middle layer of thickness 15 mm was a mixture of water and glycerin of density ρ_2 = 1.10 g/cm^3 and viscosity ν_2 = 4.5 CSt. The upper layer was benzine of density ρ_1 = 069 g/cm^3 and viscosity ν_1 = 0.77 CSt. Gelatin as a visualizing substance was added in the mixture of water and glycerin. Mass concentration of gelatin was 2%. Glycerin was only used for matching of indexes of refraction of all three layers. Optimum concentration of visualizing substance was determined by a photoelectric pickup having recorded intensity of transmitted and scattered laser light. Surface tension at the contact boundaries between aqueous solution of sodium hyposulfite and benzine, and between the glycerin and water mixture and benzine amount to 20 –30 dyne/cm.

The inner sizes of working volume of the ampoule were X_0 = 64 mm, Y_0 = 54 mm, Z_0 = 120 mm. Impulse luminous flux in the form of "sheet" illuminated the central section of the ampoule (the "light sheet" coordinate is y = 27 mm). There was a fixed mark inside the ampoule in the light sheet plane for determining of the contact boundaries initial positions and mixing fronts coordinates. A scale grid was placed inside the ampoule in the light sheet plane for preliminary determining the light channels enlargement. Initial perturbations at the contact boundaries of the liquids were created by blow with a special striker made of fluoroplastic of mass 40 g upon the ampoule cover. Specific mass of the equipped ampoule was μ = 23.9 g/cm^2.

There were performed two groups of experiments differed by initial acceleration g_1. In the first group of experiments acceleration was g_1 = 350 g, in the second one - g_1 = 100 g, where g – acceleration of the Earth's gravity. When the ampoule has passed distance 784 mm, in the first group of experiments acceleration becomes 230 g and in the second group – 66 g. In its turn every group consisted of two series of experiments differed by the range of recording. The reason was connected with availability of CB2 formed by miscible liquids with not great Atwood number A = 0.11. Because of that turbulent mixing at that contact boundary started after some delay and was developing not enough intensive for heterogeneous structure measuring in that range. It had to enlarge the ampoule displacement along the measuring channel by 500 mm to measure the

heterogeneous structure. So that the ampoule displacement was S = 784 mm in the first series of experiments and S = 1284 mm – in the second one.

5 Experimental results

Each group consisted of 20 experiments. Characteristic photo images captured in the 1st group of experiments are shown in Fig. 5. Photo images for the 2nd group are presented in Fig. 6.

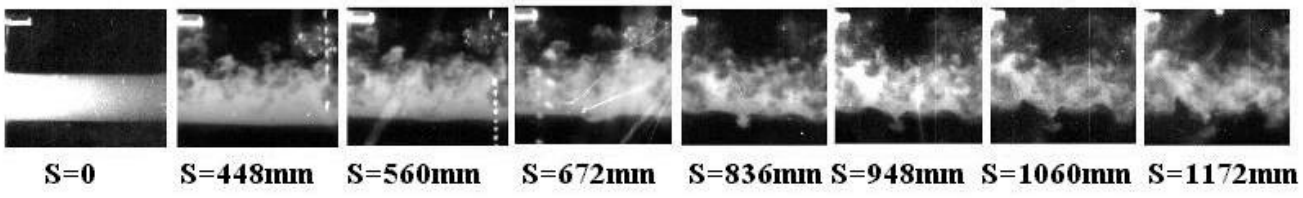

Fig. 5. Characteristic photo images of the mixing zone structure for the 1st group of experiments

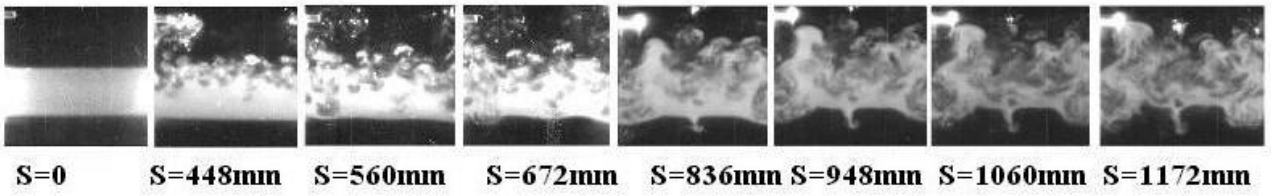

Fig. 6. Characteristic photo images of the mixing zone structure for the 2nd group of experiments

It is seen from the photo images that the turbulent mixing first develops at the contact boundary CB1 and some time later – at the contact boundary CB2.

Photo images were processing the following manner. Two-dimensional (X – Z) matrix of the film blackening intensities was produced at scanning each photo image. For arbitrary section $Z = Z_0$ the dependence of the film blackening density on coordinate X was built. Next this dependence was processing according to a special developed algorithm, which gave a possibility to obtain sizes of liquid fragments having found themselves in the light sheet section by computer. The program was developed so that it determined fragments sizes of one of the liquids, namely that liquid whose fragments at positive image were light. For determining fragments sizes of another liquid (not containing visualizing substance) it was processing negative image of the frame at which fragments images of that liquid were light. All the data obtained for the same moment of time were referred to the same statistical population. Bar charts of liquid fragments distribution at their sizes were built as the result of processing.

At each photo image, determination of liquid fragments sizes in the mixing zone was produced at the following sections (along Z-coordinate): at the section where the initial contact boundary CB1 was placed (Z = 0), and at the sections Z = ± 4mm, Z = ± 8mm. Inaccuracy of measurements of liquid fragments sizes was obtained with using of photo images of the jets, produced in model experiments. Transversal sizes of the jets were determined in ten sections along Z-coordinate by both a handle method and machine one. As a result of this measuring the maximum inaccuracy is $\boldsymbol{h}$ = 15%.

Bar charts of sizes $\boldsymbol{d}$ distributions of both light liquid fragments (of density ρ_1 =0.69 g/cm^3) and heavy ones (of density ρ_2 =1.23 g/cm^3) built at considering all fragment sizes of each liquid obtained for all displacements $\boldsymbol{S}$ and all sections $\boldsymbol{Z}$ as the same statistical population in each group of experiments are shown in Fig. 7.

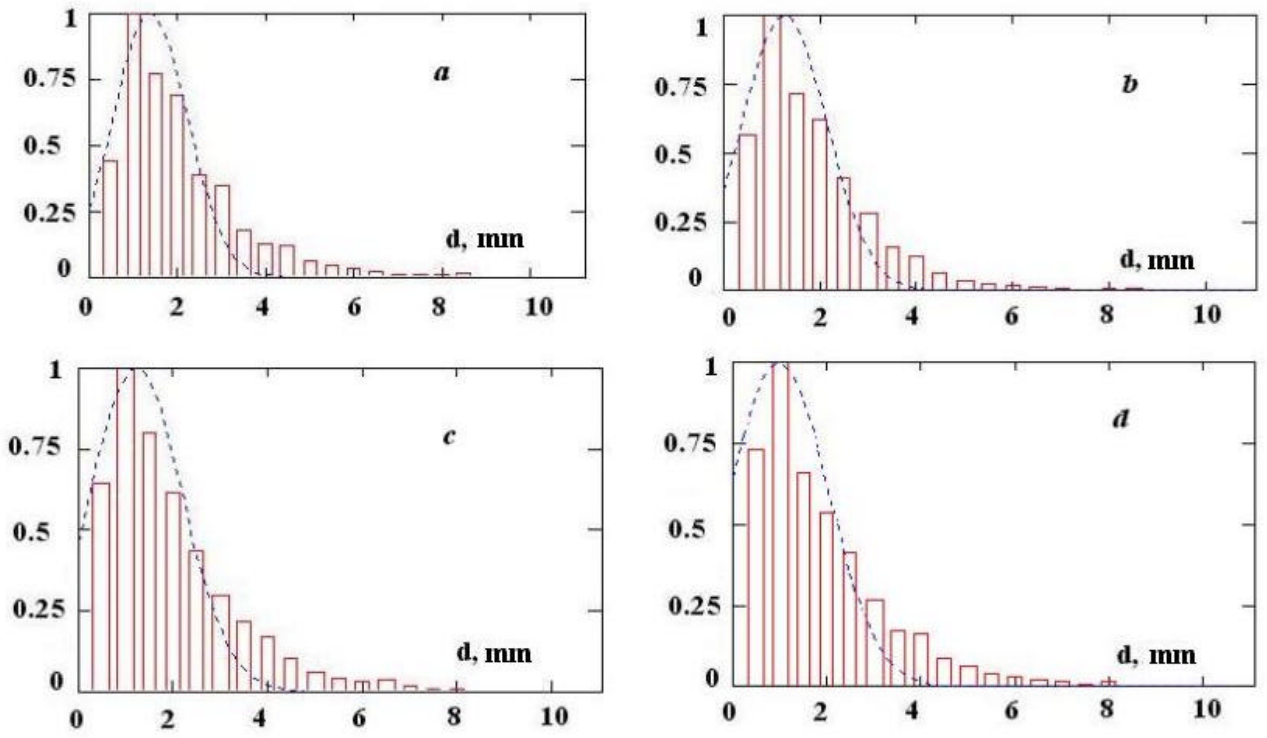

Fig. 7. Bar charts of distributions of liquids fragments sizes in the mixing zone
a – light liquid of density ρ_1, the 1st group of experiments; ***b*** – heavy liquid of density ρ_2, the 1st group of experiments; ***c*** - light liquid of density ρ_1, the 2nd group of experiments; ***d*** - heavy liquid of density ρ_2, the 2nd group of experiments

It is seen from the bar charts that in the 1st group of experiments the maximum of the distribution is $\grave{a}_1$ = 1.39 mm for the liquid of density ρ_1, and $\grave{a}_2$ = 1.26 mm for the liquid of density ρ_2. In the 2nd group of experiments the maximums of the distributions are $\grave{a}_1$ = 1.23 mm and $\grave{a}_2$ = 0.98 mm for the light and heavy liquids correspondingly.

6 Conclusion

Performed experiments showed that in developed turbulent flow produced by the Rayleigh-Taylor instability sizes of most part of fragments of immiscible liquids are in the range from 1 mm to 1.5 mm. Evaluations of minimum sizes of liquid fragments by the Polionov's relation (1) show that they are in the range from 0.5 mm to 1.1 mm for the light liquid and from 0.36 mm to 0.8 mm for the heavy one. These evaluations are in qualitative agreement with the experiment.

Literature

1. I. K. Kikoin, D. I. Voskoboinik, V. A. Dmitrievsky, V. I. Stefanov. Experimental study of turbulent mixing of liquids in an acceleration field. LIPAN Report, p.2, 1953.
2. E. E. Meshkov, A.I. Tolshmyakov. Study into turbulent mixing zone structure by scattered light. RFNC-VNIIEF Report, 1982.
3. P. F. Linden and J. M. Redondo. Molecular mixing in Rayleigh-Taylor instability. Part I: Global mixing. Phys. Fluids, A3 (5), 1991.
4. P. F. Linden, J. M. Redondo and D. L. Youngs. Molecular mixing in Rayleigh-Taylor instability. J. Fluid Mech., v. 265, 1994.

5. S. B. Dalziel, P. F. Linden and D. L. Youngs. Self-similarity and Internal Structure of Turbulence Induced by Rayleigh-Taylor Instability. Proceedings of the Sixth International Workshop on the Physics of Compressible Turbulent Mixing. Marseilles, 18 –21 June 1997.
6. M. Schneider, G. Dimonte and B. Remington. Structure of Rayleigh-Taylor Mixing from Laser Induced Fluorescence on the Linear Electric Motor (in typescript).
7. Yu. A. Kucherenko, A. P. Pylaev, V. D. Murzakov, V. N. Popov, O. R. Komarov, V. E. Savel'ev, R. Cherret, and J.-F. Haas. Experimental study into the Asymptotic Stage of the Separation of the Turbulized Mixtures in Gravitationally Stable Mode. Proceedings of the 5th International Workshop on Compressible Turbulent Mixing. Stony Brook, 18 – 21 July 1995.

Measurements of Turbulence Correlations in Low Atwood Number Rayleigh-Taylor Mixing

Malcolm Andrews & Praveen Ramaprabhu

Department of Mechanical Engineering
Texas A&M University
College Station, TX 77845
Tel: (979) 847 8843; e-mail: mandrews@mengr.tamu.edu

International Workshop on the Physics of
Compressible Turbulent Mixing
CalTech, Pasadena, CA
December 9-14, 2001
DOE Grant# DE-FG03-99DP00276/A000

Overview

- Detailed measurements of turbulent Rayleigh-Taylor have been taken in support of mix models for the description and understanding of hydrodynamic instabilities that develop during the implosion phase of ICF capsules.
- Highlights include: extensive collection of data and development of the PIV-S method.
- The intent is data to aid in the development of statistical turbulence models
- What follows is a selection of our results.

Schematic of experiment

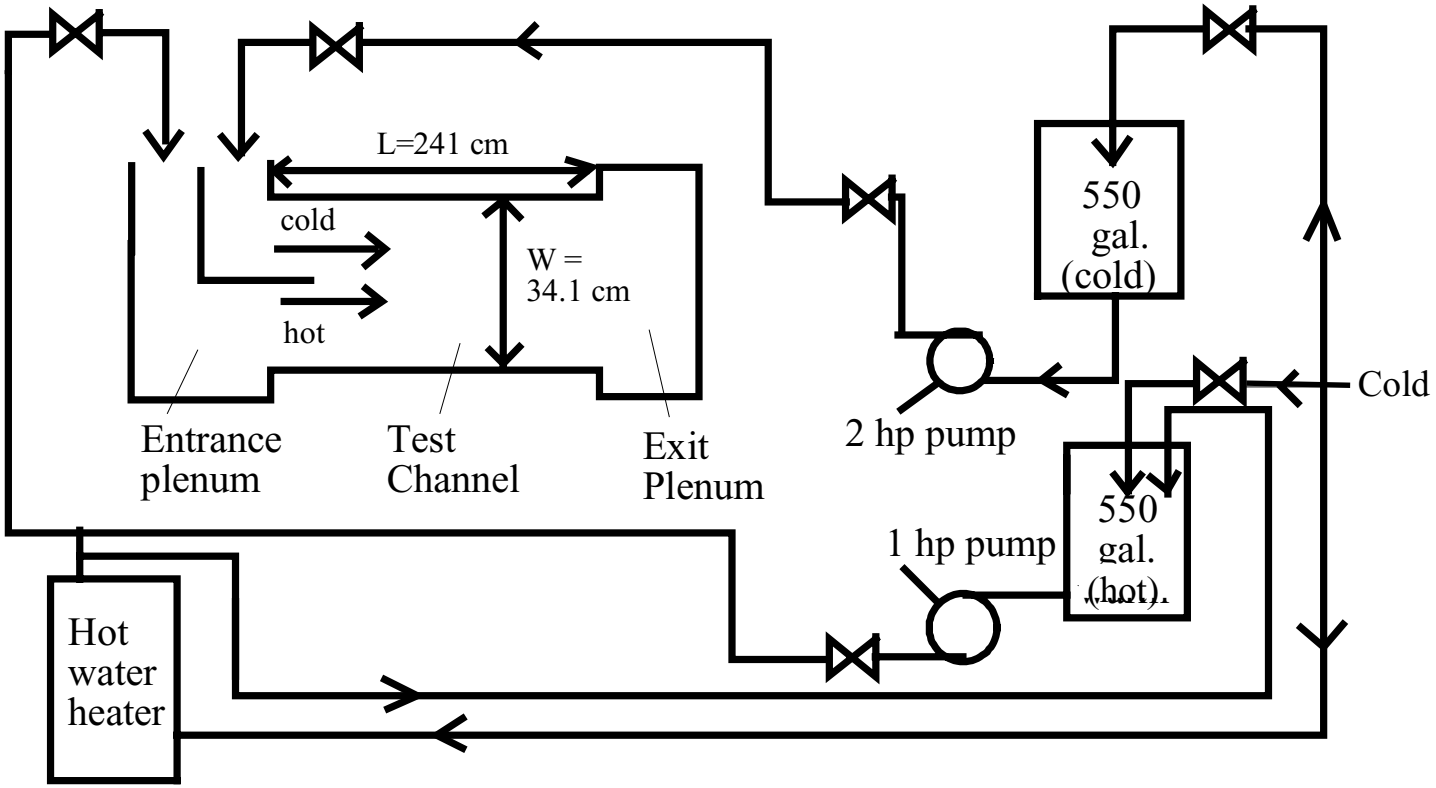

Experimental details

ATM

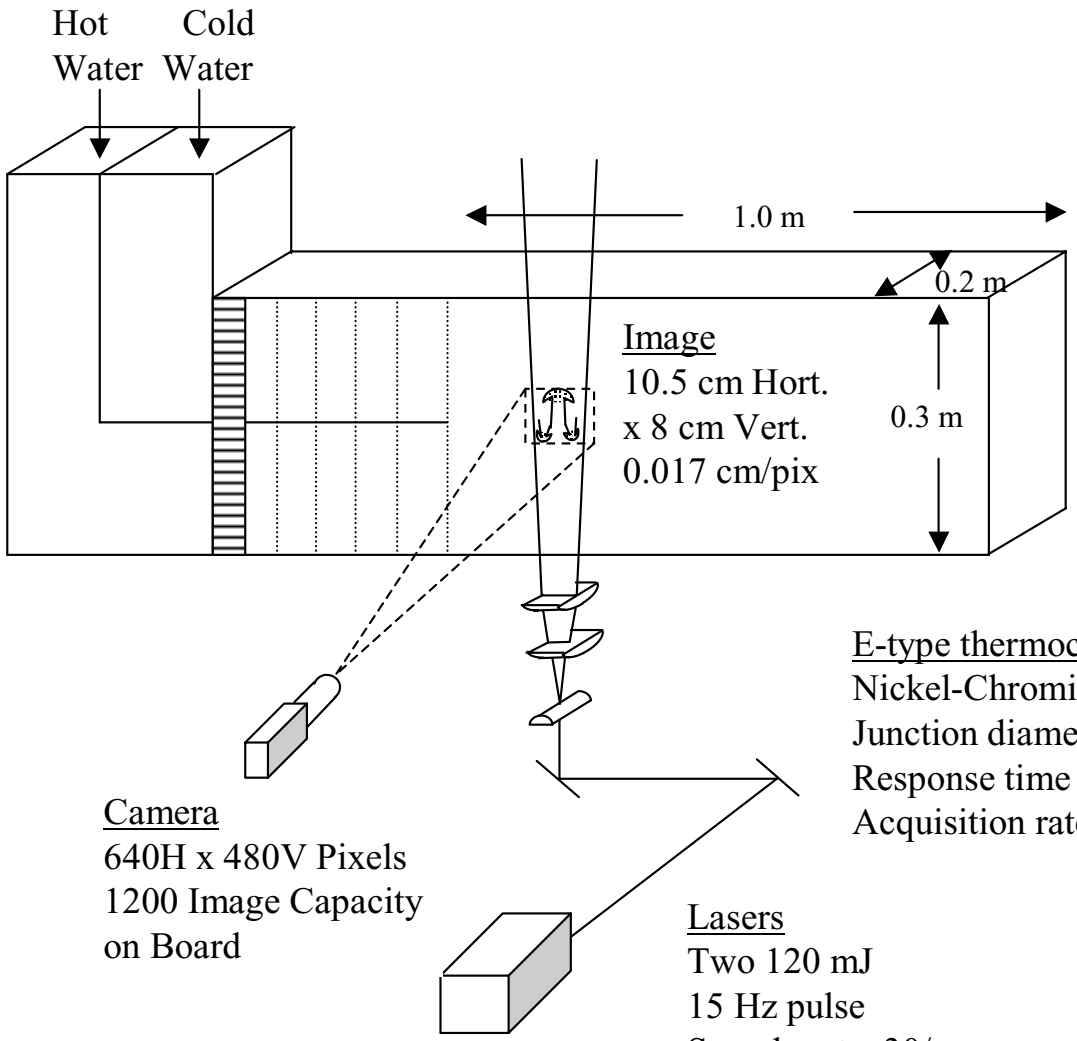

PIV particle concentration:
3mL/2000 L

<u>Camera</u>
640H x 480V Pixels
1200 Image Capacity on Board

<u>E-type thermocouples</u>
Nickel-Chromium and Constantan
Junction diameter of 0.01-0.02 cm
Response time 0.001 s/^{o}C
Acquisition rate 8 kHz.

<u>Lasers</u>
Two 120 mJ
15 Hz pulse
Sample rate: 30/sec.

Photograph from experiment

At # = 10^{-3}

$\Delta T = 5^{o}C$

U = 4 cm/s

Summary of data collected

At Atwood numbers of 10^{-3} and $5\text{x}10^{-4}$:

- Density profiles across mix; width quadratic growth rate, α
- Ensemble averaged measurements of turbulence R-T mixing correlations:

$$\overline{\rho'^2}, \overline{u'^2}, \overline{v'^2}, \overline{u'v'}, \text{and } \overline{\rho'u'}, \overline{\rho'v'}$$

- Turbulence density fluctuation energy spectra.
- Molecular mix fraction, θ
- Anisotropy tensor

ATM

Parameter definitions

$$\mathrm{B}_0 = \lim_{\mathrm{T}\to\infty} \frac{1}{\mathrm{T}} \int_0^{\mathrm{T}} \left(\rho - \overline{\rho}\right)^2 \mathrm{dt} / \Delta\rho^2 = \lim_{\mathrm{T}\to\infty} \frac{1}{\mathrm{T}} \int_0^{\mathrm{T}} \left(\rho'\right)^2 \mathrm{dt} / \Delta\rho^2$$

$$B_2 = \overline{\rho^*}\left(1 - \overline{\rho^*}\right) = f_1\left(1 - f_1\right) \qquad \theta \equiv 1 - B_0 / B_2$$

$$\rho^* = \frac{\left(\rho - \rho_{\min}\right)}{\left(\rho_{\max} - \rho_{\min}\right)} \qquad \overline{\rho^*} = \frac{\sum_1^n \rho_{\mathrm{i}}^*}{\mathrm{n}} \qquad B_0 = \frac{\mathrm{n}\sum_1^n \rho_{\mathrm{i}}^{*2} - \left(\sum_1^n \rho_{\mathrm{i}}^*\right)^2}{\mathrm{n(n-1)}}$$

$$\mathrm{B}_0(\omega_{\mathrm{n}}) = \frac{2\delta\mathrm{t}}{\mathrm{N}} \left| \sum_{i=0}^{N-1} (\rho_i^*)' \mathrm{e}^{2\pi \mathrm{j} \omega_n t_i} \right|$$

Mean density profiles

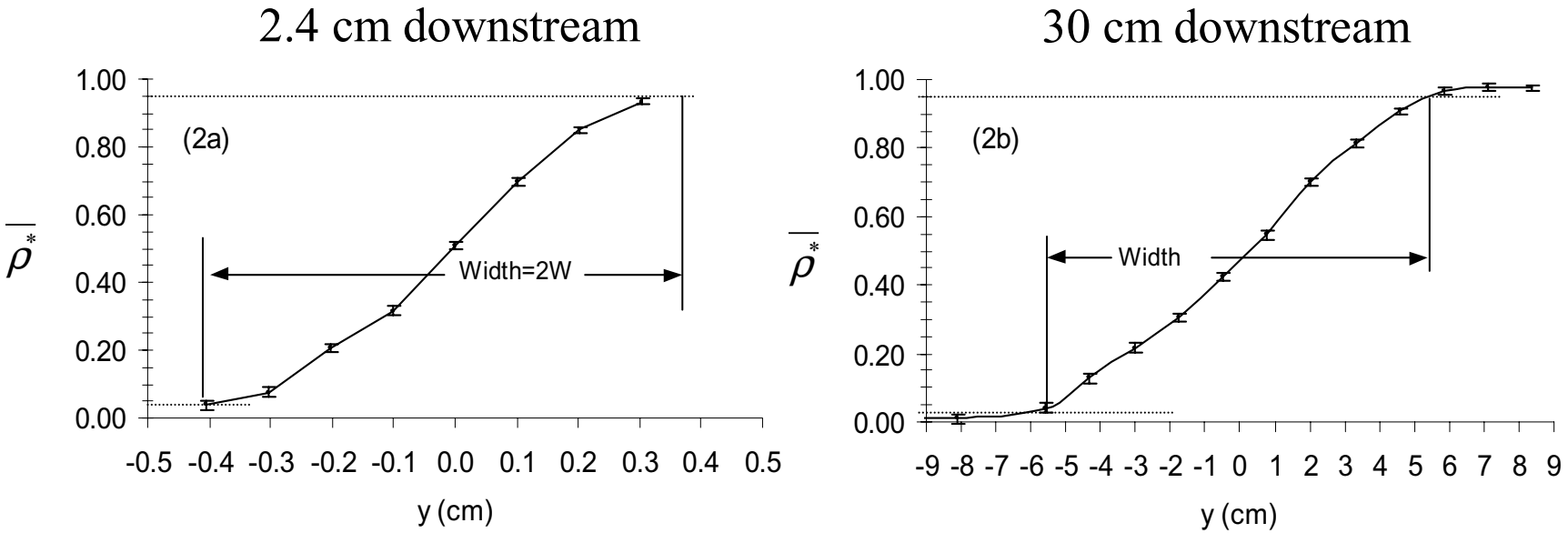

Mean density profile taken with thermocouple measurements, and showing error bars.

Density fluctuation power spectra

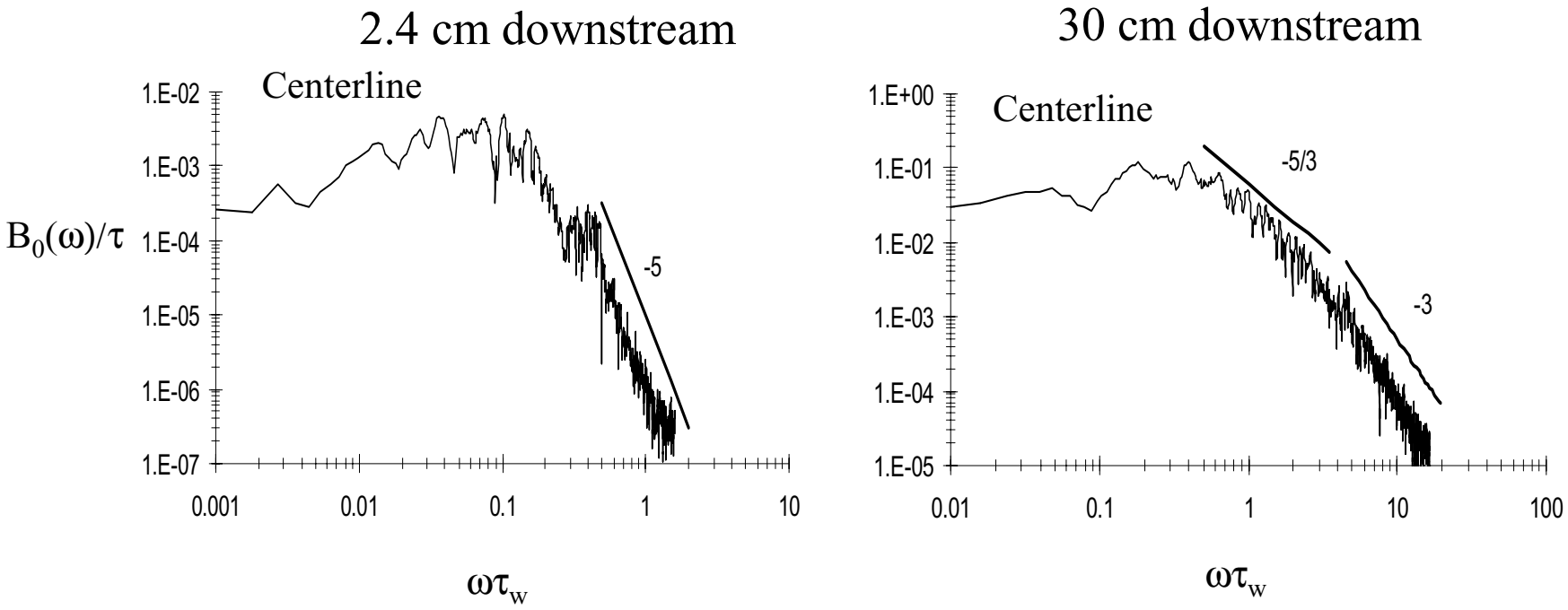

More power spectra

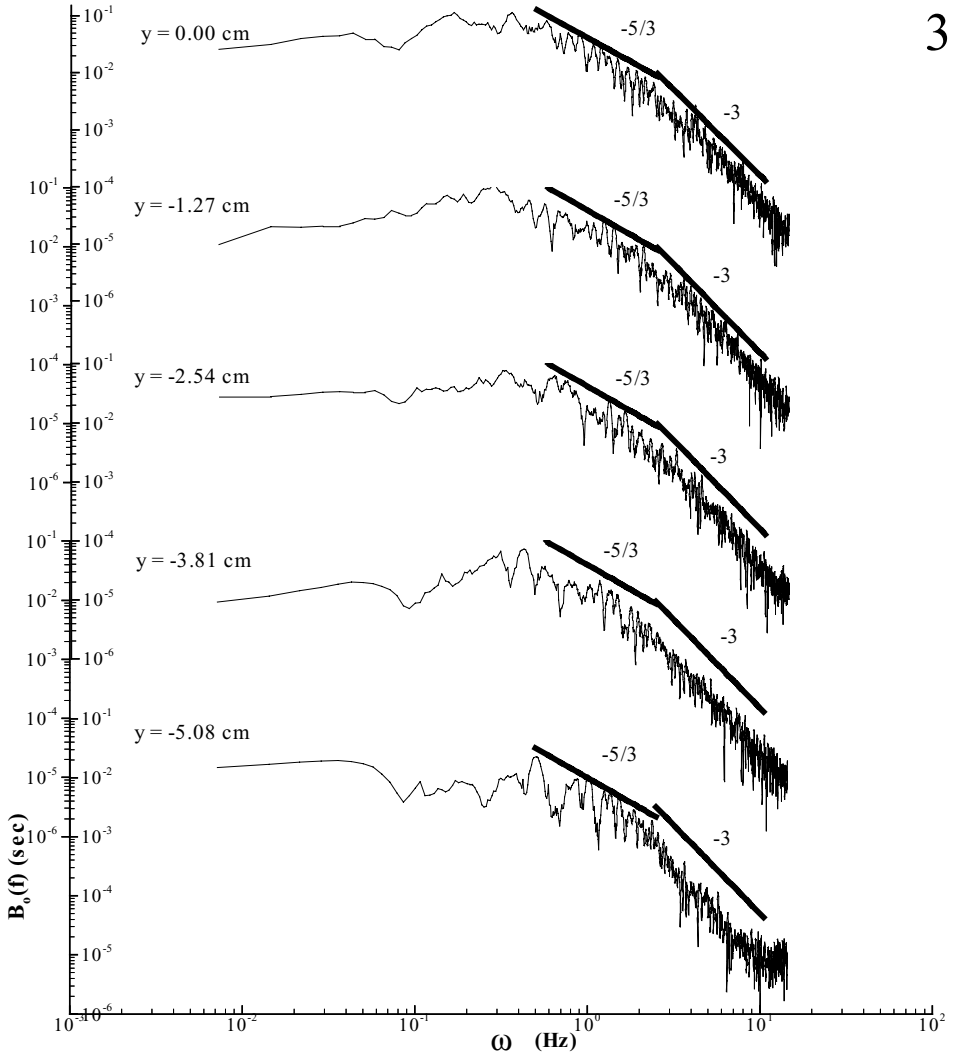

30 cm downstream

Centerline

Mix edge

PIV-S

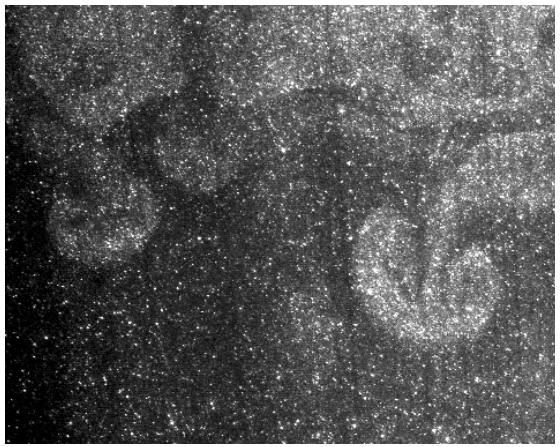

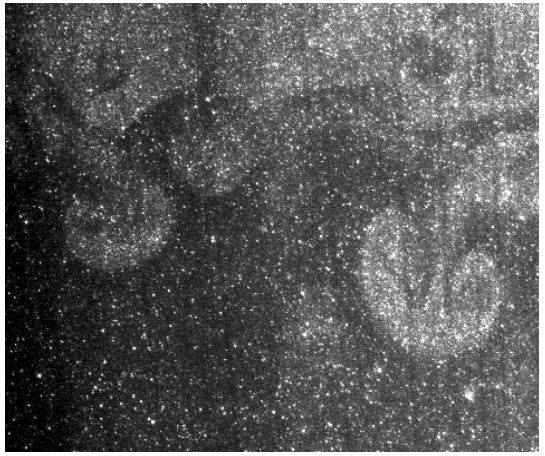

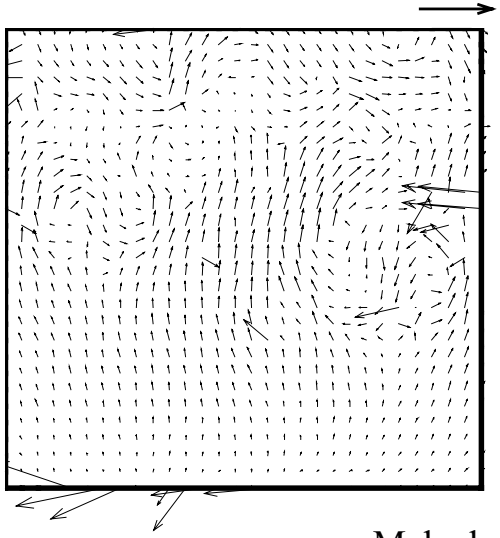

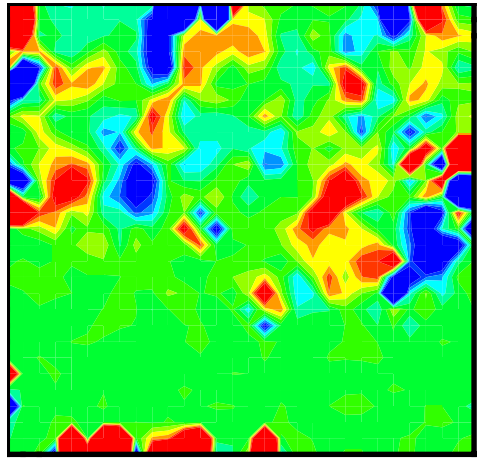

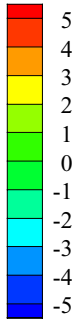

Density fluctuations

ATM

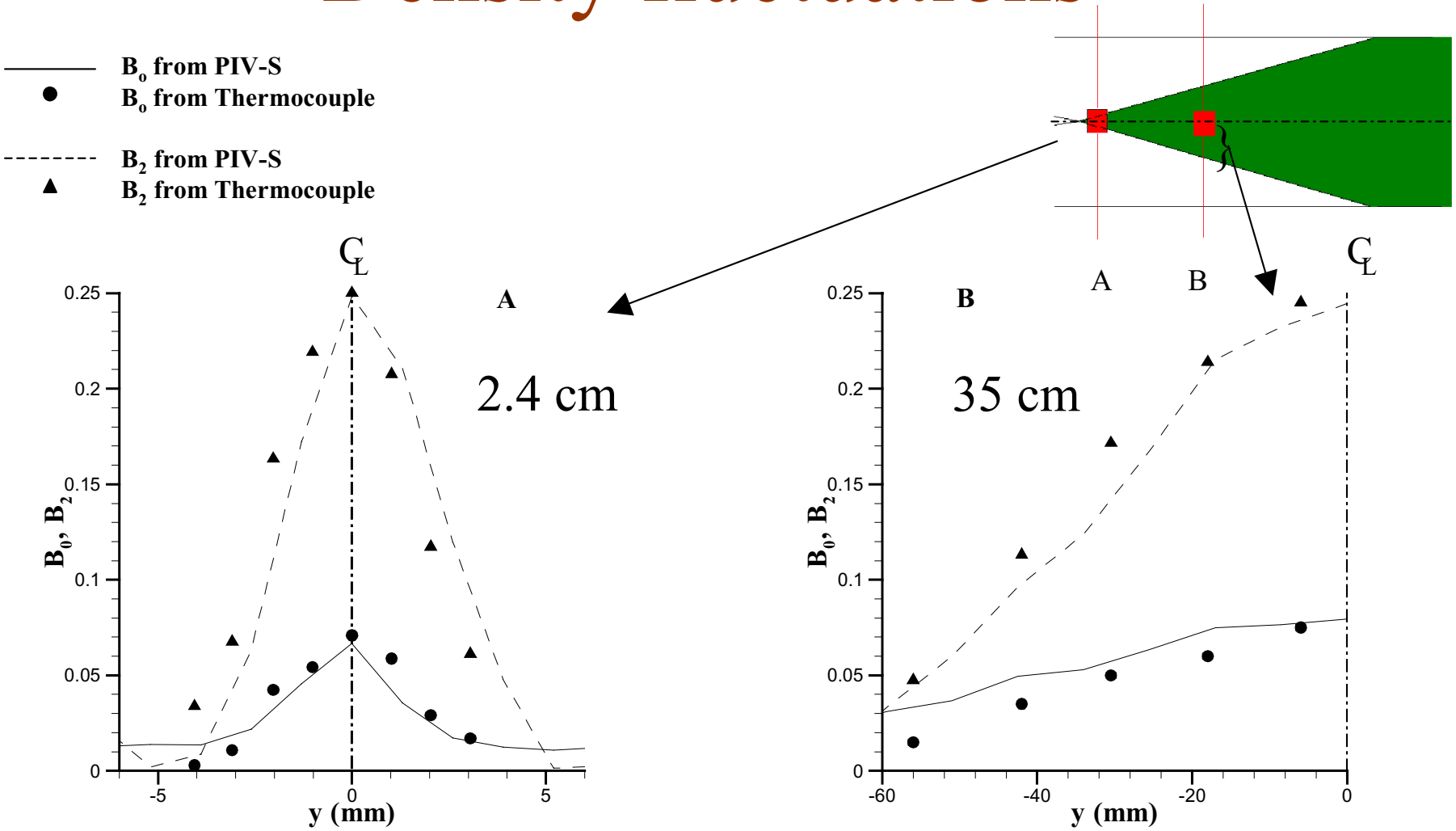

Molecular Mixing

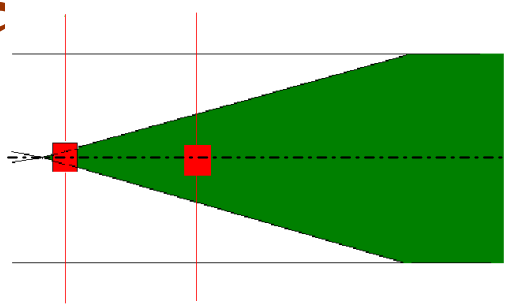

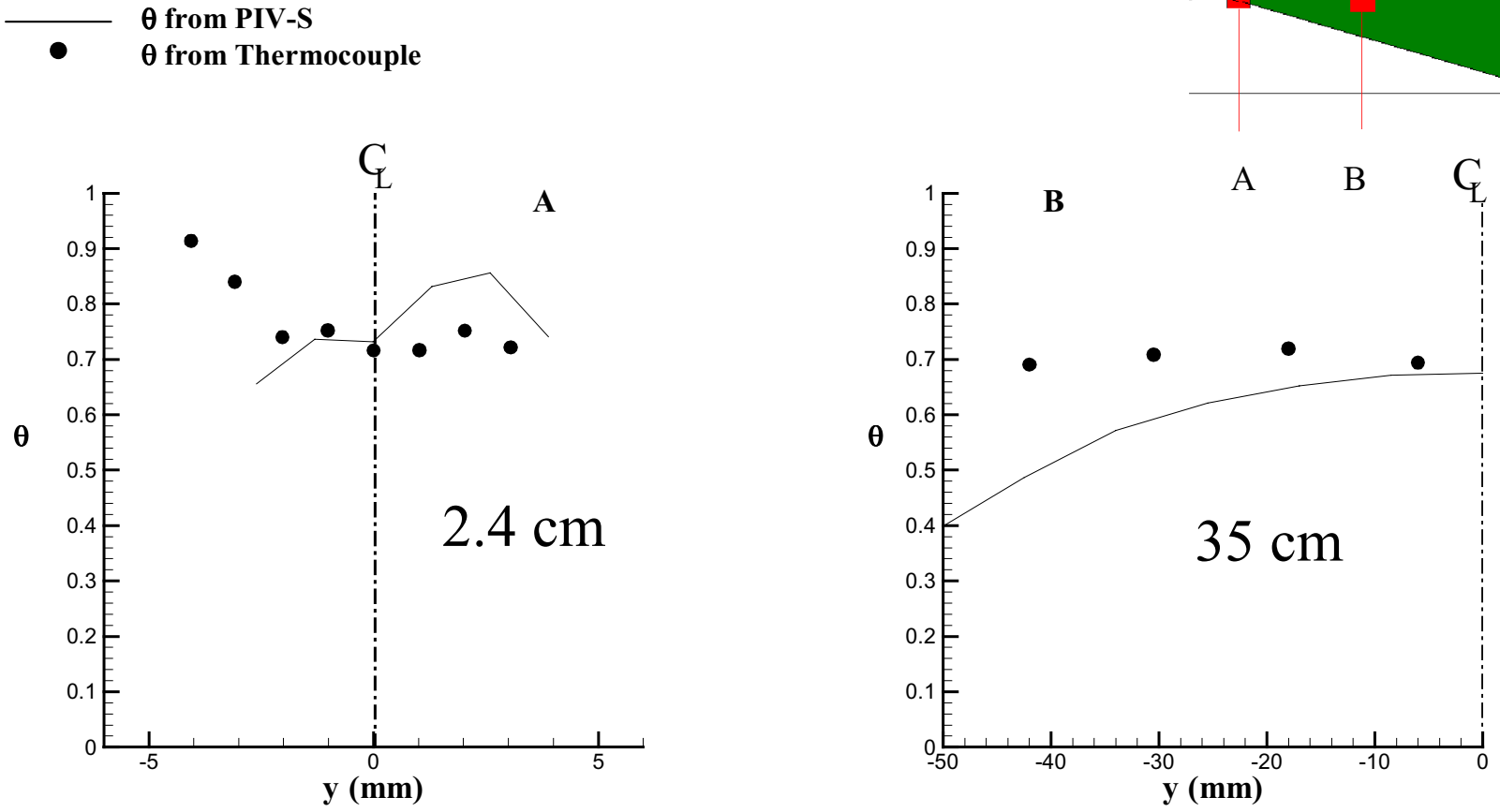

Density/Velocity Correlations ATM

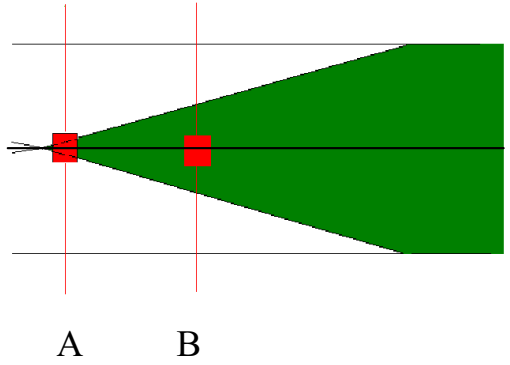

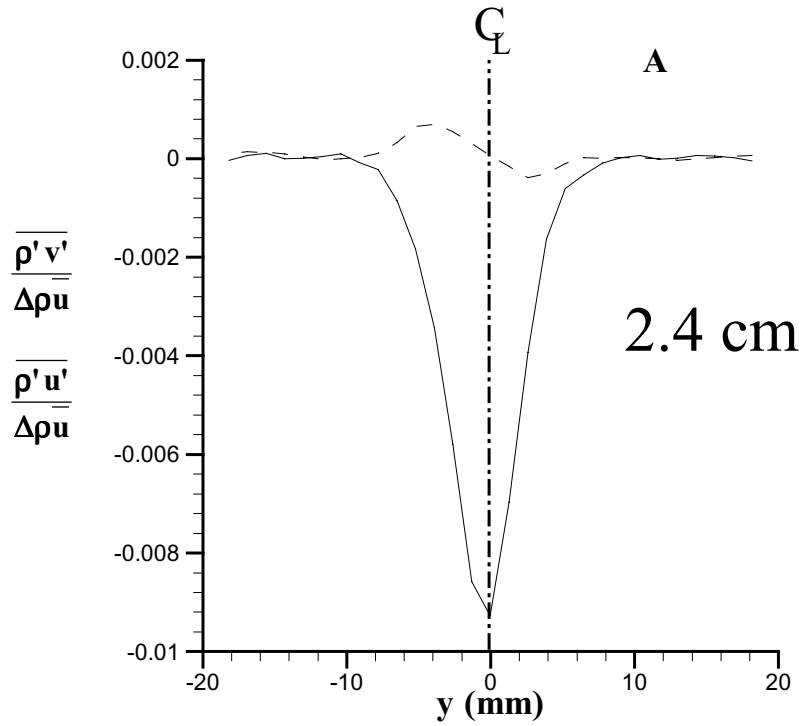

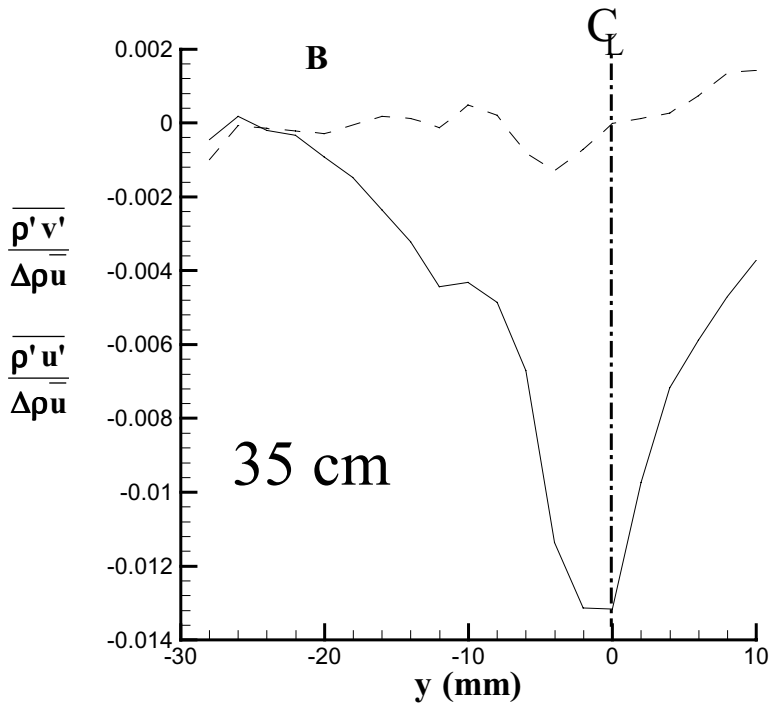

Scatter plots of velocity fluctuations

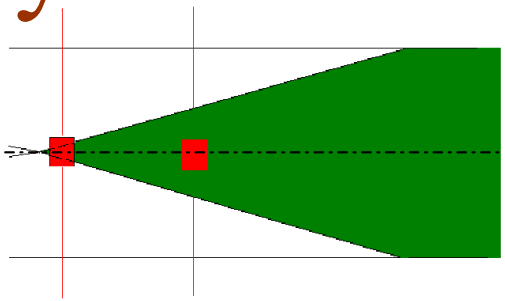

Taken at centerline

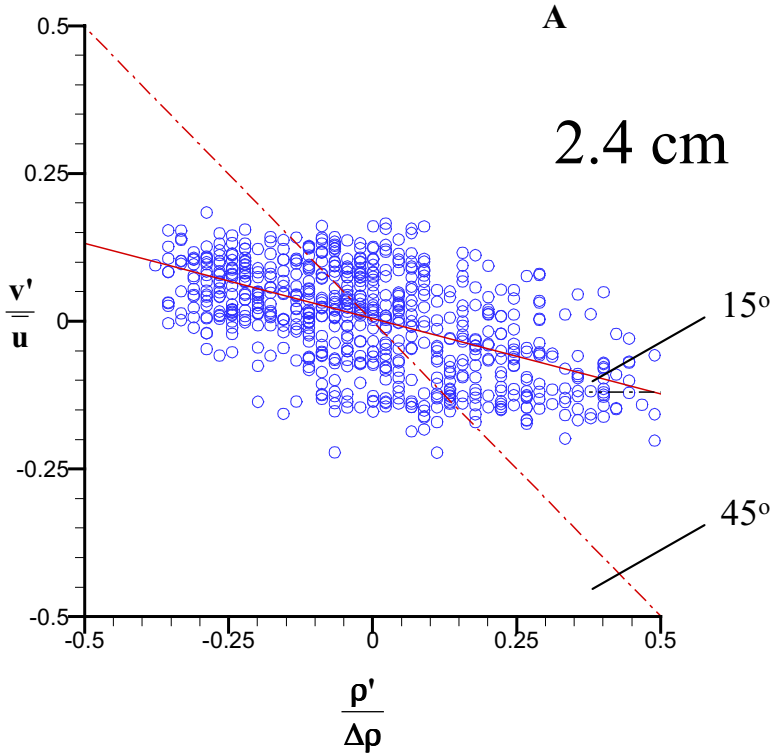

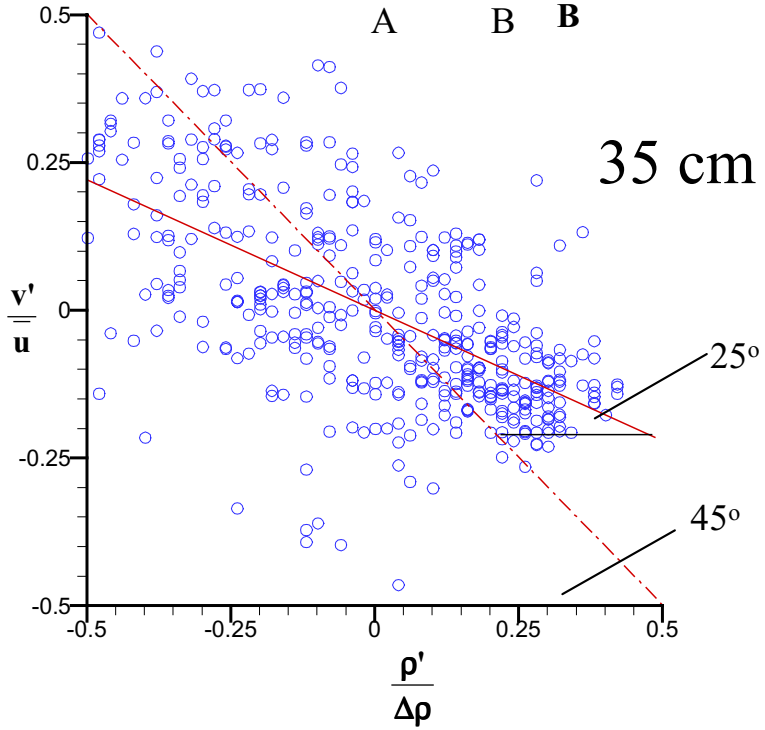

Velocity Fluctuations (35 cm)

ATM

$\frac{v_{rms}}{u_\infty}$

$\frac{u_{rms}}{u_\infty}$

$u_\infty = 0.7\sqrt{A_t g H / 4}$

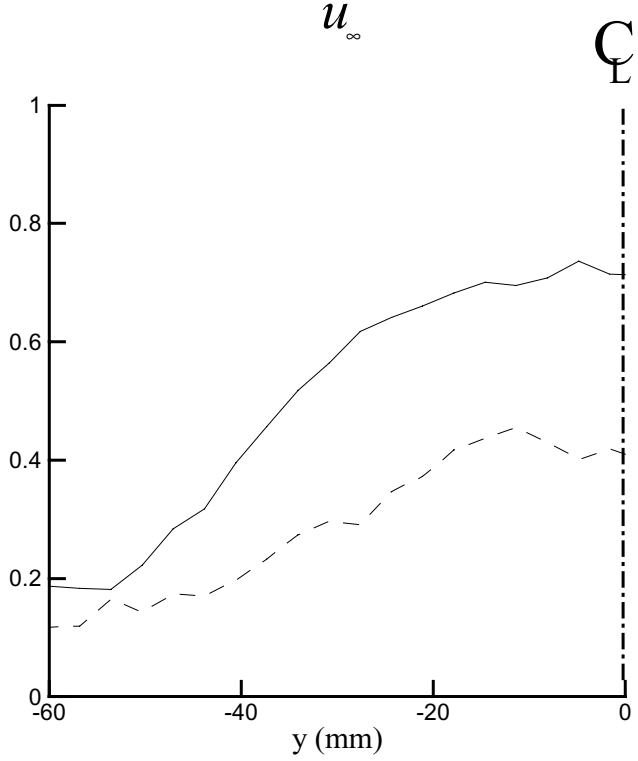

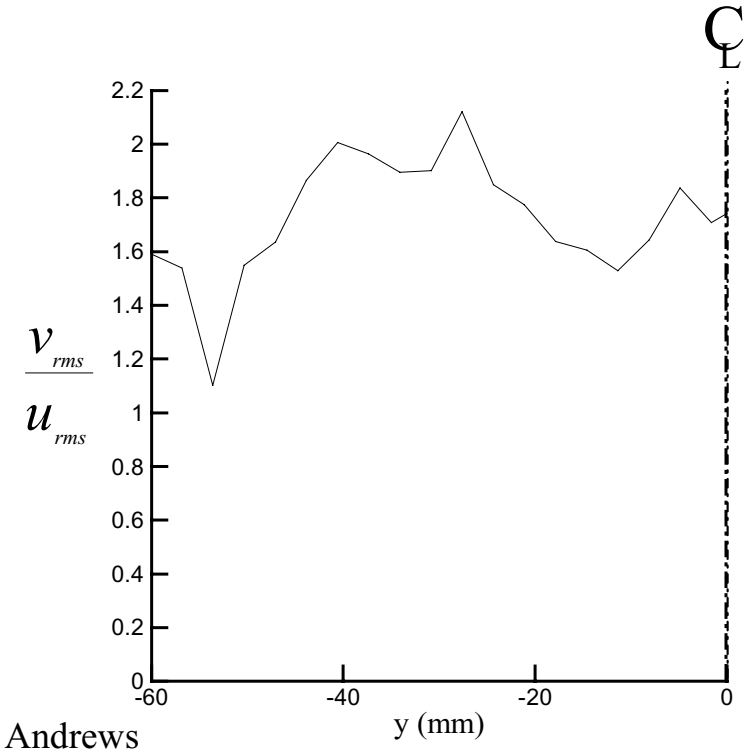

Anisotropy Tensor

ATM

$$b_{ij} = \frac{< u'_i u'_j >}{< u'_k u'_k >} - \frac{1}{3}\delta_{ij}$$

$$< u'_i \, u'_j >= 0 \quad \text{if i} \neq \text{j}$$

where $$< u'_k \, u'_k >= \overline{u'^2} + \overline{v'^2} + \overline{w'^2}$$

$$\approx 2\overline{u'^2} + \overline{v'^2}$$

Isotropy $$\Rightarrow b_{ii} = 0$$

Anisotropy Tensor

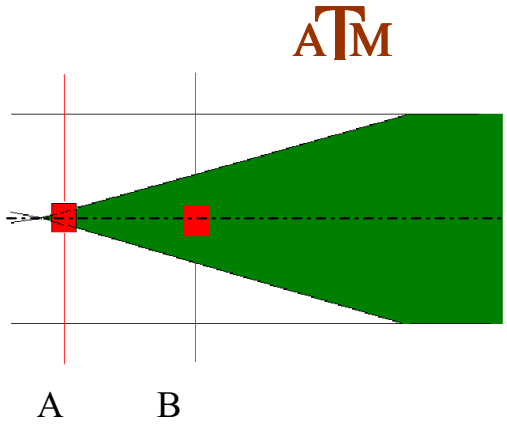

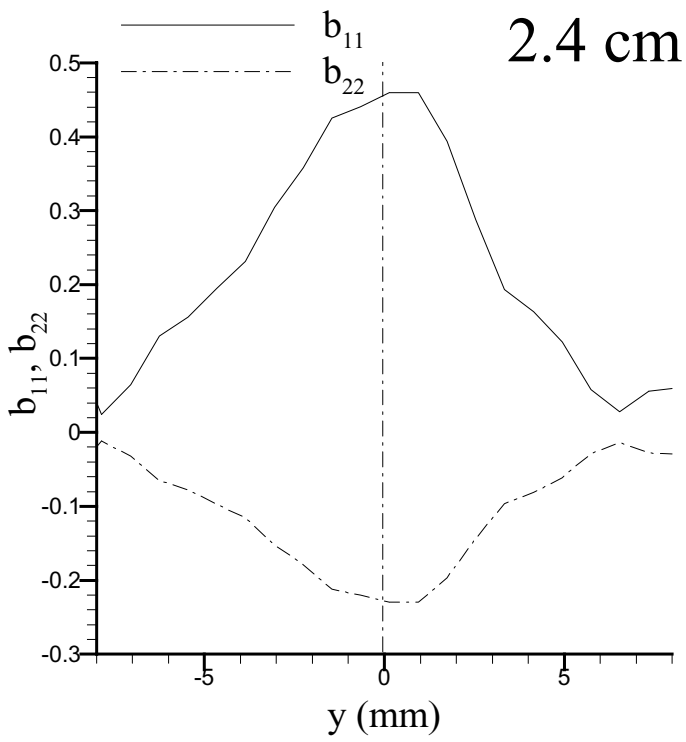

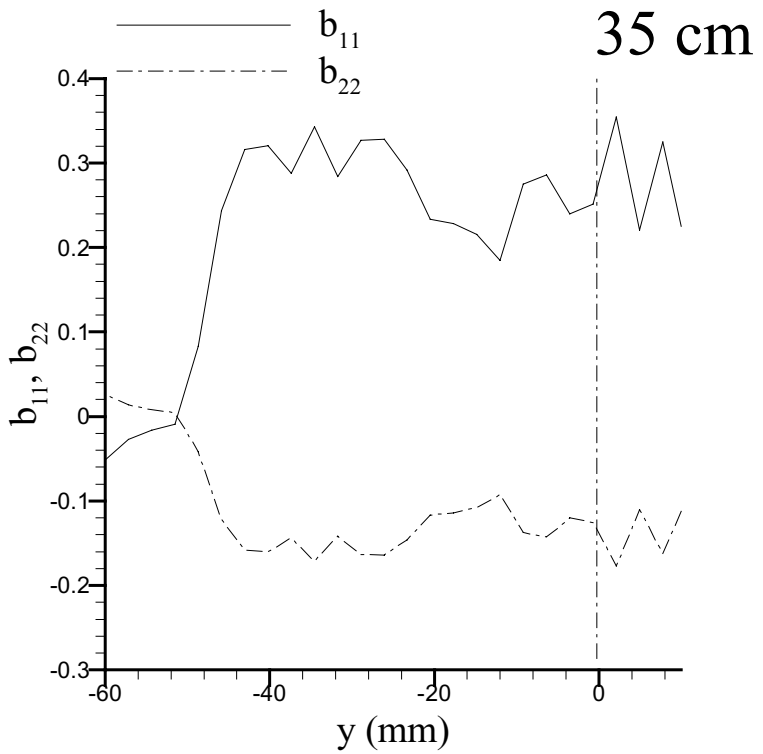

Future work

- Buoyancy and shear
- Non-equilibrium strained configurations:

  Contractions

  Obstacles
- Modeling
- Large density differences

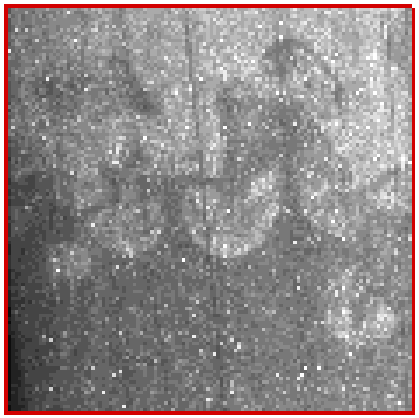

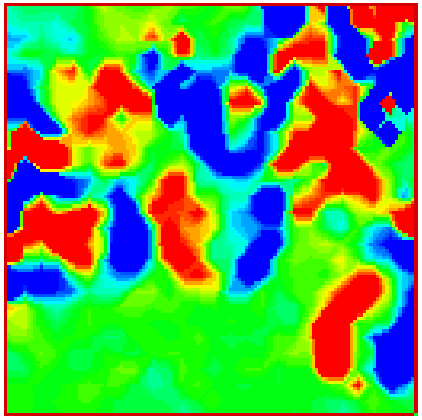

Photographs

Vorticity

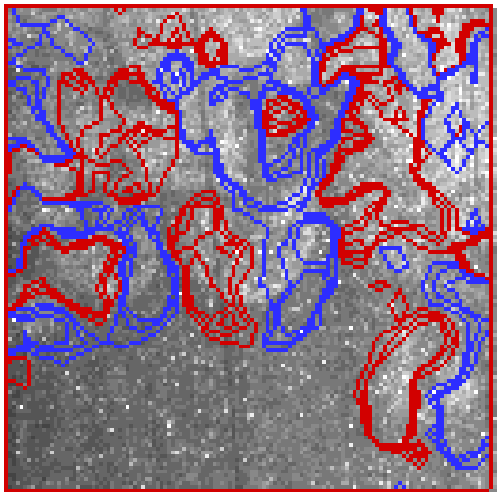

Photographs overlaid with vorticity

Experimental study of the interaction of a strong shock with a spherical density inhomogeneity

H. F. Robey[1], T. S. Perry[1], R. I. Klein[1, 2], J. A. Greenough[1],
H. Louis[1], P. Davis[1], J. O. Kane[1], T. R. Boehly[3]

[1]Lawrence Livermore National Laboratory, Livermore, California 94550
[2]U. C. Berkeley, Department of Astronomy
[3]Laboratory for Laser Energetics, University of Rochester, Rochester, NY

Presented at the 8th Meeting of the
International Workshop on the Physics of Compressible Turbulent Mixing
Pasadena, CA
December 9-14, 2001

This work was performed under the auspices of the U. S. Department of Energy by the University of California, Lawrence Livermore National Laboratory under Contract No. W-7405-Eng-48.

Summary

- Experiments have been conducted on the Omega Laser to study the interaction of a strong shock (M>10) with a spatially localized density inhomogeneity (Cu sphere)
- The interaction is diagnosed with x-ray radiography simultaneously from two orthogonal directions
- The evolution of the shocked sphere is observed to proceed as an initial roll-up into a double vortex ring structure followed by the appearance of an azimuthal instability which ultimately results in the three-dimensional breakup of the sphere.
- Numerical simulations are performed in both two and three-dimensions, and results are in good agreement with experiment.

Outline

- **Background / motivation**
- **Omega Experimental Results**
- **Numerical simulations**
- **Conclusions**

These experiments recreate in a controlled setting the interaction of a strong shock with a dense molecular cloud

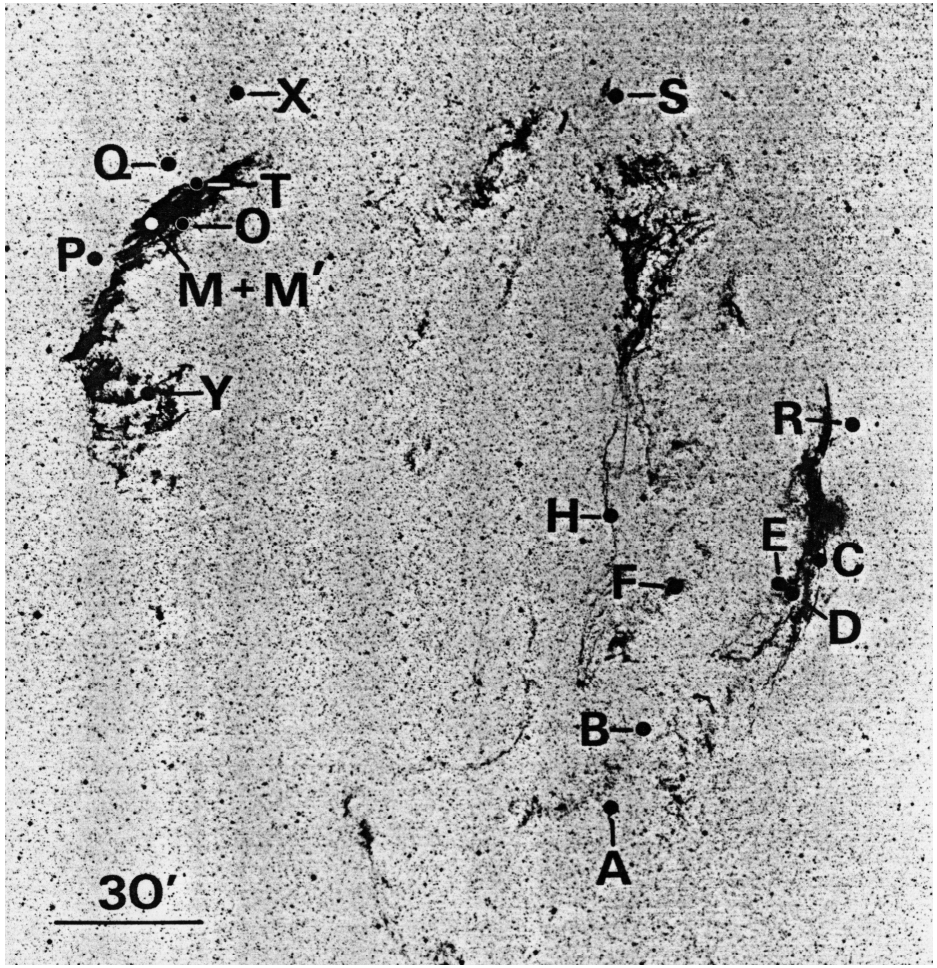

From Fesen el al., Ap.J. 262, 171 (1982):

"The Cygnus Loop is the classic example of a moderately old supernova remnant (SNR). its structure and physical properties are the result of a supernova-generated shock wave interacting with the surrounding interstellar medium."

"Comparisons with published shock models indicate significant differences between the models and observations …"

The interaction of a shock with a dense spherical inhomogeneity has previously been studied only at low mach number

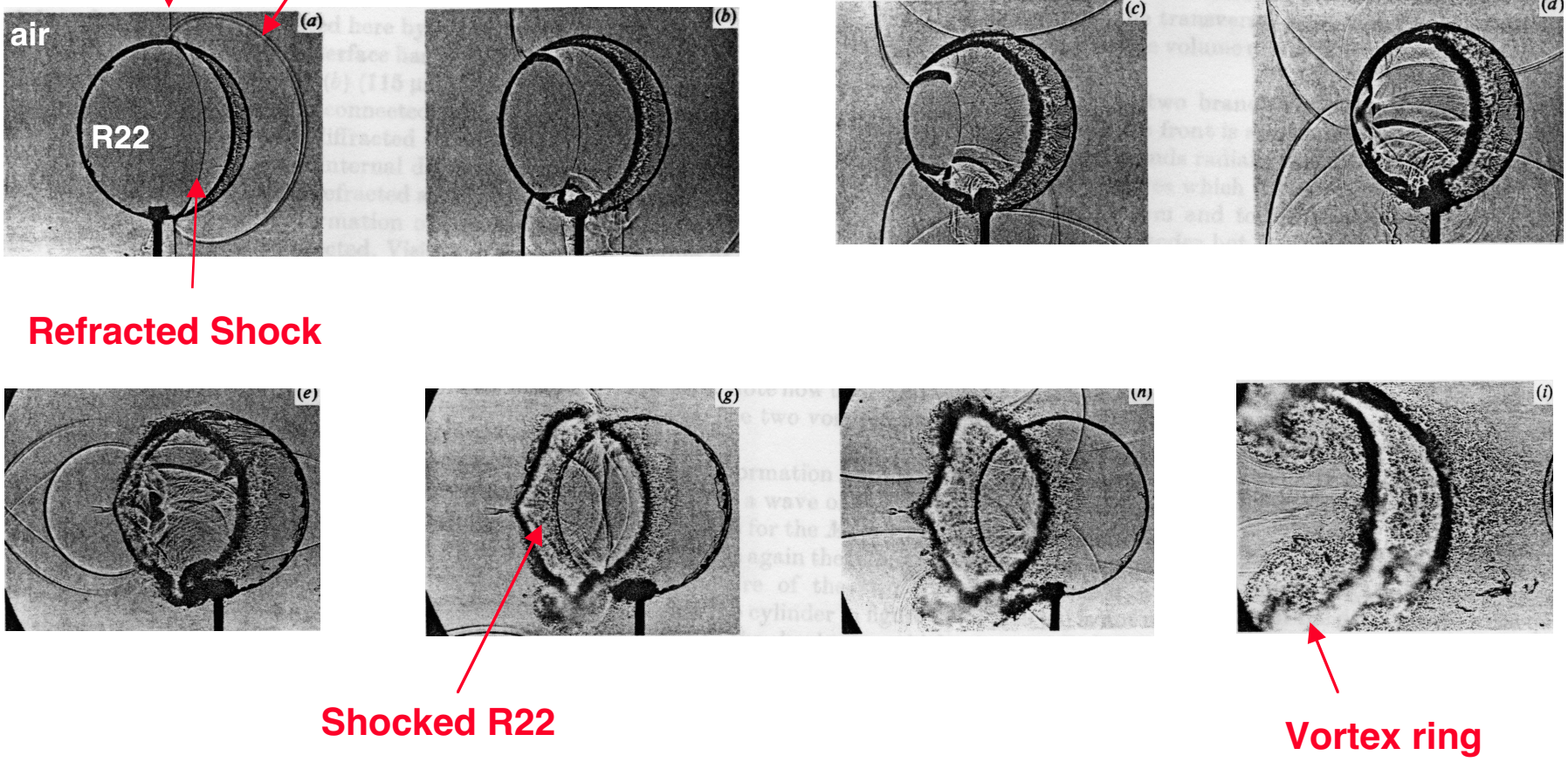

From M = 1.2 shock tube experiments of
Haas & Sturtevant, JFM 181, 41 (1987)

Once formed, a vortex ring is subject to a 3D azimuthal bending mode instability

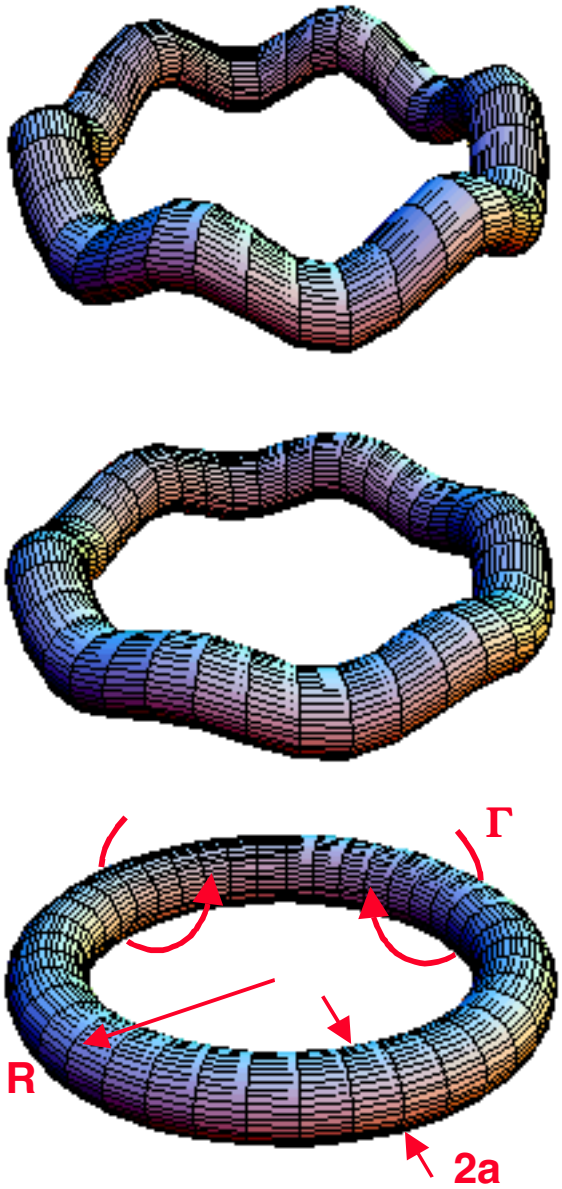

time

Mode number, n vs. non-dimensional ring translation velocity, $\tilde{V}$

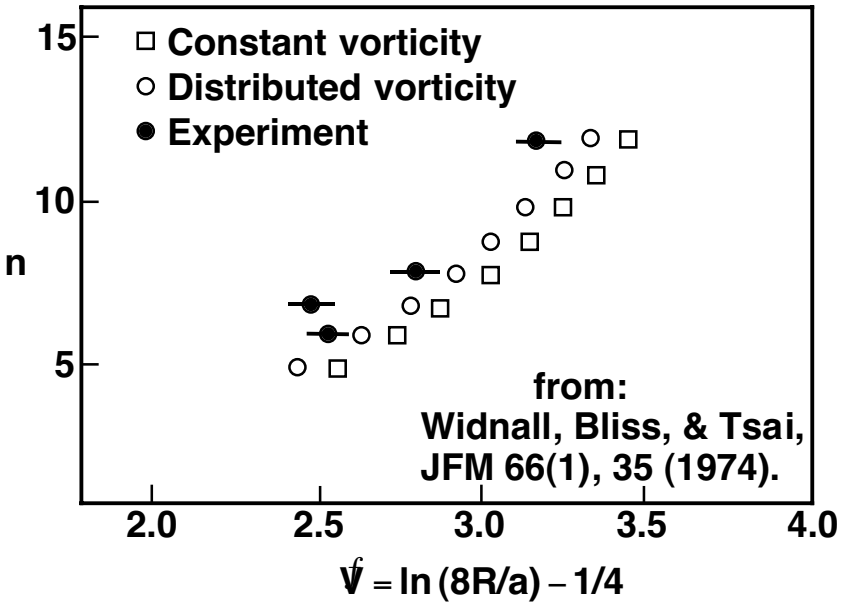

The mode number is a function of the ring radius R and thickness a

Outline

- Background / motivation
- **Omega Experimental Results**
- Numerical simulations
- Conclusions

The Omega experiments are conducted in a very small Beryllium shock tube

2D slice through target

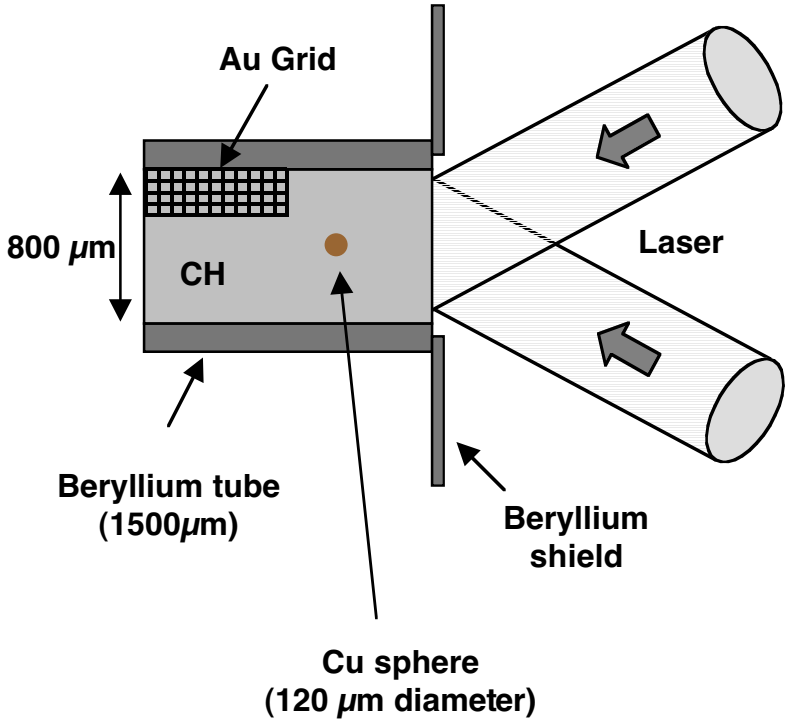

3D view of target

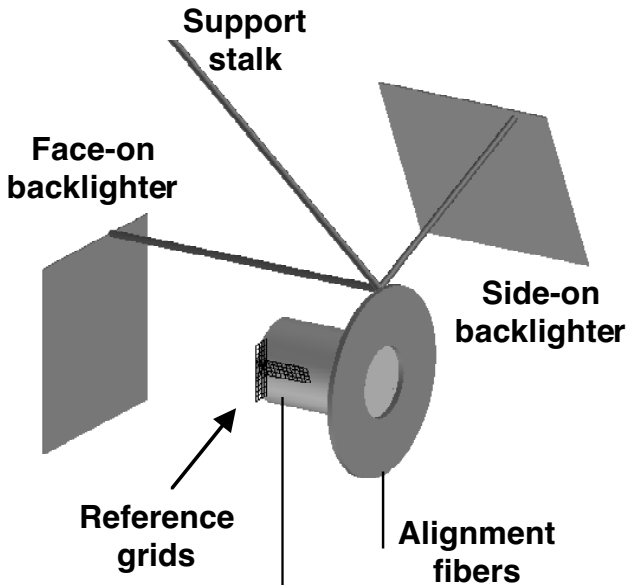

Multiple beams of the Omega laser are used to both drive the strong shock and diagnose the interaction

Target CAD drawing with Omega beam orientations

Side-on backlighter beams

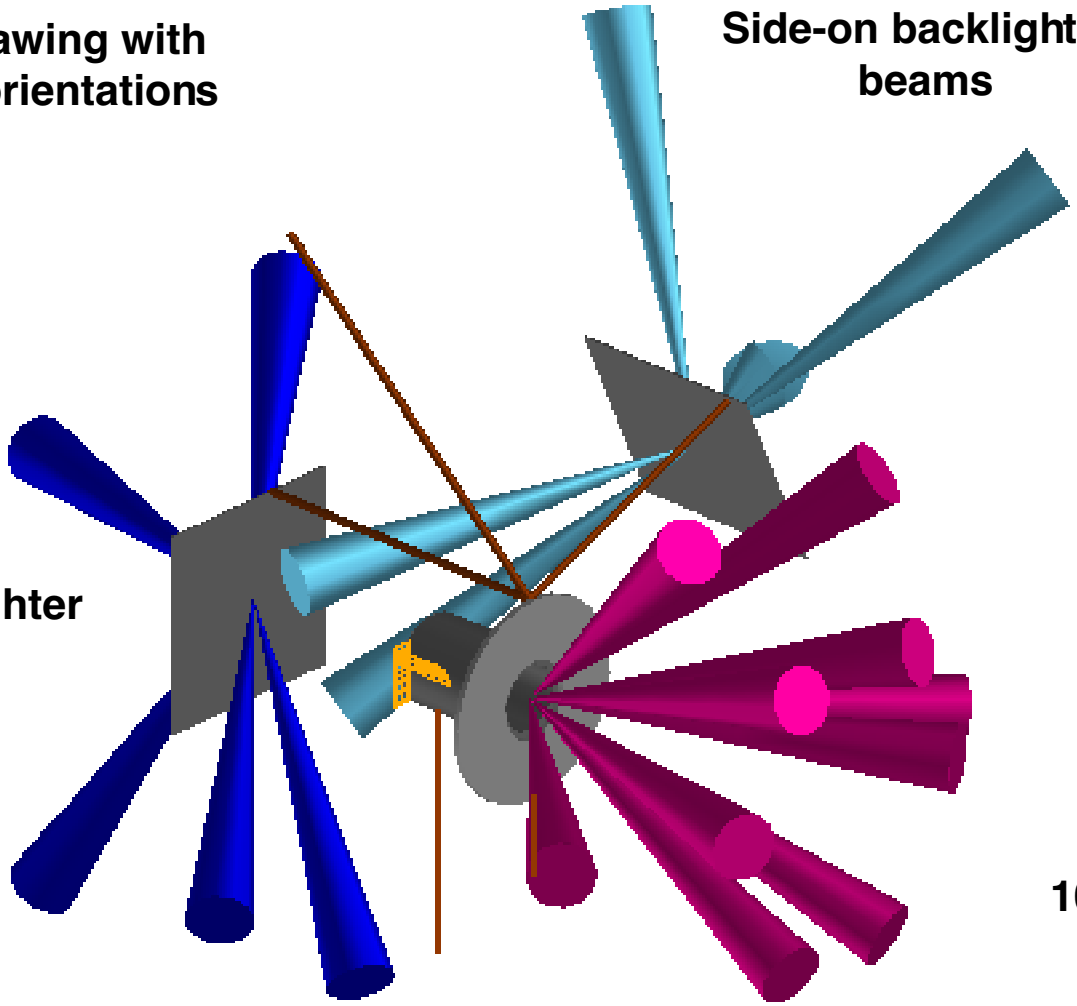

Face-on backlighter beams

Drive beams
10 beams @ 500J
~ 600 μm spot

Simultaneous side-on and face-on images of shock / sphere interaction with 120 μm diameter Cu sphere

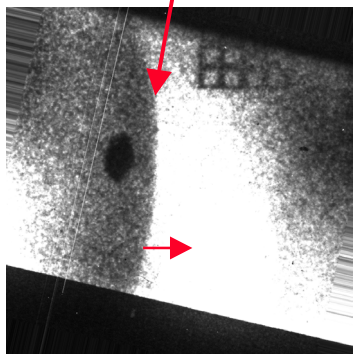

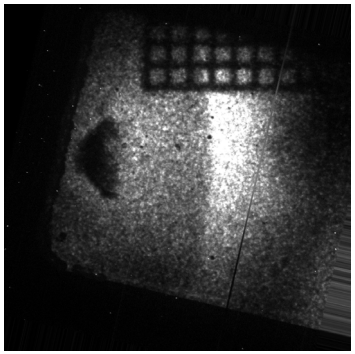

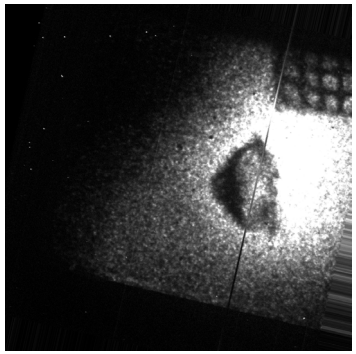

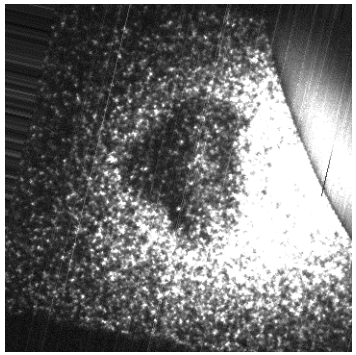

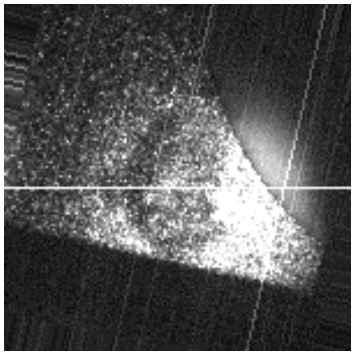

19728 # 19736 # 19732 # 20637 # 20645

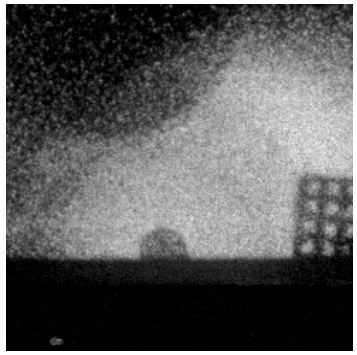

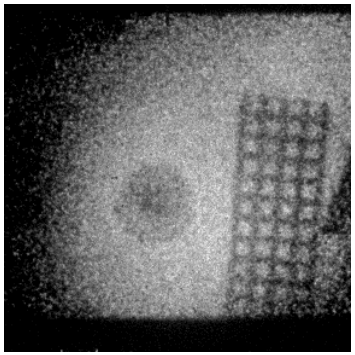

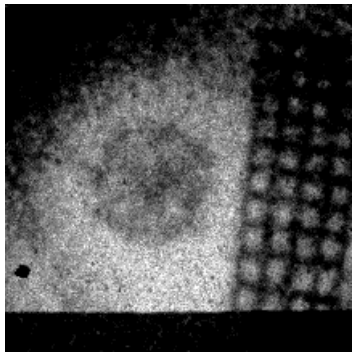

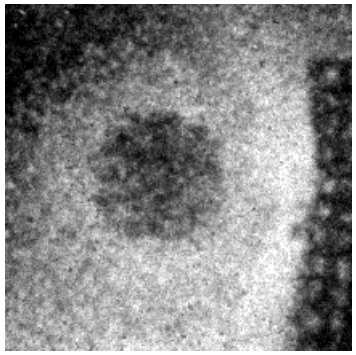

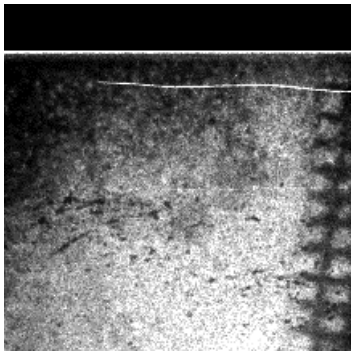

t = 13 ns t = 26 ns t = 39 ns t = 52 ns t = 78 ns

Omega data of April, 2000

Omega data of Aug 2-3, 2000

Simultaneous side-on and face-on images of shock / sphere interaction with 240 μm diameter Cu sphere

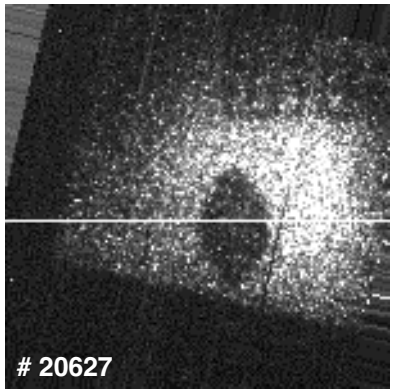

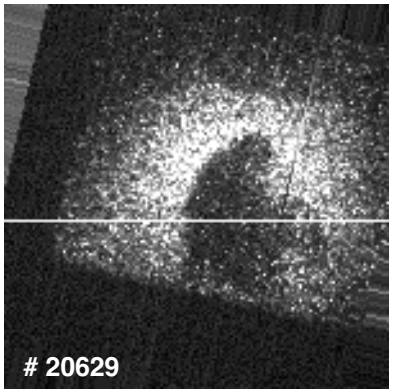

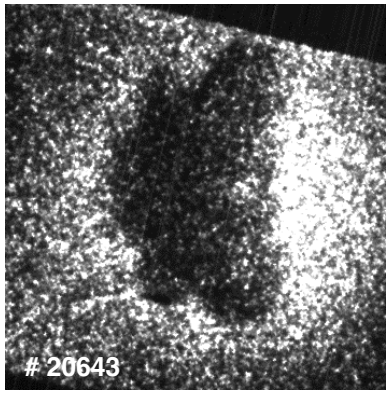

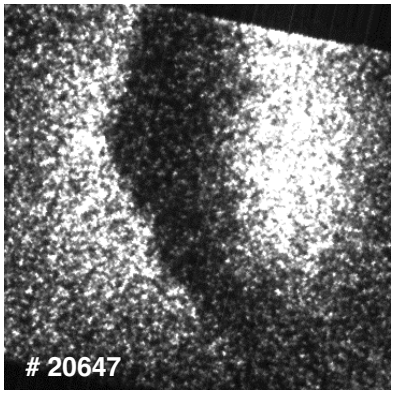

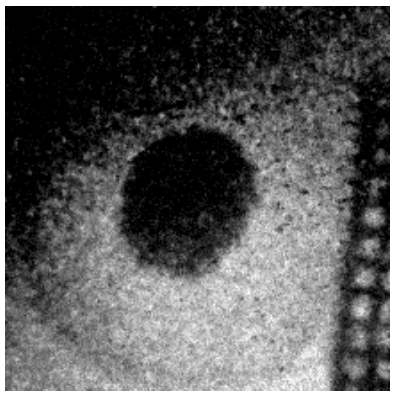

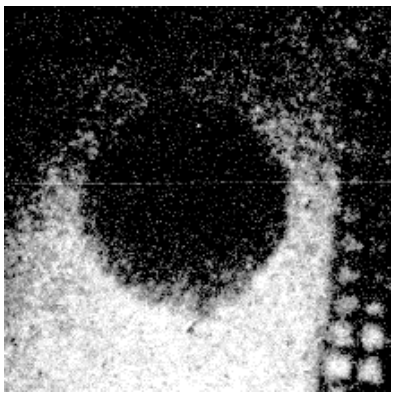

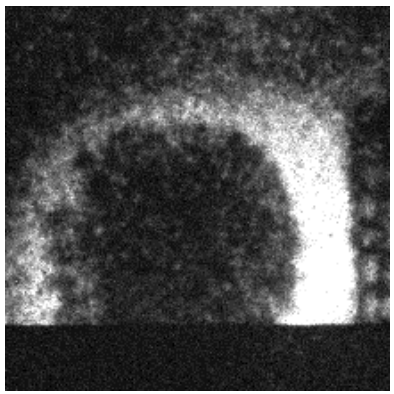

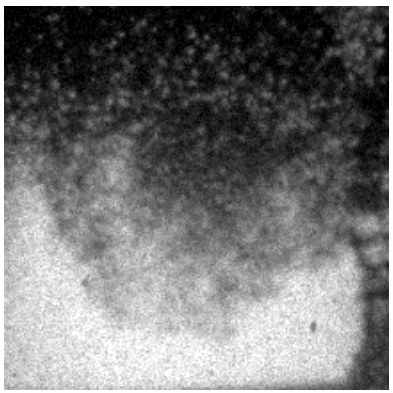

t = 27 ns | t = 54 ns | t = 78 ns | t = 105 ns

Omega data of Aug 2-3, 2000

Large-scale features appear repeatable from shot-to-shot, but small-scale details differ

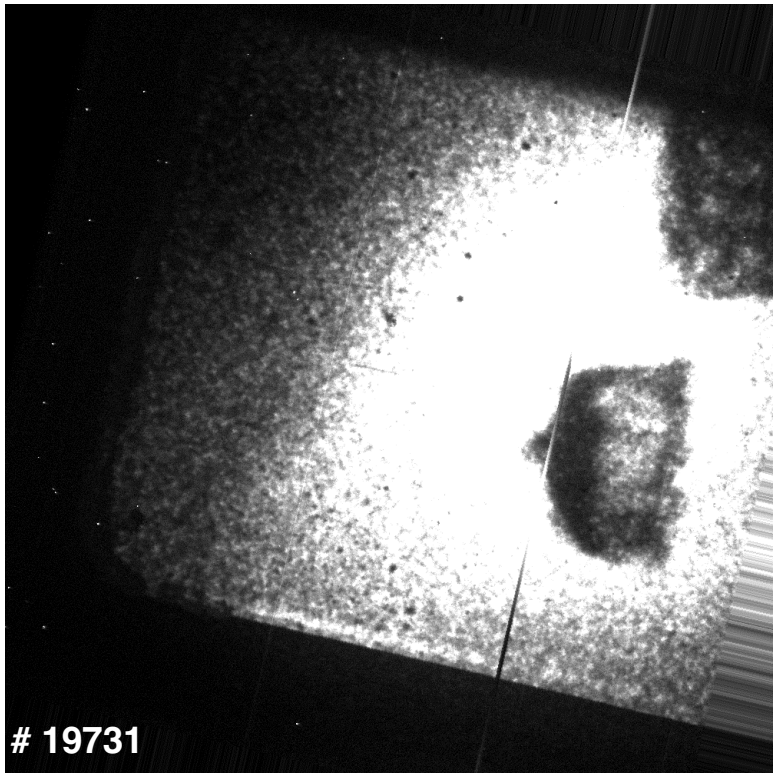

t= 39 ns
V-backlighter

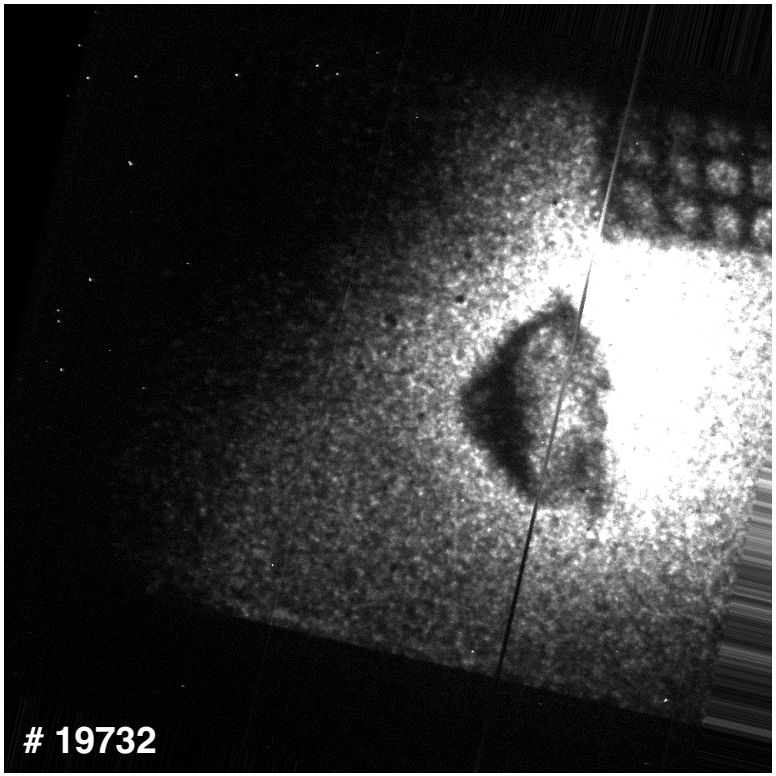

t= 39 ns
Fe-backlighter

The two orthogonal diagnostic views help to reveal the 3D morphology of this flow

Illustration of 3D morphology

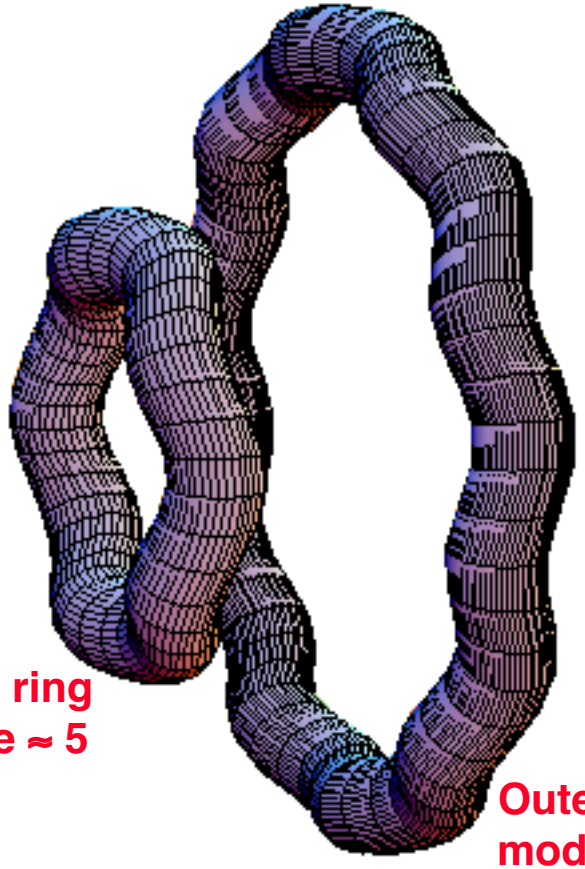

Inner ring mode ≈ 5

Outer ring mode ≈ 15

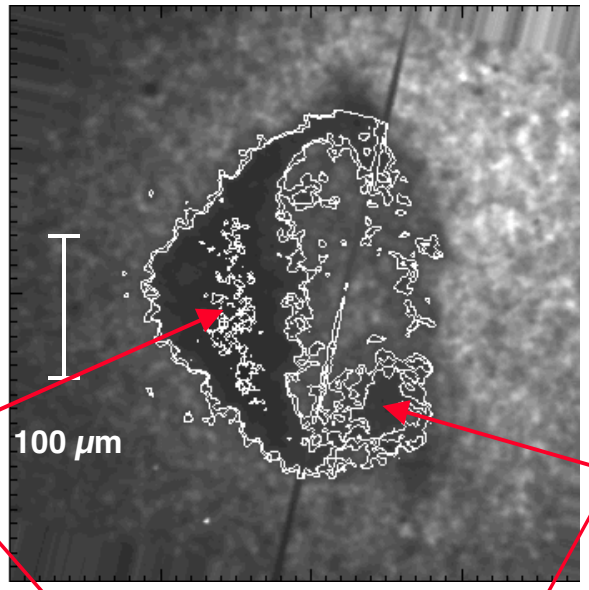

Inner ring

Outer ring

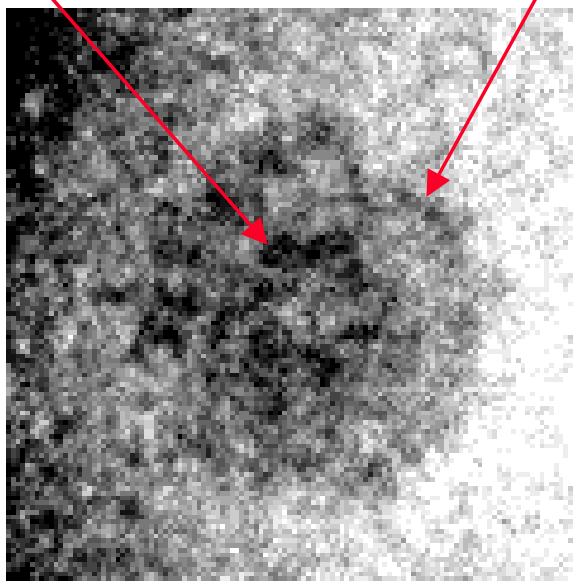

Analysis of Omega shock / sphere data quantifies the three-dimensional instability and breakup of the sphere

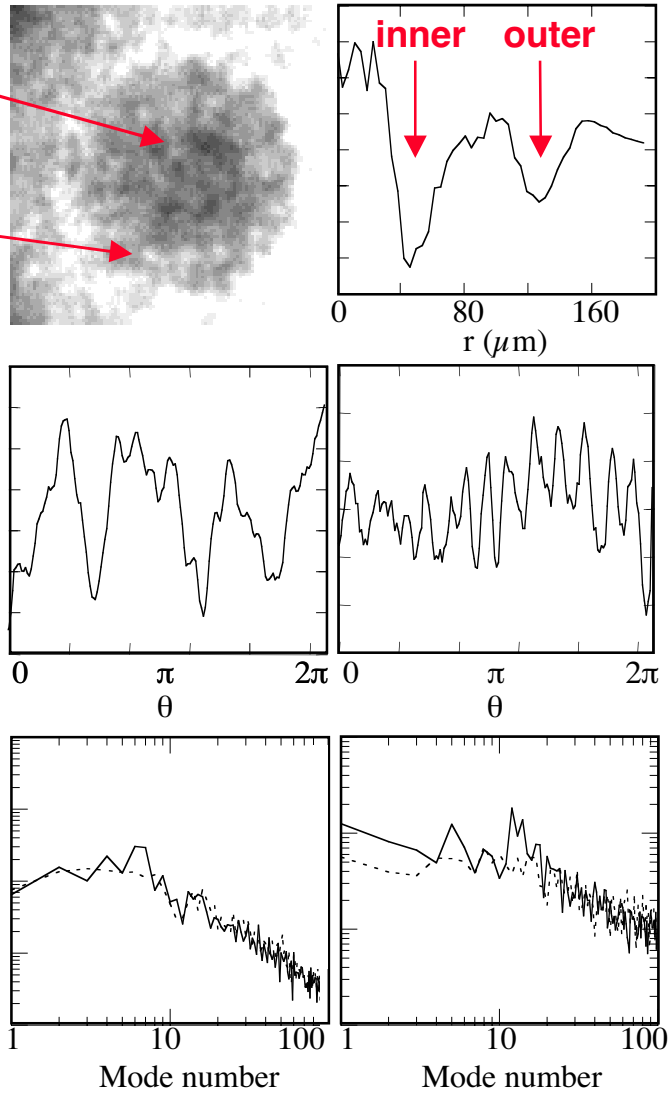

Azimuthally averaged radial lineout

Azimuthal lineout through inner ring

Azimuthal lineout through outer ring

Spectrum of inner azimuthal lineout

Spectrum of outer azimuthal lineout

From Robey et al., submitted to PRL (May, 2001)

Mode number spectra from face-on images of shock / sphere interaction reveal a dominant azimuthal mode

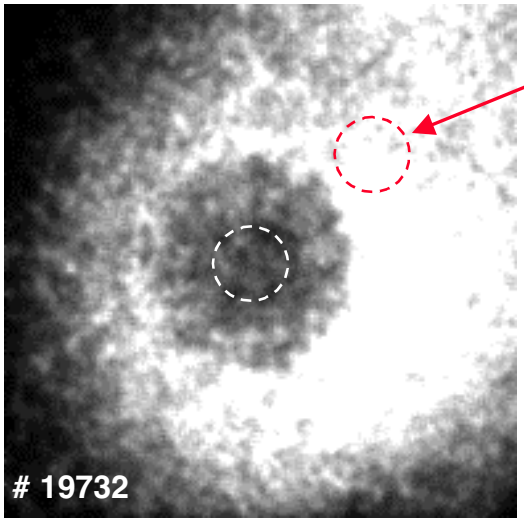

Background line-outs

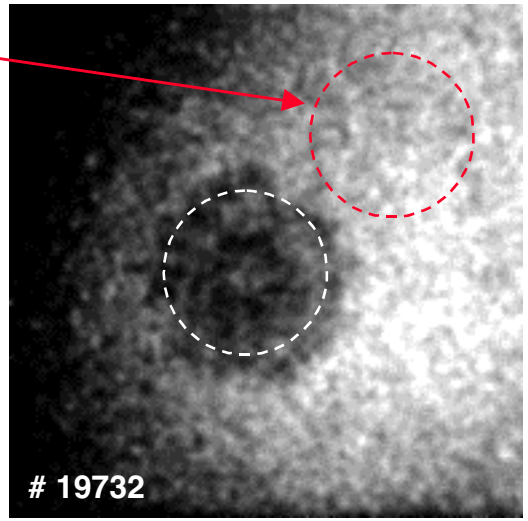

Power spectrum of circular line-out through central feature (r=50 μm)

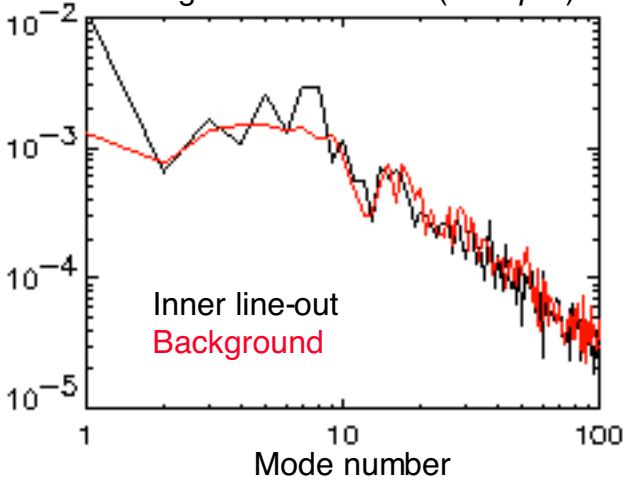

Power spectrum of circular line-out through outer feature (r=127 μm)

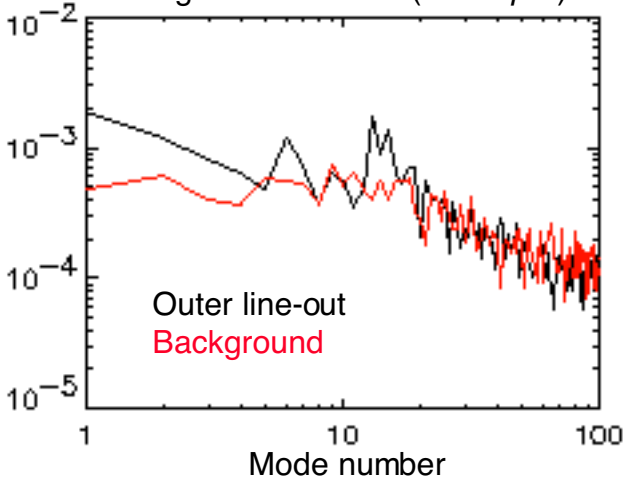

The observed azimuthal mode number agrees well with the prediction from Widnall's theory

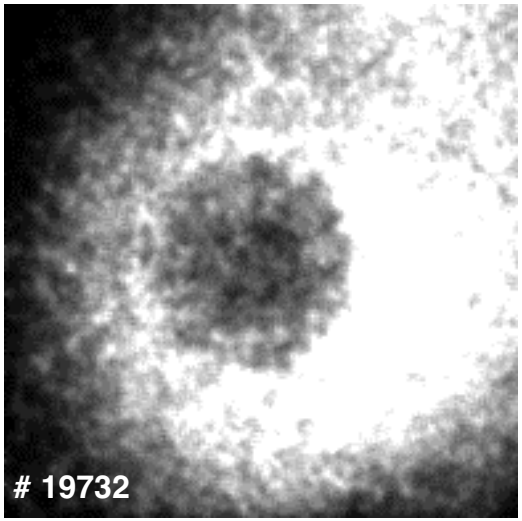

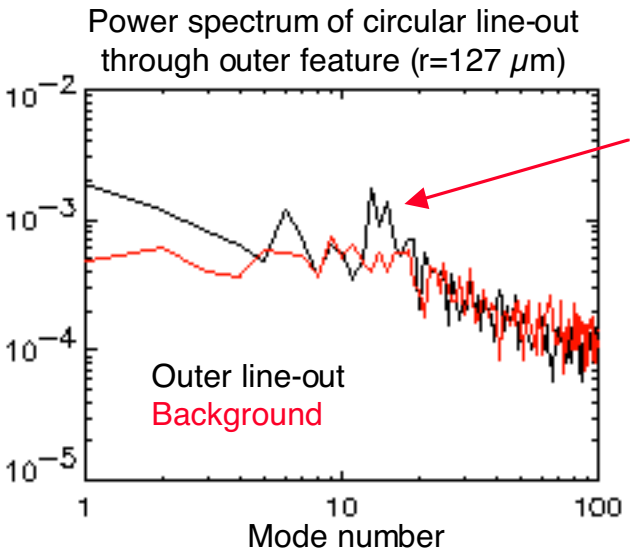

Observed peak at 15

Mode number, n vs. non-dimensional ring translation velocity, $\tilde{V}$

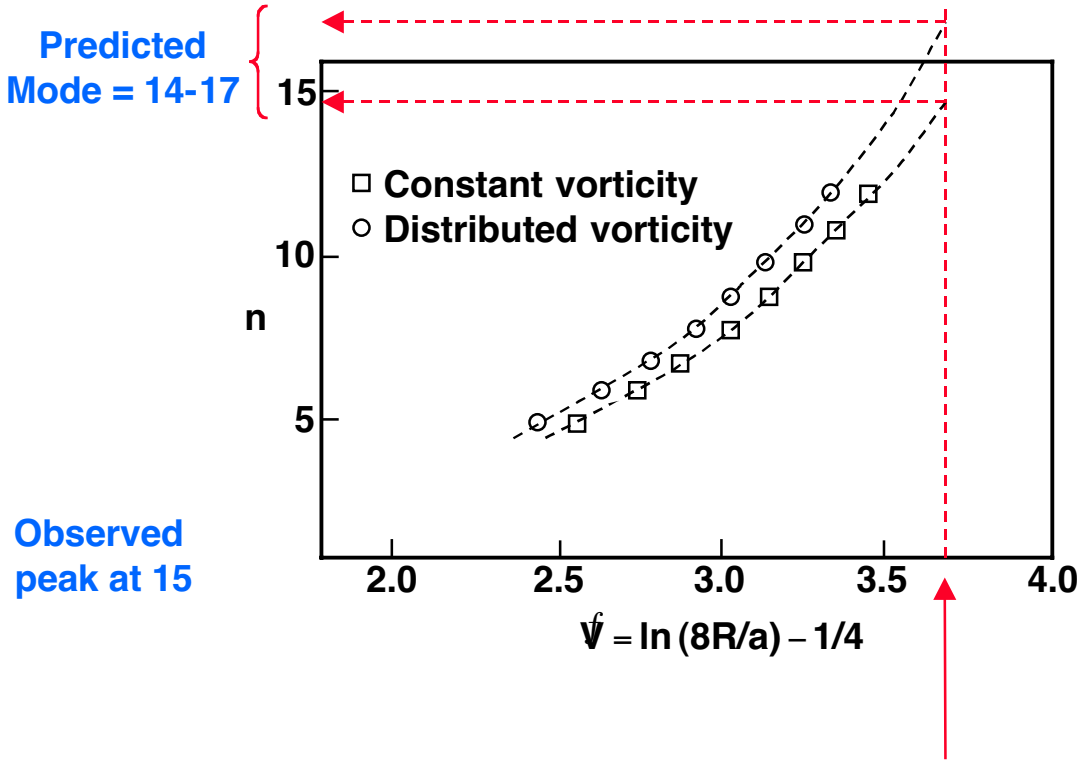

From azimuthal lineouts

a = 20 μm
R = 127 μm

$\tilde{V} = 3.67$

SNR should be greatly improved using a backlit pinhole due to greatly decreased pinhole-to-target distance

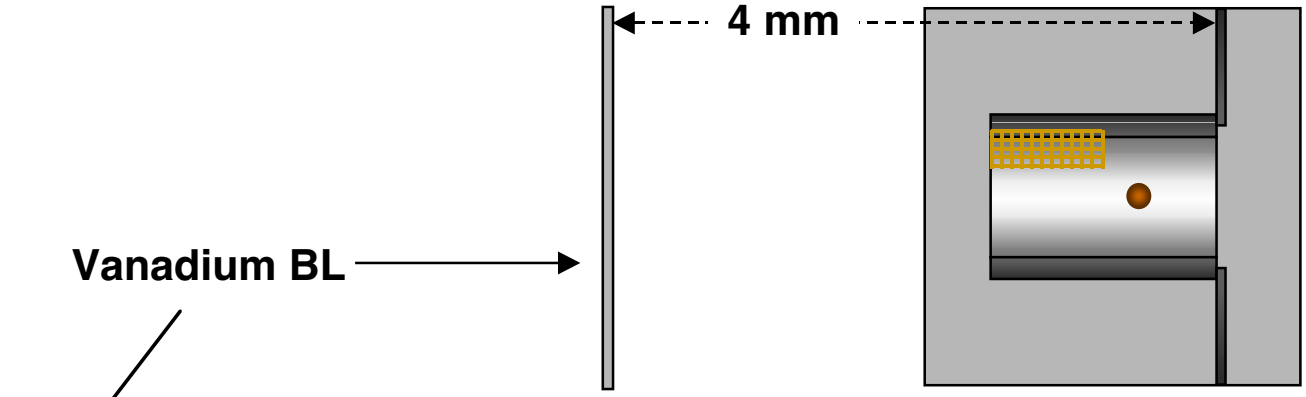

Pinhole-to-target,
u = 64 mm
(6x magnification)

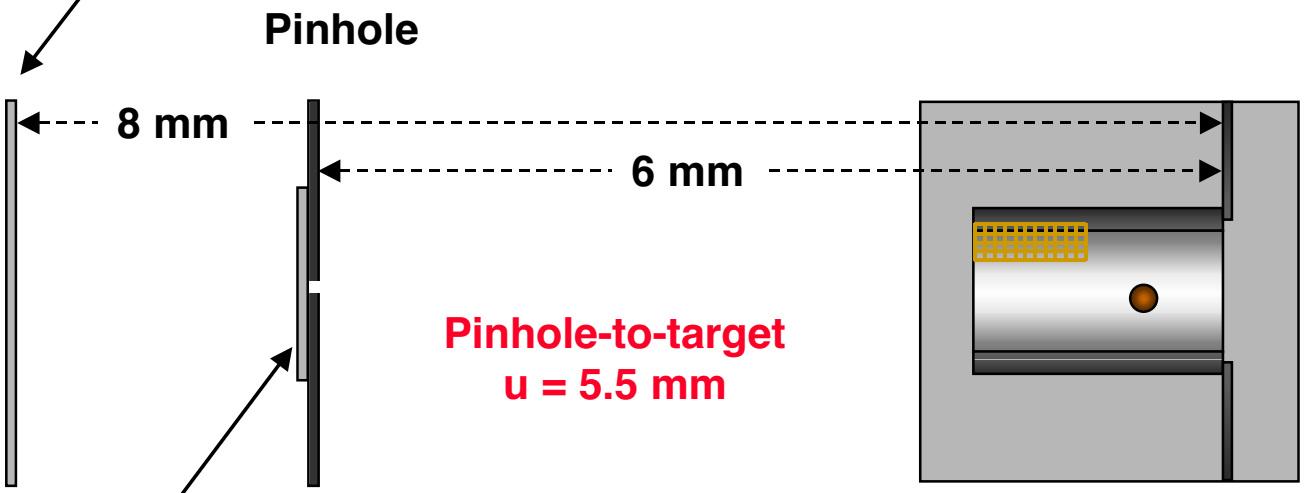

Pinhole-to-target
u = 5.5 mm

photons / resolution element ~ u^{-2}, and SNR = $\sqrt{\#\ photons}$

Backlit pinhole increases SNR by factor of 11

We have begun investigating the ability to seed the azimuthal instability with machined initial perturbations

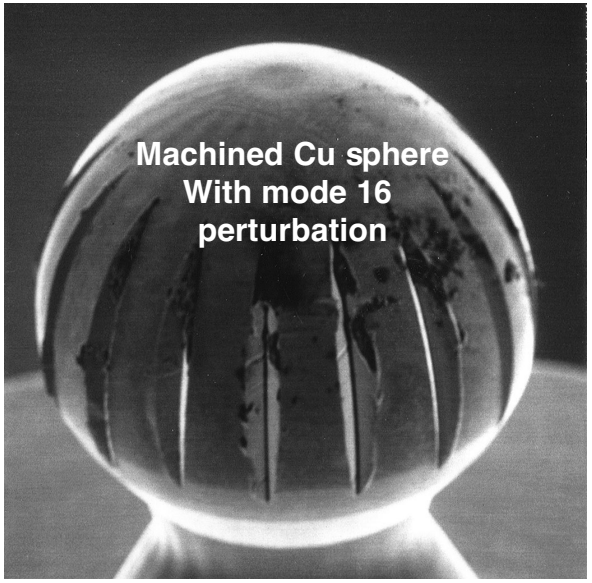

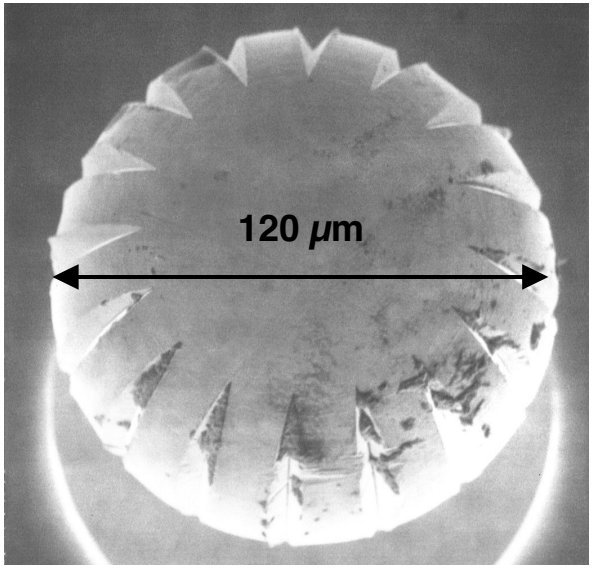

Face-on view using point projection backlighting

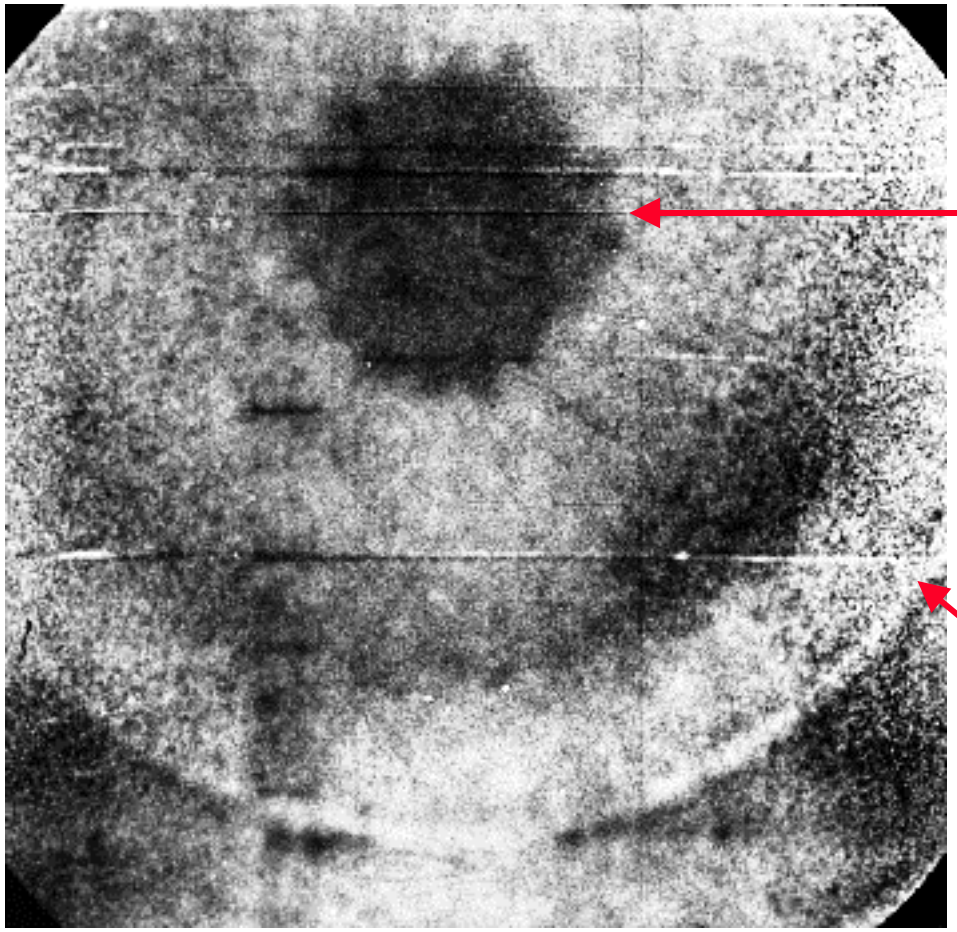

Shot #24527

Outline

- Background / motivation
- Omega Experimental Results
- Numerical simulations
- Conclusions

2D simulations of the experiment performed with CALE predict the basic evolution of the sphere into a vortex ring

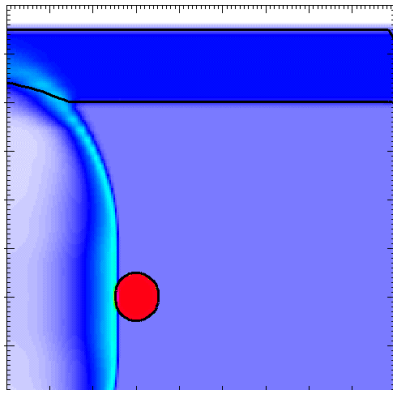

t= 10 ns

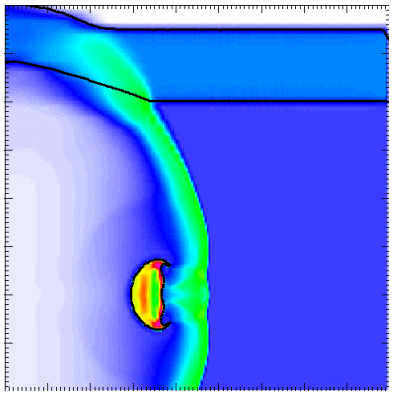

t= 20 ns

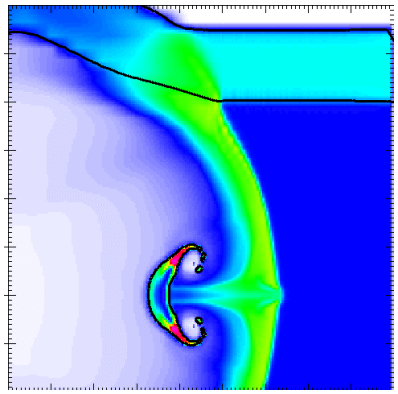

t= 30 ns

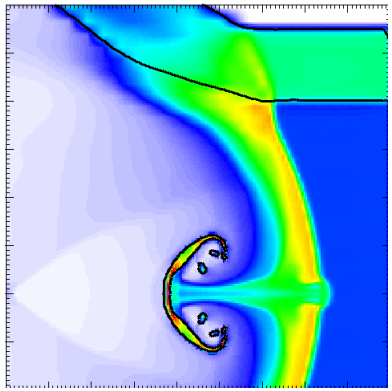

t= 40 ns

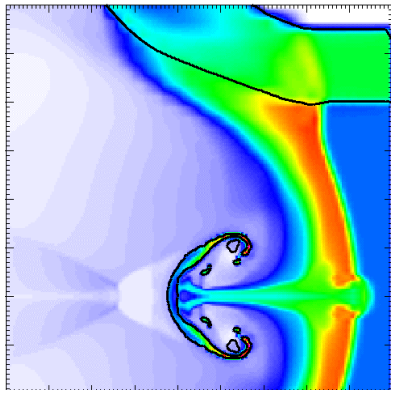

t= 50 ns

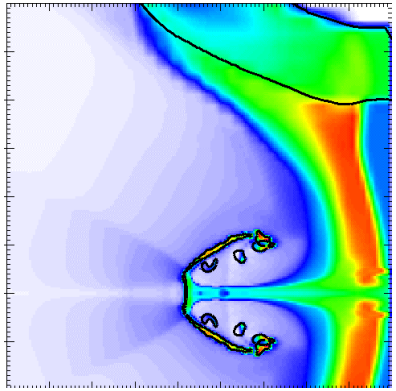

t= 60 ns

Simulations by J. O. Kane

3D simulations of the experiment have been performed with an AMR code

Simulated radiograph of side-on view

Simulated radiograph of face-on view

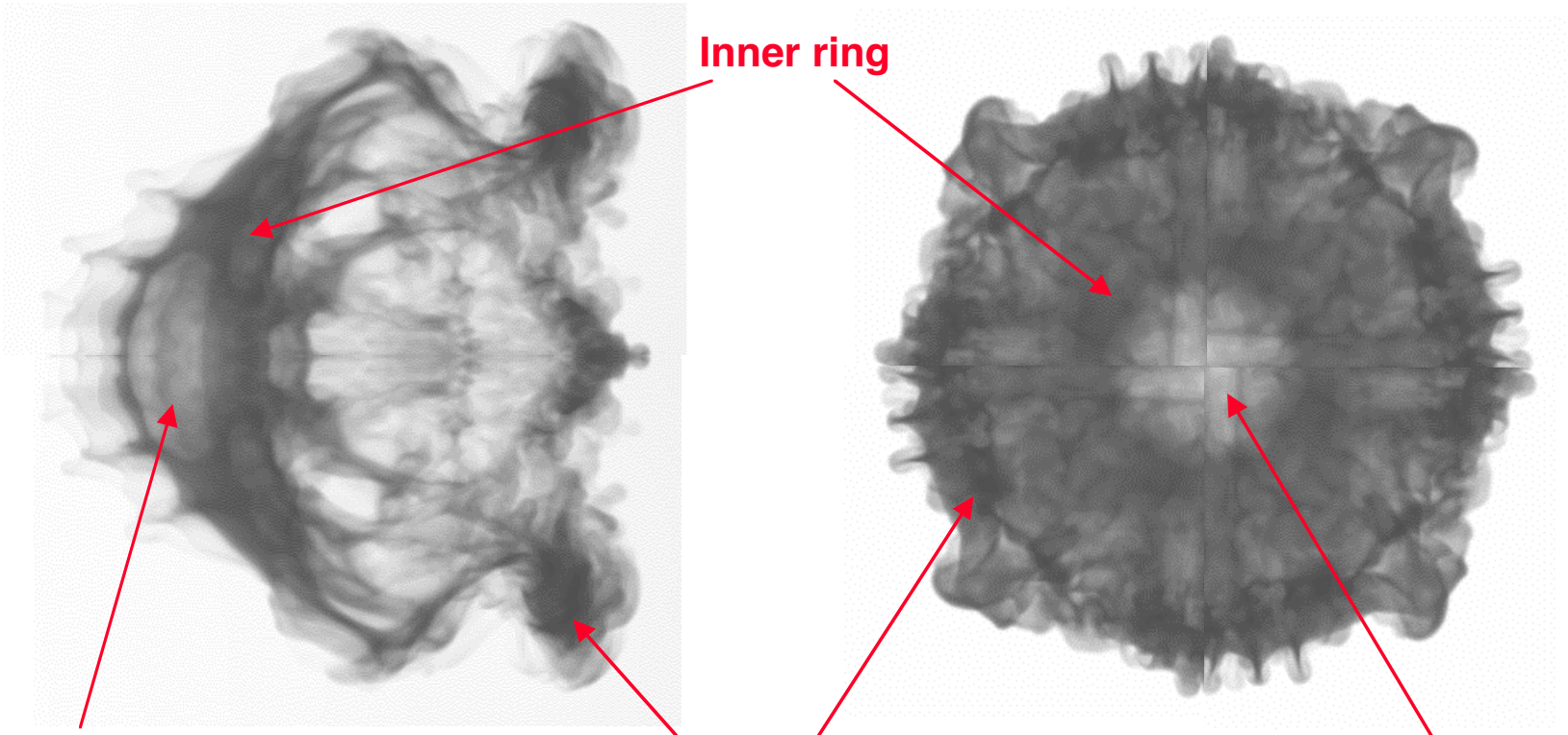

Simulations by J. A. Greenough

Mode number spectra of the experimental and the AMR face-on images are in good agreement

Experiment

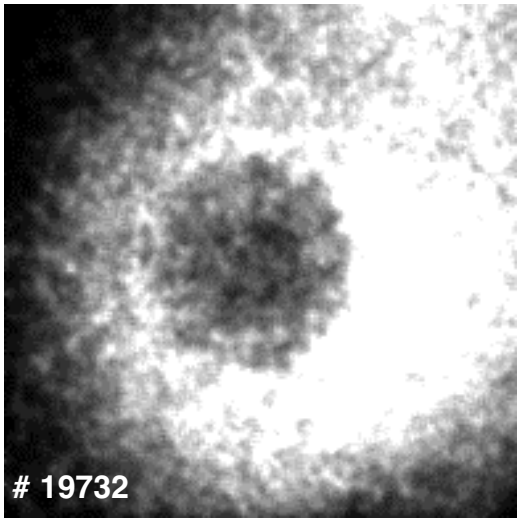

AMR simulation

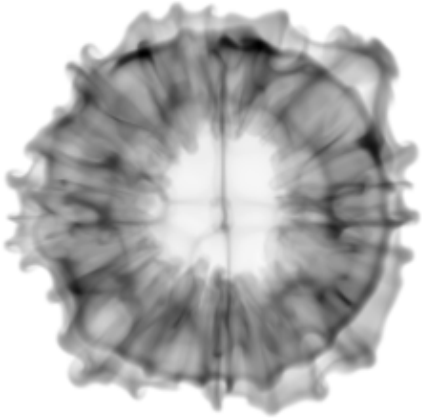

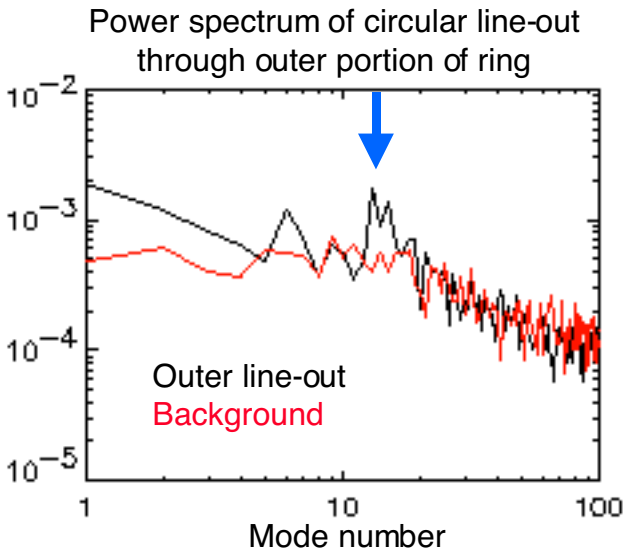

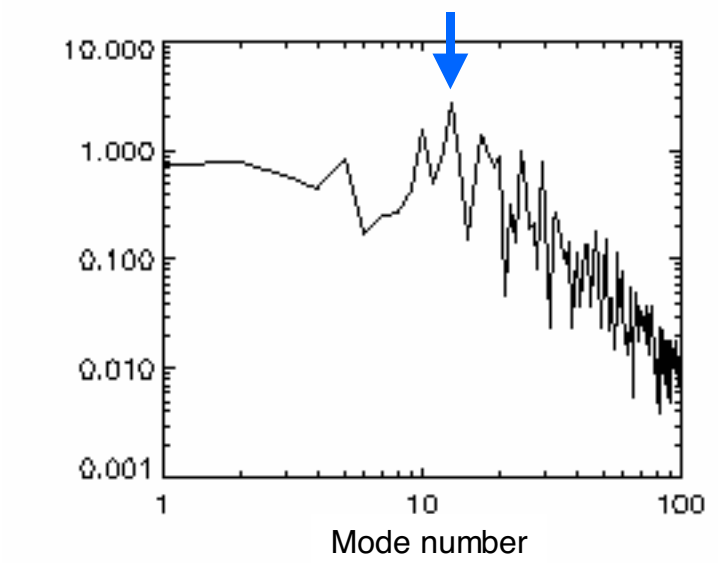

Conclusion

- Experiments have been conducted on the Omega laser to explore the interaction of a strong shock with a dense sphere

- The experiment has been diagnosed simultaneously from two orthogonal directions

- The experimentally observed azimuthal mode number is in good agreement with both incompressible theory of Widnall and 3D numerical simulations.

- Future work will focus on shock interaction with less-dense objects and interactions with multiple objects

Turbulent transition in a high Reynolds number, Rayleigh-Taylor unstable plasma flow

H. F. Robey, Y. K. Zhou, A. C. Buckingham, P.Keiter,
B. A. Remington, and R. P. Drake

Lawrence Livermore National Laboratory
Livermore, California 94550

Presented at the 8th Meeting of the
International Workshop on the Physics of Compressible Turbulent Mixing
Pasadena, CA
December 9-14, 2001

This work was performed under the auspices of the U. S. Department of Energy by the University of California, Lawrence Livermore National Laboratory under Contract No. W-7405-Eng-48.

Summary

- The transition to turbulence in a high Reynolds number, Rayleigh-Taylor unstable plasma flow is studied.

- 1D numerical simulations (HYADES) are used to determine the plasma flow parameters (P,ρ,T, Z) from which the kinematic viscosity is then determined.

- The Reynolds number is determined using the experimentally measured perturbation amplitude and growth rate together with the plasma kinematic viscosity determined from the 1D numerical simulations.

- It is observed that the Reynolds number is sufficiently greater than the mixing transition threshold of Dimotakis (i.e. $Re >> 2 \times 10^4$) for much of the experiment, yet the flow has not transitioned to turbulence.

- An extension of the Dimotakis mixing transition to non-stationary flows of short time-duration is presented.

Outline

- Experimental setup and results of Omega laser experiment

- Results from 1D HYADES simulation of the experiment

  Basic plasma flow parameters (P,ρ,T, Z)
  Derived flow parameters (ν, D)
  Estimation of the Reynolds number

- Extension of Dimotakis mixing transition to non-stationary flows of short time-duration

- Conclusions

The experiments are conducted on the Omega laser in a very small Beryllium shock tube

Schematic of target

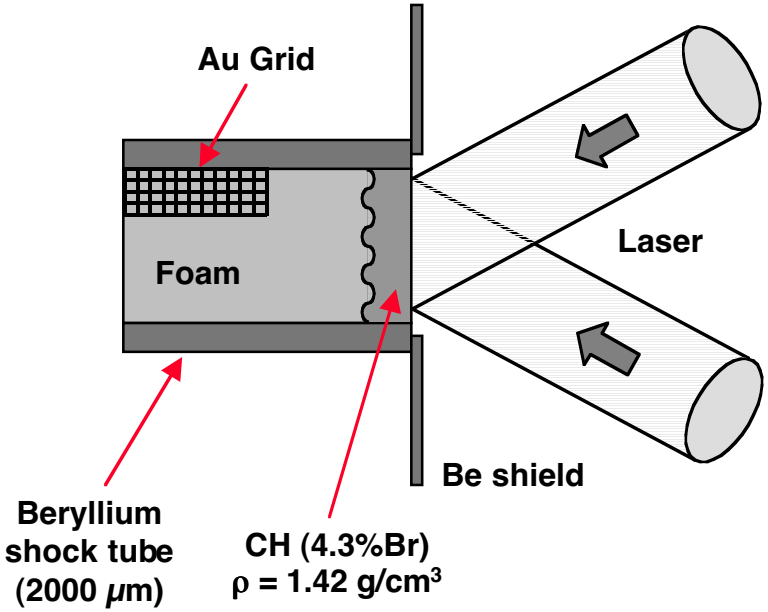

3D CAD rendering of target

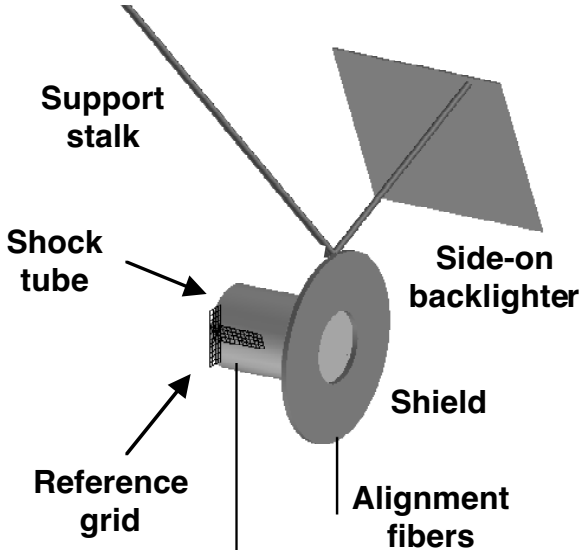

Face-on view of target

The target has a radiographic tracer strip which is density matched to the surrounding material

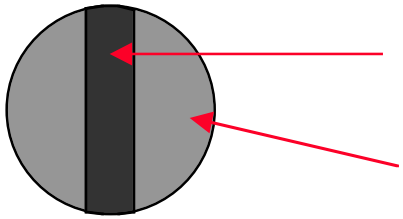

1.42 g/cm^3 CH (4.3%Br) tracer

1.41 g/cm^3 polyimide

Multiple beams of the Omega laser are used to both drive the strong shock and diagnose the interaction

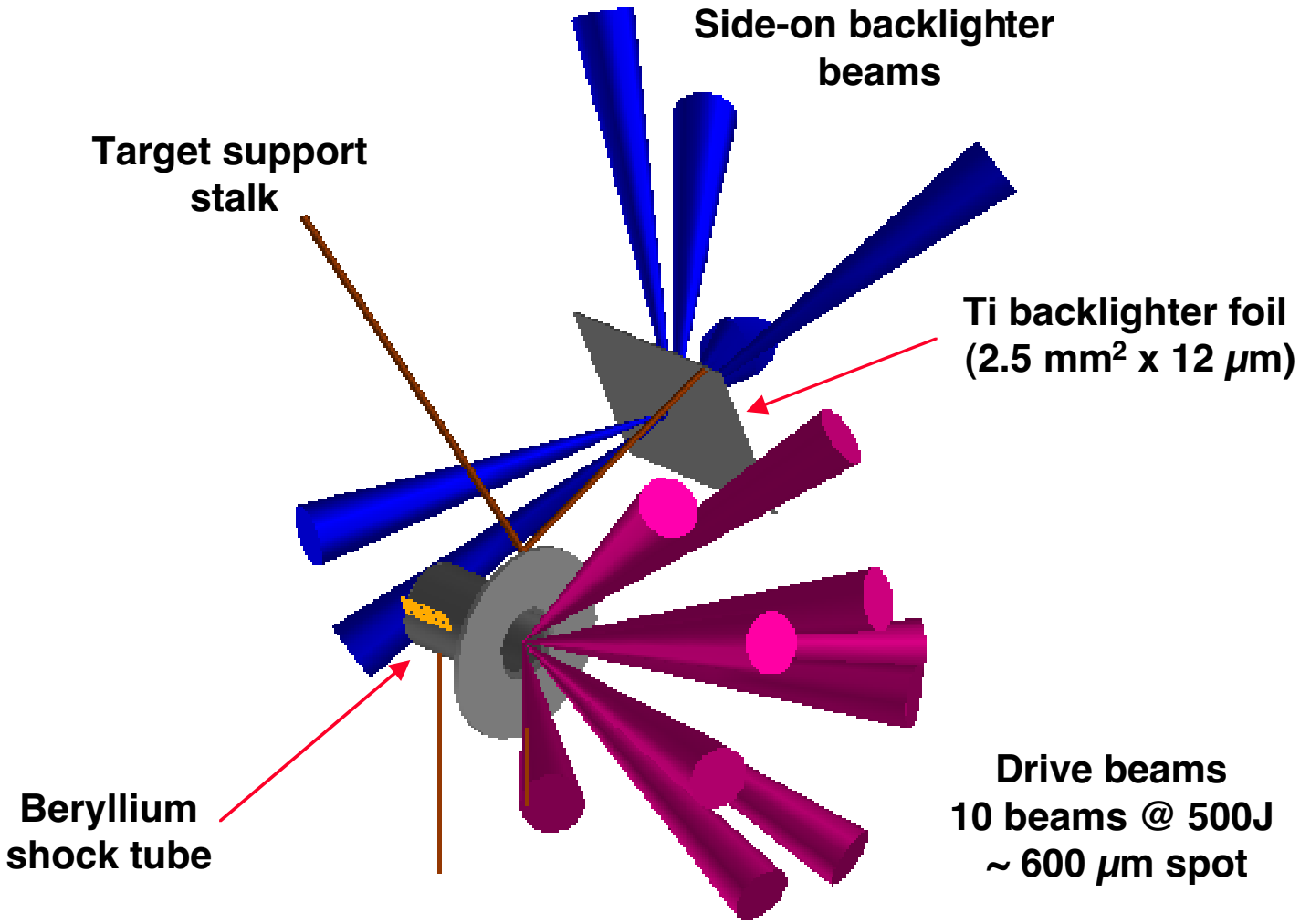

The evolution of a 2D single-mode perturbation (λ=50μm, a_0=2.5μm) is observed with x-ray radiography

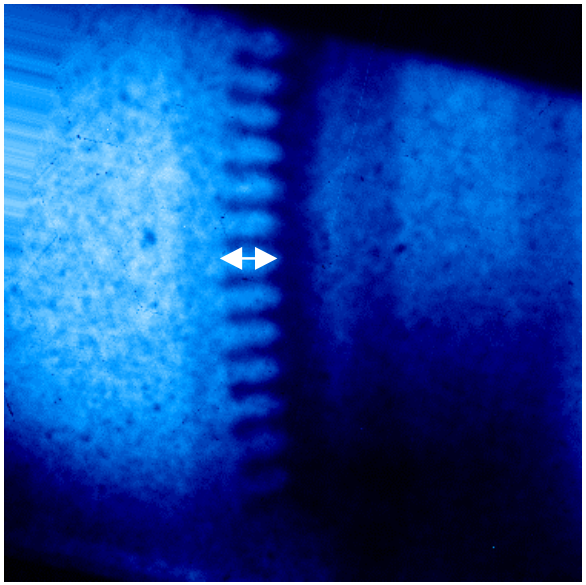

t = 8 ns

$a_{P\text{-}V}$ = 83 μm

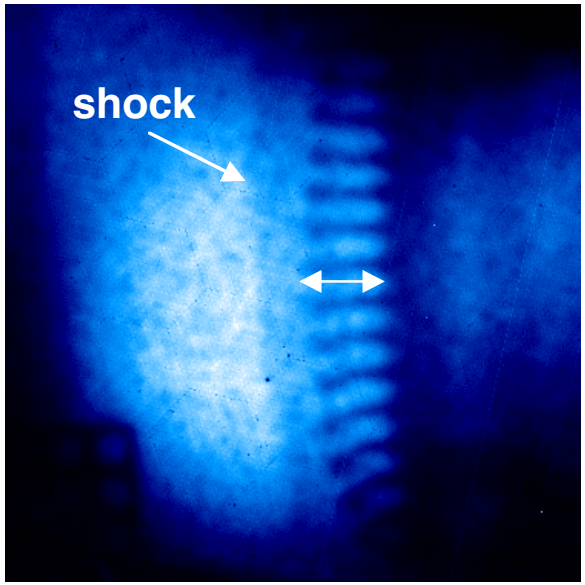

t = 12 ns

$a_{P\text{-}V}$ = 121 μm

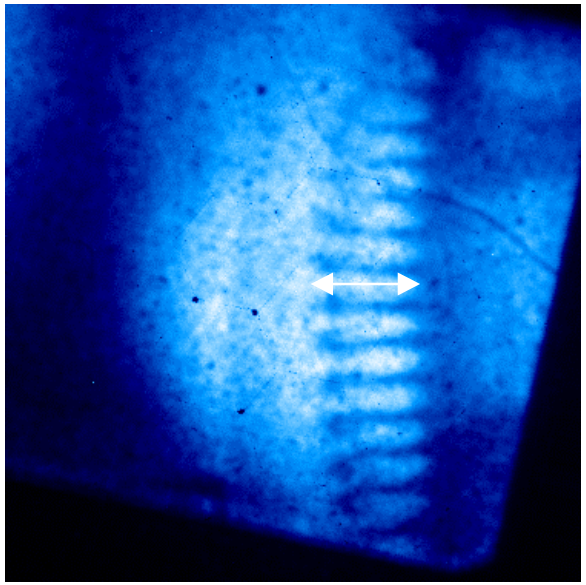

t = 14 ns

$a_{P\text{-}V}$ = 157 μm

Radiographic images obtained with 4.7keV Ti He-α x-rays imaged onto a gated x-ray framing camera

Results from 1D numerical simulation of the experiment

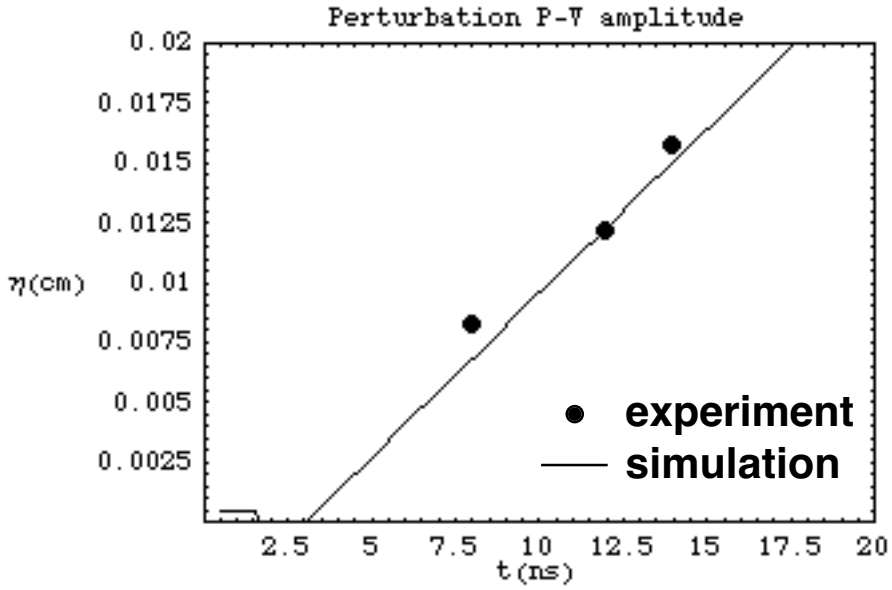

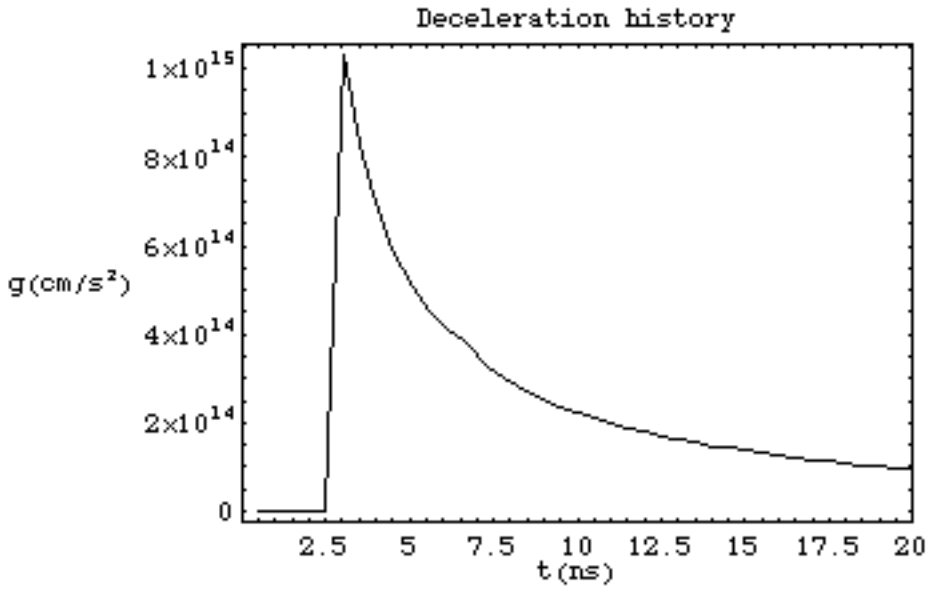

The effect of decompression of the interface has been taken into account

Outline

- Experimental setup and results of Omega laser experiment

- Results from 1D HYADES simulation of the experiment

  Basic plasma flow parameters (P,ρ,T, Z)
  Derived flow parameters (ν, D)
  Estimation of the Reynolds number

- Extension of Dimotakis mixing transition to non-stationary flows of short time-duration

- Conclusions

Time dependent values of the basic flow parameters (pressure, density, temperature, and degree of ionization)

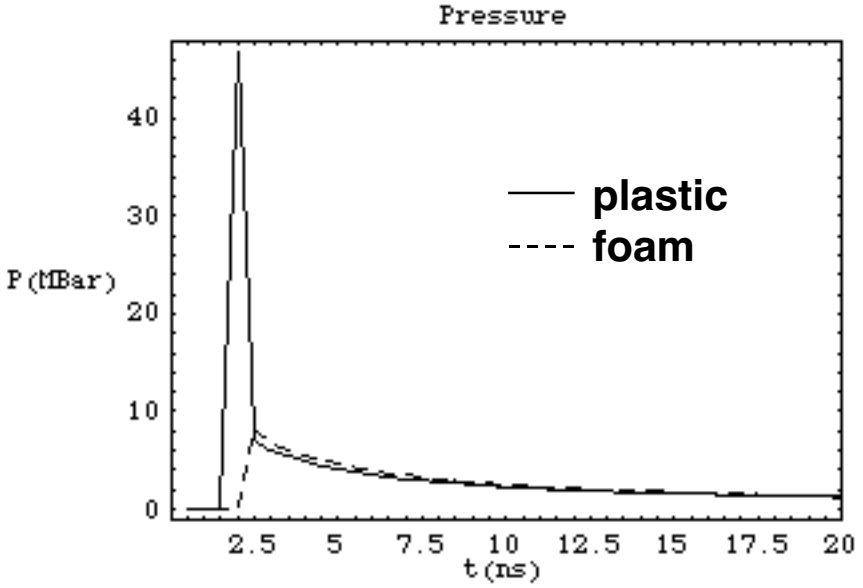

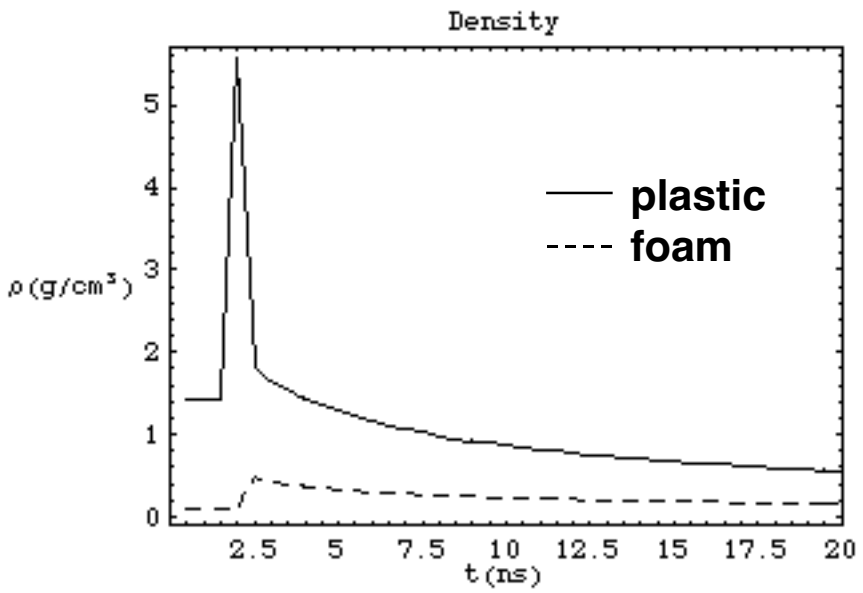

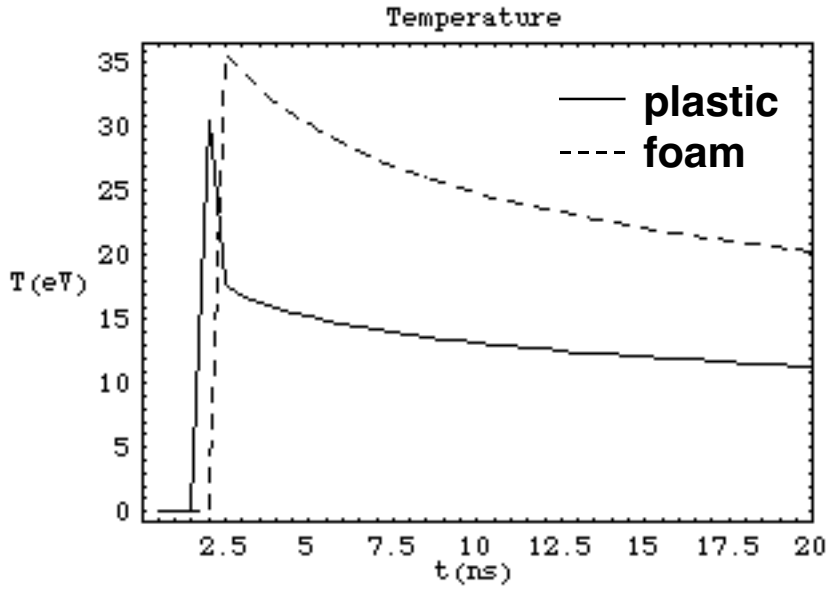

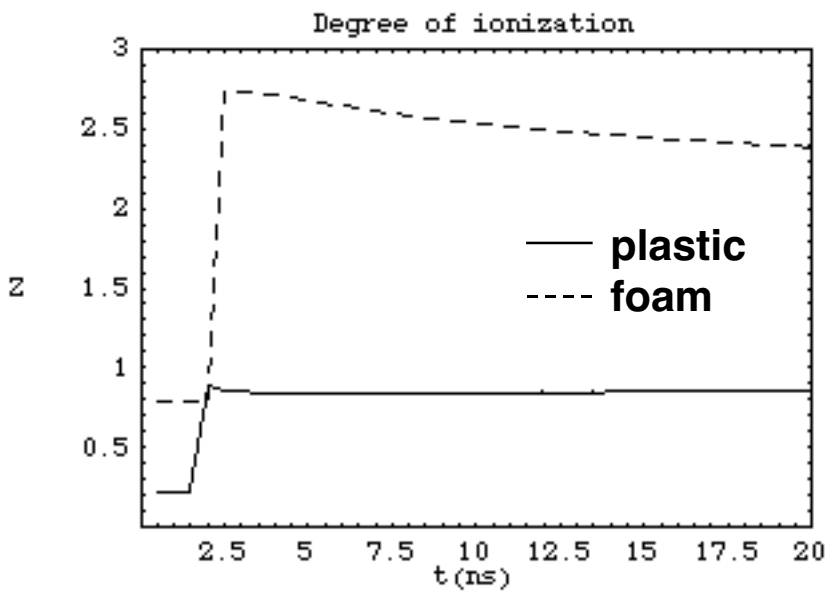

Time dependent values of related flow quantities (Atwood number, adiabatic index, and Mach number)

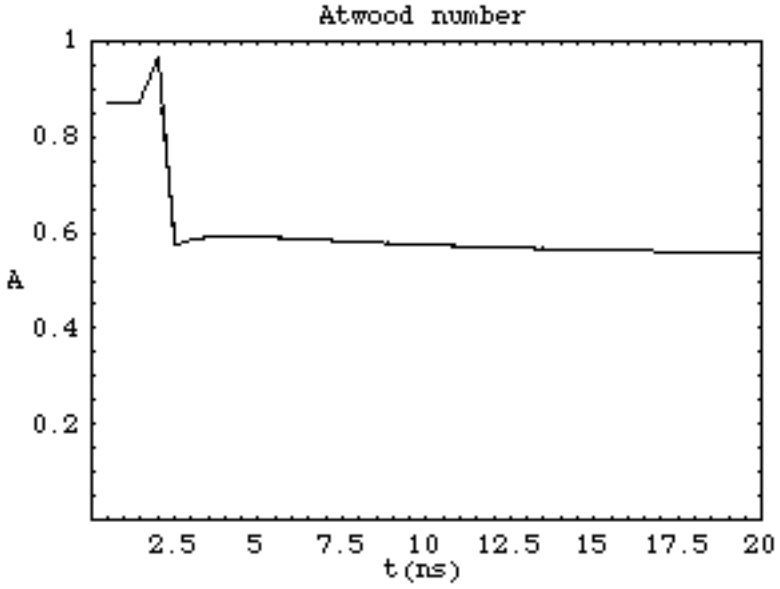

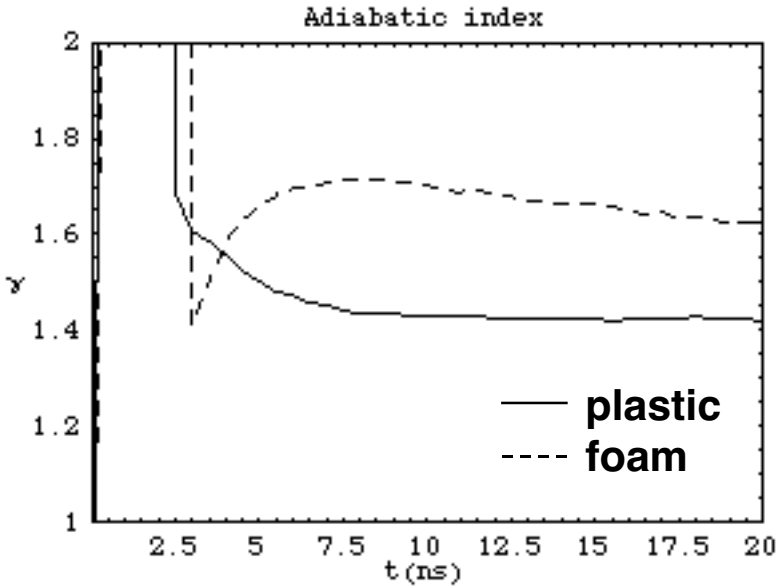

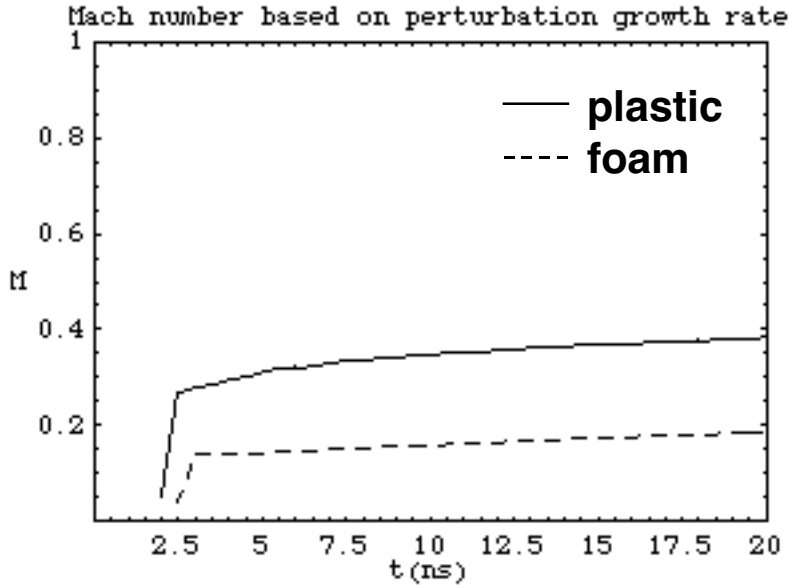

$$A^* = \frac{\rho_1^* - \rho_2^*}{\rho_1^* + \rho_2^*}$$

$$\gamma = \partial \ln(P) / \partial \ln(\rho)$$

$$M = \frac{k_{bubble-spike}}{\sqrt{\gamma P / \rho}}$$

Time dependent values of the plasma coupling parameter, Γ

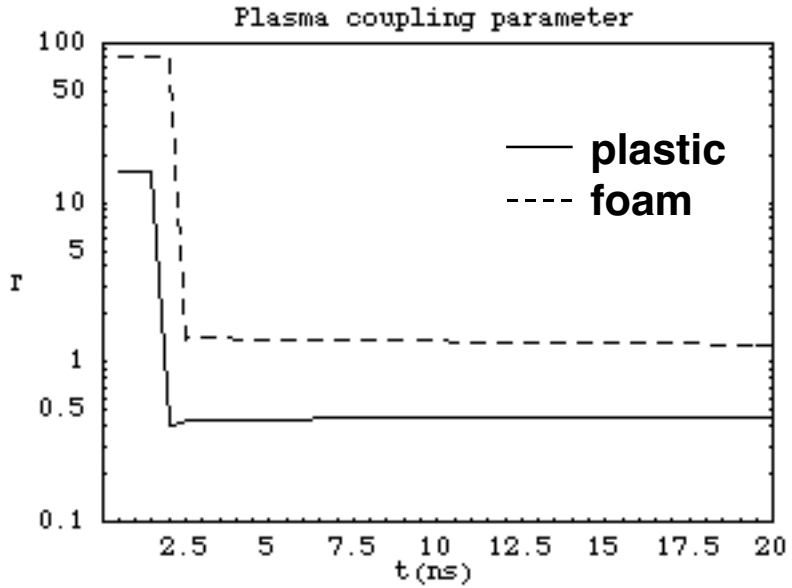

$$\Gamma = \frac{Z^2 e^2}{k_B T \lambda_i} \quad , \quad \lambda_i = \left(\frac{3}{4\pi N_i} \right)^{1/3}$$

The plasma coupling parameter is in the "uncomfortable" range, i.e neither weakly coupled (Γ<<1) where kinetic theory applies nor strongly coupled (Γ>>1) where molecular dynamics simulations can provide rigorous transport properties

Time dependent values of the kinematic viscosity, ν

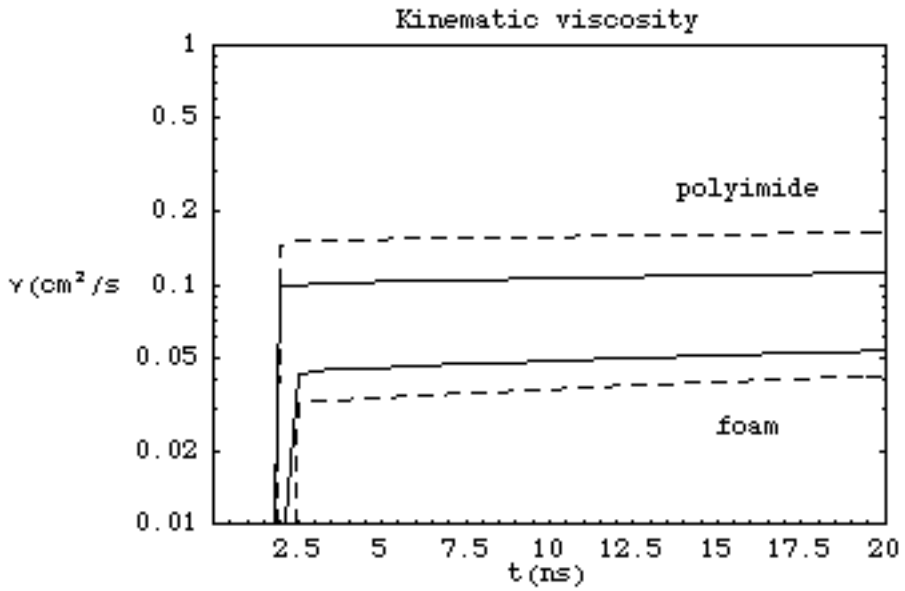

------ S.I. Braginskii, in *Reviews of Plasma Physics*, New York, Consultants Bureau (1965).

——— J.G. Clerouin, M.H. Cherfi, and G. Zerah, *EuroPhys. Lett.* **42**, 37 (1998).

- **The kinematic viscosity is relatively constant throughout the experiment**
- **The value differs by more than a factor of 2 across the interface**
- **The Braginskii and Clerouin models show significant differences**

Time dependent values of the Reynolds number

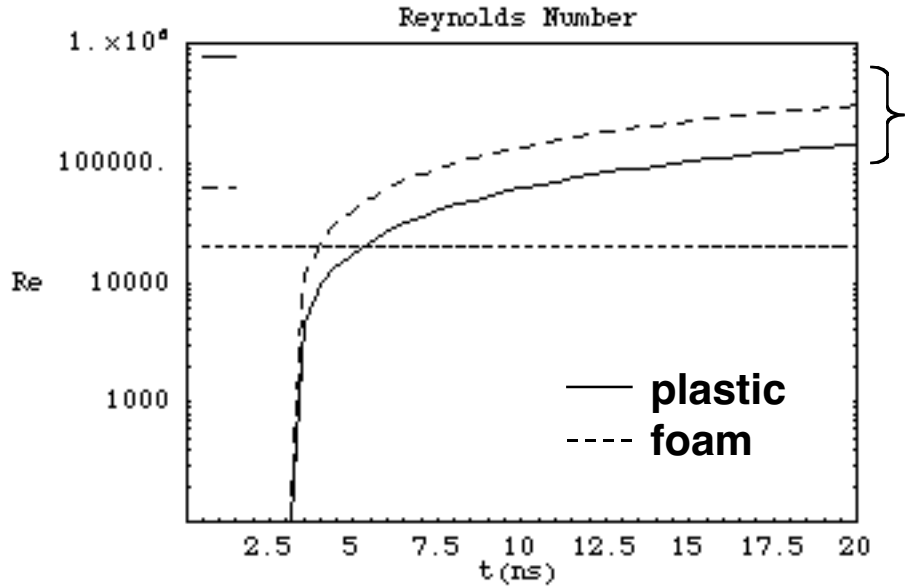

Different values due to differences in kinematic viscosity on either side of the interface

The Reynolds number exceeds the mixing transition threshold of Dimotakis* (Re_{crit} = 2 x 10^4) on both sides of the interface for t > 5ns.

***P.E. Dimotakis, *JFM* 409, 69 (2000)**

The binary mass diffusivity at the interface and the Schmidt number have been calculated as well

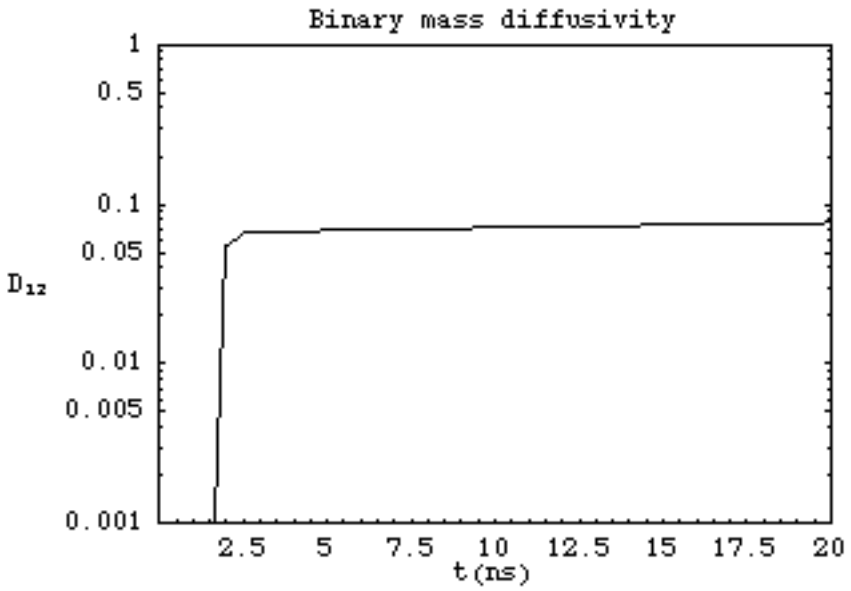

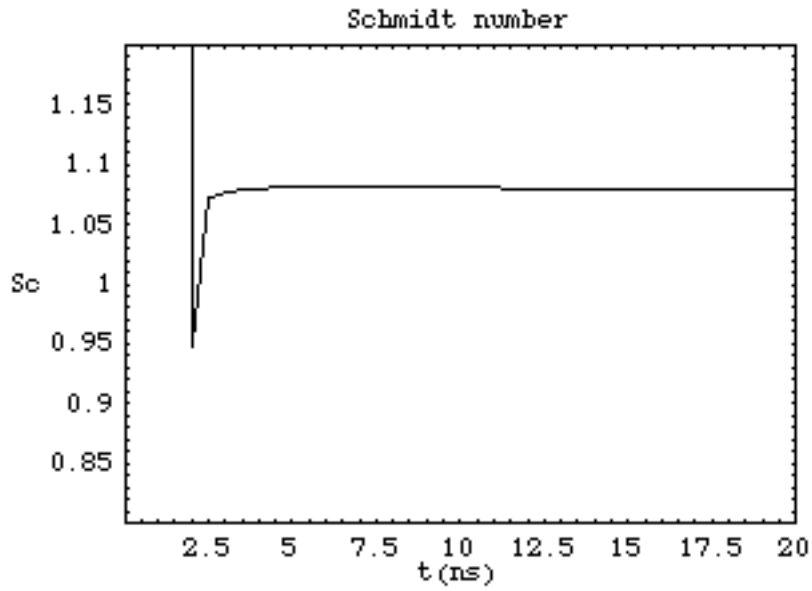

Binary mass diffusivity calculation follow the method outlined in :

C. Paquette et al., *Astrophys. J. Suppl. Ser.* 61, 177 (1986).

From the kinematic viscosity ν and mass diffusivity *D*, the Rayleigh-Taylor growth rate dispersion curve can be calculated

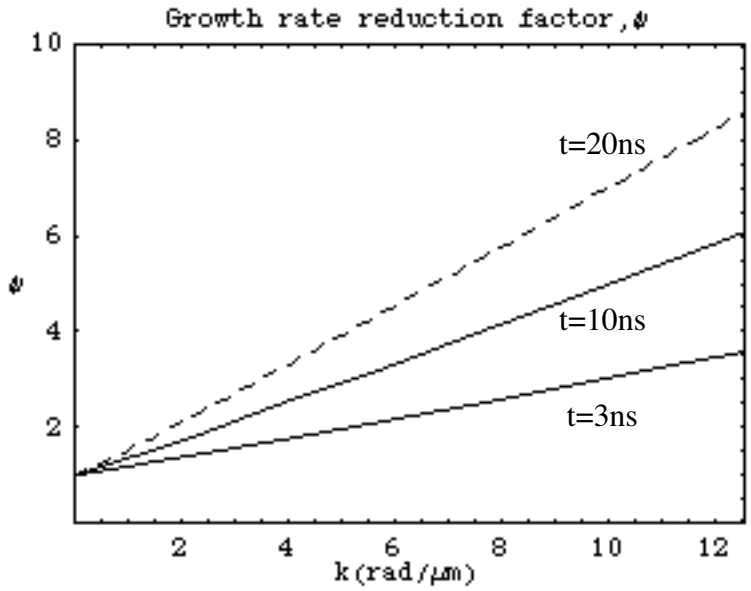

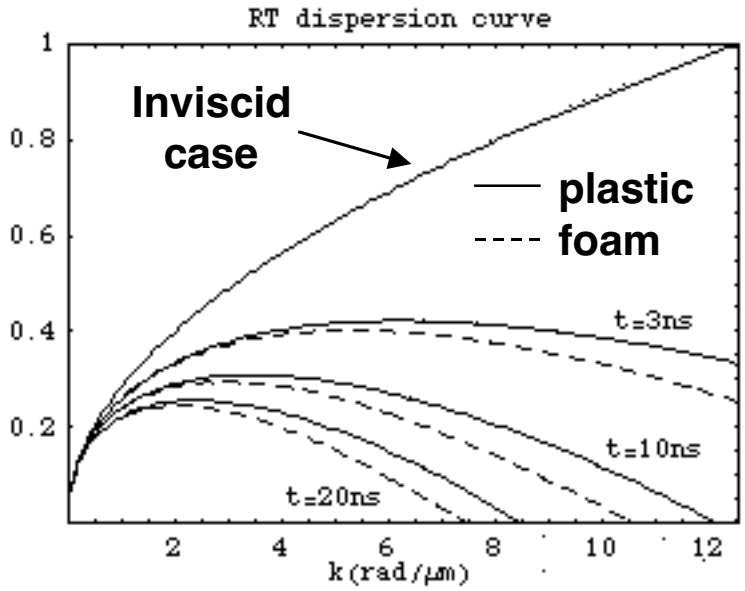

The Rayleigh-Taylor dispersion curve is :

$$\eta_{\nu,D} = \sqrt{\frac{A\,k\,g}{\psi(k,t)} + \nu^2\,k^4} - (\nu + D)\,k^2$$

where Ψ(k,t) is the growth rate reduction factor due to a finite density gradient and is found as the solution of the following eigenvalue equation :

$$\frac{d}{dz}\left(\rho\,\frac{dw}{dz}\right) = w\,k^2\left(\rho - \frac{\psi}{A\,k}\,\frac{d\rho}{dz}\right)$$

From Duff, Harlow, and Hirt, "*Effects of diffusion on interface instability between gases*", Phys. Fluids **5**(4), 417 (1962).

A sufficient range of Rayleigh-Taylor unstable scales exists to populate a turbulent spectrum

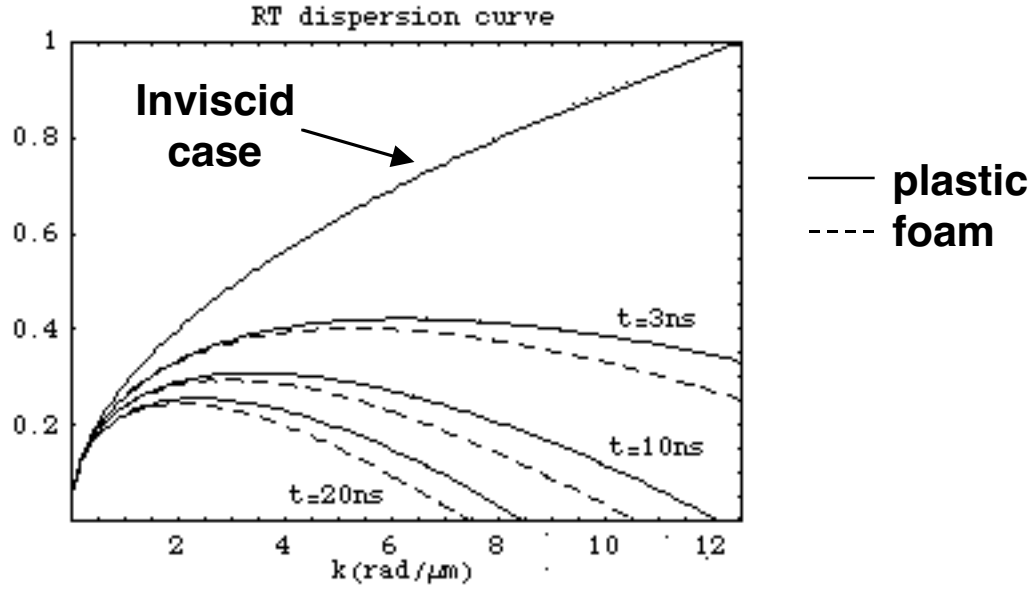

- The initially imposed perturbation has wavelength $\lambda = 50\ \mu m$, or $k = 0.126$ rad / μm.
- At t = 20 ns, perturbations with $k > 8$ rad/μm ($\lambda < 1.3\ \mu m$) are completely stablized.
- At t = 20 ns, the peak growth rate occurs at $k = 2.5$ rad/μm ($\lambda = 2.5\ \mu m$)
- A sufficient range of scales exists, subject to RT instability which can populate a turbulent spectrum

Outline

- Experimental setup and results of Omega laser experiment

- Results from 1D HYADES simulation of the experiment

  Plasma flow parameters (P,ρ,T, Z)
  Derived flow parameters (ν, D)
  Estimation of the Reynolds number

- Extension of Dimotakis mixing transition to non-stationary flows of short time-duration

- Conclusions

Dimotakis has identified a critical Reynolds number at which a rather abrupt transition to a well mixed state occurs

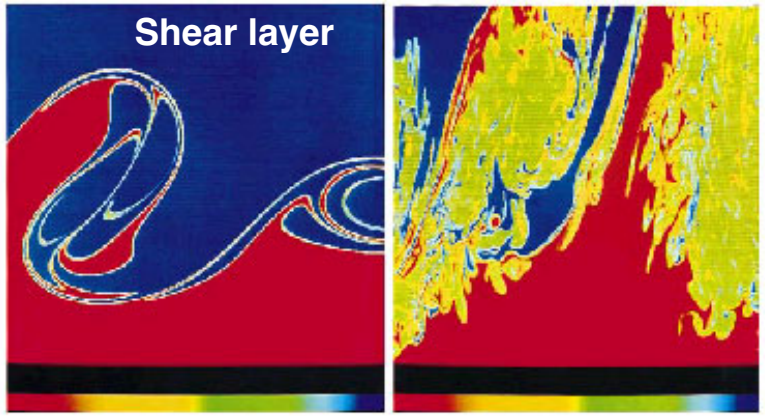

FIGURE 2. Laser-induced fluorescence streak images of the scalar field in a liquid-phase shear layer, for $Re \simeq 1.75 \times 10^4$ (*a*) and $Re \simeq 2.3 \times 10^4$ (*b*). From KD86, figures 7*b* and 9, respectively.

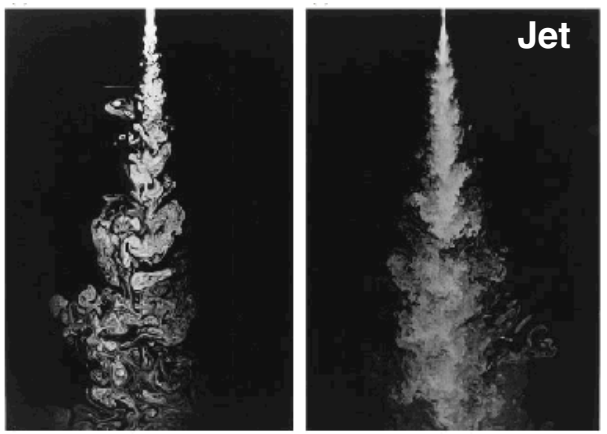

FIGURE 5. Jet-fluid concentration in the plane of symmetry of a round turbulent jet. (*a*) $Re \simeq 2.5 \times 10^4$ ($0 < z/d_e < 35$). (*b*) $Re \simeq 10^6$ ($0 < z/d_e < 200$). Data from Dimotakis *et al.* (1983, figures 5 and 9).

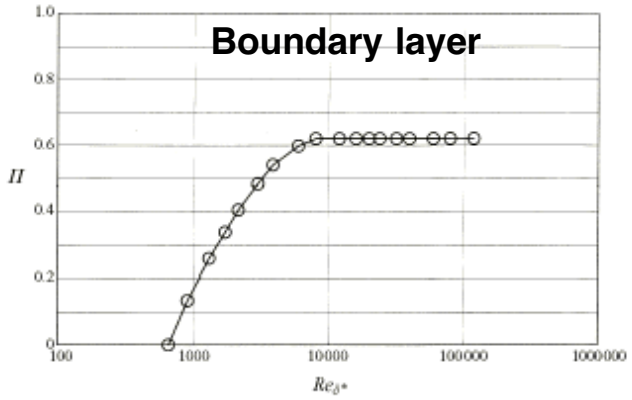

FIGURE 12. Turbulent boundary-layer Π parameter vs. Re_{δ^*}. Skin-friction-law fit data (Collins *et al.* 1978, table 4).

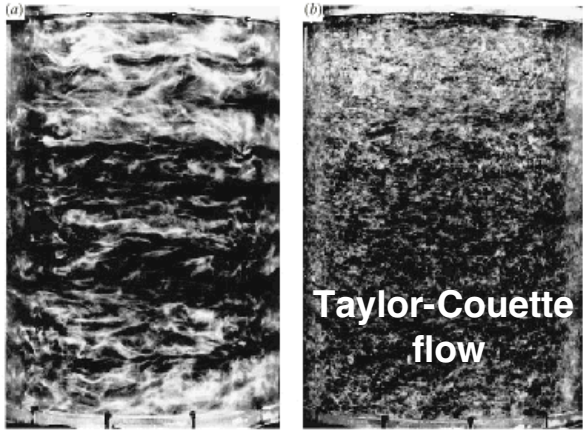

FIGURE 16. Couette–Taylor flow-visualization data at (*a*) $Re = 0.6 \times 10^4$, and (*b*) $Re = 2.4 \times 10^4$. From Lathrop *et al.* (1992*b*, figures 5*a*,*b*). Reproduced by kind permission of Professor H. Swinney.

This mixing transition at Re ≈ 2 x 10^4 is observed to occur in a very wide range of stationary flows

All figures from P.E. Dimotakis, *JFM* 409, 69 (2000)

This transition is co-incident with the appearance of a range of scales decoupled from both large-scale and viscous effects

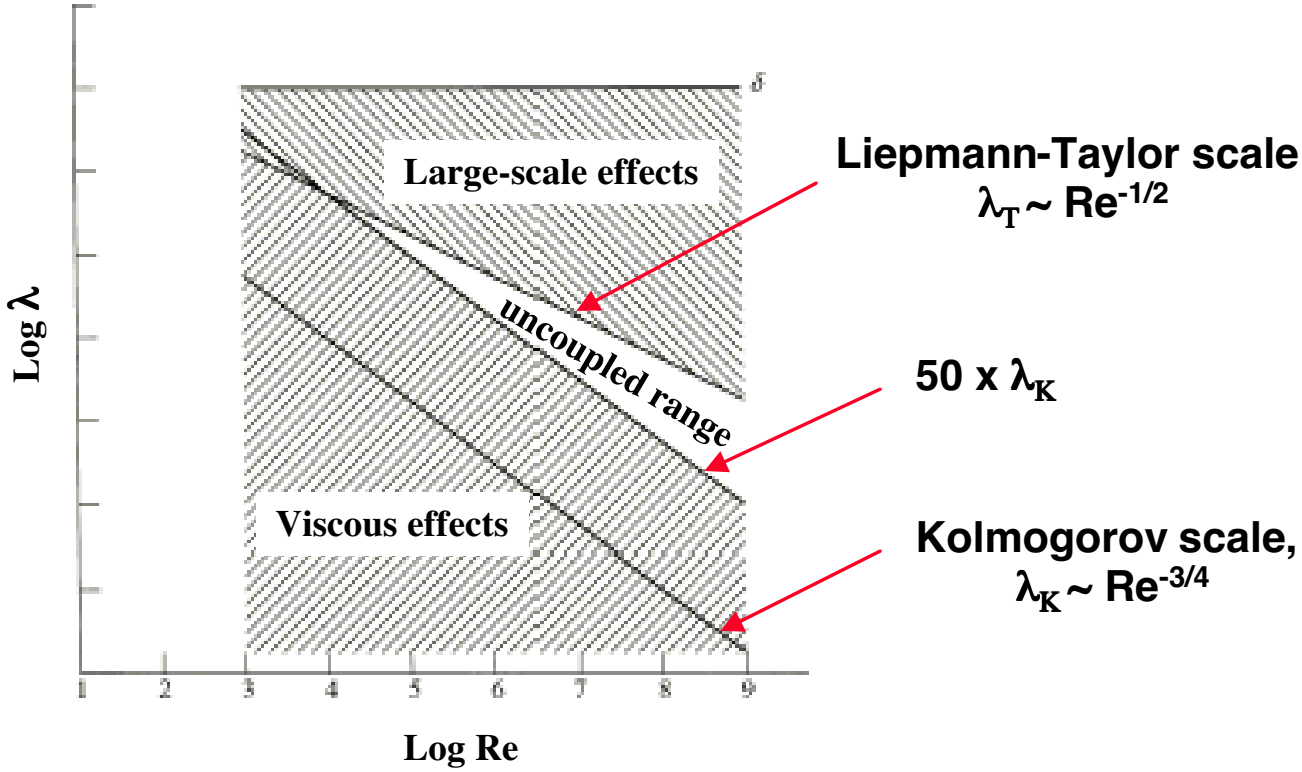

Figure 19. Reynolds number dependence of spatial scales for a turbulent jet

Figure 19 from P.E. Dimotakis, *JFM* 409, 69 (2000)

In high Re flows of short time duration, the Taylor microscale may not have sufficient time to reach its asymptotic value

The Taylor microscale (for stationary, homogeneous, isotropic flows) depends on the integral scale δ and the Reynolds number as :

$$\lambda_T \sim \delta \, \mathrm{Re}_\delta^{-1/2}$$

This dependence is analogous to the development of a laminar viscous boundary layer on a flat plate :

$$\lambda_\nu \sim x \, \mathrm{Re}_x^{-1/2}$$

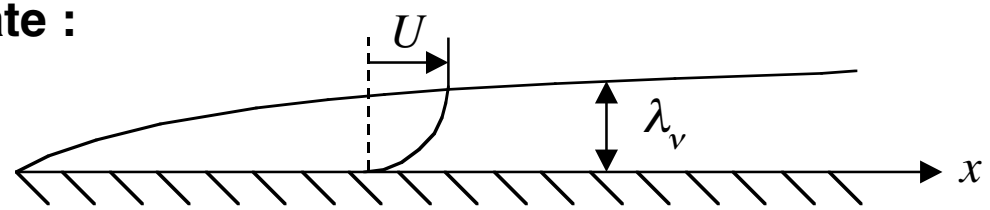

For an impulsively accelerated plate, however, the boundary layer development will initially grow as :

$$\lambda_\nu(t) \sim \sqrt{\nu t}$$

We propose a modification to the mixing transition as the time at which the smaller of the Taylor microscale and the viscous diffusion scale exceeds the dissipation scale (50 x Kolmogorov scale) :

$$Min(\sqrt{\nu t}, \lambda_T) > 50\lambda_K$$

Time dependent values of the Taylor microscale, Kolmogorov scale, and viscous diffusion scale

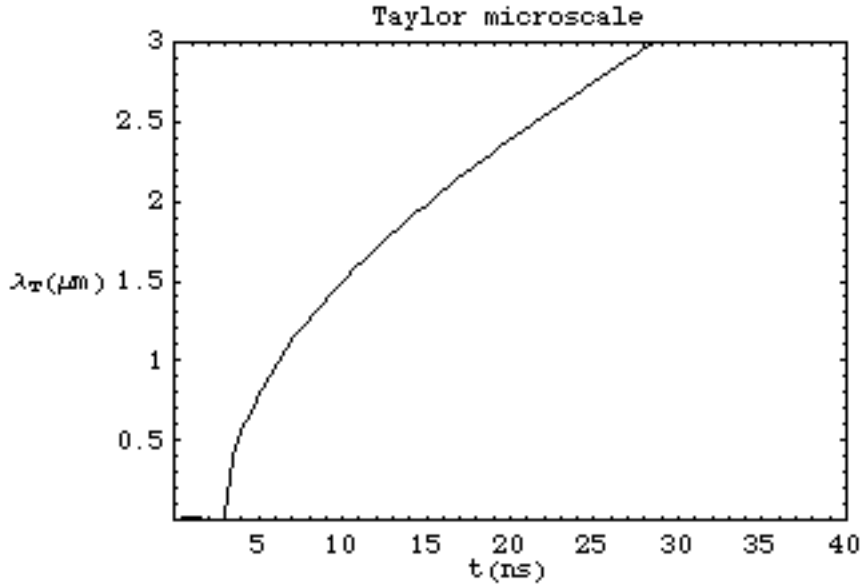

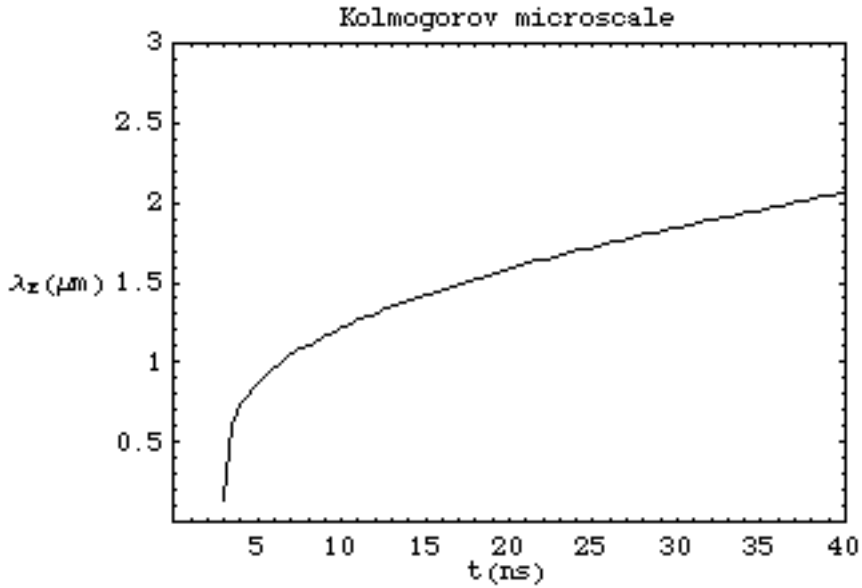

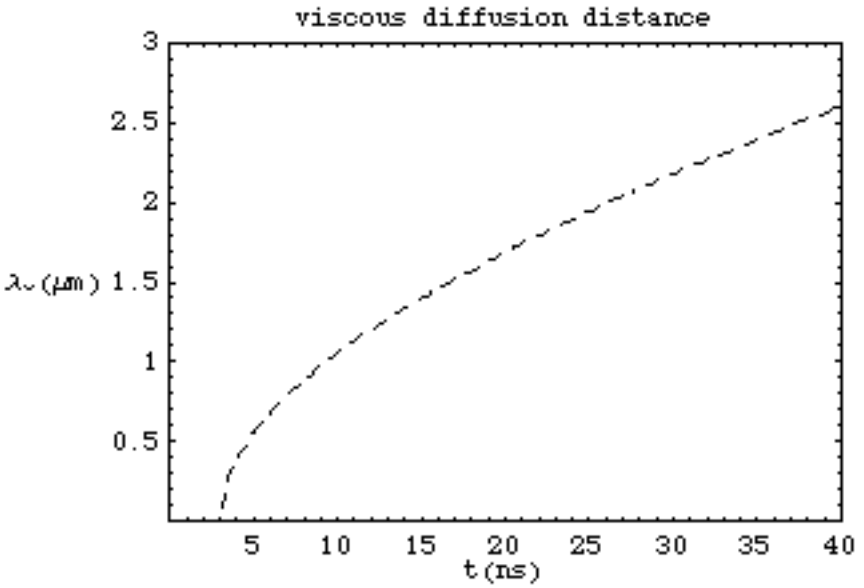

For the present experiment, the viscous diffusion scale is less than the Taylor microscale for the entire duration of the flow.

Therefore the viscous diffusion scale sets the time for a time-dependent mixing transition.

A comparison of viscous length scales shows the appearance of a decoupled range of scales for t > 17 ns

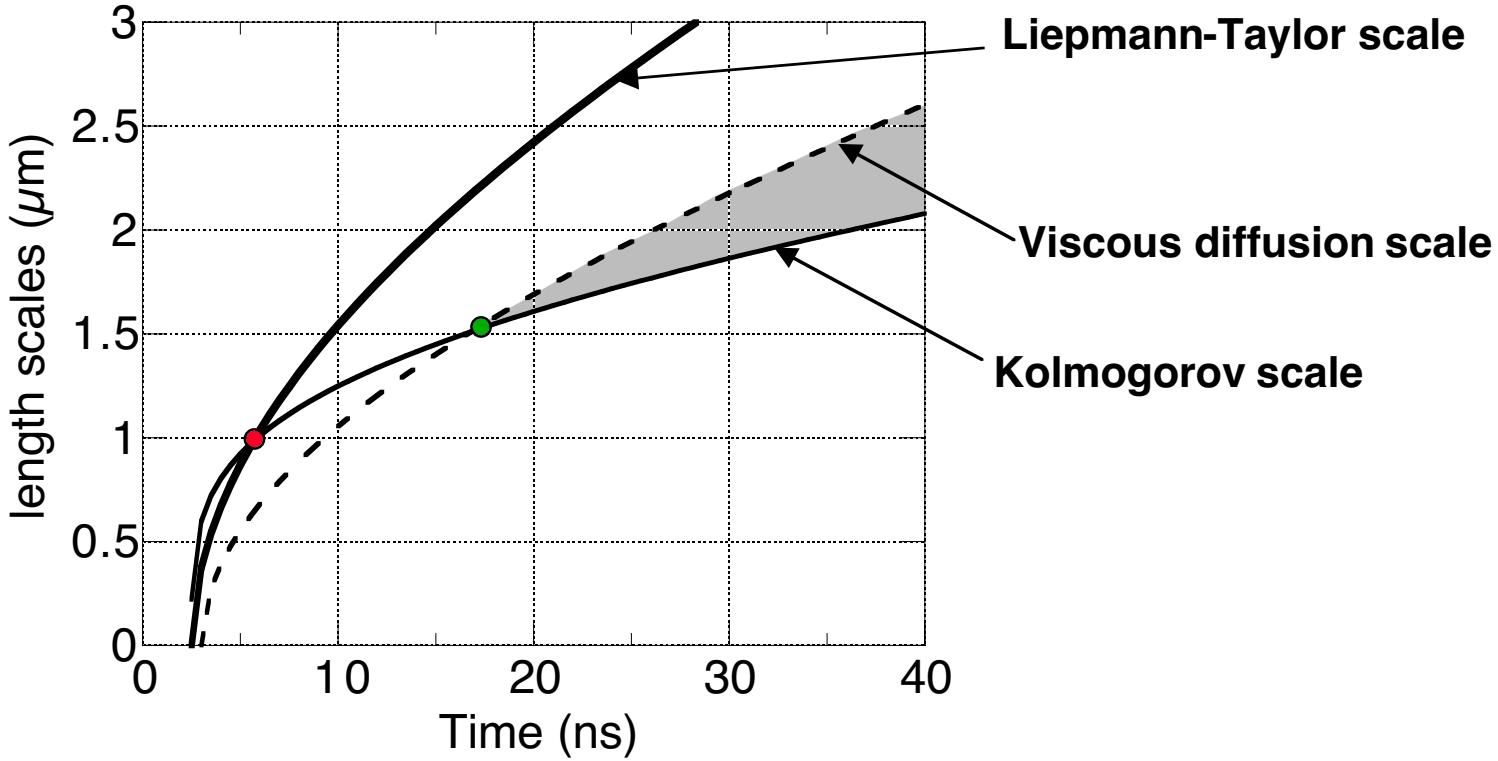

- The red dot indicates the Dimotakis criterion for transition in a stationary flow. This occurs at t ≈ 5.5 ns or Re ≈ 2 x 10^4.
- The green dot indicates the present criterion for transition in a temporally-limited flow. This occurs at t ≈17 ns or Re ≈ 10^5.

This method has been applied to estimate the turbulent transition time in the LANL gas curtain experiment *

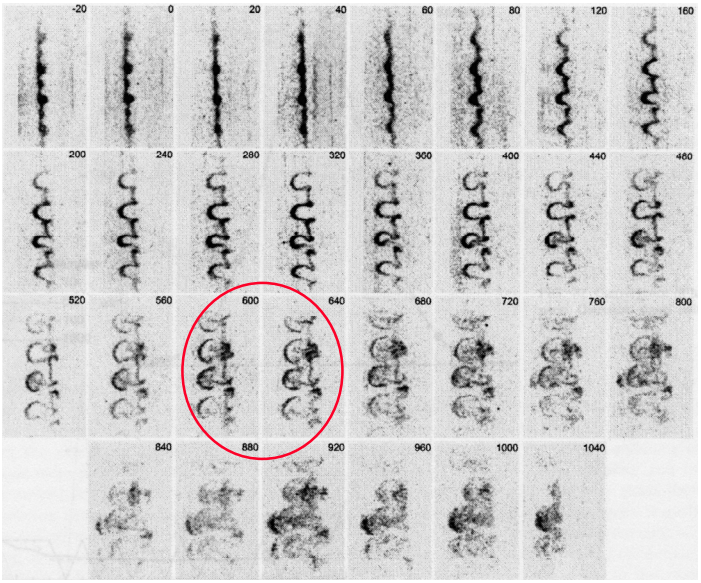

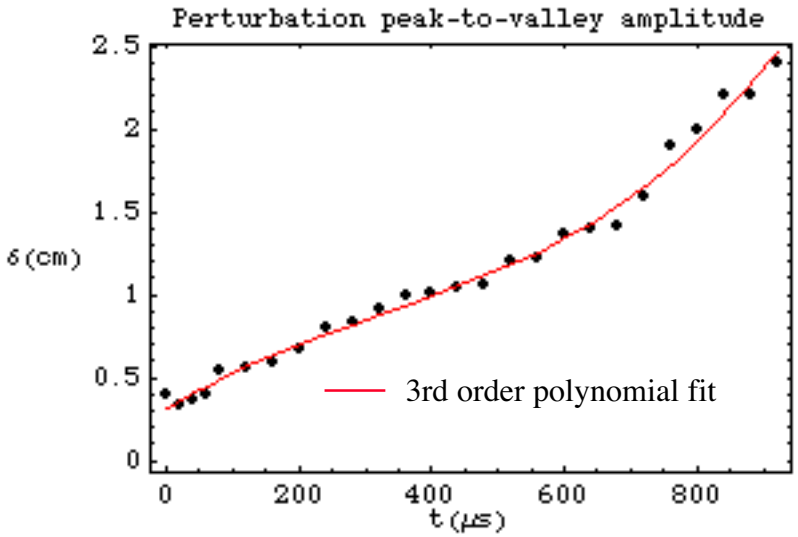

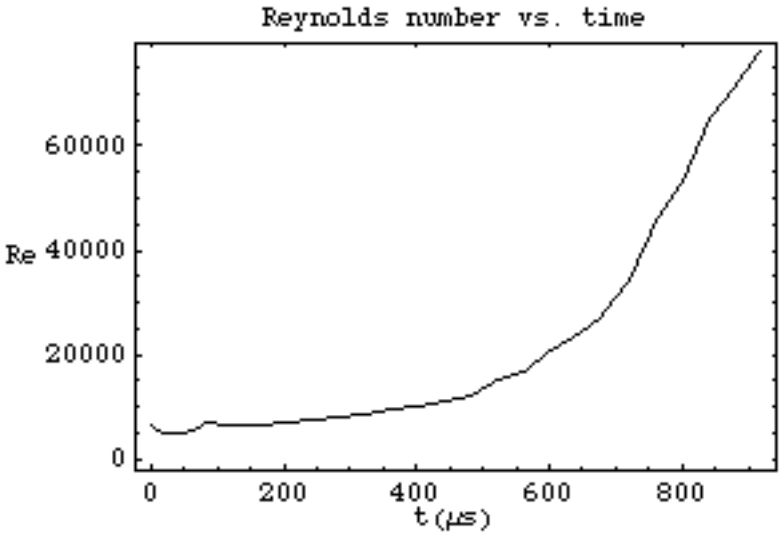

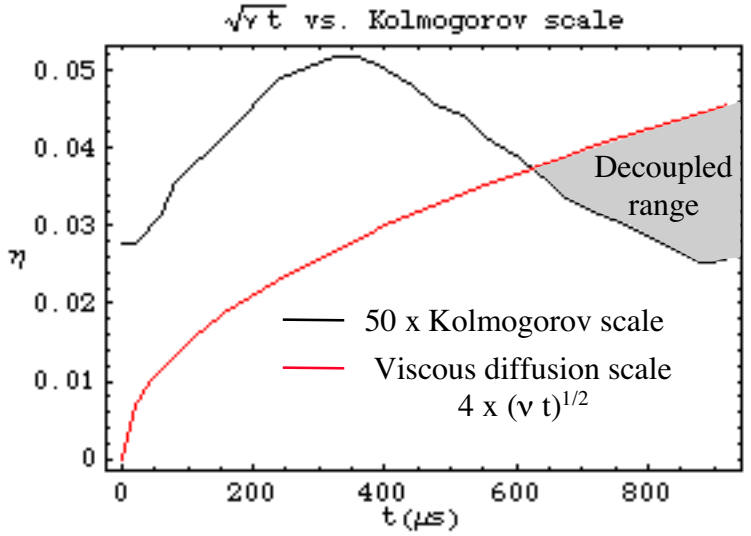

* From Rightly, Vorobieff, Martin, & Benjamin, Phys. Fluids 11(1), 186 (1999)

Current and future work on Omega will focus on the role of modal content and dimensionality of the initial perturbation

2D, single-mode @ 13 ns

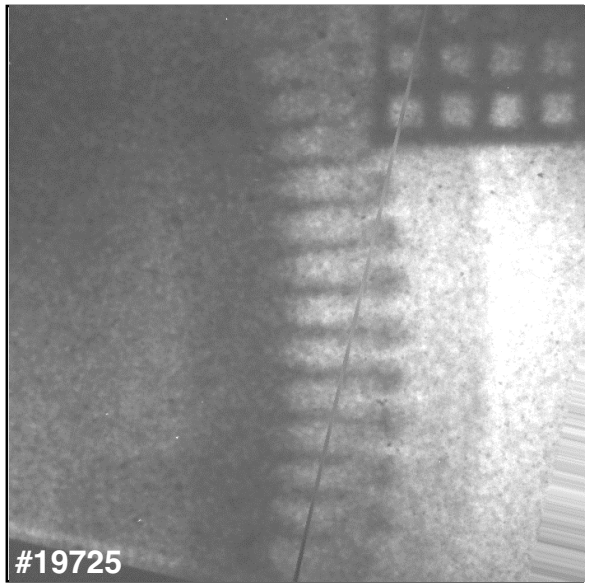

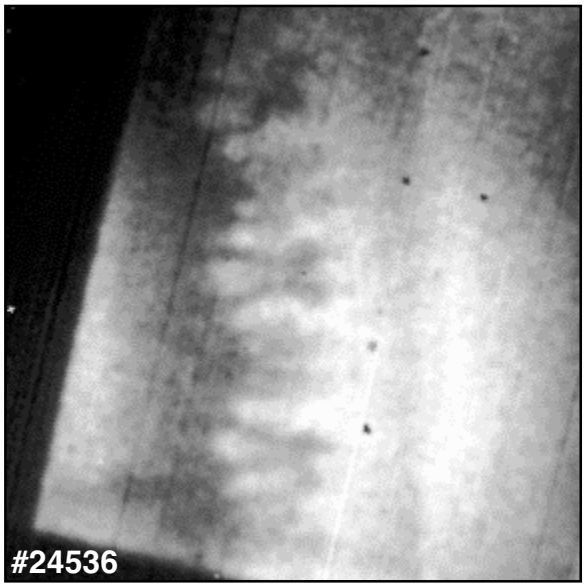

2D, 8-mode @ 13 ns

2D, 2-mode @ 13 ns

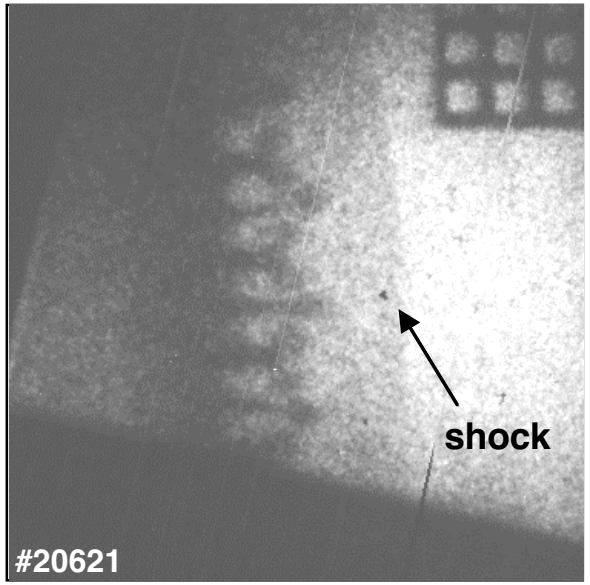

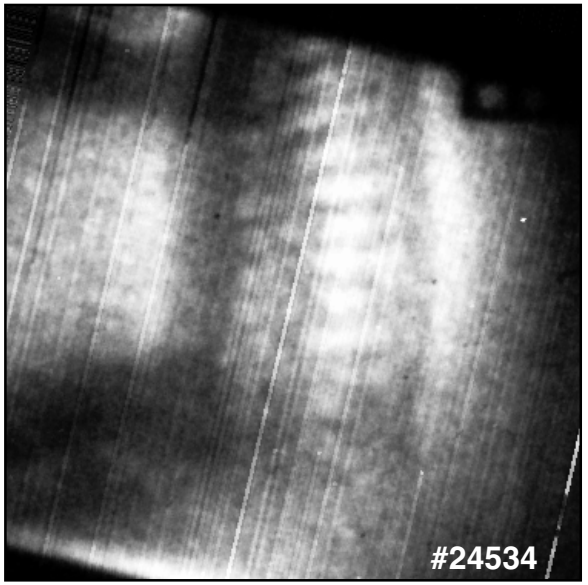

3D, single-mode @ 13 ns

Conclusions

The transition to turbulence in a high Reynolds number, Rayleigh-Taylor unstable plasma flow has been studied experimentally.

The following observations are made :

- **The Reynolds number exceeds the mixing transition threshold of Dimotakis (i.e. $Re >> 2 \times 10^4$) for much of the experiment, yet no transition to turbulence is observed.**

- **An extension of the Dimotakis mixing transition to non-stationary flows of short time-duration is presented. This method illustrates that the temporal duration of the present flow is insufficient to allow for the appearance of a mixing transition.**

MIX2001

High Mach Number and High Initial Amplitude Effects on the Evolution of the Single-Mode Richtmyer-Meshkov Instability An Experimental Study

O. Sadot[1,2], A. Rikanati[1,2], D. Oron [1], A. Yosef-Hai[2],
G. Ben-Dor [2], D. Shvarts [1,2]

1) Nuclear Research Center Negev, ISRAEL.
2) Ben-Gurion University of the Negev, ISRAEL.

Theory: The case of a single-mode RM instability

Small initial amplitude: (Richtmyer Impulsive model)

Using:

1) Incompressible flow after the shock passes the interface.
2) Modeling the shock as:

$$g(t) = U_0 d(t)$$

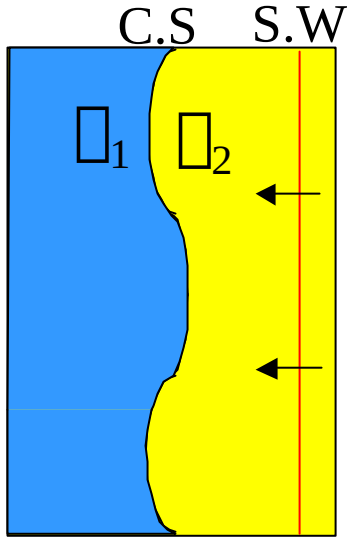

Leads to a linear growth:

$$U_{bubble} = U_0 \times k \times \frac{r_1 - r_2}{r_1 + r_2} a_+$$

k wave-number

U_0-shock wave induced velocity of the contact surface

a_+- initial post shock amplitude

ρ_1, ρ_2 - densities ahead and behind the contact surface

t -time

Reduction from the impulsive model

Aleshin *et al.* (1997) M=2.5 - 4.5

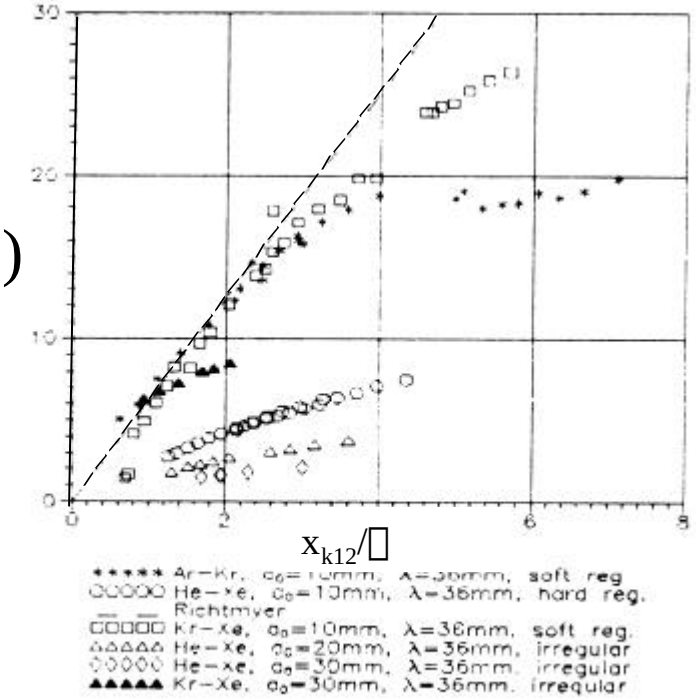

$$\tilde{a}(t) = (a_{k12}(x_{k12}) - a(0)_{k12})/(\dot{a}_{k12} A t)$$

Dimonte *et al.* (1996) M=15.3

Holmes *et al.* (1997) a_k=0.63

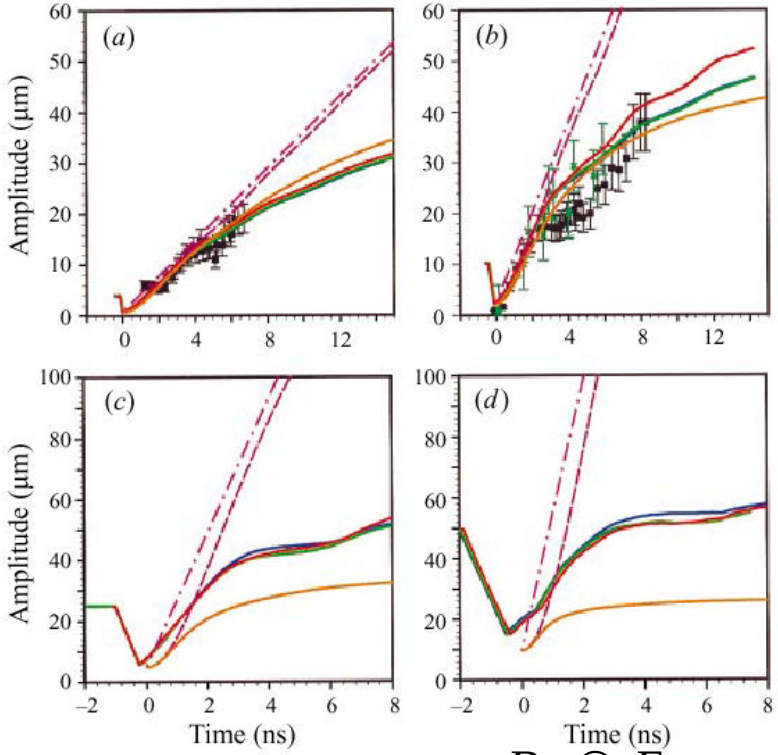

Be ® Foam

At high Mach numbers:

$$U = \min(U_{richtmyer}, U_{Transmitted} - U_{Interface})$$

The reduction is a high Mach number effect

Experimental results: reduction from the impulsive model

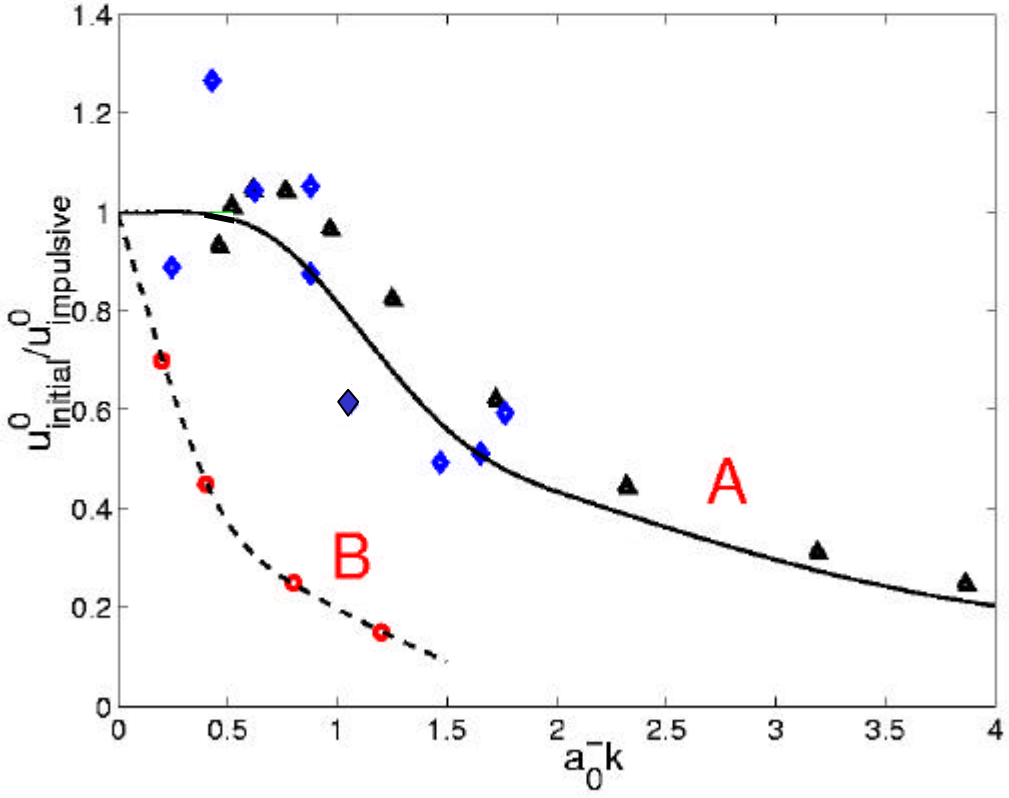

- Dimonte Be ® Foam (M=15.3)
- Aleshin Ar ® Xe (M=2.5)
- Aleshin He ® Xe (M=2.5)

Experimental Apparatus

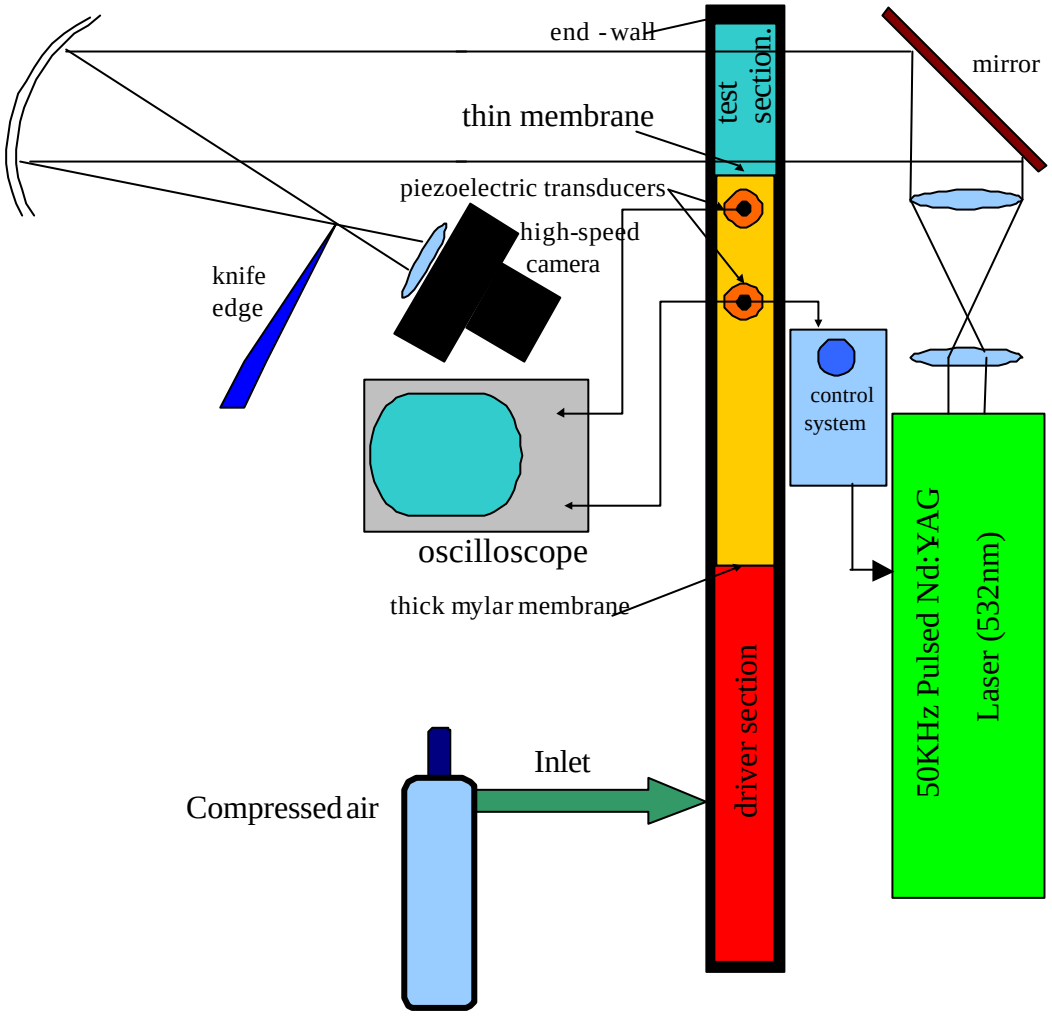

Control and diagnostic

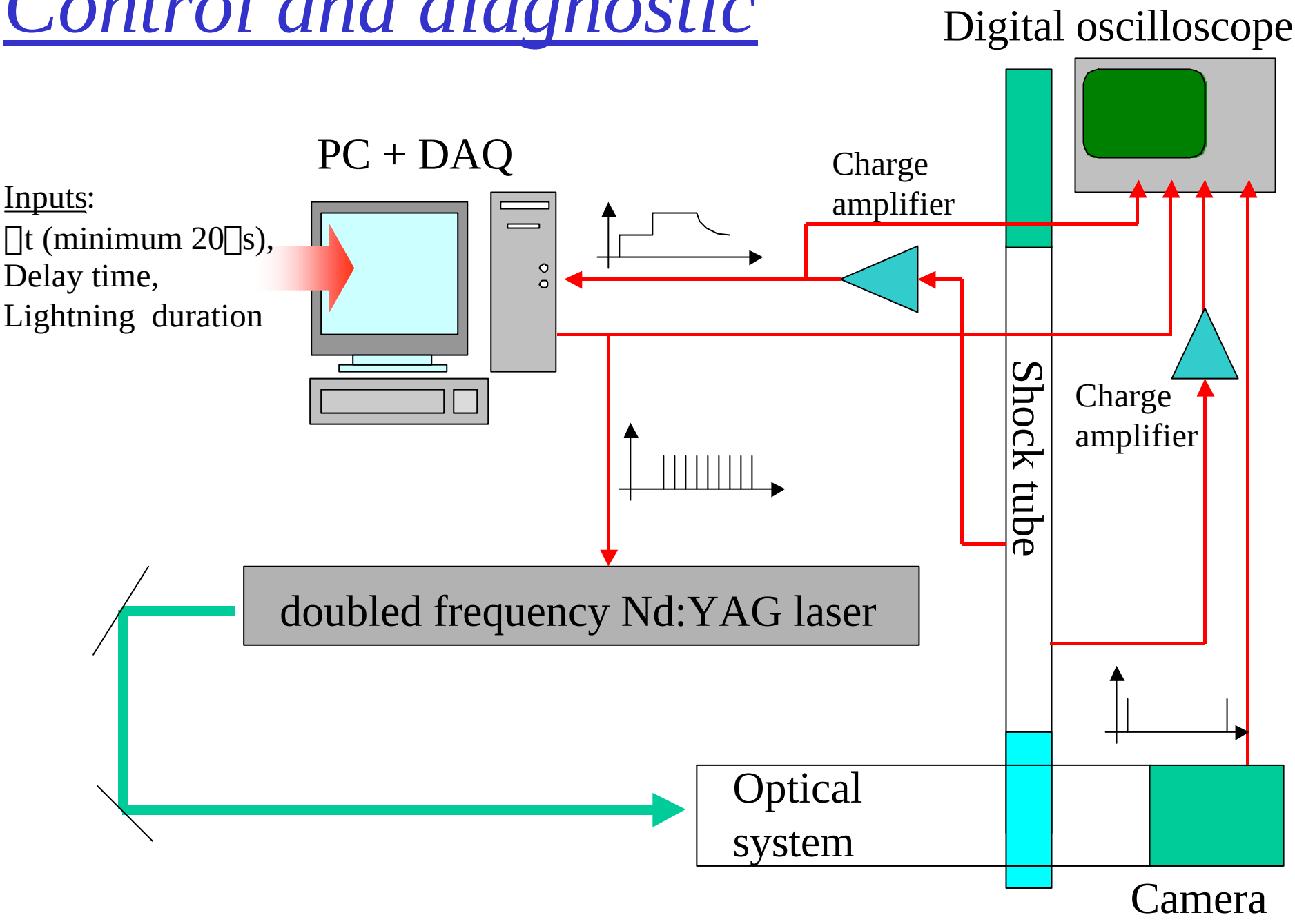

Experimental apparatus The membrane

Mach number M=1.2

□	a_	a_k
80mm	40mm	3.14
26mm	10mm	2.45
40mm	12mm	1.9
80mm	20mm	1.57
40mm	7mm	1.1
40mm	3mm	0.5

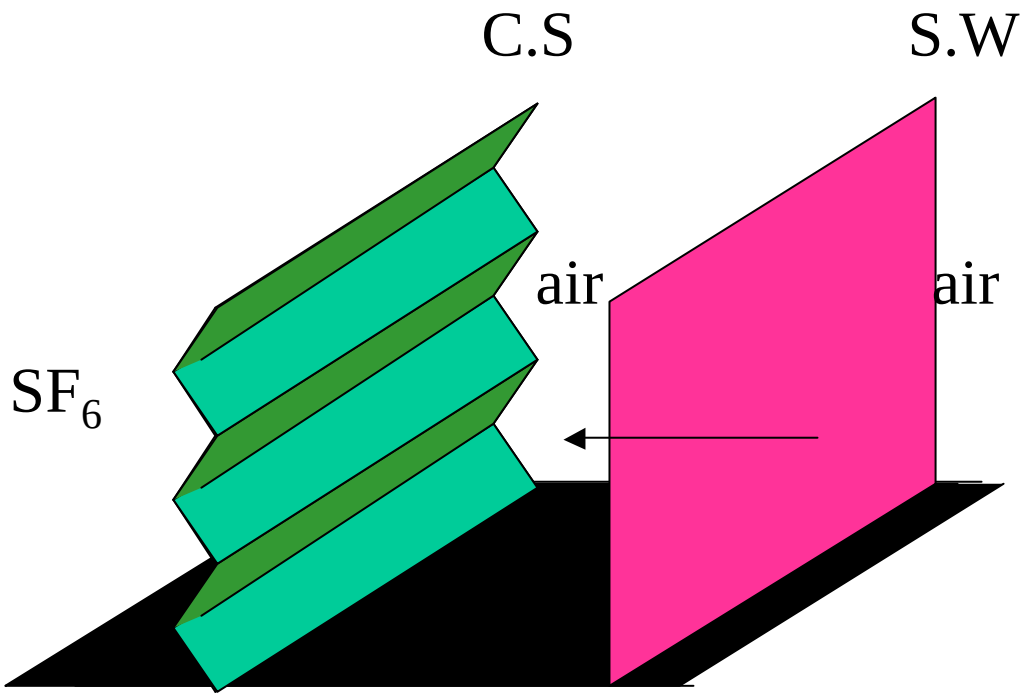

Experimental results (M=1.2)

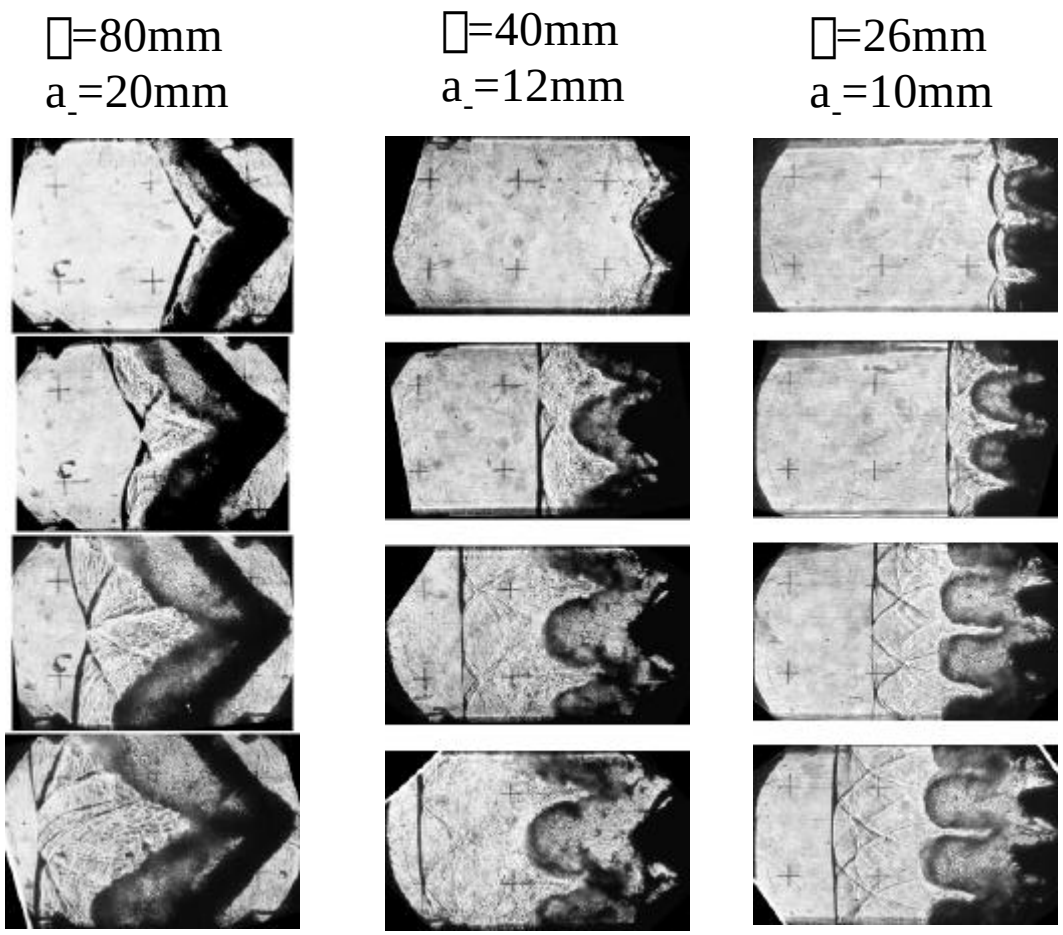

Numerical simulation

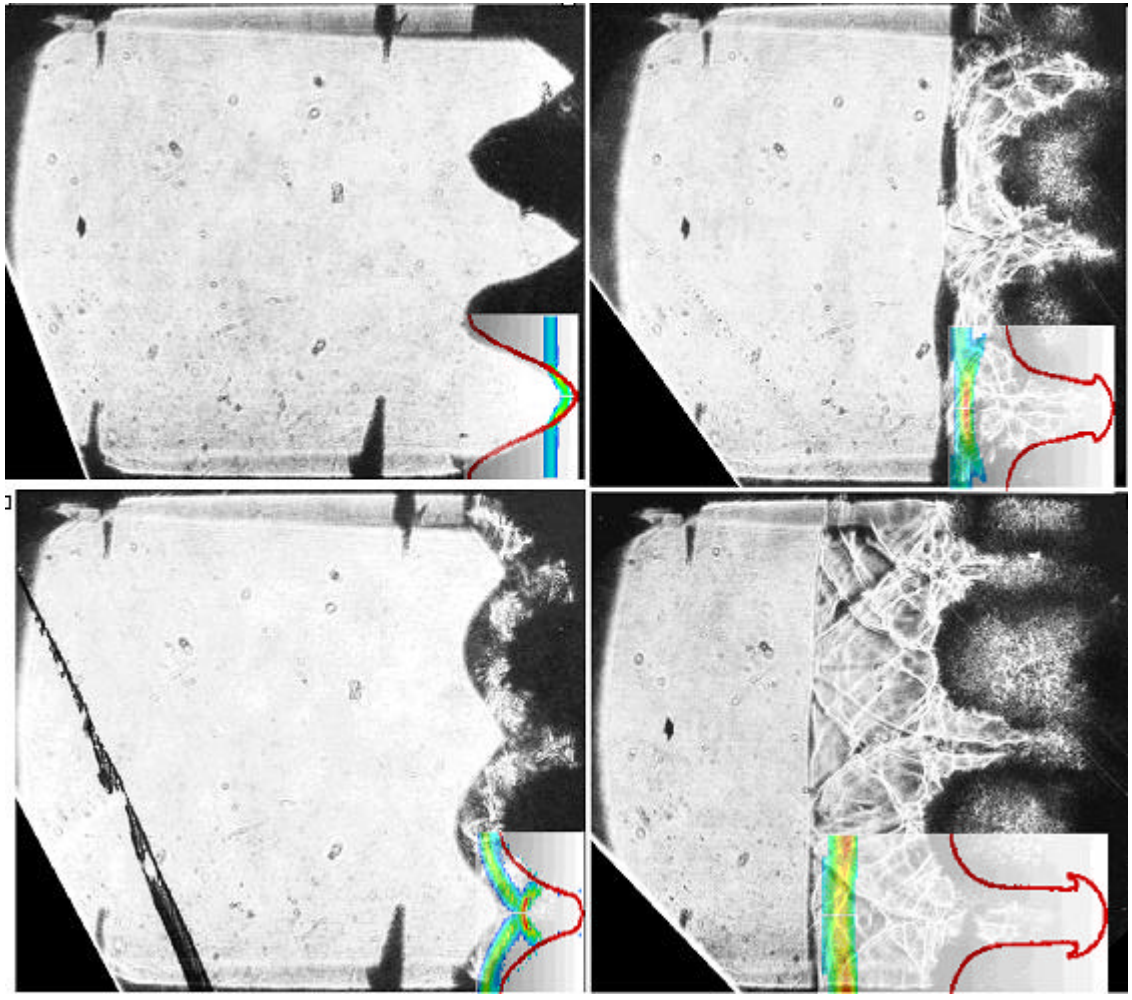

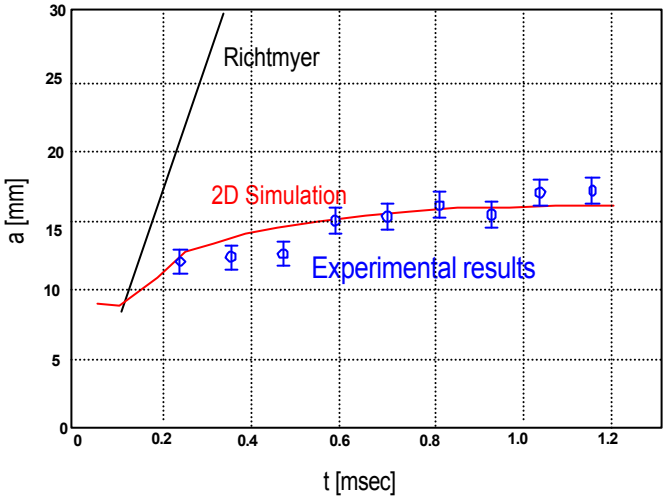

The initial velocity was found from the simulation

Reduction from the impulsive model: Results of experiment, model and simulation

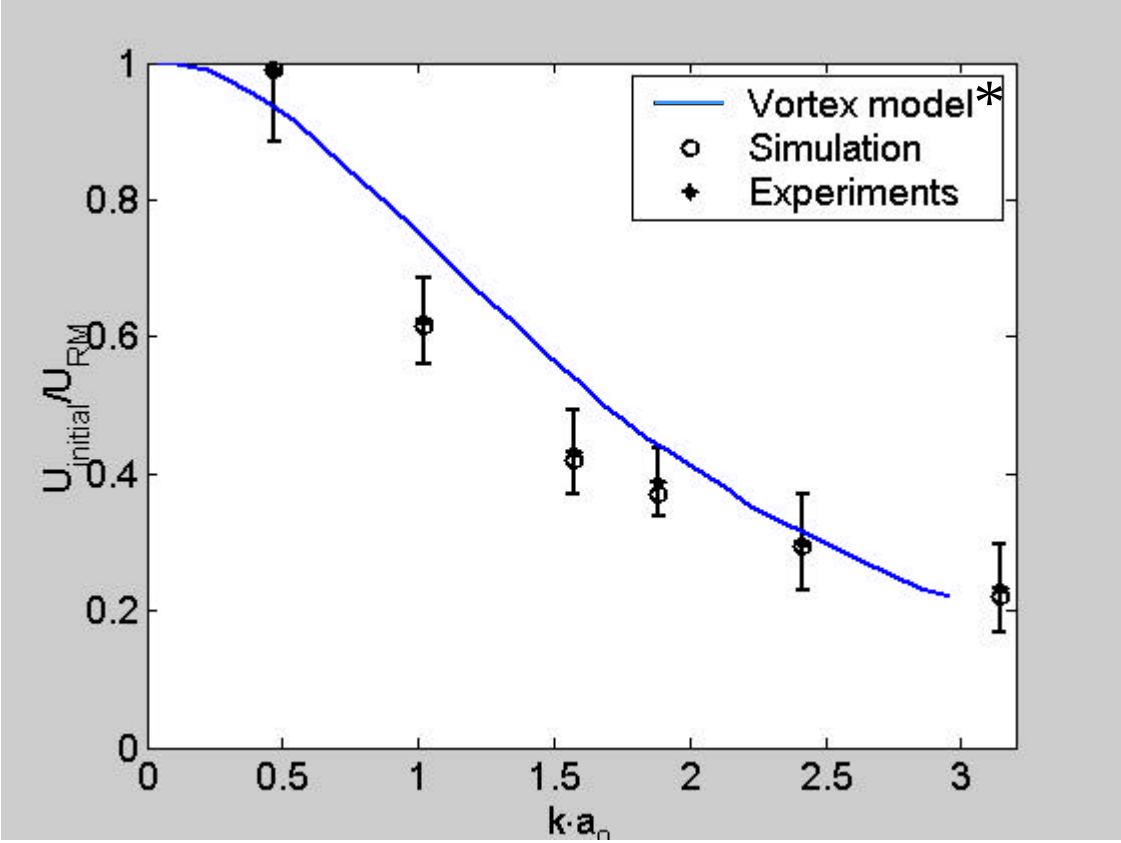

* See Rikanati Thursday T23.

Experimental results: reduction from the impulsive model

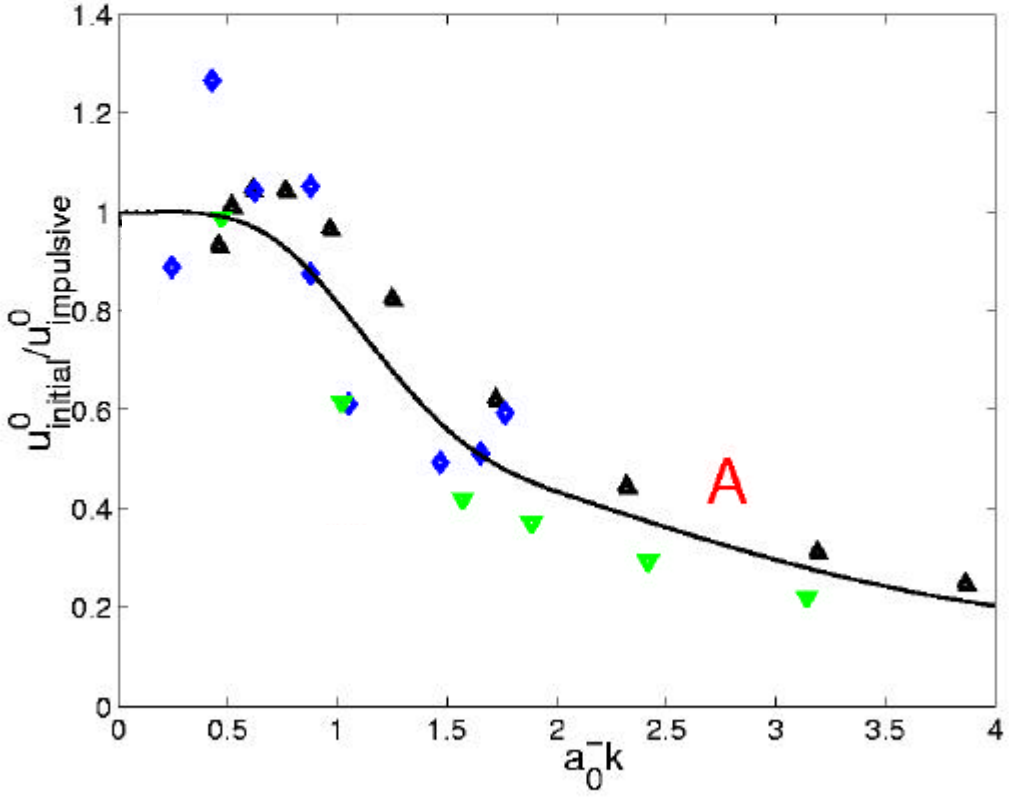

- Dimonte Be ® Foam (M=15.3)
- Aleshin Ar ® Xe (M=2.5)
- Sadot Air ® SF_6 (M=1.2)

High initial amplitude effect

Bubble late time evolution in the large amplitude experiment

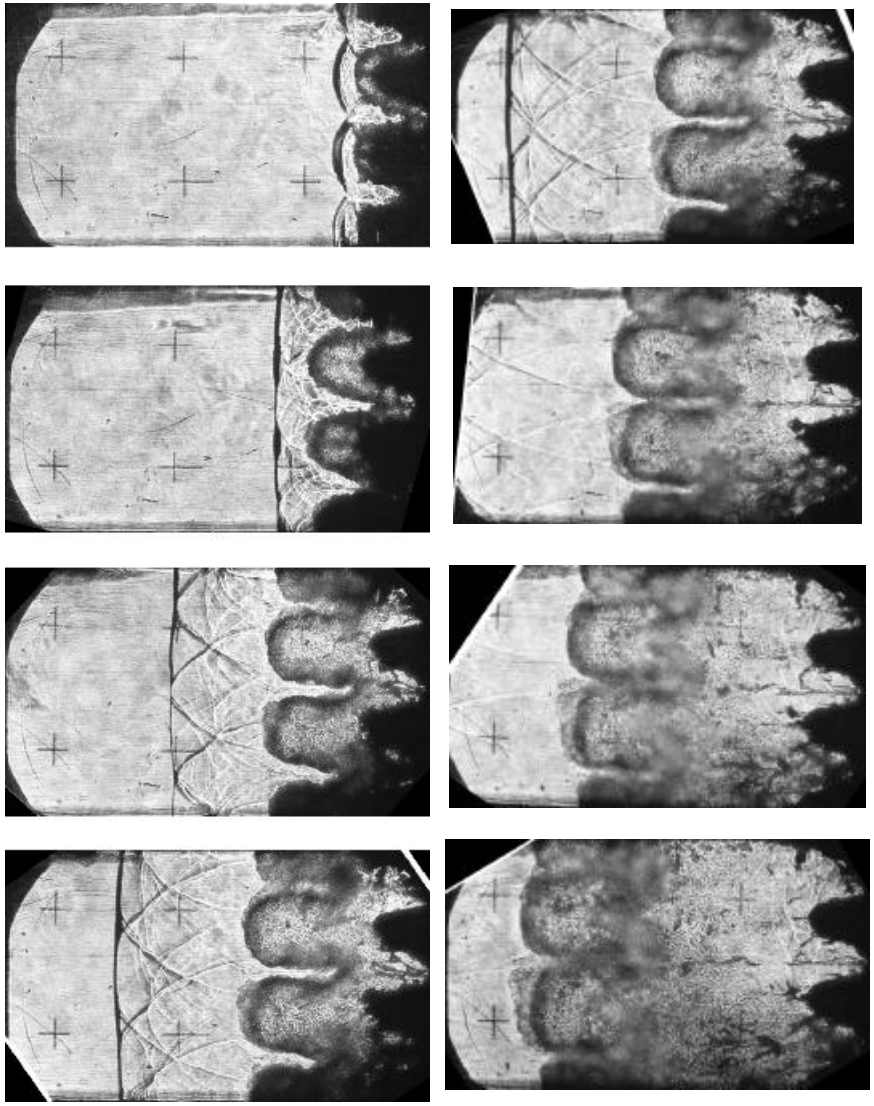

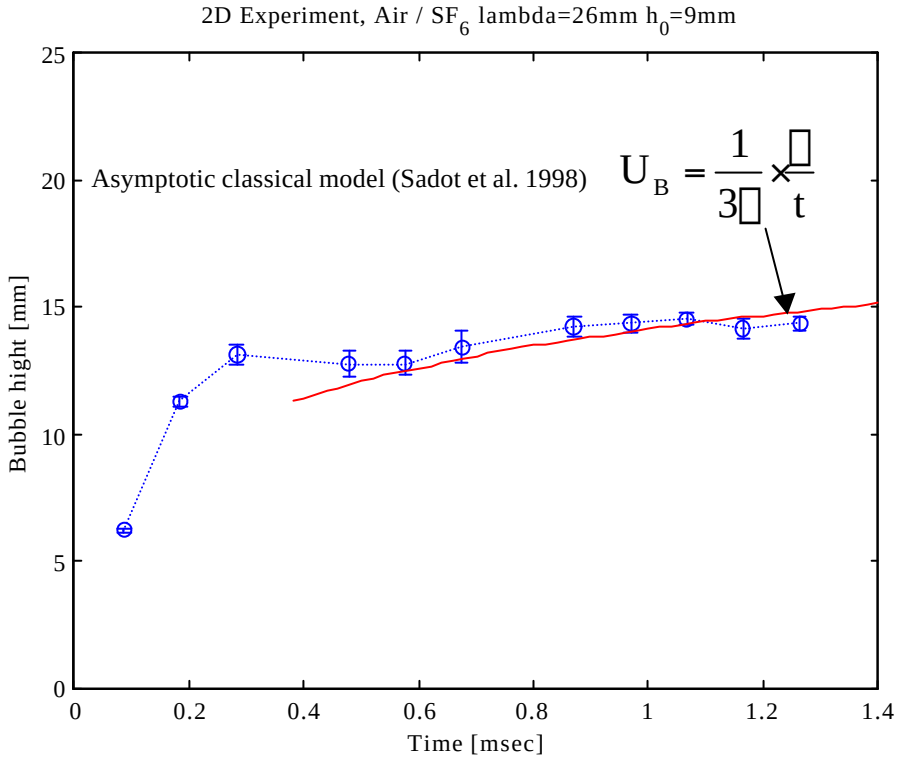

Late time reduction from the classical models due to high Mach number effects

a_0=3mm, M =2

air to SF_6 ($\gamma_{SF_6} = 1.09$)

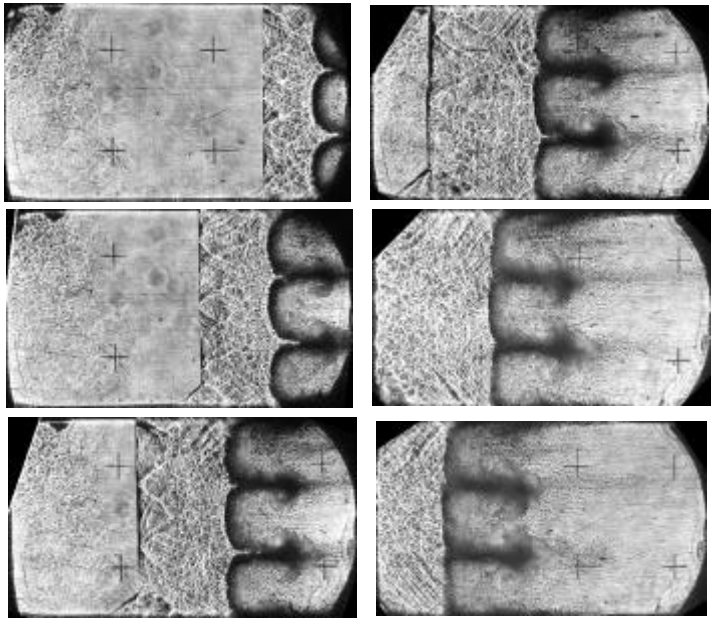

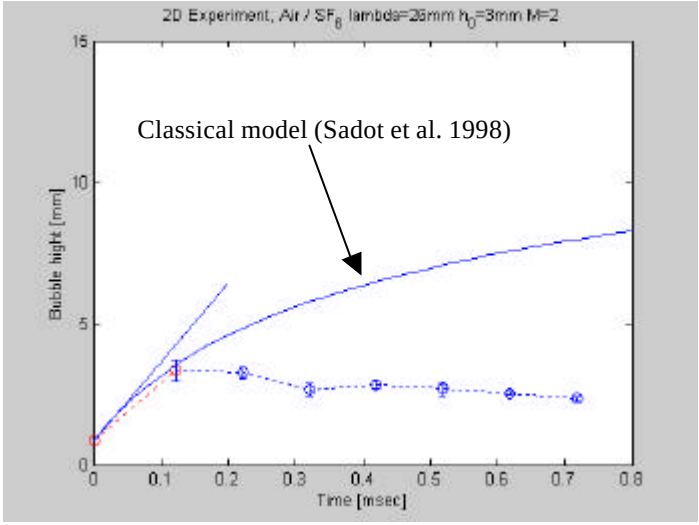

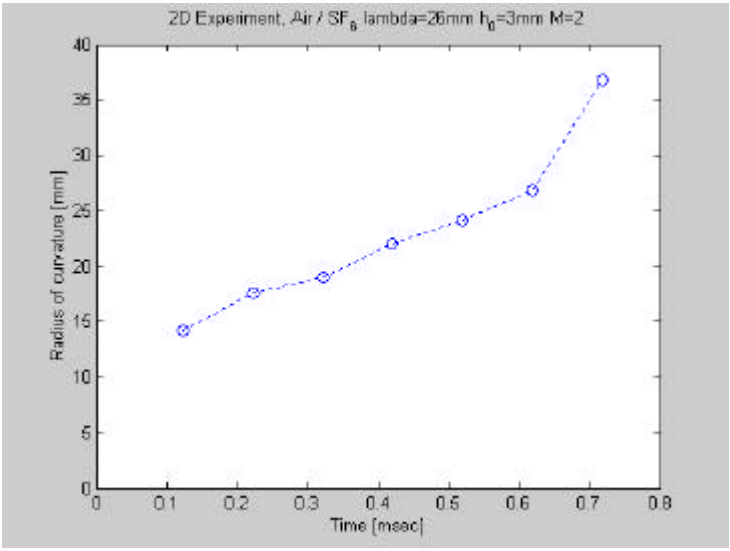

The radius of curvature of the bubble:

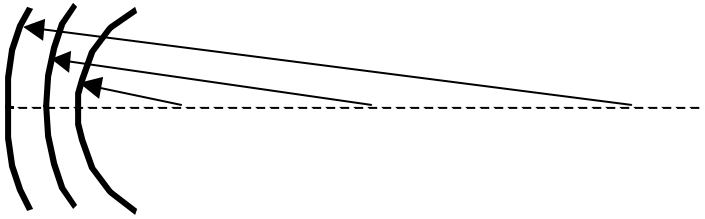

At late time the shock reverberation reduces the bubble growth rate

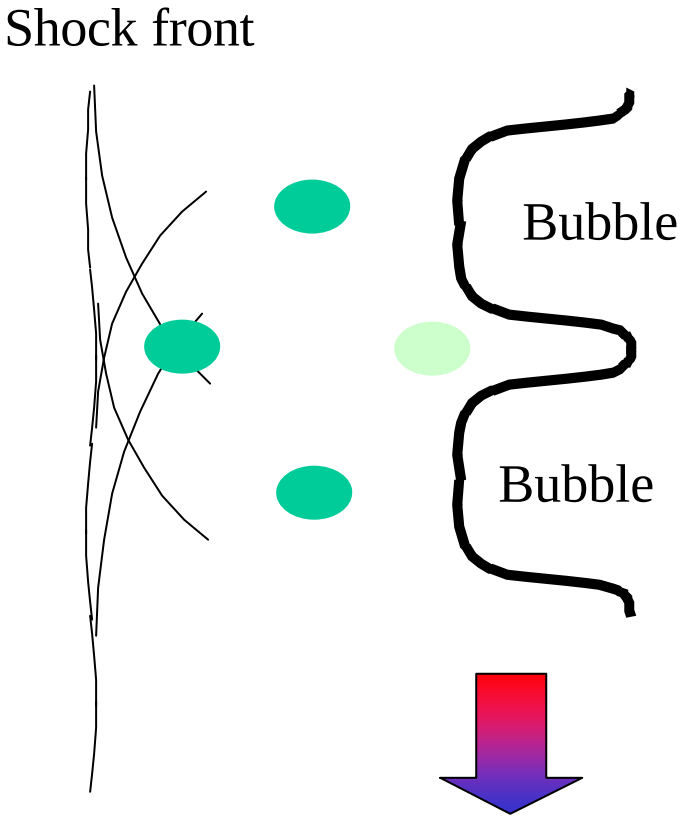

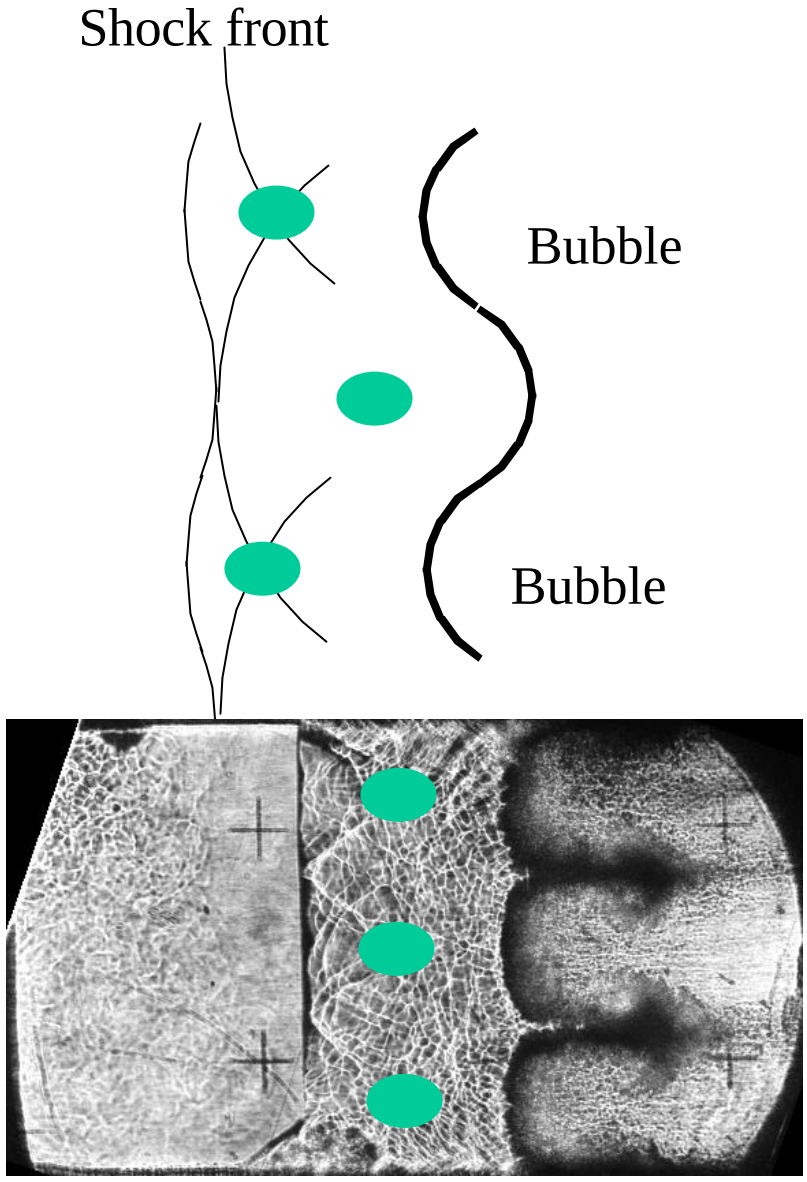

The growth velocity is reduced
The radius of curvature is increased

Summary

Effects of high initial amplitudes were quantified experimentally for the early linear stages of the flow.

The reduction from the Richtmyer initial velocity occur even at low Mach number (M=1.2).

For the late nonlinear stages of the flow:

- The initial amplitudes effect was forgotten and the bubble evolves as in the classical case (depends only on the wave length).
- New effect was observed for high Mach numbers which decreases the bubble asymptotic velocity.

MEASUREMENTS WITHIN A RICHTMYER-MESHKOV MIXING ZONE USING A TRIPLE HOT WIRE PROBE TECHNIQUE

L. SCHWAEDERLE*, G. JOURDAN*, L.HOUAS* and J.-F. HAAS♣

*IUSTI, UMR CNRS 6595, Université de Provence, Technopôle de Château-Gombert, 5 rue Enrico Fermi, 13453 Marseille Cedex 13, FRANCE

♣CEA-DAM, Ile de France, BP 12, 91680 Bruyères-le-Chatel, FRANCE

I- INTRODUCTION

Present research topic: Characterization of a turbulent mixing zone (TMZ) induced by the Richtmyer- Meshkov instability (RMI) in a shock tube

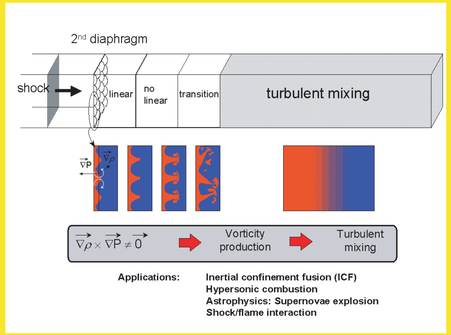

- Global characterization : visual structures, thickness
- Time evolution of local measurements (molar fraction and velocity)
- Turbulent energy level

Schlieren visualizations
+
Laser Doppler anemometry (CEA/DAM)
Constant temperature hot wire anemometry (IUSTI)

II- EXPERIMENTAL SET-UP

Schileren + Hot wire anemometry

-Constant temperature
-Single probes (5µm diam x 1.5mm length)
-Cut-off frequency : 80kHz
-Probe spacing : ~1 cm
-Sampling : 1 MHz/n probes

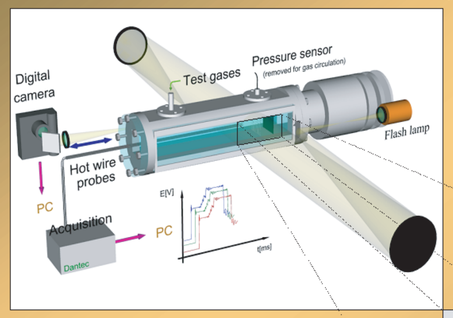

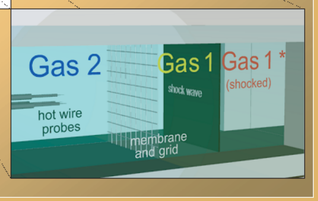

Double diaphragm shock tube
- Square cross section 85x85 mm2
- 1st diaphragm : aluminium membrane (0.8 mm thick)
- 2nd diaphragm : mylar (0.9 µm thick) or nitrocellulose (0.5 µm thick) film resting over a 100 cells or a 7225 cells grid

III- PRINCIPLE OF MEASUREMENTS

HWA output versus time

- Reynolds number
- species molar fraction
- velocity

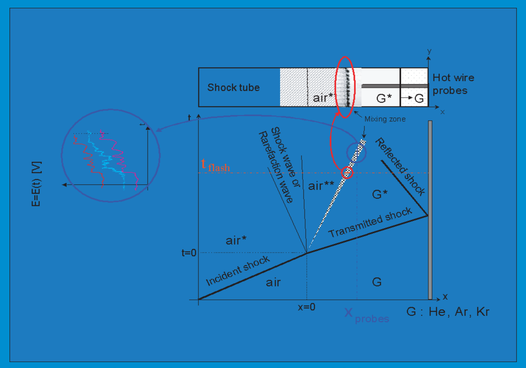

Principle Heat transfer from the heated wire to the gaseous flow which depends on both the properties of the gas (µ, λ) and the parameters of the flow (U, T, ρ)

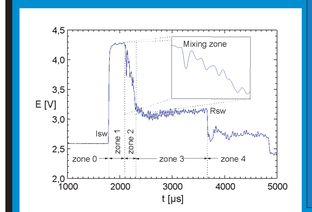

✔ *Infinitely long wire:*

$$\frac{R_W}{(R_1+R_L+R_W)^2}\frac{E^2}{T_W-T}\frac{1}{\lambda}=[0{,}42\,\pi\,Pr^{0{,}2}]+[0{,}57\,\pi\,Pr^{0{,}33}]\left(\frac{\rho U d}{\mu}\right)^{0{,}5}$$

$$E=f(T,\rho,U,\lambda,\mu)$$

E depends on both the electrical bridge data (known) and the instantaneous variations of the flow parameters

✔ *Finite length wire:*

$$\frac{R_W}{(R_1+R_L+R_W)^2}\frac{E^2}{T_W-T}\frac{1}{\lambda}=A'+B'\left(\frac{\rho U d}{\mu}\right)^{n'}$$

A', B' and n obtained by calibration

Q_{cond}

Hypothesis: constant temperature within the mixing

➡ E=f(x,U,A,B,n)

Two ways of calibration :
- graphical method (in pure and pre-mixed gases)
- direct method (A, B and n determined for each run)

➡ E=f(x,U)
- resolution of the system (inverse method)

IV- INITIAL CONDITIONS

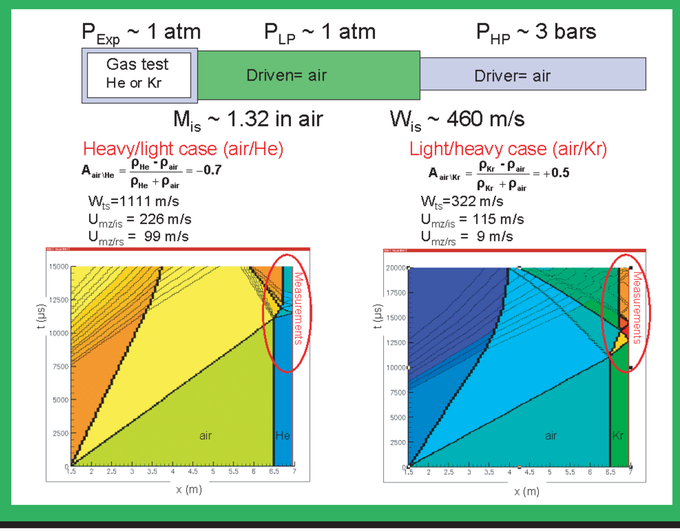

V- RESULTS

Optimal conditions

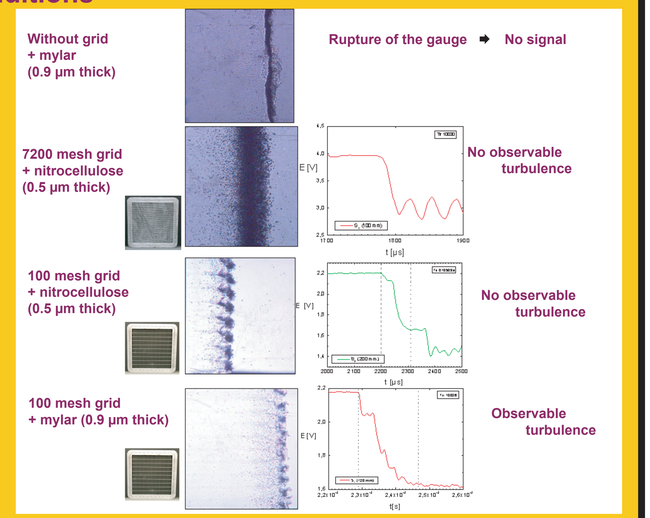

Species molar fraction and velocity profiles

Heavy/light case air/He

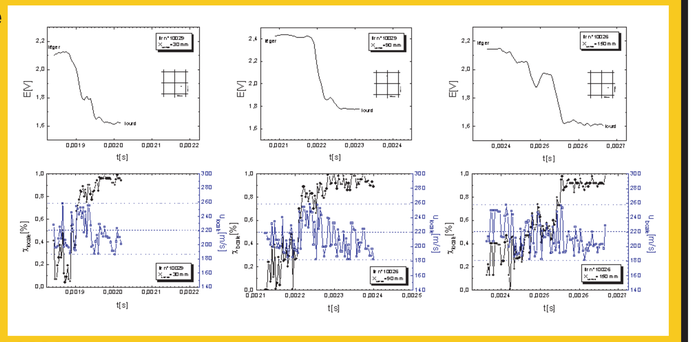

Light/heavy case air/Kr

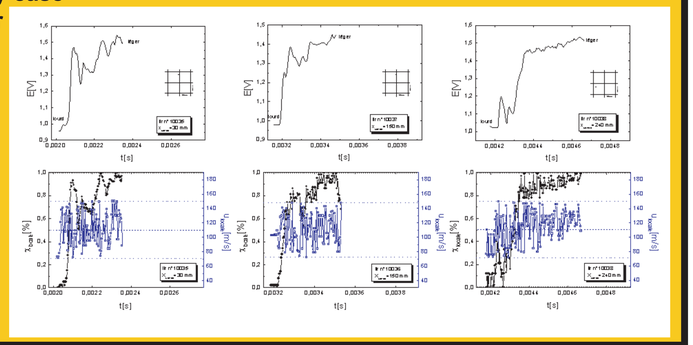

VI- CONCLUSION

- First exploitation of the constant temperature hot wire anemometry for the study of a turbulent mixing induced by Richtmyer-Meshkov instability in shock tube.
- Special experimental conditions have permitted the hypothesis of constant temperature within the mixing.
- Suitable calibration and signal data processes have allowed to determine the local species molar fraction and velocity within the mixing zone.

Paper at the VIII International Workshop on Physics of Compressible Turbulent Mixing
Technological Institute, Pasadena, California, USA

EXPERIMENTAL INVESTIGATION INTO THE SELF-SIMILAR MODE OF MIXING OF DIFFERENT DENSITY GASES IN THE EARTH`S GRAVITATIONAL FIELD

Yu.A.Kucherenko, O.E.Shestachenko, Yu.A.Piskunov, E.V.Sviridov, V.M.Medvedev, A.I.Baishev

Russian Federal Nuclear Center – Academician E. I. Zababakhin
All-Russian Research Institute of Technical Physics
456770 Snezhinsk, Russia

Abstract

At the installation OSA the experiments on the investigation of the self-similar mixing of different density gases in the Earth's gravitational field have been performed. At the same time, the light gas was found under the heavy one, and the gases were separated by a specter-diaphragm. At some instant of time the specter-diaphragm was ruptures into small-scale fragments by the external force. At the formed contact boundary of two different density gases the Rayleigh-Taylor instability and the unstationary zone of turbulent mixing evolved. For three values of Atwood number the experiments were performed. In the experiments the mixing front trajectories in the light gas and the heavy one were recorded. According to the results of experiments the mixing asymmetry coefficient and the constant α defining the nondimensional rate of mixing have been determined.

1. Introduction

In many gasdynamic phenomena such situations are widely met when a heavy medium accelerates the light one and vice versa. Depending on the acceleration profile and direction, at the contact boundary the Rayleigh-Taylor or Richtmyer-Meshkov instabilities can arise. At the same time, at the contact boundary of two different density media the unstationary mixing zone arises. The given work is devoted to the investigation of the self-similar mode of different density gases in the Earth's gravitational field.

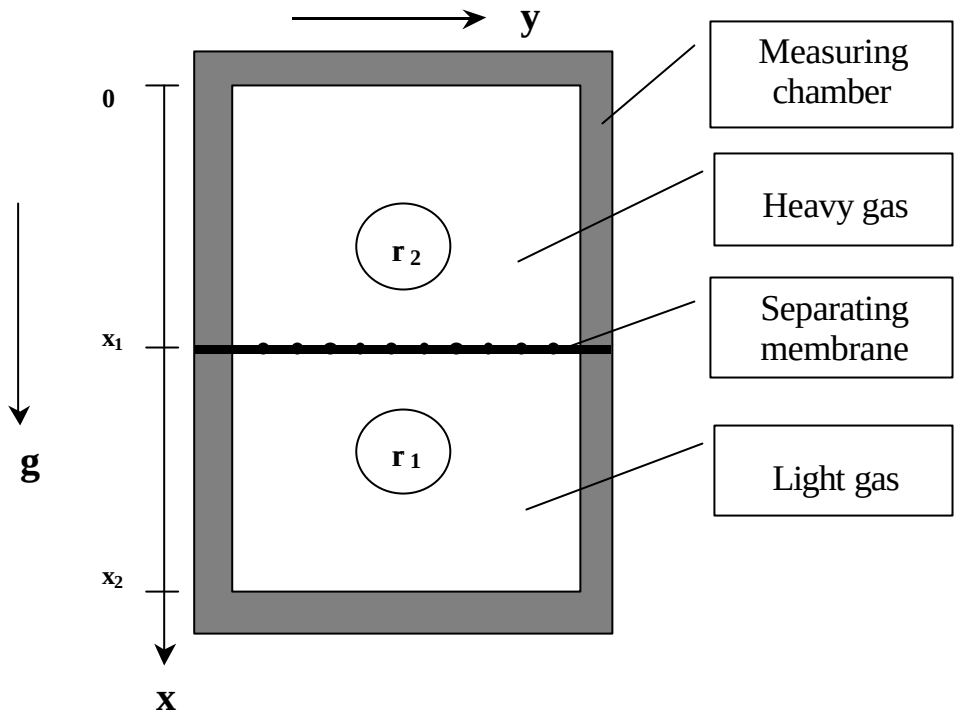

Fig.1 Physical scheme to perform an experiment measuring chamber

The physical scheme of experiments is shown in Fig.1. In the region $0 < x < x_1$ there is gas 2 of density ρ_2, and in region $x_1 < x < x_2$ there is gas 1 of density ρ_1. In the point $x = x_1$ a separating membrane is placed which prevents from mixing of working gases during the experiment preparation. At the specified instant of time the separating membrane is ruptured into fragments of definite size under the action of the external force, and different density gases begin to interact between themselves. In so far as the heavy gas ρ_2 is found under light gas ρ_1 and the Earth's gravitational acceleration is directed from the heavy gas to the light one, then at the contact boundary the Rayleigh-Taylor instabilities arises. The process of the gravitational turbulent mixing zone evolution is visualized by means of schlieren-technique and is recorded on the photographic film.

2. Set-up of experiment

In Fig.2 the functional scheme to perform experiments is shown. The gases being investigated were located in the measuring chamber with transparent walls and the internal cross-section equal to 138 x 138 mm^2. The gases are separated by the separating membrane to prevent from the interaction between themselves at the stage of the experiment preparation.

Filling up with gases was carried out by means of the gas filling system, which supported the pressure drop $\Delta P < 10$ Pa on both sides of the separating membrane. This is necessary to provide the conservation of the separating membrane, which withstands the limiting pressure drop $\Delta P \approx 40$ Pa.

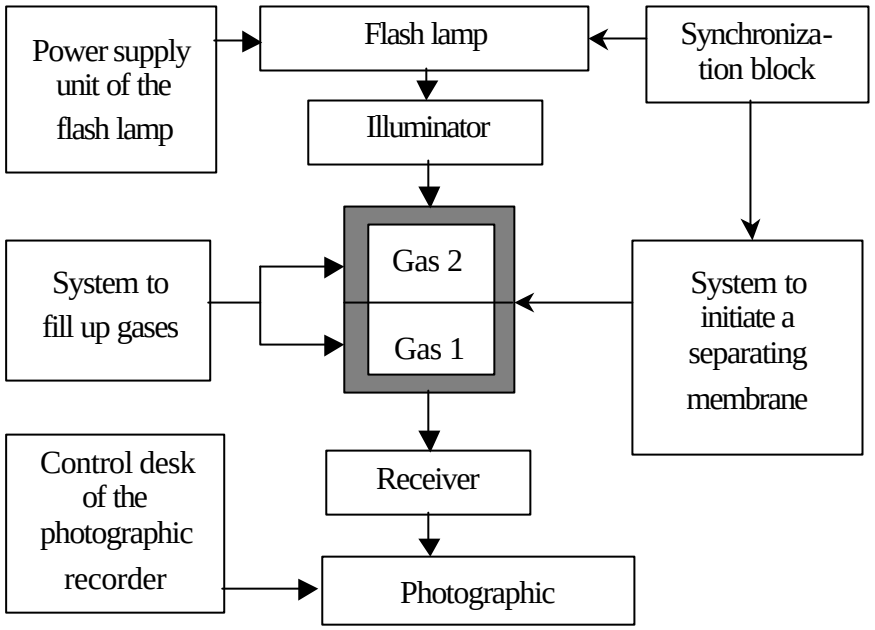

Fig 2 Functional scheme of experiments

At instant of time t= 0 an electrical pulse is applied to the grid of microconductors from the capacitor bank which is the part of the initiation system of the separating membrane (capacitor bank capacity C = 0.25 μF, voltage U = 12 kV). At the same instant of time, the flash lamp begins to operate in a stroboscopic mode illuminating the measuring chamber. Optical nonuniformities are visualized by means of the light and shade device IAB – 451. The turbulent mixing process evolution is recorded on the photographic film by means of a drum-type photographic recorder.

The distinctive features of the given scheme to perform experiments are:

- Constancy of acceleration at the contact boundary of gases. In the other experiments on gases the contact boundary acceleration is quasi-constant.
- Absence of gases compression and the gravitational turbulent mixing zone during the whole experiment. This makes possible to perform the unambiguous interpretation of the turbulent mixing zone width.
- Constancy of Atwood number on the contact boundary of gases during the whole experiment even for gases with different adiabatic indices.

- Absence of parietal flows, because the turbulent mixing zone, upon the whole, does not move relative to the measuring chamber walls.
- Absence of the turbulent mixing zone motion as the whole. This makes possible to determine the asymmetry coefficient of the gravitational turbulent mixing for gases.

Real gases are possessed of viscosity and in order that this parameter does not exert any influence on the mixing process, it is necessary to satisfy the condition $g1 >> v^2 \cdot L^{-3}$, where g_1 – contact boundary acceleration, v – viscosity, L – turbulent mixing zone width. For such a gas as helium $v \sim 10^{-4}$ m^2/s, and if measurements are made at L > 5 mm, then for the realization of the above shown inequality it would be sufficient to reach

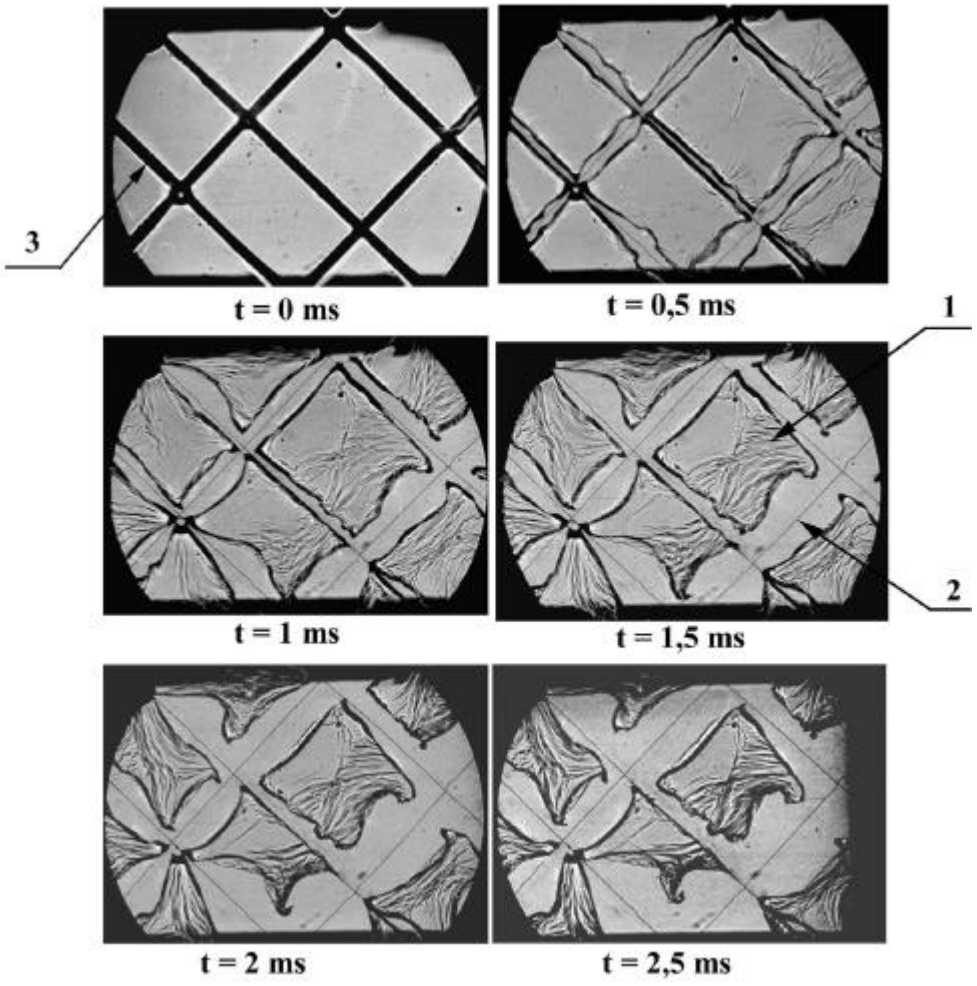

Fig.3 Characteristic photographic images of the rupture process of the liquid film.

$g_1 >> 0.09$ m/s^2. For heavier gases (air, argon, krypton) the shown inequality is satisfied at L > 1 mm and $g_1 >> 0.18$ m/s^2. Thus, viscosity of gases does not exert any influence on the gravitational turbulent mixing zone evolution at the contact boundary acceleration $g_1 = g_0$.

The separating membrane represents an interlaced grid of microconductors, 20 μm in diameter, with a 4 mm spacing. The liquid film of soap solution is applied on this grid. The film thickness is ~ 1 μm. At the specified instant of time the electric current is conducted through the grid. Microconductors get warm and the liquid film begins to be ruptured in the places of contact with microconductors. Then the surface tension forces

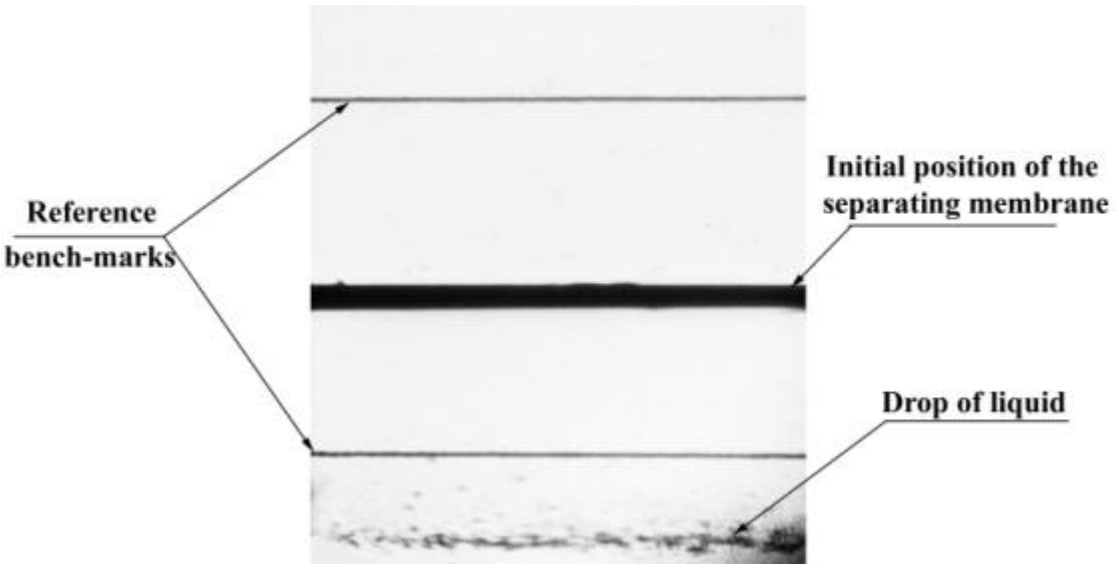

Fig.4 Characteristic photographic images of the separating membrane residues motion.

pull together the liquid film pieces into small balls which under the action of the Earth's gravitational field begins to fall down and do not take part subsequently in the turbulent mixing process.

Fig.3 shows the characteristic photographic images of the rupture process of the separating membrane for different instants of time. Microconductors are denoted by number 1, liquid film pieces – by number 2, a microconductor with a liquid film around it – by number 3. From the figure it is seen that after applying the electric current pulses to the grid the liquid film begins to be separated from the microconductor and then, under the action of surface tension forces, it is tightened into a drop.

The characteristic photographic images of the separating membrane residues (liquid drops) are shown in Fig. 4. It is seen that the drops of liquid fly in the form of a plane being parallel to that of the separating membrane. Hence, it is possible to conclude that the separating membrane rupture takes place simultaneously all over the plane.

3. Discussion of results

In the given work three groups of experiments were performed with different working gases: helium He (density ρ = 0.178 kg/m^3), argon Ar (density ρ = 1.78 kg/m^3), SF_6 gas (density ρ = 6.0 kg/m^3), krypton Kr (density ρ = 3.74 kg/m^3). In each group eight experiments have been carried out. The relation of densities and Atwood numbers for different groups are shown in Table.

Group number	Pair of gases	Relation of densities	Atwood number
1	**SF_6 – Ar**	**3,37**	**0,54**
2	**SF_6 - He**	**33,7**	**0,94**
3	**Kr - Ar**	**2,1**	**0,35**

Fig. 5 shows the characteristic photographic images of the gravitational turbulent mixing process in the Earth's gravitational field. Heavy gas is denoted by number **1**, light gas – by number **2**. Time t is counted off since the moment of applying the current pulse to the grid of

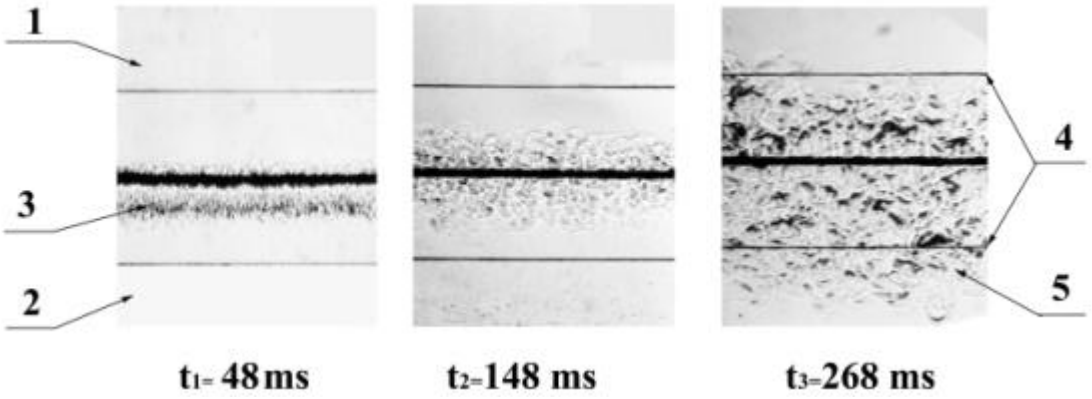

Fig. 5. The characteristic photographic images of the turbulent mixing process.

microconductors. At the first photo a number of drops **3** can be seen which fall down under the action of gravitational forces. At the following two photos the growth of the turbulent mixing zone **5** is seen. For the accurate determination of the scale and the coordinates of the mixing front the reference bench-marks **4** are set before the measuring chamber glasses.

Fig. 6a, 6b and 6c show dependencies of the mixing front coordinate of the light gas into the heavy one on the parameter S. The parameter $S = gt^2/2$, where g is acceleration of the Earth's gravitational field and t is time since the moment of the separating membrane rupture.

From the presented plots it can be seen that beginning from some value of the parameter S the mixing front coordinate L_{12} is growing according to the linear law $L_{12} = 2\alpha A S$, where A is Atwood number and α is constant which determines the nondimensional rate of mixing. If all the experimental points for all three groups of experiments are processed as a single set, then it is possible to obtain the value of α equal to 0.078.

According to the results of experiments the mixing asymmetry coefficient $k = L_{21}/L_{12}$. For different values of the parameter S the asymmetry coefficient is changed from 1.1 to 1.7.

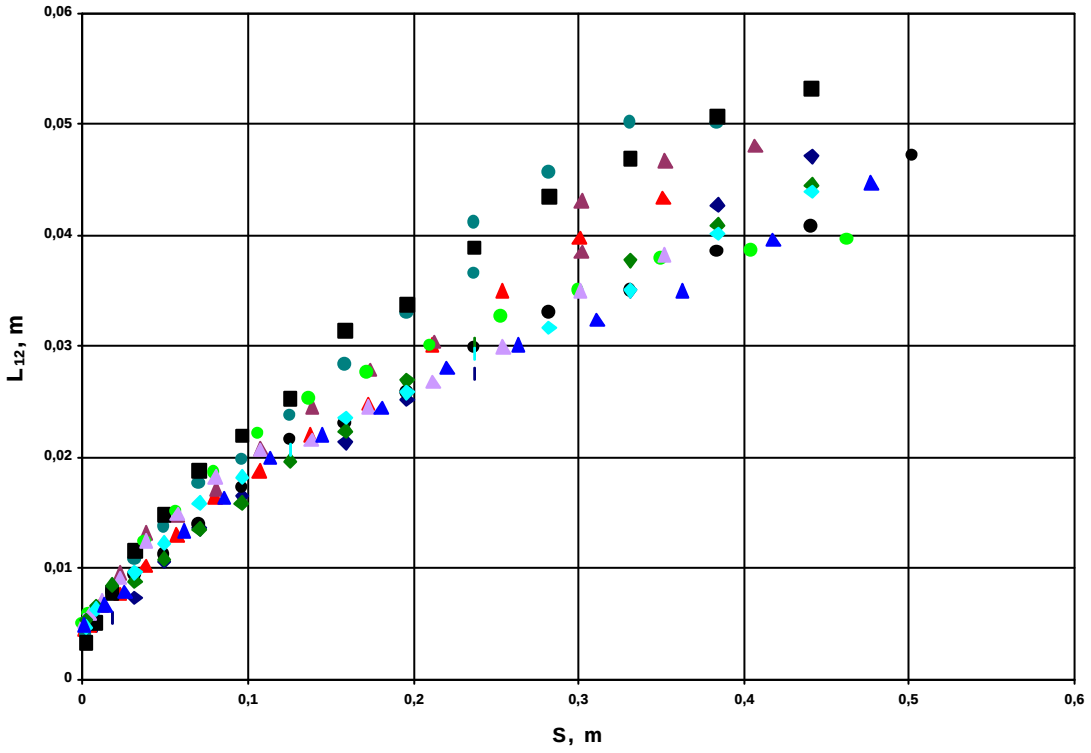

Fig. 6a Dependence of the mixing front coordinate L_{12} on the parameter S for the first group of experiments (SF_6 – Ar).

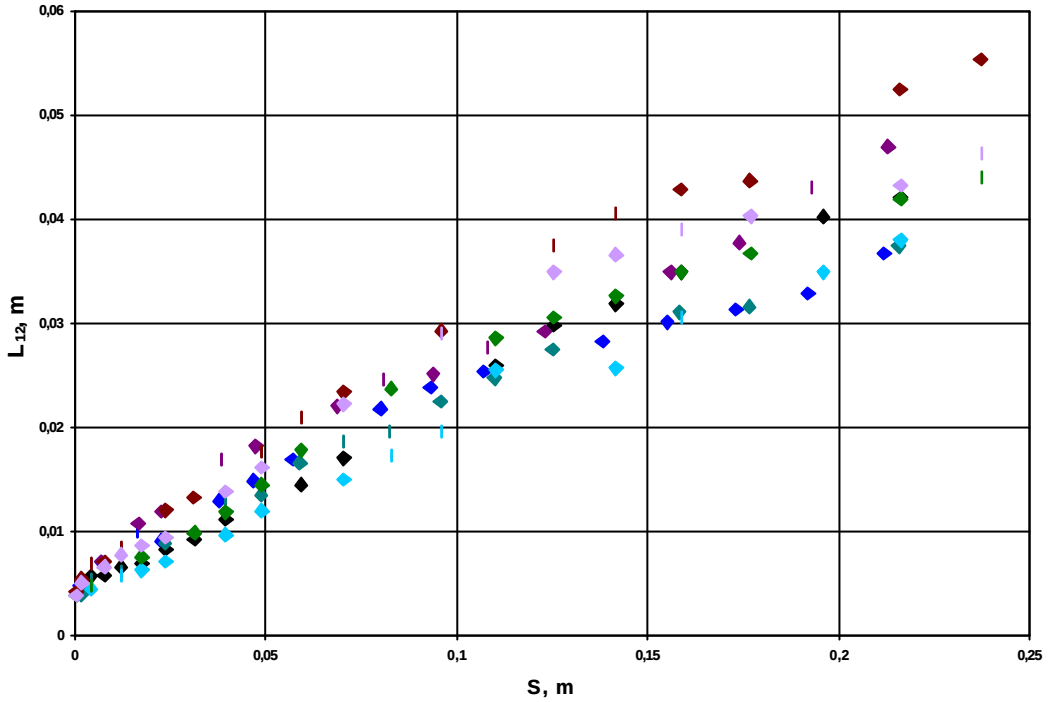

Fig. 6b Dependence of the mixing front coordinate L_{12} on the parameter S for the second group of experiments (SF_6 - He).

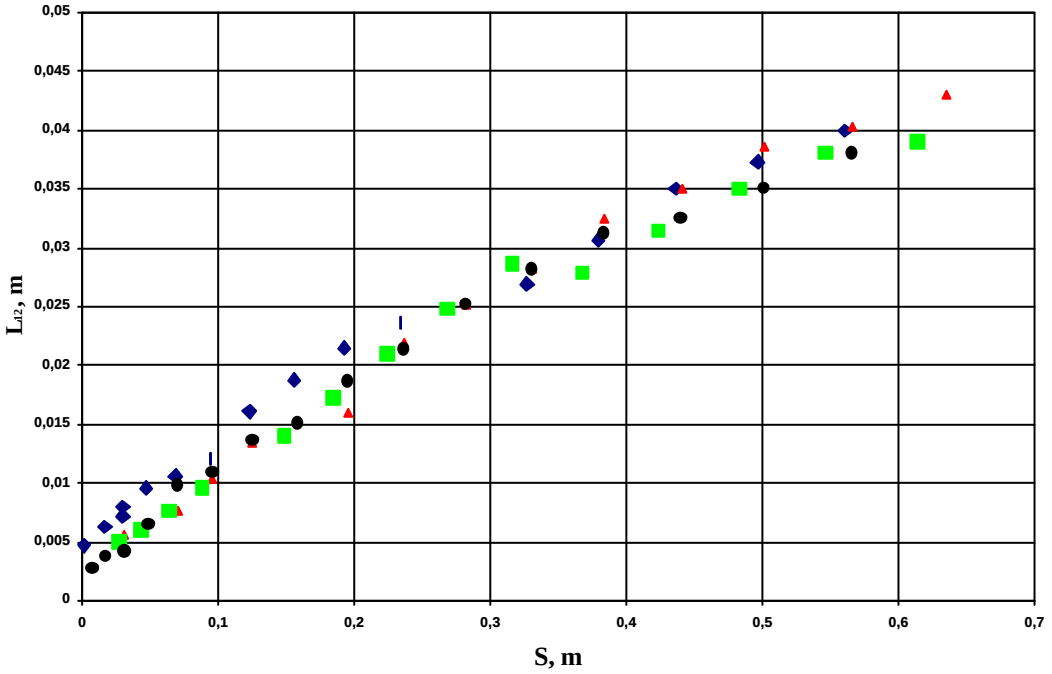

Fig. 6c Dependence of the mixing front coordinate L_{12} on the parameter S for the third group of experiments (Kr – Ar).

Conclusion

At the installation OSA the experiments have been performed with respect to the investigation of the self-similar mixing of different density gases in the Earth's gravitational field. In these experiments the controlled separating membrane of a new type with a liquid film was used. This separating membrane made it possible to carry out experiments with gases at the acceleration of the contact boundary $g_1 = g_0$. The distinctive feature of a new membrane is its low density. At the specified instant of time the membrane was ruptured under the external force action into pieces whose characteristic size $\delta \approx 4$ mm. At the contact boundary the gravitational turbulent mixing zone growing with time was formed.

Three groups of experiments with different working gases have been performed. The density ratio and Atwood numbers for different groups of experiments are shown in Table.

Group number	Pair of gases	Density ratio	Atwood number
1	**SF_6 – Ar**	**3,37**	**0,54**
2	**SF_6 - He**	**33,7**	**0,94**
3	**Kr - Ar**	**2,1**	**0,35**

According to the results of experiments, the mixing asymmetry coefficient $k = 1.1 \div 1.7$ (for different values of the parameters S) and constant $\alpha = 0.078$ defining the nondimensional rate of mixing were determined.

Shock Tube Experiments on Richtmyer-Meshkov Instability across a Chevron Profiled Interface

A V Smith, D A Holder, C J Barton, A P Morris
D L Youngs

AWE, Aldermaston, Reading, Berkshire, RG7 4PR, UK

© Crown Copyright 2000
This document is of United Kingdom origin and contains proprietary information which is the property of the Secretary of State for Defence. It is furnished in confidence and may not be copied, used or disclosed in whole or in part without prior written consent of the Director Commercial 2, Defence Procurement Agency, Ash 1b #3110, MoD Abbey Wood, Bristol. BS34 8JH England.

Content

- Show experimental mix results from a chevron interface perturbation
  - comparable to numerical test problem #1 and
  - similar to experiments of Meshkov et al (5th IWPCTM)
- Compare these to 3D code results
- Illustrate the potential benefits of Intensified CCD imaging to overcome Multiple Scattering
- Future work
- Video of results

Perturbation

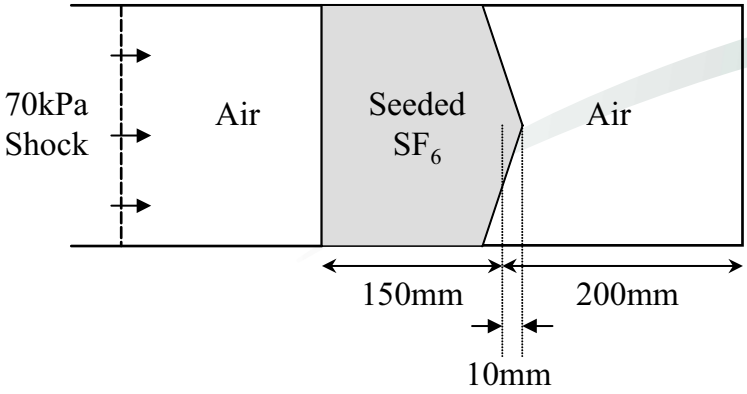

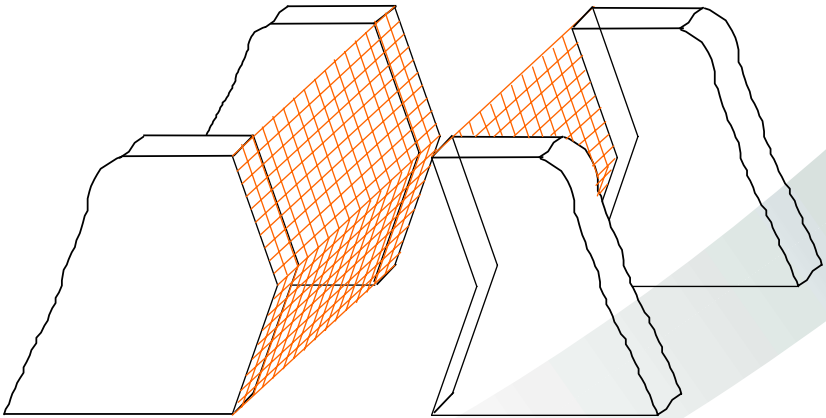

Seeded SF_6 region constrained with microfilm membranes supported on wire meshes.

Meshes on both interfaces are made from horizontal and vertical 25∞m wires with 4mm spacing.

the total flow blockage is 1.25%

Perturbation (cont.)

The chevron was conceived as a progression from the work of Meshkov et al and Test Problem #1.

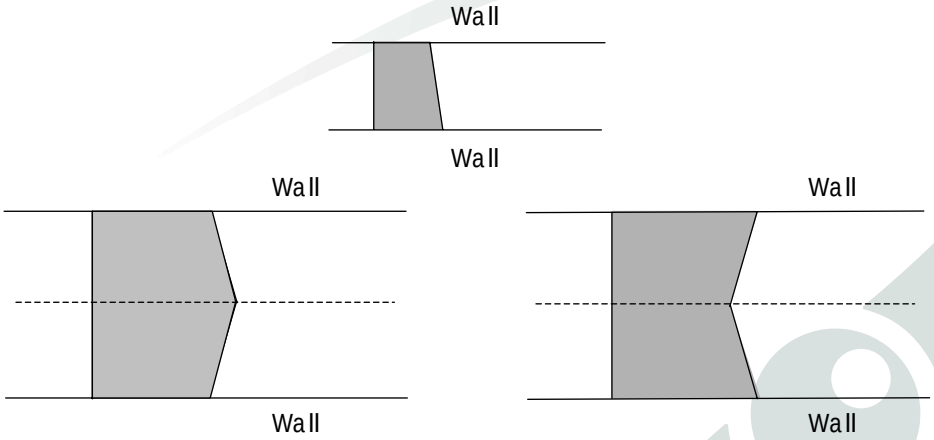

Presented Future Work

The chevron takes advantage of a larger shock tube to eliminate any possible constraining effect of one wall and also to investigate boundary layer effects.

The two chevron experiments will together complement the previous work

200 x 100 mm Shock Tube

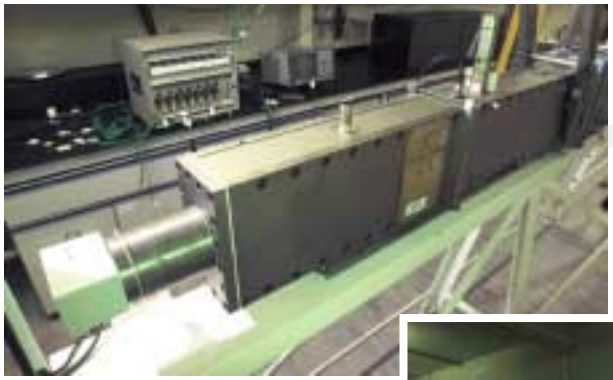

Compression Chamber
Pressurised with Air
to 2 bar

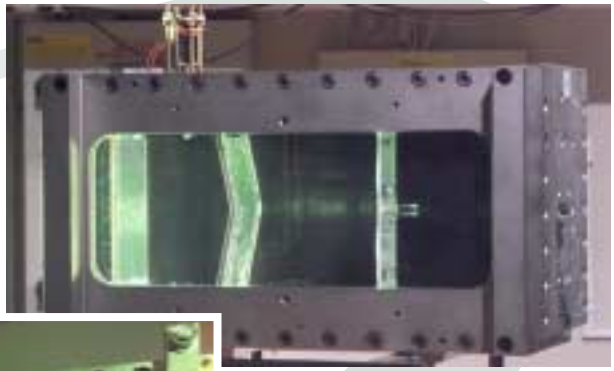

Test Cell
Chevron Interface Profile
SF_6 gives Atwood
Number, A=0.67

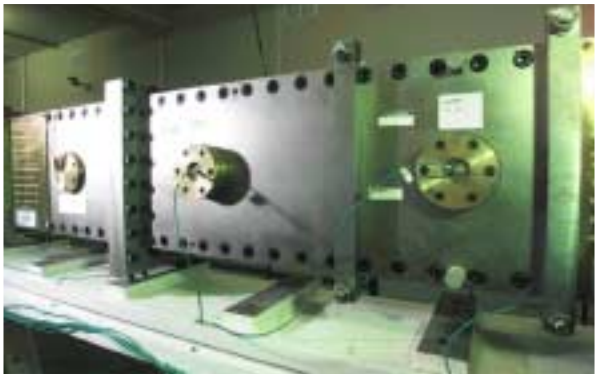

Shock of 70kPa
Overpressure and
7ms Duration

Shock Mach Number
1.26

Pressure Profile

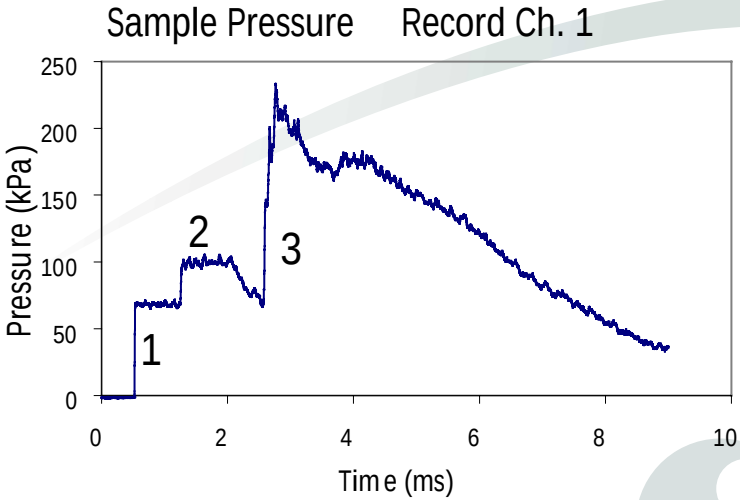

Pressure transducers monitor shock passage and record waveforms. This is a typical waveform from the pressure gauge nearest the test cell.

1. Incident shock
2. First shock reflection from dense gas region
3. First shock reflection from end wall

Laser Sheet Arrangement

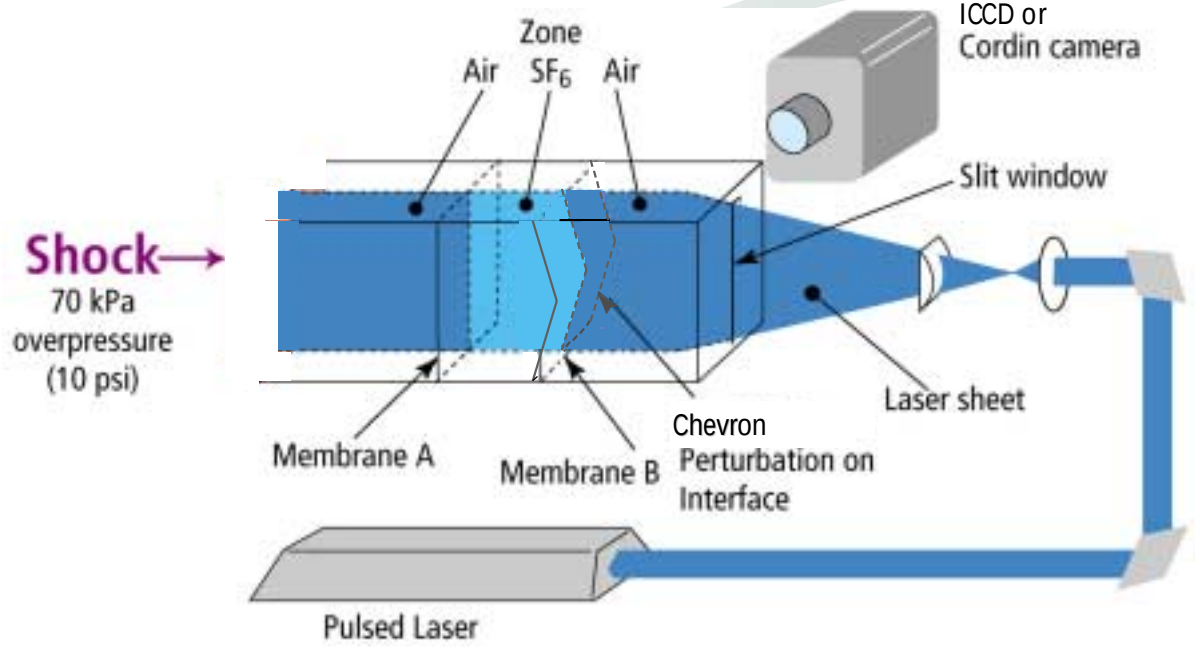

Chevron Experiment

Sequence of selected images from a single experiment

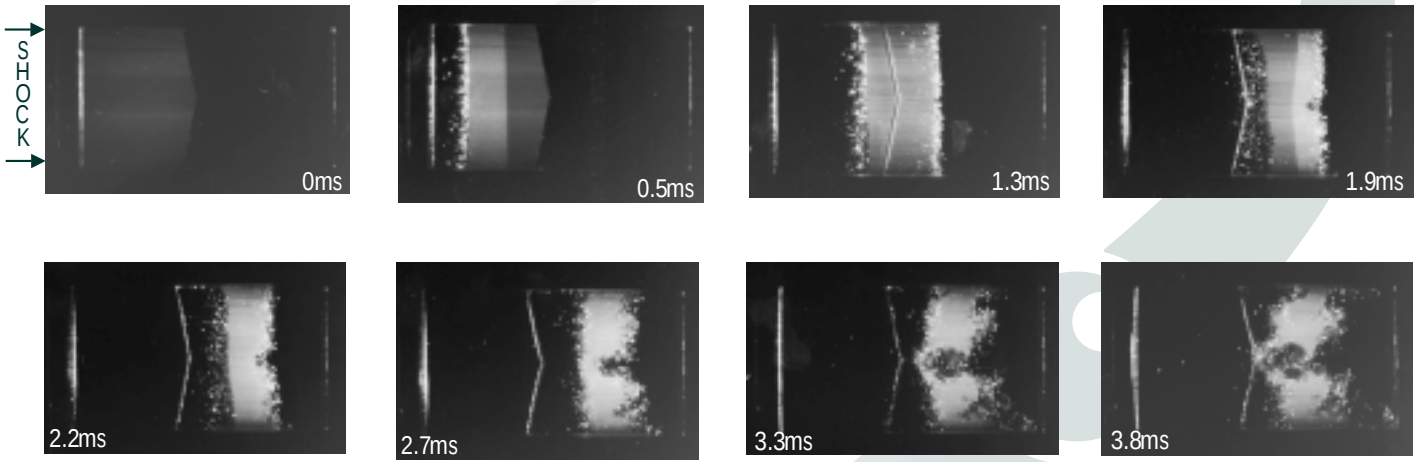

TURMOIL 3D Calculations

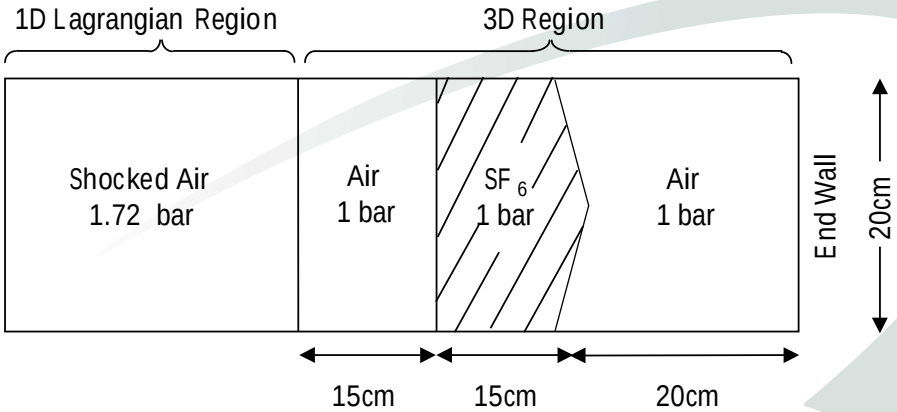

Zoning used in 3D region : 400 x 320 x 160

Semi-Lagrangian calculation : x-direction mesh moves with the mean fluid velocity.

Random initial perturbation at air/SF6 interfaces:

Wavelengths = 0.5 to 5cm

R.M.S. amplitude = 0.01cm

Experiment and Code Comparison (0 - 1.9ms)

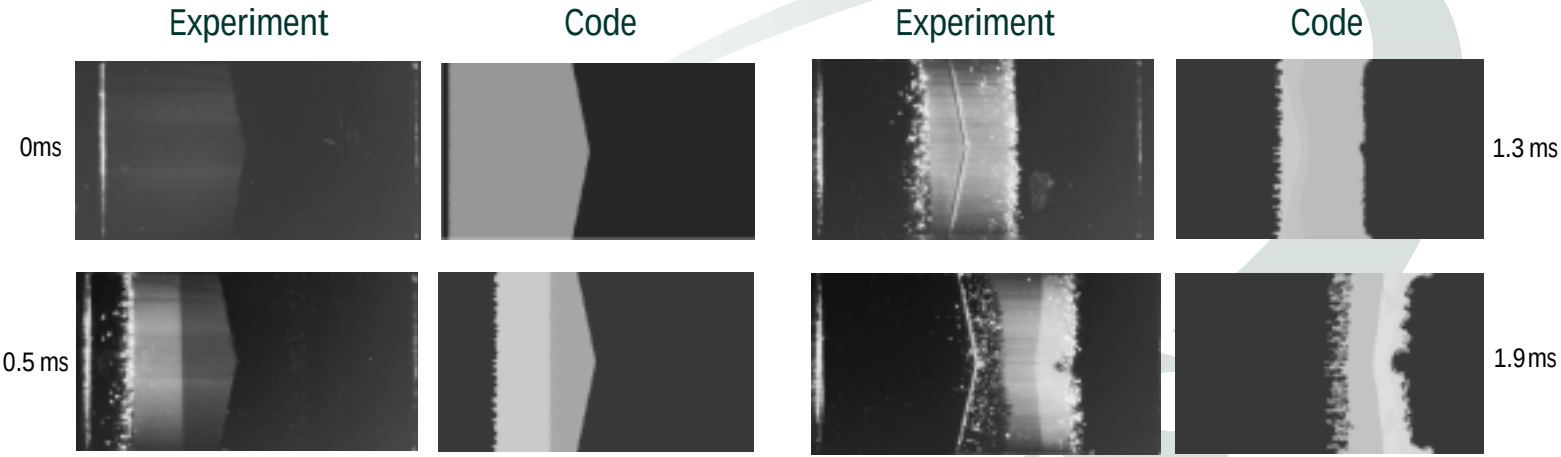

Experiment and Code Comparison (2.2 - 3.8ms)

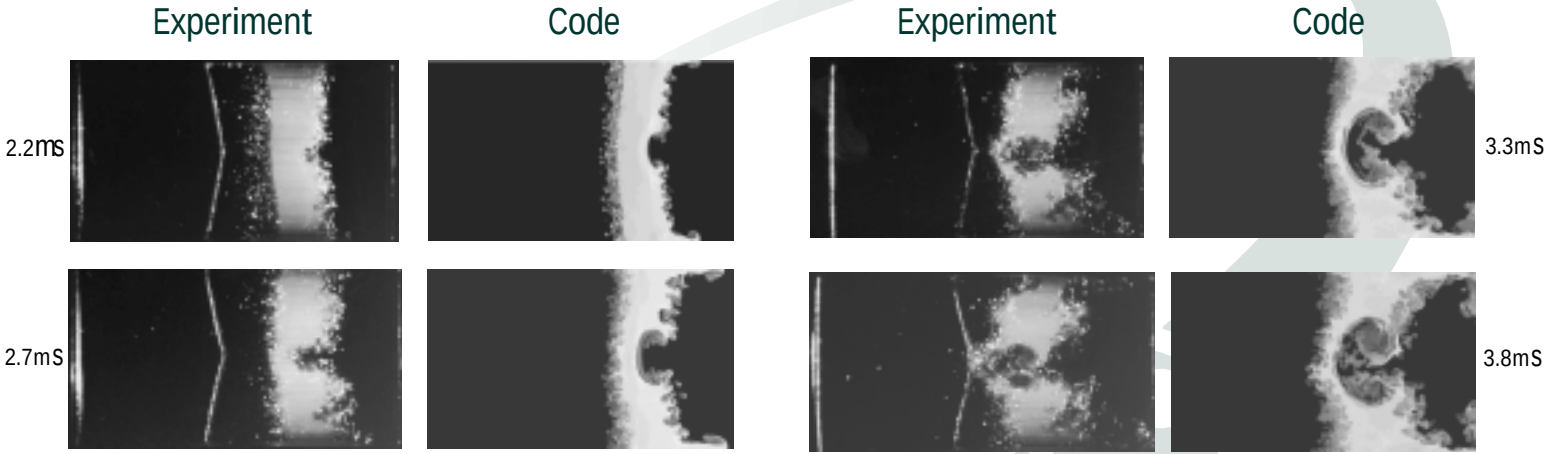

Multiple Scattering

A Monte Carlo multiple scattering simulation has been devised to successfully 'add' multiple scattering to the mix code results.

Ref: Giddings et.al. 7th IWPC TM
Holder et.al. 23rd ISSW

Multiple scattering in experiment

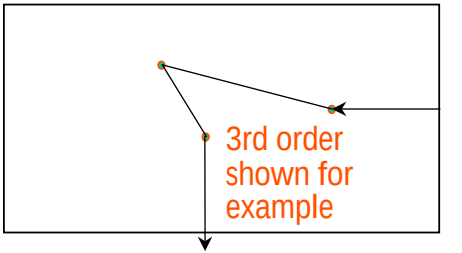

Monte Carlo code simulation

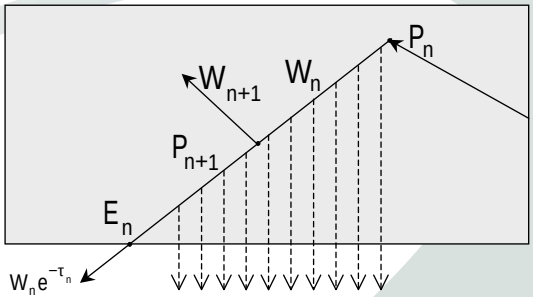

Contributions to scattered image

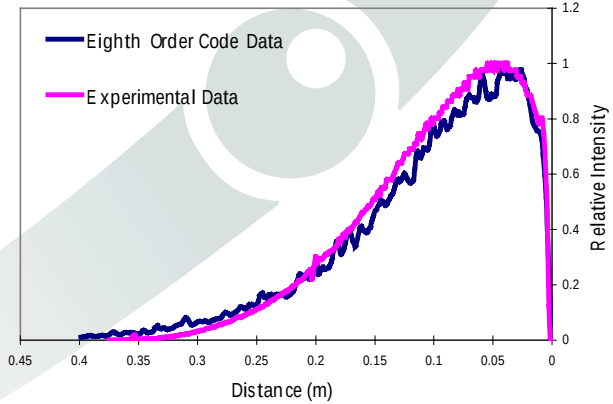

Multiple Scattering Example

Experiment

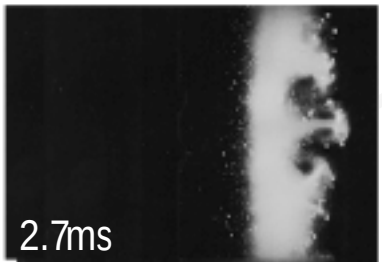

Code

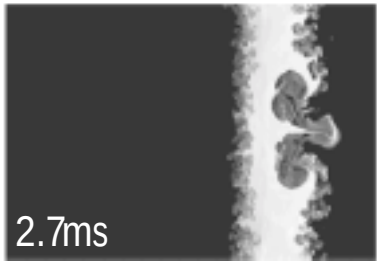

Code + Scattering

These are images from a single time (2.7ms) from a double bump experiment presented to ISSW 23.

These are an experimental image, a plane section through a mix calculation and the same calculation with the Monte Carlo simulation applied.

The Monte Carlo scattering code greatly improves qualitative comparison between experiment and code results.

Wall Effects

Code results at 2.2 and 3.3 ms

Spikes of dense gas are seen to advance along the top and bottom.

Are these due to the Chevron pert urbation, boundary layer interactions, or a combination of both ?

The bubble of air penetrating into the dense gas is not axi-symmetric. Would the presence of a wall, as in numerical Test Problem #1 prevent this occurring?

Conclusions

- Chevron perturbation appears to produce feed-through in the experiments, but not in the code results.
- Acceptable agreement between experiment and code has not yet been achieved. The experiment will have to be repeated.
- Inverse chevron experiment to
  - further investigate boundary layer effects
  - investigate asymmetric effects
- Further use of ICCD imaging and fluorescent seeding
  - allows a reduction in multiple scattering
  - promising for future, allowing quantitative analysis
- Chevron experiments are useful to validate test problem calculations in addition to the work of Meshkov et al..

See next page for **Video of Results**

Code Data

Move cursor over image and click to play

Experimental Data

Move cursor over image and click to play

The evolution and interaction of two shock-accelerated, unstable gas cylinders

Chris Tomkins, Kathy Prestridge,
Paul Rightley, Mark Marr-Lyon,
Robert Benjamin
Summer students: James Doyle and Michael Schneider
Dynamic Experimentation Division, Los Alamos National Laboratory

Peter Vorobieff
Department of Mechanical Engineering, University of New Mexico

Cindy Zoldi
Applied Physics Division, Los Alamos National Laboratory

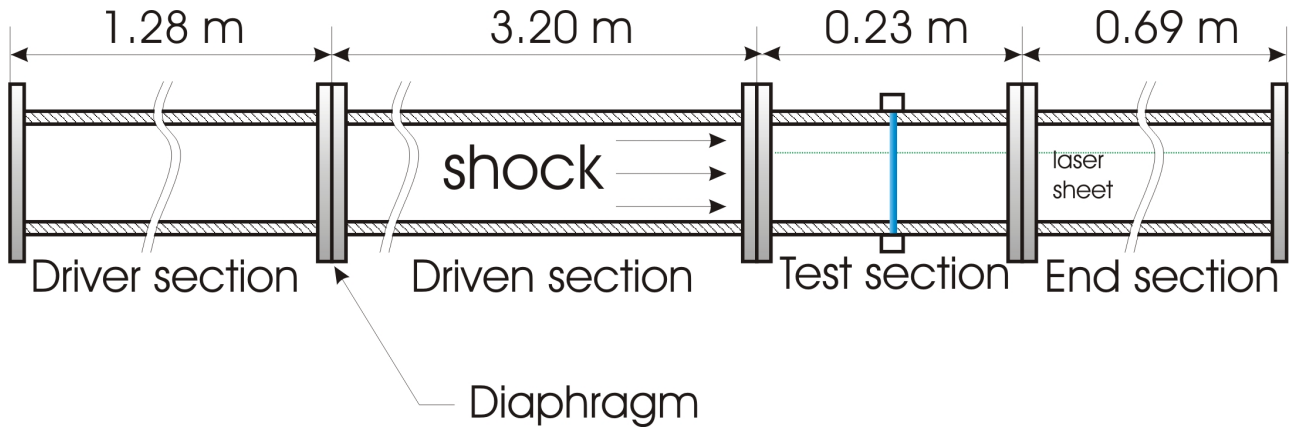

Experimental setup: shock tube

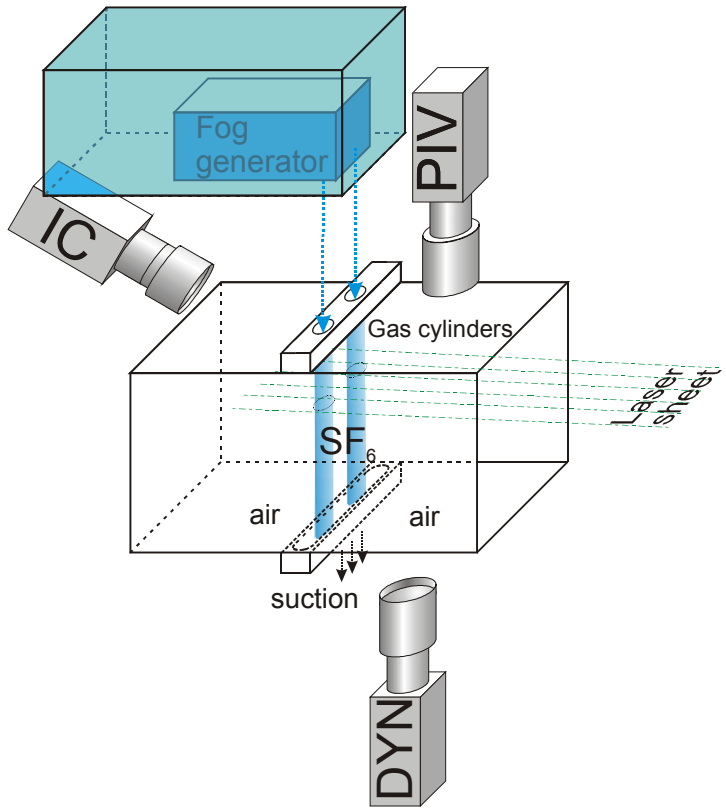

Overview

- Examine interaction of planar shock with 2 gas cylinders, separated spanwise.
- S = 1.2D to 2.0D.
  (D = cylinder diameter)

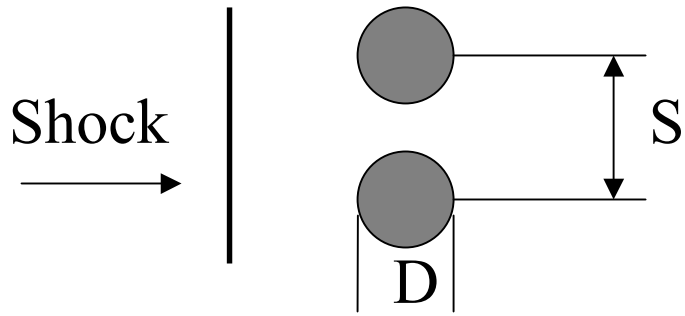

- Goal: Investigate the evolution of the interacting, RM-unstable cylinders. Issues of interest include:
  - What is the effect of the interaction on the resulting flow morphologies? On the initial vorticity deposition? On the post-shock vortex development?
  - How sensitive is the flow evolution to the initial separation S?

Single shock-accelerated cylinder

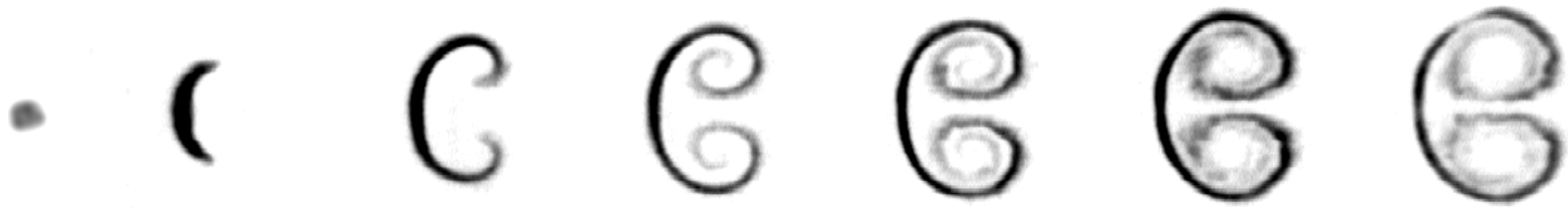

Double-cylinder "vortex blob" simulation

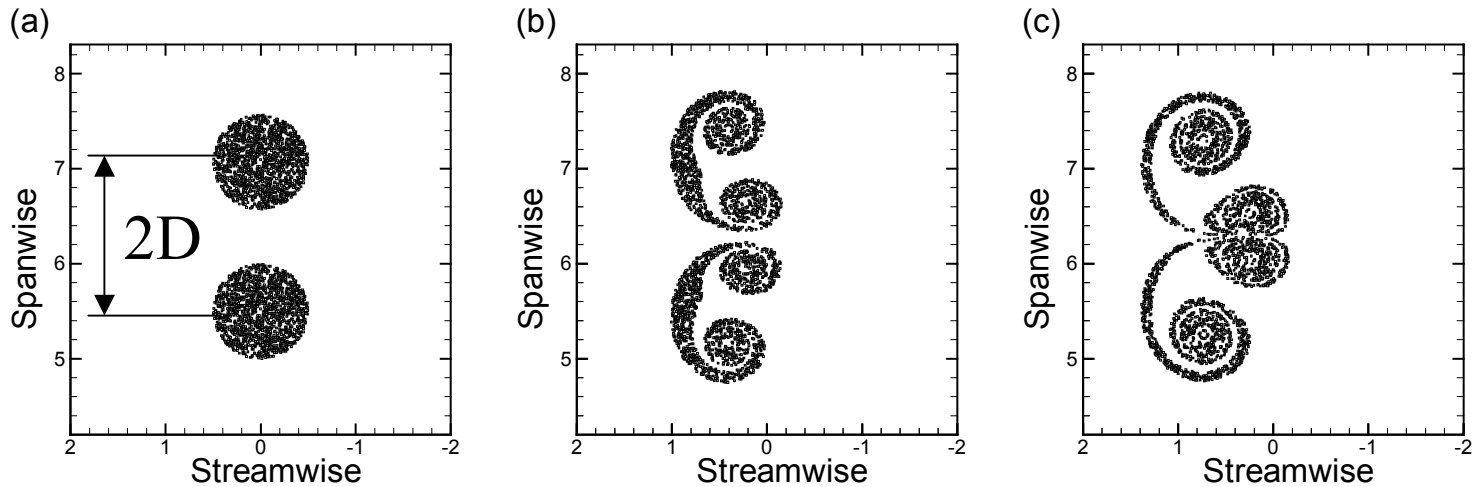

Double-cylinder interaction: weak

S ≈ 2.0D

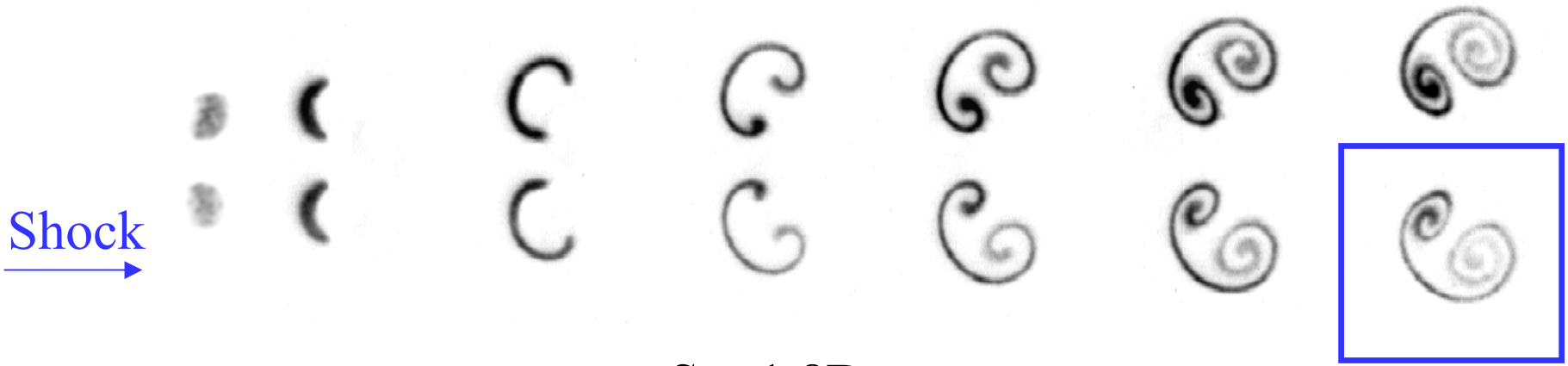

S ≈ 1.8D

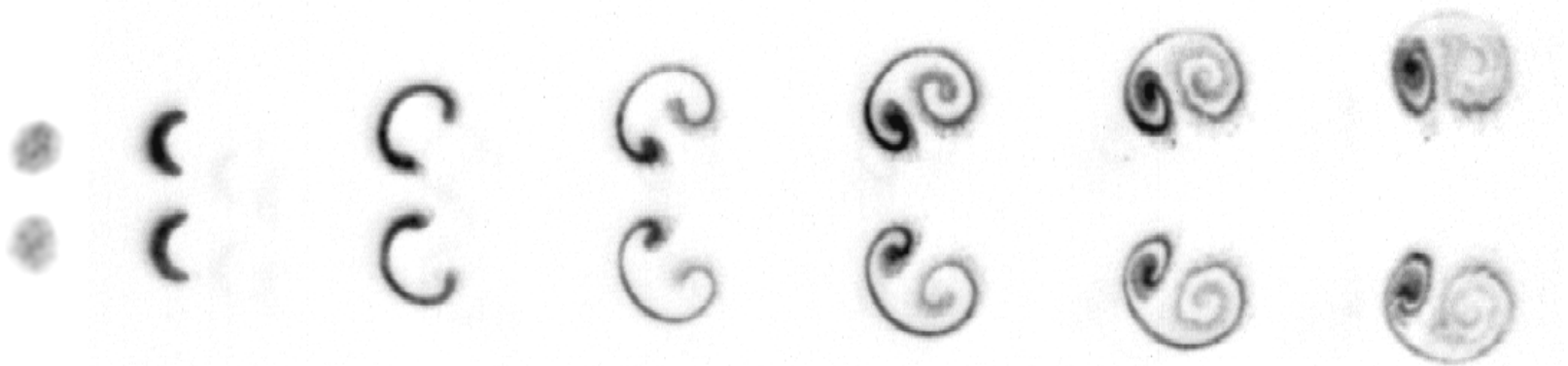

Double-cylinder interaction: moderate

S ≈ 1.6D

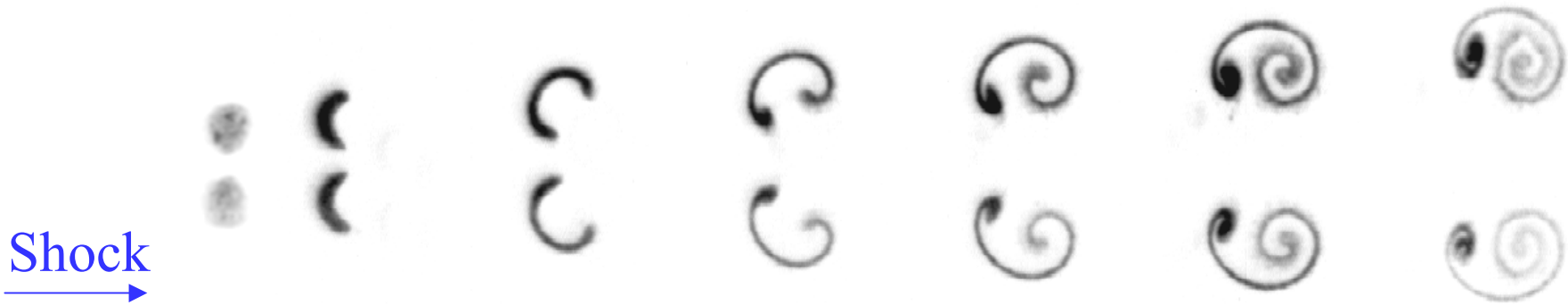

S ≈ 1.5D

Double-cylinder interaction: strong

S ≈ 1.4D

S ≈ 1.2D

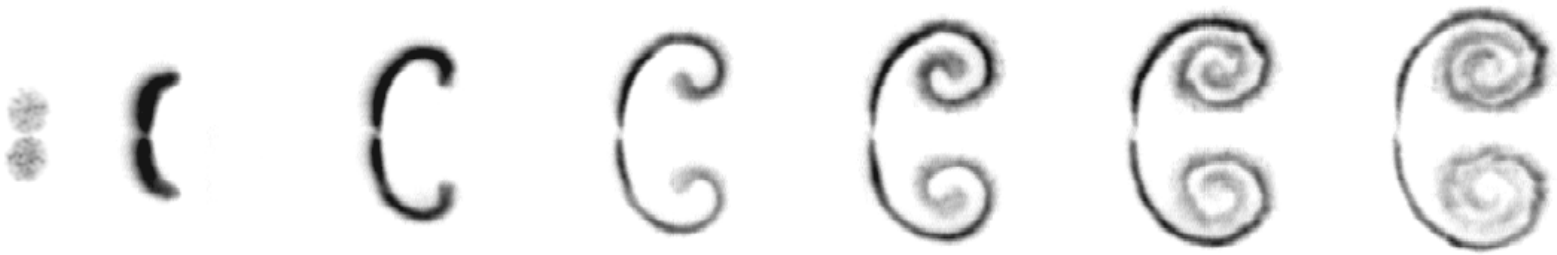

PIV images: double cylinder

- Two-frame cross-correlation, flow left to right, 6th pulse
- S = 2.0D. Note non-uniform seeding.

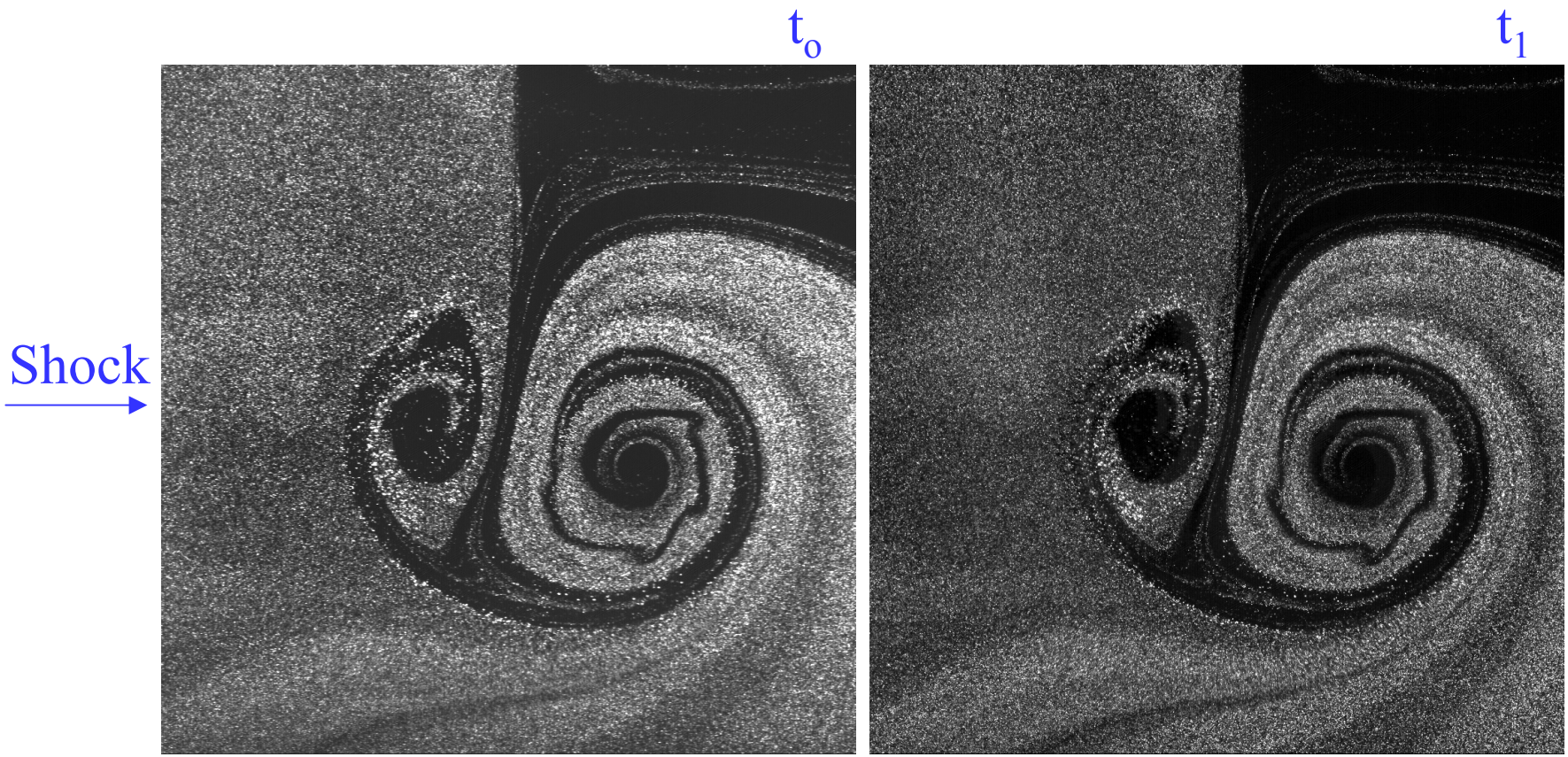

Double-cylinder velocity field: PIV

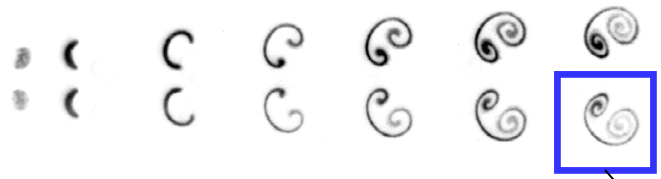

- Double-cylinder data, 6th pulse, S = 2.0D
- Two-frame cross-correlation (Christensen et al., 2000)
- Not smoothed
- Contours are fluctuating velocity magnitude

Shock

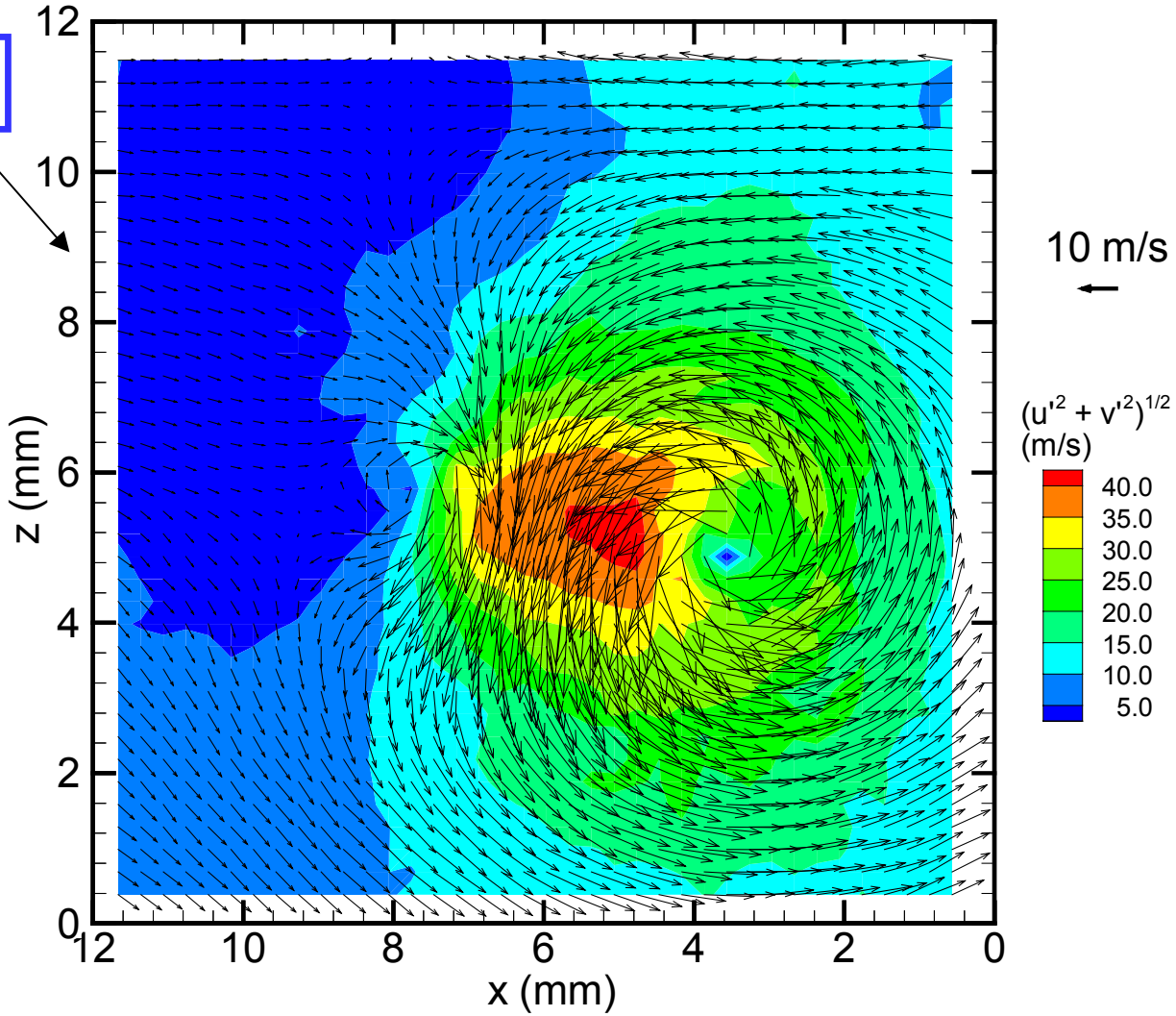

Double-cylinder vorticity field

- Same realization
- Vorticity contours
- Not smoothed

Shock

- And the ratio of circulations is

$$\frac{\Gamma_{outer}}{\Gamma_{inner}} \approx 3$$

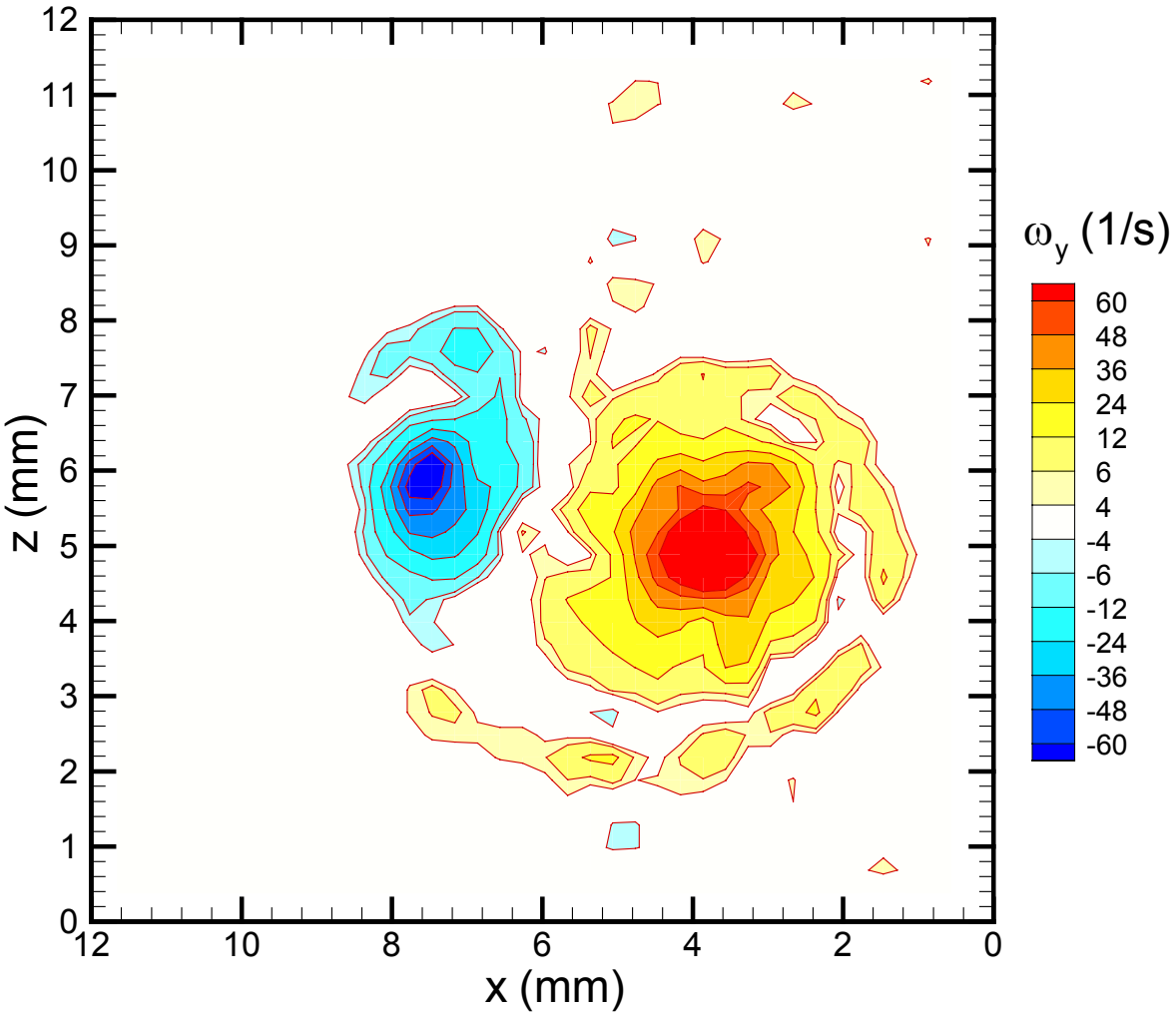

Correlation-based ensemble averaging

Match one image (template) to each individual realization.
Desire optimum match between template
and image, i.e. minimize mean sq. error: $e = \int \left| I(\underline{x}) - I_t(\underline{x} - \underline{x_0}) \right|^2 dA$

This requires maximizing $\int_D I(\mathbf{x}) \bullet I_t(\mathbf{x} - \mathbf{x}_o) dA$ w.r.t. $\mathbf{X}o$

Do for each realization, then extract and average (Soloff, 1997)
Yields cond. avg.: $< I(\mathbf{x} - \mathbf{x}_o) \mid \mathbf{x}_o >$

This avg. becomes the new template.

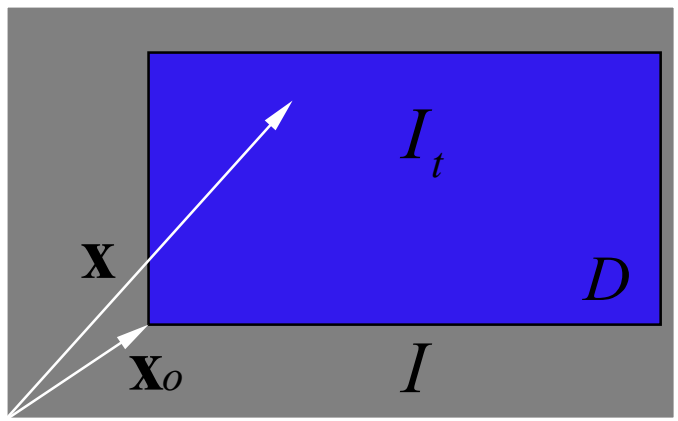

Properties:
-Minimizes dependence on initial choice of template.
-Converges quickly.

Correlation-based ensemble average

S ≈ 1.2D, Ensemble average

Shock

S ≈ 1.2D, Individual realization

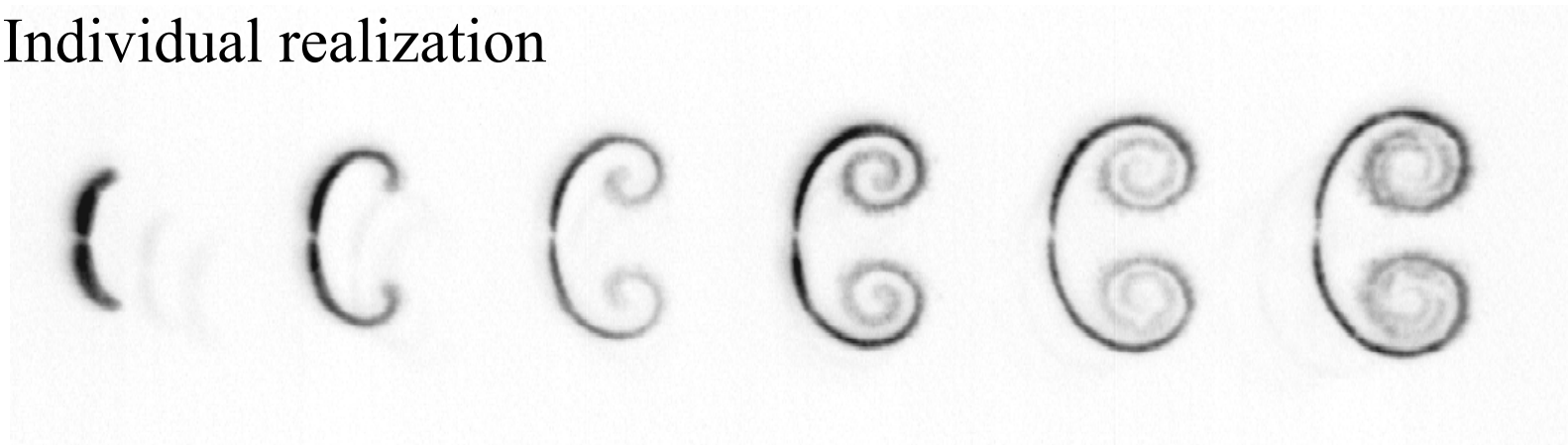

Fluctuating intensity fields, S = 1.2D

$t = 470\,\mu s$

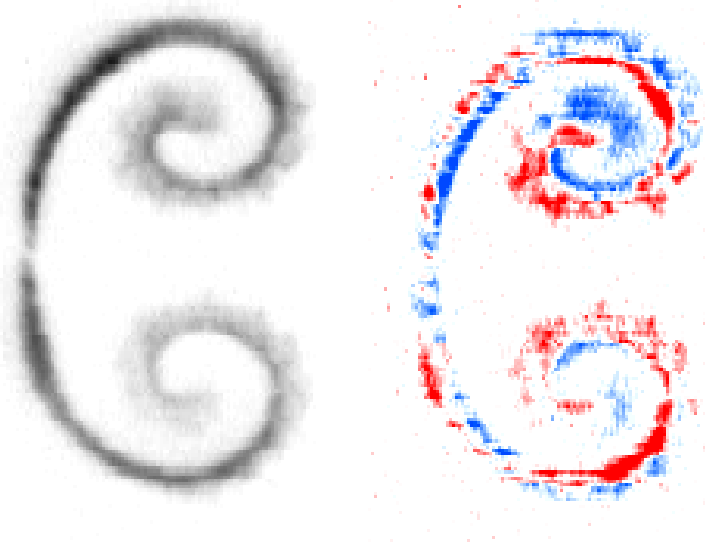

Total Fluctuating

$t = 750\,\mu s$

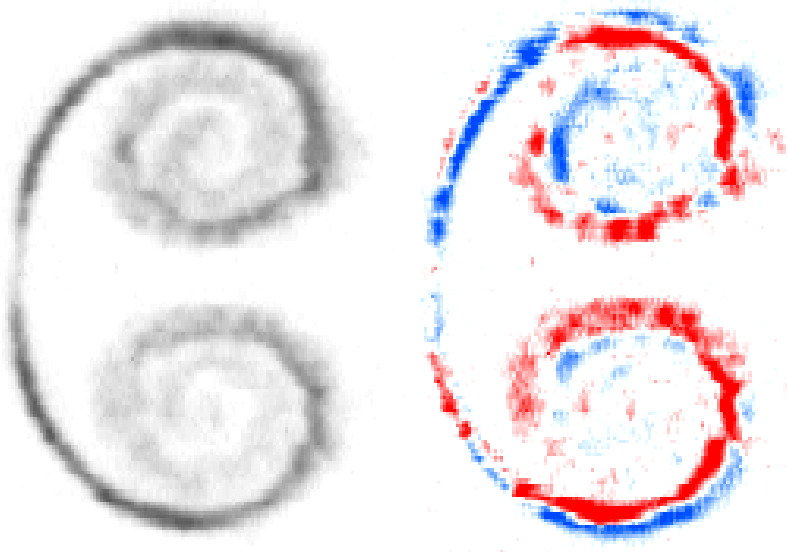

Total Fluctuating

RMS of fluctuating intensity

RMS Intensity vs. Time for several values of S/D.

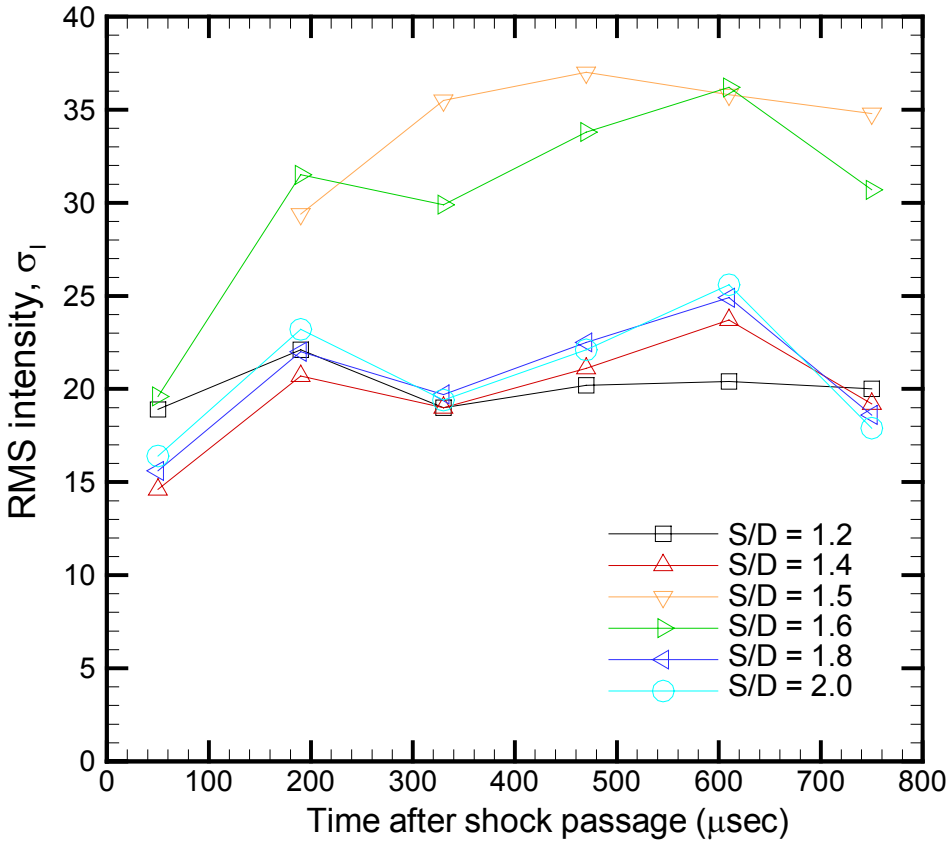

RMS of Initial Conditions

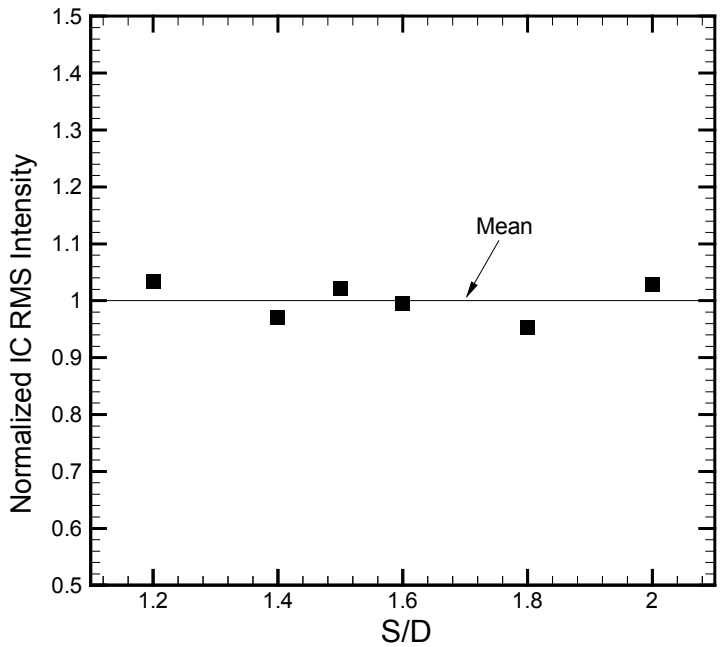

Small-scale activity: single cylinder

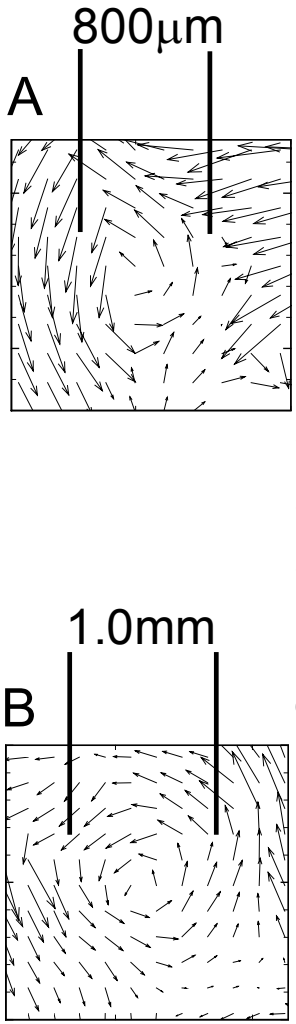

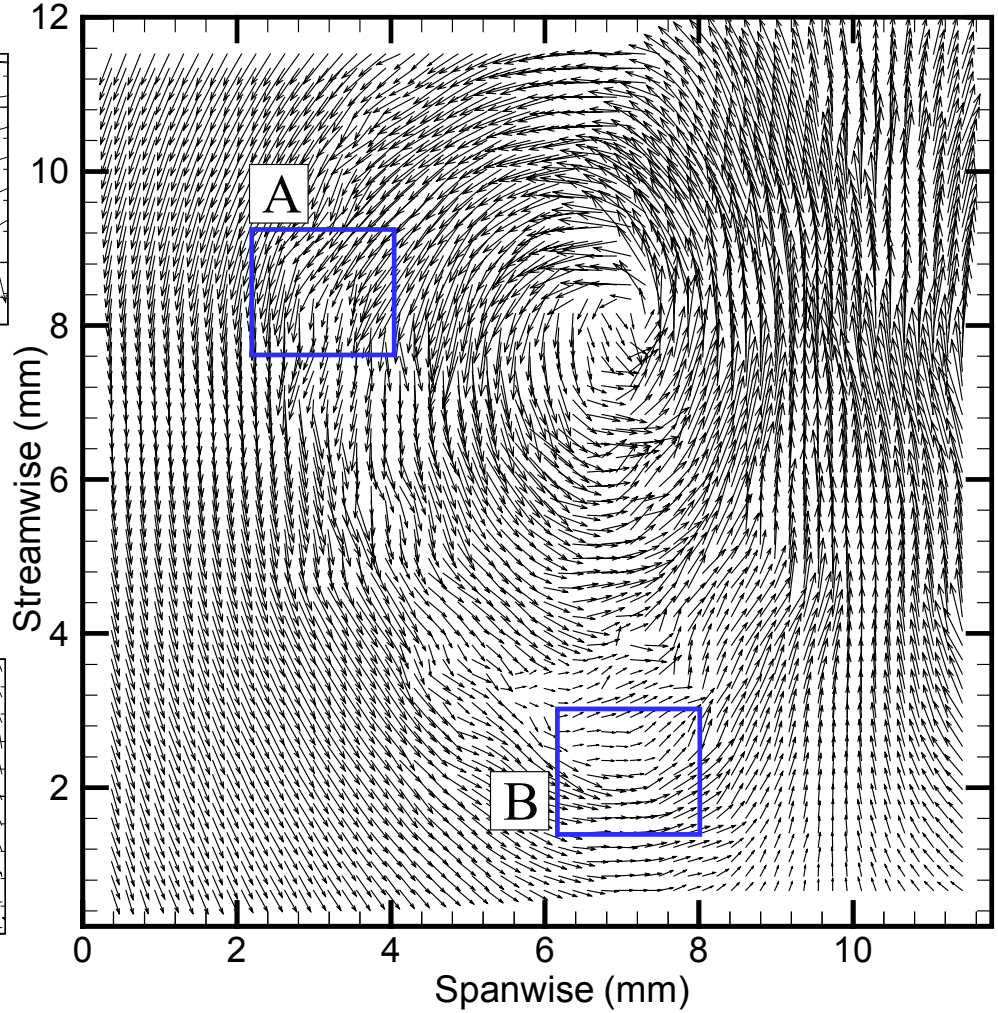

Vorticity and swirling strength

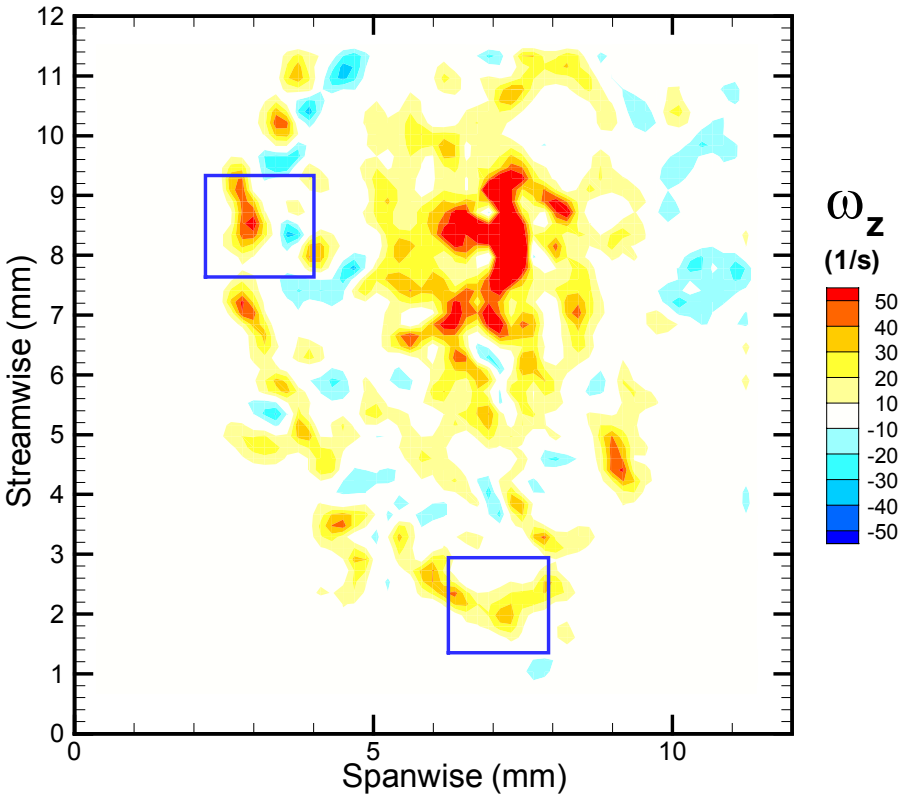

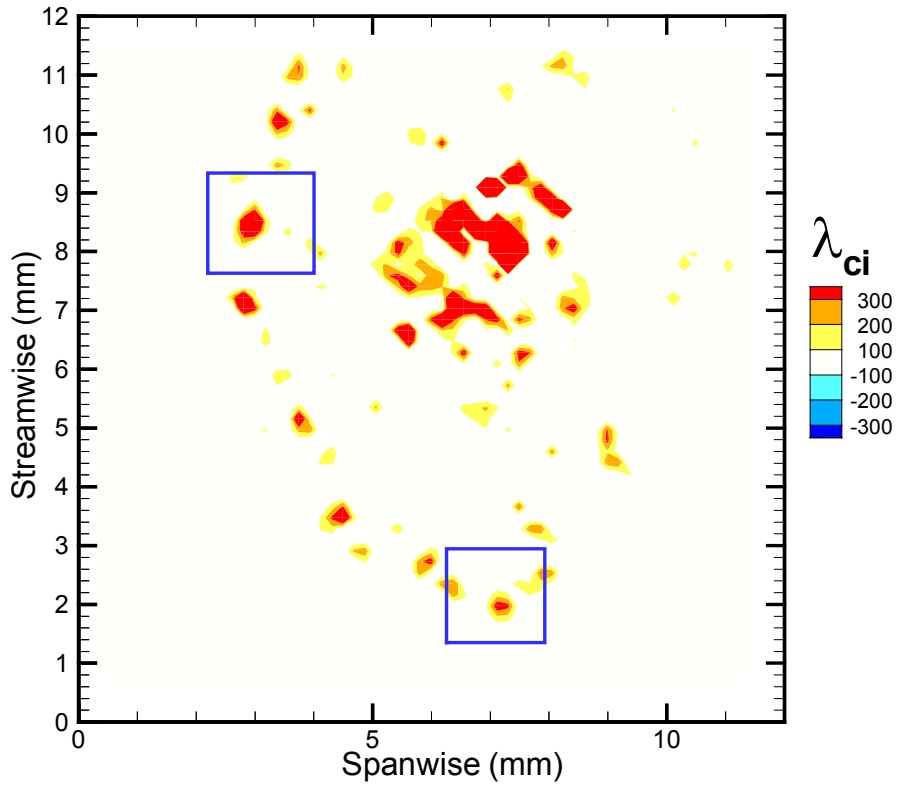

Conclusions

- The degree of cylinder-cylinder interaction, and hence the resulting flow morphology, is highly sensitive to the initial cylinder separation.
  - Different separations may lead to weak, moderate, or strong interactions.
- An idealized "vortex blob" simulation leads to very different flow morphologies than experiment, suggesting that the inner vortices are weakened by interaction.
- Vorticity fields calculated from high-resolution PIV measurements confirm that the inner vortices are significantly weaker, even for S/D = 2.0:

$$\Gamma_{outer} / \Gamma_{inner} \approx 3$$

Conclusions

- A correlation-based ensemble averaging procedure effectively captures the large and intermediate scales of the flow, providing confirmation of the experimental repeatability, and permitting decomposition of the density field into mean and fluctuating components.
- The RMS intensity fluctuations based on this decomposition are substantially greater for the case of “moderate” interaction than for the “strong” or “weak” interaction cases, despite comparable initial RMS values.
- High-resolution PIV data resolves mm-scale vortices being convected around the vortex cores.

The Interaction of Supernova Blast Waves with Interstellar clouds: Experiments on the Omega Laser

Richard I. Klein
University of California LLNL and
Berkeley, Department of Astronomy

Collaborators
Harry Robey, Ted Perry, Jave Kane, Jeff Greenough,
Marty Marinak

Lawrence Livermore National Laboratory

Four Stages of Shock-Sphere Interaction

- Initial development of reflected, transmitted and diffracted shocks
- Shock compression, convergence and multiple shock interaction ⇒ triple point flow and vorticity production
- Re-expansion and shear flow instabilities
- Destruction by instabilities and differential forces

The interaction of shock waves with clouds in the ISM is a problem of fundamental importance

Composite image from the ROSAT satellite

Graham *et al.*, ApJ 1997

yellow = X ray
blue = H-α
green = H-α + OIII + X ray

Shock waves from supernovae

shocks heat the coronal phase of the ISM

determine the velocity dispersion of clouds

↓

governs the scale height of the ISM

may effectively destroy clouds

↓

mixing of clouds with ISM

compression of clouds

↓

gravitational collapse

↓

star formation

Kimberly S. Budil *et al.*, *1998 Joint APS/AAPT Meeting*

KLEIN et al. 1990, 1994, 1995, 1996, 1999, 2000, 2001
Zabusky (??)

There is ample evidence of the aftermath of shock-cloud interations in the Cygnus Loop supernova remnant

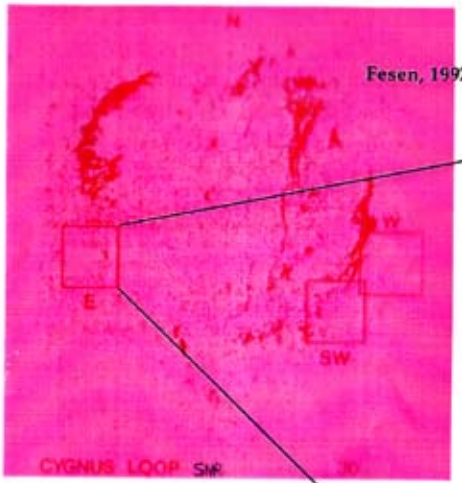

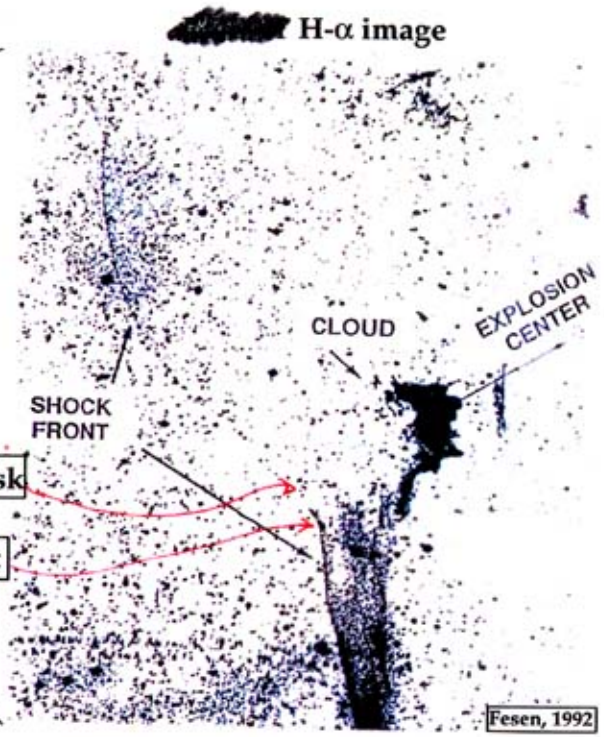

$R_{cloud} \sim 0.5$ pc

$n_{cloud} \sim 1$

$R_{shock} \sim 5.2 \times 10^{18}$

$v_{shock} \sim 4 \times 10^{7}$ cm/s

$t \sim 4.1 \times 10^{3}$ year

Understanding and Modeling the Evolution of 3D Hydrodynamic Instabilities and Turbulence is Crucial for Code Validation

- The shock-sphere experiments are rich in shock physics relevant to code validation
  - Multiple shock structure interactions from reflected, transmitted, diffracted shocks
  - Multiple shock-shock interactions with Mach stems, triple points, shear flows
  - Non-Linear hydrodynamics instabilities such as R-M, R-T, K-H
  - Vortex ring instabilities (bending mode) that cause large-scale vorticity and mixing
  - Turbulent flows

Timescales continued

Pressures comparable

$$V_s \approx (\rho_{Io}/\rho_{co})^{1/2} V_b \text{(non radiative)}$$

if $\dot{V}_s, \dot{V}_b < 0 \Rightarrow$ accurate to ≈ 1.5

if shock is radiative $\rho_{I1} >> \rho_{I0}$ typically $\rho_{I1} \gtrsim \rho_{I0}$

$\Rightarrow V_s$ (radiative) $>> V_s$ (non-radiative)

Timescale for shock to sweep across sphere

$$t_{ic} \equiv \frac{2a_o}{V_b}$$ Intercloud Crossing time

Timescale for sphere to be crushed by shock moving into the sphere

$$t_c \equiv \frac{a_o}{V_s} = \frac{\chi^{1/2} a_o}{V_b}$$ Cloud Crushing Time

t_c is the basic timescale governing the evolution of the sphere

$\{\chi, m\}$ characterize evolution $\Rightarrow$ scaling

After the shock has swept over the sphere, the shocked sphere is subject to Kelvin-Hemholtz and Rayleigh-Taylor instabilities

For $\chi >> 1$, the time-scale t_{KH} for growth of K-H instabilities for perturbations of wavenumber k parallel to relative V_{rel} between sphere and surrounding medium is

$$t^{-1}_{KH} = k\, v_{rel}/\chi^{1/2}$$

$$\Rightarrow \frac{t_{KH}}{t_c} = \frac{V_b / V_{rel}}{ka_o} \rightarrow \text{K-H growth time-tc,}$$

Shortest wavelength cause the fastest growth

It can also be shown for Rayleigh-Taylor

$$\Rightarrow \frac{t_{RT}}{t_c} \cong \frac{1}{(ka_o)^{1/2}} \Rightarrow \text{sphere undergoes severe instabilities in few } t_c$$

SNR age

For Sedov-Taylor

Blast Wave $t \equiv \frac{\alpha R_b}{V_b} = \frac{2}{5}\frac{R_b}{V_b}$ $\left(V_b = \frac{dR_b}{dt} = \alpha t^{\alpha-1}\right)$

$R_{blast} \propto t^{\alpha}\ (\alpha = 2/5)$

If $\chi >> 1 \Rightarrow t_{cc} > t_{ic}$, Clouds are characterized in 3 sizes

Small clouds $t > t_{cc} \Rightarrow a << \frac{0.1R}{\chi^{1/2}}$

SNR does not evolve significantly during cloud crushing – cloud is promptly crushed. V_s ~ constant pressure on cloud ≈ steady.

Medium clouds $t_{cc} > t > t_{lc} \Rightarrow \frac{0.1R}{\chi^{1/2}} < a < 0.05R$ V_s decelarated

Blast wave does evolve during the time to crush the cloud.

Large clouds $t < t_{lc} \Rightarrow a > 0.05R$

Blast wave weakens significantly over time to cross clouds

Force on clouds impulsive

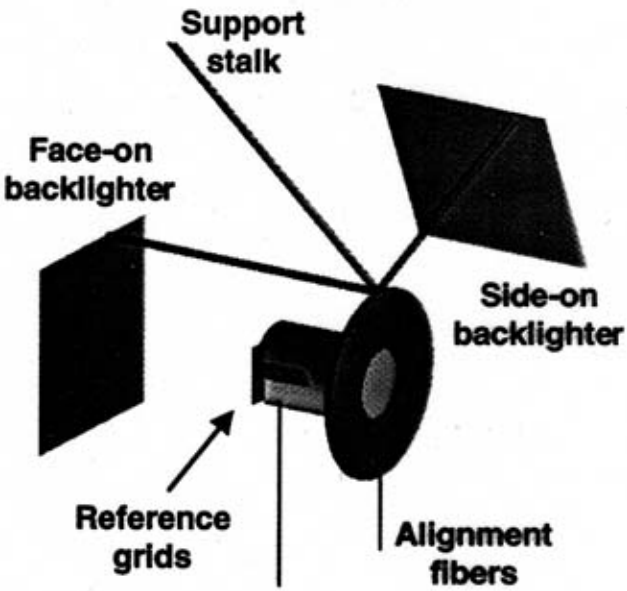

Figure 1(b), Robey, Phys. Rev. Lett.

Experimental Setup

- Achieve strong shock conditions with direct 10 beams with 500 J/beam, flat pulse length 10 ns and laser wavelength of 0.351 μm onto target
- Beams have super-Gaussian spatial intensity

$$I/Io = \exp\ [-(r/412\ \mu m)]^{4.7}$$

- Target Diameter is 800 μm
- Berryllium shield was used to delay shock propagation around target and generate planar shock propagation.
- Direct -drive laser illumination used to permit face-on imagining of target

⇒ Previous experiments (Klein et al. 2000 - 2001) used indirect-drive

Experimental Setup - con't

- Cu sphere with 120 μm diameter (**representing interstellar cloud**) and density 8.95g/cm^3 embedded in Beryllium shock tube filled with polystyrene (CH) at density 1.044g/μm^3 (**representing interstellar medium**)
- Interaction is imaged with 5.2 KeV x-rays with 7 additional Omega beams

Experimental Setup - con't

- Advantages of indirect-Drive $\Rightarrow$ produces a more uniform radiation flux and shocks of greater planarity
- Disadvantages: Plasma blown off the walls prohibits late-time imaging of interaction from face-on direction.
- Direct-Drive maintains face-on access for duration of the experiment

Experimental Radiographs

Side-on Face-on

t = 13 ns
shock passes
over sphere

t = 26 ns
shock is
well passed
sphere

t = 39 ns
shock is out
of field of view

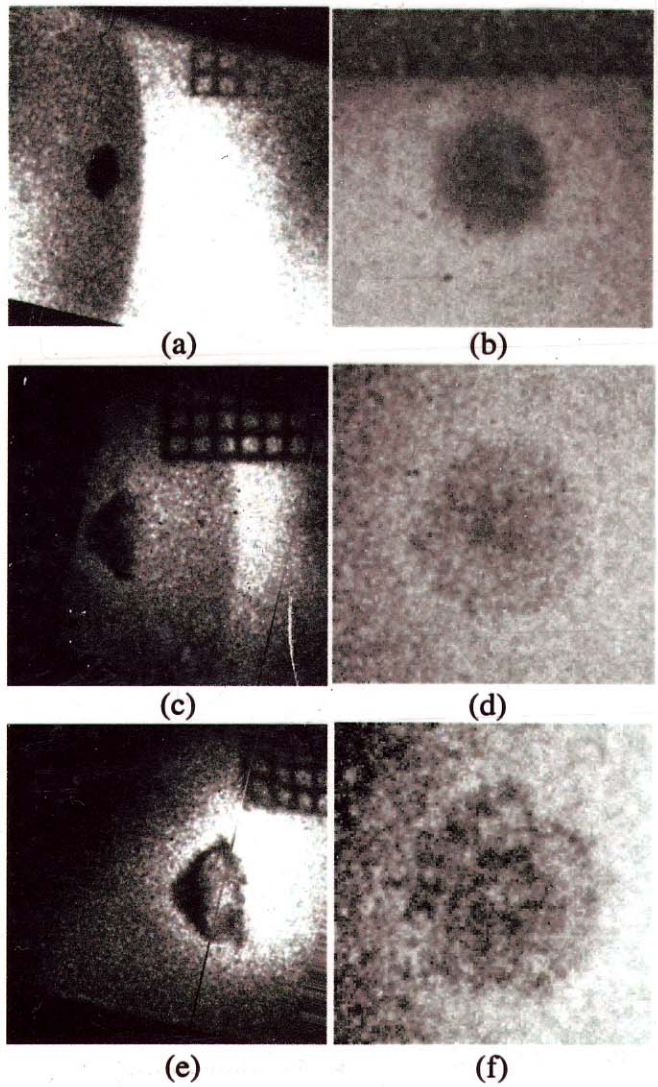

Figure 2, Robey, Phys. Rev. Lett.

Experimental Results

- Experimental radiographs show interaction with "simultaneous" side-on and face-on images

t=12 ns

- Sphere compressed in axial direction with little radial compression

t=26 ns

- Sphere undergoes severe axial compression. Baroclinic vorticity generated at sphere-CH interface

- Vorticity generated during initial passage of shock over spherical cloud

Experimental Results - con't

- Vorticity generated during subsequent post-shock flow at cloud-intercloud boundary
- Flow around cloud produces high-pressure Mach reflected shock into back side of cloud
- Side shocks weaker than front and aft shocks due to pressure minimum at sides

$\Rightarrow$ Results in strong axial compression - sphere begins to pancake

Experimental Results - con't

- Emergence of double ring structure seen in face-on radiograph

t=39ns

- Strong vortex roll up noted on sides of sphere
- Face-on view shows distinct double ring structure which tracks development of double vortex ring
  - Klein and McKee (1994) showed that 3-D vorticity field of cloud is well tracked by full density field ⇒ Vortex Ring Instability

Azimuthal line-outs from face-on images of shock / sphere interaction at t = 39 ns

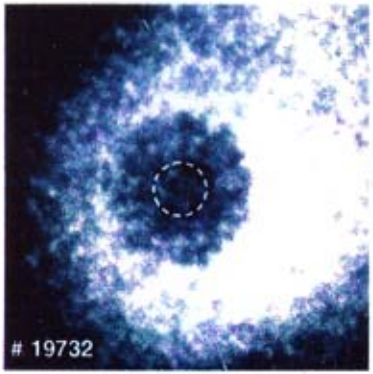

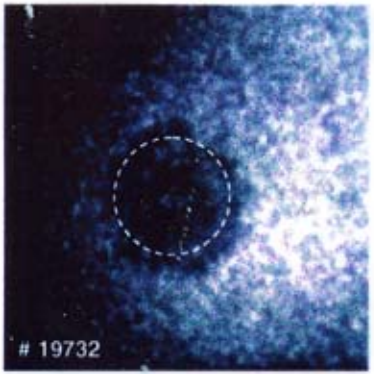

Azimuthal line-out
through central feature (r=36 μm)

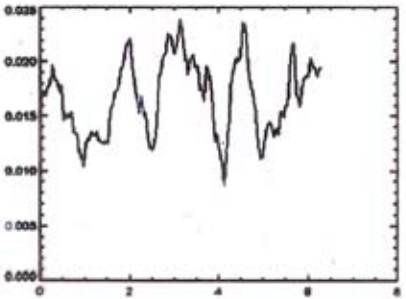

Azimuthal line-out
through outer feature (r=80 μm)

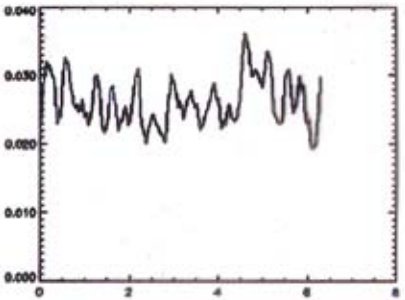

Modal Analysis of Double Vortex Ring at t = 39 ns

Double Vortex Ring structure

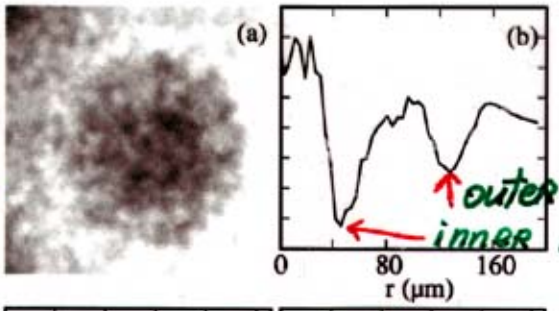

radial transparency of double ring

Azimuthal mode structure
Azimuthal Lineouts

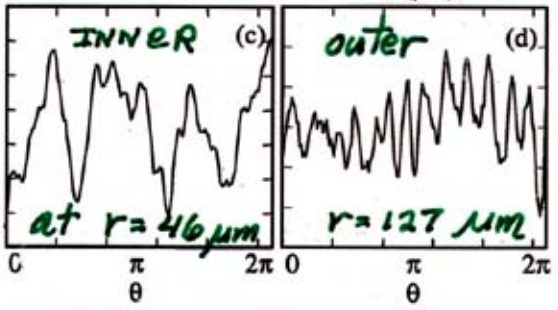

Power Density spectrum of Azimuthal Lineouts

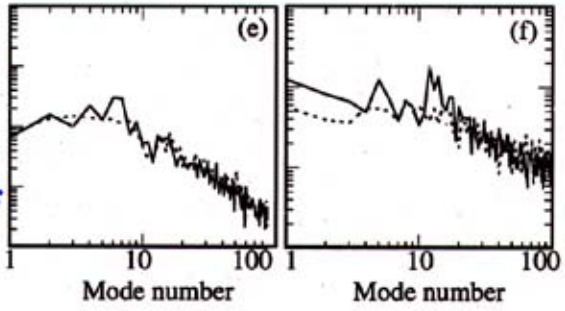

INNER Vortex Ring Dominant mode n = 5-8

OUTER Vortex Ring Dominant mode n = 15

Figure 3, Robey, Phys. Rev. Lett.

Modal Analysis of Double Vortex Ring Structure

- 3-D simulations show development of 2 Vortex Rings associated with cloud that undergo bending mode instability (Klein and McKee, 1994; Marinak, Klein and Perry 2001)
- Azimuthally averaged radial lineouts of experimental radiograph show unambiguous double ring structure
- Azimuth lineouts at radial location of each ring show periodic azimuthal modulation suggesting a dominant mode number of 5 for inner ring and higher mode number of 14-16 for the outer ring

Modal Analysis of Double Vortex Ring Structure - con't

- Power density spectrum of azimuthal lineouts confirm dominant mode number of 5-8 for inner ring and dominant mode number 15 for outer ring

Experimental-Theoretical Comparison of Vortex Ring Modal Structure

- At t=39ns, shocks have left sphere and sphere advects essentially as an incompressible fluid
- Applying incompressible theory to describe an incompressible bending mode instability in vortex ring to experimental face-on radiographs $\Rightarrow$ dominant unstable mode for inner ring n=5-7 and n=15-17 for outer ring
- Theoretically determined dominant modes in non-axisymmetric unstable vortex rings are in remarkable agreement with experimentally determined unstable modes

Contours showing location of Inner and Outer Vortex Rings

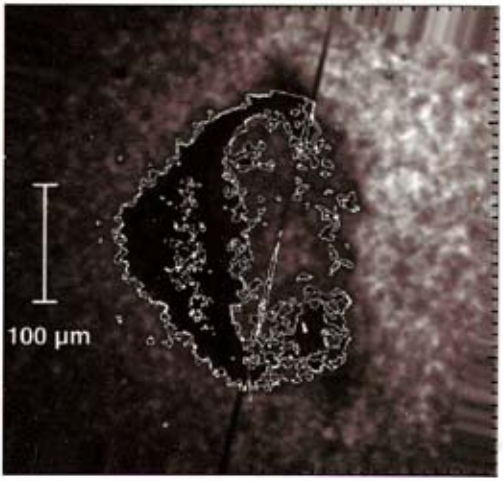

Figure 4, Robey, Phys. Rev. Lett.

3-D High Resolution AMR Simulations

- Side on view of simulation shows well separated front and back part of the sphere due to instabilities
- Side on view models inner transparent bubble seen in experimental radiograph
- Face on view shows clear evidence of inner and outer vortex rings seen in experimental radiograph
- Inner ring shows low mode structure and outer ring shows high mode structure as in radiographs
- Overall morphology of 3-D simulations in excellent agreement with experimental radiographs

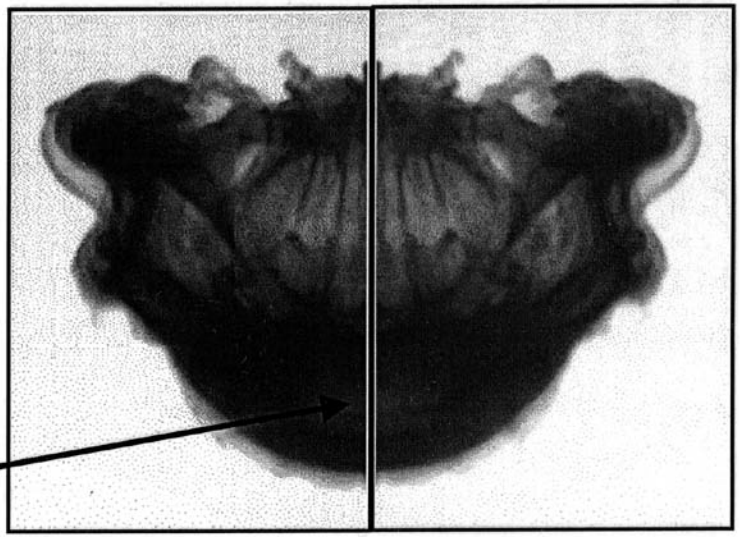

Figure X(a)

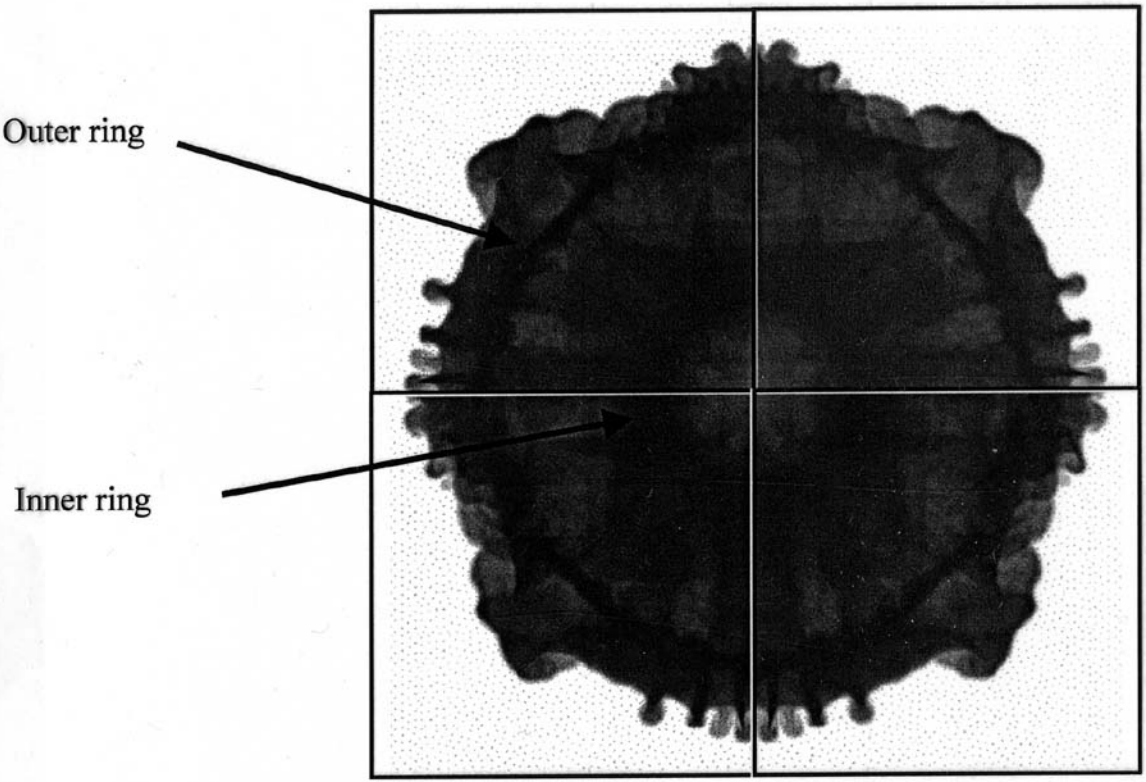

Figure X(b)

Conclusions

- The interaction of a supernova blast wave with interstellar clouds can be well scaled to an HED Omega laser experiment
- Development of vortex flow gives rise to strong vortex rings unstable to Widnall Bending Mode instabilities. **These are shown for the first time in HED laser experiment**
- At 39 ns (~3 t_c) hydrodynamic instabilities (R-T, K-H and Widnall) destroy sphere (cloud) resulting in turbulent mixing of cloud with surrounding medium (ISM)
- Power density spectrum of face-on radiographs determine dominant mode of inner and outer vortex rings to be n = 5-8 and n = 15
- Incompressible vortex ring theory shows remarkable agreement in predicting dominant unstable modes of vortex rings
- High resolution 3-D AMR simulations capture all essential morphological features of side-on and face-on experimental radiographs including appearance of double vortex rings

Ablative Rayleigh-Taylor Instability at Short Wavelengths

Moire Interferometry

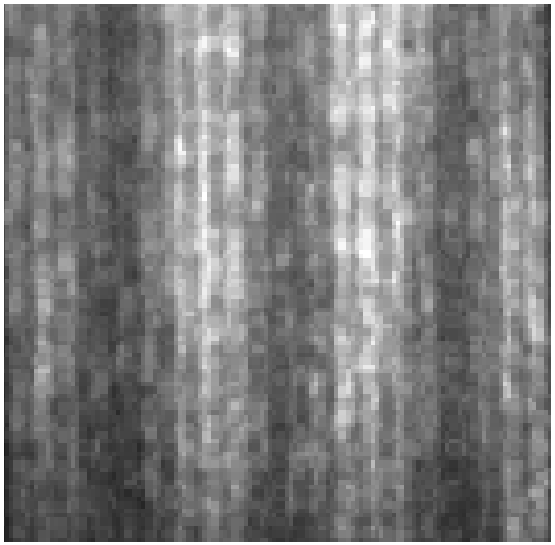

Penumbral Imaging

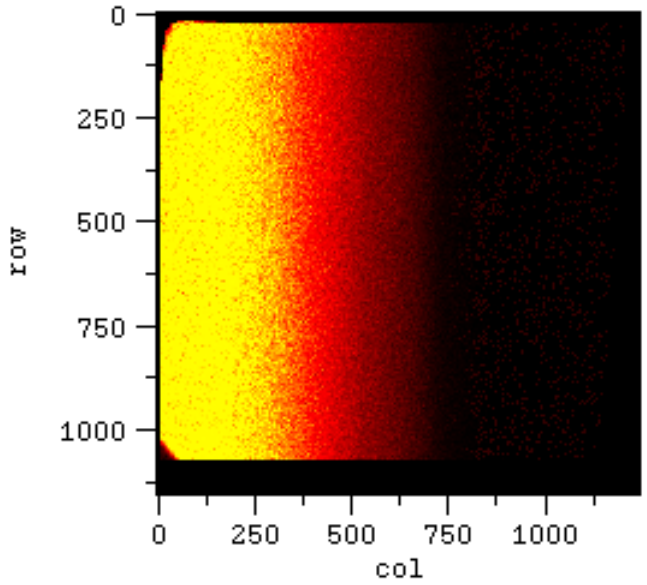

Fresnel Phase Zone Plate

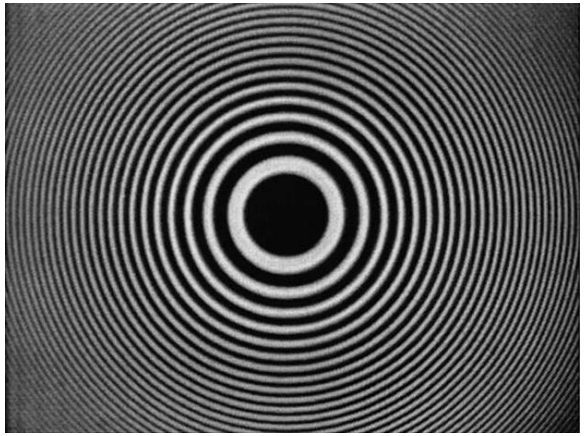

H. Azechi *et al.*
Institute of Laser Engineering
Osaka University
IWPCTM 2001 Paper# E-45
9-14 Dec 2001,
Pasadena, USA

Primary obstacle of IFE is Rayleigh-Taylor instability.

ILE OSAKA

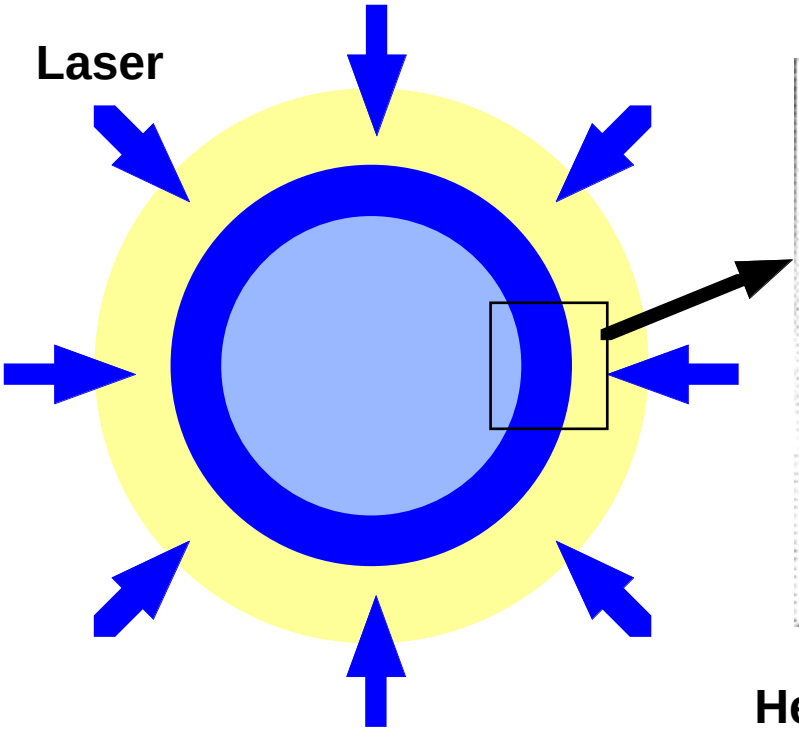

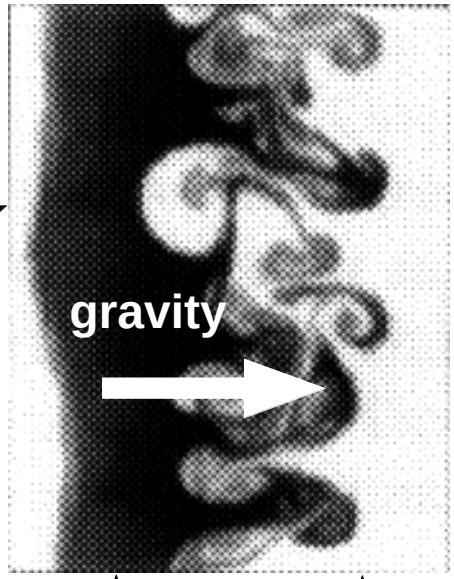

Guy Dimonte, C. Eric Frerking
and Marilyn Schneider,
Phys. Rev. Lett. **74**, 4855, (1995)

Heavy Fluids **Light Fluids**

Typical wavelength = several tens μm
time scale = ns
High resolution advanced diagnostics are required.

X-ray **Moire interferometry**
Fresnel phase zone plate
Penumbral imaging

Ablative Rayleigh-Taylor instabilities

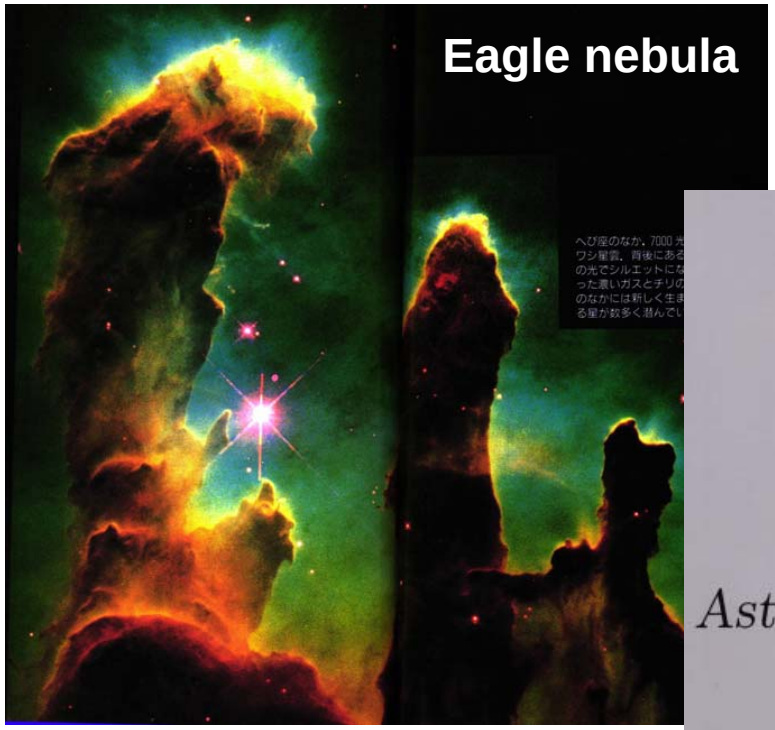

Type Ia supernovae

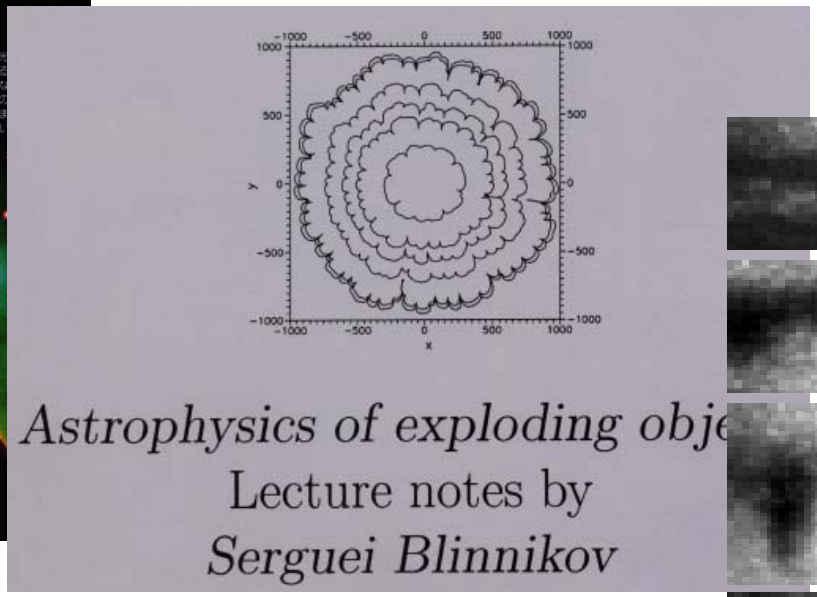

Laser exp't

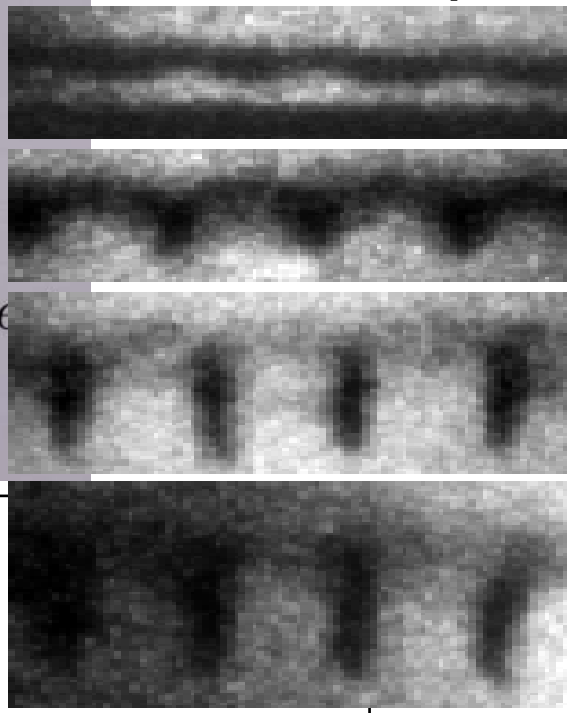

Perturbation amplitude $a = a_0 e^{\gamma t}$

$$\gamma = \sqrt{\frac{kg}{1+kL}} - \beta k v_a$$

v_a=fluid velocity across the unstable surface

β = depends on the ablation structure.

Motivation

New method is needed for the measurement of short wavelength Rayleigh-Taylor (RT) Growth.

ILE Osaka

It is necessary to measure short wavelength RT growth in order to understand the mechanism of the ablative stabilization.

Dispersion curve of the Rayleigh-Taylor instability

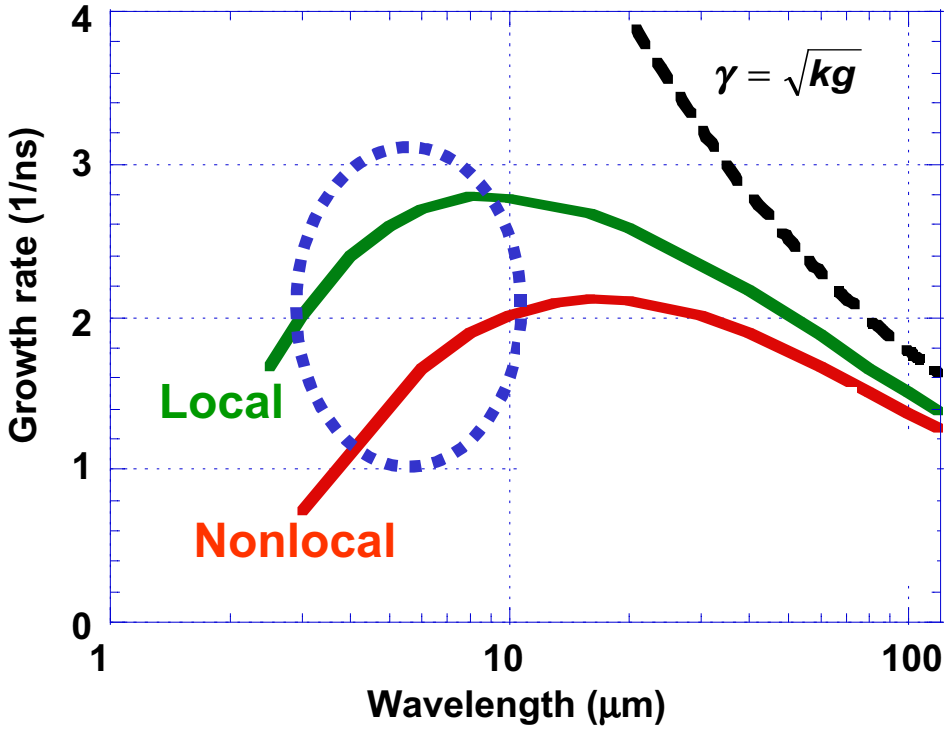

- Short wavelength RT
  Moire interferometry
- Independent test
  Penumbral imaging
  Fresnel phase zone plate

Moire interferometry / short wavelength Rayleigh-Taylor

Experimental procedure

Schematic view of the experimental setup

ILE Osaka

Setup

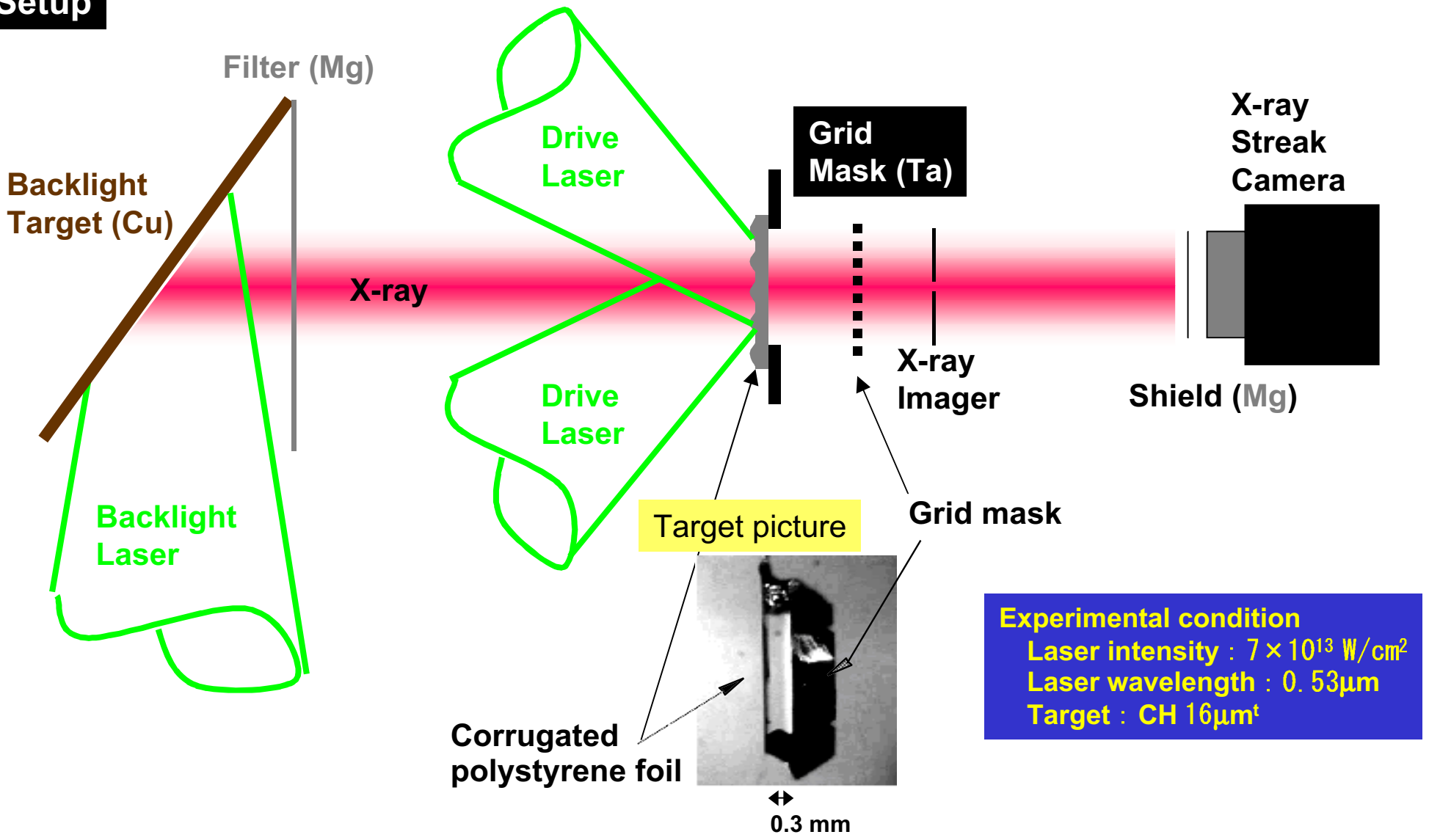

Experimental condition
- Laser intensity : 7×10^{13} W/cm^2
- Laser wavelength : 0.53μm
- Target : CH 16μm^t

Moiré interferometry

Moiré interferometry is very useful for measurements of the RT instability at short wavelength.

ILE Osaka

Principle

Perturbation wavelength

$\lambda_{Perturb.} = 12\ \mu m$

Grid mask

$\lambda_{Grid} = 10\ \mu m$

Moiré interferometry

$\lambda_{Moiré} = \underline{60}\ \mu m$

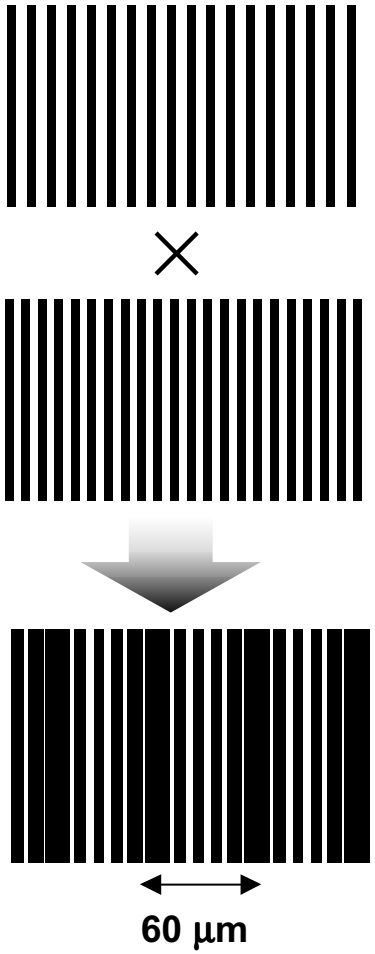

$$k_{Moire} = |k_{Perturb.} \pm k_{Grid}|$$

Due to the moiré interference, the short wavelength perturbation is converted to longer wavelength perturbation.

M. Matsuoka *et al*., Rev. Sci. Instrum., **70**, 637 (1999)

Raw image

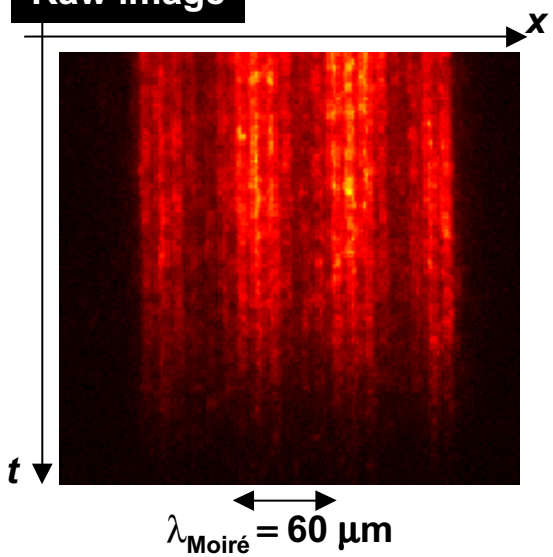

Experimental results

Raw data of Rayleigh-Taylor instability observed with moiré interferometry

ILE Osaka

λ= 12μm
a_0 = 0.1μm

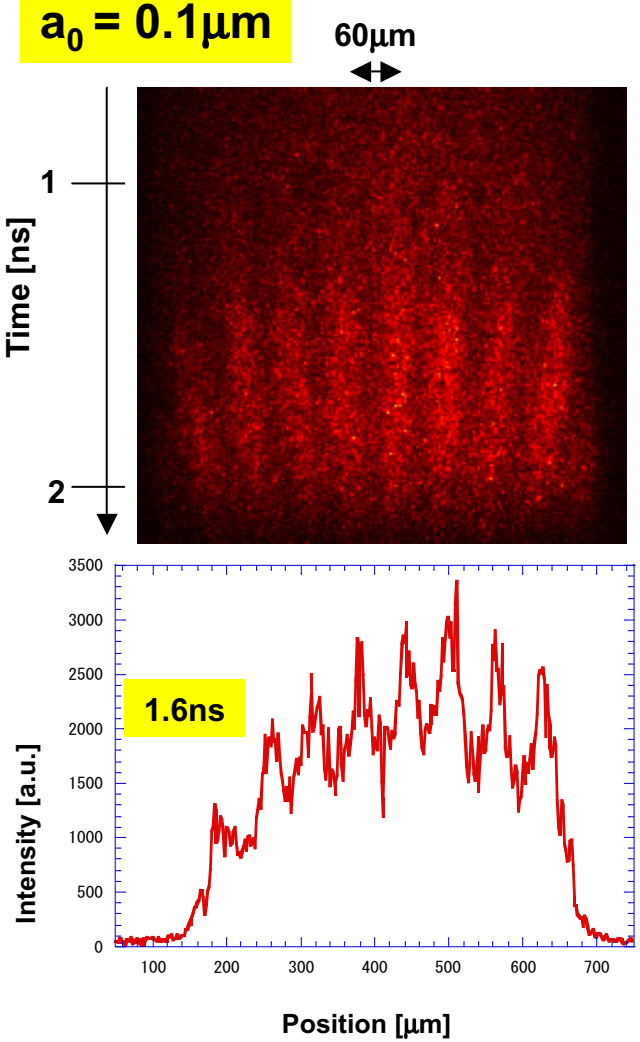

λ= 8.5μm
a_0 = 0.1μm

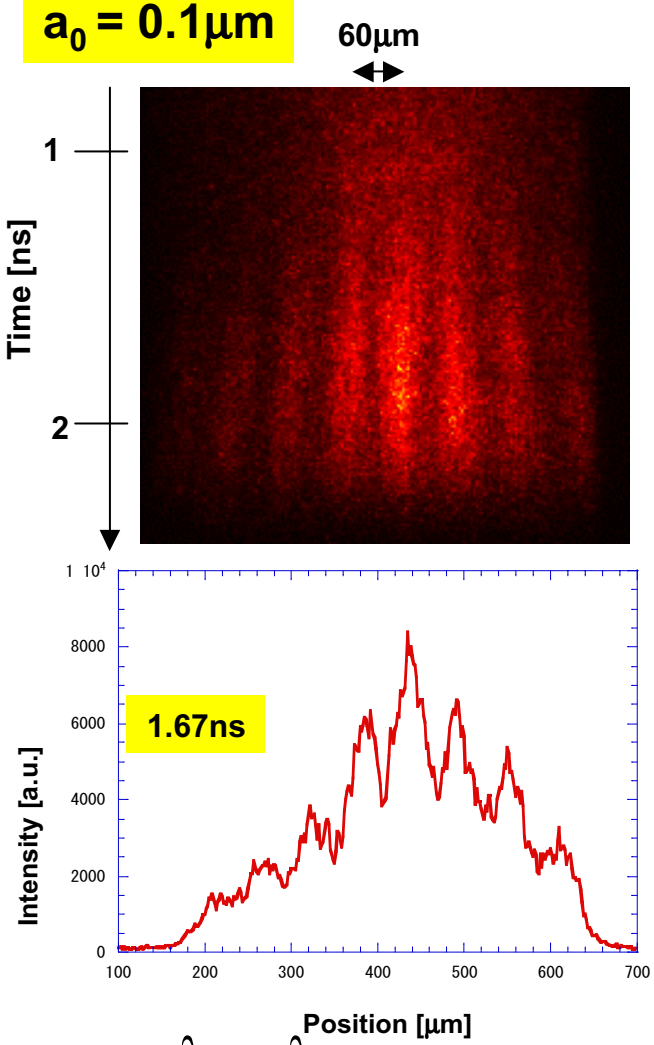

λ= 4.7μm
a_0 = 0.05μm

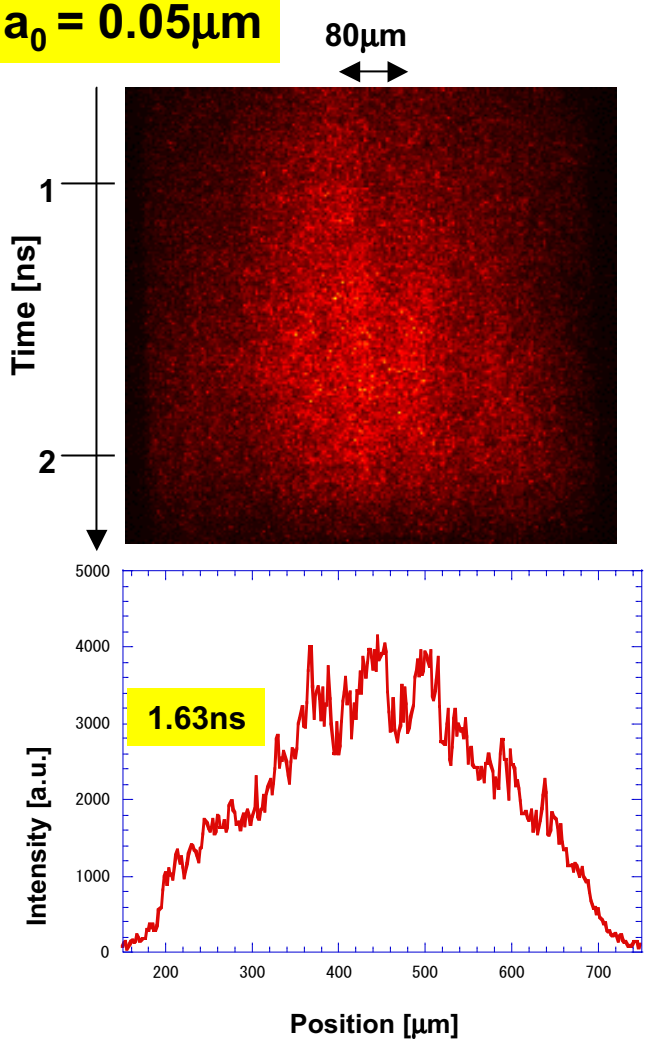

$$\lambda_M = \frac{\lambda_1 + \lambda_2}{\lambda_1 - \lambda_2}$$ sensitive to $\Delta\lambda$

Large Rayleigh-Taylor growth was observed up to 5-μm wavelength.

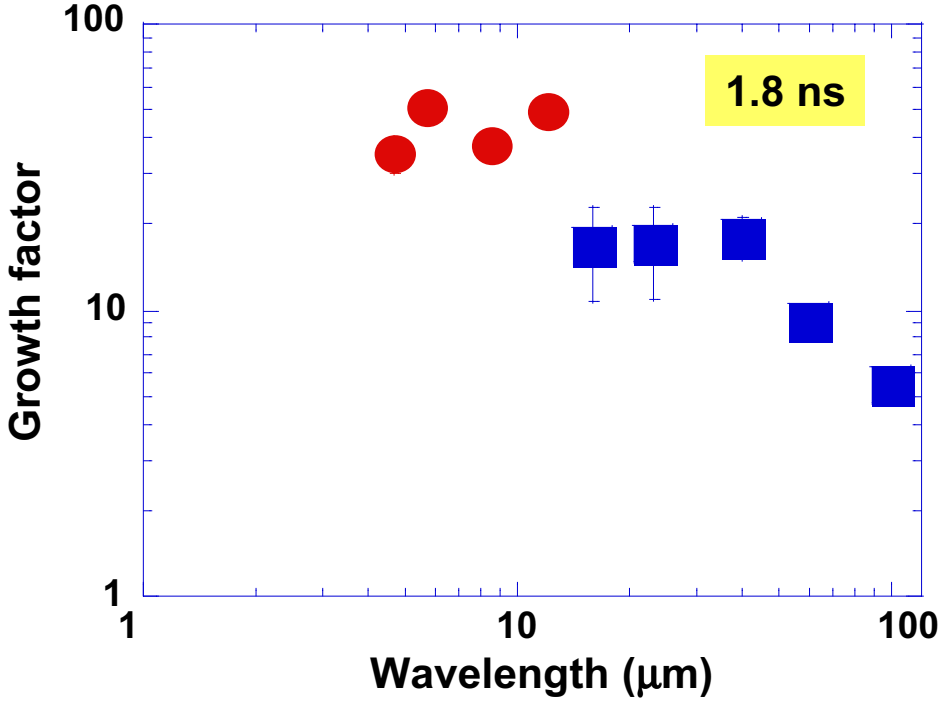

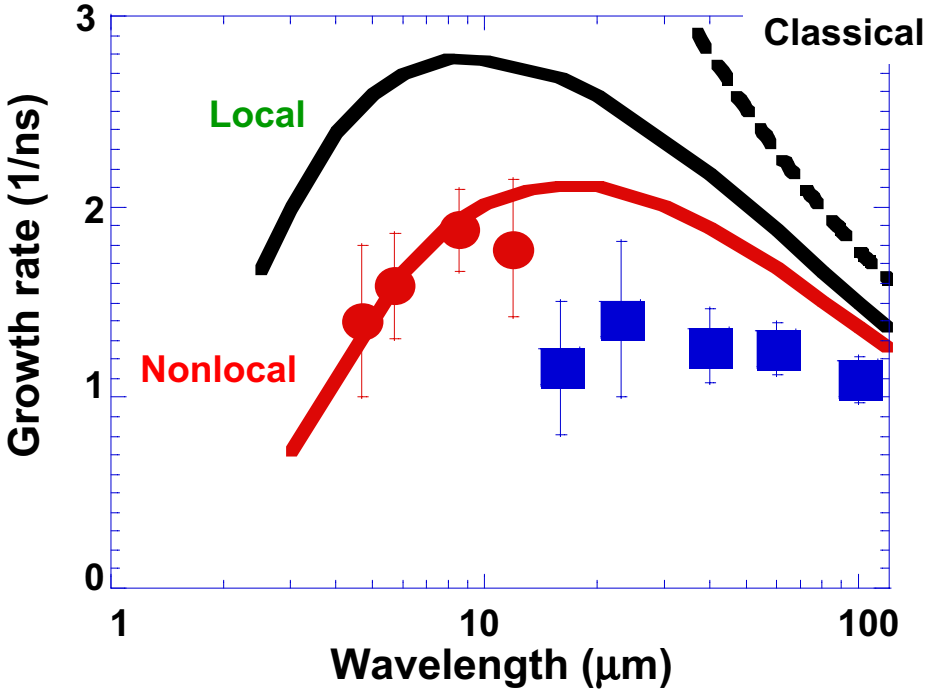

- This exp't suggests that nonlocal heat transport plays a role in ablative stabilization.
- However, for unambiguous clarification, we need to make independent observation.

Reduction of the target density with nonlocal heat transport

ILE Osaka

Density profile at 1.3 ns

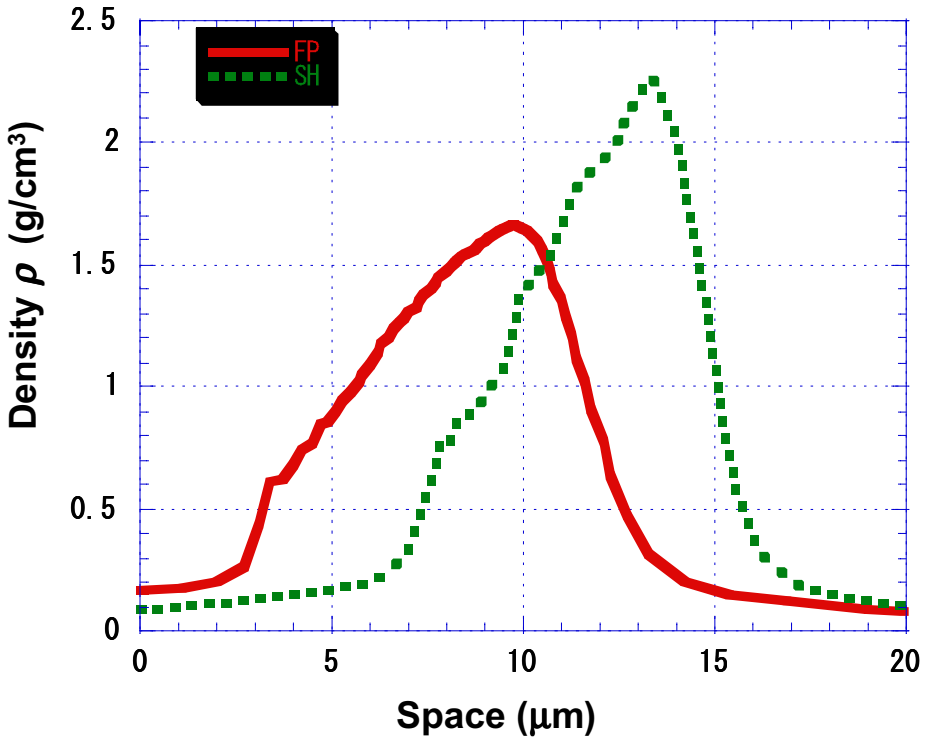

Spitzer-Härm (SH)
Local heat transport :

- **Diffusion approximation of electron thermal conduction**

Fokker-Planck (FP)
Nonlocal heat transport :

- **High-energy electrons in the tail of Maxwellian distribution penetrate into the target and preheat it.**

Target expansion → Density reduction

Ablation velocity increases

Stabilization

if $\dot{m} = \rho_a v_a \cong const$

A. Sunahara *et al.*, "Nonlocal Electron Transport" (2000)

Method of Density Measurement

Density profile was obtained from the x-ray backlighting image of the planar target.

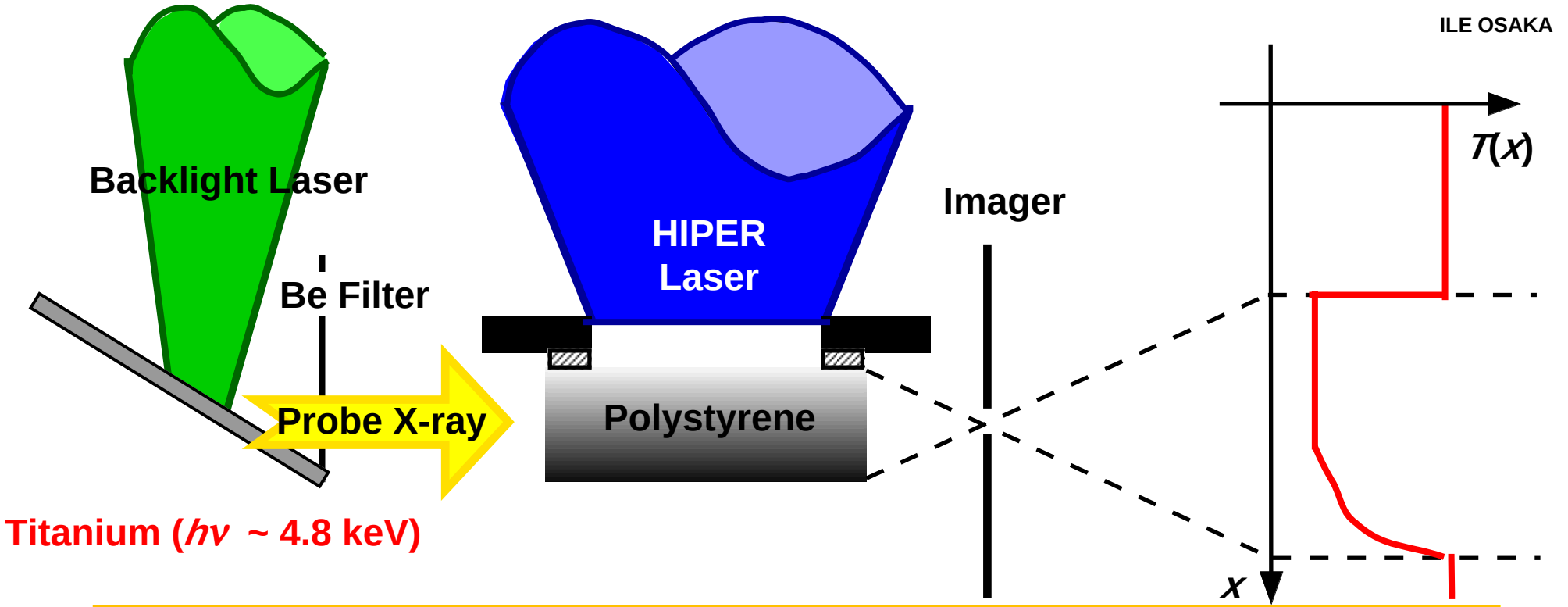

$$T = \exp(-\mu\rho l)$$

T : Transmission, μ : mass absorption coeff.

l : material thickness, ρ : density

Fresnel phase zone plate / density profile

The principle of the FPZP imaging

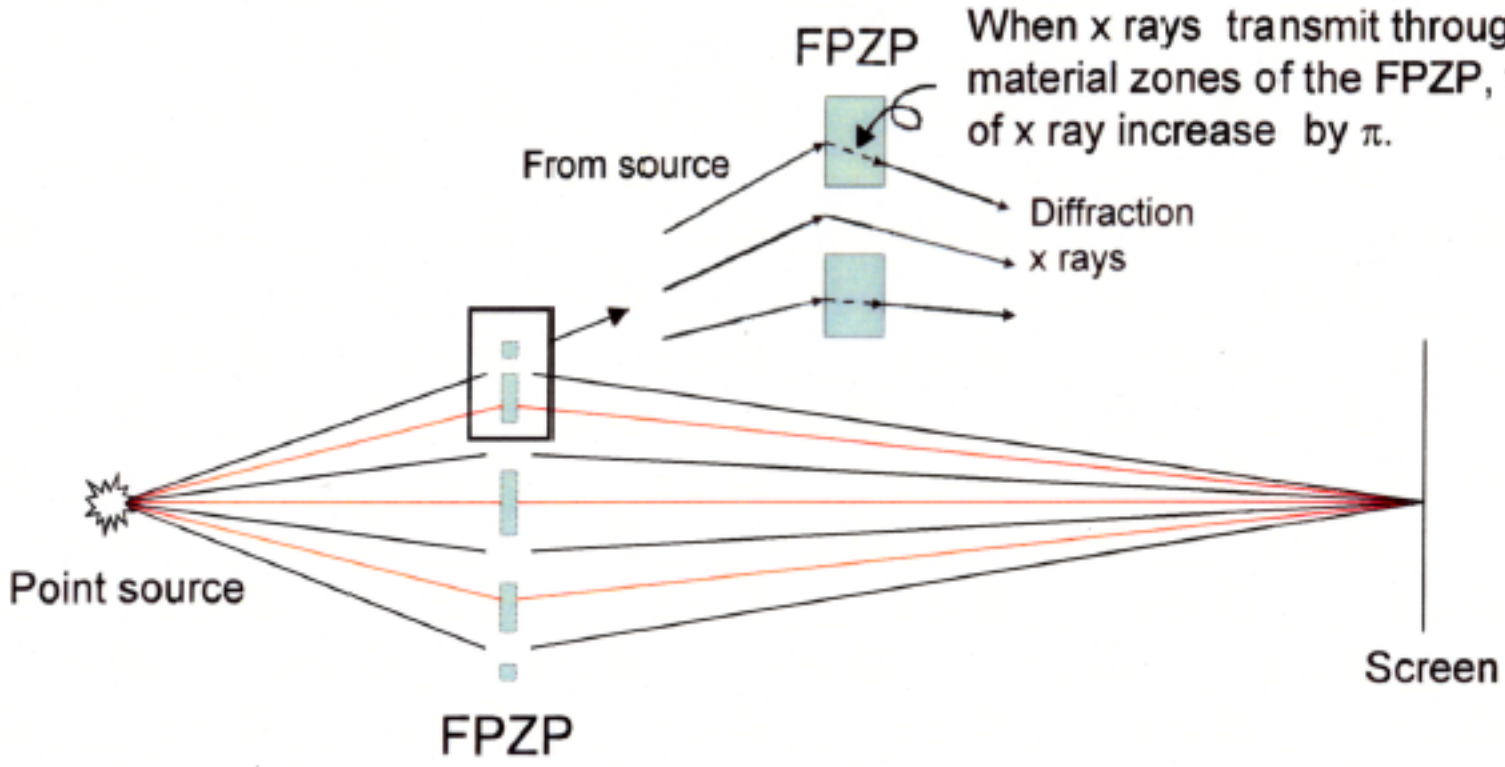

Advantage

- High spatial resolution 2.2 μm
- Hard x-ray imaging 4.7 keV

Disadvantage

- Chromatic aberration — Possible to obtain ~μm spatial resolution
- Background

Spatial resolution test of FZP

Ta grid mask
10.0 μm pitch
Thickness: 2.2 μm

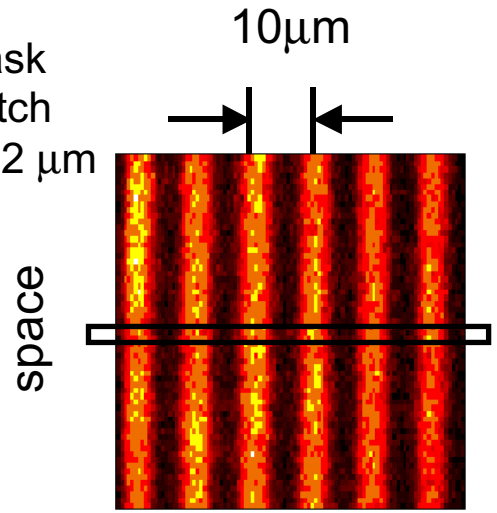

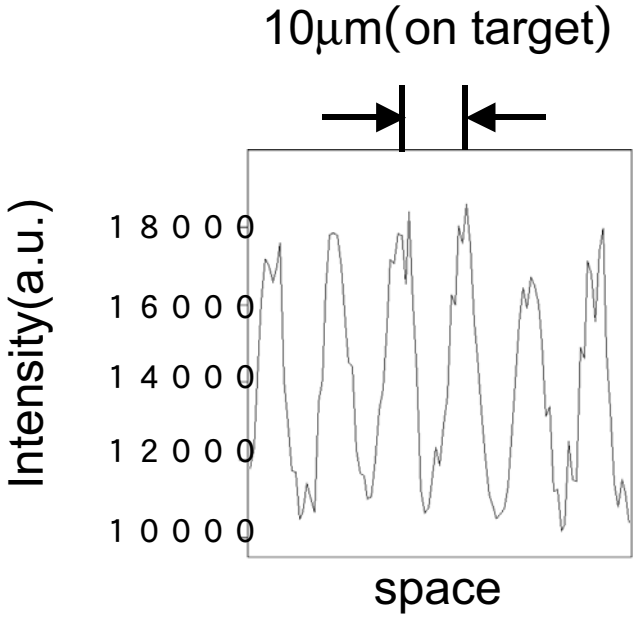

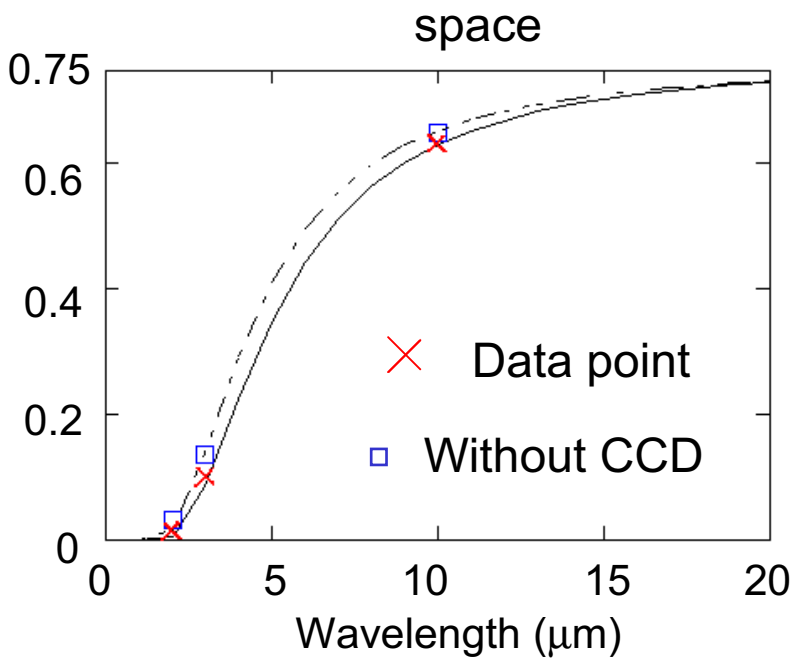

CCD camera MTF is removed by Calculation.

The wavelength at which the MTF becomes 5 % is 2.2 μm.

Ablation density profile

Obtained data

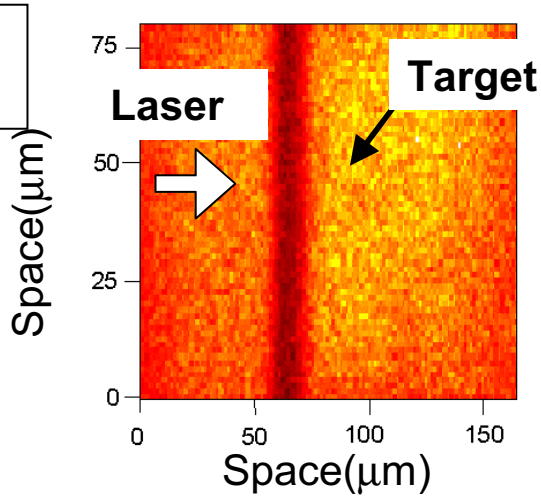

Spectrum breadth	2~3 %
Target thickness	2~3 %
The target bend	negligible
Intensity profile of the probe x rays	<1 %
Contribution of the background	**<20 %**

t= 1.3 ns: the early phase of acceleration

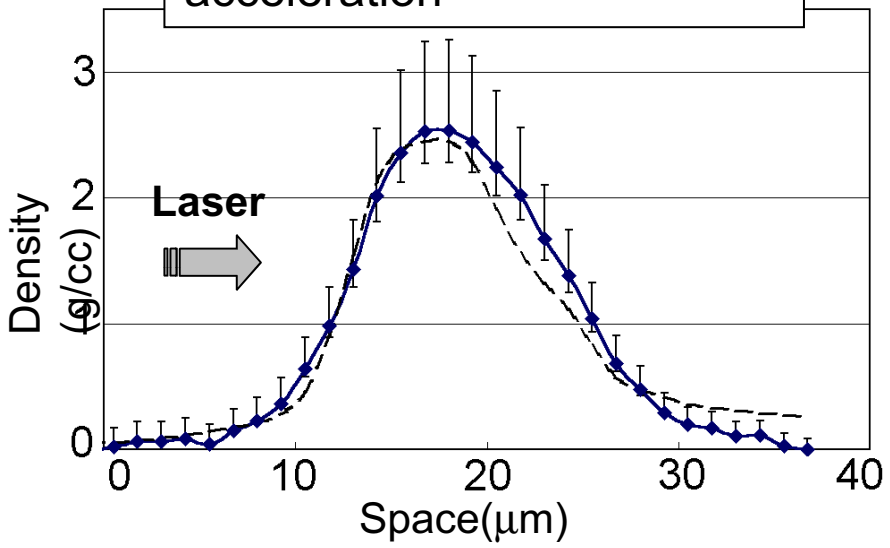

t= 2.2 ns: the late phase of acceleration

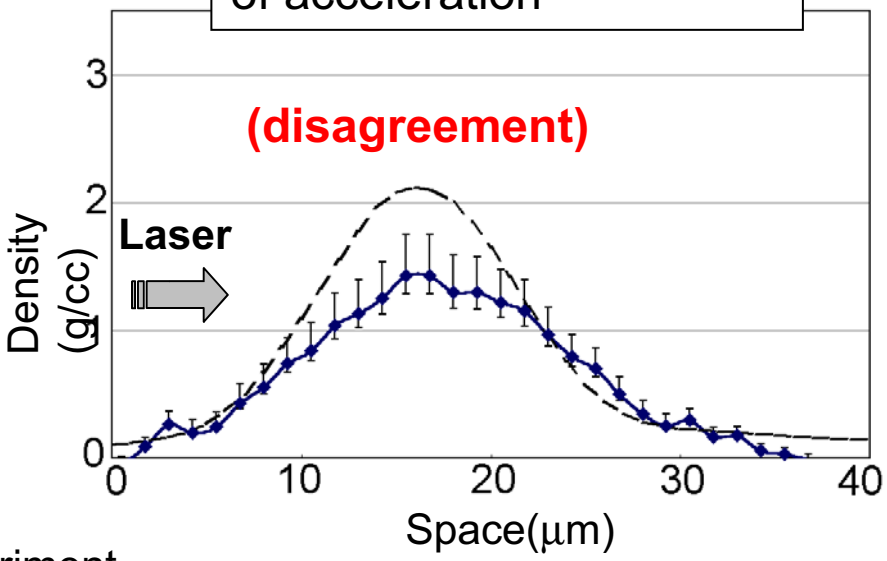

Experiment

Simulation+Smear

Penumbral Imaging / density profile

Proof of Principle experiment

The proper density profile of the laser-undriven polystyrene target was obtained with penumbral imaging coupled with a side-on x-ray backlighting.

ILE OSAKA

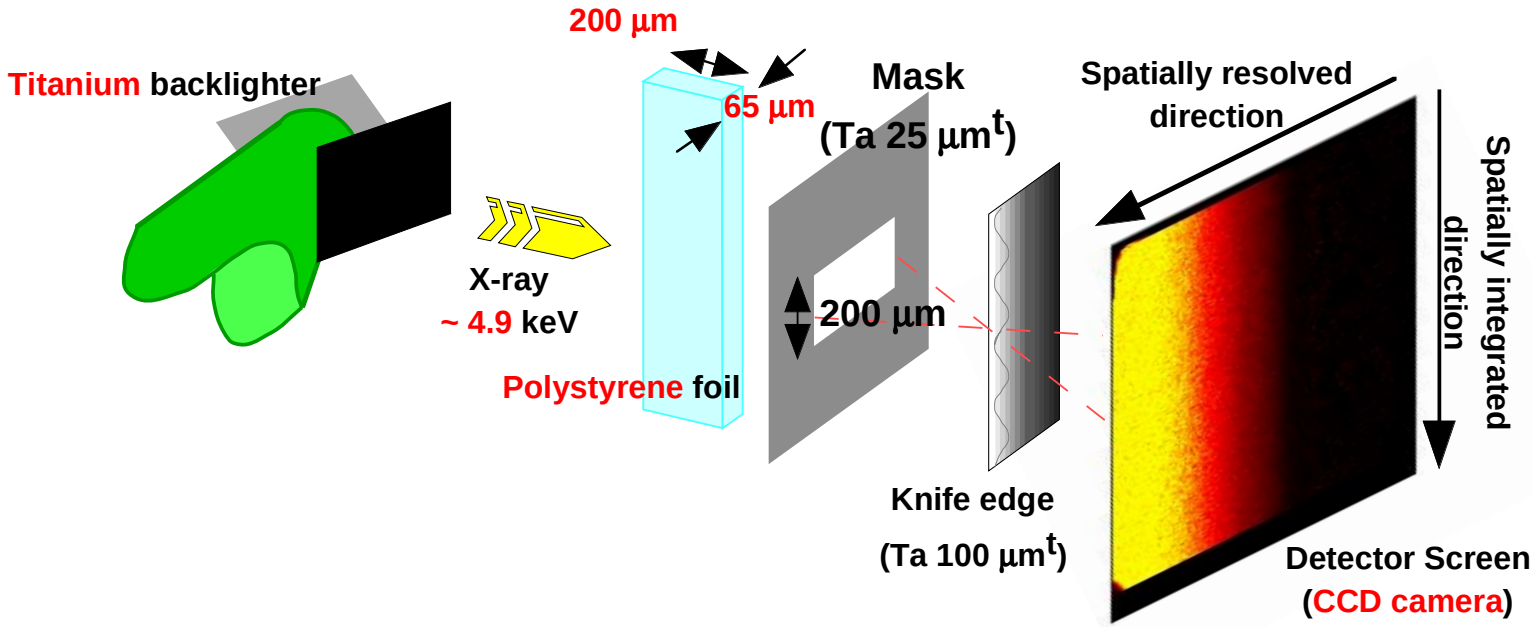

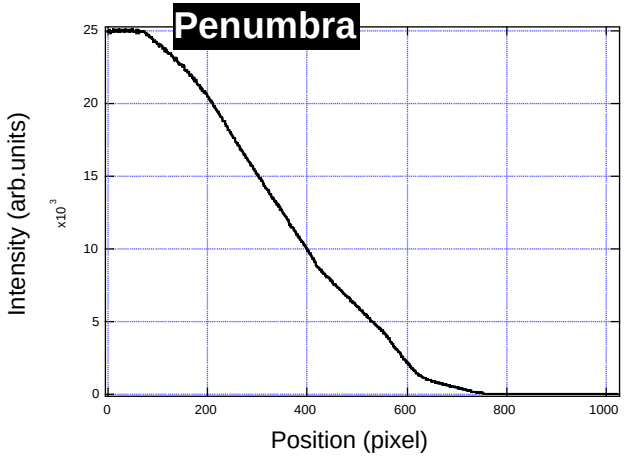

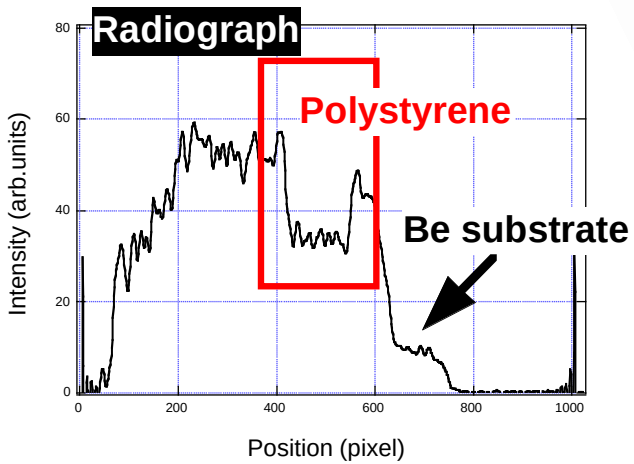

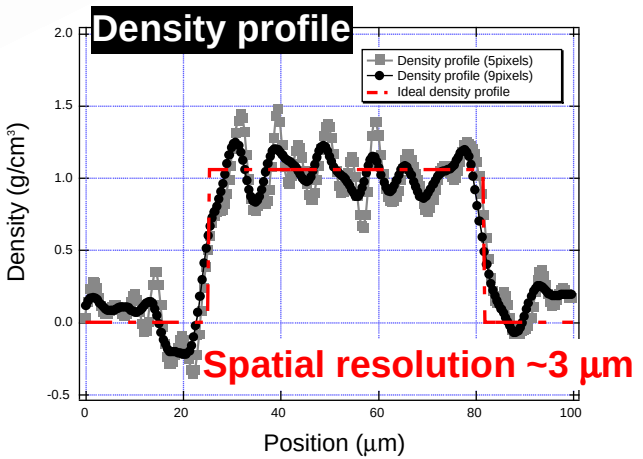

Density measurement with penumbral imaging

The density profiles in target plasmas driven by the HIPER laser were observed from shock transit to target acceleration.

S. Fujioka
(ILE. Osaka)

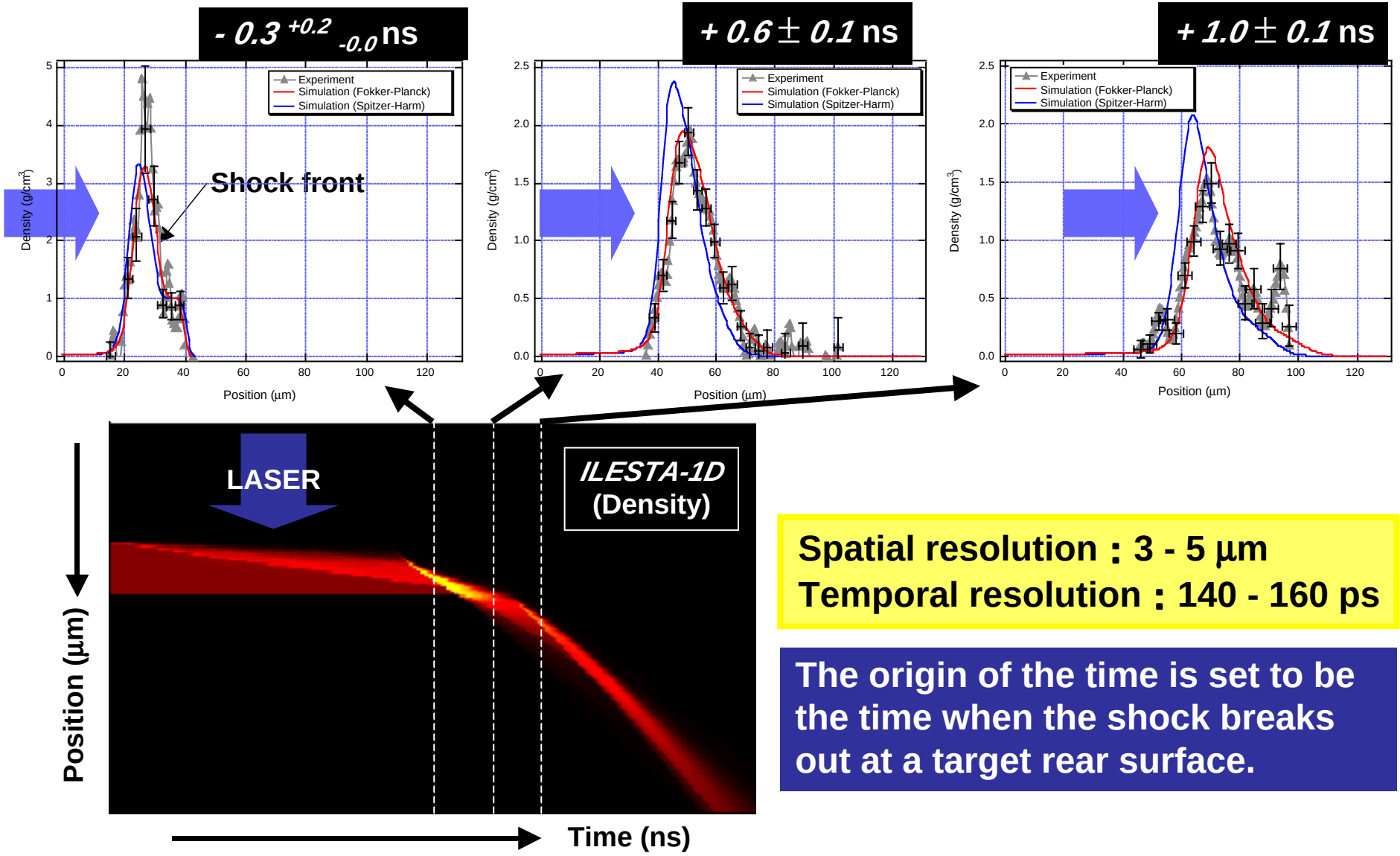

Spatial resolution : 3 - 5 μm
Temporal resolution : 140 - 160 ps

The origin of the time is set to be the time when the shock breaks out at a target rear surface.

Density measurement with penumbral imaging

Kinetic effects on electron energy transport are not negligible even in the case of relatively low intensity blue laser irradiation (I_L = 0.7 x 10^{14} W/cm^2, λ_L = 0.35 μm).

S. Fujioka
(ILE. Osaka)

+ 0.6 ns (corresponding to the beginning of a target acceleration)

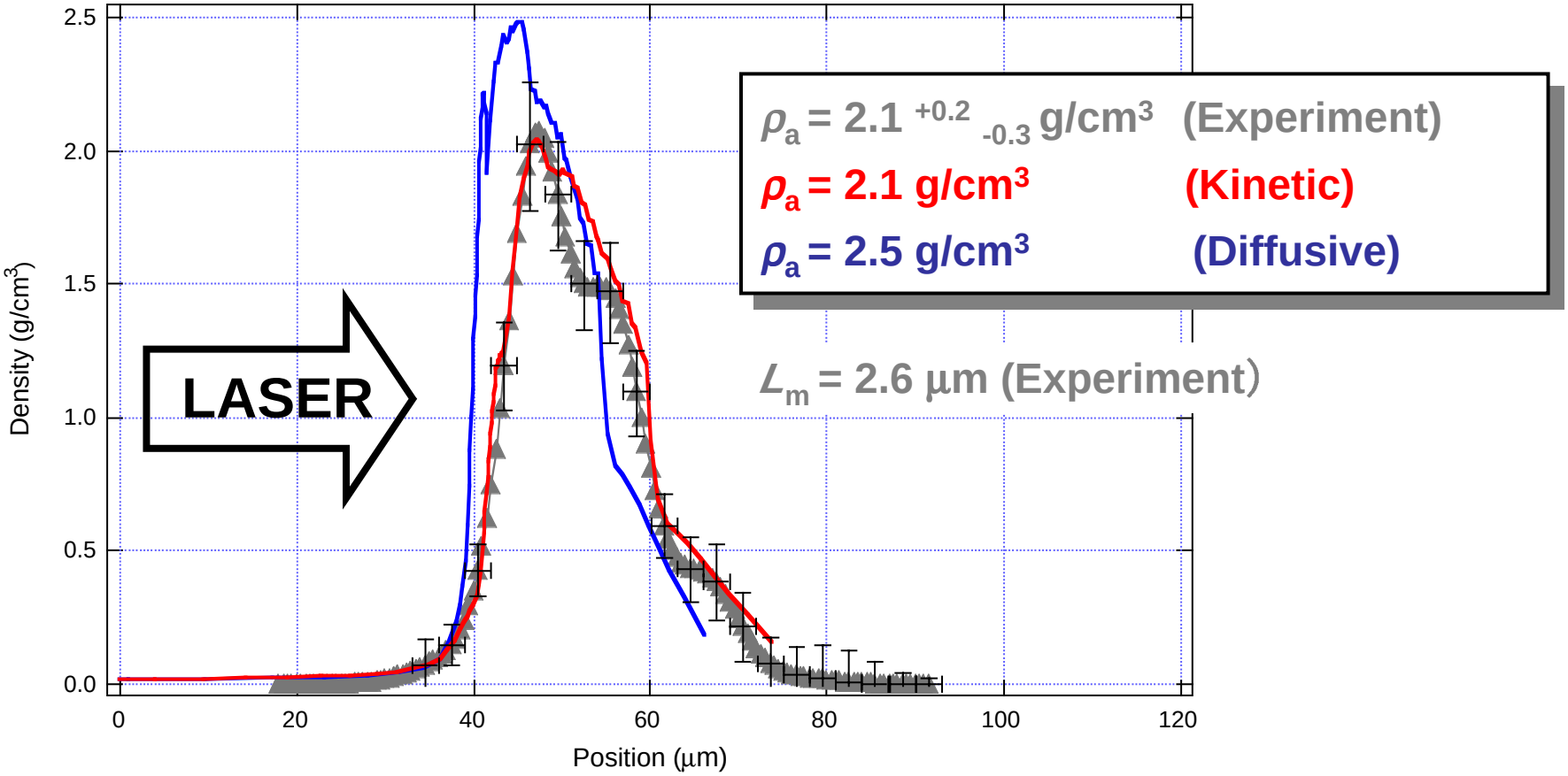

Motion blurring were cleared away by a deconvolution process with measured temporal history of backlight x-rays and velocity of targets.

summary

With advanced diagnostic techniques, we are approaching to better understanding of the Raylei-Taylor instability.

- Rayleigh-Taylor (RT) is the critical physics for high-gain IFE
- Energy transport can modify the RT growth at short wavelengths.
- Moire interferometry first observed the short wavelength RT growth.
- The observed RT growth suggests that nonlocal transport plays a role in ablative stabilization. But there is some ambiguity due to saturation.
- For independent test of the transport effect, we are measuring the ablation density with high-resolution imaging techniques.
- Initial test result is supportive to the nonlocal transport.

Our strategy is to measure all necessary quantities (γ, k, g, m, ρ_a, L) to test various RT theories.

A Vortex Model for Studying the Effect of Shock Proximity on Richtmyer-Meshkov Instability at High Mach Number

H. F. Robey, S. G. Glendinning, J. A. Greenough, & S. V. Weber

Lawrence Livermore National Laboratory
Livermore, California 94550

Presented at the 8th Meeting of the
International Workshop on the Physics of Compressible Turbulent Mixing
Pasadena, CA
December 9-14, 2001

This work was performed under the auspices of the U. S. Department of Energy by the University of California, Lawrence Livermore National Laboratory under Contract No. W-7405-Eng-48.

Issue: At high Mach number, the transmitted shock can remain in close proximity to an R-M unstable interface

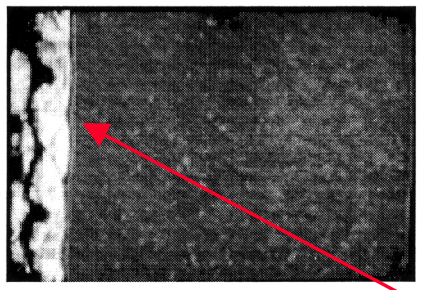

t = 2 μs

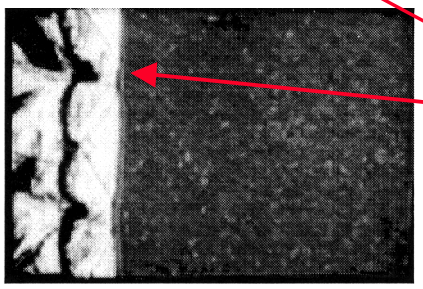

t = 12 μs

t = 37 μs

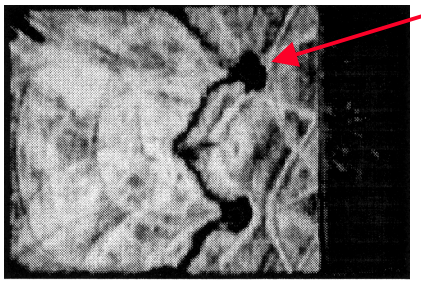

t = 57 μs

Data of Aleshin et al.
M = 4.5, ka_0 = 1.745, A = 0.45,
λ= 36 mm, a_0 = 10 mm

Shock

Perturbed interface

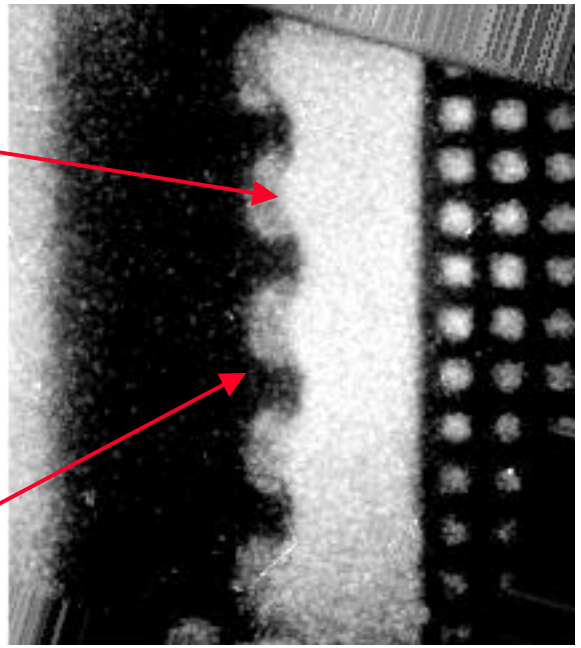

Omega data of Glendinning
M ≈ 10, ka_0 = 0.9, A = 0.47
λ = 150 μm, a_0 = 22 μm

At these high Mach number conditions, the presence of the shock can affect the Richtmyer-Meshkov growth rate

Shock proximity effect not included

Shock proximity effect included

Shock

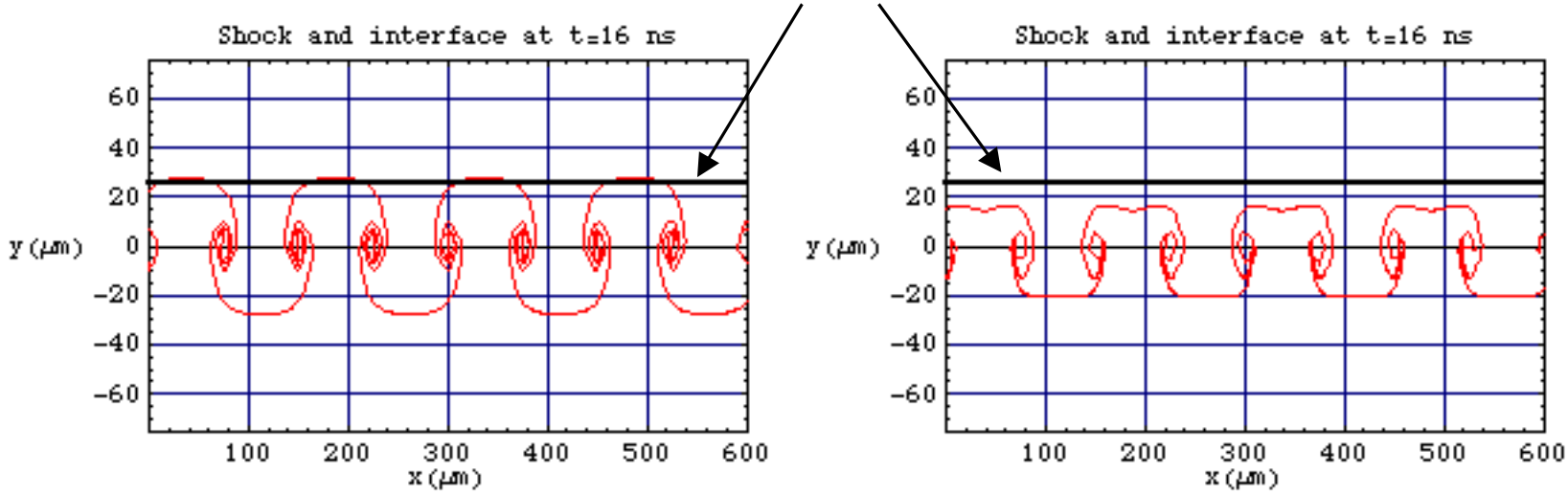

- In certain cases, the predicted linear growth rate can exceed the speed of the transmitted shock relative to the interface
- In this study, point vortex methods are used as a simple means of incorporating the effect of a transmitted shock on the instability growth

Point vortex methods can be used to approximate the evolution of interfacial perturbations throughout the non-linear regime

Following Jacobs & Sheeley*, interfacial vorticity is modeled by an alternating array of point vortices of circulation, Γ :

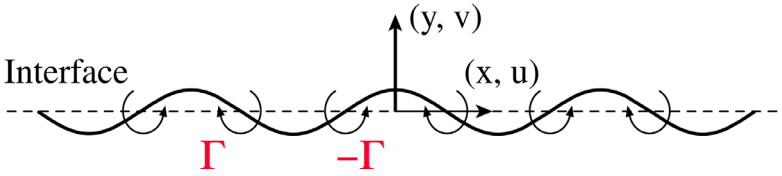

The flow evolution is obtained from a streamfunction of the form:

$$\psi = \frac{\Gamma}{4\pi} \ln\left(\frac{\cosh(ky)+\sin(kx)}{\cosh(ky)-\sin(kx)}\right)$$

$$u = \partial\psi / \partial y \quad , \quad v = -\partial\psi / \partial x$$

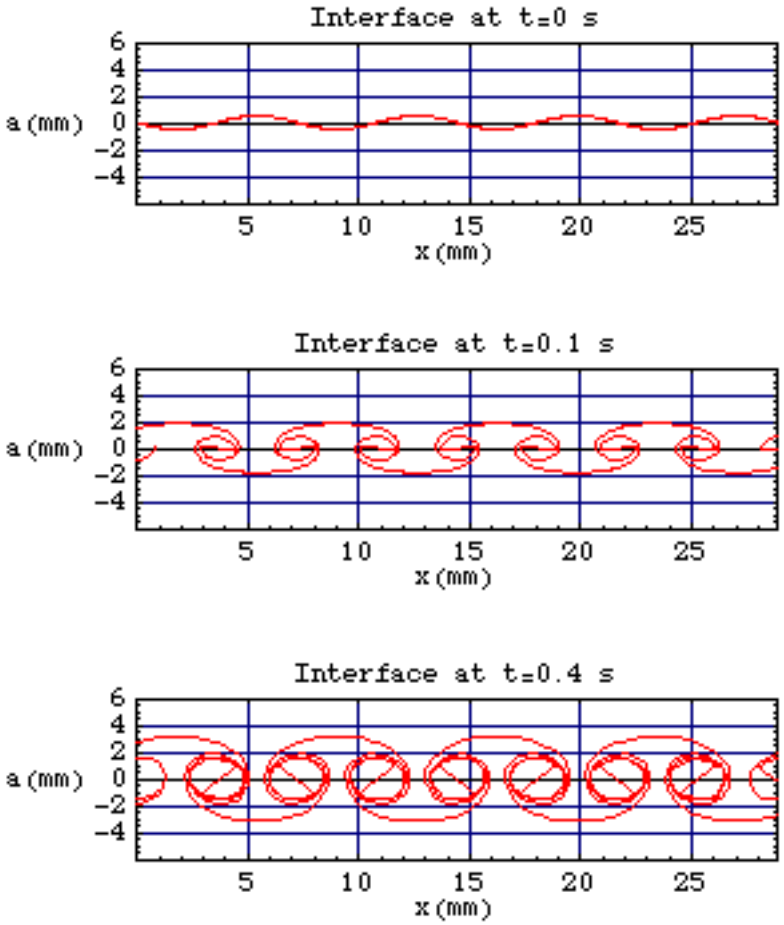

*Phys. Fluids 8(2), 405 (1996)

The incompressible, A = 0.155 experiments of Jacobs & Sheeley are well modeled by point vortex methods

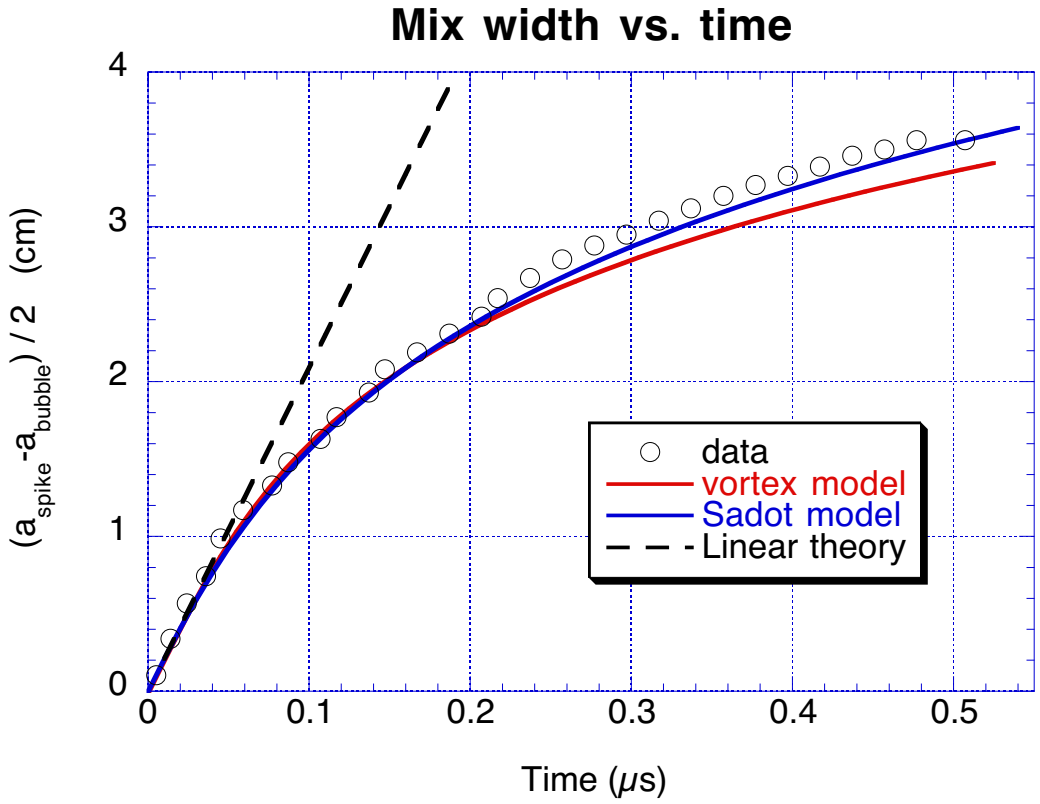

The circulation Γ is defined as that required to reproduce the initial linear growth rate :

$$\Gamma = 2\pi\, v_{IM} / k$$

- **The model of Sadot et al., PRL 80(8), 1654 (1998) is in excellent agreement with the data**

- **The vortex model predicts an amplitude slightly below the data at later time, but is within 6% of the data and the Sadot model.**

An image vortex model can be used to incorporate the effect of a transmitted shock as a downstream boundary condition

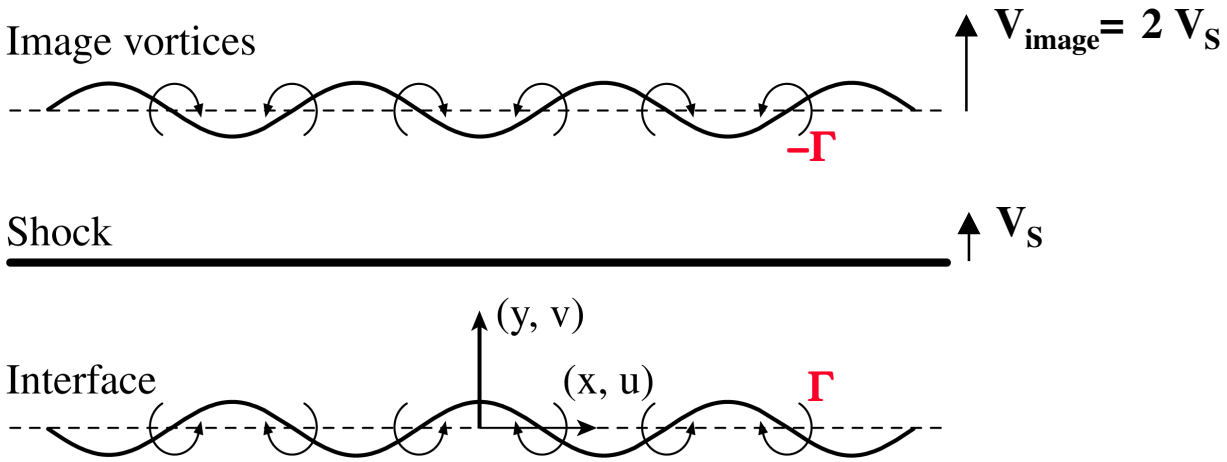

The image vortex array moves away from the interface at twice the shock-to-interface velocity

The streamfunction is now given by :

$$\psi = \frac{\Gamma}{4\pi}\left[\ln\left(\frac{\cosh(ky)+\sin(kx)}{\cosh(ky)-\sin(kx)}\right) - \ln\left(\frac{\cosh(k\,(2\,(a_0^* + V_{st}\,t) - y)) + \sin(kx)}{\cosh(k\,(2\,(a_0^* + V_{st}\,t) - y)) - \sin(kx)}\right)\right]$$

Interface vortices **Image vortices**

Though derived from potential flow theory, this model includes effects due to compressibility and finite Atwood number

Compressibility enters through the circulation which depends on the post-shock Atwood number and compressed perturbation amplitude

$$\Gamma = \frac{2\pi v_{IM}}{k} \quad \& \quad v_{IM} = kA^* \frac{(a_0 + a_0^*)}{2} u_C$$

where the post-shock Atwood number is : $A^* = \frac{\rho_1^* - \rho_2^*}{\rho_1^* + \rho_2^*}$

and post-shock perturbation amplitude is approximated as : $a_0^* = a_0 (1 - \frac{u_C}{V_{SI}})$

All model parameters are obtained from the solution of the associated Riemann problem for the unperturbed interface

Example 1: The image vortex model has been applied to the M = 4.5 shock tube experiments of Aleshin et al.

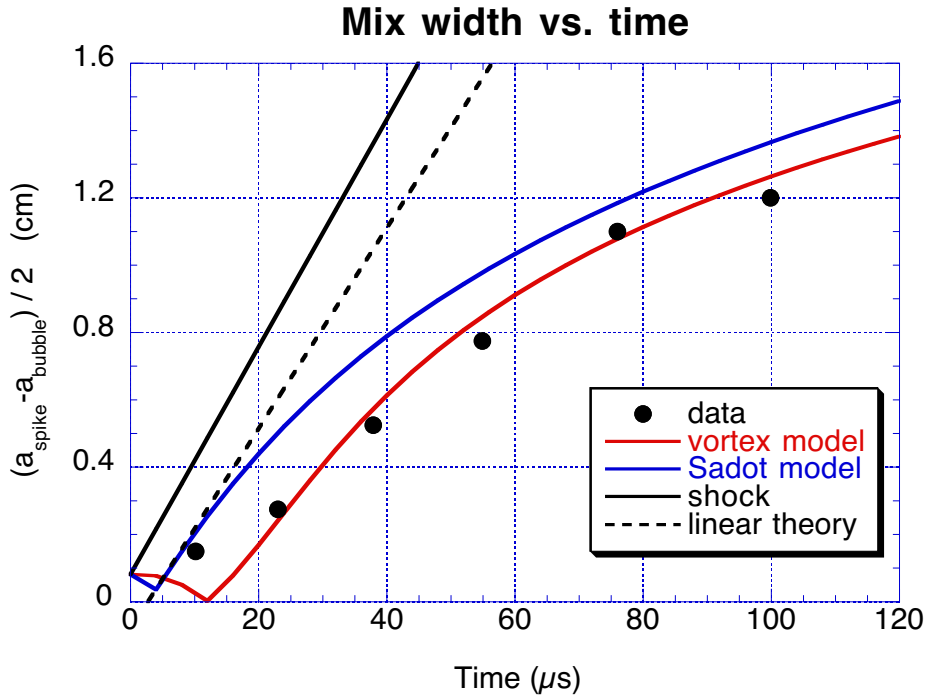

Aleshin et al., run #630B

Xe -> Ar, M = 4.5,
A = 0.45, λ = 36 mm
$2a_0$ = 20 mm (P-V)
ka_0 = 1.745

- **The data falls well below the linear theory for the entire experiment**
- **After phase inversion, the vortex model agrees well with the data**
- **The Sadot model predicts an amplitude consistently above the data.**

A look at the development of individual spike and bubble amplitudes reveals further differences

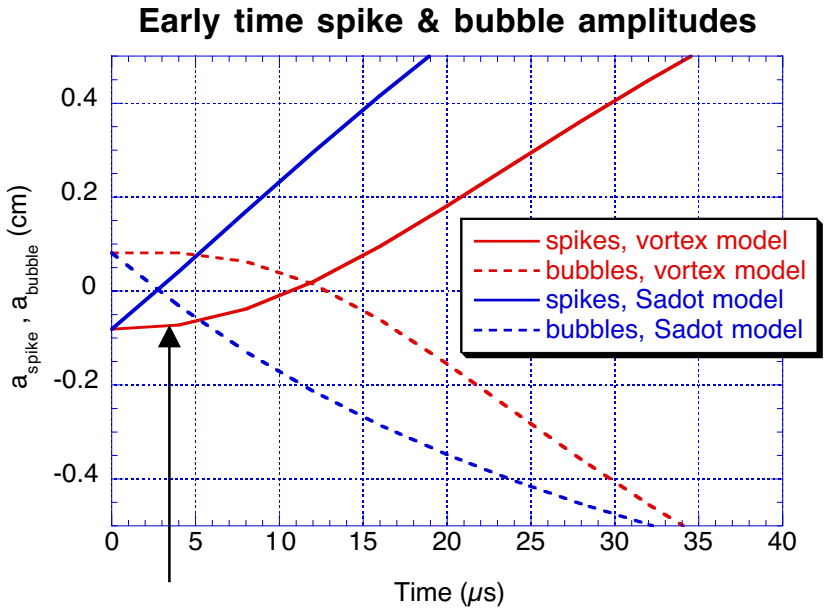

Suppressed growth early in time

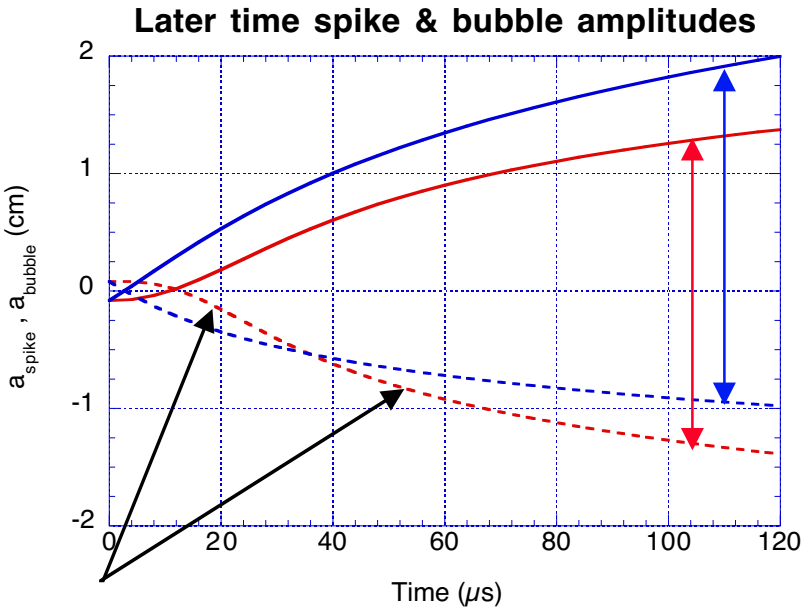

Bubble growth is initially suppressed, but later rebounds

- **The vortex model exhibits a suppressed growth early in time when the shock (and therefore the image vortex system) are close to the interface**

- **Later in time, the spike growth continues to be suppressed since the spikes remain in close proximity to the shock, whereas the bubble growth rebounds. This results in a more symmetrical bubble-to-spike development.**

The spike and bubble growth rates and asymptotic behavior also show the effect of shock proximity

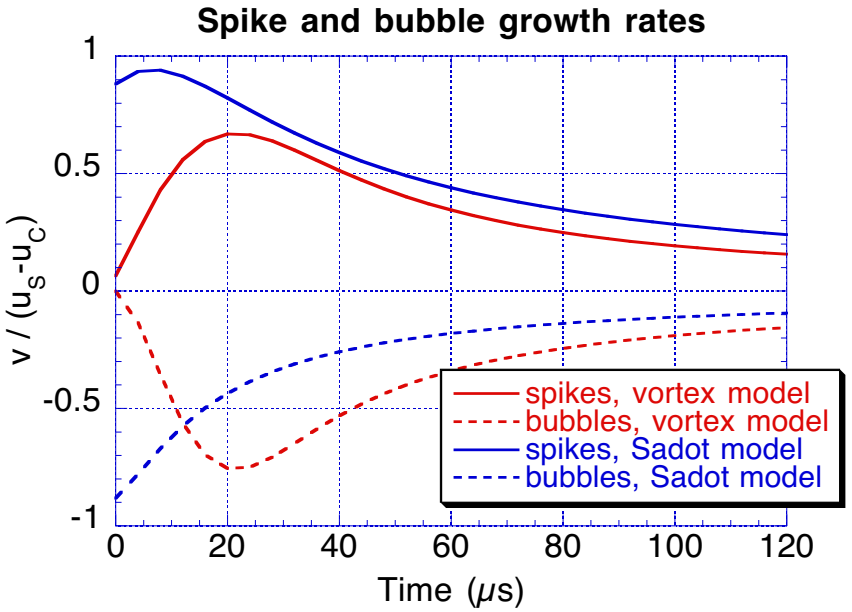

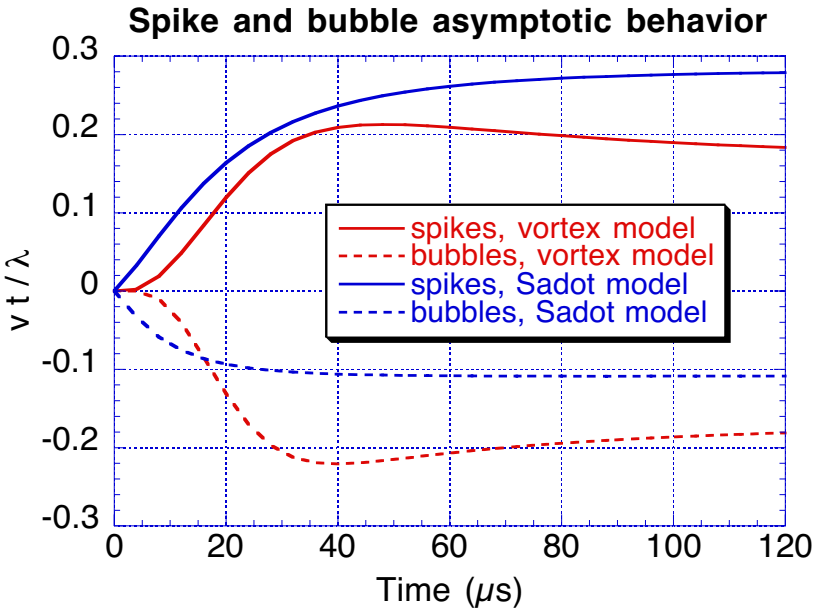

- **The growth rate of the vortex model exhibits a peak which is both reduced in magnitude and delayed in time.**
- **The delayed peak growth is qualitatively consistent with the fully compressible linear theory of Yang, Zhang, & Sharp, Phys. Fluids 6, 1856 (1994)**
- **At late time, all models asymptote to a t^{-1} behavior.**

The ratio of spike-to-bubble amplitudes quantifies a very important difference resulting from shock proximity

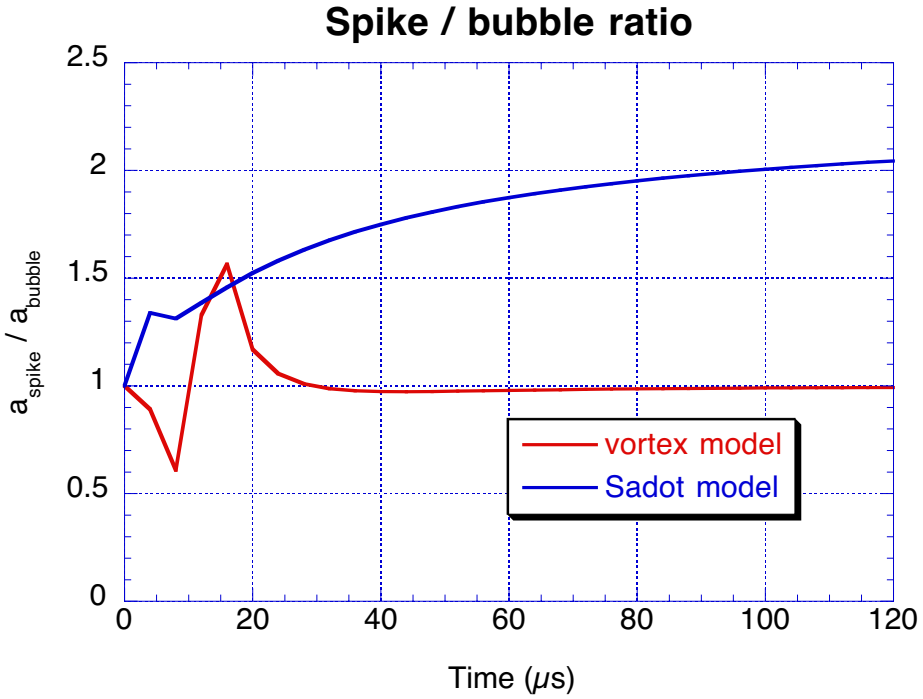

- Clearly, the spike to bubble ratio of the vortex model is due to the single fluid (A=0) assumption and is therefore wrong, right?

- To answer this question, we turn to numerical simulation

Numerical simulations of Aleshin experiment N630B have been performed using a 2D ALE code, HYDRA

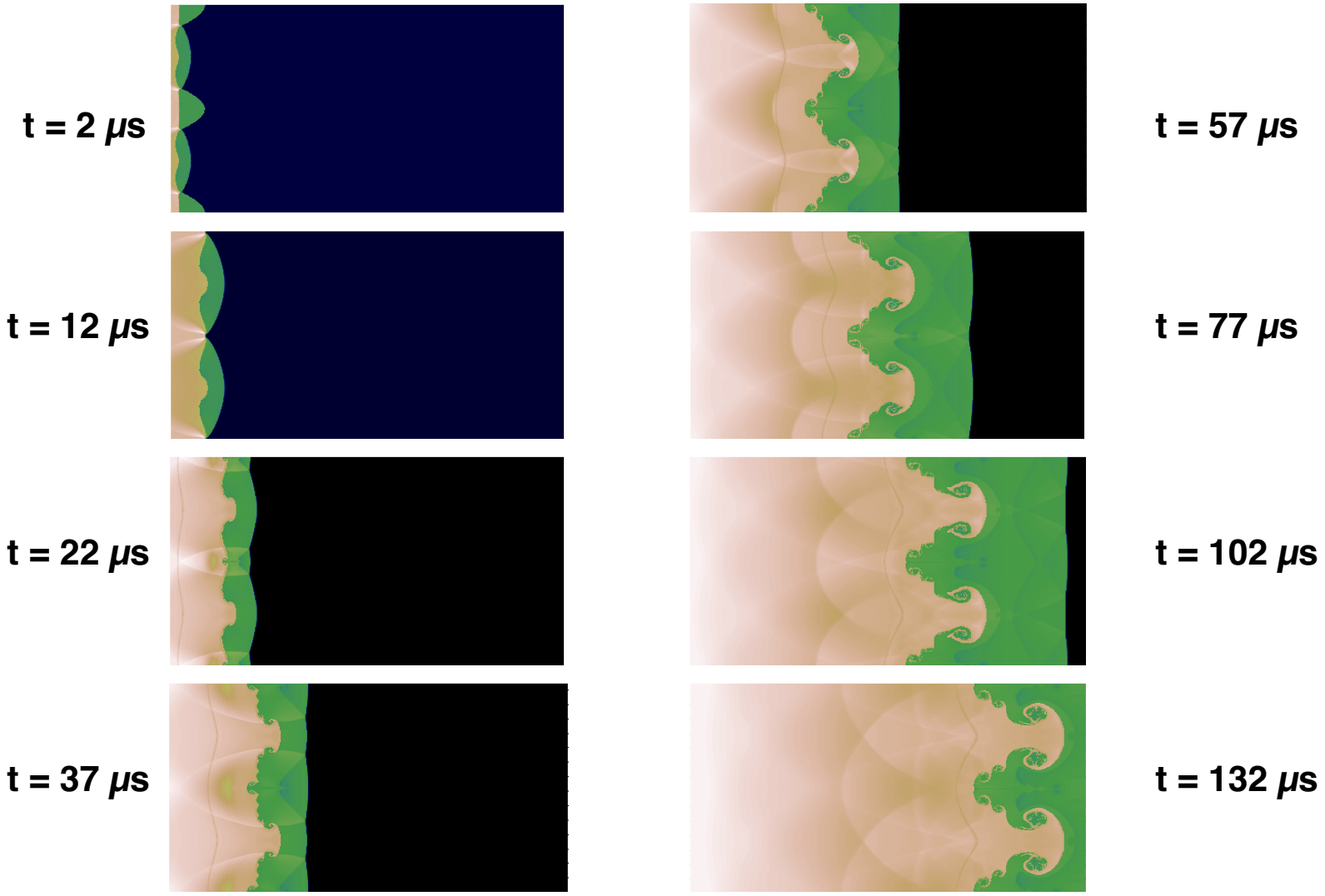

Simulations of S. V. Weber, resolution = 512 zones / wavelength

Numerical simulations of Aleshin experiment N630B have also been performed using a 2D AMR code

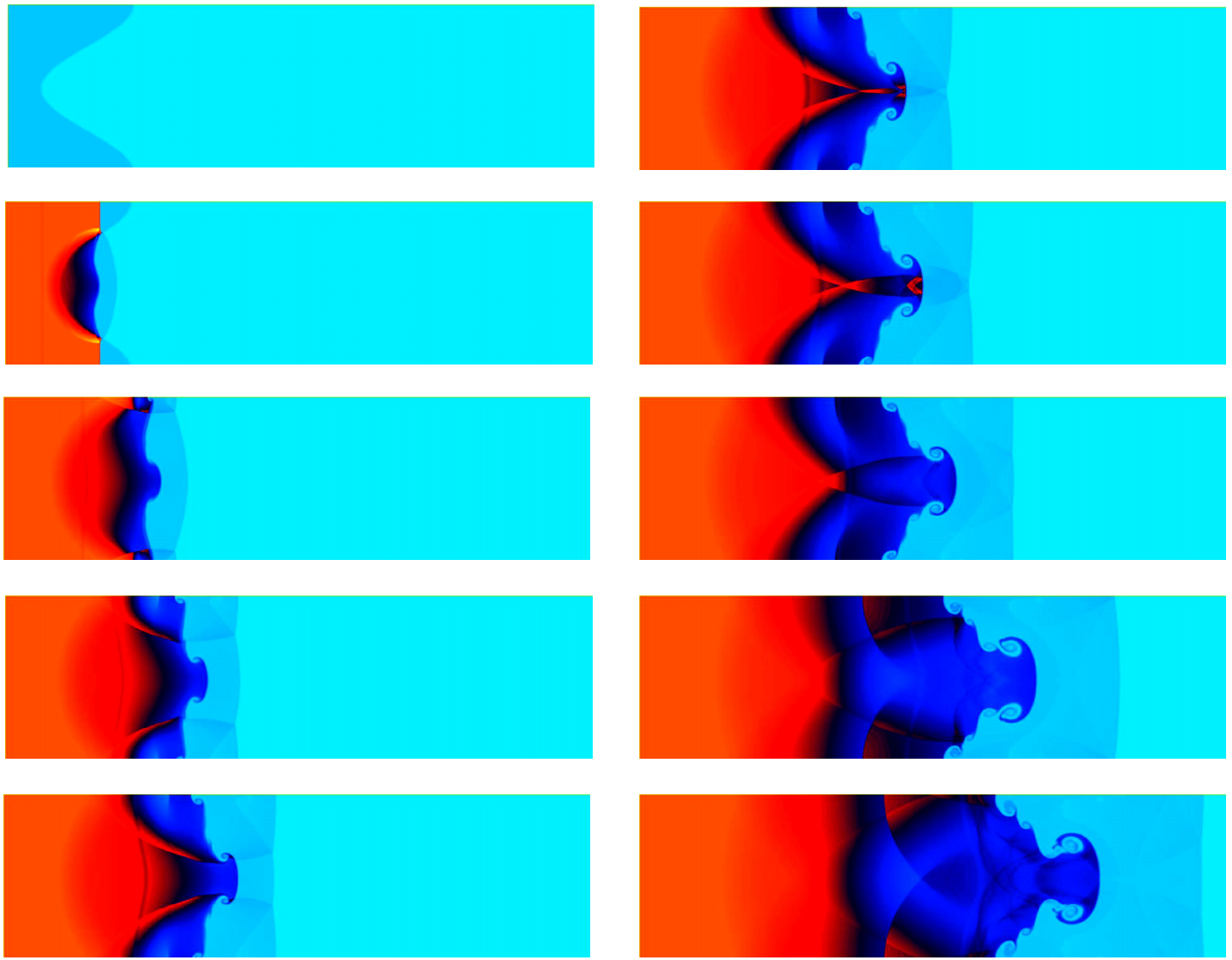

Simulations of J. A. Greenough, resolution = 2560 zones / wavelength

Both numerical simulations are in reasonable agreement with the image vortex model

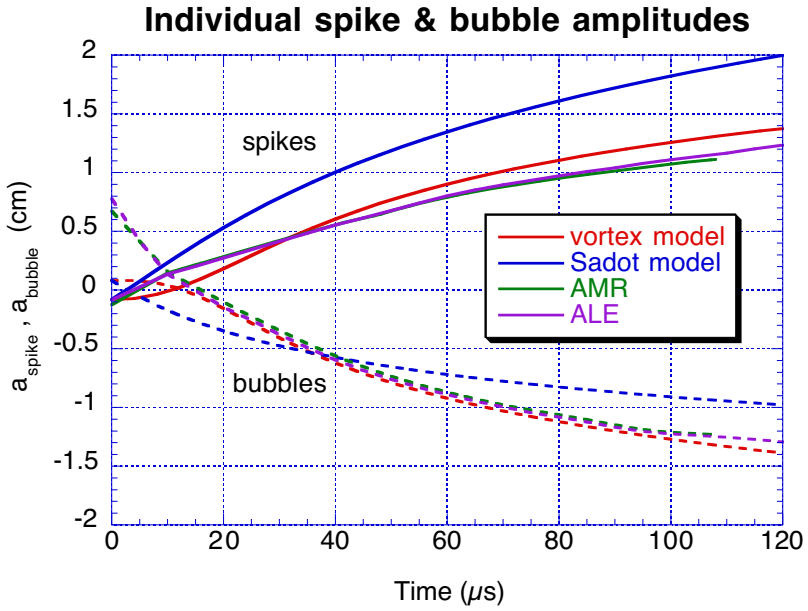

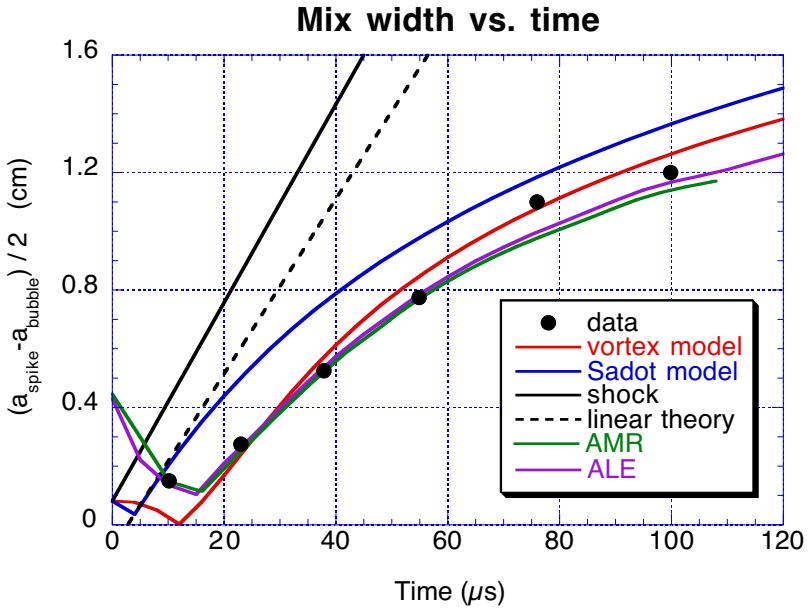

Both simulations show :

- **A delayed phase inversion due to reduced growth early in time**
- **Reduced spike growth throughout the duration of the experiment**
- **more symmetrical spike-to-bubble development**

The spike / bubble ratio obtained from the numerical simulations also agrees with the image vortex model

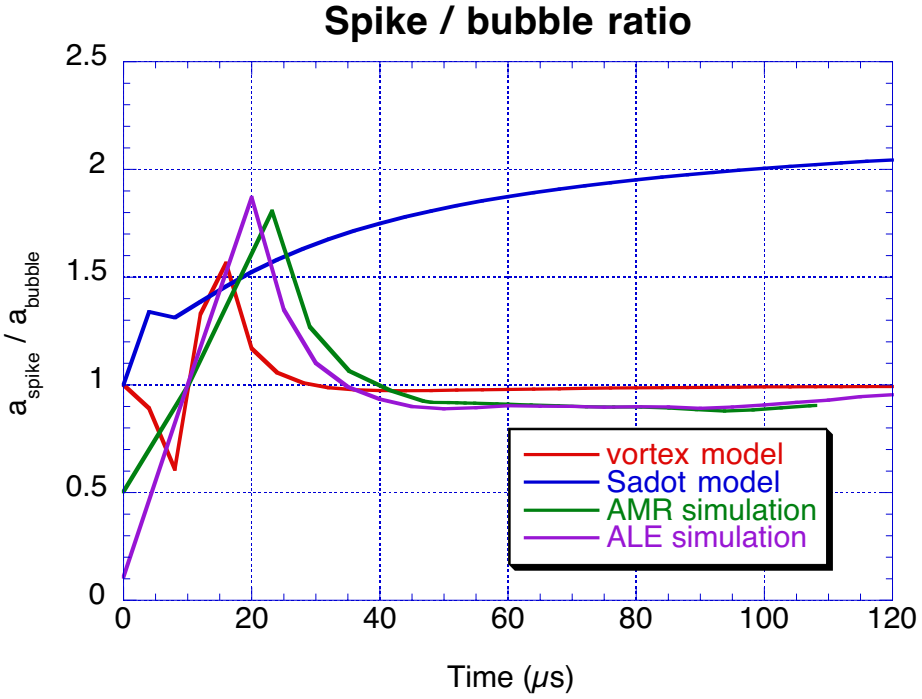

- Differences are again observed at early time as the interface inverts phase, but later the amplitude of the spikes remains less than that of the bubbles.

- This effect is not observed at lower Mach number and is an essential effect due to shock proximity.

Example 2: The image vortex model has also been applied to the Omega experiments of Glendinning et al.

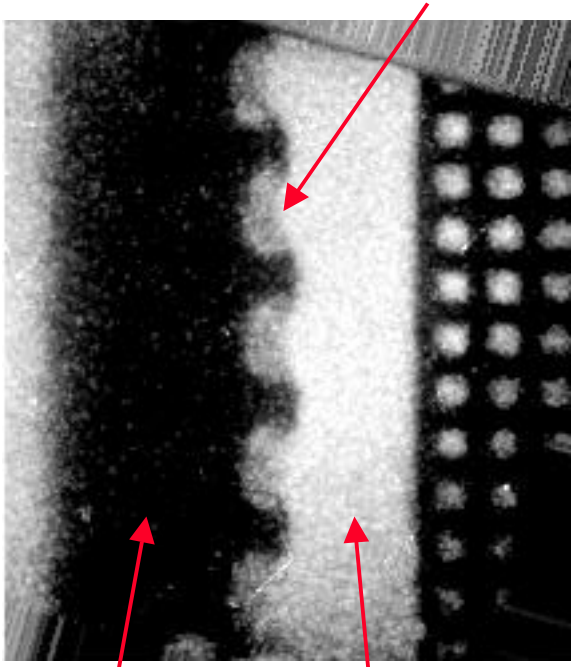

X-ray radiograph
@ t = 22 ns

This experiment differs from that of Aleshin et al. in the following :

- Higher Mach number, M ≈ 10
- Lower initial perturbation amplitude $ka_0 = 0.92$ (vs. $ka_0 = 1.745$)
- Linear theory (Meyer-Blewett) predicts a growth rate which exceeds the shock-to-interface velocity
- Phase inversion of the perturbation is completed by the end of shock refraction
- The effect of shock proximity is more pronounced than before.

The image vortex model does a reasonable job of predicting the perturbation amplitude vs. time

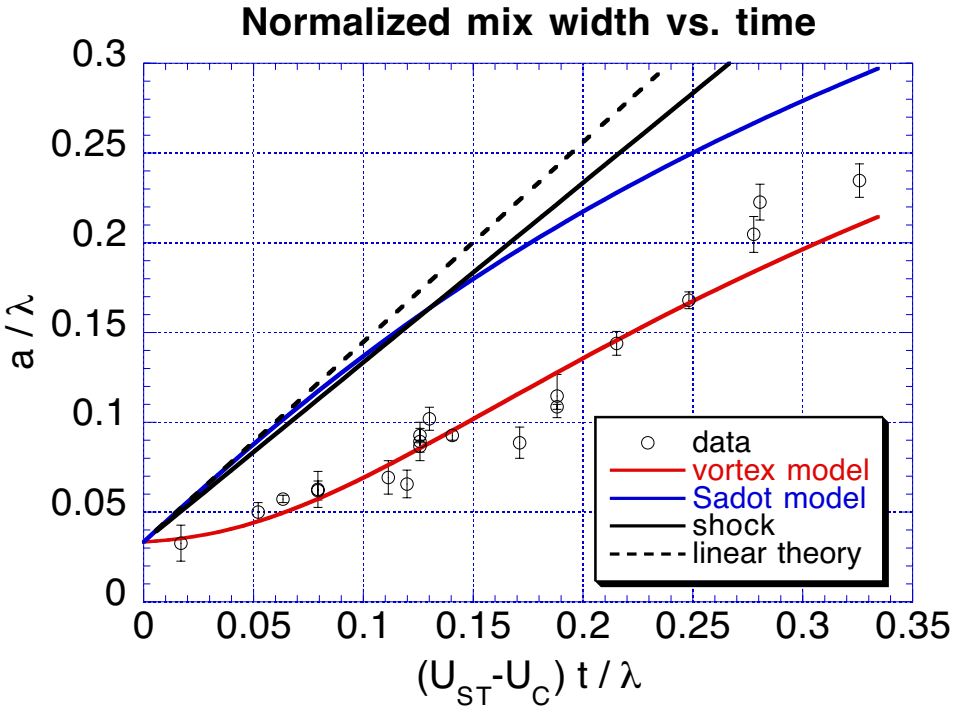

- The data is well below the linear theory at all times.
- The data shows a distinct increase in the growth rate later in time, when the normalized amplitude is small ($a / \lambda = 0.1$)
- The shock separation distance from the interface is only 0.33 λ at the latest time observed in the experiment.

Large differences are again seen in the spike and bubble growth rates due to shock proximity

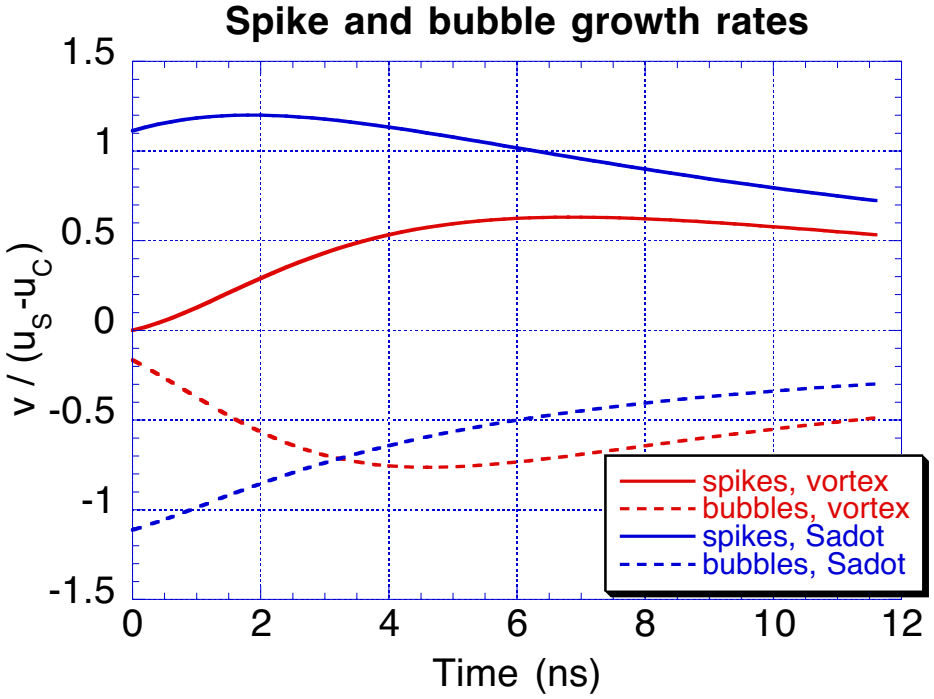

- In this case, the linear theory predicts a spike growth rate which is faster than the velocity of the transmitted shock.

- The vortex model again predicts a spike growth rate which is at all times lower than that of the Sadot model. The peak growth rate does not occur until ~ 6ns after passage of the shock

The spike / bubble ratio again shows large differences

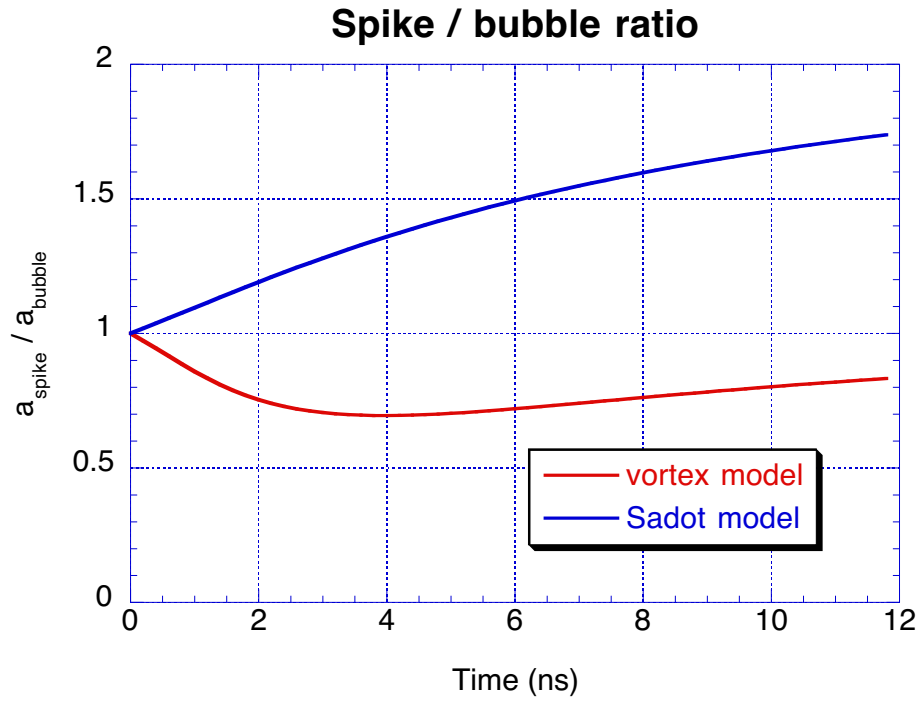

- **The large supression of the spike growth results in a spike amplitude which remains considerably lower (20-30%) than the amplitude of the of the bubbles.**

Conclusions

- An image vortex model has been presented as a simple means of incorporating the effect of a transmitted shock as a downstream boundary condition on the growth of a Richtmyer-Meshkov unstable interface.

- At low Mach number, the vortex model agrees well with the incompressible experiments of Jacobs and Sheeley and also agrees well with the model of Sadot et al.

- At high Mach number, the image vortex model agrees well with shock tube experiments of Aleshin et al. (M=4.5) and laser-driven experiments of of Glendinning et al. (M>10).

Conclusions, continued

The effect of shock proximity is distinguished from saturation effects due to large perturbation amplitude in the following:

- **For shock propagation from heavy to light, the Atwood number dependence observed at lower Mach number is significantly altered due to the presence of the shock boundary. For the two cases discussed, the spike amplitude remains slightly less than that of the bubbles throughout the experiment.**

- **The perturbation growth immediately following passage of the shock is significantly smaller than that given by the linear theory. As the shock departs from the interface, the growth rate increases. Later in time, as the perturbation amplitude increases, normal growth rate saturation effects are seen.**

Review on RTI, RMI and TM experiments

J-F Haas CEA/DIF & S G Zaytsev ENIN

a discussion based on the analysis of past (5th, 6th & 7th) workshops and other meetings : 21, 22 & 23rd ISSW (International Shock Wave Symposia), 51 & 53rd APS/DFD (American Physical Society, Division of Fluid Dynanics), 43rd APS/DPP (Division of Plasma Physics), recent ECLIM & IFSA conferences.

Acknowlegements to CEA colleagues with whom some of these meetings were analysed for our official trip reports, recent IWPCTM organizers, contributors of the 23rd ISSW who let us consult their very recent work (July 2001) and colleagues who spontaneouly sent their papers.

Apologies to all contributors for any omissions, distorsions, low quality reproduction of their high quality work and general imperfections for this difficult exercise.

See this as a draft for our contribution to the summary experimental roundtable ?

Outline of this review

- Introductory statistics

We cite the conclusions of roundtable for experiments at mix 99 and add comments

- Incompressible experiments
- Shock-tube for planar shock waves
- Convergent flows
- Explosively driven flows
- Laser driven flows

There is a wide spectrum of experiments
but we have a clearer view of shock tubes

- Conclusions

Relative importance of experimental contributions in CTM workshop series averages 40 %

1st Princeton 1988 : ? (misplaced Proceedings)

2nd Pleasanton 1989 : ? (misplaced Proceedings)

3rd Royaumont 1991: poster 6/24, oral 12/25

summary 18 exp / 49 total = 37%

4th Cambridge 1993: RT 10/17, RM 9/14, KH 2/8, laser 4/4, converging flows 2/7 : summary 27 exp / 61 total = 44% *

5th Stony Brook 1995: 23 exp / 53 total = 43 % *

6th Marseille 1997: 44 exp / 96 total = 46% *

7th Saint Petersburg 1999: 53 exp / 126 total = 42 % *

8th Pasadena 2001: poster 25/63, oral 25/66,

summary 50 exp /129 total = 39%

* does a proportion above 40% correlate with stronger russian attendance ?

mix 99 : summary roundtable for experiments :

incompressible domain (J. Jacobs spokesman),

Interpreted by E. Meshkov, L. Houas & JF Haas for report in the ERCOFTAC bulletin (2000) and the proceedings of the 7thIWPCTM

It had been pointed out that even if a lot of experiments, for both low Atwood numbers in the miscible and high Atwood numbers in the non-miscible ranges, have been successfully undertaken, the initial conditions generally still remain unknown.

Consequently, it was suggested for future work to carry large Atwood number experiments for miscible liquids, as well as to evaluate the importance of the surface tension in the RTI development.

In any case, the emphasis was made on the fact that the initial conditions must be known. From the other hand, more complex geometry experiments (multi-layer) are welcome for a better understanding of the influence on the exponent a of the mixing zone thickness evolution law.

In a near future, the influence of medium on the 2D-3D transition will also be greatly interesting.

Cold and slow Rayleigh-Taylor experiments allow the most precise measurements and richest interplay with theory

- **Ordinary set-ups (as seen by the fluid mechanics community):**
  - Texas A & M : stationary mixing of co-flowing liquids under earth gravity @ low Atwood (small DT):
    - thermo-couples measurements for (long) time evolution of local density, statistics compared with spectral models (LANL),
    - PIV-S (for scalar) for combined instantaneous maps of velocity and density, velocity-density correlations
  - continuous mixing of co-flowing gases in curved channels (ancient CalTech work in Roshko's group)
  - Some work was in progress at Univ. of Washington (Breidenthal)
  - We need to communicate with the « non RTI-induced » mixing community (for instance, in Europe the ERCOFTAC 's Special Interest Group on variable density low speed turbulent flows).

Cold and slow, incompressible experiments (continued)

Conventional Rayleigh-Taylor set-ups

• Cambridge : great attention to the control & analysis of perturbations induced by the separating barrier removal, double interface, tilted interface, concentration measurements from fluorescent dye in arc lamp light sheet

•CalTech : RTI for miscible fluids

•Univ. of Arizona : tank accelerated downwards by weights (g above gravity)

Non-conventional (i.e. non shock-induced) Richtmyer-Meshkov set-ups

•Univ. of Arizona : falling tank bouncing on springs with long inertial flight thereafter: laser sheet visualisation of incompressible linear & non-linear RMI

•Univ. of Catalunya : similar principle reported by Redondo in 1993 : falling tank suddenly stopped on foam pad.

More vigorous incompressible RTI experiments : a VNIITF specialty but the Linear Electric Motor facility of LLNL has become famous

At VNIITF, the setups EKAP and SOM have an high acceleration range : 100-1000 g and provide various acceleration histories (acceleration, braking, inertial)

Vertical gas guns for propelling experimental packages with various liquids :

(various Atwood, unmiscible and soon miscible, various interface geometries)

Various diagnostics : shadowgraph, X-rays, laser sheet soon ?

At LLNL, the LEM is characterized by controllable acceleration, state of the art diagnostics and imaginative liquids (yogurt)

Sorry, for this very uncomplete overview, the « alpha » group should take over...

mix 99 : summary roundtable for experiments (continued).

Planar shock tube experiments (JF Haas et al.)

There are 12 experimental laboratories involved with the conventional shock tube experiments :
AWE : (Aldermaston), ENIN (Moscow), CEA (France), IUSTI (Marseille), LANL, University of Arizona, University of the Negev (Beer-Sheva, Israel), University of Wisconsin (Madison), CalTech (Pasadena), SWRC (Tohoku University, Sendai), VNIIEF (Sarov) and VNIITF (Snejinsk).

Flow definition

In a first plot we attempted to classify the various flows to be studied :
-horizontal axis for flow compressibility, connected to the incident shock Mach #
-vertical axis for instability strength : At k h
An issue loosely linked to the issue of deterministic vs. random initial interface

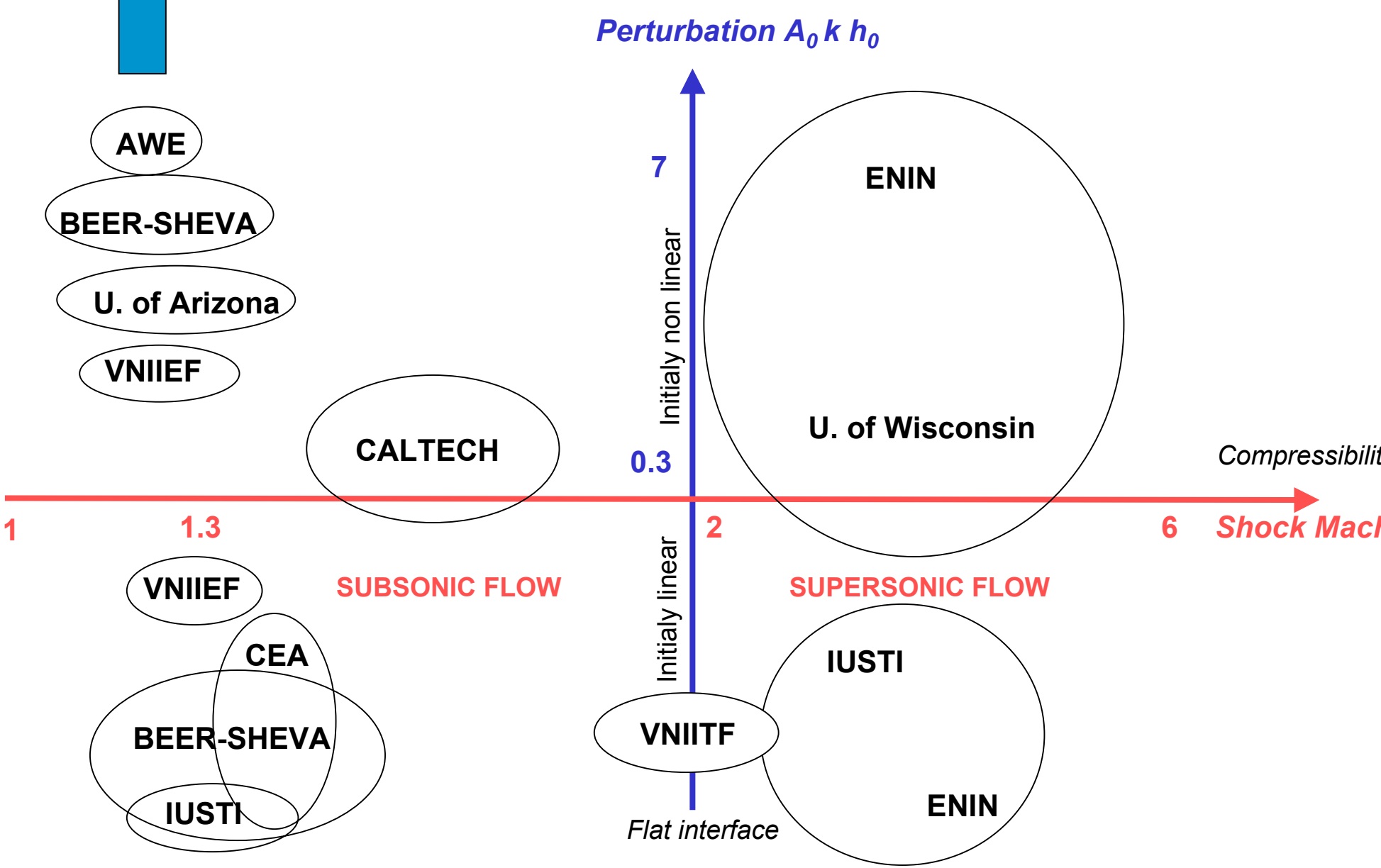
Perturbation $A_0 k h_0$
AWE
BEER-SHEVA
U. of Arizona
VNIIEF
CALTECH
7
Initialy non linear
ENIN
U. of Wisconsin
0.3
Compressibilit
1
1.3
2
6
Shock Mach
VNIIEF
SUBSONIC FLOW
SUPERSONIC FLOW
CEA
BEER-SHEVA
IUSTI
Initialy linear
IUSTI
VNIITF
ENIN
Flat interface

mix 99 : summary roundtable for experiments (continued).

Planar shock tube experiments (diagnostics)

Schlieren and shadowgraph visualizations,
the laser sheet with the following principles : Mye scattering by particles
planar laser induced fluorescence (PLIF) using tracer molecules,
the Rayleigh diffusion (differential among gases)
the particle image velocimetry (PIV), the laser Doppler velocimetry (LDV),
the hot wire anemometry (HWA), the CO_2 infrared emission and absorption,
the X-ray absorption (X-Ray),
the interferometry (ENIN, SWRC), differential interferometry (CEA).

In a second plot, we sought to relate the performance of diagnostics to its usefulness for physical understanding, hence modelling and simulation : not so simple !

It should be obvious that an experiment has to be imaginatively designed before spending time and money on sophisticated diagnostics

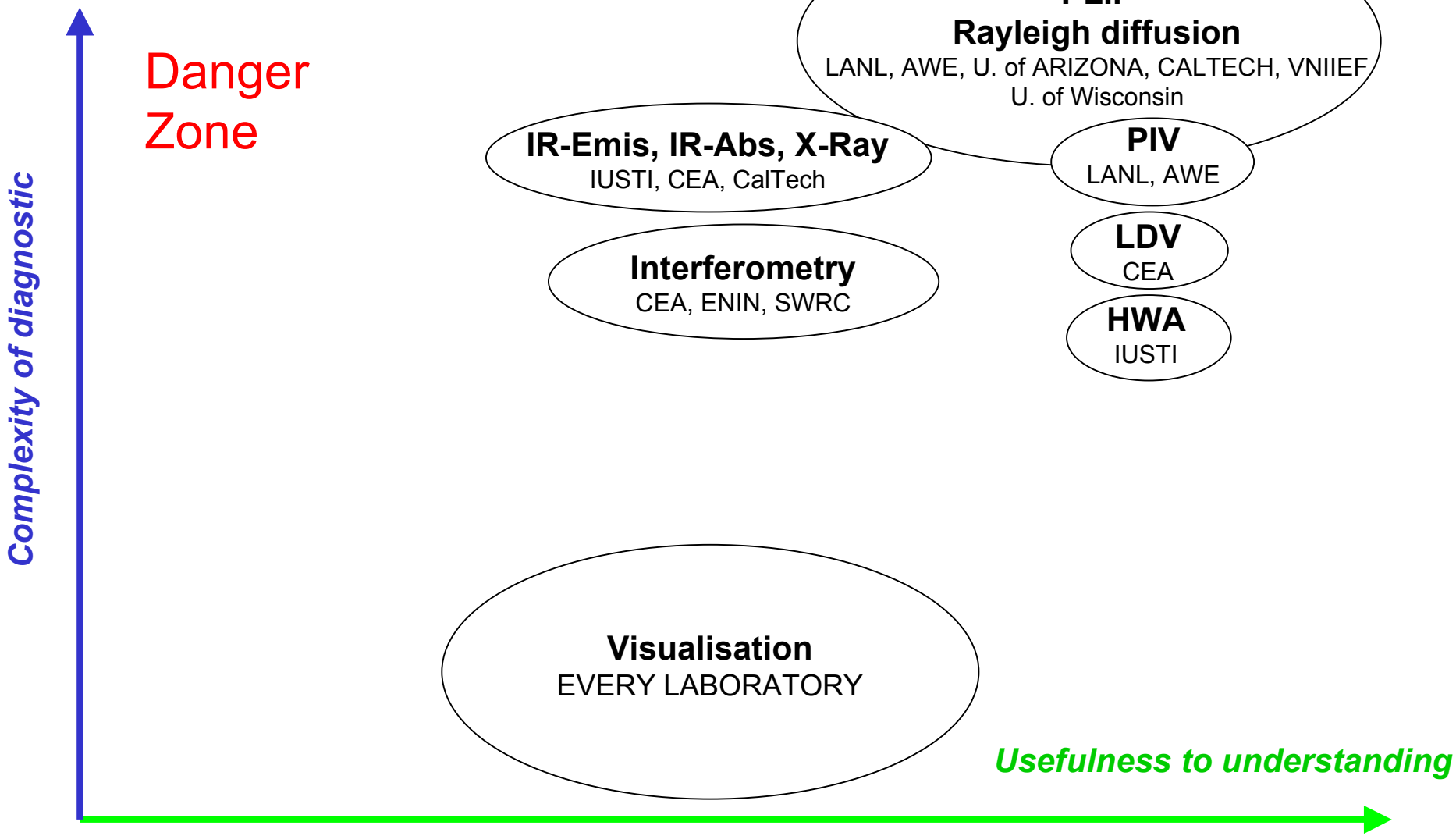
Danger Zone
Complexity of diagnostic
Usefulness to understanding
Mye Scattering
PLIF
Rayleigh diffusion
LANL, AWE, U. of ARIZONA, CALTECH, VNIIEF
U. of Wisconsin
IR-Emis, IR-Abs, X-Ray
IUSTI, CEA, CalTech
PIV
LANL, AWE
LDV
CEA
Interferometry
CEA, ENIN, SWRC
HWA
IUSTI
Visualisation
EVERY LABORATORY

mix 99 : summary roundtable for experiments.

Shock tube experiments (continued)

The choice of the "usefulness to understanding" axis on the second graph was problematic as no laboratory would like to be positioned on the left side !

As an afterthought, we could have drawn instead a map with two axis, one dedicated to the measurement of the density field, the other for the velocity field.

The distance from the origin could be proportional to the probed volume (local vs. global).

Most of the presently used diagnostics would then be positioned on the density axis, LDV and PIV on the velocity axis and the HWA somewhere in between (probably closer to the density as explained on the poster E37).

Density versus velocity diagnostics,

distance from origin : probed volume

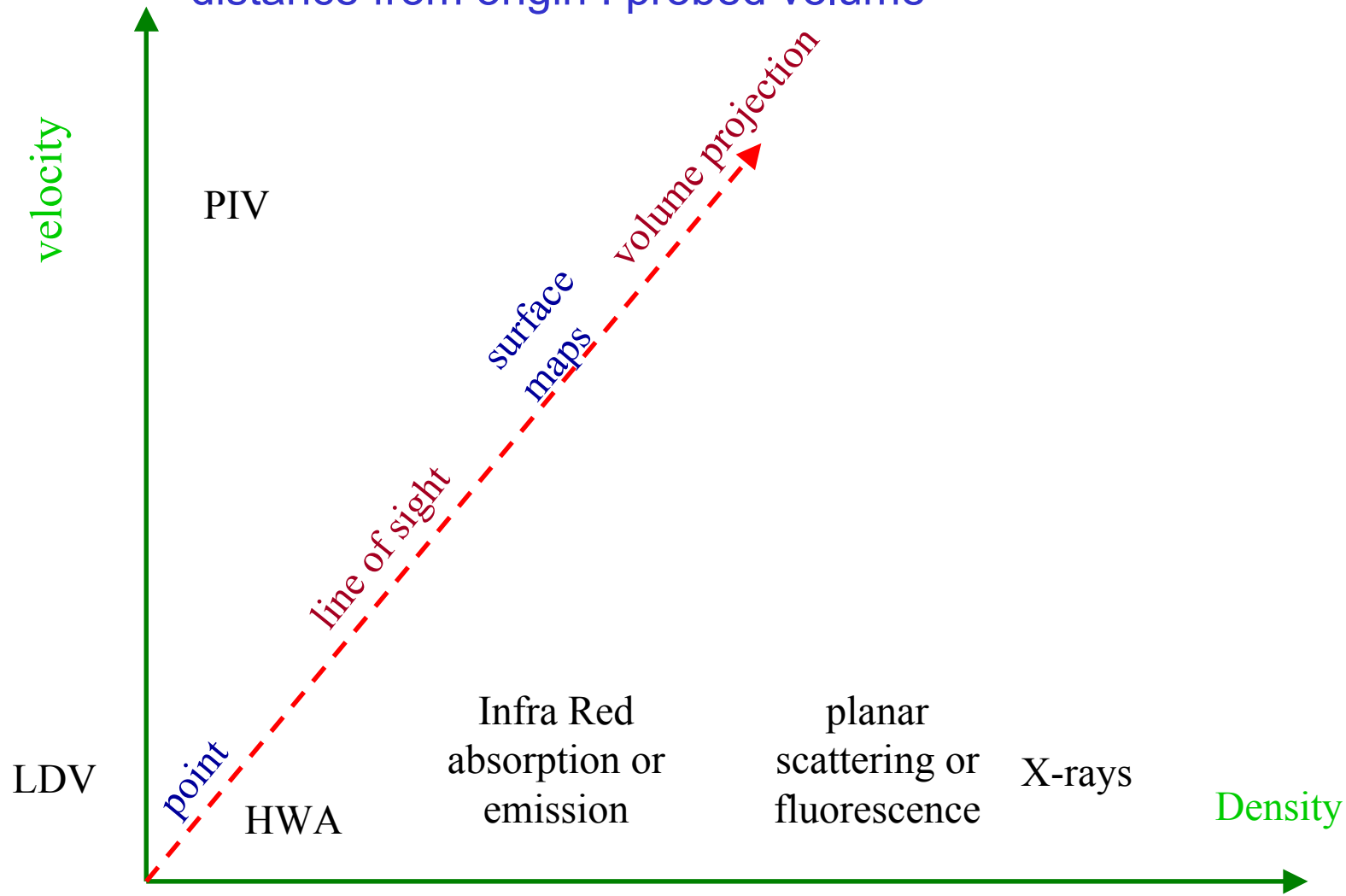

mix 99 : summary roundtable for experiments.

Shock tube experiments (continued)

The discussion pointed out the parameters such as interface geometry, the shock tube dimension and the initial interface control.

Again, it appears that the initial conditions, both wavelengths and amplitudes of the perturbations and the mechanical properties of the membrane, must be known.

An effort has to be undertaken on this fundamental point of interest for the next conference.

Richtmyer-Meshkov shock tube experiments : some issues on flow definition

single mode interface (Arizona, Wisconsin, Caltech)
deterministic multiple mode (ENIN, Beer-Sheva)
simple geometries : transverse curtain, round jet, tilted plane, step, bubbles (LANL, AWE, VNIIEF)
undetermined, multimode planar interface (CEA, IUSTI, VNIIEF, VNIITF, ENIN)

continuous or discontinuous interfaces : the killing of small scale turbulence or the membrane problem ?

low / high Mach # : incompressible / compressible flow

the Reynolds # : transition to turbulence, boundary layers

shock and reshock (of variable strength, ENIN)

Review on RT, RM & TM experiments
The issues on shock tube diagnostics

Shadowgraph & Schlieren (AWE, Beer Sheva, Marseille)

Interferometry (Sendai, Moscow, CEA)

Flash X-rays (CalTech, CEA-Vaujours)

Laser sheet visualization

- Mye scattering (VNIIEF, AWE)
- Rayleigh scattering (CalTech & Los Alamos, Madison)
- Planar laser induced fluorescence

Velocity measurements : PIV (Los-Alamos), LDV (CEA)

Combined velocity & concentration : HWA (Marseille)

Cleanest looking results for membrane-less experiments and macroscopic perurbations with laser sheet diagnostics

•Excellent measurement of RMI growth rate @ Mach 1.1-1.2 for single mode linear & non-linear regimes (U. of Arizona) : comparison with analytical models.

•Turbulent mixing soon arising from RMI @ Mach 3 (U of Wisconsin) :

after schlieren observations of discontinuous interfaces (with code comparisons), the initial interface is now controlled by gravity-induced RTI after sinusoidal plate removal and observed using planar Mye scattering.

Precise comparison of experiments of shocked SF6 curtain or cylindrical SF6 jet @ Mach 1.2 with simulations (Los Alamos) :

good agreement for concentration field, but low experimental velocities as compared to code, very detailed discussions about codes : first order « better » than second order, use of turbulence models.

•Archetypal (late 8O's) shocked SF6 or Helium gas cylindrical jet at Caltech using PLIF (Jacobs) and Rayleigh scattering (Budzinski) in large shock tube @ Mach 1.1 - 2.0

•Wish from a simulation specialist: good measures of mixed mass of accelerated heavy gas jets ?

But membrane based interfaces still have a future : they can enhance TM at small scale and can be destroyed

VNIIEF relies on irregular membranes or on burning by combustible gas mixture prior shock

VNIITF has invented the MIRAGE membrane with controlled burning

ENIN lets the hot shocked gases burn the membrane

CEA and IUSTI slice the membrane with a very fine wire mesh

An important effort on the analysis of laser sheet based diagnostics :

AWE experiments on shocked SF6 layers with discrete downstream defects and membrane : good agreement with 2D or 3D code using postprocessor for multiple scattering (now 10th order, see Holder et al.).

Other important issues were presented by the AWE team in Marseille : characterisation of photographic film and laser sheet intensity, removal of membrane fragments : a good example for the recently started effort at IUSTI and the one just starting one at CEA.

Other shock-tube experiments with laser sheet diagnostics have been long around or are just starting.

VNIIEF(Sarov) : tilted and step interface with cigarette smoke, comparison with 2D or 3D code

IUSTI (Marseille) : multimode air/helium and air/krypton interface using Mye scattering in new large shock tube with pulsed copper vapor laser (as in AWE, see poster E17 by Houas et al.)

CEA (Bruyères) : preliminary shots on planar interfaces using Mye scattering from prehistorical single pulse 2 Joule ruby laser (see abstract E21 by Lassis et al., but poster is not available).

Other visualization and densitometry methods

Classical refractive visualisation (shadowgraph, schlieren) still in use : Beer Sheva, IUSTI, ENIN (Moscow), VNIITF, VNIIEF, CEA

Interferometry at ENIN and SWRC (Sendai, Japan)

Differential interferometry, useless in turbulence, just as qualitative as color schlieren (CEA, reported in mix 95, to be revived?)

Flash X-ray densitometry (Caltech, mix 89, CEA, mix 93&95, to be revived), needs xenon as absorber of low energy X-rays but provides an excellent averaged concentration in turbulence

Laser interferometric tomography (Bashurin et al., Sarov) : the principle of LIT was described in Stony Brook and its application to a propane jet in air and to wire explosion in air was shown in Marseille : application to RT&RM induced mixing ?

Infrared emission and absorption was explored at IUSTI from 1985 to 1995.

Point velocity and density measurements are motivated by modelling needs in 1D code, 2D exp. maps are better suited to comparison to 2D & 3D simulation ?

•Laser Doppler Velocimetry (LDV): was used on planar air/SF6 interfaces in CEA-Vaujours (Poggi et al., mix 97) : direct measurement of velocity, no detection of mixing zone passage by itself. To be used again in CEA-Bruyères in a larger shock tube (abstract E21). Non intrusive but seeding required, OK for reshock.

•Constant temperature hot wire anemometry (CTA) explored in IUSTI since 1997 : the signal is a fonction of concentration and velocity. Recent analysis (poster E37) shows that the density is better resolved than velocity. Intrusive method, problematic for reshock.

•Simultaneous measurements of LDV and CTA in CEA in 2002 ?

•Small scale resolution : LDV OK, CTA and PIV problematic ?

•PIV seems ideal for large structures, long time development of instability.

85 mm × 85 mm test section of IUSTI 's shock tube for hot wire measurement of RMI-induced Mixing Zones

The wire is 1.25 mm long has a diameter of 5 µm and breaks too often !

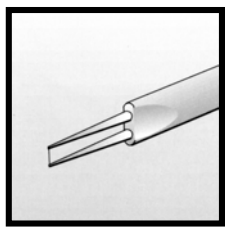

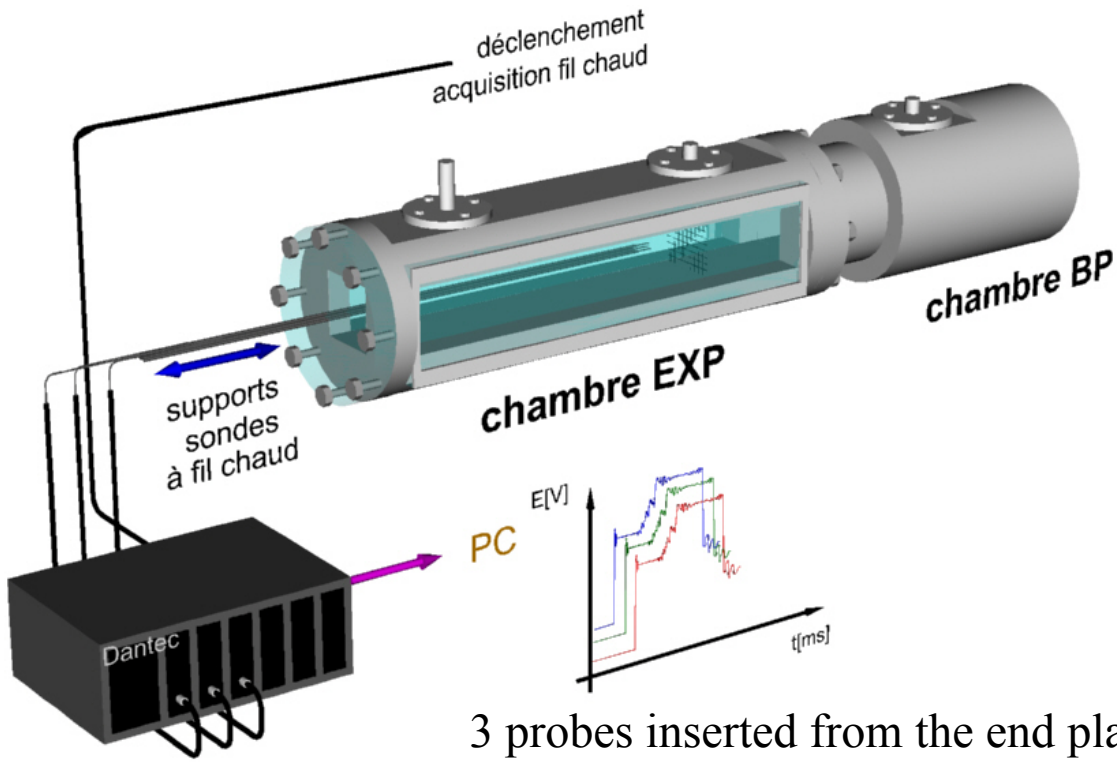

3 probes inserted from the end plate

Borrowed from Laurent Schwaederlé 's presentation for his succesful thesis defense on December 7th 2001

Constant temperature hot wire anemometry @ IUSTI Marseille

The signal clearly shows the mixing zone passage and yields the local density time evolution

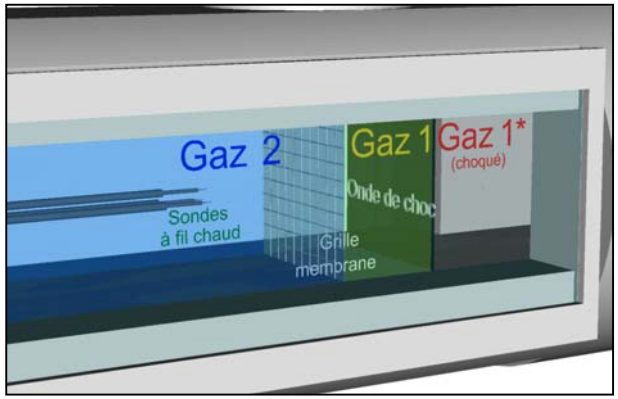

But the probes are intrusive and will disturb the reshock phase

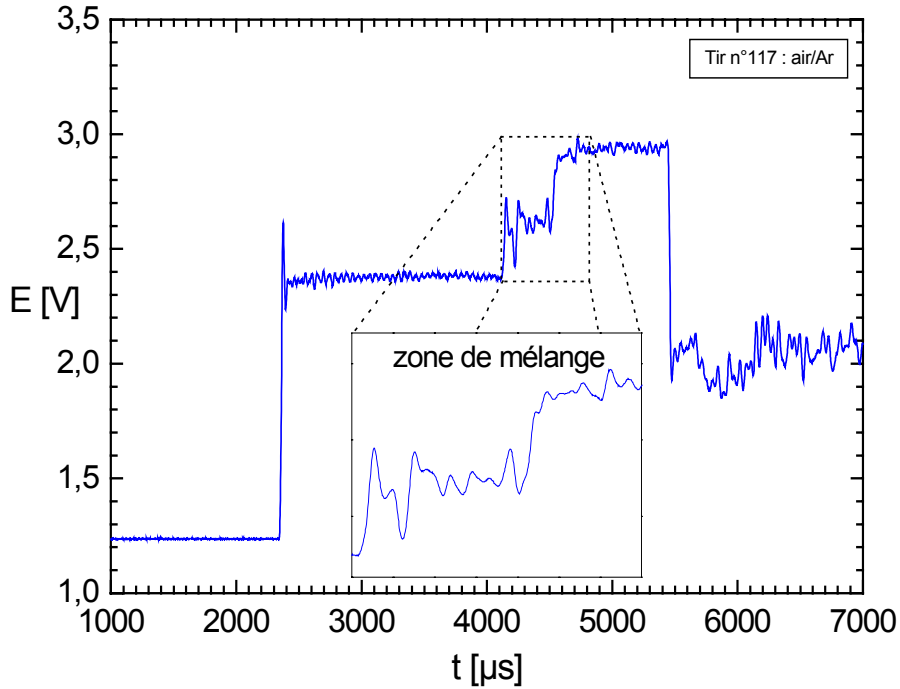

Meet Dr Schwaederlé in front of his poster E37 to learn about the first application of this ancient technique to our difficult flows !

Gas detonation driven experiments on jelly layers or gas interfaces : a VNIIEF tradition followed at LLNL

Easiest method to study material with strength and with well defined defects:

•in mix 99 : accelerated layer in square box at VNIIEF (Zhidov)

•applications to security against accidental explosions : protective liquid layers

•subject left to be commented by the specialists !

Vertical combustion tube for nonstationary compressible RTI flows

listen to review presentation by Zaytsev tomorrow, see poster E43

Ectromagnetic shock tube for Rayleigh-Taylor mixing at high gas speeds in VNIIEF , also multipurpose OSA facility: initial RMI phase due to strong shock, then constant acceleration for stable or unstable RTI phase.

mix 99 : convergent shock experiments (K. Takayama, spokesman)

The measurement of the behavior of converging shock waves is useful for the study of the evolution of the interface perturbation from the linear to the non-linear (still deterministic) regime. In the last few years, novel converging shock experiments have appeared.

The cylindrical implosion can be obtained from the coalescence into a detonation wave of spherical explosions from a large number of point sources. At AWE : the large chamber (30° sector, 1 m radius) is a difficult undertaking but with promising laser sheet diagnostics.

From VNIIEF, we have seen results obtained with smaller, fully circular detonation chamber, with traditional visualisation.

It can also be generated using a diaphragmless vertical shock tube (SWRC, Sendai).

At VNIIEF, spherical chambers have been used with diagnostics from wall mounted pressure transducers (timing and intensity of reflected waves with or without TMZ inside.
A pertinent suggestion was made about the visualization of a spherically converging flow inside a cone by the holographic interferometry technique (SWRC, Sendai). We certainly hope to be able to discuss such experiments during the next workshop.

Unfinished business ….

High explosive experiments

a russian domain of excellence

Z-pinch experiments

a competitor to laser experiments ?

Laser driven experiments

At mix 99 : Bruce Remington, the spokesman for the laser experiments subgroup brillantly summarized the goals of laser (and all) experiments:

We must demonstrate that we can access to interesting scientific domains: i.e. the linear and non-linear regimes (ICF) of the RT/RM-I as well as to turbulent mixing (supernovae), but also the behavior of liquids (or solids) at high pressure (planetary interior) and the coupled radiation hydrodynamics (photo evaporation front).

But experiments have to be improved to facilitate independence of their results from the facility (an issue of science versus “facility calibration”). For this, we need to derive scaling laws in each domain (test of "scalability") and to develop the required numerous diagnostics. We are not there yet.

The action items for future laser facilities (LIL, NIF, LMJ) are: progress towards longer steady drive, large enough ground facilities allowing turbulent regimes, bright source of hard X-rays combined to spectroscopy, codes to grasp all domains, use of the spallation experiments for demonstrating facility independence, specific diagnostics for astrophysics motivated experiments, spherical effects in explosions, convergence effects in spherical implosions. In any case, we have a long and interesting way to do in this domain which is still full of promises.

We like laser experiments which mimic shock tubes or supernovae !

T. Peyser wrote in 1995: « Nova, the world's largest laser, was used to drive one of the world 's smallest shock tube » and obtain various exciting flows :

•non linear RMI growth from sawtooth initial perturbations @ Mach 20 (1995)
•hypervelocity jet from hemispheric defect (1995)
•developped mixing from broad spectrum multimode perturbations (1997)
•reshock @ Mach 15 of a primary shock induced mixing zone (1999)

We will see some careful checks of theories for RMI in the compressible , non-linear regime from experimental results obtained on Omega @ Mach 10 with comparisons with shock tube results from ENIN (@ Mach 3).

Note that mixing experiments in large size and at large Reynolds for Mach 10 to 20 shocks could be obtained in the (intermediate) shock tube section of free piston facilities such as T5 here at CalTech (1998 proposal by Bradford Sturtevant).

At mix 99 , Evgenij Meshkov insisted on practical and peaceful applications of RT&RMI & TM experiments.

Finally, it is about time for our scientific community to harness turbulent mixing in nature and ordinary technology and try to bring some (more?) contribution to humanity.

Some Sarov colleagues have already pointed out some interesting ways such as the fighting of forest fires by explosive methods (joint project VNIIEF-IUSTI), the conception of new explosive light sources and of protective liquid wall against explosions (VNIIEF, after an idea from the czar Peter the Great ?).

The common point of these three methods is the development of turbulent mixing arising from the evolution of hydrodynamic interface instability.

Preliminary conclusions….

Experimental investigators should collaborate with theory and simulation specialists :

by proposing and carrying out imaginative experiments with reasonnable diagnostics

but the diagnostics can also be simulated in code postprocessors

The experiments should be fun (because these flows are exciting)

to be continued in the experimental discussion, tuesday 11, 16:15-16:45

Summary of the 8th International Workshop on the Physics of Compressible Turbulent Mixing (9-14 December 2001, Pasadena, CA)

Oleg Schilling

Chairman of the 8th International Workshop on the Physics of Compressible Turbulent Mixing

University of California, Lawrence Livermore National Laboratory

P.O. Box 808, L-22

Livermore, CA 94551

(925) 423-6879, schilling1@llnl.gov

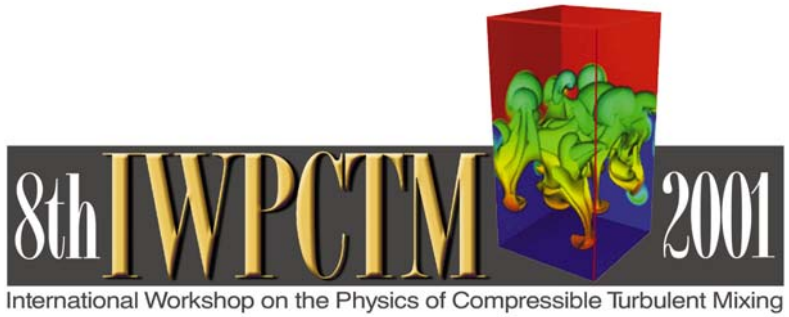

This work was performed under the auspices of the U.S. Department of Energy by the University of California, Lawrence Livermore National Laboratory under Contract No. W-7405-Eng-48

Outline of IWPCTM summary/synthesis

- Introduction
  - Background, previous venues, and 2003 location of the IWPCTM
  - Demographics: how many attendees and from where
  - Difference in format from previous conferences
- Technical summary
  - Experimental research
  - Computational research
  - Theoretical research
- Observations on the IWPCTM
  - Past
  - Present
  - Future

The 8th International Workshop on the Physics of Compressible Turbulent Mixing is a biennial conference originally established by LLNL

- Previous venues
  1) Princeton, NJ, USA (1988) [LLNL]
  2) Pleasanton, CA, USA (1989) [LLNL]
  3) Royaumont, France (1991) [CEA]
  4) Cambridge, UK (1993) [AWE/Cambridge University]
  5) Stony Brook, NY, USA (1995) [SUNY Stony Brook]
  6) Marseille, France (1997) [Université de Provênce]
  7) St. Petersburg, Russia (1999) [RFNC-VNIIEF]
  8) Pasadena, CA, USA (2001) [LLNL]
- Venue for the 9th IWPCTM
  – Cambridge, UK (tentatively Spring 2003) [AWE/Cambridge University]

The 8th IWPCTM was very well attended, with approximately 1/3 of participants from the academic community

- 123 Total Attendees
  - USA: 74
  - Russia: 20
  - France: 8
  - Israel: 8
  - UK: 6
  - Japan: 4
  - Canada: 2
  - Spain: 1

Invited review talks were presented, and more presentations were given than during past workshops

- One hour talks given at beginning of Experimental, Computational, and Theoretical sessions to review state-of-the-art
  - Experimental: "Review on RTI, RMI and TM Experiments" (Haas & Zaytsev) and "The Experimental Study of Excitation and Development of the Hydrodynamic Instability in the Mixing Zone Separating Gases of Different Densities at Their Accelerated Motion" (Zaytsev)
  - Computational: "Review of Numerical Simulation of Mixing due to Rayleigh-Taylor and Richtmyer-Meshkov Instabilities" (Youngs)
  - Theoretical: "Three Dimensional Multi-Mode Rayleigh-Taylor and Richtmyer-Meshkov Instabilities at All Density Ratios" (Kartoon et al.)
- This further stimulated the Panel Discussions at the conclusion of each of the three sessions
- 126 total oral and poster presentations
  - 67 oral presentations
  - 59 poster presentations (staggered format used for more coverage)

Summary of experimental research

- "Complex" Rayleigh-Taylor instability experiments
  - Combined Rayleigh-Taylor and Kelvin-Helmholtz instability
  - "Demixing" experiments
  - Helium-driven gelatin experiments
- Diagnostic developments for Rayleigh-Taylor instability experiments
  - Scalar PIV
  - Wavelet post-processing
  - Moiré interferometry, Fresnel phase zone plate/penumbral imaging
- "Complex" Richtmyer-Meshkov instability experiments
  - Retractable plate shock tube experiments
  - Experiments to study velocity reduction due to large *Ma* and initial amplitude
  - Converging geometry experiments
- Diagnostic developments for Richtmyer-Meshkov instability experiments
  - PLIF, PIV
  - Hot-wire anemometry, laser sheet visualization, and LDV
  - Shadowgraphy
- High-energy density (laser) experiments
- "Laboratory astrophysics"

"Complex" Rayleigh-Taylor instability experiments with shear and "demixing" were reported

- Combined effects of Rayleigh-Taylor instability and shear in tilted interface experiments using double-shielded barrier plate withdrawal (Holford, Dalziel & Youngs E14)
  - Similar to Cambridge University experiments reported in JFM in 1999
  - Shear results in competition between large λ (large-scale) overturning and small λ (large k) Rayleigh-Taylor instability growth
  - Turbulence models examining combined shear-buoyancy are under development (Wilson, Andrews & Harlow T33)
  - Chemically-reactive experiments resulting in a fluorescent product envisaged
- "Demixing" experiments in liquids with three different *At* with sign of acceleration reversed (Kucherenko et al. E2)
- 3D periodic perturbation influence on turbulent mixing using gelatin driven by He compressed to 13 atm with $g \sim 3 \times 10^6$ cm/s^2 giving $\alpha = 0.1$ (Bliznetsov et al. E7)

New diagnostics used in Rayleigh-Taylor instability experiments to measure *statistical*, in addition to integral (large-scale), properties

- Splitter-plate experiment similar to classical shear flow experiments (Ramaprabhu & Andrews E32)
  - Small Atwood number ($At \sim 10^{-3}$) in a water channel
  - Cold and hot horizontally-moving streams of water achieving $Re \sim O(10^3)$
  - Scalar PIV with different particle concentrations used to simultaneously measure ρ and v_i fields to obtain $\langle \rho'^2 \rangle$, $\langle v_x'^2 \rangle$, $\langle v_y'^2 \rangle$, $\langle v_x' v_y' \rangle$, $\langle \rho' v_x' \rangle$, $\langle \rho' v_y' \rangle$ and 2D spectra (needed for DNS, LES, and turbulence models)
  - Results in good agreement with previous thermocouple experiments
  - Chemically-reactive fluids to diagnose molecular mixing possible also
- Wavelet post-processing of sequential density data from experiments to denoise, compress, and detect patterns (Afeyan, Ramaprabhu & Andrews T39)
- Moiré interferometry used to diagnose ablative Rayleigh-Taylor instability at small wavelengths and Fresnel phase zone plate/penumbral imaging used for density measurements on lasers (Azechi et al. E45)

Progress in Richtmyer-Meshkov instability experiments was reported, especially at larger Mach numbers and in convergent geometries

- Retractable Cu plate vertical shock tube experiments at *Ma* = 2.9 with imposed perturbations in air/CO_2 (Anderson et al. E27)
  - Heavy $\rightarrow$ light Rayleigh-Taylor followed by Richtmyer-Meshkov instability diagnosed with Mie scattering
- Experiments studying velocity reduction due to large *Ma* and large initial amplitude with *Ma* = 5 achievable (Sadot et al. E36) and large cross-section shock tube facility (Houas et al. E17)
- Classical and high-energy density convergent experiments reported
  - Detonation-driven 2D shock tube experiments with *Ma* = 2-3 (Holder et al. E13; Hosseini & Takayama E15, E16)
  - "Chevron" (notch) shock tube experiments at *Ma* = 1.26 diagnosed with Mie scattering (Smith et al. E39)
  - Cylindrical direct-drive experiments on OMEGA (Barnes et al. E4; Batha et al. E5; Parker et al. C28)
- Shock/flame interactions studied (Bliznetsov et al. E6)
- Kelvin-Helmholtz instability studied in analysis of impact of oblique metal plates (Bakrakh et al.)

New diagnostics have also been proposed for better imaging and measuring additional quantities in Richtmyer-Meshkov instability experiments

- "Membraneless" shock tube experiments in air/SF_6 at *Ma* = 1.3 (Jacobs & Krivets E18)
  - PLIF shows that interface evolution depends strongly on degree of nonlinearity at time of onset of *second* shock
- Impulsive Richtmyer-Meshkov experiments (Niederhaus & Jacobs E26)
- PIV used to study interaction of a shock with one cylinder (Prestridge et al. E30) and two cylinders (Tomkins et al. E40)
- Triple probe, constant temperature hot-wire anemometry measurements of ρ, v_i, and T at *Ma* = 1.25 (Schwaederlé et al. E37)
- Planar laser sheet visualization and laser Doppler velocimetry (LDV) measurements (Lassis et al. E21)
- Shadowgraphy used to diagnose interaction of a *Ma* = 1.5 shock with a Kr bubble (Layes et al. E22); shock/bubble interactions also simulated using ALE code LEEOR2D (Levy et al. E23)
- Development of a liquid film conductor to rupture membrane with an electric current prior to shock passage (Kucherenko et al. E20, E28, E38)
- Design of novel miniature KrF laser shock tube for experiments with *Ma* > 20 and p > 10 kbar in liquids (Lebo & Zvorykin C25)

High-energy density experiments on OMEGA continue to be valuable for studying nonlinear Richtmyer-Meshkov instability growth and ICF

- Study of effects of shock proximity on linear/nonlinear instability growth at *Ma* ~ 10 in C foam with a polycarbonate pusher (Glendinning et al. E12; Robey et al. E46)
- CALE simulations of *Ma* ~ 10 experiments (Miles, Edwards & Glendinning C57); also Mikaelian T20
- 1D/2D CALE simulations compared to 1D/2D FCI simulations (using a K-ε model) of *Ma* ~ 30 RM instability experiments (Seytor & Legrand C35; see Souffland & Renaud C36)
- NIF ignition target development (Haan et al. C22)
- ICF implosion experiments simulated in 2D (Srebro et al. C37)
- High-strain-rate material strength experiments (Kalantar et al. E19; Pollaine et al. E29)
- Rayleigh-Taylor mode-coupling experiments on NOVA simulated using ALE code (Darlington & Budil C9)

"Laboratory astrophysics" continues to motivate High-energy density experiments on OMEGA

- Shock-sphere interaction experiments
  - Study vortex structure and evolution (Robey et al. E34; see Brouillette & Hébert E8 for classical fluid experiments on vortex rings)
  - Paradigm for interaction of supernova blast wave interaction with interstellar clouds (Klein et al. E42)
  - Simulations of shock-sphere/shock-cylinder interactions using PPM (Peng et al. C29) and shock-planar curtain interactions (Zhang & Zabusky C48)
- Compressible turbulent mixing experiments in support of astrophysics (Drake et al. E9, E10)
- Compressible MHD turbulence application to radiating molecular clouds discussed (Ryutov T25)

Summary of computational research

- Differences between DNS, LES, and MILES
- MILES of variable acceleration Rayleigh-Taylor flow
- Code intercomparisons
  - Spectral/compact, Godunov, and CENO simulations of Shu-Osher problem, Richtmyer-Mehskov instability, and Taylor-Green vortex
  - RAGE, Cuervo, Raptor simulations of shock/cylinder interaction
- High-order and high-resolution methods
  - Filtered spectral and WENO schemes
  - PPM scheme
- Sensitivity of Rayleigh-Taylor mixing to initial conditions and studies of self-similarity
- Effects of small scales on large scales
  - Stabilizing effects of a transitional layer
  - Compressibility effects on supersonic, reacting shear layers
  - Spherical combustion layers
  - Stability of converging shocks
- Numerical simulations and comparisons to bubble merger models
- Subgrid-scale model development and LES of interfacial instability-driven turbulence

Systematic comparisons between simulation methods (direct numerical simulation, large-eddy simulation, and monotone integrated LES) are being conducted

- Differences between DNS, LES and MILES discussed (Youngs)
  - Reynolds-Averaged Navier-Stokes models will still continue to be needed (Youngs C46)
- MILES of variable acceleration Rayleigh-Taylor flow (Youngs & Llor C47)
- Simulations of 1D density-shock interaction, 2D air-acetone/SF_6 *Ma* = 1.2 Richtmyer-Meshkov instability experiment, and 3D Taylor-Green vortex using spectral/compact, Godunov, and CENO schemes to assess numerical effects (Cook et al. C8)
- Eulerian codes RAGE, Cuervo, and Raptor compared in 2D simulations of *Ma* = 1.2 shock acceleration of a diffuse, dense gas cylinder (Greenough et al. C16; Rider, Kamm & Zoldi C31; Zoldi C50)
- 2D simulations of shocked interfaces using high-order and high-resolution methods
  - Aleshin et al. *Ma* = 4.5 experiment using high-order filtered spectral and WENO schemes (Don et al. C54)
  - WENO and PPM schemes (Zabusky et al. C20)
  - Interaction of blast waves with cylindrical/spherical bubbles (Zhang et al. C49)
  - Efficient solver developed (Wang et al. C41)

The sensitivity of Rayleigh-Taylor mixing to the numerical algorithm used remains undetermined, and the "determination" of α remains inconclusive

1952-2002

- 3D simulations (256^2 x 512) using different numerical methods (PPM, ALE, etc.) and same initial conditions have not conclusively determined that α is universal (Dimonte et al. C10; see Weber, Dimonte & Marinak C42 and Dimits C55)
  - Mixing (entrainment) changes the effective *At* at the mixing layer front
  - Now being recognized that the front-tracking result $\alpha = 0.07$ may be an overestimate as this method inhibits mixing at the interface, i.e., as in immiscible fluids (Dutta et al. C11)
  - Immiscible experiments and simulations inhibit energy cascade to small-scales and dissipation (mixing) at large *Re*, resulting in a more rapid mixing layer growth and larger α
  - Simulations using highly diffusive algorithms result in excessive (numerical) "mixing", reducing *At* locally and the mixing layer growth (giving a small α)
- 3D simulations using TREK code for ρ_1/ρ_2 = 3-40 gave α = 0.06-0.16 (Yanilkin et al. C44); TREK also used for simulating instabilities in plasma clouds during expansion in a magnetic field (Gavrilova et al. C14)
- A turbulence model was developed for magnetohydrodynamic Rayleigh-Taylor instability evolution at the interface of an accelerated plasma and magnetic field (Gubkov, Zhmailo & Yanilkin C19)

The effects of small scales (molecular mixing) on the dynamics of the large scales was an important experimental, numerical, and theoretical theme

- Stabilizing effects of an intermediate, transitional layer due to molecular diffusion studied (Kucherenko et al. E3, E31)
- DNS of moderate *Re* Rayleigh-Taylor instability examined sensitivity of large-scale properties (mixing widths) and statistics (such as molecular mixing rate) to initial conditions (Cook, Dimotakis & Mattner C56)
- Reduction of growth rate and other effects of compressibility (increasing Ma_c) studied in DNS of a supersonic, reacting shear layer (Pantano & Sarkar C27)
- 3D AMR simulations of a spherical combustion layer resulting from a TNT explosion (Kuhl & Ferguson T37)
- Molecular dynamics simulations to study stability of converging shocks and Richtmyer-Meshkov instability in a dense Lennard-Jones fluid (Nishihara, Zhakhovskii & Abe C26)
- Mechanisms of turbulent diffusion in solar-type stars studied numerically (Toqué C39)

Numerical simulations showed qualitative consistency with statistical bubble merger models

- A general buoyancy-drag model was developed to include shock compression and spherical convergence (Elbaz et al. T11, C12)
  - Multi-mode perturbation evolution is described by evolution of a single, effective λ (mode)
  - Internal density profile of mixing layer studied using a diffusion model
- Bubble merger results in a pure front of low density fluid rising in higher density fluid (Rikanati, Alon & Shvarts T22)
  - Effectively leads to a single bubble of light fluid on top and heavy fluid on bottom
  - In this 2D model, mixing occurs at center and bottom of mixing layer due to Kelvin-Helmholtz instabilities generated when falling spikes shear rising bubbles
- 3D ALE simulations of random perturbation growth with different ρ_1/ρ_2 using front-tracking consistent with this bubble merger model (Kartoon et al. T14)
- Thermonuclear burning in a Type IA supernova explosion modeled using this merger model (Takabe et al. C38)

Limited progress has been made on the development/application of explicit subgrid-scale models for interfacial instability-driven turbulence

- Large-eddy simulation (LES) of Richtmyer-Meshkov unstable turbulent flows generated by a *Ma* = 10 shock (Samtaney et al. C33)
  - Used the Pullin stretched-vortex subgrid-scale model
  - 5th- and 7th-order WENO schemes
  - Evolution of mixing layer, spectra, and statistics studied (with reshock)
- A methodology was extended to study interaction between small and large scales (subgrid-scale dynamics) in Rayleigh-Taylor and Richtmyer-Meshkov instability (Schilling & Cook T28)
  - Applied to a 512^2 x 2040 Rayleigh-Taylor mixing spectral/compact DNS dataset (Cabot, Schilling & Zhou, submitted to *Physics of Fluids*)
  - Examined transfer dynamics of small and large scales as a function of scale and vertical height
  - Extracted eddy viscosity and backscatter

Summary of theoretical research

- Development of models
  - Bubble merger, two-phase flow, and buoyancy-drag models
  - Potential flow, vorticity deposition, and shell models
  - One-dimensional turbulence model
- Modeling of nonlinear instability growth and transition to turbulence
  - Application of Dimotakis transition criterion at $Re \sim 10^4$
  - Modeling of combined shear and buoyancy instabilities
  - Effects of heat transfer and ablation
  - Modified Zhang-Sohn model
  - Compressible Rayleigh-Taylor instability
  - Stability of converging/diverging shock waves
- Turbulent transport and mixing models
  - Two-fluid model for combined Rayleigh-Taylor, Richtmyer-Meshkov, and Kelvin-Helmholtz instabilities
  - Two-equation, single-velocity turbulence models
  - Two-scale turbulence model
  - Simulations using multi-fluid models in ALE and AMR codes

Progress has been made in the theoretical study of nonlinear instability evolution using bubble merger, two-phase flow, and simple models

- A model for mixing layer width evolution was described (Cheng, Glimm & Sharp T7)
  - Bubble merger model based on a renormalization group fixed-point
  - Center-of-mass model coupling bubble and spike mixing zone edges
  - Buoyancy-drag model calibrated against above models
- A buoyancy-drag model was used to model dependence of spatial dimensionality and density ratio on Richtmyer-Meshkov instability evolution (Yosef-Hai et al. T35)
- A vorticity deposition model was developed for single-mode Richtmyer-Meshkov instability growth at large *Ma* and large initial amplitude (Rikanati et al. T23)
- Extensions of Layzer potential flow model used to study bubble/spike front evolution with modal interactions (Abarzhi T1, T3; Abarzhi, Glimm & der Lin T2)
  - Regular and singular asymptotic solutions studied for $At < 1$
  - Group theoretical methods used to study morphology/topology of large-scale structure of periodic bubble/spike arrays (Inogamov et al. T12, T13)
- Layzer-type and *shell* models including effects of entrainment and diffusion on mixing layer growth used to study Rayleigh-Taylor evolution and examine α (Dalziel T10)
- One-dimensional Turbulence (ODT) model used to study large *At*, small *Ma* mixing (Ashurst & Kerstein C4)
- A model of inhibition of Rayleigh-Taylor mixing was developed (Breidenthal T5)

Progress has been made in the theoretical study of nonlinearity and the transition to turbulence

- Dimotakis criteria for transition to turbulence at *Re* ~ 10^4 applied as a function of time to:
  - Cambridge University experiment and an OMEGA experiment (Zhou et al. T36)
  - Rayleigh-Taylor unstable plasma flow (Robey et al. E35)
- Turbulence modeling of combined shear and buoyancy instabilities (Wilson, Andrews & Harlow T33)
- Effects of heat transfer/ablation on turbulent mixing investigated (Clark & Harlow T8)
- Predictions of Nikiforov's turbulence model in the VIKHR code was shown to be in good agreement with:
  - LEM data (Kozlov, Razin & Sapozhnikov C51)
  - Poggi et al. RM instability data (Kozlov & Razin C52)
- A modified Zhang-Sohn model was developed for single-mode, nonlinear growth of the Rayleigh-Taylor and Richtmyer-Meshkov instability (Vandenboomgaerde T31; Vandenboomgaerde et al. T32)
- Growth rates of linear (Wouchuk T34) and nonlinear (Nishihara, Matsuoka & Fukuda T19) Richtmyer-Meshkov instability studied
- Rayleigh-Taylor instability in compressible fluids was studied (Tricottet & Bouquet T30)
- The stability of diverging shock waves (Ktitorov T15) and of converging shock waves (Ktitorov T16) was studied

Progress has been made in turbulent transport model development for turbulent mixing induced by interfacial instabilities

- A 1D two-fluid model incorporating combined Rayleigh-Taylor/Richtmyer-Meshkov/Kelvin-Helmholtz instabilities with arbitrary *g(t)* was developed (Bailly & Llor T4)
  - Mass transfer between fluids and diffusion (*K*-ε model) included
  - Self-similarity studied in "0D", i.e., as a function of time only (Llor T18)
- A family of two-equation models was developed for 2D/3D single-velocity, compressible, multi-component flow (*K*-*Z*: *K*-ε, *K*-*l*, *K*-ω, *K*-τ) (Schilling T26)
  - Includes closures for compressibility, reaction terms not previously included
  - Special cases studied analytically (decay, shear layer, boundary layer, jet)
- A 1D two-scale *K*-ε model was formulated using spectral and scaling concepts,and preliminary validation studies were performed in the ALE code sKULL (Eliason, Cabot & Zhou C53)
- Youngs multi-fluid turbulence model was implemented in the 2D finite-element ALE code CORVUS (Grieves C17)
- Multi-fluid simulations of Rayleigh-Taylor mixing using 2D AMR code (Vold C40)
- A 1D diffusive mixing model was used to study neutron and charged-particle yields in laser implosion experiments (Epstein et al. C13)
- A *K*-ε model was developed for applications to the atmospheric surface layer (Anuchin, Neuvazhayev & Parshukov C2)

Concluding observations: past, present, and future of the IWPCTM

- In the past, many presentations had limited relevancy to *compressibility*, *turbulence*, or *mixing*
  - Experiments and simulations limited to very small *Re* and *Ma*
  - Euler simulations generated “numerical mixing” and “numerical turbulence”
  - Analytical models were limited to linear and weakly-nonlinear regimes
- Presentations this year were more focused on the subjects of the Waorkshop, with good progress in:
  - Experimental designs/diagnostics,especially for classical fluid experiments
  - Higher accuracy and higher resolution simulations in 2D and 3D
  - Multi-fluid interpenetration, turbulent transport and mixing model development
- Future focus should include:
  - Diagnostic methods that can experimentally measure statistical quantities
  - Experiments, simulations, and modeling of *reacting* turbulent flows
  - Analysis of DNS data, and development of subgrid-scale models
  - LES of compressible turbulent mixing
  - Refined turbulence models validated against experiments and LES

Nonlinear evolution of unstable fluid interface

S.I. Abarzhi

Department of Applied Mathematics and Statistics

State University of New-York at Stony Brook

LIGHT FLUID ACCELERATES HEAVY FLUID

misalignment PRESSURE and DENSITY gradients

INSTABILITY TURBULENT MIXING

Rayleigh-Taylor instability sustained acceleration (gravity)

Richtmyer-Meshkov instability impulsive acceleration (shock)

- thermonuclear flashes on surface of stars; supernova explosion
- inertial confinement fusion; interaction of laser with matter

Basic objective: reliable description of turbulent mixing

Fundamental issues:

- the cascades of energy
- the dynamics of small-scale structures
- the dynamics of the large-scale coherent structure

Coherent structure

an array of bubble and spikes periodic in the plane normal to the direction of acceleration (shock)

- Dynamics of 3D and 2D nonlinear structures in RMI
- Properties of the 3D-2D dimensional crossover in RMI

INTERFACE	**active** regions	**passive** regions
Aref[1989]	**small** scales	**large** scales
	intensive vorticity	simple advection

	large-scale coherent motion	scalar fields
	spectral approach	group theory
Abarzhi[1996] (RTI)		

Group theory

coherent structure periodicity

group of invariance 17 plane crystallographic symmetry groups

$\boldsymbol{G}$ translations in the plane + rotations + reflections

The COHERENT STRUCTURE is OBSERVABLE

- A significant part of the fluid energy is concentrated in the coherent motion

  a DOMINANT mode **K** governs macroscopic dynamics
- The structure is stable under modulations

$\boldsymbol{K}+\xi$: $\varphi(\boldsymbol{K}+\xi)\approx\varphi(\boldsymbol{K})+F(\boldsymbol{K})\xi^2$ $\boldsymbol{K}\leftrightarrow-\boldsymbol{K}$

a scalar macroscopic function

$\boldsymbol{G}$ is a **symmorphic group** with **inversion** in the plane

3D: p6mm, p4mm, p2mm, cmm, p2 **2D**: pm11

LARGE-SCALE COHERENT MOTION

time t potential $\Phi(x, y, z, t)$ free surface $z^*(x, y, t)$

$$\Delta\Phi = 0, \qquad \nabla\Phi\big|_{z=+\infty} = 0$$

$$\frac{\partial z^*}{\partial t} + \nabla z^* \nabla\Phi - \frac{\partial\Phi}{\partial z}\Big|_{z=z^*} = 0, \quad \frac{\partial\Phi}{\partial t}\Big|_{z=z^*} + \frac{1}{2}(\nabla\Phi)^2 + g(t)z\Big|_{z=z^*} = 0$$

$g \geq 0$ - instability: RT $g > 0$ RM $g = 0$

Initial conditions: $z^*(x, y, t_0)$ $\boldsymbol{v}(x, y, t_0)$

length scale $\lambda\ (\sim \lambda_{\max})$ time scale $\tau \sim \lambda / |v_0|$

Symmetry: periodic, symmorphic + inversion in the plane (x, y)

difficulty **SINGULARITY** **interplay of harmonics**

2D RTI: Taylor[1950], Fermi[1952], Layzer[1955], Garabedian[1957], Birkgoff[1957], Zuffiria[1986], Inogamov[1990], Tanveer[1993], Hazak[1997]

3D RTI: Abarzhi[1995]

LOCAL EXPANSIONS *ASYMPTOTIC SOLUTIONS*

2D & 3D RMI: Shvarts[1995], Inogamov[1995], Mikaelian[1998], Zhang[1998], Abarzhi[2000]

Layzer-type approach single-mode approximation

- Expansion in terms of orthogonal functions:

$$\Phi = \sum_{n=1}^{\infty} \Phi_n(t) \left(\frac{1}{\gamma_n} \exp\left(-\gamma_n (z - z_0(t)) + i \sum_j \boldsymbol{k}_j \boldsymbol{r} n_j \right) + c.c \right)$$

irreducible representations of group $\boldsymbol{G}$ wave-vectors $\boldsymbol{k}$, $\boldsymbol{G}_{\boldsymbol{k}}$

project operators Fourier expansion

- Local expansion at a highly symmetric point of the interface $x \approx 0, y \approx 0, z \approx z_0(t)$:

$$z^*(x, y, t) = z_0(t) + \sum_{i+j=1}^{\infty} \zeta_{ij}(t) x^{2i} y^{2j}, \qquad N = i + j = 1,2,...\infty$$

Dynamical system of ordinary differential equations

$$\sum_{i+j=1}^{\infty} D_{ij}(\dot{M}, M, \zeta) x^{2i} y^{2j} = 0 \qquad \sum_{i+j=1}^{\infty} K_{ij}(\dot{\zeta}, M, \zeta) x^{2i} y^{2j} = 0$$

$\zeta = \{\zeta_{ij}\}$; $M = \{M_n\}$ moments $M_n = \sum_{m=1}^{\infty} \Phi_m (km)^n$

- Local dynamics, any time t; the length scale(s) λ is invariable
- Multiple harmonics presentation
- 3D flows with general type of symmetry and 2D flows
- Desired accuracy, $x \approx 0, y \approx 0, z \approx z_0(t)$, $N = i + j = 1,2,...\infty$

REGULAR ASYMPTOTIC SOLUTIONS

$$\sum_{i+j=1}^{\infty} D_{ij}\left(\dot{M}, M, \zeta\right) x^{2i} y^{2j} = 0 \qquad \sum_{i+j=1}^{\infty} K_{ij}\left(\dot{\zeta}, M, \zeta\right) x^{2i} y^{2j} = 0$$

regular asymptotic solutions $t/\tau >> 1$

Richtmyer-Meshkov **bubble**: $v(t) \sim \lambda/t,\ \zeta(t) \sim 1/\lambda$

Layzer-type expansion: regular asymptotic solutions are absent in general case

- non-linearity is non-local
- singularities determine the interplay of harmonics

At a fixed length scale(s) λ, shape of the regular bubble is free and is parameterised by the principal curvature(s)

number of the parameters N_p *symmetry of the* 3D (2D) *flow*

$$N_p \le 3$$

2D pm11, 3D p4mm, p6mm $N_p = 1$ 3D p2mm $N_p = 2$

✓ to capture the interplay of harmonics

✓ to show existence and convergence for solutions in the family

✓ to involve all bubbles allowed by symmetry of the flow

✓ to choose the physically dominant (i.e. the fastest stable) solution

RICHTMYER-MESHKOV bubbles

Curvature radius R (radii $R_{x,y}$) $kR_{cr} \le kR \le \infty$

Velocity $v = L(k,R)/t$ surface variables $\zeta_n = \zeta_n(k,R)$

Fourier amplitudes $\Phi_n = \varphi_n(k,R)/t$

$$|\Phi_n/\Phi_1| \sim \exp(-pn)$$

Asymptotic stability $v - L(k,R)/t \sim t^{\beta-1}$, $\zeta_n(t) - \zeta_n(k,R) \sim t^{\beta}$

$\beta = \beta(kR)$ for stable solutions $\mathrm{Re}[\beta] < 0$

Properties

1. The physically dominant solution in the family corresponds to a bubble with a flattened surface, $kR \to \infty$
2. The bubble flattens in time as $kR \sim (t/\tau)^{|\beta_\infty|}$
3. For highly symmetric 3D flows: $kR_{3D} \sim (t/\tau)^{|\beta_\infty|}$, $v_{3D} \sim 4/kt$
4. The local dynamics of 3D highly symmetric flows is universal; near-circular contour $z^* \sim \zeta_1(x^2 + y^2)$
5. 3D anisotropic bubbles tend to conserve a near-circular contour
6. 3D anisotropic bubbles are unstable
7. 3D Layzer-type “square” solution is the point of bifurcation
8. The dimensional crossover is discontinuous, $\beta_{3D-2D} > 0$
9. NO 2D flows

Family of regular asymptotic solutions in RMI

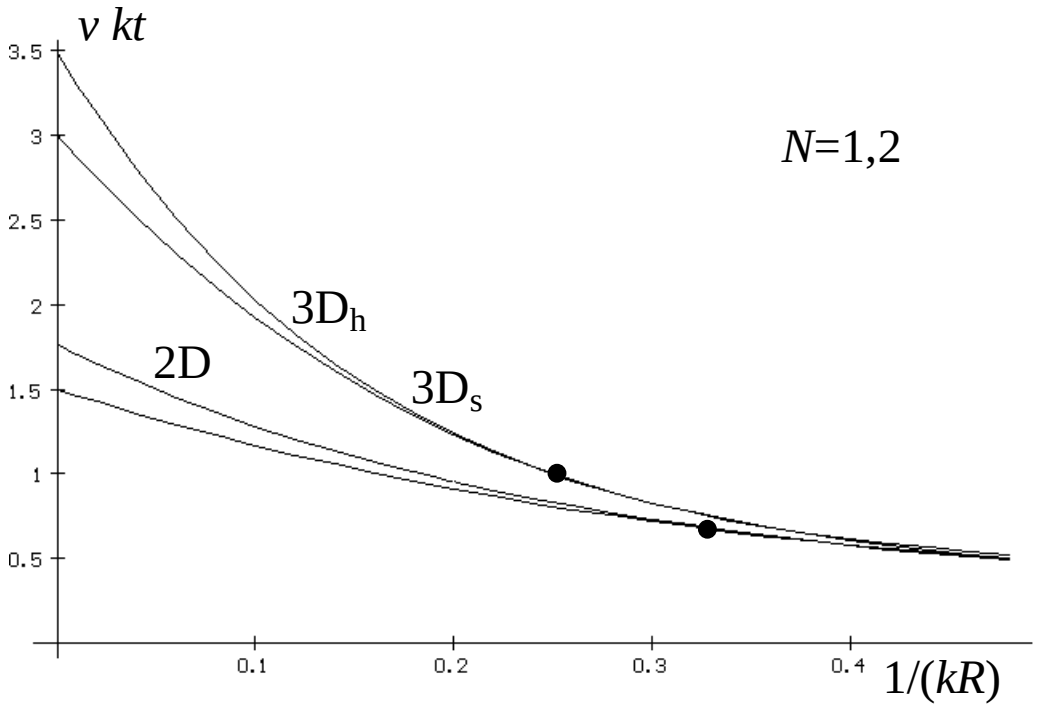

Velocity v as the function on the radius of curvature R

Three-dimensional flows with hexagonal ($3D_h$) and square ($3D_s$) symmetry and two-dimensional flow (2D); k is the wave-vector, t is time, N is order of approximation.

Black circles mark the Layzer-type solutions with

$R_L = 4/k, v_L = 1/kt$ in 3D and $R_L = 3/k$, $v_L = 2/3kt$ in 2D.

Family of regular asymptotic solutions in RMI

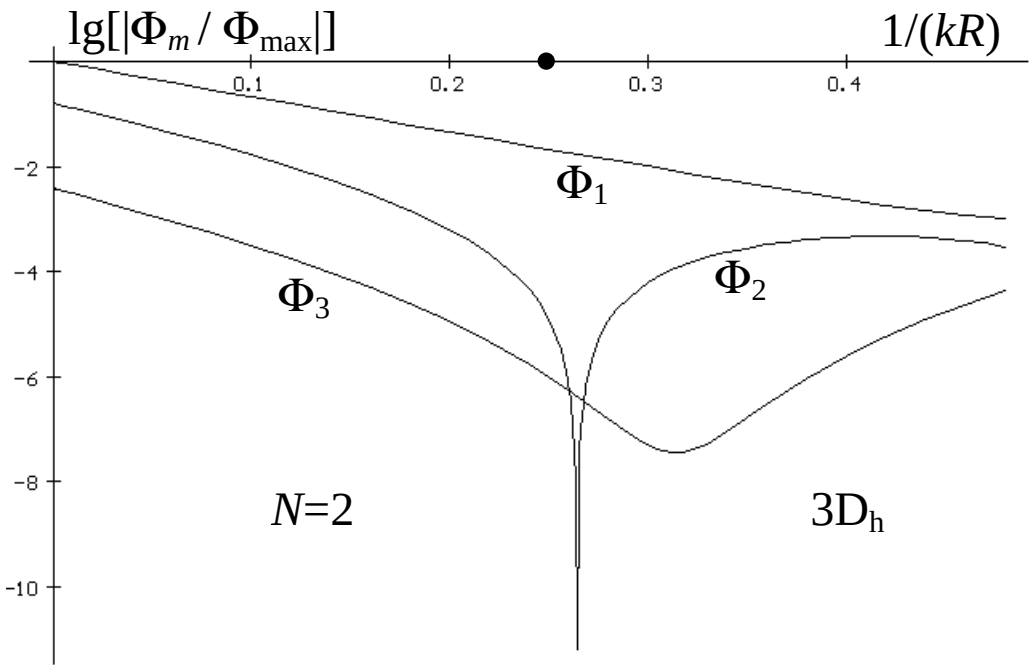

Exponential decay of the Fourier-amplitudes

with an increase in their number.

Three-dimensional flows with hexagonal symmetry p6mm ($3D_h$); $\Phi_{\max} = \Phi_1(kR \equiv \infty)$; black circle corresponds to the Layzer-type bubble.

Family of regular asymptotic solutions in RMI

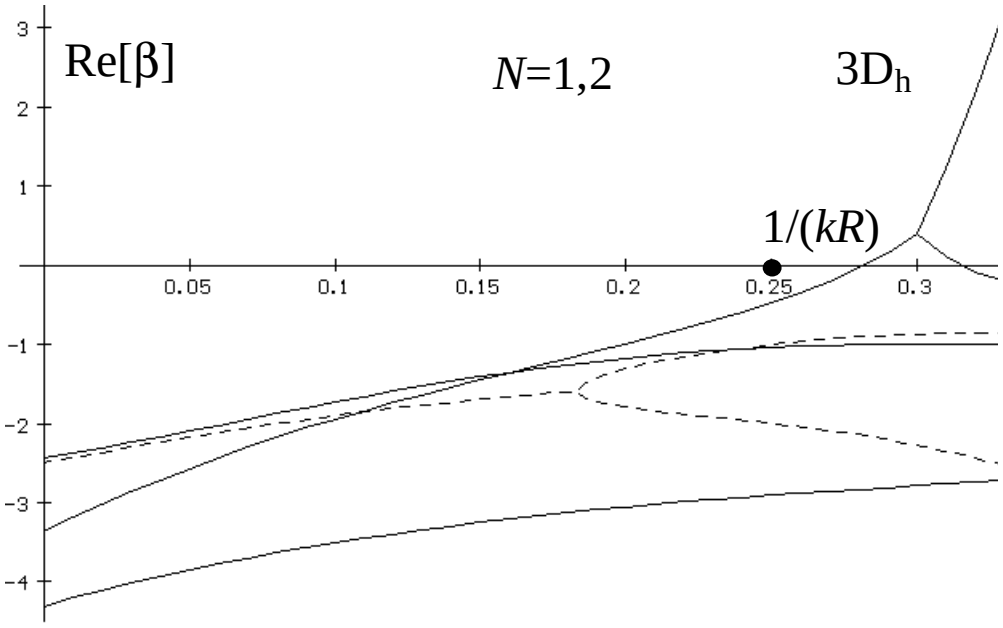

Stability analysis for the family of regular asymptotic solutions

Real parts of exponents β as functions on the radius of curvature *R*

Dashed lines correspond to *N*=1, solid lines – to *N*=2, black circle corresponds to the Layzer-type solution.

Evolution of the bubble front in RMI

Highly symmetric 3D and 2D coherent structures

time scale $\tau \sim 1/v_0 k$

$t << \tau$: curvature $\zeta_1(t) \sim -k\, t/\tau$, velocity $v(t) - v_0 \sim v_0\, t/\tau$

$t \sim \tau$: curvature $\zeta_1(t) \sim -k$

$t >> \tau$: curvature $\zeta_1(t) \sim -k\,(t/\tau)^{-|\beta_\infty|}$, velocity $v(t) \sim C_\infty / k\, t$

Dynamic trajectories

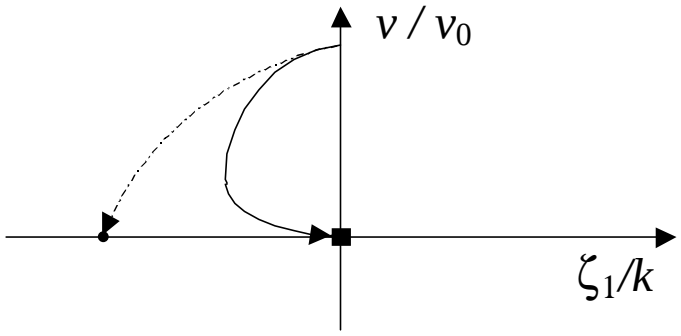

Solid line corresponds to multiple harmonic solution, and black square - to the flattened bubble. Dashed line corresponds to Layzer-type single-mode solution, and black circle – to the Layzer-type bubble.

Evolution of the bubble front in RMI

RM bubbles flatten **RM bubbles decelerate**

- Qualitative agreement with experiments
- Bubble velocity $v_\infty \sim C_\infty / kt$ $v_L \sim C_L / kt$

  $C_\infty / C_L \sim 3-4$ $\Delta h \sim C \ln(t/\tau)$
- Bubble shape $\zeta_1(t) \sim -k\,(t/\tau)^{-|\beta_\infty|}$ reliable parameter
- Existence of an exact analytical solution

- a rigid body curvature $\sim 1/R$ drag force = $\rho v^2 R^2$

For a two-fluid system, Atwood number < 1

- the Layzer-type approach requires MASS FLUX through the interface
- Flattened RM bubble is a multiple-harmonic solution with NO MASS FLUX through the interface

Family of regular asymptotic solutions in RMI

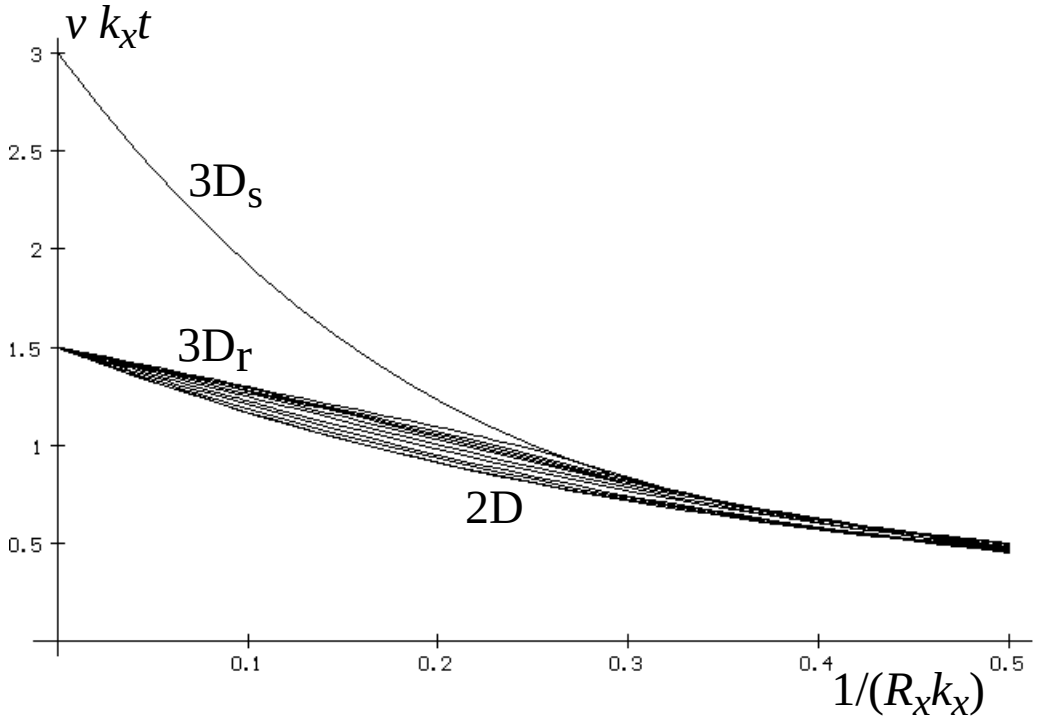

Dependence of velocity $v = L\left(R_{x,y}, k_{x,y}\right)/t$ on the bubble shape

Low-symmetric bubbles with rectangular symmetry $3D_r$, two-parameter family; various values of the aspect ratio; the highest curve $3D_s$ is the family of solutions for 3D square bubbles with $R_y = R_x$ and $k_x/k_y = 1$; the lowest curve 2D is the family of solutions for 2D bubbles flat in the *y*-direction with $R_y \equiv \infty$

Family of regular asymptotic solutions in RMI

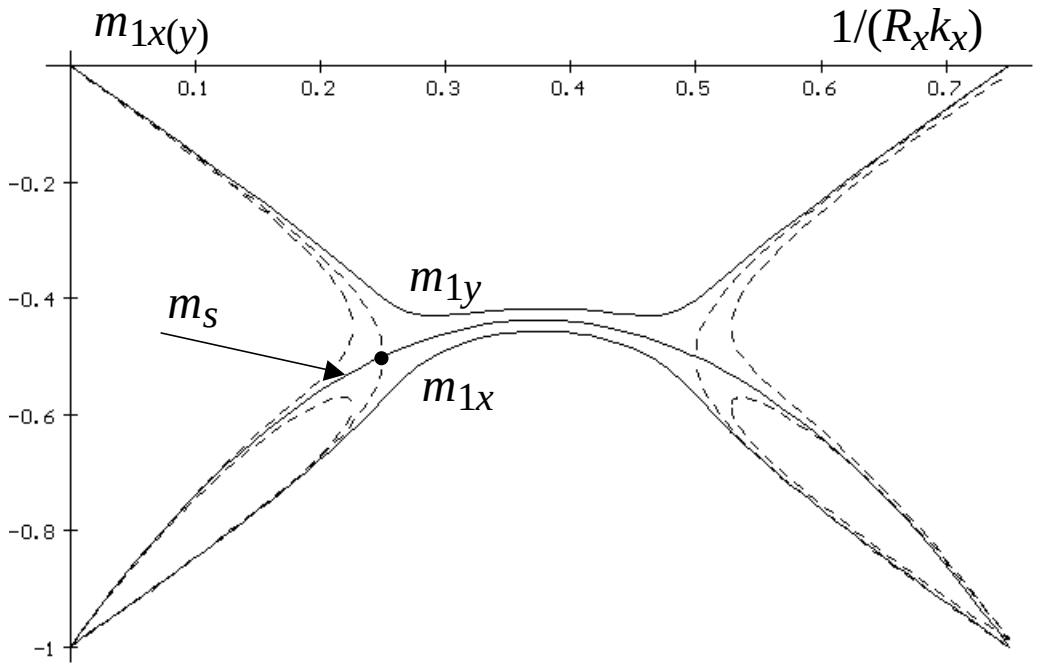

Bifurcation of the Layzer-type square solution (black point) for nearly symmetric flows with $k_x \sim k_y$ and $R_x \sim R_y$

Family of regular asymptotic solutions in RMI

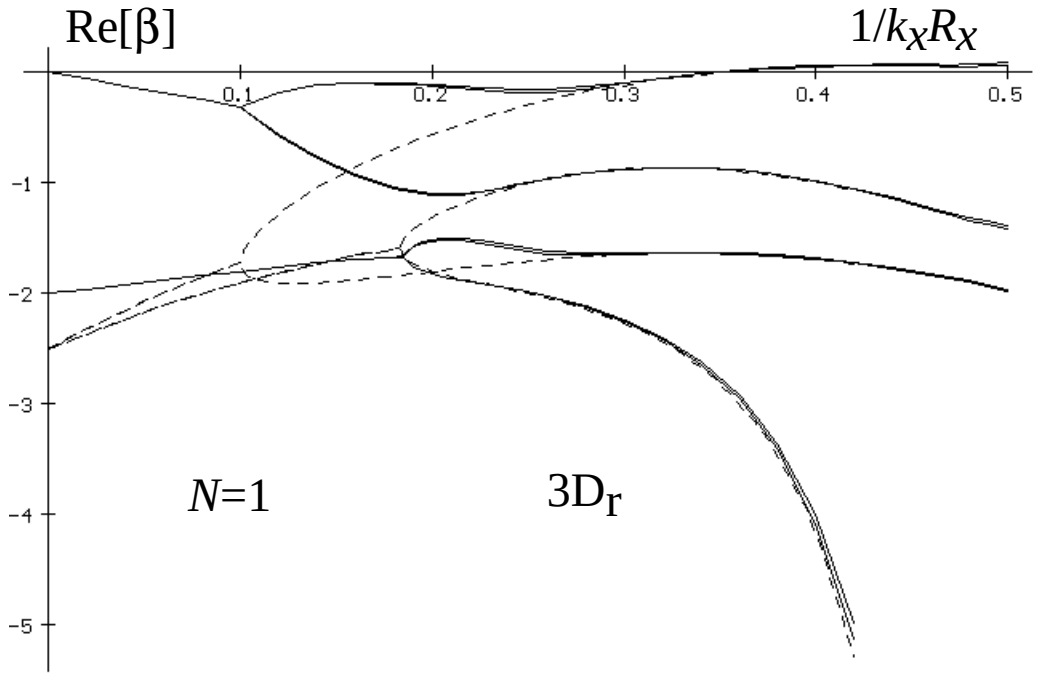

Stability analysis for low-symmetric RM bubbles

Dashing lines corresponds to highly symmetric 3D square solutions with $k_x = k_y$ and $R_x = R_y$. Solid lines correspond to nearly symmetric solutions with $k_x \sim k_y$ and $R_x \sim R_y$. Non-symmetric solutions are unstable.

Evolution of the bubble front in RMI

Low-symmetric 3D coherent structures

The dimensional 3D-2D crossover

2D bubbles under 3D modulations

time scale $\tau \sim 1/|v_0|k_x$

$t << \tau \qquad \zeta_{1x}(t) \sim -k_x\, t/\tau \qquad\qquad \zeta_{1y} \sim -k_y\, t/\tau$

$t >> \tau \qquad \zeta_{1x}(t) \sim -k_x (t/\tau)^{-|\beta_\infty|} \qquad \zeta_{1y} \sim -k_x (t/\tau)^{|\beta_{3D-2D}|}$

the dimensional crossover is discontinuous, $\beta_{3D-2D} > 0$

Secondary instabilities

- Secondary instabilities in RMI are “slow” in contrast to RTI

SINGULAR ASYMPTOTIC SOLUTIONS

Richtmyer-Meshkov **spikes** small-scale structure dynamics

Singular asymptotic solutions to dynamical system

Zhang[1998], Abarzhi[2000]

$t >> \tau$: shape $z^*(t) \sim \sum_{n=1} C_n \left(\exp(t/\tau) r^2\right)^n$, velocity $v(t) \sim -v_0$

- Tanveer 1993, Baker and Meiron 1989, Pullin[2001]…
- For a two-fluid system, Atwood number < 1, the singular asymptotic solutions requires mass flux through the interface

Conclusion

- ✓ Large-scale coherent motion in RMI
- ✓ Separation of scales active regions passive regions
- ✓ Group symmetry large-scale coherent motion
- ✓ Local dynamics of regular bubbles and singular spikes
- ✓ Consideration of 3D flows with general type of symmetry
- ✓ Singularity – interplay of harmonics – shape of the bubble
- ✓ Family of regular asymptotic solutions – symmetry of the flow
- ✓ The physically dominant solution in the family
- ✓ Multiple harmonic solution
- ✓ Universality of local dynamics for 3D highly symmetric flows
- ✓ Conservation of a near-circular contour of 3D bubbles
- ✓ Discontinuous 3D-2D dimensional crossover
- ✓ Singular asymptotes
- ✓ Comparison between the local dynamics in RTI and RMI
- ✓ Different types of the bubble front evolution in RTI and RMI
- ✓ Layzer-type bubbles in RTI and RMI
- ✓ New type of the evolution of the bubble front in RMI
- ✓ Integral (velocity) and internal (shape) diagnostic parameters
- ✓ Theory works effectively for a two-fluid system

Discussion

??? turbulent mixing in RMI and RTI

Nonlinear asymptotic solutions to Rayleigh-Taylor and Richtmyer-Meshkov problems for fluids with a finite density contrast

S. Abarzhi, J. Glimm, A. der Lin

Department of Applied Mathematics and Statistics

State University of New York at Stony Brook, USA

LIGHT FLUID ACCELERATES HEAVY FLUID

INSTABILITY of the interface

TURBULENT MIXING of the fluids

Rayleigh-Taylor instability sustained acceleration (gravity)

Richtmyer-Meshkov instability impulsive acceleration (shock)

Fundamental issues:

- the cascades of energy
- the dynamics of the large-scale coherent structure

Coherent structure: a spatially periodic array of bubble and spikes

basic scales: period λ, gravity g (RTI), initial velocity v_0 (RMI)

time scale $\tau \sim \sqrt{\lambda / Ag}$ (RTI) $\tau \sim \lambda / A|v_0|$ (RMI)

Atwood number $A = (\rho_h - \rho_l)/(\rho_h + \rho_l)$

density ratio is a determining physical factor in RTI/RMI dynamics

Heuristic models

RTI, traditional approach $g \to Ag$ Sharp 1984

RMI, buoyancy-drag model $g \to (2A/(1+A))g$ for bubbles

Shvarts 1995 $g \to (2A/(1-A))g$ for spikes

more formal theoretical approach and a systematic study

INTERFACE	**active** regions	**passive** regions
	small scales	**large** scales
	intensive vorticity	simply advected

large-scale coherent motion — scalar fields

time t — coordinates (x, y, z) — free surface $z^*(x, y, t)$

$z^*(x, y, t) < z < +\infty$ — density $\rho = \rho_h$ — velocity $\boldsymbol{v} = \boldsymbol{v}_h$

$z^*(x, y, t) > z > -\infty$ — density $\rho = \rho_l$ — velocity $\boldsymbol{v} = \boldsymbol{v}_l$

scalar function $\theta(x, y, z, t) = z^*(x, y, t) - z$

Conservation laws:

$$\nabla \cdot \boldsymbol{v} = 0$$

momentum $(\dot{\boldsymbol{v}}_h + (\boldsymbol{v}_h \nabla)\boldsymbol{v}_h - \boldsymbol{g})\rho_h|_{\theta=0} = (\dot{\boldsymbol{v}}_l + (\boldsymbol{v}_l \nabla)\boldsymbol{v}_l - \boldsymbol{g})\rho_l|_{\theta=0}$

mass $(\dot{\theta} + \boldsymbol{v}_h \nabla\theta)\rho_h\big|_{\theta=0} = (\dot{\theta} + \boldsymbol{v}_l \nabla\theta)\rho_l\big|_{\theta=0}$

no mass flux $(\dot{\theta} + \boldsymbol{v}_h \nabla\theta)\rho_h\big|_{\theta=0} = (\dot{\theta} + \boldsymbol{v}_l \nabla\theta)\rho_l\big|_{\theta=0} = 0$

boundary conditions $\boldsymbol{v}_h\big|_{z=+\infty} = \boldsymbol{v}_l\big|_{z=-\infty} = 0$

$g \geq 0$ - instability: RTI $g > 0$, RMI $g = 0$

$0 < A \le 1$ no significant energy cascade potential approximation

$$\boldsymbol{v}_{h(l)} = \nabla \Phi_{h(l)}$$

- Fourier expansion

$$\Phi = \sum_{n=0}^{\infty} \Phi_n(t) \left(\frac{1}{\gamma_n} \exp\left(-\gamma_n (z - z_0(t)) + i \sum_j \boldsymbol{k}_j \boldsymbol{r} n_j \right) + c.c \right)$$

$\Phi_h \Rightarrow \{\Phi_n\}, \quad \Phi_l \Rightarrow \{\tilde{\Phi}_n\}, \quad \boldsymbol{r} = (x, y), \quad \boldsymbol{k}$-wave-vectors

- Spatial expansion at a highly symmetric point of the interface

$$x \approx 0, y \approx 0, z \approx z_0(t) \quad z^*(x, y, t) - z_0(t) = \sum_{i+j=N=1}^{\infty} \zeta_{ij}(t) x^{2i} y^{2j}$$

Conservation laws $x^{2i} y^{2j}$ $i + j = N = 1,2,...\infty$

are reduced to dynamical system of ODE in terms of

surface variables $\xi_{ij}(t)$ and

moments $M_n(t) = \sum_{m=0}^{\infty} \Phi_m(t) (km)^n$, $\tilde{M}_n(t) = \sum_{m=0}^{\infty} \tilde{\Phi}_m(t) (km)^n$

with $v = \partial z_0 / \partial t = -M_0 = \tilde{M}_0$

- Local dynamics at any time *t*; the length scale λ is unchanged
- Multiple harmonics analysis, $m = 0,1,2,...\infty$
- Desired accuracy, $i + j = N = 1,2,...\infty$
- 3D flows with general type of symmetry and 2D flows

2D Rayleigh-Taylor and Richtmyer-Meshkov instabilities

N=1: $z^* - z_0 \approx \zeta_1(t)x^2$ principal curvature $\zeta_1(t)$

$$\left(\dot{M}_1/2 + \zeta_1\dot{M}_0 - M_1^2/2 + \zeta_1 g\right)\rho_h = \left(\tilde{\dot{M}}_1/2 - \zeta_1\tilde{\dot{M}}_0 - \tilde{M}_1^2/2 + \zeta_1 g\right)\rho_l$$

$$\left(\dot{\zeta}_1 - 3\zeta_1 M_1 - M_2/2\right)\rho_h = \left(\dot{\zeta}_1 - 3\zeta_1\tilde{M}_1 + \tilde{M}_2/2\right)\rho_l$$

no mass flux: $\left(\dot{\zeta}_1 - 3\zeta_1 M_1 - M_2/2\right)\rho_h = \left(\dot{\zeta}_1 - 3\zeta_1\tilde{M}_1 + \tilde{M}_2/2\right)\rho_l = 0$

Layzer-type expansion

amplitudes Φ_1 and $\tilde{\Phi}_1$

Regular asymptotic solutions

A=1 Layzer 1955

Rayleigh-Taylor bubbles time scale $\tau = 1/\sqrt{Agk}$

$t << \tau$ $v, \zeta_1 \sim \exp(t/\tau)$

$t >> \tau$ $\zeta_1 = \zeta_L = -Ak/6$ $v_L = \sqrt{Ag/3k}$

re-scaling Layzer-type steady bubble *A*=1

Richtmyer-Meshkov bubbles time scale $\tau = 1/Akv_0$

$t << \tau$ $\quad \zeta_1 = -(k/A)(t/\tau)$ $\quad v - v_0 = -v_0(t/\tau)$

$t >> \tau$ $\quad \zeta_1 = \zeta_L = -Ak/6$ $\quad v_L = \left(1 - A^2/3\right)/Akt$

Singular asymptotic solutions

A=1 Zhang 1998, Abarzhi 2000

Rayleigh-Taylor spikes time scale $\tau = 1/\sqrt{Agk}$

$t << \tau$ $\quad v, \zeta_1 \sim \exp(t/\tau)$

$t >> \tau$ $\quad \zeta_1 \approx k \exp\left((3/2)(t/A\tau)^2\right)$ $\quad v \approx -g\,t$

Richtmyer-Meshkov spikes time scale $\tau = 1/Akv_0$

$t << \tau$ $\quad \zeta_1 = -(k/A)(t/\tau)$ $\quad v - v_0 = -v_0(t/\tau)$

$t >> \tau$ $\quad \zeta_1 \approx k \exp\left(C\left(t/\tau A^2\right)\right)$ $\quad v - Cv_0 \approx \exp\left(C\left(t/\tau A^2\right)\right)$

finite – time singularities:

Baker, Meiron 1980s, Moore 1980s, Tanveer 1990s

!!! **Layzer-type expansion requires**

MASS FLUX through the interface

NON-LINEAR REGULAR ASYMPTOTIC SOLUTION

NO MASS FLUX through the INTERFACE

1. Non-linearity is non-local
2. Interplay of harmonics bubble shape singularities
3. Multiple harmonics analysis
4. The bubble shape is free principal curvature
5. Family of regular asymptotic solutions with no mass flux through the interface
6. The fastest solution in the Family physically dominant
7. Family of asymptotic solutions at A=1 in 2D RTI (Garabedian) and 3D RTI and 3D/2D RMI (Abarzhi)

Family of regular asymptotic solutions

Rayleigh-Taylor bubbles, 3D/2D:

$t >> \tau$ $v = v(\zeta_1, A)$

the fastest solution in the family $\zeta_1 = \zeta_A$ $v = v_A$

Richtmyer-Meshkov bubbles, 3D/2D

$t >> \tau$ $v = v(\zeta_1, A, t) = L(\zeta_1, A)/t$

the fastest solution in the family $\zeta_1 = \zeta_A$ $v = v_A = L_A/t$

!!! lowest-order harmonics $\Phi_1, \tilde{\Phi}_1$ are dominant

2D Rayleigh-Taylor bubble

$t >> \tau$ ζ_A v_A

$A \approx 1,\ \zeta_A \approx -(k/6)(1-(1-A)/8),\ v_A \approx \sqrt{g/3k}\,(1-3(1-A)/16)$

$A \approx 0,\ \zeta_A \approx -(k/2)A^{1/3},\qquad v_A \approx (3/2)^{3/2}\sqrt{Ag/3k}$

!!! For $0 < A \le 1$, velocity v_A is quite close (10-15%) to

$v_L = \sqrt{Ag/3k}$ traditional empirical approach

$v_D = \sqrt{2A/(1+A)}\sqrt{g/3k}$ drag model

Bubble curvature is a more sensitive parameter

2D Richtmyer-Meshkov bubble

$t >> \tau$ $\zeta_A = 0$ $v_A = 3/2\,Akt$

!!! Agreement with multiple harmonic analysis at A=1 (S.A. 2000)

!!! Qualitative agreement with experiments

RM bubbles decelerate RM bubbles flatten

$$v_A/v_L = 3/2\left(1 - A^2/3\right)$$

$v_A, v_L \sim C/kt$ $\Delta h \sim C\ln(t/\tau)$

!!! Bubble curvature is a more sensitive parameter

!!! $A \to 0$ and $(t/\tau) \to \infty$ $v(kt) >> 1$

SIMULATIONS

Front Tracking method FronTier (Glimm, 1988)

- 2D compressible adiabatic Navier-Stokes equation

Euler equations augmented viscous forces and heat flux

- weakly compressible fluids
- contribution of viscous and thermal terms is small to yield a slightly stabilized but nearly inviscid calculations

mesh refinement: 80 x 800, 160 x 1600, 320 x 3200

$A < 0.05$ slow evolution no satisfactorily late-time convergence

$A > 0.85$ certain numerical restrictions late-time dynamics

$$0.3 < A < 0.8$$

Nonlinear regime

Bubble: terminal velocity accompanied by slight oscillations

oscillations: small amplitude sensitive to A

$A > 0.7$: terminal velocity

Comparison

numerical data quasi-terminal regime for each A

averaged values **deviations 3-8%**

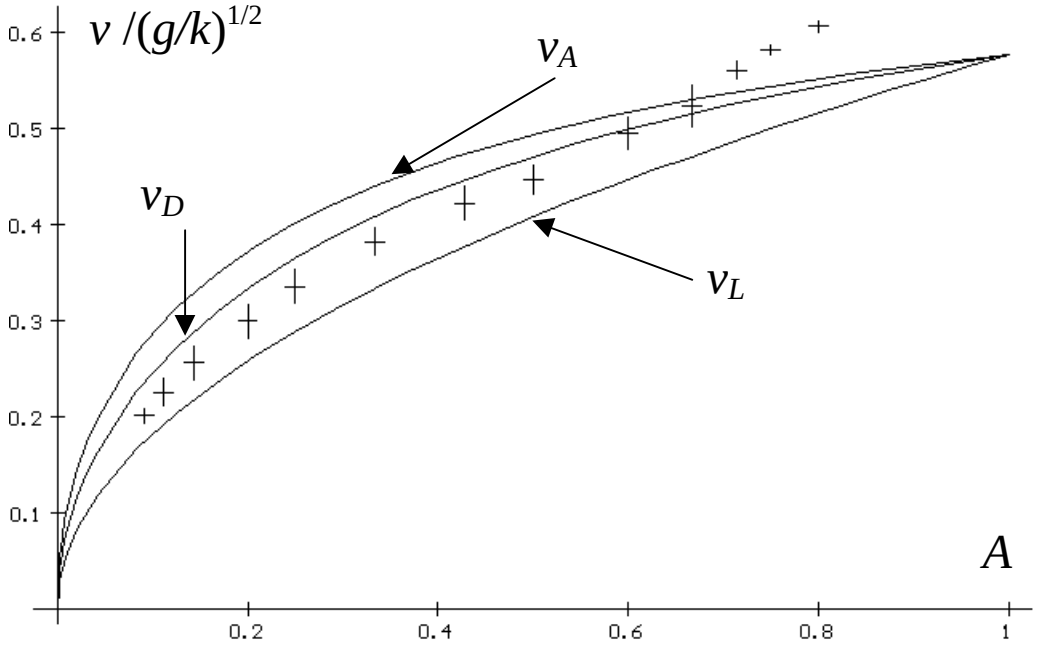

2D RTI

Dependence of the quasi-steady velocity on the Atwood number.

$v_L = \sqrt{Ag/3k}$ is the velocity of the Layzer-type bubble,

$v_D = \sqrt{g/3k}\sqrt{2A/(1+A)}$ corresponds to drag model, and

v_A corresponds to nonlinear solution with no mass flux through the interface.

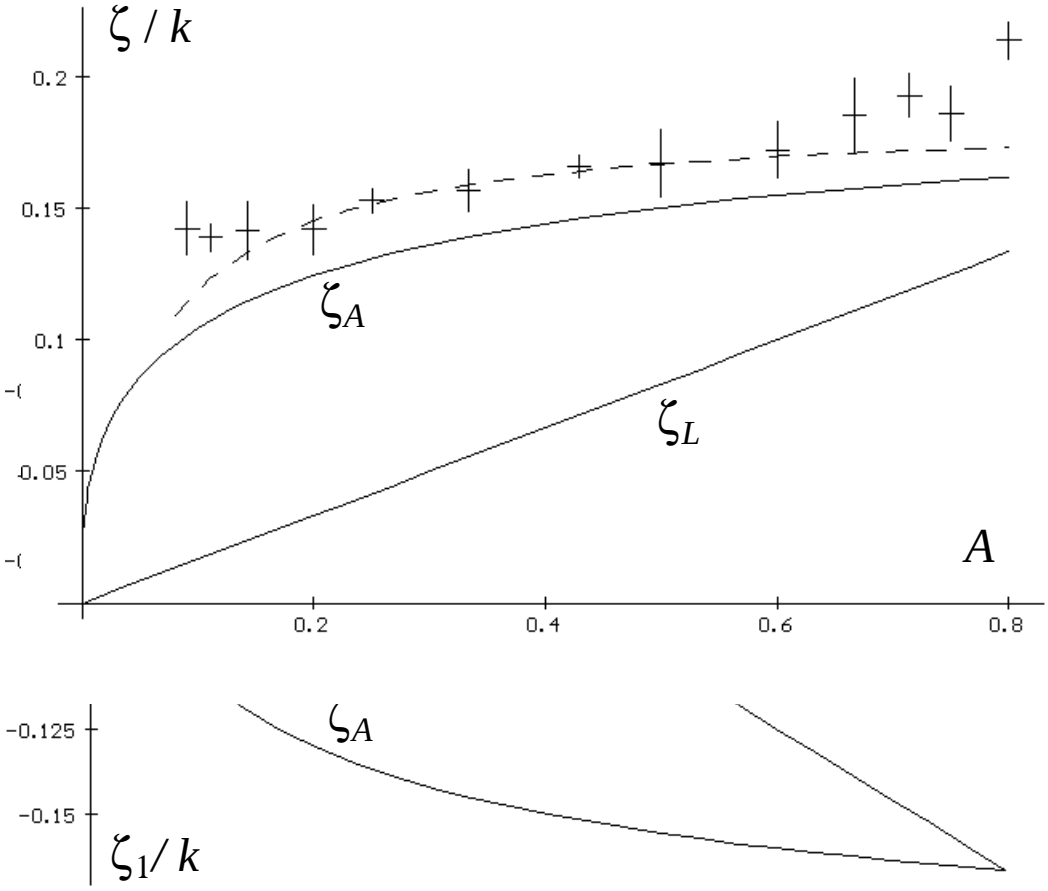

2D RTI:

Dependence of the curvature of the quasi-steady bubble on the Atwood number. The curvature of the Layzer-type bubble is $\zeta_L = -Ak/6$; the curvature corresponding to the nonlinear solution with no mass flux is ζ_A.

LIMITATIONS:

NON-LINEAR SOLUTIONS are “QUASI-STEADY”

vorticity energy cascade time-dependence

$A \to 0$ applicability of the theory

NON-LINEAR SINGULAR ASYMPTOTIC SOLUTIONS

$A \approx 1$ finite-time singularities

$A < 1$ vorticity energy cascade

small-scale structures dispersive properties of the flow

ADVANTAGES:

3D Rayleigh-Taylor and Richtmyer-Meshkov instabilities for fluids with a finite density contrast

!!! CHAOTIC REGIME

RTI width of the mixing zone $h \approx \alpha A g t^2$

re-scaling $g \to Ag$ mass flux $\alpha = \alpha(A)$

CONCLUSIONS

1. Rayleigh-Taylor and Richtmyer-Meshkov instabilities for fluids with a finite density contrast in 3D and 2D
2. Analytical solutions for the conservation laws
3. Layzer-type solution in RTI/RMI, re-scaling
4. Layzer-type approach requires mass flux through the interface
5. Approximate nonlinear solution with no mass flux
6. Parameters of the RT and RM bubbles
7. RT bubble is curved, RM bubble is flat
8. The bubble curvature is a more sensitive parameter than the bubble velocity
9. Good quantitative agreement between theory and simulations in RTI
10. Comparison with heuristic models
11. Limitations

Turbulent mixing in RTI as order-disorder process

S.I. Abarzhi

Department of Applied Mathematics and Statistics

State University of New York at Stony Brook, USA

LIGHT FLUID ACCELERATES HEAVY FLUID

the misalignment of the PRESSURE and DENSITY gradients

the INSTABILITY of the interface

TURBULENT MIXING of the fluids

Rayleigh-Taylor instability	sustained acceleration (gravity)
Richtmyer-Meshkov instability	impulsive acceleration (shock)

Basic Objective: reliable description of turbulent mixing

Fundamental issues:

- the cascades of energy
- the dynamics of the large-scale coherent structure

DYNAMICS of the COHERENT STRUCTURE of BUBBLES and SPIKES in 3D RTI / RMI

to PUT BACK a REGULARITY into the flow

INTERFACE	**active** regions	**passive** regions
	small scales	**large** scales
	intensive vorticity	simply advected
	large-scale coherent motion	scalar fields
	spectral approach	group theory

GROUP THEORY

An array of bubbles and spikes periodic in the plane normal to the direction of gravity

- NO travelling waves $\sim e^{iwt}$, NO convection
- The flow dynamics in the direction of gravity is much faster than the evolution of large scales in the normal plane

Periodicity Equivalence of points and directions

17 plane crystallographic symmetry groups

translations in the plane + rotations + reflections

irreducible representations of crystallographic space groups $\boldsymbol{G}$

wave-vectors $\boldsymbol{k}$ in the reciprocal lattice with subgroups $\boldsymbol{G_k}$

A STRUCTURE is OBSERVABLE

Structure group $\boldsymbol{G}$ wave-vector $\boldsymbol{K}$

- A significant part of the fluid energy is concentrated in the coherent motion

A DOMINANT mode $\boldsymbol{K}$ governs the macroscopic dynamics

- The structure is stable under large-scale modulations

a scalar function of the macroscopic motion

$$\boldsymbol{K}+\xi: \qquad \varphi(\boldsymbol{K}+\xi)\approx\varphi(\boldsymbol{K})+F(\boldsymbol{K})\xi^2, \qquad \boldsymbol{K}\leftrightarrow-\boldsymbol{K}$$

subgroup $\boldsymbol{G_K}$ inversion in the plane

$\boldsymbol{G}$ is a **symmorphic group** with **inversion in the plane**

3D: p6mm, p4mm, p2mm, cmm, p2 2D: pm11

- Rayleigh-Taylor instability: the structure is isotropic in the plane normal to the direction of gravity

3D: p6mm, p4mm 2D: pm11

TURBULENT MIXING and GROUP THEORY

inverse cascade *transitions with the length scale growth*

3D flow symmetry group $\boldsymbol{G}$ representations $\{\boldsymbol{k}, \boldsymbol{G_k}\}$

Transitions between **structures** with **various** wave-vectors $\boldsymbol{k}$

Stability under large-scale modulations

$\boldsymbol{k}+\xi$ $\varphi(\boldsymbol{k}+\xi) \approx \varphi(\boldsymbol{k}) + f(\boldsymbol{k})\xi^2$, $\boldsymbol{k} \leftrightarrow -\boldsymbol{k}$, $G_{\boldsymbol{k}}$

wave-vectors $\boldsymbol{k}$ subgroup $\boldsymbol{G_k}$ inversion in the plane

Lifshits[1940] order-disorder transitions

2D flow, $\boldsymbol{G}$=pm11: $\boldsymbol{k}=0, \boldsymbol{G_k}=m$, length scale $\Lambda = \lambda$

$\boldsymbol{k}=1/2, \boldsymbol{G_k}=m$, length scale $\Lambda = 2\lambda$

2D: scale growing as doubling of the spatial period

3D flow, ***G***=p6mm:

$\boldsymbol{k}=0, \boldsymbol{G_k}=6mm$ length scale $\Lambda=\lambda$ hexagonal p6mm

$\boldsymbol{k}=(1/2,0), \boldsymbol{G_k}=2mm$ $\vec{\Lambda}=(2\lambda,\lambda)$ rectangular p2mm

$\boldsymbol{k}=(1/3,1/3), \boldsymbol{G_k}=3m$ 2 ray star triangular p31m

3D flow, ***G***=p4mm:

$\boldsymbol{k}=0, \boldsymbol{G_k}=4mm$ length scale $\Lambda=\lambda$ square p4mm

$\boldsymbol{k}=(1/2,0), \boldsymbol{G_k}=2mm$ $\vec{\Lambda}=(2\lambda,\lambda)$ rectangular p2mm

$\boldsymbol{k}=(1/2,1/2), \boldsymbol{G_k}=4mm$ $\vec{\Lambda}=(2\lambda,2\lambda)$ square p4mm

4 bubble interaction special modulation

3D: scale growing symmetry lowering anisotropy

To keep isotropy of the RT flow, a balance is required between the inverse and direct cascades merging and splitting

An internal coherent structure with hexagonal symmetry and with the length scale $\Lambda=O(\lambda_{\max})$

CONCLUSION

Group theory

- formulation and general requirements
- structural stability order-disorder
- 3D flow with general type of spatial symmetry
- structural transitions
- isotropy, inverse and direct cascades
- internal coherent structure

??? Concept of self-similarity of turbulent mixing

??? Dynamical symmetry

A New Turbulent Two-Fluid RANS Model for KH, RT and RM Mixing Layers

Pascal BAILLY, Antoine LLOR

Commissariat à l'Energie Atomique
B.P.12 91680 Bruyères-le-Châtel Cedex

December 14th, 2001

Abstract

Our aim is to develop an accurate turbulent mixing model for combined RT, RM and KH types of instabilities, with arbitrarily variable accelerations.

Following the recent analysis of the RT and RM cases by G. Dimonte 2000, and of the self-similar variable acceleration RT flows (SSVARTs) by A. Llor in an other presentation to the present workshop, we have considered as crucial to capture the following physical aspects by using the corresponding model features:
– the directed transport by a two-fluid approach,
– the correct buoyancy force by including mass transfer between the fluids,
– the turbulence diffusion by including most of the standard k-e features,
– the geometrical aspects by consistent closures of the length scales.

Identifying the large scale transport structures and including the above physical aspects, we developped the TTT model (Two-structure Two-fluid Two-turbulence) whose specific and original features will be discussed. Preliminary 1D numerical results of the TTT model will be presented for self-similar RT flows.

I Introduction

I.1 Aim and strategy

Our aim is to craft a RANS model applicable to:

- Kelvin-Helmoltz,
- Richtmyer-Meshkov,
- Rayleigh-Taylor,
- and SSVARTs (self-similar variable g RT, see Llor)

and able to capture consistently:

- TMZ growth laws ($L(t)$),
- global energy balance (K_I, K_D, K_T),
- and length scales
- (Von Kármán numbers $K^{3/2}/EL$, KH≈ 0.63, RT≈ 0.09).

Our strategy is to combine as much as possible
the relevant features from simple and efficient existing models:

Turbulence dynamics (KH and RM)	$\longleftrightarrow$	k–ε model,
Directed transport (RT, SSVARTs)	$\longleftrightarrow$	Two-fluid model (Youngs 1989),
Buoyancy (RT, SSVARTs)	$\longleftrightarrow$	Mass exchange (Youngs 1995).

The model has to be a closure of RANS equations
to permit calibrations using measured correlations
$\longrightarrow$ avoid a phenomenological length equation.

I.2 Starting point

Young's two-fluid model (1989) as starting point:

- mass conservation, $\alpha^{\pm}\rho^{\pm}$,
- 2 eq. momentum conservation, $\alpha^{\pm}\rho^{\pm}U^{\pm}$,
- 1 eq. turbulent kinetic energy, K,
- 1 eq. characteristic length scale, λ,

with main closures:

- drag $\propto (\delta U)^2/\lambda$,
- turbulent integral length scale $\propto \lambda$,
- length scale production term $\propto \|\delta\vec{U}\|$.

Problems:

- no equation for dissipation, ε,
- no extension of turbulence to pure fluids,
- debatable closures and coefficients,
- λ equation not RANS based,
- singular behavior of λ at TMZ edges,
- overestimates Von Kármán number in RT by factor 6.5.

I.3 Preliminary attempt, k–ε–Σ

Ideas:

- add ε equation "as in k–ε",
- replace λ by $\Sigma \approx \alpha^+\alpha^-/\lambda$, interfacial area density (RANS),
- add interaction between turbulent and geometrical lengths.

$\longrightarrow$ "k–ε–Σ" model
(Vallet 2000)

Failed because of incompatible behavior at TMZ edges:

$\lambda_i \to 0$ for standard k–ε,

$\lambda_d \to$ Constant in usual two-fluid models.

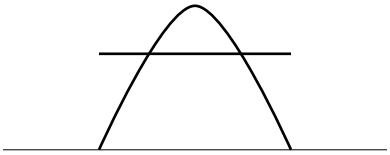

Schematic mean profiles of drag and integral length scales in typical TMZ.

However, raised the basic issues:

What are the transported/transporting structures in TMZ ?
What mechanisms control the length/drag of the structures ?
How can length singularities be avoided at edges of TMZ ?

II The TTT model

II.1 The transport structure concept

Large structures $\approx$ Large turbulent eddies $\approx$ Bubbles $\approx$ Plumes $\approx$ ... $\approx$ Basic building block for transport and mixing.

Assumption holds because:
- separation of fluids inside large eddies cannot occur (small size, large drag, high turbulence),
- experimentally, bubble sizes match Von Kármán number, (Dimonte 2000...),
- in simulations, visual correlation of turbulence and density, (Dalziel 1999, Inogamov 2001...).

Solves length scale paradox at edges:

$\lambda_i/\lambda_d \rightarrow$ Constant in structures at edges,
but $\langle\lambda_i\rangle \rightarrow 0$ because of intermittency
(structures at edges enter laminar zones when TMZ grows).

Simple modeling should be accessible
since plumes are appropriatly captured by adapted k–ε models.

Averaging over the TMZ, modeling demands:
- two velocities (plume shearing),
- mass exchange (entrainment in plumes),
- two turbulence fields (intermittency between plumes).

II.2 Two-structure RANS equations

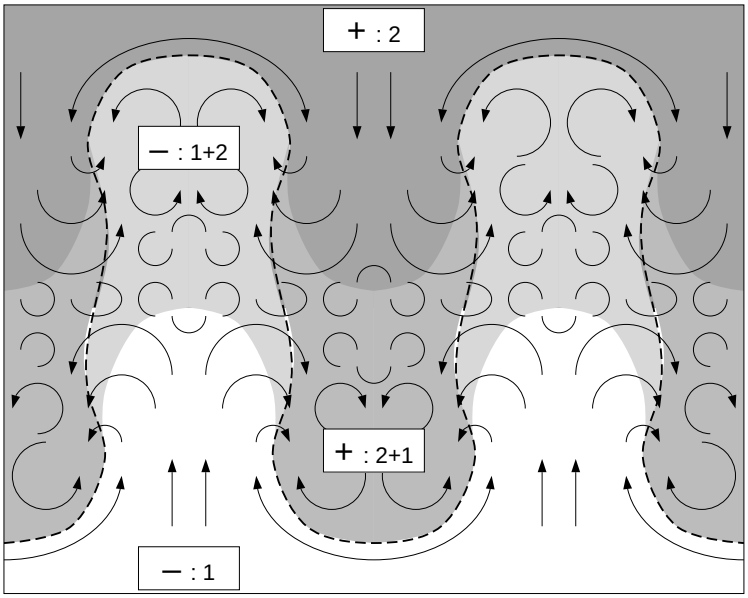

Schematic representation of the Two-structure, Two-fluid, Two-turbulent TMZ; dashed line: $b^{\pm}$ boundary; gray shading: $c^{1,2}$ levels.

Structures + and − defined by presence functions $b^{\pm}$ (=0 or 1).

Structure evolution defined by velocity field $\vec{w}$ for $b^{\pm}$:

$$\frac{\partial}{\partial t} b^{\pm} + w_j \, b^{\pm}_{,j} = 0. \qquad (1)$$

Evolution equations for hydro quantities a:

$$\frac{\partial}{\partial t}(\rho a) + (\rho a u_j)_{,j} = s - (\theta_j)_{,j}, \qquad (2)$$

where $a = c^{1,2}$ (fluid mass fractions), u_i, k, ε, e...

$c^1 = b^-$ and $c^2 = b^+$ in initial state (separate fluids).

Conditional averaging by $b^{\pm}$ yields two-structure RANS :

$$\frac{\partial}{\partial t}(\alpha^{\pm}\rho^{\pm}A^{\pm}) + (\alpha^{\pm}\rho^{\pm}A^{\pm}U_j^{\pm})_{,j} = S^{\pm} - (\Theta_j^{\pm})_{,j} - (\Phi_j^{\pm})_{,j} \mp X \mp \Psi \quad (3)$$

where:

$\alpha^{\pm} = \overline{b^{\pm}}$	structure volume fractions,
$\rho^{\pm} = \overline{b^{\pm}\rho}/\alpha^{\pm}$	structure densities,
$A^{\pm} = \overline{b^{\pm}\rho a}/(\alpha^{\pm}\rho^{\pm})$	structure quantities,
$U_i^{\pm} = \overline{b^{\pm}\rho u_i}/(\alpha^{\pm}\rho^{\pm})$	structure velocities,
$S^{\pm} = \overline{b^{\pm}s}$	structure source terms,
$\Theta_i^{\pm} = \overline{b^{\pm}\theta_i^{\pm}}$	structure fluxes,
$\Phi_i^{\pm} = \overline{b^{\pm}\rho a u_i^{\pm}}$	structure turbulent fluxes,
$u_i^{\pm} = u_i - U_i^{\pm}$	structure velocity fluctuations,

$\boxed{X = \pm\, \overline{b^{\pm}_{,j}\theta_j^{\pm}}}$ inter-structure flux term ($\rightarrow$ buoyancy + drag),

$\boxed{\Psi = \pm\, \overline{b^{\pm}_{,j}\rho a(w_j - u_j)}}$

inter-structure turbulent-flux and exchange term.

Closures of standard terms are adapted
from usual single fluid approaches and not discussed here.

Closures of exchange terms X and Ψ are crucial.

Presently, $b^{\pm}$ is loosely defined
to match the turbulent/laminar areas in flow.
Eventually, $b^{\pm}$ will be more precisely given
by analysis of density/velocity fields in simulations.

However, closure of $b^{\pm}$-involving average terms is possible now.

II.3 TTT: the closed modeled equations

TTT = Two-structure, Two-fluid, Two-k–ε. "Minimal".

Incompressible version (extension to compressibility and shocks to be published).

Single pressure is assumed (two pressure version also possible, but weak effect).

$$
\left\{
\begin{aligned}
&(\alpha^{\pm}\rho^{\pm})_{,t} + (\alpha^{\pm}\rho^{\pm}U_j^{\pm})_{,j} = \mp\,\Psi \\
&(\alpha^{\pm}\rho^{\pm}C^{m\pm})_{,t} + (\alpha^{\pm}\rho^{\pm}C^{m\pm}U_j^{\pm})_{,j} = -\,\Phi_{j,j}^{m\pm} \mp \Psi^m \\
&(\alpha^{\pm}\rho^{\pm}U_i^{\pm})_{,t} + (\alpha^{\pm}\rho^{\pm}U_i^{\pm}U_j^{\pm})_{,j} = -\,\alpha^{\pm}P_{,i} + \alpha^{\pm}\rho^{\pm}g_i \\
&\qquad\qquad - R_{ij,j}^{\pm} \mp D_i \mp M_i \mp X_i^U \mp \Psi_i^U \\
&(\alpha^{\pm}\rho^{\pm}K^{\pm})_{,t} + (\alpha^{\pm}\rho^{\pm}K^{\pm}U_j^{\pm})_{,j} = +\,\Pi^{\pm} + \xi^{\pm}\Pi^d + \chi^{\pm}\Pi^{\Psi} \\
&\qquad\qquad - \alpha^{\pm}\rho^{\pm}\varepsilon^{\pm} - \Phi_{j,j}^{K\pm} \mp \Psi^K \\
&(\alpha^{\pm}\rho^{\pm}\varepsilon^{\pm})_{,t} + (\alpha^{\pm}\rho^{\pm}\varepsilon^{\pm}U_j^{\pm})_{,j} = \\
&\qquad\qquad + C_{\varepsilon 1}\tfrac{\varepsilon^{\pm}}{K^{\pm}}(\Pi^{\pm} + \xi^{\pm}\Pi^d + \chi^{\pm}\Pi^{\Psi}) \\
&\qquad\qquad - C_{\varepsilon 2}\,\alpha^{\pm}\rho^{\pm}\tfrac{(\varepsilon^{\pm})^2}{K^{\pm}} - \Phi_{j,j}^{\varepsilon\pm} \mp \Psi^{\varepsilon}
\end{aligned}
\right. \qquad (4)
$$

Production of $K^{\pm}$ by structure shear, $\Pi^{\pm}$, drag dissipation, Π^d,
and momentum exchange due to mass exchange, Π^{Ψ}.
Weighing of productions on $\pm$ according to $\xi^{\pm}$ and $\chi^{\pm}$.

Single-fluid ε equation is assumed valid in each structure:
$K^{\pm}$ production and dissipation mirrored with $C_{\varepsilon 1}$ and $C_{\varepsilon 2}$.

Reduces to standard k–ε for identical structures/fluids.

II.4 k–ε like closures

Turbulence characteristics:

$$\nu_t^{\pm} = C_\mu (K^{\pm})^2/\varepsilon^{\pm}, \qquad \sigma^{\pm} = \varepsilon^{\pm}/K^{\pm}, \qquad \lambda^{\pm} = (K^{\pm})^{3/2}/\varepsilon^{\pm}.$$

First gradient assumption for turbulent fluxes in structures:

$$\Phi_j^{A\pm} \stackrel{\text{m}}{=} \alpha^{\pm}\rho^{\pm}\left(\frac{\nu_t^{\pm}}{\sigma_a} + D_W\right) A_{,j}^{\pm} + \text{correction for } \rho_{,j}^{\pm}, \tag{5a}$$

$$R_{ij}^{\pm} \stackrel{\text{m}}{=} \alpha^{\pm}\rho^{\pm}\left[\frac{2}{3}(K^{\pm} + \nu_t^{\pm} U_{k,k}^{\pm})\delta_{ij} - \nu_t^{\pm}(U_{i,j}^{\pm} + U_{j,i}^{\pm})\right]. \tag{5b}$$

Turbulent kinetic energy production by Reynolds stresses:

$$\Pi^{\pm} = -R_{ij}^{\pm}\,(U_{i,j}^{\pm} - U_{k,k}^{\pm}\delta_{ij}/3). \tag{6}$$

Conpensation of spurious production by turbulent pressure demands presence of momentum exchange term:

$$X_i^U = -\tfrac{2}{3}\left[\,\alpha_{,i}^{+}(\alpha^{+}\rho^{+}K^{+} + \alpha^{-}\rho^{-}K^{-}) + (\alpha^{+}\alpha^{-}(\rho^{+}K^{+} - \rho^{-}K^{-}))_{,i}\,\right] \tag{7}$$

here called turbulent buoyancy.

II.5 Mass exchange and structure growth closure

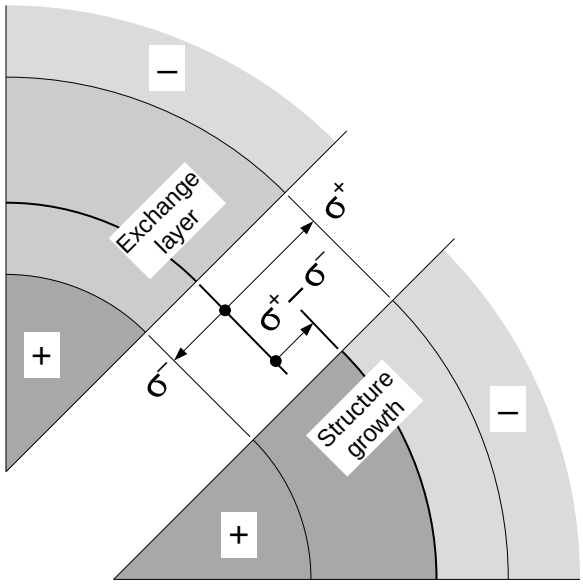

Schematic representation of inter-structure mass transfer and structure growth.

Closure of Ψ^a obtained by extension of Youngs' approach (1995).

Ψ^a is proportional to interface density $\approx \alpha^+\alpha^-$.
Affected volume fractions per time unit are proportional to $\sigma^\pm$.
Mixing layer thus defined is assumed homogeneous.
Rate of volume fraction transfer is proportional to $\sigma^+ - \sigma^-$.
Conserved quantities in layer are then attributed to $\pm$ structures.

Therefore:

$$\Psi \stackrel{\text{m}}{=} C_\psi\, \alpha^+\alpha^- \left(\xi^-\sigma^-\rho^+ - \xi^+\sigma^+\rho^-\right) \tag{8a}$$
$$\Psi^m \stackrel{\text{m}}{=} C_\psi\, \alpha^+\alpha^- \left(\xi^-\sigma^-\rho^+C^{m+} - \xi^+\sigma^+\rho^-C^{m-}\right) \tag{8b}$$
$$\Psi_i^U \stackrel{\text{m}}{=} C_\psi\, \alpha^+\alpha^- \left(\xi^-\sigma^-\rho^+U_i^+ - \xi^+\sigma^+\rho^-U_i^-\right) \tag{8c}$$
$$\Psi^K \stackrel{\text{m}}{=} C_\psi\, \alpha^+\alpha^- \left(\xi^-\sigma^-\rho^+K^+ - \xi^+\sigma^+\rho^-K^-\right) \tag{8d}$$
$$\Psi^\varepsilon \stackrel{\text{m}}{=} C_\psi\, \alpha^+\alpha^- \left(\xi^-\sigma^-\rho^+\varepsilon^+ - \xi^+\sigma^+\rho^-\varepsilon^-\right) \tag{8e}$$

where $\xi^\pm = \sigma^\pm \,/\, (\sigma^+ + \sigma^-)$.

Dissipation of directed energy by momentum exchange
results in total turbulent kinetic energy production:

$$\begin{aligned}\Pi^\psi &= \left[\Psi_i^U - \Psi(U_i^+ + U_i^-)/2\right] \delta U_i \\ &= C_\psi\, \alpha^+\alpha^- \left(\xi^-\sigma^-\rho^+ + \xi^+\sigma^+\rho^-\right) \delta U_i \delta U_i/2,\end{aligned} \tag{9}$$

distributed on $\pm$ structures according to $\xi^\pm$.

Matching the dissipation rate of density fluctuations
in homogeneous isotropic turbulence yields $C_\psi \approx 1$.

II.6 Drag closure

Analogy with Π^{ψ} suggest to choose drag as:

$$D_i \stackrel{\text{m}}{=} C_d\,\alpha^+\alpha^-\left(\sigma^+\rho^+ + \sigma^-\rho^-\right)(\delta U_i - W_i), \tag{10}$$

where $C_d \approx 0.3$ for invicid bubble of size $2\lambda^{\pm}$ in viscous liquid.

Is not a Newton regime drag in $(\delta\vec{U})^2$!

Is a Stokes regime drag in $\delta\vec{U}$ because
structure size and turbulent viscosity yield Re ≈ 1.7.

Thus, drag length scale is implicit combination of λ^+ and λ^-.

Can be interpreted by assuming that
shear due to δU_i is evenly spread on structures,
where structure viscosities induce dissipation.

Total turbulent kinetic energy production by drag,
$\Pi^d = D_i\delta U_i$, spread on structures according to:

$$\chi^{\pm} = \sigma^{\pm}\rho^{\pm} \,/\, \left(\sigma^+\rho^+ + \sigma^-\rho^-\right). \tag{11}$$

Dispersion drift velocity is given by

$$W_i \stackrel{\text{m}}{=} D_W \left(\frac{(\alpha^+\rho^+)_{,i}}{\alpha^+\rho^+} - \frac{(\alpha^-\rho^-)_{,i}}{\alpha^-\rho^-}\right). \tag{12}$$

Since $D_W \propto (\delta\vec{U})^2$, drag vanishes if $\delta\vec{U} = \vec{0}$.

II.7 Added mass closure

Various motivations for including added mass energy, K_A:
- significant in energy balance since $K_A \approx K_D$,
- important at TMZ edges (dominant in invicid laminar flow),
- may affect evolution in demixing and SSVARTs at $n \to -2$,
- makes $k^{\pm} - k_a$ and $(U^{\pm})^2/2 + k_a$ continuous,
- represents large scale contribution to $k^{\pm}$ spectra,
- provides rationale of drag closure.

In two-field RANS equations, k_a is included in $k^{\pm}$,
and should be separated and modeled by evolution equation.

Here, algebraic closure will be assumed:

$$K_A \stackrel{\text{m}}{=} C_a \, \alpha^+ \alpha^- \, (\rho^+ + \rho^-) \, \delta U_i \delta U_i / 2. \tag{13}$$

where $C_a \approx 0.5$ for bubbles in liquid.

Drag can now be interpreted as
dissipation of added mass energy in each structure.

An associated term in momentum equation can be found as:

$$M_i \stackrel{\text{m}}{=} C_a \, \alpha^+ \alpha^- \, (\rho^+ + \rho^-) \, \Big[\Big(\frac{\mathsf{d}^+}{\mathsf{d}t} U_i^+ - \frac{\mathsf{d}^-}{\mathsf{d}t} U_i^- \Big) - \Big(\alpha^+ U_{i,j}^+ + \alpha^- U_{i,j}^- \Big)^S \delta U_j - \Big(\tfrac{\overline{\rho}_{,j}}{\rho^+ + \rho^-} + \alpha_{,j}^+ \Big) \delta U_j \delta U_i / 2 \Big] \tag{14}$$

without $M_i \delta U_i$ dissipation in $K^{\pm}$ equations.

Will be rederived in near future from least action principle.

II.8 Diffusion from added mass velocity fluctuations

Added mass energy is contained in velocity fluctuations
which induce diffusion, described by D_W:

$$D_W \stackrel{\text{m}}{=} C_W \, \alpha^+ \alpha^- \, \frac{(\delta \vec{U})^2}{\alpha^+ \sigma^- + \alpha^- \sigma^+} \tag{15}$$

D_W obtained assuming:
- characteristic velocity fluctuations are $\|\delta \vec{U}\|$,
- characteristic "interaction time" is average of $\sigma^{\pm}$,
- average is weighed by less present structure
(avoids singularities at TMZ edges).

Added mass diffusion dominates turbulent diffusion,
increases transport slightly, and damps elliptic instabilities.

II.9 Summary of constants

Standard k–ε						TTT extension			
C_μ	σ_c	σ_k	σ_ε	$C_{\varepsilon 1}$	$C_{\varepsilon 2}$	C_ψ	C_d	C_a	C_W
0.09	0.7	1.0	1.3	1.47	1.92	0.8	0.15	0.17	3

C_ψ, C_d, C_a and C_W ajusted on RT to match respectively:
- molecular mixing fraction Θ (Youngs 1995),
- growth rate coefficient $\mathcal{Y}_0$,
- estimated added mass energy in internal shear,
- damping of elliptical modes (Youngs 1989...).

III Results of TTT on SSVARTs

III.1 Numerical conditions

Used 1D all-purpose test code :

compressible, artificial viscosity,
explicit, no splitting, second order RK2,
bi-lagrangian + TVD projection (ALE),
non-diffusive evolution of TMZ edges,
(P.-H. Cournède 2001)

TTT model adapted for compressibility effects.

Calculation conditions :

- $x \in [0, 1]$,
- 100 cells,
- $g(t) \propto t^n$,
- energy source term to compensate $g(t)$
  (see Youngs, this conference)
- t_0 and $g(t_0)$ ajusted so
  $L(t_0) \approx 0.4\Delta x$ and $L(1) \approx 1$ for selected n,
- isentropic stratification of perfect gases at $\gamma = 5/3$,
- maximum Mach number below 5%,
- At $= 0.2$ at interface for $t = t_0$,
- Initial turbulence in pure fluids with $\sigma \ll \sigma_{\mathsf{TMZ}}$ and $K \ll K_{\mathsf{TMZ}}$.

III.2 Typical TTT profiles in RT TMZ

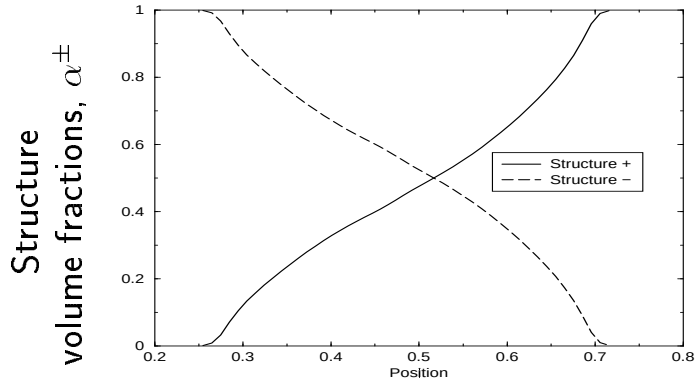

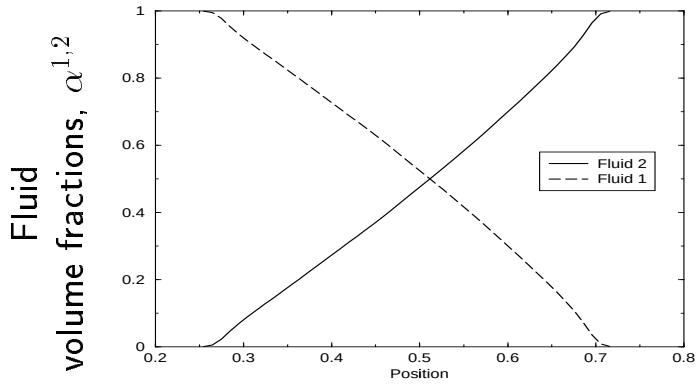

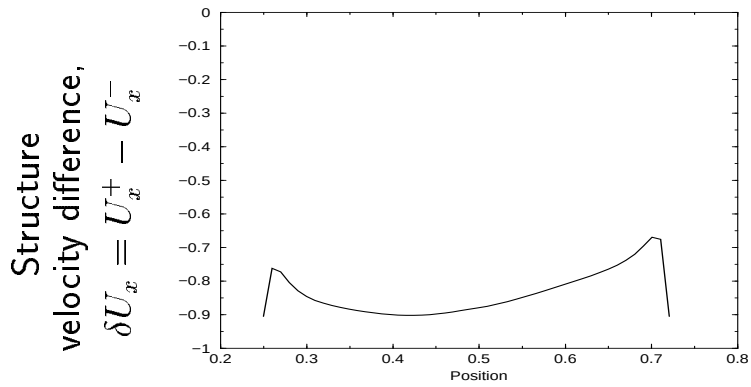

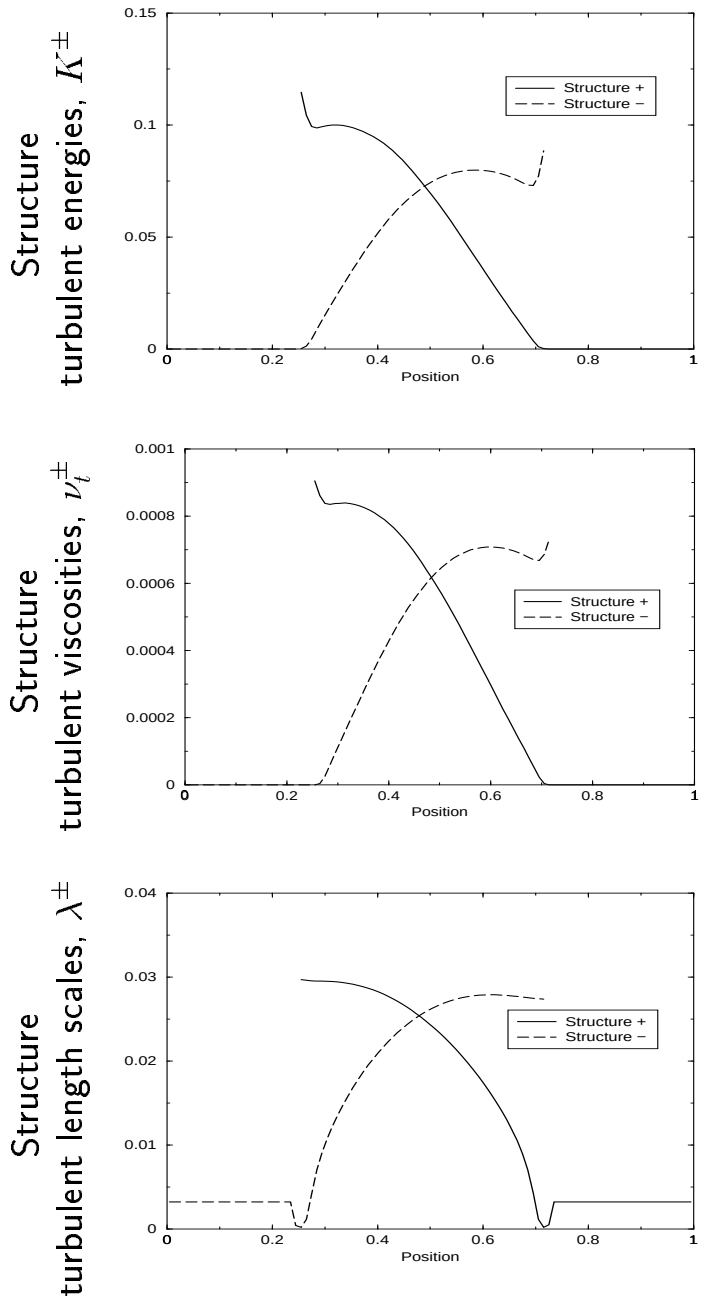

Profiles are very similar for explored SSVARTs at $n = -1$ to 1.

Slight artifacts at TMZ edges for $\alpha^{\pm} \to 0$ are numerical.

III.3 Typical TTT "0D" parameters in RT TMZ

Three main "0D" parameters :

- growth rate, $\mathcal{Y}_0 \approx 0.12$,
- molecular mixing fraction, $\Theta \approx 0.83$,
- Von Kármán number, $\kappa \approx 0.13$,

are defined by:

$$L(t) = 6 \int \alpha^+ \alpha^- dx, \tag{16a}$$

$$\Theta(t) = \int \alpha^+ \alpha^{2+} \alpha^{1+} + \alpha^- \alpha^{2-} \alpha^{1-} dx \; / \int \alpha^2 \alpha^1 dx, \tag{16b}$$

$$E(t) = \int \alpha^+ \rho^+ \varepsilon^+ + \alpha^- \rho^- \varepsilon^- dx \; / \int \alpha^+ \rho^+ + \alpha^- \rho^- dx, \tag{16c}$$

$$K(t) = \ldots = K^+ + K^- + K_D + K_A, \tag{16d}$$

$$\kappa(t) = K^{3/2} \, / \, E \, L. \tag{16e}$$

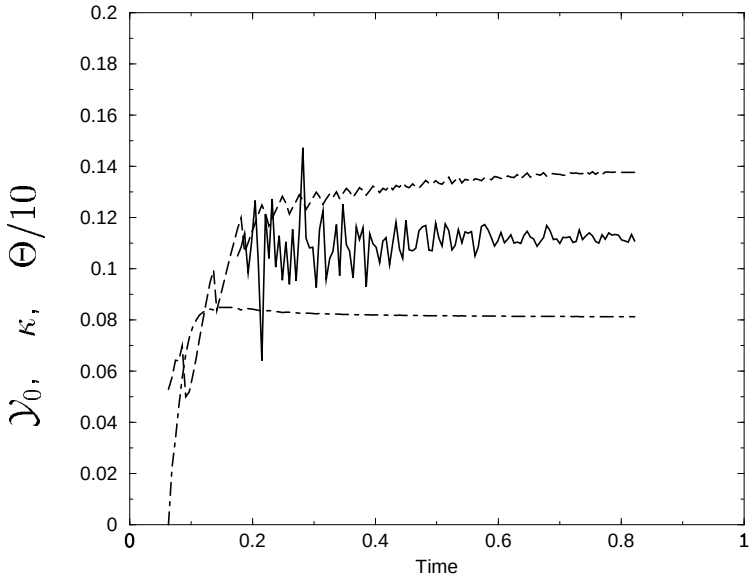

Time evolution of "0D" parameters: $\mathcal{Y}_0$ (continuous), Θ (dot–dashed), and κ (dashed).

Von Kármán number captured within 20% without ajustments.

For Richtmyer-Meshkov, TTT yields $n_0 \approx 0.3$ as k–ε.

III.4 Growth rate compared to other models

Estimate of growth coefficient
corrected for transient and relaxation effects:

$$L(t) = \mathcal{Y}_n \, \mathsf{At} \, g(t) \, t^2 \times \left[1 + \frac{\delta t}{t} + \frac{\tau^2}{t^2}\right]^{n+2} \tag{17}$$

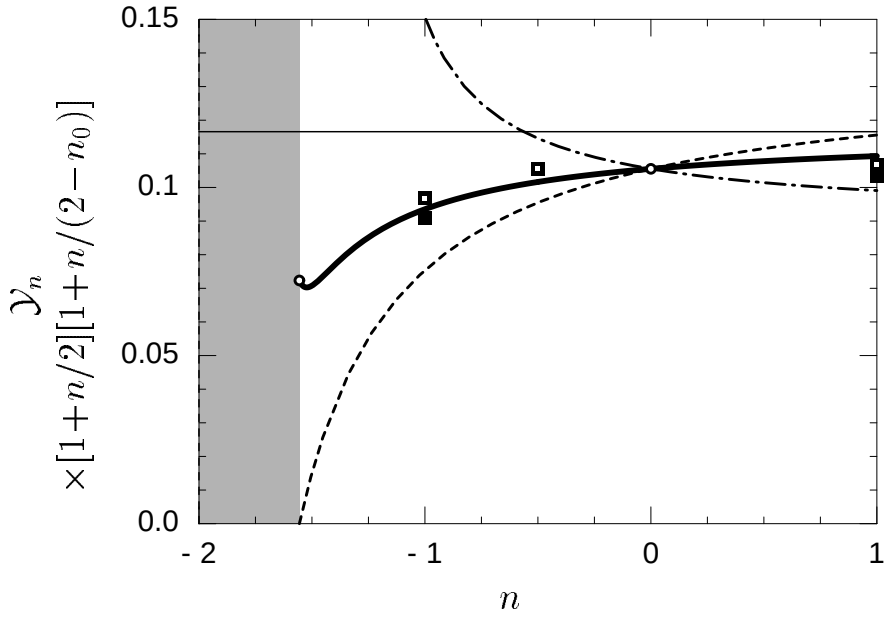

Normalized growth rates of various models: TTT (squares),
Youngs' two-fluid (dot-dashed), free fall (dashed) Read's formula (dotted),
and Youngs' preliminary simulations presented at this conference (filled squares).

Molecular mixing fraction and Von Kármán number,
Θ_n and κ_n, are practically independent of n for $-1 < n < 1$.

IV Conclusions

A two-structure, two-fluid, two-k–ε model (TTT)
has been developped which:

- derives from two-field RANS closure,
- provides physically consistent picture of RT/SSVARTs TMZs,
- contains single fluid k–ε ($\rightarrow$ KH, RM),
- captures Von Kármán numbers,
- is potentially accurate on a range of SSVARTs and demixing,
- involves few unknown ajustable constants.

TTT is currently being improved regarding:

- Atwood number influence,
- added mass closure,
- response to KH,
- dispersion by added mass velocity fluctuations,
- shocks and compressibility effects.
- confirmation of closures from simulated correlations.

Acknowledgements

Benoît Dejardins (Commissariat à l'Energie Atomique, Bruyères-le-Châtel, France),

Olivier Simonin, Ariane Vallet

(Institut de Mécanique des Fluides de Toulouse, France),

David L. Youngs (Atomic Weapons Establishment, United Kingdom),

Paul-Henry Cournède (Ecole Centrale de Paris, France),
Laurent Chodorge (Commissariat à l'Energie Atomique, Fontenay-aux-Roses, France).

References

P.-H. Cournède, Thèse de Doctorat, Ecole Centrale de Paris, France (2001).

S.B. Dalziel, P.F. Linden, and D.L. Youngs, *J. Fluid Mech.* **399**, 1 (1999).

G. Dimonte, Phys. Plasmas **7**, 2255 (2000).

G. Dimonte, and M. Schneider, *Phys. Fluids* **12**, 304 (2000).

N.A. Inogamov, A.M. Oparin, A.Yu. Dem'yanov, L.N. Dembitskii, and V.A. Khokhlov, *J. Exp. Theor. Phys.* **92**, 715 (2001).

A. Llor, CEA Report in print R–5983, France, 2001.

A. Llor, This conference.

A. Vallet, O. Simonin, and A. Llor, Proceedings of "Trends in numerical and physical modelling for industrial multiphase flows", Carghese, France 27-29/09/00.

D.L. Youngs, *Physica* **D37**, 270 (1989).

D.L. Youngs, *Laser and Particle Beams* **12**, 725 (1994).

D.L. Youngs, in Proceedings of the 5th International Workshop on Compressible Turbulent Mixing, Stony Brook, New York, August 1995, edited by R. Young, J. Glimm, and B. Boston, World Scientific, Singapore, 1995.

D.L. Youngs, and A. Llor, This conference.

How to inhibit Rayleigh-Taylor mixing

Robert E. Breidenthal
University of Washington

Self-similar flow

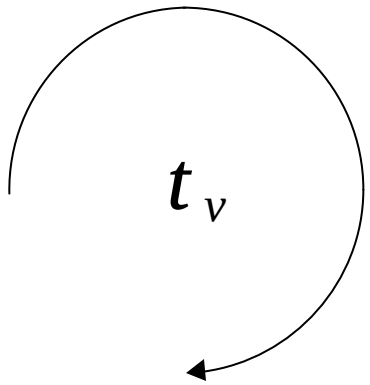

Self-similarity means the next rotation period is always proportional to the current one.

$$\tau_v(t + \tau_v(t)) = \text{const.}\ \tau_v(t).$$

In other words, the fractional decrease in rotation period per rotation is a constant, independent of time,

$$[\tau_v(t) - \tau_v(t + \tau_v(t))]/\tau_v(t) = \text{const.} = \varepsilon.$$

Proof that $t_v(t)$ must linear if self similar

Assume

$$\Delta_v(t) = \Delta_v(0) + a_1 t + a_2 t^2 + \ldots a_n t^n.$$

Then

$$[-a_1(\Delta_0 + a_1 t + a_2 t^2 + \ldots a_n t^n) + \text{terms up to } t^{n2}]/(\Delta_0 + a_1 t + a_2 t^2 + \ldots a_n t^n) = \Delta.$$

Satisfied iff $n^2 - n = 0$. So n = 0 or 1.

Thus $a_j = 0$ for all $j > 1$, and $a_1 = -\Delta$.

The only possible self-similar evolution is $\Delta_v(t) = \Delta_v(0) - \Delta t = \Delta_0 - \Delta t$.

Example - Inertial subrange

One eddy 'turnover time'

$$\tau_\ell = \ell / v_\ell = \ell^{2/3} / \varepsilon^{1/3} = (\ell/L)^{2/3} \tau_L$$

Time interval from scale ℓ to (ℓ ℓ $d\ell$)

$$dt = const. \ell^{2/3} d\ell / (\varepsilon^{1/3} \ell)$$

(Kulkarny & Broadwell)

Total elapsed time to reach scale ℓ

starting from scale L is

$$t(\ell) = [1 - (\ell/L)^{2/3}] \tau_L,$$

so

$$\ell / L = 1 - t(\ell)/\tau_L \quad \ldots \text{linear}$$

in t

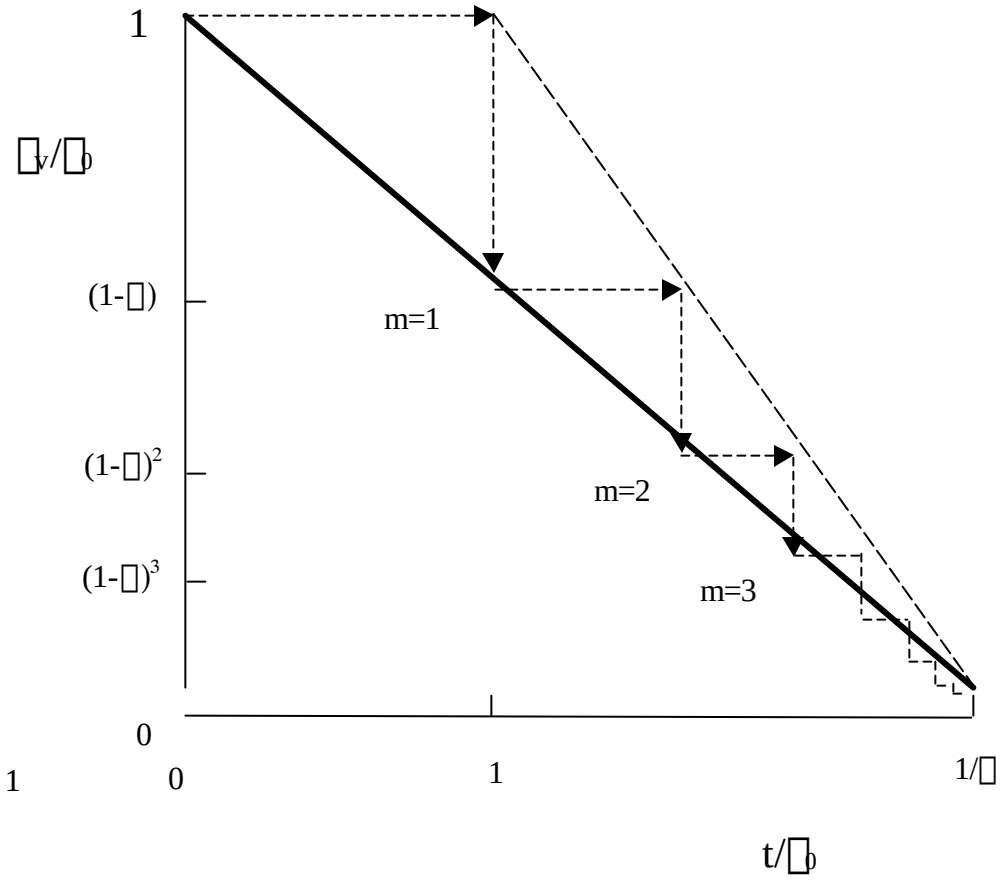

Vortex rotation period $\tau_v(t)$ for $\alpha > 0$

.

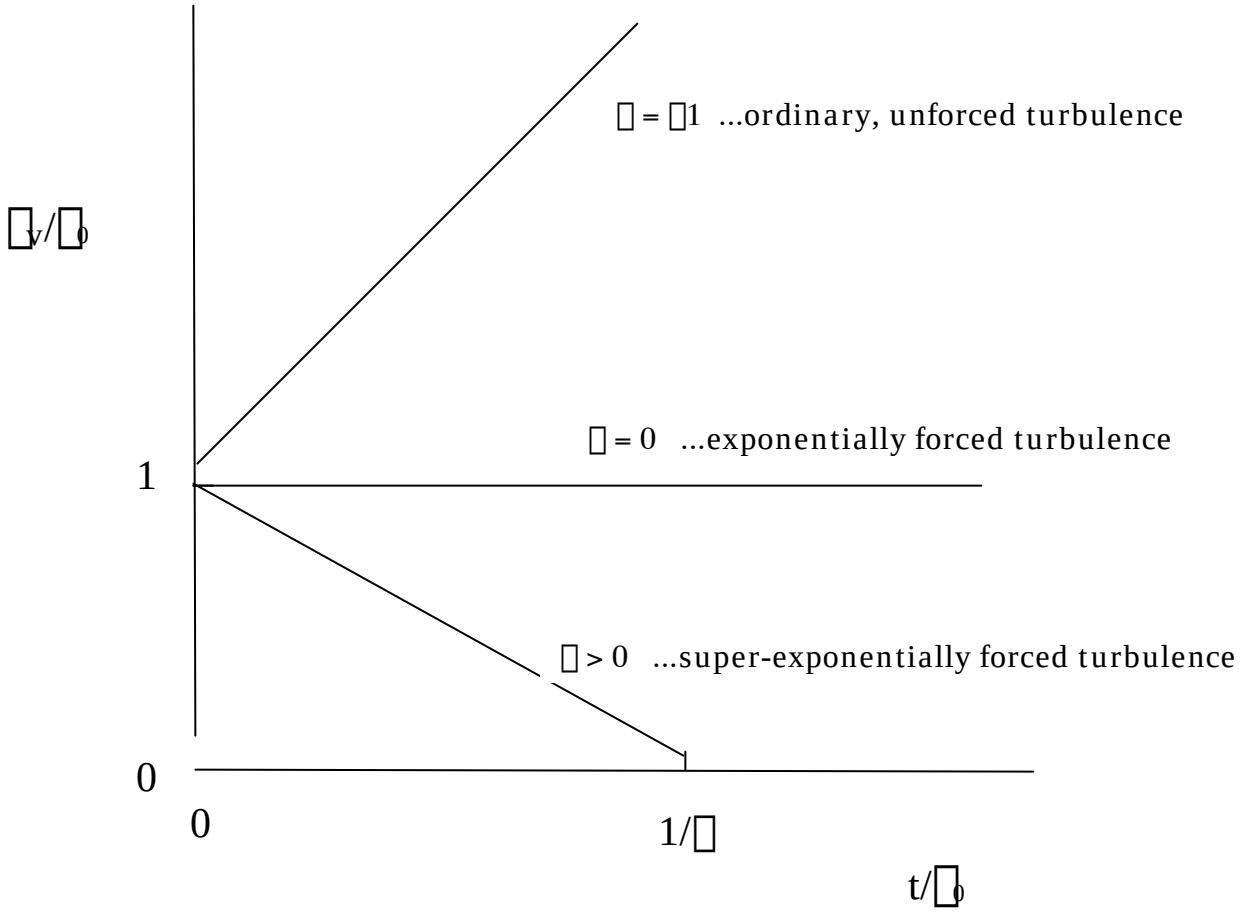

Vortex rotation period $\tau_v(t)$ for all self-similar flows

Vortex stretching

$$Dw/Dt = (\tilde{N}\mathbf{u})\, w$$

Symmetry arguments imply

$$mag((\tilde{N}\mathbf{u})\, w) = c\, \omega^2$$

$$D\omega/Dt = c\, \omega^2.$$

$$\omega(t)/\omega(0) = 1/(1 - ct/\lambda_v(0)),$$

identical to

$$\lambda_v(t)/\lambda_v(0) = 1 - \alpha t/\lambda_v(0)$$

for $\alpha = 1/\lambda_v$ and $c = \alpha$.

Rayleigh-Taylor

$$g' = \frac{\Delta r}{\bar{r}} g$$

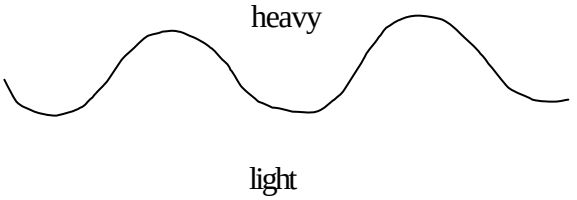

Impose an e-folding time scale $\tau_v(t) = \tau_0 - \beta t$.

So force with "super-exponential"

acceleration $\frac{g(t)}{g_0} = e^{\left(\frac{t}{t_0 - bt}\right)}$.

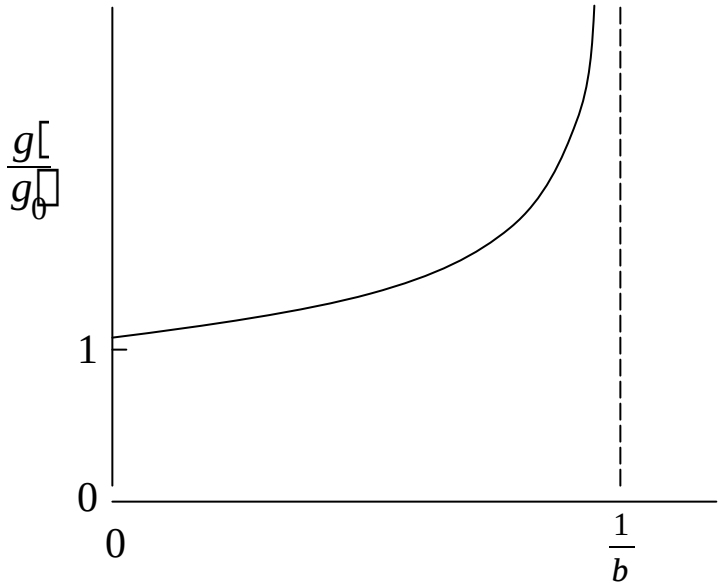

$\frac{t}{t_0}$

How to inhibit Rayleigh-Taylor entrainment?

Instead of constant acceleration, use super-exponential, e.g.

$$\frac{g'}{g'_0} = \exp\left(\frac{t}{t_0 - bt}\right).$$

As $b \to 1$, entrainment is inhibited for all perturbation wavelengths $\lambda > g_o' \lambda_o^2$.

2D inviscid simulations

Christian Anitei

Randy Leveque's CLAWPACK code (suggested by Hamid Johari)
Derek Bale
James Rossmanith

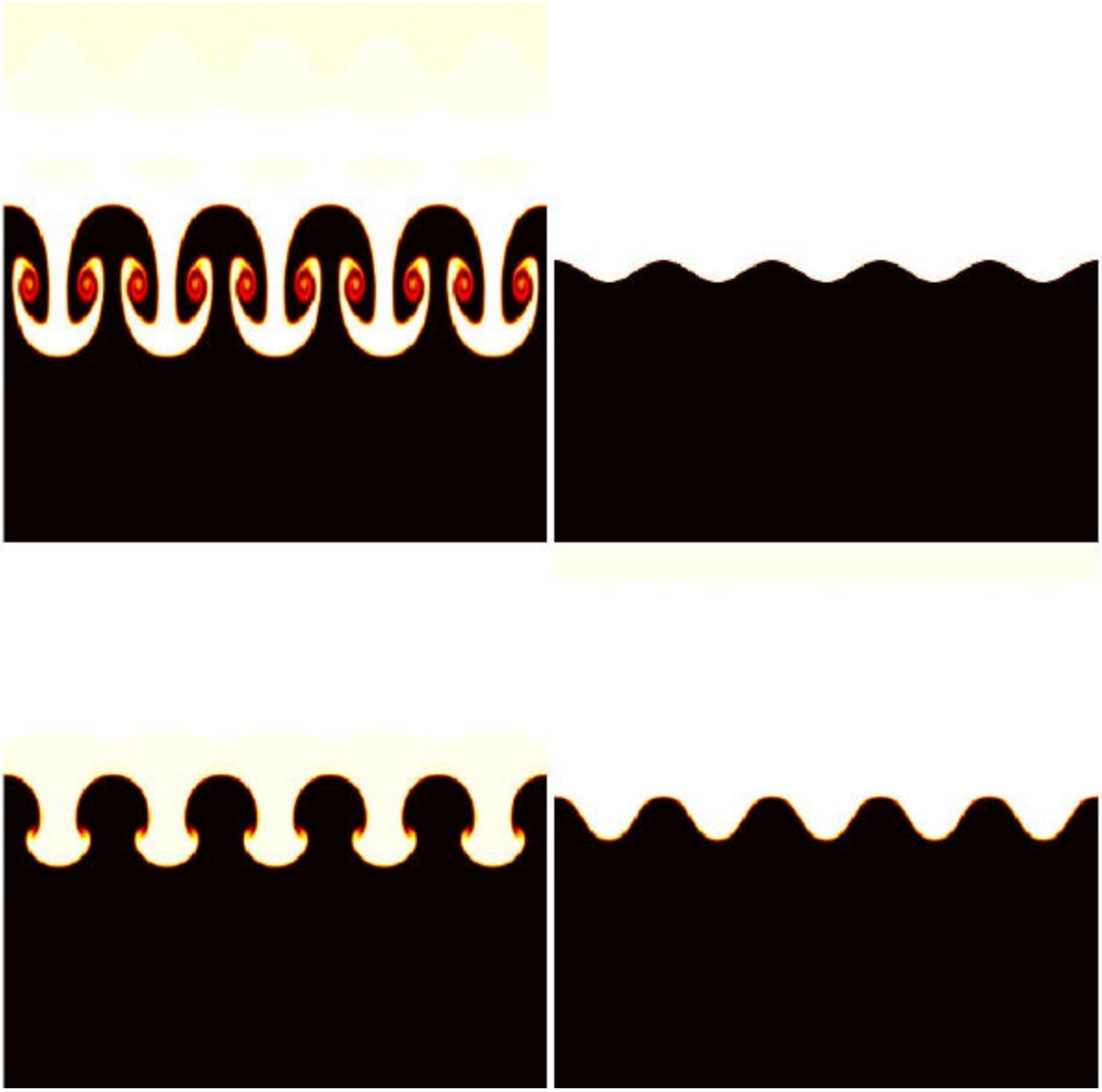

□ = □□

Time progresses clockwise from upper right

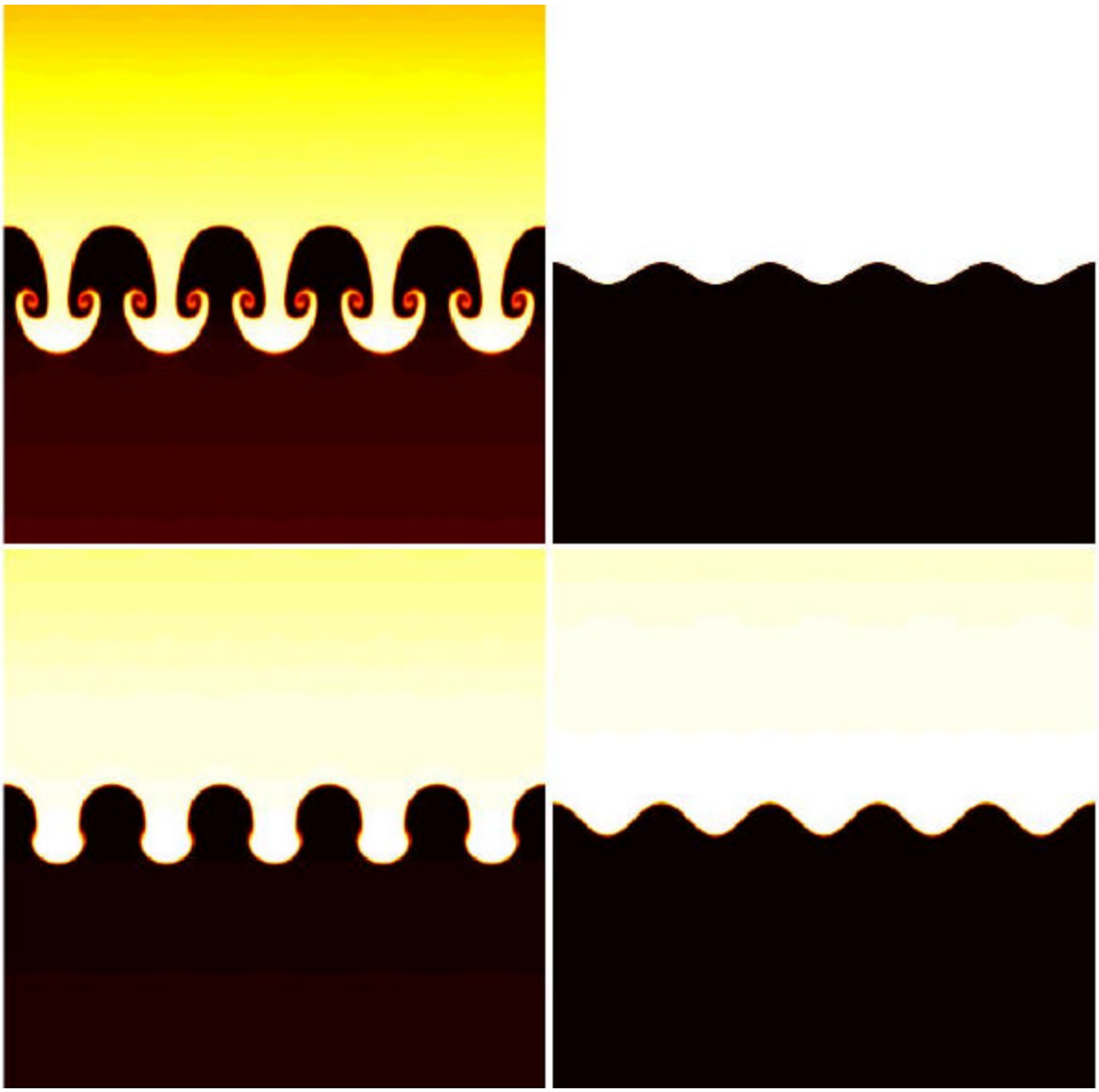

$\theta = 0$

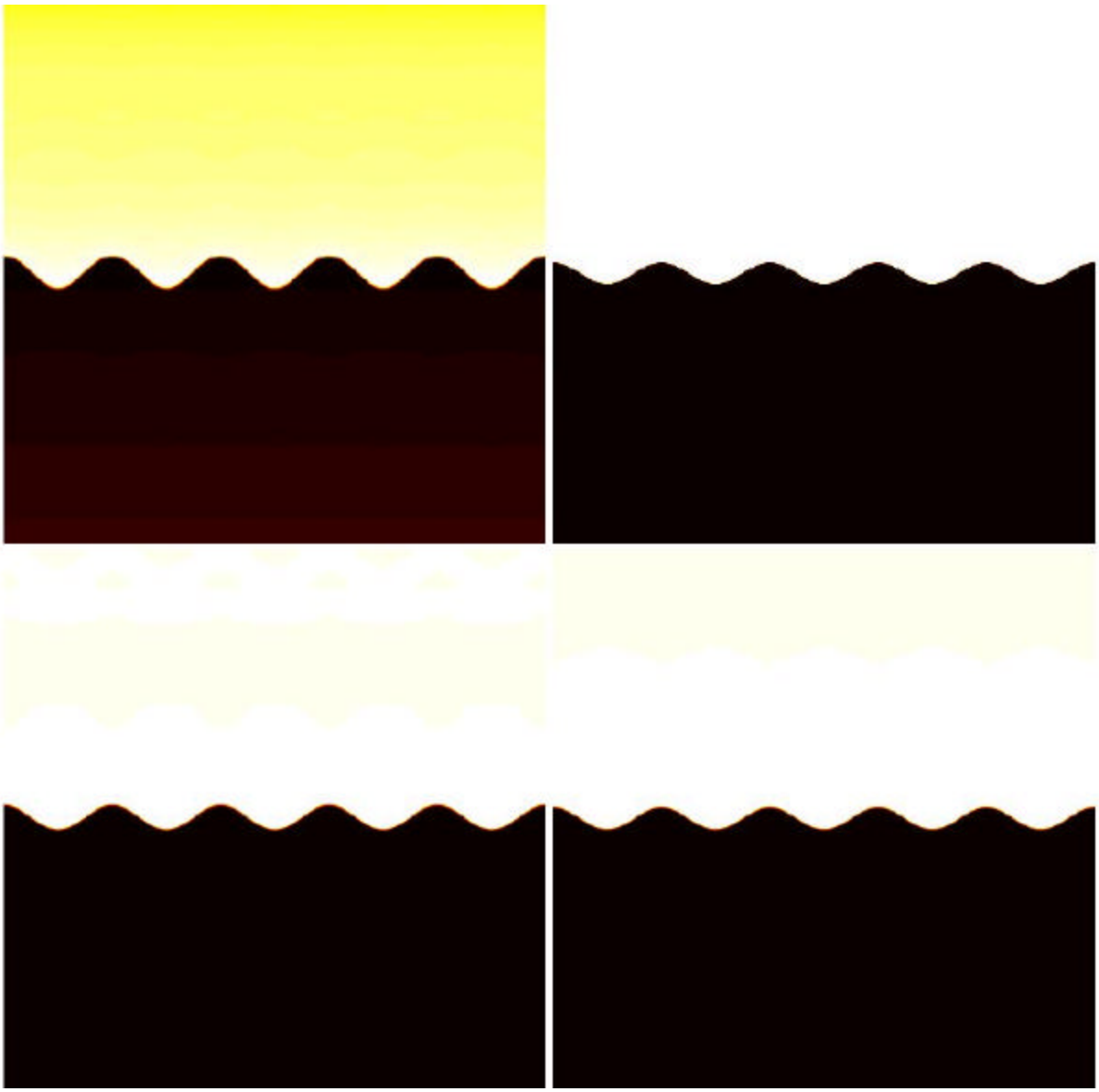

$\theta = 1$

Physical interpretation

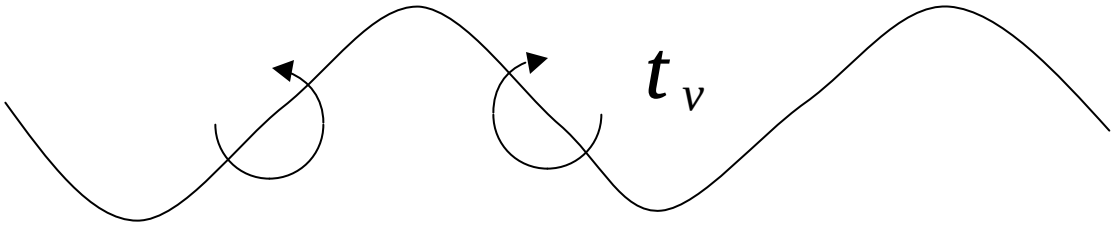

It takes time for a vortex sheet to roll up. If at every instant, the required roll-up time is just equal to the remaining available time (Γ=1), there can be no roll up. Even more that this, the acceleration provides a stabilization.

$\Delta = 1$

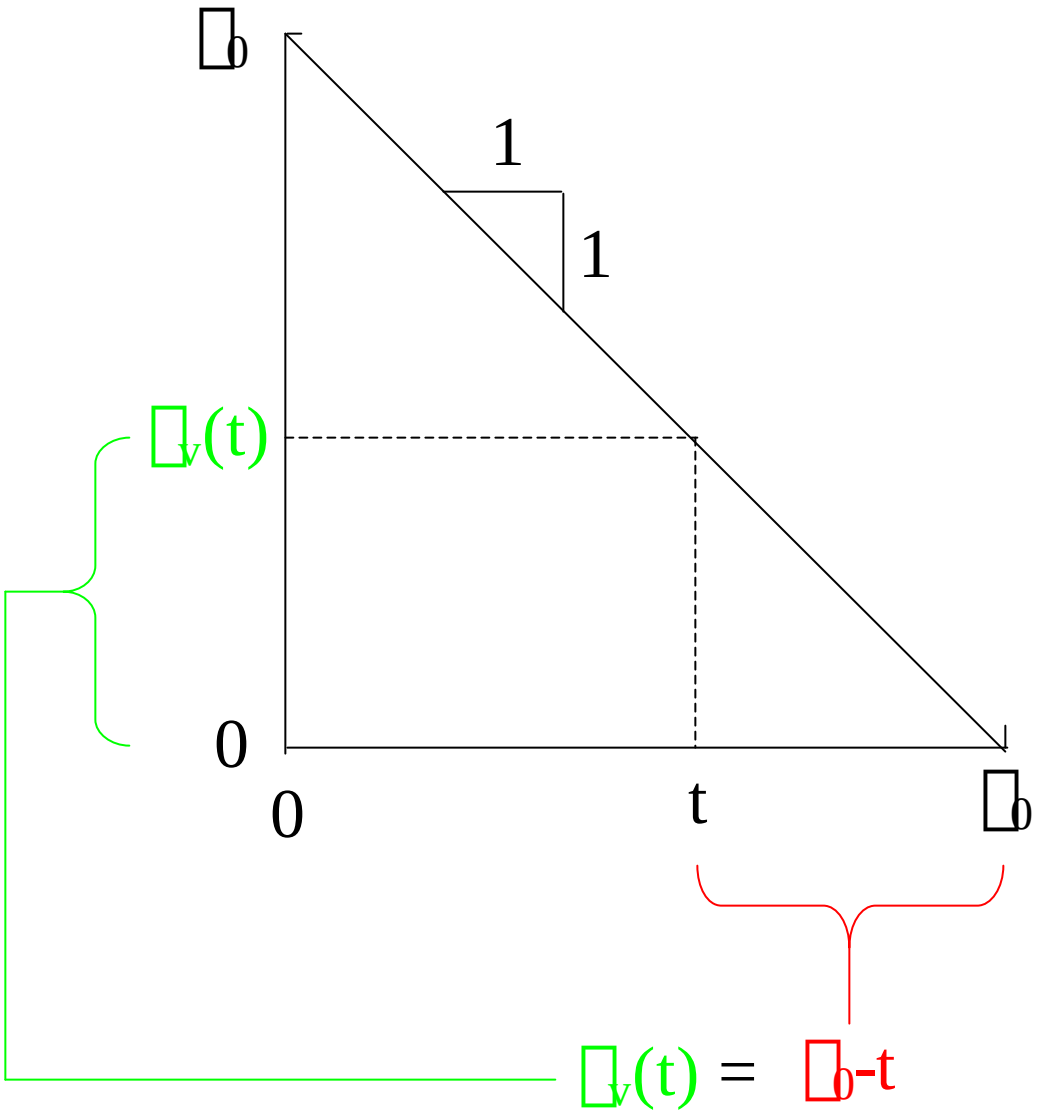

At every instant, the current rotation period is just equal to the remaining time.

Conclusions

- For all self-similar turbulence, the vortex rotation period is a linear function of time,

  $\tau_v = \tau_0 - \alpha t$.

- Entrainment and dissipation are inhibited as $\alpha \to 1$.

- For $\alpha=1$, Rayleigh-Taylor entrainment is suppressed for all wavelengths

  $\lambda > g_0' \tau_0^2$.

Theoretical Methods for the Determination of Mix

Baolian Cheng, James Glimm and David Sharp

Los Alamos National Laboratory

Los Alamos, NM

Department of Applied Mathematics & Statistics
State University of New York
Stony Brook, NY 11794-3600

Center for Data Intensive Computing
Brookhaven National Laboratory
Upton, NY 11973-5000

- in collaboration with -

Hyeonseong Jin

Main Results

1. Buoyancy drag mixing edge motion equations --
   - Agree with bubble merger model, experiments, FT simulation and A = 1 theory
   - Spike -- bubble coupling (Center of Mass)
   - All drag coefficients determined
   - Lower than leading order asymptotics
2. Improved two phase mix model equations --
   - mathematically stable and thermodynamically determinate
   - Closure specified from asymptotic analysis
3. Turbulent diffusivity derived from mix model

Comparison of Bubble Merger Model with Experiments, Simulation

$Z_b(t) =$ penetration distance of light fluid into heavy

$$= \alpha_b A g t^2$$

$\alpha_b =$ 0.05 -- 0.077 (Experiment)
0.05 -- 0.06 (Theory)
0.07 (Simulation - tracked)

Bubble height / bubble width = 3.3 (experiment)
= 2.3 (theory)

A Bubble Merger Model

Statistical Models of Interacting Bubbles

Bubble Merger Models

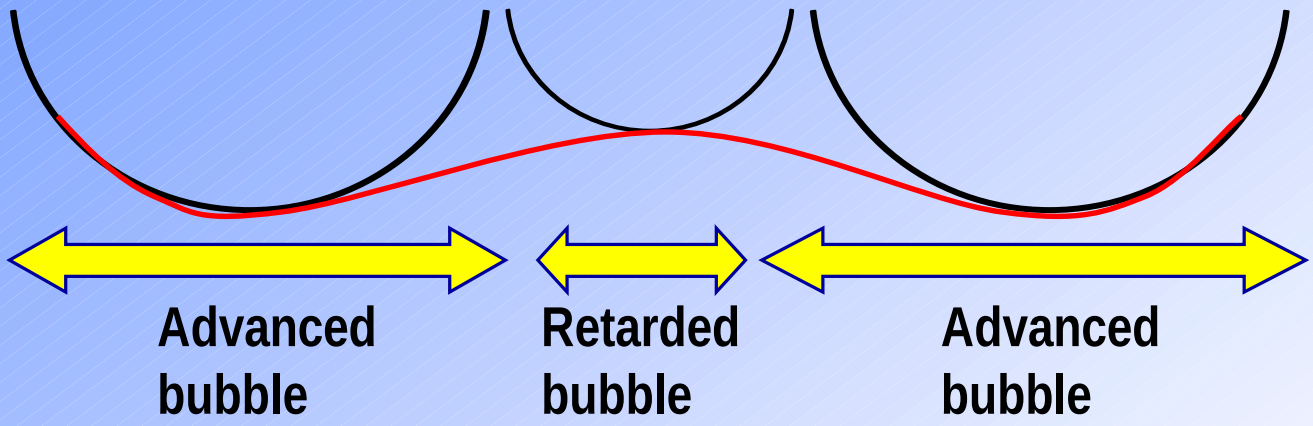

Bubble velocity = single mode velocity + envelope velocity

Bubble Merger Criterion

Envelope velocity > 0 advanced bubble

Envelope velocity < 0 retarded bubble

Remove bubble from ensemble where velocity = 0:

$|\text{single mode velocity}| = |\text{envelope velocity}|$

$$\alpha_b \approx \text{ 0.5 -- 0.6}$$

Scaled Variables

r = mean bubble radius

t_m = time to bubble merger

$t_m' =$ scaled time to merger

$dt' = (Ag / r)^{1/2} dt$

$\langle \; \rangle_*$ = fixed point expectation

Renormalization group (RNG) fixed point equation for bubble radius

$$\frac{dr}{dt} = \Delta r \times \text{merger rate} = kr \times \text{merger rate}$$

$$= kr\left\langle \frac{1}{t_m} \right\rangle = k\sqrt{Ag}\left\langle \frac{1}{t_m'} \right\rangle r^{1/2}$$

k = fractional increase in radius due to one merger event; t_m = time to merger

$$r = \frac{k^2}{4}\left\langle \frac{1}{t_m'} \right\rangle^* Agt^2; \quad \alpha_r = \frac{k^2}{4}\left\langle \frac{1}{t_m'} \right\rangle^*$$

Bubble height variables

k = geometric factor, $\approx .43$

$\bar{h}$ = mean bubble height

h_m = bubble height separation for merger

$h = \bar{h} + h_m / 2$

Derive rate equation for h in RNG scaling

RNG Bubble Height Equation

$$\alpha_b = \frac{1}{2} c_b \alpha_r^{1/2} + \left[\frac{1}{2k} + \frac{1}{2} \right] \alpha_{h_m}$$

c_b = terminal velocity coefficient for single (periodic) bubble

Average of three Smeeton and Youngs experiments:

LHS = 0.067; RHS = 0.0695;
Fixed Point Calculation = 0.056

Center of Mass (COM) Hypothesis

$$Z_{\mathrm{COM}} = \alpha_{\mathrm{COM}} A g t^2$$

$$\alpha_{\mathrm{COM}} = \frac{7}{60}\alpha_s A^{\gamma}; \quad \gamma = 3 - 17$$

$$\approx 0 \text{ unless } A \approx 1$$

fits data and theory (A = 1). α_s / α_b = solution of quadratic equation

$$\alpha_s = \alpha_s(\alpha_b)$$

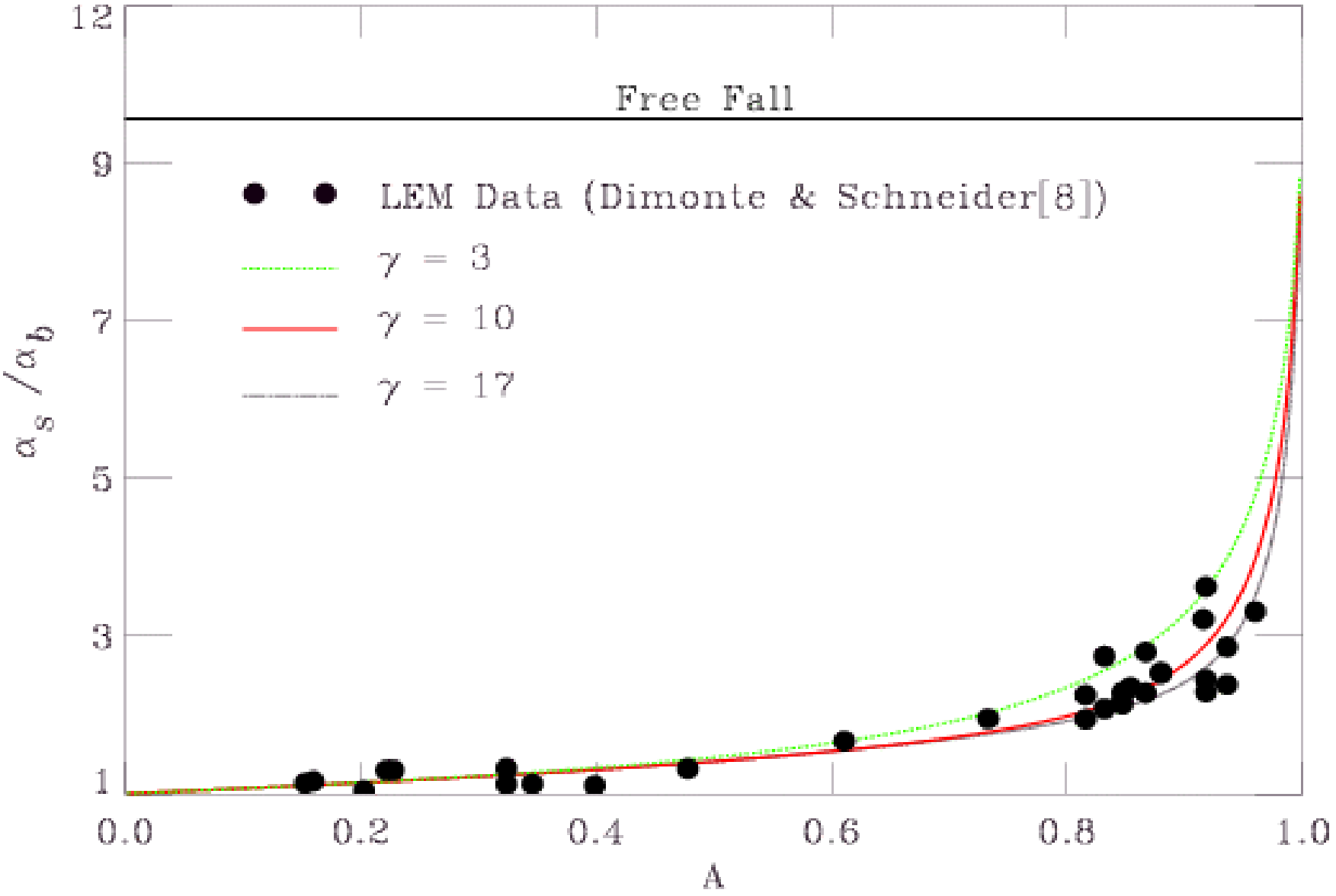
Free Fall
LEM Data (Dimonte & Schneider[8])
γ = 3
γ = 10
γ = 17
a_s / a_b
A
12
9
7
5
3
1
0.0
0.2
0.4
0.6
0.8
1.0

Mixing Zone Edge Models

$Z_{b,s}(t) = h_{b,s} = \alpha_{bs}\ Agt^2$ in RT case

Buoyancy Drag equation for $Z_{b,s}(t)$:

$$\left(\rho_{b,s} + k\rho_{s,b}\right)\ddot{Z}_{b,s}(t) = \left(\rho_b - \rho_s\right)g - \rho_{s,b}C_{b,s}\dot{Z}_{b,s}^{\ 2} / Z_{b,s}$$

Determine $C_{b,s}$ from RT edge motion theory.
ODE valid for arbitrary acceleration

k = 1 from standard fluid dynamics and from bubble geometry

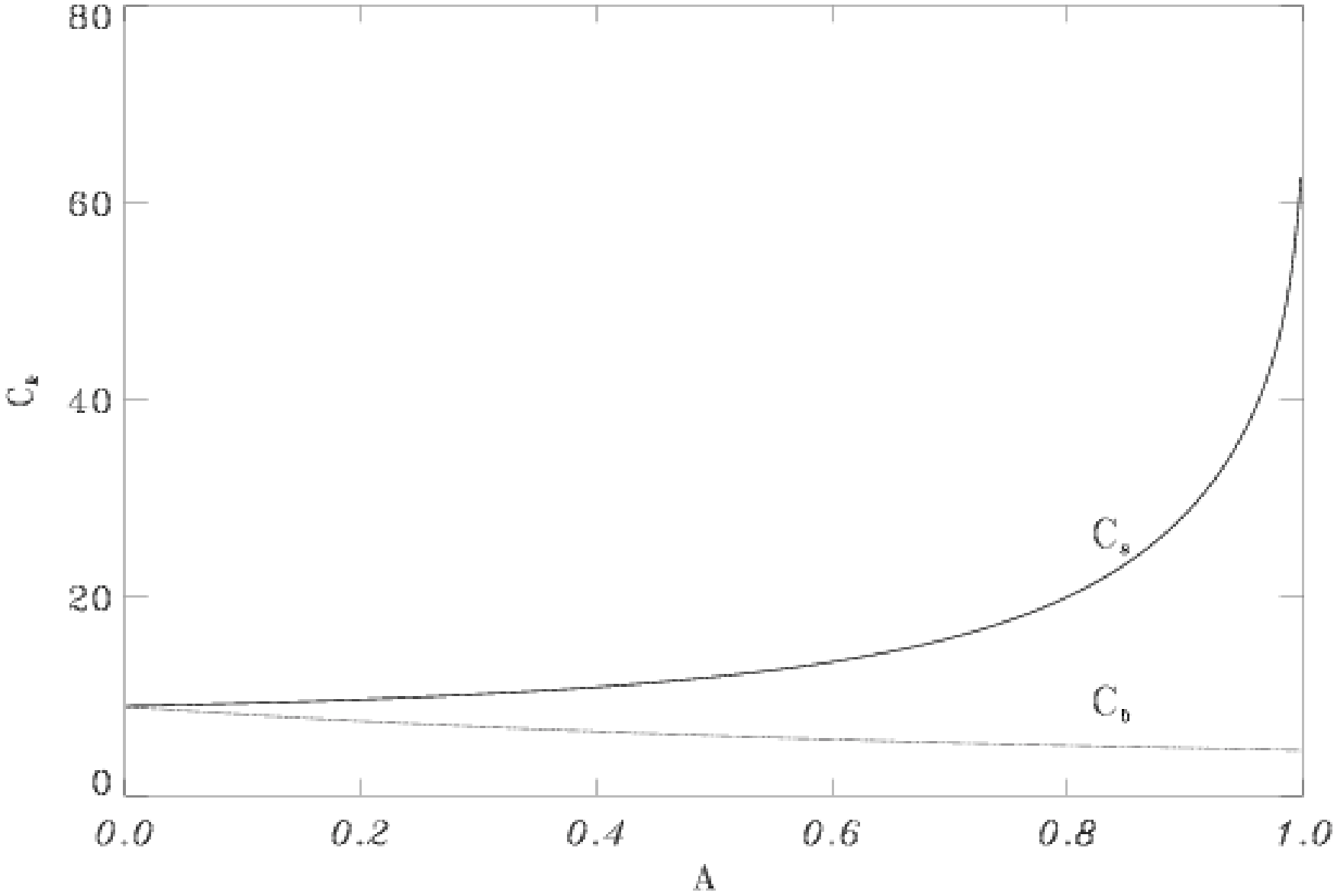
80
60
40
20
0
C_s
0.0
0.2
0.4
0.6
0.8
1.0
A
C_s
C_b

Non-leading Order Terms in RT Asymptotics

$$Z(\mathrm{t}) = \alpha\ Agt^{2} + \beta t + \gamma$$

β, γ depend on initial data :

$$t_0, Z_0, V_0$$

α does not depend on initial data

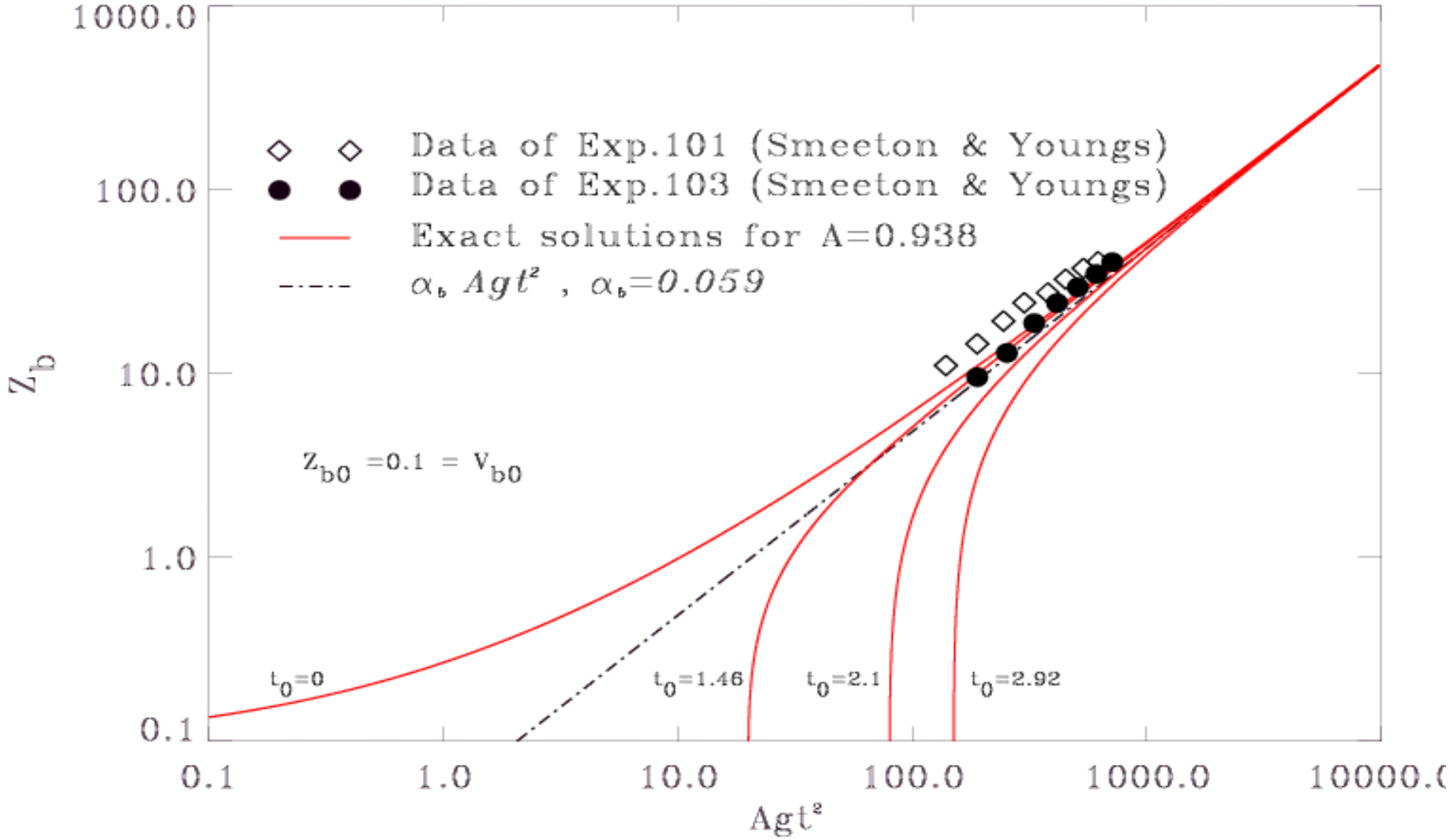
1000.0
100.0
10.0
1.0
0.1
Z_b
Data of Exp.101 (Smeeton & Youngs)
Data of Exp.103 (Smeeton & Youngs)
Exact solutions for A=0.938
$\alpha_b\, Agt^2$, α_b=0.059
Z_{b0} =0.1 = V_{b0}
t_0=0
t_0=1.46
t_0=2.1
t_0=2.92
0.1
1.0
10.0
100.0
1000.0
10000.0
Agt^2

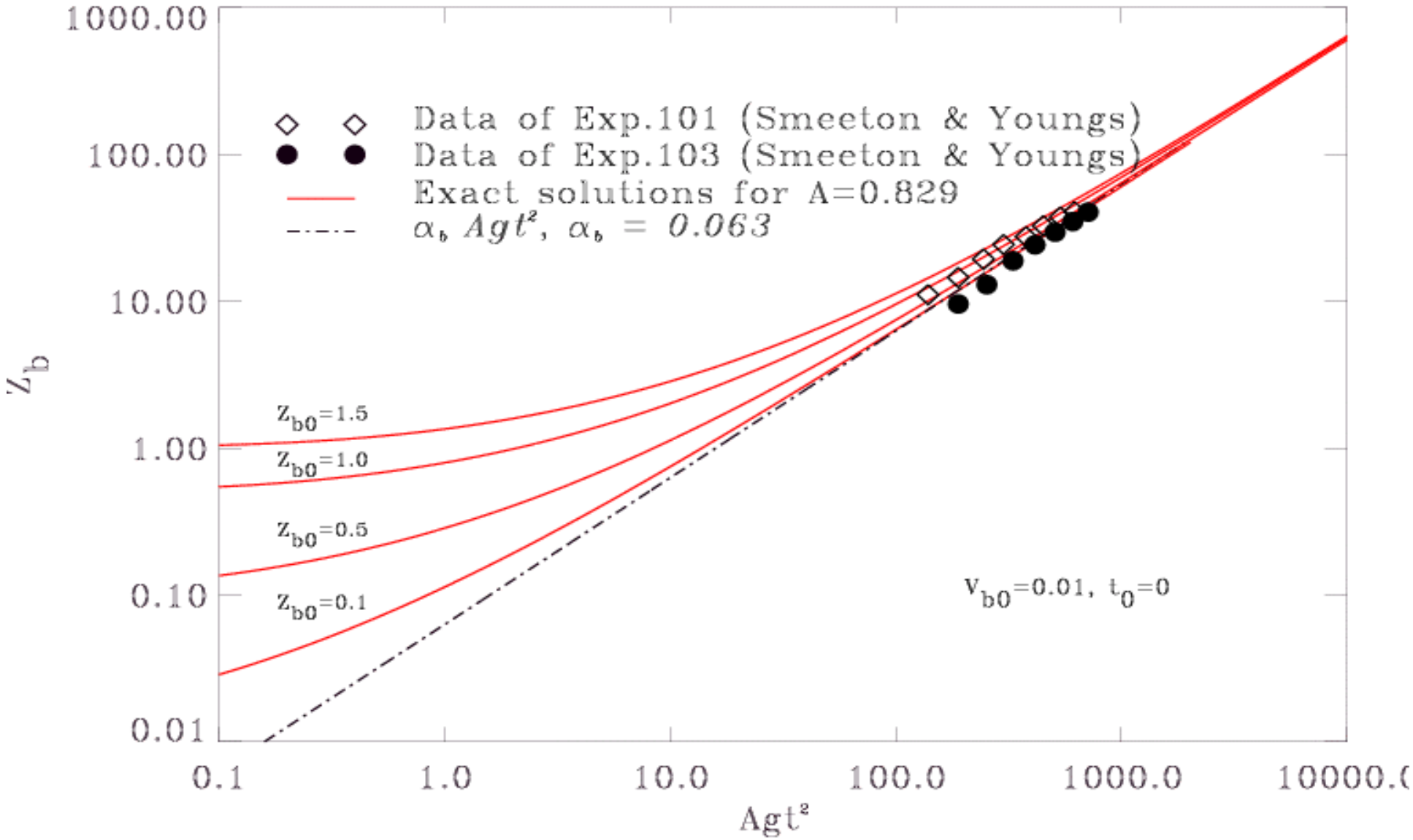
1000.00
100.00
10.00
1.00
0.10
0.01
Z_b
0.1
1.0
10.0
100.0
1000.0
10000.0
Agt^2
Data of Exp.101 (Smeeton & Youngs)
Data of Exp.103 (Smeeton & Youngs)
Exact solutions for A=0.829
$\alpha_b\, Agt^2$, $\alpha_b = 0.063$
Z_{b0}=1.5
Z_{b0}=1.0
Z_{b0}=0.5
Z_{b0}=0.1
v_{b0}=0.01, t_0=0

Chunk Mix Model

- Complete fluid variables for each fluid
  -- Mathematically stable equations
- Improved physics model for mix
  -- Pressure difference forces ~ drag
- Thermodynamics is process independent
- New closure proposed and tested
  -- Zero parameters (incompressible flow)
- Analytic solution for incompressible case

Multiphase Averaged Equations

Microphysics: $U_t + \nabla F(U) = 0$

Macrophysics: $\bar{U}_t + \nabla \overline{F(U)} = 0$

$$\overline{F(U)} \neq F(\bar{U})$$

$$F_{ren}(\bar{U}) \approx \overline{F(U)}$$

$$\bar{U}_t + \nabla F_{ren}(\bar{U}) = 0$$

Closure Problem: Determine F_{ren}

Ensemble Averages

Assume two fluids, labeled k=1 (light) and k=2 (heavy). Define

$$\mathbf{X}_k(x, y, z, t) = \begin{cases} 1 & \text{if } (x, y, z) \text{ is in fluid k at time t} \\ 0 & \text{otherwise} \end{cases}$$

Let $\langle \cdot \rangle$ denote (ensemble) average.

Microphysics

$$\frac{\partial \mathbf{X}_k}{\partial t} + v \cdot \nabla \mathbf{X}_k = 0$$

Define v^*:

$$\langle v \cdot \nabla \mathbf{X}_k \rangle \equiv v^* \nabla \boldsymbol{\beta}_k$$

Macrophysics

$$\boldsymbol{\beta}_k = \langle \mathbf{X}_k \rangle$$

$$\frac{\partial \boldsymbol{\beta}_k}{\partial t} + \langle v \cdot \nabla \mathbf{X}_k \rangle = 0$$

Thus

$$\frac{\partial \boldsymbol{\beta}_k}{\partial t} + v^* \cdot \nabla \boldsymbol{\beta}_k = 0$$

Closure

Assume: v^* depends on v_1 and v_2 and spatially dimensionless quantities only.

Assume: regularity of v*.

Theorem: $$\upsilon^* = \mu_2^{\upsilon}\upsilon_1 + \mu_1^{\upsilon}\upsilon_2$$

(convex combination) and related expressions for p* and *(pv)**

Assume: all μ's depend on β_k and t only.

Explicit Model: Zero Parameters

Exact calculation: μ_k^{υ} is fractional linear. Assume same for μ_k^{p}. Assume dependence on β_k alone. Then

$$\mu_k^q = \frac{\beta_k}{\beta_k + c_k^q \beta_{k'}}$$

with k' denoting the other fluid index and $c_1^q c_2^q = 1 \qquad q = \upsilon \quad \text{or} \quad q = p.$

With the mixing zone boundaries $Z_k(t)$, and velocities $V_k(t)$,

$$c_k^{\upsilon} = \frac{|V_{k'}|}{|V_k|}, \qquad c_k^{p} = \frac{\rho_{k'}}{\rho_k}$$

for incompressible flow. Boundary accelerations $\ddot{Z}_k(t)$ must be must be supplied externally to this model.

$\ddot{Z}_k(t) =$ Drag + buoyancy

Analytic Solution: Incompressible Case

$$\upsilon_k(\beta_k, t) = V_k \mu^{\upsilon}_{k'}$$

$$\upsilon^*(\beta_k, t) = \frac{V_k V_{k'}(V_k \beta_k^2 + V_{k'} \beta_{k'}^2)}{(|V_k|\beta_k + |V_{k'}|\beta_{k'})^2}$$

$$z(\beta_k, t) = z_0(\beta_k) + \int_0^t \upsilon^*(\beta_k, s)ds$$

Let

$$\overline{p} = \beta_1 p_1 + \beta_2 p_2, \qquad p_{diff} = \frac{p_2}{\rho_2} - \frac{p_1}{\rho_1},$$

$$\frac{D_k}{D_t} = \frac{\partial}{\partial t} + \upsilon_k \frac{\partial}{\partial_z} \quad .$$

Then

$$\overline{p}(z, t) = p_2(Z_1) + \int_{Z_1}^{z} \sum_{k=1}^{2} \beta_k \rho_k (g - \frac{D_k \upsilon_k}{Dt})dz$$

$$p_{diff} = p_{diff}(Z_1) - \int_{Z_1}^{z} \left(\frac{D_2 \upsilon_2}{Dt} - \frac{D_1 \upsilon_1}{Dt} \right) dz$$

Asymptotic Expansion in Powers of M = Mach Number

0th order = incompressible v, β

1st order = correction v, β

2nd order = incompressible p_1, p_2

+ v, β correction

2nd order p_1, p_2 = incompressible p_1, p_2

$\Rightarrow$ constraint:

"missing" incompressible pressure equation

Also resolves "missing" compressible closure.

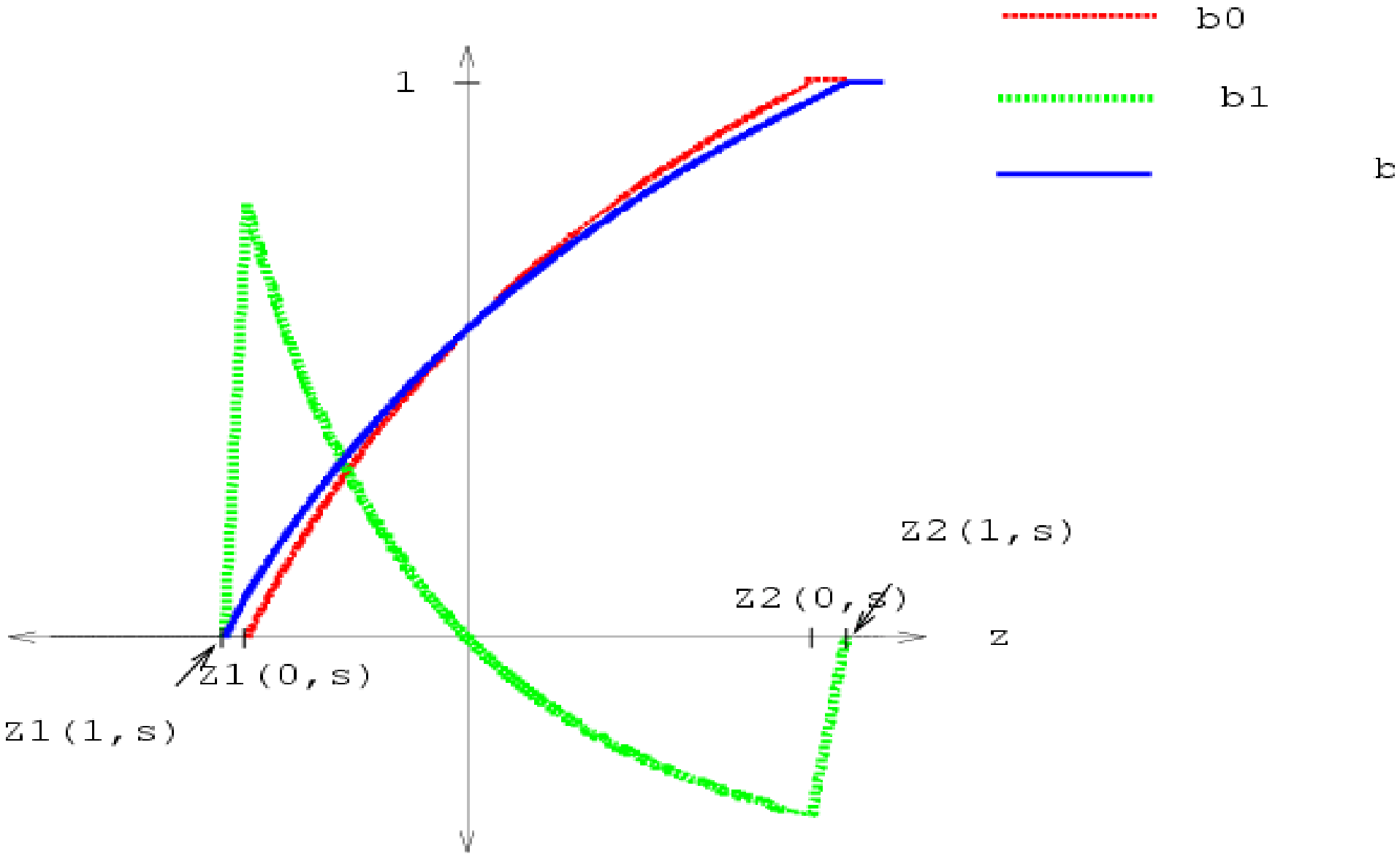
b0
b1
b
1
z2(1,s)
z2(0,s)
z
z1(0,s)
z1(1,s)

Reduced Models: Equilibrated Pressures and Velocities

Equilibrated pressures $(p_1 = p_2)$ requires equilibrated velocities for hyperbolic equations.

Equilibrated velocities requires a diffusion term to move phase particles.

Diffusion can be computed within the Chunk Mix model.

RT and RM Diffusion Coefficients

RT diffusion coefficient:

$$D = 2A^2 g^2 t^3 \left[\beta_2 \alpha_2^{\,2} \left(\frac{\alpha_1 \beta_1}{\alpha_1 \beta_1 + \alpha_2 \beta_2} \right)^3 + \beta_1 \alpha_1^{\,2} \left(\frac{\alpha_2 \beta_2}{\alpha_1 \beta_1 + \alpha_2 \beta_2} \right)^3 \right]$$

RM diffusion coefficient (s = entrainment time, obtained from solution of ODE):

$$D = \frac{\alpha_2^{\,2} \theta_2 \beta_2 s_1^{\,\theta_2}}{1+\tau} t^{\theta_2 - 1} + \frac{\alpha_1^{\,2} \theta_1 \beta_1 \tau s_2^{\,\theta_1}}{1+\tau} t^{\theta_1 - 1}$$

$$\tau = \frac{\alpha_2 \beta_2 \theta_2}{\alpha_1 \beta_1 \theta_1} t^{\theta_2 - \theta_1}$$

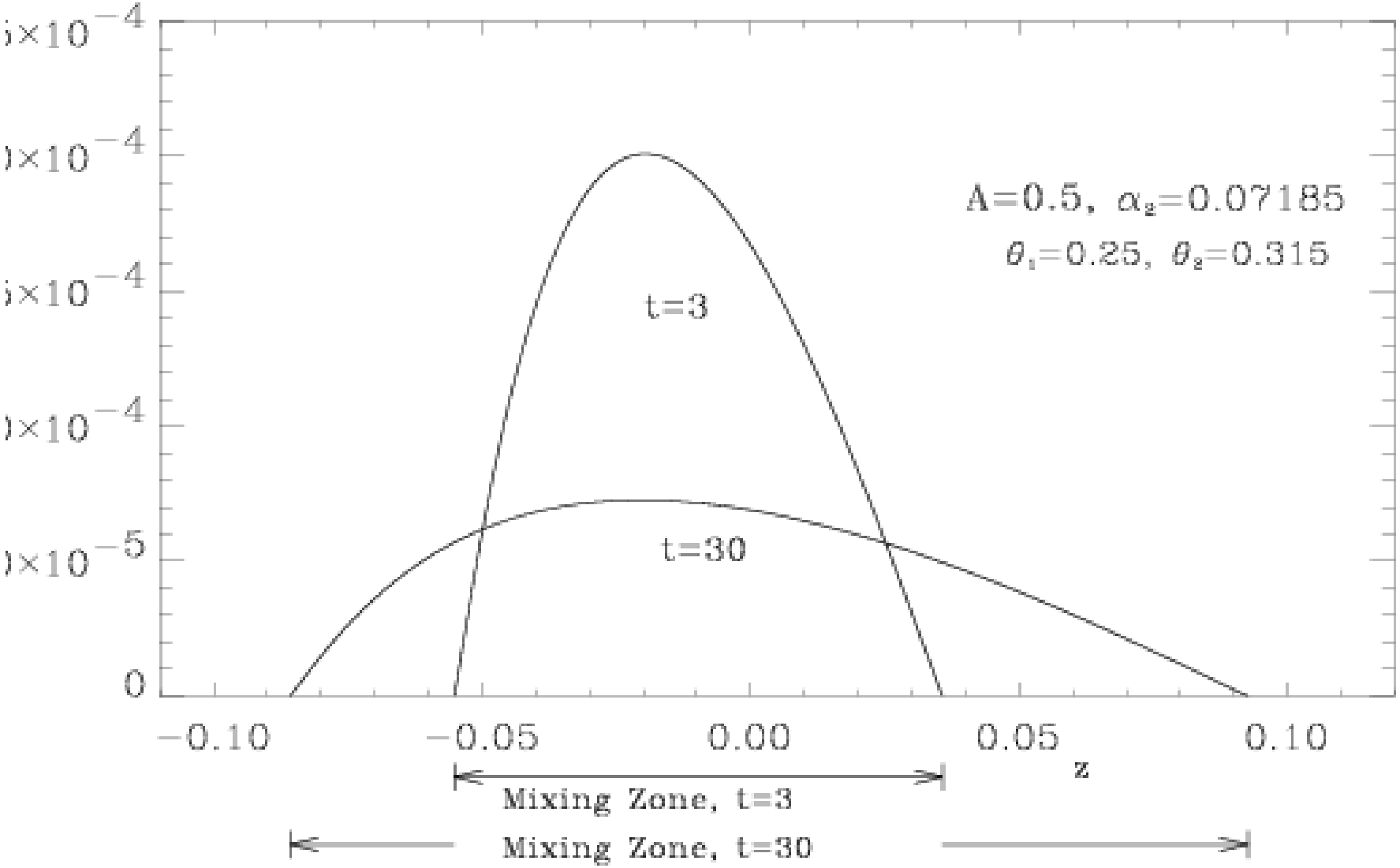
A=0.5, α_2=0.07185
θ_1=0.25, θ_2=0.315
t=3
t=30
0
−0.10
−0.05
0.00
0.05
0.10
z
Mixing Zone, t=3
Mixing Zone, t=30

Summary: A Predictive Science for Mix

- Consistent theory, simulation and experiment for 3D Rayleigh-Taylor fluid mixing
- Determine the mixing zone edge motions for general accelerations in agreement with experiment and A = 1 theory
- Lower than leading order asymptotics with explicit dependence on intial conditions
- Improved mix model equations: Stable mathematically and thermodynamically determinate
- Asmptotics defined; closure improved

Modeling Radiation Effects in Mixing Layers

Tim Clark (T-13)

Frank Harlow (T-3)

Theoretical Division

Los Alamos National Laboratory

December, 2001

Background/Goals

- Models of Rayleigh-Taylor and Richtmyer-Meshkov mixing layers are relatively sophisticated.
  - Multiphase flow models, turbulent models, hybrid models…
- Additional physical phenomena must be included for many practical circumstances.
  - Material strength, heat flux, evaporation….
- Goal: To develop a simple model to describe the effects of radiative heat transfer and ablation on a turbulent mixing layer.
  - Emphasis is on simplicity--fidelity will be assessed by comparison to experiment or simulations, possibly motivating additional complications.
  - Competition between instability growth rate and ablative growth rate; depends on the initial scale of the perturbations.

Strategy/Problem Formulation

- Multi-material flow formulation.
  - Appropriate for multi-material problems...
- Simple drag model for multi-field interaction.
  - May include more sophisticated models later, as needed.
- Radiation diffusion approach.
  - For simplicity...
- Simple heat transport model.
  - Heat exchange occurs in a thin “skin” of the cold material.
  - Heat transfer to cold material leads to ablation, not temperature increase.
  - Ablated “cold” material becomes “hot fluid” (e.g. melting ice in water etc.)
  - Cold material and hot fluid experience PdV work (and temperature change).

Heat Transfer Model

- Prescription for area for heat transfer per unit volume
  - Uniform distribution of "spheres" of varying sizes.
  - (Similar to simple spherical-particle model for multi-fluid drag models?)
- Quasi-steady state for local heat flux at particle surface.
- Model:

$$Q = \left(\frac{12\pi}{7}\right) \frac{\alpha_1 \alpha_2 \kappa(T_2)}{\rho_2 r^2 \left[1 - \left(\frac{3\alpha_1}{4\pi}\right)^{1/3}\right]} \left(T_2^4 - T_1^4\right)$$

- We also have an equation for r ("radius"):

$$\frac{\partial r}{\partial t} + u_{1n} \frac{\partial r}{\partial x_n} = -\frac{r}{3\rho_1} \left\{ \frac{d\rho_1}{dt} + \frac{1}{\alpha_1} \left(\frac{Q}{C_{v1} T_{c1} + L_{H1}} \right) \right\}$$

Two-Field Continuity Equation

- Cold material (1) is heated and becomes hot fluid (2).

$$\frac{\partial \rho_k \alpha_k}{\partial t} + \frac{\partial \rho_k \alpha_k u_{kn}}{\partial x_n} = (-1)^k \frac{Q}{C_{v1} T_{c1} + L_{H1}}$$

- Material exchange rate is related to heat transfer rate, Q.
  - More complicated model could be incorporated, involving temperature increase and then "evaporation."

- Adjustable rate base on $C_{v1}\, T_{c1} + L_{H1}$

Momentum Equation

- Momentum equation
  - Changes in momentum enter through pressure and changes in mass fractions.

$$\frac{\partial \rho_k \alpha_k u_{ki}}{\partial t} + \frac{\partial \rho_k \alpha_k u_{ki} u_{kn}}{\partial x_n} = -\alpha_k \frac{\partial P}{\partial x_i} + \bar{\rho} \kappa_D \left(u_{k'i} - u_{ki} \right)$$

- Drag coefficient is based on a simple spherical particle drag model (courtesy of B. Kashiwa, T-3)(Note Re is very large…).
  - We need additional guidance from simulation or experiment to improve this model for ablating materials.

$$\kappa_D = \frac{3 C_D}{8 r} \frac{\alpha_1 \alpha_2}{\rho} |u_1 - u_2| \qquad C_D = 0.44 + \frac{24.0}{\mathrm{Re}} + \frac{6}{1 + \mathrm{Re}^{1/2}}$$

Equations of State (present example…)

- Simple equation of state for sample calculation.
  - Model does not require a particular thermodynamic EOS.
  - May need better EOS for comparison to experiments.
- Hot fluid (2) has radiation pressure contribution.
  - May require radiation pressure and heat transfer/temperature increase in cold material if T_c is much hotter than T_1.
- Pressure equilibration between phases.
  - Restrictive assumption-- presents difficulties when temperature difference is very large….

$$p_1 = c_{v1}(\gamma_1 - 1)\rho_1 T_1 \qquad p_2 = c_{v2}(\gamma_2 - 1)\rho_2 T_2 + \frac{4\sigma}{3c} T_2^4$$

$$I_1 = c_{v1} T_1 \qquad I_2 = c_{v2} T_2 + \frac{4\sigma}{\rho_2 c} T_2^4$$

Energy Equation

- Energy equations

$$\frac{\partial \rho_1 \alpha_1 I_1}{\partial t} + \frac{\partial \rho_1 \alpha_1 u_{1i} I_1}{\partial x_n} = +P_1 \frac{\alpha_1}{\rho_1} \frac{d\rho_1}{dt}$$

$$\frac{\partial \rho_2 \alpha_2 I_2}{\partial t} + \frac{\partial \rho_2 \alpha_2 u_{2i} C_{v2} T_2}{\partial x_n} = \frac{\partial}{\partial x_n} \left\{ \frac{\alpha_2}{\rho_2} \kappa_2 (T_2) \frac{\partial T_2^4}{\partial x_n} \right\} + P_2 \frac{\alpha_2}{\rho_2} \frac{d\rho_2}{dt} - Q$$

- Opacity: $\mu(T_2) = \mu_0 \left(\frac{T_0}{T_2} \right)^3 + \mu_{scattering}$
- Transmissivity: $\kappa(T_2) = \frac{1}{\mu(T_2)}$

Turbulence Model?

- Current formulation does not have a detailed model for turbulence.
  - Need more comparison to simulations/experiments for motivation
- We could add hybrid multi-phase model.
  - Cranfill's hybrid model, Youngs model etc.
- Modification of turbulence model for ablated materials?
  - Fluctuating velocity is not solenoidal, pressure fluctuations tied to radiation (i.e., opacity....), and material transfer, et cetera.
- Such modifications would require simulations and experiment for guidance...

Sample Problem

- Problem is statistically one-dimensional.
- Hot fluid (2) is 1.5 keV, cold fluid (2) is 0.2 keV
- Boundary conditions:
  - Hot side (left) is constant temperature, no mass flux or velocity.
  - Cold side (right) is simple out-flow boundary (dp/dx = 0).
- Pressure equilibration in mixed zone requires some artful choices.
  - Assume that pressure in mixing zone has a smooth transition from hot side to cold side.

- Choice of constants based on iron properties (and expedience)...

Sample Problem Parameters

- Constants:

$$\Sigma_0 = 10^4 \frac{cm^2}{gm}, \qquad \Sigma_{scatter} = 0.2 \frac{cm^2}{gm}$$

$$C_{v1} = C_{v2} = 6.856 \times 10^{-3} \frac{j}{gm \;\; keV}$$

$$\gamma_1 = \gamma_2 = 0.6667$$

$$T_c = 0.2 \;\; keV, \qquad L_H = 0.2 \frac{j}{gm}$$

$$\text{Pressure is in} \left(\frac{j}{cm^3} \right), \quad \text{Energy, } I_k \text{ is in} \left(\frac{j}{gm} \right)$$

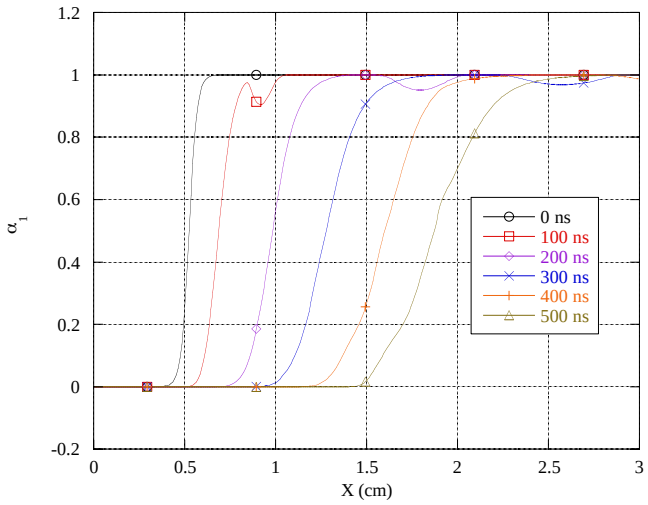

Volume Fraction of Cold Fluid
R_0=1.0 cm

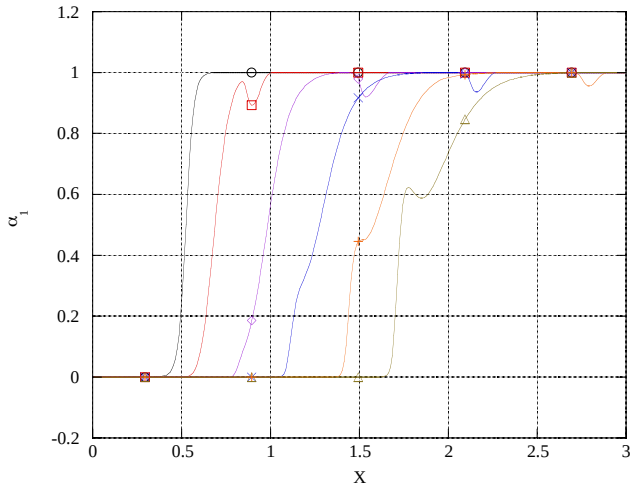

Volume Fraction of Cold Fluid
R_0=1.0x10^{-1} cm

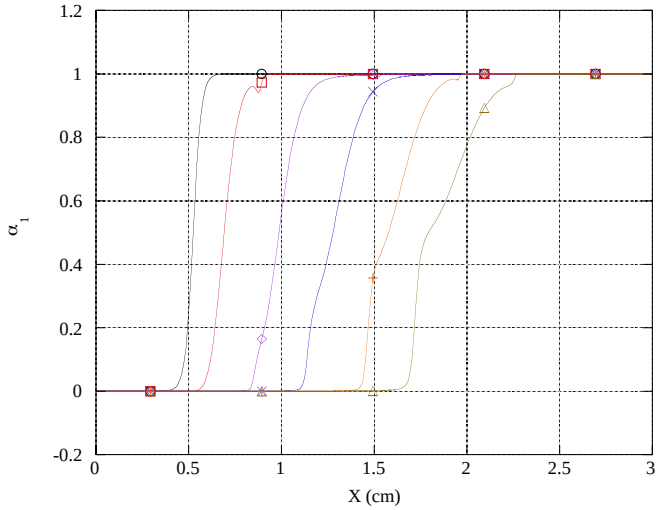

Volume Fraction of Cold Fluid
R_0=1.0x10^{-2} cm

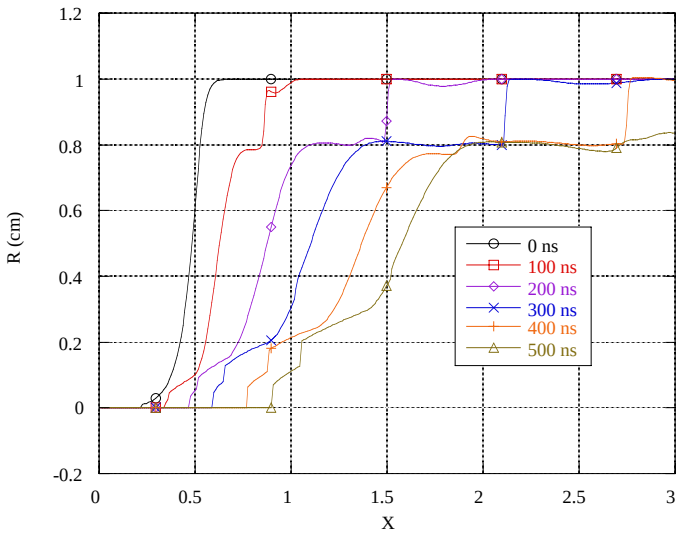

Radius of Characteristic "Droplet"

R_0 = 1.0 cm

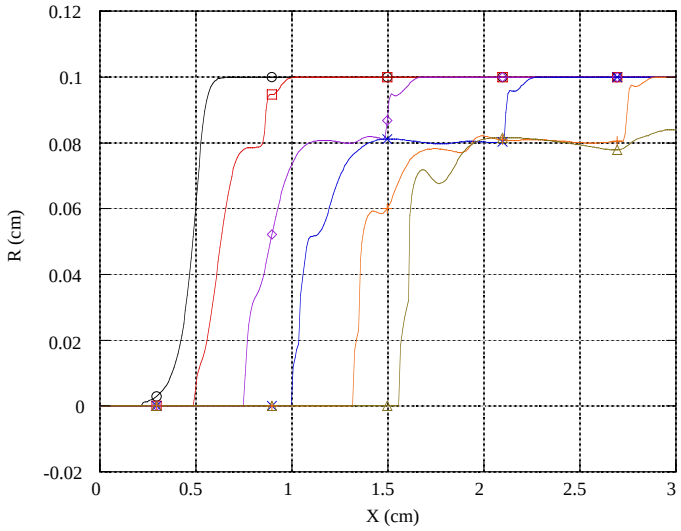

Radius of Characteristic "Droplet"

R_0 = 1.0x10^{-1} cm

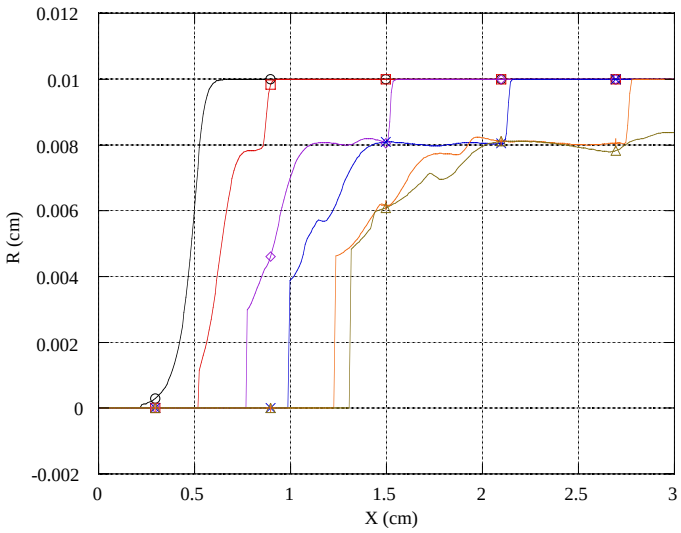

Radius of Characteristic "Droplet"

R_0 = 1.0x10^{-2} cm

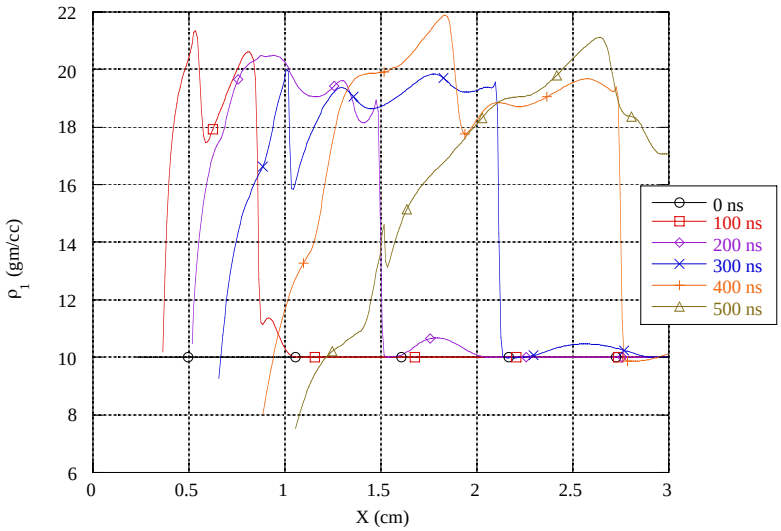

Density of Cold Fluid
R_0 =1.0 cm

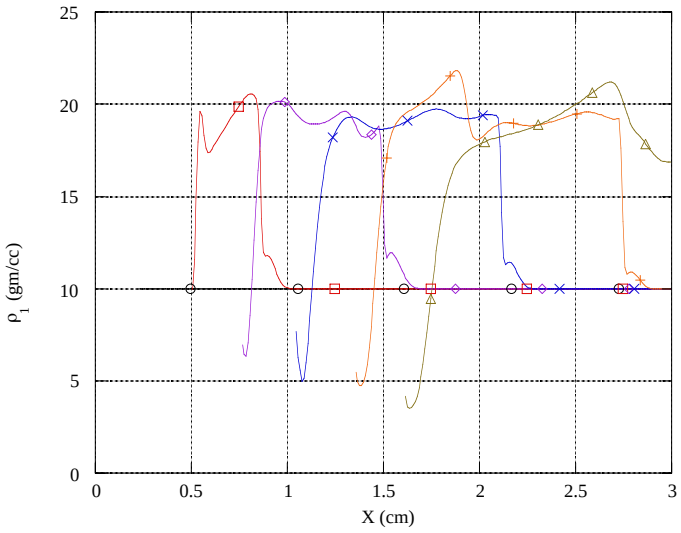

Density of Cold Fluid
R_0 =1.0x10^{-1} cm

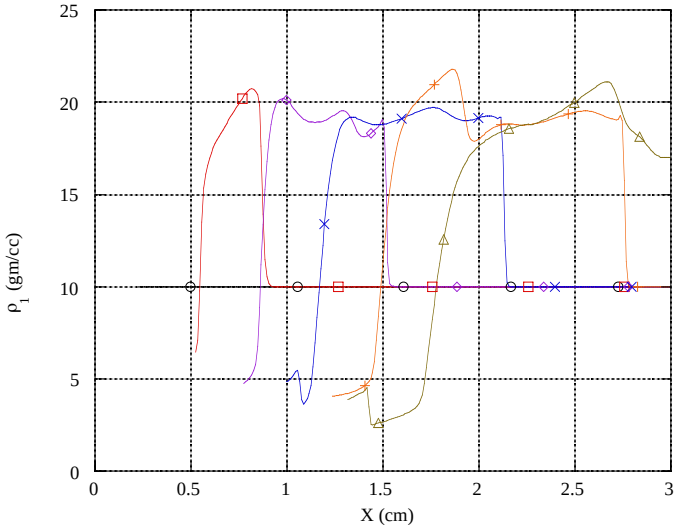

Density of Cold Fluid
R_0 =1.0x10^{-2} cm

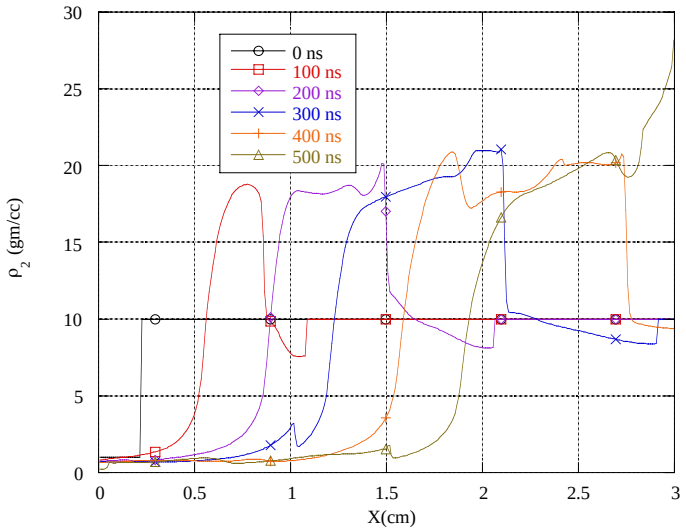

Density of Hot Fluid
R_0 = 1.0 cm

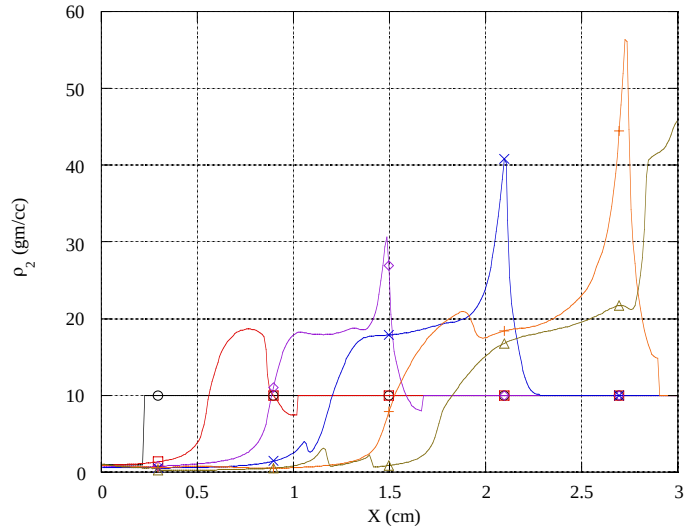

Density of Hot Fluid
R_0 = 1.0x10^{-1} cm

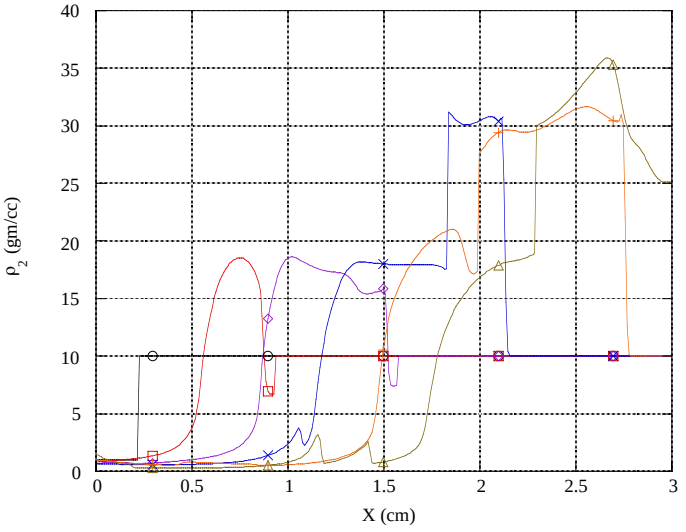

Density of Hot Fluid
R_0 = 1.0x10^{-2} cm

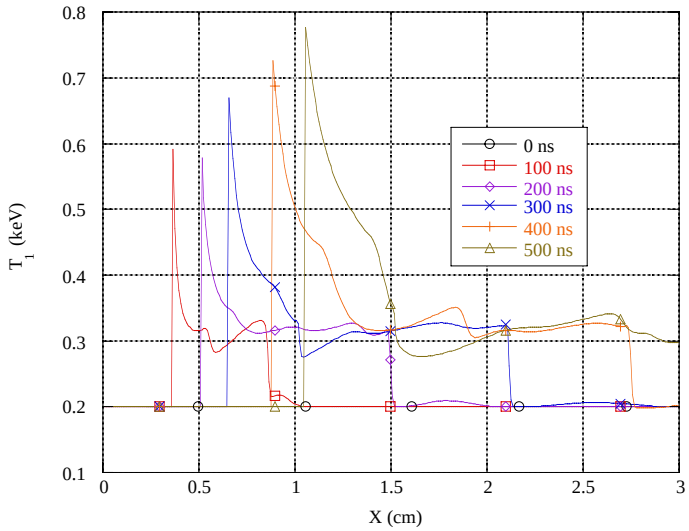

Temperature of Cold Fluid
R_0 = 1.0 cm

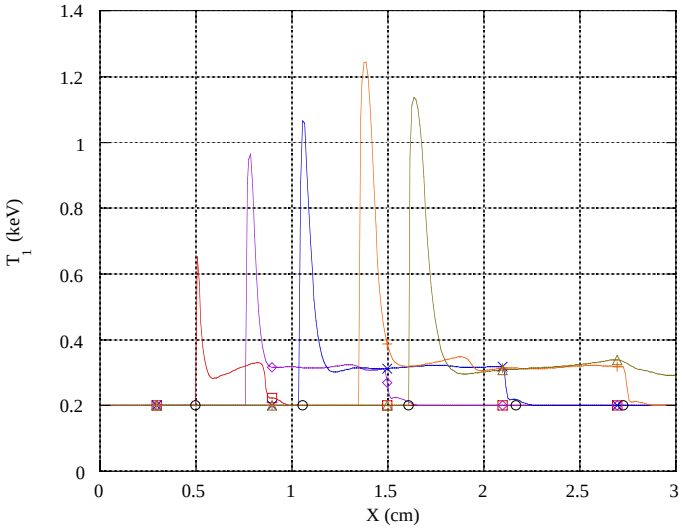

Temperature of Cold Fluid
R_0 = 1.0x10^{-1} cm

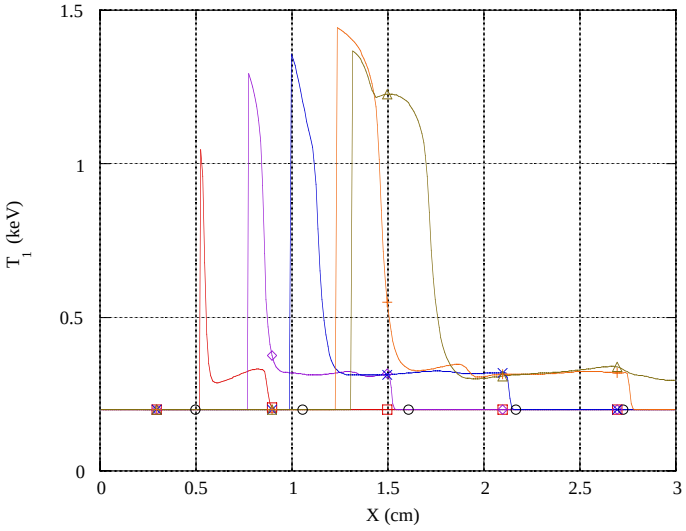

Temperature of Cold Fluid
R_0 = 1.0x10^{-2} cm

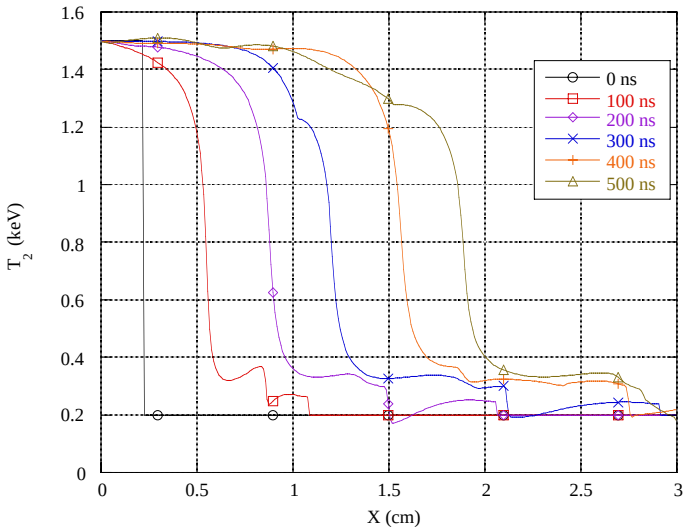

Temperature of the Hot Fluid

R_0 = 1.0 cm

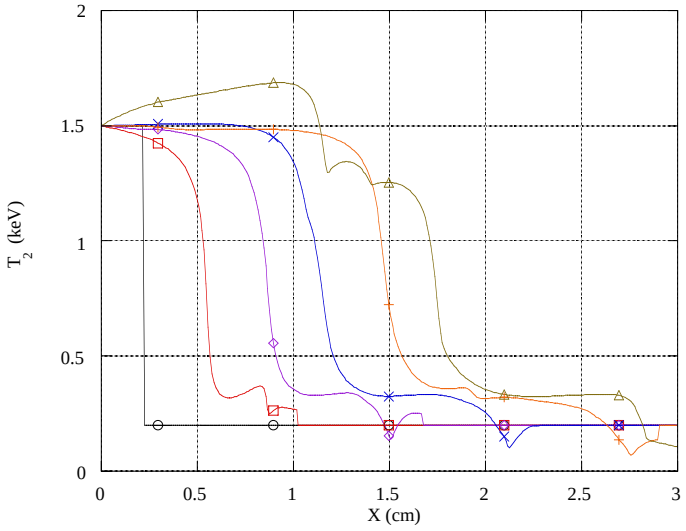

Temperature of the Hot Fluid

$R_0 = 1.0 \times 10^{-1}$ cm

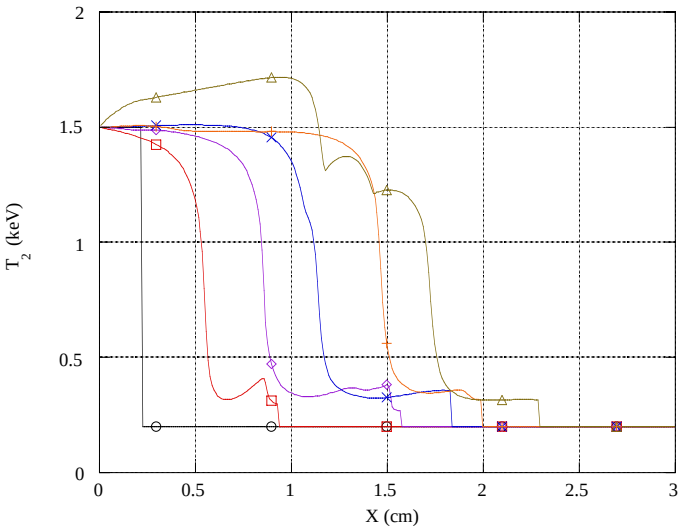

Temperature of the Hot Fluid

$R_0 = 1.0 \times 10^{-2}$ cm

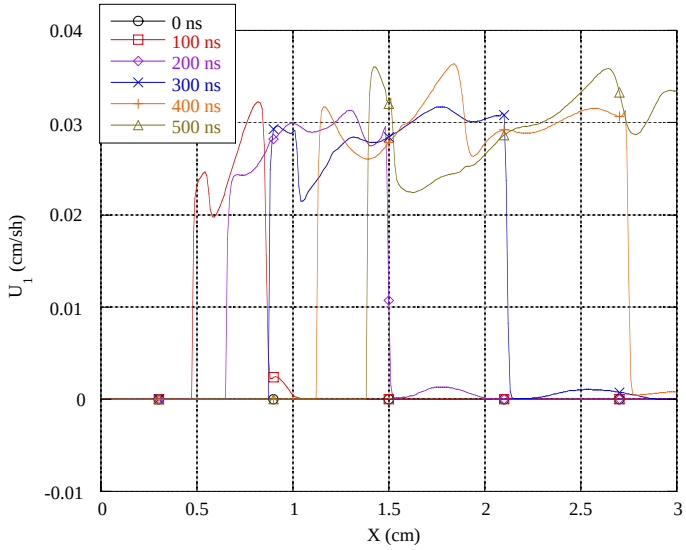

Velocity of Cold Fluid

R_0 = 1.0 cm

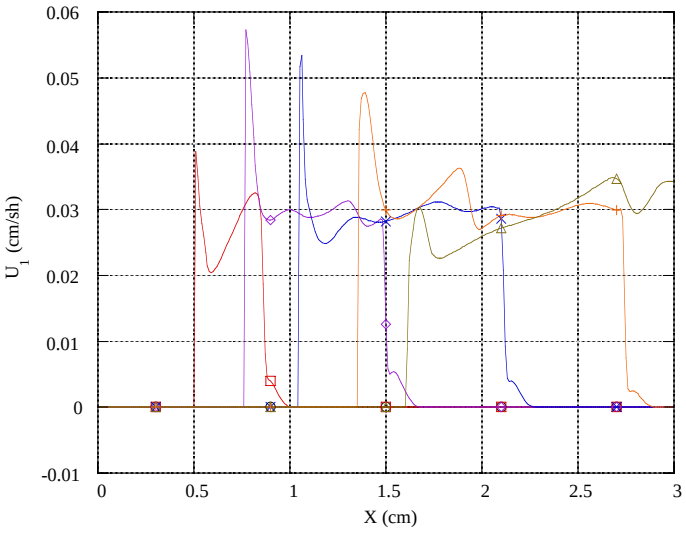

Velocity of Cold Fluid

$R_0 = 1.0 \times 10^{-1}$ cm

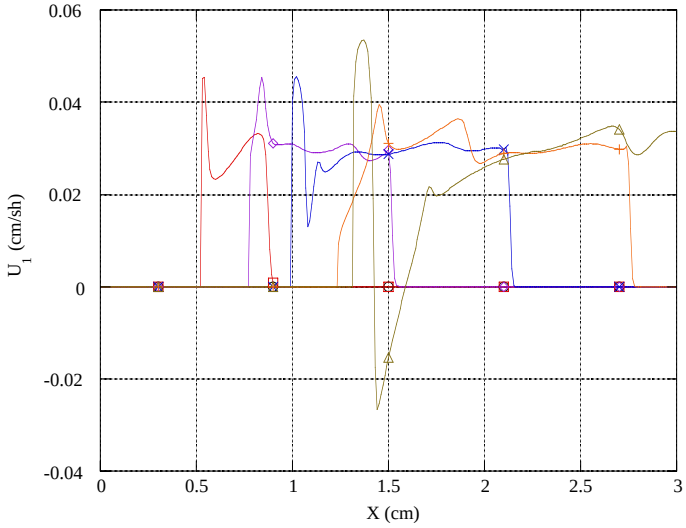

Velocity of Cold Fluid

$R_0 = 1.0 \times 10^{-2}$ cm

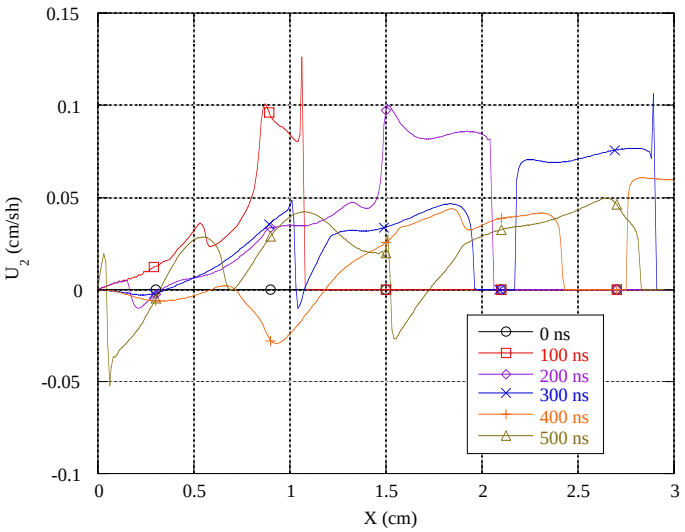

Velocity of Hot Fluid
R_0 = 1.0 cm

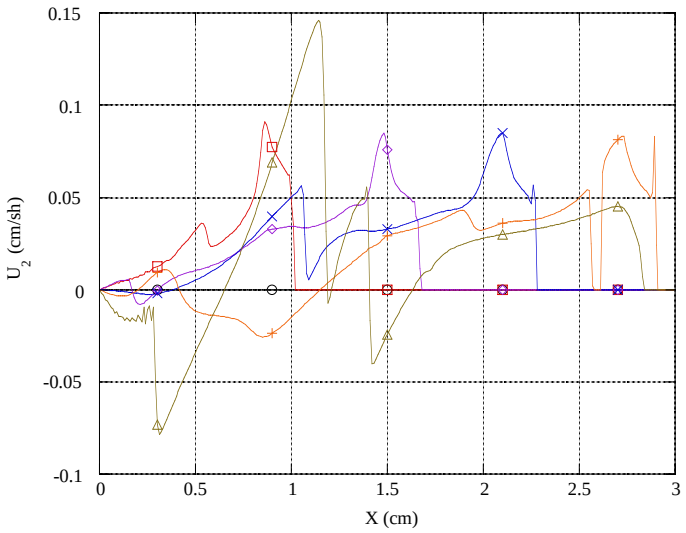

Velocity of Hot Fluid
R_0 = 1.0x10^{-1} cm

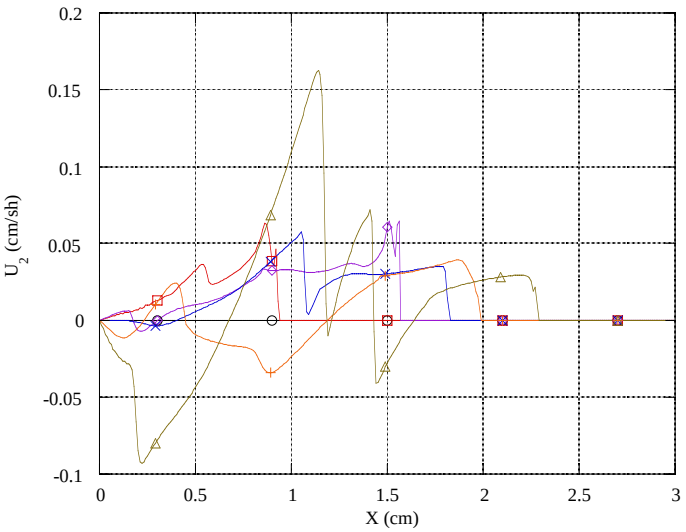

Velocity of Hot Fluid
R_0 = 1.0x10^{-2} cm

Conclusions

- Model represents a simple, tractable approach to account for radiation and phase change in a two-phase flow.
  - Length scale for radiation transfer (spherical model) is consistent with the drag model.
  - Can be extended to multiple fluids, and more complicated prescriptions for drag, turbulence, heat exchange.
- Demonstrates ablative phenomenon.
  - Have not fully explored parameter regimes.
- We now need detailed comparisons to experiments, simulations and observations.
  - Laser-driven flyer plates, Cepheid variables, Computer simulations.

Toy models for Rayleigh-Taylor instability:

Stuart Dalziel

Department of Applied Mathematics and Theoretical Physics
University of Cambridge

International Workshop on the Physics of Compressible Turbulent Mixing

14 December 2001

(9:10 – 9:30)

with thanks to

Joanne Holford (DAMTP)

David Youngs (AWE)

The growth question:

$$h = \alpha A g t^2, \text{ where } A = \frac{\rho_1 - \rho_2}{\rho_1 + \rho_2}$$

But what is α ?

◊ 0.10, … 0.07, 0.06, … 0.03, 0.02 ?

Timescale: $$T = \sqrt{\frac{H}{Ag}}$$

If $\delta = h/H$, and $\tau = t/T$,

then $$\delta = \alpha \tau^2$$

Experiments

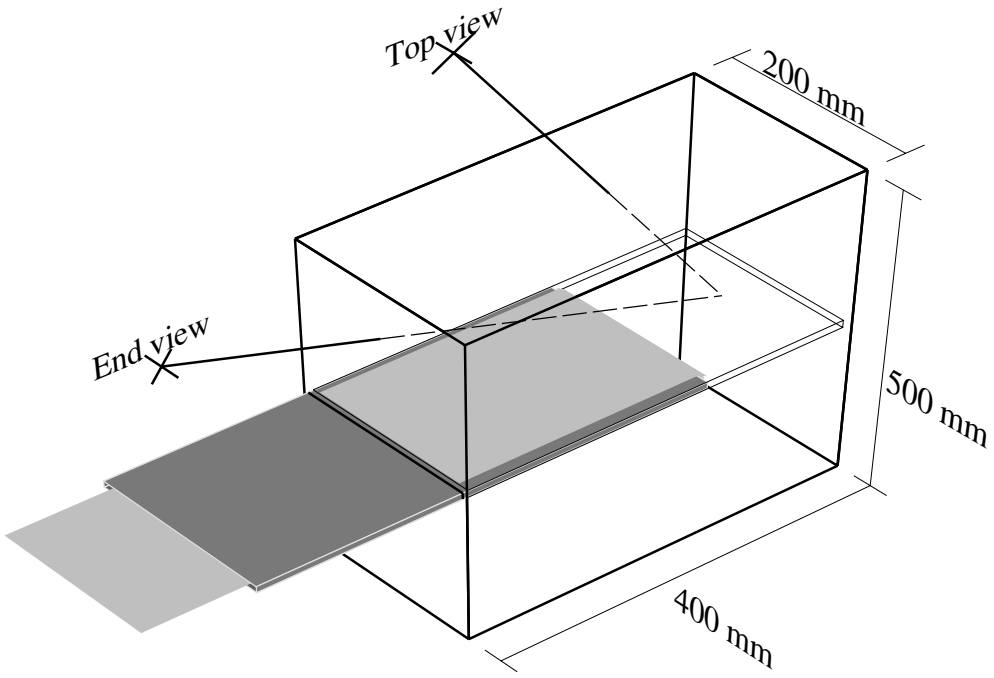

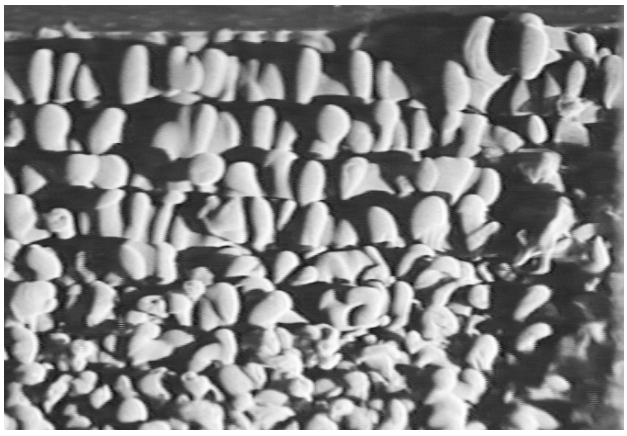

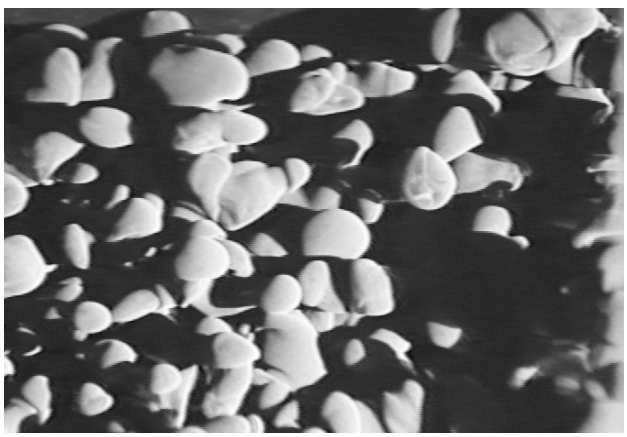

Appropriate modelling (?)

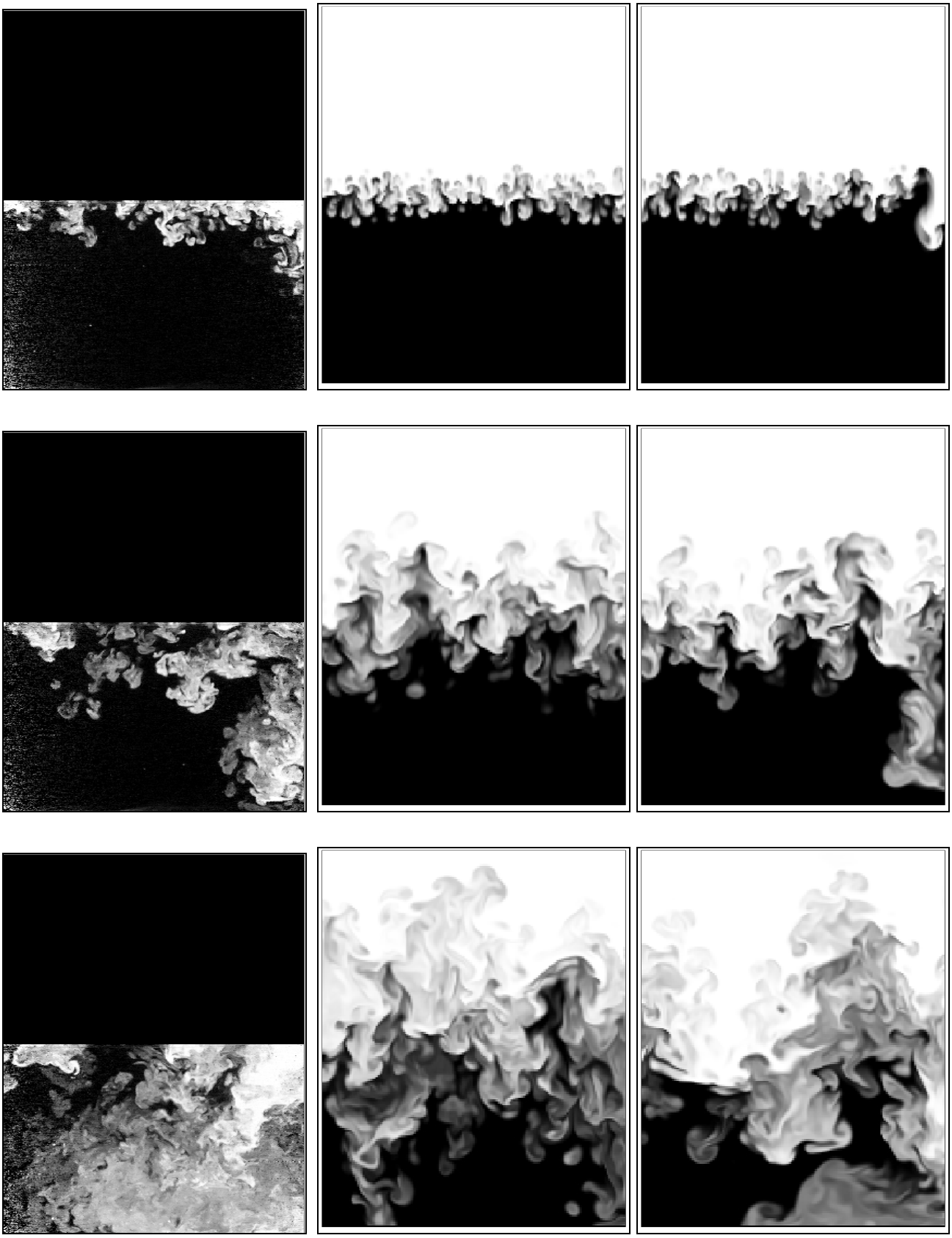

Growth

Dimensional analysis/similarity theory

$$h = \alpha A g t^2.$$

Single mode

Layzer (1955)

For $$\zeta(x,y) = a_0 \cos\frac{2\pi x}{\lambda}$$

if $$\frac{dh}{dt} = w,$$

then $$(2+E)\frac{dw}{dt} = Ag(1-E) - C_D\frac{w^2}{\lambda},$$

where

$$E = \exp\left(\frac{-6\pi h}{\lambda}\right).$$

Experimentally $C_D \sim 10$

◊ Does this make sense?

Early time → linear theory $\frac{d^2h}{dt^2} = \frac{2\pi Ag}{\lambda}h$

Late time → constant velocity $w_\infty = \sqrt{\frac{Ag\lambda}{C_D}}$

$$\Rightarrow h \to w_\infty(t - t_0)$$

Structure

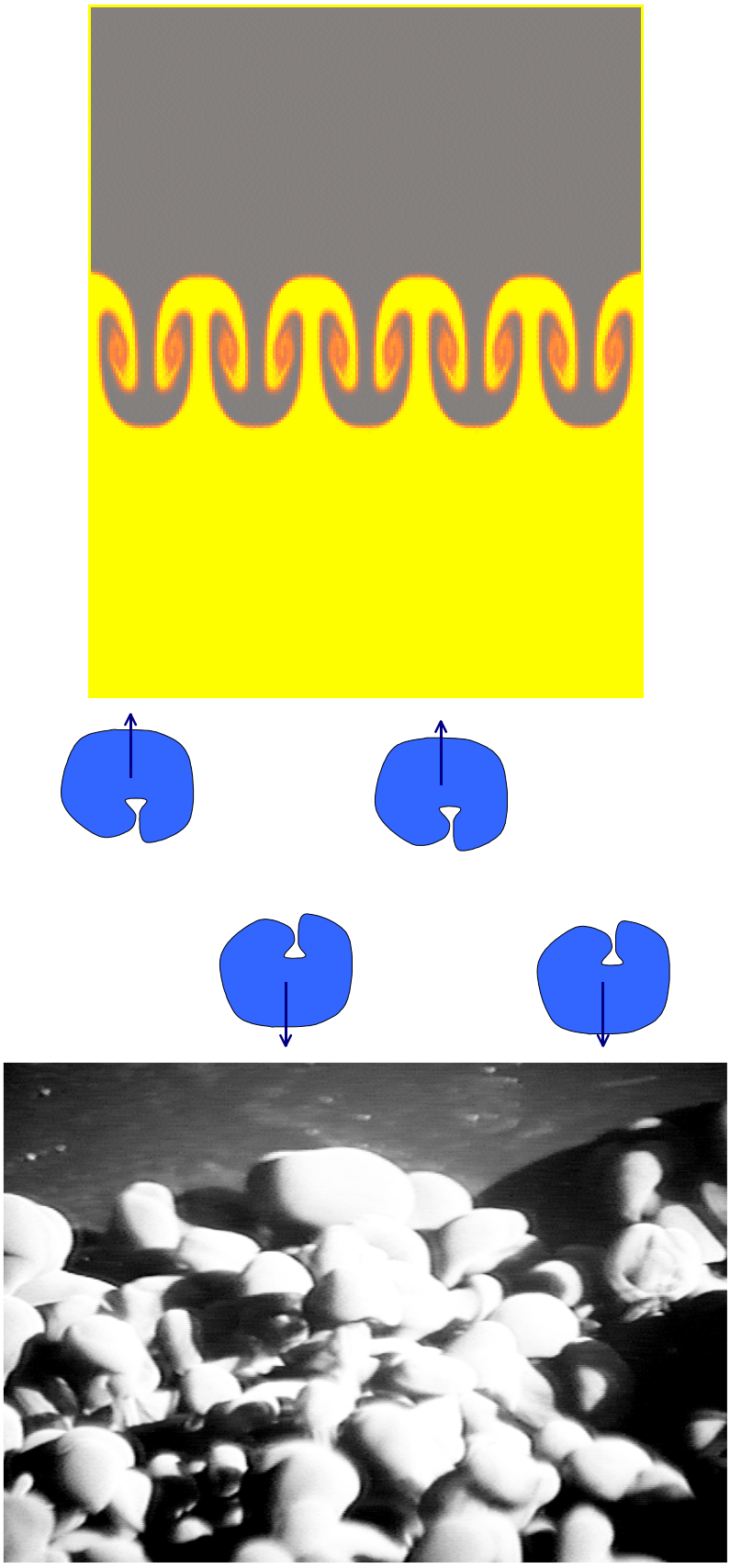

Often described as ‘bubbles’…

…but more like ‘thermals’ in miscible fluids

Thermals

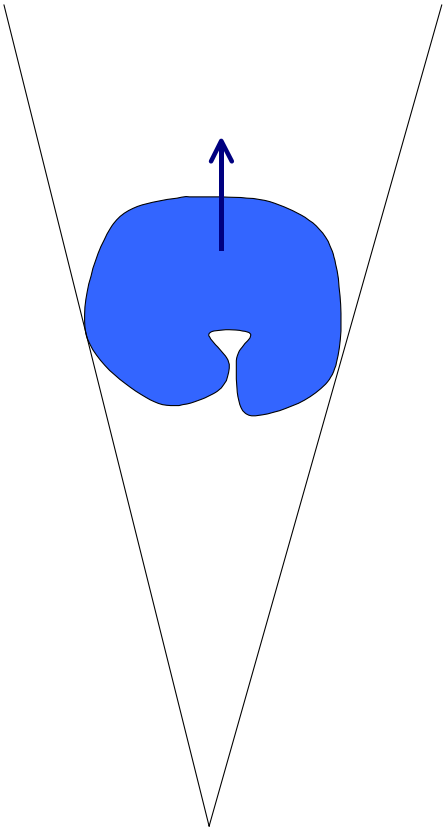

Self-similar

$$r = \theta z$$

$$V = \gamma r^3.$$

Buoyancy conserved

$$g' V = g' \gamma r^3 = g'_0 V_0.$$

Constant Froude number

$$F^2 = \frac{w^2}{g' r}$$

Integrating $w = dz/dt$

$$\frac{\gamma^{1/2}\theta}{2F\left(g'_0 V_0\right)^{1/2}} z^2 = t$$

Experimental results $\rightarrow F \approx 1.2$.

Rayleigh-Taylor as thermals

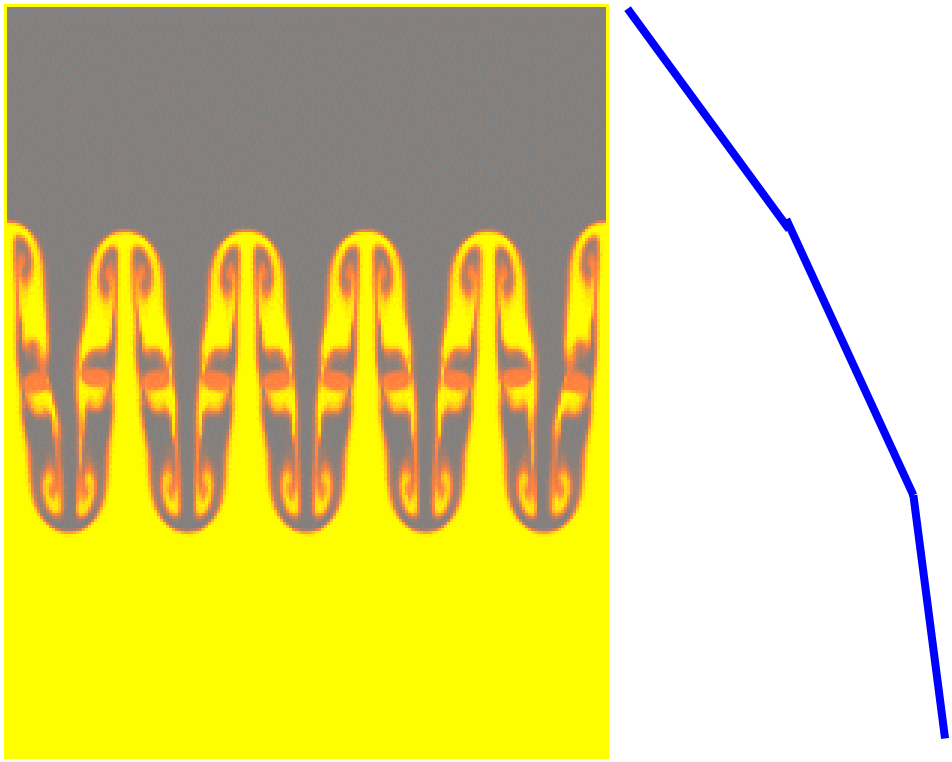

Froude number ~ 1.2 (aspect ratio 0.72) $\Rightarrow C_{Thermal} \approx 1.3$.

Rayleigh-Taylor bubbles a little like thermals $\rightarrow C_D \approx 1.3$

But in Rayleigh-Taylor environment

- Density field not hydrostatic in ambient
  - ◊ Hydrostatic in mean density $\Rightarrow$ halve buoyancy force $\rightarrow C_D \approx 2.6$
- Flow around bubble affected by bubble moving in opposite direction
  - ◊ Drag due to twice rise speed of bubble $\rightarrow C_D \approx 10.4$

In agreement with single mode experiments

BUT natural R-T has more than one mode

Multi-mode

What happens if λ grows with h?

Let $\lambda = \psi h$

Late times approximation:

$$\frac{dh}{dt} = \left(\frac{Ag}{C_D}(1-E)\psi \right)^{1/2} h^{1/2}$$

$$\Rightarrow \qquad h = \frac{Ag}{C_D}(1-E)\psi(t-t_0)^2 = \alpha Ag(t-t_0)^2$$

For $C_D = 10$ and $\psi = 1$, $\alpha = 0.025$.

[Full Layzer growth with $\psi = 1$ gives $\alpha = 0.023$.]

Growth rate maximised with $\psi \sim 10$ giving $\alpha \sim 0.103$

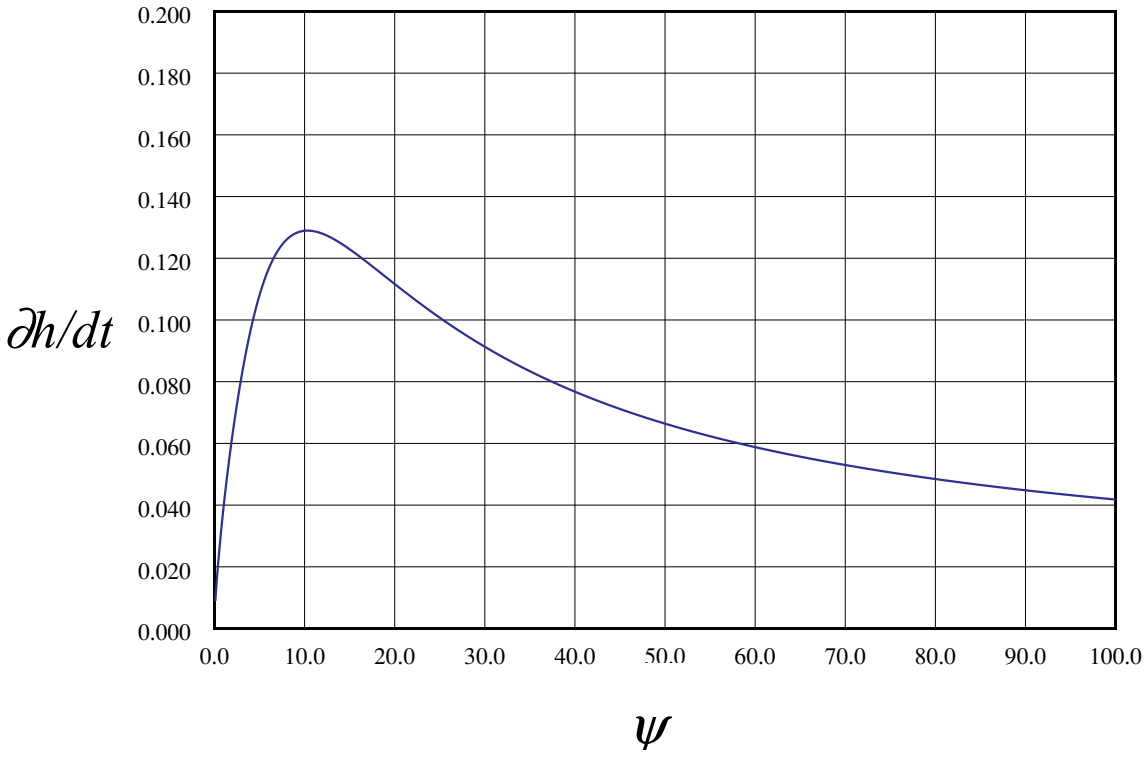

Where do the modes begin? How do they interact?

- ◊ Nonlinear interaction?
- ◊ Initial perturbation?

If modes independent and equal amplitude:

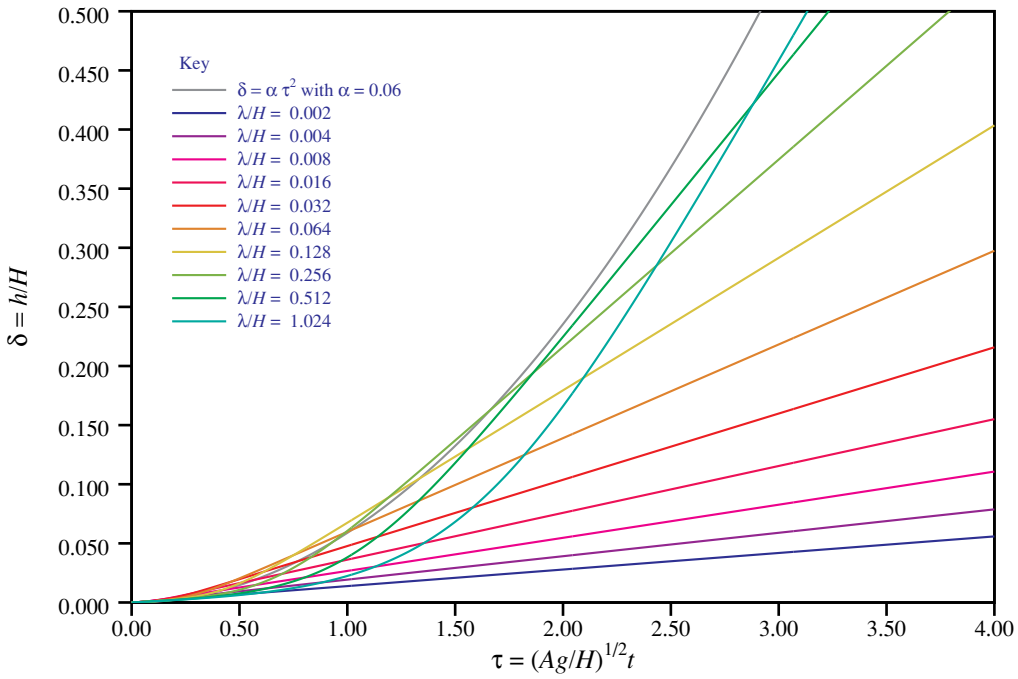

Instantaneous nonlinear mode halving interaction when $h = \lambda$:

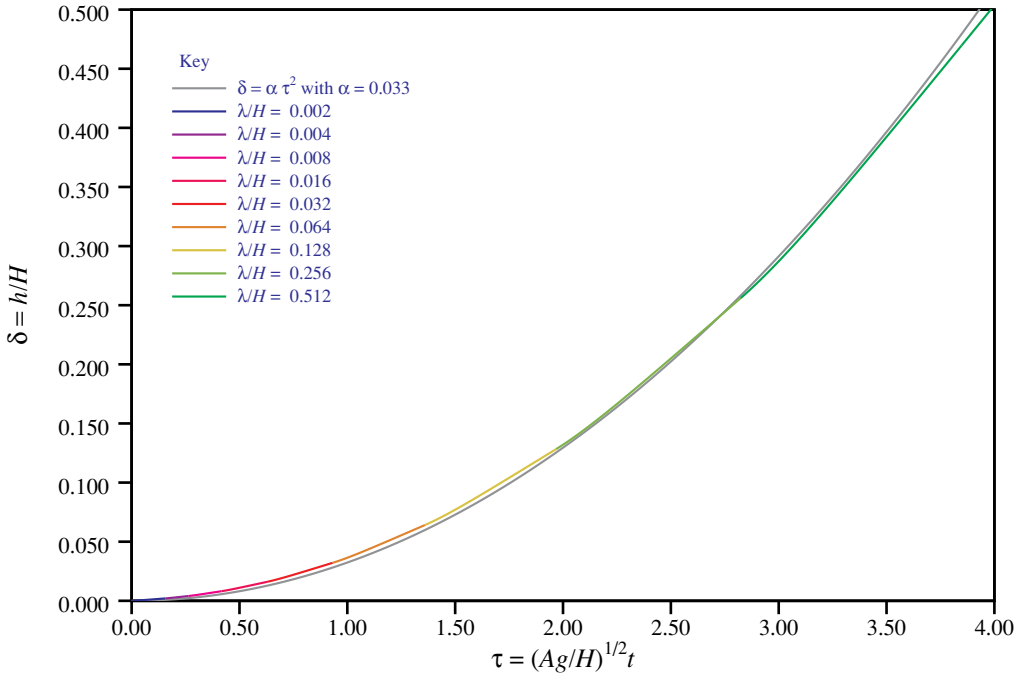

Which is it?

Mixing

See talk by Joanne Holford

Energy budget

Can decompose *PE* into **Background PE** and **Available PE**.

PE_{back} is the minimum energy state that is achieved by adiabatic rearrangement of fluid parcels.

Mixing increases PE_{back} – it cannot decrease it!

PE_{avail} is the component of *PE* that can be converted into *KE*, heat (through dissipation) and, if mixing occurs, into PE_{back}.

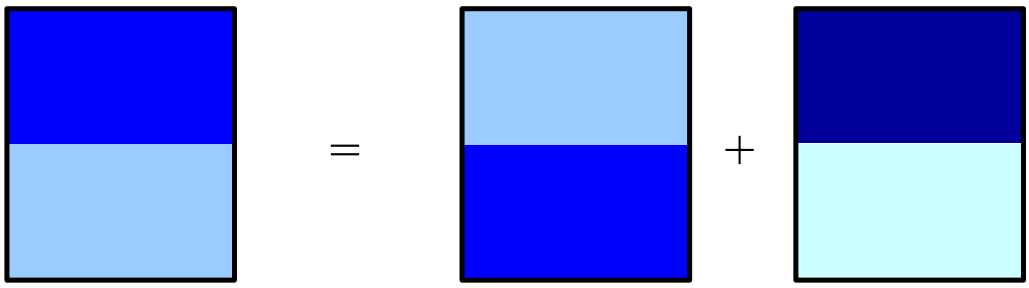

In the absence of external work:

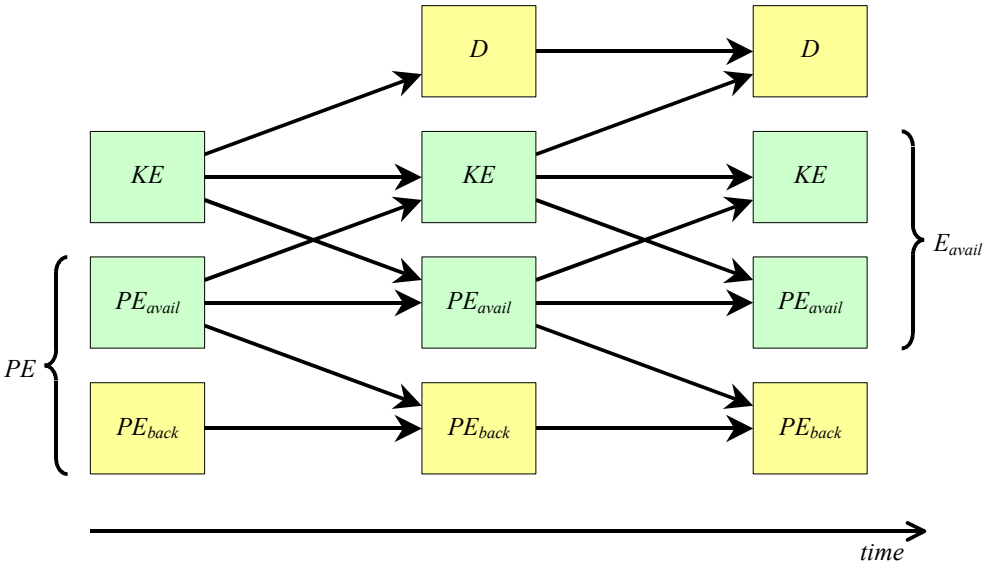

Mixing efficiency

*

$$\eta_{Integral} = -\frac{\Delta E_{back}}{\Delta E_{avail}} = \frac{\Delta PE_{Back}}{\Delta PE_{Back} + \int \varepsilon \, dt} = \frac{\Delta PE_{Back}}{-\left(\Delta KE + \Delta PE_{Avail}\right)}$$

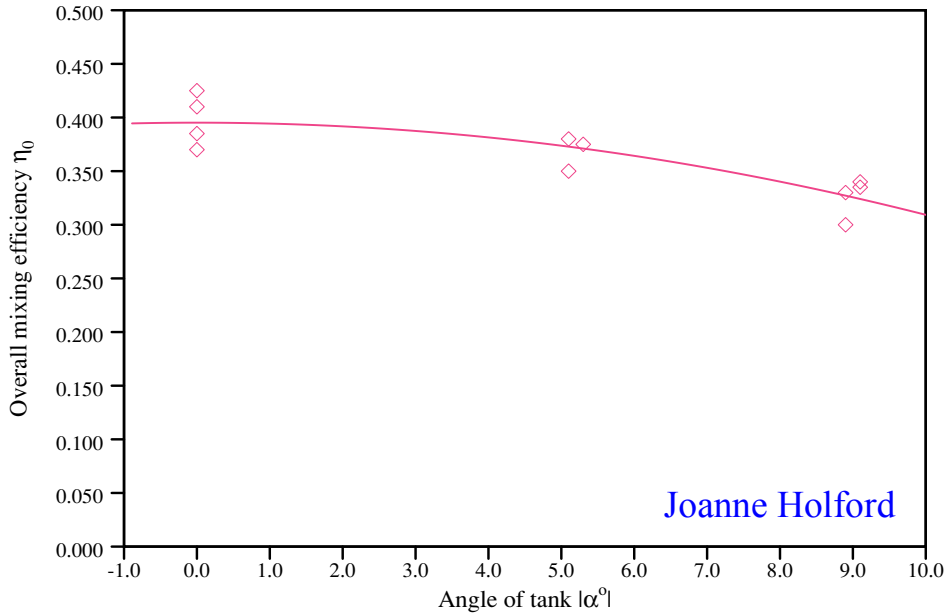

$$\eta_{instantaneous} = \frac{\delta PE_{Back}}{-\delta E_{Avail}} = \frac{\delta PE_{Back}}{\delta KE + \delta PE_{Avail}}$$

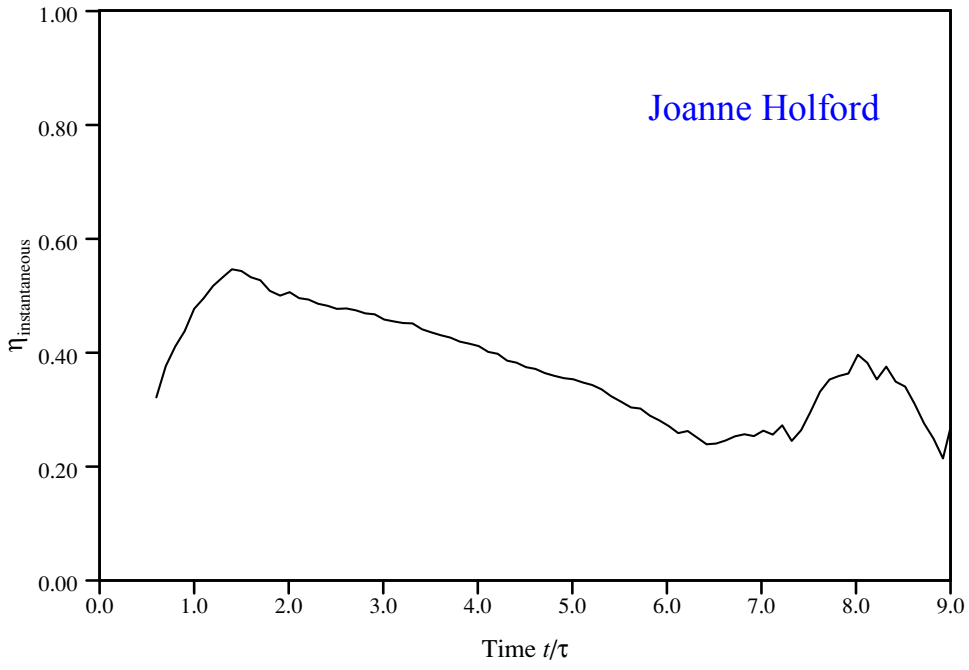

Thermal

Entrainment into a thermal

$$\frac{dV}{dt} = \beta w A$$

...

$$\beta = 0.18.$$

Energetics of a thermal

Mixing efficiency not well defined: depends on size of domain!

Rayleigh-Taylor

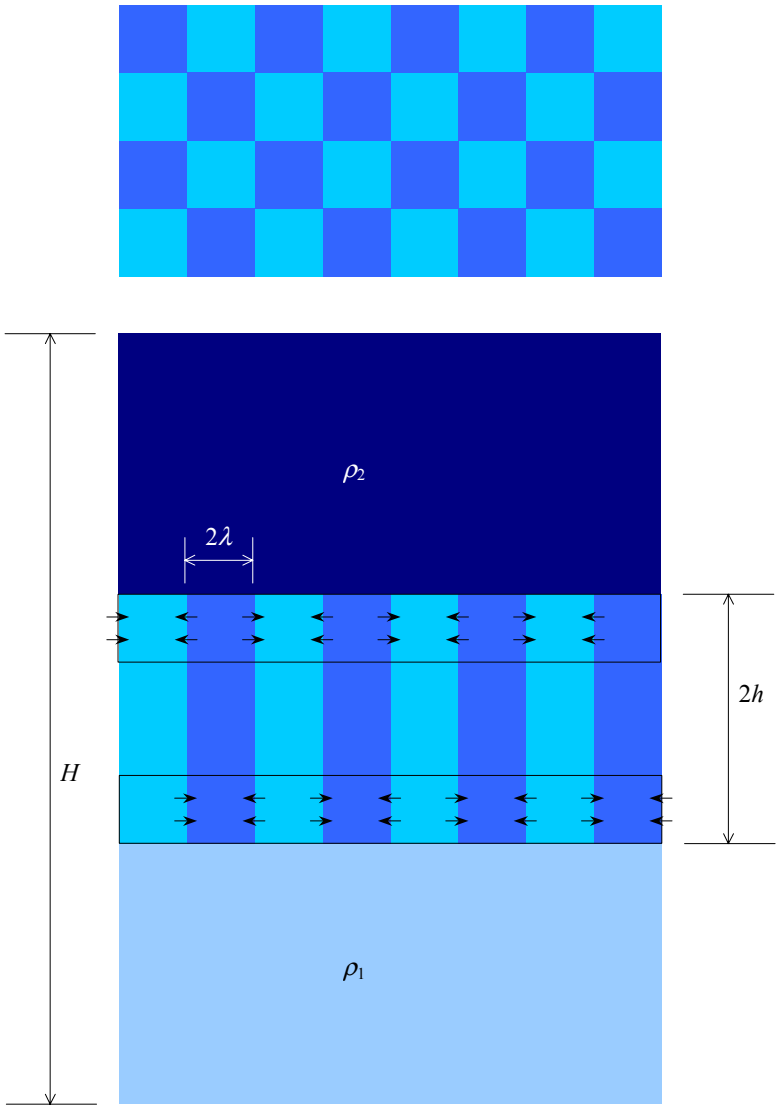

$$h = \alpha A g t^2 \qquad \delta = \alpha \tau^2$$

$$w = 2\alpha A g t \qquad \omega = 2\alpha\tau$$

$$V = 2L^2 h$$

Total potential energy

$$PE^*_{Total} = \frac{PE_{Total}}{PE_0} = 1 - 4\alpha^2\tau^4$$

Background potential energy

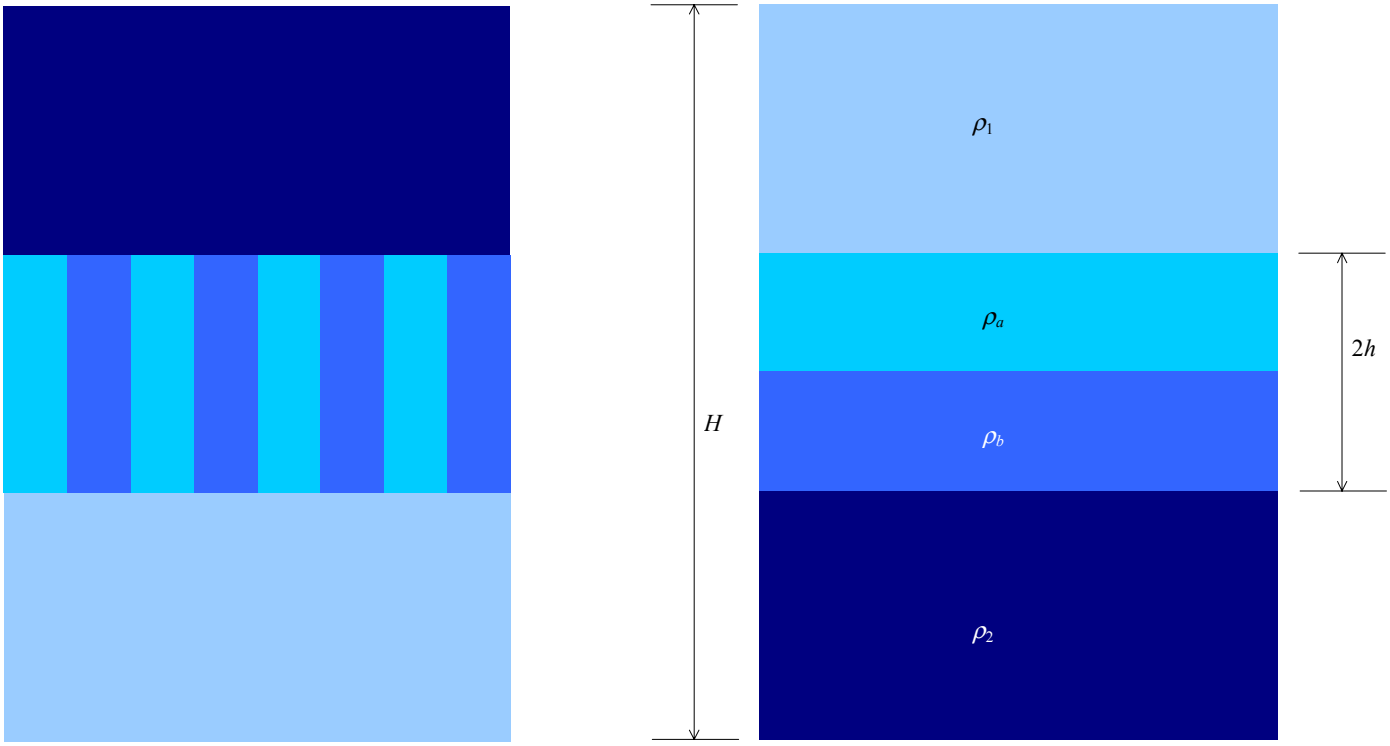

Changes due to entrainment between counter-flowing streams.

Invoke entrainment hypothesis: $u_e = \beta w$

Area of entrainment independent of h

$\Leftrightarrow$ depth of entrainment comparable with λ

$\Rightarrow$ *entraining area* $= \varphi \times$ *plan area*.

$$PE^*_{Back} = -\left(1 - \varphi\beta\alpha^2\tau^4\right)$$

Available potential energy

$$PE^*_{Avail} = PE^*_{Tot} - PE^*_{Back} = 2 - (4 + \varphi\beta)\alpha^2\tau^4$$

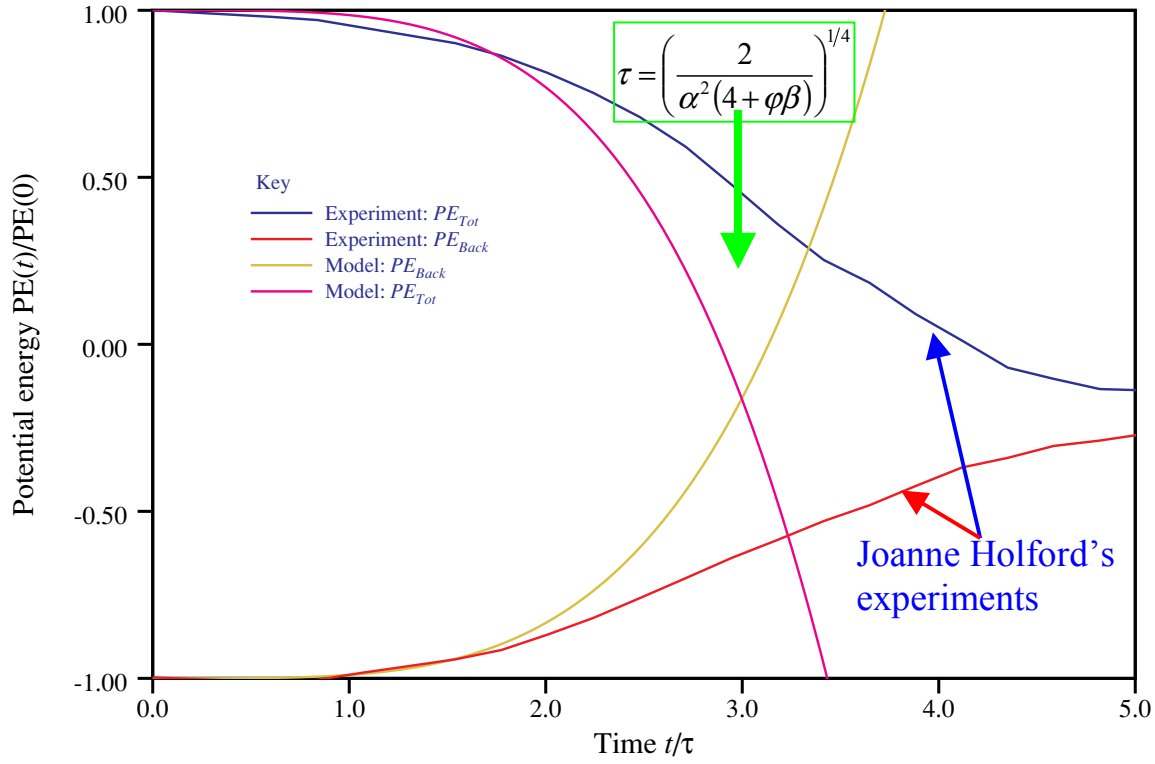

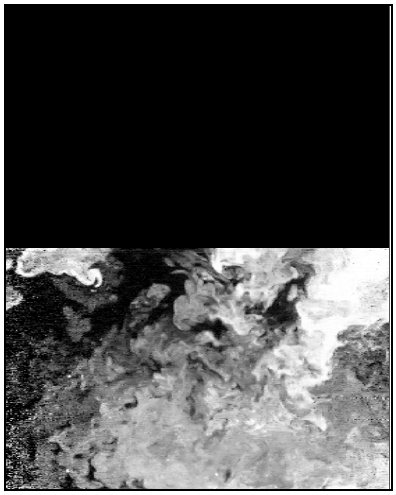

Kinetic energy

$$KE^* = 16\sigma\alpha^3\tau^4$$

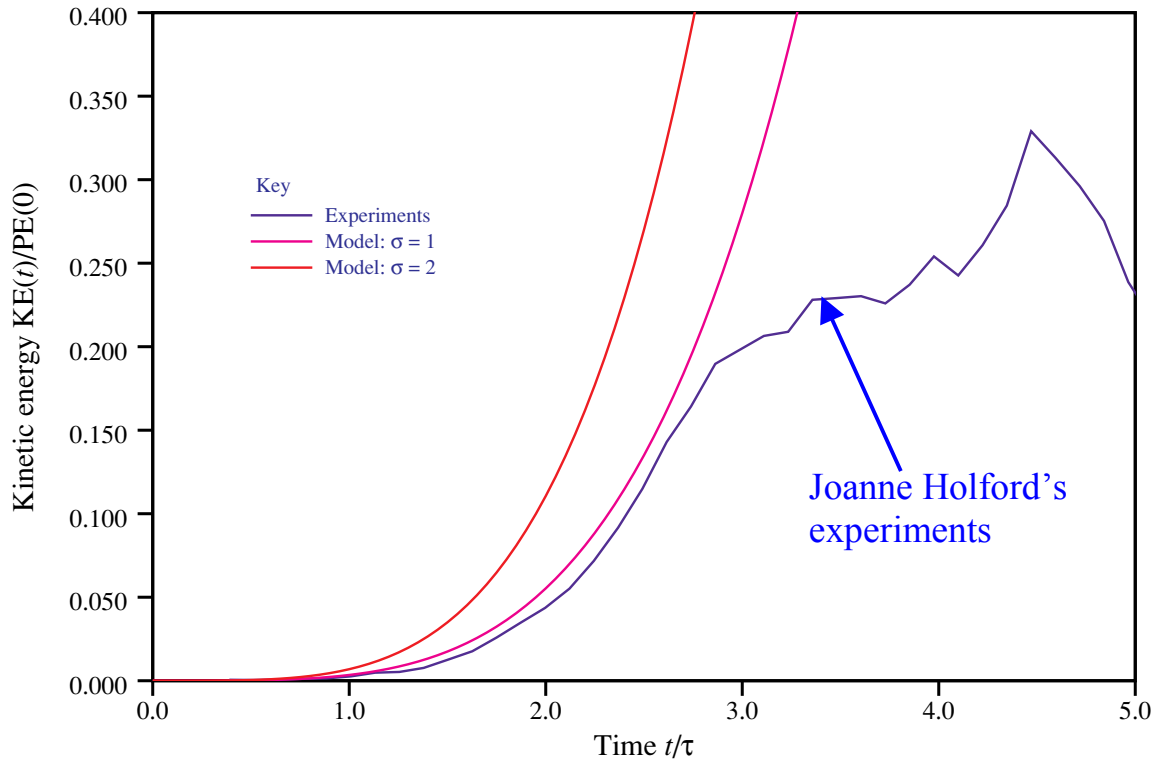

Available energy changing

$$\frac{dE^*_{Avail}}{d\tau} = \frac{dKE^*}{d\tau} + \frac{dPE^*_{Avail}}{d\tau}$$

$$= -4\left(4 + \varphi\beta - 16\sigma\alpha\right)\alpha^2\tau^3$$

Hence, energy is lost whenever $\alpha < ¼$ (for $\beta = 0$, $\sigma = 1$).

Instantaneous mixing efficiency

$$\eta_{Inst} = -\frac{\dfrac{dPE^*_{Back}}{d\tau}}{\dfrac{dPE^*_{Avail}}{d\tau} + \dfrac{dKE^*}{d\tau}}$$

$$= \frac{\varphi\beta}{4 + \varphi\beta - 16\sigma\alpha}$$

So for $\varphi = 16$, $\beta = 0.18$, $\sigma = 1$, and $\alpha = 0.06$, then $\eta_{Inst} = 0.49$.

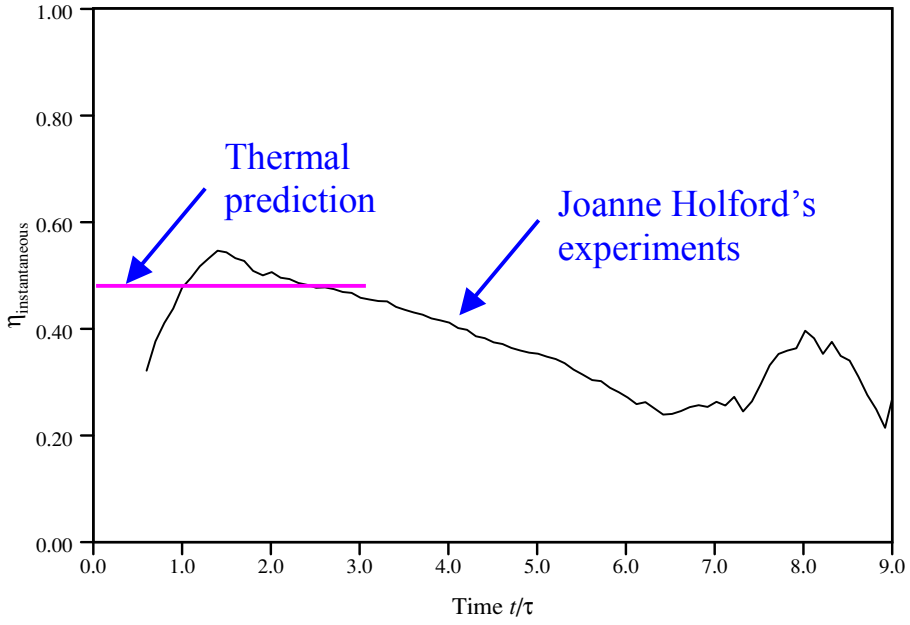

Integral mixing efficiency

If there no mixing after reaching the bottom…

$$\eta_{Integral} = \frac{PE_{Back}^{(bot)} - PE_{Back}^{(0)}}{PE_{Avail}^{(0)}}$$

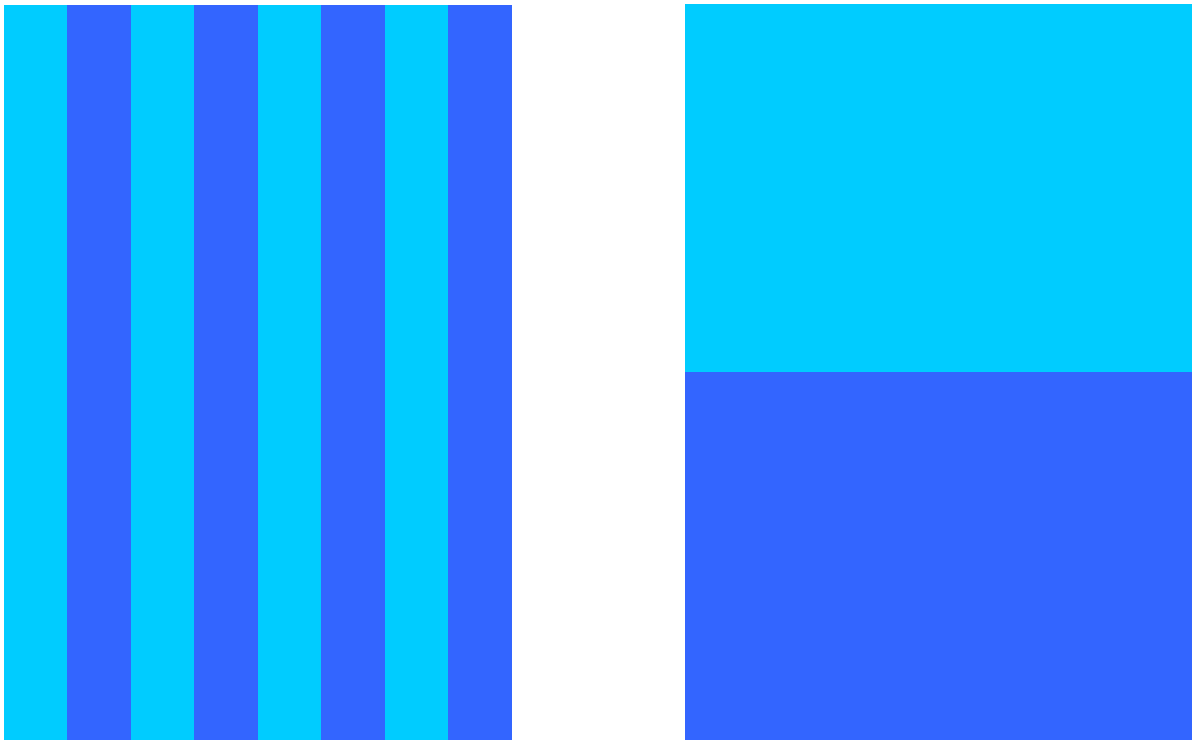

$$\eta_{Integral} = \frac{1}{8}\varphi\beta$$

For $\varphi = 16$ and $\beta = 0.18$, then $\eta_{Integral} = 0.36$.

If there is mixing after reaching the bottom…

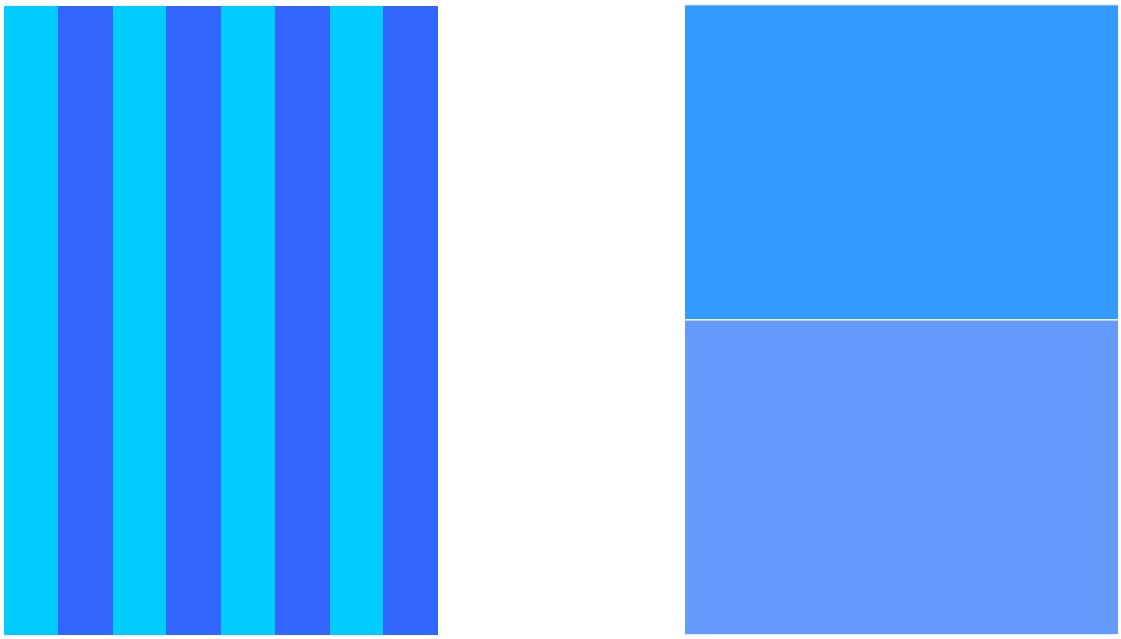

$$E_{Avail}^{*(bot)} = \left(1 + 4\sigma\alpha - \frac{1}{4}\varphi\beta\right)$$

If $\Delta E_{Back}^{(After\,bot)} = \eta_{stab} E_{Avail}^{(bot)}$, then

$$\eta_{Integral} = \frac{1}{8}\varphi\beta + \frac{1}{2}\eta_{stab}\left(1 + 4\sigma\alpha - \frac{1}{4}\varphi\beta\right)$$

For $\eta_{stab} = 0.2$, then $\eta_{Integral} = 0.41$.

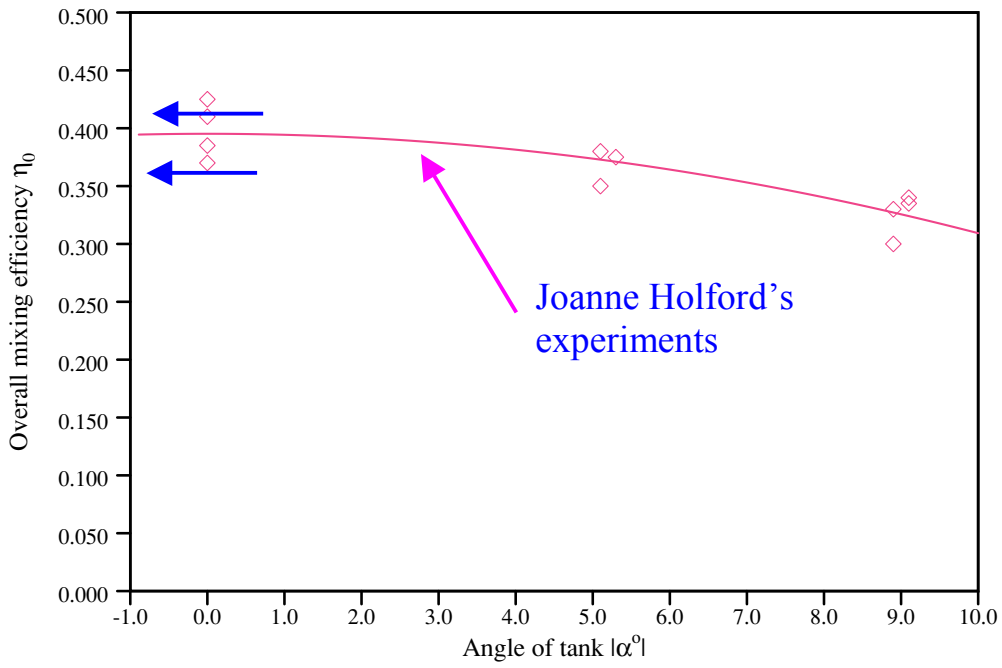

Extensions *

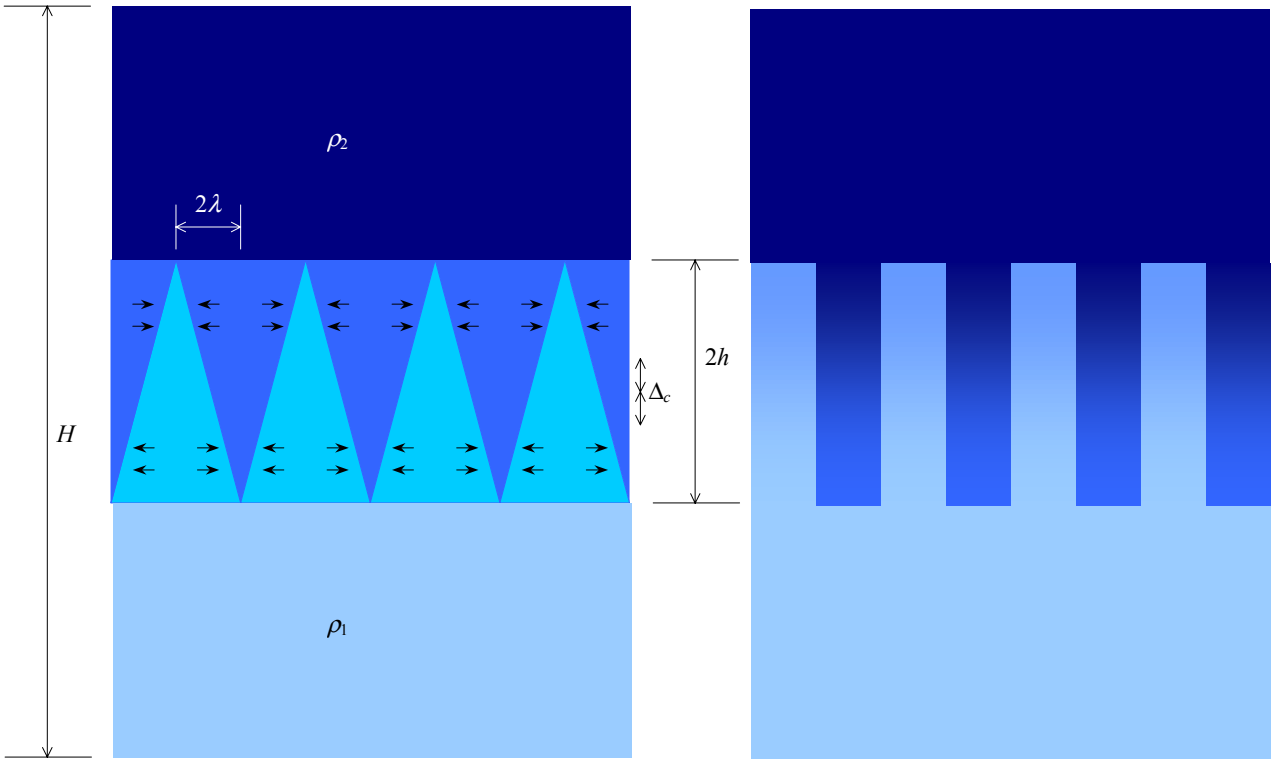

Let Δ_c be the fractional displacement of the centroid of the *bubble* from $z = 0$.

→

$$\eta_{Inst} = -\frac{\delta PE^*_{Back}}{\delta PE^*_{Avail} + \delta KE^*}$$

$$= \frac{\varphi\beta}{4 + \varphi\beta - 4(4 - \varphi\beta)\Delta_c - 16\sigma\alpha}$$

Pyramid ($\Delta_c = 1/4$): $\eta_{Inst} = 0.6$.

Parabolic ($\Delta_c = 1/6$): $\eta_{Inst} = 0.56$.

(gives linear mean concentration)

How can we avoid having to specify C_D?

Shell model

GOY model (Gledzer–Ohkitani–Yamada):

$$\frac{dU_n}{dt} = \left(ak_n U_{n+1}^* U_{n+2}^* + bk_{n-1} U_{n-1}^* U_{n+1}^* + ck_{n-2} U_{n-1}^* U_{n-2}^*\right)$$

$$-\nu k_n^2 U_n + F_n$$

with $k_n = \beta^n k_0$, $a = 1$, $b = -\varepsilon$ and $c = -1 + \varepsilon$.

In Rayleigh-Taylor instability, energy input at all scales.

$$\frac{dU_n}{dt} = \left(k_n U_{n+1} U_{n+2} - \varepsilon\, k_{n-1} U_{n-1} U_{n+1} - (1-\varepsilon) k_{n-2} U_{n-1} U_{n-2}\right)$$

$$-\nu k_n^2 U_n + F_n$$

Recall Layzer model: $(2+E)\dfrac{dw}{dt} = Ag(1-E) - C_D \dfrac{w^2}{\lambda}$

Hence $F_n = A_n g \dfrac{1-E_n}{2+E_n}$, where

$$E_n = \exp\left(-\frac{6\pi\, h_n}{\lambda_n}\right) \quad \text{and} \quad A_n = A\, h_n/h.$$

The mode penetrations h_n and total penetration h are obtained from

$$\frac{dh_n}{dt} = U_n \qquad \text{and} \qquad h = \max_n h_n .$$

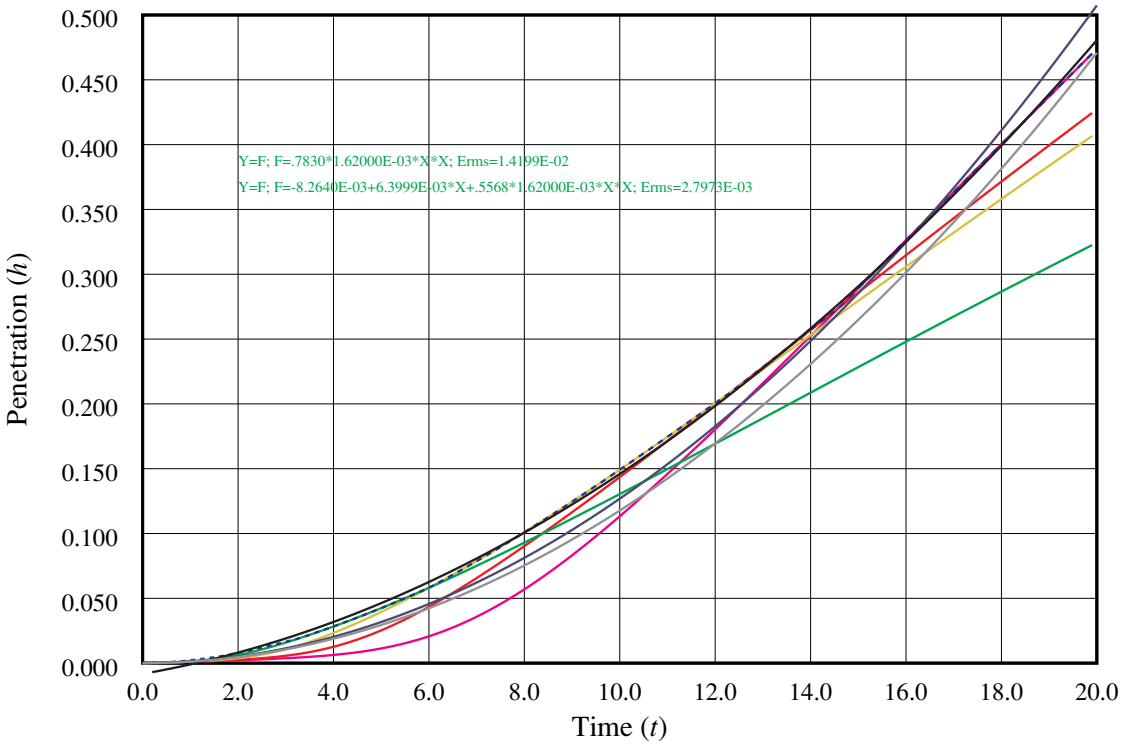

◊ Approximate quadratic growth

◊ Coefficient depends on initial spectrum

◊ Possible to replicate $\alpha \sim 0.06$

Conclusions

General

- Initial conditions are important for gross features
- Internal details relatively insensitive to initial conditions
- Appropriate modelling of initial conditions gives close agreement

Thermals model

- Single-mode growth rate consistent with isolated thermal
- Simple model for transfer between modes replicates t^2 growth
- Mixing efficiency consistent with thermal entrainment

Shell model

- Baroclinic input at all scales
- Very simple model replicates t^2 growth
- Growth rate sensitive to initial spectrum

An explanation?

No, but it helps.

A General Buoyancy-Drag Model for the Evolution of the Rayleigh-Taylor and Richtmyer-Meshkov Instabilities

Y. Elbaz, Y. Srebro, O. Sadot and D. Shvarts

Nuclear Research Center - Negev, Israel.

Ben-Gurion Universiy, Beer-Sheva, Israel.

Abstract

The growth of a single-mode perturbation is described by a buoyancy-drag equation, which describes all instability stages (linear, non-linear and asymptotic) at time-dependant Atwood number and acceleration profile. The evolution of a multi-mode spectrum of perturbations from a short wavelength random noise is described using a single characteristic wavelength. The temporal evolution of this wavelength allows the description of both the linear stage and the late time self-similar behavior. The model includes additional effects, such as shock compression and spherical convergence.
Model results are compared to full 2D numerical simulations and shock-tube experiments of random perturbations, studying the various stages of the evolution.

Ideal Model Requirements

- Calculate mix region for:
  - general acceleration profile (RT and RM).
  - all instability stages (linear, early nonlinear, asymptotic)
  - general geometry (planar, cylindrical, spherical)
  - compressibility and coupling to 1D flow.
  - ablation.
- Describe internal structure of mixing zone:
  - density, temperature and pressure of every material.
  - degree of mixing.
- Feedback to 1D simulation:
  - material flow.

Definitions

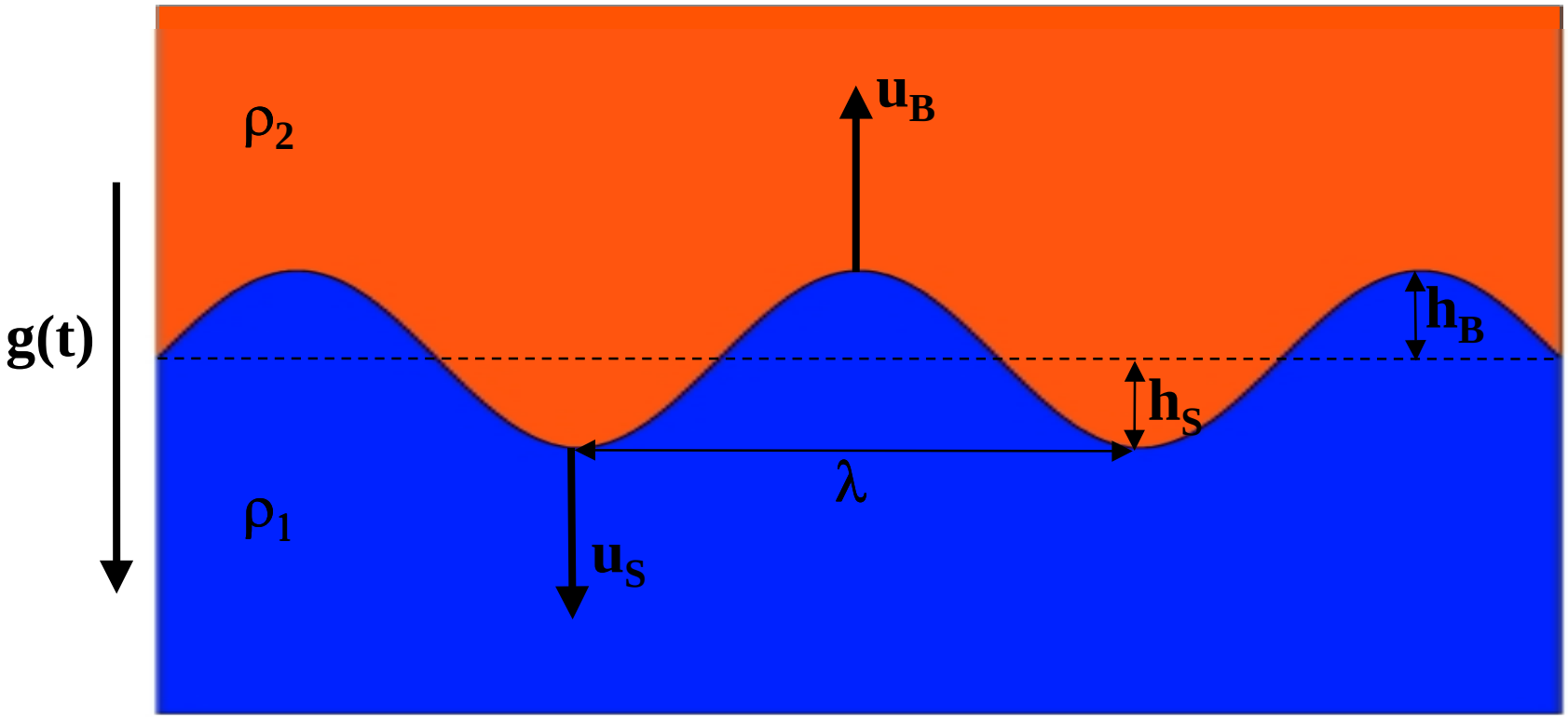

Atwood number

$$A = \frac{\rho_2 - \rho_1}{\rho_2 + \rho_1}$$

$$k = \frac{2\pi}{\lambda}$$

Layzer model

(2D) $$\frac{du_B}{dt} = \left(\frac{1-E}{2+E}\right)\cdot g(t) - \left(\frac{6\pi}{2+E}\right)\cdot\frac{u_B^2}{\lambda} \quad , \quad E = e^{-3kh_B}$$

(3D) $$\frac{du_B}{dt} = \left(\frac{1-E}{1+E}\right)\cdot g(t) - \left(\frac{2\pi}{1+E}\right)\cdot\frac{u_B^2}{\lambda} \quad , \quad E = e^{-2kh_B}$$

- Single mode (periodic array of bubbles and spikes).
- Describes all instability stages.
- Valid for a general acceleration profile.
- Limited to A=1.

Buoyancy-drag equations

$$\left(\rho_1 + C_a \rho_2\right)\frac{du_B}{dt} = \left(\rho_2 - \rho_1\right)\cdot g(t) - \frac{C_d}{\lambda}\rho_2 \cdot u_B^2$$

$$\left(\rho_2 + C_a \rho_1\right)\frac{du_S}{dt} = \left(\rho_2 - \rho_1\right)\cdot g(t) - \frac{C_d}{\lambda}\rho_1 \cdot u_S^2$$

- Single mode (periodic array of bubbles and spikes).
- Describes only asymptotic stage.
- Valid for a general acceleration profile.
- Valid for every A.

New model for single-mode perturbation

- We combine Layzer model with buoyancy-drag equations.
- C_a, C_d, C_e are determined from Layzer model for A=1, and assumed to be Atwood independent.

$$\left[\left(C_a \cdot E(t)+1\right)\rho_1+\left(C_a+E(t)\right)\rho_2\right]\frac{du_B}{dt}=$$

$$\left(1-E(t)\right)\cdot\left(\rho_2-\rho_1\right)\cdot g(t)-\frac{C_d}{\lambda}\rho_2\cdot u_B^2$$

$$\left(E(t)=e^{-C_e\cdot k\cdot h_B}\right)$$

Multimode evolution

Mixing fronts (bubbles and spikes) are described by one characteristic wavelength: $\langle\lambda\rangle=\langle\lambda_{BUB}\rangle$.

- Linear stage: $\dfrac{d\langle\lambda\rangle}{dt}=0$

- Asymptotic self-similar behavior:

$$\frac{h_B}{\langle\lambda\rangle}=b(A) \quad \Rightarrow \quad \frac{d\langle\lambda\rangle}{dt}=\frac{u_B}{b(A)}$$

- Transition from linear to asymptotic is at:

$$h_B=\langle\lambda_0\rangle\cdot b(A)$$

Model properties

- Linear stage:

reproduces theoretical result (first order):

$$\ddot{h}(t) = Akgh(t)$$

- Early nonlinear stage:

for A$\rightarrow$1, correct to second order (Layzer model)

- Asymptotic stage:

buoyancy-drag equation for all A.

Limited to planar geometry and incompressible flow.

1D Hydrodynamic coupling

The dynamic front equation is solved coupled to the 1D lagrangian motion:

- Change in Atwood number:

$$\rho_i = \left| \int_{h_{1d}}^{h_i} \rho_i V dx \right| \Big/ \left| \int_{h_{1d}}^{h_i} V dx \right| \qquad i = 1,2$$

- 1D Lagrangian “drift” of the mixing zone boundaries:

$$u_B \rightarrow u_B + U_{1d}(h_B)$$

$$u_S \rightarrow u_S + U_{1d}(h_S)$$

Corrections required for non-planar geometry

Non-planar geometry introduces two effects:

- change in amplitude due to 1D motion (Bell-Plesset)

  - included in 1D coupling to lagrangian flow.

- Change in wavelength (conservation of wavenumber, $\ell = \lambda/R$).

  - geometric term added to wavelength equation:

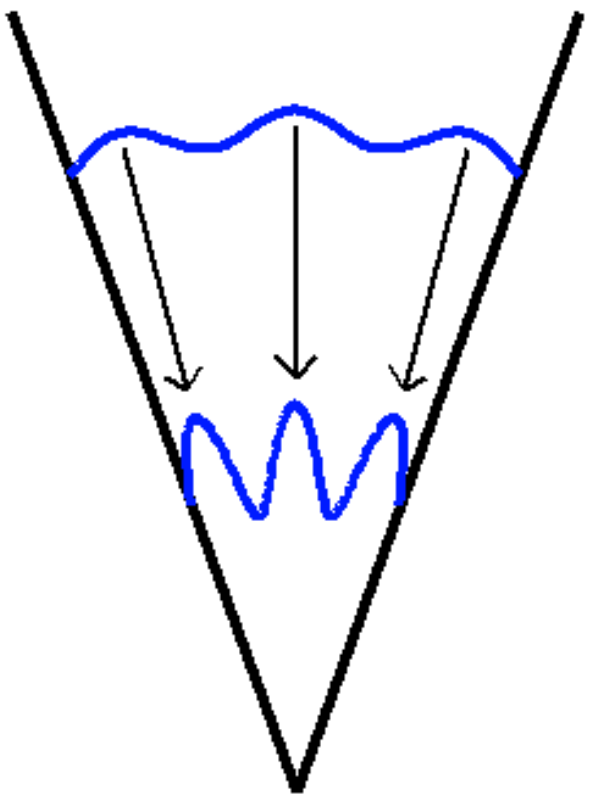

$$\frac{d\langle\lambda\rangle}{dt} \rightarrow \frac{d\langle\lambda\rangle}{dt} + \left(\frac{d\langle\lambda\rangle}{dt}\right)_{geometry}$$

$$\left(\frac{d\langle\lambda\rangle}{dt}\right)_{geometry} = \langle\lambda(t)\rangle \frac{U_{1d}(t)}{R_{1d}(t)}$$

Shock tube experiments

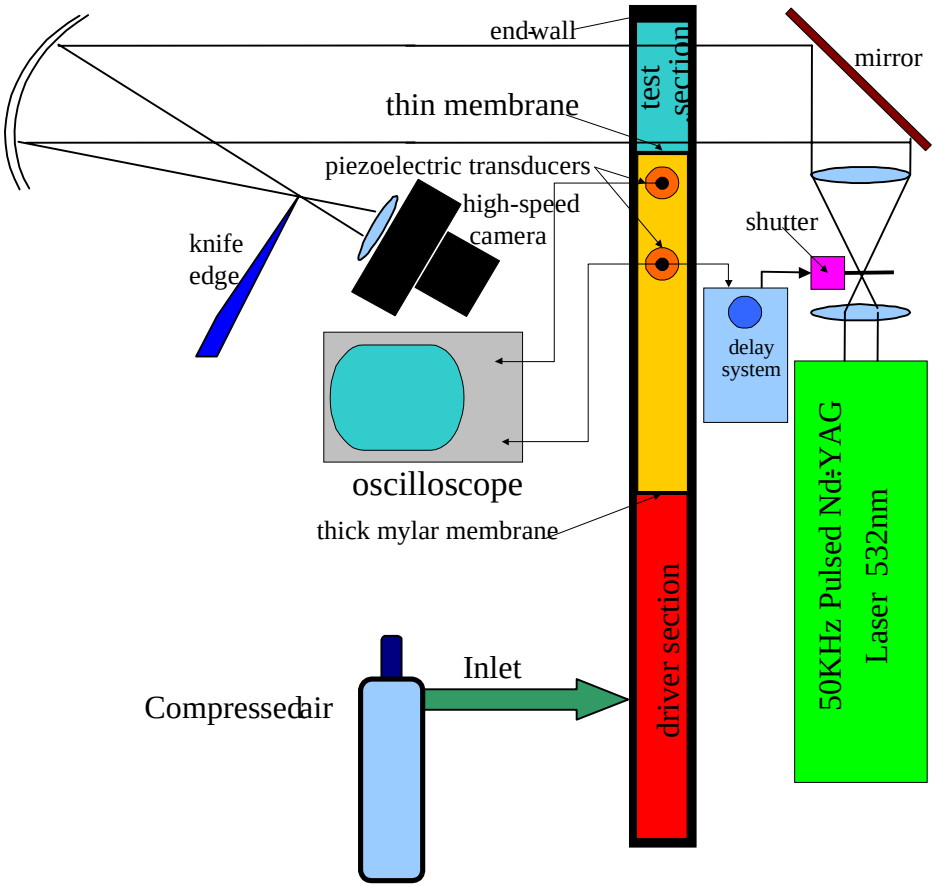

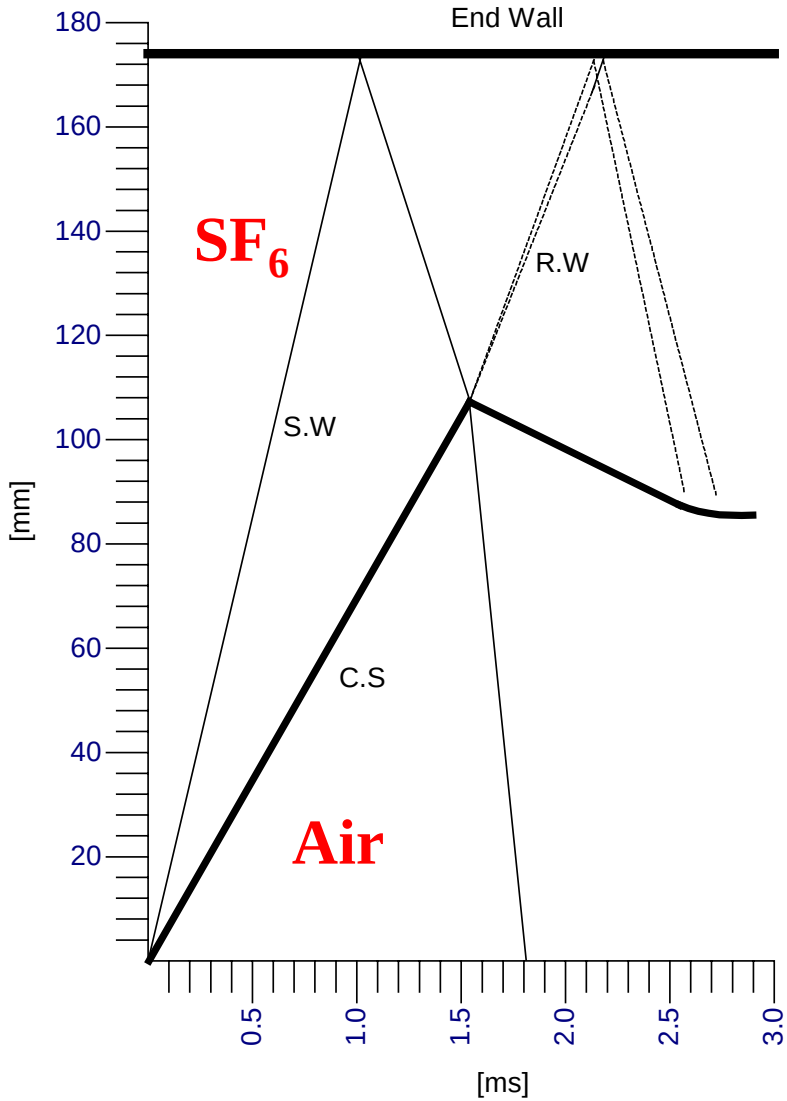

Mach=1.2

Experimental results
(random initial conditions)

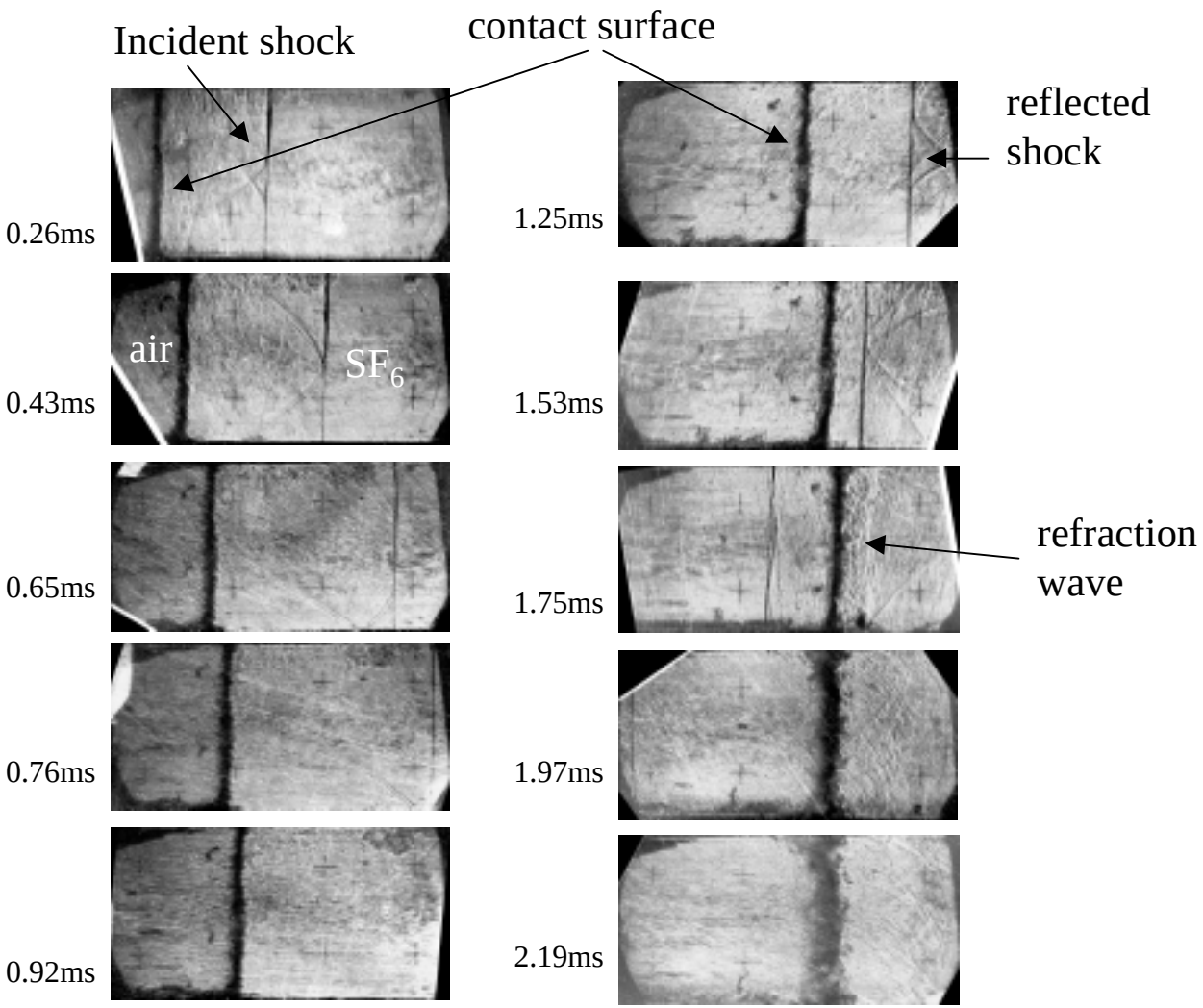

2D numerical simulations

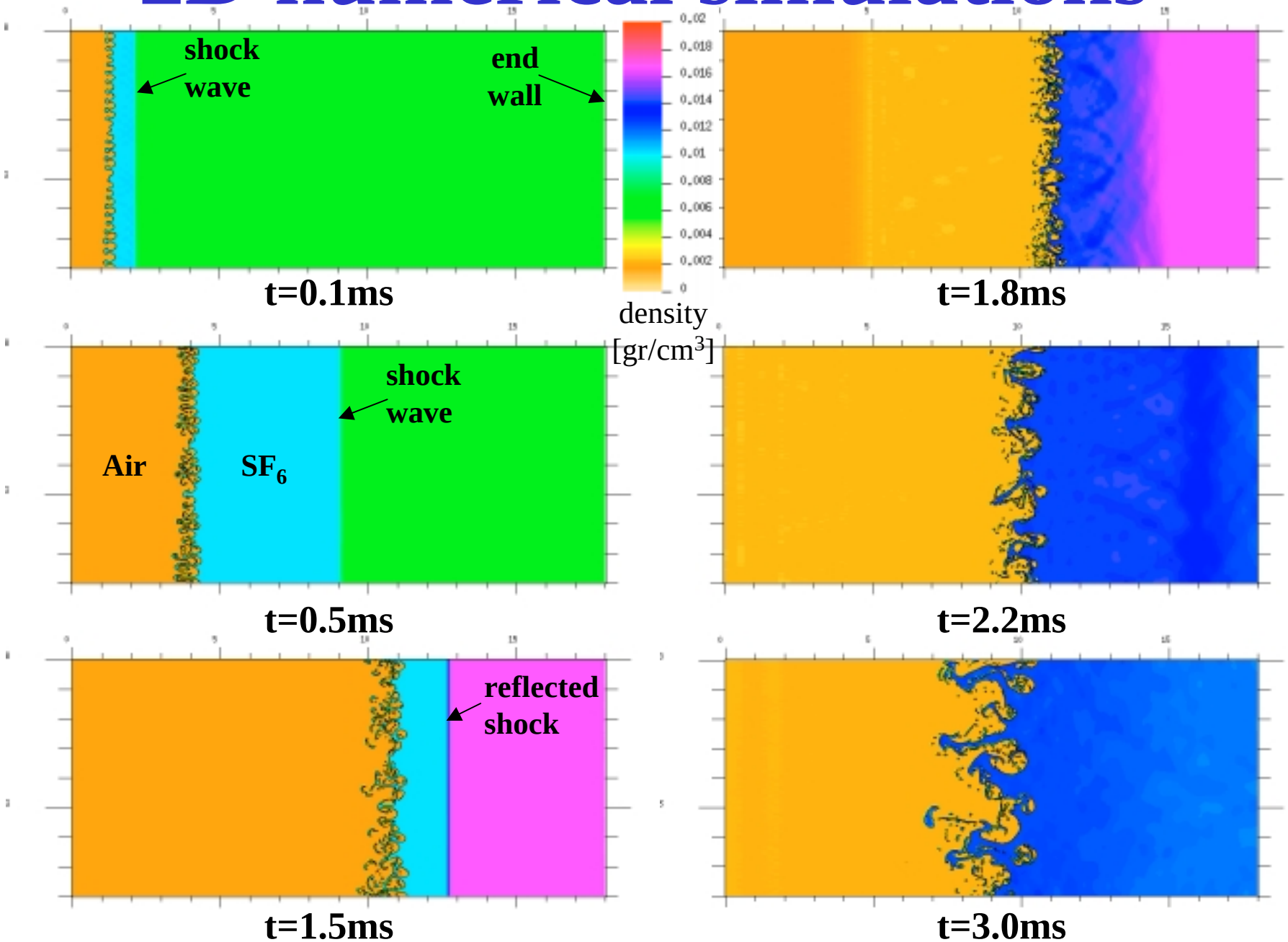

Good agreement between mix model and 2D simulation

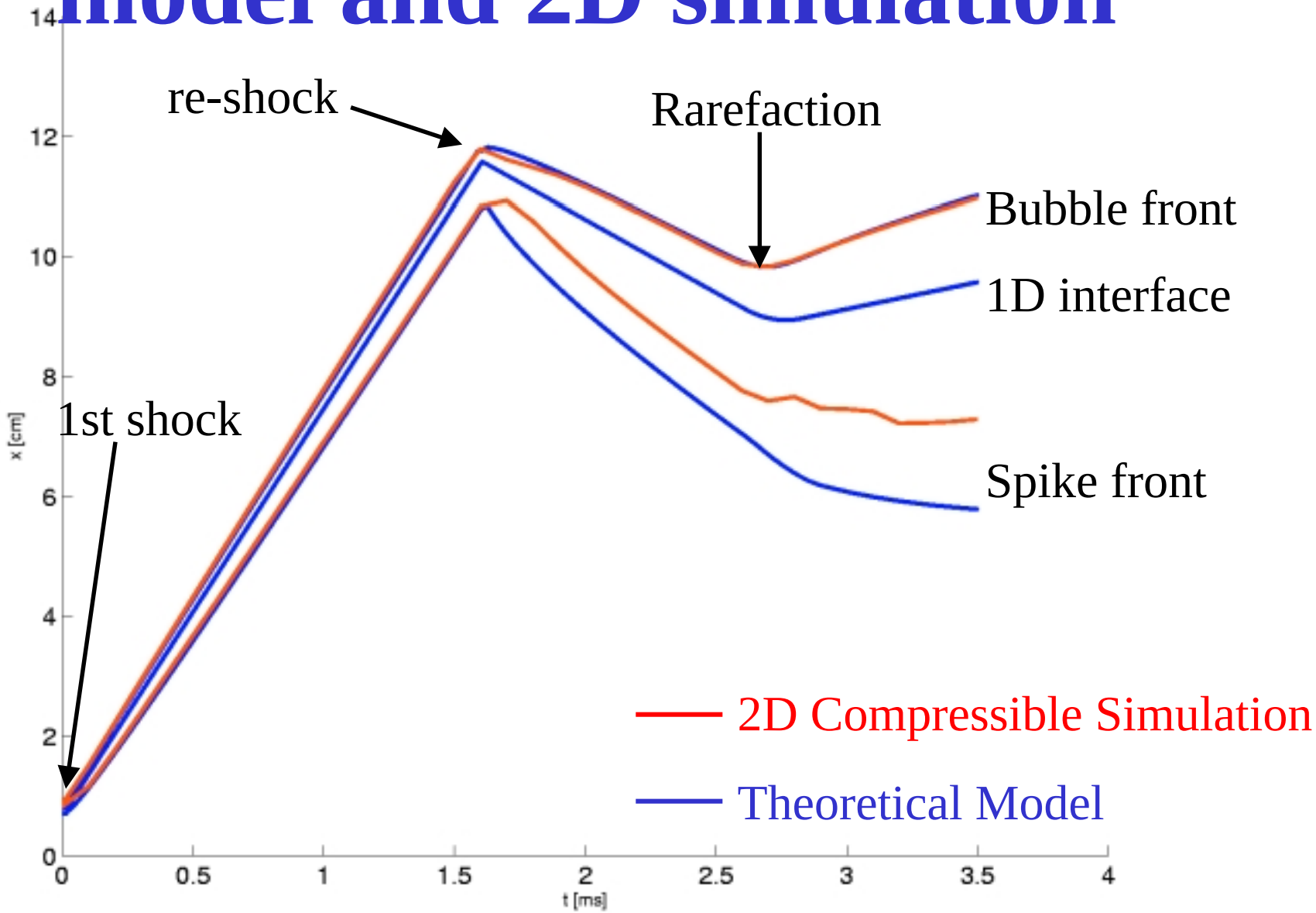

Model agrees with experimental results

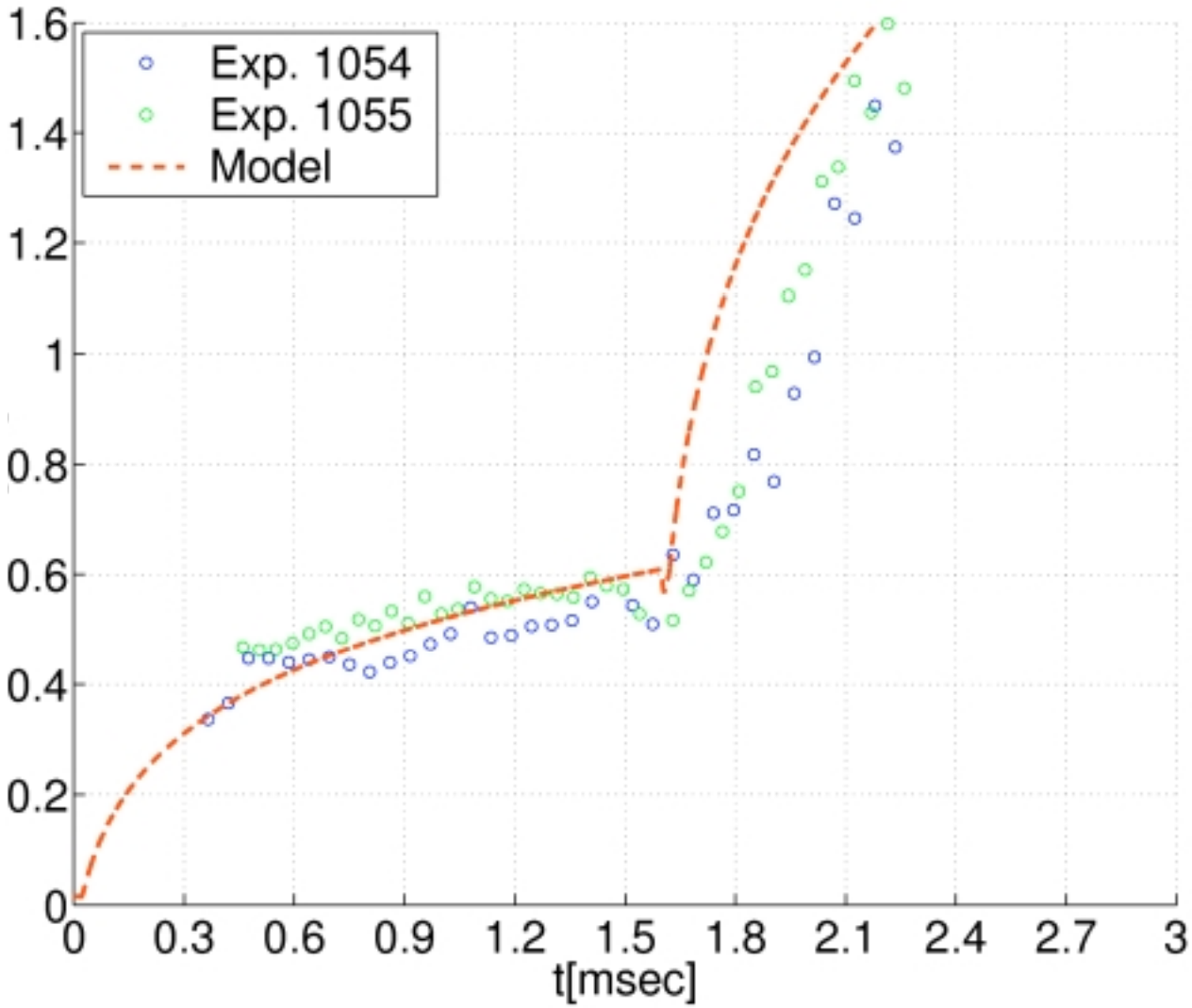

Summary

- Layzer model and buoyancy-drag equation have been combined to describe all instability stages for all Atwood numbers and a general acceleration profile.
- Multi-mode spectrum is described by one characteristic wavelength.
- 1D compressibility and scale change effects are introduced through Lagrangian “drift” of the mixing zone boundaries and by time dependant Atwood number.
- Model results have been compared to experiments and to full 2D numerical simulations.
- Non-planar geometry may be introduced by modifying characteristic wavelength.

NON LINEAR RT and RM SINGLE MODES (ANALYTIC)

- Nail INOGAMOV (MOSCOU)
- Matthieu TRICOTTET (CEA - PARIS)
- Alexei OPARIN (MOSCOU)
- Serge BOUQUET (CEA - PARIS)

Astro-ph
0104024

OUTLINE

- ASSUMPTIONS
  + INITIAL 2D/3D PERTURBATION

- ANALYTICAL MODEL

- STRUCTURE OF THE INTERFACE

- SHAPE FACTOR

- COMP. OTHER WORKS.

ASSUMPTIONS :

- $g = f(t)$ arbitrary
  - $g \sim$ cste RTI
  - $g \sim \delta(t)$ RMI

- INCOMPRESSIBLE
  (compressible - Linear)

- POTENTIAL FLOW

$$\vec{V} = \vec{\nabla}\phi \Rightarrow \boxed{\nabla^2\phi = 0}$$

- $At = \dfrac{\rho_H - \rho_L}{\rho_H + \rho_L} \longrightarrow 1$

- SINGLE MODE STUDY
  2D and 3D

- INFLUENCE OF THE LATTICE (PERIODIC)
  B3 (J6), B4 (J4), B6 (J3)

Perturbations

- 2D

RIPPLES

- 3D B4

3D PERIODIC LATT.

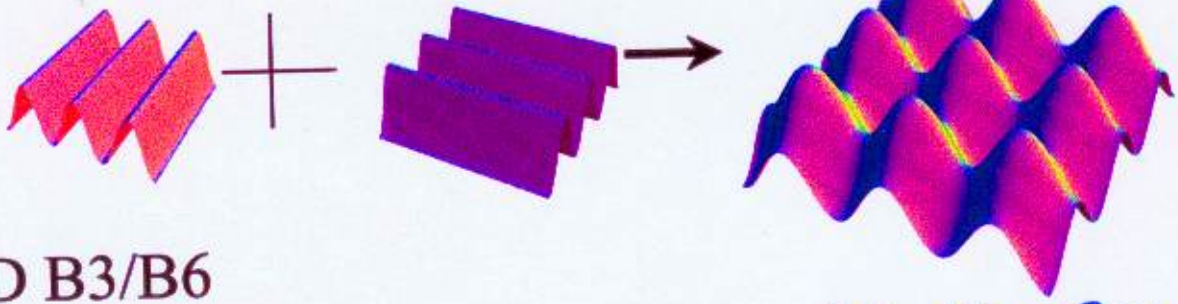

B4 - Egg Box

- 3D B3/B6

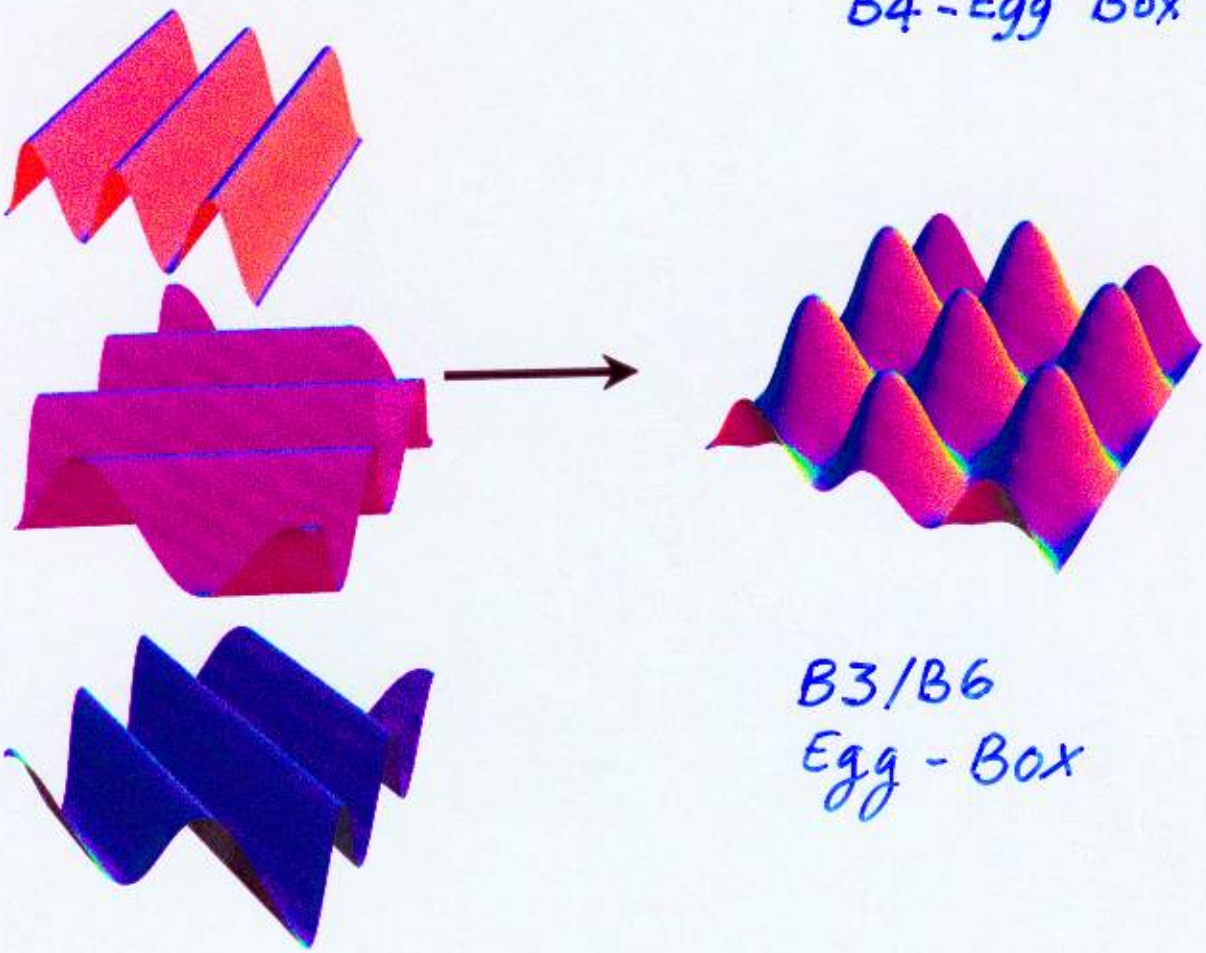

B3/B6
Egg - Box

EQUATIONS

- INTERFACE $\begin{cases} 2D & z = \eta(x,t) \\ 3D & z = \eta(x,y,t) \end{cases}$

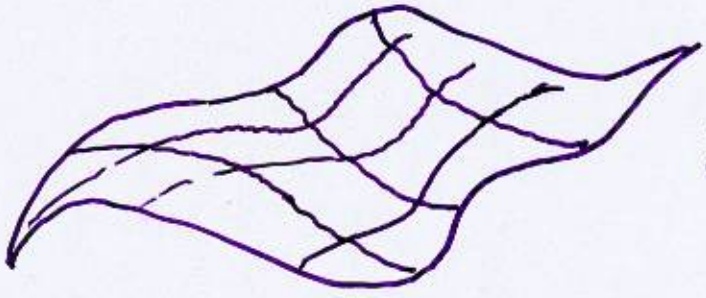

3D

$z = \eta(x,y,t)$

- PARTICLES of FLUID ATTACHED TO THE INTERFACE

$$\frac{\partial \eta}{\partial t} = v_z - v_x \frac{\partial \eta}{\partial x} - \underbrace{v_y \frac{\partial \eta}{\partial y}}_{3D}$$

- BERNOUILLI EQUATION

$$\frac{\partial \phi}{\partial t} = \frac{1}{2}(\vec{v})^2 + g(t)\,\eta$$

MODEL

Extension of LAYZER Approach

ApJ 122 1 (1955)

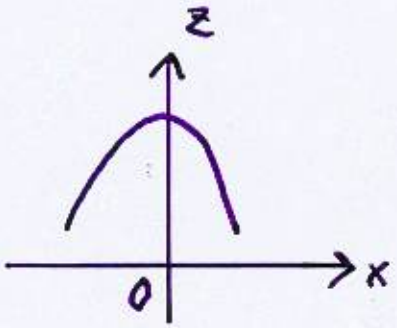

Top of a bubble:

1) $\eta(x,t) = \eta_0(t) + \frac{1}{2}\eta_1(t)x^2 + \cdots$

2) monomode potential

$\phi(x,z,t) \sim a(t)(\cos kx)e^{-kz}$

OUR WORK:

2D: $\phi(x,z,t) = \sum_{n=1}^{N}{}' \phi_n(t)\cos(nx)e^{-nz}$

$\eta = \eta_0 + \sum_{n=1}^{N}{}' K_n(t)\frac{x^{2n}}{(2n)!}$

N - TRUNCATION NUMBER
(Up to 6 for J, for the first time)

3D $\begin{cases} \phi \sim \sum_{n,m}^{n+m<N}{}' \phi_{nm}(t)\cos nx \cos my\, e^{-q_{nm}z} \\ \eta \sim \sum' K_{nm}(t)\frac{x^{2n}}{(2n!)}\frac{y^{2m}}{(2m!)} \end{cases}$

STAGNATION POINTS

- TOP OF BUBBLES
- TIP OF JETS
- SADDLE POINTS

for the first time

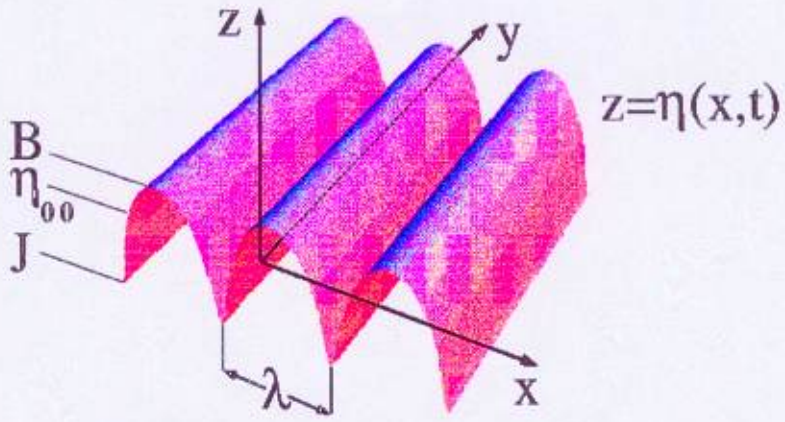

2D – Nonlinear Analytical Study (parrallel ripples)

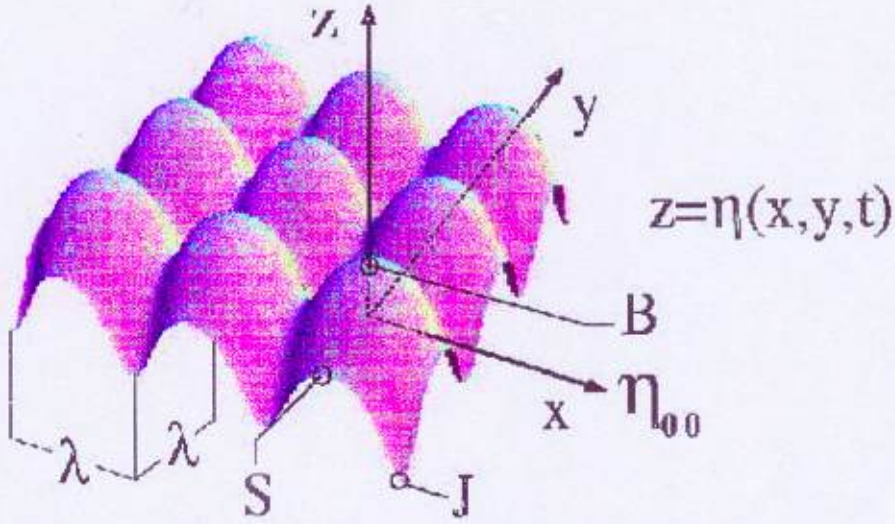

2D – Nonlinear Analytical Study (egg box type initial perturbation)

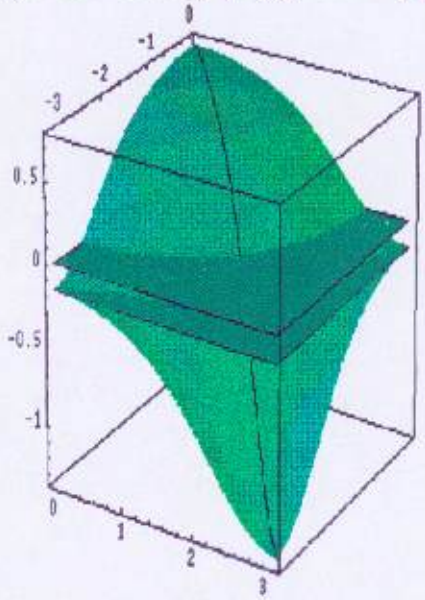

Detail of a Local System « Bubble+Jet+Saddle Point »

BLOW-UP
B + S + J

$h_B \simeq 0.7$
$l_J \simeq 1.4$
$\Big\} \; l_J \simeq 2 h_B$ Highly NL

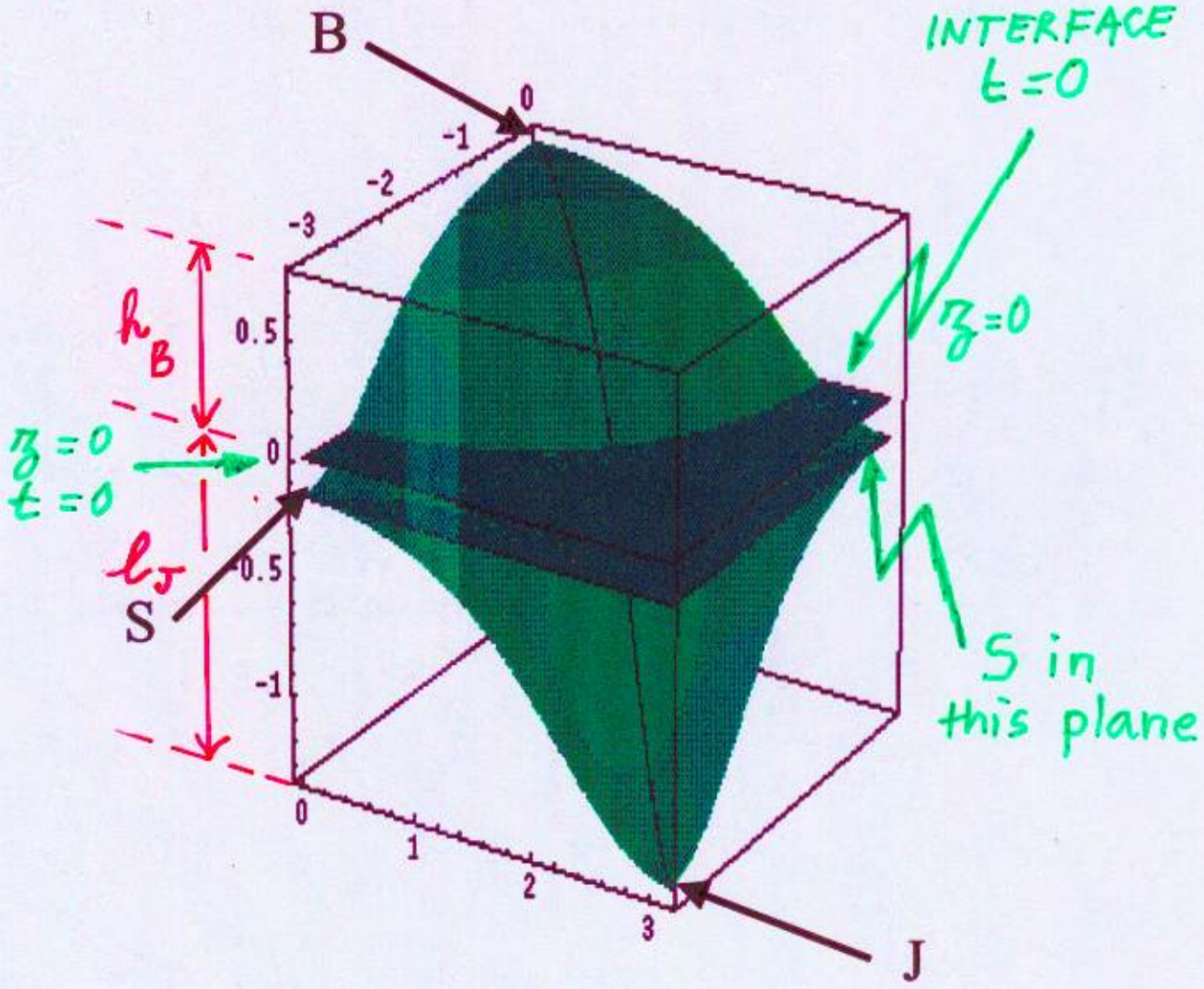

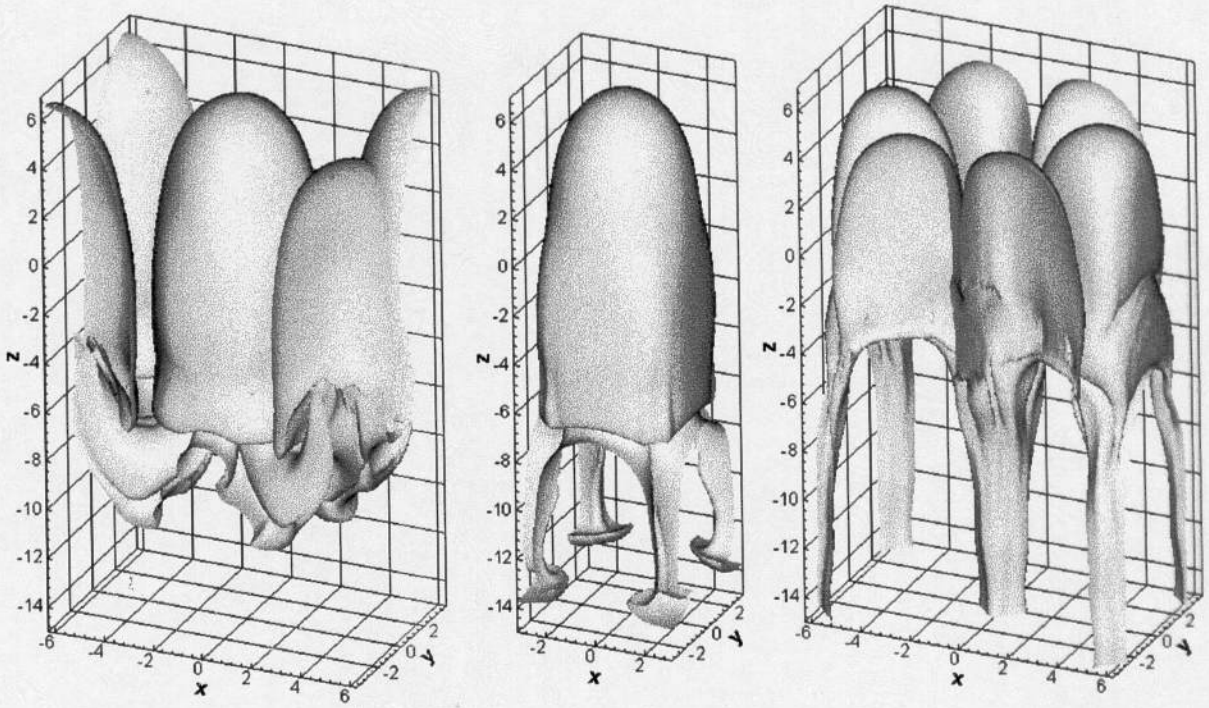

Numerical Simulation of the Rayleigh-Taylor Instability (B6, B4, B3)

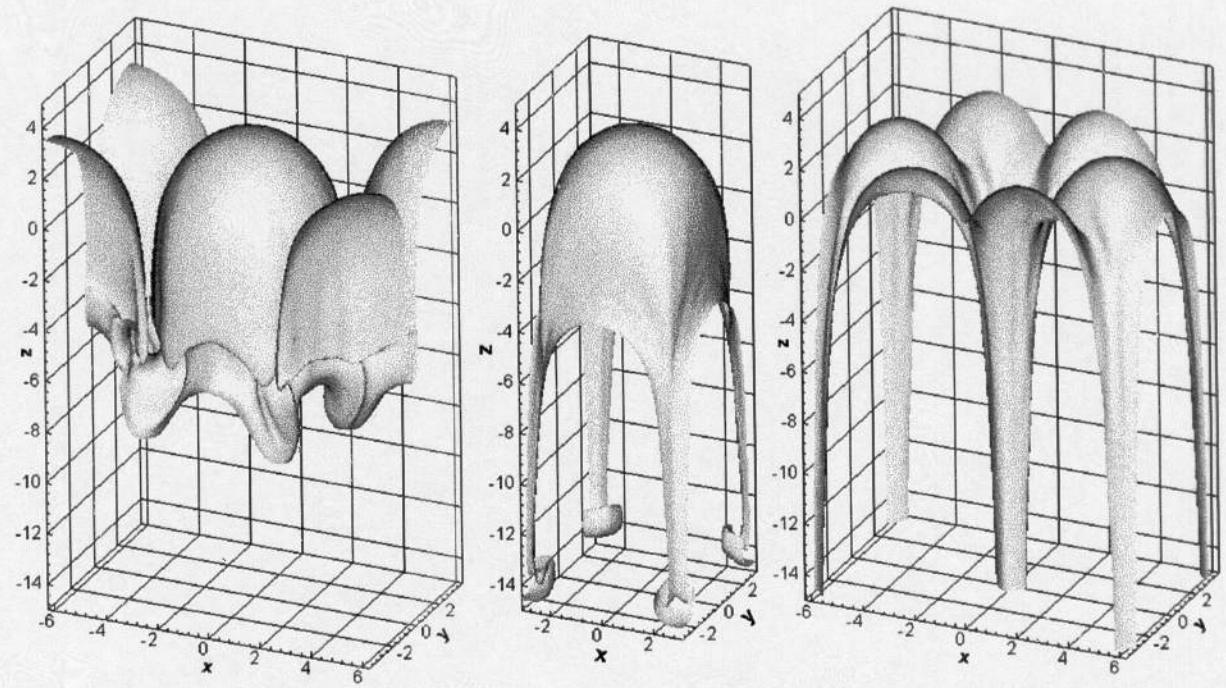

Numerical Simulation of the Richtmyer-Meshkov Instability (B6, B4, B3)

RTI

$$\Gamma = \frac{d(B-\bar{J})}{d(B-J)}$$

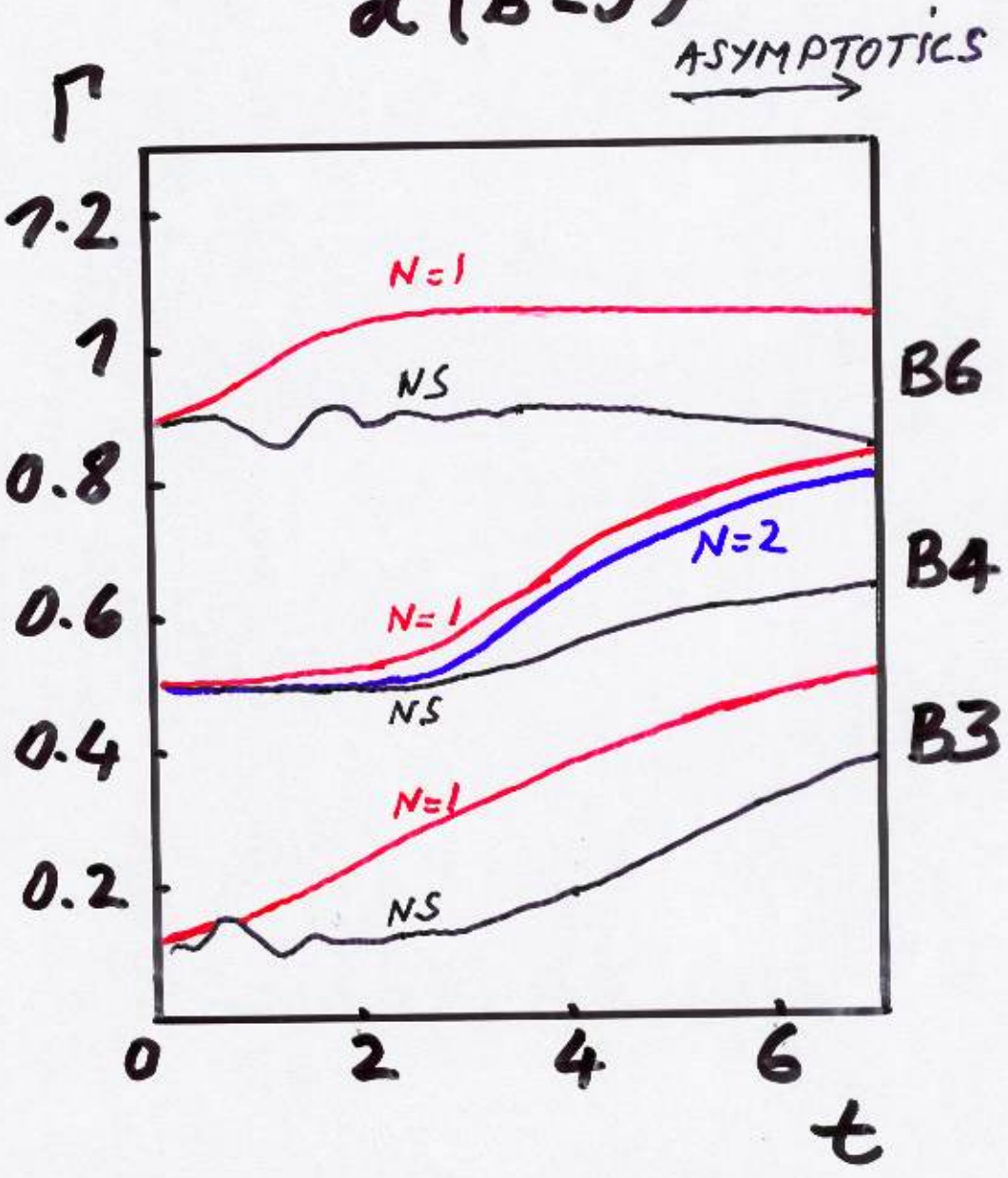

— Num. Sim. (OPARIN)

— Theory N=1

— Theory N=2

GOOD TENDENCY (Γ is global)

RMI

$$\Gamma = \frac{d(B-S)}{d(B-J)}$$

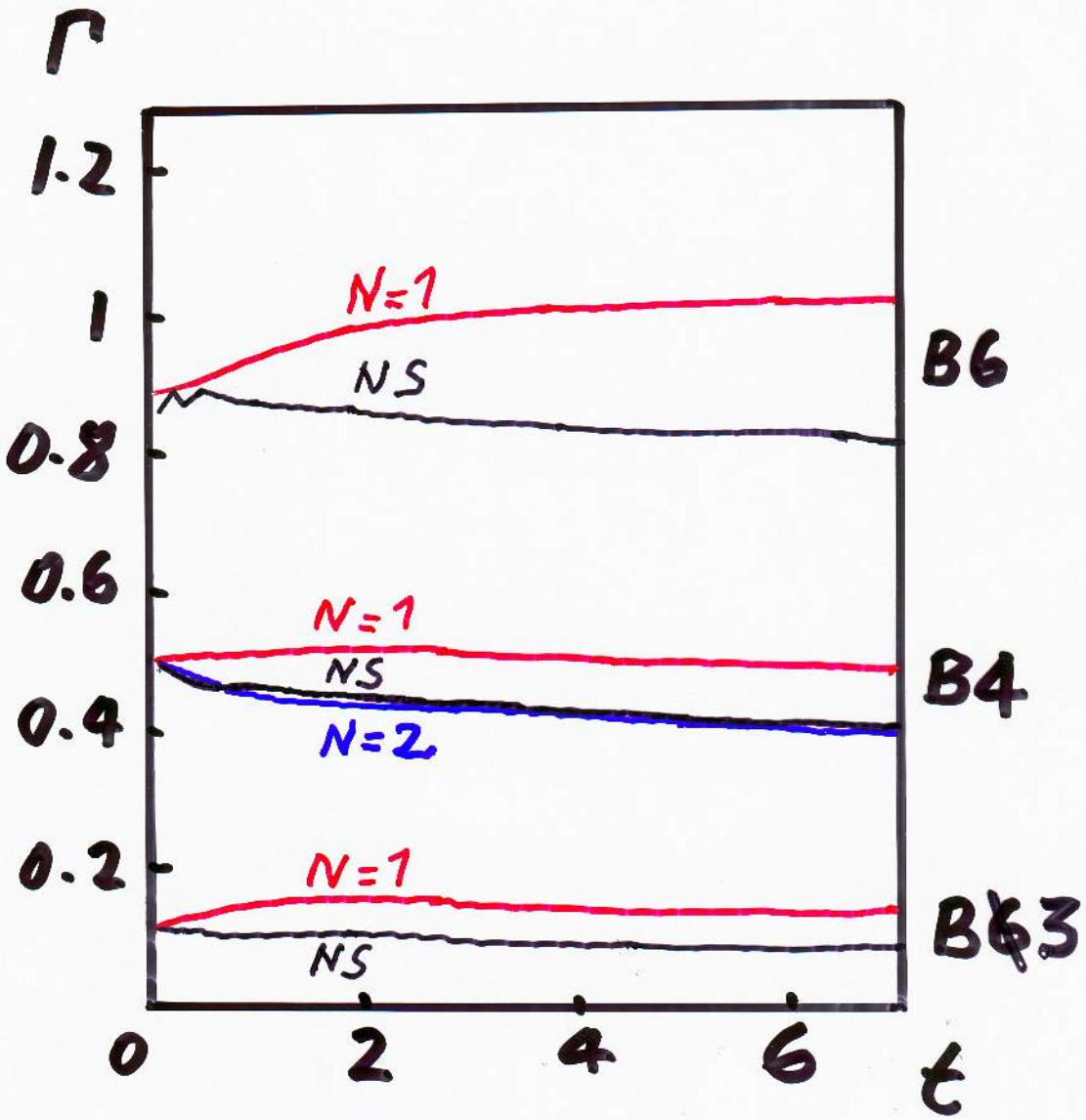

N=2 Good agreement.
Rather good " for asymptotic values.

COMP. WNL APPROACH $a_0 k \alpha t \lesssim 1$
-RMI-

expansion parameter about $t=0$

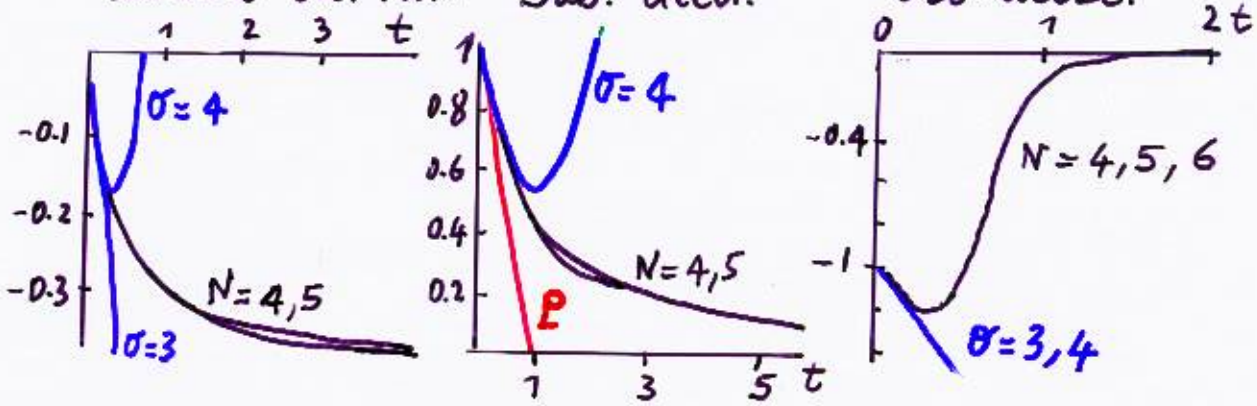

— WNL — Pade — ITOB

RIGHT MODELING OF THE LINEAR PHASES.

$R_b = 2.6$

$V_b = \frac{\alpha}{t}$

$\alpha = 0.60$

↑

WNL approach can only follow bubble curvature up to 40% of the asymtotic valve

CONCLUSION

- Analytical NL asymtotic stages (+ transients)

- comparisons with 2D/3D CODES wich compute hydro in such NL regimes

IWPCTM 2001

Three Dimensional Multi-Mode Rayleigh-Taylor and Richtmyer-Meshkov Instabilities at All Density Ratios

D. Kartoon[1,2], D. Oron[3], L. Arazi[4], A. Rikanati[1,2], O. Sadot[1,5], A. Yosef-Hai[1,5], U. Alon[3], G. Ben-Dor[5] and D. Shvarts[1,2,5]

1. *Dept. of Physics, Nuclear Research Center Negev, Israel*
2. *Dept. of Physics, Ben-Gurion University, Beer-Sheva, Israel*
3. *Fac. of Physics, The Weizmann Institute of Science, Rehovot, Israel*
4. *School of Physics and Astronomy, Tel-Aviv University, Tel-Aviv, Israel*
5. *Dept. of Mech. Eng., Ben-Gurion University, Beer-Sheva, Israel*

Relevant Publications

Oron et al. PoP 2001.

Alon et al, PRL 1994, 1995.

Hecht et al. PoF 1994.

Oron et al. PoP 1998.

Rikanati et al. PRE 1998.

Sadot et al. PRL 1998.

Layzer APJ 1955.

Dimonte PoF, PoP 2000.

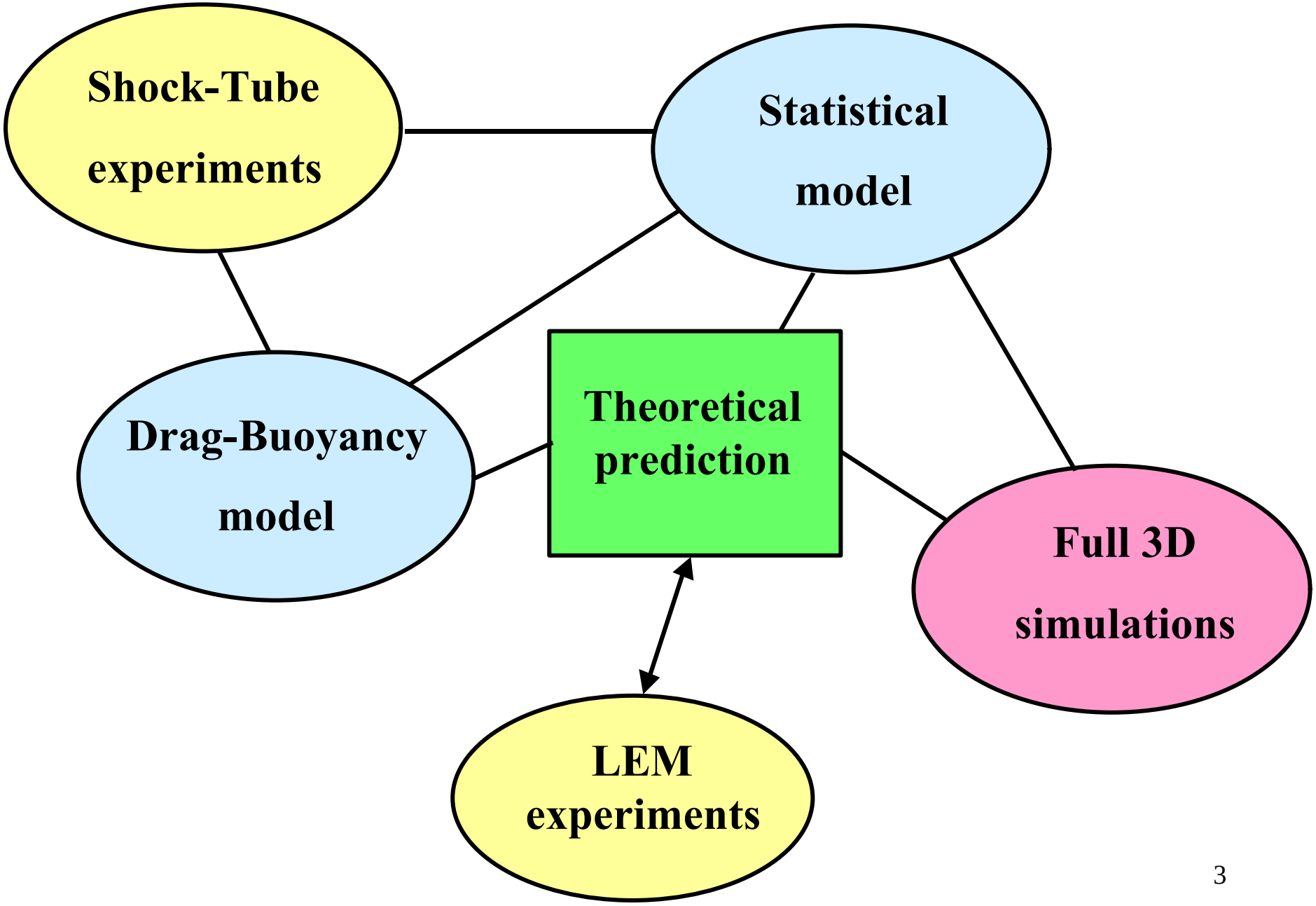
Shock-Tube experiments
Statistical model
Drag-Buoyancy model
Theoretical prediction
Full 3D simulations
LEM experiments

Outline

The Drag-Buoyancy Model for Bubbles

2D Statistical Model

Full 3D Numerical Simulations

3D Statistical Model

The Drag-Buoyancy Model for Spikes

Conclusion

Single Mode Nonlinear Stage

$$(\rho_l \times V + C_a \times \rho_h \times V) \times \frac{du}{dt} = (\rho_h - \rho_l) V \times g \quad - \quad \rho_h \times S \times u^2$$

(inertia) + (added mass) = (buoyancy) (kinematic drag)

Where V/S →

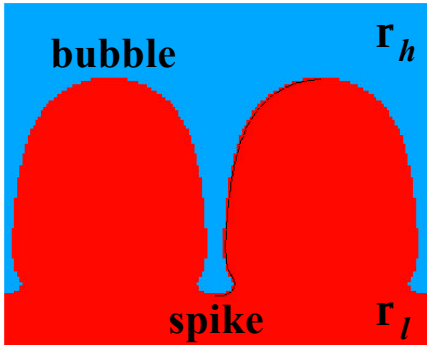

$$(\rho_l + C_a \rho_h)\dot{u} = (\rho_h - \rho_l) \times g - \frac{C_d}{l} \rho_h \times u^2$$

Where C_a and C_d are geometric constants.

Single Mode Asymptotic Velocities

$$(\rho_l + C_a \rho_h)\dot{u} = (\rho_h - \rho_l)g - \frac{C_d}{l}\rho_h u^2$$

RT: $$u_B = \sqrt{\frac{1}{C_d}\left(\frac{2A}{1+A}\right)g}$$

RM: $$u_B = \frac{1}{C_d}\left(\frac{1-A}{1+A} + C_a\right)\frac{\Delta x}{t}$$

The geometric constants depend on the dimensionality:

$$C_a^{2D} = 2, \qquad C_d^{2D} = 6$$
$$C_a^{3D} = 1, \qquad C_d^{3D} = 2$$

RM Single Mode Experimental Results

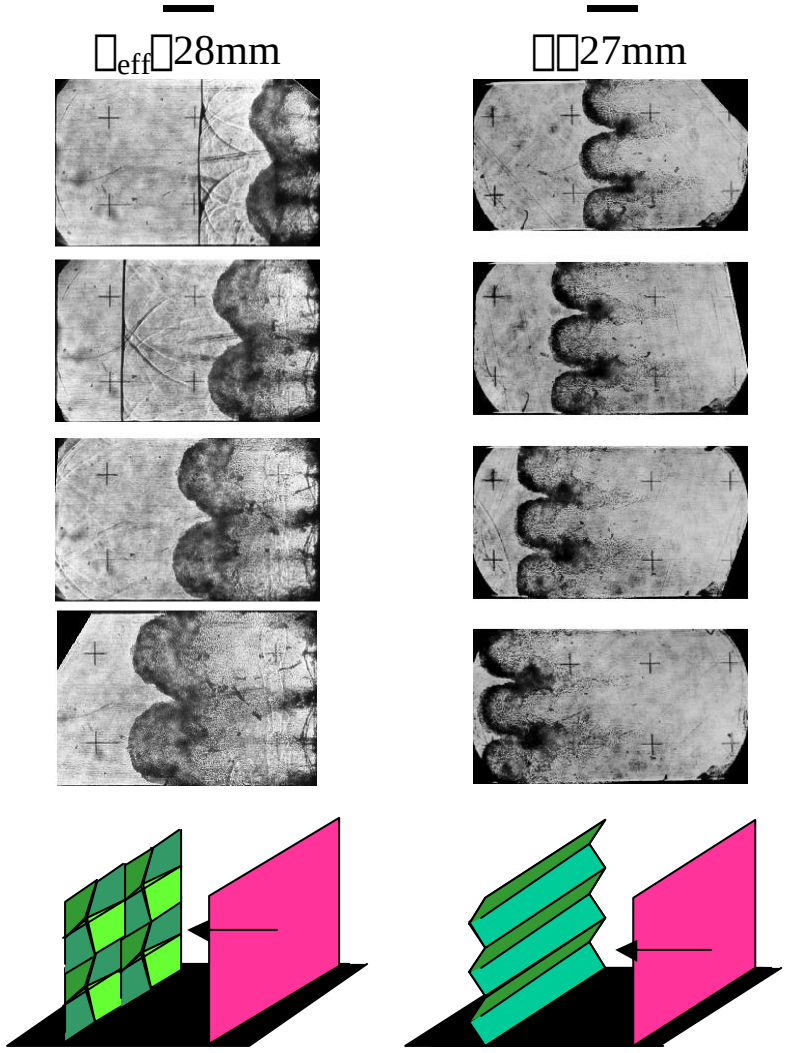

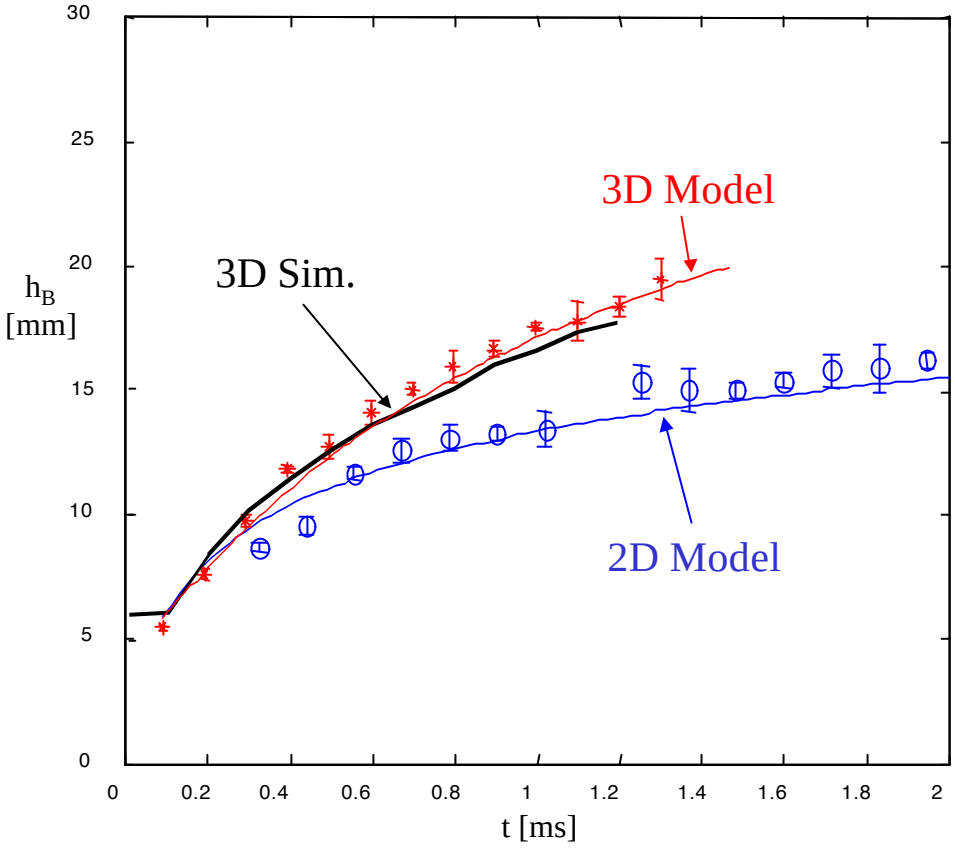

Multi Mode Drag Buoyancy Model

Generalization of the drag-buoyancy equation, using the *self-similarity* assumption:

$$h_B^{(MM)}(t) = b(A) \times \langle l \rangle (t)$$

RT: $u = \dot{h} = \sqrt{c_1(A) \times g \times h / b(A)} = a \times A \times g t^2$

RM: $u = \dot{h} = c_2(A) \times h / b(A) \times \frac{1}{t} = c \times t^q$

$$\alpha = \frac{1}{2(1+A)} \frac{1}{C_d} \frac{1}{b^{RT}(A)}$$

$$\alpha = \left(\frac{1-A}{1+A} + C_a \right) \times \frac{1}{C_d} \times \frac{1}{b^{RM}(A)}$$

3D Multi Mode the a q b Relations

Using the 3D coefficients in the expressions relating □, □ and b, and assuming that $b^{(RM)}=b^{(RT)}$, the differences between 2D and 3D bubble front growth are obtained:

	2D ($C_a=2$, $C_d=6$□)	**3D** ($C_a=1$, $C_d=2$□)
assumed a	0.05	0.05
q	0.1(A+3) (=0.3-0.4)	0.2
b	$\frac{1}{2(A+1)}$ (=0.25-0.5)	$\frac{3}{2(A+1)}$ (=0.75-1.5)

Outline

The Drag-Buoyancy Model for Bubbles

2D Statistical Model

Full 3D Numerical Simulations

3D Statistical Model

The Drag-Buoyancy Model for Spikes

Simulation of 2D Multimode Perturbation Evolution

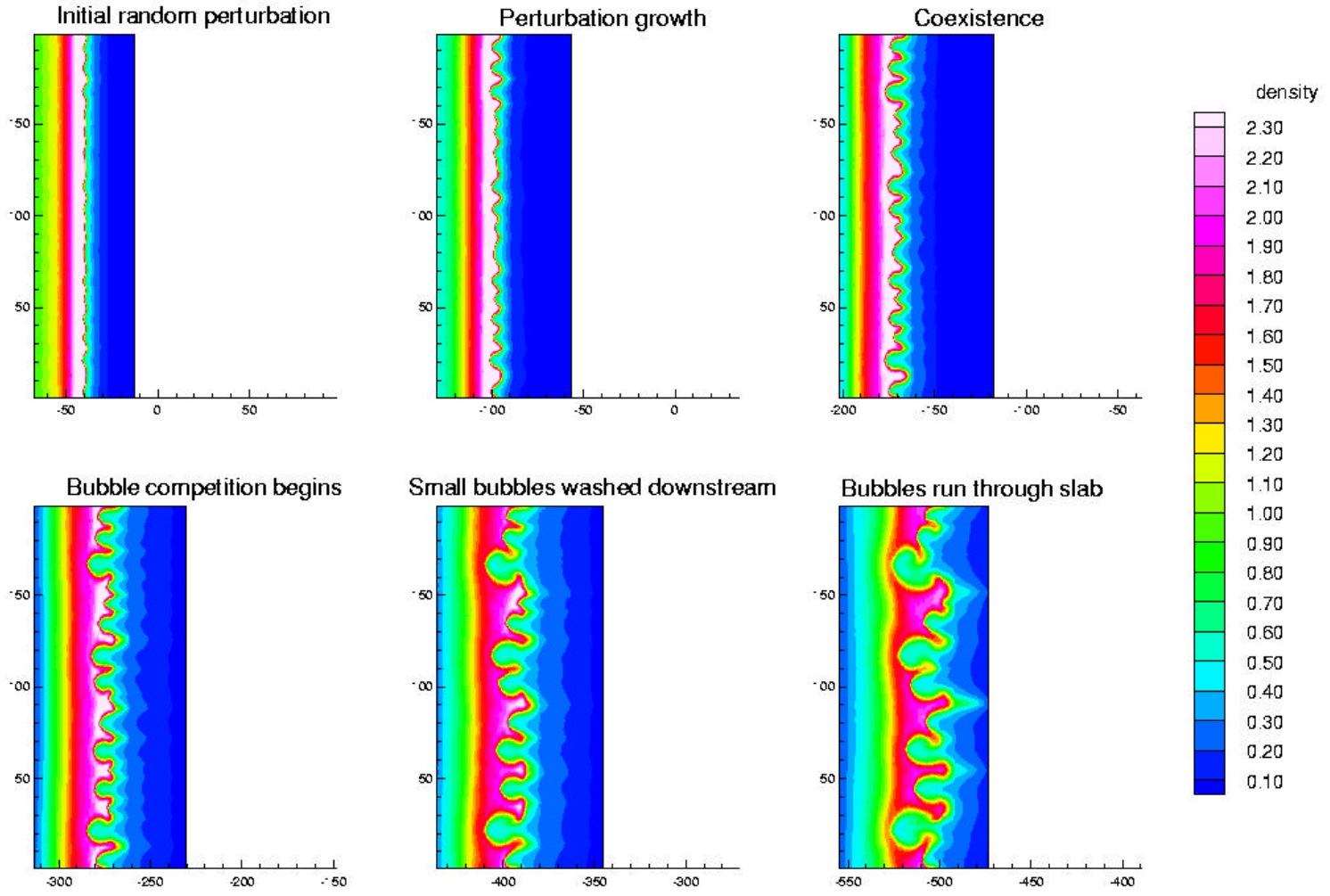

Multi Mode 2D Statistical Model (Alon et. Al.)

Bubble Envelope (Simulation)

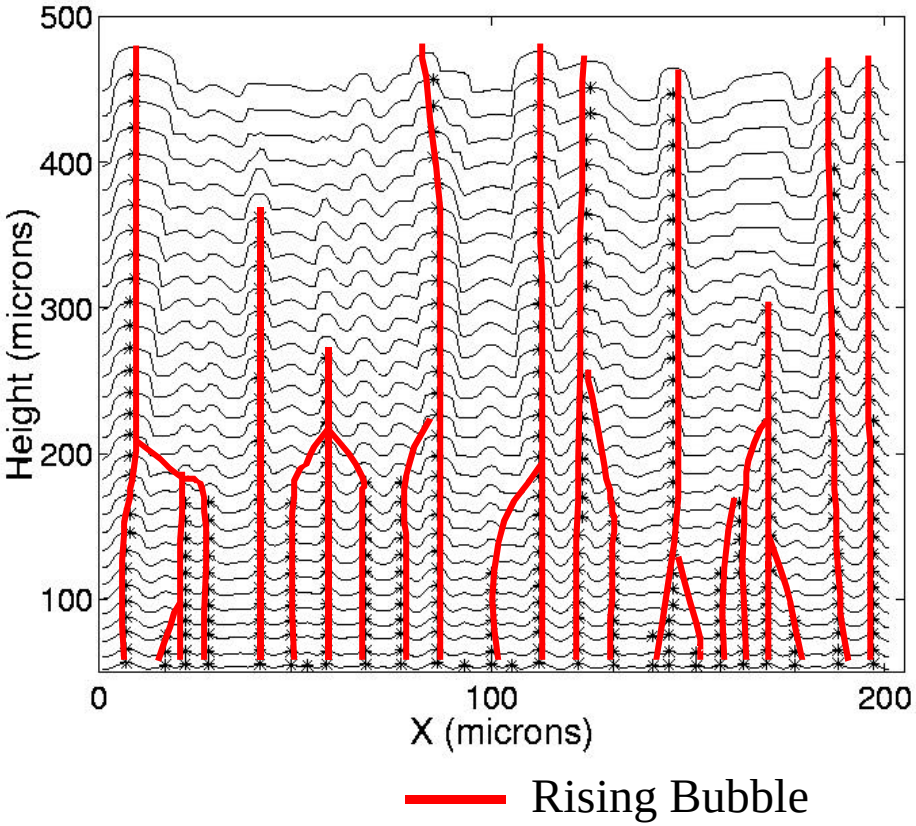

Each bubble grows with its asymptotic velocity, according to its wavelength:

$$u_i = u_{2D}^{(asy)}\left(l_i, t\right)$$

Multi Mode Bubble Merger

Velocity evolution of two non-identical adjacent bubbles:

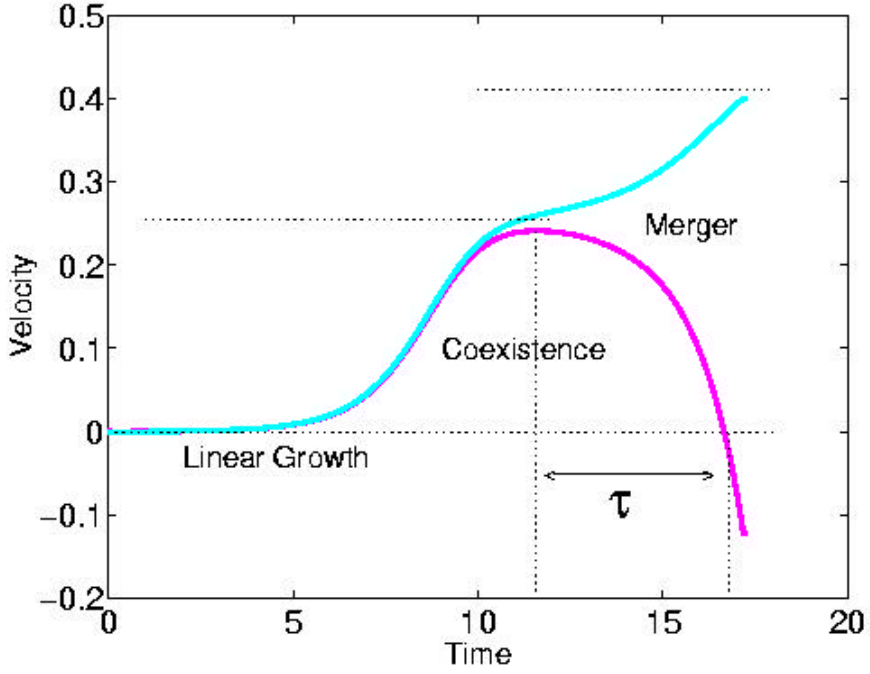

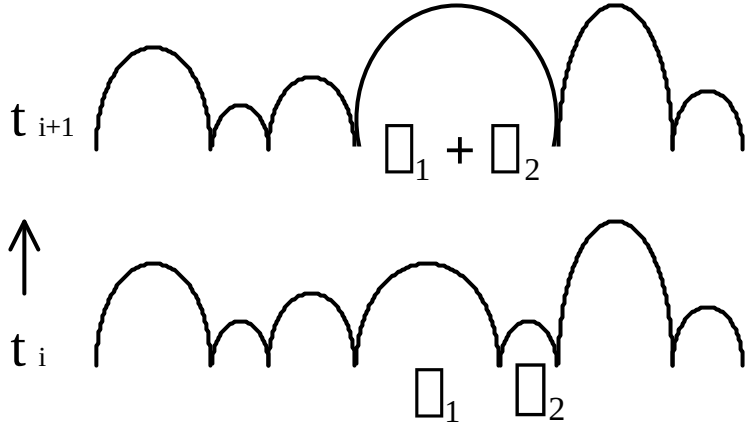

Merger Rate:

(l_i, l_{i+1})

$\Rightarrow \quad w_{merge}(l_i, l_{i+1}, t) \sim 1/t$

$(l_i + l_{i+1})$

Multi Mode 2D Statistical Model

$$N(t)\times\frac{\partial g(\lambda,t)}{\partial t} = -2g(\lambda,t)\int_0^{\infty} g(\lambda',t)w(\lambda,\lambda')d\lambda' \qquad \text{death}$$

$$+\int_0^{\infty} g(\lambda-\lambda',t)g(\lambda',t)w(\lambda-\lambda',\lambda')d\lambda' \qquad \text{birth}$$

Where g(λ,t) is the number of bubbles with wavelength λ within interval dλ at time t, and N(t) is the total number of bubbles:

$$\frac{\partial N(t)}{\partial t} = -\langle w\rangle_g \times N(t)$$

Multi Mode 2D Statistical Model Results

1. The distribution reaches an asymptotic function:

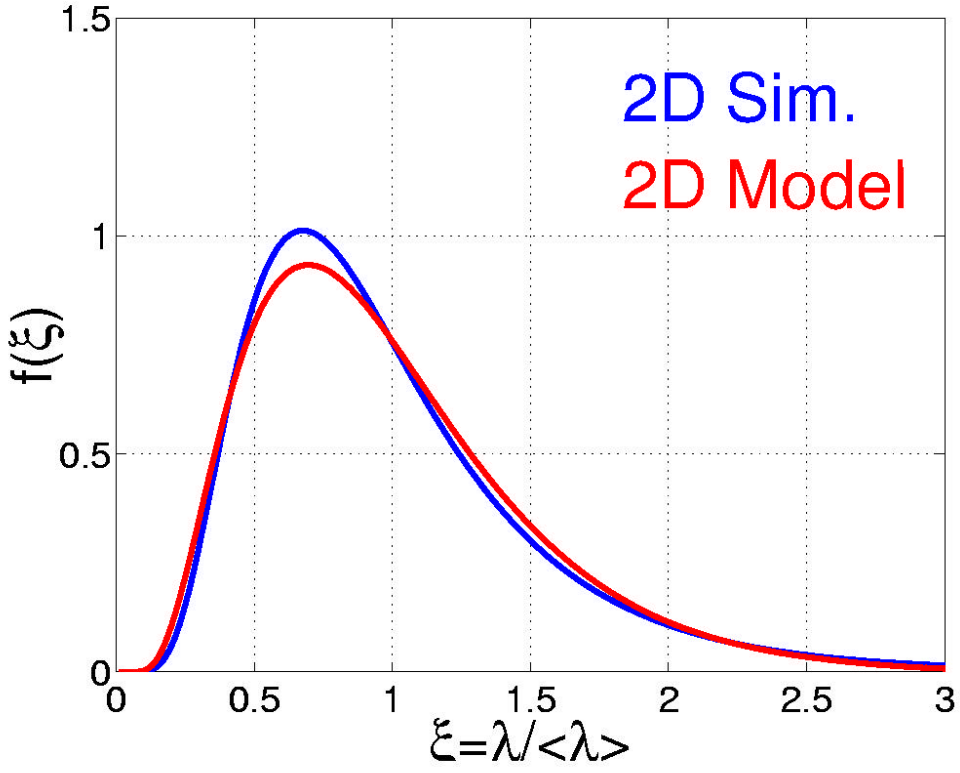

RT simulation,
A=0.5

Multi Mode 2D Statistical Model Results

2. The average bubble and spike heights are obtained for both the RT and the RM case:

RT: $u_B^{asy} \propto \sqrt{g\lambda}$ $\Rightarrow$ self-similarity $\Rightarrow$ $\dot{h}_B \propto \sqrt{gh}$ $\Rightarrow$ $h_B = \alpha_B \times gt^2$

RM: $u_B^{asy} \propto \frac{\lambda}{t}$ $\Rightarrow$ self-similarity $\Rightarrow$ $\dot{h}_B \propto \frac{h_B}{t}$ $\Rightarrow$ $h_B = c \times t^{\theta_B}$

Self-similarity parameter: $b^{RT} = b^{RM} = \frac{h_B}{\langle \lambda \rangle}$

2D Statistical Model Results:

$\alpha_B \approx 0.05$ $\quad \theta_B \approx 0.4$ $\quad b \approx 0.2$

LEM Experimental Results

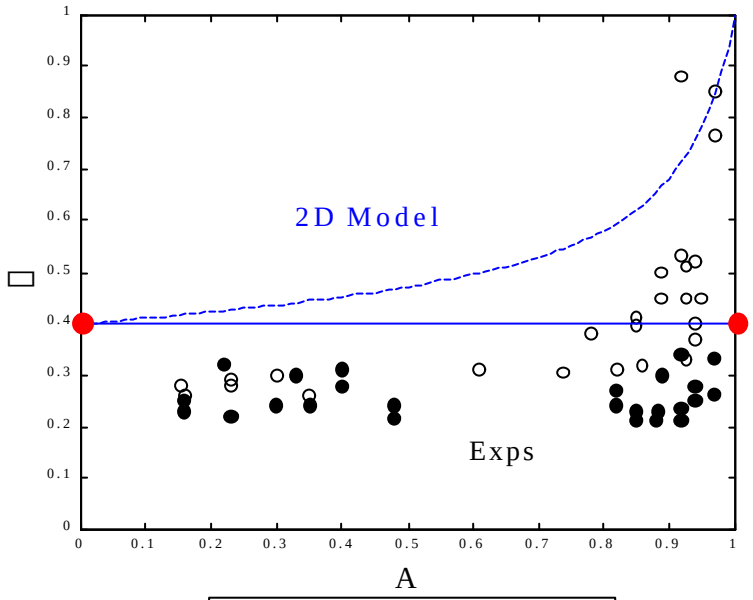

RM: $h_{B/S} = a_0 \times t^{\square_{B/S}}$

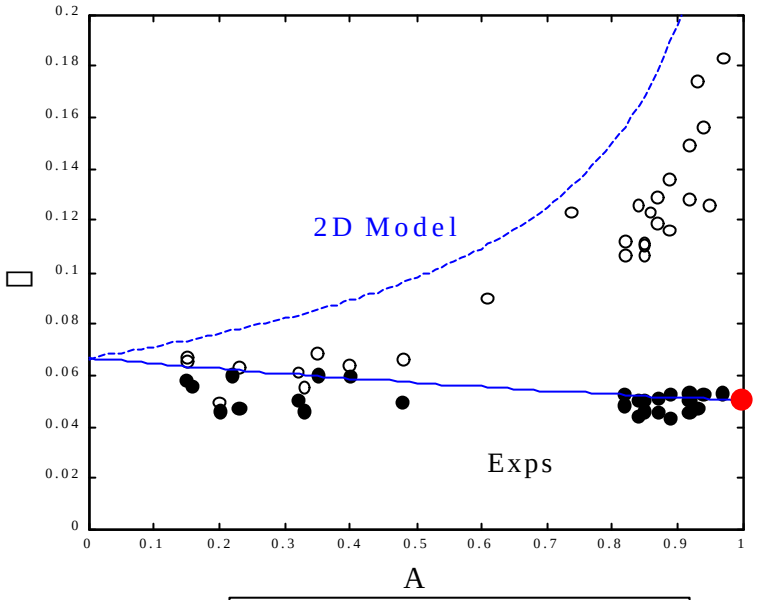

RT: $h_{B/S} = \square_{B/S} \times Agt^2$

Drag-Buoyancy Model
Effective 1-Mode

2D Statistical Model

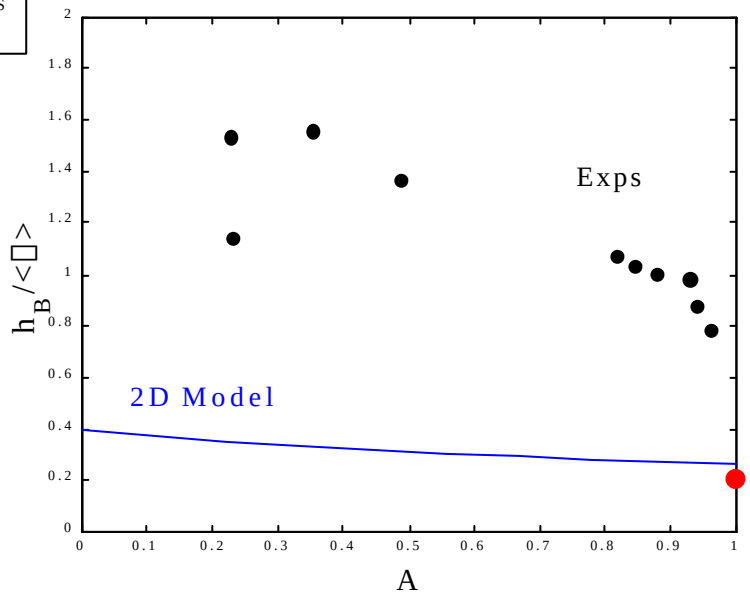

Outline

The Drag-Buoyancy Model for Bubbles

2D Statistical Model

Full 3D Numerical Simulations

3D Statistical Model

The Drag-Buoyancy Model for Spikes

Full 3D Numerical Simulation of the RT A=0.5 Case

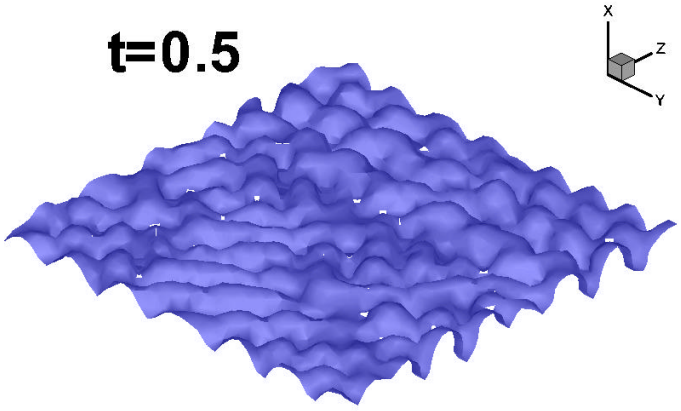

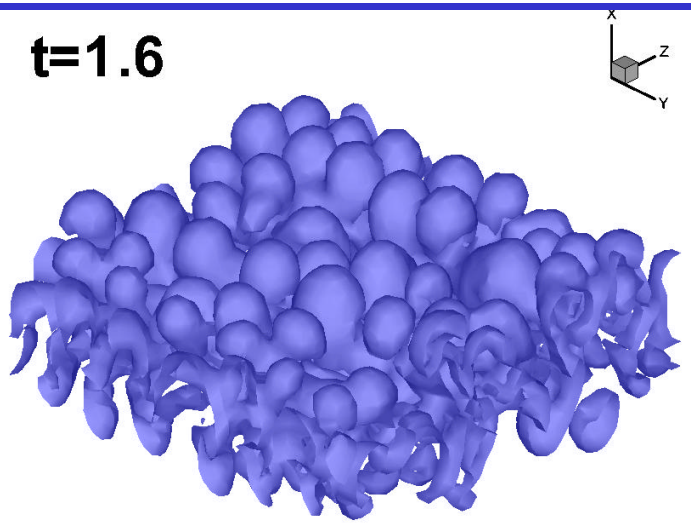

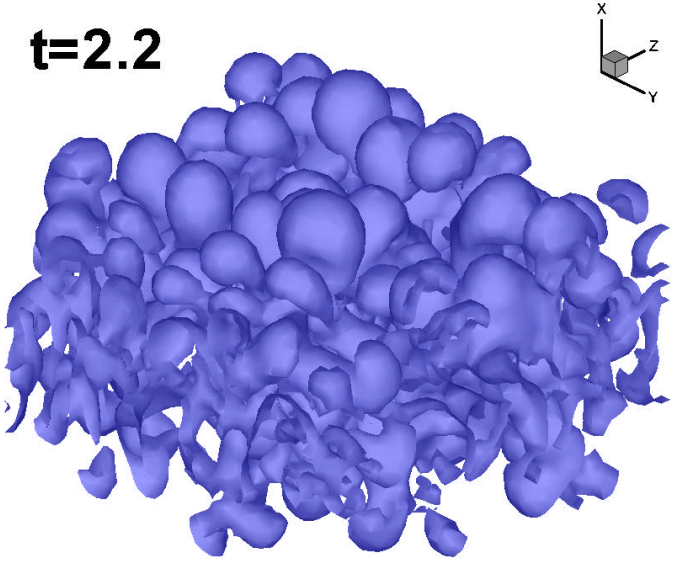

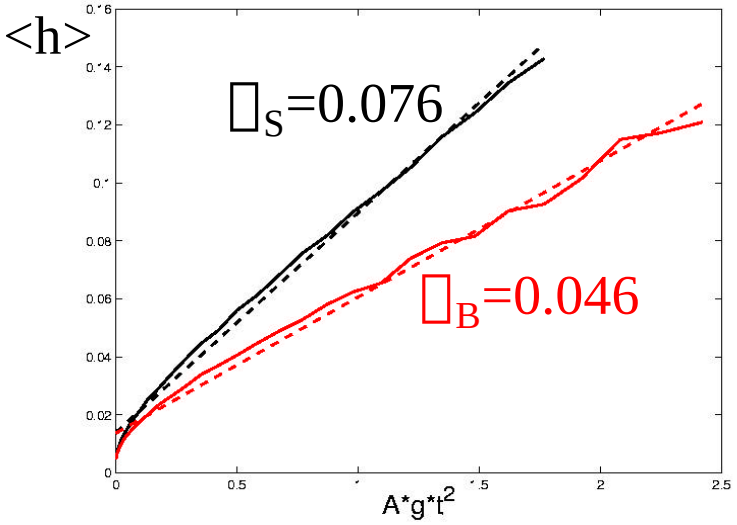

Voronoi Cell Structure of the Bubble Front Demonstrates the 3D Bubble Merger

t=0.28

n=260

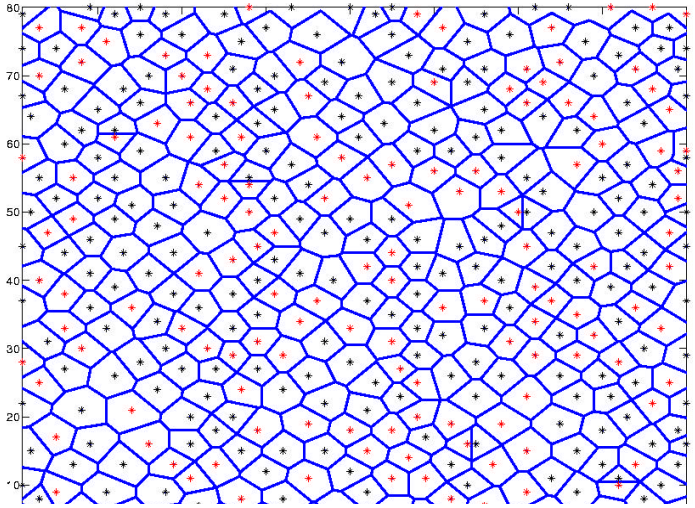

t=1.4

n=112

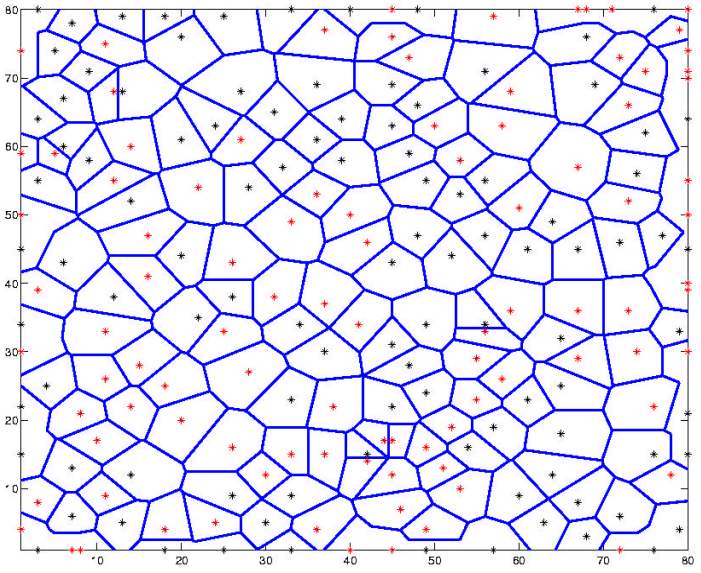

t=2.2

n=30

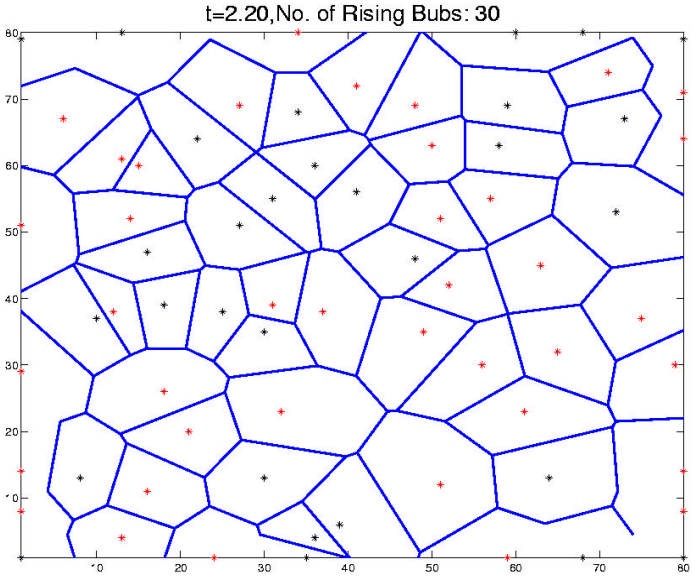

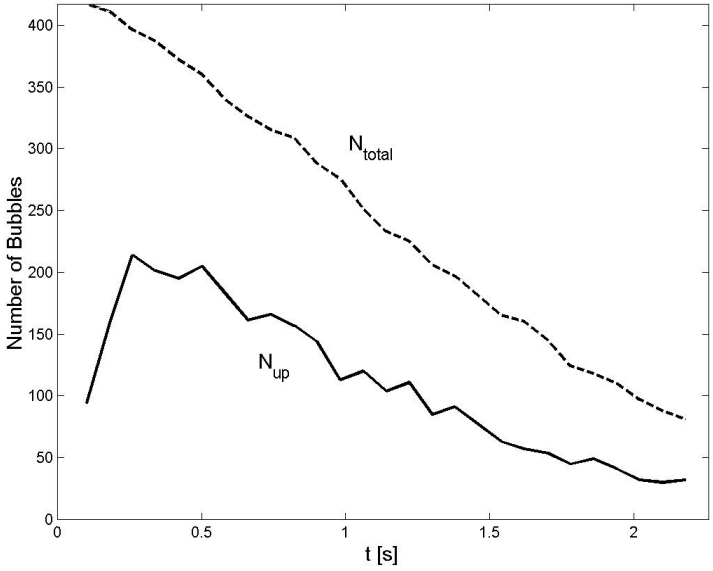

3D Simulation Results

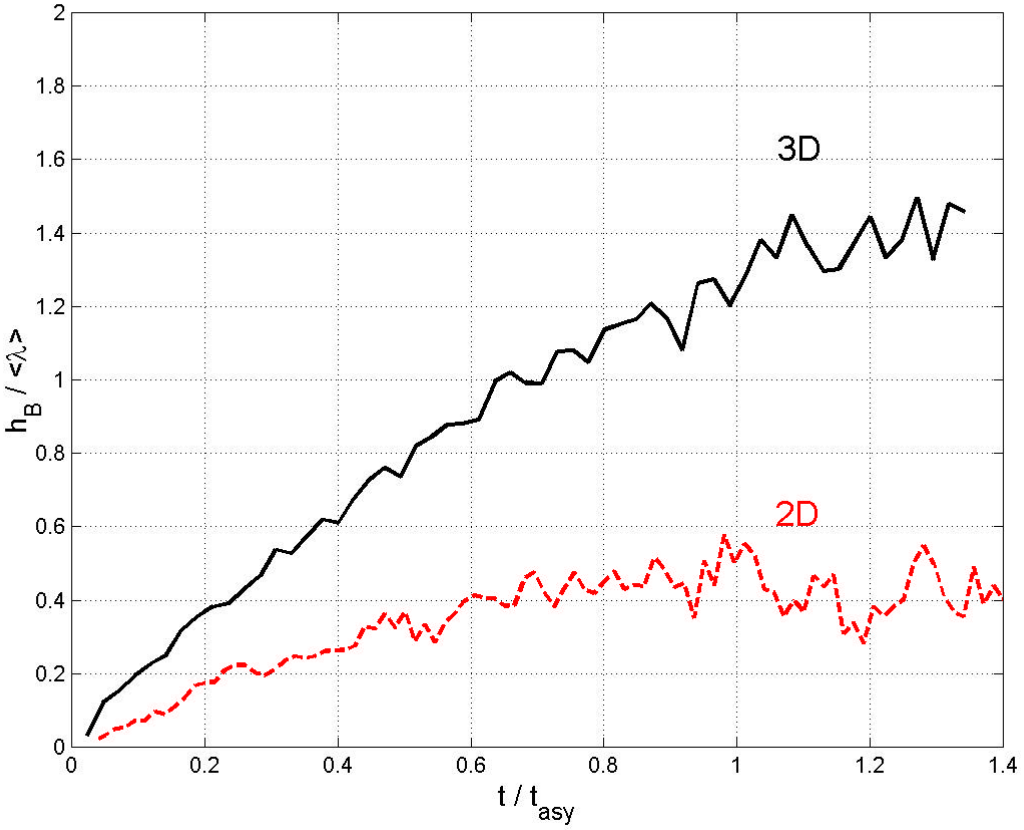

2D Simulation

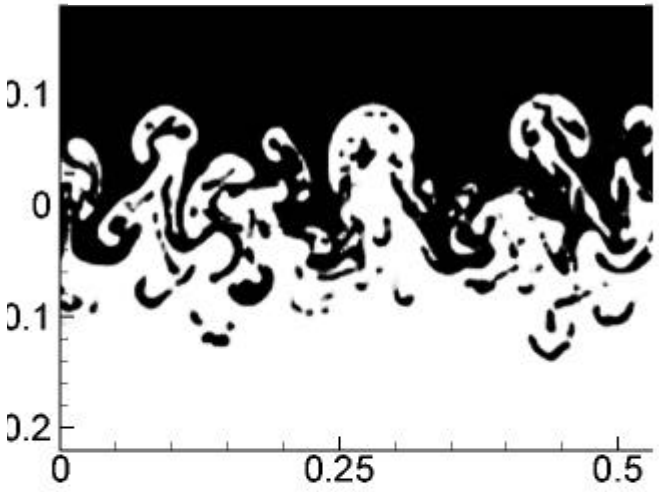

3D Simulation slice

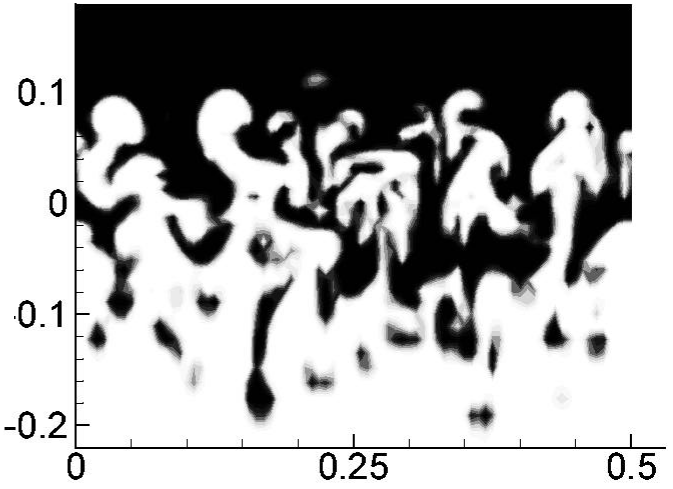

Outline

The Drag-Buoyancy Model for Bubbles

2D Statistical Model

Full 3D Numerical Simulations

3D Statistical Model

The Drag-Buoyancy Model for Spikes

Multi Mode 3D Statistical Model

Dimensionality effects on the statistical model:

Asymptotic velocity of each bubble 1.5-2 times higher than in the 2D case: $u_{3D}=1.5\text{-}2u_{2D}$

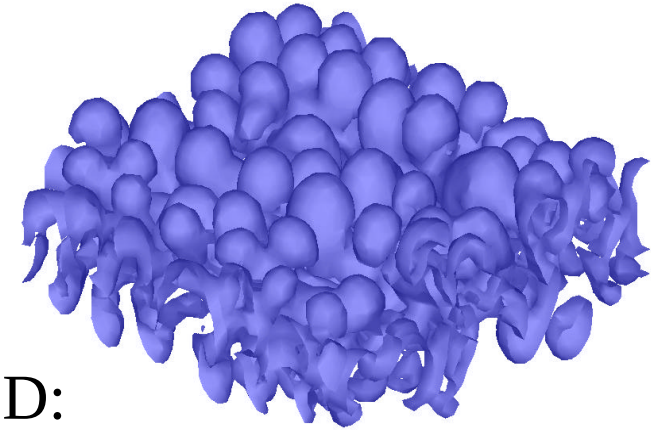

Average number of neighbors per bubbles□6 in 3D, rather than 2 in 2D:

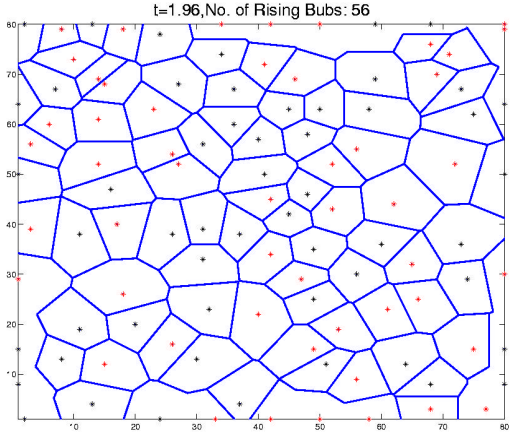

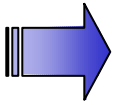

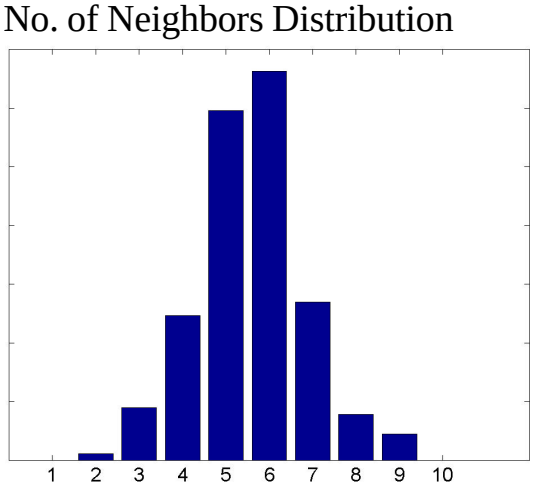

Multi Mode 3D Statistical Model

Dimensionality effects on the bubble merger:

Bubble merging in 3D conserves <u>area</u>, rather than length in 2D:

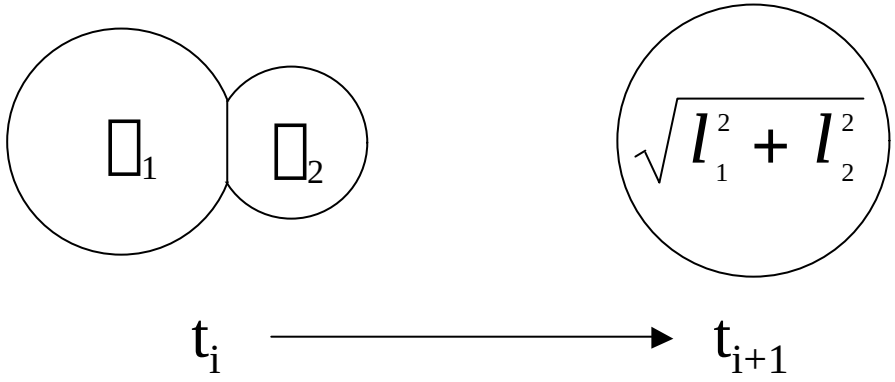

The merges occur with rate $\Gamma(\lambda_1, \lambda_2)$. At first step Γ^{3D} was taken to be equal to $\left(u_{3D}^{asy} / u_{2D}^{asy}\right) \times \Gamma^{2D}$

Because of the area conservation, a 3D bubble has to merge with more of its neighbors in order to reach the same l. This effect reduces dl/dt, which in turn reduces both a and q (and increases b).

Multi Mode 3D Statistical Model Results

The segment distribution g`(d) is obtained from the simulation:

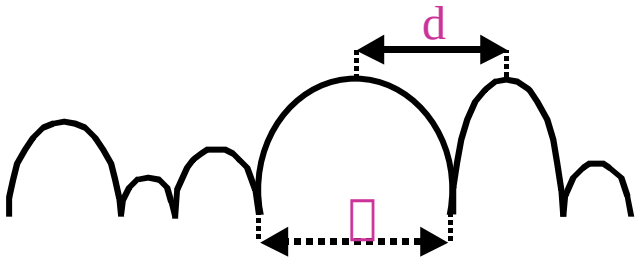

The relation between g`(d) and g(□) is given by:

$$g`(d) = 2\int_0^d g(2d - 2l)\,g(2l)\,dl$$

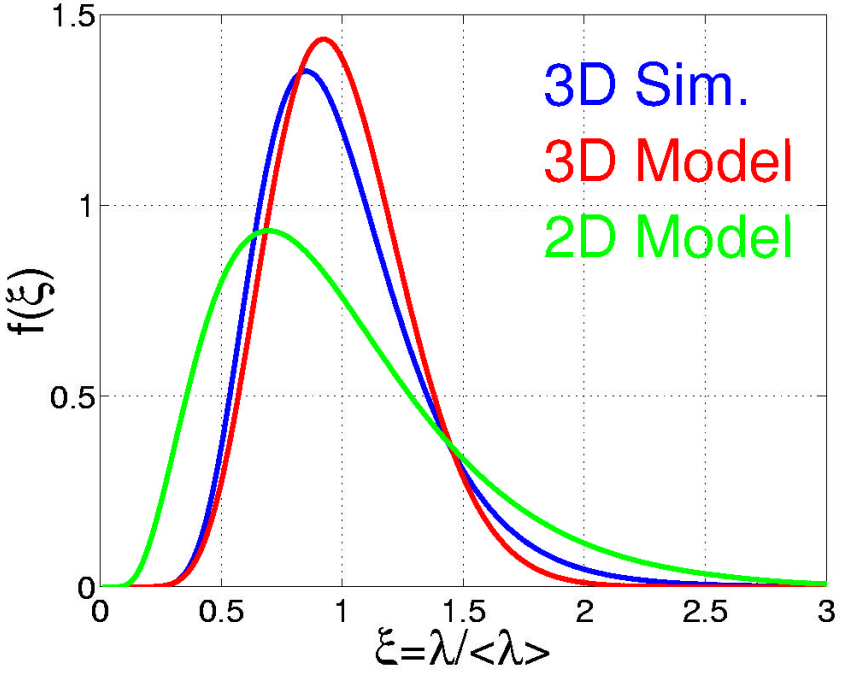

Multi Mode 3D Statistical Model Results

3D Statistical model results agree well with 3D Simulations.

$\Gamma_B = 0.055 \qquad \Gamma_B = 0.18 \qquad b = 0.67$

The 3D wavelength distribution is narrower than the 2D distribution. The narrowing of the Γ distribution is due to:

a) Reduction of $d\Gamma/dt$.

b) Increased number of neighbors.

Simulations results indicate that the 3D statistical model may be applicable to a wide range of A:

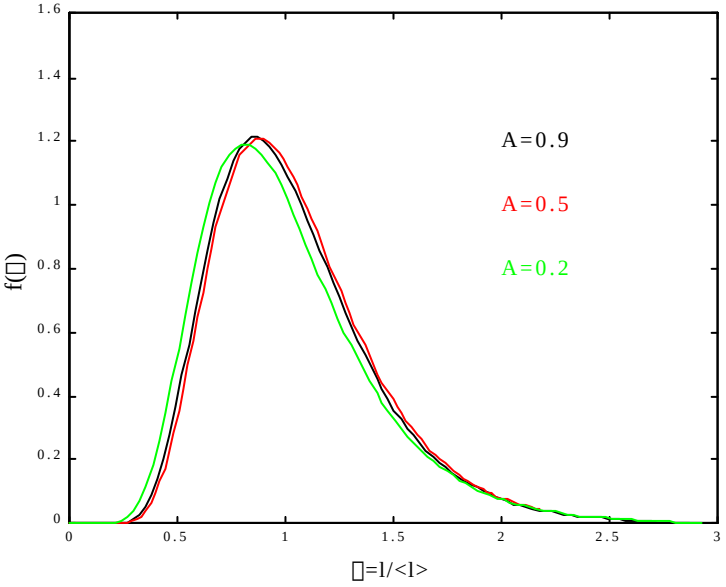

3D Statistical Model Dependence on Initial Distribution

Using the initial wavelength distribution derived from the voronoi diagram in the statistical model gives the dependence on the generation number:

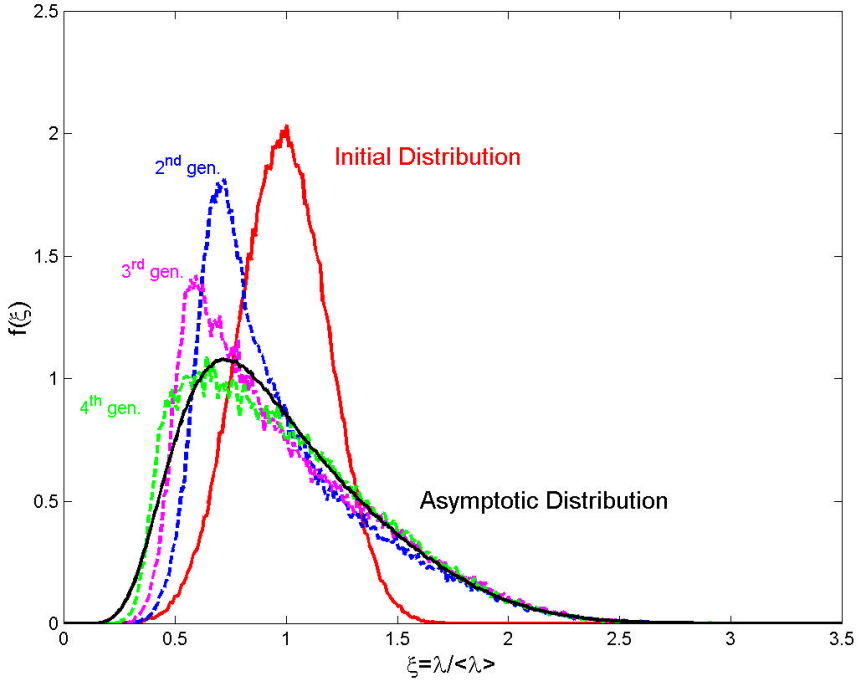

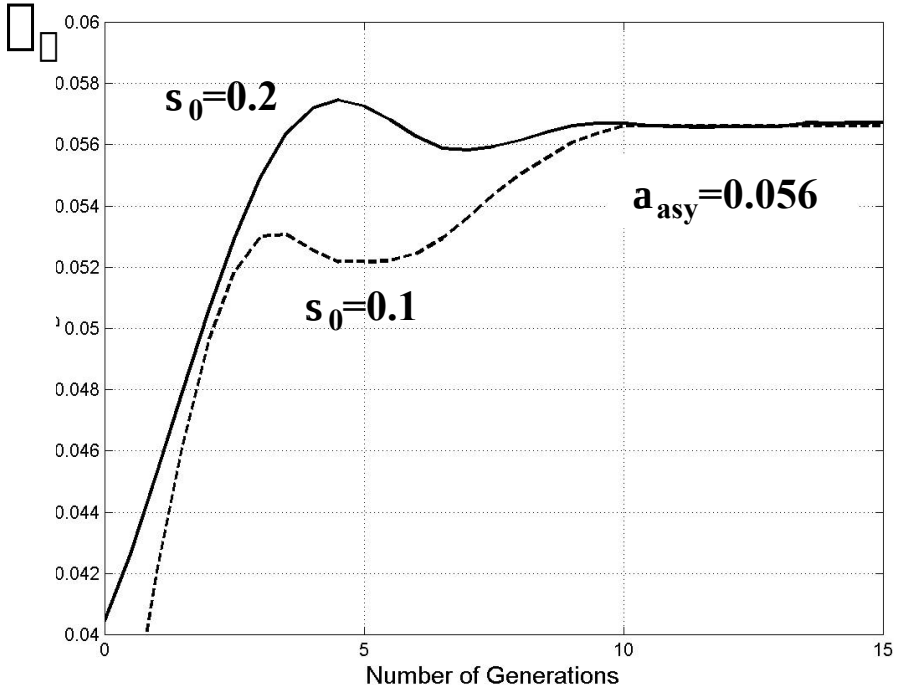

LEM Experimental Results Vs. 3D Models and Simulations

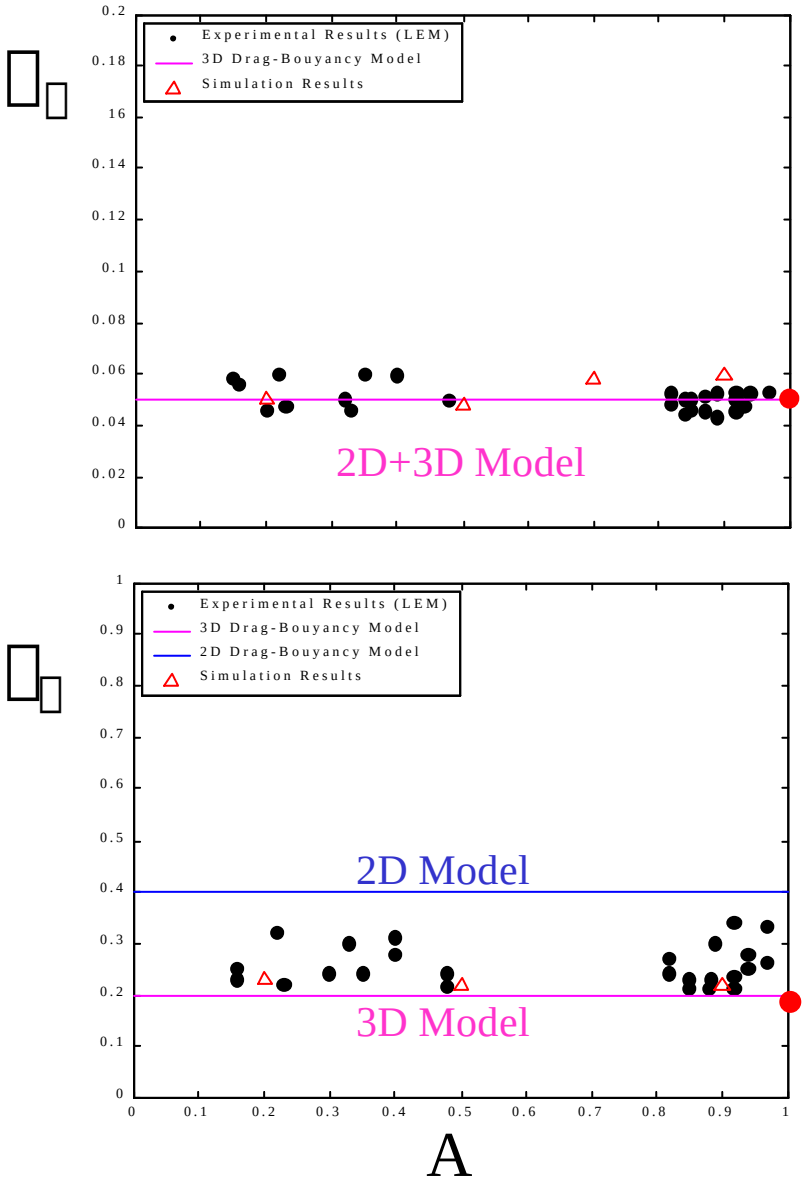

$h_{\square}/\langle\square\rangle$

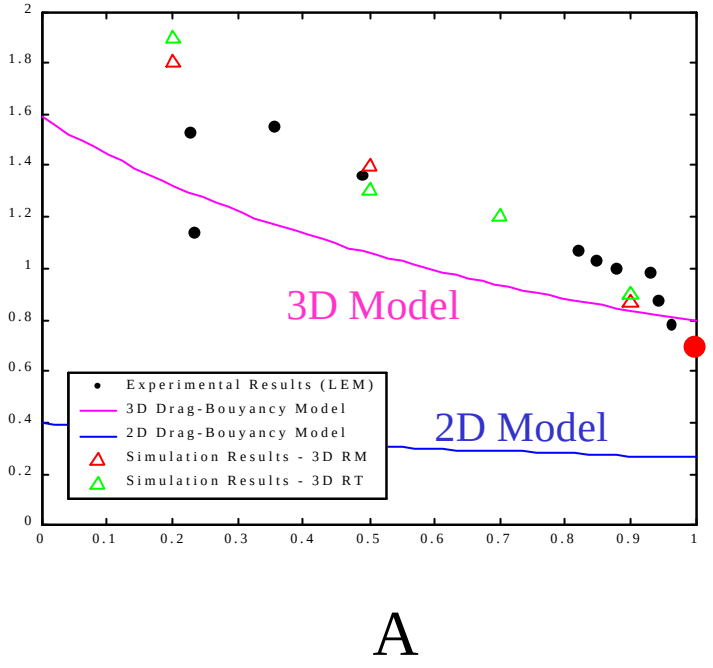

LEM Experimental Results Vs. 3D Simulations

Alpha - Spike

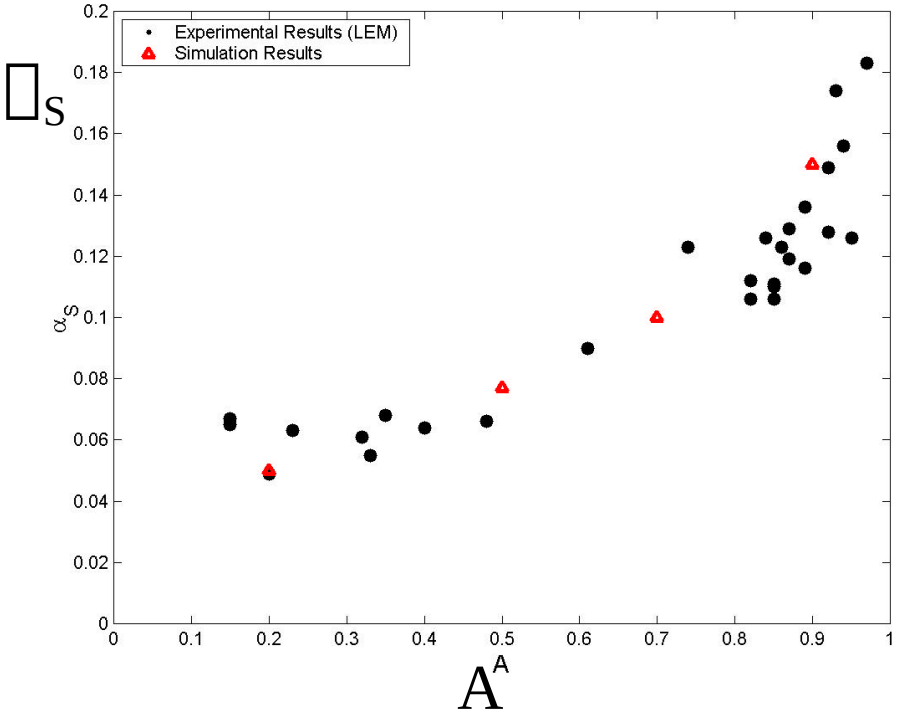

Theta - Spike

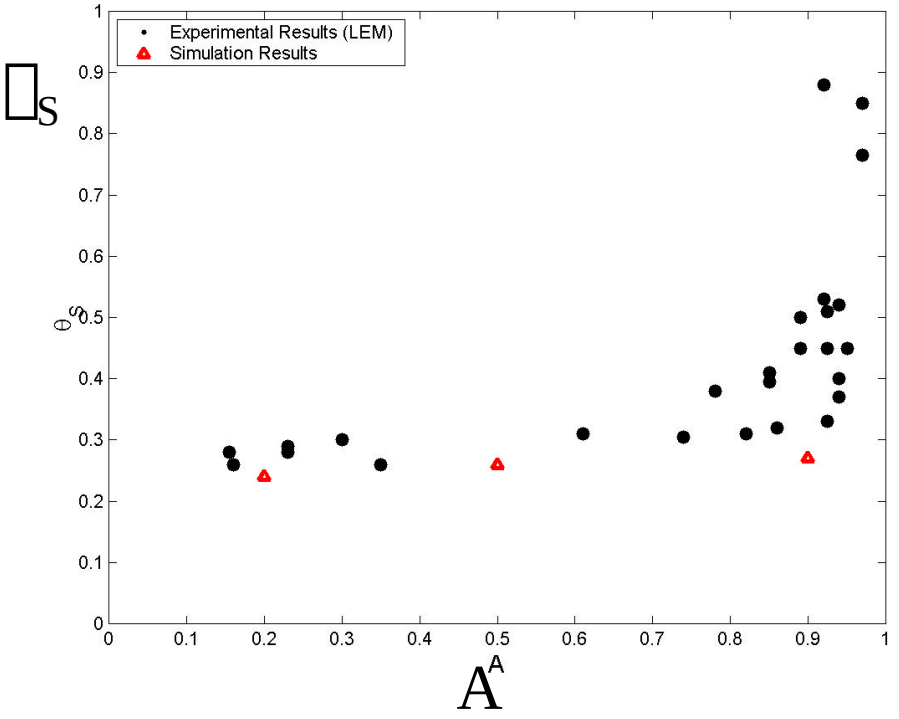

Sensitivity of q_S to percentage criterion

Alpha - Spike

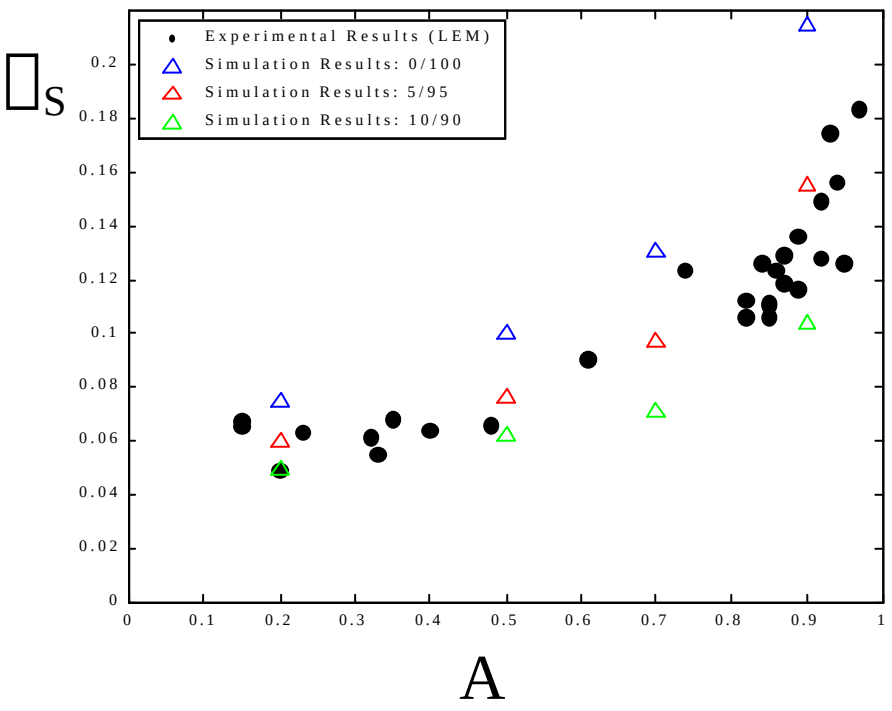

Theta - Spike

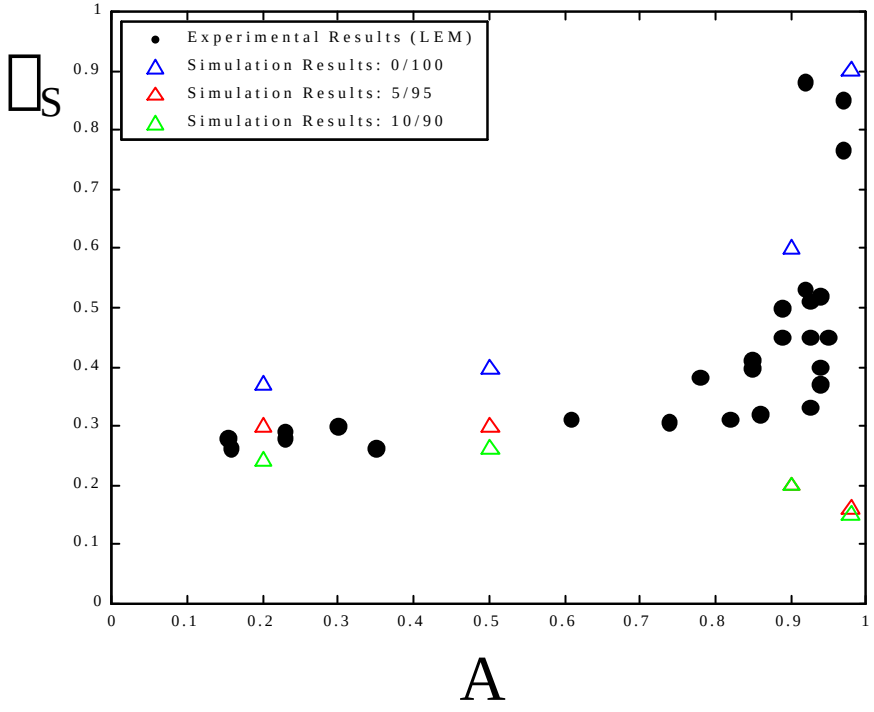

q_B is not sensitive to percentage criterion

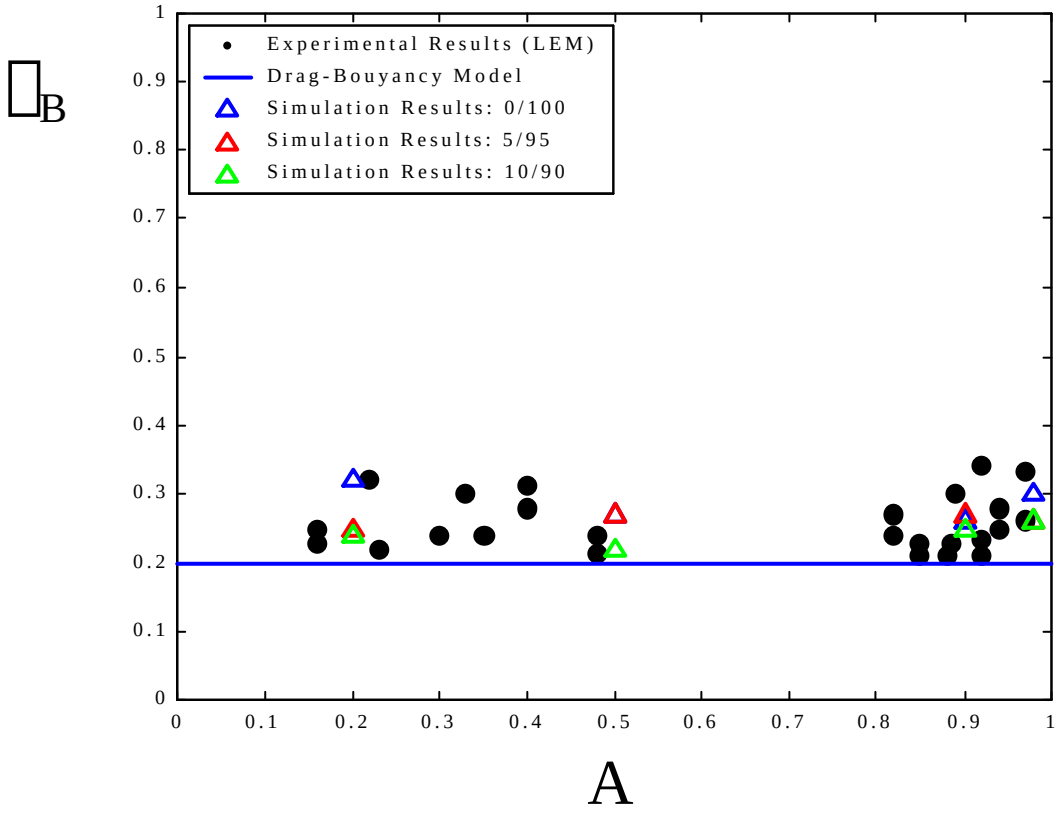

Outline

The Drag-Buoyancy Model for Bubbles

2D Statistical Model

Full 3D Numerical Simulations

3D Statistical Model

The Drag-Buoyancy Model for Spikes

Drag-Buoyancy Model for the Spike Front - I. Single Mode

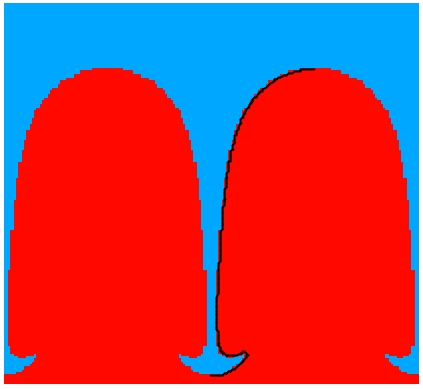

Since the spikes develop a rounded tip, one can apply the drag-buoyancy equation to them:

$$(\rho_h + C_a \rho_l)\dot{u}_S = (\rho_h - \rho_l) \times g - \frac{C_d}{\lambda} \rho_l \times u_S^2$$

The spikes velocity is obtained using the assumptions:

$$C_{dS}(A) = C_{dB}(A) = \begin{cases} 6 & 2D \\ 2 & 3D \end{cases}$$

$$C_{aS}(A) = C_{aB}(A) = \begin{cases} 2 & 2D \\ 1 & 3D \end{cases}$$

Drag-Buoyancy Model for the Spike Front - I. Single Mode Shock Tube Experimental Results

$$U_{asy} = C \times \sqrt{\frac{}{t}}$$

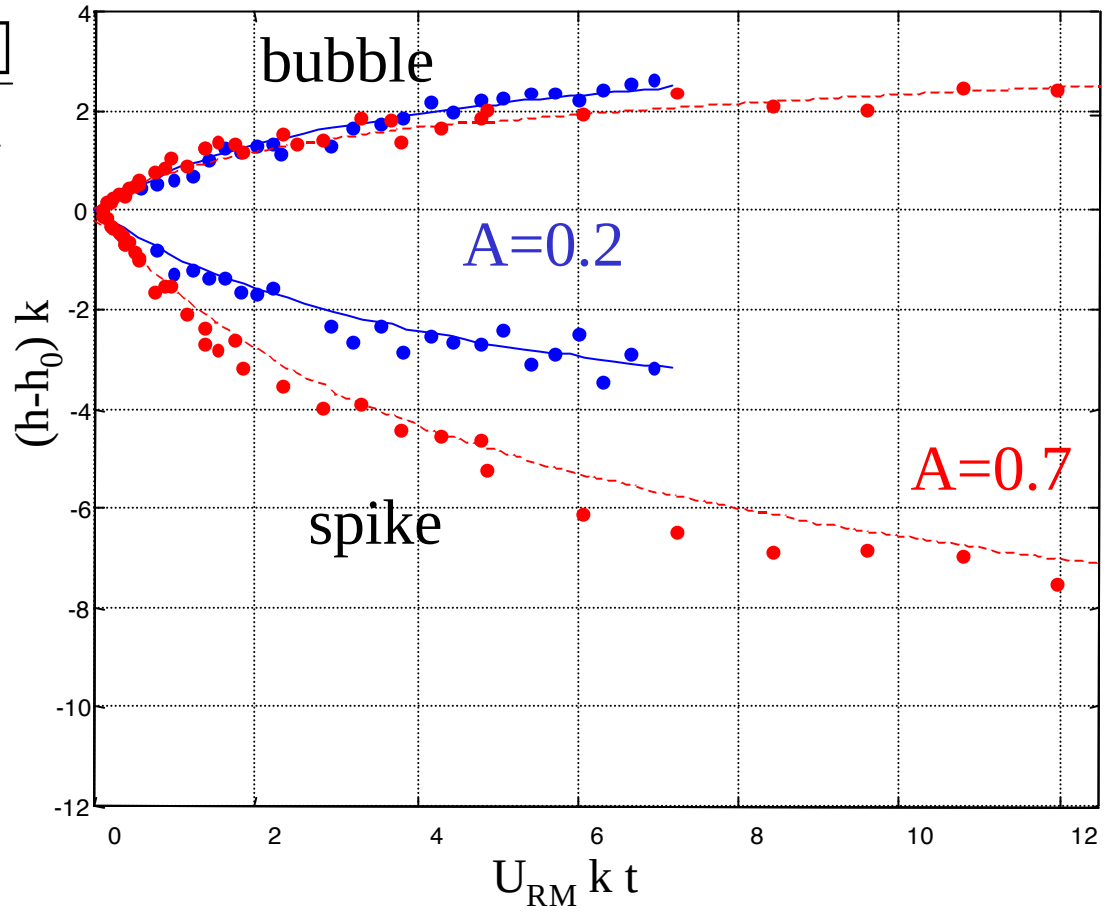

Drag-Buoyancy Model for the Spike Front - II. Multi Mode

1st assumption:

Periodicity of the spikes Periodicity of the bubbles

$\alpha_S(t) \quad \alpha_B(t)$

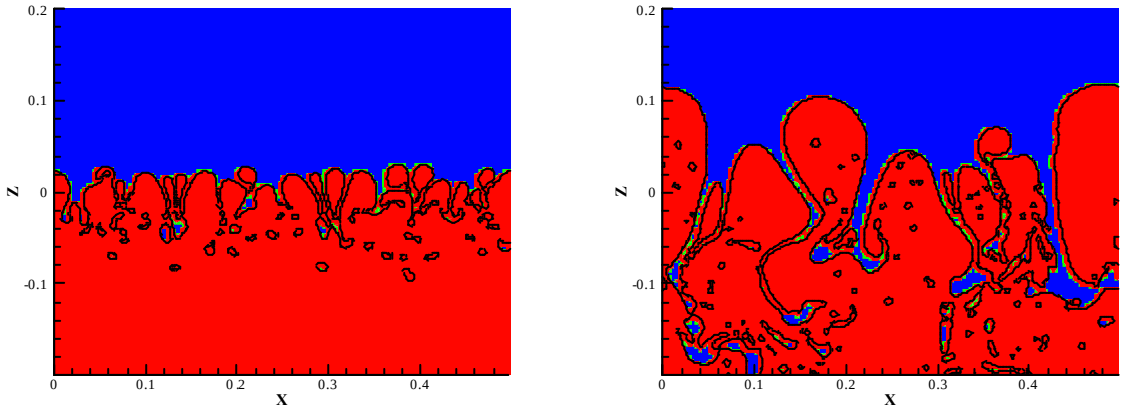

2D RT Simulation with A=0.9

Drag-Buoyancy Model for the Spike Front - II. Multi Mode - RT

Naïve approach:

The ratio between the momentary velocities of the spikes and the bubbles equals the ratio between their asymptotic velocities:

$$\frac{u_S(t)}{u_B(t)} = \frac{2\alpha_S Agt}{2\alpha_B Agt} = \frac{\alpha_S}{\alpha_B} = \frac{u_S^{asy}}{u_B^{asy}} = \sqrt{\frac{1+A}{1-A}} = \sqrt{\frac{\alpha_h}{\alpha_l}}$$

2nd assumption:

The ratio between the momentary velocities of the spikes and the bubbles equals the ratio between their velocities at the time t_b in which the bubbles height reaches its self-similar value: $h_B(t_b)=b\alpha$

$$\frac{u_S(t)}{u_B(t)} = \frac{2\alpha_S Agt}{2\alpha_B Agt} = \frac{\alpha_S}{\alpha_B} = \frac{u_S(t_b)}{u_B(t_b)} \equiv \frac{u_S(t_b)}{u_B^{asy}}$$

Drag-Buoyancy Model for the Spike Front - II. Multi Mode - RT Results

3D:

$$\frac{\alpha_S}{\alpha_B} = \sqrt{\frac{1+A}{1-A}} \times \tanh\left[\sqrt{\frac{1-A}{1+A}} \times \cosh^{-1} \times \exp\left(-b(1+A)\right)\right]$$

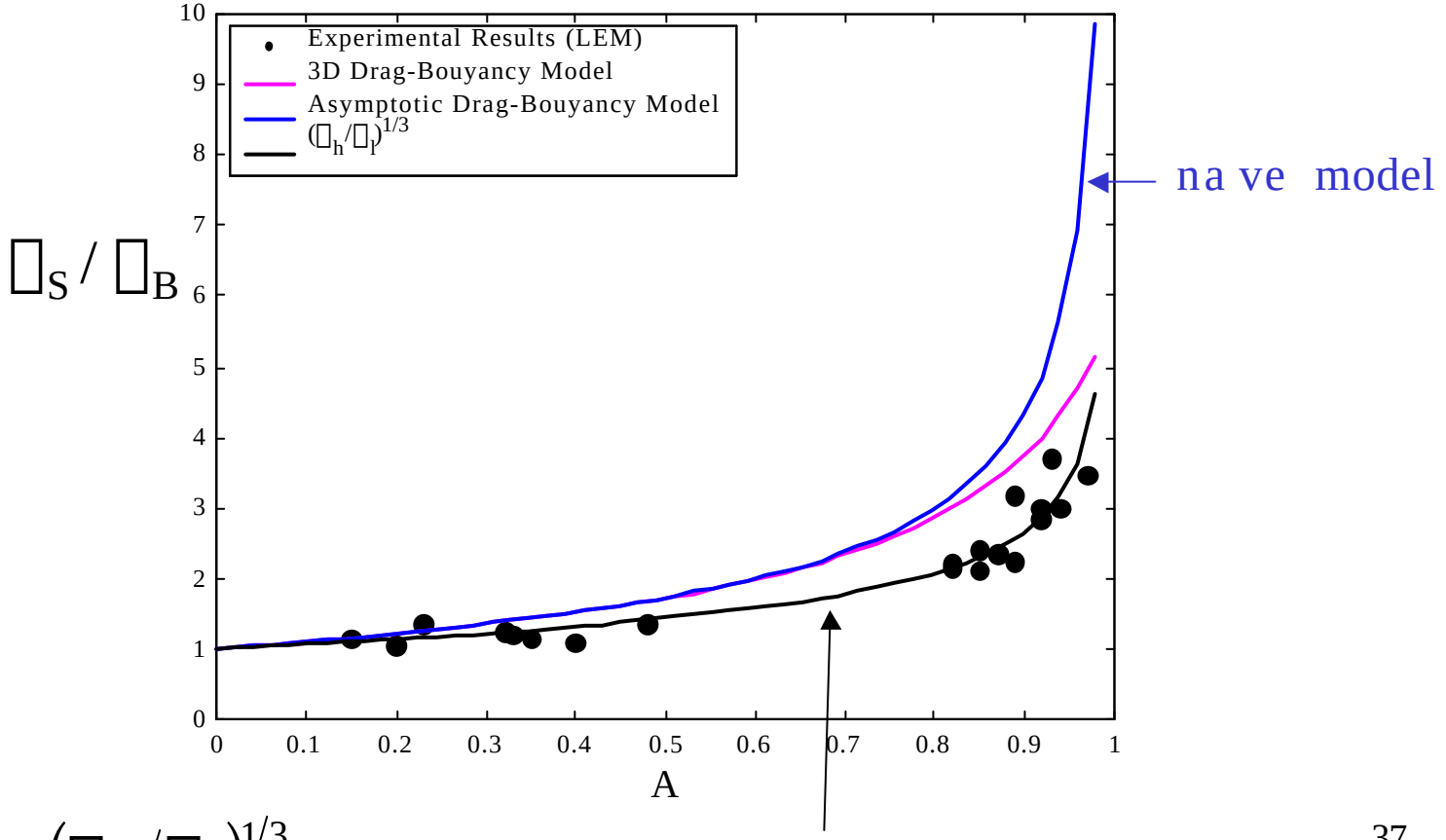

naïve model

$\alpha_S/\alpha_B \sim (\alpha_h/\alpha_l)^{1/3}$: Best fit by Dimonte et. Al.

Drag-Buoyancy Model for the Spike Front - II. Single Mode - RM

At late times, the bubble velocity in RM goes like α/t.

At finite time t its velocity can be expressed by a time-dependent coefficient $\alpha(t)$:

$$\frac{u_B(t)}{u_0} = \left(\frac{u_0 t}{\alpha}\right)^{\theta_B(t)} \qquad \theta_B(t \to \infty) = -1 \quad \textit{for all A s}$$

$$\frac{u_S(t)}{u_0} = \left(\frac{u_0 t}{\alpha}\right)^{\theta_S(t)} \qquad \theta_S(t \to \infty) = \begin{cases} -1 & A < 1 \\ 0 & A = 1 \end{cases}$$

Where, from assumption 1: $\langle \alpha(t) \rangle = \frac{h_B(t)}{b} \propto t^{\theta_B}$

Drag-Buoyancy Model for the Spike Front - II. Multi Mode - RM

$$\Rightarrow u_S^{MM} \propto t^{\theta_S(t_b)\times(1-\theta_B)} \qquad \textit{also:} \quad u_S^{MM}(t) = \frac{dh_S(t)}{dt} \propto t^{\theta_S - 1}$$

$$\boxed{\theta_S = 1 + \theta_S(t_b)\times(1-\theta_B)}$$

Naïve approach:

$$\theta_S^{asy} = \begin{cases} 0 & A = 1 \Rightarrow \theta_S = 1 \\ -1 & A < 1 \Rightarrow \theta_S = \theta_B \end{cases}$$

Drag-Buoyancy Model for the Spike Front - II. Multi Mode - RM Results

3D: $$\alpha_S = 1 + \alpha_S(t_b) \times (1 - \alpha_B) = 1 - \frac{\left(\frac{1-A}{1+A}\right) \div \times (\exp(-b(1+A)) - 1)}{1 + \left(\frac{1-A}{1+A}\right) \div \times (\exp(-b(1+A)) - 1)} \times (1 - \alpha_B)$$

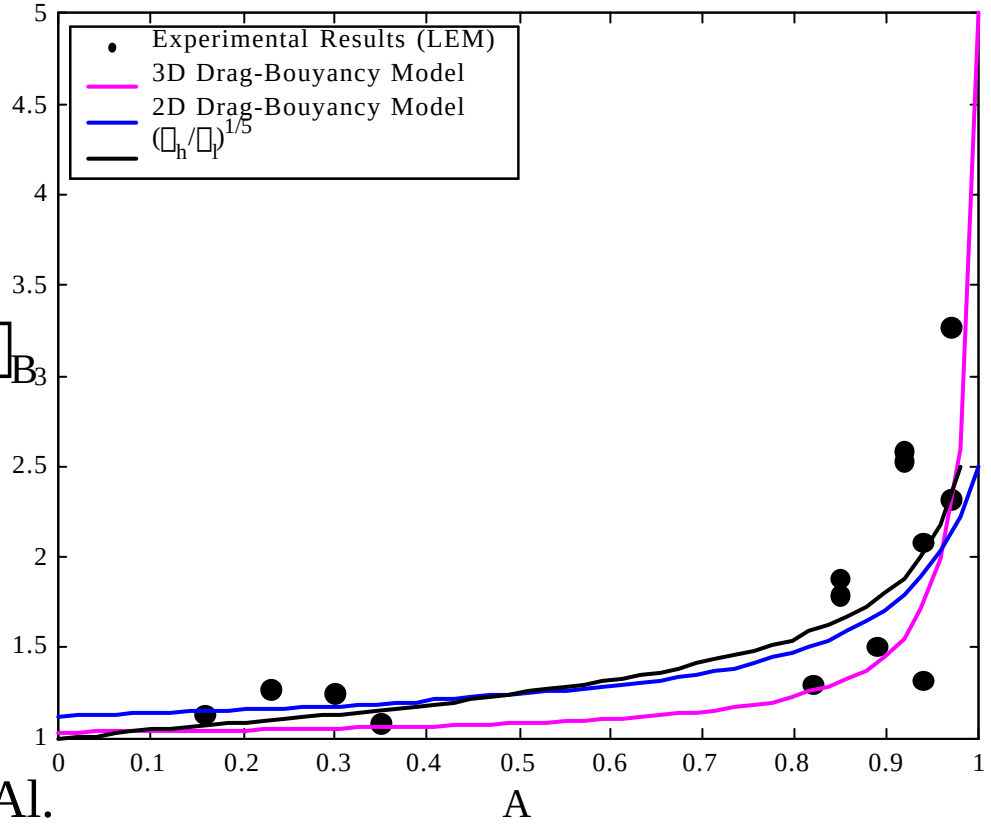

$$\alpha_S / \alpha_B \sim (\rho_h / \rho_l)^{1/5}$$

Best fit by Dimonte et. Al.

Summary

Good agreement between 3D drag-buoyancy model, statistical model, full 3D simulations and experimental results.

2D and 3D RT and RM scaling laws:

RT: $h_{B(S)} = \alpha_{B(S)} A g t^2$

RM: $h_{B(S)} = a_{B(S)} t^{\theta_{B(S)}}$

Geometrical effect results in different scaling parameters:

α_B	$\approx$ 0.05	in 2D and 3D
α_B	$\approx$ 0.2-0.3	in 3D
	Vs. 0.4	in 2D
b	$\approx$ 0.75-1.5	in 3D
	Vs. 0.25-0.5	in 2D

Spikes scaling laws are obtained from the drag-buoyancy model.

STABILITY 0F DIVERGING SHOCK WAVES

V.M.Ktitorov
Russian Federal Nuclear Center (VNIIEF), Sarov, RU

Introduction

The problem of a search for cases of unstable evolution of expanding shock waves with non-radial perturbations growing in amplitude was formulated long ago but there was no essential progress in this field until 1980-ths. The first proof of an existence of the unstable regime of perturbation evolution was published in the paper by E.Vishniac (Ref.1) where stability of point blast wave in an ideal gas with a specific heat ratio equal to unit ($\gamma=1$) was considered. In this case the gas behind the shock front is compressed into thin dense layer moving under influence of pressure of hot gas in the center region. The calculation of this layer movement can be done simply by application of conservation laws. This calculation was made in Ref. 1 for small blast wave perturbations those being expanded in spherical harmonics. Results of these calculations were as follows:

- small perturbation evolution had oscillating pattern,
-perturbations with big enough harmonic numbers were growing in amplitude with power dependence of time the power exponent being complex number,
- the discovered instability was Raleigh-Taylor type.

Later investigations revealed that all these features are characteristic for the perturbations evolution in the general case of an arbitrary value of γ.

V.Ktitorov[2] and E.Vishniac and D.Ryu[3] first published the solution of the point blast wave stability problem in the general case of an arbitrary $\gamma>1$. There was considered the point blast wave in a uniform gas with constant density. There were found values determining the perturbation evolution: the increment of perturbation growth, and the period of oscillations. These values were calculated for a large number of sets: harmonic number *n* and gas specific heat ratio γ.

The critical value of γ determining the blast wave stability was found too (Ref.2): $\gamma_c=1.20$. If γ were greater than this value the blast wave would be stable with respect to perturbations of all harmonic numbers; if $\gamma<1.20$, on the contrary, there would exist growing in amplitude harmonics.

Later there was found an experimental validation of these calculation results (Ref.4,5)[5].

This solution was obtained owing to using in Refs. 2,3 a self-similar approach for calculation of perturbation structure. The physical sense of this approach was in considering an asymptotically regime of perturbation evolution. This regime takes place when time of perturbation evolution is large enough to make the influence of initial conditions become negligibly small. The analogy could be made between the role of this solution in describing the perturbation evolution and the role of the well-known Taylor-Sedov solution Ref.6 in describing an evolution of spherically symmetric blasts.

Later on the number of systems with blast waves that were studied using the self-similar approach was extended; and the following cases were considered:

- Cylindrical blast wave (Ref.7),
- Isothermal blast wave (Ref.8),
- Blast wave in gas which has initial density depending on radius as power function (Ref.9),
- Blast wave in a non-ideal gas, which specific heat ratio γ is a function of gas density ρ (Ref.10).

In this paper we use the self-similar approach in order to consider the stability problem of these and some other systems in the unified manner.

1.STABILITY 0F A POINT BLAST WAVE IN AN IDEAL GAS

1.1 Formulating the stability problem

Let us consider a spherical *(s=3)* or cylindrical (*s=2*) blast wave in an ideal gas in the case when the initial gas density ρ_0 is a power function of radius *r*: $r_0 \sim r^k$. According to[2] we shall write the hydrodynamic system of equations in the Lagrangian form.

The following notation is used below:

$\bar{R}$ - the Eulerian co-ordinates

$\bar{r}$ - the Lagrangian co-ordinates (the initial co-ordinates before shock front are taken as the Lagrangian co-ordinates),

$\frac{d^3(\bar{R})}{d^3(\bar{r})} \equiv \frac{D(R^3, \cos\Theta, \Phi)}{D(r^3, \cos\theta, \varphi)}$ - the Jacobian of the transformation from the Lagrangian to the Eulerian co-ordinates,

P - pressure, *r* - density, r_0 - the initial density $(r_0 \sim r^k)$,

We start considering the stability problem from writing 3D hydrodynamic equations in the Lagrangian form: (here time derivative is to be understood in the Lagrangian sense - it is the derivative along the flow line). The first two equations are obvious:

$$\frac{\partial}{\partial t}\left(\frac{P}{\rho^\gamma}\right) = 0, \tag{1}$$

$$\frac{\rho_0}{\rho} = \frac{d^3(\bar{R})}{d^3(\bar{r})} \tag{2}$$

The equation of motion (the third equation) can be deduced from its Eulerian form (for the sake of simplicity we use here Cartesian coordinates $\bar{R} = (X_1, X_2, X_3)$ and $\bar{r} = (x_1, x_2, x_3)$):

$$\frac{\partial^2 X_k}{\partial t^2} = -\frac{\partial P}{\rho \partial X_k} \tag{3}$$

We change the arguments in the equation of motion written in the Eulerian form using formula:

$$\frac{\partial}{\partial x_i} = \sum_k \frac{\partial X_k}{\partial x_i} \frac{\partial}{\partial X_k} \tag{4}$$

And we get finally:

$$\frac{\partial P}{\rho \partial x_i} = -\sum_k \frac{\partial X_k}{\partial x_i} \frac{\partial^2 X_k}{\partial t^2} \tag{5}$$

For the non-perturbed blast wave the system of equation (1),(2),(5) looks as follows:

$$\frac{\partial}{\partial t}\left(\frac{P}{\rho^\gamma}\right) = 0, \tag{6}$$

$$\frac{\rho_0(r)}{\rho} = \frac{R^{s-1}\partial R}{r^{s-1}\partial r} \tag{7}$$

$$\frac{\partial P}{\rho \partial r} = -\frac{\partial R}{\partial r}\frac{\partial^2 R}{\partial t^2} \tag{8}$$

The corresponding spherically (or cylindrically) symmetric self-similar solution of Eqs. (6-8) is well known. It can be written using the shock wave radius value $S(t) \sim t^{2/(k+s+2)}$ and functions *x(z), p(z), r(z)* of the self-similar argument *z=r/S,*:

$$R_0(t,r) = Sx(z),$$
$$P_0\ (t,r) = \frac{2}{\gamma+1}\rho^0(S)\dot{S}^2 p(z),$$
$$\rho_0(t,r) = \frac{\gamma+1}{\gamma-1}\rho^0(S)\rho(z), \qquad (9)$$
$$\Theta_0 = \theta,$$
$$\Phi_0 = \varphi$$

where *x, P, r* should satisfy to ordinary differential equations:

$$\rho = \frac{\gamma-1}{\gamma+1}\frac{z^{s+k}}{x^s w},$$
$$p = \frac{\rho^\gamma}{x^s z^s}, \qquad (10)$$
$$\frac{p'}{p} = -\gamma\frac{ab}{w};$$

With boundary conditions: *x(1)=p(1)=r(1)=1,*

Here we denote:

$$w = \frac{zdx}{xdz} = \frac{x'z}{z},$$
$$a = w'z + (w-1)(w + \frac{s+k}{2}), \qquad (11)$$
$$b = \frac{\gamma+1}{2\gamma}\frac{wz^{s+k}}{px};$$

We insert to the system of equations (1),(2),(5) hydrodynamic values corresponding to the perturbed blast wave ($\widetilde{\overline{R}}, \widetilde{P}, \widetilde{\rho}$) presented as sums of the non-perturbed blast wave values ($\overline{R}, P, \rho$), and small perturbations ($\overline{R}_1, P_1, \rho_1$):

$$\widetilde{\overline{R}}(t,\bar{r}) = R(t,r) + R_1(t,\bar{r}),$$
$$\widetilde{\Theta}(t,\bar{r}) = \theta + \Theta_1(t,\bar{r}),$$
$$\widetilde{\Phi}(t,\bar{r}) = \varphi + \Phi_1(t,\bar{r}), \qquad (12)$$
$$\widetilde{P}(t,\bar{r}) = P(t,r) + P_1(t,\bar{r}),$$
$$\widetilde{\rho}(t,\bar{r}) = \rho(t,r) + \rho_1(t,\bar{r}).$$

Also we suppose that an angular motion is the potential one:

$$\Theta_1 = \frac{\partial F_1}{\partial\cos\theta}, \Phi_1 = \frac{\partial F_1}{\partial\varphi}, \qquad (13)$$

and that supposition will make the Jacobian being equal to:

$$\frac{d^3(\overline{R}+\overline{R}_1)}{d^3\bar{r}} = \frac{R^2\partial R}{r^2\partial r}(1+\Delta_{\theta\varphi}F_1) + \frac{\partial R^2 R_1}{r^2\partial r} \qquad (14)$$

We insert expressions (12,13) to the system of equations Eqs.(1,2,5), and after finishing linearization procedure we get the following equations for perturbations:

Equation of entropy conservation:

$$\frac{\partial}{\partial t}(\frac{P_1}{P} - \gamma\frac{\rho_1}{\rho}) = 0 \qquad (15)$$

Continuity equation:

$$\frac{\rho_1}{\rho} + \Delta_{\theta\varphi} F_1 + \frac{\dfrac{\partial (R^{s-1} R_1)}{r^{s-1} \partial r}}{\dfrac{R^{s-1} \partial R}{r^{s-1} \partial r}} = 0 \qquad (16)$$

Angular component of the equation of motion (here we denote: $\dot{R} \equiv \frac{\partial R}{\partial t}$):

$$\frac{P_1}{\rho} + R_1 \ddot{R} + (R^2 \dot{F}_1^{\cdot}) = 0 \qquad (17)$$

Radial component of the equation of motion:

$$\frac{\partial P_1}{\rho \partial r} + \ddot{R} \frac{\partial R_1}{\partial r} + \ddot{R}_1 \frac{\partial R}{\partial r} - \frac{\rho_1 \partial P}{\rho^2 \partial r} = 0 \qquad (18)$$

Here and after S stands for the non-perturbed shock front radius, $S(t) \sim t^{2/(k+s+2)}$, and S_1 stands for the value of the shock front radius perturbation.

Boundary conditions for the system of equations Eqs.(15-18) should be put on the shock front ($r=S+S_1$) using the following scheme:

$$\begin{aligned}
&(R + R_1)(r = S + S_1, t) = S + S_1 \\
&(R + R_1)(r = S + S_1, t) = R(r = S + S_1, t) + R_1(r = S + S_1, t) \\
&R(r = S + S_1, t) = R(r = S, t) + S_1 \frac{\partial R}{\partial r}(r = S, t) = S + S_1 \cdot \frac{wx}{z}(z = 1) \\
&R_1(r = S + S_1, t) = R_1(r = S, t)
\end{aligned} \qquad (19)$$

From Eqs.(10,11) we have:

$$w(1) = \frac{\gamma - 1}{\gamma + 1}, x(1) = 1. \qquad (20)$$

Hence we get:

$$R_1(r = S, t) = \frac{2}{\gamma + 1} S_1 \qquad (21)$$

The next front conditions are calculated in the same way. We get:

$$\begin{aligned}
&F_1(r = S, t) = 0 \\
&\dot{F}_1(r = S, t) = -\frac{2}{\gamma + 1} \frac{\dot{S}}{S^2} S_1 \\
&P_1(r = S, t) = \frac{2\rho_0}{\gamma + 1} \frac{\dot{S}^2}{S} S_1 (2\lambda + s + 2 + a(1)) \\
&\rho(r = S, t) = \frac{(\gamma + 1)\rho_0}{\gamma + 1} \frac{S_1}{S} a(1)
\end{aligned} \qquad (22)$$

According to Ref. 2 the perturbations are expanded in spherical harmonics $Y_{nm} \sim P_{nm}(\cos\theta) e^{im\varphi}$ (or in axial harmonics $e^{in\varphi}$ in the cylindrical case), and the components of expansion are presented in the self-similar form.

Shock wave radius perturbations are expanded too: ($S_1 = \sum S_{1mn} Y_{mn}$). We suppose that the components of expansion are power functions of time for each harmonic number:

$$S_{1mn} \sim S^{\lambda_{mn}+1} \sim t^{\frac{2(\lambda_{mn}+1)}{k+s+2}}, \qquad (23)$$

Here λ_{mn} is a complex number.

So we write:

$$\widetilde{R}(t,\bar{r}) = R(t,r) + \frac{2}{\gamma+1}\sum_{nm} S_{1nm}(t)x(z)x_{1nm}(z)z^{\lambda_{nm}}Y_{nm}(\theta,\varphi),$$

$$\widetilde{P}(t,\bar{r}) = P(t,r) + \frac{2}{\gamma+1}\rho_0(r)\frac{\dot{S}^2(t)}{S}\sum_{nm} S_{1nm}(t)p_{1nm}(z)z^{\lambda_{nm}+S+k}Y_{nm}(\theta,\varphi),$$

$$\widetilde{\rho}(t,\bar{r}) = \rho(t,r) + \frac{\gamma+1}{\gamma-1}\rho_0(r)\frac{1}{S}\sum_{nm} S_{1nm}(t)\rho_{1nm}(z)z^{\lambda_{nm}}Y_{nm}(\theta,\varphi), \qquad (24)$$

$$\Theta(t,\bar{r}) = \theta + \frac{2}{\gamma+1}\frac{1}{S}\sum_{nm} S_{1nm}(t)f_{1nm}(z)z^{\lambda_{nm}}\frac{\partial Y(\theta,\varphi)}{\partial\cos\theta},$$

$$\Phi(t,\bar{r}) = \varphi + \frac{2}{\gamma+1}\frac{1}{S}\sum_{nm} S_{1nm}(t)f_{1nm}(z)z^{\lambda_{nm}}\frac{\partial Y(\theta,\varphi)}{\partial\varphi};$$

1.2 Formulating an eigenvalue problem.

At first, using boundary conditions we integrate adiabatic equation (15) . We get (here and after we omit indices *n,m* of p_1, r_1, x_1, f_1, l, S_1):

$$\frac{P_1}{P} - \gamma\frac{\rho_1}{\rho} = (2\lambda+s+2)z^{\lambda}\frac{S_1}{S} \qquad (25)$$

After that using the assumption of the self-similarity (24) we convert the system of equations (16), (17), (18), (25) into the system of ordinary differential equations. We write it having excluded ρ_1 :

$$bp_1 + (\frac{zd}{dz} + \lambda + sw)x_1 - n(n+s-1)wf_1 = \frac{\gamma+1}{2\gamma}(2\lambda+s+k+2)w, \qquad (26)$$

$$wp_1 + ax_1 - (\frac{zd}{dz} + 2w + \frac{s+k-2}{2})\frac{zd}{dz}f_1 = 0, \qquad (27)$$

$$[\frac{zd}{dz} + \lambda + s + k - (s+k-2)w]p_1 + \left[(\frac{zd}{dz} + 2w + \frac{s+k-2}{2})\frac{zd}{dz} - (s+k-2)a\right]x_1 + \qquad 28)$$

$$+ n(n+s-1)af_1 = 0;$$

With boundary conditions as follows:

- On the right edge *z=1* (shock front):

$$f_1(1) = 0,$$

$$f_1'(1) = 1,$$

$$x_1(1) = 1, \qquad (29)$$

$$p_1(1) = 2\lambda + \frac{6\gamma+2-s(3\gamma-1)+k(\gamma+1)}{(\gamma+1)^2};$$

- On the left edge *z=0* (at the center):

$$p_1(1)=0; \qquad (30)$$

The system of equations Eqs.(26-28) is of the forth order one, so four edge conditions Eqs.(29) construct the complete set of boundary conditions necessary for solution. The fifth edge condition Eq.(30) at *z=0* converts the problem of solving the Eqs.(26-29) to an eigenvalue problem. Solving this problem includes calculation of the complex exponent λ as eigenvalue. Coefficients in (26)-(30) are independent of index *m*, so $\lambda \equiv \lambda(n)$.

1.3 Numerical solution results

In general the case $\gamma > 1$ the eigenvalue problem Eqs.(26-30) was solved numerically. The values of the complex exponents λ_n were calculated in the wide region of γ , and *n* for spherical

(*s=3*) and cylindrical (*s=2*) blast waves. The values of *k* were *k=0,-1,-2*. The results are presented on Figs.1,2.

The instability region on the plane n - γ is shown on Fig.3. Blast wave is unstable in the right lower corner of the chart. If the function $\gamma_0(n)$ corresponds to the boundary line of the instability region then the critical value of specific ratio γ_c can be defined:

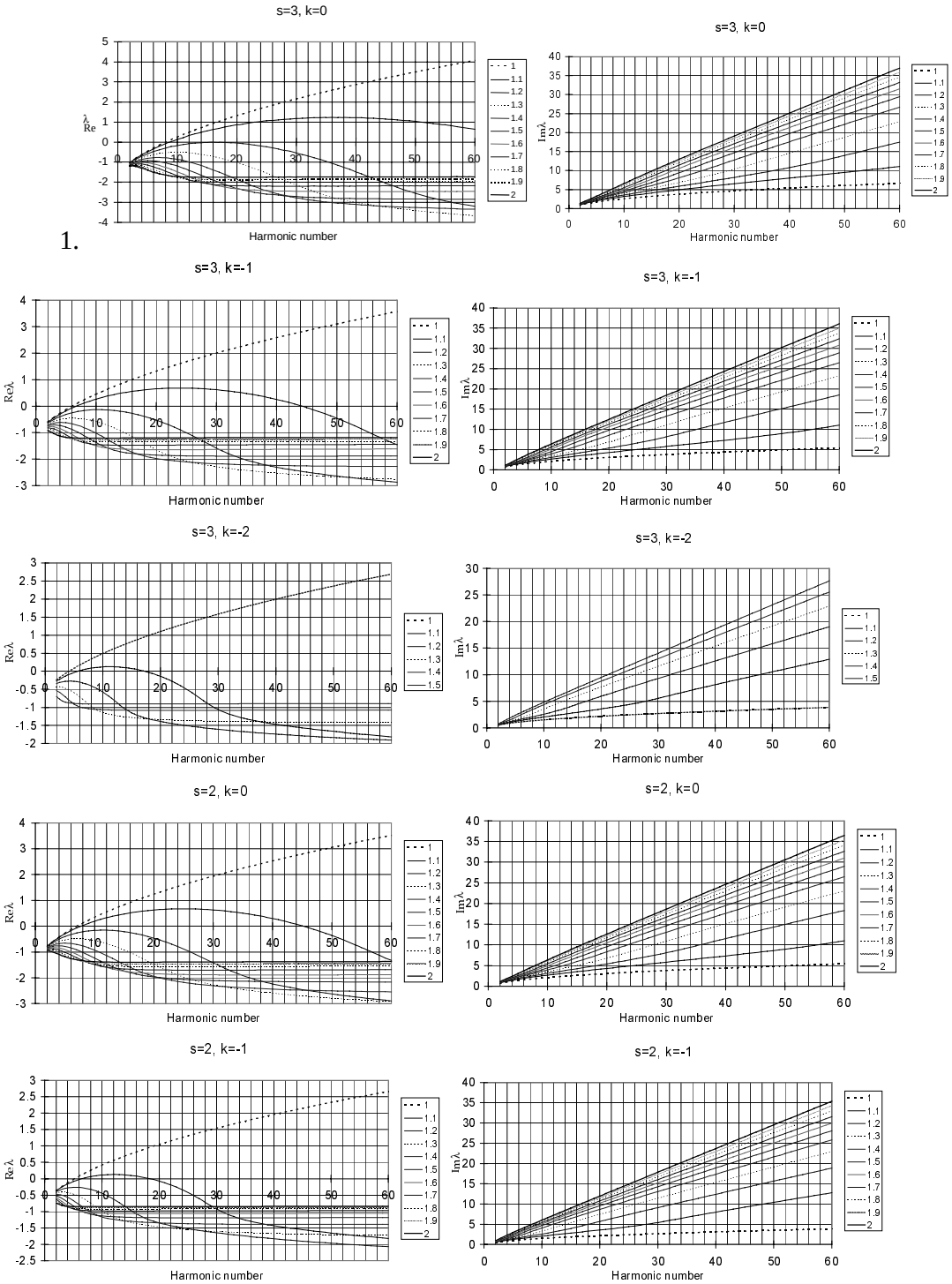

Fig.1 Values of complex exponent λ in the cases of spherical *(s=3)* and cylindrical *(s=2)* blast wave in a gas which initial density ρ_0 is power function of radius: $\rho_0 \sim r^k$ for a number of values of gas specific ratio γ. For the case γ=1 values are calculated using analytic expressions Eq.(36).

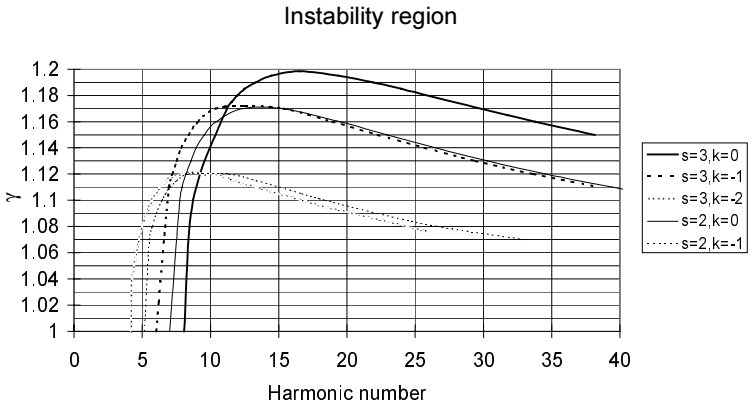

Fig.2 Instability region on the plane n-γ

1.4 Analytical solution results

Let us consider some cases when eigenvalue problem has an analytical solution .

1.4.1 Thin shell approximation: $\gamma - 1 \ll 1$

The problem has an analytic solution in the case when the value of g is close to unit. In this case we let in the equations (26)-(30): $\gamma = 1$, $w = 0$, $a=-(s+k)/2$, $b=0$.

We get:

$$(\frac{zd}{dz} + \lambda)x_1 = 0, \tag{31}$$

$$-\frac{s+k}{2}x_1 + (\frac{zd}{dz} + \frac{s+k-2}{2})\frac{zd}{dz} f_1 = 0, \tag{32}$$

$$(\frac{zd}{dz} + \lambda + s + k)\, p_1 + ((\frac{zd}{dz} + \frac{s+k-2}{2})\frac{zd}{dz} + (s+k-2)\frac{s+k}{2})x_1 - \\ - n(n+s-1)\frac{s+k}{2} f_1 = 0 \tag{33}$$

with boundary conditions:

$$f_1(1) = 0,$$
$$f_1'(1) = 1,$$
$$x_1(1) = 1, \tag{34}$$
$$p_1(1) = 2\lambda + \frac{4-s+k}{2},$$
$$(p_1 z^{s+k})(z \to 0) = 0$$

Solution of (31)-(34) is as follows:

$$x_1 = z^{-\lambda},$$

$$f_1 = \frac{s+k}{2\lambda(\lambda - \frac{s+k-2}{2})} z^{-\lambda} - \frac{2}{s=k-2}\frac{\lambda+1}{\lambda - \frac{s+k-2}{2}} z^{-\frac{s+k-2}{2}} + \frac{2}{s=k-2}\frac{\lambda + \frac{s+k}{2}}{\lambda},$$

$$p_1 = [\frac{\lambda(\lambda - \frac{s+k-2}{2}) - \frac{(s+k-2)(s+k)}{2}}{s+k} + \frac{n(n+s-1)(s+k)}{2\lambda(\lambda - \frac{s+k-2}{2})}]z^{-\lambda} - \quad (35)$$

$$- \frac{(s+k)(\lambda+1)n(n+s-1)}{(\lambda - \frac{s+k-2}{2})(\lambda + \frac{s+k+2}{2})} z^{-\frac{s+k-2}{2}} + \frac{(s+k)(\lambda + \frac{s+k}{2})n(n+s-1)}{\lambda(\lambda - +s+k)},$$

-and after simple calculations we get the equation for λ (note that it is possible to get this equation in a simpler way applying conservation laws for calculating thin layer motion[1]):

$$(\lambda+s+k)^2(\lambda + \frac{s+k+2}{2})^2 - \frac{s(s+k)}{2}(\lambda+s+k)(\lambda + \frac{s+k+2}{2}) + \quad (36)$$

$$+ n(n+s-1)\frac{(s+k)^2}{4} = 0;$$

One of two pairs of the complexly conjugated roots of this equation with the greater real part is the solution of the problem in the case *n>1*.

In the case *n=1* the equation (34) has four real negative roots. The two of them satisfying boundary condition at the center are solutions:

One of these solutions is determined with formula:

$$\lambda = -\frac{s+k}{2}, \quad (37)$$

this case corresponds to explosion direct motion with momentum conservation. This value of l can be calculated from dimension consideration.

The other is the greater root of equation:

$$\lambda^2 + \lambda\frac{3s+3k+2}{2} + \frac{(s+k)(k+3)}{2} = 0 \quad (38)$$

it is equal to *-1 if k=0*; this case corresponds to the blast being displaced.

.We can continue analytical calculations if we take into account next terms of expansion of solution of eigenvalue problem (26)-(30) by powers of the small parameter *(g-1)*:

$\lambda=\lambda^{(0)}+(\gamma-1)\,\lambda^{(1)}$, (39)

where $\lambda^{(0)}$ is determined by (36)

In this case we get for the first approximation terms the equation system with constant coefficients analogous to (31) but with non-uniform equations. The right parts of these equations are of the first order of smallness. This equation system is integrated quite similar to that was done for (31,32), and (omitting cumbersome transformations) we arrive to the following formula[2,7] for the first order correction of *l* (to avoid bulky expressions here we present only the special case *s=3, k=0)* ; here *b(a)* stands for integral $\beta(\alpha) = \int_0^1 \frac{t^\alpha dt}{1+t}$, and *l* is from (36)):

$$\lambda^{(1)} = \frac{1}{3}\frac{(\lambda+1)(\lambda+\frac{3}{2})(\lambda+\frac{5}{2})(\lambda+3)(\lambda+4)}{(\lambda+\frac{11}{4})(\lambda^2+\frac{11}{2}\lambda+\frac{21}{4})}\{(1-2\ln 2\frac{(\lambda+\frac{3}{2})(\lambda+\frac{5}{2})}{\lambda(\lambda-\frac{1}{2})}- \\ -\frac{4}{3}(\lambda+\frac{5}{2})[\frac{(\lambda^2+6\lambda+\frac{9}{2})}{\lambda}\beta(\frac{\lambda+3}{3})-\frac{(\lambda^2+\frac{11}{2}\lambda+3)}{\lambda-\frac{1}{2}}\beta(\frac{\lambda+\frac{5}{2}}{3})]\} \quad (40)$$

The results of (39),(40) are in a good agreement with the results of numerical calculation for the imaginary parts of l and in the worse one for the real parts. For example, in the case: *s=3, k=0, n=8, γ=1.2,* we have[2]: $\lambda_{analyt} = 0.15 + 3.14i$, and $\lambda_{numer} = -0.30 + 3.07i$.

1.4.2 The first harmonic: *n=1*

Note that both solutions (35,38): λ = *-1*, and $\lambda = -(s+k)/2$, are independent of γ, and they are solutions of eigenvalue problem (26)-(30) in the general case of an arbitrary *γ>1:*

1) The displacement solution. λ=-1

We can verify it by a direct substitution of the following expressions to the system of equations (26)-(28):

$$n = 1, k = 0, \lambda = -1,$$

$$f_1 = \frac{\gamma+1}{2}(\frac{z}{x}-1)$$

$$x_1 = \frac{\gamma+1}{2}(\frac{z}{x}-w) \quad (42)$$

$$p_1 = \frac{\gamma+1}{2}a$$

So λ=*-1* is the correct solution for the case: *n=1, k=0*

2) $n = 1, \lambda = -\frac{s+k}{2}$,

We subtract equation (27) from equation (28) multiplied by *(s-1),* and integrate the result. Then we get:

$$p_1 + (\frac{zd}{dz} + w + \frac{s+k}{2})x_1 + (\frac{zd}{dz} + w + \frac{s+k}{2})f_1 = 0 \quad (41)$$

This equation together with Eqs.(25,27) forms equation system. It can easily be shown that all solutions of this system have the required convergence at the center independently of shock front boundary conditions. So $\lambda = -\frac{s+k}{2}$, is the correct solution of the eigenvalue problem for *n=1*.

1.4.3 Investigation of the features of the solution in the limit *n*→∞.

The next case of analytical approach to solving the eigenvalue problem is a short wavelength approximation: *n>>1*. In this case we seek for the solution, which looks like:

$\exp(\int\frac{q(z)dz}{z})$, where $|q| \sim |l| \sim n >> 1$. (43)

We substitute so defined values to Eqs. (26-28), remove all terms of the lowest order, and get the following equation system:

$$bp_1 + (q+\lambda)x_1 - n^2 w f_1 = \frac{\gamma+1}{\gamma}\lambda w,$$
$$wp_1 + q^2 f_1 = 0, \qquad (44)$$
$$(q+\lambda)p_1 + q^2 x_1 = 0,$$

and boundary conditions:

$$x_1(z=1) = 1,$$
$$f_1(z=1) = 0,$$
$$\frac{zd}{dz} f_1(z=1) = 1, \qquad (45)$$
$$p_1(z=1) = 2\lambda,$$
$$\mathrm{Re}\, al(q) > 0,$$

Solution of (44),(45) is as follows:

$$x_1(z) = \frac{\gamma^2-1}{2\gamma^2}(\exp(\int_1 \frac{q(z)dz}{z}) - 1) - \frac{\lambda}{\gamma}\ln z + 1,$$
$$f_1(z) = -\frac{\gamma^2-1}{2\gamma^2\lambda}(\exp(\int_1 \frac{q(z)dz}{z}) - 1) - \frac{1}{\gamma}\ln z, \qquad (46)$$
$$p_1(z) = 2\lambda \exp(\int_1 \frac{q(z)dz}{z})$$

where

$$\lambda = in\sqrt{\frac{\gamma-1}{\gamma+1}}, \qquad (47)$$

and $q(z)$ is the root with a positive real part of the following equation:

$$q^2(1-b) + 2\lambda q + \lambda^2 - n^2 w^2 = 0, \qquad (48)$$

Data of Fig.1 show that formula Eq.(47) is in a reasonable agreement with numerical results. We should note also that Eq.(47) has the right limit of $n \to \infty$, it is in an agreement with the corresponding formulas describing perturbation oscillations in plane shock waves.[10]

2. Evolution of shock front radius small perturbations in the case when the gas density before shock front has small perturbation.

We considered above free oscillations of blast wave . We can develop an analogy between the blast wave perturbations and other oscillating systems and consider the perturbations generated by perpetually operating external sources. One of these cases is when perturbations of density before shock front $r_{o1} \sim r^{l+1}$ take place. This problem was considered earlier in Ref. 2. In this case hydrodynamic equation system for perturbations coincides with (16),(17),(18),(22) except for continuity equation which has a non-zero right part:

$$\frac{\rho_1}{\rho} + \Delta_{\theta\varphi} F_1 + \frac{\frac{\partial(R^{s-1}R_1)}{r^{s-1}\partial r}}{\frac{R^{s-1}\partial R}{r^{s-1}\partial r}} = \frac{\rho_{01}(r)}{\rho_0(r)} \qquad (49)$$

and for boundary conditions:

$$P_1(r=S,t) = \frac{2\rho_0}{\gamma+1}\frac{\dot{S}^2}{S}S_1(2\lambda+s+2+a(1))$$
$$\rho(r=S,t) = \frac{(\gamma+1)\rho_0}{\gamma+1}\frac{S_1}{S}a(1) \qquad (50)$$

Using that we get the self-similar equation system and boundary conditions analogous to Eqs. (26)-(30). The difference between eigenvalue problem in this case and stability problem considered above is that the role of eigenvalues is played by the ratio of shock front radius perturbation to initial density perturbation *d*:

$$d = d(\lambda, n) = \frac{\frac{S_1}{S}(r)}{\frac{\rho_{10}}{\rho}(r)}; \qquad (51)$$

The eigenvalue problem is linear of 1/d. The system of equations is the following::

$$\begin{aligned}
&bp_1 + (\frac{zd}{dz} + \lambda + sw)x_1 - n(n+s-1)wf_1 = \frac{\gamma+1}{2\gamma}(2\lambda + s + k + 2 + \frac{1}{d})w, \\
&wp_1 + ax_1 - (\frac{zd}{dz} + 2w + \frac{s+k-2}{2})\frac{zd}{dz} f_1 = 0, \\
&(\frac{zd}{dz} + \lambda + s + k - (s+k-2)w)p_1 + ((\frac{zd}{dz} + 2w + \frac{s+k-2}{2})\frac{zd}{dz} - (s+k-1))ax_1 + \\
&+ n(n+s-1)af_1 = -\frac{\gamma+1}{2}\frac{a}{d};
\end{aligned} \qquad (52)$$

Boundary conditions are the same as in (29,30), except:

$$p_1(1) = 2\lambda + \frac{6\gamma + 2 - s(3\gamma - 1) + k(\gamma + 1)}{(\gamma+1)^2} + \frac{1}{d};$$

2.1 The forced oscillations of the shock front radius.

Earlier the case of $\lambda = 0$ was considered in Ref. 2.

In this paper we consider pure imaginary values of *l:* $l = iw$. The problem is solved numerically. The calculated values of $|d(w,n)|$ are presented on Fig.3. The sharp resonance pattern (in the vicinity of $\omega = \sqrt{\frac{\gamma-1}{\gamma+1}}n$) is demonstrated for $\gamma=1.2$ and the smeared one is demonstrated for $\gamma=5/3$.

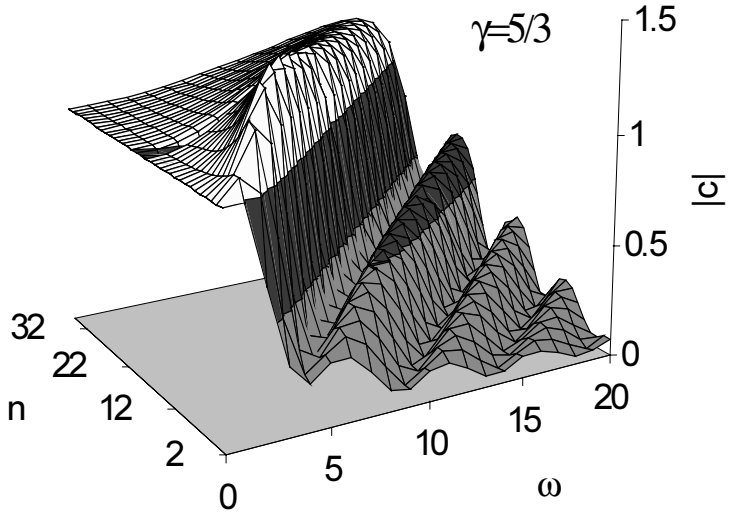

Fig.4a. Resonance patterns $|c(\omega,n)|$ for γ=1.667. Results are normalized to $q(0,n)$:

$c(\omega,n) = \left|\frac{q(\omega,n)}{q(0,n)}\right|$. (Note that $q(0,n) \cong \frac{1}{n}\sqrt{\frac{\gamma+1}{2\gamma}}$ for $n>>1$)

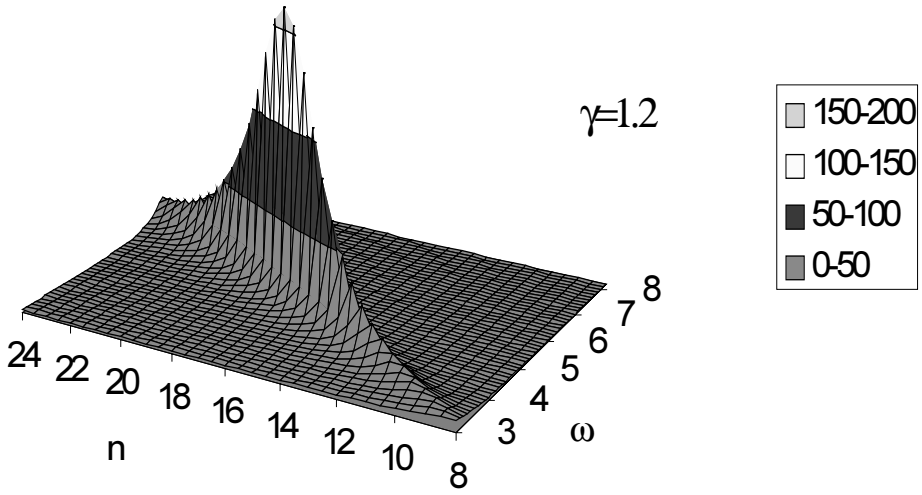

Fig.4b. Resonance patterns $|c(\omega,n)|$ for γ=1.2. Results are normalized to $q(0,n)$: $c(\omega,n)=\left|\frac{q(\omega,n)}{q(0,n)}\right|$.

Analytical solution can be obtained for *n>>1, k=0.*

We again seek solution of (43) type, reduce equation system (52), and get finally the following solution:

$$q = nw\sqrt{\frac{1}{1-b}}, \qquad d = -\frac{1}{n}\sqrt{\frac{\gamma+1}{2\gamma}} \tag{53}$$

This result is in a good agreement with the well-known formulas for front perturbations in a stationary shock wave (Ref.11).

3. Stability of the blast wave in a non-ideal gas.

For the sake of convenience of comparison with an experiment we however need a solution of the stability problem for the case of non-ideal gas. In actual practice gas adiabatic exponent is a function of density and temperature: it's getting lower while degree of ionization is increasing, that is while density is lowing or temperature is rising. In Ref.12 the authors considered the stability problem for one of the cases of blast wave in non-ideal gas, namely, the only case when the blast wave in the non-ideal gas is self-similar: we supposed that the gas adiabatic exponent γ was a function of the gas density (i.e. γ was independent from the gas energy). In this case we can use the self-similar technique for solving the blast wave stability problem.

In Ref.13 the authors supposed that the gas equation of state (EOS) was as follows:

$P=(\gamma^*(\rho)-1)\rho E$ (54)

where coefficient γ* was a two-parameter function of ρ:

$$\gamma^*(\rho)-1=\frac{\gamma_c-1}{1-\frac{\gamma_f-\gamma_c}{\gamma_f+1}\rho} \tag{55}$$

Here parameters: γ_c,γ_f stand for values of the gas adiabatic exponent in the blast center and at the shock front.

The eigenvalue problem in this case is the same (See Ref.13) as in Eqs.(26-31). Fig.4 presents results of numerical solution of the eigenvalue problem.

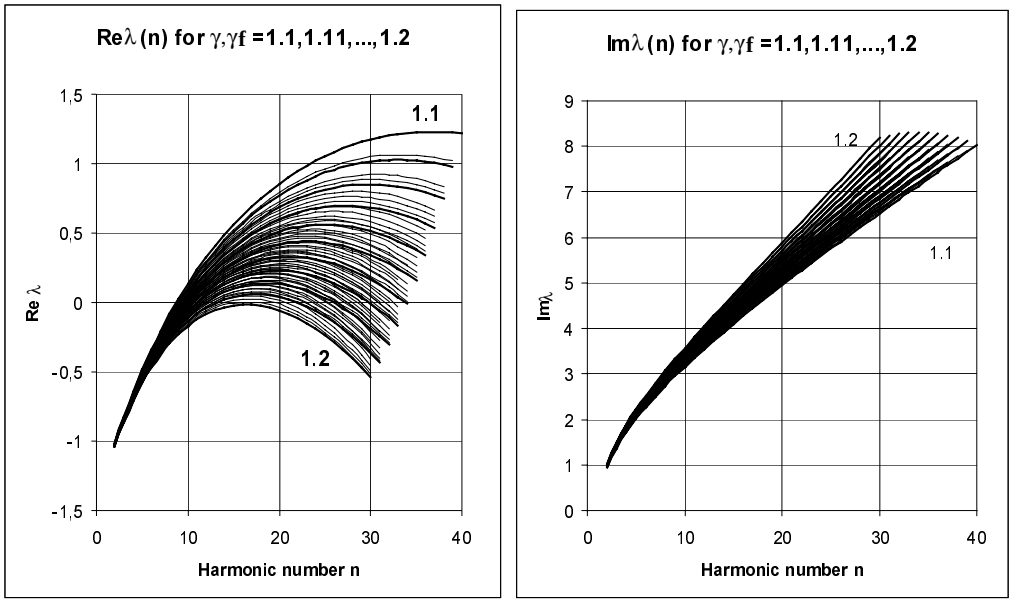

Fig.4 The components of complex eigenvalue λ for some sets of values of parameters of gas EOS. Heavy curves correspond to the cases of ideal gas with $\gamma_f=\gamma_c=\gamma=1.10,1.11,1.12,\ldots1.20$. the other lines correspond to the cases when $\gamma_f>\gamma_c$.

Conclusion

Blast wave perturbation evolution was considered. The solutions obtained have applications in laboratory physics and astrophysics; they also can serve the tests for elaboration of the 2D and 3D hydrodynamic codes.

Stability of some cases of spherical or cylindrical blast wave was considered using self-similar approach in the unified manner. Namely, stability of the cases in which gas density before shock front was a power function of radius (with power exponent being equal to *k*) was considered. Blast wave small perturbations were expanded in spherical harmonics. The perturbation value was supposed to be a power function of time (with complex exponent), stability problem was reduced to eigenvalue problem, and the increments of perturbation growth and periods of oscillation were calculated as the eigenvalues for each harmonic number. The calculations were made numerically both for spherical and cylindrical blasts for a large set of blast wave parameters: gas specific heat ratio γ, harmonic number *n*, value of *k*. The instability region on the plane n - γ was determined. The critical value of specific heat ratio γ_c was calculated for each case considered.

The evolution of perturbations generated by perpetually operating external sources was considered too. Namely, there were considered the forced oscillations of shock front radius perturbations caused by a presence of spatially oscillating perturbations of initial gas density. The eigenvalue problem in this case was formulated using the self-similar technique.

4. The short wavelength approximation was used to obtain an analytical solution of eigenvalue problem. It was shown that the obtained solutions agreed with the corresponding solutions describing plane shock wave perturbations.

5. The analytical solutions of stability problem were also obtained in the case of values of *g* being close to unit. In this case expansion of the solution by powers of γ-1 was used. The terms of the zero order, and the first order of negligibility were calculated. It was shown that they were in a reasonable agreement with the numerical results.

6. The spherical (or cylindrical) blast wave stability was considered using the self-similar approach. Using this technique helped us to reduce rather complicated 3D hydrodynamic

problem of small perturbation evolution to the simpler eigenvalue problem. Blast wave should satisfy two conditions to be studied using this approach: it should be self-similar and 1D solution for this blast wave should be smooth at the center. A sound speed should tend to infinity, and a particle velocity should be negligible compared with the sound speed at the center.

The main assumptions of the self-similar approach are:

- Pattern of the perturbation evolution is a self-similar one.
- The value of pressure small perturbations tends to zero at the center.

In the spherical case one more assumption was made. It is:

- Pattern of an angular motion is a potential one.

It seems to us that all three these assumptions were proved in experiments (see Ref. 4 where perturbation oscillation period was measured and the period value proved to be in a good agreement with the self-similar theory results). But for the better proof of the third assumption we need direct computer simulation of blast waves using 3D hydrodynamic codes.

Acknowledgments

This work was sponsored by the International Science and Technology Center (Project No222,No874).

References

1.E.T.Vishniac,"The dynamic and gravitational instabilities of spherical shocks," Astrophys.J. 274, p.152 (1983);

2.V.M.Ktitorov, "Asymptotical development of point blast wave small perturbations," Voprosy Atomnoi Nauki i Tekhniki, Ser.Teoreticheskaya i Prikladnaya.Fizika (Atomic Science and Technique Issues, Ser. Theoretical and Applied Physics), No2, p.28, (1984);

3.D.Ryu and E.T.Vishniac, "The growth of linear perturbations of adiabatic shock waves," Astrophys.J. 313, 820 (1987);

4.J.Grun, J.Stamper, C.Manca, et al., "Instabilities of Taylor-Sedov blast wave propagating through uniform gas," Phys.Rev.Let., V.66, No21, p.2738, (1991);

5.C.Manca, J.Grun, J.Stamper, et al., "Images of unstable Taylor-Sedov Blast Waves propagating through uniform gas," IEEE Transactions on Plasma Science vol.24,No1, p.35,(1995);

6.L.D.Landau, and E.M.Lifshits, Fluid Mechanics, 2-nd ed. (Pergamon, NY 1987);

7.V.M.Ktitorov, "Cylindrical blast wave stability and two-dimensional perturbation development," Voprosy Atomnoi Nauki i Tekhniki, Ser.Teoreticheskaya i Prikladnaya.Fizika (Atomic Science and Technique Issues, Ser. Theoretical and Applied Physics), No2, p.37, (1985);

8.E.T.Vishniac and D.Ryu, Astrophys.J "On the stability of decelerating shocks," 337, 917 (1989);

9.V.M.Ktitorov, "Stability of blast wave propagating through a gas with a power depending density", Khimicheskaya Fizika (Chemical Physics Issues) V.14, No 2-3, p.169, (1995);

10.R.M.Zeidel, "Perturbation evolution in plane shock waves," Zhurnal Prikladnoi Matematiki I Tekhnicheskoi Fiziki (Applied Mathematics and Physics Journal) v.4, p.30, (1968);

11.V.M.Ktitorov, "Perturbations of stationary shock wave moving along a channel", Khimicheskaya Fizika (Chemical Physics Issues) V.14, No 2-3, p.171, (1995);

12. V.M.Ktitorov,V.Yu.Meltsas, "Study of point blast wave instability in numerical experiment", Proceedings of the 6th IWPCTM, p.251

13. V.M.Ktitorov, "Stability of Blast wave in non–ideal gas", Report at the 7th IWPCTM, St-Peterbourg,, July,1999

STABILITY 0F REFLECTED FROM THE CENTER SELF-SIMILAR CONVERGING SHOCK WAVE

V.M.Ktitorov

Russian Federal Nuclear Center (VNIIEF), Sarov, RU

In this paper the technique first used in Ref.1,2 for solving the point blast wave stability problem is applied for the one of the self-similar converging shock wave after focusing.

Equations for the case of converging self-similar shock wave

The obtained in Ref.1-4 system of equations can be applied for the case under consideration.

Let us consider the uniform equation for perturbations (we use the notification of Ref.4):

$$\frac{P_1}{\rho} +_1 +\gamma\frac{(R^2R_1)'}{R^2R'} - n(n+1)\gamma F_1 = 0 \qquad (1)$$

$$\frac{P_1}{\rho} + R_1\ddot{R} + (R^2\dot{F}_1\dot{}) = 0 \qquad (2)$$

$$\frac{P_1'}{\rho} + \ddot{R}\frac{R_1}{R} + \ddot{R}_1 + n(n+1)\ddot{R}F_1 = 0 \qquad (3)$$

With boundary conditions:

$$\begin{aligned} &R_(R=S,t) = R_1(1-R') + \frac{s_1}{3}R'(S) \\ &F(S,t) = \frac{\lambda+3}{3N}s_1(S) \\ &\dot{F}(S,t) = -\frac{\dot{R}(S)}{\dot{S}} \\ &P_(S,t) = P_1(Shock) - \frac{s_1}{3}P'(S) \end{aligned} \qquad (4)$$

According to the self-similar approach we look for the solution in the self-similar form:

$(F_1,R_1,P_1) \sim r^\lambda f(r/S)$, and: $s_1 \sim r^\lambda$ (5)

After inserting of self-similar variables (functions of $z=r/S$) we get:

$$\begin{aligned} &P_1b - (D+\lambda+3w)r_1 - NwF_1 = 0 \\ &P_1w + r_1a + (D+2w+\frac{1}{\alpha}-1)DF_1 = 0 \\ &(D+\lambda+3-w)P_1 + ((D+2w+\frac{1}{\alpha}-1)D-a)r_1 + NaF_1 = 0 \end{aligned} \qquad (6)$$

(Here D stands for differential operator: $Df \equiv \frac{d}{d\ln z}f$)

Because of presence of non-zero initial velocity before shock front (we denote this velocity u_0) the mass conservation equation is changing:

$$\frac{1}{\rho} = \frac{1}{1+u_0}\frac{R^{s-1}\partial R}{r^{s-1}\partial r} \tag{7}$$

So coefficients in (Eqs.27) look like as follows:

$$\begin{aligned} w &= \frac{Dx}{x} \\ a &= Dw + (w-1)(w+\frac{1}{\alpha}-1) \\ b &= (1+u_0)\frac{wz^3}{\gamma x P} \end{aligned} \tag{8}$$

(Here variables $x=R/S$, $P=P/S^2$ are functions of z), the front value of coefficient w is $w(1) = \frac{1+u_0}{\delta}$, (here δ stands for front compression), the front value of coefficient a(1) is calculated from spherically symmetric solution.

Equation system (6) has the fourth order; there are four boundary conditions on the front edge (z=1):

$$\begin{aligned} x_1(1) &= 1 - \frac{1+u_0}{\delta} + \frac{s_1}{3}\frac{1+u_0}{\delta} \\ F_1(1) &= \frac{\lambda+3}{3N}s_1 \\ DF_1(1) &= 1 - \frac{1+u_0}{\delta} \\ P_1(1) &= P_1(Shock) + \frac{s_1}{3}a(1) \end{aligned} \tag{9}$$

These conditions construct full set of boundary conditions necessary to determine a solution. (To derive the conditions one should take into account the characteristics of gas flow before the shock front because values P_1 *(shock)* and s_1 in (31) depend on values of gradients of pressure and velocity before the shock front).

In order to construct the eigenvalue problem we add the fifth boundary condition (at the center):

$$P_1(0)=0 \tag{10}$$

We solve the eigenvalue problem (Eqs.6,9,10) and we calculate the values of power exponent λ (see Eq.5) as eigenvalues.

We used the simultaneous solving of spherically symmetric equations and equations for perturbations. The variables *P1, F1, x1* are expressed as functions of w and coefficients *a, b,* in Eq.6 are also expressed as functions of w:

$$a = \frac{b}{1-b}\left[(w-1)(w-1+\frac{1}{\alpha}) - 3w(w-1+\frac{2/\alpha-2}{3\gamma})\right]$$

$$D \equiv \left[a-(w-1)(w-1+\frac{1}{\alpha})\right]\frac{d}{dw} \qquad (11)$$

$$\frac{db}{bdw} = \frac{6-3\gamma+w(3\gamma-1)(b-1)}{3w(w-1+\frac{2/\alpha-2}{3\gamma}) - b(w-1)(w-1+\frac{1}{\alpha})} + \frac{\gamma+1}{w}$$

Using this approach the eigenvalue problem was solved numerically. The values of λ were calculated as eigenvalues. The dependence of λ on γ and harmonic number n is shown on Fig.1, Fig2.

The case under consideration differs from other cases with diverging shock waves considered earlier. Curves on figures look like irregular ones. The reason of it is that self-similar solutions exist only in small region on the plane n-γ. For big harmonic numbers (n≥15 for γ=1.2, γ=1.4 and n≥7 for γ=1.667) self-similar solution supposedly does not exist at all.

Fig.3, Fig.4 present the computer validation of self-similar results shown on Fig.1, Fig.2. V.Yu Meltsas performed the computer modeling of the reflected from the center shock wave in the way he did it in Ref.5 . The results of computer modeling agree the results of self-similar calculations: we see the exponential perturbation grow on Fig. 3 and oscillation regime of perturbation evolution for the case n=2, γ=1.667 on Fig.4.

Acknowledgments

The author wishes to acknowledge the financial support by ISTC (Project No 874).

References:

1. V.M.Ktitorov (Russian Atomic Science and Technique Issues, Ser. Theoretical and Applied Physics), No2, p.28, (1984);
2. D.Ryu and E.T.Vishniac, Astrophys.J. 313, 820 (1987);
3. V.M.Ktitorov, Khimicheskaya Fizika (Chemical Physics Issues) V.14, No 2-3, p.169, (1995)
4. V.M.Ktitorov Stability of Diverging Shock Waves, Report at the 8th IWCTM, Pasadena, Dec, 9-14, 200112.
5. V.M.Ktitorov,V.Yu.Meltsas, “Study of point blast wave instability in numerical experiment”, Proceedings of the 6th IWPCTM, p.251

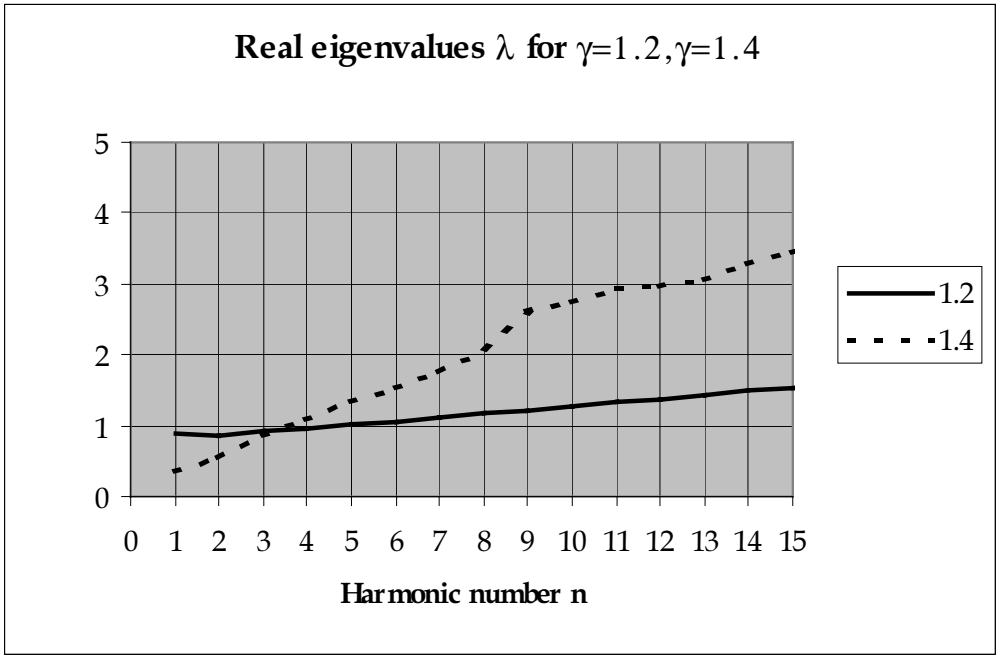

Fig. 1 Real eigenvalues λ(n) for γ=1.2, γ=1.4. Shock wave is unstable with respect to perturbations of all harmonic numbers.

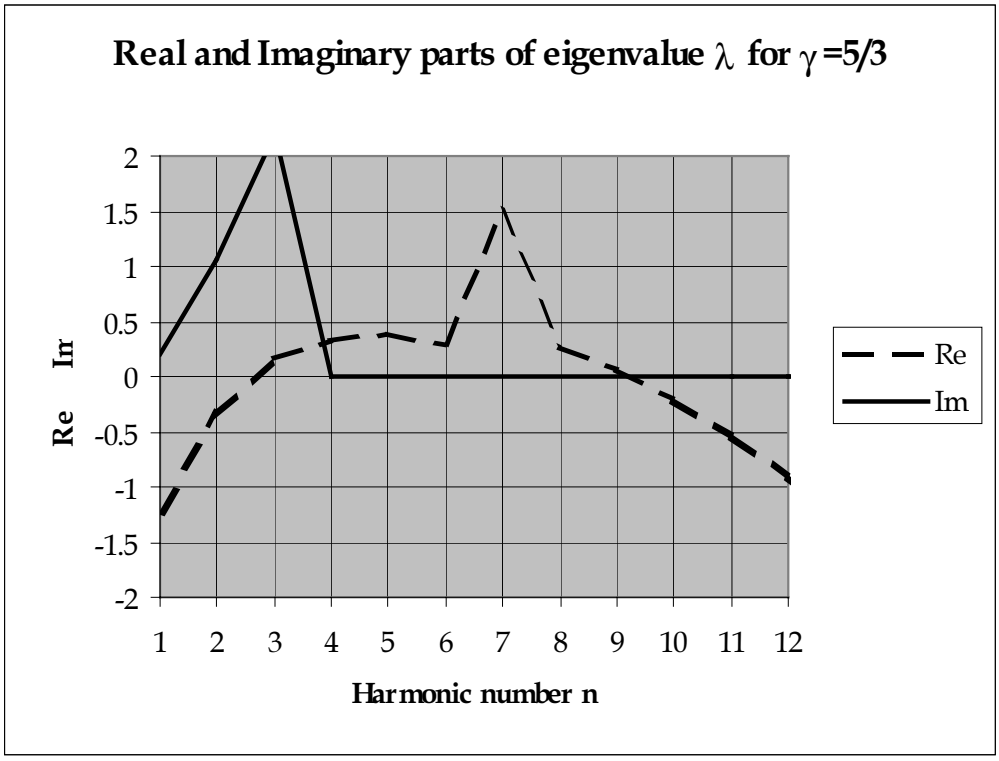

Fig.2 Complex (for n=1,2,3) and real (for n>3) power exponents (eigenvalues) $\lambda(n)$ for gases with γ=1.667. There appears to be no self-similar perturbations for n>6.

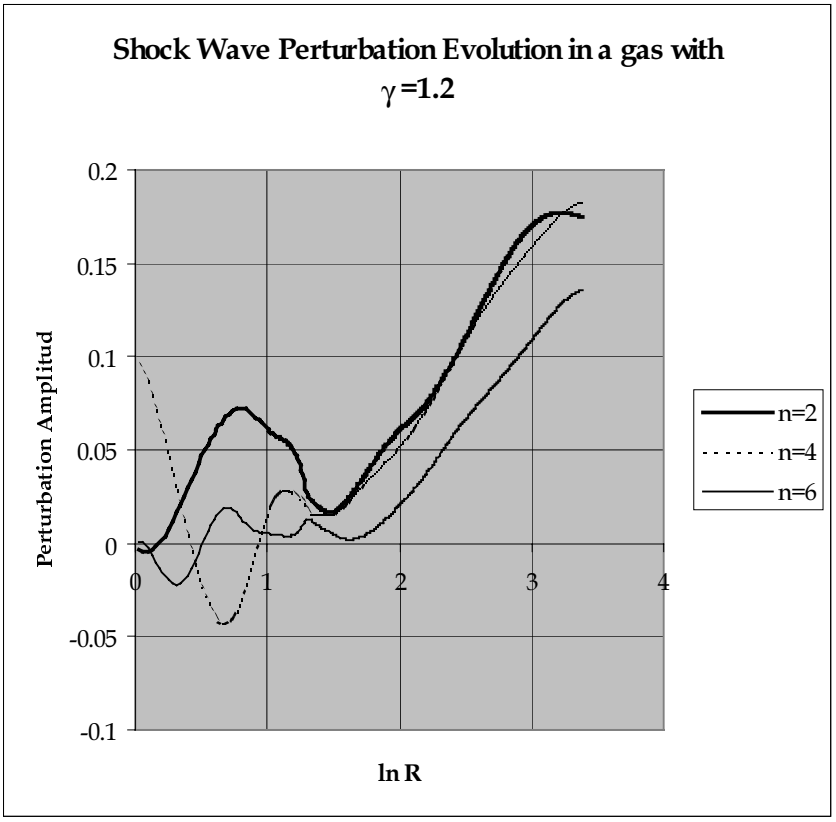

Fig.3 Perturbation evolution for shock wave in a gas with γ=1.2

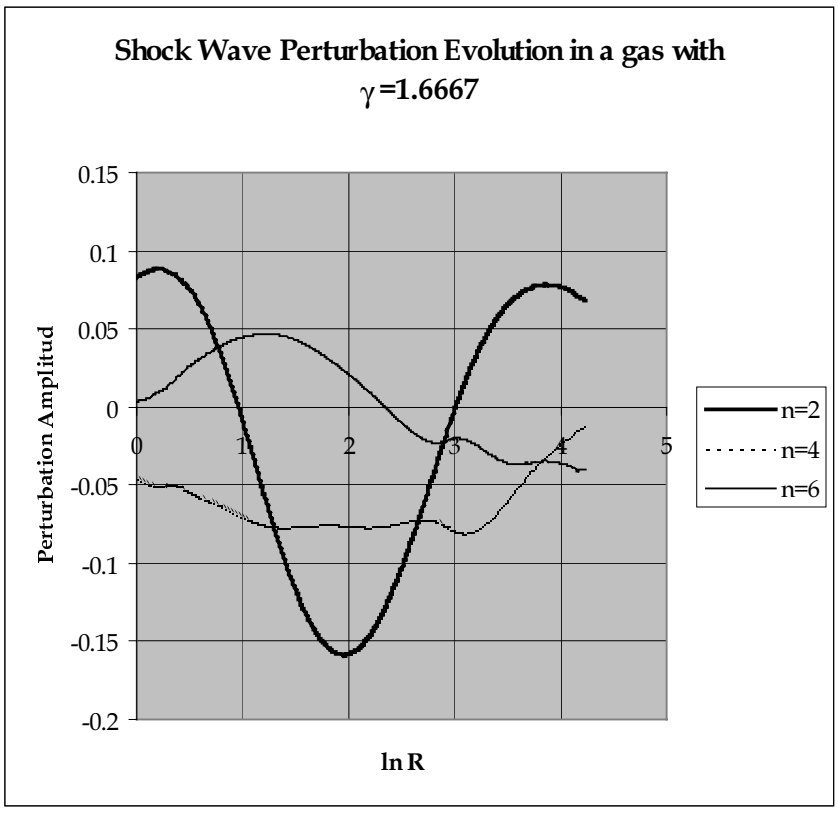

Fig.4 Perturbation evolution for shock wave in a gas with γ=1.667

Response of Turbulent RANS Models to Self-Similar Variable Acceleration RT-Mixing: an Analytical "0D" Analysis

Antoine LLOR

Commissariat à l'Energie Atomique
B.P.12 91680 Bruyères-le-Châtel Cedex

December 13th, 2001

Abstract

So far, the validation of RANS models applicable to variable acceleration RT mixing flows (as found in ICF) has mostly been carried out by fitting experimental or numerical data obtained for constant (RT) and impulsive (RM) accelerations. Further checks are also possible on the few available data for variable acceleration, such as in mixing-demixing flows induced by reverting the gravity field. Although this approach is widely applied and accepted, it is unsatisfactory because of the complex relationship between the model features and coefficients and the experimental measurements.

It is shown here that self-similar variable acceleration RT (SSVART) provides an appealing alternative since it extends the usual calibration techniques of turbulent RANS models based on simple self-similar flows. The general model equations in 1D (PDEs) are still too complex for full analytical calculations of SSVART flows, but using reasonable assumptions, simple 0D (ODEs) approximations can be derived and solved analytically.

This approach is applied to an extended k–ε model derived from Andronov's (1979) and to Youngs' (1989) two-fluid model. The behaviour of the mixing layer growth rate and integral turbulent scales provides important informations on the accuracy of these models.

Finally, general qualitative arguments will be discussed showing the importance and the difficulty of capturing accurately a broad range of SSVARTs with a single simple model.

I Introduction

Qualitative understanding of large scale turbulence
in Rayleigh-Taylor (RT)
and incompressible Richtmyer-Meshkov (IRM)
is not available as in other mixing layers (wakes, jets...).

Our aim is to provide such analysis for:

- ideal incompressible self-similar turbulent regime,
- vanishingly small density differences ($\mathcal{A} \to 0$),
- and "0D" (global) energy balance.

"0D" approximation is averaging over TMZ width, $L(t)$.

Two-fluid analysis will be applied.

Kelvin-Helmoltz (KH) will be used as reference.

Experimental, simulated and modeled results will be examined.

Extension to SSVARTs will be considered
(Self-Similar Variable Acceleration Raleigh-Taylor mixing).

II "0D" averaging

II.1 Fluid motion

In $\mathcal{A} \to 0$ limit

experiments and simulations show

linear profiles of fluid volume fractions:

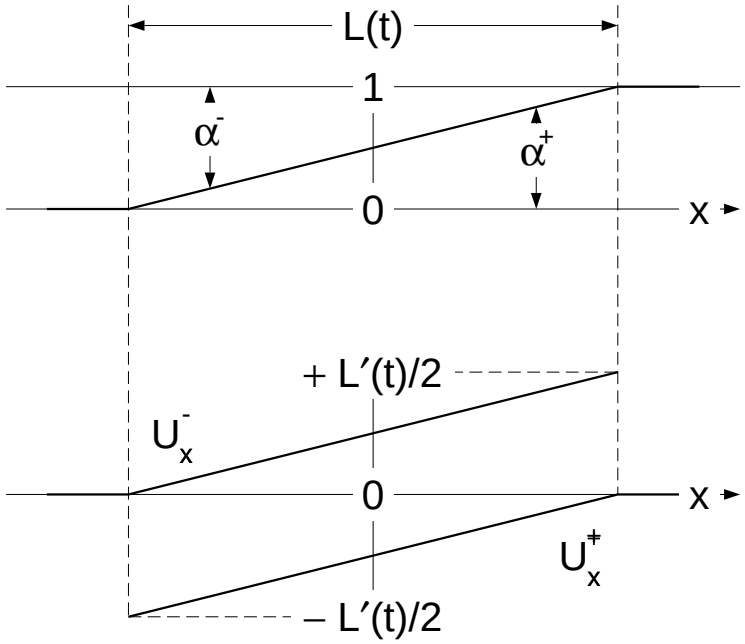

From mass conservation equations for fluids $+$ and $-$,

fluid velocities $U^{\pm}$ are also found linear.

Therefore:

$$\delta U_x = U_x^+ - U_x^- = \frac{\mathrm{d}}{\mathrm{d}t} L(t) \qquad (1)$$

II.2 TMZ-growth related energies

From growth law and fluid velocities, one can extract:

• Total input of energy:

$$K_I = \frac{-2\,g}{(\rho^+ + \rho^-)\,L}\left(\int_{-L/2}^{+L/2}(\alpha^+(x)\rho^+ + \alpha^-(x)\rho^-)\,x\,\mathrm{d}x - \int_{-L/2}^{0}\rho^- x\,\mathrm{d}x - \int_{0}^{+L/2}\rho^+ x\,\mathrm{d}x\right). \qquad (2)$$

• Mean kinetic energy:

$$\begin{aligned} K_M &= \int_{-L/2}^{+L/2}\overline{\rho}(U_x)^2/2\,\mathrm{d}x \Big/ \int_{-L/2}^{+L/2}\overline{\rho}\,\mathrm{d}x \\ &\approx \tfrac{1}{15}\,\mathcal{A}^2(\delta U_x)^2 \quad \text{for } \mathcal{A}\to 0. \end{aligned} \qquad (3)$$

• Directed kinetic energy:

$$\begin{aligned} K_D &= \int_{-L/2}^{+L/2}[\alpha^+\rho^+(U_x^+)^2 + \alpha^-\rho^-(U_x^-)^2 - \overline{\rho}(U_x)^2]/2\,\mathrm{d}x \Big/ \int_{-L/2}^{+L/2}\overline{\rho}\,\mathrm{d}x \\ &\approx \tfrac{1}{12}\,(\delta U_x)^2 = \tfrac{1}{48}\,(L')^2 \quad \text{for } \mathcal{A}\to 0. \end{aligned} \qquad (4)$$

K_M will thus be ignored.

Instability	RT	IRM	KH
$L(t)$	$\mathcal{Y}_0 \times \mathcal{A}gt^2$	$L_0 \left(\frac{t}{t_0}\right)^{n_0}$	$\mathcal{X}_0 \times \Delta U_y t$
K_I	$\frac{\mathcal{Y}_0}{12} \times (\mathcal{A}gt)^2$	$K_{I0} \left(\frac{t}{t_0}\right)^{-n_0}$	$\frac{1}{12} \times (\Delta U_y)^2$
K_D	$\frac{\mathcal{Y}_0^2}{12} \times (\mathcal{A}gt)^2$	$\frac{n_0^2}{48} \times \frac{L_0^2}{t_0^2}\left(\frac{t}{t_0}\right)^{-2(1-n_0)}$	$\frac{\mathcal{X}_0^2}{48} \times (\Delta U_y)^2$
K_D/K_I	$\mathcal{Y}_0$	$\frac{n_0^2}{48} \times \frac{L_0^2}{K_{I0}\, t_0^2} \left(\frac{t}{t_0}\right)^{-(2-3n_0)}$	$\frac{\mathcal{X}_0^2}{4}$

Since $\mathcal{Y}_0 \approx \mathcal{X}_0 \approx 0.1$,

K_D/K_I levels largely motivate use of two-fluid models for RT.

II.4 Energy balance

The knowledge of the total kinetic energy in TMZ, K,
obtained from experiments or simulations,
completes balance and provides dissipation, E.

The ratio of integral length scale to TMZ width:

$$\kappa_T = \frac{K_T^{3/2}}{E\,L}, \tag{5}$$

will be called **Von Kármán number**

by analogy with the Von Kármán Constant of turbulent boundary layers,

with the two-fluid turbulence defined as:

$$K_T = K - K_D \tag{6}$$

Instability	RT	IRM	KH
Growth coefficient	$\mathcal{Y}_0$=0.12	n_0=0.3	$\mathcal{X}_0$=0.1
K_T/K_D	3	58	116
κ_T	0.09	0.3	0.63

see references in Llor 2001.

The Von Kármán number is 7 times smaller in RT than in KH:
assuming there is one large eddy in KH TMZ,
there are seven large eddies in RT TMZ !

(confirmed in experiments or simulations, Dimonte 2000, Dalziel 1999, Inogamov 2001...)

III Results from "0D" averaged models

III.1 "0D" averaging of model PDEs

From equation for hydro quantity a in model:

$$\frac{\partial}{\partial t}a + (\phi^a_x)_{,x} = s^a, \tag{7}$$

averaging over TMZ width, $A = \langle a \rangle$, yields:

$$\frac{1}{L}\frac{\mathrm{d}(LA)}{\mathrm{d}t} = \frac{\mathrm{d}A}{\mathrm{d}t} + \frac{\mathrm{d}L}{L\,\mathrm{d}t}\,A = S^a, \tag{8}$$

since (usually) $\phi^a_x = 0$ at edges of TMZ.

Supplementary asumptions/approximations are needed to provide closed expression of S^a.

For instance, center of TMZ is often dominant, so:

$$S^a \approx \frac{1}{\zeta}\, s^a\left(\zeta\, B\right), \tag{9}$$

if $s^a = s^a(b)$ and defining $\zeta \approx a(0)/A \approx b(0)/B \approx 3/2$.

Models are thus reduced from PDEs to ODEs.

Two models considered here:

- Andronov's modified single-fluid k–ε model (1979),
- Youngs' two-fluid model (1989).

III.2 PDEs of modified k–ε and two-fluid models

Basic relevant PDEs for Andronov's modified k–ε:

$$\begin{cases} \frac{\partial}{\partial t}\,\overline{\rho c^{\pm}} \;\ldots \;=\; \ldots - (\overline{\rho c^{\pm} u_i''})_{,i} \stackrel{\text{m}}{=} \left(\overline{\rho}\frac{\nu_t}{\sigma_c}\widetilde{c^{\pm}}_{,i}\right)_{,i} & \Rightarrow \frac{\mathsf{d}}{\mathsf{d}t}L(t) \\ \frac{\partial}{\partial t}\,\overline{\rho k} \;\ldots \;=\; \ldots - \overline{p}_{,i}\overline{u_i''} \stackrel{\text{m}}{=} -\frac{\nu_t}{\sigma_\rho}\frac{\overline{p}_{,i}\overline{\rho}_{,i}}{\overline{\rho}} & \Rightarrow \text{“RT” prod.} \\ \frac{\partial}{\partial t}\,\overline{\rho\epsilon} \;\ldots \;=\; \ldots \stackrel{\text{m}}{=} -C_{\epsilon 0}\frac{\nu_t}{\sigma_\rho}\frac{\overline{p}_{,i}\overline{\rho}_{,i}}{\overline{\rho}} & \end{cases}$$

with $\sigma_\rho \approx 2$ and $C_{\epsilon 0} \approx 0.85$ (other constants as usual).

Basic relevant PDEs for Youngs' two-fluid:

$$\begin{cases} \frac{\partial}{\partial t}\,(\alpha^{\pm}\rho^{\pm}) \;\ldots \;=\; \ldots & \\ \frac{\partial}{\partial t}\,(\alpha^{\pm}\rho^{\pm}U_i^{\pm}) \;\ldots \;=\; \ldots - (R_{ij})_{,j} \mp D_i(\lambda_d) & \Rightarrow \frac{\mathsf{d}}{\mathsf{d}t}L(t) \\ \frac{\partial}{\partial t}\,(\overline{\rho}k_b) \;\ldots \;=\; \ldots \pi_{\mathsf{KH}} + D_i\delta U_i & \\ \frac{\partial}{\partial t}\,\lambda_d \;\ldots \;=\; \ldots \sqrt{\frac{2\overline{\rho}}{\rho^+ + \rho^-}}\, n_i \delta U_i & \Rightarrow \text{Length scale} \end{cases}$$

$$D_i \stackrel{\text{m}}{=} C_d\overline{\rho}\frac{\alpha^+\alpha^-}{\lambda_d}\| U_i^+ - U_i^- - \vec{W} \| (U_i^+ - U_i^- - W_i) + a.m. + \ldots$$

$$\nu_t = C_\mu\sqrt{k_b}\,\lambda_i, \qquad\qquad \lambda_i = \frac{C_i}{C_\mu}\lambda_d,$$

with $C_d \approx 20$ and $C_i \approx 0.105$ (other constants as usual).

III.3 ODEs of modified k–ε and two-fluid models

"0D" ODEs for Andronov's modified k–ε:

$$\left\{\begin{array}{rcl} \dfrac{\mathrm{d}}{\mathrm{d}t}L &=& \dfrac{8\,\zeta\,C_\mu}{\sigma_c}\dfrac{K^2}{E\,L}, \\ \dfrac{\mathrm{d}}{\mathrm{d}t}K &=& -\dfrac{\mathrm{d}L}{L\,\mathrm{d}t}\,K + \Pi_K - E, \\ \dfrac{\mathrm{d}}{\mathrm{d}t}E &=& -\dfrac{\mathrm{d}L}{L\,\mathrm{d}t}\,E + C_{\epsilon\pi}\dfrac{E}{K}\,\Pi_K - C_{\epsilon 2}\,\dfrac{E^2}{K}, \end{array}\right. \tag{10}$$

$$\Pi_K^{\boxed{\mathrm{RT}}} \approx \frac{2C_\mu}{\sigma_\rho}\,\frac{K^2}{E\,L}\,\mathcal{A}\,\Gamma, \qquad \Pi_K^{\boxed{\mathrm{KH}}} \approx C_\mu\frac{K^2}{E}\,\left(\frac{\Delta U_y}{L}\right)^2.$$

"0D" ODEs for Youngs' two-fluid:

$$\left\{\begin{array}{rcl} \dfrac{\mathrm{d}}{\mathrm{d}t}L &=& 4\sqrt{3\,K_D}, \\ \dfrac{\mathrm{d}}{\mathrm{d}t}K_D &=& -\dfrac{\mathrm{d}L}{L\,\mathrm{d}t}\,K_D - \Pi_D + \dfrac{2}{3}\,\mathcal{A}\Gamma\sqrt{3\,K_D}, \\ \dfrac{\mathrm{d}}{\mathrm{d}t}K_T &=& -\dfrac{\mathrm{d}L}{L\,\mathrm{d}t}\,K_T + \Pi_D - \dfrac{2\,C_\mu}{C_i}\sqrt{\zeta}\,\dfrac{K_T^{3/2}}{L}, \end{array}\right. \tag{11}$$

$$\Pi_D = \left[\tfrac{C_d}{2\,L}\left(2\sqrt{3\,K_D} - 4C_i\sqrt{\zeta K_T}\right)^2 + \frac{\mathrm{d}}{\mathrm{d}t}\tfrac{\sqrt{3\,K_D}}{4} + \tfrac{3\,K_D}{2\,L}\right]\,\tfrac{2\sqrt{3\,K_D}}{\zeta}.$$

KH more complex but can be treated in similar way.

Self-similar solutions are analytical for both models (explicit for k–ε),
and yield the following numerical results
(for recommended values of the coefficients):

Source	Exp. & Sim.			Modified k–ε			Young's two-fluid		
Instability	RT	IRM	KH	RT	IRM	KH	RT	IRM	KH
$\mathcal{Y}_0$, n_0, $\mathcal{X}_0$	0.12	0.3	0.1	0.054	0.3	0.077	0.106	0.44	0.105
K_T/K_D	3	58	116	4.9	117	106	6.2	26	93
κ_T	0.09	0.3	0.63	1.4	0.42	0.53	0.58	0.58	0.76

Deviations below 30% due to exp. errors, "0D" averaging and modeling.
However, significant discrepancies in RT:
– $\mathcal{Y}_0$ is 50% too low in k–ε,
– κ_T is too high by factors 15 and 6 in k–ε and two-fluid respectively.

III.5 Conclusion on models

Inconsistencies for k–ε due to purely diffusive TMZ growth.

In k–ε, directed transport in RT
is replaced by enhanced diffusion (sufficient for KH and IRM).

$L(t)$ equation in (10) for RT case can be rewritten as:

$$1 = \frac{2\,\zeta\,C_\mu}{\sigma_c}\,\kappa\,\sqrt{\frac{K}{3K_D}}, \tag{12}$$

which yields unphysically small value $\sigma_c \approx 10^{-2}$,
for known estimates of κ and $\sqrt{K/K_D}$.

In two-fluid model,
production term of λ is $\propto \delta U$ ($\approx$ uniform over TMZ).
Therefore, $\kappa_T = \langle\lambda\rangle/L = C_i/(2C_\mu) \approx 0.58$ is constant.

Variations in κ cannot be reproduced;
but it has little consequence since
diffusion is properly captured in IRM and KH,
whereas transport is dominated by directed energy in RT.

IV Expanding horizons: SSVARTs

IV.1 Definition and usefulness of SSVARTs

Self-Similar Variable Acceleration Rayleigh-Taylor flows,
or SSVARTs, defined by acceleration profiles:

$$\begin{array}{ll} \text{if } \; n > -2, \; g \propto t^n & \text{for } \; t > 0, \\ \text{if } \; n < -2, \; g \propto (-t)^n & \text{for } \; t < 0. \end{array} \tag{13}$$

Since $L(t) \propto t^{n+2}$,
growth of $L(t)$ demands the $-t$ inversion for $n < -2$.

May be out of reach from experiments,
but can be studied numerically (Youngs, this conference).

Will be assumed to exist as Reynolds (ensemble) averages.

Response will be:

$$L(t) = \mathcal{Y}_n \mathcal{A}\, g(t)\, t^2 \quad \text{where} \quad \mathcal{Y}_n > 0. \tag{14}$$

Testing models in variable acceleration is difficult,
but SSVARTs are helpful in testing robustness and accuracy,
since they represent a "basis" set of all possible $g(t)$.

IV.2 Stability of SSVARTs

Self-similar $g(t)$ can always be considered,
but response of system is VART that may not be SSVART.

For stability (and existence),
a SSVART must be an attractor of motion
and eventually forget its initial condition.

Behavior of input energy provides criterion:

- $g(t)$ energy input from t_0 to t behaves as $K_I \propto (\pm t)^{2n+2}$,
- initially present energy at t_0 is dilluted as $K_0 \propto (\pm t)^{-(n+2)}$.

Therefore, initial condition is not forgotten if:

$K_0/K_I \to \infty$ for $\pm\, t \to \infty$ or 0,
which yields $-2 < n < -4/3$.

Since K_0 is both diluted and dissipated during growth,
the forbiden interval is less restrictive :

$$-2 < n < -2 + n_0, \tag{15}$$

Within this range of "forbidden" values,
SSVARTs eventually behave as Richtmyer-Meshkov, $L(t) \propto t^{n_0}$
(the evolution is dominated by the initial energy).

IV.3 SSVARTs as seen by "0D" models

• For Andronov's modified k–ε:

$$\mathcal{Y}_n \;=\; \frac{2C_\mu}{\sigma_\rho}\frac{(C_{\epsilon 2}-C_{\epsilon 0})^2}{[(3C_{\epsilon 2}-3)n+(4C_{\epsilon 2}-3)][(3C_{\epsilon 0}-3)n+(4C_{\epsilon 0}-3)]}. \quad (16)$$

• For Youngs' two-fluid model:

$$\mathcal{Y}_n \;=\; \frac{1/(1+n/2)}{C_d\left(1-\sqrt{2}C_i\,\mathcal{U}_n\right)^2(1+n/2)+3(1+3n/4)/2}, \quad (17)$$

where $\mathcal{U}_n = \sqrt{K_T/K_D}$ is largest real solution of:

$$C_\mu\,\mathcal{U}_n^3 \;-\; 4\sqrt{2}C_i\left[2C_i^2C_d-\frac{4+3n}{2(2+n)}\right]\mathcal{U}_n^2 + \;16C_i^2C_d\,\mathcal{U}_n \;-\; 2\sqrt{2}C_i\left[C_d+\frac{4+3n}{2(2+n)}\right] \;=\; 0. \quad (18)$$

• For scaled free fall
(obtained by canceling Π in two-fluid K_D equation):

$$\mathcal{Y}_n \;=\; \frac{\mathcal{Y}_0}{(1+n/2)(1+3n/4)}, \quad (19)$$

• For Read's formula ($L \propto \mathcal{A}\left(\int\sqrt{g}\right)^2$):

$$\mathcal{Y}_n \;=\; \frac{\mathcal{Y}_0}{(1+n/2)^2}, \quad (20)$$

All models generate two main poles for $\mathcal{Y}_n$.

k–ε provides negative values outside pole interval $[-1.7, 0.89]$
for recommended values of σ_ρ and $C_{\epsilon 0}$.
Positive values outside interval $[-2, -1.7]$ requires $C_{\epsilon 0} \geq 3/2$,
but then $\mathcal{Y}_0 \approx 10^{-3}$!
Again k–ε cannot capture directed transport
which is enhanced as n is increased.

Behavior of all other models is similar (common $n = -2$ pole)
except near poles associated with IRM growth coefficients:

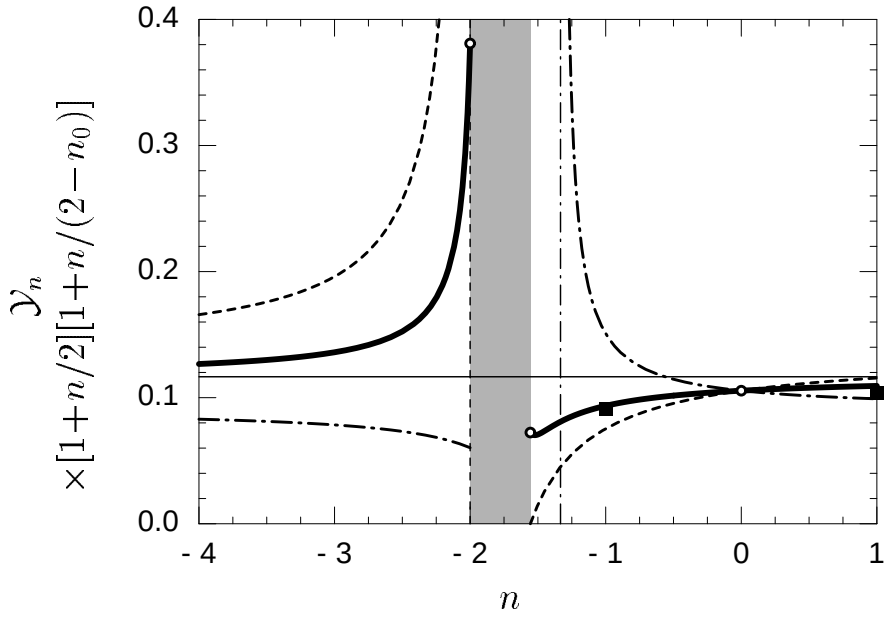

Normalized growth rates of various models:

Youngs' two-fluid (dot-dashed), free fall (dashed) Read's formula (dotted),

and Youngs' preliminary simulations presented at this conference (filled squares).

Free fall and Read's formula respectively provide
highest ($n = -4/3$) and lowest ($n = -2$) positions
of "IRM" pole.

Youngs' two-fluid model is intermediate
between free fall and Read's formula.

Free fall and Read's formula are good approximations around RT,
but can diverge severly in other regimes.

Three continuously connected regimes are found:

- $n_0 - 2 < n < -1$:
directed transport is dominated by diffusion,
- $-1 < n$ and $n < -5/2$:
directed transport is limited by turbulent viscosity,
- $-5/2 < n < -2$:
directed transport is limited by free fall.

Single-fluid models seem limited to first regime,
approximate models are accurate to 30% over second regime,
but only two-fluid approaches can capture all three.

V Conclusions

RANS models can efficiently be analysed as "0D" averages,
without heavy numerical developments.

Such analysis show importance,
of energy balance and Von Kármán number
in characterizing transport and turbulence structure.

Two-fluid approaches seem superior to single-fluid approaches
in capturing directed transport with robust behaviour.

SSVARTs have been shown to provide
a useful set of benchmark flows for models.

Appropriate capture of SSVARTs seems to require two-fluid model.

RT and IRM are limiting cases of SSVARTs.

SSVARTs are currently being investigated by DNS/LES.

Extention of SSVARTs to complex n ?

Acknowledgements

Benoît Dejardins, Philippe Mignon, Eric Van Renterghem...
(Commissariat à l'Energie Atomique, Bruyères-le-Châtel, France),

David L. Youngs (Atomic Weapons Establishment, United Kingdom),

References

V.A. Andronov, S.M. Bakhrakh, V.N. Mokhov, V.V. Nikiforov, and A.V. Pevnitskii, Pis'ma Zh. Eksp. Teor. Fiz. **1**, 62 (1979) and Sov. Phys. JETP Lett. **29**, 57 (1979); M. Bonnet, S. Gauthier, and P. Spitz, in Proceedings of the 1st International Workshop on the Physics of Compressible Turbulent Mixing, Princeton, New Jersey, October 1988, edited by W.P. Dannavik, A.C. Buckingham, and C.E. Leith, LLNL Report Conf-8810234, 1992; M. Bonnet, and S. Gauthier, Phys. Fluids A **2**, 1685 (1990).

S.B. Dalziel, P.F. Linden, and D.L. Youngs, *J. Fluid Mech.* **399**, 1 (1999).

G. Dimonte, and M. Schneider, *Phys. Fluids* **12**, 304 (2000).

N.A. Inogamov, A.M. Oparin, A.Yu. Dem'yanov, L.N. Dembitskii, and V.A. Khokhlov, *J. Exp. Theor. Phys.* **92**, 715 (2001).

A. Llor, CEA Report in print R–5983, France, 2001.

D.L. Youngs, *Physica* **D37**, 270 (1989).

D.L. Youngs, and A. Llor, This conference.

Nonlinear Evolution of an Interface in the Richtmyer-Meshkov Instability

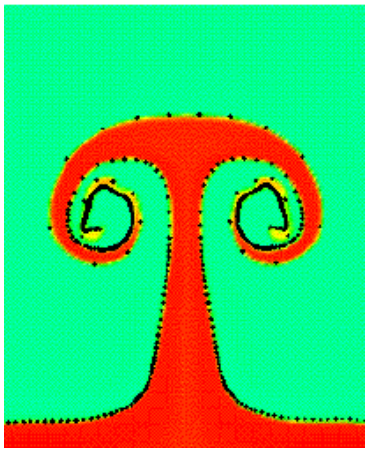

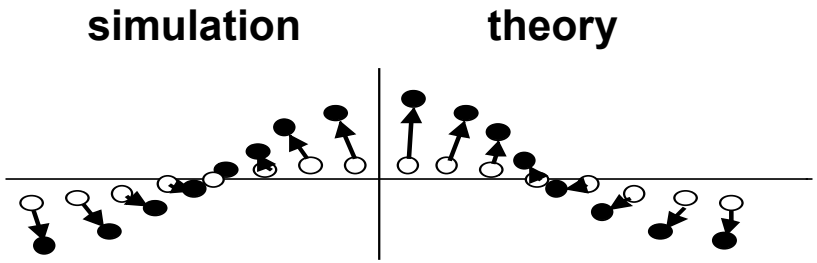

vorticity along interface

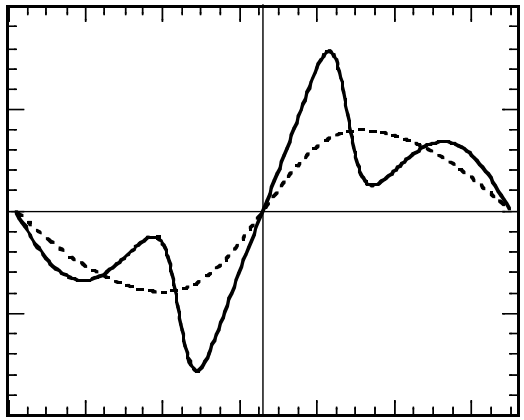

K. Nishihara , C. Matsuoka[a], Y. Fukuda

Institute of Laser Engineering, Osaka University

a) Facluty of Science, Ehime University

18 IWPCTM

Dec. 10-14, 2001

Pasadena, USA

Introduction

Wouchuk-Nishihara formula(1997) of RMI growth rate indicates that RM instability is driven by velocity shear left by the shocks at the interface without the impulsive gravitational acceleration.

ILE-OSAKA

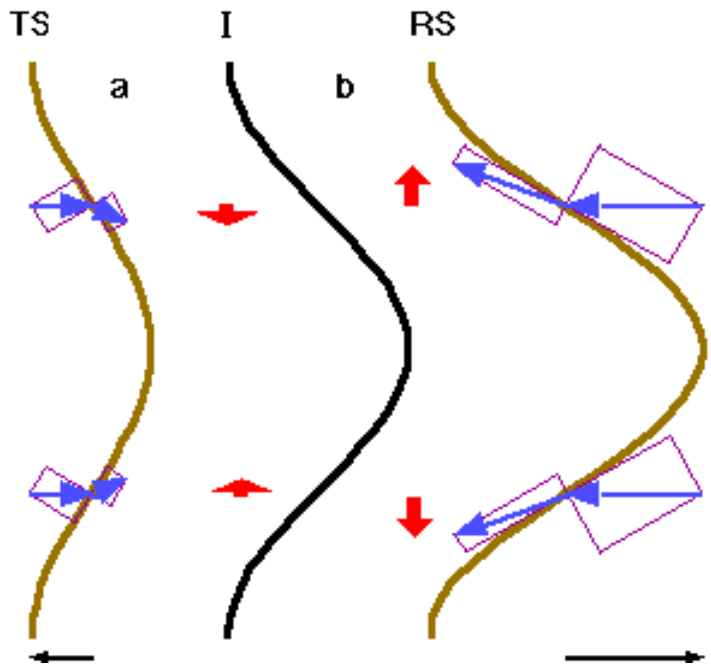

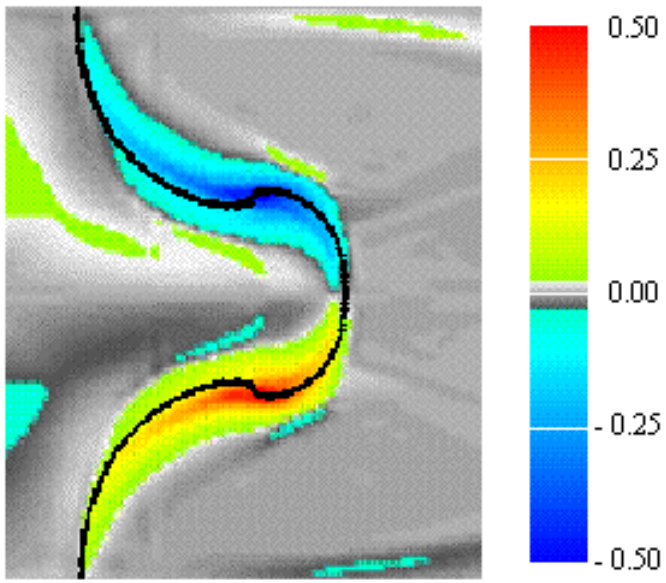

vorticity

$$v_{liu} = \frac{\rho^b \delta v_o^b - \rho^a \delta v_o^a}{\rho^a + \rho^b}$$

$$\delta v_o^a = k\xi_o \left(1 - \frac{u_{st}}{u_{si}}\right) v_i$$

$$\delta v_o^b = k\xi_o \left(1 + \frac{u_{sr}}{u_{si}}\right) (v_l - v_i)$$

Executive summary

- **Nonlinear evolution of Richtmyer-Meshkov instability is described with nonlinear self-interaction of a vortex sheet with a density jump across the sheet.**

- **Lagrangian description of the vortex sheet reveals nonlinear dynamics, such as local stretching and shrinking of the sheet.**

- **Theory shows local increase and decrease of vorticity along the sheet. They results in spiral formation of spike and appearance of opposite vorticity sign at joint of mushroom umbrella, respectively.**

- **We have investigated dependence of nonlinear growth and nonlinear evolution of circulation on the sheet on the Atwood number and initial corrugation amplitude of the sheet.**

Outline of Talk

- Shocked interface vs vortex sheet
- Analytical model for nonlinear dynamics of vortex sheet

  Lagrangian description, finite Atwood number
- Result and comparison with simulations

  nonlinear growth of spike and bubble

  local strethcing and shrinking of interface

  local increase and decrease of vorticity along interface

  dependence of nonlinear growth and circulation on interface on Atwood number and initial corrugation amplitude

By treating the interface as a vortex sheet,
fully nonlinear evolution of RM instability is described.

ILE-OSAKA

M=2, **before shock** $A_0=0.4$ $\xi_0/\lambda=0.0362$

after shock $A'_0=0.376$ $\xi'_0/\lambda=0.02$ $\xi'_0=\xi_0(1-u_{st}/u_{si})$

shock

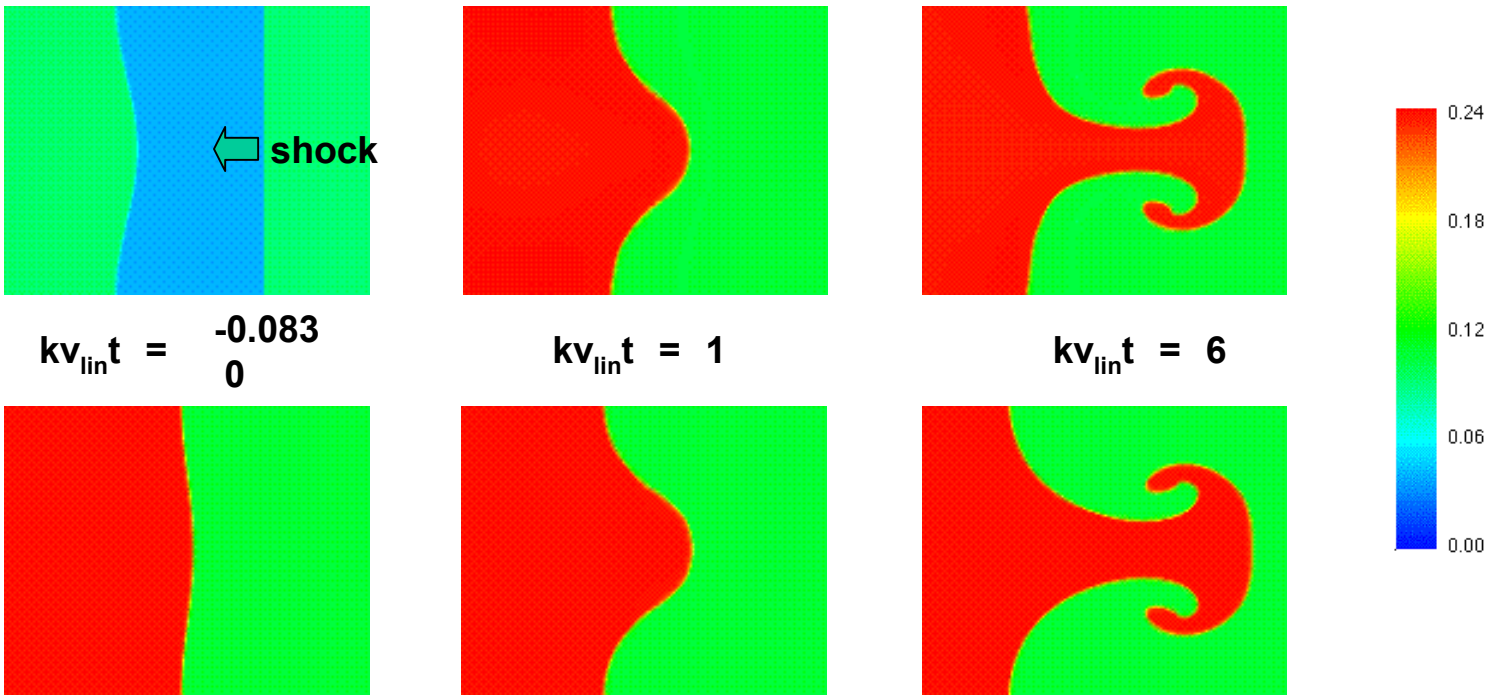

$kv_{lin}t$ = -0.083 0 $kv_{lin}t$ = 1 $kv_{lin}t$ = 6

velocity shear

$$\frac{\mathbf{v}}{\mathbf{v}_{lin}}=\left(-\frac{\partial}{\partial x}\psi,\frac{\partial}{\partial y}\psi,\right) \qquad \psi=e^{\mp kx}\sin ky$$

In case of finite Atwood number, baroclinic term induces vorticity on interface, and streching and shrinking of interface occurs locally in tangential direction

---

By introducing fluid velocity on the interface

$$\mathbf{u}_+ \equiv \frac{\rho_1 \mathbf{u}_1 + \rho_2 \mathbf{u}_2}{\rho_1 + \rho_2}$$

we obtain from Euler equation

$$\frac{\mathbf{D}\Gamma}{\mathbf{Dt}} = \left(\frac{\partial}{\partial \mathbf{t}} + \mathbf{u}_+ \cdot \nabla \right) \Gamma = 2\mathbf{A} \left[\frac{\mathbf{D}\Phi}{\mathbf{Dt}} - \frac{1}{2}\mathbf{q}\cdot\mathbf{q} - \frac{1}{8}\boldsymbol{\kappa}\cdot\boldsymbol{\kappa} + \frac{\mathbf{A}}{2}\boldsymbol{\kappa}\cdot\mathbf{q} \right]$$

where

$\mathbf{A} = \dfrac{\rho_2 - \rho_1}{\rho_2 + \rho_1}$ **(Atwood number) ,** $\Gamma = \phi_1 - \phi_2$ **(circulation),** $\Phi = \phi_1 + \phi_2$

$\boldsymbol{\kappa} = \nabla\Gamma = \mathbf{u}_1 - \mathbf{u}_2$ **(vorticity),** $\mathbf{q} = \dfrac{1}{2}(\mathbf{u}_1 + \mathbf{u}_2)$, $\mathbf{u}_\mathbf{i} = \nabla\phi_\mathbf{i} (\mathbf{i} = 1,2)$

Modified Birkhoff-Rott equation becomes

$$\frac{\partial}{\partial \mathbf{t}} \mathbf{Z}^* = \mathbf{u}_+ = \mathbf{q} - \frac{\mathbf{A}}{2}\boldsymbol{\kappa} = \frac{1}{2\pi\mathbf{i}} \int \frac{\boldsymbol{\kappa} \mathbf{ds}'}{\mathbf{Z} - \mathbf{Z}'} - \frac{\mathbf{A}}{2}\boldsymbol{\kappa}, \quad \mathbf{Z}(\mathbf{t}) = \mathbf{x} + \mathbf{iy}$$ **(position of the interface)**

Nonlinear Theory of a Vortex Sheet(1): Basic Equations

Circulation on vortex sheet

$$\frac{\mathbf{D}}{\mathbf{Dt}}\Gamma = \left(\frac{\partial}{\partial \mathbf{t}} + \mathbf{u}_+ \cdot \nabla\right)\Gamma = 2\mathbf{A}\left[\frac{\mathbf{D}\Phi}{\mathbf{Dt}} - \frac{1}{2}\mathbf{q}\cdot\mathbf{q} - \frac{1}{8}\boldsymbol{\kappa}\cdot\boldsymbol{\kappa} + \frac{\mathbf{A}}{2}\boldsymbol{\kappa}\cdot\mathbf{q}\right]$$

where

$$\mathbf{A} = \frac{\rho_2 - \rho_1}{\rho_2 + \rho_1} \quad , \quad \Gamma = \phi_1 - \phi_2 \quad , \quad \Phi \equiv \phi_1 - \phi_2 \quad ,$$

$$\mathbf{u}_+ = \frac{\rho_1 \mathbf{u}_1 + \rho_2 \mathbf{u}_2}{\rho_1 + \rho_2} \quad , \quad \boldsymbol{\kappa} = \mathbf{u}_1 - \mathbf{u}_2 \quad , \quad \mathbf{q} = \frac{1}{2}(\mathbf{u}_1 + \mathbf{u}_2)$$

incompressible and irrotational fluid

$$\nabla^2 \phi_{\mathbf{i}} = 0 \quad , \quad \mathbf{u}_{\mathbf{i}} = \nabla \phi_{\mathbf{i}} \, (\mathbf{i} = 1,2)$$

kinematic boundary conditions

$$\mathbf{r}_{\mathbf{t}} \cdot \mathbf{n} = \mathbf{u}_+ \cdot \mathbf{n} \quad , \quad \mathbf{r}_{\mathbf{t}} \cdot \mathbf{t} = \mathbf{u}_+ \cdot \mathbf{t} \quad , \quad \mathbf{u}_1 \cdot \mathbf{n} = \mathbf{u}_2 \cdot \mathbf{n}$$

Nonlinear Theory of a Vortex Sheet(2) : Expantion

Lagrangian marker of vortex sheet

$$x(t) = \theta + X(\theta, t)$$
$$y(t) = Y(\theta, t)$$

expansion

$$X = \sum_n \varepsilon^n X^{(n)} \quad , \quad Y = \sum_n \varepsilon^n Y^{(n)}$$

$$\phi_1 = \sum_n \varepsilon^n \phi_i^{(n)} e^{\mp nky} \cos nkx \quad ,$$

By introducing normalization, kx , $kv_{lin}t$, and $k\phi_i / v_{lin}$, nonlinear evolution of a vortex sheet is determined from two parameters

A (Atwood number) and $k\xi_0$ (initial corrugation of sheet),

where $v_{lin} = \dfrac{\rho_1 \delta v_{10} - \rho_2 \delta v_{20}}{\rho_1 + \rho_2}$, **(Wouchuk – Nishihara formula)**

Comparison of Nonlinear Growth Rates (Spike grows faster than bubble)

ILE OSAKA

$M=2 \quad A_0=0.4 \quad \xi'_0/\lambda=0.02$

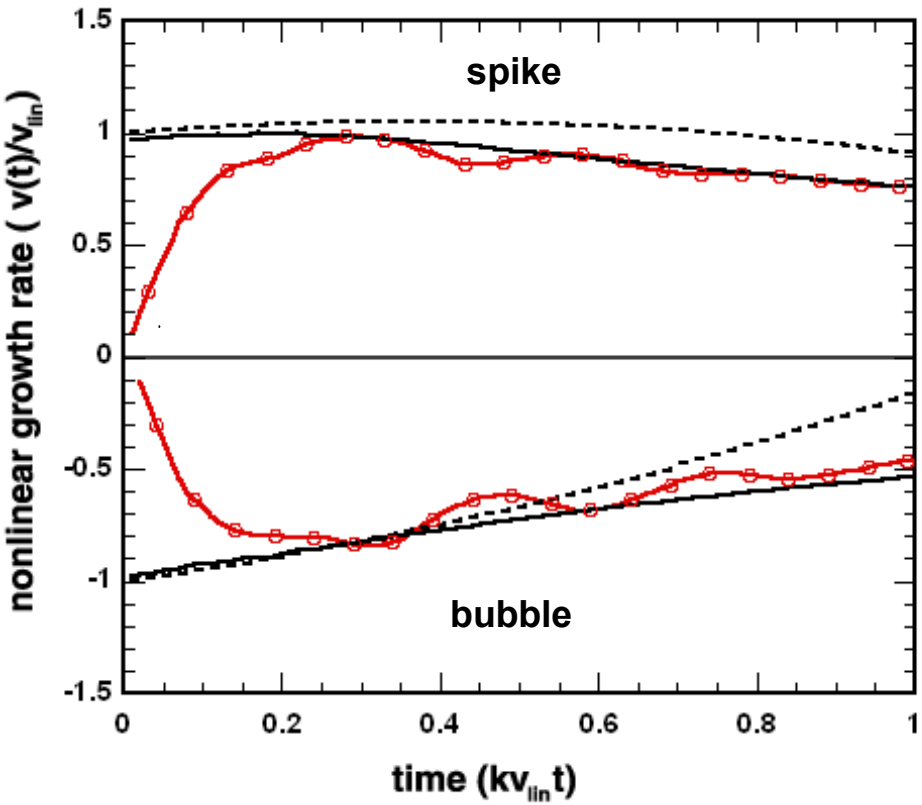

Incident shock hits corrugated interface

Nonuniform velocity shear at corrugated interface

3rd order nonlinear theory of vortex sheet

Theoretical dependence of nonlinear growth and vorticity on Atwood number and corrugation amplitude agrees well simulations

ILE OSAKA

vorticity density

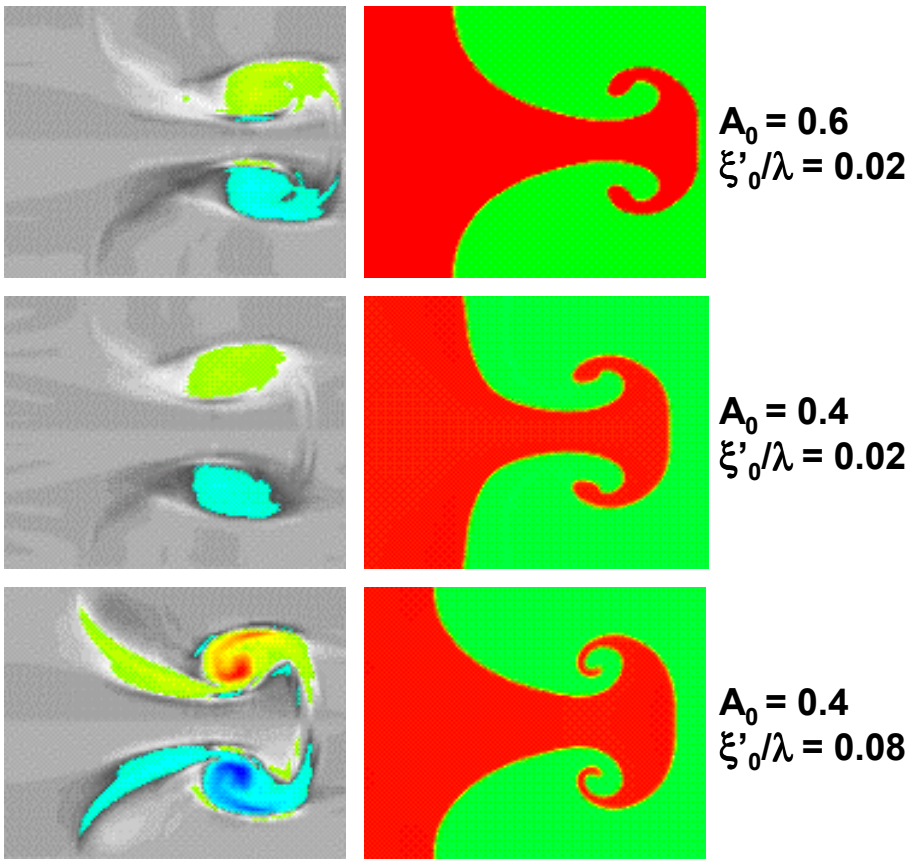

$A_0 = 0.6$
$\xi'_0/\lambda = 0.02$

$A_0 = 0.4$
$\xi'_0/\lambda = 0.02$

$A_0 = 0.4$
$\xi'_0/\lambda = 0.08$

$kv_{lin}t = 6$

Larger Atwood number leads to larger nonlinear growth

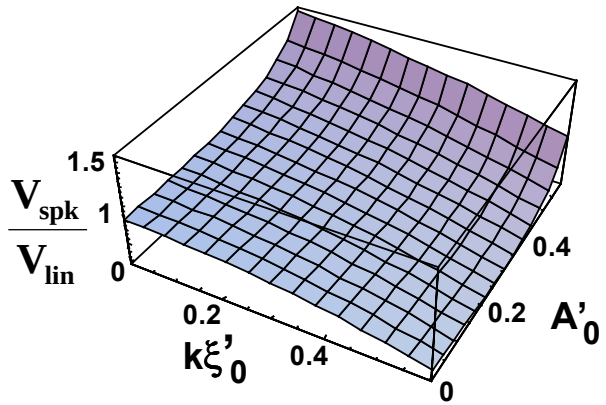

Larger corragation amplitude lead to rapid increase of circulation

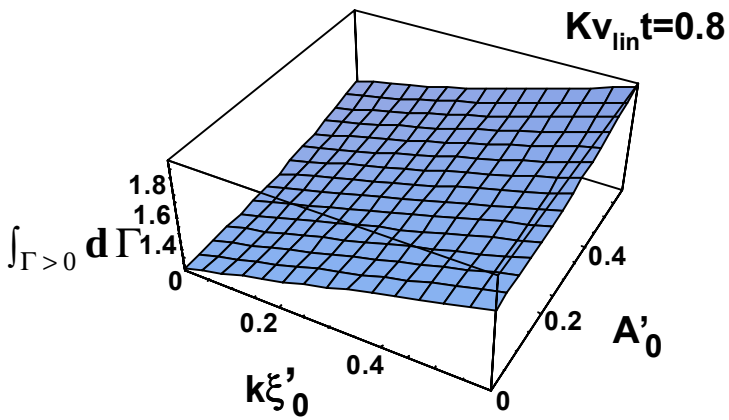

Lagrangian markers move both x and y directions.
Stretch and shrink of vortex sheet occur locally.

Theoretical results agrees well with simulations

simulation
(shocked interface)

simulation
(vortex sheet)

theory
(x(θ ,t) , y(θ ,t))

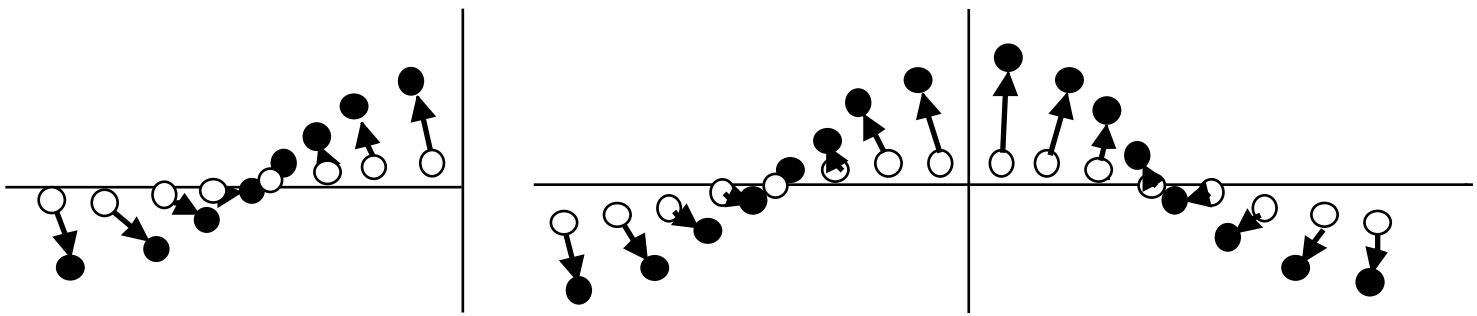

- ● $Kv_{lin}t = 0.80$
- ○ $Kv_{lin}t = 0.05$

$A_0' = 0.376$

$x'_0/\lambda = 0.02$

$M = 2$

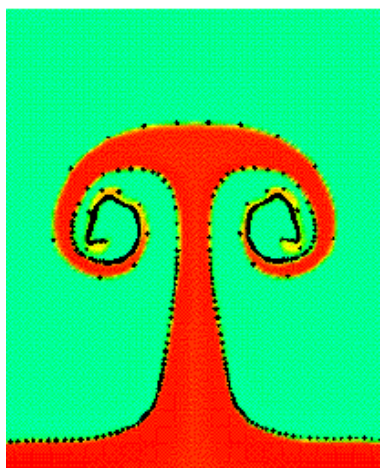

Theory shows local increase of vorticity (tip of spiral), and local decrease of vorticity (joint of mushroom umbrella).

ILE OSAKA

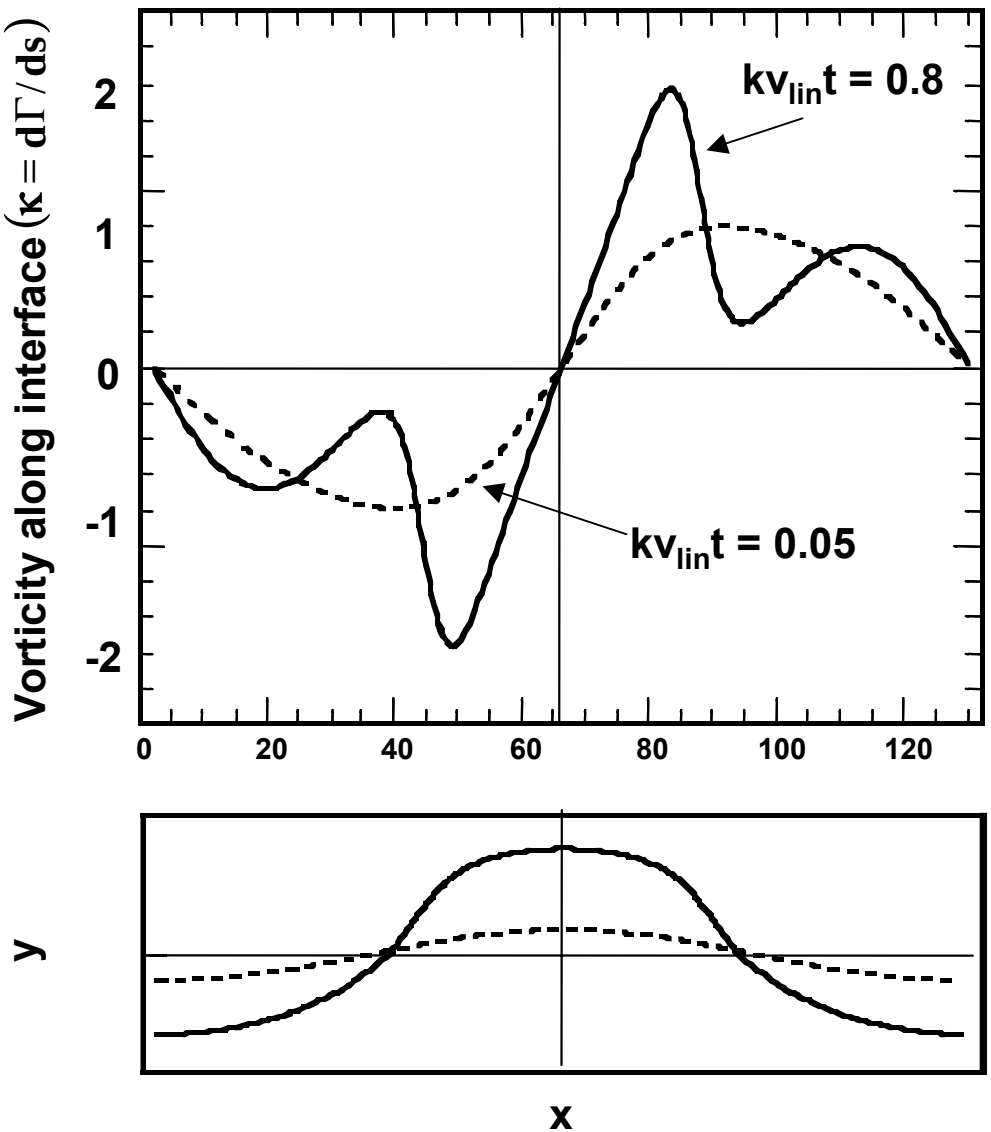

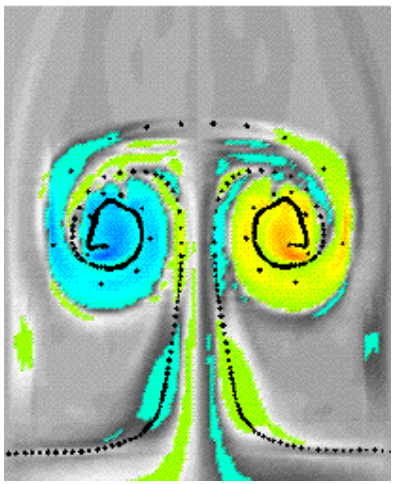

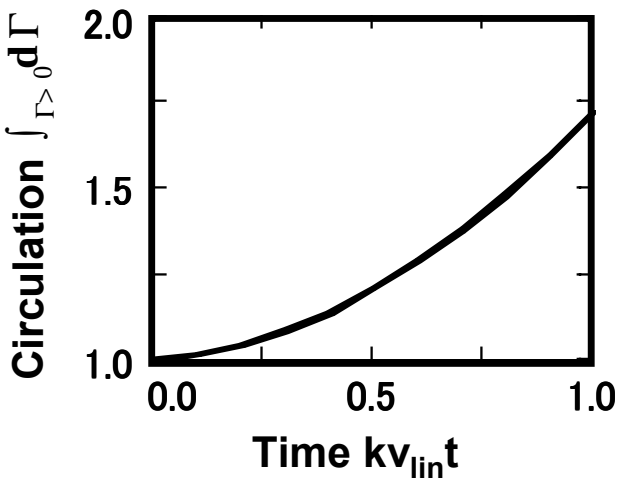

Conclusion

- Nonlinear evolution of Richtmyer-Meshkov instability is described with nonlinear self-interaction of a vortex sheet with a density jump across the sheet.
- Lagrangian description of the vortex sheet reveals nonlinear dynamics, such as local stretching and shrinking of the sheet.
- Theory shows local increase and decrease of vorticity along the sheet. They results in spiral formation of spike and appearance of opposite vorticity sign at joint of mushroom umbrella, respectively.
- We have investigated dependence of nonlinear growth and nonlinear evolution of circulation on the sheet on the Atwood number and initial corrugation amplitude of the sheet.

Vortex-Merger Statistical Model for the Late Time Self-Similar Evolution of the Kelvin-Helmholtz Instability

Avi Rikanati[1,2], U. Alon[3], Dov Shvarts[1,2]

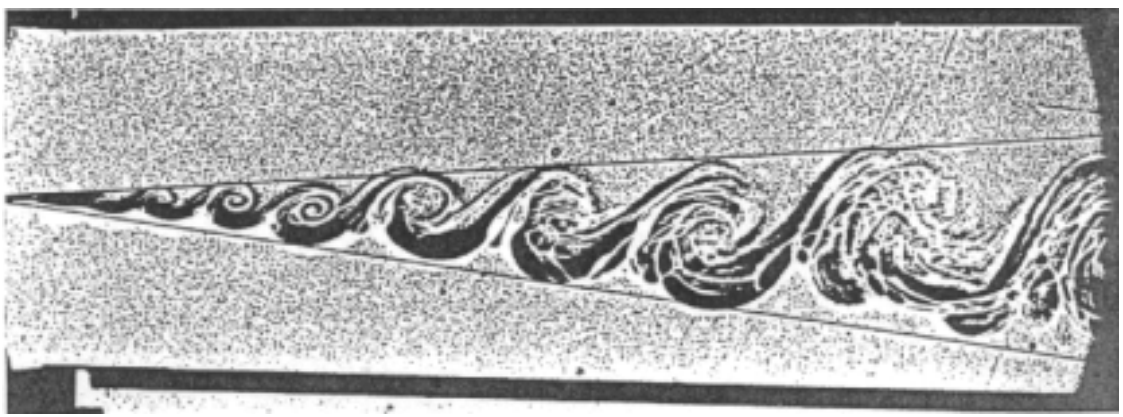

[1] Nuclear Research Center, Negev, ISRAEL

[2] Ben Gurion University, Beer-Sheva, ISRAEL

[3] Weizmann Institute of Science, Rehovot, ISRAEL

Abstract

The nonlinear growth of the multi-mode incompressible Kelvin-Helmholtz (KH) shear flow instability at all density ratios is treated by a non empirical large scale statistical-mechanics eddy-pairing model, based on the single eddy behavior and the process of two eddy-pairing. From the model, a linear time growth of the mixing zone is obtained, resulting in the linear time growth coefficient for several density ratios as well as an asymptotic lognormal eddy size distribution and the average eddy life time probability. Very good agreement with previous works, full numerical simulations and experiments is achieved.

Example of Shadowgraph Photography*

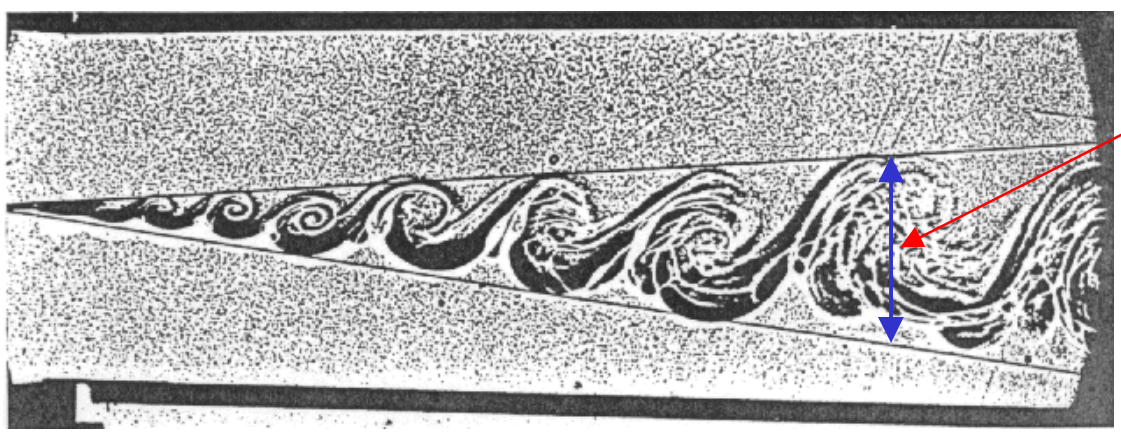

*Roshko & Brown, J. Fluid Mech, 1974.

Numerical Simulations for the Single Mode case

Material interface

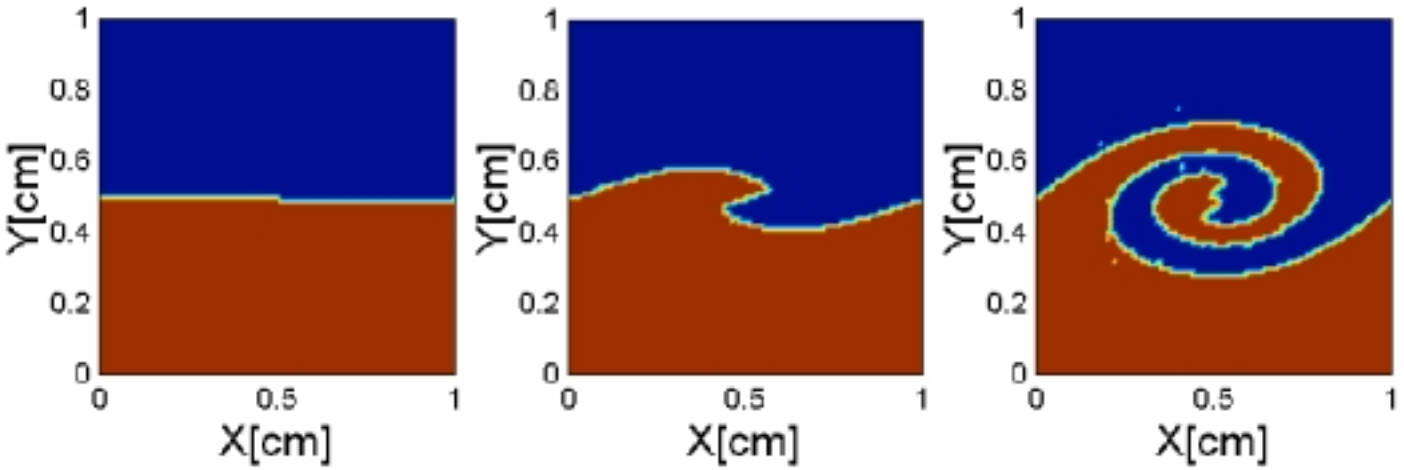

Vorticity Colormaps

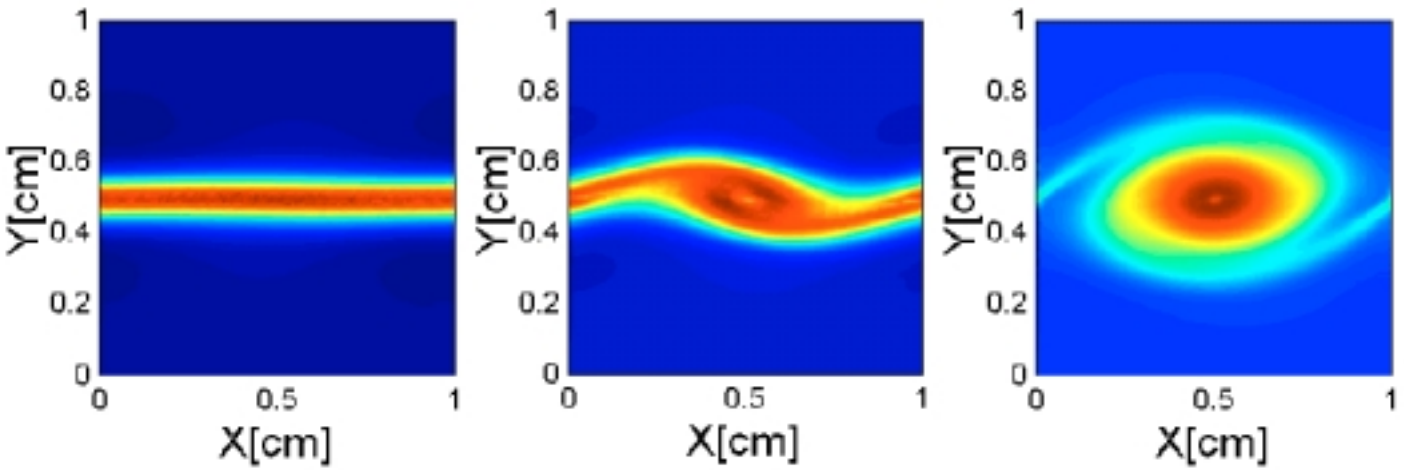

Fast
Vortex
Formation

Vortex Line - Analytical Solution

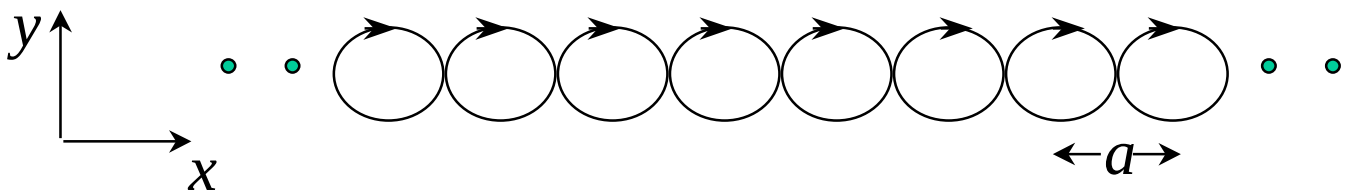

- Vorticity Definition: $\vec{\omega} = \nabla \times V$
- Vortex Strength set by Kelvin Theorem of Circulation:

$$\Gamma = \int_{Surface} \vec{\omega} \cdot ds = \oint_{Contour} v \cdot dl = Const$$

- Resulting Complex Potential of a Vortex Line :

$$W(z) = \sum_{n=-\infty}^{\infty} \left(i \cdot \frac{\Gamma}{2\pi} \right) \ln(z - na) = \frac{i \cdot \Gamma}{2\pi} \ln\left(Sin(\pi \cdot z / a)\right)$$

$$(z = x + i \cdot y)$$

Vortex Model for a Single Mode Initial Perturbation

Velocity field calculated as a derivative of the complex potential

$$u(z) - i \cdot v(z) = \frac{dW(z)}{dZ}$$

Interface Evolution

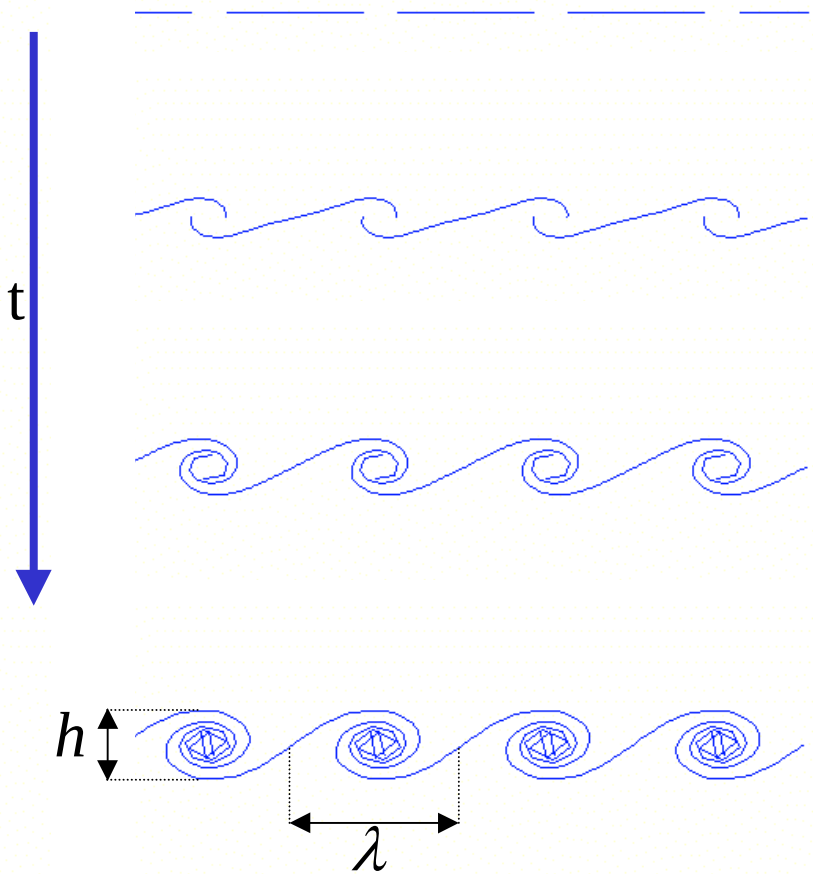

Eddy Height Vs. Time*

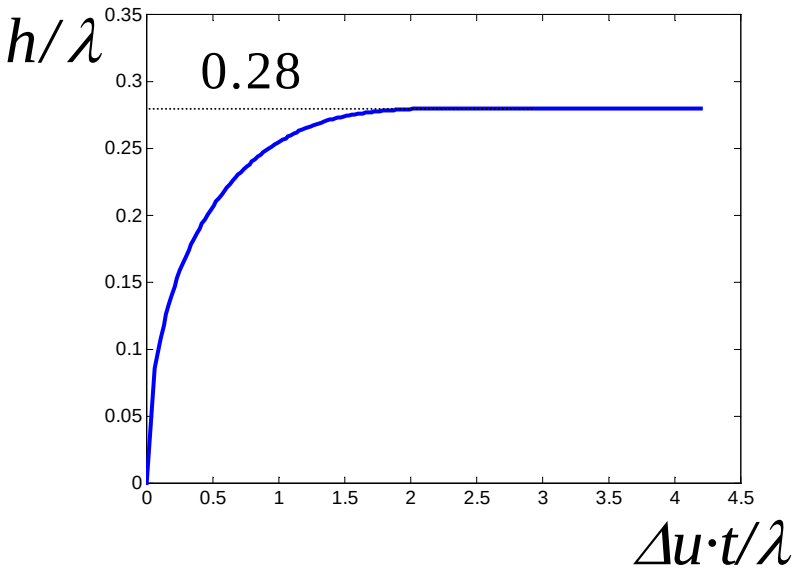

$$h(\lambda, t \to \infty) = 0.28\lambda$$

*Analytical Solution by Y. Elbaz

Experimental eddies trajectories show the vortex merger dominance

Vortex Trajectories*

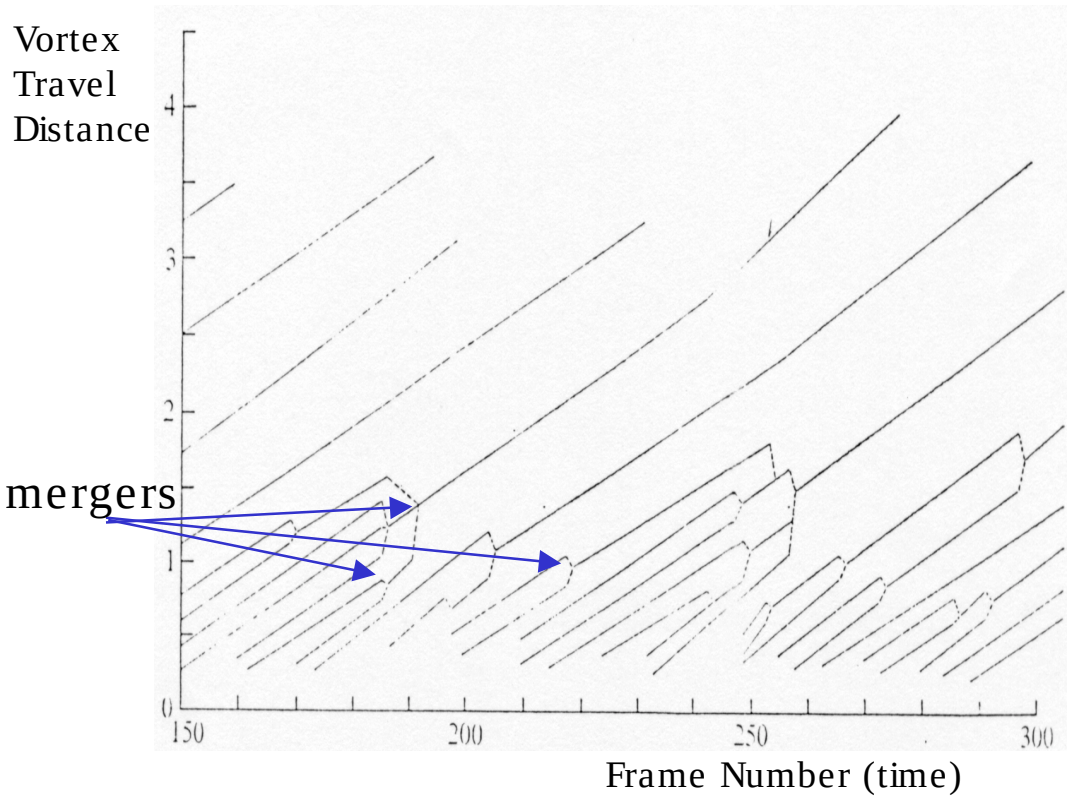

Single Vortex Merger**

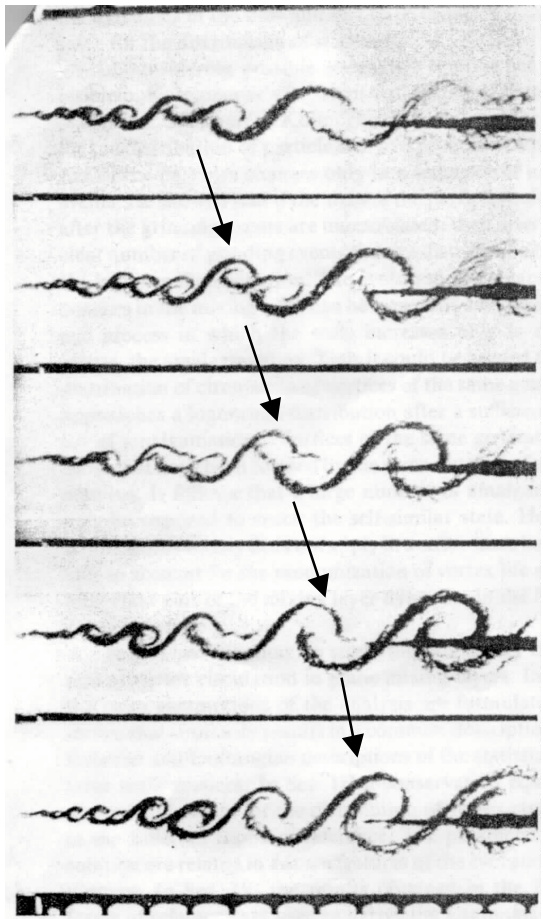

* Roshko & Brown (1974)
** Bernal (1988)

Two Vortex Pairing - Model Results

Two Vortex Setup

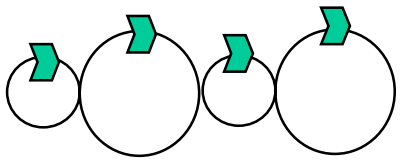

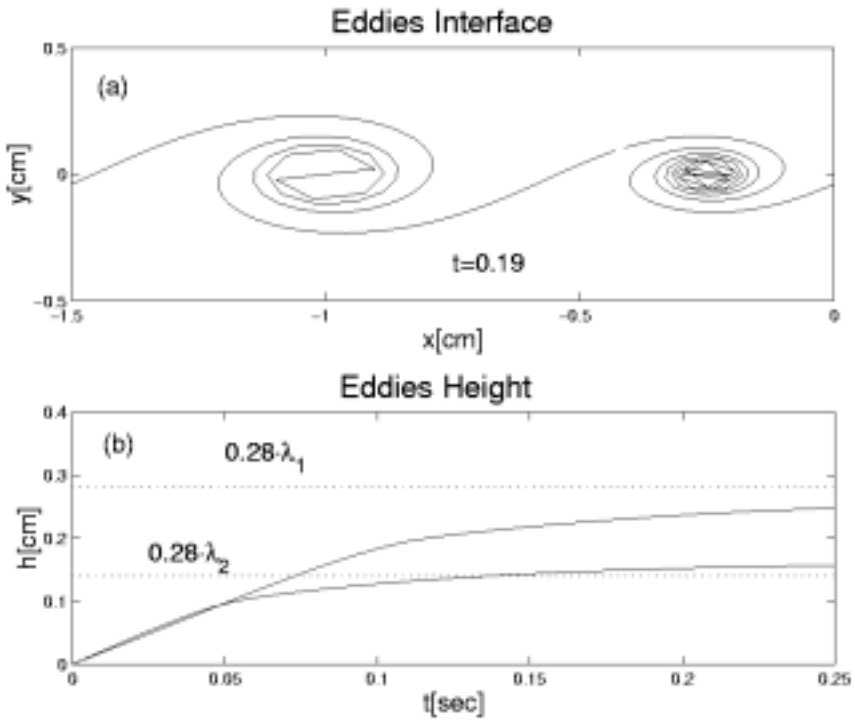

NO MERGER!
3 eddies must be introduced

Three Vortex Setup

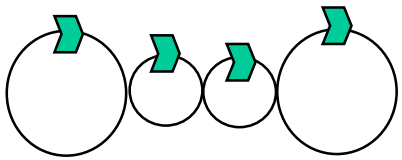

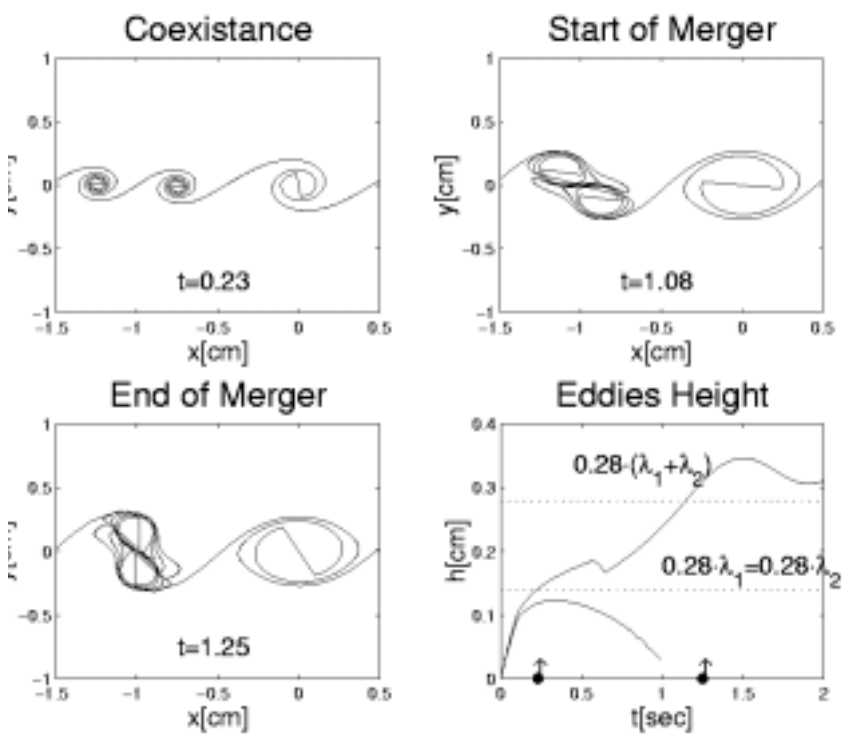

New vortex at predicted height of $\lambda_1+\lambda_2$

Statistical Mechanics Model for the Multi Mode Kelvin-Helmholtz Instability

A large ensemble of eddies is set along a line.

Each eddy is assumed to possess its asymptotic height according to the vortex model.

$$h(\lambda, t) = 0.28\lambda$$

Eddies increase in size through occasional mergers, according to the previously calculated merger rate.

$$\lambda_i \, , \, \lambda_{i+1}$$

$$\omega(\lambda_i \, , \, \lambda_{i+1})$$

$$\lambda_i + \lambda_{i+1}$$

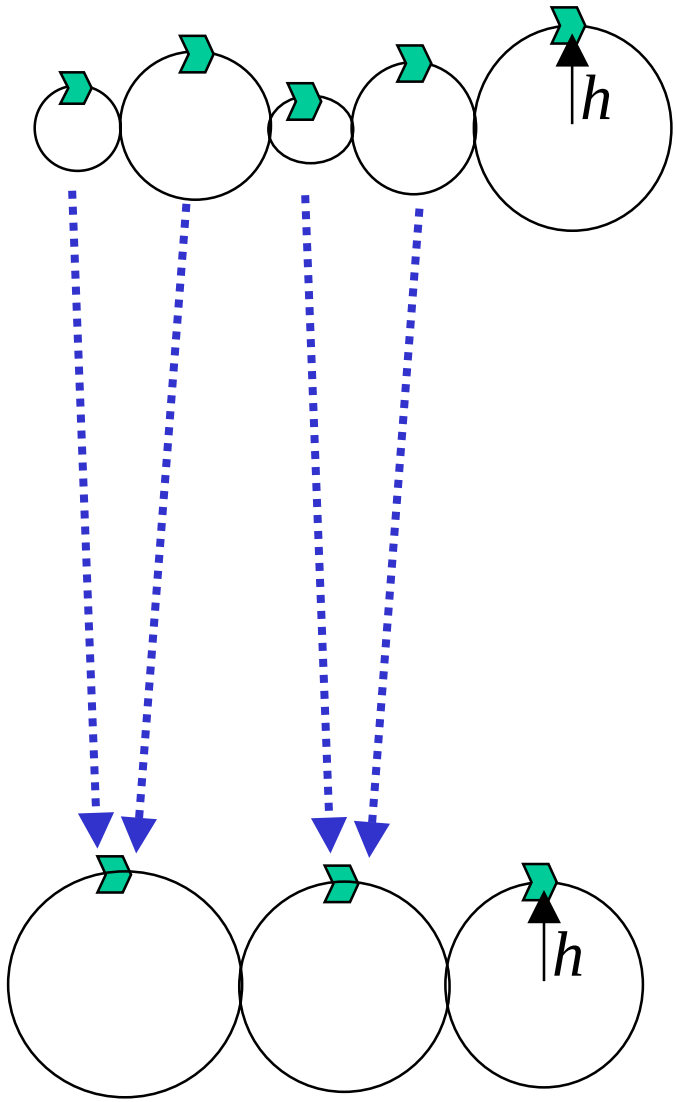

Self-Similar Analyses of the Multi-Mode KH Instability

- Average width: $\langle h(t)\rangle = 0.56\langle\lambda\rangle = 0.56L/N(t)$
- Number of eddies change through mergers: $d(N(t))/dt = -\langle\omega\rangle N(t)/2$
- Merger rate scales as: $\langle\omega\rangle = \Delta u\langle\omega_0\rangle/\langle\lambda\rangle$
- Resulting number of eddies: $N(t) = 0.56L/(\Delta u \cdot t)/\langle\omega_0\rangle$

Integrating the above, linearity is achieved through simple arguments.

$$\langle h(t)\rangle = \langle\omega_0\rangle \Delta u \cdot t$$

Results from the Large-Scale Statistical Model

Statistical Model

$$h_{mix}(t) = a_0 \cdot t \quad ; \quad a_0 \approx \underline{0.2}$$

Experiment

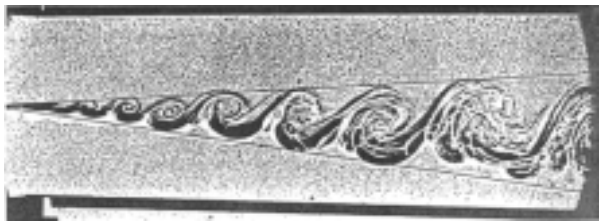

$h_{mix}(t) = a_0 \cdot t$

$a_0(\rho_1 = \rho_2) \approx \underline{0.2}$

Eddy Size Distribution

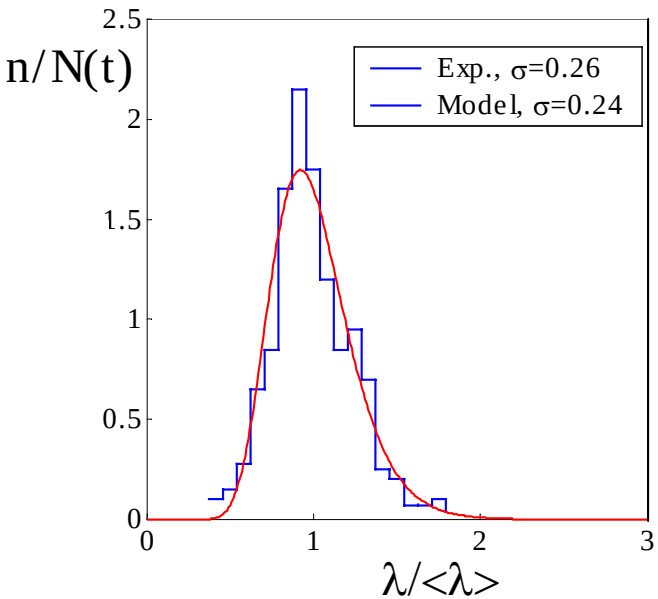

Life-time Probability

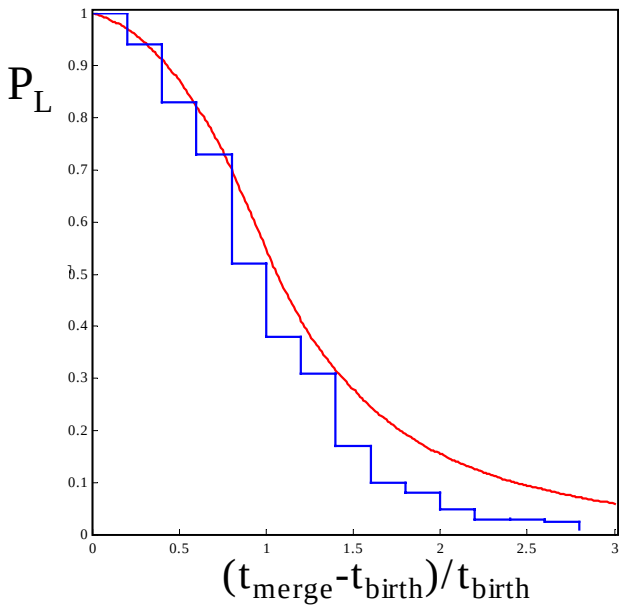

Experimental results taken from Roshko & Brown, J. Fluid Mech, 1974 & L.P. Bernal, Phys Fluids (1988).

Multi Mode Numerical Simulation

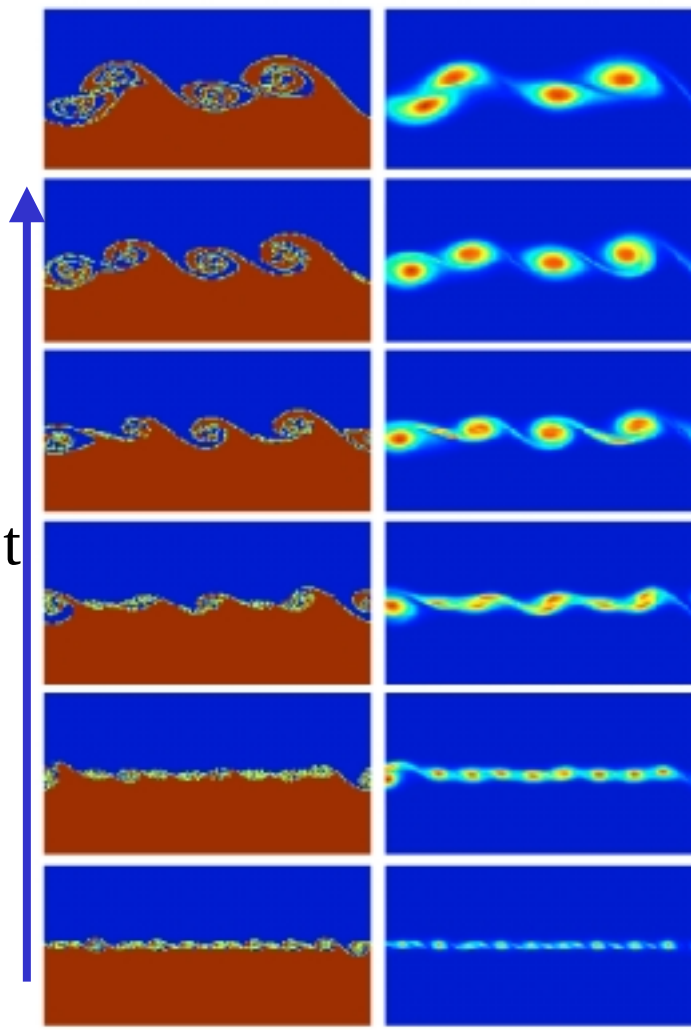

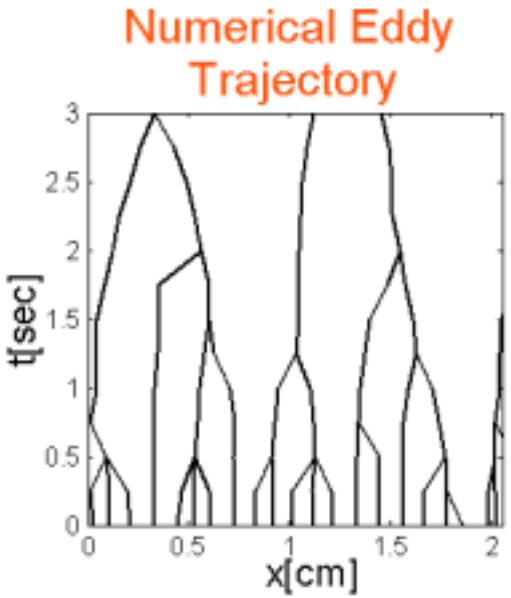

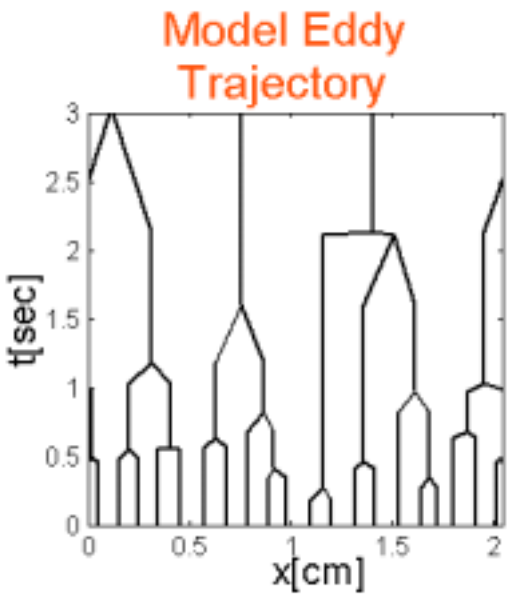

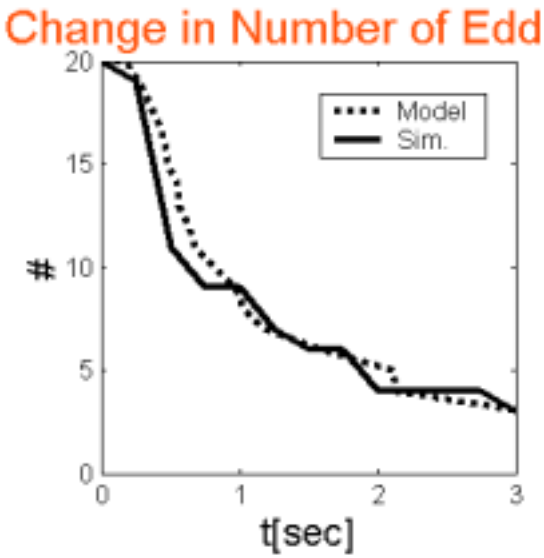

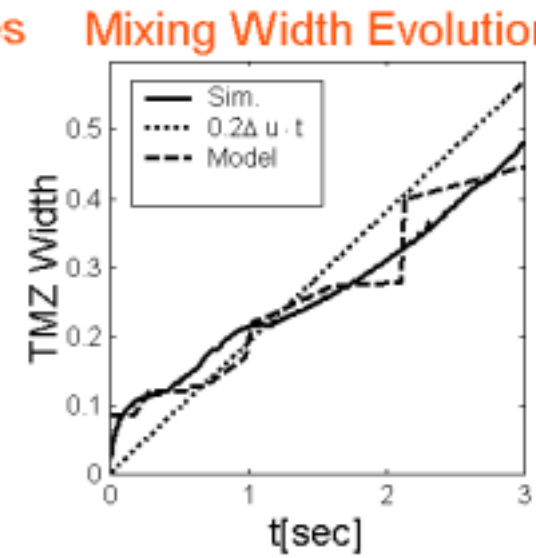

Density Ratio Effects on the KH Instability: Single Mode - Numerical Simulations

$\rho_1=\rho_2$; $v_1=v_2$

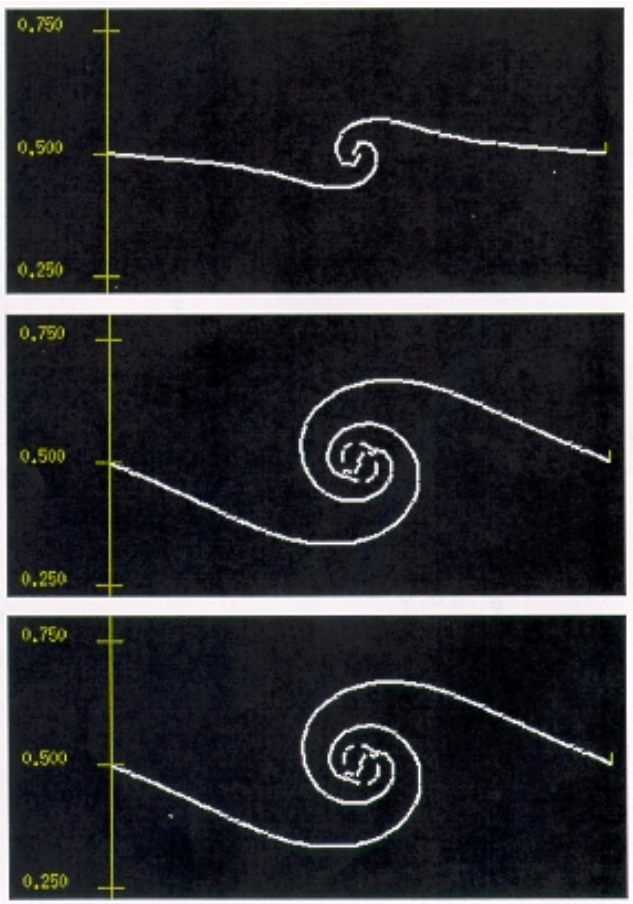

$\rho_1=7\rho_2$; $v_1=v_2$

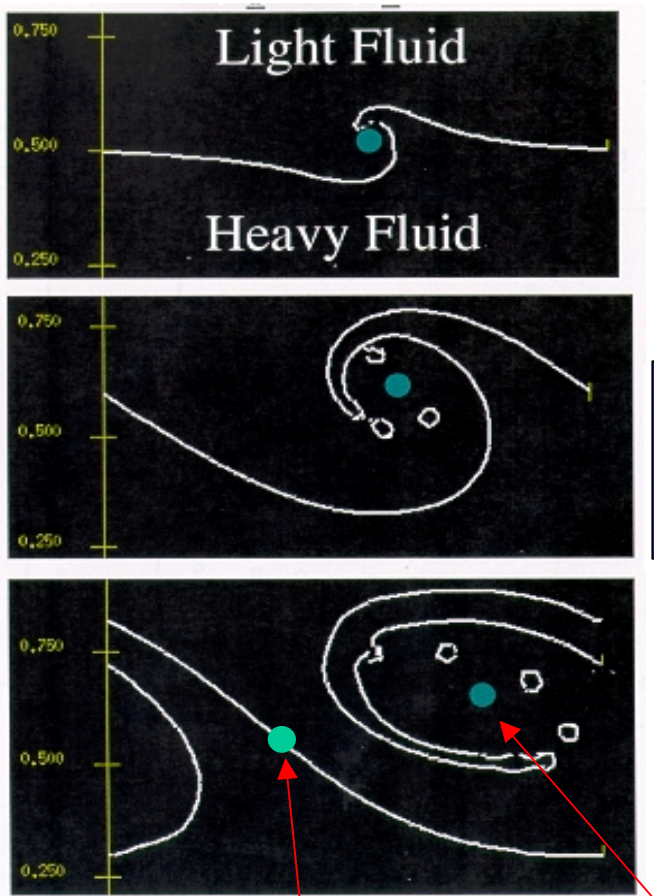

Vortex drifts at

$$v_c \neq \frac{v_1 + v_2}{2}$$

according to pressure equilibrium on stagnation points between neighboring vortices*:

$$\rho_1(v_1 - v_c)^2 = \rho_2(v_c - v_2)^2$$

Stagnation point

Vortex

*Dimotakis et. Al., AIAA J. **24**, 1791 (1986)

Multi-Mode Case: Numerical Simulation

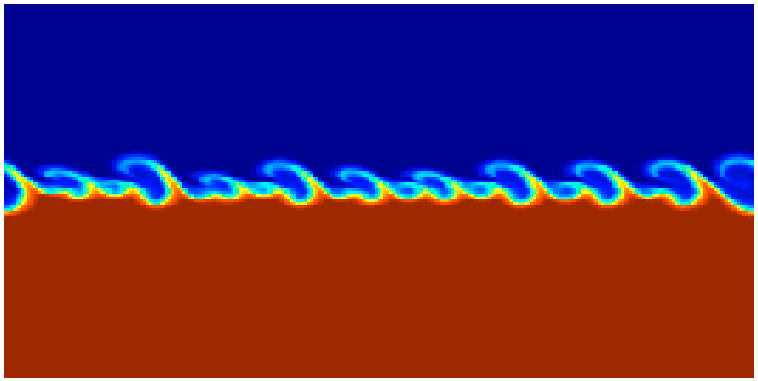

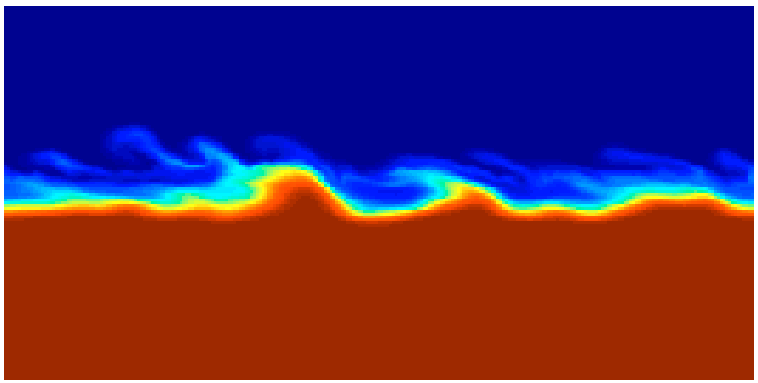

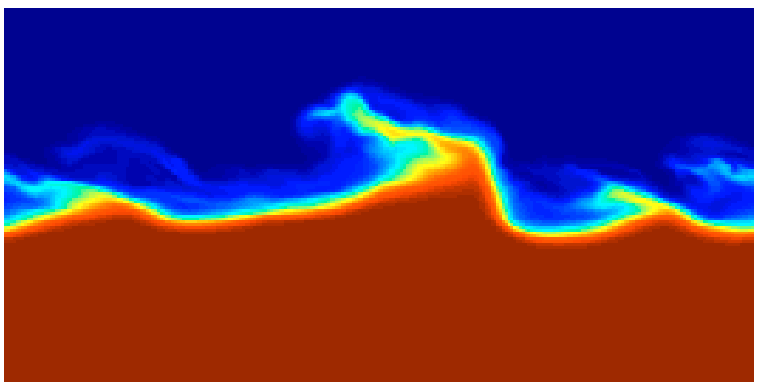

Mixing Width Comparison

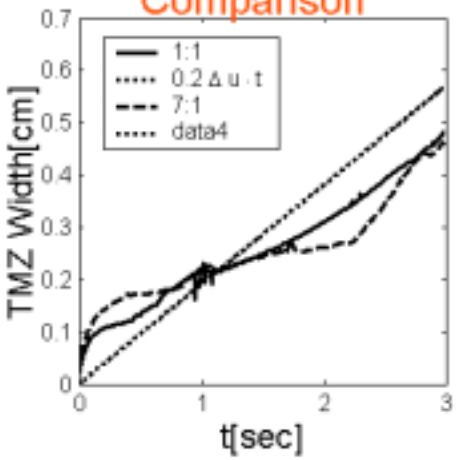

Trajectories Comparison

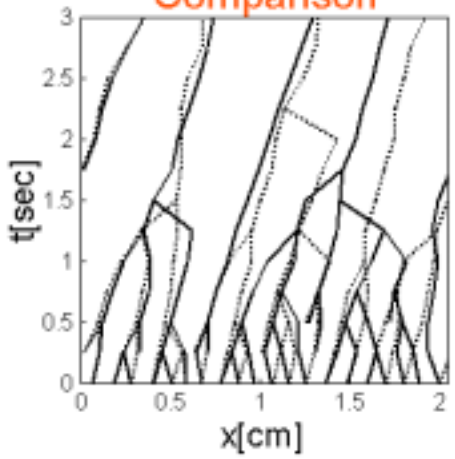

Width Comparison

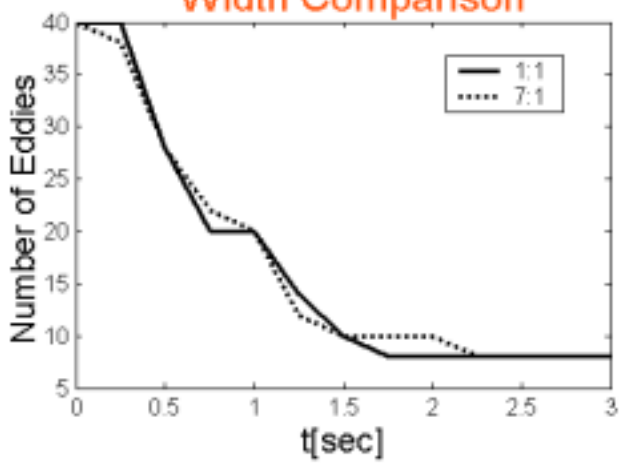

No true density ratio effects on the large scale evolution of the flow

Drift Velocity Effect on the Linear Growth Coefficient

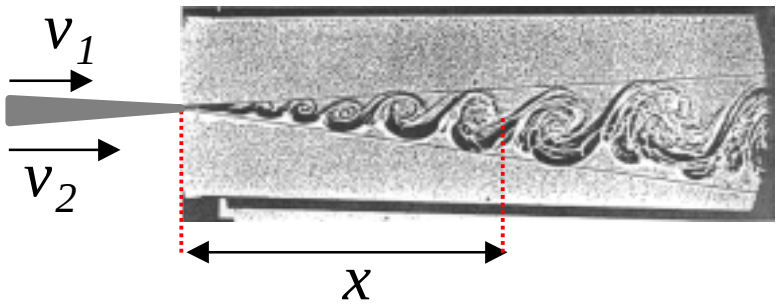

$$\bar{v} = (v_1 + v_2)/2$$

v_d = *drift velocity*

$t(x) = ?$

$v_d = 0 \ (\rho_1 = \rho_2)$ | $v_d \neq 0 \ (\rho_1 \neq \rho_2)$

$$t = \frac{x}{\bar{v}}$$

$$h_{mix} = 0.2 \cdot \Delta u \cdot t = 0.4 \frac{v_1 - v_2}{v_1 + v_2} x$$

$$t = \frac{x}{v_c} = \frac{x}{\bar{v} + v_d}$$

$$h_{mix} = 0.2 \cdot \Delta u \cdot t = 0.4 \frac{f}{1 \pm c \cdot f} x$$

$$with \quad f = \frac{v_1 - v_2}{v_1 + v_2}$$

Linear Growth Coefficient in Agreement with Experiments

For mixing zone height of: $h(x)=\delta \cdot x$

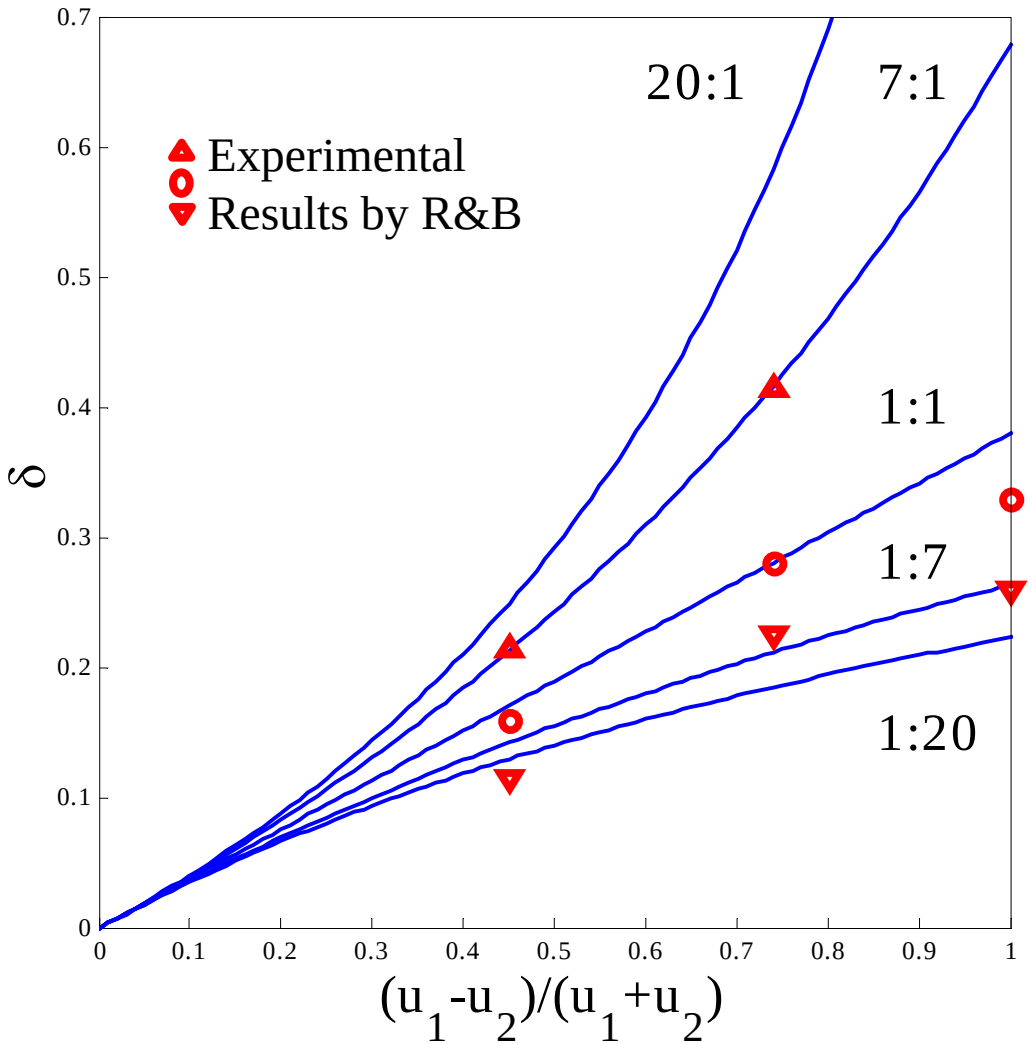

$h_{mix}(x)$ not linear with Δu for $v_d \neq 0$

Summary

- A large scale statistical model for the KH instability was developed resulting in:
  - Linear growth rate coefficient for all density ratios.
  - Full statistical characterization of the flow.
  - The vortex merger is established as the growth mechanism of the mixing zone.
- Very good agreement with simulations and experiments is achieved.

High Mach Number and High Initial Amplitude Effects on the Evolution of the Single-Mode Richtmyer-Meshkov Instability – Theoretical Study

A. Rikanati, D. Oron, O. Sadot & D. Shvarts

Impulsive Models for the Small Amplitude Single-Mode RM Instability

Assuming low mach (SW effects as a - delta function acceleration) and small amplitudes (ak<<1):

$$u_{bubble} = \Delta u_{1d} \cdot k \cdot \frac{\rho_1 - \rho_2}{\rho_1 + \rho_2} a_0$$

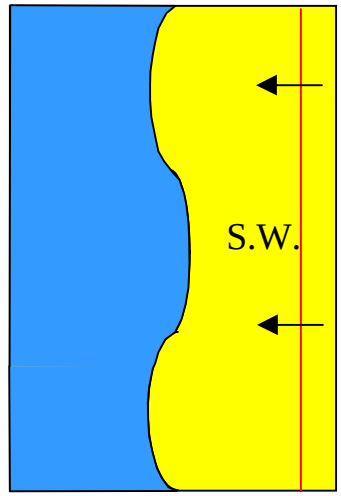

k – wavelength

Δu_{1d}-velocity of unperturbed contact surface induced by shock wave

ρ_1, ρ_2 - shocked densities before and after contact surface

Fast - Slow interaction

Richtmyer Formula :

$$a_0 = a_0^+$$

a_0^+ - post shock amplitude

Slow - Fast interaction (phase inversion)

Meyer-Blewett correction :

$$a_0 = \frac{a_0^+ + a_0^-}{2}$$

a_0^+ - post shock amplitude

a_0^- - pre shock amplitude

Results from New Shock Tube Experimental by Sadot et. al. M=1.2 (E36)

λ=80mm
a=20mm

λ=40mm
a=12mm

λ=26mm
a=10mm

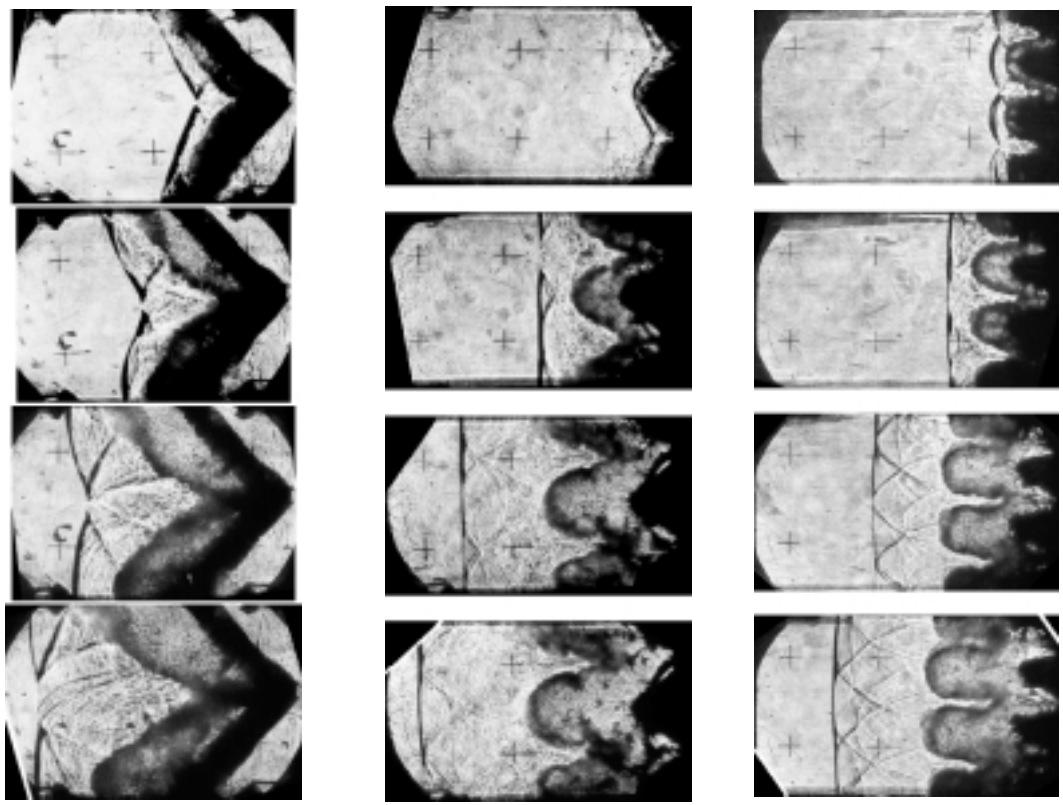

Experimental Velocity Reduction

Class A Experiments:

Similar reduction at a range of Mach numbers (1.2-15.3)

Apparent High Amplitude Effect

Class B Experiments:

Can be High Mach Effect

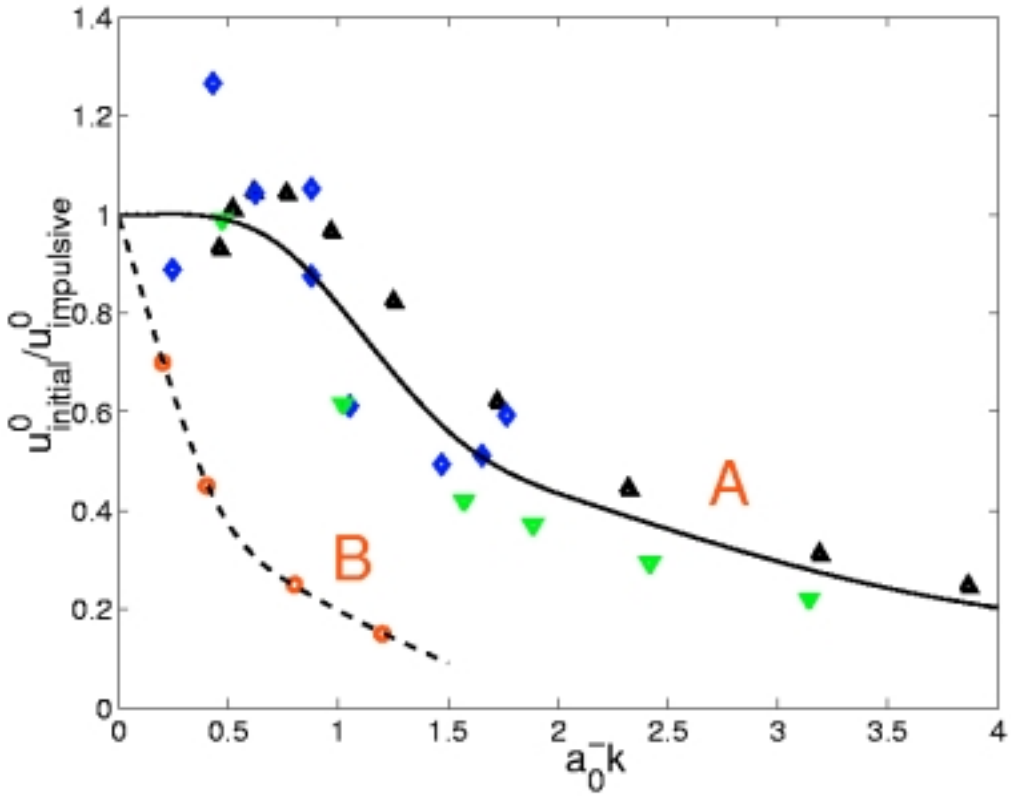

- Dimonte Be → Foam (M=15.3)
- Aleshin Ar → Xe (M=2.5)
- Sadot Air → SF_6 (M=1.2)
- Aleshin He → Xe (M=2.5)

Vorticity Deposition Model

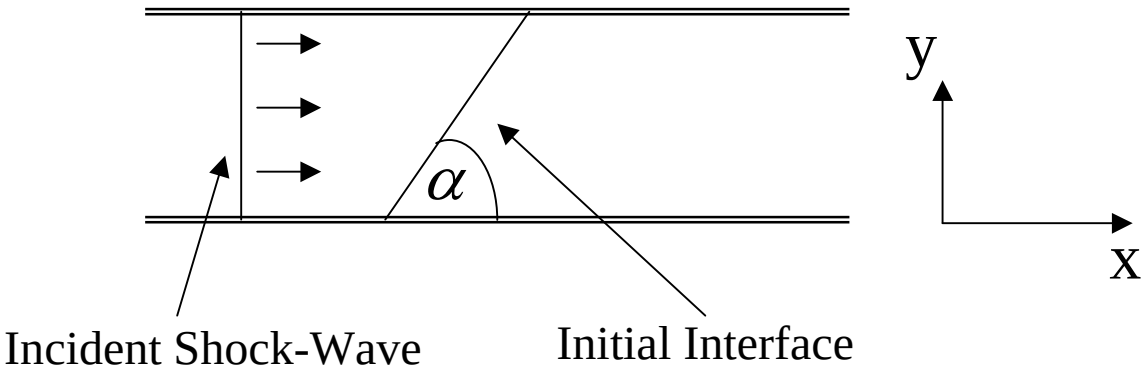

- Local vorticity deposition per unit length*:

$$\Gamma ds = \Gamma_0(M, \gamma_1, \gamma_2, \rho_1, \rho_2)\sin(\alpha)ds$$

- Bubble tip velocity:

$$u(z) - i \cdot v(z) = 2\pi \int_{\text{interface}} \Gamma(z)\cot((z - z') \cdot \pi / d)dz'$$

$$z = x + i \cdot y$$

* R. Samtaney and N. J. Zabusky, Phys. Fluids A **5**, 1285 (1993)

Model Velocity Reduction Compared with class ‘A’ Experiments and Simulations

Experiments by Dimonte and Aleshin

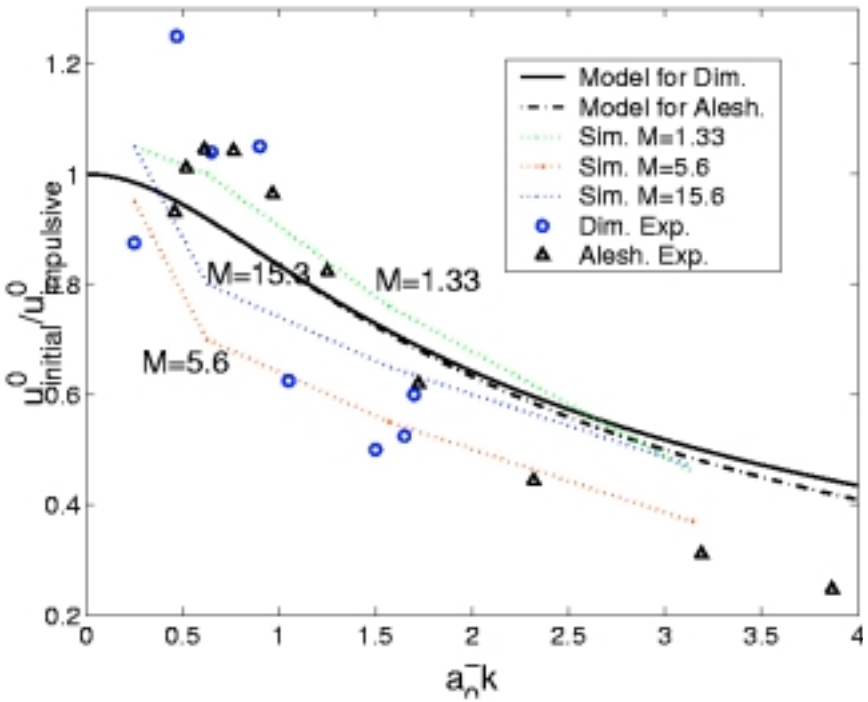

New shock Tube Experiments

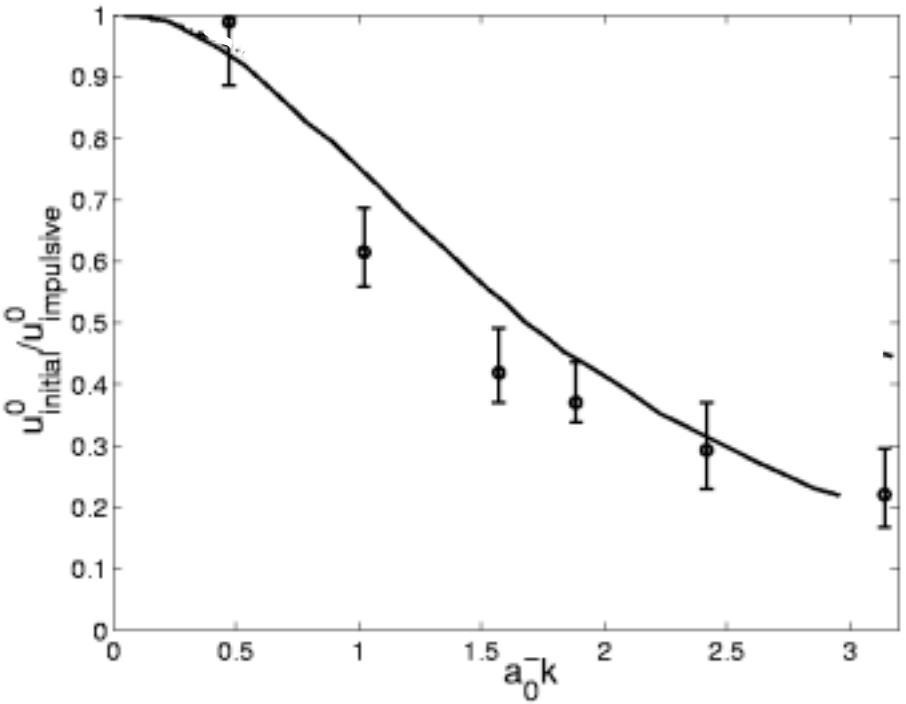

In class ‘A’ experiments the velocity reduction is mainly attributed to high amplitudes effects.

Compressibility dominated regimes

Compressibility effects are expected to dominate the flow when the shock wave is in proximity with the interface.

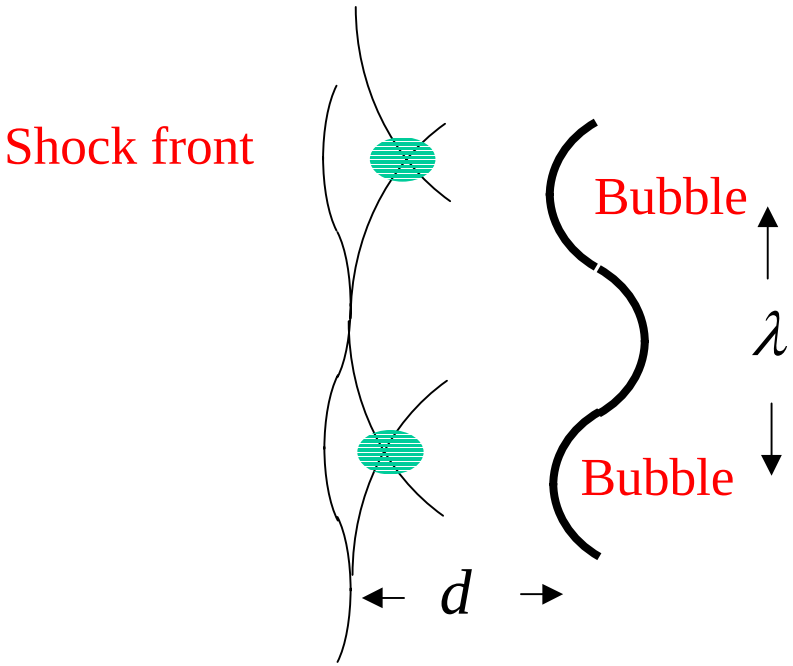

Proximity criterion:

$$f_c = \frac{u_{bouble}}{u_{shock} - u_{1d}}$$

Conjecture: f_c characterizes the flow at moderate Mach numbers

$f_c = 1$ contour lines

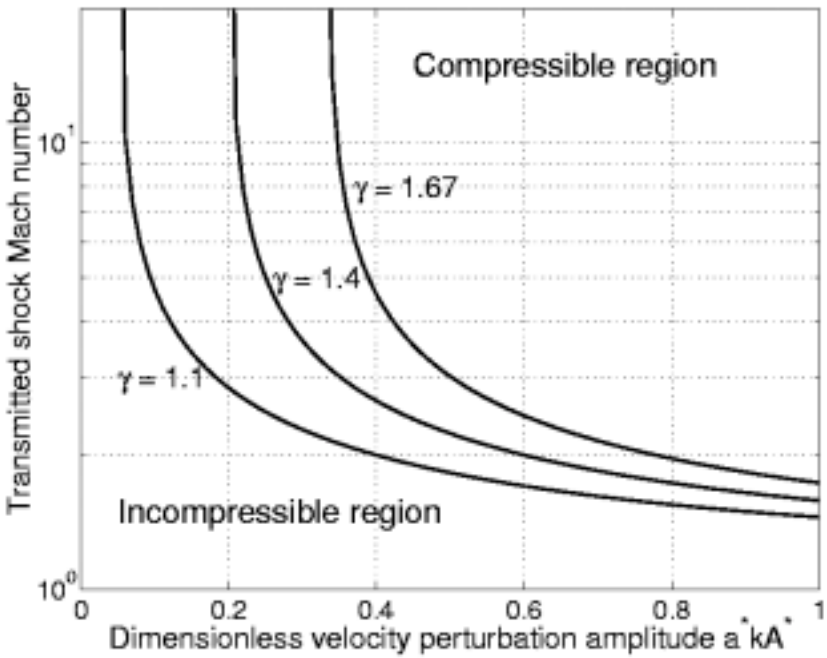

“Wall” model for moderate Mach RM instability

- Shock wave is treated as a rigid straight wall moving in the *1d* shock velocity.
- Secondary high pressure points are not considered.
- Model reduction depends only on f_c.
- Model is solved by using previous models* while inhibiting the shock as a moving boundary condition.

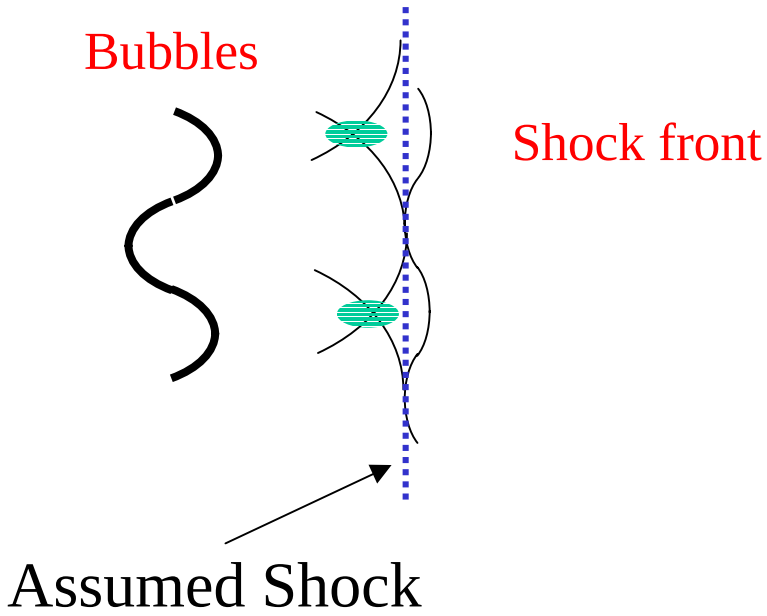

* Potential model for A close to 1 and Vortex model for A close to 0.

Example of results from the Wall model

- As the shock velocity increases (f_c decreases) the velocity profile is closer to the incompressible case.

- The reduction factor is calculated by:

$$\frac{Reduced\ Velocity}{Richtmyer\ Velocity}$$

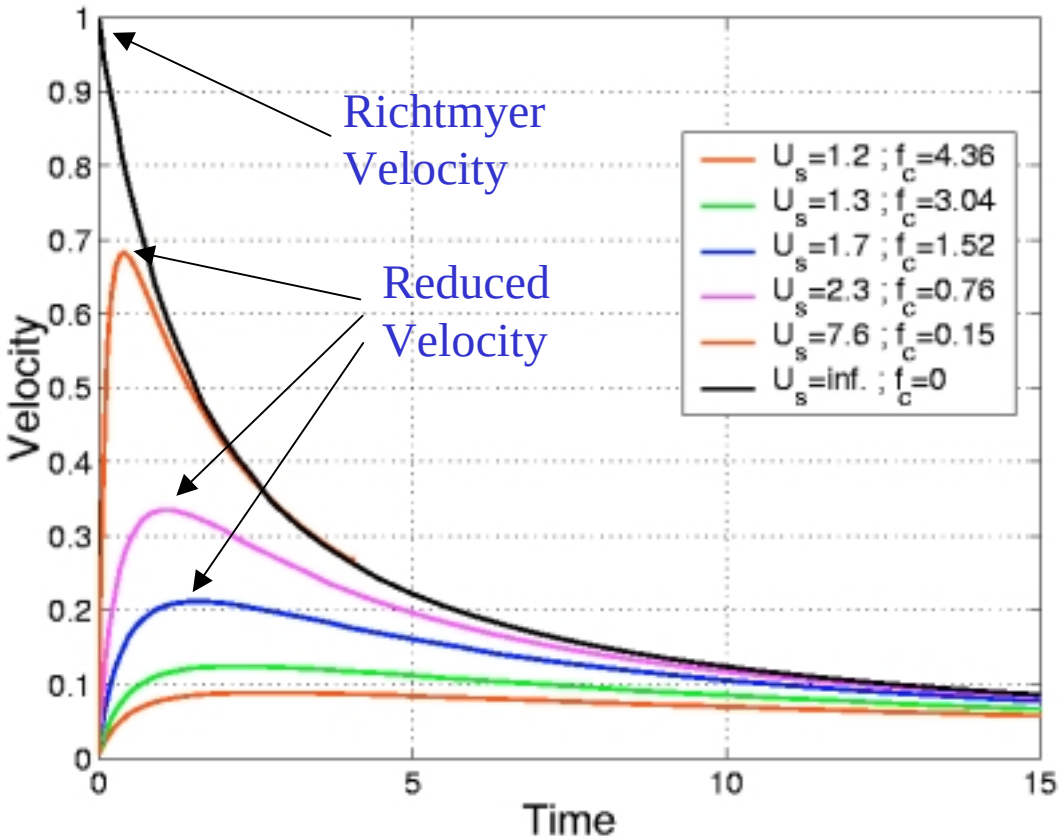

Comparison with Aleshin He → Xe experiments

Rictmyer Veloctiy

Classical Model

Wall Model

Sim./Exp.

Reverberation arrivel time

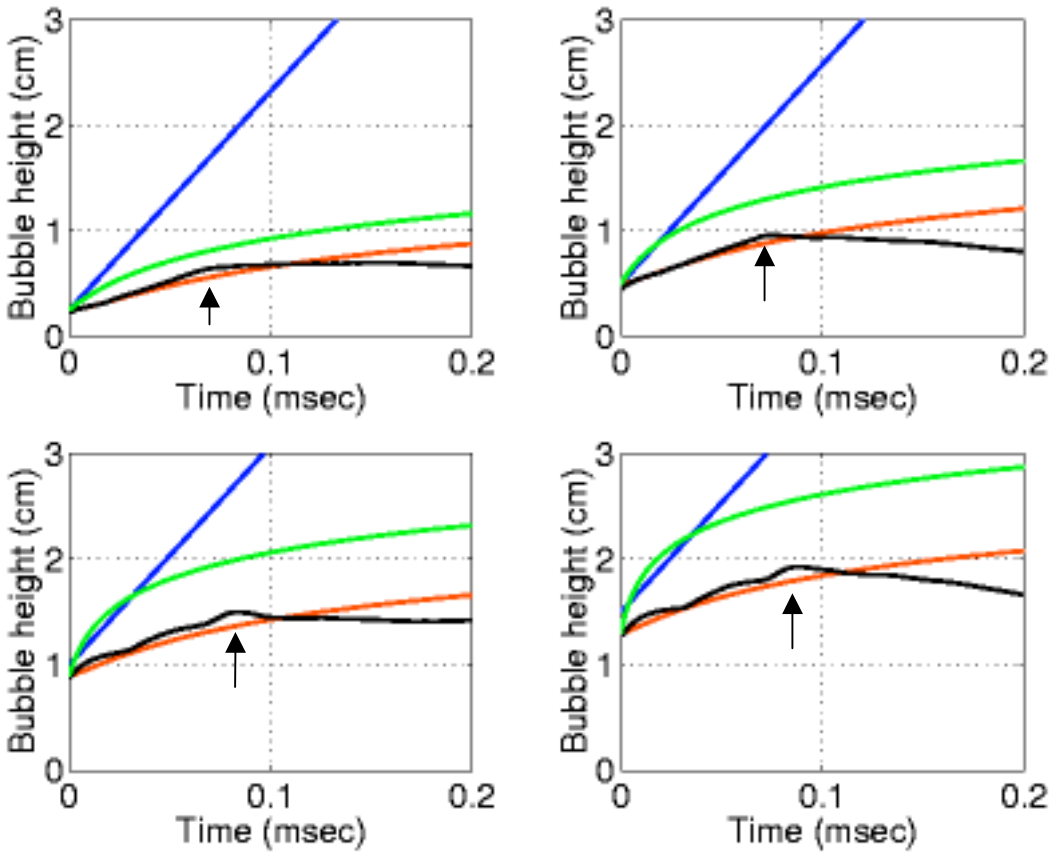

⇒ By Introducing f_c to the potential model, good agreement is achieved with experiments.

Class B Reduction Factor - Theory Vs. Experiments

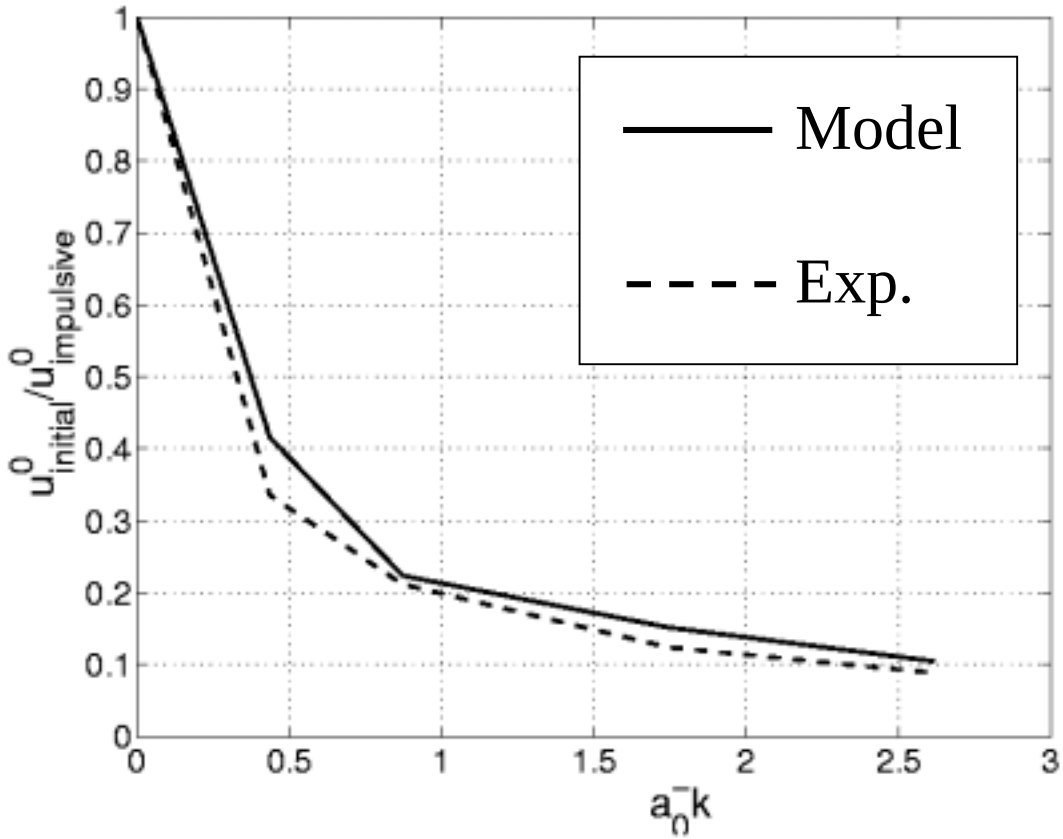

In class ‘B’ experiments the velocity reduction is mainly attributed to high Mach effects.

Late Nonlinear Stages of the Flow - Numerical Simulations at f_c=0.05 and ak=0.175 - 1.75.

Normelized Velocity

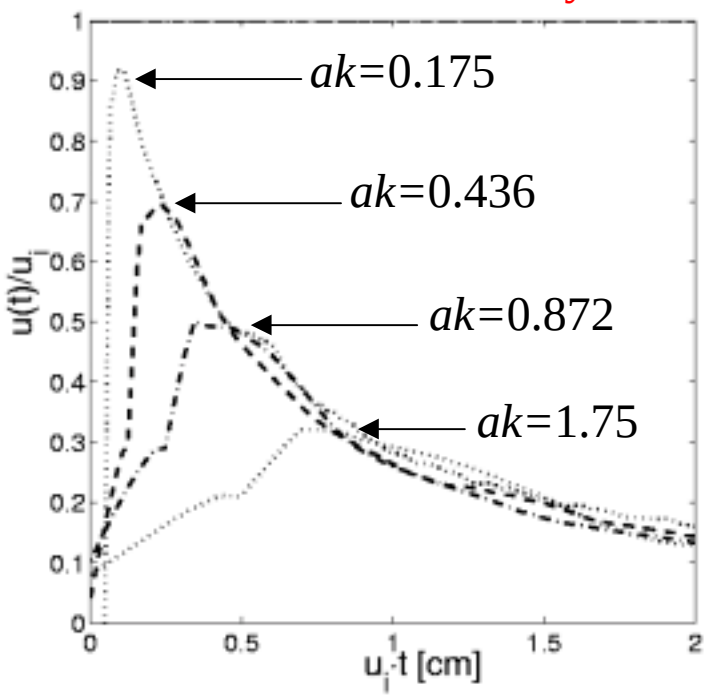

Normelized Velocity Multiplied by Time

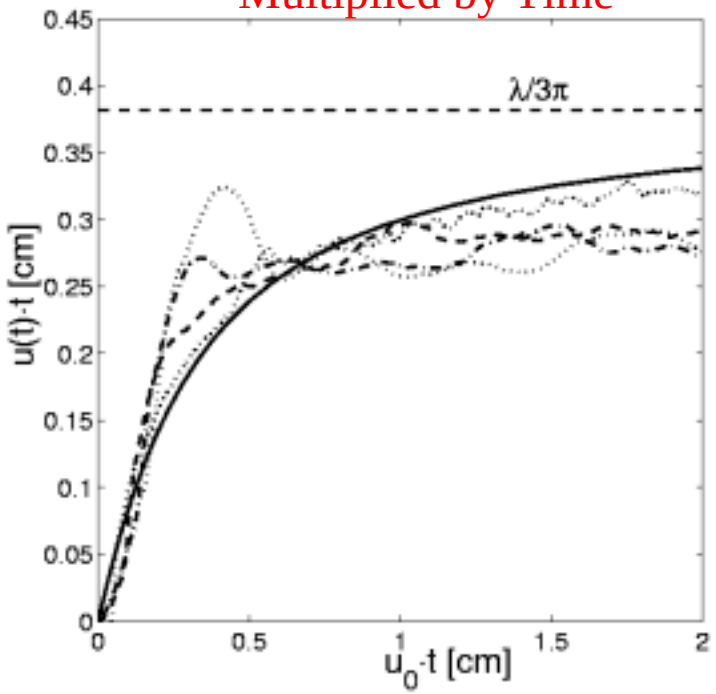

⇒ Normalizing the late stages of the flow by the initial velocity from the High Amplitudes Model, deduces high amplitudes effects. Hence the classic behavior is regained.

Late Nonlinear Stages of the Flow - Numerical Simulations for f_c=0.05 - 0.625 and ak=0.43.

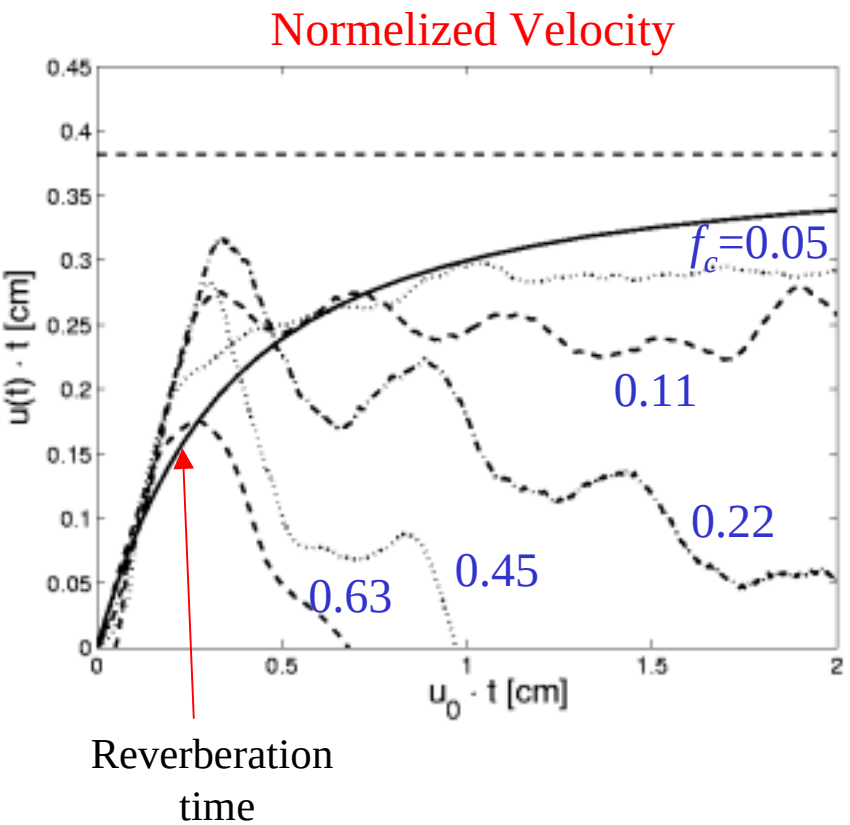

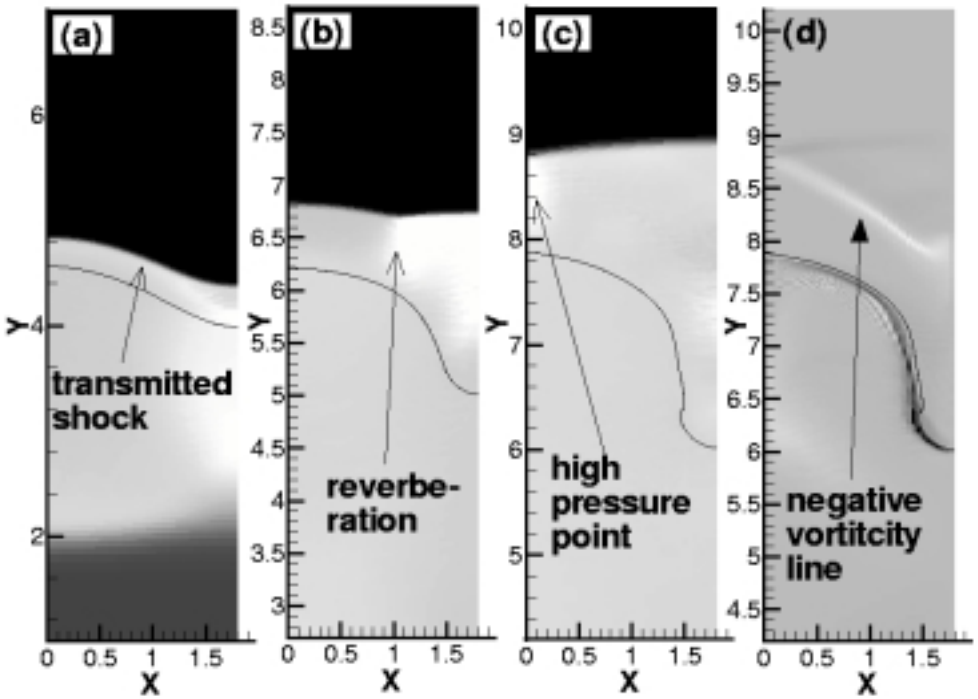

⇒ At High values of f_c new phenomena arises due to secondary high pressure points, drastically affecting the flow.

Summary

- Effects of high initial amplitudes and Mach numbers were quantified for the early linear stages of the flow.

- Classes ‘A’ and ‘B’ of experiments were recognized, distinguishing between the two effects.

- For the late nonlinear stages of the flow:

  - No true effects were found for high initial amplitudes.

  - New dominant effects were found for high Mach numbers.

Poster T25

Compressible MHD Turbulence in Strongly Radiating Molecular Clouds in Astrophysics*

D.D. Ryutov

LLNL, Livermore, CA 94551, USA

Presented at 8th International Workshop on the Physics of Compressible Turbulent Mixing, December 10-14, 2001, Pasadena CA

*Work performed for the U.S. DoE by UC LLNL under contract W-7405-Eng-48.

ABSTRACT

Molecular clouds in astrophysics are often subjected to intense irradiation by nearby young stars. The ablation process ensues and a strong shock is driven into the cloud. In a number of cases, the radiative cooling time of the shocked matter is much shorter than the dynamical time of the cloud evolution. In such situations, possible pre-existing turbulent motions and turbulent magnetic fields can potentially contribute to the "stiffness" of the shocked material. We suggest simple models allowing quick evaluation of these effects. We conclude that the presence of a turbulent magnetic field can play a significant role, provided its amplitude is beyond some critical level, whereas the turbulent ram pressure of the unmagnetized medium can play only a relatively minor role. Implications for the dynamics of astrophysical molecular clouds are discussed.

Work performed under the auspices of the U.S. Department of Energy by University of California Lawrence Livermore National Laboratory under contract W-7405-Eng-48.

Eagle Nebula

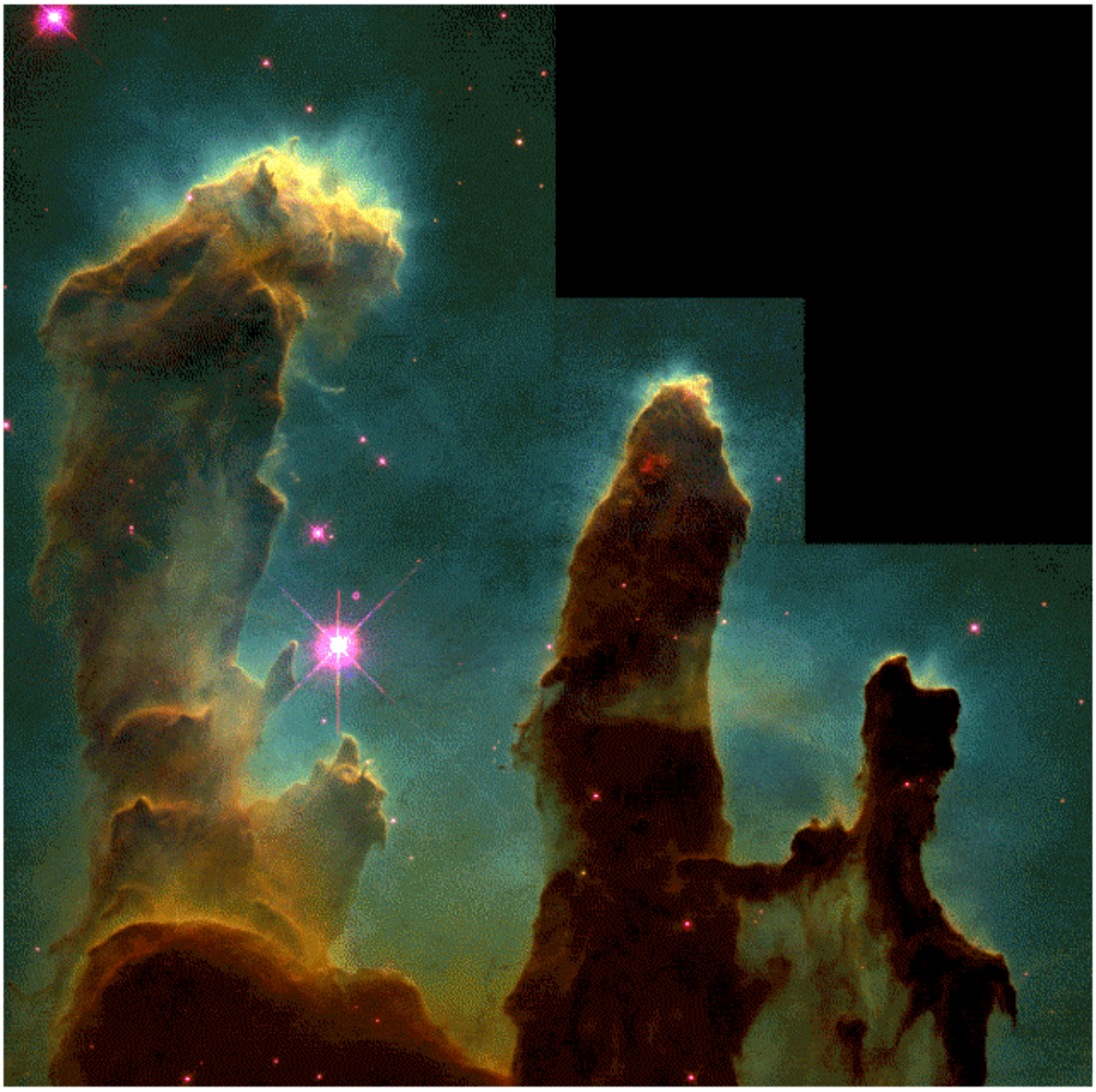

OUTLINE

Formulation of the problem (supersonic turbulence decays very quickly)

Possible experiment on the temporal evolution of the trans-sonic turbulence.

MHD turbulence: can it provide necessary stiffness? – Probably, not, if radiation is fast.

“Static” MHD turbulence (random, force-free magnetic field) – Yes, it can provide necessary stiffness.

Acknowledgment: discussions with Bruce Remington (LLNL), Jave Kane (LLNL) and Marc Pound (U. of Maryland, College Park) are gratefully acknowledged

A PROBLEM:

The molecular matter stays at a low temperature ~30 K: at higher temperatures, extremely strong heat losses begin (radiation in 1 mm range)

The gas pressure inferred from simple hydrodynamic arguments is much (10 to 100 times) higher than the pressure found as a product of density and temperature.

A “canonical” solution: attribute the hydrodynamic pressure to the turbulent ram pressure of a small-scale hydrodynamic turbulence. This explanation to be valid, one has to assume that the turbulence is strongly supersonic. This, in turn, would mean extremely fast dissipation (~ 1 turn-over time for characteristic vortex size), incompatible with any available energy sources.

A conclusion: hydrodynamic turbulence cannot provide required “stiffness” to molecular clouds.

A CONCEPT OF A LASER EXPERIMENT

As it would be desirable to obtain a direct experimental information on the decay of a transonic turbulence, we suggest the following experiment:

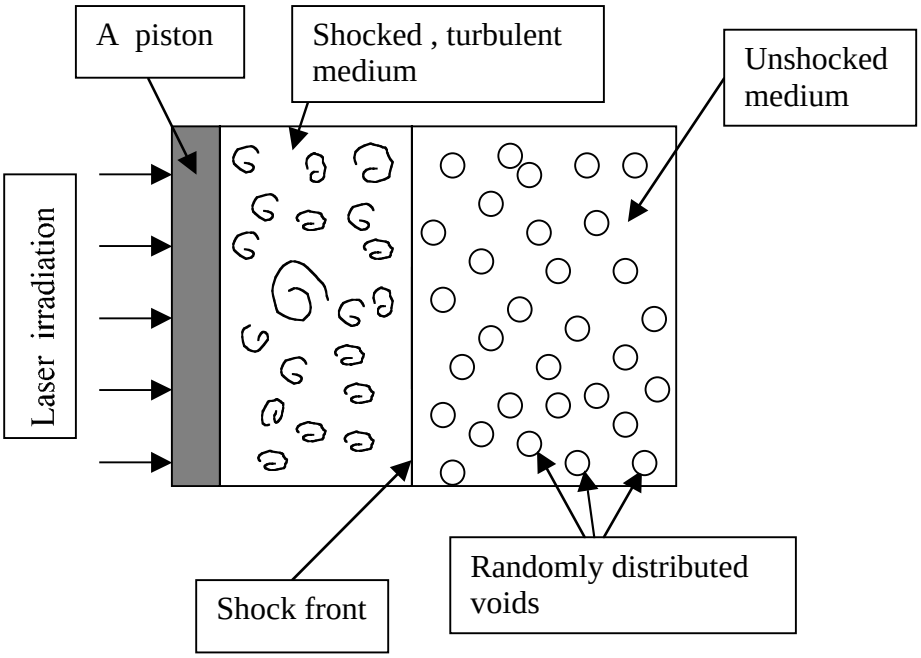

Using voids as a source of turbulent vortices is attractive because it allows one to eliminate complexities associated with mixing of different materials. Filling factor ~ 1. The shape of voids is not very important.

For a strong shock, the fluid behind the shock will be strongly turbulent, with a characteristic pulsation velocity of order of the sound velocity in the shocked material.

How to observe: add a strip seeded with a tracer; its turbulent broadening will be a measure of the turbulent diffusion.

One can introduce a spherical marker (no alignment issues). Both face-on radiography, and a side-on radiography are possible. The side-on radiography can be used to study possible anisotropy of the turbulence.

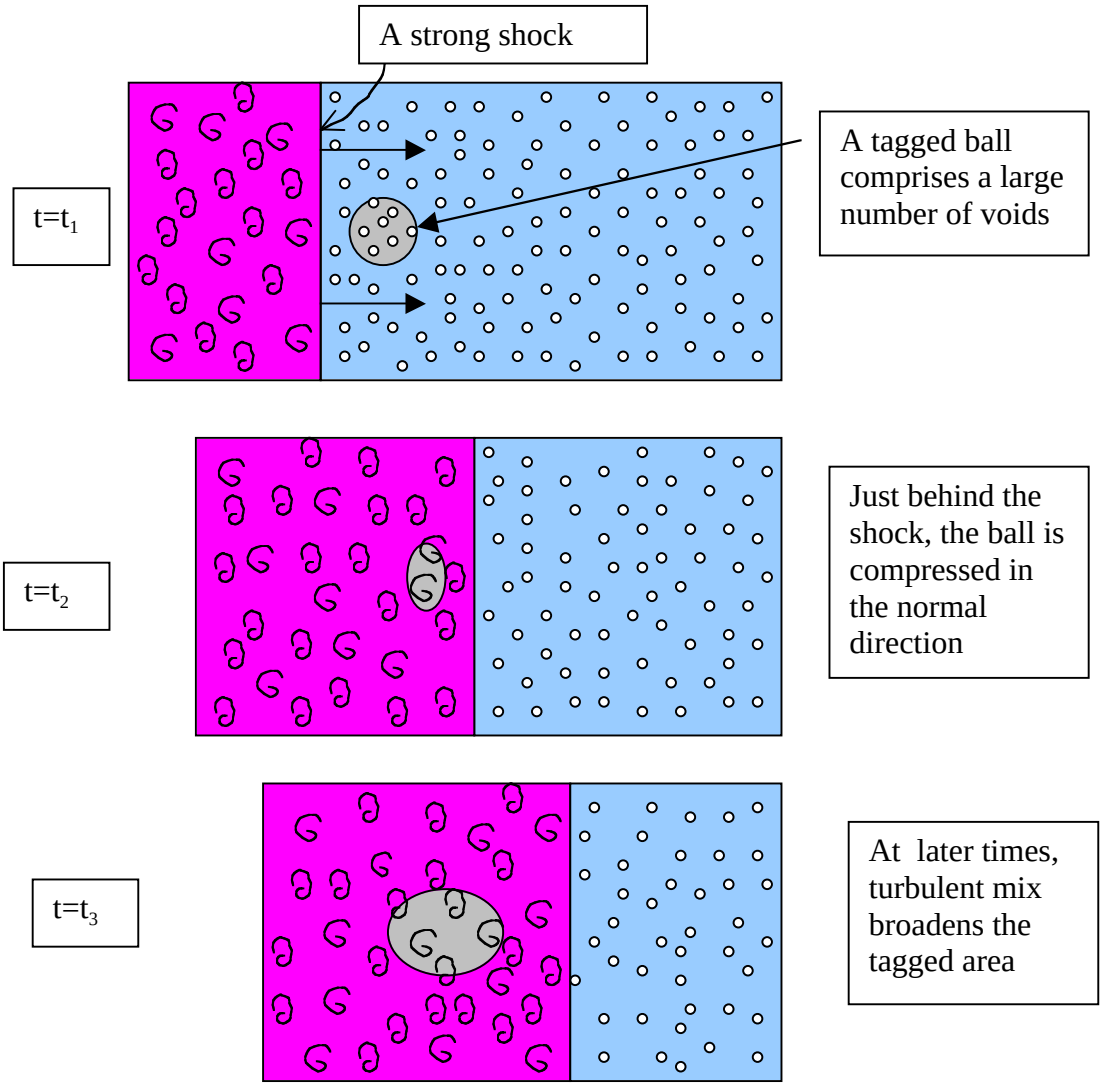

Reference experiment: compressing a “uniform” matter.

SUSTAINING SUPERSONIC TURBULENCE

In the molecular cloud, the cooling time is typically orders of magnitude shorter than the sound transit time. Whence, even if initially the matter was hot and the turbulence was initially subsonic, very quickly the turbulent velocity becomes greater than the sound velocity. The resulting formation of shocks gives rise to a much faster decay of the turbulence than in the case of a subsonic (incompressible) turbulence.

One can try to study this process experimentally, by using the following techniques:

1) Creating conditions where the shock-heated plasma would be strongly radiating (rapidly cooling).

2) Letting the turbulent plasma to expand (e.g., in the rarefaction wave).

3) Compressing the turbulent plasma

The first approach would require reaching high temperatures of the shocked matter (may become feasible with the NIF facility)

The second (the third) approach works for the matter with a “stiff” (“soft”) equation of state [effective adiabat index higher (lower) than 5/3]

MHD TURBULENCE ALSO CANNOT PROVIDE NECESSARY STIFFNESS

By MHD turbulence we mean flows with a tangled magnetic field, with the average magnetic field much less than the turbulent field.

This

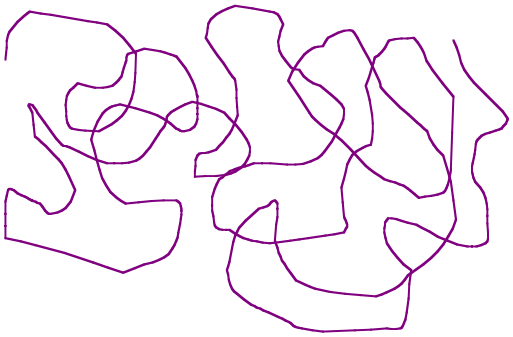

Not this

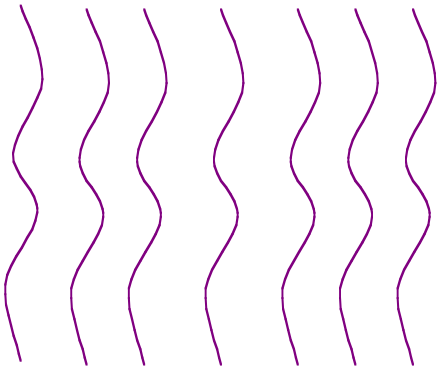

Mac Low et al (1998): turbulent energy decays as

$$W_{turb} \sim t^{-\eta}, \quad 0.85 < \eta < 1.2$$

Decay occurs within a few turn-over times for the largest-scale vortices

(M.-M. Mac Low, R.S. Klessen, A. Burkert, M.D. Smith. “Decay Timescales of MHD Turbulence in Molecular Clouds.“ In: *Interstellar turbulence*, J. Franco, A Caraminiana, Editors, Cambridge University Press, 1999. p. 256; E.C. Ostriker, J.M. Stone, C.F. Gammie. “Density, velocity, and magnetic field structure in turbulent molecular cloud models. Astropysical Journal, **546**, 980, 2001)

EXISTING MODELS OF THE STIFFNESS OF MOLECULAR CLOUDS

A Model	Main difficulty	Representative reference
Supersonic turbulence	Very high dissipation rate related to shocks	Mestel. MNRAS, 6, 161 (1965)
MHD turbulence	Formation of shocks parallel to the magnetic field and very fast dissipation of the turbulence	McLow et al., PRL, 80, 2754 (1998)
A medium composed of clumps and non-interacting shells moving at supersonic velocities	A relatively short time for collisions between dense structures (?)	Melnick et al, In "*Interstellar turbulence.*" J. Franco, A Caraminiana, Editors, Cambridge University Press, 1999, p. 148
A large-scale magnetic field permeating a cloud	In most cases, the observed magnetic field strength is insufficient to provide a required stiffness	R.M. Crutcher, Ap.J. 520, 706 (1991)

POSSIBLE LONG-LASTING TURBULENT SUPPORT: "STATIC" MHD TURBLENCE

Force-free magnetic field

$$\nabla\times\mathbf{B}=\lambda\mathbf{B}\ (\mathbf{j}=4\pi\lambda\mathbf{B}/c)$$

Characteristic vortex size: $1/\lambda$. The parameter λ may vary in space and time.

A plausible scenario leading to a formation of a force-free random magnetic field:

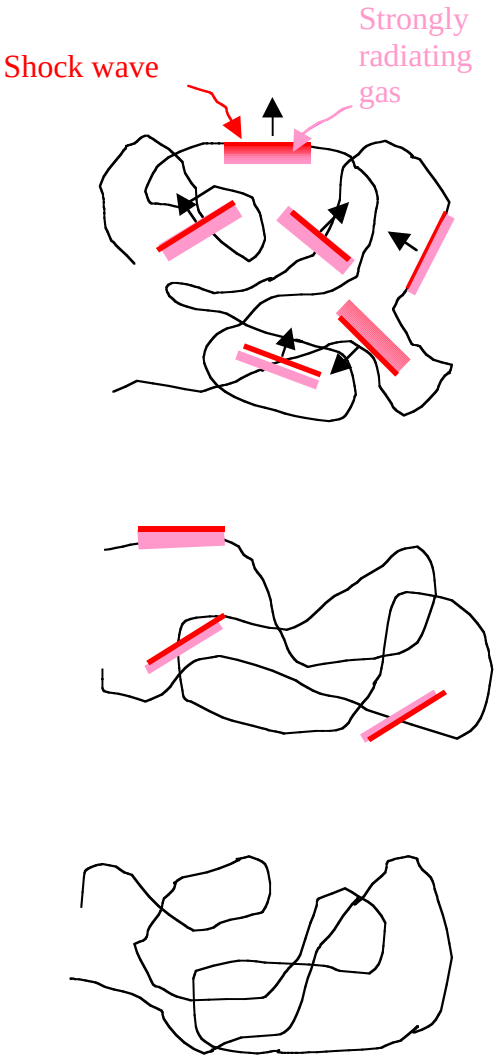

1) Initial (not a force-free) MHD turbulence stirs the gas, generates shocks, and transfers energy to the gas that quickly radiates it; the gas pressure remains low during this whole process;

2) The system evolves in the direction of a force-free state, leading to a gradual slowing down of a stirring (and dissipation);

3) A force-free state is reached whose lifetime is determined by a very slow resistive dissipation

REACTION OF A "STATIC" TURBULENCE TO COMPRESSION

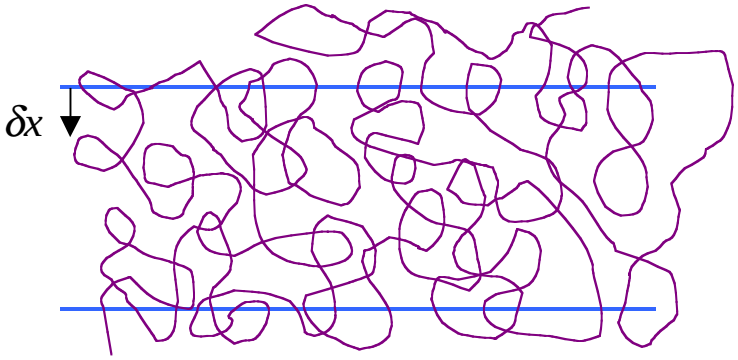

$$p=<p_M>/3;\ \ p_M=B^2/8\pi$$

The energy density:

$$W=<p_M>$$

The adiabat index

$$\gamma=4/3$$

(because $p=W/3$)

A DERIVATION:

Magnetic field stress tensor

$$\pi_{\alpha\beta} = -p_M b_\alpha b_\beta + p_M(\delta_{\alpha\beta} - b_\alpha b_\beta),\ \boldsymbol{b}=\boldsymbol{B}/|\boldsymbol{B}|$$

For a surface oriented perpendicularly to an axis z, the p_{zz} component (the “pressure” acting on this surface) is

$$\pi_{zz} = \frac{B_x^2 + B_y^2 - B_z^2}{8\pi}$$

For isotropic turbulence,

$$p = \langle p_{zz} \rangle = \langle p_M \rangle / 3$$

REACTION OF A STATIC TURBULENCE TO SHEAR DEFORMATION

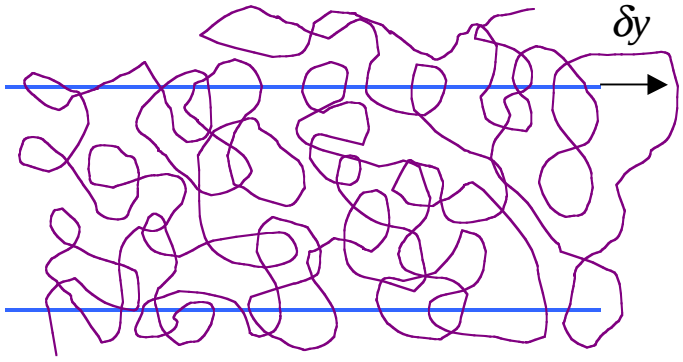

Shear stress:

$$\sigma=-(p_M/6)(d\delta y/dx)$$

There is a rheological decay of the shear stress.

DISSIPATIVE PROCESSES

Generally speaking, both compression and shear deformation trigger reconnection process that leads to some dissipation

This gives rise to appearance of the following terms in the momentum equation:

$$\sigma_{\alpha\beta} = \eta\left(\frac{\partial v_\alpha}{\partial x_\beta} + \frac{\partial v_\beta}{\partial x_\alpha} - \frac{2}{3}\delta_{\alpha\beta}\frac{\partial v_\gamma}{\partial x_\gamma}\right) + \varsigma\delta_{\alpha\beta}\frac{\partial v_\gamma}{\partial x_\gamma}$$

with

$$\varsigma \approx 3\eta = \frac{p_M}{\tau}$$

where τ is a characteristic time of the reconnection over the scale $1/\lambda$.

SUMMARY OF THE "STATIC TURBULENCE" EFFECTS

"Static turbulence" has a very long decay time and is, therefore, an excellent candidate for a factor providing "stiffness" of molecular clouds

When a medium with initially present "static turbulence" is forced to move, the reaction is the following:

- For compressional waves, γ=4/3

- For shear waves, the shear stress is present, with a rheological decay

- Dissipative processes accompany both compressional and shear flow

A random magnetic field would not contribute a lot to a line-of sight average of polarization; small measured $<\mathbf{B}>$ may correspond to a large $<B^2>^{1/2}$

WHAT IS THE SOURCE OF THE STATIC TURBULENCE?

Initial large-scale weak magnetic field threading the cloud would be tangled in the course of fluid convection during the early stage of the cloud existence.

The magnetic pressure of this random field will be of the order of the gaseous pressure.

When the ablation pressure “turns on,” the random magnetic field is compressed and its pressure provides the necessary stiffness.

Observed line broadening in molecular transitions can be explained by two effects: radiation of the just shocked matter; the presence of non-uniform large-scale motions integrated along the line of sight.

Direct observations of the line shapes show that there exists considerable suprathermal broadening, How can this be compatible with the “static” turbulence?

An answer: locally static turbulence is compatible with supersonic velocity variation of the global flow .

A relevant quotation:

“A clear isolation of the effects of turbulent motions from observed line profiles, however, is not readily obtainable, because of the uncertainties introduced by the possible existence of large scale mass motions along the line of sight”

G. Munch. “Turbulence in the Interstellar Medium: a Retrospective Review,” In: “*Interstellar turbulence.*” J. Franco, A Caraminiana, Editors, Cambridge University Press, 1999. p.1.

Another possibility: the line radiation comes predominantly from the just shocked hot regions

SUMMARY

An experiment directed towards studies of decaying compressible turbulence has been proposed

“Static” (force-free) magnetic turbulence has been suggested as a slowly-decaying agent providing a necessary stiffness to molecular clouds

Basic equations describing effects of such turbulence on macroscopic motions of matter have been formulated

Single-Velocity, Multi-Component Turbulent Transport Models for Interfacial Instability-Driven Flows

Oleg Schilling

University of California, Lawrence Livermore National Laboratory

P.O. Box 808, L-22, Livermore, CA 94551

(925) 423-6879, schilling1@llnl.gov

Presented at the

8th International Workshop on the Physics of Compressible Turbulent Mixing

California Institute of Technology, Pasadena, CA

9-14 December 2001

This work was performed under the auspices of the U.S. Department of Energy by the University of California, Lawrence Livermore National Laboratory under Contract No. W-7405-Eng-48

Outline of presentation

- Motivation
  - The need for turbulent transport and mixing models
  - Single- vs. multiple-velocity, multi-component fluid formulations
- Derivation of the Favre-Reynolds averaged single-velocity equations
- Two-equation turbulence models
  - The general *K*-*Z* model
  - The *K*-ε model
  - Derivation of consistent *K*-*l*, *K*-ω, and *K*-τ models
- Work in progress: *a priori* model tests
  - Determination of model coefficients from experimental data
  - Determination of model coefficients from simulation data
- Conclusions

An *averaged* description of turbulent transport and mixing is needed due to the very wide range of spatio-temporal scales in turbulent mixing layers

- Direct numerical simulation (DNS) cannot attain parameter regimes of interest for astrophysical and inertial confinement fusion (ICF) applications
- Large-eddy simulation (LES) is not yet sufficiently developed
- Interim solution: turbulent transport and mixing models, which have similarities with LES

- Transport models are based on closing terms in the density-weighted averaged equations
  - Reynolds stress tensor
  - Density and energy flux
- These quantities are modeled using an eddy viscosity approximation

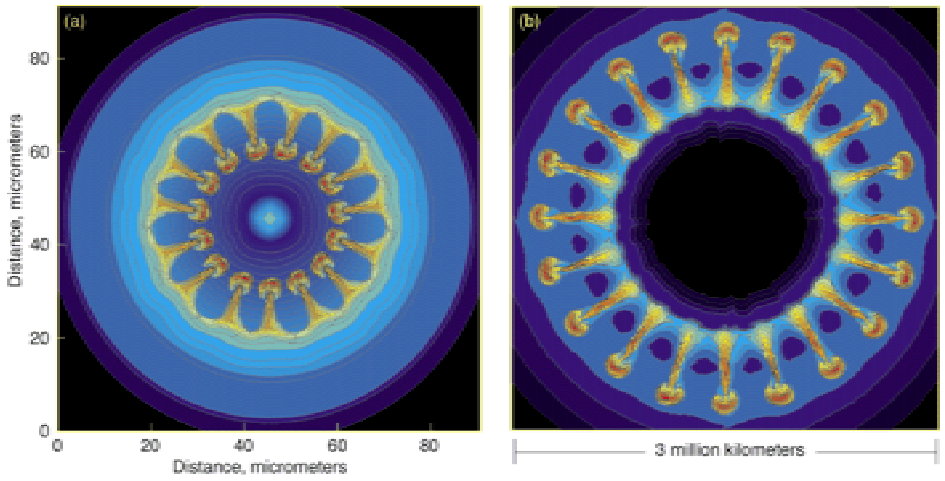

Striking similarities exist between hydrodynamic instabilities in (a) inertial confinement fusion capsule implosions and (b) core-collapse supernova explosions. [Image (a) is from Sakagami and Nishihara, *Physics of Fluids B* **2**, 2715 (1990); image (b) is from Hachisu *et al.*, *Astrophysical Journal* **368**, L27 (1991).]

ICF **supernova**

Single-velocity formulations of multi-component flow are significantly less complex than multiple-velocity formulations

- Single-velocity, multi-component fluid formulations:
  - Equations systematically derived from reacting flow theory
  - Equations have nearly the same form as the *single-fluid*, compressible fluid dynamics equations
  - Additional fluxes involving a diffusion velocity are present
  - The diffusion velocity is obtained, and these fluxes are expressed in terms of a mass diffusion flux
- Multiple-velocity, multi-component fluid formulations:
  - Require multiple advection terms equal to number of fluids
  - Require fluid dynamic fields for every fluid, so the number of equations to model and solve is large
  - Require phenomenological modeling of interfacial source terms arising from interfacial averaging: drag, added mass terms, etc.

The derivation of the single-velocity equations begins with the full, *N*-fluid equations expressing mass, momentum, and energy conservation

- In compact form, these equations are (*r* labels each fluid):

$$\frac{\partial}{\partial t}(\rho^r \phi^r_\alpha) + \frac{\partial J^r_{\alpha\beta}[\phi^r]}{\partial x_\beta} = F^r_\alpha + S^r_\alpha$$

  - where the fields, fluxes, forces, and sources are

$$\rho^r \phi^r_\alpha = \begin{pmatrix} \rho^r \\ \rho^r v^r_\alpha \\ \rho^r e^r \\ \rho^r \phi^r \end{pmatrix}, \quad J^r_{\alpha\beta} = \begin{pmatrix} \rho^r v^r_\beta \\ \rho^r v^r_\alpha v^r_\beta + p^r \delta_{\alpha\beta} - \sigma^r_{\alpha\beta} \\ (\rho^r e^r + p^r) v^r_\beta - v^r_\alpha \sigma^r_{\alpha\beta} + \Phi^{\mathrm{rad},r}_\beta \\ \rho^r \phi^r v^r_\beta + \Phi^{\phi,r}_\beta \end{pmatrix}$$

$$F^r_\alpha = \begin{pmatrix} 0 \\ \rho^r g_\alpha \\ 0 \\ 0 \end{pmatrix}, \quad S^r_\alpha = \begin{pmatrix} R^r \\ v^r_\alpha R^r \\ H^r R^r + \rho^r g_\alpha v^r_\alpha \\ \phi^r R^r \end{pmatrix}$$

These fields are defined so that summing appropriate expressions over each fluids recovers the non-reacting, single-fluid equations

- The quantities ρ^r, v_α^r, U^r, φ^r, $\Phi_\alpha^{rad,r}$, Φ^r, g_α, R^r, and H^r are the density, velocity, internal energy, scalar, radiative flux, scalar flux, acceleration, reaction rate, and heat of formation
- The pressure, viscous stress tensor, and total energy are

$$p^r = p^r(\rho^r, U^r)$$

$$\sigma_{\alpha\beta}^r \equiv \mu^r \left(\frac{\partial v_\alpha^r}{\partial x^\beta} + \frac{\partial v_\beta^r}{\partial x^\alpha} \right) + \left(\xi^r - \frac{2\mu^r}{d} \right) \delta_{\alpha\beta} \frac{\partial v_\gamma^r}{\partial x_\gamma}$$

$$e^r = \frac{v_r^2}{2} + U^r + \rho m^r H^r - \mathbf{g} \cdot \mathbf{x}$$

- Consistency with the single-fluid equations is obtained with the constraints

$$\sum_{r=1}^N \rho^r \phi_\alpha^r = \rho \phi_\alpha \quad , \quad \sum_{r=1}^N J_{\alpha\beta}^r = J_{\alpha\beta}$$

$$\sum_{r=1}^N F_\alpha^r = F_\alpha \quad , \quad \sum_{r=1}^N S_\alpha^r = S_\alpha$$

$$\sum_{r=1}^N R^r = 0 \quad , \quad \sum_{r=1}^N \phi_\alpha^r R^r = 0$$

The single-velocity equations are obtained by decomposing the velocity into a mean velocity plus a diffusion velocity

- Introduce the local mass fraction of fluid *r*

$$m^r(\mathbf{x},t) \equiv \frac{\rho^r}{\rho} \quad , \quad \sum_{r=1}^{N} m^r(\mathbf{x},t) = 1$$

- Write the velocity of fluid *r* as

$$\mathbf{v}^r = \mathbf{v} + \mathbf{V}^r \quad , \quad \mathbf{v} \equiv \sum_{r=1}^{N} m^r \mathbf{v}^r$$

where V^r is the diffusion velocity, which expresses the molecular transport caused by the concentration gradient in fluid *r*

- The identity

$$\sum_{r=1}^{N} m^r \mathbf{V}^r = 0$$

is central to the derivation of the single-velocity equations

The single-velocity equations are a consequence of the previous identities

- Substituting the velocity decomposition into the multi-component equations, summing, and using the previous identities gives the single-velocity equations

$$\frac{\partial}{\partial t}(\rho\phi_\alpha) + \frac{\partial J_{\alpha\beta}}{\partial x_\beta} = F_\alpha + S_\alpha$$

- The fields and fluxes are

$$\rho\phi_\alpha = \begin{pmatrix} \rho \\ \rho v_\alpha \\ \rho e \\ \rho\phi \end{pmatrix} \qquad J_{\alpha\beta} = \begin{pmatrix} \rho v_\beta \\ \rho v_\alpha v_\beta + p\delta_{\alpha\beta} - \sigma_{\alpha\beta} \\ (\rho e + p)v_\beta - v_\alpha \sigma_{\alpha\beta} + \Phi_\beta^{\mathrm{rad}} \\ \rho\phi v_\beta + \Phi_\beta^{\phi} \end{pmatrix} + \begin{pmatrix} 0 \\ -\sigma_{\alpha\beta}^{D} \\ J_\beta^{e} \\ J_\beta^{\phi} \end{pmatrix}$$

where the last term in $J_{\alpha\beta}$ depends on the diffusion velocity and must be modeled

The forces, sources, and other quantities are defined as follows

- The forces and sources are

$$F_\alpha = \begin{pmatrix} 0 \\ \rho g_\alpha \\ 0 \\ 0 \end{pmatrix} \qquad S_\alpha = \begin{pmatrix} 0 \\ 0 \\ \rho g_\alpha v_\alpha \\ 0 \end{pmatrix} + \sum_{r=1}^{N} \begin{pmatrix} 0 \\ 0 \\ H^r R^r \\ 0 \end{pmatrix}$$

- The total density, pressure, radiative flux, viscous stress tensor, dynamic viscosity, and bulk viscosity are

$$\rho \equiv \sum_{r=1}^{N} \rho^r \qquad p \equiv \sum_{r=1}^{N} p^r(\rho^r, U^r) \qquad \Phi_\alpha^{\text{rad}} \equiv \sum_{r=1}^{N} \Phi_\alpha^{\text{rad},r}$$

$$\sigma_{\alpha\beta} \equiv \mu\left(\frac{\partial v_\alpha}{\partial x^\beta} + \frac{\partial v_\beta}{\partial x^\alpha}\right) + \left(\xi - \frac{2\mu}{d}\right)\delta_{\alpha\beta}\frac{\partial v_\gamma}{\partial x_\gamma}$$

$$+\sum_{r=1}^{N} \mu^r\left(\frac{\partial V_\alpha^r}{\partial x^\beta} + \frac{\partial V_\beta^r}{\partial x^\alpha}\right) + \left(\xi^r - \frac{2\mu^r}{d}\right)\delta_{\alpha\beta}\frac{\partial V_\gamma^r}{\partial x_\gamma}$$

$$\mu \equiv \sum_{r=1}^{N} \mu^r \quad , \quad \xi \equiv \sum_{r=1}^{N} \xi^r$$

The diffusive fluxes are defined as follows

- The multi-component viscous diffusion stress tensor is

$$\sigma^{D}_{\alpha\beta} \equiv -\rho \sum_{r=1}^{N} m^{r} V^{r}_{\alpha} V$$

- The diffusive energy flux is

$$J^{e}_{\alpha} \equiv \rho \sum_{r=1}^{N} m^{r} e^{r} V^{r}_{\alpha}$$

- The diffusive scalar flux is

$$J^{\phi}_{\alpha} \equiv \rho \sum_{r=1}^{N} m^{r} \phi^{r} V^{r}_{\alpha}$$

The averaged equations are obtained by introducing the Favre-Reynolds decompositions and averaging

- The Favre-Reynolds decompositions are

$$\phi_\alpha^r(\mathbf{x},t) = \tilde{\phi}_\alpha^r(\mathbf{x},t) + \phi_\alpha^r(\mathbf{x},t)''$$

$$\rho^r(\mathbf{x},t) = \overline{\rho}^r(\mathbf{x},t) + \rho^r(\mathbf{x},t)' \qquad p^r(\mathbf{x},t) = \overline{p}^r(\mathbf{x},t) + p^r(\mathbf{x},t)'$$

- The Favre average is

$$\tilde{\phi}_\alpha \equiv \frac{\overline{\rho\phi_\alpha}}{\overline{\rho}}$$

- The Favre-averaged multi-component fluid dynamics equations are

$$\frac{\partial}{\partial t}(\overline{\rho}\,\tilde{\phi}_\alpha) + \frac{\partial \overline{J}_{\alpha\beta}}{\partial x_\beta} = \overline{F}_\alpha + \overline{S}_\alpha$$

The Favre-averaged fields and fluxes are defined as follows

- The fields and fluxes are

$$\overline{\rho}\,\widetilde{\phi}_\alpha = \begin{pmatrix} \overline{\rho} \\ \overline{\rho}\,\widetilde{v}_\alpha \\ \overline{\rho}\,\widetilde{e} \\ \overline{\rho}\,\widetilde{\phi} \end{pmatrix}$$

$$\overline{J}_{\alpha\beta} = \begin{pmatrix} \overline{\rho}\,\widetilde{v}_\beta \\ \overline{\rho}\,\widetilde{v}_\alpha\,\widetilde{v}_\beta + \overline{p}\,\delta_{\alpha\beta} - \widetilde{\sigma}_{\alpha\beta} - \widetilde{\sigma}^D_{\alpha\beta} \\ (\overline{\rho}\,\widetilde{e} + \overline{p})\widetilde{v}_\beta - \widetilde{v}_\alpha\,\widetilde{\sigma}_{\alpha\beta} + \overline{\Phi}^{\mathrm{rad}}_\beta + \widetilde{J}^e_\beta \\ \overline{\rho}\,\widetilde{\phi}\,\widetilde{v}_\beta + \overline{\Phi}^{\phi}_\beta + \widetilde{J}^{\phi}_\beta \end{pmatrix} + \begin{pmatrix} 0 \\ -\overline{\sigma''_{\alpha\beta}} - \overline{\sigma^{D\prime\prime}_{\alpha\beta}} + \overline{\rho}\,\widetilde{v''_\alpha\,v''_\beta} \\ \overline{p'\,v''_\beta} - \overline{v''_\alpha\,\sigma''_{\alpha\beta}} + \overline{\Phi^{\mathrm{rad}\prime\prime}_\beta} + \overline{J^{e\prime\prime}_\beta} + \overline{\rho}\,\widetilde{e''\,v''_\beta} \\ \overline{\Phi^{\phi\prime\prime}_\beta} + \overline{J^{\phi\prime\prime}_\beta} + \overline{\rho}\,\widetilde{\phi''\,v''_\beta} \end{pmatrix}$$

The Favre-averaged forces and sources are defined as follows

- The forces and sources are

$$\overline{F}_\alpha = \begin{pmatrix} 0 \\ \overline{\rho}\, g_\alpha \\ 0 \\ 0 \end{pmatrix}$$

$$\overline{S}_\alpha = \begin{pmatrix} 0 \\ 0 \\ \overline{\rho}\, g_\alpha \widetilde{v}_\alpha \\ 0 \end{pmatrix} + \begin{pmatrix} 0 \\ 0 \\ \overline{\rho' v''_\alpha}\, g_\alpha + \sum_r \left(\overline{H}^r \overline{R}^r + \overline{H^{r\prime\prime} R^{r\prime\prime}} \right) \\ 0 \end{pmatrix}$$

- At large Reynolds numbers, the viscous stress terms and diffusive fluxes are assumed to be negligible compared to the Reynolds stress tensor and turbulent fluxes

A gradient diffusion approximation is usually used to model the turbulent stresses and fluxes

- The gradient diffusion approximation is

$$\overline{\rho \phi_\alpha'' v_j''} = \overline{\rho}\,\widetilde{\phi_\alpha'' v_\beta''} = -\frac{\partial}{\partial x^j}\left(\frac{\nu_t}{\sigma_{\phi\alpha}}\,\overline{\rho}\,\tilde{\phi}_\alpha\right)$$

$$\tau_{ij} \equiv \overline{\rho v_i'' v_j''} = \overline{\rho}\,\widetilde{v_i'' v_j''}$$

$$= 2\,\overline{\rho}\,\widetilde{E''}\,\frac{\delta_{ij}}{3} - 2\,\overline{\rho}\,\nu_t\left(\tilde{S}_{kj} - \frac{\delta_{kj}}{3}\,\frac{\partial \tilde{v}_l}{\partial x_l}\right)$$

$$\overline{\rho' v_j''} = -\frac{\partial}{\partial x_j}\left(\frac{\nu_t}{\sigma_\rho}\,\overline{\rho}\right)$$

- The eddy viscosity

$$\nu_t = C_\mu \left(\widetilde{E''}\right)^{\frac{m+2n}{n}} \left(\widetilde{Z''}\right)^{-\frac{1}{n}}$$

is determined by the solution of transport equations for two turbulence variables K (= E'') and

$$\widetilde{Z''} \equiv C_Z \left(\widetilde{E''}\right)^m \left(\widetilde{\epsilon''}\right)^n$$

The turbulent kinetic energy equation is closed as follows

- The unclosed turbulent kinetic energy equation is

$$\frac{\partial}{\partial t}\left(\overline{\rho}\,\widetilde{E''}\right)+\frac{\partial}{\partial x_j}\left(\overline{\rho}\,\widetilde{E''}\,\widetilde{v}_j\right)$$

$$=\underbrace{\left(\overline{\rho}\,\overline{v_i''}+\overline{\rho' v_i''}\right)g_i}_{\text{force production}}-\underbrace{\frac{\partial}{\partial x_j}\left(\frac{\overline{\rho v''^2 v_j''}}{2}+\overline{p' v_j''}-\overline{v_i''\sigma_{ij}''}-\overline{v_i''\sigma_{ij}^{D''}}\right)}_{\text{turbulent diffusion}}$$

$$+\underbrace{\widetilde{v}_i\frac{\partial}{\partial x_j}\left(\overline{\rho v_i'' v_j''}\right)}_{\text{mean velocity production}}-\underbrace{\overline{v_i''}\frac{\partial\overline{p}}{\partial x_i}}_{\text{pressure work}}+\underbrace{\overline{p'\frac{\partial v_j''}{\partial x_j}}}_{\text{pressure-dilatation}}-\underbrace{\overline{\sigma_{ij}''\frac{\partial v_i''}{\partial x_j}}-\overline{\sigma_{ij}^{D''}\frac{\partial v_i''}{\partial x_j}}}_{\text{kinetic energy dissipation rate}}$$

- Use the gradient diffusion approximation to close the diffusion term and density flux, and (Ma_t is the turbulent Mach number)

$$\overline{p'\frac{\partial v_i''}{\partial x_j}}=\overline{\rho}\left(\alpha_2\,\tau_{ij}\frac{\partial\widetilde{v}_i}{\partial x_j}+\alpha_3\,Ma_t\,\widetilde{\epsilon''}\right)Ma_t^2$$

$$\overline{v_i''}=-\frac{\overline{\rho' v_i''}}{\overline{\rho}}=\frac{\nu_t}{\overline{\rho}\,\sigma_\rho}\frac{\partial\overline{\rho}}{\partial x^i}$$

The modeled turbulent kinetic energy dissipation rate transport equation is obtained as follows

- The turbulent kinetic energy dissipation rate equation is obtained by multiplying the turbulent kinetic energy equation by ε/K and a dimensionless constant for each term:

$$\frac{\partial}{\partial t}\left(\overline{\rho}\,\widetilde{\epsilon''}\right)+\frac{\partial}{\partial x_j}\left(\overline{\rho}\,\widetilde{\epsilon''}\,\widetilde{v}_j\right)$$

$$=\underbrace{C_{\epsilon 0}\,\frac{\widetilde{\epsilon''}}{\widetilde{E''}}\left(\overline{\rho}\,\overline{v_i''}+\overline{\rho' v_i''}\right)g_i}_{\text{force production}}+\underbrace{C_{\epsilon 1}\,\frac{\widetilde{\epsilon''}}{\widetilde{E''}}\,\widetilde{v}_i\,\frac{\partial}{\partial x_j}\left(\overline{\rho\, v_i'' v_j''}\right)}_{\text{mean velocity production}}$$

$$-\underbrace{C_{\epsilon 2}\,\overline{\rho}\,\frac{\left(\widetilde{\epsilon''}\right)^2}{\widetilde{E''}}}_{\text{kinetic energy dissipation rate}}-\underbrace{\frac{\partial}{\partial x_j}\left(\frac{\mu_t}{\sigma_\epsilon}\,\frac{\partial\widetilde{\epsilon''}}{\partial x^j}\right)}_{\text{turbulent diffusion}}$$

$$-\underbrace{C_{\epsilon 3}\,\frac{\widetilde{\epsilon''}}{\widetilde{E''}}\,\overline{v_i''}\,\frac{\partial\overline{p}}{\partial x_i}}_{\text{pressure work}}+\underbrace{C_{\epsilon 4}\,\frac{\widetilde{\epsilon''}}{\widetilde{E''}}\,\overline{p'\,\frac{\partial v_i''}{\partial x_i}}}_{\text{pressure-dilatation}}$$

The modeled *Z* transport equation is obtained from the *K* and ε equations as follows

- Using the *K* and ε equations,

$$\frac{\partial}{\partial t}\left(\overline{\rho}\,\widetilde{Z''}\right)+\frac{\partial}{\partial x_j}\left(\overline{\rho}\,\widetilde{Z''}\,\widetilde{v}_j\right)=\overline{\rho}\left(\frac{\partial}{\partial t}+\widetilde{v}_j\frac{\partial}{\partial x_j}\right)\widetilde{Z''}$$

$$=\overline{\rho}\,\widetilde{Z''}\left[\frac{m}{\widetilde{E''}}\left(\frac{\partial}{\partial t}+\widetilde{v}_j\frac{\partial}{\partial x_j}\right)\widetilde{E''}+\frac{n}{\widetilde{\epsilon''}}\left(\frac{\partial}{\partial t}+\widetilde{v}_j\frac{\partial}{\partial x_j}\right)\widetilde{\epsilon''}\right]$$

$$=m\frac{\widetilde{Z''}}{\widetilde{E''}}\left[\frac{\partial}{\partial t}\left(\overline{\rho}\,\widetilde{E''}\right)+\frac{\partial}{\partial x_j}\left(\overline{\rho}\,\widetilde{E''}\,\widetilde{v}_j\right)\right]$$

$$+n\frac{\widetilde{Z''}}{\widetilde{\epsilon''}}\left[\frac{\partial}{\partial t}\left(\overline{\rho}\,\widetilde{\epsilon''}\right)+\frac{\partial}{\partial x_j}\left(\overline{\rho}\,\widetilde{\epsilon''}\,\widetilde{v}_j\right)\right]$$

$$=\frac{\widetilde{Z''}}{\widetilde{E''}}\left(m+n\,C_{\epsilon_K}\right)\left[\frac{\partial}{\partial t}\left(\overline{\rho}\,\widetilde{E''}\right)+\frac{\partial}{\partial x_j}\left(\overline{\rho}\,\widetilde{E''}\,\widetilde{v}_j\right)\right]$$

The turbulent diffusion term is transformed as follows

- Substituting

$$\widetilde{\epsilon''} = \left[\frac{\widetilde{Z''}}{C_Z \left(\widetilde{E''} \right)^m} \right]^{1/n}$$

it follows that

$$\widetilde{Z''} \left[\frac{m}{\widetilde{E''}} \frac{\partial}{\partial x_j} \left(\frac{\mu_t}{\sigma_k} \frac{\partial \widetilde{E''}}{\partial x^j} \right) + \frac{n}{\widetilde{\epsilon''}} \frac{\partial}{\partial x_j} \left(\frac{\mu_t}{\sigma_\epsilon} \frac{\partial \widetilde{\epsilon''}}{\partial x^j} \right) \right]$$

$$= \frac{m \widetilde{Z''}}{\widetilde{E''}} \frac{\partial}{\partial x_j} \left(\frac{\mu_t}{\sigma_k} \frac{\partial \widetilde{E''}}{\partial x^j} \right) + \frac{\partial}{\partial x_j} \left[\frac{\mu_t}{\sigma_\epsilon} \left(\frac{\partial \widetilde{Z''}}{\partial x^j} - \frac{m \widetilde{Z''}}{\widetilde{E''}} \frac{\partial \widetilde{E''}}{\partial x^j} \right) \right]$$

$$+ \frac{\mu_t}{n \sigma_\epsilon} \left(\frac{\partial \widetilde{Z''}}{\partial x^j} - \frac{m \widetilde{Z''}}{\widetilde{E''}} \frac{\partial \widetilde{E''}}{\partial x^j} \right) \left(\frac{1-n}{\widetilde{Z''}} \frac{\partial \widetilde{Z''}}{\partial x_j} - \frac{m}{\widetilde{E''}} \frac{\partial \widetilde{E''}}{\partial x_j} \right)$$

Finally, the modeled form of the *Z* transport equation is as follows

$$\frac{\partial}{\partial t}\left(\overline{\rho}\,\widetilde{Z''}\right)+\frac{\partial}{\partial x_j}\left(\overline{\rho}\,\widetilde{Z''}\,\widetilde{v}_j\right)=\overline{\rho}\left(\frac{\partial}{\partial t}+\widetilde{v}_j\,\frac{\partial}{\partial x_j}\right)\widetilde{Z''}$$

$$=\underbrace{C_{Z0}\,\frac{\widetilde{Z''}}{\widetilde{E''}}\left(\overline{\rho}\,\overline{v_i''}+\overline{\rho' v_i''}\right)g_i}_{\text{force production}}+\underbrace{C_{Z1}\,\frac{\widetilde{Z''}}{\widetilde{E''}}\,\widetilde{v}_i\,\frac{\partial}{\partial x_j}\left(\overline{\rho\,v_i''\,v_j''}\right)}_{\text{mean velocity production}}-\underbrace{C_{Z2}\,\overline{\rho}\,\frac{\widetilde{Z''}\widetilde{\epsilon''}}{\widetilde{E''}}}_{\text{kinetic energy dissipation rate}}$$

$$\underbrace{-\frac{\partial}{\partial x_j}\left[\left(\mu+\frac{\mu_t}{\sigma_\epsilon}\right)\frac{\partial\widetilde{Z''}}{\partial x^j}\right]-\frac{m\widetilde{Z''}}{\widetilde{E''}}\,\frac{\partial}{\partial x_j}\left(\frac{\mu_t}{\sigma_k}\,\frac{\partial\widetilde{E''}}{\partial x^j}\right)}_{\text{turbulent diffusion}}$$

$$\underbrace{+m\,\frac{\partial}{\partial x_j}\left(\frac{\mu_t}{\sigma_\epsilon}\,\frac{\widetilde{Z''}}{\widetilde{E''}}\,\frac{\partial\widetilde{E''}}{\partial x^j}\right)-\frac{\mu_t}{n\sigma_\epsilon}\left(\frac{\partial\widetilde{Z''}}{\partial x^j}-\frac{m\widetilde{Z''}}{\widetilde{E''}}\,\frac{\partial\widetilde{E''}}{\partial x^j}\right)\left(\frac{1-n}{\widetilde{Z''}}\,\frac{\partial\widetilde{Z''}}{\partial x_j}-\frac{m}{\widetilde{E''}}\,\frac{\partial\widetilde{E''}_k}{\partial x_j}\right)}_{\text{turbulent diffusion}}$$

$$\underbrace{-C_{Z3}\,\frac{\widetilde{Z''}}{\widetilde{E''}}\,\overline{v_i''}\,\frac{\partial\overline{p}}{\partial x_i}}_{\text{pressure work}}+\underbrace{C_{Z4}\,\frac{\widetilde{Z''}}{\widetilde{E''}}\,\overline{p'\,\frac{\partial v_i''}{\partial x_i}}}_{\text{pressure-dilatation}}$$

The coefficients in the modeled *Z* transport equation are obtained from those in the ε equation

- The coefficients in the standard *K*-ε model are

$$\sigma_k = 1.0 \quad , \quad \sigma_\epsilon = 1.3 \quad , \quad C_{\epsilon 1} = 1.44 \quad , \quad C_{\epsilon 2} = 1.92$$

$$C_{\epsilon 0} = C_{\epsilon 4} = 1.0$$

- The coefficients in the *Z* equation are

$$C_{Z0} \equiv m + n\,C_{\epsilon 0} \quad , \quad C_{Z1} \equiv m + n\,C_{\epsilon 1} \quad , \quad C_{Z2} \equiv m + n\,C_{\epsilon 2}$$

$$C_{Z3} \equiv m + n\,C_{\epsilon 3} \quad , \quad C_{Z4} \equiv m + n\,C_{\epsilon 4}$$

- Different choices of *m* and *n* yield different 2-equation models:
  - $\widetilde{E''}$-$\widetilde{\epsilon''}$ with *m* = 0 and *n* = 1 (turbulent energy dissipation)
  - $\widetilde{E''}$-$\widetilde{\ell''}$ with *m* = 3/2 and *n* = -1 (turbulent lengthscale)
  - $\widetilde{E''}$-$\widetilde{\omega''}$ with *m* = -1 and *n* = 1 (turbulent frequency)
  - $\widetilde{E''}$-$\widetilde{\tau''}$ with *m* = 1 and *n* = -1 (turbulent timescale)

The *K-Z* model simplifies for several special types of turbulent flows, which can be used to tune the model coefficients

- Isotropic turbulence: power-law decaying solutions
  - Production terms proportional to τ_{ij}, the turbulent diffusion terms, and the mean velocity vanish

- Free shear flows (plane wake; mixing layer; plane, round, and radial jet): far-field, self-similar, statistically-stationary solutions
  - Solutions depend on the similarity variable $\eta = y/x$

- Turbulent boundary layers: power-law solutions in the logarithmic layer
  - Sufficiently far from the boundary, the eddy viscosity dominates the molecular viscosity and the advection terms are negligible

The *K*-*Z* model equations have power-law solutions for isotropic turbulence

- The model equations reduce to coupled ordinary differential equations

$$\frac{dK}{dt} = -\epsilon \qquad \frac{dZ}{dt} = -C_{Z2}\frac{Z}{K}\epsilon$$

- The initial conditions are $K(0) = K_0$ and $Z(0) = Z_0 = C_Z K_0^m \epsilon_0^n$
- The corresponding solutions are

$$\frac{K(t)}{K_0} = \left[1 + \left(\frac{C_{Z2}-m-n}{n}\right)\frac{\epsilon_0}{K_0}t\right]^{-n/(C_{Z2}-m-n)}$$

$$= \left[1 + (C_{\epsilon 2}-1)\frac{\epsilon_0}{K_0}t\right]^{-1/(C_{\epsilon 2}-1)}$$

$$\frac{Z(t)}{Z_0} = \left[\frac{K(t)}{K_0}\right]^{C_{Z2}} = \left[\frac{K(t)}{K_0}\right]^{m+nC_{\epsilon 2}}$$

- Experimentally, $K(t) \propto t^{1.34}$, which determines $C_{\varepsilon 2}$ (or C_{Z2})

The *K-Z* model equations have similarity solutions for free shear flows

- The model equations reduce to (and are solved by transforming to the similarity variable)

$$\left(\overline{v}_x \frac{\partial}{\partial x} + \overline{v}_y \frac{\partial}{\partial y}\right)K = \tau_{xy} \frac{\partial \overline{v}_x}{\partial y} - \epsilon + \frac{1}{y^r} \frac{\partial}{\partial y}\left(y^r \frac{\nu_t}{\sigma_k} \frac{\partial K}{\partial y}\right)$$

$$\left(\overline{v}_x \frac{\partial}{\partial x} + \overline{v}_y \frac{\partial}{\partial y}\right)Z = C_{Z1} \frac{Z}{K} \nu_t \left(\frac{\partial \overline{v}_i}{\partial x_j}\right)^2 - C_{Z2} \frac{Z}{K} \epsilon$$

$$+\frac{1}{y^r} \frac{\partial}{\partial y}\left(y^r \frac{\nu_t}{\sigma_\epsilon} \frac{\partial Z}{\partial y}\right) + \frac{mZ}{Ky^r} \frac{\partial}{\partial y}\left(y^r \frac{\nu_t}{\sigma_k} \frac{\partial K}{\partial y}\right) - \frac{m}{y^r} \frac{\partial}{\partial y}\left(y^r \frac{\nu_t}{\sigma_\epsilon} \frac{Z}{K} \frac{\partial K}{\partial y}\right)$$

$$+\frac{\nu_t}{n\sigma_\epsilon}\left(\frac{\partial Z}{\partial y} - \frac{mZ}{K} \frac{\partial K}{\partial y}\right)\left(\frac{1-n}{Z} \frac{\partial Z}{\partial y} - \frac{m}{K} \frac{\partial K}{\partial y}\right)$$

where $r = 1$ corresponds to a round jet and $r = 0$ otherwise, and the shear stress is

$$\tau_{xy} = \nu_t \frac{\partial \overline{v}_x}{\partial y}$$

The *K-Z* model equations have similarity solutions for the mixing layer

- The solutions have the form

$$\overline{v}_x(x,y) = \Delta v\, \overline{v}_x(\eta)$$

$$K(x,y) = (\Delta v)^2 K(\eta)$$

$$Z(x,y) = C_Z (\Delta v)^{2m} K(\eta)^m \left[\frac{(\Delta v)^3}{x} \right]^n \epsilon(\eta)^n$$

where $v = v_1 - v_2$ is the velocity difference between the two streams

The *K*-*Z* model equations have solutions consistent with the law-of-the-wall in bounded flows

- The Reynolds-averaged and *K*-*Z* equations reduce to

$$\frac{\partial}{\partial y}\left(\mu_t \frac{\partial \overline{v}_x}{\partial y}\right) = 0$$

$$\mu_t \left(\frac{\partial \overline{v}_x}{\partial y}\right)^2 + \frac{\partial}{\partial y}\left(\frac{\mu_t}{\sigma_K}\frac{\partial K}{\partial y}\right) - \rho\epsilon = 0$$

$$C_{Z1}\frac{Z}{K}\mu_t\left(\frac{\partial \overline{v}_x}{\partial y}\right)^2 - C_{Z2}\,\rho\frac{Z}{K}\epsilon + \frac{\partial}{\partial y}\left(\frac{\mu_t}{\sigma_\epsilon}\frac{\partial Z}{\partial y}\right)$$

$$+\frac{mZ}{K}\frac{\partial}{\partial y}\left(\frac{\mu_t}{\sigma_k}\frac{\partial K}{\partial y}\right) - m\frac{\partial}{\partial y}\left(\frac{\mu_t}{\sigma_\epsilon}\frac{Z}{K}\frac{\partial K}{\partial y}\right)$$

$$+\frac{\mu_t}{n\sigma_\epsilon}\left(\frac{\partial Z}{\partial y} - \frac{mZ}{K}\frac{\partial K}{\partial y}\right)\left(\frac{1-n}{Z}\frac{\partial Z}{\partial y} - \frac{m}{K}\frac{\partial K}{\partial y}\right) = 0$$

- The solutions have the form (where v_τ is the friction velocity, κ is the von Kármán constant, and *C*, *D*, C_Z are constants)

$$\overline{v}_x = \frac{v_\tau}{\kappa}\log y + C \quad , \quad K = D v_\tau^2 \quad , \quad Z = C_Z D^m v_\tau^{2m+3n}\left(\frac{1}{\kappa y}\right)^n$$

Application to asymptotically self-similar Rayleigh-Taylor mixing

- The turbulence production term is of the form

$$P_Z = C_{Z1} \frac{\widetilde{Z''}}{\widetilde{E''}} \tau_{ij} \frac{\partial \widetilde{v}_i}{\partial x_j}$$

- Assume that at sufficiently late times, the scaling of the mixing layer width is

$$h(t) = \alpha A t g t^2$$

  and that turbulence variables are proportional to this lengthscale and the corresponding velocity scale

- Then, K, ε, and Z are

$$\widetilde{E''} = \frac{\widetilde{v''^2}}{2} \propto \left(\frac{dh}{dt}\right)^2 \propto 4(\alpha A t g)^2 t^2 \qquad \widetilde{\epsilon''} = \frac{\partial \widetilde{E''_k}}{\partial t} \propto 8(\alpha A t g)^2 t$$

$$\widetilde{Z''} = C_Z \left(\widetilde{E''}\right)^m \left(\widetilde{\epsilon''}\right)^n \propto (\alpha A t g)^{2m+2n} t^{2m+n}$$

In Rayleigh-Taylor mixing the eddy viscosity and Reynolds stress tensor scale as follows

- The eddy viscosity scales as

$$\nu_t = \left(\widetilde{E''}\right)^{\frac{m+2n}{n}} \left(\widetilde{Z''}\right)^{-\frac{1}{n}} \propto (\alpha A t g)^2 t^3$$

- The Reynolds stress scales as

$$\tau_{ij} = 2\overline{\rho}\,\widetilde{E''}\,\frac{\delta_{ij}}{d} - 2\overline{\rho}\,\nu_t\left(\widetilde{S}_{ij} - \frac{\delta_{ij}}{d}\,\frac{\partial \widetilde{v}_k}{\partial x_k}\right)$$

$$\propto 2\overline{\rho}(\alpha A t g)^2 t^2\left[\frac{4}{d}\delta_{ij} - \left(\widetilde{S}_{ij} - \frac{\delta_{ij}}{d}\,\frac{\partial \widetilde{v}_k}{\partial x_k}\right)t\right]$$

- Therefore, if the Favre-averaged strain-rate tensor dimensionally scales as (q_{ij} is dimensionless)

$$\widetilde{S}_{ij} = \frac{1}{2}\left(\frac{\partial \widetilde{v}_i}{\partial x_j} + \frac{\partial \widetilde{v}_j}{\partial x_i}\right) \propto q_{ij}\,\frac{1}{h(t)}\,\frac{dh(t)}{dt} \propto \frac{1}{t}$$

then $\tau_{ij} \propto 2\overline{\rho}(\alpha A t g)^2 t^2\left(\frac{5}{d}\delta_{ij} - q_{ij}\right)$ and

$$P_Z \propto (\alpha A t g)^{2(m+n)}\, t^{2m+n-1}\,\overline{\rho}\left(\frac{5}{d}\delta_{ij} - q_{ij}\right)q_{ij}$$

Conclusions

- The methodology presented here provides a systematic and self-consistent approach to the derivation of 2-equation turbulent transport models
  - This provides an improved *l* transport equation
  - Also provides a consistent expression for the diffusion and cross diffusion terms, which are important in many flow (e.g., near a boundary)
- Several canonical turbulent flows can be used to reduce the model equations and specify model parameters before application to interfacial-instability induced turbulence
- The general *Z* equation is consistent with the t^2 scaling of the mixing layer width
- Both an ω and a τ equation were derived as alternatives to the ε and *l* equation
  - τ may be a better physical variable than ε and *l*

Work in progress

- Completion of solutions for canonical turbulent flows
- Completion of solutions for Rayleigh-Taylor instability-induced turbulence
- Commencement of examination of model parameters and forms of modeled terms using high-resolution DNS data
- Eventually, application to Richtmyer-Meshkov instability-induced turbulence

Large- and Small-Scale Dynamics of Variable-Density Rayleigh-Taylor Instability-Induced Turbulent Mixing

Oleg Schilling and Andrew W. Cook

University of California, Lawrence Livermore National Laboratory

P.O. Box 808, L-22, Livermore, CA 94551

(925) 423-6879, schilling1@llnl.gov

Presented at the

8th International Workshop on the Physics of Compressible Turbulent Mixing

California Institute of Technology, Pasadena, CA

9-14 December 2001

This work was performed under the auspices of the U.S. Department of Energy by the University of California, Lawrence Livermore National Laboratory under Contract No. W-7405-Eng-48

The dynamical effects of 'small' (unresolved) scales on 'large' (resolved) scales cannot be neglected in a turbulent mixing layer

- The dynamical effect of small scales on large scales is a bi-directional, competing process
  - Energy transferred up and down scale through 'backscatter' and a cascade, respectively, over a wide range of eddies
  - As *Re* increases, contribution from the small scales increases
- *Rate of scalar mixing* is proportional to dissipation rate of the squared scalar ($\langle \cdot \rangle$ is an average and *D* is the scalar diffusion coefficient)

$$\langle \epsilon_\phi \rangle \equiv -\frac{\partial}{\partial t}\left\langle \frac{\phi^2}{2} \right\rangle = D\langle \phi \nabla^2 \phi \rangle$$

  - *Contribution to this quantity is dominated by the small scales*, where gradients are large
- Turbulent quantities (e.g., the kinetic energy) are contributed by all scales, not only by large-scale, integral quantities
- Simulation of Rayleigh-Taylor mixing requires capability to simulate smaller scales as well as the largest scales

Schematic of direct numerical simulation (DNS) and large-eddy simulation (LES) for turbulent mixing

- Turbulence enhances mass, momentum, energy transport
  - Coherent bubble/spike structures associated with energy containing subrange
- Energy *transferred* among eddies at all scales
  - Inertial subrange 'mediates' between largest and smallest scales
- Molecular (atomic) mixing associated with dissipation subrange, in which structures are too small to be resolved

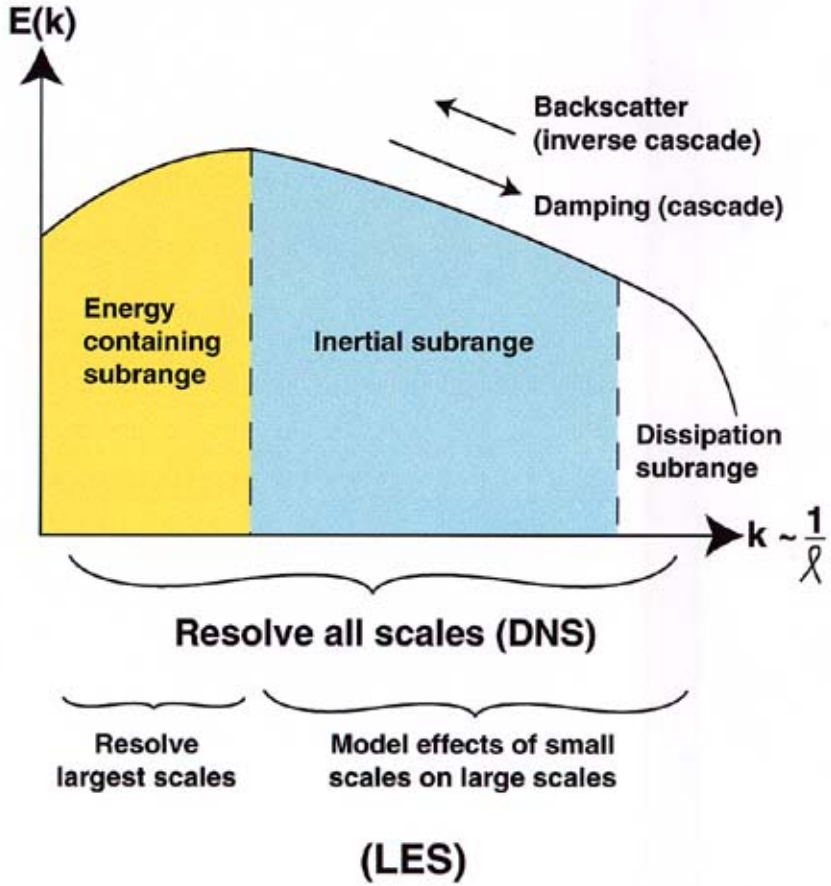

The approaches used thus far to simulate Rayleigh-Taylor mixing have important physical and computational limitations

- Monotone integrated LES (MILES)
  - Implicit numerical dissipation (finite-volume simulations of the non-dissipative equations)
  - Advantage: modest computational requirements
  - Disadvantage: small-scale structures and statistics not estimated well, while large-scale structures and lowest-order integral properties are

- DNS
  - Physical dissipation (spectral and finite-difference simulations of the dissipative equations)
  - Advantage: all structures and statistics estimated well
  - Disadvantage: very high computational and data storage/processing requirements

High-resolution DNS is too computationally expensive to simulate Rayleigh-Taylor mixing: an LES capability is needed

- DNS is too expensive to simulate a mixing layer that exceeds the *mixing transition Reynolds number* $Re \sim 10^4$
  - Issue is more acute for miscible, reacting flows in which all scales are below any possible grid resolution

- Therefore, development of a true LES capability to predict mean hydrodynamic fields and lowest-order transport and mixing statistics is essential

$Re \sim 2.5 \times 10^3$ $Re \sim 1 \times 10^4$

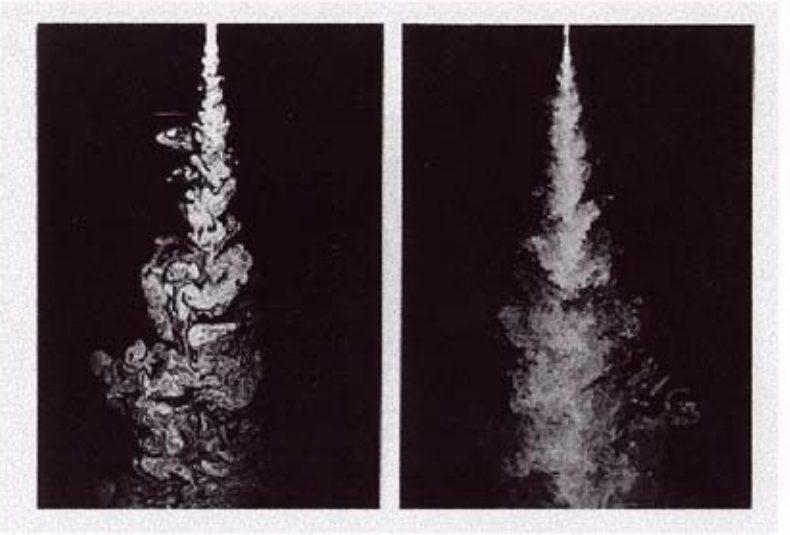

Liquid-jet concentration in a round turbulent jet (Dimotakis 1983)

To develop an LES capability, an examination of interaction between unresolved and resolved scales in Rayleigh-Taylor mixing layers is needed

- Study transfer (exchange) of $\rho^2/2$ and $v^2/2$ among different wavenumber regions (corresponding to spatial scales or eddies)
  - ρ and v_i fields obtained from high-resolution DNS data
  - An artificial cutoff scale is used to partition scales into computationally resolved and unresolved scales
- Fourier space representation determines magnitude and other properties of transfer process as a function of scale k and height in the domain
  - Wavelet transforms can also be used to add information *as a function of position*
- Data obtained from this study will be used to develop and assess subgrid-scale and backscatter models for LES
  - Work will improve the classical Smagorinsky eddy viscosity and scale-similarity subgrid-scale models

A high-resolution ($512^2 \times 2040$) DNS was performed for miscible, variable-density, Rayleigh-Taylor unstable fluids with $At = 1/2$

Density isosurface at times 1, 2, 3, 4, 5, 6
red: $\rho = 3$; green: $\rho = 2$; blue: $\rho = 1$

- Spectral/8th-order compact finite-difference method with 3rd-order, Adams-Bashforth time-evolution
- Small-scale initial perturbations on fluid interface
- Turbulence attains late-time Reynolds number based on mixing layer width

$$Re_h(t) = \frac{(\rho_1 + \rho_2)}{2\mu} h(t) \frac{dh(t)}{dt}$$

$$\approx 5.5 \times 10^3$$

Similarly, the analysis of kinetic energy transfer dynamics begins with a 2-dimensional Fourier transform of the momentum equation

- Applying the Fourier transform to the momentum equation in homogeneous directions gives ($V = 1/\rho$ is the specific volume)

$$\frac{\partial v_i(\mathbf{k}_\perp,z,t)}{\partial t} \equiv \underbrace{F_i(\mathbf{k}_\perp,z,t)}_{\text{forcing term}} + \underbrace{N_i(\mathbf{k}_\perp,z,t)}_{\text{advection term}} + \underbrace{D_i(\mathbf{k}_\perp,z,t)}_{\text{dissipation terms}}$$

$$= -g(t)\,\delta_{i3}$$

$$-\iint V(\mathbf{p}_\perp,z,t)\left(iq_\perp^i + \delta^{i3}\frac{\partial}{\partial z}\right)p(\mathbf{q}_\perp,z,t)\,\delta^2(\mathbf{k}_\perp-\mathbf{p}_\perp-\mathbf{q}_\perp)\,d^2p_\perp\,d^2q_\perp$$

$$-\iint v_j(\mathbf{p}_\perp,z,t)\left(iq_\perp^j + \delta^{j3}\frac{\partial}{\partial z}\right)v_i(\mathbf{q}_\perp,z,t)\,\delta^2(\mathbf{k}_\perp-\mathbf{p}_\perp-\mathbf{q}_\perp)\,d^2p_\perp\,d^2q_\perp$$

$$-\nu\left(k_\perp^2 - \frac{\partial^2}{\partial z^2}\right)v_i(\mathbf{k}_\perp,z,t) - \frac{4}{3}\nu\,k_\perp^i\,k_\perp^j\,v_j(\mathbf{k}_\perp,z,t)$$

For a given $k_\perp$, N_ρ and N_i describe the integrated nonlinear interactions of *all other scales* with $k_\perp$

- Decompose nonlinear terms into partial sum N_ρ^A and N_i^A corresponding to different disjoint regions A э $k_\perp$
  - Each term represents nonlinear interactions contributed by any 2 such regions
- Define regions

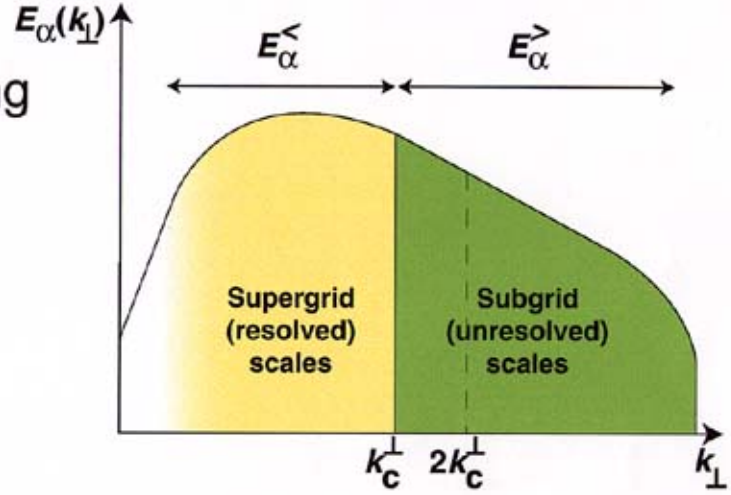

$$k_0^\perp = 0 < k_1^\perp = k_c^\perp < k_2^\perp = 2k_c^\perp < k_3^\perp = k_{max}^\perp$$

where $k_c^\perp$ and $k_{max}^\perp$ are cutoff and maximum wavenumbers

- Partial nonlinear terms computed by truncating v_i and ρ to region A,

$$\phi_\alpha^{\mathcal{A}}(\mathbf{k}_\perp, z, t) \equiv \begin{cases} \phi_\alpha(\mathbf{k}_\perp, z, t) & \mathbf{k}_\perp \in \mathcal{A} \\ 0 & \text{otherwise} \end{cases}$$

The kinetic energy spectrum at the midplane ($z = 0$) evolves to a state with a very short inertial subrange

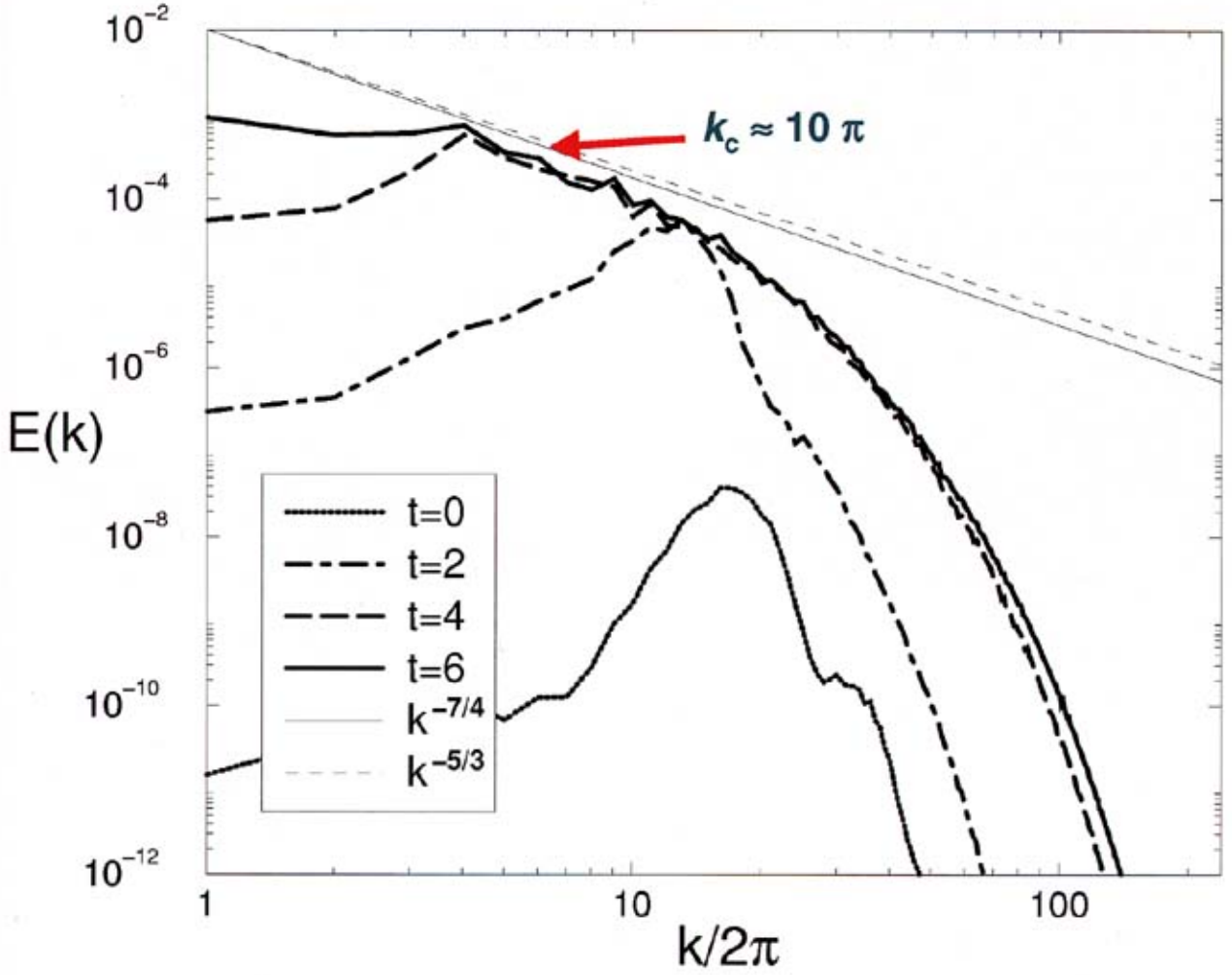

Previous decomposition of nonlinear terms can be used to derive expressions for supergrid and subgrid nonlinear terms

- The nonlinear term describing interactions of modes $k_\perp \in K$ with modes in regions P and Q can be expressed as a sum

$$N_\alpha(\mathbf{k}_\perp, z, t) = \sum_{\mathcal{K}=1}^{3} \sum_{\mathcal{P}=1}^{3} \sum_{\mathcal{Q}\geq\mathcal{P}=1}^{3} N_\alpha^{\mathcal{K}\mathcal{P}\mathcal{Q}}(\mathbf{k}_\perp, z, t)$$

- Supergrid (resolved) nonlinear terms corresponding to modes $k_\perp < k_c^\perp$ and to modes $k_\perp < k_2^\perp = 2\, k_c^\perp$:

$$N_\alpha^{<}(\mathbf{k}_\perp | \mathbf{k}_\perp^c, z, t) = N_\alpha^{111}$$

$$N_\alpha^{<}(\mathbf{k}_\perp | 2\mathbf{k}_\perp^c, z, t) = N_\alpha^{111} + N_\alpha^{121} + N_\alpha^{221} + N_\alpha^{112} + N_\alpha^{122} + N_\alpha^{222}$$

- Subgrid (unresolved) nonlinear terms corresponding to modes $k_\perp > k_c^\perp$ and to modes $k_c^\perp > k_2^\perp = 2\, k_c^\perp$:

$$N_\alpha^{>}(\mathbf{k}_\perp | \mathbf{k}_\perp^c, z, t) = N_\alpha^{121} + N_\alpha^{131} + N_\alpha^{221} + N_\alpha^{231} + N_\alpha^{331}$$

$$N_\alpha^{>}(\mathbf{k}_\perp | 2\mathbf{k}_\perp^c, z, t) = N_\alpha^{131} + N_\alpha^{231} + N_\alpha^{331} + N_\alpha^{132} + N_\alpha^{232} + N_\alpha^{332}$$

The supergrid and subgrid energy density evolution equations can be formed in terms of the nonlinear terms

- Partial transfer spectra describe rate of $\rho^2/2$ and $v^2/2$ change in modes $k_\perp \in K$ due to nonlinear interactions between modes $p_\perp \in P$ and $q_\perp \in Q$:

$$T_\alpha^{KPQ}(\mathbf{k}_\perp, z, t) = \mathrm{Re}\left[\phi_\alpha(\mathbf{k}_\perp, z, t)^* N_\alpha^{KPQ}(\mathbf{k}_\perp, z, t)\right]$$

- Introducing large-scale density and velocity truncated at $k_2^\perp = 2\, k_c^\perp$,

$$\rho^< = \rho^1 + \rho^2 \quad , \quad v_i^< = v_i^1 + v_i^2$$

the supergrid (resolved) density squared and kinetic energy are

$$E_\rho^<(\mathbf{x}, t) = \frac{\rho^<(\mathbf{x},t)^2}{2} \quad , \quad E^<(\mathbf{x}, t) = \frac{v^<(\mathbf{x},t)^2}{2}$$

- The equations for these quantities contain the supergrid and subgrid transfers

The subgrid-scale energy transfer spectra $T_\alpha(k_\perp|k_\perp^c;z,t)$ provide information on *magnitude* and *direction* of the energy transfer

- Computation of subgrid-scale energy transfers requires summation over all $k_\perp$ in a spherical shell centered around $k_\perp$:

$$T_\alpha^{>}(k_\perp|k_c^\perp;z,t) = \sum_{k_\perp-\frac{\Delta k_\perp}{2}<|\mathbf{k}_\perp|<k_\perp+\frac{\Delta k_\perp}{2}} T_\alpha^{>PQ}(k_\perp|k_c^\perp;z,t)$$

  where P and Q are spherical wavenumber bands centered around $p_\perp$ and $q_\perp$

- Computation involves interactions in which components of the sum can be either positive or negative
  - Positive component (forward energy cascade):

$$T_\alpha^{(+)>}(k_\perp|k_c^\perp;z,t) \equiv \frac{T_\alpha^{>}(k_\perp|k_c^\perp;z,t)+|T_\alpha^{>}(k_\perp|k_c^\perp;z,t)|}{2}$$

  - Negative component (backward energy cascade):

$$T_\alpha^{(-)>}(k_\perp|k_c^\perp;z,t) \equiv \frac{T_\alpha^{>}(k_\perp|k_c^\perp;z,t)-|T_\alpha^{>}(k_\perp|k_c^\perp;z,t)|}{2}$$

Net eddy viscosities $\nu_\alpha^n(k_\perp|k_\perp^c;z,t)$ can be defined for $k_\perp < k_\perp^c$ in terms of eddy and backscatter viscosities

- *Net* eddy viscosities:

$$\nu_\alpha^n(k_\perp|k_c^\perp;z,t) \equiv -\frac{T_\alpha^{>}(k_\perp|k_c^\perp;z,t)}{2k_\perp^2 E_\alpha^{<}(k_\perp,z,t)}$$

- Eddy viscosities: (representing energy removal by small scales)

$$\nu_\alpha(k_\perp|k_c^\perp;z,t) \equiv -\frac{T_\alpha^{(+)>}(k_\perp|k_c^\perp;z,t)}{2k_\perp^2 E_\alpha^{<}(k_\perp,z,t)}$$

- Backscatter viscosities: (representing energy transfer from small to larger scales)

$$\nu_\alpha^b(k_\perp|k_c^\perp;z,t) \equiv \frac{T_\alpha^{(-)>}(k_\perp|k_c^\perp;z,t)}{2k_\perp^2 E_\alpha^{<}(k_\perp,z,t)}$$

- Thus, net viscosities are

$$\nu_\alpha^n(k_\perp|k_c^\perp;z,t) = \nu_\alpha(k_\perp|k_c^\perp;z,t) - \nu_\alpha^b(k_\perp|k_c^\perp;z,t)$$

Eddy viscosity

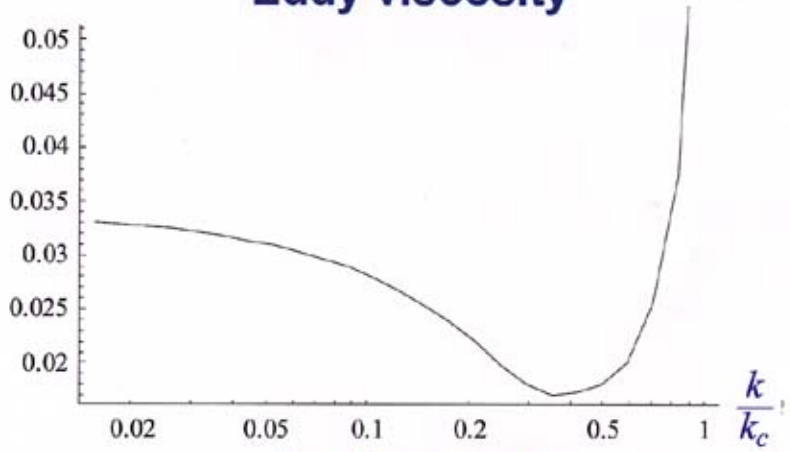

Backscatter

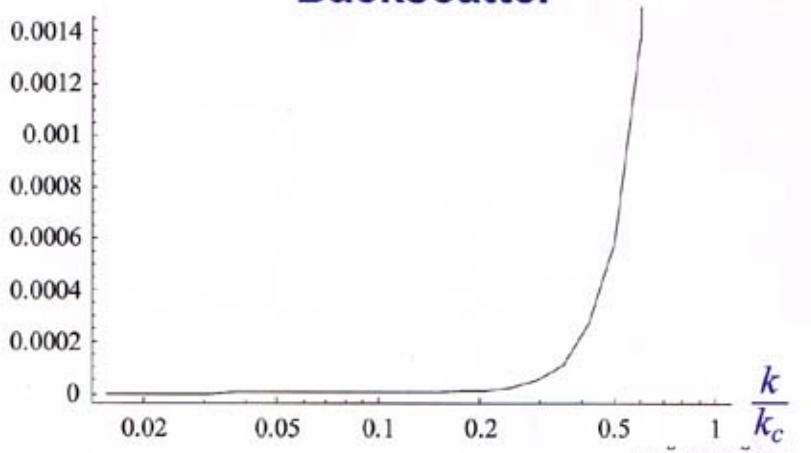

Given the eddy and backscatter viscosities, a subgrid-scale model can be defined

- Large-eddy equations have the form (only the Navier-Stokes equation is shown)

$$\frac{\partial}{\partial t}(\rho^{<} v_i^{<}) + \frac{\partial}{\partial x_j}\left(\rho^{<} v_i^{<} v_j^{<} + p\delta_{ij} - \sigma_{ij}\right) - \rho^{<} g_i = -\frac{\partial \tau_{ij}}{\partial x_j}$$

- Left side is computed explicitly
- Right side involves the Reynolds stress tensor τ_{ij}
  - The Smagorinsky model is

$$\tau_{ij} = \frac{\delta_{ij}}{3}(\nu^{<})^2 - \nu_t\left(\frac{\partial v_i^{<}}{\partial x_j} + \frac{\partial v_j^{<}}{\partial x_i}\right)$$

- A similar parameterization may be reasonable for resolved density equation

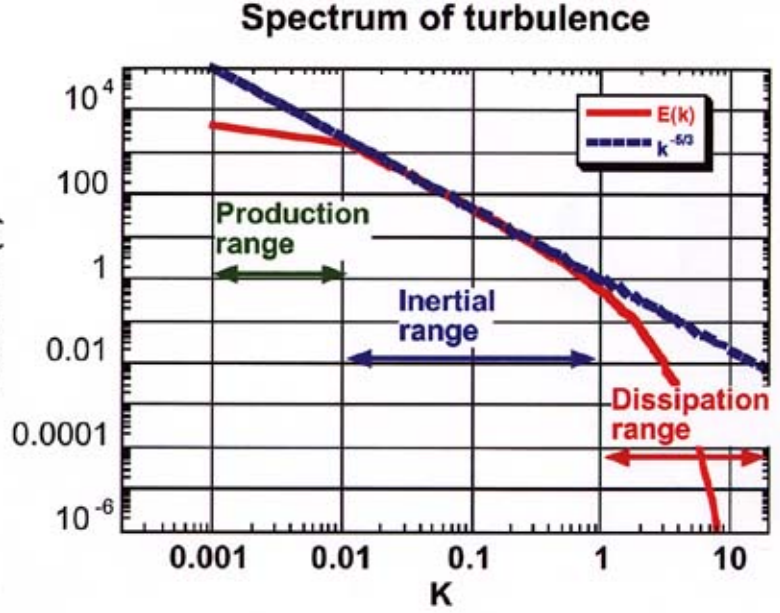

Turbulence dynamics of enstrophy (vorticity squared) transfer is particularly relevant to interfacial instability-induced turbulent mixing

- Dynamics of enstrophy $\rho\,\Omega = \rho\,\omega^2 / 2$ will also be examined (dissipation terms are not written)

$$\frac{\partial}{\partial t}(\rho\Omega) + \frac{\partial}{\partial x_j}(\rho\Omega v_j) = \underbrace{\epsilon_{ijk}\,\frac{\omega^i}{\rho}\,\frac{\partial\rho}{\partial x_j}\,\frac{\partial p}{\partial x_k}}_{\text{baroclinic production}} + \underbrace{\rho\,\omega_i S^{ij}\,\omega_j}_{\text{enstrophy stretching}} - \underbrace{2\,\rho\Omega\,\frac{\partial v_j}{\partial x_j}}_{\text{dilatation}}$$

  - Baroclinic production term is an instability source term, existing due to misalignment of $\nabla\rho$ and ∇p
  - Stretching term is related to development of turbulence
  - Dilatation term is small in a variable-density flow, but is important in a compressible (Richtmyer-Meshkov) flow
- Baroclinic production and stretching terms exist in 3D, but only the former exists in 2D
  - Nature of turbulent energy and enstrophy cascades is, therefore, very different in 2D and 3D

Conclusions and work in progress

- A subgrid-scale transfer analysis can be applied to Rayleigh-Taylor and Richtmyer-Meshkov mixing layers
  - Provides time- and scale-dependent measure of energy transfer process
  - Provides parameterizable eddy viscosities/backscatters for LES of Rayleigh-Taylor mixing at large *Re*
  - Also provides information for scale-similarity and more recent deconvolution subgrid-scale models
- Data processing at LLNL requires 256 IBM SP nodes (1,024 CPUs) and sufficient computer time
- Purpose of this research is to acquire physical insight into coupling of the large and small scales, in order to develop and assess subgrid-scale models for LES

ANALYTICAL STUDY of the RTI in COMPRESSIBLE FLUIDS

M. TRICOTTET (PhD-St.)

Serge BOUQUET

COMMISSARIAT ENERGIE ATOMIQUE
-CEA-
Dept. App. Theor. Physics

bouquet@bruyeres.cea.fr

USE of COMPRESSIBILITY for the RTI

Sound speed : $c_s^2 = (\Delta p / \Delta \rho)_{adiab.}$

Incompressible fluids : $\Delta \rho$ finite $\rightarrow \Delta p = \infty$!

$c_s \rightarrow \infty$

NOT NECESSARLY REPRESENTATIVE OF PHYSICS

- ICF
- ASTROPHYSICS

H-envelope Type II -SN progenitor :

$T \simeq 10^6$ K , $\rho \simeq 10^{-3}$ g/cc , $D \simeq c/10$ **M ≃ 100's !**

INCOMPRESSIBILITY IS NO LONGER VALID

1980's:

- Bernstein-Book (1983): $\alpha_{comp} > \alpha_{incomp.}$
- Baker (1983): compressibility either enhance or decrease α
- Sharp (1984): $\alpha_{comp} < \alpha_{incomp.}$

Since .... very few analytical work

DIMENSIONAL ANALYSIS

INCOMPRESS. $[g] = LT^{-2}$, $[\lambda] = L$ $([\rho] = ML^{-3})$

→ no dimensionless number

→ characteristic time $\begin{cases} \tau = \sqrt{\lambda/g} \\ \alpha^2 \sim kg \end{cases}$

$[\rho]$? M should disappear

$\rho_1 \to \rho_2$ $\quad R \equiv \rho_1/\rho_2 \to$ **At.**

COMPRESSIBLE : $[g] = LT^{-2}$, $[\lambda] = L$, $[c_s] = LT^{-1}$

π-Theorem : $\pi = c_s^2/(\lambda g)$

$$\begin{cases} c_s \text{ finite} \\ \lambda \to 0 \end{cases} \simeq \begin{cases} c_s \to \infty \\ \lambda \text{ finite} \end{cases} \qquad (\pi \to \infty)$$

small λ's ($\lambda \ll c_s^2/g$) not affected by compress.

(Sharp 1983)

3 QUANT. REPRESENT. of. COMPRESS.

	$c_s^2 < \infty$	$\nabla\rho$	θ'
STATIC (g = cste)	×	×	
		×	
DYNAM.	×	↑	×

neglected if $\lambda \ll (\nabla\rho/\rho)^{-1}$

scale of stratif.

$\nabla\rho$: stratif

$\theta' \equiv \dfrac{\partial v}{\partial z}$ exp. velocity

$\vec{\nabla} \cdot \vec{v} \neq 0$

ASSUMPTIONS

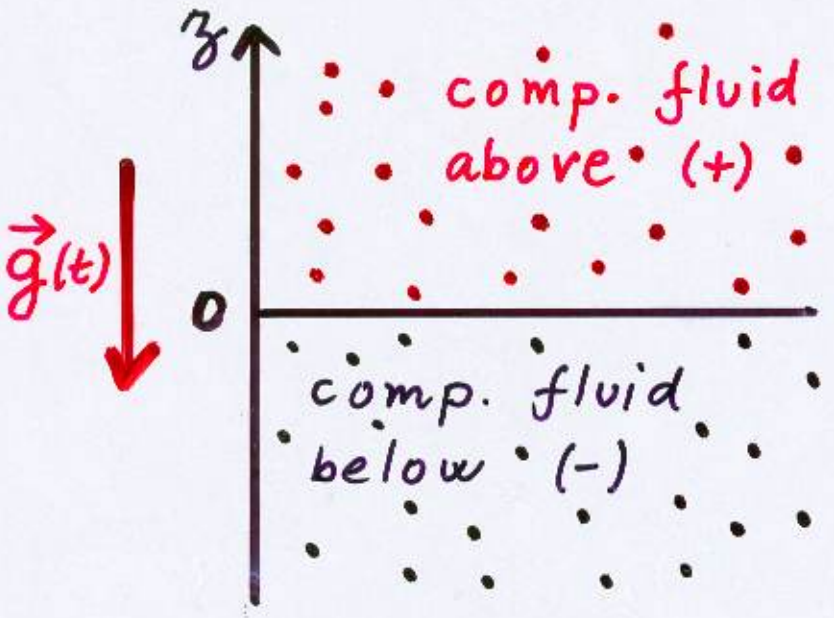

$\begin{cases} \dot{g} = 0 & \text{STATIC} \\ \dot{g} \neq 0 & \text{DYNAM.} \end{cases}$ $\rightarrow (\theta' \equiv \partial V/\partial z)$

Assume: – initial state "0" ($\vec{V}_0 = 0$ or $\vec{V}_0 \neq 0$)

– no vorticity $\vec{V} = \vec{\nabla}\phi$

$\frac{d}{dt}\int \vec{v}.d\vec{l} = cste = \frac{d}{dt}\int (\vec{\nabla}\wedge\vec{v})\, d\vec{S} = \vec{0}$ if $\vec{V}_0 = 0$

$\Rightarrow \vec{\nabla}\wedge\vec{V} = 0 \Rightarrow \vec{V} = \vec{\nabla}\phi$

Idem $V_0 \neq 0$

– arbitrary EOS : $p^{\pm} = f^{\pm}(\rho^{\pm})$

especially $p \sim \rho^{\gamma}$, $\gamma = \frac{1+n}{n}$ $(\gamma^+ \neq \gamma^-)$

For "+" and "–", hydro. Eqs. are:

$$\begin{cases} \rho \nabla^2\phi + \vec{\nabla}\phi.\vec{\nabla}\rho + \partial\rho/\partial t = 0 \\ \partial\phi/\partial t + (\vec{\nabla}\phi)^2/2 + g z + \underline{h} = 0 \end{cases}$$

$\begin{cases} \underline{h} : \text{enthalpy} \\ dh = dp/\rho = f'(\rho)\, d\rho/\rho \\ \text{Id. Gas} : h = c_s^2/(\gamma-1) \end{cases}$

THE PERTURBATION (STATIC)

Phys. quantity: $q(x,y,z;t) = \underbrace{q_0(z)}_{\text{Eq.}} + \underbrace{q_1(x,y,z;t)}_{\text{1rst o. pert.}}$

3D+t analytical stability analysis

4 dimensions !!!

Velocity potential: $\boxed{\phi(\vec{r};t) = \phi_{dim}\, S(x,y)\, Z(z)\, T(t)}$

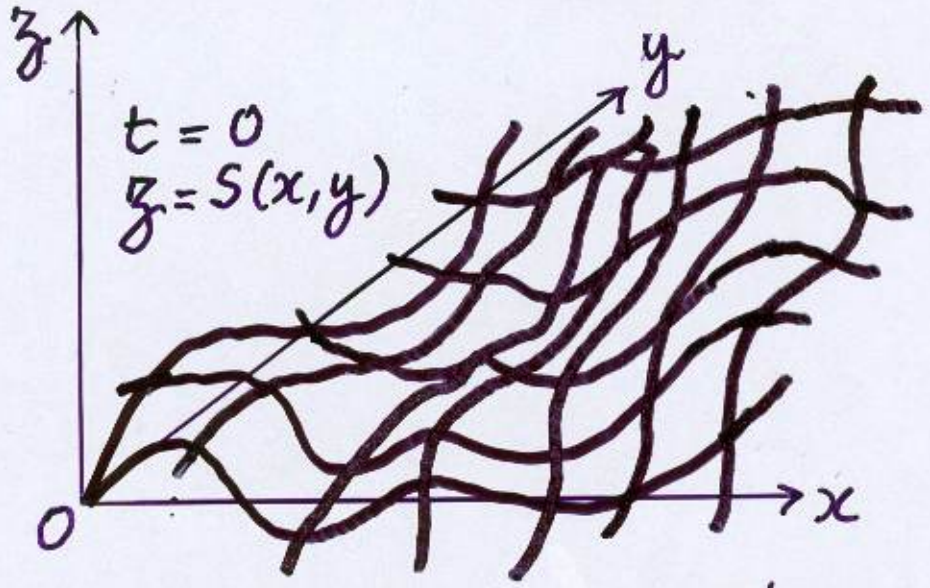

$z = S(x,y)$

3D-interface

LINEAR SYSTEM OF 3-ODE'S:

- $\ddot{T}(t) - \alpha^2 T(t) = 0 \Rightarrow T(t) = e^{\alpha t}$; α = G.Rate
  Exponential (OK!)
- $\partial_x^2 S(x,y) + \partial_y^2 (x,y) = -k^2 S(x,y)$
  k^2: eigen values of 2D-∇^2
- $c_0^2(z)\, Z''(z) - g\, Z'(z) - [k^2 c_0^2(z) + \alpha^2] Z(z) = 0$; $c_0 = \frac{dp}{d\rho} = f'(\rho)$
  (g: $\dot{g} = 0$)

NO EXPONENTIAL SOLUTION !!!

→ YET DISPERSION RELATION

ISOTHERMAL CASE $p^{\pm} = K^{\pm} \rho^{\pm}$

$$\tilde{\alpha}^2 = 2\left(\frac{1}{R} - 1\right) \frac{\left[1 - (1+\tilde{\alpha}^2+\tilde{k}^2)^{1/2}\right]\left[1 + (1+R\tilde{\alpha}^2+R^2\tilde{k}^2)^{1/2}\right]}{(1+\tilde{\alpha}^2+\tilde{k}^2)^{1/2} + (1+R\tilde{\alpha}^2+R^2\tilde{k}^2)^{1/2}}$$

IMPLICIT!

$$\begin{cases} \tilde{\alpha} = \alpha / (g/2\sqrt{K^+}) \\ \tilde{k} = k / (g/2K^+) \end{cases}$$ dimensionless

UNIVERSAL 1-PARAMATER R-CURVES

$R = \rho^+/\rho^-$ instead of $At = (R-1)/(R+1)$

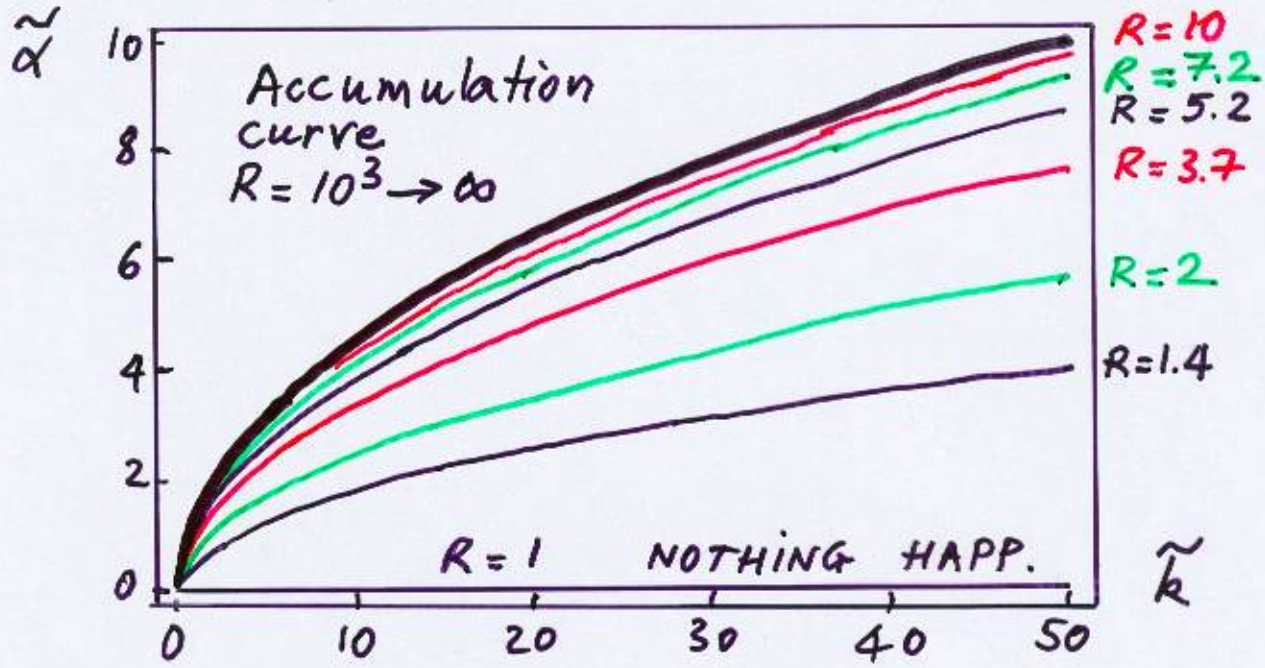

- $R \gg 1$ $(At \to 1)$: $\alpha = \sqrt{kg}$
- $\tilde{k} \gg 1$ $(\lambda \to 0, c_{s0} \to \infty)$: $\alpha = \sqrt{At\, kg}$
- $\tilde{k} \ll 1$ $(\lambda g / c_{s0}^2 \to \infty)$: $\alpha = \sqrt{2At}\, c_{os}^+ k \sim \frac{1}{\lambda}$

incompress. $\alpha_{inc} \sim \frac{1}{\sqrt{\lambda}}$

$\alpha_{comp} < \alpha_{incomp.}$

POLYTROPIC CASE $p^{\pm} = K^{\pm}(\rho^{\pm})^{\Gamma^{\pm}}$

2 parameters (R, Γ) universal family curves

$R = \rho^{+}/\rho^{-} = 1.1$ (At # 0.05)

HIGHLY IMPLICIT !!!

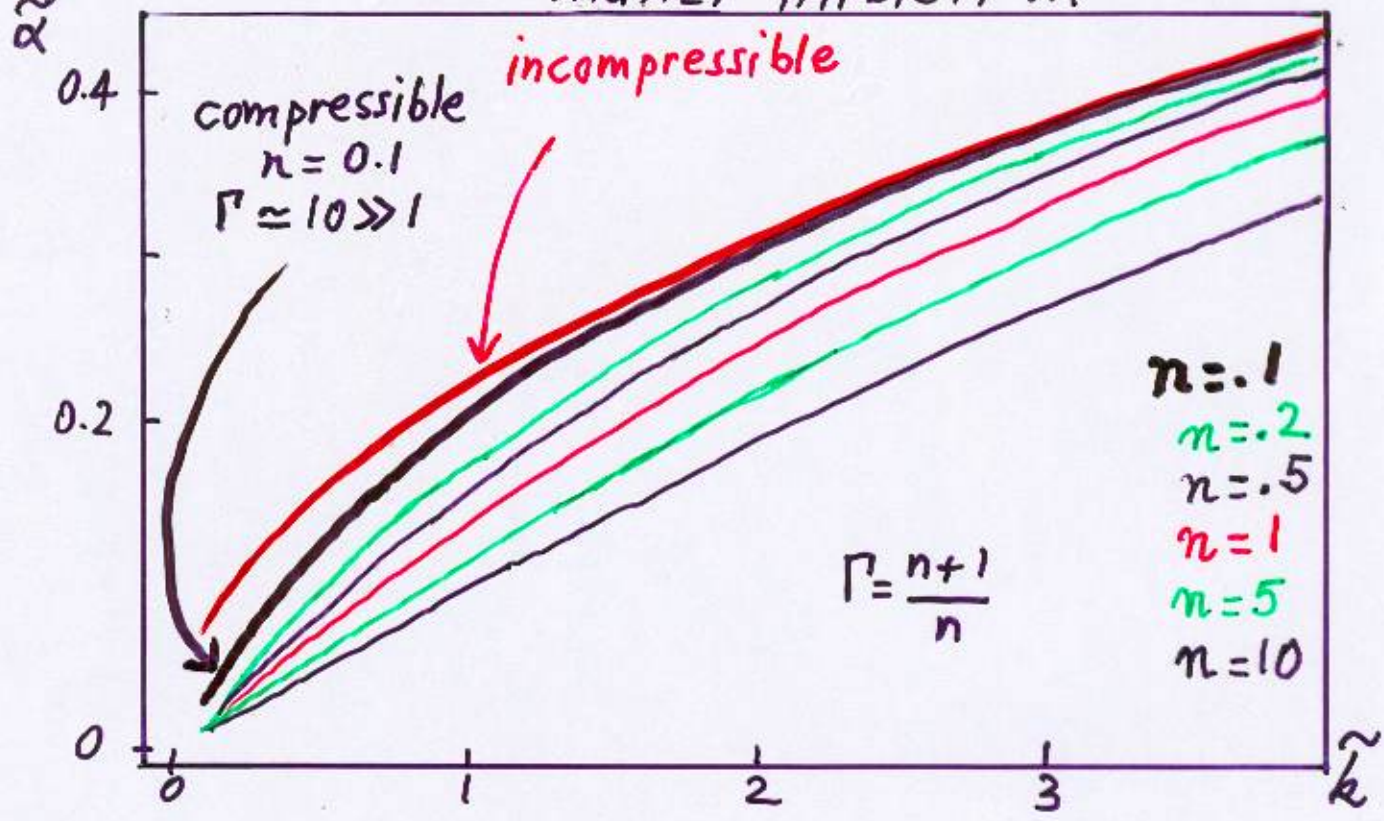

- $\tilde{k} \gg 1$: $\alpha \to \sqrt{A_t k g}$
- $n \to 0$, $\Gamma \to \infty$: ——— $\neq$ ——— $\tilde{k} < 2$

  large λ $\alpha_{comp.} < \alpha_{incomp.}$ (— below —)
- comparison : $\tilde{k} = 2$

$\begin{cases} \tilde{\alpha}_{comp} \simeq .15 \\ \tilde{\alpha}_{inc} \simeq .3 \end{cases}$ $\sim 50\%$ deviation !!!

(and into an exponential)

DYNAMICAL CASE
POLYTROPE Γ
$\dot{g}/g \ll \alpha$

1-D background motion $\vec{v} = v(z,t)\,\vec{e}_z$ and $\theta' = \partial v/\partial z$ $(\vec{\nabla}.\vec{v} \neq 0)$

$$\alpha(\alpha-\theta') = g^2(\rho^+-\rho^-)\frac{\{[1+4c_0^{+}(\alpha^2+\alpha a^{+}+c_0^{+2}k^2)/g^2]^{1/2}-1\}\{-\text{ superscript }+\}}{2\rho^{+}c_0^{+2}\{-\}+2\rho^{-}c_0^{-2}\{+\}}$$

$$\alpha^{\pm} = \theta'(\Gamma-1)$$

ASYMPTOTICS :

- $k \to \infty$: $\alpha(\alpha-\theta') \to \alpha_{incomp}^2 = Atkg$

$$\alpha \to \frac{\theta' + \sqrt{\theta'^2+4\alpha_{inc}^2}}{2} \qquad \theta'=0,\ \alpha=\alpha_{inc}$$

$\begin{cases}\theta'>0 \text{ (expansion)} & \alpha > \alpha_{inc}\\ \theta'<0 \text{ (contraction)} & \alpha < \alpha_{inc}\end{cases}$

- $c_0^{\pm} \to \infty$: same as for $k \to +\infty$.

CONCLUSION

- Compressibility requires careful study (comparison with incomp. should continued)
- Equilibrium initial State :

$\alpha_{comp} < \alpha_{incomp} = \sqrt{A_t k g}$

Similar to $\alpha_\nabla \simeq \sqrt{\frac{A_t k g}{1 + k L_\nabla}}$

Stratification due to compressibility similar to the existence of a $\vec{\nabla}\rho$

- Incompressible :
$\vec{V} = \vec{\nabla}\Phi$ and $\vec{\nabla}.\vec{V} = 0 \Rightarrow \nabla^2\Phi = 0$

<u>Compressible</u> $\phi = \phi_{dim}\, S(x,y)\, Z(z)\, T(t)$

with $\nabla^2 S = -k^2 S$

Similar to $\nabla^2\Phi = 0$, but ...

... additional equation for $Z(z)$, $T(t)$!

- To be used as a starting point for :
  - Non Linear Study
  - Comparison with codes.

ANALYTICAL GROWTH RATE OF A NON-

M. Vandenboomgaerde - Commissariat à l'Energie Atomique -

ACCURATE APPROXIMATE PERTURBATION

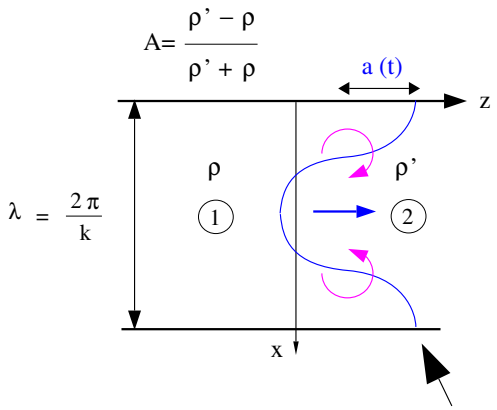

$z = \eta\,(x,t)$

$$k\eta = \sum_{n=1}^{\infty} (a_0 k \sigma t)^n \sum_{j=1}^{n} a_j^{(n)} \cos(\, jkx\,) \quad \Rightarrow$$

$$P1[A] = 1$$

$$P3[A] = \frac{-1 + 2 * A^2}{6}$$

$$P5[A] = \frac{19 - 125 * A^2 + 92 * A^4}{240}$$

$$P7[A] = \frac{-264 + 3686 * A^2 - 6997 * A^4 + 3234 * A^6}{5040}$$

* See T32 Oral : Efficient perturbation method for the RM and the RT instabilities: Weakly nonlinear stage and beyond

LINEAR SINGLE-MODE R-M INSTABILITY

BP 12 - 91680 Bruyeres-Le-Chatel- FRANCE

E-mail: marc.vandenboomgaerde@cea.fr

THEORY* GIVES SIMPLE FORMULA FOR a(T)

$$k\,a(T) = \sum_{p=0}^{\infty} P_{2p+1}[A]\,T^{2p+1} \quad \text{with} \quad T = a_0 k \sigma t$$

$$P9[A] = \frac{117663 - 2855274 * A^2 + 10086083 * A^4 - 11093856 * A^6 + 3805728 * A^8}{2903040}$$

$$P11[A] = (-5507319 + 206796915 * A^2 - 1168865775 * A^4 + 2250383605 * A^6 - 1755444326 * A^8 + 483163144 * A^{10})/15966720$$

$$P13[A] = (311713933 7 - 167864265395 * A^2 + 1387729381613 * A^4 - 4085608349133 * A^6 + 5380115327442 * A^8 - 3272269554968 * A^{10} + 7556535876 48 * A^{12})/99632332800$$

$P_{2\,P+1}[A]$ POLYNOMIALS HAVE PECULIAR SHAPES

$P_{2P+1}[A]$

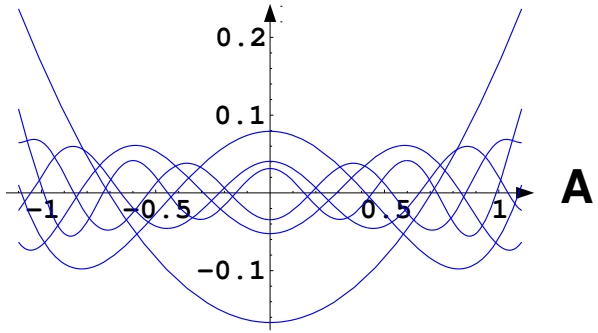

JACOBI'S POLYNOMIALS

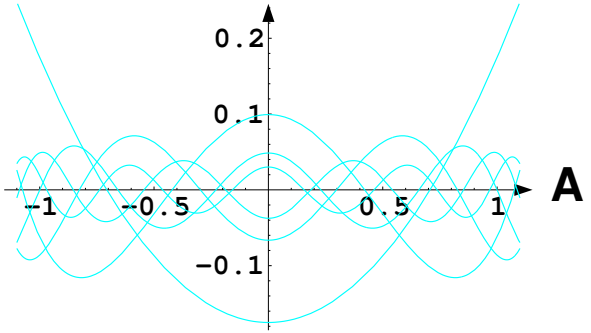

HYPOTHESIS 1 : $P_{2P+1}[A] = \frac{1}{P+2}$ **JACOBIP[2 P, 0.1, 0.1, 0.79 A]**

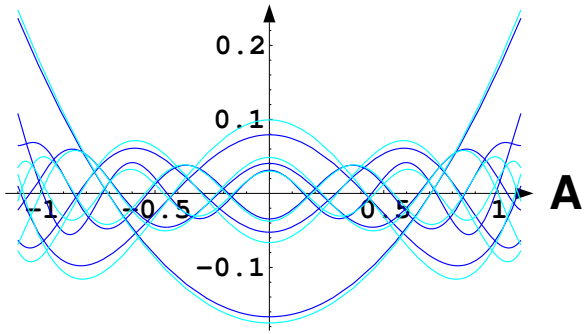

A BASIS OF JACOBI'S POLYNOMIALS IS USED FOR a(T)

$$k(a(T)-a_0)=\sum_{p=0}^{\infty} P_{2p+1}[A]T^{2p+1}=\sum_{p=0}^{\infty}\frac{1}{p+2}\,\mathbf{JacobiP}\,[2p,0.1,0.1,0.79A]\;T^{2p+1}+remainder_{2p+1}[A]T^{2p+1}$$

$$=\frac{1}{2}T+\frac{1}{T^3}\int_0^T\frac{\tau^3}{2}\{F(A,\tau)+F(A,-\tau)\}d\tau \qquad +\ RemainderFunction[A,T]$$

$F(A,\tau)$ = Generating function of Jacobi's polynomials

HYPOTHESIS 2 : $k(a(T)-a_0)\approx\frac{1}{2}T+\frac{1}{T^3}\int_0^T\frac{\tau^3}{2}\{F(A,\tau)+F(A,-\tau)\}d\tau$

EXTENDED GROWTH RATE BY GENERATING FUNCTION FITS WITH TAYLOR EXPANSION

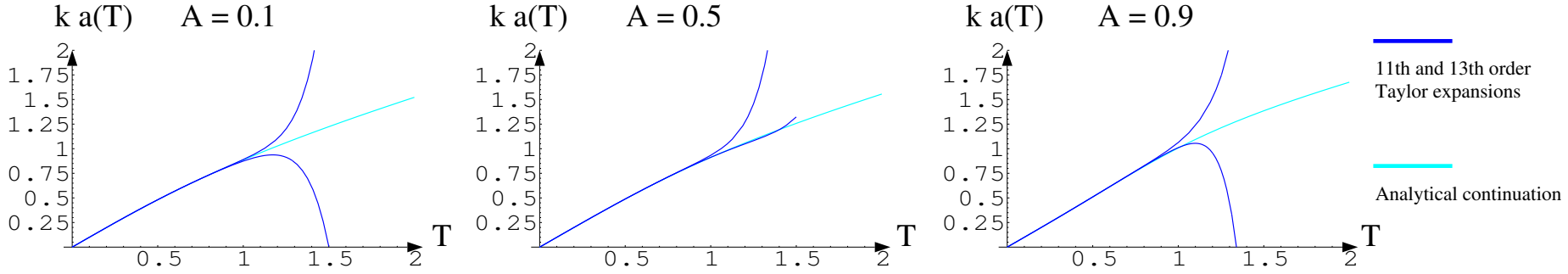

EXTENTED GROWTH RATE BY GENERATING FUNCTION FITS NONLINEAR R-M INSTABILITIES

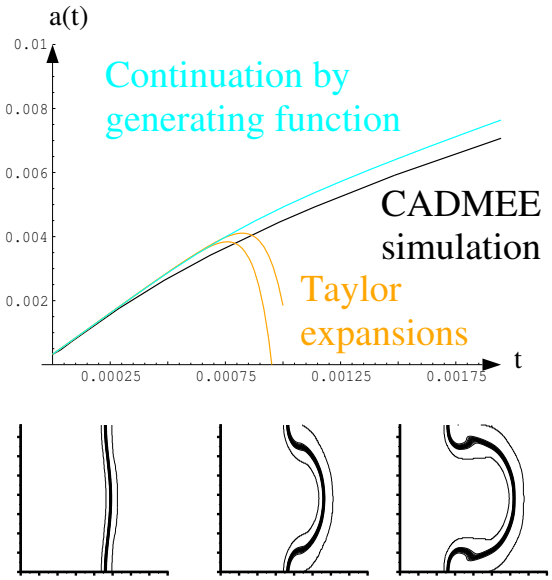

CADMEE simulation

He/Air M_0= 1.09
k=224.855
A= 0.764
a_0=0.35 mm

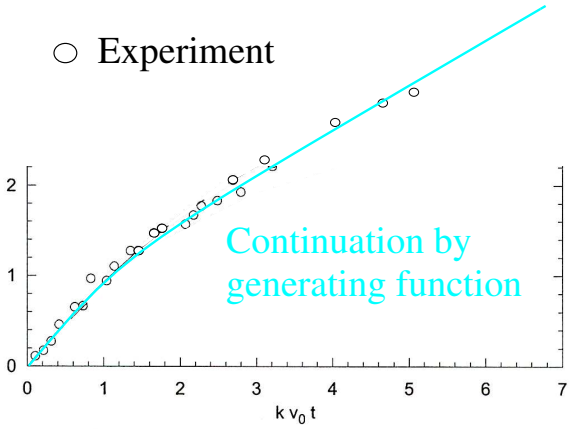

From Jacobs & Krivets 2001
Proceedings of the 23rd ISSW

Air/SF6 M_0=1.3
a_0k=0.23
A=0.635

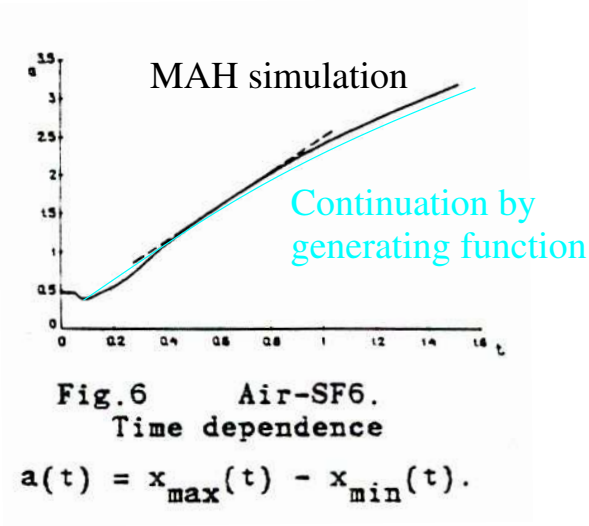

From Anuchina & Volkov
Proceedings IWPCTM 91

Air/SF6 M_0=1.32
k=1.112
A=0.585
a_0=0.183

ANALYTICAL CONTINUATION IS ACCURATE FOR a(T) k < 5.5

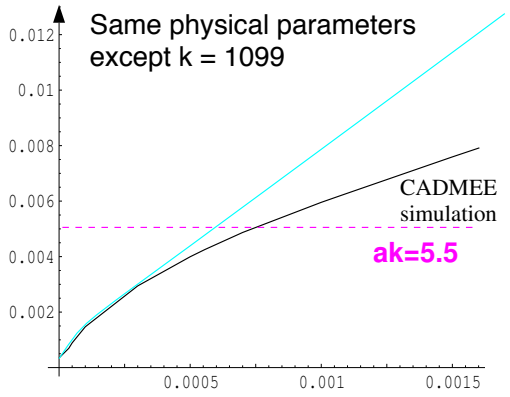

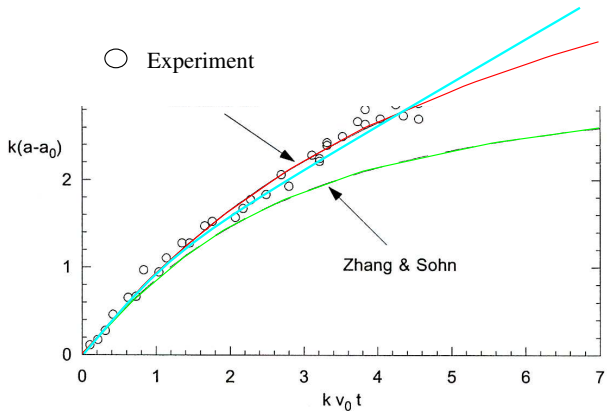

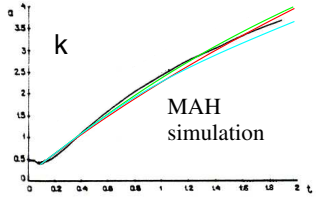

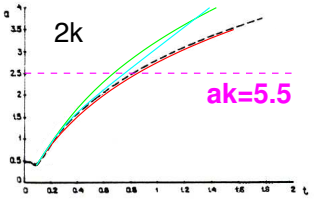

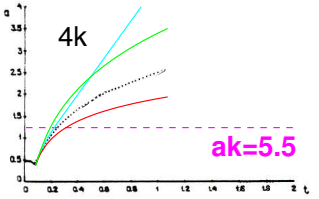

Fig.10 Air-SF6. Time dependences a(t) for some various wavelengths.

Analytical continuation

Sadot's model $\dfrac{da_{b/s}}{dt} = \dfrac{a_0 k\sigma(1+a_0 k\sigma t)}{1+(1\pm A)a_0 k\sigma t + \dfrac{1}{2\pi C}\left(\dfrac{1+A}{1\pm A}\right)(a_0 k\sigma t)^2}$ $C = \dfrac{1}{3}\pi$ for $A > 0.5$ $C = \dfrac{1}{2}\pi$ for $A \to 0$

Zhang's model $\dfrac{da}{dt} = \dfrac{a_0\sigma}{1+a_0^2 k^2\sigma t + \mathrm{Max}\left[0, a_0^2 k^2 - A^2 + \frac{1}{2}\right](a_0 k\sigma t)^2}$

ANALYTICAL CONTINUATION HAS A RELIABLE RANGE OF VALIDITY

CONCLUSIONS

- Continuation of the growth rate by generating function has a reliable range of validity

  * for ak< 5.5 Relative error < 15%

  * for ak>5.5 non-physical linear behavior :
    - remainder part no more negligeable
    - other polynomial basis should be used
    - single-evaluated interface model has reached its limit

- No adjustable parameter in the model
- The growth rate is solution of governing equations

Efficient perturbation methods for Richtmyer-Meshkov and Rayleigh-Taylor instabilities: Weakly nonlinear stage and Beyond.

M. Vandenboomgaerde, S. Gauthier, D. Galmiche, C. Cherfils, P.A. Raviart

CEA/DAM - Ile de France - DCSA

- I- Perturbation methods for the Richtmyer-Meshkov instability
  Summary, new approach and applications
- II- Beyond the weakly nonlinear stage
  Inferences and numerical tests
- III- Accurate approximation for the Rayleigh-Taylor instability
  Some examples
- Concluding remarks

I-Perturbation methods for the Richtmyer-Meshkov instability

Principle and hypothesis

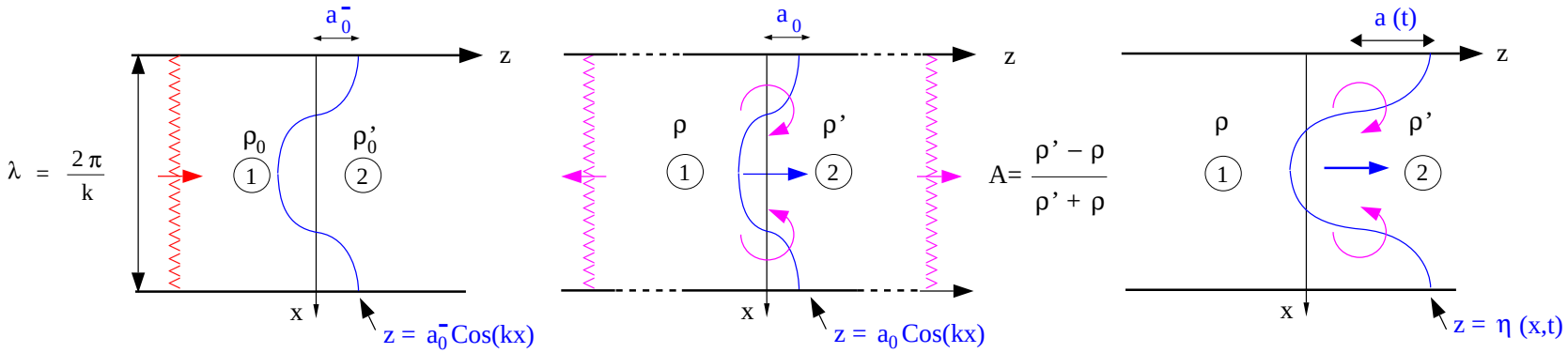

- Fluids are considered **incompressible** and **irrotational**
- No more effect of the reflected and transmitted waves

Equations

- Velocities derive from potentials: $\vec{v} = -G\vec{r}ad\ \Phi \qquad \vec{v'} = -G\vec{r}ad\ \Phi'$
- Motion of the interface: $-\frac{\partial \Phi}{\partial z} = \frac{\partial \eta}{\partial t} - \frac{\partial \Phi}{\partial x}\frac{\partial \eta}{\partial x}$ and $-\frac{\partial \Phi'}{\partial z} = \frac{\partial \eta}{\partial t} - \frac{\partial \Phi'}{\partial x}\frac{\partial \eta}{\partial x}$ at $z = \eta$
- Bernoulli's equation: $-\rho'\frac{\partial \Phi'}{\partial t} + \rho\frac{\partial \Phi}{\partial t} + \frac{1}{2}\rho'[(\frac{\partial \Phi'}{\partial x})^2 + (\frac{\partial \Phi'}{\partial z})^2] - \frac{1}{2}\rho[(\frac{\partial \Phi}{\partial x})^2 + (\frac{\partial \Phi}{\partial z})^2] = 0$ at $z = \eta$

I-Perturbation methods for the Richtmyer-Meshkov instability

Summary of the full perturbation theory

- Find a small parameter: $a_0 k << 1$
- Expand unknowns η, Φ, Φ' as series: $\eta = \sum \eta^{(n)}$ with $\eta^{(n)} \# (a_0 k)^n$
- Introduce expansions in the 3-equation system
- Collect terms of the same order
- Solve resulting systems $\Longrightarrow$ appearance of "secular terms"

  Ex: $X^{(n)} = (a_0 k)^n \times \left(x_1^{(n)} t^n + x_2^{(n)} t^{n-1} + ... + x_n^{(n)} \right)$

- At the nth order, $3n^2$ coefficients must be evaluated

$$k\eta^{(3)} = -\frac{1}{24}(a_0 k)^3[(4A^2+1)(\sigma t)^3 + 3(\sigma t)^2 + 6\sigma t]\, cos kx + \frac{1}{8}(a_0 k)^3[(4A^2-1)(\sigma t)^3 - 3(\sigma t)^2]\, cos 3kx$$

I-Perturbation methods for the Richtmyer-Meshkov instability

How to simplify the full perturbation theory

C.M. Bender, S.A. Orszag, "Advanced mathematical methods ... ", 1978

At each order, keep ONLY the MOST SECULAR TERMS

- A new small parameter: $a_0 k\sigma t << 1$
- Expand unknowns η, Φ, Φ' as series: $\eta = \sum \eta^{(n)}$ with $\eta^{(n)} \# (a_0 k\sigma t)^n$
- Introduce expansions in the 3-equation system
- Collect terms of the same order $\Longleftrightarrow$ at the nth order, $\frac{\partial \eta}{\partial t} \Rightarrow t^{n-1}$ terms
- Solve resulting systems: results are written in a new form

Ex: $$X^{(n)} = (a_0 k)^n \times \left(x_1^{(n)} t^n + x_2^{(n)} t^{n-1} + ... + x_n^{(n)} \right)$$

$$\Downarrow$$

$$X^{(n)} \approx (a_0 k)^n \times x_1^{(n)} t^n$$

- At the nth order, only $3n$ coefficients must be evaluated

$$k\eta^{(3)} = -\frac{1}{24}(a_0 k)^3[(4A^2+1)(\sigma t)^3 + 3(\sigma t)^2 + 6\sigma t]\, cos kx + \frac{1}{8}(a_0 k)^3[(4A^2-1)(\sigma t)^3 - 3(\sigma t)^2]\, cos 3kx$$

$$\Downarrow$$

$$k\eta^{(3)} \approx (a_0 k\sigma t)^3 \left[-\frac{1}{24}(4A^2-1) cos\ kx + \frac{1}{8}(4A^2-1) cos\ 3kx \right]$$

- Same algorithm for multimode configuration

I-Perturbation methods for the Richtmyer-Meshkov instability

Some remarks about the approximate perturbation theory

- The approximate pertubation theory gives accurate results within its range of validity
- The range of validity is clearly defined: $a_0 k \sigma t_v = 1$
- The approximation makes solution easier and faster: n^2-algorithm $\rightarrow$ n-algorithm
- The approximation makes multimode configurations tractable
- Sign of the initial amplitudes (or the phase between modes) have effects upon the mode-competition process

$$\Downarrow$$

Mode-competition models must take into account the phases of the initial perturbation spectrum

Comparisons approximate theory/simulations
Single mode dynamics

3 modes are considered: $k_1 = 274.855 \;\; k_2 = 3/7\; k1 \;\; k_3 = 4/7\; k1$

$$a_{01}^{-} = -0.35\ 10^{-3} m \;\; a_{02}^{-} = -1.9055\ 10^{-3} m \;\; a_{03}^{-} = -1.072\ 10^{-3} m$$

Physical parameters: He/Air $M_0 = 1.0962 \;\; A^{-} = 0.75724$

$$t_v = 0.67 ms$$

Simulations: 2D CADMEE code: 2nd order in time and space

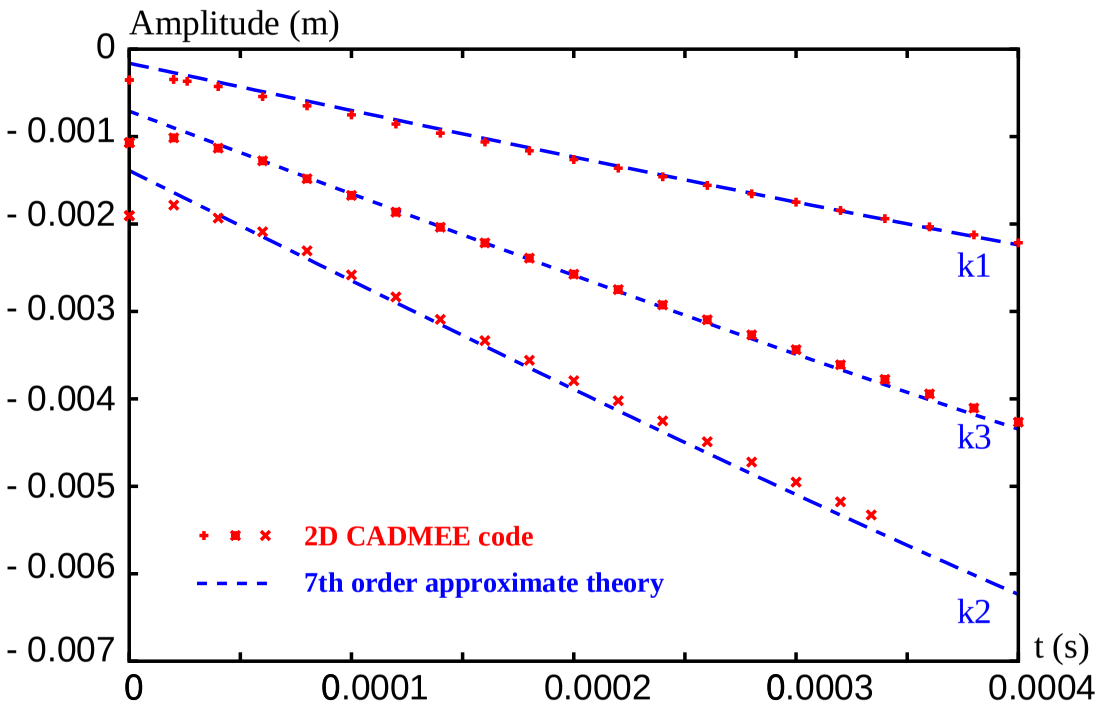

Multimode dynamics: negative initial amplitude

$a_{01}^{-} = -0.35\ 10^{-3} m \quad a_{02}^{-} = -1.9055\ 10^{-3} m \quad a_{03}^{-} = -1.072\ 10^{-3} m$

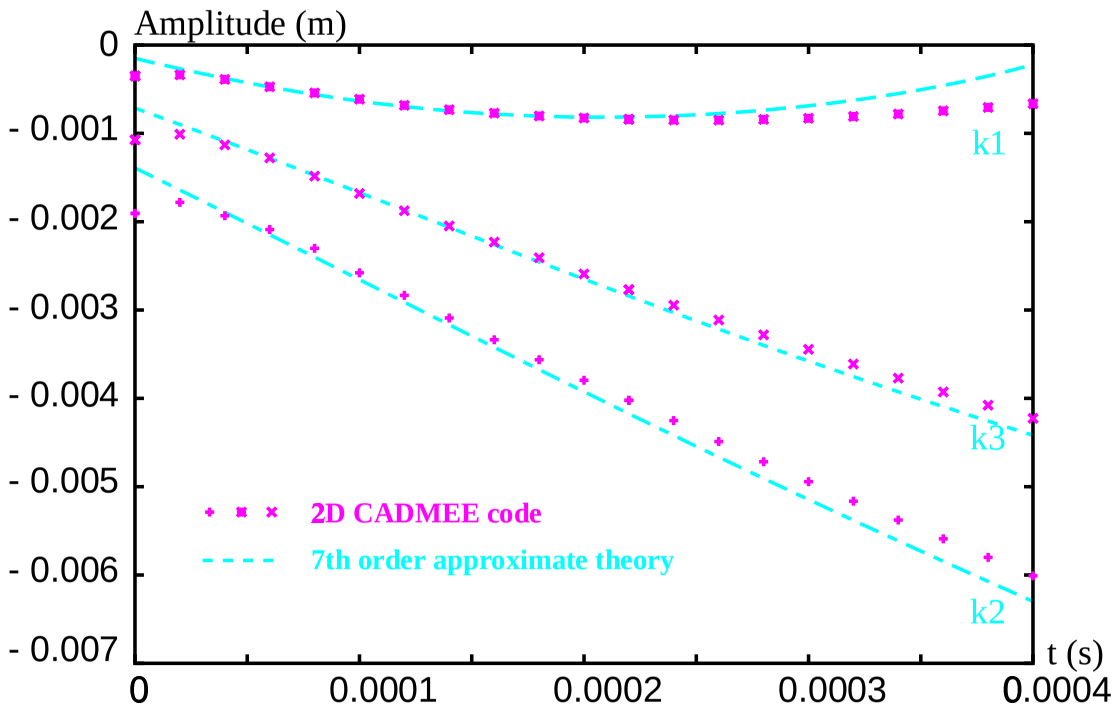

The growth of the mode k_1 is strongly reduced by k_2 and k_3.

Multimode dynamics: positive initial amplitude

$a_{01}^{-} = +0.35\ 10^{-3} m \quad a_{02}^{-} = +1.9055\ 10^{-3} m \quad a_{03}^{-} = +1.072\ 10^{-3} m$

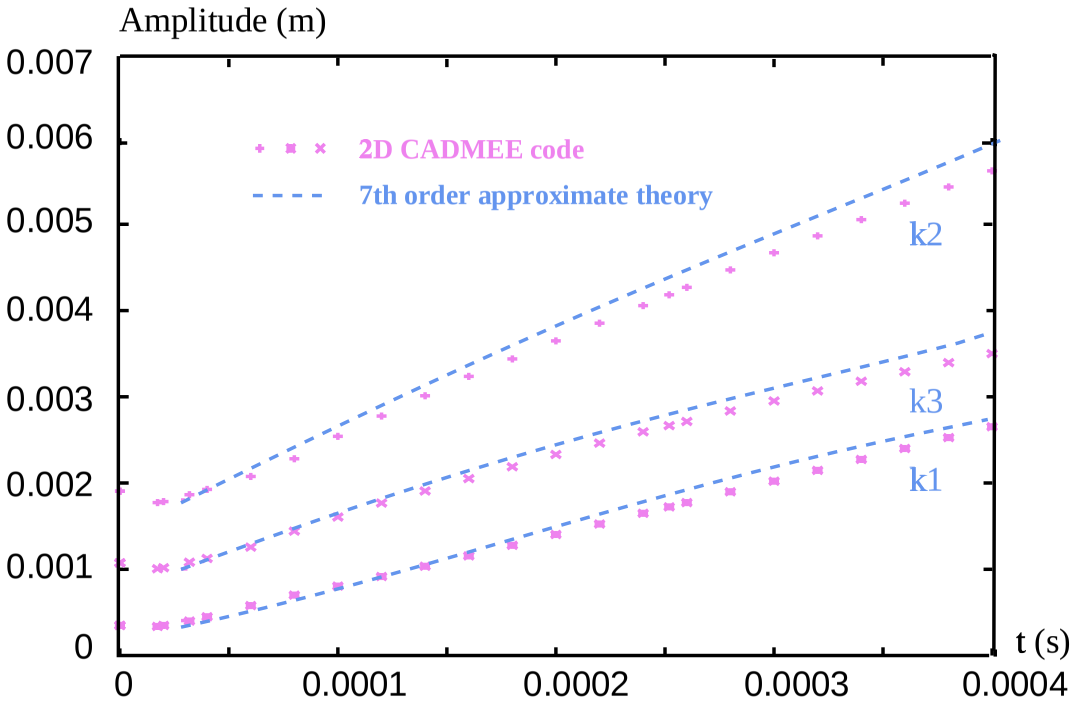

The growth of the mode k_1 is unaffected by k_2 and k_3.

A-Late time 2-mode competition:

influence of the values of the initial amplitude

2 nearby modes are studied: $k_1 = 274.855 \quad k_2 = 8/7 k_1 = 314.159$

2 initial amplitudes are used: $a_{01}^- = 10^{-3}$ or $a_{02}^- = 0.35\ 10^{-3} m$

Physical parameters: He/Air $M_0 = 1.26 \quad A^- = 0.756$

CADMEE results for configuration $(k_1, a_{02}^-), (k_2, a_{01}^-)$-$t_v = 0.24\ ms$

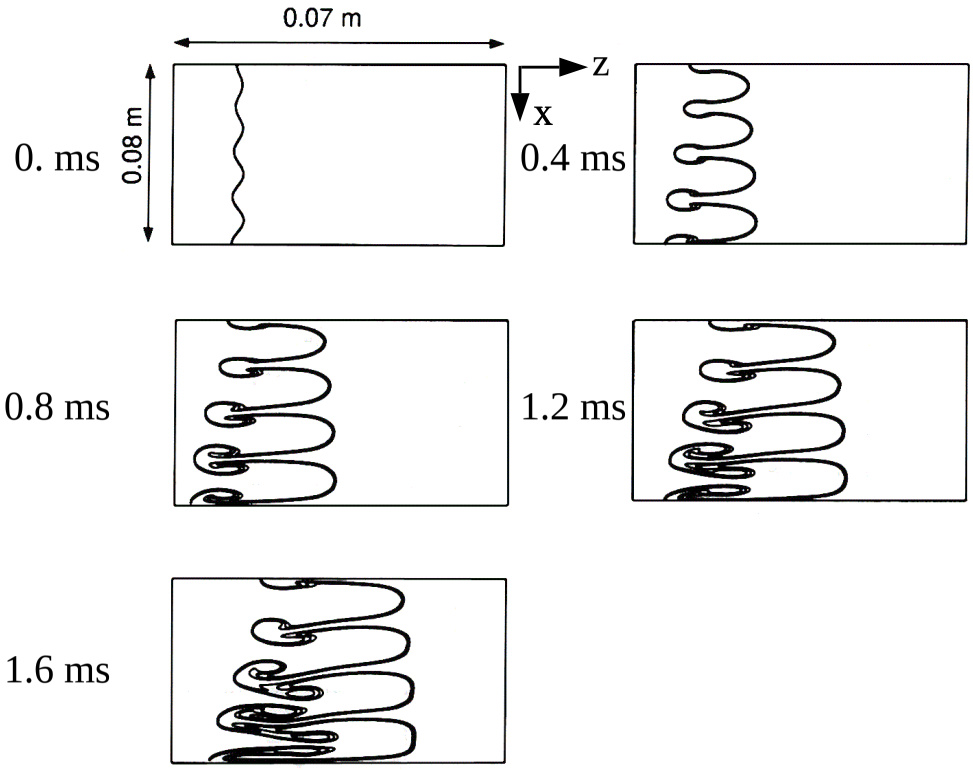

A spectral analysis is performed:

- z-integration of the density: $\rho(x) = \int \rho(z, x) dz$
- Fourier transform of $\rho(x)$

Growth of the 2 dominant modes

CADMEE results

5th order approximate theory extended with Padé approximants

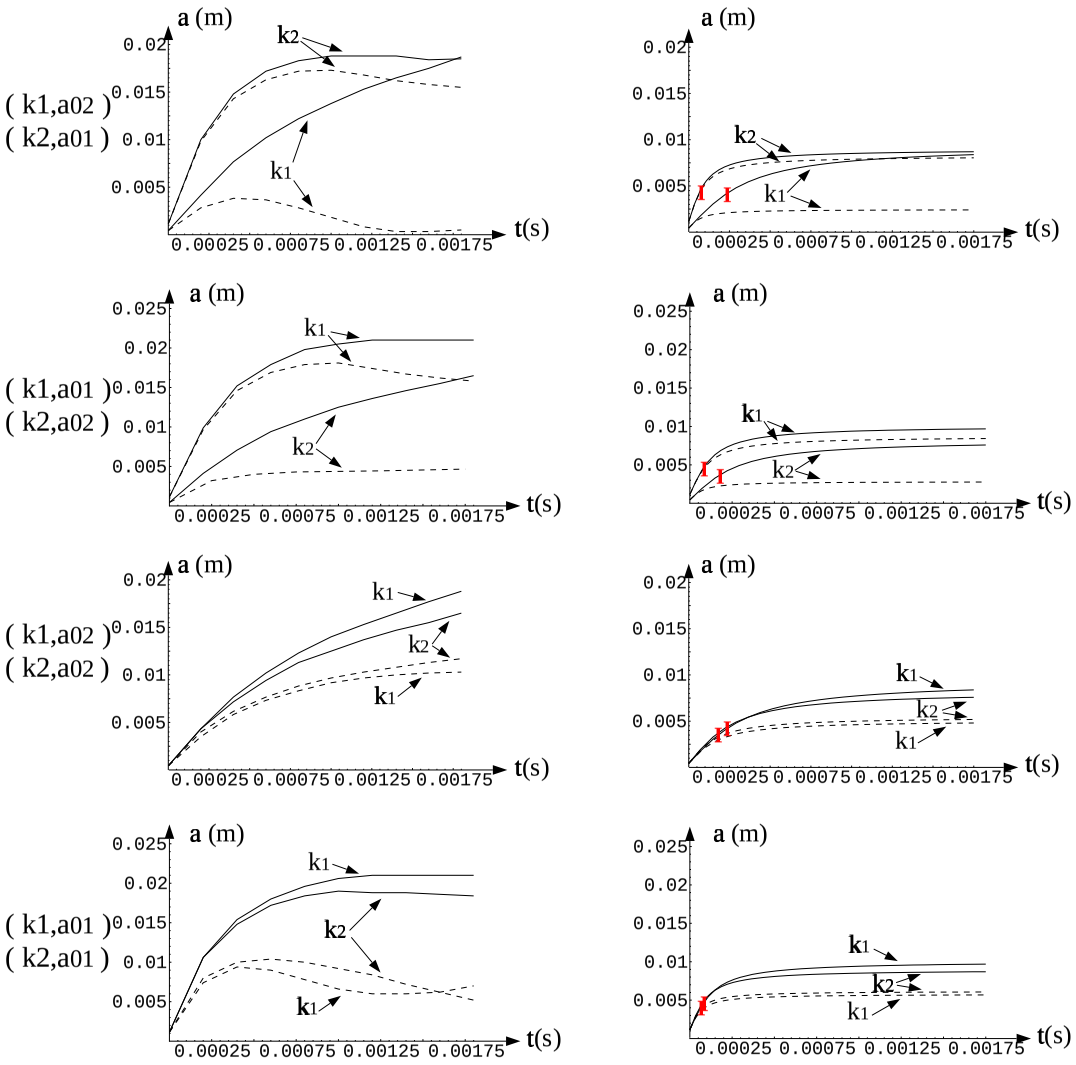

- The values of the initial amplitudes dictate the selection process:
  - the mode with the lower initial amplitude is suppressed
  - if the amplitude are the same, both modes are equally lowered
- Qualitative agreement between simulation and theory: behavior and selection process are correctly predicted
- Quantitative discrepancies: Padé approximants underestimate the late-time nonlinear growth
- Late-time nonlinear behaviors seems settled since the early nonlinear stage

B-Class of homothetic single-mode perturbations

Perturbation expansion can be considered as Taylor expansion of an unknown function $\mathcal{F}$:

$$k\eta = \sum k\eta^{(n)} = \sum_{n=1}^{\infty} (a_0 k\sigma t)^n \sum_{j=1}^{n} a_j^{(n)} \cos(jkx)$$

$$\Downarrow$$

$$k\,(a(T) - a_0) = \sum_{p=0}^{\infty} P_{2p+1}[A]\; T^{2p+1} = \sum_{p=0}^{\infty} \frac{1}{p!} \left.\frac{\partial^p \mathcal{F}}{\partial T^p}\right|_0 T^p = \mathcal{F}(A,T)$$

$$\text{with } T = a_0 k\sigma t$$

$$\Downarrow$$

If two perturbations 1 and 2 are such that:

$$A_1 = A_2 \text{ and } a_{01} k_1 \sigma_1 = a_{02} k_2 \sigma_2 \Longleftrightarrow a_{01} k_1^2 = a_{02} k_2^2$$

$$\text{Then } a_1(t) = \frac{k_2}{k_1}\,(a_2(t) - a_{02}) + a_{01}$$

Application to numerical simulations:

$$\text{He/Air} \quad M_0 = 1.26 \quad A^- = 0.756$$

$$(a_{01}, k_1) = (0.35\ 10^{-3}, 274.855) \quad (a_{02}, k_2) = (0.525\ 10^{-3}, 224.418)$$

$$a_{01} k_1^2 = a_{02} k_2^2$$

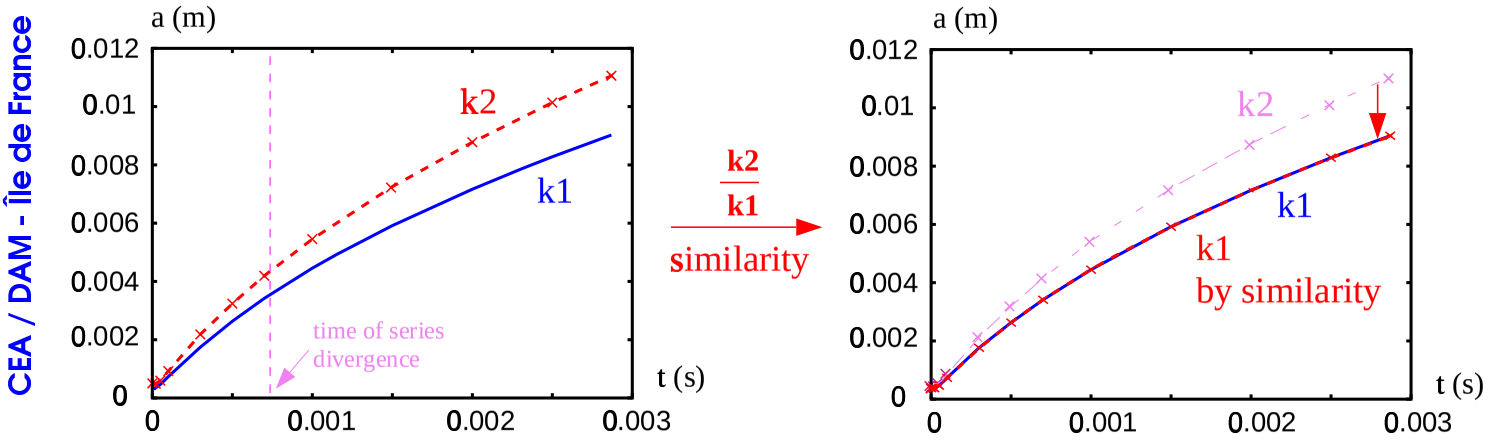

The similarity still stands during the mushroom stage

$$a_{02} = 0.525mm > a_{01} = 0.35mm \qquad \lambda_2 = 2.8cm > \lambda_1 = 2.3cm$$

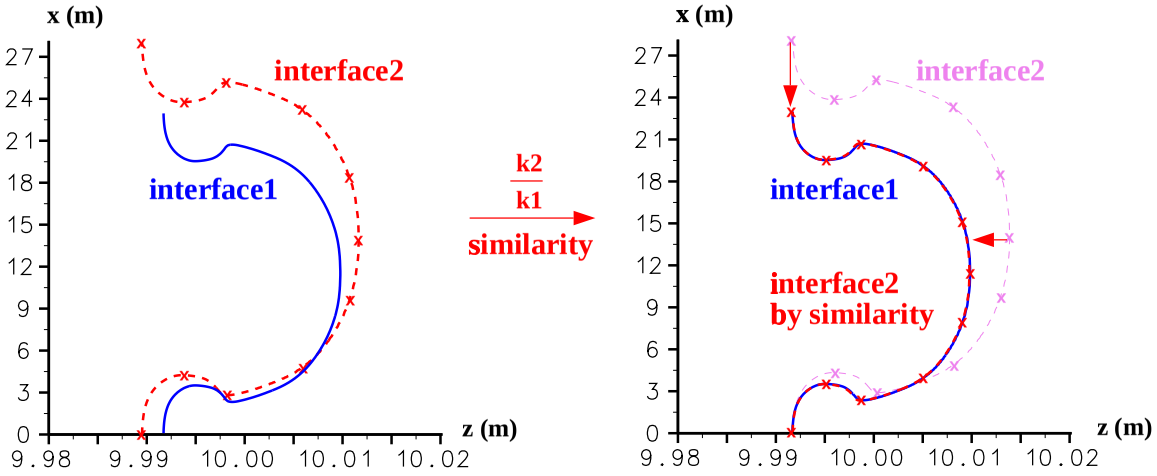

Some remarks

- A class of homothetic perturbated interfaces is inferred from the approximate perturbation theory:

$$A_i = A_j \qquad a_{0i}k_i^2 = a_{0j}k_j^2$$

- The theory is accurate
- The similarity stands during the late-time nonlinear stage: the shapes are homothetic even in the Kelvin-Helmholtz vortex area
- Large perturbations can be used to study small ones
  - Advantages for numerical simulations: less limiting CFL conditions (cpu time 2 = 78% cpu time 1)
  - Advantages for experiments: $(\lambda, a_0) = (10\mu m, 0.1\mu m) \Longleftrightarrow (31.62\mu m, 1\mu m) \Longleftrightarrow (1cm, 4mm)$

III- Accurate approximation for the Rayleigh-Taylor instability

- Same hypothesis for the fluids as for the RM instability
- Same 3-equation system as for the RM instability except for the additional

  $(\rho' - \rho) g\eta$ term in Bernoulli's equation

- Same solution algorithm except that the "secular" terms write as

  $(a_0 k e^{\gamma t})^i$ with $\gamma = \sqrt{Agk}$

- Unknowns are written in a similar form:

$$\eta = \sum \eta^{(n)} = \sum (a_0 k e^{\gamma t})^n \sum_{j=1}^{n} a_j^{(n)} cos(jkx)$$

- Range of validity: $a_0 k e^{\gamma t_v} = 1$
- Same advantage: n^2-algorithm $\rightarrow$ n-algorithm
- Example:

$$k\eta^{(2)} = -\tfrac{1}{4} A a_0^2 k^2 \left[2\, Cosh(\sqrt{2}\gamma t) - 1 - Cosh(2\gamma t) \right] \cos 2kx$$

$$\downarrow$$

$$k\eta^{(2)} = -\tfrac{A}{8} (a_0 k)^2 e^{2\gamma t} \cos 2kx$$

Comparisons approximate theory / simulations

Trajectories of the tip of the bubble and the tip of the spike

Menikoff et Zemach, JCP **51**, 28-64 (1983)

$A = 1; g = 1; k = 1; a_0 = -0.01 \Rightarrow t_v = 4.6$

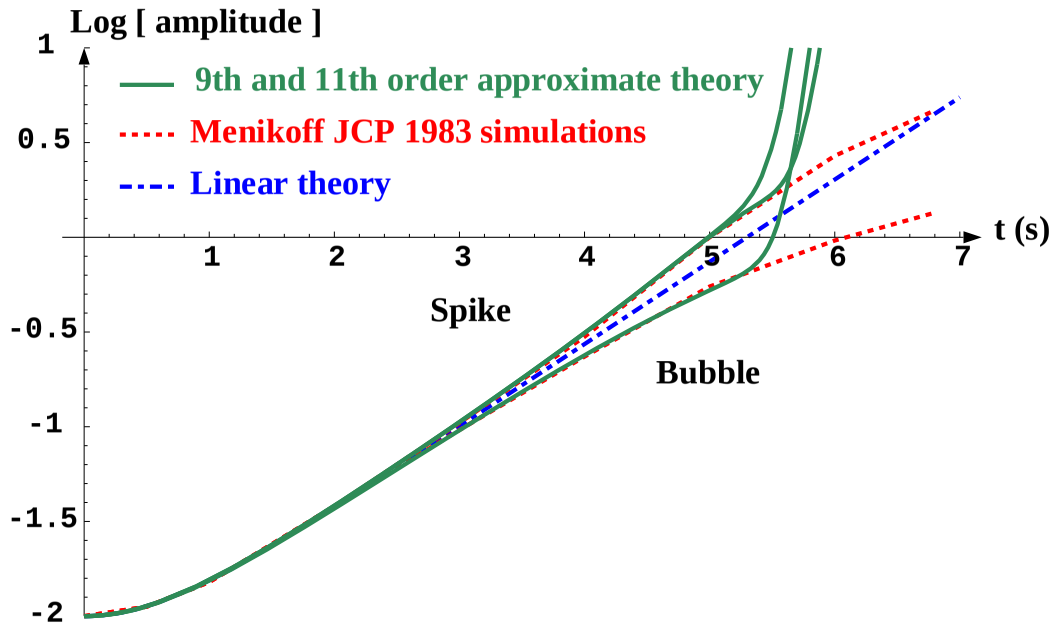

Influence of the Atwood number:

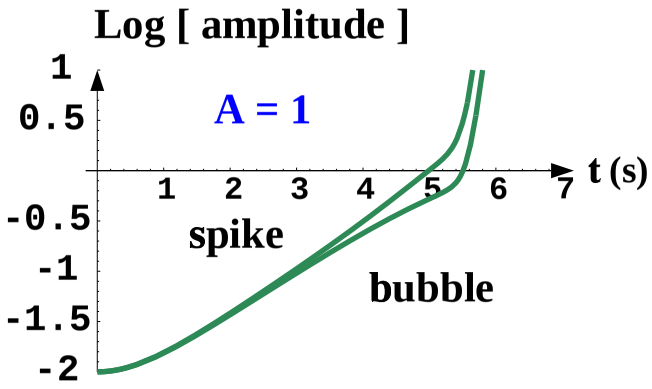

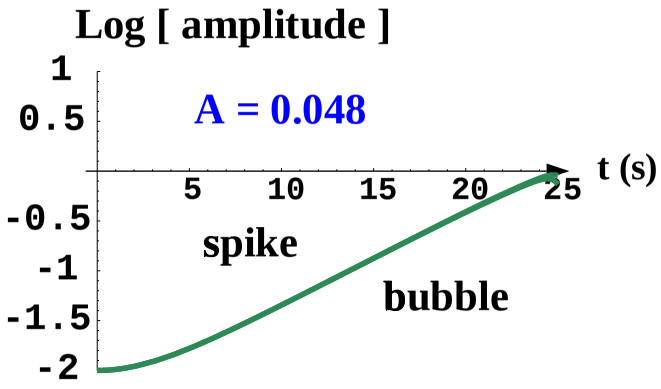

- If $A \approx 1$, the spike grows faster than the bubble.
- If $A \approx 0$, bubble and spike have the same growth.
- Same conclusions as Baker *et al.*, Phys. Fluids **23**(8), 1980.

Concluding remarks

- Approximate perturbation theory is accurate within its range of validity for RM and RT instabilities
- Solutions are easier and faster: n^2-algorithm $\rightarrow$ n-algorithm
- For the Richtmyer-Meshkov instabilities:
  - Approximate theory makes multimode configurations tractable
  - Padé extended approximate theory allows us to predict late-time selection process: the origin of such process occurs in the weakly nonlinear stage
  - Mode spectrum, amplitude values but also, the phase between modes must be known to determine the modes leading to the bubble stage.
  - Existence of a class of homothetic perturbated interfaces:

$$A_i = A_j \quad \text{and} \quad a_{0i}\, k_i^2 = a_{0j}\, k_j^2$$

Combined Shear and Buoyancy Instabilities

Peter Wilson, Malcolm Andrews and Francis Harlow

8th International Workshop on the Physics of Compressible Turbulent Mixing

Pasadena, CA

December 9-14, 2001

Spectral Turbulence Model for Variable Density Turbulence

- Steinkamp, Clark and Harlow, Int. J. of Multiphase Flow (1999)

- $\hat{R}_{ij}(\vec{x},\vec{k},t) = \iiint_{-\infty \text{ to } \infty} R_{ij}(\vec{x}_1,\vec{x}_2,t)e^{-i\vec{k}\vec{r}}d\vec{r}$

  where $\vec{x} = \frac{\vec{x}_1 + \vec{x}_2}{2}$, $\vec{r} = \vec{x}_2 - \vec{x}_1$

- $R_{ij}(\vec{x},k,t) = \int_{\Omega_k} \hat{R}_{ij}(\vec{x},\vec{k},t)\frac{k^2 d\Omega_k}{(2\pi)^3}$

- $R_{ij}(\vec{x},t) = \int_0^\infty R_{ij}(\vec{x},k,t)dk$

Advantages of Spectral Transport Models Over Single-Point Models (i.e., k-ε):

- More generality, such as in the case of non-equilibrium transients
- Does not require a length scale or dissipation equation
- Greater flexibility with modeling, such as with non-local interactions in both physical and wavenumber space

Disadvantages:

- Greater Complexity
- More computationally expensive
- More Flexibility!

Governing Equations

$$\frac{D\tilde{u}_i}{Dt} = -\frac{1}{\bar{\rho}}\left[\frac{\partial R_{in}}{\partial x_n} + \frac{\partial \bar{p}}{\partial x_i}\right] + \upsilon_m \frac{\partial^2 \bar{u}_i}{\partial x_n^2} + g_i$$

$$\tilde{u}_i = \frac{\overline{\rho u_i}}{\bar{\rho}}, \quad R_{in} = \overline{\rho u_i'' u''_n} \qquad \text{where } u_i = \tilde{u}_i + u_i''$$

$$\frac{\partial \bar{\rho}}{\partial t} + \frac{\partial \bar{\rho}\tilde{u}_n}{\partial x_n} = 0$$

$$\frac{DR_{ij}(k)}{Dt} = \iiint_{-\infty to \infty}\left[a_i(k)\frac{\partial \bar{p}}{\partial x_j} + a_j(k)\frac{\partial \bar{p}}{\partial x_i}\right]_{\bar{x}'} \hat{f}(\vec{x}, \vec{x}')d\vec{x}' - R_{in}\frac{\partial \tilde{u}_j}{\partial x_n} - R_{jn}\frac{\partial \tilde{u}_i}{\partial x_n}$$

$$+ c_d \frac{\partial}{\partial x_n}\left[\upsilon_t \frac{\partial R_{ij}}{\partial x_n}\right] + c_m\left(\frac{1}{3}\delta_{ij}R_{nn} - R_{ij}\right)\int_0^\infty \sqrt{\frac{kR_{nn}}{\bar{\rho}}}dk$$

$$+ \frac{\partial}{\partial k}\left\{k^2\sqrt{\frac{kR_{nn}}{\bar{\rho}}}\left[-c_1 R_{ij} + c_2 k\frac{\partial R_{ij}}{\partial k}\right]\right\}$$

$$+ \text{Non - Local}(T(k))$$

where $a_i(\vec{x}_1, \vec{x}_2, t) = -\overline{u_i''(\vec{x}_1)\rho(\vec{x}_1)v(\vec{x}_2)}$ and $\upsilon_t = \int_0^\infty \sqrt{\frac{kR_{nn}}{\bar{\rho}}}\frac{dk}{k^2}$

Governing Equations (cont.)

$$\frac{Da_i(k)}{Dt} = \frac{b(k)}{\bar{\rho}}\frac{\partial \bar{p}}{\partial x_i} - \frac{R_{in}}{\bar{\rho}^2}\frac{\partial \bar{\rho}}{\partial x_n} + c_d \frac{\partial}{\partial x_n}\left[\upsilon_t \frac{\partial a_i}{\partial x_n}\right]$$

$$-\left[c_{r1}k^2\sqrt{a_n a_n} + c_{r2}k\sqrt{\frac{kR_{nn}}{\bar{\rho}}}\right]a_i$$

$$+\frac{\partial}{\partial k}\left\{k^2\sqrt{\frac{kR_{nn}}{\bar{\rho}}}\left[-c_1 a_i + c_2 k\frac{\partial a_i}{\partial k}\right]\right\}$$

where $b(\vec{x}_1, \vec{x}_2, t) = -\overline{\rho'(\vec{x}_1)v'(\vec{x}_2)}$

$$\frac{Db(k)}{Dt} = u_n\frac{\partial b}{\partial x_n} + \frac{2\bar{\rho} - \rho_1 - \rho_2}{\rho_1\rho_2}\frac{\partial \bar{\rho}a_n}{\partial x_n} + c_d\frac{\partial}{\partial x_n}\left[\upsilon_t\frac{\partial b}{\partial x_n}\right]$$

$$-c_{fb}\left[\bar{v}^2\frac{\partial \bar{\rho}/\bar{v}}{\partial x_n}\right]\frac{\partial k a_n}{\partial k} + \frac{\partial}{\partial k}\left\{k^2\sqrt{\frac{kR_{nn}}{\bar{\rho}}}\left[-c_1 b + c_2 k\frac{\partial b}{\partial k}\right]\right\}$$

$$-2\upsilon_t k^2 b$$

Non-Local Behavior in Physical and Wavenumber Space

Physical Space:

$$\frac{DR_{nn}}{Dt} = 2\int_{-\infty}^{\infty} a_2(y')\frac{\partial \overline{p}}{\partial y'}\hat{f}(y,y')dy' + \cdots$$

$$\int_{-\infty}^{\infty}\hat{f}(y,y')dy = 1$$

$$\hat{f}(y,y') = \frac{\exp(-2k|y-y'|)}{\int_{-\infty}^{\infty}\exp(-2k|y-y''|)dy''}$$

Wavenumber Space: Kraichnan and Spiegal Model for Energy Transfer (1962)

$$T(k) = \int[S_a(k/p) - S_e(k/p)]dp$$

$$S_e(p/k) = \eta\sqrt{pE(p)}E(p)\left(\frac{p}{k}\right)^m g\left(\frac{p}{k}\right)$$

$$S_a(k/p) = S_e(p/k)$$

$$T(k) = -\Sigma(k) + \int\Sigma(p)\breve{f}(k,p)dp \quad \text{where} \quad \Sigma(k) = \eta[kE(k)]^{\frac{3}{2}}$$

$$\text{and} \quad \breve{f}(k,p) = p^{-1}\left(\frac{k}{p}\right)^m g\left(\frac{k}{p}\right)$$

Modeling Constants

c_1, c_2, c_m, c_{r1}, c_{r2}, c_d also η and $g(x)$

$c_1/c_2 = 2$ for equipartition of energy ($c_1 = .5$)

$c_{r1} \approx c_{r2} = 5.0$ to match buoyancy experiments

$c_m = 1.0$ original SCH model constant

Given that $\int \tilde{f}(k,p)dk = 1 \Rightarrow \int x^m g(x)dx = 1$ where $x = k/p$

Let $g(x) = \exp\left[-\alpha(x + x^{-1})\right]/N$

and for 2k coupling ($m = -2, \alpha = 2/3$)

Lastly,

$$\varepsilon = \int_{k}^{\infty}\int_{0}^{k} S(q/p)dpdq$$

$$\eta = C_k^{-3/2}\left[\int_1^{\infty} \ln(x)(x^m - x^{-m-2})g(x)dx\right]^{-1} \Rightarrow \eta = 1.36$$

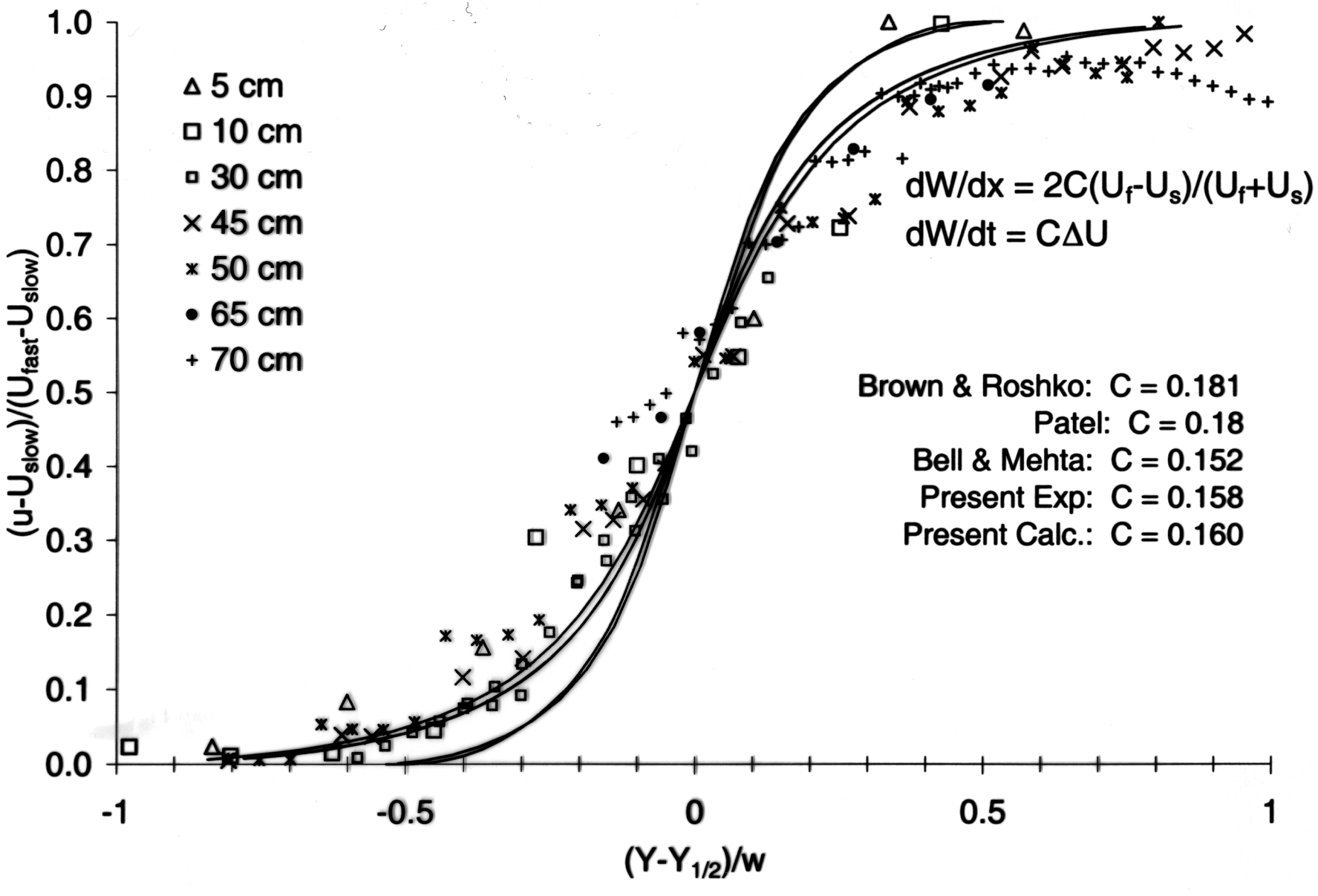
5 cm
10 cm
30 cm
45 cm
50 cm
65 cm
70 cm
dW/dx = 2C(Uf-Us)/(Uf+Us)
dW/dt = CΔU
Brown & Roshko: C = 0.181
Patel: C = 0.18
Bell & Mehta: C = 0.152
Present Exp: C = 0.158
Present Calc.: C = 0.160
(u-Uslow)/(Ufast-Uslow)
(Y-Y1/2)/w
1.0
0.9
0.8
0.7
0.6
0.5
0.4
0.3
0.2
0.1
0.0
-1
-0.5
0
0.5
1

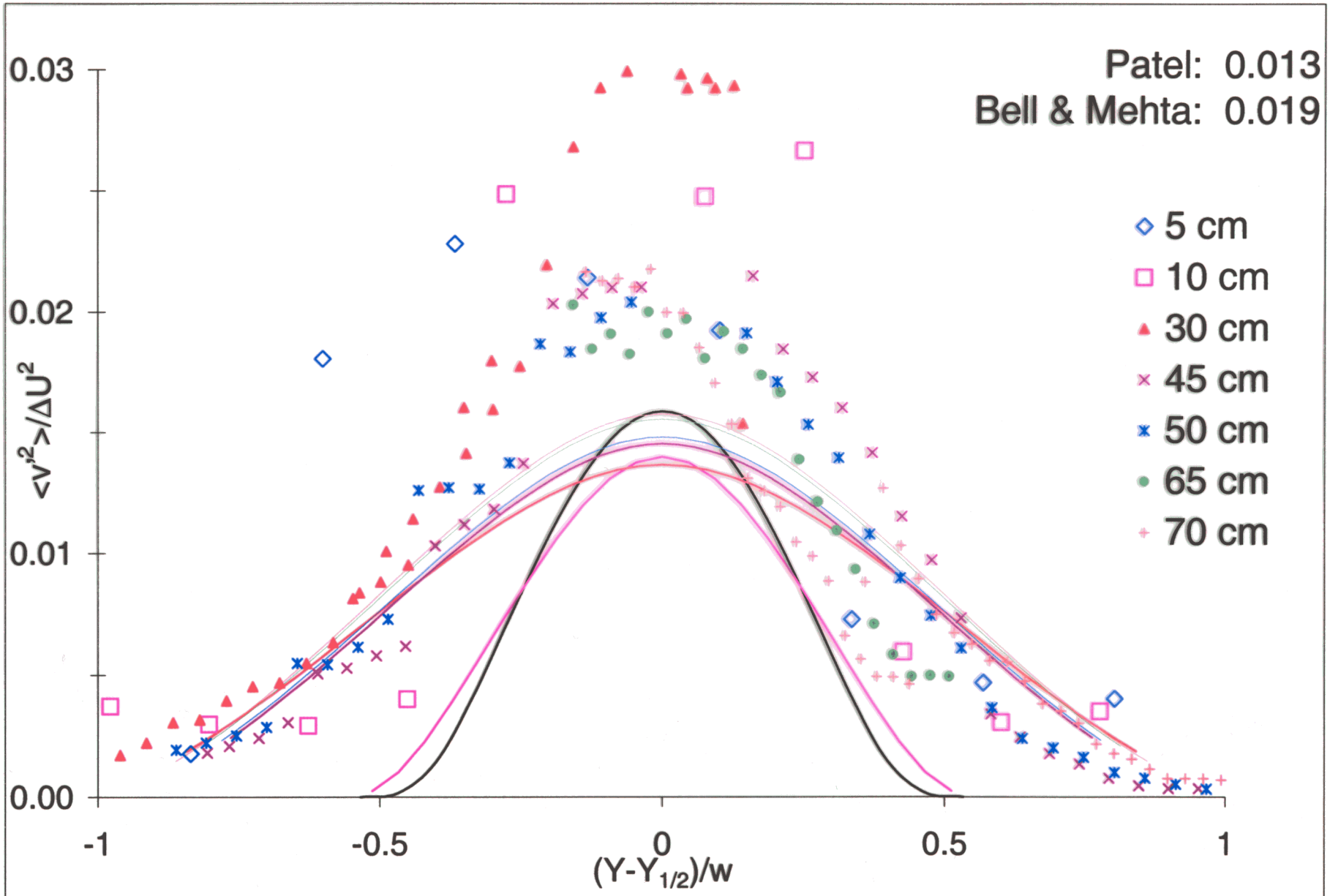
Patel: 0.013
Bell & Mehta: 0.019
5 cm
10 cm
30 cm
45 cm
50 cm
65 cm
70 cm
0.03
0.02
0.01
0.00
<v'²>/ΔU²
-1
-0.5
0
0.5
1
(Y-Y1/2)/w

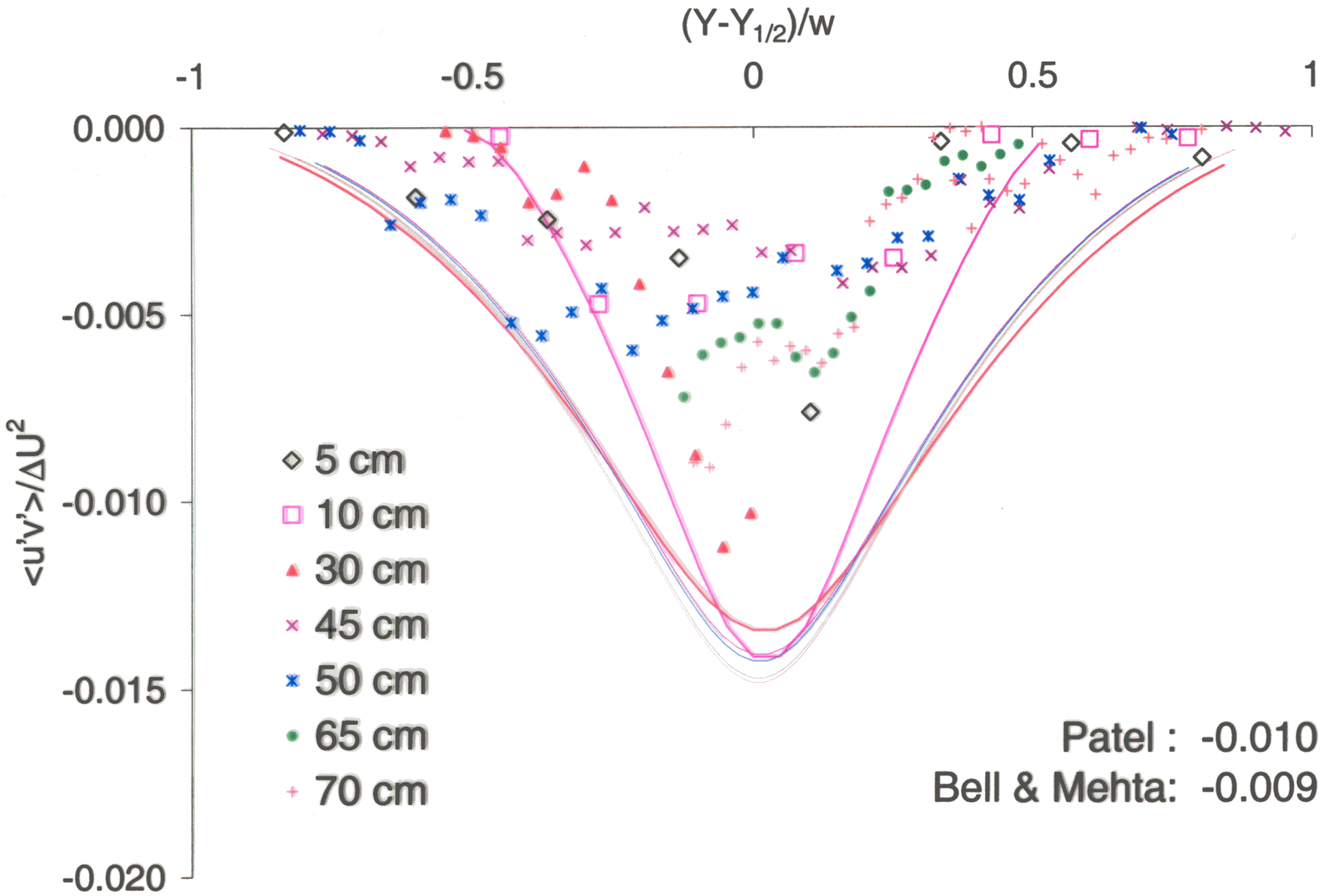
(Y-Y1/2)/w
-1
-0.5
0
0.5
1
0.000
-0.005
-0.010
-0.015
-0.020
<u'v'>/ΔU2
5 cm
10 cm
30 cm
45 cm
50 cm
65 cm
70 cm
Patel : -0.010
Bell & Mehta: -0.009

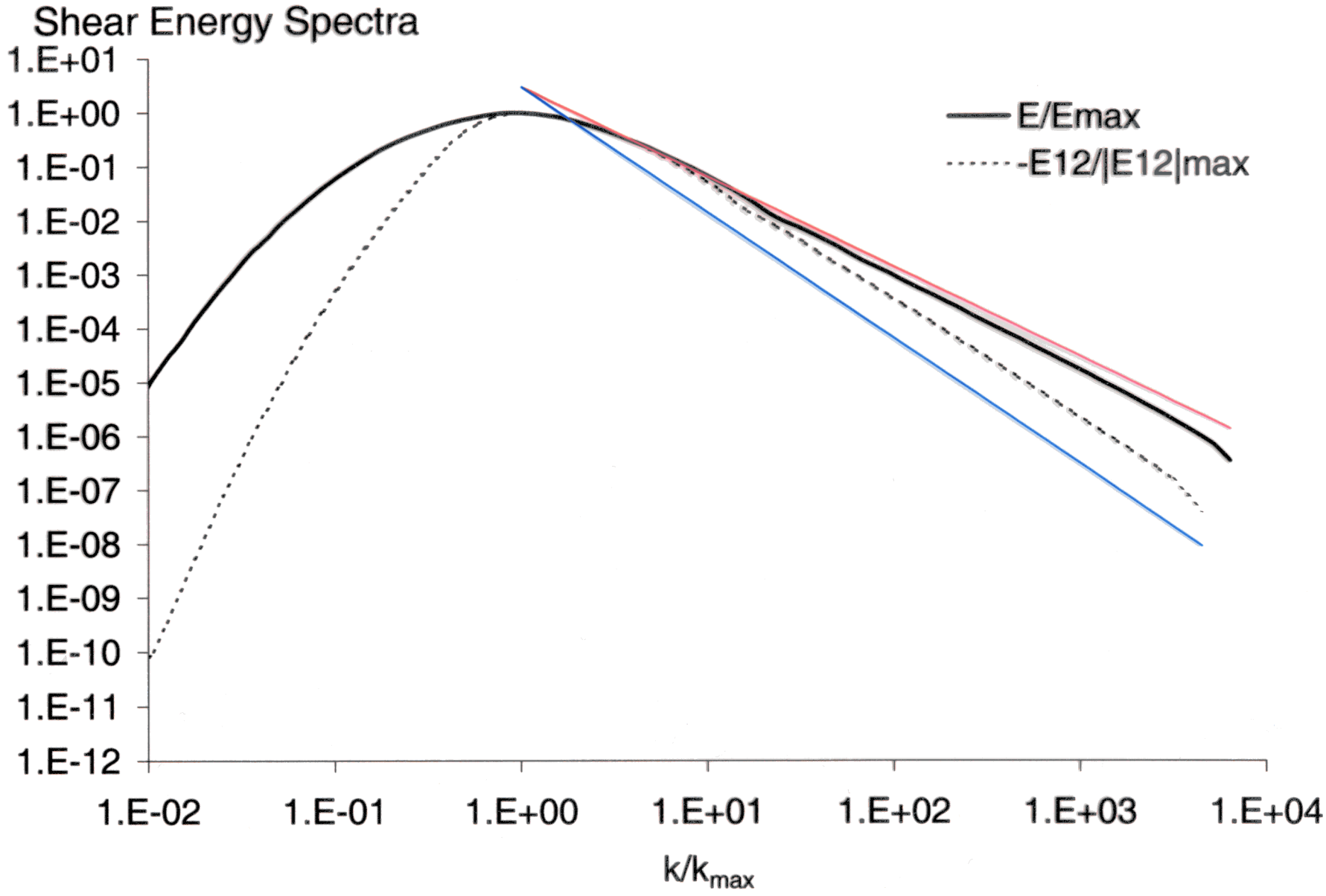
Shear Energy Spectra
1.E+01
1.E+00
1.E-01
1.E-02
1.E-03
1.E-04
1.E-05
1.E-06
1.E-07
1.E-08
1.E-09
1.E-10
1.E-11
1.E-12
E/Emax
-E12/|E12|max
1.E-02
1.E-01
1.E+00
1.E+01
1.E+02
1.E+03
1.E+04
k/k_max

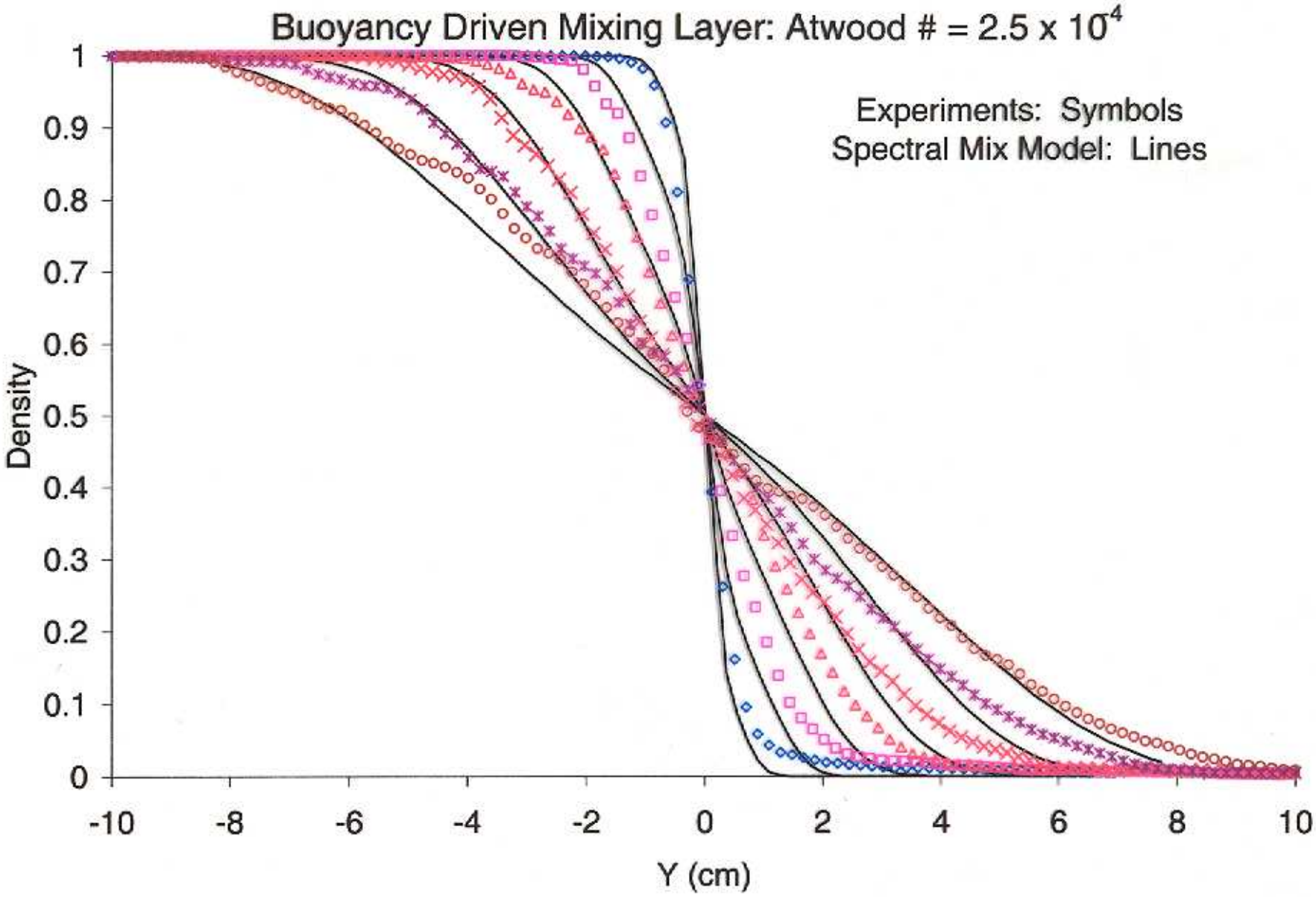
Buoyancy Driven Mixing Layer: Atwood # = 2.5 x 10^4
Experiments: Symbols
Spectral Mix Model: Lines
Density
Y (cm)
1
0.9
0.8
0.7
0.6
0.5
0.4
0.3
0.2
0.1
0
-10
-8
-6
-4
-2
0
2
4
6
8
10

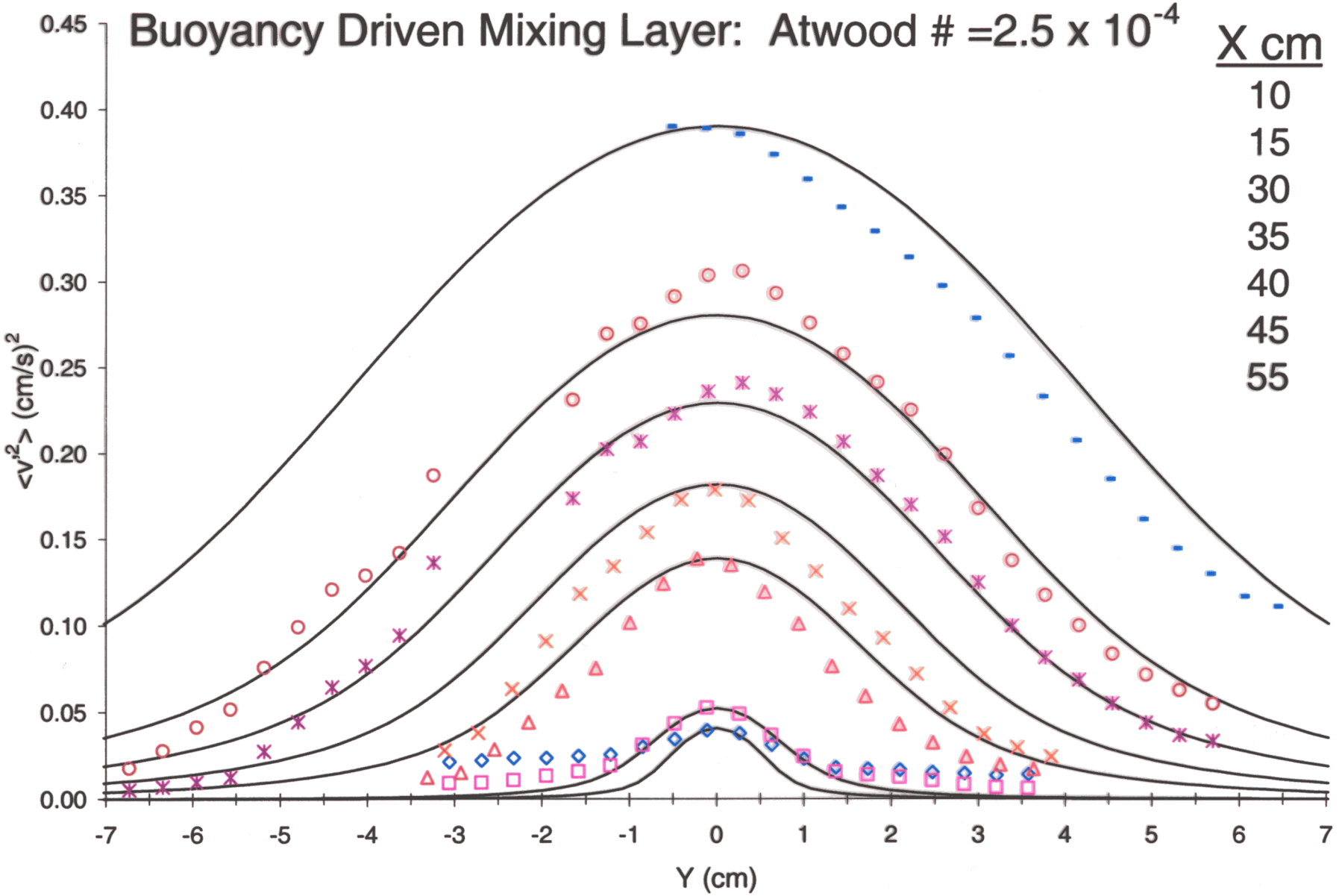
Buoyancy Driven Mixing Layer: Atwood # =2.5 x 10-4
X cm
10
15
30
35
40
45
55
<v'2> (cm/s)2
0.45
0.40
0.35
0.30
0.25
0.20
0.15
0.10
0.05
0.00
-7
-6
-5
-4
-3
-2
-1
0
1
2
3
4
5
6
7
Y (cm)

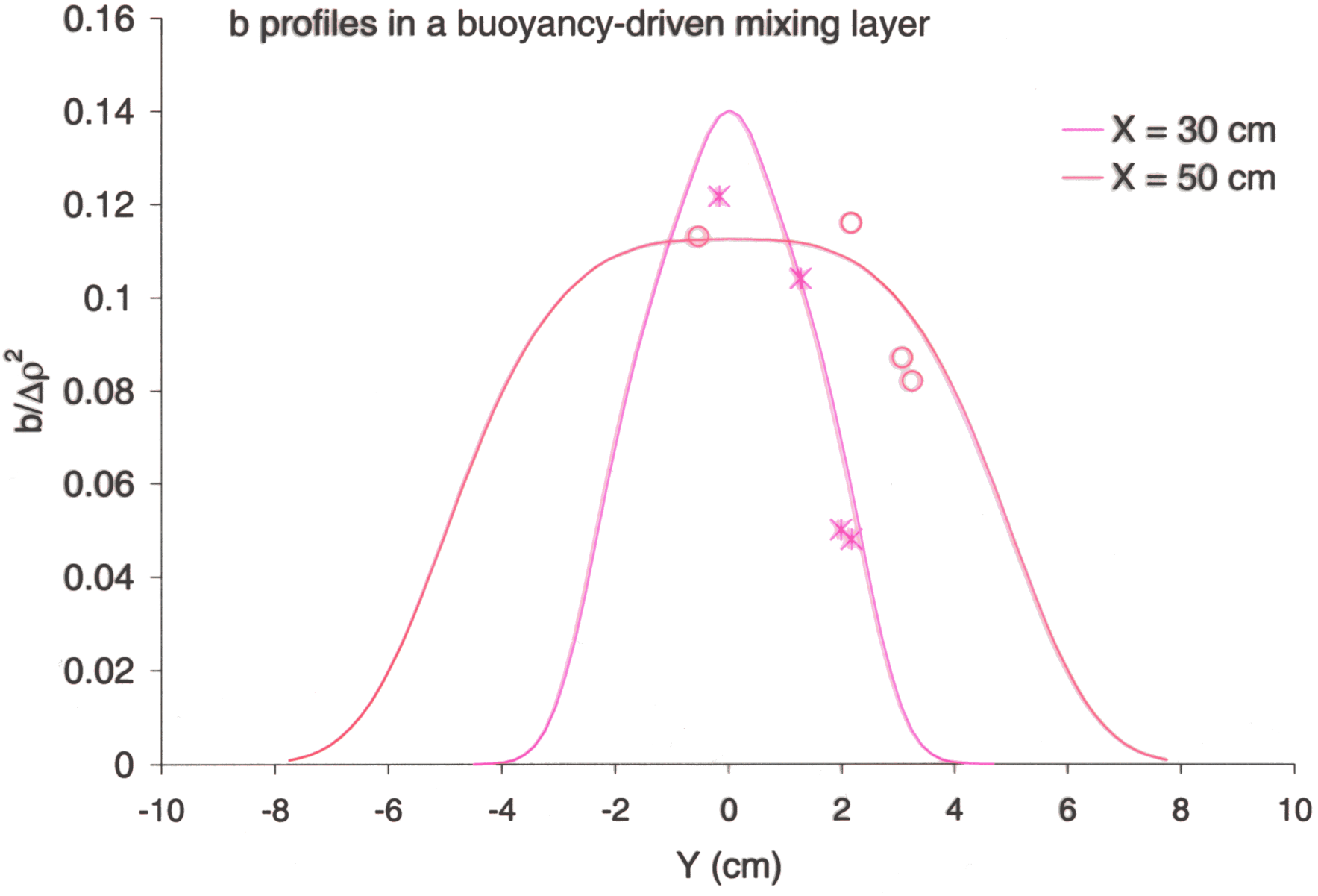
b profiles in a buoyancy-driven mixing layer
X = 30 cm
X = 50 cm
b/Δρ²
0.16
0.14
0.12
0.1
0.08
0.06
0.04
0.02
0
-10
-8
-6
-4
-2
0
2
4
6
8
10
Y (cm)

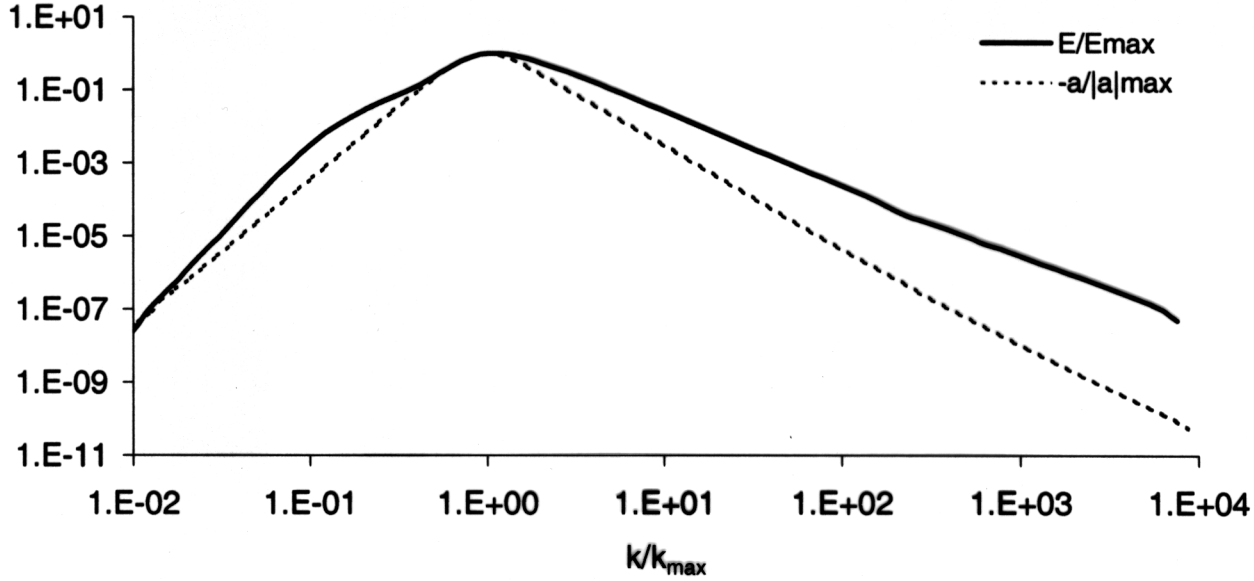
1.E+01
1.E-01
1.E-03
1.E-05
1.E-07
1.E-09
1.E-11
1.E-02
1.E-01
1.E+00
1.E+01
1.E+02
1.E+03
1.E+04
k/k_max
E/Emax
-a/|a|max

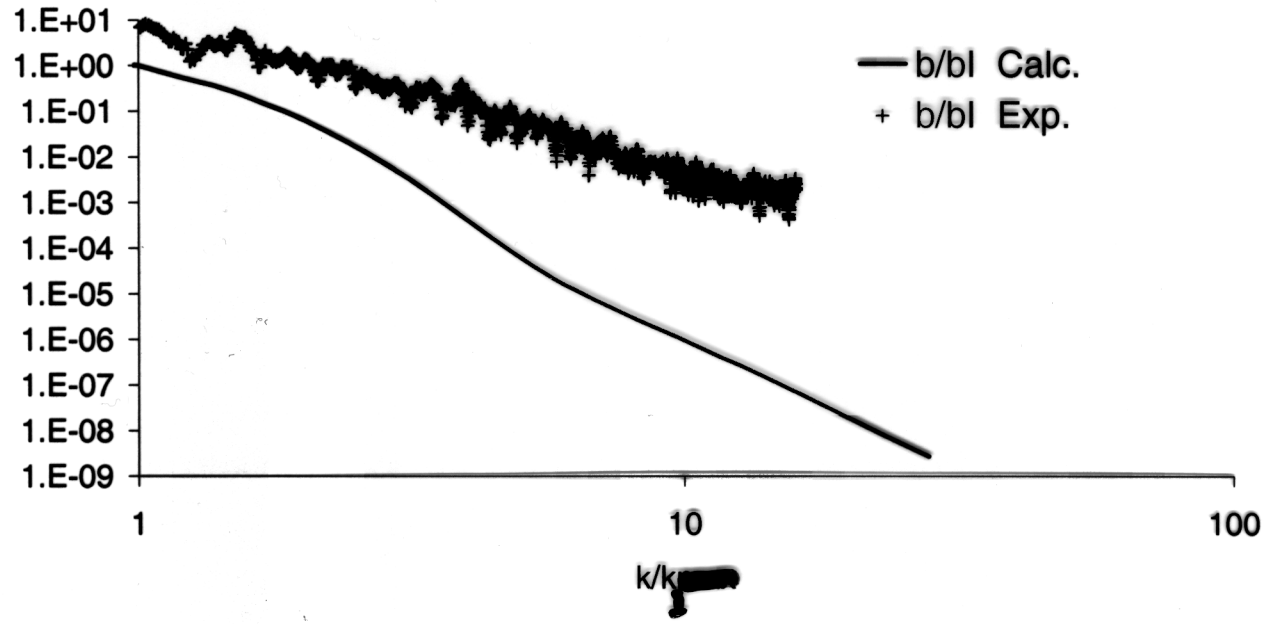
1.E+01
1.E+00
1.E-01
1.E-02
1.E-03
1.E-04
1.E-05
1.E-06
1.E-07
1.E-08
1.E-09
1
10
100
b/bl Calc.
b/bl Exp.

Rate of growth of the linear Richtmyer-Meshkov instability

J. G. Wouchuk

E.T.S.I.Industriales
University of Castilla La Mancha
Ciudad Real
Spain

Presented at the 8th IWPCTM
California Institute of Technology
December 2001

RM instability**:** *perturbation growth due to the vorticity generation at both sides of a contact surface by means of corrugated shock fronts.*

We distinguish two situations:

1) A shock is reflected back or,

2) a rarefaction is reflected instead

Two possible approaches to get the growth rate are:

1-heuristic models based on an impulsive formulation (RM, VMG, MB),

2-rigorous linear theory:

-numerical solution as in Richtmyer, CPaAM 13, 297 (1960) or in Yang, Zhang and Sharp (PoF 6, 1856 (1994)),
- series expansions as in Velikovich, PoF 8, 1666 (1996), Wouchuk and Nishihara, PoP 3, 3761 (1996).
-closed analytical formulas deduced from linear theory [Fraley, PoF 29, 376 (1986) Wouchuk and Nishihara, PoP 3,3761 (1996);4, 1028 (1997)]

It is clear that an estimate by means of a closed formula would be useful be it for numerical or experimental studies.

It is always possible to get asymptotic expressions of the rate of growth truncating the temporal expansions. However, the validity of such expressions is limited to very weak incident shocks.

The same restriction applies to any heuristic approach like the ones based on an impulsive formulation of the instability.

Before discussing an exact formulation that leads to a very accurate determination of the growth rate, we discuss some of the hypothesis underlying the heuristic models.

The impulsive formulations make the assumptions:

a) ***Incompressible*** *fluid flow after shock transit, and*

*b****) Irrotational*** *perturbations left by the shocks.*

The general form of the vorticity profile left by a rippled shock is:

$$\delta\omega(x,y) = \Omega \quad \delta p(x, t = \frac{x}{U_s})\sin(ky)$$

$$\delta\omega(x,y) = \Omega \quad \delta p_s(kx / \sinh(\theta_s))\sin(ky)$$

$$\delta\omega(x,y) = \sum_{n\geq 0} A_{2n+1} J_{2n+1}\left(kx / \sinh(\theta_s)\right) \quad \sin(ky)$$

We see that vorticity production could be substantial, and this fact depends on fluids properties as well as on the incident shock intensity.

The vorticity left by the shock fronts is the memory of the effect of the "rippled compression" of the fluid elements.

For a strictly planar shock the flow behind it will be trivially irrotational.

For a corrugated front, the flow behind it will be rotational.

The vorticity deposited in the interior of the fluids will have a definite effect on the interface growth as we are going to see. It can not be neglected for strong shocks or highly compressible fluids.

Tangential velocity:

$$\frac{\partial v_y}{\partial t} = \delta p_i(t) \quad \xrightarrow{\int_{0+}^{\infty} ...dt} \quad \rho_{af}(\delta v_{ya}^{\infty} - \delta v_{ya}^{0}) = \rho_{bf}(\delta v_{yb}^{\infty} - \delta v_{yb}^{0})$$

Normal velocity:

$$\frac{\partial \delta v_x}{\partial t} = -\frac{1}{\rho_{mf}} \frac{\partial \delta p_i}{\partial x} \quad \xrightarrow{\int_{0+}^{\infty} ...dt} \quad \delta v_i^{\infty}$$

$$\delta v_i^{\infty}, \quad \delta v_{ya}^{\infty}, \quad \textit{and} \quad \delta v_{yb}^{\infty}$$

are not equal in the general case.

In fact, the parameters:

$$F_a = \delta v_{ya}^{\infty} + \delta v_i^{\infty},$$
$$F_b = \delta v_{yb}^{\infty} - \delta v_i^{\infty}$$

are different from zero and become important for very strong shocks and highly compressible fluids.

How do we relate the parameters F_a and F_b with the shock compression history?

Asymptotic velocity fields:

-Incompressibility:

$$\frac{d\delta v_x}{dx} + \delta v_y = 0,$$

-Vorticity:

$$\frac{d\delta v_y}{dx} + \delta v_x = \Omega \delta p(x/\sinh\theta_s)$$

We get, for example:

$$\frac{d^2 \delta v_x}{dx^2} - \delta v_x = -\Omega \delta p(x / \sinh\theta_s)$$

The right hand side can not be made zero for moderate to strong shocks.

In fact, not only the qualitative form of the velocity profile is modified because of the bulk vorticity: the asymptotic value of the interface velocity could be seriously inferior to any value deduced from an irrotational assumption.

*An **<u>exact expression</u>** of the linear asymptotic growth rate is obtained:*

$$\delta v_i^{\infty} = \frac{\rho_{bf}\delta v_{yb}^0 - \rho_{af}\delta v_{ya}^0}{\rho_{bf} + \rho_{af}} + \frac{-\rho_{bf}F_b + \rho_{af}F_a}{\rho_{bf} + \rho_{af}}$$

F_a and F_b must be related with the compressible evolution of the instability.

For very weak shocks we have the scaling laws:

$$\begin{cases} F_a & \propto & (M_t^2 - 1)^{7/2} \\ F_b & \propto & (M_r^2 - 1)^{7/2} \end{cases} \qquad \begin{cases} \delta v_{ya}^0 & \propto & (M_t^2 - 1) \\ \delta v_{ya}^0 & \propto & M_r^2 - 1 \end{cases}$$

And then, an irrotational estimation for the asymptotic velocity is justified:

$$\delta v_{irrot}^{\infty} = \frac{\rho_{bf}\delta v_{yb}^0 - \rho_{af}\delta v_{ya}^0}{\rho_{bf} + \rho_{af}}$$

We make a Laplace transform of the equation for δv_x and get:

$$\delta V_{xb}(\sigma) \quad = \quad \frac{\sigma \delta v_i^{\infty} - \delta v_{yb}^{\infty} - \Omega_b \sinh\theta_r \delta P_r(\sigma \sinh\theta_r)}{\sigma^2 - 1}$$

A similar equation holds in fluid "a".

The function δP is the time Laplace transform of the shock front pressure perturbations.

To get bounded perturbations, we see that it must be:

$$F_b = -\delta v_i^{\infty} + \delta v_{yb}^{\infty} = \Omega_b \sinh\theta_r \delta P_r(\sinh\theta_r)$$

And an analogous relationship holds in fluid "a".

If a rarefaction were reflected, then: $F_b = 0$.

Thus, to get the values of F_a *and* F_b*, we need temporal averages of the shock pressure functions.*

How do we calculate the parameters F_a ***and*** F_b***?***

We change to the coordinate system:

$$\begin{cases} kx = r\sinh\theta \\ kc_f t = r\cosh\theta \end{cases}$$

The shock-fronts coordinates are defined by:

$$\tanh\theta_t = -\frac{U_t}{c_{af}} \qquad\qquad \tanh\theta_r = \frac{U_r}{c_{bf}}$$

It can also be seen that the Laplace transform of the shock pressure in each fluid can be written as:

$$\delta P_m(\theta, q) = \frac{F_{m1}(q-\theta) + F_{m2}(q+\theta)}{\cosh q}$$

Where "q" is related to the Laplace variable "s" through:

$$s = \sinh q$$

In principle we have four unknown functions:

$$\begin{cases} F_{a1}(q_a), F_{a2}(q_a) \\ F_{b1}(q_b), F_{b2}(q_b) \end{cases}$$

After some algebra, at the shock fronts and at the interface, we can relate Fa1 and Fb2 in the following way:

$$\begin{cases} F_{a1}(q_a) + \phi_{b3} F_{b2}(q_b) = \phi_{b1} + \phi_{b2} F_{b2}(q_b + 2\theta_r) \\ F_{b2}(q_b) + \phi_{a3} F_{a1}(q_a) = \phi_{a1} + \phi_{a2} F_{a1}(q_a - 2\theta_t) \end{cases}$$

Besides, it can be seen that the desired parameters F_a and F_b are easily related to specific values of F_{a1} and F_{b2}:

$$\begin{cases} F_a = \varepsilon_{a1} F_{a1}(-2\theta_t) + \varepsilon_{a0} \\ F_b = \varepsilon_{b1} F_{b2}(2\theta_r) + \varepsilon_{b0} \end{cases}$$

A very fast and accurate algorithm can be implemented to get F_a and F_b.

We define an iteration sequence:

$$F_a^{[n]} \qquad \textit{and} \qquad F_b^{[n]}$$

with which we get the parameters F_a and F_b.

With just the starting values (n = 0) we can get up to 3 digits in the asymptotic velocities even for very strong shocks and highly compressible fluids.
For details see Phys. Plasmas ***8****, 2890 (2001), Phys. Rev. E 63, 056303 (2001).*

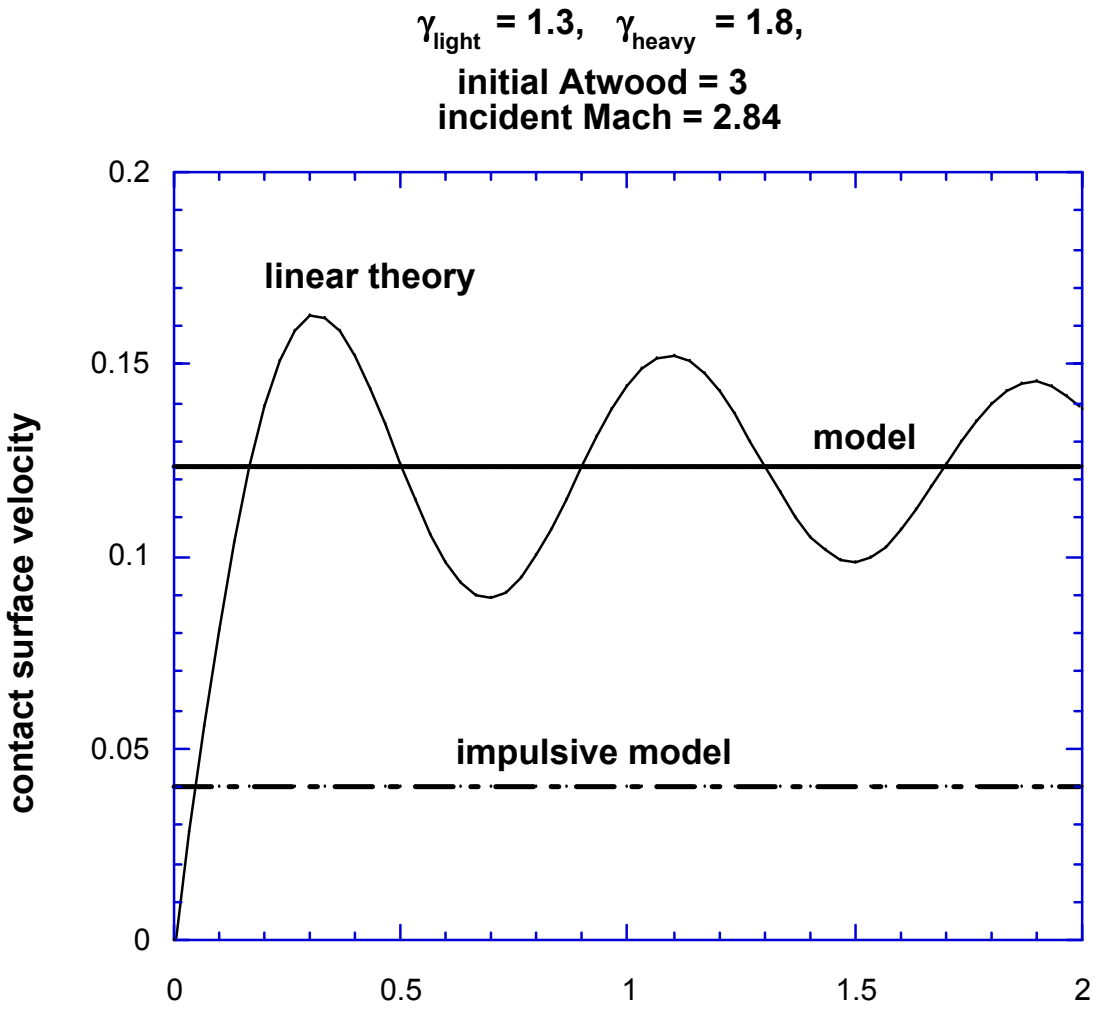
γ_{light} = 1.3, γ_{heavy} = 1.8,
initial Atwood = 3
incident Mach = 2.84
linear theory
model
impulsive model
contact surface velocity
0.2
0.15
0.1
0.05
0
0
0.5
1
1.5
2

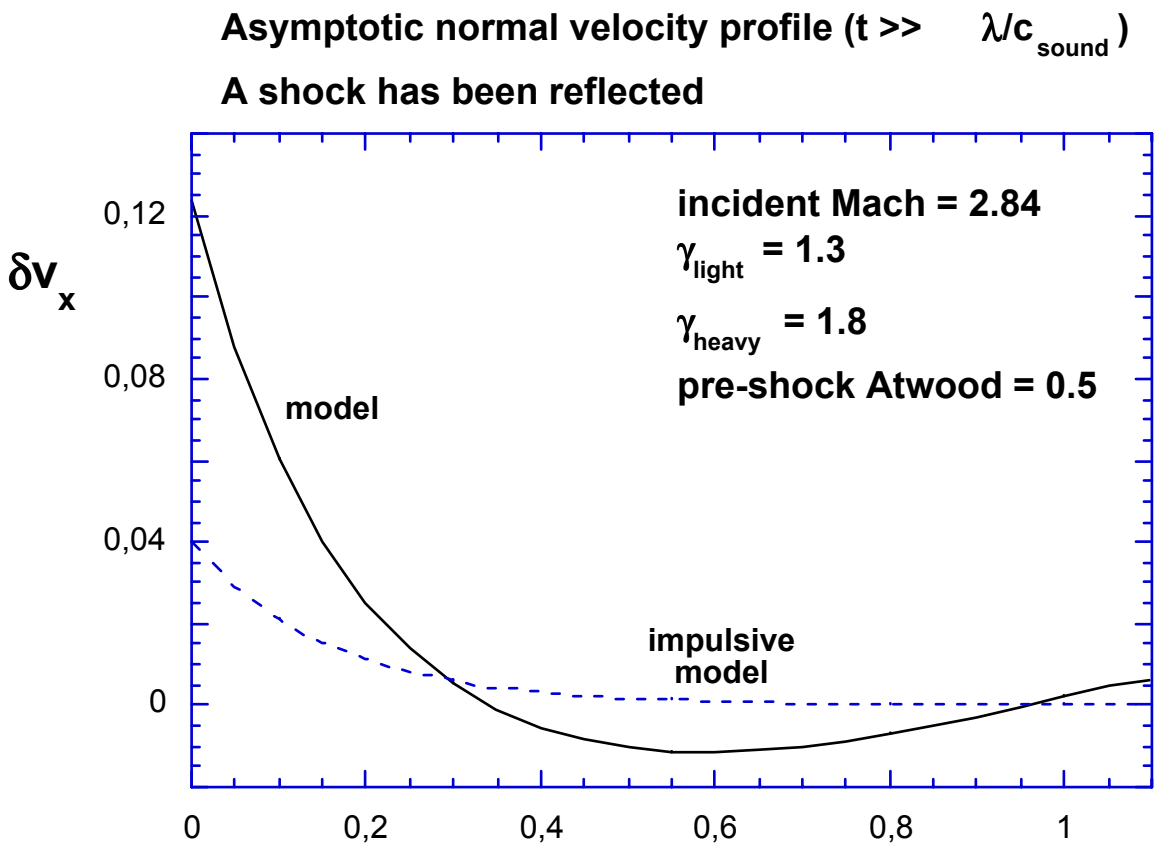
Asymptotic normal velocity profile (t >> λ/c sound)
A shock has been reflected
δv x
0,12
0,08
0,04
0
0
0,2
0,4
0,6
0,8
1
incident Mach = 2.84
γ light = 1.3
γ heavy = 1.8
pre-shock Atwood = 0.5
model
impulsive model

Comparison between the model and simulations together with two impulsive prescriptions. A shock has been reflected.

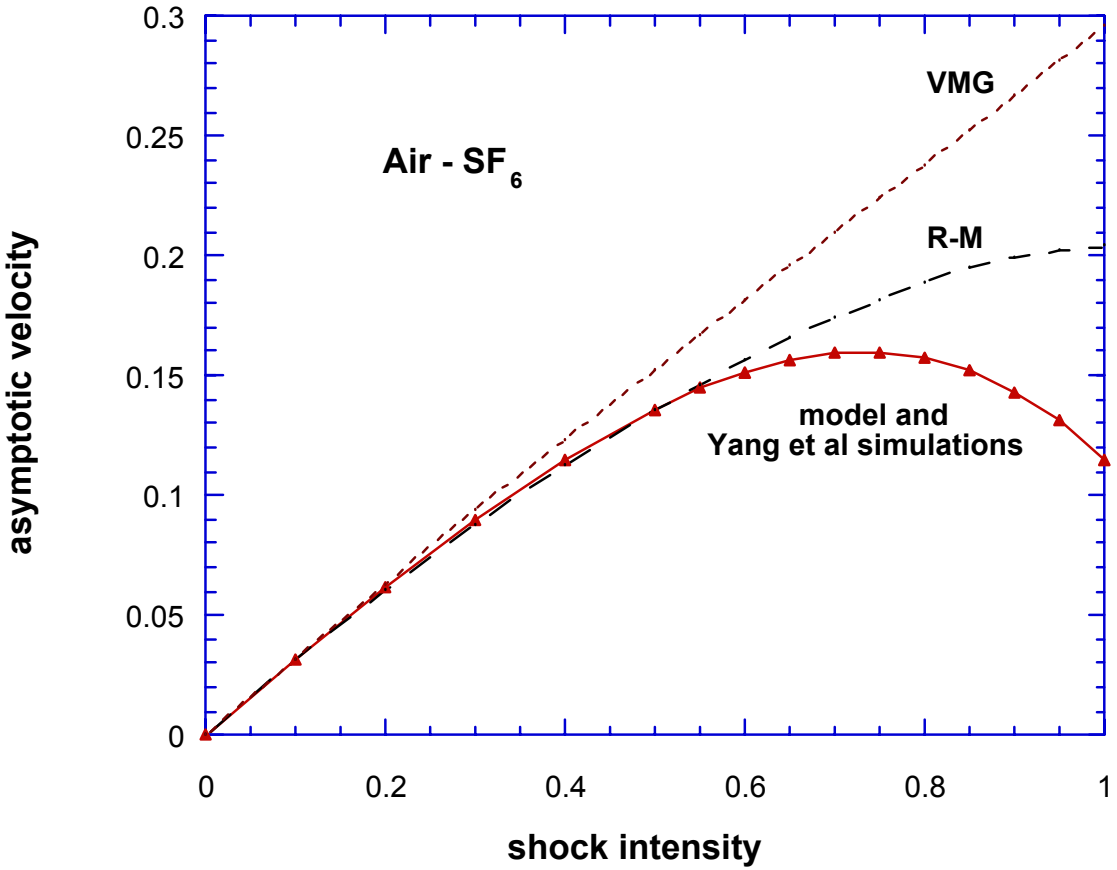

**Comparison between the model and the irrotational approx.
which does not include the vorticity corrections.
A shock impinged upon a Air-He interface**

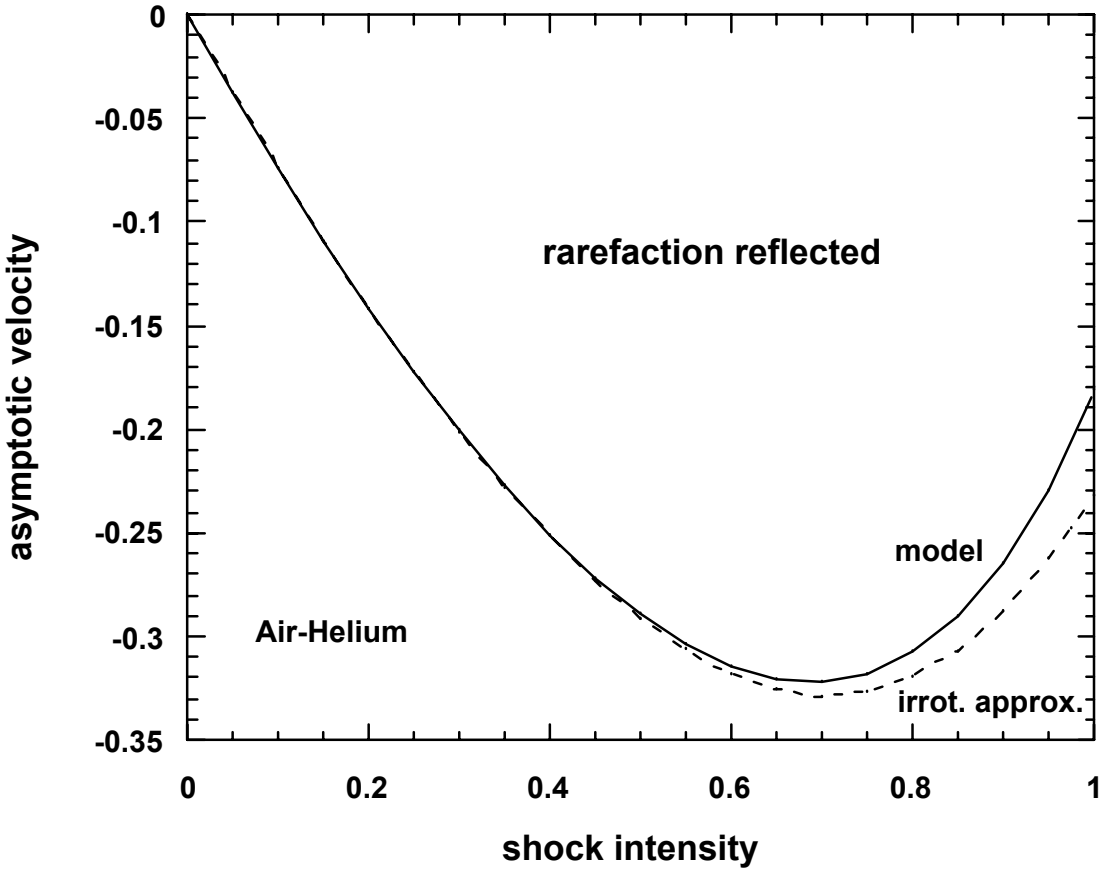

The same as the former picture but with a comparison to different impulsive prescriptions.

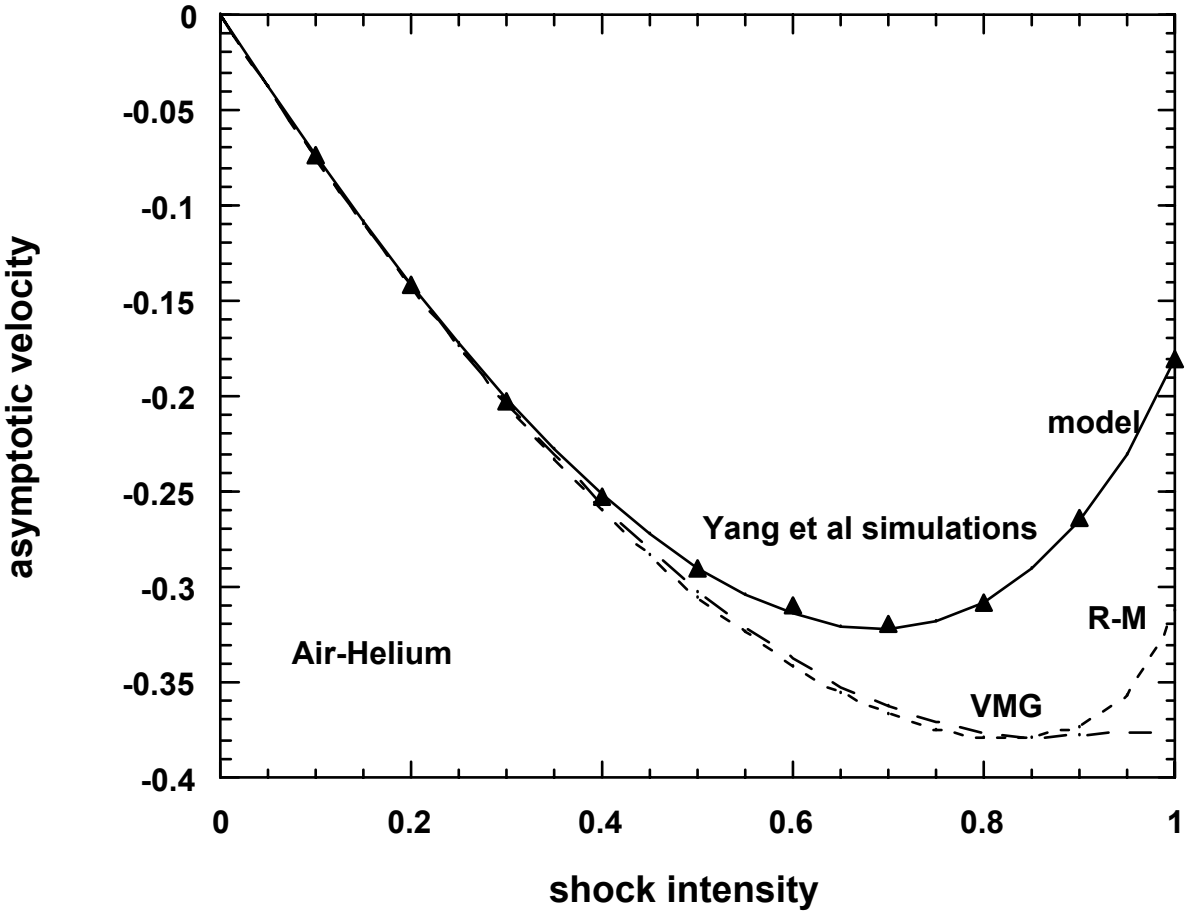

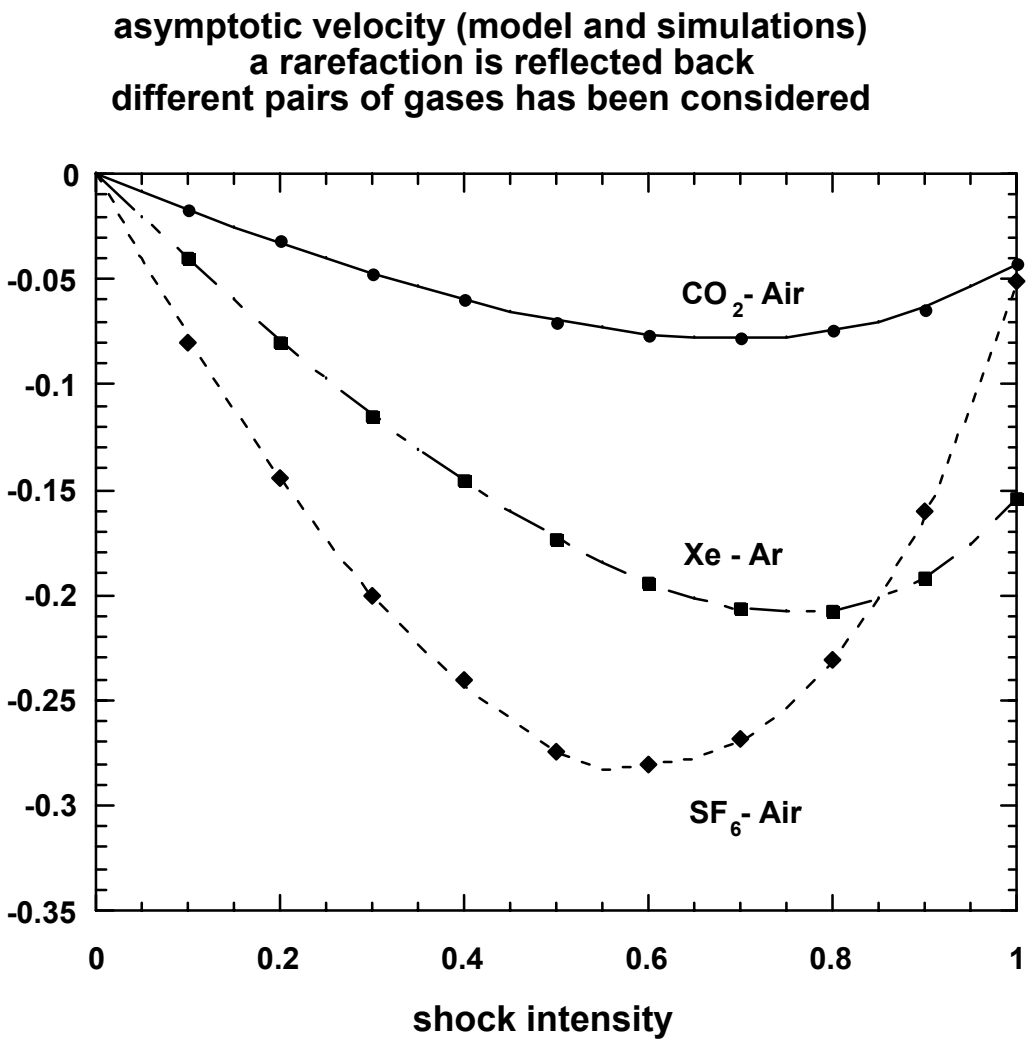
asymptotic velocity (model and simulations)
a rarefaction is reflected back
different pairs of gases has been considered
0
-0.05
-0.1
-0.15
-0.2
-0.25
-0.3
-0.35
0
0.2
0.4
0.6
0.8
1
shock intensity
CO2- Air
Xe - Ar
SF6- Air

Spherical Combustion Layer in a TNT Explosion

A. L. Kuhl† & R. E. Ferguson*

†Lawrence Livermore National Laboratory, Livermore, CA

*Krispin Technologies, Inc, Rockville, MD

8th Int. Workshop on the Physics of Compressible Turbulent Mixing

California Institue of Technology

Pasadena, California

December 9-14, 2001

UCRL-JC-14658

Background: mixing at HE-air interface

1977: S. I. Anisimov & Ya. B. Zel'dovich, "Rayleigh-Taylor instabilitiy of the boundary between deotnation products and gas in a spherical explosion", *Pis'ma Zh. Eksp. Teor. Fiz*, **3**, pp. 1081-1084.

1983: S. I. Anisimov, Ya. B. Zel'dovich, M. A. Inogamov & M. F. Ivanov, " "Taylor instability of contact boundary between expanding detonation products and a surrounding gas", Shock Waves, Explosions & Detonations" *Prog. Astronautics & Astronautics Series,* **87**, AIAA, Wash., DC, pp 218-227.

1996: A. L. Kuhl, "Spherical Mixing Layers in Explosions", *Dynamics of Exothermicity*, Ed. J. R. Bowen, Gordon & Breach, Amsterdam, pp. 291-320.

LLNL Bomb Calorimeter (V=5.28 l)

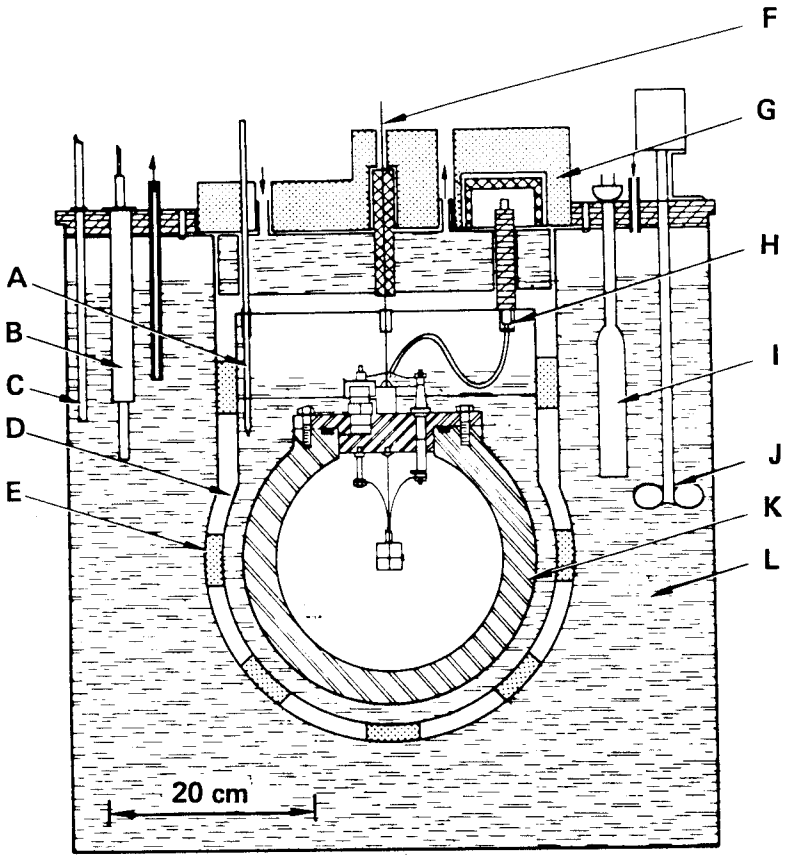

Composition: *TNT products in O_2 & vacuum*

Experimental conditions		Atmosphere: Vacuum, detonation	Atmosphere: Carbon dioxide, detonation	Atmosphere: Oxygen, detonation
Balance level attempted		-	CO and H_2O	CO_2 and H_2O
Pressure, atm (absolute)		-	1.66	2.46
$-\Delta H$ detonation[c]				
Experimental		1093 ± 11	1116 ± 11	3575 ± 35
Calculated from products		1133 ± 15	1105 ± 15	3594 ± 60
Products, mol/mol TNT	N_2	1.32	1.22	1.54
	H_2O	1.60	1.55	2.65
	CO_2	1.25	1.19[c]	6.82
	CO	1.98	2.05	0.38
	C(s)	3.65	3.65	Not detected
	H_2	0.46	0.45	0.050
	NH_3	0.16	0.19	0.0050
	CH_4	0.099	0.099	0.0011
	HCN	0.020	0.009	0.0005
	NO	Not detected	Not detected	0.0011
	C_2H_6	0.004	0.003	Not detected
Material recovery, mol%	C	47.9	48.2	103
	H	100	99.9	109
	N	94.1	88.1	103
	O	101	99.7	101

Multi-Fluid Model

FORMULATION: *turbulent combustion in un-mixed gases*

- **Three Fluids:** Fuel-*F,* Air-*A* & Products-*P* defined by: $\{\rho_K, u_K\}$ where $K = F, A, P$
- **Asymptotic Limit:** $Re = Pe = Da \to \infty$
- **Compressible Flow:** $M > 0$

CONSERVATION EQUATIONS: *mixture*

- **Mass:** $\partial_t \rho_m + \nabla \cdot \rho_m \mathbf{u} = 0$
- **Momentum:** $\partial_t \rho_m \mathbf{u} + \nabla \cdot \rho_m \mathbf{u}\mathbf{u} = -\nabla p_m$
- **Energy:** $\partial_t \rho_m U_T + \nabla \cdot \rho_m U_T \mathbf{u} = -\nabla \cdot (p_m \mathbf{u})$ where $U_T = u_m + \mathbf{u} \cdot \mathbf{u}/2$

THERMODYANMIC FIELDS: *fluids*

- **Fuel:** $\partial_t \rho_F + \nabla \cdot \rho_F \mathbf{u} = -\rho_s$ & $\partial_t \rho_F u_F + \nabla \cdot \rho_F u_F \mathbf{u} = -p_F \nabla \cdot \mathbf{u} - \rho_s u_F$
- **Air:** $\partial_t \rho_A + \nabla \cdot \rho_A \mathbf{u} = -\sigma \rho_s$ & $\partial_t \rho_A u_A + \nabla \cdot \rho_A u_A \mathbf{u} = -p_A \nabla \cdot \mathbf{u} - \sigma \rho_s u_A$
- **Products:** $\partial_t \rho_P + \nabla \cdot \rho_P \mathbf{u} = (1+\sigma)\dot{\rho}_s$ & $\partial_t \rho_P u_P + \nabla \cdot \rho_P u_P \mathbf{u} = -p_P \nabla \cdot \mathbf{u} + (1+\sigma)\dot{\rho}_s u_P$
- **Stoichiometric Source:** $\dot{\rho}_s = \begin{cases} \rho_F(\mathbf{x}_s, t_s)\delta(t - t_s) & \text{for } \lambda_e \geq 1 \\ \rho_A(\mathbf{x}_s, t_s)\delta(t - t_s)/\sigma & \text{for } \lambda_e < 1 \end{cases}$
- **Adiabatic Constraint:** $\sum_K \dot{\rho}_K u_K = 0$

SOLUTION: *high-order Godunov scheme & AMR to follow turbulent mixing*

Thermodynamic Model

Equations of State: *fluid K (=F, A & P)*

- Perfect Gas Equation: $p_K v_K \equiv w_K \equiv R_K T_K$

- Caloric Equation: $u_K = F_K(w_K) \cong -|q_K| + C_K\, w_K \;\Leftrightarrow\; w_K = F_K^{-1}(u_K) \cong [u_K + |q_K|]/C_K$

Pressures & Temperatures

- *fluid K*: $p_K \equiv \rho_K w_K = \rho_K [u_K + |q_K|]/C_K \quad \& \quad T_K = w_K / R_K$

- *mixture m:* $p_m \equiv \rho_m w_m = \rho_m [u_m + |q_m|]/C_m \quad \& \quad T_m = w_m / R_m$

where

$$\rho_m \equiv \sum_K \rho_K \;;\; Y_K \equiv \rho_K / \rho_m \;;\; u_m \equiv \sum_K Y_K u_K \;;\; w_m \equiv \sum_K Y_K w_K \;;\; q_m \equiv \sum_K Y_K\, q_K \;;\; C_m = \sum_K Y_K C_K w_K / w_m$$

Le Chatelier Diagram: *combustion of TNT in air*

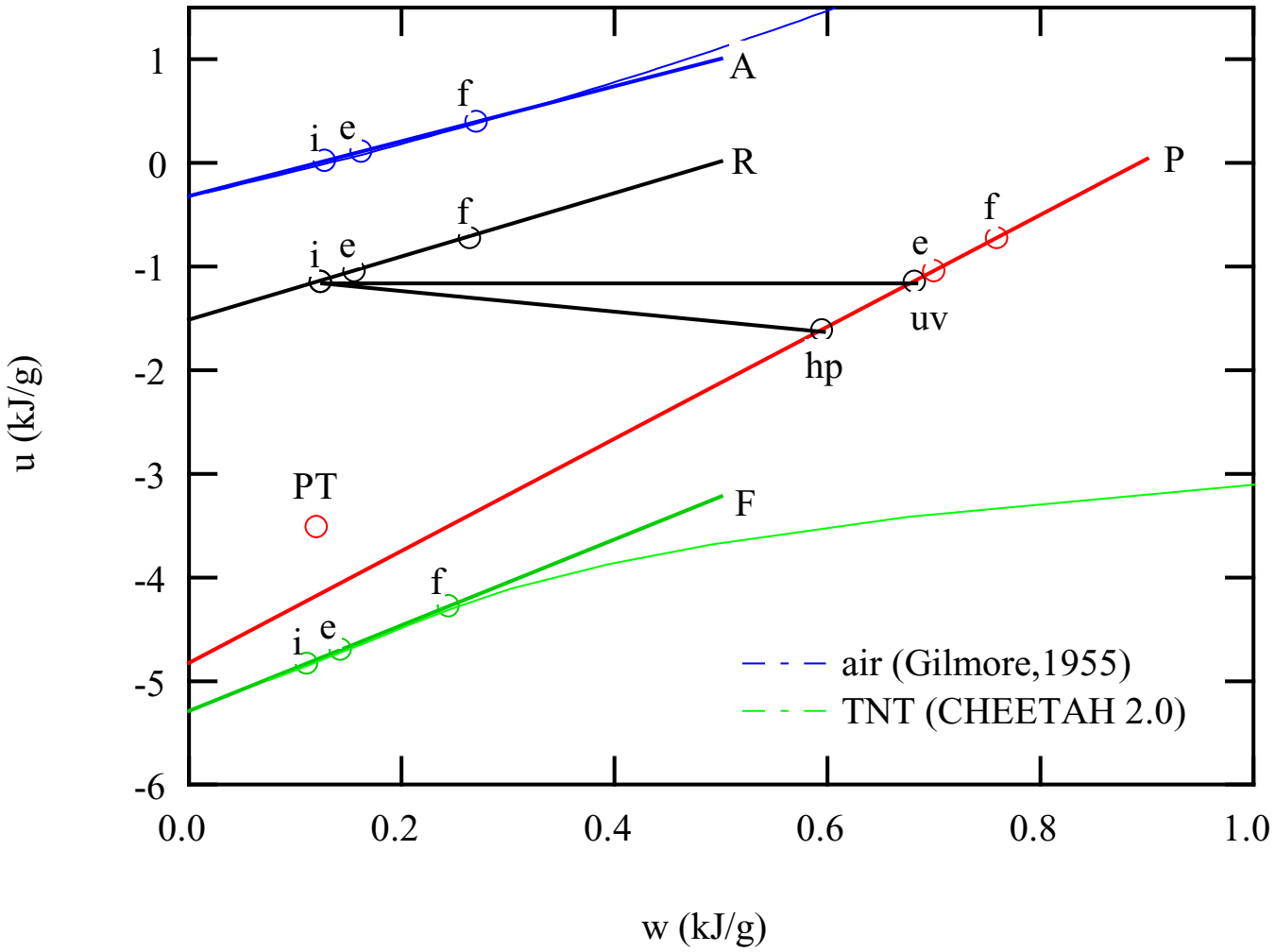

Combustion Model

1. Reactants Formation: *stoichiometric sub-grid mass mixing*:

$$u_R = (u_F + \sigma u_A)/(1+\sigma) \quad \& \quad w_R = (w_F + \sigma w_A)/(1+\sigma)$$

2. Combustion ≡ *material transformations in the Le Chatelier plane*

- at *uv* = *constant* (closed systems): $u_P = u_R$
- at *hp* = *constant* (deflagrations): $u_P = u_R - \dfrac{\Delta Q - (C_P - C_R) w_R}{C_P + 1}$

3. Thermal Equilibration ⇔ *sub-grid energy mixing*: $T_K^e = T_m$

$$w_K^e = R_K T_m$$
$$u_K^e = -|q_K| + C_K w_K^e$$

Initial Conditions: *Self-Similar CJ Detonation*

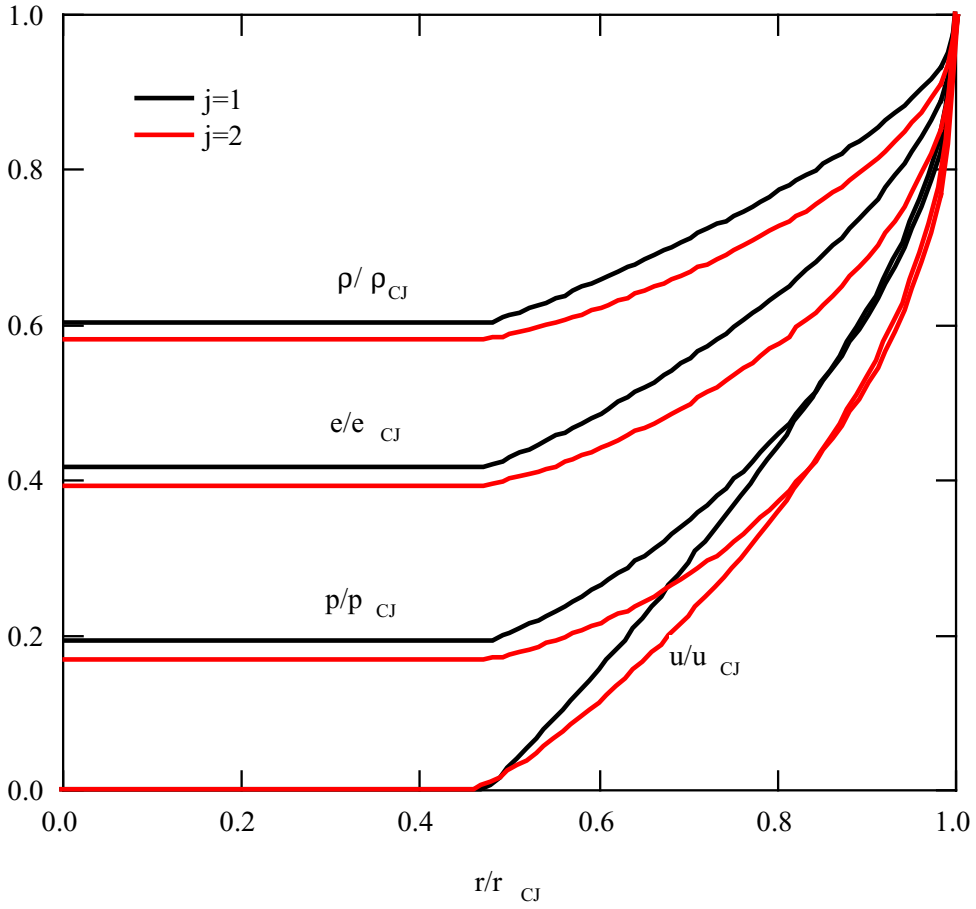

Evolution: Material & Vorticity Fields

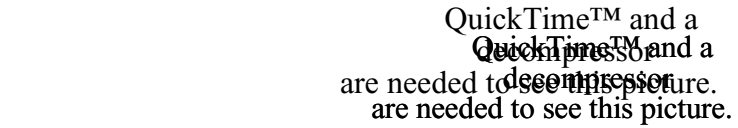

QuickTime™ and a
decompressor
are needed to see this picture.

QuickTime PICT

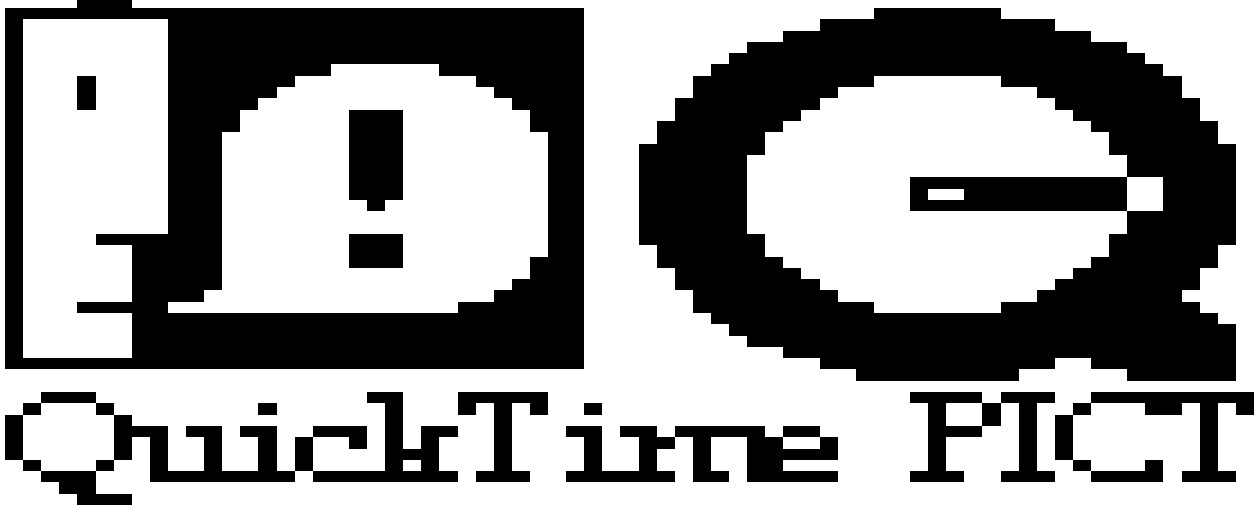
QuickTime PICT

QuickTime PICT

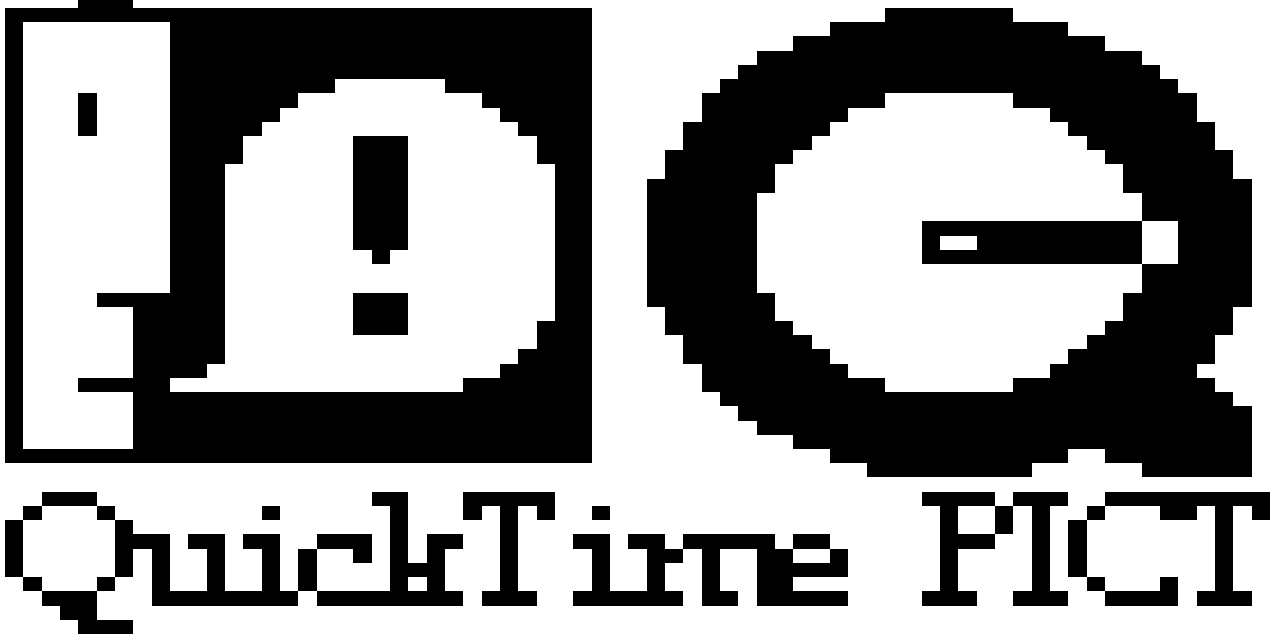
QuickTime PICT

QuickTime PICT
QuickTime PICT

QuickTime PICT

QuickTime PICT

QuickTime PICT
QuickTime PICT

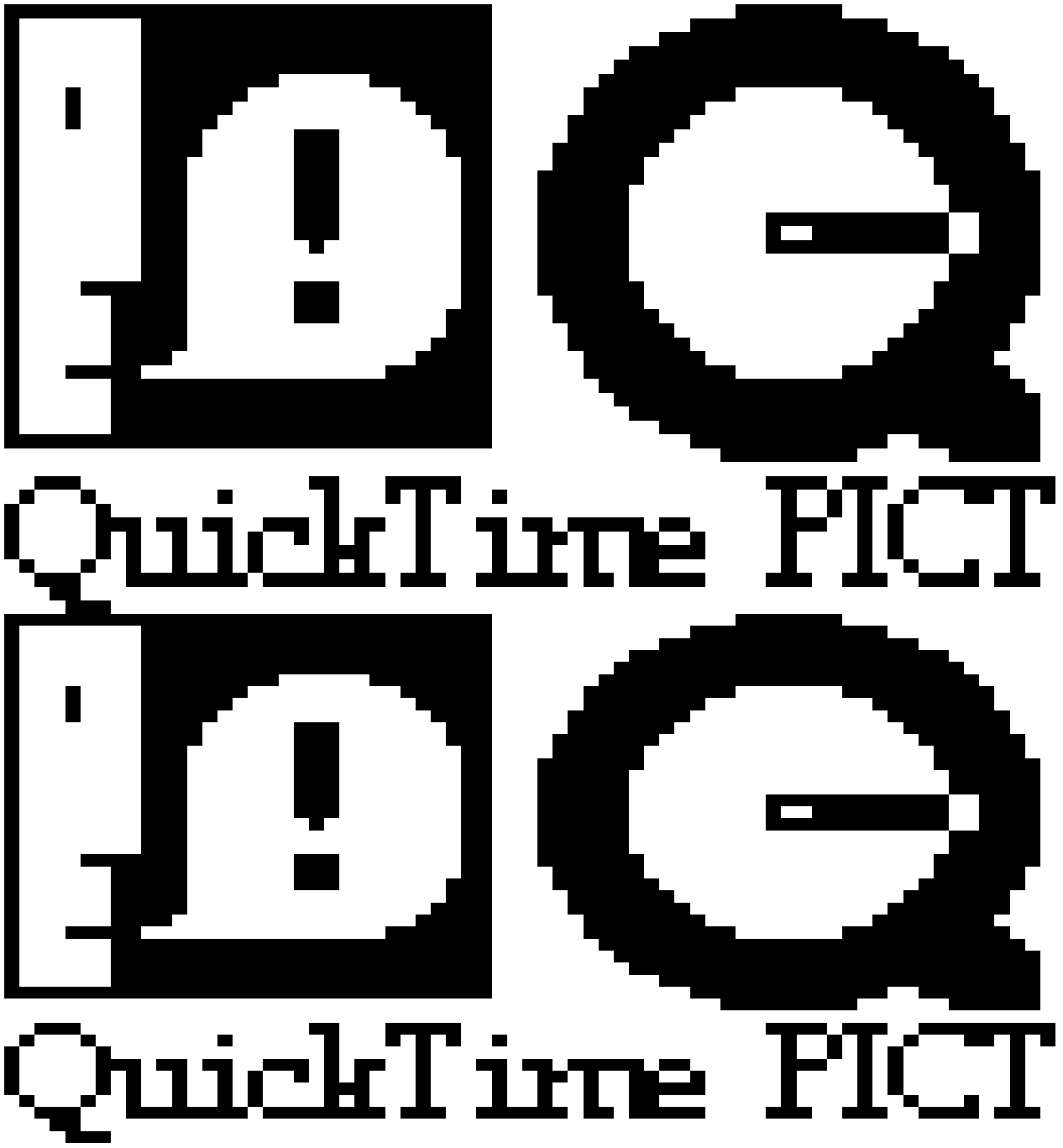
QuickTime PICT
QuickTime PICT

QuickTime PICT
QuickTime PICT

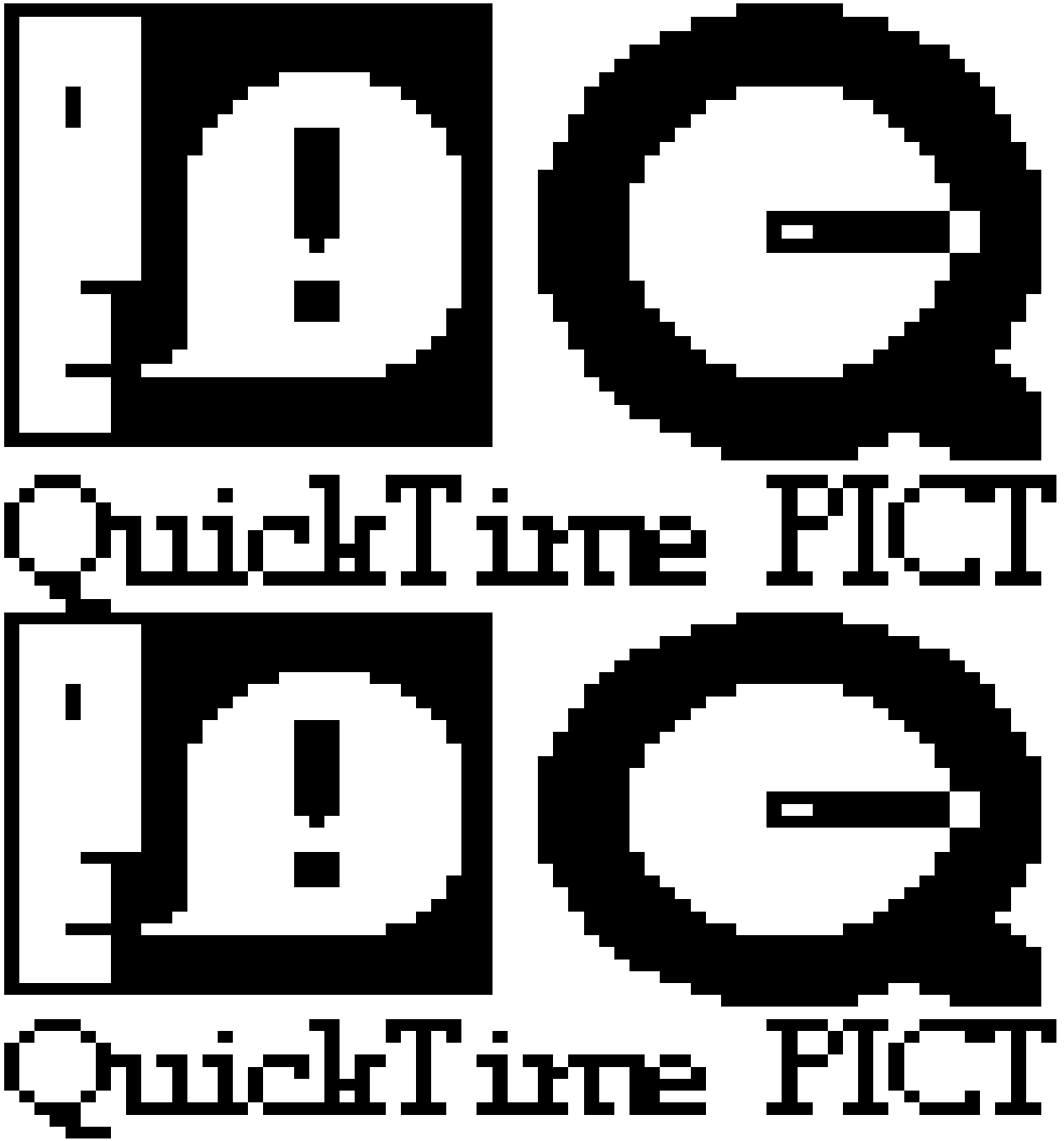
QuickTime PICT
QuickTime PICT

Visualization of Exothermic Fields

material fields

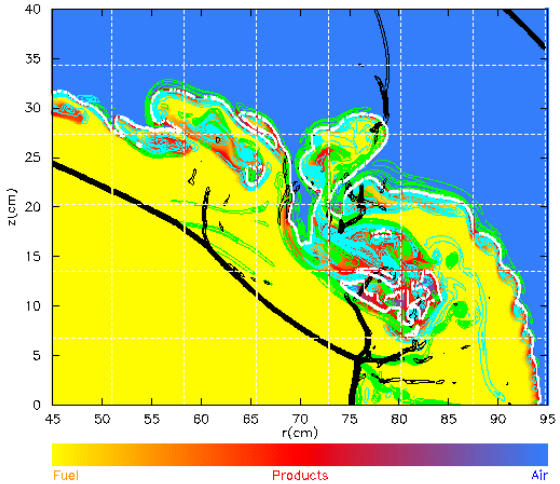

vorticity field

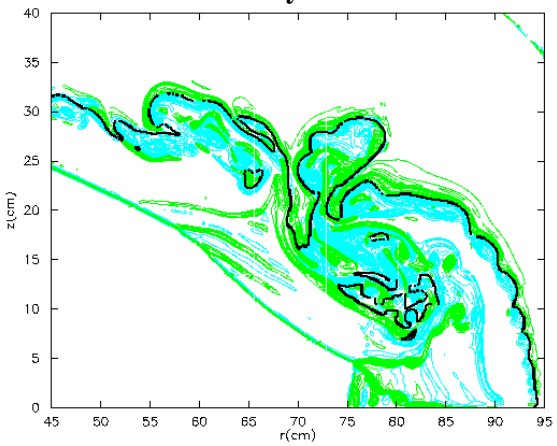

pressure field

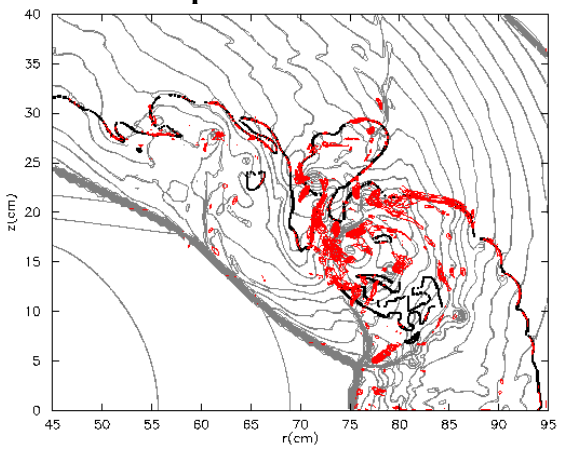

dilatation field

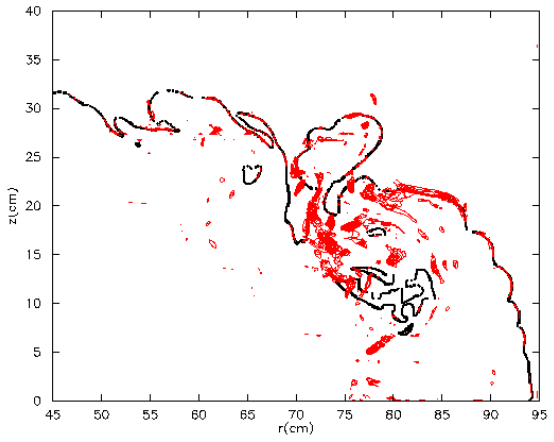

Post-Explosion Combustion of HE in Chamber

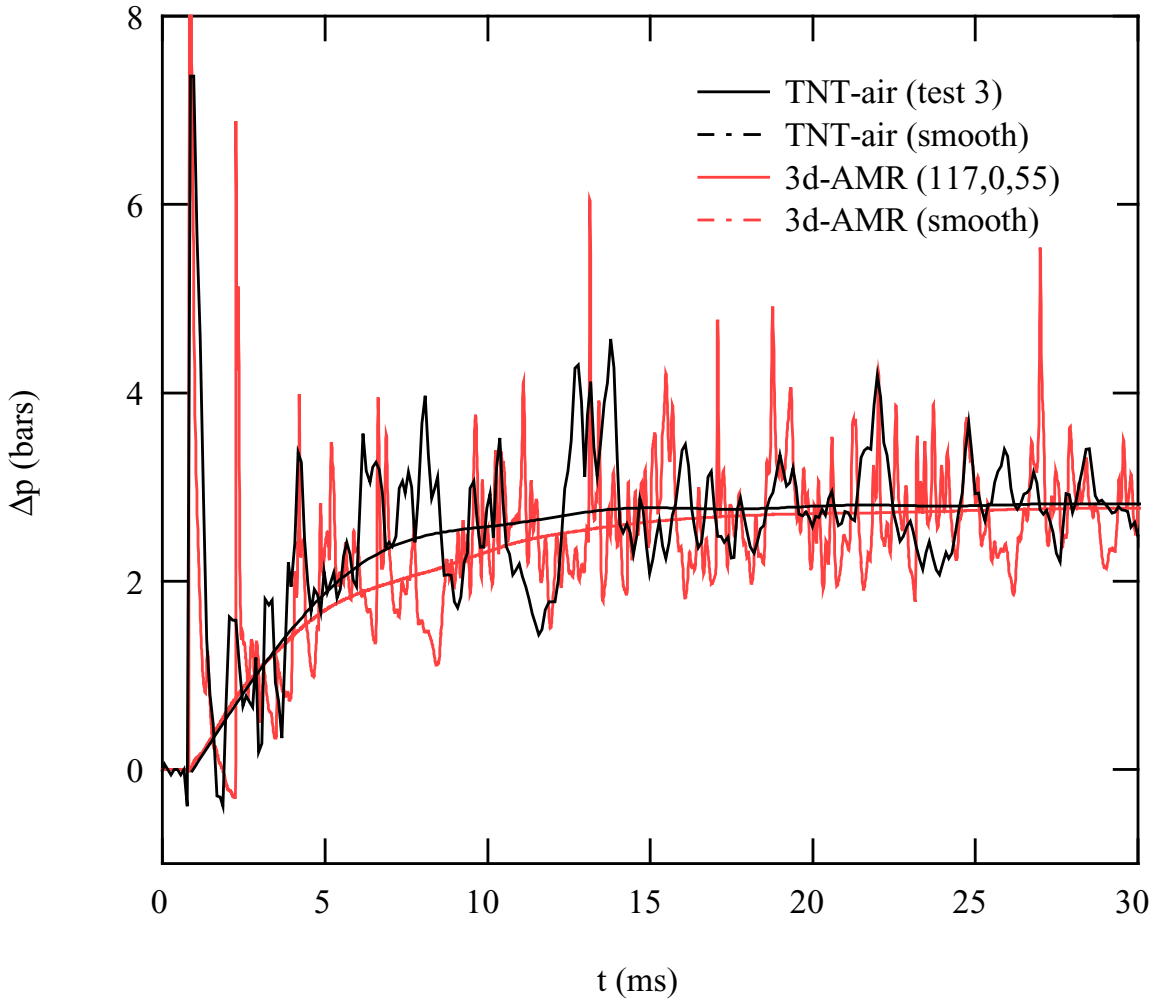

Fuel Consumption

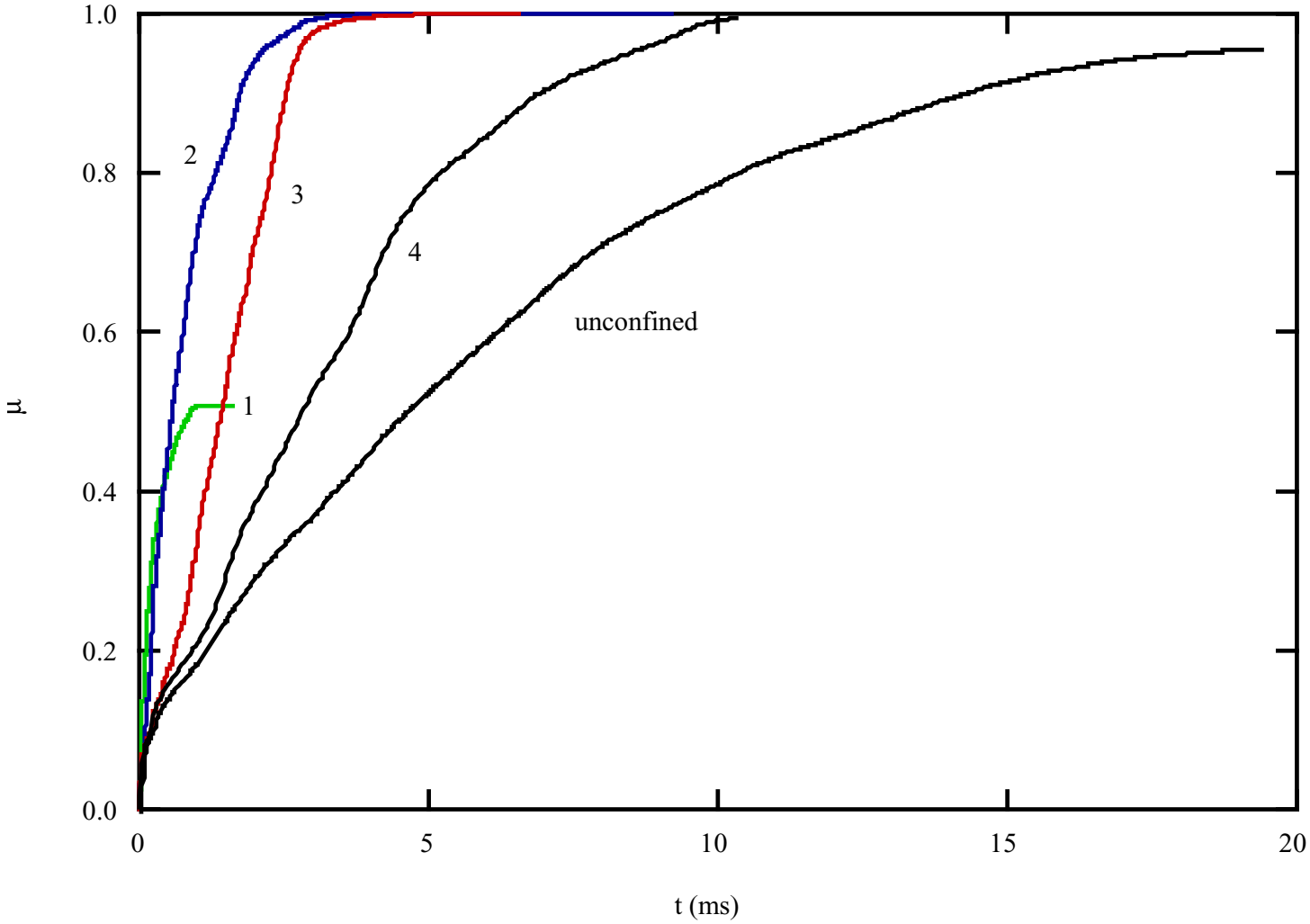

Résumé

Multi-fluid Model

- Gas-dynamic Conservation Equations for the mixture
- Mass & Energy Conservation Equations for each fluid, with source/sink terms

Thermodynamic Model

- *Equations of State*: for each fluid
- *Thermodynamic-Equilibrium Relations*: for mixed cells

Combustion Model

- combustion occurs at thin exothermic sheets: $\mathbf{x}_s(t_s)$ (stoichiometric surface)
- **sink** for *Fuel* & *Air* mass and energy
- **source** for *Products* mass and energy
- Combustion ≡ material transformations in the Le Chatelier plane:

$$u_R(w_R) \Rightarrow u_P(w_P)$$

Conclusions

- This **Model** elucidates the link between **turbulence** (≡ **vorticity**) and **exothermicity** (≡ **dilatation**) in the limit of fast chemistry.

- It thus illustrates the dynamics of turbulent combustion where **exothermic effects** are controlled by mixing — rather than by the reaction-diffusion mechanism of Zel'dovich & Frank-Kamenetzkii (1938)

Discrete Wavelet Transform Techniques for Denoising, Pattern Detection and Compression of Turbulent Rayleigh-Taylor Mix Data

Bedros Afeyan, Polymath Research Inc.
Praveen Ramaprabhu & **Malcolm J. Andrews,** Texas A&M University

International Workshop on the Physics of Compressible Turbulent Mixing
Cal Tech
Pasadena, CA
December 9-14, 2001

What Are Wavelets?
Start @ (www.wavelets.org) surf (Mathsoft, amara, ...)

Mallat, Meyer, Daubechies, Beylkin, Coifman, Strang, Sweldens, Jawerth...

- Wavelets are localized kernels or atoms in PHASE SPACE.
- You may think of them as basis functions with prescribed dilation and translation properties.
- They may or may not be orthonormal or have compact support or be differentiable everywhere, or be fractal, or have many zero momemts.
- Wavelets are like breathing wave packets which can home in on structures in phase space better than FT or WFT ever could.

$$\psi_{j,k}(x) = 2^{j/2}\,\Psi\left[2^j\left(x - \frac{k}{2^j}\right)\right];\; j,k \in \mathbf{Z}$$

$$\Psi_n(x) = (-1)^n \frac{d^n}{dx^n}\left[\exp\left(-\kappa(x - x_c)^2/2\right)\right]$$

When the scale is decreased translation steps between wavelets should likewise be decreased

What is MRD or Multi-resolution Decomposition?

- Multiresolution: Zoom in and out on a number of successively finer scales in a sequence of nested approximation subspaces $\{V_j\}_{j \text{ in } Z}$.
- In general, get an overcomplete basis set in $L_2(R)$. Approximate (or truncate) by bounding the scales of interest.

Scaling functions and the scaling equation:

Low pass filter

$$\varphi(x) = 2\sum_{k=0}^{2N-1} h_k \varphi(2x-k)$$

$$\sum_k h_k = 1 \qquad \int_{-\infty}^{\infty} \varphi(x)\,dx = 1$$

The Wavelets:

High pass filter

$$\psi(x) = 2\sum_{k=0}^{2N-1} g_k \varphi(2x-k)$$

$$g_k = (-1)^k h_{2N-1-k}$$

These filters decompose a sampled signal into 2 sub-sampled channels: the coarse approximation of the signal and the missing details at finer scales. The original signal can be reconstructed from these channels by interpolation.

What Are Discrete Wavelet Decompositions Good for?

- Wavelet decompositions are very useful for the analysis of intermittent or bursty data.
- Spatial and scale localized information is efficiently represented.
- Because the trends you want are captured efficiently (get large coefficients in the expansion)very high quality denoising is possible.
- Similarly, pattern recognition and detection capability is enhanced.
- Compression is achieved where a few coefficients can represent what is needed in the data.
- All this depends on nonlinear (or largest coefficient)thresholding and not scale or level thresholding . The latter is rather reminiscent of what is done with Fourier expansions.

The Scaling Function and Wavelet for Haar or Daubechies 1 in X-Space

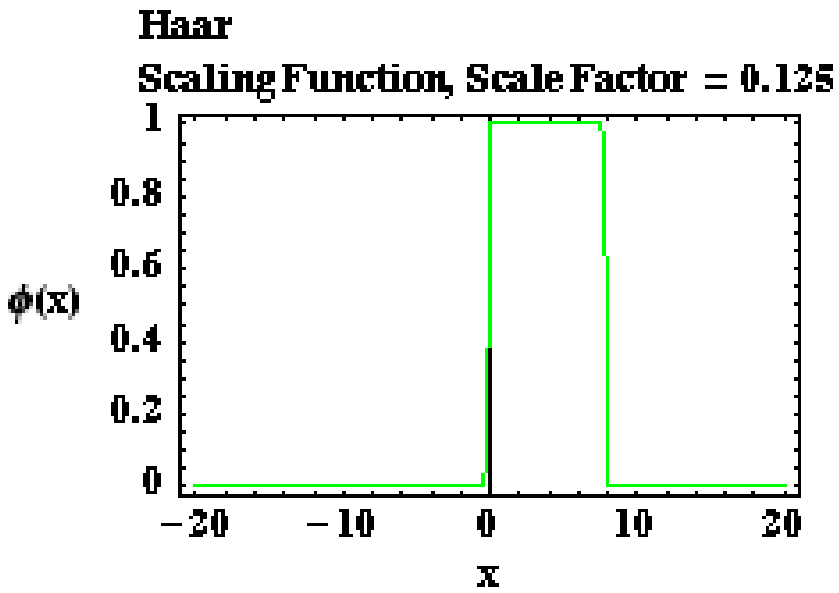

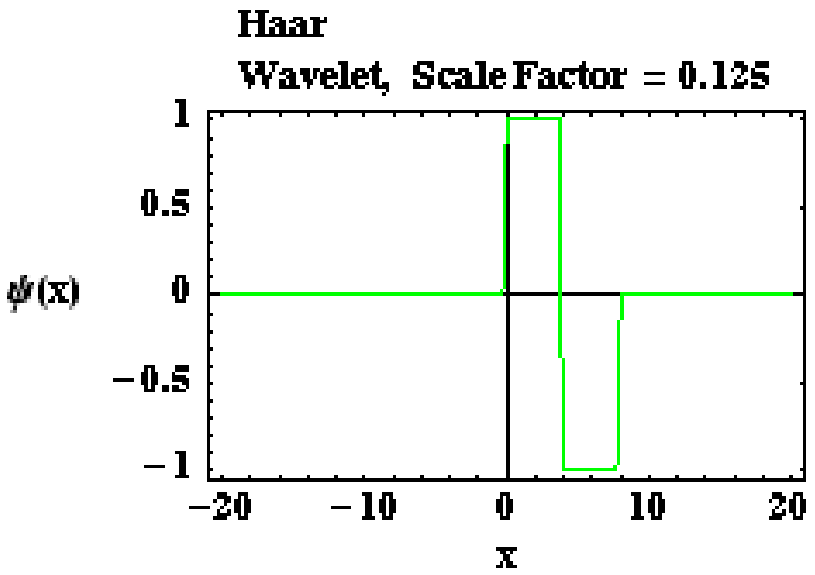

The Scaling Function and Wavelet for Haar or Daubechies 1 in K- Space

Polymath Research Inc.

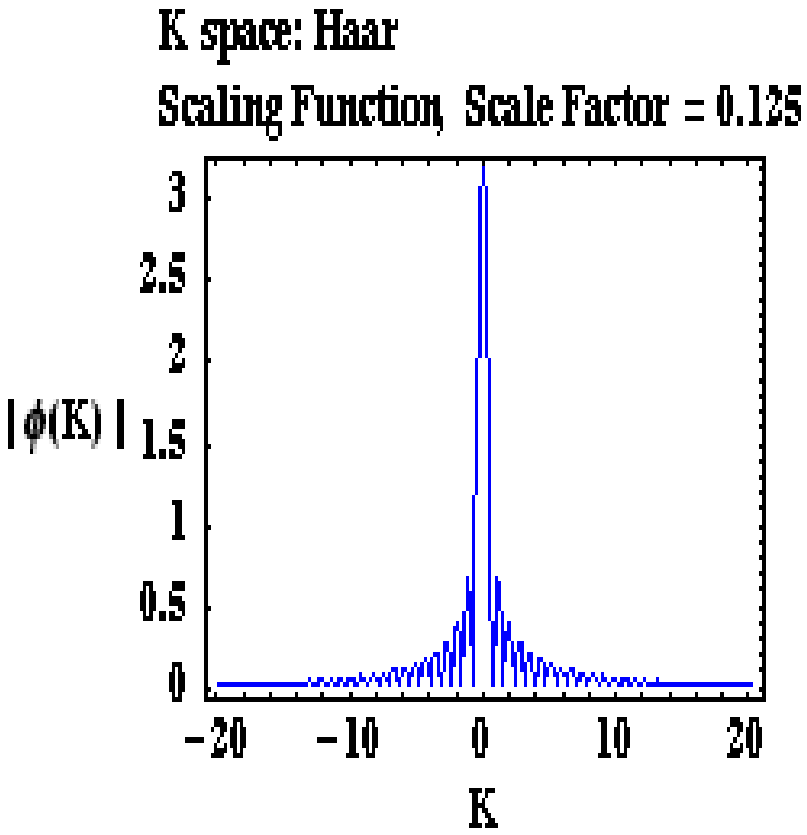

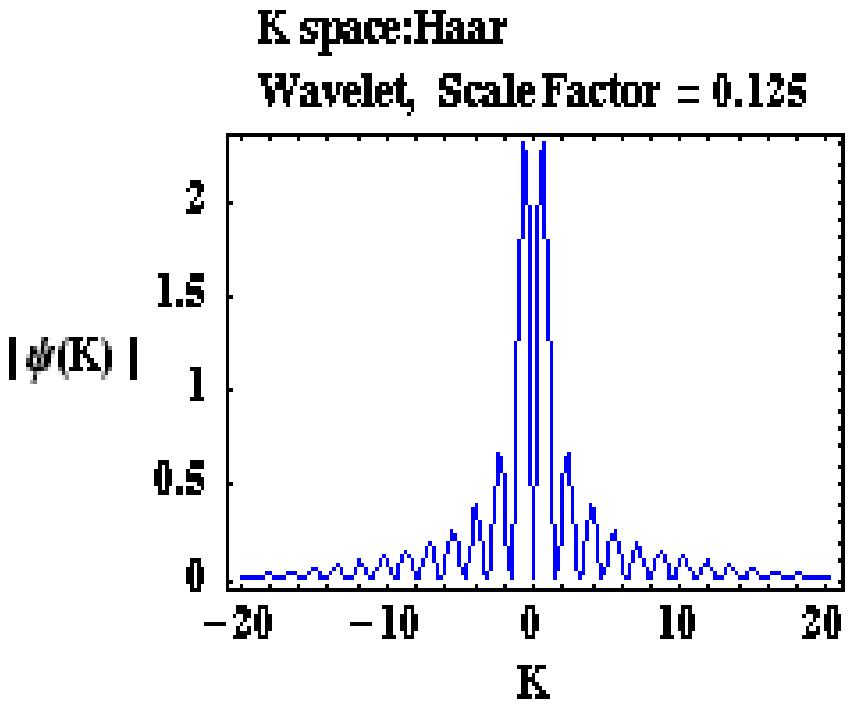

The Scaling Functions and Wavelets for Daubechies 2-6 in X-Space

Polymath Research Inc.

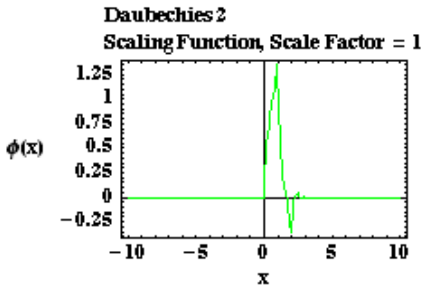

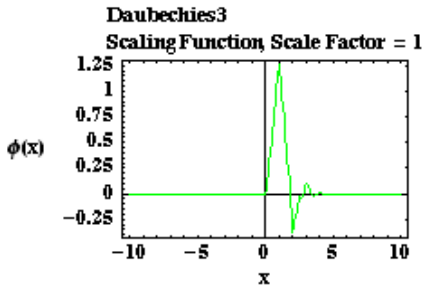

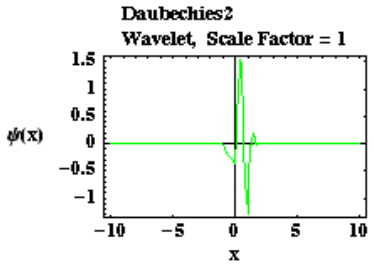

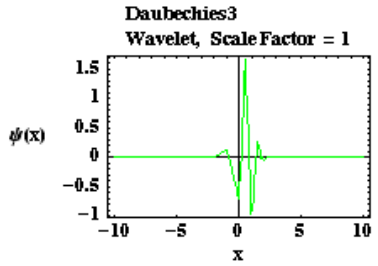

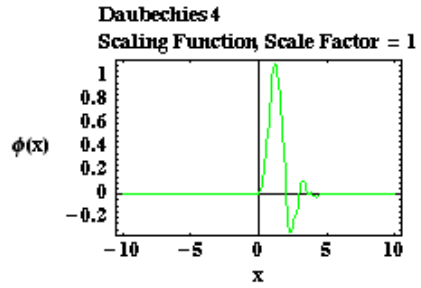

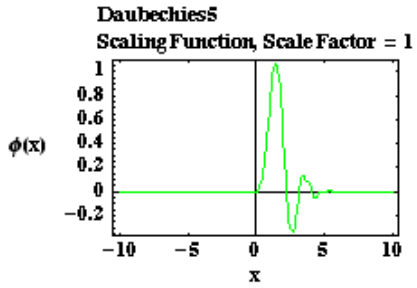

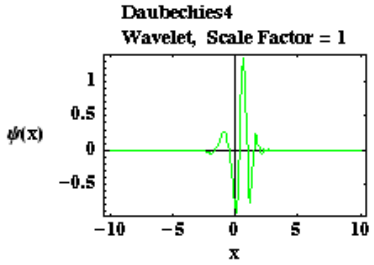

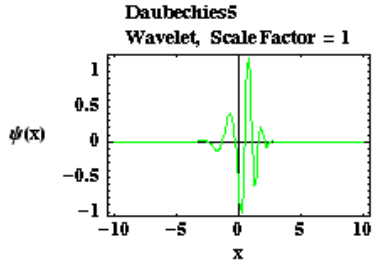

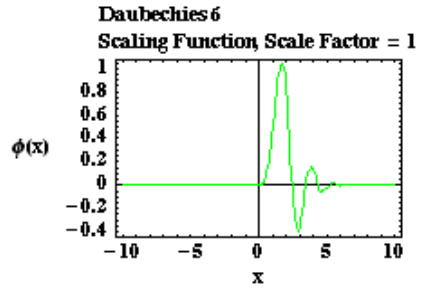

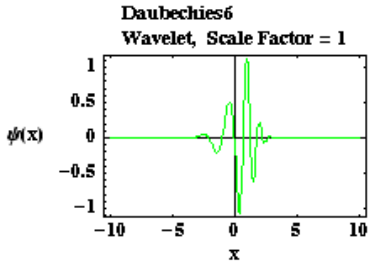

The Scaling Functions and Wavelets for Daubechies 2-6 in k-Space

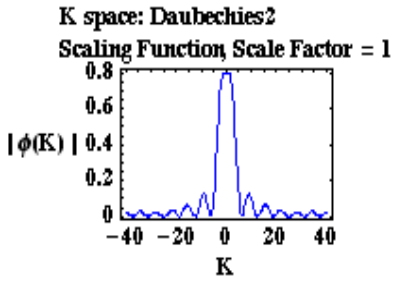

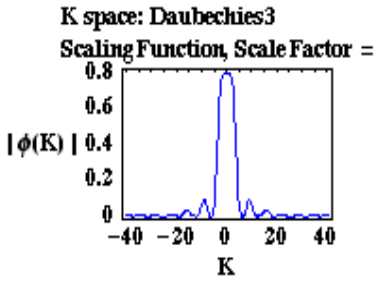

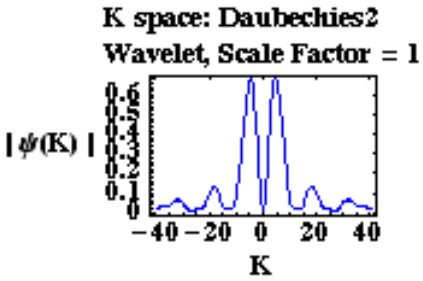

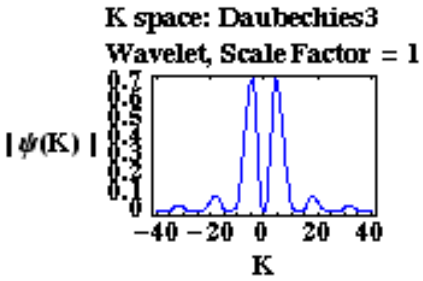

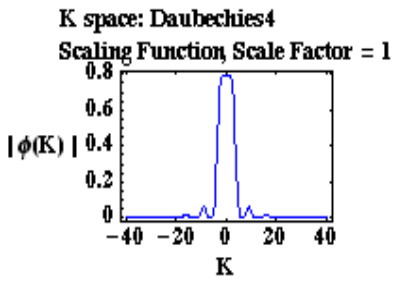

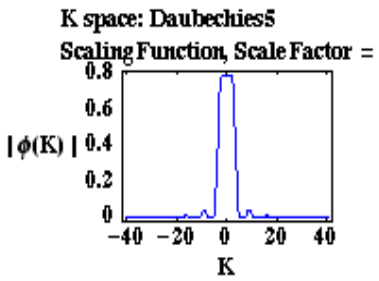

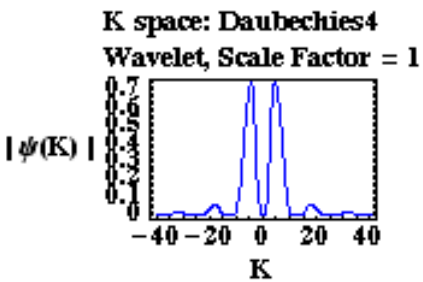

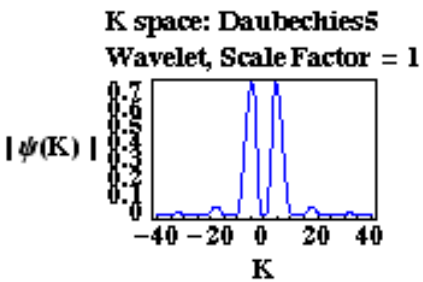

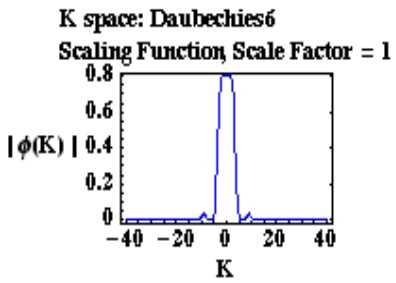

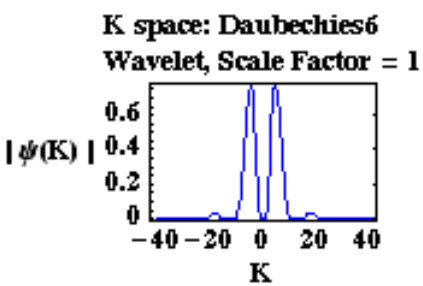

Raw Thermocouple RT Strong Mix Data (30 cm Downstream, theta ~ 0.71) from Texas A&M

Polymath Research Inc.

$$\frac{T - T_{AVE}}{T_{MAX} - T_{AVE}}$$

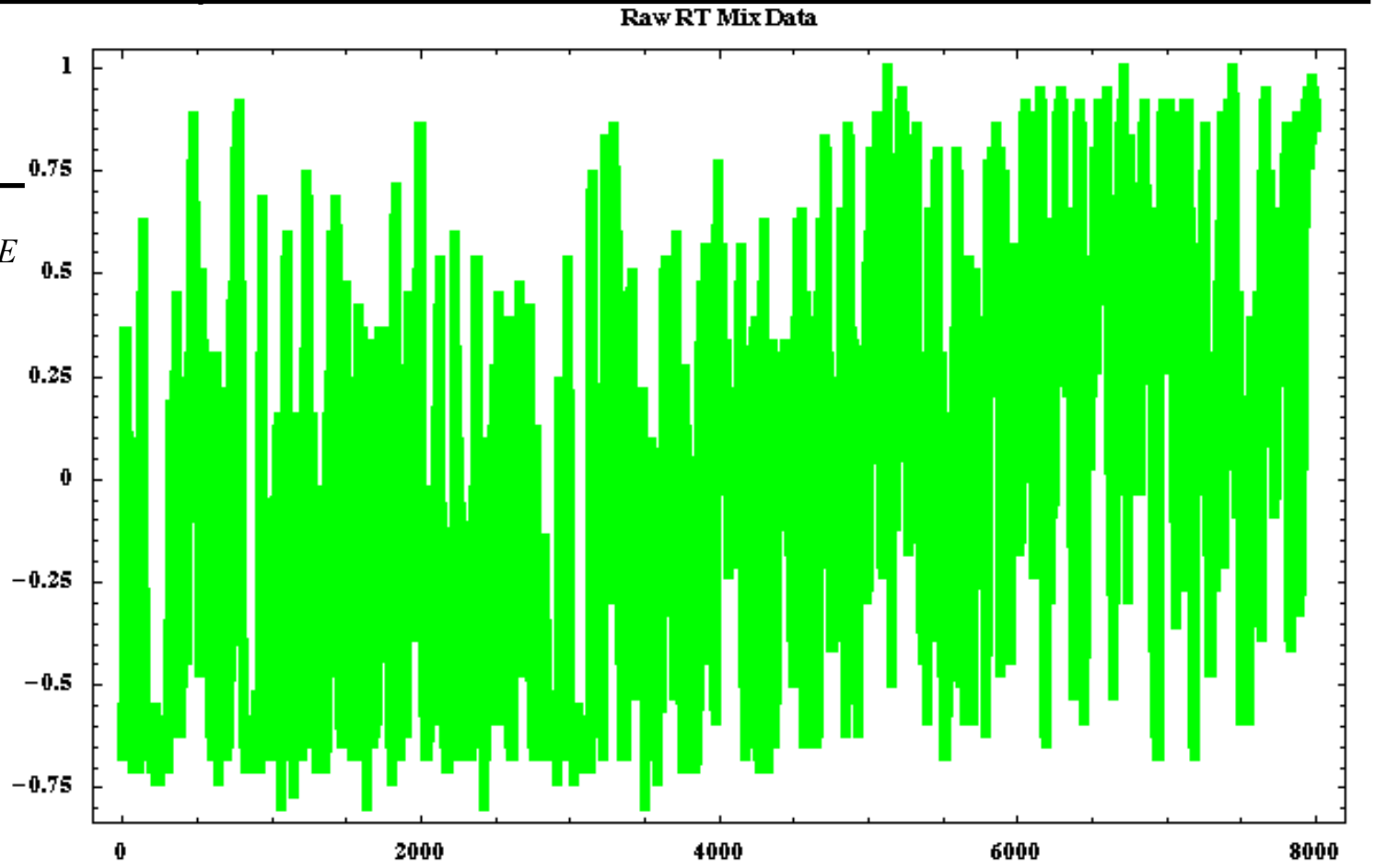

Time, arb. units (Delta t=0.012 sec, Sampling Rate = 85 Hz)

The Faded and Padded Version of the Data 8192 Points Long

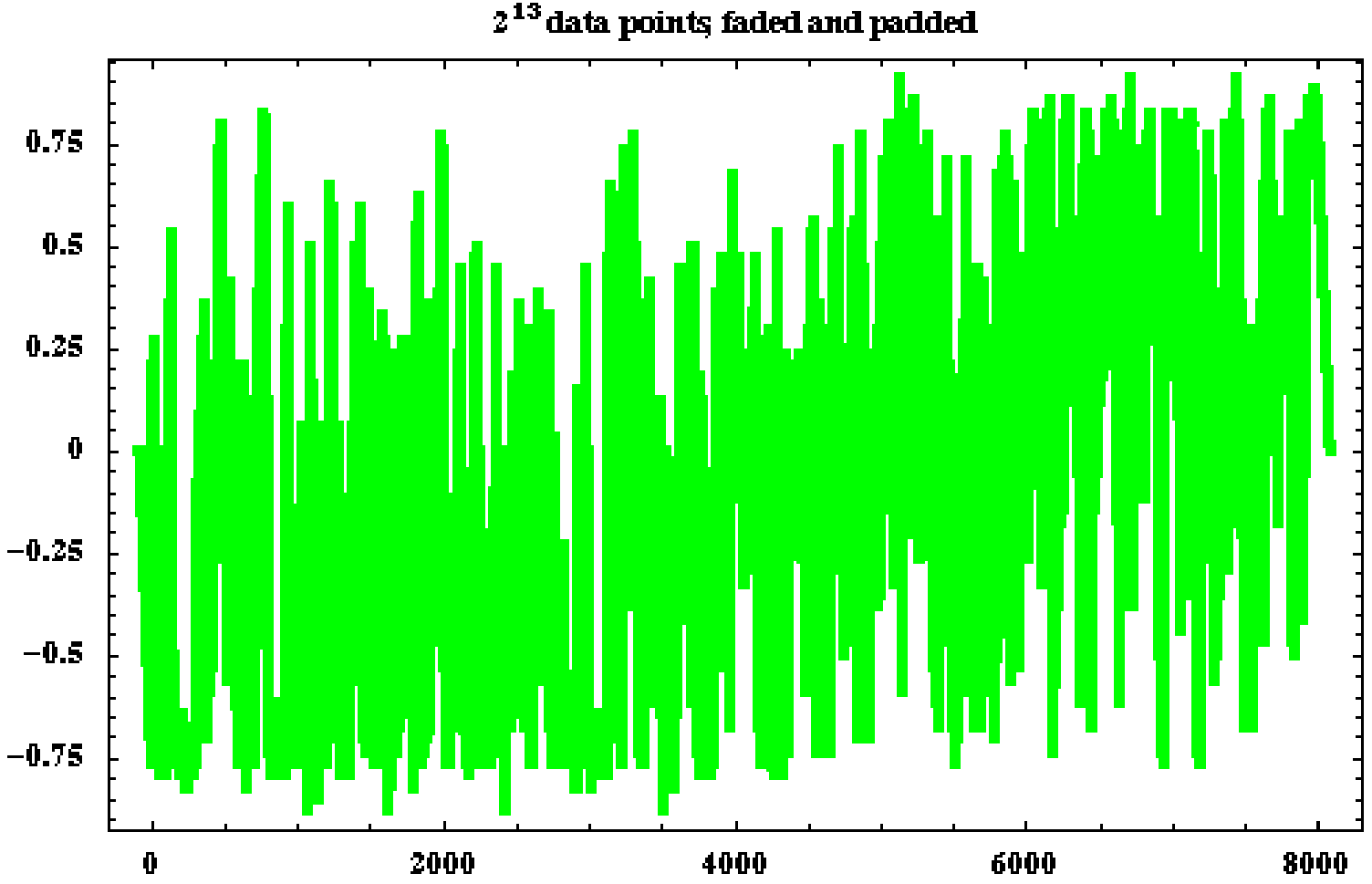

80 pts to fade
16 pts to pad
per side

The Fourier Transform of the RT Mix Data

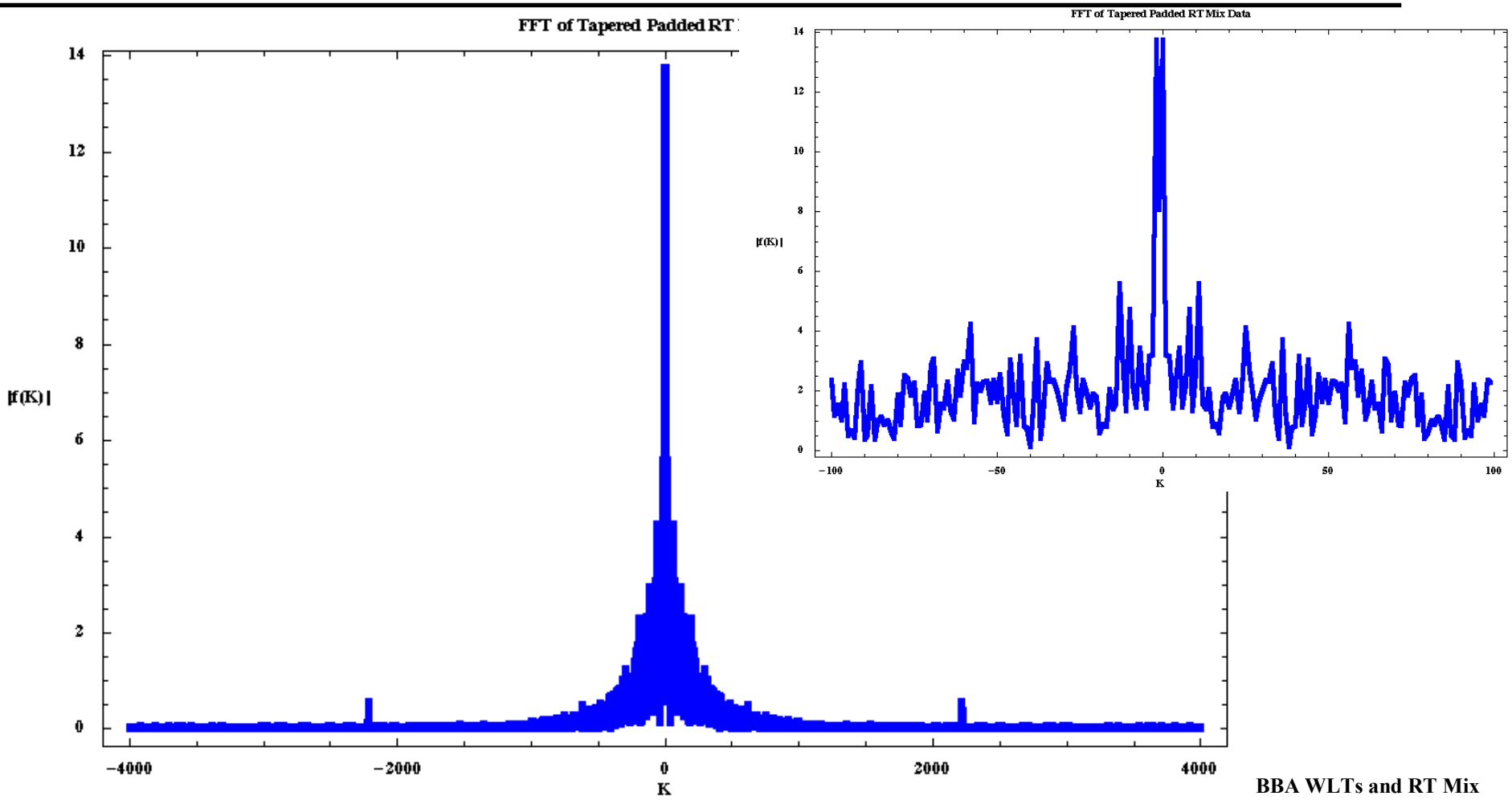

MRDs of the RT Mix Data in 6 Different Daubechies WLT Bases

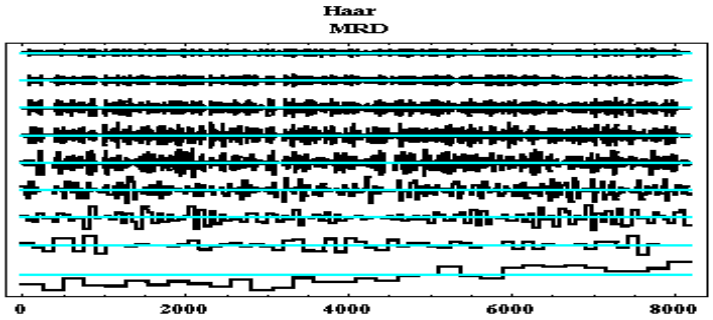

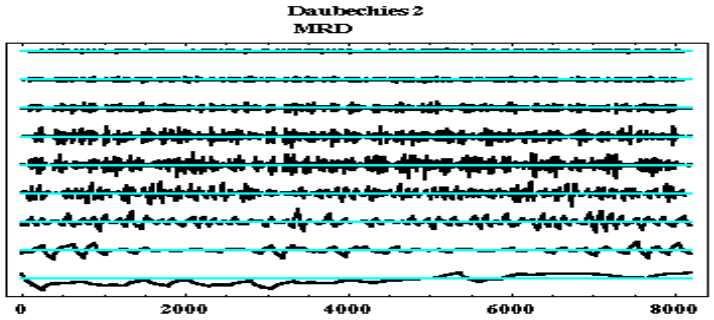

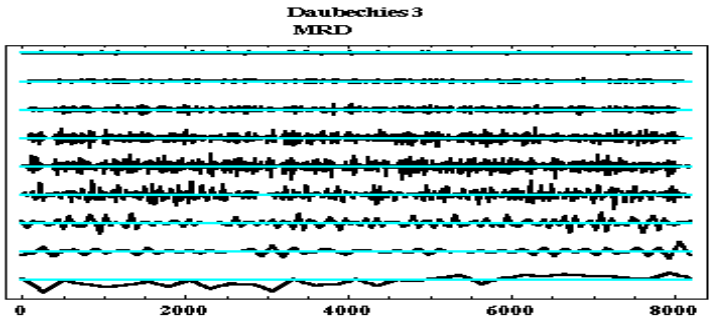

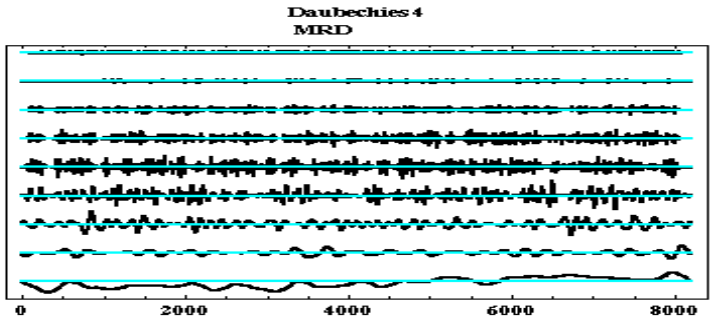

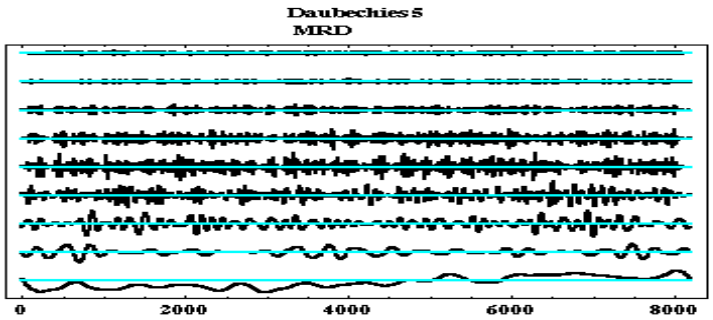

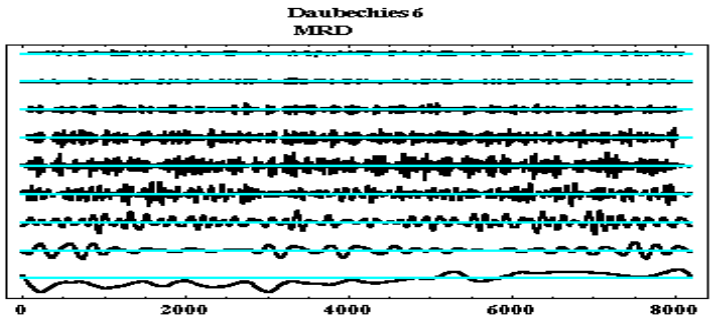

Decay Rate of Largest Coefficient vs Number of Coefficients Kept in 6 Different Daub WLT Decomps

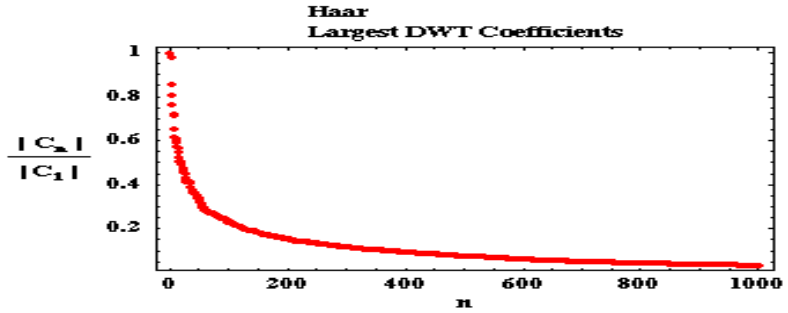

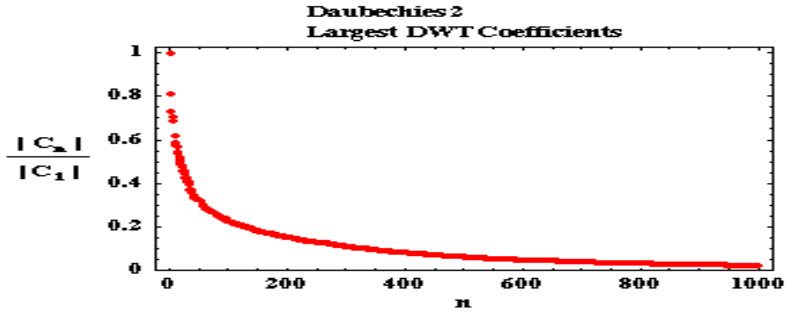

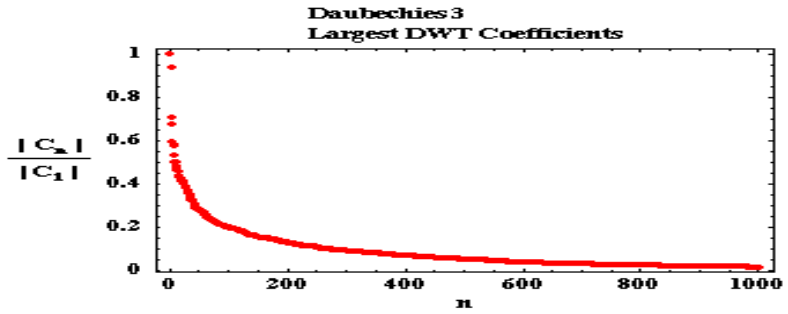

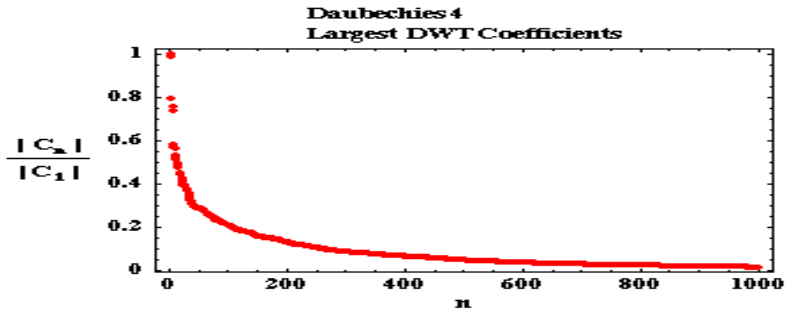

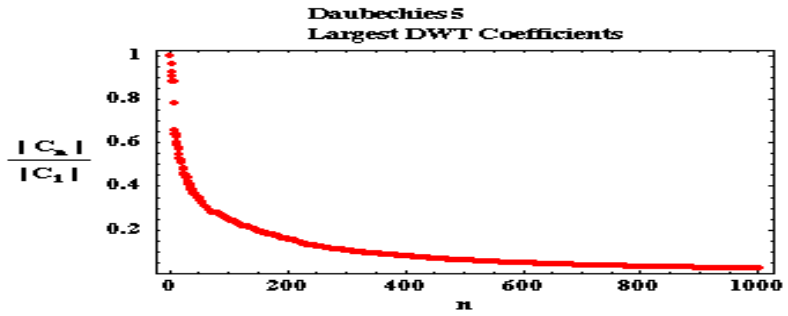

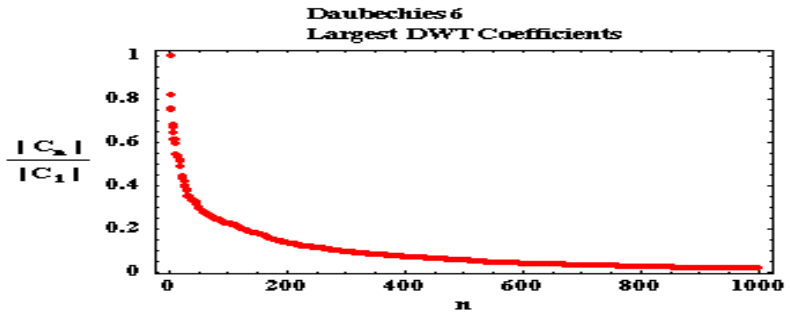

Energy Accumulation Rate in Coefficient Space vs # of WLTs Kept in 6 Different Daub Decomps

Polymath Research Inc.

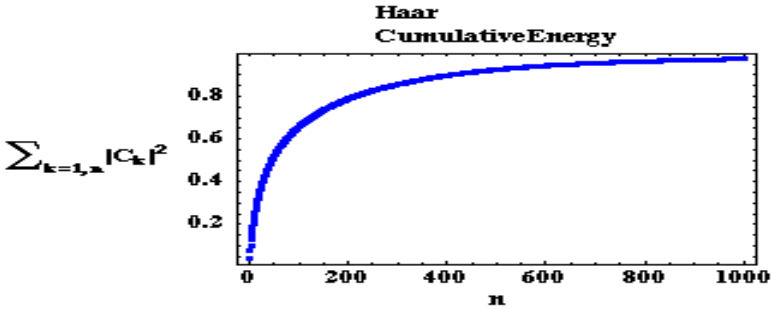

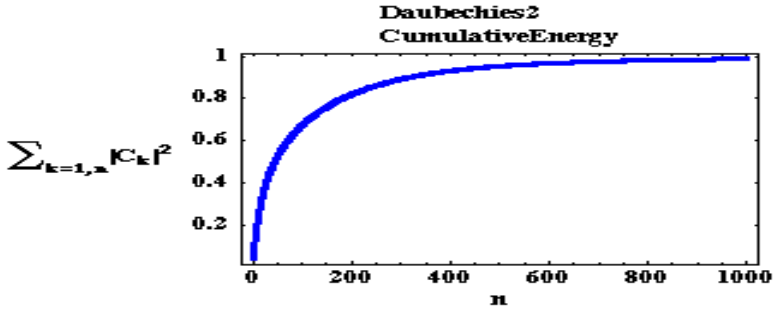

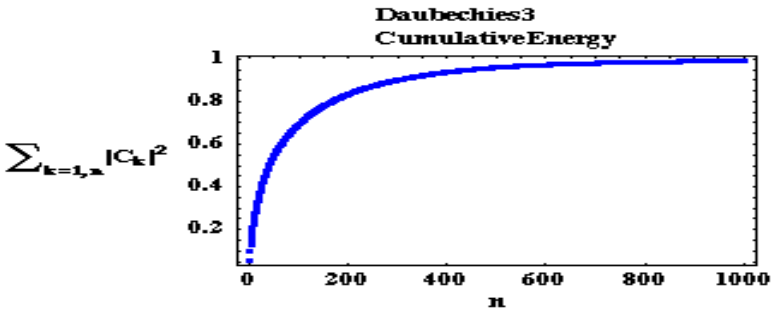

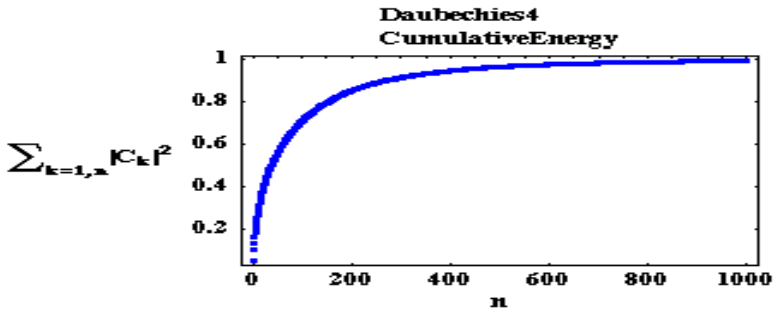

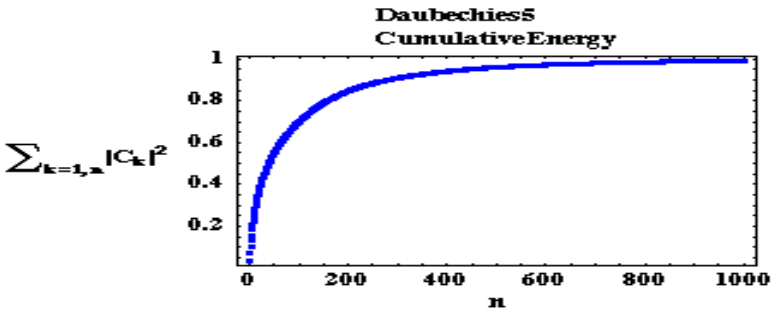

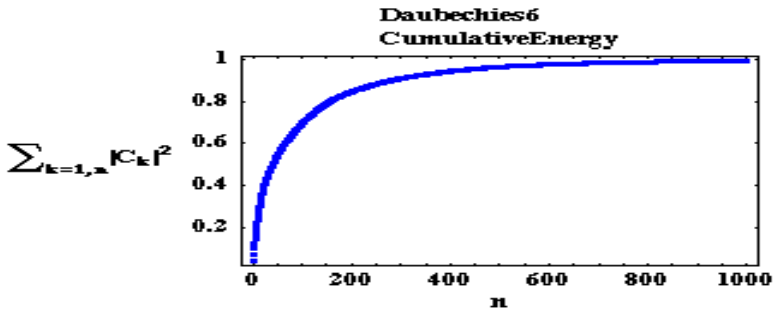

Scaleograms: Waveleters Preferred Way of Judging Tiling in Scale-Translation Space

Polymath Research Inc.

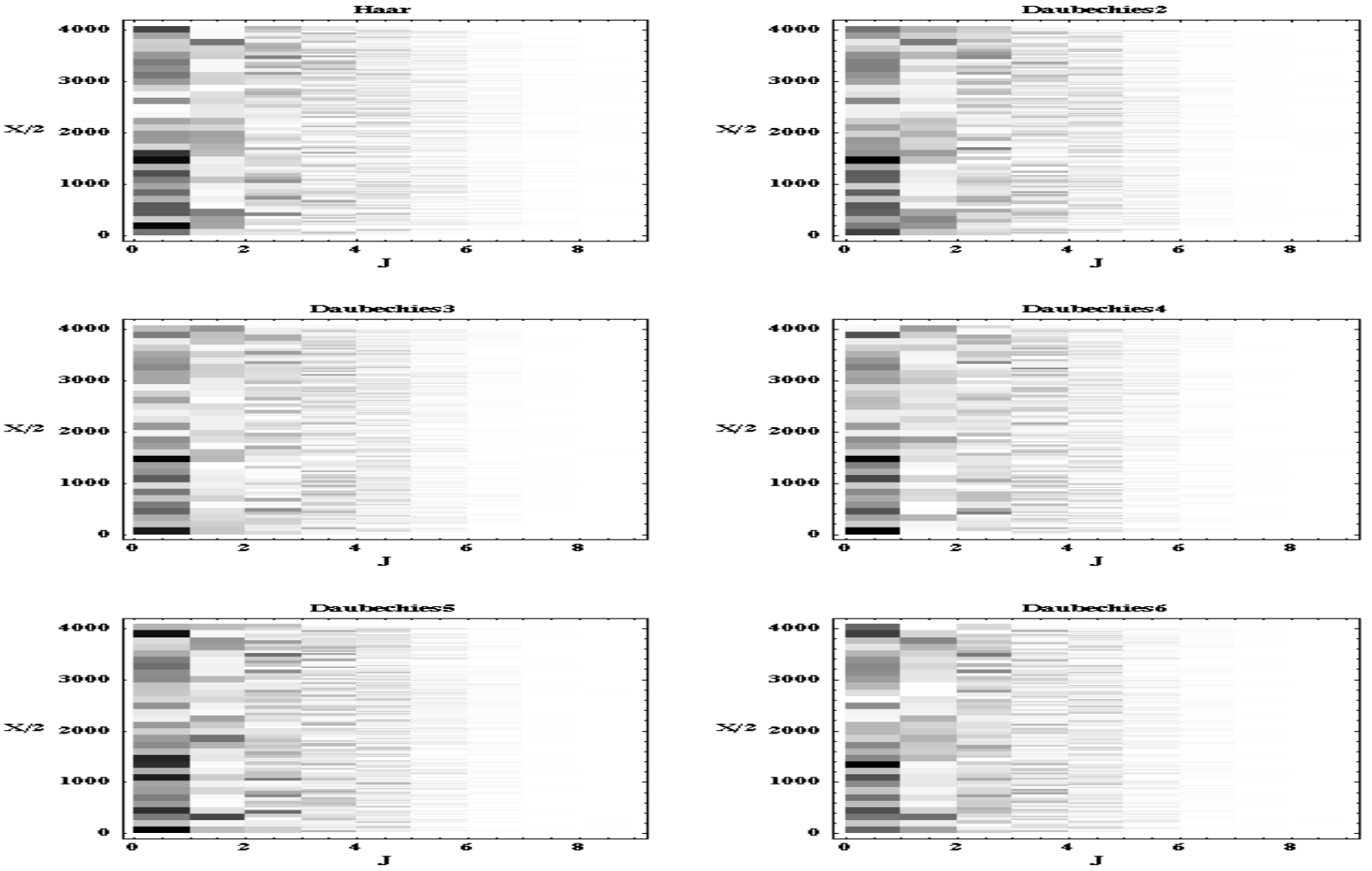

Least Square Error Incurred By Truncating the WLT Series at N of its Largest Coefficients

Polymath Research Inc.

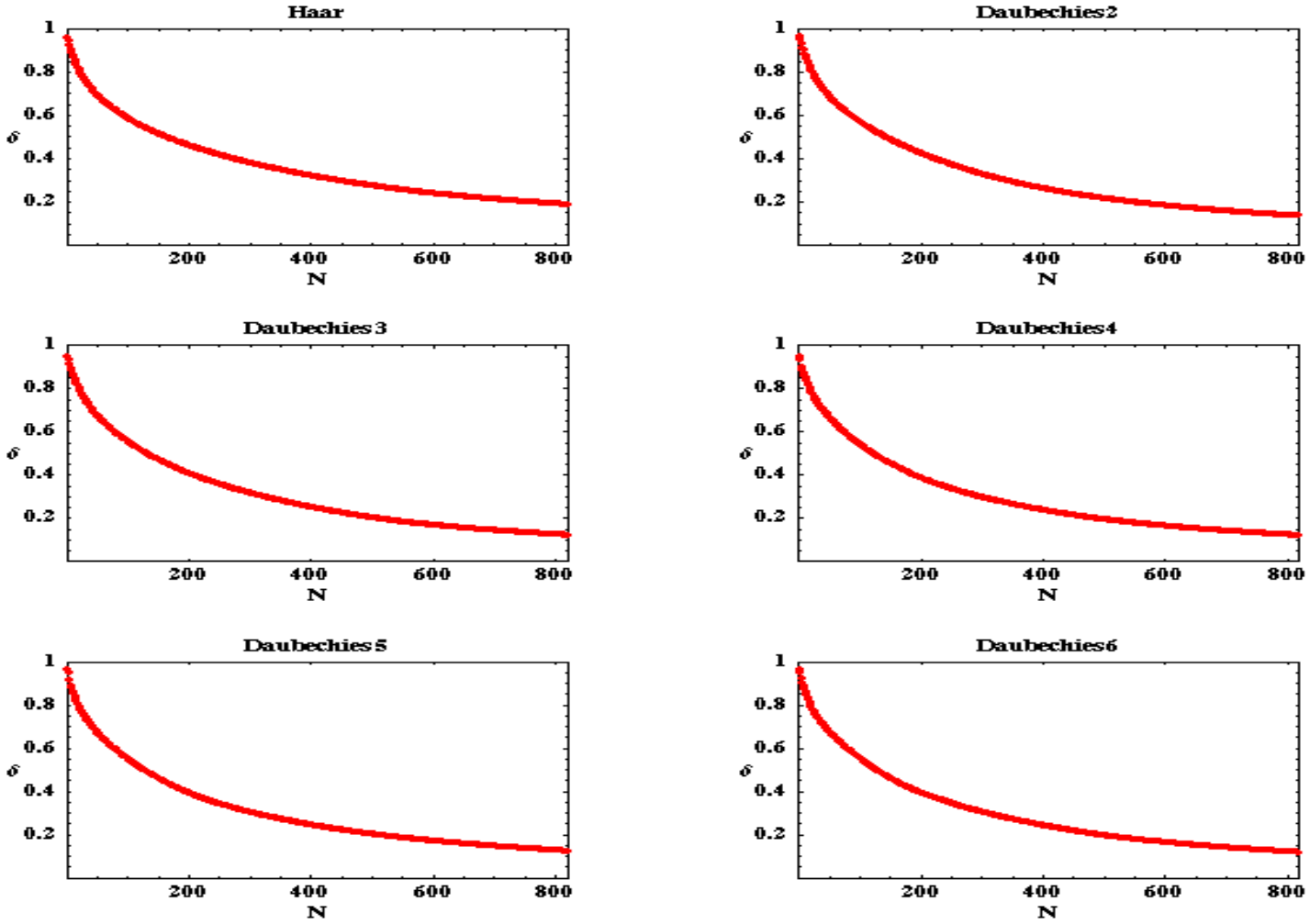

Least Square Error Incurred by Level Thresholding the DWT

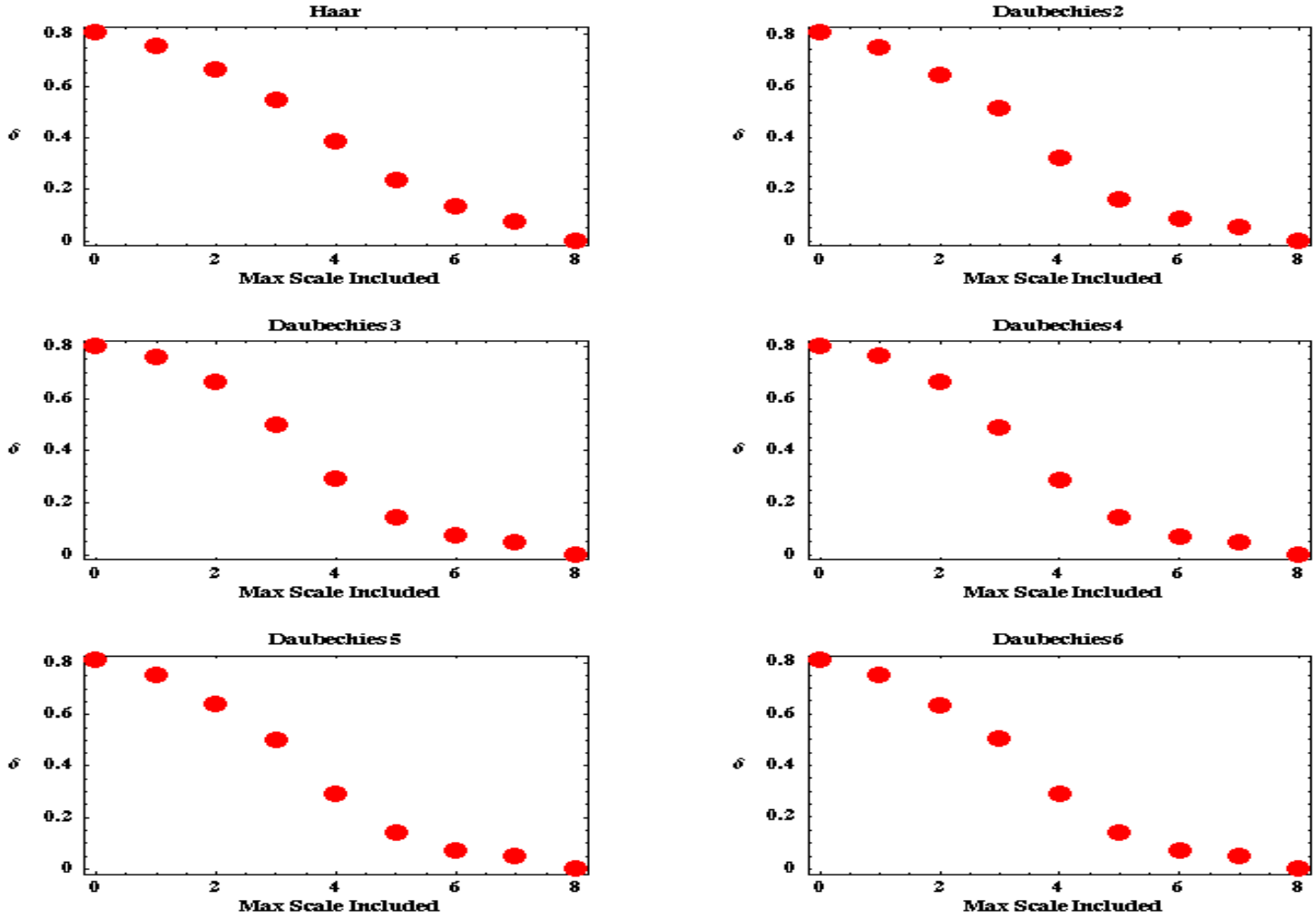

Daubechies 5 Does Much Better than Haar: 5 Quantitative Measures

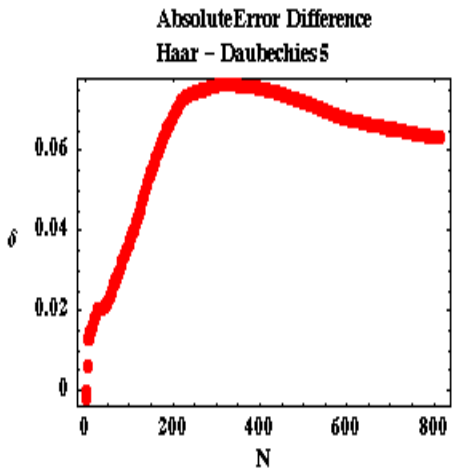

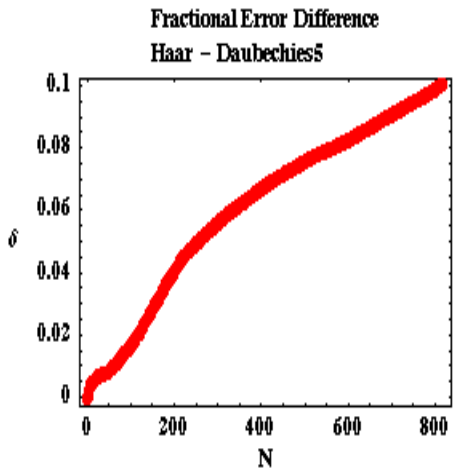

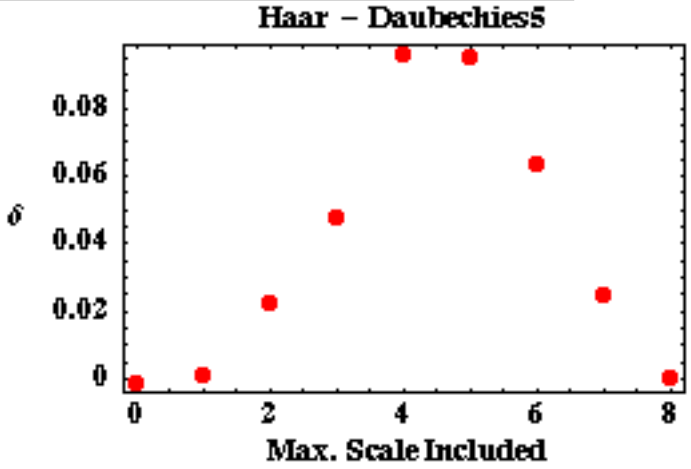

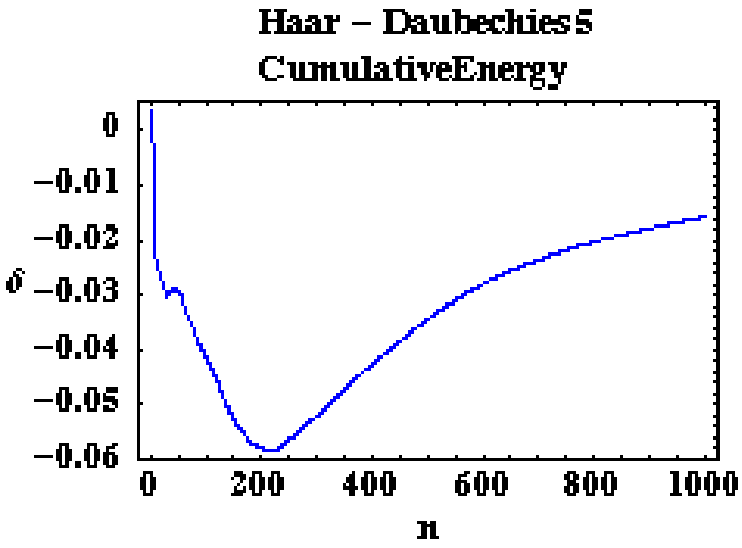

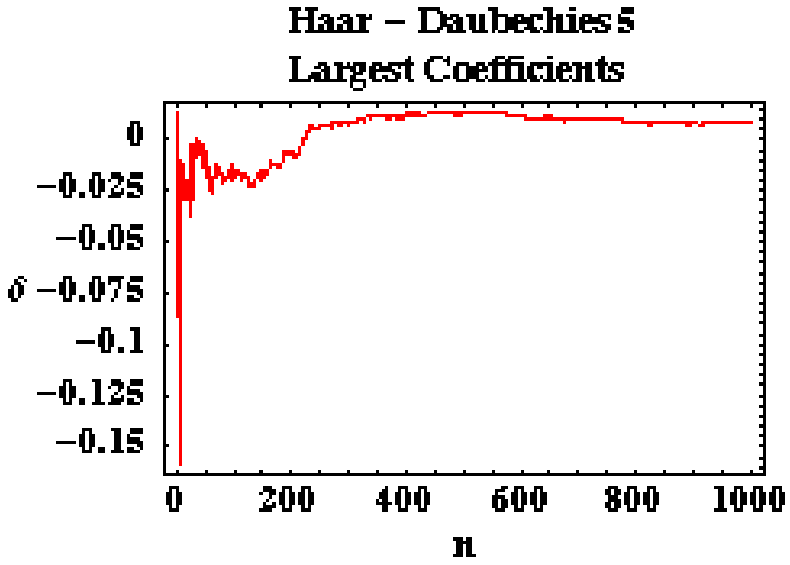

Level by Level Decomposition of the RT Mix Data Using Daub5 WLTs

Polymath Research Inc.

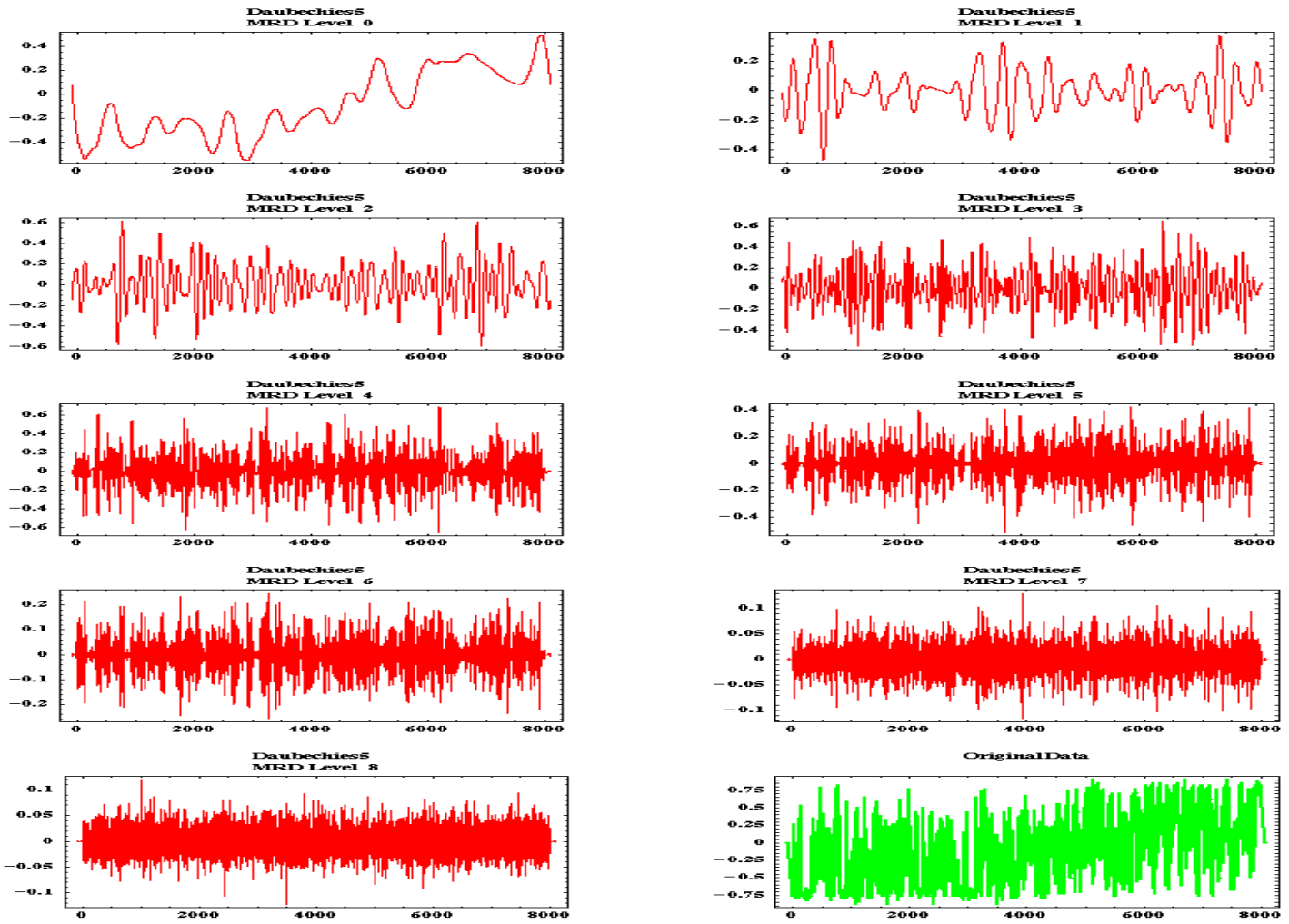

Reconstruction of the Data Using the 5 Largest WLT Coefficients

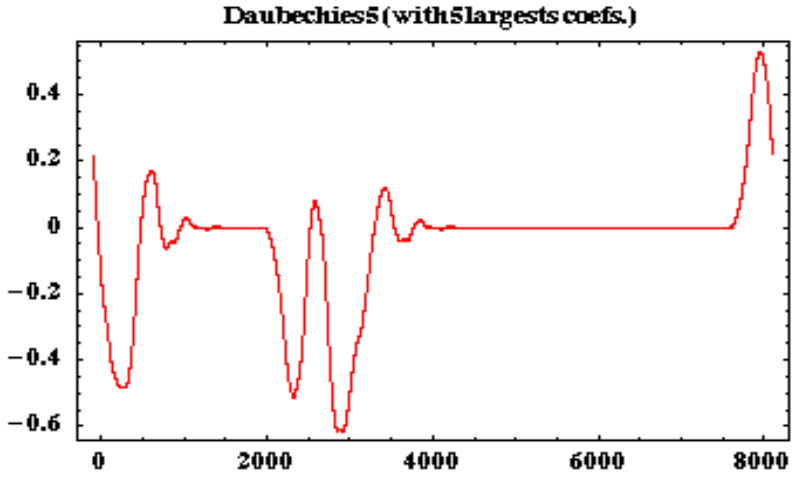

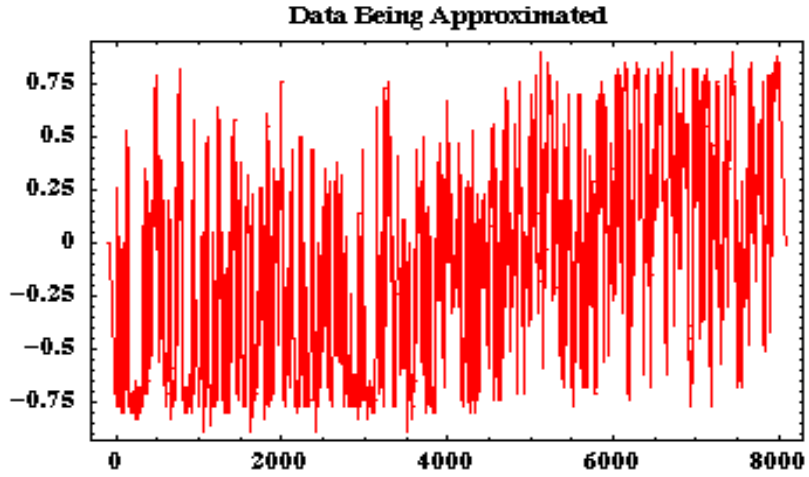

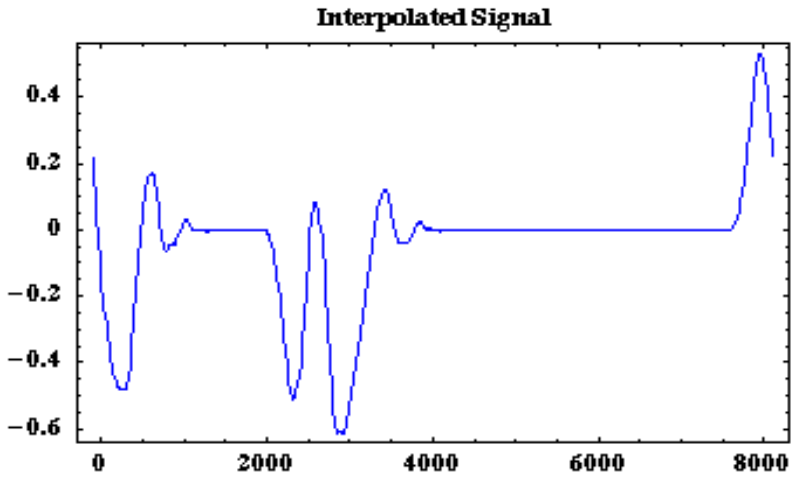

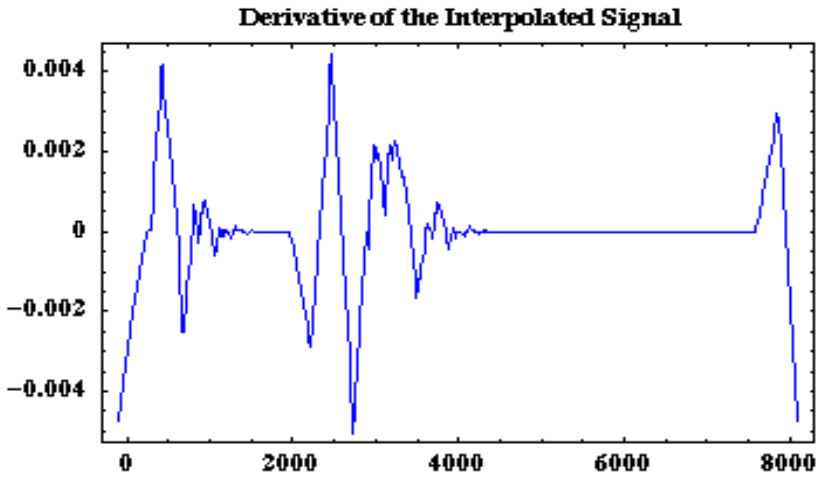

Reconstruction of the Data Using the 10 Largest WLT Coefficients

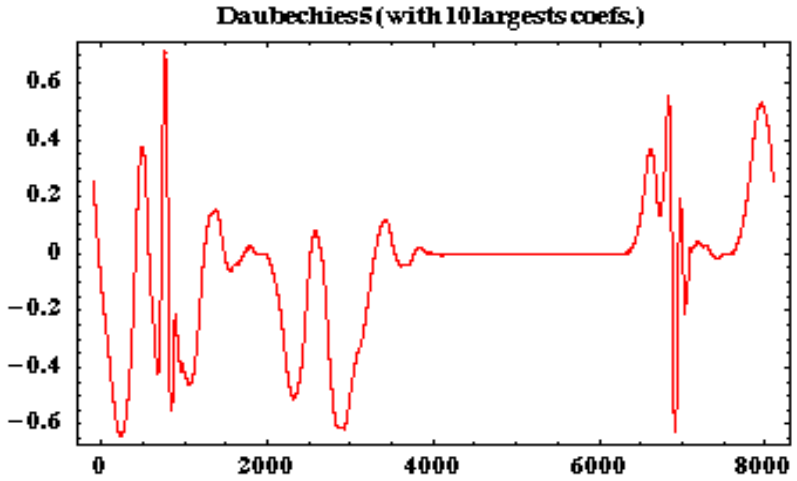

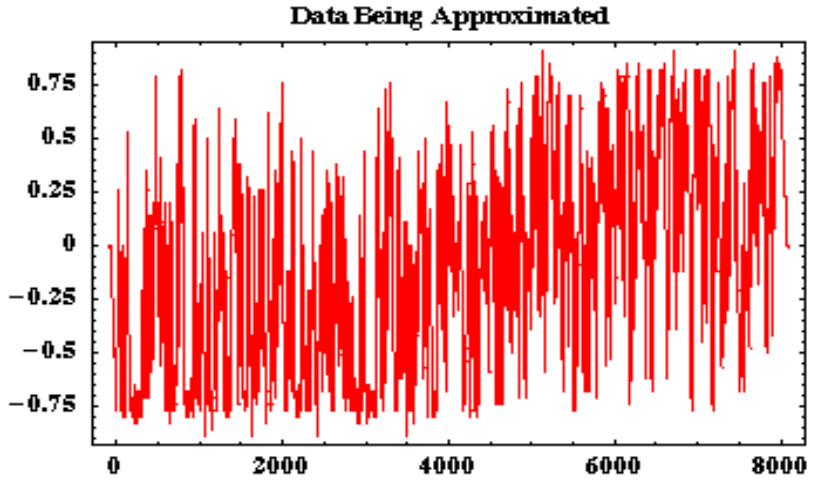

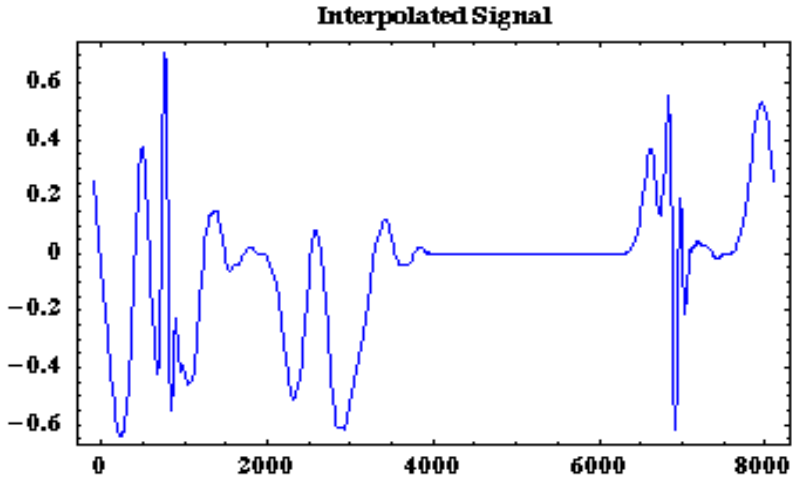

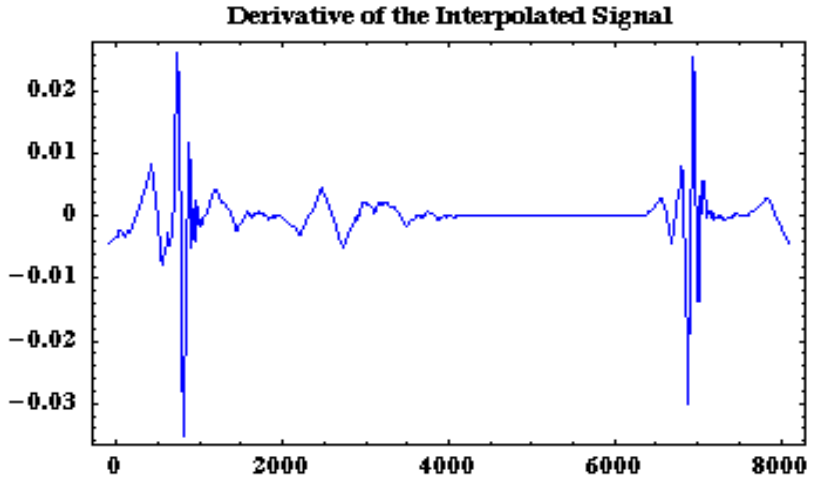

Reconstruction of the Data Using the 15 Largest WLT Coefficients

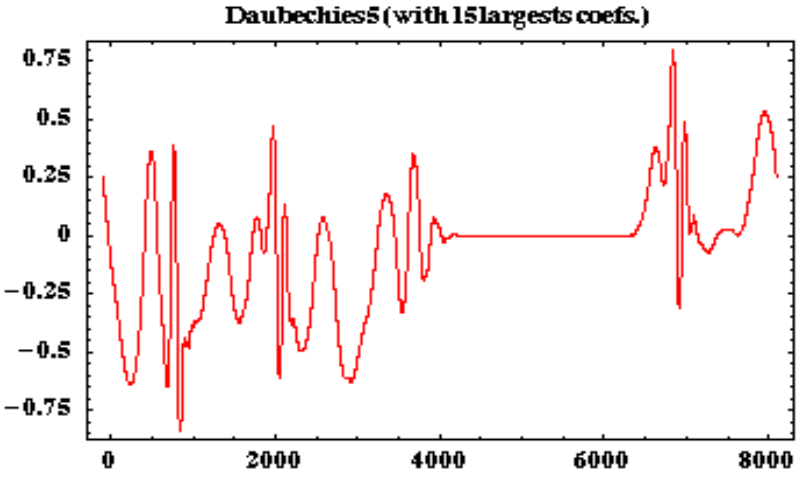

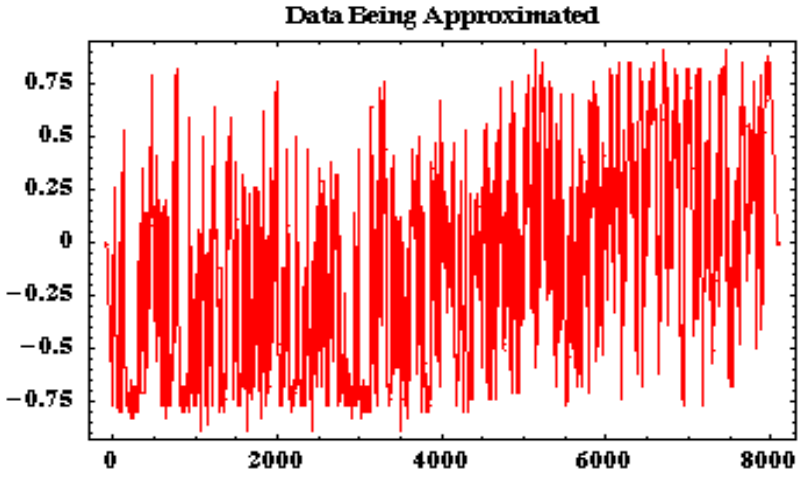

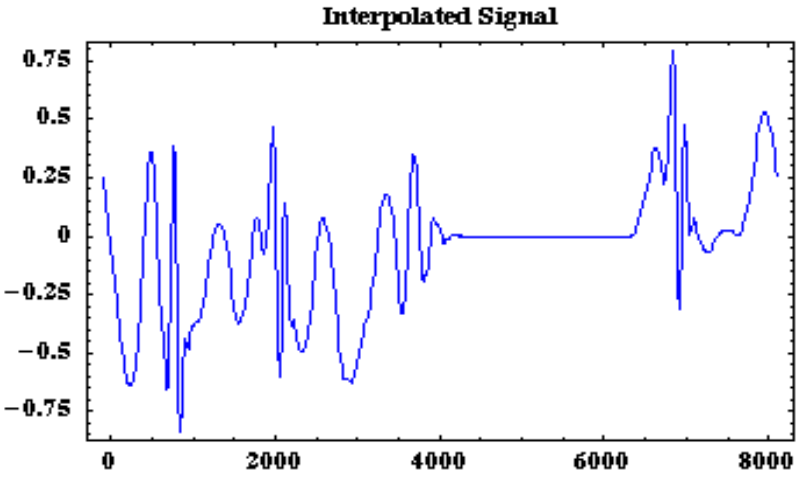

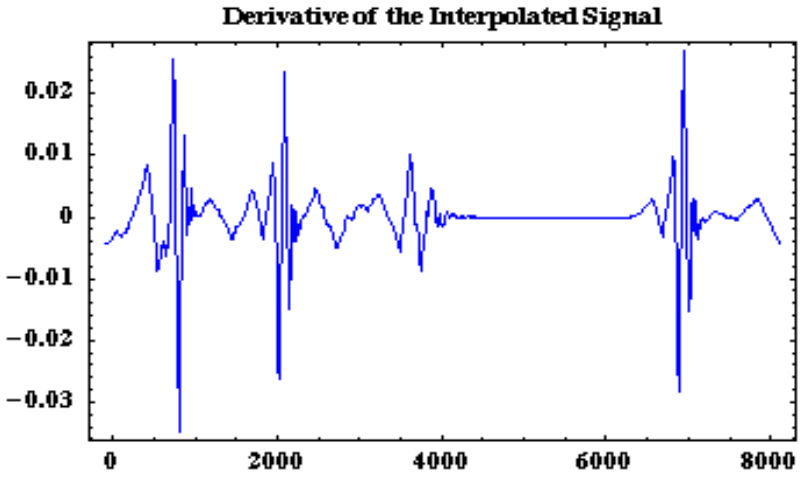

Reconstruction of the Data Using the 20 Largest WLT Coefficients

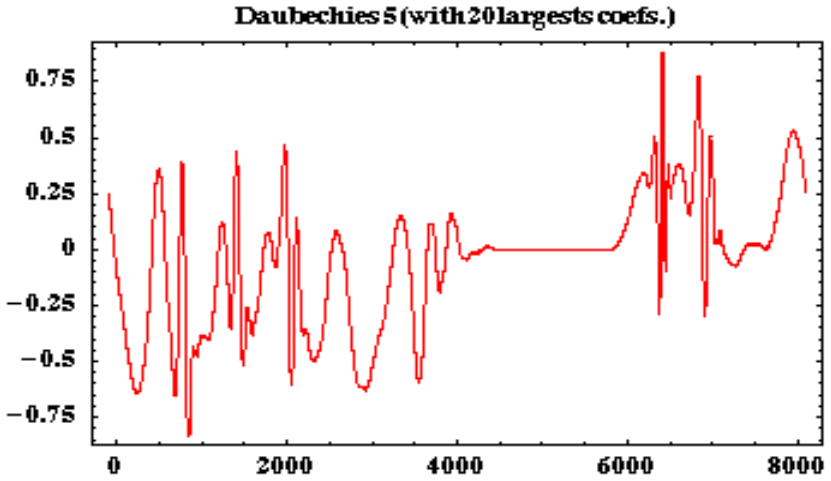

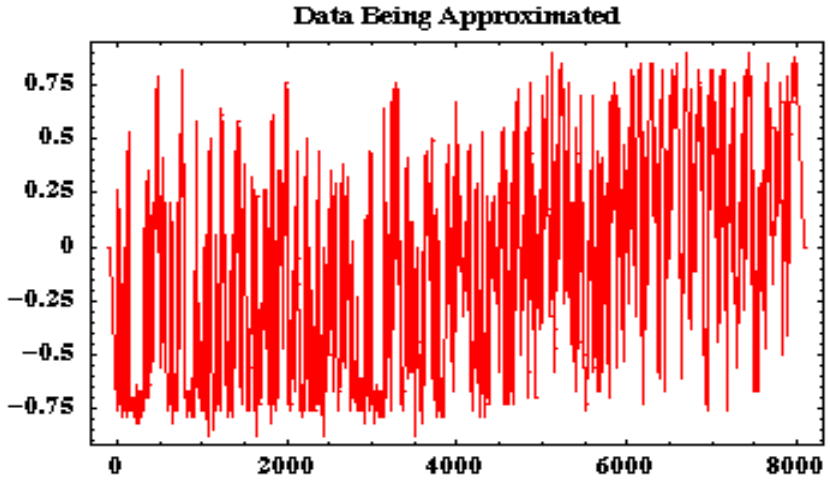

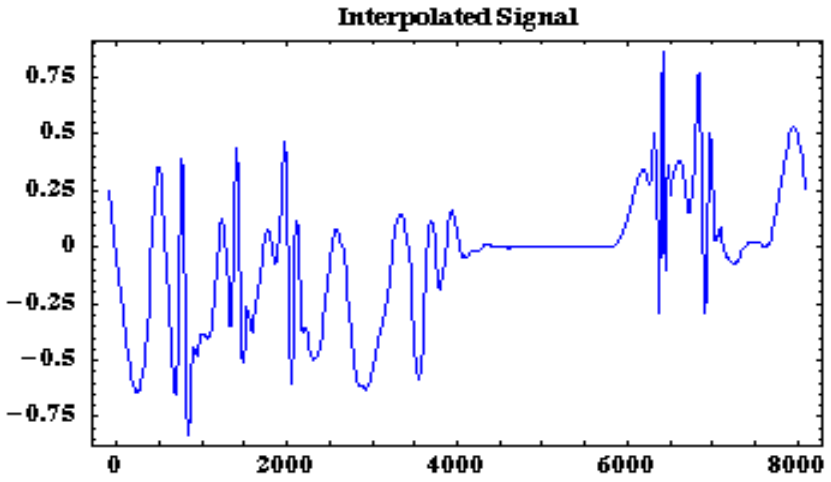

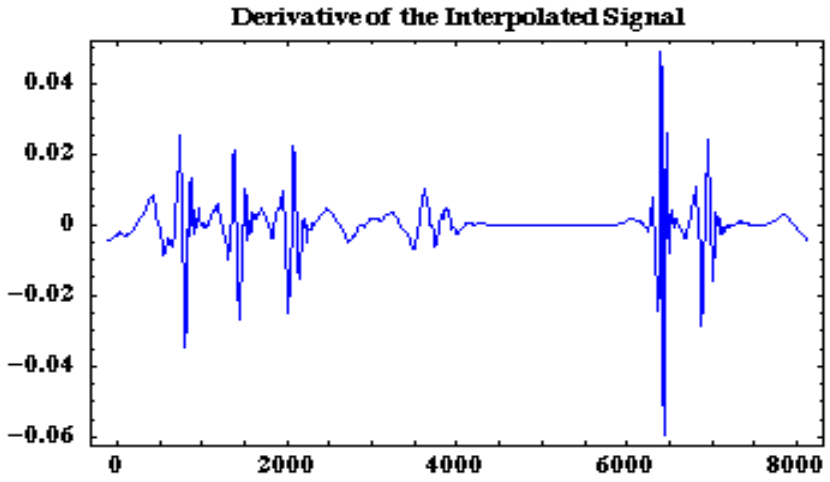

Reconstruction of the Data Using the 30 Largest WLT Coefficients

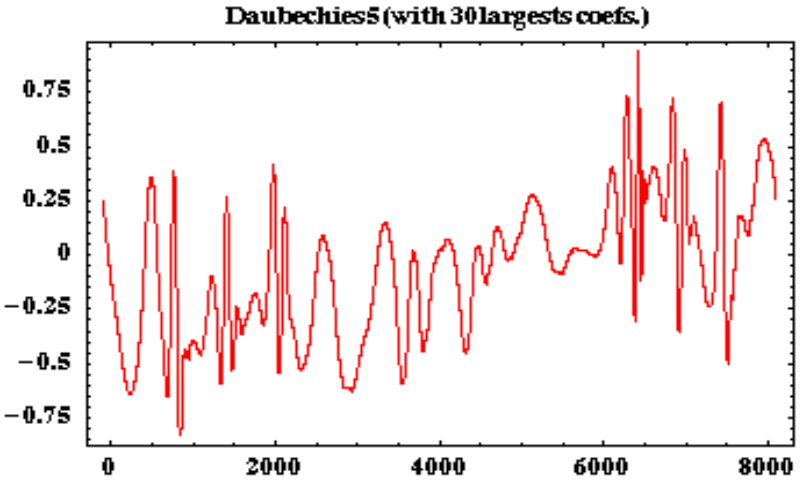

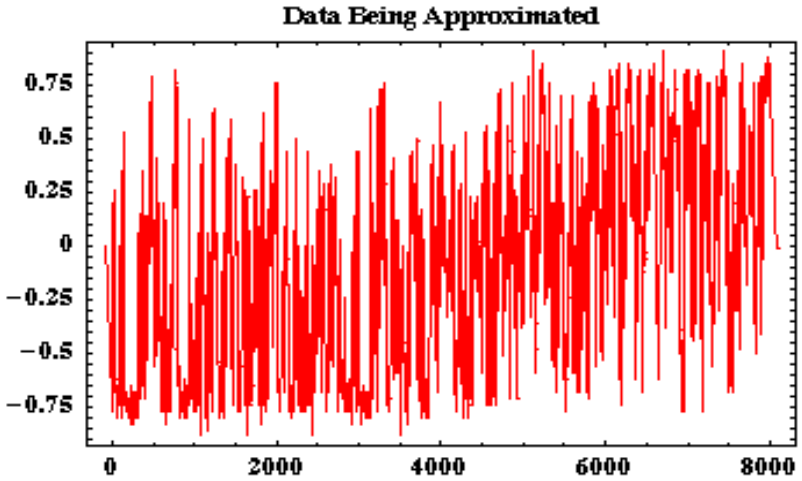

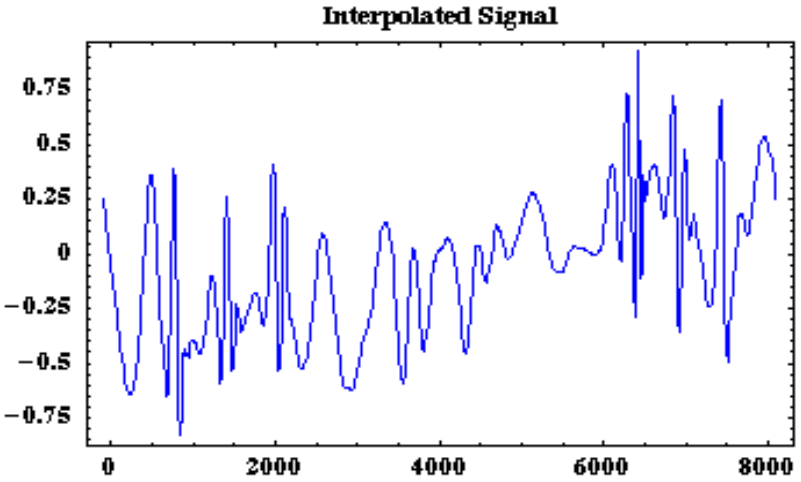

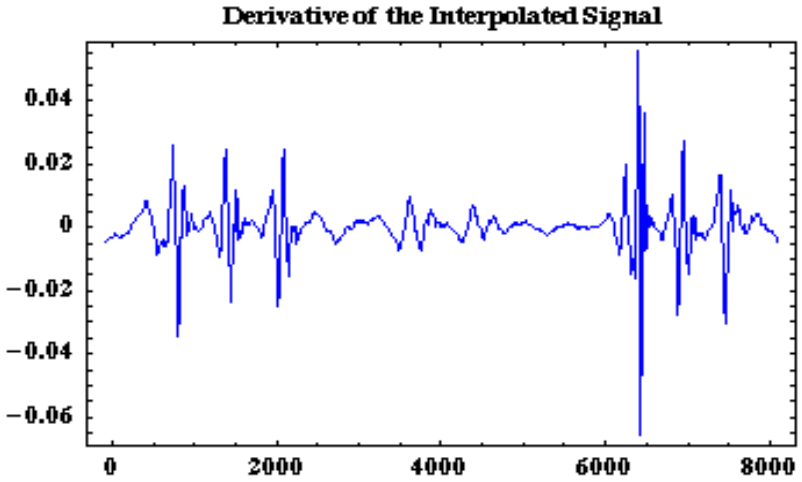

Reconstruction of the Data Using the 50 Largest WLT Coefficients

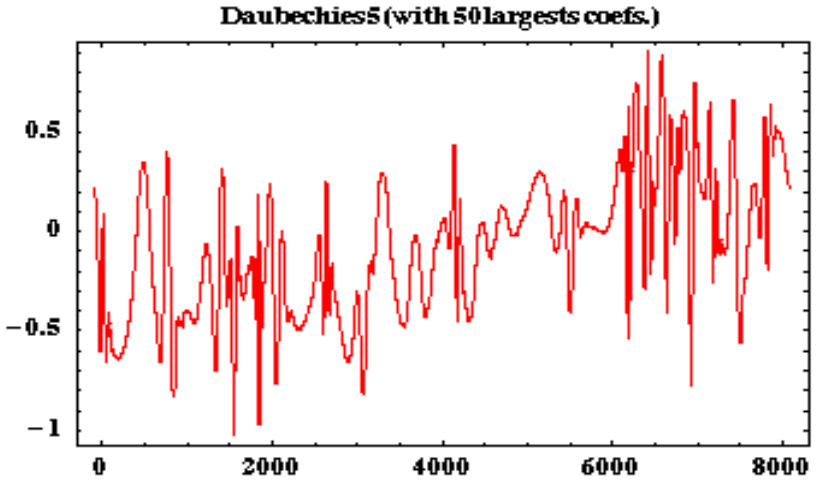

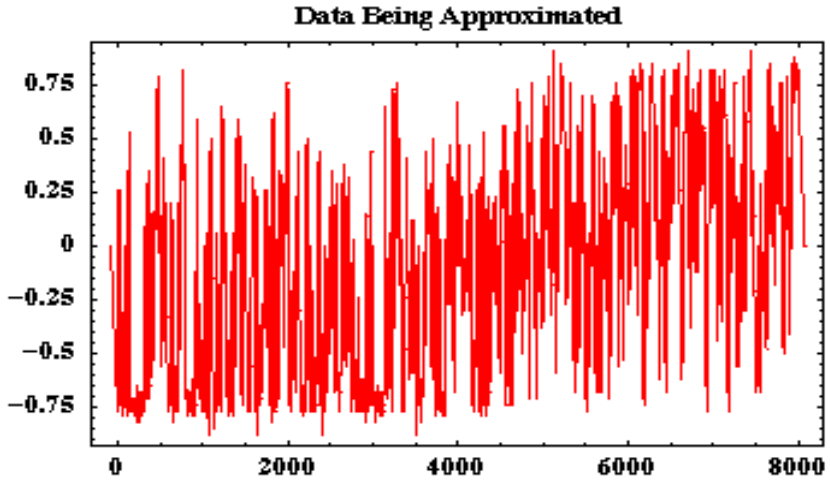

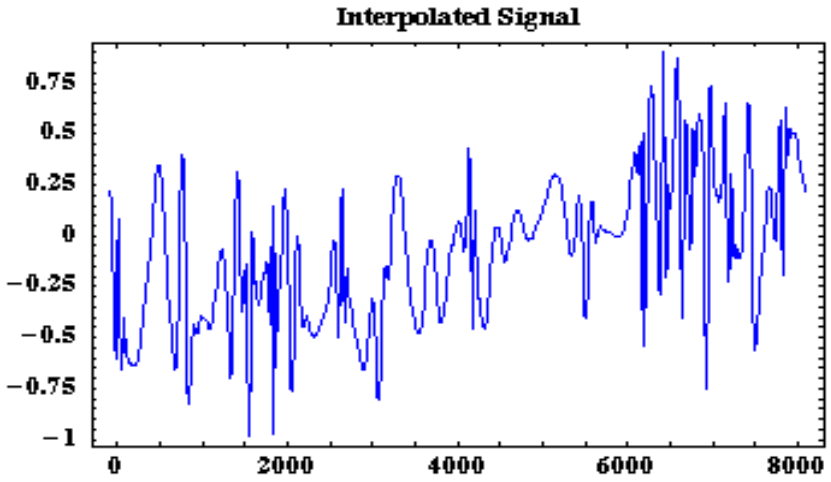

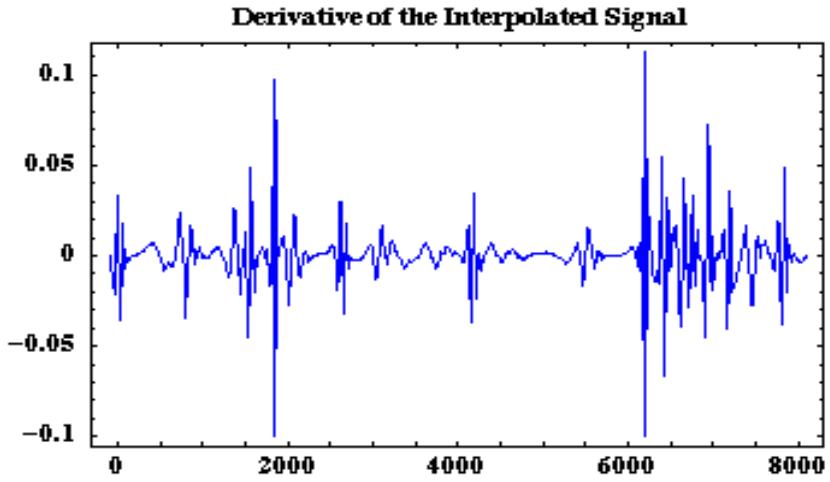

Reconstruction of the Data Using 100 Largest WLT Coefficients

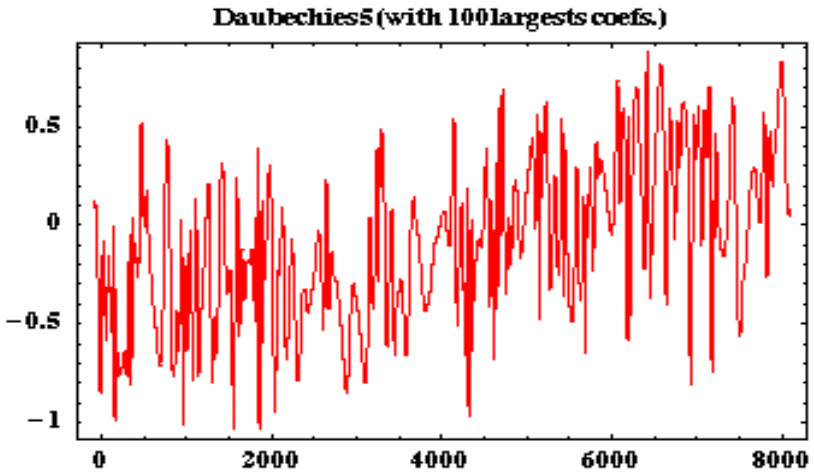

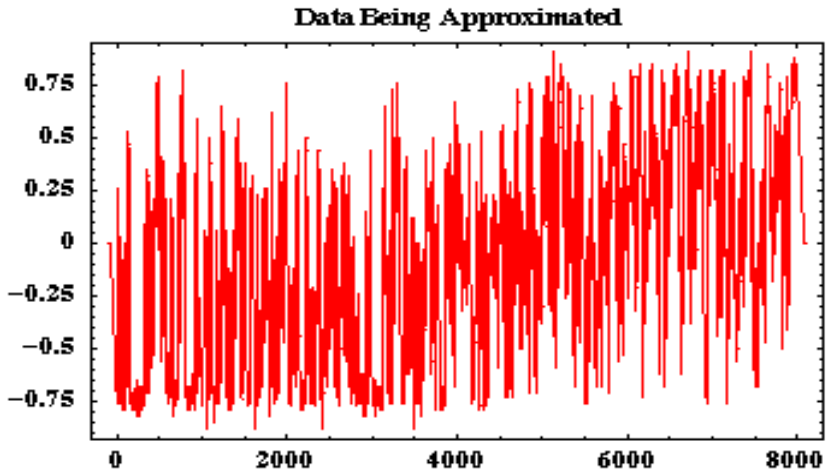

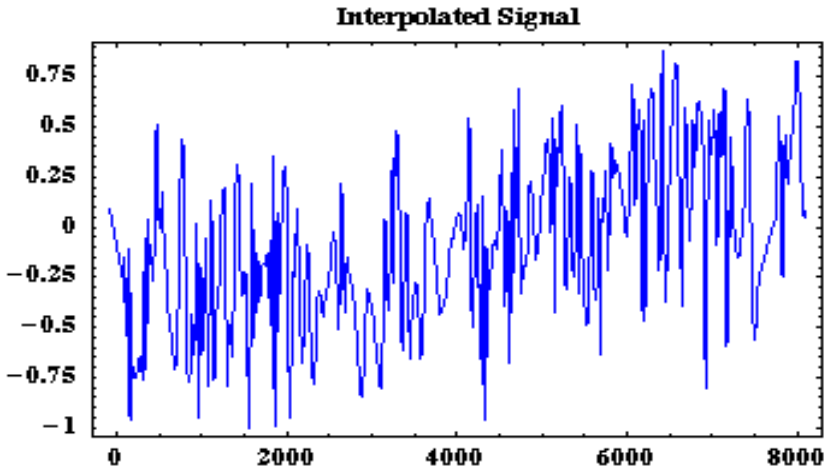

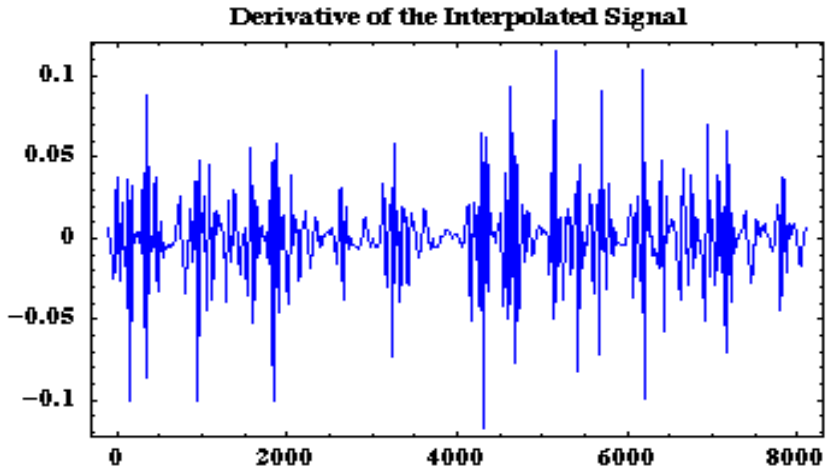

Reconstruction of the Data Using 200 Largest WLT Coefficients

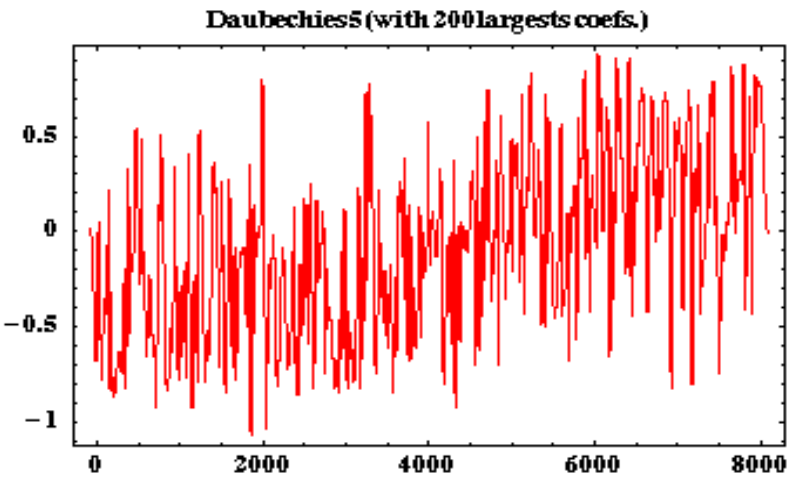

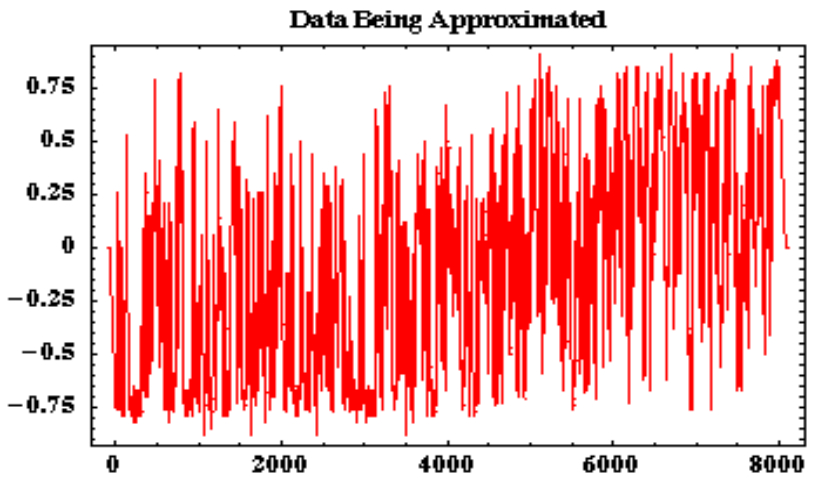

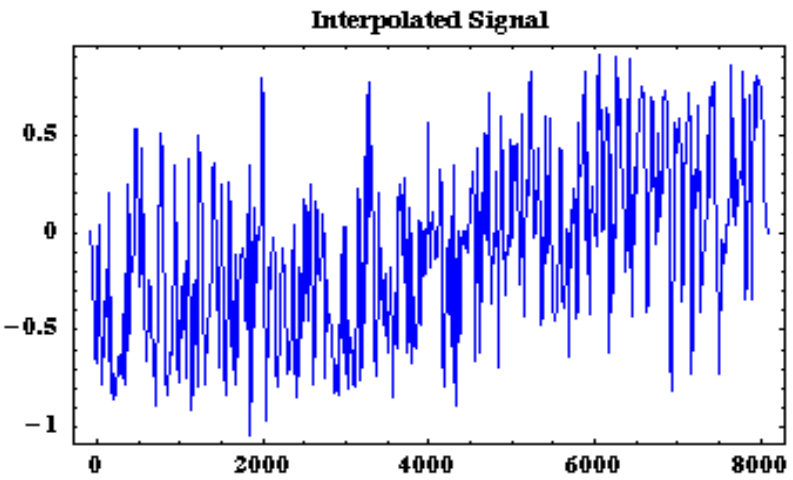

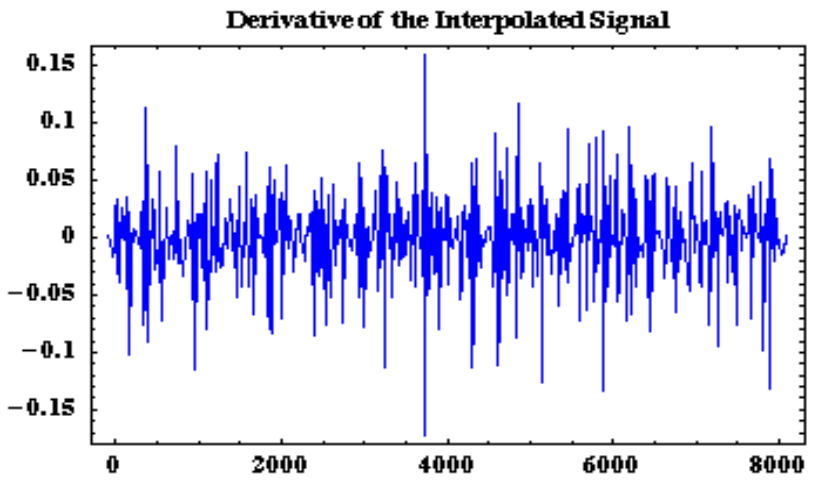

Reconstruction of the Data Using 400 Largest WLT Coefficients

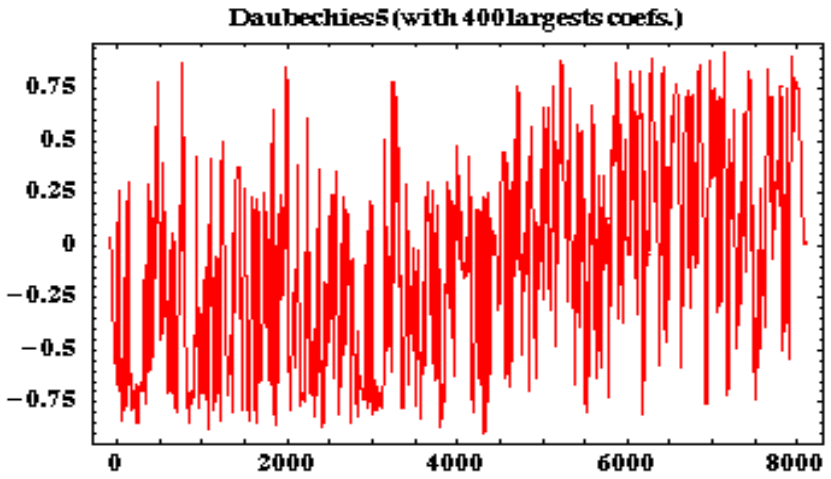

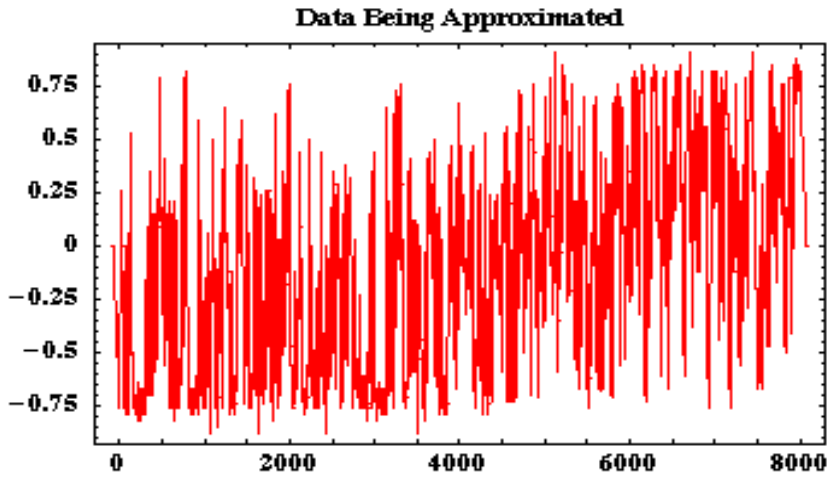

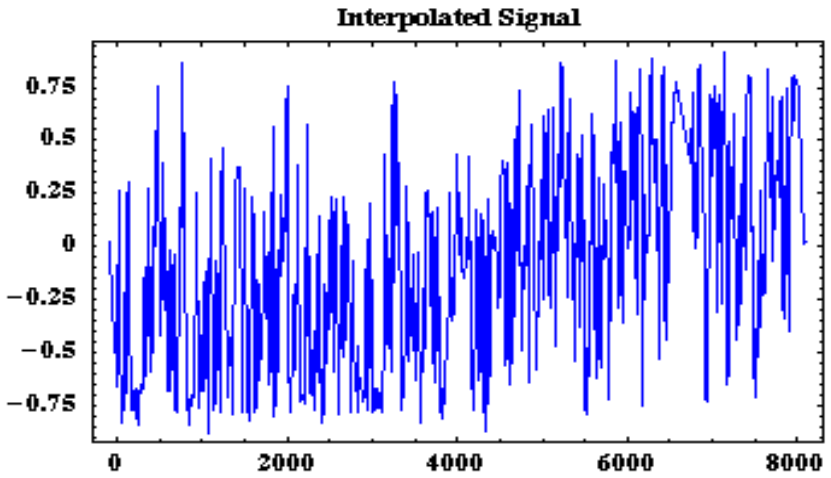

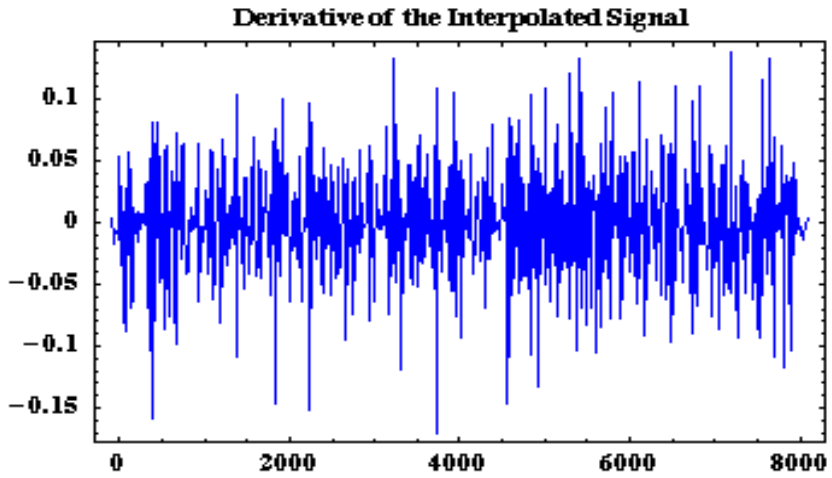

Reconstruction of the Data Using Up to 0.75 times the Largest WLT Coefficient

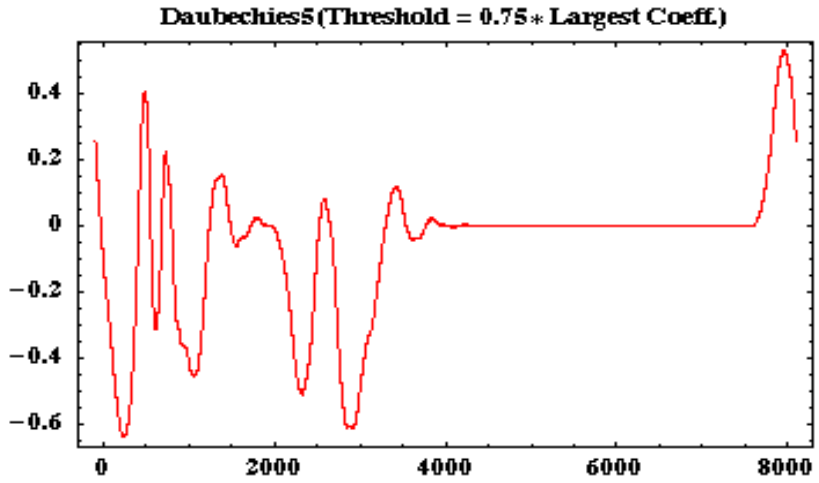

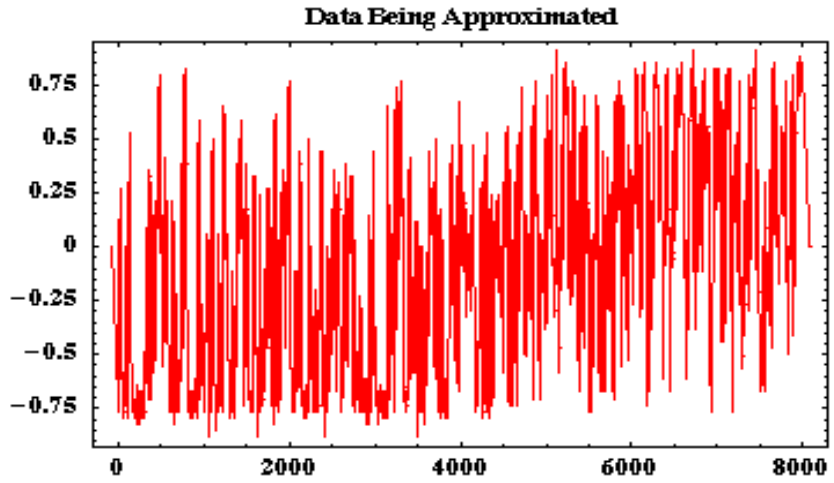

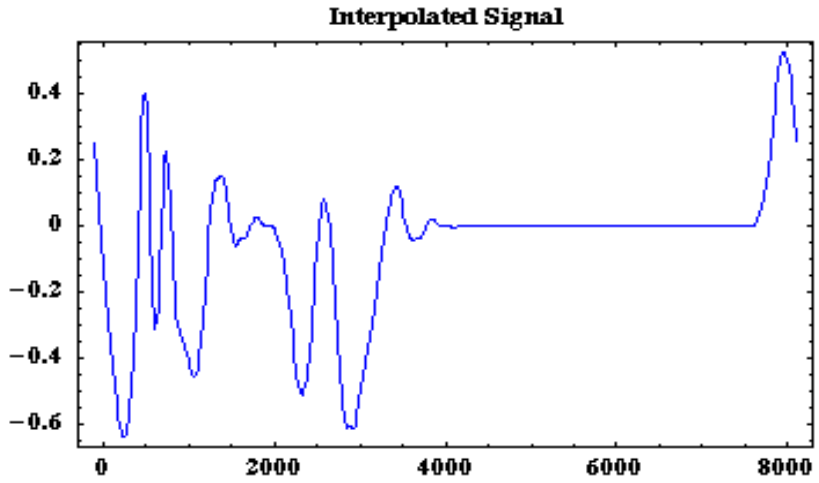

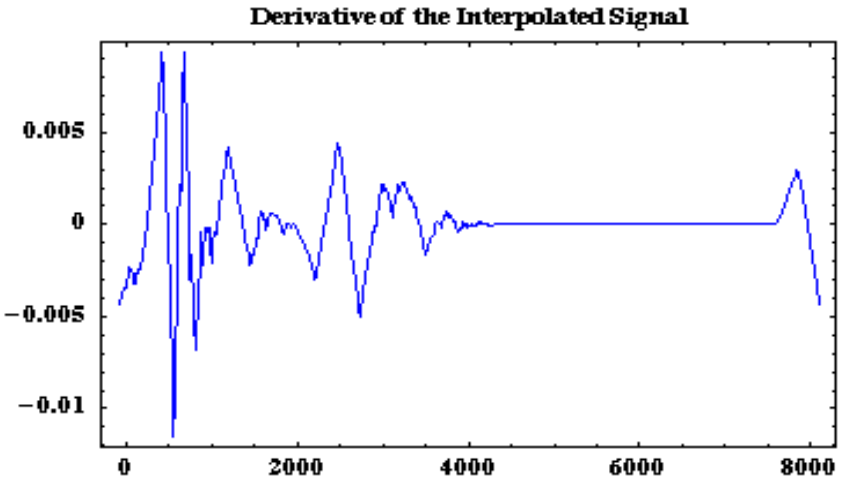

Reconstruction of the Data Using Up to 0.5 times the Largest WLT Coefficient

Polymath Research Inc.

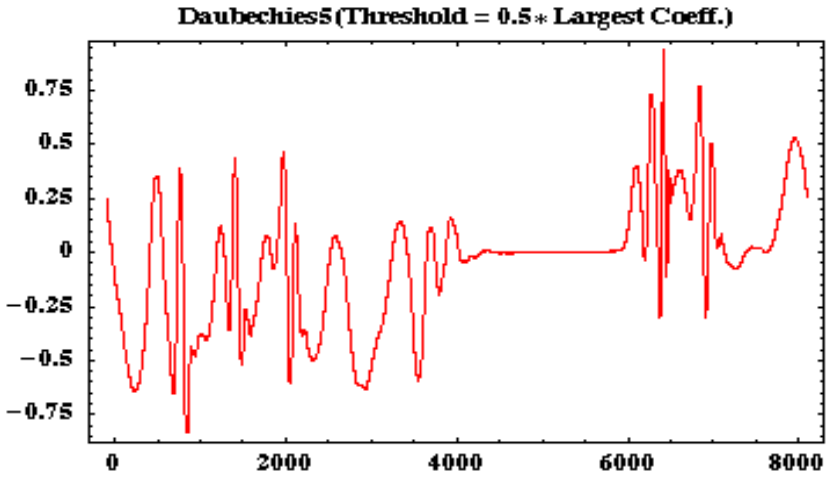

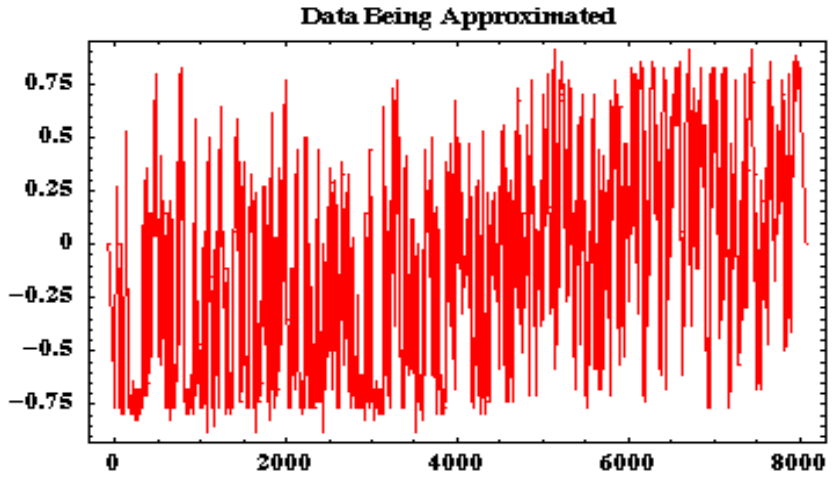

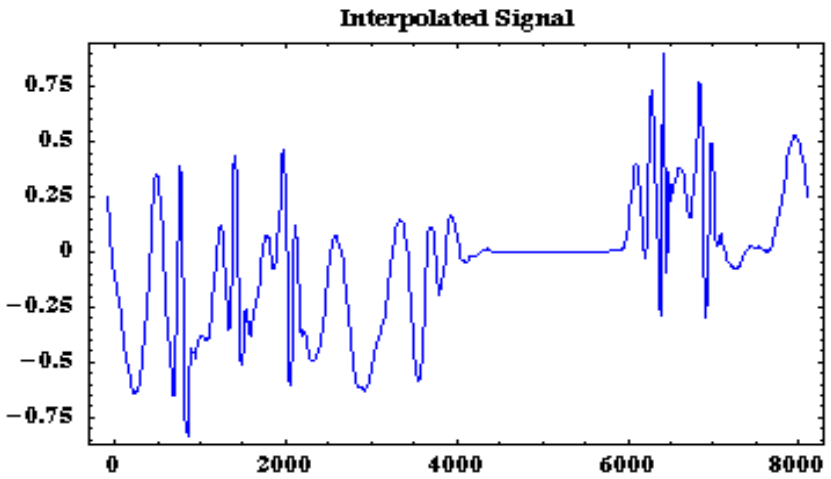

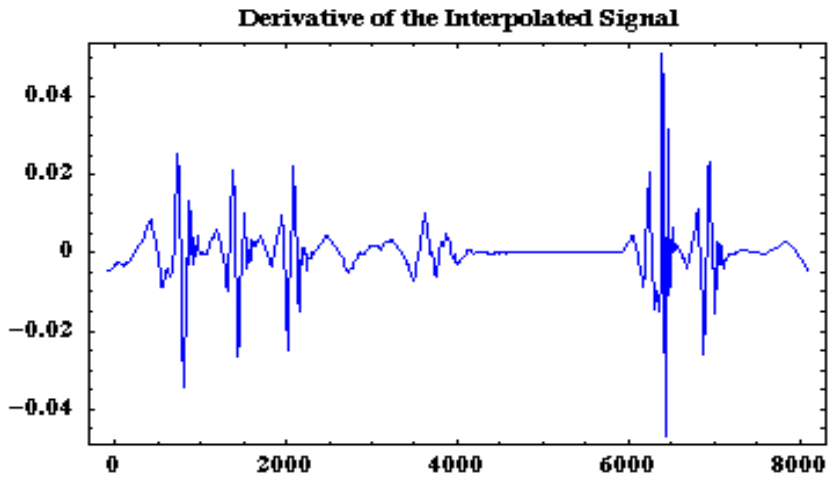

Reconstruction of the Data Using Up to 0.25 times the Largest WLT Coefficient

Polymath Research Inc.

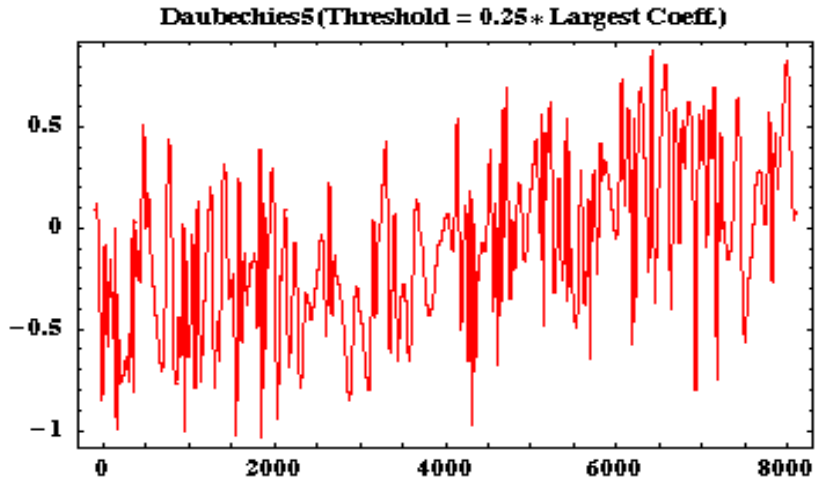

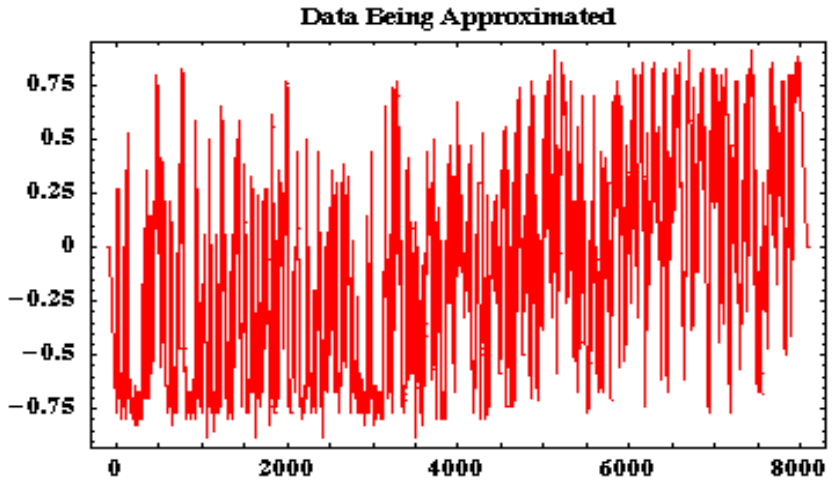

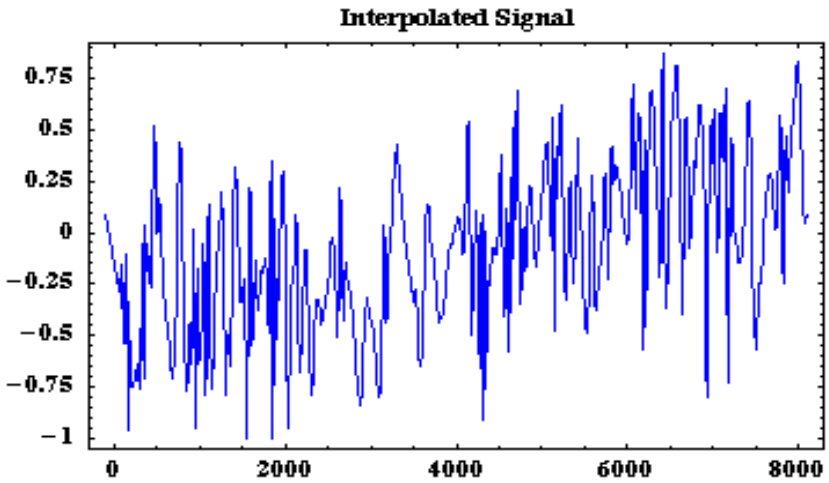

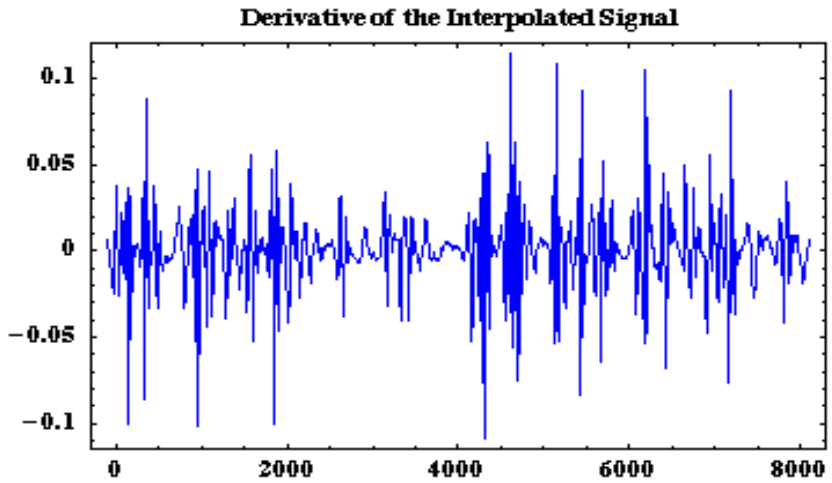

Reconstruction of the Data Using Up to 0.1 times the Largest WLT Coefficient

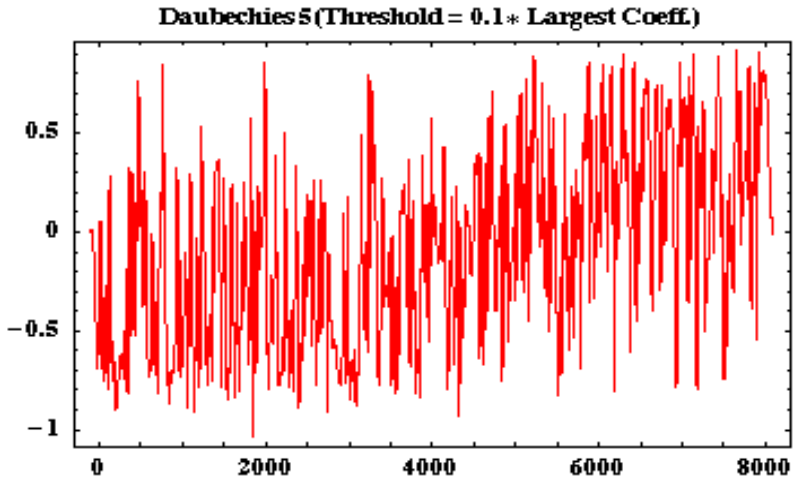

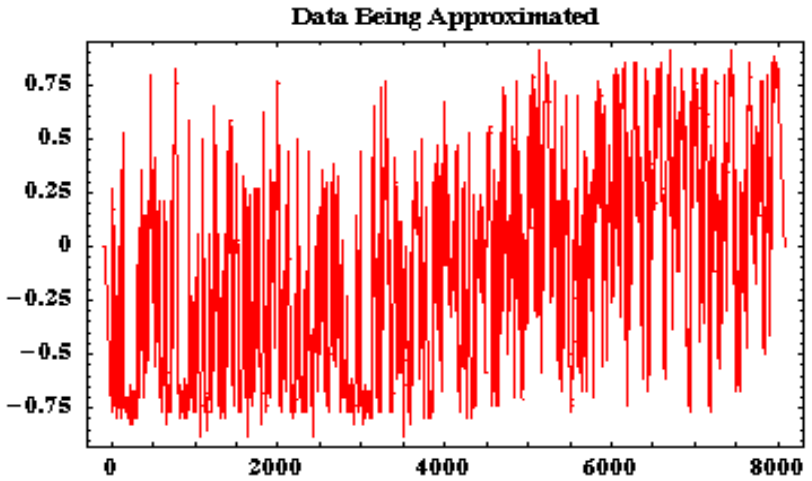

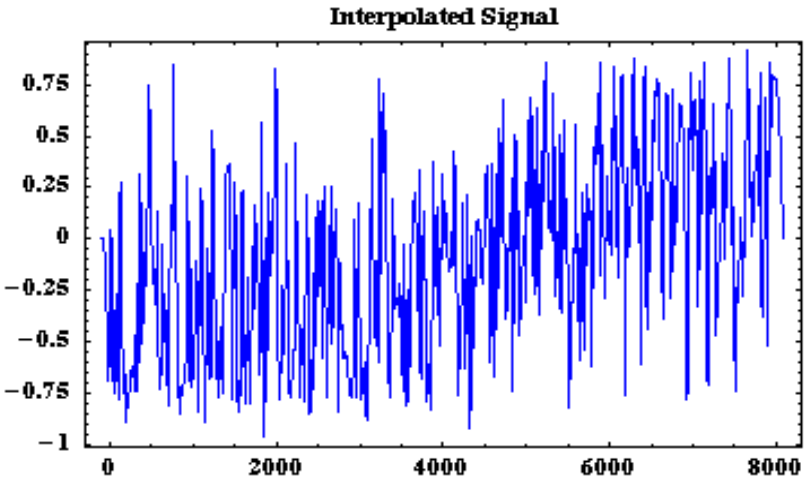

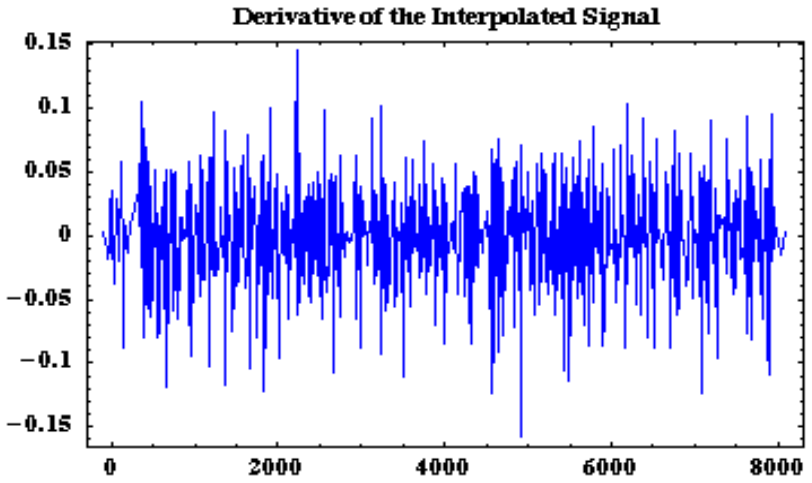

Reconstruction of the Data Using Up to 0.05 times the Largest WLT Coefficient

Polymath Research Inc.

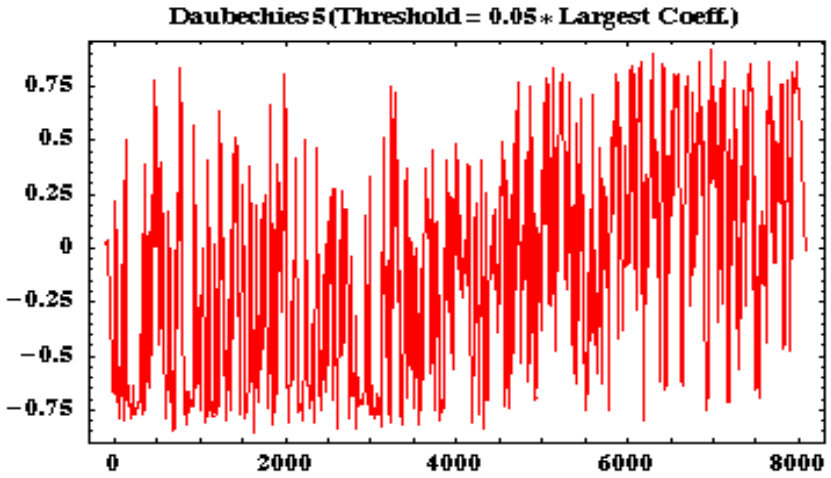

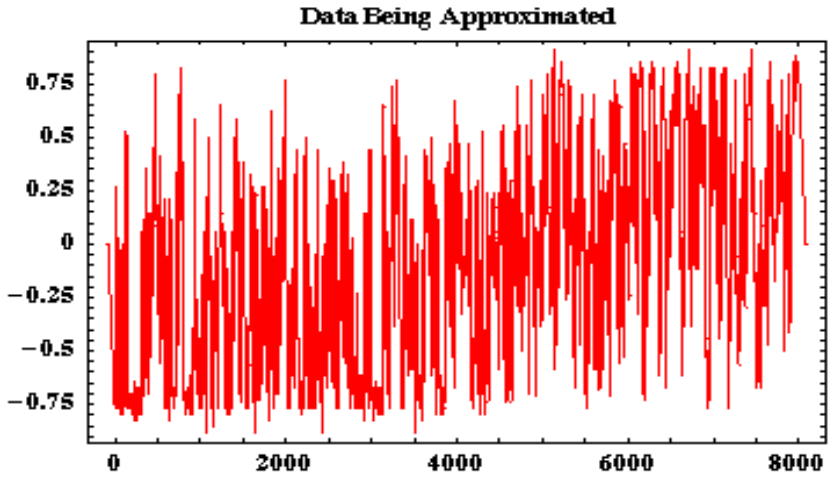

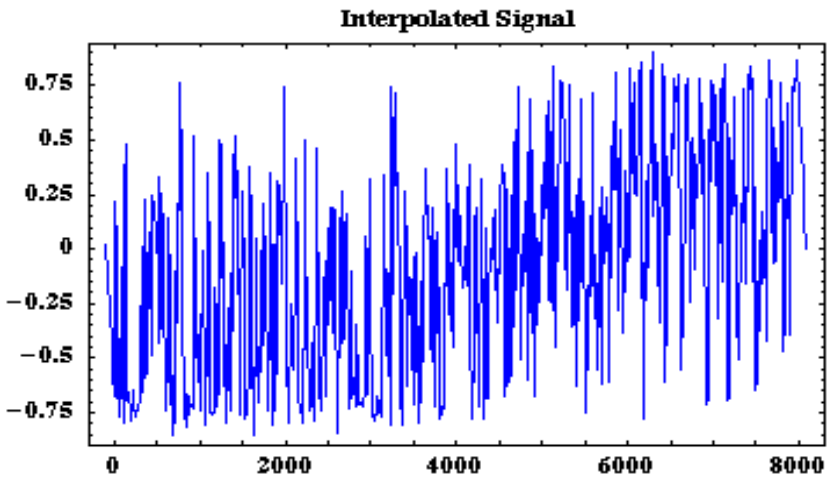

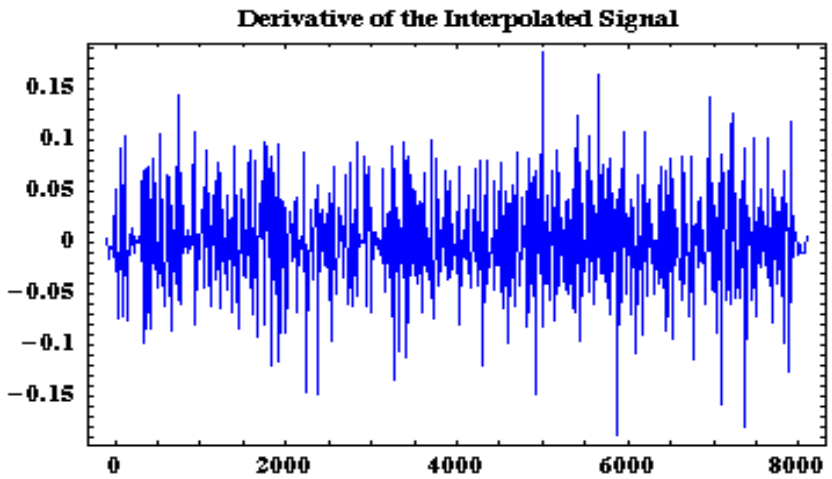

Reconstruction of the Data Using the First (of 10) Level of the MRD

Polymath Research Inc.

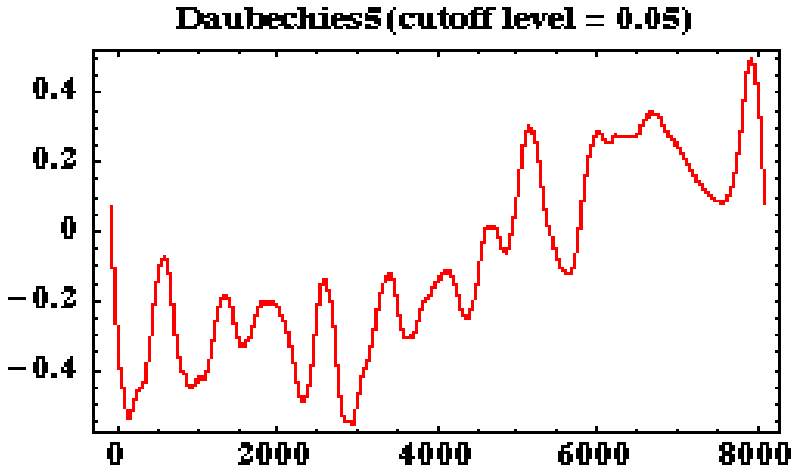

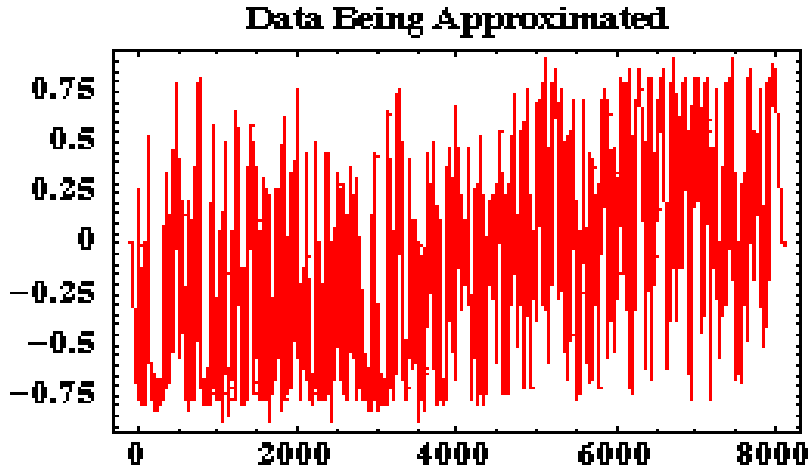

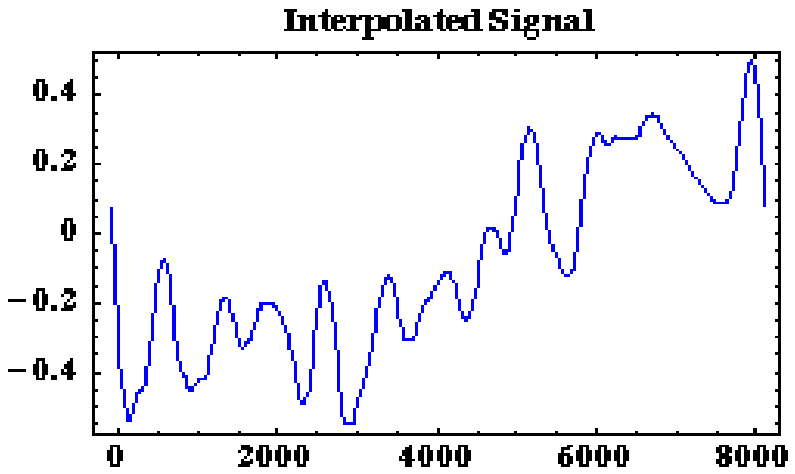

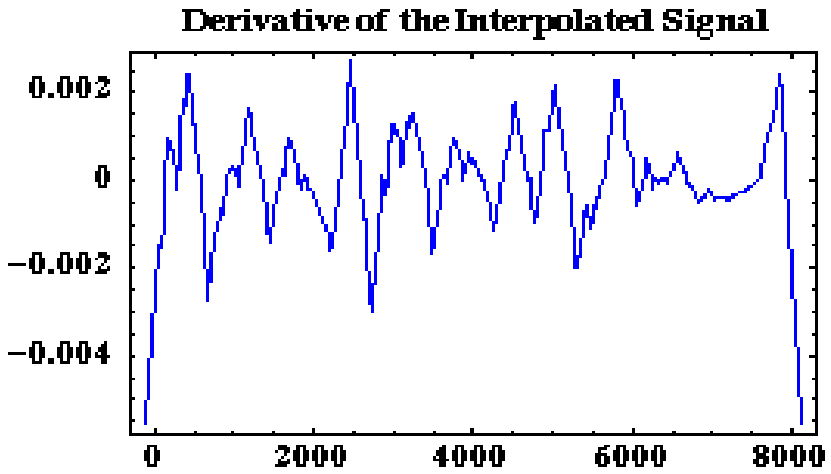

Reconstruction of the Data Using the First Two (of 10) Levels of the MRD

Polymath Research Inc.

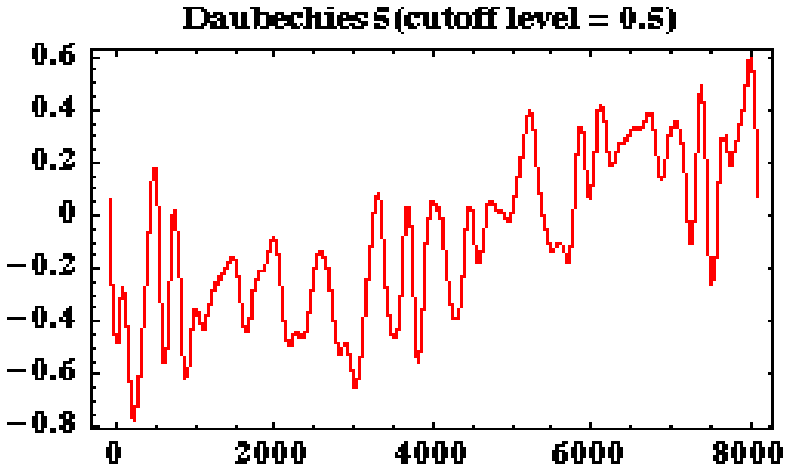

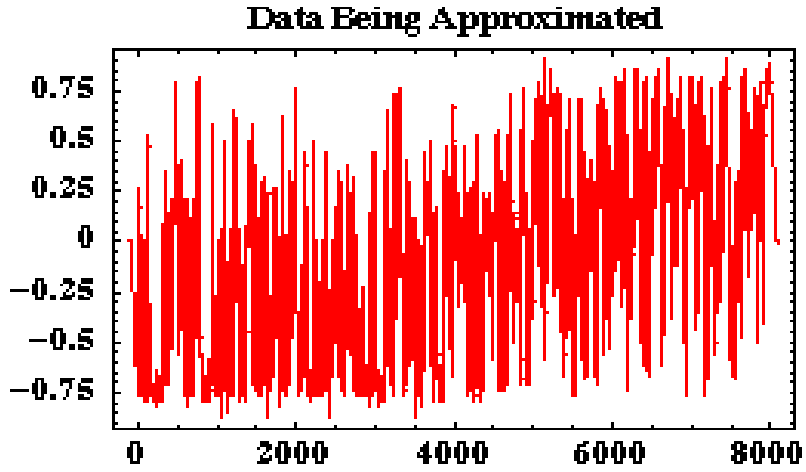

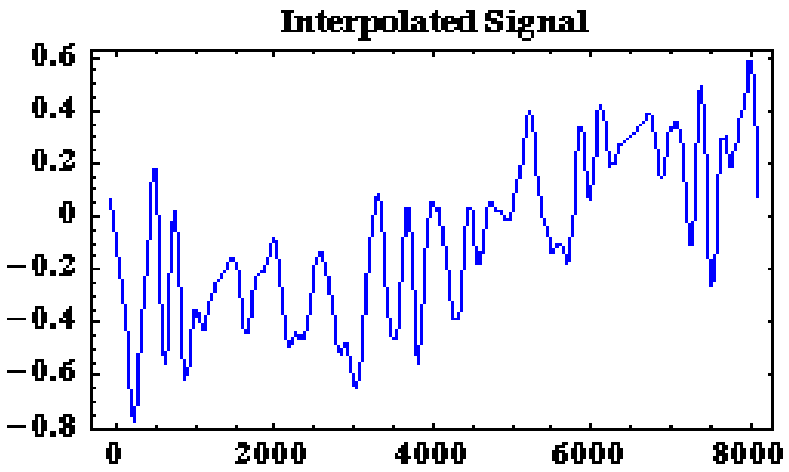

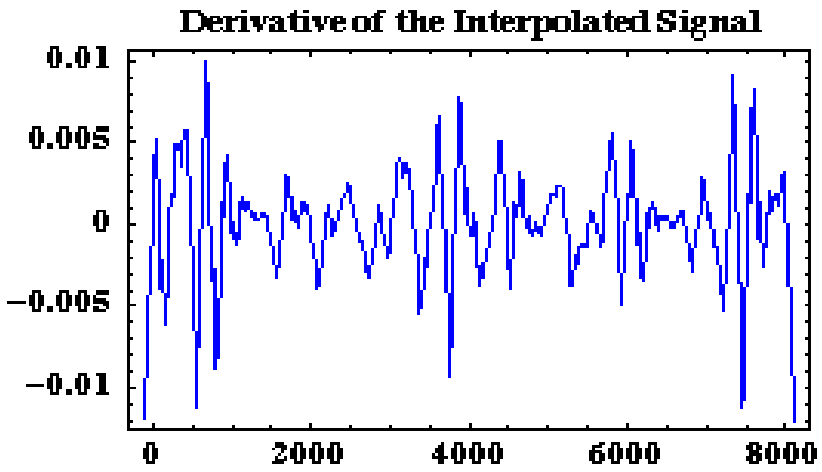

Reconstruction of the Data Using the First Three (of 10) Levels of the MRD

Polymath Research Inc.

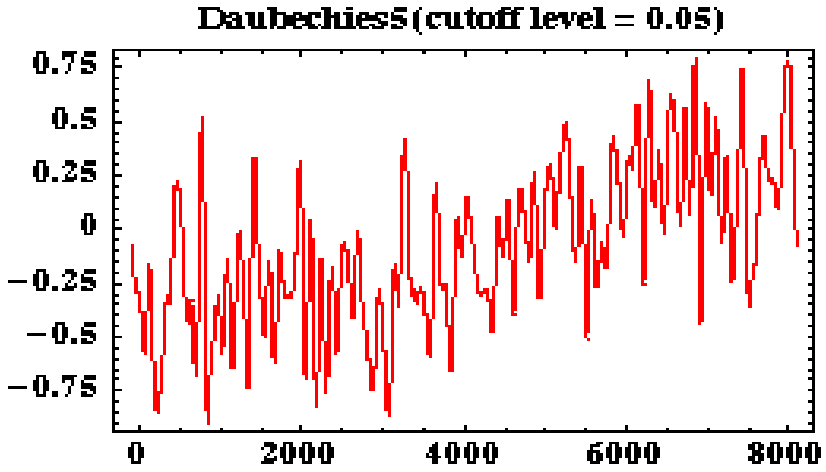

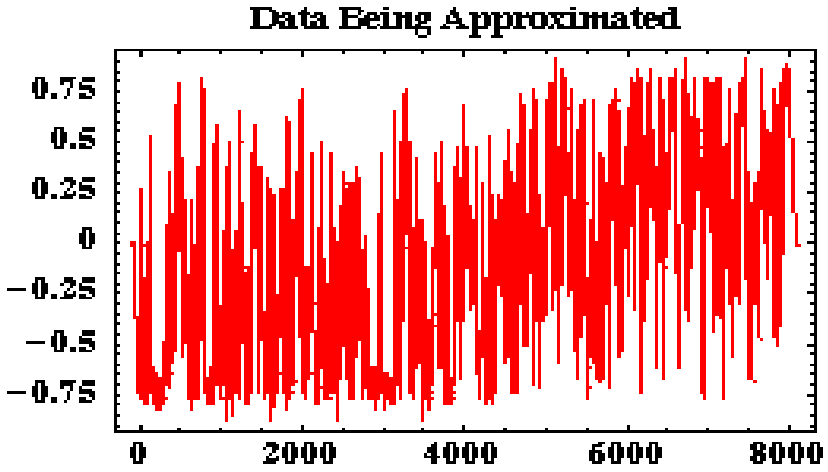

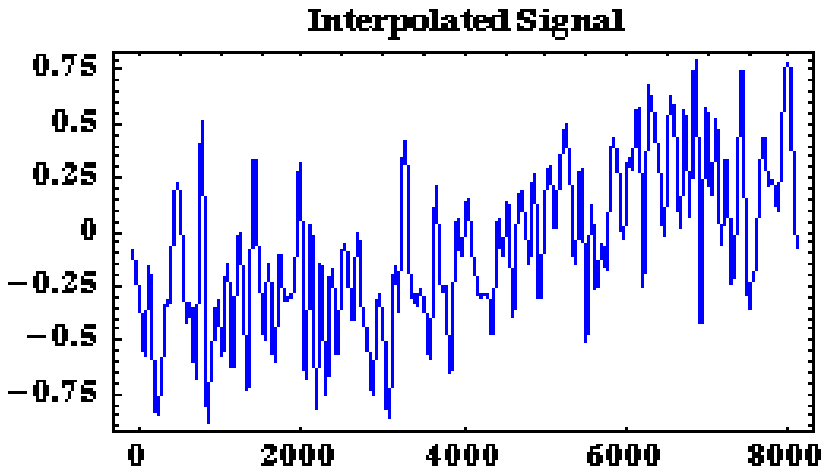

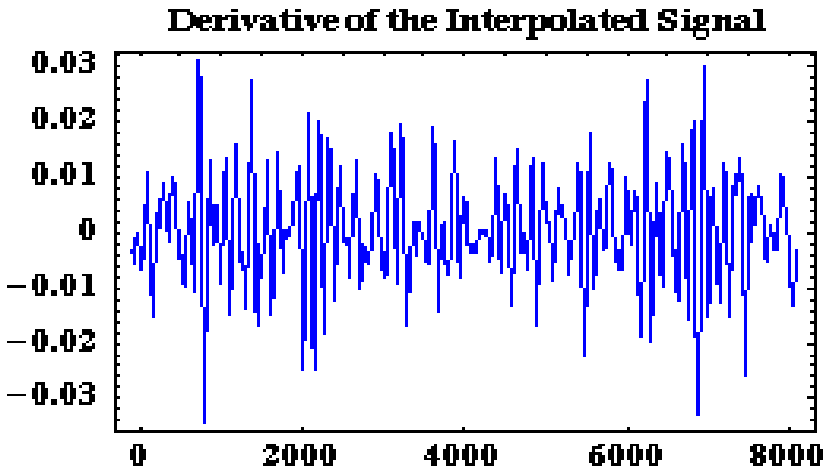

Reconstruction of the Data Using the First Four (of 10) Levels of the MRD

Polymath Research Inc.

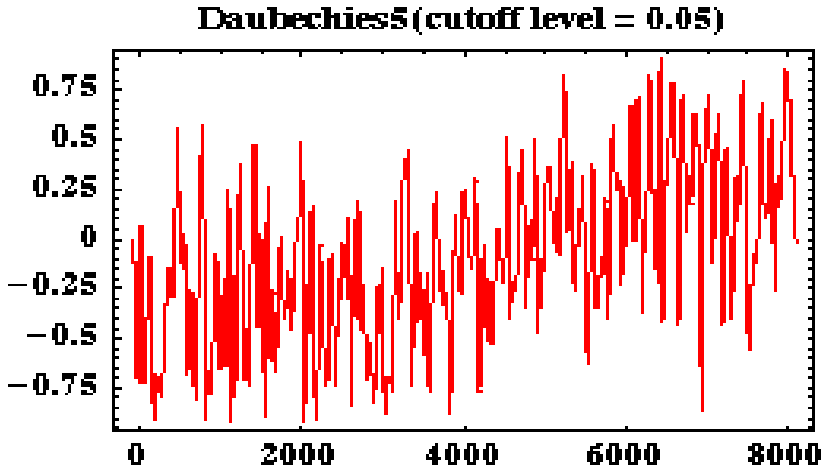

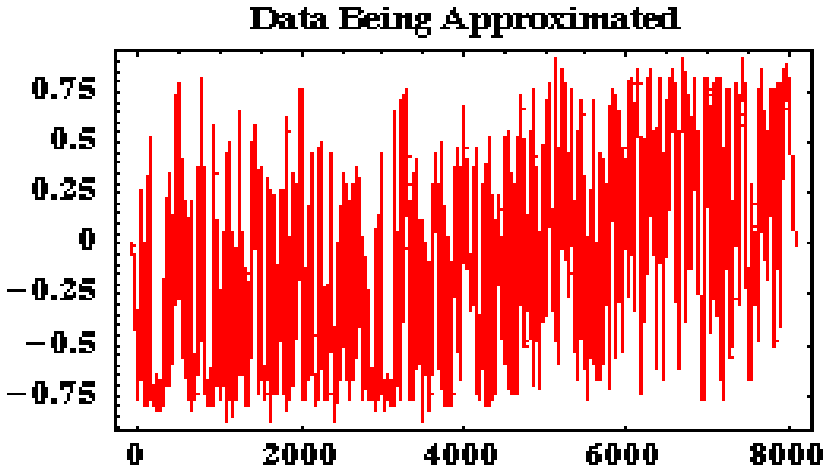

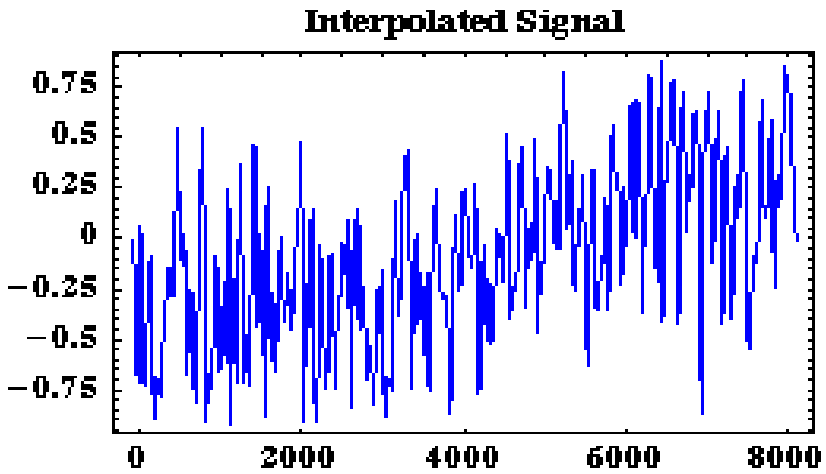

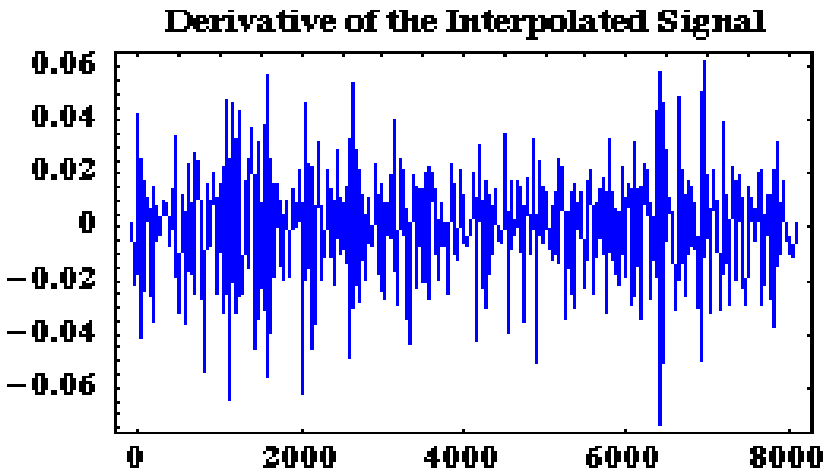

Reconstruction of the Data Using the First Five (of 10) Levels of the MRD

Polymath Research Inc.

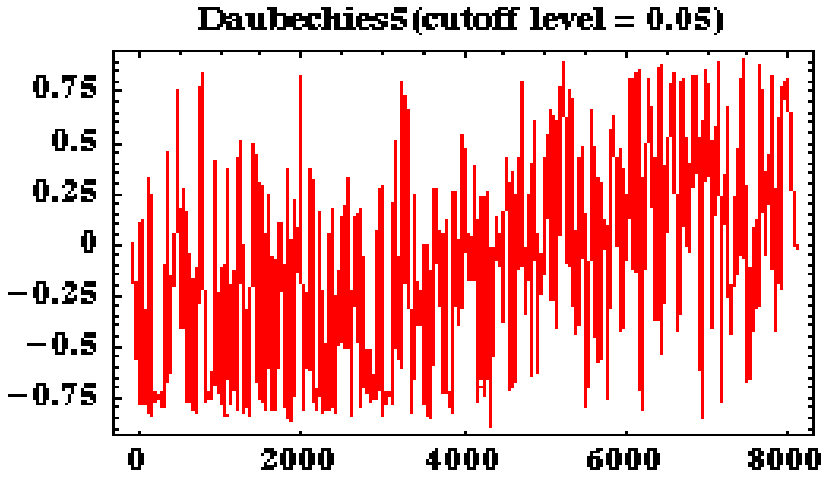

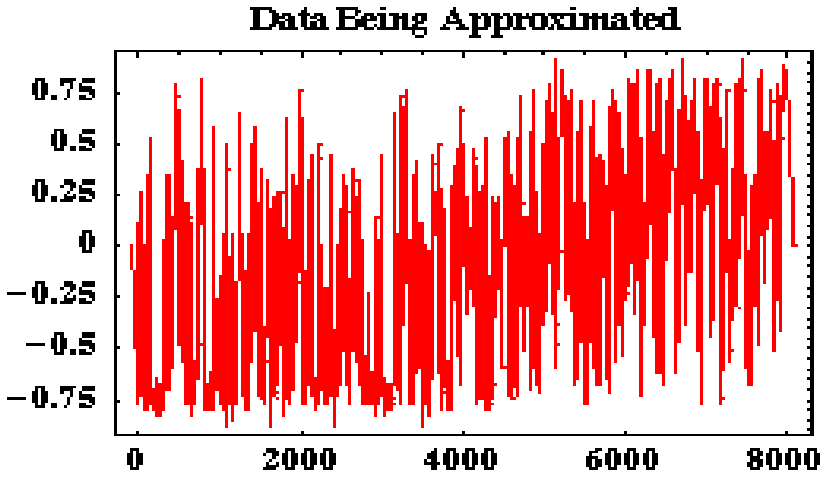

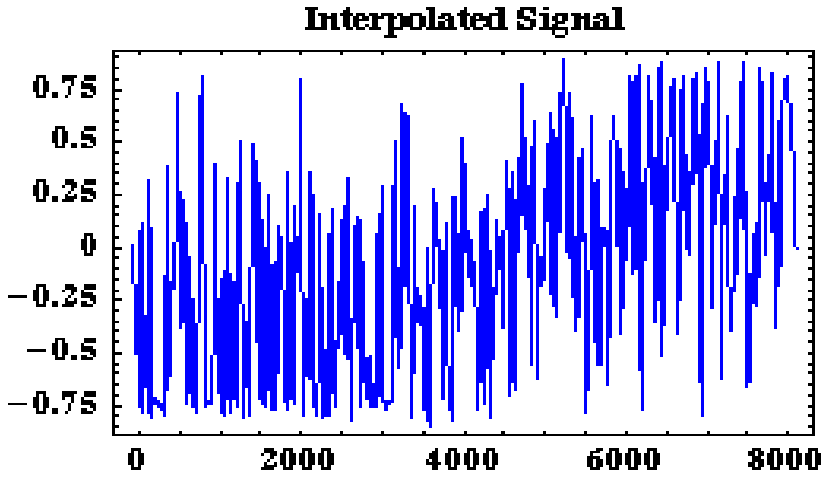

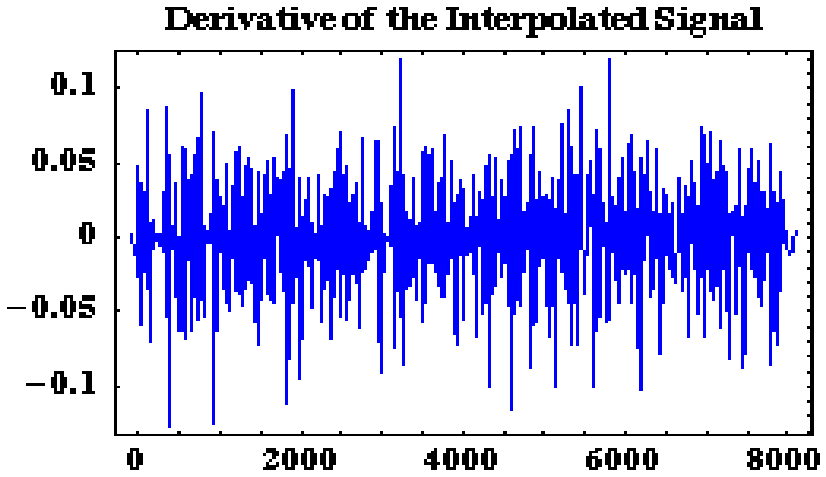

Reconstruction of the Data Using the First Six (of 10) Levels of the MRD

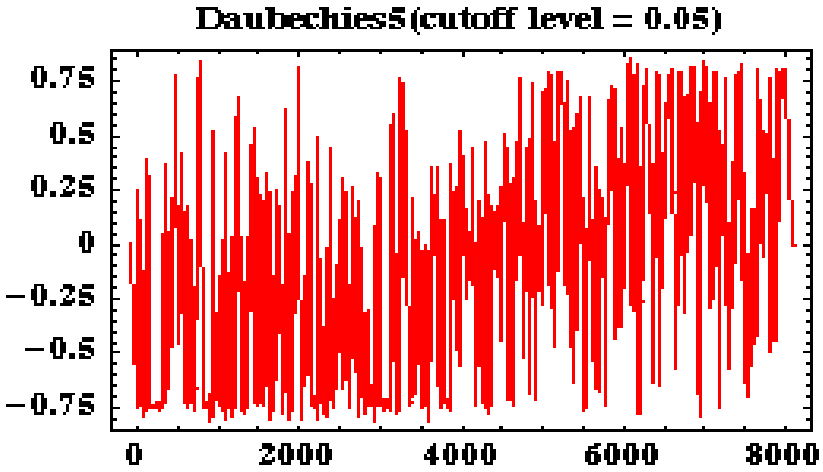

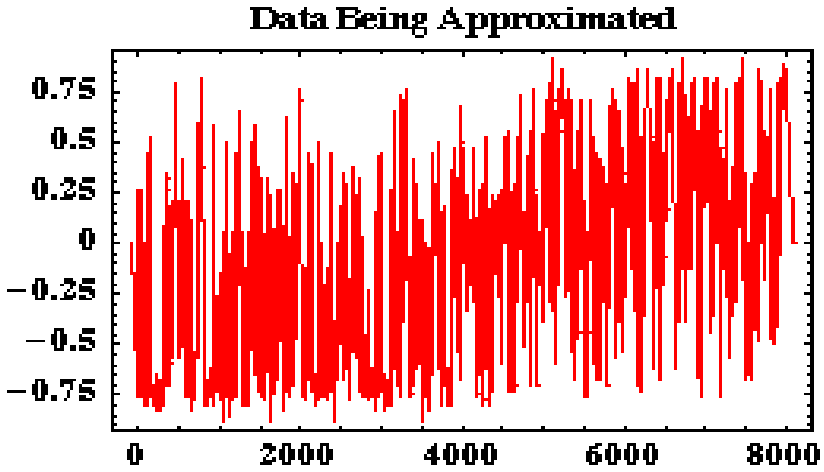

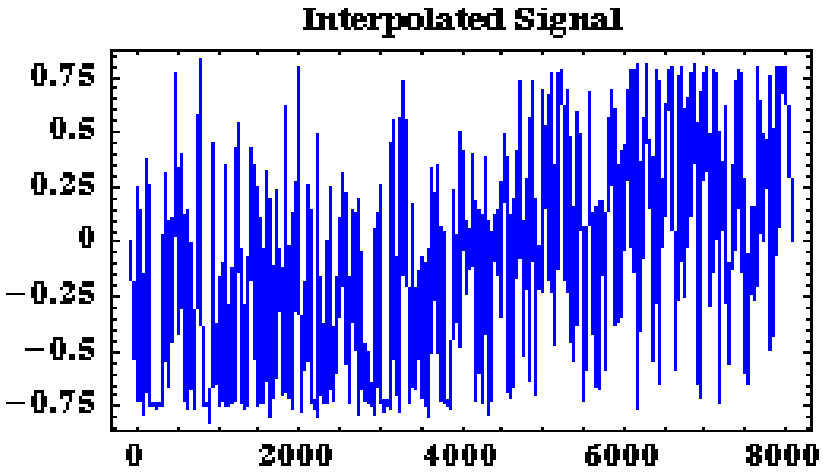

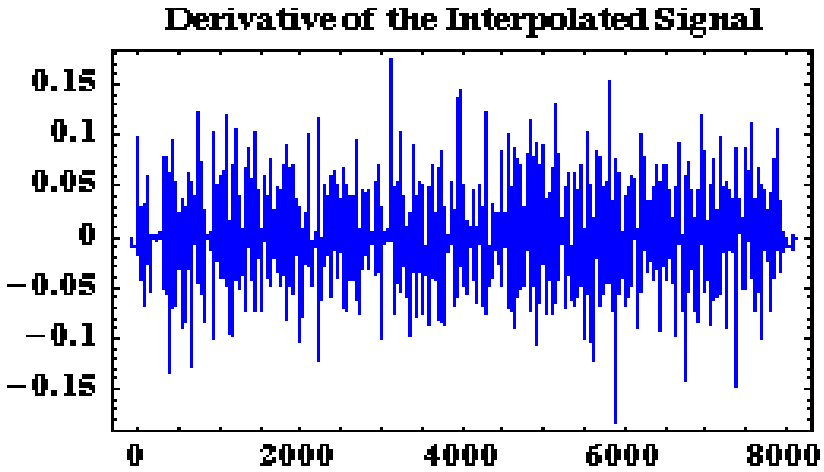

Reconstruction of the Data Using the First Seven (of 10) Levels of the MRD

Polymath Research Inc.

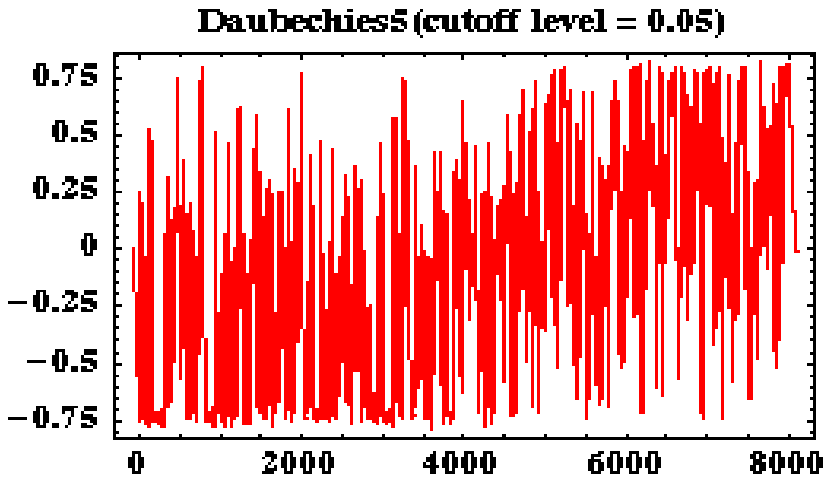

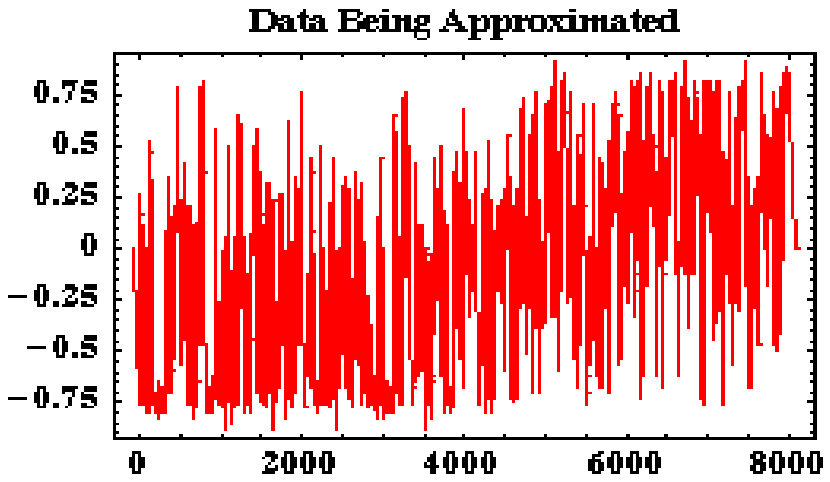

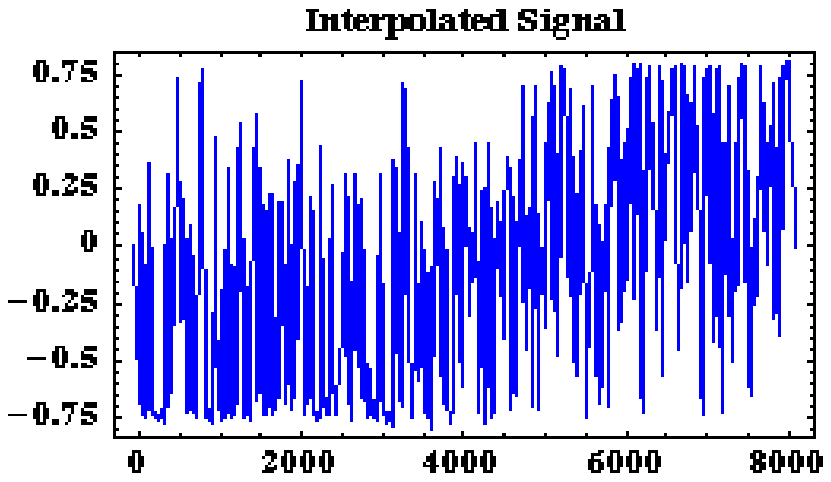

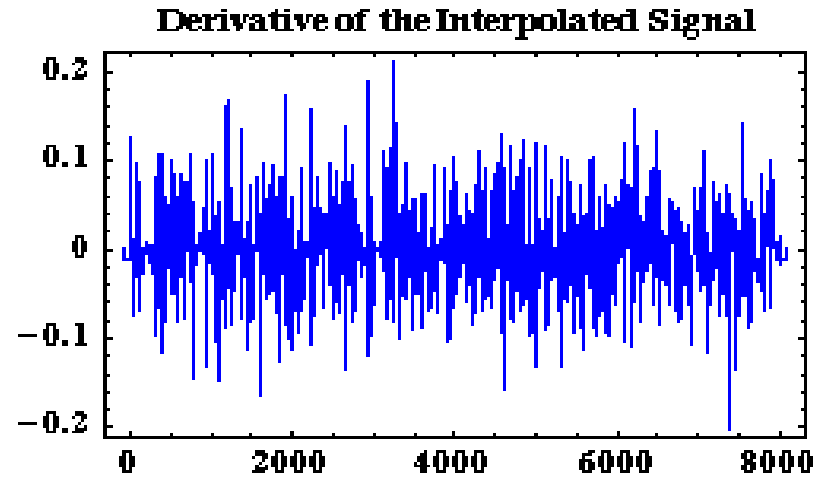

Conclusions on Raw RT Mix Data Analysis Using DWT

- Compression of around a factor of 20 seems likely with full data set.
- Will see what low pass filtering will do to initial data and its subsequent WLT analysis.
- Looks like 25% of the largest coefficients are enough to reconstruct the clean parts of the data.
- We should compare different stages of evolution of RT Mix in terms of their optimum WLT representations.
- Significant dynamical degrees of freedom vs insignificant ones which vary more slowly or not at all or randomly might be obtainable if we keep at it!

Low Pass Filtered RT Mix Data

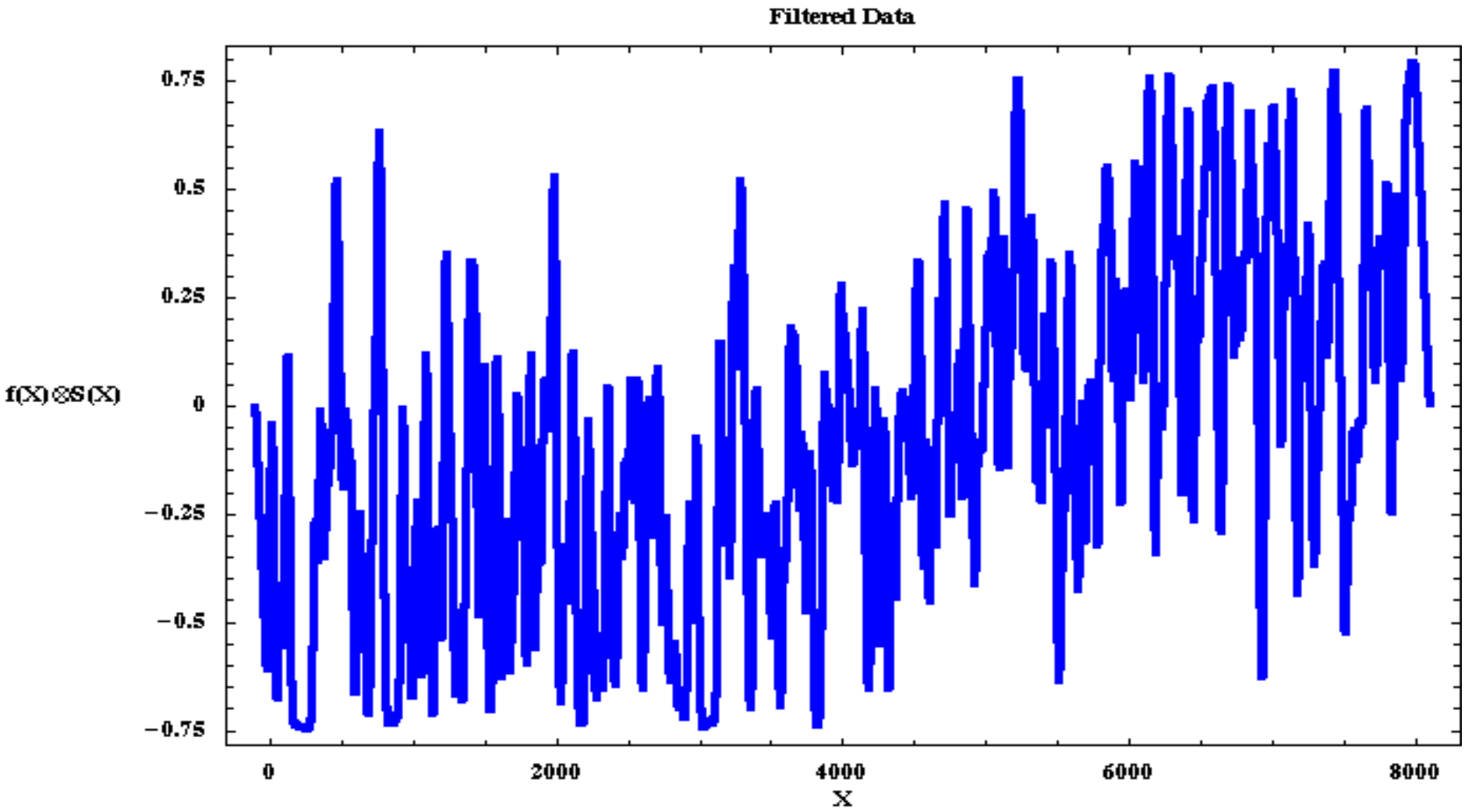

The Filtering Has This Form and Effect in k-Space

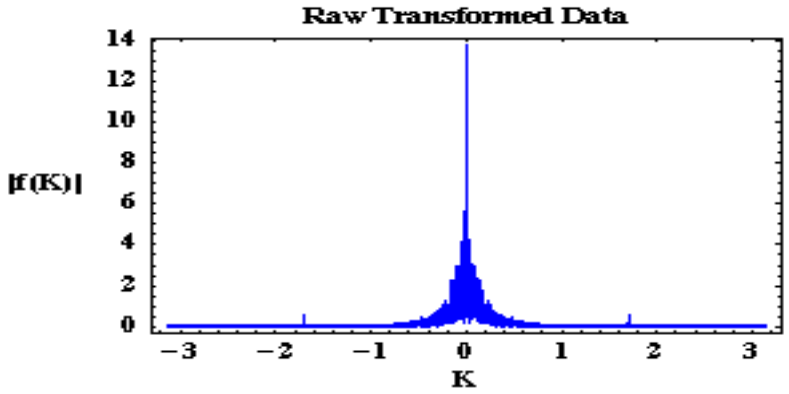

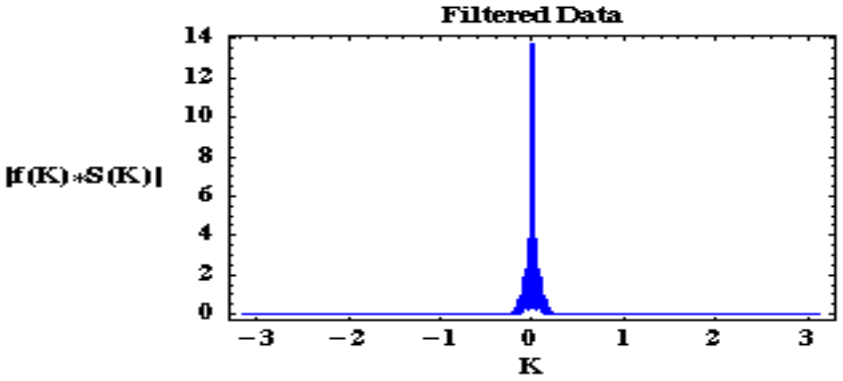

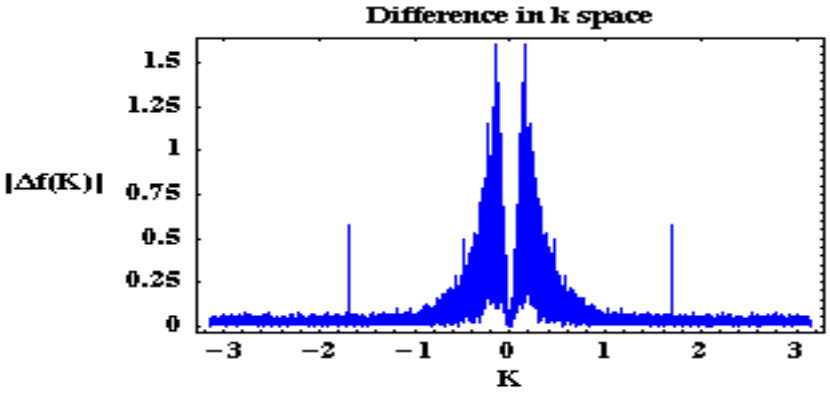

Filter was of the form:

$$S(k) = \exp\left[-\left(\frac{k}{k_{width}} \right)^{2\alpha} \right]$$

Where α=5 and k_{width} = 400

MRDs of the LP Filtered RT Mix Data in 6 Different Daubechies WLT Bases

Haar
MRD

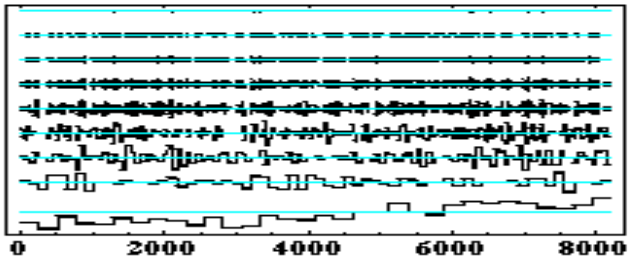

Daubechies2
MRD

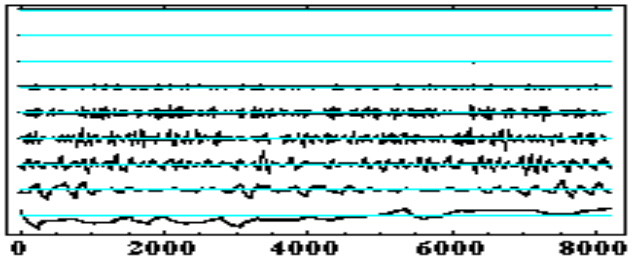

Daubechies3
MRD

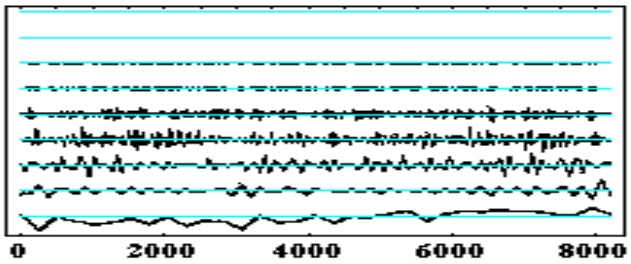

Daubechies4
MRD

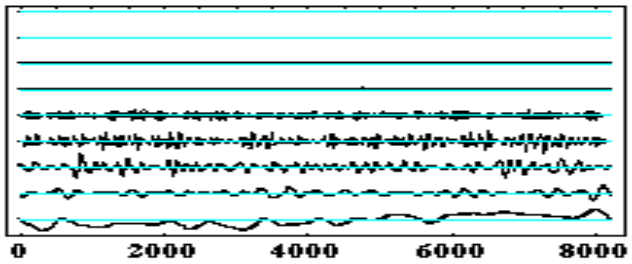

Daubechies5
MRD

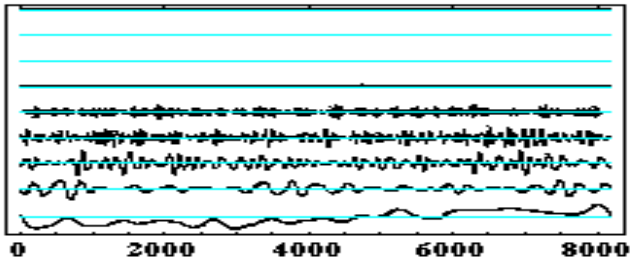

Daubechies6
MRD

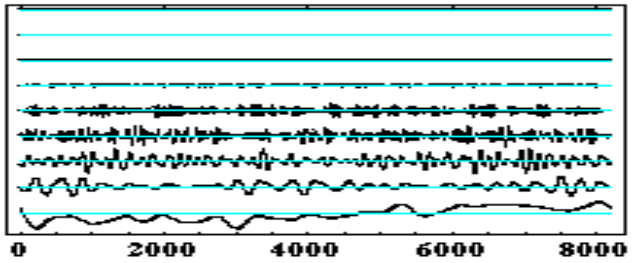

Decay Rate of Largest Coefficient vs Number of Coeffs Kept in LPF RT Mix Data

Polymath Research Inc.

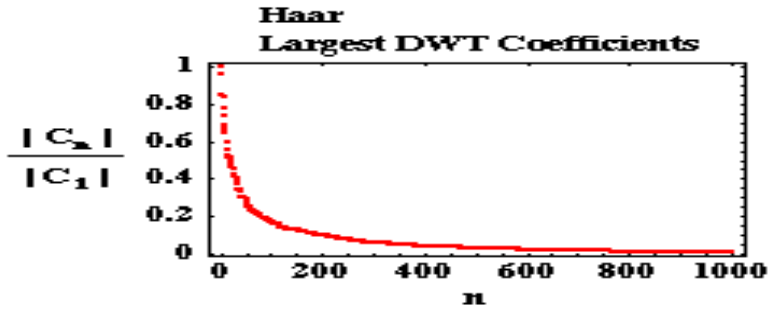

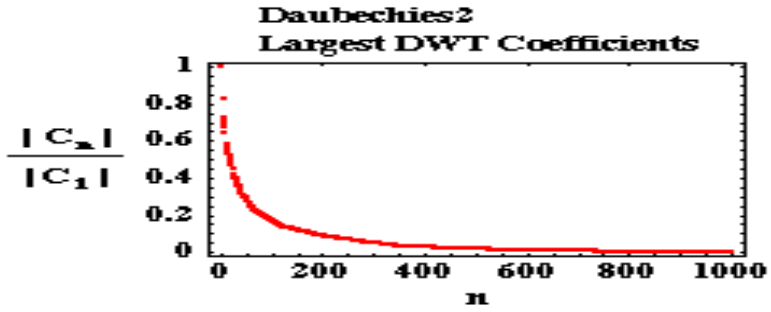

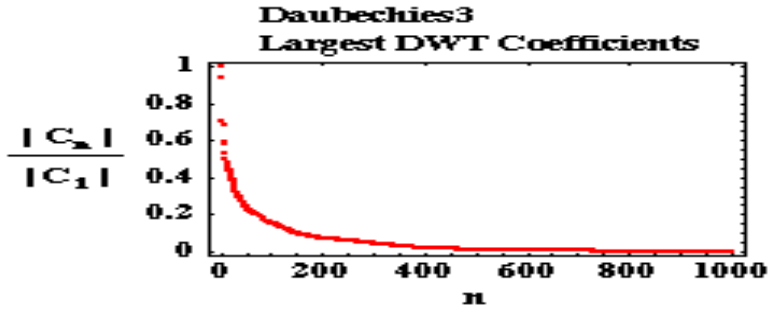

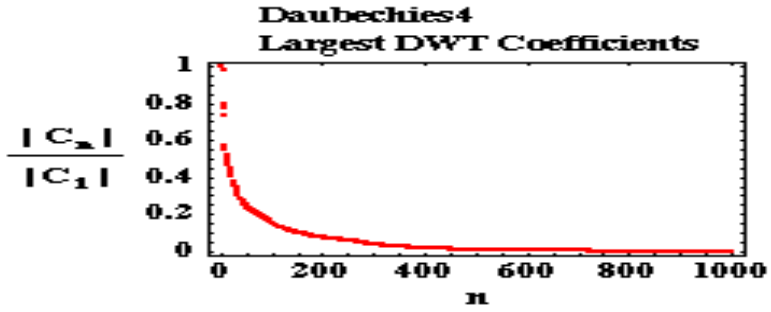

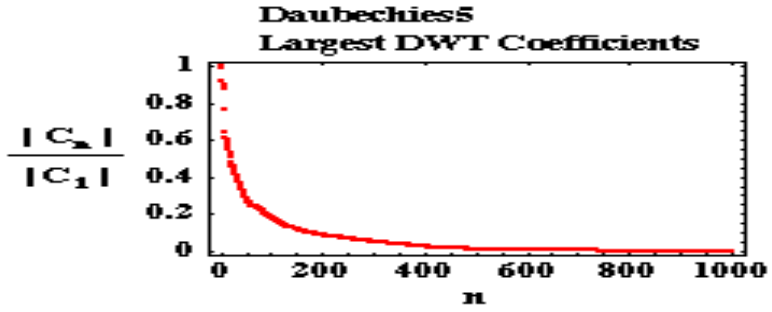

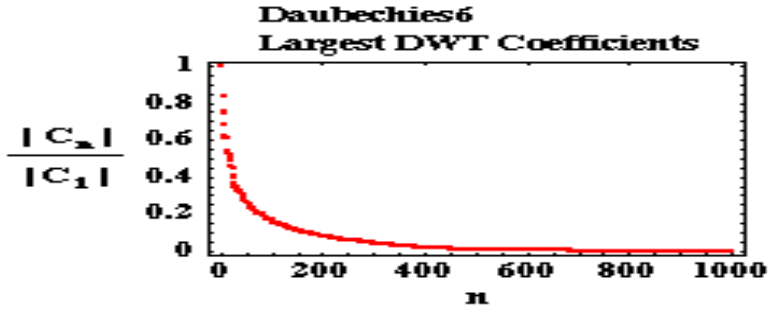

Energy Accumulation Rate in Coefficient Space vs # of WLTs Kept for LPF RT Mix Data

Polymath Research Inc.

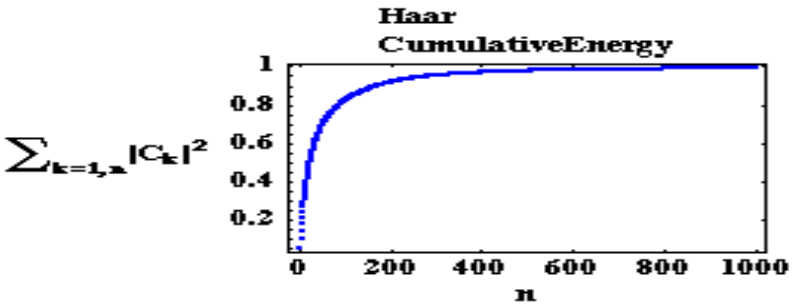

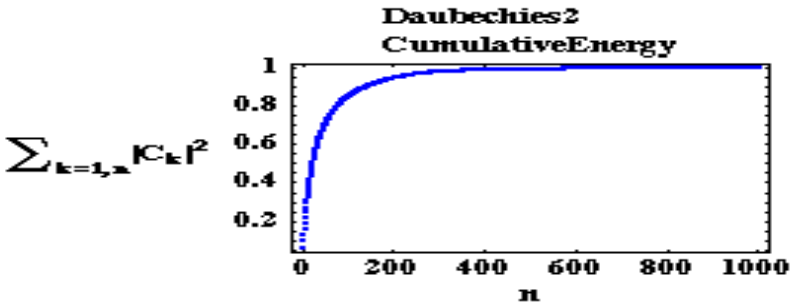

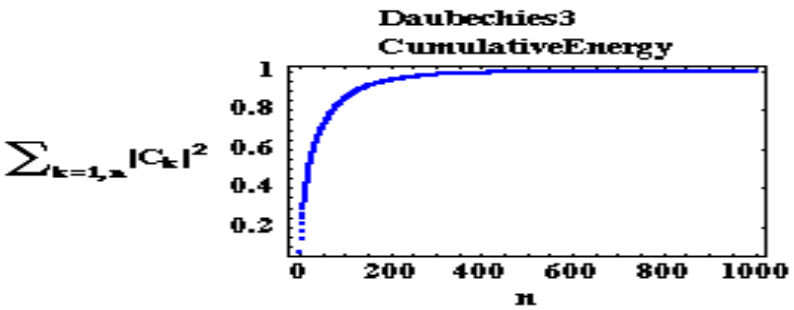

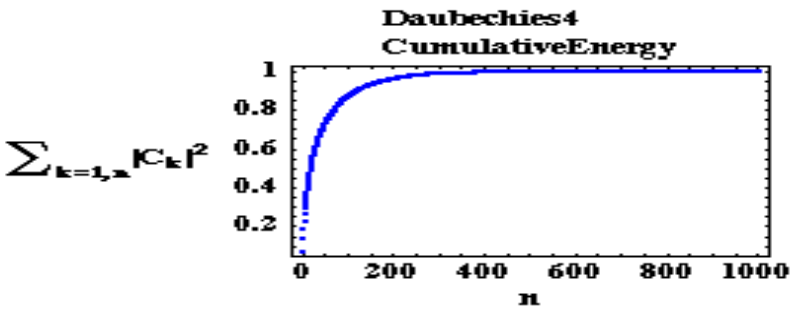

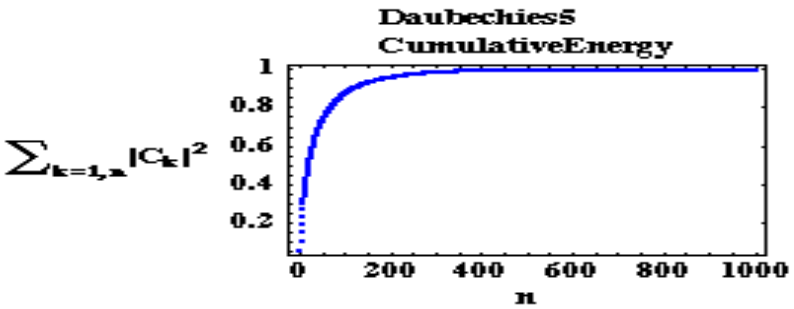

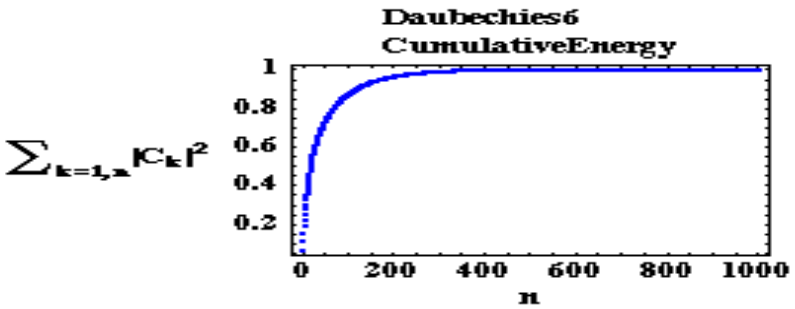

Scaleograms: Waveleters Preferred Way of Judging Tiling in Scale-Translation Space for LPF RT Mix

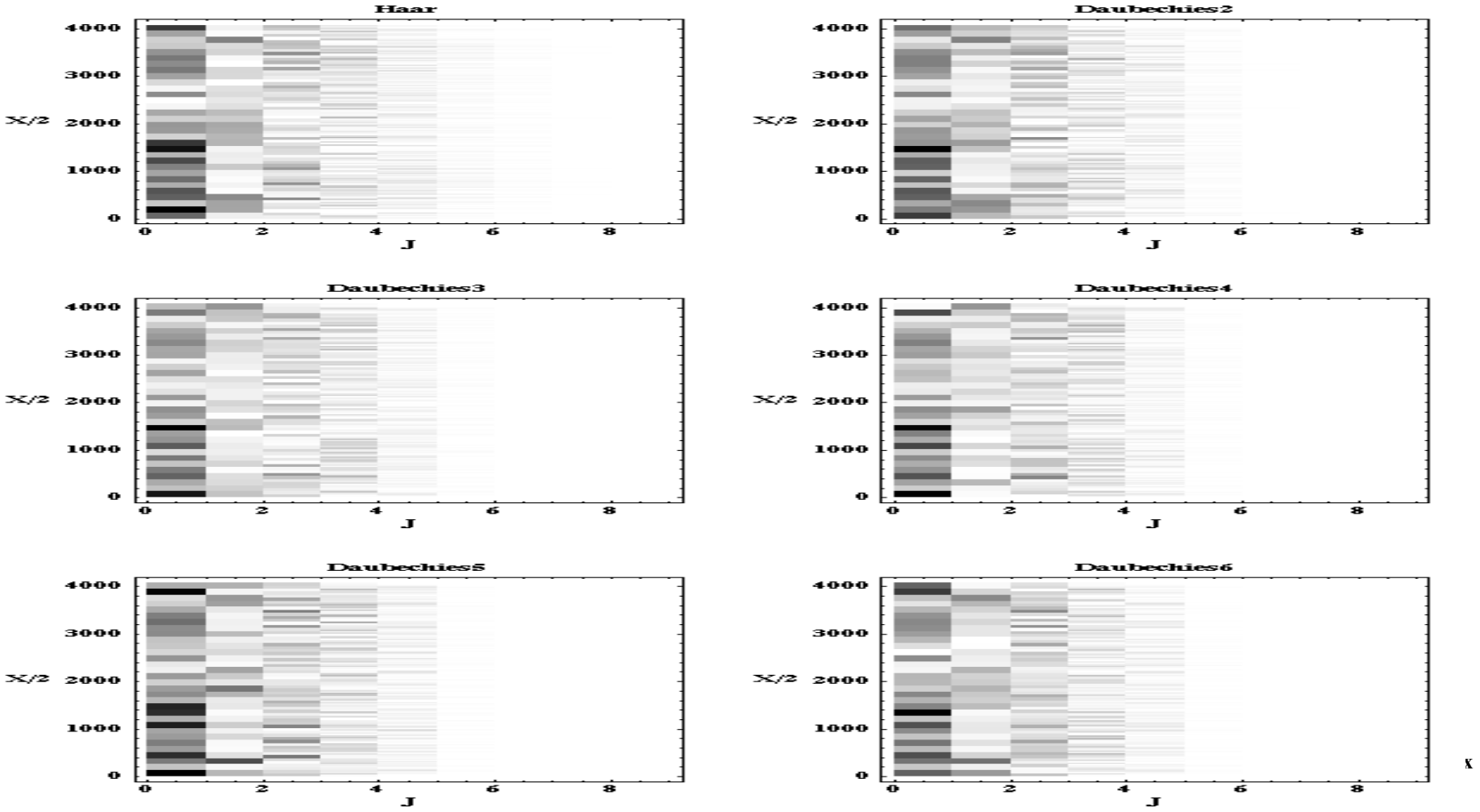

Least Square Error Incurred By Truncating the WLT Series at N of its Largest Coeffs LPF RT Mix Data

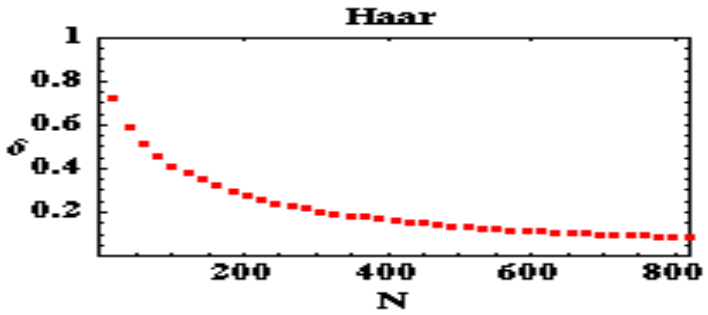

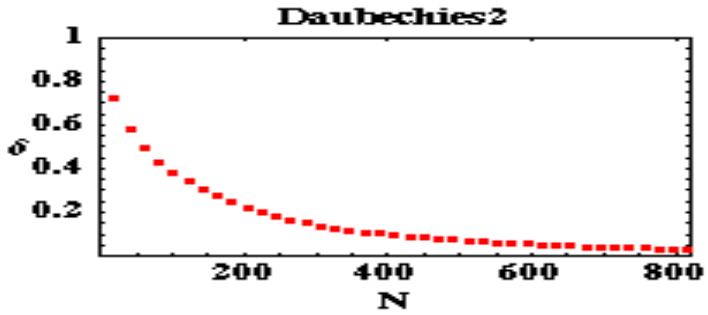

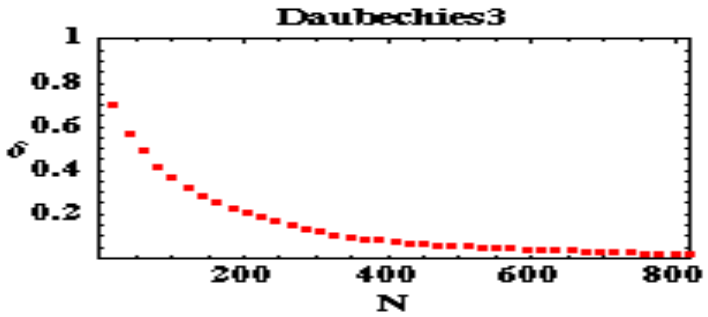

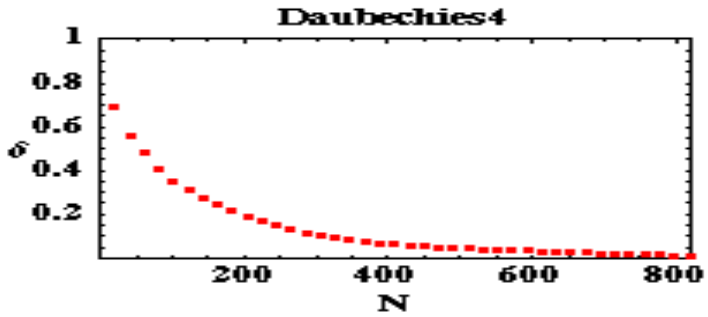

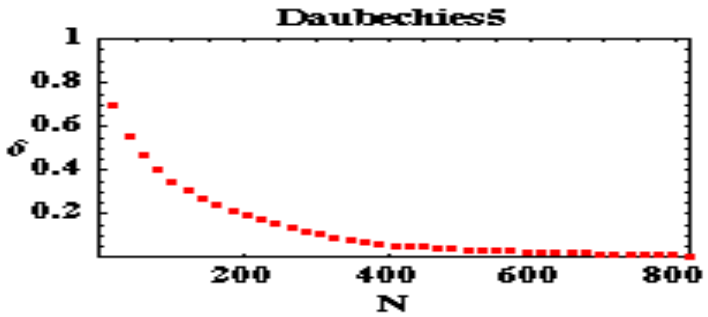

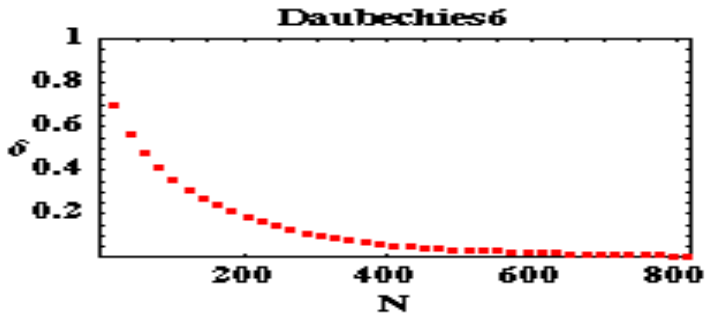

Least Square Error Incurred by Level Thresholding the DWT of LPF RT Mix Data

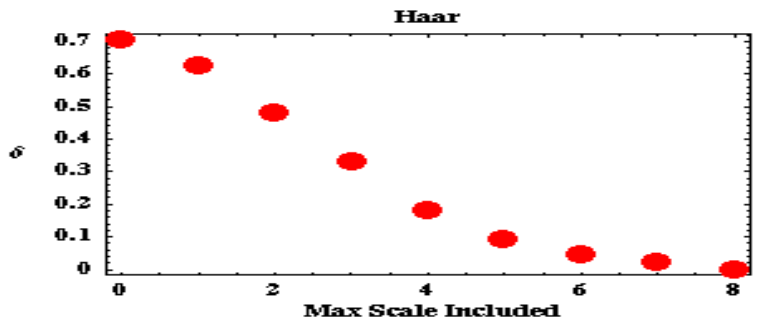

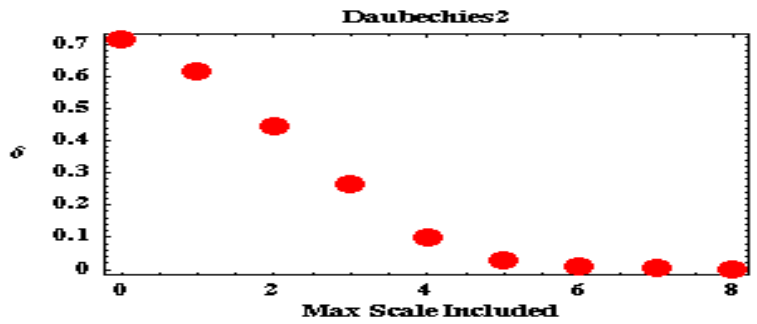

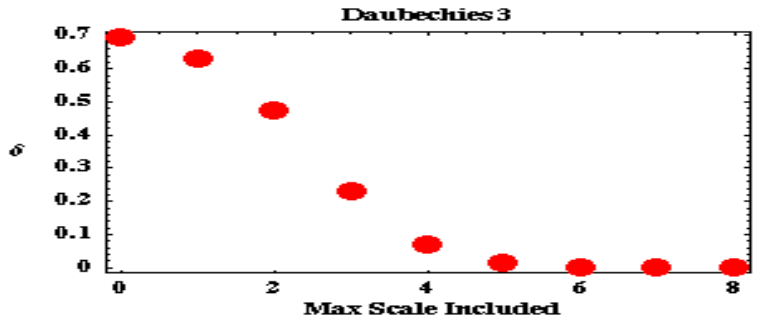

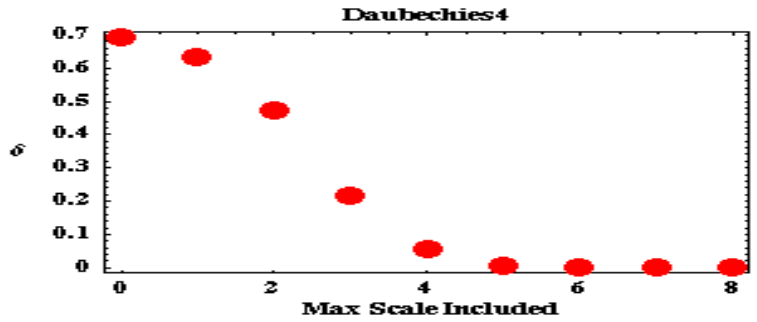

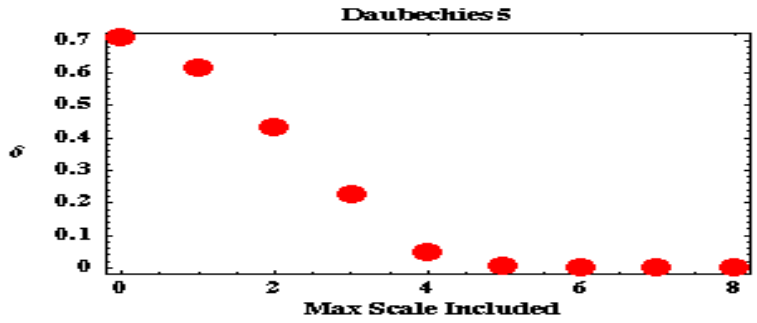

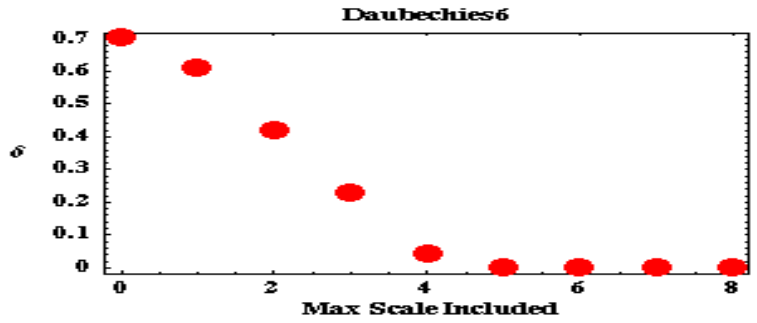

Daubechies 5 Does Much Better than Haar: 5 Quantitative Measures for LPF RT Mix Data

Polymath Research Inc.

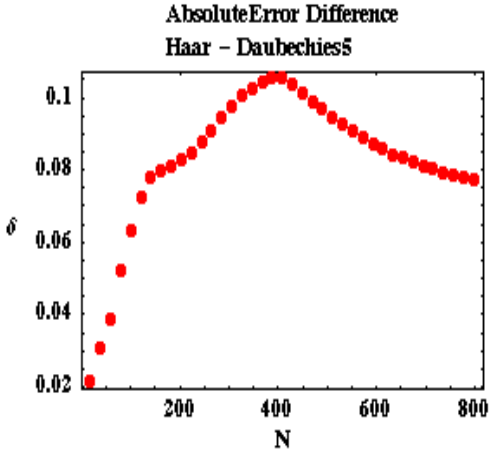

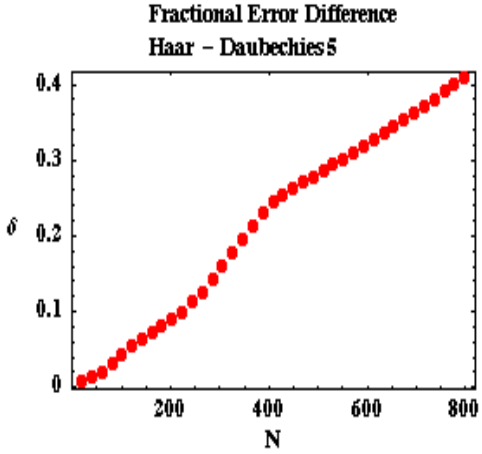

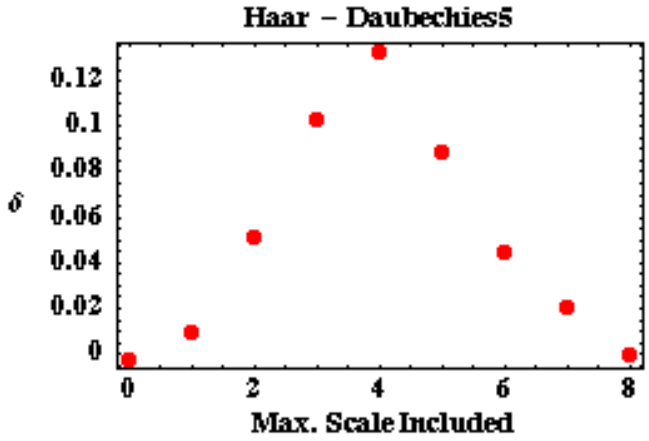

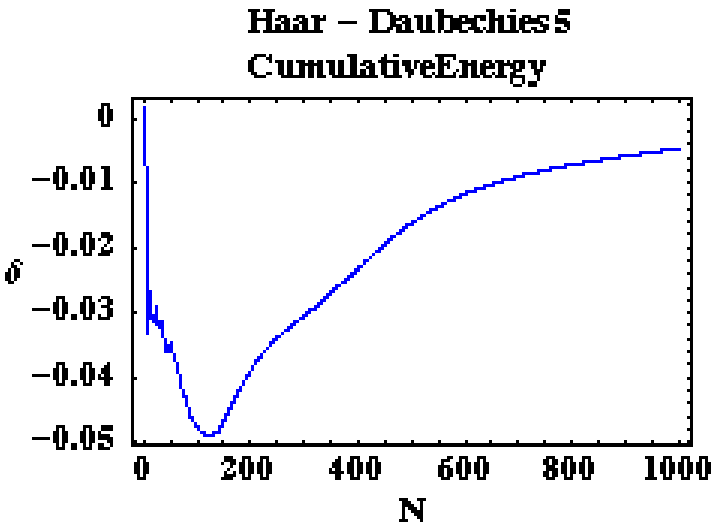

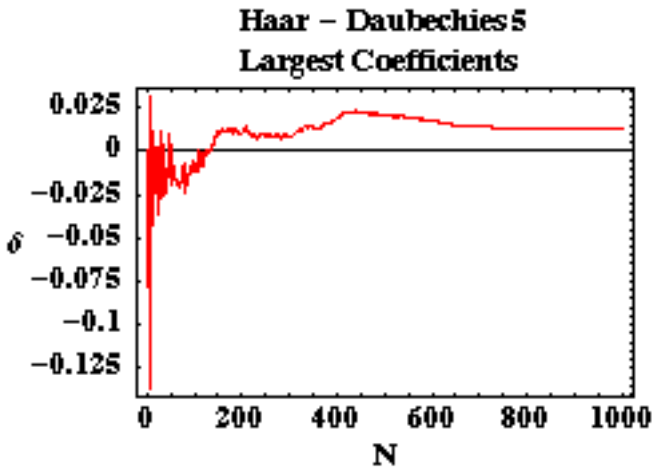

Level by Level Decomposition of the LPF RT Mix Data Using Daub5 WLTs

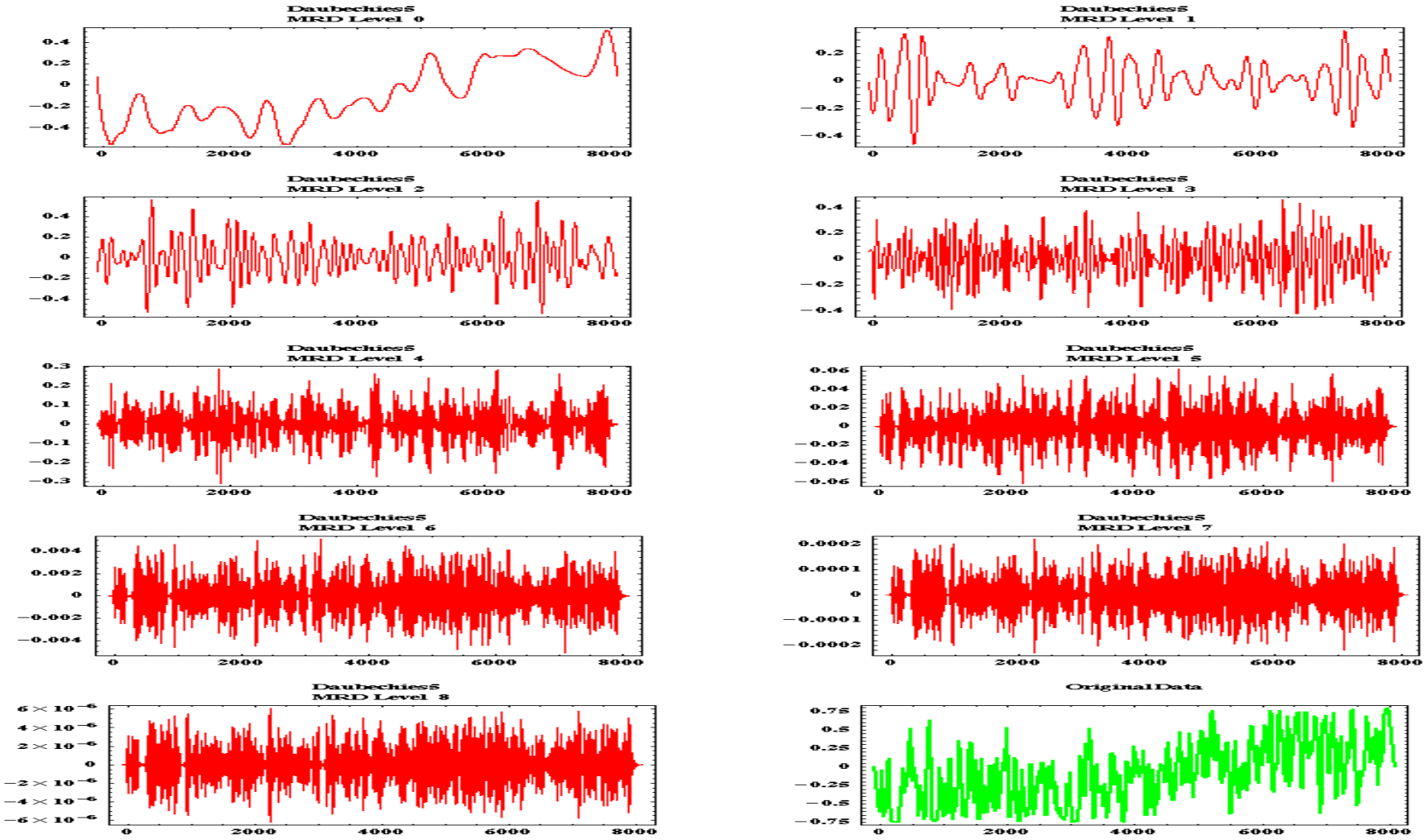

Reconstruction of the LPF Data with 5 Largest WLT Coeffs

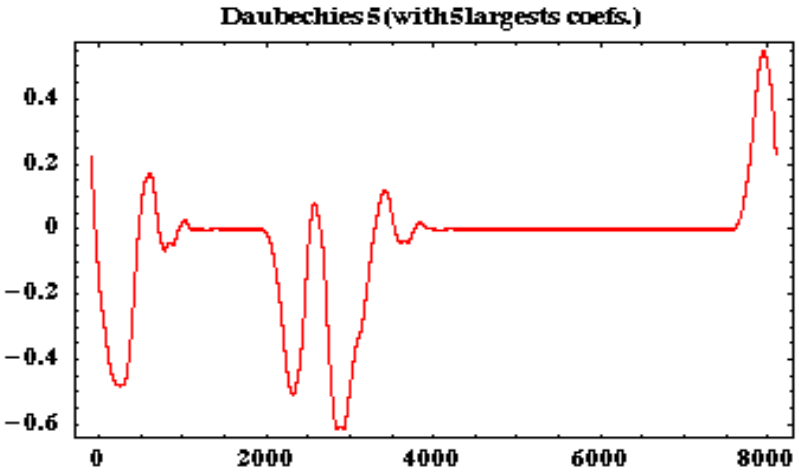

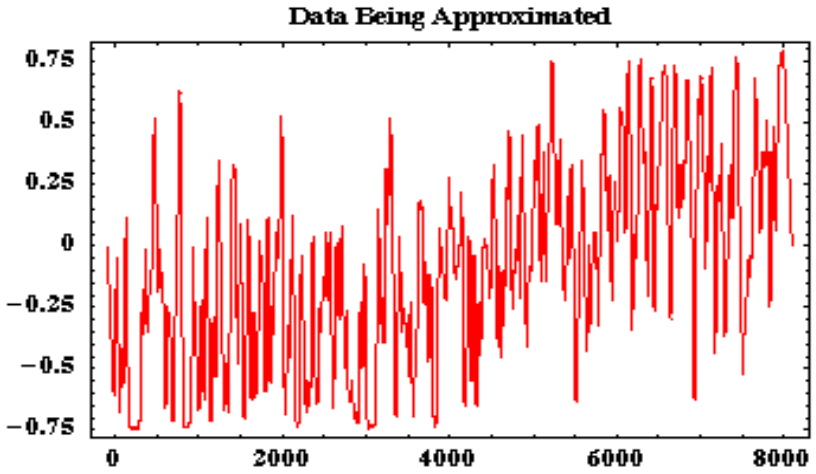

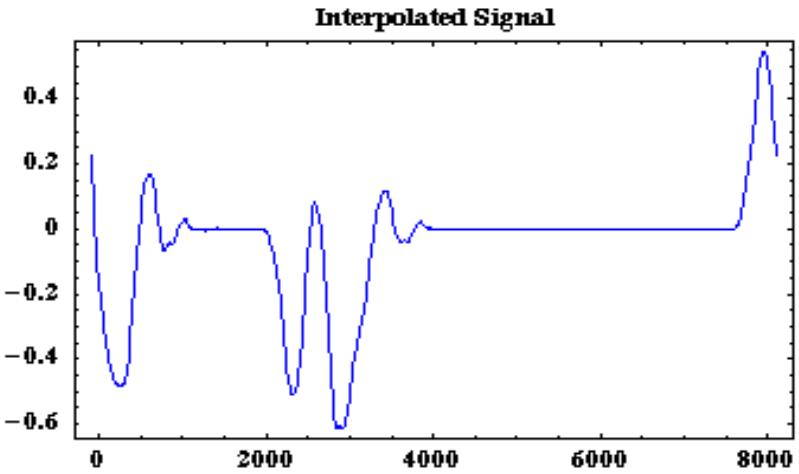

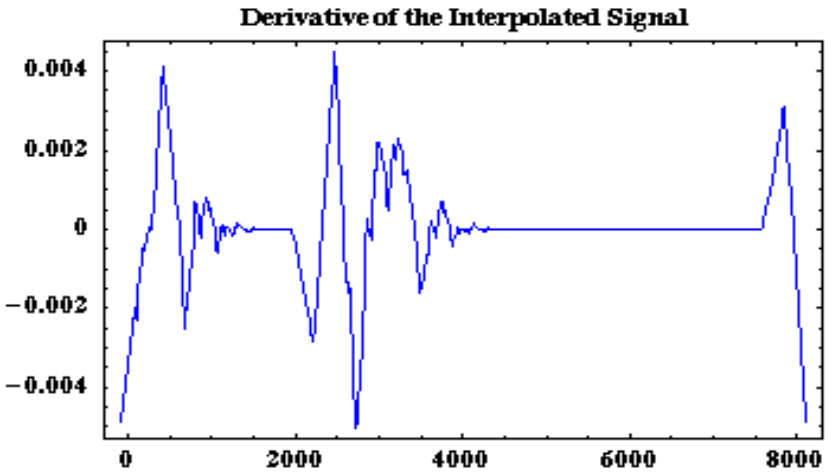

Reconstruction of the LPF Data with 10 Largest WLT Coeffs

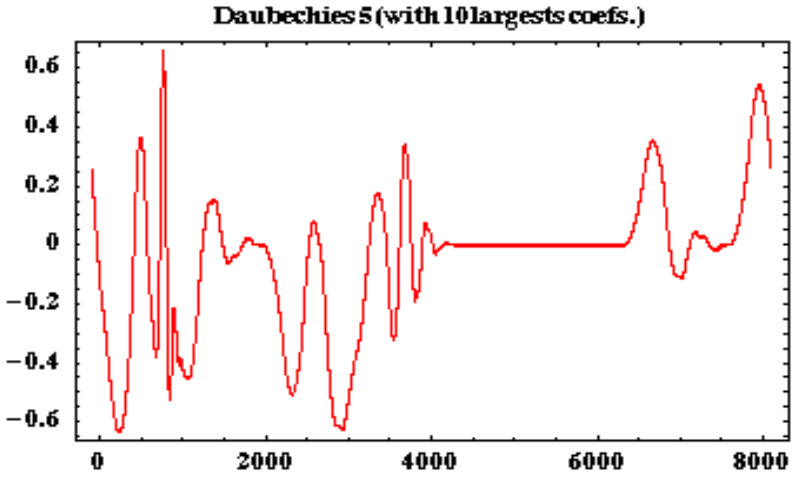

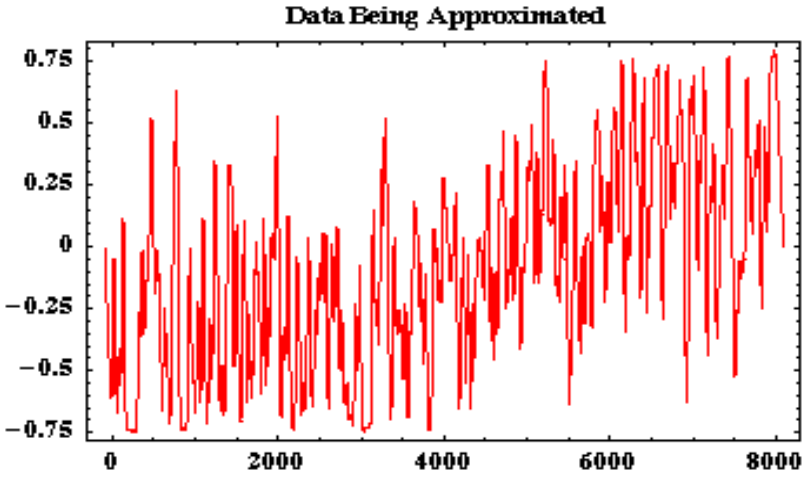

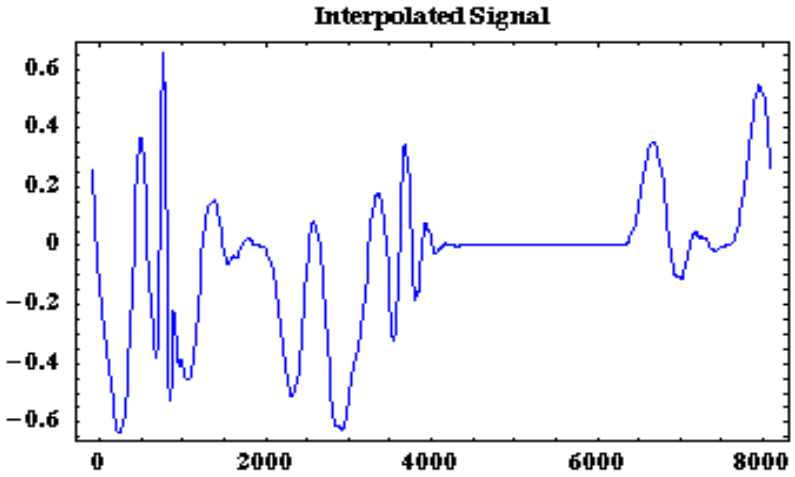

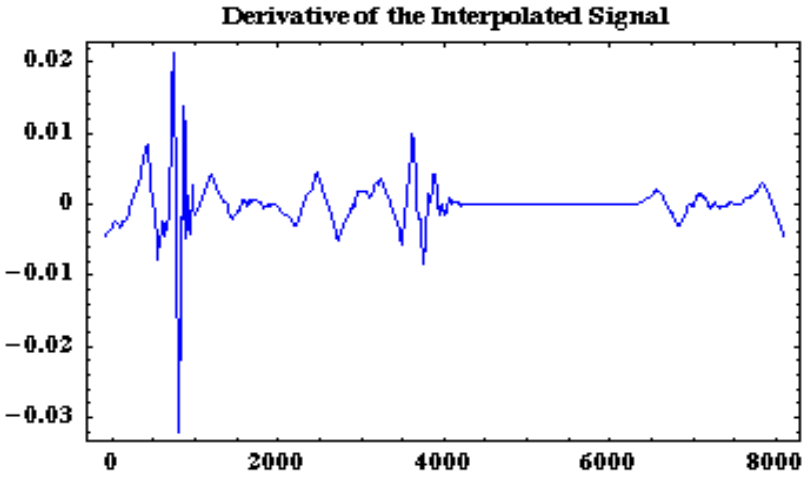

Reconstruction of the LPF Data with 15 Largest WLT Coeffs

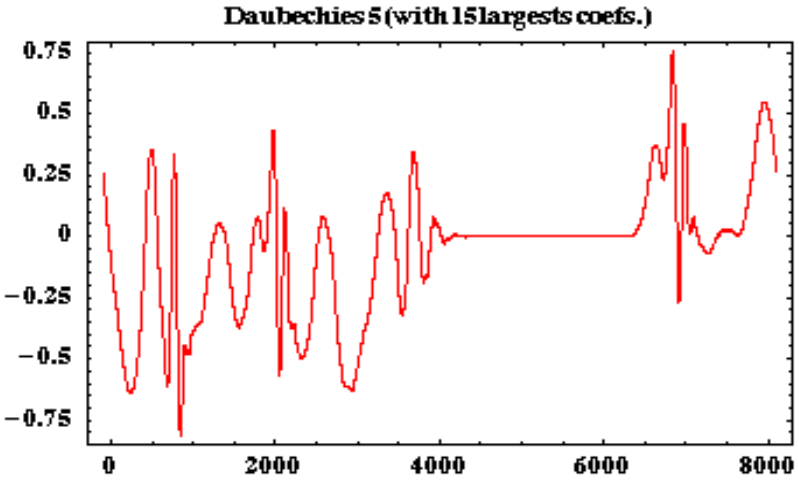

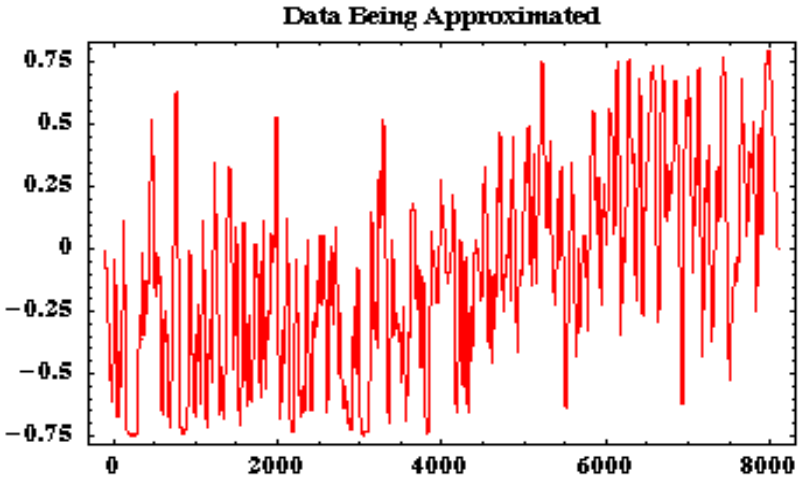

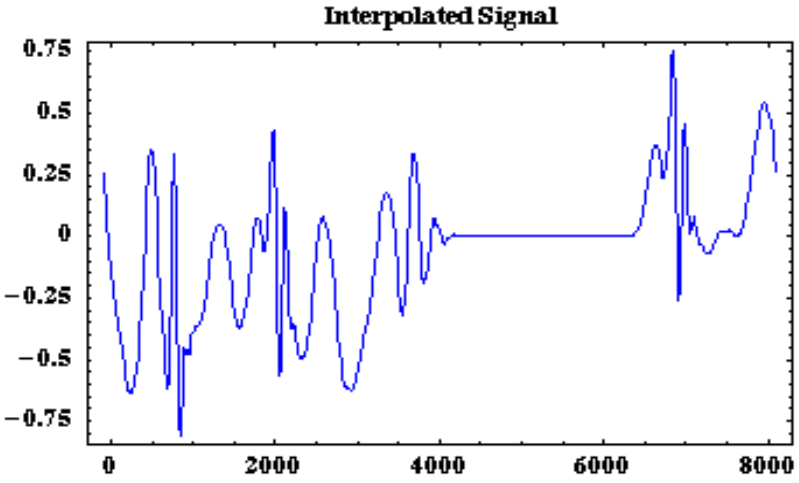

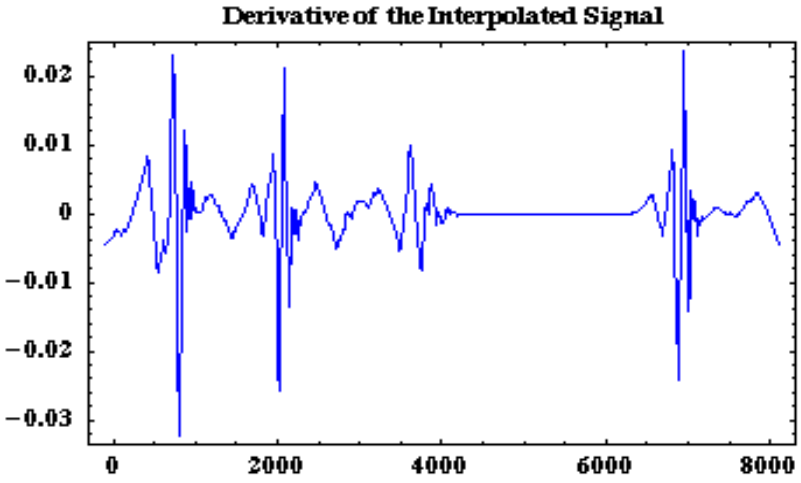

Reconstruction of the LPF Data with 20 Largest WLT Coeffs

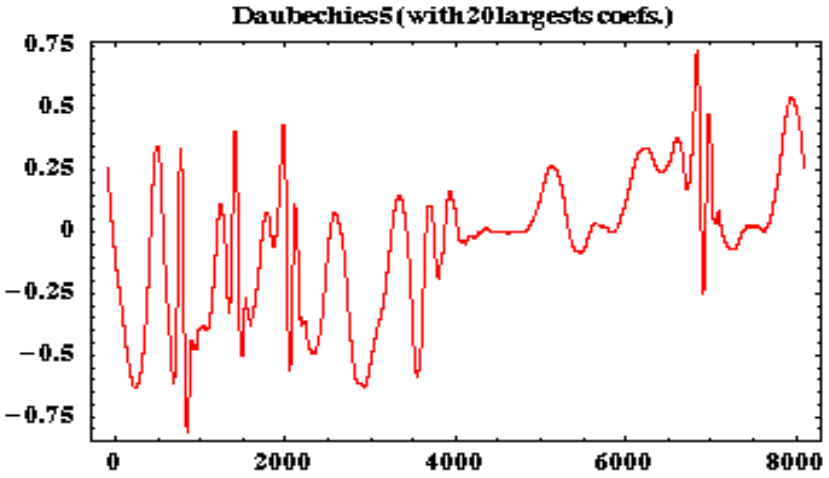

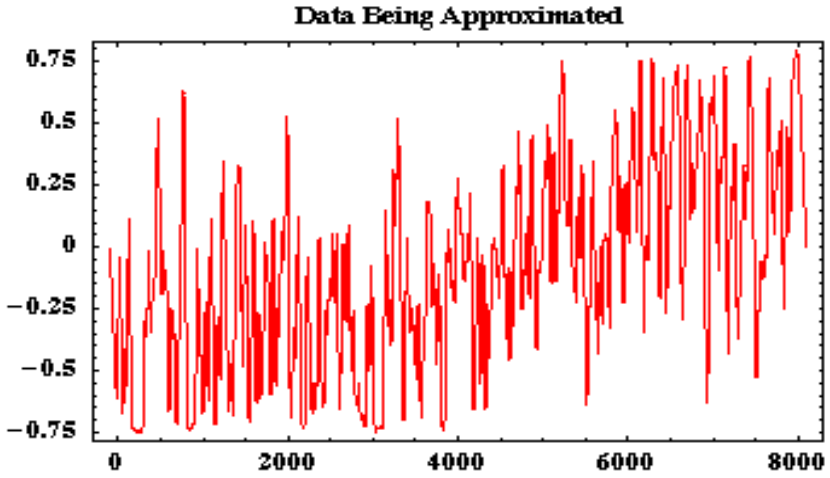

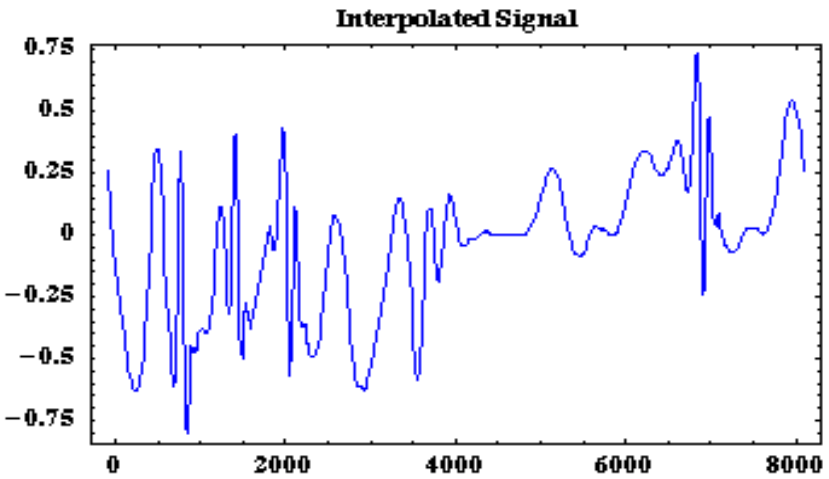

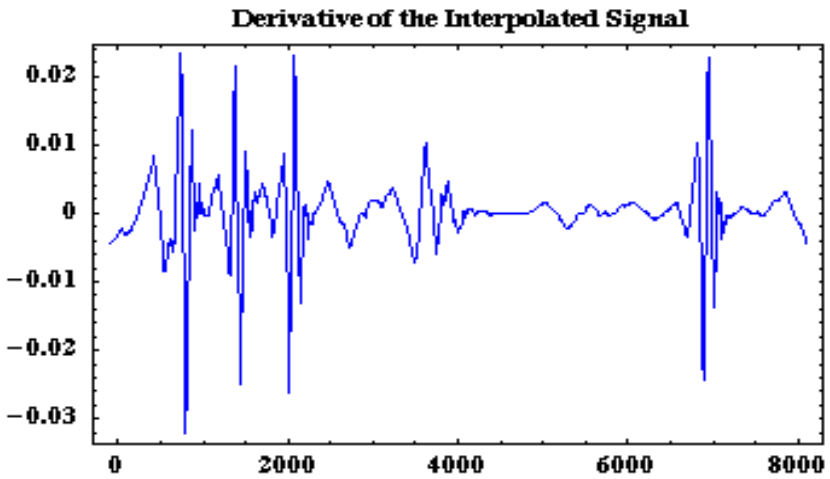

Reconstruction of the LPF Data with 30 Largest WLT Coeffs

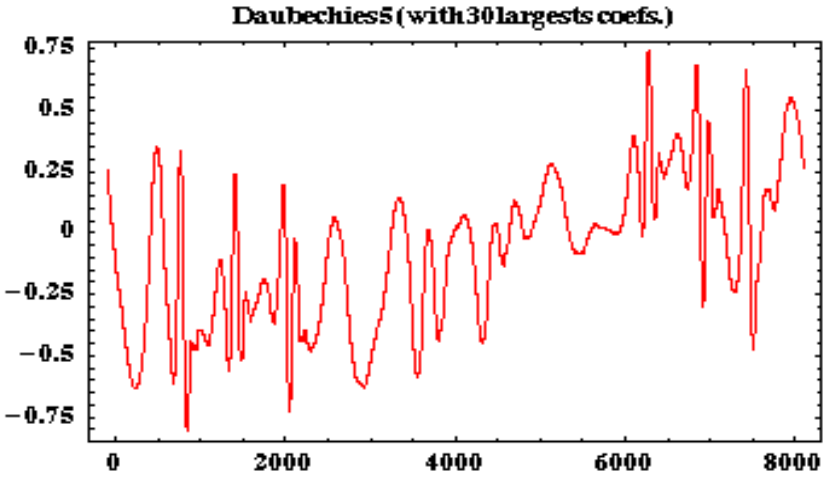

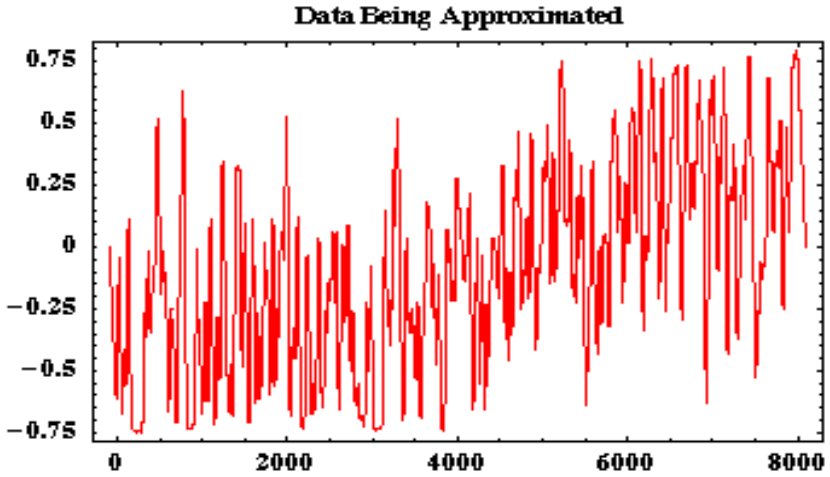

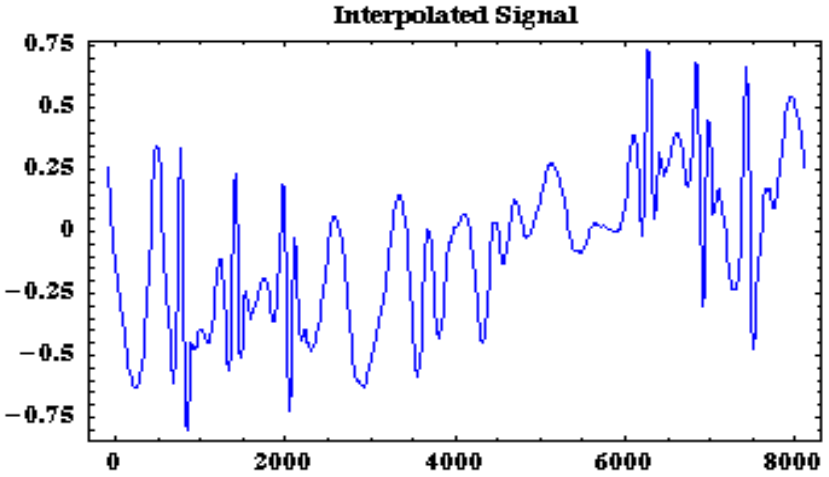

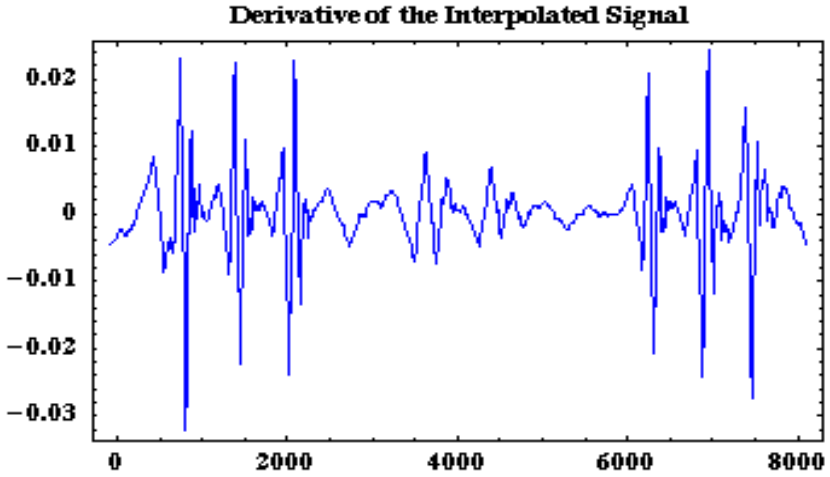

Reconstruction of the LPF Data with 50 Largest WLT Coeffs

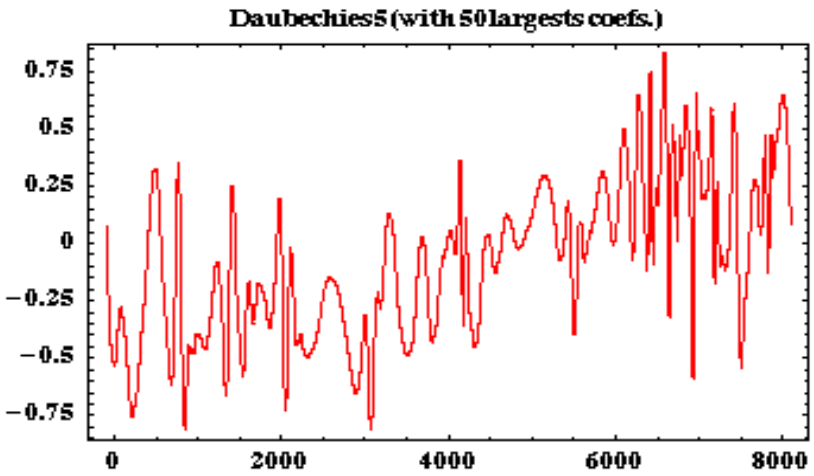

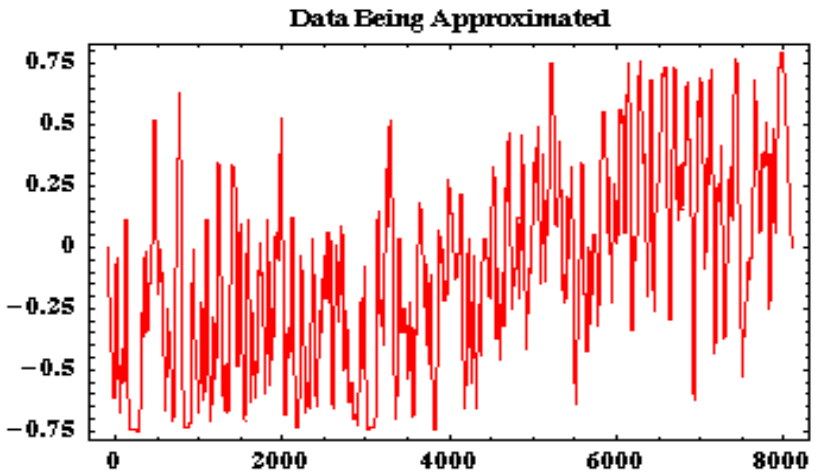

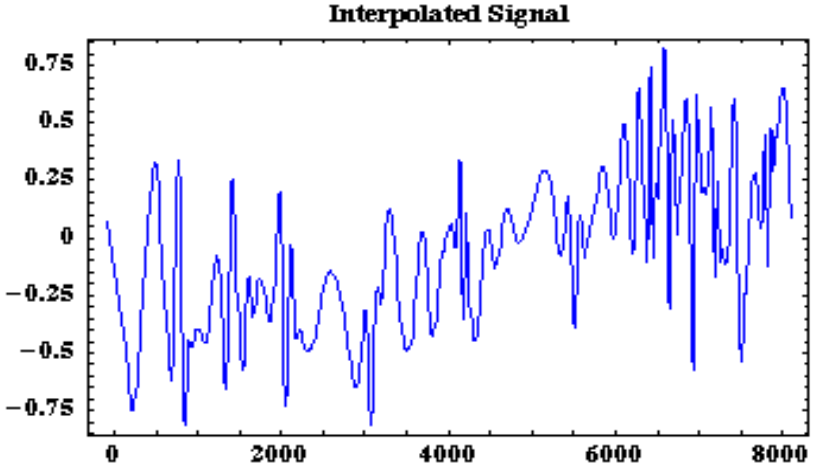

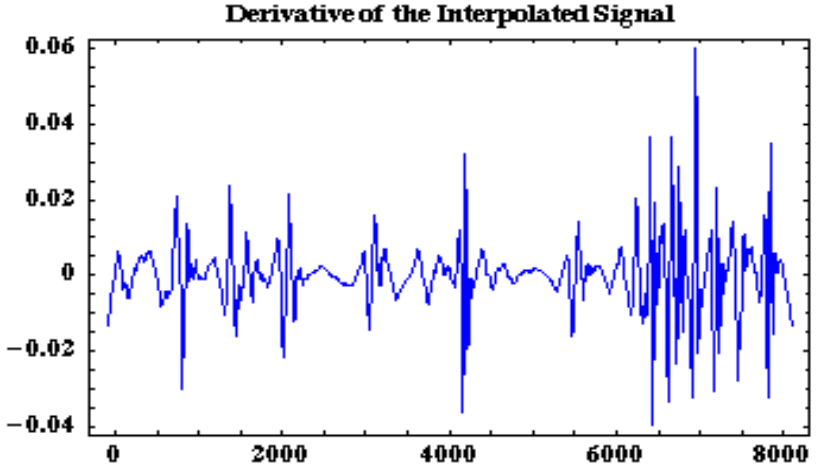

Reconstruction of the LPF Data with 100 Largest WLT Coeffs

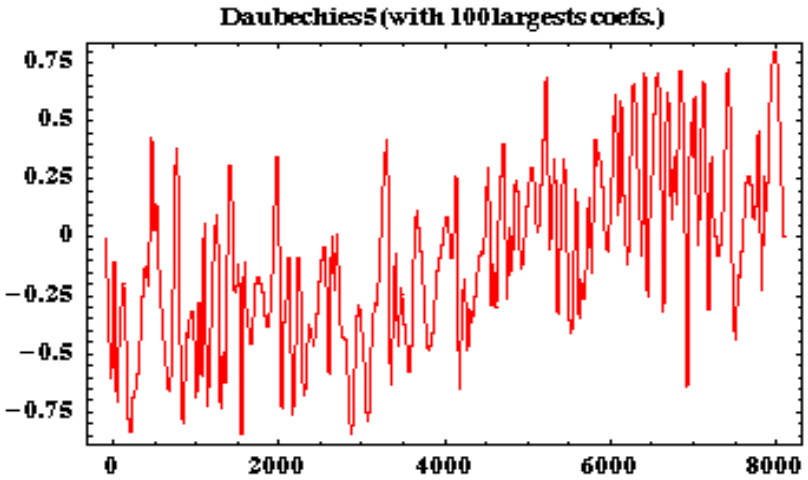

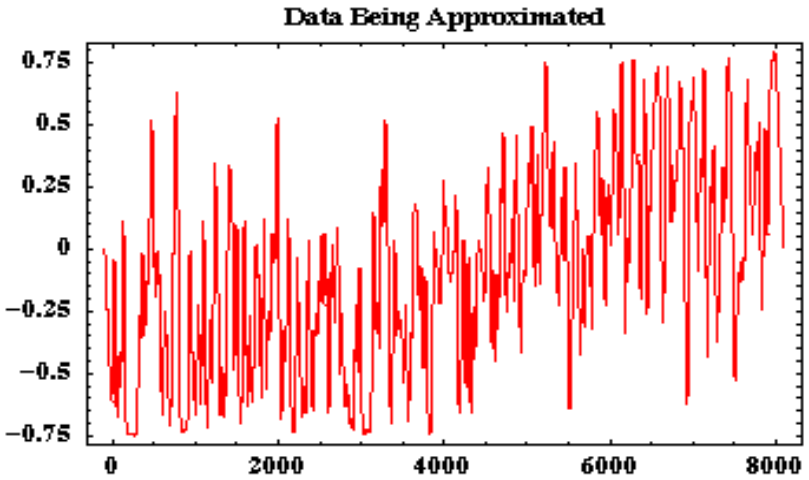

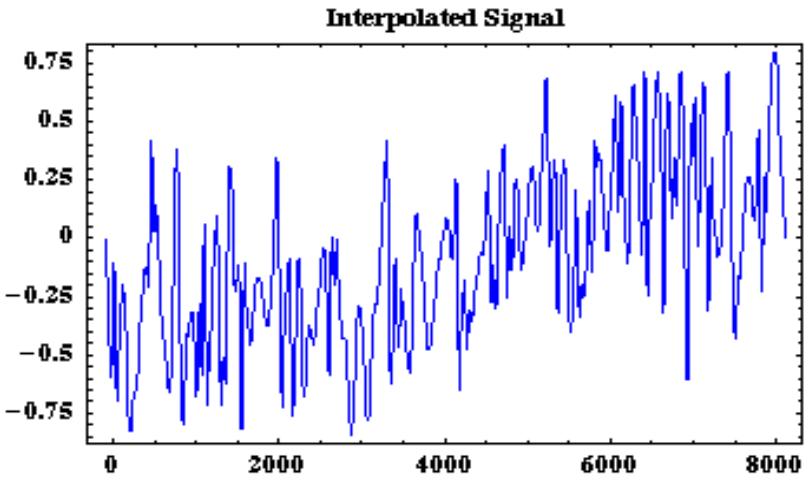

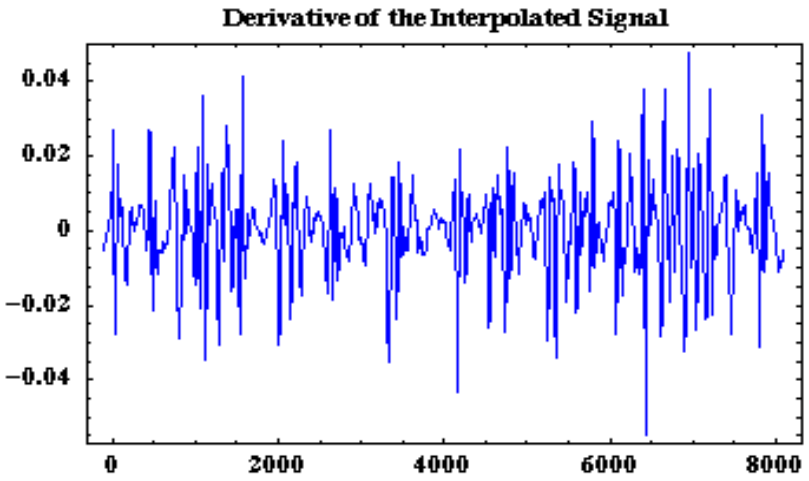

Reconstruction of the LPF Data with 200 Largest WLT Coeffs

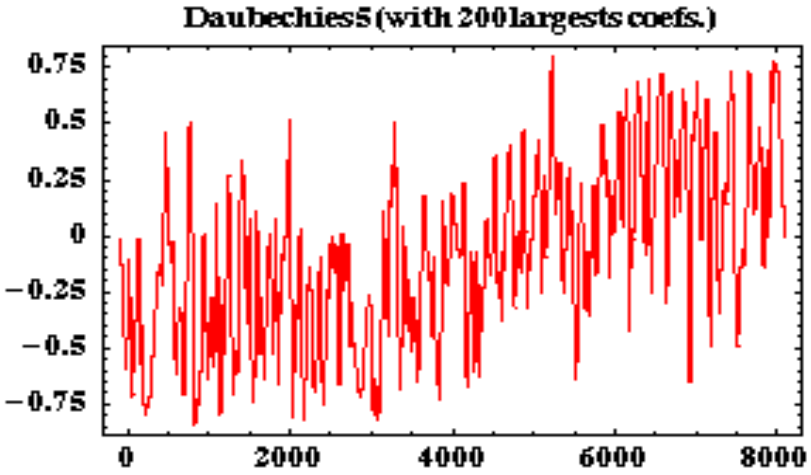

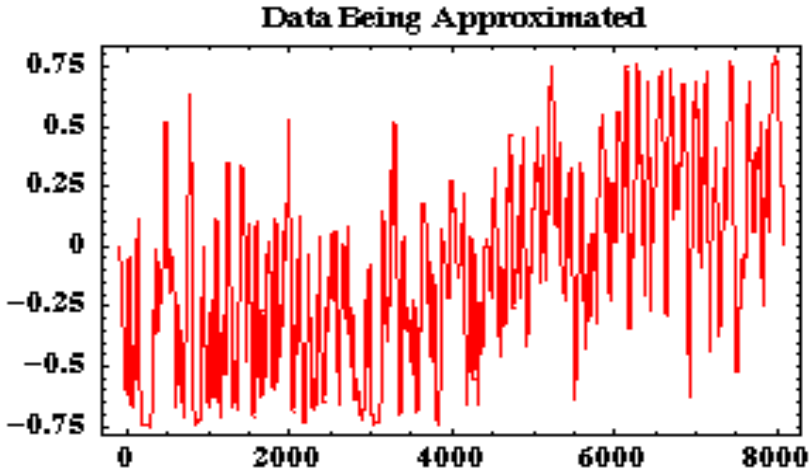

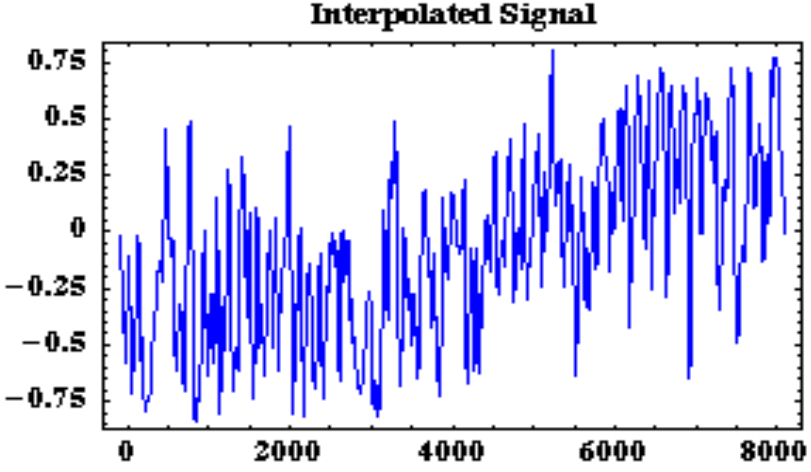

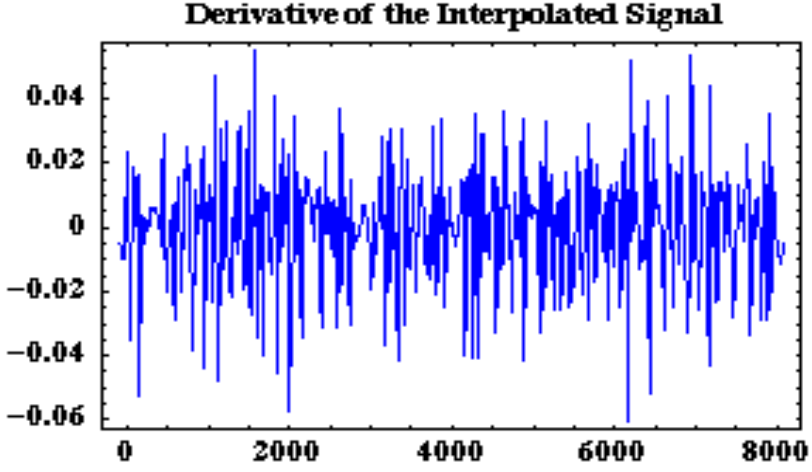

Reconstruction of the LPF Data with 400 Largest WLT Coeffs

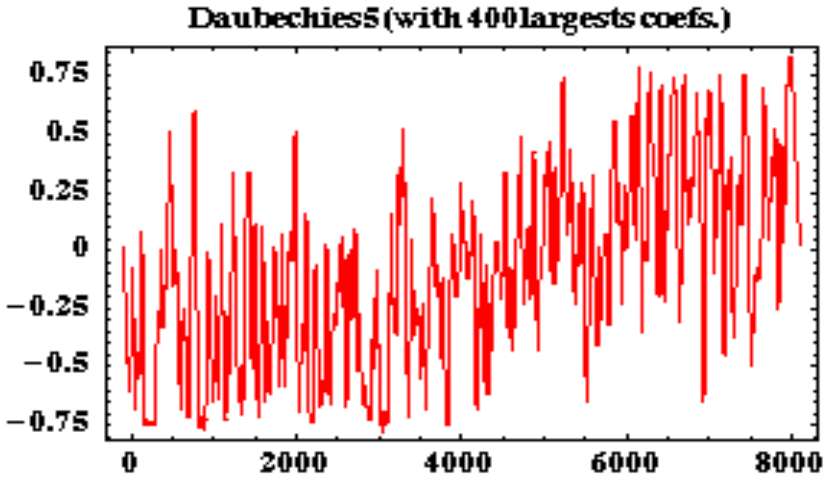

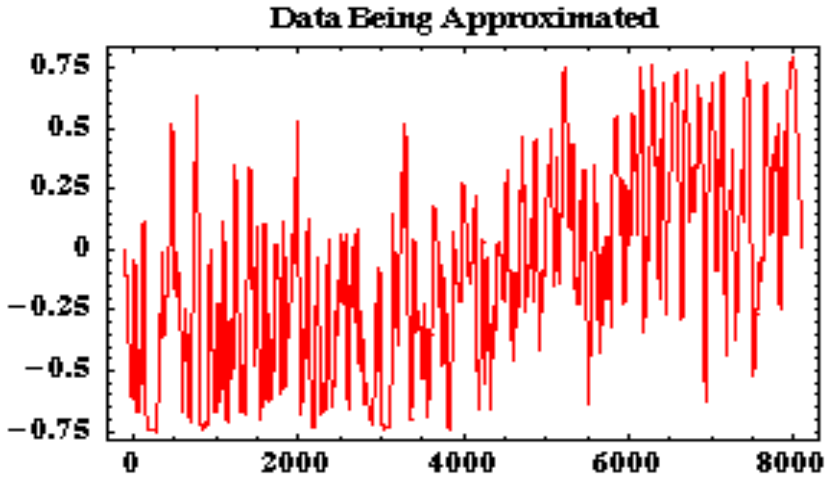

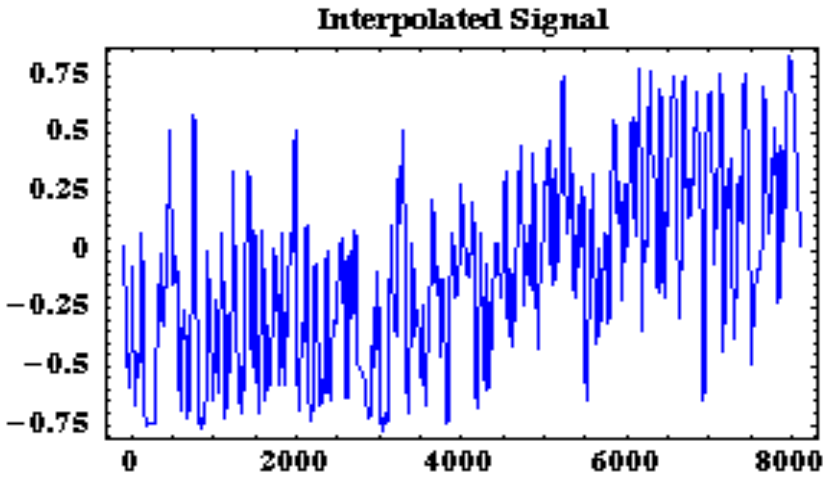

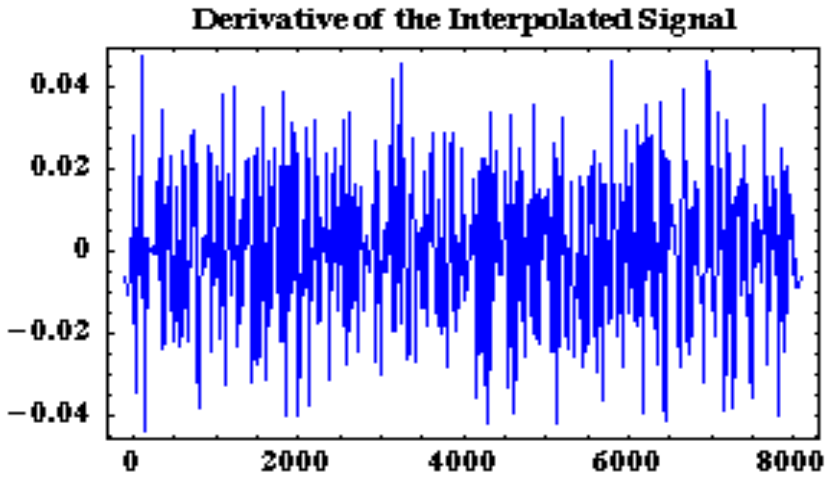

Recons. of the LPF Data Using Up to 0.75 x the Largest WLTs

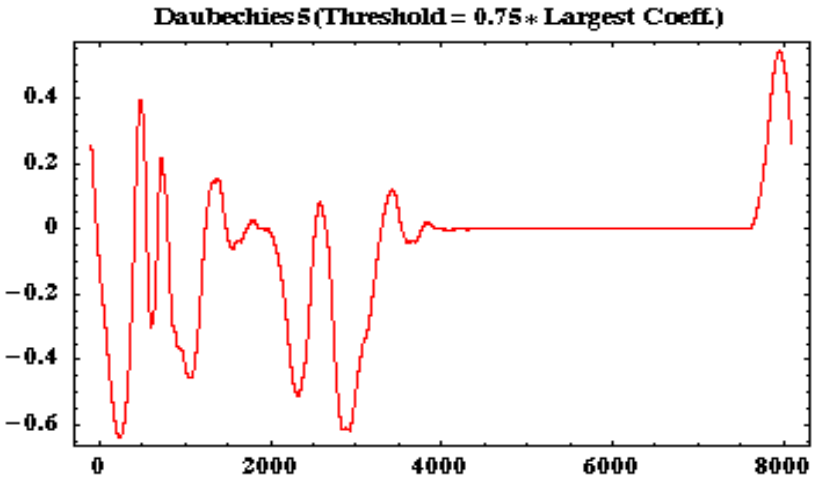

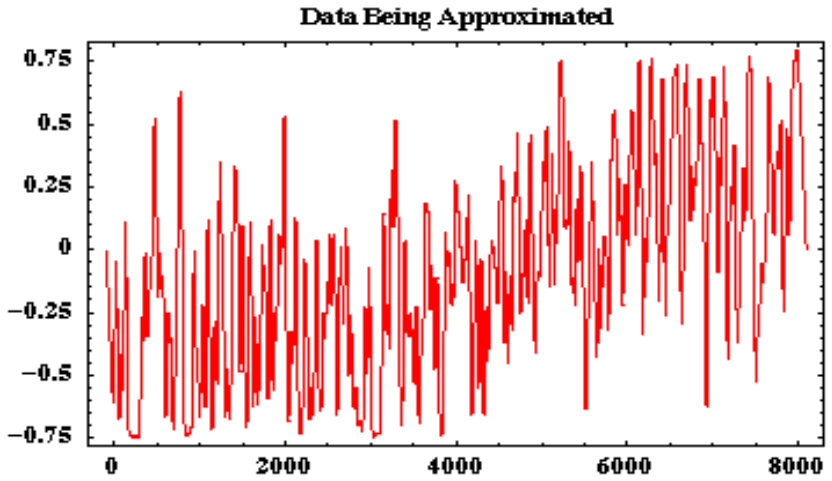

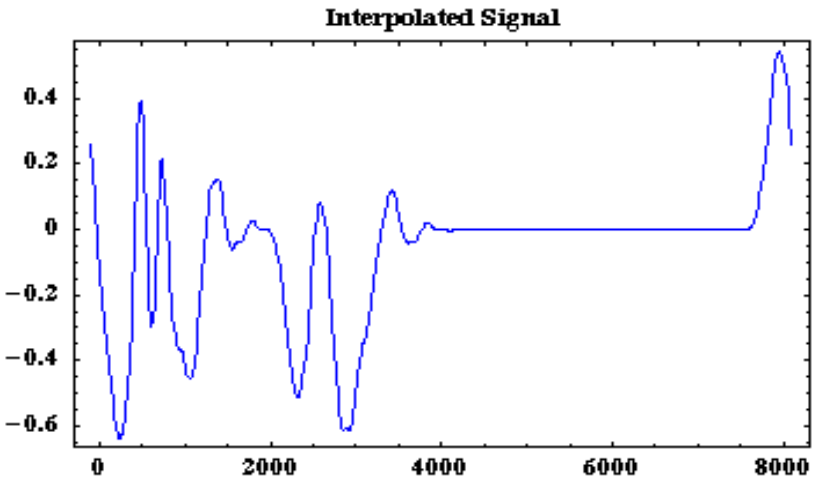

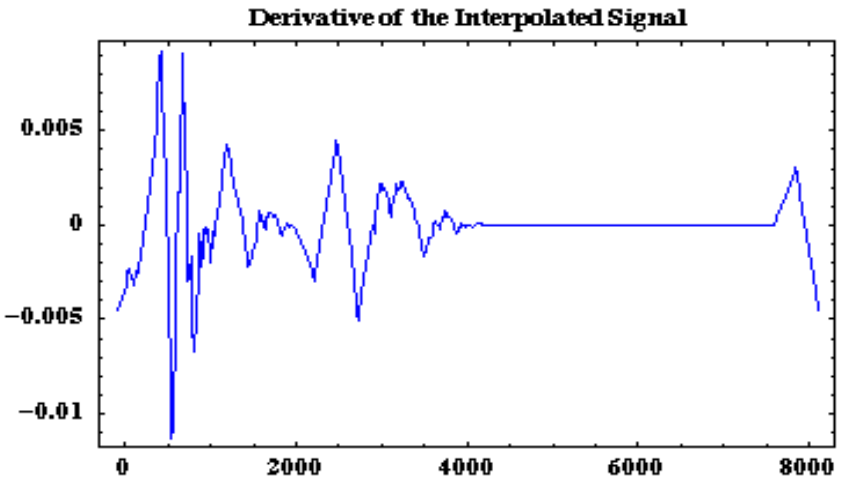

Recons. of the LPF Data Using Up to 0.5 x the Largest WLTs

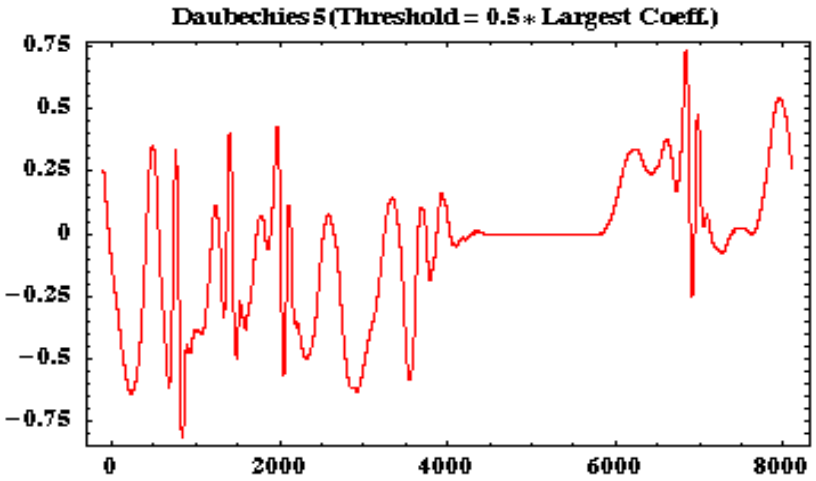

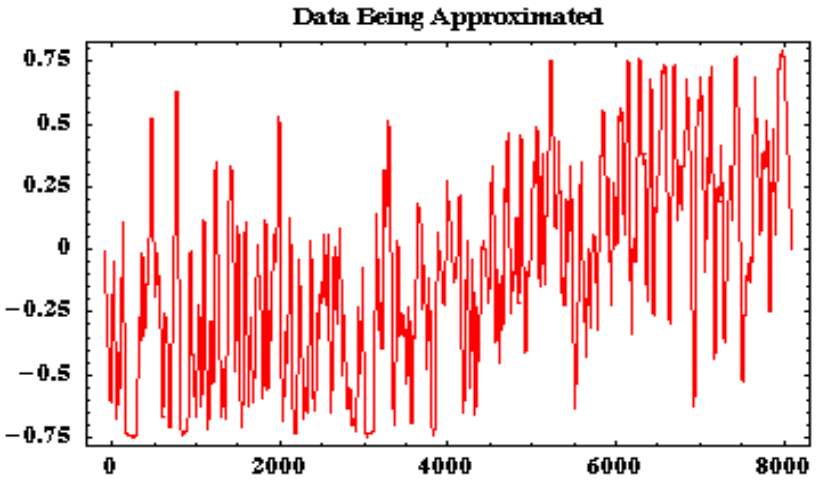

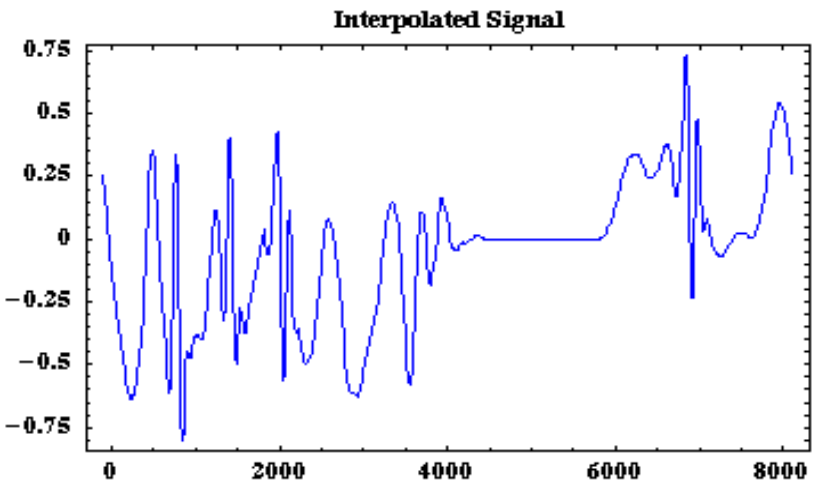

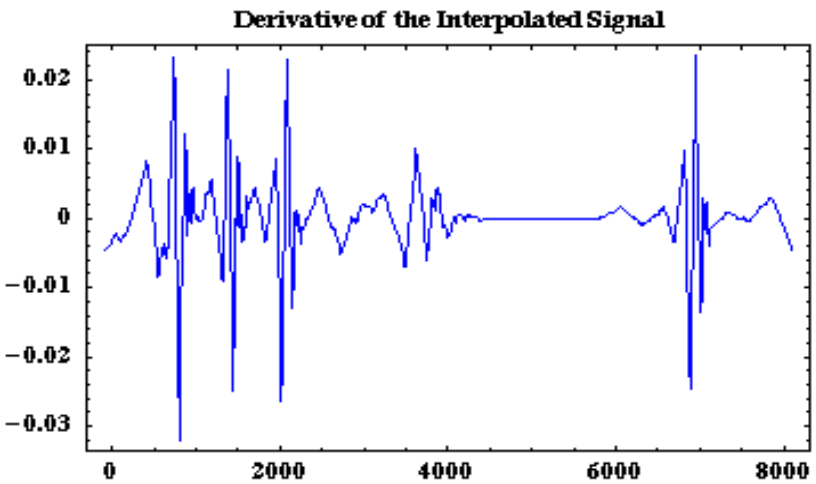

Recons. of the LPF Data Using Up to 0.25 x the Largest WLTs

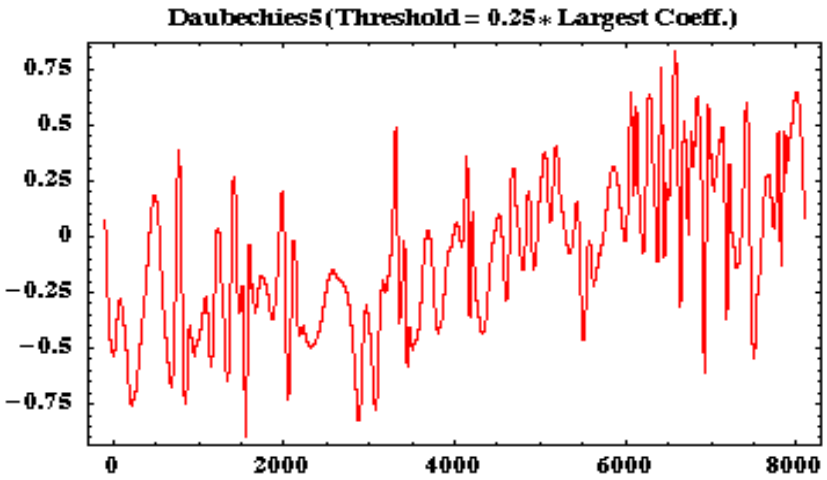

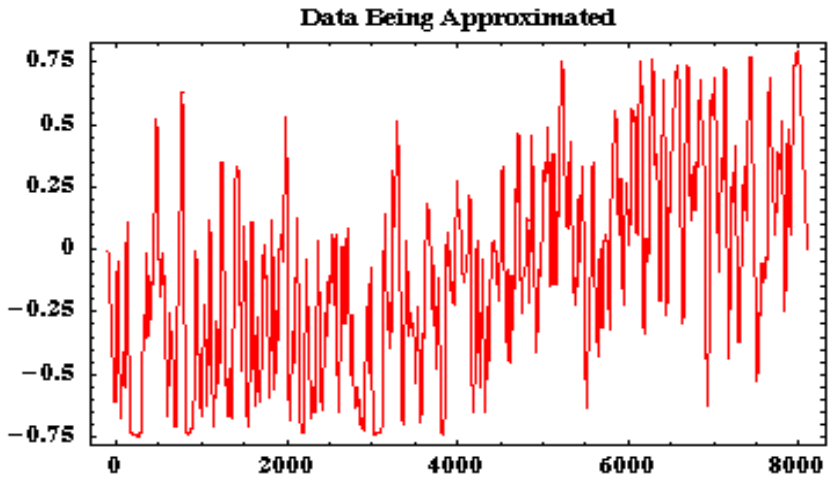

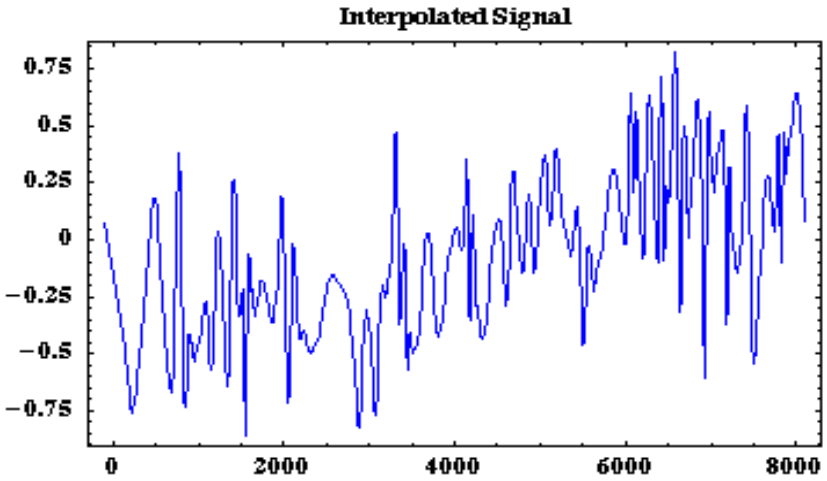

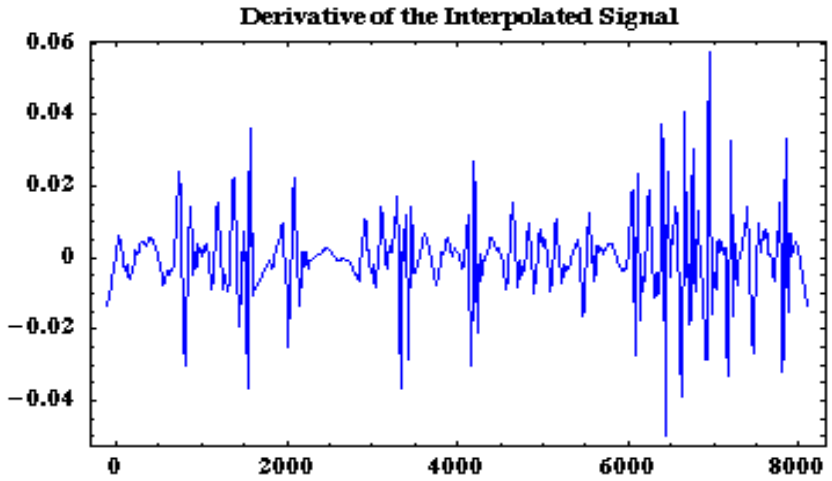

Recons. of the LPF Data Using Up to 0.1 x the Largest WLTs

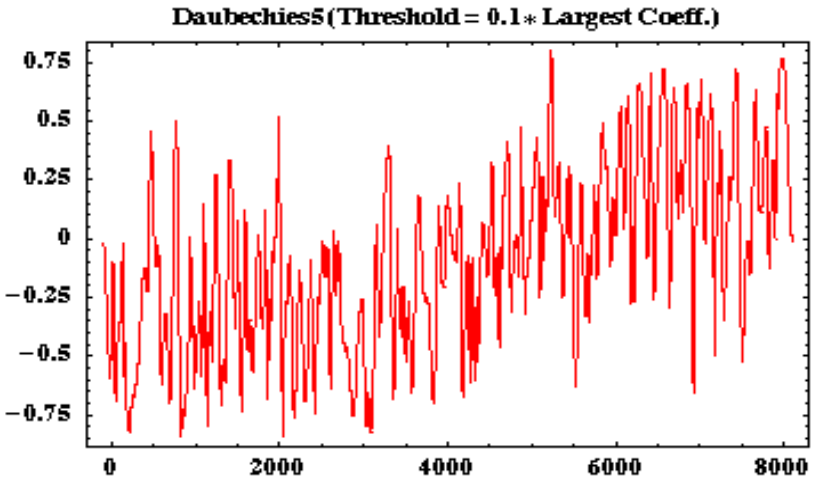

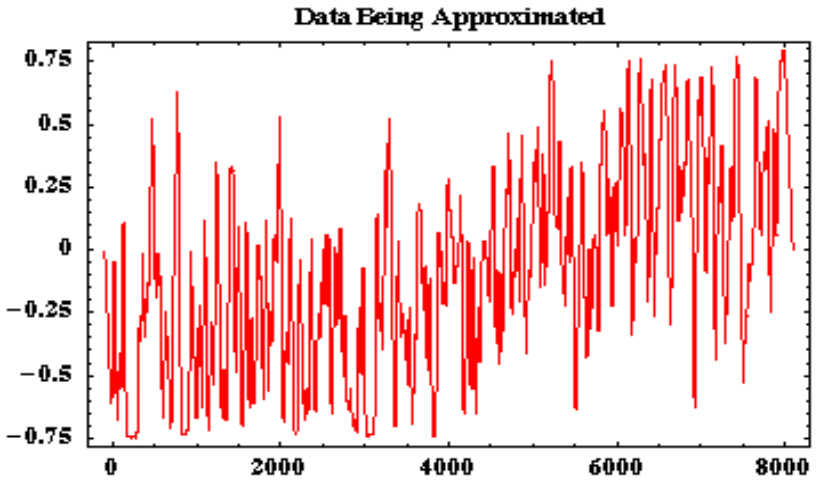

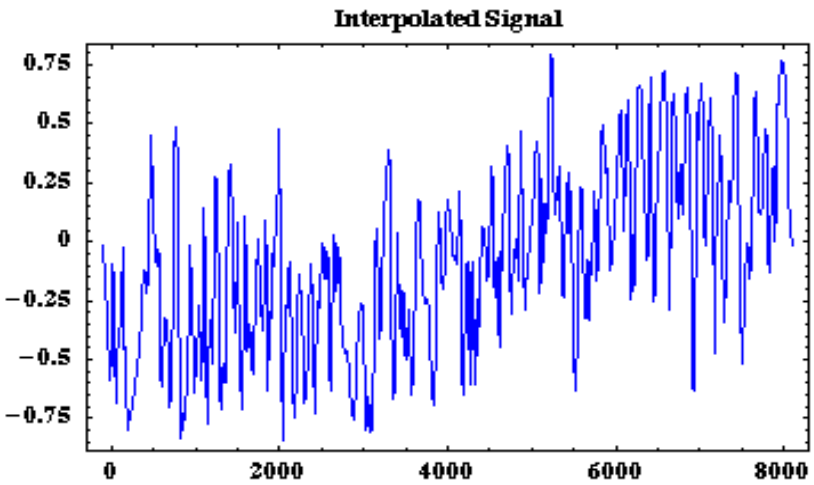

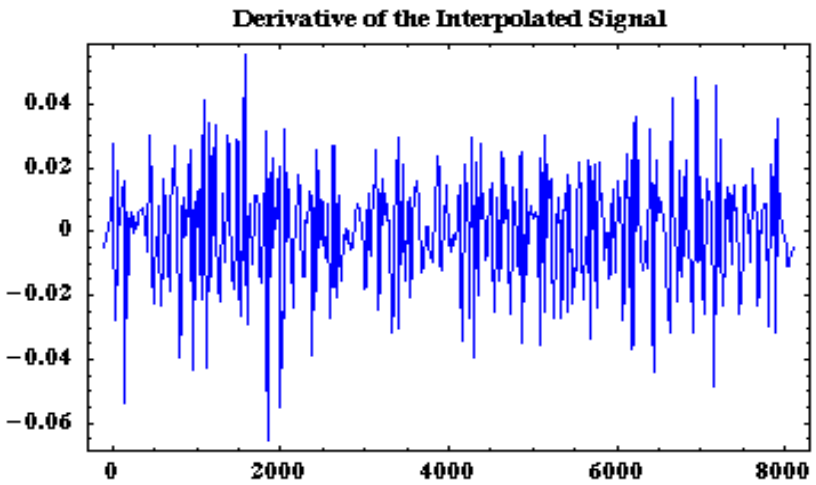

Recons. of the LPF Data Using Up to 0.05 x the Largest WLTs

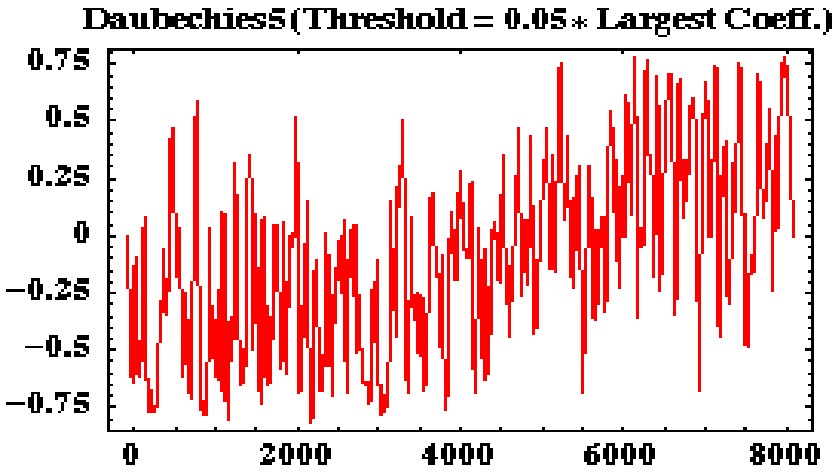

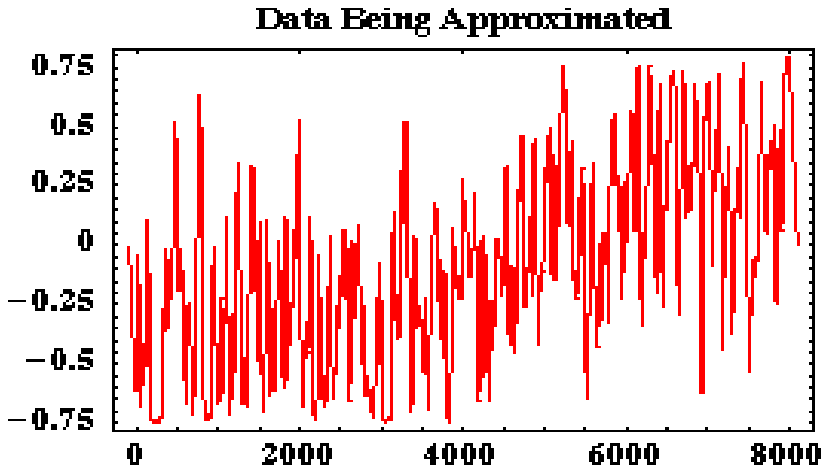

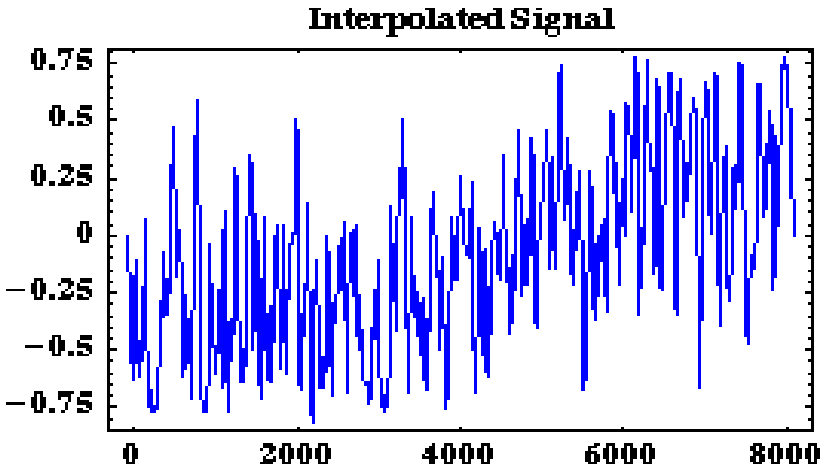

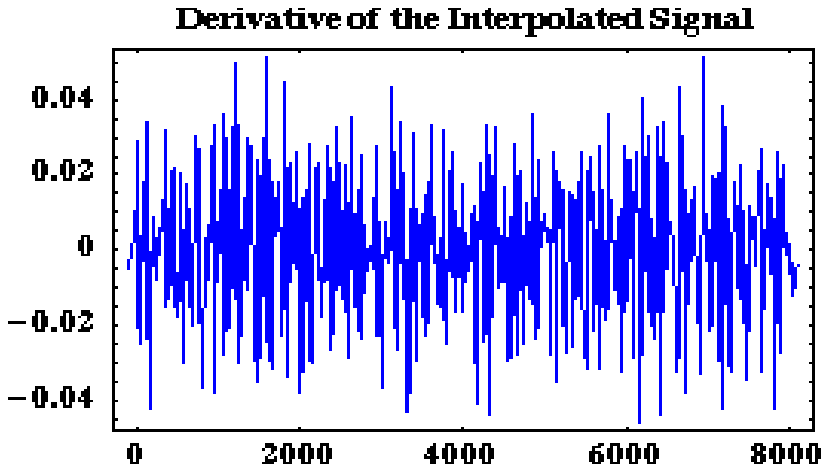

Reconstruction of the LPF Data Using the First MRD Level

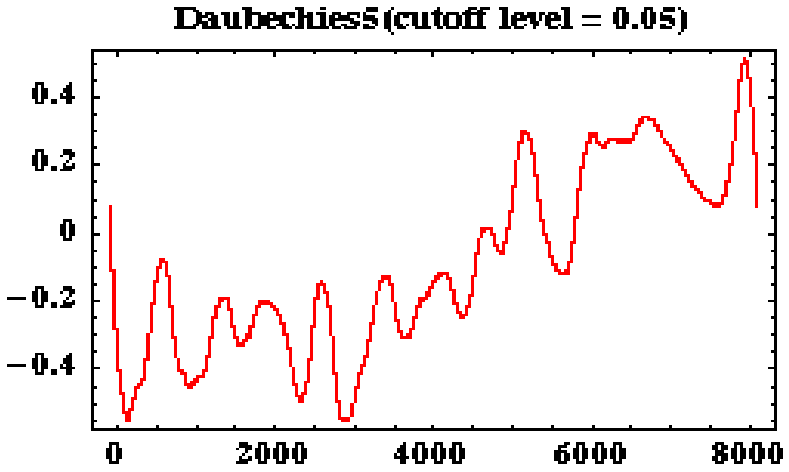

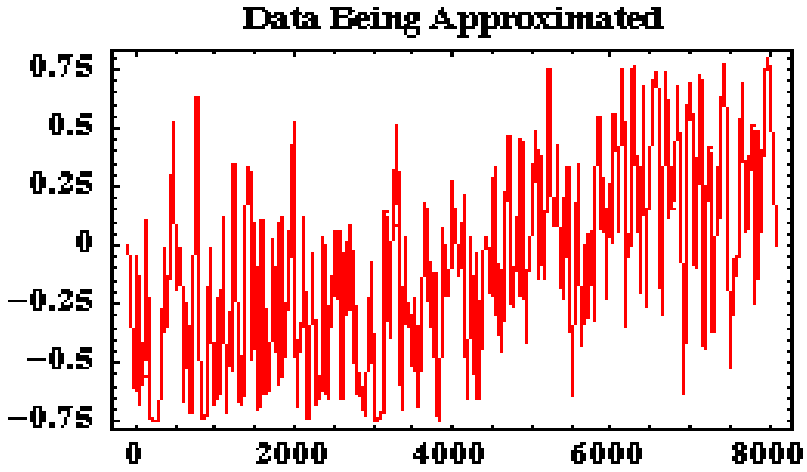

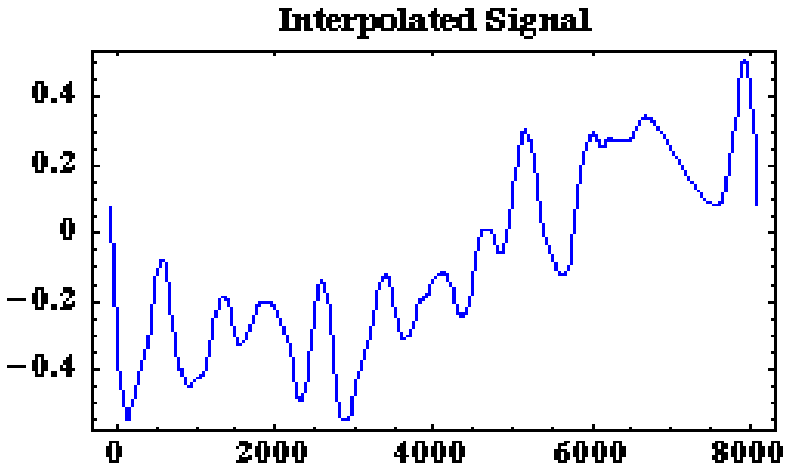

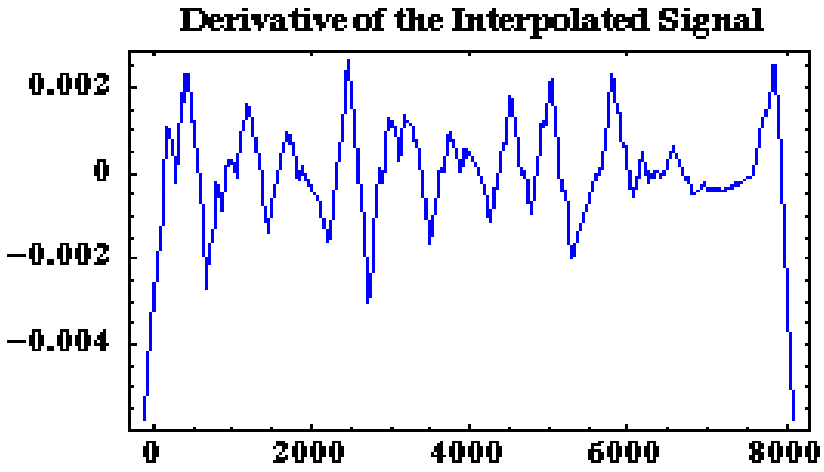

Reconstruction of the LPF Data Using the First 2 MRD Levels

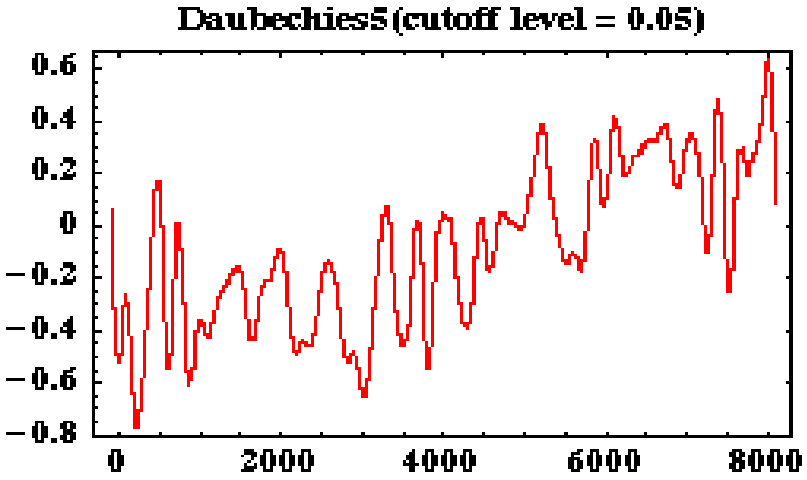

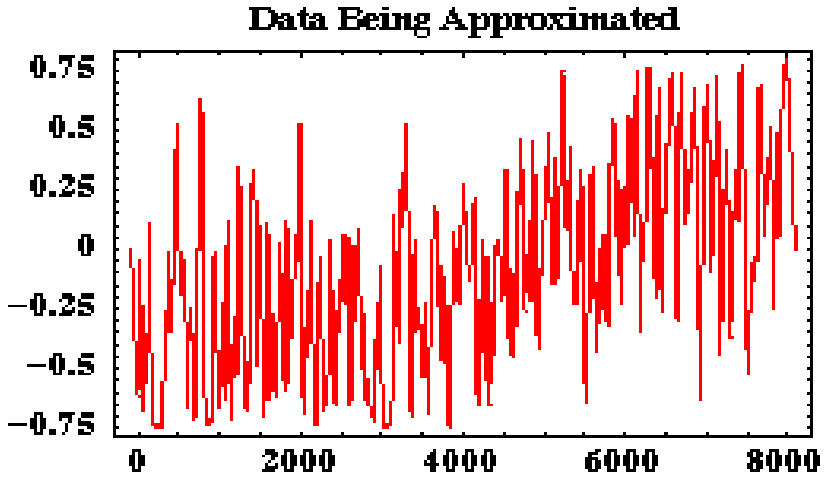

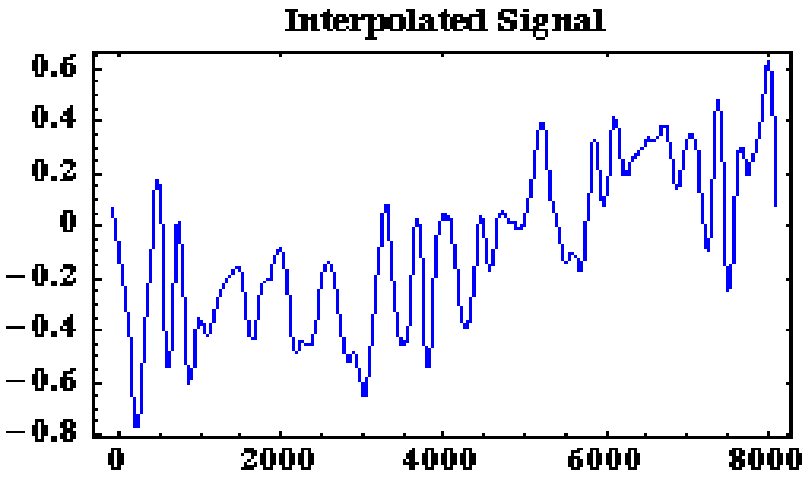

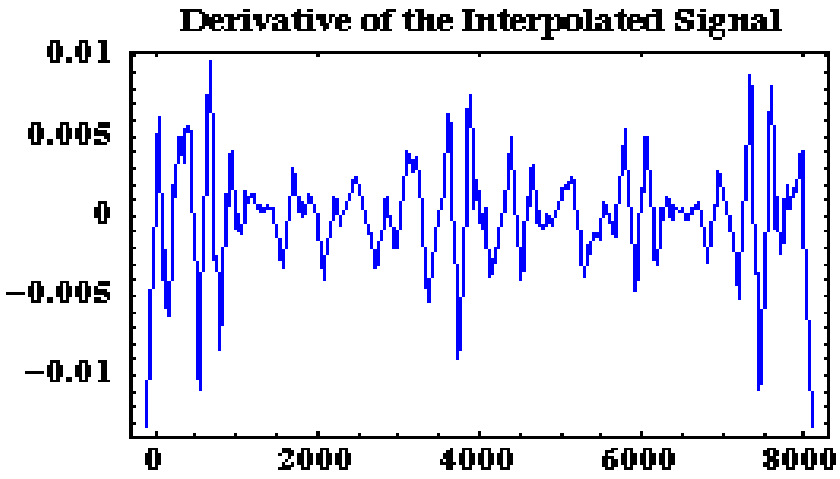

Reconstruction of the LPF Data Using the First 3 MRD Levels

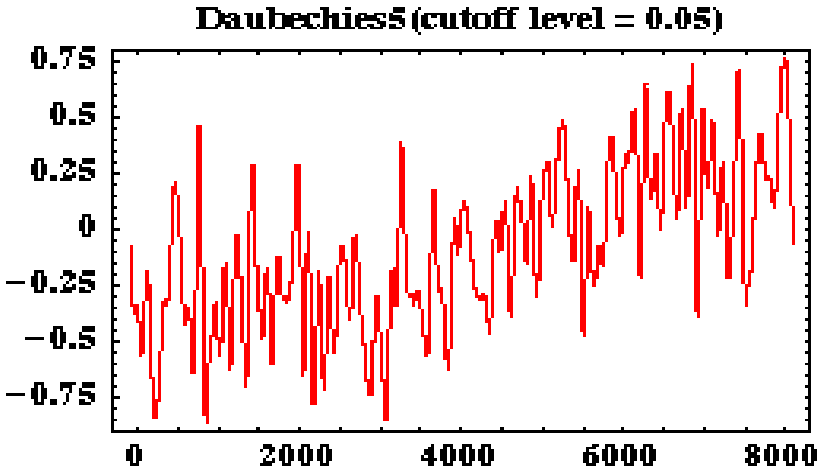

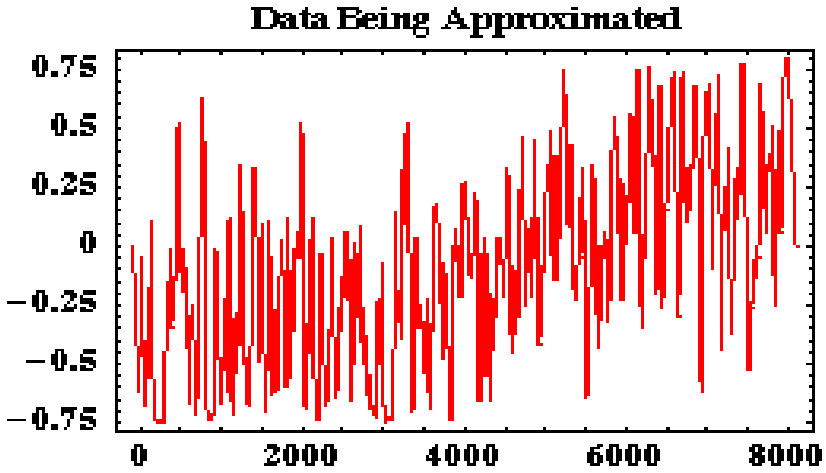

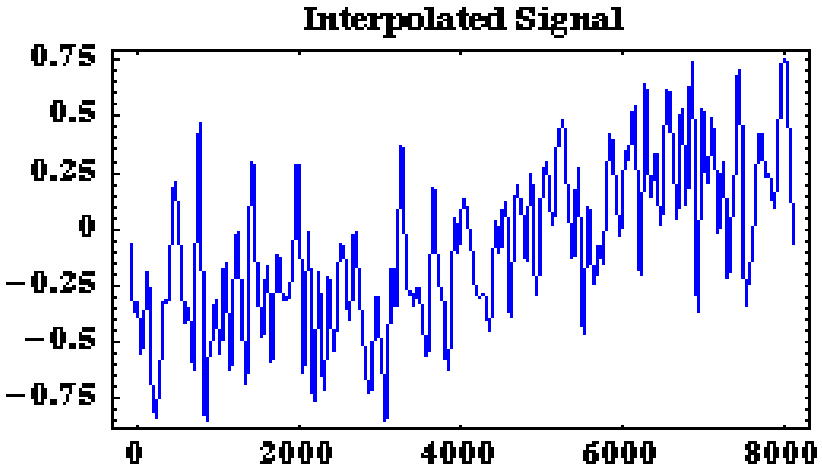

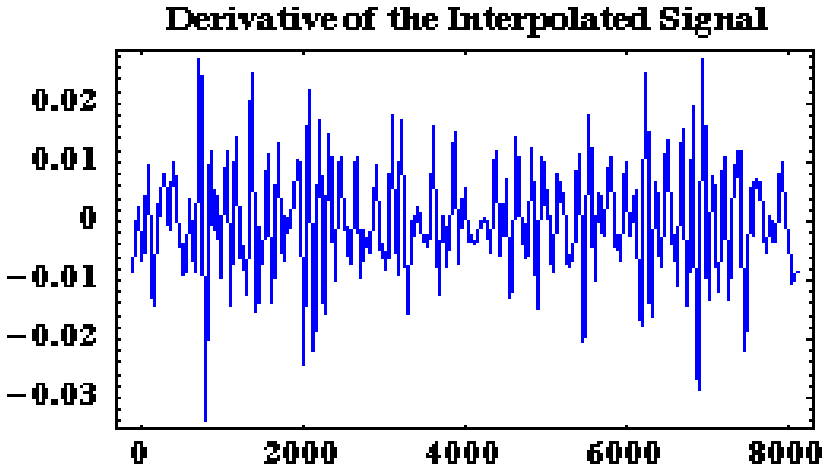

Reconstruction of the LPF Data Using the First 4 MRD Levels

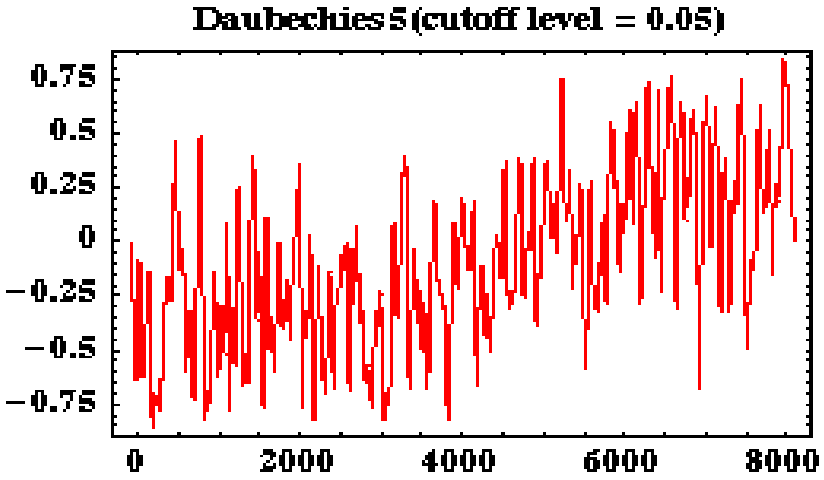

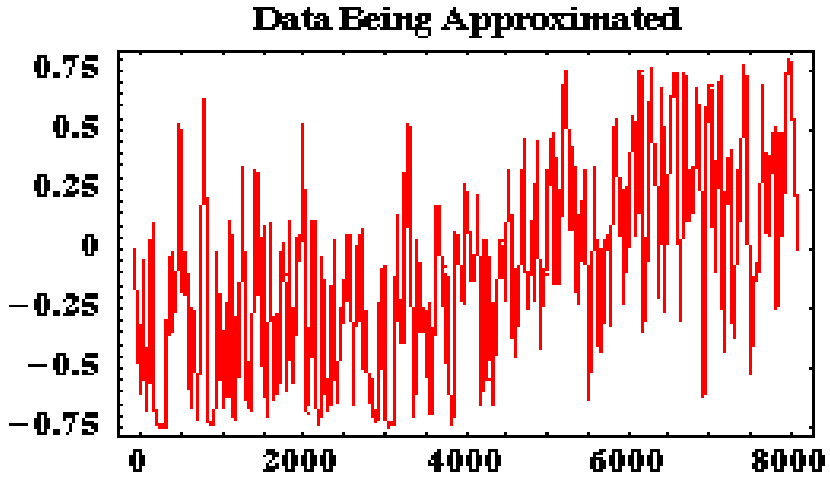

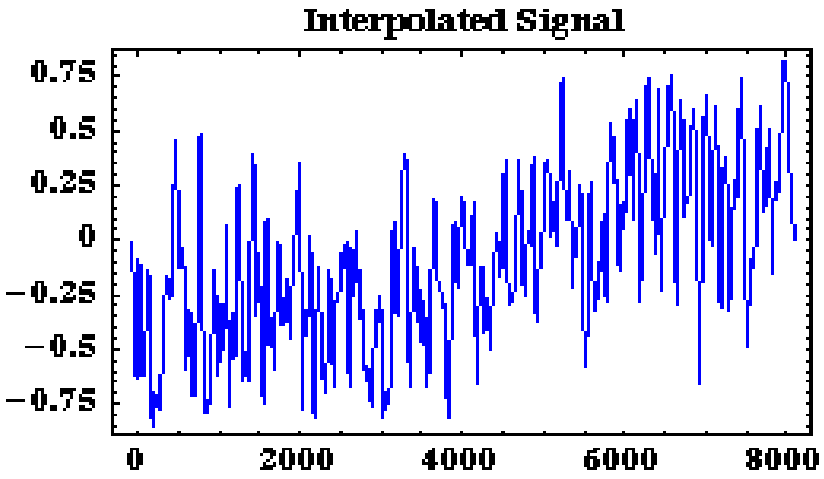

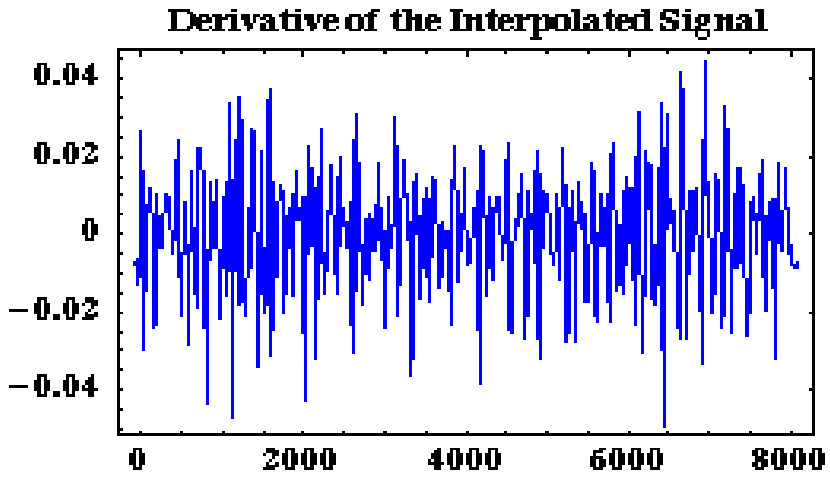

Reconstruction of the LPF Data Using the First 5 MRD Levels

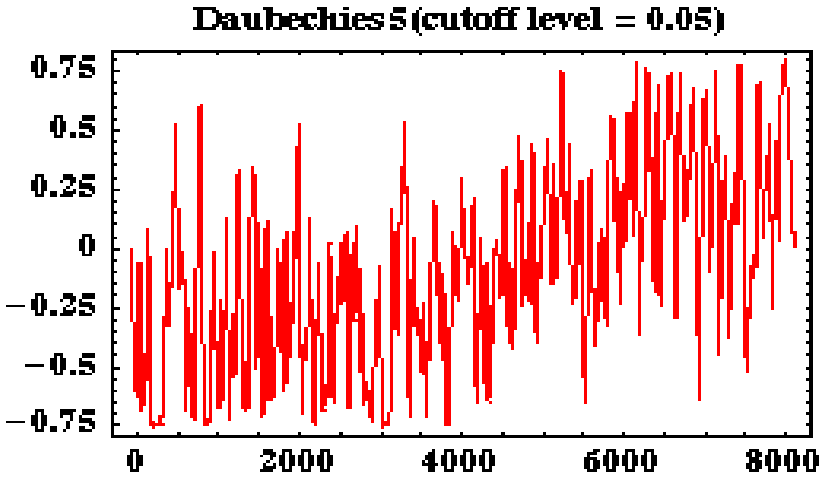

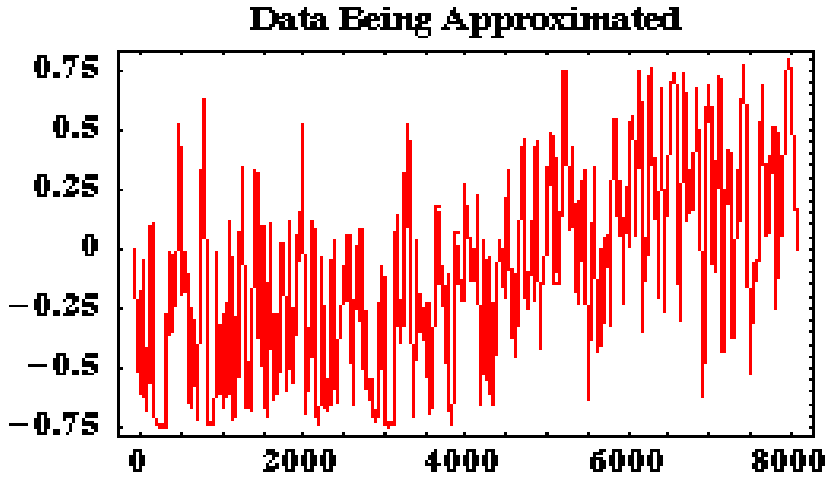

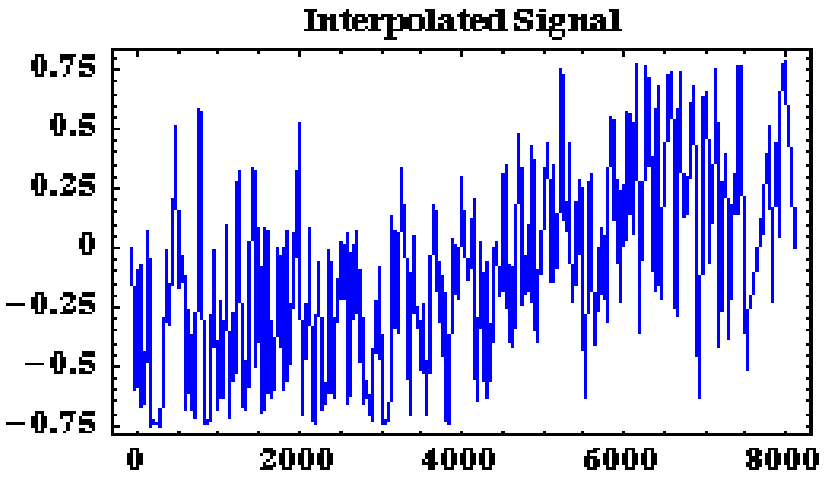

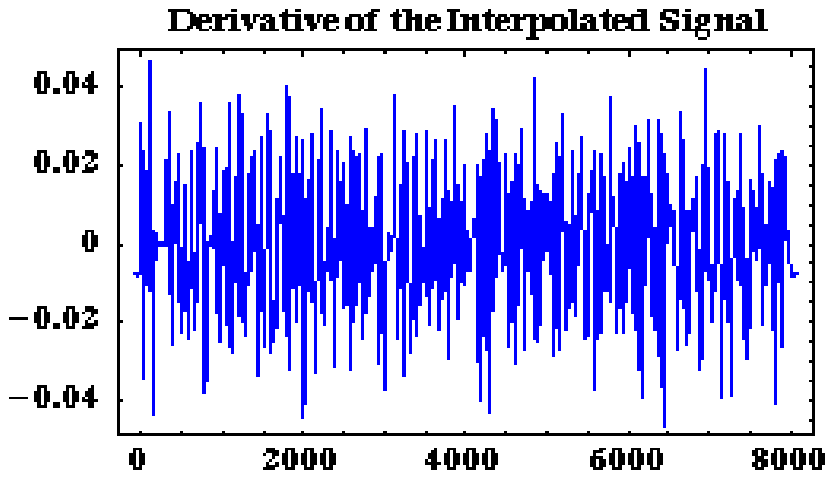

Conclusions Regarding the WLT Analysis of the LPF RT Mix Data

- Far better compression and denoising is achieved once a modest amount of initial low pass filtering is done on the data.
- Note the extremely small contributions levels 5 and above make to the MRD while with the unfiltered data that contribution was of order 1 or 0.1
- Far cleaner structures are observable in levels 1, 2 and 3, periodic correlations in time, or so it seems to the eye!
- The reconstruction with largest wavelets kept shows long patches of flatness surrounded by localized structures which could be indicative of the correlation properties of the data.
- More to come!

Raw RT Weak Mix Data (2 cm Downstream, Theta = 0.7) from Texas A&M

Polymath Research Inc.

$$\frac{T - T_{AVE}}{T_{MAX} - T_{AVE}}$$

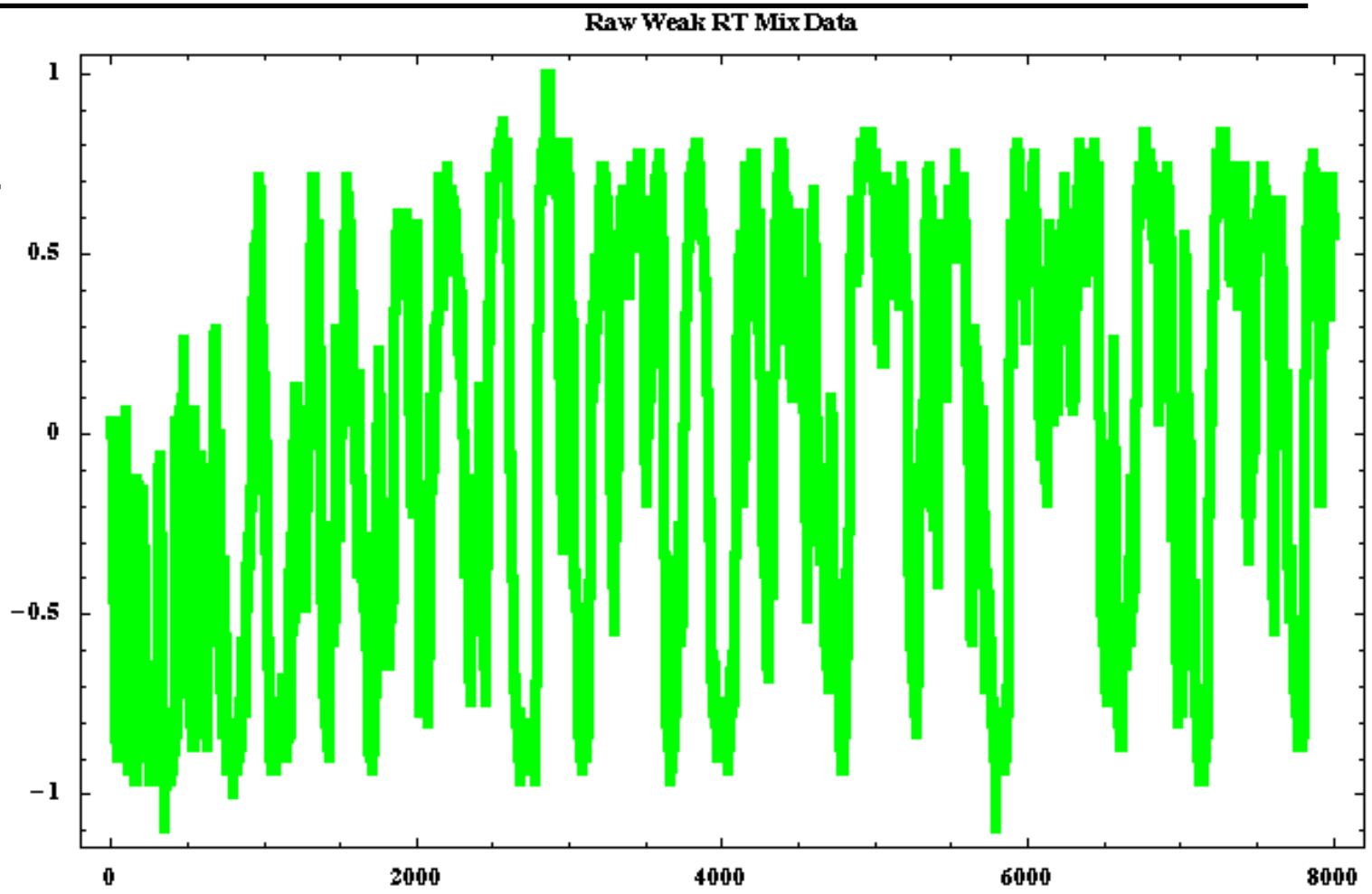

The Faded and Padded Version of the RT Weak Mix Data: 8192 Points

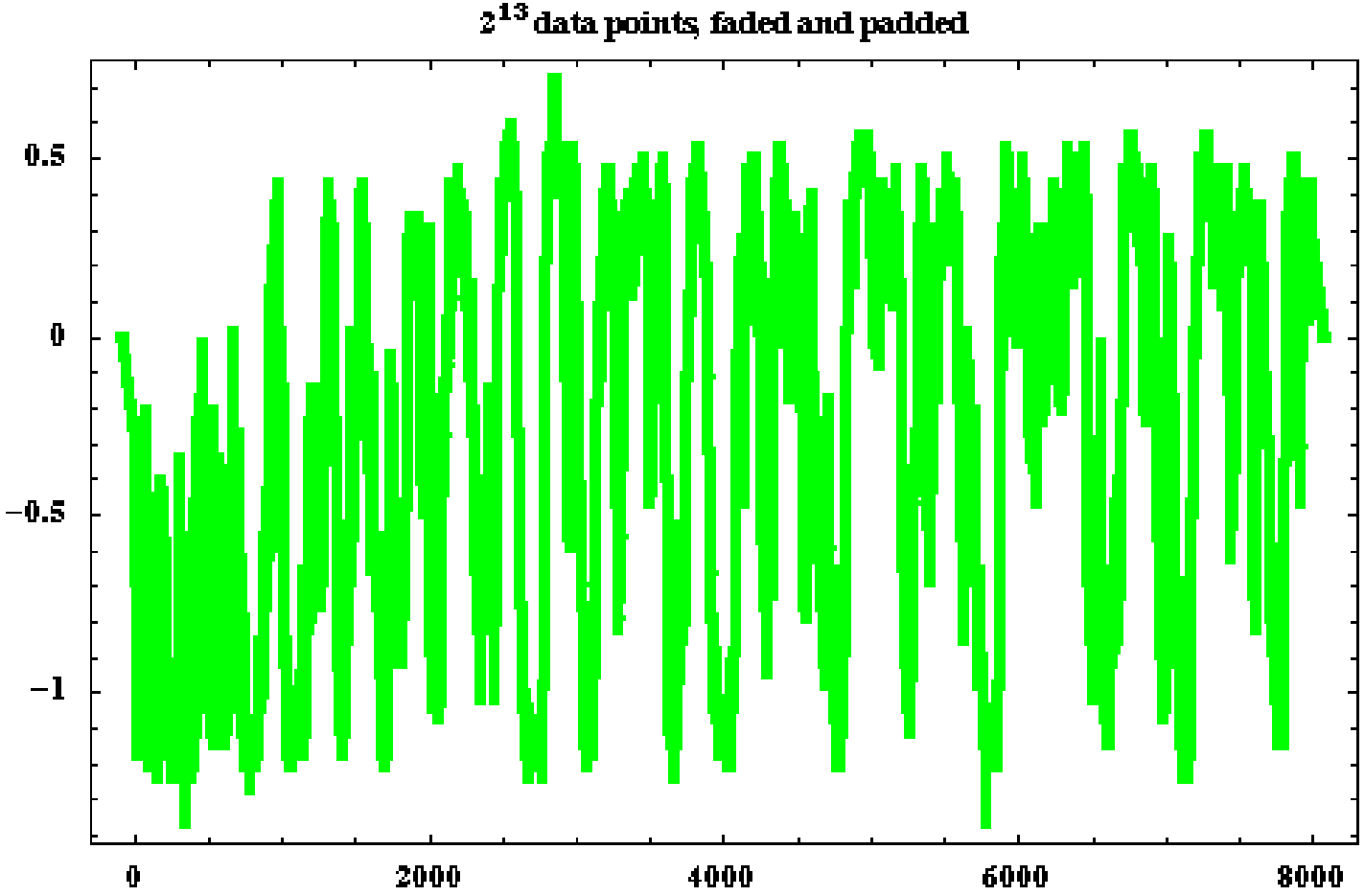

BBA WLTs and RT Mix
Cal Tech Pasadena CA
8th IW PCTM 12-11-01

The Fourier Transform of the RT Weak Mix Data

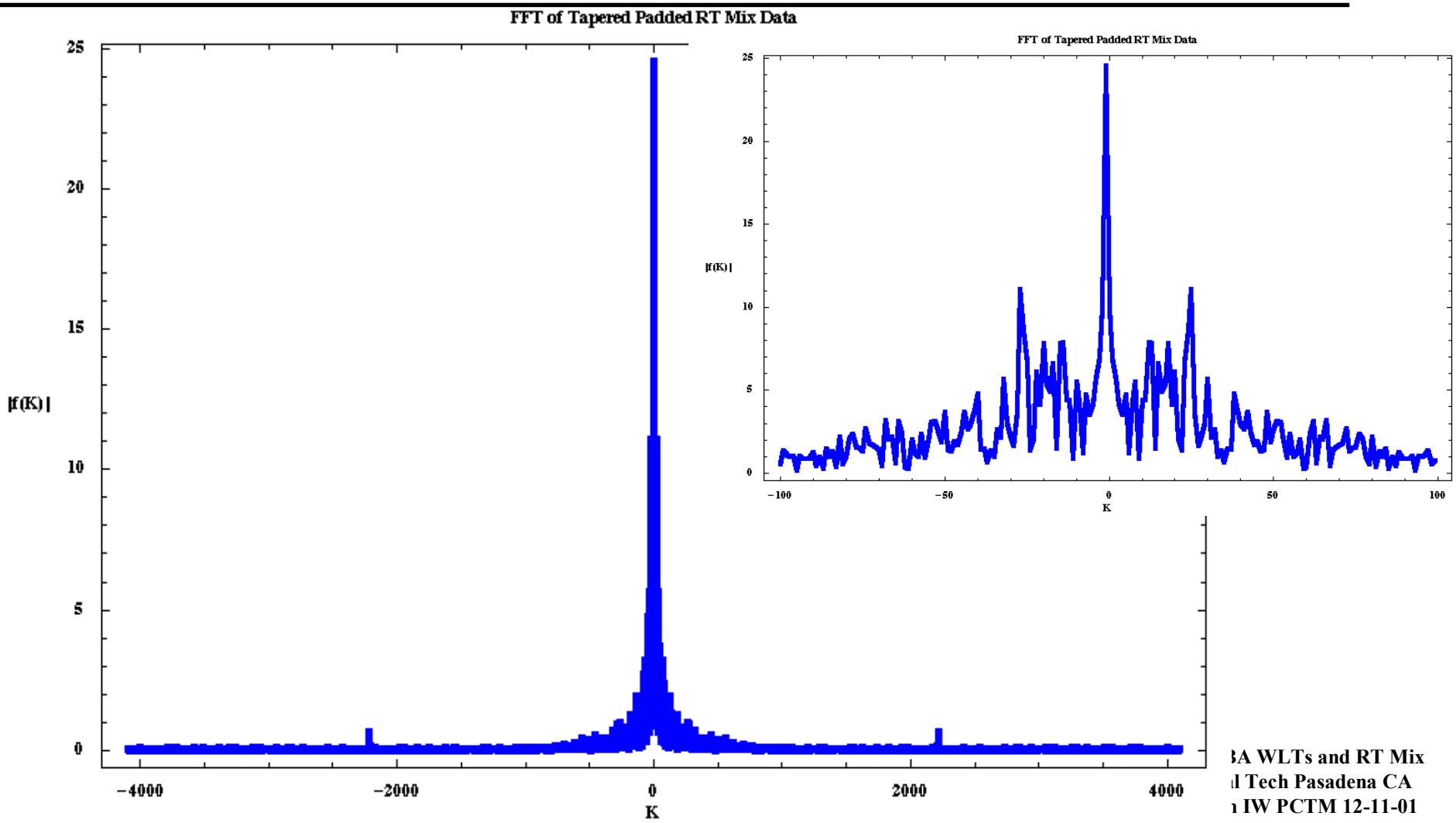

MRD Coefficients of the RT Weak Mix Data in 6 Different Daubechies WLT Bases

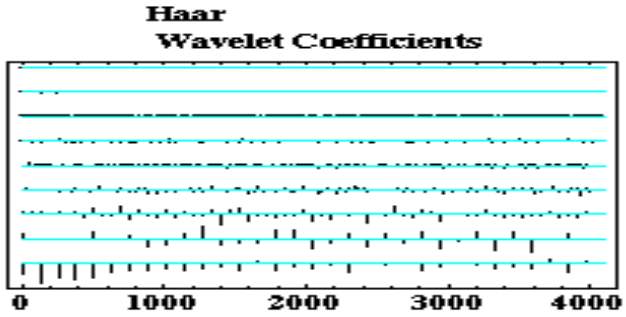

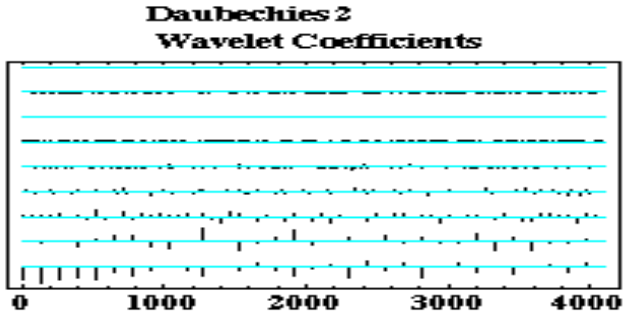

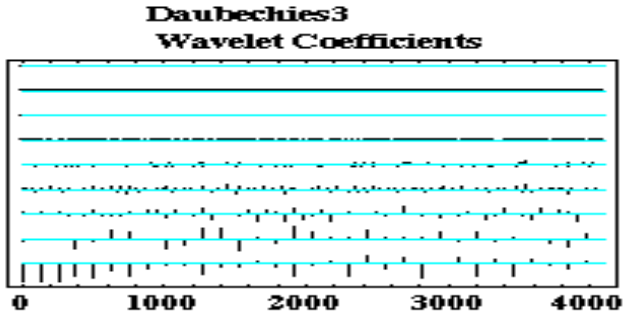

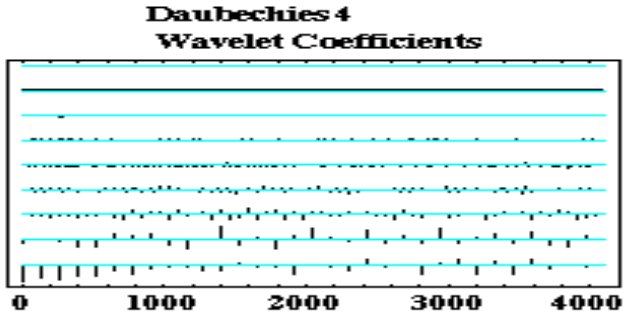

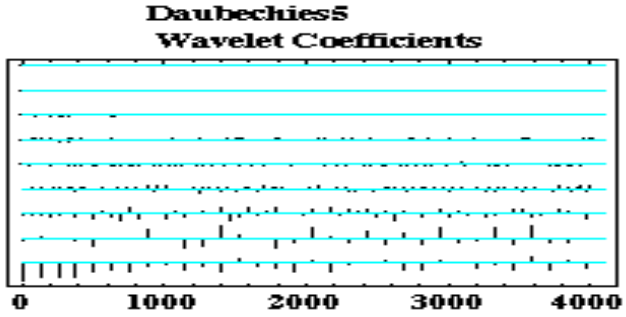

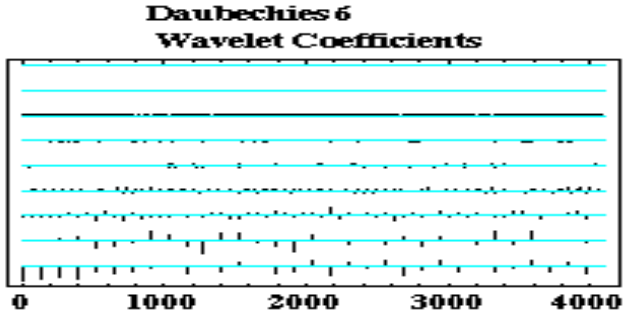

Actual MRDs of the RT Weak Mix Data in 6 Different Daubechies WLT Bases

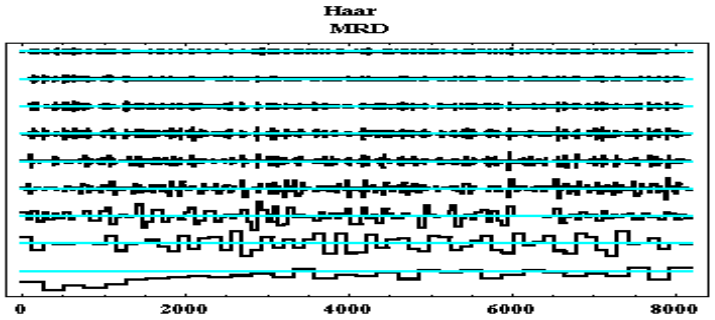

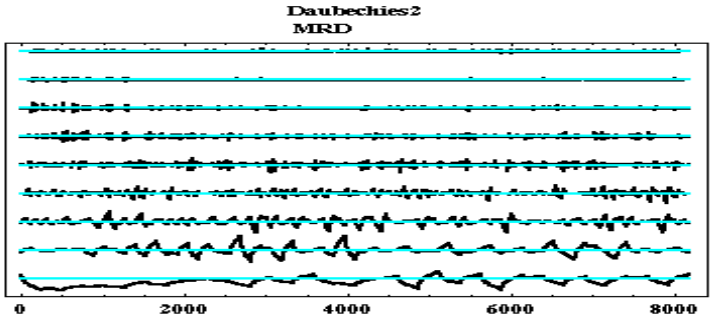

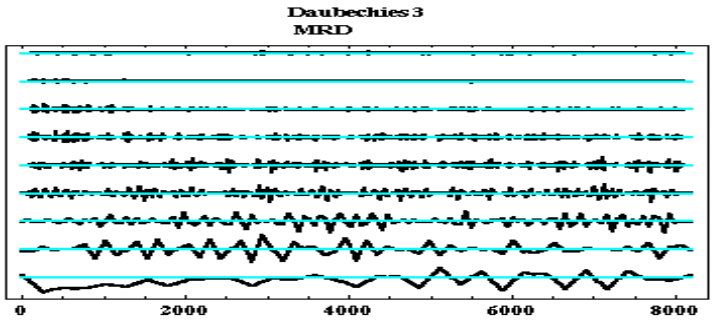

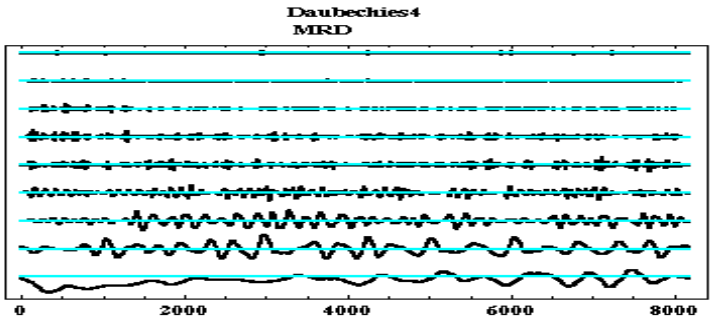

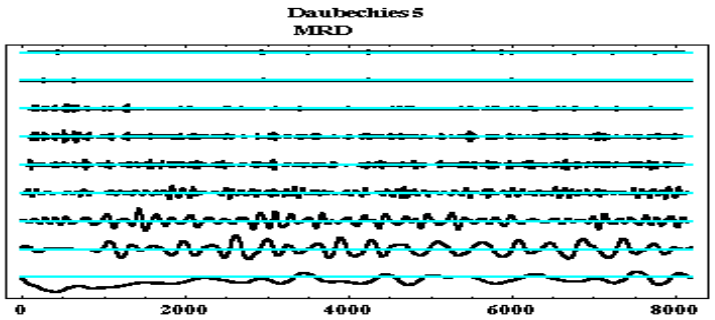

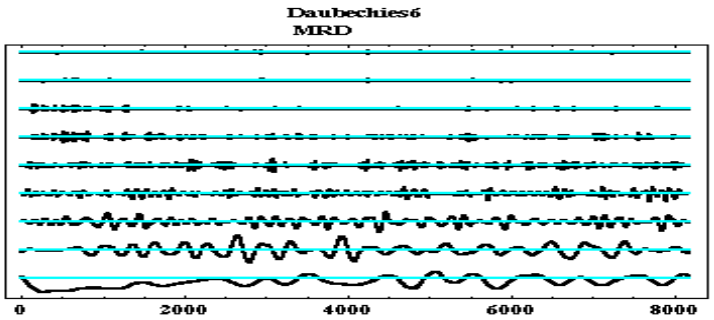

Decay Rate of Largest Coefficient vs Number of Coefficients Kept in 6 Different Daub WLT Decomps

Polymath Research Inc.

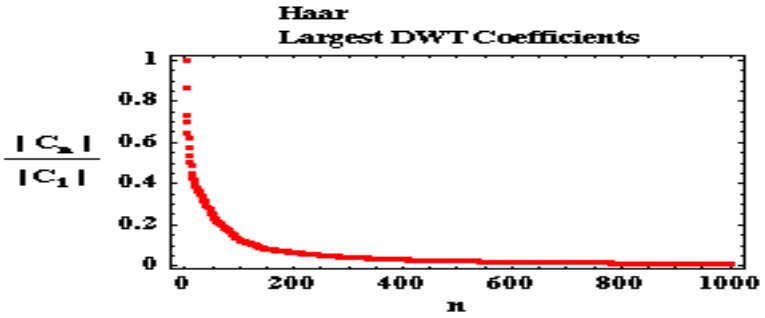

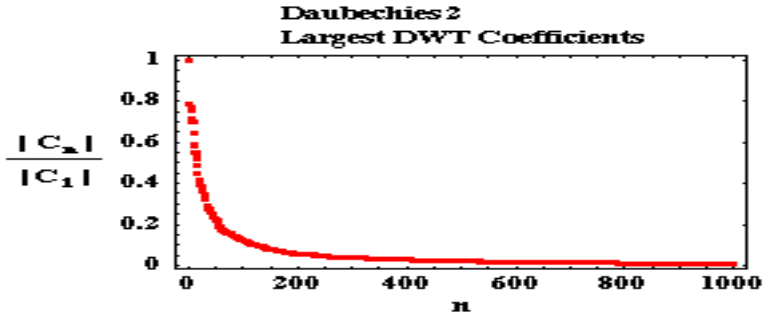

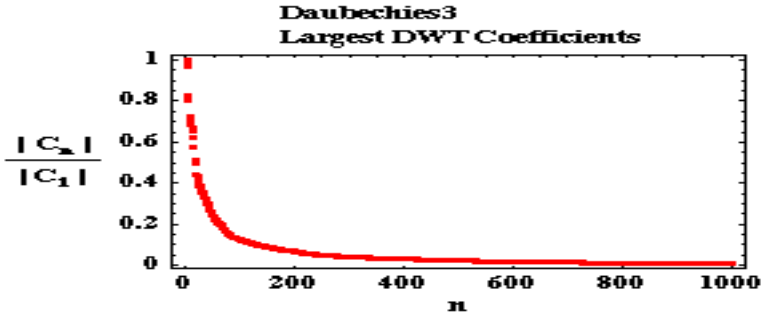

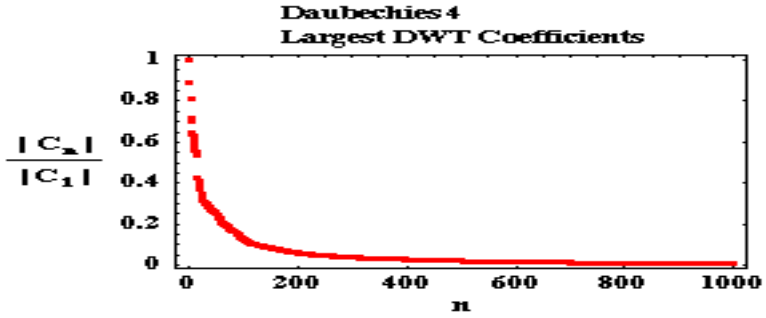

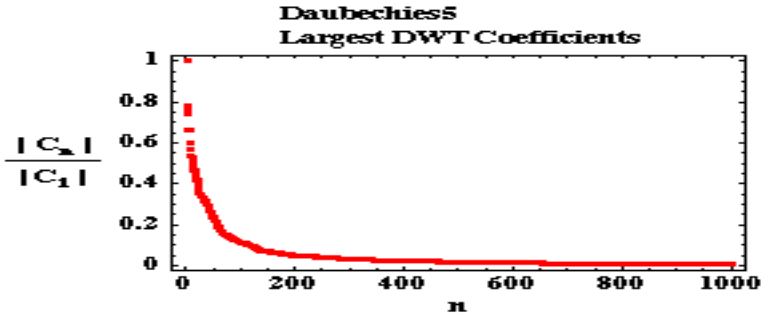

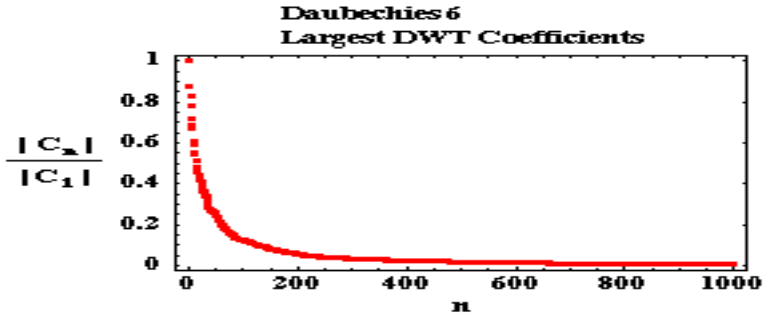

Energy Accumulation Rate in Coefficient Space vs # of WLTs Kept in 6 Different Daub Decomps

Polymath Research Inc.

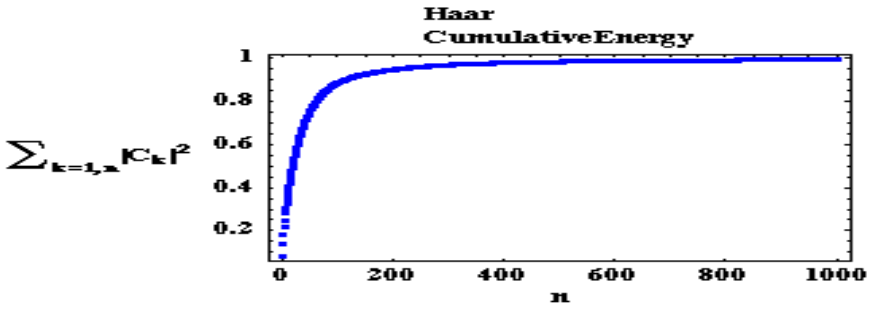

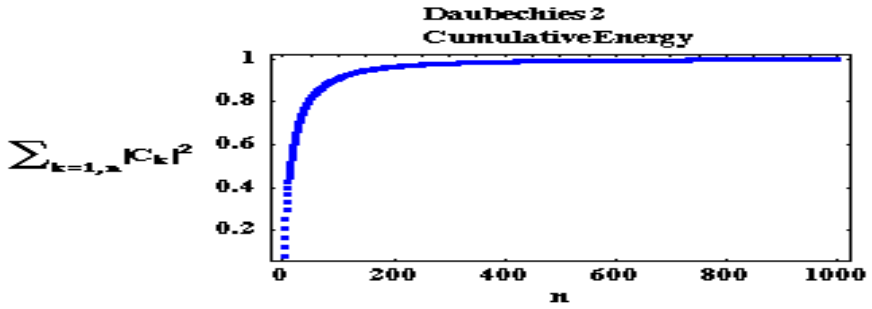

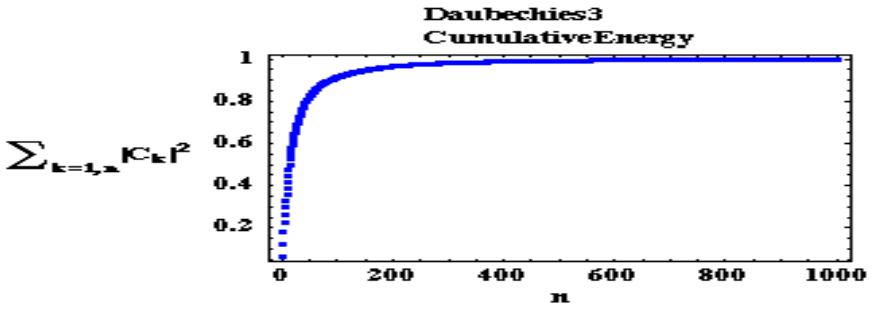

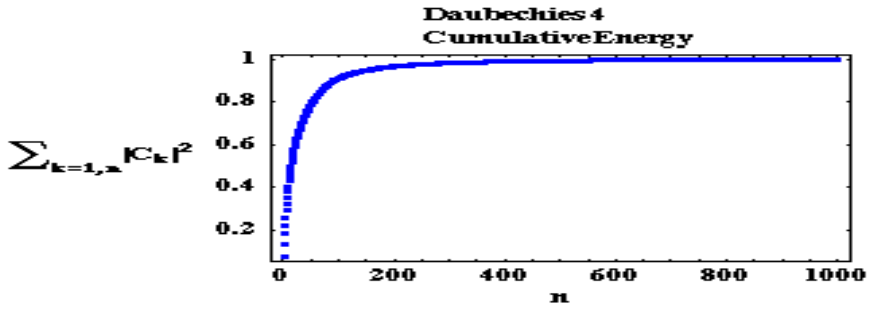

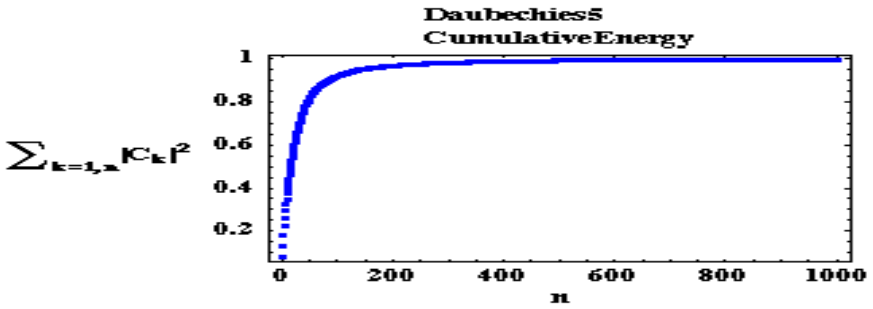

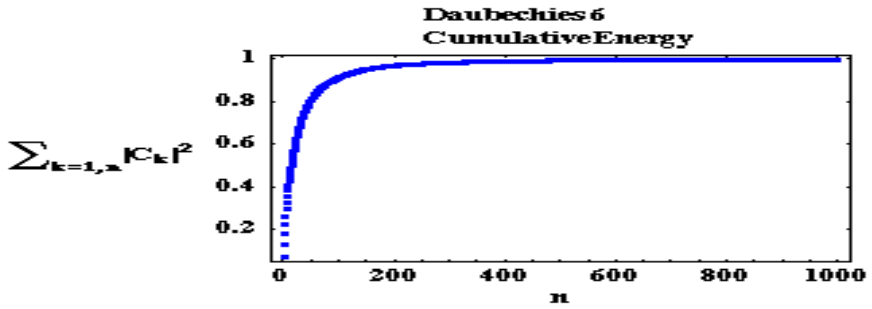

Scaleograms: Waveleters Preferred Way of Judging Tiling in Scale-Translation Space

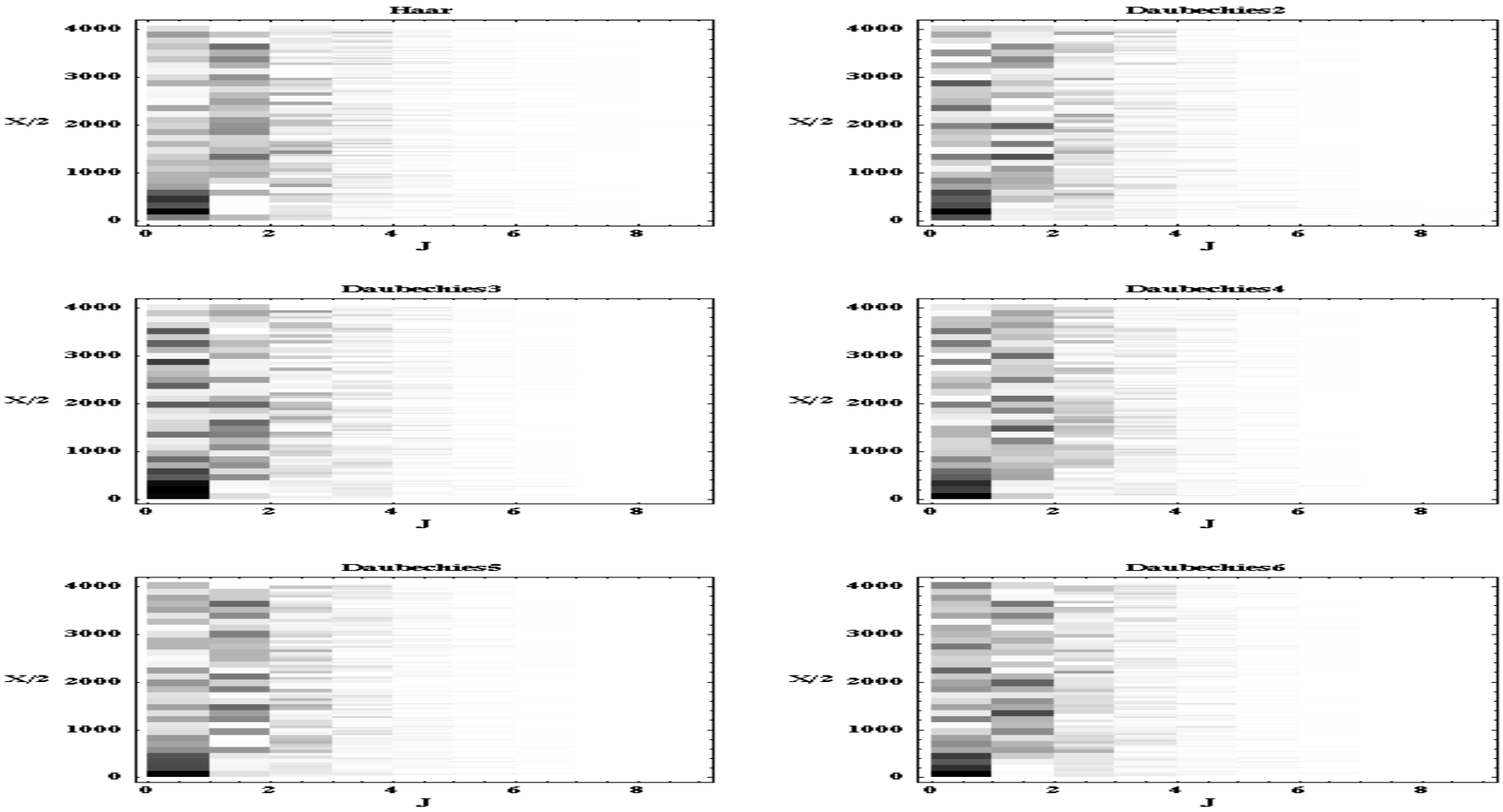

Least Square Error Incurred By Truncating the WLT Series at N of its Largest Coefficients

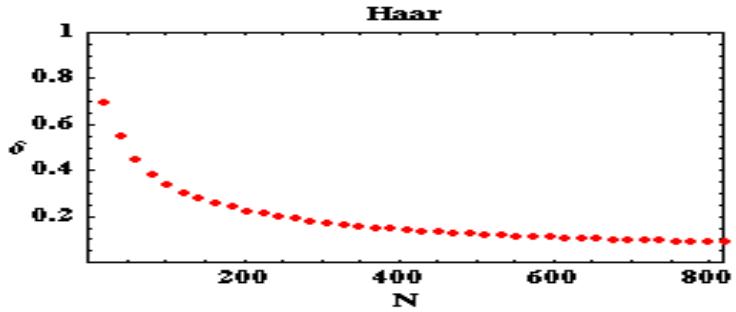

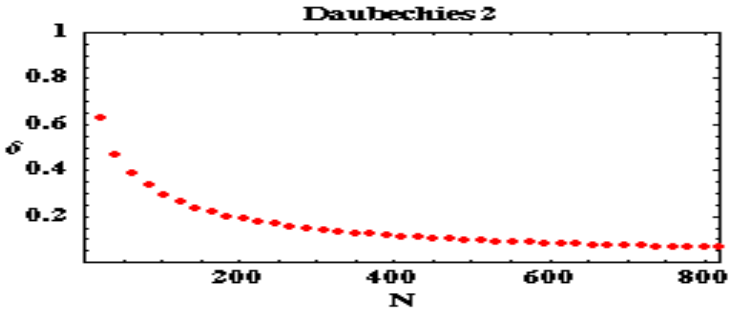

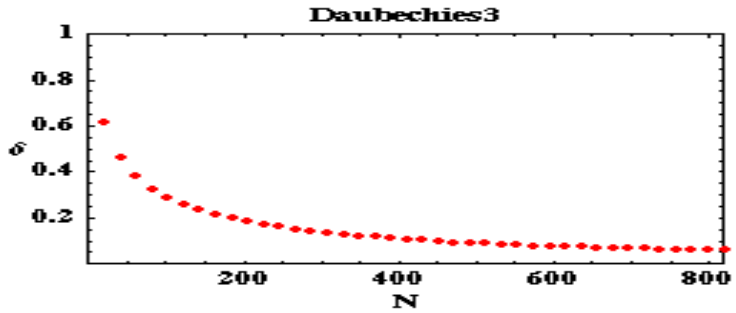

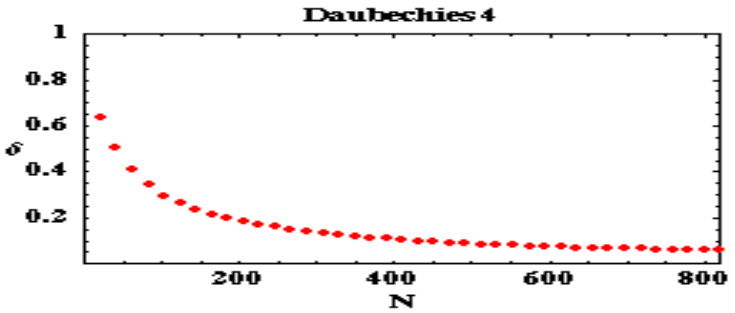

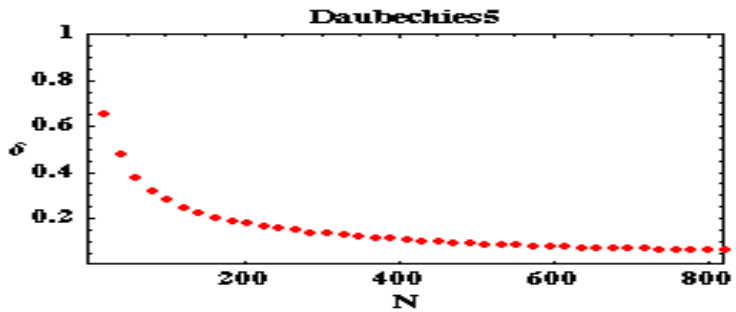

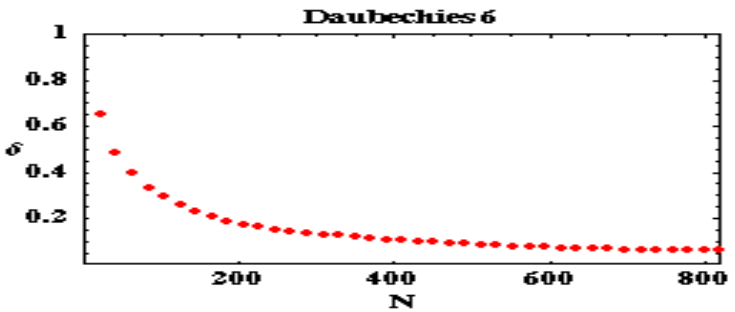

Least Square Error Incurred by Level Thresholding the DWT

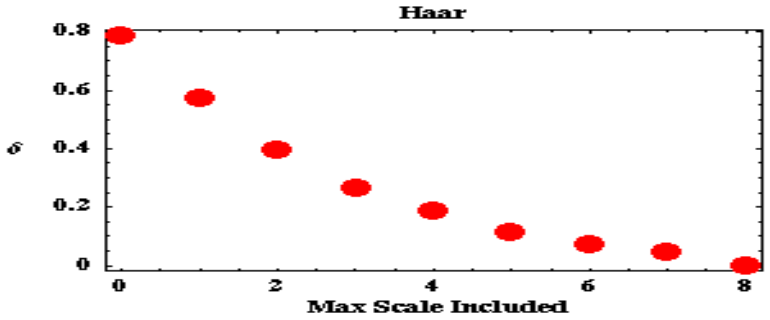

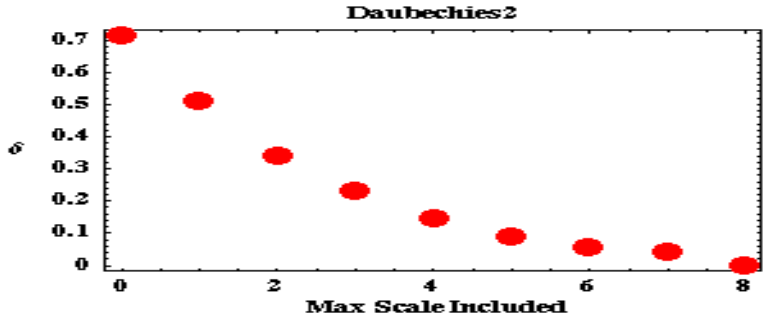

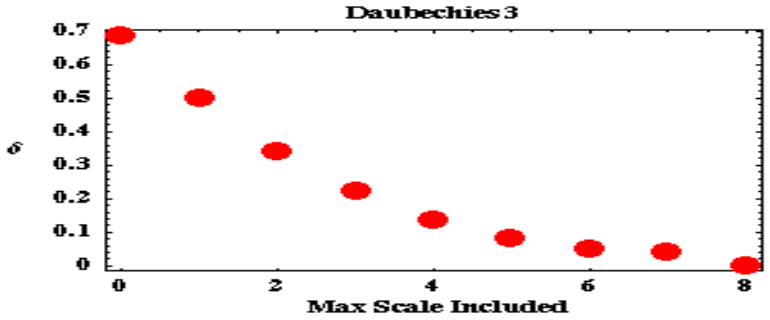

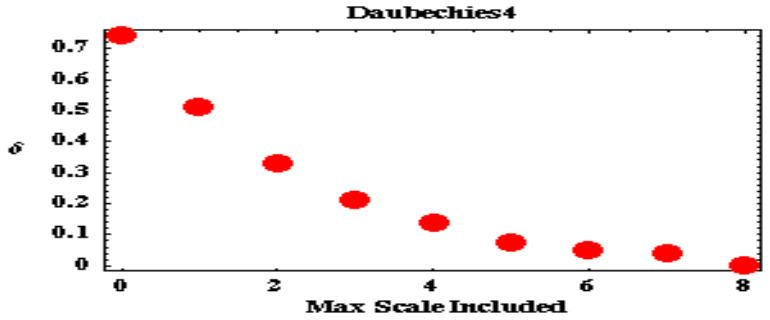

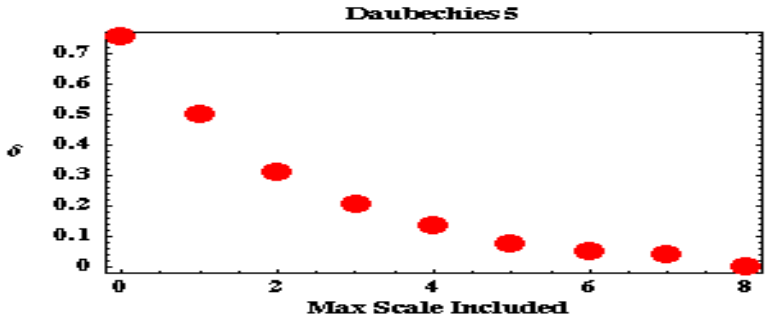

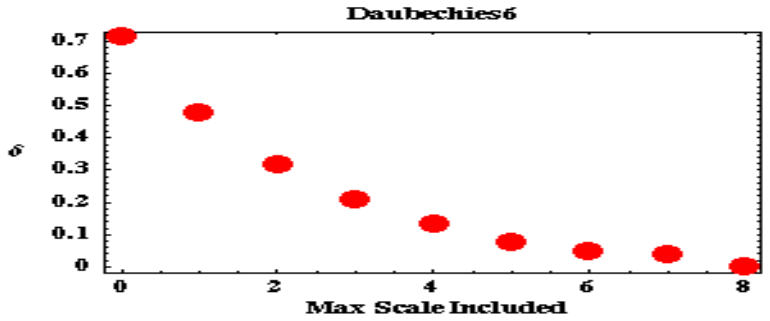

Daubechies 5 Does Much Better than Haar: 5 Quantitative Measures

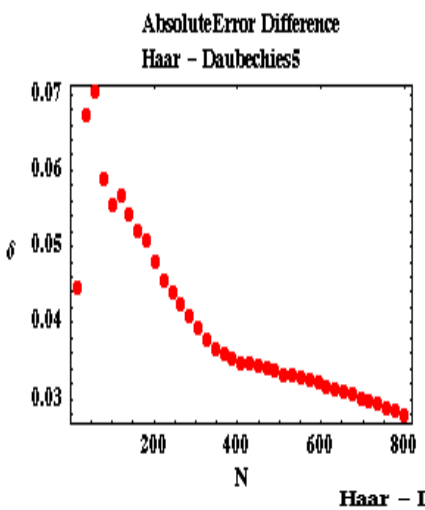

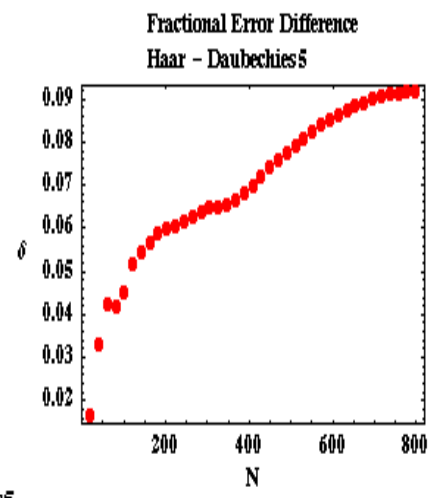

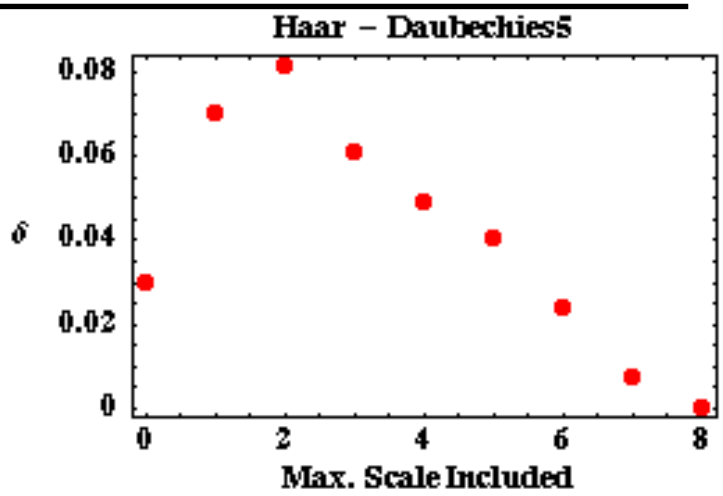

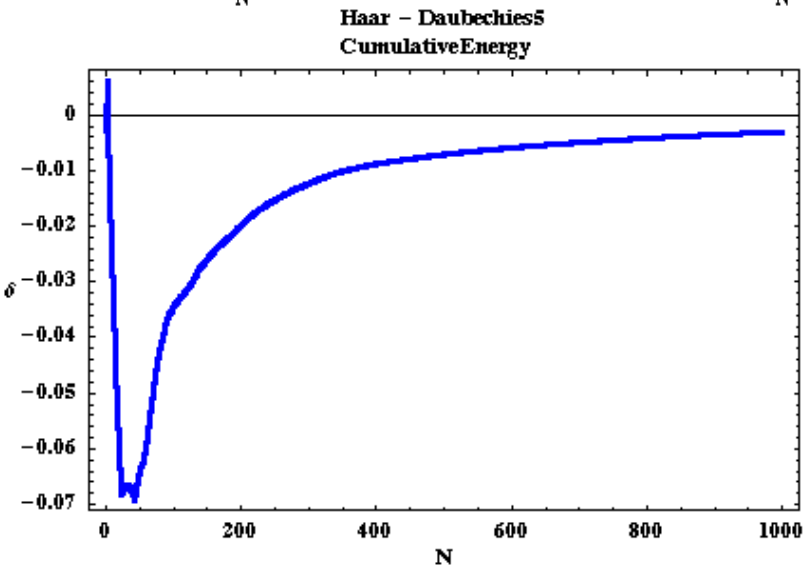

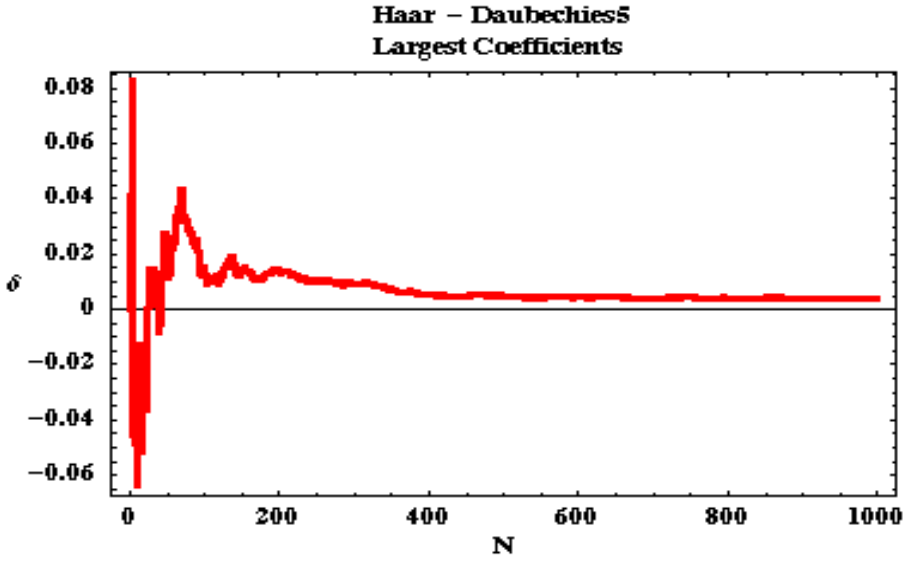

Level by Level Decomposition of the RT Weak Mix Data Using Daub5 WLTs

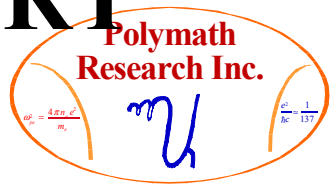

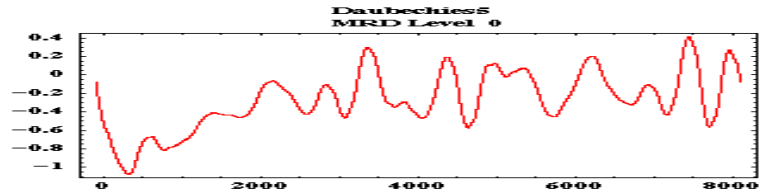

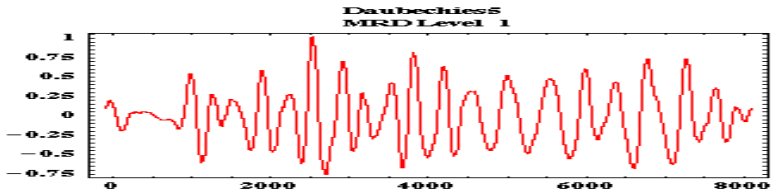

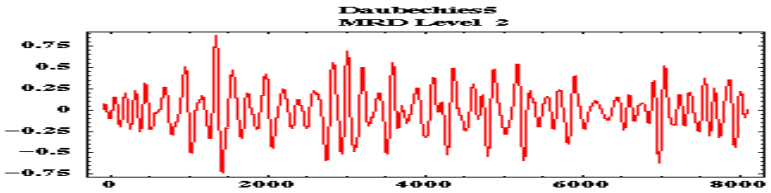

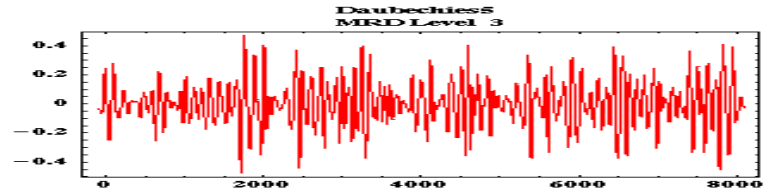

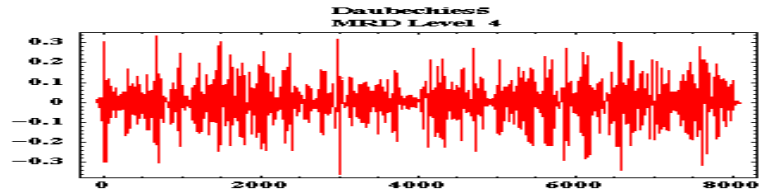

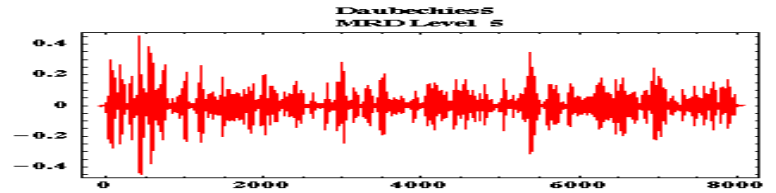

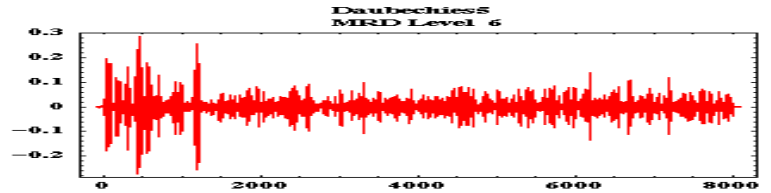

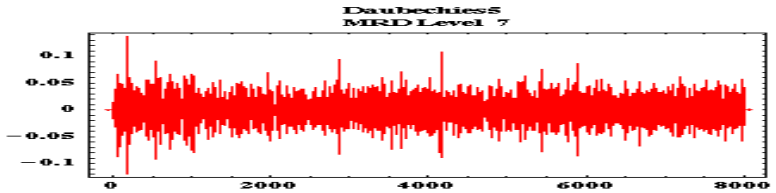

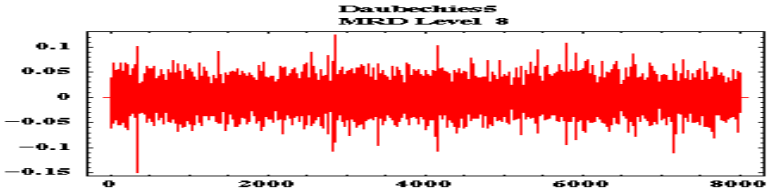

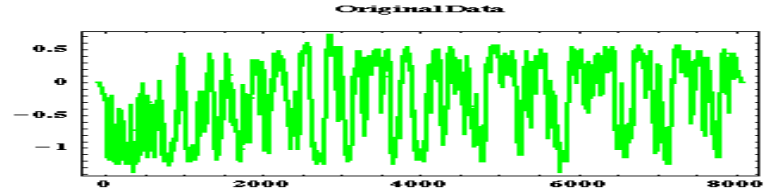

Reconstruction of the Data Using the 5 Largest WLT Coefficients

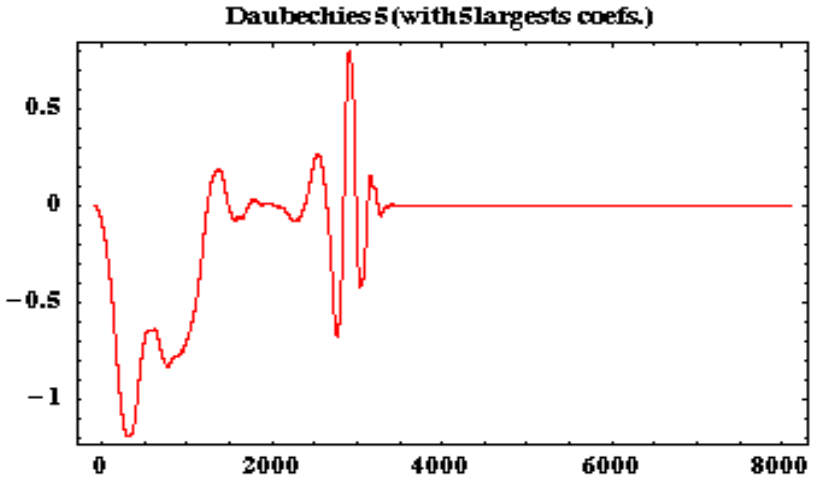

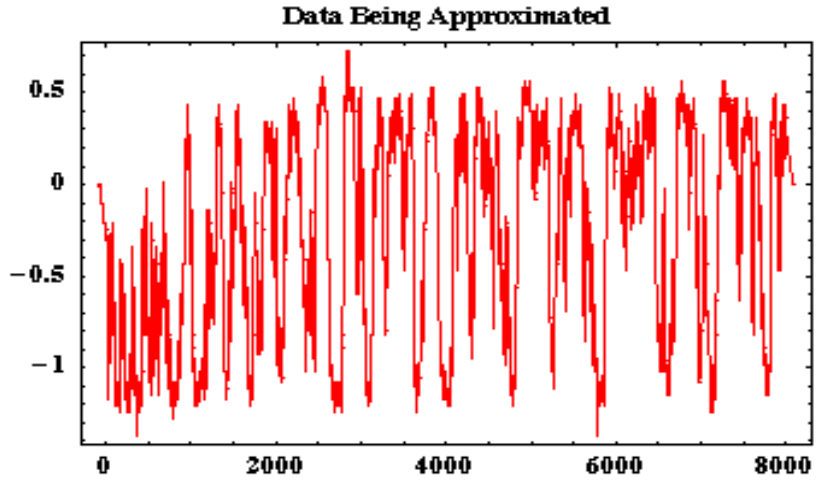

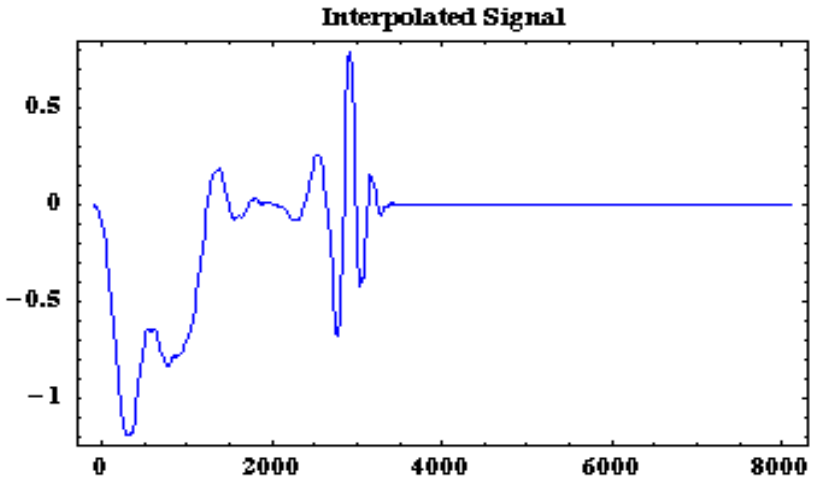

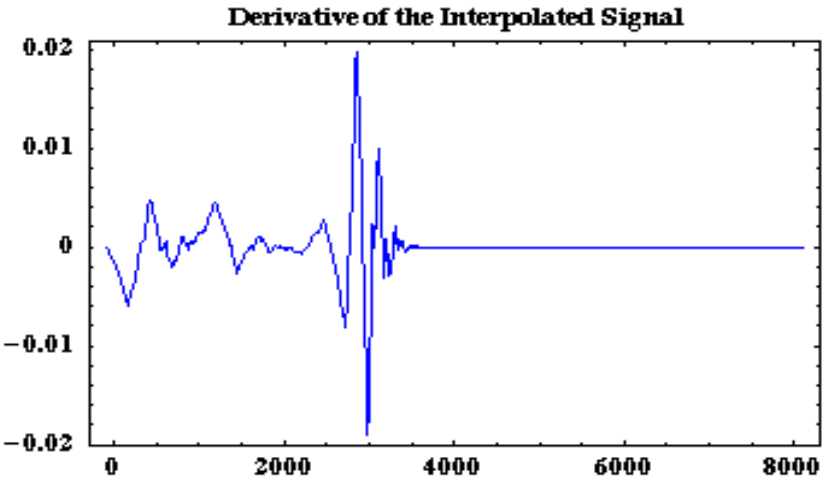

Reconstruction of the Data Using the 10 Largest WLT Coefficients

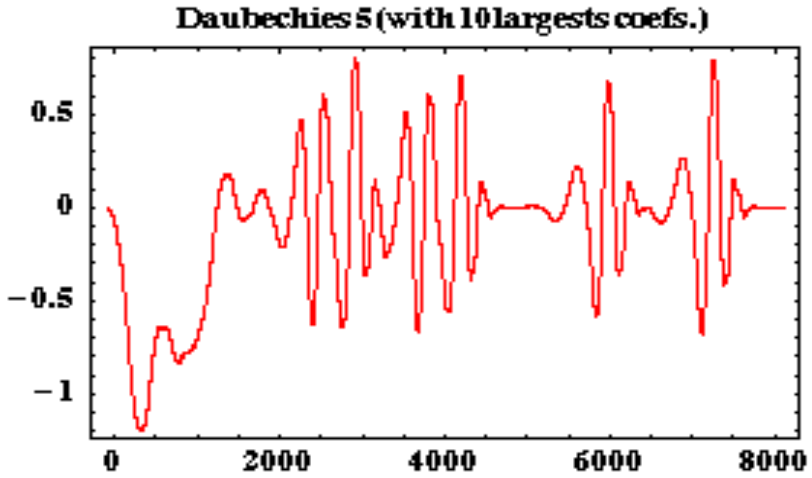

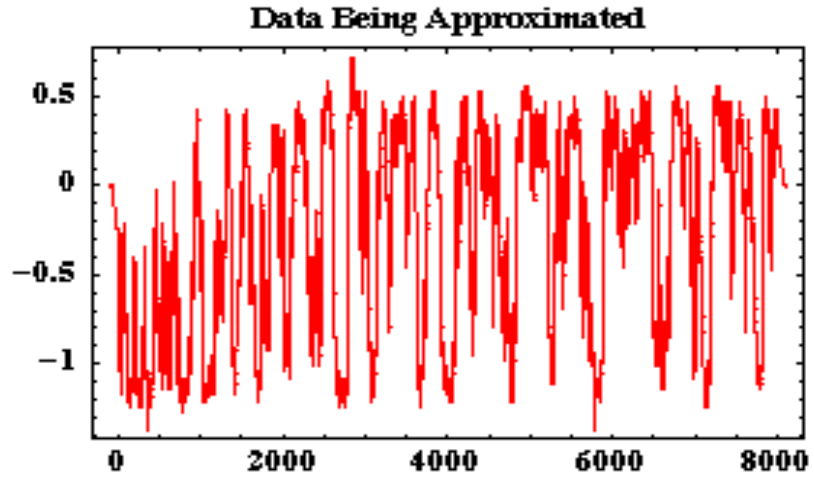

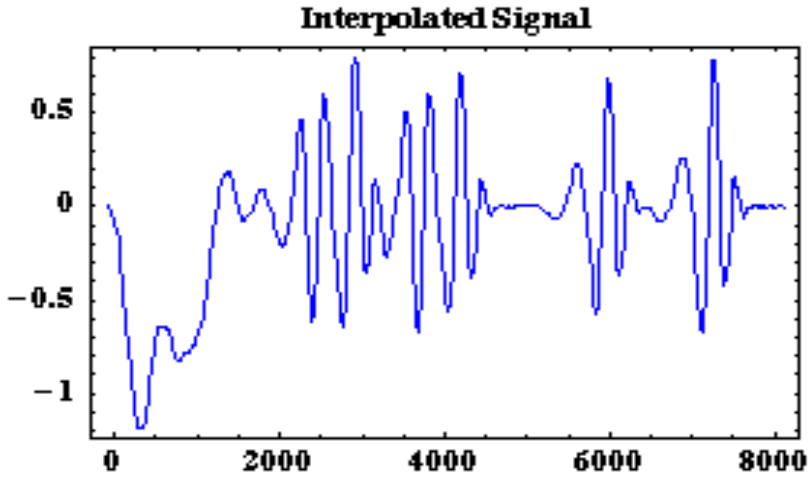

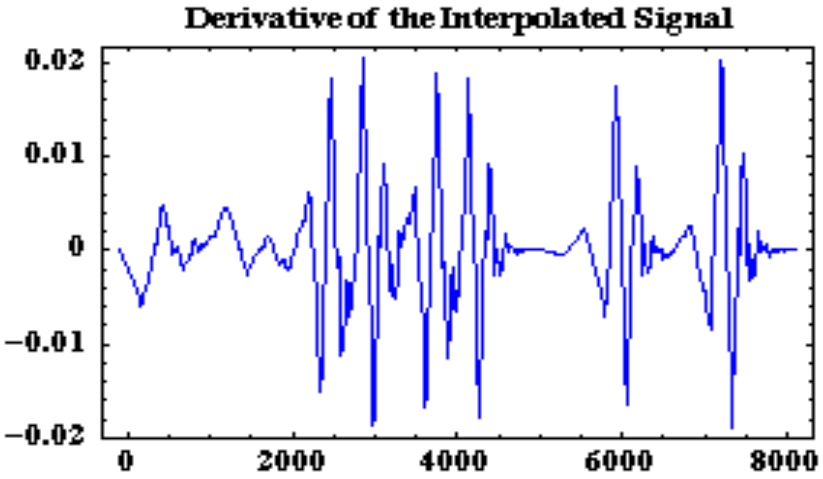

Reconstruction of the Data Using the 15 Largest WLT Coefficients

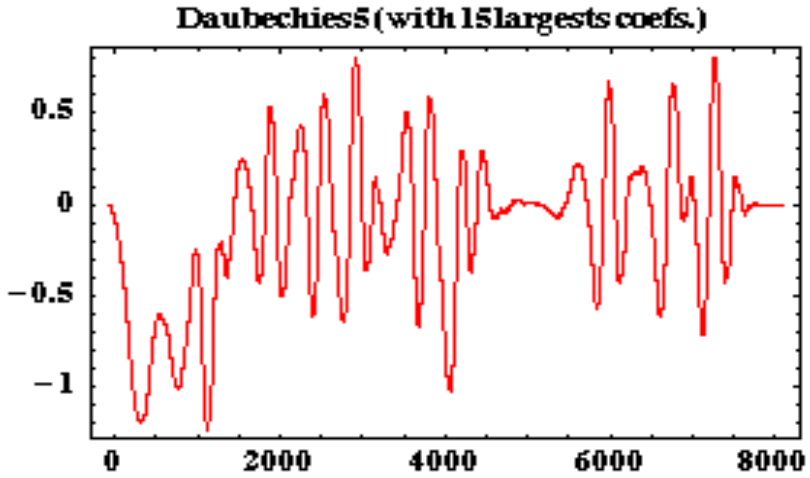

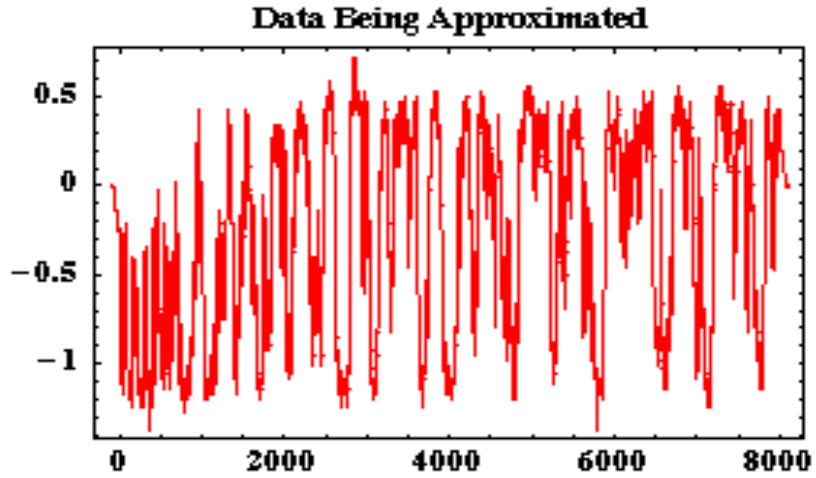

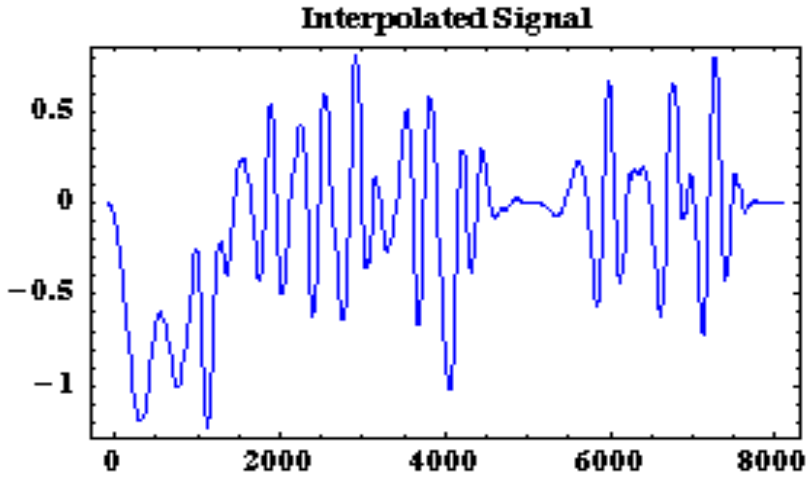

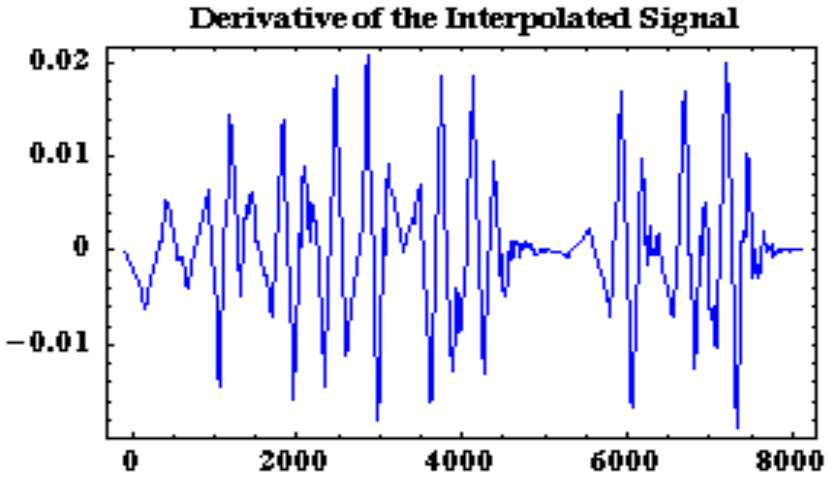

Reconstruction of the Data Using the 20 Largest WLT Coefficients

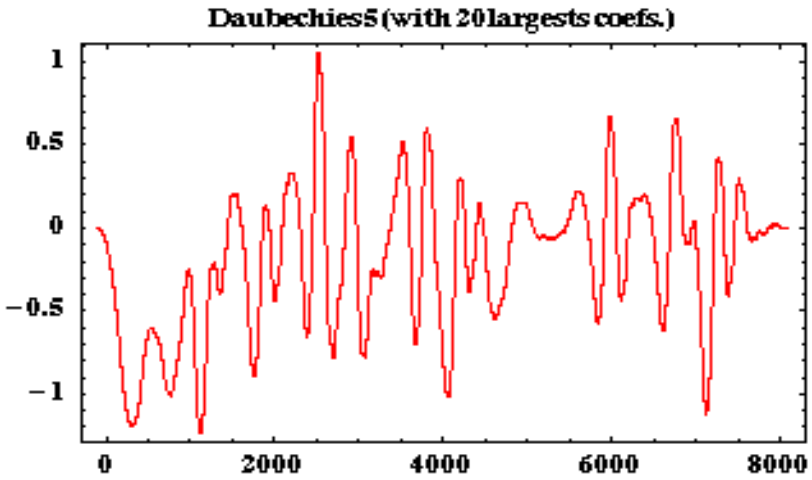

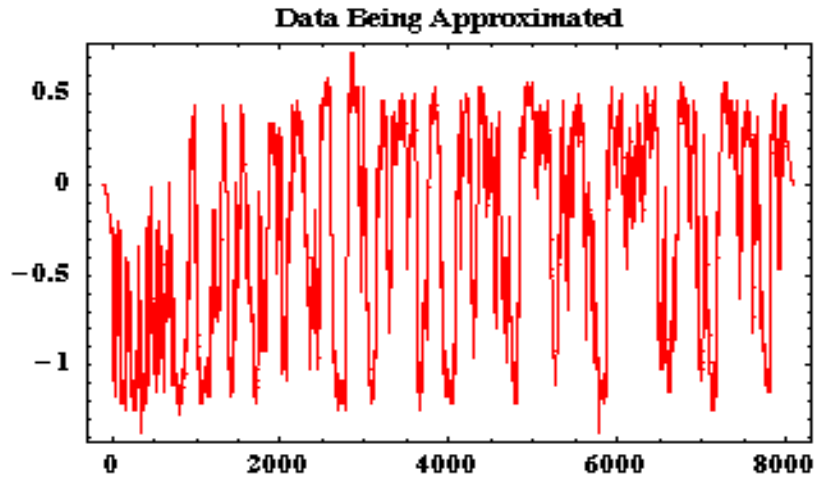

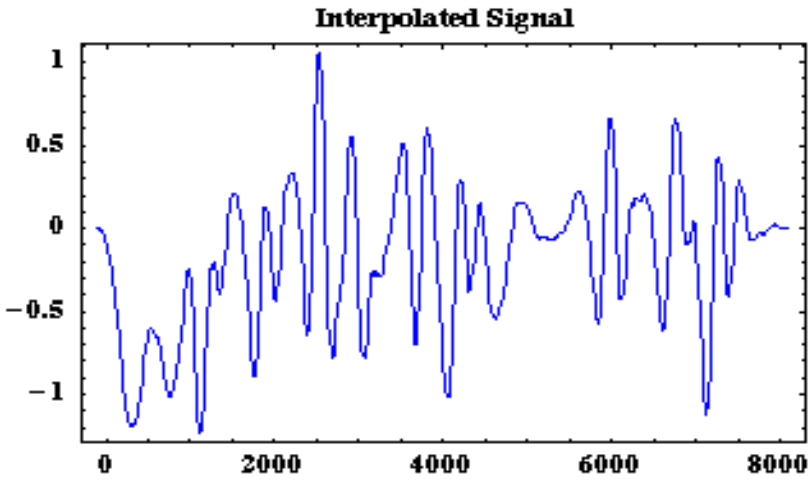

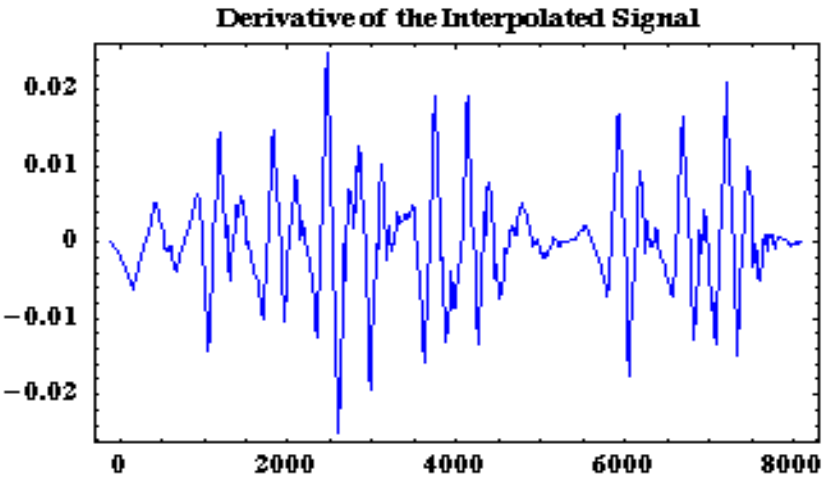

Reconstruction of the Data Using the 25 Largest WLT Coefficients

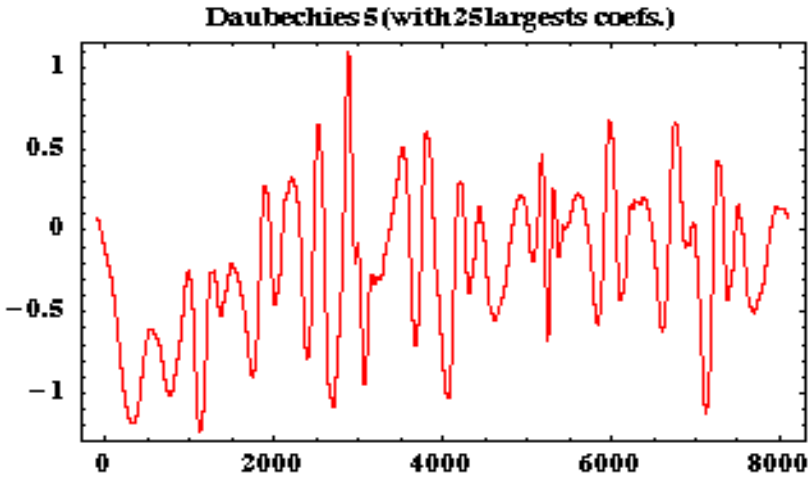

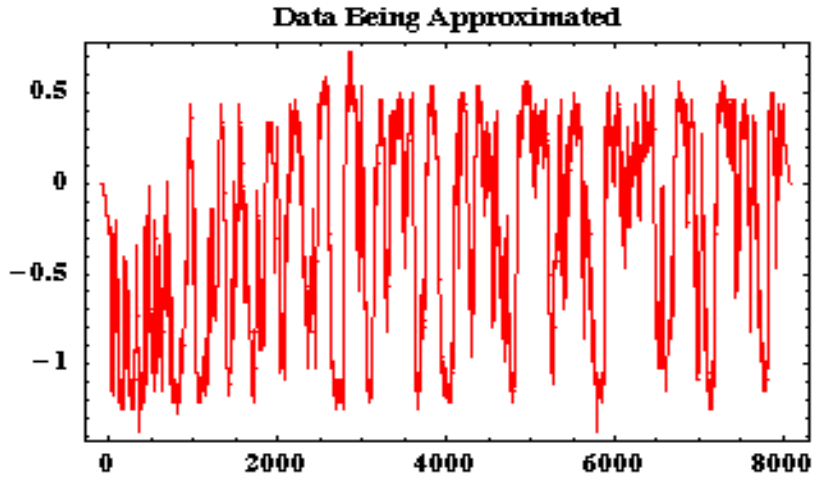

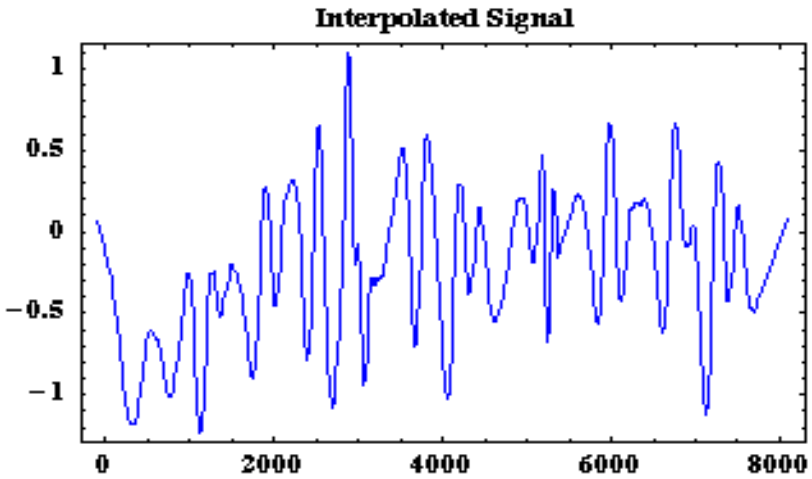

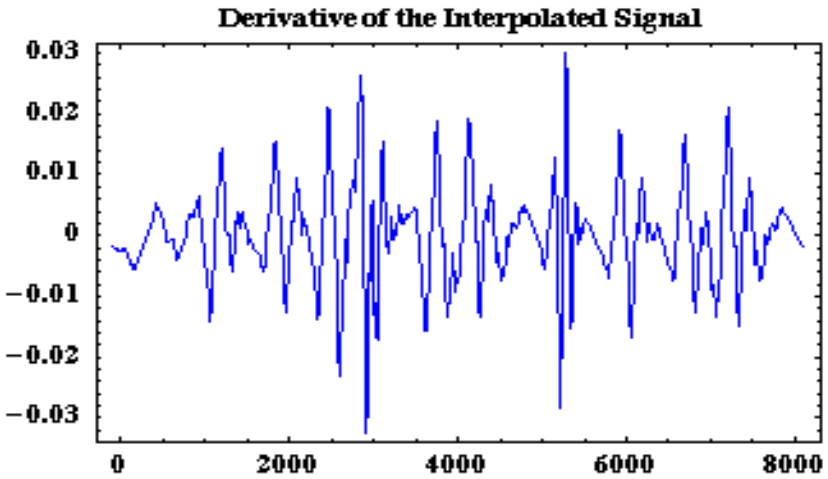

Reconstruction of the Data Using the 30 Largest WLT Coefficients

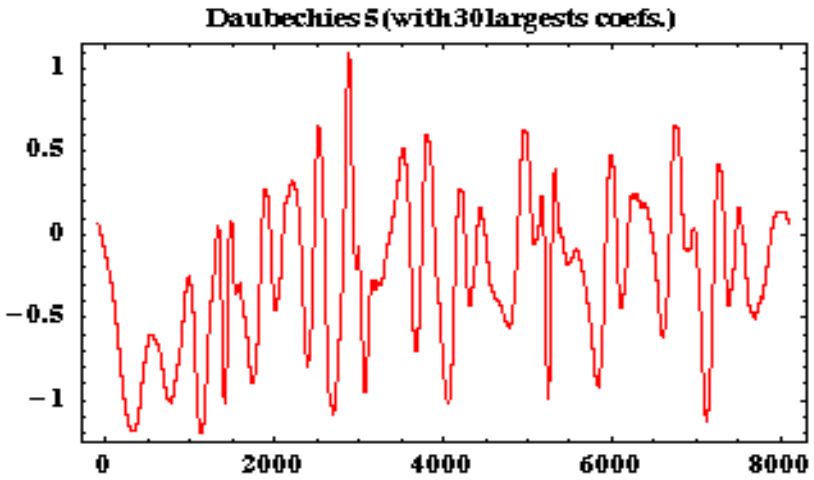

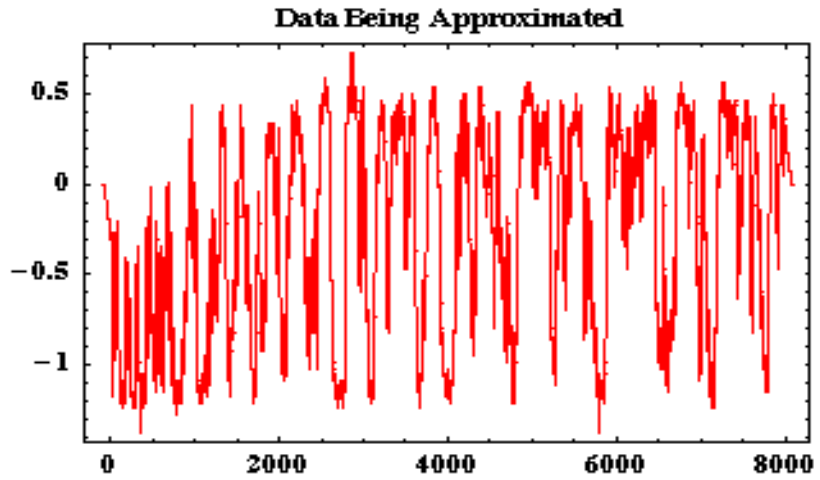

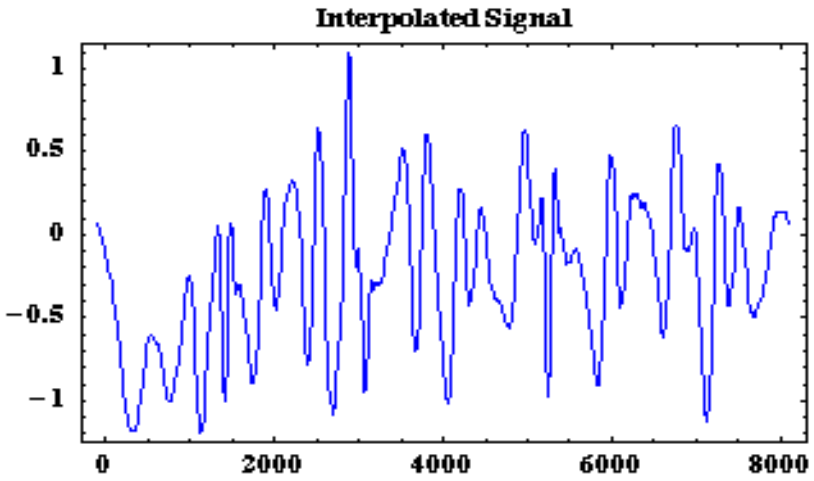

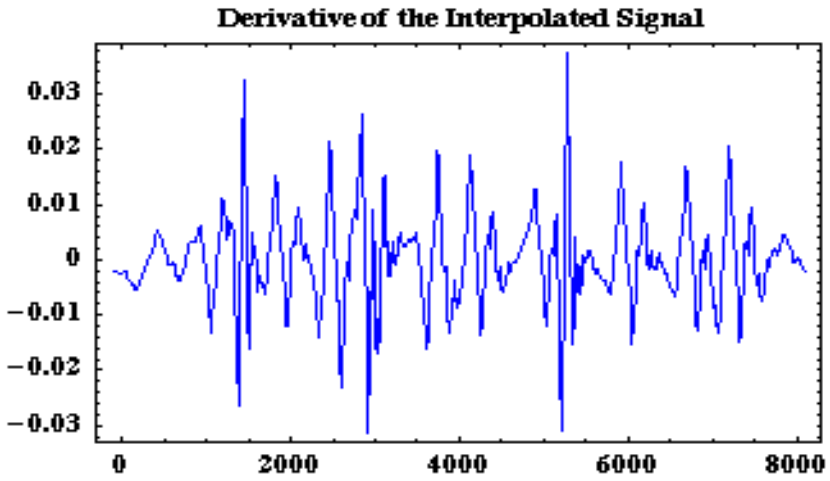

Reconstruction of the Data Using the 35 Largest WLT Coefficients

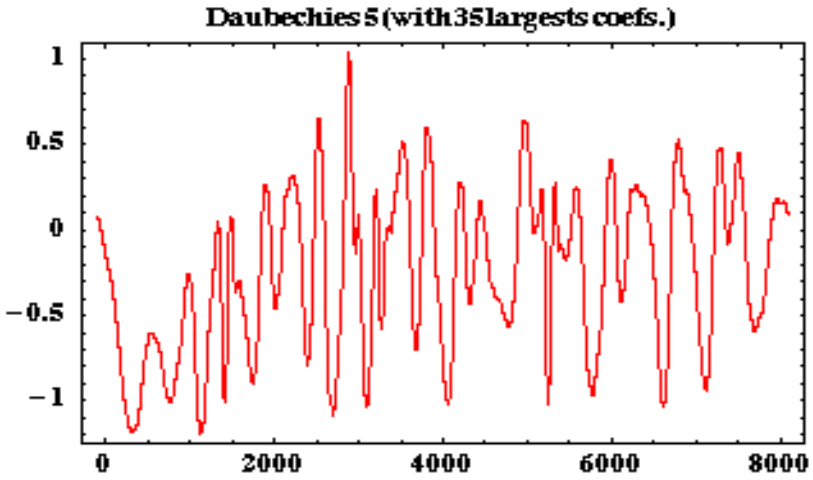

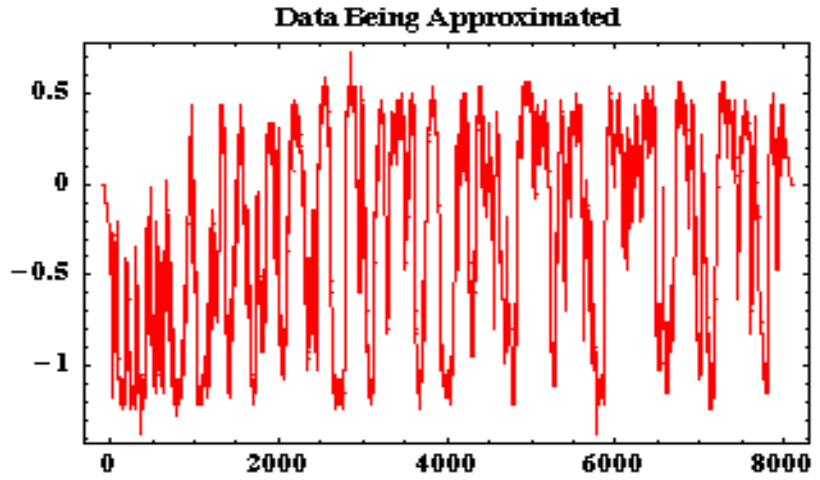

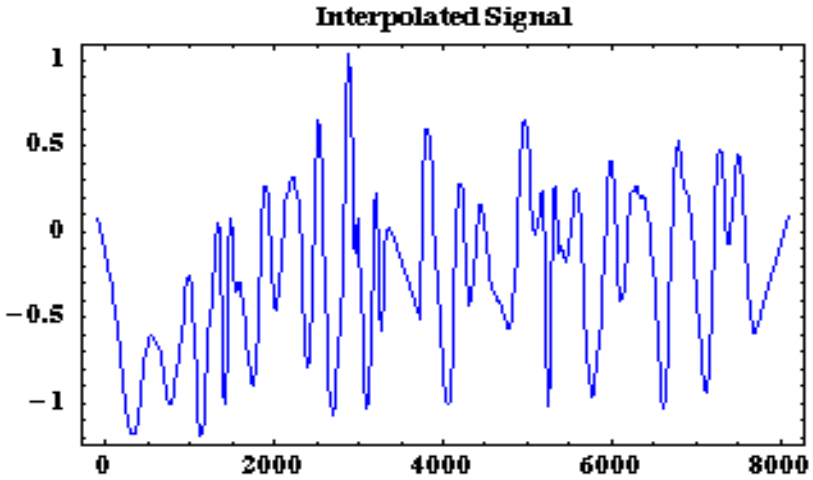

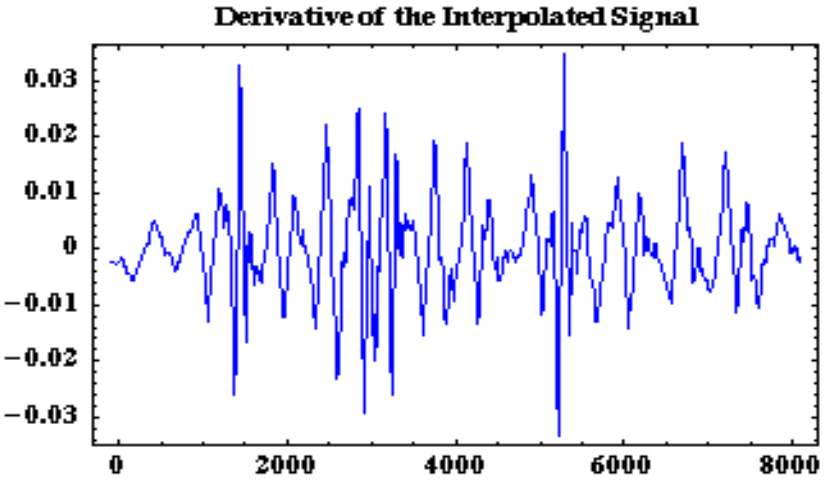

Reconstruction of the Data Using the 40 Largest WLT Coefficients

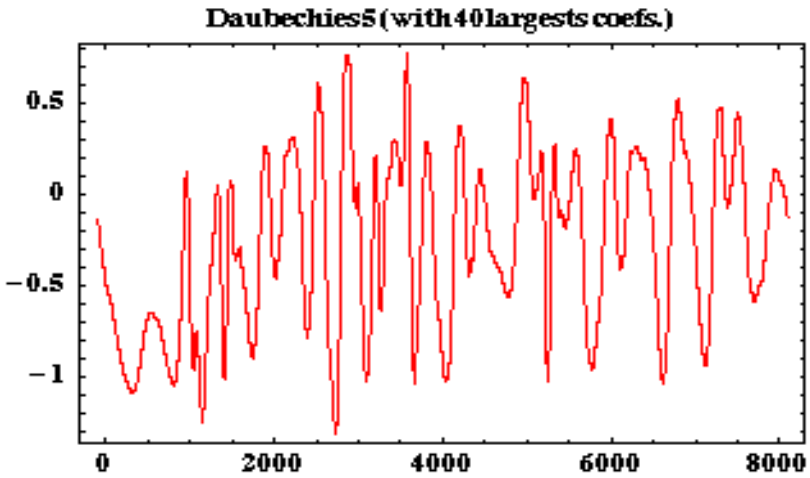

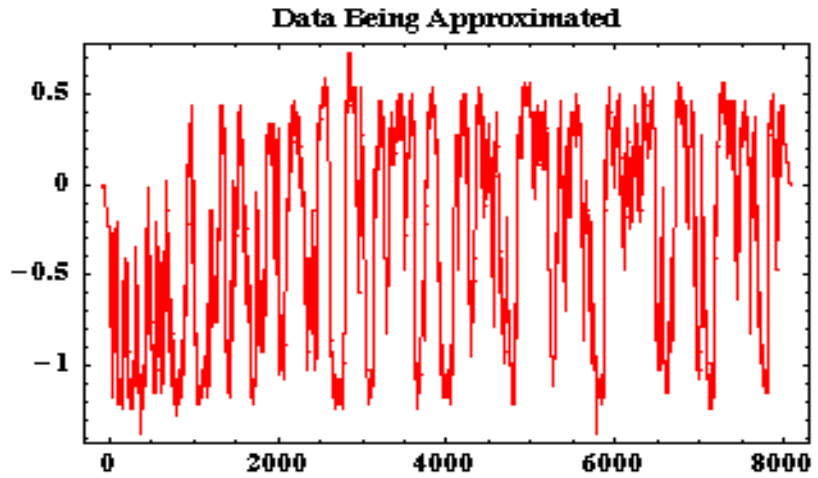

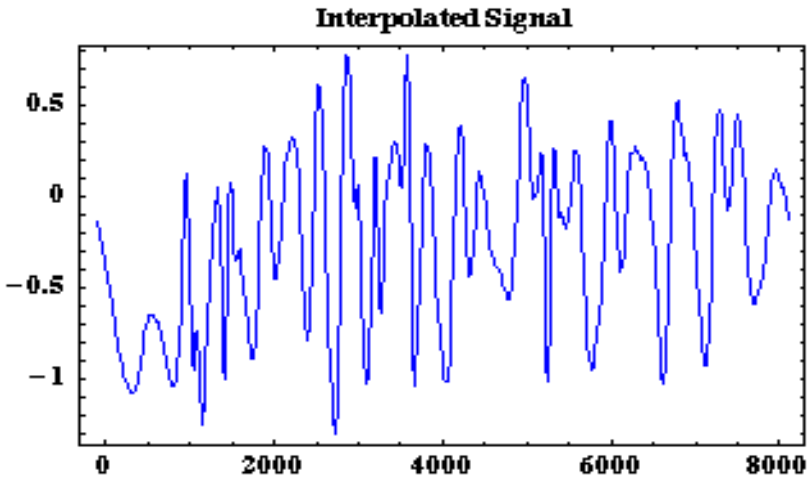

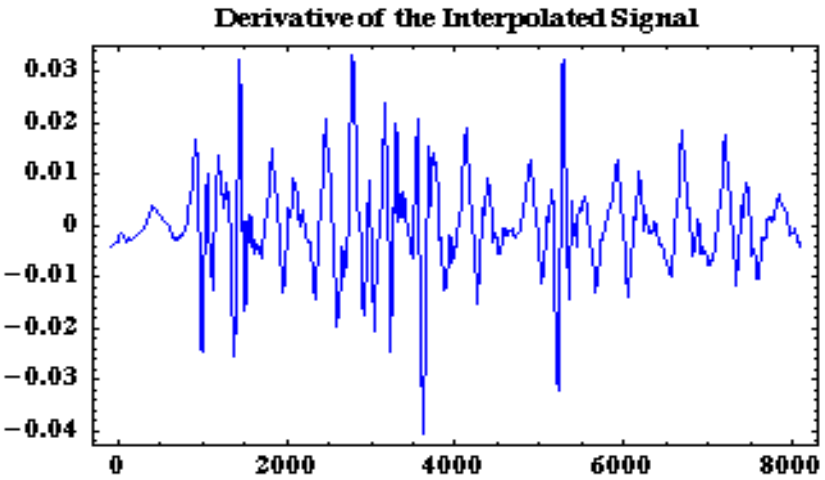

Reconstruction of the Data Using the 45 Largest WLT Coefficients

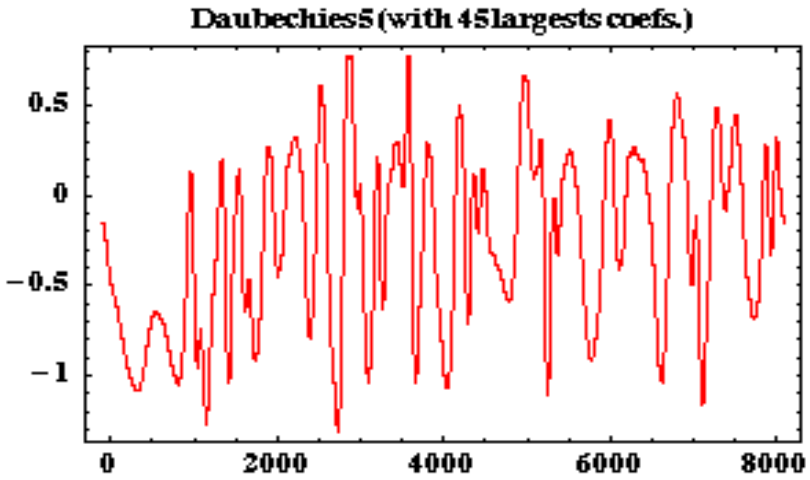

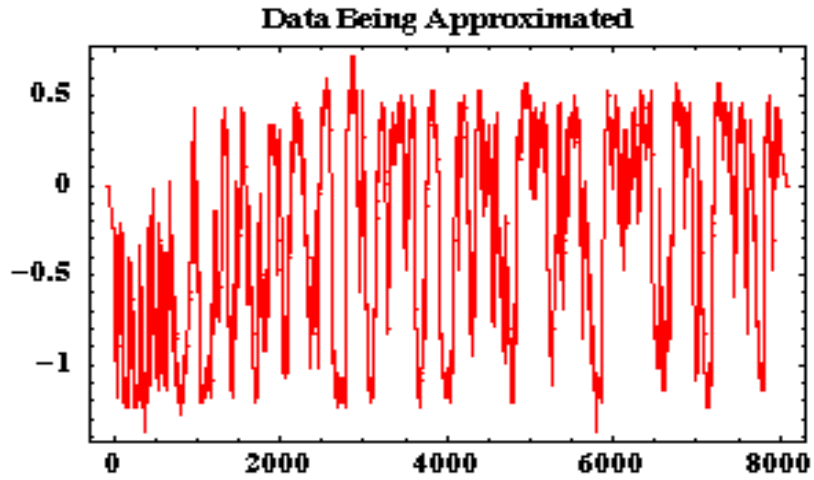

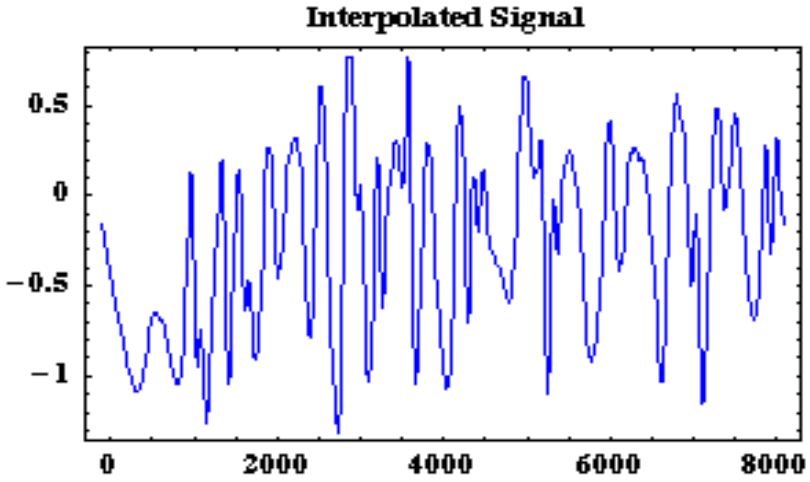

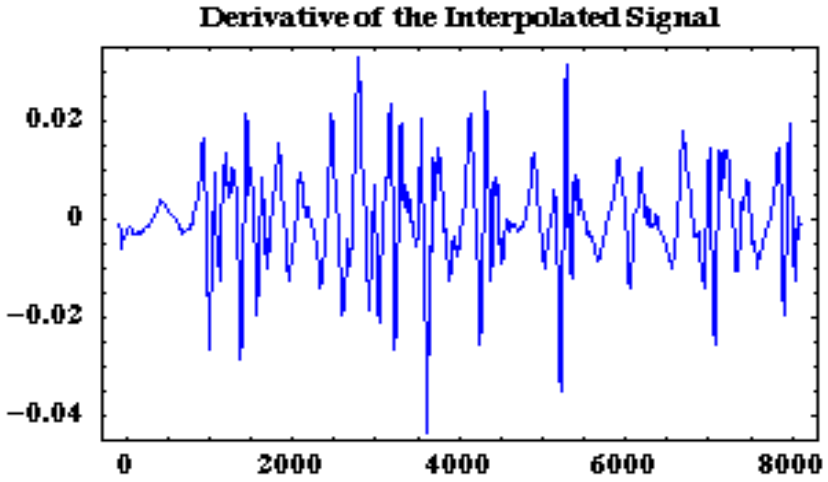

Reconstruction of the Data Using the 50 Largest WLT Coefficients

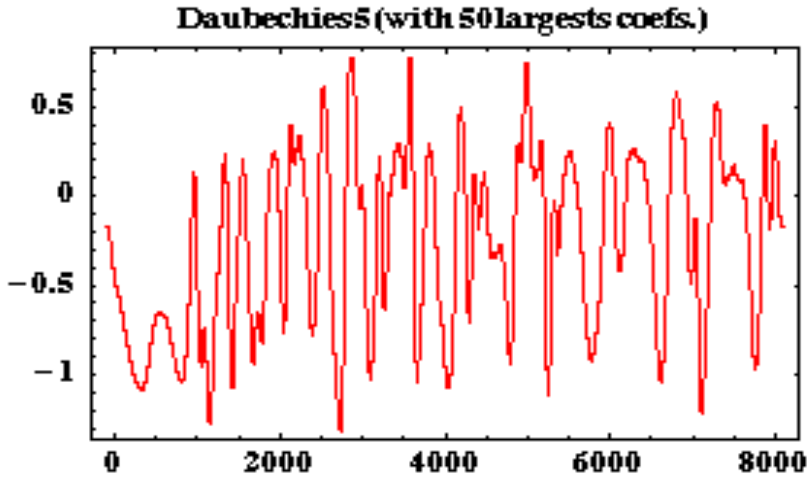

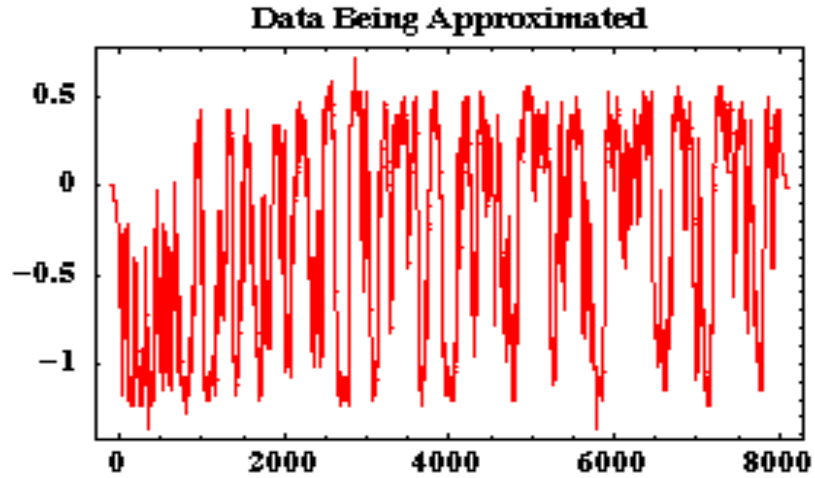

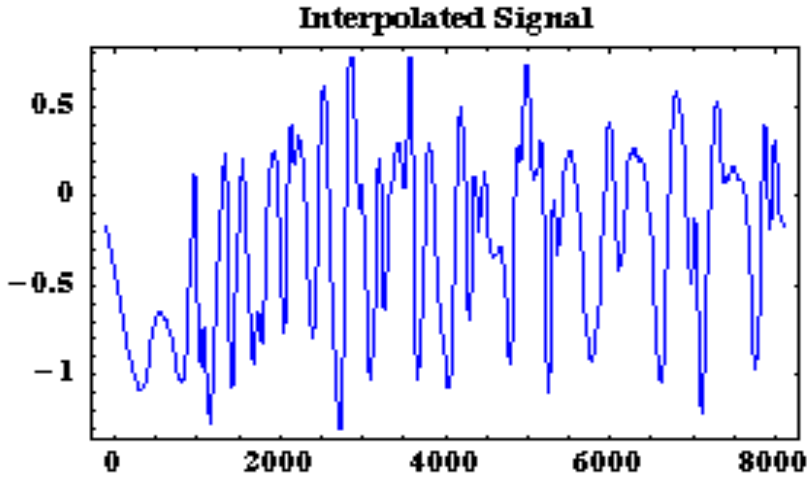

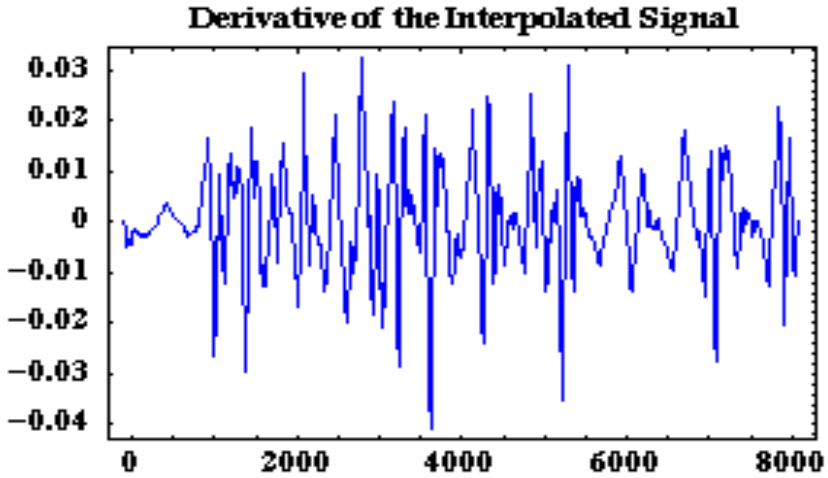

Reconstruction of the Data Using the 100 Largest WLT Coefficients

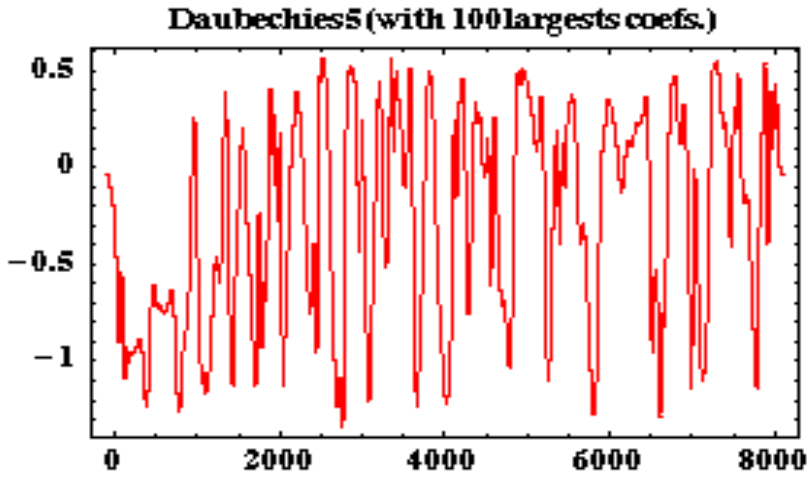

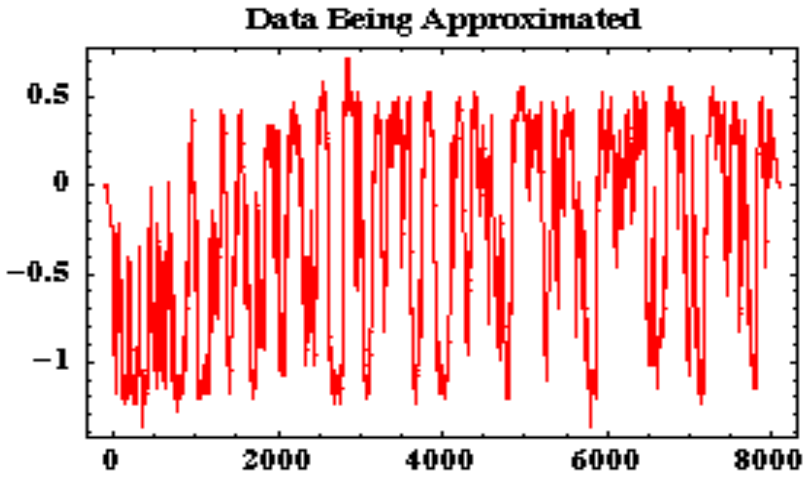

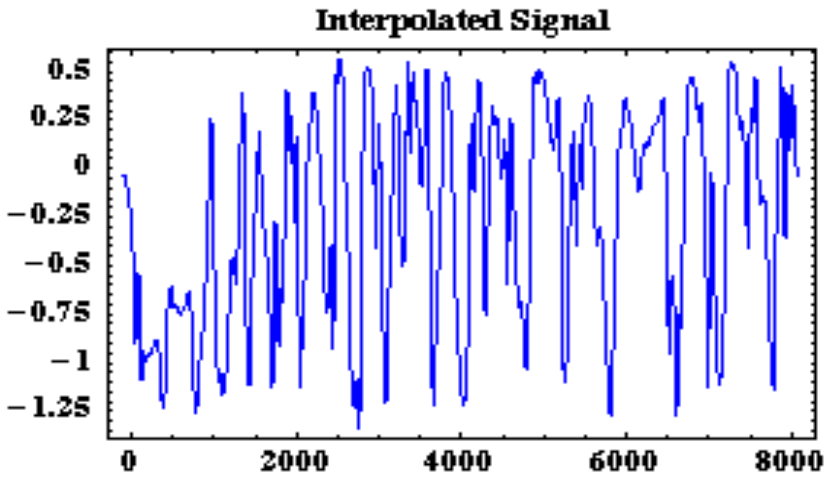

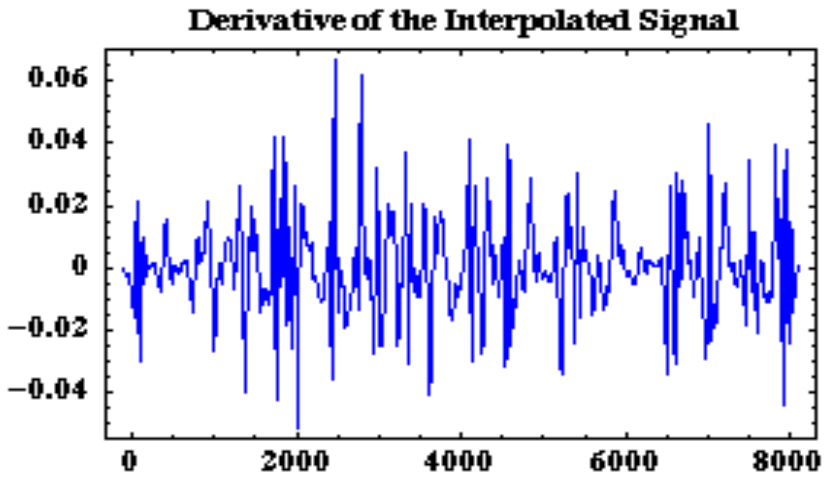

Reconstruction of the Data Using the 200 Largest WLT Coefficients

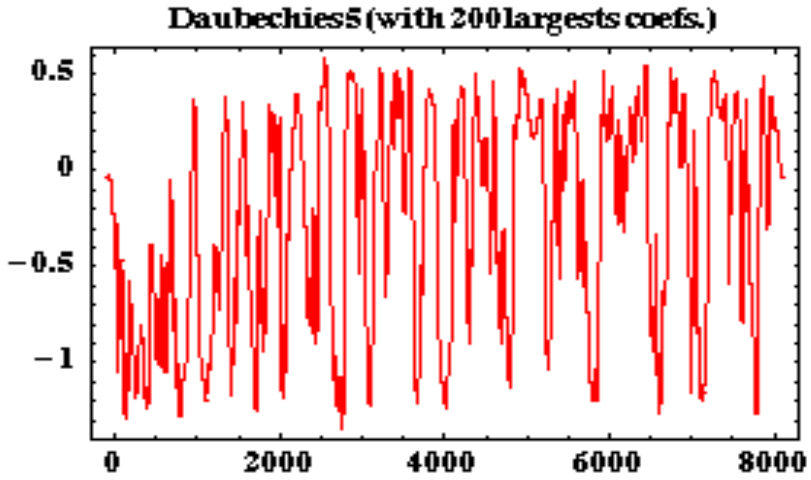

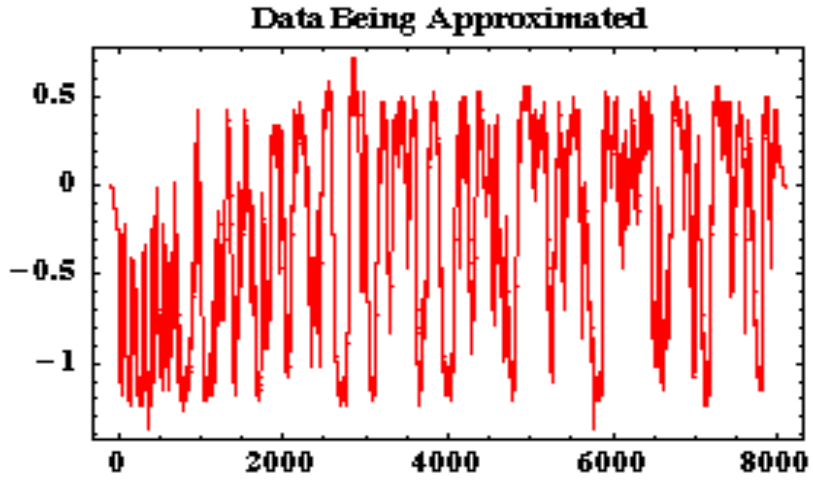

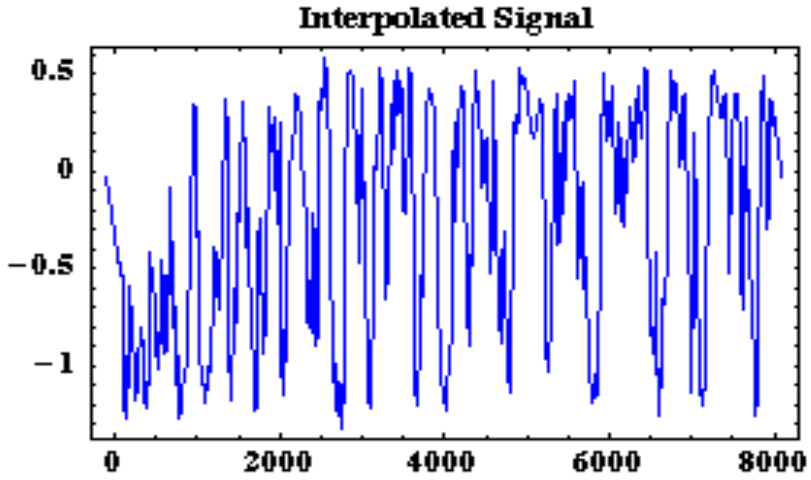

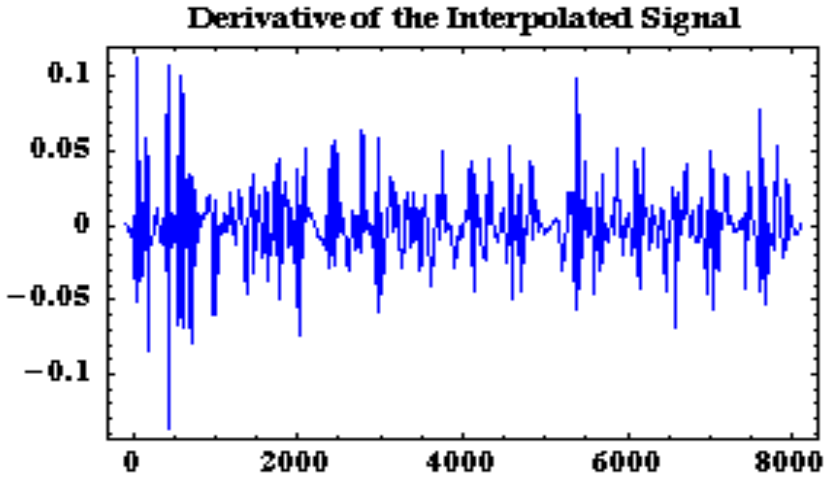

Reconstruction of the LPF Data Using the First MRD Level

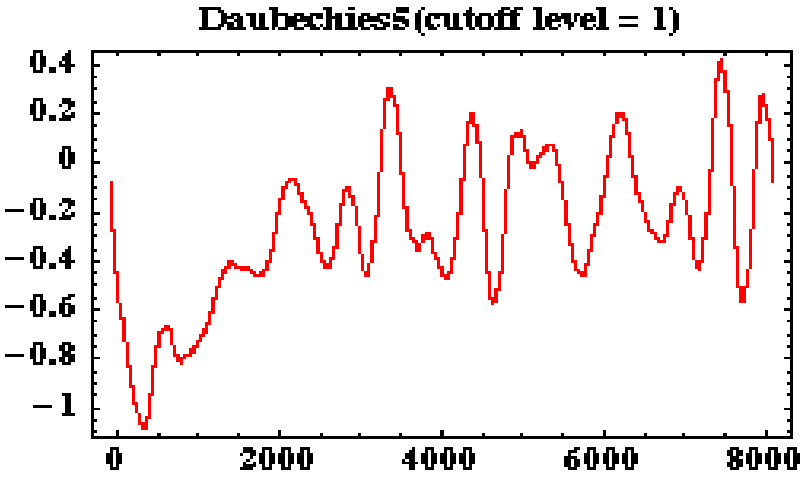

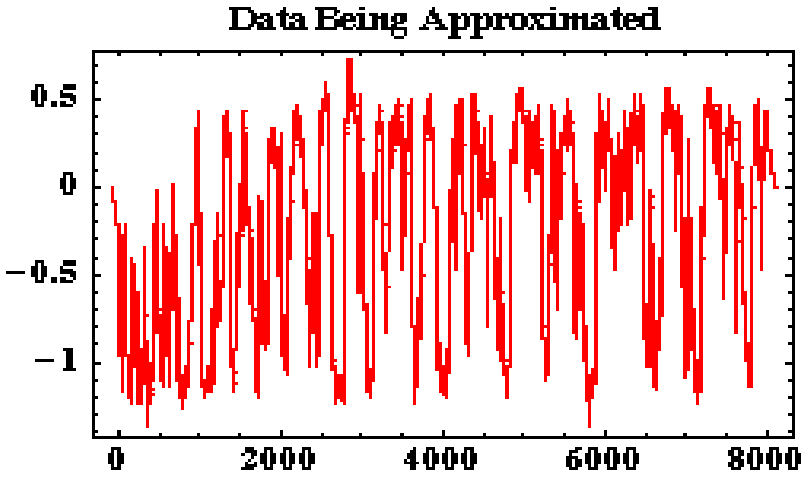

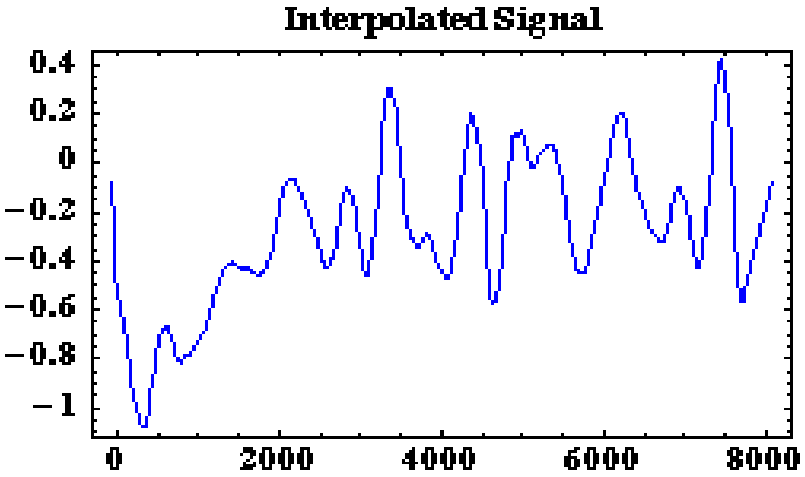

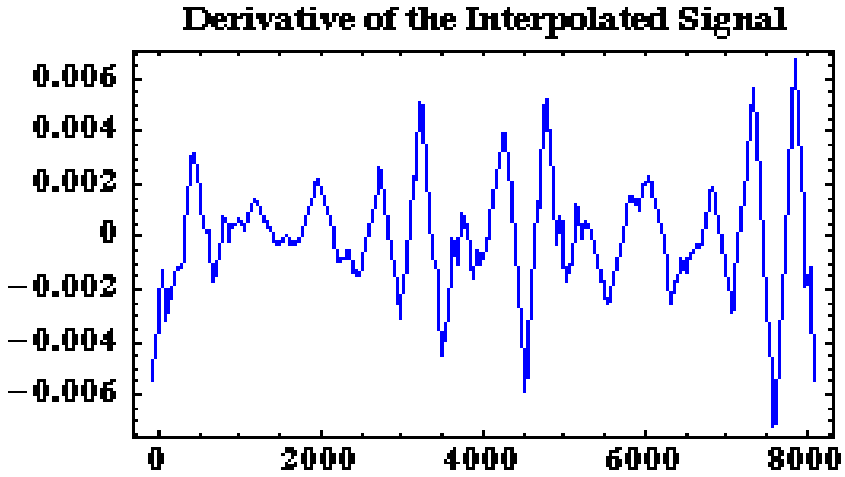

Reconstruction of the Weak Mix Data Using First 2 MRD Levels

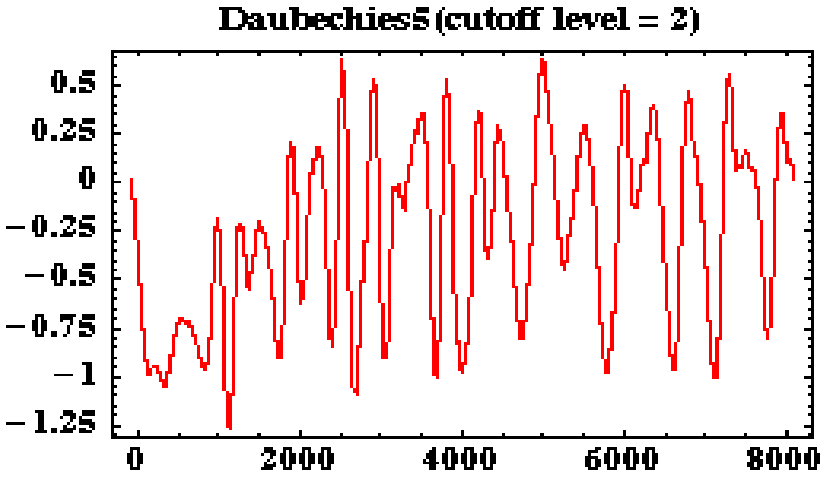

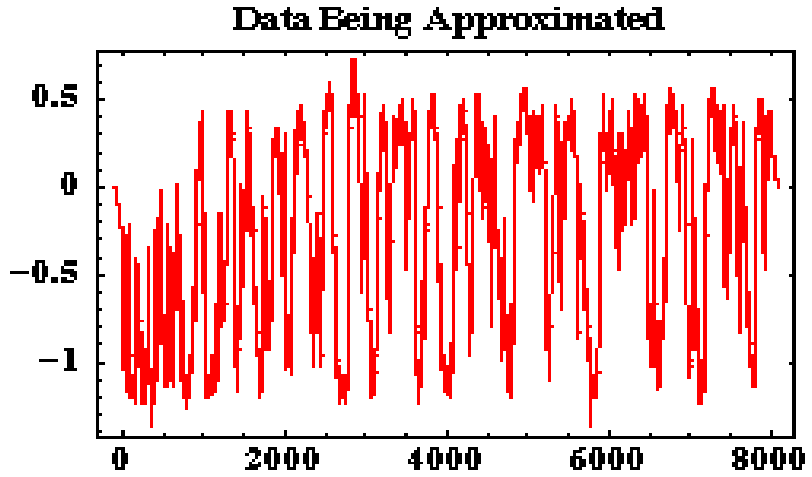

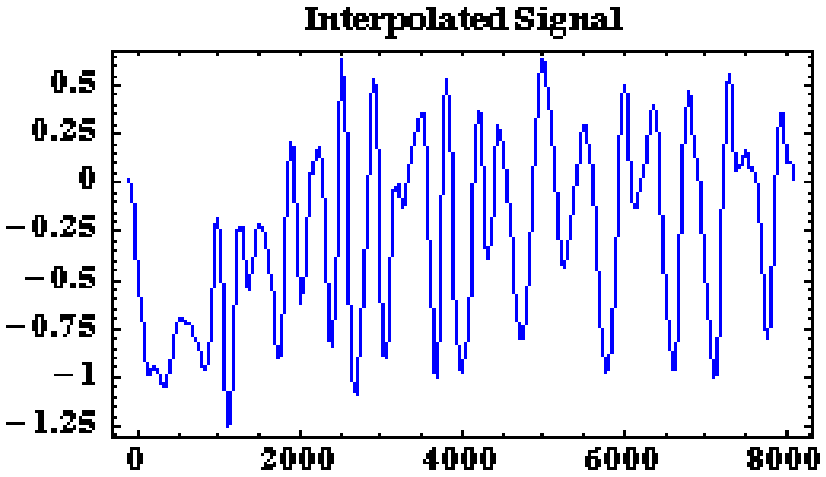

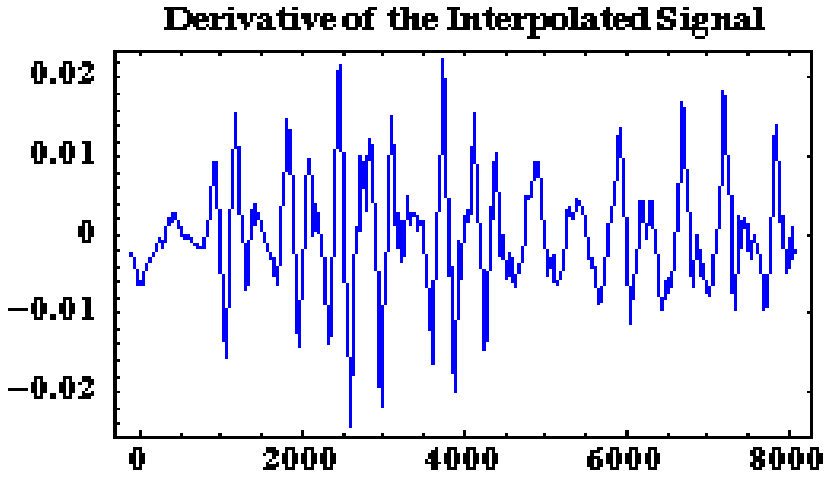

Reconstruction of the Weak Mix Data Using First 3 MRD Levels

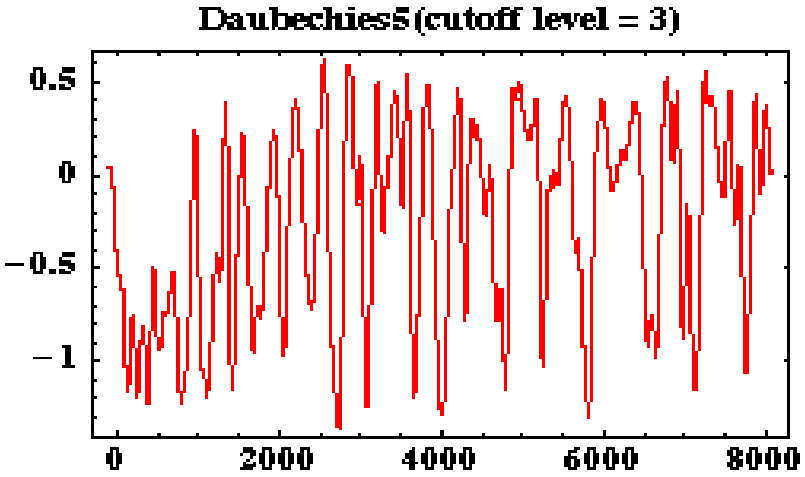

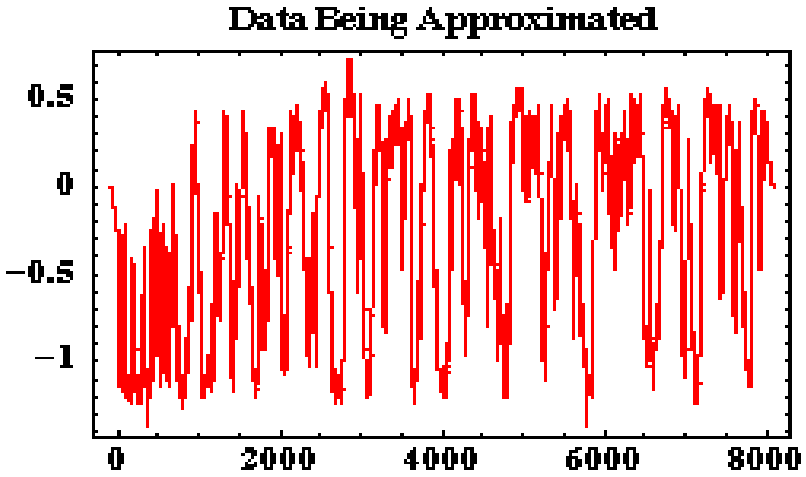

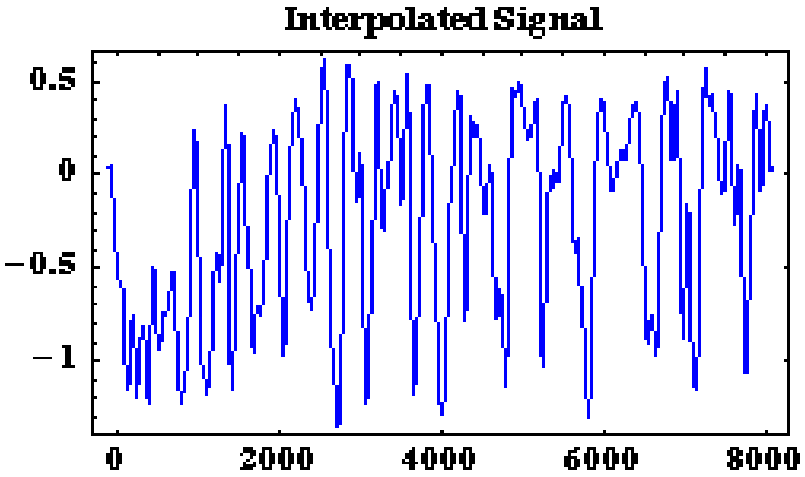

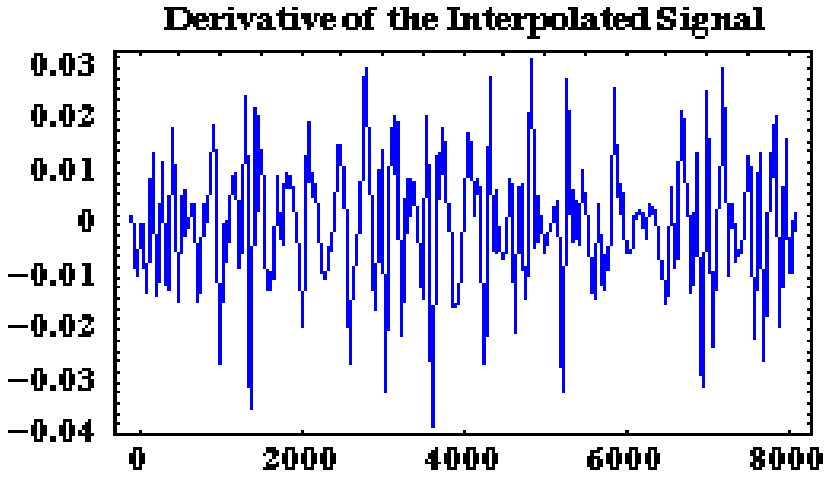

Reconstruction of the Weak Mix Data Using First 4 MRD Levels

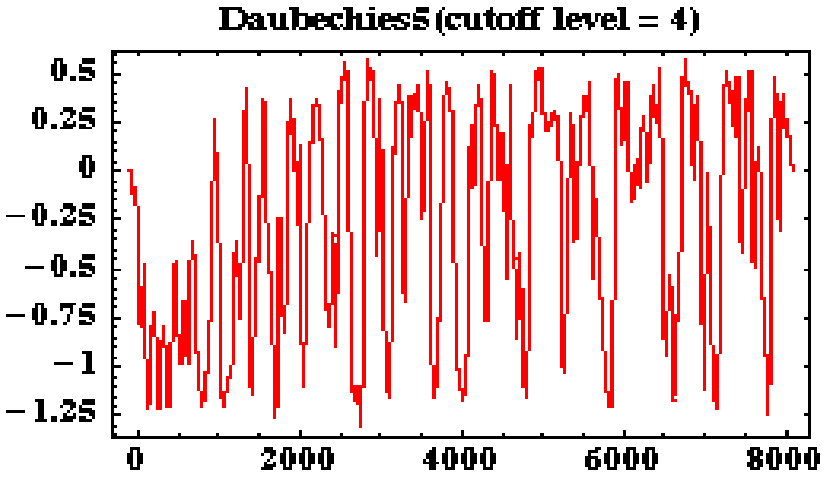

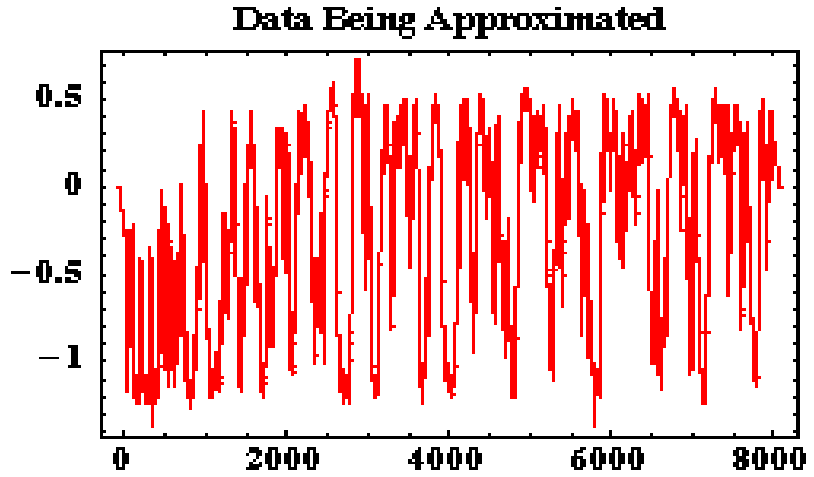

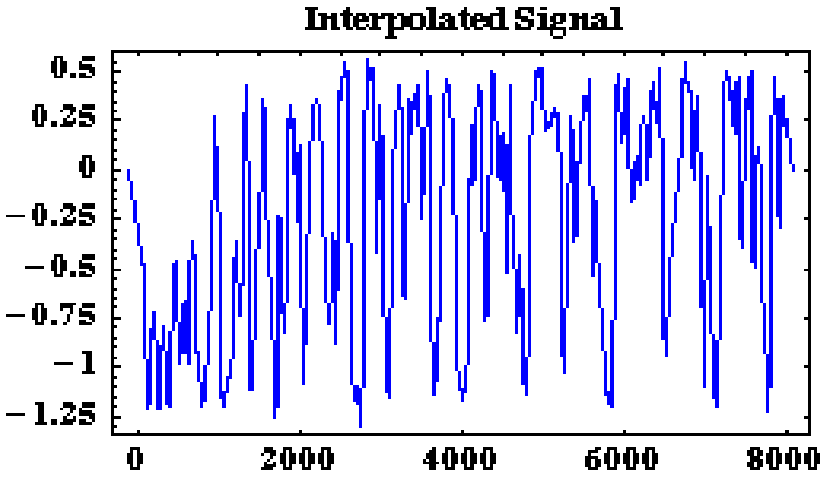

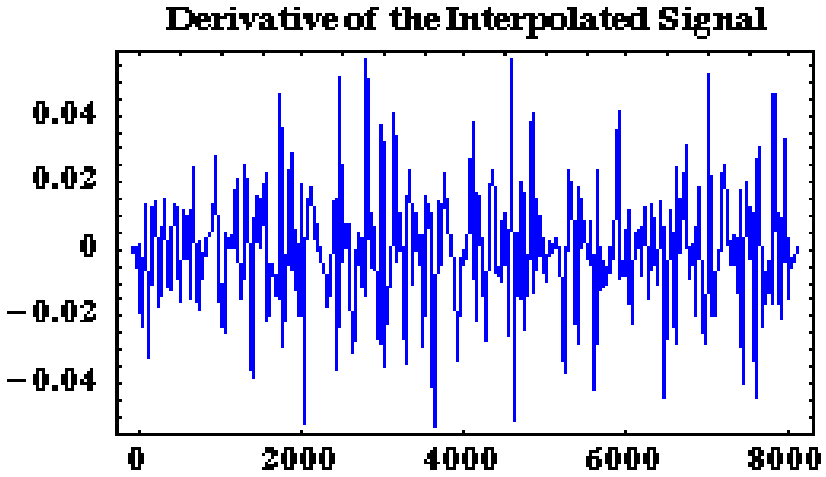

Reconstruction of the Weak Mix Data Using First 5 MRD Levels

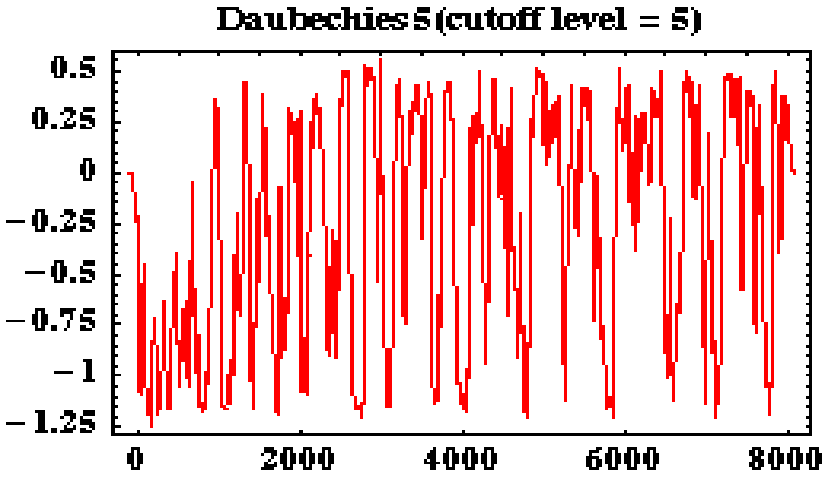

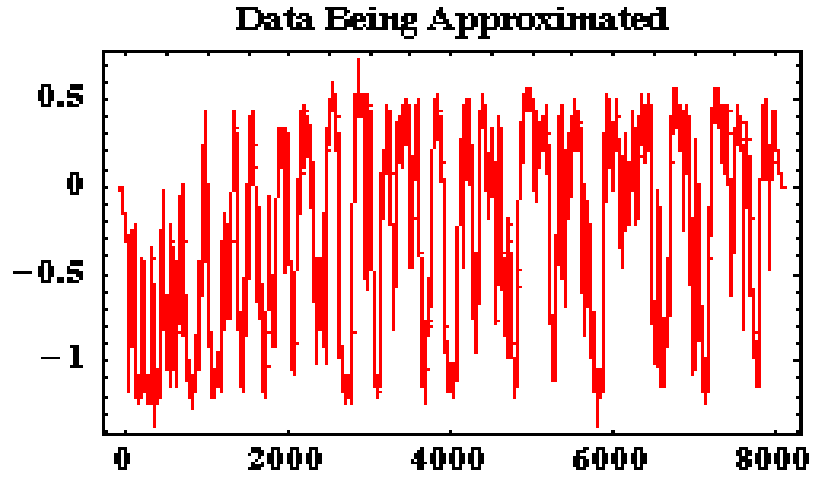

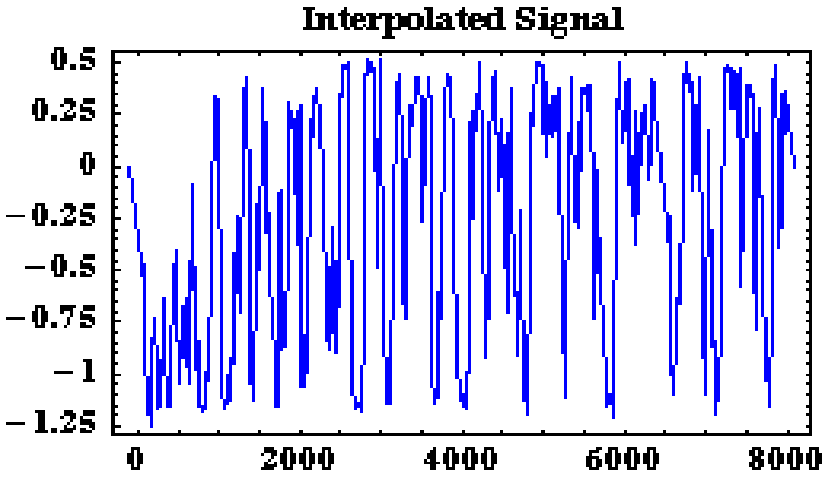

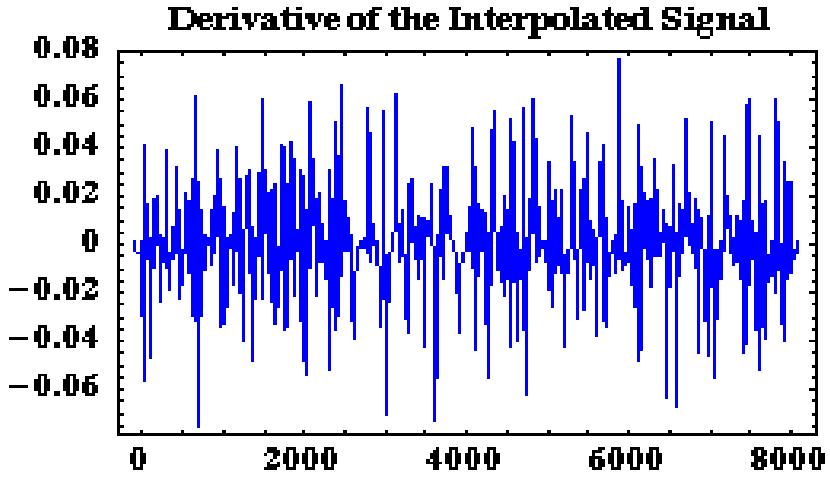

Conclusions Regarding the WLT Analysis of the RT Weak Mix Data

Low Pass Filtered (LPF) Padded and Faded RT Weak Mix Data

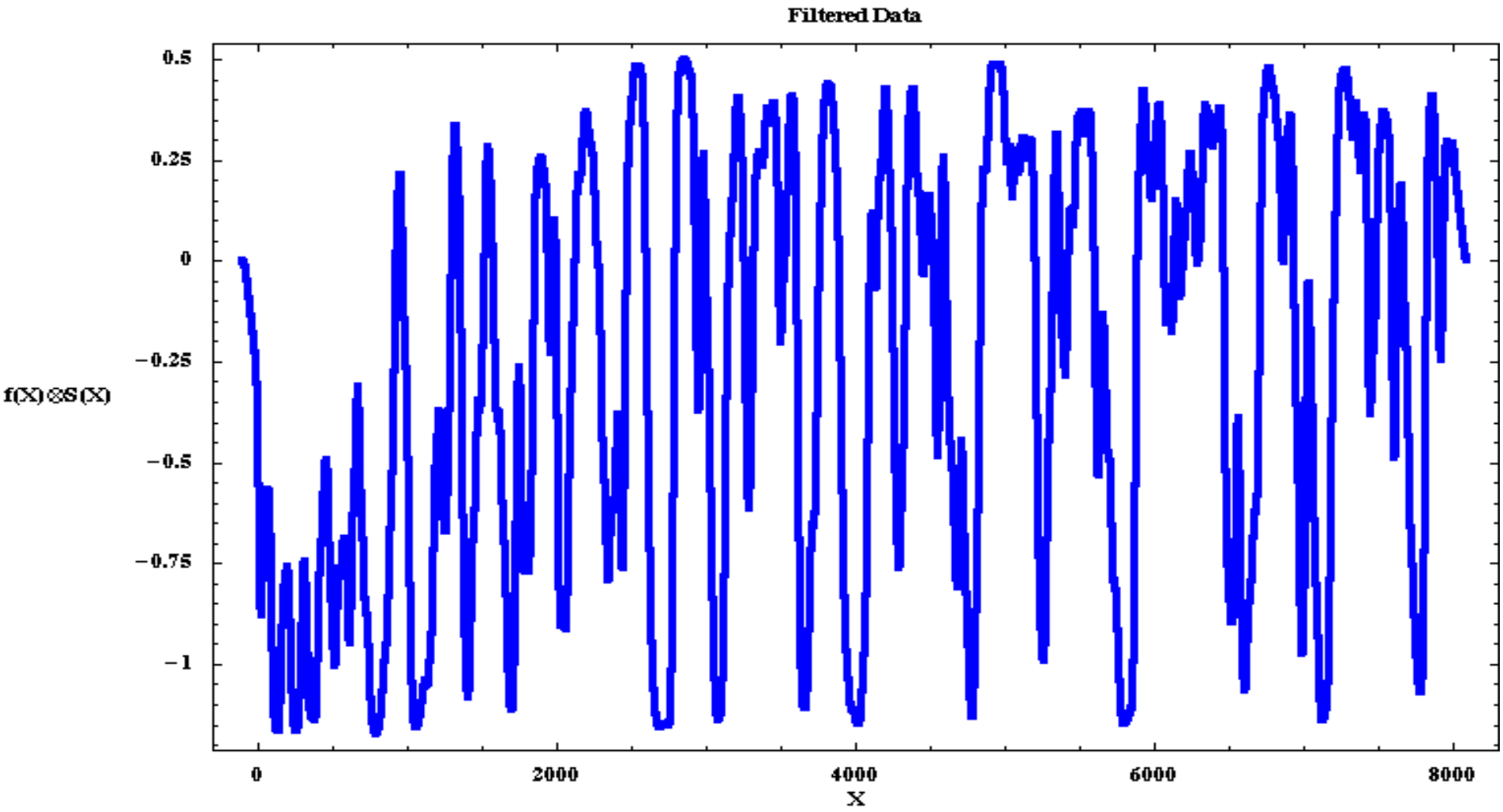

The Filtering Has This Form and Effect on the Data in k-Space

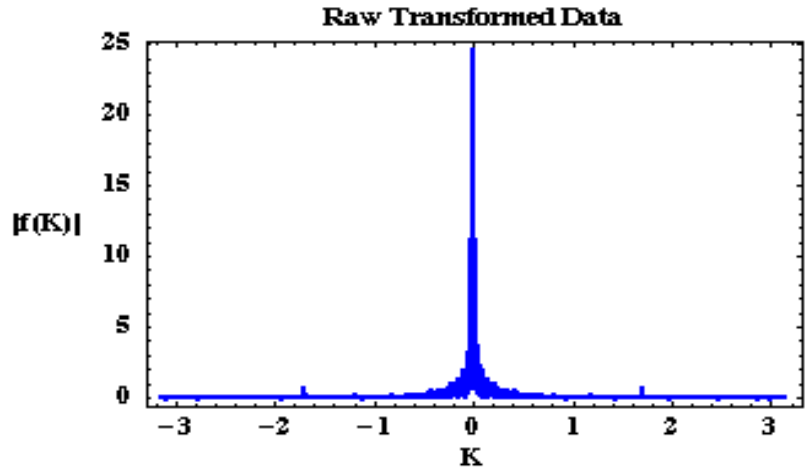

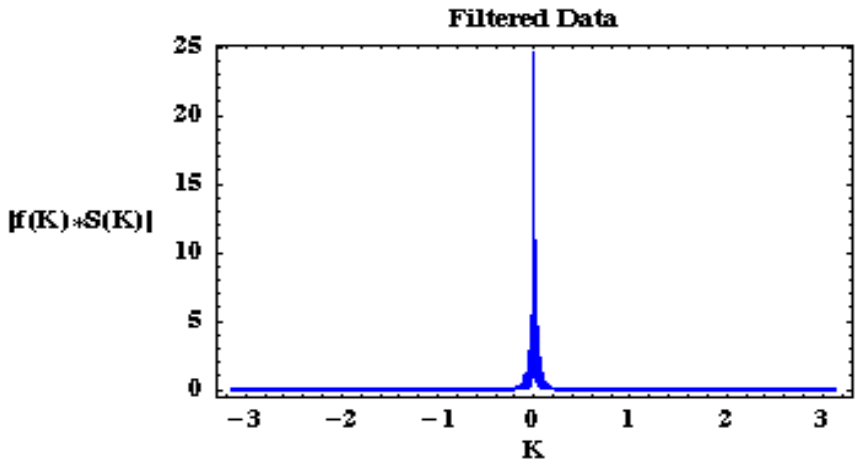

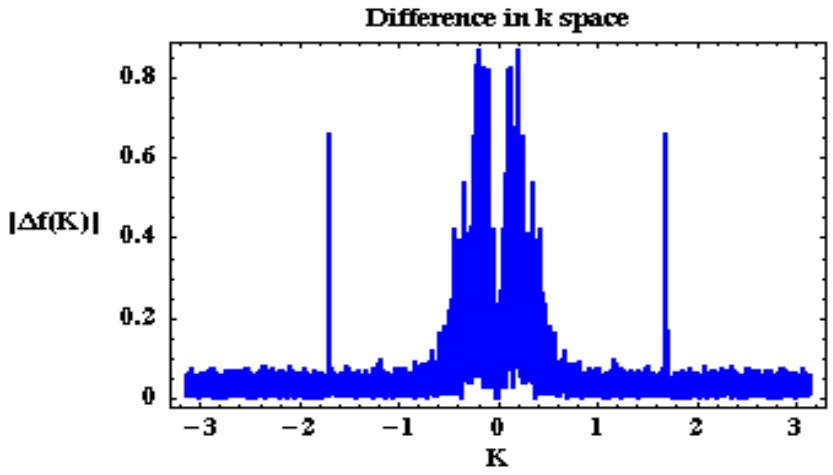

Filter was of the form:

$$S(k) = \exp\left[-\left(\frac{k}{k_{width}}\right)^{2\alpha}\right]$$

Where α=5 and k_{width} = 400

MRD Coefficients of the LPF RT Weak Mix Data in 6 Different Daubechies WLT Bases

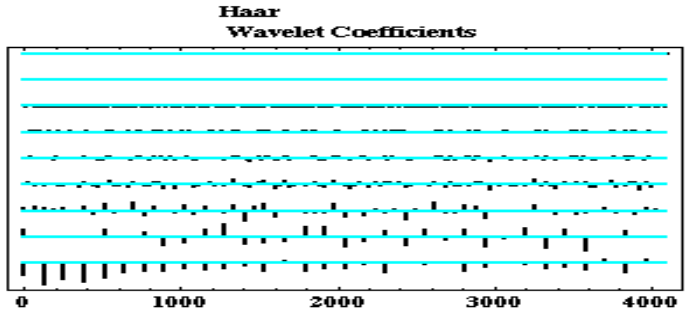

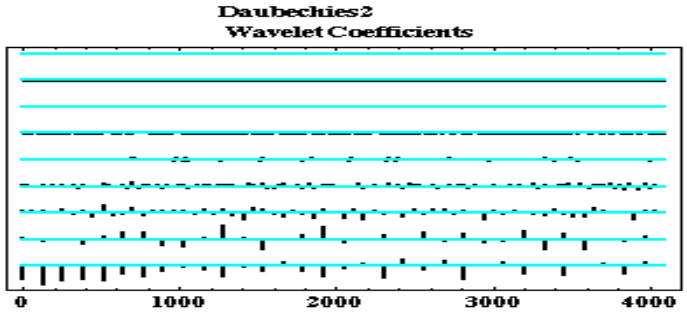

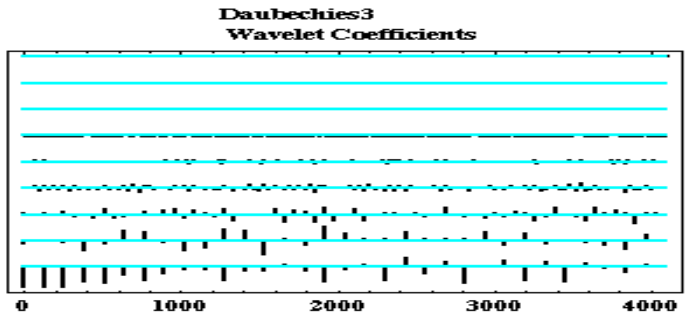

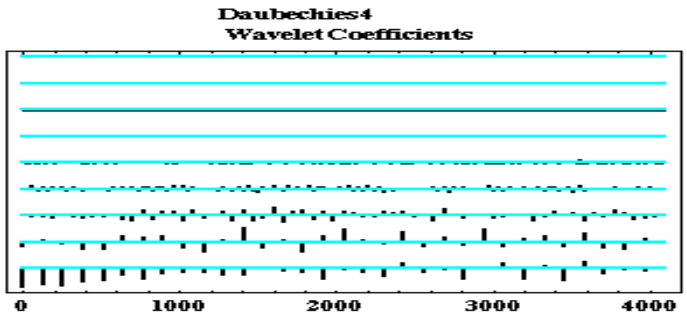

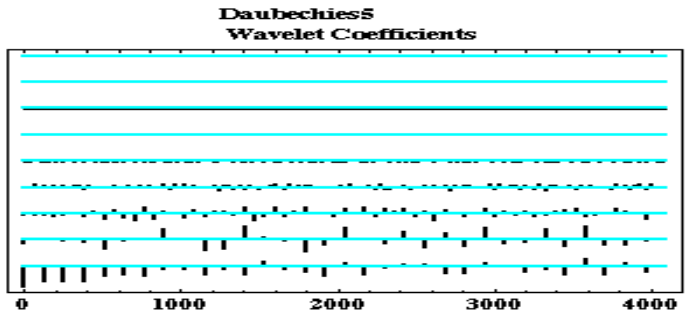

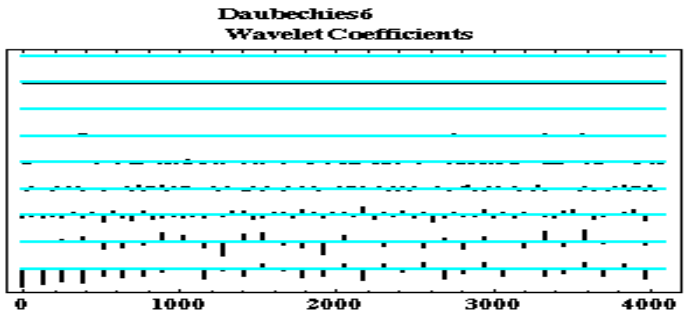

Actual MRDs of the LPF RT Weak Mix Data in 6 Different Daubechies WLT Bases

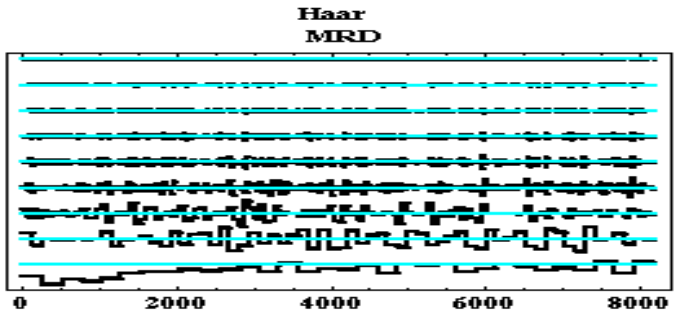

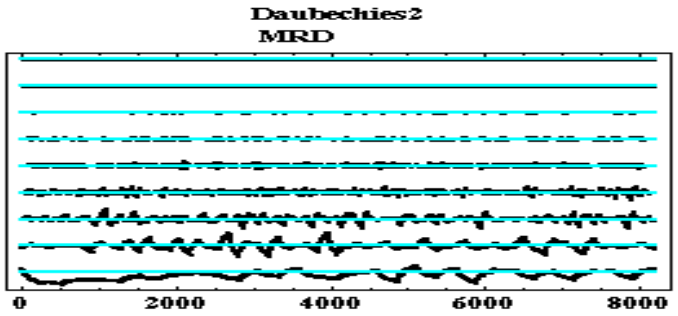

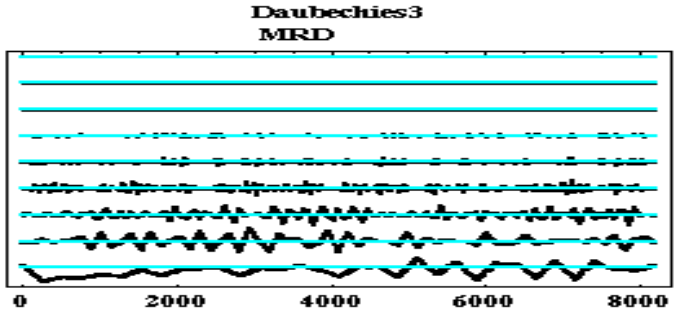

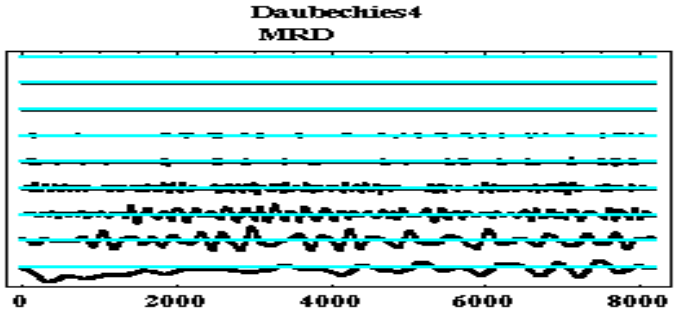

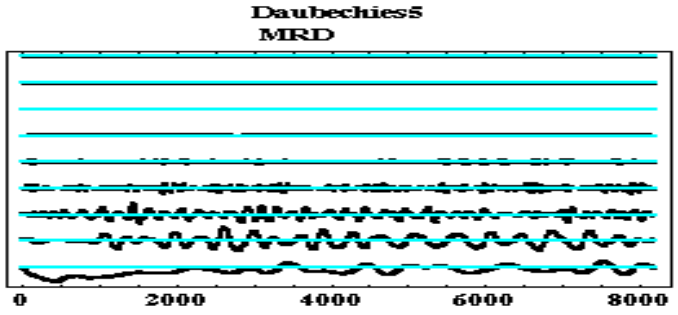

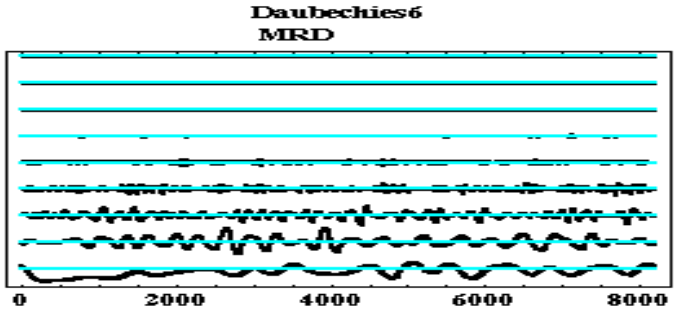

Decay Rate of Largest Coefficient vs Number of Coefficients Kept in 6 Different Daub WLT Decomps

Polymath Research Inc.

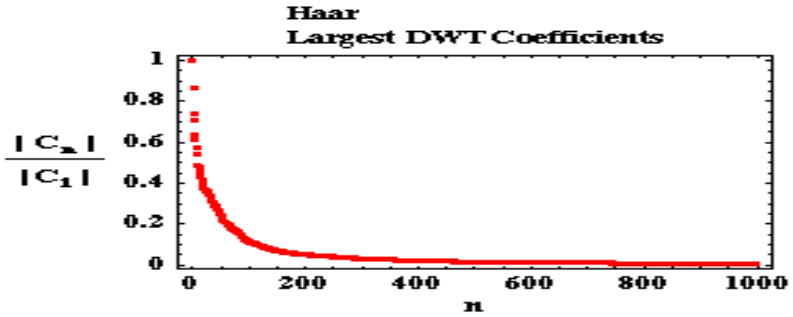

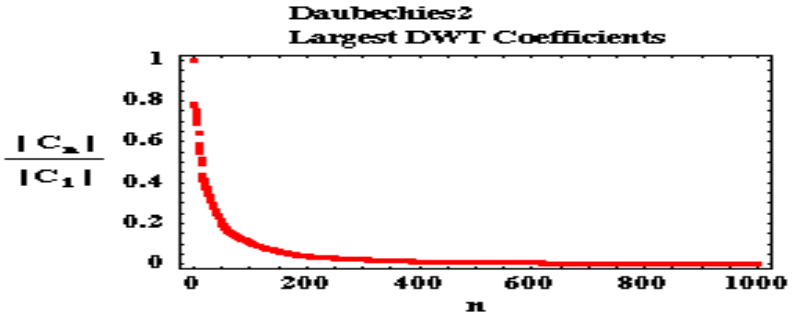

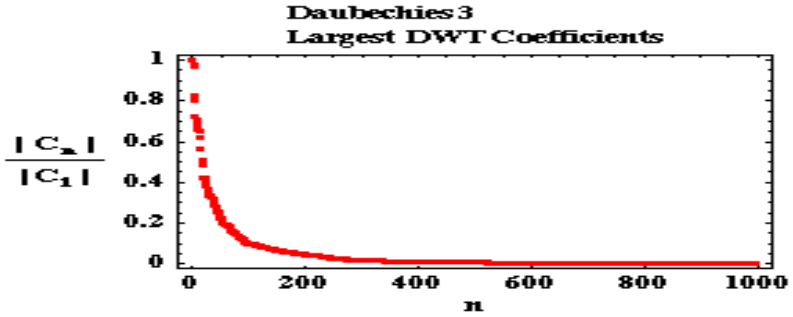

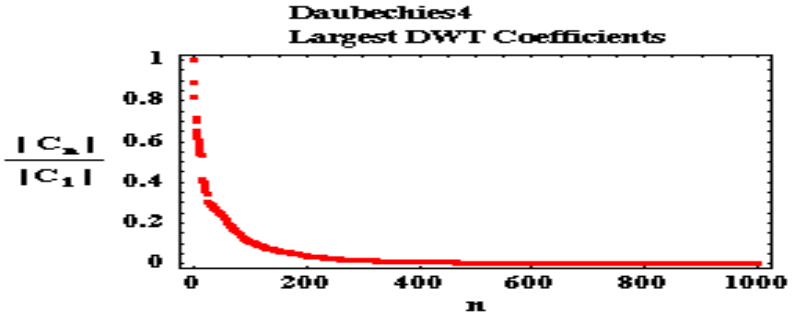

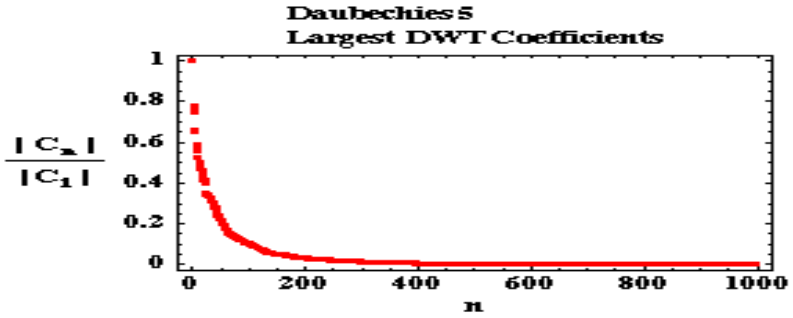

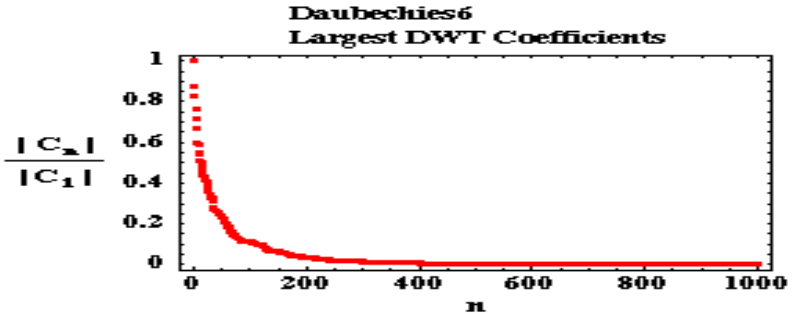

Energy Accumulation Rate in Coefficient Space vs # of WLTs Kept in 6 Different Daub Decomps.

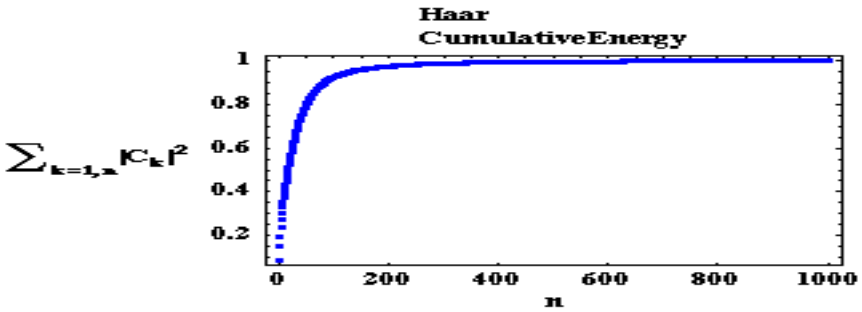

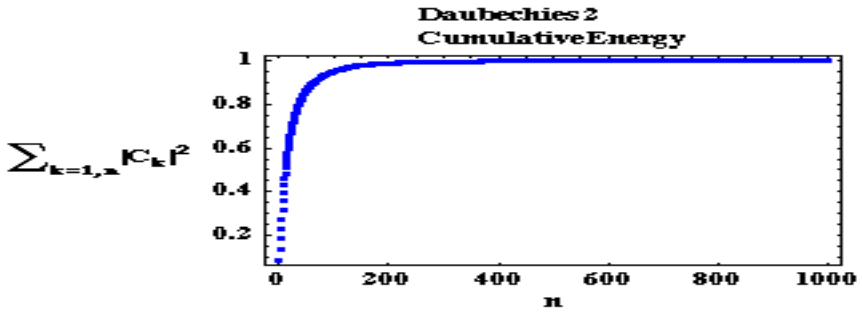

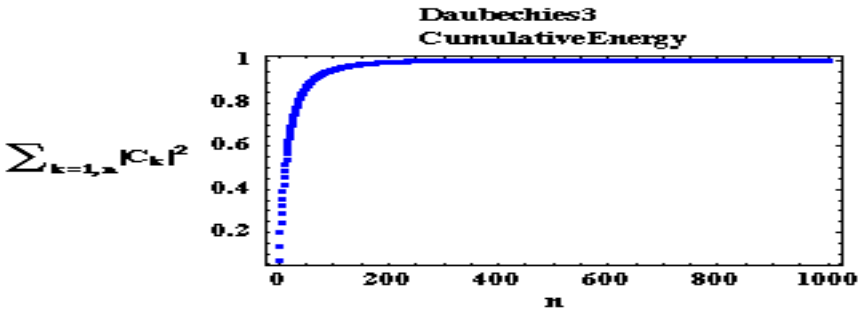

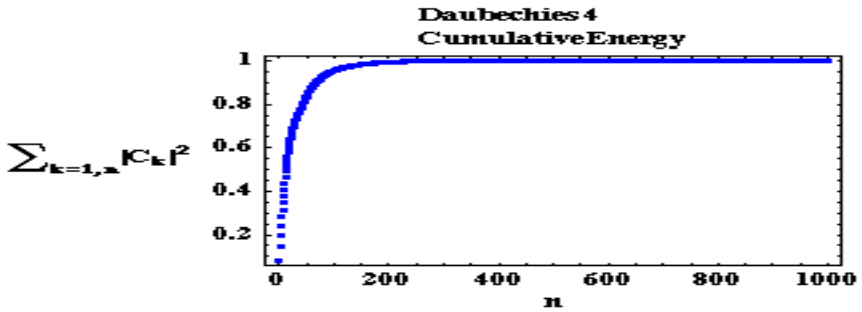

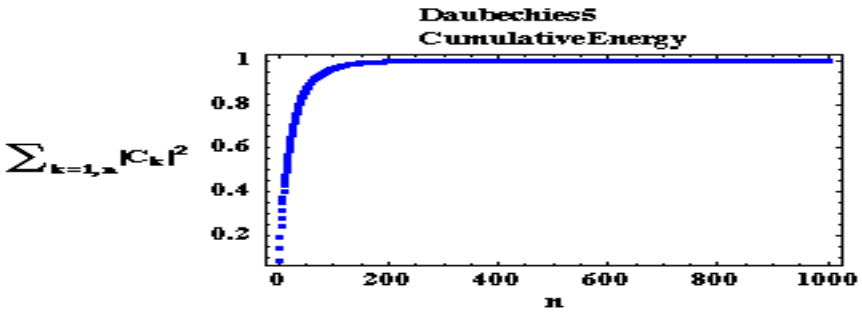

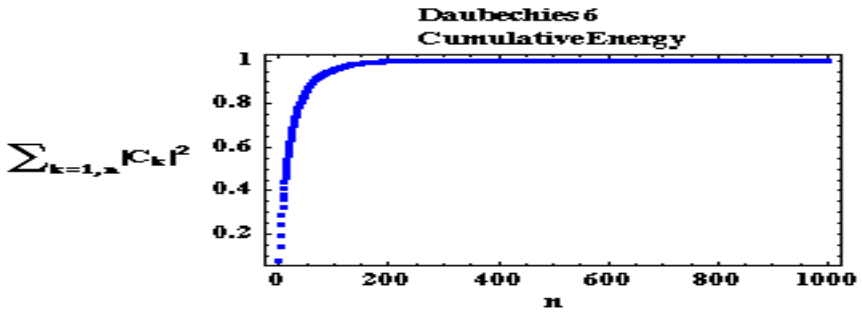

Scaleograms: Waveleters Preferred Way of Judging Tiling in Scale-Translation Space

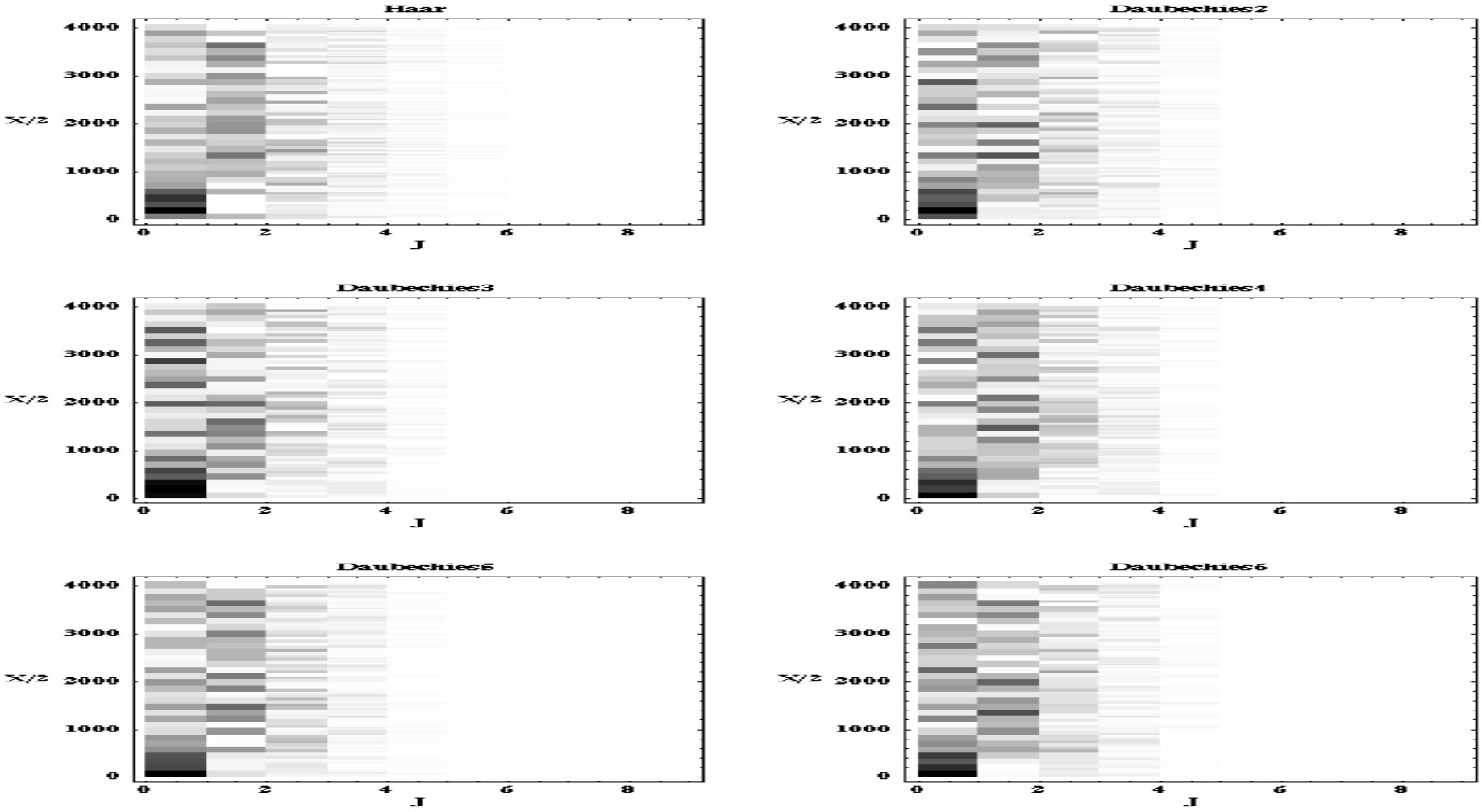

Least Square Error Incurred By Truncating the WLT Series at N of its Largest Coefficients

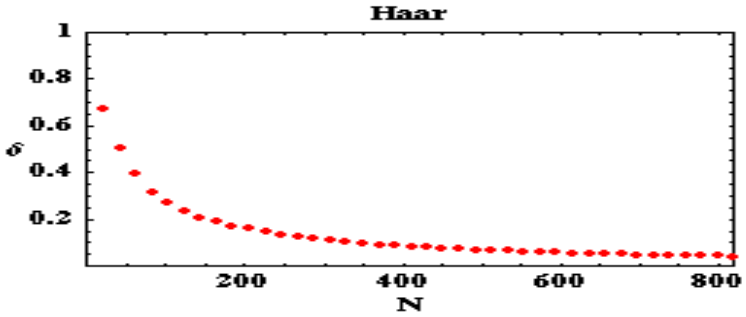

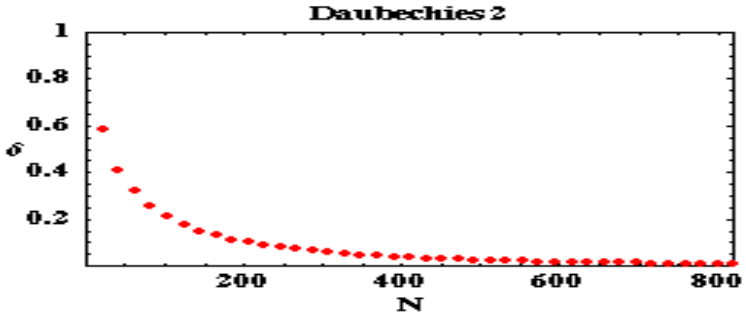

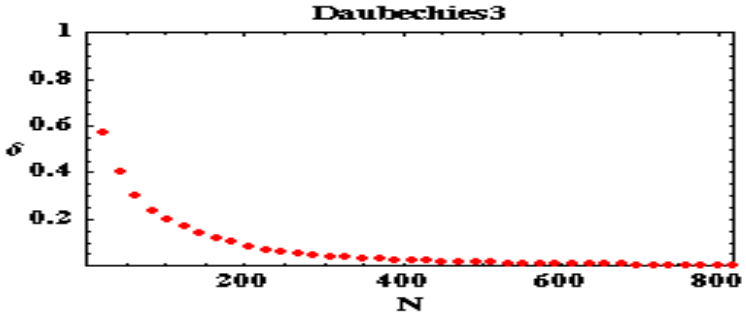

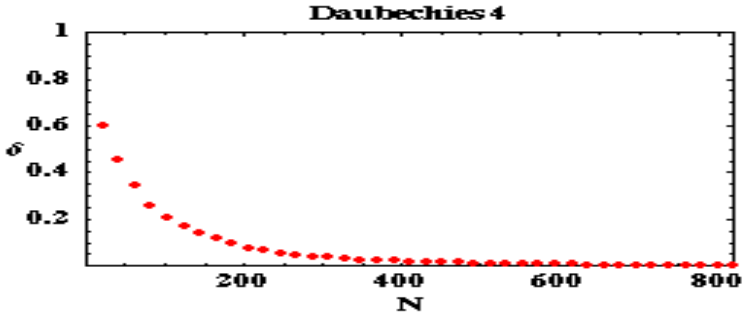

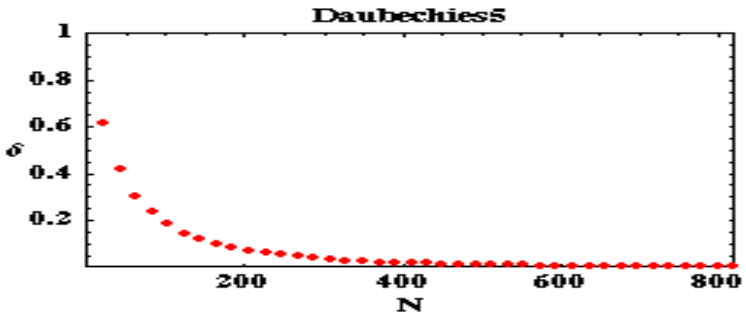

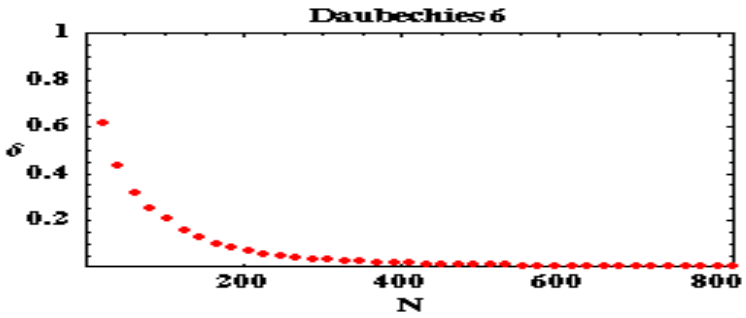

Least Square Error Incurred by Level Thresholding the DWT

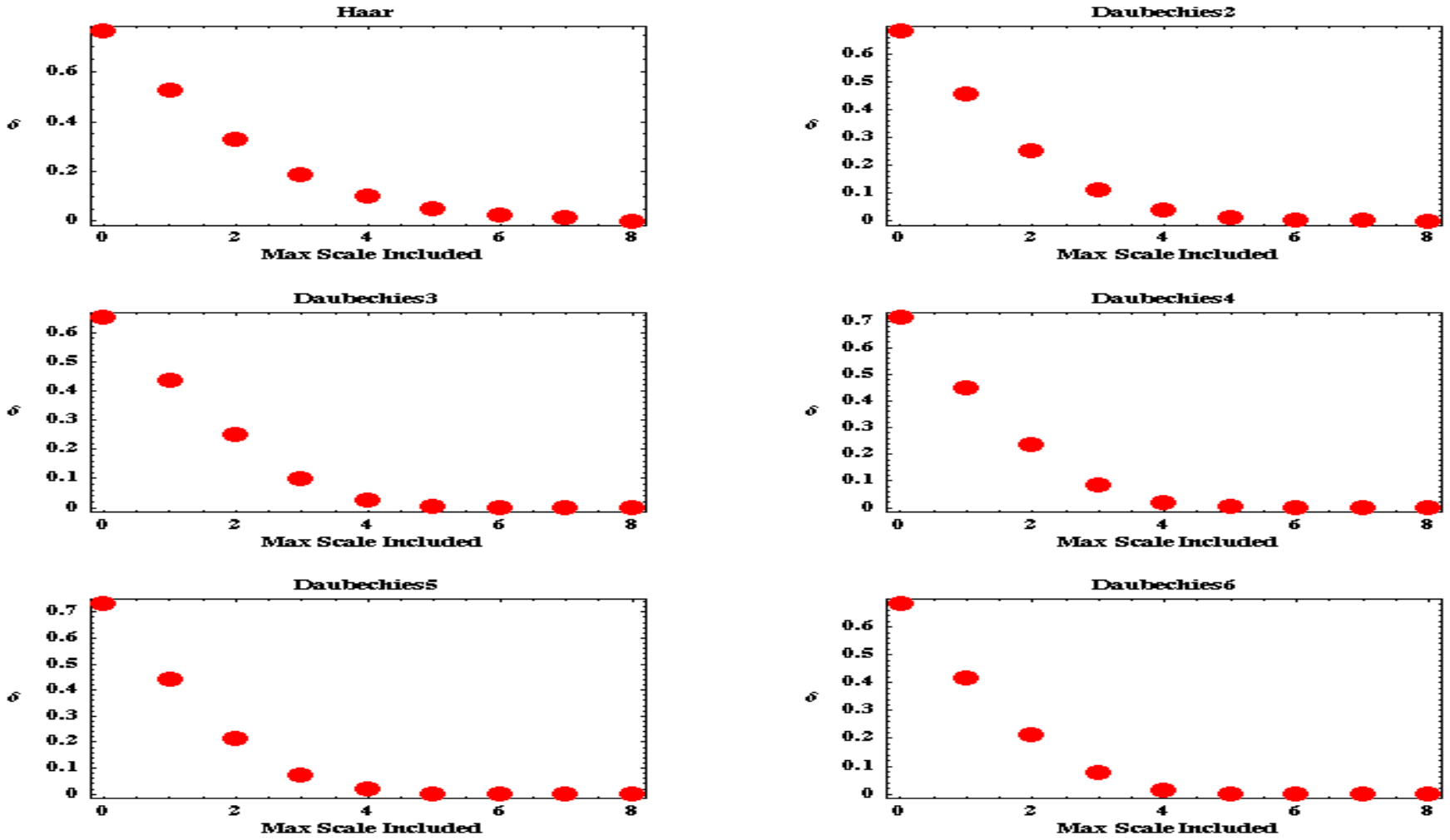

Daubechies 5 Does Much Better than Haar: 5 Quantitative Measures

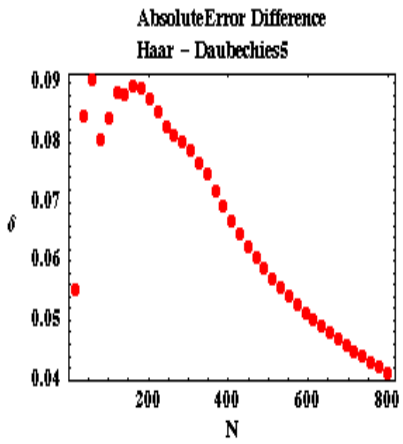

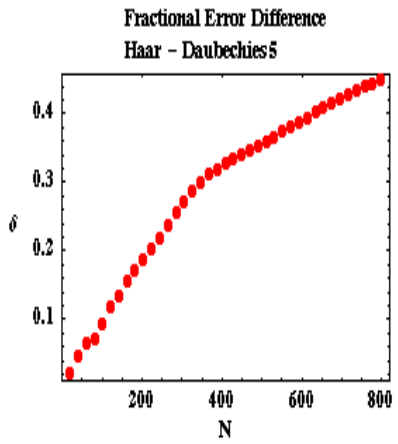

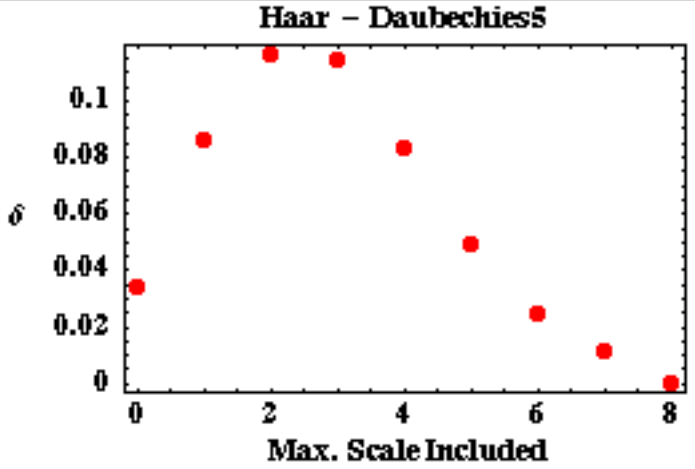

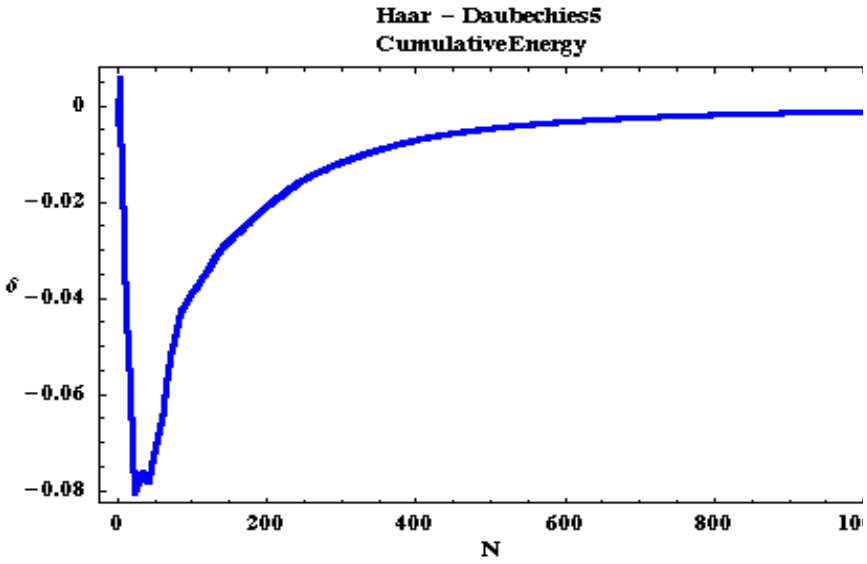

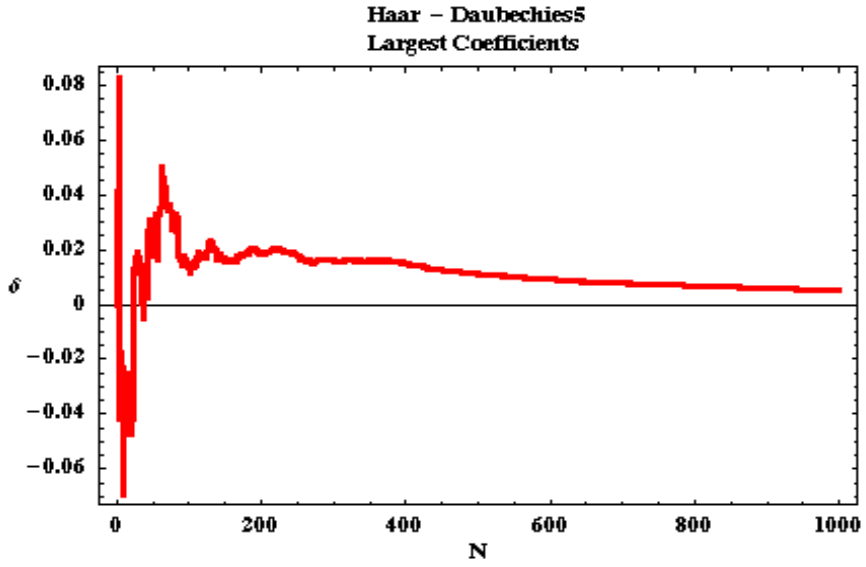

Level by Level Decomposition of the LPF RT Weak Mix Data Using Daub5 WLTs

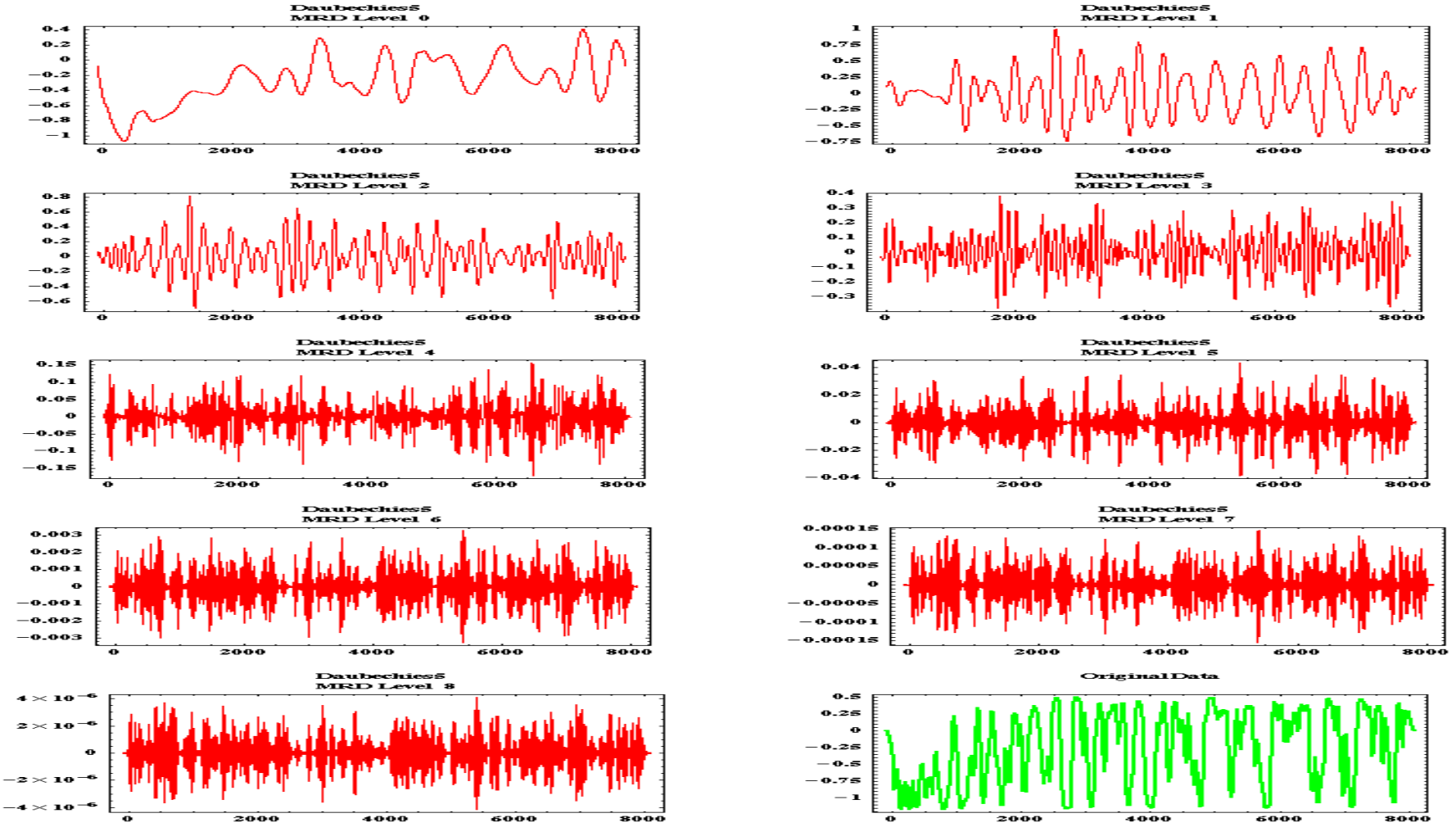

Reconstruction of the LPF RT Weak Mix Data Using the 5 Largest WLT Coefficients

Polymath Research Inc.

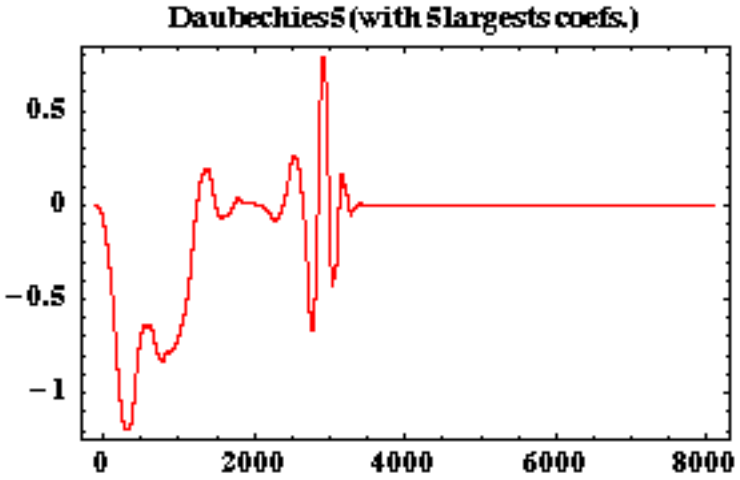

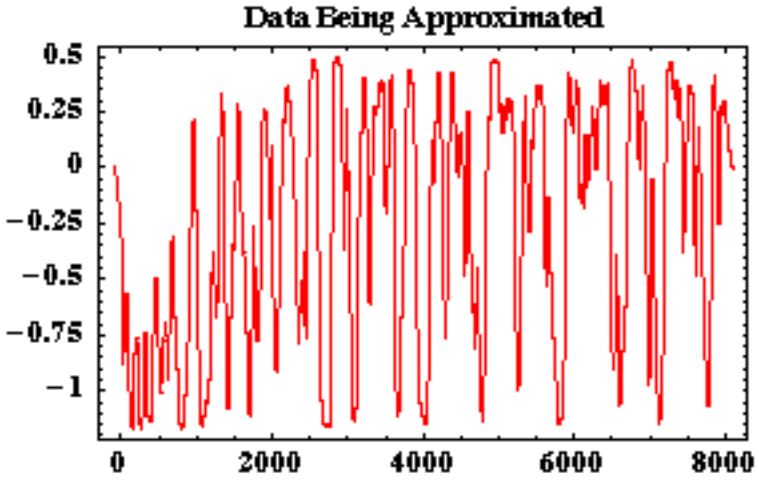

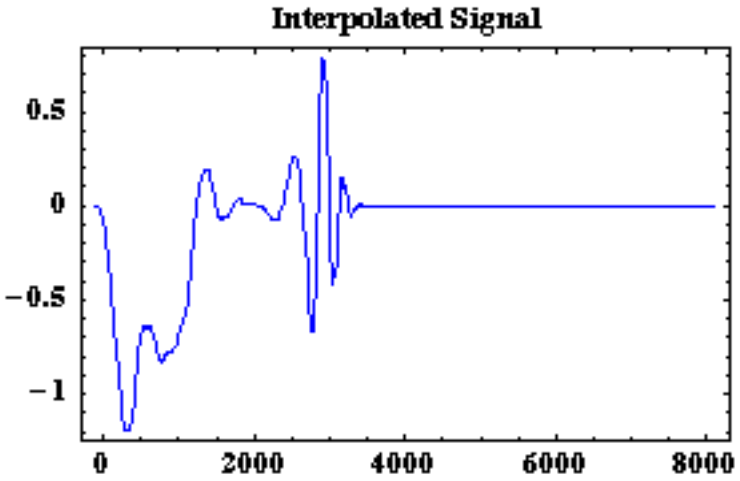

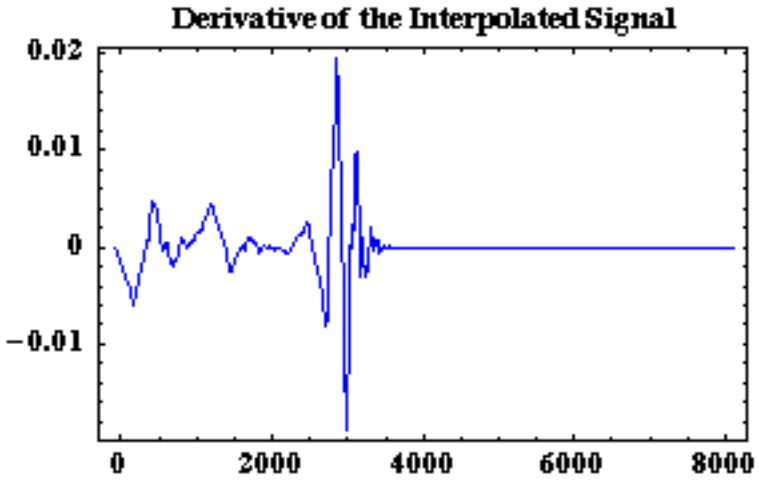

Reconstruction of the LPF RT Weak Mix Data Using the 10 Largest WLT Coefficients

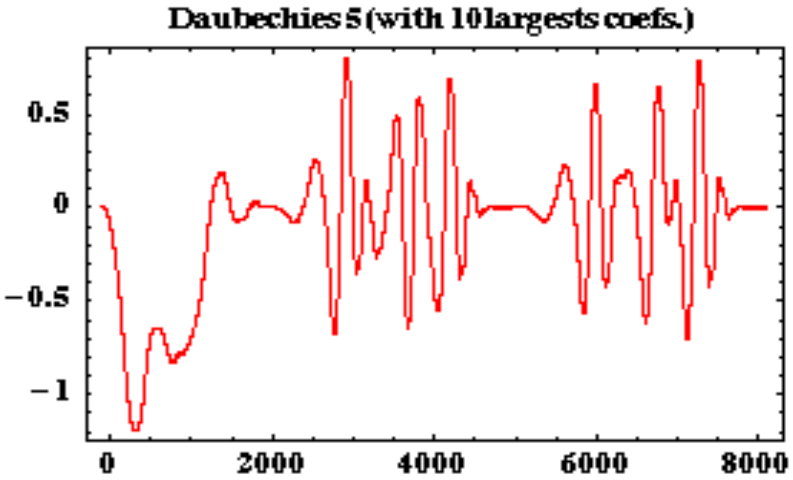

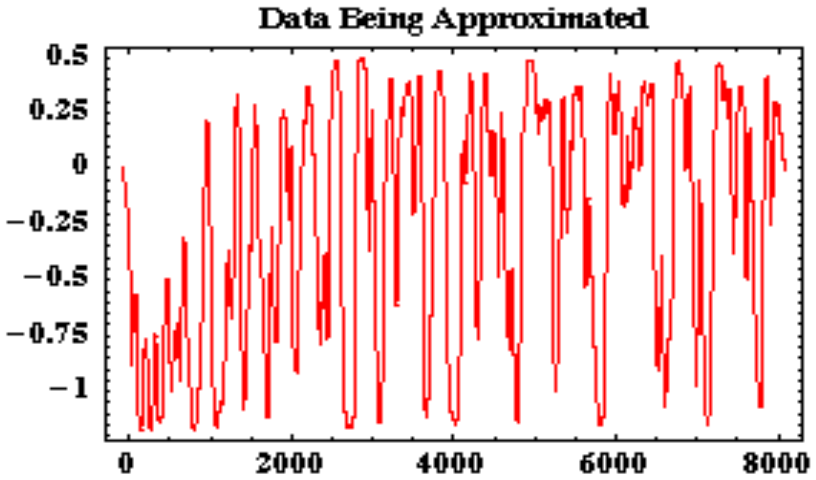

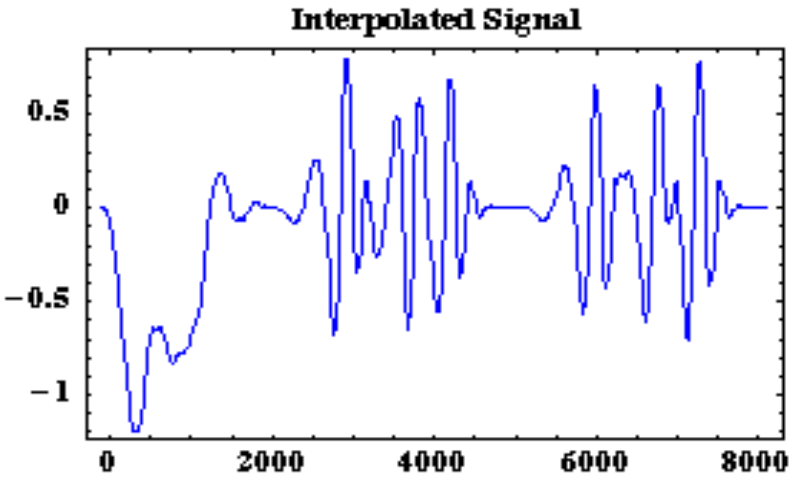

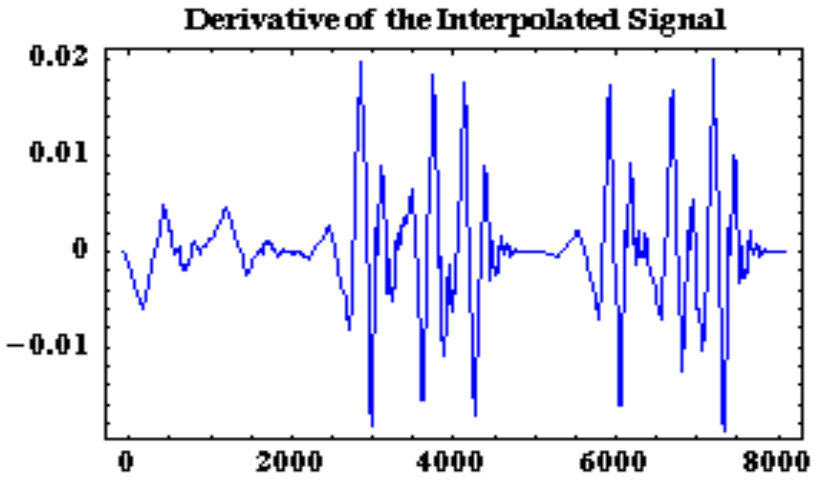

Reconstruction of the LPF RT Weak Mix Data Using the 15 Largest WLT Coefficients

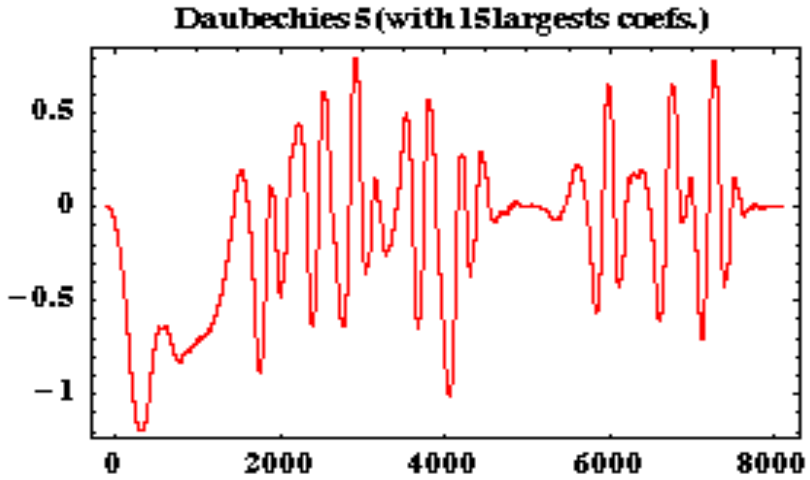

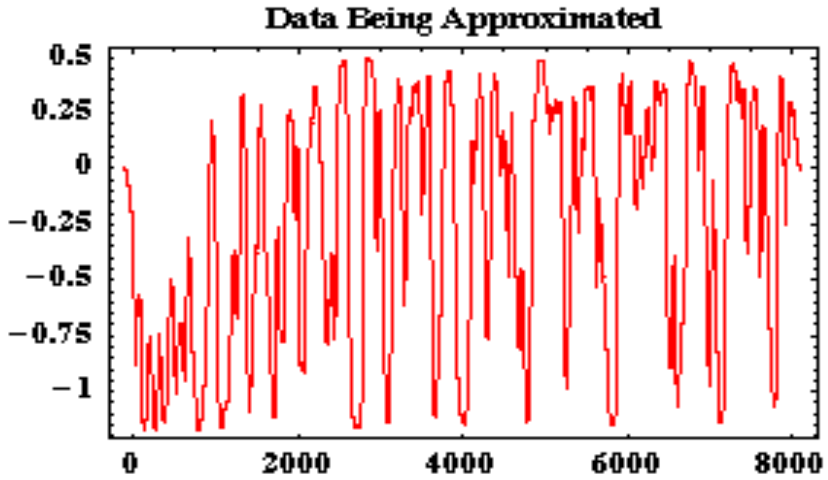

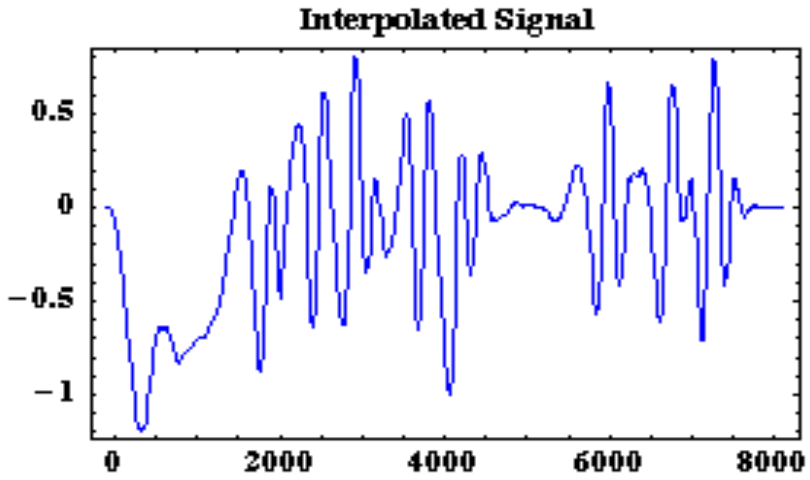

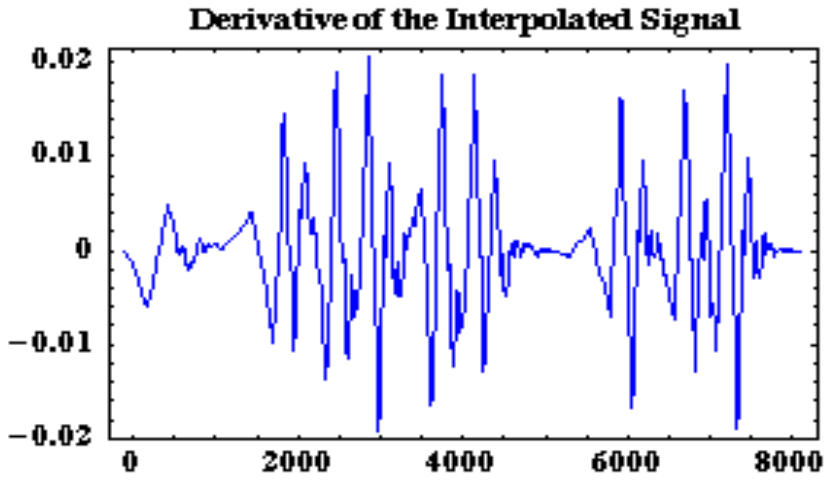

Reconstruction of the LPF RT Weak Mix Data Using the 20 Largest WLT Coefficients

Polymath Research Inc.

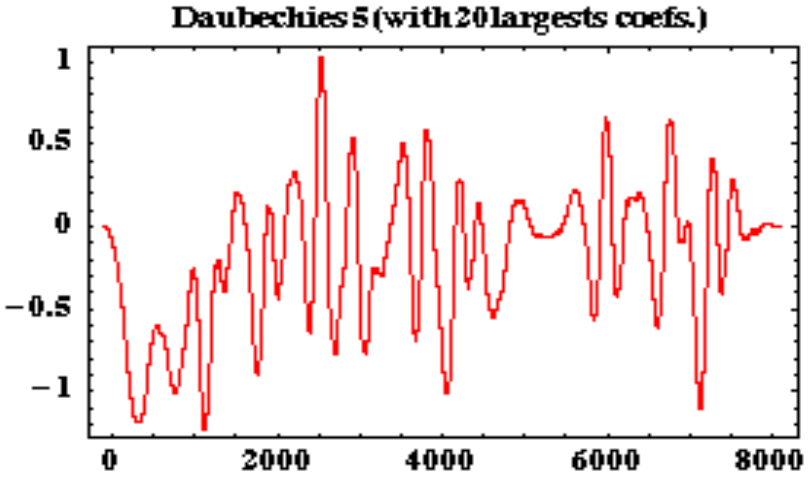

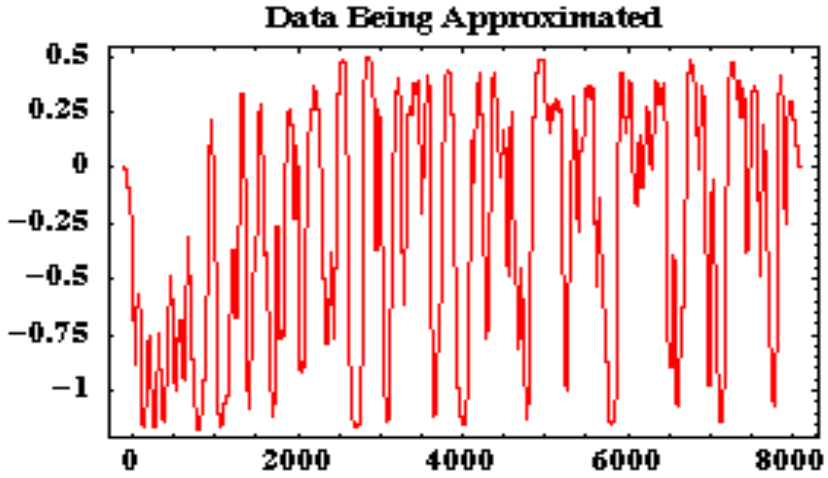

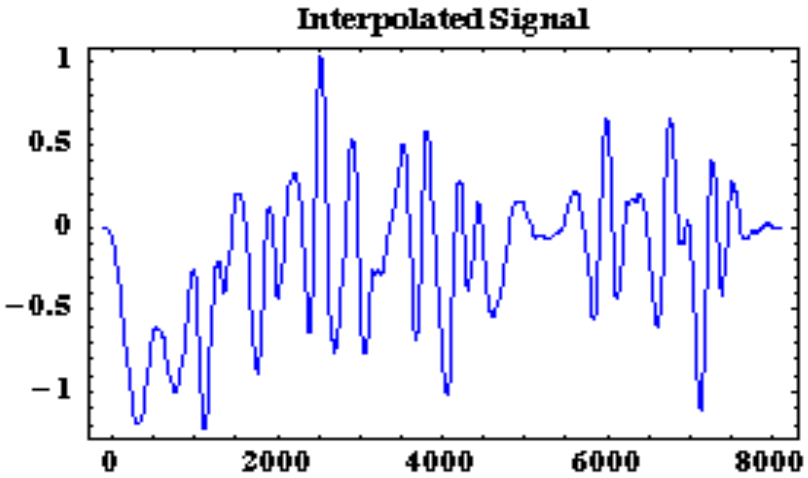

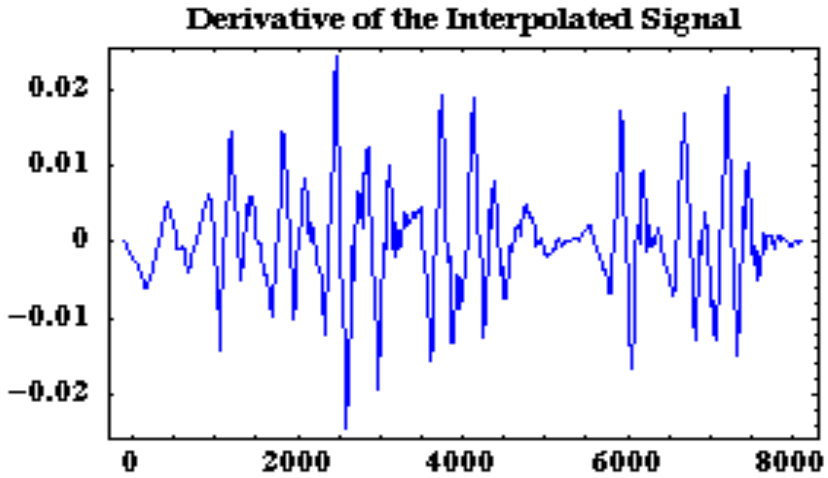

Reconstruction of the LPF RT Weak Mix Data Using the 25 Largest WLT Coefficients

Polymath Research Inc.

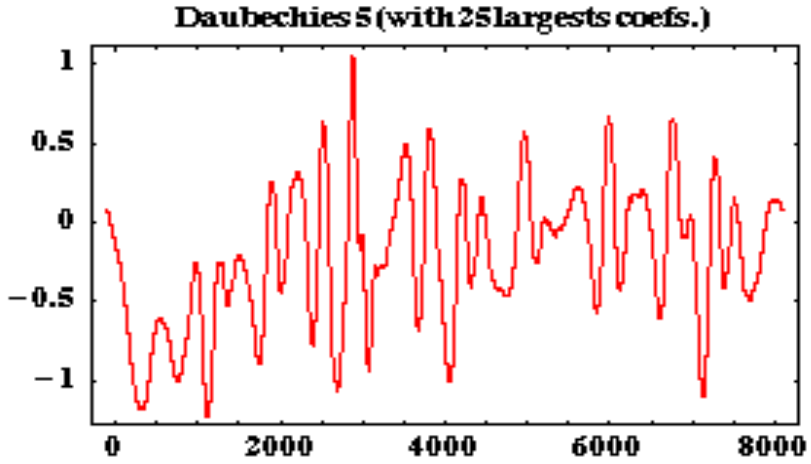

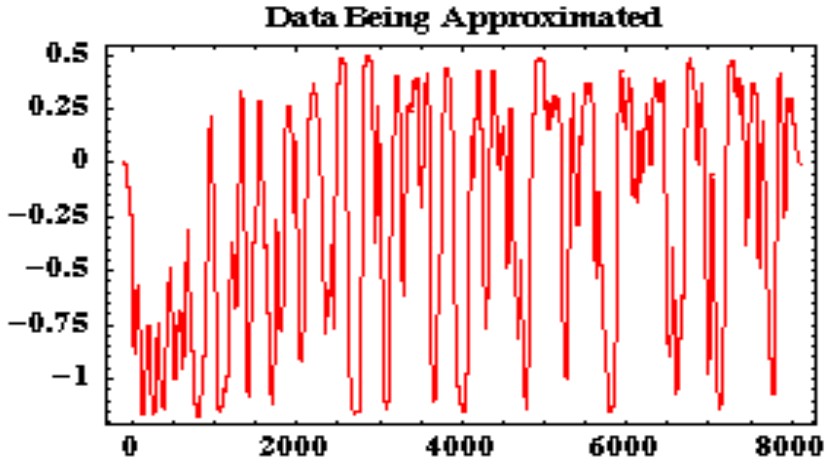

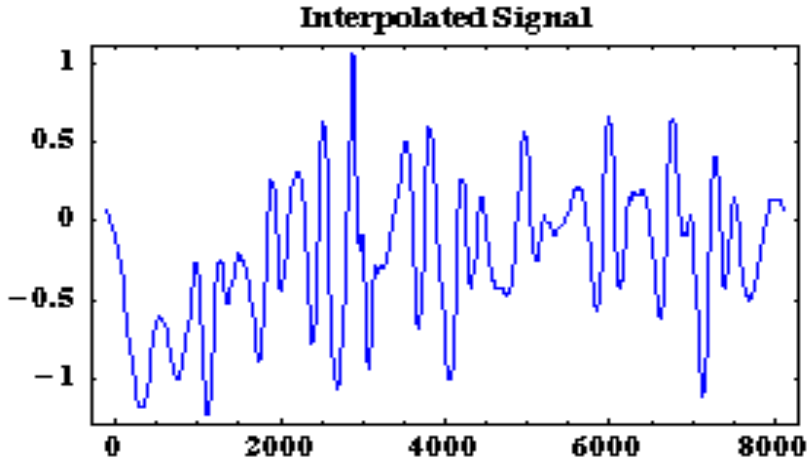

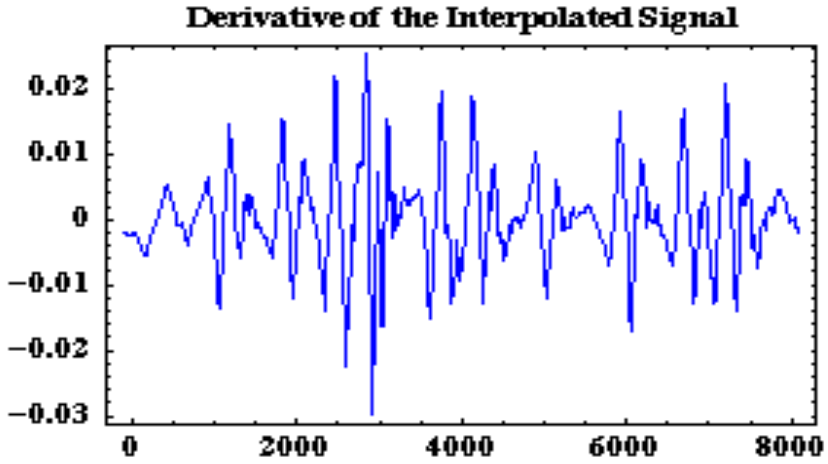

Reconstruction of the LPF RT Weak Mix Data Using the 30 Largest WLT Coefficients

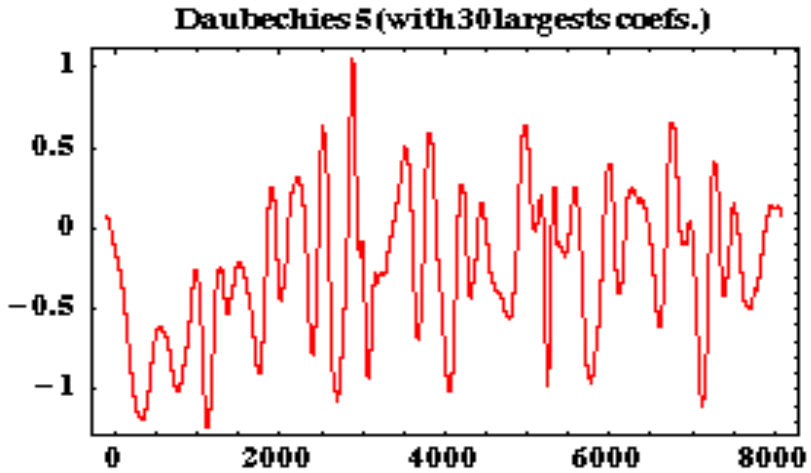

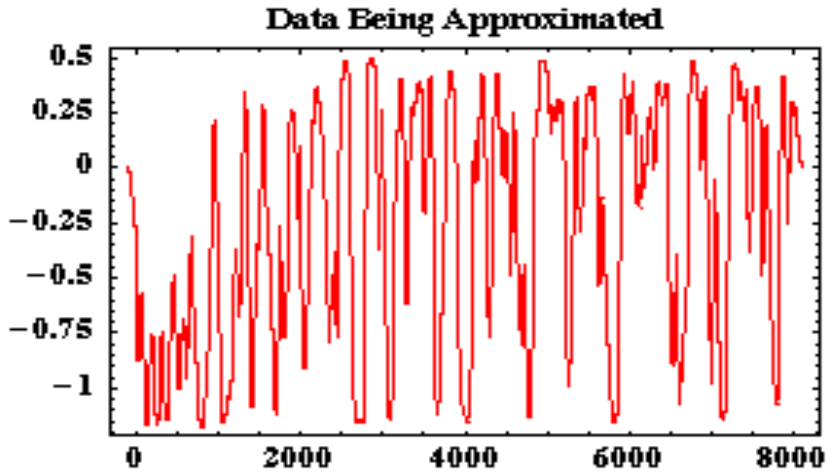

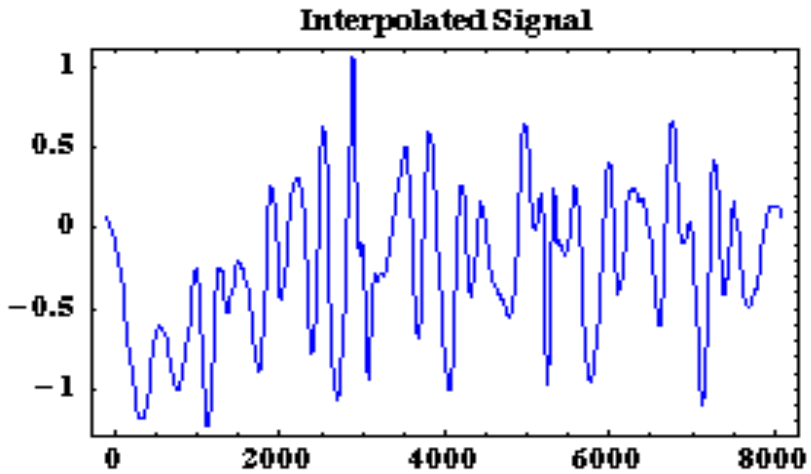

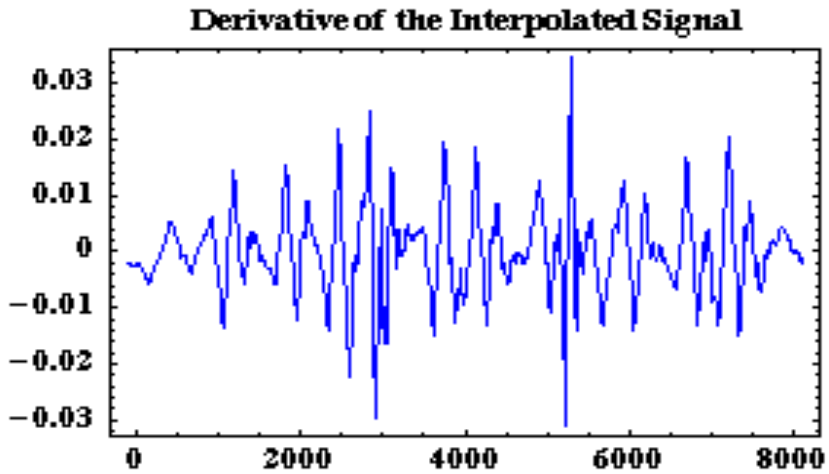

Reconstruction of the LPF RT Weak Mix Data Using the 35 Largest WLT Coefficients

Polymath Research Inc.

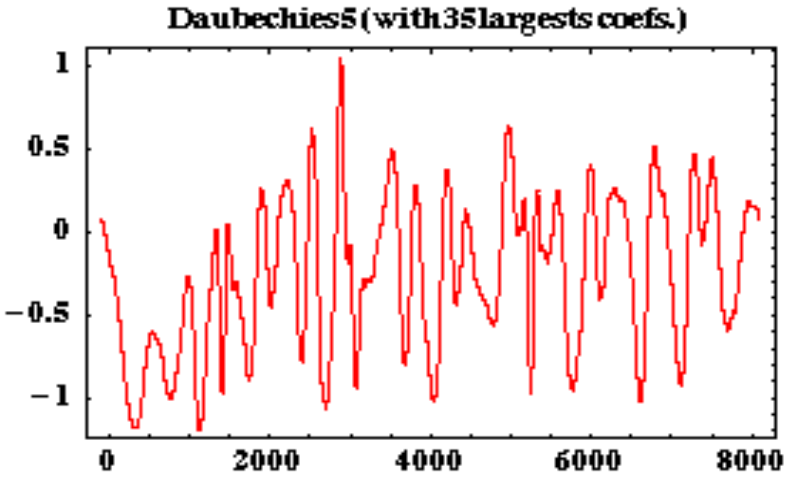

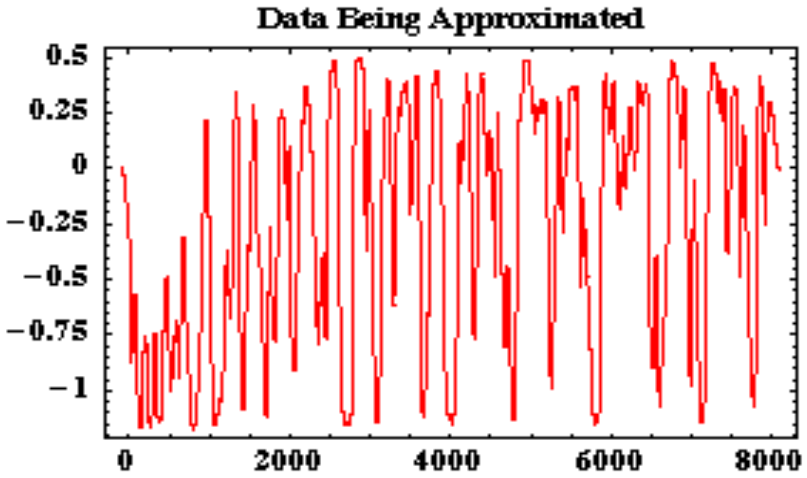

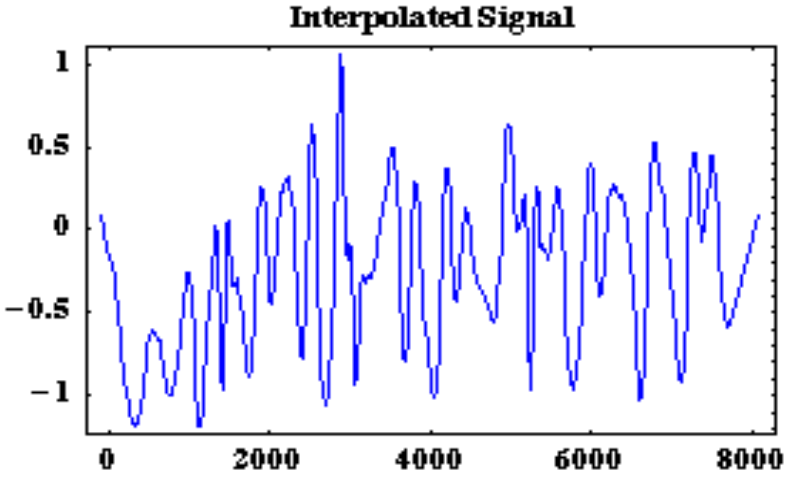

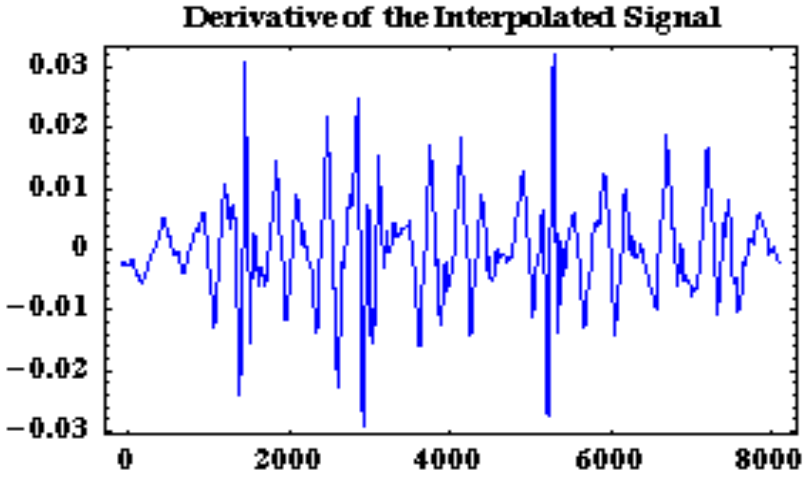

Reconstruction of the LPF RT Weak Mix Data Using the 40 Largest WLT Coefficients

Polymath Research Inc.

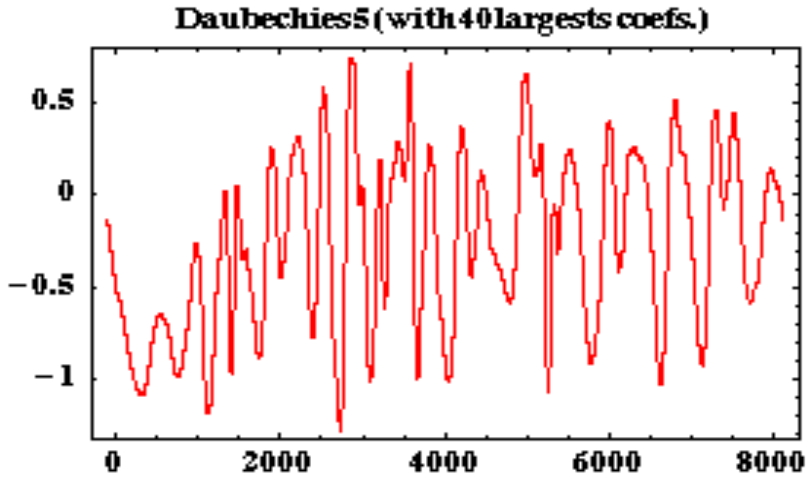

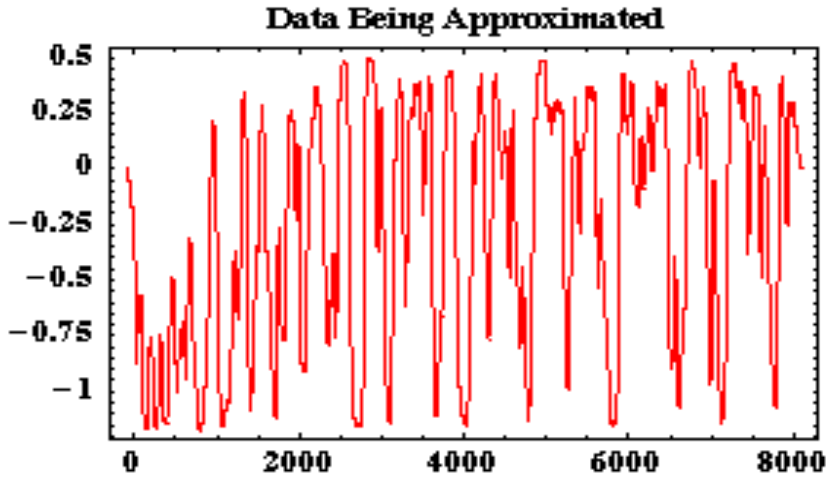

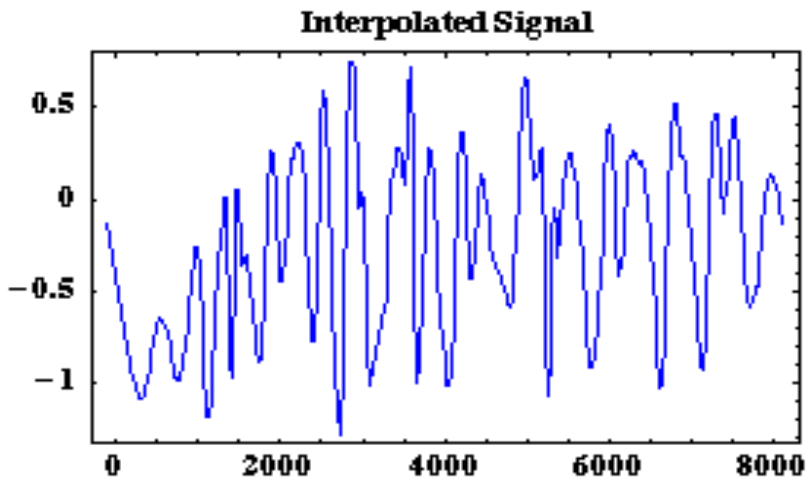

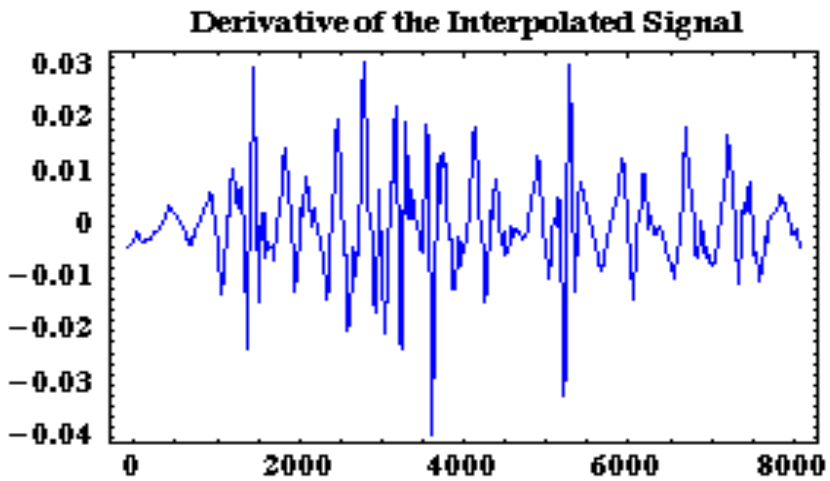

Reconstruction of the LPF RT Weak Mix Data Using the 45 Largest WLT Coefficients

Polymath Research Inc.

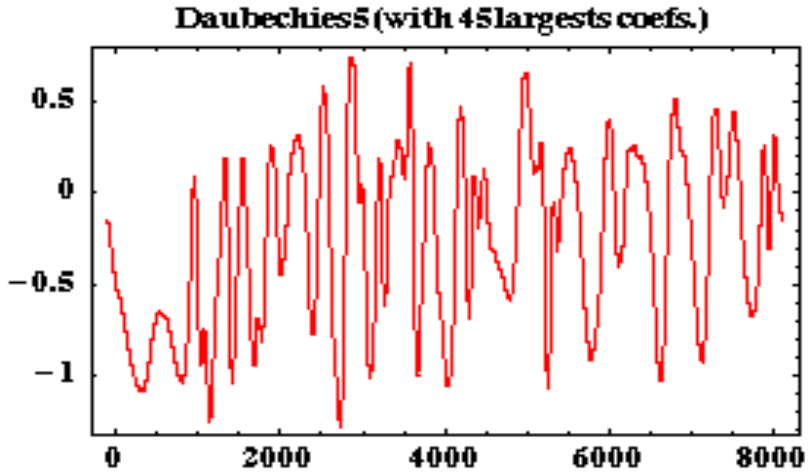

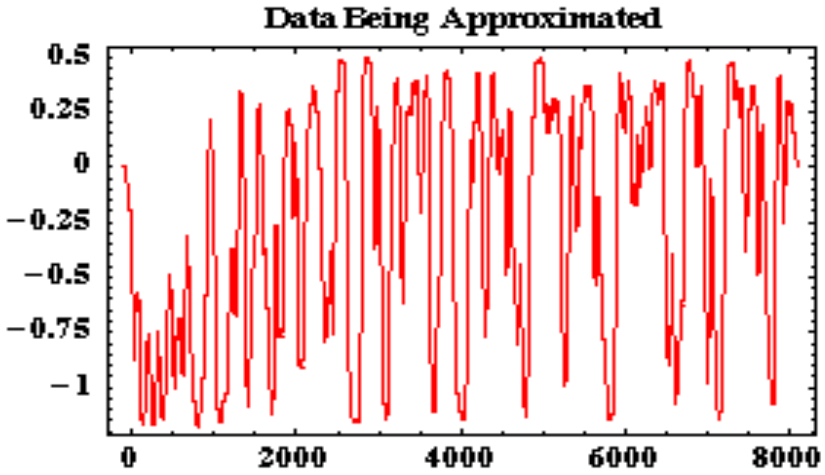

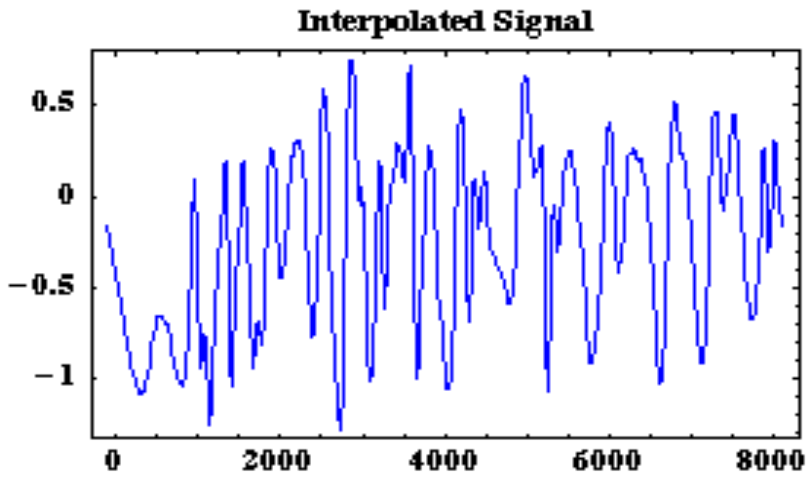

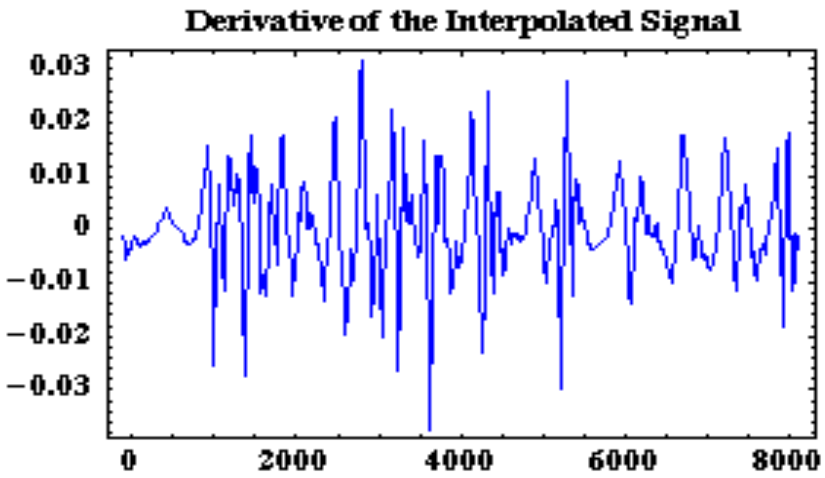

Reconstruction of the LPF RT Weak Mix Data Using the 50 Largest WLT Coefficients

Polymath Research Inc.

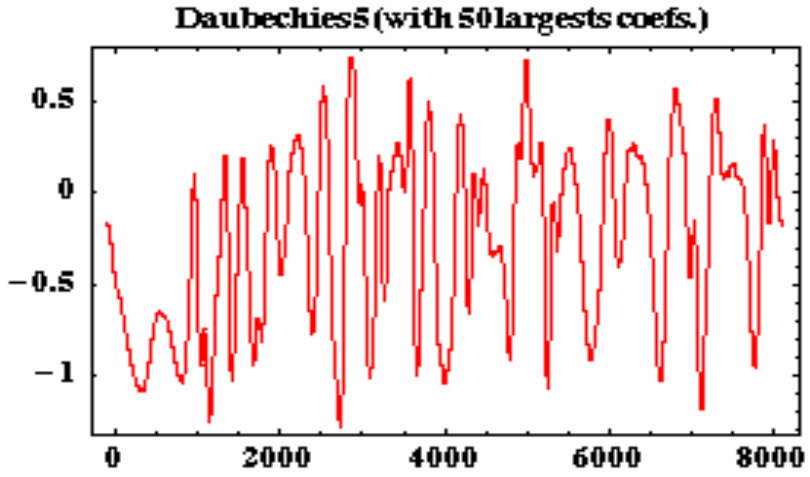

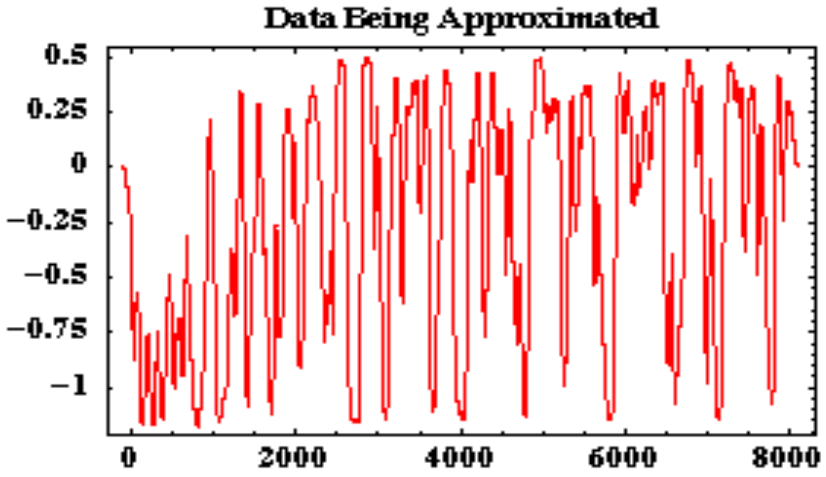

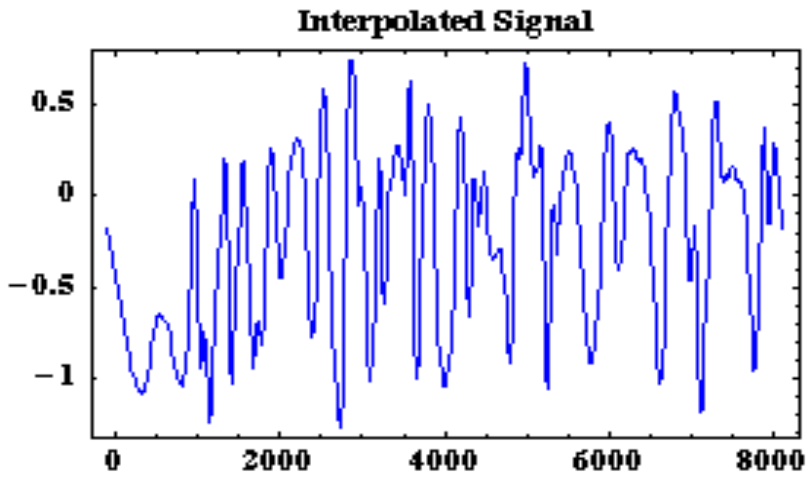

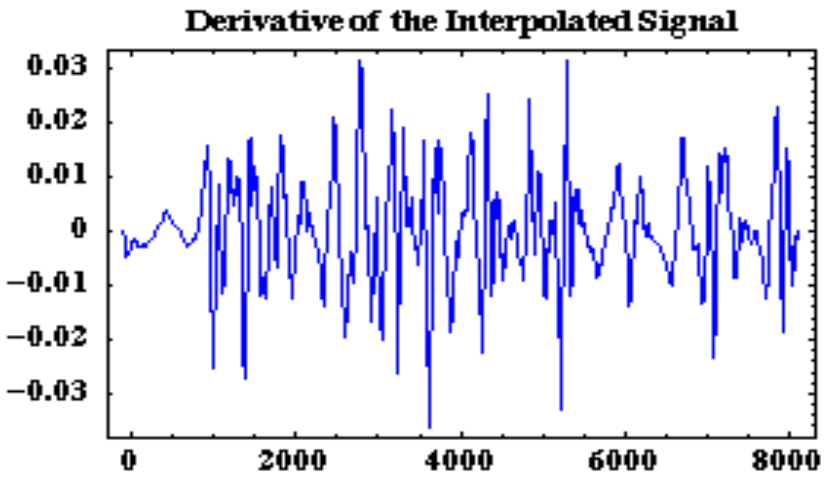

Reconstruction of the LPF RT Weak Mix Data Using the 100 Largest WLT Coefficients

Polymath Research Inc.

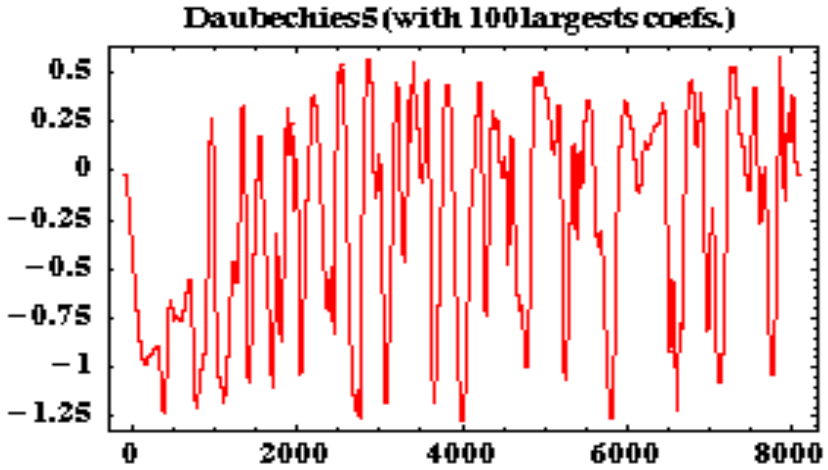

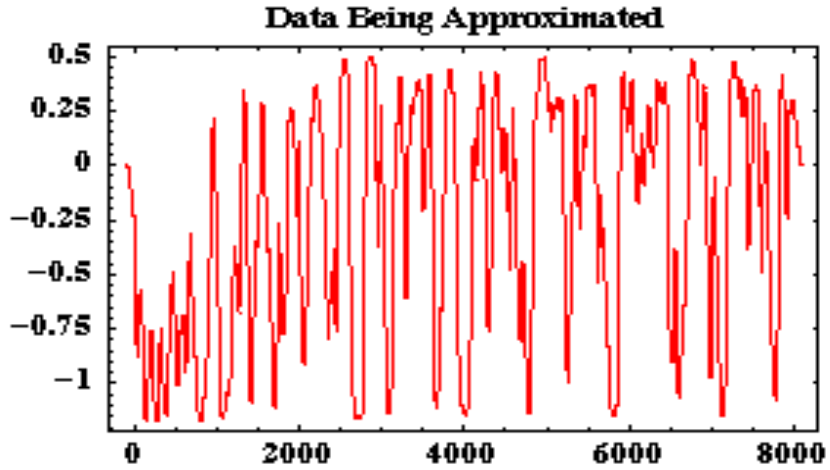

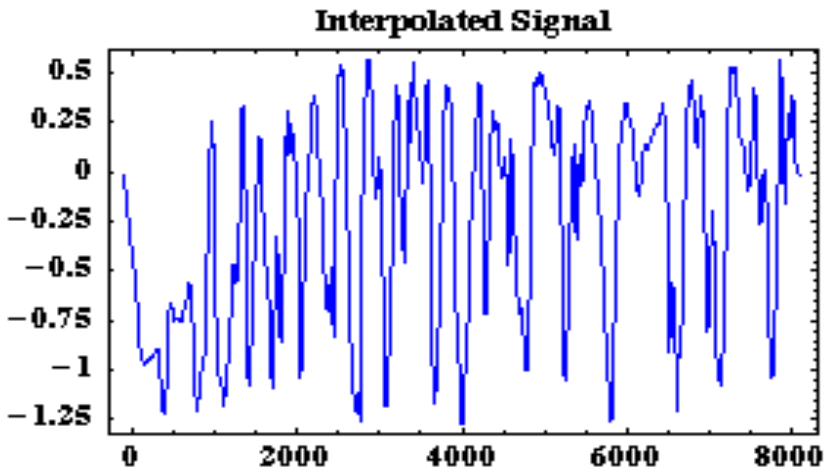

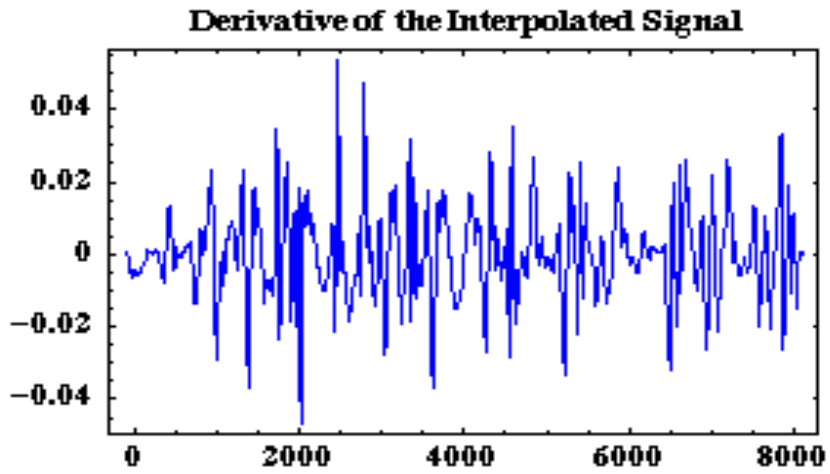

Reconstruction of the LPF RT Weak Mix Data Using the 200 Largest WLT Coefficients

Polymath Research Inc.

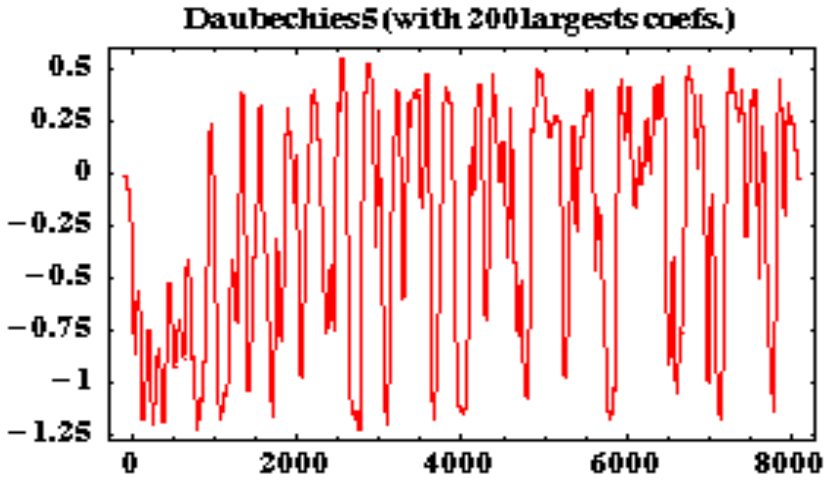

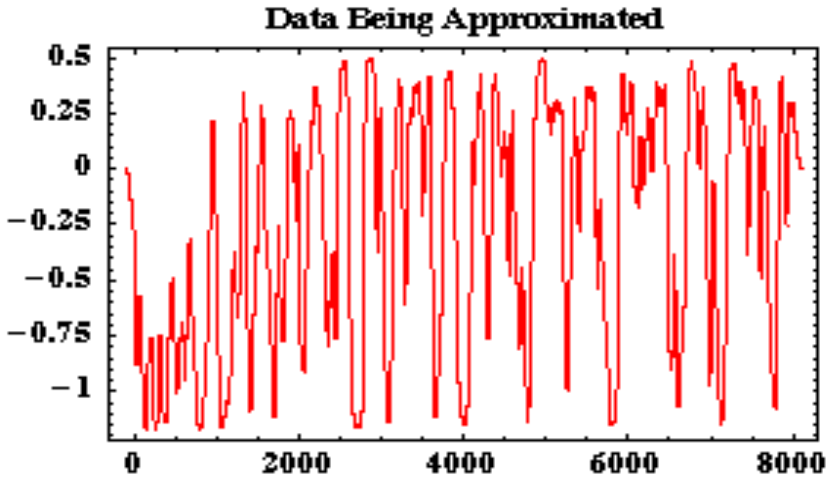

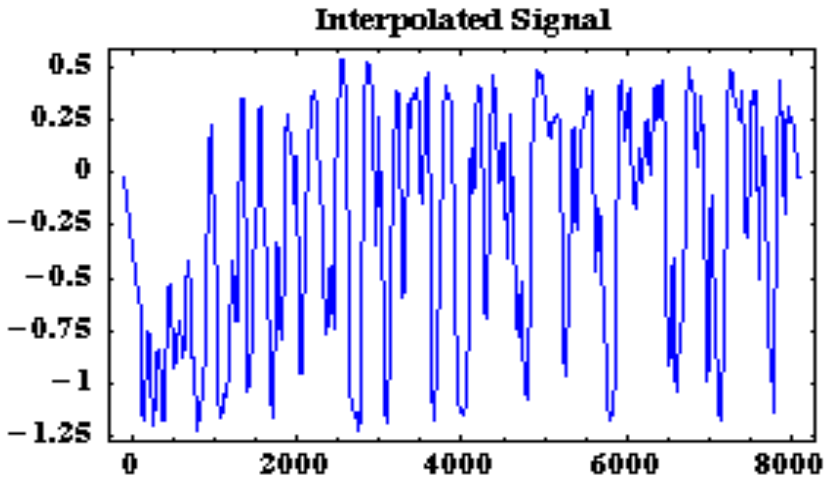

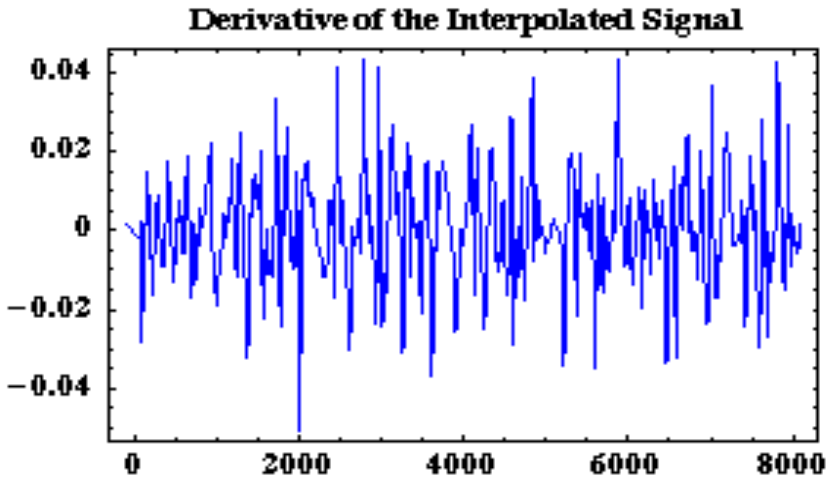

Reconstruction of the LPF RT Weak Mix Data Using the First MRD Level

Polymath Research Inc.

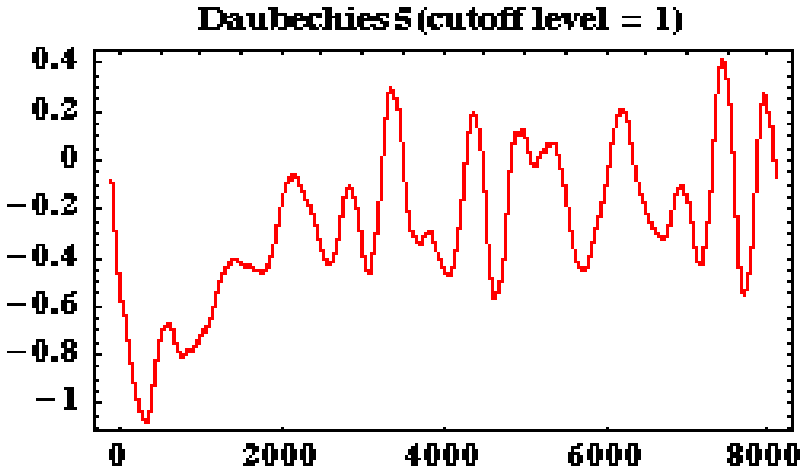

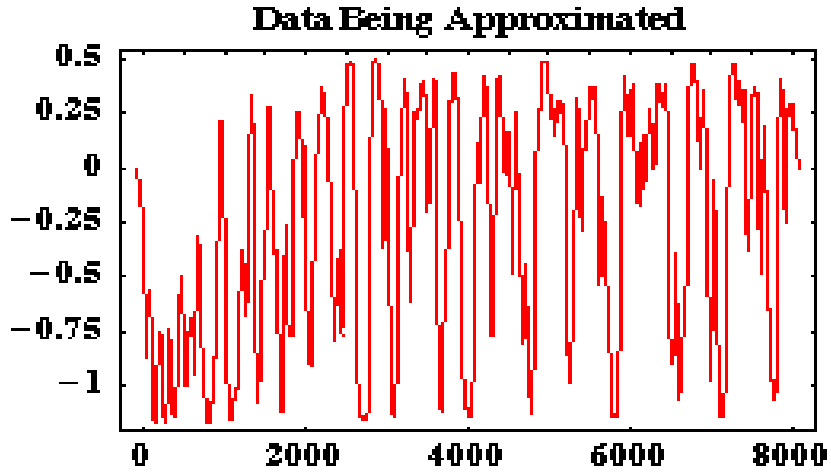

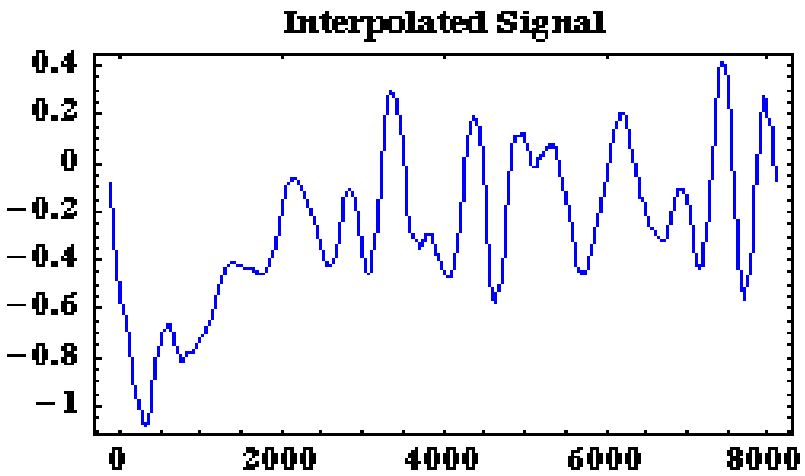

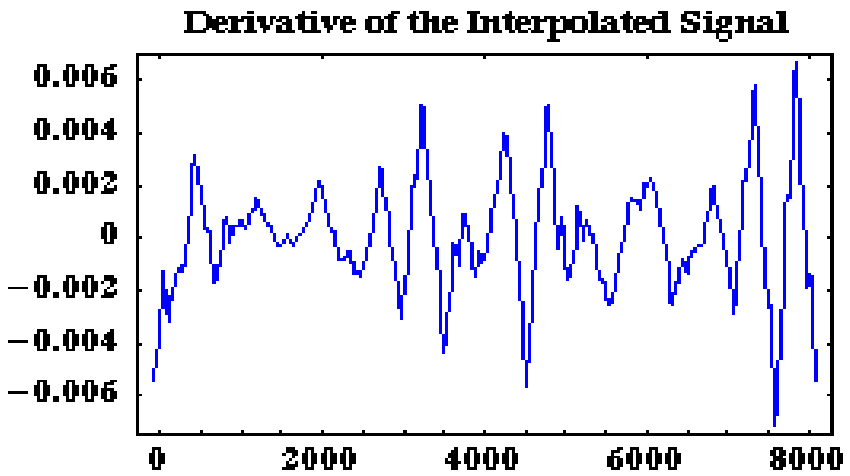

Reconstruction of the LPF RT Weak Mix Data Using the First 2 MRD Levels

Polymath Research Inc.

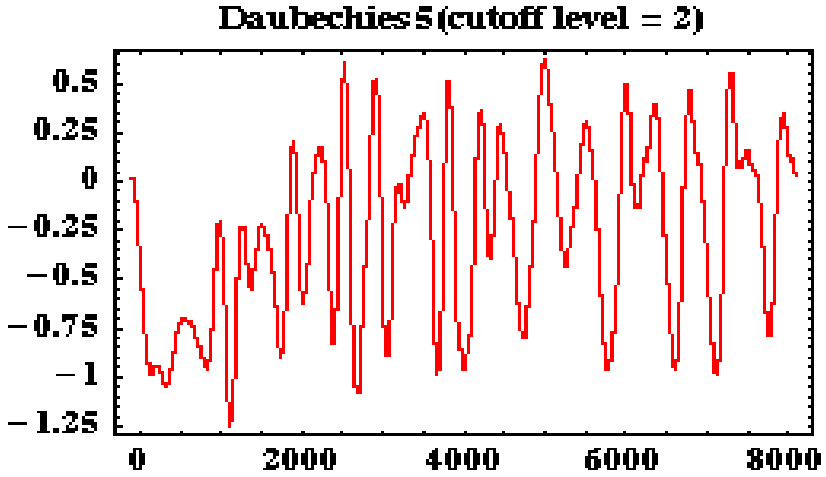

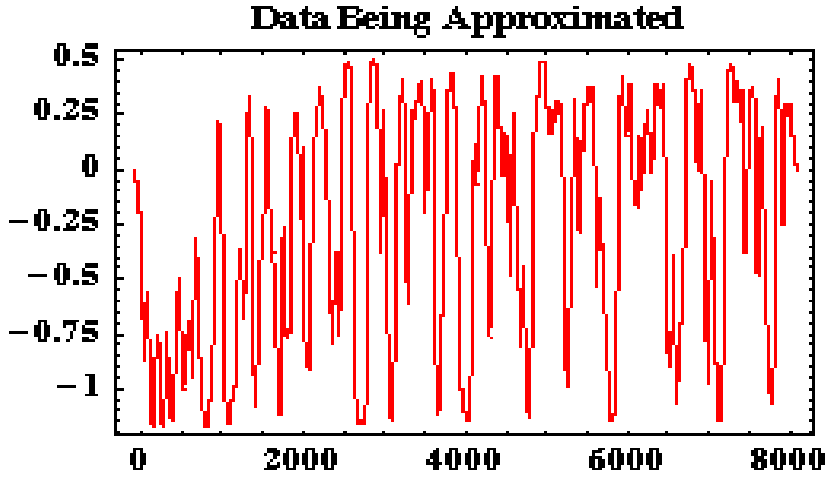

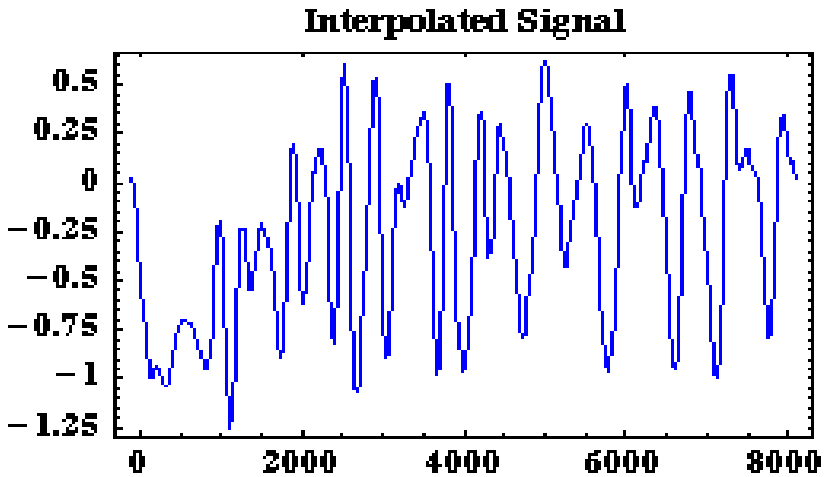

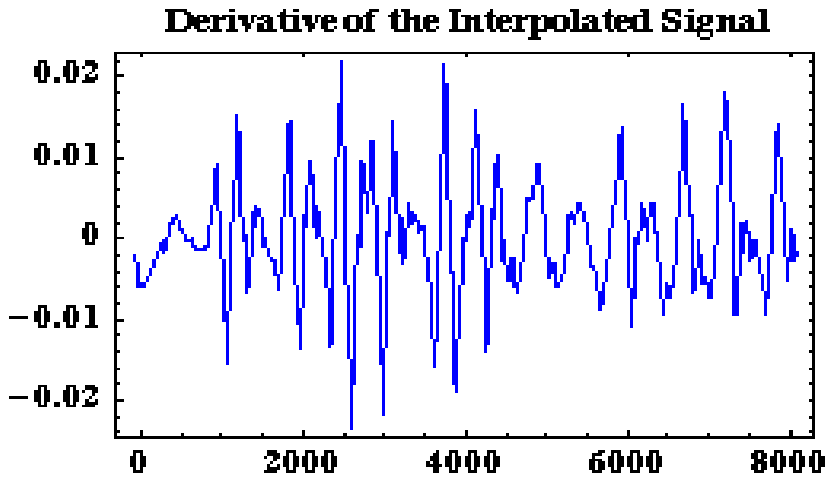

Reconstruction of the LPF RT Weak Mix Data Using the First 3 MRD Levels

Polymath Research Inc.

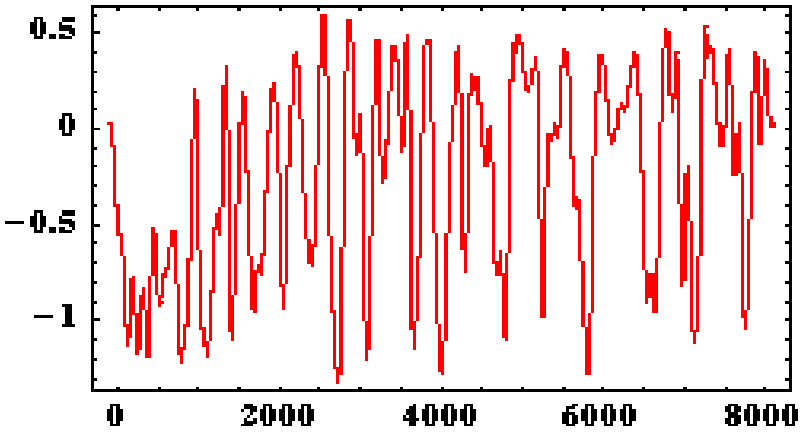

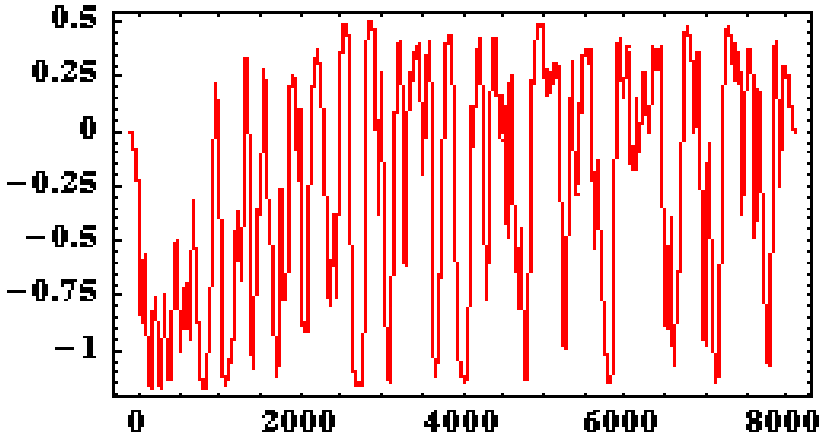

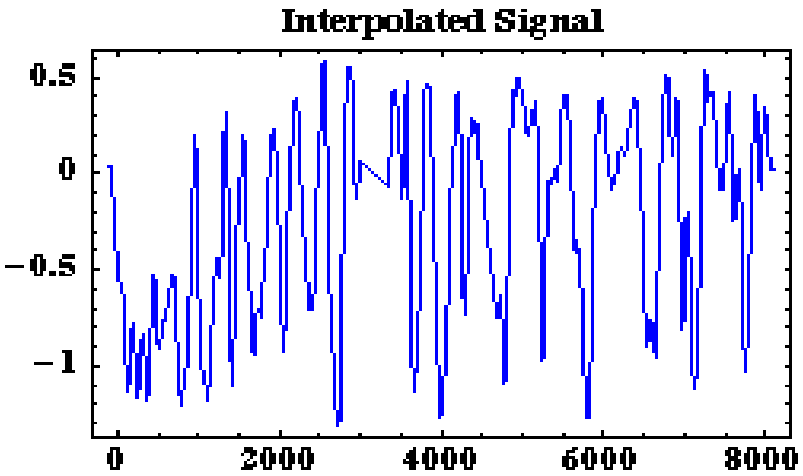

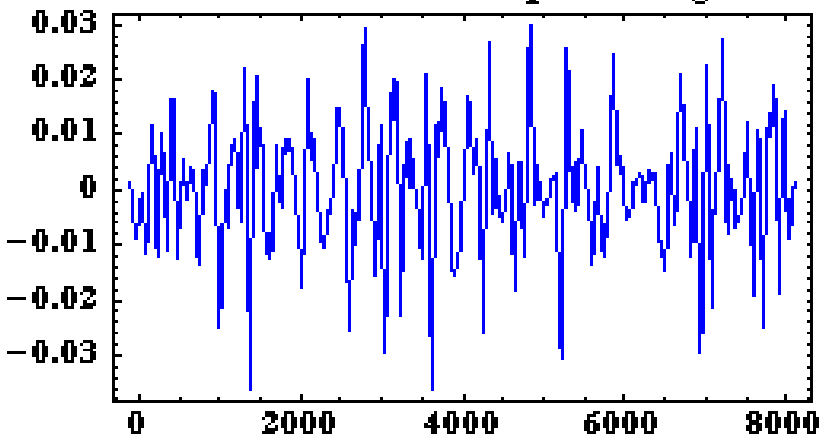

Reconstruction of the LPF RT Weak Mix Data Using the First 4 MRD Levels

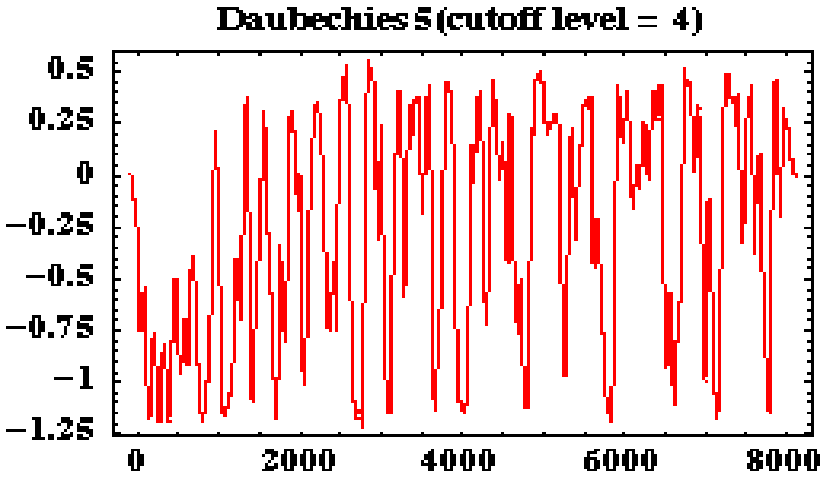

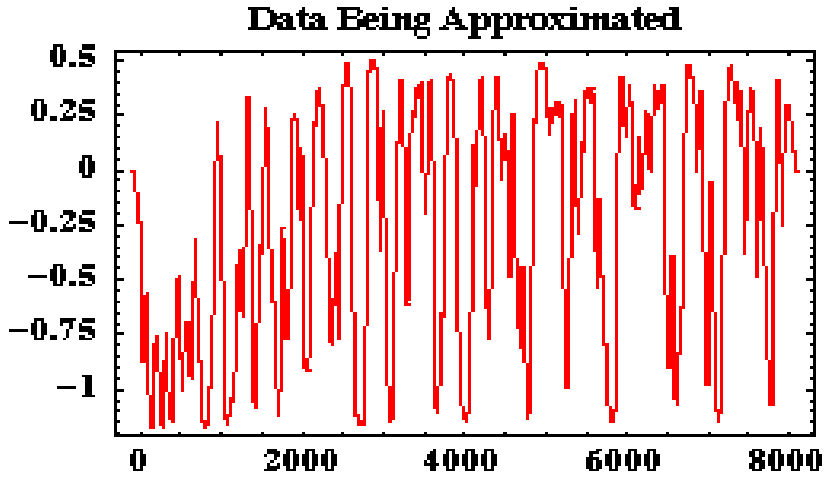

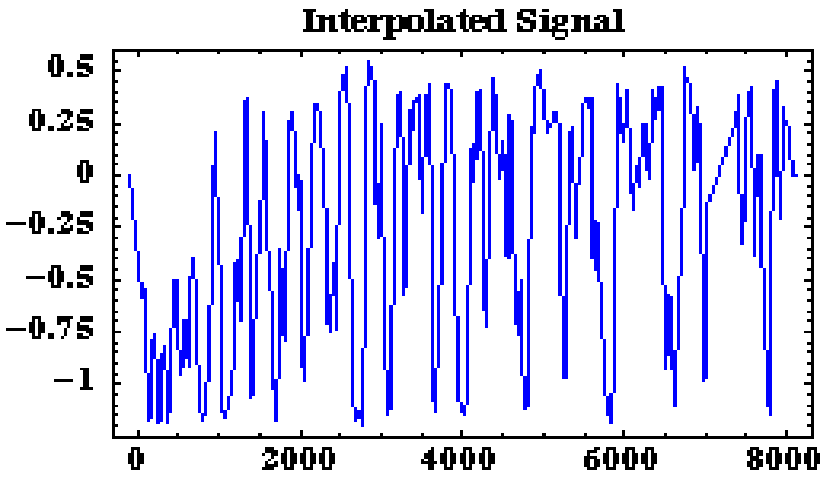

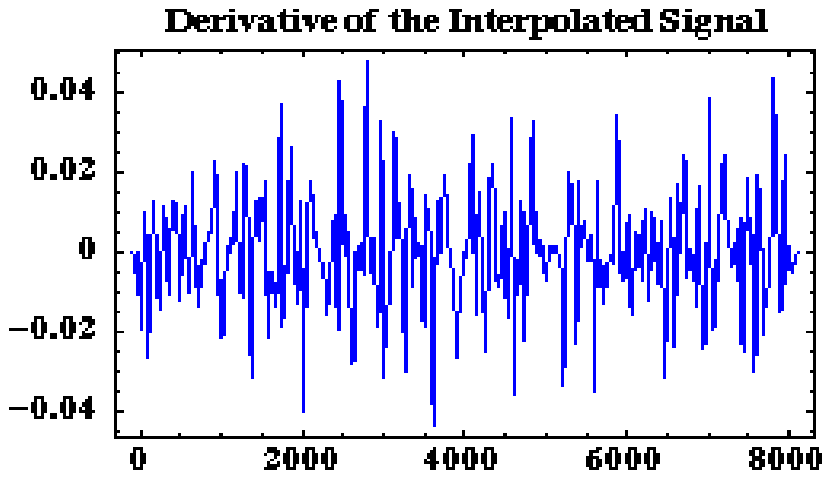

Reconstruction of the LPF RT Weak Mix Data Using the First 5 MRD Levels

Polymath Research Inc.

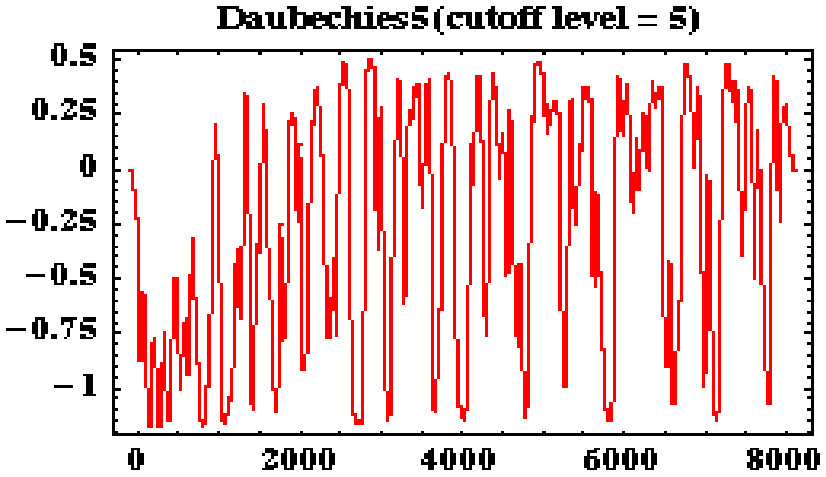

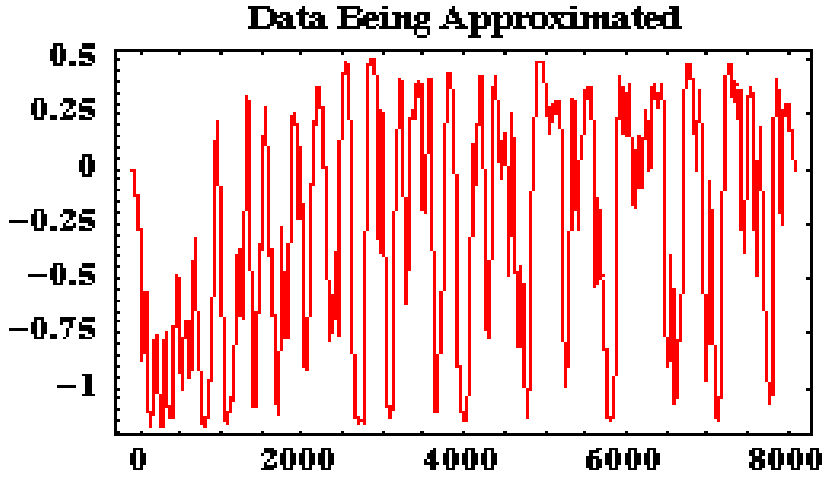

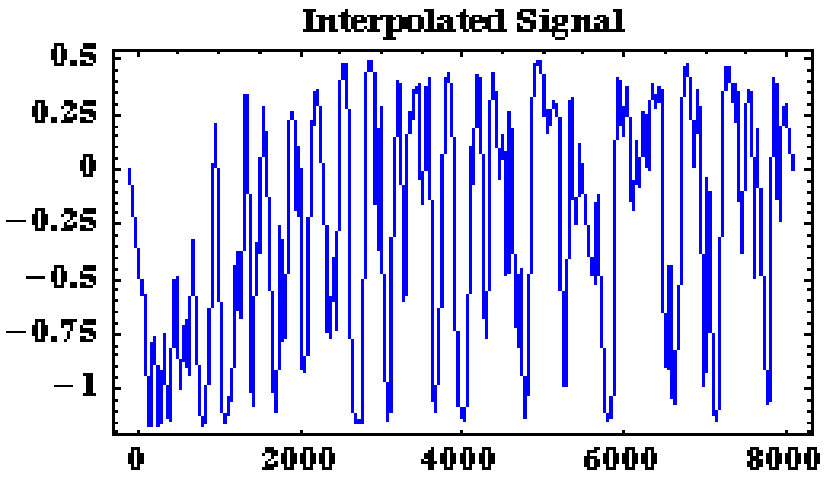

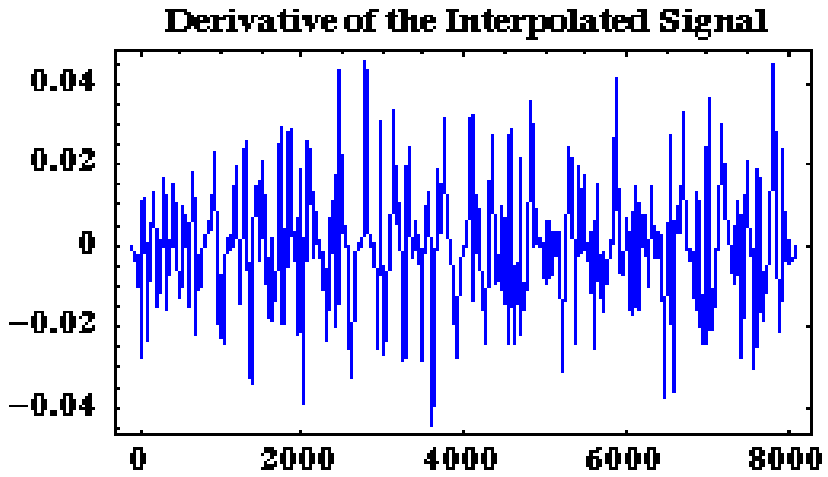

Conclusions Based on the LPF RT Weak Mix Data's WLT Analyses

REVIEW OF NUMERICAL SIMULATION OF MIXING DUE TO RAYLEIGH-TAYLOR AND RICHTMYER-MESHKOV INSTABILITIES

David Youngs

AWE

Aldermaston

UK

Scope: 2D and 3D numerical simulation (DNS or LES) of the non-linear growth of Rayleigh-Taylor and Richtmyer-Meshkov instabilities.

Reasons for numerical simulation

(a) gain understanding of the mixing processes which is not available from experiment

(b) explain experimental results

(c) design experiments

(d) provide results for the calibration of engineering models (eg RANS models)

(e) full simulation of engineering applications

(a) **2D single mode**

(b) 2D multimode

(c) Additional physics

(d) 3D single mode/few modes

(e) 3D turbulence
modelling of the unresolved scales

(f) Future role of numerical simulation
AWE examples

Aim to illustrate the progress made with examples – not a complete review of all the work done.

Turbulent mixing is a 3D process.

However, the dynamics of the large scale structures within the mixing layer is the key aspect of mixing and much has been/can still be learnt about this from single-mode or 2D multimode simulations.

The fine-scale structure (dissipation at high wave numbers) is essentially a 3D process and for this 3D simulation is essential.

The possibilities of 3D simulation on present-day super computers should be fully exploited – however, simpler 2D simulation still has an essential role especially for complex problems with additional physics.

2D SINGLE MODE

The first 2D simulations of RT were carried out in Frank Harlow's group at LANL in the late 1960s.

e.g. B J Daly, Phys Fluids Vol 10, p297 (1967)

MAC code: **incompressible**
'Marker and Cell'

$\frac{\rho_1}{\rho_2} = 1.1, 2, 10$

Roll-up of the spike due to Kelvin-Helmholtz instability seen for

$\frac{\rho_1}{\rho_2} = 1.1, \text{and } 2,$ **but not for** $\frac{\rho_1}{\rho_2} = 10.$

not observed experimentally until Ratafia, Phys Fluids Vol 16 p1207 (1973).

results explained by drag force on bubble and spike – as in buoyancy – drag models which are widely used today.

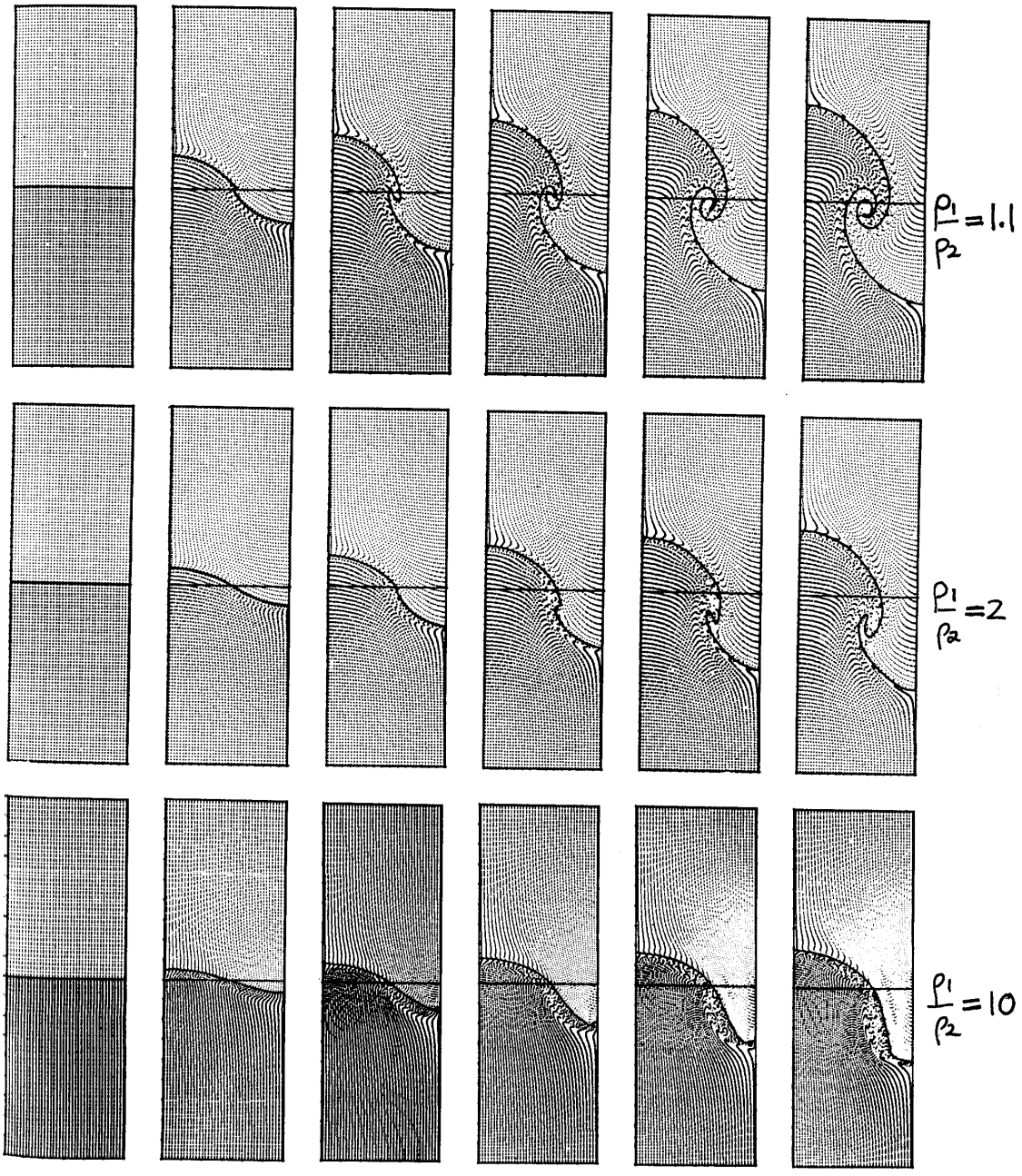

Physics of Fluids, vol 10, p297 (1967)

Youngs, Physica 12D, p32 (1984)

2D Eulerian code

- **Interface tracking (VOF technique)**
- **Monotonic advection method of Van Leer for all fluid variables**

  $\Rightarrow$ **improved numerical stability over the earlier hydrocodes**

Shows KH instability on the spike at high density ratio, $\frac{\rho_1}{\rho_2} = 20$

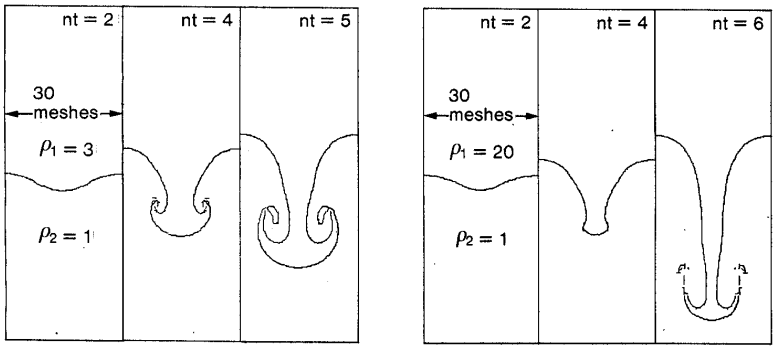

Fig. 1. Rayleigh–Taylor instability, single wavelength initial perturbation.

Youngs, Physica 12D, p19 (1984)

2D Multimode Rayleigh-Taylor triggered by short wavelength random perturbations. Incompressible hydrocode similar to MAC code but interface tracking was abandoned as fine-scale mixing expected.

Solved equation for fluid 1 volume fraction

$$\frac{\partial f_1}{\partial t} + \mathrm{div}\left(f_1 \underline{u}\right) = 0$$

Showed self-similar growth with bubble penetration (h_1) given by

$$h_1 = \alpha \frac{\rho_1 - \rho_2}{\rho_1 + \rho_2} g t^2$$

$\alpha \approx$ **0.04 to 0.05 independent of density ratio, for growth by mode coupling.**

Subsequent experiments, Read, Physica 12D, p45 (1984) gave $\alpha \sim$ **0.06 to 0.07.**

At the time difference between α **in calculation and experiment was attributed to 2D vs 3D effects – but this has not turned out to be so simple.**

I-L Chern, J Glimm et al
J Comp Phys, vol 62, p64 (1986)

Fron Tier: **Accurate front tracking technique (more accurate than the VOF techniques)**

Applied to multimode 2D RT in Glimm et al Phys Fluids A2 p2046 (1990)

Note that most of RT experiments use immiscible liquids – so need to eliminate mass diffusion.

Results used to develop bubble merger models.

For two generations of bubble merger simulations give $\alpha \sim 0.055$ to 0.065 in agreement with experiment.

For more than two generations α drops to ~ 0.04 (fine-scale structure develops).

Glimm et al (1990)

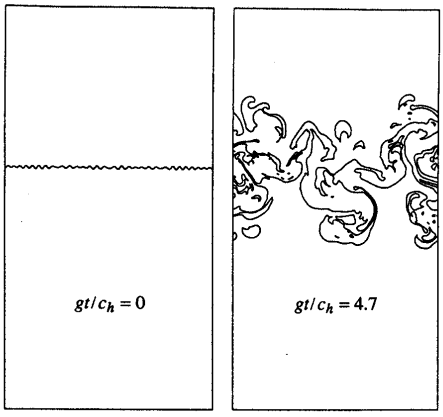

FIG. 10. Plots of interfaces in the random disturbance simulation of Rayleigh–Taylor instability. The Atwood number is $A = \frac{1}{3}$ and the compressibility is $M^2 = 0.1$. The acceleration rate of the bubble envelope has good agreement with the experiment of Read for $1\frac{1}{2}$ generations of bubble merger. The acceleration rate decreases after this time because of the multiphase connectivity, which is different in the exactly two-dimensional computation and in the approximately two-dimensional experiments.

Inogamov (3rd IWPCTM) argued that self similar gt^2 growth should be obtained if a multimode perturbation with

$$\frac{\text{amplitude}}{\text{wavelength}} = \varepsilon \text{ (a constant)}$$

is used. In this case α depends weakly on the initial conditions.

2D multimode calculations described by Atzeni and Guerrieri, Europhys Lett, Vol 22, p603 (1993).

α ~ 0.04 to 0.05 lower bound for mix evolution.

Demonstrates the very useful role which numerical simulation can play in understanding the effect of initial conditions on turbulent mixing.

What happens in real problems?

Growth via mode coupling

or growth directly from initial perturbations.

RICHTMYER-MESHKOV: 2D SINGLE MODE

Impulsive linear model (Richtmyer)

$$\frac{da}{dt} = \frac{2\pi}{\lambda} A^+ a_o^+ \Delta U$$

A^+, a_o^+: **post shock Atwood Number and amplitude**

2D numerical simulation very useful in understanding the correct effect of compressibility on the linear theory and also the non-linear behaviour.

Highlight recent paper:-

Holmes, Dimonte, Fryxell, Gittings, Grove, Schneider, Sharp, Velikovich, Weaver, Zhang. J Fluid Mech, Vol 389, p55 (1999)

Compare three different hydrocodes (RAGE, PROMETHEUS and Fron Tier) with non-linear theory, and with a NOVA experiment.

Fron Tier:	**interface tracking**
RAGE:	**no interface tracking, AMR**
PROMETHEUS:	**no interface tracking (MUSCL)**

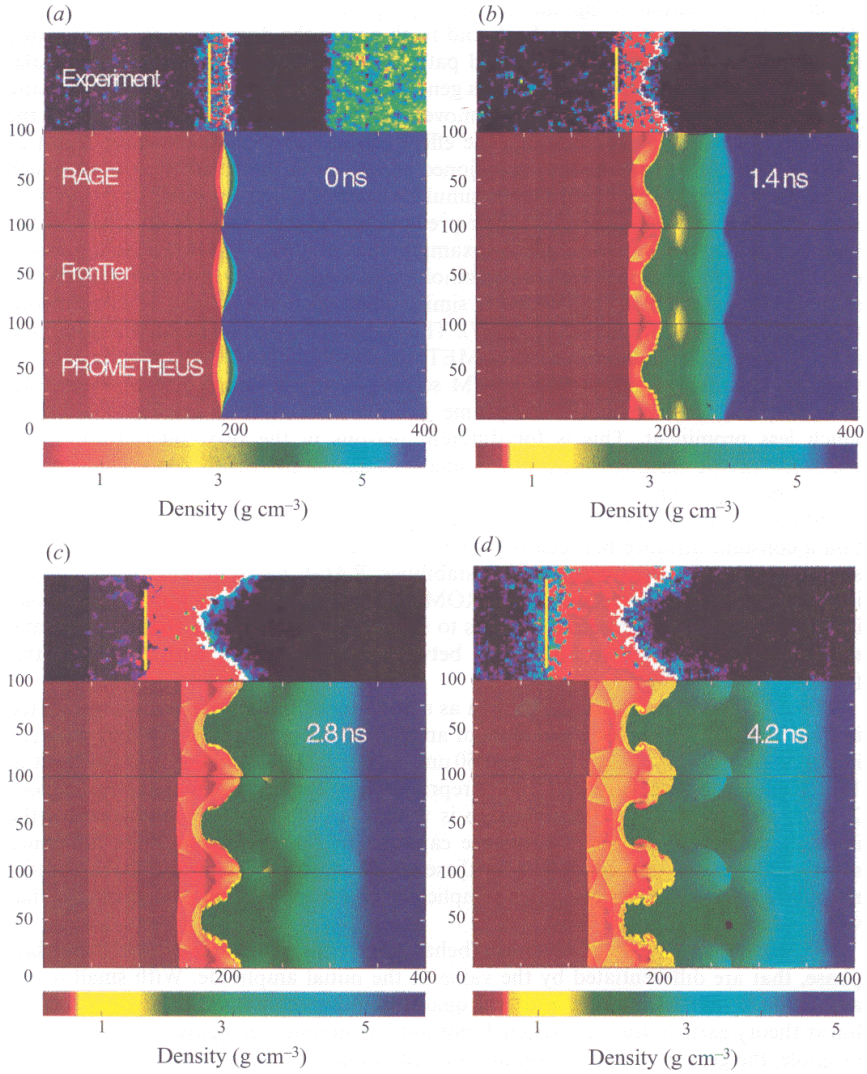

FIGURE 3. Simulation density plots and experimental radiographs for case 10/15.3. (*a*) $t = 0.0$ ns, (*b*) $t = 1.4$ ns, (*c*) $t = 2.8$ ns, (*d*) $t = 4.2$ ns. Each figure shows the results obtained with the three codes (RAGE, FronTier and PROMETHEUS, top-to-bottom) along with an experimental image. The incident shock moves from right to left. The experimental radiograph is an averaged composite over four wavelengths. Note that at later times the experimental wavelength increases due to expansion of the experimental target.

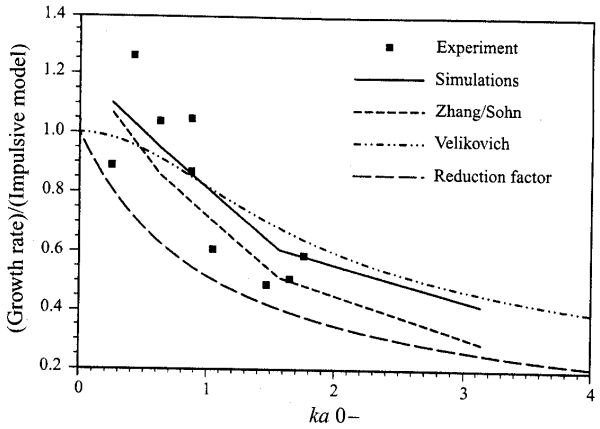

FIGURE 7. Comparison of experimental, simulation and theoretical peak growth rates as a function of initial amplitude with incident Mach number 15.3. Growth rates are scaled to the Meyer–Blewett formulation of the Impulsive Model. For the simulations we averaged the peak growth rates of each of the three codes.

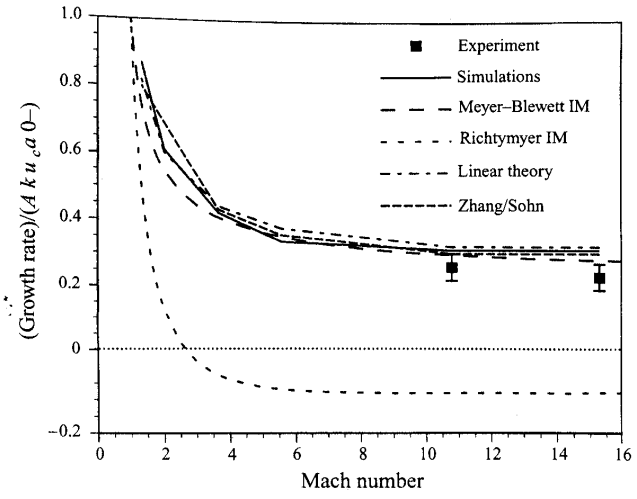

FIGURE 10. Comparison of experimental, simulation and theoretical peak growth rates as a function of incident shock Mach number. The growth rate is scaled by $Aku_c a_{0-}$.

Richtmyer-Meshkov: Late-time behaviour (Multimode)

Theory suggests $h \sim t^{\theta}$ for single shock RM

Nova experiment (Dimonte, Frerking, Schneider, PRL, vol 74, p4855 (1995)

Be/foam interface, random perturbations experiment gives $\theta \sim 0.6$.

2D CALE simulation with representation of the measured surface finish.

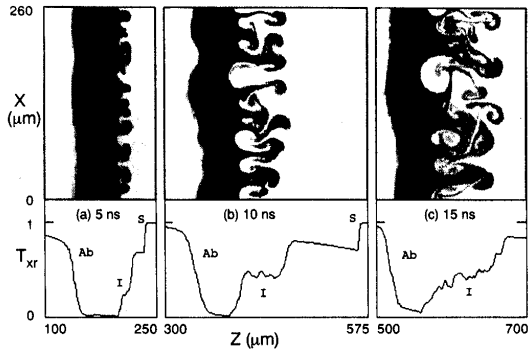

FIG. 4. Simulation side-on radiographs and spatial x-ray transmission profiles at $t = 0$, 5, and 10 ns.

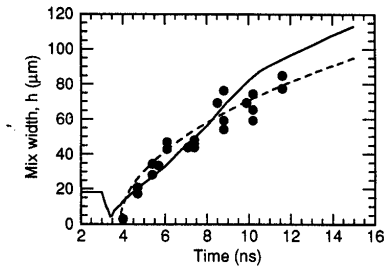

FIG. 5. The turbulent mix width at the interface vs time for the experiment (points), CALE (solid line), and Eq. (3) (dashed line) with $\eta_{\rm rms} \sim 4.6$ μm, $h^*_{0e} = 5.6$ μm, and $t_i = 3.9$ ns.

Mügler and Gauthier. Physics of Fluids, vol 12, p1783 (2000)

2D multimode RM mixing compare with shock tube experimental data.

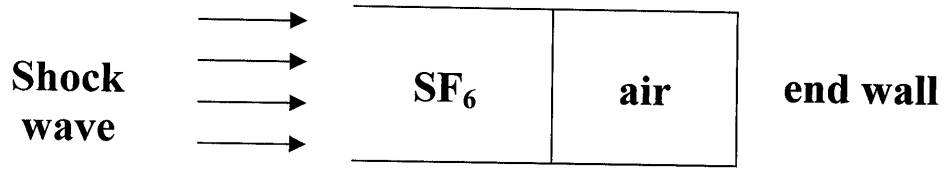

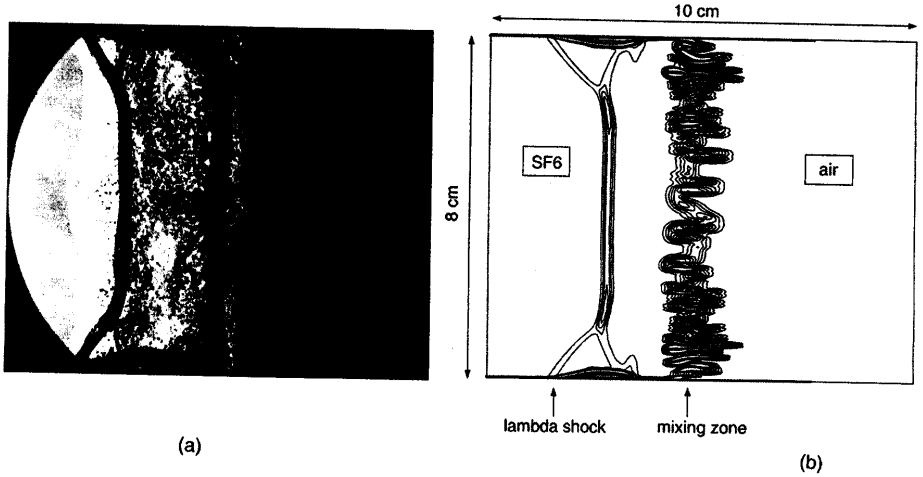

FIG. 7. (Color) (a) Experimental, from Galametz (Ref. 5), and (b) numerical schlieren pictures at a time t just after the first reflected shock wave–mixing zone interaction. Because of its interaction with the boundary layer, the transmitted shock in the SF_6 bifurcates.

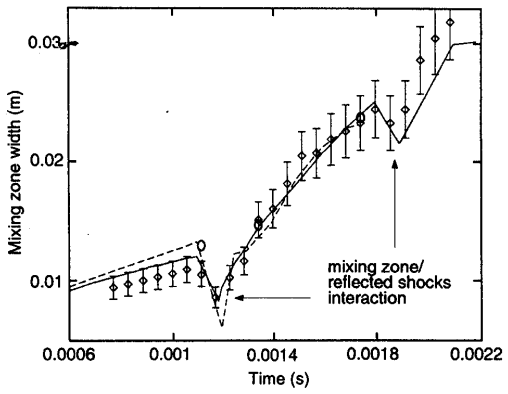

FIG. 2. Evolution of the mixing-zone width vs time. Diamonds correspond to the experimental width measured from schlieren pictures. The errorbars of this visual measurement are equal to ±10%. The three small circles correspond to microdensitometry measurements of some schlieren pictures. Full and dotted lines correspond to numerical widths obtained from the coarse and fine grids, respectively.

ADDITIONAL PHYSICS

Numerical simulation has played a major role in the understanding of additional physics on RT/RM instability.

(a) Material strength (solids)

(b) Density gradient stabilisation

(c) Ablation front stabilisation

Effect of Material Strength

Linear theory not straightforward.
Growth rate depends on
- **amplitude**
- **wavelength**
- **shear modulus**
- **yield strength**

Simplest model : amplitude threshold (Drucker)

Initial paper : J F Barnes et al J Appl Phys, vol 45, p727 (1974) **(LANL)**

Also : Swegle and Robinson. J Appl Phys, vol 66, p2838 (1989) **(SNLA)**

2D Lagrangian numerical simulation.

Swegle and Robinson

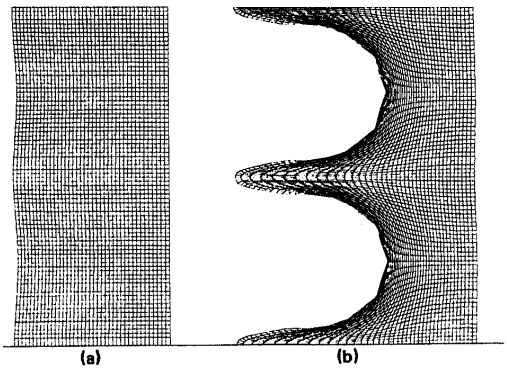

FIG. 2. Typical mesh plot for an unstable calculation. The small initial perturbation in (a) grows to that in (b) after a few microseconds of application of the driving pressure. There are 40 zones through the plate thickness of 2 mm, with 80 zones in the other direction.

Hydrodynamic Instability in Strong Media – UCRL – CR – 126710 (LLNL)

- Review of open VNIIEF publications

Theory, experiment, numerical simulation

2D (planar) vs 3D (axisymmetric)
2D grows faster than 3D (opposite to the fluid case)

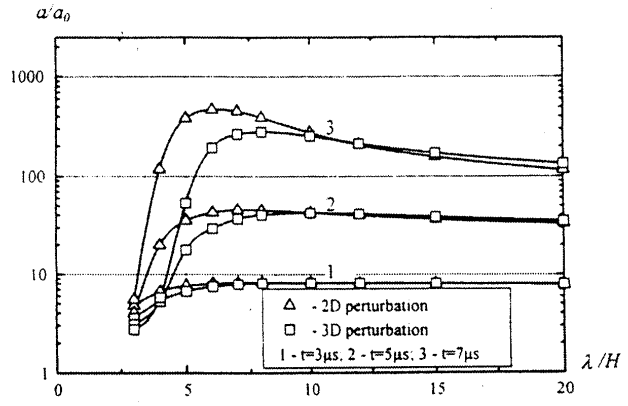

Fig. 4.3-14. Perturbation amplitude vs wavelength at various times for 2D and 3D perturbations. a_0=3.3 μm, σ_T=1.5 GPa, $\Delta\tau$=2 μs.

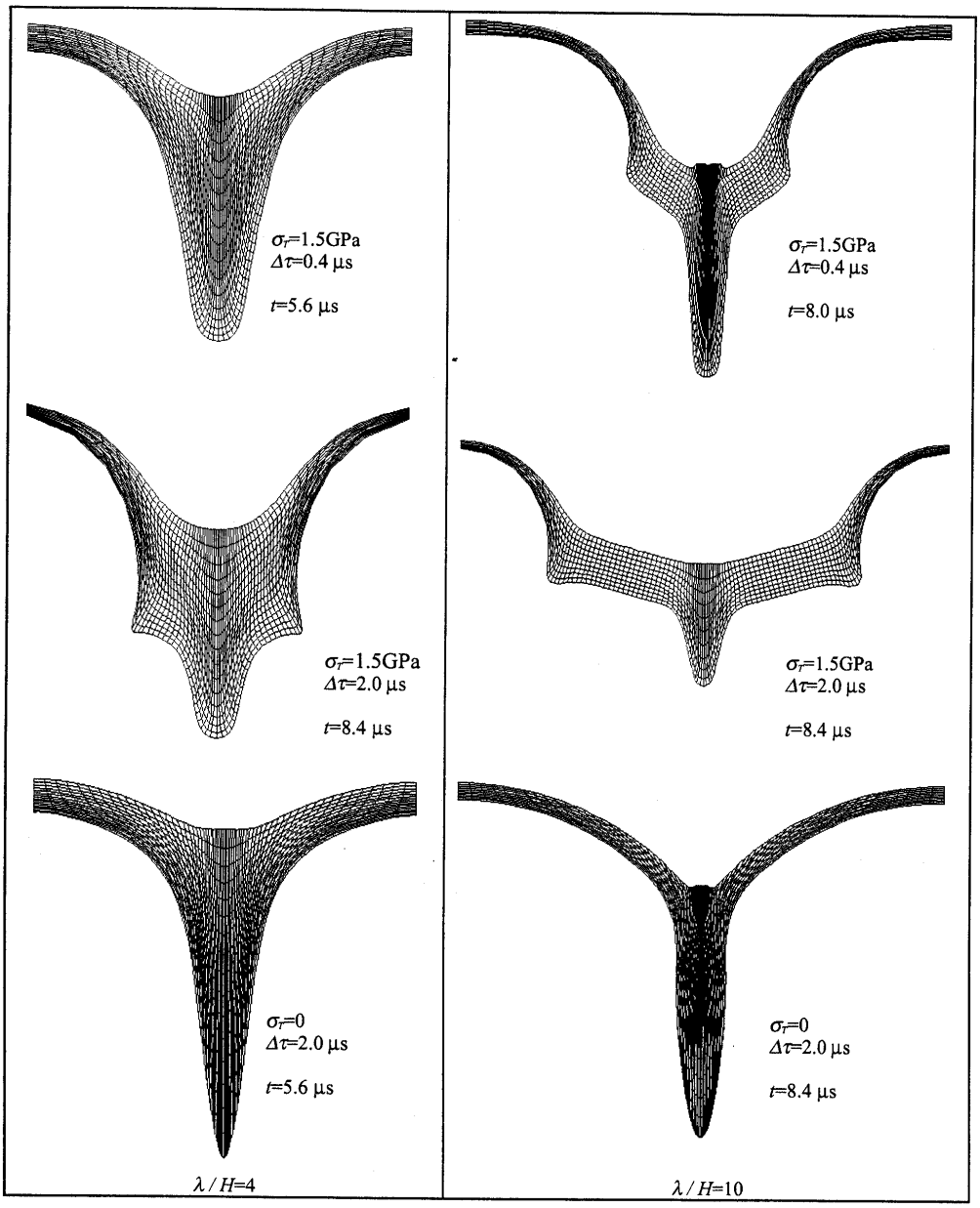

Fig. 4.3-13. Characteristic layer shapes.

Density gradient stabilisation

Pham and Meiron, Physics of Fluids, vol A5, p344 (1993)

RM + continuously stratified fluids
2D single mode and multimode.

Implusive acceleration

$$\rho(\mathbf{x},\mathbf{y})=\frac{\mathbf{1}}{\mathbf{2}}\left[\mathbf{1}+\mathbf{A}\tanh\left\{\frac{\mathbf{y}-\zeta(\mathbf{x})}{\mathbf{L}}\right\}\right]$$

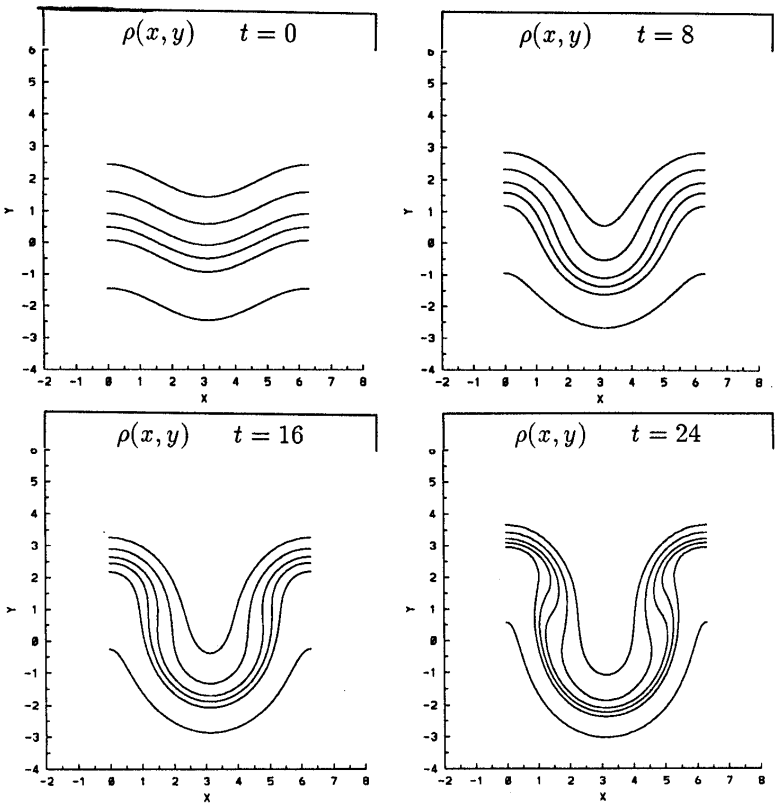

FIG. 1. Time evolution of the density contours for the single-scale profile $L=1.0$, $A=-0.5$, $\epsilon=0.5$, $t=0,8,16,24$. The contours are at $\rho=0.26,0.3,0.4,0.5,0.6,0.74$ in that order from top to bottom of each figure.

Ablative Rayleigh-Taylor instability

Ablation stabilisation is a key issue for direct-drive ICF as this reduces the growth of Rayleigh-Taylor instability.

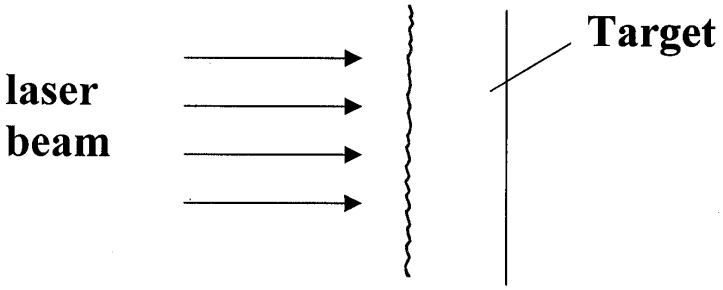

2D and 3D numerical simulations of ablative RT have been performed by the NRL group – also some of the first 3D RT calculations – Dahlburg and Gardner, Phys Rev A, vol 41, p5695 (1990) – mixing rate higher in 3D that 2D

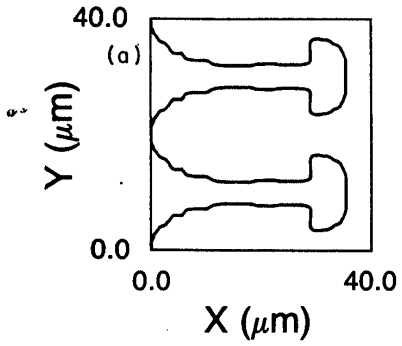

2D

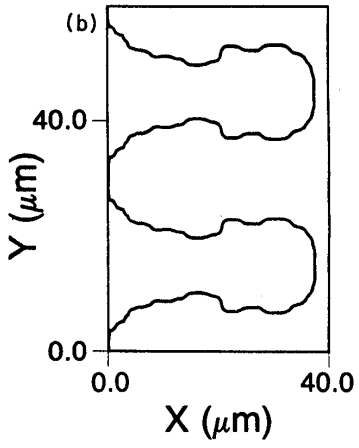

3D

3T Multimode ablative RT instability

Dahlburg et al, Phys Plasmas, vol 2, p2453 (1995)

FAST3D code – FCT method

220 x 128 x 128 cells

Random perturbation k^{-2} spectrum

In the case considered, ablative RT did not give fully developed turbulence.

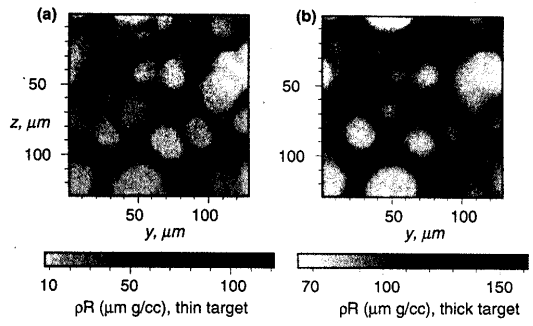

FIG. 4. Comparison of ρR between the thinner (a) and thicker (b) targets, at 4 ns when the thinner target has burned through. In these plots, the darkest shades of gray scale indicate the regions of greatest ρR.

3D SIMULATION

(a) Single mode/few modes

Difference between the behaviour of large scale structure in 2D and 3D.

3D growth rate is higher than 2D growth rate.

(Layzer theory).

Use of interface tracking is an advantage.

(b) Turbulent Mixing

Formation of a Kolmogorov-like $\left(k^{-\frac{5}{3}}\right)$ inertial range .

Dissipation in 3D much higher than in 2D. Counteracts the higher growth rate of the large scale structures in 3D.

Tryggvason and Unverdi Phys Fluids, vol A2, p656 (1990)

Single mode RT (2D vs 3D)
Boussinesq limit + viscosity
Accurate interface tracking method. Interface represented by triangular elements.

3D growth greater than 2D growth.

FIG. 2. The large-amplitude stage for a single initial mode. Here $t = 2.75$.

FIG. 1. The evolution of an interface disturbed by two modes. The nondimensional times are 2.0, 2.5, and 3.0.

RT Single Mode at Higher Atwood No.

Oparin and Abarzhi. Phys Fluids, vol 11, p3306 (1999) quasi-monotonic grid – characteristic method.

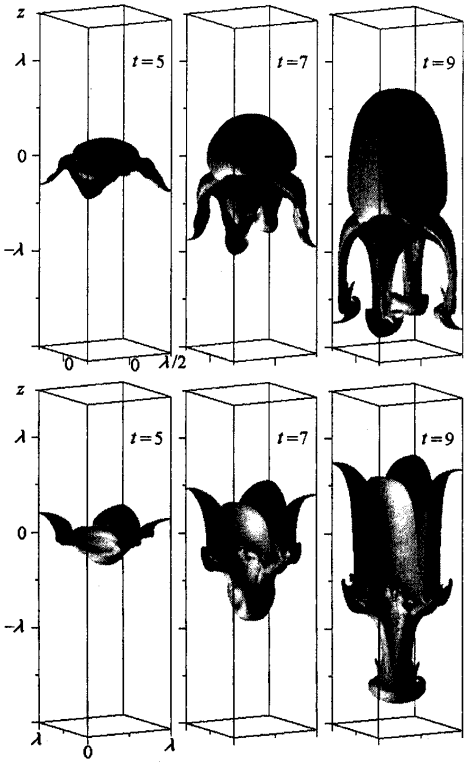

$\frac{\rho_1}{\rho_2} = 10$

FIG. 1. Bubble (above) and jet (below) evolution. Grid 30×30×210.

He, Zhang, Chen and Doolen. Physics of Fluids Vol 11, p1143 (1999) – Lattice Boltzmann scheme

Mixing of immiscible fluids.

$\frac{\rho_1}{\rho_2} = 3$

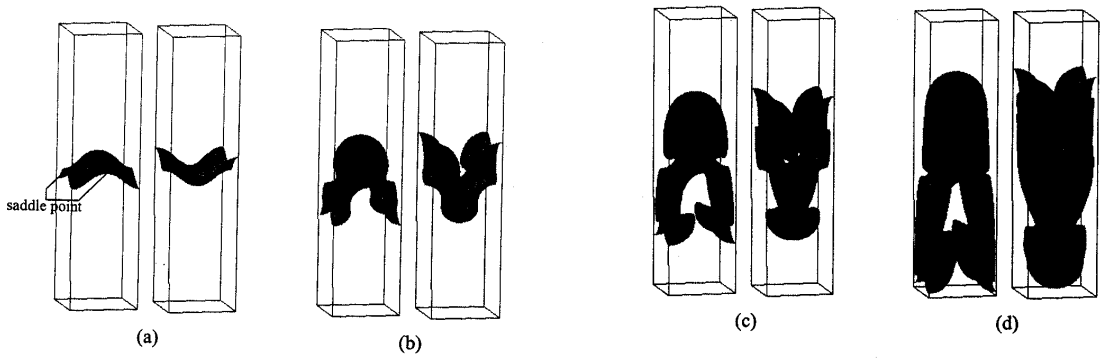

V.V.Nikishin et al. 6th IWPCTM (Marseille, 1997)

Institute for Mathematical Modelling
Lebedev Institute

3D single single mode/ few mode RM

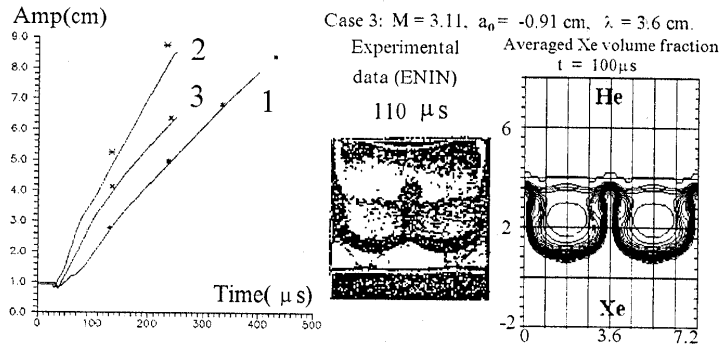

Figure 5. Comparison $He - Xe$ 3D results (ENIN,IMM,AWE).

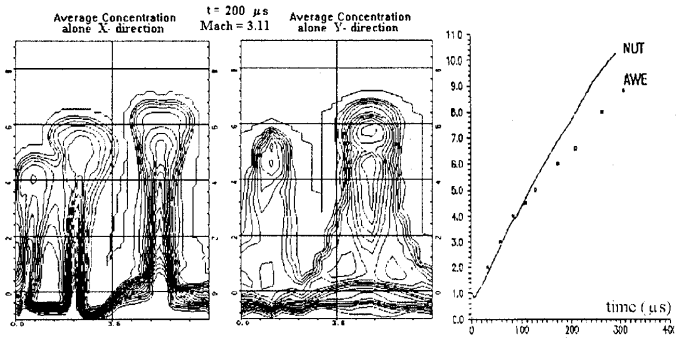

Figure 6. Multimode $He - Xe$ 3D results.

Li and Zhang. **Phys Fluids, vol 9, p3069 (1997)**

2D and 3D single mode
TVD method + Artificial Compression

Single shock : good agreement with non-linear theory of Zhang and Sohn.
3D growth > 2D growth.

Also single shock + reflected shock.

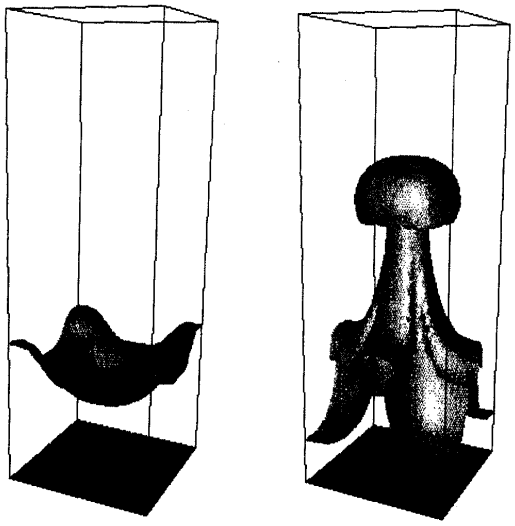

$t = 22.1$ $t = 58.6$

FIG. 10. Evolution of fluid interface in the Richtmyer-Meshkov re-shock experiment. The fluid interface first moves downward after transition of the incident shock. It is then hit by the reflected shock. Since the reflected shock travels from heavy fluid to light fluid, it is the reflected rarefaction case which reverses the phase of the interface motion. A mushroom-like spike is formed at $t = 58.6$.

SPHERICAL IMPLOSIONS (ICF)

Sakagami and Nishihara – PRL, vol 65, p432 (1990)

Town and Bell – PRL, vol 67, p1863 (1991)

(r, θ, ϕ) grid : $\frac{1}{120}$ of the sphere.

RT at inner fuel/shell interface.
Single mode spherical harmonic perturbation.

3D growth > 2D growth.

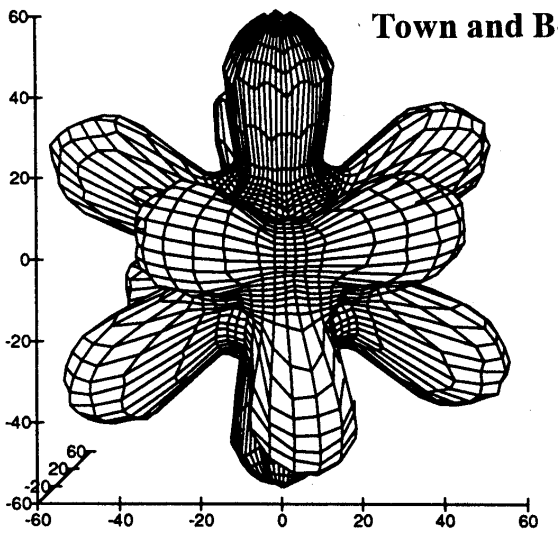

FIG. 1. The inner surface of the shell (defined as the surface of constant density equal to $1/e$ of the maximum density) at 1.226 ns. This shows the bubble-ridge arrangement.

Marinak et al, **Physics of Plasmas, vol 5, p1125 (1998)**

3D multimode RT calculations for NIF capsules.

(r, θ, ϕ) mesh
170 x 64 x 64 zones

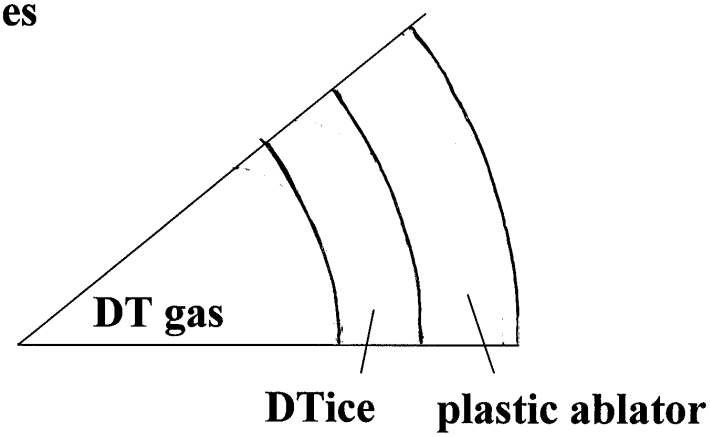

Realistic surface finish

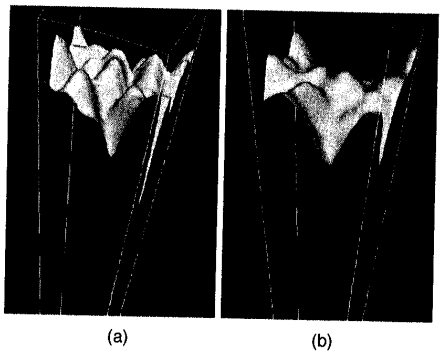

FIG. 9. Density isosurfaces close to the ablator–fuel interface 20 ps before the respective ignition time for each capsule. (a) For the PT capsule and (b) for the BeCu capsule.

3D TURBULENCE SIMULATION

Most detailed analysis for RT mixing – the simple case ρ_1, ρ_2, g constant – for which bubble growth is given by

$$h_1 = \alpha \frac{\rho_1 - \rho_2}{\rho_1 + \rho_2} gt^2$$

Major area of controversy is the treatment of the small scales

Techniques used

- **Direct Numerical Simulation (DNS) – viscosity and diffusivity included in the calculation – all scales present are resolved**
- **Interface tracking - for immiscible mixing**
- **Large Eddy Simulation (LES) - only large scales resolved - dissipation at small scales modelled**

The high-Reynolds number limit

In high-Reynolds number turbulent mixing, turbulence KE and density fluctuations are dissipated by a cascade to high wave numbers.

Power spectrum: $\sigma^2 = \int_0^\infty P(k)\, dk$

where $\sigma^2 = \left\langle \left(\mathbf{u}_i - \bar{\mathbf{u}}_i \right)^2 \right\rangle$ **or** $\left\langle (\rho - \bar{\rho})^2 \right\rangle$

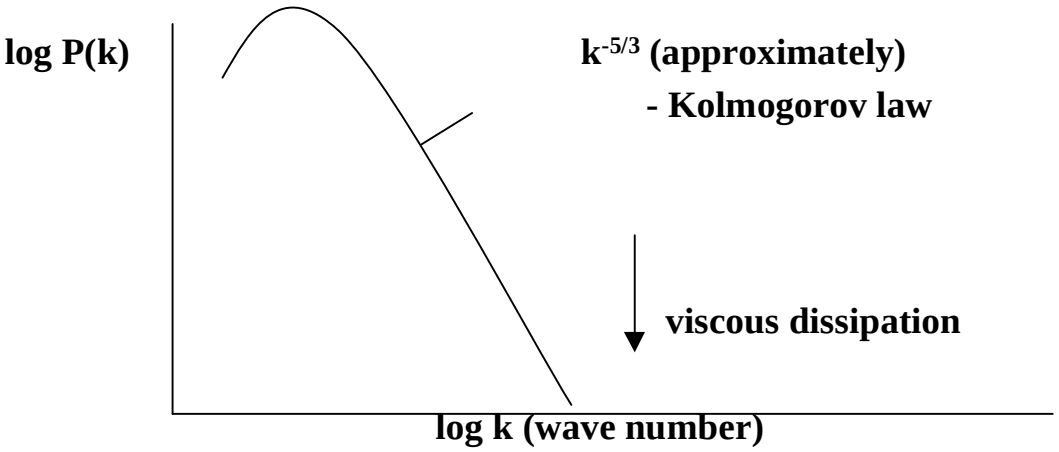

Viscosity/diffusivity determines the scale at which dissipation occurs, not the rate.

LES works if some of the $k^{-5/3}$ spectrum can be resolved – dissipation occurs at an artificially large scale determined by the mesh resolution.

(Conclusions given here are not necessarily applicable to simulation of turbulent boundary layers.

Experimental density fluctuation spectra

J Fluid Mech, vol 399, p1 (1999)

S. B. Dalziel, P. F. Linden and D. L. Youngs

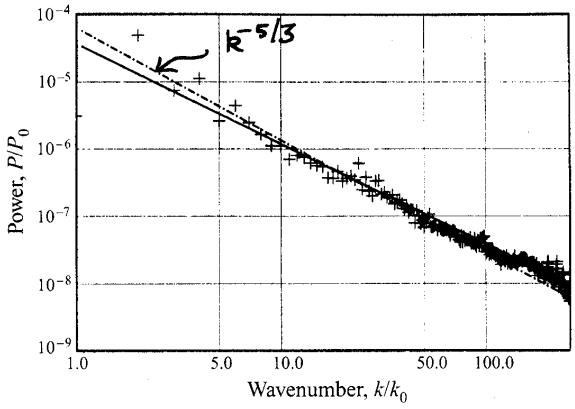

Sc=1000

Wilson and Andrews, Phys. Fluids, vol 14, p938 (2002)

Pr (Sc)=7

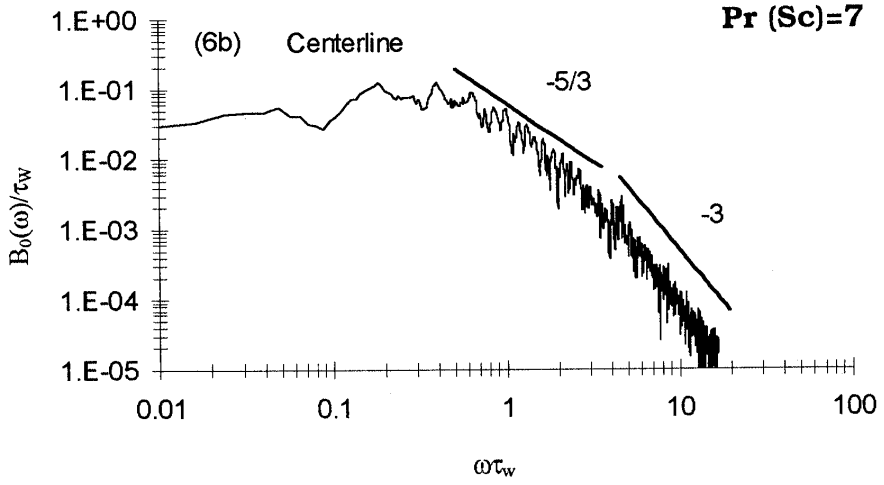

Two approaches to LES

See recent text books:-

Turbulent Flows: Stephen Pope, Cambridge University Press (2000)

Numerical Simulation of Reactive Flow (second edition) : Elaine Oran and Jay Boris, Cambridge University Press (2000)

(a) **The numerical method should have negligible dissipation.**
> 80% of the turbulence KE should be resolved
A sub-grid scale model should be used to represent the effect of the unresolved scales.

(b) **Many numerical schemes (FCT, van Leer, TVD) have implicit dissipation at high-wave numbers. No additional sub-grid model should be used.**
- **MILES, Monotone Integrated Large–Eddy Simulation**

(a) is most popular within the turbulence community – a controversial issue but not given much attention so far at the IWPCTMs.

Limited application of sub-grid models to RT/RM mixing.

LES + Smagorinsky model

Simplest and most well-known sub-grid model.

For incompressible uniform density flow

$$\frac{\partial u_i}{\partial t}+\frac{\partial}{\partial x_j}\left(u_i u_j\right)=-\frac{1}{\rho}\frac{\partial p}{\partial x_i}$$

$\bar{u}_i$ **= filtered value of** u_i **ie averaged over a small region of space just sufficient for** $\bar{u}i$ **to be resolved by the numerical mesh**

$$\frac{\partial \bar{u}_i}{\partial t}+\frac{\partial}{\partial x_j}\left(\bar{u}_i\,\bar{u}_j\right)=-\frac{1}{\rho}\frac{\partial \bar{p}}{\partial x_i}+\tau_{ij}$$

$$\tau_{ij}=\bar{u}_i\,\bar{u}_j-\overline{u_i u_j}$$

$$=2\nu_t\,\bar{S}_{ij}+\frac{1}{3}\tau_{kk}\delta_{ij}$$

$$\bar{S}_{ij}=\frac{1}{2}\left(\frac{\partial \bar{u}_i}{\partial x_j}+\frac{\partial \bar{u}_j}{\partial x_i}\right)$$

$$\nu_t=C_d\,\Delta x^2\left|\bar{S}\right| \qquad \text{where} \quad \bar{S}^2=\bar{S}_{ij}\,\bar{S}_{ij}$$

$\frac{1}{3}\tau_{kk}$ **add to** $\bar{p}$

Vremen et al J Fluid Mech, Vol 399, p357, (1997)

Six subgrid scale models applied to the free shear layer (32^3 grid).

Smagorinsky model with constant coefficient did not perform well – too dissipative in laminar regions.

Best results with dynamic eddy–viscosity model, Germano, J Fluid Mech, Vol 238, p325 (1992).

$$\tau_{ij} = c_d \Delta x^2 \left|\overline{S}\right| \overline{S}_{ij}$$

c_d: a variable coefficient estimated from the velocity field filtered at two different levels Δx and $2\Delta x$.

Subgrid Scale Models

Theoretical analysis available.

eg for Smagorinsky model (Fureby et al, Physics of Fluids, Vol 9, p1416, 1997) – assuming spectrum

$$\nu_t = \mathbf{c}_D \Delta^2 |\mathbf{S}|$$

$$\mathbf{C}_D = \frac{4}{\pi^2} \frac{1}{\left(3\,\mathbf{C}_K\right)^{3/2}} = 0.042$$

Δ = **filter width**

$\mathbf{C}_K$ = **Kolmogorov constant**

MILES technique

Theoretical analysis lacking, except for recent work by Margolin and Rider, ECCOMAS, Swansea, UK (2001).

Analysis of truncation terms in nonoscillatory finite volume schemes – relate to SGS models.

"It appears that the reluctance of the community in general to accept implicit turbulence modelling is more due to lack of justification of the approach rather than any failure of application."

DNS - low to moderate Reynolds no.

needed to understand the transition to Turbulence.

Understand the behaviour of the high – wave number end of the spectra.

Effect of Schmidt no.

LES or MILES

- used to model the high–Reynolds number limit – relevant to many applications eg shock tube experiments.

INTERFACE TRACKING

- useful to understand the effect of `surface tension for mixing of immiscible fluids (a number of RT experiments have used immiscible fluids).

Immiscible fluids with negligible surface tension should give fine–scale mixing which behaves like miscible

mixing, at high Reynolds number.

TURMOIL3D experience

Numerical method used based on the 2D Eulerian technique for multimaterial flow developed ~ 1980.

- **Lagrangian phase + rezone (advection) phase**
- **Interface tracking**
- **Monotonic advection method of van Leer used in rezone phase for all fluid variables.**

Van Leer method very successful at giving a robust method with low numerical diffusion.

Applied to a wide range of compressible flows with shocks and density discontinuities.

- **TURMOIL3D – same basic numerical method as the 2D code**
- **As simple as possible eg perfect gas EoS**
- **Interface tracking not used, as dissipation of density fluctuations at small scales expected**
- **Use of the van Leer method implied non- linear numerical dissipation at scales of order the mesh size**

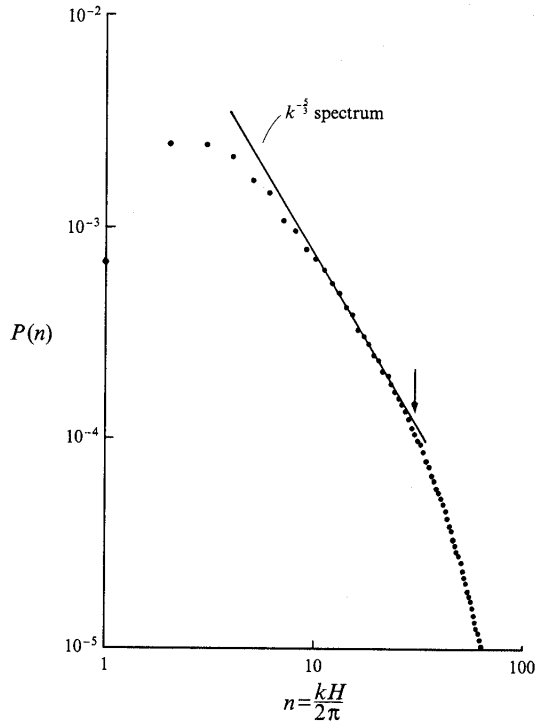

FIGURE 14. Power spectrum $P(n)$ for concentration fluctuations at $\tau = 3$ from the numerical calculation without the long-wave perturbation. The line drawn corresponds to a $k^{-\frac{5}{3}}$ spectrum, where $k = (k_x^2 + k_y^2)^{\frac{1}{2}}$. The arrow indicates the point where the wavelength $2\pi/k$ equals 6 mesh widths.

TURMOIL3D density fluctuation spectrum

Linden, Redondo, Youngs J Fluid Mech, vol 265, p97 (1994)

No need for additional sub-grid dissipation model

Could be argued that there is more high-wavenumber dissipation than desirable

MILES vs LES with explicit sub-grid model

TVD schemes (such as the van Leer advection method used in TURMOIL3D) have become very popular for compressible flow with shocks and contact discontinuities. It seems appropriate to continue using them for compressible turbulent flow. The dissipation implicit in the numerical scheme should be sufficient to make sub-grid models unnecessary $\rightarrow$ MILES approach.

The rationale for LES + explicit sub-grid model requires the use of a basic numerical technique with negligible dissipation $\Rightarrow$ TVD schemes cannot be used.

Does this mean that this approach is most useful for uniform density incompressible flow?

Many disagreements about best method to use for 3D RT turbulent mixing.

Need to compare results for agreed test problems.

Guy Dimonte (alpha group comparison).

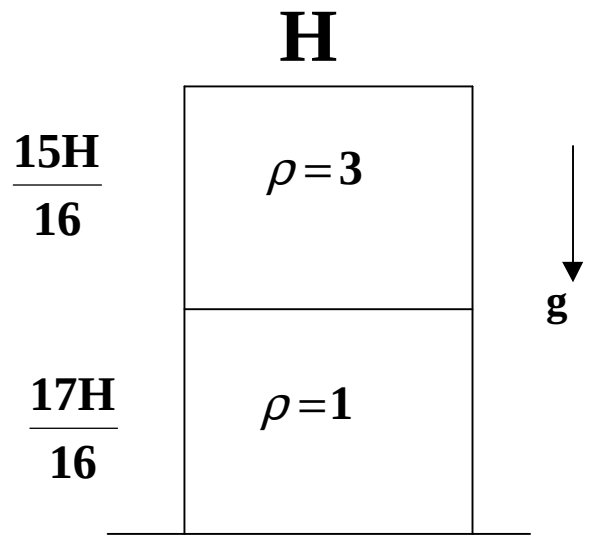

256 x 256 x 512 zones

Initial perturbation : wavelengths in the range 4 Δx to 8 Δx.

Growth by mode coupling $\Rightarrow$ loss of memory of the initial conditions.

$$h_1 = 3.3\int \overline{f_1} \cdot \overline{f_2}\, dz$$

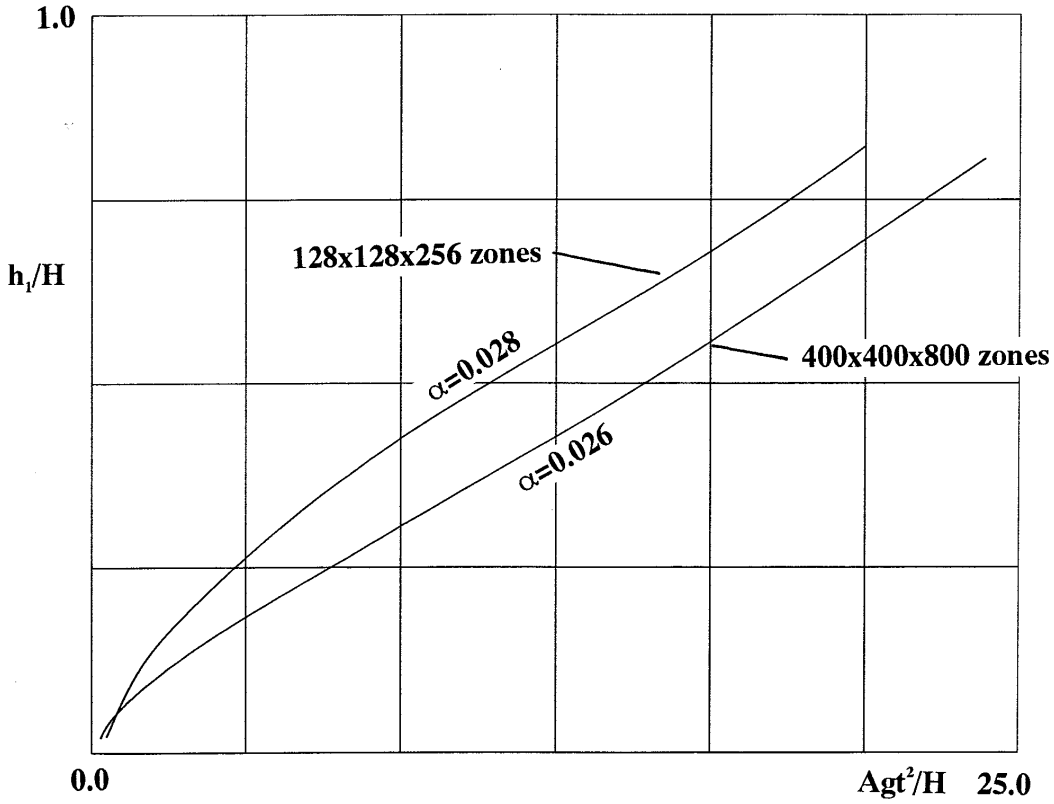

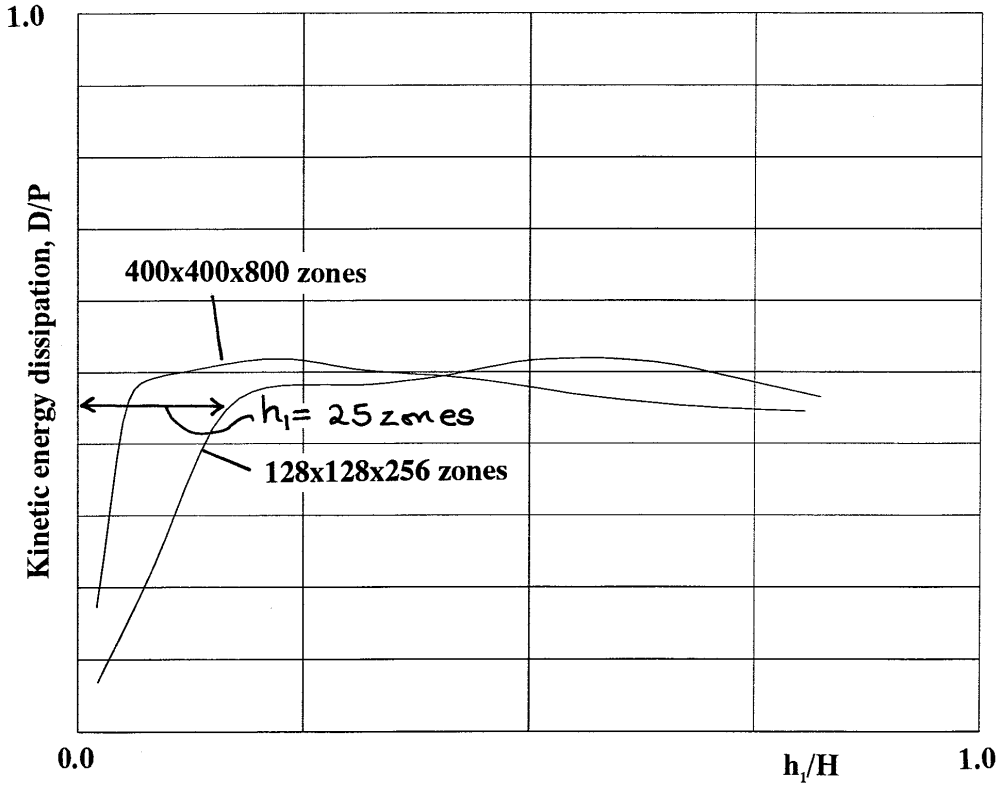
1.0
Kinetic energy dissipation, D/P
400x400x800 zones
h_1= 25 zones
128x128x256 zones
0.0
h_1/H
1.0

$$\theta = \frac{\int \overline{f_1 f_2}\, dz}{\int \overline{f_1}.\,\overline{f_2}\, dz}$$

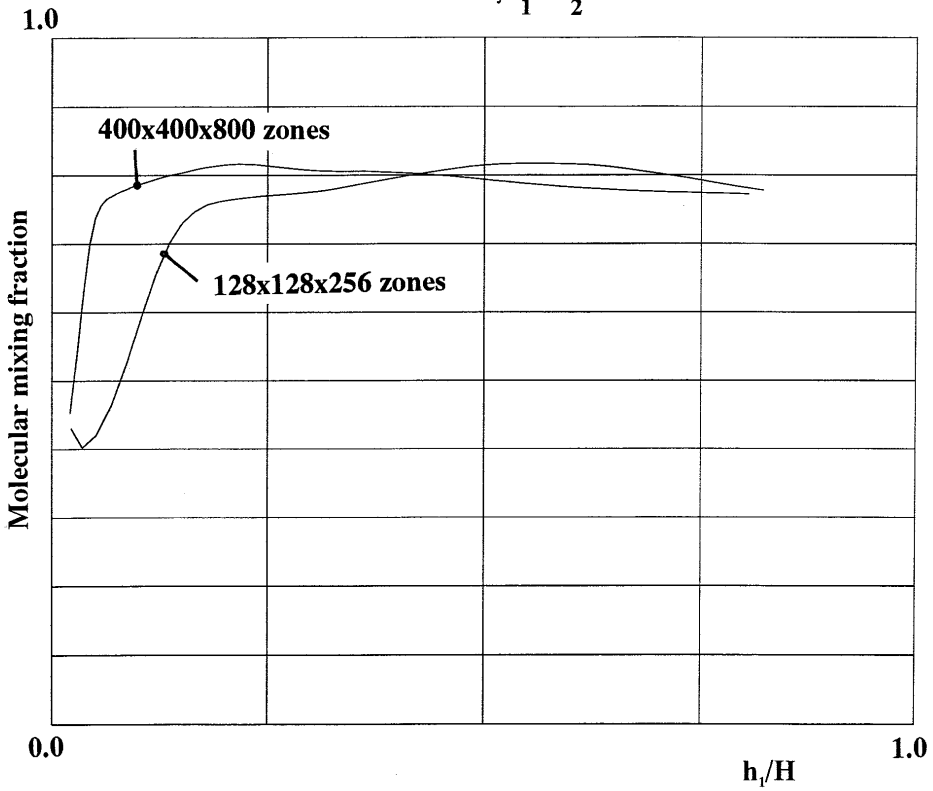

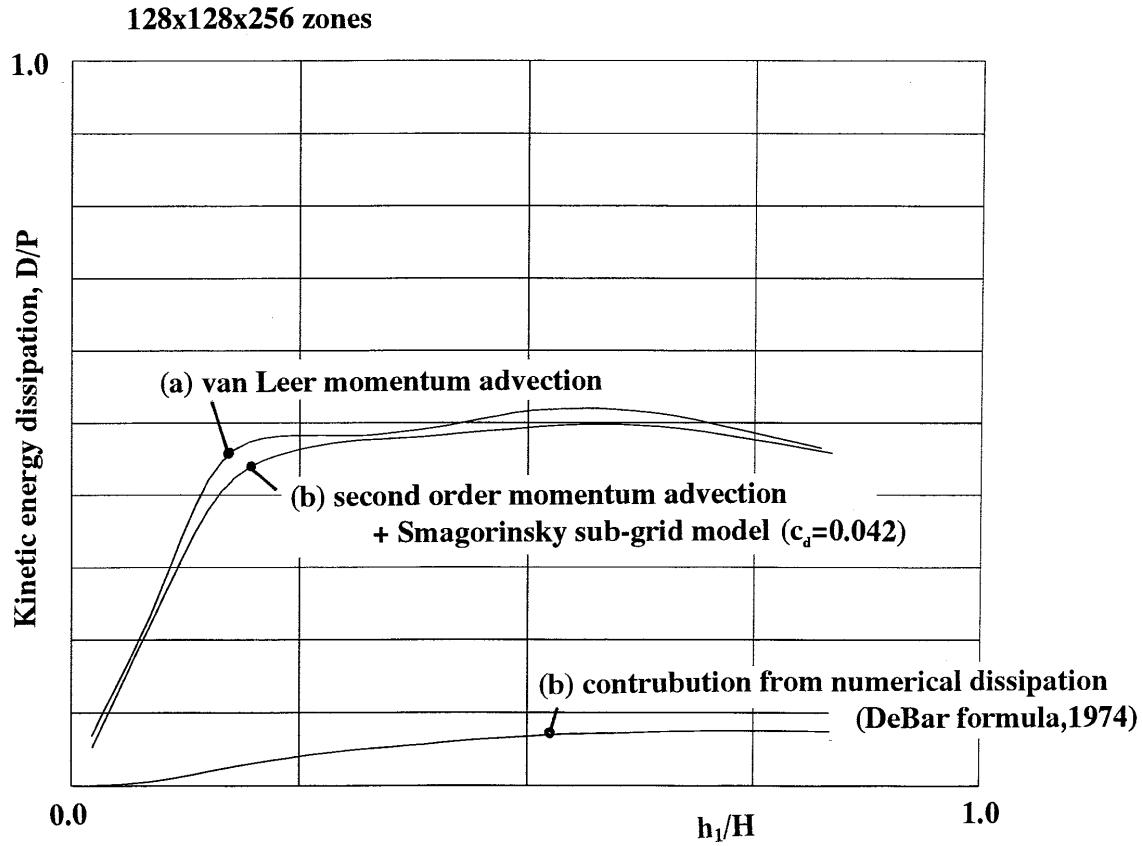
128x128x256 zones
1.0
Kinetic energy dissipation, D/P
(a) van Leer momentum advection
(b) second order momentum advection
+ Smagorinsky sub-grid model (c_d=0.042)
(b) contrubution from numerical dissipation
(DeBar formula,1974)
0.0
h_1/H
1.0

THE INITIAL PERTURBATION

RT experiments with constant g give bubble penetration

$$h_1 = \alpha \frac{\rho_1 - \rho_2}{\rho_1 + \rho_2} gt^2 \quad \text{, with } \alpha \sim 0.05 \text{ to } 0.06$$

TURMOIL3D calculations with short wavelength initial perturbations (growth purely by mode coupling) give

$\alpha \sim 0.03.$

Need to assume long wavelength initial perturbations with amplitude $\propto$ wavelength (as proposed by Inogamov) to give self-similar growth with $\alpha \sim 0.05$.

Perturbation used $\zeta(x,y) = \zeta_S + \zeta_L$

ζ_S **: wavelengths** $4\Delta x$ **to** $8\Delta x$

s.d $= 0.005\,\Delta x$

ζ_L **: power spectrum P(k)**

$$\sigma_\lambda = \left\{ \int_{2\pi/\lambda}^{\infty} P(k)\,dk \right\}^{\frac{1}{2}} = \varepsilon\,\lambda$$

$$\Rightarrow P(k) \propto 1/k^3 \text{ (ocean surface spectrum)}$$

$$\varepsilon = 0.0005$$

wavelengths in the range $4\Delta x$ **to** $\frac{H}{2}$

$\left(\text{ICF surface finish } P(k) \propto 1/k^2 \right)$

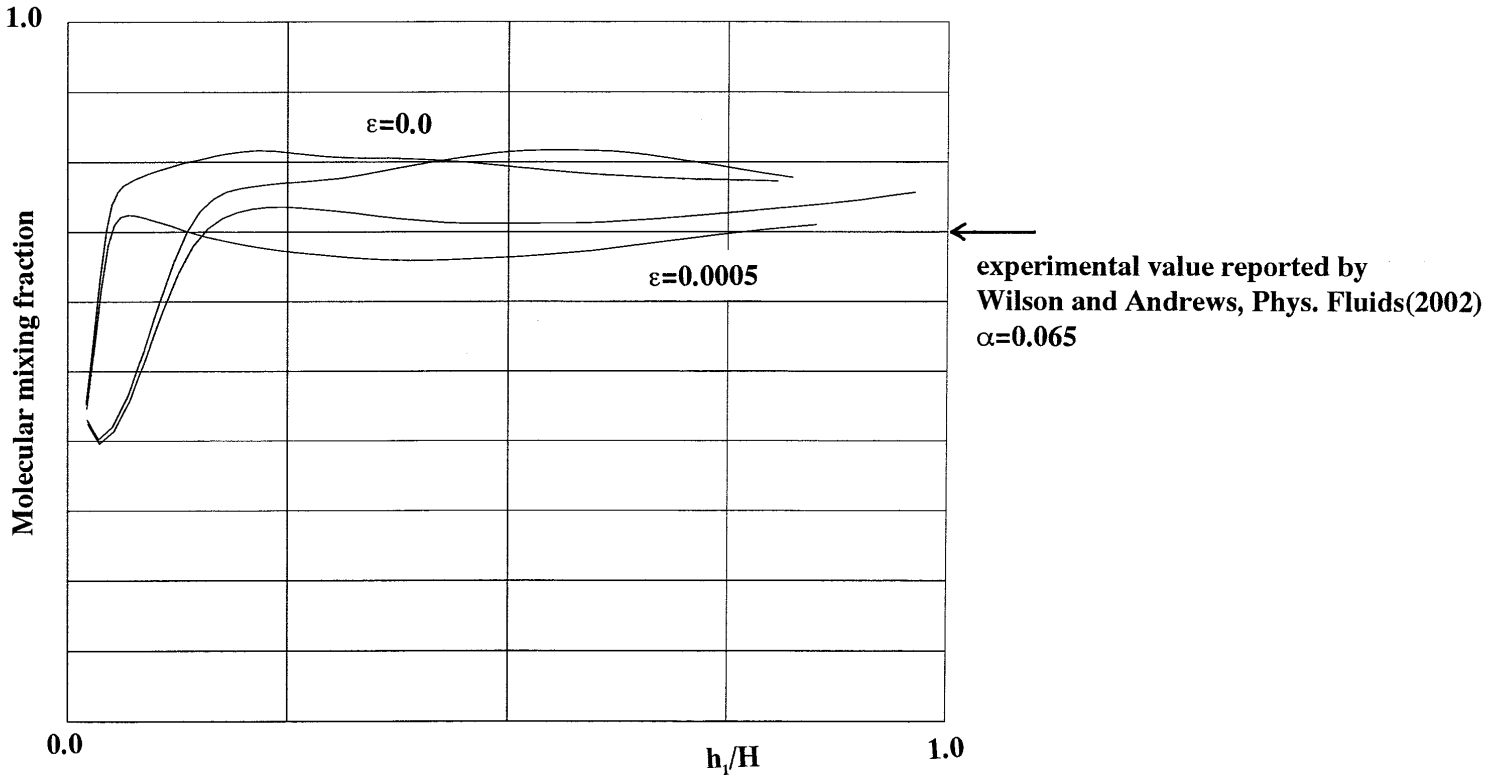
1.0
ε=0.0
ε=0.0005
Molecular mixing fraction
0.0
h1/H
1.0
experimental value reported by
Wilson and Andrews, Phys. Fluids(2002)
α=0.065

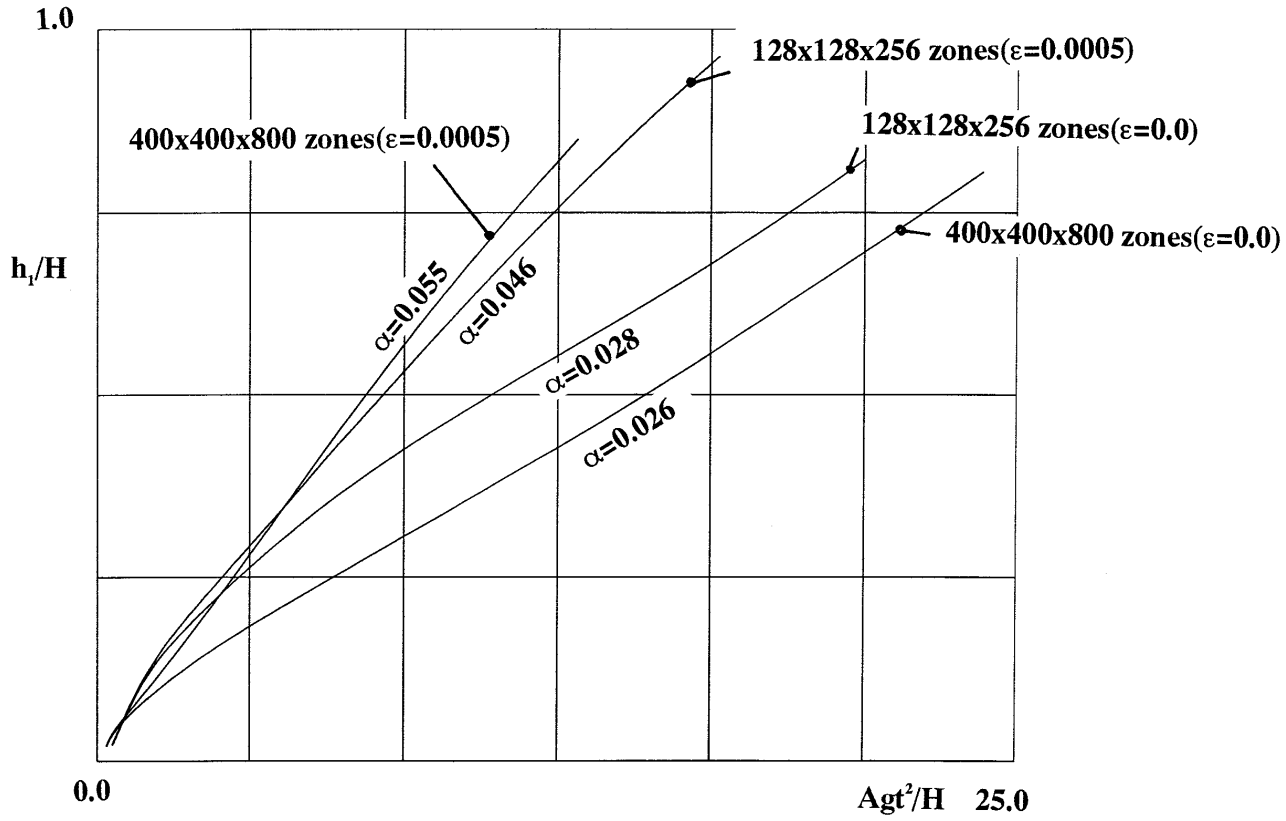
1.0
128x128x256 zones(ε=0.0005)
400x400x800 zones(ε=0.0005)
128x128x256 zones(ε=0.0)
400x400x800 zones(ε=0.0)
h1/H
α=0.055
α=0.046
α=0.028
α=0.026
0.0
Agt²/H 25.0

Figure7 : Probability distributions for f_1 within a plane z=constant

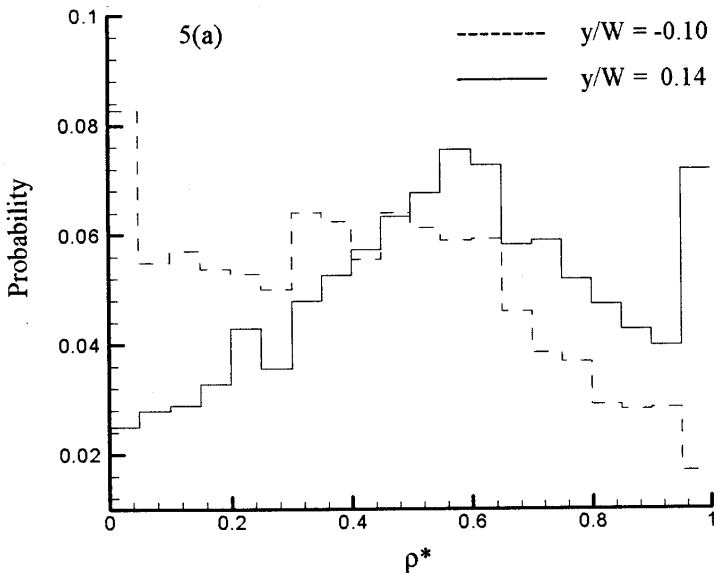

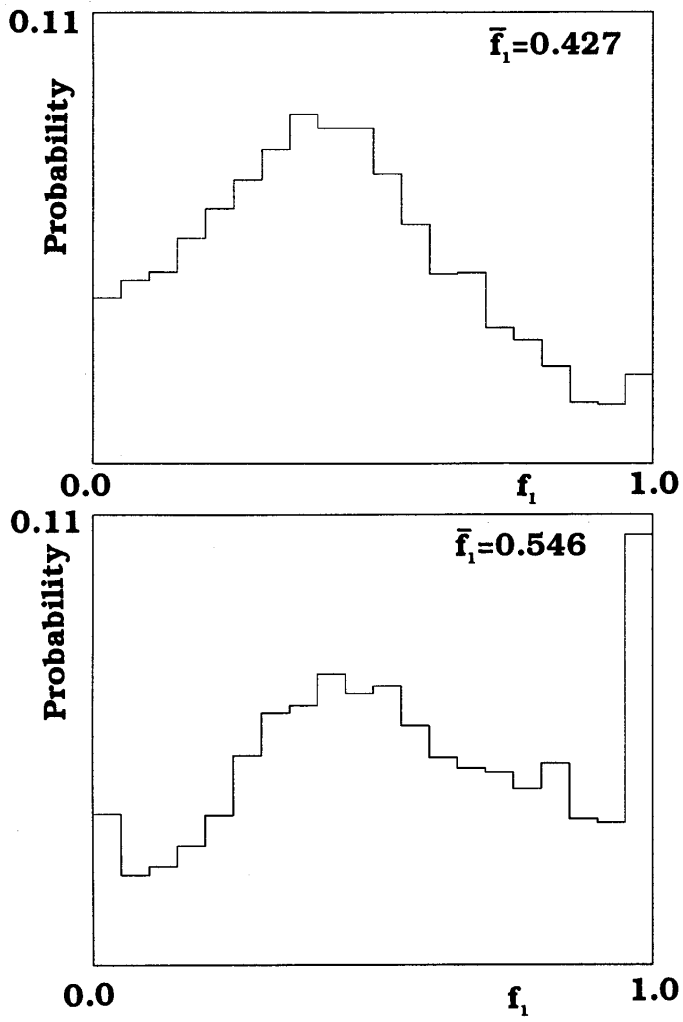

TURMOIL3D calculation
At=0.5
128x128x256 zones

g=constant

Cook and Dimotakis, J Fluid Mech, vol 443, p69 (2001)

DNS : 256 x 256 x 1024 zones

Sc = 1, Re ~ 140, $\rho_1/\rho_2 = 3$

Diffuse initial interface

Eighth-order compact scheme (Lele 1992) – spectral-like resolution.

Calculated transition to turbulence, which was found to be very dependent on the initial conditions.

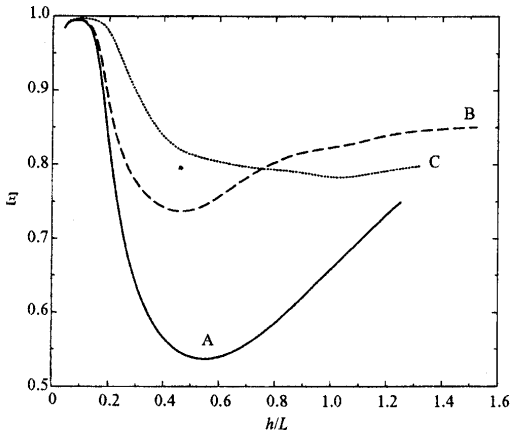

FIGURE 16. Mixing parameter, Ξ, *vs.* h/L, for the three cases.

Young, Tufo, Dubey, Rosner (Chicago U) – J Fluid Mech, vol 447, p377 (2001)

Miscible RT

Spectral method or spectral-element method
Low Atwood no. (Boussinesq approximation)
256 x 256 x 512 zones.
Initial modes with wavelengths around 8Δx.

2D $\alpha \sim 0.017$?

3D $\alpha \sim 0.03$

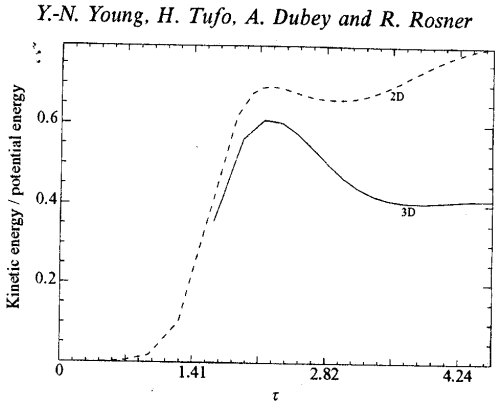

FIGURE 8. Ratio of kinetic energy to gravitational potential energy: two-dimensional versus three-dimensional simulations. The kinetic energy is the volume integral of the kinetic energy density, and the potential energy is the volume integral of the potential energy available in the system. For $\tau \leqslant 1.4$, the growth is exponential and is similar for both two and three dimensions, after this period, two-dimensional motions are much more efficient in extracting potential energy than three-dimensional motions.

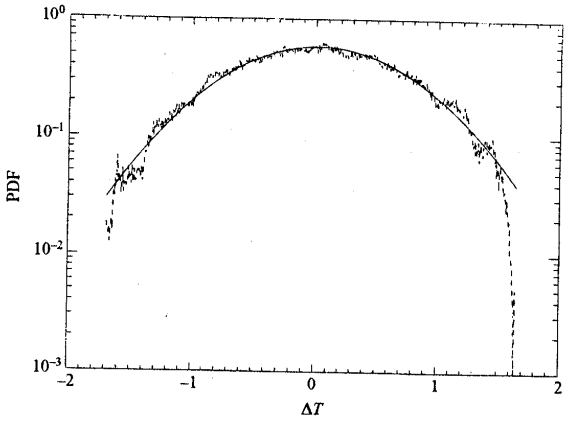

FIGURE 13. PDF of the temperature fluctuation ($\delta T = T - T_0$) within the mixing zone ($\Delta z = 0.025$) at the position of the original interface ($z = 0.06$).

Calculations with Interface Tracking

A number of researchers have considered turbulent mixing of immiscible fluids using interface tracking techniques.

J Glimm et al J Comp Phys, Vol 162, p652 (2001)

Frontier method – represents both the velocity and density discontinuity at the interface.

112 x 112 x 224 zones

α ~ 0.07

Oron, Arazi, Kartoon, Rikanati, Alon, Shvarts Physics of Plasmas, Vol 8, p2883 (2001). See also Shvarts et al Shock-Induced instability of interfaces, in Handbook of Shock Waves, Vol 2, Academic Press (2001).

80 x 80 x 80 zones

α ~ 0.05

Anuchina et al – Proceeding of 5th Zababakhin Scientific Talks (1999).

60 x 60 x 60 zones **α = 0.064**

120 x 120 x 120 zones **α = 0.074**

Evidence for $k^{-5/3}$ energy spectrum.

(Also, Yu. V. Yanilkin, VNIIEF, 120^3 mesh, α = 0.06)

Rayleigh-Taylor Summary

- **Many 3D calculations with significant differences between results**

  α ~ 0.03 to 0.07

- **Effect of initial conditions important – very good reason for pursuing the numerical simulation.**

- **Controversy over the numerical techniques which should be used.**

  Use of sub-grid scale models is recommended by many but has not been widely used here.

  Interface tracking calculations have given higher values of α but have not used the highest resolution.

- **Need some test problems to resolve the disagreements (see talk by Guy Dimonte).**

RM Turbulent Mixing

Fewer 3D simulations available.

Scaling laws for single shock RM :

Bubbles	**:**	$h_B \sim t^{\theta B}$
Spikes	**:**	$h_S \sim t^{\theta S}$

Youngs, Laser and Particle Beams, Vol 12, p725, (1994)

160 x 160 x 270 zones, assumed $\theta_B = \theta_S$

then $\theta \simeq 0.30$ **(based on growth of integral mix width)**

for a flat spectrum

P(k) = const for 0 < k < k_{max}

$k_{max} = \dfrac{2\pi}{\lambda_{min}}$, $\lambda_{min} = 16\Delta x$

Cohen et al. IWPCTM6 (Marseille)

High resolution RM calculations up to 512^3

PPM method

Single-shock and double shock calculations

Single – shock random perturbations, but with longer wavelengths present

θ = 0.75

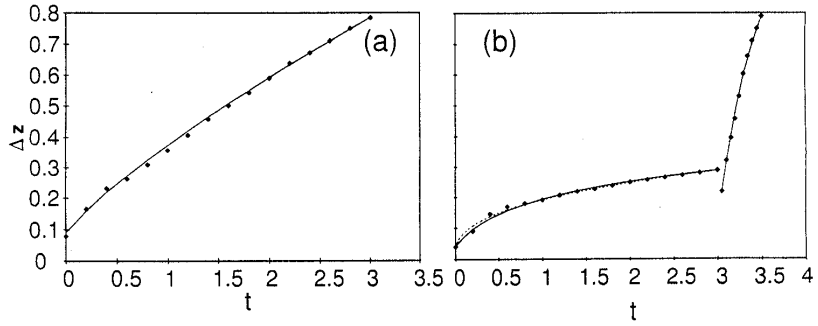

Figure 1. Mixing layer growth vs. time for (a) random-phase sum initial condition; (b) single mode initial condition with two shocks

Oron, Arazi, Kartoon, Rikanati, Alon, Shvarts

Physics of Plasmas, vol 8, p2883 (2001)

LEEOR-3D (interface tracking)

80 x 80 x 80 zones

$\theta_B \simeq 0.35\,(2D) \quad , \quad \sim 0.22\,(3D)$

$\theta_S \simeq 0.45\,(2D) \quad , \quad \sim 0.3\,(3D)$

Results used to construct a simple buoyancy – drag model.

Theta bubble:

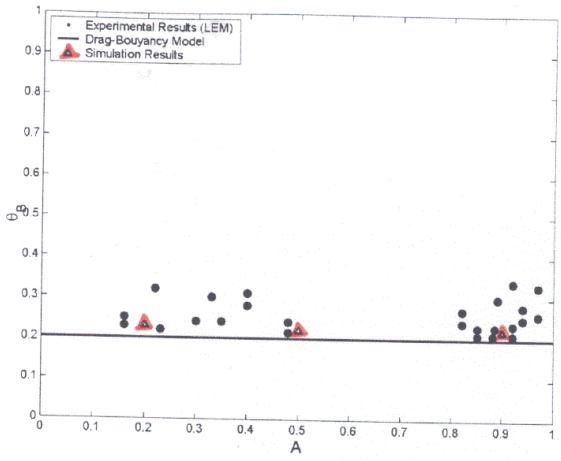

Theta spike:

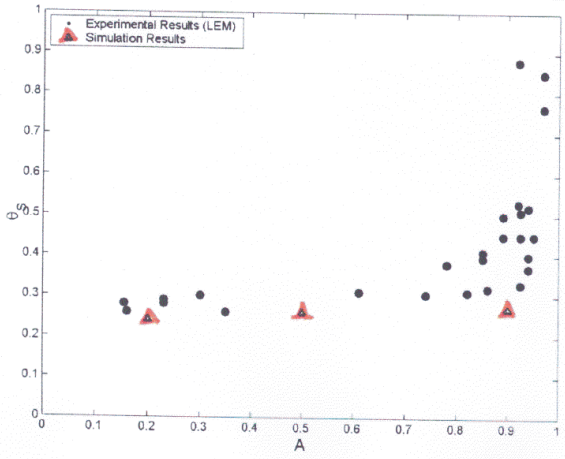

Single Shock RM

3D simulation should be used to investigate the effect of initial conditions in more detail.

An initial amplitude spectrum

$$P(k) \sim k^{-2}$$

may be more appropriate to real applications $\Rightarrow$ higher values of θ_S , θ_B ?

Double Shock RM

3D simulation has been applied to experiments where several shocks are present.

However, no detailed 3D studies (development of scaling laws) for double shock RM.

Second shock : shock-turbulence interaction and shock-density fluctuation interaction.

FUTURE ROLE OF NUMERICAL SIMULATION

2D Simulation

- **Will continue to be essential for complex problems with additional physics**

3D Simulation

- **Fundamental understanding of turbulent mixing in simple flows (DNS and LES)**
- **More complex flows – LES now feasible**
- **LES results should be used to validate engineering models (Bouyancy – drag models, RANS models)**
- **Not yet feasible for complex real applications**

AWE SHOCK TUBE EXPERIMENT

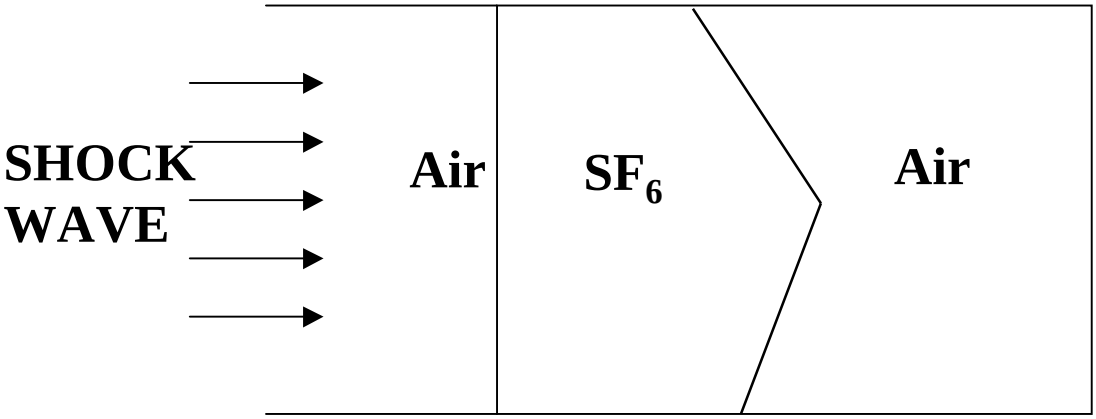

The purpose of the shock tube experiment is validation of a 2D RANS model

Experiment is 2D on average

3D Simulation (TURMOIL3D) : 400 x 320 x 160 zones interfaces randomly perturbed

2D turbulence model (RANS model) calculation

: 200 x 160 zones

Compare average behaviour extracted from 3D simulation with 2D RANS model

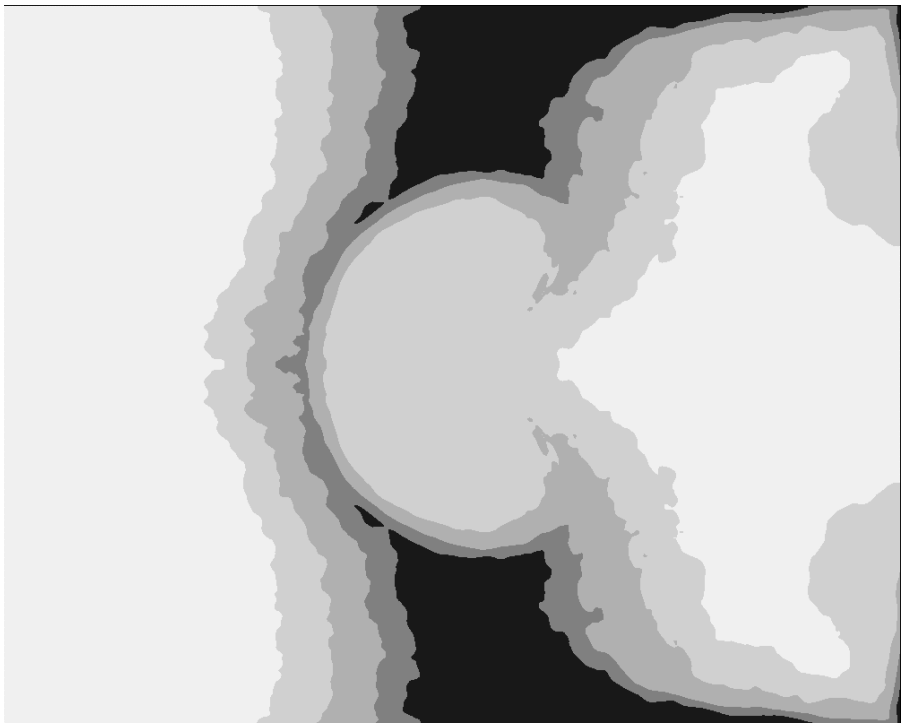

3D simulation at t = 4.0ms

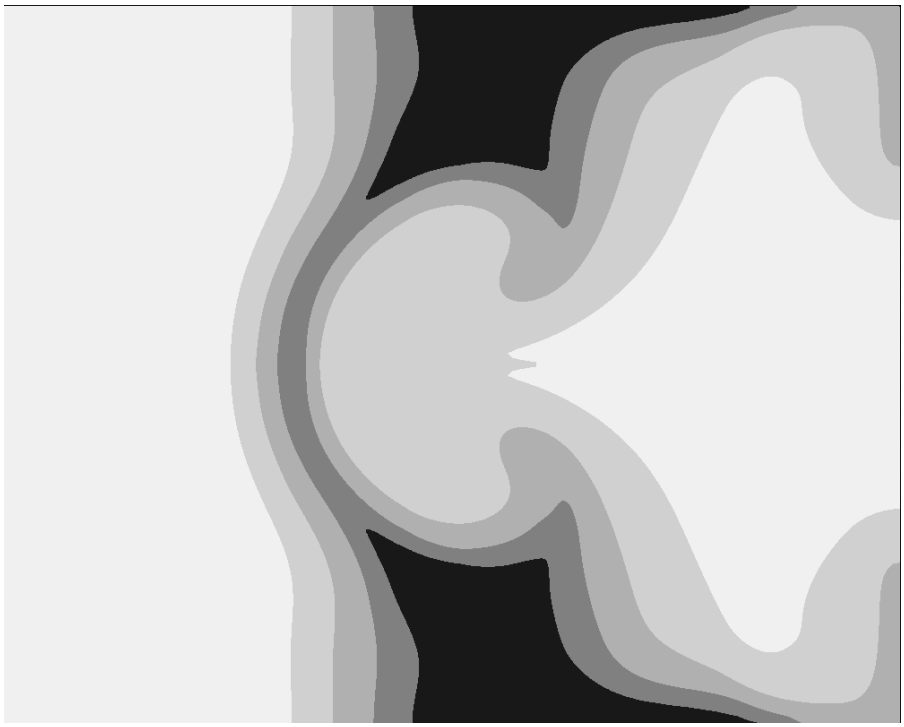

2D RANS model at t = 4.0ms

Mean volume fraction levels -

0.0,0.05,0.3,0.7,0.95,1.0

FINAL REMARKS

- **Numerical simulation has made a major contribution to the understanding of RT and RM instability over the last 40 years.**

- **Need to focus more now on 3D turbulence simulation.**

- **Reasonably good 3D LES can be performed with mesh sizes ~ 256^3, well within the capability of present-day supercomputers.**

- **3D simulation not yet practical for complex real applications but can have a major impact on engineering models.**

Authors Contact Information

Abarzhi, Snejana I.
Department of Applied Mathematics
State University of New York at Stony Brook
Stony Brook, NY 11794-3600
Phone: 631-632-9360
Fax: 631-632-8490
E-mail: snezha@ams.sunysb.edu

Abe, M.
Institute of Laser Engineering
Osaka University
Suita, Osaka 565 Japan

Afeyan, Bedros
Polymath Research Incorporated
827 Bonde Court
Pleasanton, CA 94566
Phone: (925) 417-0609
Fax: (925) 417-0684
E-mail: bedros@polymath-usa.com

Allen, A. M.
University of Oxford
University Offices
Wellington Square
Oxford OX1 2JD. UK
Phone: +44 1865 270000
Fax: +44 1865 270708

Alon, U.
Weizmann Institute of Science
PO Box 26
Rehovot 76100 Israel
Phone: + 972-8-934-2111
Fax: + 972-8-934-4107
E-mail: uri.alon@weizmann.ac.il

Anderson, M. H.
University of Wisconsin at Madison
1500 Engineering Drive
Madison, WI 53706
Phone: (608) 263-2802
Fax: (608) 263-7541
E-mail: manderson@engr.wisc.edu

Andrews, Malcolm
Department of Mechanical Engineering
Texas A & M University
MS 3123
College Station, TX 77843-3123
Phone: (409) 847-8843
Fax: (409) 845 3081
E-mail: malcolm@chagal.tamu.edu

Anisimov, V. I.
Russian Federal Nuclear Center-VNIITF
P.O. Box 245
456770 Snezhinsk, Russia
E-mail: v.i.anisimov@vniitf.ru

Anuchin, M. G.
Russian Federal Nuclear Center-VNIITF
P.O. Box 245
456770 Snezhinsk, Russia

Arazi, L.
Tel Aviv University
P.O. Box 39040
Tel Aviv 69978
Israel

Ardashova, R. I.
Russian Federal Nuclear Center-VNIITF
P.O. Box 245
456770 Snezhinsk, Russia

Arnett, D.
The University of Arizona
P.O. Box: 210096
Tucson, AZ 85721
Phone: (520) 621-9587
E-mail:: darnett@as.arizona.edu

Ashurst, William T.
Sandia National Laboratory
P.O. Box 969, MS 9051
Livermore, CA 94551-0969
Phone: (925) 294-2274
Fax: (925) 294-2595
E-mail:: ASHURS@sandia.gov

Azechi, Hiroshi
Institute of Laser Engineering
Osaka University
Suita, Osaka 565 Japan
Phone: 81-879-8770
Fax: 81-877-4799
E-mail: azechi@ile.osaka-u.ac.jp

Bailly, P.
Commissariat à l'Energie Atomique
BP 12 - 91680 Bruyères-le-Châtel

Baishev, A. I.
Russian Federal Nuclear Center-VNIITF
P.O. Box 245
456770 Snezhinsk, Russia

Balabin, Serguei
Russian Federal Nuclear Center-VNIITF
P.O. Box 245
456770 Snezhinsk, Russia
Fax: (351-72) 3 20 77
E-mail: kucherenko@five.ch70.chel.su

Barnes, Christopher W.
Los Alamos National Laboratory
P.O. Box 1663
Los Alamos, NM 87545
Phone: (505) 665-5687
E-mail:: cbarnes@lanl.gov

Barton, C.
Atomic Weapons Establishment
Aldermaston
Reading, Berkshire
RG7 4PR UK
Phone: +44 (0)1734 814111
Fax: +44 (0)1734 815320

Batha, Steven
Los Alamos National Laboratory
P.O. Box 1663, MS E526
Los Alamos, NM 87545
Phone: (505) 665-5898
Fax: (505) 665-4409
E-mail: sbatha@lanl.gov

Belak, James F.
Lawrence Livermore National Laboratory
P.O. Box 808, L-045
Livermore, CA 94551
Phone: (925) 422-6061
Fax: (925) 422-2851
E-mail: belak1@llnlg.gov

Belomestnih, A. V.
Russian Federal Nuclear Center-VNIITF
P.O. Box 245
456770 Snezhinsk, Russia

Ben-Dor, Gabi
Ben-Gurion University of the Negev
Faculty of Engineering Sciences
Beer Sheva, 84105, Israel
Phone: 972-7-6461212
Fax: 972-7-6472936
E-mail: bendor@menix.bgu.ac.il

Benjamin, Robert F.
Los Alamos National Laboratory
P.O. Box 1663, MS P940
Los Alamos, NM 87545
Phone: (505) 667-8116
Fax: (505) 665-3359
E-mail: rfb@lanl.gov

Biello, J.
University of Chicago
933 East 56th Street
Chicago, IL 60637
Phone: (773) 702-1234

Bliznetsov, M. V.
Russian Federal Nuclear Center-VNIIEF
Mir Avenue, 37, Sarov
Nizhnii Novgorod Region, 607190, Russia
Fax: (831-30) 459-58
E-mail: root@gdd.vniief.ru

Boehly, T. R.
Laboratory for Laser Energetics
University of Rochester
250 East River Road
Rochester, New York 14623-1299
Phone: (716) 275-0254
E-mail: trb@lle.rochester.edu

Bonazza, Riccardo
Department of Engineering. Physics
University of Wisconsin at Madison
1500 Engineering Drive
Madison, WI 53706
Phone: (608) 265-2337
Fax: (608) 262-6707
E-mail: bonazza@engr.wisc.edu

Bouquet, Serge
Commissariat à l'Energie Atomique
PDPTA-BP 12
Bruyeres-le-Chatel, France 91680
Phone: +33-1-69-26-51-83
Fax: +33-1-69-26-71-06
E-mail: bouquet@bruyeres.cea.fr

Braun, David G.
Lawrence Livermore National Laboratory
P.O. Box 808, L-031
Livermore, CA 94551
Phone: (925) 423-6275
Fax: (925) 423-9969
E-mail: braun1@llnl.gov

Breidenthal, Robert
Department of Aeronautics and Astronautics
University of Washington
Box 352400
Seattle, WA 98195-2400
Phone: (206) 685-1098
Fax: (206) 685-0217
E-mail: breidenthal@aa.washington.edu

Brouillette, Martin
Department of Mechanical Engineering
Université de Sherbrooke
Sherbrooke, Quebec J1K 2R1 Canada
Phone: (819) 821-7144
Fax: (819) 821-7163
E-mail: martin.brouillette@gme.usherb.ca

Buckingham, Alfred C.
Lawrence Livermore National Laboratory
P.O. Box 808, L-23
Livermore, CA 94551
Phone: (925) 423-4828
Fax: (925) 422-2644
E-mail: alfredcb@llnl.gov

Budil, Kimberly S.
Lawrence Livermore National Laboratory
P. O. Box 808, L-97
Livermore, CA 94551
Phone: (925) 423-8098
Fax: (925) 422-0779
E-mail: budil1@llnl.gov

Cabot, William H.
Lawrence Livermore National Laboratory
P.O. Box 808, L-22
Livermore, CA 94551
Phone: (925) 423-9272
Fax: (925) 423-0925
E-mail: cabot1@llnl.gov

Calder, A. C.
Department of Astronomy and Astrophysics
University of Chicago
5640 South Ellis Ave.
Chicago, IL 60637
Phone: (773) 834-3904
Fax: (773) 834-3230
E-mail:: calder@flash.uchicago.edu

Chebotareva, E. I.
Krzhizhanovsky Power Engineering Institute
ENIN, Leninsky pr. 19, GSP-1
Moscow, 117927 Russia
Phone: (7-095) 955-31-07
Fax: (7-095) 954-42-50
E-mail: S.G.Zaytsev@mtu-net.ru

Cheng, Baolian
Los Alamos National Laboratory
P.O. Box 1663, MS D413
Los Alamos, NM 87545
Phone: (505) 667-4701
Fax: (505) 667-3726
E-mail: bcheng@lanl.gov

Clark, Timothy T.
Los Alamos National Laboratory
P.O. Box 1663, MS B213
Los Alamos, NM 87545
Phone: (505) 665-4858
Fax: (505) 665-3003
E-mail: ttc@llnl.gov

Clerouin-Cherfils, Catherine
Commissariat à l'Energie Atomique
CEA/DRIF
BP 12, 91680, Bruyeres-le-Chatel, France
Phone: 33 1 69 26 57 38
Fax: 33 1 69 26 70 94
E-mail: cherfils@bruyeres.cea.fr

Colvin, Jeffrey. D.
Lawrence Livermore National Laboratory
P.O. Box 808, L-021
Livermore, CA 94551
Phone: (925) 422-3273
Fax: (925) 423-8945
E-mail: colvin5@llnl.gov

Cook, Andrew W.
Lawrence Livermore National Laboratory
P.O. Box 808, L-22
Livermore, CA 94551
Phone: (925) 423-2856
Fax: (925) 423-0925
E-mail: awcook@llnl.gov

Dalziel, Stuart
DAMTP, University of Cambridge
Silver Street, Cambridge CB3 9EW, England
Phone: (44) (1223) 337 911
Fax: (44) (1223) 337 918
E-mail: s.dalziel@damtp.cam.ac.uk

Dannenberg, K.
University of Michigan
Space Research Lab, Rm 1216
2245 Hayward
Ann Arbor, MI 48104

Darlington, Rebecca M.
Lawrence Livermore National Laboratory
P.O. Box 808, L-95
Livermore, CA 94551
Phone: (925) 424-3422
E-mail: darlington1@llnl.gov

Delettrez, J. A.
Laboratory for Laser Energetics
University of Rochester
Rochester, NY 14623-1299
Phone: (716) 275-5374
E-mail: jdel@lle.rochester.edu

Demyanov, A. Yu.
Landau Institute for Theoretical Physics
Kosygnina St. 2, Moscow
117940, GSP-1
V-334 RUSSIA

Dimits, Andris M.
Lawrence Livermore National Laboratory
P.O. Box 808, L-630
Livermore, CA 94551
Phone: (925) 422-0211
Fax: (925) 423-3484
E-mail: dimits1@llnl.gov

Dimonte, Guy
Lawrence Livermore National Laboratory
P.O. Box 808, L-43
Livermore, CA 94551
Phone: (925) 423-0596
Fax: (925) 423-5998
E-mail: dimonte1@llnl.gov

Dittrich, Thomas R.
Lawrence Livermore National Laboratory
P.O. Box 808, L-023
Livermore, CA 94551
Phone: (925) 422-4706
Fax: (925) 423-8945
E-mail: dittrich1@llnl.gov

Don, Wai-Sun
Division of Applied Mathematics
Brown University
Box F
Providence, RI 02912
Phone: (401) 863-2250
E-mail:: Wai-Sun_Don@brown.edu

Drake, R. Paul
University of Michigan
2245 Hayward
Ann Arbor, MI 48104
Phone: (734) 763-4072
Fax: (734) 647-3083
E-mail: rpdrake@umich.edu

Drennov, O. B.
Russian Federal Nuclear Center-VNIIEF
Mir Avenue, 37, Sarov
Nizhnii Novgorod Region, 607190, Russia
Fax: (831-30) 459-58
E-mail: root@gdd.vniief.ru

Dudin, V. D.
Russian Federal Nuclear Center-VNIIEF
Mir Avenue, 37, Sarov
Nizhnii Novgorod Region, 607190, Russia
Fax: (831-30) 459-58
E-mail: root@gdd.vniief.ru

Dulov, A. V.
Russian Federal Nuclear Center-VNIITF
P.O. Box 245
456770 Snezhinsk, Russia

Dunne, A. M.
Atomic Weapons Establishment
Aldermaston
Reading, Berkshire
RG7 4PR UK

Dursi, L.
Department of Astronomy and Astrophysics
University of Chicago
5640 South Ellis Ave.
Chicago, IL 60637
Phone: (773) 834-1059
Fax: (773) 834-3230

Dutta, S.
State University of New York at Stony Brook
P-138A Math Tower
Stony Brook, NY 11794-3600

Edwards, Michael J.
Lawrence Livermore National Laboratory
P.O. Box 808, L-21
Livermore, CA 94551
Phone: (925) 422-1189
Fax: (925) 423-8945
E-mail: edwards39@llnl.gov

Elbaz, Y.
Ben-Gurion University
Beer-Sheva
Israel 84015
Phone: 972-8-6568836
Fax: 972-8-6567878
E-mail: elbazyo@bgumail.bgu.ac.il

Eliason, Donald E.
Lawrence Livermore National Laboratory
P.O. Box 808, L-103
Livermore, CA 94551
Phone: (925) 423-5625
Fax: (925) 422-6388
E-mail: eliason@merlin.llnl.gov

Epstein, Reuben
Laboratory for Laser Energetics
University of Rochester
Rochester, NY 14623-1299
Phone: (716) 275-5405
E-mail: reps@lle.rochester.edu

Farley, David
Institute of Laser Engineering
Osaka University
Suita, Osaka 565, Japan
E-mail: dfarley@epri.com

Fryxell, Bruce
Enrico Fermi Institute and Laboratory for Astrophysics and
Space Research
University of Chicago
933 East 56th Street
Chicago, IL 60637
Phone: (773) 704-3226
Fax: (773) 704-3230
E-mail:: fryxell@uffda.asci.uchicago.edu

Fujioka, S.
Institute of Laser Engineering,
2-6, Yamada-oka, Suita,
Osaka 565-0871 Japan

Fukuda, Y.
Institute of Laser Engineering,
2-6, Yamada-oka, Suita,
Osaka 565-0871 Japan

Galmiche, Didier Jean Marie
Commissariat à l'Energie Atomique
BP12 91680 Bruyeres-le-Chatel, France
Phone: 33 1 69 26 40 05
Fax: 33 1 69 26 70 94
E-mail: galmiche@bruyeres.cea.fr

Garasi, C.
Sandia National Laboratory
P.O. Box 969, 0819
Livermore, CA 94551-0969
Phone: (505) 284-2691
Fax: (505) 844-0918
E-mail: CJGARAS@sandia.gov

Gauthier, Serge
Centre d'Etudes de Limeil-Valenton
BP 27 Villeneuve St. Georges cedex
94195, FRANCE
E-mail: gauthier@limeil.cea.fr

Gavrilova, E. S.
Russian Federal Nuclear Center-VNIIEF
Mir Avenue, 37, Sarov
Nizhnii Novgorod Region, 607190, Russia
Fax: (831-30) 459-58
E-mail: root@gdd.vniief.ru

George, E.
State University of New York at Stony Brook
P-138A Math Tower
Stony Brook, NY 11794-3600

Gerasimov, Serguei
Russian Federal Nuclear Center, VNIIEF
Mir Avenue, 37, Sarov
Nizhnii Novgorod Region, 607190, Russia
Phone: (7-83130) 45 009
Fax: (7-83130) 45 958
E-mail: root@gdd.vniief.ru

Glebov, V. Yu.
Laboratory for Laser Energetics
University of Rochester
250 East River Road
Rochester, New York 14623-1299
Phone: (716) 275-7454
E-mail: vgle@lle.rochester.edu

Glendinning, Gail
Lawrence Livermore National Laboratory
P.O. Box 808, L-21
Livermore, CA 94551
Phone: (925) 423-3065
Fax: (925) 423-8945
E-mail: glendinning1@llnl.gov

Glimm, James
Department of Applied Mathematics and Statistics
State University of New York at Stony Brook
P-138A Math Tower
Stony Brook, NY 11794-3600
Phone: (631) 632-8355
FAX: (631) 632-8490
E-mail: glimm@ams.sunysb.edu

Goncharov, V. N.
Laboratory for Laser Energetics
University of Rochester
250 East River Road
Rochester, New York 14623-1299
Phone: (716) 275-1017
E-mail: vgon@lle.rochester.edu

Goodwin, Bruce T.
Lawrence Livermore National Laboratory
P.O. Box 808, L-160
Livermore, CA 94551
Phone: (925) 423-7736
Fax: (925) 424-2723
E-mail: goodwin2@llnl.gov

Gottlieb, David I.
Division of Applied Mathematics
Brown University
Providence, RI 02912
Phone: (401) 863-2266
E-mail:: David.Gottlieb@brown.edu

Graham, Mary J.
Lawrence Livermore National Laboratory
P.O. Box 808, L-312
Livermore, CA 94551
Phone: (925) 424-4222
Fax: (925) 422-8920
E-mail: mjgraham@llnl.gov

Greenough, Jeffrey A.
Lawrence Livermore National Laboratory
P.O. Box 808, L-30
Livermore, CA 94551
Phone: (925) 423-3211
Fax: (925) 424-6764
E-mail: greenough1@llnl.gov

Grieves, Brian
Atomic Weapons Establishment
Aldermaston
Reading, Berkshire
RG7 4PR UK
Phone: +44 (0)1734 814111
Fax: +44 (0)1734 815320
E-mail:: brian.grieves@awe.co.uk

Grove, John W.
Los Alamos National Laboratory
P.O. Box 1663, MS D413
Los Alamos, New Mexico, 87545
Phone: (505) 667-0723
Fax: (505) 665-4972
E-mail: jgrove@lanl.gov

Gubkov, E. V.
Russian Federal Nuclear Center-VNIIEF
Mir Avenue, 37, Sarov
Nizhnii Novgorod Region, 607190, Russia
Phone: (831-30) 450 09
Fax: (831-30) 459 58
E-mail: root@gdd.vniief.ru

Gulak, Y.
Department of Mechanical and Aerospace Engineering
Rutgers University
98 Brett Rd.
Piscataway, NJ 08854
Phone: (732) 445-5627
Fax: (732) 445-3124
E-mail: YGULAK@RCI.RUTGERS.EDU

Gupta, S.
Department of Mechanical and Aerospace Engineering
Rutgers University
98 Brett Rd.
Piscataway, NJ 08854
Phone: (732) 445-5627
Fax: (732) 445-3124

Haan, Steven W.
Lawrence Livermore National Laboratory
P.O. Box 808, L-023
Livermore, CA 94551
Phone: (925) 422-4715
Fax: (925) 423-8945
E-mail: haan1@llnl.gov

Haas, Jean Francois
Commissariat à l'Energie Atomique
CEA/DIF/DCRE/SCSE BP 12
Bruyeres le Chatel, 91680
France
Phone: 33-1-69-26-52-94
Fax: 33-1-69-26-70-62
E-mail: jean-francois.haas@cea.fr

Harlow, Francis H.
Los Alamos National Laboratory
P.O. Box 1663, MS B216
Los Alamos, NM 87545
Phone: (505) 667-9090
E-mail: fhharlow@lanl.gov

Hatchett, Stephen P.
Lawrence Livermore National Laboratory
P.O. Box 808, L-016
Livermore, CA 94551
Phone: (925) 422-5916
Fax: (925) 423-5112
E-mail: hatchett1@llnl.gov

Hauer, A.
Los Alamos National Laboratory
P.O. Box 1663
Los Alamos, NM 87545
Phone: (505) 667-5167
Fax: (505) 667-0405
E-mail: hauer@lanl.gov

Hébert, C. H.
Department of Mechanical Engineering
Université de Sherbrooke
Sherbrooke, Quebec J1K 2R1 Canada

Hinkel, Denise
Lawrence Livermore National Laboratory
P.O. Box 808, L-038
Livermore, CA 94551
Phone: (925) 423-2626
Fax: (925) 423-2157
E-mail: hinkel1@llnl.gov

Holder, David
Atomic Weapons Establishment
Building H27, Aldermaston
Reading, Berkshire, RG7 4PR, United Kingdom
Phone: 0118 982 5592
Fax: 0118 982 4816
E-mail:: david.holder@awe.co.uk

Holford, Joanne M.
University of Cambridge
Silver Street
Cambridge , UK CB3 9EW
Phone: +44 1223 337858
Fax: +44 1223 337918
E-mail:: J.M.Holford@DAMTP.CAM.AC.UK

Holmes, Richard L.
Los Alamos National Laboratory
P.O. Box 1663, MS B220
Los Alamos, NM 87545
Phone: (505) 667-3598
Fax: (505) 665-2227
E-mail: holmes@lanl.gov

Hosseini, S. H. R.
Shock Wave Research Center, Institute of Fluid Science
Tohoku University
2-1-1 Katahira, Aoba-ku
Sendai 980-77, Japan
E-mail:: hosseini@rainbow.ifs.tohoku.ac.jp

Houas, Lazhar
I.U.S.T.I. / Umr CNRS 6595
Technopole de Chateau Gombert
5 rue Enrico Fermi
13453 Marseille Cedex 13 France
Phone: 33 (0)4 91 10 69 30
Fax: 33 (0)4 91 10 69 69
E-mail: houas@iusti.univ-mrs.fr

Hsing, Warren W.
Lawrence Livermore National Laboratory
P.O. Box 808, L-21
Livermore, CA 94551
Phone: (925) 423-2849
Fax: (925) 423-8945
E-mail:: hsing@llnl.gov

Hurricane, Omar
Lawrence Livermore National Laboratory
P.O. Box 808, L-22
Livermore, CA 94551
Phone: (925) 424-2701
Fax: (925) 423-0925
E-mail: hurricane1@llnl.gov

Inogamov, Nail
Landau Inst. for Theor. Phys.
Kosygnina St. 2, Moscow
117940, GSP-1
V-334 RUSSIA
Phone: 095 425 8767
FAX: 095 938 2077
E-mail: itf@ips.ac.msk.su

Jacobs, Jeffrey W.
Department of Aerospace and Mechanical Engineering
University of Arizona
Bldg. 16, Room 301
Tucson, AZ 85721
Phone: (602) 621-8459
Fax: (602) 621-8191
E-mail: jacobs@ame.arizona.edu

Jameson, Leland M.
Lawrence Livermore National Laboratory
P.O. Box 808, L-312
Livermore, CA 94551
Phone: (925) 424-6160
E-mail: jameson3@llnl.gov

Jones, Oggden
Lawrence Livermore National Laboratory
P.O. Box 808, L-030
Livermore, CA 94551
Phone: (925) 423-1872
Fax: (925) 423-9969
E-mail:: jones96@llnl.gov

Jourdan, Georges
Universite de Provence
IUSTI-CNRS Umr 139
Centre Saint Jerome -- Case 321
13397 Marseille Cedex 20 France
Phone: 33 (0) 491106930
Fax: 33 (0) 491106969
E-mail: jourdan@iusti-dipha.univ-mrs.fr

Kalantar, Daniel
Lawrence Livermore National Laboratory
P.O. Box 808, L- 472
Livermore, CA 94551
Phone: (925) 422-6147
Fax: (925) 422-8395
E-mail: kalantar1@llnl.gov

Kamm, R. J.
Los Alamos National Laboratory
P.O. Box 1663
Los Alamos NM, 87545
Phone: (505) 667-1918
E-mail:: kammj@lanl.gov

Kane, Jave O.
Lawrence Livermore National Laboratory
P.O. Box 808, L-411
Livermore, CA 94551
Phone: (925) 424-5805
Fax: (925) 423-2463
E-mail:: jave@llnl.gov

Kang, Young-Gwang
Kwangju Institute of Science and Technology
1 Oryong-dong
Kwangju, 500-712, South Korea
Phone: 82-62-970-2310
Fax: 82-62-970-2304
E-mail: ygkang@kjist.ac.kr

Kartoon, Daniela
Department of Physics
Nuclear Research Center Negev
P.O. Box 9001
Beer-Sheva, 84190, Israel
Phone: 972-8-6568845
Fax: 972-8-6567878
E-mail:: danyk@bgumail.bgu.ac.il

Keiter, P.
University of Michigan
Space Research Lab, Rm 1216
2245 Hayward
Ann Arbor, MI 48104

Kerstein, Alan R.
Sandia National Laboratory
P.O. Box 969, MS 9051
Livermore, CA 94551-0969
Phone: (925) 294-2390
Fax: (925) 294-1004
E-mail: kerstein@ca.sandia.gov

Kim, H.
Department of Mechanical and Aerospace Engineering
Rutgers University
98 Brett Rd.
Piscataway, NJ 08854

Klein, Richard I.
Lawrence Livermore National Laboratory
P.O. Box 808, L-023
Livermore, CA 94551
Phone: (925) 422-3548
Fax: (925) 423-0925
E-mail: rklein@llnl.gov

Knauer, J.
Department of Mechanical and Aerospace Engineering
Rutgers University
98 Brett Rd.
Piscataway, NJ 08854

Kobayashi, K.
Osaka University
2-6, Yamada-oka, Suita,
Osaka 565-0871 Japan

Korreck, K. E.
University of Michigan
Space Research Lab, Rm 1216
2245 Hayward
Ann Arbor, MI 48104

Kozelkov, O. E.
Russian Federal Nuclear Center-VNIITF
P.O. Box 245
456770 Snezhinsk, Russia

Kozlov, V. I.
Russian Federal Nuclear Center-VNIIEF
Mir Avenue, 37, Sarov
Nizhnii Novgorod Region, 607190 Russia
Fax: (831-30) 4-57-72
E-mail: otd1_0903@spd.vniief.ru

Ktitorov, Vladimir M.
Russian Federal Nuclear Center-VNIIEF
Mir Avenue, 37, Sarov
Nizhnii Novgorod Region, 607190 Russia
Phone: 831-30 1-36-65
Fax: 831-30 5-45-65
E-mail: mvn_072e@rfnc.nnov.su

Kucherenko, Yuri A.
Russian Federal Nuclear Center-VNIITF
P.O. Box 245
456770 Snezhinsk, Russia
Fax: (351-72) 3 20 77
E-mail: kucherenko@five.ch70.chel.su

Kuhl, Allen L.
Lawrence Livermore National Laboratory
P.O. Box 808, L-30
Livermore, CA 94551
Phone: (925) 422-4777
Fax: (925) 424-6764
E-mail: kuhl2@llnl.gov

Kumar, M.
Department of Physics
Nuclear Research Center Negev
P.O. Box 9001
Beer-Sheva, 84190, Israel

Kushnir, D.
Department of Physics
Nuclear Research Center Negev
P.O. Box 9001
Beer-Sheva, 84190, Israel

Lanier, N. E.
Los Alamos National Laboratory
P.O. Box 1663, MS
Los Alamos NM, 87545
Phone: (505) 665-0236
Fax: (505) 665-3686
E-mail:: nlanier@lanl.gov

Lasinski, Barbara F.
Lawrence Livermore National Laboratory
P.O. Box 808, L-038
Livermore, CA 94551
Phone: (925) 422-5443
Fax: (925) 423-9208
E-mail:: blasinski@llnl.gov

Lassis, A.
Commissariat à l'Energie Atomique
BP 12
Bruyeres le Chatel, 91680, France

Layes, G.
IUSTI
Technopole Chateau-Gombert – 5,
Rue Enrico Fermi
Marseille, 13013 France

Lebedev, Alexander
Russian Federal Nuclear Center-VNIIEF
Mir Avenue, 37, Sarov
Nizhnii Novgorod Region, 607190, Russia
Phone: (831-30) 450 09
Fax: (831-30) 459 58
E-mail: root@gdd.vniief.ru

Lebo, Ivan
Laser Fusion Department
PN Lebedev Physics Institute
Leninsky prospect 53
117294 Russia, Moscow
Phone: 095-132-68-47
Fax: 095-132-11-96
E-mail: lebo@sci.fian.msk.su

Legrand, Michel
Commissariat à l'Energie Atomique
DAM Ile de France
BP12, Bruyeres le Chatel, 91680, France
Phone: 33-1-69-26-57-09
Fax: 33-1-69-26-70-94
E-mail: michel.legrand@cea.fr

Levy, Kedem
Physics Department
Ben Gurion University of the Negev
P.O. B 653, Beer-Sheva 84105, Israel
Phone: 972-8-6568844
Fax: 972-8-6567878
E-Mail: klevy@bgumail.bgu.ac.il

Li, Xiaolin
Department of Applied Mathematics and Statistics
State University of New York at Stony Brook
1-119 Math Tower
Stony Brook, NY 11794-3600
Phone: (631) 632-8353
Fax: (631) 632-8490
E-mail: linli@ams.sunysb.edu

Linn, Rodman R.
Los Alamos National Laboratory
P.O. Box 1663
Los Alamos NM, 87545
Phone: (505) 665-6254
E-mail:: rrl@lanl.gov

Llor, Antoine
Commissariat à l'Energie Atomique
BP 12
Bruyeres le Chatel, 91680, France
Phone: 33 1 69 26 49 38
Fax: 33 1 69 26 70 97
E-mail: antoine.llor@cea.fr

Logvinov, A.
Russian Federal Nuclear Center, VNIIEF
Mir Avenue, 37, Sarov
Nizhnii Novgorod Region, 607190, Russia
E-mail: root@gdd.vniief.ru

Lorenz, Karl T.
Lawrence Livermore National Laboratory
P.O. Box 808, L-472
Livermore, CA 94551
Phone: (925) 424-4200
E-mail: lorenz3@llnl.gov

Louis, Hedley
Lawrence Livermore National Laboratory
P.O. Box 808, L-472
Livermore, CA 94551
Phone: (925) 4242-9937
E-mail: louis1@llnl.gov

Loveridge –Smith, A.
Oxford University
University Offices
Wellington, Oxford, OX1 2JD UK
Phone: +44 1865 270000
Fax: +44 1865 270708

MacNeice, P.
NASA Goddard Space Flight Center
Greenbelt, MD

Magelssen, Glenn R.
Los Alamos National Laboratory
P.O. Box 1663
Los Alamos NM, 87545
Phone: (505) 667-6519
E-mail:: grm@lanl.gov

Magnaudet, J.
Institut de Mécanique des Fluides de Toulouse
31400 Toulouse
Toulouse, France

Marchese, A.
State University of New York at Stony Brook
P-138A Math Tower
Stony Brook, NY 11794-3600

Marinak, Michael M.
Lawrence Livermore National Laboratory
P.O. Box 808, L-023
Livermore, CA 94551
Phone: (925) 423-8458
Fax: (925) 423-9969
E-mail:: marinak1@llnl.gov

Matsuoka, C.
10-13,Dogo-Himata,Matsuyama 790-8577
Japan

Mazilin, I. M.
Krzhizhanovsky Power Engineering Institute
ENIN, Leninsky pr. 19, GSP-1
Moscow, 117927 Russia

McAbee, Thomas L.
Lawrence Livermore National Laboratory
P.O. Box 808, L-170
Livermore, CA 94551
Phone: (925) 422-3398
Fax: (925) 424-2723
E-mail: mcabee@viper.llnl.gov

McCray, R.
University of Colorado, Boulder
Colorado 80309
Phone: (303) 492-1411

McKenty, P. W.
Laboratory for Laser Energetics
University of Rochester
250 East River Road
Rochester, New York 14623-1299

Medvedev, V. M.
Russian Federal Nuclear Center-VNIITF
P.O. Box 245
456770 Snezhinsk, Russia

Meiron, Daniel I.
Department of Applied and Computational Mathematics
California Institute of Technology
MC 217-50
Pasadena, CA 91125
Phone: (626) 395-4563
Fax: (626) 578-0124
E-mail: dim@acm.caltech.edu

Meshkov, Evgeni E.
Russian Federal Nuclear Center-VNIIEF
Mir Avenue, 37, Sarov
Nizhnii Novgorod Region, 607190, Russia
Fax: 831-305-4565
E-mail: root@gdd.vniief.ru

Meyers, M. A.
University of California at San Diego
9500 Gilman Drive
La Jolla, CA 92093-0411

Mikaelian, Karnig O.
Lawrence Livermore National Laboratory
P.O. Box 808, L-97
Livermore, CA 94551
Phone: (925) 422-5449
Fax: (925) 423-7228

Mikhaylov, A. L.
Russian Federal Nuclear Center, VNIIEF
Mir Avenue, 37, Sarov
Nizhnii Novgorod Region, 607190, Russia
E-mail: root@gdd.vniief.ru

Miles, Aaron
Lawrence Livermore National Laboratory
P.O. Box 808, L-12
Livermore, CA 94551
Phone: (925) 423-8131
Fax: (925) 422-8920
E-Mail: miles15@llnl.gov

Miller, Paul L.
Lawrence Livermore National Laboratory
P.O. Box 808, L-22
Livermore, CA 94551
Phone: (925) 423-6455
Fax: (925) 423-0925
E-mail: pmiller@llnl.gov

Minich, Roger
Lawrence Livermore National Laboratory
P. O. Box 808, L-097
Livermore, CA 94551
Phone: (925) 422-4552
Fax: (925) 422-0779
E-mail:: minich1@llnl.gov

Miyanaga, N.
Osaka University
2-6, Yamada-oka, Suita,
Osaka 565-0871 Japan

Mizuta, A.
Osaka University
2-6, Yamada-oka, Suita,
Osaka 565-0871 Japan

Montlaurent, P.
Commissariat à l'Energie Atomique
BP 12, 91680
Bruyeres-le-Chatel, France

Moreno, Juan
Lawrence Livermore National Laboratory
P. O. Box 808, L-031
Livermore, CA 94551
Phone: (925) 423-4170
Fax: (925) 424-6764
E-mail:: jcmoreno@llnl.gov

Morris, A. P.
Atomic Weapons Establishment
Aldermaston
Reading
Berkshire RG7 4PR England

Munro, David H.
Lawrence Livermore National Laboratory
P. O. Box 808, L-023
Livermore, CA 94551
Phone: (925) 422-5428
Fax: (925) 423-9969
E-mail:: dmunro@llnl.gov

Murphy, T. J.
Los Alamos National Laboratory
P.O. Box 1663
Los Alamos NM, 87545
Phone: (505) 665-5697
Fax: (505) 996-4366
E-mail:: tjmurphy@lanl.gov

Murzakov, V. D.
Russian Federal Nuclear Center-VNIITF
P.O. Box 245
456770 Snezhinsk, Russia

Nagatomo, H.
Osaka University
2-6, Yamada-oka, Suita,
Osaka 565-0871 Japan

Nakai, M.
2-6, Yamada-oka, Suita,
Osaka 565-0871 Japan

Nash, Jeffrey K.
Lawrence Livermore National Laboratory
P. O. Box 808, L-15
Livermore, CA 94551
Phone: (925) 422-7255
E-mail:: jknash@llnl.gov

Neuvazhayev, Vladimir
Russian Federal Nuclear Center-VNIITF
P.O. Box 245
456770 Snezhinsk, Russia
Phone: 351-72-55675
Fax: 351-72-32077
E-mail: nio3@ch70.chel.su

Nevmerzhitsky, Nikolay
Russian Federal Nuclear Center, VNIIEF
Mir Avenue, 37, Sarov
Nizhnii Novgorod Region, 607190, Russia
Phone: (831-30) 450 09
Fax: (831-30) 459 58
E-mail: root@gdd.vniief.ru

Niederhaus, Charles E.
NASA Glenn Research Center
21000 Brookpark Rd., MS-77-5
Cleveland, OH 44135
Phone: (216) 433-5461
Fax: (216) 433-8050
E-mail:: charles.niederhaus@grc.nasa.gov

Nikishin, Vladislav
Institute for Mathematical Modeling (IMM)
Russian Academy of Science
Miusskaya 4a, 125047, Moscow, Russia
Phone: 007(095) 250-79-35
Fax: 007(095) 972-07-23
E-mail: nikishin\#4@imamod.msk.su

Nikulin, A.
Russian Federal Nuclear Center-VNIIEF
Mir Avenue, 37, Sarov
Nizhnii Novgorod Region, 607190 Russia
E-mail:: root@gdd.vniief.ru

Nishihara, Katsunobu
Institute of Laser Engineering
Osaka University
2-6, Yamada-oka, Suita,
Osaka 565-0871 Japan
Phone: 81-6-6879-8725
Fax: 81-6-6877-4799
E-mail: nishihara@ile.osaka-u.ac.jp

Nishikino, M.
2-6, Yamada-oka, Suita,
Osaka 565-0871 Japan

Nizovtsev, P. N.
Russian Federal Nuclear Center-VNIIEF
Mir Avenue, 37, Sarov
Nizhnii Novgorod Region, 607190 Russia
E-mail:: root@gdd.vniief.ru

Nomoto, K.
University of Tokyo
7-3-1 Hongo, Bunkyo-ku, Tokyo 113-8654, Japan
Phone: +81-3-3812-2111

Oakley, J. G.
Department of Engineering. Physics
University of Wisconsin at Madison
1500 Engineering Drive
Madison, WI 53706

Olson, K.
NASA Goddard Space Flight Center
Greenbelt, MD

Oparin, A. M.
Institute for Computer Aided Design,
Vtoraya Brestskaya ul., 19/18, 123056
Moscow, Russia
Phone: (095) 250-96-30
Fax: (095) 250-89-28
E-mail: oparin@cpd.landau.ac.ru

Oron, Dan
Department of Physics
Nuclear Research Center - Negev
P.O. Box 9001
Beer-Sheva, 84190, Israel
Phone: 972-7-6568736
Fax: 972-7-6567878
E-mail: danor@bgumail.bgu.ac.il

Paisley, Dennis
Los Alamos National Laboratory
P.O. Box 1663
Los Alamos NM, 87545
Phone: (505) 667-7837
E-mail:: dxp@lanl.gov

Pantano, C.
University of California at San Diego
9500 Gilman Drive
La Jolla, CA 92093-0411

Parker, Kenneth W.
Atomic Weapons Establishment
Aldermaston
Reading
Berkshire RG7 4PR England
Phone: +44 118 9827578
Fax: +44 118 9824844
E-mail:: Kenneth.W.Parker@awe.co.uk

Parshukov, I. E.
Russian Federal Nuclear Center-VNIITF
P.O. Box 245
456770 Snezhinsk, Russia

Peng, O.
Rutgers University
98 Brett Rd.
Piscataway, NJ 08854

Perry, Theodore S.
Lawrence Livermore National Laboratory
P.O. Box 808, L-23
Livermore, CA 94551
Phone: (925) 423-2065
Fax: (925) 424-3294
E-mail: tedperry@llnl.gov

Peyser, Thomas A.
Lawrence Livermore National Laboratory
P.O. Box 808, L-23
Livermore, CA 94551
Phone: (925) 423-6454
Fax: (925) 423-0925
E-mail: tpeyser@llnl.gov

Piskunov, Yu. A.
Russian Federal Nuclear Center-VNIITF
P.O. Box 245
456770 Snezhinsk, Russia

Polionov, Arkadi
Russian Federal Nuclear Center
Institute of Technical Physics
Chelyabinsk 70
P.O. Box 245, Russia
Phone: 351-722-3977
Fax: 351-723-2077
E-mail: nio3@ch70.chel.su

Pollaine, Steven
Lawrence Livermore National Laboratory
P.O. Box 808, L-30
Livermore, CA 94551
Phone: (925) 422-5950
Fax: (925) 423-9208
E-mail: pollaine@llnl.gov

Popov, V. N.
Russian Federal Nuclear Center-VNIITF
P.O. Box 245
456770 Snezhinsk, Russia

Pound, M.
University of Maryland
College Park, MD 20742
Phone (301) 405-1000

Prestridge, Katherine P.
Los Alamos National Laboratory
P.O. Box 1663, MS P940
Los Alamos NM, 87545
Phone: (505) 667-8861
Fax: (505) 665-3359
E-mail: kpp@lanl.gov

Pullin, Dale I.
Department of Aeronautics
California Institute of Technology
1200 East California Boulevard, MS 105-50
Pasadena, CA 91125
Phone: (626) 395-6081
Fax: (626) 441-2222
E-mail:: dale@galcit.caltech.edu

Pylaev, Anatoly
Russian Federal Nuclear Center-VNIITF
P.O. Box 245
456770 Snezhinsk, Chelyabinsk region, Russia
Fax: (351-72) 3 20 77
E-mail: kucherenko@five.ch70.chel.su

Radha, P. B.
Laboratory for Laser Energetics
University of Rochester
Rochester, NY 14623-1299

Raevskii, Viktor
All Russian Sci & Research Institute of Experimental Physics
607200, Arzamas - 16
Nizhny Novgorod Region, Russia
Fax: 831-305-4565
E-mail: otd3_2305@rfnc.nnov.su

Rampaprabhu, P.
Department of Mechanical Engineering
Texas A & M University
MS 3123
College Station, TX 77843-3123

Raviard, P. A.
Commissariat à l'Energie Atomique
BP 12, 91680
Bruyeres-le-Chatel, France

Rayer, C.
Commissariat à l'Energie Atomique
BP 12, 91680
Bruyeres-le-Chatel, France

Razin, A. N.
Russian Federal Nuclear Center-VNIIEF
Mir Avenue, 37, Sarov
Nizhnii Novgorod Region, 607190
E-mail:: root@gdd.vniief.ru

Rebrov, S. V.
Russian Federal Nuclear Center-VNIIEF
Mir Avenue, 37, Sarov
Nizhnii Novgorod Region, 607190
E-mail:: root@gdd.vniief.ru

Remington, Bruce A.
Lawrence Livermore National Laboratory
P.O. Box 808, L-21
Livermore, CA 94551
Phone: (925) 423-2712
Fax: (925) 422-8395
E-mail: remington2@llnl.gov

Renaud, Francois
Commissariat à l'Energie Atomique
CEA/DRIF/DCSA/SET
BP 12, 91680
Bruyeres-le-Chatel, France
Phone: 33 1 69 26 40 81
Fax: 33 1 69 26 71 02

Ricker, P.
University of Chicago
933 East 56th Street
Chicago, IL 60637

Rider, William J.
Los Alamos National Laboratory
P.O. Box 1663, MS D413
Los Alamos NM, 87545
Phone: (505) 665-4162
Fax: (505) 667-3726
E-mail: wjr@lanl.gov

Rightley, Paul M.
Los Alamos National Laboratory
P.O. Box 1663, MS P940
Los Alamos NM, 87545
Phone: (505) 667-0460
Fax: (505) 665-3359
E-mail: pright@lanl.gov

Rikanati, Avi
Physics Department
Nuclear Research Center - Negev
P.O. Box 9001
Beer-Sheva, 84190, Israel
Phone: 972-7-6568736
Fax: 972-7-6567878
E-mail: rkavi@bgumail.bgu.ac.il

Robey, Harry F.
Lawrence Livermore National Laboratory
P.O. Box 808, L-21
Livermore, CA 94551
Phone: (925) 423-5669
FAX: (925) 422-3358
E-mail: robey1@llnl.gov

Robinson, A.
Sandia National Laboratory
P.O. Box 969, MS 9051
Livermore, CA 94551-0969

Rosner, Robert L.
Enrico Fermi Institute and Laboratory for Astrophysics
and Space Research
University of Chicago
933 East 56th Street
Chicago, IL 60637
Phone: (773) 702-0560
Fax: (773) 704-3230
E-mail:: rosner@uchicago.edu

Rothman, S.
Atomic Weapons Establishment
Aldermaston
Reading
Berkshire RG7 4PR England

Roualdes, P.
Centre d'Etudes de Gramat
Gramat. France

Rozanov, I. A.
Lebedev Physical Institute
Leninsky Pr. 53
117924, Moscow, Russia
E-mail:: Rozanov@sci.lebedev.ru

Rozanov, Vladislav
Lebedev Physical Institute
Leninsky Pr. 53
117924, Moscow, Russia
Phone: (095)-132-68-47
Fax: (095)-132 -11-96
E-mail: lebo@neur.lpi.msk.su

Ryutov, Dimitri D.
Lawrence Livermore National Laboratory
P.O. Box 808, L-630
Livermore, CA 94551
Phone: (925) 422-9832
E-mail: ryutov1@llnl.gov

Sadot, Oren
Department of Physics
Nuclear Research Center - Negev
P.O.B. 9001, Beer-Sheva 84109, Israel
Phone: 972-7-6567278
Fax: 972-7-6567878
E-mail: sorens@bgumail.bgu.ac.il

Sakaiya, T.
Institute of Laser Engineering
Osaka University
2-6 Yamadaoka Suita
Osaka, 565 Japan

Samtaney, Ravi
Department of Aeronautics
California Institute of Technology
MS 205-45
Pasadena, CA 91125
Phone: (626) 395-8030
Fax: (626) 449-2677
E-mail: ravi@ama.caltech.edu

Sapozhnikov, I. V.
Russian Federal Nuclear Center-VNIIEF
Mir Avenue, 37, Sarov
Nizhnii Novgorod Region, 607190, Russia

Sarid, Eli
Physics Department
Nuclear Research Center - Negev
P.O. Box 9001
Beer-Sheva, 84190, Israel
Phone: 972-7-6568736
Fax: 972-7-6567878
E-mail: fnsarid@weizmann.weizmann.ac.il

Sarkar, Sutanu
Department of Mechanical and Aerospace Engineering
University of California at San Diego
9500 Gilman Drive
La Jolla, CA 92093-0411
Phone: (858) 534-8243
Fax: (858) 534-7599
E-mail:: sarkar@mae.ucsd.edu

Schilling, Oleg
Lawrence Livermore National Laboratory
P.O. Box 808, L-22
Livermore, CA 94551
Phone: (925) 423-6879
Fax: (925) 423-0925
E-mail: schilling1@llnl.gov

Schurtz, G.
Commissariat à l'Energie Atomique
CEA/DRIF/DCSA/SET
BP12, 91680 Bruyeres-le-Chatel, France

Schwaederlè, Laurent
IUSTI
Technopole Chateau-Gombert – 5,
Rue Enrico Fermi
Marseille, 13013 France
Phone: 04 91 10 69 35
Fax: 04 91 10 69 69
E-Mail: schwaed@iusti.univ-mrs.fr

Sharp, David H.
Los Alamos National Laboratory
P.O. Box 1663, MS B285
Los Alamos, NM 87545
Phone: (505) 667-5266
Fax: (505) 665-3003
E-mail: dhs@lanl.gov

Shestachenko, Oleg
Russian Federal Nuclear Center-VNIITF
P.O. Box 245
456770 Snezhinsk, Chelyabinsk region, Russia
Fax: (351-72) 3 20 77
E-mail: kucherenko@five.ch70.chel.su

Shestakov, Alex
Lawrence Livermore National Laboratory
P.O. Box 808, L-38
Livermore, CA 94551
Phone: (925) 422-4213
Fax: (925) 423-9208
E-mail: shestakov1@llnl.gov

Shigemori, K.
Institute of Laser Engineering
Osaka University
2-6 Yamadaoka Suita
Osaka, 565 Japan

Shiraga, H.
Institute of Laser Engineering
Osaka University
2-6 Yamadaoka Suita
Osaka, 565 Japan

Shu, Chi-Wang
Division of Applied Mathematics
Brown University
Providence, RI 02912
Phone: (401) 863-2549
E-mail:: Chi-Wang_Shu@brown.edu

Shvarts, Dov
Department of Physics
Nuclear Research Center - Negev
P.O. Box 9001
Beer-Sheva, 84190, Israel
Phone: 972-7-6567500
Fax: 972-7-6567665
E-mail: shvarts@bgumail.bgu.ac.il

Silvani, X.
Institut de Mécanique des Fluides de Toulouse
31400 Toulouse
Toulouse, France

Sinitsina, S. N.
Russian Federal Nuclear Center-VNIIEF
Mir Avenue, 37, Sarov
Nizhnii Novgorod Region, 607190, Russia
E-mail:: root@gdd.vniief.ru

Sinkova, O. G.
Russian Federal Nuclear Center-VNIIEF
Mir Avenue, 37, Sarov
Nizhnii Novgorod Region, 607190, Russia
E-mail:: root@gdd.vniief.ru

Skupsky, S.
Laboratory for Laser Energetics
University of Rochester
Rochester, NY 14623-1299

Smalyuk, V. A.
Laboratory for Laser Energetics
University of Rochester
Rochester, NY 14623-1299

Smith, Alan V.
Building H27
Atomic Weapons Establishment
Aldermaston
Reading
Berkshire RG7 4PR England
Phone: 01189-825592
Fax: 01734-815320
E-mail: alan.smith@awe.co.uk

Sotskov, E.A.
Russian Federal Nuclear Center-VNIIEF
Mir Avenue, 37, Sarov
Nizhnii Novgorod Region, 607190, Russia
Fax: (831-30) 459 58
E-mail: root@gdd.vniief.ru

Souffland, Denis
Commissariat à l'Energie Atomique
CEA/DRIF/DCSA/SET
BP12, 91680 Bruyeres-le-Chatel, France
Phone: 33 1 69 26 59 77
Fax: 33 1 69 26 70 94
E-mail: soufflan@bruyeres.cea.fr

Srebro, Yair
Department of Physics
Ben-Gurion University of the Negev
Beer Sheva, 84105, Israel
Phone: 972-8-6568416
Fax: 972-8-656-7878
E-mail:: sibo@bgumail.bgu.ac.il

Stadnik, A. L.
Russian Federal Nuclear Center-VNIIEF
Mir Avenue, 37, Sarov
Nizhnii Novgorod Region, 607190, Russia
E-mail: root@gdd.vniief.ru

Statsenko, V. P.
Russian Federal Nuclear Center-VNIIEF
Mir Avenue, 37, Sarov
Nizhnii Novgorod Region, 607190, Russia
E-mail: root@gdd.vniief.ru

Steinkamp, Michael J.
Los Alamos National Laboratory
P.O. Box 1663, MS D413
Los Alamos, NM 87545
Phone: (505) 667-5837
Fax: (505) 667-3726
E-mail: steinmj@lanl.gov

Stoeckl, C.
Laboratory for Laser Energetics
University of Rochester
Rochester, NY 14623-1299

Stone, J.
University of Maryland
College Park, MD 20742
Phone (301) 405-1000

Sunahara, A.
Institute of Laser Engineering
Osaka University
2-6 Yamadaoka Suita
Osaka, 565 Japan
Phone: 81-6-879-8742
Fax: 81-6-877-4799
E-mail: suna@ile.osaka-u.ac.jp

Suter, Laurance
Lawrence Livermore National Laboratory
P. O. Box 808, L-031
Livermore, CA 94551
Phone: (925) 422-5423
Fax: (925) 423-9969
E-mail:: suter1@llnl.gov

Sviridov, E. V.
Russian Federal Nuclear Center-VNIITF
P.O. Box 245
456770 Snezhinsk, Russia

Takabe, Hideaki
Institute of Laser Engineering
Osaka University
Yamada-oka 2-6, Suita
Osaka 565, Japan
Phone: 81-6-877-5111 Ext. 6553
Fax: 81-6-877-4779
E-mail: takabe@ile.osaka-u.ac.jp

Takayama, Kazuyoshi
Shock Wave Research Center
Institute of Fluid Science
Tohoku University
2-1-1 Katahira, Aoba-ku
Sendai 980-77, Japan
Phone: 81-22-263-0895
Fax: 81-22-227-7390
E-mail: paul@bellanca.ifs.tohoku.ac.jp

Tamari, Y.
Institute of Laser Engineering (ILE)
Osaka University
2-6 Yamadoaka
Suita, Osaka 565-0871, Japan

Teyssier, R.
Commissariat a 'Energie Atomique
BP 12, 91680
Bruyeres-le-Chatel, France

Timmes, F.
University of Chicago
933 East 56th Street
Chicago, IL 60637

Tishkin, Vladimir
Institute for Mathematical Modeling
Russian Academy of Science
Miusskaya 4a
125047, Moscow, Russia
Phone: 007(095) 250-79-35
Fax: 007(095) 972-07-23
E-mail: tishkin@imamod.msk.su

Titov, S. N.
Krzhizhanovsky Power Engineering Institute
ENIN, Leninsky pr. 19, GSP-1
Moscow, 117927 Russia

Tomkins, Christopher
Los Alamos National Laboratory
P.O. Box 1663, MS 0454
Los Alamos, NM 87545
Phone: (505) 665-6228
Fax: (505) 665-4507
E-mail:: ctomkins@lanl.gov

Toqué, Nathalie
Universite de Montreal
#1, 6685 Saint Denis
Montreal, Canada H-85-851
Phone: 514-276-9014
E-mail:: Toque@astro.umontreal.ca

Tricottet, Matthieu
Commissariat à l'Energie Atomique
BP 12, 91680
Bruyeres-le-Chatel, France
E-mail:: Matthieu.Tricottet@cea.fr

Tufo, H.
University of Chicago
933 East 56th Street
Chicago, IL 60637

Turano, Edward J.
Lawrence Livermore National Laboratory
P.O. Box 808, L-15
Livermore, CA 94551
Phone: (925) 424-3508
E-mail:: turano1@llnl.gov

Turner, N.
University of Maryland
College Park, MD 20742
Phone (301) 405-1000

Tyaktev, A. A.
Russian Federal Nuclear Center-VNIITF
P.O. Box 245
456770 Snezhinsk, Russia

Uchayev, A. Ya.
Russian Federal Nuclear Center, VNIIEF
Mir Avenue, 37, Sarov
Nizhnii Novgorod Region, 607190, Russia

Vandenboomgaerde, Marc
Commissariat à l'Energie Atomique
BP 12, 91680
Bruyeres-le-Chatel, France
Phone: 33 01 69 26 66 68
Fax: 33 01 69 26 70 94
E-mail: marc.vandenboomgaerde@bruyeres.cea.fr

Verdon, Charles P.
Lawrence Livermore National Laboratory
P.O. Box 808, L-30
Livermore, CA 94551
Phone: (925) 423-4449
Fax: (925) 423-9969
E-mail:: verdon1@llnl.gov

Vlasov, Yu.
Russian Federal Nuclear Center, VNIIEF
Mir Avenue, 37, Sarov
Nizhnii Novgorod Region, 607190, Russia

Voelkl, Tobias
Department of Applied and Computational Mathematics
California Institute of Technology
M/C 217-50
Pasadena, CA 91125
Phone: (626) 395-8534
E-mail: tobias@its.caltech.edu

Vold, Erik L.
Los Alamos National Laboratory
P.O. Box 1663, MS D413
Los Alamos, NM 87545
Phone: (505) 665-5646
Fax: (505) 667-3726
E-mail: elv@lanl.gov

Volkov, V. I.
Russian Federal Nuclear Center-VNIITF
P.O. Box 245 456770
Snezhinsk, Chelyabinsk Region, Russia
E-mail: v.a.gordeychuk@vniitf.ru

Vorobieff, Peter V.
Department of Mechanical Engineering
University of New Mexico
ME Bldg. Rm. 424
Albuquerque, NM 87131
Phone: (505) 277-8347
Fax: (505) 277-1571
E-mail: kalmoth@me.unm.edu

Ward, David J.
Lawrence Livermore National Laboratory
P.O. Box 808, L-30
Livermore, CA 94551
Phone: (925) 423-3211
Fax: (925) 424-6764
E-mail: djw@llnl.gov

Ward, Richard A.
Lawrence Livermore National Laboratory
P.O. Box 808, L-13
Livermore, CA 94551
Phone: (925) 423-2679
Fax: (925) 422-4643
E-mail: raward@llnl.gov

Wark, J. S.
Oxford University
University Offices
Wellington, Oxford, OX1 2JD UK
Phone: +44 1865 270000
Fax: +44 1865 270708

Weber, Stephen V.
Lawrence Livermore National Laboratory
P.O. Box 808, L-16
Livermore, CA 94551
Phone: (925) 422-5433
Fax: (925) 423-9208
E-mail: svweber@llnl.gov

Wiley, Larry G.
Lawrence Livermore National Laboratory
P.O. Box 808, L-97
Livermore, CA 94551
Phone: (925) 423-2461
Fax: (925) 422-0779
E-mail: wiley1@llnl.gov

Wilson, P. N.
Department of Mechanical Engineering
Texas A & M University
MS 3123
College Station, TX 77843-3123

Wolfer, Wilhelm G.
Lawrence Livermore National Laboratory
P.O. Box 808, L-97
Livermore, CA 94551
Phone: (925) 423-1501
Fax: (925) 423-7040
E-mail:: wolfer1@llnl.gov

Wouchuk, Juan G.
E.T.S.I. Industriales
Universidad Castilla-La Mancha
Campus Universitario s/n
13071 Ciudad Real, Spain
Phone: (34) 926-29-53-00 x3826
Fax: (34) 926-29-53-61
E-mail: gwouchuk@ind-cr.uclm.es

Wunsch, Scott E.
Sandia National Laboratory
P.O. Box 969, MS 9051
Livermore, CA 94551-0969
Phone: (925) 294-4621
Fax: (925) 294-2595
E-mail: sewunsch@sandia.gov

Xu, Z.
State University of New York at Stony Brook
P-138A Math Tower
Stony Brook, NY 11794-3600

Yamada, Shoichi
Institute of Laser Engineering (ILE)
Osaka University
2-6 Yamadoaka
Suita, Osaka 565-0871, Japan
Phone: 81-6-6879-8747
Fax: 81-6-6879-8747
E-mail: syamada@ile.osaka-u.ac.jp

Yanilkin, Yury
Russian Federal Nuclear Center-VNIIEF
Mir Avenue, 37, Sarov
Nizhnii Novgorod Region, 607190, Russia
Phone: (831-30) 111 90
Fax: (831-30) 546 65
E-mail: yan@md08.vniief.ru

Yosef-Hai, Arnon
Department of Physics
Nuclear Research Center-Negev
P.O.B. 9001 Beer-Sheva, 84190, Israel
Phone: 972-8-6568913
Fax: 972-8-6567878
E-mail: ajoseph@bgumail.bgu.ac.il

Young, Y.-N.
University of Chicago
933 East 56th Street
Chicago, IL 60637

Youngs, David L.
Atomic Weapons Establishment
Building E3, AWE(A)
Reading, Berkshire
RG7 4PR, England
Phone: 0118 9826766
Fax: 0118 9815320
E-mail: dyoungs@awe.co.uk

Zabusky, Norman J.
Department of Mechanical and Aerospace Engineering
Rutgers University
98 Brett Rd.
Piscataway, NJ 08854
Phone: (732) 445-5869
Fax: (732) 445-3124
E-mail: nzabusky@caip.rutgers.edu

Zaytsev, Sergey G.
Krzhizhanovsky Power Engineering Institute
ENIN, Leninsky pr. 19, GSP-1
Moscow, 117927 Russia
Phone: (7-095) 955-31-07
Fax: (7-095) 954-42-50
E-mail: S.G.Zaytsev@mtu-net.ru

Zhakhovskii, V.
Institute of Laser Engineering
Osaka University
Suita, Osaka 565 Japan

Zhang, S.
Department of Mechanical and Aerospace Engineering
Rutgers University
98 Brett Rd.
Piscataway, NJ 08854

Zhang, Y.
State University of New York at Stony Brook
P-138A Math Tower
Stony Brook, NY 11794-3600

Zhmailo, Vadim A.
Russian Federal Nuclear Center-VNIIEF
Mir Avenue, 37, Sarov
Nizhnii Novgorod Region, 607190, Russia
Fax: 83130 54565
E-mail: rvg_092C@rfnc.nnov.su

Zhou, Ye K.
Lawrence Livermore National Laboratory
P.O. Box 808, L-23
Livermore, CA 94551
Phone: (925) 424-3624
E-mail:: zhou3@llnl.gov

Zingdale, N. V.
University of Chicago
933 East 56th Street
Chicago, IL 60637

Zmitrenko, Nikolay
Institute for Mathematical Modeling
Russian Academy of Science
Miusskaya 4a, 125047, Moscow, Russia
Phone: 007(095) 250-79-16
Fax: 007(095) 972-07-23
E-mail: nickzmit\#9@imamod.msk.su

Zoldi, Cindy A.
Los Alamos National Laboratory
P.O. Box 1663, MS B220
Los Alamos, NM 87544
Phone: (505) 667-6455
Fax: (505) 665-2227
E-mail: czoldi@lanl.gov

Zvorykin, V. D.
PN Lebedev Physics Institute
Leninsky prospect 53
117294 Russia, Moscow

Author Index

Abarzhi, S. I. ……..103, 104, 105
Abe, M. ……..73
Afeyan, B. B. ……..138
Allen, A. M. ……..25, 35
Alon, U. ……115, 123
Anderson, M. H. ……..33, 87
Andrews, M. J. ……..38, 59, 131, 138
Anisimov, V. I. ……...54
Anuchin, M. G. ……....55
Arazi, L. ……..115
Ardashova, R. I. ……....7, 8
Arnett, D. ……....15, 71
Ashurst, Wm. T. ……...56
Azechi, H. ……51
Bailly, P. ……..106
Baishev, A. I. ……..34, 44
Balabin, S. I. ……..7, 8, 26
Barnes, C. W. ……...9, 10, 76
Barton, C. ……....18, 45
Batha, S. H. ……..9, 10, 76
Belak, J. ……..25, 35
Belomestnih, A. V. ……..37
Ben-Dor, G. ……..30, 41, 133
Benjamin, R. F. ……..36, 46, 94
Biello, J. ……...59
Bliznetsov, M. ……11, 12
Boehly, T.R. ……....35, 39
Bonazza, R. ……..33, 87
Bouquet, S. ……..49, 113, 114, 128
Braun, D. G. ……..17
Breidenthal, R. E. ……..107
Brouillette, M. ……..13
Buckingham, A. C. ……..40, 135
Budil, K. S. ……..47, 58, 64
Cabot, W. H. ……...57, 97
Calder, A. ……..15, 59
Chebotareva, E. I. ……..49
Cheng, B. ……...108
Cherfils, C. ……..130
Clark, T. ……..109
Colvin, J. D. ……25, 31, 35, 110
Cook, A. W. ……..57, 100, 127
Dalziel, S. B. ……..19, 111
Dannenberg, K. ……..15
Darlington, R. M. ……58
Delettrez, J. A. ……62
Demiris, A. ……...47
Dem'yanov, A. Yu. ……..122

Dimits, A. ……59, 99
Dimonte, G. ……59, 88
Dimotakis, P. E. ……100
Dittrich, T. ……70
Don, W.-S. ……98
Drake, R. P. ……14, 15, 40
Drennov, O. B. ……16
Dudin, V. D. ……11
Dulov, A. V. ……8
Dunne, A. M. ……9, 10, 76
Dursi, L. ……59
Dutta, S. ……60
Edwards, M. J. ……17, 31, 35, 34, 101
Elbaz, Y. ……30, 61, 83, 112
Eliason, D. E. ……97
Epstein, J. A. ……62
Ferguson, R. E. ……136
Fryxell, B. ……15, 59
Fujioka, S. ……51
Fukuda, Y. ……120
Galmiche, D. ……130
Garasi, C. ……59
Gauthier, S. ……130
Gavrilova, E. S. ……63
George, E. ……60
Gerasimov, S. ……11
Glebov, V. Yu. ……62
Glendinning, S. G. ……17, 52, 71, 101
Glimm, J. ……15, 60, 108
Goncharov, V. N. ……62
Gottlieb, D. ……98
Graham, M. J. ……64
Greenough, J. A. ……39, 48, 57, 65
Grieves, B. ……66
Grove, J. ……15, 60, 64, 67
Gubkov, E. V. ……63, 68
Gulak, Y. ……69
Gupta, S. ……69
Haan, S. W. ……70
Haas, J.-F. ……2, 27, 42, 49
Harlow, F. ……109, 118, 131
Hatchett, S. ……70
Hauer, A. ……35
Hérbert, C. H. ……13
Hinkel, D. ……70
Holder, D. A. ……18, 45
Holford, J. M. ……19
Hosseini, S. H. R. ……20, 21
Houas, L. ……11, 22, 29, 42
Hsing, W. W. ……17

Hurricane, O. A. ……15
Inogamov, N. A. ……113, 114, 122
Jacobs, J. W. ……24, 32
Jameson, L. ……98
Jones, O. ……70
Jourdan, G. ……11, 22, 29, 42
Kalantar, D. H. ……25, 31, 35
Kamm, R. J. ……65, 79
Kane, J. O. ……15, 39, 71
Kang, Y.-G. ……93
Kartoon, D. ……115, 133
Keiter, P. ……15, 40
Kerstein, A. R. ……56
Kim, H. ……93
Klein, R. ……39, 48
Knauer, J. ……15
Kobayashi, K. ……84
Korreck, K. E. ……15
Kozelkov, O. E. ……7, 8
Kozlov, V. I. ……95, 96
Krivets, V. V. ……24, 49
Ktitorov, V. M. ……116, 117
Kucherenko, Yu. A. ……7, 8, 26, 34, 37, 44
Kuhl, A. L. ……136
Kumar, M. ……25
Kushnir, D. ……83
Lanier, N. E. ……9, 10, 76
Lasinski, B. F. ……17
Lassis, A. ……27
Layes, G. ……29
Lebedev, A. ……50
Lebo, I. G. ……72
LeGrand, M. ……81, 110
Levy, K. ……30
Li, X. ……60
Linn, R. R. ……118
Llor, A. ……91, 106, 119
Logvinov, A. ……11
Lorenz, K. T. ……25, 31, 35
Louis, H. ……17, 47
Loveridge-Smith, A. ……25, 35
MacNeice, P. ……59
Magelssen, G. R. ……9, 10, 76
Magnaudet, J. ……91
Marchese, A. ……60
Marinak, M. M. ……70, 88
Matsuoka, C. ……120
Mazilin, I. M. ……49
McCray, R. ……15
McKenty, P. W. ……62

Medvedev, V. M. ……34, 44
Meshkov, E. ……11, 12, 22
Meyers, M. A. ……25, 35
Mikaelian, K. O. ……25, 35, 121
Mikhaylov, A. L. ……16
Miles, A. ……101
Miller, P. L. ……47
Minich, R. ……35
Miyanaga, N. ……51
Mizuta, A. ……84
Montlaurent, P. ……27
Moreno, J. ……17
Morris, A. P. ……45
Munro, D. ……70
Murphy, T. J. ……9, 10, 76
Murzakov, V. D. ……7, 37
Nagatomo, H. ……51
Nakai, M. ……51
Nash, J. ……71
Neuvazhayev, V. E. ……55
Nevmerzhitzky, N. ……12
Niederhaus, C. E. ……32
Nikishin, V. V. ……49
Nikulin, A. ……12
Nishihara, K. ……73, 93, 120
Nishikino, M. ……51
Nizovtsev, P. N. …… 16, 50
Nomoto, K. ……84
Oakley, J. G. ……33, 87
Olson, K. ……59
Oparin, A. M. ……113, 114, 122
Oron, D. ……30, 41, 61, 115, 124, 133
Paisley, D. ……35
Pantano, C. ……74
Parker, K. W. ……9, 10, 76
Parshukov, I. E. ……55
Peng, G. ……77
Perry, T. ……15, 39, 48
Peyser, T. A. ……17, 47
Piskunov, Yu. A. ……34, 44
Polionov, A. V. ……54
Pollaine, S. ……25, 35, 70
Popov, V. N. ……37
Pound, M. ……71
Prestridge, K. ……36, 46, 94
Pullin, D. I. ……80
Pylaev, A. P. ……7, 26, 37
Radha, P. B. ……62
Raevskii, V.A. ……16, 50, 78
Ramaprabhu, P. ……38, 59, 138

Raviard, P. A. ……..130
Rayer, C. ……..27
Razin, A. N. ……...95, 96
Rebrov, S. V. ……89
Remington, B. A. ……15, 17, 25, 31, 35, 40, 47, 64, 71, 110, 125
Renaud, F. ……82
Ricker, P. ……..59
Rider, W. J. ……65, 79
Rightley, P. M. ……36, 46, 94
Rikanati, A. ……41, 61, 115, 123, 124
Robey, H. A. ……15, 17, 39, 40, 48, 52, 135
Robinson, A. ……59
Romanov, I. A. ……8
Rosner, R. ……15, 59
Rothman, S. ……9, 10, 76
Roualdes, P. ……29
Ryutov, D. D. ……15, 71, 125
Sadot, O. ……30, 41, 112, 124, 133
Sakaiya, T. ……51
Samtaney, R. ……69, 80
Sapozhnikov, I. V. ……95
Sarid, E. ……133
Sarkar, S. ……74
Schilling, O. ……126, 127
Schurtz, G. ……110
Schwaederlé, L. ……22, 42
Scott, J. M. ……9, 10, 76
Selchenkova, N. I. ……89
Senkovsky, E. ……12
Seytor, P. ……81
Sharp, D. H. ……60, 108
Shestachenko, O. E. ……26, 34, 44
Shigemori, K. ……51
Shiraga, H. ……51
Shu, C.-W. ……98
Shvarts, D. ……5, 30, 41, 61, 83, 112, 115, 123, 124, 133
Silvani, X. ……91
Sinitsina, S. N. ……78
Sinkova, O. G. ……89
Skupsky, S. ……62
Smalyuk, V. A. ……62
Smith, A. V. ……18, 45
Sotskov, E. ……12
Souffland, D. ……82
Srebro, Y. ……30, 83, 112
Stadnik, A. L. ……89
Statsenko, V. P. ……89
Stoeckl, C. ……62
Stone, J. ……15
Sunahara, A. ……51

Suter, L. ……70
Sviridov, E. V. ……34, 44
Takabe, H. ……51, 84
Takayama, K. ……20, 21
Tamari, Y. ……51
Teyssier, R. ……15
Timmes, F. ……59
Tishkin, V. F. ……49, 137
Titov, S. N. ……49
Tomkins, C. ……46
Toqué, N. ……85
Tricottet, M. ……113, 114, 128
Tufo, H. ……59
Turano, E. J. ……17
Turner, N. ……15
Tyaktev, A. A. ……37
Uchayev, A. Ya. ……89
Vandenboomgaerde, M. ……129, 130
Verdon, C. P. ……17
Vlasov, Yu. ……11
Voelkl, T. ……80
Vold, E. ……86
Vorobieff, P. ……36
Wallace, R. J. ……15, 47
Wang, S. P. ……87
Ward, D. J. ……47
Wark, J. S. ……25, 35
Weber, S. V. ……25, 35, 59, 88, 110
Wiley, L. G. ……25, 35
Wilson, P. N. ……131
Wolfer, W. G. ……34
Wouchuk, J. G. ……132
Wunsch, S. ……59
Xu, Z. ……60
Yamada, S. ……84
Yanilkin, Yu. V. ……63, 68, 78, 89
Yosef-Hai, A. ……30, 41, 133
Young, Y.-N. ……59
Youngs, D. L. ……4, 9, 10, 19, 45, 59, 76, 90, 91
Zabusky, N. J. ……69, 77, 92, 93
Zaytsev, S. G. ……2, 3, 49
Zhakhovskii, V. ……73
Zhang, S. ……92, 93
Zhang, Y. ……15, 60
Zhmailo, V. A. ……63, 68
Zhou, Y. ……17, 40, 97, 135
Zingale, M. ……59
Zmitrenko, N. V. ……137
Zoldi, C. A. ……36, 46, 65, 79, 94
Zvorykin, V. D. ……72

Authors Contact Information

Abarzhi, Snejana I.
Department of Applied Mathematics
State University of New York at Stony Brook
Stony Brook, NY 11794-3600
Phone: (631) 632-9360
Fax: (631) 632-8490
E-mail: snezha@ams.sunysb.edu

Abe, M.
Institute of Laser Engineering
Osaka University
Suita, Osaka 565 Japan

Afeyan, Bedros
Polymath Research Incorporated
827 Bonde Court
Pleasanton, CA 94566
Phone: (925) 417-0609
Fax: (925) 417-0684
E-mail: bedros@polymath-usa.com

Allen, A. M.
University of Oxford
University Offices
Wellington Square
Oxford OX1 2JD United Kingdom
Phone: +44 1865 270000
Fax: +44 1865 270708

Alon, Uri
Weizmann Institute of Science
PO Box 26
Rehovot 76100 Israel
Phone: + 972-8-934-2111
Fax: + 972-8-934-4107
E-mail: uri.alon@weizmann.ac.il

Anderson, M. H.
University of Wisconsin at Madison
1500 Engineering Drive
Madison, WI 53706
Phone: (608) 263-2802
Fax: (608) 263-7541
E-mail: manderson@engr.wisc.edu

Andrews, Malcolm
Department of Mechanical Engineering
Texas A & M University
MS 3123
College Station, TX 77843-3123
Phone: (409) 847-8843
Fax: (409) 845 3081
E-mail: malcolm@chagal.tamu.edu

Anisimov, V. I.
Russian Federal Nuclear Center-VNIITF
P.O. Box 245
456770 Snezhinsk, Russia
E-mail: v.i.anisimov@vniitf.ru

Anuchin, M. G.
Russian Federal Nuclear Center-VNIITF
P.O. Box 245
456770 Snezhinsk, Russia

Arazi, L.
Tel Aviv University
P.O. Box 39040
Tel Aviv 69978 Israel

Ardashova, Rufina I.
Russian Federal Nuclear Center-VNIITF
P.O. Box 245
456770 Snezhinsk, Russia

Arnett, David
University of Arizona
P.O. Box 210096
Tucson, AZ 85721
Phone: (520) 621-9587
E-mail: darnett@as.arizona.edu

Ashurst, William T.
Sandia National Laboratory
P.O. Box 969, MS 9051
Livermore, CA 94551-0969
Phone: (925) 294-2274
Fax: (925) 294-2595
E-mail: ashurs@sandia.gov

Azechi, Hiroshi
Institute of Laser Engineering
Osaka University
Suita, Osaka 565 Japan
Phone: 81-879-8770
Fax: 81-877-4799
E-mail: azechi@ile.osaka-u.ac.jp

Bailly, P.
Commissariat à l'Energie Atomique
BP 12 - 91680 Bruyères-le-Châtel France

Baishev, A. I.
Russian Federal Nuclear Center-VNIITF
P.O. Box 245
456770 Snezhinsk, Russia

Balabin, Serguei
Russian Federal Nuclear Center-VNIITF
P.O. Box 245
456770 Snezhinsk, Russia
Fax: (351-72) 3 20 77
E-mail: kucherenko@five.ch70.chel.su

Barnes, Christopher W.
Los Alamos National Laboratory
P.O. Box 1663
Los Alamos, NM 87545
Phone: (505) 665-5687
E-mail: cbarnes@lanl.gov

Barton, C.
Atomic Weapons Establishment
Aldermaston
Reading, Berkshire
RG7 4PR United Kingdom
Phone: +44 (0)1734 814111
Fax: +44 (0)1734 815320

Batha, Steven
Los Alamos National Laboratory
P.O. Box 1663, MS E526
Los Alamos, NM 87545
Phone: (505) 665-5898
Fax: (505) 665-4409
E-mail: sbatha@lanl.gov

Belak, James F.
Lawrence Livermore National Laboratory
P.O. Box 808, L-45
Livermore, CA 94551
Phone: (925) 422-6061
Fax: (925) 422-2851
E-mail: belak1@llnlg.gov

Belomestnih, A. V.
Russian Federal Nuclear Center-VNIITF
P.O. Box 245
456770 Snezhinsk, Russia

Ben-Dor, Gabi
Faculty of Engineering Sciences
Ben-Gurion University of the Negev
Beer Sheva, 84105, Israel
Phone: 972-7-6461212
Fax: 972-7-6472936
E-mail: bendor@menix.bgu.ac.il

Benjamin, Robert F.
Los Alamos National Laboratory
P.O. Box 1663, MS P940
Los Alamos, NM 87545
Phone: (505) 667-8116
Fax: (505) 665-3359
E-mail: rfb@lanl.gov

Biello, J.
University of Chicago
933 East 56th Street
Chicago, IL 60637
Phone: (773) 702-1234

Bliznetsov, M. V.
Russian Federal Nuclear Center-VNIIEF
Mir Avenue, 37, Sarov
Nizhnii Novgorod Region, 607190, Russia
Fax: (831-30) 459-58
E-mail: root@gdd.vniief.ru

Boehly, T. R.
Laboratory for Laser Energetics
University of Rochester
250 East River Road
Rochester, New York 14623-1299
Phone: (716) 275-0254
E-mail: trb@lle.rochester.edu

Bonazza, Riccardo
Department of Engineering Physics
University of Wisconsin at Madison
1500 Engineering Drive
Madison, WI 53706
Phone: (608) 265-2337
Fax: (608) 262-6707
E-mail: bonazza@engr.wisc.edu

Bouquet, Serge
Commissariat à l'Energie Atomique
PDPTA-BP 12
Bruyeres-le-Chatel, France 91680
Phone: +33-1-69-26-51-83
Fax: +33-1-69-26-71-06
E-mail: bouquet@bruyeres.cea.fr

Braun, David G.
Lawrence Livermore National Laboratory
P.O. Box 808, L-31
Livermore, CA 94551
Phone: (925) 423-6275
Fax: (925) 423-9969
E-mail: braun1@llnl.gov

Breidenthal, Robert
Department of Aeronautics and Astronautics
University of Washington
Box 352400
Seattle, WA 98195-2400
Phone: (206) 685-1098
Fax: (206) 685-0217
E-mail: breidenthal@aa.washington.edu

Brouillette, Martin
Department of Mechanical Engineering
Université de Sherbrooke
Sherbrooke, Quebec J1K 2R1 Canada
Phone: (819) 821-7144
Fax: (819) 821-7163
E-mail: martin.brouillette@gme.usherb.ca

Buckingham, Alfred C.
Lawrence Livermore National Laboratory
P.O. Box 808, L-23
Livermore, CA 94551
Phone: (925) 423-4828
Fax: (925) 422-2644
E-mail: alfredcb@llnl.gov

Budil, Kimberly S.
Lawrence Livermore National Laboratory
P. O. Box 808, L-97
Livermore, CA 94551
Phone: (925) 423-8098
Fax: (925) 422-0779
E-mail: budil1@llnl.gov

Cabot, William H.
Lawrence Livermore National Laboratory
P.O. Box 808, L-22
Livermore, CA 94551
Phone: (925) 423-9272
Fax: (925) 423-0925
E-mail: cabot1@llnl.gov

Calder, A. C.
Department of Astronomy and Astrophysics
University of Chicago
5640 South Ellis Ave.
Chicago, IL 60637
Phone: (773) 834-3904
Fax: (773) 834-3230
E-mail: calder@flash.uchicago.edu

Chebotareva, E. I.
Krzhizhanovsky Power Engineering Institute
ENIN, Leninsky pr. 19, GSP-1
Moscow, 117927 Russia
Phone: (7-095) 955-31-07
Fax: (7-095) 954-42-50
E-mail: S.G.Zaytsev@mtu-net.ru

Cheng, Baolian
Los Alamos National Laboratory
P.O. Box 1663, MS D413
Los Alamos, NM 87545
Phone: (505) 667-4701
Fax: (505) 667-3726
E-mail: bcheng@lanl.gov

Clark, Timothy T.
Los Alamos National Laboratory
P.O. Box 1663, MS B213
Los Alamos, NM 87545
Phone: (505) 665-4858
Fax: (505) 665-3003
E-mail: ttc@llnl.gov

Clerouin-Cherfils, Catherine
Commissariat à l'Energie Atomique
CEA/DRIF
BP 12, 91680, Bruyeres-le-Chatel, France
Phone: 33 1 69 26 57 38
Fax: 33 1 69 26 70 94
E-mail: cherfils@bruyeres.cea.fr

Colvin, Jeffrey. D.
Lawrence Livermore National Laboratory
P.O. Box 808, L-21
Livermore, CA 94551
Phone: (925) 422-3273
Fax: (925) 423-8945
E-mail: colvin5@llnl.gov

Cook, Andrew W.
Lawrence Livermore National Laboratory
P.O. Box 808, L-22
Livermore, CA 94551
Phone: (925) 423-2856
Fax: (925) 423-0925
E-mail: awcook@llnl.gov

Dalziel, Stuart
DAMTP, University of Cambridge
Silver Street, Cambridge CB3 9EW, United Kingdom
Phone: (44) (1223) 337 911
Fax: (44) (1223) 337 918
E-mail: s.dalziel@damtp.cam.ac.uk

Dannenberg, K.
University of Michigan
Space Research Lab, Rm 1216
2245 Hayward
Ann Arbor, MI 48104

Darlington, Rebecca M.
Lawrence Livermore National Laboratory
P.O. Box 808, L-95
Livermore, CA 94551
Phone: (925) 424-3422
E-mail: darlington1@llnl.gov

Delettrez, J. A.
Laboratory for Laser Energetics
University of Rochester
Rochester, NY 14623-1299
Phone: (716) 275-5374
E-mail: jdel@lle.rochester.edu

Demyanov, A. Yu.
Landau Institute for Theoretical Physics
Kosygnina St. 2, Moscow
117940, GSP-1
V-334 Russia

Dimits, Andris M.
Lawrence Livermore National Laboratory
P.O. Box 808, L-630
Livermore, CA 94551
Phone: (925) 422-0211
Fax: (925) 423-3484
E-mail: dimits1@llnl.gov

Dimonte, Guy
Lawrence Livermore National Laboratory
P.O. Box 808, L-43
Livermore, CA 94551
Phone: (925) 423-0596
Fax: (925) 423-5998
E-mail: dimonte1@llnl.gov

Dittrich, Thomas R.
Lawrence Livermore National Laboratory
P.O. Box 808, L-23
Livermore, CA 94551
Phone: (925) 422-4706
Fax: (925) 423-8945
E-mail: dittrich1@llnl.gov

Don, Wai-Sun
Division of Applied Mathematics
Brown University
Box F
Providence, RI 02912
Phone: (401) 863-2250
E-mail: Wai-Sun_Don@brown.edu

Drake, R. Paul
University of Michigan
2245 Hayward
Ann Arbor, MI 48104
Phone: (734) 763-4072
Fax: (734) 647-3083
E-mail: rpdrake@umich.edu

Drennov, O. B.
Russian Federal Nuclear Center-VNIIEF
Mir Avenue, 37, Sarov
Nizhnii Novgorod Region, 607190, Russia
Fax: (831-30) 459-58
E-mail: root@gdd.vniief.ru

Dudin, V. D.
Russian Federal Nuclear Center-VNIIEF
Mir Avenue, 37, Sarov
Nizhnii Novgorod Region, 607190, Russia
Fax: (831-30) 459-58
E-mail: root@gdd.vniief.ru

Dulov, A. V.
Russian Federal Nuclear Center-VNIITF
P.O. Box 245
456770 Snezhinsk, Russia

Dunne, A. M.
Atomic Weapons Establishment
Aldermaston
Reading, Berkshire
RG7 4PR United Kingdom

Dursi, J. L.
Department of Astronomy and Astrophysics
University of Chicago
5640 South Ellis Ave.
Chicago, IL 60637
Phone: (773) 834-1059
Fax: (773) 834-3230

Dutta, S.
State University of New York at Stony Brook
P-138A Math Tower
Stony Brook, NY 11794-3600

Edwards, Michael J.
Lawrence Livermore National Laboratory
P.O. Box 808, L-21
Livermore, CA 94551
Phone: (925) 422-1189
E-mail: edwards39@llnl.gov

Elbaz, Y.
Ben-Gurion University
Beer-Sheva Israel 84015
Phone: 972-8-6568836
Fax: 972-8-6567878
E-mail: elbazyo@bgumail.bgu.ac.il

Eliason, Donald E.
Lawrence Livermore National Laboratory
P.O. Box 808, L-103
Livermore, CA 94551
Phone: (925) 423-5625
Fax: (925) 422-6388
E-mail: eliason@merlin.llnl.gov

Epstein, Reuben
Laboratory for Laser Energetics
University of Rochester
Rochester, NY 14623-1299
Phone: (716) 275-5405
E-mail: reps@lle.rochester.edu

Farley, David
Institute of Laser Engineering
Osaka University
Suita, Osaka 565, Japan
E-mail: dfarley@epri.com

Fryxell, Bruce
Enrico Fermi Institute and Laboratory for Astrophysics and
Space Research
University of Chicago
933 East 56th Street
Chicago, IL 60637
Phone: (773) 704-3226
Fax: (773) 704-3230
E-mail: fryxell@uffda.asci.uchicago.edu

Fujioka, S.
Institute of Laser Engineering,
2-6, Yamada-oka, Suita,
Osaka 565-0871 Japan

Fukuda, Y.
Institute of Laser Engineering,
2-6, Yamada-oka, Suita,
Osaka 565-0871 Japan

Galmiche, Didier Jean Marie
Commissariat à l'Energie Atomique
BP12 91680 Bruyeres-le-Chatel, France
Phone: 33 1 69 26 40 05
Fax: 33 1 69 26 70 94
E-mail: galmiche@bruyeres.cea.fr

Garasi, C.
Sandia National Laboratory
P.O. Box 969, 0819
Livermore, CA 94551
Phone: (505) 284-2691
Fax: (505) 844-0918
E-mail: cjgaras@sandia.gov

Gauthier, Serge
Centre d'Etudes de Limeil-Valenton
BP 27 Villeneuve St. Georges
94195, France
E-mail: gauthier@limeil.cea.fr

Gavrilova, E. S.
Russian Federal Nuclear Center-VNIIEF
Mir Avenue, 37, Sarov
Nizhnii Novgorod Region, 607190, Russia
Fax: (831-30) 459-58
E-mail: root@gdd.vniief.ru

George, E.
State University of New York at Stony Brook
P-138A Math Tower
Stony Brook, NY 11794-3600

Gerasimov, Serguei
Russian Federal Nuclear Center-VNIIEF
Mir Avenue, 37, Sarov
Nizhnii Novgorod Region, 607190, Russia
Phone: (7-83130) 45 009
Fax: (7-83130) 45 958
E-mail: root@gdd.vniief.ru

Glebov, V. Yu.
Laboratory for Laser Energetics
University of Rochester
250 East River Road
Rochester, NY 14623-1299
Phone: (716) 275-7454
E-mail: vgle@lle.rochester.edu

Glendinning, Sharon G.
Lawrence Livermore National Laboratory
P.O. Box 808, L-21
Livermore, CA 94551
Phone: (925) 423-3065
Fax: (925) 423-8945
E-mail: glendinning1@llnl.gov

Glimm, James
Department of Applied Mathematics and Statistics
State University of New York at Stony Brook
P-138A Math Tower
Stony Brook, NY 11794-3600
Phone: (631) 632-8355
Fax: (631) 632-8490
E-mail: glimm@ams.sunysb.edu

Goncharov, V. N.
Laboratory for Laser Energetics
University of Rochester
250 East River Road
Rochester, NY 14623-1299
Phone: (716) 275-1017
E-mail: vgon@lle.rochester.edu

Goodwin, Bruce T.
Lawrence Livermore National Laboratory
P.O. Box 808, L-160
Livermore, CA 94551
Phone: (925) 423-7736
Fax: (925) 424-2723
E-mail: goodwin2@llnl.gov

Gottlieb, David I.
Division of Applied Mathematics
Brown University
Providence, RI 02912
Phone: (401) 863-2266
E-mail: David.Gottlieb@brown.edu

Graham, Mary J.
Lawrence Livermore National Laboratory
P.O. Box 808, L-312
Livermore, CA 94551
Phone: (925) 424-4222
Fax: (925) 422-8920
E-mail: mjgraham@llnl.gov

Greenough, Jeffrey A.
Lawrence Livermore National Laboratory
P.O. Box 808, L-30
Livermore, CA 94551
Phone: (925) 423-3211
Fax: (925) 424-6764
E-mail: greenough1@llnl.gov

Grieves, Brian
Atomic Weapons Establishment
Aldermaston
Reading, Berkshire
RG7 4PR United Kingdom
Phone: +44 (0)1734 814111
Fax: +44 (0)1734 815320
E-mail: brian.grieves@awe.co.uk

Grove, John W.
Los Alamos National Laboratory
P.O. Box 1663, MS D413
Los Alamos, NM 87545
Phone: (505) 667-0723
Fax: (505) 665-4972
E-mail: jgrove@lanl.gov

Gubkov, E. V.
Russian Federal Nuclear Center-VNIIEF
Mir Avenue, 37, Sarov
Nizhnii Novgorod Region, 607190, Russia
Phone: (831-30) 450 09
Fax: (831-30) 459 58
E-mail: root@gdd.vniief.ru

Gulak, Y.
Department of Mechanical and Aerospace Engineering
Rutgers University
98 Brett Road
Piscataway, NJ 08854
Phone: (732) 445-5627
Fax: (732) 445-3124
E-mail: ygulak@rci.rutgers.edu

Gupta, S.
Department of Mechanical and Aerospace Engineering
Rutgers University
98 Brett Road
Piscataway, NJ 08854
Phone: (732) 445-5627
Fax: (732) 445-3124

Haan, Steven W.
Lawrence Livermore National Laboratory
P.O. Box 808, L-23
Livermore, CA 94551
Phone: (925) 422-4715
Fax: (925) 423-8945
E-mail: haan1@llnl.gov

Haas, Jean Francois
Commissariat à l'Energie Atomique
CEA/DIF/DCRE/SCSE BP 12
Bruyeres le Chatel, 91680, France
Phone: 33-1-69-26-52-94
Fax: 33-1-69-26-70-62
E-mail: jean-francois.haas@cea.fr

Harlow, Francis H.
Los Alamos National Laboratory
P.O. Box 1663, MS B216
Los Alamos, NM 87545
Phone: (505) 667-9090
E-mail: fhharlow@lanl.gov

Hatchett, Stephen P.
Lawrence Livermore National Laboratory
P.O. Box 808, L-16
Livermore, CA 94551
Phone: (925) 422-5916
Fax: (925) 423-5112
E-mail: hatchett1@llnl.gov

Hauer, A.
Los Alamos National Laboratory
P.O. Box 1663
Los Alamos, NM 87545
Phone: (505) 667-5167
Fax: (505) 667-0405
E-mail: hauer@lanl.gov

Hebert, C. H.
Department of Mechanical Engineering
Universite de Sherbrooke
Sherbrooke, Quebec J1K 2R1 Canada

Hinkel, Denise
Lawrence Livermore National Laboratory
P.O. Box 808, L-38
Livermore, CA 94551
Phone: (925) 423-2626
Fax: (925) 423-2157
E-mail: hinkel1@llnl.gov

Holder, David
AWE
Building H27, Aldermaston
Reading, Berkshire, RG7 4PR, United Kingdom
Phone: 0118 982 5592
Fax: 0118 982 4816
E-mail: david.holder@awe.co.uk

Holford, Joanne M.
University of Cambridge
Silver Street
Cambridge, United Kingdom CB3 9EW
Phone: +44 1223 337858
Fax: +44 1223 337918
E-mail: J.M.Holford@damtp.cam.ac.uk

Holmes, Richard L.
Los Alamos National Laboratory
P.O. Box 1663, MS B220
Los Alamos, NM 87545
Phone: (505) 667-3598
Fax: (505) 665-2227
E-mail: holmes@lanl.gov

Hosseini, S. H. R.
Shock Wave Research Center, Institute of Fluid Science
Tohoku University
2-1-1 Katahira, Aoba-ku
Sendai 980-77, Japan
E-mail: hosseini@rainbow.ifs.tohoku.ac.jp

Houas, Lazhar
I.U.S.T.I. / Umr CNRS 6595
Technopole de Chateau Gombert
5 rue Enrico Fermi
13453 Marseille 13 France
Phone: 33 (0)4 91 10 69 30
Fax: 33 (0)4 91 10 69 69
E-mail: houas@iusti.univ-mrs.fr

Hsing, Warren W.
Lawrence Livermore National Laboratory
P.O. Box 808, L-21
Livermore, CA 94551
Phone: (925) 423-2849
Fax: (925) 423-8945
E-mail: hsing@llnl.gov

Hurricane, Omar
Lawrence Livermore National Laboratory
P.O. Box 808, L-22
Livermore, CA 94551
Phone: (925) 424-2701
Fax: (925) 423-0925
E-mail: hurricane1@llnl.gov

Inogamov, Nail
Landau Institute for Theoretical Physics
Kosygnina St. 2, Moscow
117940, GSP-1
V-334 Russia
Phone: 095 425 8767
Fax: 095 938 2077
E-mail: itf@ips.ac.msk.su

Jacobs, Jeffrey W.
Department of Aerospace and Mechanical Engineering
University of Arizona
Bldg. 16, Room 301
Tucson, AZ 85721
Phone: (602) 621-8459
Fax: (602) 621-8191
E-mail: jacobs@ame.arizona.edu

Jameson, Leland M.
Lawrence Livermore National Laboratory
P.O. Box 808, L-39
Livermore, CA 94551
Phone: (925) 424-6160
E-mail: jameson3@llnl.gov

Jones, Oggden
Lawrence Livermore National Laboratory
P.O. Box 808, L-30
Livermore, CA 94551
Phone: (925) 423-1872
Fax: (925) 423-9969
E-mail: jones96@llnl.gov

Jourdan, Georges
Universite de Provence
IUSTI-CNRS Umr 139
Centre Saint Jerome - Case 321
13397 Marseille Cedex 20 France
Phone: 33 (0) 491106930
Fax: 33 (0) 491106969
E-mail: jourdan@iusti-dipha.univ-mrs.fr

Kalantar, Daniel
Lawrence Livermore National Laboratory
P.O. Box 808, L-472
Livermore, CA 94551
Phone: (925) 422-6147
Fax: (925) 422-8395
E-mail: kalantar1@llnl.gov

Kamm, R. J.
Los Alamos National Laboratory
P.O. Box 1663, MS
Los Alamos, NM 87545
Phone: (505) 667-1918
E-mail: kammj@lanl.gov

Kane, Jave O.
Lawrence Livermore National Laboratory
P.O. Box 808, L-411
Livermore, CA 94551
Phone: (925) 424-5805
Fax: (925) 423-2463
E-mail: jave@llnl.gov

Kang, Young-Gwang
Kwangju Institute of Science and Technology
1 Oryong-dong
Kwangju, 500-712, South Korea
Phone: 82-62-970-2310
Fax: 82-62-970-2304
E-mail: ygkang@kjist.ac.kr

Kartoon, Daniela
Department of Physics
Nuclear Research Center Negev
P.O. Box 9001
Beer-Sheva, 84190, Israel
Phone: 972-8-6568845
Fax: 972-8-6567878
E-mail: danyk@bgumail.bgu.ac.il

Keiter, P.
University of Michigan
Space Research Lab, Rm 1216
2245 Hayward
Ann Arbor, MI 48104

Kerstein, Alan R.
Sandia National Laboratory
P.O. Box 969, MS 9051
Livermore, CA 94551-0969
Phone: (925) 294-2390
Fax: (925) 294-1004
E-mail: kerstein@ca.sandia.gov

Kim, H.
Department of Mechanical and Aerospace Engineering
Rutgers University
98 Brett Road
Piscataway, NJ 08854

Klein, Richard I.
Lawrence Livermore National Laboratory
P.O. Box 808, L-23
Livermore, CA 94551
Phone: (925) 422-3548
Fax: (925) 423-0925
E-mail: rklein@llnl.gov

Knauer, J.
Department of Mechanical and Aerospace Engineering
Rutgers University
98 Brett Road
Piscataway, NJ 08854

Kobayashi, K.
Osaka University
2-6, Yamada-oka, Suita,
Osaka 565-0871 Japan

Korreck, K. E.
University of Michigan
Space Research Lab, Rm 1216
2245 Hayward
Ann Arbor, MI 48104

Kozelkov, O. E.
Russian Federal Nuclear Center-VNIITF
P.O. Box 245
456770 Snezhinsk, Russia

Kozlov, V. I.
Russian Federal Nuclear Center-VNIIEF
Mir Avenue, 37, Sarov
Nizhnii Novgorod Region, 607190, Russia
Fax: (831-30) 4-57-72
E-mail: otd1_0903@spd.vniief.ru

Ktitorov, Vladimir M.
Russian Federal Nuclear Center-VNIIEF
Mir Avenue, 37, Sarov
Nizhnii Novgorod Region, 607190 Russia
Phone: 831-30 1-36-65
Fax: 831-30 5-45-65
E-mail: mvn_072e@rfnc.nnov.su

Kucherenko, Yuri A.
Russian Federal Nuclear Center-VNIITF
P.O. Box 245
456770 Snezhinsk, Russia
Fax: (351-72) 3 20 77
E-mail: kucherenko@five.ch70.chel.su

Kuhl, Allen L.
Lawrence Livermore National Laboratory
P.O. Box 808, L-30
Livermore, CA 94551
Phone: (925) 422-4777
Fax: (925) 424-6764
E-mail: kuhl2@llnl.gov

Kumar, M.
Department of Physics
Nuclear Research Center Negev
P.O. Box 9001
Beer-Sheva, 84190, Israel

Kushnir, D.
Department of Physics
Nuclear Research Center Negev
P.O. Box 9001
Beer-Sheva, 84190, Israel

Lanier, N. E.
Los Alamos National Laboratory
P.O. Box 1663, MS
Los Alamos NM, 87545
Phone: (505) 665-0236
Fax: (505) 665-3686
E-mail: nlanier@lanl.gov

Lasinski, Barbara F.
Lawrence Livermore National Laboratory
P.O. Box 808, L-38
Livermore, CA 94551
Phone: (925) 422-5443
Fax: (925) 423-9208
E-mail: blasinski@llnl.gov

Lassis, A.
Commissariat à l'Energie Atomique
BP 12
Bruyeres le Chatel, 91680, France

Layes, G.
IUSTI
Technopole Chateau-Gombert
5 Rue Enrico Fermi
Marseille, 13013 France

Lebedev, Alexander
Russian Federal Nuclear Center-VNIIEF
Mir Avenue, 37, Sarov
Nizhnii Novgorod Region, 607190, Russia
Phone: (831-30) 450 09
Fax: (831-30) 459 58
E-mail: root@gdd.vniief.ru

Lebo, Ivan
Laser Fusion Department
PN Lebedev Physics Institute
Leninsky prospect 53
117294 Russia, Moscow
Phone: 095-132-68-47
Fax: 095-132-11-96
E-mail: lebo@sci.fian.msk.su

Legrand, Michel
Commissariat à l'Energie Atomique
DAM Ile de France
BP12, Bruyeres le Chatel, 91680, France
Phone: 33-1-69-26-57-09
Fax: 33-1-69-26-70-94
E-mail: michel.legrand@cea.fr

Levy, Kedem
Physics Department
Ben Gurion University of the Negev
P.O. B 653, Beer-Sheva 84105, Israel
Phone: 972-8-6568844
Fax: 972-8-6567878
E-Mail: klevy@bgumail.bgu.ac.il

Li, Xiaolin
Department of Applied Mathematics and Statistics
State University of New York at Stony Brook
1-119 Math Tower
Stony Brook, NY 11794-3600
Phone: (631) 632-8353
Fax: (631) 632-8490
E-mail: linli@ams.sunysb.edu

Linn, Rodman R.
Los Alamos National Laboratory
P.O. Box 1663, MS
Los Alamos, NM 87545
Phone: (505) 665-6254
E-mail: rrl@lanl.gov

Llor, Antoine
Commissariat à l'Energie Atomique
BP 12
Bruyeres le Chatel, 91680, France
Phone: 33 1 69 26 49 38
Fax: 33 1 69 26 70 97
E-mail: antoine.llor@cea.fr

Logvinov, A.
Russian Federal Nuclear Center-VNIIEF
Mir Avenue, 37, Sarov
Nizhnii Novgorod Region, 607190, Russia
E-mail: root@gdd.vniief.ru

Lorenz, Karl T.
Lawrence Livermore National Laboratory
P.O. Box 808, L-472
Livermore, CA 94551
Phone: (925) 424-4200
E-mail: lorenz3@llnl.gov

Louis, Hedley
Lawrence Livermore National Laboratory
P.O. Box 808, L-472
Livermore, CA 94551
Phone: (925) 4242-9937
E-mail: louis1@llnl.gov

Loveridge-Smith, A.
Oxford University
University Offices
Wellington, Oxford, OX1 2JD United Kingdom
Phone: +44 1865 270000
Fax: +44 1865 270708

MacNeice, P.
NASA Goddard Space Flight Center
Greenbelt, MD

Magelssen, Glenn R.
Los Alamos National Laboratory
P.O. Box 1663, MS
Los Alamos, NM 87545
Phone: (505) 667-6519
E-mail: grm@lanl.gov

Magnaudet, J.
Institut de Mécanique des Fluides de Toulouse
31400 Toulouse
Toulouse, France

Marchese, A.
State University of New York at Stony Brook
P-138A Math Tower
Stony Brook, NY 11794-3600

Marinak, Michael M.
Lawrence Livermore National Laboratory
P.O. Box 808, L-23
Livermore, CA 94551
Phone: (925) 423-8458
Fax: (925) 423-9969
E-mail: marinak1@llnl.gov

Matsuoka, C.
10-13,Dogo-Himata, Matsuyama 790-8577
Japan

Mazilin, I. M.
Krzhizhanovsky Power Engineering Institute
ENIN, Leninsky pr. 19, GSP-1
Moscow, 117927 Russia

McAbee, Thomas L.
Lawrence Livermore National Laboratory
P.O. Box 808, L-170
Livermore, CA 94551
Phone: (925) 422-3398
Fax: (925) 424-2723
E-mail: mcabee@viper.llnl.gov

McCray, R.
University of Colorado at Boulder
Boulder, CO 80309
Phone: (303) 492-1411

McKenty, P. W.
Laboratory for Laser Energetics
University of Rochester
250 East River Road
Rochester, NY 14623-1299

Medvedev, V. M.
Russian Federal Nuclear Center-VNIITF
P.O. Box 245
456770 Snezhinsk, Russia

Meiron, Daniel I.
Department of Applied and Computational Mathematics
California Institute of Technology
MC 217-50
Pasadena, CA 91125
Phone: (626) 395-4563
Fax: (626) 578-0124
E-mail: dim@acm.caltech.edu

Meshkov, Evgeni E.
Russian Federal Nuclear Center-VNIIEF
Mir Avenue, 37, Sarov
Nizhny Novgorod Region, 607190, Russia
Fax: 831-305-4565
E-mail: root@gdd.vniief.ru

Meyers, M. A.
University of California at San Diego
9500 Gilman Drive
La Jolla, CA 92093-0411

Mikaelian, Karnig O.
Lawrence Livermore National Laboratory
P.O. Box 808, L-97
Livermore, CA 94551
Phone: (925) 422-5449
Fax: (925) 423-7228

Mikhaylov, A. L.
Russian Federal Nuclear Center-VNIIEF
Mir Avenue, 37, Sarov
Nizhnii Novgorod Region, 607190, Russia
E-mail: root@gdd.vniief.ru

Miles, Aaron
Lawrence Livermore National Laboratory
P.O. Box 808, L-12
Livermore, CA 94551
Phone: (925) 423-8131
Fax: (925) 422-8920
E-Mail: miles15@llnl.gov

Miller, Paul L.
Lawrence Livermore National Laboratory
P.O. Box 808, L-22
Livermore, CA 94551
Phone: (925) 423-6455
Fax: (925) 423-0925
E-mail: pmiller@llnl.gov

Minich, Roger
Lawrence Livermore National Laboratory
P. O. Box 808, L-97
Livermore, CA 94551
Phone: (925) 422-4552
Fax: (925) 422-0779
E-mail: minich1@llnl.gov

Miyanaga, N.
Osaka University
2-6, Yamada-oka, Suita,
Osaka 565-0871 Japan

Mizuta, A.
Osaka University
2-6, Yamada-oka, Suita,
Osaka 565-0871 Japan

Montlaurent, P.
Commissariat à l'Energie Atomique
BP 12, 91680
Bruyeres-le-Chatel, France

Moreno, Juan
Lawrence Livermore National Laboratory
P. O. Box 808, L-31
Livermore, CA 94551
Phone: (925) 423-4170
Fax: (925) 424-6764
E-mail: jcmoreno@llnl.gov

Morris, A. P.
AWE Aldermaston
Reading
Berkshire RG7 4PR United Kingdom

Munro, David H.
Lawrence Livermore National Laboratory
P. O. Box 808, L-23
Livermore, CA 94551
Phone: (925) 422-5428
Fax: (925) 423-9969
E-mail: dmunro@llnl.gov

Murphy, T. J.
Los Alamos National Laboratory
P.O. Box 1663, MS
Los Alamos, NM 87545
Phone: (505) 665-5697
Fax: (505) 996-4366
E-mail: tjmurphy@lanl.gov

Murzakov, V. D.
Russian Federal Nuclear Center-VNIITF
P.O. Box 245
456770 Snezhinsk, Russia

Nagatomo, H.
Osaka University
2-6, Yamada-oka, Suita,
Osaka 565-0871 Japan

Nakai, M.
2-6, Yamada-oka, Suita,
Osaka 565-0871 Japan

Nash, Jeffrey K.
Lawrence Livermore National Laboratory
P. O. Box 808, L-15
Livermore, CA 94551
Phone: (925) 422-7255
E-mail: jknash@llnl.gov

Neuvazhayev, Vladimir
Russian Federal Nuclear Center -VNIITF
P.O. Box 245
456770 Snezhinsk, Russia
Phone: 351-72-55675
Fax: 351-72-32077
E-mail: nio3@ch70.chel.su

Nevmerzhitsky, Nikolay
Russian Federal Nuclear Center-VNIIEF
Mir Avenue, 37, Sarov
Nizhnii Novgorod Region, 607190, Russia
Phone: (831-30) 450 09
Fax: (831-30) 459 58
E-mail: root@gdd.vniief.ru

Niederhaus, Charles E.
NASA Glenn Research Center
21000 Brookpark Road
MS-77-5
Cleveland, OH 44135
Phone: (216) 433-5461
Fax: (216) 433-8050
E-mail: charles.niederhaus@grc.nasa.gov

Nikishin, Vladislav
Institute for Mathematical Modeling
Russian Academy of Science
Miusskaya 4a, 125047, Moscow, Russia
Phone: 007(095) 250-79-35
Fax: 007(095) 972-07-23
E-mail: nikishin\#4@imamod.msk.su

Nikulin, A.
Russian Federal Nuclear Center-VNIIEF
Mir Avenue, 37, Sarov
Nizhnii Novgorod Region, 607190, Russia
E-mail: root@gdd.vniief.ru

Nishihara, Katsunobu
Osaka University, Institute of Laser Engineering,
2-6, Yamada-oka, Suita,
Osaka 565-0871 Japan
Phone: 81-6-6879-8725
Fax: 81-6-6877-4799
E-mail: nishihara@ile.osaka-u.ac.jp

Nishikino, M.
2-6, Yamada-oka, Suita,
Osaka 565-0871 Japan

Nizovtsev, P. N.
Russian Federal Nuclear Center-VNIIEF
Mir Avenue, 37, Sarov
Nizhnii Novgorod Region, 607190, Russia
E-mail: root@gdd.vniief.ru

Nomoto, K.
University of Tokyo
7-3-1 Hongo, Bunkyo-ku, Tokyo 113-8654, Japan
Phone: +81-3-3812-2111

Oakley, J. G.
Department of Engineering Physics
University of Wisconsin at Madison
1500 Engineering Drive
Madison, WI 53706

Olson, K.
NASA Goddard Space Flight Center
Greenbelt, MD

Oparin, A. M.
Institute for Computer Aided Design
Vtoraya Brestskaya ul., 19/18, 123056
Moscow, Russia
Phone: (095) 250-96-30
Fax: (095) 250-89-28
E-mail: oparin@cpd.landau.ac.ru

Oron, Dan
Department of Physics
Nuclear Research Center - Negev
P.O. Box 9001
Beer-Sheva, 84190, Israel
Phone: 972-7-6568736
Fax: 972-7-6567878
E-mail: danor@bgumail.bgu.ac.il

Paisley, Dennis
Los Alamos National Laboratory
P.O. Box 1663, MS
Los Alamos, NM 87545
Phone: (505) 667-7837
E-mail: dxp@lanl.gov

Pantano, C.
University of California at San Diego
9500 Gilman Drive
La Jolla, CA 92093-0411

Parker, Kenneth W.
AWE Aldermaston
Reading
Berkshire RG7 4PR United Kingdom
Phone: +44 118 9827578
Fax: +44 118 9824844
E-mail: Kenneth.W.Parker@awe.co.uk

Parshukov, I. E.
Russian Federal Nuclear Center-VNIITF
P.O. Box 245
456770 Snezhinsk, Russia

Peng, O.
Rutgers University
98 Brett Road
Piscataway, NJ 08854

Perry, Theodore S.
Lawrence Livermore National Laboratory
P.O. Box 808, L-23
Livermore, CA 94551
Phone: (925) 423-2065
Fax: (925) 424-3294
E-mail: tedperry@llnl.gov

Peyser, Thomas A.
Lawrence Livermore National Laboratory
P.O. Box 808, L-23
Livermore, CA 94551
Phone: (925) 423-6454
Fax: (925) 423-0925
E-mail: tpeyser@llnl.gov

Piskunov, Yu. A.
Russian Federal Nuclear Center-VNIITF
P.O. Box 245
456770 Snezhinsk, Russia

Polionov, Arkadi
Russian Federal Nuclear Center-VNIITF
P.O. Box 245
456770 Snezhinsk, Russia
Phone: 351-722-3977
Fax: 351-723-2077
E-mail: nio3@ch70.chel.su

Pollaine, Steven
Lawrence Livermore National Laboratory
P.O. Box 808, L-30
Livermore, CA 94551
Phone: (925) 422-5950
Fax: (925) 423-9208
E-mail: pollaine@llnl.gov

Popov, V. N.
Russian Federal Nuclear Center-VNIITF
P.O. Box 245
456770 Snezhinsk, Russia

Pound, M.
University of Maryland
College Park, MD 20742
Phone: (301) 405-1000

Prestridge, Katherine P.
Los Alamos National Laboratory
P.O. Box 1663, MS P940
Los Alamos, NM 87545
Phone: (505) 667-8861
Fax: (505) 665-3359
E-mail: kpp@lanl.gov

Pullin, Dale I.
Department of Aeronautics
California Institute of Technology
1200 East California Boulevard, MS 105-50
Pasadena, CA 91125
Phone: (626) 395-6081
Fax: (626) 441-2222
E-mail: dale@galcit.caltech.edu

Pylaev, Anatoly
Russian Federal Nuclear Center-VNIITF
P.O. Box 245
456770 Snezhinsk, Russia
Fax: (351-72) 3 20 77
E-mail: kucherenko@five.ch70.chel.su

Radha, P. B.
Laboratory for Laser Energetics
University of Rochester
Rochester, NY 14623-1299

Raevskii, Viktor
Russian Federal Nuclear Center-VNIIEF
Mir Avenue, 37, Sarov
Nizhny Novgorod Region, 607190, Russia
Fax: 831-305-4565
E-mail: otd3_2305@rfnc.nnov.su

Rampaprabhu, P.
Department of Mechanical Engineering
Texas A & M University
MS 3123
College Station, TX 77843-3123

Raviard, P. A.
Commissariat à l'Energie Atomique
BP 12, 91680
Bruyeres-le-Chatel, France

Rayer, C.
Commissariat à l'Energie Atomique
BP 12, 91680
Bruyeres-le-Chatel, France

Razin, A. N.
Russian Federal Nuclear Center-VNIIEF
Mir Avenue, 37, Sarov
Nizhnii Novgorod Region, 607190, Russia
E-mail: root@gdd.vniief.ru

Rebrov, S. V.
Mir Avenue, 37, Sarov
Nizhnii Novgorod Region, 607190, Russia
E-mail: root@gdd.vniief.ru

Remington, Bruce A.
Lawrence Livermore National Laboratory
P.O. Box 808, L-21
Livermore, CA 94551
Phone: (925) 423-2712
Fax: (925) 422-8395
E-mail: remington2@llnl.gov

Renaud, Francois
Commissariat à l'Energie Atomique
CEA/DRIF/DCSA/SET
BP 12, 91680
Bruyeres-le-Chatel, France
Phone: 33 1 69 26 40 81
Fax: 33 1 69 26 71 02

Ricker, P.
University of Chicago
933 East 56th Street
Chicago, IL 60637

Rider, William J.
Los Alamos National Laboratory
P.O. Box 1663, MS D413
Los Alamos, NM 87545
Phone: (505) 665-4162
Fax: (505) 667-3726
E-mail: wjr@lanl.gov

Rightley, Paul M.
Los Alamos National Laboratory
P.O. Box 1663, MS P940
Los Alamos, NM 87545
Phone: (505) 667-0460
Fax: (505) 665-3359
E-mail: pright@lanl.gov

Rikanati, Avi
Physics Department
Nuclear Research Center - Negev
P.O. Box 9001
Beer-Sheva, 84190, Israel
Phone: 972-7-6568736
Fax: 972-7-6567878
E-mail: rkavi@bgumail.bgu.ac.il

Robey, Harry F.
Lawrence Livermore National Laboratory
P.O. Box 808, L-21
Livermore, CA 94551
Phone: (925) 423-5669
Fax: (925) 422-3358
E-mail: robey1@llnl.gov

Robinson, A.
Sandia National Laboratory
P.O. Box 969, MS 9051
Livermore, CA 94551-0969

Rozanov, I. A.
Lebedev Physical Institute
Leninsky Pr. 53
117924, Moscow, Russia
E-mail: Rozanov@sci.lebedev.ru

Rosner, Robert L.
Enrico Fermi Institute and Laboratory for Astrophysics
and Space Research
University of Chicago
933 East 56th Street
Chicago, IL 60637
Phone: (773) 702-0560
Fax: (773) 704-3230
E-mail: rosner@uchicago.edu

Rothman, S.
AWE Aldermaston
Reading
Berkshire RG7 4PR United Kingdom

Roualdes, P.
Centre d'Etudes de Gramat
Gramat, France

Rozanov, Vladislav
Lebedev Physical Institute
Leninsky Pr. 53
117924, Moscow, Russia
Phone: (095)-132-68-47
Fax: (095)-132 -11-96
E-mail: lebo@neur.lpi.msk.su

Ryutov, Dimitri D.
Lawrence Livermore National Laboratory
P.O. Box 808, L-630
Livermore, CA 94551
Phone: (925) 422-9832
E-mail: ryutov1@llnl.gov

Sadot, Oren
Department of Physics
Nuclear Research Center - Negev
P.O. Box 9001
Beer-Sheva 84109, Israel
Phone: 972-7-6567278
Fax: 972-7-6567878
E-mail: sorens@bgumail.bgu.ac.il

Sakaiya, T.
Institute of Laser Engineering
Osaka University
2-6 Yamadaoka Suita
Osaka, 565 Japan

Samtaney, Ravi
Department of Aeronautics
California Institute of Technology
MS 205-45
Pasadena, CA 91125
Phone: (626) 395-8030
Fax: (626) 449-2677
E-mail: ravi@ama.caltech.edu

Sapozhnikov, I. V.
Russian Federal Nuclear Center-VNIIEF
Mir Avenue, 37, Sarov
Nizhnii Novgorod Region, 607190, Russia

Sarid, Eli
Department of Physics
Nuclear Research Center - Negev
P.O. Box 9001
Beer-Sheva, 84190, Israel
Phone: 972-7-6568736
Fax: 972-7-6567878
E-mail: fnsarid@weizmann.weizmann.ac.il

Sarkar, Sutanu
Department of Mechanical and Aerospace Engineering
University of California at San Diego
9500 Gilman Drive
La Jolla, CA 92093-0411
Phone: (858) 534-8243
Fax: (858) 534-7599
E-mail: sarkar@mae.ucsd.edu

Schilling, Oleg
Lawrence Livermore National Laboratory
P.O. Box 808, L-22
Livermore, CA 94551
Phone: (925) 423-6879
Fax: (925) 423-0925
E-mail: schilling1@llnl.gov

Schurtz, G.
Commissariat à l'Energie Atomique
CEA/DRIF/DCSA/SET
BP12, 91680 Bruyeres-le-Chatel, France

Schwaederlè, Laurent
IUSTI
Technopole Chateau-Gombert
5 Rue Enrico Fermi
Marseille, 13013 France
Phone: 04 91 10 69 35
Fax: 04 91 10 69 69
E-Mail: schwaed@iusti.univ-mrs.fr

Sharp, David H.
Los Alamos National Laboratory
P.O. Box 1663, MS B285
Los Alamos, NM 87545
Phone: (505) 667-5266
Fax: (505) 665-3003
E-mail: dhs@lanl.gov

Shestachenko, Oleg
Russian Federal Nuclear Center-VNIITF
P.O. Box 245
456770 Snezhinsk, Russia
Fax: (351-72) 3 20 77
E-mail: kucherenko@five.ch70.chel.su

Shestakov, Alex
Lawrence Livermore National Laboratory
P.O. Box 808, L-38
Livermore, CA 94551
Phone: (925) 422-4213
Fax: (925) 423-9208
E-mail: shestakov1@llnl.gov

Shigemori, K.
Institute of Laser Engineering
Osaka University
2-6 Yamadaoka Suita
Osaka, 565 Japan

Shiraga, H.
Institute of Laser Engineering
Osaka University
2-6 Yamadaoka Suita
Osaka, 565 Japan

Shu, Chi-Wang
Division of Applied Mathematics
Brown University
Providence, RI 02912
Phone: (401) 863-2549
E-mail: Chi-Wang_Shu@brown.edu

Shvarts, Dov
Nuclear Research Center - Negev
Department of Physics
P.O. Box 9001
Beer-Sheva, 84190, Israel
Phone: 972-7-6567500
Fax: 972-7-6567665
E-mail: shvarts@bgumail.bgu.ac.il

Silvani, X.
Institut de Mécanique des Fluides de Toulouse
31400 Toulouse
Toulouse, France

Sinitsina, S. N.
Russian Federal Nuclear Center-VNIIEF
Mir Avenue, 37, Sarov
Nizhnii Novgorod Region, 607190, Russia
E-mail: root@gdd.vniief.ru

Sinkova, O. G.
Russian Federal Nuclear Center-VNIIEF
Mir Avenue, 37, Sarov
Nizhnii Novgorod Region, 607190, Russia
E-mail: root@gdd.vniief.ru

Skupsky, S.
Laboratory for Laser Energetics
University of Rochester
Rochester, NY 14623-1299

Smalyuk, V. A.
Laboratory for Laser Energetics
University of Rochester
Rochester, NY 14623-1299

Smith, Alan V.
Building H27
AWE Aldermaston
Reading
Berkshire RG7 4PR United Kingdom
Phone: 01189-825592
Fax: 01734-815320
E-mail: alan.smith@awe.co.uk

Sotskov, E.A.
Russian Federal Nuclear Center-VNIIEF
Mir Avenue, 37, Sarov
Nizhnii Novgorod Region, 607190, Russia
Fax: (831-30) 459 58
E-mail: root@gdd.vniief.ru

Souffland, Denis
Commissariat à l'Energie Atomique
CEA/DRIF/DCSA/SET
BP12, 91680 Bruyeres-le-Chatel, France
Phone: 33 1 69 26 59 77
Fax: 33 1 69 26 70 94
E-mail: soufflan@bruyeres.cea.fr

Srebro, Yair
Department of Physics
Ben-Gurion University of the Negev
Beer Sheva, 84105, Israel
Phone: 972-8-6568416
Fax: 972-8-656-7878
E-mail: sibo@bgumail.bgu.ac.il

Stadnik, A. L.
Russian Federal Nuclear Center-VNIIEF
Mir Avenue, 37, Sarov
Nizhnii Novgorod Region, 607190, Russia
E-mail: root@gdd.vniief.ru

Statsenko, V. P.
Russian Federal Nuclear Center-VNIIEF
Mir Avenue, 37, Sarov
Nizhnii Novgorod Region, 607190, Russia
E-mail: root@gdd.vniief.ru

Steinkamp, Michael J.
Los Alamos National Laboratory
P.O. Box 1663, MS D413
Los Alamos, NM 87545
Phone: (505) 667-5837
Fax: (505) 667-3726
E-mail: steinmj@lanl.gov

Stoeckl, C.
Laboratory for Laser Energetics
University of Rochester
Rochester, NY 14623-1299

Stone, J.
University of Maryland
College Park, MD 20742
Phone: (301) 405-1000

Sunahara, A.
Institute of Laser Engineering
Osaka University
2-6 Yamadaoka Suita
Osaka, 565 Japan
Phone: 81-6-879-8742
Fax: 81-6-877-4799
E-mail: suna@ile.osaka-u.ac.jp

Suter, Laurance
Lawrence Livermore National Laboratory
P.O. Box 808, L-31
Livermore, CA 94551
Phone: (925) 422-5423
Fax: (925) 423-9969
E-mail: suter1@llnl.gov

Sviridov, E. V.
Russian Federal Nuclear Center-VNIITF
P.O. Box 245
456770 Snezhinsk, Russia

Takabe, Hideaki
Institute of Laser Engineering
Osaka University
Yamada-oka 2-6, Suita
Osaka 565, Japan
E-mail: takabe@ile.osaka-u.ac.jp
Phone: 81-6-877-5111 Ext. 6553
Fax: 81-6-877-4779

Takayama, Kazuyoshi
Shock Wave Research Center
Institute of Fluid Science
Tohoku University
2-1-1 Katahira, Aoba-ku
Sendai 980-77, Japan
Phone: 81-22-263-0895
Fax: 81-22-227-7390
E-mail: paul@bellanca.ifs.tohoku.ac.jp

Tamari, Y.
Institute of Laser Engineering (ILE)
Osaka University
2-6 Yamadoaka
Suita, Osaka 565-0871, Japan

Teyssier, R.
Commissariat à l'Energie Atomique
BP 12, 91680
Bruyeres-le-Chatel, France

Timmes, F.
University of Chicago
933 East 56th Street
Chicago, IL 60637

Tishkin, Vladimir
Institute for Mathematical Modeling
Russian Academy of Science
Miusskaya 4a
125047, Moscow, Russia
Phone: 007(095) 250-79-35
Fax: 007(095) 972-07-23
E-mail: tishkin@imamod.msk.su

Titov, S. N.
Krzhizhanovsky Power Engineering Institute
ENIN, Leninsky pr. 19, GSP-1
Moscow, 117927 Russia

Tomkins, Christopher
Los Alamos National Laboratory
P.O. Box 1663, MS 0454
Los Alamos, NM 87545
Phone: (505) 665-6228
Fax: (505) 665-4507
E-mail: ctomkins@lanl.gov

Toqué, Nathalie
Universite de Montreal
#1, 6685 Saint Denis
Montreal, Canada H-85-851
Phone: 514-276-9014
E-mail: Toque@astro.umontreal.ca

Tricottet, Matthieu
Commissariat à l'Energie Atomique
BP 12, 91680
Bruyeres-le-Chatel, France
E-mail: Matthieu.Tricottet@cea.fr

Tufo, H.
University of Chicago
933 East 56th Street
Chicago, IL 60637

Turano, Edward J.
Lawrence Livermore National Laboratory
P.O. Box 808, L-15
Livermore, CA 94551
Phone: (925) 424-3508
E-mail: turano1@llnl.gov

Turner, N.
University of Maryland
College Park, MD 20742
Phone (301) 405-1000

Tyaktev, A. A.
Russian Federal Nuclear Center-VNIITF
P.O. Box 245
456770 Snezhinsk, Russia

Uchayev, A. Ya.
Russian Federal Nuclear Center-VNIIEF
Mir Avenue, 37, Sarov
Nizhnii Novgorod Region, 607190, Russia

Vandenboomgaerde, Marc
Commissariat à l'Energie Atomique
BP 12, 91680
Bruyeres-le-Chatel, France
Phone: 33 01 69 26 66 68
Fax: 33 01 69 26 70 94
E-mail: marc.vandenboomgaerde@bruyeres.cea.fr

Verdon, Charles P.
Lawrence Livermore National Laboratory
P.O. Box 808, L-30
Livermore, CA 94551
Phone: (925) 423-4449
Fax: (925) 423-9969
E-mail: verdon1@llnl.gov

Vlasov, Yu.
Russian Federal Nuclear Center-VNIIEF
Mir Avenue, 37, Sarov
Nizhnii Novgorod Region, 607190, Russia

Voelkl, Tobias
Department of Applied and Computational Mathematics
California Institute of Technology
M/C 217-50
Pasadena, CA 91125
Phone: (626) 395-8534
E-mail: tobias@its.caltech.edu

Vold, Erik L.
Los Alamos National Laboratory
P.O. Box 1663, MS D413
Los Alamos, NM 87545
Phone: (505) 665-5646
Fax: (505) 667-3726
E-mail: elv@lanl.gov

Volkov, V. I.
Russian Federal Nuclear Center-VNIITF
P.O. Box 245
Snezhinsk, 456770 Russia
E-mail: v.a.gordeychuk@vniitf.ru

Vorobieff, Peter V.
Department of Mechanical Engineering
University of New Mexico
ME Bldg. Rm. 424
Albuquerque, NM 87131
Phone: (505) 277-8347
Fax: (505) 277-1571
E-mail: kalmoth@me.unm.edu

Ward, David J.
Lawrence Livermore National Laboratory
P.O. Box 808, L-30
Livermore, CA 94551
Phone: (925) 423-3211
Fax: (925) 424-6764
E-mail: djw@llnl.gov

Ward, Richard A.
Lawrence Livermore National Laboratory
P.O. Box 808, L-13
Livermore, CA 94551
Phone: (925) 423-2679
Fax: (925) 422-4643
E-mail: raward@llnl.gov

Wark, J. S.
Oxford University
University Offices
Wellington, Oxford, OX1 2JD United Kingdom
Phone: +44 1865 270000
Fax: +44 1865 270708

Weber, Stephen V.
Lawrence Livermore National Laboratory
P.O. Box 808, L-16
Livermore, CA 94551
Phone: (925) 422-5433
Fax: (925) 423-9208
E-mail: svweber@llnl.gov

Wiley, Larry G.
Lawrence Livermore National Laboratory
P.O. Box 808, L-97
Livermore, CA 94551
Phone: (925) 423-2461
Fax: (925) 422-0779
E-mail: wiley1@llnl.gov

Wilson, P. N.
Department of Mechanical Engineering
Texas A & M University
MS 3123
College Station, TX 77843-3123

Wolfer, Wilhelm G.
Lawrence Livermore National Laboratory
P.O. Box 808, L-97
Livermore, CA 94551
Phone: (925) 423-1501
Fax: (925) 423-7040
E-mail: wolfer1@llnl.gov

Wouchuk, Juan G.
E.T.S.I. Industriales
Universidad Castilla-La Mancha
Campus Universitario s/n
13071 Ciudad Real, Spain
Phone: (34) 926-29-53-00 x3826
Fax: (34) 926-29-53-61
E-mail: gwouchuk@ind-cr.uclm.es

Wunsch, Scott E.
Sandia National Laboratory
P.O. Box 969, MS 9051
Livermore, CA 94551-0969
Phone: (925) 294-4621
Fax: (925) 294-2595
E-mail: sewunsch@sandia.gov

Xu, Z.
State University of New York at Stony Brook
P-138A Math Tower
Stony Brook, NY 11794-3600

Yamada, Shoichi
Institute of Laser Engineering (ILE)
Osaka University
2-6 Yamadoaka
Suita, Osaka 565-0871, Japan
Phone: 81-6-6879-8747
Fax: 81-6-6879-8747
E-mail: syamada@ile.osaka-u.ac.jp

Yanilkin, Yury
Russian Federal Nuclear Center-VNIIEF
Mir Avenue, 37, Sarov
Nizhnii Novgorod Region, 607190, Russia
Phone: (831-30) 111 90
Fax: (831-30) 546 65
E-mail: yan@md08.vniief.ru

Yosef-Hai, Arnon
Department of Physics
Nuclear Research Center-Negev
P.O. Box 9001
Beer-Sheva, 84190, Israel
Phone: 972-8-6568913
Fax: 972-8-6567878
E-mail: ajoseph@bgumail.bgu.ac.il

Young, Y.-N.
University of Chicago
933 East 56th Street
Chicago, IL 60637

Youngs, David L.
AWE
Building E3, AWE(A)
Reading, Berkshire
RG7 4PR, United Kingdom
Phone: 0118 9826766
Fax: 0118 9815320
E-mail: dyoungs@awe.co.uk

Zabusky, Norman J.
Department of Mechanical and Aerospace Engineering
Rutgers University
98 Brett Road
Piscataway, NJ 08854
Phone: (732) 445-5869
Fax: (732) 445-3124
E-mail: nzabusky@caip.rutgers.edu

Zaytsev, Sergey G.
Krzhizhanovsky Power Engineering Institute
ENIN, Leninsky pr. 19, GSP-1
Moscow, 117927 Russia
Phone: (7-095) 955-31-07
Fax: (7-095) 954-42-50
E-mail: S.G.Zaytsev@mtu-net.ru

Zhakhovskii, V.
Institute of Laser Engineering
Osaka University
Suita, Osaka 565 Japan

Zhang, S.
Department of Mechanical and Aerospace Engineering
Rutgers University
98 Brett Road
Piscataway, NJ 08854

Zhang, Y.
State University of New York at Stony Brook
P-138A Math Tower
Stony Brook, NY 11794-3600

Zhmailo, Vadim A.
Russian Federal Nuclear Center-VNIIEF
Mir Avenue, 37, Sarov
Nizhnii Novgorod Region, 607190, Russia
Fax: 83130 54565
E-mail: rvg_092C@rfnc.nnov.su

Zhou, Ye K.
Lawrence Livermore National Laboratory
P.O. Box 808, L-23
Livermore, CA 94551
Phone: (925) 424-3624
E-mail: zhou3@llnl.gov

Zingdale, N. V.
University of Chicago
933 East 56th Street
Chicago, IL 60637

Zmitrenko, Nikolay
Institute for Mathematical Modeling
Russian Academy of Science
Miusskaya 4a, 125047, Moscow, Russia
Phone: 007(095) 250-79-16
Fax: 007(095) 972-07-23
E-mail: nickzmit\#9@imamod.msk.su

Zoldi, Cindy A.
Los Alamos National Laboratory
P.O. Box 1663, MS B220
Los Alamos, NM 87544
Phone: (505) 667-6455
Fax: (505) 665-2227
E-mail: czoldi@lanl.gov

Zvorykin, V. D.
PN Lebedev Physics Institute
Leninsky prospect 53
117294 Russia, Moscow

University of California
Lawrence Livermore National Laboratory
Technical Information Department
Livermore, CA 94551